Volume I

Midwestern Regional Carbon Sequestration Partnership (MRCSP) Phase III (Development Phase).



Geologic Characterization for CO_2 Storage with Enhanced Oil Recovery in Northern Michigan

Prepared by:

Battelle
505 King Avenue
Columbus, Ohio 43201

Principal Investigator: Dr. Neeraj Gupta

Authors: Autumn Haagsma, Amber Conner, Zachary Cotter, Benjamin Grove, Joel Main, Mackenzie Scharenberg, Glenn Larsen, Samin Raziperchikolaee, Wayne Goodman, Charlotte Sullivan, and Neeraj Gupta

Submitted to:

The U.S. Department of Energy, National Energy Technology Laboratory
Program Manager: Andrea McNemar

DOE Project #DE-FC26-05NT42589

September 2020

BATTELLE

Notice

This report was prepared by Battelle as an account of work sponsored by an agency of the United States Government and other project sponsors, including Core Energy, LLC and The Ohio Development Services Agency. Neither the United States Government, nor any agency thereof, nor any of their employees, nor Battelle and other cosponsors, makes any warranty, express or implied, or assumes any liability or responsibility for the accuracy, completeness, or usefulness of any information, apparatus, product, or process disclosed, or represents that its use would not infringe privately owned rights. Reference herein to any specific commercial product, process, or service by trade name, trademark, manufacturer, or otherwise does not necessarily constitute or imply its endorsement, recommendations, or favoring by the United States Government or any agency thereof. The views and the opinions of authors expressed herein do not necessarily state or reflect those of the United States Government or any agency thereof.

Battelle does not engage in research for advertising, sales promotion, or endorsement of our clients' interests including raising investment capital or recommending investments decisions, or other publicity purposes, or for any use in litigation.

Battelle endeavors at all times to produce work of the highest quality, consistent with our contract commitments. However, because of the research and/or experimental nature of this work the client undertakes the sole responsibility for the consequence of any use or misuse of, or inability to use, any information, apparatus, process or result obtained from Battelle, and Battelle, its employees, officers, or Trustees have no legal liability for the accuracy, adequacy, or efficacy thereof.

Acknowledgements

Sponsorships - This report is part of a series of reports prepared under the Midwestern Regional Carbon Sequestration Partnership (MRCSP) Phase III (Development Phase). These reports summarize and detail the findings of the work conducted under the Phase III project. The primary funding for the MRCSP program is from the US Department of Energy's National Energy Technology Laboratory (NETL) under DOE project number DE-FC26-05NT42589 with Ms. Andrea McNemar as the DOE project manager. The past DOE project managers for MRCSP include Dawn Deel, Lynn Brickett, and Traci Rodosta. Many others in the DOE leadership supported, encouraged, and enabled the MRCSP work including but not limited to Kanwal Mahajan, John Litynski, Darin Damiani, and Sean Plasynski.

The Michigan Basin large-scale test received significant in-kind cost share from Core Energy, LLC, who also provided essential access to the field test site and related data. This contribution by Core Energy CEO Robert Mannes, VP Operations Rick Pardini, and Allan Modroo, VP Exploration, and the entire Core Energy staff is gratefully acknowledged. MRCSP work in Ohio has been supported by the Ohio Coal Development Office in the Ohio Development Services Agency under various grants (CDO D-10-7, CDO-D-13-22, CDO-D-D-13-24, and CDO-D-15-08) with Mr. Greg Payne as the OCDO project manager. Finally, several industry sponsors and numerous technical team members from State Geological Surveys, universities, and field service providers have supported MRCSP through cash and in-kind contributions over the years as listed in the individual reports.

Program Leadership – During the MRCSP Phase III project period, several Battelle staff and external collaborators contributed to the successful completion of the program through their efforts in field work, geological data analysis and interpretation, and/or reporting. The primary project managers over the MRCSP performance period have included Rebecca Wessinger, Neeraj Gupta, Jared Walker, Rod Osborne, Darrell Paul, David Ball. Additional project management support has been provided by Andrew Burchwell, Christa Duffy, Caitlin McNeil, and Jacqueline Gerst over the years.

Principal Investigator: Neeraj Gupta (614-424-3820/ gupta@battelle.org)

Report Authors and Principal Technical Contributors – Autumn Haagsma, Amber Conner, Zachary Cotter, Benjamin Grove, Joel Main, Mackenzie Scharenberg, Glenn Larsen, Samin Raziperchikolaee, Wayne Goodman, Charlotte Sullivan, and Neeraj Gupta.

Other Technical Contributors – Matthew Rine, William Harrison, Heather McCarren, Allen Modroo, and Rick Pardini

Table of Contents

Page

Acknowledgements iii

List of Acronyms xlv

1.0 Project Background and Report Scope 1
- 1.1 Project Background 1
- 1.2 Report Scope 2
- 1.3 Approach 3

2.0 Geology Overview 5
- 2.1 Introduction 5
- 2.2 Basin Structure 7
- 2.3 Lithostratigraphy 7
- 2.4 Interpreted Sequence Stratigraphy of the Reef Interval 9

3.0 Data Availability and Geologic Characterization Methodology 11
- 3.1 Data Types 11
  - 3.1.1 Wireline Logs 11
  - 3.1.2 Core Data 13
  - 3.1.3 Seismic Data 14
- 3.2 Tops Selection 14
  - 3.2.1 A-2 Carbonate 15
  - 3.2.2 A-2 Evaporite 16
  - 3.2.3 A-1 Carbonate 16
  - 3.2.4 A-1 Evaporite 16
  - 3.2.5 Brown Niagaran 16
  - 3.2.6 Gray Niagaran 16
- 3.3 Facies Selection 17
- 3.4 Sub-Regional Mapping Methodology 21
- 3.5 Wireline Log Interpretation 25
  - 3.5.1 Basic Log Analysis 25
  - 3.5.2 Advanced Log Analysis 27
  - 3.5.3 Petrophysics 31
- 3.6 Seismic Analysis 35
  - 3.6.1 Seismic Horizons 35
  - 3.6.2 Seismic Mapping 36

4.0 Dover 33 37
- 4.1 Reef History and Production Review 37
- 4.2 Wireline Log Analysis 39
  - 4.2.1 Basic Log Interpretation 40
  - 4.2.2 Advanced Log Interpretation 53
  - 4.2.3 Petrophysical Calculations 58
- 4.3 Core Analysis 60
- 4.4 Seismic Analysis 63
- 4.5 Statistical Analysis 67
- 4.6 Geologic Interpretations and Data Integration 70

5.0 Chester 16 75
5.1 Reef History and Production Review 75
5.2 Wireline Log Analysis 77
5.2.1 Basic Log Interpretation 77
5.2.2 Advanced Log Interpretation 91
5.2.3 Petrophysical Calculations 94
5.3 Core Analysis 95
5.3.1 Core from Well 28433 96
5.3.2 Core from Well 28159 98
5.3.3 Core from Well 28511 100
5.3.4 Core from the Chester 6-16 Well 102
5.3.5 Core from the Chester 8-16 well 105
5.3.6 Formation Properties from Core Analyses 109
5.4 Seismic Analysis 112
5.4.1 Basic Seismic Interpretation 112
5.4.2 Advanced Seismic Interpretation 113
5.4.3 Interpretations of Seismic Analyses 122
5.5 Statistical Analysis 128
5.5.1 A-1 Carbonate 128
5.5.2 Brown Niagaran 131
5.5.3 Core-to-Log Correlation 141
5.5.4 Conclusions of Statistical Analyses 144
5.6 Geologic Interpretations and Data Integration 144

6.0 Bagley 153
6.1 Reef History and Production Review 153
6.2 Wireline Log Analysis 154
6.2.1 Basic Log Interpretation 155
6.2.2 Petrophysical Calculations 179
6.3 Core Analysis 180
6.3.1 Grain Density 180
6.3.2 Porosity-Permeability Transform 181
6.3.3 Core Descriptions 182
6.4 Statistical Analysis 187
6.4.1 Determining Components 189
6.4.2 Determining Number of Clusters 194
6.4.3 Cluster Analysis Results 197
6.5 Geologic Interpretations 207

7.0 Charlton 19 215
7.1 Reef History and Production Review 215
7.2 Wireline Log Analysis 217
7.2.1 Basic Log Interpretation 219
7.2.2 Petrophysical Calculations 230
7.3 Seismic Analysis 231
7.4 Geologic Interpretations and Data Integration 234

8.0 Dover 35 239
8.1 Reef History and Production Review 239
8.2 Wireline Log Analysis 241

8.2.1 Basic Log Interpretation 243
8.2.2 Petrophysics Calculations 249
8.3 Seismic Analysis 250
8.4 Geologic Interpretations 251

9.0 Dover 36 255
9.1 Reef History and Production Review 255
9.2 Wireline Log Analysis 257
9.2.1 Basic Log Interpretation 259
9.2.2 Petrophysics Calculations 263
9.3 Seismic Analysis 265
9.4 Geological Interpretations 265

10.0 Charlton 30-31 269
10.1 Reef History and Production Review 269
10.2 Wireline Log Analysis 270
10.2.1 Basic Log Interpretation 272
10.2.2 Petrophysics Calculations 287
10.3 Seismic Analysis 289
10.4 Geologic Interpretations 292

11.0 Charlton 6 297
11.1 Reef History and Production Review 297
11.2 Wireline Log Analysis 298
11.2.1 Basic Log Interpretation 301
11.2.2 Petrophysics Calculations 306
11.3 Seismic Analysis 308
11.4 Geologic Interpretations 311

12.0 Chester 2 315
12.1 Reef History and Production Review 315
12.2 Wireline Log Analysis 316
12.2.1 Basic Log Interpretation 318
12.2.2 Petrophysics Calculations 328
12.3 Seismic Analysis 330
12.4 Core Analysis 334
12.5 Geologic Interpretations 337

13.0 Chester 5/6 343
13.1 Reef History and Production Review 343
13.2 Wireline Log Analysis 344
13.2.1 Basic Log Interpretation 346
13.2.2 Petrophysics Calculations 355
13.3 Core Analysis 356
13.4 Geologic Interpretations 357

14.0 Geomechanical Assessment 361
14.1 Introduction 361
14.2 Geomechanical Characterization 361
14.2.1 Introduction 361
14.2.2 Calculation of Elastic Properties 362
14.2.3 Results and Discussion 363

14.2.4 Individual Formation Evaluation Results 366
14.2.5 Shallow Formation Evaluation Results 367
14.3 In-Situ Stress Analysis 367
14.3.1 SH_{max} Orientation Interpretation 368
14.3.2 Vertical Stress Spatial Variability Analysis 378
14.3.3 In-Situ Stress Changes Due to CO_2 Injection 381
14.4 Rock Mechanical – Rock Physical Experimental Data and Interpretation 385
14.4.1 Rock Mechanical – Rock Physical Tests 385
14.4.2 Rock Mechanical Parameters (Static-Dynamic Correlation) 386
14.4.3 Biot Coefficient Estimate 388
14.4.4 Rock Failure Parameters (UCS and CCS, Mohr-Coulomb Analysis, and Tensile Strength) 390
14.5 Conclusions 393
15.0 Well Testing 395
15.1 Introduction 395
15.2 Methodology 395
15.2.1 Reservoir Pressure 395
15.2.2 Hydraulic Well Testing 397
15.2.3 Micro-Frac Tests 400
15.2.4 Fluid Characterization 401
15.3 Lawnichak 9-33 (Dover 33) 403
15.3.1 Reservoir Pressure 403
15.3.2 Hydraulic Well Tests 404
15.3.3 Fluid Characterization 421
15.4 Chester 8-16 (Chester 16) 429
15.4.1 Reservoir Pressure 429
15.4.2 Hydraulic Well Tests 432
15.4.3 Micro-Frac Tests 440
15.4.4 Summary 456
15.5 Conclusion 465
16.0 Conclusions 467
17.0 References 475
Appendix A. Literature Review of Niagaran Reef Geology A-1
Appendix B. Detailed Core Descriptions and Photographs B-1
Appendix C. Individual Well Geomechanics Evaluation Results C-1

List of Tables

Page

Table 1-1. List of reefs studied and associated task number. 2
Table 3-1. Number of wells in each reef with wireline log data..... 13
Table 3-2. Summary of available core data by reef. 14
Table 3-3. Summary of available 3D seismic data by reef. 14
Table 3-4. Summary of basic wireline logs and use. 26
Table 3-5. Methodology for describing the general behavior of electro-textures with possible interpretations. 30
Table 3-6. Grain density used to calculate average porosity logs by lithology. 31
Table 3-7. Definitions of petrophysical properties with data inputs needed. 32
Table 4-1. Summary of initial (discovery) conditions of the Dover 33 reef field..... 37
Table 4-2. Summary of available wireline log data for wells penetrating the Dover 33 reef field. 39
Table 4-3. Summary of petrophysical calculations for the A-2 carbonate in the Dover 33 reef field..... 59
Table 4-4. Summary of petrophysical calculations for the A-1 carbonate in the Dover 33 reef field..... 59
Table 4-5. Summary of petrophysical calculations for the Brown Niagaran in the Dover 33 reef field..... 60
Table 4-6. Summary of whole core porosity and permeability data in the Lawnichak 9-33 well. 60
Table 4-7. Summary of RSWC porosity and permeability data in the Lawnichak 9-33 well..... 60
Table 4-8. Summary of key potential reservoir intervals in the Lawnichak 9-33 well based on whole core analysis and images. 60
Table 4-9. Summary of log averages and ranges by lithofacies in the Brown Niagaran. 68
Table 4-10. Hypothesis test results between lithofacies pairs. 69
Table 5-1. Chester 16 reef field primary production by well. 75
Table 5-2. Chester 16 reef field initial reservoir conditions. 76
Table 5-3. Summary of available wireline log data for wells penetrating the Chester 16 reef field. 77
Table 5-4. Summary of petrophysical calculations for the A-2 carbonate in the Chester 16 reef field..... 94
Table 5-5. Summary of petrophysical calculations for the A-1 carbonate in the Chester 16 reef field..... 94
Table 5-6. Summary of petrophysical calculations for the Brown Niagaran in the Chester 16 reef field..... 94
Table 5-7. Summary of core collected by well in the Chester 16 reef field..... 95
Table 5-8. Conventional core acquisition parameters for Chester 8-16. 105
Table 5-9. Summary of porosity and permeability data from whole core in the Chester 16 reef field..... 111
Table 5-10. Lithofacies used for statistical analyses by formation..... 128
Table 5-11. Averages and ranges of log properties for lithofacies in the A-1 carbonate..... 128
Table 5-12. Average core-measured properties for the Chester 16 lithofacies of the A-1 carbonate. 130
Table 5-13. Averages and ranges of log properties for lithofacies in the Brown Niagaran. 132
Table 5-14. Tukey's HSD test results for each lithofacies pair and log. 133
Table 5-15. Averages and ranges of core-measured properties for each lithofacies in the Brown Niagaran formation. 134
Table 5-16. Statistical tests and results performed to compare core-measured properties of the lithofacies of the Brown Niagaran formation. 138

Table 5-17. Results of KMeans clustering showing which cluster the core-measured data falls into for each lithofacies. 138
Table 5-18. Results of the Mclust clustering showing which cluster the core-measured data falls into for each lithofacies. 139
Table 6-1. Summary of initial (discovery) conditions of the Bagley reef field. 153
Table 6-2. Summary of available wireline log data for wells penetrating the Bagley reef field. 155
Table 6-3. Summary of petrophysical calculations for the A-2 carbonate in the Bagley reef field. 179
Table 6-4. Summary of petrophysical calculations for the A-1 carbonate in the Bagley reef field. 179
Table 6-5. Summary of petrophysical calculations for the Brown Niagaran in the Bagley reef field. 179
Table 6-6. Summary of grain density measured from whole core in the Bagley reef field. 180
Table 6-7. List of formations, facies, and zones with respect to one another for each reef field. 188
Table 6-8. P-values for each formation pair as determined by the Tukey HSD test. Yellow highlights formation pairs with similar average. 193
Table 6-9. P-values for each facies pair as determined by the Tukey HSD test. Yellow highlights formation pairs with similar average. 193
Table 6-10. P-values for each zone pair as determined by the Tukey HSD test. Yellow highlights formation pairs with similar average. 194
Table 7-1. Summary of initial discovery conditions of the Charlton 19 reef field. 216
Table 7-2. Summary of wireline log data for the Charlton 19 reef; green shading indicates logs available by well. 217
Table 7-3. Average petrophysical calculations for the A2 Carbonate in the Charlton 19 reef. 230
Table 7-4. Average petrophysical calculations for the A1 Carbonate in the Charlton 19 reef field. 231
Table 7-5. Average petrophysical calculations for the Brown Niagaran in the Charlton 19 reef field. 231
Table 8-1. Summary of initial (discovery) conditions of the Dover 35 reef field. 240
Table 8-2. Summary of available wireline log data for wells penetrating the Dover 35 reef. 242
Table 8-3. Summary of petrophysical calculations for the A-2 carbonate in the Dover 35 reef field. 249
Table 8-4. Summary of petrophysical calculations for the A-1 carbonate in the Dover 35 reef field. 249
Table 8-5. Summary of petrophysical calculations for the Brown Niagaran in the Dover 35 reef field. 250
Table 9-1. Summary of initial (discovery) conditions of the Dover 36 reef field. 256
Table 9-2. Summary of available wireline log data for wells penetrating the Dover 36 reef field. 258
Table 9-3. Summary of petrophysical calculations for the A-2 carbonate in the Dover 36 reef field. 264
Table 9-4. Summary of petrophysical calculations for the A-1 carbonate in the Dover 36 reef field. 264
Table 9-5. Summary of petrophysical calculations for the Brown Niagaran in the Dover 36 reef field. 264
Table 10-1. Summary of initial (discovery) conditions of the Charlton 30-31 reef field. 270
Table 10-2. Summary of available wireline log data for wells penetrating the Charlton 30-31 reef field. 271
Table 10-3. Summary of petrophysical calculations for the A-2 carbonate in the Charlton 30-31 reef field. 287
Table 10-4. Summary of petrophysical calculations for the A-1 carbonate in the Charlton 30-31 reef field. 288
Table 10-5. Summary of petrophysical calculations for the Brown Niagaran in the Charlton 30-31 reef field. 288
Table 11-1. Summary of initial (discovery) conditions of the Charlton 6 reef field. 298
Table 11-2. Summary of available wireline log data for wells penetrating the Charlton 6 reef field. 299
Table 11-3. Summary of petrophysical calculations for the A-2 carbonate in the Charlton 6 reef field. 306

Table 11-4. Summary of petrophysical calculations for the A-1 carbonate in the Charlton 6 reef field.....307
Table 11-5. Summary of petrophysical calculations for the Brown Niagaran in the Charlton 6 reef field.....307
Table 12-1. Summary of initial (discovery) conditions of the Chester 2 reef field.....316
Table 12-2. Summary of available wireline log data for wells penetrating the Chester 2 reef field.....317
Table 12-3. Summary of petrophysical calculations for the A-2 carbonate in the Chester 2 reef field.....328
Table 12-4. Summary of petrophysical calculations for the A-1 carbonate in the Chester 2 reef field.....329
Table 12-5. Summary of petrophysical calculations for the Brown Niagaran in the Chester 2 reef field.....329
Table 13-1. Summary of initial (discovery) conditions of the Chester 5/6 reef field.....344
Table 13-2. Summary of available wireline log data for wells penetrating the Chester 5-6 reef field.....345
Table 13-3. Summary of petrophysical calculations for the A-2 carbonate in the Chester 5-6 reef field.....355
Table 13-4. Summary of petrophysical calculations for the A-1 carbonate in the Chester 5-6 reef field.....355
Table 13-5. Summary of petrophysical calculations for the Brown Niagaran in the Chester 5-6 reef field.....355
Table 13-6. Summary of grain density measured from whole core in Chester 5-6 reef field. 356
Table 14-1. Mean and variance values of geomechanical parameters for each formation combined across wells.....364
Table 14-2. Summary of Open Borehole MicroFrac Tests Performed in Chester 8-16.....368
Table 14-3. Fast shear wave azimuth mean and variance for Lawnichak 9-33 (bedding mean azimuth of 68 and fracture azimuth of 61). 373
Table 14-4. Fast shear wave azimuth mean and variance for Chester 8-16.....373
Table 14-5. Summary of calculated S_v values for the five wells characterized in the caprock stress analysis. 378
Table 14-6. Geomechanics Model Parameters 384
Table 14-7. Sh_{min} gradient increase due to increase pressure using hard reservoir and soft caprock scenario.....385
Table 14-8. Laboratory tests performed on core samples. 386
Table 14-9. Static elastic moduli measured using triaxial test. 387
Table 14-10. Dynamic elastic module measured using triaxial test.....387
Table 14-11. Estimated Biot's coefficient for each rock sample. 389
Table 14-12. Summary of strength parameters determined from uniaxial tests.....390
Table 14-13. Summary of strength parameters determined from triaxial tests.....390
Table 14-14. Mohr-Coulomb failure analysis results for Upper Brown Niagaran Formation in Dover 33 Reef.....391
Table 14-15. Mohr-Coulomb failure analysis results for Brown Niagaran Formation in Chester 16 Reef.....392
Table 14-16. Summary of Brazilian tensile test results.....393
Table 15-1. Pressure and mobility measurements from well 9-33.....403
Table 15-2. Depth of VITs in the 9-33 well.....404
Table 15-3. Reservoir and fluid parameters used in the analysis of the VITs. 404
Table 15-4. Reservoir properties estimated from PTA of VIT-22 straddle packer pressure data.....406

Table 15-5. Summary of key reservoir properties determined from VITs conducted in the 9-33 well (Dover 33 reef).....421
Table 15-6. Summary of fluid characterization for the 9-33 well.....421
Table 15-7. Summary of in-situ reservoir pressure and mobility measurements. 430
Table 15-8. Depth of LITs in the Chester 8-16 well. 432
Table 15-9. Summary of key reservoir properties determined from LITs conducted in the Chester 8-16 well.....440
Table 15-10. Summary of open-borehole micro-frac tests performed in the 8-16 well.....440
Table 15-11. Fracture closure pressures for micro-frac Station 1 (5861 ft MD). 445
Table 15-12. Fracture closure pressures for micro-frac Station 2 (5967 ft MD). 448
Table 15-13. Fracture closure pressures for micro-frac Station 3 (5791 ft MD). 450
Table 15-14. Fracture closure pressures for micro-frac test 4 (5765 ft MD).....452
Table 15-15. Summary of key reservoir properties determined from VITs conducted in 9-33 well (Dover 33 reef).....456
Table 15-16. Summary of key reservoir properties determined from LITs conducted in the 8-16 well (Chester 16 reef).....459
Table 15-17. Summary of fluid characterization for the 9-33 well.....462
Table 15-18. Micro-frac testing results.....462
Table 15-19. Triaxial test results for Chester 16 cores. 463
Table 16-1. Summary of data types, analyses, and outcomes used in geologic characterization. 468
Table 16-2. Summary of data tested at piggyback well locations in order of importance for geologic characterization efforts. 469
Table 16-3. Summary of reservoir controls and identification methods.....469
Table A-1. Original mineralogy of Silurian reef organisms. Arag- aragonite, LMC- low magnesium calcite, HMC-high magnesium calcite, Cal-calcite. Modified from Trout, 2012. ..... A-20
Table C-1. Mean, variance, and N (number of data values) values of geomechanical parameters within Cargas 3-2 HD1 by formation. C-7
Table C-2. Mean, variance, and N (number of data values) values of geomechanical parameters within El Mac Hills 1-18A by formation. C-14
Table C-3. Mean, variance, and N (number of data values) values of geomechanical parameters within Lawnichak 9-33 by formation..... C-21
Table C-4. Mean, variance, and N (number of data values) values of geomechanical parameters within Chester 6-16 by formation. C-28
Table C-5. Mean, variance, and N (number of data values) values of geomechanical parameters within Chester 8-16 by formation. C-35

List of Figures

Page

Figure 1-1. Map of reefs studied under Task 3, Task 4, and Task 5. 3
Figure 1-2. Three major components of geologic characterization of the Niagaran reefs and associated substeps. 4
Figure 1-3. Analyses completed by reef showing variability due to data availability. 4
Figure 2-1. Silurian Northern Niagaran Pinnacle Reef Trend within the Michigan Basin (modified from Rine, 2015, and Burgess & Benson, 1969). 5
Figure 2-2. Stratigraphy of the Silurian-age Niagaran and Salina Groups in the Michigan Basin. On left is the formal and informal Silurian stratigraphic nomenclature (modified from Trout, 2012, and Rine, 2015). On right is a conceptual model and stratigraphy of the Brown Niagaran reef interval (after Gill 1973, 1979; and Huh 1973). 6
Figure 2-3. Main structural elements and age of bedrock in the Michigan Basin (modified from Rine, 2015, and Catacosinos et al., 1991)..... 7
Figure 2-4. Major faults in the Michigan Basin (modified from Esch, 2010; Cox & Barnes, 2016). 8
Figure 2-5. Geometry of reservoirs and seals in the interval of interest (modified from Rine, 2015a, and Rine et al., 2017). 8
Figure 3-1. Map of the study area showing locations of reefs (green and red), 3D seismic data sources (colored polygons), 2D seismic data sources (blue lines), and deep wells (black). 11
Figure 3-2. Single well cross sections representing typical log signatures for key formations at the crest of the reef, flank of the reef, and off-reef. 15
Figure 3-3. Depositional facies model by Western Michigan University collaborators showing (1) windward flank, (2) windward reef talus, (3) reef core complex, (4) leeward proximal reef apron, (5) leeward distal reef apron, (6) leeward flank facies..... 18
Figure 3-4. Gamma ray curve interpretations for lithofacies suites indicating the following depositional facies: (1) windward flank, (2) windward reef talus, (3) reef core complex, (4) leeward proximal reef apron, (5) leeward distal reef apron, (6) leeward flank facies. From Rine, 2015 19
Figure 3-5. Simplified workflow for assigning facies to individual well locations in the Brown Niagaran. 21
Figure 3-6. Structure map of the Gray Niagaran (base) without the influence of reefs. 22
Figure 3-7. Structure map of the regional Brown Niagaran without the influence of reefs. 23
Figure 3-8. Structure map of the A-1 carbonate without the influence of reefs. 24
Figure 3-9. Structure map of the A-2 carbonate without the influence of the reefs. 25
Figure 3-10. Industry standard crossplot of neutron porosity and bulk density used to evaluate formation lithology, porosity, and influence of shale. 27
Figure 3-11. Elemental capture spectroscopy header log (Baker Hughes). 28
Figure 3-12. Crossplot of resistivity and neutron porosity for wells in an example reef field showing a strong decrease in resistivity with increasing porosity. Colors represent different wells. 33
Figure 3-13. Plot of predicted bulk density versus percentage of salt for different lithology and porosity scenarios. 35
Figure 3-14. Examples of the seismic horizons for the A-2 carbonate (blue), A-1 carbonate (orange), and Brown Niagaran (brown) for Chester 2 (A) and Chester 16 (B). 36
Figure 4-1. Cumulative production in the Dover 33 reef field from 1974 through 2017 showing an increase in production rates after EOR operations began in 1996..... 37

Figure 4-2. Cumulative oil and gas production maps in the Dover 33 reef field showing the highest production in the middle of the northern pod in well 29565. 38
Figure 4-3. Map of the Dover 33 reef field showing locations of wells used in the geologic analysis. 39
Figure 4-4. Neutron porosity-bulk density crossplot of well 35195 in the southern pod of the Dover 33 reef field showing high porosity in the lower A-1 carbonate and the Brown Niagaran. 40
Figure 4-5. Water saturation curve and histogram for well 35195 showing a gradual increase at the top of the Brown Niagaran (BN). 41
Figure 4-6. Neutron porosity-bulk density crossplot of well 30392 in the Dover 33 reef field showing porosity in the lower A-1 carbonate and the Brown Niagaran. 42
Figure 4-7. Water saturation curve and histogram for well 30392 showing higher water saturations in the A-1 carbonate and Brown Niagaran. 43
Figure 4-8. Neutron porosity-bulk density crossplot for well 29781 in the Dover 33 reef field showing porosity in the Brown Niagaran. 44
Figure 4-9. Water saturation curve and histogram for well 29781 showing low water saturations throughout the formations of interest. 44
Figure 4-10. Neutron porosity-bulk density crossplot of well 33830 in the Dover 33 reef field showing salts (blue) in the A-2 evaporite and porosity in the lower A-1 carbonate and the Brown Niagaran. 45
Figure 4-11. Water saturation curve and histogram for well 33830 showing an increase in water saturation in the mid-formation A-1 carbonate at the oil/water contact. 46
Figure 4-12. Neutron porosity-bulk density crossplot of well 50985 in the Dover 33 reef field showing salt (blue), anhydrite (green), and porosity (red) flags. 47
Figure 4-13. Neutron porosity-bulk density crossplot of well 35584 in the Dover 33 reef field showing salts (blue), anhydrite (green), and porosity (red) flags. 48
Figure 4-14. Neutron porosity-bulk density crossplot of well 29565 in the Dover 33 reef field showing a thick Brown Niagaran with numerous porosity flags (red). 49
Figure 4-15. Water saturation curve and histogram for well 29565 showing in increase in saturation mid-Brown Niagaran. 49
Figure 4-16. Neutron porosity-bulk density crossplot of well 29809 in the Dover 33 reef field showing porosity flags (red) in the Brown Niagaran. 50
Figure 4-17. Water saturation curve and histogram for well 29809 showing an increase in water saturation in the upper Brown Niagaran. 51
Figure 4-18. Neutron porosity-bulk density crossplot of well 61209 in the Dover 33 reef field showing porosity flags (red) in the Brown Niagaran. 52
Figure 4-19. Water saturation curve and histogram for well 61209 showing an increase in water saturation in the upper Brown Niagaran. 52
Figure 4-20. Neutron porosity comparison between data collected on a limestone matrix (blue) and dolomite matrix (red), with limestone porosity overestimating true porosity. 53
Figure 4-21. Cross section of NMR log data, select logs from the triple combo log suite, and pay flags generated from triple combo logs and neutron porosity-bulk density crossplots for the A-2 carbonate and A-2 evaporite. The NMR effective porosity log is plotted with neutron porosity, density porosity, and average porosity logs derived from the triple combo log suite. Permeability, bulk volume of movable fluid (BVM), bulk volume of irreducible fluid (BVI), clay-bound water (CBW), and T2 distributions are also shown. 54
Figure 4-22. Annotated image log of the A-1 carbonate from ~5,538 feet to 5,550 feet. Note the laminated discontinuous conductive features that occur throughout the resistive matrix, interpreted to be brecciated microbial laminites. 55

Figure 4-23. Cross section of NMR log data, select logs from the triple combo log suite, core porosity and permeability data, and pay flags generated from triple combo logs and neutron porosity-bulk density crossplots for the A-1 carbonate. The NMR effective porosity log is plotted with neutron porosity, density porosity, and average porosity logs derived from the triple combo log suite as well as core porosity. NMR permeability is shown with core permeability. BVM, BVI, CBW, and T2 distributions are also shown. Green box highlights a zone of interest. 56
Figure 4-24. Annotated FMI image log of the Brown Niagaran from ~5,564 feet to 5,575 feet. This texture is described as massive heterogeneously conductive texture where all conductive features occur within a resistive matrix. This zone is interpreted to be massively bedded mudstone with a moderate to high distribution of vuggy porosity. 57
Figure 4-25. Cross section of NMR log data, select logs from the triple combo log suite, core porosity and permeability data, and pay flags generated from triple combo logs and neutron porosity-bulk density crossplots for the Brown Niagaran. The NMR effective porosity log is plotted with neutron porosity, density porosity, and average porosity logs derived from the triple combo log suite, as well as core porosity. NMR permeability is shown with core permeability. BVM, BVI, CBW, and T2 distributions are also shown. Green boxes highlight zones of interest. 58
Figure 4-26. Compiled illustration of lithology log, core photos (ultraviolet [UV] and white light), CT scan image, core descriptions, and annotated core images of the Brown Niagaran for depths 5,749 feet to 5,752 feet. 61
Figure 4-27. Core porosity-permeability transform plot for the A-1 carbonate (yellow circles) and the Brown Niagaran (brown circles). 62
Figure 4-28. 2D cross section through 3D seismic horizon collected over the Dover 33 reef, showing two reefs identified in the Dover 33 field (brown). 63
Figure 4-29. Time horizon surface for the Brown Niagaran showing steep slopes along the edges of the Dover 33 reef. The red box outlines the Dover 33 reef field. 64
Figure 4-30. Time horizon surface for the A-1 carbonate showing moderate slopes along the edges of the Dover 33 reef. The red box outlines the Dover 33 reef field. 65
Figure 4-31. Time horizon surface for the A-2 carbonate showing gentle slopes along the edges of the Dover 33 reef. The red box outlines the Dover 33 reef field. 66
Figure 4-32. Boxplot comparison of neutron porosity by lithofacies with the reef core (blue) having the highest average. 67
Figure 4-33. Location of cross sections through the Dover 33 reef field. 70
Figure 4-34. Cross section A-A’ across the northern pod of the Dover 33 reef field showing numerous porosity flags (red and green) above and below the oil/water contact (dashed line). 71
Figure 4-35. Cross section C-C’ running south to north through the Dover 33 reef field showing the distribution of porosity flags across wells. 72
Figure 4-36. Plan view of the depositional model of the Dover 33 reef field showing the subdivision into windward (purple), reef core (green), and leeward (blue) facies. 73
Figure 4-37. Cross section A-A’ across the northern reef pod in the Dover 33 reef field showing changes in lithology and lithofacies from the southwest to the northeast. 74
Figure 5-1. Cumulative oil and gas production by well in the Chester 16 reef field showing wells with greatest production (larger radius) and wells with lower production (smaller radius). 75
Figure 5-2. Cumulative production in the Chester 16 reef field from 1971 through 2017. 76
Figure 5-3. Histogram and curve from calculated water saturations in well 28796 showing high water saturations in the flank of the Chester 16 reef field. 78

Figure 5-4. Neutron porosity-bulk density crossplot of well 28159 showing porosity in the upper A-1 carbonate. 79
Figure 5-5. Water saturation histogram and curve for well 28159 over the A-2 carbonate to the Gray Niagaran showing an increase in water saturation near the base. 80
Figure 5-6. Neutron porosity-bulk density crossplot of well 28433 showing porosity in the upper A-1 carbonate and thin intervals in the Brown Niagaran. 81
Figure 5-7. Water saturation histogram and curve for well 28433 over the A-2 carbonate to the Gray Niagaran. 81
Figure 5-8. Neutron porosity-bulk density (from sonic) crossplot of well 28511 showing very little porosity with some porosity spikes in the Brown Niagaran. 82
Figure 5-9. Water saturation histogram and curve for well 28511 over the A-2 carbonate to the Gray Niagaran showing high saturations throughout the flank interval of the Chester 16 reef field. 83
Figure 5-10. Neutron porosity-bulk density (sonic) crossplot of well 28743 in the Chester 16 reef field showing porosity in the upper A-1 carbonate and middle Brown Niagaran. 84
Figure 5-11. Histogram and curve for calculated water saturation for well 28743 showing an increase in water saturation toward the base of the Brown Niagaran. 85
Figure 5-12. Neutron porosity-bulk density (sonic) crossplot of well 28798 in the Chester 16 reef field showing no porosity. 86
Figure 5-13. Neutron porosity-bulk density (sonic) crossplot of well 28918 in the Chester 16 reef field showing no porosity. 87
Figure 5-14. Neutron porosity-bulk density (sonic) crossplot of the Chester 6-16 well showing porosity in the upper A-1 carbonate and mid-Brown Niagaran. 88
Figure 5-15. Histogram and curve for calculated water saturation for the Chester 6-16 well showing high water saturation throughout the Brown Niagaran. 89
Figure 5-16. Neutron porosity-bulk density (sonic) crossplot of the Chester 8-16 well showing porosity in the upper A-1 carbonate and mid-Brown Niagaran. 90
Figure 5-17. Histogram and curve for calculated water saturation for the Chester 8-16 well showing an increase in water saturation toward the base of the Brown Niagaran. 91
Figure 5-18. Intermediate texture zone of the A-1 carbonate. The texture was heterogeneous with two porosity zones shown in the figure (blue boxes) from 5,884 to 5,888 feet and from 5,892 to 5,903 feet. 92
Figure 5-19. Texture three within the Brown Niagaran unit of the Chester 8-16 well. Texture was interbedded homogenous and heterogenous materials. Significant porosity zone was shown from 6,141 to 6,150 feet. Note cyclical packages of homogenously resistive-to-heterogeneous materials. 93
Figure 5-20. Map of the Chester 16 reef field showing previously collected core (red) and newly Battelle-collected core (blue) by well and position in main reef structure. 95
Figure 5-21. Photographs of textures and structures observed in whole core from well 28433. 97
Figure 5-22. Simplified stratigraphic column of core in well 28433 summarizing lithology, textures, and structures in the Brown Niagaran. 98
Figure 5-23. Photographs of textures and structures observed in the whole core from well 28159. 99
Figure 5-24. Simplified stratigraphic column of core from well 28159 summarizing lithology, textures, and structures. 100
Figure 5-25. Photographs of textures and structures of whole core from well 28511. 101
Figure 5-26. Simplified stratigraphic column of core from well 28511 summarizing lithology, textures, and structures. 102
Figure 5-27. Example photographs of sidewall cores collected in the A-1 carbonate from the Chester 6-16 well. 103

Figure 5-28. Example photographs of sidewall cores collected from the Brown Niagaran in the Chester 6-16 well. 104
Figure 5-29. Compiled illustration of lithology log, core photos (UV and white light), CT scan image, core descriptions, and annotated core images of the Brown Niagaran in the Chester 8-16 well for depths 6,148 to 6,151 feet. 106
Figure 5-30. Compiled illustration of lithology log, core photos (UV and white light), CT scan image, core descriptions, and annotated core images of the Brown Niagaran in the Chester 8-16 well for depths 6,181 to 6,184 feet. 107
Figure 5-31. Compiled illustration of lithology log, core photos (UV and white light), CT scan image, core descriptions, and annotated core images of the Gray Niagaran in the Chester 8-16 well for depths 6,347 to 6,350 feet. 108
Figure 5-32. Compiled illustration of lithology log, core photos (UV and white light), CT scan image, core descriptions, and annotated core images of the Gray Niagaran in the Chester 8-16 well for depths 6,356 to 6,359 feet. 109
Figure 5-33. Histograms of the grain density for the A-1 carbonate, A-1 evaporite, and Brown Niagaran formations from whole core in the Chester 16 reef field. 110
Figure 5-34. Porosity-permeability transform for the A-1 carbonate, A-1 evaporite, and Brown Niagaran from whole core measurements in the Chester 16 reef field. 111
Figure 5-35. Example horizons for the A-2 carbonate (blue) and top of the reef structure (brown) for cross line 182 in the 3D seismic covering the Chester 16 reef field. 112
Figure 5-36. Time horizon surface of the Brown Niagaran showing steeply dipping edges of the Chester 16 reef field. 113
Figure 5-37. Results of data reprocessing show different angle stacks with and without HFE. The 31-45 angle stack with HFE improved reef resolution (upper left). 114
Figure 5-38. Map of the maximum RAI from the Chester 16 seismic data, where blues indicate salts, greens indicate porosity, and red/yellows indicate dense rock. 115
Figure 5-39. Bar plot of RAI and cumulative production for five wells in the Chester 16 reef field. 116
Figure 5-40. RAI porosity horizons in cross section view through the Chester 16 reef field showing multiple intervals of potential porosity in the Brown Niagaran and A-1 carbonate. 118
Figure 5-41. Extent of RA- identified porosity horizons within the Chester 16 reef field. 119
Figure 5-42. Average RAI maps of porosity horizons 3 (left) and 6 (right) in the Chester 16 reef field showing higher porosity at crestal positions and lower porosity in the saddle region. 120
Figure 5-43. Maps of normalized RAI for each porosity horizon showing higher porosity in horizons 3 and 6. 121
Figure 5-44. Wavelets extracted at each well location from Chester 16 3D seismic data and the correlation coefficient to well 28159. 123
Figure 5-45. Wavelet correlation maps for each well through the Chester 16 seismic data with cooler colors showing lower correlation coefficients and hotter colors having higher correlation. 124
Figure 5-46. Compilation of wavelet correlations from the Chester 16 seismic data. 125
Figure 5-47. Geologic interpretation of RAI analysis of the Chester 16 field. 126
Figure 5-48. Interpretation of the wavelet matching and RAI analysis of the Chester 16 field showing a baffle in the saddle region between reef pods. 127
Figure 5-49. Boxplots of wireline log properties for each lithofacies of the A-1 carbonate in the Chester 16 reef field. 129
Figure 5-50. Density plots of wireline log properties for each lithofacies of the A-1 carbonate in the Chester 16 reef field. 129

Figure 5-51. Density plots of the core measured porosity and permeability for the A-1 Crest and A-1 Flank lithofacies. 130
Figure 5-52. Crossplot of core-measured porosity and permeability illustrating a moderate trend with highest values in the crest (pink) of the Chester 16 reef field. 131
Figure 5-53. Boxplots of each wireline log and each lithofacies of the Brown Niagaran formation. 132
Figure 5-54. Density plots of each wireline log and lithofacies for the Brown Niagaran formation. 133
Figure 5-55. Boxplot (left) and density plot (right) of core measured porosity for each lithofacies in the Brown Niagaran formation. 135
Figure 5-56. Boxplot (left) and density plot (right) of core measured permeability for each lithofacies in the Brown Niagaran formation. 136
Figure 5-57. Core-measured porosity and permeability by lithofacies of the Brown Niagaran showing a poor correlation. 137
Figure 5-58. KMeans clustering results show porosity and permeability falling into three identified clusters as identified by colored circles and differing symbols. 139
Figure 5-59. Cluster results from Mclust using core-measured porosity and permeability with different symbols for each cluster. 140
Figure 5-60. Core-measured porosity and permeability colored by Mclust clustering results with shape showing lithofacies. 141
Figure 5-61. Log-measured porosity and core-measured porosity for all data in the Chester 16 reef field showing a strong correlation. 142
Figure 5-62. Log-measured porosity and core-measured porosity for all data in the Chester 16 reef field, by lithofacies, showing no dependence on lithofacies. 143
Figure 5-63. Cross section A-A’ through the Chester 16 reef field showing wells used and position in the reef structure. 145
Figure 5-64. Cross section A-A’ through the Chester 16 reef field showing changes in gamma ray, neutron porosity, bulk density, and water saturation in correlation with key formations. Angled well diagrams indicate deviated wells. Not drawn to scale. 146
Figure 5-65. Cross section A-A’ through the Chester 16 reef field showing a 2D interpolation of neutron porosity between wellbores. Significant porosity (red) is observed in the A-1 carbonate and as thin streaks through the Brown Niagaran. Angled well diagrams indicate deviated wells. Not drawn to scale. 147
Figure 5-66. Cross section A-A’ through the Chester 16 reef field showing a 2D interpolation of gamma ray between wellbores. High gamma ray was consistent in the mid-formation A-2 carbonate over a shaley interval and high in the porosity zone in the A-1 carbonate. Angled well diagrams indicate deviated wells. Not drawn to scale. 148
Figure 5-67. Cross section A-A’ through the Chester 16 reef field with a 2D interpolation of the water saturation showing high water saturations after the oil/water contact and where evaporites are present. Angled well diagrams indicate deviated wells. Not drawn to scale. 149
Figure 5-68. Brown Niagaran lithofacies (A) and A-1 carbonate lithofacies (B) for the Chester 16 reef field. Green represents reef core, purple is windward facies, blue is leeward facies, and orange is A-1 carbonate porosity facies. 151
Figure 5-69. Geologic interpretation of the Chester 16 reef field at cross section A-A’ showing lithofacies, formations, and highlighted features. A-2 carbonate (A2C), A-2 evaporite (A2E), A-1 carbonate reservoir (A1C Res), A-1 carbonate non-reservoir (A1C NonRes), Brown Niagaran flank (BN Flank), Brown Niagaran leeward (BN Leeward), Brown Niagaran reef core (BN Reef Core), Brown Niagaran windward (BN Windward), and Gray Niagaran (GN). 152

Figure 6-1. Cumulative production in the Bagley reef from 1973 through 2015 showing an increase in production rates after EOR operations began in 2015. 153
Figure 6-2. Map of Bagley reef field well locations indicating northern (red), middle (yellow), and southern (blue) lobes. 154
Figure 6-3. Neutron porosity–bulk density crossplot for the A-2 carbonate in the northern unit of the Bagley reef field. 156
Figure 6-4. Neutron porosity–bulk density crossplot for the A-2 carbonate in the middle unit of the Bagley reef field. 157
Figure 6-5. Neutron porosity–bulk density crossplot for the A-2 carbonate in the southern unit of the Bagley reef field. 158
Figure 6-6. Water saturation histogram over the A-2 carbonate for all wells in the Bagley reef field. 159
Figure 6-7. Neutron porosity–bulk density crossplot for the A-2 evaporite in the northern unit of the Bagley reef field. 161
Figure 6-8. Neutron porosity–bulk density crossplot for the A-2 evaporite in the middle unit of the Bagley reef field. 162
Figure 6-9. Neutron porosity–bulk density crossplot for the A-2 evaporite in the southern l unit of the Bagley reef field. 163
Figure 6-10. Water saturation histogram for the A-2 evaporite showing a high frequency of data with very low and very high saturations due to interbedded carbonates and evaporites. 164
Figure 6-11. Neutron porosity–bulk density crossplot for the A-1 carbonate in the northern unit of the Bagley reef field. 166
Figure 6-12. Neutron porosity–bulk density crossplot for the A-1 carbonate in the middle unit of the Bagley reef field. 167
Figure 6-13. Neutron porosity–bulk density crossplot for the A-1 carbonate in the southern unit of the Bagley reef field. 168
Figure 6-14. Water saturation histogram for the A-1 carbonate showing relatively low saturations. 169
Figure 6-15. Neutron porosity–bulk density crossplot for the A-1 evaporite in the middle unit of the Bagley reef field. 171
Figure 6-16. Neutron porosity–bulk density crossplot for the A-1 evaporite in the southern unit of the Bagley reef. 172
Figure 6-17. Water saturation histogram of the A-1 evaporite showing a bimodal response to interbedded carbonate and evaporite. 173
Figure 6-18. Neutron porosity–bulk density crossplot for the Brown Niagaran in the northern unit of the Bagley reef field. 175
Figure 6-19. Neutron porosity–bulk density crossplot for the Brown Niagaran in the middle unit of the Bagley reef field. 176
Figure 6-20. Neutron porosity–bulk density crossplot for the Brown Niagaran in the southern unit of the Bagley reef field. 177
Figure 6-21. Water saturation histogram across the Brown Niagaran formation showing an average of 46%. 178
Figure 6-22. Well locations in the Bagley reef field highlighting the locations (in red) of whole core. 180
Figure 6-23. Histogram of the grain density of the Bagley reef field whole core, showing an average of 2.83 g/cm^3 with end members representing salt plugging and anhydrite plugging. 181
Figure 6-24. Porosity-permeability transform of the Bagley reef field using whole core measurements. 182
Figure 6-25. Summary descriptions of core 29074 with representative photographs of each section. 183

Figure 6-26. Simplified stratigraphic column of core 29074 summarizing lithology and structure. 184
Figure 6-27. Summary descriptions of core 29085 with representative photographs of each section. 185
Figure 6-28. Simplified stratigraphic column of core 29085 summarizing lithology and structures. 186
Figure 6-29. Geostatistical workflow applied to Bagley reef field core data. 187
Figure 6-30. Boxplots of gamma ray (A), neutron porosity (B), and bulk density (C) for each formation. 190
Figure 6-31. Boxplot of gamma ray (A), neutron porosity (B), and bulk density (C), for each identified facies. 191
Figure 6-32. Boxplot of gamma ray (A), neutron porosity (B), and bulk density (C) for each zone. 192
Figure 6-33. First-pass Mclust results using three components (gamma ray, neutron porosity, and bulk density) showing eight clusters. 195
Figure 6-34. Kmeans “elbow plots” showing the ideal number of clusters for each component pair. 196
Figure 6-35. Log signatures, whole-core photographs, and core measurements for well 29085 showing a correlation between clusters, log signatures, and whole core. 198
Figure 6-36. Log signatures and whole-core photographs for well 29074 showing a correlation between Mclust clusters and changes in whole core. 199
Figure 6-37. Single well cross section of well 37794 showing Mclust clusters and correlations to log signatures and PNC interpretations. 200
Figure 6-38. Beanplots for gamma ray (A), bulk density (B), and neutron porosity (C), for each cluster. 202
Figure 6-39. Cross section A-A’ across the southern lobe of the Bagley reef field showing interpreted Mclust results. 204
Figure 6-40. Cross section B-B’ across the middle lobe of the Bagley reef field showing interpreted Mclust results. 205
Figure 6-41. Cross section C-C’ across the northern lobe of the Bagley reef field showing interpreted Mclust results. 206
Figure 6-42. Cross section of the northern lobe of the Bagley reef field showing the GR, RHOB, and NPHI for the A-2 carbonate, A-2 evaporite, A-1 carbonate, and Brown Niagaran intervals. 209
Figure 6-43. Cross section of the middle lobe of the Bagley reef field showing the XGR, RHOB, and XNPHI for the A-2 carbonate, A-2 evaporite, A-1 carbonate, A-1 evaporite, and Brown Niagaran intervals. 210
Figure 6-44. Cross section of the southern lobe of the Bagley reef field showing the XGR, RHOB, and XNPHI for the A-2 carbonate, A-2 evaporite, A-1 carbonate, A-1 evaporite, and Brown Niagaran intervals. 211
Figure 6-45. Depositional and flow zone model of the Bagley reef field in map view showing the major subdivisions. 212
Figure 6-46. Cross section through the Bagley reef field showing lithofacies and four reef lobes. 213
Figure 7-1. Cumulative production in the Charlton 19 reef from 1988 through 2017 showing an increase in production rates following EOR operations in 2017. 215
Figure 7-2. Cumulative oil and gas production by well showing the highest producers in the center of the reef pods (hot colors) and poor production along the flanks (cool colors). 216
Figure 7-3. Overview map of the Charlton 19 field showing reef geometry, well locations, and cross section A-A’. 218
Figure 7-4. Neutron porosity and bulk density cross plot of well 42766 showing high density of rock with greater than 5% porosity (red flag) in the A1 Carbonate and Brown Niagaran. 219

Figure 7-5. Water saturation histogram and curve over the A2 Carbonate to the Gray Niagaran for well 42766 in Charlton 19 reef showing high saturations throughout the Brown Niagaran. 220
Figure 7-6. Neutron porosity and bulk density cross plot of well 61197 showing best porosity (red flags) in the lower A1 Carbonate and throughout the Brown Niagaran..... 221
Figure 7-7. Water saturation histogram and curve over the A2 Carbonate through the Brown Niagaran for well 61197 in the Charlton 19 reef showing low water saturation values. 222
Figure 7-8. Neutron porosity and bulk density cross plot of well 41801 showing good porosity (red flags) in the lower A1 Carbonate and Brown Niagaran. 223
Figure 7-9. Water saturation histogram and curve over the A2 Carbonate through the Gray Niagaran for well 41801 in the Charlton 19 reef showing an increase in the Brown Niagaran at the oil water contact. 224
Figure 7-10. Neutron porosity and bulk density crossplot of well 40911 showing the best porosity (red flags) in the lower A1 Carbonate and throughout the Brown Niagaran..... 225
Figure 7-11. Water saturation histogram and curve from the A2 Carbonate through the Gray Niagaran for well 40911 in the Charlton 19 reef field showing an increase mid-Brown Niagaran at the oil water contact. 226
Figure 7-12. Neutron porosity and bulk density cross plot of well 57261 showing best porosity (red flags) in the lower A1 Carbonate and throughout the Brown Niagaran..... 227
Figure 7-13. Water saturation histogram and curve over the A2 Carbonate through the Brown Niagaran for well 57261 in the Charlton 19 reef showing low water saturation values. 228
Figure 7-14. Neutron porosity and bulk density cross plot of El Mac Hills 1-18A showing best porosity (red flags) throughout the Brown Niagaran. 229
Figure 7-15. Water saturation histogram and curve over the A2 Carbonate through the Brown Niagaran for El Mac Hills 1-18A in the Charlton 19 reef showing a high oil water contact in the Brown Niagaran. 230
Figure 7-16. Time horizon surface of the Brown Niagaran showing the geometry of the Charlton 19 reef field. 232
Figure 7-17. Time horizon surface of the A1 Carbonate over the Charlton 19 reef field. 233
Figure 7-18. Time horizon surface for the A2 Carbonate showing gentle slopes around the northern pod of Charlton 19 with a subtle high over the southern pod. 234
Figure 7-19. Lithofacies map of the Brown Niagaran in the Charlton 19 reef field showing two separate reef pods. 235
Figure 7-20. Cross section A-A’ across the Charlton 19 field showing porosity trends in the lower A1 Carbonate and throughout the Brown Niagaran. 236
Figure 7-21. Cross section A-A’ showing interpreted lithofacies in the Charlton 19 reef with a “saddle” region between reef pods. 237
Figure 8-1. Cumulative production in the Dover 35 reef field from 1982 through 2017 showing an increase in production rates after EOR operations began in 2005. 239
Figure 8-2. Cumulative oil and gas production by well showing the highest producers (red) in the center of the reef field with decreasing production along the edges (green). Black outline illustrates edge of reef structure. 240
Figure 8-3. Map of the Dover 35 reef field showing reef geometry and well locations. 241
Figure 8-4. Neutron porosity-bulk density crossplot of well 35941 in the A-2 carbonate to the Brown Niagaran. Green polygon = porosity >5%, red polygon = salt, blue polygon = anhydrite. 243

Figure 8-5. Neutron porosity-bulk density crossplot of well 29236 in the A-2 carbonate to the Brown Niagaran. Green polygon = porosity >5%. 244
Figure 8-6. Neutron porosity-bulk density crossplot of well 29947 in the A-2 carbonate to the Brown Niagaran. Green polygon = porosity >5%. 245
Figure 8-7. Neutron porosity-bulk density crossplot of well 29374 in the A-2 carbonate to the Brown Niagaran. Green polygon = porosity >5%, red polygon = salt. 246
Figure 8-8. Neutron porosity-bulk density crossplot of well 37324 in the A-2 carbonate to the Brown Niagaran. Green polygon = porosity >5%, red polygon = salt, blue polygon = anhydrite. 247
Figure 8-9. Neutron porosity-bulk density crossplot of well 37381 in the A-2 carbonate to the Brown Niagaran. Green polygon = porosity >5%, red polygon = salt, blue polygon = anhydrite. 248
Figure 8-10. Seismic time surface over the Dover 35 (yellow box) and Dover 36 (red box) reef fields for the A-2 carbonate showing faster arrival times over the reef structures..... 250
Figure 8-11. Depositional model of the Dover 35 reef field showing a single reef core (green) with the windward facies (purple) and leeward facies (blue). 251
Figure 8-12. Cross section of the Dover 35 reef field showing the XGR, RHOB, and XNPHI for the A-2 carbonate, A-2 evaporite, A-1 carbonate, A-1 evaporite, and Brown Niagaran intervals. Green represents porosity values >5%, blue represents anhydrite, and red represents salt intervals. 252
Figure 8-13. Cross section of the Dover 35 reef field showing the XGR, RHOB, and XNPHI for the A-2 carbonate, A-2 evaporite, A-1 carbonate, A-1 evaporite, and Brown Niagaran intervals. Colors represent the different lithofacies in the depositional interpretation. 253
Figure 9-1. Cumulative production in the Dover 36 reef field from 1973 through 2017 showing an increase in production rates after EOR operations began in 1997..... 255
Figure 9-2. Cumulative oil and gas production in the Dover 36 reef field showing the highest producer (red), well 52719, in the center of the reef field. 256
Figure 9-3. Map of the Dover 36 reef field showing structural geometry and well locations. 257
Figure 9-4. Neutron porosity-bulk density crossplot of well 29235 in the A-2 carbonate to the Brown Niagaran. Green polygon = porosity >5%, black polygon = secondary features. 259
Figure 9-5. Neutron porosity -bulk density crossplot of well 52719 in the A-2 carbonate to the Brown Niagaran. Green polygon = porosity >5%, red polygon = salt, blue polygon = anhydrite, black polygon = secondary features. 260
Figure 9-6. Neutron porosity-bulk density crossplot of well 29303 in the A-2 carbonate to the Brown Niagaran. Green polygon = porosity >5%, red polygon = salt. 261
Figure 9-7. Neutron porosity-bulk density crossplot of well 29348 in the A-2 carbonate to the Brown Niagaran. Green polygon = porosity >5%. 262
Figure 9-8. Neutron porosity-bulk density crossplot of well 29664 in the A-2 carbonate to the Brown Niagaran. 263
Figure 9-9. Location of cross section A-A’ (blue line) on lithofacies map of the Brown Niagaran formation in the Dover 36 reef field showing three reef pods. Where lithofacies overlap, it is expected both would be present. 266
Figure 9-10. Cross section A-A’ through the Dover 36 reef field showing the XGR, RHOB, and XNPHI for the A-2 carbonate, A-2 evaporite, A-1 carbonate, and Brown Niagaran intervals. Green flags = porosity values >5%, blue flags = anhydrite, red flags = salt intervals, and black flags = secondary features..... 267
Figure 9-11. Cross section A-A’ through the Dover 36 reef field showing three individual reef pods and formations colored by interpreted lithofacies. 268

Figure 10-1. Cumulative production in the Charlton 30/31 reef field from 1974 through 2017 showing an increase in production rates after EOR operations began in 2006. 269
Figure 10-2. Cumulative oil and gas production in the Charlton 30-31 reef field showing the highest production (red) in the northern section of the field. 270
Figure 10-3. Structure map of the Charlton 30-31 reef field showing well locations and trajectories. 271
Figure 10-4. Neutron porosity bulk-density crossplot of well 29073 from the A-2 carbonate to the Brown Niagaran showing thin intervals of porosity in the Brown Niagaran (red). 272
Figure 10-5. Water saturation curve and histogram for well 29073 showing an increase in saturation toward the base of the Brown Niagaran. 273
Figure 10-6. Neutron porosity-bulk density crossplot of well 29989 from the A-2 carbonate to the Brown Niagaran showing porosity greater than 5% in the A-1 carbonate. 274
Figure 10-7. Water saturation curve and histogram for well 29989 showing an increase in water saturation at 5,380 feet MD in the Brown Niagaran formation. 275
Figure 10-8. Neutron porosity-bulk density crossplot of well 30195 from the A-2 carbonate to the Brown Niagaran showing porosity streaks in the Brown Niagaran (red flags) with potential salt plugging (green flags). Red polygon = porosity >5%, green polygon = salt, blue polygon = anhydrite. 276
Figure 10-9. Water saturation curve and histogram for well 30195 showing an increase at 5,530 feet MD in the Brown Niagaran. 277
Figure 10-10. Neutron porosity-bulk density crossplot for well 30203 from the A-2 carbonate to the Brown Niagaran showing porosity greater than 5% (red flags) in the Brown Niagaran. Red polygon = porosity >5%, green polygon = salt, blue polygon = anhydrite. 278
Figure 10-11. Water saturation curve and histogram for well 30203 showing a gradational increase in saturation in the Brown Niagaran before the end of the curve at 6,010 feet MD. 279
Figure 10-12. Neutron porosity-bulk density crossplot of well 31287 from the A-2 carbonate to the Brown Niagaran showing streaks of porosity in the Brown Niagaran (red flags) and a thick package of salt in the A-2 evaporite (green flags). Red polygon = porosity >5%, green polygon = salt. 280
Figure 10-13. Water saturation curve and histogram for well 31287 showing an increase in saturation in the Brown Niagaran at 5,540 feet MD. 281
Figure 10-14. Neutron porosity-bulk density crossplot for well 32605 from the A-2 carbonate to the Brown Niagaran showing intervals of porosity greater than 5% in the lower A-1 carbonate and Brown Niagaran. Red polygon = porosity >5%, green polygon = salt, blue polygon = anhydrite. 282
Figure 10-15. Water saturation curve and histogram for well 32605 showing an increase in water saturation mid-Brown Niagaran at 5,510 feet MD. 283
Figure 10-16. Neutron porosity-bulk density crossplot of well 57916 from the A-2 carbonate to the Brown Niagaran showing thin intervals of porosity >5% in the Brown Niagaran (red) with potential salt plugging (green). Red polygon = porosity >5%, green polygon = salt. 284
Figure 10-17. Water saturation curve and histogram for well 57916 showing a gradational increase in water saturation mid-Brown Niagaran at 5,550 feet MD. 285
Figure 10-18. Neutron porosity-bulk density crossplot of well 59048 from the A-2 carbonate to the Brown Niagaran showing intervals of porosity >5% (red) in the Brown Niagaran. Red polygon = porosity >5%, green polygon = salt, blue polygon = anhydrite. 286

Figure 10-19. Water saturation curve and histogram for well 59048 showing a gradational increase mid-Brown Niagaran near 5,500 feet MD. 287
Figure 10-20. Time horizon surface for the A-2 carbonate showing gentle slopes along the edges of the Charlton 30-31 reef field. 289
Figure 10-21. Time horizon surface for the A-1 carbonate showing gentle slopes and low relief along the edges of the Charlton 30-31 reef field. 290
Figure 10-22. Time horizon surface for the Brown Niagaran showing steep slopes along the edges of the Charlton 30-31 reef field. 291
Figure 10-23. Lithofacies of the Brown Niagaran formation in the Charlton 30-31 reef showing three pods. 293
Figure 10-24. Cross section A-A' running south to north through the Charlton 30-31 reef field showing porosity flags (red and green) throughout the Brown Niagaran with an oil/water contact in the lower Brown Niagaran. 294
Figure 10-25. Cross section B-B' running west to east through the middle of the Charlton 30-31 reef field showing porosity in the Brown Niagaran and a mid-formation oil/water contact. 295
Figure 10-26. Depositional interpretation of the Charlton 30-31 reef field using cross section A-A' showing three closely spaced reefs. 296
Figure 11-1. Cumulative production in the Charlton 6 reef field from 1982 through 2017 showing an increase in production rates after EOR operations began in 2006. 297
Figure 11-2. Cumulative oil and gas production in the Charlton 6 reef field showing highest production (red) in the northernmost well 298
Figure 11-3. Map of the Charlton 6 reef field showing well locations. 300
Figure 11-4. Neutron porosity-bulk density crossplot of well 28895 showing very little porosity with thick salt packages. Red polygon = porosity >5%, green polygon = salt, blue polygon = anhydrite. 302
Figure 11-5. Water saturation curve and histogram for well 28895 showing high saturation values and a strong influence of evaporites on the curve. 303
Figure 11-6. Neutron porosity-bulk density crossplot of well 35209 showing porosity >5% in the Brown Niagaran. Red polygon = porosity >5%, green polygon = salt, blue polygon = anhydrite. 304
Figure 11-7. Neutron porosity-bulk density crossplot of well 59086 showing intervals of porosity >5% in the Brown Niagaran. Red polygon = porosity >5%, green polygon = salt. 305
Figure 11-8. Water saturation curve and histogram for well 59086 showing an increase in water saturation at the base of the Brown Niagaran. 306
Figure 11-9. Time horizon surface for the A-2 carbonate over the Charlton 6 reef field (red square) showing a slight increase in arrival time over the reef complex. 308
Figure 11-10. Seismic time horizons of the A-1 carbonate over the Charlton 6 reef field (red square) showing no significant changes over the reef complex due to similar lithologies. 309
Figure 11-11. Seismic time horizon for the top of the reef structure over the Charlton 6 reef field (red square) showing steep angles along the edges of the reef. 310
Figure 11-12. Lithofacies map of the Brown Niagaran formation in the Charlton 6 reef field showing a single reef core. 311
Figure 11-13. Cross section A-A' through the Charlton 6 reef showing frequent porosity flags in the Brown Niagaran and a low oil/water contact. 312
Figure 11-14. Depositional lithofacies interpretation of the Charlton 6 reef field showing one reef pod. 313

Figure 12-1. Cumulative production in the Chester 2 reef field from 1971 through 2017 showing a slight increase in production after EOR operations began in 2011. 315
Figure 12-2. Cumulative oil and gas production by well in the Chester 2 reef field showing the best producer is well 29430 (red). 316
Figure 12-3. Structural map of the Chester 2 reef field showing well locations. 317
Figure 12-4. Neutron porosity-bulk density crossplot of well 28459 showing porosity in the middle of the Brown Niagaran. Red polygon = porosity >5%, green polygon = salt plugged, blue polygon = anhydrite. 318
Figure 12-5. Water saturation curve and histogram for well 28459 showing an increase in water saturation toward the base of the Brown Niagaran. 319
Figure 12-6. Neutron porosity-bulk density crossplot of well 2845901 showing porosity in the A-2 carbonate and in the middle-lower Brown Niagaran. 320
Figure 12-7. Neutron porosity-bulk density crossplot of well 29430 showing porosity in the middle-lower Brown Niagaran. 321
Figure 12-8. Water saturation curve and histogram for well 29430 showing frequent spikes due to evaporites. 322
Figure 12-9. Neutron porosity-bulk density crossplot of well 29677 showing porosity in the top half of the A-1 carbonate and in the lower Brown Niagaran. 323
Figure 12-10. Water saturation curve and histogram for well 29677 showing an increase in water saturation near the base of the Brown Niagaran at 5,800 feet MD. 324
Figure 12-11. Neutron porosity-bulk density crossplot of well 29958 showing porosity in the top half of the A-1 carbonate and in the lower Brown Niagaran. 325
Figure 12-12. Water saturation curve for well 29958 showing relatively low water saturations throughout the intervals of interest. 326
Figure 12-13. Neutron porosity-bulk density crossplot of well 60596 showing high-porosity dolomite in the Brown Niagaran in the northern section of the well. Red polygon = porosity >5%, green polygon = salt, blue polygon = anhydrite. 327
Figure 12-14. Water saturation curve and histogram for well 60596 showing frequent spikes due to the presence of evaporites throughout the formations of interest. 328
Figure 12-15. Time horizon surface for the Brown Niagaran showing steep slopes along the edges of the Chester 2 reef field. 330
Figure 12-16. Time horizon surface for the A-1 carbonate showing no relief across the Chester 2 reef field due to similar velocities between the A-1 carbonate and Brown Niagaran. 331
Figure 12-17. Time horizon surface for the A-2 carbonate showing gentle slopes along the edges of the Chester 2 reef field. 332
Figure 12-18. Time horizon surface with sections of 3D seismic data and the trajectory of the Cargas well showing a porous zone (red polygon). 333
Figure 12-19. Photographs of whole core from Chester 2 showing tight limestone with salt filled vugs and fractures. 334
Figure 12-20. Histogram of the grain density for the Brown Niagaran from whole core analysis of well 28459. 335
Figure 12-21. Histogram of the bulk density for the Brown Niagaran from whole core analysis of well 28459. 336
Figure 12-22. Porosity-permeability transform for the A-1 carbonate, A-1 evaporite, and Brown Niagaran from whole core measurements from well 28459. 337
Figure 12-23. Map view of lithofacies and lithology extents in the Chester 2 reef field and locations of cross sections A-A’ (red) and B-B’(black). 338

Figure 12-24. Single-well cross section of horizontal well 60596 as it cuts through the Chester 2 reef field. The red rectangle highlights a high-porosity interval which has been identified in the dolomitized zone. 339
Figure 12-25. Cross section A-A' along the western side of the Chester 2 reef field showing a highly dolomitized zone to the north and little porosity to the south. 340
Figure 12-26. Cross section B-B' running west to east through the Chester 2 reef showing the changes in formation thickness transitioning from leeward to reef core positions along with the increased porosity in the dolomitized section in well 29430. 341
Figure 12-27. 3D interpretation of the dolomitized zone (green) within the Chester 2 reef field showing well locations and trajectories through the 3D volume. 342
Figure 13-1. Cumulative production in the Chester 5/6 reef field from 1973 through 2017 showing a slight increase in production rates after EOR operations began in 2011. 343
Figure 13-2. Cumulative oil and gas production by well in the Chester 5-6 reef showing the best producer (red) to be well 29067 and cross section line A-A'. 344
Figure 13-3. Structure map of the Chester 5-6 reef field showing well locations. 345
Figure 13-4. Neutron porosity-bulk density crossplot of well 29067 showing porosity in the upper A-1 carbonate and the lower Brown Niagaran with potential polyhalite. Red polygon = porosity >5%, tan polygon = polyhalite. 346
Figure 13-5. Water saturation curve and histogram for well 29067 showing a highly water-saturated well. 347
Figure 13-6. Neutron porosity-bulk density crossplot of well 29234 showing porosity flags in the lower A-1 carbonate. Red polygon = porosity >5%. 348
Figure 13-7. Water saturation curve and histogram for well 29234 showing high saturation values and a distinct shift toward the base of the A-1 carbonate 349
Figure 13-8. Neutron porosity-bulk density crossplot of well 29265 showing porosity flags in the lower A-1 carbonate. Red polygon = porosity >5%. 350
Figure 13-9. Water saturation curve and histogram for well 29265 showing high saturation values and an oil/water contact at 5,680 feet MD. 351
Figure 13-10. Neutron porosity-bulk density crossplot of well 31515 showing porosity flags throughout the A-1 carbonate and top of Brown Niagaran. Red polygon = porosity >5%, blue polygon = anhydrite. 352
Figure 13-11. Neutron porosity-bulk density crossplot of well 40169 showing porosity flags in the upper Brown Niagaran. Red polygon = porosity >5%, green polygon = salt, blue polygon = anhydrite. 353
Figure 13-12. Water saturation curve and histogram for well 40169 showing high water saturations throughout. 354
Figure 13-13. Histogram of grain density of the Chester 5-6 reef field. 356
Figure 13-14. Porosity-permeability transform of the Chester 5-6 reef field using whole core measurements. 357
Figure 13-15. Lithofacies interpretation of the Chester 5-6 reef field showing potential locations of reef core, windward facies, and leeward facies. Blue line illustrates cross section line A-A' 358
Figure 13-16. Cross section A-A' across the Chester 5-6 reef field showing porosity trends in the upper A-1 carbonate and a high oil/water contact. 359
Figure 13-17. Cross section through Chester 5-6 showing lithofacies interpretation with two reef pods represented. 360

Figure 14-1. Plot of mean and variance for (a) Poisson's ratio (b) Shear Modulus (c) Bulk Modulus (d) Young's Modulus. Formation type number in the figure: 1: Salina, 2: A-2 Carbonate, 3: A-2 Evaporate, 4: A-1 Carbonate, 5: Brown Niagaran, 6: Gray Niagaran. 365
Figure 14-2. Example of DIF recorded on acoustic image of Chester 6-16. 369
Figure 14-3. Image log interpretation of induced fracture after mini-frac test of A-1 Carbonate (upper) and the Brown Niagara (lower) in the 8-16 well. SH_{max} orientation is N62E and N6E. 370
Figure 14-4. Depth plot of fast shear wave anisotropy for Lawnichak 9-33. The depth and formation interval for each zone is mentioned in Table 14-2. 371
Figure 14-5. Depth plot of fast shear wave anisotropy for Chester 8-16. 372
Figure 14-6. Fast shear wave azimuth distribution in Lawnichak 9-33 in all zones mentioned in Table 14-3. 374
Figure 14-7. Fast shear wave azimuth distribution in Chester 8-16 in all zones mentioned in Table 14-4. 374
Figure 14-8. Direction of fast shear wave induced by in-situ stress (left) and fractured zones (right). 375
Figure 14-9. Example of natural fractures in Lawnichak 9-33 (1st track: depth, 2nd track: bedding azimuth, 3rd track: fracture azimuth, 4th track: fracture count). 376
Figure 14-10. Histogram diagram of bedding and natural fracture azimuth in Lawnichak 9-33 (bedding mean azimuth of 68 and fracture azimuth of 61). 377
Figure 14-11. Calculated vertical stress magnitude with depth for Lawnichak 9-33 and Cargas 3-2 HD1. 379
Figure 14-12. Calculated total vertical stress magnitude with depth for El Mac Hills 1-18A and Chester 6-16. 380
Figure 14-13. Calculated total vertical stress magnitude with depth for Chester 8-16. 381
Figure 14-14. (A) Reservoir section in Geomechanics model (B) soft caprock and hard reservoir (C) equal Young's modulus of caprock and reservoir (D) 3D schematic of geomechanical model grid. 382
Figure 14-15. Changes in Sh_{min}, stress increase, (top) and Sv, K stress increase, (bottom) as a function of pressure increase. 383
Figure 14-16. Relationship between static and dynamic Young's modulus (b) Relationship between static and dynamic Poisson's Ratio. 388
Figure 14-17. Relationship between static Young's modulus and compressive strength. 388
Figure 14-18. Mohr-Coulomb failure analysis. 391
Figure 14-19. Mohr-Coulomb failure analysis. 392
Figure 15-1. RCX configured with single snorkel above straddle packer. 396
Figure 15-2. Basic pressure testing involving multiple cycles to determine a representative pressure. 396
Figure 15-3. Schematic of straddle packer and an observation probe combination for a VIT (also referred to as LIT). 397
Figure 15-4. Expected flow regimes for a mini-DST (no observation probe). Radial flow provides an estimate of horizontal permeability (kxy); spherical flow is a function of horizontal and vertical permeability and can be used to isolate vertical permeability if radial flow develops. 398
Figure 15-5. Schematic of VIT: tool diagram. 398
Figure 15-6. Schematic of VIT: example pressure data from straddle packer interval and observation probe (top panel) and pressure/derivative for both intervals (bottom panel). 399

Figure 15-7. Illustration of a typical micro-frac test in which multiple injection-recovery cycles are performed. 400
Figure 15-8. Schematic of IFX absorbance analysis. 401
Figure 15-9. Output from spectral absorbance analysis. 402
Figure 15-10. Example output from tuning fork (density and viscosity) and transducer (sound speed). 402
Figure 15-11. Packers available for the Baker Hughes RCX single packer probe used to measure reservoir pressure. 404
Figure 15-12. Pumping rate and pressure response in the straddle packer interval during VIT-22. 405
Figure 15-13. PTA of VIT-22; log-log diagnostic plot of straddle packer (blue symbols) pressure response during VIT-22 buildup period, solid lines are shown for wellbore storage (slope = 1), spherical flow (slope = -1) and radial flow (slope = 0) in the straddle packer interval. 406
Figure 15-14. Matching of straddle packer data in log-log plot in VIT-22 using “partially completed well in an infinitely acting homogeneous reservoir” model. 407
Figure 15-15. Pressure history match of test interval data for the entire VIT-22. 408
Figure 15-16. Model input parameters and reservoir properties from the model history match analysis for VIT-22. 408
Figure 15-17. Pumping rate and pressure response in the straddle packer interval during VIT-23. 409
Figure 15-18. PTA of VIT-23; log-log diagnostic plot of straddle packer (blue symbols) pressure response during VIT-23 buildup period; solid lines are shown for wellbore storage (slope = 1) and spherical flow (slope = -1). 410
Figure 15-19. Matching of straddle packer data in log-log plot in VIT-23; panel a shows a constant pressure boundary model; panel b shows a radial composite model. 411
Figure 15-20. Pressure history match of the VIT-23 pumping and buildup periods (both models produce similar results). 412
Figure 15-21. Model input parameters and reservoir properties from the model history match analysis for VIT-23 (constant pressure boundary model and radial composite model). 412
Figure 15-22. Pumping rate and pressure response in the straddle packer interval during VIT-24. 413
Figure 15-23. Log-log diagnostic plot of the straddle packer (blue symbols) pressure response during VIT-24 buildup period, plus modeled pressure and pressure derivative (solid lines) in the straddle packer interval. 414
Figure 15-24. Comparison of observed pressure (blue squares) and pressure derivative (blue triangles) data to modeled pressure and pressure derivative (red lines) for the VIT-24 buildup period. 415
Figure 15-25. Pressure history match of the VIT-24 pumping and buildup periods. 415
Figure 15-26. Model input parameters and reservoir properties from the model history match analysis for VIT-24. 416
Figure 15-27. Pumping rate and pressure response in the straddle packer interval during VIT-25. 417
Figure 15-28. Log-log diagnostic plot of the straddle packer (blue symbols) pressure response during VIT-25 buildup period. 418
Figure 15-29. Comparison of observed pressure (blue squares) and pressure derivative (blue triangles) data to modeled pressure and pressure derivative (red lines) for the VIT-25 buildup period. 419
Figure 15-30. Pressure history match of the VIT-25 pumping and buildup periods. 420
Figure 15-31. Model input parameters and reservoir properties from the model history match analysis for VIT-25. 420
Figure 15-32. Absorbance spectrum for filtrate (top) and sample (bottom) for Station #1. 423

Figure 15-33. Channel subtraction (16-15) for hydrocarbon identification (green curve), gas indicator channel subtraction (M1-M2) (red), and water indicator channel subtraction (14-13) (blue) during pumping and buildup for Station #1. 423
Figure 15-34. CO_2 channel (CH21-CH15) showing a reading of 0.4 or higher during pumping, indicating the presence of CO_2 gas at Station #1. 424
Figure 15-35. Absorbance spectrum for filtrate (top) and sample (bottom) for Station #2. 425
Figure 15-36. Channel subtraction (16-15) for hydrocarbon identification (green curve), gas indicator channel subtraction (M1-M2) (red), and water indicator channel subtraction (14-13) (blue) during pumping and buildup for Station #2. 425
Figure 15-37. Absorbance spectrum for filtrate (top panel) and sample (bottom panel) for Station #3. 426
Figure 15-38. Channel subtraction (16-15) for hydrocarbon identification (green curve), gas indicator channel subtraction (M1-M2) (red), and water indicator channel subtraction (14-13) (blue) during pumping and buildup for Station #3. 427
Figure 15-39. Absorbance spectrum for filtrate (top panel) and sample (bottom panel) for Station #4. 428
Figure 15-40. Channel subtraction (16-15) for hydrocarbon identification (green curve), gas indicator channel subtraction (M1-M2) (red), and water indicator channel subtraction (14-13) (blue) during pumping and buildup for Station #4. 428
Figure 15-41. CO_2 channel (CH21-CH15) showing a reading of 0.4 or higher during pumping, indicating the presence of CO_2 gas at Station #4. 429
Figure 15-42. Reservoir pressures (yellow diamonds) measured with Baker Hughes RCX tool. 431
Figure 15-43. Pumping rate and pressure response in the straddle packer interval during LIT-1. 432
Figure 15-44. Pressure response at the observation probe during LIT-1. 433
Figure 15-45. Log-log diagnostic plot of straddle packer (blue symbols) and observation probe (green symbols) pressure response during LIT-1 showing modeled response at the straddle packer (red line) and observation probe (green line). 434
Figure 15-46. Pressure history match of test interval data (top panel) and observation probe data (bottom panel) for the entire LIT-1. 434
Figure 15-47. Model input parameters and reservoir properties from the model history match analysis for LIT-1. 435
Figure 15-48. Pumping rate and pressure response in the straddle packer interval during LIT-2. 436
Figure 15-49. Pressure response at the observation probe during LIT-2. 436
Figure 15-50. Log-log diagnostic plot of straddle packer (blue symbols) and observation probe (green symbols) pressure response during LIT-2 buildup period. 437
Figure 15-51. Comparison of observed pressure (blue squares) and pressure derivative (blue triangles) data to modeled pressure and pressure derivative (red lines) for the LIT-2 buildup period. 438
Figure 15-52. Pressure history match of the LIT-2 pumping and buildup periods. 438
Figure 15-53. Model input parameters and reservoir properties from the model history match analysis for LIT-2. 439
Figure 15-54. Test history for micro-frac test 1 in the A-1 Carbonate at 5861 ft MD. 441
Figure 15-55. Fracture breakdown pressure during FOT1 of micro-frac test 1. 442
Figure 15-56. Example square root of shut-in-time plot for fracture closure identification in station 1/cycle 1. 443
Figure 15-57. Example log-log of shut-in time plot for fracture closure identification in station 1/cycle 1. 444
Figure 15-58. Example G-function of shut-in time plot for fracture closure identification in station 1/cycle 1. 444

Figure 15-59. Test history for micro-frac test 2 in the Brown Niagaran at 5967 ft MD. 446
Figure 15-60. Fracture breakdown pressure during the FOT1 of micro-frac test 2. 447
Figure 15-61. Test history for micro-frac test 3 in the A-2 Carbonate at 5791 ft MD. 449
Figure 15-62. Test history for micro-frac test 4 in the A-2 Carbonate at 5765 ft MD. 450
Figure 15-63. Fracture breakdown pressure during the first injection cycle of micro-frac test 4. 451
Figure 15-64. Image log interpretation of induced fracture after mini-frac test of Station 1 (A-1 Carbonate, upper) and Station 2 (Brown Niagaran, lower) in the 8-16 well. SH_{max} orientation is N62E and N6E. 453
Figure 15-65. Calibration of log-derived stress parameters using measurements from micro-frac testing (see tracks 8 through 12) for the depth interval 5735 to 6455 ft in the 8-16 well. Calibration points from the micro-frac testing are shown in tracks 8 and 9. Note low values of Sh_{min} in the A-1 Carbonate and Brown Niagaran reservoir (sample points below 5850 ft) due to depleted pressure resulting from primary production compared to A-2 Carbonate caprock (sample points above 5850 ft). 455
Figure 15-66. Transmissivity values determined from four VITs in the 9-33 well, Dover 33 reef. Each symbol represents a different sample. 457
Figure 15-67. Permeability calculated from transmissivity values determined from four VITs in the 9-33 well, Dover 33 reef (assuming h = 100 ft) compared to core permeability. 458
Figure 15-68. Transmissivity values determined from two LITs in the 8-16 well, Chester 16 reef. 460
Figure 15-69. Permeability calculated from transmissivity values determined from two LITs in the 8-16 well, Chester 16 reef (assuming h = 20 ft) compared to core permeability. 461
Figure 15-70. Schematic of the Chester 16 reef showing reservoir geometry. 463
Figure 15-71. Sh_{min} changes as a function of pore pressure. 464
Figure 15-72. Effective Sh_{min} changes as a function of pore pressure. Initial Sh_{min} of 1799 psi and pore pressure of 528 psi (Table 15-18) is used to calculate Sh_{min} at higher pressures. 464
Figure 16-1. Reef properties, attributes, lithofacies, production, and reservoir pattern by reef. Green= reef core, purple= windward, and blue= leeward lithofacies. 471
Figure 16-2. Comparison of average porosity, NTG ratio, and percent recovery by reef. Along the horizontal axis, light purple shading (left) = dolomitic, light blue shading (right) = limestone, and lavender (center) = mixed carbonate. 472
Figure 16-3. Reservoir ranking plot of reefs using diagenesis and salt plugging rank with average porosity. 473
Figure 16-4. Reservoir ranking plot of reefs using diagenesis and salt plugging rank with percent oil recovery. 474
Figure A-1. Silurian Northern Pinnacle Reef Trend within the Michigan Basin (modified from Rine, 2015 and Burgess and Benson, 1969). A-1
Figure A-2. Lithostratigraphy of the Silurian Niagara reef interval, left (after Gill 1973, 1979; and Huh 1973), and comparison of formal and informal lithostratigraphic names, right (modified from Trout 2012). A-2
Figure A-3. Main structural elements and age of bedrock in the Michigan Basin (Modified from Rine, 2015 and Catacosinos et al., 1991). A-3
Figure A-4. Major faults in the Michigan Basin. (Modified from Esch, 2010; Cox and Barnes, 2016). A-3
Figure A-5. Lineaments and anticlinal traces in the Michigan Basin area. Labeled faults: AS=Albion-Scipio, HL=Howell, LM=Lucas-Monroe, SC=Sanilac (Modified from Grammer and Harrison, 2013). A-4
Figure A-6. Geometry of reservoirs and seals in the interval of interest. Modified from Rine, 2015a and Rine et al., 2017. ..... A-5

Figure A-7. Geometry of a seismic-scale sequence with three depositional systems tracts (modified after Vail 1987; Christie-Blick and Driscoll 1995). Mfs is maximum flooding surface. A-6
Figure A-8. Comparison of three-tract and four-tract sequence stratigraphic depositional models. Note that deposits formed during sea level fall are included in the lower sequence in the four-tract model. Modified from Catuneanu et al., 2011. ..... A-7
Figure A-9. Hierarchical nature of sequence stratigraphic depositional packages interpreted in the Miller –Fox 1-11 well, Oceana County. Interpretation is based on cored lithofacies, unconformities, flooding surfaces, marine hardgrounds, and wireline-log signatures. Numbered intervals represent lithofacies; red and blue triangles represent upward shallowing and deepening depositional stacking patterns (Modified from Ritter, 2008). A-8
Figure A-10. Carbonate lithofacies, as used in this study, based on classification by Dunham (1962), revised and expanded by Embry and Klovan (1971). A-9
Figure A-11. Location of reefs in Northern and Southern Reef trends mentioned in text. Modified from Miller et al. (2014) and Rine et al. (2017). A-10
Figure A-12. Interpreted third order sequences in a reef flank well (left) and on-reef well (right) from the Dover 33 reef, which lacks core, along with key to interpreted lithofacies. From Miller et al., 2014. These sequence boundaries can be now be adjusted to match recent correlations to additional cored wells by Rine et al., 2017, and Rine et al., 2018. ..... A-11
Figure A-13. Relation of the Mulde1 carbon isotope excursion to Niagaran depositional reef facies in the Columbus 3 Reef. Locations of unconformable surfaces are shown in red. Figure is courtesy of Matt Rine. A-12
Figure A-14. New sequence stratigraphic interpretation of the A-1 Carbonate. Modified from Rine et al. (2018). A-13
Figure A-15. Comparison of the sequence stratigraphic subdivisions of A) Ritter (2008); (B) Miller et al. (2014), and (C) Rine (2015a), Rine et al. (2017), and Rine et al. (2018), projected onto Huh's (1973) reef model. Subdivisions in C are considered in this report to be most correct. A-14
Figure A-16. Simplified geometry and lithofacies distribution in Niagaran reefs by Huh (A) and Gill (B). As shown, these models do not address differences in windward and leeward reef morphologies or facies zonation. Modified from Rine et al. (2017). A-15
Figure A-17. Niagaran faunal zonation of the Ray Reef in the Southern Reef trend. **Unid** is unidentified skeletal material (Modified from Trout 2012). A-17
Figure A-18. Comparison of depositional facies belts identified by Gill (1973) and Rine et al. (2017) in the Columbus III reef (St Clair County) in the Belle River Mills Field. Cross section E-E' is shown in the following Figure. Modified from Rine (2015a) and Rine et al. (2017) A-18
Figure A-19. Comparison of vertical depositional facies distribution and interpreted external reef morphology of the Columbus III reef, Belle River Mills, St. Clair County. Modified from Rine et al. (2017). A-18
Figure A-20. Realms and processes of carbonate diagenesis. Modified from Moore and Wade (2013) A-20
Figure A-21. Carbonate porosity types (modified from Choquette and Pray 1970) A-21
Figure A-22. Petrophysical carbonate porosity classification (after Lucia, 1995). Resulting permeability and reservoir performance depends on connectivity of all porosity systems. A-21

Figure A-23. Relative timing of diagenetic processes identified in the northern reef trend with increasing time towards the right. Modified from Cercone (1984) and Cercone and Lohmann (1985, 1987). A-22
Figure A-24. Major types of dolomitization. Modified from Machel, 2004. ..... A-25
Figure A-25. Generalized distribution of carbonate lithologies in the Niagaran reefs. Modified from Rine 2015b. A-26
Figure A-26. Distribution of limestone and dolomite lithology in three wells from the Chester 16 reef. Modified from Rine 2015b. A-27
Figure A-27. Comparison of Niagaran reef porosity and permeability in dolomite and limestone whole core samples, grouped by (A) reef-core and (B) leeward grain-apron depositional facies. The Kalkaska 1-21 (28676) is located in Kalkaska County. Modified from Rine, 2015b. A-28
Figure A-28. Effect of salt plugging on reef-core samples from the Columbus III field in the Southern Reef Trend. Modified from Rine, 2015b. A-29
Figure A-29. Faults and documented hydrothermal dolomite in Northern Michigan fields. Modified from Woods and Harrison (2002). A-30
Figure B-1. Nomenclature and symbology used to describe whole and sidewall cores analyzed under tasks 3, 4, and 5. ..... B-1
Figure B-2. Rotary sidewall core (RSWC) abbreviation explanation B-2
Figure B-3. Compiled illustration of lithology log, core photos (UV and white light), CT scan image, core descriptions, and annotated core images of the A-1 Carbonate for depths 5,525 ft. to 5,528 ft. B-3
Figure B-4. Compiled illustration of lithology log, core photos (UV and white light), CT scan image, core descriptions, and annotated core images of the A-1 Carbonate for depths 5,528 ft. to 5,531 ft. B-4
Figure B-5. Compiled illustration of lithology log, core photos (UV and white light), CT scan image, core descriptions, and annotated core images of the A-1 Carbonate for depths 5,531 ft. to 5,534 ft. B-5
Figure B-6. Compiled illustration of lithology log, core photos (UV and white light), CT scan image, core descriptions, and annotated core images of the A-1 Carbonate for depths 5,534 ft. to 5,537 ft. B-6
Figure B-7. Compiled illustration of lithology log, core photos (UV and white light), CT scan image, core descriptions, and annotated core images of the A-1 Carbonate for depths 5,537 ft. to 5,540 ft. B-7
Figure B-8. Compiled illustration of lithology log, core photos (UV and white light), CT scan image, core descriptions, and annotated core images of the A-1 Carbonate for depths 5,540 ft. to 5,543 ft. B-8
Figure B-9. Compiled illustration of lithology log, core photos (UV and white light), CT scan image, core descriptions, and annotated core images of the A-1 Carbonate for depths 5,543 ft. to 5,546 ft. B-9
Figure B-10. Compiled illustration of lithology log, core photos (UV and white light), CT scan image, core descriptions, and annotated core images of the Brown Niagaran for depths 5,546 ft. to 5,549 ft. B-10
Figure B-11. Compiled illustration of lithology log, core photos (UV and white light), CT scan image, core descriptions, and annotated core images of the Brown Niagaran for depths 5,549 ft. to 5,552 ft. B-11
Figure B-12. Compiled illustration of lithology log, core photos (UV and white light), CT scan image, core descriptions, and annotated core images of the Brown Niagaran for depths 5,552 ft. to 5,555 ft B-12

Figure B-13. Compiled illustration of lithology log, core photos (UV and white light), CT scan image, core descriptions, and annotated core images of the Brown Niagaran for depths 5,555 ft. to 5,558 ft. B-13
Figure B-14. Compiled illustration of lithology log, core photos (UV and white light), CT scan image, core descriptions, and annotated core images of the Brown Niagaran for depths 5,559 ft. to 5,562 ft. B-14
Figure B-15. Compiled illustration of lithology log, core photos (UV and white light), CT scan image, core descriptions, and annotated core images of the Brown Niagaran for depths 5,562 ft. to 5,565 ft. B-15
Figure B-16. Compiled illustration of lithology log, core photos (UV and white light), CT scan image, core descriptions, and annotated core images of the Brown Niagaran for depths 5,598 ft. to 5,601 ft. B-16
Figure B-17. Compiled illustration of lithology log, core photos (UV and white light), CT scan image, core descriptions, and annotated core images of the Brown Niagaran for depths 5,601 ft. to 5,604 ft. B-17
Figure B-18. Compiled illustration of lithology log, core photos (UV and white light), CT scan image, core descriptions, and annotated core images of the Brown Niagaran for depths 5,604 ft. to 5,607 ft. B-18
Figure B-19. Compiled illustration of lithology log, core photos (UV and white light), CT scan image, core descriptions, and annotated core images of the Brown Niagaran for depths 5,607 ft. to 5,610 ft. B-19
Figure B-20. Compiled illustration of lithology log, core photos (UV and white light), CT scan image, core descriptions, and annotated core images of the Brown Niagaran for depths 5,690 ft. to 5,693 ft. B-20
Figure B-21. Compiled illustration of lithology log, core photos (UV and white light), CT scan image, core descriptions, and annotated core images of the Brown Niagaran for depths 5,693 ft. to 5,696 ft. B-21
Figure B-22. Compiled illustration of lithology log, core photos (UV and white light), CT scan image, core descriptions, and annotated core images of the Brown Niagaran for depths 5,696 ft. to 5,699 ft. B-22
Figure B-23. Compiled illustration of lithology log, core photos (UV and white light), CT scan image, core descriptions, and annotated core images of the Brown Niagaran for depths 5,699 ft. to 5,702 ft. B-23
Figure B-24. Compiled illustration of lithology log, core photos (UV and white light), CT scan image, core descriptions, and annotated core images of the Brown Niagaran for depths 5,702 ft. to 5,705 ft. B-24
Figure B-25. Compiled illustration of lithology log, core photos (UV and white light), CT scan image, core descriptions, and annotated core images of the Brown Niagaran for depths 5,705 ft. to 5,708 ft. B-25
Figure B-26. Compiled illustration of lithology log, core photos (UV and white light), CT scan image, core descriptions, and annotated core images of the Brown Niagaran for depths 5,708 ft. to 5,711 ft. B-26
Figure B-27. Compiled illustration of lithology log, core photos (UV and white light), CT scan image, core descriptions, and annotated core images of the Brown Niagaran for depths 5,711 ft. to 5,714 ft. B-27
Figure B-28. Compiled illustration of lithology log, core photos (UV and white light), CT scan image, core descriptions, and annotated core images of the Brown Niagaran for depths 5,714 ft. to 5,717 ft. B-28

Figure B-29. Compiled illustration of lithology log, core photos (UV and white light), CT scan image, core descriptions, and annotated core images of the Brown Niagaran for depths 5,718 ft. to 5,721 ft. B-29
Figure B-30. Compiled illustration of lithology log, core photos (UV and white light), CT scan image, core descriptions, and annotated core images of the Brown Niagaran for depths 5,721 ft. to 5,724 ft. B-30
Figure B-31. Compiled illustration of lithology log, core photos (UV and white light), CT scan image, core descriptions, and annotated core images of the Brown Niagaran for depths 5,724 ft. to 5,727 ft. B-31
Figure B-32. Compiled illustration of lithology log, core photos (UV and white light), CT scan image, core descriptions, and annotated core images of the Brown Niagaran for depths 5,727 ft. to 5,730 ft. B-32
Figure B-33. Compiled illustration of lithology log, core photos (UV and white light), CT scan image, core descriptions, and annotated core images of the Brown Niagaran for depths 5,730 ft. to 5,733 ft. B-33
Figure B-34. Compiled illustration of lithology log, core photos (UV and white light), CT scan image, core descriptions, and annotated core images of the Brown Niagaran for depths 5,733 ft. to 5,736 ft. B-34
Figure B-35. Compiled illustration of lithology log, core photos (UV and white light), CT scan image, core descriptions, and annotated core images of the Brown Niagaran for depths 5,736 ft. to 5,739 ft. B-35
Figure B-36. Compiled illustration of lithology log, core photos (UV and white light), CT scan image, core descriptions, and annotated core images of the Brown Niagaran for depths 5,739 ft. to 5,742 ft. B-36
Figure B-37. Compiled illustration of lithology log, core photos (UV and white light), CT scan image, core descriptions, and annotated core images of the Brown Niagaran for depths 5,742 ft. to 5,745 ft. B-37
Figure B-38. Compiled illustration of lithology log, core photos (UV and white light), CT scan image, core descriptions, and annotated core images of the Brown Niagaran for depths 5,745 ft. to 5,748 ft. B-38
Figure B-39. Compiled illustration of lithology log, core photos (UV and white light), CT scan image, core descriptions, and annotated core images of the Brown Niagaran for depths 5,748 ft. to 5,751 ft. B-39
Figure B-40. Compiled illustration of lithology log, core photos (UV and white light), CT scan image, core descriptions, and annotated core images of the Brown Niagaran for depths 5,749 ft. to 5,752 ft. B-40
Figure B-41. Compiled illustration of lithology log, core photos (UV and white light), CT scan image, core descriptions, and annotated core images of the Brown Niagaran for depths 5,752 ft. to 5,755 ft. B-41
Figure B-42. Compiled illustration of lithology log, core photos (UV and white light), CT scan image, core descriptions, and annotated core images of the Brown Niagaran for depths 5,755 ft. to 5,758 ft. B-42
Figure B-43. Compiled illustration of lithology log, core photos (UV and white light), CT scan image, core descriptions, and annotated core images of the Brown Niagaran for depths 5,758 ft. to 5,761 ft. B-43
Figure B-44. Annotated RSWC images with corresponding core descriptions of the A-2 Carbonate for depths 5,330 ft. to 5,330.5 ft. B-44
Figure B-45. Annotated RSWC images with corresponding core descriptions of the A-2 Carbonate for depths 5,374 ft. to 5,374.5 ft. B-45

Figure B-46. Annotated RSWC images with corresponding core descriptions of the A-2 Carbonate for depths 5,378 ft. to 5,390 ft. B-46
Figure B-47. Annotated RSWC images with corresponding core descriptions of the A-2 Carbonate and A-2 Evaporite for depths 5,393 ft. and 5,409 ft. B-47
Figure B-48. Annotated RSWC images with corresponding core descriptions of the A-2 Evaporite for depths 5,415 ft. and 5,430 ft. B-48
Figure B-49. Annotated RSWC images with corresponding core descriptions of the A-2 Evaporite for depths 5,440 ft. and 5,451 ft. B-49
Figure B-50. Annotated RSWC images with corresponding core descriptions of the A-2 Evaporite and A-1 Carbonate for depths 5,454 ft. to 5,455 ft. B-50
Figure B-51. Annotated RSWC images with corresponding core descriptions of the A-1 Carbonate for depths 5,456 ft. to 5,458 ft. B-51
Figure B-52. Annotated RSWC images with corresponding core descriptions of the A-1 Carbonate for depths 5,465 ft. to 5,467 ft. B-52
Figure B-53. Annotated RSWC images with corresponding core descriptions of the A-1 Carbonate for depths 5,472 ft. to 5,477 ft. B-53
Figure B-54. Annotated RSWC images with corresponding core descriptions of the A-1 Carbonate for depths 5,482 ft. to 5,485 ft. B-54
Figure B-55. Annotated RSWC images with corresponding core descriptions of the A-1 Carbonate for depths 5,490 ft. to 5,495 ft. B-55
Figure B-56. Annotated RSWC images with corresponding core descriptions of the A-1 Carbonate for depths 5,503 ft. and 5,509 ft. B-56
Figure B-57. Annotated RSWC images with corresponding core descriptions of the A-1 Carbonate for depths 5,511 ft. to 5,514 ft. B-57
Figure B-58. Annotated RSWC images with corresponding core descriptions of the A-1 Carbonate for depths 5,520 ft. to 5,523 ft. B-58
Figure B-59. Annotated RSWC images with corresponding core descriptions of the Brown Niagaran for depths 5,570 ft. and 5,576.5 ft. B-59
Figure B-60. Annotated RSWC images with corresponding core descriptions of the Brown Niagaran for depths 5,580 ft. to 5,583 ft. B-60
Figure B-61. Annotated RSWC images with corresponding core descriptions of the Brown Niagaran for depths 5,587.5 ft. to 5,588 ft. B-61
Figure B-62. Annotated RSWC images with corresponding core descriptions of the Brown Niagaran for depths 5,595 ft. and 5,608 ft. B-62
Figure B-63. Annotated RSWC images with corresponding core descriptions of the Brown Niagaran for depths 5,615 ft. and 5,625 ft. B-63
Figure B-64. Annotated RSWC images with corresponding core descriptions of the Brown Niagaran for depths 5,627 ft. to 5,630 ft. B-64
Figure B-65. Annotated RSWC images with corresponding core descriptions of the Brown Niagaran for depths 5,633 ft. and 5,639 ft. B-65
Figure B-66. Annotated RSWC images with corresponding core descriptions of the Brown Niagaran for depths 5,643 ft. to 5,647.5 ft. B-66
Figure B-67. Annotated RSWC images with corresponding core descriptions of the Brown Niagaran for depths 5,655 ft. and 5,663 ft. B-67
Figure B-68. Annotated RSWC images with corresponding core descriptions of the Brown Niagaran for depths 5,665.5 ft. to 5,669 ft. B-68
Figure B-69. Annotated RSWC images with corresponding core descriptions of the Brown Niagaran for depths 5,676 ft. and 5,685 ft. B-69

Figure B-70. Annotated RSWC images with corresponding core descriptions of the Brown Niagaran for depths 5,773 ft. and 5,782 ft. B-70
Figure B-71. Annotated RSWC images with corresponding core descriptions of the Brown Niagaran for depths 5,793 ft. and 5,800 ft. B-71
Figure B-72. Annotated RSWC images with corresponding core descriptions of the Brown Niagaran for depths 5,805 ft. and 5,815 ft. B-72
Figure B-73. Annotated RSWC images with corresponding core descriptions of the Brown Niagaran for depths 5,817 ft. to 5,820 ft. B-73
Figure B-74. Annotated RSWC images with corresponding core descriptions of the Brown Niagaran for depths 5,830 ft. to 5,833 ft. B-74
Figure B-75. Annotated RSWC images with corresponding core descriptions of the Brown Niagaran for depths 5,847 ft. and 5,865 ft. B-75
Figure B-76. Annotated RSWC images with corresponding core descriptions of the Brown Niagaran and Gray Niagaran for depths 5,867 ft. to 5,868 ft. B-76
Figure B-77. Annotated RSWC images with corresponding core descriptions of the Gray Niagaran for depths 5,873 ft. to 5,899 ft. B-77
Figure B-78. Compiled illustration of lithology log, core photos (UV and white light), CT scan image, core descriptions, and annotated core images of the Brown Niagaran for depths 6,148 ft. to 6,150 ft. B-78
Figure B-79. Compiled illustration of lithology log, core photos (UV and white light), CT scan image, core descriptions, and annotated core images of the Brown Niagaran for depths 6,151 ft. to 6,153 ft. B-79
Figure B-80. Compiled illustration of lithology log, core photos (UV and white light), CT scan image, core descriptions, and annotated core images of the Brown Niagaran for depths 6,154 ft. to 6,156 ft. B-80
Figure B-81. Compiled illustration of lithology log, core photos (UV and white light), CT scan image, core descriptions, and annotated core images of the Brown Niagaran for depths 6,157 ft. to 6,159 ft. B-81
Figure B-82. Compiled illustration of lithology log, core photos (UV and white light), CT scan image, core descriptions, and annotated core images of the Brown Niagaran for depths 6,160 ft. to 6,162 ft. B-82
Figure B-83. Compiled illustration of lithology log, core photos (UV and white light), CT scan image, core descriptions, and annotated core images of the Brown Niagaran for depths 6,163 ft. to 6,165 ft. B-83
Figure B-84. Compiled illustration of lithology log, core photos (UV and white light), CT scan image, core descriptions, and annotated core images of the Brown Niagaran for depths 6,166 ft. to 6,168 ft. B-84
Figure B-85. Compiled illustration of lithology log, core photos (UV and white light), CT scan image, core descriptions, and annotated core images of the Brown Niagaran for depths 6,169 ft. to 6,171 ft. B-85
Figure B-86. Compiled illustration of lithology log, core photos (UV and white light), CT scan image, core descriptions, and annotated core images of the Brown Niagaran for depths 6,172 ft. to 6,174 ft. B-86
Figure B-87. Compiled illustration of lithology log, core photos (UV and white light), CT scan image, core descriptions, and annotated core images of the Brown Niagaran for depths 6,175 ft. to 6,177 ft. B-87
Figure B-88. Compiled illustration of lithology log, core photos (UV and white light), CT scan image, core descriptions, and annotated core images of the Brown Niagaran for depths 6,178 ft. to 6,180 ft. B-88

Figure B-89. Compiled illustration of lithology log, core photos (UV and white light), CT scan image, core descriptions, and annotated core images of the Brown Niagaran for depths 6,181 ft. to 6,183 ft. B-89
Figure B-90. Compiled illustration of lithology log, core photos (UV and white light), CT scan image, core descriptions, and annotated core images of the Brown Niagaran for depths 6,184 ft. to 6,186 ft. B-90
Figure B-91. Compiled illustration of lithology log, core photos (UV and white light), CT scan image, core descriptions, and annotated core images of the Brown Niagaran for depths 6,187 ft. to 6,189 ft. B-91
Figure B-92. Compiled illustration of lithology log, core photos (UV and white light), CT scan image, core descriptions, and annotated core images of the Brown Niagaran for depths 6,190 ft. to 6,192 ft. B-92
Figure B-93. Compiled illustration of lithology log, core photos (UV and white light), CT scan image, core descriptions, and annotated core images of the Brown Niagaran for depths 6,193 ft. to 6,195 ft. B-93
Figure B-94. Compiled illustration of lithology log, core photos (UV and white light), CT scan image, core descriptions, and annotated core images of the Brown Niagaran for depths 6,196 ft. to 6,198 ft. B-94
Figure B-95. Compiled illustration of lithology log, core photos (UV and white light), CT scan image, core descriptions, and annotated core images of the Brown Niagaran for depths 6,199 ft. to 6,201 ft. B-95
Figure B-96. Compiled illustration of lithology log, core photos (UV and white light), CT scan image, core descriptions, and annotated core images of the Brown Niagaran for depths 6,202 ft. to 6,204 ft. B-96
Figure B-97. Compiled illustration of lithology log, core photos (UV and white light), CT scan image, core descriptions, and annotated core images of the Brown Niagaran for depths 6,205 ft. to 6,207 ft. B-97
Figure B-98. Compiled illustration of lithology log, core photos (UV and white light), CT scan image, core descriptions, and annotated core images of the Brown Niagaran for depths 6,208 ft. to 6,210 ft. B-98
Figure B-99. Compiled illustration of lithology log, core photos (UV and white light), CT scan image, core descriptions, and annotated core images of the Brown Niagaran for depths 6,211 ft. to 6,213 ft. B-99
Figure B-100. Compiled illustration of lithology log, core photos (UV and white light), CT scan image, core descriptions, and annotated core images of the Brown Niagaran for depths 6,214 ft. to 6,216 ft. B-100
Figure B-101. Compiled illustration of lithology log, core photos (UV and white light), CT scan image, core descriptions, and annotated core images of the Brown Niagaran for depths 6,217 ft. to 6,219 ft. B-101
Figure B-102. Compiled illustration of lithology log, core photos (UV and white light), CT scan image, core descriptions, and annotated core images of the Brown Niagaran for depths 6,220 ft. to 6,222 ft. B-102
Figure B-103. Compiled illustration of lithology log, core photos (UV and white light), CT scan image, core descriptions, and annotated core images of the Brown Niagaran for depths 6,223 ft. to 6,225 ft. B-103
Figure B-104. Compiled illustration of lithology log, core photos (UV and white light), CT scan image, core descriptions, and annotated core images of the Brown Niagaran for depths 6,226 ft. to 6,228 ft. B-104

Figure B-105. Compiled illustration of lithology log, core photos (UV and white light), CT scan image, core descriptions, and annotated core images of the Brown Niagaran for depths 6,229 ft. to 6,231 ft. B-105
Figure B-106. Compiled illustration of lithology log, core photos (UV and white light), CT scan image, core descriptions, and annotated core images of the Brown Niagaran for depths 6,232 ft. to 6,234 ft. B-106
Figure B-107. Compiled illustration of lithology log, core photos (UV and white light), CT scan image, core descriptions, and annotated core images of the Brown Niagaran for depths 6,235 ft. to 6,237 ft. B-107
Figure B-108. Compiled illustration of lithology log, core photos (UV and white light), CT scan image, core descriptions, and annotated core images of the Brown Niagaran for depths 6,238 ft. to 6,240 ft. B-108
Figure B-109. Compiled illustration of lithology log, core photos (UV and white light), CT scan image, core descriptions, and annotated core images of the Brown Niagaran for depths 6,241 ft. to 6,243 ft. B-109
Figure B-110. Compiled illustration of lithology log, core photos (UV and white light), CT scan image, core descriptions, and annotated core images of the Brown Niagaran for depths 6,244 ft. to 6,246 ft. B-110
Figure B-111. Compiled illustration of lithology log, core photos (UV and white light), CT scan image, core descriptions, and annotated core images of the Brown Niagaran for depths 6,247 ft. to 6,249 ft. B-111
Figure B-112. Compiled illustration of lithology log, core photos (UV and white light), CT scan image, core descriptions, and annotated core images of the Brown Niagaran for depths 6,250 ft. to 6,252 ft. B-112
Figure B-113. Compiled illustration of lithology log, core photos (UV and white light), CT scan image, core descriptions, and annotated core images of the Brown Niagaran for depths 6,253 ft. to 6,255 ft. B-113
Figure B-114. Compiled illustration of lithology log, core photos (UV and white light), CT scan image, core descriptions, and annotated core images of the Brown Niagaran for depths 6,256 ft. to 6,258 ft. B-114
Figure B-115. Compiled illustration of lithology log, core photos (UV and white light), CT scan image, core descriptions, and annotated core images of the Brown Niagaran for depths 6,259 ft. to 6,261 ft. B-115
Figure B-116. Compiled illustration of lithology log, core photos (UV and white light), CT scan image, core descriptions, and annotated core images of the Brown Niagaran for depths 6,262 ft. to 6,264 ft. B-116
Figure B-117. Compiled illustration of lithology log, core photos (UV and white light), CT scan image, core descriptions, and annotated core images of the Brown Niagaran for depths 6,265 ft. to 6,267 ft. B-117
Figure B-118. Compiled illustration of lithology log, core photos (UV and white light), CT scan image, core descriptions, and annotated core images of the Brown Niagaran for depths 6,268 ft. to 6,270 ft. B-118
Figure B-119. Compiled illustration of lithology log, core photos (UV and white light), CT scan image, core descriptions, and annotated core images of the Brown Niagaran for depths 6,271 ft. to 6,273 ft. B-119
Figure B-120. Compiled illustration of lithology log, core photos (UV and white light), CT scan image, core descriptions, and annotated core images of the Brown Niagaran for depths 6,274 ft. to 6,276 ft. B-120

Figure B-121. Compiled illustration of lithology log, core photos (UV and white light), CT scan image, core descriptions, and annotated core images of the Brown Niagaran for depths 6,277 ft. to 6,279 ft. B-121
Figure B-122. Compiled illustration of lithology log, core photos (UV and white light), CT scan image, core descriptions, and annotated core images of the Brown Niagaran for depths 6,280 ft. to 6,282 ft. B-122
Figure B-123. Compiled illustration of lithology log, core photos (UV and white light), CT scan image, core descriptions, and annotated core images of the Brown Niagaran for depths 6,283 ft. to 6,285 ft. B-123
Figure B-124. Compiled illustration of lithology log, core photos (UV and white light), CT scan image, core descriptions, and annotated core images of the Brown Niagaran for depths 6,286 ft. to 6,288 ft. B-124
Figure B-125. Compiled illustration of lithology log, core photos (UV and white light), CT scan image, core descriptions, and annotated core images of the Brown Niagaran for depths 6,289 ft. to 6,291 ft. B-125
Figure B-126. Compiled illustration of lithology log, core photos (UV and white light), CT scan image, core descriptions, and annotated core images of the Brown Niagaran for depths 6,292 ft. to 6,294 ft. B-126
Figure B-127. Compiled illustration of lithology log, core photos (UV and white light), CT scan image, core descriptions, and annotated core images of the Brown Niagaran for depths 6,295 ft. to 6,297 ft. B-127
Figure B-128. Compiled illustration of lithology log, core photos (UV and white light), CT scan image, core descriptions, and annotated core images of the Brown Niagaran for depths 6,298 ft. to 6,300 ft. B-128
Figure B-129. Compiled illustration of lithology log, core photos (UV and white light), CT scan image, core descriptions, and annotated core images of the Brown Niagaran for depths 6,299 ft. to 6,301 ft. B-129
Figure B-130. Compiled illustration of lithology log, core photos (UV and white light), CT scan image, core descriptions, and annotated core images of the Brown Niagaran for depths 6,302 ft. to 6,304 ft. B-130
Figure B-131. Compiled illustration of lithology log, core photos (UV and white light), CT scan image, core descriptions, and annotated core images of the Brown Niagaran for depths 6,305 ft. to 6,307 ft. B-131
Figure B-132. Compiled illustration of lithology log, core photos (UV and white light), CT scan image, core descriptions, and annotated core images of the Brown Niagaran for depths 6,308 ft. to 6,310 ft. B-132
Figure B-133. Compiled illustration of lithology log, core photos (UV and white light), CT scan image, core descriptions, and annotated core images of the Brown Niagaran for depths 6,311 ft. to 6,313 ft. B-133
Figure B-134. Compiled illustration of lithology log, core photos (UV and white light), CT scan image, core descriptions, and annotated core images of the Brown Niagaran for depths 6,314 ft. to 6,316 ft. B-134
Figure B-135. Compiled illustration of lithology log, core photos (UV and white light), CT scan image, core descriptions, and annotated core images of the Brown Niagaran for depths 6,317 ft. to 6,319 ft. B-135
Figure B-136. Compiled illustration of lithology log, core photos (UV and white light), CT scan image, core descriptions, and annotated core images of the Brown Niagaran for depths 6,320 ft. to 6,322 ft. B-136

Figure B-137. Compiled illustration of lithology log, core photos (UV and white light), CT scan image, core descriptions, and annotated core images of the Brown Niagaran for depths 6,323 ft. to 6,325 ft. B-137
Figure B-138. Compiled illustration of lithology log, core photos (UV and white light), CT scan image, core descriptions, and annotated core images of the Brown Niagaran for depths 6,326 ft. to 6,328 ft. B-138
Figure B-139. Compiled illustration of lithology log, core photos (UV and white light), CT scan image, core descriptions, and annotated core images of the Brown Niagaran for depths 6,329 ft. to 6,331 ft. B-139
Figure B-140. Compiled illustration of lithology log, core photos (UV and white light), CT scan image, core descriptions, and annotated core images of the Gray Niagaran for depths 6,332 ft. to 6,334 ft. B-140
Figure B-141. Compiled illustration of lithology log, core photos (UV and white light), CT scan image, core descriptions, and annotated core images of the Gray Niagaran for depths 6,335 ft. to 6,337 ft. B-141
Figure B-142. Compiled illustration of lithology log, core photos (UV and white light), CT scan image, core descriptions, and annotated core images of the Gray Niagaran for depths 6,338 ft. to 6,340 ft. B-142
Figure B-143. Compiled illustration of lithology log, core photos (UV and white light), CT scan image, core descriptions, and annotated core images of the Gray Niagaran for depths 6,341 ft. to 6,343 ft. B-143
Figure B-144. Compiled illustration of lithology log, core photos (UV and white light), CT scan image, core descriptions, and annotated core images of the Gray Niagaran for depths 6,344 ft. to 6,346 ft. B-144
Figure B-145. Compiled illustration of lithology log, core photos (UV and white light), CT scan image, core descriptions, and annotated core images of the Gray Niagaran for depths 6,347 ft. to 6,349 ft. B-145
Figure B-146. Compiled illustration of lithology log, core photos (UV and white light), CT scan image, core descriptions, and annotated core images of the Gray Niagaran for depths 6,350 ft. to 6,352 ft. B-146
Figure B-147. Compiled illustration of lithology log, core photos (UV and white light), CT scan image, core descriptions, and annotated core images of the Gray Niagaran for depths 6,353 ft. to 6,355 ft. B-147
Figure B-148. Compiled illustration of lithology log, core photos (UV and white light), CT scan image, core descriptions, and annotated core images of the Gray Niagaran for depths 6,356 ft. to 6,358 ft. B-148
Figure B-149. Compiled illustration of lithology log, core photos (UV and white light), CT scan image, core descriptions, and annotated core images of the Gray Niagaran for depths 6,359 ft. to 6,361 ft. B-149
Figure B-150. Annotated RSWC images with corresponding core descriptions of the A-2 Carbonate for depths 5,760 ft. to 5,760.5 ft. B-150
Figure B-151. Annotated RSWC images with corresponding core descriptions of the A-2 Carbonate for depths 5,761 ft. and 5,778 ft. B-151
Figure B-152. Annotated RSWC images with corresponding core descriptions of the A-2 Evaporite for depths 5,819 ft. to 5,819.5 ft. B-152
Figure B-153. Annotated RSWC images with corresponding core descriptions of the A-2 Evaporite and A-1 Carbonate for depths 5,820 ft. to 5,846 ft. B-153
Figure B-154. Annotated RSWC images with corresponding core descriptions of the A-1 Carbonate for depths 5,884 ft. to 5,887 ft. B-154

Figure B-155. Annotated RSWC images with corresponding core descriptions of the A-1 Carbonate for depths 5,864 ft. to 5,871 ft. B-155
Figure B-156. Annotated RSWC images with corresponding core descriptions of the A-1 Carbonate for depths 5,884 ft. to 5,887 ft. B-156
Figure B-157. Annotated RSWC images with corresponding core descriptions of the A-1 Carbonate for depths 5,890 ft. to 5,893 ft. B-157
Figure B-158. Annotated RSWC images with corresponding core descriptions of the A-1 Carbonate for depths 5,896 ft. to 5,903 ft. B-158
Figure B-159. Annotated RSWC images with corresponding core descriptions of the A-1 Carbonate and the Brown Niagaran for depths 5,914 ft. to 5,916 ft. B-159
Figure B-160. Annotated RSWC images with corresponding core descriptions of the Brown Niagaran for depths 5,923 ft. to 5,940 ft. B-160
Figure B-161. Annotated RSWC images with corresponding core descriptions of the Brown Niagaran for depths 6,012 ft. to 6,015 ft. B-161
Figure B-162. Annotated RSWC images with corresponding core descriptions of the Brown Niagaran for depths 6,049 ft. to 6,076 ft. B-162
Figure B-163. Annotated RSWC images with corresponding core descriptions of the Brown Niagaran for depths 6,095 ft. to 6,121 ft. B-163
Figure B-164. Annotated RSWC images with corresponding core descriptions of the Brown Niagaran for depths 6,137 ft. to 6,145 ft. B-164
Figure B-165. Annotated RSWC images with corresponding core descriptions of the A-1 Carbonate for depths 5,927 ft. and 5,934 ft. B-165
Figure B-166. Annotated RSWC images with corresponding core descriptions of the A-1 Carbonate for depths 5,938 ft. and 5,961 ft. B-166
Figure B-167. Annotated RSWC images with corresponding core descriptions of the A-1 Carbonate for depths 5,962 ft. and 5,968 ft. B-167
Figure B-168. Annotated RSWC images with corresponding core descriptions of the Brown Niagaran for depths 5,970 ft. to 5,971 ft. B-168
Figure B-169. Annotated RSWC images with corresponding core descriptions of the Brown Niagaran for depths 6,015 ft. and 6,032 ft. B-169
Figure B-170. Annotated RSWC images with corresponding core descriptions of the Brown Niagaran for depths 6,032.5 ft. to 6,033 ft. B-170
Figure B-171. Annotated RSWC images with corresponding core descriptions of the Brown Niagaran for depths 6,033.5 ft. to 6,036 ft. B-171
Figure C-1. Depth plots of Poisson’s ratio and dynamic shear modulus for Cargas 3-2 HD1..... C-2
Figure C-2. Depth plots of bulk modulus and Young’s modulus for Cargas 3-2 HD1. ..... C-3
Figure C-3. Histograms of Poisson’s ratio and dynamic shear modulus for Cargas 3-2 HD1. Two of the histograms include the Salina Formation, and two of the histograms don’t include the Salina Formation for visual resolution purposes. C-5
Figure C-4. Histograms of bulk modulus and Young’s Modulus for Cargas 3-2 HD1. Two of the histograms include the Salina Formation, and two of the histograms don’t include the Salina Formation for visual resolution purposes..... C-6
Figure C-5. Depth plots of Poisson’s ratio and dynamic shear modulus for El Mac Hills 1-18A. C-9
Figure C-6. Depth plots of bulk modulus and Young’s modulus for El Mac Hills 1-18A. C-10
Figure C-7. Histograms of Poisson’s ratio and dynamic shear modulus for El Mac Hills 1-18A. Two of the histograms include the Salina Formation, and two of the histograms don’t include the Salina Formation for visual resolution purposes. C-12

Figure C-8. Histograms of bulk modulus and Young's Modulus for El Mac Hills 1-18A. Two of the histograms include the Salina Formation, and two of the histograms don't include the Salina Formation for visual resolution purposes..... C-13
Figure C-9. Depth plots of Poisson's ratio and dynamic shear modulus for Lawnichak 9-33. ..... C-16
Figure C-10. Depth plots of bulk modulus and Young's modulus for Lawnichak 9-33. ..... C-17
Figure C-11. Histograms of Poisson's ratio and dynamic shear modulus for Lawnichak 9-33. Two of the histograms include the Salina Formation, and two of the histograms don't include the Salina Formation for visual resolution purposes. C-19
Figure C-12. Histograms of bulk modulus and Young's Modulus for Lawnichak 9-33. Two of the histograms include the Salina Formation, and two of the histograms don't include the Salina Formation for visual resolution purposes..... C-20
Figure C-13. Depth plots of Poisson's ratio and dynamic shear modulus for Chester 6-16. ..... C-23
Figure C-14. Depth plots of bulk modulus and Young's modulus for Chester 6-16..... C-24
Figure C-15. Histograms of Poisson's ratio and dynamic shear modulus for Chester 6-16. Two of the histograms include the Salina Formation, and two of the histograms don't include the Salina Formation for visual resolution purposes..... C-26
Figure C-16. Histograms of bulk modulus and Young's Modulus for Chester 6-16. Two of the histograms include the Salina Formation, and two of the histograms don't include the Salina Formation for visual resolution purposes..... C-27
Figure C-17. Depth plots of Poisson's ratio and dynamic shear modulus for Chester 8-16. ..... C-30
Figure C-18. Depth plots of bulk modulus and Young's modulus for Chester 8-16..... C-31
Figure C-19. Histograms of Poisson's ratio and dynamic shear modulus for Chester 8-16. Two of the histograms include the Salina Formation, and two of the histograms don't include the Salina Formation for visual resolution purposes..... C-33
Figure C-20. Histograms of bulk modulus and Young's Modulus for Chester 8-16. Two of the histograms include the Salina Formation, and two of the histograms don't include the Salina Formation for visual resolution purposes..... C-34

List of Equations

Page

Equation 3-1 31
Equation 3-2 31
Equation 3-3 32
Equation 3-4 32
Equation 3-5 34
Equation 3-6 34
Equation 5-1 112
Equation 5-2 112
Equation 5-3 112
Equation 6-1 181
Equation 6-2 181
Equation 12-1 336
Equation 13-1 357
Equation 14-1 362
Equation 14-2 362
Equation 14-3 363
Equation 14-4 363
Equation 14-5 378
Equation 14-6 388
Equation 15-1 462

List of Attachments

Page

Attachment 1. Cargas 3-2 HD1 Horizontal Well Wireline and Pipe-Conveyed Log Analysis: Chester 2 Niagaran Reef Piggyback Well 1-1
Attachment 2. Lawnichak 9-33 Horizontal Well Wireline and Core Analysis: Dover 33 Niagaran Reef Piggyback Well 2-1
Attachment 3. Chester 6-16 Wireline and Core Analysis: Chester 16 Niagaran Reef Piggyback Well 3-1
Attachment 4. Chester 8-15 Wireline and Core Analysis: Chester 16 Niagaran Reef Piggyback Well 4-1
Attachment 5. El Mac Hills 1-18A Wireline Log Analysis: Charlton 19 Niagaran Reef Piggyback Well 5-1
Attachment 6. Dover 33 Niagaran Reef Alternative Conceptual Static Earth Models (SEM): Level 1 Lithostratigraphic and Level 2 Sequence Stratigraphic Models 6-1

List of Acronyms

ANOVA	Analysis of Variance
API	American Petroleum Institute
bbl	Barrel
BO	Breakout
BVI	Bulk Volume of Irreducible Fluid
BVM	Bulk Volume of Movable Fluid
CBW	Clay-bound Water
CCS	Confined Compressive Strength
CCUS	Carbon Capture Utilization and Storage
CO_2	Carbon Dioxide
CT	Computed Tomography
DIF	Drilling-induced Fracture
DOE	Department of Energy
DPHI	Computed Porosity from Density
DT	Sonic Travel Time
DT_c	Compressional-wave Slowness
DT_s	Shear-wave Slowness
EOR	Enhanced Oil Recovery
FMI	Formation Micro Image
ft/hr	feet per hour
g/cc	grams per cubic centimeter
g/cm^3	grams per cubic centimeter
HFE	High-frequency Enhancement
HSD	(Tukey's) Honest Significance Difference
LAS	Log ASCII Standard
µs/ft	microseconds per foot
MCF	thousand cubic feet
MCRS	Midcontinent Rift System
mD	millidarcy
MD	Measured Depth
MGRRE	Michigan Geological Repository for Research and Education
MICP	Mercury Injection Capillary Pressure
MRCSP	Midwest Regional Carbon Sequestration Partnership
MReX	Magnetic Resonance eXplorer
MT	Metric ton
MVA	Monitoring, Verification and Accounting
NATCARB	National Carbon Sequestration Database and Geographic Information System
NETL	National Energy Technology Laboratory
NMR	Nuclear Magnetic Resonance
NNPRT	Northern Niagaran Pinnacle Reef Trend
NTG	Net to Gross
ohm-m	Ohm-meter
OOIP	Original Oil in Place

P_p	Pore Pressure
p.u.	Porosity Unit
PNC	Pulsed Neutron Capture
psi	pounds per square inch
PSTM	Post-stack Time Migration
QA/QC	Quality Assurance/Quality Control
RAI	Relative Acoustic Impedance
ROP	Rate of Penetration
SEM	Static Earth Model
SH_{max}	Maximum Horizontal Stress
Sh_{min}	Minimum Horizontal Stress
S_v	Vertical Stress
T_2	NMR Dephasing Time
TD	Total Depth
TVD	True Vertical Depth
UCS	Uniaxial Compressive Strength
UV	Ultraviolet
XPHIA	Computed Average Neutron and Density Porosity

1.0 Project Background and Report Scope

1.1 Project Background

The Midwest Regional Carbon Sequestration Partnership (MRCSP) was established to assess the technical potential, economic viability, and public acceptability of carbon sequestration within its region. It was established by the Department of Energy (DOE) National Energy Technology Laboratory (NETL) as part of its overall strategy to (1) develop technologies that will support industries' ability to predict carbon dioxide (CO_2) storage capacity in geologic formations to within ±30 percent; (2) develop technologies to demonstrate that 99 percent of injected CO_2 remains in the injection zones; and (3) contribute technical expertise and lessons learned for development of Best Practices Manuals.

A primary goal of the MRCSP Development Phase effort is to execute a large-scale CO_2 injection test on a scale of 1 million metric tons. The most practical opportunity for conducting this large-volume injection test in the MRCSP region was to plan and execute it in collaboration with enhanced oil recovery (EOR) activities, an approach which also allows research on concurrent utilization of CO_2.

In the MRCSP region, CO_2 for such large-scale injection is available from Antrim-shale gas processing plants. Some of this CO_2 is already utilized for oil recovery from pinnacle carbonate reefs located in the northern part of the lower peninsula of Michigan. About 700 such carbonate reefs have been found in the area, and carbonate formations also form potential CO_2 storage targets in much of the MRCSP region. The reef structures are in various stages of the production life-cycle, including undiscovered and pre-production reefs, reefs in primary production, reefs undergoing EOR, and post-EOR depleted reefs.

The large-scale field test leverages existing EOR operations in the MRCSP region to examine and optimize methods and technologies used to obtain and interpret data on geologic, hydrologic, geomechanical, and geochemical properties. The overall objective of the large-volume geologic injection of CO_2 is to address issues relevant to future carbon capture utilization and storage (CCUS) projects, including the following specific goals:

- Proving adequate injectivity and available capacity
- Proving storage permanence
- Determining the areal extent of plume and potential leakage pathways
- Developing risk assessment strategies
- Developing best practices
- Engaging in public outreach and education
- Contributing to improved efforts to address permitting requirements

These objectives were accomplished by (1) injecting 1 million metric tons of CO_2 into oil fields at different stages in their life cycles; (2) using oil and gas fields as test beds for innovative monitoring, verification and accounting (MVA) technologies; (3) performing reservoir modeling, augmented by hydraulic, geophysical, and system monitoring; and (4) integrating the results into the National Carbon Sequestration Database and Geographic Information System (NATCARB), participating in technical working groups, and communicating the results to MRCSP members.

The CO_2 procurement, injection, and monitoring operations in the oil fields (i.e., Niagaran-age reefs) are categorized according to stages in the life cycle of EOR operations, designated as follows: Category 1

(nearly depleted reefs); Category 2 (active CO_2-EOR reefs); and Category 3 (newly targeted reefs). For the CO_2 injection test, wells and pipelines were instrumented to obtain geological and operational data. The data has been used to validate reservoir simulation models and help account for material balance of EOR system components to determine how much CO_2 is retained in the formations. Category 1 (nearly depleted) Niagaran reefs are late-stage EOR reefs that have undergone extensive primary and secondary oil recovery and are pressure depleted. Category 2 (active) Niagaran reefs are operational EOR reefs, in which primary oil recovery is completed and secondary oil recovery phase is currently under way using CO_2 injection. Category 3 (newly targeted) Niagaran reefs typically have undergone primary oil recovery, but no secondary oil recovery using CO_2 has been attempted. As new wells were drilled for EOR operations in these reefs, MRCSP had the opportunity to collect extensive data in the form of core samples, advanced wireline logs, and advanced reservoir well tests and thus obtain valuable additional information about the subsurface geology.

The host/partner, Core Energy, LLC, provided injection-ready CO_2 for the large-scale injection test in a composition consistent with Class II permits. Core Energy also provided the infrastructure (wells, compressors, pipelines, and controls) needed for CO_2 injection for the project.

1.2 Report Scope

This report compiles the results of geologic characterization of Task 3 (late-stage reef), Task 4 (active EOR reefs), and Task 5 (new EOR reefs) to demonstrate developed methodologies, geologic variability, and reservoir potential (Figure 1-1). Table 1-1 lists the reefs studied by task number.

Table 1-1. List of reefs studied and associated task number.

Reef Name	Task
Dover 33	3
Bagley	4
Charlton 19	4
Dover 35	4
Dover 36	4
Charlton 30/31	4
Charlton 6	4
Chester 5/6	4
Chester 2	4
Chester 16	5

The goals of MRCSP Tasks 3, 4, and 5 are to evaluate CO_2 injection potential, determine migration within the subsurface, and understand the potential for CO_2 storage in the three that represent the conditions defined in Section 1.1 for Categories 1, 2, and 3.

Conducting CO_2 injection and monitoring in these settings will provide significant insights for addressing the project objectives: assessment of injectivity in complex carbonate reef deposits; assessing CO_2 trapping mechanisms in a closed reservoir system; assessing any final oil recovery from transitional or residual oil zones in a field where CO_2 flooding is nearing completion; evaluating the transition from EOR to storage of CO_2; assessing regional commercialization; assessing new technologies for tracking CO_2, brine, and oil movements underground; and monitoring options in a closed reservoir with oil, residual oil, and water zones.

Several challenges and questions exist for CO_2 storage in oil and gas fields, but also in a discontinuous, compartmentalized environment. The geologic characterization efforts were aimed at addressing the following questions and reducing uncertainty:

1. The reefs cannot be treated as traditional oil and gas or saline reservoirs because they are disconnected, individual fields. Can a standardized approach be used to assess and characterize the reefs consistently?
2. There is significant variability in data availability by reef. Which data and analyses are most important?
3. The reservoirs are complex carbonates. What are the key controls on reservoir quality, and which are important for modeling?

4. What is the variability of reef geology?
5. Battelle participated in several piggyback wells to improve characterization. What was learned?
6. Confining units are a crucial part of the storage system. What are the units and properties?

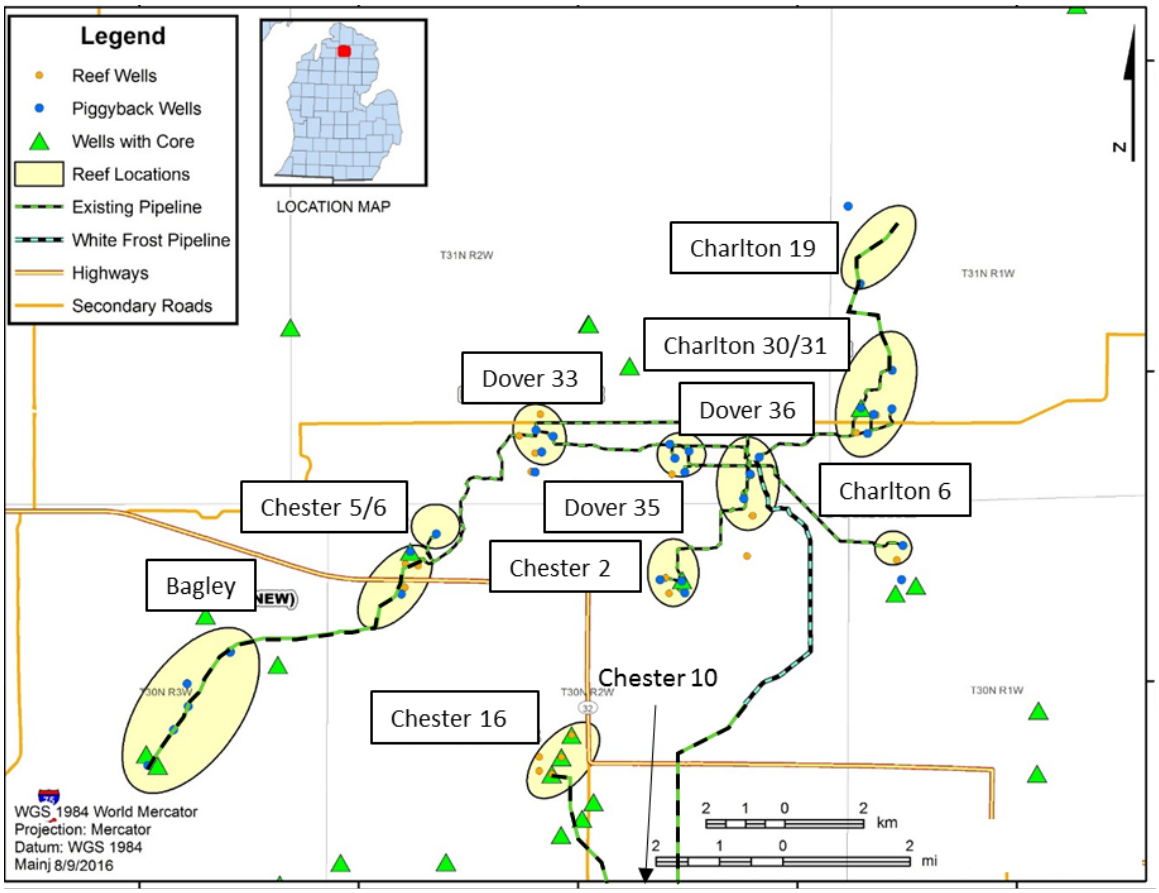


Figure 1-1. Map of reefs studied under Task 3, Task 4, and Task 5.

1.3 Approach

Geologic characterization and static earth modeling (SEM) of reefs consisted of three main components: (1) geological characterization using wireline logs, whole core observations and analyses, petrophysics, and seismic records, (2) statistics to determine and validate modeling decisions, and (3) construction of the SEM. Each part was a multi-step, iterative process as shown in Figure 1-2. The level of characterization varied by reef and was dependent on data availability. Figure 1-3 lists the types of analyses completed for each reef under each task number.

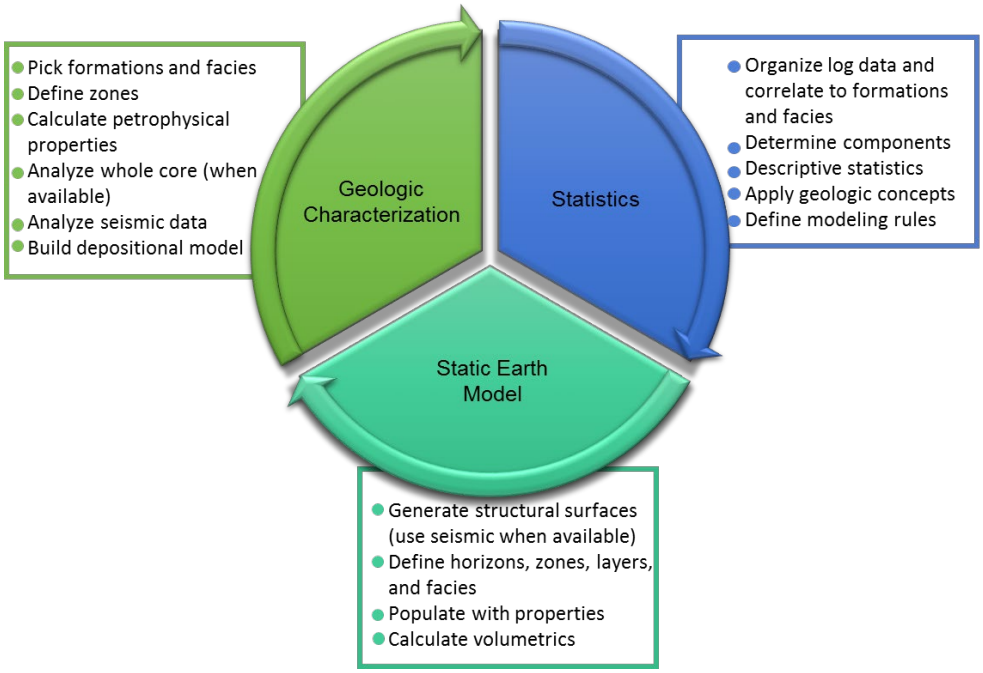


Figure 1-2. Three major components of geologic characterization of the Niagaran reefs and associated substeps.

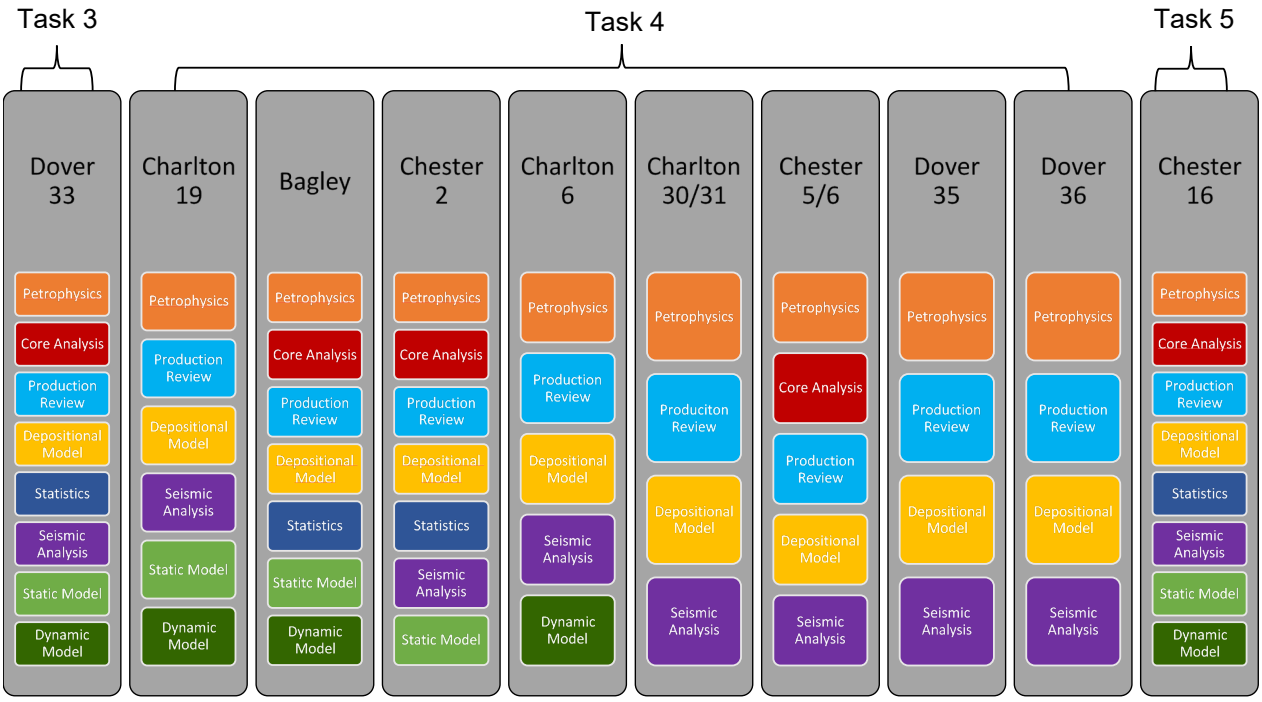


Figure 1-3. Analyses completed by reef showing variability due to data availability.

2.0 Geology Overview

2.1 Introduction

This geology overview summarizes published and MRCSP Development Phase results on the geologic setting of the Northern Niagaran Pinnacle Reef Trend (NNPRT), and on the structural, sequence stratigraphic, depositional, and diagenetic controls on geologic variability of reservoir and seal development. Appendix A provides a more comprehensive overview of the NNPRT geology.

Upper Silurian carbonate platforms developed along arches that separate the Michigan, Ohio, and Illinois Basins (Sarg, 2001); the NNPRT developed along the northern slope of the Michigan Basin (Briggs et al., 1980; Harrison III, 2010). Individual reef complexes developed on the slope and margins of the Michigan Basin (Figure 2-1). These reefs range from 2,000 feet to over 6,000 feet deep, with many occurring at depths of 3,500 to 5,000 feet. Individual reefs are closely spaced and compartmentalized from the enclosing rock; they average 50 to 400 acres in area and up to 700 feet in height, with steep flanks of 30° to 45°, thus fitting the definition of pinnacles by Shouldice (1955).

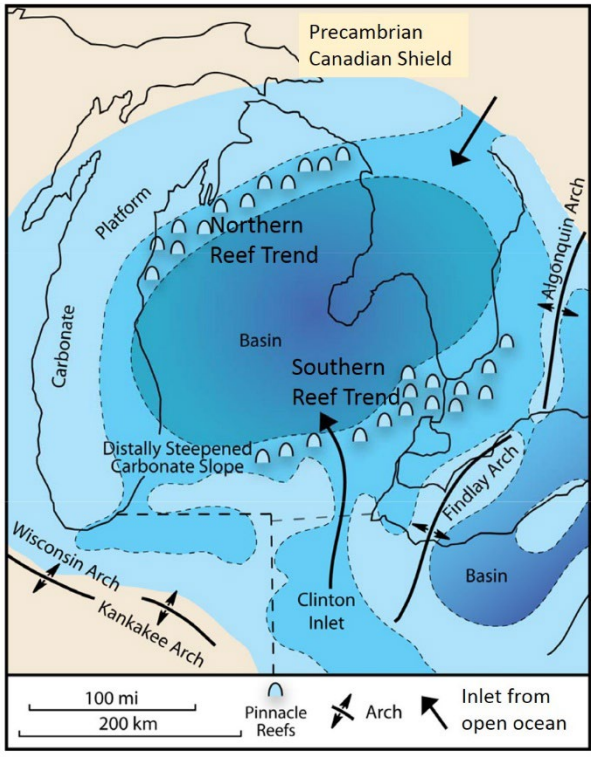


Figure 2-1. Silurian Northern Niagaran Pinnacle Reef Trend within the Michigan Basin (modified from Rine, 2015, and Burgess & Benson, 1969).

Approximately 800 fields in the NNPRT, originally developed in the 1970s-1980s, have undergone primary production; some have also undergone secondary recovery by water flood and tertiary recovery by CO_2 (Grammer et al., 2009; Harrison III, 2010; Barnes et al., 2013; Haagsma et al., 2017). Reef reservoir rocks develop in the Brown Niagaran lithostratigraphic interval of the Guelph formation (Figure 2-2) and may be completely dolomitized, essentially all limestone, or a heterogeneous mix. Reservoir quality is generally enhanced by dolomitization, and upper parts of reefs often, but not always, are more dolomitized than the lower parts. Hydrothermal dolomite is locally present and is related to structure, fractures, and migration of deep fluids (Grammer, 2007).

The principal source rock for oil accumulation in the NNPRT is the off-reef fine-grained facies of the A-1 carbonate of the Salina Group (Rullkotter et al., 1986; Rine et al., 2017); the Brown Niagaran is a secondary source (Gardner & Bray, 1984). Multiple episodes of hydrocarbon migration occurred between the Mississippian and the Middle Jurassic (Cercone & Lohmann, 1987).

Seals for the hydrocarbon reservoirs include the flanking A-1 evaporite, which transitions from anhydrite near the reefs to halite in the basin center, and the A-2 evaporite, which overlies the reef and which is dominantly halite in the NNPRT (Figure 2-2). The A-2 evaporite thins to zero thickness northward toward the Niagaran carbonate platform that rims the basin margin (Cercone & Lohmann, 1985; Harrison & Voice, 2018). In flanking and off-reef areas, the Rabbit Ears anhydrites form thin (2- to 20-foot) vertical baffles and barriers to flow within the A-1 carbonate.

System	Epoch	N. American Series	Michigan Basin Lithostratigraphy		
			Subsurface Group	Subsurface Formation	Informal Nomenclature
Devonian	Lower	Ulsterian			
Silurian	Upper	Cayugan	Bass Islands		
			Salina		G Unit
					F Unit
					E Unit
					D Unit
					C Unit
					B Unit
					A-2 Carbonate
					A-2 Evaporite
				Ruff	A-1 Carbonate
					A-1 Evaporite
				Cain	A-0 Carbonate
	Lower	Niagaran	Niagara	Guelph Dol	Brown Niagara
				Lockport Dol	Gray Niagara
					White Niagara

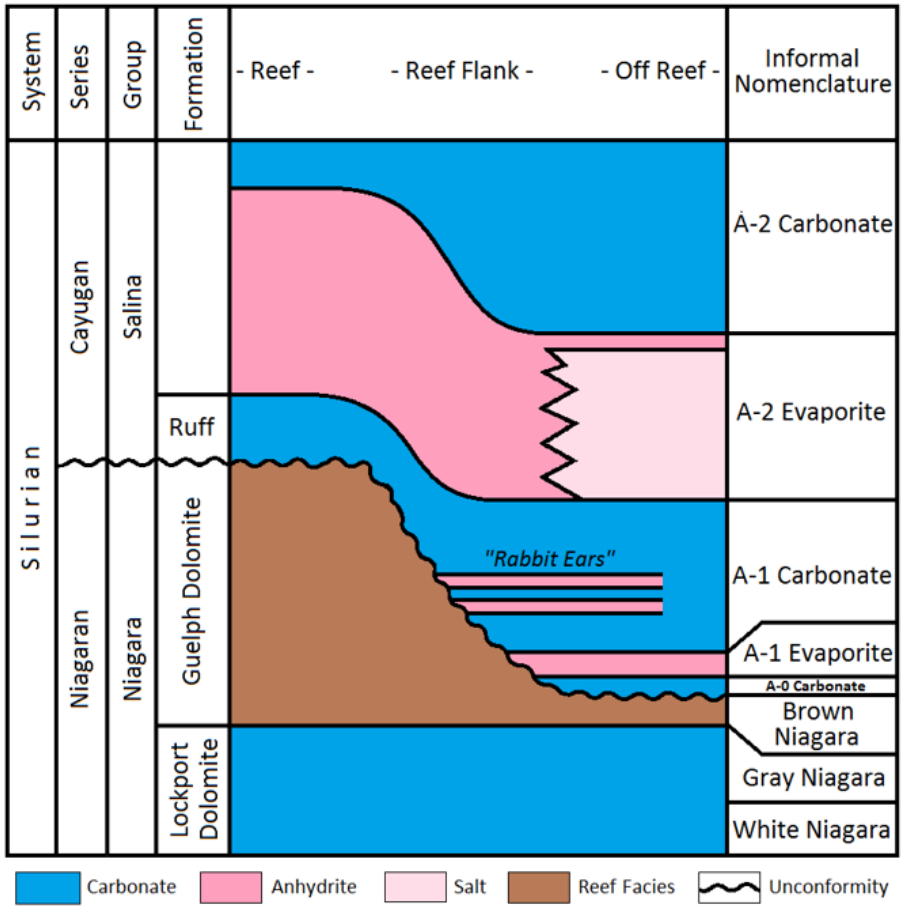


Figure 2-2. Stratigraphy of the Silurian-age Niagaran and Salina Groups in the Michigan Basin. On left is the formal and informal Silurian stratigraphic nomenclature (modified from Trout, 2012, and Rine, 2015). On right is a conceptual model and stratigraphy of the Brown Niagaran reef interval (after Gill 1973, 1979; and Huh 1973).

2.2 Basin Structure

The main structural elements of the Michigan Basin are shown in Figure 2-3. The initial basin appears to have started as an elongate Upper Cambrian to Lower Ordovician continuation of the extensional Reelfoot rift-Illinois Basin (Howell & van der Pluijm, 1990). Howell & van der Pluijm (1990; 1999) concluded that there were at least six distinct episodes of subsidence in the 200-million-year history of the Michigan Basin, with several episodes related to the orogenic events in the Appalachian Basin.

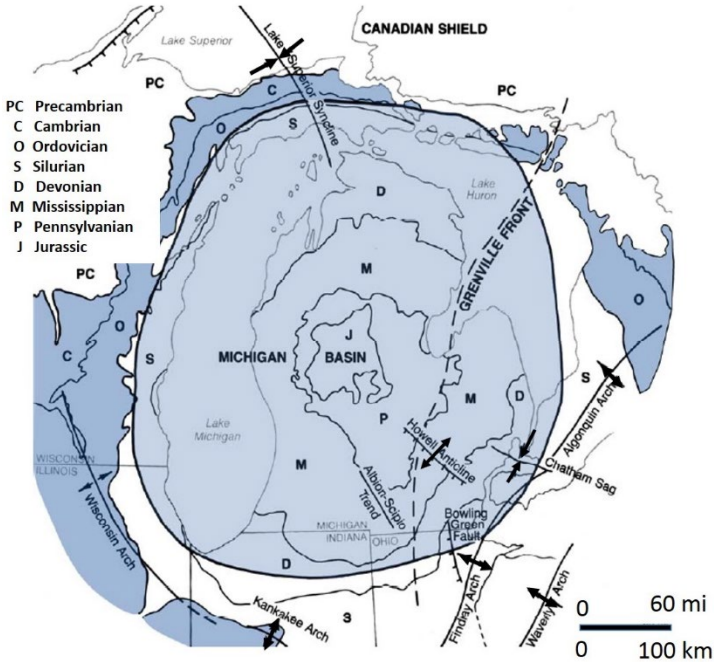


Figure 2-3. Main structural elements and age of bedrock in the Michigan Basin (modified from Rine, 2015, and Catacosinos et al., 1991).

Major faults (Figure 2-4) generally trend northwest-southeast. Most faults appear to terminate at or below middle Devonian age strata (Woods & Harrison, 2002). Woods & Harrison (2002) reported that a complex fracture pattern in strata in the center of the Michigan Basin is related to the Precambrian Keweenawan-age Midcontinent Rift System (MCRS). The eastern arm of the MCRS extends from the northwest to the southeast across the central part of the basin (Figure 2-4). Reactivation of basement faults occurred during the Mississippian (Fisher et al., 1988; Towne et al., 2013) related to northwest/southeast Alleghenian compression (Woods & Harrison, 2002). Distribution and diagenetic overprints of the Niagaran reefs are influenced by structure and late-stage hydrothermal dolomitization resulting from fluid migration along faults (Grammer, 2007).

2.3 Lithostratigraphy

As shown in Figure 2-2, reefs developed in the upper portion of the Niagaran Group, which is subdivided into the Guelph dolomite and Lockport dolomite formations (Catacosinos et al., 2000, 2001). Historically, the oil industry subdivides the Niagaran Group into Brown, Gray, and White Niagaran formations based on color, texture, and wireline log signature (Carter et al., 2010). The reefal Brown Niagaran is stratigraphically equivalent to the Guelph dolomite, and the underlying Gray and White Niagaran are equivalent to the Lockport dolomite. The reefal buildups in the Brown Niagaran are overlain and encased by cyclic carbonate and evaporite beds of the Salina Group.

The Brown Niagaran and A-1 carbonate are the reservoirs in the Silurian reefs (Figure 2-5). The distinctive color of the Brown Niagaran can be attributed to dolomitization as well as, in some cases, oil staining. The underlying Gray and White Niagaran form the base of the reservoir. The Gray and White Niagaran reach a thickness of approximately 500 feet near the basin margin, and become thinner and have a more reddish color toward the center of the basin (Huh, 1973; Huh et al., 1977; Charbonneau, 1990). The regional Gray Niagaran tends to be slightly thicker below Brown Niagaran reefs.

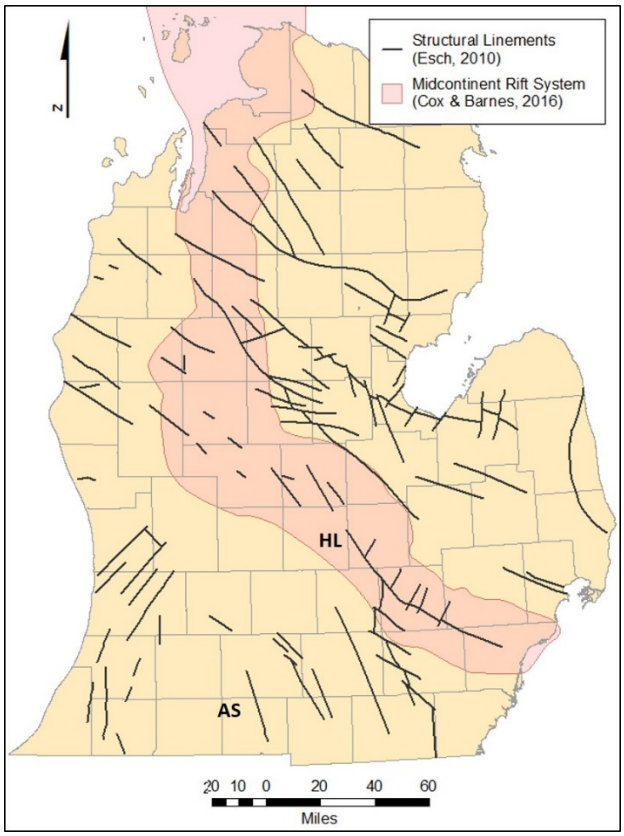


Figure 2-4. Major faults in the Michigan Basin (modified from Esch, 2010; Cox & Barnes, 2016).

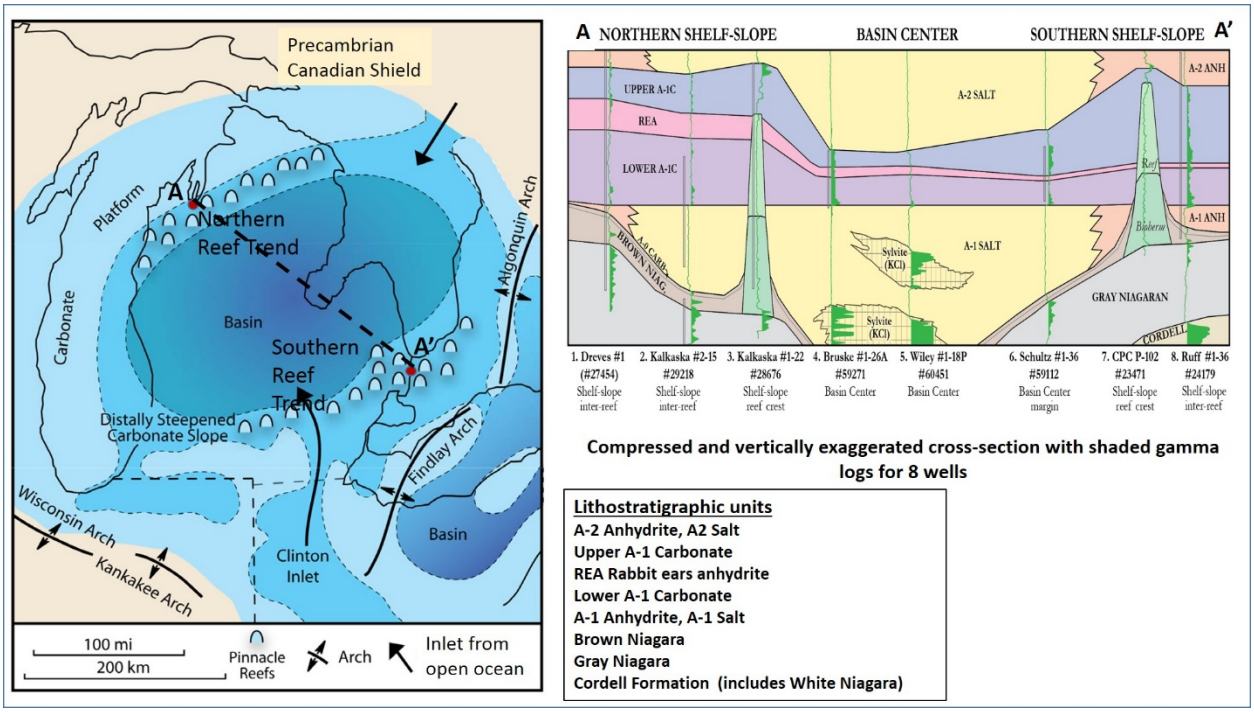


Figure 2-5. Geometry of reservoirs and seals in the interval of interest (modified from Rine, 2015a, and Rine et al., 2017).

The A-0 carbonate is a thin (10- to 40-foot) unit that overlies Brown Niagaran reef-associated conglomerates on reef flanks (Catacosinos et al., 2001; Suhaimi, 2016). The superjacent A-1 evaporite regionally transitions from halite and sylvite in the basin center to anhydrite on reef flanks, forming a sealing lithology. The A-1 carbonate, subsurface equivalent to the Ruff formation, overlies the Brown Niagaran on reef crests and overlies the A-1 evaporite on off-reef locations. Off-reef, the upper part of the A-1 carbonate includes the thin, regionally correlative Rabbit Ears anhydrites. The A-1 carbonate may act as seals on the flanks of the reefs but can develop dolomitic intercrystalline reef top and proximal flank reservoirs as well as microporous reservoirs off-reef. Variations in on-reef upper A-1 carbonate thickness indicate differential subsidence along the north and south basin margins (Rine et al., 2017).

The A-2 evaporite occurs as a thin bed of anhydrite or halite above the tops of reefs and as bedded halite in the inter-reef deposits (Huh et al., 1977; Gill, 1977). The A-2 carbonate is a 100- to 120-foot thick regional tight limestone. Rapid changes in the anhydrite/halite composition of the Niagaran and Salina evaporites surrounding the reefs make the acquisition of a full suite of density and acoustic logs critical in mapping reservoir boundaries and calibrating seismic response.

2.4 Interpreted Sequence Stratigraphy of the Reef Interval

The subdivision of the rock record encountered in an exploration wellbore traditionally is lithostratigraphic and is based on sharp changes in lithology (sandstone, dolostone, limestone, shale, etc.). In contrast, sequence stratigraphy is a method of grouping rock strata based on their depositional relationships, with major boundaries formed by unconformities or their correlative downdip surfaces. Rock units that lie between unconformities are assumed to be more closely related than units that are separated by unconformities.

Sarg (1991) and Liebold (1992) appear to be among the first to apply sequence stratigraphic concepts to the Michigan Basin. Dr. Michael Grammer and his students at Western Michigan University evaluated the Michigan reef core- and log-based sedimentological work of Huh and others (Huh, 1973, Huh et al., 1977; Gill, 1973) in terms of a sequence stratigraphic framework. Recognition of unconformity-bounded packages by Huh (1973) and Gill (1973) greatly influenced later sequence stratigraphic interpretations.

The importance of the sequence stratigraphic analysis of the Niagaran reefs is that it allows an understanding of the relative age of the Brown Niagaran, the A-0 carbonate, the A-1 anhydrite, and the A-1 carbonate, and more realistically allows lateral assignment of lithofacies and petrophysical properties within static models. The correlation of a major platform exposure event (Smith et al., 1993) to the top of bioherm buildups near the southern basin margin provides better understanding of lateral depositional events and the possibility of unexploited dolomite porosity development in reefs within the reef trends.

Appendix A contains a detailed discussion on sequence stratigraphic analysis, application, and evolution of the currently used depositional models of the Brown Niagaran reef reservoirs.

3.0 Data Availability and Geologic Characterization Methodology

3.1 Data Types

The data analyzed for these tasks were obtained from Core Energy, LLC; the Michigan Geological Repository for Research and Education (MGRRE); and Battelle/MRCSP-collected data. Multiple types of data were acquired, including wireline logs, core data, 3D seismic data, and well tests. Wireline logs are one of the most prevalent forms of subsurface data available, while core provides a physical rock specimen that can be analyzed by a geologist and/or laboratory. 3D seismic data are used to define the boundaries and geometries of the reefs. Well tests provide real measurements of reservoir injectability. The dataset includes more than 4,200 wells, wireline log data, formation tops, 60+ square miles of 3D seismic data, 160+ miles of 2D seismic data, seismic horizons, and whole core, along with archived porosity and permeability measurements of part of the available core. Figure 3-1 shows the data types and distribution within the study area.

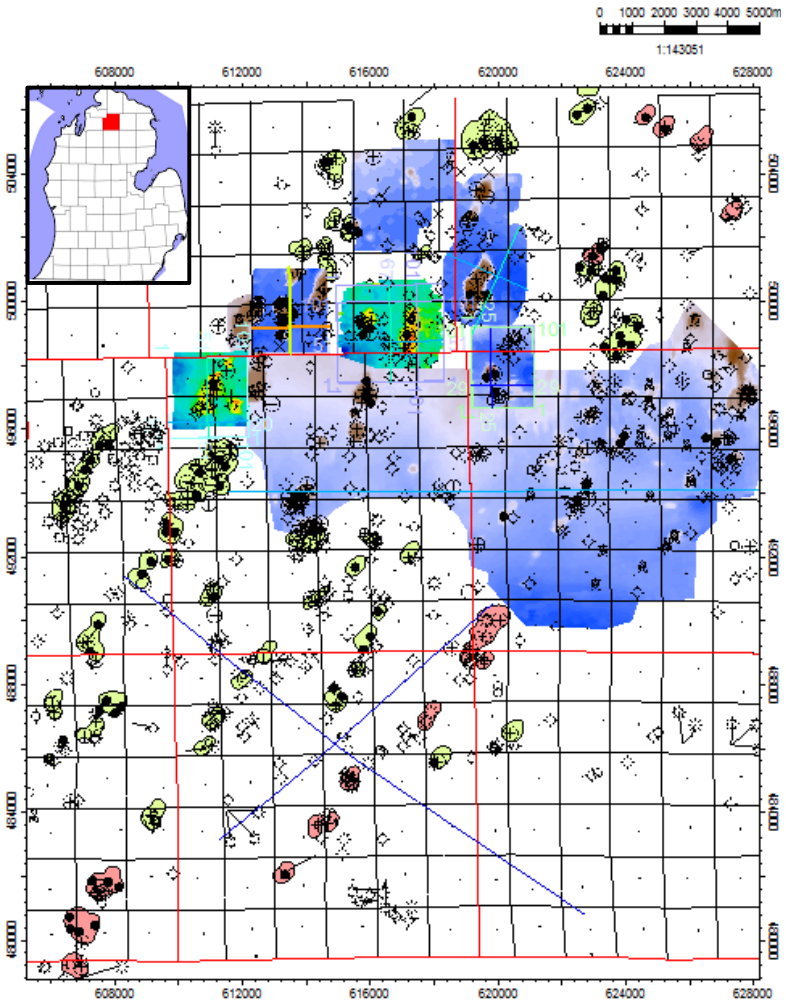


Figure 3-1. Map of the study area showing locations of reefs (green and red), 3D seismic data sources (colored polygons), 2D seismic data sources (blue lines), and deep wells (black).

3.1.1 Wireline Logs

Wireline logs are detailed, continuous, depth-based records of rock properties obtained by lowering a string of tools into a borehole. Each tool measures a unique property of the formations into which the borehole is drilled. Some of the most useful and commonly used tools are gamma ray, resistivity, and density-neutron logs, referred to collectively as a triple combo.

The gamma ray tool records a log of the total natural radioactivity in a borehole, measured in American Petroleum Institute (API) units. The measurement can be made in open holes and through well casing, meaning they are often complete records of the borehole from ground surface to total depth. Different

rock types typically have different gamma ray signatures that can be correlated between wells. For example, shales tend to read very high on the gamma ray log, while sandstones tend to read very low. Thus, gamma ray logs are often useful for interpreting lithology and comparing formations across multiple boreholes and for correlating measurements from open hole logs and cased hole work, such as completion and perforating.

The resistivity tool measures the electrical resistivity of a formation, expressed in ohm-meters (ohm-m). Resistivity is useful for formation evaluation because all formation waters conduct electricity, whereas the more crystalline rock matrices do not. Although the most common use of resistivity logs is to quantify fluid saturation, the level of resistivity can serve as a qualitative indicator of porosity and permeability. An electrical current flows with little resistivity in a brine-filled reservoir with good porosity and permeability (good connectivity between pores).

The density tool measures the bulk density (the mass of a solid over a given volume, including pore spaces) of a formation. The reading is based on the reduction in gamma ray flux between a source and a detector due to a phenomenon known as Compton scattering. It is calculated from a reference density, typically limestone (2.71 grams per cubic centimeter [g/cm^3]). To the extent that a density reading is less than the assumed known value, that difference can be attributed to void space (density-porosity). The log is interpreted under the assumption that the rock has a unique mineralogy of known density; however, a rock rarely has a single mineral composition. Therefore, estimates of rock composition must be made before calculating density-porosity. In this way, sediment crystalline and cement mineralogy is considered to estimate a formation-specific density. The density porosity log must also be screened for suspected shale content, included clays, and accessory mineralogies, as these can skew density log results.

The neutron log is a measure of porosity that is based on the effect a formation has on the number of fast neutrons emitted by a source. Hydrogen, which has the greatest effects on these emissions, slows down and captures neutrons. Since hydrogen is found mainly in the pore fluids, the neutron log responds principally to porosity; however, the matrix and the type of fluid also have an effect. Basic reservoir fluids are composed of water, oil, and gas, all of which contain hydrogen. Porosity is interpreted based on the amount of hydrogen detected by the sensor. This works well for water and oil. However, gas has a low molecular density and may escape detection by the sensor in part or in whole. Consequently, a neutron porosity log may indicate a reduced presence or even absence of hydrogen in gas-filled reservoirs, returning erroneously low porosity values. Like the density log, blended mineralogies can produce inaccurate values for porosity, particularly for rocks with shale and clay inclusions. This is because shale and clays are capable of holding large volumes of bound water, which show false high porosity. Interbedded shale and included clays must be screened in the neutron porosity log. Both porosity measurements are calibrated to read the correct porosity (assuming that the pores are filled with fresh water) for a given matrix (limestone, sandstone, or dolomite). It is presented in units of porosity (vol/vol or porosity unit [p.u.]) for the matrix chosen.

Advanced logs, such as sonic logs and image logs, are more expensive to obtain and are thus less common. A sonic tool emits an acoustical signal into the rocks and measures the travel speed of the wave echoes through the formations. Both compressional (P) and shear (S) wave velocities can be used to calculate geomechanical properties. The data provided in resistivity-based image logs allow an assessment of the formation on a very fine scale (1 foot of well length is represented by 1 inch of data). The data can be used to assess fractures, identify bedding planes, and determine the introduction of fluid, texture changes, stratification type, and vugular porosity. The primary asset is a visual clue to the nature and controls on the porosity indicated on density or neutron logs.

For each of the study area wells, all wireline logs were either obtained from Core Energy, LLC, gathered during piggyback operations, or obtained from historical databases. Wireline logs were acquired in two different forms: as rasters or Log ASCII Standard (LAS) files. Rasters are uncalibrated images of the logs. Many rasters, particularly of older logs, are scans of paper logs and are of varying quality. At a minimum, rasters must be depth-calibrated prior to being used in geological software such as Petra®. Raster curves must also be digitized prior to being used for petrophysical calculations (described in Section 3.5). The process of digitization requires a user to trace the curve in Petra® in order to assign values to each depth. LAS files, on the other hand, provide digitized representations of log curves and are thus preferable to raster images.

Log quality and availability varied widely from well to well and reef to reef (Table 3-1). Whenever possible, formation tops were picked using a full triple combo suite of logs. In the event a well did not have at least a gamma ray log and either a density or porosity log associated with it, the formation tops picks were caveated for future scrutiny in the event they did not match formation tops picks of surrounding wells. Other caveats included complicating geologic factors (e.g., faults or geologic structures that affect the relatedness of proximate wells) and formation picks made from poor-quality logs.

Table 3-1. Number of wells in each reef with wireline log data.

Reef Name	# of Wells with Wireline Logs
Dover 33	17
Bagley	16
Charlton 19	4
Dover 35	9
Dover 36	5
Charlton 30/31	9
Charlton 6	3
Chester 5/6	9
Chester 2	8
Chester 16	7

3.1.2 Core Data

When a well is drilled, sections of rock, ranging from tens to hundreds of feet long, are sometimes cut and saved for future use and analysis. These rock sections, known as core, are invaluable resources for obtaining direct information about target formations. Core can be used to inform, confirm, or calibrate the interpretation of wireline logs by providing an observable section of rock. Each core can inform a geological interpretation in up to three ways. First, the core is often retained and is available for inspection. Second, when core is obtained, it is often logged and interpreted by a geologist. Finally, small portions of the core, referred to as plugs, can be sent to laboratories for analysis. These analyses yield information about rock properties such as porosity, permeability, and mineralogy.

The amount of core available for geologic characterization varied by reef field. Table 3-2 shows the core data available for each reef field. Core was described and photographed by geologists at Battelle, Core Laboratories, and MGRRE.

Table 3-2. Summary of available core data by reef.

Data	Chester 16	Bagley	Chester 2	Chester 5/6	Charlton 6	Dover 33
# of Cores	5	2	1	1	2	1
Formations	A-1 carbonate, Brown Niagaran	A-1 carbonate, Brown Niagaran	A-1 carbonate, Brown Niagaran	A-1 carbonate	Off reef	A-1 carbonate, Brown Niagaran
Descriptions	X	X	X	X	NA	X
Photographs	X	X	X	X	NA	X
Porosity	X	X	X	X	X	X
Permeability	X	X	X	X	X	X
Grain Density	X	X	X	X	X	X
CT Scans	X	NA	NA	NA	NA	X
Thin Sections	NA	NA	NA	NA	NA	X
Advanced Analyses	X	NA	NA	X	NA	X

3.1.3 Seismic Data

Core Energy, LLC provided over 60 square miles of 3D seismic data to Battelle. The data covers nine out of the ten reefs in this study. Core Energy also provided seismic horizons to aid in mapping and boundary definition. Table 3-3 summarizes seismic data available by reef.

Table 3-3. Summary of available 3D seismic data by reef.

Reef Name	3D Seismic Data
Dover 33	X
Bagley	NA
Charlton 19	X
Dover 35	X
Dover 36	X
Charlton 30/31	X
Charlton 6	X
Chester 5/6	X
Chester 2	X
Chester 16	X

3.2 Tops Selection

The common reservoir characteristics that define each formation are understood through correlative information such as core data, field data from outcrops, wireline logs, and interpretations of an aggregation of all wells drilled and logged in the last 100+ years within the region. These separate data are combined to create a general framework of each formation, and to help understand where transitions occur between formations and the signatures found at these transitions. Because the purpose of this study was to characterize the reservoir, the tops of formations were picked on wireline logs primarily based on each formation's common wireline characteristics (neutron porosity, density, and lithology). Other wireline logs (e.g., gamma ray, sonic, resistivity) were used as secondary indicators for each formation if porosity, density, and lithology were insufficient indicators. This method allows for development of a regional framework of the formations, and also helps better define the individual formations through an increased incorporation of data. Formation tops were selected for the entire length of the wireline logs, but only formations that will be used in the SEMs are described in this section.

Log signatures and lithology can be different between the crest of the reef, flank, and off-reef positions. Three representative well cross sections were created to illustrate typical log signatures for key formations and how they vary, based on reef position. Individual formations are described below.

3.2.1 A-2 Carbonate

The A-2 carbonate is a low porosity, low permeability (referred to as tight in oil and gas) carbonate that is overlain by the Salina B-salt and overlies the A-2 evaporite. Wireline curves show a sharp contact between the Salina B-salt and the A-2 carbonate which was used to identify the top of the A-2 carbonate interval. This contact occurs in wireline logs where there is a sharp increase in the bulk density curve and a slight increase in the neutron porosity curve (Figure 3-2). Additionally, the A-2 carbonate has a high gamma marker informally named the “A-2 shale” mid-formation. The A-2 shale is a muddy carbonate. The thickness of the A-2 carbonate varies slightly across a reef structure, being thinnest overlying the crest of the reef and thicker off-reef.

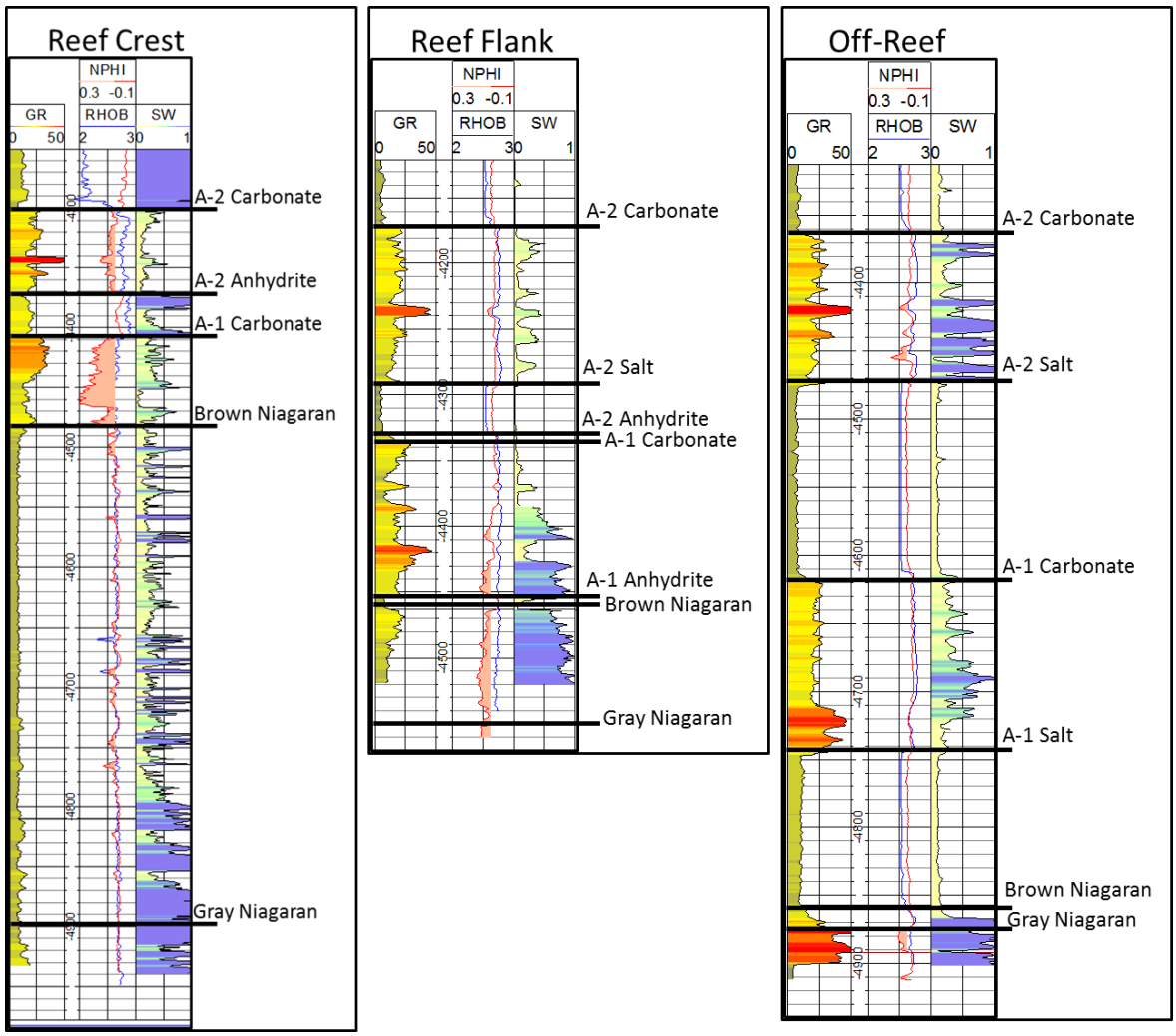


Figure 3-2. Single well cross sections representing typical log signatures for key formations at the crest of the reef, flank of the reef, and off-reef.

3.2.2 A-2 Evaporite

The A-2 evaporite is a thin anhydrite bed when situated at the top of a pinnacle reef, and halite in inter-reef deposits. Gamma log signatures for anhydrite and halite layers are similar and show distinctive contacts between the A-2 carbonate base and A-2 evaporite top. There is a sharp change in bulk density that is congruent with a slight decrease of the neutron porosity curve (Figure 3-2). Additionally, the gamma ray curve and the neutron porosity curve are uniform and have relatively straight line signatures. Resistivity and density curves permit immediate distinction between the anhydrite and halite. The thickness varies from thin on top of the reef to a thick package off-reef.

3.2.3 A-1 Carbonate

The A-1 carbonate is mostly dolomite across the reef trend. The contact with overlying A-2 evaporite has a distinct log signature with an increase in gamma ray and neutron porosity (Figure 3-2). Porosity tends to be higher toward the basin and lower up-dip due to over-dolomitization. Poker-chip shales (source rock) are present along the reef flank and off-reef positions and are notable by high gamma at the base and within the lower A-1 carbonate. Additionally, the A-1 carbonate thins over the crest of the reef and thickens toward off-reef.

3.2.4 A-1 Evaporite

The A-1 evaporite is composed of thin anhydrite beds (Rabbit Ears anhydrites) and halite. Gamma log signatures for anhydrite and halite layers are similar and show distinctive contacts between the A-1 carbonate and A-1 evaporite. There is a sharp change in bulk density that is congruent with a slight decrease of the neutron porosity curve (Figure 3-2). Additionally, the gamma ray curve and the neutron porosity curve are uniform and have relatively straight line signatures. Resistivity and density curves permit immediate distinction between the anhydrite and halite. The A-1 evaporite is absent on the crest of the reef, occurs as anhydrite along the flanks, and is a thick package of halite off-reef.

3.2.5 Brown Niagaran

The Brown Niagaran is a carbonate formation that varies from limestone (basin-ward) to dolomite (up-dip). The top of the Brown Niagaran has a distinct contact with the A-1 evaporite or A-1 carbonate, depending on reef position, with a decrease in gamma ray (see Figure 3-2). The gamma ray remains low throughout the formation and is the best indicator as other log properties vary along the trend. Porosity tends to be highest in dolomitic reefs and decreases as a reef becomes limestone. Reef thicknesses also vary along the trend, with the tallest reefs (500 feet or greater) toward the center of the basin and the shortest reefs (300 to 350 feet) up-dip.

3.2.6 Gray Niagaran

The Gray Niagaran is a carbonate formation mostly composed of mottled limestone with low porosity and permeability. The top of the Gray Niagaran can be identified by an increase in gamma ray which is a result of bentonite beds and increased clay content (see Figure 3-2). Most wells do not fully penetrate the Brown Niagaran into the Gray Niagaran, so formation tops are scarce. The Gray Niagaran has also been historically misidentified due to increasing gamma ray of the muddy bioherm at the base of the reef, which can cause a poor estimate in overall thickness of the overlying Brown Niagaran.

3.3 Facies Selection

The students of Western Michigan University, partners of MRCSP, used the extensively available whole core at MGRRE to subdivide the Niagaran reefs into lithofacies (e.g., crinoid wackestone, coral boundstone) and depositional facies (Figure 3-3). Whole core observations were correlated to available wireline logs to aid in interpretation of depositional facies and lithofacies in wells with little to no core data, with the goal of building 3D models of geobodies with more predictable ranges of porosity and permeability. Additionally, lithofacies picks were then constrained to gamma ray curve signatures (Figure 3-4) to compensate and address limited log coverage for the NNPRT.

Gamma ray signatures were redisplayed at a scale of 0 to 50 API with greater than 25 API shaded indicators. Defined in this section, prominent increases or high gamma ray responses are indicated where the signature is above 25 API. Moderate responses are defined as 10 to 25 API, and low is defined by less than 10 API with a calm, more uniform signature. Typical gamma ray log signatures associated with core-based lithofacies suites were interpreted to represent the following depositional facies on a typical reef: windward reef flank, windward reef talus, reef core, leeward proximal reef apron, leeward distal reef apron, and leeward flank facies.

Windward Flank

The windward flank depositional facies is characterized by a moderately thick A-2 carbonate and A-2 salt with a relatively thin A-1 carbonate, A-1 anhydrite, A-0 carbonate, clean reef flank carbonate, and bioherm toe intervals. The gamma ray curve (Figure 3-4, panel 1) shows an increase at the top of the A-1 carbonate with moderate gamma spikes occurring in the interval. The thin A-1 anhydrite, A-0 carbonate, windward flank, and bioherm toe intervals are noted by thin transitions in the gamma ray curve, from calm and low gamma ray signatures to moderate to high gamma ray signatures. The base of this interval is interpreted at the top of the Gray Niagaran shown by a large increase and high gamma ray signature spike.

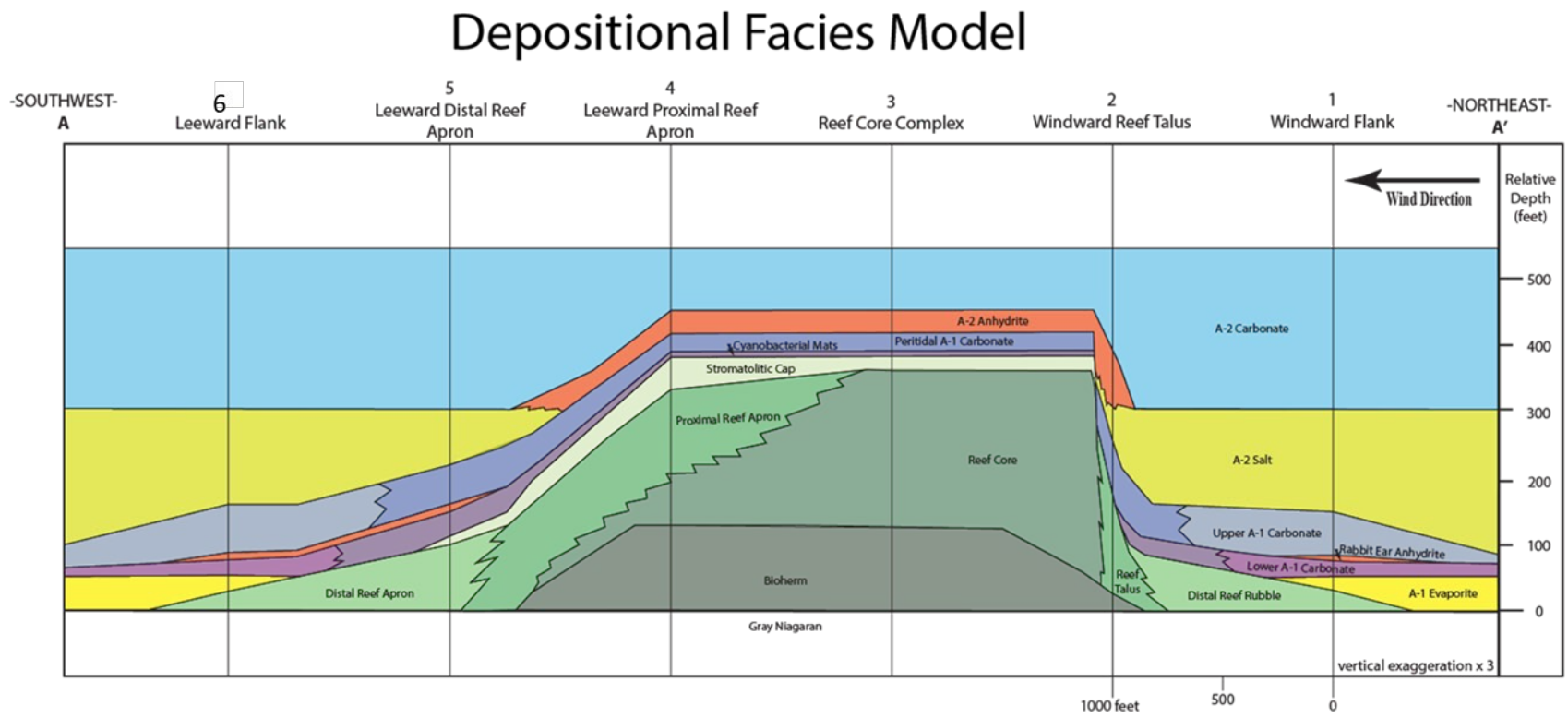


Figure 3-3. Depositional facies model by Western Michigan University collaborators showing (1) windward flank, (2) windward reef talus, (3) reef core complex, (4) leeward proximal reef apron, (5) leeward distal reef apron, (6) leeward flank facies.

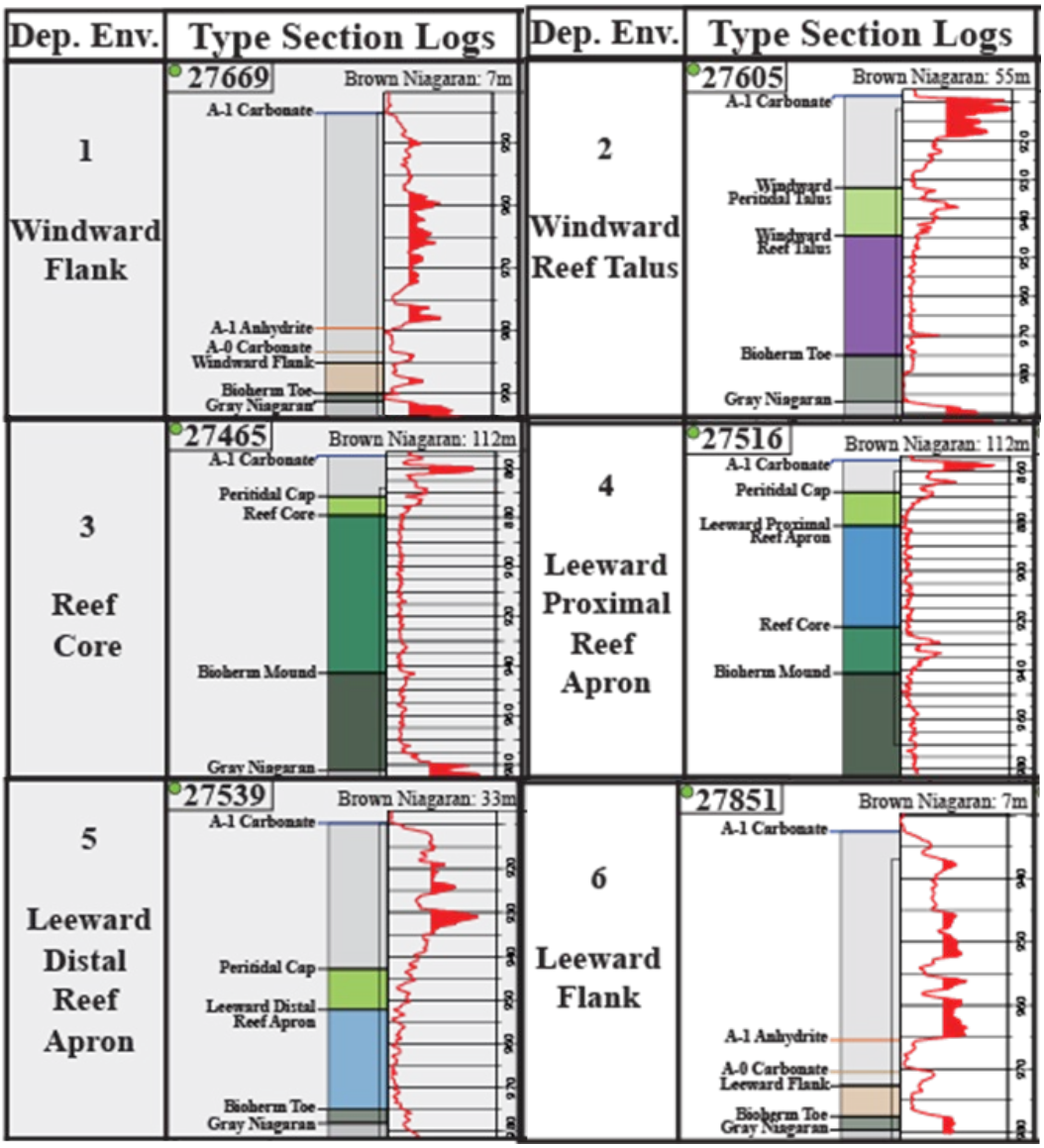


Figure 3-4. Gamma ray curve interpretations for lithofacies suites indicating the following depositional facies: (1) windward flank, (2) windward reef talus, (3) reef core complex, (4) leeward proximal reef apron, (5) leeward distal reef apron, (6) leeward flank facies. From Rine, 2015

Windward Reef Talus

The windward reef talus depositional facies generally contains a moderately thick A-2 carbonate with a thin A-2 anhydrite interval. The A-2 salt interval, if present, will underlie the A-2 anhydrite and will be an extremely thin to moderately thick interval. The A-1 carbonate is relatively thin and is overlying the moderately thick proximal reef rubble, which includes broken debris from the reef core and bioherm toe. Gamma ray signatures on the interpreted windward reef talus side (Figure 3-4, panel 2) show a sharp and high increase at the top of the A-1 carbonate. There is a short interval with a decrease in gamma ray intensity. There is a moderate gamma increase at the top of the windward reef talus and a cleaner gamma at the top of the bioherm toe. The base of this interpreted interval is shown at top of the Gray Niagaran, which is indicated by a large increase and high gamma ray signature spike.

Reef Core

The reef core depositional facies generally displays a moderately thick A-2 carbonate that overlies a thin A-2 anhydrite layer, in turn overlying relatively thin overlying A-1 carbonate and peritidal cap lithofacies with moderately thick reef core and bioherm intervals. A moderate intensity gamma ray signature with a sharp spike (Figure 3-4, panel 3) occurs in the A-1 carbonate. Gamma ray intensity decreases and is relatively calm at the top of the peritidal cap and stays clean with a slight sawtooth signature to the top of the bioherm mound. There is a slight increase in gamma ray at the top of the bioherm mound. A high gamma ray spike at the top of the Gray Niagaran represents the base of the reef core interval interpretation.

Leeward Proximal Reef Apron

The leeward proximal reef apron depositional facies is characterized by a moderately thick A-2 carbonate overlying thin A-2 anhydrite, A-1 carbonate, and peritidal cap intervals. A moderately thick leeward proximal reef apron lithofacies overlies a thin reef core interval and a moderately thick bioherm mound. On the leeward proximal side of the reef (Figure 3-4, panel 4), gamma ray signatures show a moderate and thin intensity through the A-1 carbonate that decreases and is calm at the peritidal cap. There is a slight increase, still low and calm intensity, at the top of the leeward proximal reef apron depositional facies. This interval can display a low amplitude sawtooth pattern similar to reef core. The reef core interval shows a moderate gamma ray intensity, which decreases at the top of the underlying bioherm mound interval. The base of this interval is interpreted at the top of the Gray Niagaran and is marked by a higher gamma ray signature spike.

Leeward Distal Reef Apron

The leeward distal reef apron depositional facies can be interpreted where there is a moderately thick A-2 carbonate which overlies a moderate thick A-2 salt. The A-1 carbonate is a thin to moderate interval that overlies thin peritidal cap, leeward distal reef apron, and bioherm toe intervals. The gamma ray curve (Figure 3-4, panel 5) shows an increase at the top of the A-1 carbonate with moderate spikes occurring in the interval. Gamma ray intensity decreases and is relatively calm at the top of the peritidal cap and continues to decrease as the interval deepens toward the base of the interval. At the top of the bioherm mound is a thin gamma ray increase. The base of this interval is interpreted at the top of the Gray Niagaran, which is shown by a large increase and high amplitude gamma ray signature spike.

Leeward Flank

The leeward flank depositional facies is interpreted where there is a moderately thick A-2 carbonate overlying a moderate thick A-2 salt with relatively thin A-1 carbonate, A-1 anhydrite, A-0 carbonate, windward flank, and bioherm toe intervals. The gamma ray curve (Figure 3-4, panel 6) shows an increase at the top of the A-1 carbonate with moderate spikes occurring in the interval. The thin A-1 anhydrite, A-0 carbonate, windward flank, and bioherm intervals are noted by thin transitions in the gamma ray curve, from calm and low gamma ray signatures to moderate to high gamma ray signatures. The base of this interval is interpreted at the top of the Gray Niagaran, which is shown by a large increase and high gamma ray signature spike. The leeward flank has similar gamma ray signatures as the windward flank. As such, multiple wells should be used to determine the reef orientation and proximity of the facies intervals.

For the purposes of characterization and modeling, reef facies have been lumped into windward, leeward, and reef core. Most wells do not fully penetrate the entire reef, making it difficult to subdivide the Brown Niagaran into smaller facies. Additionally, log signatures are similar on the leeward side and windward side due to same material composition. Brown Niagaran facies, then, are being determined based on reef location, formation thicknesses, and presence of evaporites (Figure 3-5).

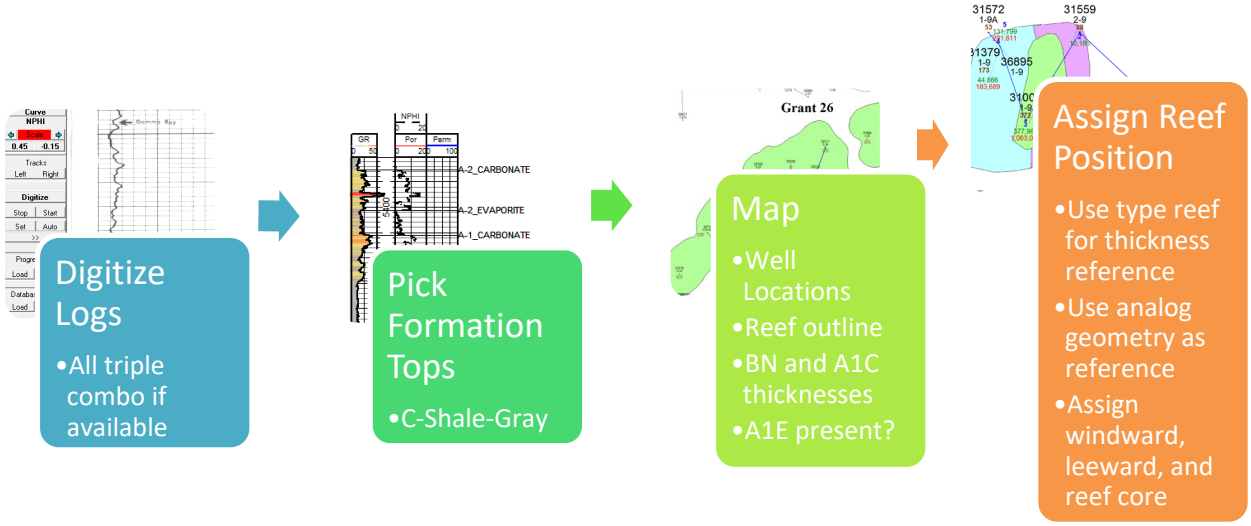


Figure 3-5. Simplified workflow for assigning facies to individual well locations in the Brown Niagaran.

3.4 Sub-Regional Mapping Methodology

Sub-regional structure and isopach maps were created for both reservoir formations (A-1 carbonate and Brown Niagaran) plus two confining formations: the Gray Niagaran (base) and the A-2 carbonate (seal) (Figure 3-6 through Figure 3-9). Wells that were drilled into Niagaran reef facies were excluded from the dataset to establish regional trend maps without the influence of the reefs. Default settings were used for the convergent interpolation method in Petrel™. There was still some influence of the reefs on the structure maps, so the resulting maps were hand-edited to remove any extreme peaks or troughs. All surfaces were smoothed over five grid cells and two iterations. Off-reef formation trends are important to guide and control the boundaries in a SEM.

All structure maps show the same trend of dipping rocks toward the Michigan Basin (north to south). The Gray Niagaran (Figure 3-6) is the smoothest surface because it has the least impact from Niagaran reefs.

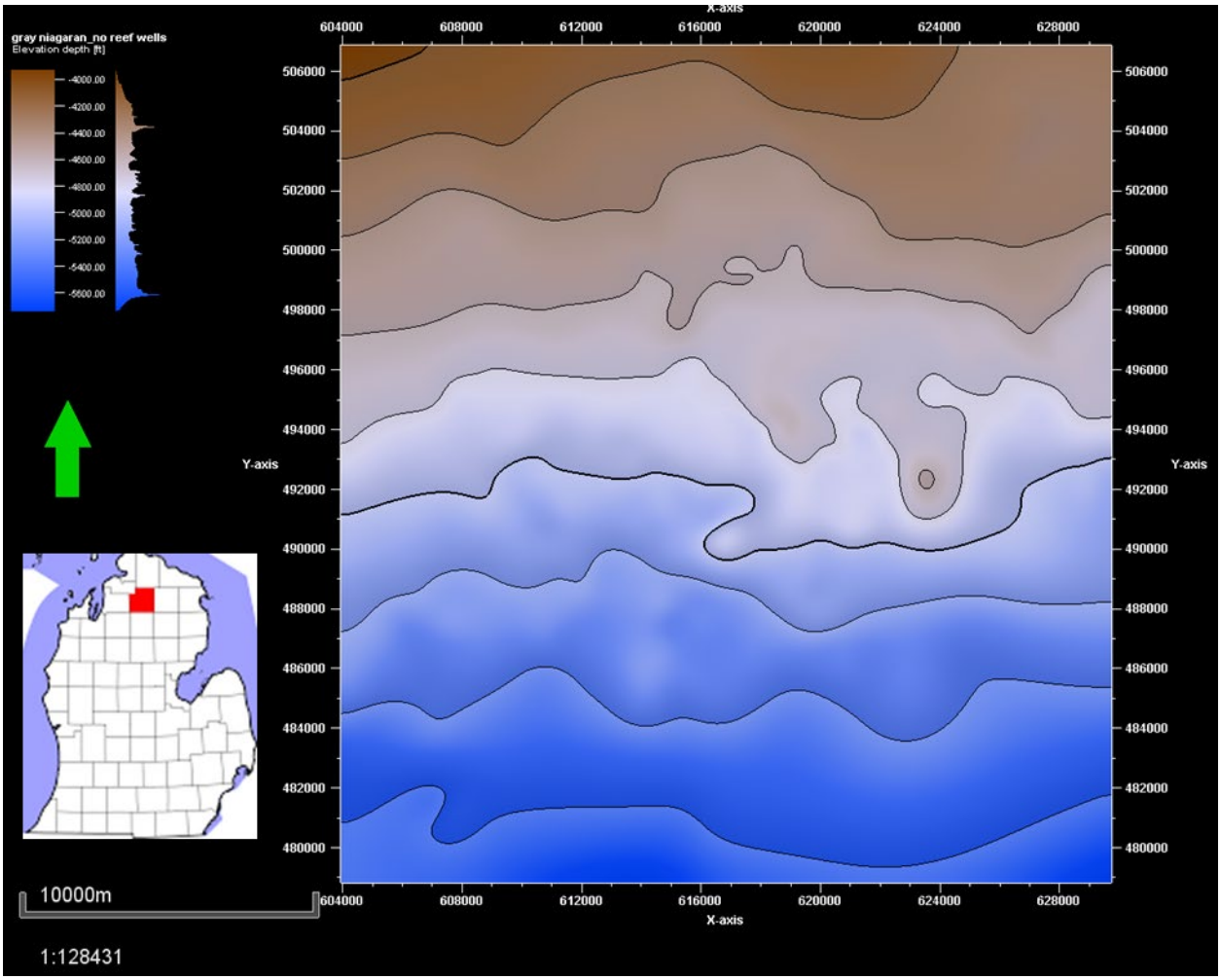


Figure 3-6. Structure map of the Gray Niagaran (base) without the influence of reefs.

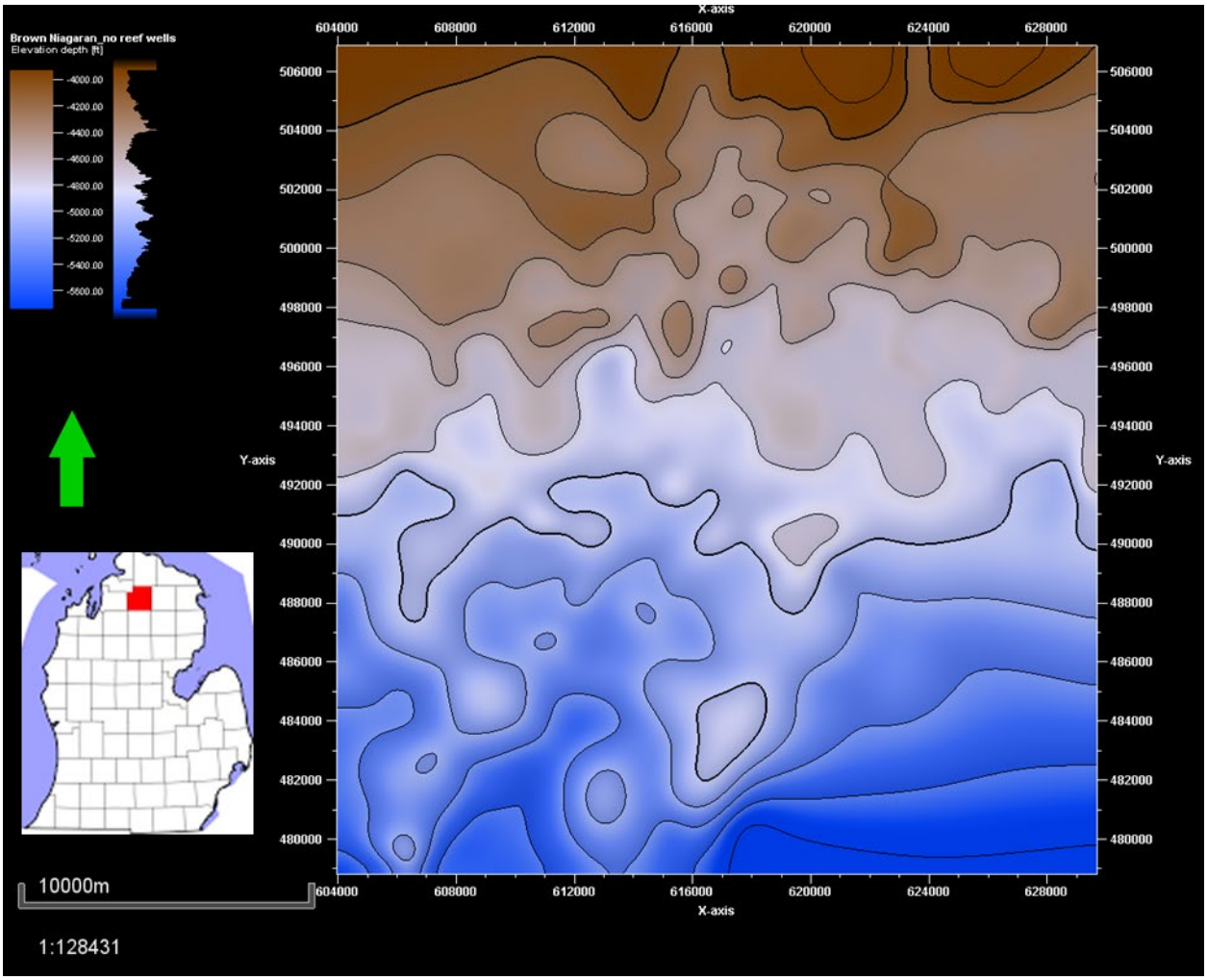


Figure 3-7. Structure map of the regional Brown Niagaran without the influence of reefs.

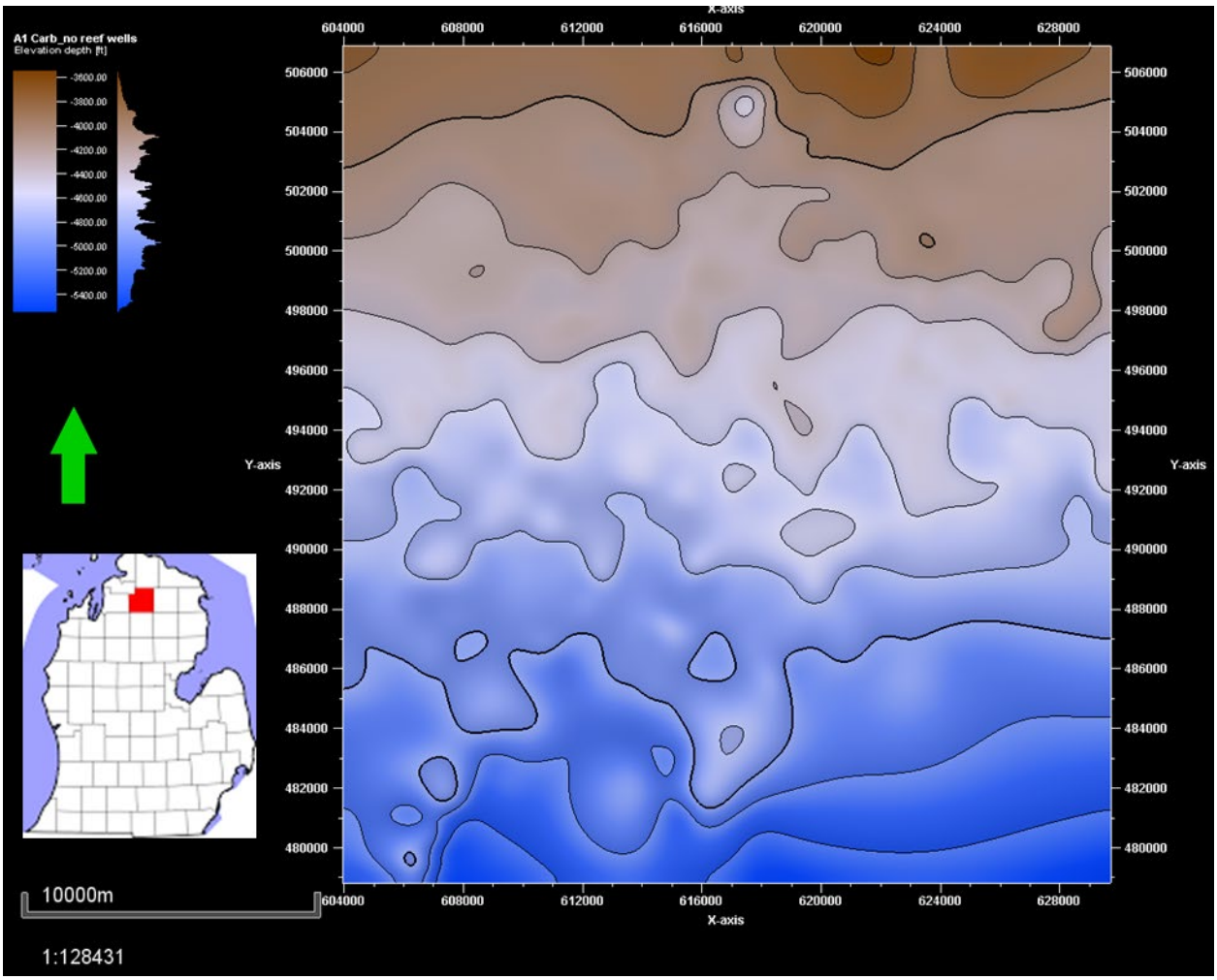


Figure 3-8. Structure map of the A-1 carbonate without the influence of reefs.

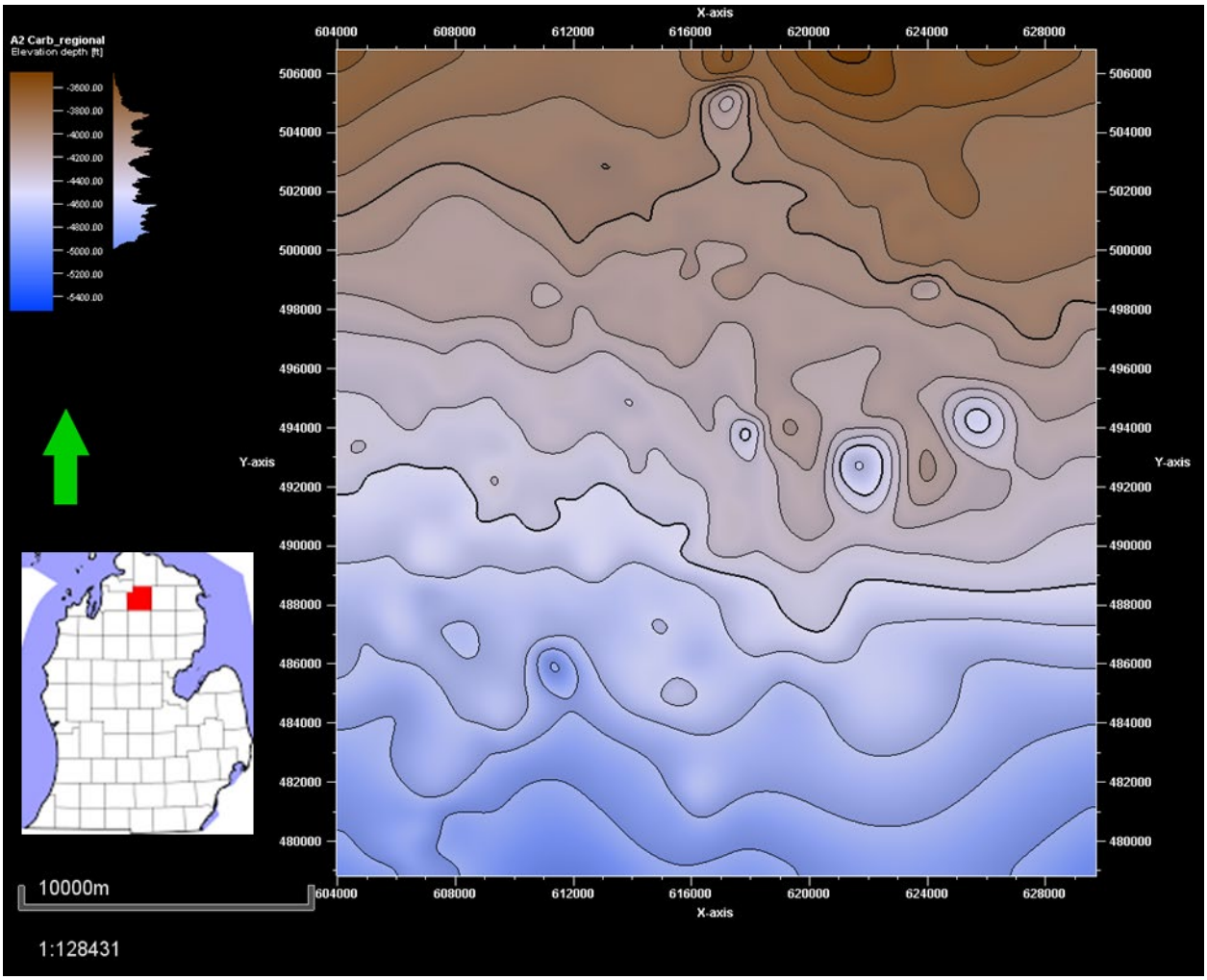


Figure 3-9. Structure map of the A-2 carbonate without the influence of the reefs.

3.5 Wireline Log Interpretation

3.5.1 Basic Log Analysis

Basic log analyses include gamma ray, bulk density, neutron porosity, and photoelectric index logs for defining formations and zones, characterizing lithology, and developing reservoir flags. First, logs were quality-checked to eliminate erroneous data. Log averages were calculated for each zone to evaluate distributions and geographical variations. Table 3-4 lists the wireline logs used and the information learned from each log.

Table 3-4. Summary of basic wireline logs and use.

Log Code	Description	Data Uses
GR	Gamma ray	GR was used to correlate formation tops. The GR log is also used as a shale/clay index to determine the reservoir fraction of the deep saline formation.
NPHI	Neutron porosity	NPHI was used to estimate porosity.
RHOB	Bulk density	RHOB was used as a lithology indicator and to estimate density porosity.
PE	Photoelectric index	PE was used as a lithology indicator to identify changes throughout the formation.

Crossplot analyses were also used to evaluate changes in formation lithology and porosity. Neutron porosity was plotted against bulk density data on an industry standard crossplot (Figure 3-10). Additionally, crossplot porosity greater than 5% was flagged to highlight intervals of higher reservoir potential.

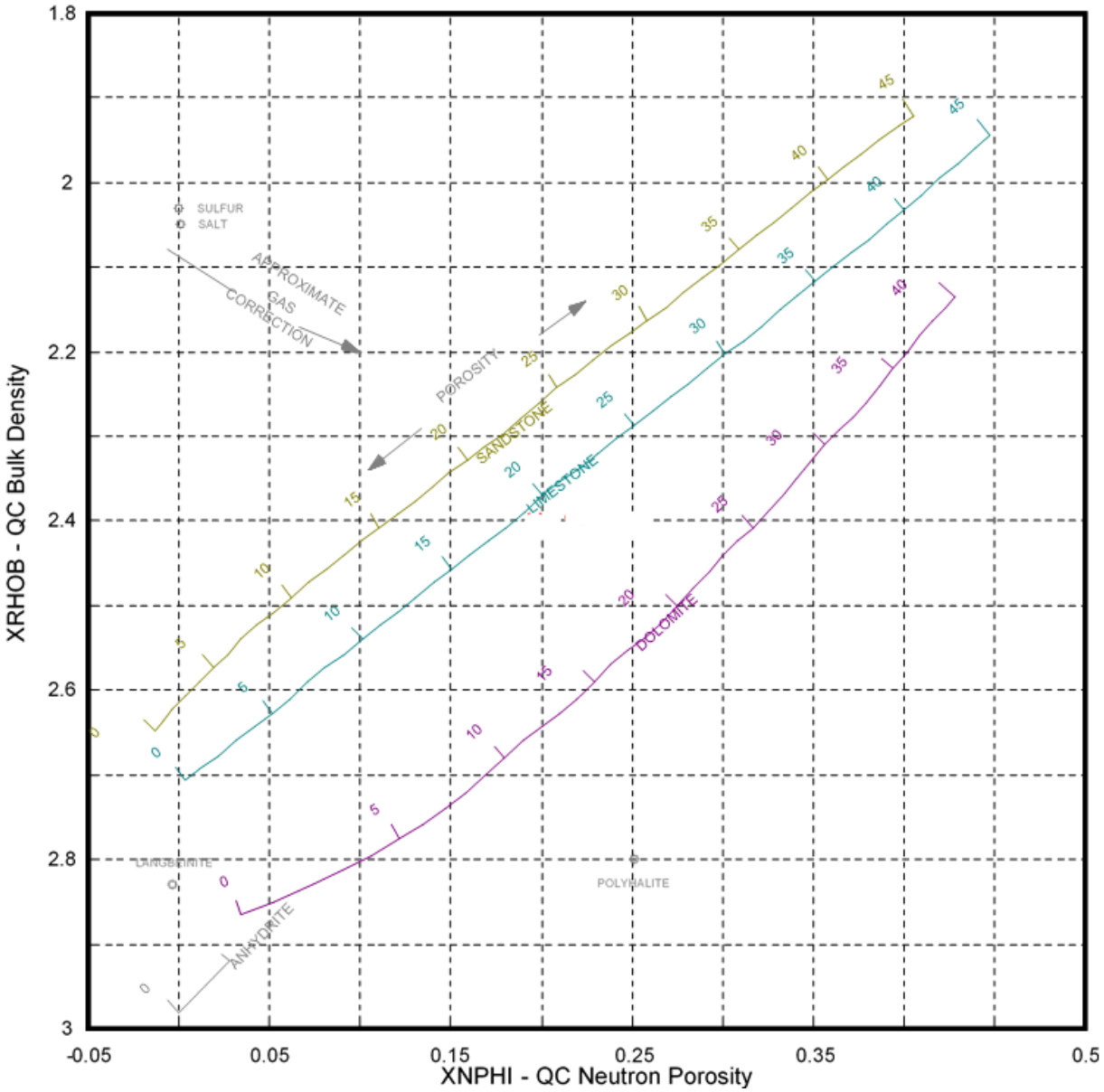


Figure 3-10. Industry standard crossplot of neutron porosity and bulk density used to evaluate formation lithology, porosity, and influence of shale.

3.5.2 Advanced Log Analysis

Advanced logs were not routinely available but were analyzed when collected. These include elemental spectroscopy and image logs. The elemental spectroscopy incudes gamma ray, borehole caliper, porosity, spectra logs, mineral brittleness index, and elemental spectroscopy mineralogy curves. Spectral logs include elemental analysis of potassium (K), thorium (Th), uranium (U), silicon (Si), calcium (Ca), magnesium (Mg), iron (Fe), aluminum (Al), and sulfur (S) curves. Log analysis combined these data with regional knowledge to calculate bulk volumetric and lithological zones of interest.

The primary elemental spectroscopy analysis technique consists of plotting weighted fractions of elements on ternary diagrams to derive mineralogical and lithological data. The elemental spectroscopy tool operates by generating a pulse of high-energy neutrons, subsequently measuring the inelastic and

captured gamma ray radioactive decay reactions of the subsurface formations. The tool provides a detailed breakdown of lithology components which furthers the understanding of specific formation compositions and changes. Figure 3-11 is an example header of an elemental spectroscopy log showing the elemental and lithology breakdown.

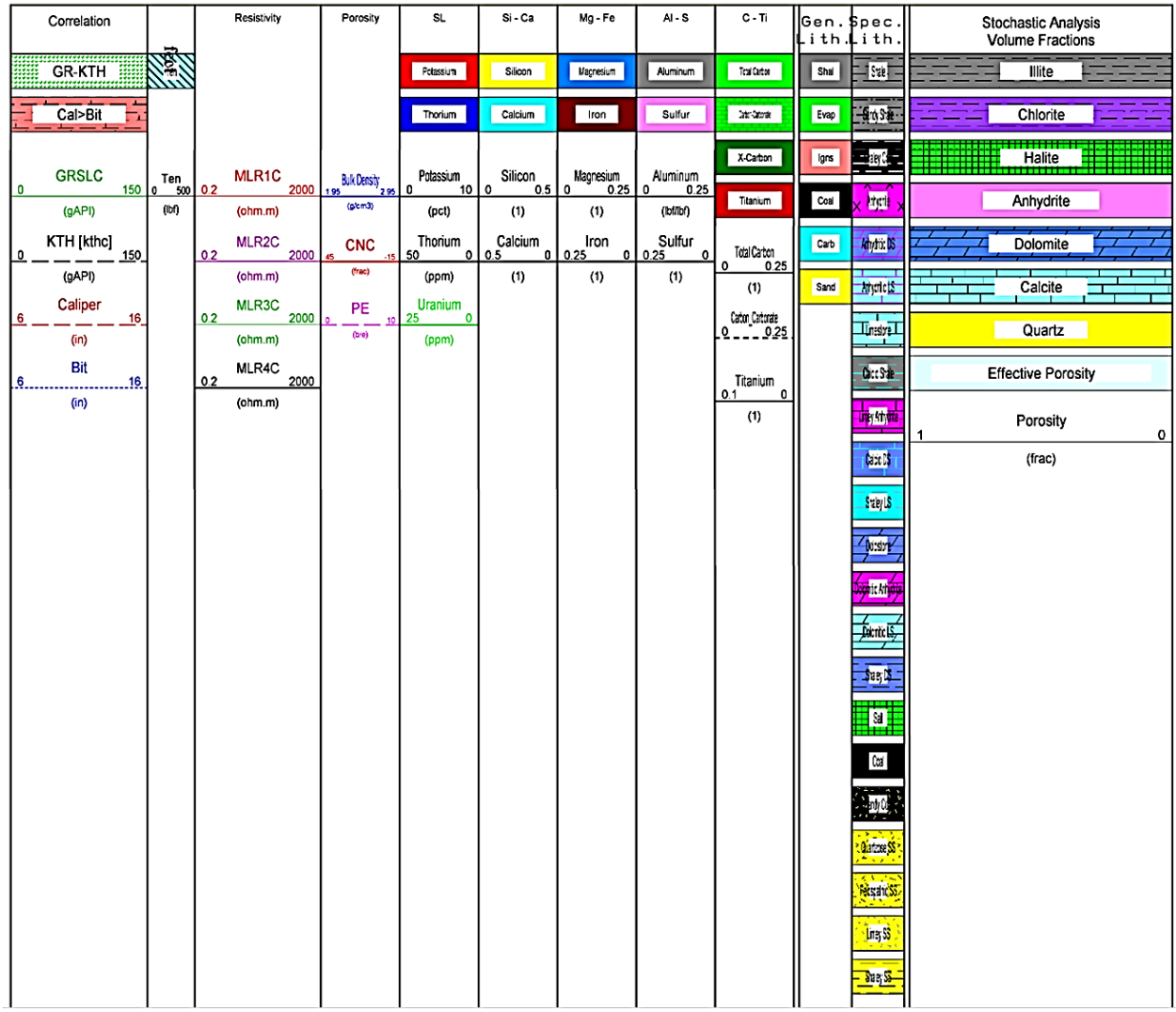


Figure 3-11. Elemental capture spectroscopy header log (Baker Hughes).

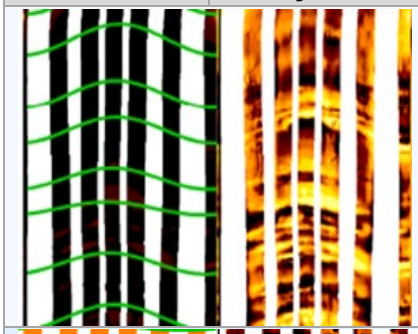
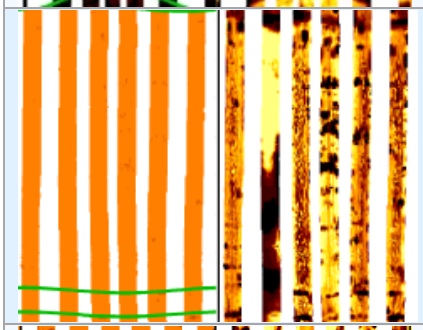
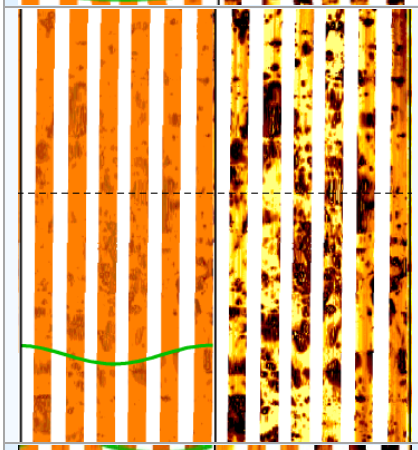
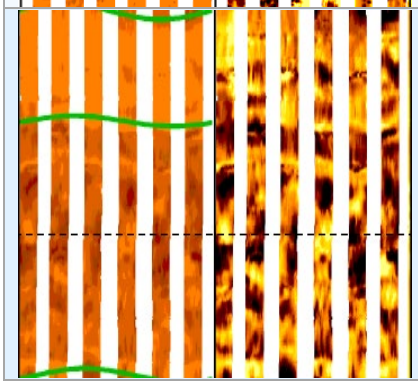
This image log analysis focuses on identifying stratigraphic/structural trends and features, bedding orientations, and electro-textures, in addition to intervals with significant amounts of porosity. The analysis was based almost entirely off the resistivity image; however, within some intervals, large fractures and pores showed up in acoustic images, serving as a good verification agent.

Acoustic and electric borehole image logging plays a vital role in modern reservoir characterization, leading to successful hydrocarbon and carbon storage ventures. Acoustic imaging tools are elongate devices that contain a rotating piezoelectric transducer that operates in a pulse echo mode at an ultrasonic frequency. The transducer acts as both transmitter and receiver, recording the travel time and amplitude of an acoustic pulse, which is reflected off the borehole wall or casing. Magnetometers provide azimuthal data for each scan the piezometer makes (Prensky, 1999). Acoustic travel time is a function of the distance to the borehole wall or casing and the velocity of the borehole fluid, which in turn is related to the density of the borehole fluid. The acoustic amplitude is a function of acoustic impedance (product of density and velocity) (Prensky, 1999). Modern micro-resistivity devices are pad-type devices that consist of multiple independent arms, with each arm consisting of an array of closely spaced microelectrodes. These pads propagate current into the formation, and microelectrodes measure current density across the pad, keeping a constant potential relative to the return electrode. Any variation in current density is due to formation resistivity (Prensky, 1999).

Acoustic and resistivity images are presented in both *static* and *dynamic* views, which differ by normalization of image features. In static normalization, histogram equalization techniques are used, where a range of resistivity values for the entire well is computed and partitioned into 256 color hues, setting the color spectrum. This type of normalization is best used for identification of large-scale resistivity variations. Dynamic normalization is used to enhance smaller-scale resistivity features that are subdued during static normalization. The color intensity of dynamic view is continuously rescaled over a small interval (a few meters), resetting the hue spectrum with respect to depth (Prensky, 1999). For consistency within this report, the static view is used to identify features, and the dynamic view is used only to aid in interpretation.

Changes resistivity image-measured electro-textures were described by examining factors such as continuity, shape, size, and distribution of conductive/resistive features within the image profile. Electro-textures may be generally described as homogenously resistive/conductive, heterogeneous, or a mixed (interbedded) homogenous and heterogeneous texture. Table 3-5 shows typical textures that are encountered, briefly describes the textures, and provides corresponding interpretations of the electro-textures. Interpretations of lithology and zones of high porosity development were checked with gamma ray, bulk density, photoelectric, and neutron porosity logs. When possible, core photos were compared with borehole image logs for improved accuracy.

Table 3-5. Methodology for describing the general behavior of electro-textures with possible interpretations.

STAR Profile		Description	Possible Interpretations
Static	Dynamic		
		• Homogenously conductive • Static view	• Uniform show of water content • Micro-porosity (if limestone) • Shale (clay-bound water) • Intercrystalline porosity (If dolomite)
		• Homogenously resistive • Static view	• Uniform lack of water content • No porosity, tight rock • Tight dolomite, limestone, sandstone, micrite • Lack of bedding contacts ~ thickly or massively bedded
		• Heterogenous materials • Static view	• Presence of primary and secondary porosity development (pore types may be inferred by the scale, shape, size of features) • Increasing heterogeneity • Occurrence of discontinuous conductive features could suggest increasing degrees of bioclastic constituents and thus changes in carbonate lithology
		• Mixed homogenous/ heterogeneous textures	• Interbedded intervals with an array of interpretations associated with heterogeneous and homogenous textures discussed above • Interbedded nature suggests a complex depositional environment with shifting conditions that may or may not be cyclical in occurrence

3.5.3 Petrophysics

Reservoir Calculations

Petrophysical analyses were conducted using wireline logs and core data. First, average porosity logs were calculated by (1) using grain density from core data (Table 3-6) to calculate density porosity from bulk density logs, and (2) taking the average of neutron porosity and density porosity. Density porosity was calculated from Equation 3-1:

$$\phi_D = (\rho_{ma} - \rho_b)/(\rho_{ma} - \rho_{fl}) \qquad \textbf{Equation 3-1}$$

where:

ϕ_D = density porosity
ρ_{ma} = matrix density (based on core data)
ρ_b = bulk density (from the density log)
ρ_{fl} = fluid density (assumed brine: 1.15 g/cm^3)

Table 3-6. Grain density used to calculate average porosity logs by lithology.

Lithology	Grain Density (g/cm^3)
Limestone	2.71
Dolomite	2.83
Mixed Carbonate	2.77
Anhydrite	3.0

Average porosity was calculated using both density and neutron porosities with Equation 3-2:

$$\phi_A = (\phi_D + \phi_N) / 2 \qquad \textbf{Equation 3-2}$$

where:

ϕ_A = average porosity
ϕ_D = density porosity
ϕ_N = neutron porosity

Average porosities are used as representative values of formation porosity because neutron and density log porosity derivations are each susceptible to inaccuracies under certain conditions, such as the presence of gas, washouts, and atypical mineralogy.

Next, evaluation of reservoir petrophysical properties included calculation of net thickness, net-to-gross (NTG) ratio, porosity thickness, and average net porosity. Petrophysical properties are further defined in Table 3-7.

Table 3-7. Definitions of petrophysical properties with data inputs needed.

Property	Definition	Data Input/Quantification
Total Reservoir	Portion of the deep saline formation composed of sedimentary lithologies with conventional reservoir potential (e.g., sandstones and carbonates)	Bulk volume of the subsurface unit estimated to have gamma ray values ≤ 50 gAPI
Net Reservoir	Portion of the total reservoir associated with interconnected porosity that is potentially accessible to injected CO_2	Bulk volume of the subsurface unit estimated using gamma ray and porosity cutoffs
NTG Ratio	Ratio of net reservoir to total reservoir	Thickness of net reservoir/thickness of total reservoir
Porosity Thickness	Thickness of available pore space that is potentially accessible to injected CO_2	Porosity multiplied by net reservoir thickness
Average Net Porosity	Average porosity of the net reservoir	Average porosity after meeting gamma ray and porosity cutoffs

Bulk Density from Sonic

Many wells in the Michigan Basin do not have bulk density logs available due to age or operator preference. However, acoustic travel time (sonic, travel time [DT]) logs were often available. Where bulk density was missing, Gardner's equation (Equation 3-3) was used to estimate the bulk density from sonic logs. Standard values were used. Gardner's equation is mostly used for carbonate rocks and does not estimate bulk density accurately for salts. Anhydrites will have similar bulk density as carbonates due to similar rock velocities.

$$\rho = \alpha V_p^{\beta}$$

Equation 3-3

where:

ρ = bulk density of the rock
Vp = p-wave velocity of the rock from sonic logs
α and β = derived constants set to 0.23 and 0.25, respectively

Water Saturation (S_w) from Resistivity

Water saturation calculations are performed to determine the percentage of the pore space that is filled with water and, thus, inversely, what percentage of available pore space is filled with hydrocarbons. Water saturation was calculated using the Archie equation, a standard oil and gas formula shown in Equation 3-4:

$$S_w = \left(\frac{a * R_w}{R_t * \emptyset^m}\right)^{\frac{1}{n}}$$

Equation 3-4

where:

S_w = water saturation of the uninvaded zone (%)
R_w = formation water resistivity (ohm-ft)
R_t = formation resistivity (ohm-ft)
Ø = porosity (%)
a = tortuosity factor
m = cementation exponent
n = saturation exponent

Values for formation resistivity (R_t) and porosity (ø) were derived from the wireline logs. Formation water resistivity (R_w) value was determined at each reef field dependent on salinity. Constants a, m, and n were set to industry standard values of a=1, m=2, and n=2.

Water resistivity values were estimated using a resistivity and porosity crossplot and the salinity of the formation fluids. The resistivity curve trends with the neutron porosity by decreasing with increasing porosity. The Archie equation (Equation 3-4) was used to calculate water saturation trends to fit the cross-plot data (Figure 3-12). A Rw value of 0.1 ohm-m was used because it best captured the range of resistivity values. Additionally, estimated salinities greater than 300,000 parts per million and temperatures near 100ºF have recorded Rw values of 0.1 ohm-m or less.

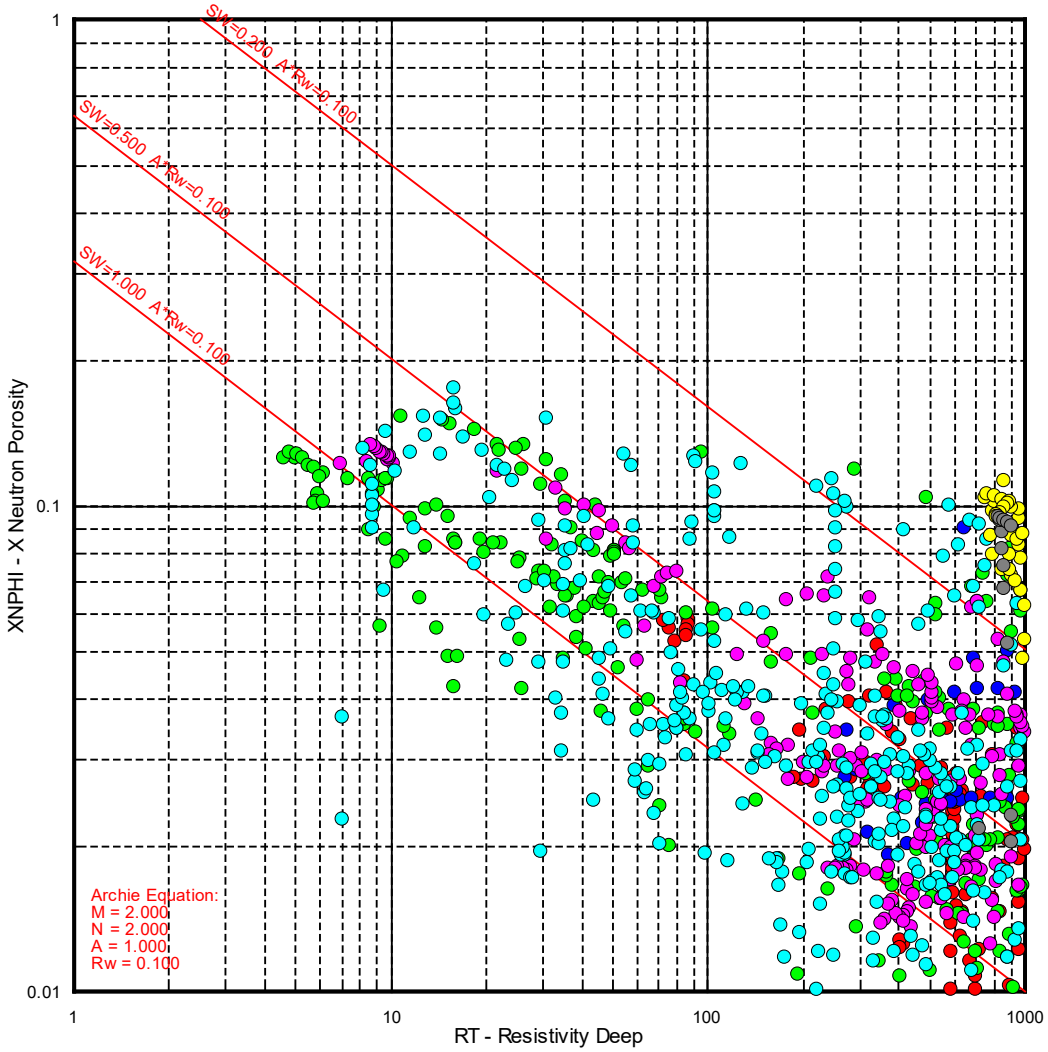


Figure 3-12. Crossplot of resistivity and neutron porosity for wells in an example reef field showing a strong decrease in resistivity with increasing porosity. Colors represent different wells.

Influence of Salt on Bulk Density

Salt plugging in carbonate intervals can greatly decrease porosity and permeability in the reservoirs; thus, it is important to identify and trace its occurrence through the reef complexes. Salt has a low bulk density of 2.04 g/cm^3, where dolomite is on average 2.83 g/cm^3 and limestone is 2.71 g/cm^3. The influence of a lower-density mineral, such as salt, in a carbonate will lower the total bulk density of the rock. Preliminary plots were created to predict the influence of salt in a carbonate to aid with interpretation using Equation 3-5 and Equation 3-6.

$$\rho_b = (1 - \emptyset)\rho_m + \emptyset\rho_f$$

Equation 3-5

$$\rho_m = S_s\rho_s + S_c\rho_c$$

Equation 3-6

where:

ρ_b= bulk density (g/cm^3)
ρ_s = density of salt (g/cm^3)
ρ_c = density of carbonate (g/cm^3)
ρ_m = matrix density (g/cm^3)
ρ_f = fluid density (g/cm^3)
ø = porosity
S_s = percentage of salt
S_c = percentage of carbonate

Salt plugging can be detected using bulk density in a pure limestone and pure dolomite case by identifying decreases in bulk density. However, for mixed carbonate systems, there is an overlap between salt-plugged limestone and dolomite where the resulting bulk density could indicate either scenario. Figure 3-13 illustrates predicted bulk densities based on salt percentage, lithology, and porosity scenarios. The bulk density can be used as an indicator in end member carbonates but not for mixed carbonates. The predicted trends were used in cross-plot analysis to assist with interpretations of carbonates and salt plugs.

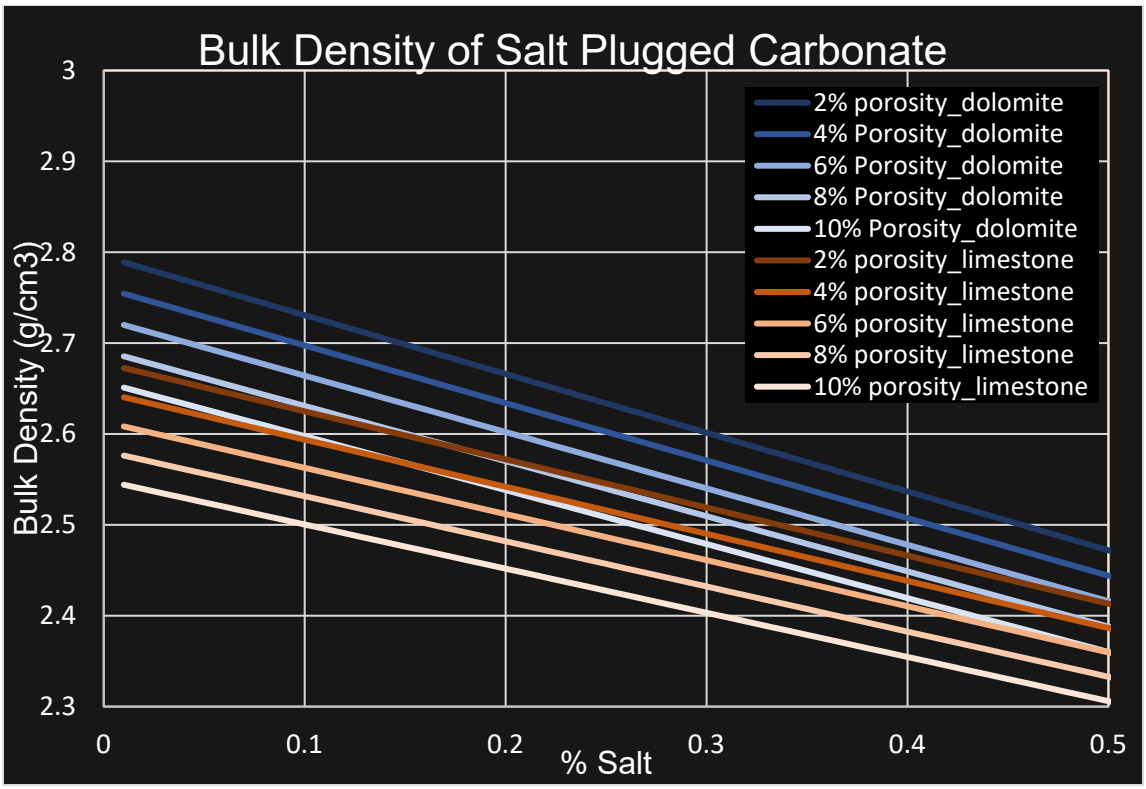


Figure 3-13. Plot of predicted bulk density versus percentage of salt for different lithology and porosity scenarios.

3.6 Seismic Analysis

The seismic interpretation of the Niagaran reef fields is critical to understanding the geometry of the reefs and the reservoir changes within the reefs. Large amounts of 3D seismic data have been acquired by Core Energy, LLC, and shared with Battelle (see Figure 3-1). Key seismic horizons were selected by Core Energy, LLC, and interpreted by a geophysicist at Battelle. This section describes the features used to identify key formations.

3.6.1 Seismic Horizons

A-2 Carbonate

The A-2 carbonate is a strong positive reflector located between 900 and 1,000 milliseconds (ms), depending on depth. On the edges of the reef and off reef, the top of a package of strong peaks and troughs represent alternating carbonate and salt. There is a slight plateau over the crest of the reef. The horizon on the reef crest is often picked the same as the Brown Niagaran due to little to no velocity contrast. The A-2 carbonate and Brown Niagaran are separated by carbonates and anhydrites instead of salt. Figure 3-14 outlines typical A-2 carbonate horizons in blue.

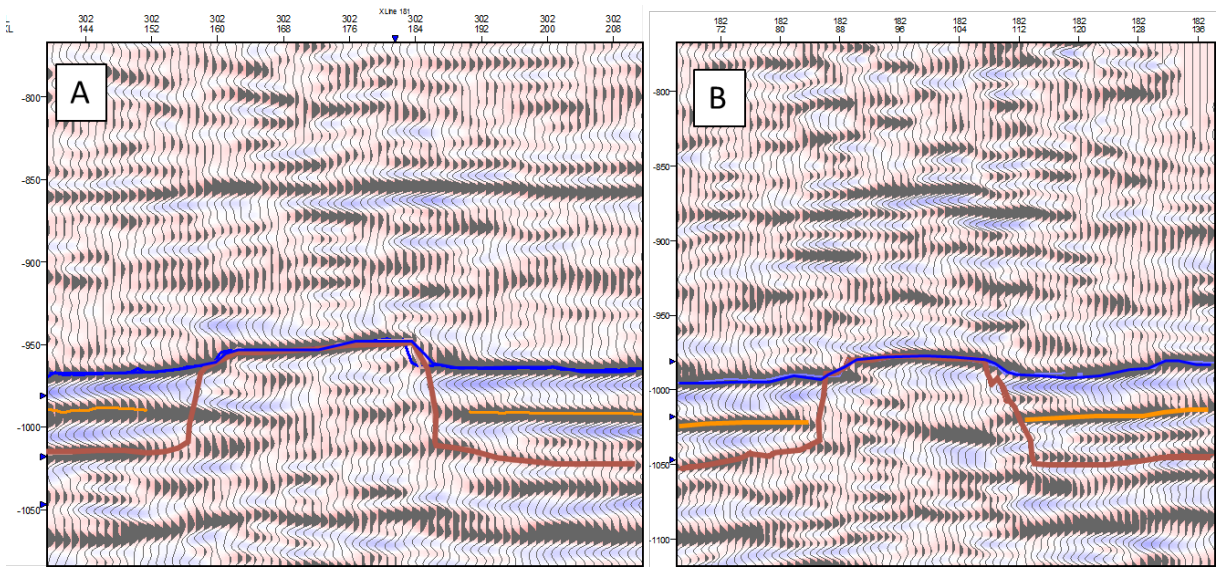


Figure 3-14. Examples of the seismic horizons for the A-2 carbonate (blue), A-1 carbonate (orange), and Brown Niagaran (brown) for Chester 2 (A) and Chester 16 (B).

A-1 Carbonate

The A-1 carbonate is a strong positive reflector located about 25 ms below the A-2 carbonate. The A-1 carbonate and A-2 carbonate are separated by a strong trough on the edges of the reef and off reef and which represents salt. The horizon cannot be traced over the Brown Niagaran due to little to no velocity contrast between formations. Figure 3-14 outlines typical A-1 carbonate horizons in orange.

Brown Niagaran

The Brown Niagaran is a strong positive reflector located about 25 ms below the A-1 carbonate off reef and at the base of the A-2 carbonate along the reef crest. It is noticeable by subtle plateaus along the horizons and the discontinuous A-1 carbonate. Internally, the Brown Niagaran has poor reflectors that do not have detail due to the high angles of the reef edges. Figure 3-14 outlines typical Brown Niagaran horizons in brown.

3.6.2 Seismic Mapping

Seismic horizons for the A-2 carbonate, A-1 carbonate, and Brown Niagaran, were used to generate seismic horizon maps. The convergent interpolation method was used in Petrel with a grid cell size of 50 x 50 meters. A smoothing algorithm was applied to each seismic horizon using one iteration across three grid cells. The resulting maps were used to define the geometry of each reef for the SEMs.

4.0 Dover 33

4.1 Reef History and Production Review

The initial (discovery) conditions of the Dover 33 reef field, summarized in Table 4-1, consist of original oil in place (OOIP), oil API gravity, discovery pressure and temperature, and fluid saturations. Initial gas saturations were recorded at zero, as gas was produced as it came out of solution during the production of oil.

Table 4-1. Summary of initial (discovery) conditions of the Dover 33 reef field.

		Discovery		Saturation		
OOIP (bbls)	API Gravity	Pressure (psi)	Temperature (°F)	Oil	Gas	Water
3,500,000	43.6	2,894	108	66.25%	0%	33.75%

The primary production period occurred at Dover 33 between the years of 1974 and 1996. CO_2 injection and EOR began in 1996. CO_2 injection was halted in 2007 and resumed in 2013. As of 12/31/2017, about 1,788,000 cumulative barrels (bbls) of oil have been produced and 1,555,400 metric tons (MT) of CO_2 have been injected into the Dover 33 field (Figure 4-1). Well 29565 had the highest cumulative oil and gas production of any other well in the reef field (Figure 4-2).

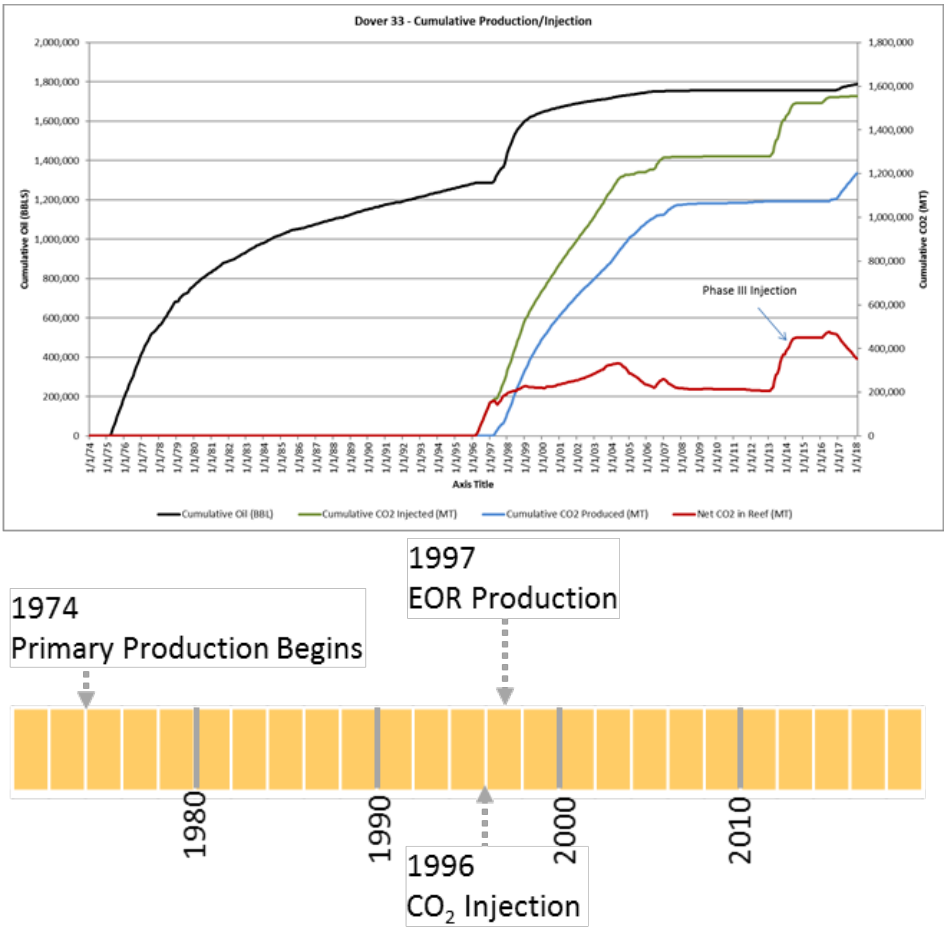


Figure 4-1. Cumulative production in the Dover 33 reef field from 1974 through 2017 showing an increase in production rates after EOR operations began in 1996.

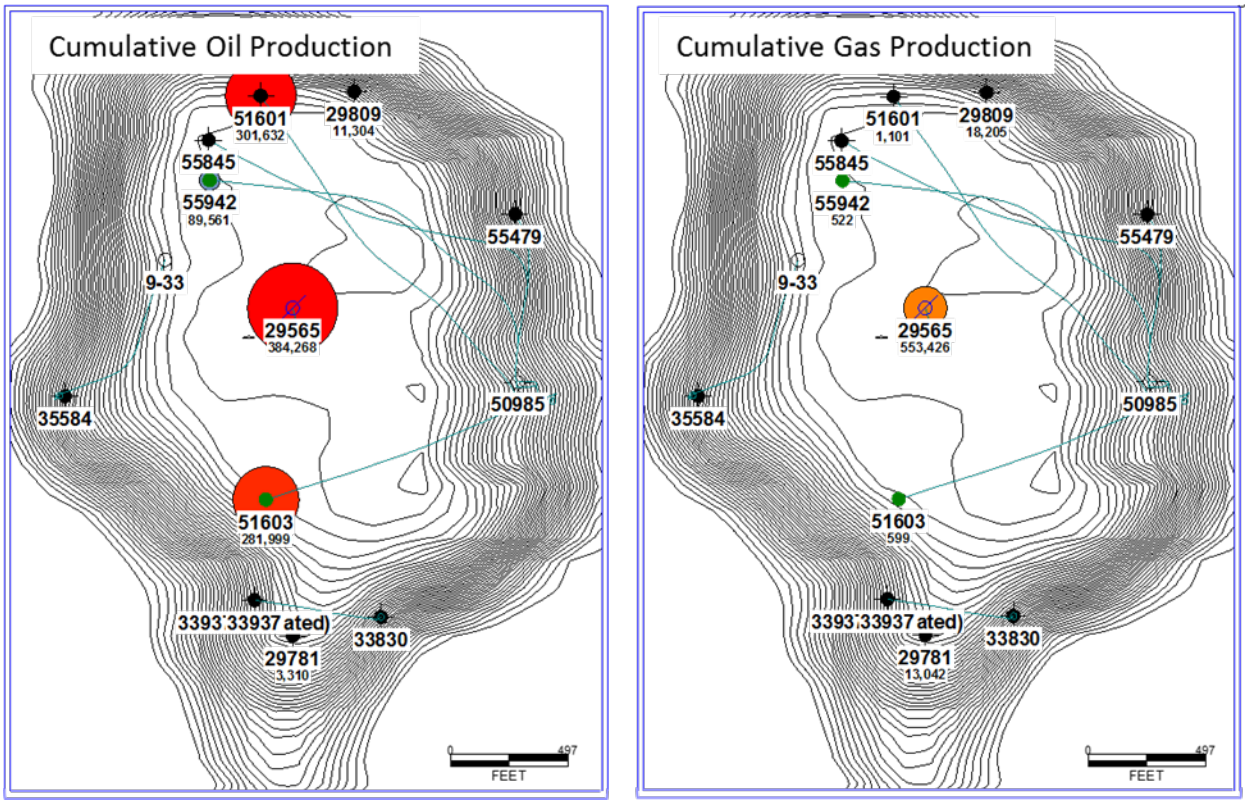


Figure 4-2. Cumulative oil and gas production maps in the Dover 33 reef field showing the highest production in the middle of the northern pod in well 29565.

4.2 Wireline Log Analysis

There are 20 wells that penetrate the Dover 33 reef system. Of these 20 wells, 18 have multiple LAS and/or raster logs available. All 18 have gamma ray, 15 have neutron porosity, and 6 have bulk density. Additionally, 8 wells have sonic logs; in cases where bulk density logs were not present, the sonic logs were used to calculate bulk density following the methodology outlined in Section 3.5.3. In addition, 12 wells have advanced logs available such as photoelectric index, pulsed neutron capture (PNC), and resistivity. Table 4-2 summarizes the wireline log data available for the 20 wells in the Dover 33 reef field; Figure 4-3 illustrates the well locations.

Table 4-2. Summary of available wireline log data for wells penetrating the Dover 33 reef field.

	Well UWI	2113729565000	2113729781000	2113729809000	2113729840000	2113730392000	2113731108000	2113731228000	2113731303000	2113732298000	2113733830000	2113733830010	2113735195000	2113735584000	2113750985000	2113751603000	2113751603000	2113755479000	2113755845000	2113755942000	2113706520000
CAL	Caliper																				
DT	Sonic																				
GR	Gamma Ray																				
LLD	Latero-Log Deep (Resistivity)																				
LLS	Latero-Log Shallow (Resistivity)																				
NPHI	Neutron Porosity																				
RES	Resistivity																				
PNC	Pulsed Neutron Capture	2												3		3					
RHOB	Bulk Density																				
SNP	Sidewall Neutron Porosity																				
XMAC	Acoustic log																				
BHP	Bottom Hole Pressure Monitoring																				

Note: Green shading indicates logs available by well and number indicated repeat collection.

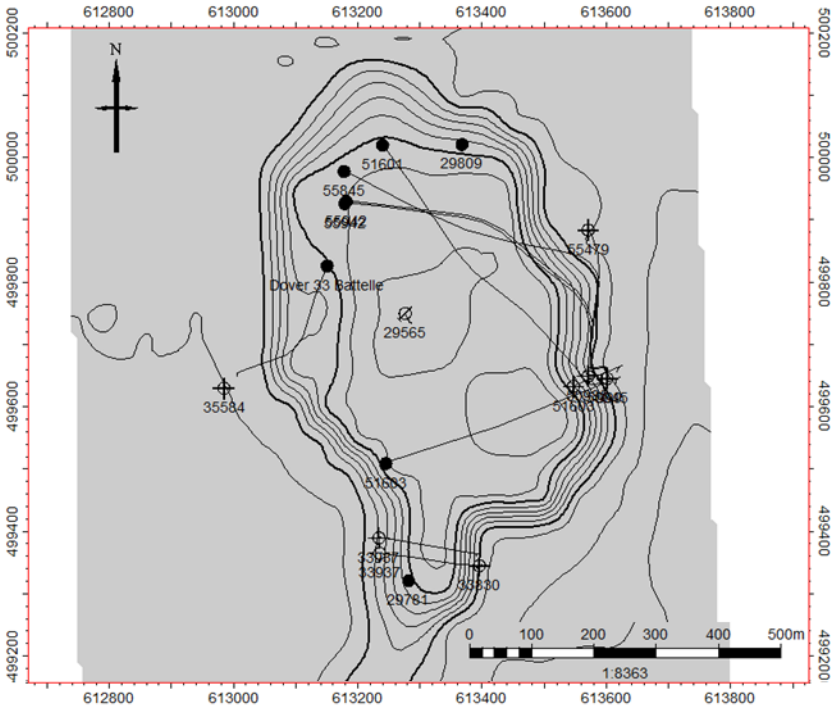


Figure 4-3. Map of the Dover 33 reef field showing locations of wells used in the geologic analysis.

4.2.1 Basic Log Interpretation

Well 35195

Well 35195 is located along the eastern edge of the southern reef pod. There are thin intervals of salt plugging and anhydrite at the top of the A-2 carbonate and A-1 carbonate, as indicated by the green and blue flags in Figure 4-4. Crossplot porosity greater than 5% occurs at the base of the A-1 carbonate and throughout the Brown Niagaran. The thin porosity flag in the A-2 Carbonate is due to a muddier matrix, informally called the A-2 Shale. The presence of salt in the A-2 evaporite indicates a flank location within the windward interval. Figure 4-4 shows the neutron porosity-bulk density crossplot for well 35195.

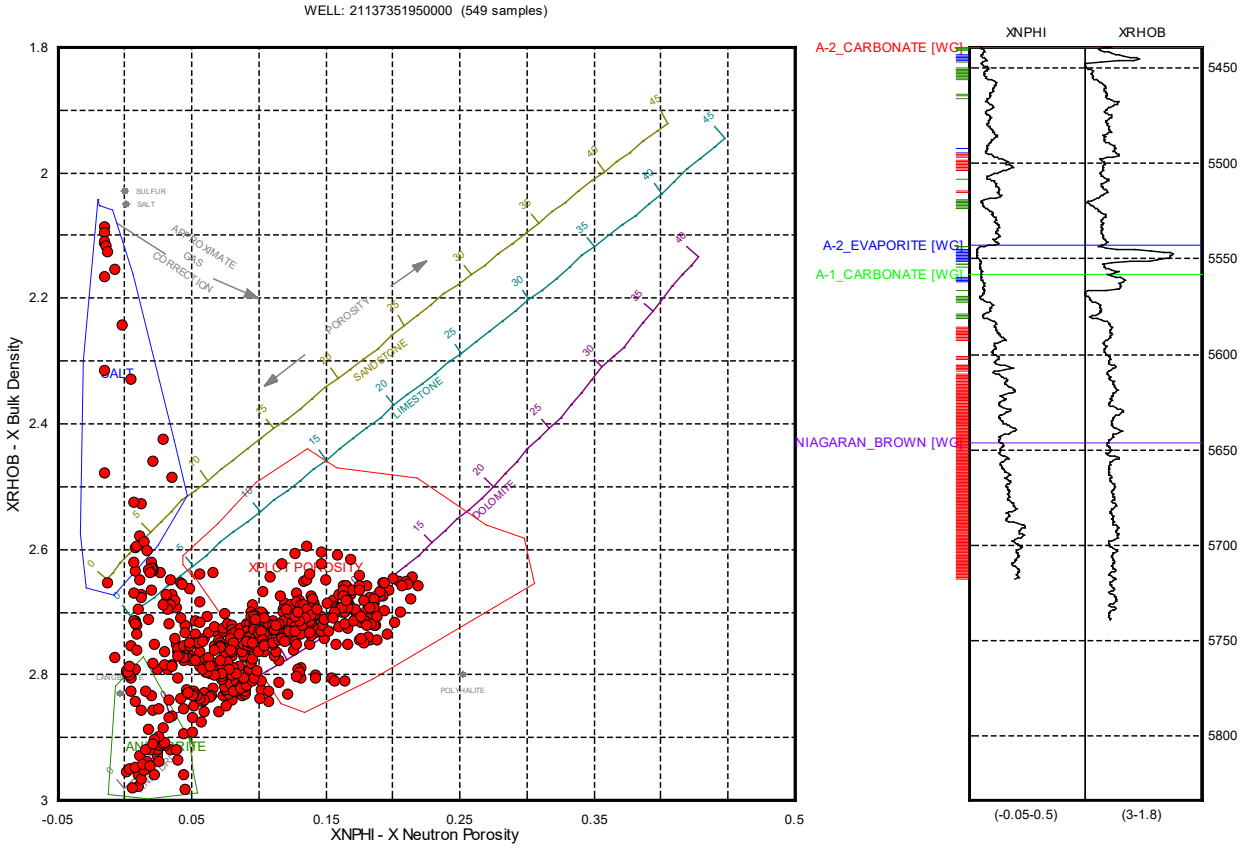


Figure 4-4. Neutron porosity-bulk density crossplot of well 35195 in the southern pod of the Dover 33 reef field showing high porosity in the lower A-1 carbonate and the Brown Niagaran.

The water saturation remained low for most of the formations but gradually increased near the top of the Brown Niagaran. Values were greater than 50% after 5,690 feet measured depth (MD), and the Brown Niagaran had an average of 43%. This limits the available reservoir to the top of the Brown Niagaran and the A-1 carbonate. Figure 4-5 is the resulting water saturation curve and histogram.

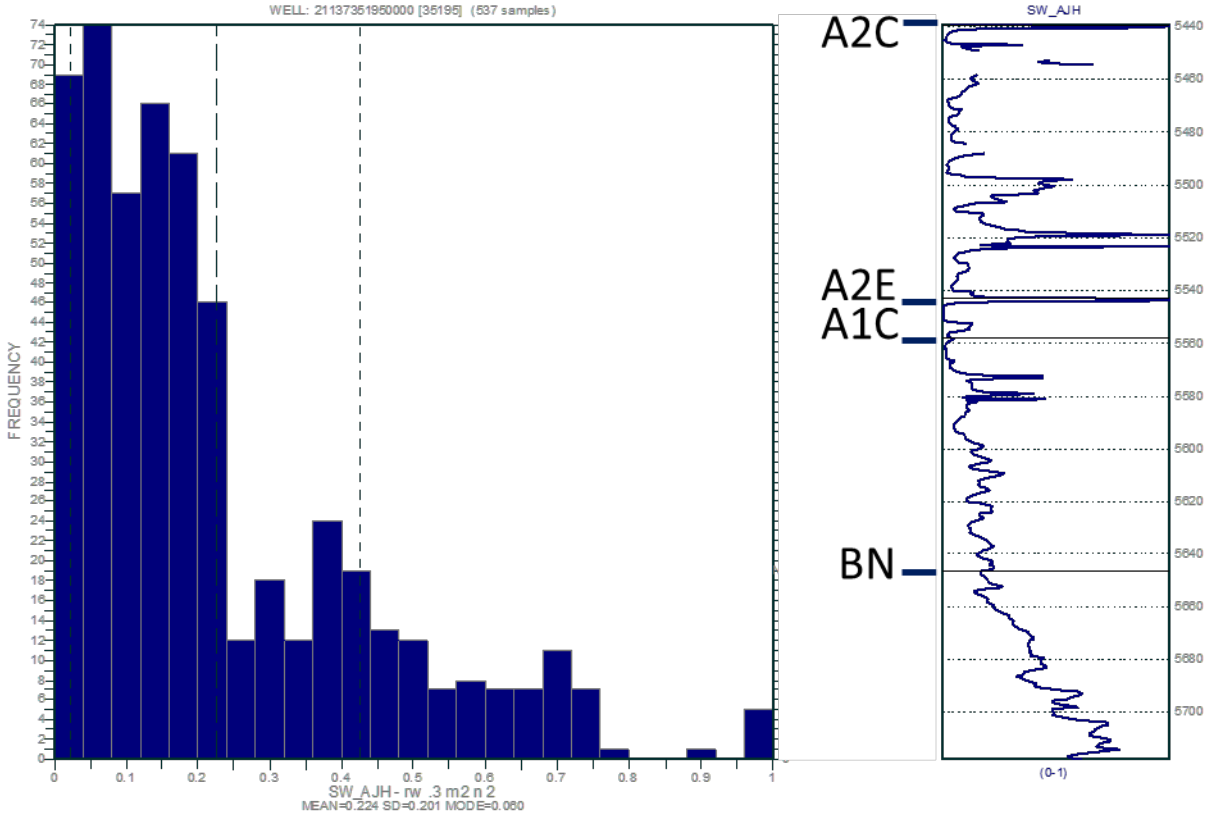


Figure 4-5. Water saturation curve and histogram for well 35195 showing a gradual increase at the top of the Brown Niagaran (BN).

Well 30392

Well 30392 is located in the northern flank of the southern pod in the Dover 33 reef field. There are thin intervals of potential anhydritic beds in the A-2 carbonate and A-1 carbonate, with the A-2 evaporite showing as a package of salt. Crossplot porosity greater than 5% occurs at the base of the A-1 carbonate and throughout the Brown Niagaran. The Brown Niagaran is thinner here (~100 feet), with a thicker A-2 salt (which is typical of a flank well). Figure 4-6 shows the neutron porosity-bulk density crossplot.

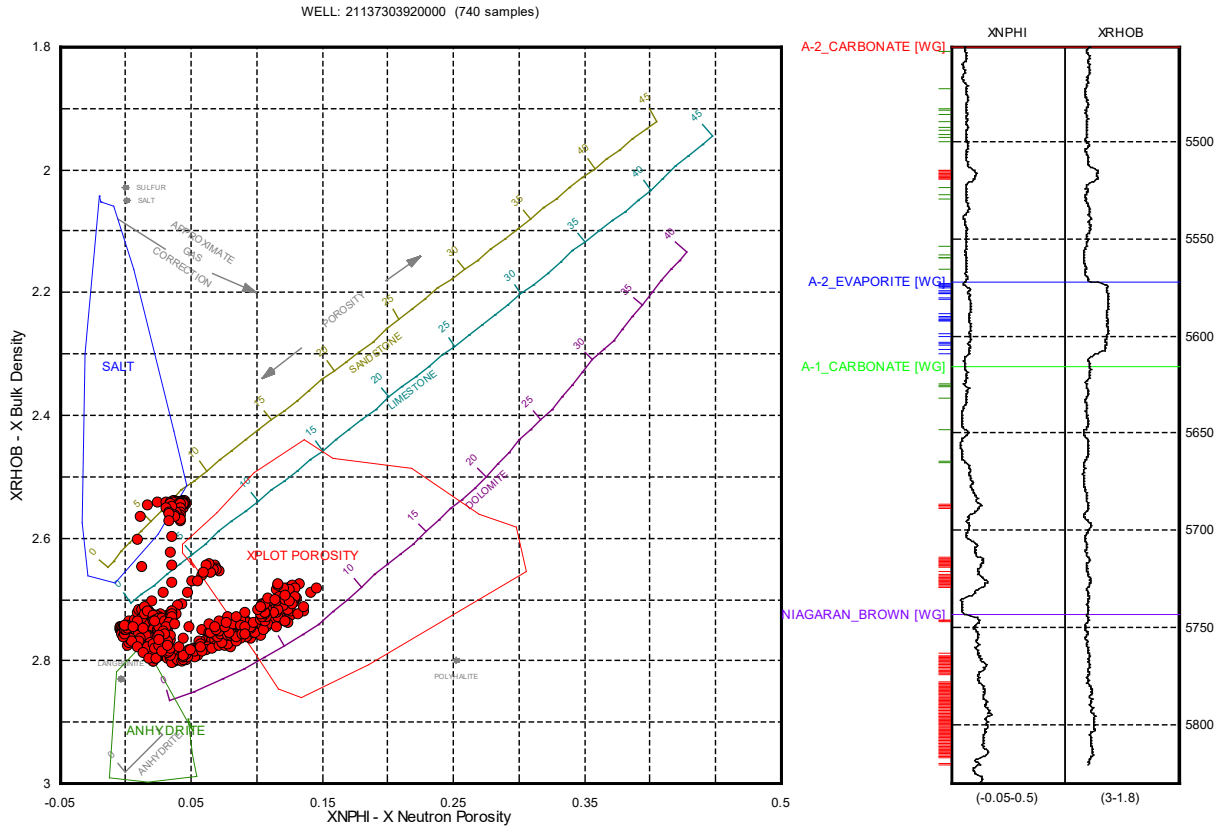


Figure 4-6. Neutron porosity-bulk density crossplot of well 30392 in the Dover 33 reef field showing porosity in the lower A-1 carbonate and the Brown Niagaran.

The water saturation was high (>40%) throughout this well due to its location along the flank. The water saturation increases in the mid-formation A-1 carbonate, near 5,660 feet MD. The Brown Niagaran is fully saturated, with an average water saturation of 80%. The porosity flags occur only in water-saturated intervals, which leave little to no reservoir potential over the formations of interest. Figure 4-7 is the resulting water saturation curve and histogram.

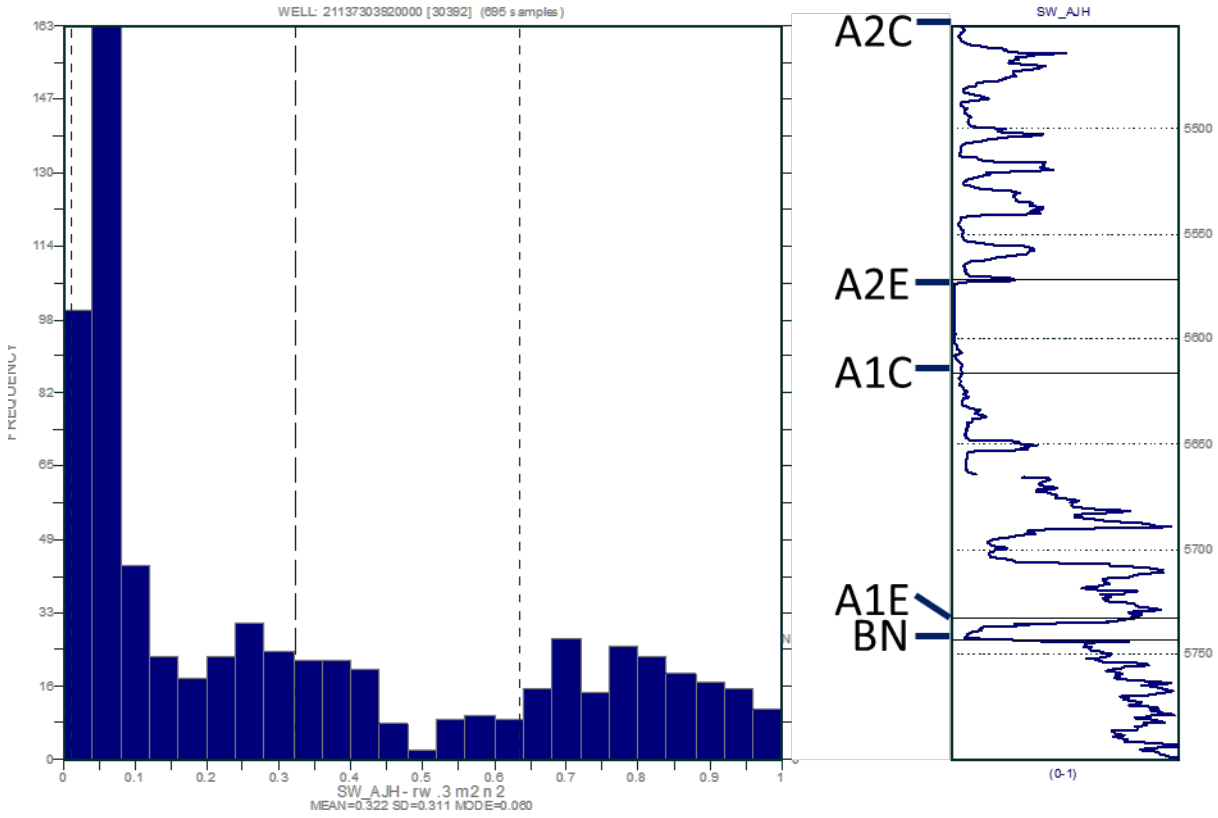


Figure 4-7. Water saturation curve and histogram for well 30392 showing higher water saturations in the A-1 carbonate and Brown Niagaran.

Well 29781

Well 29781 is located in the southern section of the northern reef pod. There are no indicators of salt plugging but some thin intervals of anhydrite occur in the A-2 carbonate. Crossplot porosity greater than 5% primarily occurred in the Brown Niagaran. The Brown Niagaran is relatively thin, which is consistent with a flank location. Figure 4-8 shows the neutron porosity-bulk density crossplot.

Water saturations remain low throughout the formations, with spikes in the presence of anhydritic layers. The saturations increase gradually in the Brown Niagaran formation, where saturation averages 13%. The logged interval in well 29781 might not have reached the oil/water contact at this location. The porosity identified in the Brown Niagaran has reservoir potential with low fluid saturations. Figure 4-9 shows the water saturation curve and histogram over the A-2 carbonate through total depth (TD).

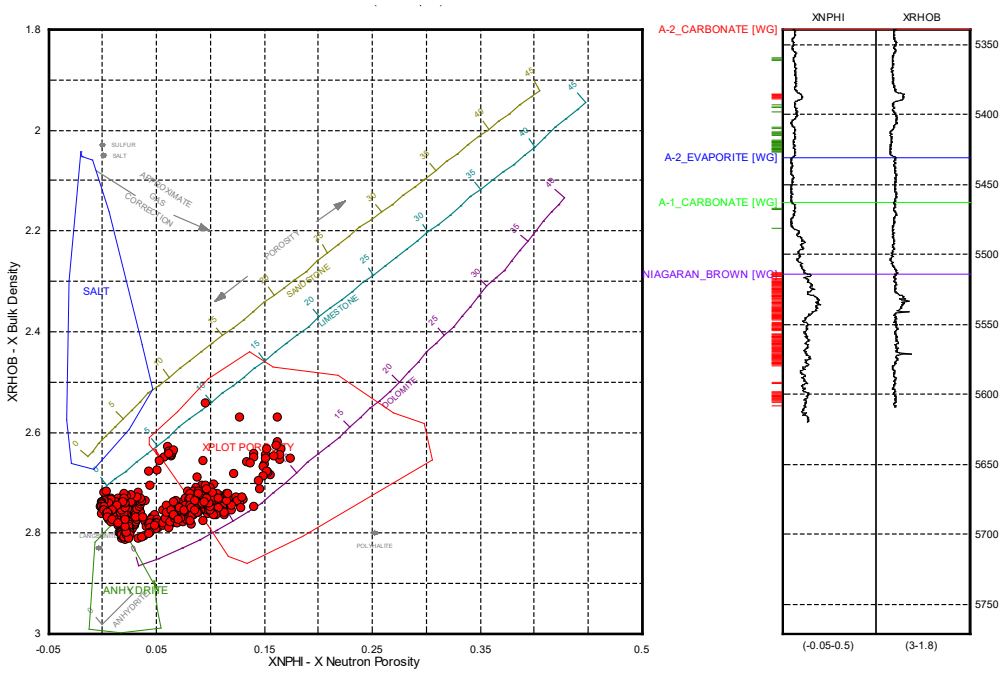


Figure 4-8. Neutron porosity-bulk density crossplot for well 29781 in the Dover 33 reef field showing porosity in the Brown Niagaran.

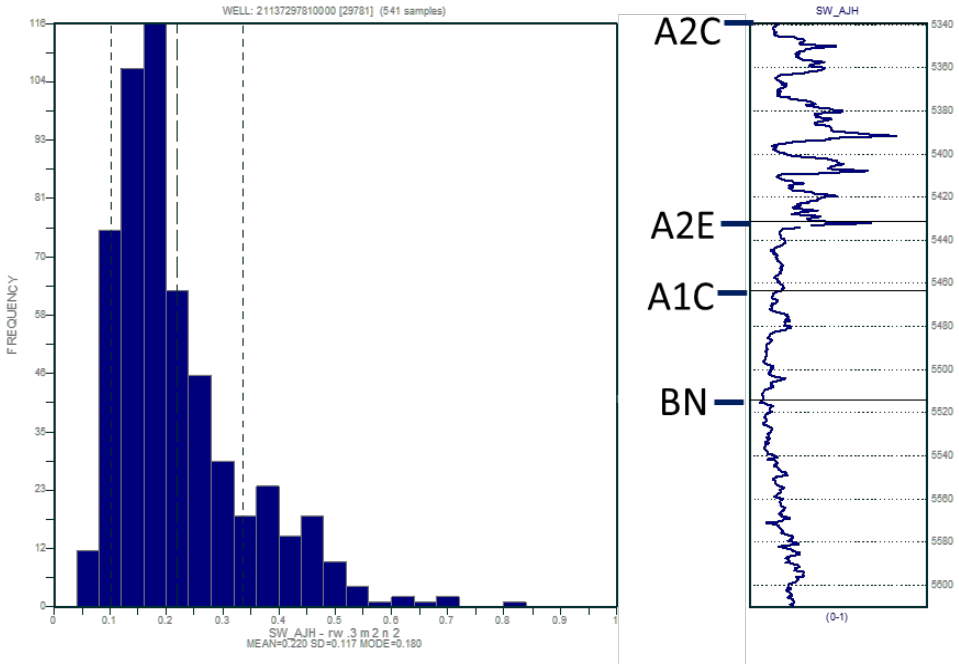


Figure 4-9. Water saturation curve and histogram for well 29781 showing low water saturations throughout the formations of interest.

Well 33830

Well 33830 is located in the southern flank of the northern reef pod. The A-2 evaporite is composed of salt with a relatively thin Brown Niagaran (which is consistent with a flank well). Crossplot porosity greater than 5% occurs in the base of the A-1 carbonate and through the Brown Niagaran (Figure 4-10). The water saturation increases rapidly in the A-1 carbonate at the oil/water contact. Where the porosity flags occurred, the formations are water-saturated, which limits the reservoir potential. Figure 4-11 is the resulting water saturation curve and histogram.

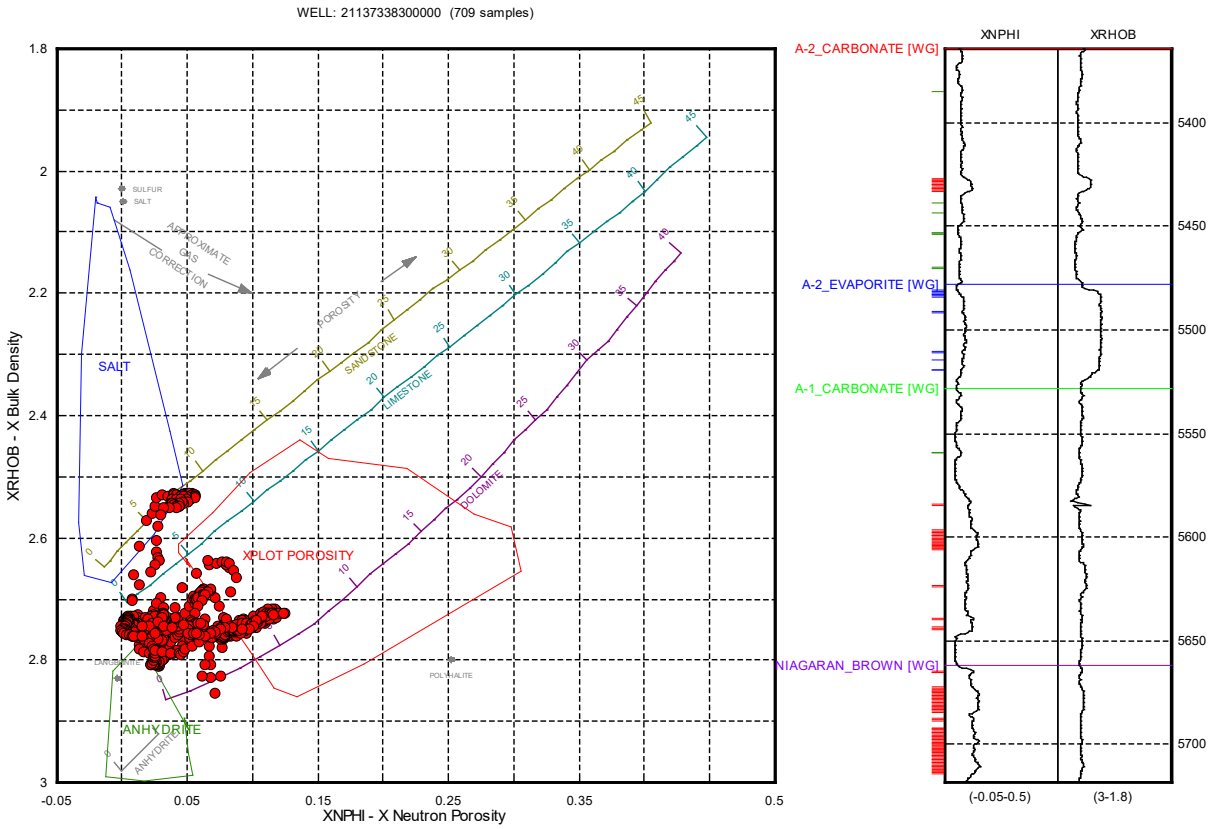


Figure 4-10. Neutron porosity-bulk density crossplot of well 33830 in the Dover 33 reef field showing salts (blue) in the A-2 evaporite and porosity in the lower A-1 carbonate and the Brown Niagaran.

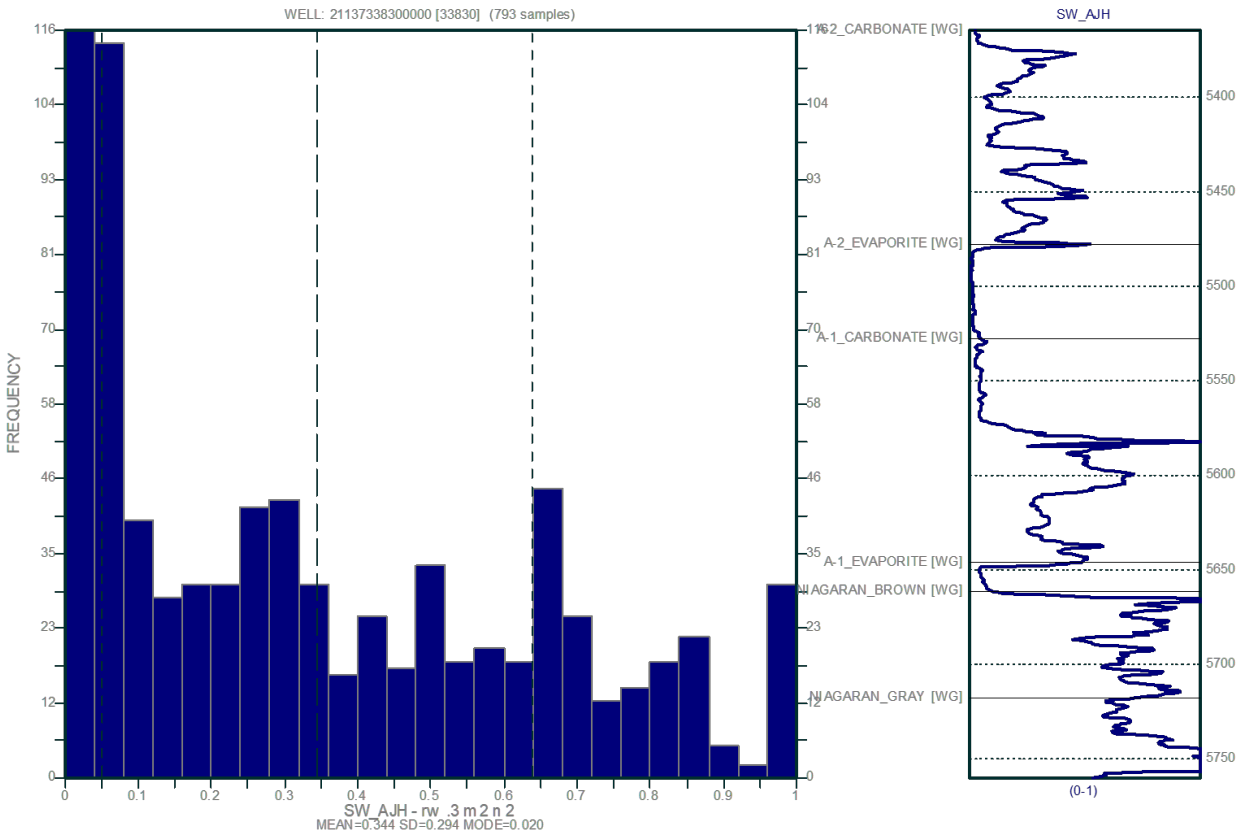


Figure 4-11. Water saturation curve and histogram for well 33830 showing an increase in water saturation in the mid-formation A-1 carbonate at the oil/water contact.

Well 50985

Well 50985 is located along the eastern edge of the Dover 33 reef field. The A-2 evaporite is composed of salt, which is indicated by the decrease in bulk density. Anhydrite occurs in intervals throughout the A-1 carbonate, indicated by the green flags in Figure 4-12. The increased presence of evaporites and a relatively thin Brown Niagaran is consistent with a flank position. Crossplot porosity greater than 5% was flagged in the base of the A-1 carbonate and through the Brown Niagaran (Figure 4-12). Resistivity logs were not available for this well, so no water saturations were calculated. Based on the high oil/water contact observed in similar wells, the oil/water contact in well 50985 is projected to occur in the mid-formation A-1 carbonate, resulting in low reservoir potential.

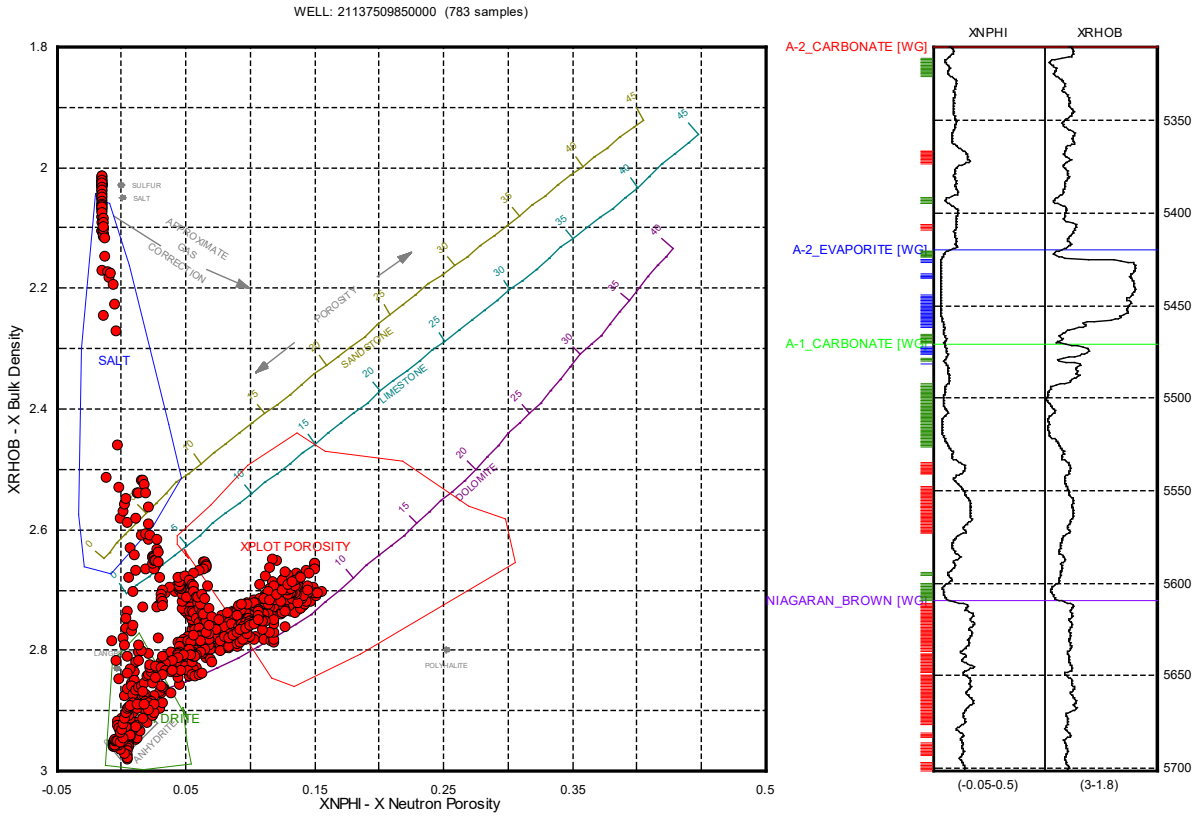


Figure 4-12. Neutron porosity-bulk density crossplot of well 50985 in the Dover 33 reef field showing salt (blue), anhydrite (green), and porosity (red) flags.

Well 35584

Well 35584 is located on the western edge of the Dover 33 reef field. The A-2 evaporite is composed of salt, and anhydrite occurs frequently in the A-1 carbonate. The presence of evaporites and the relative thin Brown Niagaran are consistent with a flank position. Crossplot porosity greater than 5% (red) occurs in the lower A-1 carbonate and the Brown Niagaran. Resistivity logs were not available for this well, so water saturation was not calculated. Based on the flank position of the well, the oil/water contact was projected to occur in the mid-formation A-1 carbonate, leaving little to no available storage space. Figure 4-13 shows the neutron porosity-bulk density crossplot.

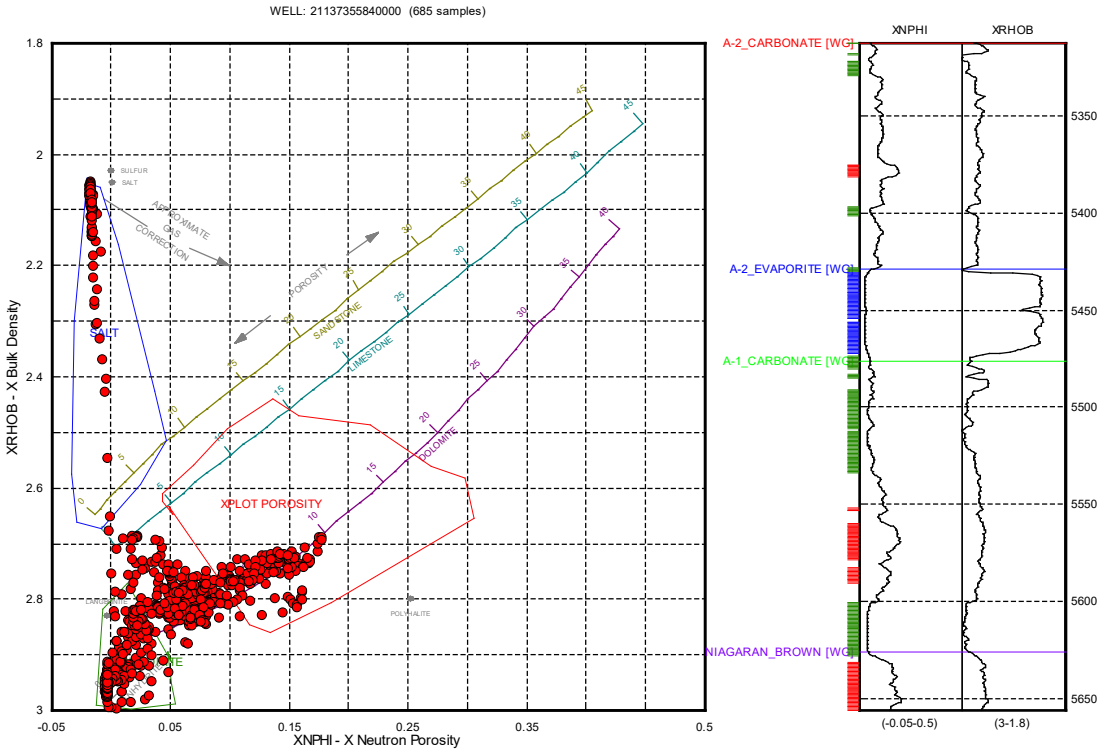


Figure 4-13. Neutron porosity-bulk density crossplot of well 35584 in the Dover 33 reef field showing salts (blue), anhydrite (green), and porosity (red) flags.

Well 29565

Well 29565 is the injection well located in the center of the Dover 33 reef field. There were no indicators of salt plugging through the formations of interest, but some thin layers of anhydrite occur. The Brown Niagaran is thickest at this well location, with numerous porosity flags throughout (Figure 4-14). The water saturation gradually increases in the Brown Niagaran mid-formation, at 5,490 feet MD near the oil/water contact. Below 5,490 feet, the water saturation increases to an average of 75%, leaving 100 feet of Brown Niagaran as potential reservoir. Figure 4-15 shows the resulting water saturation curve and histogram.

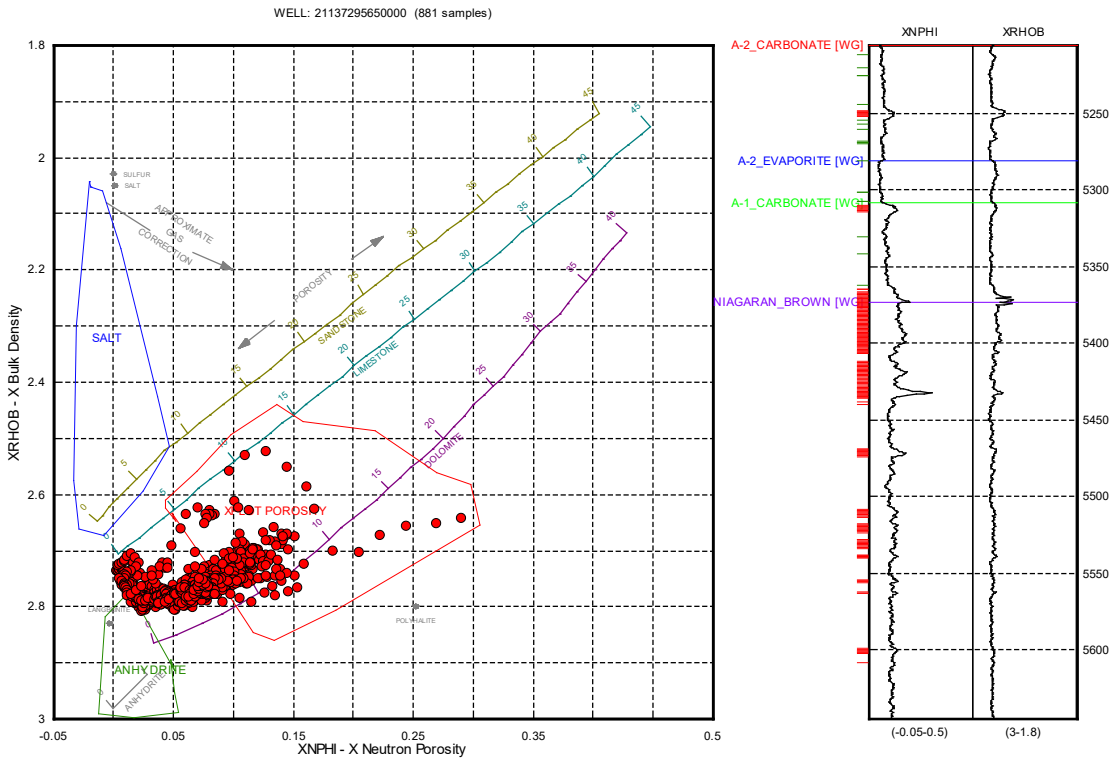


Figure 4-14. Neutron porosity-bulk density crossplot of well 29565 in the Dover 33 reef field showing a thick Brown Niagaran with numerous porosity flags (red).

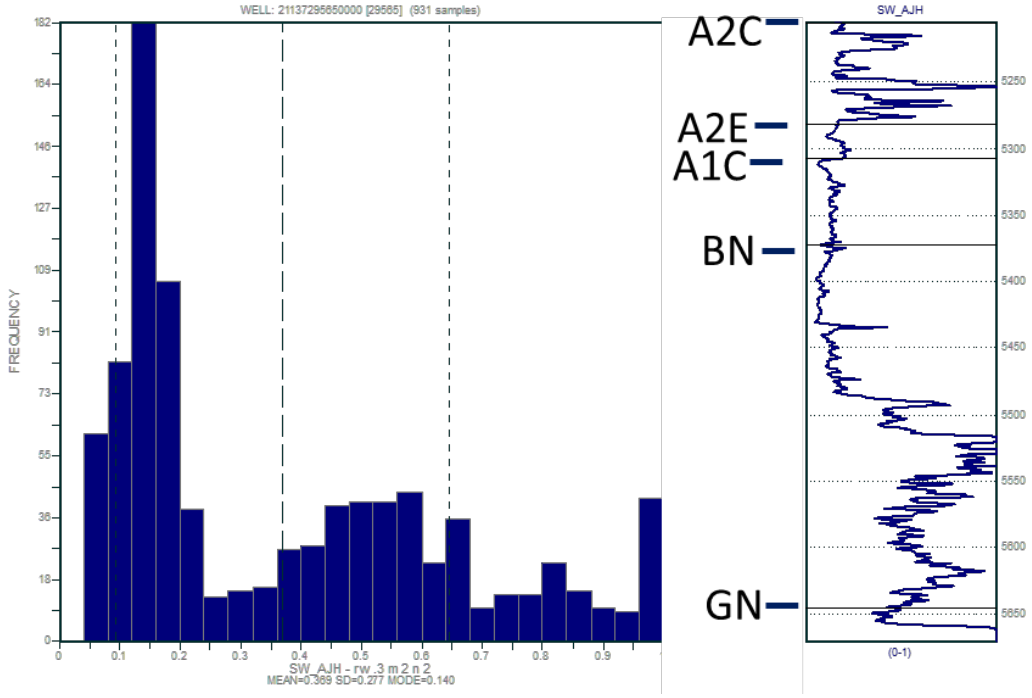


Figure 4-15. Water saturation curve and histogram for well 29565 showing in increase in saturation mid-Brown Niagaran.

Well 29809

Well 29809 is located in the northern section of the Dover 33 reef field. The A-2 evaporite is composed of salt and the Brown Niagaran is relatively thinner, consistent with a flank location. Crossplot porosity greater than 5% was flagged throughout the Brown Niagaran (Figure 4-16). However, the water saturation increases near the top of the Brown Niagaran, leaving only 10 feet of unsaturated dolomite. The water saturation in the Brown Niagaran is on average 56%, with values up to 100%. Figure 4-17 is the resulting water saturation curve and histogram.

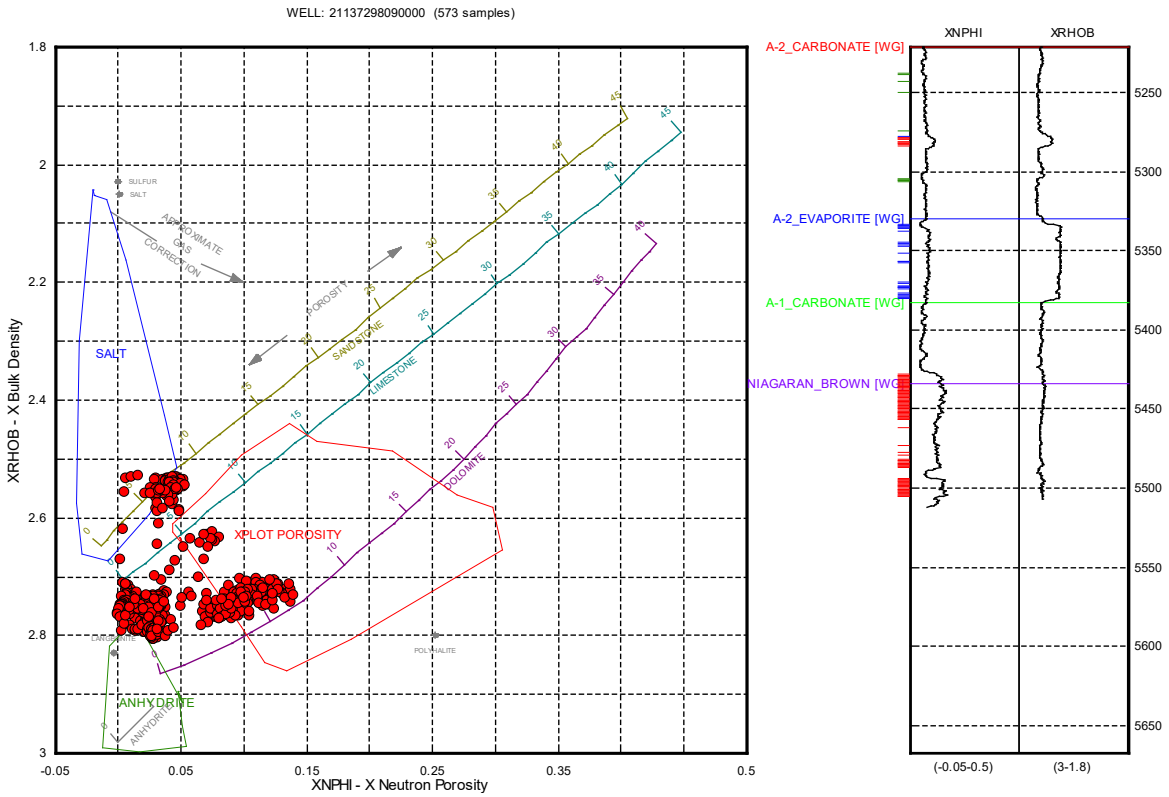


Figure 4-16. Neutron porosity-bulk density crossplot of well 29809 in the Dover 33 reef field showing porosity flags (red) in the Brown Niagaran.

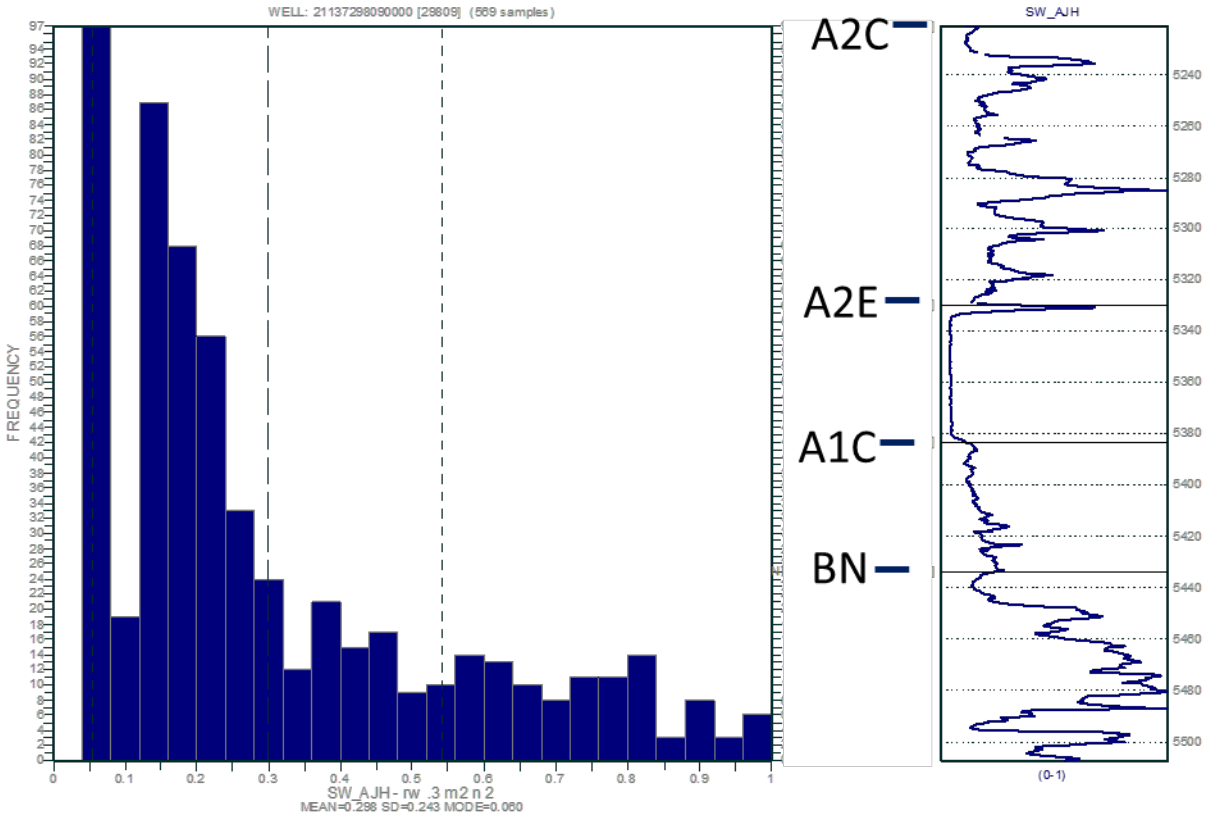


Figure 4-17. Water saturation curve and histogram for well 29809 showing an increase in water saturation in the upper Brown Niagaran.

Well 61209 (Lawnichak 9-33)

Well 61209 was recently drilled (2016) along the western side of the Dover 33 reef field post primary and secondary recovery. The A-2 carbonate is composed of anhydrite (green) and tight carbonate (which is indicative of being higher up on the reef structure), along with a thick Brown Niagaran. Crossplot porosity greater than 5% was flagged throughout the Brown Niagaran, showing uncharacteristically high porosity (Figure 4-18). The water saturation in the Brown Niagaran had an average of 26%, with values increasing to 60% past the oil/water contact (Figure 4-19). The crossplot shows the Brown Niagaran to be dolostone, while the original neutron porosity log was run on a limestone matrix. The difference in matrix properties can result in an overprediction of porosity. The porosity log was then corrected to a dolomite matrix (Figure 4-20), which decreases the porosity to be near 5% rather than 10 to 15%.

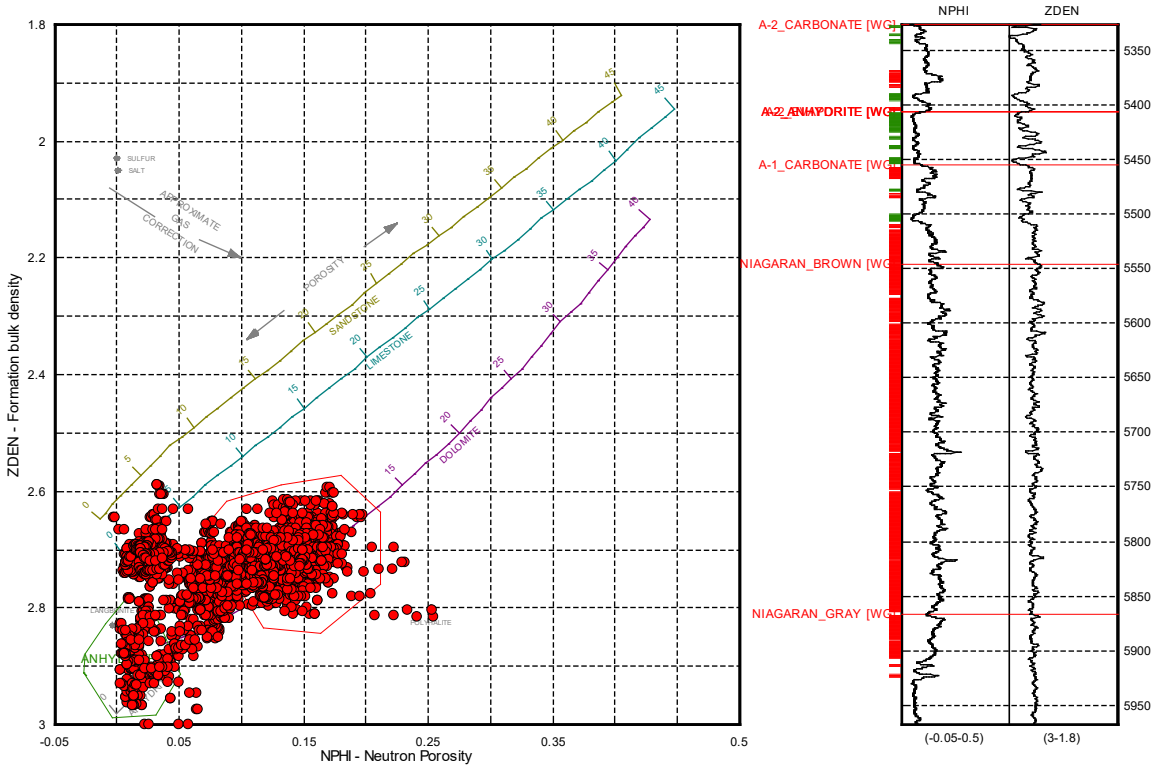


Figure 4-18. Neutron porosity-bulk density crossplot of well 61209 in the Dover 33 reef field showing porosity flags (red) in the Brown Niagaran.

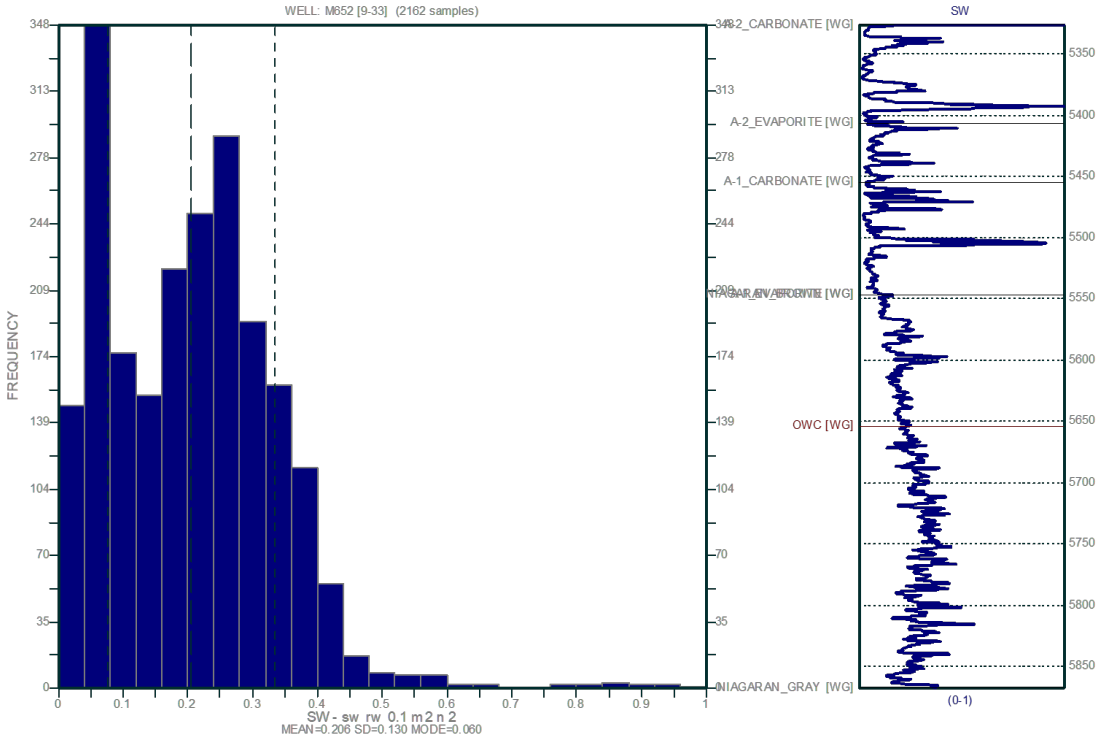


Figure 4-19. Water saturation curve and histogram for well 61209 showing an increase in water saturation in the upper Brown Niagaran.

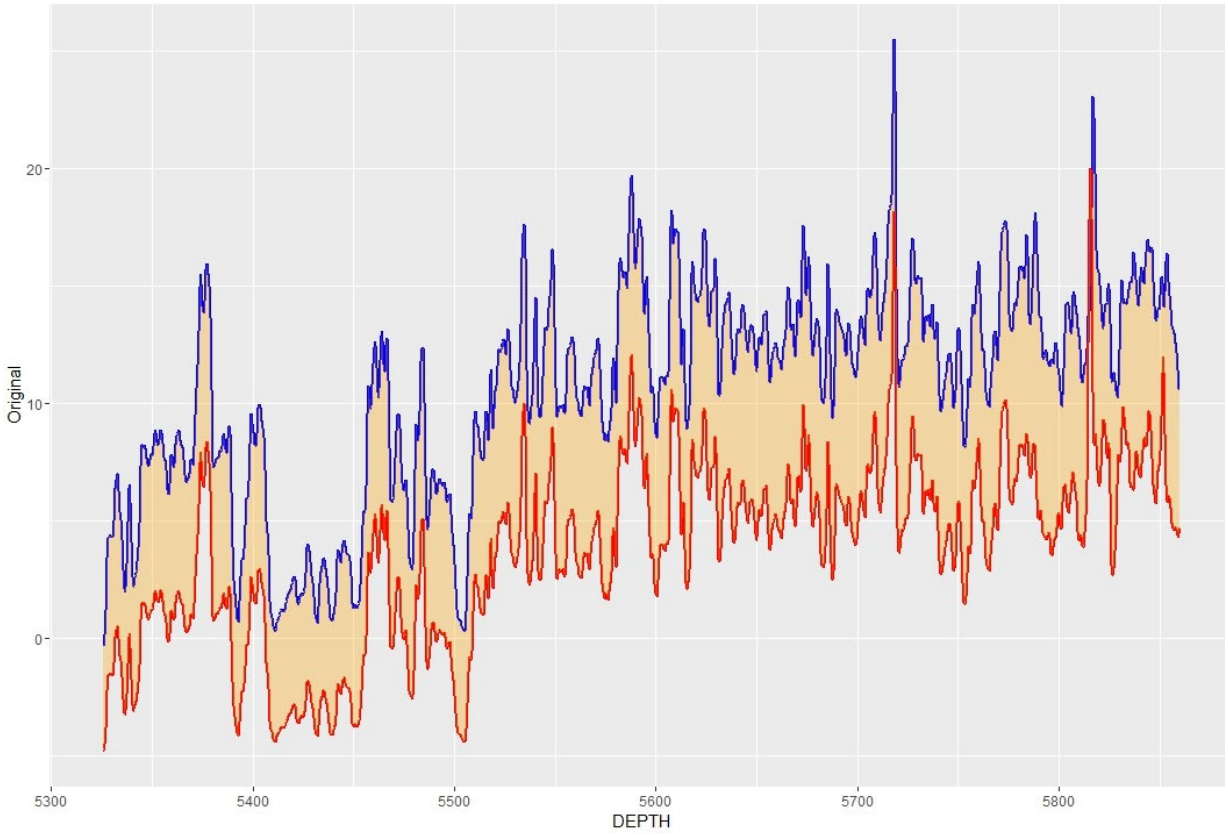


Figure 4-20. Neutron porosity comparison between data collected on a limestone matrix (blue) and dolomite matrix (red), with limestone porosity overestimating true porosity.

4.2.2 Advanced Log Interpretation

Advanced wireline log data was collected in the Lawnichak 9-33 well (permit 61209), which included image logs, nuclear magnetic resonance (NMR), and elemental spectroscopy. Key observations are summarized in this section; the detailed report can be found in Attachment 2.

Confining Units

The A-2 carbonate and A-2 evaporite were found to be interbedded anhydrite-bearing carbonates due to high bulk densities, photoelectric index, and fluctuating gamma ray. Image logs and NMR did not show any significant features of porosity or permeability. Figure 4-21 shows a single well cross section of NMR and triple combo data.

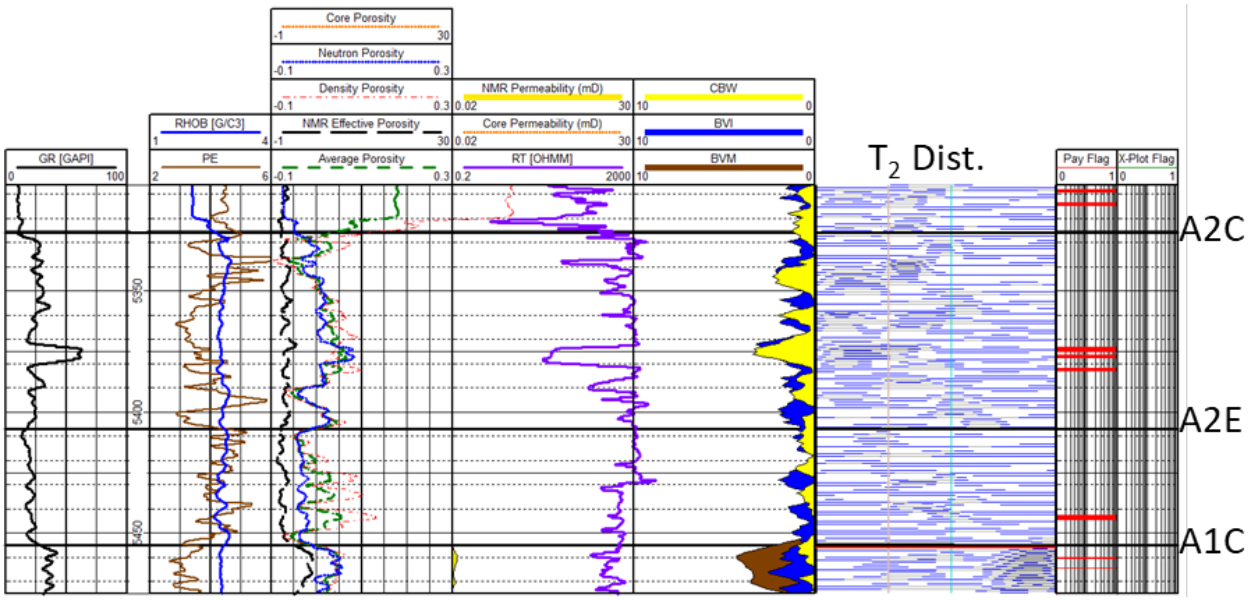


Figure 4-21. Cross section of NMR log data, select logs from the triple combo log suite, and pay flags generated from triple combo logs and neutron porosity-bulk density crossplots for the A-2 carbonate and A-2 evaporite. The NMR effective porosity log is plotted with neutron porosity, density porosity, and average porosity logs derived from the triple combo log suite. Permeability, bulk volume of movable fluid (BVM), bulk volume of irreducible fluid (BVI), clay-bound water (CBW), and T2 distributions are also shown.

Reservoirs

Both the A-1 carbonate and Brown Niagaran formations were found to have high reservoir potential. The lower A-1 carbonate showed vuggy porosity with an increase in NMR permeability (Figure 4-22 and Figure 4-23). However, logs also indicated the matrix may be mud supported with limited connectivity between larger pore spaces.

The Brown Niagaran had intervals with high distribution of vugs and fractures observed on the image logs (Figure 4-24). Additionally, NMR showed a distinct interval from 5,546 to 5,640 feet MD of relatively high permeability which occurred at the same intervals of vugs and fractures (Figure 4-25).

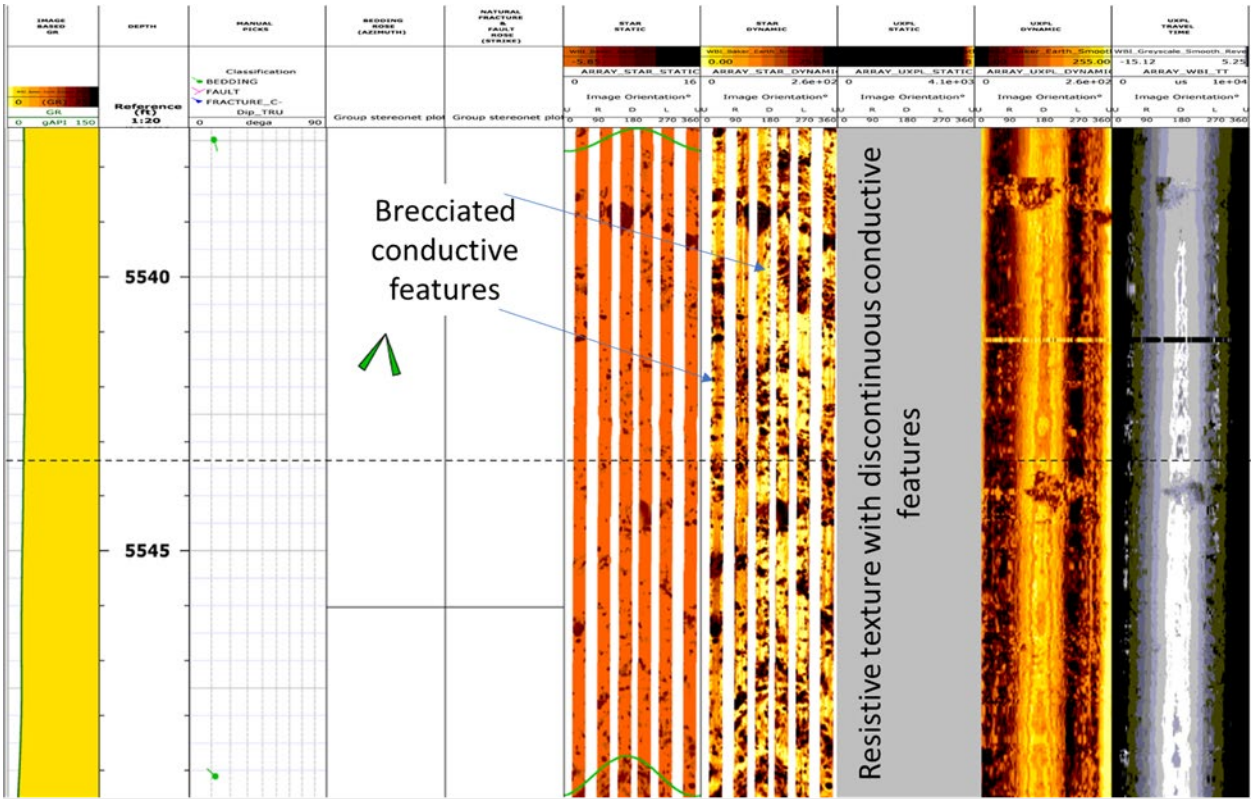


Figure 4-22. Annotated image log of the A-1 carbonate from ~5,538 feet to 5,550 feet. Note the laminated discontinuous conductive features that occur throughout the resistive matrix, interpreted to be brecciated microbial laminites.

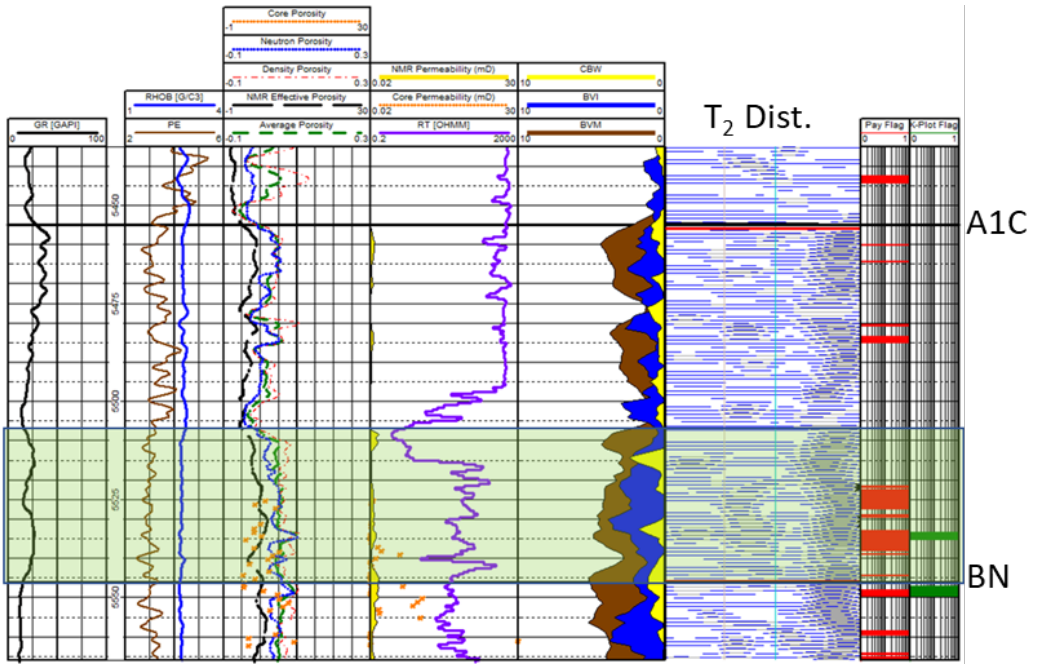


Figure 4-23. Cross section of NMR log data, select logs from the triple combo log suite, core porosity and permeability data, and pay flags generated from triple combo logs and neutron porosity-bulk density crossplots for the A-1 carbonate. The NMR effective porosity log is plotted with neutron porosity, density porosity, and average porosity logs derived from the triple combo log suite as well as core porosity. NMR permeability is shown with core permeability. BVM, BVI, CBW, and T2 distributions are also shown. Green box highlights a zone of interest.

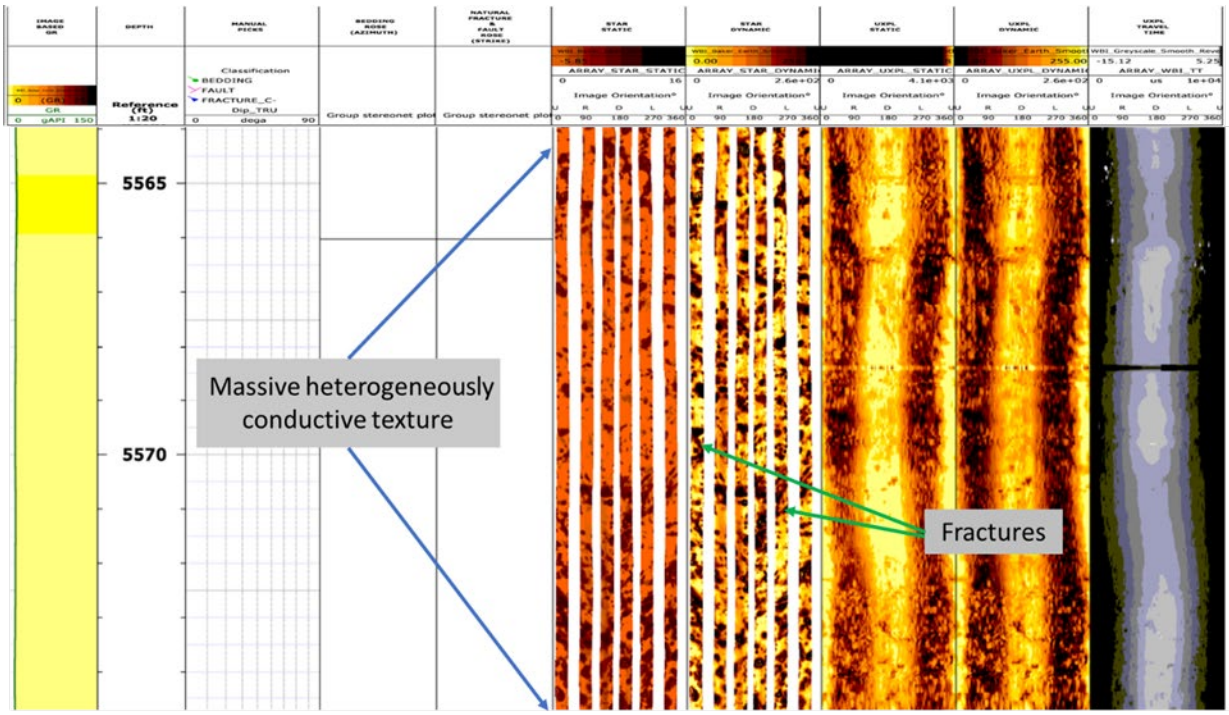


Figure 4-24. Annotated FMI image log of the Brown Niagaran from ~5,564 feet to 5,575 feet. This texture is described as massive heterogeneously conductive texture where all conductive features occur within a resistive matrix. This zone is interpreted to be massively bedded mudstone with a moderate to high distribution of vuggy porosity.

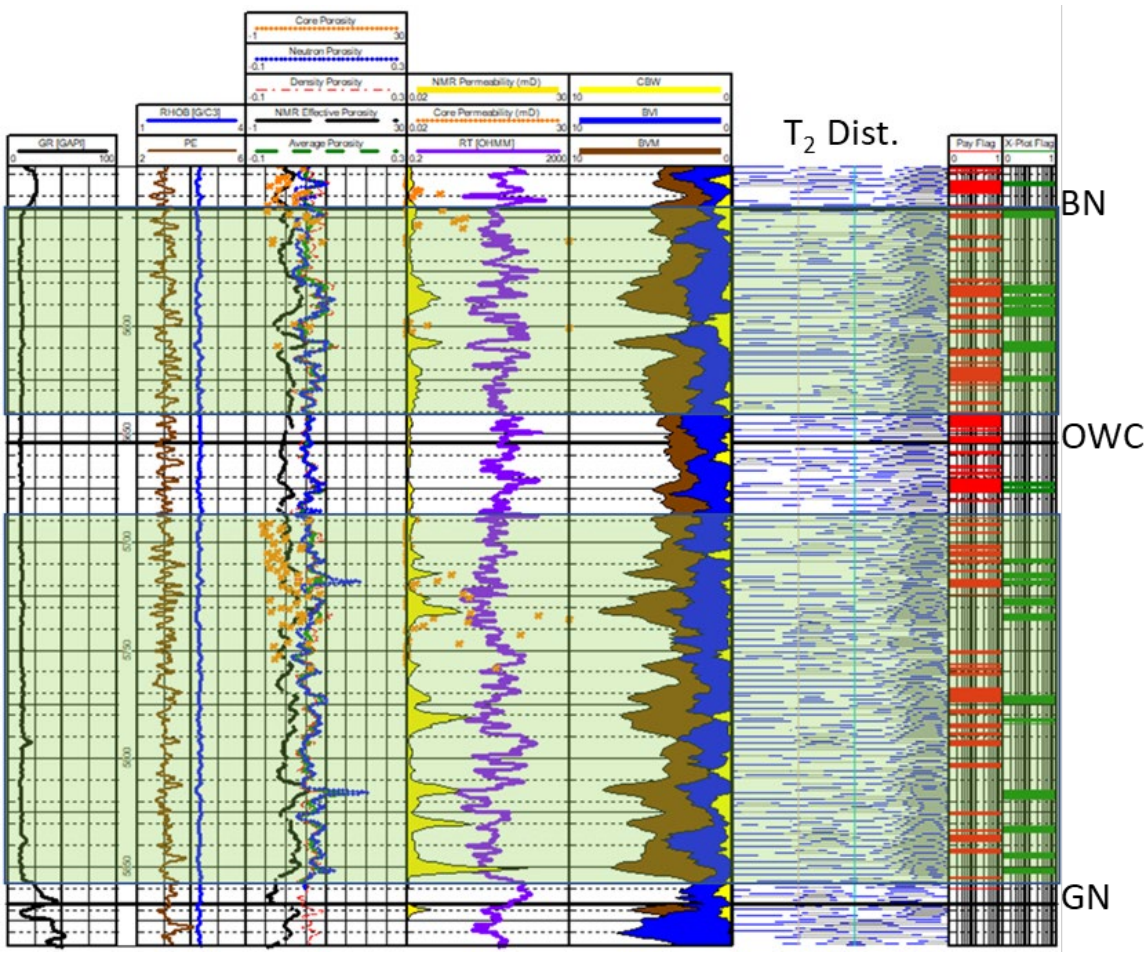


Figure 4-25. Cross section of NMR log data, select logs from the triple combo log suite, core porosity and permeability data, and pay flags generated from triple combo logs and neutron porosity-bulk density crossplots for the Brown Niagaran. The NMR effective porosity log is plotted with neutron porosity, density porosity, and average porosity logs derived from the triple combo log suite, as well as core porosity. NMR permeability is shown with core permeability. BVM, BVI, CBW, and T2 distributions are also shown. Green boxes highlight zones of interest.

4.2.3 Petrophysical Calculations

The A-2 carbonate has an overall thickness of 68 to 127 feet with an average thickness of 101 feet. The formation thins out over the crest of the reef structure and is thicker on the flanks. The average porosity is 3.5% and remains below 5% at all well locations. The presence of evaporites can sometimes increase the porosity. Using a 5% porosity cutoff, the net thickness had a range of 6 to 64 feet with an average NTG ratio of 0.15. A water saturation cutoff of 40% was later applied to represent available storage and eliminate the influence of evaporites. The net thickness using a water saturation cutoff had a smaller range of 1.5 to 32 feet with an average NTG ratio of 0.07 (Table 4-3). The reservoir quality of the A-2 carbonate is poor with disconnected thin intervals of porosity, which makes for a strong confining layer.

Table 4-3. Summary of petrophysical calculations for the A-2 carbonate in the Dover 33 reef field.

Interval: A-2 Carbonate						
Avg. Thickness	Avg. Porosity	Avg. Net Thickness	Avg. NTG	Avg. SW	Avg. Net Thickness (Sw<40%)	Avg. NTG (Sw<40%)
107 ft	3.8%	19 ft	.15	25%	7.4 ft	0.07

A-2 Evaporite

The A-2 evaporite on the crest of the reef structure was composed of interbedded carbonate and anhydrite; on the flanks, it was composed of salt. Wireline logs can be sensitive to the presence of evaporites and often cause skewed porosity values. Petrophysical calculations were not computed for this zone due to false high porosities.

A-1 Carbonate

The A-1 carbonate was mostly unsaturated dolomite with some thin intervals of anhydrite. The thickness ranged from 51 feet on the crest of the reef to 168 feet on the flanks of the reef. The average porosity ranged from 1% to 7% with an average of 4%. Using a 5% porosity cutoff, the resulting net thickness ranged from 6 to 78 feet with an average of 36 feet. The NTG ratio had an average of 0.34. A water saturation cutoff was applied to eliminate water-saturated intervals and evaporites. The resulting average net thickness decreased to 18 feet with an average NTG ratio of 0.22 (Table 4-4). Overall, the A-1 carbonate had frequent intervals of porosity in the lower section of the formation. The water saturation remained low except for some flank wells where the A-1 carbonate was partially saturated.

Table 4-4. Summary of petrophysical calculations for the A-1 carbonate in the Dover 33 reef field.

Interval: A-1 Carbonate						
Avg. Thickness	Avg. Porosity	Avg. Net Thickness	Avg NTG	Avg. SW	Avg. Net Thickness (Sw<40%)	Avg. NTG (Sw<40%)
97 ft	4%	36 ft	0.34	22%	18 ft	0.22

A-1 Evaporite

The A-1 evaporite ranged in thickness from 0 feet on-reef to 126 feet off-reef. It was composed of interbedded anhydrite and carbonate on top of the reef and salt on the flanks. Due to the evaporites, petrophysical calculations were not performed.

Brown Niagaran

The Brown Niagaran ranged from 8 feet thick off-reef to 271 feet thick on the crest of the reef. The thicknesses are not representative of the true thickness of the formation because many wireline logs ended prior to the Gray Niagaran. The thickness and associated values are for the logged intervals only. The porosity ranged from 0% to 16% with an average of 8.2%. Using a porosity cutoff of 5% resulted in a net thickness of 18 to 224 feet and an average NTG ratio of 0.68. The oil/water contact was high in the Dover 33 reef, leaving approximately 100 feet of unsaturated dolomite in the middle of the reef while being fully saturated on the flanks. A water saturation cutoff of 40% was incorporated into the calculations, which resulted in an average net thickness of 62 feet and an average NTG ratio of 0.44 (Table 4-5). Overall, the upper Brown Niagaran had frequent porosity flags greater than 5% with low water saturations. The middle to lower Brown Niagaran was fully saturated with little to no available pore space.

Table 4-5. Summary of petrophysical calculations for the Brown Niagaran in the Dover 33 reef field.

Interval: Brown Niagaran						
Avg. Thickness	Avg. Porosity	Avg. Net Thickness	Avg. NTG	Avg. SW	Avg. Net Thickness (Sw<40%)	Avg. NTG (Sw<40%)
105 ft	8.2%	81 ft	0.68	56%	62 ft	0.44

4.3 Core Analysis

Conventional core samples were collected across the A-1 carbonate and Brown Niagaran formations, and rotary sidewall core (RSWC) samples were collected across the A-2 carbonate, A-2 evaporite, A-1 carbonate, Brown Niagaran, and Gray Niagaran formations. This section presents a summary of key reservoir intervals and features as determined from core analysis and images. Table 4-6 and Table 4-7 show summary statistics of porosity and permeability by formation for conventional and RSCW respectively. Table 4-8 shows the depths of key potential reservoir intervals with porosity ≥5% as determined by core analysis and intervals with visible porosity as observed in core images and computed tomography (CT) scans. Overall, the 9-33 core is dominated by a porous dolomite lithology with some isolated zones of high porosity. Visible porosity, as seen on the core images and CT scans, is predominantly in the form of small to medium vugs and significant moldic porosity (Figure 4-26).

Table 4-6. Summary of whole core porosity and permeability data in the Lawnichak 9-33 well.

Formation	Porosity (%)			Permeability (mD)		
	Min	Max	Average	Min	Max	Average
A-1 Carbonate	3.16	10.72	6.69	0.00	6.04	0.70
Brown Niagaran	1.51	14.16	7.14	0.00	204.28	6.53

Table 4-7. Summary of RSWC porosity and permeability data in the Lawnichak 9-33 well.

Formation	Porosity (%)			Permeability (mD)		
	Min	Max	Average	Min	Max	Average
A-2 Carbonate	4.3	5.1	4.7	0.00	17.7	8.9
A-2 Evaporite	0.36	0.64	0.48	-	-	-
A-1 Carbonate	0.11	8.08	4.19	0.00	0.86	0.09
Brown Niagaran	1.27	8.62	14.88	0.00	14.34	1.646
Gray Niagaran	1.83	6.39	4.72	0.00	0.31	0.10

Table 4-8. Summary of key potential reservoir intervals in the Lawnichak 9-33 well based on whole core analysis and images.

Formation	Reservoir Intervals [ϕ ≥ 5%] (ft)	Intervals with Visible Porosity (ft)
A-1 Carbonate	5525.5-5534.5, 5536.6-5540.5, 5542.4-5543.5, 5545.5	5527-5528, 5534-5544, 5549-5552
Brown Niagaran	5548.5-5559.5, 5561.5, 5599.5-5602.65, 5609.5, 5690.5, 5693.5-5694.5, 5698.5-5699.5, 5702.5-5704.5, 5708.5, 5710.5-5711.5, 5713.5-5726.5, 5728.5, 5730.5-5731.5, 5733.5-5752.5, 5757.65-5759.4	5549-5555, 5598-5609, 5690-5695, 5697-5725, 5726-5760

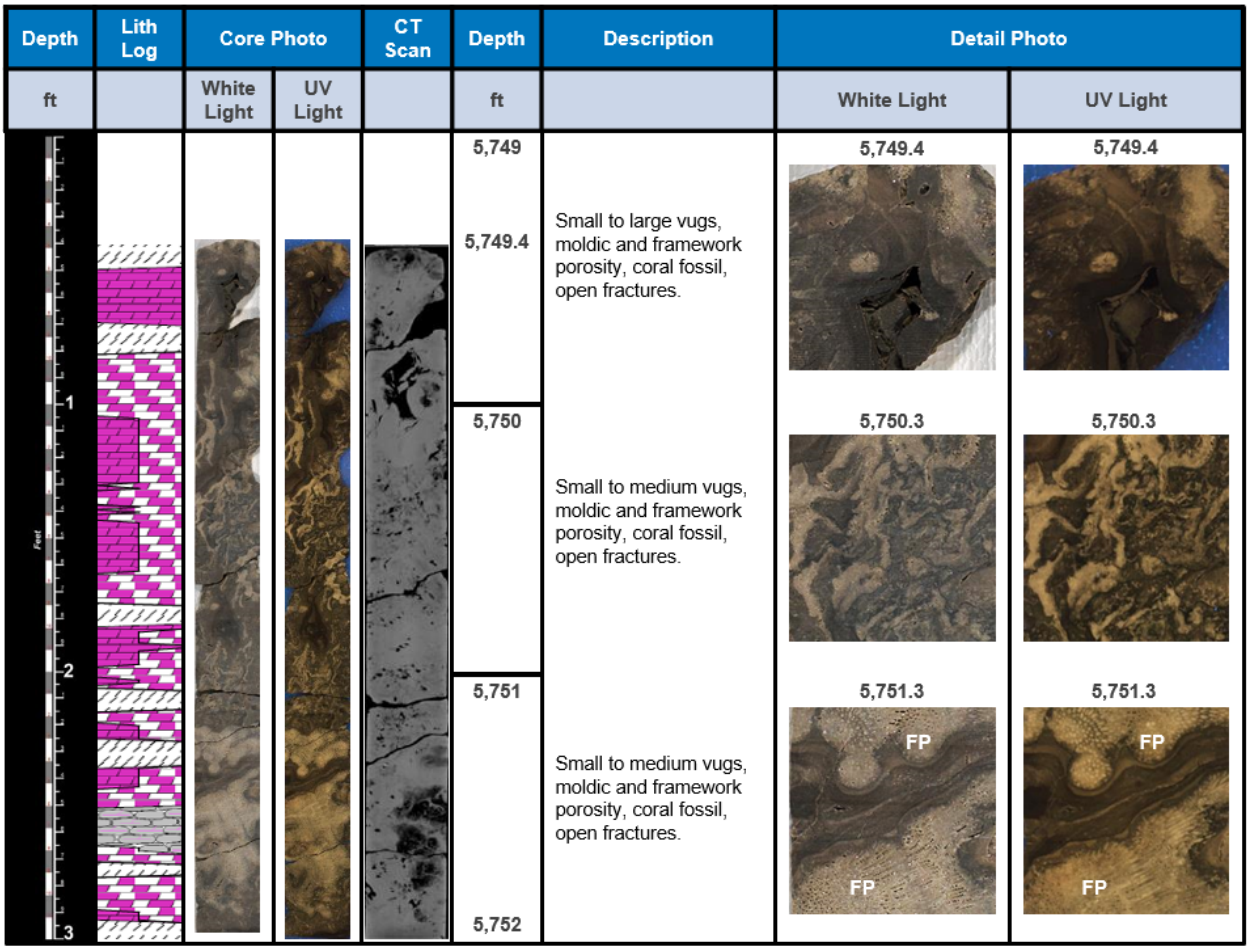


Figure 4-26. Compiled illustration of lithology log, core photos (ultraviolet [UV] and white light), CT scan image, core descriptions, and annotated core images of the Brown Niagaran for depths 5,749 feet to 5,752 feet.

The A-1 carbonate had a porosity range from 3.16% to 10.72% with a permeability range from 0.00 to 6.04 millidarcys (mD). The Brown Niagaran had a porosity range from 1.51% to 7.14% with a permeability range from 0.00 to 204.28 mD. These data are plotted in Figure 4-27 with respective transforms between porosity and permeability. For more detailed results of core analyses, refer to Attachment 2.

Additional photographs and descriptions are provided in Appendix B.

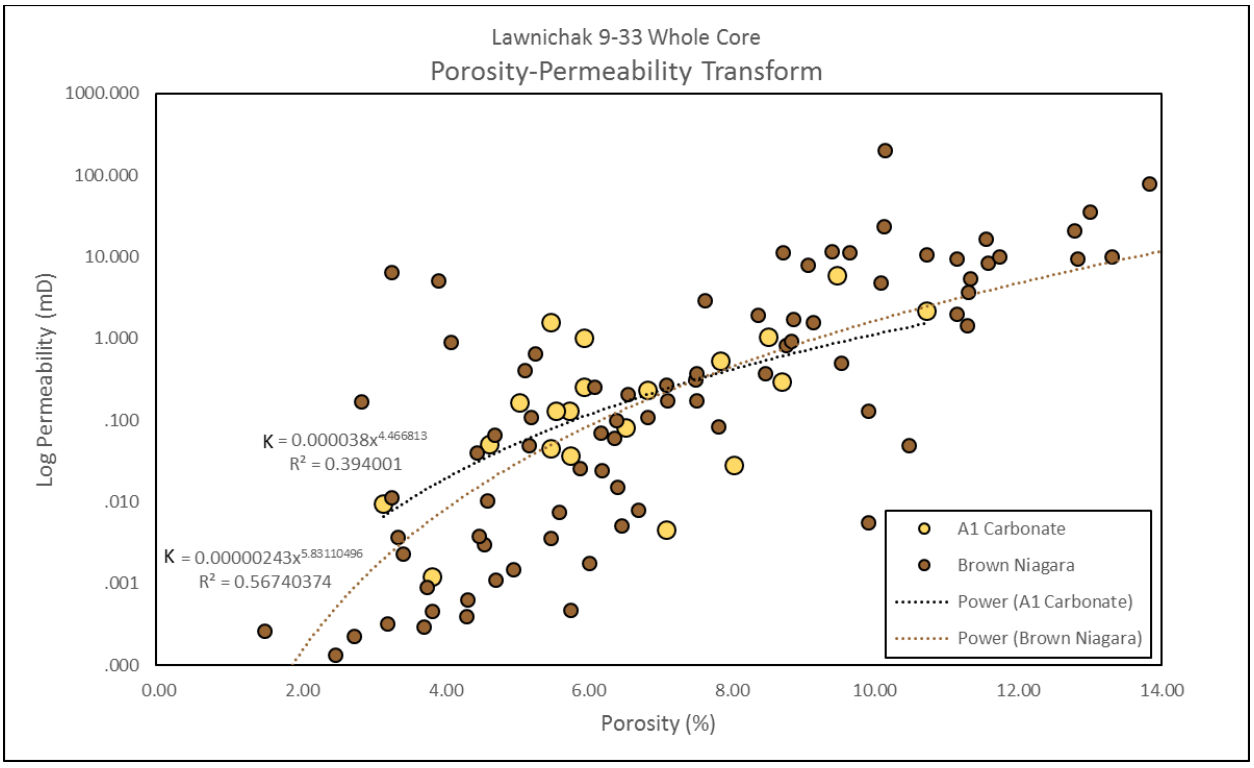


Figure 4-27. Core porosity-permeability transform plot for the A-1 carbonate (yellow circles) and the Brown Niagaran (brown circles)

4.4 Seismic Analysis

The Dover 33 reef field has sharp boundaries in seismic time where the reef has faster arrival times than the surrounding Brown Niagaran surface due to higher elevations (Figure 4-28 and Figure 4-29). The A-1 carbonate drapes over the Brown Niagaran with little relief observed in seismic time (Figure 4-30). This is due to similar rock velocities between the A-1 carbonate and Brown Niagaran. There is not enough contrast for separate horizons along the reef crest. The A-2 carbonate has gentle slopes with minor indications of an underlying reef complex (Figure 4-31).

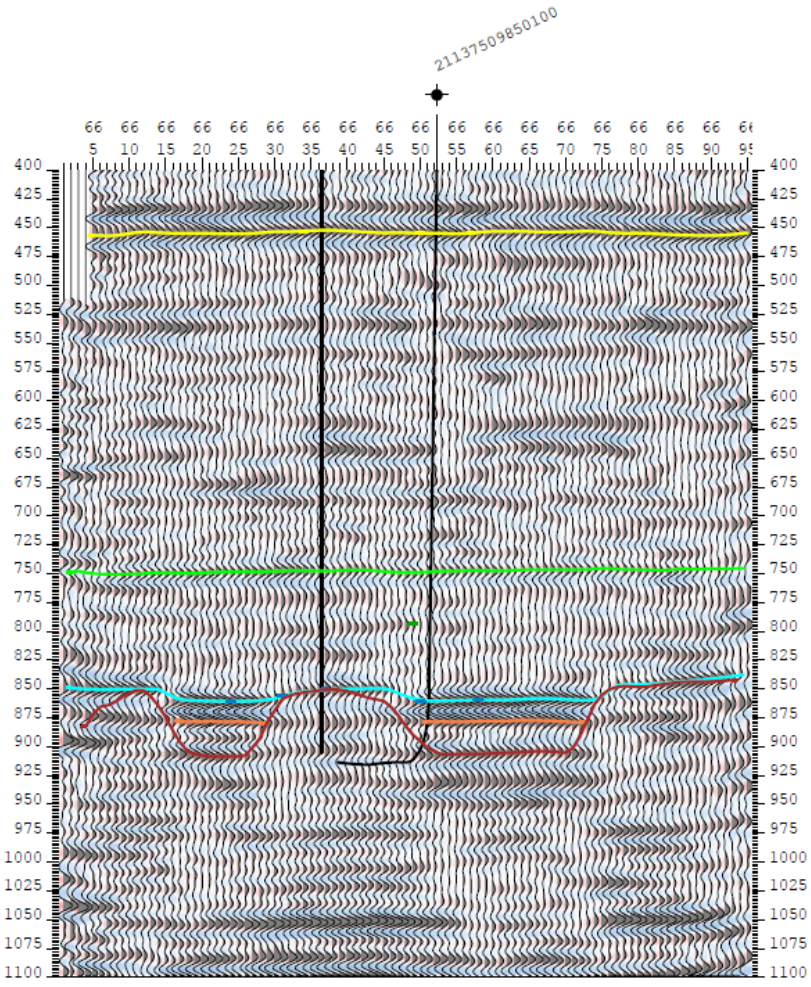


Figure 4-28. 2D cross section through 3D seismic horizon collected over the Dover 33 reef, showing two reefs identified in the Dover 33 field (brown).

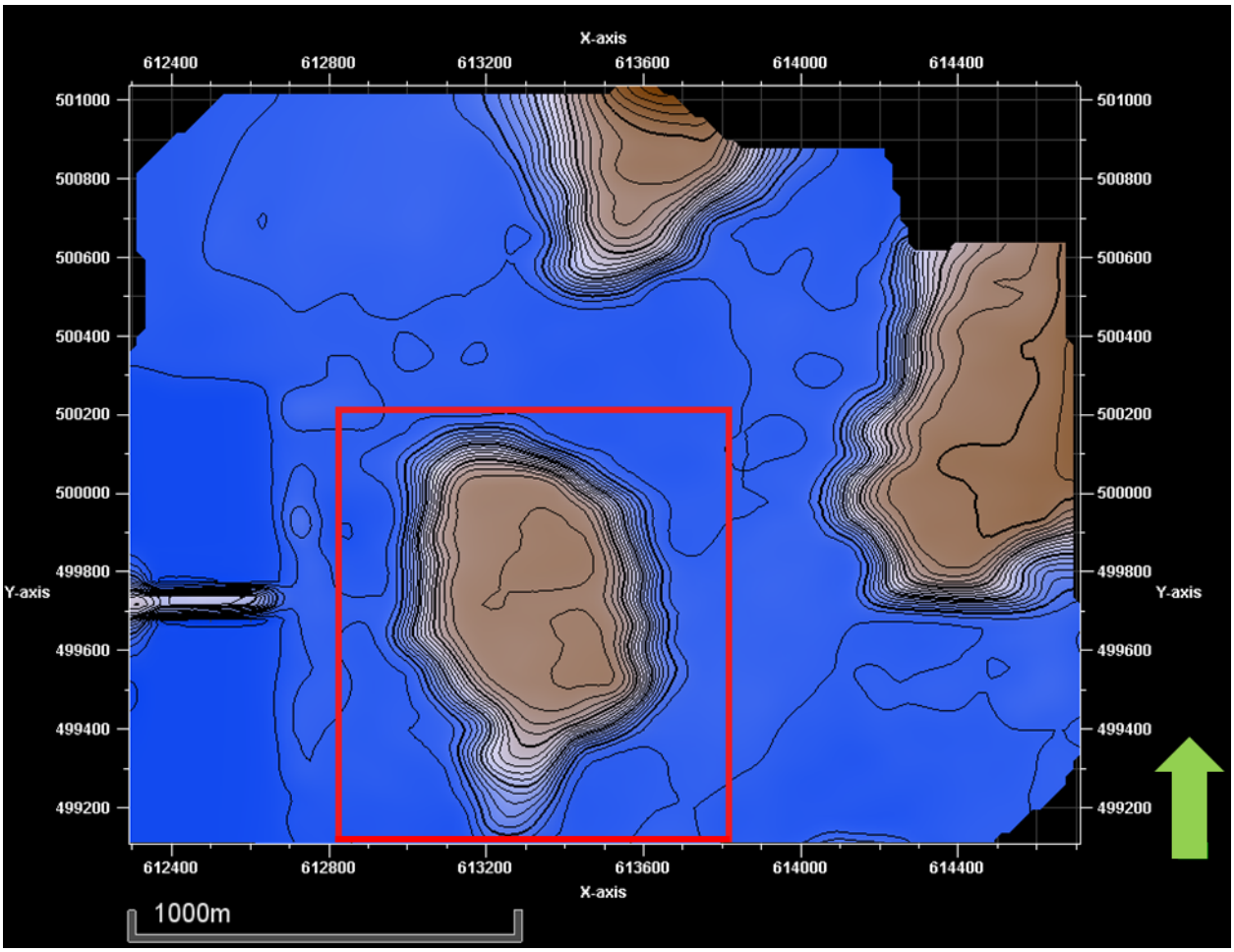


Figure 4-29. Time horizon surface for the Brown Niagaran showing steep slopes along the edges of the Dover 33 reef. The red box outlines the Dover 33 reef field.

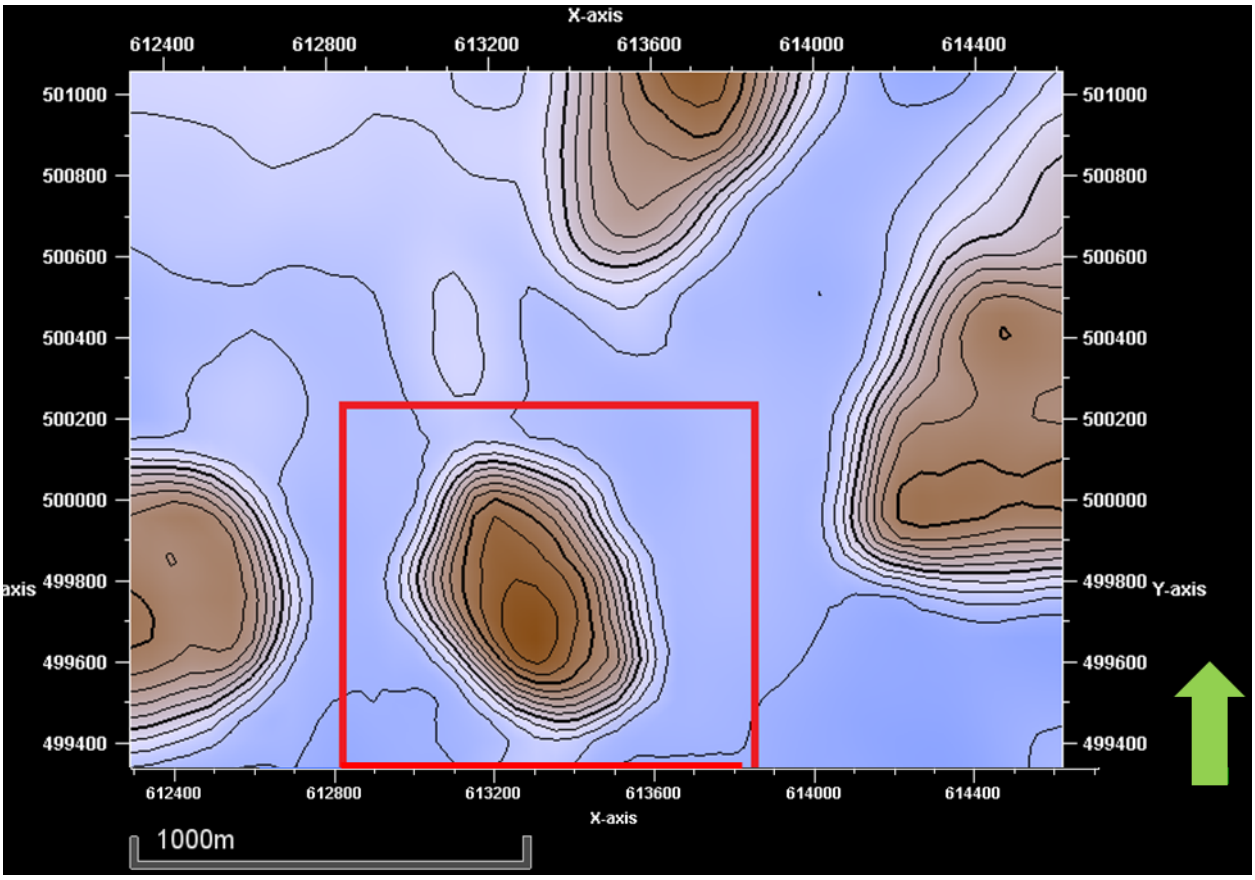


Figure 4-30. Time horizon surface for the A-1 carbonate showing moderate slopes along the edges of the Dover 33 reef. The red box outlines the Dover 33 reef field.

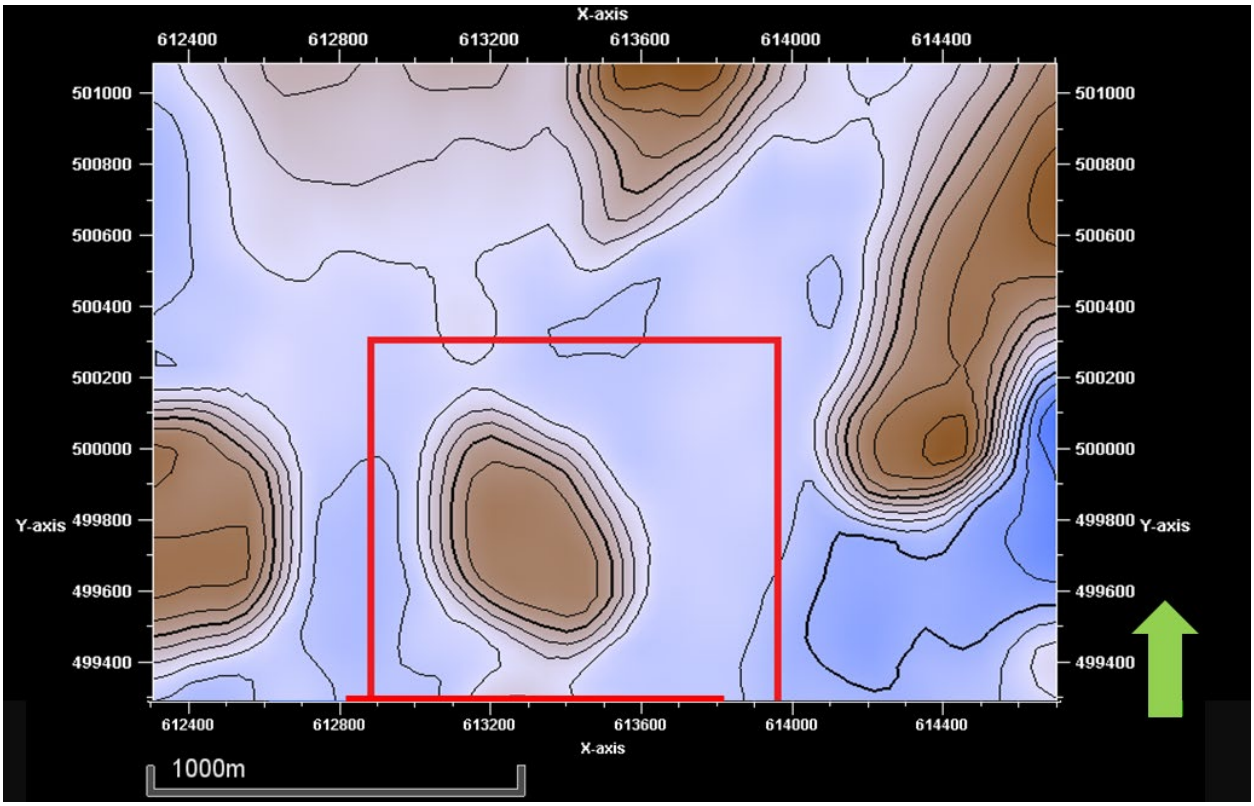


Figure 4-31. Time horizon surface for the A-2 carbonate showing gentle slopes along the edges of the Dover 33 reef. The red box outlines the Dover 33 reef field.

4.5 Statistical Analysis

A dataset of wireline log data (gamma ray, neutron porosity, bulk density, and resistivity) was compiled for the Dover 33 reef field. Each depth was assigned a lithofacies for statistical analyses which included reef core, windward, leeward, and off-reef/flank Brown Niagaran. Analyses included descriptive/exploratory statistics and hypothesis tests to determine if each lithofacies should be treated separately. Prior to statistical analyses, logs were upscaled to a vertical resolution of 2 feet to imitate the upscaling process to be conducted during modeling.

Statistical plots and averages were generated for each lithofacies and each log. The reef core lithofacies had the highest average gamma ray due to the presence of a muddy bioherm at the base. It also exhibited the highest average porosity compared to other lithofacies (Table 4-9). Resistivity was notably lower in the reef core and windward facies, which could be attributed to the presence of more oil than the flanks and leeward facies. Additionally, the reef core and windward lithofacies had the lowest bulk density averages, which could be a result of porosity and fluids. Figure 4-32 shows a boxplot of neutron porosity by lithofacies illustrating the highest average in the reef core.

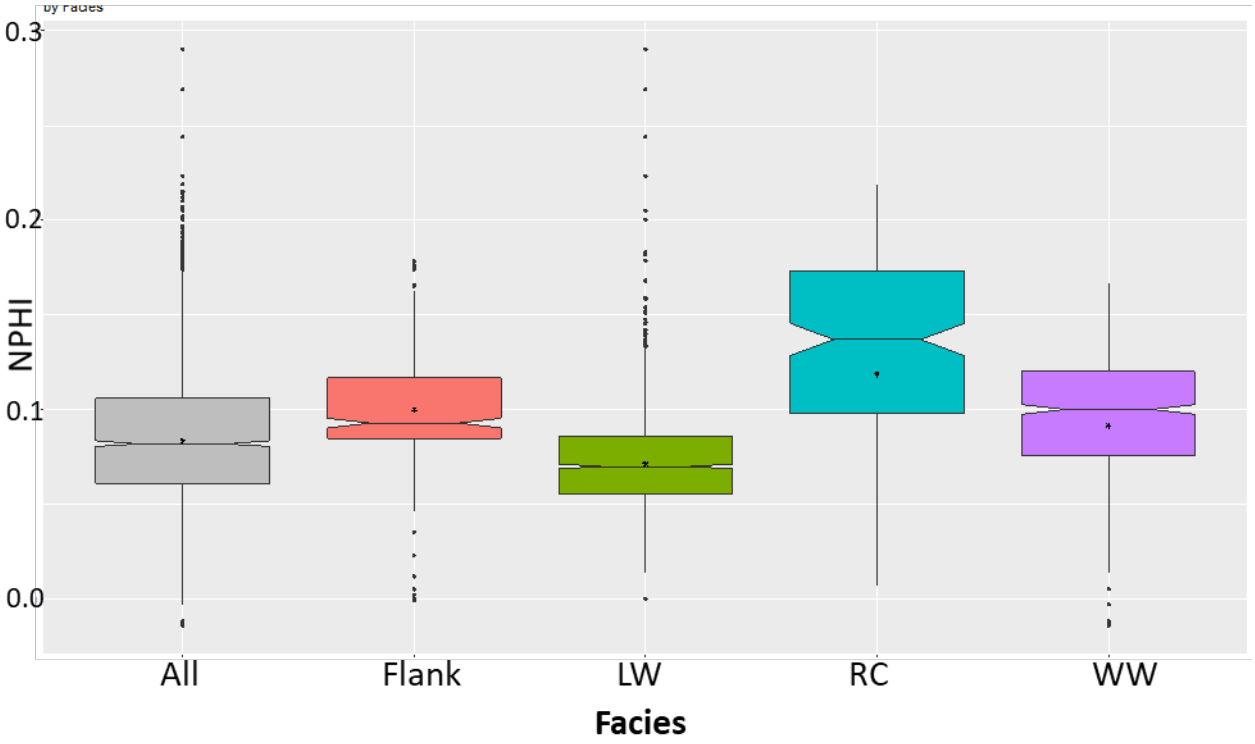


Figure 4-32. Boxplot comparison of neutron porosity by lithofacies with the reef core (blue) having the highest average.

Table 4-9. Summary of log averages and ranges by lithofacies in the Brown Niagaran.

	Flank				Leeward				Reef Core				Windward			
	GR	NPHI	RHOB	RT	GR	NPHI	RHOB	RT	GR	NPHI	RHOB	RT	GR	NPHI	RHOB	RT
Average	20.43	0.10	2.76	643.49	15.85	0.07	2.74	385.47	46.94	0.12	2.69	105.40	15.13	0.09	2.71	130.81
Minimum	1.10	0.00	2.69	245.94	6.45	0.00	2.53	1.96	14.81	0.01	1.23	10.71	0.93	-0.01	2.64	8.14
Maximum	42.58	0.18	2.92	4103.45	89.48	0.29	2.82	9288.64	228.42	0.22	2.78	629.50	47.05	0.17	2.85	1651.37

To further explore the differences between lithofacies, the means were compared using Tukey's honest significance difference (HSD) test, which tests the hypothesis that the means are statistically the same. The Tukey test computes an HSD value and compares it to the Tukey's critical value (a look-up table). If the difference is significant, it produces a p-value of 1, indicating that the means are the same between two groups. If the difference is insignificant, it produces a p-value of 0, indicating that the means are different between two groups. However, the Tukey test assumes a normal distribution, which is not always the case; therefore, additional tests were run. Table 4-10 lists the results between pairs and different hypothesis tests. Results show mostly null results (0, different means), except the Wilcoxon test showed similarities between windward (WW) and flank facies and the F-Test showed similar variances between the Leeward and Flank.

Table 4-10. Hypothesis test results between lithofacies pairs.

Test	RC-LW	RC-WW	RC-Flank	WW-LW	WW-Flank	LW-Flank
K-S	Different Distributions	Different Distributions	Different Distributions	Different Distributions	Different Distributions	Different Distributions
Wilcoxon	Different Medians	Different Medians	Different Medians	Different Medians	Similar Medians	Different Medians
T-Test	Different Medians	Different Medians	Different Medians	Different Medians	Different Medians	Different Medians
F-Test	Different Variances	Different Variances	Different Variances	Different Variances	Different Variances	Similar Variances

Note: RC = reef core, LW = leeward, WW = windward.

Overall, the high-level statistical analysis showed differences in log properties between lithofacies. This emphasizes the need to treat the lithofacies separately and incorporate them into modeling efforts.

4.6 Geologic Interpretations and Data Integration

Three cross sections were constructed across the Dover 33 reef field to determine changes in the reef structure and continuity of reservoir conditions. All cross sections were flattened on the top of the A-2 carbonate/base of the B-salt. The logs included are the gamma ray, bulk density, neutron porosity, and water saturation. Also included are two porosity flags: a crossplot porosity flag of greater than 5% porosity (red), and a log porosity flag of porosity greater than 5% with water saturation less than 40% (green). Figure 4-33 illustrates the locations of each cross section in map view.

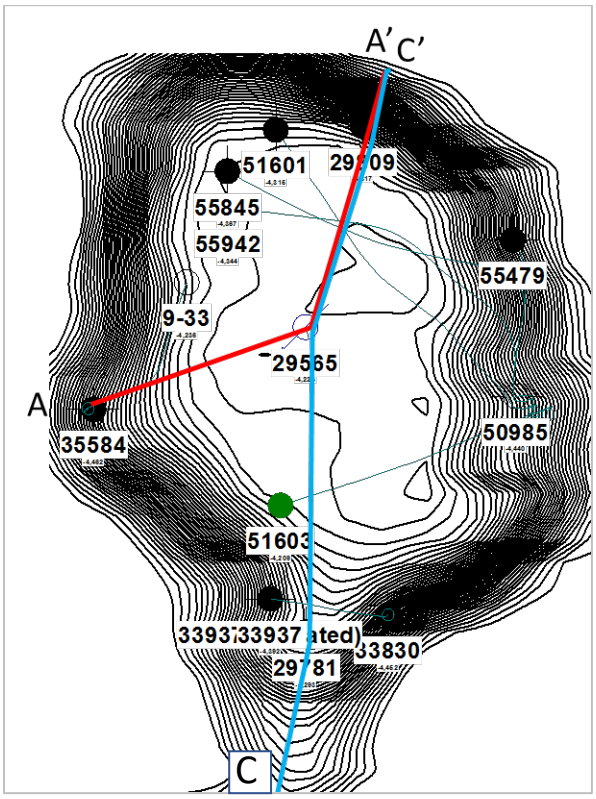


Figure 4-33. Location of cross sections through the Dover 33 reef field.

Cross Section A-A'

Cross section A-A' runs through the northern reef pod of the Dover 33 reef field, cross-cutting changes in lithology. The westernmost well (35584) has very thin, water-saturated Brown Niagaran with thin intervals of porosity. The A-1 carbonate is also mostly water-saturated in this well, which eliminates the porosity flags as viable reservoir. Well 29565, located in the center of the reef field, has a thick Brown Niagaran. Approximately 100 feet of Brown Niagaran is unsaturated, and it shows frequent porosity flags. Well 29809 has a mostly saturated Brown Niagaran with very few porosity flags above the oil/water contact. The A-2 carbonate has a high gamma response consistently throughout the middle of the formation with an assosiated porosity flag. This could be a carbonate mudstone with microporosity. Figure 4-34 shows cross section A-A' over the intervals of interest.

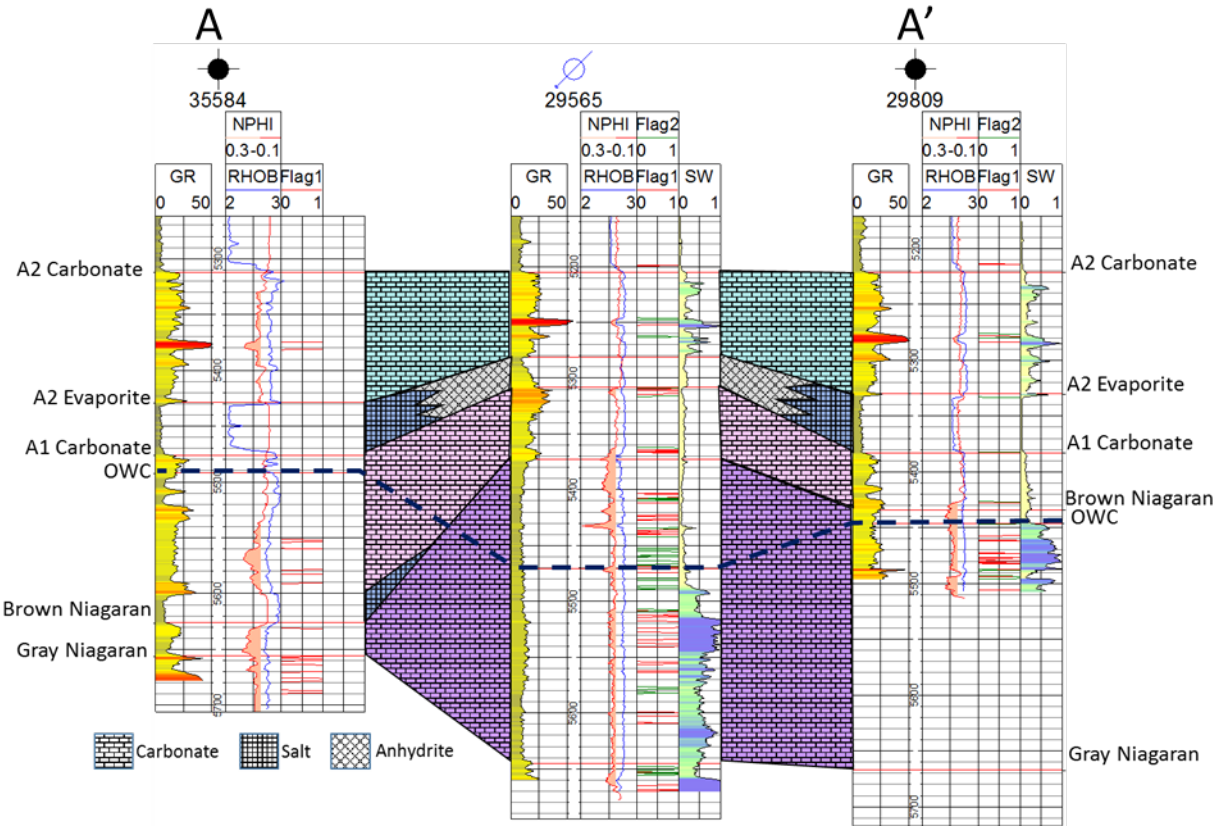


Figure 4-34. Cross section A-A' across the northern pod of the Dover 33 reef field showing numerous porosity flags (red and green) above and below the oil/water contact (dashed line).

Cross Section C-C'

Cross section C-C' runs south to north through both reef pods in the Dover 33 reef field. Porosity flags are found in the A-1 carbonate in all wells and in the upper Brown Niagaran when not water-saturated. The A-2 carbonate has a consistent high gamma spike traceable well to well. Porosity flags in the Brown Niagaran occur less frequently in the southern reef pod (well 35195) than in the northern reef pod. Figure 4-35 shows cross section C-C' over the intervals of interest.

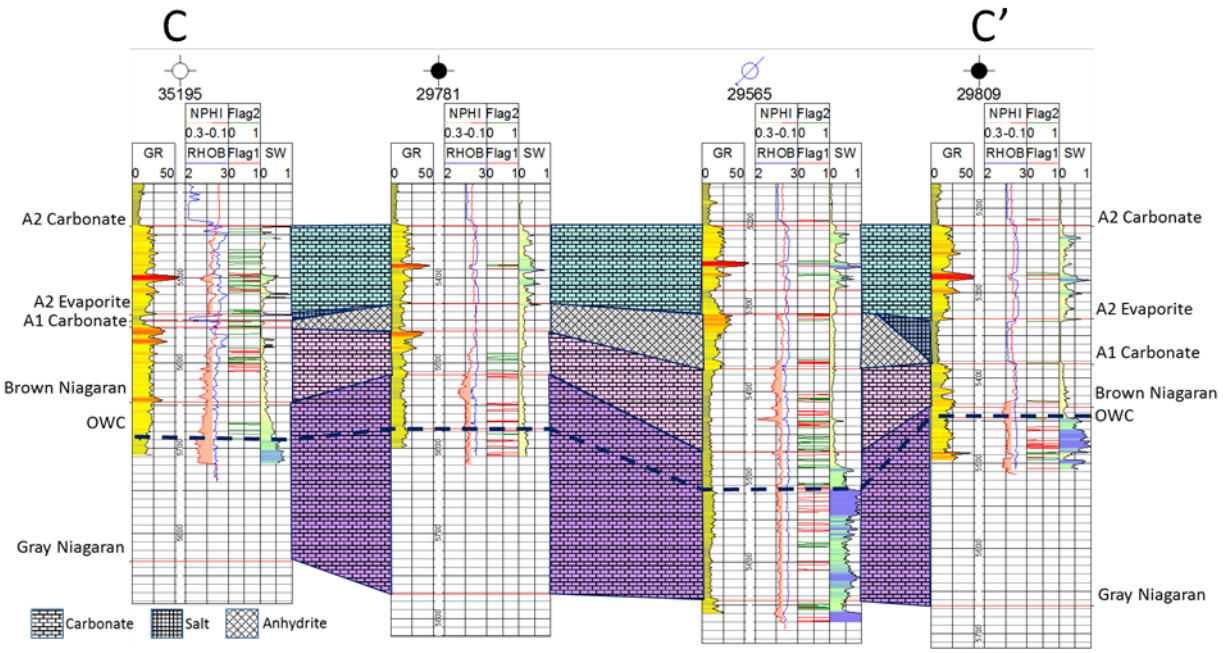


Figure 4-35. Cross section C-C' running south to north through the Dover 33 reef field showing the distribution of porosity flags across wells.

Depositional Model

Wireline logs for 13 wells were analyzed by Western Michigan University and Battelle for the Dover 33 field. The reef core, reef apron, and bioherm were composed of mixed limestone and dolomite with moderate to high porosity. The A-1 carbonate showed moderate porosity with occasional salt plugs. Moderate porosity/storage potential was observed along the flanks of the reef in the distal reef apron and rubble where there was vugular dolomite.

The interpretations of the log data were used to subdivide the reef into zones based on reservoir potential. Figure 4-36 illustrates the subdivisions of the interpreted flow zones in map view. Four zones were defined. Zone 1 (purple) includes the windward facies with high flow potential. Zone 2 (green) includes the reef core facies with moderate to high flow potential. Zone 3 (blue) includes the leeward facies with low to moderate flow potential. Zone 4 includes the flanks and off-reef Brown Niagaran with no flow potential.

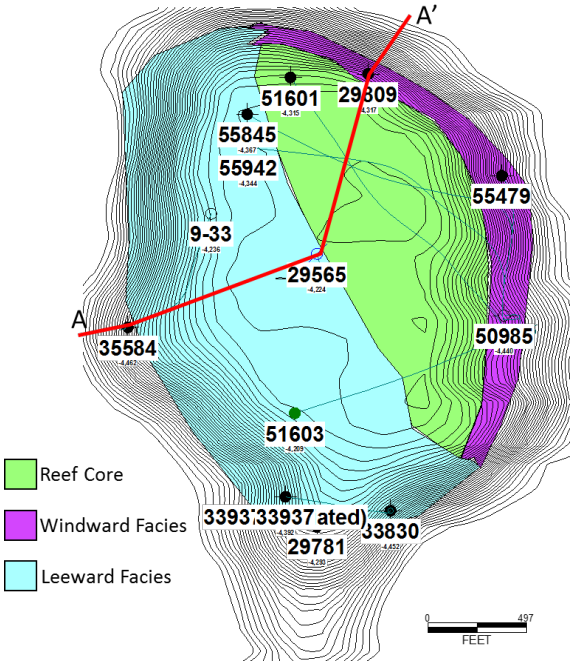


Figure 4-36. Plan view of the depositional model of the Dover 33 reef field showing the subdivision into windward (purple), reef core (green), and leeward (blue) facies.

One interpreted cross section was constructed across the northern (A-A') reef pod to illustrate the changes in lithology and the locations of the zones/lithofacies. Cross section A-A' (Figure 4-37) illustrates the thicker salts and carbonates off reef and the thinning of the A-1 and A-2 formations on the crest of the reef. Internally, the leeward facies are to the southwest, the reef core is central, and the windward facies are to the northeast.

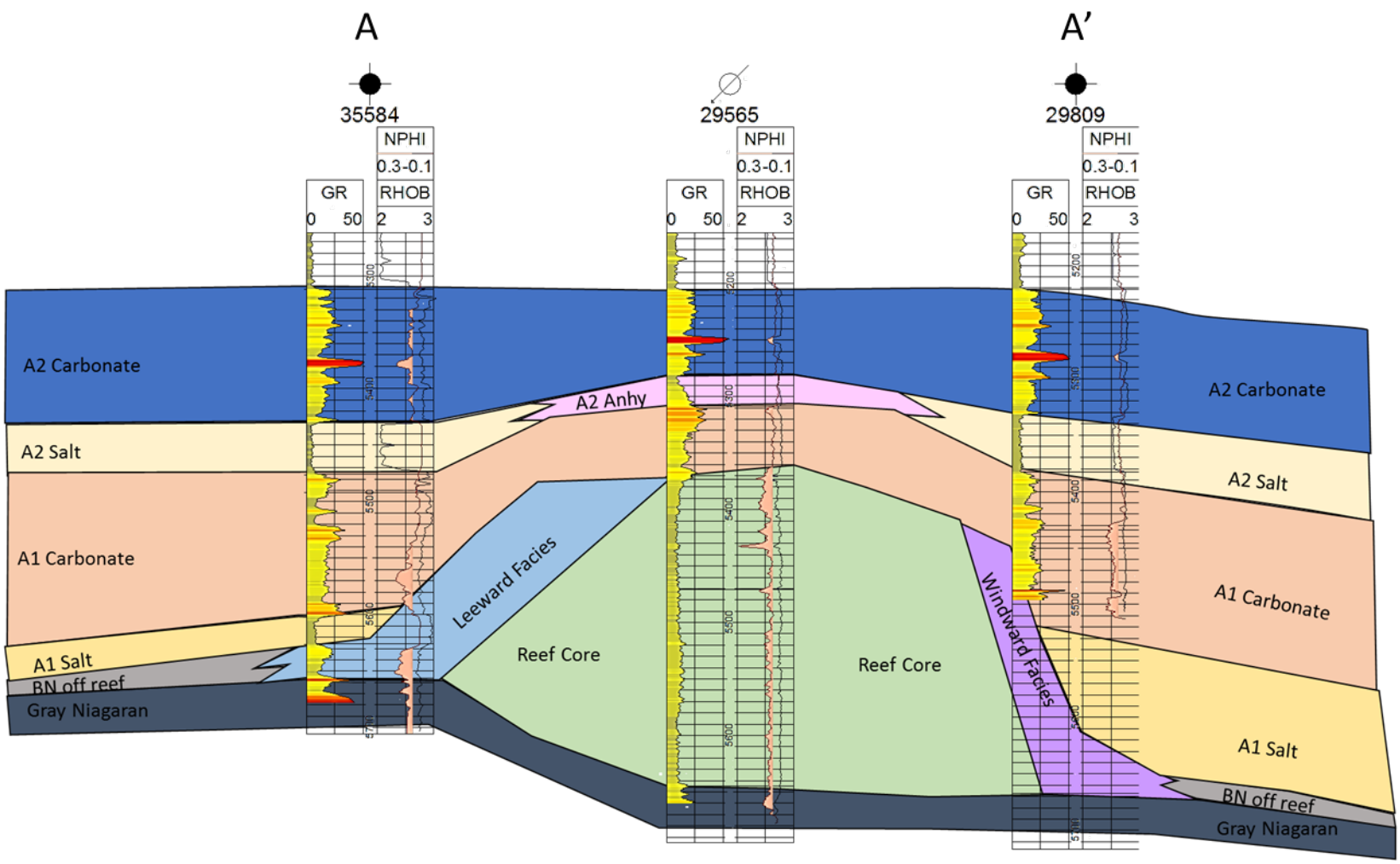


Figure 4-37. Cross section A-A' across the northern reef pod in the Dover 33 reef field showing changes in lithology and lithofacies from the southwest to the northeast.

5.0 Chester 16

5.1 Reef History and Production Review

All wells in the Chester 16 reef field were drilled and completed in the early 1970s. All wells except well 28743 were perforated throughout the Brown Niagaran and A-1 carbonate at completion. Well 28743 was perforated initially in the Brown Niagaran and then 10 years later in the A-1 carbonate. The Chester 16 reef field produced 2,584,555 MCF (thousand cubic feet) of gas and 3,001,429 bbls of oil. The greatest producers were in the center of the reef field (Figure 5-1); the poorest producers were located on the flanks. Well 28159 had the greatest recorded production, accounting for 52% of the total oil production and 51% of the total gas production. The total oil produced from all five primary production wells, 3,001,429 bbls, represents 43.8% of the OOIP produced by July 1990. Figure 5-2 shows the cumulative production for the entire Chester 16 reef field with a relative timeline of events. Table 5-1 summarizes production by well.

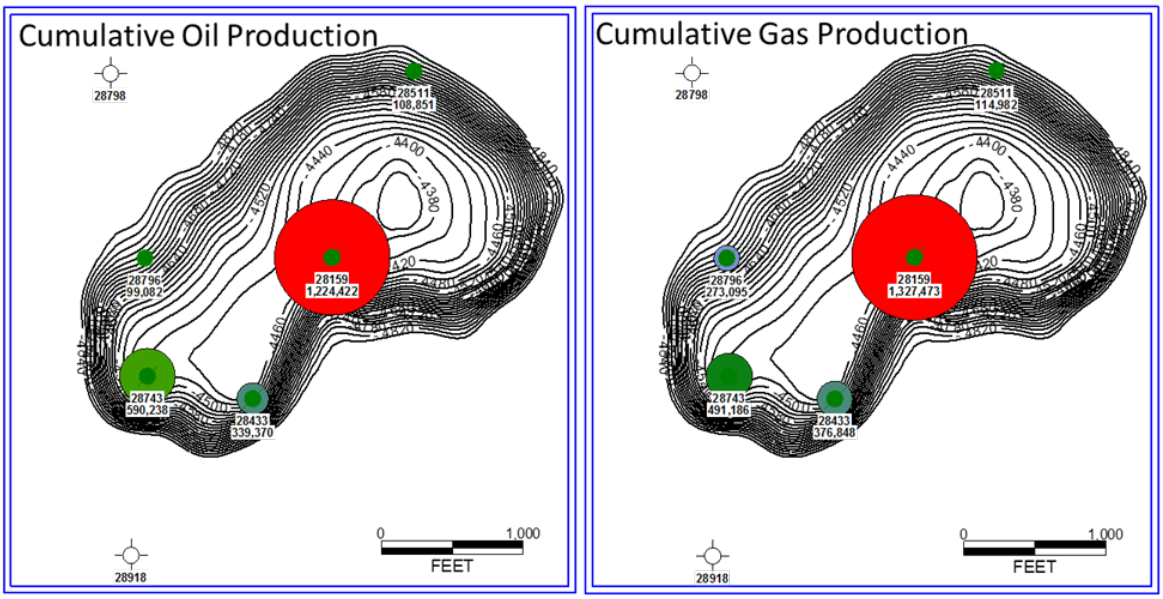


Figure 5-1. Cumulative oil and gas production by well in the Chester 16 reef field showing wells with greatest production (larger radius) and wells with lower production (smaller radius).

Table 5-1. Chester 16 reef field primary production by well.

Well Name	Well Permit	Start Date	End Date	Oil Produced (bbls)	Gas Produced (MCF)	Water Produced (bbls)
Gaylord Mortgage & Realty 1-16	28159	Jan-71	Jul-90	1,224,635	1,444,041	0
Gaylord Mortgage & Realty 2-16	28511	Sep-71	Jan-84	110,942	199,939	0
Gaylord Mortgage & Realty 3-16	28795	Sep-72	Jan-84	99,082	328,476	0
Veraghan 4-21	28433	Jul-71	Dec-84	339,370	458,236	0
Veraghan-Rypkowski 5-21	28743	Mar-72	Jan-84	596,218	570,737	0

In 1984, the Chester 16 reef field underwent a water flood. During the primary production period, one well, well 28743, was used to inject 2,166,550 barrels of water from February 1984 to June 1990 in an attempt to conduct a water-flood EOR operation. Based on the data in Figure 5-2, the water flood was ineffective at increasing oil production.

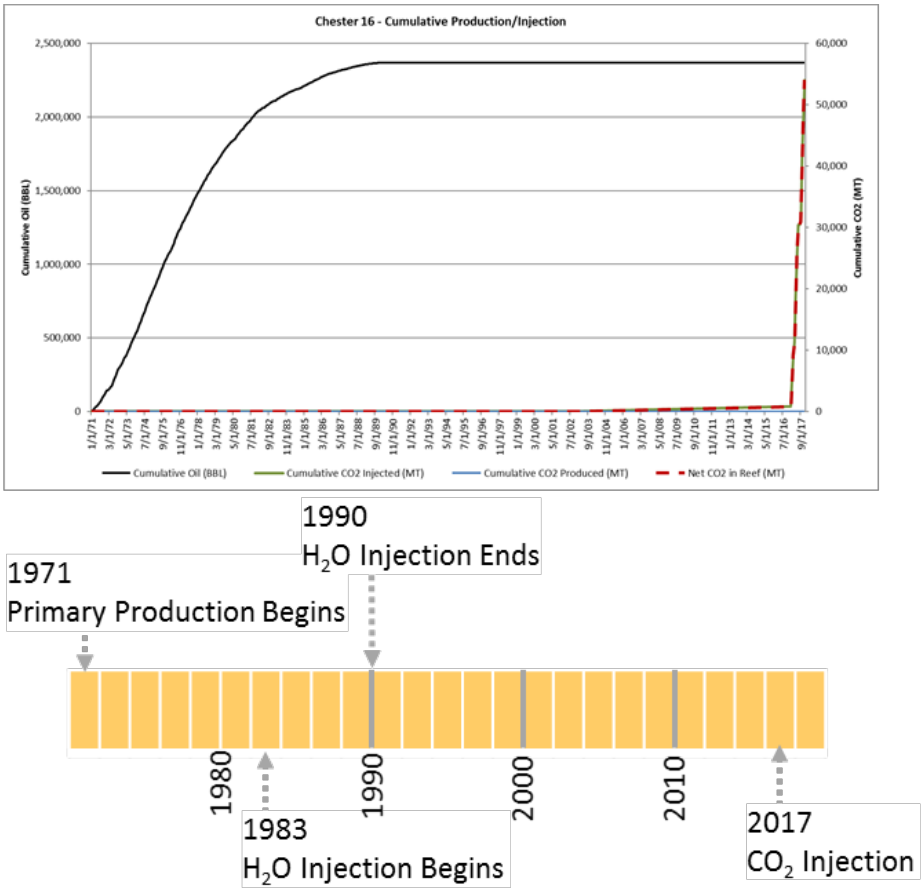


Figure 5-2. Cumulative production in the Chester 16 reef field from 1971 through 2017.

The initial (discovery) reservoir conditions of the Chester 16 reef field prior to the start of production are described in Table 5-2. These conditions are OOIP, oil API gravity, discovery pressure and temperature, and oil/gas/water saturations. Note that initial gas saturations were recorded at zero; however, gas was produced from the wells as it came out of solution during production of oil.

Table 5-2. Chester 16 reef field initial reservoir conditions.

		Discovery		Saturation		
OOIP (bbls)	**API Gravity**	**Pressure (psig)**	**Temperature (°F)**	**Oil**	**Gas**	**Water**
6,855,000	43	3,148	110	90%	0%	10%

Note: Information acquired from Core Energy, LLC.

5.2 Wireline Log Analysis

There are nine wells (seven existing wells and two new wells) in the Chester 16 reef field. Two wells are located off-reef and provide insight into how the geology changes outside the reef. Two of the seven wells are located along the flanks of the reef; the remaining five wells penetrate the reef structure. All wells have gamma ray, neutron porosity, and resistivity logs. Bulk density was available for three wells; where it was unavailable, sonic logs were used to compute bulk density. Advanced data was collected on the new wells, Chester 6-16 and 8-16. The advanced data included image logs, elemental spectroscopy, PNC data, acoustic and geomechanics data, and well testing data. The acquisition timeframe for wireline log data collectively ranged from 1971 to 2017. All data was thoroughly vetted using quality assurance/quality control (QA/QC) checks; raster logs were digitized to fill data gaps. Data availability is summarized in Table 5-3.

Table 5-3. Summary of available wireline log data for wells penetrating the Chester 16 reef field.

	Well UWI	2113728159000	2113728433000	2113728511000	2113728743000	2113728796000	2113728798000	2113728918000	2113761186000	2113761189000
CAL	Caliper									
DT	Sonic									
GR	Gamma Ray									
LLD	Latero-Log Deep (Resistivity)									
LLS	Latero-Log Shallow (Resistivity)									
MLL	MicroLatero-Log									
NPHI	Neutron Porosity									
RES	Resistivity									
PNC	Pulsed Neutron Capture									2
RHOB	Bulk Density									
SNP	Sidewall Neutron Porosity									
XMAC	Acoustic log									
IMAGE	Borehole image log									
BHP	Bottom Hole Pressure Monitoring									

Note: Green shading indicates logs available by well and number indicated repeat collection.

5.2.1 Basic Log Interpretation

Well 28796

Well 28796 is located along the northwest edge of the Chester 16 reef field. Bulk density log was not available, therefore crossplot analyses was not conducted. Sonic logs were also not available for substitute. Resistivity logs were available and were used to calculate the water saturation values. The water saturations fluctuate through the formations of interest due to interbedded evaporites in the flank. The Brown Niagaran on average has a water saturation of 72% with very few unsaturated intervals. Figure 5-3 shows the histogram and curve of the calculated water saturation for well 28796.

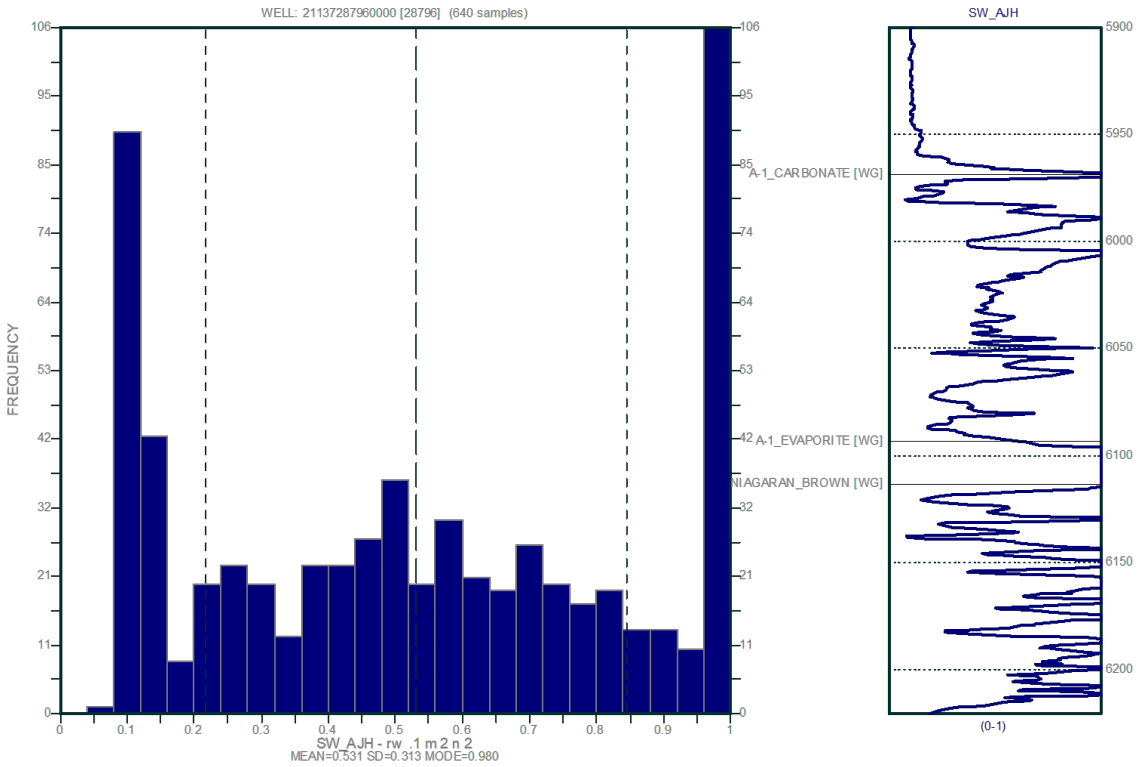


Figure 5-3. Histogram and curve from calculated water saturations in well 28796 showing high water saturations in the flank of the Chester 16 reef field.

Well 28159

Well 28159 is located in the middle of the Chester 16 reef field. A limited amount of bulk density data was available for crossplot analysis from a section of whole core. This section covers the A-1 carbonate. The A-1 carbonate plotted as a limestone with some trends toward the dolomite line. One interval of good porosity occurred in the upper section of the A-1 carbonate. There are minor spikes of porosity within the Brown Niagaran, but none have bulk density available. Figure 5-4 shows the neutron porosity-bulk density crossplot of well 28159.

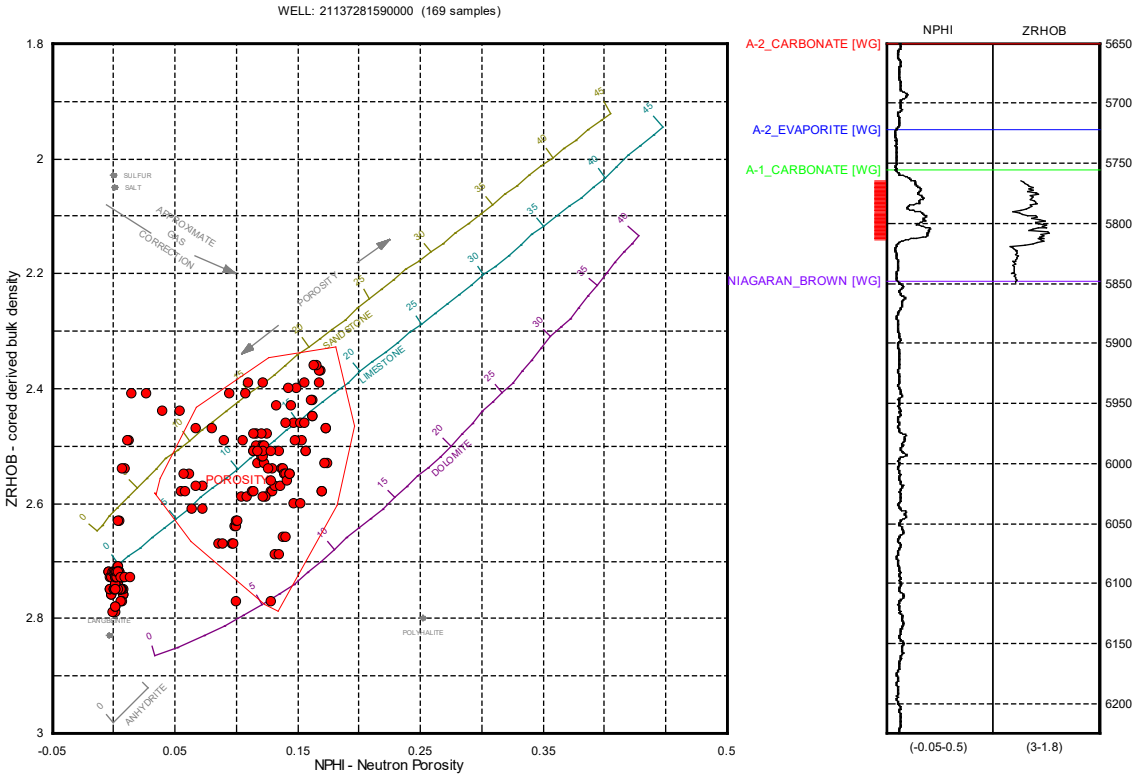


Figure 5-4. Neutron porosity-bulk density crossplot of well 28159 showing porosity in the upper A-1 carbonate.

Water saturation was estimated from the deep resistivity log and shows higher saturations in the presence of evaporites. The water saturation increases near 6,140 feet MD as it transitions from oil to water-saturated. The average water saturation for the Brown Niagaran is 33%. Figure 5-5 shows the resulting histogram and water saturation curve.

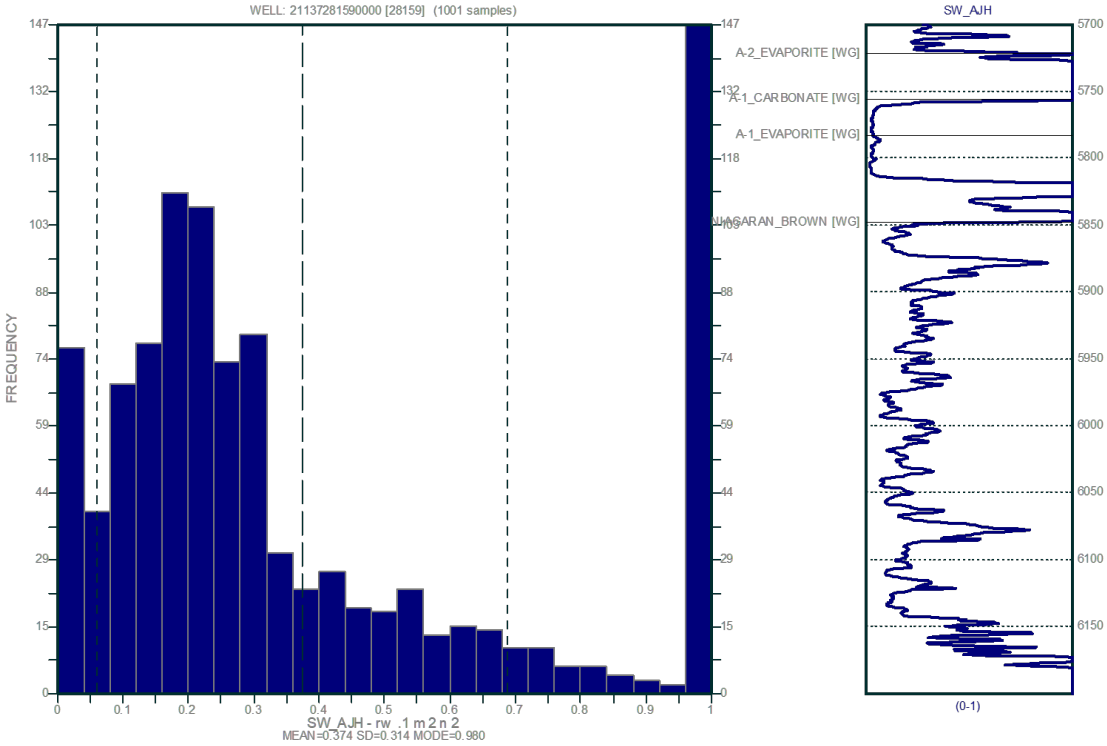


Figure 5-5. Water saturation histogram and curve for well 28159 over the A-2 carbonate to the Gray Niagaran showing an increase in water saturation near the base.

Well 28433

Well 28433 is located in the southern portion of Chester 16 near the edge of the reef. The interval of interest is mostly tight limestone with some sections of porous dolomite. The thickest interval of porosity was the upper portion of the A-1 carbonate, which had crossplot porosity up to 13%. There are 1-foot intervals of porosity within the upper 100 feet of the Brown Niagaran. Figure 5-6 shows the neutron porosity-bulk density crossplot of well 28433.

The estimated water saturation showed high saturations in the presence of evaporites. There is an increase in water saturation near 6,145 feet MD where there is a transition from oil to water within the Brown Niagaran formation. The average water saturation over the Brown Niagaran is 26% with an average of 42% after the oil/water contact. Figure 5-7 shows the histogram and curve of the water saturation estimates.

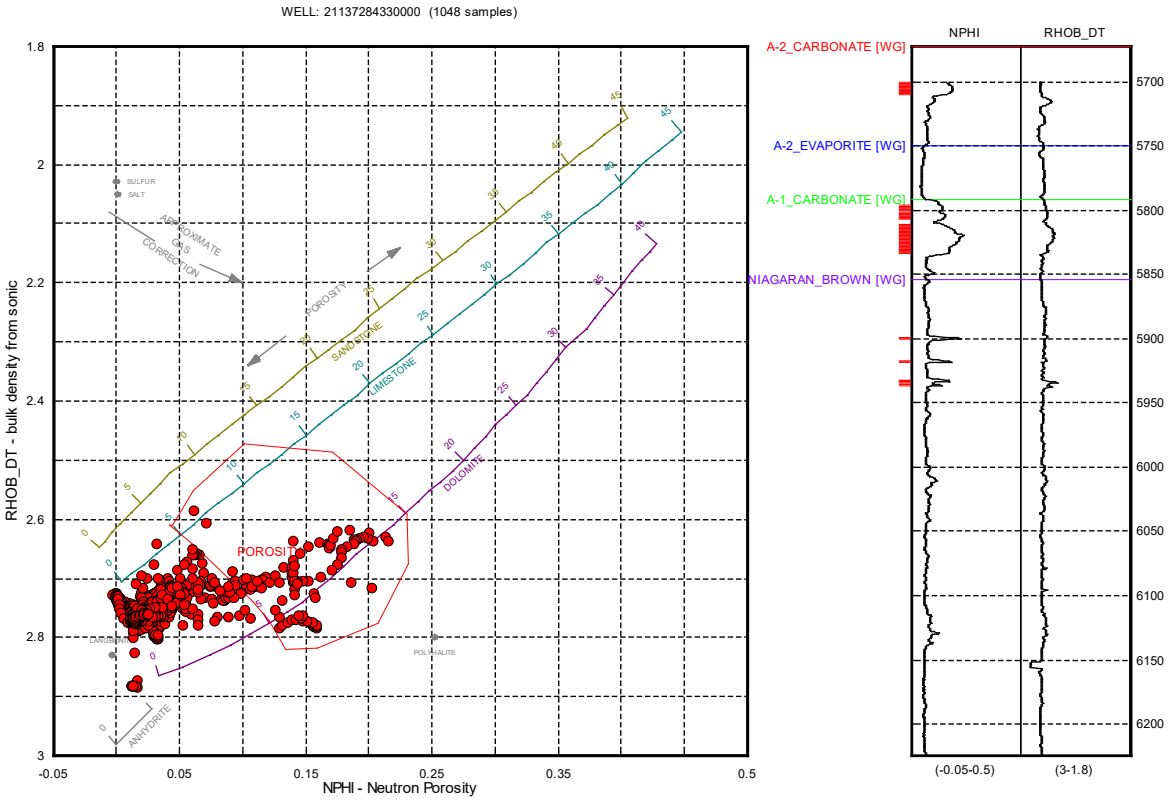


Figure 5-6. Neutron porosity-bulk density crossplot of well 28433 showing porosity in the upper A-1 carbonate and thin intervals in the Brown Niagaran.

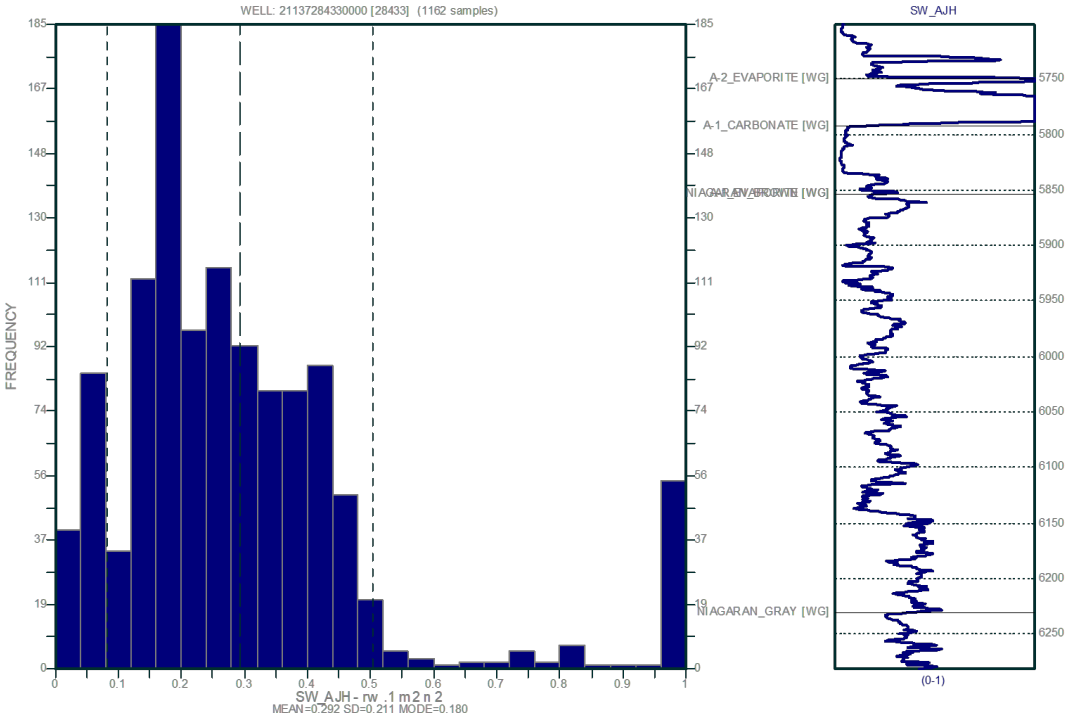


Figure 5-7. Water saturation histogram and curve for well 28433 over the A-2 carbonate to the Gray Niagaran.

Well 28511

Well 28511 is located in the most northern section of Chester 16 near the reef edge. The data in this well trend between the limestone and dolomite lines, indicating a mixed lithology. Very little porosity is observed in this well, with minor crossplot porosity spikes in the base of the A-2 carbonate and the upper Brown Niagaran. Porosity is observed in the neutron porosity curve at the top of the A-1 carbonate, but it does not plot above 5% crossplot porosity. The data which plots between the sandstone and limestone lines is a result of salt and falls within the A-2 evaporite. Figure 5-8 shows the neutron porosity-bulk density crossplot of well 28511.

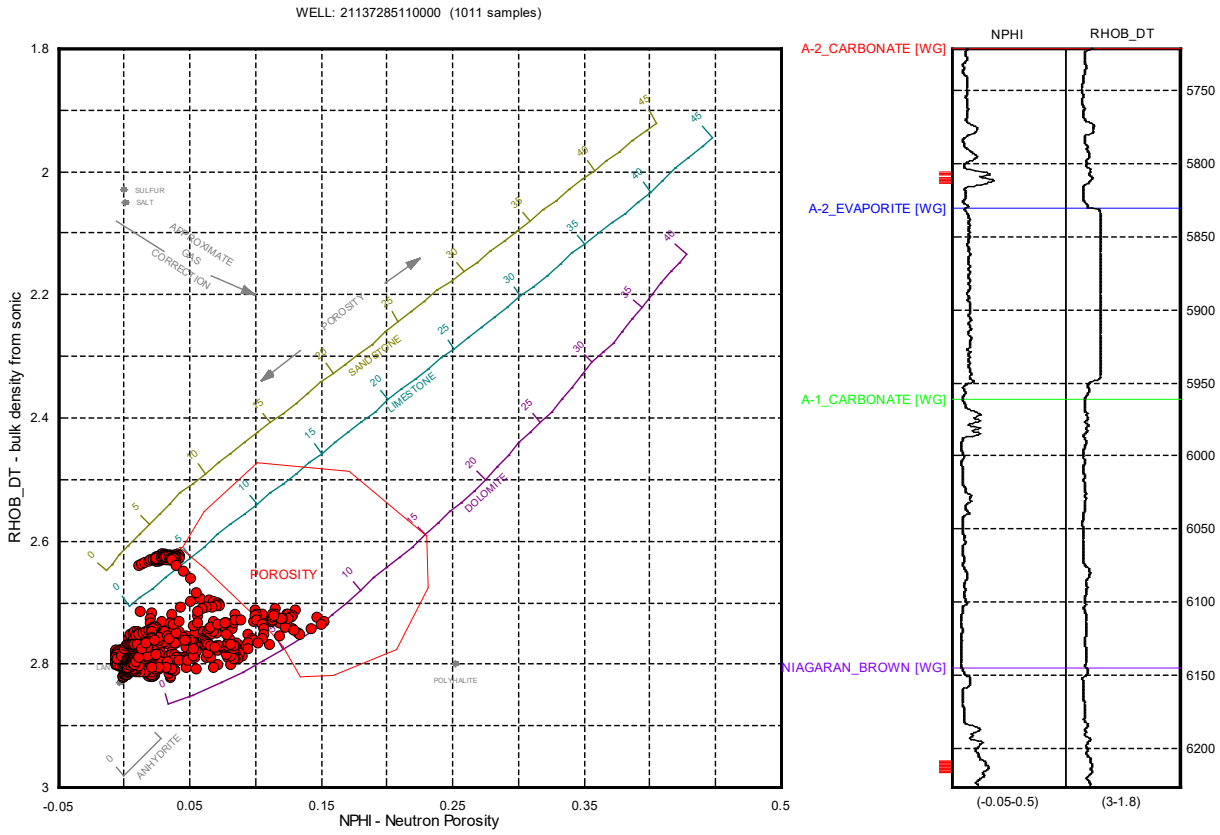


Figure 5-8. Neutron porosity-bulk density (from sonic) crossplot of well 28511 showing very little porosity with some porosity spikes in the Brown Niagaran.

The estimated water saturation curve for well 28511 showed high saturation values through the zones of interest. This could be attributed to interbedded evaporites because the well is located along the flank of the reefs. The Brown Niagaran is very thin and not likely of reservoir quality, with an average water saturation of 88% (Figure 5-9).

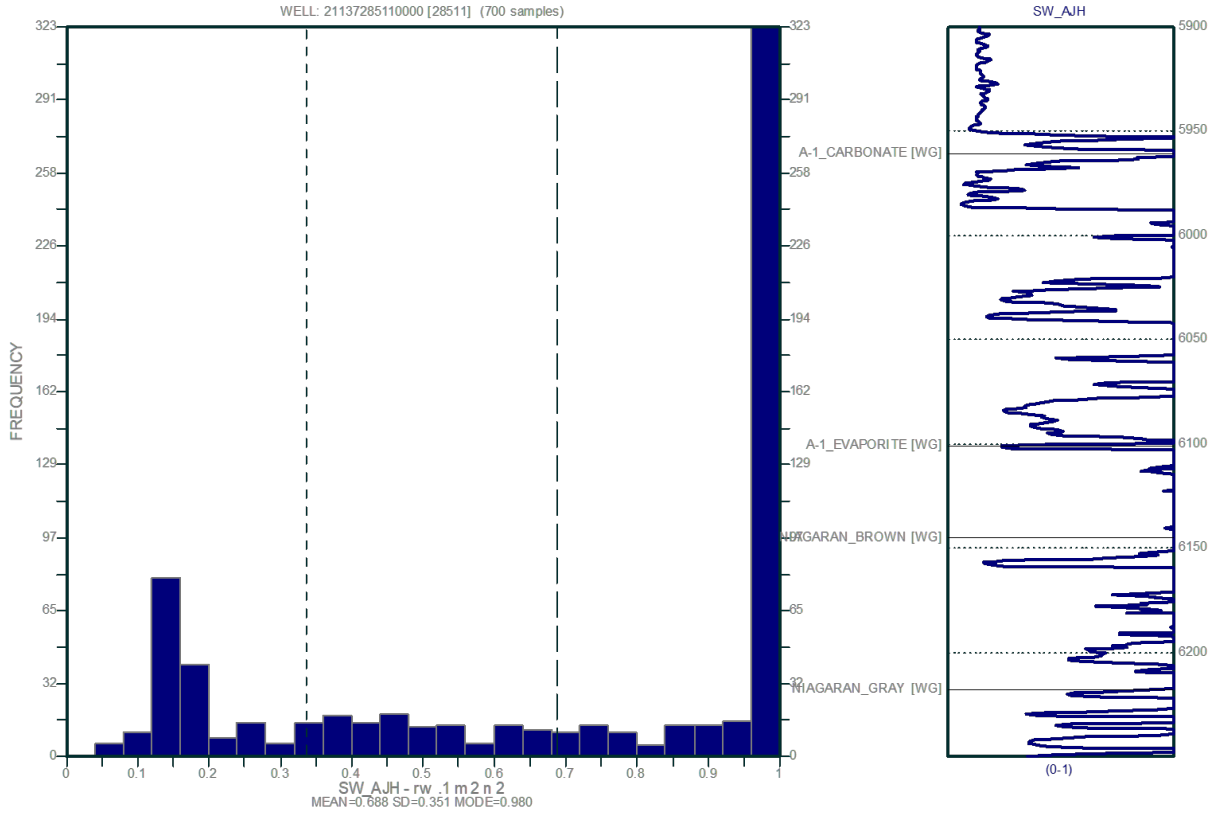


Figure 5-9. Water saturation histogram and curve for well 28511 over the A-2 carbonate to the Gray Niagaran showing high saturations throughout the flank interval of the Chester 16 reef field.

Well 28743

Well 28743 is in the southern section of the Chester 16 reef. Data falls between the limestone and dolomite lines, indicating a mixed lithology. Porosity was observed in the upper A-1 carbonate and in thin intervals in the middle of the Brown Niagaran. Some porosity points plotted between the sandstone and limestone line, which is an indication of salt plugging and might not represent true porosity. Figure 5-10 shows the neutron porosity-bulk density crossplot of well 28743.

The water saturation values remain low through the carbonates, with high values in the evaporate. The water saturation gradually increases toward the base of the Brown Niagaran near 6,113 feet MD, where the oil/water contact was identified. The average water saturation over the Brown Niagaran is 34% with an increase to 60% in the water saturated interval.
Figure 5-11 shows the histogram and calculated water saturation curve.

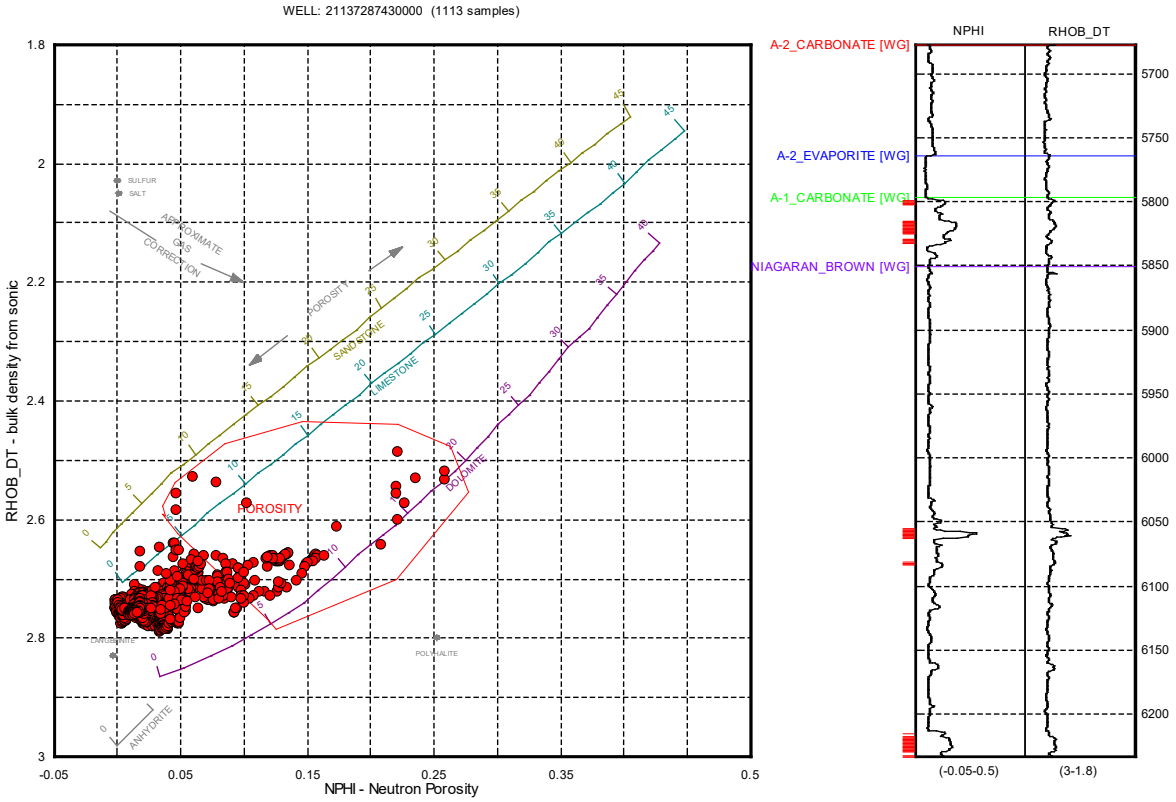


Figure 5-10. Neutron porosity-bulk density (sonic) crossplot of well 28743 in the Chester 16 reef field showing porosity in the upper A-1 carbonate and middle Brown Niagaran.

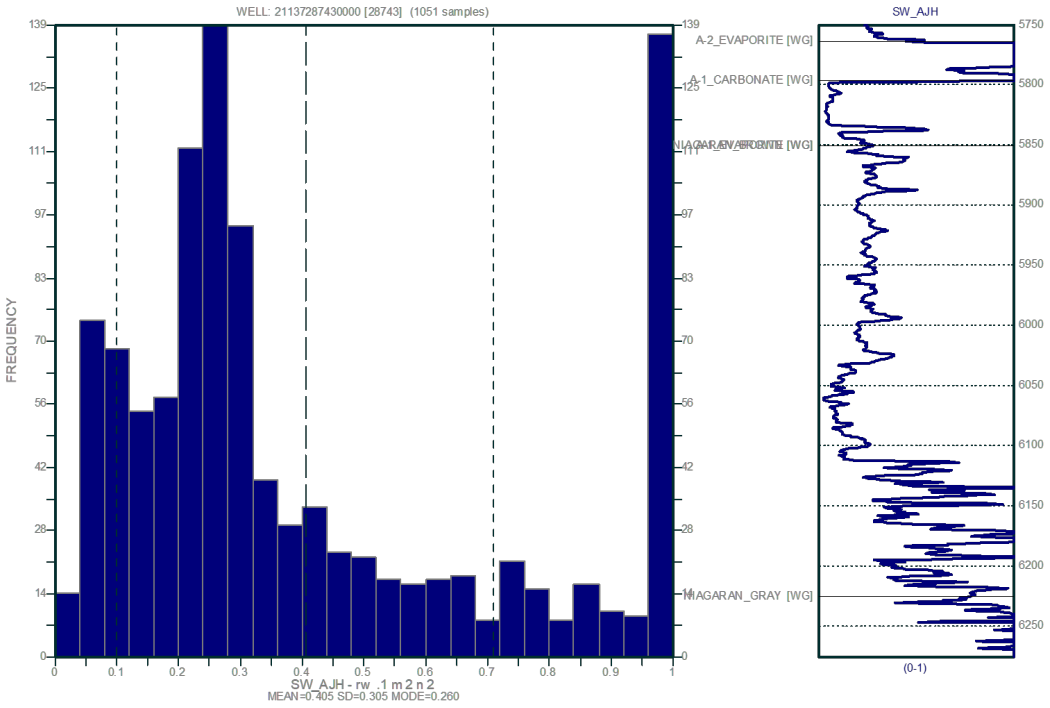


Figure 5-11. Histogram and curve for calculated water saturation for well 28743 showing an increase in water saturation toward the base of the Brown Niagaran.

Well 28798

Well 28798 is located off-reef to the northwest of Chester 16. This interval is composed of mostly limestone and salt. No porosity is observed at this location. The log data is consistent with off-reef geology. The neutron porosity-bulk density crossplot of well 28798 (Figure 5-12) shows no crossplot porosity in the formations of interest. Due to the off-reef location of this well, the Brown Niagaran northwest of the reef field has been determined to be fully water saturated.

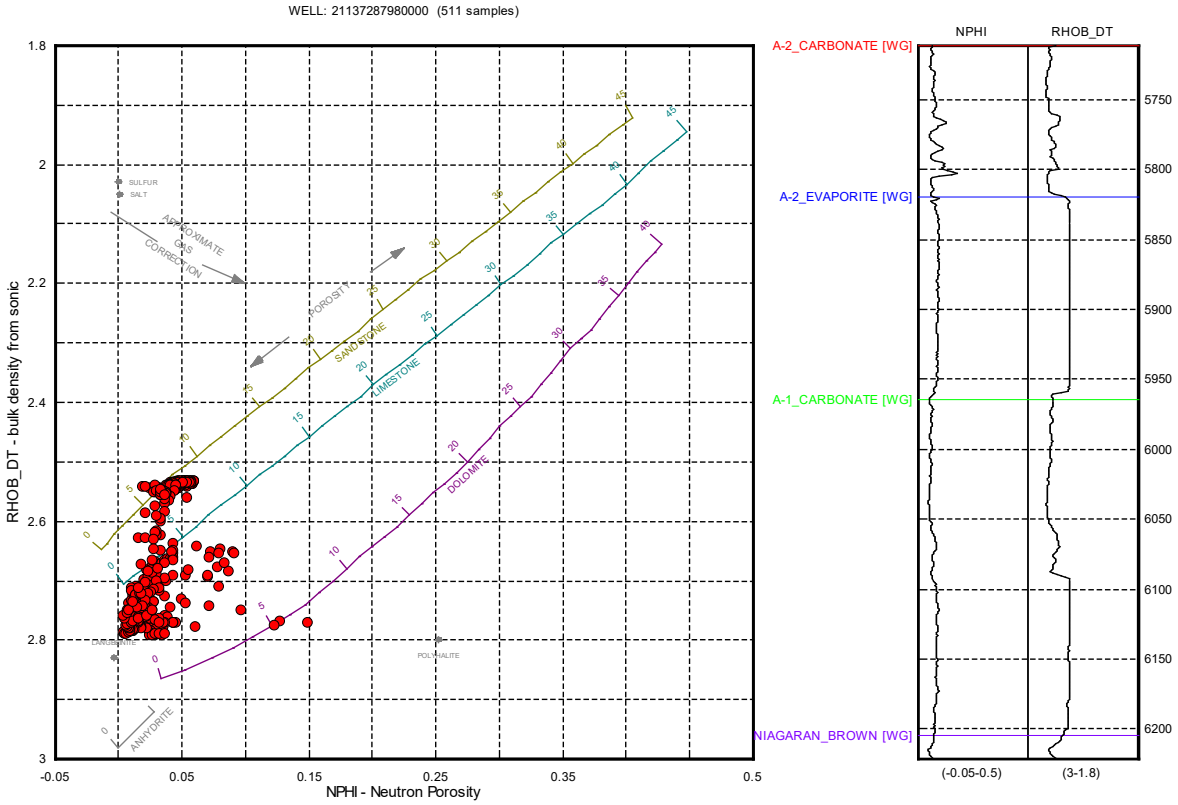


Figure 5-12. Neutron porosity-bulk density (sonic) crossplot of well 28798 in the Chester 16 reef field showing no porosity.

Well 28918

Well 28918 is an off-reef well located south of Chester 16. The formations of interest are mostly limestone with some dolomite and intervals of salt. No crossplot porosity was observed. The neutron porosity-bulk density crossplot of well 28918 (Figure 5-13) shows no crossplot porosity in the formations of interest. Water saturation estimates were not available at this well location, but considering this is an off-reef well, the Brown Niagaran south of the reef field has been determined to be fully saturated.

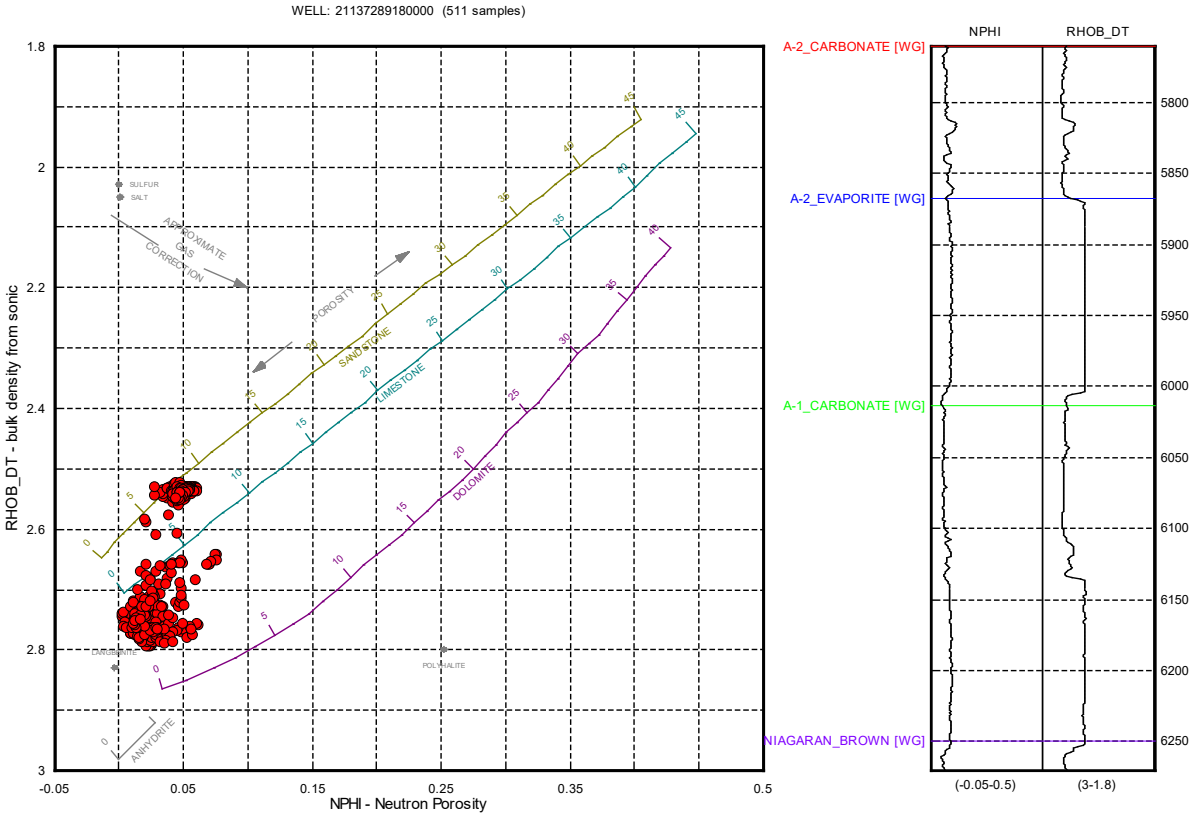


Figure 5-13. Neutron porosity-bulk density (sonic) crossplot of well 28918 in the Chester 16 reef field showing no porosity.

Chester 6-16

The Chester 6-16 well is located in the southern part of the Chester 16 reef field. The A-1 carbonate plots as mostly dolomitic with a porosity greater than 5% occurring for a significant thickness of the formation (Figure 5-14). The Brown Niagaran is a thick interval of tight limestone with thin intervals of porosity greater than 5% occurring mid-formation. The water saturation profile is sporadic and high throughout the Brown Niagaran (Figure 5-15), which could be a result of being closely located to an existing water injection well.

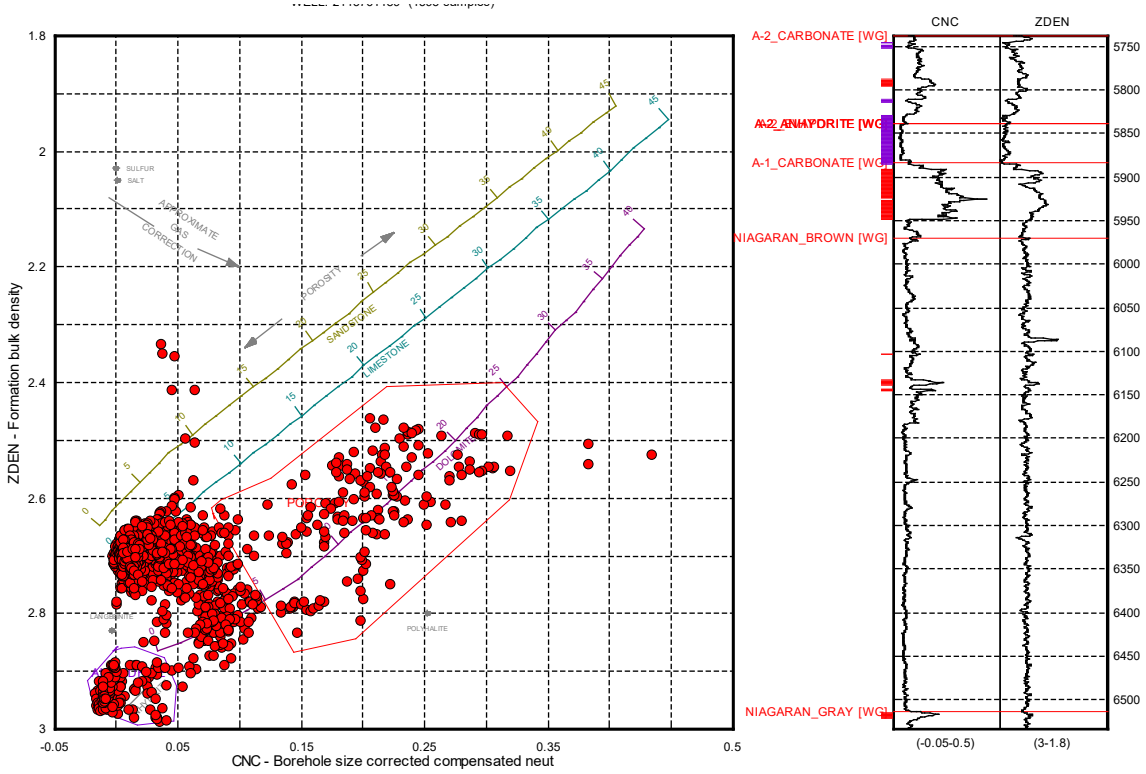


Figure 5-14. Neutron porosity-bulk density (sonic) crossplot of the Chester 6-16 well showing porosity in the upper A-1 carbonate and mid-Brown Niagaran.

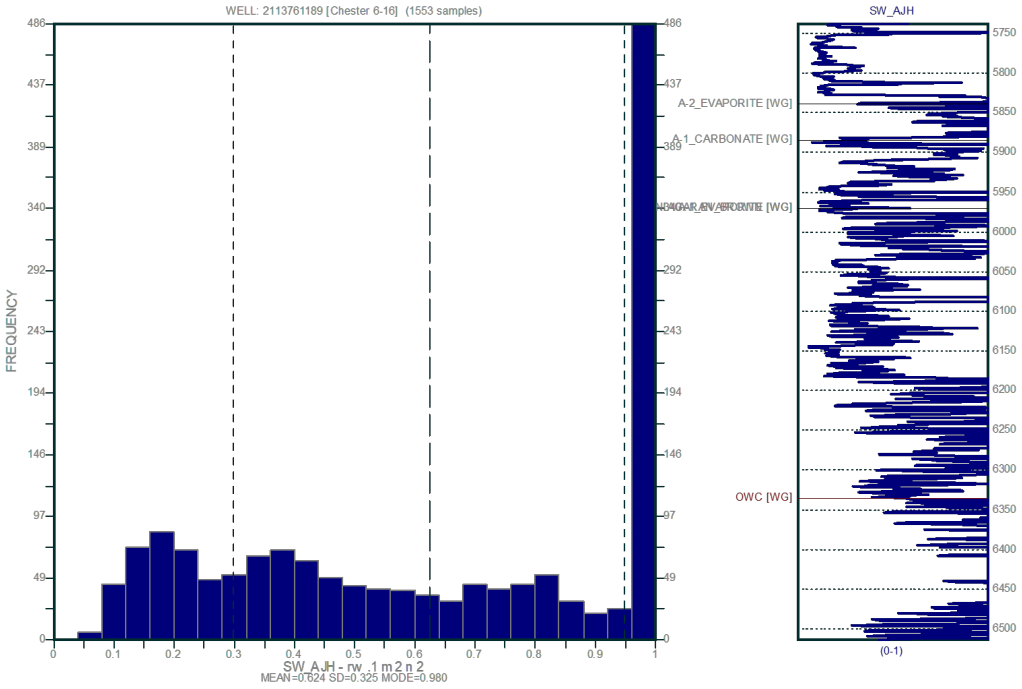


Figure 5-15. Histogram and curve for calculated water saturation for the Chester 6-16 well showing high water saturation throughout the Brown Niagaran.

Chester 8-16

The Chester 8-16 well is located in the middle of the reef field. The A-1 carbonate presents as mostly dolomitic with the entire formation having porosity greater than 5% (Figure 5-16). The Brown Niagaran formation is thick at this well location and is mostly tight limestone. Thin intervals of porosity greater than 5% occur throughout. The water saturation in the Brown Niagaran is higher than typical (Figure 5-17), which could be a result of post waterflooding activities.

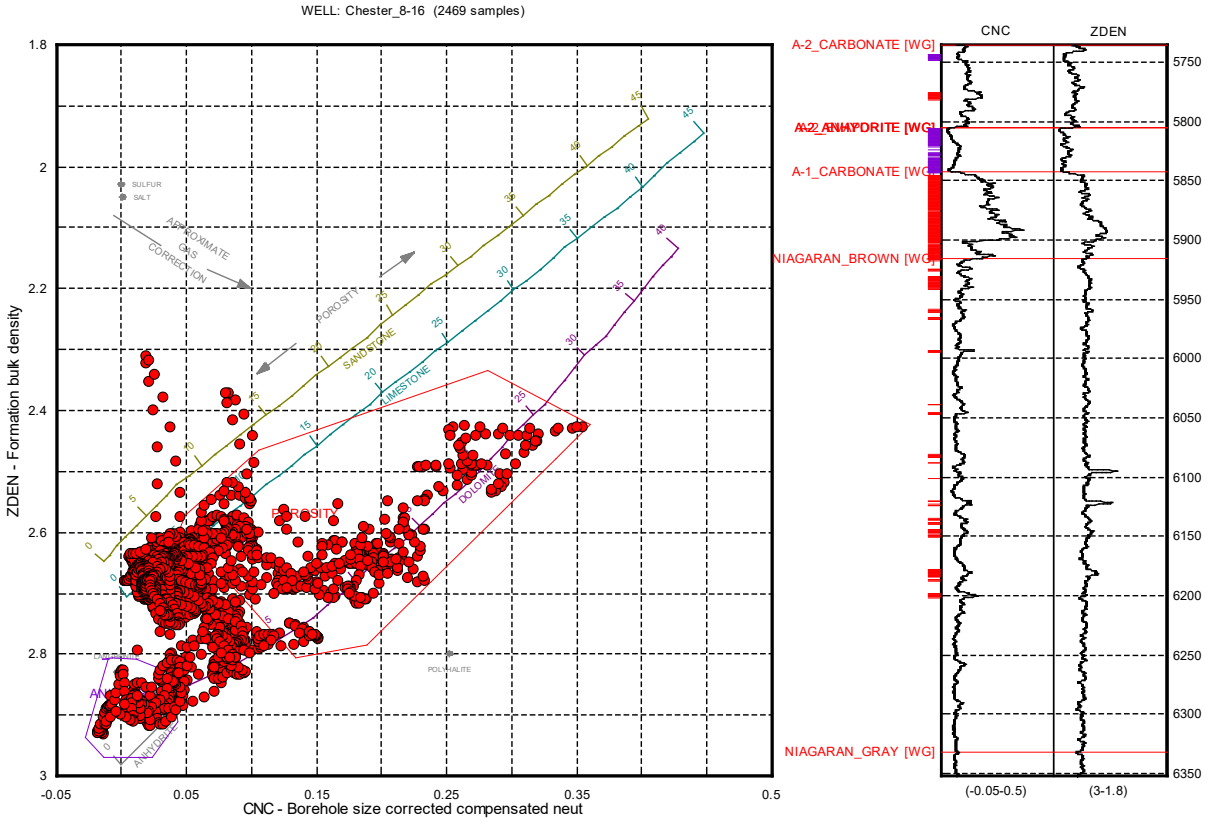


Figure 5-16. Neutron porosity-bulk density (sonic) crossplot of the Chester 8-16 well showing porosity in the upper A-1 carbonate and mid-Brown Niagaran.

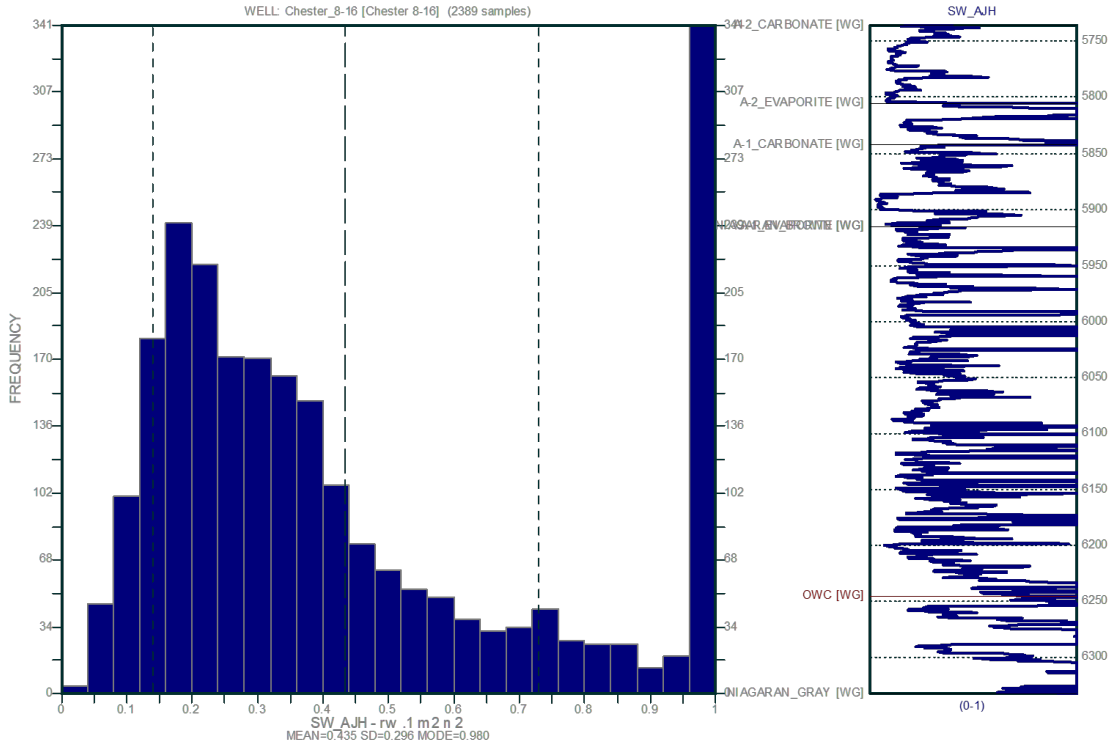


Figure 5-17. Histogram and curve for calculated water saturation for the Chester 8-16 well showing an increase in water saturation toward the base of the Brown Niagaran.

5.2.2 Advanced Log Interpretation

Advanced wireline log data was collected for the Chester 6-16 and Chester 8-16 wells as part of piggyback operations with Core Energy, LLC. The data suite consisted of elemental spectroscopy, image logs, and advanced acoustic. Key observations are provided in this section; for more details, Attachments 3 and 4 cover the detailed log analyses of the Chester 6-16 and 8-16 wells, respectively.

A-2 Carbonate and A-2 Evaporite

The A-2 carbonate was found to consist of mostly tight dolomite with thin intervals of anhydrite and shales. The image log did not show any evidence of fractures, vugs, or significant porosity. The image log and elemental spectroscopy showed that the A-2 evaporite unit was composed of interbedded intervals of anhydrite, shale, and limestone. The findings are consistent with rock properties needed for ideal confining units.

A-1 Carbonate

Elemental spectroscopy logs showed a mostly dolomitic matrix in the A-1 carbonate with a mixed carbonate unit at the base. This lower interval has been associated with stromatolitic caps in adjacent reefs and tends to lack porosity and behave as a baffle. Image log analysis showed the middle portion of the A-1 carbonate to have potential for significant porosity development due to heterogeneous textures (Figure 5-18).

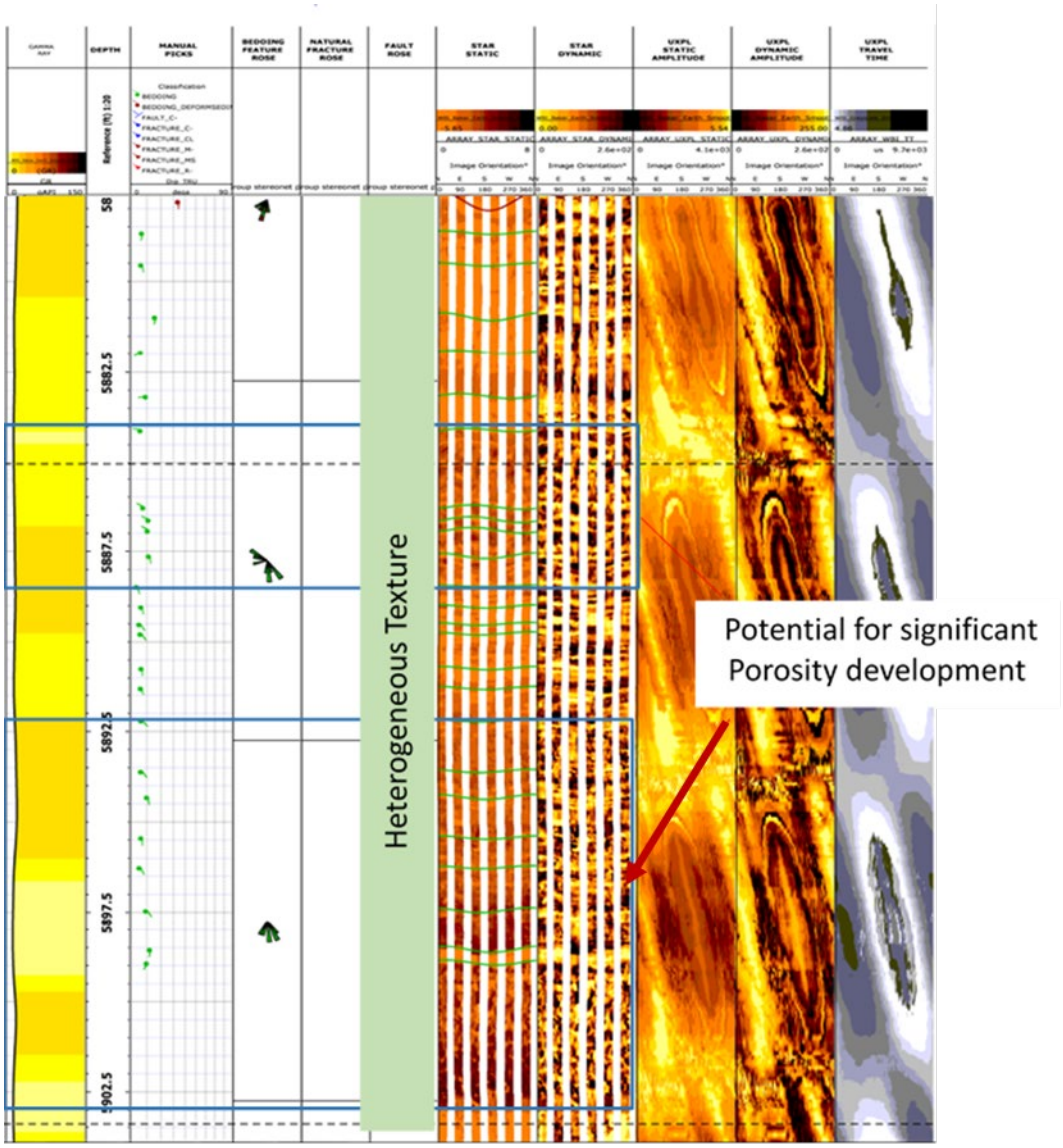


Figure 5-18. Intermediate texture zone of the A-1 carbonate. The texture was heterogeneous with two porosity zones shown in the figure (blue boxes) from 5,884 to 5,888 feet and from 5,892 to 5,903 feet.

Brown Niagaran

Elemental spectroscopy logs over the Brown Niagaran formation showed a mostly limestone matrix with thin intervals of dolomite. Where dolomite was observed, porosity increased. The image log analysis revealed mostly tight limestone with intervals of significant porosity development in the form of fractures and vugs (Figure 5-19). Both logs indicate that the porosity intervals are thin and disconnected.

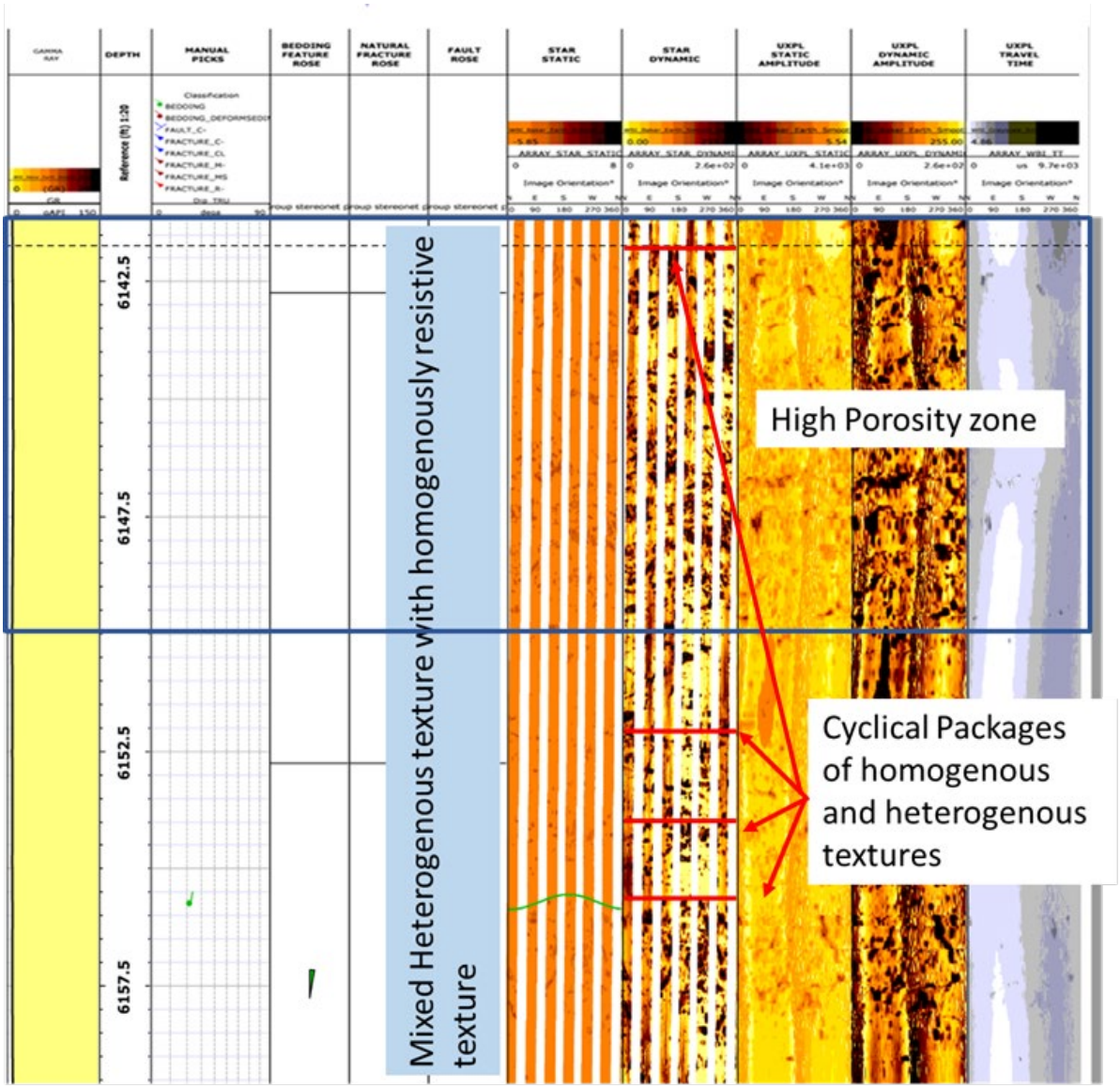


Figure 5-19. Texture three within the Brown Niagaran unit of the Chester 8-16 well. Texture was interbedded homogenous and heterogenous materials. Significant porosity zone was shown from 6,141 to 6,150 feet. Note cyclical packages of homogenously resistive-to-heterogeneous materials.

5.2.3 Petrophysical Calculations

A-2 Carbonate

The A-2 carbonate was on average 91 feet thick and mostly composed of dolomite with little to no porosity. The water saturation values remained low, except where evaporites were present. Basic petrophysical calculations yielded an average net thickness of 7 feet and the resulting NTG ratio of 0.10. The average porosity-feet was 0.5%-ft. The petrophysical calculations for the A-2 carbonate are summarized in Table 5-4.

Table 5-4. Summary of petrophysical calculations for the A-2 carbonate in the Chester 16 reef field.

Interval: A-2 Carbonate					
Avg. Thickness	**Avg. Porosity**	**Avg. Net Thickness**	**Avg. NTG**	**Avg. Porosity-Feet**	**Avg. SW**
91 ft	4.5%	7 ft	0.10	0.5%-ft	43%

A-1 Carbonate

The A-1 carbonate varied from 240 feet thick off-reef to 55 feet thick on the crest of the reef. The average neutron porosity by well ranged from 1.3% to 18.9% with an average of 7.8% for the entire formation. The water saturation was low for wells on-reef and increased in flank wells due to increased evaporites. The average water saturation was 36%. The average net thickness was 50 feet with a resulting NTG ratio of 0.44. However, wells which were on the crest of the reef had a NTG ratio above 0.50. The porosity-feet ranged from 0.6% to 8.6%-ft with an average of 4.8%-ft. Calculations are summarized in Table 5-5 for the A-1 carbonate.

Table 5-5. Summary of petrophysical calculations for the A-1 carbonate in the Chester 16 reef field.

Interval: A-1 Carbonate					
Avg. Thickness	**Avg. Porosity**	**Avg. Net Thickness**	**Avg. NTG**	**Avg. Porosity-Feet**	**Avg. SW**
128 ft	7.8%	50 ft	0.44	4.8%-ft	36%

Brown Niagaran

The thickness of the Brown Niagaran ranged from 35 feet off-reef to 416 feet at the crest of the reef. The average neutron porosity by well ranged from 2.0% to 5.3% with an overall average of 3.6%. The reef was approximately one-third water-saturated, resulting in an average of 55%. The average net thickness was 24 feet with a resulting NTG ratio of 0.08. The porosity-feet was low throughout with an average of 1.8%-ft. Overall, the Brown Niagaran showed low reservoir potential with disconnected porosity intervals. The petrophysical calculations for the Brown Niagaran are summarized in Table 5-6.

Table 5-6. Summary of petrophysical calculations for the Brown Niagaran in the Chester 16 reef field.

Interval: Brown Niagaran					
Avg. Thickness	**Avg. Porosity**	**Avg. Net Thickness**	**Avg. NTG**	**Avg. Porosity-Feet**	**Avg. SW**
270 ft	3.6%	24 ft	0.08	1.8%-ft	55%

5.3 Core Analysis

Whole core and sidewall cores were available from five wells in the Chester 16 reef field (Figure 5-20). Three wells (red circles) were previously acquired and available through the MGRRE for viewing. MRCSP collected whole core and sidewall cores from the two new wells (blue circles) to help fill in crucial data gaps. Whole core was available over the A-1 carbonate, A-1 evaporite, Brown Niagaran, and Gray Niagaran formations. Sidewall cores suplemented the dataset and were available in the A-2 carbonate, A-2 evaporite, A-1 carbonate, and Brown Niagaran formations. Table 5-7 summarizes the core data available and collected by well.

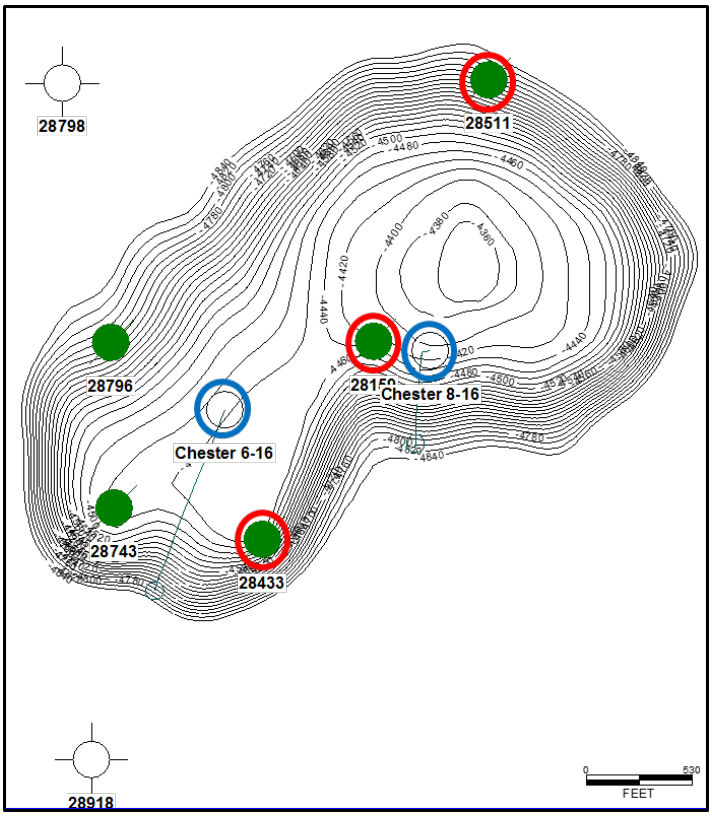


Figure 5-20. Map of the Chester 16 reef field showing previously collected core (red) and newly Battelle-collected core (blue) by well and position in main reef structure.

Table 5-7. Summary of core collected by well in the Chester 16 reef field.

Well	A-2 Carbonate	A-2 Evaporite	A-1 Carbonate	A-1 Evaporite	Brown Niagaran	Gray Niagaran
28433	-	-	-	-	WC	-
28159	-	-	WC	WC	WC	-
28511	-	-	WC	-	WC	-
Chester 6-16	-	-	SC	-	SC	SC
Chester 8-16	SC	SC	SC	-	WC	WC

Note: WC = whole core; SC = sidewall core.

Standard core analysis was conducted for core available through MGRRE, which included porosity, permeability, fluid saturation, bulk density, and grain density measurements. The core was described foot by foot, which included lithology and sedimentary structures. High-resolution photographs were taken of each section of core.

5.3.1 Core from Well 28433

Well 28433 is located in the southern part of the Chester 16 reef field along the edge of the reef. Core from this well was taken during drilling. The core covered an interval of 5,962 to 6,028 feet MD and only included the Brown Niagaran. The Brown Niagaran was dark- to light-gray carbonate. Stylolites were abundant and varied from low to high amplitudes with some high angles. Pinpoint to 1-inch vugs were visible along with moldic porosity. Bioclastic debris was common toward the end of the core. The structures observed were consistent with rock from the flank of the reef or the leeward facies. Figure 5-21 shows representative photographs of the varying textures and structures. Figure 5-22 is a simplified stratigraphic column of core from well 28433.

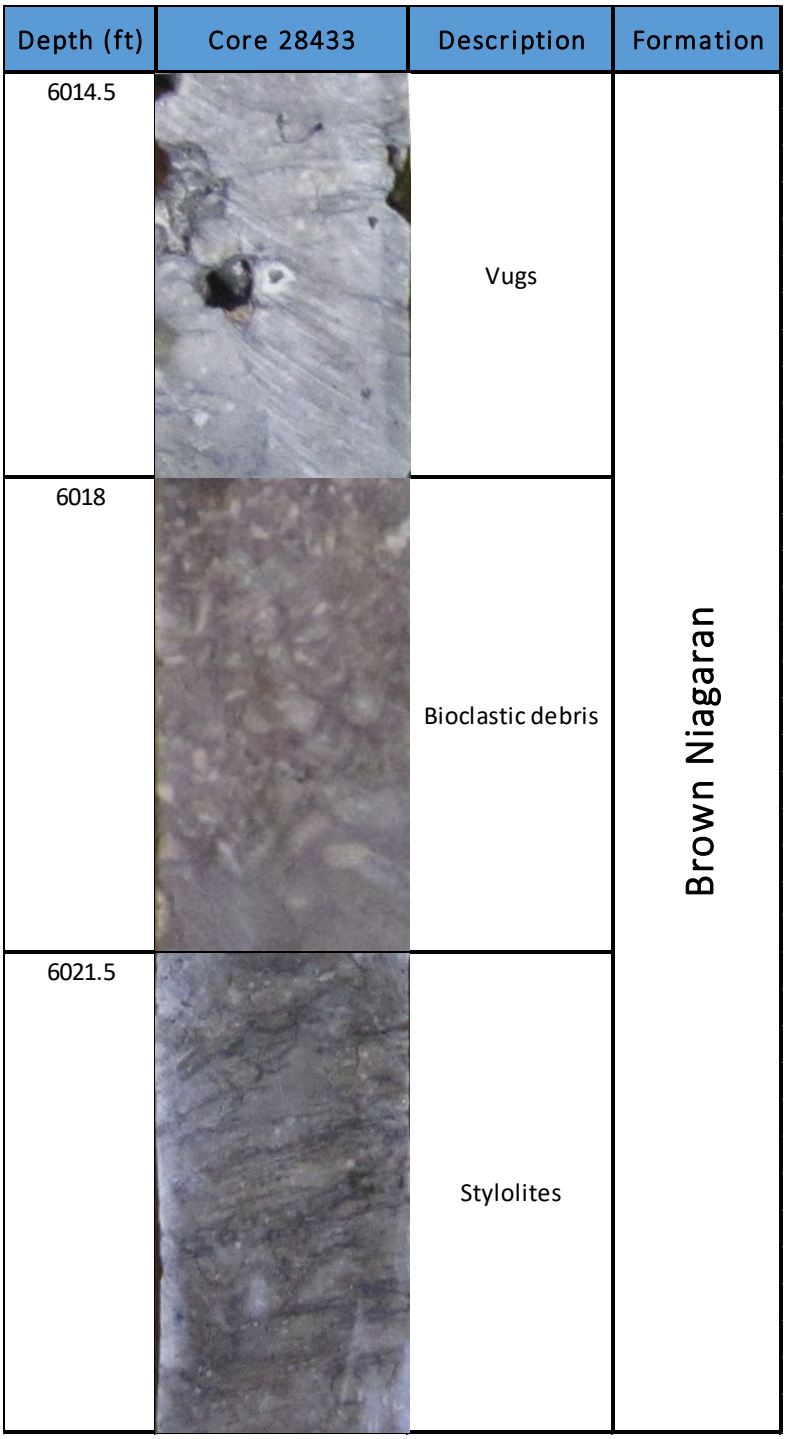


Figure 5-21. Photographs of textures and structures observed in whole core from well 28433.

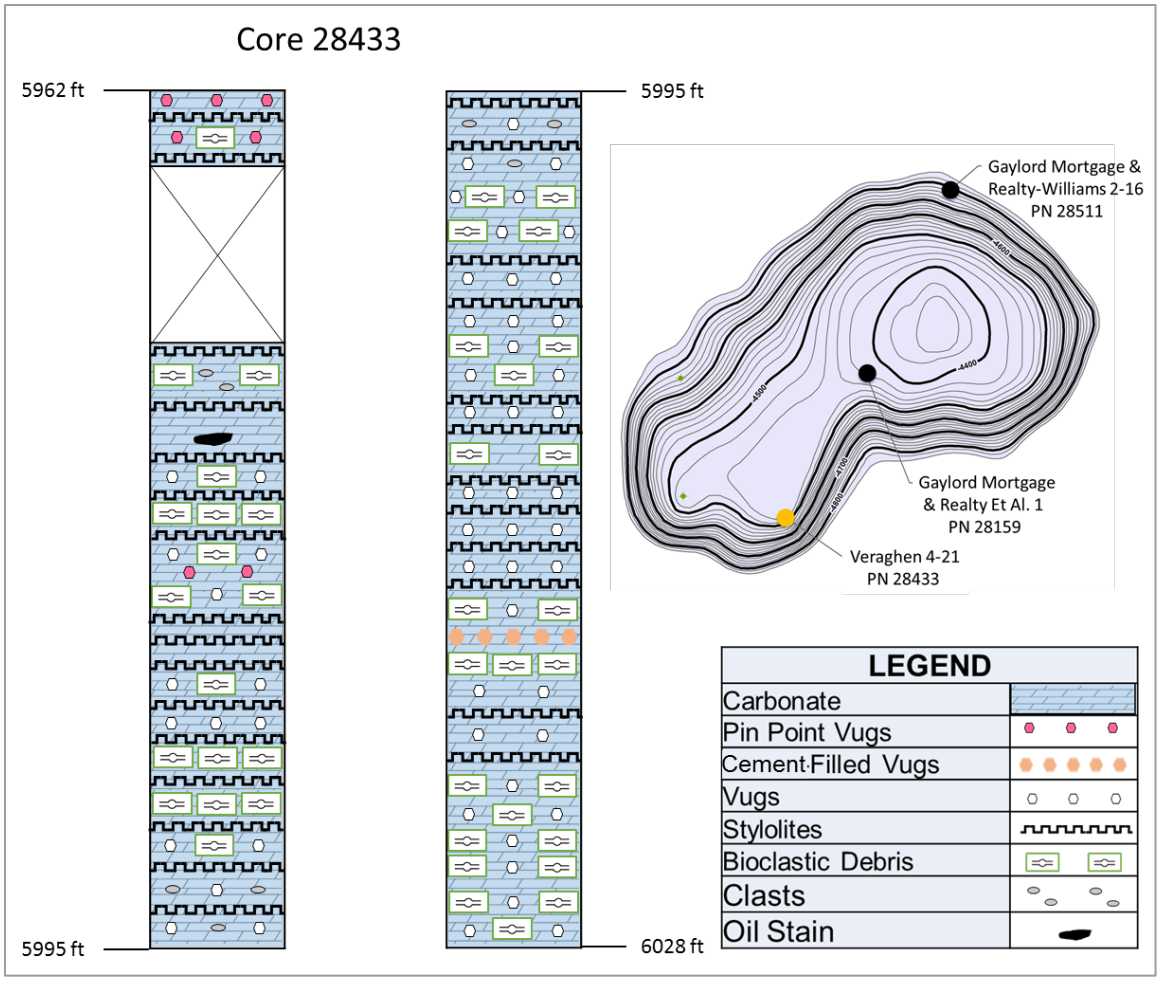


Figure 5-22. Simplified stratigraphic column of core in well 28433 summarizing lithology, textures, and structures in the Brown Niagaran.

5.3.2 Core from Well 28159

Core from well 28159, located in the middle of the Chester 16 reef field, covered an interval from 5,765 to 5,849 feet MD. The A-1 carbonate, A-1 evaporite, and Brown Niagaran were covered. The A-1 carbonate was light- to medium-gray carbonate with some stromatolite beds dipping at 25º to 30º. Algal beds were abundant along with wispy silt laminations. No visible matrix or secondary porosity was observed. The A-1 evaporite was a medium- to light-gray carbonate with abundant anhydrite beds, stylolites, and silty wisps. Stromatolites were present at the base of the A-1 evaporite along with anhydrite cement. The Brown Niagaran was light- to medium-gray carbonate with minor pinpoint vugs and anhydrite cement. Little to no porosity was seen. Overall, the presence of anhydrite and the A-1 evaporite plus little porosity in the A-1 carbonate and Brown Niagaran suggested that the well was composed of flank facies. Figure 5-23 shows representative photographs of textures and structures. Figure 5-24 is the simplified stratigraphic column of core from well 28159.

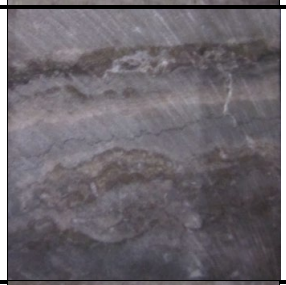
Depth (ft)	Core 28159	Description	Formation
5769		Algal beds	A1 Carbonate
5821		Stylolites	A1 Evaporite
5830.5		Stylolites Anhydrite beds	
5845		Stylolites Anhydrite cement	Brown Niagaran

Figure 5-23. Photographs of textures and structures observed in the whole core from well 28159.

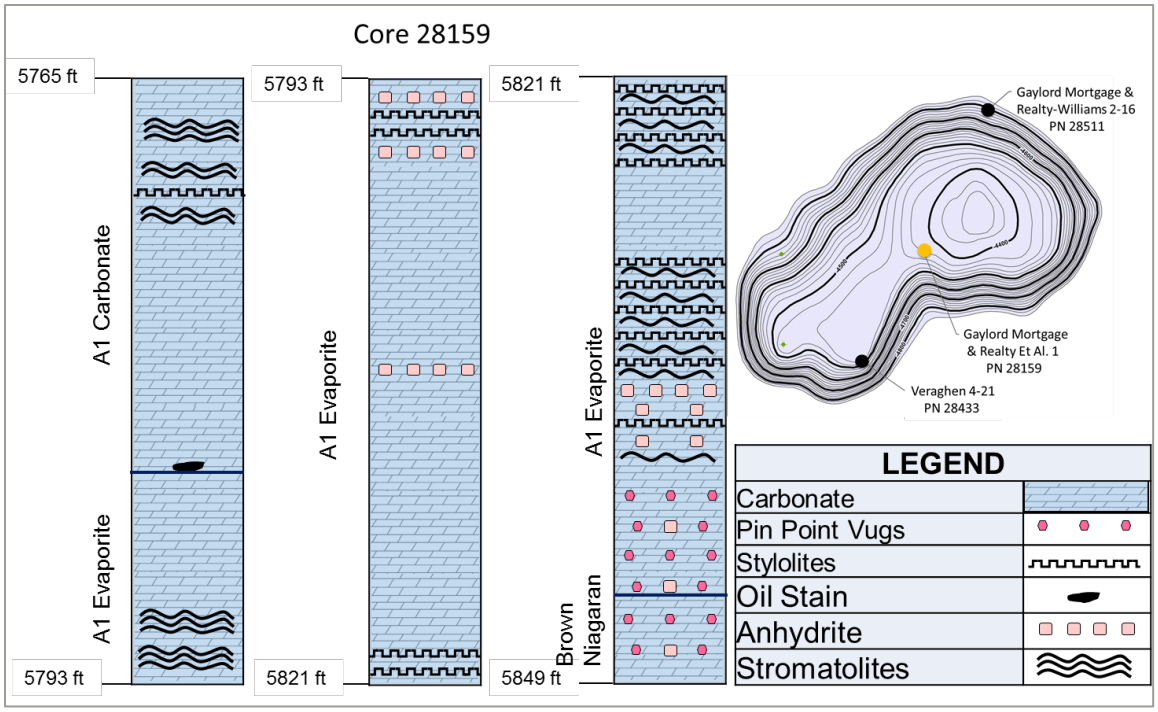


Figure 5-24. Simplified stratigraphic column of core from well 28159 summarizing lithology, textures, and structures.

5.3.3 Core from Well 28511

Core from well 28511, located in the northern part of the Chester 16 reef field along the reef edge, covered an interval of 5,982 to 6,224 feet MD. The upper 10 feet of the A-1 carbonate cored interval was composed of dark-gray carbonate mudstone with poker-chip shale. This transitioned in gray carbonate with some anhydrite beds, stylolites, and fractures. Little to no porosity was observed in the A-1 carbonate. Interval 6,062 to 6,149 feet MD was missing. The Brown Niagaran was medium-gray carbonate which was often a grainstone. Stylolites and fractures were abundant. Pinpoint vugs were occasionally present. Toward the base of the cored Brown Niagaran, there was a porosity change which correlated with a large grain-sized carbonate and churned-up clastic material. The presence of poker-chip shale in the A-1 carbonate and increased grain size in the Brown Niagaran indicated a windward flank location along the reef structure. Figure 5-25 shows representative photographs of textures and structures. Figure 5-26 is a simplified stratigraphic column of core from well 28511.

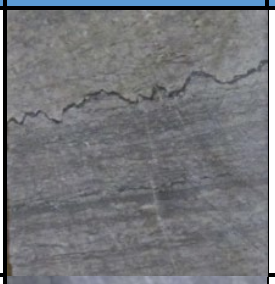
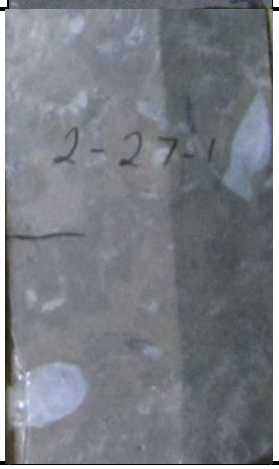
Depth (ft)	Core 28511	Description	Formation
5987		Stylolites	A1 Carbonate
5991.5		Anhydrite beds	
6193		Vugs Salt	Brown Niagaran
6197		Stylolites	
6223		Churned clastic material	

Figure 5-25. Photographs of textures and structures of whole core from well 28511.

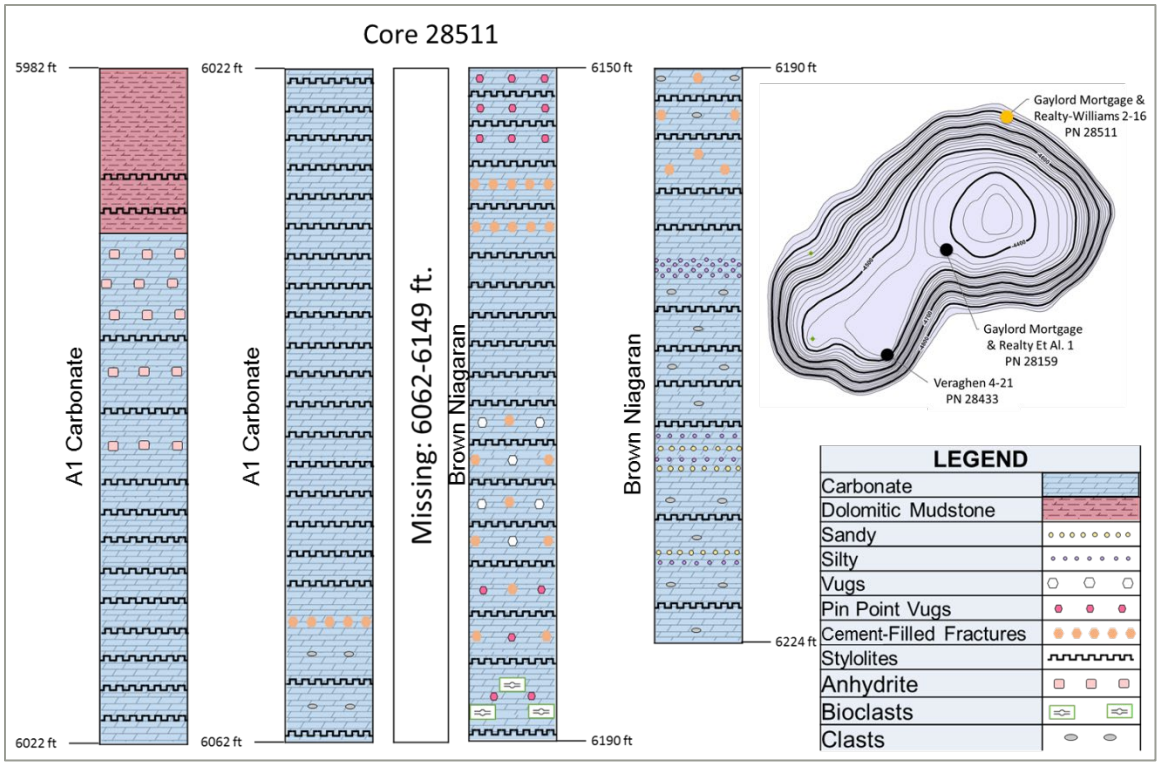


Figure 5-26. Simplified stratigraphic column of core from well 28511 summarizing lithology, textures, and structures.

5.3.4 Core from the Chester 6-16 Well

A total of 32 RSWCs were acquired during open-hole wireline operations for the Chester 6-16 well using the Baker Hughes MAXCOR tool. The sampling interval, which included the Brown Niagaran and Gray Niagaran formations (5,957 to 6,583 feet MD), was identified in the field by Battelle technical staff from log signatures. Detailed results of the core analyses can be found in Attachment 3.

A-1 Carbonate

Sidewall core photos of the A-1 carbonate at the Chester 6-16 well show that the A-1 is predominantly a gray carbonate with some zones of alternating dark- and light-gray laminations. Small vugs (some of which are salt-filled), stylolites, and filled fractures are present throughout the core (Figure 5-27). The ultraviolet (UV) images show potential residual oil throughout the formation.

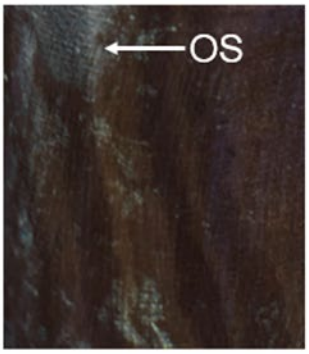
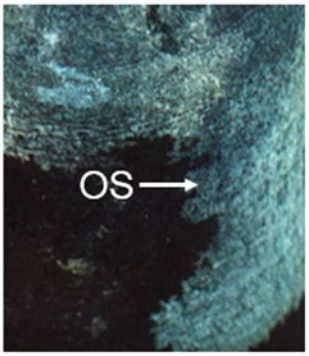
Depth Ft.	White Light Primary Features	UV Light Primary Features	Descriptions
5,962			White Light: Carbonate matrix, filled fracture, alternating dark gray and light gray laminations. UV Light: Light blue UV response due to potential residual oil.
5,968			White Light: Gray carbonate. UV Light: Light blue UV response due to potential residual oil.

Figure 5-27. Example photographs of sidewall cores collected in the A-1 carbonate from the Chester 6-16 well.

Brown Niagaran

Sidewall core photos of the Brown Niagaran at the Chester 6-16 well show that the Brown Niagaran is predominantly a gray carbonate with significant vugular porosity. Vugs are present throughout the formation, except for the basal section of the Brown Niagaran, and range from small to large with some filled moldic and some salt-filled vugs. Open and filled fractures are present throughout, as well as minor stylolites. The UV images show potential residual oil throughout the formation (Figure 5-28).

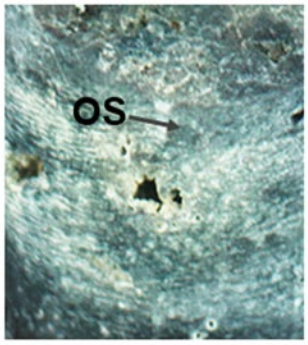
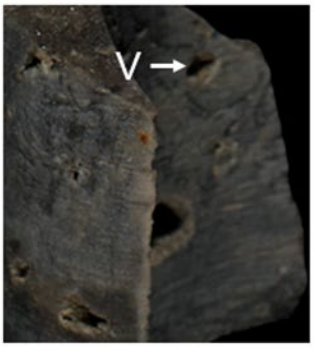
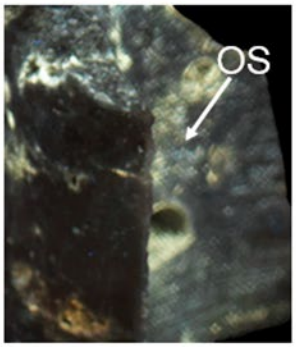
Depth Ft.	White Light Primary Features	UV Light Primary Features	Descriptions
6,015			White Light: Gray carbonate, medium/small vugs. UV Light: Light blue UV response due to potential residual oil throughout sample.
6,032			White Light: Gray carbonate, medium/small vugs, core fragment. UV Light: Light blue UV response due to potential residual oil.

Figure 5-28. Example photographs of sidewall cores collected from the Brown Niagaran in the Chester 6-16 well.

Gray Niagaran

Sidewall core photos of the Gray Niagaran at the Chester 6-16 well show that the Gray Niagaran is predominantly a homogenous gray carbonate that is relatively devoid of sedimentary structures and without secondary porosity. Stylolites are present throughout the cored interval. The UV images show potential residual oil staining throughout the formation.

5.3.5 Core from the Chester 8-16 well

A total of 210.9 feet of whole core was recovered from the Chester 8-16 well with an additional 30 sidewall cores. The cored interval spans a continuous section of the Brown Niagaran and the upper section of the Gray Niagaran formation from 6,148 to 6,358 feet MD. Acquisition was divided into four separate coring runs with an average rate of penetration (ROP) of 7.3 feet per hour (ft/hr) while coring. Details for depth ranges, recovery rates, and ROP for each run are listed in Table 5-8. Refer to Attachment 4 for additional details and results.

Table 5-8. Conventional core acquisition parameters for Chester 8-16.

Core Run #	Coring Vendor	Start Depth	End Depth	Core Cut	Core Recovered	Core Recovery	ROP
		ft MD				%	ft/hr
1	Baker Hughes	6,148	6,178	30	29.15	97%	7.5
2	Baker Hughes	6,178	6,238	60	59.83	100%	7.1
3	Baker Hughes	6,238	6,298	60	61.25	102%	4.8
4	Baker Hughes	6,298	6,358	60	60.7	101%	10.0

Brown Niagaran

The Brown Niagaran formation at the Chester 8-16 well is mostly composed of tight dolomitic limestone with thin intervals of dolomite. Figure 5-29 and Figure 5-30 illustrate common features observed. Features such as vugs and fractures result in a heterogeneous reservoir containing isolated zones of high porosity and permeability. Stylolites and bioclastic debris were observed throughout. Oil stains, salt-filled fractures, and vugs were observed in the UV light images. Significant moldic porosity was observed throughout most of the relatively continuous core.

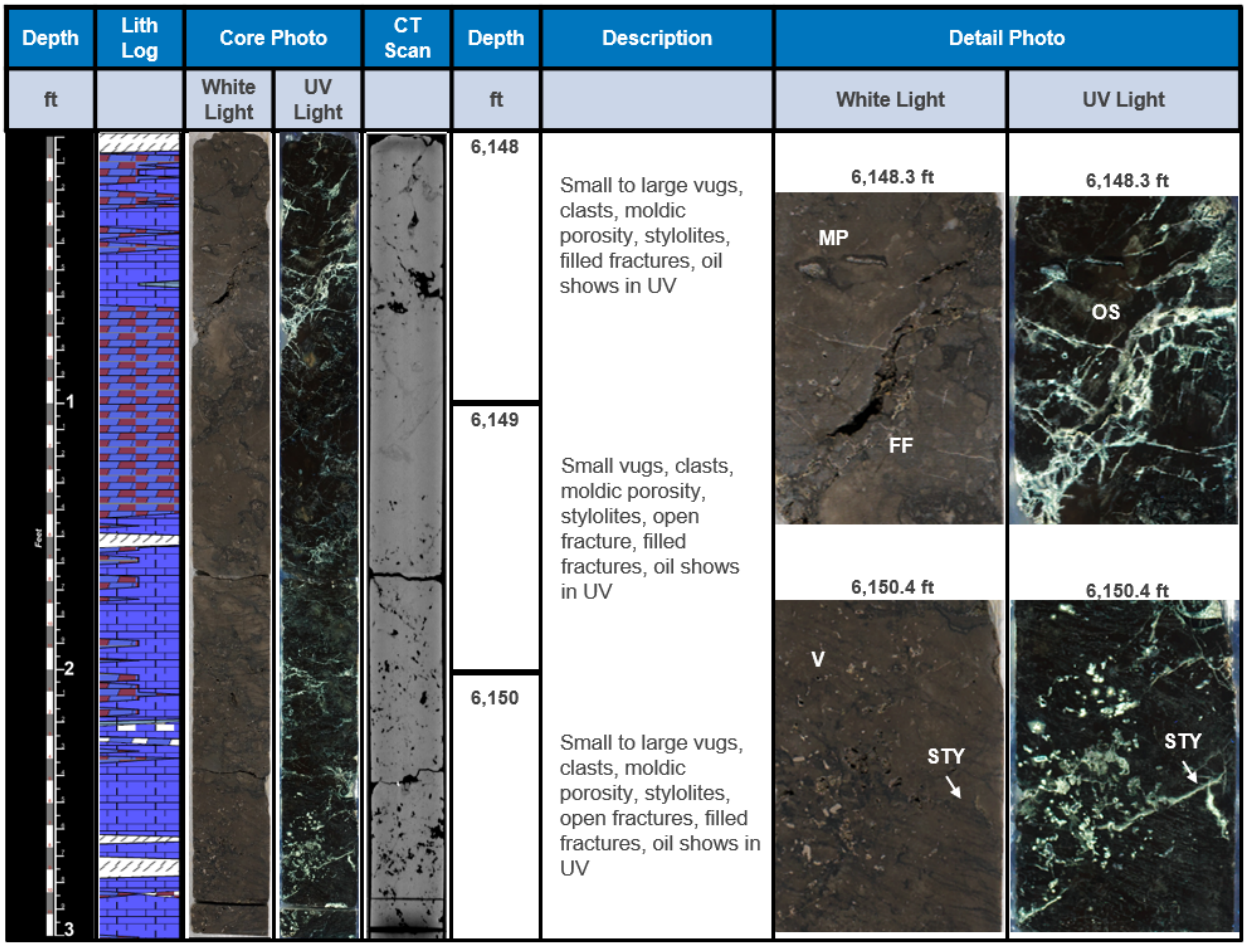


Figure 5-29. Compiled illustration of lithology log, core photos (UV and white light), CT scan image, core descriptions, and annotated core images of the Brown Niagaran in the Chester 8-16 well for depths 6,148 to 6,151 feet.

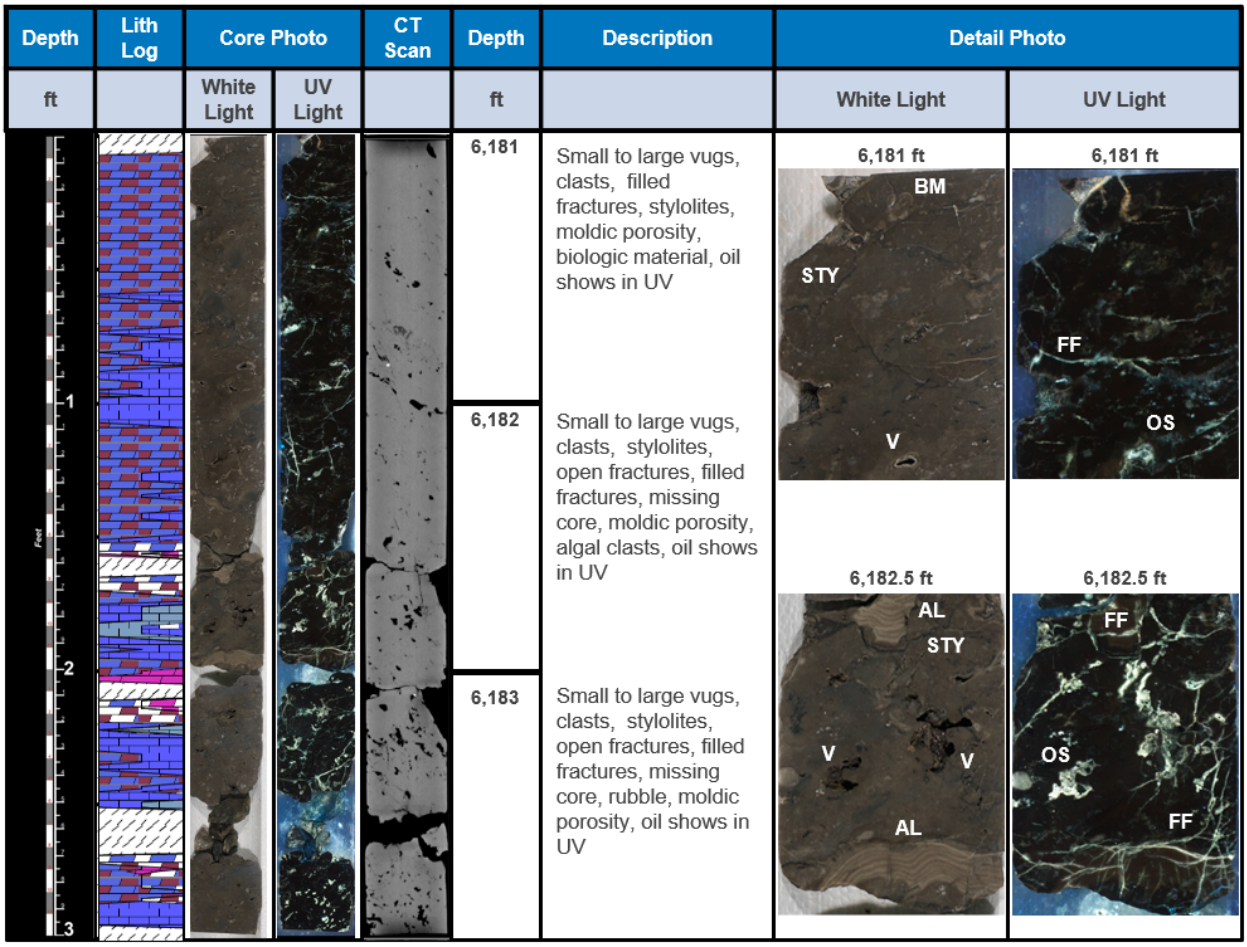


Figure 5-30. Compiled illustration of lithology log, core photos (UV and white light), CT scan image, core descriptions, and annotated core images of the Brown Niagaran in the Chester 8-16 well for depths 6,181 to 6,184 feet.

Gray Niagaran

The Gray Niagaran formation at the Chester 8-16 well is mostly composed of tight dolomitic limestone with some thin intervals of dolomite and rubble. Figure 5-31 and Figure 5-32 illustrate common features observed in the Gray Niagaran. Small vugs and open fractures were present throughout the formation, resulting in isolated zones of high porosity. Minor biologic material was present toward the basal section of core. A small oil show was present toward the base of the core, as seen in the UV light image in Figure 5-32.

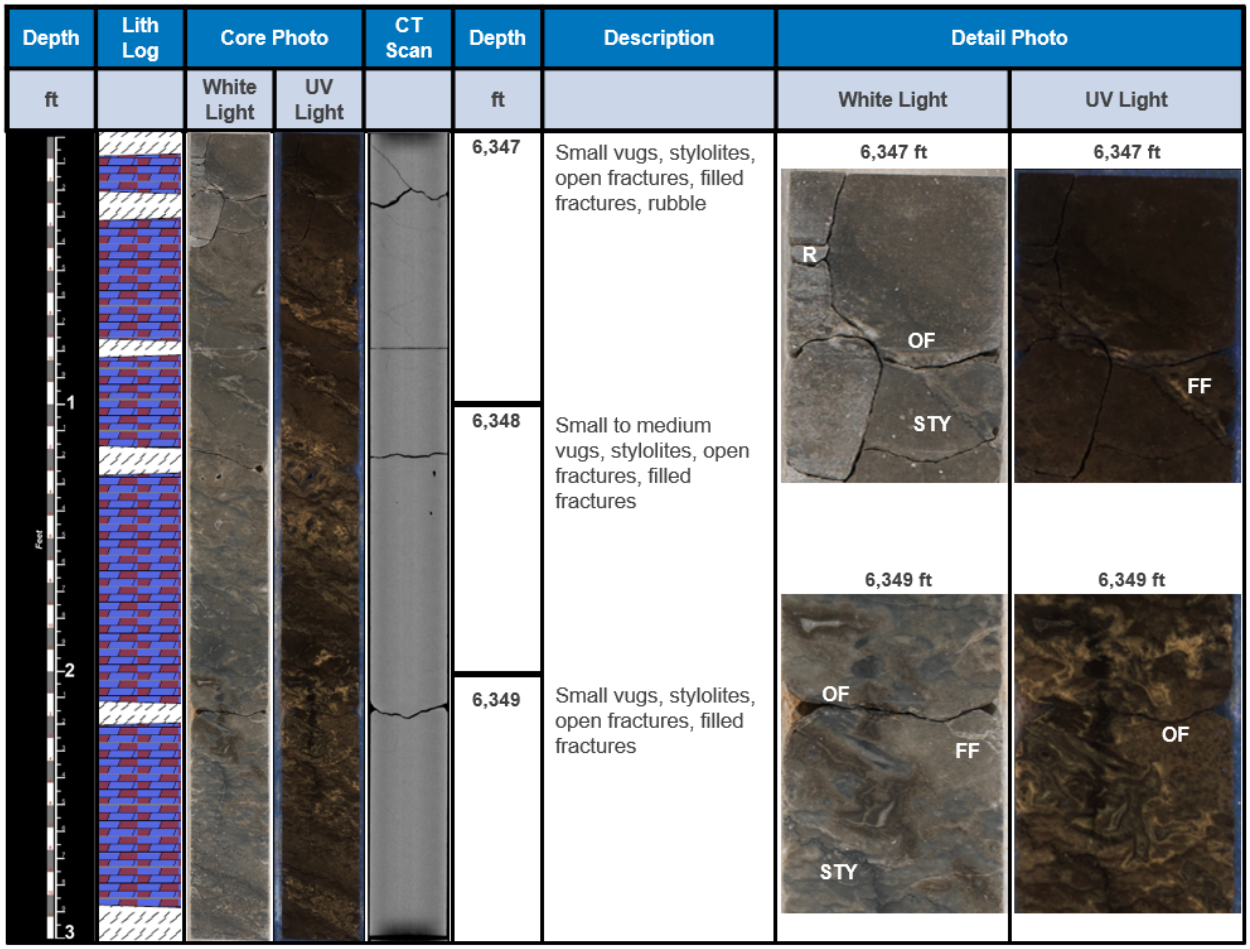


Figure 5-31. Compiled illustration of lithology log, core photos (UV and white light), CT scan image, core descriptions, and annotated core images of the Gray Niagaran in the Chester 8-16 well for depths 6,347 to 6,350 feet.

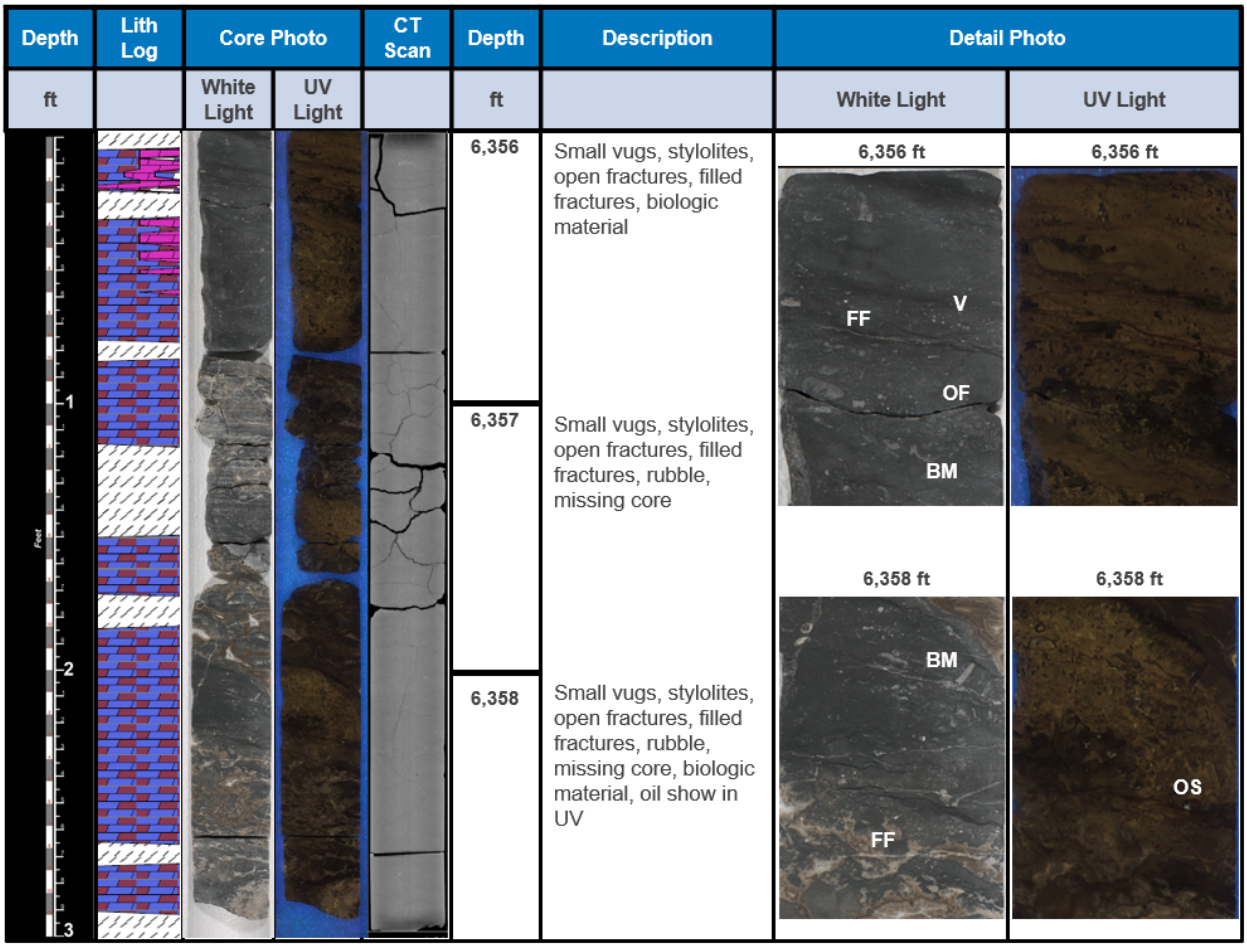


Figure 5-32. Compiled illustration of lithology log, core photos (UV and white light), CT scan image, core descriptions, and annotated core images of the Gray Niagaran in the Chester 8-16 well for depths 6,356 to 6,359 feet.

5.3.6 Formation Properties from Core Analyses

Grain Density

Grain density measurements were available through MGRRE for three whole cores in the Chester 16 reef field (wells 28433, 28511, and 28159). The A-1 carbonate had an average grain density of 2.78 g/cm^3, which was consistent with a mixture of limestone and dolomite. Intervals of the A-1 carbonate had grain densities as low as 2.67 g/cm^3 and as high as 2.89 g/cm^3. These end members could be due to the presence of salt and anhydrite observed in these formations. The A-1 evaporite had an average of 2.80 g/cm^3 with a range of 2.72 to 2.91 g/cm^3. The average was higher than other formations due to anhydrites. The Brown Niagaran had an average grain density of 2.74 g/cm^3 with a range of 2.70 to 2.87 g/cm^3. This was consistent with a dominantly limestone lithology with some presence of dolomite. Figure 5-33 shows the resulting histograms of the grain density for each formation covered by whole core.

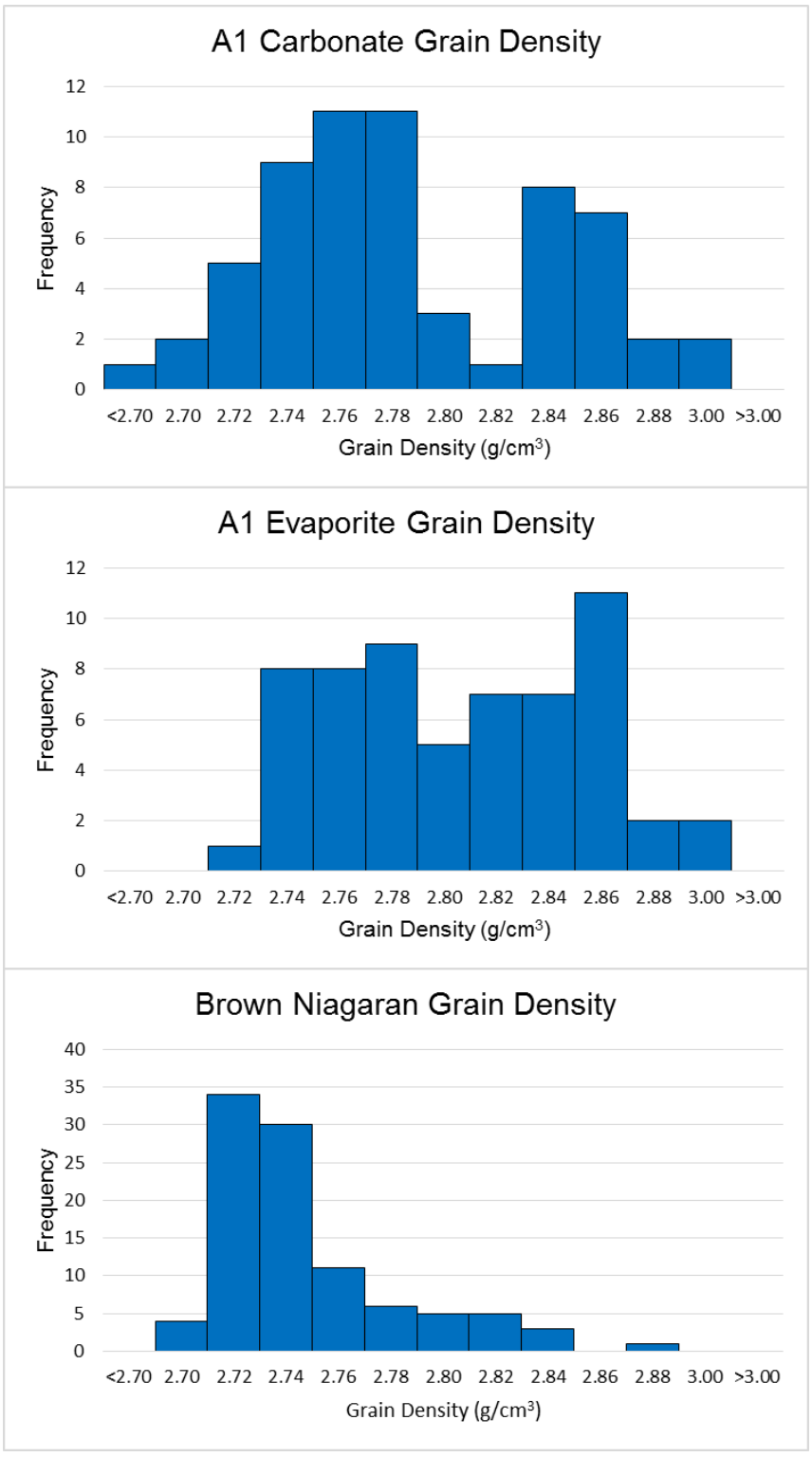


Figure 5-33. Histograms of the grain density for the A-1 carbonate, A-1 evaporite, and Brown Niagaran formations from whole core in the Chester 16 reef field.

Porosity and Permeability

Porosity and permeability data was available through MGRRE for three whole cores in the Chester 16 reef field. The A-1 carbonate had a porosity range of 0.4% to 15.5%, with permeability ranging from 0.01 to 33.1 mD. The A-1 evaporite had a porosity range of 0.7% to 16.8%, with a permeability range of 0.01 to 25.8 mD which is not reflective of true formation properties as salt tends to dissolve during collection and testing. The Brown Niagaran had a porosity range of 0.4% to 13.7%, with a permeability range of 0.01 to 450 mD. Secondary porosity features such as vugs and fractures resulted in intervals of high permeabilities not necessarily reflective of true formation permeability.

Table 5-9 summarizes the porosity and permeability data by formation. The data are plotted in Figure 5-34, with the coordinating transform equations expressed in Equation 5-1, Equation 5-2, and Equation 5-3.

Table 5-9. Summary of porosity and permeability data from whole core in the Chester 16 reef field.

Formation	Porosity (%)	Average Porosity (%)	Permeability (mD)	Average Permeability (mD)
A-1 Carbonate	0.4 - 15.5	5.0	0.01 - 33.1	10.1
A-1 Evaporite	0.7 - 16.8	7.9	0.01 - 25.8	7.0
Brown Niagaran	0.4 - 13.7	3.3	0.01 - 450	23.4

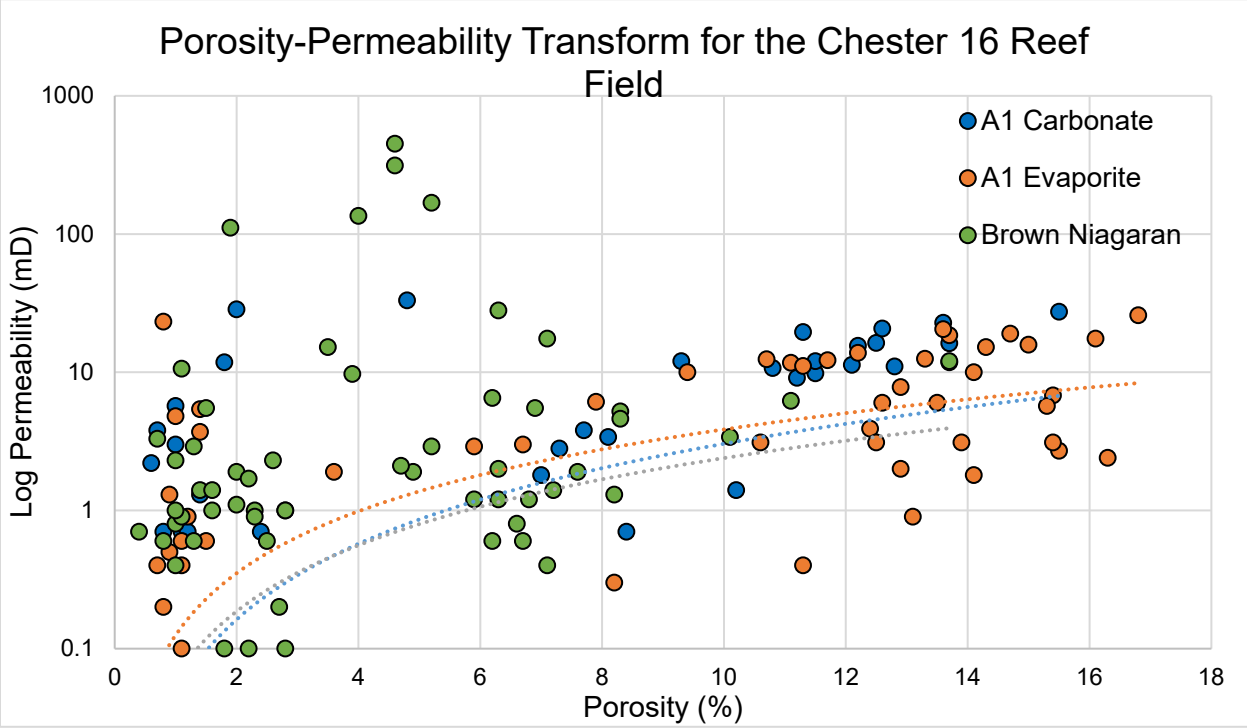


Figure 5-34. Porosity-permeability transform for the A-1 carbonate, A-1 evaporite, and Brown Niagaran from whole core measurements in the Chester 16 reef field.

$$K_{A1C} = .046\emptyset^{1.82}$$ **Equation 5-1**

$$K_{A1E} = .125\emptyset^{1.49}$$ **Equation 5-2**

$$= .062\emptyset^{1.59}$$ **Equation 5-3**

where:

K_{A1C} = permeability of the A-1 carbonate (mD)
K_{A1E} = permeability of the A-1 evaporite (mD)
K_{BN} = permeability of the Brown Niagaran (mD)
ø = porosity (%)

The A-1 carbonate and A-1 evaporite formations had r^2 values of 0.41 and 0.50, respectively, whereas the Brown Niagaran had a poor-fitting r^2 value of 0.19.

5.4 Seismic Analysis

5.4.1 Basic Seismic Interpretation

Seismic data (3D seismic) was available over the Chester 16 reef field as part of a larger 3D volume (referred to as CD-J). The seismic data was used to help develop the geometry to guide the SEM and confirm a two-reef pod interpretation. The A-2 carbonate was identified as a strong reflector due to the density contrast of the carbonate with the overlying B-salt. There was a slight plateau over the crest of the reef. The horizon over the reef crest was picked as the same as the Brown Niagaran because there was little or no velocity contrast between carbonate formations. The A-2 carbonate and Brown Niagaran were separated by carbonates and anhydrites instead of salts, which have similar velocities. Figure 5-35 shows an example from cross line 182 with horizon picks of the A-2 carbonate (blue) and top of the reef (brown).

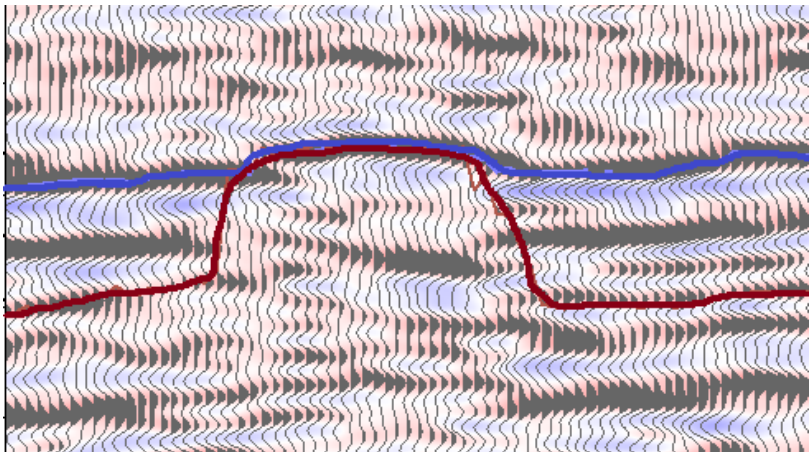


Figure 5-35. Example horizons for the A-2 carbonate (blue) and top of the reef structure (brown) for cross line 182 in the 3D seismic covering the Chester 16 reef field.

Seismic horizons for the A-2 carbonate, A-1 carbonate, and Brown Niagaran were used to generate seismic horizon maps. The convergent interpolation method was used in Petrel™ with a grid cell size of 50 x 50 feet. A smoothing algorithm was applied to each seismic horizon using one iteration across three grid cells. The resulting maps were used to define the geometry of each reef for the SEMs. The time

horizon in Figure 5-36 shows the outline of the Chester 16 reef field with a slight pinching and decrease in travel times in the middle of the reef. This suggests two reef pods instead of one.

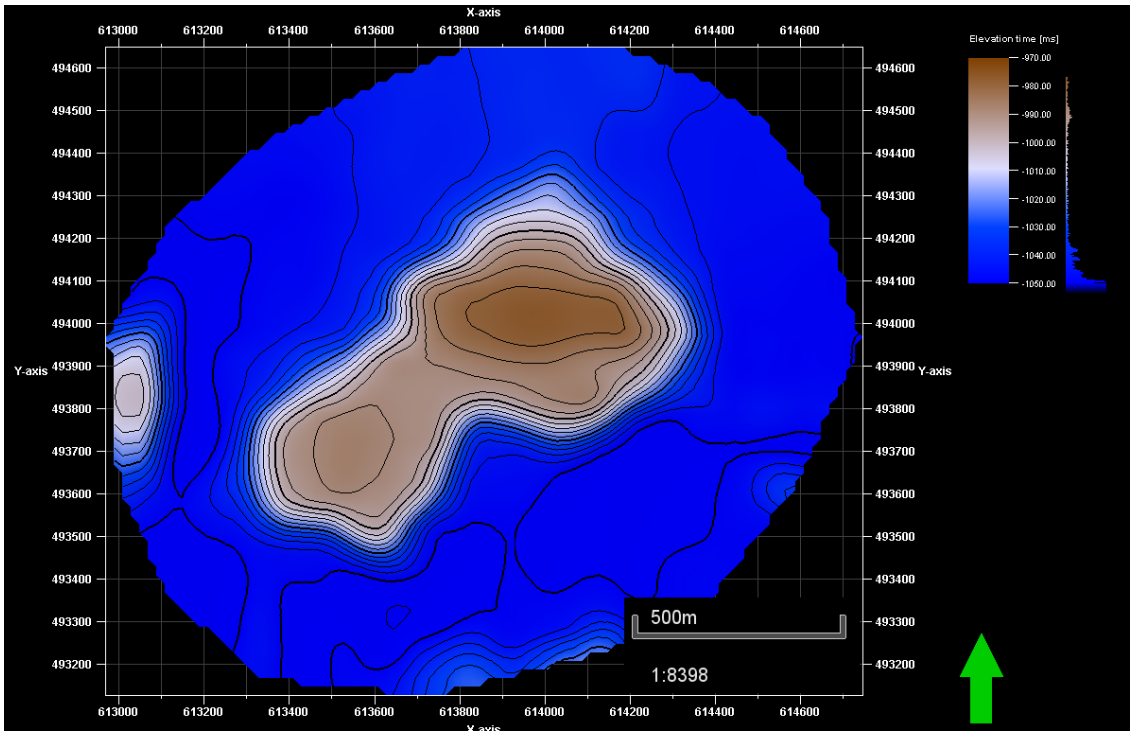


Figure 5-36. Time horizon surface of the Brown Niagaran showing steeply dipping edges of the Chester 16 reef field.

5.4.2 Advanced Seismic Interpretation

Battelle worked in collaboration with Core Energy, LLC, and INEXS to apply advanced techniques to the Chester 16 3D seismic to identify porosity zones and extents. These analyses included data reprocessing, relative acoustic impedance mapping, and wavelet extraction and matching.

Data Reprocessing

Seismic data collection and quality can be challenging in northern Michigan due to thick glacial deposits (~1,000 feet in the study area) which cause energy loss and poor reflections. Additionally, the high angle of the reef edges does not allow energy returns from internal to the reef structure, producing only an outline of the reef structure. INEXS reprocessed the 3D seismic data to decrease the effects of high angles and glacial deposits and enhance the internal signals. This was completed by creating a series of angle stacks of 0-15, 16-30, and 31-45 degrees. High-frequency enhancement was applied to each series. It was determined that the angle stack of 31-45 degrees with a high-frequency enhancement improved the resolution of the reef structure. Figure 5-37 is an example crossline through the seismic data showing the standard post-stack time migration (PSTM) and different angle stacks. It also showed whether a sample had high-frequency enhancement (HFE).

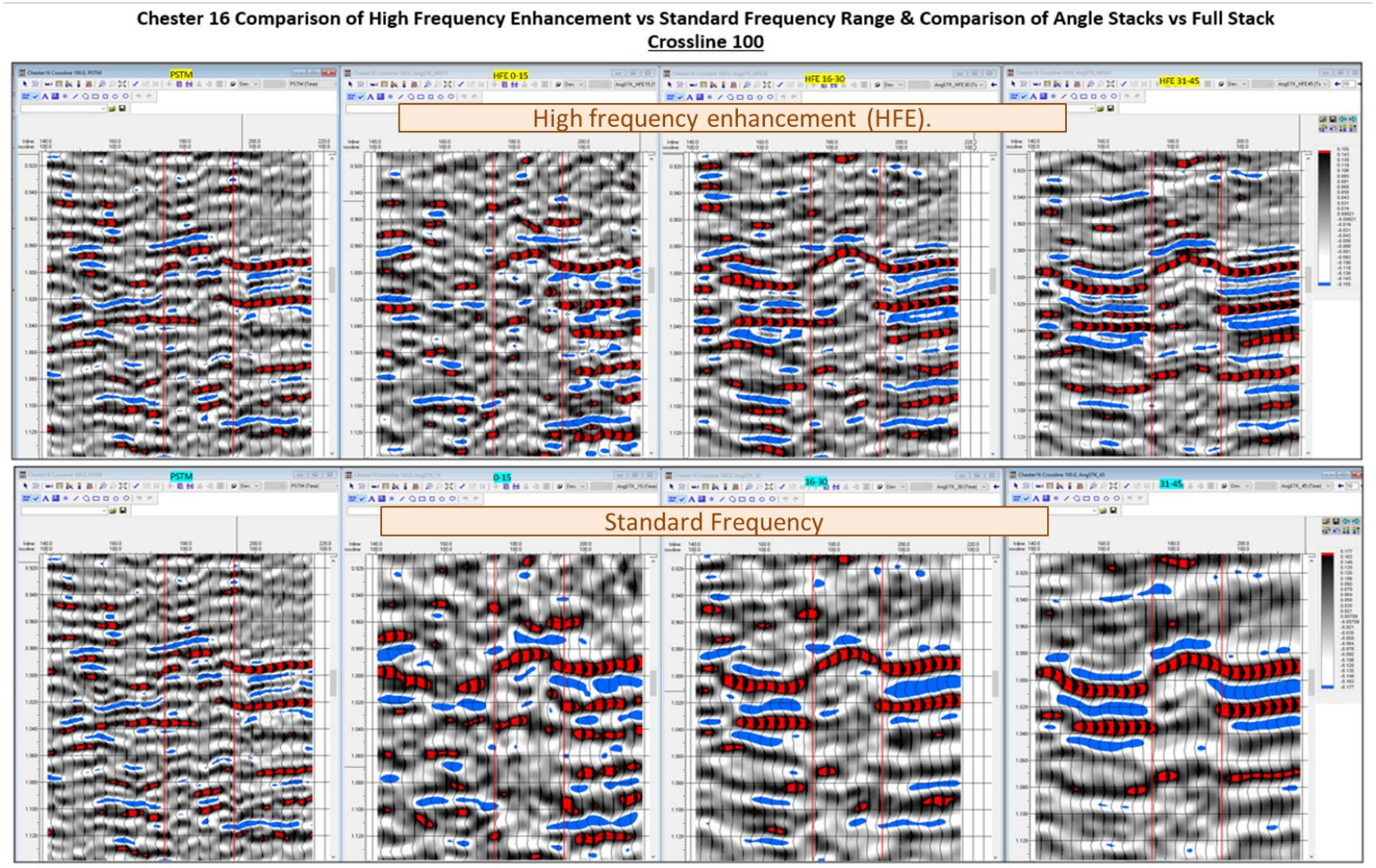


Figure 5-37. Results of data reprocessing show different angle stacks with and without HFE. The 31-45 angle stack with HFE improved reef resolution (upper left).

Relative Acoustic Impedance Analysis

Relative acoustic impedance (RAI) is the product of a rock's density and velocity, which is dependent on depth, porosity, and fluids. RAI is not typically equivalent to log-computed acoustic impedance, but it has been known to be a proxy for porosity. A map of the maximum negative RAI was generated to represent the slowest, or less dense, rock (Figure 5-38). The blue is the most negative and represents the salt along the edges of the reef and inter-reef area. Green represents slightly higher RAIs but not as low as salt; this is representative of potential porosity zones. Since significant salt plugging was not observed in core data, the decreased velocity/density is most likely a result of increased porosity. Reds and yellows represent the highest RAIs with relatively lower porosities. The RAI porosity proxy shows areas in the central portion of the northern reef and the western portion of the southern reef.

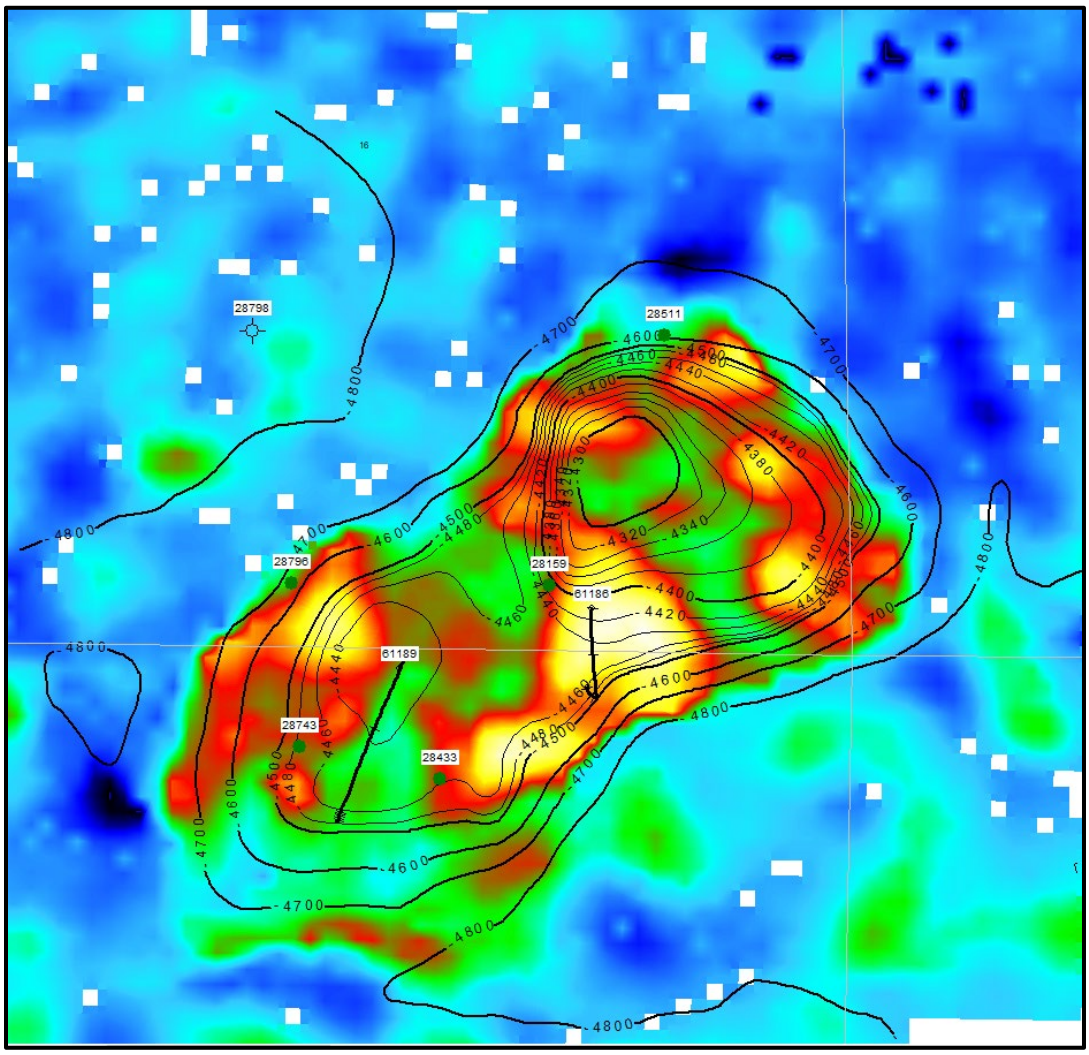


Figure 5-38. Map of the maximum RAI from the Chester 16 seismic data, where blues indicate salts, greens indicate porosity, and red/yellows indicate dense rock.

Cumulative production at five well locations was compared to extracted RAI for comparison. The greatest producer was well 28159, which had a higher RAI than the wells that produced less, such as 28511. However, wells 28511 and 28798 are along the edges of the reef and could be influenced by increased salt. The comparison of RAI to production does not show a positive correlation, but the changes in lithology could be influencing the RAI (Figure 5-39).

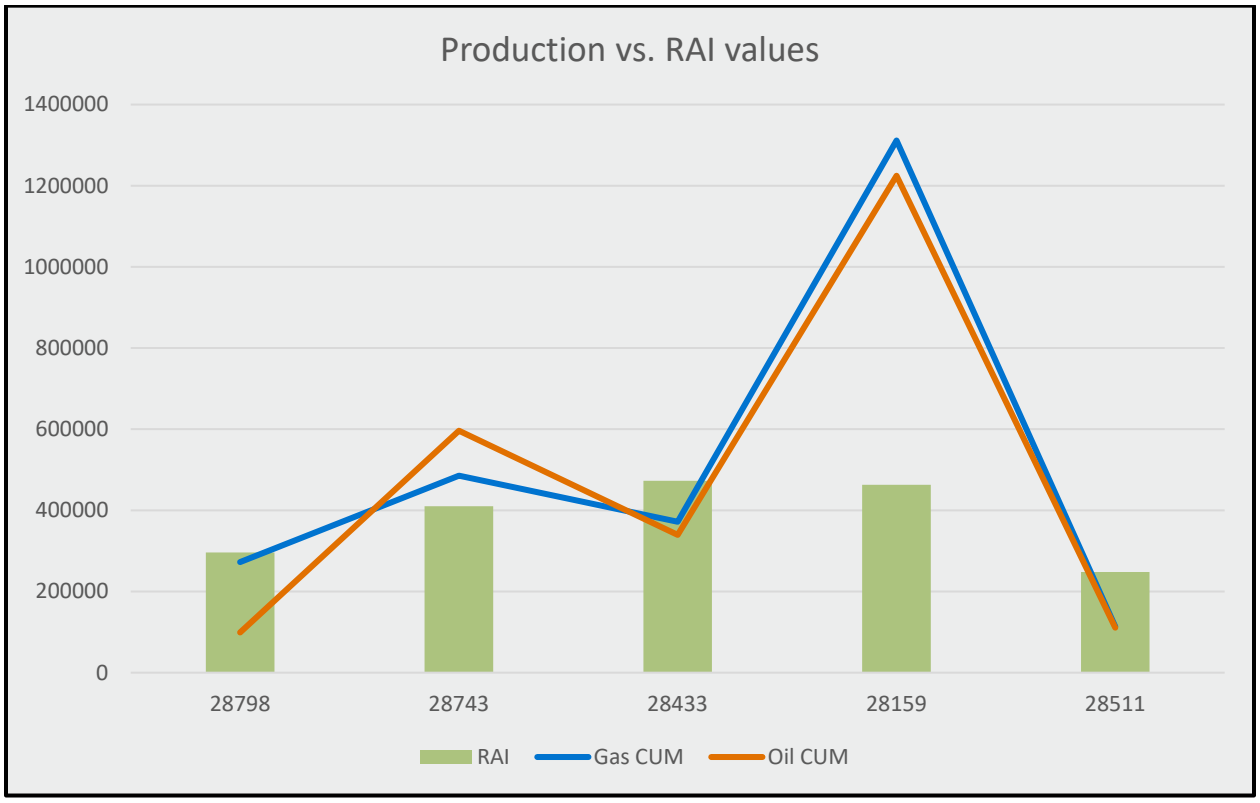


Figure 5-39. Bar plot of RAI and cumulative production for five wells in the Chester 16 reef field.

Next, porosity horizons were traced through the 3D seismic data by following continuous zones of negative RAI. This resulted in the identification of six porosity intervals (Figure 5-40). Porosity horizons 1 and 2 likely occur below the oil/water contact and within the bioherm facies (fine-grained, micro-porosity carbonate). Zone 3 occurs along major perforation intervals within the Brown Niagaran at or near the contact of the bioherm facies and the main reef growth. Porosity horizons 4 and 5 occur near the top of the Brown Niagaran, while horizon 6 is the porosity interval in the A-1 carbonate. Extreme negative RAIs occur along the edges of the reef, which are due to salt and not porosity.

Each porosity horizon was mapped in 2D to show the extent of the area. Porosity horizons 1 and 2 have small coverage, each occurring over the center areas of the reef pods. This is consistent with potentially being the bioherm facies. Porosity horizon 3 is more continuous, covering 105 acres, and appears to cut across the entire field independent of facies. It also occurs where the wells were perforated, which would have been an initial reservoir target. Porosity horizons 4 and 5 have smaller extents and tend to be more continuous within a reef pod, suggesting a depositional control. Finally, porosity horizon 6 is continuous across the top of the reef structure, consistent with the porosity development in the A-1 carbonate on top of the reef. Figure 5-41 shows the structural outline of the reef and extent of each porosity horizon.

Porosity horizons 3 and 6 were examined further as likely reservoir intervals. The average RAIs for the horizons were mapped in 2D, with hotter colors corresponding to lower RAI and higher porosity and cool colors corresponding to higher RAI and lower porosity (Figure 5-42). Porosity horizon 3 shows increased porosity near the crest of each reef pod and decreases in the saddle region between the pods. This region occurs where material was being deposited from the leeward side of the northern reef pod and the windward side of the southern reef pod. Due to the close proximity of the pods to each other during reef growth, the deposited material could have been lower-energy and finer-grained material.

Porosity horizon 6 follows a similar trend as horizon 3, where porosity is higher along the crestal position and lower in the saddle region between reef pods. The saddle region does not have well data to characterize, but it has the potential to develop finer-grained rock and evaporites while not having as much exposure as rock higher up on the crest of the reef.

Additionally, RAI was normalized across porosity horizons to compare the relative porosity between horizons. Porosity horizons 3 and 6 had the highest porosity, while horizons 4 and 5 were significantly lower. Porosity horizons 1 and 2 exhibited a range of values, with the highest points occurring near the center of each reef pod. Figure 5-43 shows the resulting normalized RAI maps of each porosity horizon.

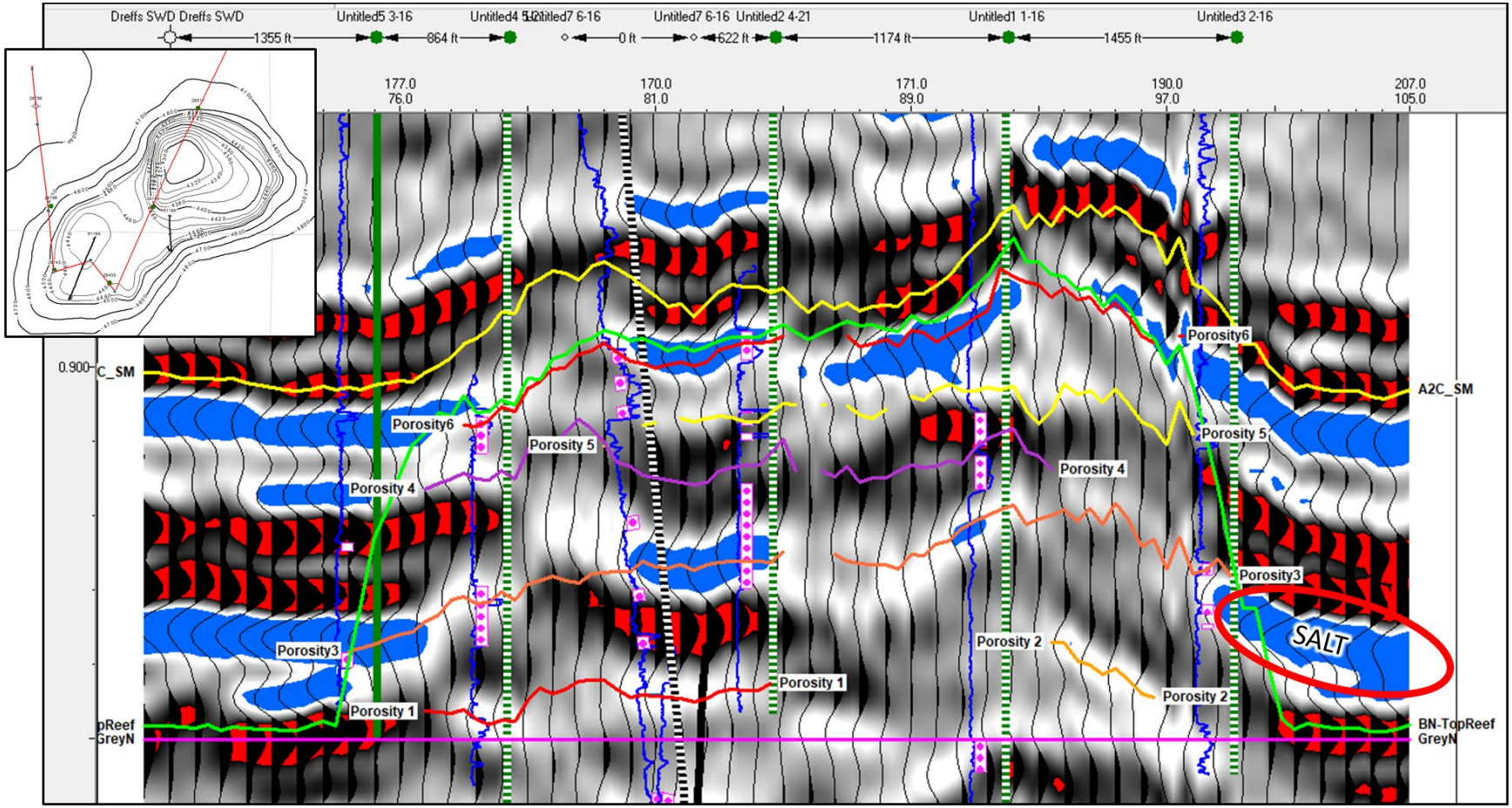


Figure 5-40. RAI porosity horizons in cross section view through the Chester 16 reef field showing multiple intervals of potential porosity in the Brown Niagaran and A-1 carbonate.

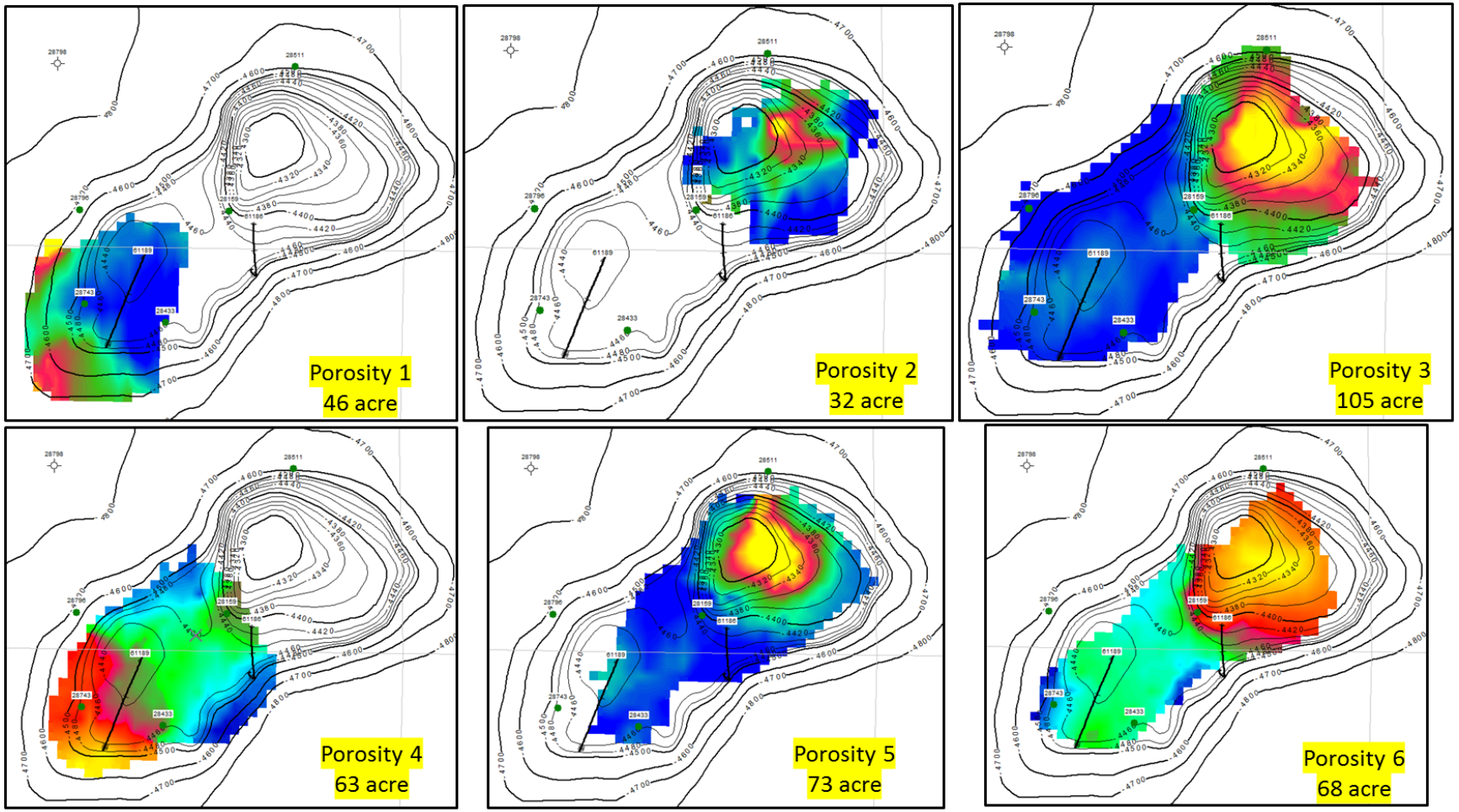


Figure 5-41. Extent of RA- identified porosity horizons within the Chester 16 reef field.

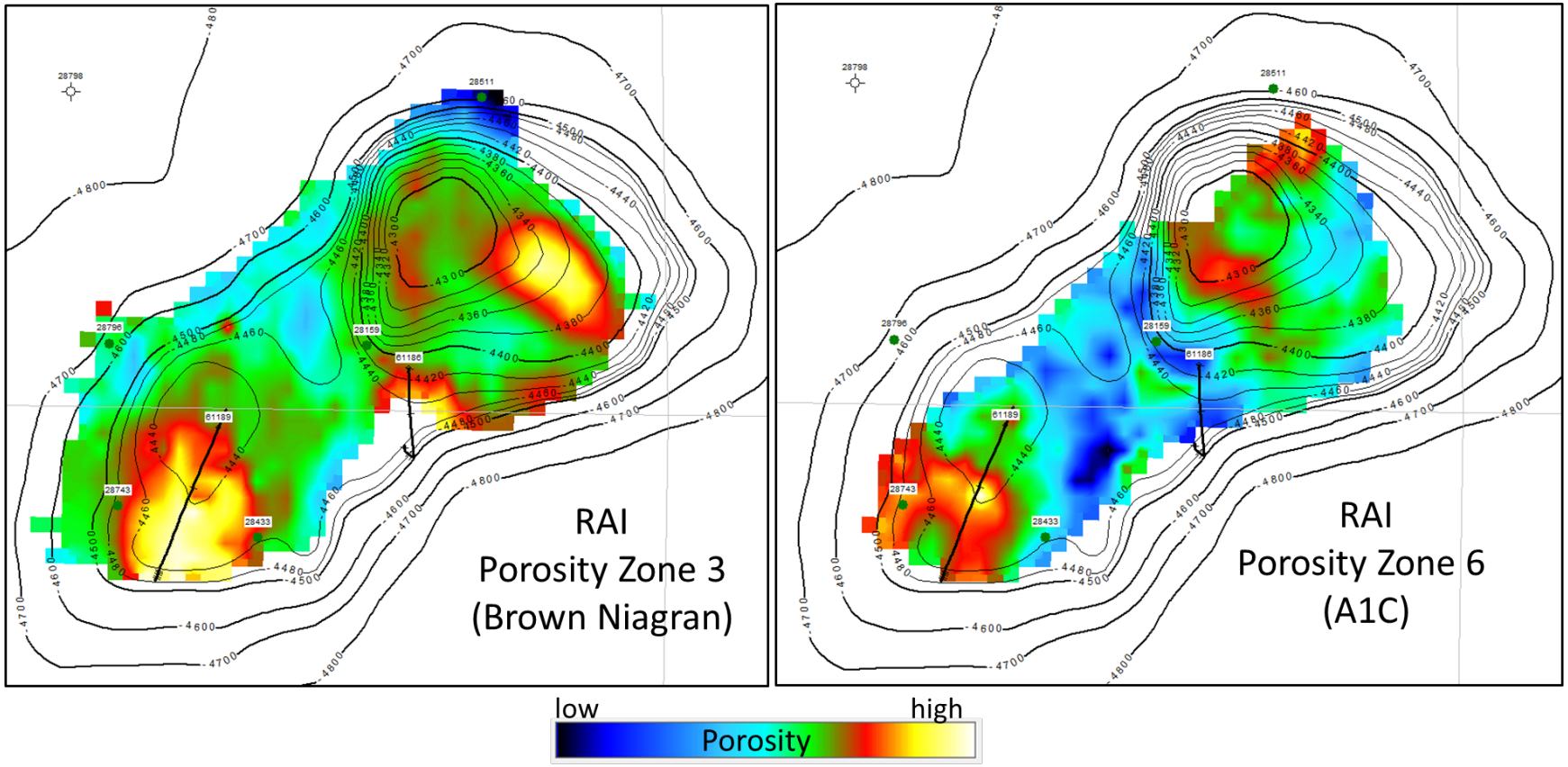


Figure 5-42. Average RAI maps of porosity horizons 3 (left) and 6 (right) in the Chester 16 reef field showing higher porosity at crestal positions and lower porosity in the saddle region.

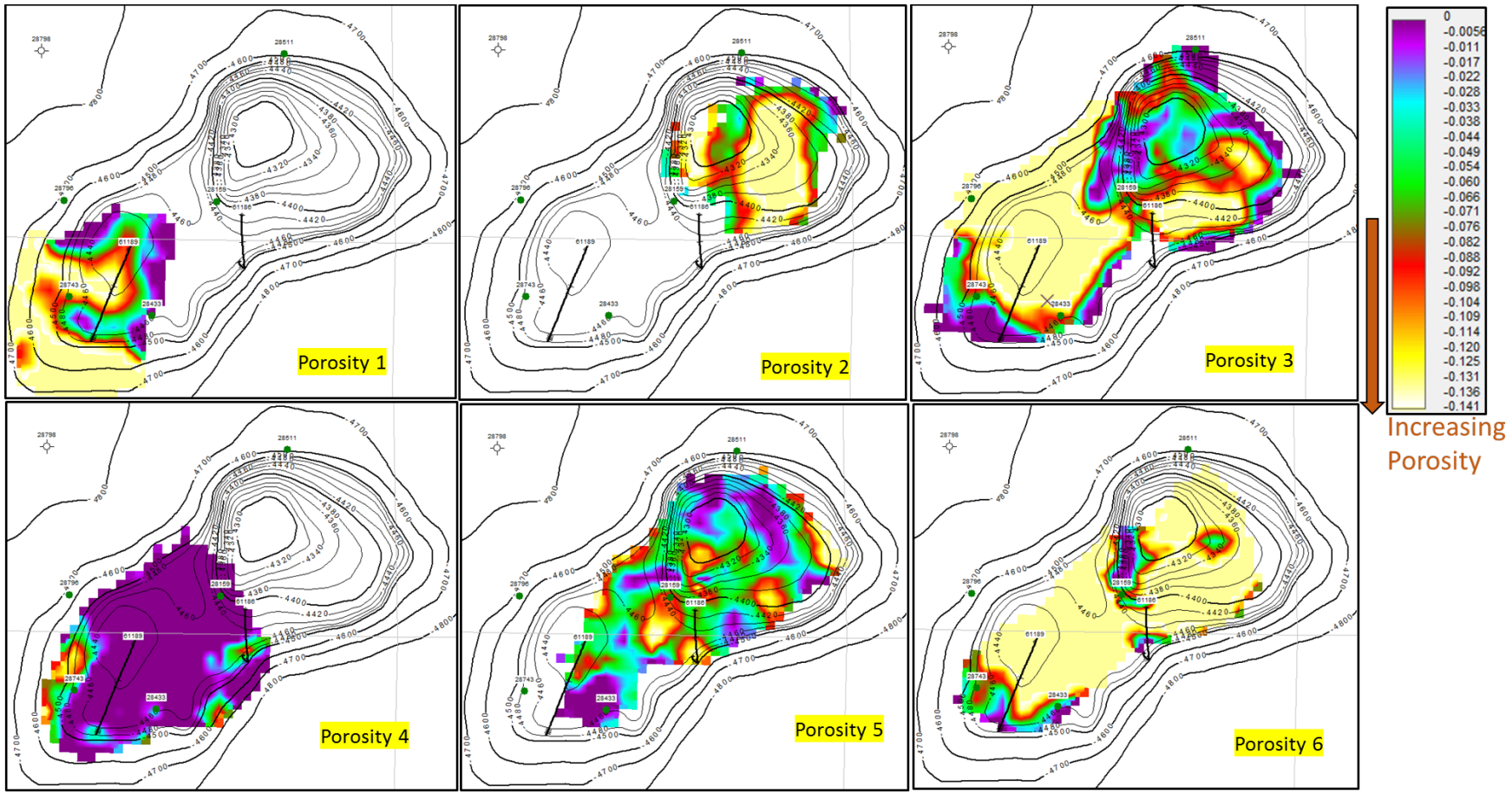


Figure 5-43. Maps of normalized RAI for each porosity horizon showing higher porosity in horizons 3 and 6.

Wavelet Matching Analysis

A wavelet matching analysis was conducted to correlate wavelets at well locations throughout the seismic volume. This analysis extracted a wavelet over the A-1 carbonate through Brown Niagaran interval from the seismic data and correlated it to wavelets at all locations. Figure 5-44 shows example wavelets extracted from each wellbore location and the resulting correlation with example well 28159. Well 28159 was the greatest producer and had the strongest correlation with well 28433 (52%) which produced approximately one-third of well 28159. Well 28743 was the second-best producer, having produced approximately one-half of well 28159, but it only had a correlation of -4.6. Individual maps of wavelet correlations were generated for each well (Figure 5-45) and were compiled into a composite wavelet map (Figure 5-46).

Well 28159 is located at the western side of the northern lobe. The highest correlations with the wavelet occur in the crestal positions in both the northern and southern lobes. Well 61186 is located near well 28159 on the western side of the northern lobe. The highest correlations ring both reef pods. Well 28433 is located along the southeastern side of the southern lobe, with greatest correlation in the crestal region of the southern pod and in the eastern edge of the northern pod. Wells 28511 and 28796 are located along the flanks or edges of the reef, resulting in high correlations which ring the edges of the identified reef. Well 28743 is located on the western side of the southern pod, near the crestal position. The highest correlations follow contours around the two reef crests. Well 61189 is located on the northeastern side of the southern pod, with the greatest correlations occurring near the wellbore and again on the eastern side of the northern pod. Individually, the extracted wavelets appear to follow the structure and potentially depositional facies of the reef.

The composite map of wavelets mimics depositional facies of the reef. Wells located in the crestal positions of the reef pods correlate most strongly near that position. A distinct zone present between the reef pods could be a potential baffle in the saddle region. Flank-position wells correlate strongly to each other and along the edges of the reef.

5.4.3 Interpretations of Seismic Analyses

The seismic analyses showed two distinct reef pods encased in tight carbonates and salt (Figure 5-47). Two significant porosity horizons occur in the A-1 carbonate on top of the reef structure and mid-reef in both reef pods. The Brown Niagaran porosity feature is continuous across each reef, suggesting that it is diagenetic in nature, potentially from a period of exposure. The A-1 carbonate on top of the reef structure would have had higher elevation and more exposure, which would create an environment for enhancing porosity. The area between the two reef pods, notated as the saddle, shows a break in porosity horizons. Both the wavelet matching and RAI mapping indicate an area of poor porosity which acted as a baffle and could explain the poor water-flood results (Figure 5-48).

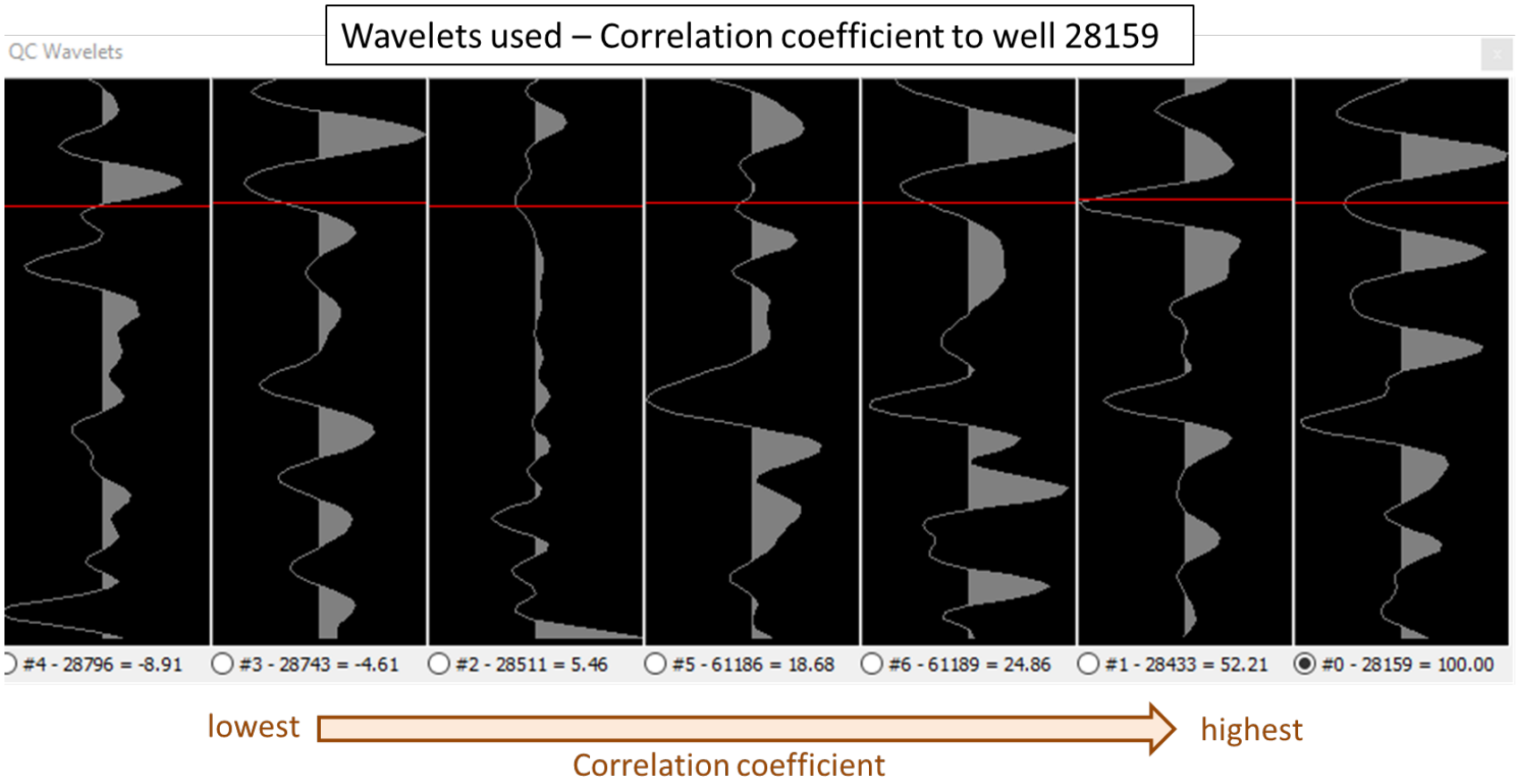


Figure 5-44. Wavelets extracted at each well location from Chester 16 3D seismic data and the correlation coefficient to well 28159.

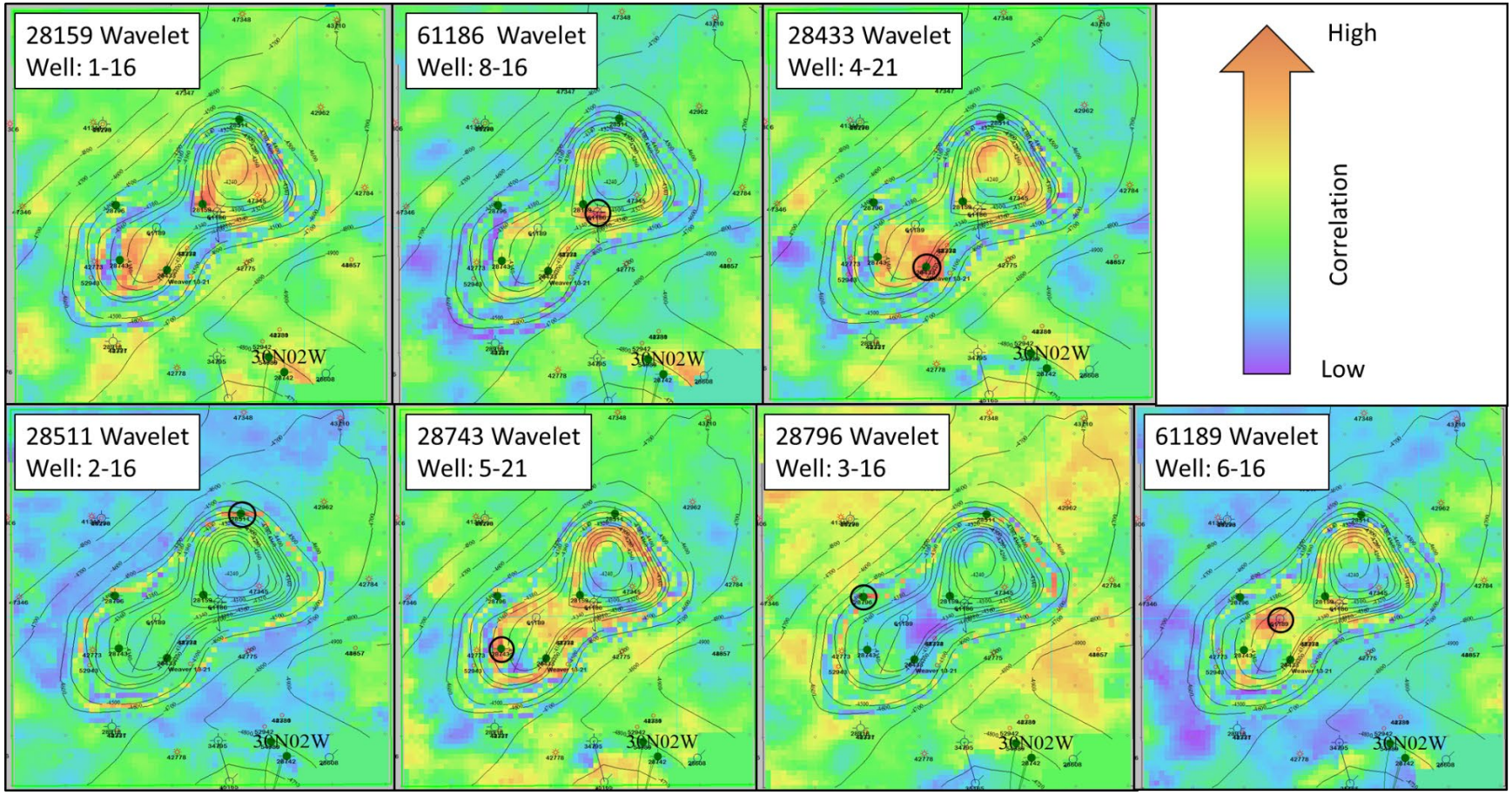


Figure 5-45. Wavelet correlation maps for each well through the Chester 16 seismic data with cooler colors showing lower correlation coefficients and hotter colors having higher correlation.

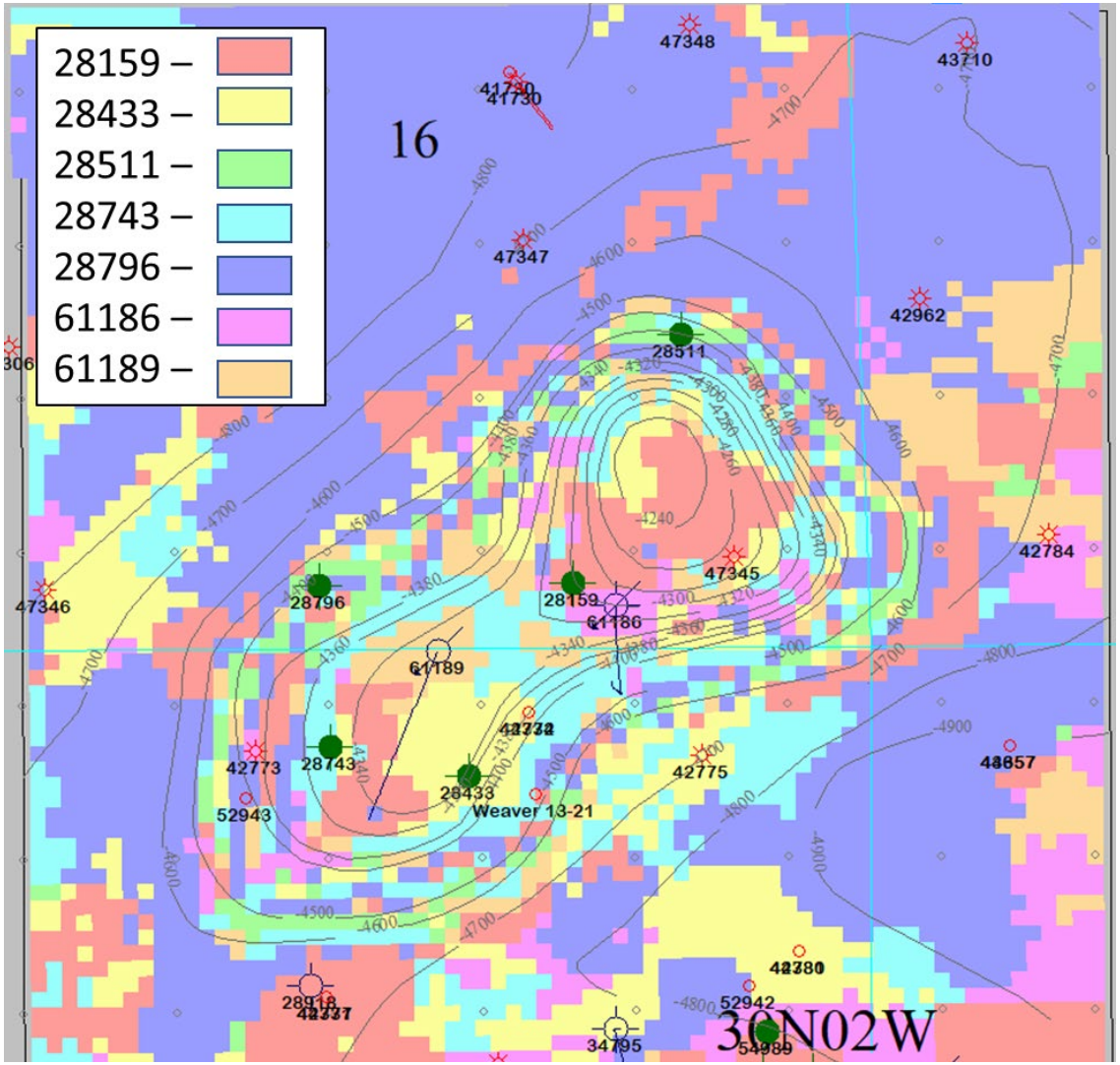


Figure 5-46. Compilation of wavelet correlations from the Chester 16 seismic data.

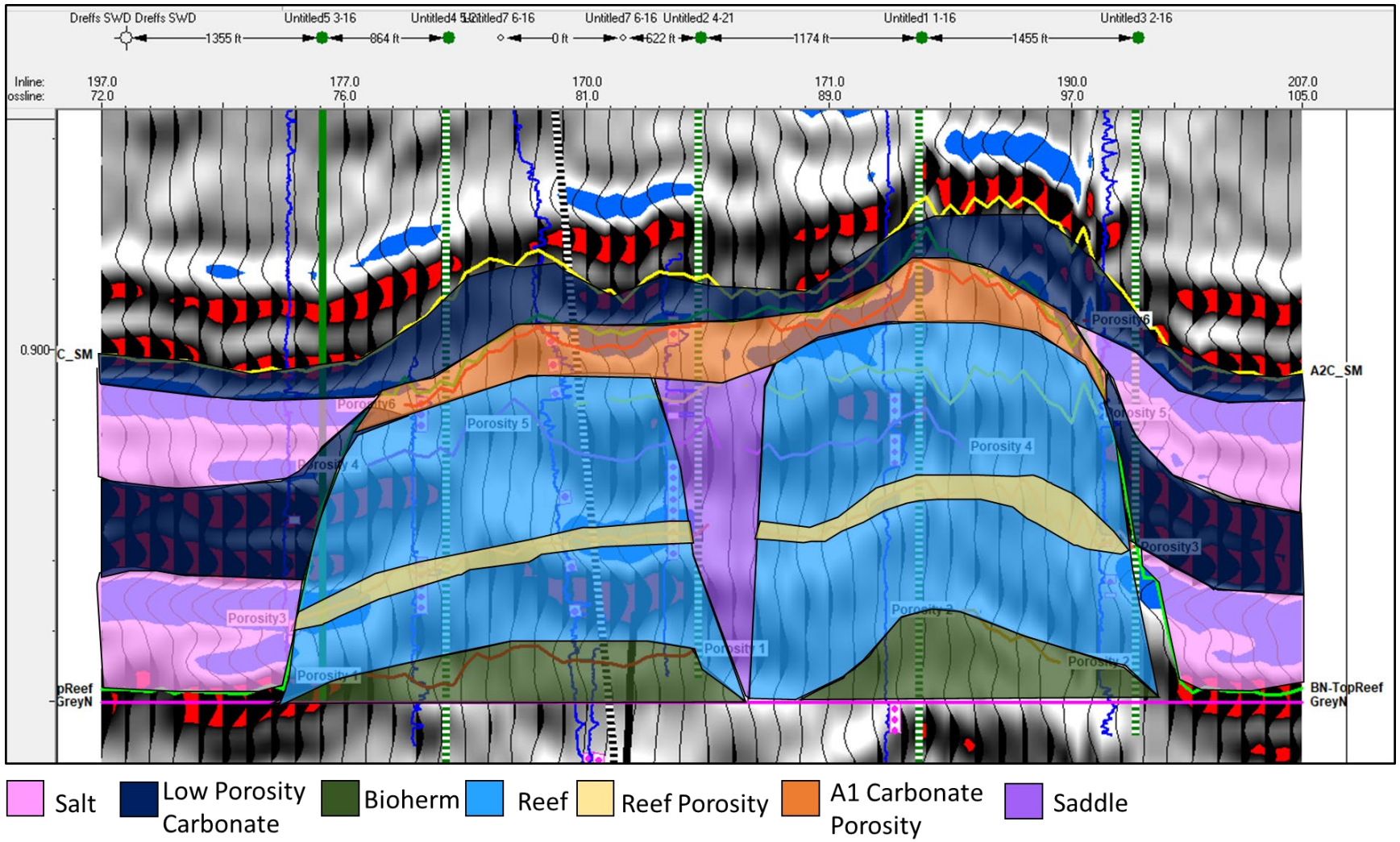


Figure 5-47. Geologic interpretation of RAI analysis of the Chester 16 field.

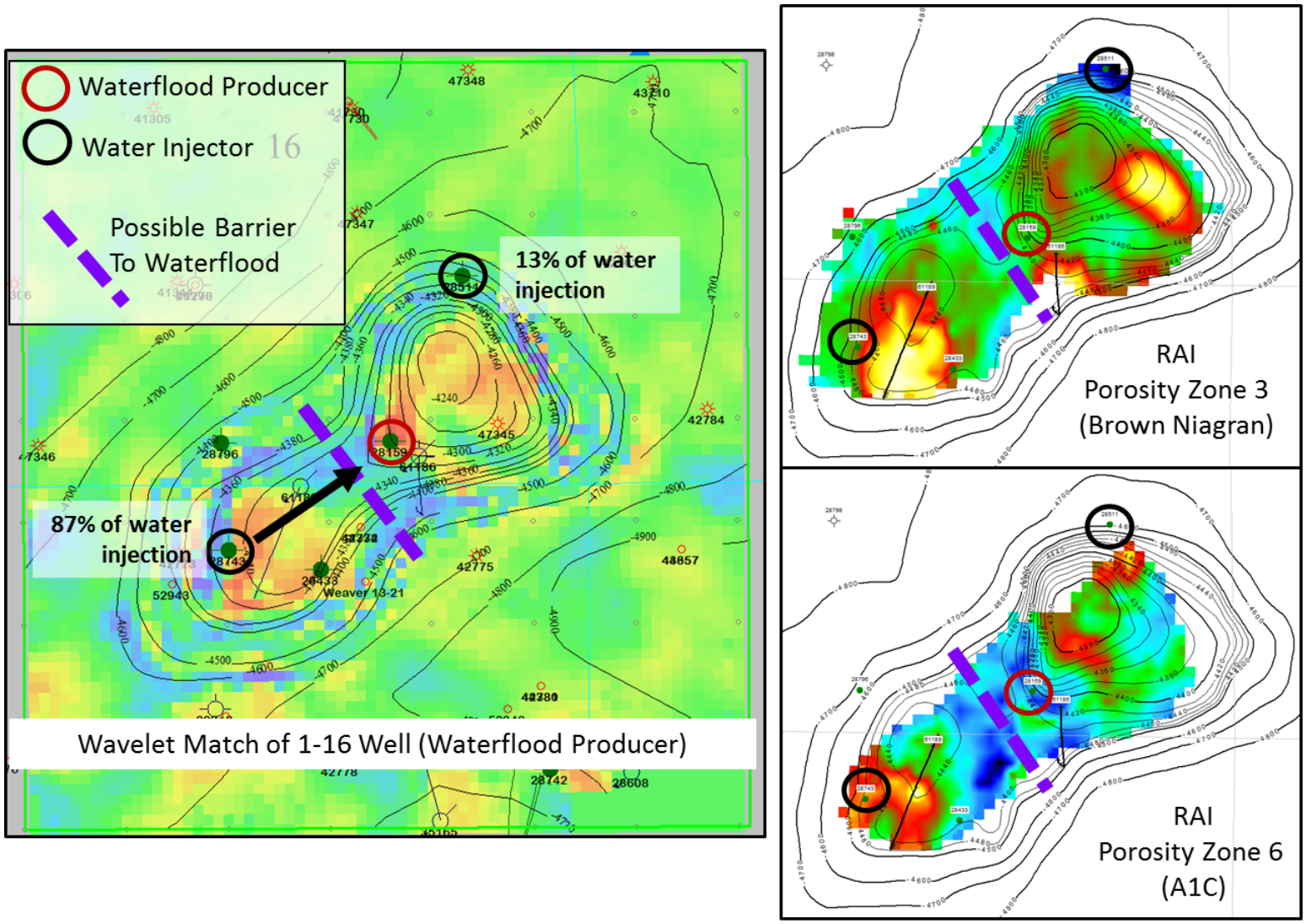


Figure 5-48. Interpretation of the wavelet matching and RAI analysis of the Chester 16 field showing a baffle in the saddle region between reef pods.

5.5 Statistical Analysis

A dataset of wireline log data (gamma ray, neutron porosity, bulk density, and travel time) and whole core and sidewall core was compiled for the Chester 16 reef field. Each depth was assigned a lithofacies (Table 5-10) for statistical analysis. Analyses included descriptive/ exploratory statistics, hypothesis tests, and cluster analyses to determine whether each lithofacies should be treated separately in static and dynamic modeling. Prior to statistical analyses, logs were upscaled to a vertical resolution of 5 feet to match the modeling resolution.

Table 5-10. Lithofacies used for statistical analyses by formation

A-1 Carbonate	Brown Niagaran
A-1 Crest	Reef Core
A-1 Flank	Windward
A-1 Off-reef	Leeward

5.5.1 A-1 Carbonate

Core-measured properties were available from four wells from whole core and sidewall cores, totaling 78 data points: 42 data points in the A-1 crest and 36 in the A-1 flank. Upscaled log data was available in the A-1 crest, A-1 flank, and A-1 off-reef lithofacies, including gamma ray, neutron porosity, and travel time.

Wireline Log Properties

Boxplots and density plots were generated for gamma ray, neutron porosity, and travel time for each lithofacies in the A-1 carbonate (Figure 5-49 and Figure 5-50). Bulk density was only available in the A-1 crest and was not included in the analyses. The off-reef A-1 carbonate shows a higher average gamma ray and distribution than the other lithofacies, which is due to the presence of shales. The A-1 crest had slower travel times and highest porosity compared to the flank and off-reef data. The difference in travel time is attributed to more porosity/pore space for an acoustic signal to travel through. The flank and off-reef porosities had similar means and distributions. Table 5-11 summarizes the ranges and averages for the log properties by lithofacies.

Table 5-11. Averages and ranges of log properties for lithofacies in the A-1 carbonate.

	A-1 Crest				A-1 Flank				A-1 Off-reef			
	DT	GR	NPHI	RHOB	DT	GR	NPHI	RHOB	DT	GR	NPHI	RHOB
Average	51.92	24.11	0.14	2.64	46.04	18.75	0.02	NA	51.49	29.12	0.02	NA
Maximum	59.44	48.81	0.32	2.84	49.60	36.03	0.09	NA	68.19	61.98	0.05	NA
Minimum	44.28	11.04	0.01	2.44	44.30	6.59	-0.01	NA	46.56	19.57	0.01	NA

Note: DT = travel time; GR = gamma ray; NPHI = neutron porosity; RHOB = bulk density.

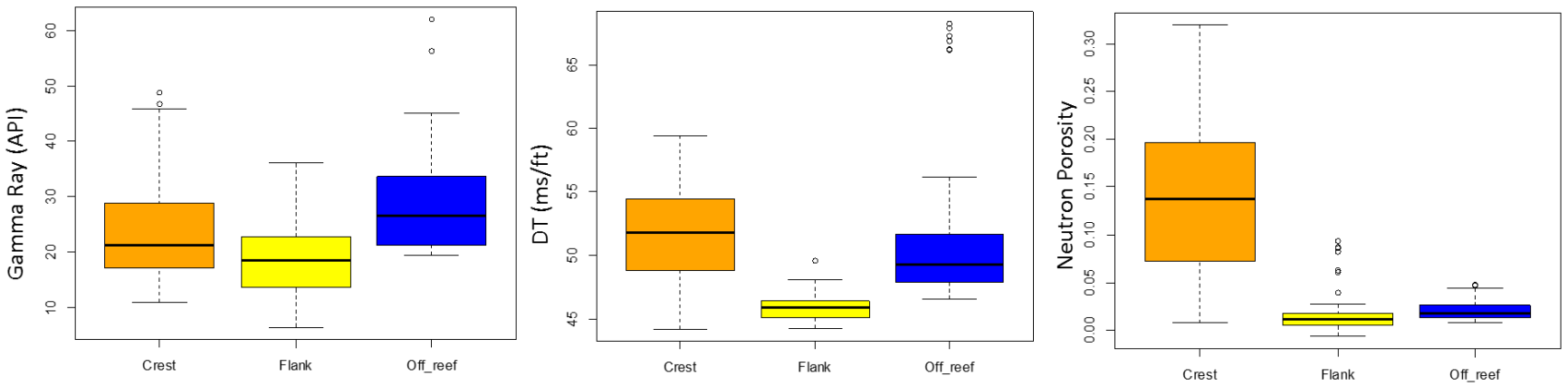


Figure 5-49. Boxplots of wireline log properties for each lithofacies of the A-1 carbonate in the Chester 16 reef field.

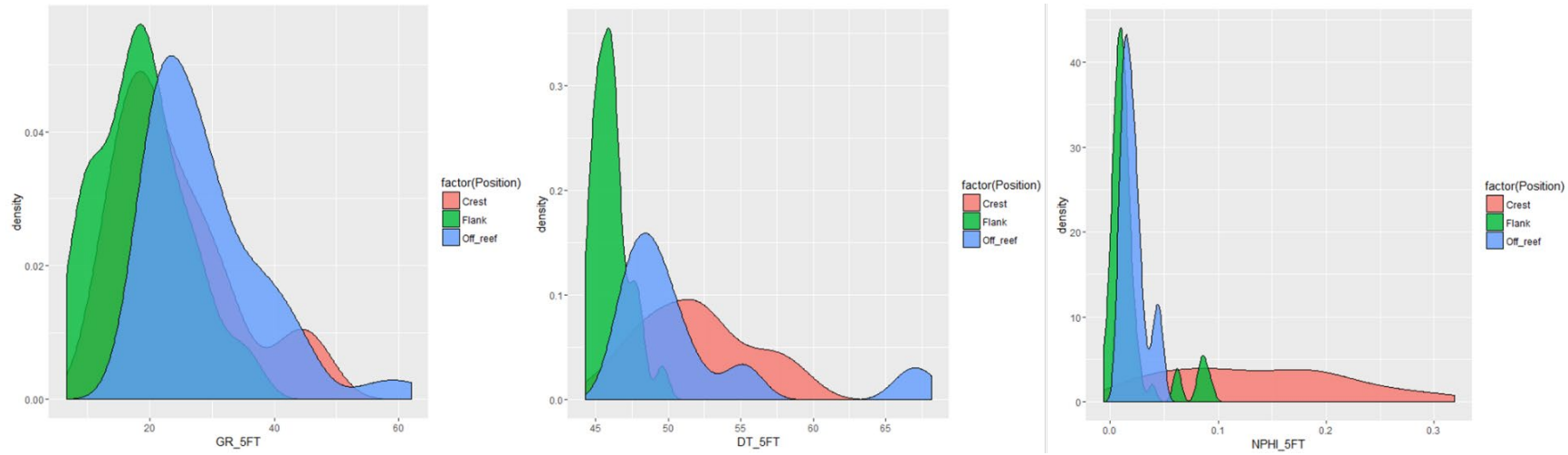


Figure 5-50. Density plots of wireline log properties for each lithofacies of the A-1 carbonate in the Chester 16 reef field.

Core-Measured Properties

Core-measured properties were not available for off-reef A-1 carbonate but were available for the A-1 crest and the A-1 flank of the Chester 16 reef field. Density plots were created (Figure 5-51) for both lithofacies. The A-1 crest had the highest porosity and permeability, while the flank remained low (Table 5-12). A crossplot of porosity and permeability also illustrates the higher values in the Crest compared to the Flank (Figure 5-52).

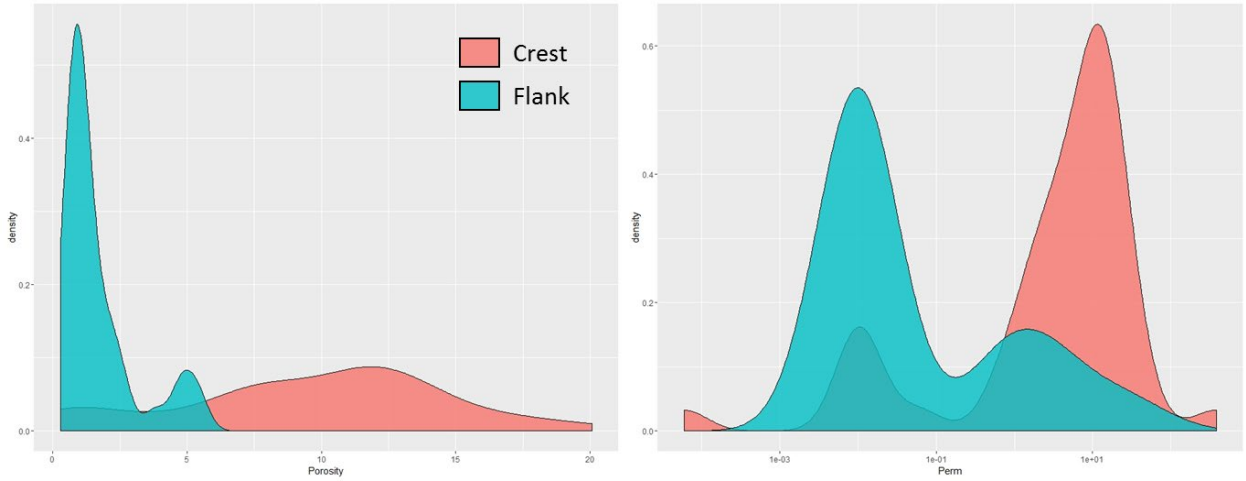


Figure 5-51. Density plots of the core measured porosity and permeability for the A-1 Crest and A-1 Flank lithofacies.

Table 5-12. Average core-measured properties for the Chester 16 lithofacies of the A-1 carbonate.

Property	A-1 Crest	A-1 Flank
Average Porosity	9.63	1.67
Average Permeability (mD)	17.69	2.24
Geometric Mean Permeability (mD)	2.40	0.06

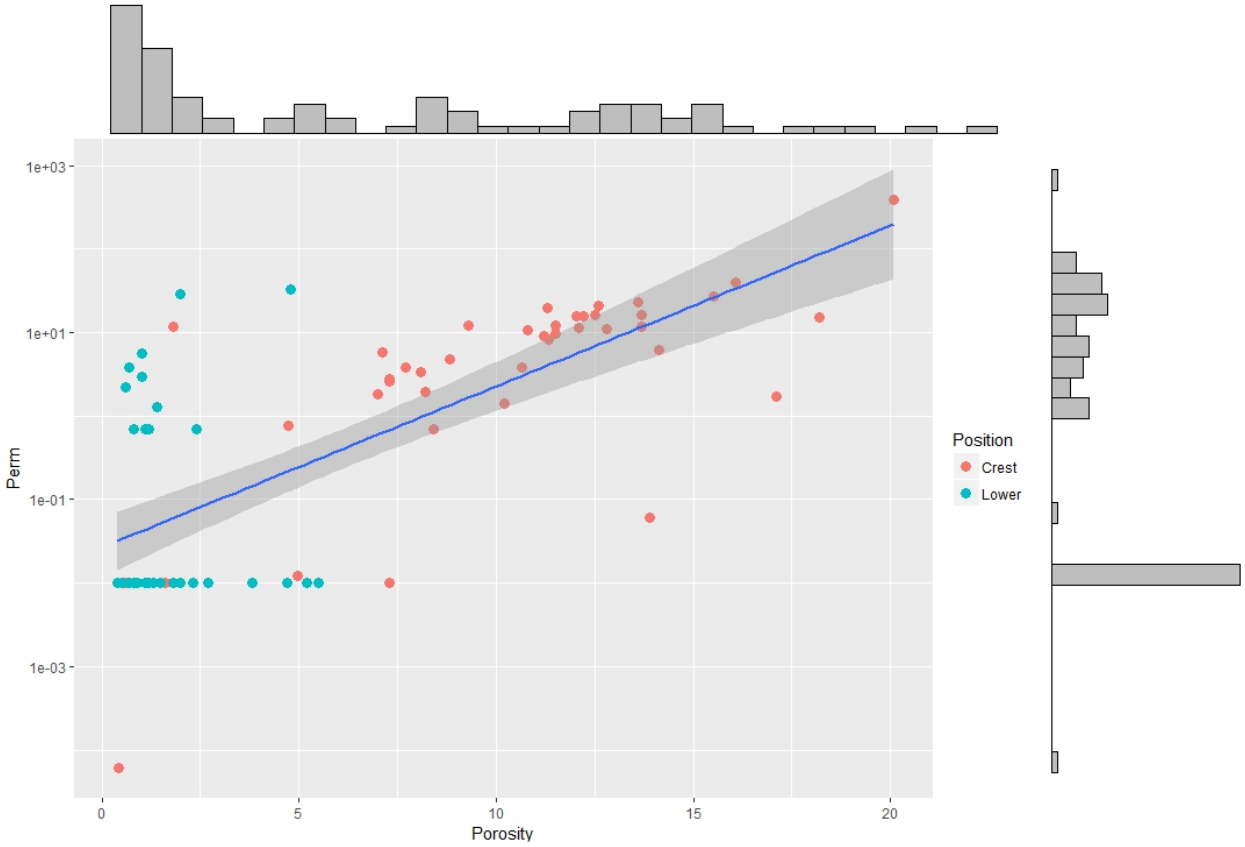


Figure 5-52. Crossplot of core-measured porosity and permeability illustrating a moderate trend with highest values in the crest (pink) of the Chester 16 reef field.

Summary

Both log and core-measured properties showed a significant difference between the A-1 crest, A-1 flank, and A-1 off-reef. The descriptive statistics were sufficient to represent the differences between lithofacies; therefore, no additional statistical analyses were performed on the A-1 carbonate.

5.5.2 Brown Niagaran

Wireline log data was available for the reef core, windward, and leeward facies of the Brown Niagaran formation. Log data covered seven wells and included gamma ray, neutron porosity, travel time, and bulk density. Bulk density data was available only in the reef core and leeward lithofacies. Whole core and sidewall core data was available from five wells; the data consisted of 57 data points in the leeward, 130 in the reef core, and 35 in the windward lithofacies.

Wireline Log Properties

Boxplots, density plots, and averages were generated for each lithofacies and each log (Figure 5-53 and Figure 5-54). The reef core had the lowest gamma ray and lowest bulk density, which is consistent with a clean limestone formation. The windward lithofacies had the highest mean porosity with the highest gamma ray. The leeward lithofacies had the slowest travel time, higher bulk density, with low average porosity. The differences between windward and the other two lithofacies was higher than differences observed between leeward and reef core. Table 5-13 summarizes the ranges and averages of the log properties for each lithofacies.

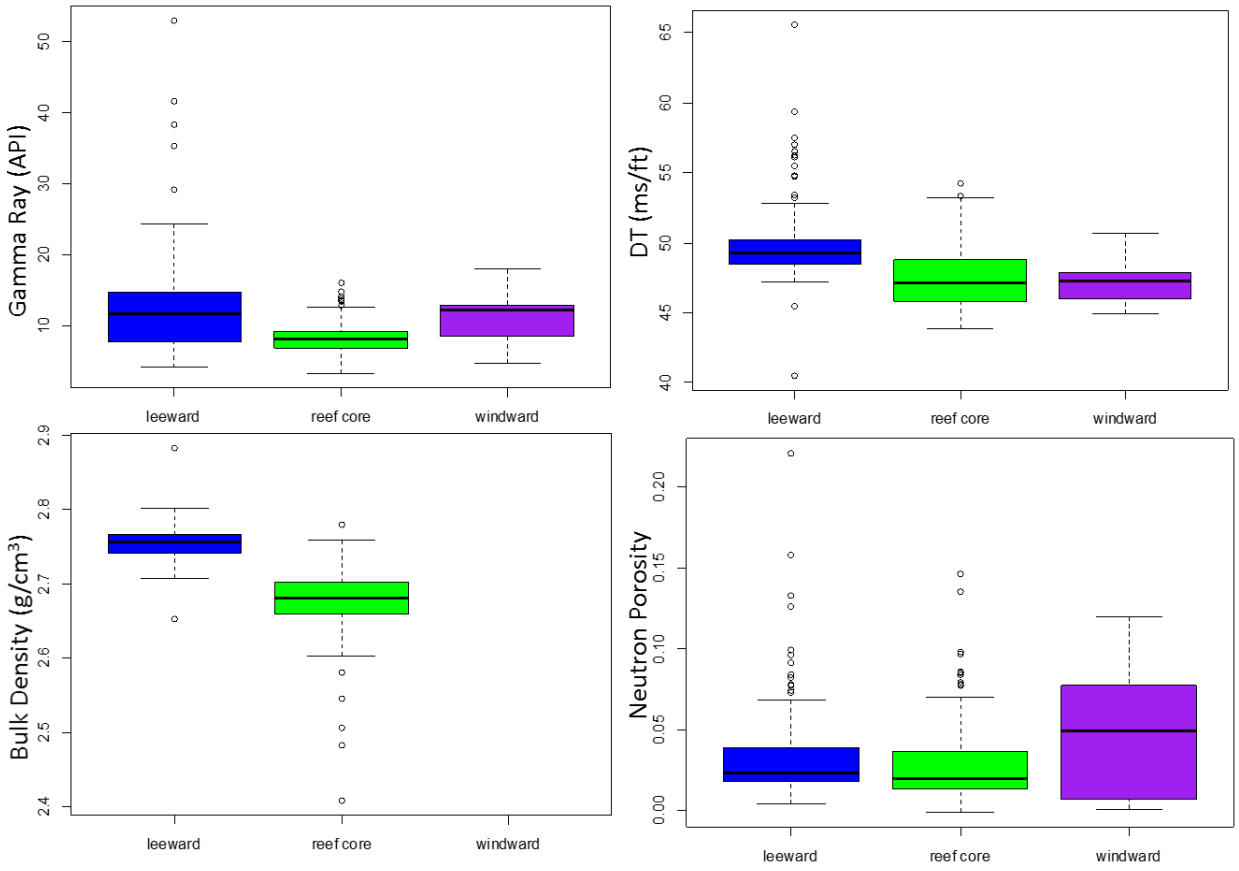


Figure 5-53. Boxplots of each wireline log and each lithofacies of the Brown Niagaran formation.

Table 5-13. Averages and ranges of log properties for lithofacies in the Brown Niagaran.

	Reef Core				Leeward				Windward			
	DT	GR	NPHI	RHOB	DT	GR	NPHI	RHOB	DT	GR	NPHI	RHOB
Average	47.39	8.33	0.03	2.68	49.89	12.27	0.03	2.75	47.38	11.01	0.05	NA
Maximum	54.25	16.01	0.15	2.78	65.59	53.09	0.22	2.88	50.66	17.98	0.12	NA
Minimum	43.90	3.31	0.00	2.41	40.50	4.20	0.00	2.65	44.94	4.64	0.00	NA

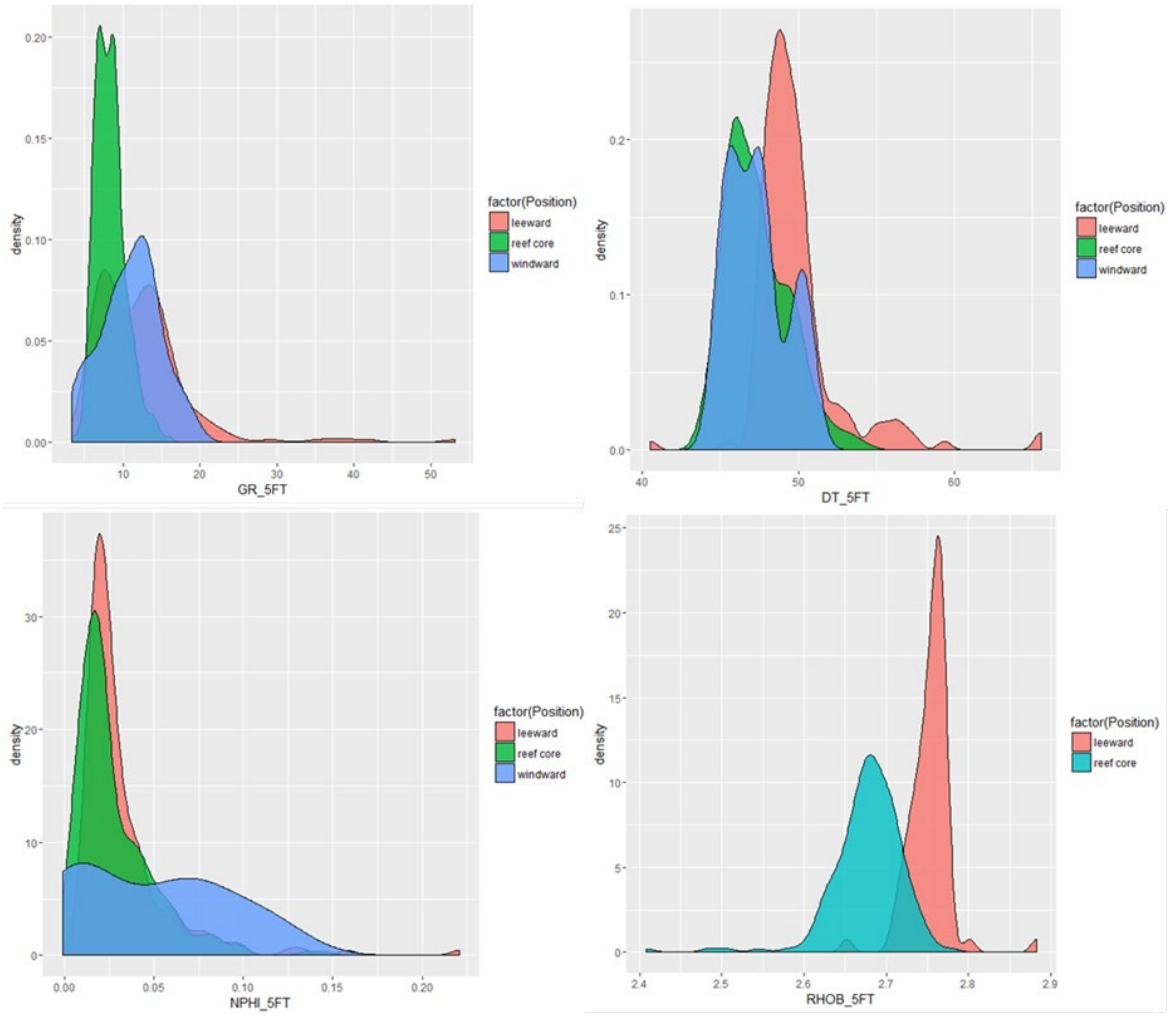


Figure 5-54. Density plots of each wireline log and lithofacies for the Brown Niagaran formation.

To further explore the differences between lithofacies, the means were compared using Tukey's HSD test, which tests the hypothesis that the means are statistically the same. The Tukey test computes an HSD value and compares it to the Tukey's critical value (a look-up table). If the difference is significant, it produces a p-value of 1, indicating that the means are the same between two groups (highlighted significant values in Table 5-14). If the difference is insignificant, it produces a p-value of 0, indicating that the means are different between two groups. However, the Tukey test assumes a normal distribution, which is not always the case, as seen in Figure 5-54. Table 5-14 lists the resulting p-value between pairs and logs. Results show mostly null results (0, different means) except for gamma ray between windward and leeward and travel time between windward and reef core. The neutron porosity means between each lithofacies is statistically different.

Table 5-14. Tukey's HSD test results for each lithofacies pair and log.

	GR		DT		NPHI	
	Difference	P-value	Difference	P-value	Difference	P-value
RC-LW	-3.94	0	-2.50	0	-0.005	0.10
WW-LW	-1.26	0.56	-2.51	0	0.015	0.04
WW-RC	2.68	0.07	-0.011	1	0.021	0.003

Core-Measured Properties

Whole core and sidewall core data was compiled for the Brown Niagaran and assigned a lithofacies. Boxplots and density plots were generated for porosity and permeability to illustrate the differences and similarities between lithofacies (Figure 5-55 and Figure 5-56). The windward lithofacies had the highest mean porosity and broadest distribution. The reef core had significantly lower mean porosity and a narrower distribution of values; however the core was collected in the lower reef, which traditionally has lower reservoir properties. The leeward lithofacies had similar porosity and permeability as the windward, with slight differences in means and distributions (Table 5-15). Permeability in the windward and leeward lithofacies showed a bimodal distribution which could be a result of secondary porosity.

Table 5-15. Averages and ranges of core-measured properties for each lithofacies in the Brown Niagaran formation.

Property		Reef Core	Windward	Leeward
Porosity (%)	Average	1.46	4.16	2.25
	Maximum	9.9	11.10	13.7
	Minimum	0.30	0.40	0.40
Permeability (mD)	Average	0.16	4.86	20.79
	Geometric Mean	0.001	0.325	0.272
	Maximum	11.10	111.00	450
	Minimum	0	0.001	0.01

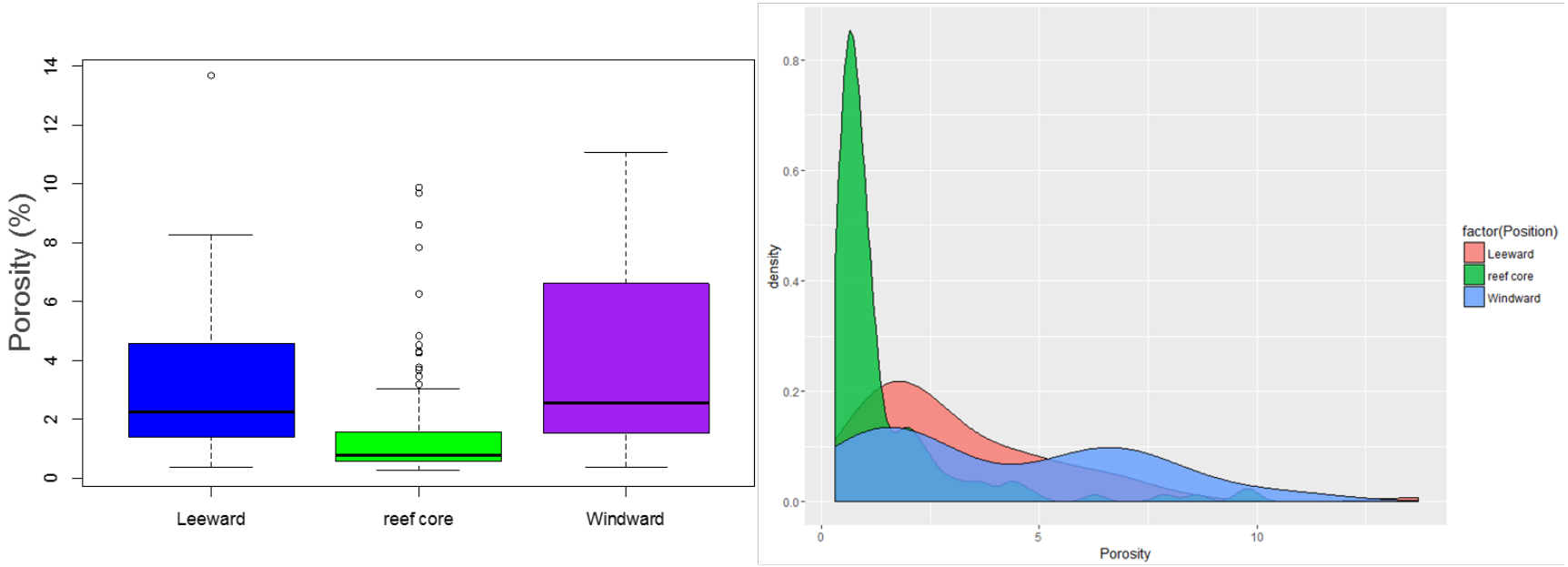


Figure 5-55. Boxplot (left) and density plot (right) of core measured porosity for each lithofacies in the Brown Niagaran formation.

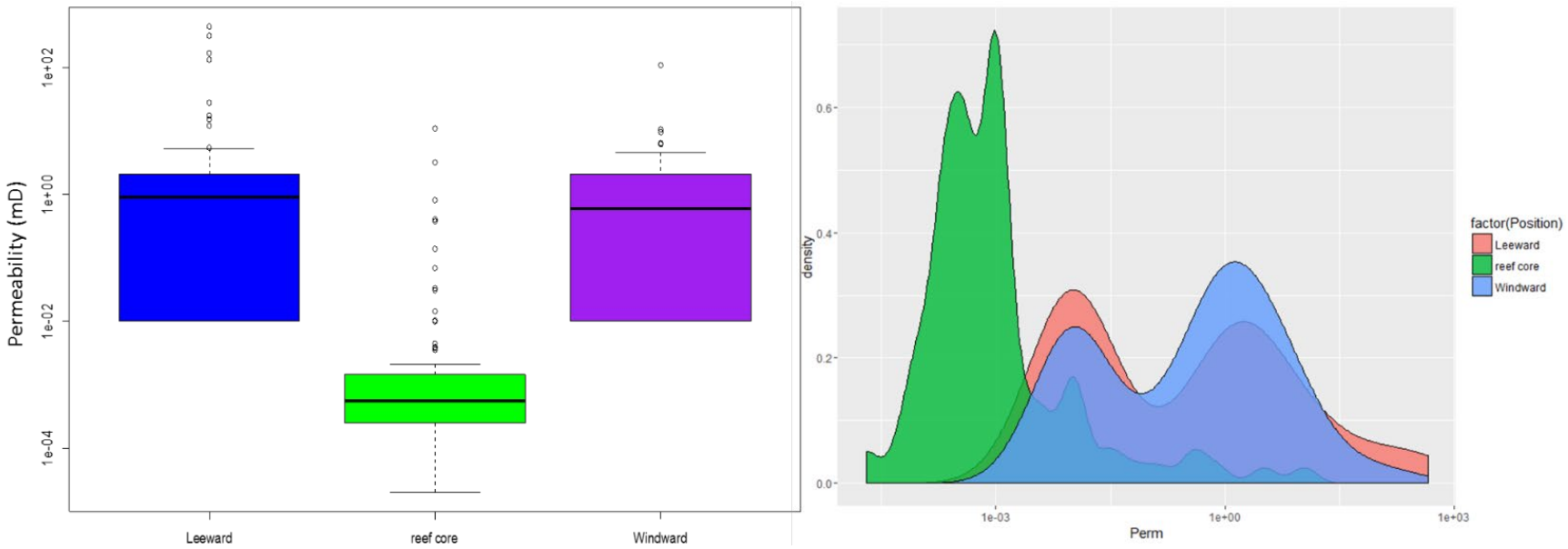


Figure 5-56. Boxplot (left) and density plot (right) of core measured permeability for each lithofacies in the Brown Niagaran formation.

Core-measured porosity and permeability were plotted to determine a transform for the Brown Niagaran formation (Figure 5-57). There was a poor correlation between properties for the Brown Niagaran and when split by lithofacies. The resulting R^2 values were less than 0.3 for each scenario. Due to the poor correlations, a transform was not developed for the Brown Niagaran.

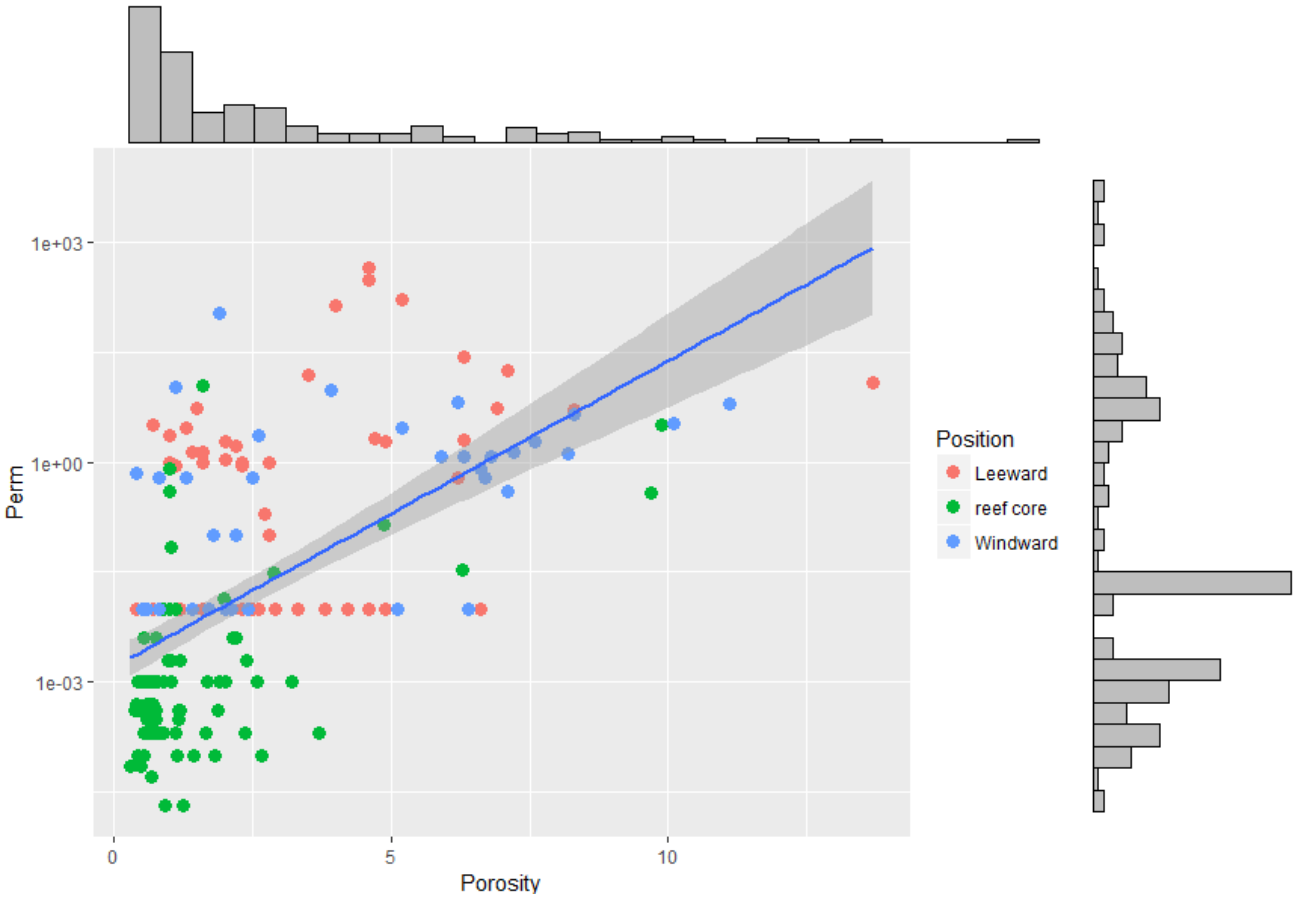


Figure 5-57. Core-measured porosity and permeability by lithofacies of the Brown Niagaran showing a poor correlation.

A series of statistical tests were performed to determine whether the core-measured properties were statistically different. The tests included an analysis of variance (ANOVA) test, Bartlett test, Kruskal-Wallis test, and Tukey's HSD test. The ANOVA test, Bartlett test, and Tukey's test all assumed a normal distribution. For these tests, an additional set was run using the log of the values. Table 5-16 summarizes the tests performed and the results. The results of the hypothesis tests all conclude that the lithofacies are statistically different.

Table 5-16. Statistical tests and results performed to compare core-measured properties of the lithofacies of the Brown Niagaran formation.

Test	Description	Assumption	Hypothesis	Results
ANOVA	Analysis of variance which compares the means of a pair	Normal distribution	Means are the same	Null: means are not the same
ANOVA-LOG	Analysis of variance which compares the means of a pair	Normal distribution of log values	Means are the same	Null: means are not the same
Bartlett	Compares the variances of each group	Normal distribution	Variances are the same	Null: variances are not the same
Bartlett-LOG	Compares the variances of each group	Normal distribution of log values	Variances are the same	Null: variances are not the same
Tukey	Compares the means of each group	Normal distribution	Means are the same	Null: means are not the same
Tukey-LOG	Compares the means of each group	Normal distribution of log values	Means are the same	Null: means are not the same
Kruskal-Wallis	Compares population distributions	Does not assume normal distribution	Distributions are the same	Null: distributions are not the same

Additionally, a preliminary cluster analysis was performed to determine how the data naturally clusters. Cluster analysis applies several algorithms to determine how data groups together. Once grouped, the data points within a group are more similar to each other than to data points in other groups. Two common algorithms in *RGui*, an open-source statistical program, are *Mclust* and *KMeans. Mclust* applies several model-based clustering algorithms and chooses the method that best fits the data. *KMeans* minimizes the sum of squares for each data point and clusters them around a center mean for the defined number of clusters. A cluster analysis was conducted to quantitatively determine whether the reef can be statistically subdivided and, if so, what the subdivisions are.

KMeans requires an input of number of clusters. It was initially run assuming three clusters to determine whether the three lithofacies would fall into separate clusters (Figure 5-58). Under this scenario, the reef core clustered by itself, while there was significant overlap between windward and leeward data between clusters (Table 5-17). KMeans was run assuming four and five clusters with similar results. KMeans did not yield unique clusters which matched the identified lithofacies.

Table 5-17. Results of KMeans clustering showing which cluster the core-measured data falls into for each lithofacies.

Lithofacies	Cluster 1	Cluster 2	Cluster 3
Reef Core	91	3	5
Windward	11	14	10
Leeward	25	13	19

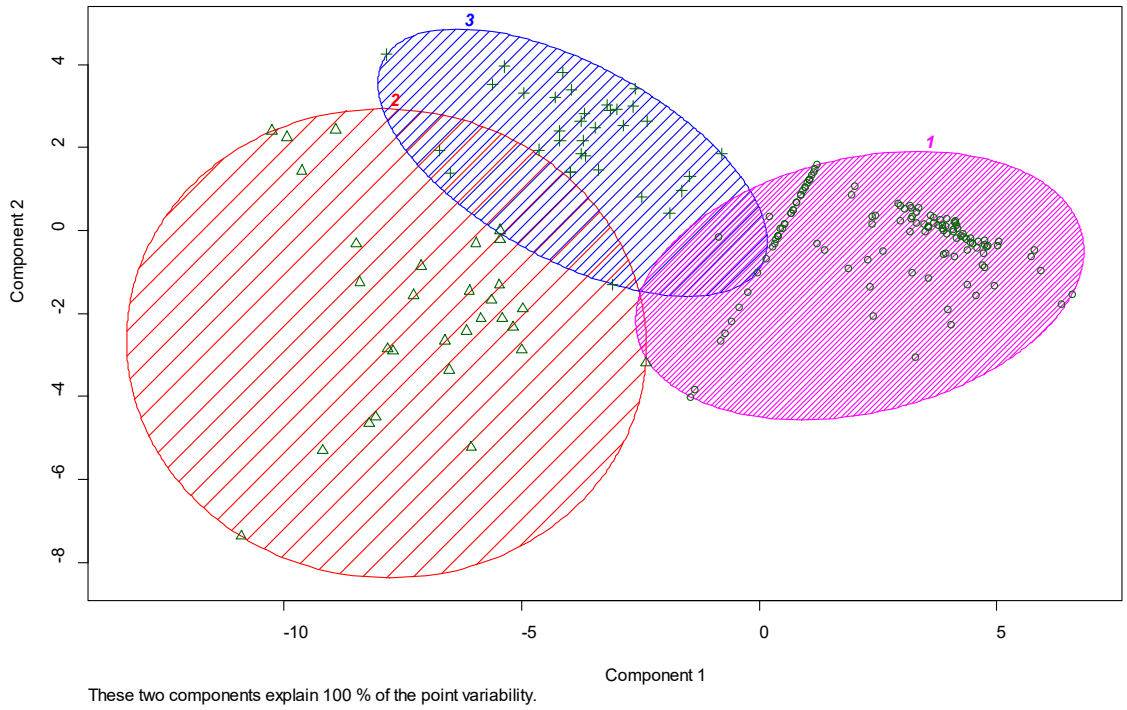


Figure 5-58. KMeans clustering results show porosity and permeability falling into three identified clusters as identified by colored circles and differing symbols.

Mclust determines the number of clusters as best fits the data. The resulting number of clusters identified was eight (Figure 5-59). This produced a range of clusters for each lithofacies; however, each lithofacies did have a dominant cluster that was not the same as another lithofacies (Table 5-18). The reef core dominantly fell into cluster 8 (60%) with a few points in five other clusters. The Leeward facies dominantly fell into cluster 2 (32%) with 23% into cluster 1. The Windward facies fell dominantly into cluster 6 (40%) with 26% falling into cluster 2. Figure 5-60 plots the core measured porosity and permeability colored by cluster with a shape based on lithofacies.

Table 5-18. Results of the Mclust clustering showing which cluster the core-measured data falls into for each lithofacies.

Lithofacies	Cluster							
	1	2	3	4	5	6	7	8
Leeward	13	18	4	5	7	10	0	0
Reef Core	11	6	2	0	0	3	17	60
Windward	5	9	4	1	2	14	0	0

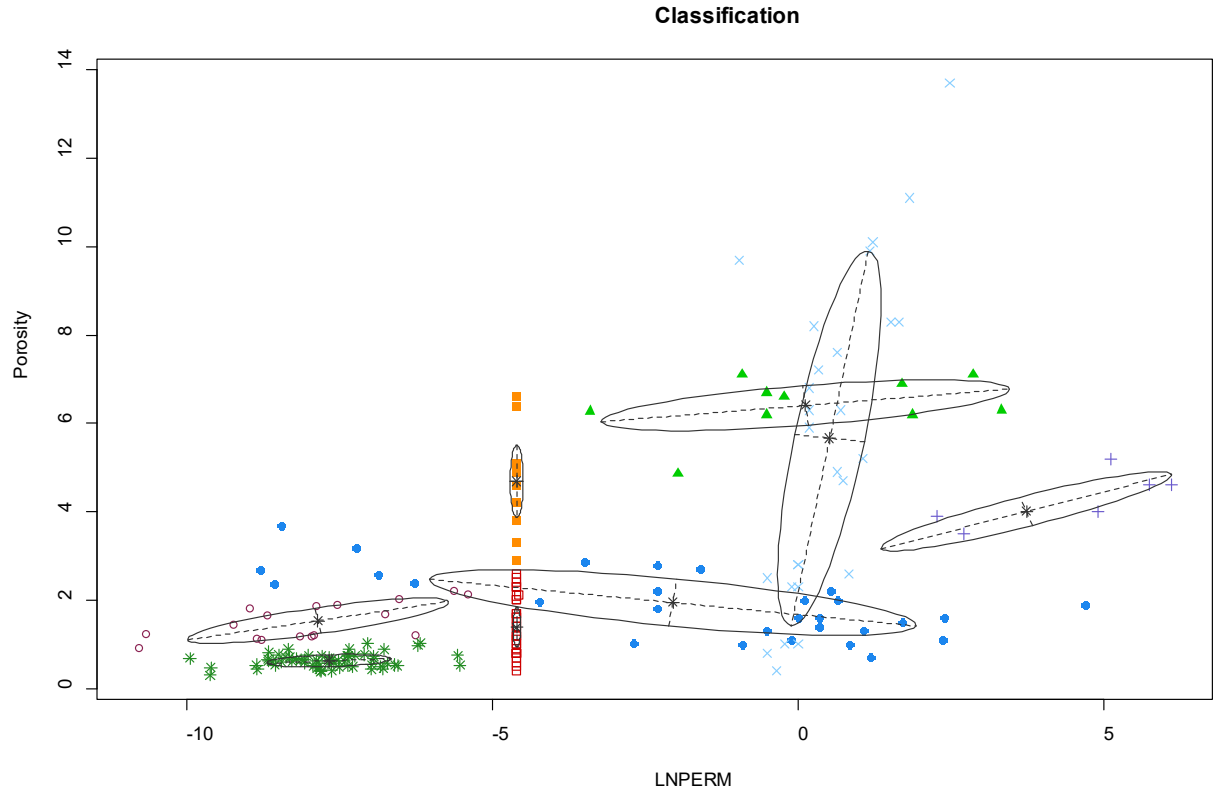


Figure 5-59. Cluster results from Mclust using core-measured porosity and permeability with different symbols for each cluster.

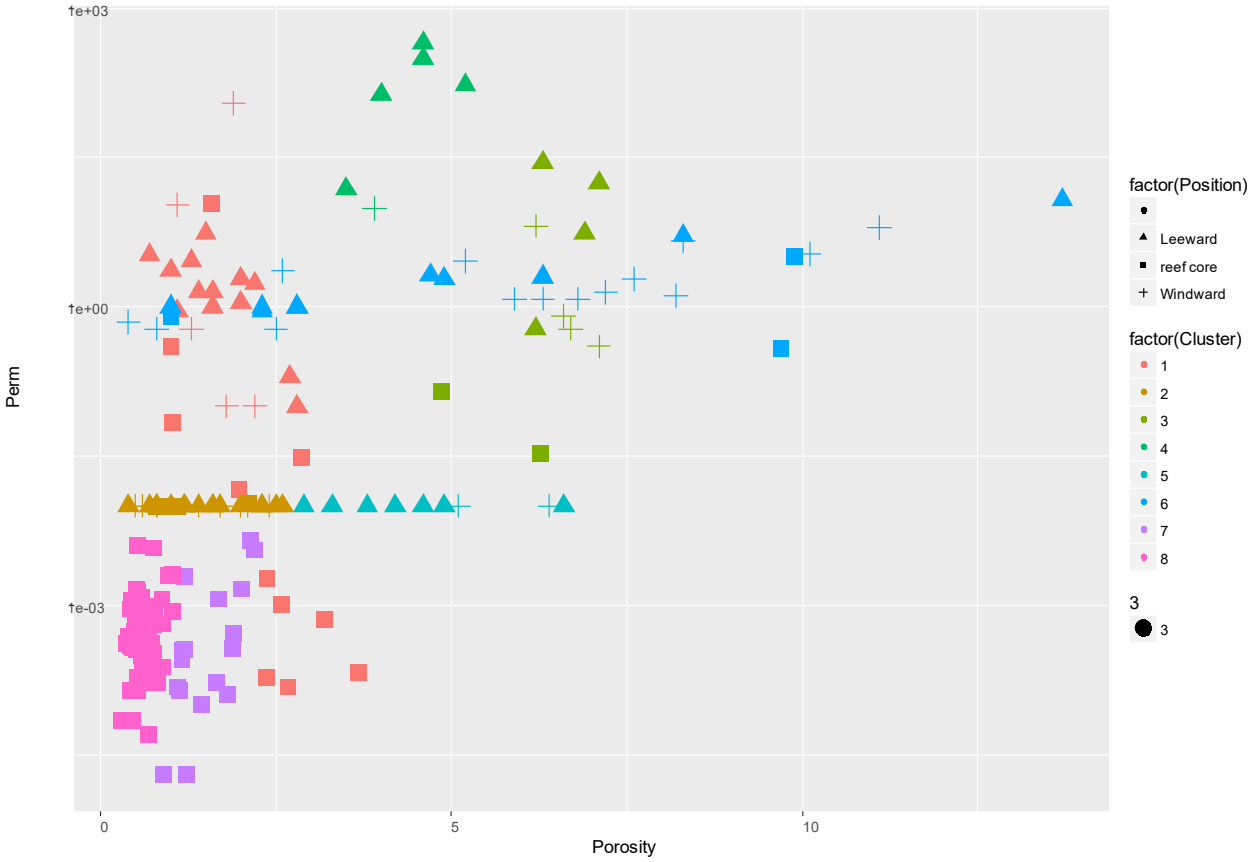


Figure 5-60. Core-measured porosity and permeability colored by Mclust clustering results with shape showing lithofacies.

5.5.3 Core-to-Log Correlation

Core data was depth-matched to log data to determine whether the log porosity measurements were representative of the direct measurements. The following five-step process was used to determine the correlation:

1. Depth-match log porosity to core-measured porosity.
2. Plot neutron porosity vs core porosity.
    a. Compare peaks/troughs and patterns in each well to determine whether a depth shift was needed.
3. Calculate the percent difference between core and log porosity.
4. Plot core vs log porosity for all wells.
5. Plot core vs log porosity for each lithofacies.

The results produced a linear correlation which was nearly one-to-one (Figure 5-61). The greatest differences occurred when core porosity was less than 2%, which is consistent with the limitations of the downhole wireline logs. Furthermore, the correlation did not change with lithofacies (Figure 5-62).

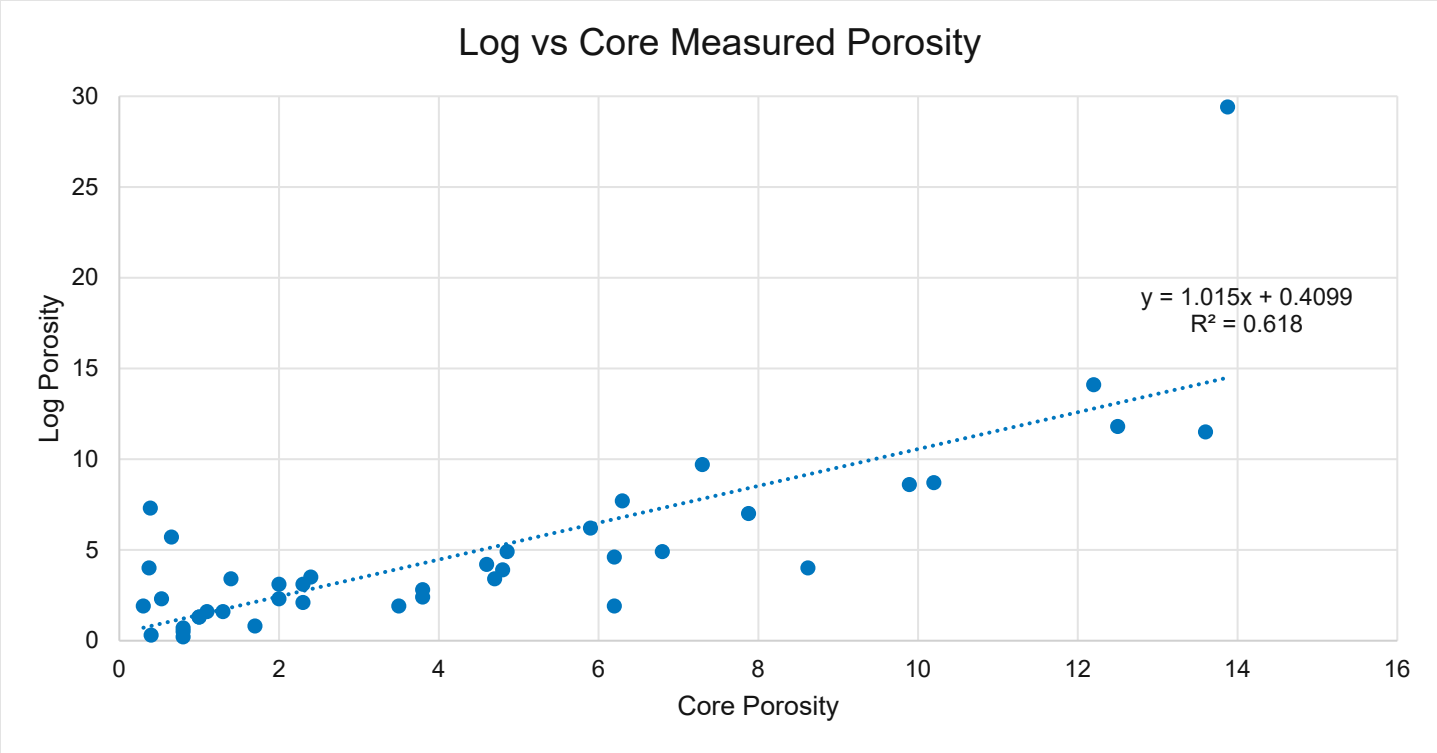


Figure 5-61. Log-measured porosity and core-measured porosity for all data in the Chester 16 reef field showing a strong correlation.

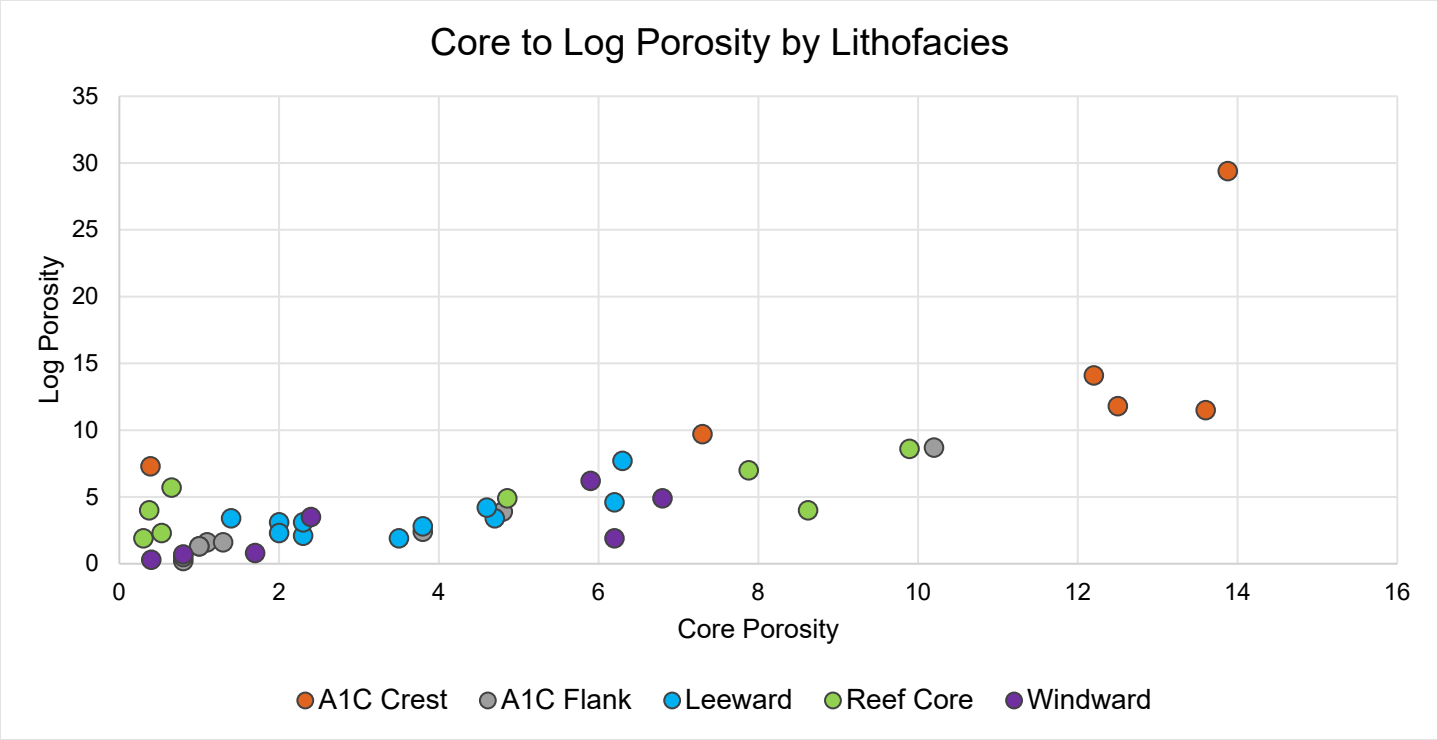


Figure 5-62. Log-measured porosity and core-measured porosity for all data in the Chester 16 reef field, by lithofacies, showing no dependence on lithofacies.

5.5.4 Conclusions of Statistical Analyses

Descriptive statistics and plots were sufficient to demonstrate that the A-1 carbonate should be subdivided into the A-1 crest and A-1 flank using both log and core data. The Brown Niagaran lithofacies were explored in more detail due to closer means and distributions of log and core properties. A series of statistical hypothesis tests all resulted in the same conclusion: the Brown Niagaran lithofacies are statistically different. A cluster analysis was performed to compare the natural clustering of core-measured properties with the identified lithofacies to determine whether the lithofacies naturally clustered into unique clusters. The two methods showed overlap between lithofacies and clusters, but the lithofacies did identify with a dominant cluster that was not dominant in another lithofacies.

The statistical analyses were limited by available log and core data. Even though the results show the lithofacies to be statistically different, the core data coverage is insufficient for a full cluster analysis. The reef core data was only collected at the base of the reef and did not represent the upper reef, which tends to have higher reservoir quality based on analog reefs.

In conclusion, the A-1 carbonate and Brown Niagaran should be modeled based on lithofacies and not as single zones. The log-measured porosity (neutron porosity) well represented the core-measured porosity and can be used to develop porosity models.

5.6 Geologic Interpretations and Data Integration

A cross section was constructed across the Chester 16 reef field to determine changes in the reef structure and continuity of reservoir conditions. The cross section was flattened on the top of the A-2 carbonate/base of the B-salt. The logs included are the gamma ray, bulk density, neutron porosity, and water saturation. Also included are two porosity flags: a crossplot porosity flag of greater than 5% porosity (red), and a log porosity flag of porosity greater than 5% with water saturation less than 40% (green).

Cross section A-A’ transects the western flank to the northeastern most well (Figure 5-63). Wells 28796 and 28511 were flank wells with increased amounts of evaporites (salt and anhydrite). The A-2 carbonate had a continuous gamma ray marker mid-formation representing a thin interval carbonate mudstone/ shale. The porosity in the A-1 carbonate changes significantly from flank wells to crestal wells as the lithology becomes porous dolomite. Anhydrite and salt layers are also evident in the A-1 carbonate along the flanks of the reef. There were thin porosity spikes in the Brown Niagaran which could be fractures or dolomitic intervals. The intervals appear at different depths in every well, but there is some potential for connectivity between wells. The lower third of the Brown Niagaran was water-saturated, as marked by increased water saturation values which correlated with the original oil/water contacts. The underlying Gray Niagaran had higher gamma ray values with minor porosity and was fully water saturated. The cross section illustrates the geologic framework of the Chester 16 reef field by revealing low-porosity immediate confining units, higher-porosity reservoirs, and then a water-saturated underlying confining unit (Figure 5-64). Figure 5-65 through Figure 5-67 show 2D interpolated properties (neutron porosity, gamma ray, and water saturation) that illustrate the geologic trends and concepts interpreted in the Chester 16 reef field.

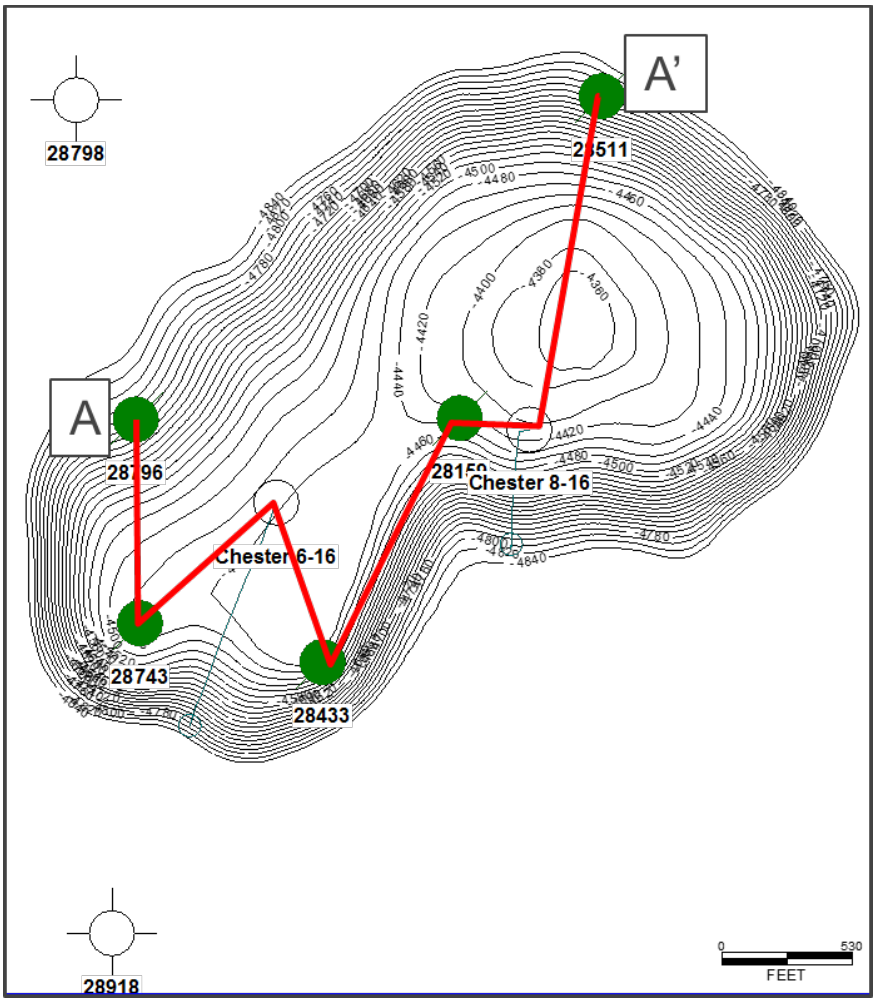


Figure 5-63. Cross section A-A' through the Chester 16 reef field showing wells used and position in the reef structure.

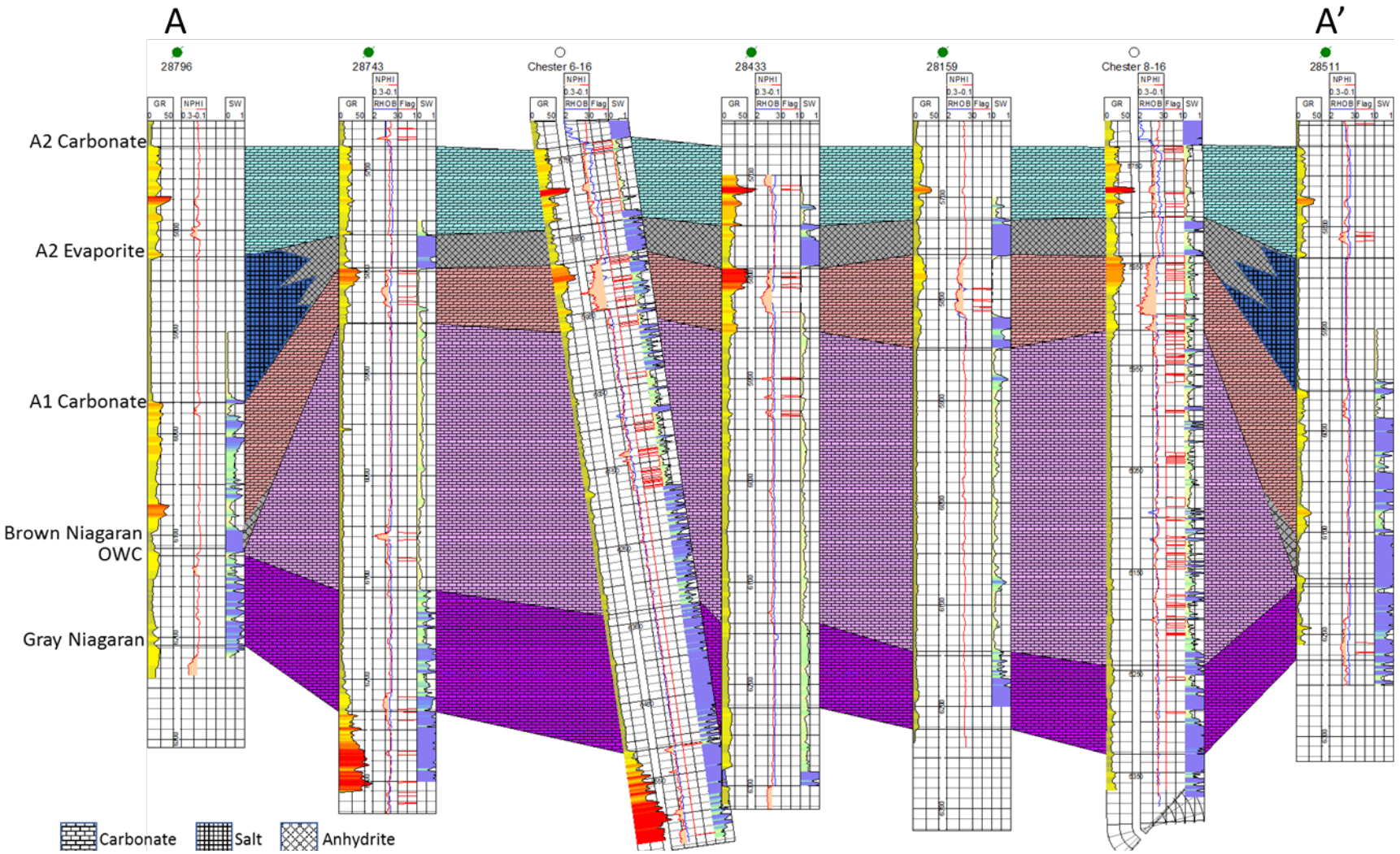


Figure 5-64. Cross section A-A' through the Chester 16 reef field showing changes in gamma ray, neutron porosity, bulk density, and water saturation in correlation with key formations. Angled well diagrams indicate deviated wells. Not drawn to scale.

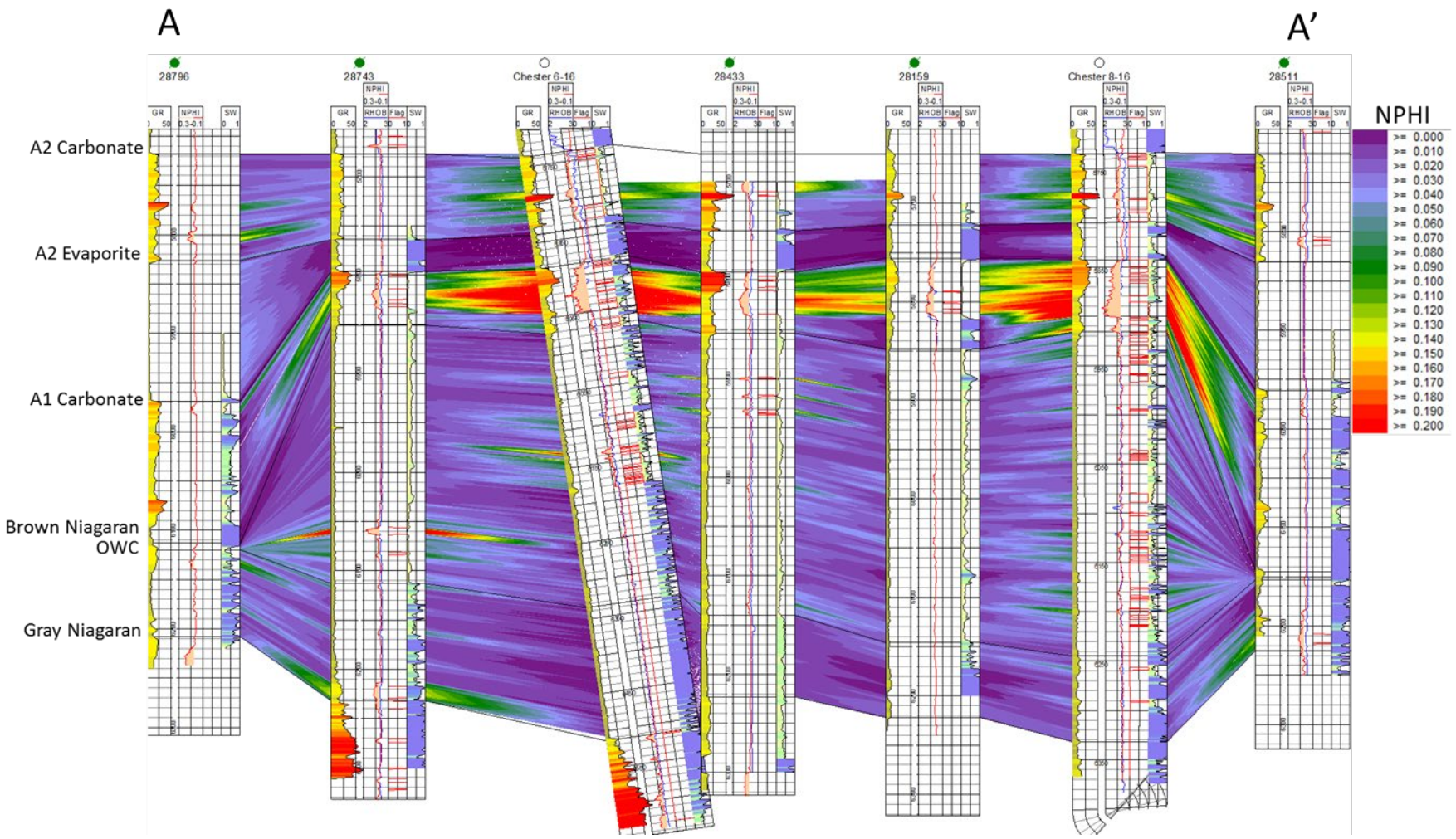


Figure 5-65. Cross section A-A' through the Chester 16 reef field showing a 2D interpolation of neutron porosity between wellbores. Significant porosity (red) is observed in the A-1 carbonate and as thin streaks through the Brown Niagaran. Angled well diagrams indicate deviated wells. Not drawn to scale.

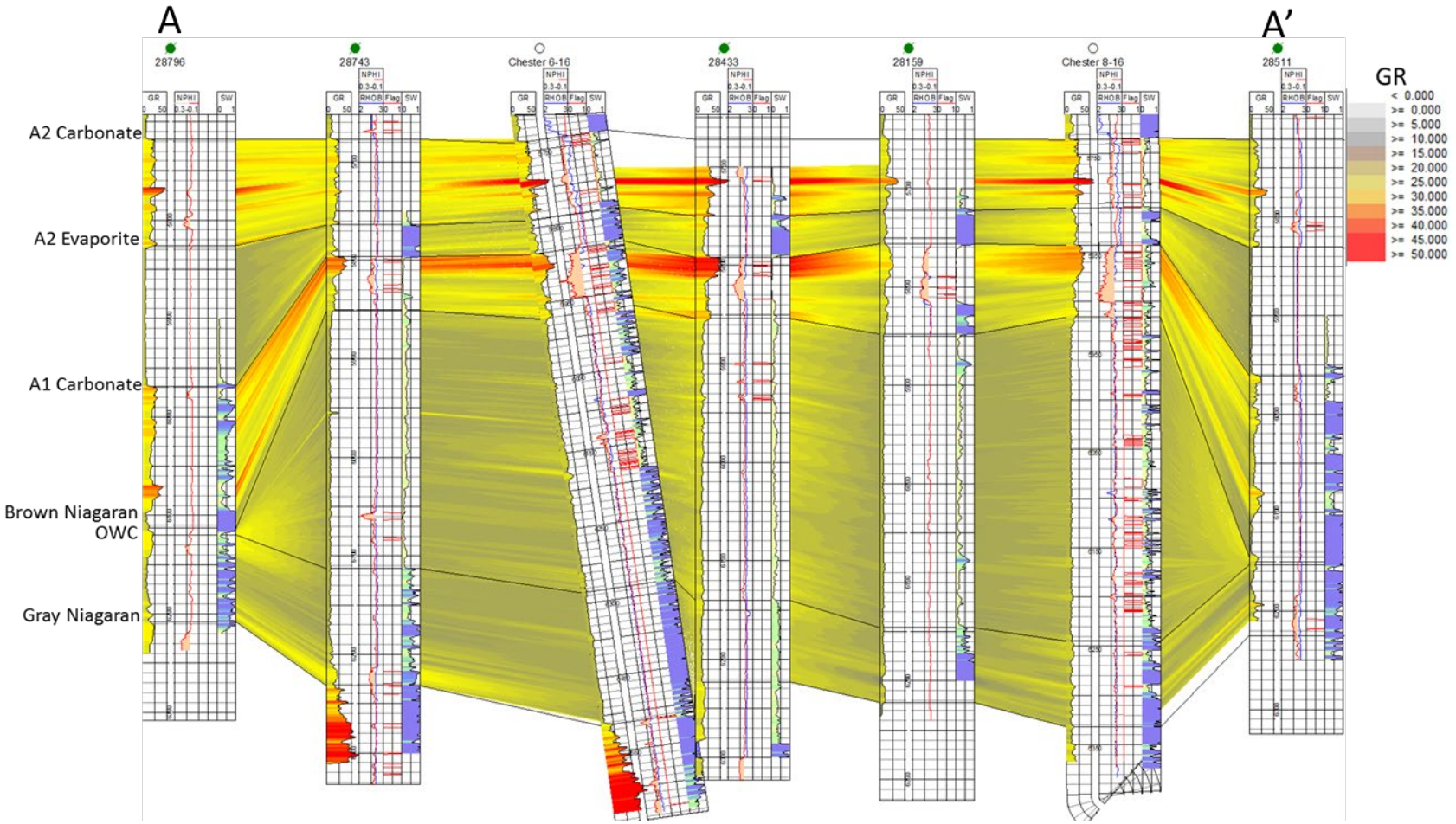


Figure 5-66. Cross section A-A' through the Chester 16 reef field showing a 2D interpolation of gamma ray between wellbores. High gamma ray was consistent in the mid-formation A-2 carbonate over a shaley interval and high in the porosity zone in the A-1 carbonate. Angled well diagrams indicate deviated wells. Not drawn to scale.

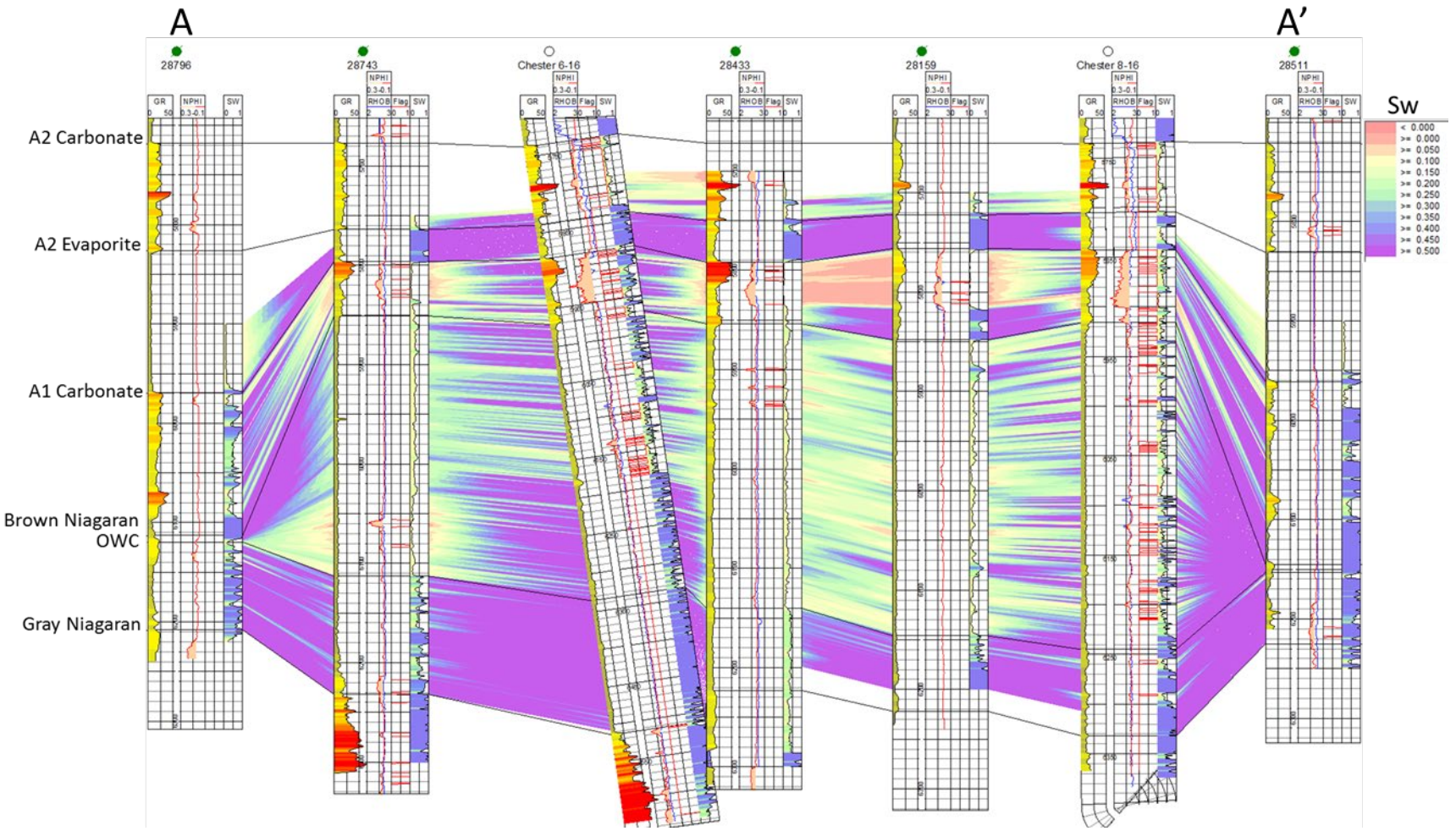


Figure 5-67. Cross section A-A' through the Chester 16 reef field with a 2D interpolation of the water saturation showing high water saturations after the oil/water contact and where evaporites are present. Angled well diagrams indicate deviated wells. Not drawn to scale.

The immediate confining units are the A-2 carbonate and A-2 evaporite. The A-2 carbonate is composed of mostly limestone with intervals of evaporites along contacts and a thin interval of shale/mudstone. Triple combo logs highlighted a shale/mudstone mid-formation with an increase in neutron porosity. Sidewall cores were taken in the shale unit and, along with image logs, showed that there was no major porosity, only microporosity. The A-2 evaporite is composed of interbedded limestone and anhydrite along the crest of the reef structure, which transitioned to salt along the flanks. Evaporites showed no porosity across logs and sidewall cores. Data confirmed that the immediate confining units made ideal seals by exhibiting a lack of porosity, tight lithologies, and no major fractures.

The reservoir units are identified as the A-1 carbonate and Brown Niagaran formations.
Figure 5-68 shows the lithofacies for these two formations. The A-1 carbonate shows significant porosity along the crest of the reef structure. Triple combo logs indicated porosity up to 20% in the upper to middle sections. Image logs in the Chester 8-16 well confirmed porosity textures in the form of vugs and moldic porosity. Sidewall cores also showed significant presence of vugs but also high-matrix porosity due to sugary/grainy dolomite. At well 28159 (the center of the reef field), the A-1 evaporite is present in the form of anhydrite. This finding was confirmed by whole core available at MGRRE. The decrease in reservoir properties and the presence of anhydrite at that location indicated a leeward position along with a double-lobe reef field. Figure 5-68(B) shows the extent of the reservoir zone in the upper A-1 carbonate (orange), with the remaining area being tight, non-reservoir rock. Porosity features are also highlighted in Figure 5-69 where core was present.

The Brown Niagaran formation is composed mostly of tight limestone with thin intervals of dolomite and high porosity. Log signatures and seismic geometry confirmed a two-lobe reef field. The northern lobe had the largest reef core with the greatest height. Whole core data and image logs confirmed intervals with porosity features in the form of vugs, fractures, and moldic porosity. There were minor amounts of salt and anhydrite plugs throughout. The lithofacies of the Brown Niagaran are shown in Figure 5-68(A) with the main reef core in green, leeward facies in blue, windward facies in purple, and flank/off-reef in gray. Intervals of porosity are seen in Figure 5-69, where there are spikes in porosity logs and whole core showing vugs.

The underlying confining unit, or Gray Niagaran, had limited data available. The addition of two new wells provided the opportunity to better characterize the formation. The triple combo logs showed high gamma ray values with thin intervals of potential porosity. However, the Gray Niagaran was fully water-saturated and provides an ideal underlying confining unit. Whole core was collected in the 8-16 well and showed intervals of secondary porosity which were not connected through matrix. Gamma ray values indicated the possible presence of bentonite beds; these have not yet been confirmed pending whole core tests.

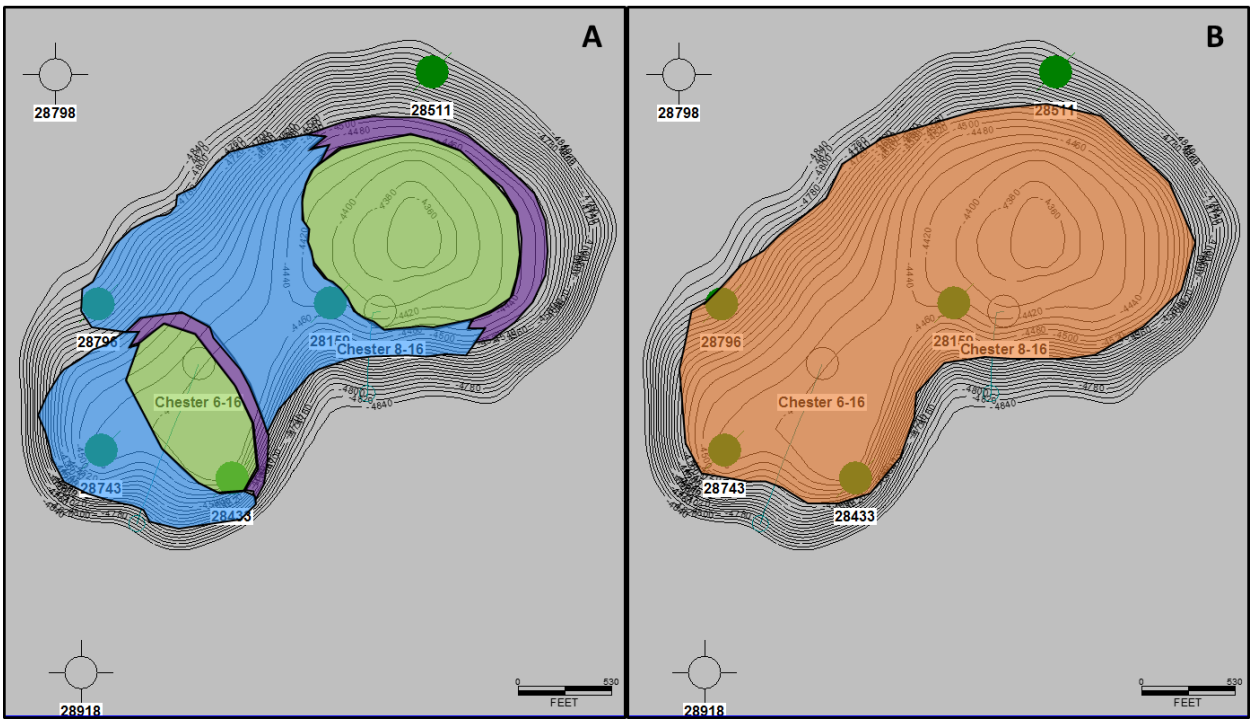


Figure 5-68. Brown Niagaran lithofacies (A) and A-1 carbonate lithofacies (B) for the Chester 16 reef field. Green represents reef core, purple is windward facies, blue is leeward facies, and orange is A-1 carbonate porosity facies.

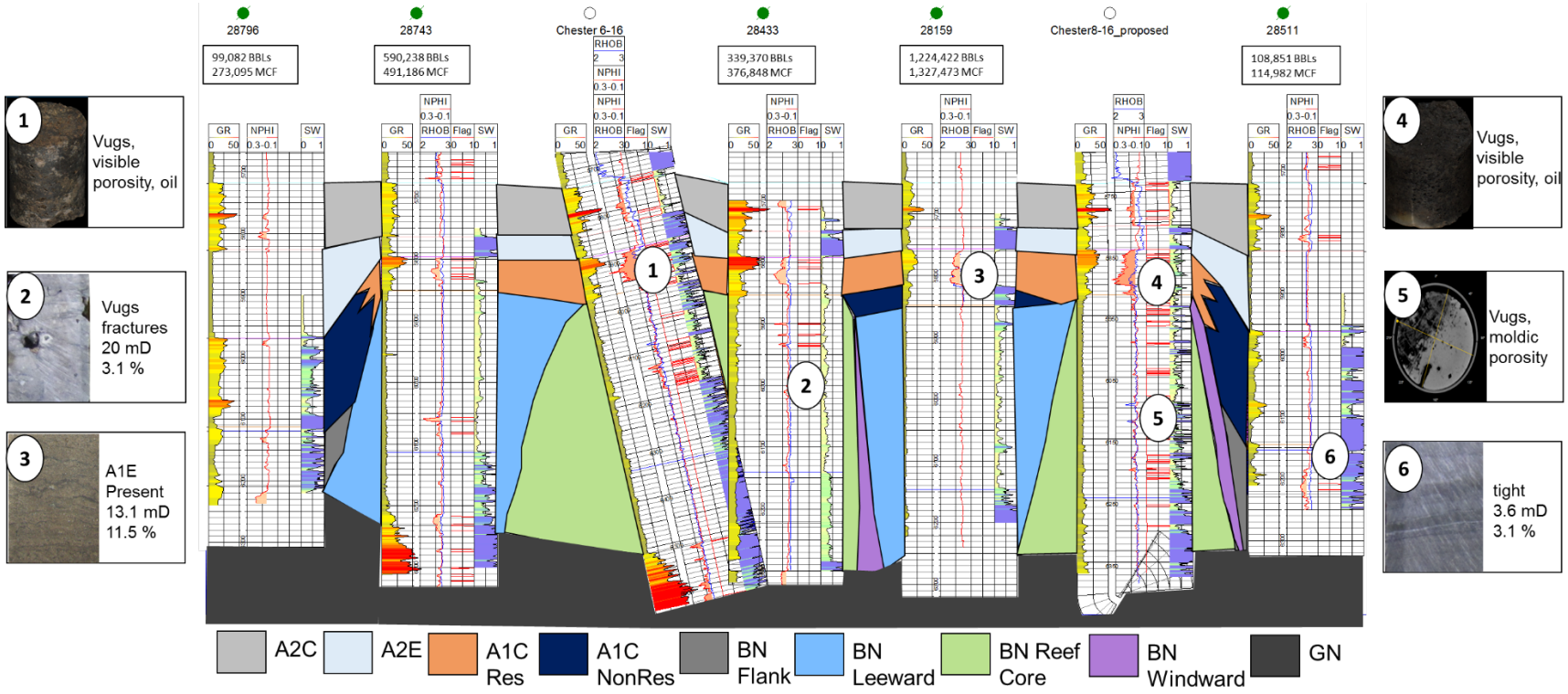


Figure 5-69. Geologic interpretation of the Chester 16 reef field at cross section A-A' showing lithofacies, formations, and highlighted features. A-2 carbonate (A2C), A-2 evaporite (A2E), A-1 carbonate reservoir (A1C Res), A-1 carbonate non-reservoir (A1C NonRes), Brown Niagaran flank (BN Flank), Brown Niagaran leeward (BN Leeward), Brown Niagaran reef core (BN Reef Core), Brown Niagaran windward (BN Windward), and Gray Niagaran (GN).

6.0 Bagley

6.1 Reef History and Production Review

The initial (discovery) data for the Bagley reef field, summarized in Table 6-1, consists of OOIP, oil API gravity, discovery pressure and temperature, and fluid saturations. Initial gas saturations were recorded at zero, as gas was produced as it came out of solution during the production of oil.

Table 6-1. Summary of initial (discovery) conditions of the Bagley reef field.

		Discovery		Saturation		
OOIP (bbls)	API Gravity	Pressure (psi)	Temperature (°F)	Oil	Gas	Water
9,046,704	37.4	3,096	104	76.72%	0%	23.28%

Primary production at the Bagley reef field commenced in 1973 with one well; a second well was added in October 1975. Oil production plateaued with increasing water cut beginning in 1979 until reaching approximately 265,000 cumulative bbls in 1984 (Figure 6-1). A significant increase in oil production occurred in 1985 when three additional wells were brought online, eventually leveling off at about 2,919,000 bbls of cumulative oil production before CO_2 gas injection began in 2015. As of December 31, 2017, 264,879 MT of CO_2 had been injected into the Bagley reef field.

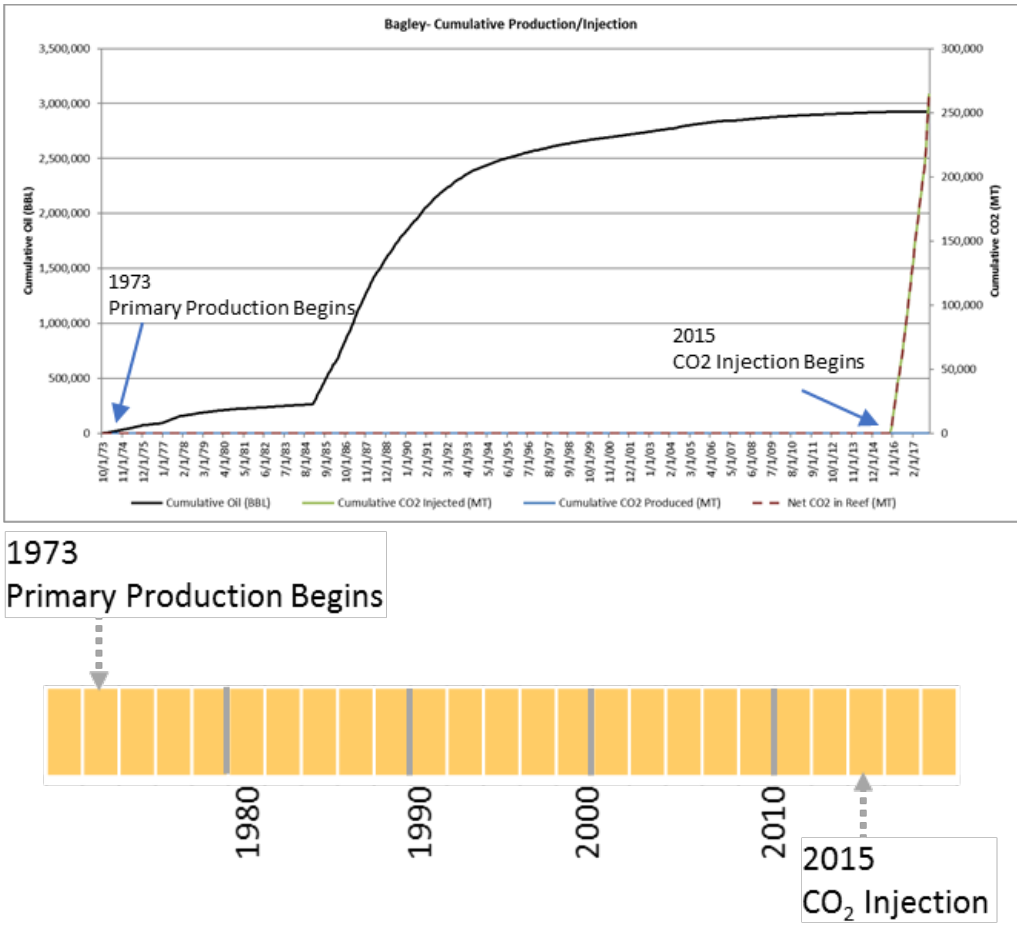


Figure 6-1. Cumulative production in the Bagley reef from 1973 through 2015 showing an increase in production rates after EOR operations began in 2015.

6.2 Wireline Log Analysis

The Bagley reef field was divided into three units—the northern, middle, and southern—to accommodate petrophysical analyses of the reef (Figure 6-2) instead of a well-by-well analysis. The northern unit contains three wells, the middle unit contains six wells, and the southern unit contains five wells. There are 18 wells which penetrate the Bagley reef field in Michigan. Of the 18 wells, 2 did not have digital or raster logs; however, the other 16 wells have gamma ray logs, and 14 have bulk density and neutron porosity logs. The Bagley reef field does not have available sonic logs and only two wells have available advanced logs. Table 6-2 summarizes the log data available for the 16 wells in the Bagley reef field.

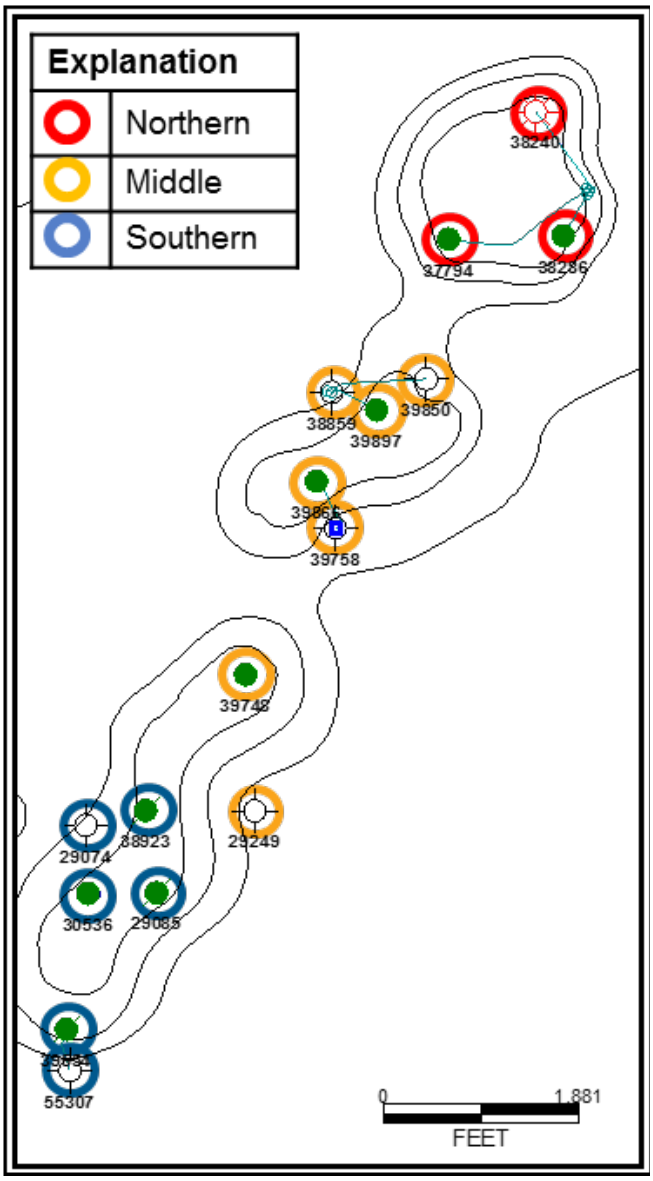


Figure 6-2. Map of Bagley reef field well locations indicating northern (red), middle (yellow), and southern (blue) lobes.

Table 6-2. Summary of available wireline log data for wells penetrating the Bagley reef field.

	Well UWI	2113729074000	2113729085000	2113729249000	2113730536000	2113737794000	2113738240000	2113738286000	2113738859010	2113738859010	2113738859020	2113738923000	2113739554000	2113739554010	2113739748000	2113739758000	2113739758010
CAL	Caliper				■	■	■	■							■	■	■
DT	Sonic																
GR	Gamma Ray	■	■	■	■	■	■	■	■	■	■	■	■	■	■	■	■
LLD	Latero-Log Deep (Resistivity)				■	■	■	■	■		■			■	■	■	■
LLS	Latero-Log Shallow (Resistivity)				■	■	■	■	■		■			■	■	■	■
NPHI	Neutron Porosity	■	■	■	■	■	■	■	■	■	■	■	■	■	■	■	■
RES	Resistivity	■			■				■			■	■		■	■	■
PNC	Pulsed Neutron Capture					2				2							
RHOB	Bulk Density	■	■	■	■	■	■	■		■		■	■	■	■	■	■
BHP	Bottom Hole Pressure Monitoring				■	■		■							■	■	■

Note: Green shading shows log availability and nubmer indcates repeat collection.

6.2.1 Basic Log Interpretation

A-2 Carbonate

The A-2 carbonate, a dolostone carbonate with thin anhydrite intervals, was present in all wells in the northern, middle, and southern units of the Bagley reef field.

Northern Unit

The A-2 carbonate in the northern unit has a gross porosity thickness ranging from 76 to 121 feet with the greatest thickness in the reef flanks. The calculated net thickness ranges from 60 to 104 feet, resulting in NTG ratio ranging between .78 and .87. The porosity ranges from 0% to 20% in the A-2 carbonate northern lobe, with an average porosity range from 3% to 7%.

The neutron porosity–bulk density crossplot (Figure 6-3) shows a dolostone with some limestone intervals. Average apparent crossplot porosities range from 2% to 3%. Data points plotting in porosity fields greater than 5% trend along the dolomite line, with a scatter of data trailing from the limestone to the dolomite line.

Middle Unit

The A-2 carbonate in the middle unit has a gross porosity thickness ranging from 58 to 122 feet with the greatest thickness in the reef flank. The calculated net thickness ranges from 55 to 109 feet, resulting in NTG ratio ranging between 69% and 97%. The porosity range in the A-2 carbonate is between 0% and 21% with an average porosity range from 1% to 5%.

The neutron porosity–bulk density crossplot (Figure 6-4) shows the majority of the data clustering along the dolomite line with some data scattered along the anhydrite and salt intervals. Average apparent crossplot porosities plot from 1% to 2%. A few data points plotting in porosity fields greater than 5% trend along the limestone line and just below the dolomite line. Data points that plot toward the salt interval create an increase in porosity indicators and are not true high porosities.

Southern Unit

The A-2 carbonate in the southern lobe shows a gross thickness ranging from 86 to 147 feet. The calculated net thickness ranges from 68 to 122 feet, resulting in NTG ratio ranging between 79% and

89%. The porosity in the A-2 carbonate southern lobe ranges from less than 1% to 19% with an average porosity range of 3% to 6%.

The neutron porosity–bulk density crossplot (Figure 6-5) shows the majority of the data clustering along the dolomite line with some data scattered along the limestone, anhydrite, and salt intervals. Average apparent crossplot porosities plot from 2% to 3%. There is a large scatter of data points plotting in porosity fields greater than 5% which trend along the dolomite line. A few data points plot greater than 5% at the limestone line and along the sandstone line. These data points could potentially show higher porosities as they trend toward the salt interval. One well in the southern lobe, WSN # 1383, has porosities as high as 19%. This well is located in the reef apron and could be the result of a salt-plugged interval.

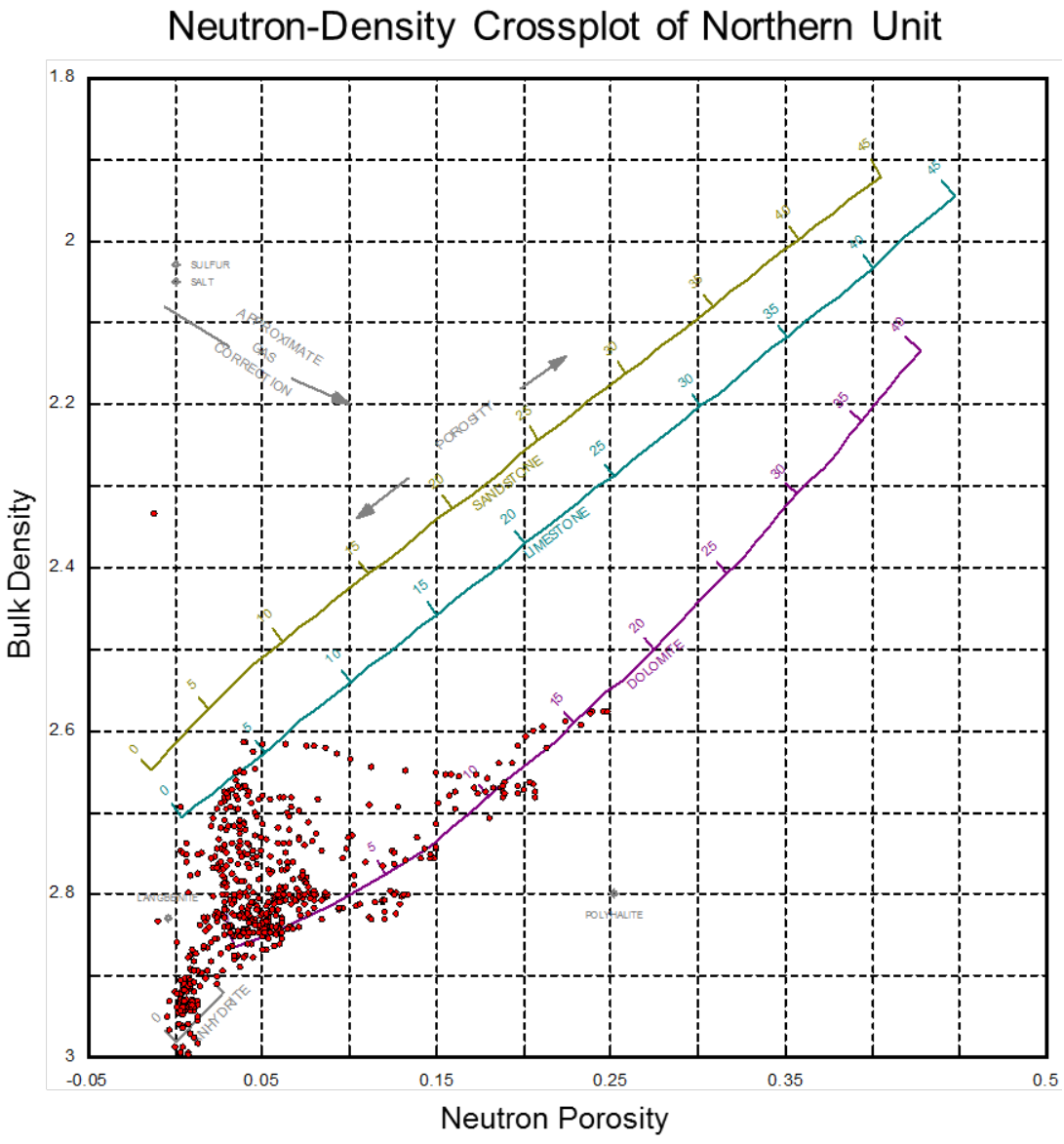


Figure 6-3. Neutron porosity–bulk density crossplot for the A-2 carbonate in the northern unit of the Bagley reef field.

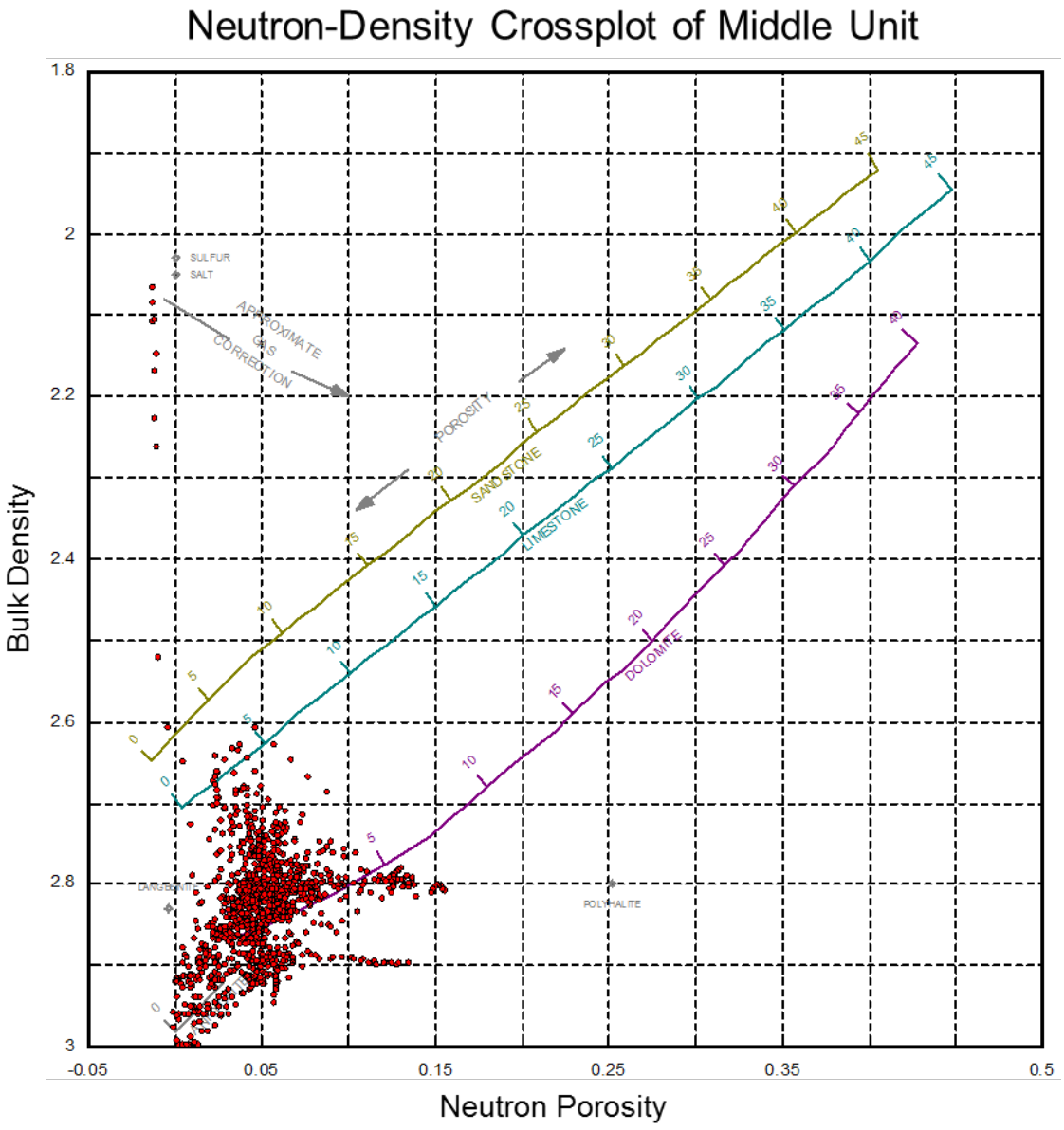


Figure 6-4. Neutron porosity–bulk density crossplot for the A-2 carbonate in the middle unit of the Bagley reef field.

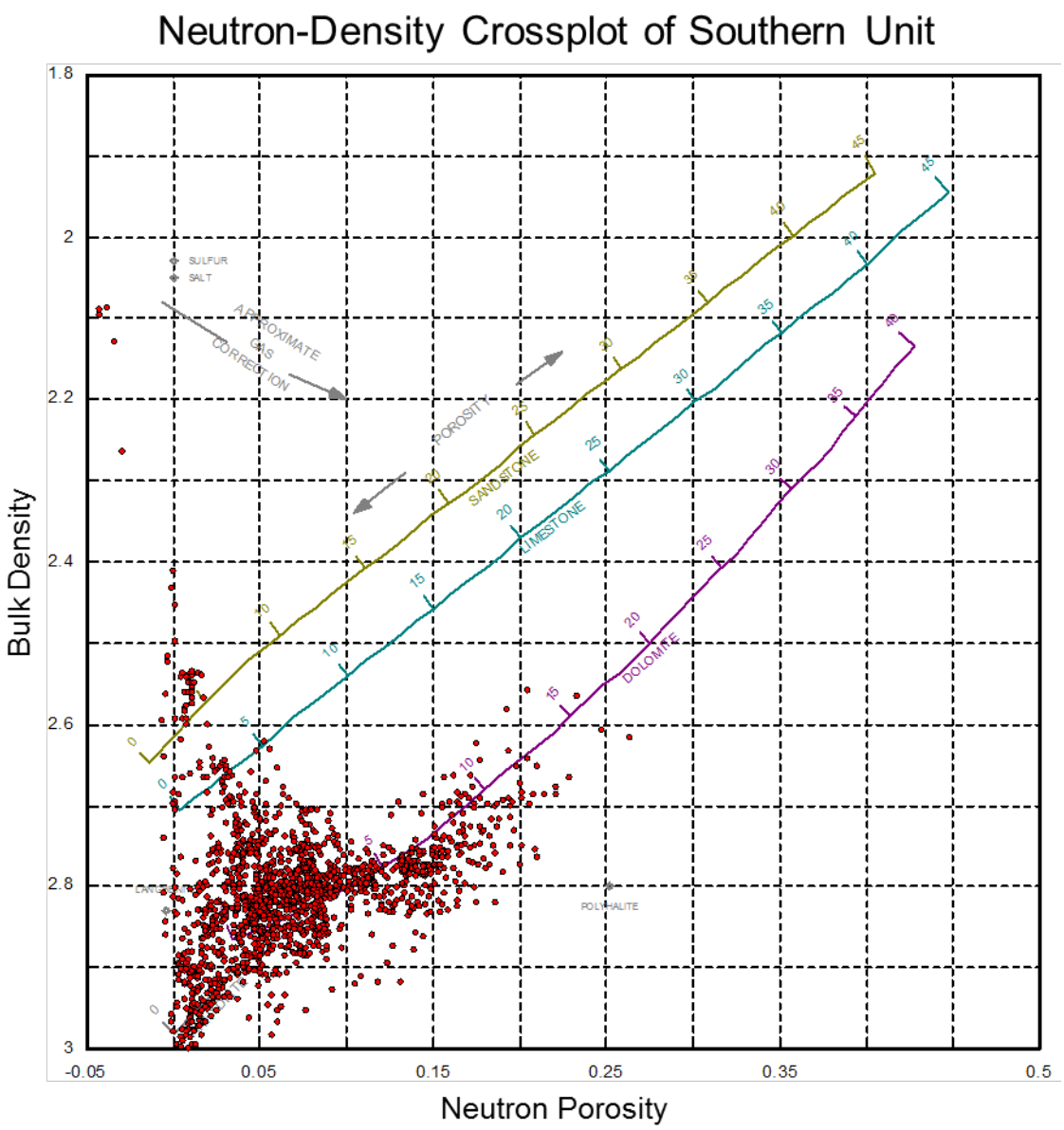


Figure 6-5. Neutron porosity–bulk density crossplot for the A-2 carbonate in the southern unit of the Bagley reef field.

Water Saturation

Water saturation in the A-2 carbonate ranged from 0 to 100%. The presence of interbedded evaporites caused erroneous high values, resulting in an average water saturation of 46%. Removing the influence of evaporites, the water saturation in the A-2 carbonate averages 25%. Figure 6-6 shows the histogram of the calculated water saturation in the A-2 carbonate.

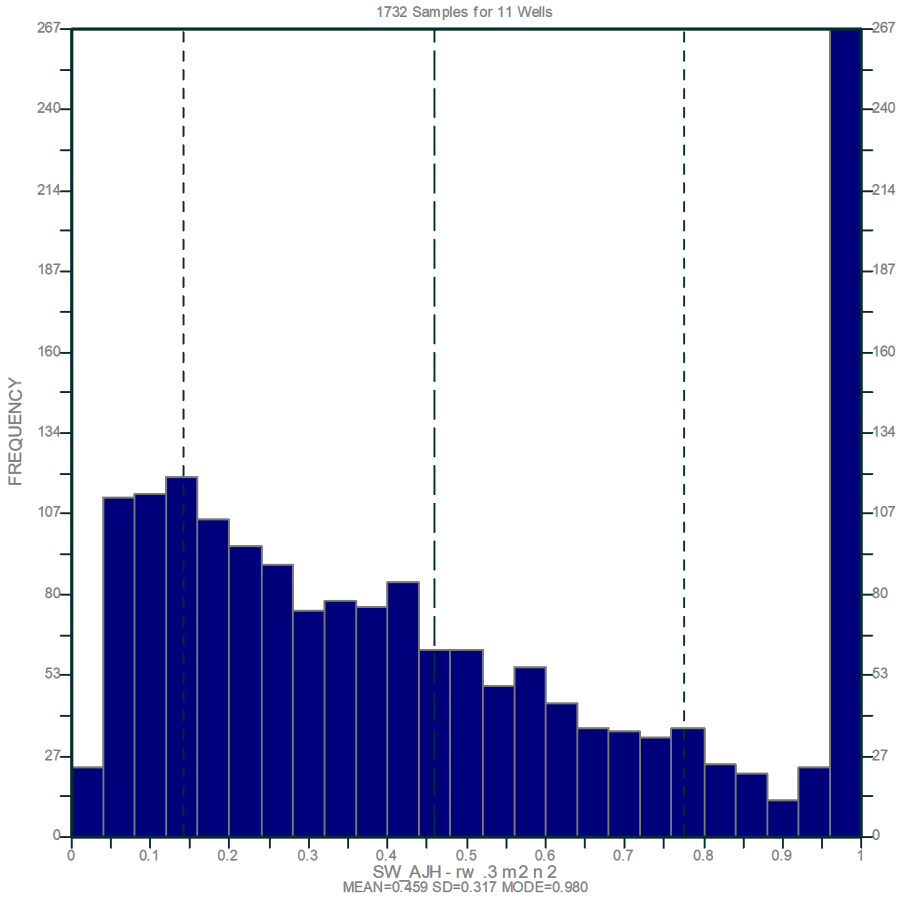


Figure 6-6. Water saturation histogram over the A-2 carbonate for all wells in the Bagley reef field.

A-2 Evaporite

The A-2 evaporite, an anhydrite/salt interval with rare occurrences of thin carbonate intervals, was present in 12 of the 16 wells in the Bagley reef field. The A-2 evaporite was identified in all wells in the northern lobe; however, it was not identified in one well in the middle lobe and one well in the southern lobe. This evaporite interval shows high porosities in the northern, middle, and southern lobes which can be attributed to anhydrite and salt (halite) layers in the same interval. Anhydrite and halite occurrences are problematic as the bulk density goes from an anhydrite interval (approximately 2.96 g/cm^3) to a halite interval (approximately 2.04 g/cm^3). Data points trend through the limestone and sandstone zones toward the halite zone. Additionally, neutron porosity is essentially a hydrogen detector; as such, trapped water in evaporite layers can increase the neutron porosity in these layers.

Northern Unit

The A-2 evaporite in the northern unit has a gross porosity thickness ranging from 17 to 46 feet with the greatest thickness in the flanks The calculated net thickness ranges from 5 to 17 feet, resulting in NTG ratio ranging from 9% to 100%. The porosity range for the A-2 evaporite is from 0% to 36% with an average porosity range from 1% to 26%.

The neutron porosity–bulk density crossplot (Figure 6-7) shows that the majority of the data clusters in the anhydrite region and then scatters as it trends toward the salt zone.

Middle Unit

The A-2 evaporite in the middle unit has a gross porosity thickness ranging from 20 to 75 feet with the greatest thickness in the reef flank. The calculated net thickness ranges from 7 to 73 feet, resulting in NTG ratio ranging from 36% to 100%. The porosity range is from 0% to 22% with an average porosity in the A-2 evaporite middle lobe that ranges from 2% to 20%.

The neutron porosity–bulk density crossplot (Figure 6-8) shows that the majority of the data is clustered in the anhydrite and salt zones with considerable scattering between the zones.

Southern Unit

The A-2 evaporite in the southern unit has a gross thickness ranging from 35 to 156 feet. The calculated net thickness ranges from 16 to 111 feet resulting in a net-to-gross range between 45% and 94%. The porosity in the A-2 evaporite southern lobe ranges from less than 1% to 30% with an average porosity range from 1% to 16%.

The neutron porosity–bulk density crossplot (Figure 6-9) shows that the majority of the data is clustered in the anhydrite and salt zones with considerable scattering between the zones. A few data points show a slight linear trend between the limestone and dolomite zones, which could suggest that there is a carbonate layer in this formation.

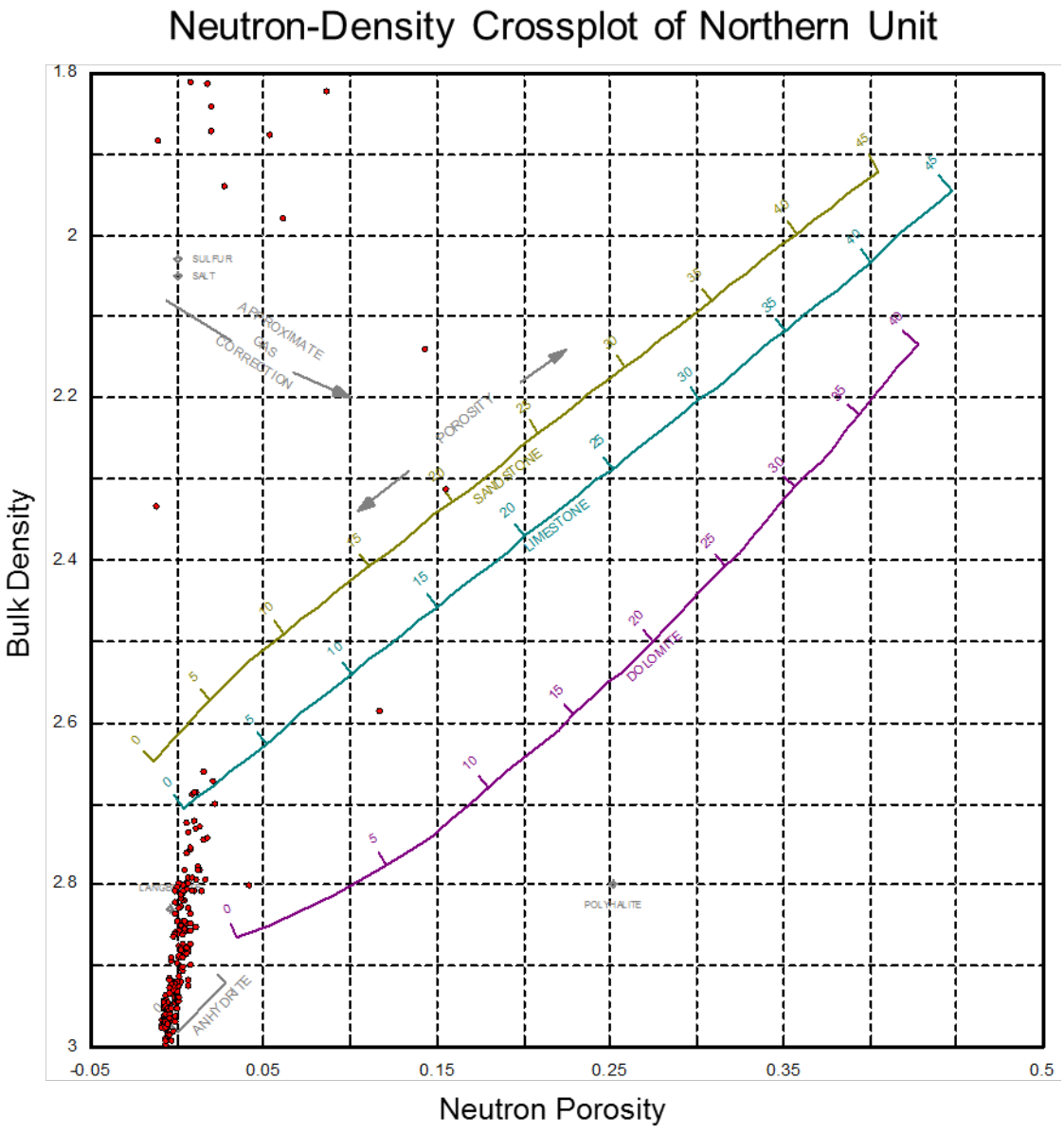


Figure 6-7. Neutron porosity–bulk density crossplot for the A-2 evaporite in the northern unit of the Bagley reef field.

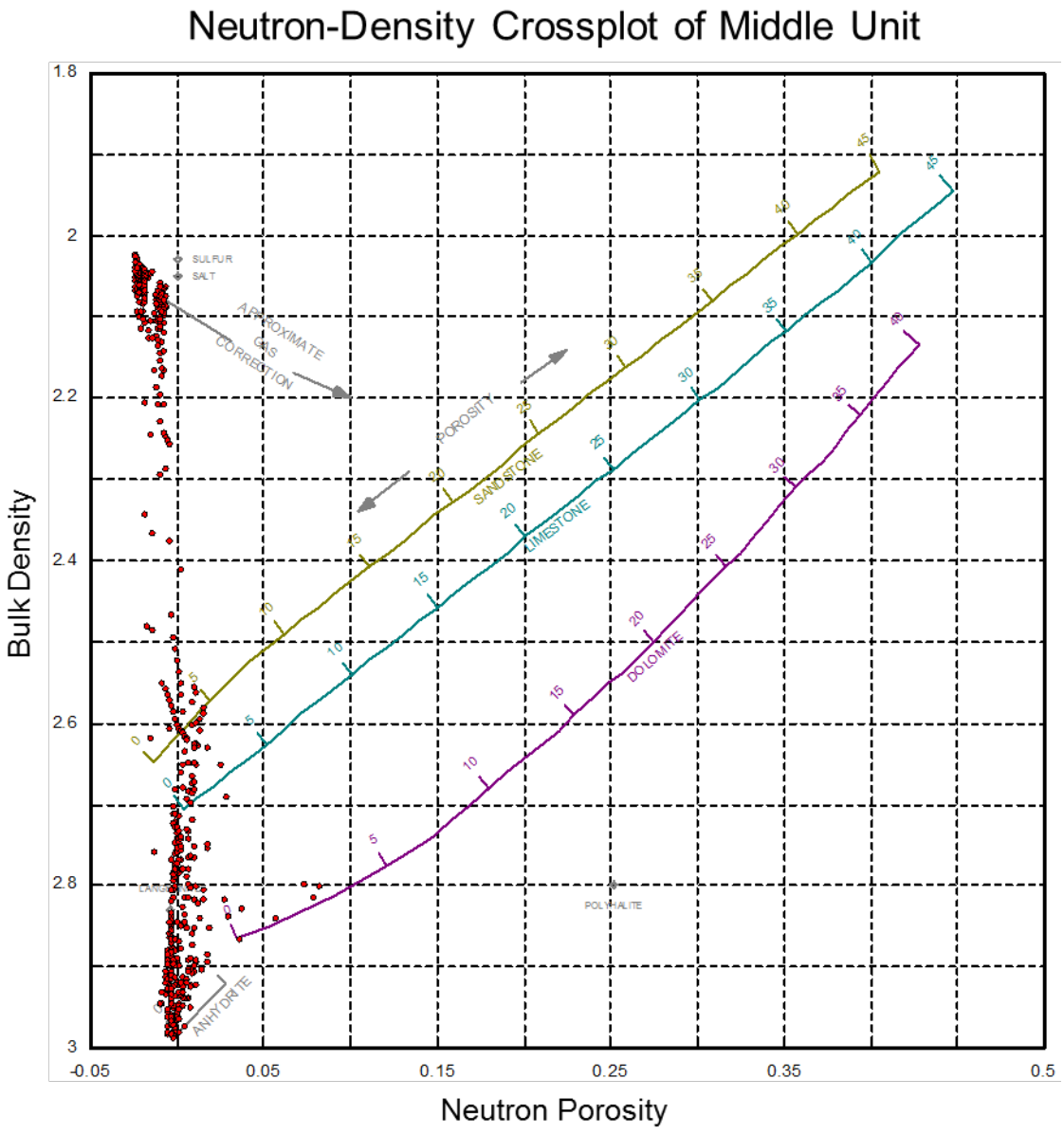


Figure 6-8. Neutron porosity–bulk density crossplot for the A-2 evaporite in the middle unit of the Bagley reef field.

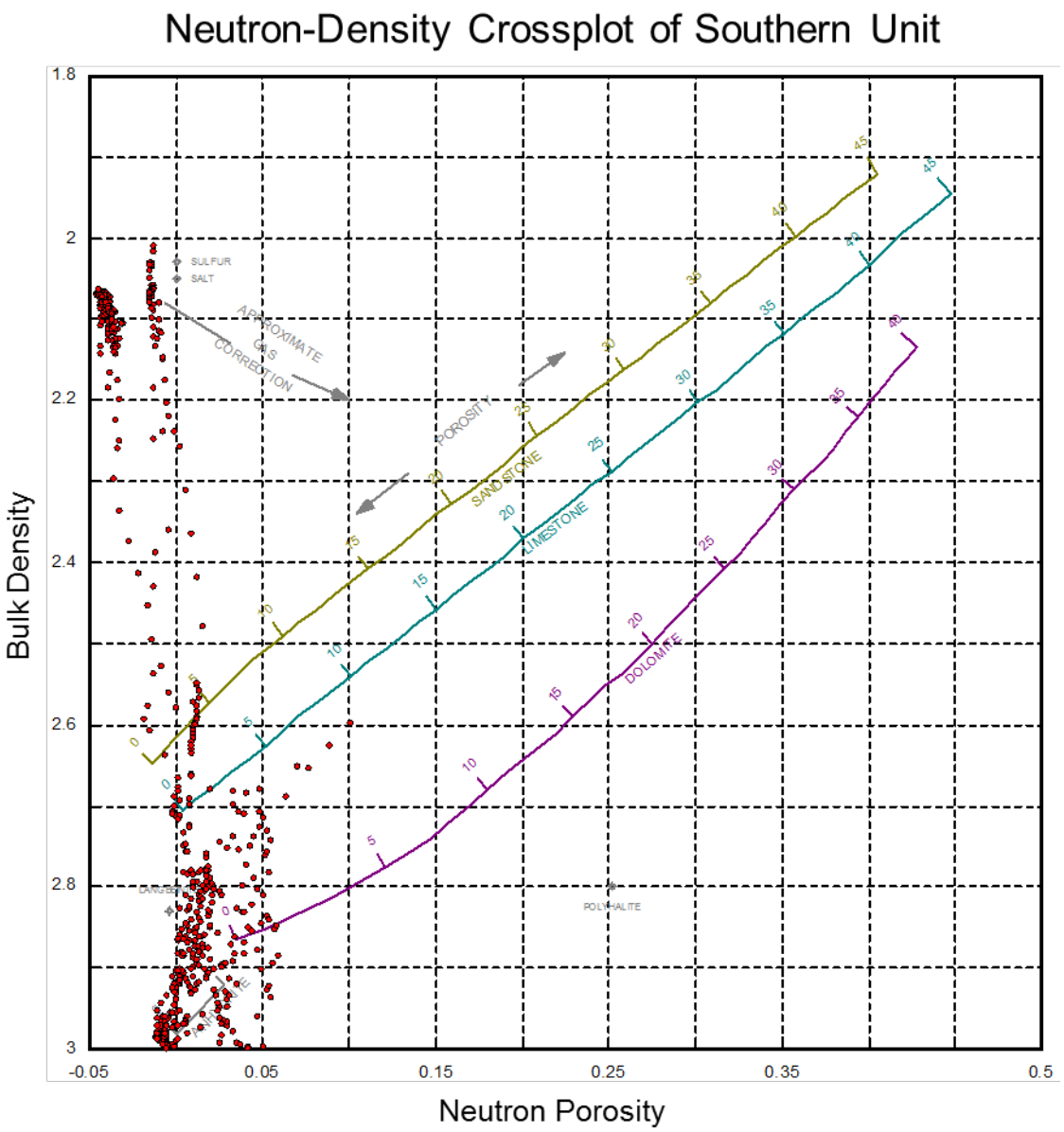


Figure 6-9. Neutron porosity–bulk density crossplot for the A-2 evaporite in the southern I unit of the Bagley reef field.

Water Saturation

The A-2 evaporite had a bimodal water saturation distribution of either less than 10% or 100% due to the interbedded carbonates and evaporites. Figure 6-10 is the resulting histogram for the water saturation across the A-2 evaporite.

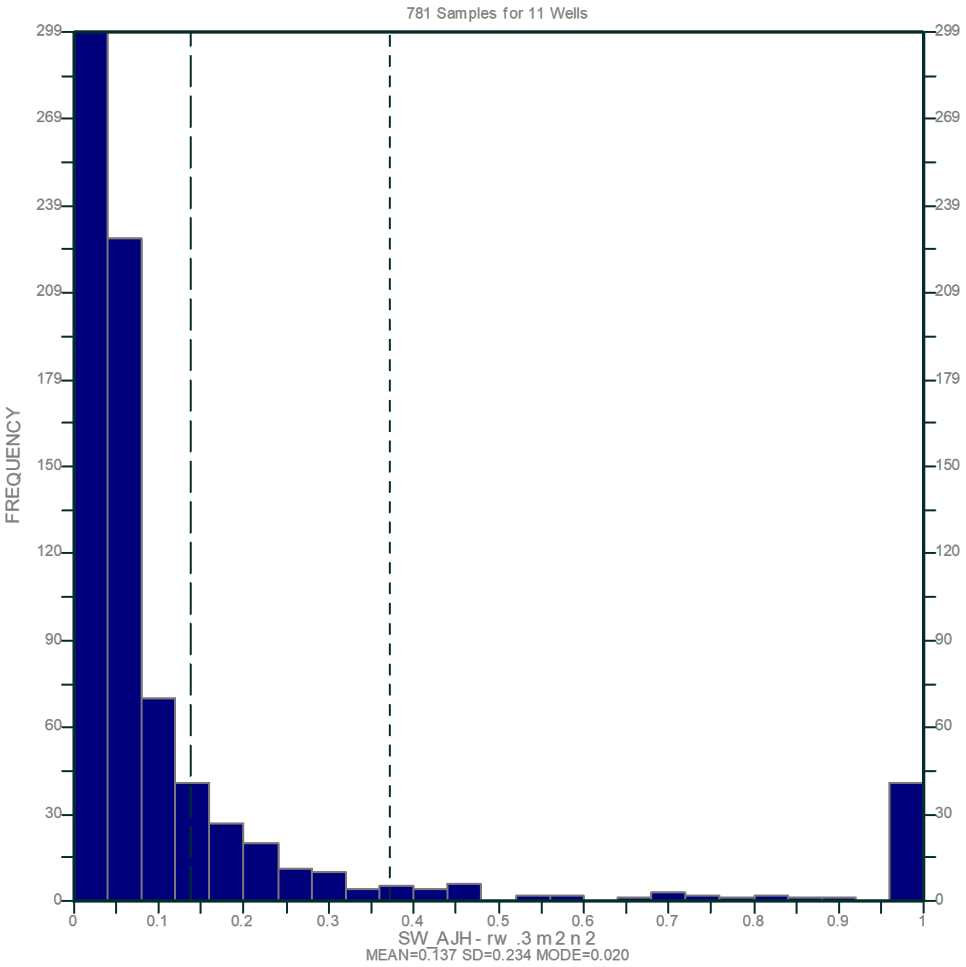


Figure 6-10. Water saturation histogram for the A-2 evaporite showing a high frequency of data with very low and very high saturations due to interbedded carbonates and evaporites.

A-1 Carbonate

The A-1 carbonate, primarily a dolostone carbonate with some limestone and thin anhydrite intervals, was present in all wells except one well in the southern lobe of the Bagley reef field.

Northern Unit

The A-1 carbonate in the northern unit has a gross porosity thickness ranging from 58 to 96 feet with the greatest thickness in the reef flanks. The calculated net thickness ranges from 46 to 96 feet, resulting in NTG ratio ranging from 80% to 99%. The porosity ranges from 0% to 11% with an average porosity range from 4% to 7% in the A-1 carbonate northern lobe.

The neutron porosity–bulk density crossplot (Figure 6-11) shows primarily a dolostone with some data scattered in the limestone zone. A small cluster of anhydrite data points suggests the presence of anhydrite layers in the A-1 carbonate interval. Average apparent crossplot porosities plot from 3% to 6%. Data points plotting in porosity fields greater than 5% trend along the dolomite line.

Middle Unit

The A-1 carbonate in the middle unit has a gross porosity thickness ranging from 54 to 217 feet with the greatest thickness in the reef flank. The calculated net thickness ranges from 52 to 78 feet, resulting in NTG ratio ranging from 59% to 96%. The porosity ranges from 0% to 15% in the A-1 carbonate middle lobe and has an average porosity range of 4% to 6%.

The neutron porosity–bulk density crossplot (Figure 6-12) shows the majority of the data clustering along the dolomite line, with some data plotting around the limestone zone. Additionally, there is a small data cluster in the anhydrite zone for the A-1 carbonate. Average apparent crossplot porosities plot from 3% to 4%. Data points plotting in porosity fields greater than 5% are primarily along the dolomite line and range as high as 9% porosity. One data point plotted near the salt zone and gave a porosity of 19%. However, this data point is not representative of the highest porosity in the carbonate interval.

Southern Unit

The A-1 carbonate in the southern unit shows a gross thickness ranging from 28 to 99 feet.
The calculated net thickness ranges from 28 to 93 feet, resulting in NTG ratio ranging between 94% and 100%. The porosity in the A-1 carbonate southern lobe ranges from 0% to 12% with an average porosity range from 3% to 8%.

The neutron porosity–bulk density crossplot (Figure 6-13) shows the majority of the data clustering along the dolomite line with some data scattered along the limestone, sandstone, and anhydrite intervals. Average apparent crossplot porosities plot from 3% to 4%. Data points plotting in porosity fields greater than 5% are primarily along the dolomite line and range as high as 15% porosity.

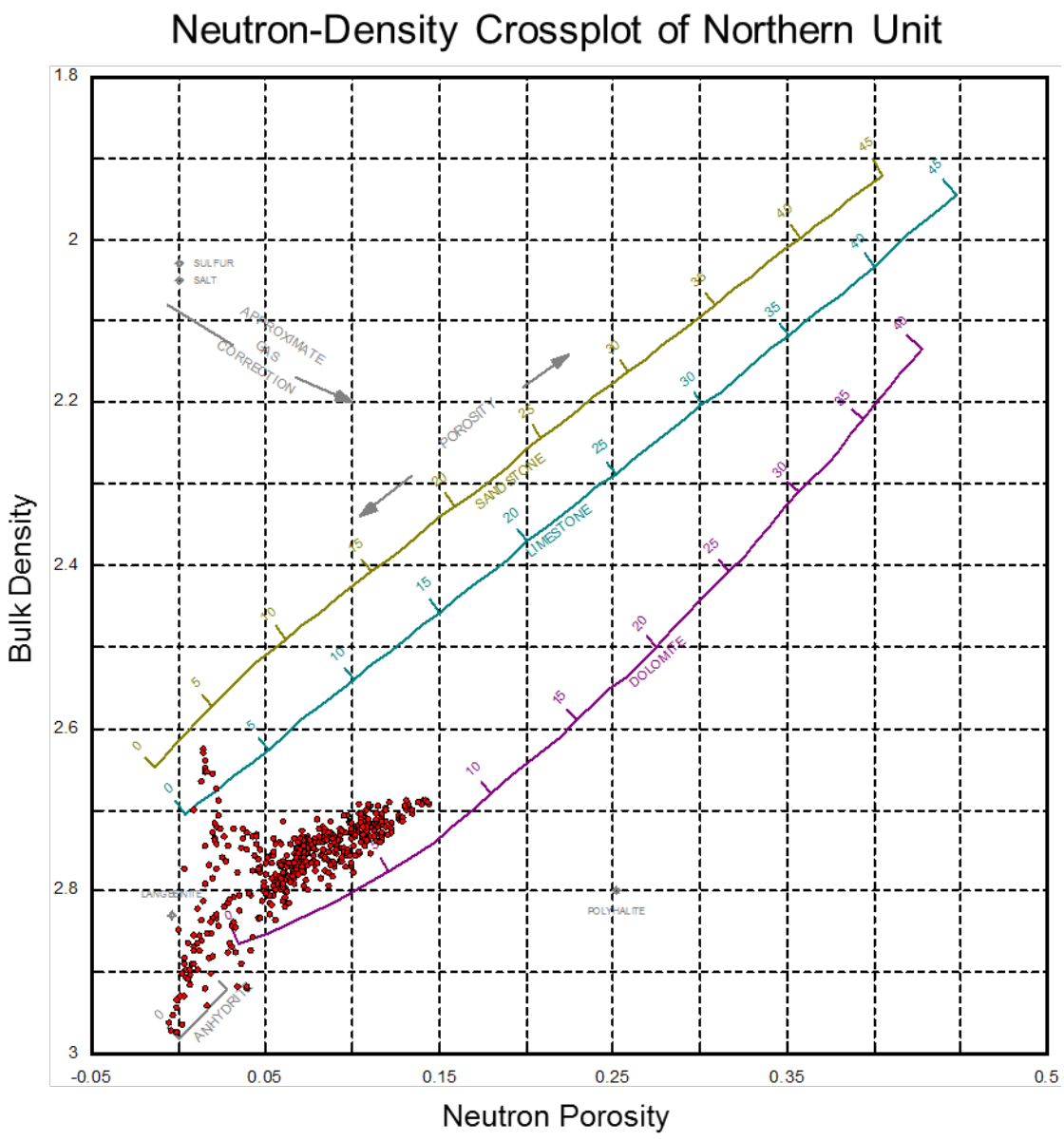


Figure 6-11. Neutron porosity–bulk density crossplot for the A-1 carbonate in the northern unit of the Bagley reef field.

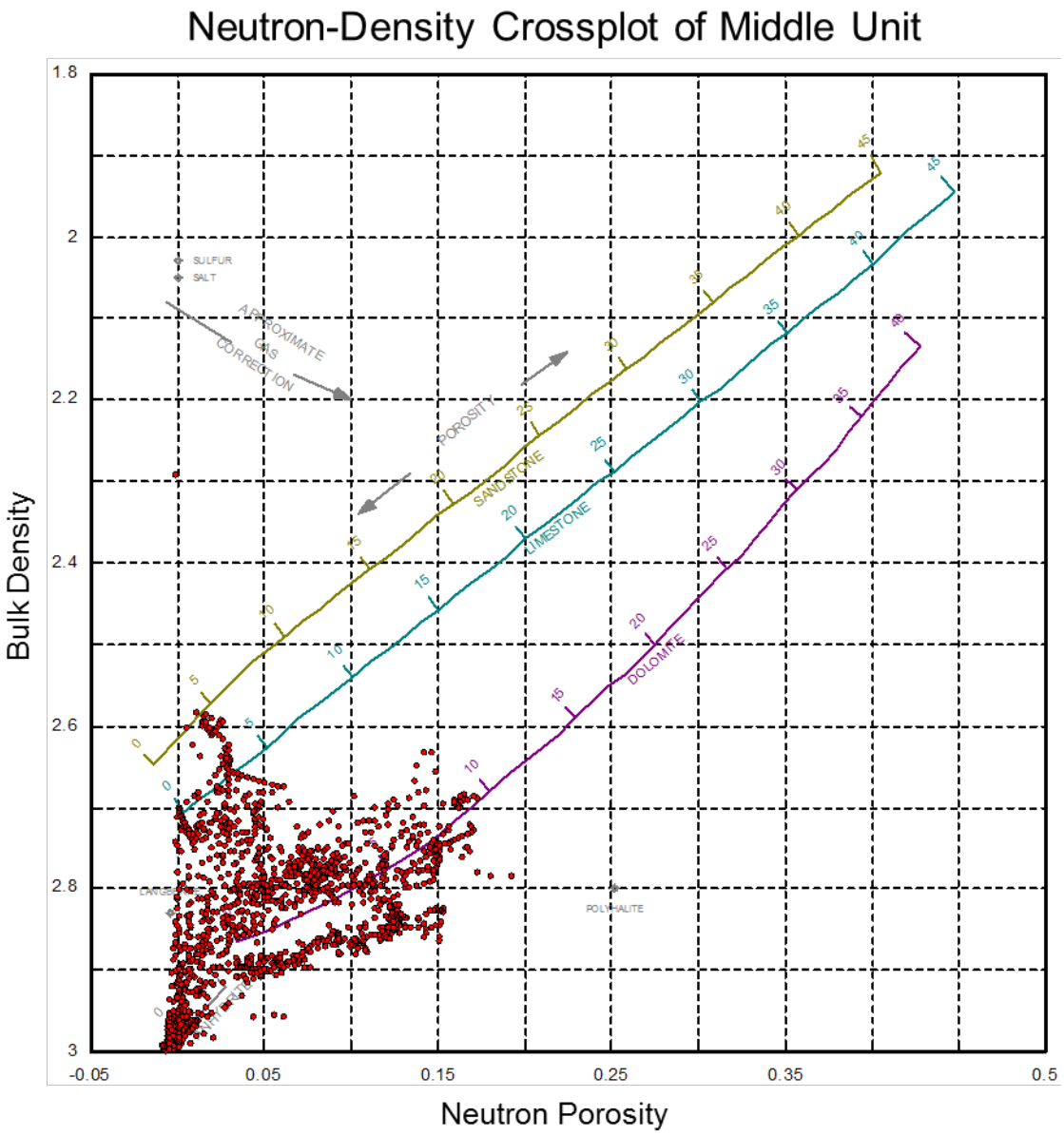


Figure 6-12. Neutron porosity–bulk density crossplot for the A-1 carbonate in the middle unit of the Bagley reef field.

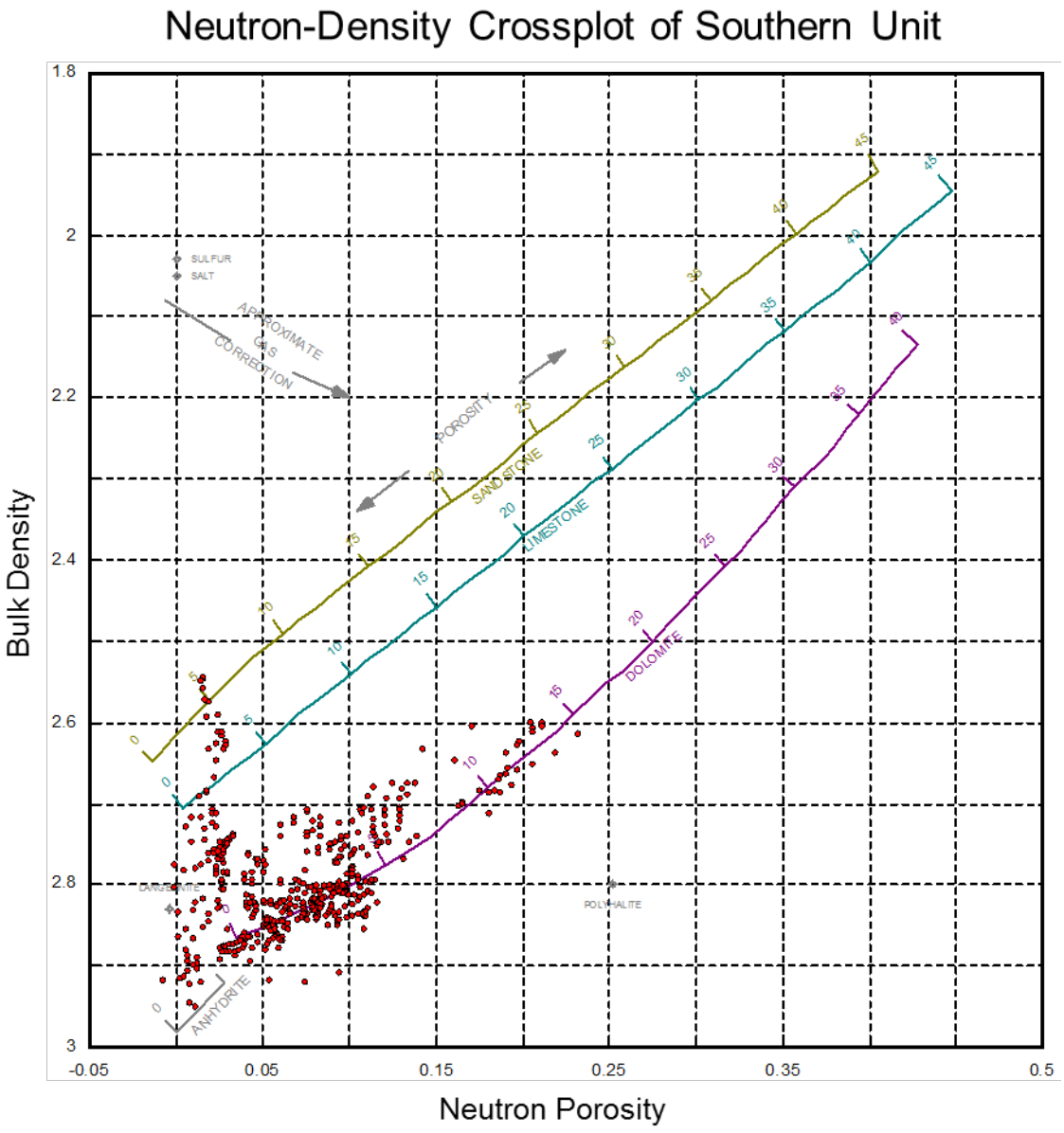


Figure 6-13. Neutron porosity–bulk density crossplot for the A-1 carbonate in the southern unit of the Bagley reef field.

Water Saturation

The A-1 carbonate has low water saturation of 26%, with the highest frequencies occurring less than 10%. There is not a strong influence of evaporites through this interval. Figure 6-14 shows the histogram of water saturation in the A-1 carbonate.

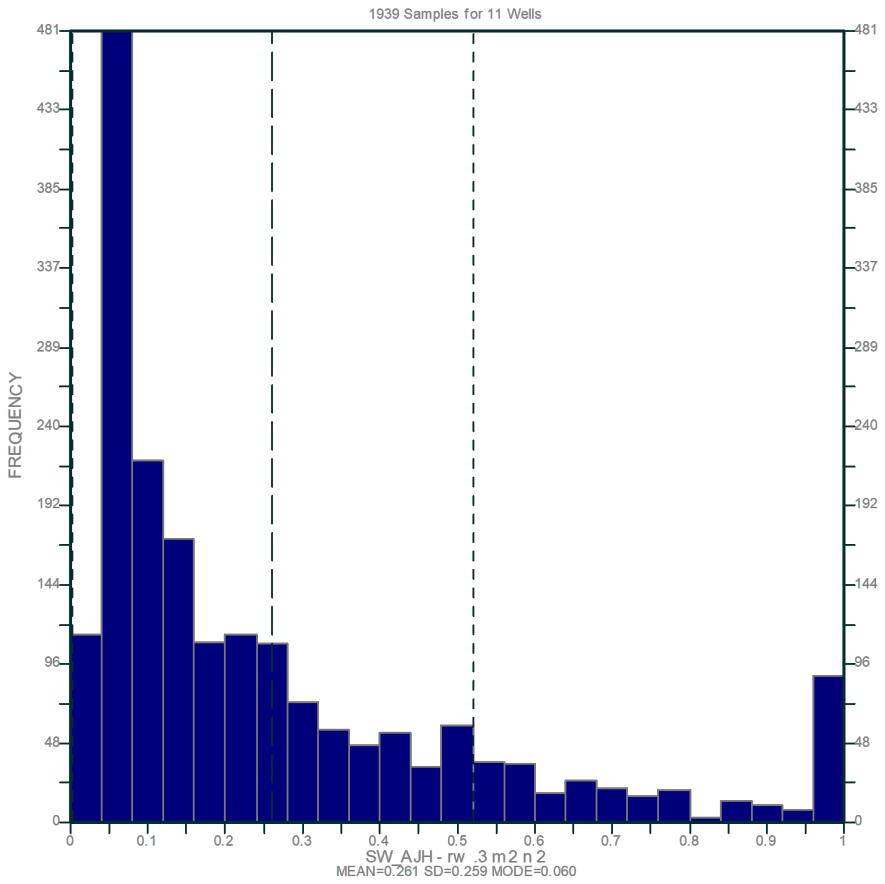


Figure 6-14. Water saturation histogram for the A-1 carbonate showing relatively low saturations.

A-1 Evaporite

The A-1 evaporite, an anhydrite/salt interval with rare occurrences of thin carbonate intervals, was present in four wells, three in the middle lobe and one in the southern lobe of the Bagley reef field. The A-1 evaporite was not identified in any of the wells in the northern lobe. The southern lobe A-1 evaporite well was determined, from crossplot analysis, to be an entire anhydrite layer. Due to negative porosities created by anhydrites, petrophysics for the southern lobe were not conducted, so only the crossplots are discussed for this section. Salts in this evaporite interval show moderately high porosities in the middle lobe, which can be attributed to anhydrite and salt (halite) layers in the same interval. Anhydrite and halite occurrences are problematic as the bulk density goes from an anhydrite interval (approximately 2.96 g/cm^3) to a halite interval (approximately 2.04 g/cm^3). Data points trend through the limestone and sandstone zones toward the halite zone. Additionally, neutron porosity is essentially a hydrogen detector; as such, trapped water in evaporite layers can increase the neutron porosity in these layers.

Northern Unit

The A-1 evaporite was not identified in the northern unit. Crossplots and petrophysics are not available for this lobe.

Middle Lobe

The A-1 evaporite in the middle unit has a gross porosity thickness ranging from 6 to 43 feet with the greatest thickness in the reef flank. The calculated net thickness ranges from 4 to 43 feet, resulting in a NTG ratio ranging between 58% and 100%. The porosity range in the A-1 evaporite middle lobe ranges from 0% to 19% with an average porosity range of 1% to 15%.

The neutron porosity–bulk density crossplot (Figure 6-15) shows a data cluster in the anhydrite, salt, and dolomite zones. The dolomite cluster shows that the majority of the porosity is above 5% and may represent a small porosity zone.

Southern Unit

The neutron porosity–bulk density crossplot (Figure 6-16) shows that all of the data plots in the anhydrite zone. This creates negative porosities, so petrophysics for the southern lobe were not conducted.

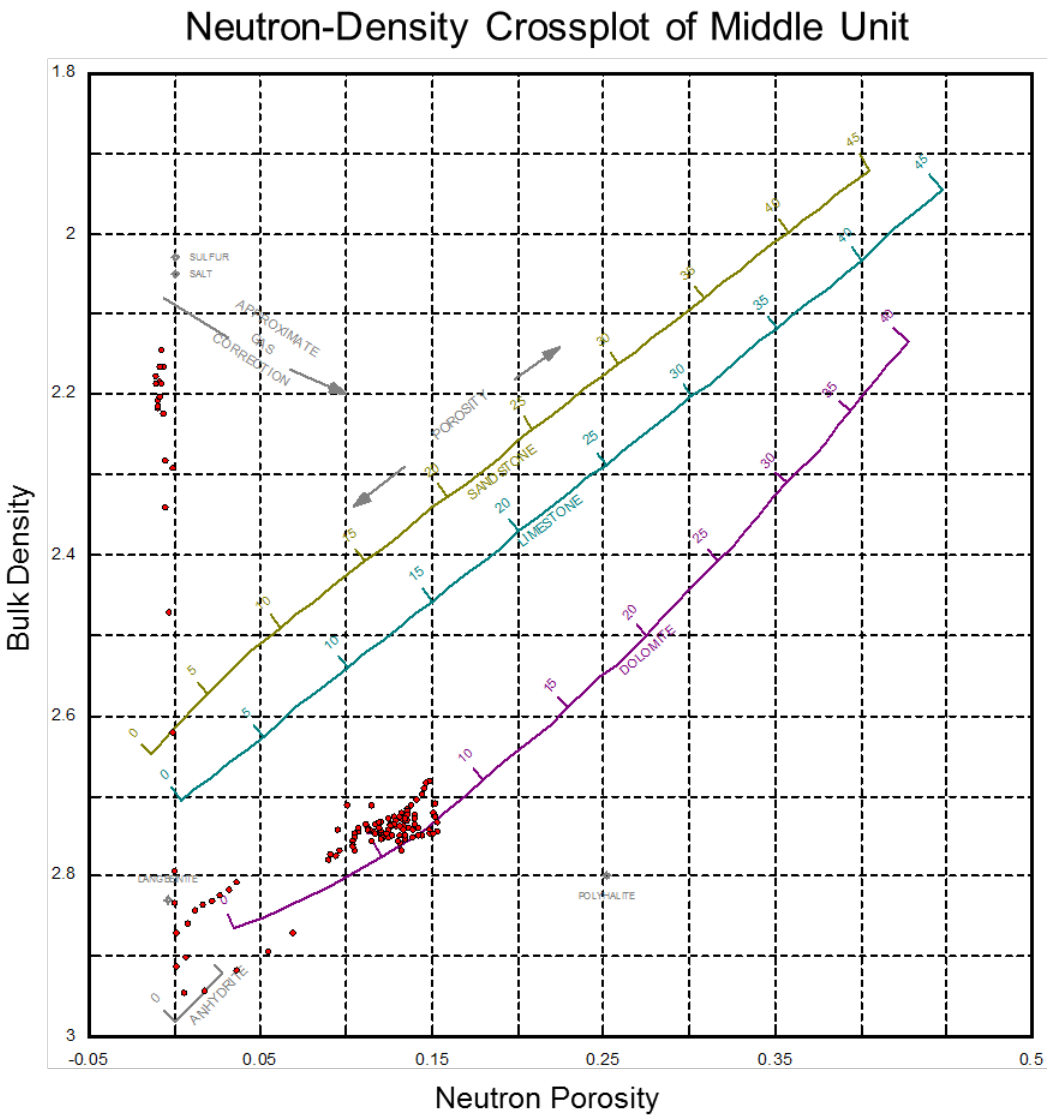


Figure 6-15. Neutron porosity–bulk density crossplot for the A-1 evaporite in the middle unit of the Bagley reef field.

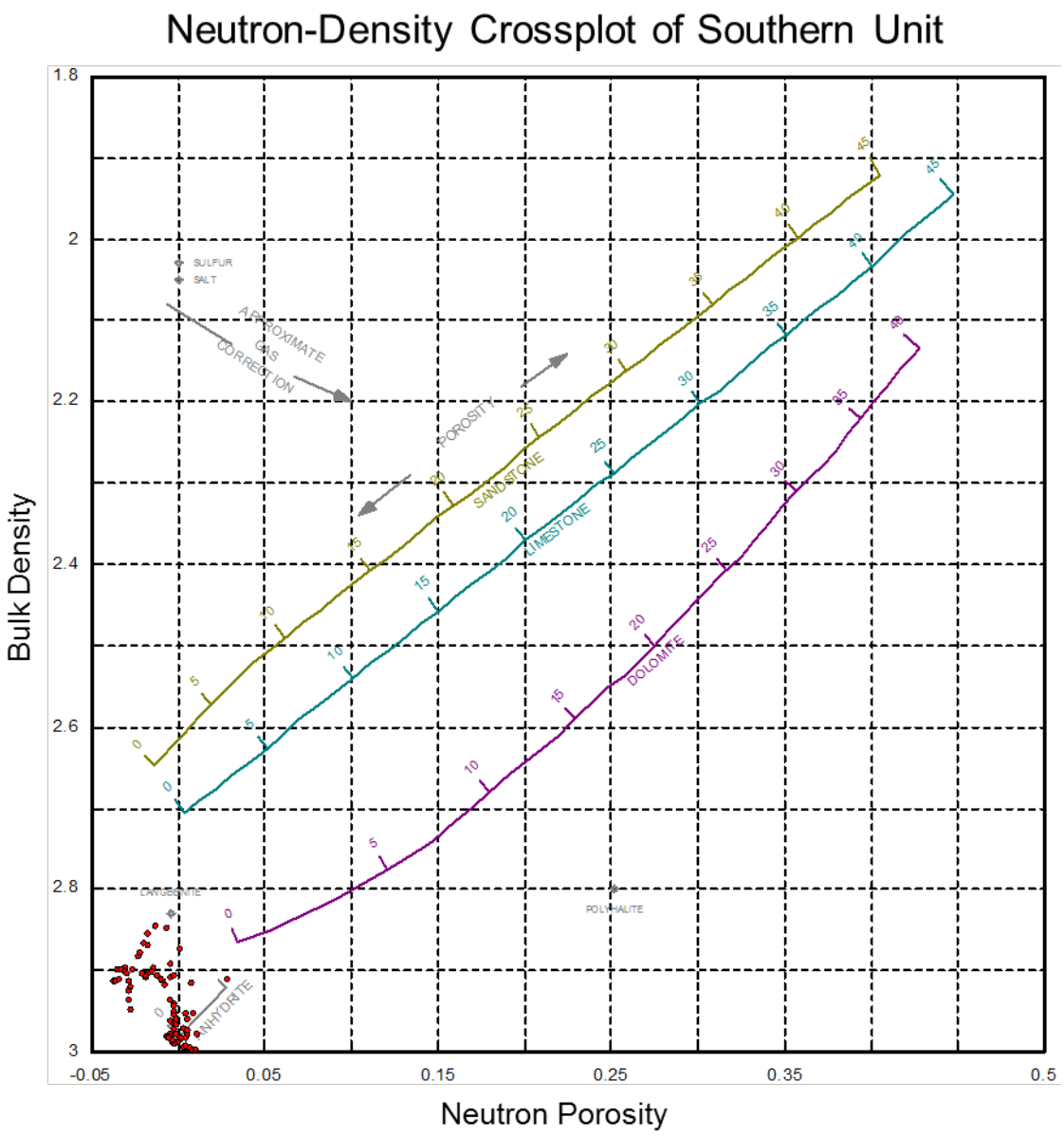


Figure 6-16. Neutron porosity–bulk density crossplot for the A-1 evaporite in the southern unit of the Bagley reef.

Water Saturation

The water saturation for the A-1 evaporite had a bimodal behavior with high frequencies of 10% and 60%, which is reflective of interbedded carbonate and evaporites. Figure 6-17 shows the histogram of the water saturation.

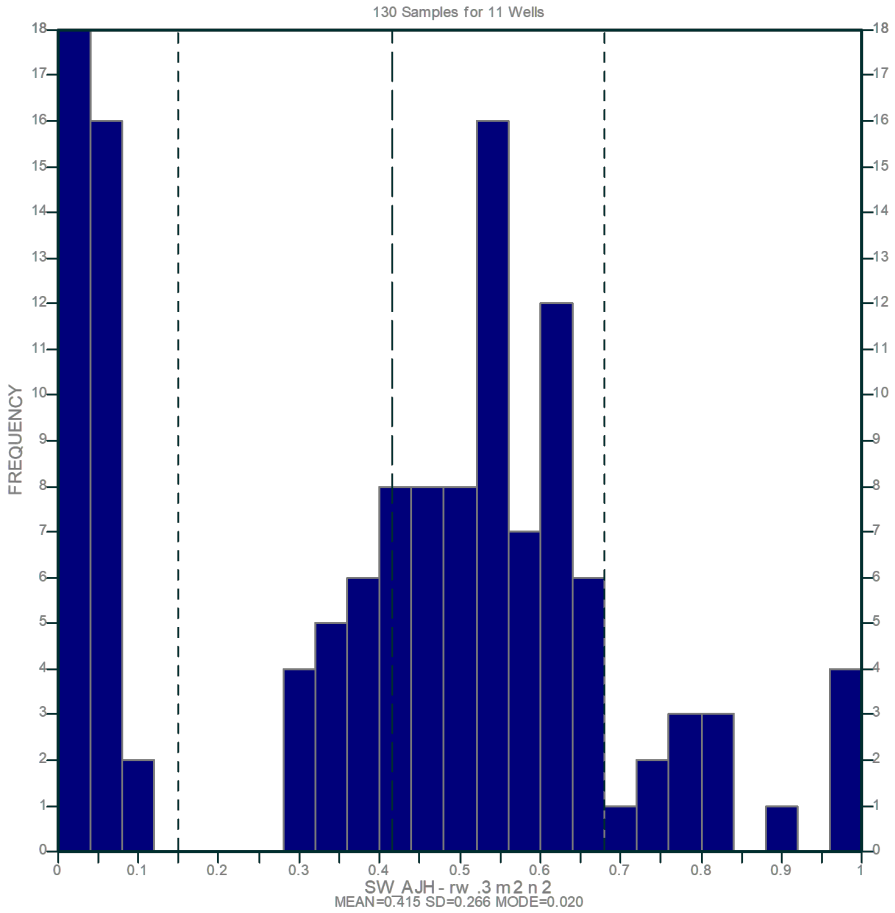


Figure 6-17. Water saturation histogram of the A-1 evaporite showing a bimodal response to interbedded carbonate and evaporite.

Brown Niagaran

The Brown Niagaran, a dolostone carbonate, was present in all wells in the northern, middle, and southern lobes of the Bagley reef field.

Northern Unit

The Brown Niagaran in the northern unit has a gross porosity thickness ranging from 179 to 268 feet. The calculated net thickness ranges from 122 to 268 feet, resulting in NTG ratio ranging from 68% to 100%. The porosity ranges from 2% to 50% with an average porosity range of 7% to 9% in the Brown Niagaran northern unit.

The neutron porosity–bulk density crossplot (Figure 6-18) shows the data plotting as a dolostone. A few data points are scattered and plot along the limestone and sandstone zones. These points show high porosity and could potentially represent washout or logging errors. Average apparent crossplot porosities plot from 4% to 5%. Data points plotting in porosity fields greater than 5% trend along the dolomite line. Data points that plot above 15% along the limestone and sandstone are not considered to be true porosity indicators.

Middle Unit

The Brown Niagaran in the middle unit has a gross porosity thickness ranging from 28 to 251 feet. The calculated net thickness ranges from 3 to 251 feet, resulting in NTG ratio ranging from 8% to 100%. The main porosity in the Brown Niagaran ranges from 0% to 16% with some data points as high as 50%. The average porosity in the Brown Niagaran middle lobe ranges from 5% to 10%.

The neutron porosity–bulk density crossplot (Figure 6-19) shows the majority of the data clustering in the dolomite zone with some data clustering in the anhydrite zone. Some scattered data points plot between the dolomite and the sandstone zones with a few plotting above the sandstone. These data points show high porosities and could potentially be evidence of washout zones in the middle lobe wells. Average apparent crossplot porosities plot from 4% to 5%. Data points plotting in porosity fields greater than 5% trend along the dolomite zone. Data points that plot above 15% along the limestone and sandstone are not considered to be true porosity indicators.

Southern Unit

The Brown Niagaran in the southern unit shows a gross thickness ranging from 24 to 322 feet. The calculated net thickness ranges from 24 to 275 feet, resulting in NTG ratio ranging from 80% to 100%. The porosity in the Brown Niagaran southern unit ranges from 0% to 20% with an average porosity range of 7% to 10%.

The neutron porosity–bulk density crossplot (Figure 6-20) shows the majority of the data clustering the dolomite zone with some data clustering in the anhydrite, sandstone, and limestone zones. Average apparent crossplot porosities plot range from 4% to 5%. Data points plotting in porosity fields greater than 5% cluster primarily in the dolomite zone; however, there are porosities greater than 5% along the limestone zone and a few in the sandstone region.

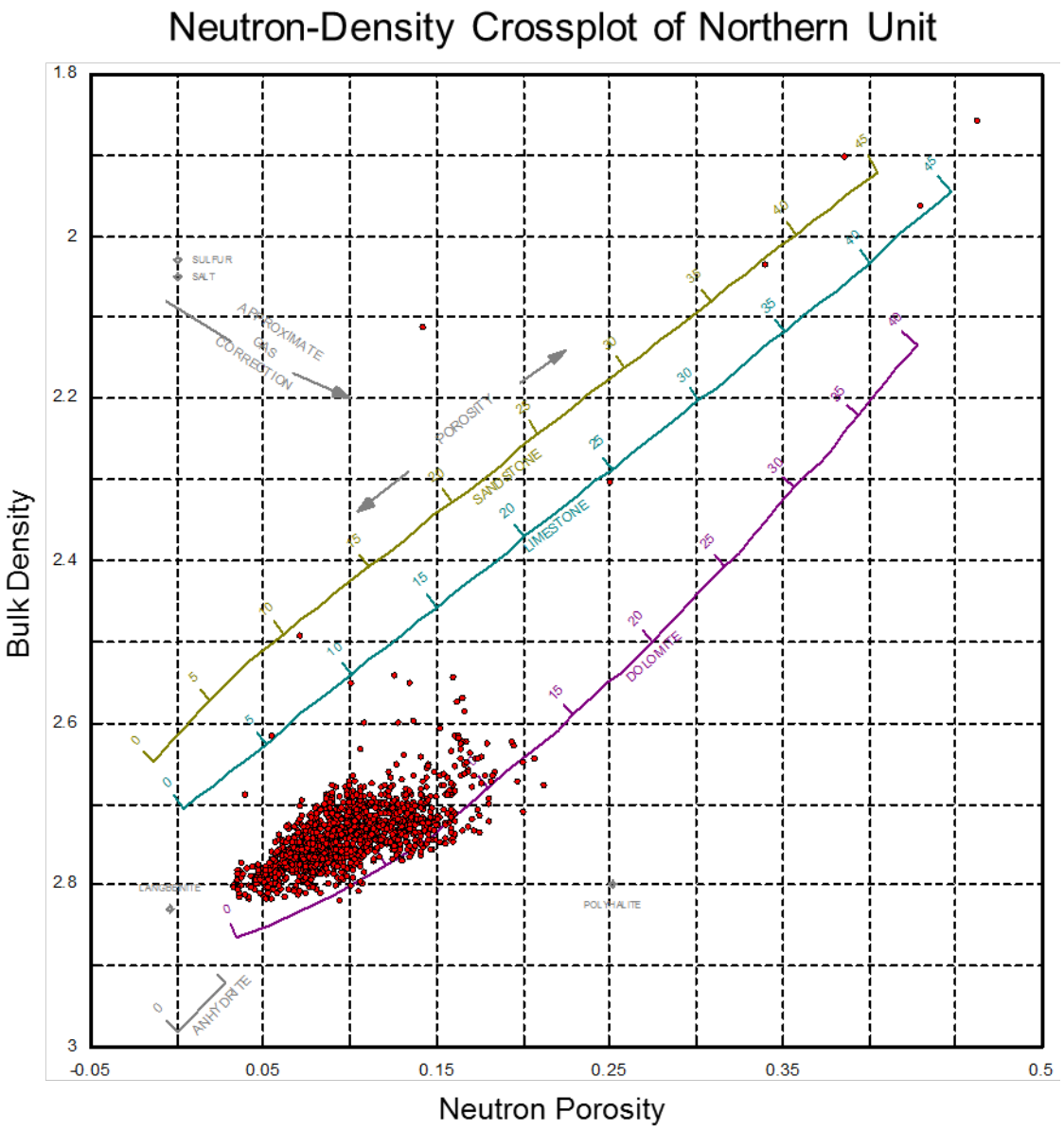


Figure 6-18. Neutron porosity–bulk density crossplot for the Brown Niagaran in the northern unit of the Bagley reef field.

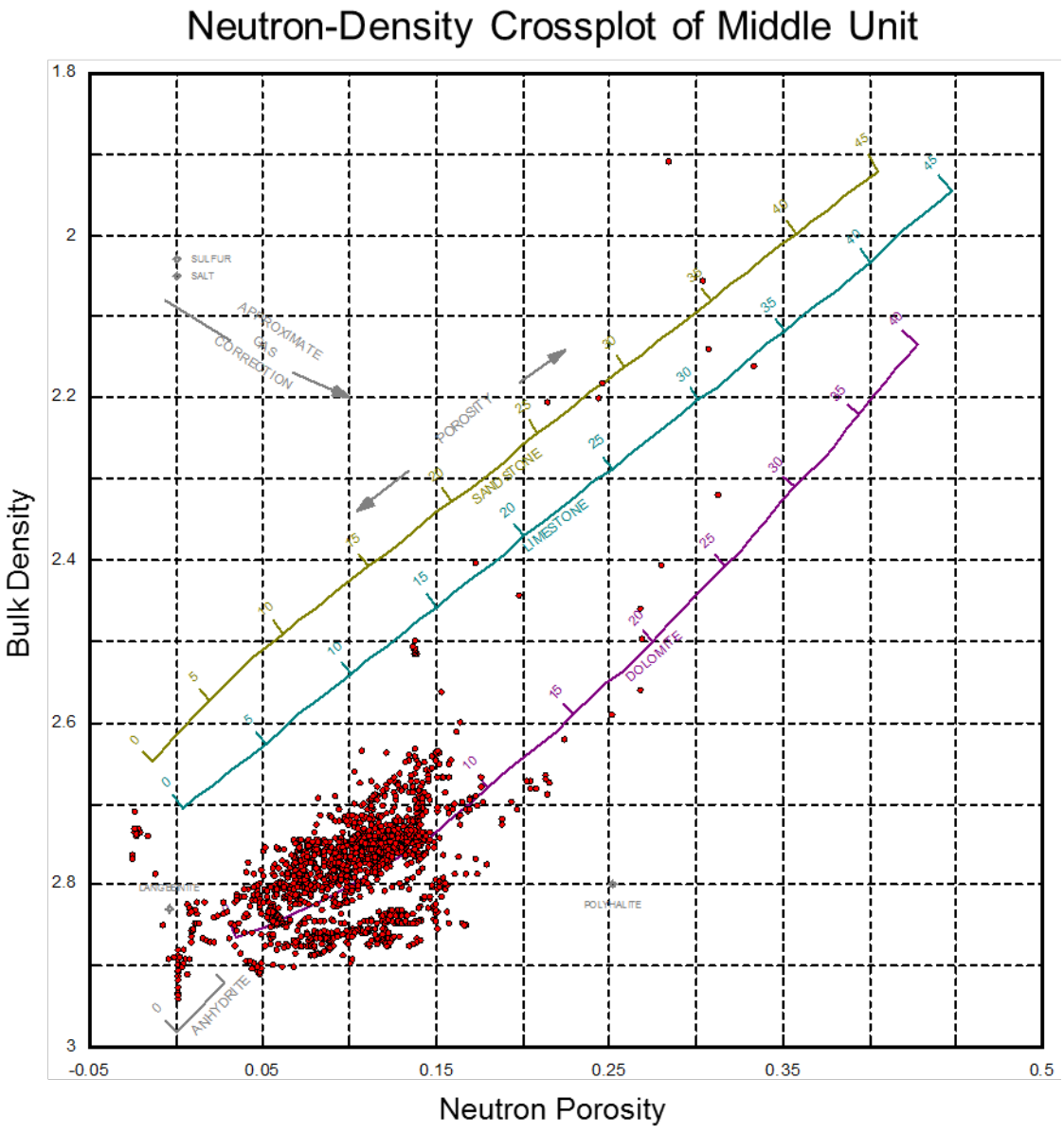


Figure 6-19. Neutron porosity–bulk density crossplot for the Brown Niagaran in the middle unit of the Bagley reef field.

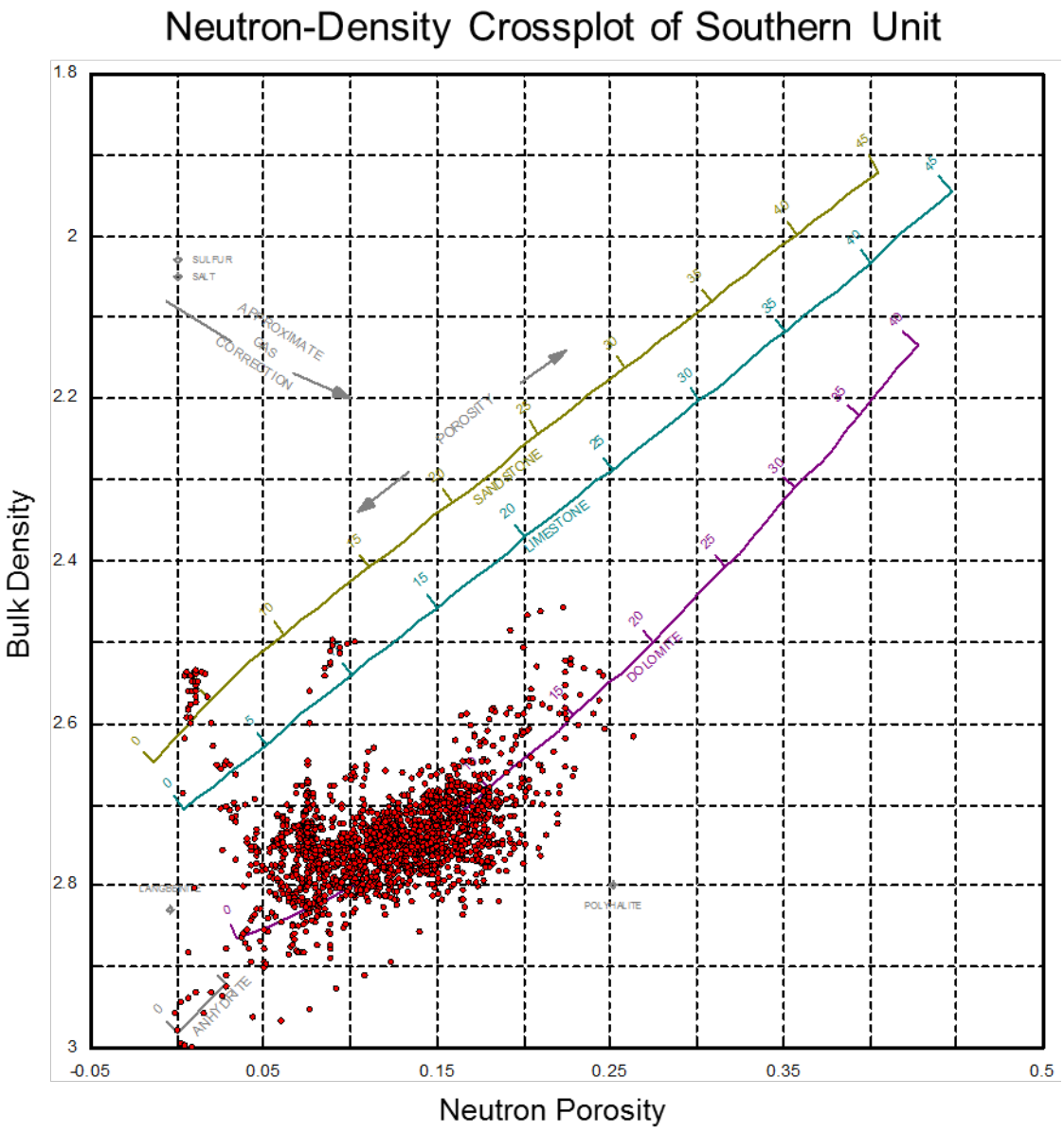


Figure 6-20. Neutron porosity–bulk density crossplot for the Brown Niagaran in the southern unit of the Bagley reef field.

Water Saturation

The water saturation in the Brown Niagaran averaged 47% with higher frequencies across high saturations than other formations due to the presence of the oil/water contact. On-reef wells showed a gradual increase toward the middle of the Brown Niagaran, while flank wells were highly saturated throughout. Figure 6-21 shows the resulting histogram of the water saturation.

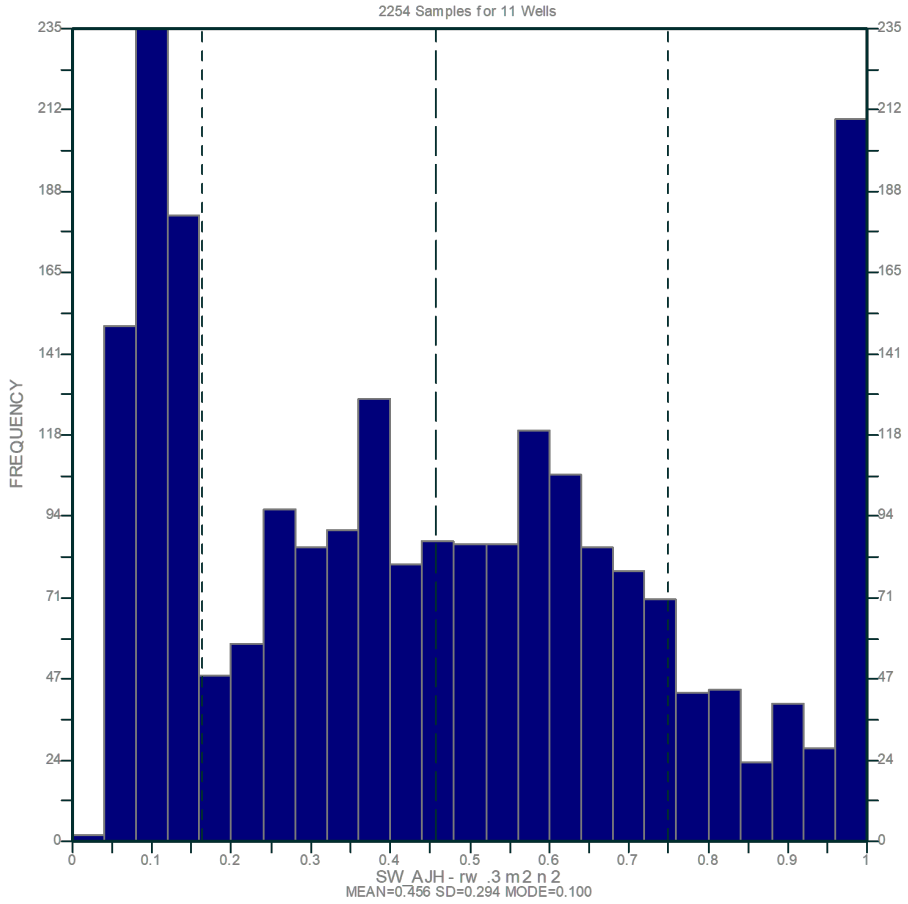


Figure 6-21. Water saturation histogram across the Brown Niagaran formation showing an average of 46%.

6.2.2 Petrophysical Calculations

A-2 Carbonate

The A-2 carbonate is predominantly dolomitic. The thickness ranges from 58 to 147 feet with an average thickness of 102 feet. The porosity values range from 0% to 7% with an average of 4.1%. The net thickness averages 87 feet with NTG ratio of 0.85. Salt plugging and anhydrite are commonly found in this formation, which can influence the porosity. A water saturation cutoff of 40% was applied which reduced the average net thickness to 16 feet and the NTG ratio to 0.54 (Table 6-3).

Table 6-3. Summary of petrophysical calculations for the A-2 carbonate in the Bagley reef field.

Interval: A-2 Carbonate						
Avg. Thickness	**Avg. Porosity**	**Avg. Net Thickness**	**Avg. NTG**	**Avg. SW**	**Avg Net Thickness (SW<40%)**	**Avg. NTG (SW<40%)**
102 ft	4.1%	87 ft	.85	17%	16 ft	0.54

A-1 Carbonate

The A-1 carbonate is dolomite with notable salt plugging in the upper 10 to15 feet. The thickness ranges from 28 feet near the crest of the reef system to 217 feet along the flanks. The porosity ranges from 3% to 9% with an average of 5.8%. A porosity cutoff of 5% resulted in an average net thickness of 79 feet with a NTG ratio of 0.88 (Table 6-4). A water saturation cutoff of 40% was applied to eliminate evaporites and saturated rock, which reduced the net thickness to 37 feet with a NTG ratio of 0.5.

Table 6-4. Summary of petrophysical calculations for the A-1 carbonate in the Bagley reef field.

Interval: A-1 Carbonate						
Avg. Thickness	**Avg. Porosity**	**Avg. Net Thickness**	**Avg. NTG**	**Avg. SW**	**Avg. Net Thickness (SW<40%)**	**Avg. NTG (SW<40%)**
94 ft	5.8%	79 ft	0.88	20%	37 ft	0.50

Brown Niagaran

The Brown Niagaran is dolomitic with minor evaporite plugging. The thickness ranges from 24 feet off-reef to 322 feet, and the porosity ranges from 5% to 10% with an average of 7.9% near the reef crest. Using a porosity cutoff of 5%, the net thickness is reduced to 182 feet with a NTG ratio of 0.91. The oil/water contact is located mid-formation to base of the Brown Niagaran. A water saturation cutoff of 40% was applied to eliminate water-saturated rock. The net thickness decreased to 88 feet with a NTG ratio of 0.45. Table 6-5 summarizes the petrophysical calculations for the Brown Niagaran.

Table 6-5. Summary of petrophysical calculations for the Brown Niagaran in the Bagley reef field.

Interval: Brown Niagaran						
Avg. Thickness	**Avg. Porosity**	**Avg. Net Thickness**	**Avg. NTG**	**Avg. SW**	**Avg. Net Thickness (SW<40%)**	**Avg. NTG (SW<40%)**
200 ft	7.9%	182 ft	0.91	52%	88 ft	0.45

6.3 Core Analysis

Two whole cores were available within the southern lobe of the Bagley reef field in the A-1 carbonate and Brown Niagaran, with a total of 117 feet of coverage. Standard core analysis was conducted, which included porosity, permeability, fluid saturation, bulk density, and grain density measurements. The core was described foot by foot, including lithology and sedimentary structures. High-resolution photographs were taken of each section of core. Figure 6-22 shows the locations of the two whole cores.

6.3.1 Grain Density

The grain density for the Bagley cores ranges from 2.59 to 2.97 g/cm^3 with an average of 2.83 g/cm^3. The A-1 carbonate has an average grain density of 2.84 g/cm^3; the Brown Niagaran has an average grain density of 2.83 g/cm^3. Salt plugging was recorded along 10 feet of core. The grain density over this interval was much lower with an average of 2.64 g/cm^3. Where anhydrite was present, the grain density was higher with an average of 2.91 g/cm^3. Table 6-6 summarizes the grain density averages for the two Bagley cores. Figure 6-23 shows the distribution of the grain density data.

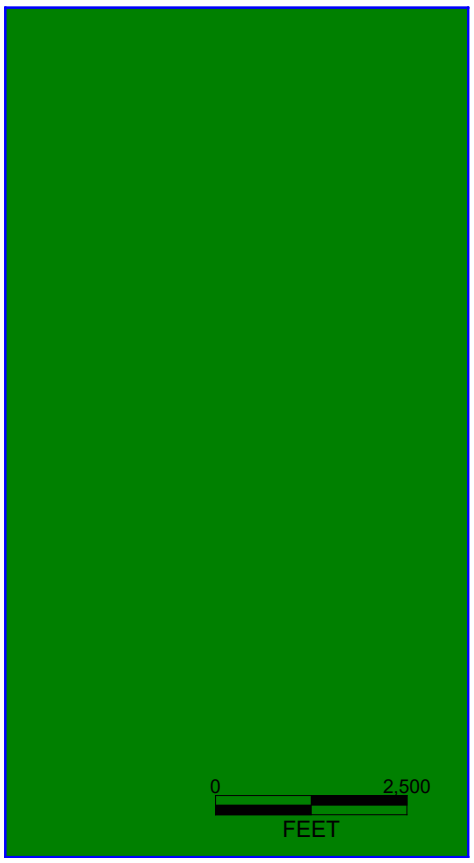


Figure 6-22. Well locations in the Bagley reef field highlighting the locations (in red) of whole core.

Table 6-6. Summary of grain density measured from whole core in the Bagley reef field.

Interval	Range (g/cm^3)	Average (g/cm^3)
All Core	2.59-2.97	2.83
A-1 Carbonate	2.59-2.97	2.84
Brown Niagaran	2.78-2.85	2.83
Salt Plugged	2.59-2.73	2.64
Anhydrite Plugged	2.87-2.97	2.91

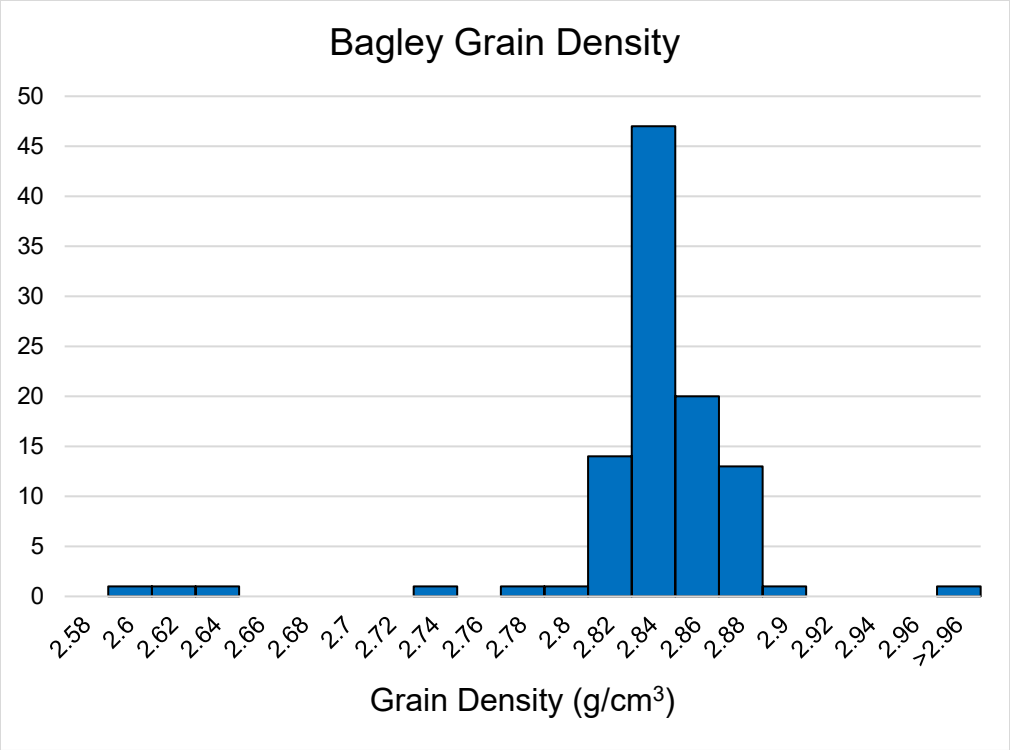


Figure 6-23. Histogram of the grain density of the Bagley reef field whole core, showing an average of 2.83 g/cm^3 with end members representing salt plugging and anhydrite plugging.

6.3.2 Porosity-Permeability Transform

The A-1 carbonate had a porosity range of 0.5% to 17%, with permeability ranging from 0.01 to 42.3 mD. Salt and anhydrite plugged available pore space and decreased the porosity and permeability. The salt- and anhydrite-plugged interval of the A-1 carbonate had an average porosity of 3% with an average permeability of 2.2 mD. The Brown Niagaran had a porosity range of 1.5% to 14.1% with a permeability range of 0.01 to 528.3 mD. The data was plotted (Figure 6-24) with the coordinating transform equations represented in Equation 6-1 and Equation 6-2.

$$K_{A1C} = .0813e^{.4291\phi} \quad \textbf{Equation 6.1}$$

$$K_{BN} = .0203e^{.7551\phi} \quad \textbf{Equation 6.2}$$

where:

K_{A1C} = permeability of the A-1 carbonate (mD)
K_{BN} = permeability of the Brown Niagaran (mD)
ø = porosity (%)

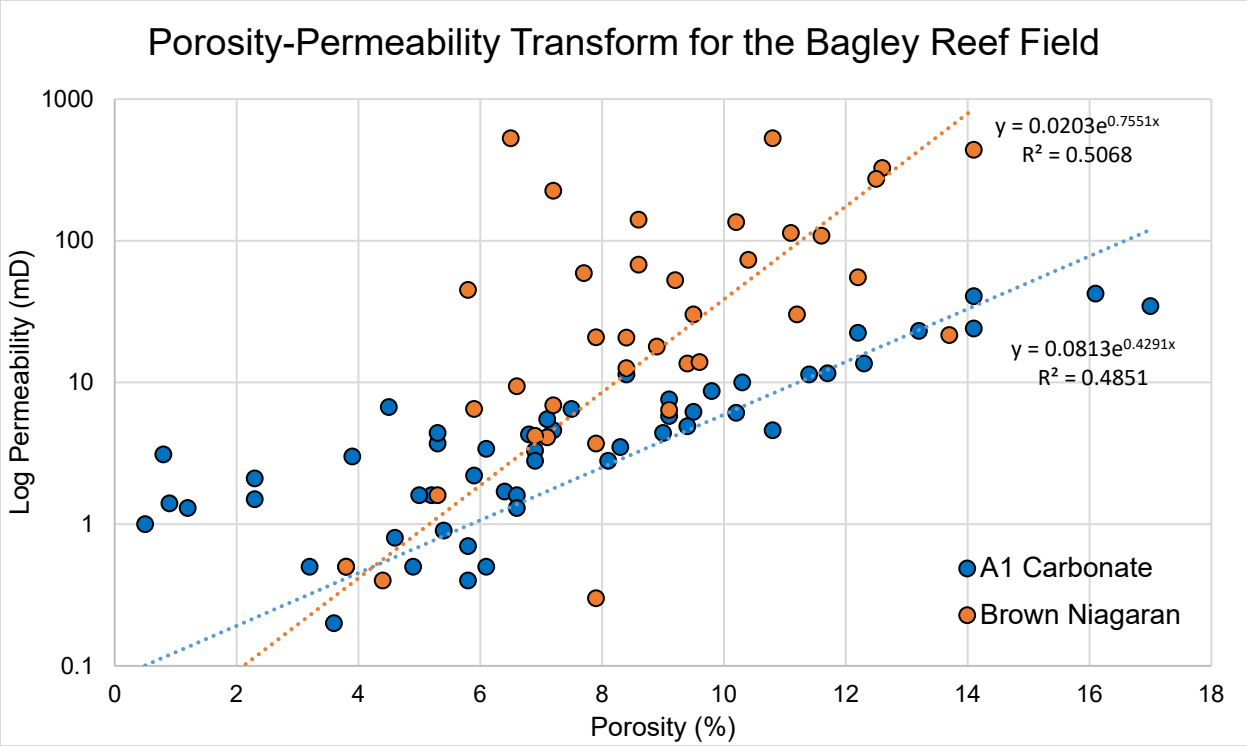


Figure 6-24. Porosity-permeability transform of the Bagley reef field using whole core measurements.

6.3.3 Core Descriptions

Core 29074

The A-1 carbonate is a medium- to light-gray dolomite with intervals of high-angle beds. Stylolites were abundant, along with intervals of poker-chip shales. The high angle, structures, and lithology suggest that the core represents the A-1 carbonate on the flank of the reef. The Brown Niagaran varies from a light- to dark-gray dolomite. High-angle beds and poker chips were present along with abundant stylolites, vugs, moldic porosity, and calcite cement-filled vugs and fractures. Bioclasts and rip-up clasts were common, which is consistent with a reef flank environment. Figure 6-25 summarizes the key rock descriptions with representative photographs from each section of core. Figure 6-26 is a simplified stratigraphic column of core 29074.

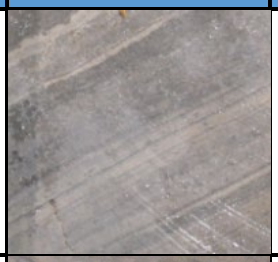
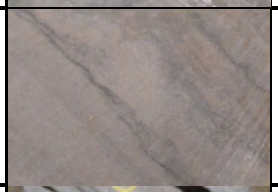
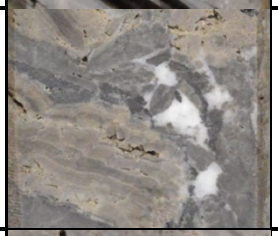
Depth (ft)	Core 29074	Description	Formation
5998.5		High angle beds	A1 Carbonate
6029.5		Stylolites	
6013.5		Poker chip shales	
6042		Calcite cement filled vugs Open vugs Moldic porosity	Brown Niagaran
6048.5		Vugs	
6052.5		Rip up clasts	

Figure 6-25. Summary descriptions of core 29074 with representative photographs of each section.

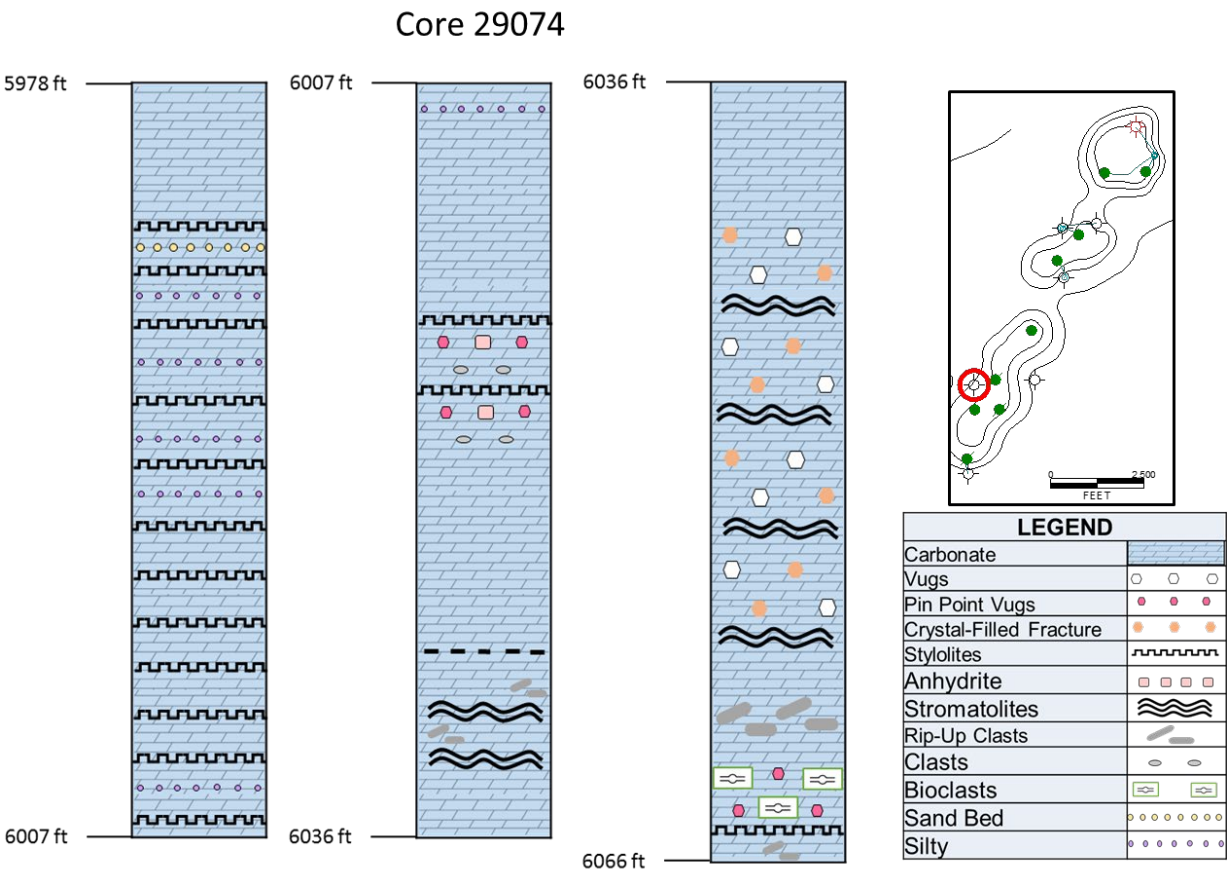


Figure 6-26. Simplified stratigraphic column of core 29074 summarizing lithology and structure.

Core 29085

The upper 15 feet of the A-1 carbonate was salt-plugged with a few feet of anhydrite plugging. The lithology was light- to dark-gray dolomite with stromatolites, moldic porosity, stylolites, and vugs. The Brown Niagaran was represented only in the lower 2 feet of core, which showed medium-gray dolomite with vugs and moldic porosity. Figure 6-27 summarizes the key rock descriptions with representative photographs from each section of core. Figure 6-28 is a simplified stratigraphic column of core 29085.

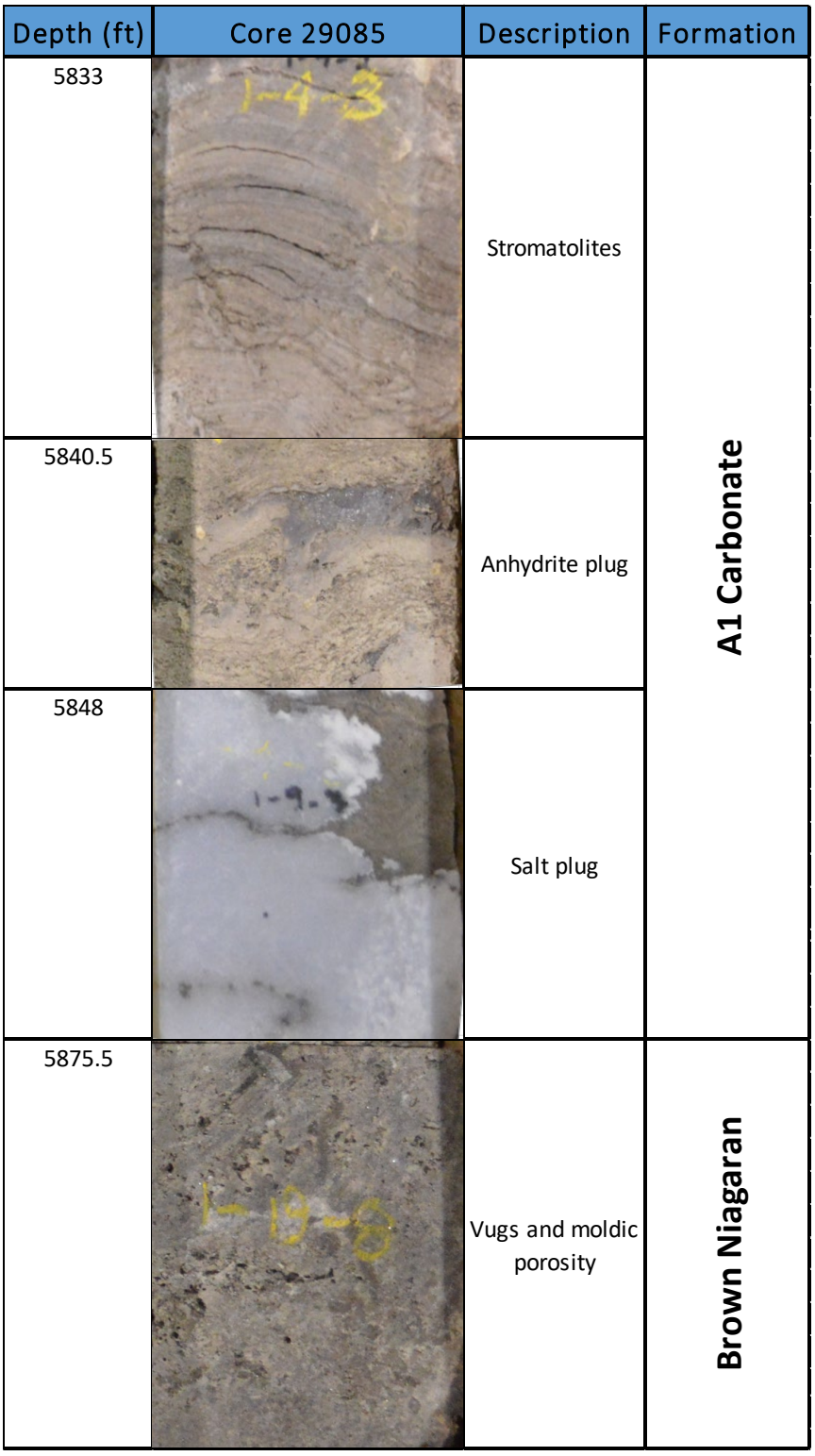


Figure 6-27. Summary descriptions of core 29085 with representative photographs of each section.

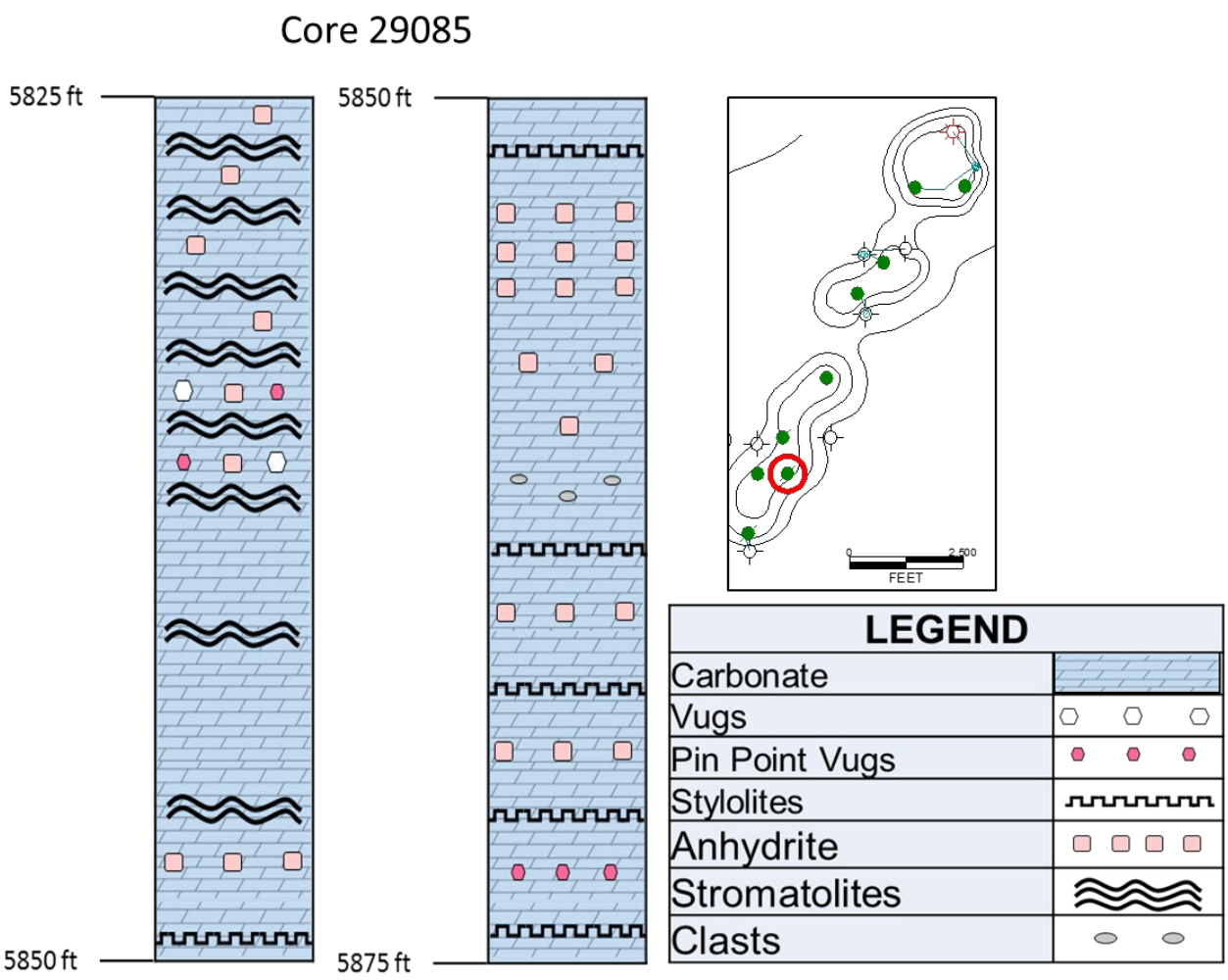


Figure 6-28. Simplified stratigraphic column of core 29085 summarizing lithology and structures.

6.4 Statistical Analysis

In preparation for the structural framework models, it was important to examine the subdivisions of the reefs beyond the qualitative observations of the wireline logs and whole core. This was accomplished by statistically determining the subdivisions using cluster analysis following the workflow described in Figure 6-29.

The reefs have traditionally been subdivided into six formations: A-2 carbonate, A-2 evaporite, A-1 carbonate, A-1 evaporite, Brown Niagaran, and Gray Niagaran. Based on the work done by Rine (2015), the reefs were subdivided into 16 individual facies. Many of the facies share reservoir characteristics and were further grouped into six flow zones. Additional zones were proposed based on production data, which yielded three main zones with a cap and a base. Each scenario was evaluated to determine the best subdivisions to use in the SEMs. Table 6-7 lists the formations, facies, and zones with respect to one another.

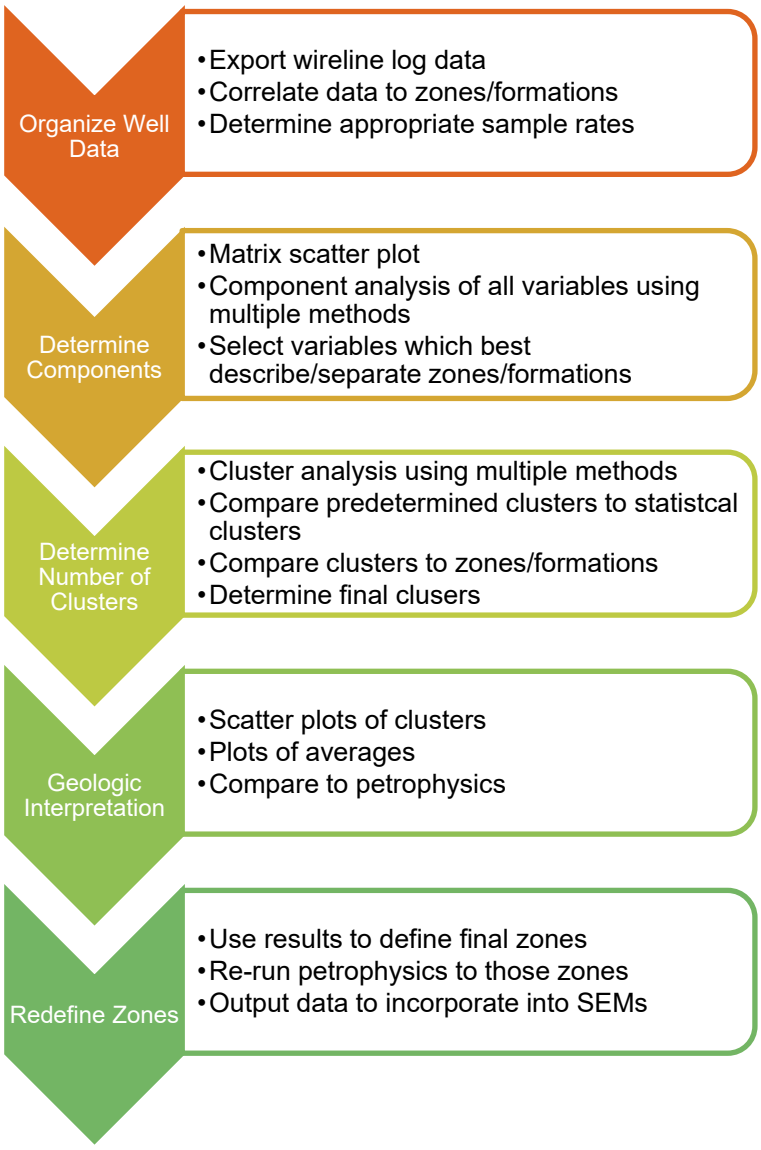


Figure 6-29. Geostatistical workflow applied to Bagley reef field core data.

Table 6-7. List of formations, facies, and zones with respect to one another for each reef field.

Formation	Facies	Flow Zone	Production Zone
A-2 Carb	A-2 Carb	Zone A	Cap
A-2 Evap	A-2 Evap		
A-1 Carb	Peritidal A-1 Carb	Zone 3	Reservoir
	Upper A-1 Carb		
	Lower A-1 Carb		Flank
	A0 Carb		
	Rabbit Ear Anhydrite (REA)		
	Peloidal Wackestone	Zone 2	Reservoir
A-1 Evap	A-1 Evaporite	Zone B	Baffle
Brown Niagaran	Thrombolitic Boundstone	Zone 1	Reservoir
	Stromatolitic Cap		
	Reef Core		
	Proximal Reef Apron	Zone 4	Flank
	Proximal Reef Rubble		
	Distal reef apron		
	Distal reef rubble		
	Muddy bioherm	Zone 1	Water Saturated
Gray Niagaran	Gray Niagaran	Zone 0	Base

Cluster analysis is the process of applying several algorithms to determine how data should be grouped together. Once grouped, the data points within a group are more similar to each other than to data points in other groups. Two common algorithms in *RGui*, an open source statistical program, are *Mclust* and *KMeans. Mclust* applies several model-based clustering algorithms and chooses the method that best fits the data. *KMeans* minimizes the sum of squares for each data point and clusters them around a center mean for the defined number of clusters. A cluster analysis was conducted to quantitatively determine whether the reefs can be statistically subdivided and, if so, what the subdivisions are. This was completed using the following steps: (1) determine which components best describe the dataset, (2) determine the number of clusters using resulting components, (3) apply geologic concepts to clusters.

6.4.1 Determining Components

Three wireline logs (gamma ray, bulk density, and neutron porosity) were consistently available for the wells with wireline log data. Each component showed strong variations between formations, but some formations had a broad range of values. Seven facies and one unknown group were identified. The A-1 anhydrite (A1A) and A-1 evaporite (A1E) showed strong differences from the carbonates. The Brown Niagaran facies, distal reef apron (D_R_A), distal reef rubble (D_R_R), and the reef core, had similar porosity and bulk density values, with the greatest variation being in the gamma ray. Three zones were selected: *the base* included the Gray Niagaran, *the flank* included the A-1 carbonate, A-1 evaporite, and Brown Niagaran on the edges of the reef, and *the reservoir* included the A-1 carbonate on the crest of the reef and the Brown Niagaran reef core. The three zones have broad ranges of values, with the reservoir having the highest neutron porosity and the lowest bulk density and gamma ray averages. The flank zone has the broadest range of values due to the inclusion of end members (salt and anhydrite). Figure 6-30 through Figure 6-32 show the boxplots of each wireline log for each formation, facies, and zone.

Next, the means were compared using Tukey's HSD test, which tests the hypothesis that the means are statistically the same and produces a p-value. A p-value of 1 indicates that the means are the same between two groups, and a p-value of 0 indicates that the means are different between two groups. Table 6-8 through Table 6-10 summarize the p-value between each pair for formations, facies, and zones, respectively. There were similar means between the A1E and A1C as well as the A2E and A1C, which could be due to salt plugging within the A1C as observed in whole core. The A2E and A1E also had similar gamma ray averages because they are both evaporate packages. The GN and A1E had similar neutron porosity averages because they are both non-reservoir formations.

There were many similarities between facies. These occurred most often between facies of similar lithologies or the same formation. The Tukey test in this case showed that these facies are not uniquely different and might not represent the best subdivisions in the reef.

Only one pair had a similar neutron porosity average: the flank and base. This is due to low reservoir potential in the flanks and the Gray Niagaran. The zones were statistically different according to the Tukey test, but it does not recognize important features such as salt plugging, anhydrite, and best reservoir dolomite.

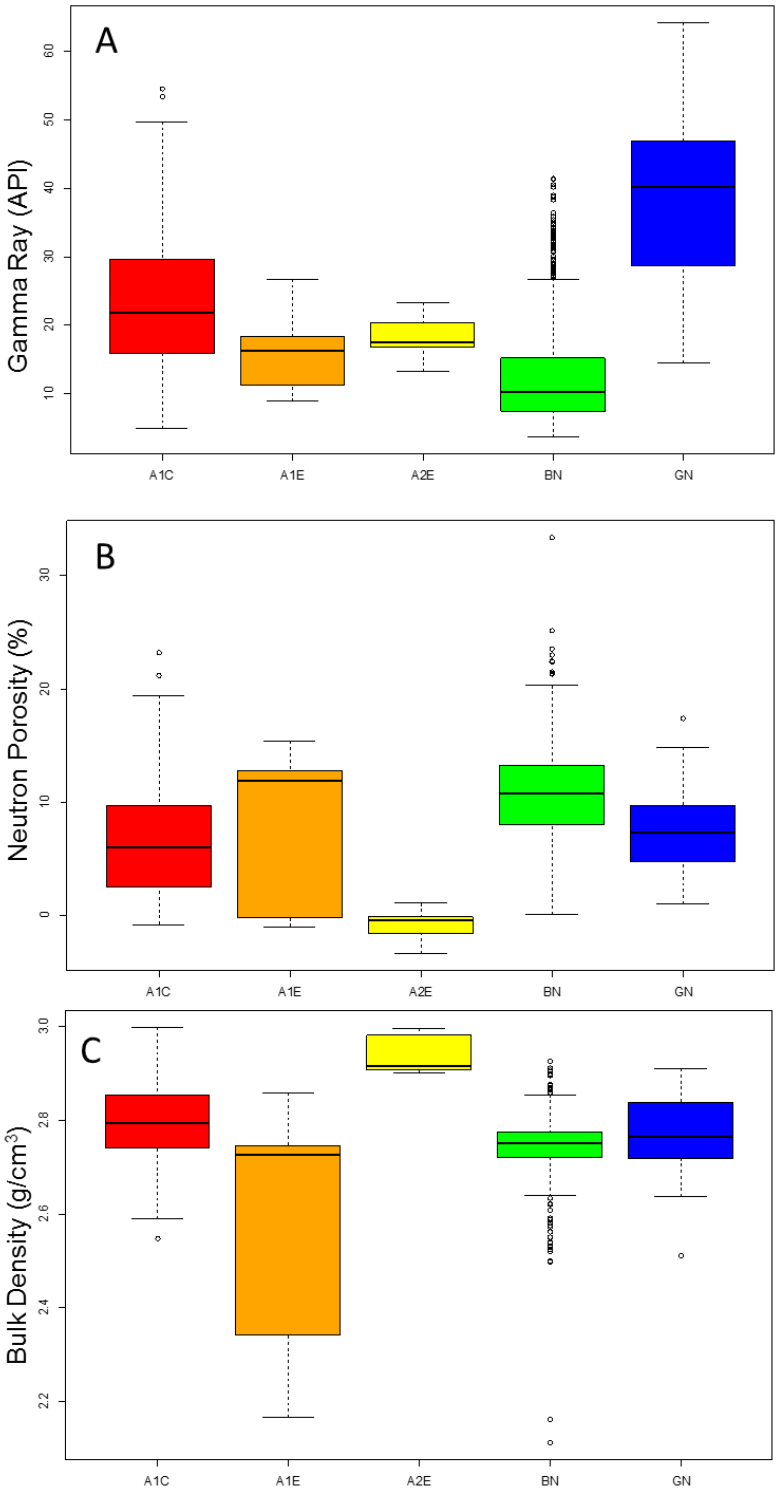


Figure 6-30. Boxplots of gamma ray (A), neutron porosity (B), and bulk density (C) for each formation.

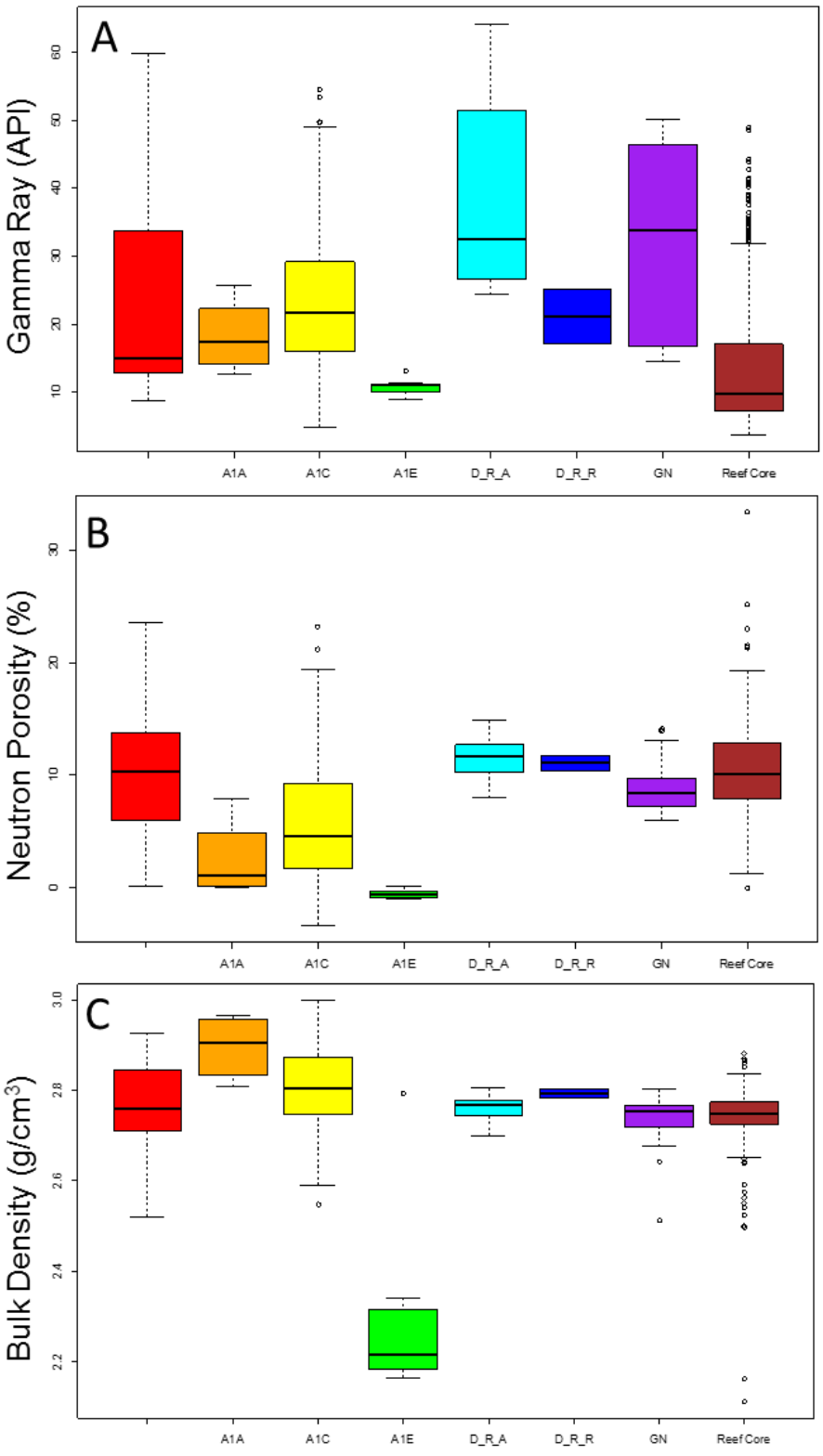


Figure 6-31. Boxplot of gamma ray (A), neutron porosity (B), and bulk density (C), for each identified facies.

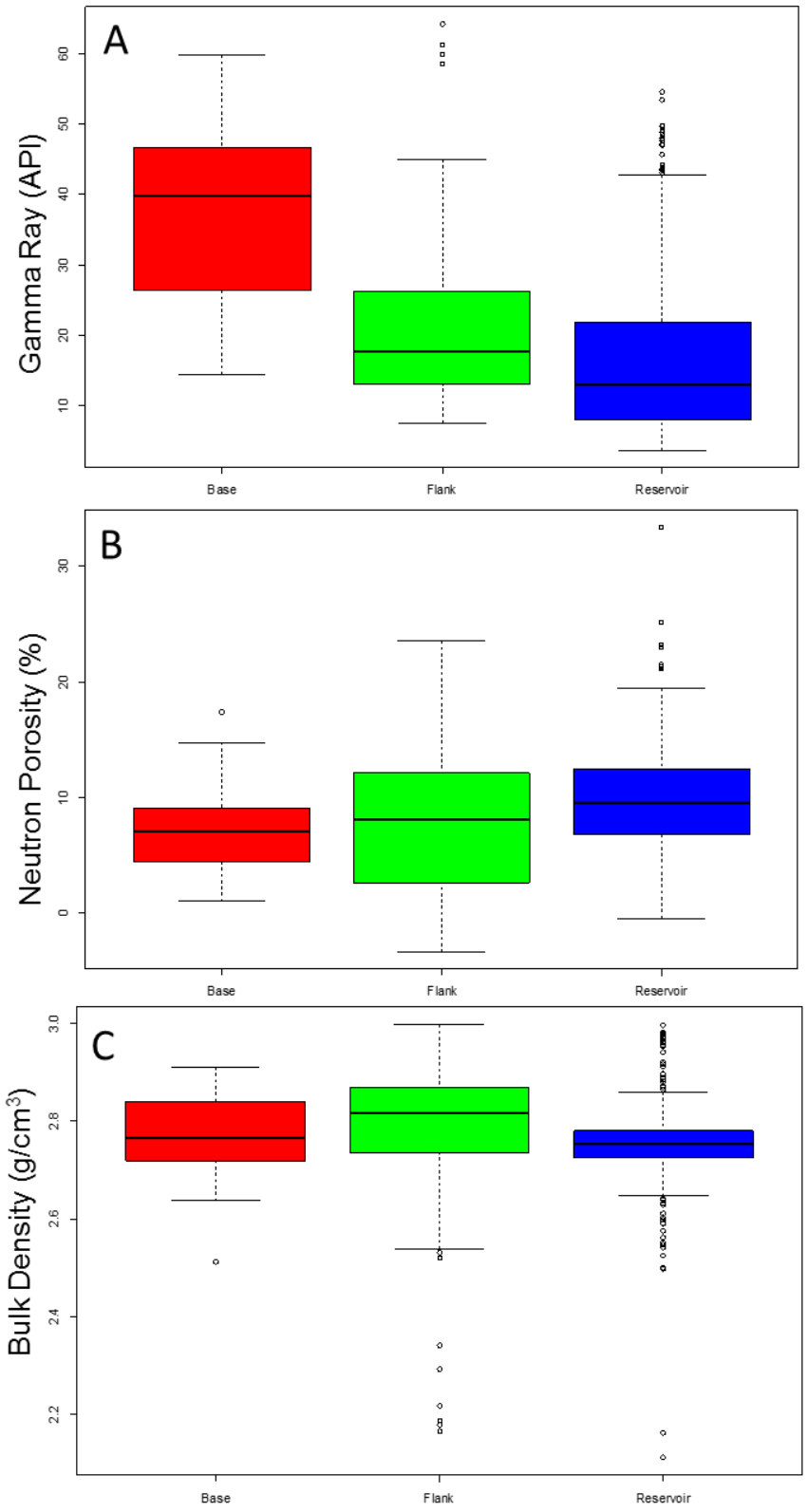


Figure 6-32. Boxplot of gamma ray (A), neutron porosity (B), and bulk density (C) for each zone.

Table 6-8. P-values for each formation pair as determined by the Tukey HSD test. Yellow highlights formation pairs with similar average.

Formation Pair	P-value		
	GR	NPHI	RHOB
A1E-A1C	0.00	0.37	0.00
A2E-A1C	0.26	0.00	0.00
BN-A1C	0.00	0.00	0.00
GN-A1C	0.00	0.06	0.01
A2E-A1E	0.98	0.00	0.00
BN-A1E	0.61	0.01	0.00
GN-A1E	0.00	0.99	0.00
BN-A2E	0.41	0.00	0.00
GN-A2E	0.00	0.00	0.00
GN-BN	0.00	0.00	0.01

Table 6-9. P-values for each facies pair as determined by the Tukey HSD test. Yellow highlights formation pairs with similar average.

Facies Pair	P-Value		
	GR	NPHI	RHOB
A1A-Unk	0.99	0.01	0.02
A1C-Unk	1.00	0.00	0.00
A1E-Unk	0.06	0.00	0.00
D_R_A-Unk	0.00	0.89	1.00
D_R_R-Unk	1.00	1.00	1.00
GN-Unk	0.00	0.76	0.29
Reef Core-Unk	0.00	0.96	0.00
A1C-A1A	0.98	0.78	0.36
A1E-A1A	0.96	0.95	0.00
D_R_A-A1A	0.01	0.00	0.03
D_R_R-A1A	1.00	0.28	0.76
GN-A1A	0.20	0.09	0.00
Reef Core-A1A	0.99	0.01	0.00
A1E-A1C	0.04	0.00	0.00
D_R_A-A1C	0.00	0.00	0.10
D_R_R-A1C	1.00	0.66	1.00
GN-A1C	0.00	0.00	0.00
Reef Core-A1C	0.00	0.00	0.00
D_R_A-A1E	0.00	0.00	0.00
D_R_R-A1E	0.93	0.02	0.00
GN-A1E	0.00	0.00	0.00
Reef Core-A1E	0.99	0.00	0.00
D_R_R-D_R_A	0.36	1.00	1.00
GN-D_R_A	0.46	0.41	0.97
Reef Core-D_R	0.00	0.97	0.99

Facies Pair	P-Value		
	GR	NPHI	RHOB
GN-D_R_R	0.84	1.00	0.97
Reef Core-D_R	0.98	1.00	0.98
Reef Core-GN	0.00	0.33	1.00

Table 6-10. P-values for each zone pair as determined by the Tukey HSD test. Yellow highlights formation pairs with similar average.

Zone-Pair	P-Value		
	GR	NPHI	RHOB
Flank-Base	0.00	0.55	0.05
Reservoir-Base	0.00	0.00	0.07
Reservoir-Flank	0.00	0.00	0.00

6.4.2 Determining Number of Clusters

A first pass at clustering was conducted using the package Mclust. Mclust was initially used to statistically determine the number of clusters needed to describe a combined dataset of gamma ray, neutron porosity, and bulk density. Eight clusters were used to encompass the dataset. Figure 6-33 is a matrix scatter plot of the resulting clusters with gamma ray (XGR), neutron porosity (XNPHI), and bulk density (XRHOB).

KMeans was also used to determine the appropriate number of clusters needed to classify the dataset. A range of clusters, 0-20, was calculated and plotted with respect to the sum of squares in each group. The “elbow” of the plot determines the best number of clusters to use. The sum of squares after the “elbow” converges to a minimum sum of squares. An elbow plot was generated for each component pair, since KMeans only considers two components. Figure 6-34 is the plot of number of clusters and sum of squares within groups. The “elbow,” or best number of clusters, is four to six clusters. Using gamma ray and neutron porosity showed a less distinct turning point before convergence than the other two pairs (gamma ray and bulk density; neutron porosity and bulk density).

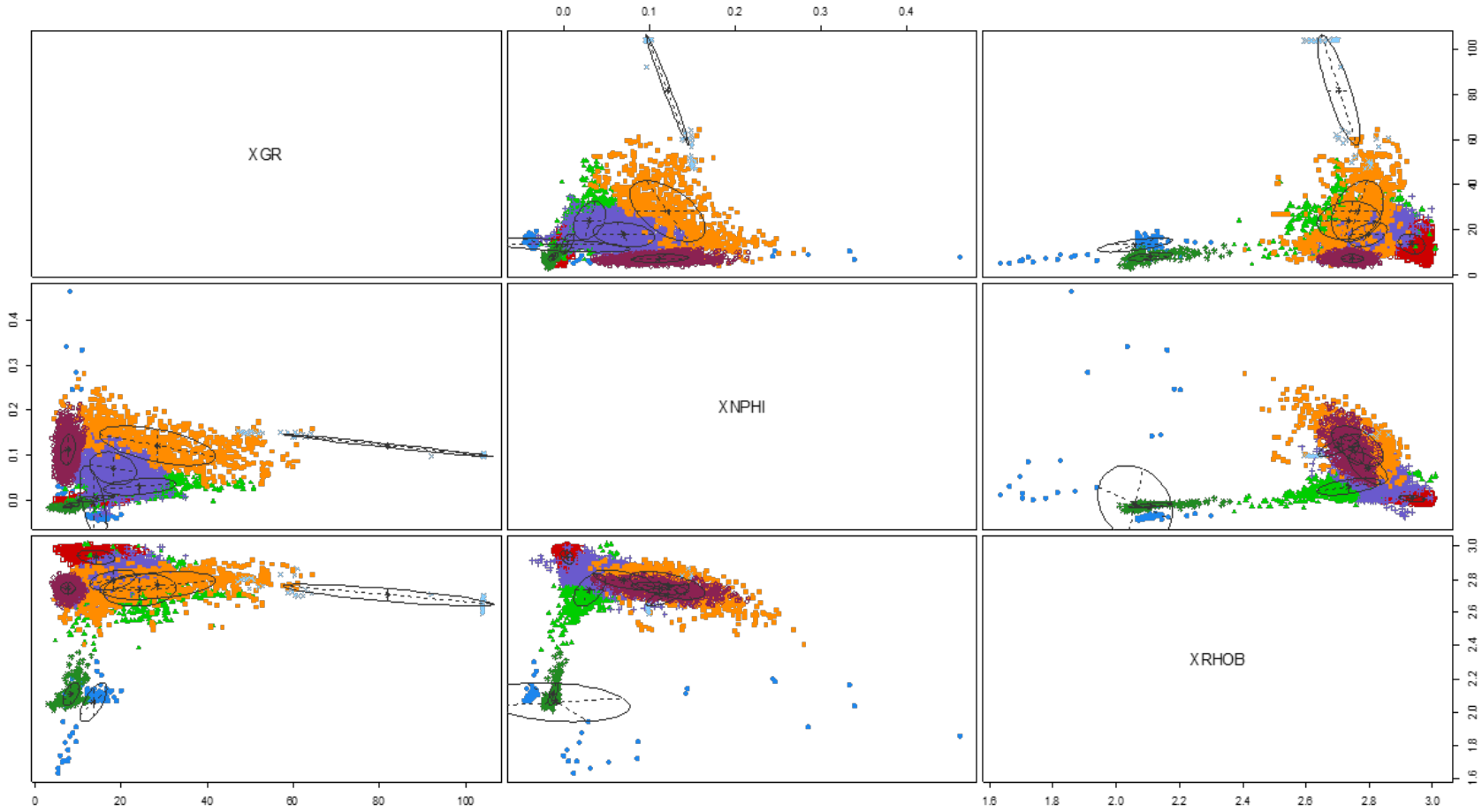


Figure 6-33. First-pass Mclust results using three components (gamma ray, neutron porosity, and bulk density) showing eight clusters.

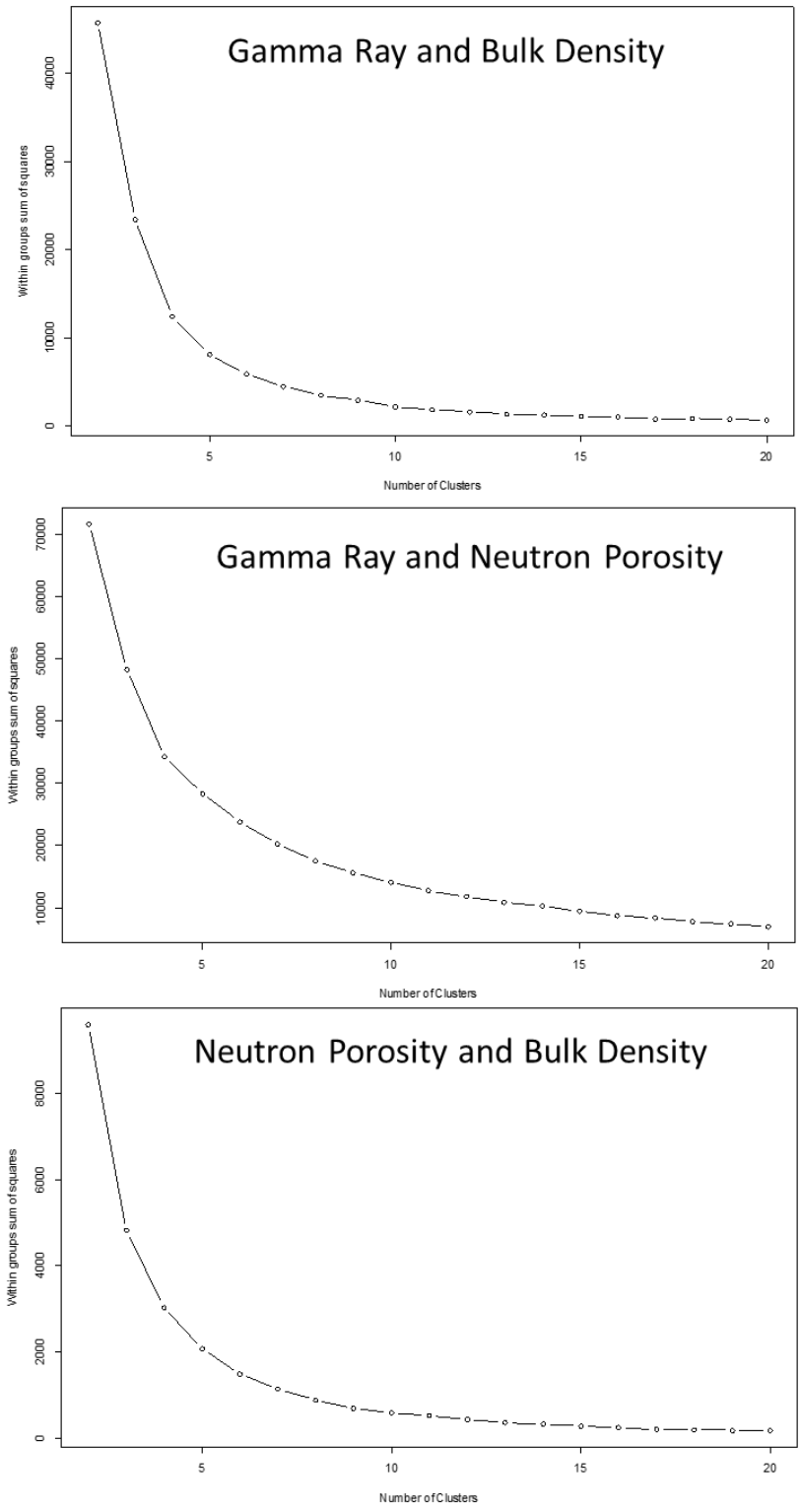


Figure 6-34. Kmeans "elbow plots" showing the ideal number of clusters for each component pair.

6.4.3 Cluster Analysis Results

Kmeans was run for multiple clustering scenarios and compared to the formations, facies, and zones to determine the best grouping for use in SEMs. Kmeans had too much overlap between clusters and only split clusters along the gamma ray without any subdivisions based on neutron porosity and bulk density. This method did not represent the data geologically.

Mclust clusters were compared to formations, facies, and zones using confusion matrixes and boxplots. Many formations, facies, and zones did not fall within a unique cluster but were composed of multiple clusters. The Mclust clusters were then formatted as a LAS and loaded into Petra to compare clusters with log signatures, whole core, and distributions within the reef.

Well 29085

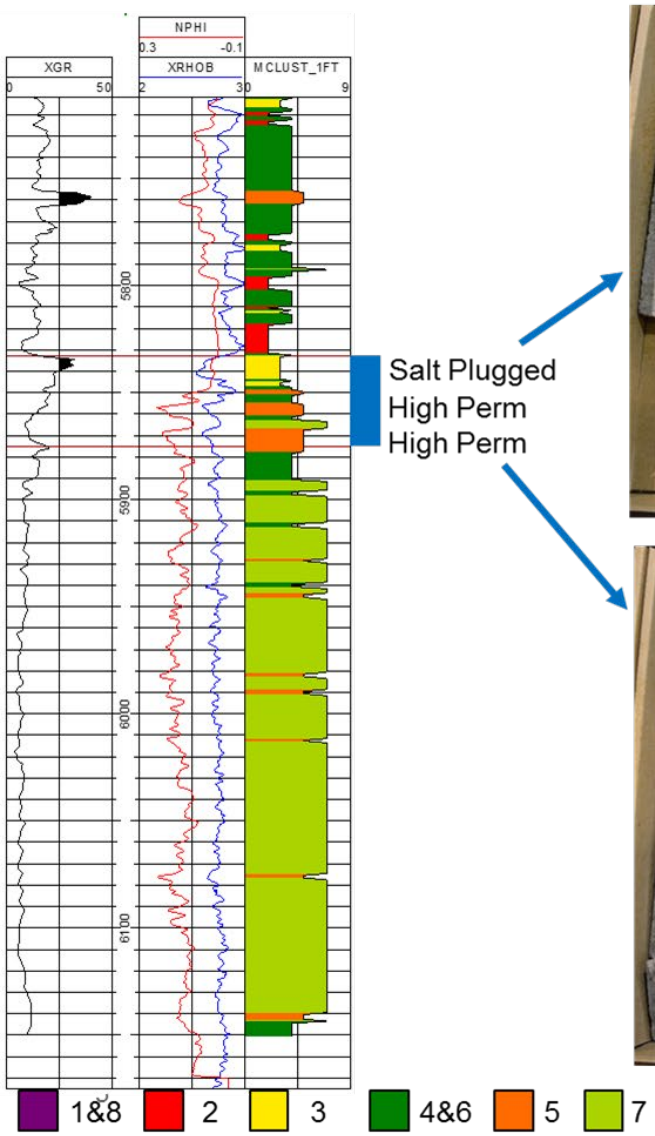
Well 29085 is in the southern reef lobe and has whole core over the A-1 carbonate interval. The top of the A-1 carbonate was within cluster 3. This interval had low bulk density and neutron porosity and correlated with a salt-plugged interval in whole core. The base of the A-1 carbonate fell within clusters 4, 5, and 7. Cluster 5 had the highest neutron porosity and core-measured porosity and permeability. Clusters 4 and 7 had lower neutron porosity and core-measured porosity and permeability. Figure 6-35 shows the resulting Mclust clusters in a single well cross section with correlating core photographs and core measurements.

Well 29074

Well 29074 is in the southern reef lobe and has whole core over the Brown Niagaran interval. The Brown Niagaran alternates between cluster 5, cluster 4, and cluster 6. Cluster 5 correlates with sections of whole core which have visible moldic porosity and high core-measured porosity and permeability. Clusters 4 and 6 correlates with a section of core which is visibly tight, contains sections of poker chips, and permeabilities below 5 mD. Figure 6-36 shows the resulting Mclust clusters in a single well cross section with correlating core photographs.

Well 37794

Well 37794 is in the northern reef lobe and has PNC logs which are used to identify fluid saturations, salt plugging, and anhydrite plugging (Conner et al., 2020). From 5,800 to 5,945 feet MD, PNC log signatures were interpreted as salt and anhydrite plugging. Where the sigma curve (SGFC) was highest (salts) it correlated with Mclust cluster 3. The upper 10 feet of the A-1 carbonate was composed of cluster 3, which is consistent with well 29085 and the salt-plugged interval. The upper Brown Niagaran was composed of mostly cluster 4 and 6 with thin intervals of cluster 7. This correlates with higher gas-saturated zones. The middle to the base of the Brown Niagaran was mostly composed of cluster 7 and thin intervals of cluster 5. This correlated with oil-saturated zones. Figure 6-37 shows the resulting Mclust clusters in a single well cross section with correlating PNC interpretations.





DEPTH	PERM MAX	POROSITY GEX
5833	2.1	2.3
5836	1	0.5
5839	1.3	1.2
5842	1.4	0.9
5847	3.1	0.8
5850	6.2	9.5
5853	0.4	5.8
5854	2.8	6.9
5855	7.6	9.1
5856	42.3	16.1
5857	34.6	17
5858	4.6	10.8
5859	13.6	12.3
5860	11.4	11.4
5861	1.6	6.6
5862	0.5	6.1
5863	1.3	6.6
5864	6.5	7.5
5865	3.5	8.3
5866	4.9	9.4
5867	11.6	11.7
5868	24	14.1
5869	40.6	14.1
5870	22.4	12.2
5871	23.1	13.2
5872	10	10.3
5873	8.7	9.8
5874	6.1	10.2
5875	6.4	9.1

Figure 6-35. Log signatures, whole-core photographs, and core measurements for well 29085 showing a correlation between clusters, log signatures, and whole core.

6.0. Bagley

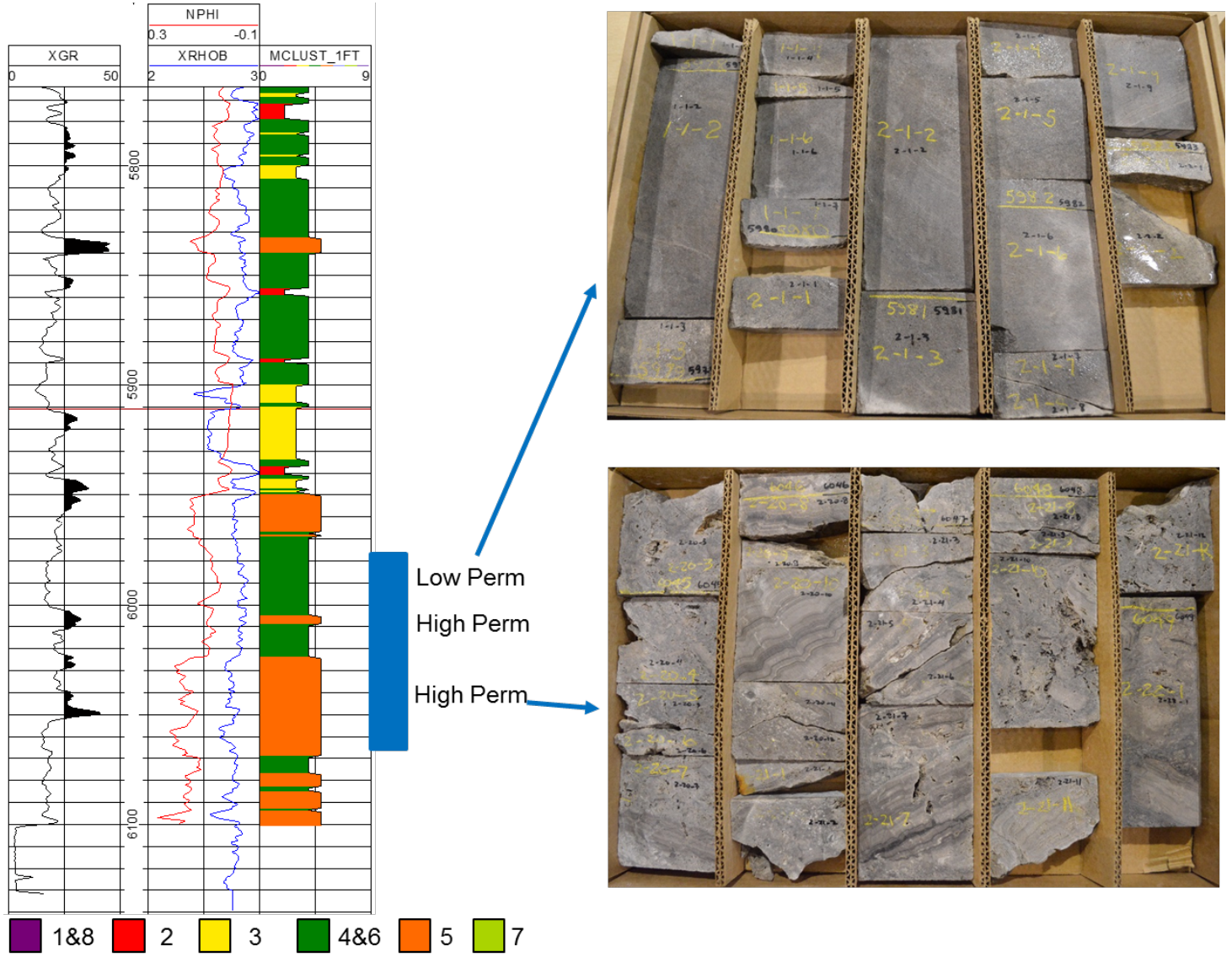


Figure 6-36. Log signatures and whole-core photographs for well 29074 showing a correlation between Mclust clusters and changes in whole core.

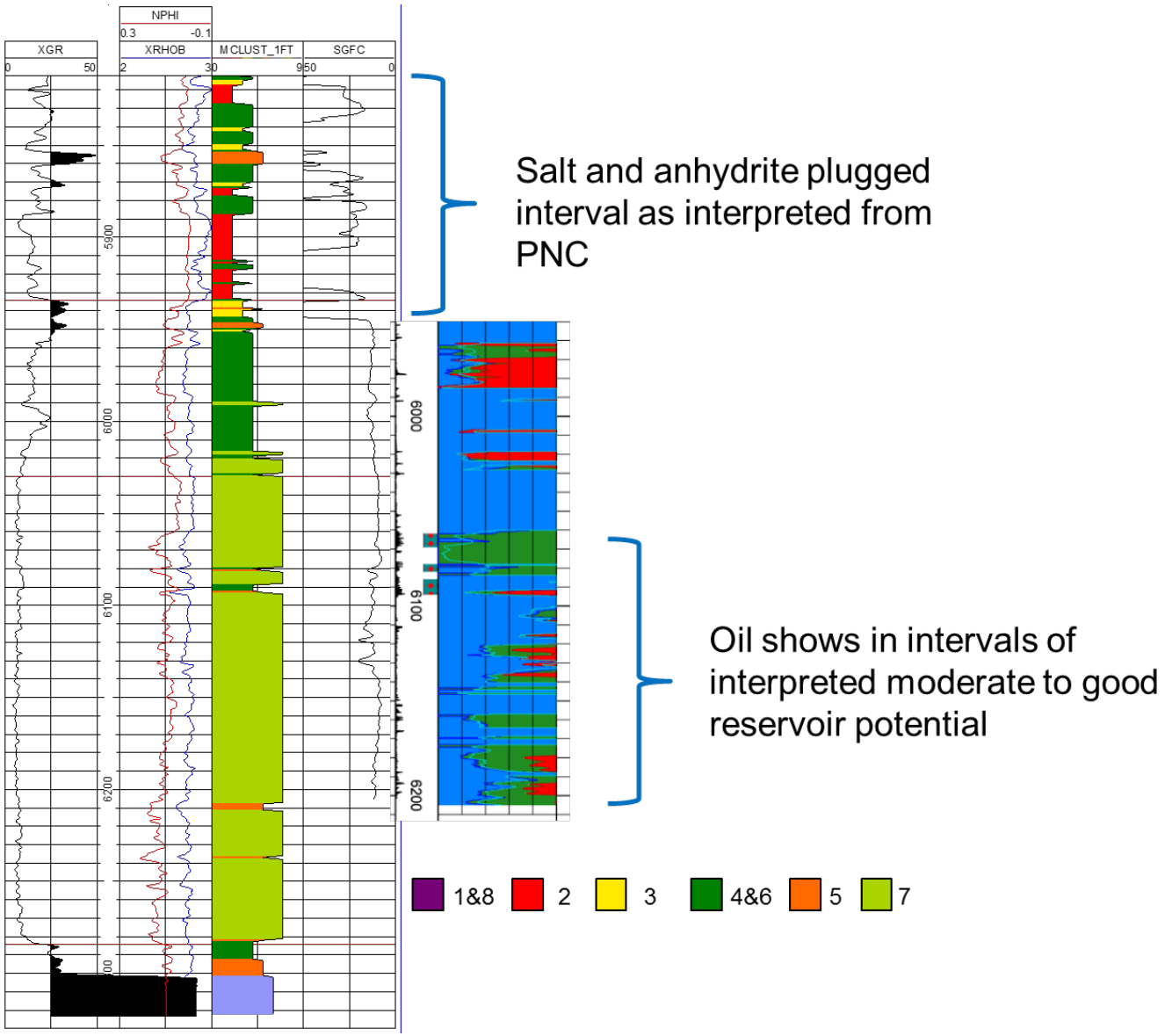


Figure 6-37. Single well cross section of well 37794 showing Mclust clusters and correlations to log signatures and PNC interpretations.

6.0. Bagley

Cluster Beanplots

Beanplots were generated to compare clusters for each component (gamma ray, neutron porosity, and bulk density). A beanplot is a combination of a boxplot and histogram which shows the density distribution of the data and the mean. Figure 6-38 shows beanplots for gamma ray, bulk density, and neutron porosity.

For gamma ray (Figure 6-38(A)), cluster 6 shows a bimodal distribution. This correlated with the Gray Niagaran, which often had skewed log signatures because it was at the end of the logged interval. Clusters 3 and 5 had uniform distributions with gamma ray ranging from 0 to 60 API. The remaining clusters (1, 2, 4, 7, and 8) had a more normal distribution, with the highest density of data around the mean.

Clusters 1 and 8 had low bulk densities, near 2.0 g/cm^3 (Figure 6-38(B)). This correlates with the bulk density for salt. Cluster 2 had the highest bulk density, near 3.0 g/cm^3, which correlates with anhydrite. Cluster 3 had a bulk density near 2.75 g/cm^3, which is close to limestone. This could be due to the presence of salts in a dolomite, which would decrease the overall bulk density of the rock. Clusters 4 through 7 had means near 2.83 g/cm^3, which correlates with dolomite.

Clusters 1 and 8 had the lowest neutron porosity, with some scattered points above 40% (Figure 6-38(C)). Neutron porosity tools are sensitive to salts and often have erroneous porosity data over those intervals. Cluster 5 had the highest neutron porosity, and cluster 7 had a similar distribution as cluster 5.

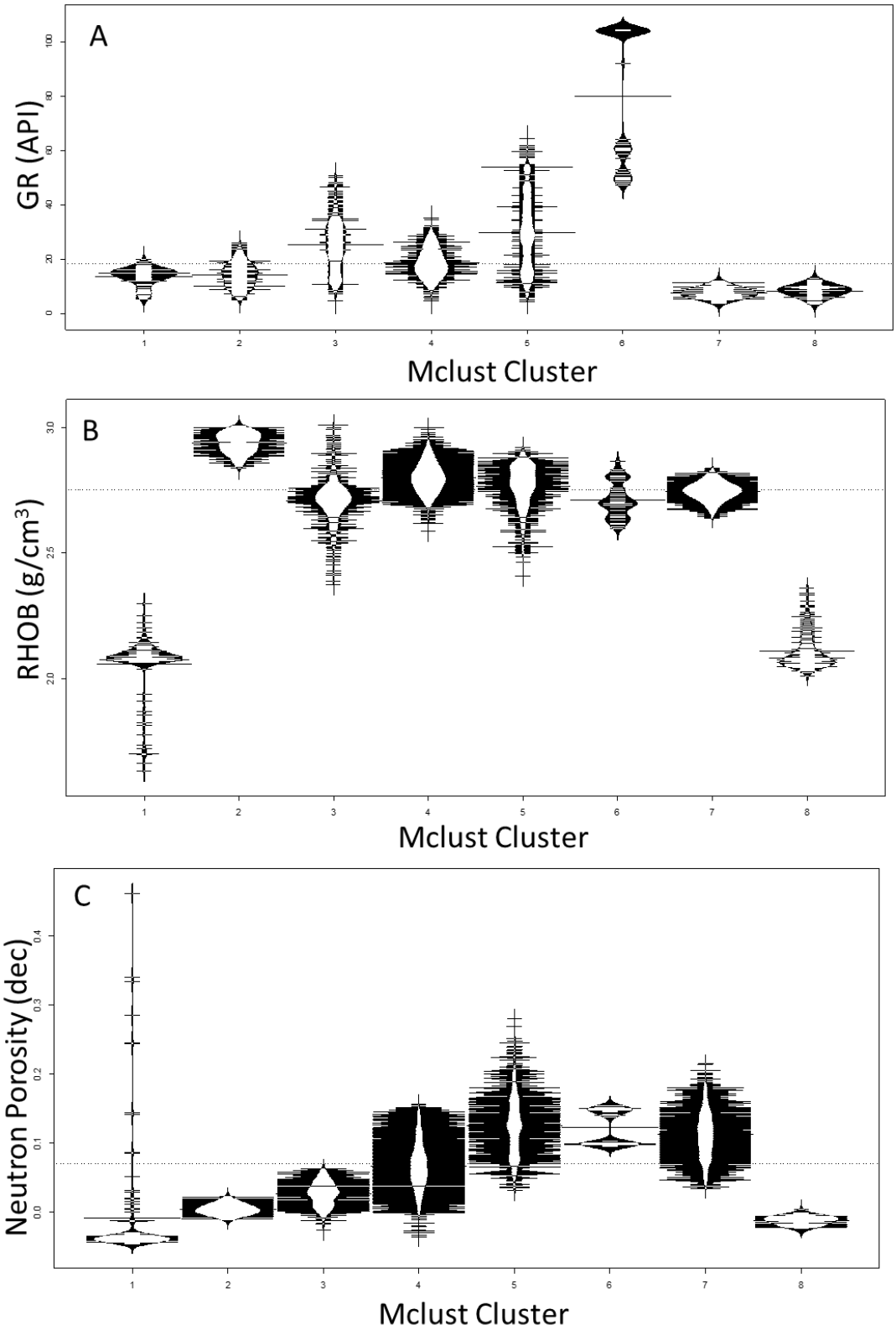


Figure 6-38. Beanplots for gamma ray (A), bulk density (B), and neutron porosity (C), for each cluster.

Mclust Interpretation

Clusters 1 and 8 had low bulk densities and were classified as salt packages. Cluster 2 had the highest bulk density with low porosity and was classified as anhydrite. Cluster 3 had bulk densities similar to a limestone but correlated with salt-plugging zones in whole core and PNC interpretations. Cluster 3 was classified as salt-plugged dolomite, which would have log signatures similar to limestone. Cluster 4 had bulk densities of dolomite with low porosities and correlated with whole core zones of tight dolomite. This was classified as low-reservoir-potential dolomite. Cluster 5 had bulk densities of dolomite with high porosities and correlated with whole core zones of porous dolomite. This was classified as high-reservoir-potential dolomite. Cluster 6 was observed only in the Gray Niagaran and was also classified as low-reservoir-potential dolomite. Cluster 7 also had bulk densities of a dolomite but had higher porosities and correlated to intervals of whole core with permeabilities between 5 and 10 mD. Cluster 7 was classified as moderate-reservoir-potential dolomite.

A series of cross sections were generated to correlate the interpreted Mclust clusters throughout the Bagley reef field. The Mclust model is only applicable to the A-1 Carbonate and Brown Niagaran formations. Cross section A-A’ (Figure 6-39) runs southwest to northeast through the southern lobe. Salt plugging was common in the upper 10 to 20 feet of the A-1 carbonate, and anhydrite was predicted in the A-1 carbonate on the flanks. The Brown Niagaran had moderate to high reservoir potential predicted throughout the reef core and intermittently along the flanks. Figure 6-39 shows log signatures with interpreted Mclust results for cross section A-A’.

Cross section B-B’ (Figure 6-40) runs southwest to northeast through the middle lobe. Salt plugging and anhydrites were interpreted in the A-1 carbonate along the flanks of the reef and a thin interval in the upper 10 feet over the crest of the reef. The Brown Niagaran was interpreted to have moderate to high reservoir potential throughout the main reef core and on the northern flank. Figure 6-40 shows log signatures with interpreted Mclust results for cross section B-B’.

Cross section C-C’ (Figure 6-41) runs through the center of the northern lobe. Salt plugging was interpreted in the upper 15 feet of the A-1 carbonate. The lower A-1 carbonate was interpreted as having low reservoir potential The Brown Niagaran had moderate to high reservoir potential with poor reservoir potential in the northernmost well. Figure 6-41 shows log signatures with interpreted Mclust results for cross section C-C’.

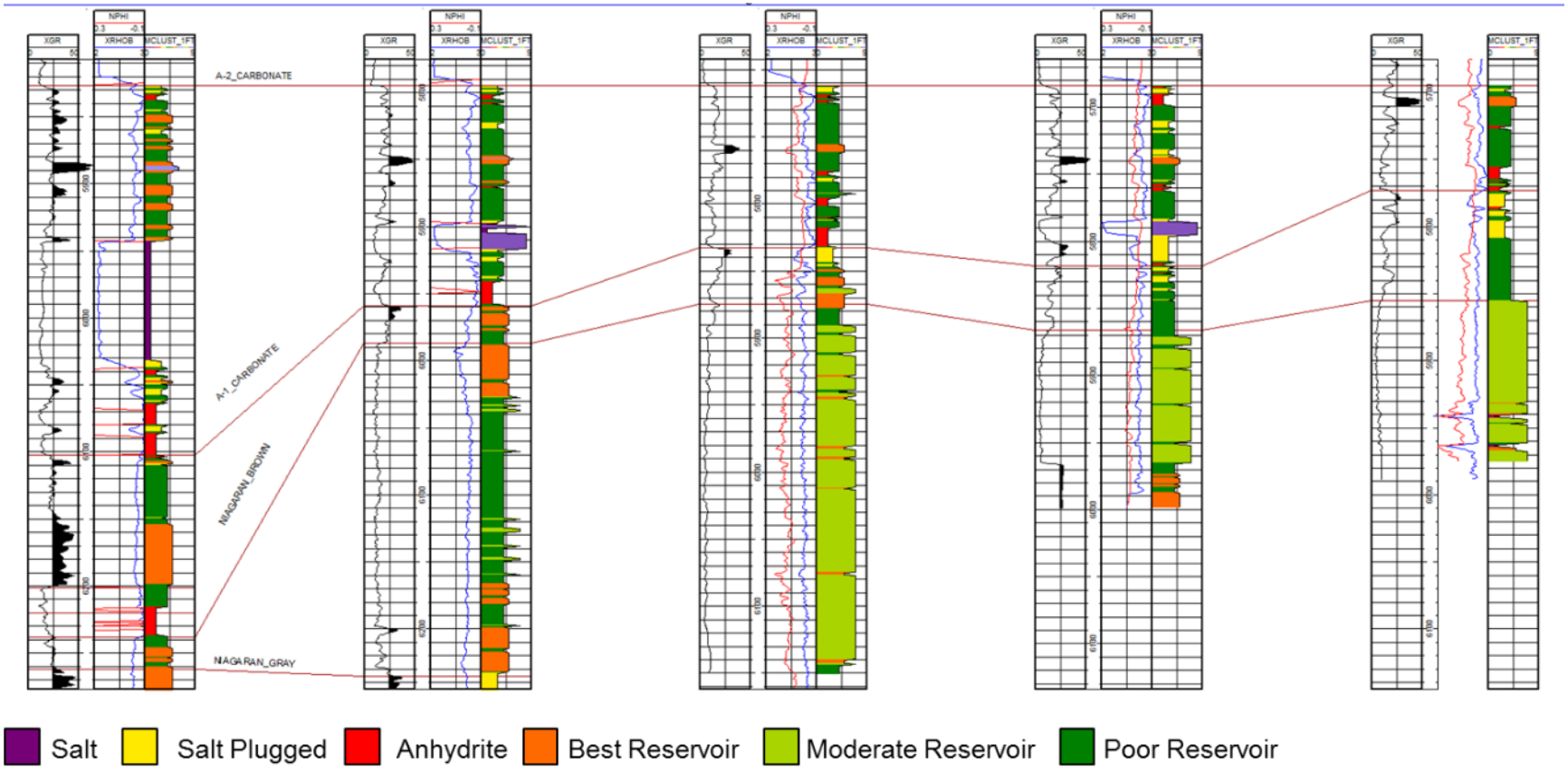


Figure 6-39. Cross section A-A' across the southern lobe of the Bagley reef field showing interpreted Mclust results.

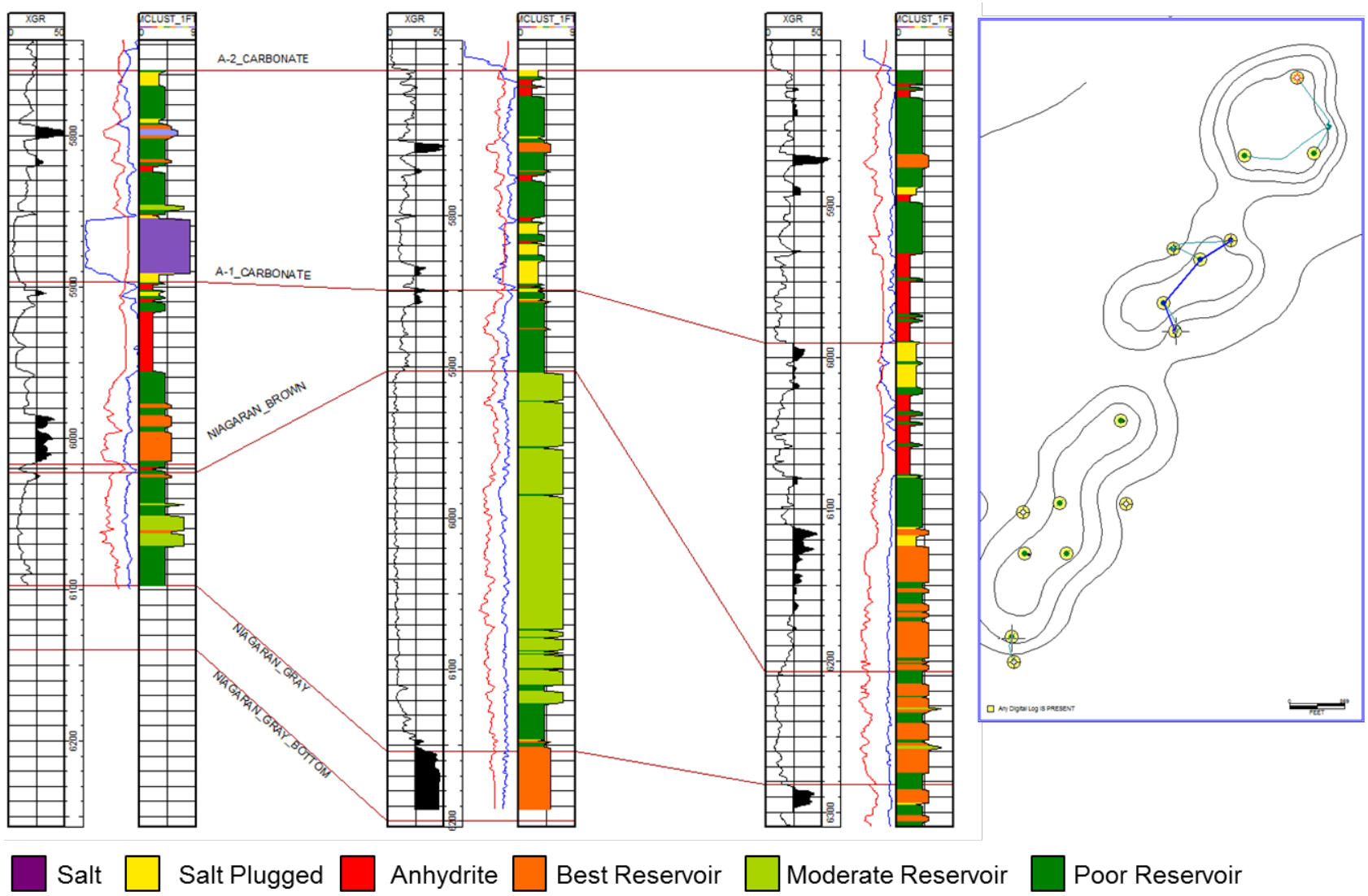


Figure 6-40. Cross section B-B' across the middle lobe of the Bagley reef field showing interpreted Mclust results.

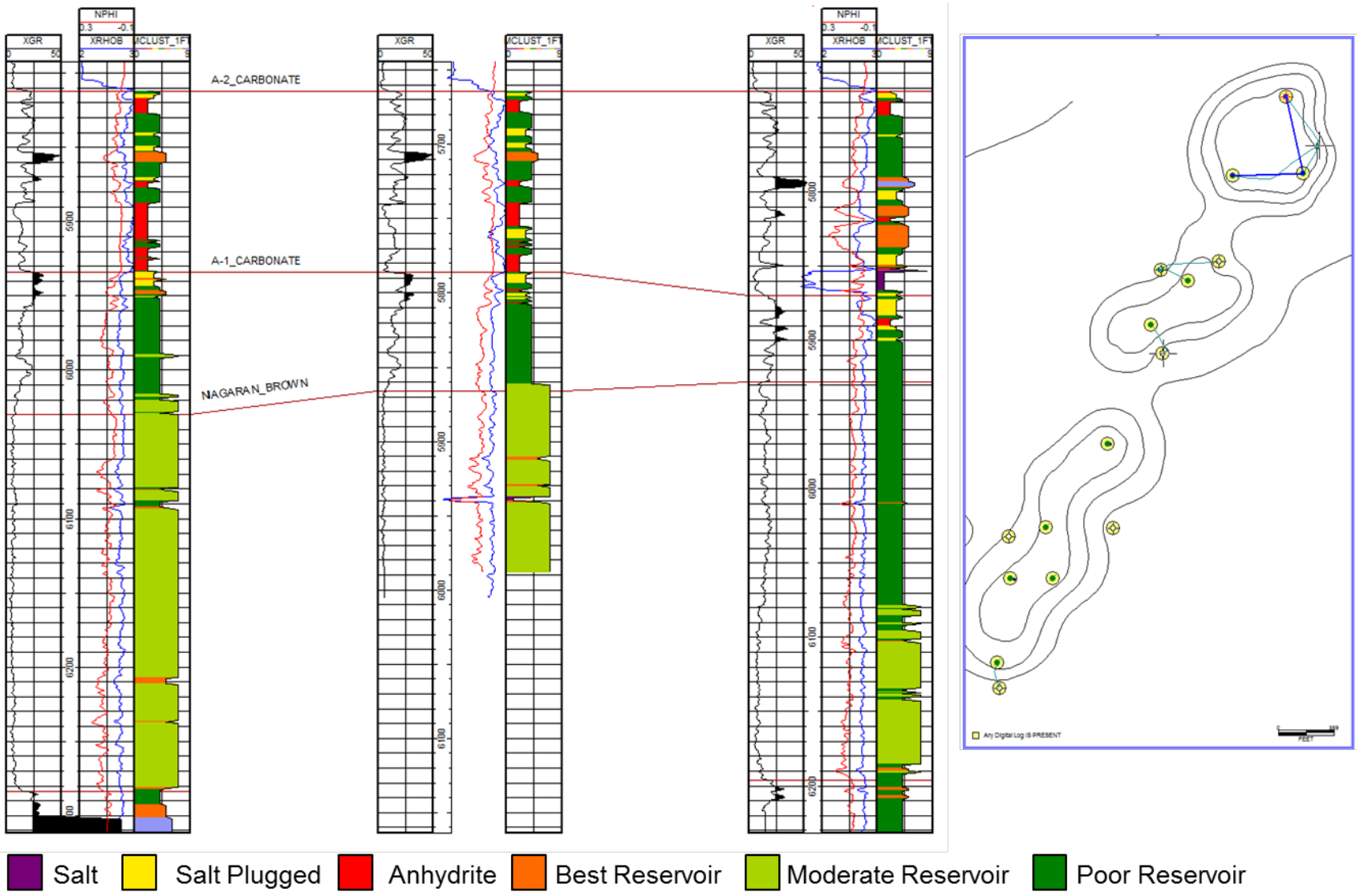


Figure 6-41. Cross section C-C' across the northern lobe of the Bagley reef field showing interpreted Mclust results.

Conclusions

Cluster analysis of the Bagley reef field showed that subdividing the reef by formations, facies, or zones did not always produce statistically different groups. Kmeans methods did not cluster data in a geologically meaningful way, but Mclust did. Mclust clusters correlated well with log data, whole core, and whole core-measured data. Salt, salt plugging, anhydrite, and different reservoir quality dolomites were successfully identified by clusters and correlated with geologic expectations.

6.5 Geologic Interpretations

The cross sections for the Bagley reef field were subdivided into the northern, middle, and southern lobes. The cross sections contain the A-2 carbonate through the Brown Niagaran intervals. All intervals except the A-1 evaporite were present in the northern lobe wells. In the middle lobe, the A-2 evaporite was not present in well 39850, and the A-1 evaporite was not present in three wells: 39850, 39748, and 39866. In the southern lobe, the A-2 evaporite, A-1 carbonate, and A-1 evaporite were not present in well 29074, and the A-1 evaporite interval was not present in three wells: 29085, 38923, and 39554.

Cross section images included gamma ray (XGR), bulk density (RHOB), and neutron porosity (XNPHI) curves for the northern, middle, and southern lobes in the Bagley reef field.

Northern Lobe

The cross-section analysis for the northern lobe in the Bagley reef field shows potential porosity in the A-2 carbonate, A-1 carbonate, and Brown Niagaran intervals for all three wells: 38240, 38286, and 37794. The porosity in the A-2 carbonate is seen in the reef core complex (well 38240), and the leeward distal reef apron (well 38286). Porosities in well 38240 are as high as 20% and occur in the lower portion of the interval. Gamma ray signatures are below 50 API, and the bulk density indicates a dolostone with some limestone indications (density less than 2.81 gm/cm^3). Thin anhydrite beds, where the RHOB trends toward 3 g/cm^3, are indicated at the top of the A-2 carbonate interval for all three wells in the northern lobe. Well 38286 in the leeward distal reef apron has a thin potential-porosity indicator in the middle of the A-2 carbonate interval. The gamma ray peaks right at 50 API, and the RHOB indicates a dolomite lithology. Potential-porosity indications were not seen in the reef core complex well 37794.

Potential-porosity indications were observed in all three northern lobe wells for the A-1 carbonate and Brown Niagaran intervals (Figure 6-42). Well 38240 had the least amount of potential porosity in the A-1 carbonate. The majority of the upper interval of this well is an anhydrite layer, indicated by the bulk density trending toward 3 g/cm^3. The lower interval is a dolomite with moderately calm gamma ray and no porosity. Wells 38286 and 37794 do not have potential porosity in the uppermost interval; however, there are porosity indications, as high as 11% (bulk density-neutron porosities) in the middle and lower intervals of the A-1 carbonate. The Brown Niagaran interval for well 38240 does not show potential porosity in the upper zone of this interval. However, as the bulk density decreases and the gamma ray calms, there is an increase in porosity indicators toward the base of the Brown Niagaran. Wells 38286 and 37794 show potential porosity in the upper, middle, and lower portions of the Brown Niagaran. The potential-porosity indication shows bulk density of dolomite and calm gamma ray signatures.

Middle Lobe

The middle lobe cross-section analysis for the Bagley reef field shows potential porosity in the A-2 carbonate, A-1 carbonate, and Brown Niagaran intervals. Cross-section analysis of the A-2 carbonate shows thin potential-porosity intervals in the reef flank (well 38859), in the reef apron (wells 39866 and 39758), and in the reef core (well 39748). The porosity indicators for each well shows a spike in gamma ray (approximately 50 API) and an increase in neutron porosity data. Thin anhydrite beds were observed in the uppermost portion of the A-2 carbonate for all of the wells except wells 39748 and 39758.

Porosity indicators were observed in all of the middle lobe wells except well 29249 in the A-1 carbonate and Brown Niagaran intervals (Figure 6-43). The bulk density for these wells show moderately thick anhydrite zones in the A-1 carbonate for reef flank wells 39850 and 29249. These anhydrites range from approximately 50 to 60 feet in thickness and show no porosity. Porosity zones in the A-1 carbonate trend toward the base of the formation, except in the reef apron (well 39866). Porosity indications in well 39866 are throughout the interval, and the anhydrite layer is absent. The Brown Niagaran has porosity indicators for all wells except well 29249 through the majority of the logged interval. Low and calm gamma ray signatures are seen where porosity indications are prevalent in this interval.

Southern Lobe

The cross-section analysis for the southern lobe in the Bagley reef field shows potential porosity in the A-2 carbonate, A-1 carbonate, and Brown Niagaran intervals. The A-2 carbonate porosity is seen in the reef talus (well 29074), reef core complex (well 29085), and reef apron (wells 39554 and 55307). Gamma ray signatures are below 50 API, and the bulk density indicates a dolostone with some limestone indications. Thin anhydrite intervals, where the RHOB trends toward 3 g/cm^3, are indicated at the top of the A-2 carbonate for all of the wells in the southern lobe. Well 38923, located on the edge of the reef core, did not show porosity indicators for this interval.

The A-1 carbonate is present in all wells except well 29074 (reef talus). Potential-porosity indications were observed in both reef core wells (38923 and 29085) and in one reef apron well (39554). (Figure 6-44). Gamma ray signatures are moderately low for these wells in this interval, and the bulk density, approximately 2.96 g/cm^3, is high in the uppermost portion of the zone for all wells. Reef core well 29085 shows porosity indications throughout the entire interval. The Brown Niagaran interval shows potential porosity in all of the southern lobe wells. Gamma ray signatures are relatively calm and combined with bulk density signatures that show a dolostone interval. Reef apron well 55307 shows moderate gamma ray signatures toward the base of the logged interval. This well is at the edge of the reef apron.

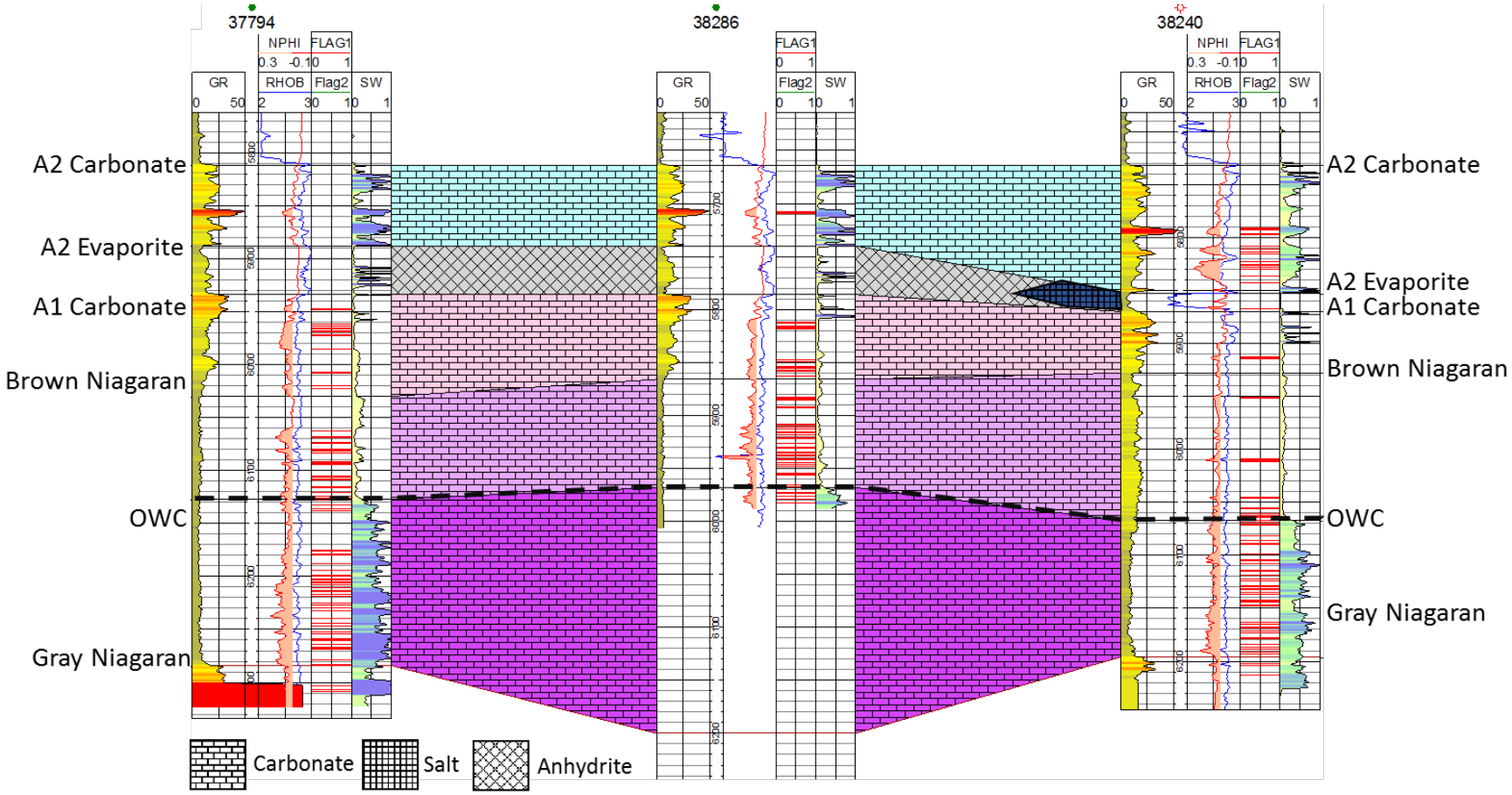


Figure 6-42. Cross section of the northern lobe of the Bagley reef field showing the GR, RHOB, and NPHI for the A-2 carbonate, A-2 evaporite, A-1 carbonate, and Brown Niagaran intervals.

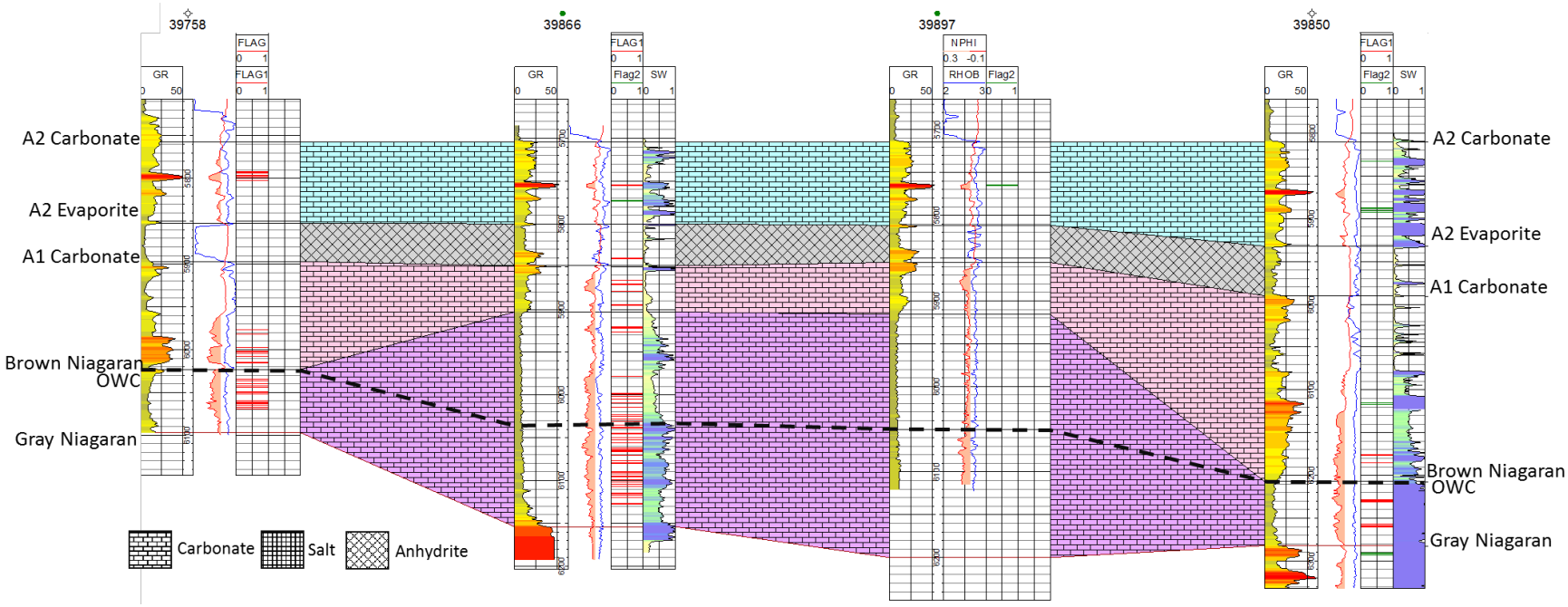


Figure 6-43. Cross section of the middle lobe of the Bagley reef field showing the XGR, RHOB, and XNPHI for the A-2 carbonate, A-2 evaporite, A-1 carbonate, A-1 evaporite, and Brown Niagaran intervals.

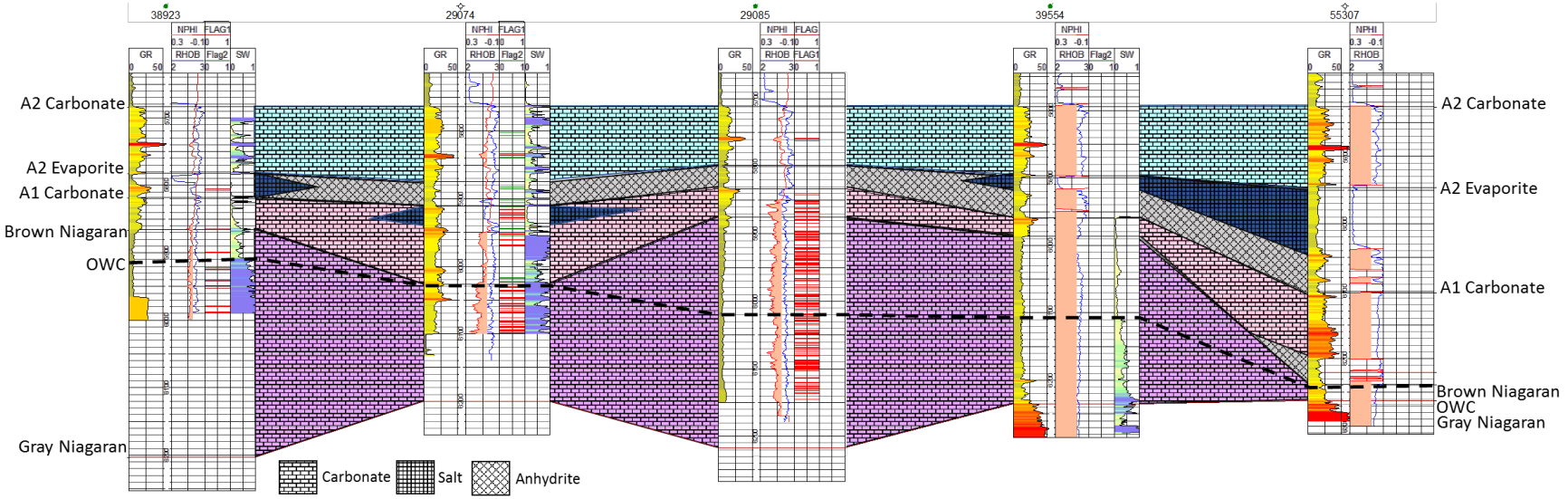


Figure 6-44. Cross section of the southern lobe of the Bagley reef field showing the XGR, RHOB, and XNPHI for the A-2 carbonate, A-2 evaporite, A-1 carbonate, A-1 evaporite, and Brown Niagaran intervals.

Geologic interpretations were developed in collaboration between Western Michigan University and Battelle for the Bagley field. The reef core, reef apron, and bioherm were composed of dolomite with moderate to high porosity. The upper section of the A-1 carbonate was composed of salt-plugged dolomite with little to no porosity. Moderate porosity/storage potential was observed along the flanks of the reef in the distal reef apron and rubble where there was vugular dolomite. Figure 6-45 illustrates the subdivisions of the interpreted flow zones in map view, and Figure 6-46 illustrates the interpreted lithofacies in a 2D cross section through the field.

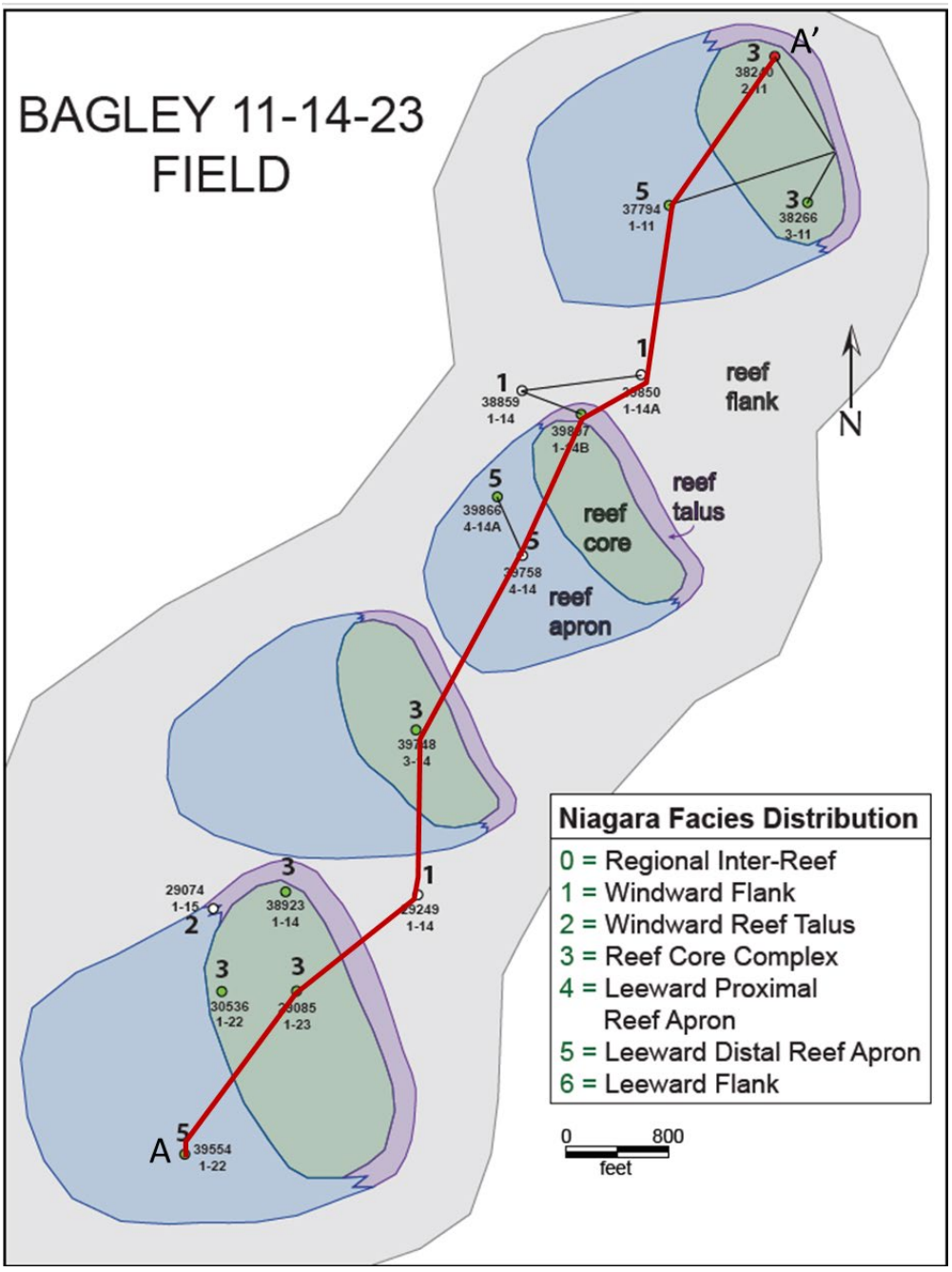


Figure 6-45. Depositional and flow zone model of the Bagley reef field in map view showing the major subdivisions.

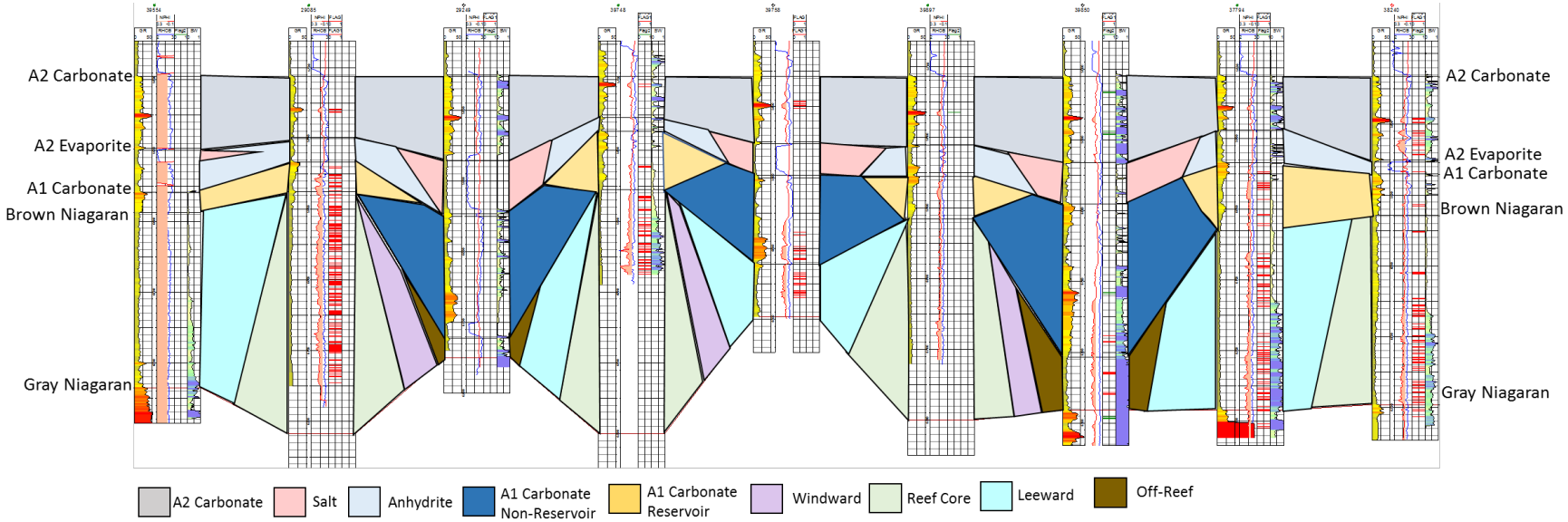


Figure 6-46. Cross section through the Bagley reef field showing lithofacies and four reef lobes.

7.0 Charlton 19

7.1 Reef History and Production Review

Production began at Charlton 19 in 1988 with a single well. A second and third well were added in 1989 and 1990 respectively. Production rates tapered off before CO_2 injection began in 2014 and subsequent EOR production in 2017 (Figure 7-1). As of 12/31/2017, 1,126,488 cumulative Bbl of oil have been produced from and 264,175 MT of CO_2 have been injected into the Charlton 19 reef. The southern pod is significantly smaller volume than the northern pod but accounts for nearly 40% of the production in the Charlton 19 reef. All wells were produced from the A1 Carbonate and Brown Niagaran formations. Figure 7-2 illustrates the cumulative production by well in the Charlton 19 reef.

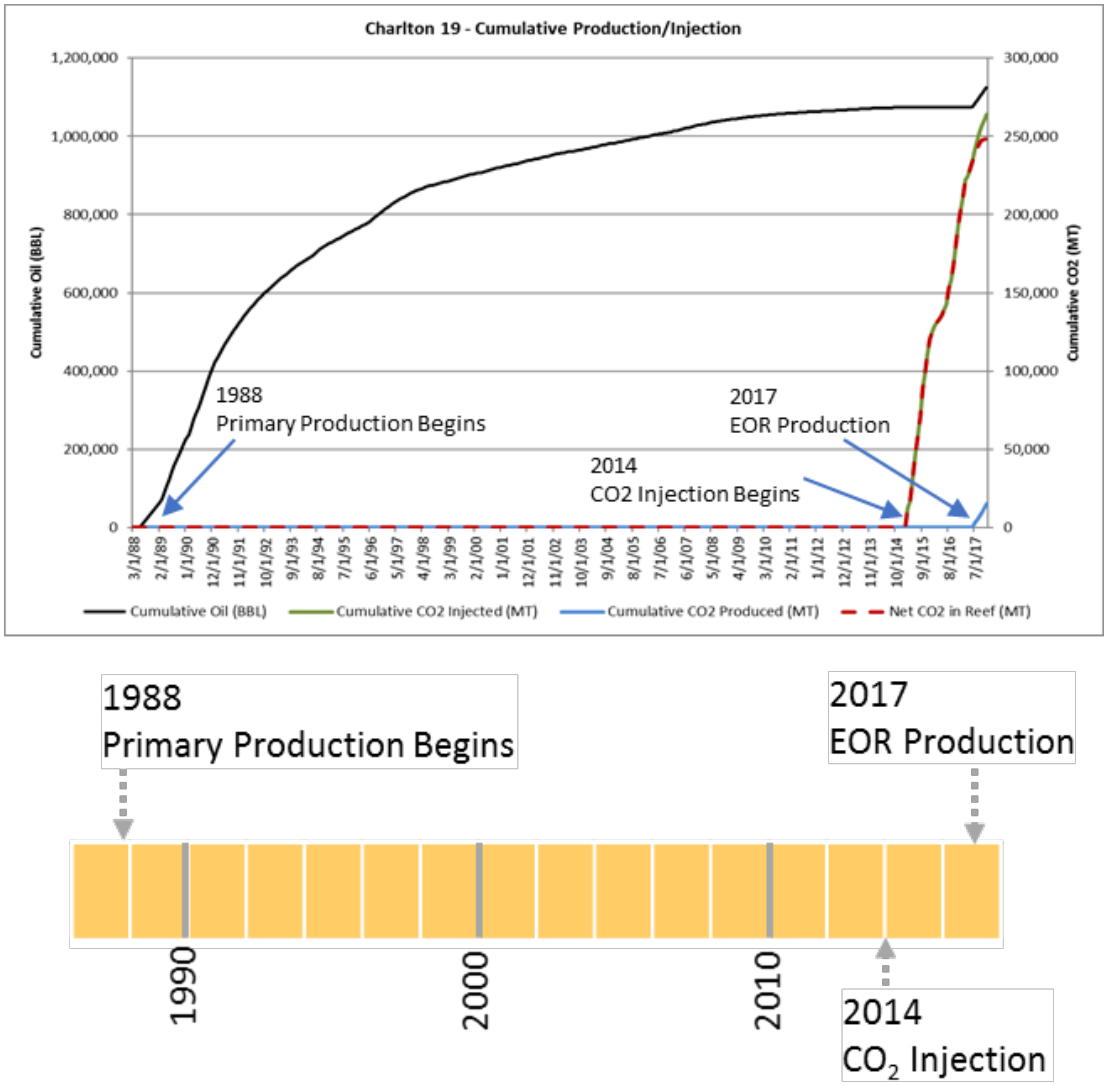


Figure 7-1. Cumulative production in the Charlton 19 reef from 1988 through 2017 showing an increase in production rates following EOR operations in 2017.

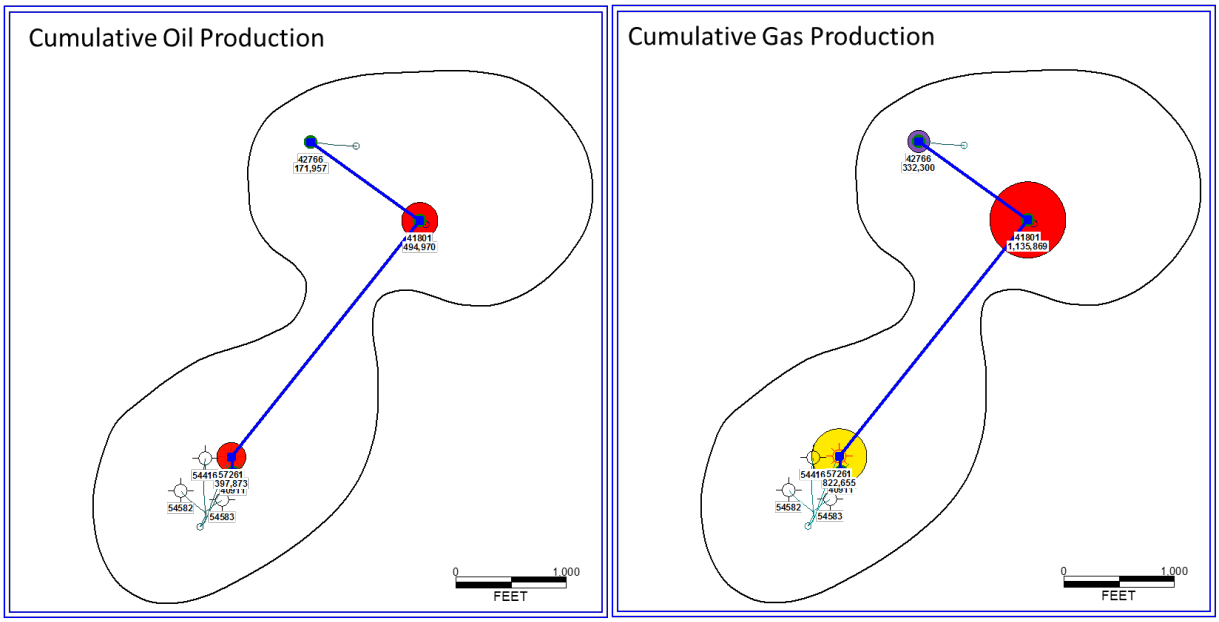


Figure 7-2. Cumulative oil and gas production by well showing the highest producers in the center of the reef pods (hot colors) and poor production along the flanks (cool colors).

The initial discovery data are summarized in Table 7-1, which includes original oil in place (OOIP), oil API gravity, discovery pressure and temperature, and fluid saturations. Initial gas saturations were recorded at zero, as gas was produced as it came out of solution during production of oil.

Table 7-1. Summary of initial discovery conditions of the Charlton 19 reef field.

		Discovery		Saturation		
Original Oil in Place (BBL)	**API Gravity**	**Pressure (PSI)**	**Temperature (oF)**	**Oil**	**Gas**	**Water**
2,634,000	42a 48.9b	2,774	103	76.72%	0%	11.35%

7.2 Wireline Log Analysis

There are eight wells which penetrate the Charlton 19 reef field in Michigan. Of these wells, five have digitized logs, and none have raster logs available. All five wells have gamma ray, bulk density, and neutron porosity logs available (Table 7-2). These wells also have various additional logs such as modern resistivity and photoelectric effect. These wells also have formation tops identified from the Glacial Drift Base to the Gray Niagaran. The three wells which do not have log data available are directional kickoffs from well 21137409110000 (Figure 7-3).

Table 7-2. Summary of wireline log data for the Charlton 19 reef; green shading indicates logs available by well.

	Well UWI	21137409110000	21137409110100	21137409110200	21137409110300	21137409110400	21137418010100	21137418010000	21137427660000
CAL	Caliper								
DT	Sonic								
GR	Gamma Ray								
LLD	Latero-Log Deep (Resistivity)								
LLS	Latero-Log Shallow (Resistivity)								
NPHI	Neutron Porosity								
PNC	Pulsed Neutron Capture					2	1		1
RHOB	Bulk Density								
BHP	Bottom Hole Pressure Monitoring								
	Permit Number	40911	54416	54582	54583	57261	61197	41801	42766
	Common Name	El Mac Hills 1-19	El Mac Hills 1-19 A	El Mac Hills 1-19 B	El Mac Hills 1-19 C	El Mac 1-19D	El Mac Hills 1-18A	El Mac Hills 1-18	El Mac 2-18

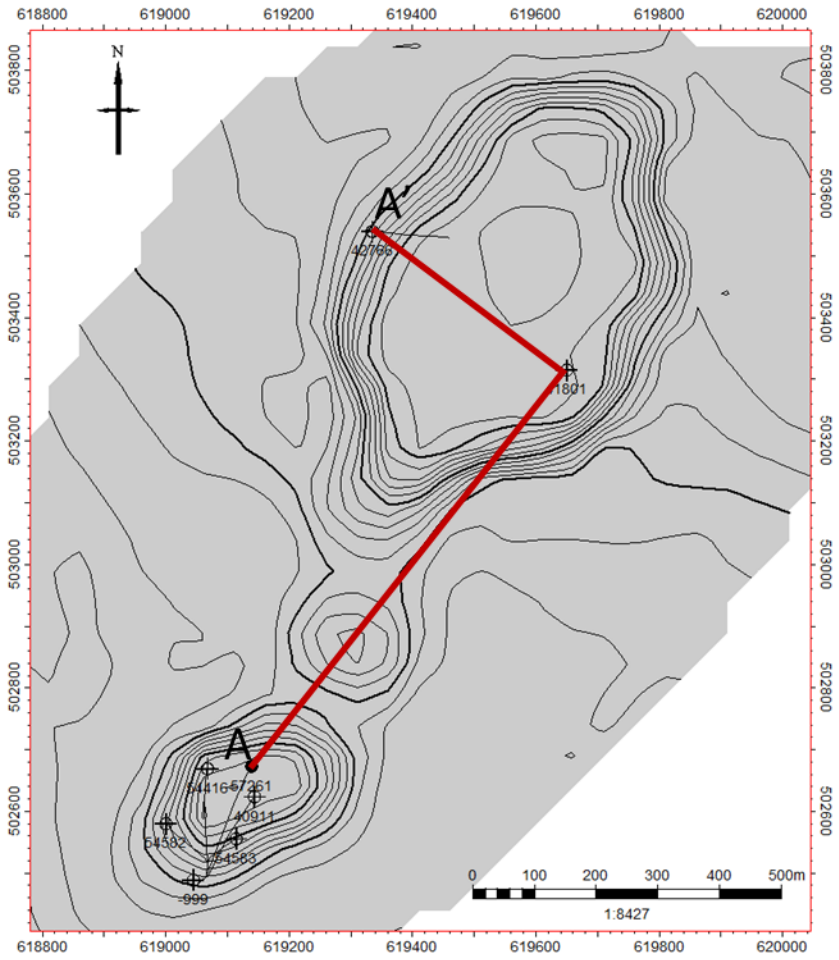


Figure 7-3. Overview map of the Charlton 19 field showing reef geometry, well locations, and cross section A-A'.

7.2.1 Basic Log Interpretation

Well 42766

Well 42766 is in the northern lobe in the Charlton 19 reef. The intervals of interest are mostly dolomite with some layers of anhydrites and salts. The anhydrite (blue flag) and salt (green flag) fall within the A2 Evaporite unit with thin intervals in the upper A1 Carbonate. Porosity above 5% (red flag) was observed primarily in the A1 Carbonate and Brown Niagaran with little to no porosity observed in the A2 Carbonate. Figure 7-4 is the neutron porosity and bulk density cross plot of well 42766.

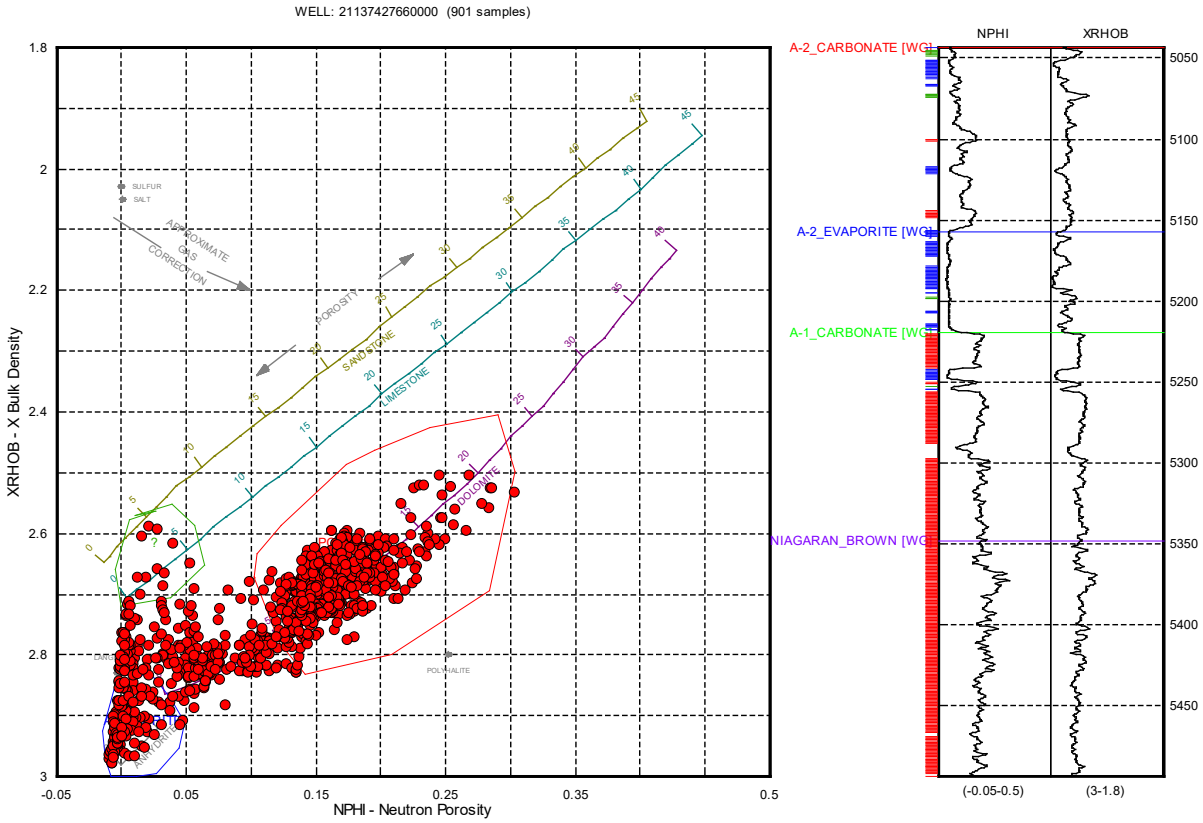


Figure 7-4. Neutron porosity and bulk density cross plot of well 42766 showing high density of rock with greater than 5% porosity (red flag) in the A1 Carbonate and Brown Niagaran.

Water saturations in the formations of interest averaged 35% with higher saturations in the presence of evaporites. The location of the well is on the flank which results in a more saturated Brown Niagaran. The Brown Niagaran had an average water saturation of 67% with a gradational increase at the top of the formation near the oil water contact. This limits the available reservoir space to the A1 Carbonate. Figure 7-5 is the histogram and water saturation curve for the A2 Carbonate to the Gray Niagaran.

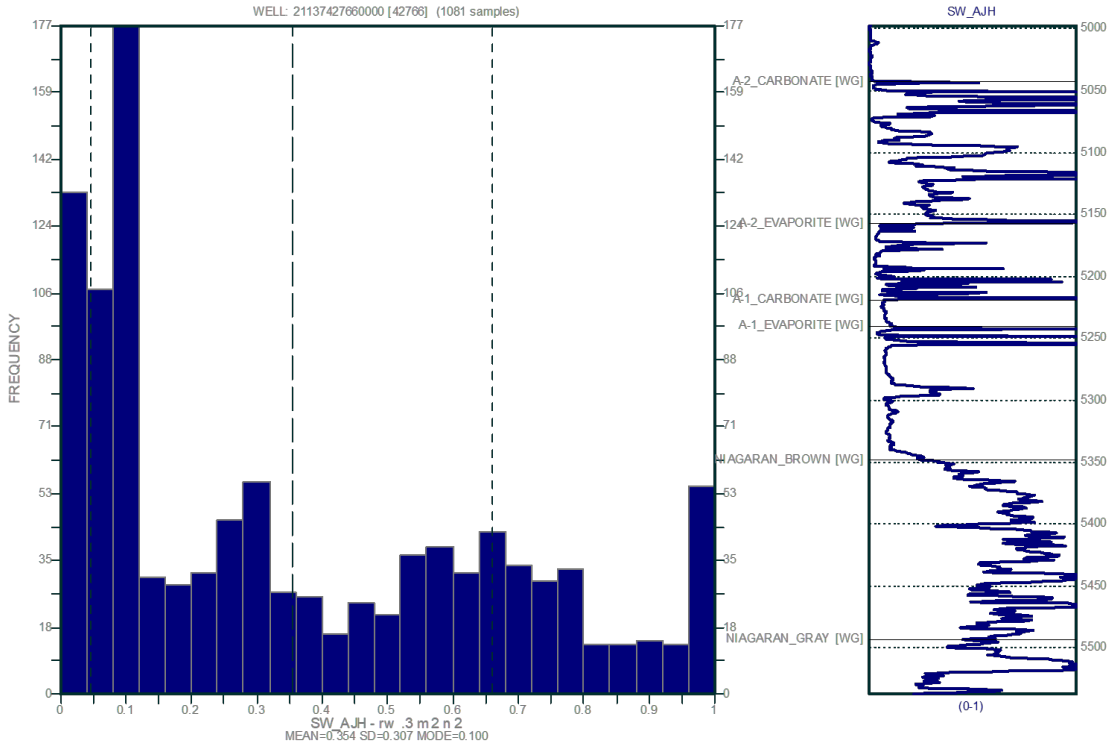


Figure 7-5. Water saturation histogram and curve over the A2 Carbonate to the Gray Niagaran for well 42766 in Charlton 19 reef showing high saturations throughout the Brown Niagaran.

Well 61197

Well 61197 is a directional well located in the southern lobe of the Charlton 19 reef. The data plotted between the dolomite and limestone lines indicates a mixed carbonate lithology with some anhydrite layers (blue). The anhydrite is present in thin intervals in the A2 Carbonate, A2 Evaporite, and upper A1 Carbonate. The best porosity (red flag) was observed in the lower A1 Carbonate and throughout the Brown Niagaran. Figure 7-6 is the neutron porosity and bulk density crossplot of well 61197.

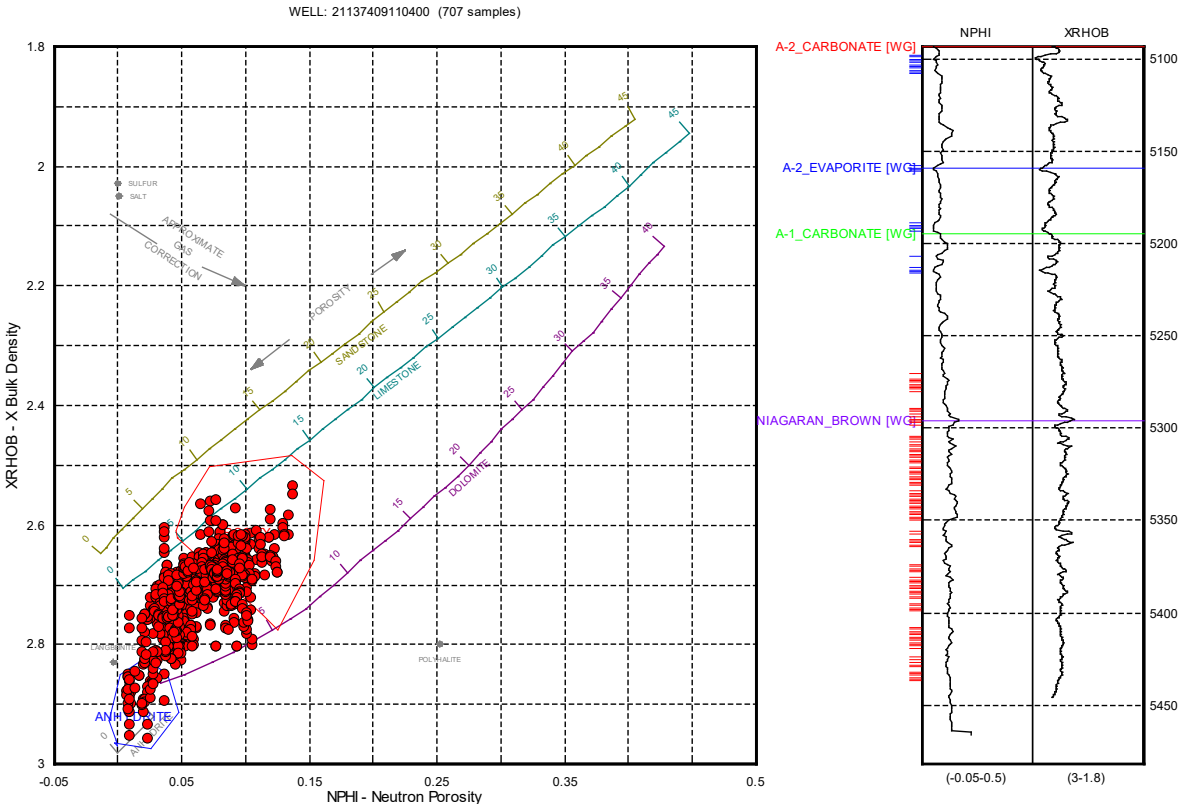


Figure 7-6. Neutron porosity and bulk density cross plot of well 61197 showing best porosity (red flags) in the lower A1 Carbonate and throughout the Brown Niagaran.

Water saturations in the formations of interest were 20% with highs in the evaporites, which is due to immoveable water. The Brown Niagaran had an overall low water saturation with an average of 28% with some values near 50% mid-Brown Niagaran. The oil-water contact is not identified due to the logging interval not covering the entire formation. There is approximately 140 ft of unsaturated Brown Niagaran present in this well. Figure 7-7 illustrates the histogram and water saturation curve over the A2 Carbonate through the mid-Brown Niagaran.

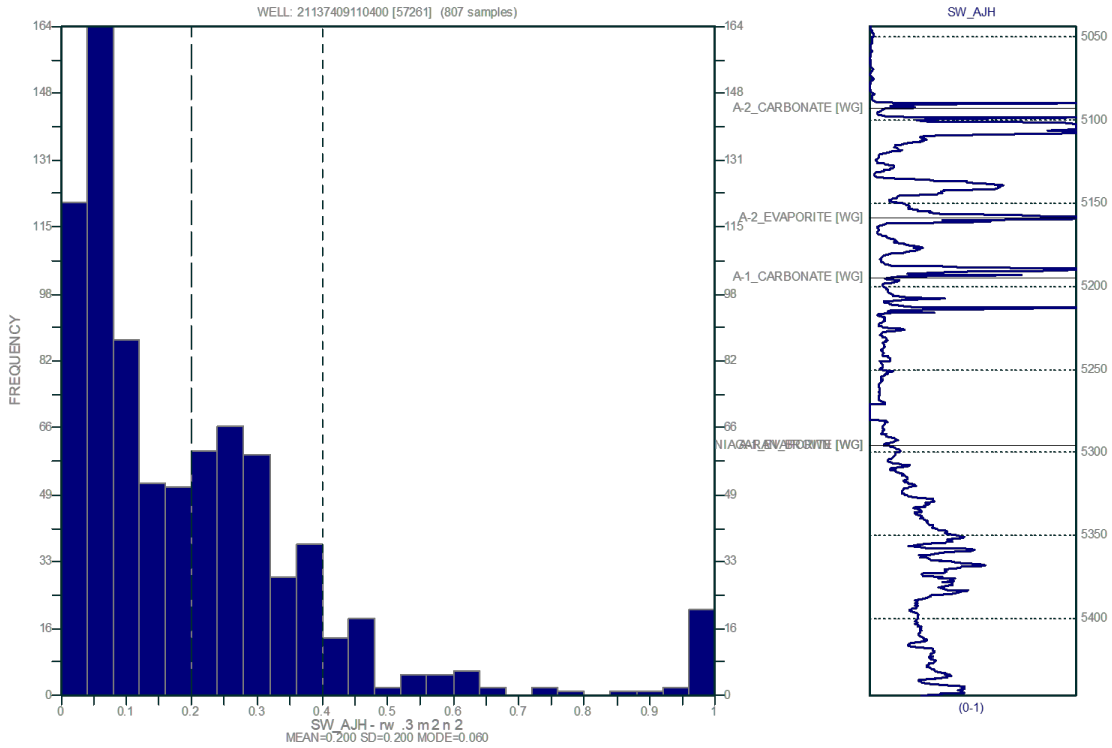


Figure 7-7. Water saturation histogram and curve over the A2 Carbonate through the Brown Niagaran for well 61197 in the Charlton 19 reef showing low water saturation values.

Well 41801

Well 41801 is in the northern lobe of the Charlton 19 reef. The intervals of interest are predominantly dolomite with intervals of anhydrite (blue flag) and salt plugging (green flag). The anhydrite was observed in the A2 Evaporite and thin intervals in the A2 Carbonate. Potential salt plugging, identified by low bulk density and erroneous neutron porosity, correlates with a series of spikes within the Brown Niagaran. This could be a result of salt plugging, but other errors are possible such as borehole conditions or logging tool issues. Porosity greater than 5% (red flag) was observed in the lower A1 Carbonate and most of the Brown Niagaran. The upper section of the A1 Carbonate has a high bulk density and low neutron porosity which could be due to anhydrite plugging. Figure 7-8 is the neutron porosity and bulk density cross plot.

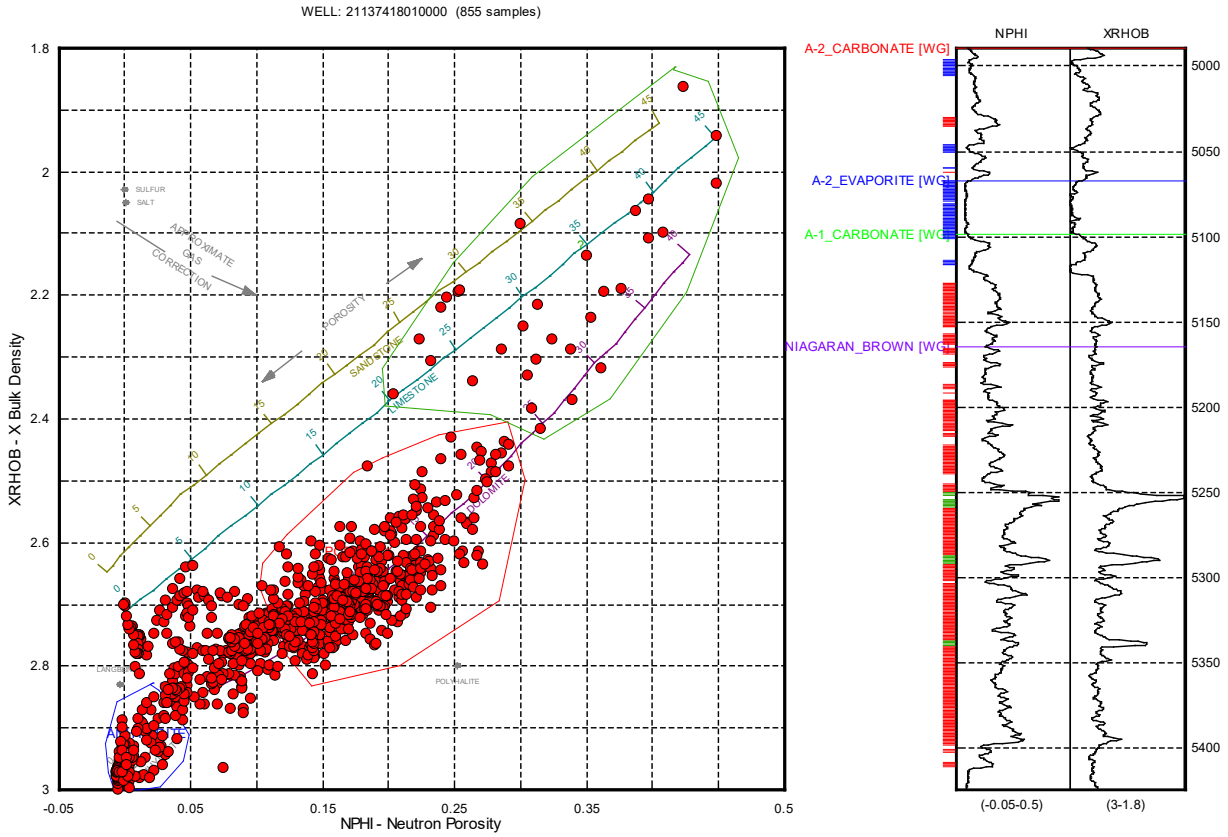


Figure 7-8. Neutron porosity and bulk density cross plot of well 41801 showing good porosity (red flags) in the lower A1 Carbonate and Brown Niagaran.

Water saturations in the formations of interest averaged 37% with higher saturations in evaporites. The oil water contact was evident mid-Brown Niagaran with a transitional zone between 5420-5480 ft MD. The Brown Niagaran had an average water saturation of 55% with approximately 100 feet of non-saturated rock. Figure 7-9 is the histogram and water saturation curve for the A2 Carbonate to the Gray Niagaran.

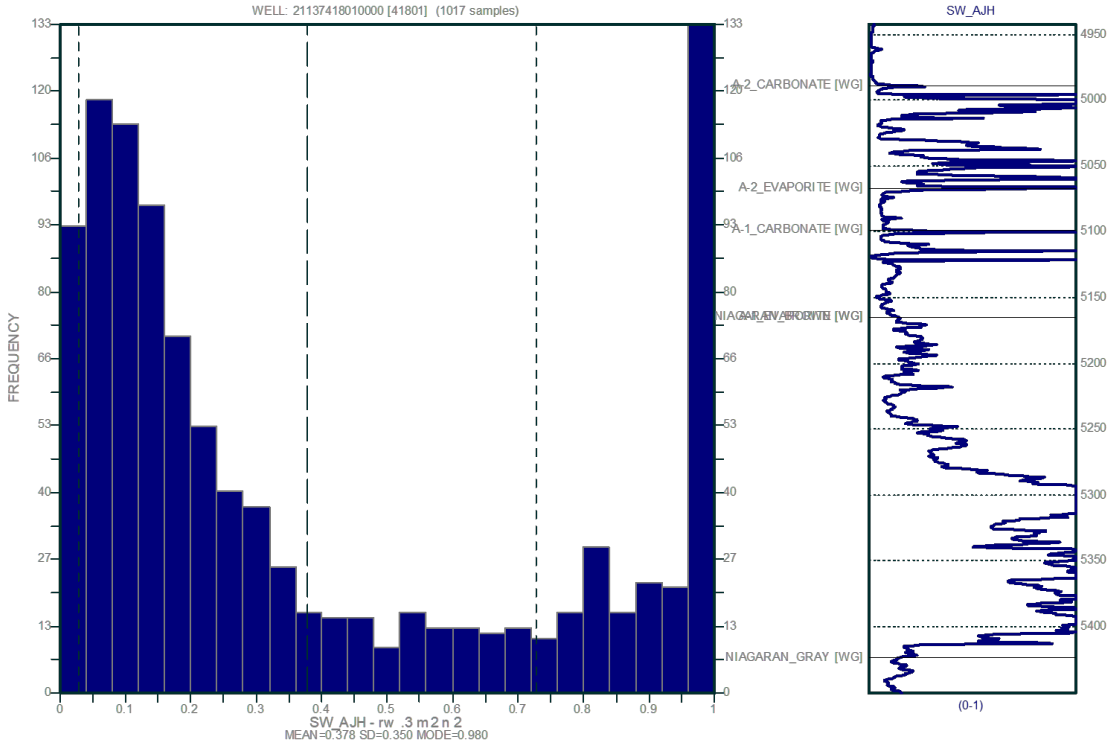


Figure 7-9. Water saturation histogram and curve over the A2 Carbonate through the Gray Niagaran for well 41801 in the Charlton 19 reef showing an increase in the Brown Niagaran at the oil water contact.

Well 40911

Well 40911 is in the southern lobe of the Charlton 19 reef. The intervals of interest are predominantly dolomite with some anhydrite (blue flag) and salts (green flags). The anhydrites and salts mostly occur in the A2 Evaporite with some thin intervals in the A2 Carbonate and upper A1 Carbonate. The best porosity (red flag) was observed in the lower A1 Carbonate and throughout the Brown Niagaran. Figure 7-10 is the neutron porosity and bulk density cross plot.

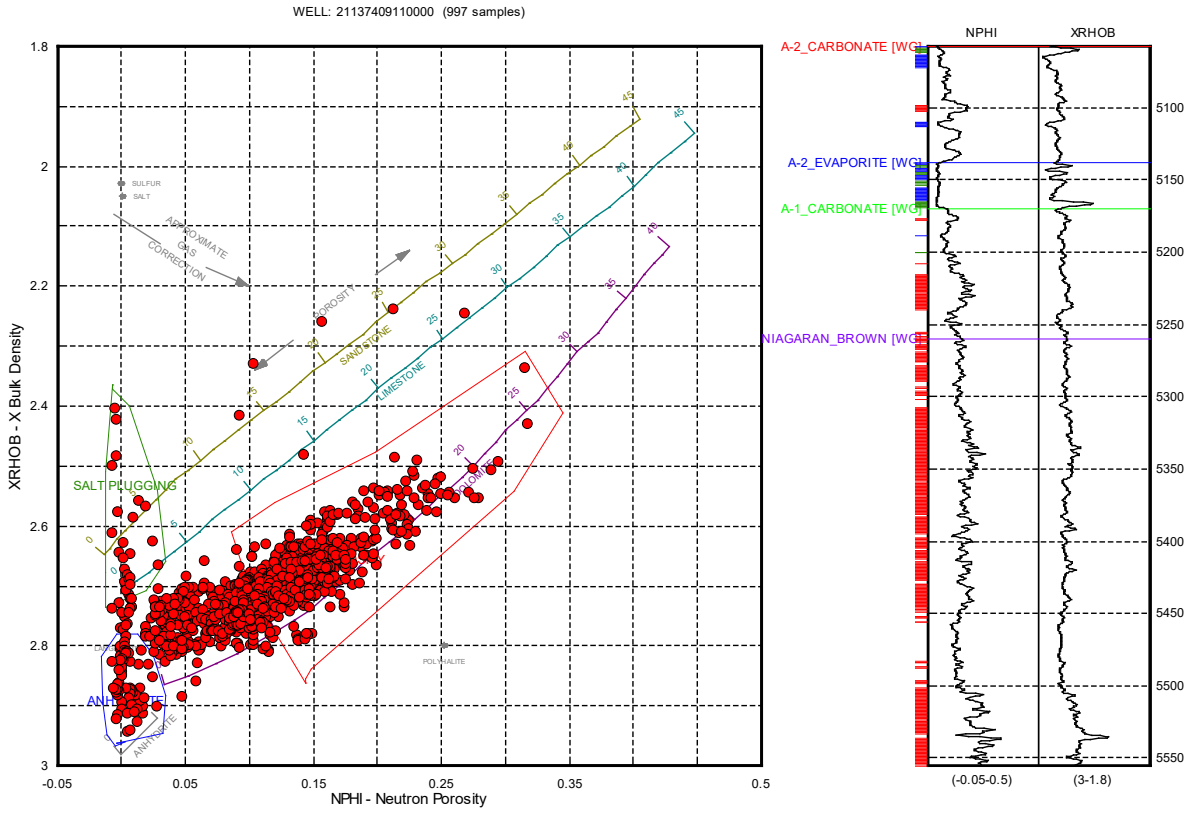


Figure 7-10. Neutron porosity and bulk density crossplot of well 40911 showing the best porosity (red flags) in the lower A1 Carbonate and throughout the Brown Niagaran.

The average water saturation was 33% over the formations of interest with higher values in the evaporites due to immoveable water. The oil water contact was identified mid-Brown Niagaran near 5380 ft MD. The Brown Niagaran had approximately 120 ft of unsaturated reservoir with an overall average of 40%. Figure 7-11 illustrates the histogram and water saturation curve for the A2 Carbonate through the Gray Niagaran.

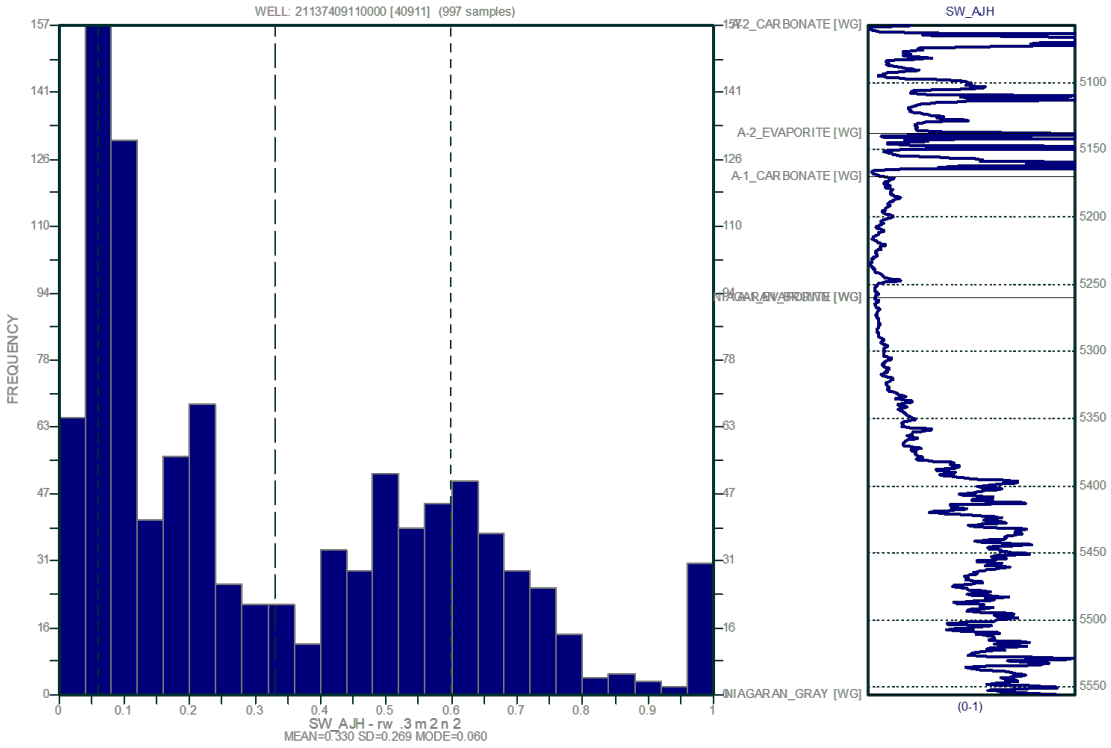


Figure 7-11. Water saturation histogram and curve from the A2 Carbonate through the Gray Niagaran for well 40911 in the Charlton 19 reef field showing an increase mid-Brown Niagaran at the oil water contact.

Well 57261

Well 57261 is a directional well located in the southern lobe of the Charlton 19 reef. The data plotted between the dolomite and limestone lines indicating a mixed carbonate lithology with some anhydrite layers (blue). The anhydrite occurred in thin intervals in the A2 Carbonate, A2 Evaporite, and upper A1 Carbonate. The best porosity (red flag) was observed in the lower A1 Carbonate and throughout the Brown Niagaran. Figure 7-12 is the neutron porosity and bulk density crossplot.

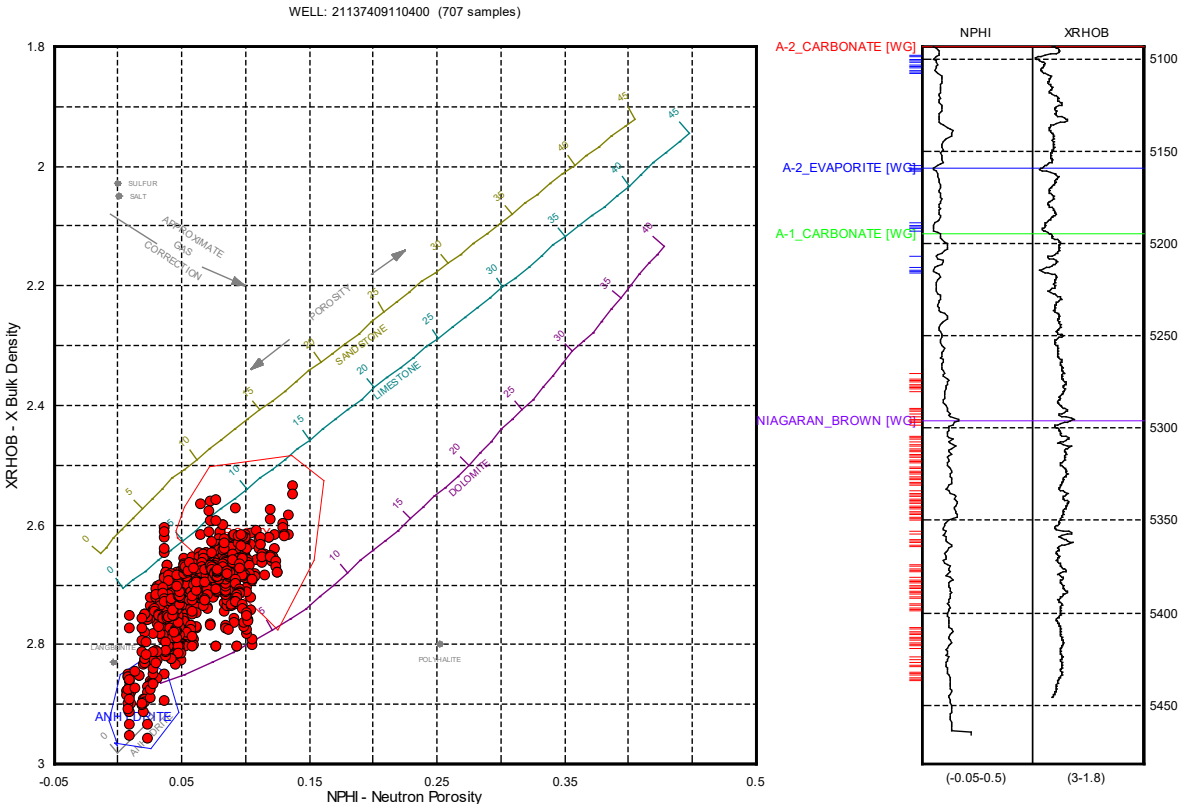


Figure 7-12. Neutron porosity and bulk density cross plot of well 57261 showing best porosity (red flags) in the lower A1 Carbonate and throughout the Brown Niagaran.

The average water saturation over the formations of interest was 20% with highs in the evaporites due to immoveable water. The Brown Niagaran had an overall low water saturation with an average of 28% with some saturations near 50% mid-Brown Niagaran. The oil-water contact could not be identified due to the logging interval not covering the entire formation. There is approximately 140 ft of unsaturated Brown Niagaran in this well. Figure 7-13 illustrates the histogram and water saturation curve over the A2 Carbonate through the mid-Brown Niagaran.

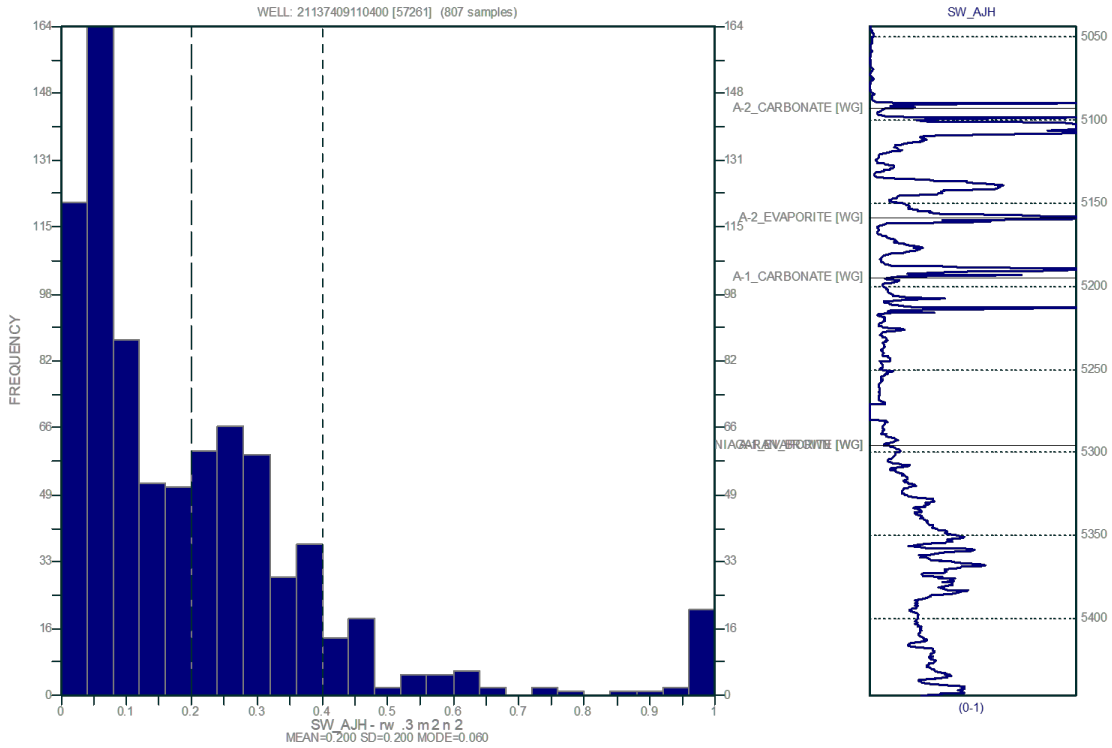


Figure 7-13. Water saturation histogram and curve over the A2 Carbonate through the Brown Niagaran for well 57261 in the Charlton 19 reef showing low water saturation values.

El-Mac Hills 1-18A

The El-Mac Hills 1-18A well was drilled in the northern reef along the southern edge. The A1 Carbonate plots and a mixed carbonate with very little porosity. It has one thin interval of porosity greater than 5% mid-formation (Figure 7-14). The Brown Niagaran is relatively thick and plots as a mixed carbonate to dolomitic with significant porosity development throughout. The water saturation is high through most of the Brown Niagaran, leaving approximately 50 feet between the oil water contact and reef top (Figure 7-15). For more detailed log analysis of the El-Mac Hills 1-18A see Attachment 4.

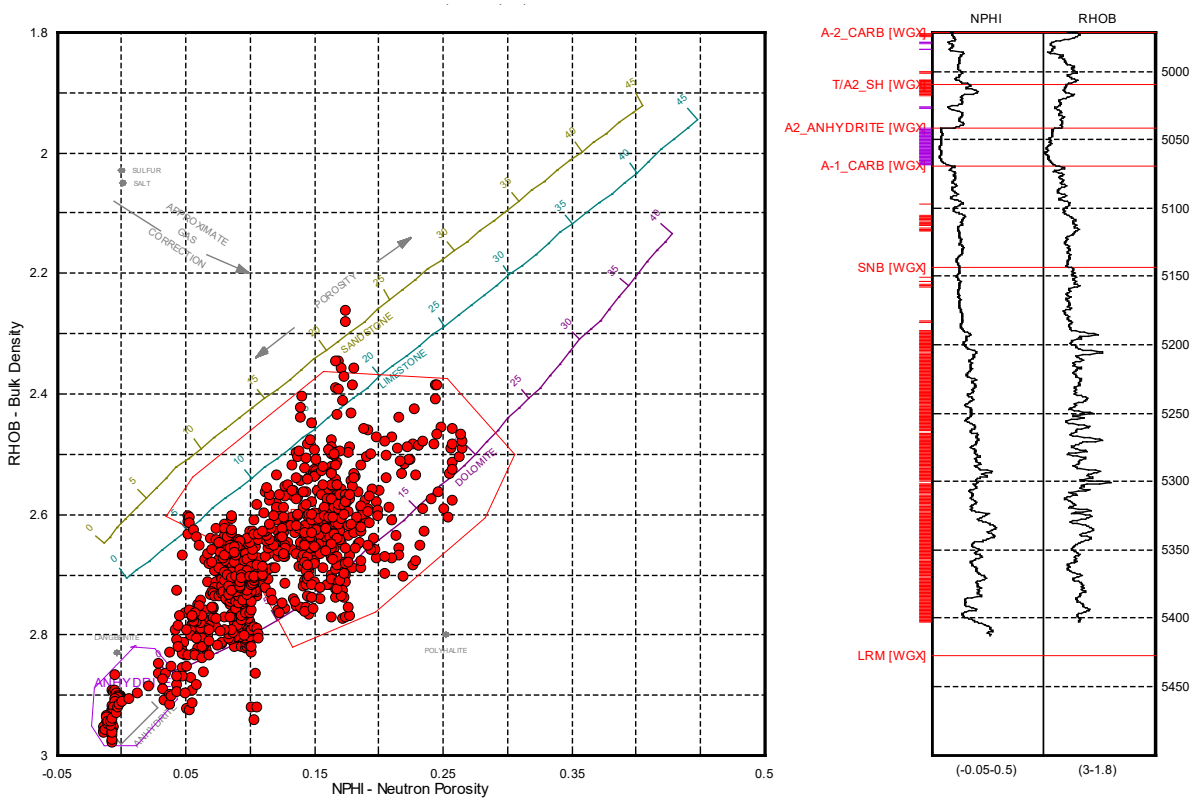


Figure 7-14. Neutron porosity and bulk density cross plot of El Mac Hills 1-18A showing best porosity (red flags) throughout the Brown Niagaran.

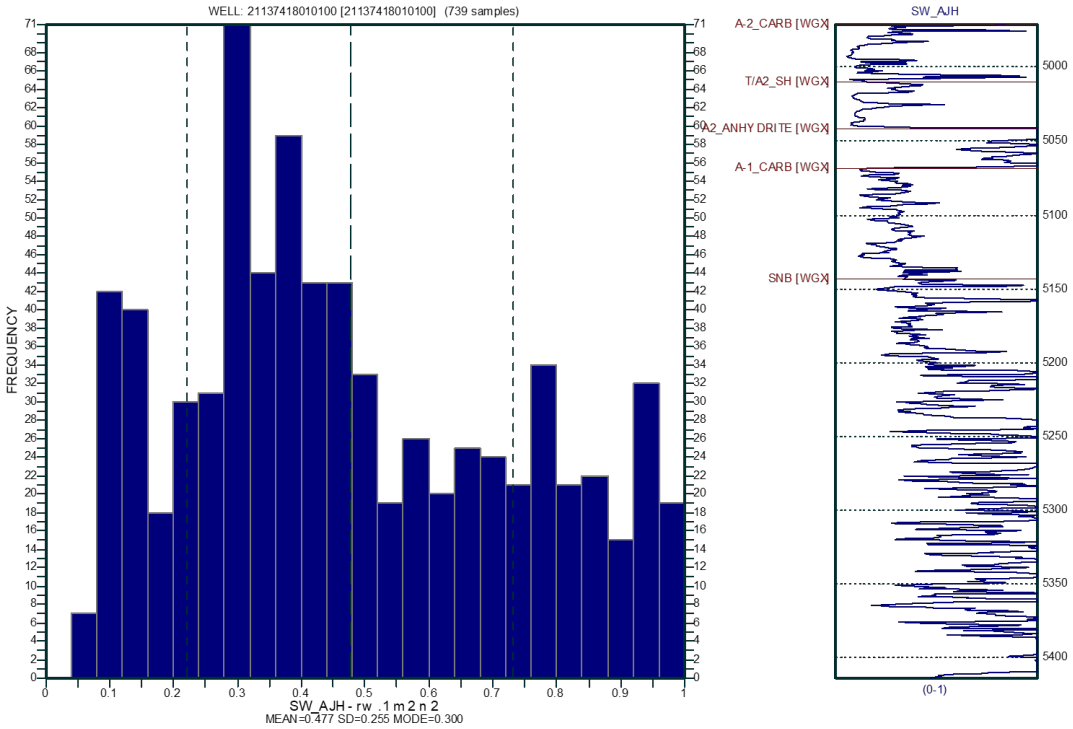


Figure 7-15. Water saturation histogram and curve over the A2 Carbonate through the Brown Niagaran for El Mac Hills 1-18A in the Charlton 19 reef showing a high oil water contact in the Brown Niagaran.

7.2.2 Petrophysical Calculations

For consistency across wells and log vintages, neutron porosity was used for petrophysical calculations. The original neutron porosity logs were collected on a limestone matrix which is known to overestimate dolomitic rocks. The reported values are likely overestimated due to the high dolomite content.

A2 Carbonate

The A2 Carbonate is mostly dolomite with up to 34% limestone and thin intervals of anhydrite. The thickness ranged from 62 ft to 114 ft with the net thickness ranging from 20 to 63 feet using a 5% porosity cutoff. The average porosity ranged from 4.6% to 8.3%. Using a water saturation cutoff of 40%, the net thickness and NTG decreased. This is due to the sensitivity of the resistivity tool to evaporites. The porosity curves overestimate the porosity in evaporites and the water saturation cutoff excludes the evaporites for a more realistic calculation**.** Table 7-3 summarizes the petrophysical calculations for the A2 Carbonate.

Table 7-3. Average petrophysical calculations for the A2 Carbonate in the Charlton 19 reef.

Avg. Thick.	Avg. Porosity	Avg. Net Thick.	Avg NTG	Avg. SW	Avg. Net Thick (Sw<40%)	Avg. NTG (Sw<40%)
80 ft	6.0%	35 ft	.44	36%	28 ft	.36

A1 Carbonate

The A1 Carbonate is mostly dolomitic with up to 50% limestone and thin intervals of anhydrite. Anhydrite only occurs in the upper 10-20 feet. The thickness ranged from 66 to 129 feet with a net thickness range of 48 to 116 feet using a 5% porosity cutoff. The average porosity ranged from 6% to 13.8%. The best porosity was consistently observed in the lower section of the A1 Carbonate. Applying a water saturation cutoff of 40% did not significantly influence the petrophysical calculations. Table 7-4 summarizes the petrophysical calculations for the A1 Carbonate.

Table 7-4. Average petrophysical calculations for the A1 Carbonate in the Charlton 19 reef field.

Avg. Thick.	Avg. Porosity	Avg. Net Thick.	Avg NTG	Avg. SW	Avg. Net Thick (Sw<40%)	Avg. NTG (Sw<40%)
89 ft	9.2%	75 ft	.80	11%	72 ft	.79

Brown Niagaran

The Brown Niagaran is mostly dolomitic with up to 36% limestone and thin intervals of potential salt plugging. The thickness ranged from 140 feet to 284 feet with a net thickness range of 145 to 283 feet using a 5% porosity cutoff. The best porosity was observed throughout most of the Brown Niagaran interval. Applying a water saturation cutoff of 40% greatly decreased the net thickness and NTG due to the oil water contact occurring mid-formation. Table 7-5 summarizes the petrophysical calculations for the Brown Niagaran.

Table 7-5. Average petrophysical calculations for the Brown Niagaran in the Charlton 19 reef field.

Avg. Thick.	Avg. Porosity	Avg. Net Thick.	Avg NTG	Avg. SW	Avg. Net Thick (Sw<40%)	Avg. NTG (Sw<40%)
216 ft	14.4%	224 ft	.98	48%	78 ft	.39

7.3 Seismic Analysis

The Charlton 19 reef has steep boundaries on the time horizons outlining the reef. There are two distinct pods; one northern and one southern (Figure 7-16). The time horizons suggest some connectivity between the two pods with a saddle in between. The A1 Carbonate was too thin over the Brown Niagaran to be traced (Figure 7-17). The resulting surface shows a higher build-up in the northern pod. The A2 Carbonate was a continuous horizon and shows subtle increases in elevation over the northern most pod with a slight high over the southern pod (Figure 7-18).

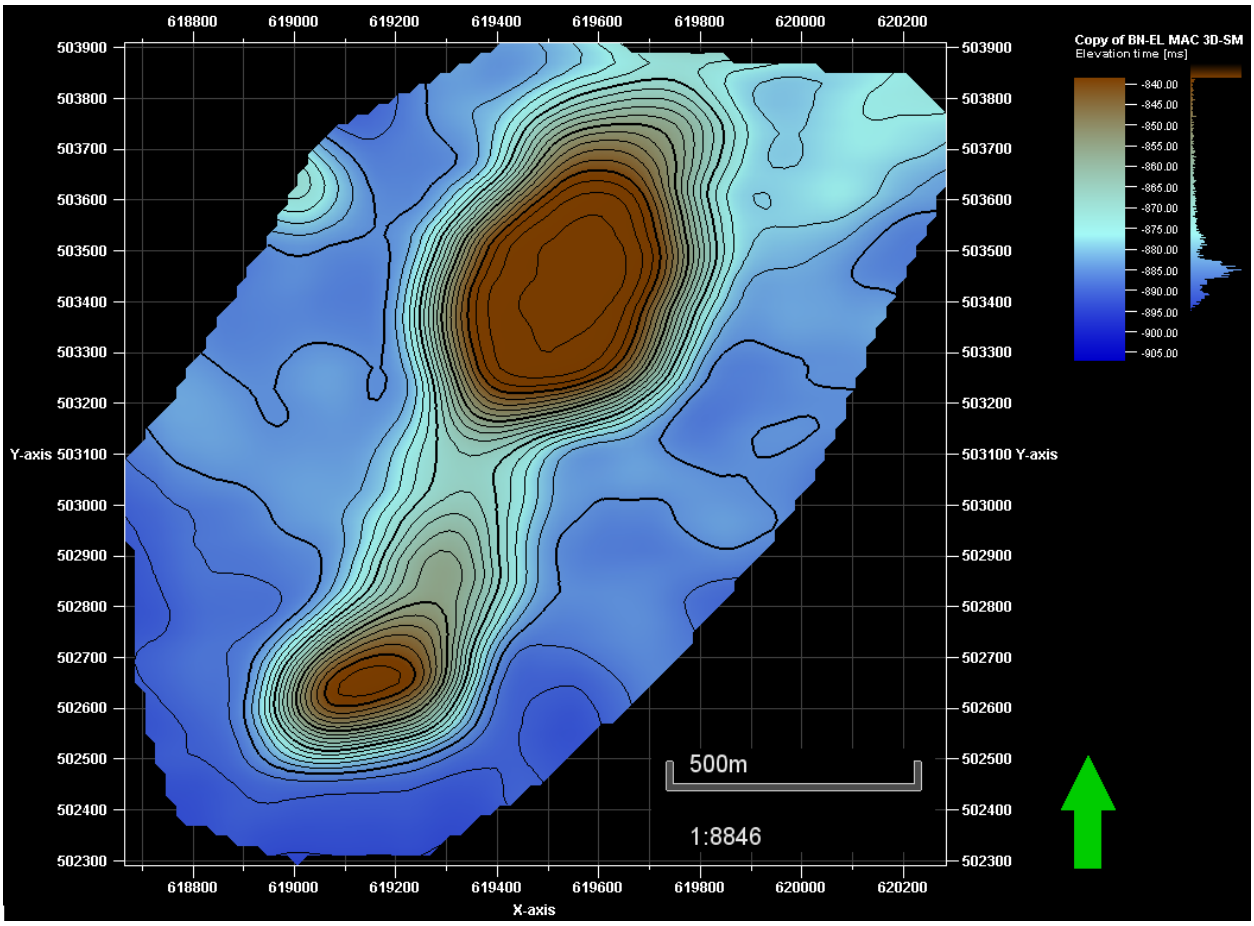


Figure 7-16. Time horizon surface of the Brown Niagaran showing the geometry of the Charlton 19 reef field.

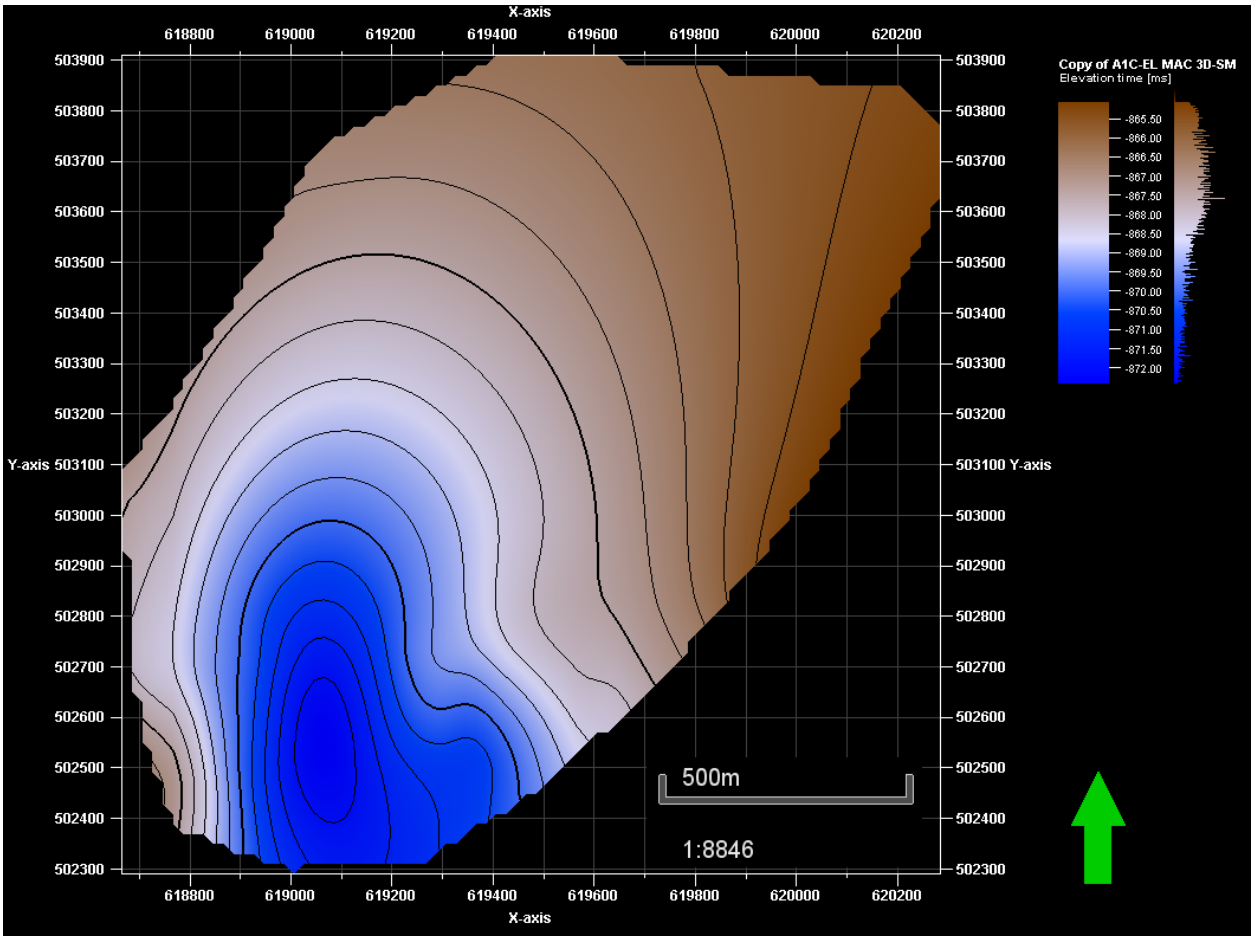


Figure 7-17. Time horizon surface of the A1 Carbonate over the Charlton 19 reef field.

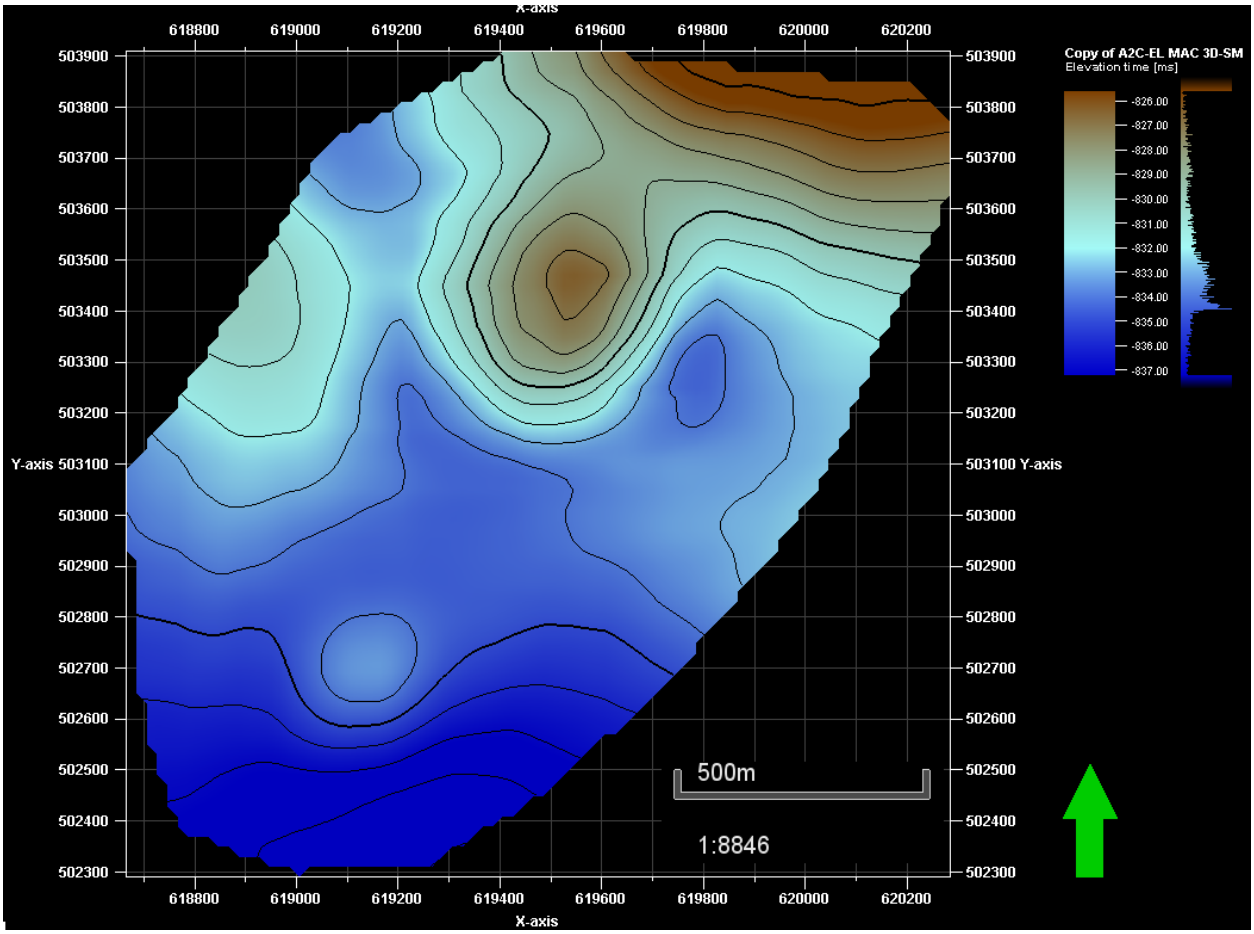


Figure 7-18. Time horizon surface for the A2 Carbonate showing gentle slopes around the northern pod of Charlton 19 with a subtle high over the southern pod.

7.4 Geologic Interpretations and Data Integration

The cross section for the Charlton 19 reef field contained the A2 Carbonate through the Brown Niagaran intervals. The cross section was flattened on the top of the A2 Carbonate. Cross section displays included gamma ray (GR), bulk density (RHOB), average neutron-bulk density porosity, and intervals of interest (flag). Figure 7-3 shows the location of cross section A-A' across the Charlton 19 reef field.

Cross section A-A' has two wells in the southern lobe and two wells in the northern lobe. Wells 40911, 57261, 61197, and 41801 are all located in the main reef core. Well 42766 is a flank well marked by the increased thickness of the A2 Carbonate and A1 Carbonate and a decreased in the Brown Niagaran thickness. Porosity in the A1 Carbonate is in the base of the A1 Carbonate. The upper A1 Carbonate in the northern lobe has spikes of high bulk density and low porosity which is indicative of anhydrite intervals. The northern lobe could also have some salt plugging as indicated by low bulk density and high porosity. The water saturation curve shows the oil water contact mid-Brown Niagaran where the saturation increases above 40%. Figure 7-19 is cross section A-A' through the Charlton 19 field.

The Charlton 19 reef field was interpreted to have two separate reef pods with little to no connection between pods. The northern most pod is the largest with only two wells penetrating the leeward facies. The southern pod is significantly smaller with all wells occurring either in the flank or in the leeward facies. Well 57261 might have penetrated the reef cores, however the well was not drilled to the Gray Niagaran

so full thickness of the Brown Niagaran is unknown. Figure 7-20 is a lithofacies map of the Brown Niagaran for the Charlton 19 reef field while Figure 7-21 is a cross section depicting geologic interpretation of the reef.

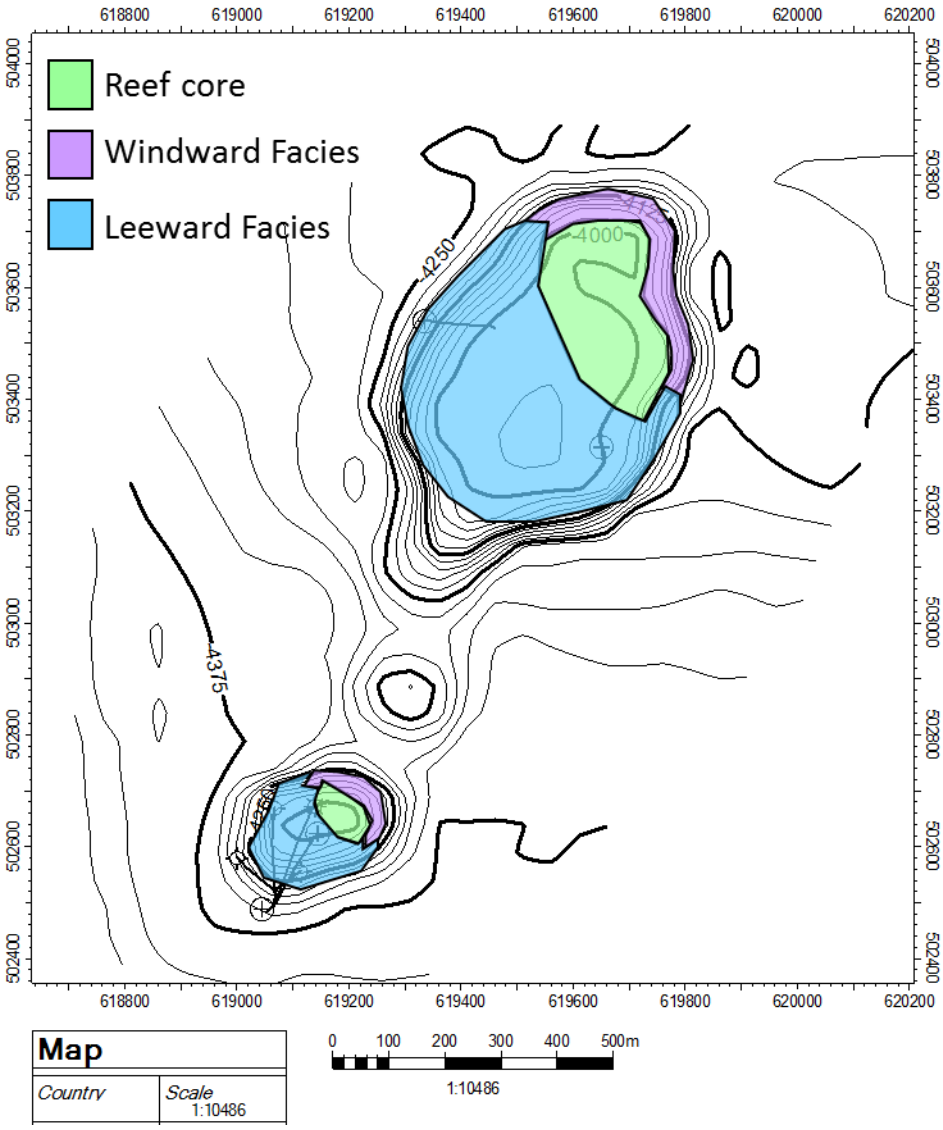


Figure 7-19. Lithofacies map of the Brown Niagaran in the Charlton 19 reef field showing two separate reef pods.

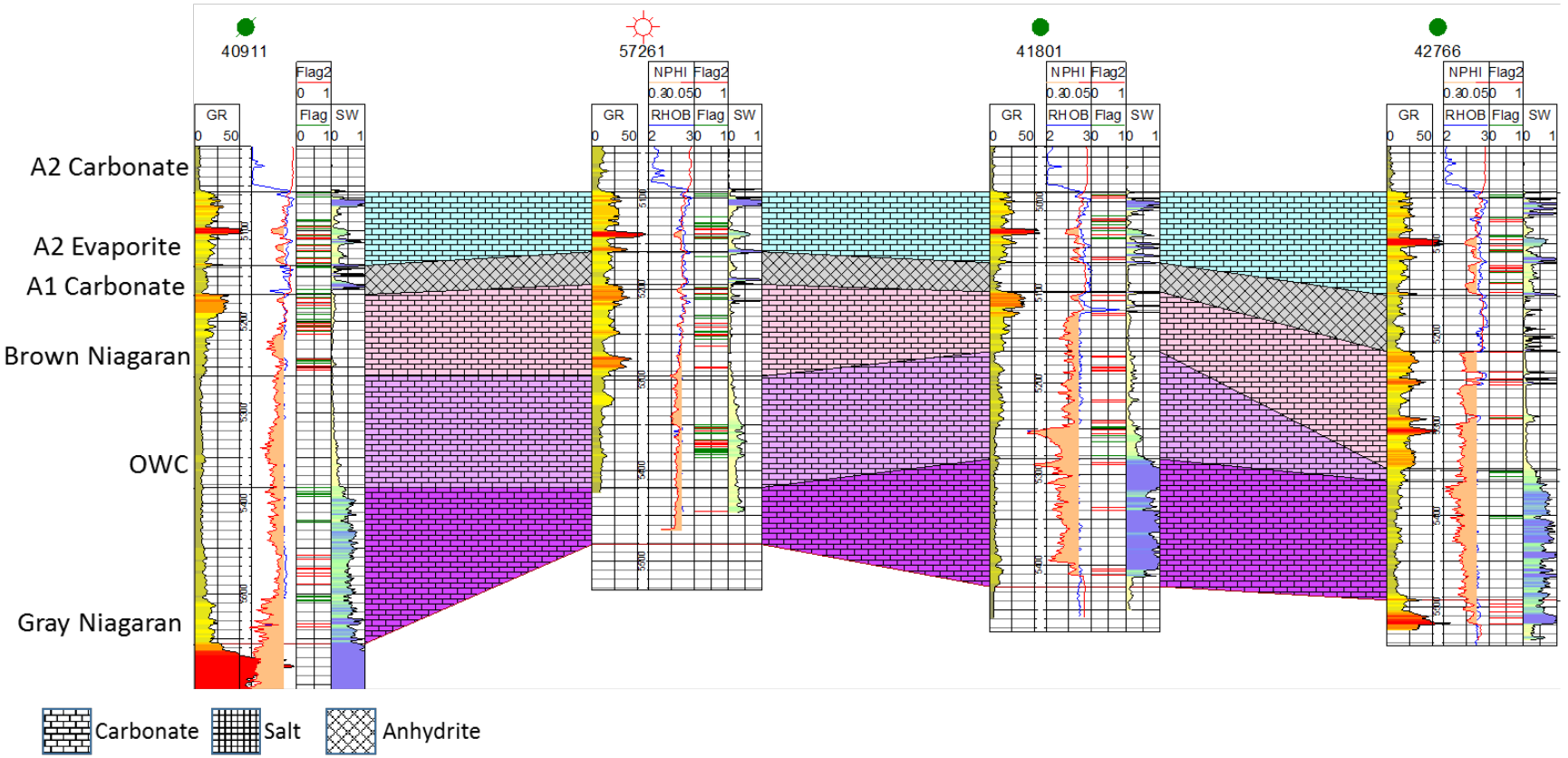


Figure 7-20. Cross section A-A' across the Charlton 19 field showing porosity trends in the lower A1 Carbonate and throughout the Brown Niagaran.

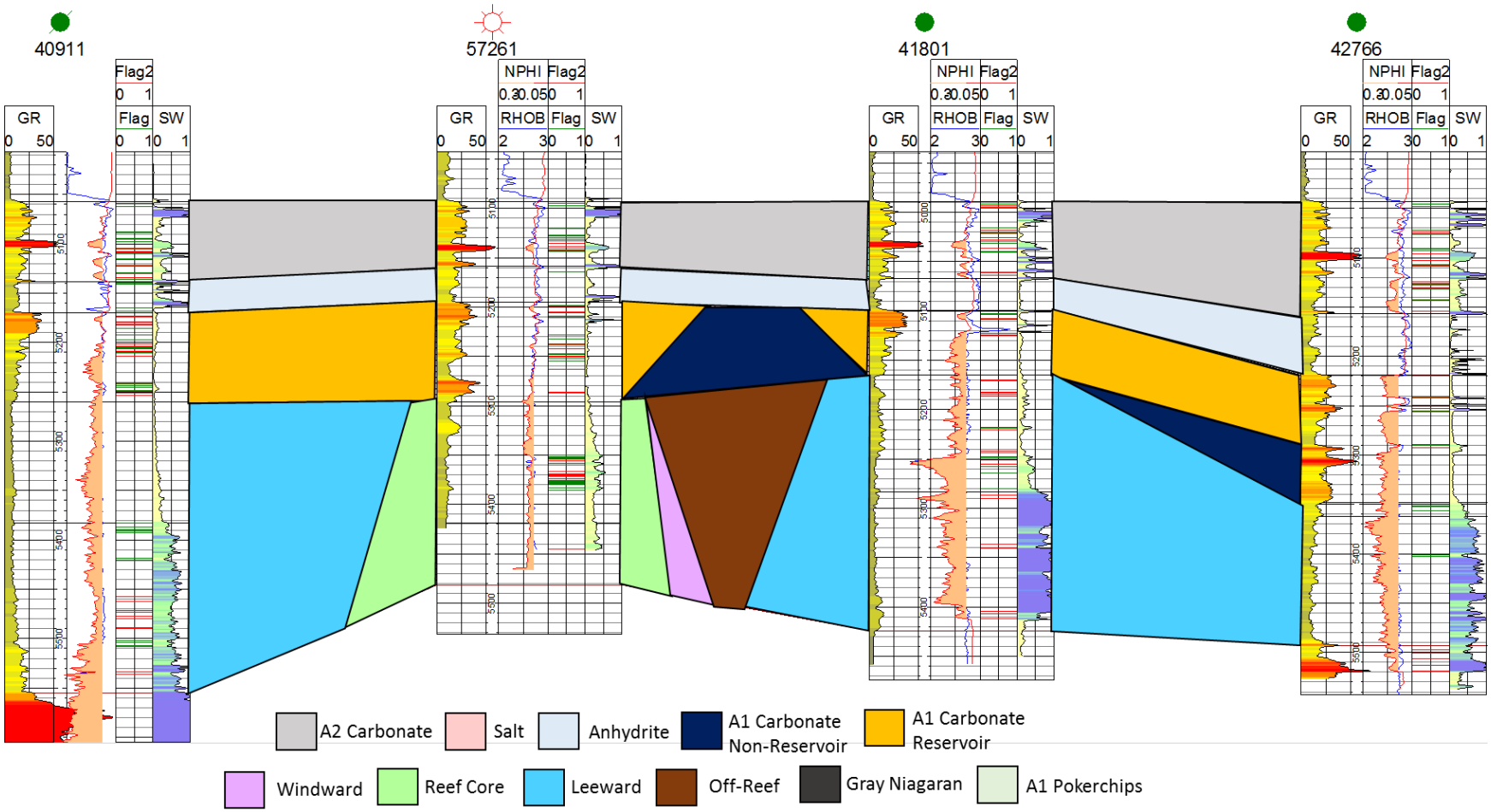


Figure 7-21. Cross section A-A' showing interpreted lithofacies in the Charlton 19 reef with a "saddle" region between reef pods.

8.0 Dover 35

8.1 Reef History and Production Review

Production in the Dover 35 reef began when well 29236 was completed in 1973. Primary production was recorded from 1973 through 2004. In late 2004, EOR operations began (Figure 8-1). There was a sharp increase in cumulative production in 2005, and production peaked in 2008 before a gentle decline began during the EOR phase. As of December 31, 2017, about 1,408,000 bbls of oil had been produced, with nearly 500,000 bbls produced after EOR operations began. The highest producer is well 29236 in the center of the reef field (Figure 8-2). The remaining producing wells on the western side of the reef field yielded significantly less oil.

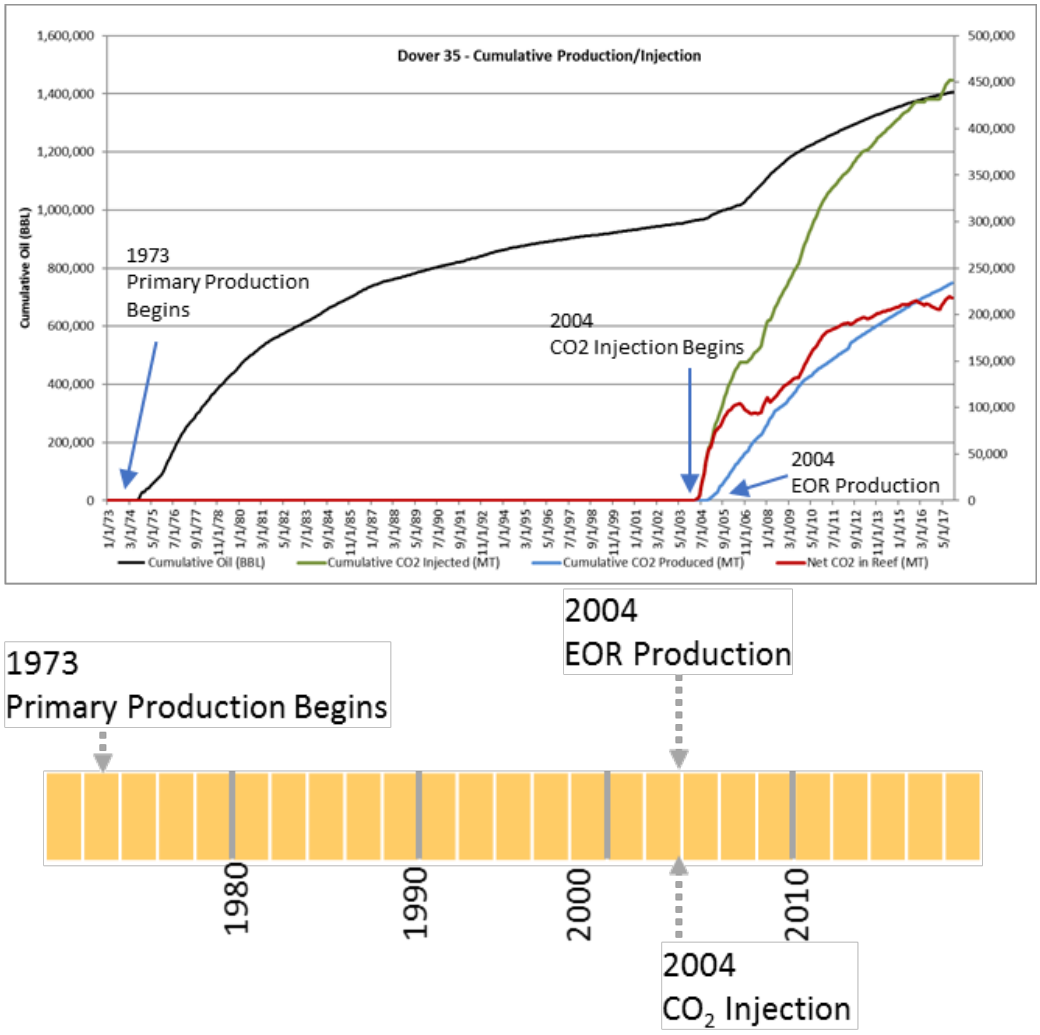


Figure 8-1. Cumulative production in the Dover 35 reef field from 1982 through 2017 showing an increase in production rates after EOR operations began in 2005.

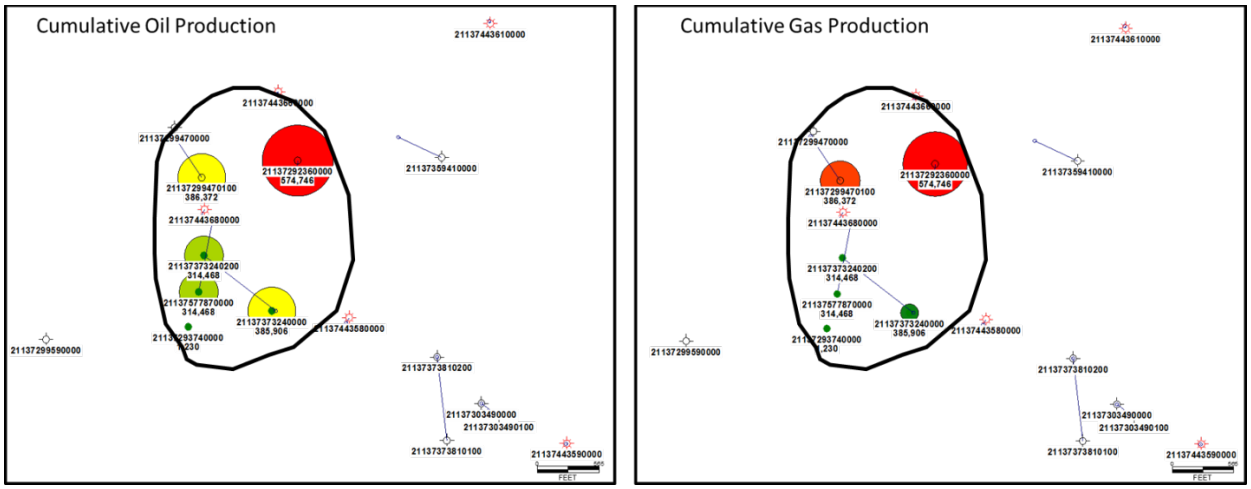


Figure 8-2. Cumulative oil and gas production by well showing the highest producers (red) in the center of the reef field with decreasing production along the edges (green). Black outline illustrates edge of reef structure.

The initial (discovery) conditions of the Dover 35 reef field, summarized in Table 8-1, consist of OOIP, oil API gravity, discovery pressure and temperature, and fluid saturations. Initial gas saturations were recorded at zero, as gas was produced as it came out of solution during the production of oil.

Table 8-1. Summary of initial (discovery) conditions of the Dover 35 reef field.

		Discovery		Saturation		
OOIP (bbls)	**API Gravity**	**Pressure (psi)**	**Temperature (°F)**	**Oil**	**Gas**	**Water**
2,480,000	41.5	2946	104	71.88%	0%	28.12%

8.2 Wireline Log Analysis

Nine wells penetrate the Dover 35 reef (Figure 8-3), with multiple digitized and raster logs available. Of these nine wells, seven have gamma ray, six have neutron porosity, three have bulk density, and four have bulk density calculated from sonic logs. Table 8-2 summarizes the log data available for Dover 35.

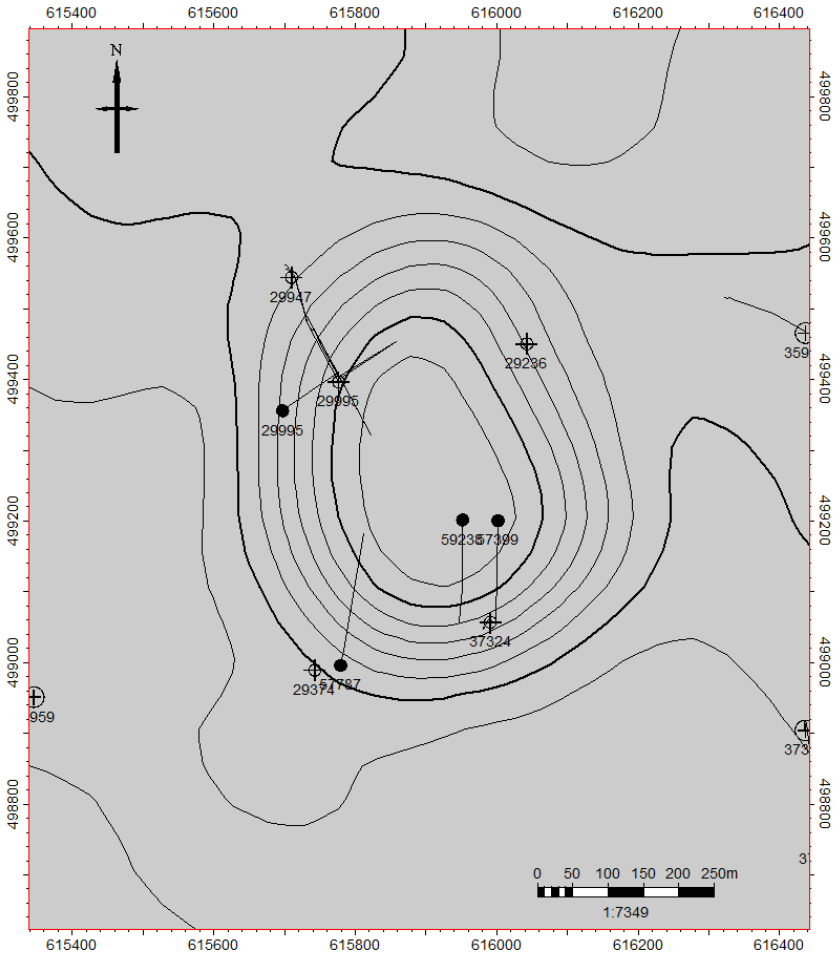


Figure 8-3. Map of the Dover 35 reef field showing reef geometry and well locations.

Table 8-2. Summary of available wireline log data for wells penetrating the Dover 35 reef.

	Well UWI	2113729236000	2113729374000	2113729947000	2113729947010	2113737324000	2113737324020	2113744366000	2113744368000	2113757787000
CAL	Caliper	■	■	■			■			■
DT	Sonic	■	■	■	■					
GR	Gamma Ray	■	■	■	■	■	■			■
LLD	Latero-Log Deep (Resistivity)	■	■		■	■	■			■
LLS	Latero-Log Shallow (Resistivity)	■	■		■	■	■			■
NPHI	Neutron Porosity	■	■		■	■	■			■
RES	Resistivity									■
RHOB	Bulk Density					■	■			■
SNP	Sidewall Neutron Porosity	■	■		■					
BHP	Bottom Hole Pressure Monitoring	■				■				■

Note: Green shading indicates logs available by well.

8.2.1 Basic Log Interpretation

Well 35941

Well 35941 is located off-reef to the east of the Dover 35 reef field. There are short intervals of greater than 5% porosity within the A-2 carbonate, A-1 carbonate, and Brown Niagaran, which mostly plot as dolomite. The less than 5% porosity intervals tend toward a mixed limestone-dolomite. Anhydrite and halite occurrences are problematic for petrophysics in this well as the bulk density goes from an anhydrite interval (approximately 2.96 g/cm^3) to a halite interval (approximately 2.04 g/cm^3). Data point scatter will trend through the limestone and sandstone zones toward the halite zone in evaporite layers due to mixed anhydrite/halite log readings. The A-2 carbonate plots as a dolomite trending toward limestone, possibly due to the presence of a salt plug. The A-1 carbonate plots as a mixed dolomite-limestone; however, the areas of high porosity trend toward a dolomite. The Brown Niagaran is only 15 feet thick in this well and shows dolomitic porosity. These features are consistent with other off-reef locations. Figure 8-4 shows the neutron porosity-bulk density crossplot of the A-2 carbonate through the Brown Niagaran in well 35941.

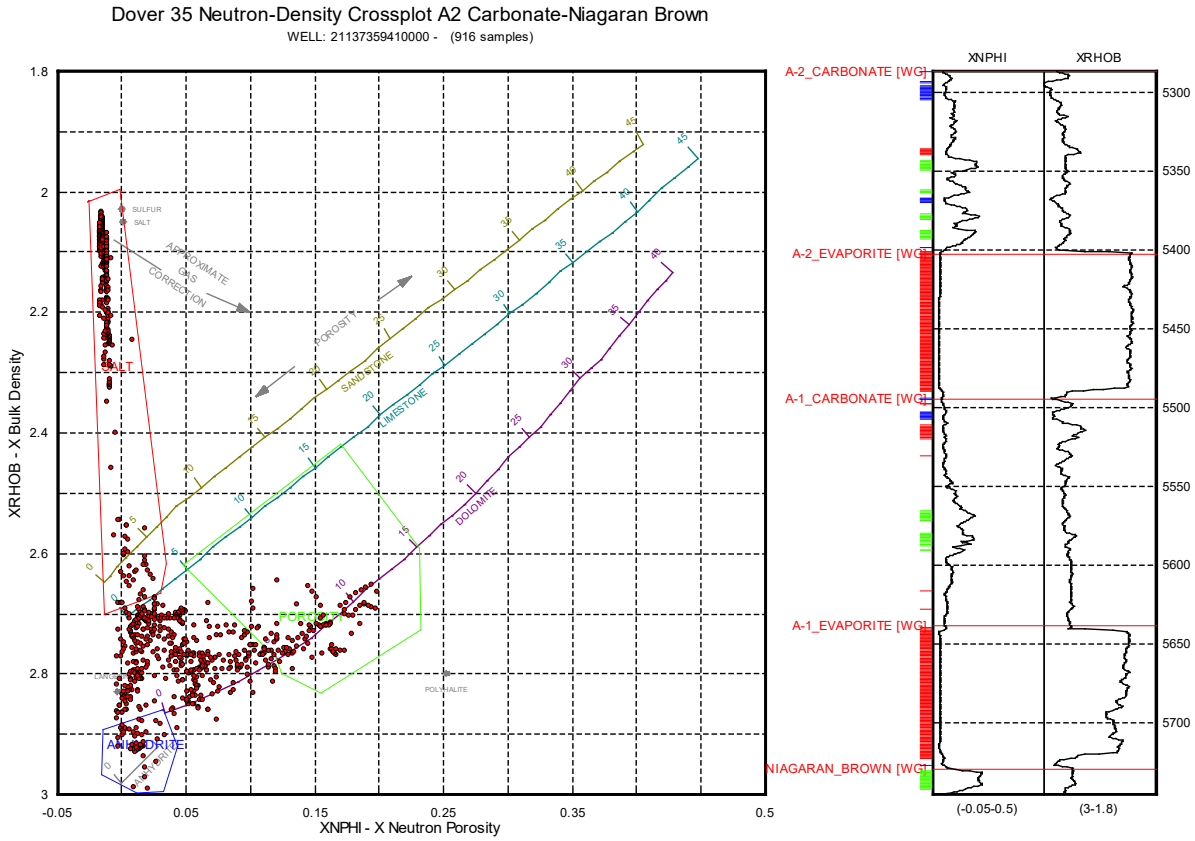


Figure 8-4. Neutron porosity-bulk density crossplot of well 35941 in the A-2 carbonate to the Brown Niagaran. Green polygon = porosity >5%, red polygon = salt, blue polygon = anhydrite.

Well 29236

Well 29236 is located on the northeastern crest of the Dover 35 reef field. There are two significant intervals of greater than 5% porosity in the A-1 carbonate and the Brown Niagaran. The A-2 carbonate has thin intervals of high porosity and appears as a mixed limestone-dolomite. The A-2 evaporite is only a foot thick at this well. The high-porosity interval in the A-1 carbonate is a dolomitized zone within the formation. The A-1 evaporite is not present at this well. There are two types of intervals with greater than 5% porosity in the Brown Niagaran: one larger interval is a dolomitized zone, while smaller intervals are mixed carbonates. Figure 8-5 shows the neutron porosity-bulk density crossplot of the A-2 carbonate through the Brown Niagaran in well 29236.

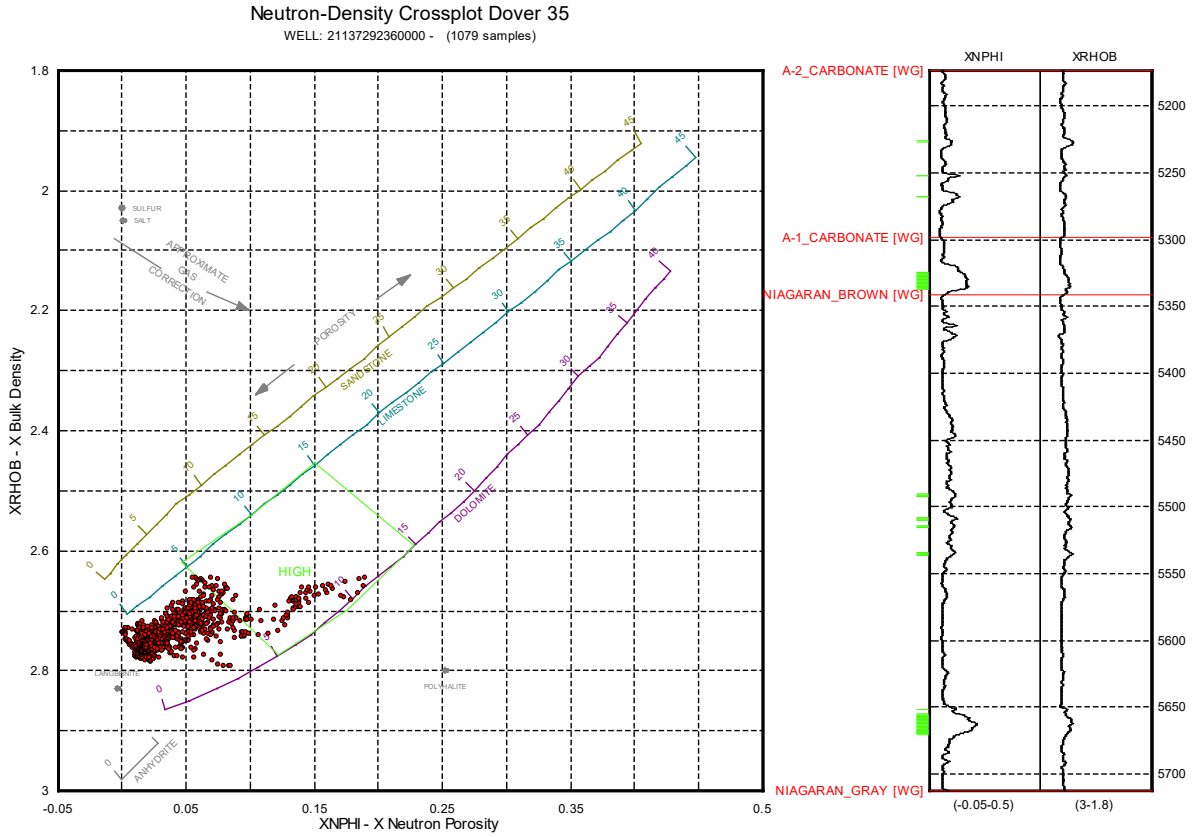


Figure 8-5. Neutron porosity-bulk density crossplot of well 29236 in the A-2 carbonate to the Brown Niagaran. Green polygon = porosity >5%.

Well 2994701

Well 2994701 is located on the western crest of the Dover 35 reef field. Two intervals of greater than 5% porosity are present: one in the A-1 carbonate and the other in the Brown Niagaran. The A-2 carbonate does not show any porosity. The A-1 carbonate plots as a mixed limestone-dolomite with the greater-than-5% interval trending as a dolomite. The A-1 evaporite is not present in this well. There is a single spike in the porosity in the Brown Niagaran formation. In general, the Brown Niagaran plots as a tight mixed carbonate; however, the interval of high porosity trends as a dolomite, with porosities reaching as high as 10%. Figure 8-6 shows the neutron porosity-bulk density crossplot of the A-2 carbonate through the Brown Niagaran in well 2994701.

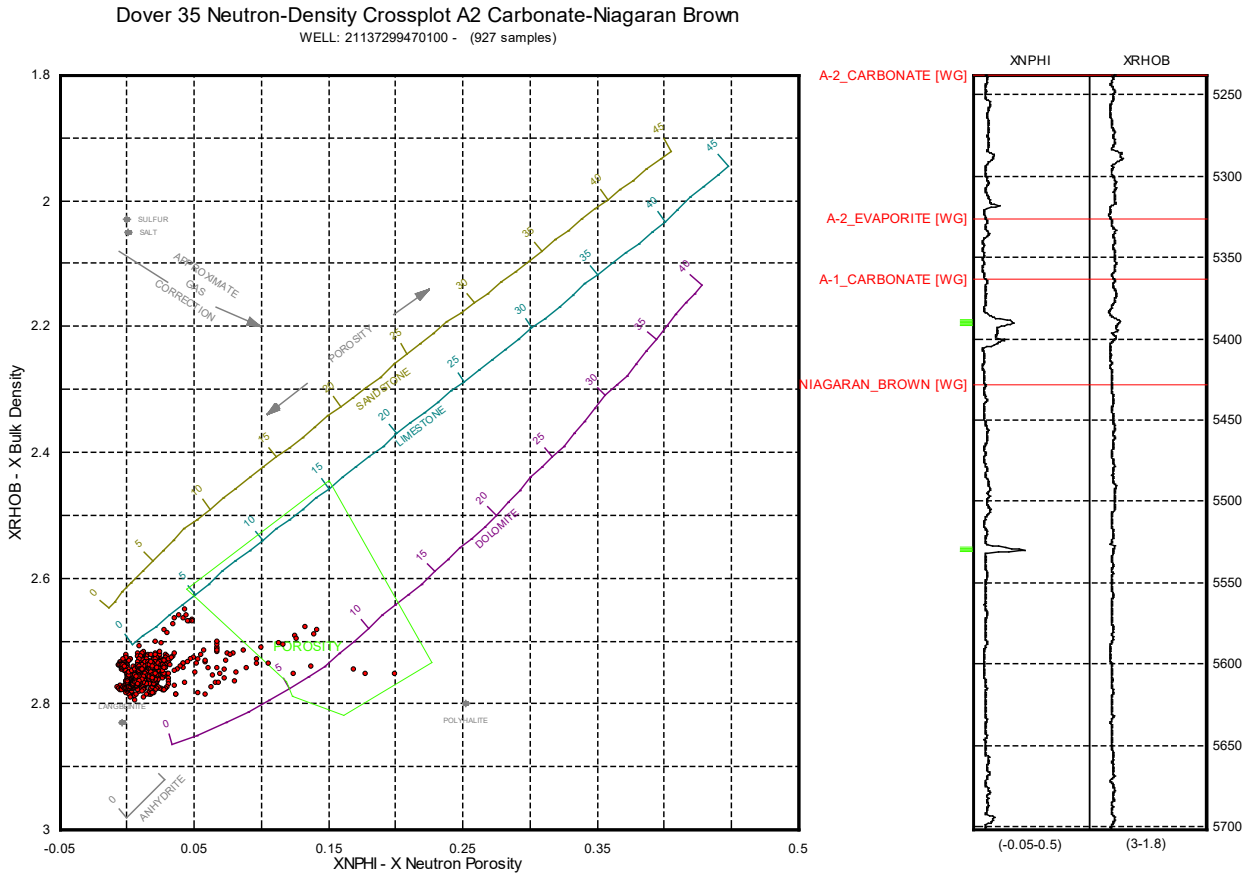


Figure 8-6. Neutron porosity-bulk density crossplot of well 29947 in the A-2 carbonate to the Brown Niagaran. Green polygon = porosity >5%.

Well 29374

Well 29374 is located in the southern portion of the Dover 35 reef field. This section of the reef is a tight carbonate with extensive salt plugging and limited porosity. The A-2 carbonate shows only a thin interval of mixed carbonates with greater than 5% porosity and multiple intervals of salt plugs. The A-2 evaporite is only a foot thick in this well and appears as a salt interval. The A-1 carbonate has one thin interval of porosity greater than 5%, with no notable salt plugging throughout. Most of the high-porosity intervals appear in the Brown Niagaran, which plots as a tight mixed carbonate with intervals of greater than 5% porosity showing a greater degree of dolomitization. Figure 8-7 shows the neutron porosity-bulk density crossplot of the A-2 carbonate through the Brown Niagaran in well 29374.

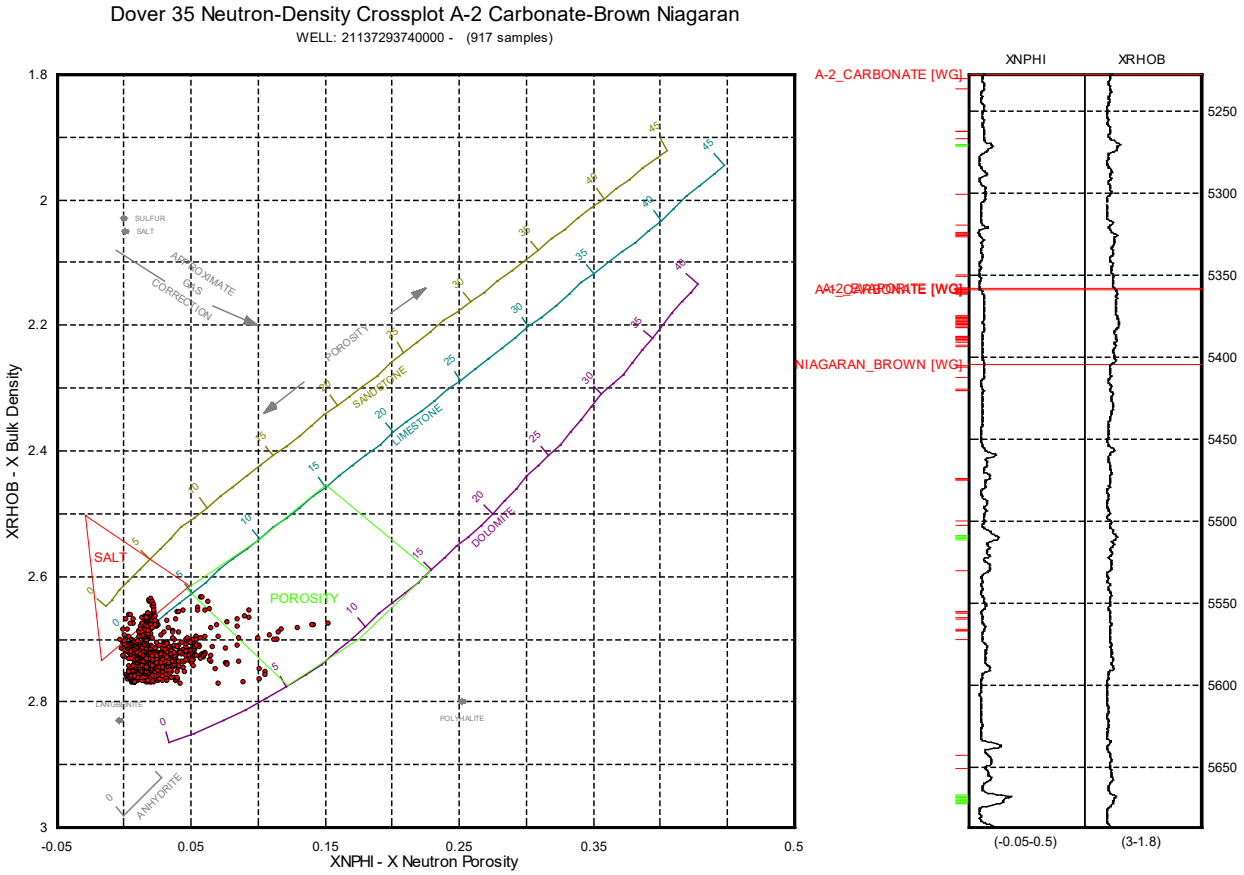


Figure 8-7. Neutron porosity-bulk density crossplot of well 29374 in the A-2 carbonate to the Brown Niagaran. Green polygon = porosity >5%, red polygon = salt.

Well 37324

Well 37324 is located just off of the Dover 35 reef field to the southeast. The crossplot for this well shows extensive scattering of the data; this is due to the presence of both salt plugs and anhydrite. Anhydrite and halite occurrences are problematic as the bulk density goes from an anhydrite interval (approximately 2.96 g/cm^3) to a halite interval (approximately 2.04 g/cm^3). Data point scatter will trend through the limestone and sandstone zones toward the halite zone in evaporite layers due to mixed anhydrite/halite log readings. The A-2 carbonate is a mixed carbonate with salt and anhydrite plugs present; it has one significant interval of greater than 5% porosity that underwent a higher degree of dolomitization. The A-2 evaporite plots as an anhydrite layer with a weak trend toward salt. The A-1 carbonate is difficult to analyze due to the presence of extensive evaporite plugging; however, it plots as a tight mixed carbonate without any significant porosity. Due to the bulk density problem, the A-1 evaporite does not plot as either a salt or an anhydrite. The Brown Niagaran plots as a mixed carbonate and shows a single interval of dolomitized porosity at the top of the formation. Increased salt in the A-2 evaporite and A-1-evaporite indicates a flank well location. Figure 8-8 shows the neutron porosity-bulk density crossplot of the A-2 carbonate through the Brown Niagaran in well 37324.

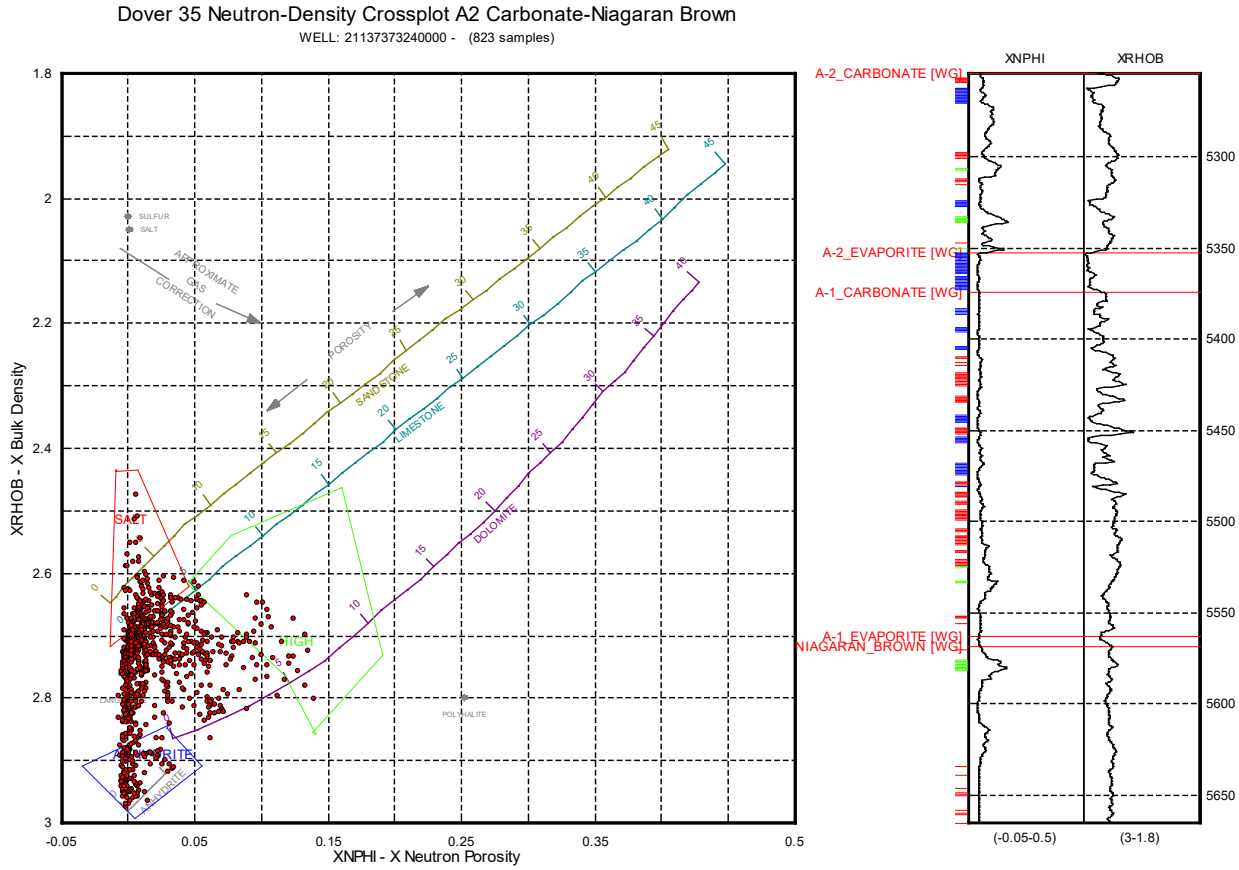


Figure 8-8. Neutron porosity-bulk density crossplot of well 37324 in the A-2 carbonate to the Brown Niagaran. Green polygon = porosity >5%, red polygon = salt, blue polygon = anhydrite.

Well 37381

Well 37381 is located off-reef to the east of the Dover 35 reef field and to the south of well 35941. There are intervals of greater than 5% porosity within the A-2 carbonate, A-1 carbonate, and Brown Niagaran which mostly plot as dolomite (Figure 8-9). The less than 5% porosity intervals tend toward a mixed limestone-dolomite Anhydrite and halite occurrences are problematic as the bulk density goes from an anhydrite interval (approximately 2.96 g/cm^3) to a halite interval (approximately 2.04 g/cm^3). Data point scatter will trend through the limestone and sandstone zones toward the halite zone in evaporite layers due to mixed anhydrite/halite log readings. The A-2 carbonate plots as a mixed carbonate with evaporite plugging; there is also a significant interval of greater than 5% porosity that has dolomitized at the bottom of the formation. The A-2 evaporite is a thick layer of salt. The A-1 carbonate plots as a limestone-dolomite carbonate with two significant intervals of greater than 5% porosity that have dolomitized in the middle of the formation. The A-1 evaporite is a thick layer of salt with a thin layer of anhydrite at the bottom of the formation. Well 37381 penetrates only a thin interval of the Brown Niagaran, which plots entirely as a dolomite with greater than 5% porosity. The thin Brown Niagaran and thick salt packages are consistent with other off-reef wells.

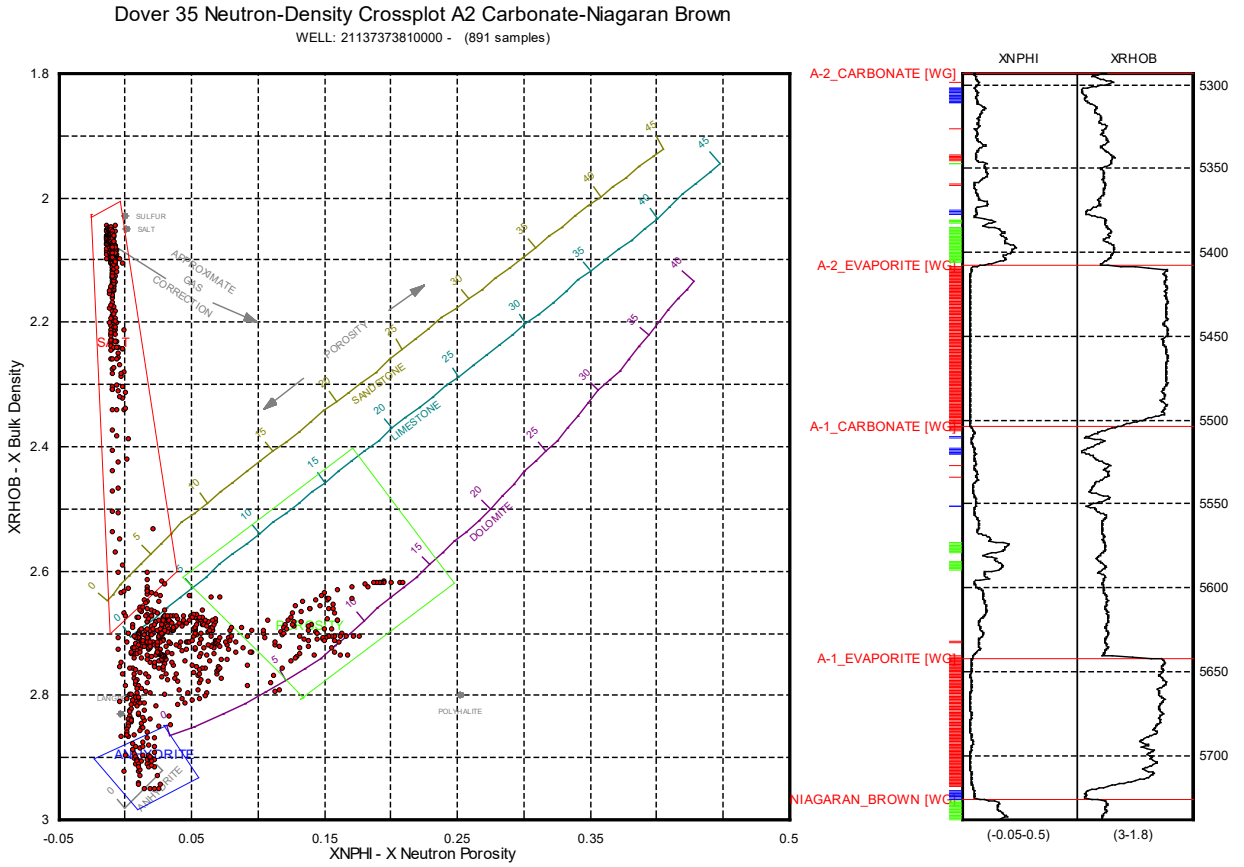


Figure 8-9. Neutron porosity-bulk density crossplot of well 37381 in the A-2 carbonate to the Brown Niagaran. Green polygon = porosity >5%, red polygon = salt, blue polygon = anhydrite.

8.2.2 Petrophysics Calculations

A-2 Carbonate

The A-2 carbonate in the Dover 35 reef field plots as a mixed limestone-dolomite carbonate with most of the high porosity present in the dolomitized intervals. The thickness of this interval varies from 124 feet (well 29236) to 99 feet (well 37324). The average net porosity for the A-2 carbonate is 7.4% with a high of 13.5% and a NTG ratio of 0.157 (Table 8-3). In the off-reef wells, this formation shows evaporite plugs.

Table 8-3. Summary of petrophysical calculations for the A-2 carbonate in the Dover 35 reef field.

Interval: A-2 Carbonate				
Avg. Thickness	**Gross Avg. Porosity**	**Avg. Net Porosity**	**Avg. Net Thickness**	**Avg. NTG**
112 ft	2.8%	7.4%	16.8 ft	0.157

A-2 Evaporite

The A-2 evaporite is present in every well; however, in two wells (29236 and 29374) this formation is only a foot thick. Petrophysics were not calculated for this zone due to anhydrite and halite.

A-1 Carbonate

The A-1 carbonate in the Dover 35 reef field plots as a mixed limestone-dolomite carbonate with dolomitized high-porosity intervals. Salt plugging influenced the bulk density at times which displayed as porous zones. The thickness of this interval varies from 189 feet (well 37324) to 43 feet (well 29236) with an average thickness of 103 feet. The average net porosity for the A-1 carbonate is 6.8% with the maximum porosity of 8.2% in well 29236 and a gross average porosity of 3.1% (Table 8-4). This formation has an average NTG ratio of 0.22.

Table 8-4. Summary of petrophysical calculations for the A-1 carbonate in the Dover 35 reef field.

Interval: A-1 Carbonate				
Avg. Thickness	**Gross Avg. Porosity**	**Avg. Net Porosity**	**Avg. Net Thickness**	**Avg. NTG**
103 ft	3.1%	6.8%	22.6 ft	0.22

A-1 Evaporite

The A-1 evaporite is present in three wells (35941, 37324, and 37381). Petrophysics were not calculated for this zone due to anhydrite and halite.

Brown Niagaran

The Brown Niagaran in the Dover 35 reef field plots as a mixed limestone-dolomite carbonate with dolomitized high-porosity intervals. The thickness of this formation varies from 371 feet (well 29236) on-reef to 12 feet (well 37381) off-reef. The average net porosity for this formation is 8.2% with a maximum porosity of 10.9% in well 35941 off-reef. The gross average porosity is 4.7% with a NTG ratio of 0.362 (Table 8-5).

Table 8-5. Summary of petrophysical calculations for the Brown Niagaran in the Dover 35 reef field.

Interval: Brown Niagaran				
Avg. Thickness	**Gross Avg. Porosity**	**Avg. Net Porosity**	**Avg. Net Thickness**	**Avg. NTG**
174 ft	4.7%	8.2%	22.4 ft	0.362

8.3 Seismic Analysis

A 3D seismic survey was shot over the Dover 35 and Dover 36 reef fields. Dover 35 was identified in the west-central portion of the survey, and Dover 36 was in the east-central portion of the survey. The A-2 carbonate horizon was picked showing faster arrival times over the reef complex with steeply dipped edges (Figure 8-10). The Dover 36 reef field had faster arrival times, indicating a taller reef complex than the smaller Dover 35. The A-1 carbonate and Brown Niagaran horizons could not confidently be picked due to the presence of multiples (multiple reflections from the same horizon).

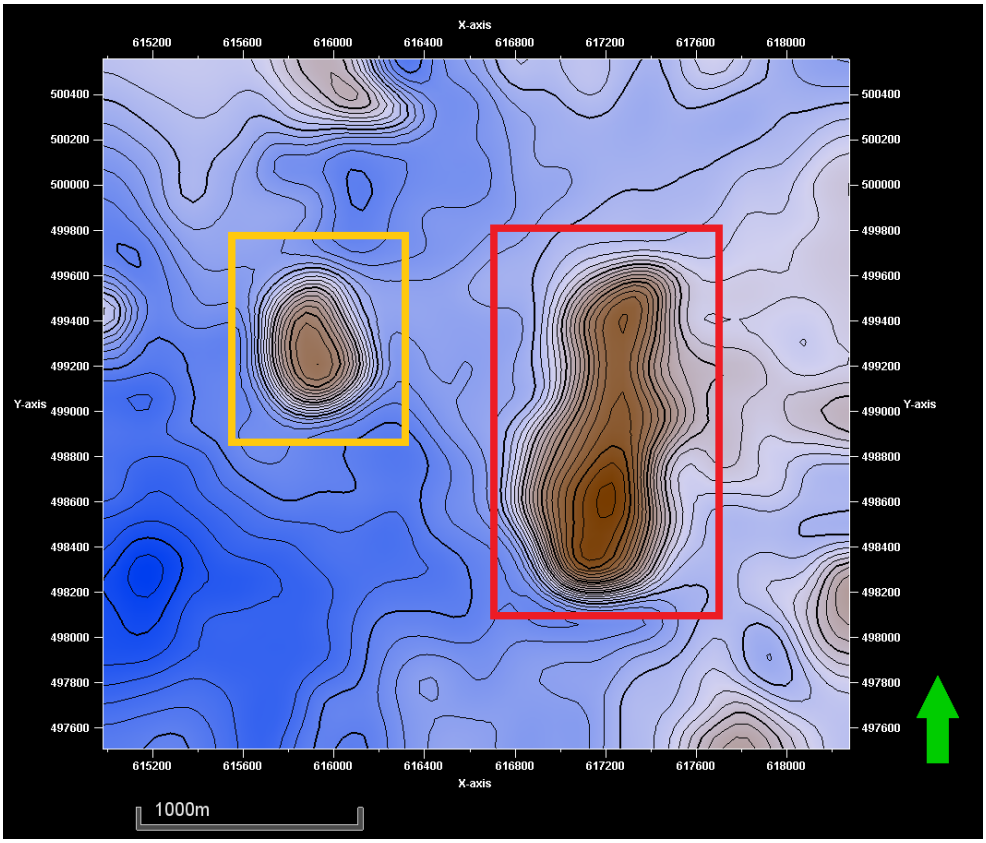


Figure 8-10. Seismic time surface over the Dover 35 (yellow box) and Dover 36 (red box) reef fields for the A-2 carbonate showing faster arrival times over the reef structures.

8.4 Geologic Interpretations

Cross section A-A' tracks from off-reef, through the reef field, and back to off-reef to show the reef structure (Figure 8-11). Starting with well 37381, there are thick packages of salt with thin Brown Niagaran, which is consistent with an off-reef position. Thin porosity streaks are present in the A-1 carbonate and Brown Niagaran, which does not correlate with nearby wells. The Brown Niagaran thickens toward the center of the reef, and the A-1 thins out with less evaporites. There are porosity streaks in the A-1 carbonate along the crest of the reef, and thin intervals of porosity are present inside the Brown Niagaran. The thin porosity in the Brown Niagaran is traceable well to well, cross cutting lithofacies which could be an unconformity. The A-2 carbonate has a continuous high gamma marker mid-formation attributed to carbonate mudstone. Figure 8-12 shows cross section A-A' through the Dover 35 reef field.

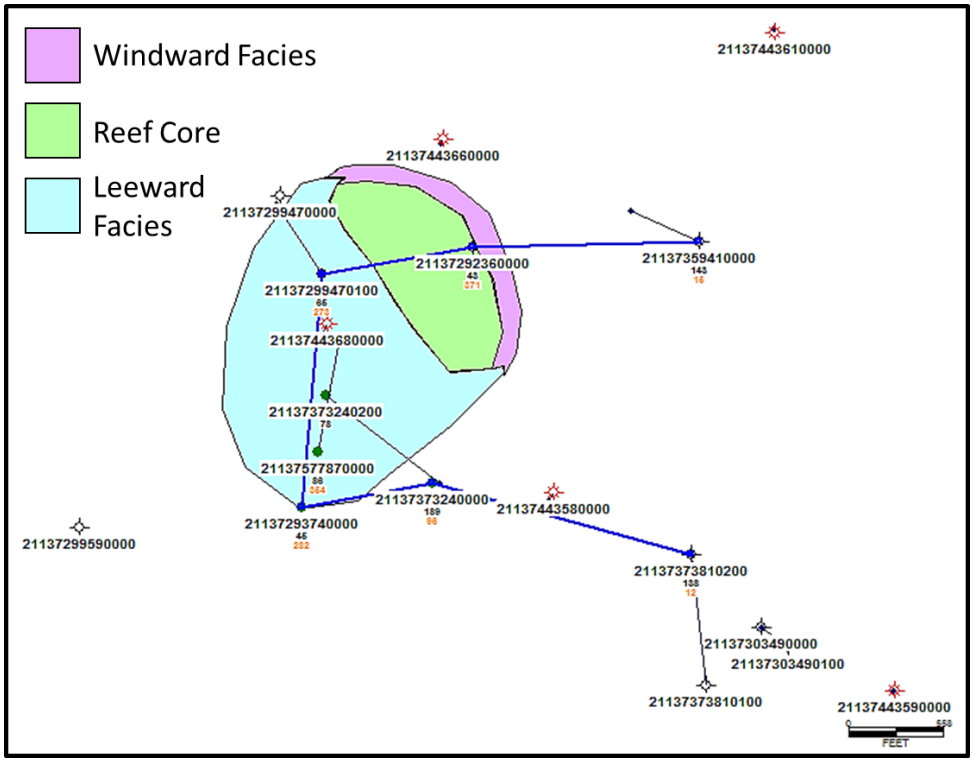


Figure 8-11. Depositional model of the Dover 35 reef field showing a single reef core (green) with the windward facies (purple) and leeward facies (blue).

The geometry of the reef field was defined from seismic data. The thicknesses of the Brown Niagaran and A-1 carbonate formations were used to interpret boundaries of the lithofacies within the reef boundary. Well 29236 had the thickest Brown Niagaran with little to no evaporites, which is consistent with a reef crest. The majority of the wells fell into the leeward reef facies, as indicated by a thinning Brown Niagaran and a thickening A-1 carbonate with increased evaporites. The map view of the Dover 35 reef field in Figure 8-11 shows interpreted locations of the reef core (green), windward facies (purple), and leeward facies (blue). Figure 8-13 shows a 2D cross section of the interpreted lithofacies of the Dover 35 reef.

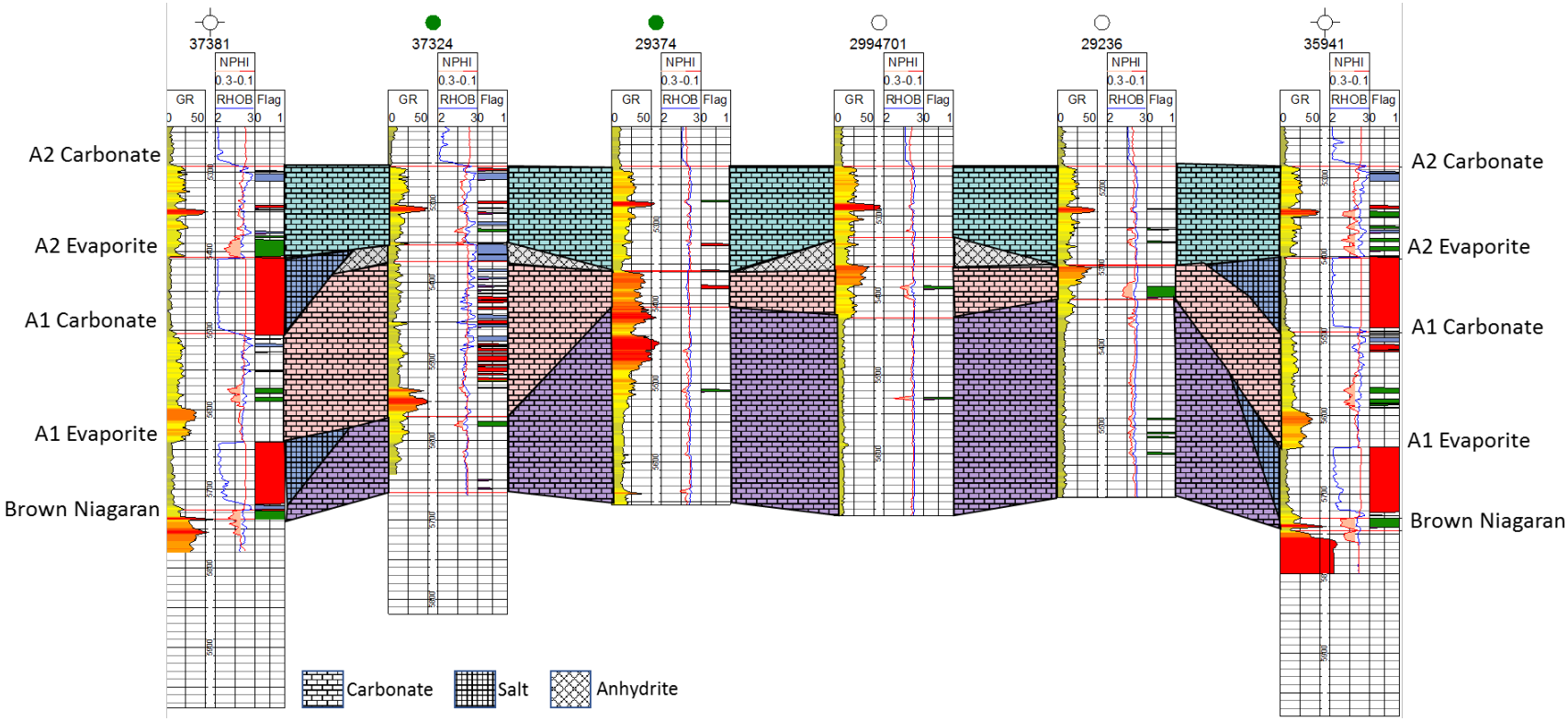


Figure 8-12. Cross section of the Dover 35 reef field showing the XGR, RHOB, and XNPHI for the A-2 carbonate, A-2 evaporite, A-1 carbonate, A-1 evaporite, and Brown Niagaran intervals. Green represents porosity values >5%, blue represents anhydrite, and red represents salt intervals.

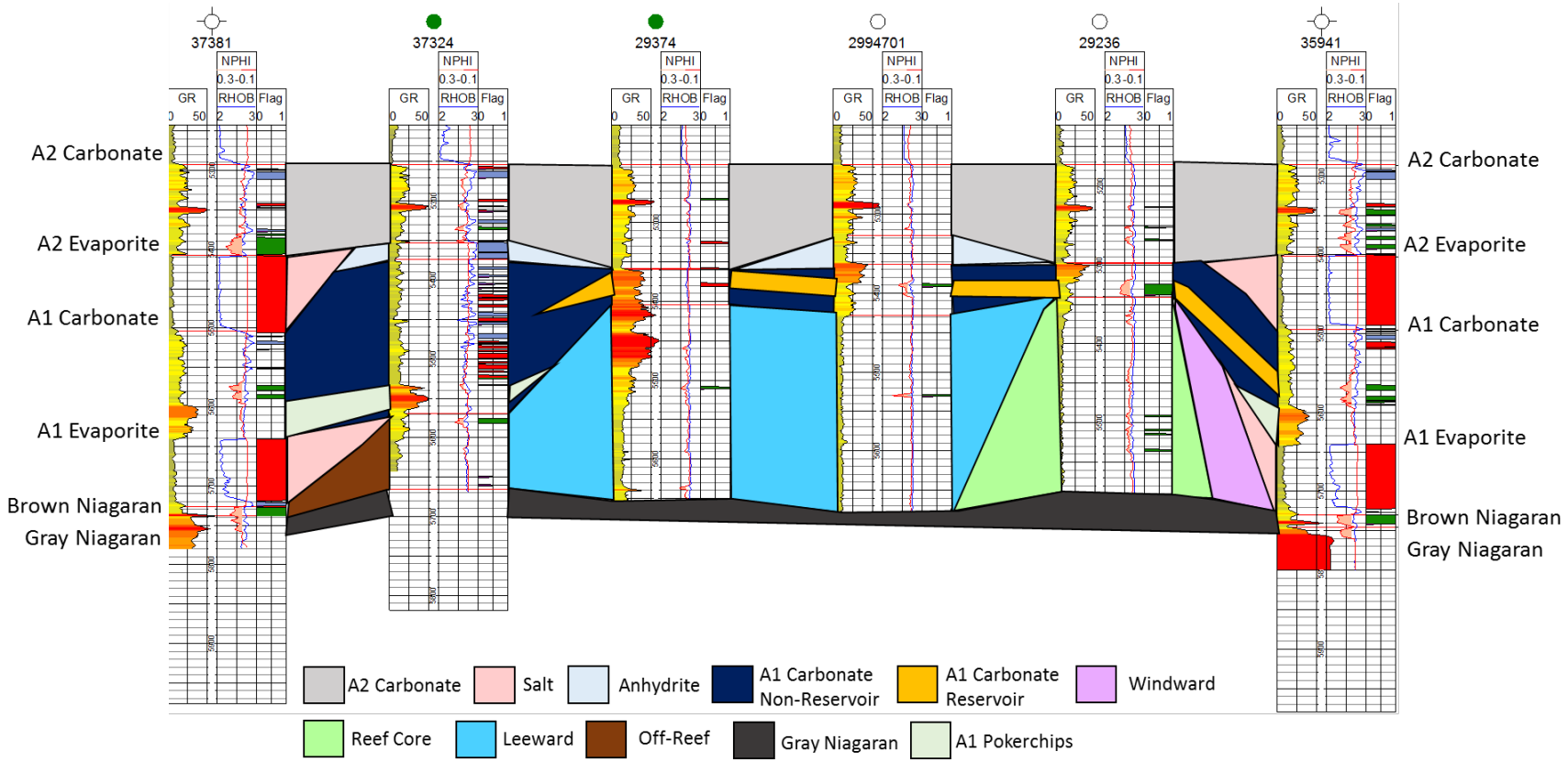


Figure 8-13. Cross section of the Dover 35 reef field showing the XGR, RHOB, and XNPHI for the A-2 carbonate, A-2 evaporite, A-1 carbonate, A-1 evaporite, and Brown Niagaran intervals. Colors represent the different lithofacies in the depositional interpretation.

9.0 Dover 36

9.1 Reef History and Production Review

Production began in the Dover 36 reef in 1973. Annual field production peaked in 1974 and followed a steady, predictable decline from 1982 through 1997, when operations stopped for CO_2 injection. Injection operations began in 1998 with a marked increase in production peaking in the first full year of operations in 1999 (Figure 9-1). The second well drilled during the field's primary phase, well 29303, had the field's highest cumulative oil production. Approximately 59% of the field's primary oil production came from this well, located in the west-central location of the reef field. (well 52719 was drilled as an EOR well, and its PRU (Production Reporting Unit) production is the PRU comprising the total EOR production since that time). As of December 31, 2017, about 1,758,000 bbls of oil have been produced. Figure 9-2 is a cumulative oil and gas production map for all wells in the Dover 36 reef field.

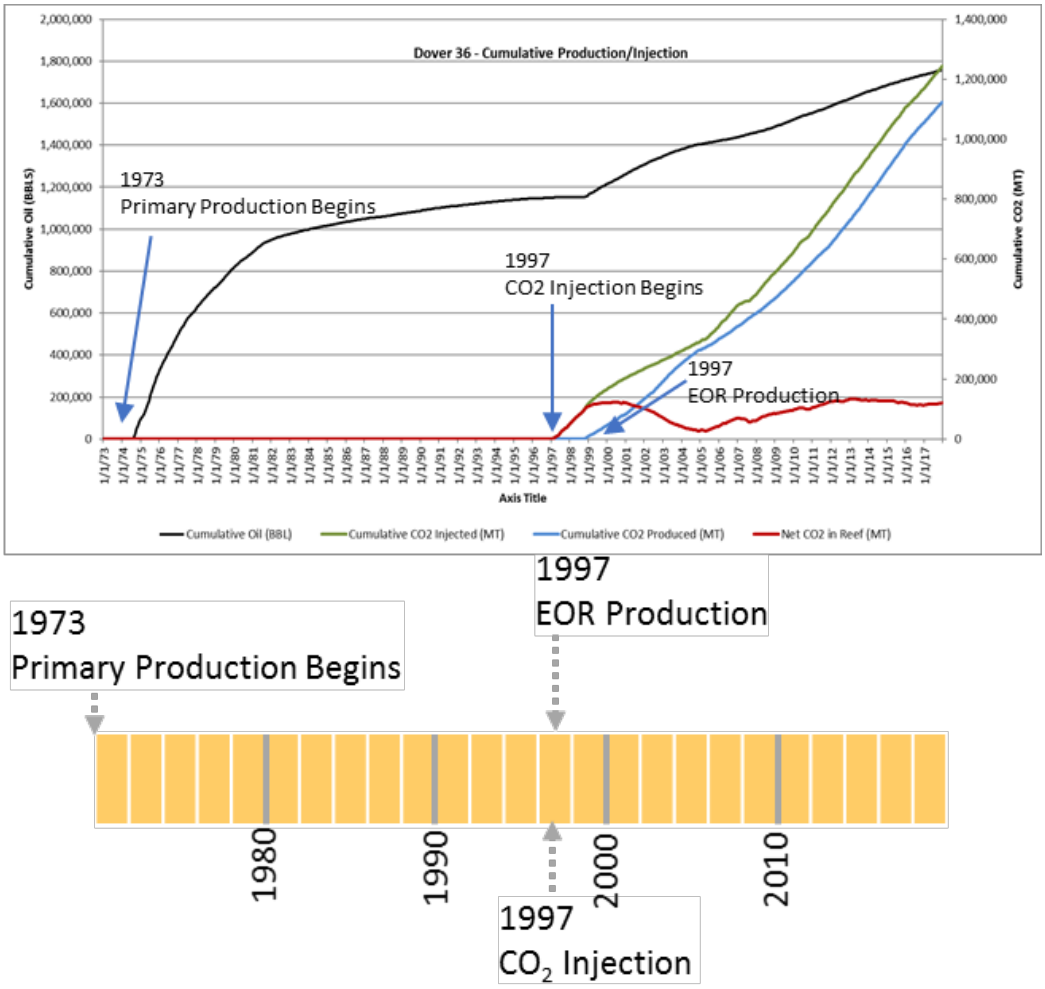


Figure 9-1. Cumulative production in the Dover 36 reef field from 1973 through 2017 showing an increase in production rates after EOR operations began in 1997.

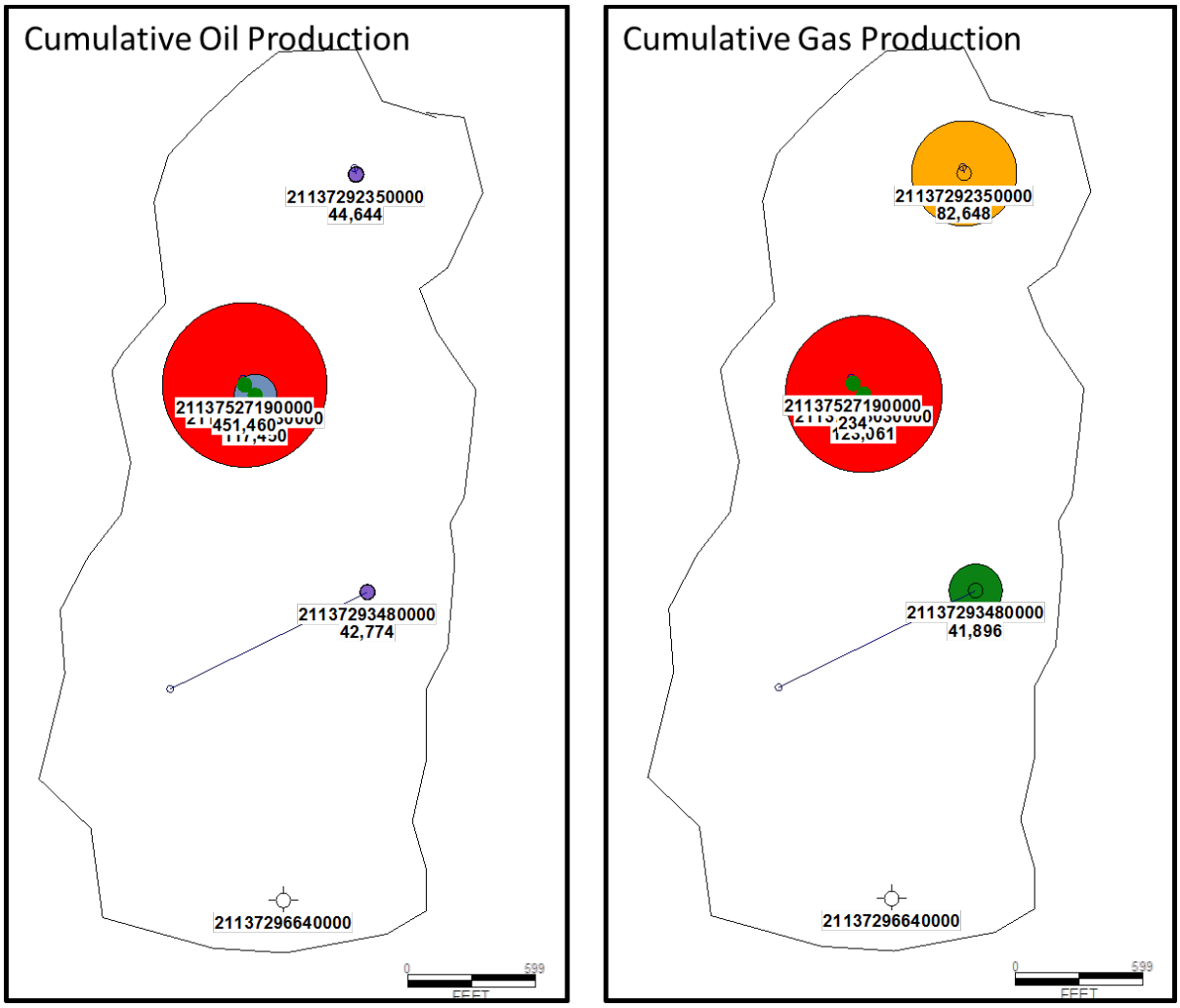


Figure 9-2. Cumulative oil and gas production in the Dover 36 reef field showing the highest producer (red), well 52719, in the center of the reef field.

The initial (discovery) data for the Dover 36 reef field, summarized in Table 9-1,consists of OOIP, oil API gravity, discovery pressure and temperature, and fluid saturations. Initial gas saturations were recorded at zero, as gas was produced as it came out of solution during production of oil.

Table 9-1. Summary of initial (discovery) conditions of the Dover 36 reef field.

		Discovery		Saturation		
OOIP (bbls)	**API Gravity**	**Pressure (psi)**	**Temperature (°F)**	**Oil**	**Gas**	**Water**
3,728,000	42.8	2,996	108	63.53%	0%	36.47%

9.2 Wireline Log Analysis

Five wells penetrate the Dover 36 reef field (Figure 9-3), all of which have been digitized and raster logs available. Of these five wells, five have gamma ray, five have neutron porosity, one has bulk density, and four have bulk density calculated from sonic logs. Table 9-2 summarizes the log data available for the Dover 36 reef field.

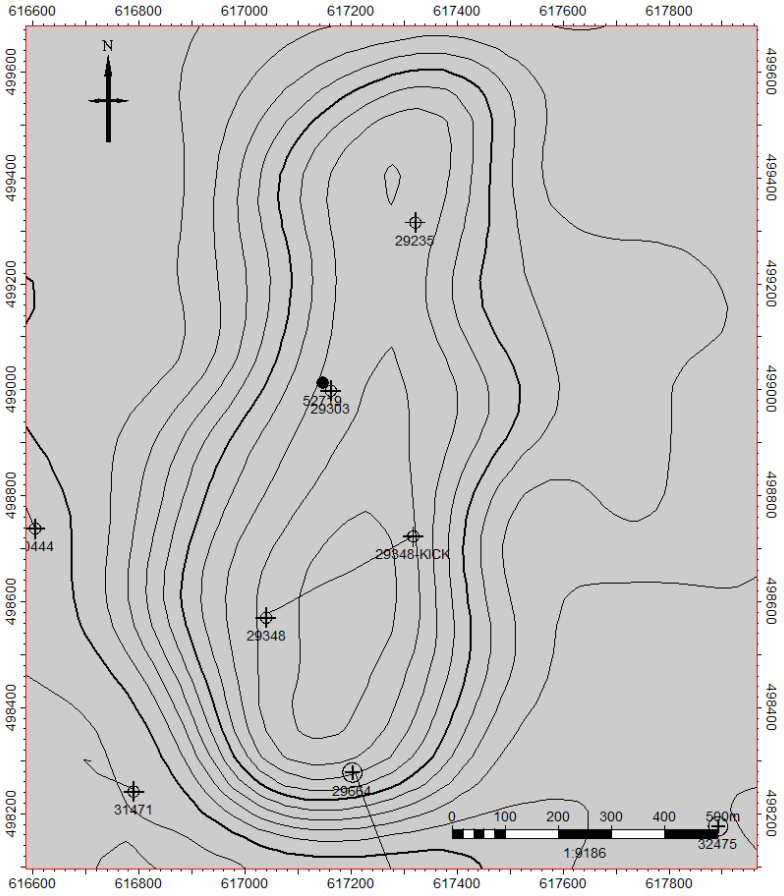


Figure 9-3. Map of the Dover 36 reef field showing structural geometry and well locations.

Table 9-2. Summary of available wireline log data for wells penetrating the Dover 36 reef field.

	Well UWI	2113729235000	2113729303000	2113729348000	2113729664000	2113752719000
CAL	Caliper	■	■	■	■	■
DT	Sonic	■	■	■	■	
GR	Gamma Ray	■	■	■	■	■
LLD	Latero-Log Deep (Resistivity)	■	■	■		
LLS	Latero-Log Shallow (Resistivity)	■	■			
NPHI	Neutron Porosity	■	■	■	■	■
RHOB	Bulk Density					■
SNP	Sidewall Neutron Porosity				■	
BHP	Bottom Hole Pressure Monitoring	■		■		■

Note: Green shading indicates logs available by well.

9.2.1 Basic Log Interpretation

Well 29235

Well 29235 is located on the northern reef crest of the Dover 36 reef field. There are short intervals of greater than 5% porosity within the A-2 carbonate and A-1 carbonate and multiple larger intervals within the Brown Niagaran. The A-2 carbonate is a tight limestone formation with a small interval of greater than 5% porosity mid-formation. While the A-2 evaporite is present in this well, it is only a foot thick and lacks a log signature for salt or anhydrites. In this well, the A-1 carbonate appears to be a tight limestone at the top of the formation that transitions into a mixed limestone-dolomite with an interval of high porosity. The A-1 evaporite is not present in this well. Most of the high-porosity intervals are present in the Brown Niagaran, which presents as a mixed carbonate. Figure 9-4 shows the neutron porosity-bulk density crossplot of the A-2 carbonate through the Brown Niagaran for well 29235. A section of greater than 10% porosity shown in Figure 9-4 may be due to a secondary feature such as a karst washout, fracture, or lithology change.

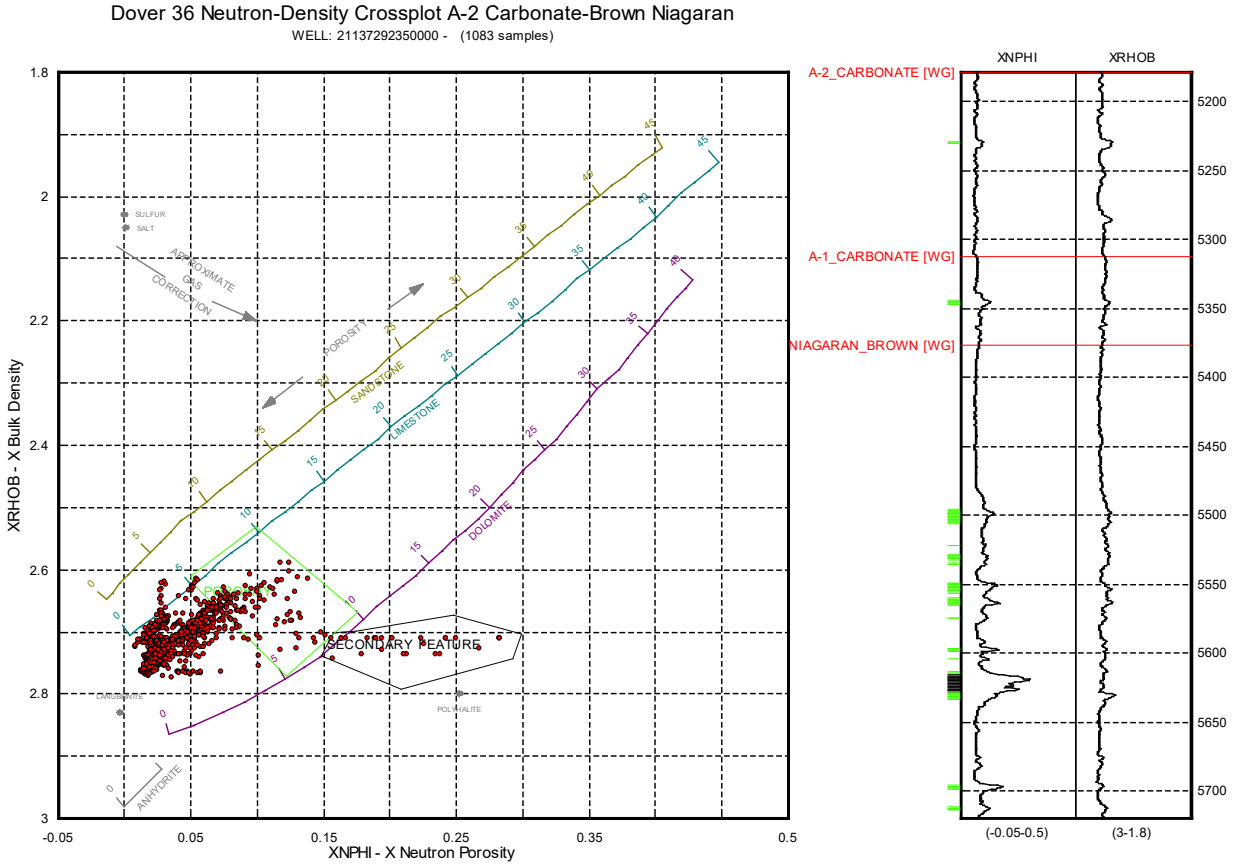


Figure 9-4. Neutron porosity-bulk density crossplot of well 29235 in the A-2 carbonate to the Brown Niagaran. Green polygon = porosity >5%, black polygon = secondary features.

Well 52719

Well 52719 is located in the center of the reef crest of the Dover 36 reef field. There are thin layers of greater than 5% porosity in the A-2 carbonate and the Brown Niagaran. Anhydrite and halite are present in this well as the bulk density goes from an anhydrite interval (approximately 2.96 g/cm^3) to a halite interval (approximately 2.04 g/cm^3). Data points trend through the limestone and sandstone zones toward the halite zone in evaporite layers due to mixed anhydrite/halite log readings. The A-2 carbonate is a tight limestone formation with a small interval of greater than 5% porosity. This formation also contains significant intervals of anhydrite and a thin layer of salt. The A-2 evaporite contains both salt and anhydrite layers. The A-1 carbonate is a tight limestone with no significant porosity that contains large intervals of salt. The A-1 evaporite is not present in this well. The Brown Niagaran is a limestone formation that contains most of the porosity present in this well; there are also thin intervals of salt plugging in the Brown Niagaran. Figure 9-5 shows the neutron porosity-bulk density crossplot of the A-2 carbonate through the Brown Niagaran for well 52719. The section of abnormal porosity shown in Figure 9-5 may be due to a secondary feature such as a karst washout, fracture, or lithology change.

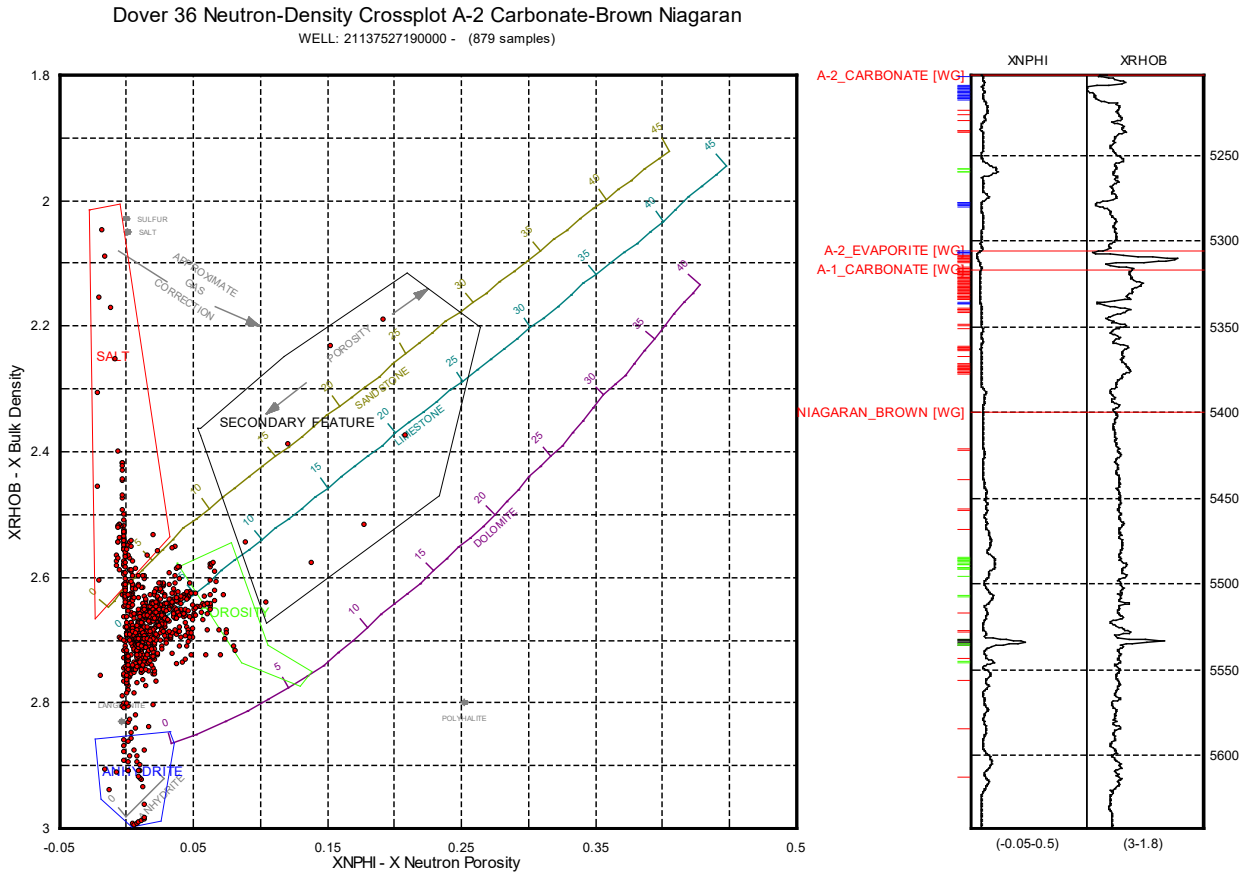


Figure 9-5. Neutron porosity -bulk density crossplot of well 52719 in the A-2 carbonate to the Brown Niagaran. Green polygon = porosity >5%, red polygon = salt, blue polygon = anhydrite, black polygon = secondary features.

Well 29303

Well 29303 is located in the center of the reef crest of the Dover 36 reef field, adjacent to well 52719. This well penetrates a tight limestone with some dolomitization occurring in the Brown Niagaran. The A-2 carbonate does not have any intervals of greater than 5% porosity, but it does have an interval of salt at the bottom of the formation. The A-2 evaporite is present in this well; however, it is only one foot thick. The A-1 carbonate is a tight limestone that does not contain any significant porosity or evaporites. The A-1 evaporite is not present in this well. All the porosity in this well is located at the bottom of the Brown Niagaran formation. This formation also contains the secondary feature seen in the other wells penetrating this reef. Figure 9-6 shows the neutron porosity-bulk density crossplot of the A-2 carbonate through the Brown Niagaran in well 29303.

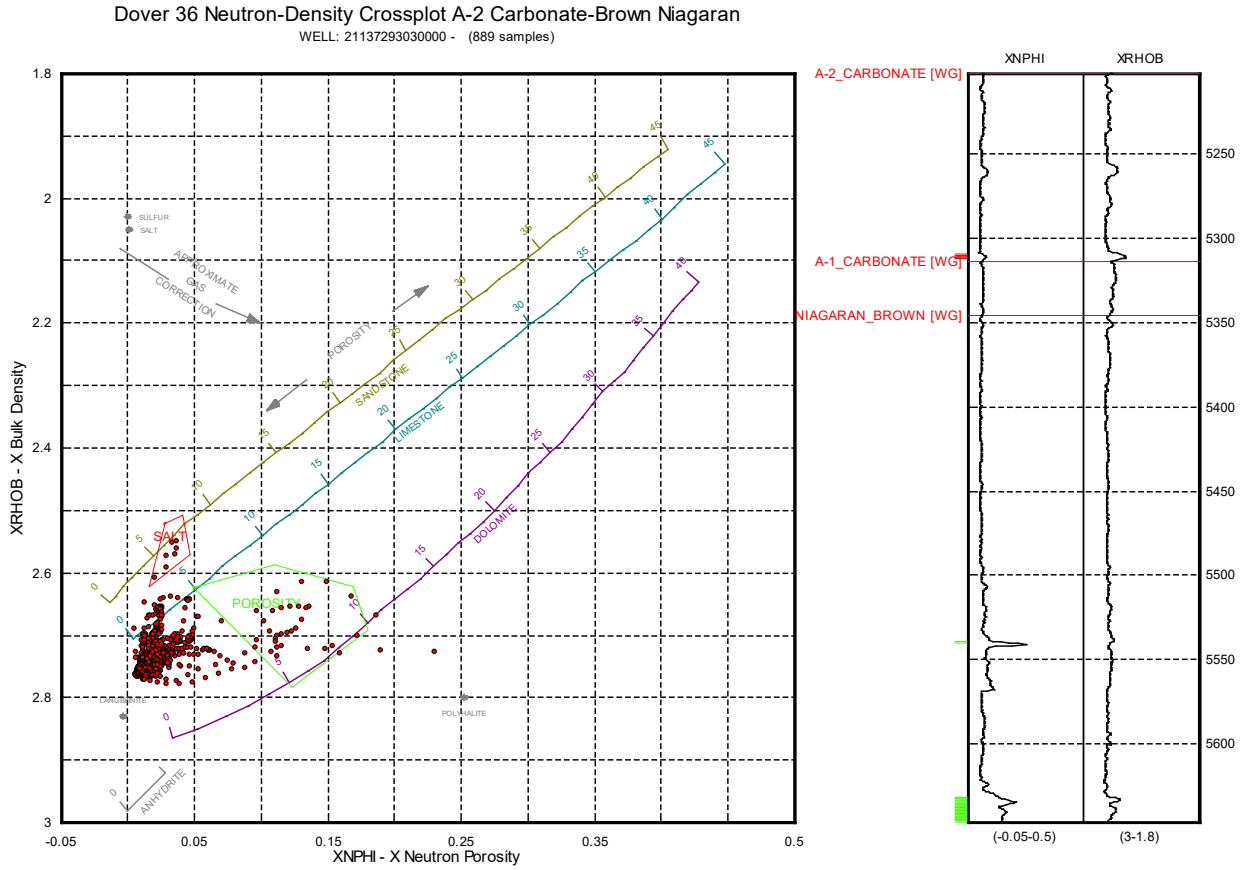


Figure 9-6. Neutron porosity-bulk density crossplot of well 29303 in the A-2 carbonate to the Brown Niagaran. Green polygon = porosity >5%, red polygon = salt.

Well 29348

Well 29348 is located on the crest of the Dover 36 reef field south of wells 29303 and 52719. This section of the reef is a tight, mixed carbonate with only minor intervals of greater than 5% porosity in the A-2 carbonate and the Brown Niagaran. The A-2 carbonate is a tight mixed carbonate with an extremely thin interval of greater than 5% porosity mid-formation. The A-2 evaporite appears as a thin layer; otherwise, there appear to be no significant traces of evaporites in this formation. The A-1 carbonate has intervals of tight limestone and tight mixed carbonates; it does not contain significant porosity. The A-1 evaporite is not present in this well. The only interval containing significant porosity is the Brown Niagaran, which appears as a mixed carbonate. It is important to note that the interval of greater than 5% porosity is laterally in line with the secondary features seen in the previous wells. Figure 9-7 shows the neutron porosity-bulk density crossplot of the A-2 carbonate in the A-2 carbonate through the Brown Niagaran in well 29348.

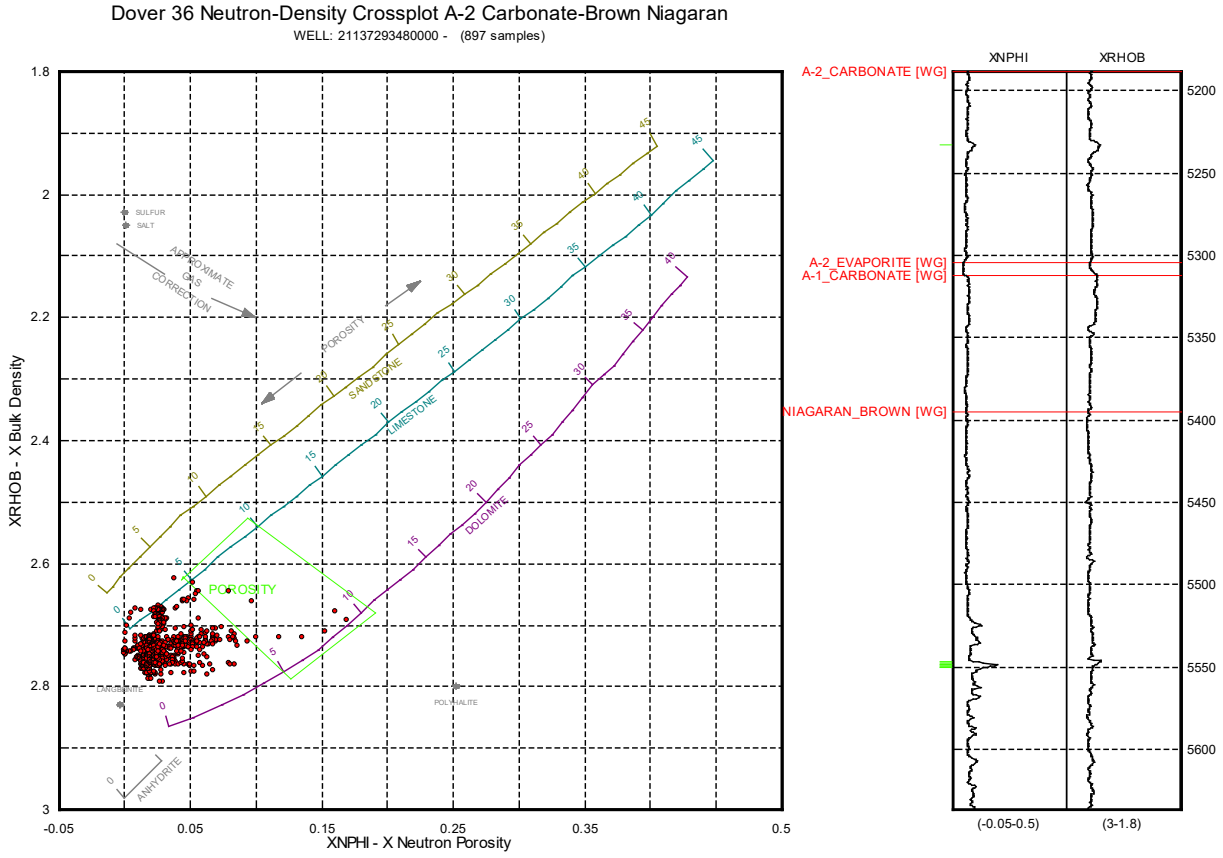


Figure 9-7. Neutron porosity-bulk density crossplot of well 29348 in the A-2 carbonate to the Brown Niagaran. Green polygon = porosity >5%.

Well 29664

Well 29664 is located on the southern portion of the Dover 36 reef field. This well penetrates a portion of the reef that does not contain any intervals of greater than 5% porosity. It is partially tight limestone and a tight mixed carbonate. The A-2 carbonate is a tight limestone without any intervals of note. The A-2 evaporite appears as a thin layer; otherwise, there appear to be no significant traces of evaporites in this formation. The A-1 carbonate ranges from a tight limestone to a tight mixed carbonate. The A-1 evaporite is not present in this well. The Brown Niagaran appears as a tight mixed carbonate. Unlike the previous wells, the Brown Niagaran does not contain an interval of greater than 5% porosity. The small changes and "flatness" of the wireline log suggest poor data quality. Figure 9-8 shows the neutron porosity-bulk density crossplot of the A-2 carbonate through the Brown Niagaran in well 29664.

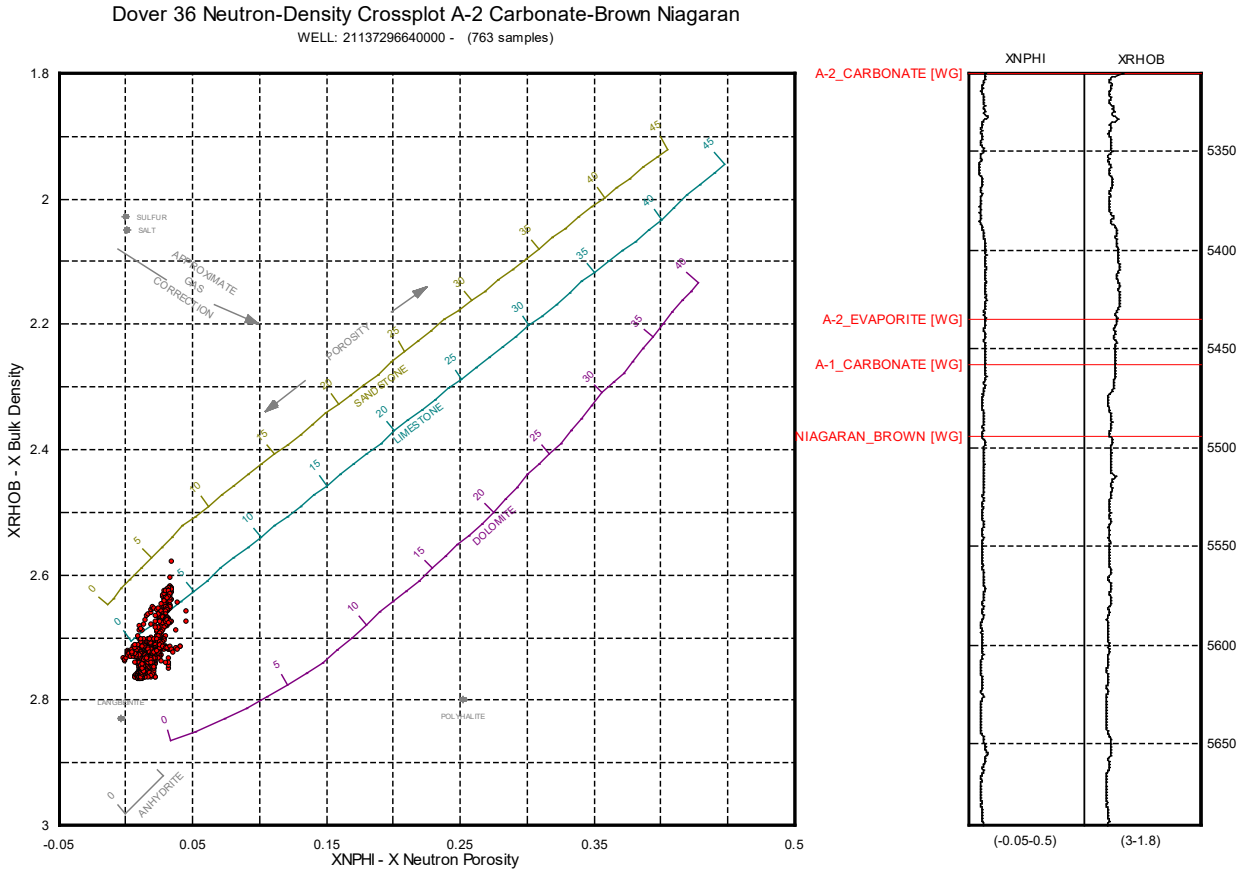


Figure 9-8. Neutron porosity-bulk density crossplot of well 29664 in the A-2 carbonate to the Brown Niagaran.

9.2.2 Petrophysics Calculations

A-2 Carbonate

The A-2 carbonate in the Dover 36 reef field plots as a mixed limestone-dolomite carbonate with portions plotting as a tight limestone. The thickness of this interval varies from 103 feet (well 52719) to 133 feet (well 29235), averaging 117 feet. The average net porosity for the A-2 carbonate is 5.7% with a maximum of 6.1%. It is important to note that only two wells contain significant porosity. The NTG ratio is 0.011 (Table 9-3).

Table 9-3. Summary of petrophysical calculations for the A-2 carbonate in the Dover 36 reef field.

Interval: A-2 Carbonate				
Avg. Thickness	**Gross Avg. Porosity**	**Avg. Net Porosity**	**Avg. Net Thickness**	**Avg. NTG**
117 ft	0.68%	5.7%	1.3 ft	0.011

A-2 Evaporite

The A-2 evaporite is present in every well; however, in two of the wells (29235 and 29303), this formation is only a foot thick. Petrophysics were not calculated for this zone due to anhydrite and halite lithology, which does not have pore space.

A-1 Carbonate

The A-1 carbonate in the Dover 36 reef field plots partially as a mixed limestone-dolomite carbonate and partially as a limestone. The thickness of this interval varies from 32 feet (well 29303) to 83 feet (wells 52719 and 29348) with an average thickness of 59.6 feet. The average porosity for the A-1 carbonate is 6.2% with a maximum porosity of 6.3% in well 52719. It is important to note that only two wells have significant porosity. There is a gross average porosity of 1.7% (Table 9-4). This formation has an average NTG ratio of 0.114.

Table 9-4. Summary of petrophysical calculations for the A-1 carbonate in the Dover 36 reef field.

Interval: A-1 Carbonate				
Avg. Thickness	**Gross Avg. Porosity**	**Avg. Net Porosity**	**Avg. Net Thickness**	**Avg. NTG**
59.6 ft	1.7%	6.2%	8.875 ft	0.114

A-1 Evaporite

The A-1 evaporite is not present in the wells in this reef field.

Brown Niagaran

The Brown Niagaran in the Dover 36 reef field plots as a mixed limestone-dolomite carbonate with high-porosity intervals in both the dolomitized and mixed carbonate zones. The thickness of this formation varies from 197 feet (well 29664) to 300 feet (well 29303) averaging 246 feet (Table 9-5). The average net porosity for this formation is 1.4% with a maximum porosity of 9.2% in well 52719 in the reef crest. The gross average porosity is 1.4% with a NTG ratio of 0.082.

Table 9-5. Summary of petrophysical calculations for the Brown Niagaran in the Dover 36 reef field.

Interval: Brown Niagaran				
Avg. Thickness	**Gross Avg. Porosity**	**Avg. Net Porosity**	**Avg. Net Thickness**	**Avg. NTG**
246 ft	1.4%	7.8%	20.9 ft	0.082

9.3 Seismic Analysis

Seismic analysis was conducted with the Dover 35 reef field and is discussed in Section 8.3.

9.4 Geological Interpretations

The Dover 36 reef field was interpreted to contain three reef pods which are highly connected through the overlap of leeward and windward facies and through the A-1 carbonate. The Dover 36 reef field boundaries were interpreted by the geometry of the reef and the changes in thickness of the Brown Niagaran and A-1 carbonate. The Brown Niagaran was thickest in the reef crest or the reef core facies while the A-1 carbonate was thinnest. Brown Niagaran in wells in the windward facies changed thickness more rapidly than in the leeward facies due to steeper angles. The presence of evaporites was also used to determine if wells were in a flank position.

Cross section A-A’ runs south to north through the Dover 36 reef field. The cross section traverses the three reef pods and changes in lithology. The A-2 carbonate has a continuous high gamma spike, observed in other reef fields, that could be a carbonate mudstone. The A-1 carbonate is thin in all wells due to the wells being on-reef. Wells 52719 and 29303 have potential salt plugging at the top of the A-1 carbonate due to leaching from the overlying A-2 salt. The salt plugging was also noted in the mudlogs. There is minor porosity in the A-1 carbonate, with no porosity flags to indicate good reservoir. The Brown Niagaran has porosity flags mid-formation, with the greatest porosity observed in well 29235. The porosity flags in the Brown Niagaran also connect laterally across reef pods and lithofacies. This suggests a potential unconformity which has enhanced the porosity mid-reef.

Figure 9-9 shows the location of cross section A-A’ superimposed on a lithofacies map of the Brown Niagaran. Figure 9-10 shows the resulting cross section A-A’ through the A-2 carbonate, A-2 evaporite, A-1 carbonate, and Brown Niagaran intervals. Figure 9-11 shows cross section A-A’ cross section through the Dover 36 reef field revealing the three individual reef pods and formations colored by interpreted lithofacies.

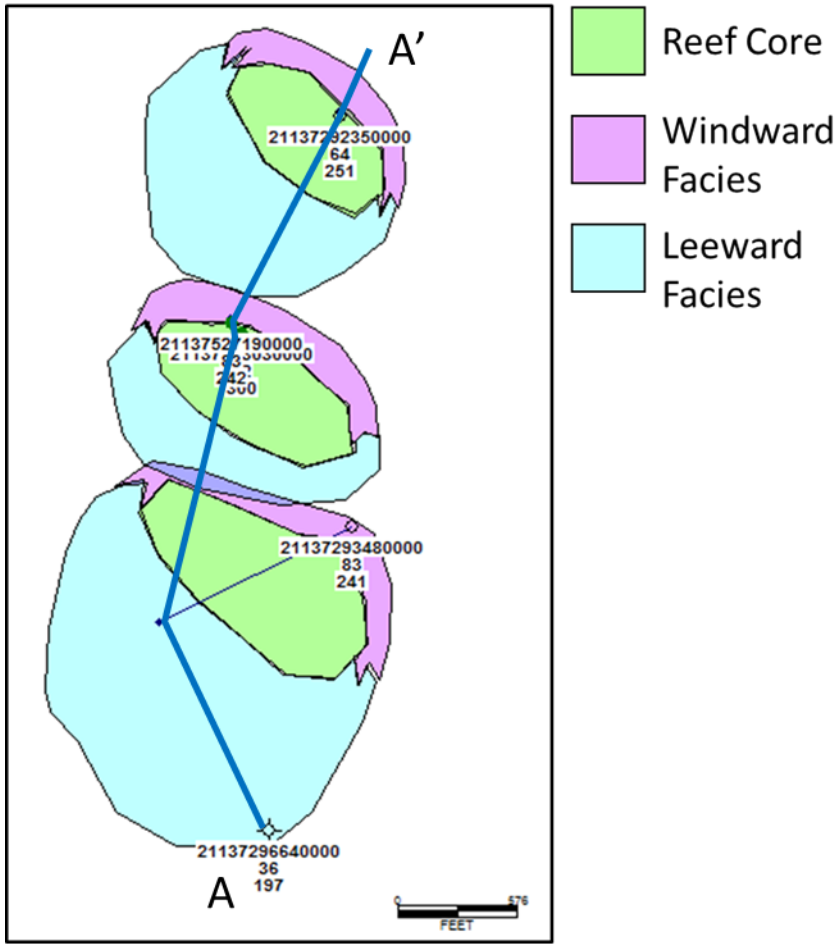


Figure 9-9. Location of cross section A-A' (blue line) on lithofacies map of the Brown Niagaran formation in the Dover 36 reef field showing three reef pods. Where lithofacies overlap, it is expected both would be present.

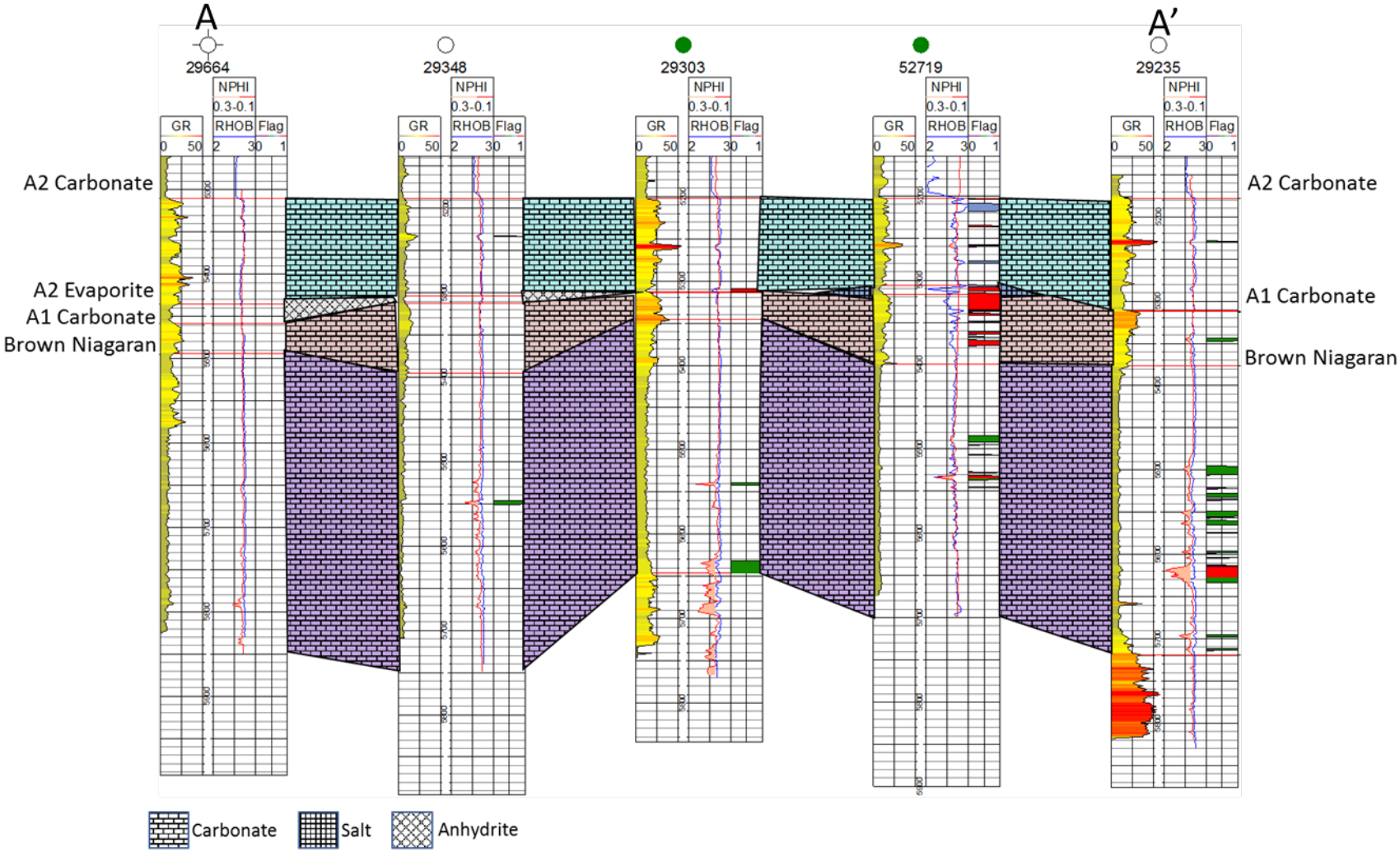


Figure 9-10. Cross section A-A' through the Dover 36 reef field showing the XGR, RHOB, and XNPHI for the A-2 carbonate, A-2 evaporite, A-1 carbonate, and Brown Niagaran intervals. Green flags = porosity values >5%, blue flags = anhydrite, red flags = salt intervals, and black flags = secondary features.

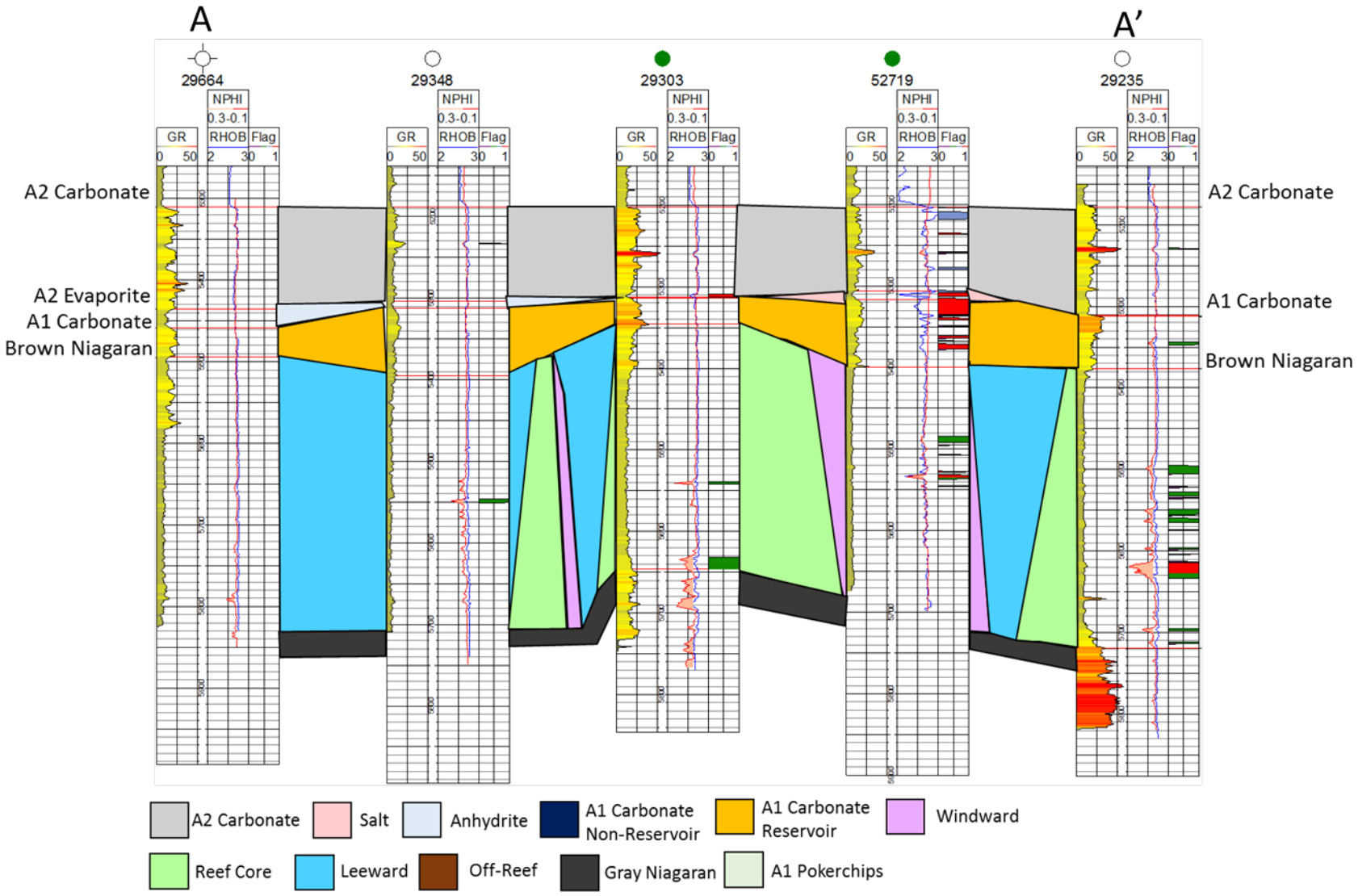


Figure 9-11. Cross section A-A' through the Dover 36 reef field showing three individual reef pods and formations colored by interpreted lithofacies.

10.0 Charlton 30-31

10.1 Reef History and Production Review

Production in the Charlton 30-31 field began with the completion of well 29073 in 1973. Since that time, several additional wells have been completed. The best production was from well 30203 in the northern section, which produced 35% of the oil during primary recovery. Well 29073, in the southern pod, produced 29% of the primary recovery oil and was the second-best producer. Considerably lesser volumes were produced by the other wells in the field, located between these two productive wells. Oil production peaked in 1977, early in the field's history, and steadily declined until 1998 when production ceased. The field was then acquired by Core Energy and additional wells were drilled. EOR operations began in 2006 with a steady increase in production through 2012 (Figure 10-1). As of December 31, 2017, approximately 2,987,800 bbls of oil have been produced. Figure 10-2 shows the cumulative oil and gas production by well.

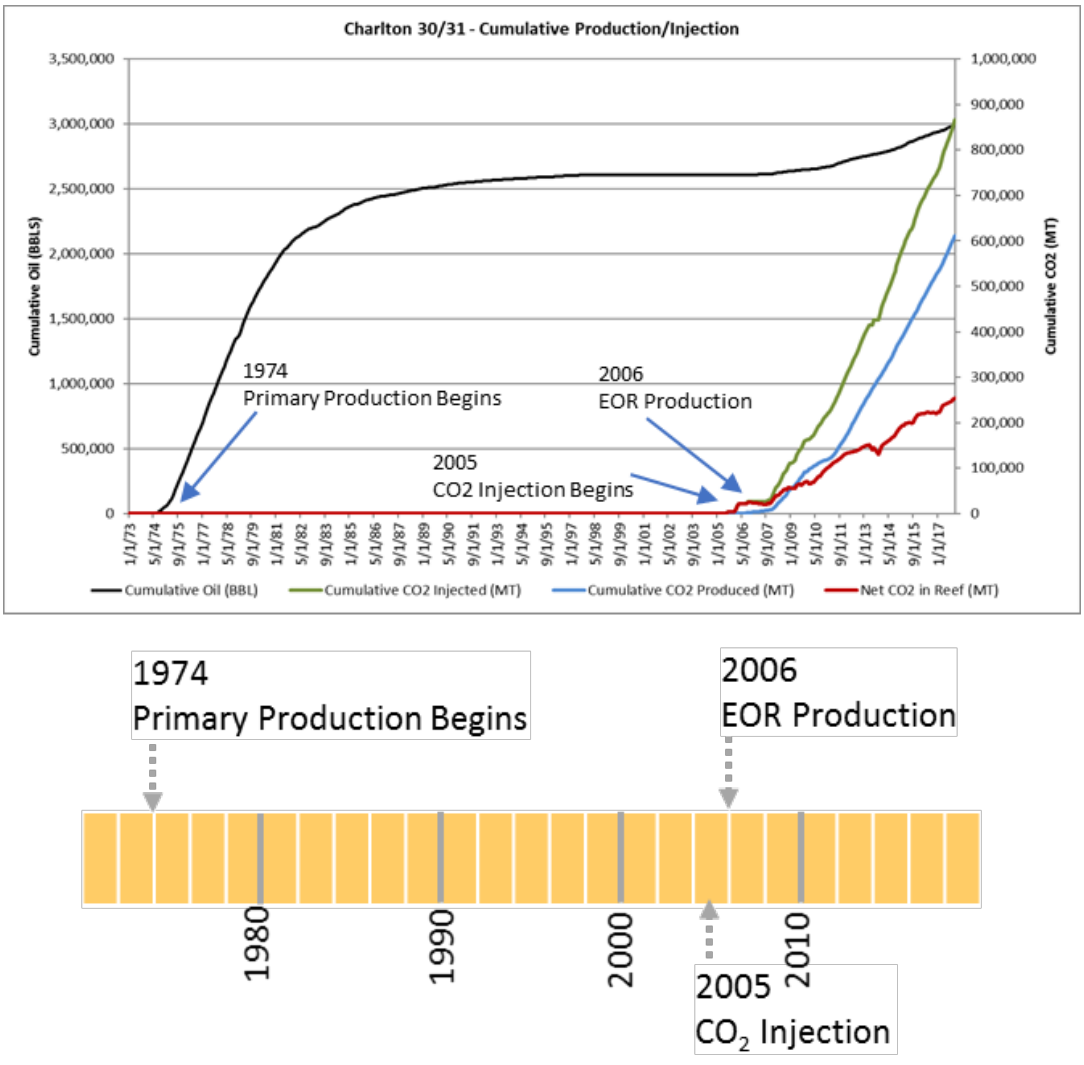


Figure 10-1. Cumulative production in the Charlton 30/31 reef field from 1974 through 2017 showing an increase in production rates after EOR operations began in 2006.

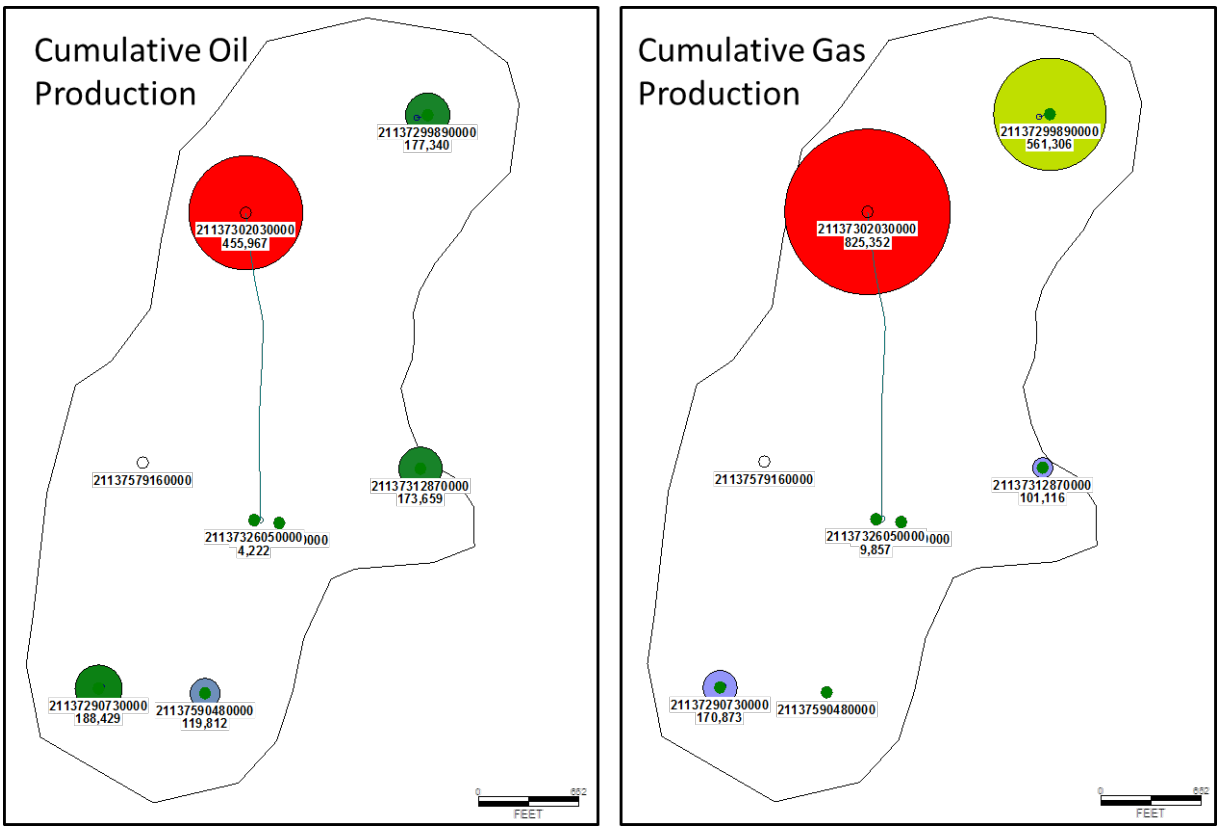


Figure 10-2. Cumulative oil and gas production in the Charlton 30-31 reef field showing the highest production (red) in the northern section of the field.

The initial (discovery) data for the Charlton 30-31 reef field, summarized in Table 10-1, consists of OOIP, oil API gravity, discovery pressure and temperature, and fluid saturations. Initial gas saturations were recorded at zero, as gas was produced as it came out of solution during production of oil as production continued.

Table 10-1. Summary of initial (discovery) conditions of the Charlton 30-31 reef field.

		Discovery		Saturation		
OOIP (bbls)	**API Gravity**	**Pressure (psi)**	**Temperature (oF)**	**Oil**	**Gas**	**Water**
6,800,000	44.2	2,954	103	61.23%	0%	38.77%

10.2 Wireline Log Analysis

Nine wells penetrate the Charlton 30-31 reef field. All of these wells have gamma ray, caliper, neutron porosity, and bulk density logs, or bulk density calculated from sonic (DT); these logs were used in the petrophysical analysis. Table 10-2 summarizes the available wireline log data for the Charlton 30/31 reef field. Figure 10-3 is a structure map of the reef field with well locations.

Table 10-2. Summary of available wireline log data for wells penetrating the Charlton 30-31 reef field.

	Well UWI	2113729073000	2113729989000	2113730195000	2113730203000	2113731287000	2113732605000	2113751603001	2113757916000	2113759048000
CAL	Caliper	■	■	■	■				■	
DT	Sonic	■	■			■			■	
GR	Gamma Ray	■	■	■	■	■	■	■	■	■
NPHI	Neutron Porosity	■	■	■		■		■	■	■
PNC	Pulsed Neutron Capture							2		2
RES	Resistivity	■	■	■	■	■	■		■	■
RHOB	Bulk Density	■	■	■	■	■	■	■	■	■
BHP	Bottom Hole Pressure Monitoring		■		■	■		■	■	■

Note: Green shading indicates logs available by well and numbers indicate repeat collection.

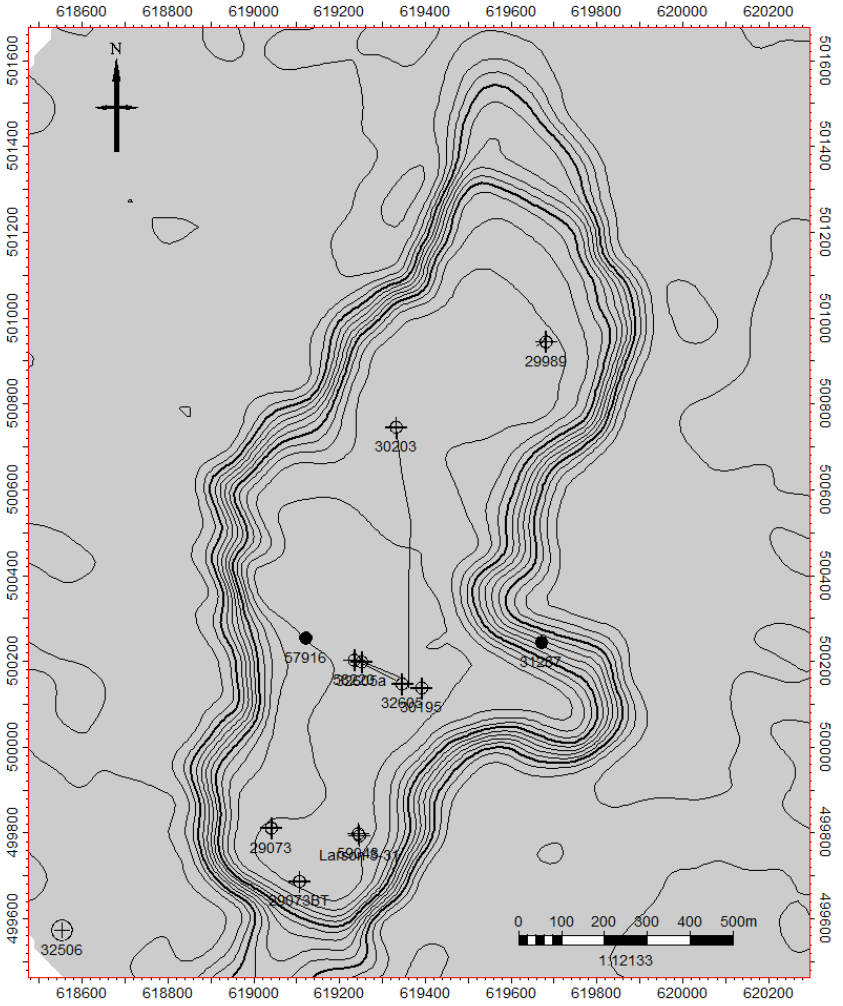


Figure 10-3. Structure map of the Charlton 30-31 reef field showing well locations and trajectories.

10.2.1 Basic Log Interpretation

Well 29073

Well 29073 is located in the southwest portion of the Charlton 30-31 reef field. The A-2-carbonate plots as a mixed limestone-dolomite matrix that is dominated by limestone. This region contains anhydrite in its upper and lower intervals. The A-1 carbonate was predominantly a limestone and contained thin zones of anhydrite in its lower intervals. The Brown Niagaran contained the only porosity in this well that is greater than 5%. The Brown Niagaran is a mixed limestone-dolomite matrix. Figure 10-4 is the neutron porosity-bulk density crossplot from the A-2 carbonate to the Brown Niagaran. The red polygon indicates the zones with porosity of greater than 5% and have been flagged on the XNPHI and RHOB logs accordingly, while the blue polygon indicates anhydrite.

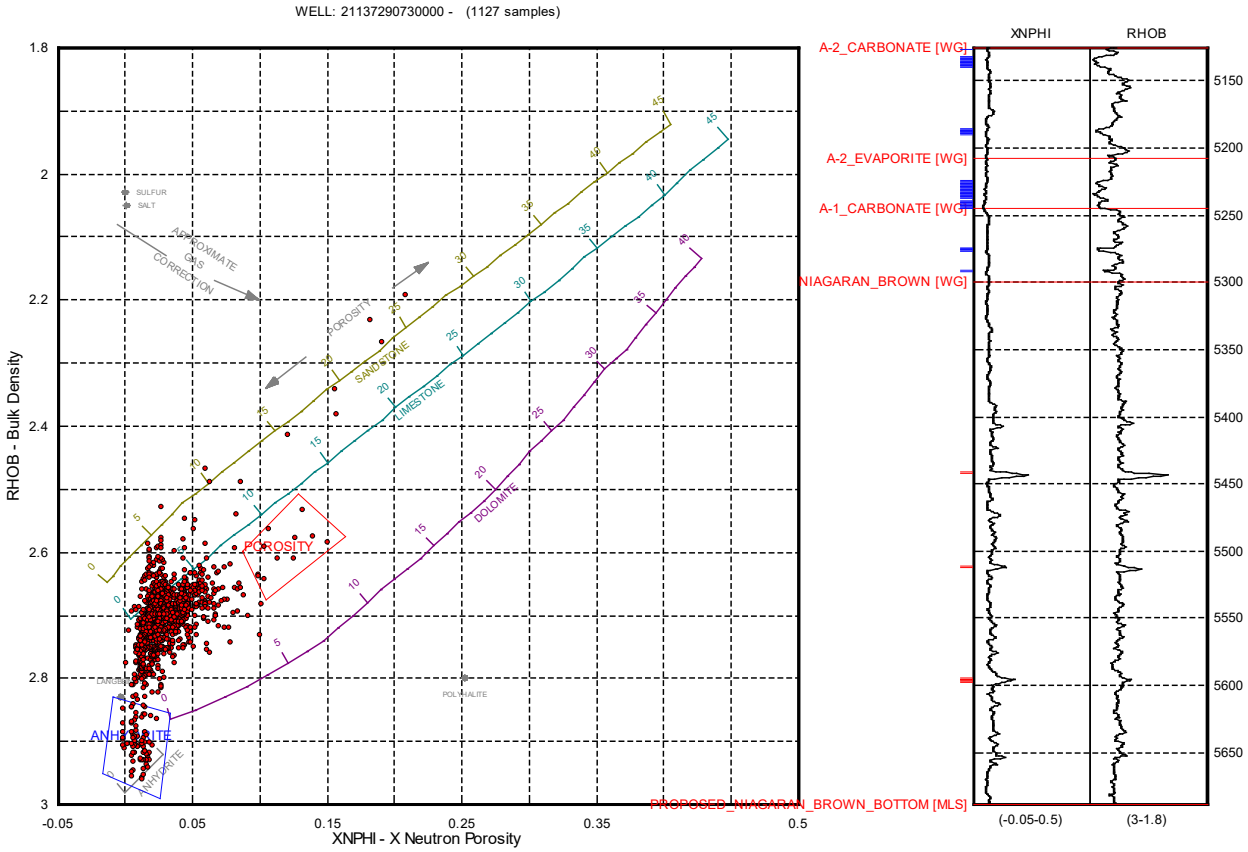


Figure 10-4. Neutron porosity bulk-density crossplot of well 29073 from the A-2 carbonate to the Brown Niagaran showing thin intervals of porosity in the Brown Niagaran (red).

High water saturations were calculated for well 29073 where evaporites are present. The water saturation gradually increases mid-Brown Niagaran and remains high at 5,545 feet MD at the apparent oil/water contact. This leaves approximately 245 feet of unsaturated Brown Niagaran. On average, the Brown Niagaran has a water saturation of 36%, which increases to an average of 71% below 5,545 feet MD. Figure 10-5 shows the water saturation curve and histogram.

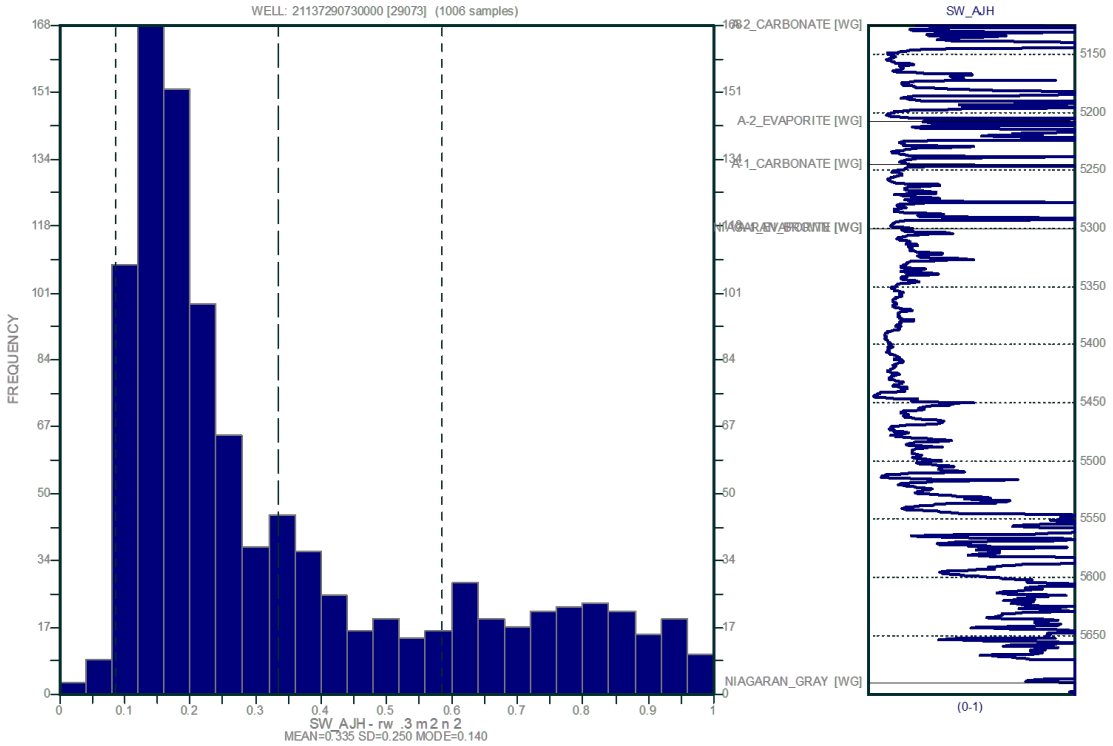


Figure 10-5. Water saturation curve and histogram for well 29073 showing an increase in saturation toward the base of the Brown Niagaran.

Well 29989

Well 29989 is located in the northeast portion of the Charlton 30-31 reef field. The A-2 carbonate had a mixed limestone-dolomite matrix but is dominated by dolomite. This zone contained minor amounts of porosity that were greater than 5%. The A-1 carbonate had a mixed limestone-dolomite matrix with the highest porosity value. The middle and lower intervals of the A-1 carbonate both had porosity greater than 5%. The Brown Niagaran also had a mixed limestone-dolomite matrix and contained some porosity greater than 5%. Figure 10-6 is the neutron porosity-bulk density crossplot from the A-2 carbonate to the Brown Niagaran in well 29989. The red rectangle indicates the zones with porosity of greater than 5% and have been flagged on the XNPHI and RHOB logs accordingly.

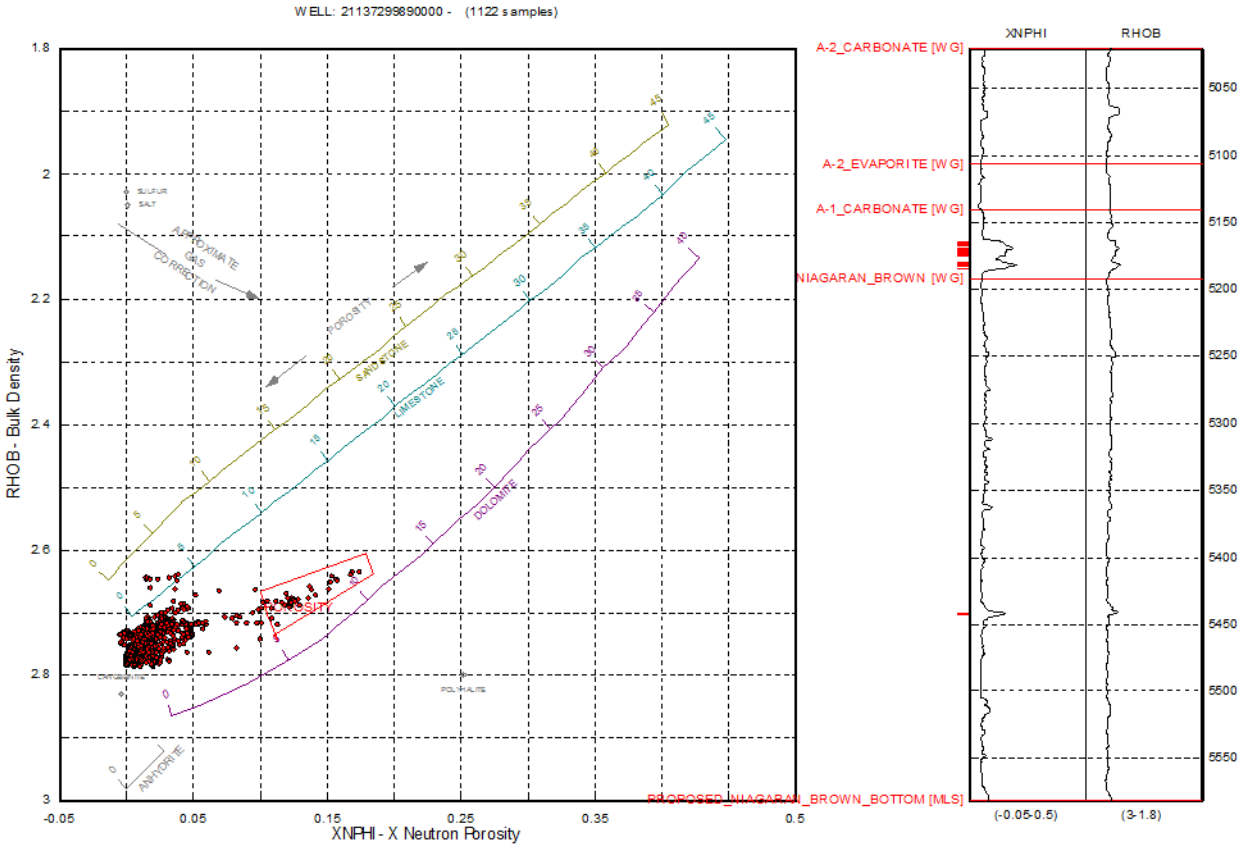


Figure 10-6. Neutron porosity-bulk density crossplot of well 29989 from the A-2 carbonate to the Brown Niagaran showing porosity greater than 5% in the A-1 carbonate.

Water saturation was calculated for well 29989 and showed spikes in saturation in the presence of evaporites. These spikes occurred throughout the A-2 carbonate, the upper A-2 evaporite, and the top of the Brown Niagaran. The water saturation had a sharp increase mid-Brown Niagaran at 5,380 feet MD and again at 5,450 feet MD. The original oil/water contact was recorded at 5,520 feet MD, implying the high intervals above could be due to a transitional zone. The Brown Niagaran had an average water saturation of 33%, which increased to 54% below 5,380 feet MD. Figure 10-7 shows the water saturation curve and histogram for well 29989.

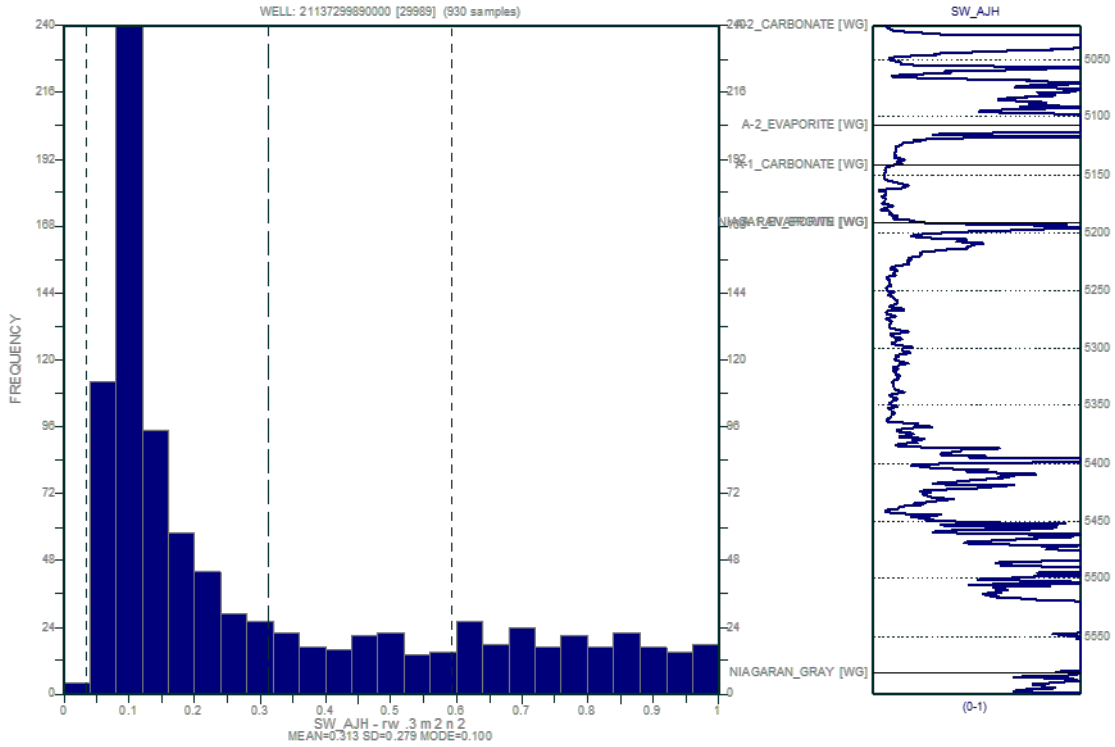


Figure 10-7. Water saturation curve and histogram for well 29989 showing an increase in water saturation at 5,380 feet MD in the Brown Niagaran formation.

Well 30195

Well 30195 is located in the south-central portion of the Charlton 30-31 reef field. The A-2 carbonate plotted as a mixed limestone-dolomite. This area contained anhydrite in the upper and lower intervals. The A-1 carbonate had a mixed limestone-dolomite matrix but was dominated by limestone. This formation contained anhydrite in its upper and middle intervals. The Brown Niagaran was dominated by limestone in its upper intervals and by dolomite in its lower intervals. There was some indication of salt plugging in the upper intervals as well. This is the only interval in this well that contained porosity greater than 5%. Figure 10-8 is the neutron porosity-bulk density crossplot from the A-2 carbonate to the Brown Niagaran. The red polygon indicates the zones with porosity greater than 5% and have been flagged on the neutron porosity and bulk density logs accordingly, while the blue polygon indicates anhydrite and the green indicates salt.

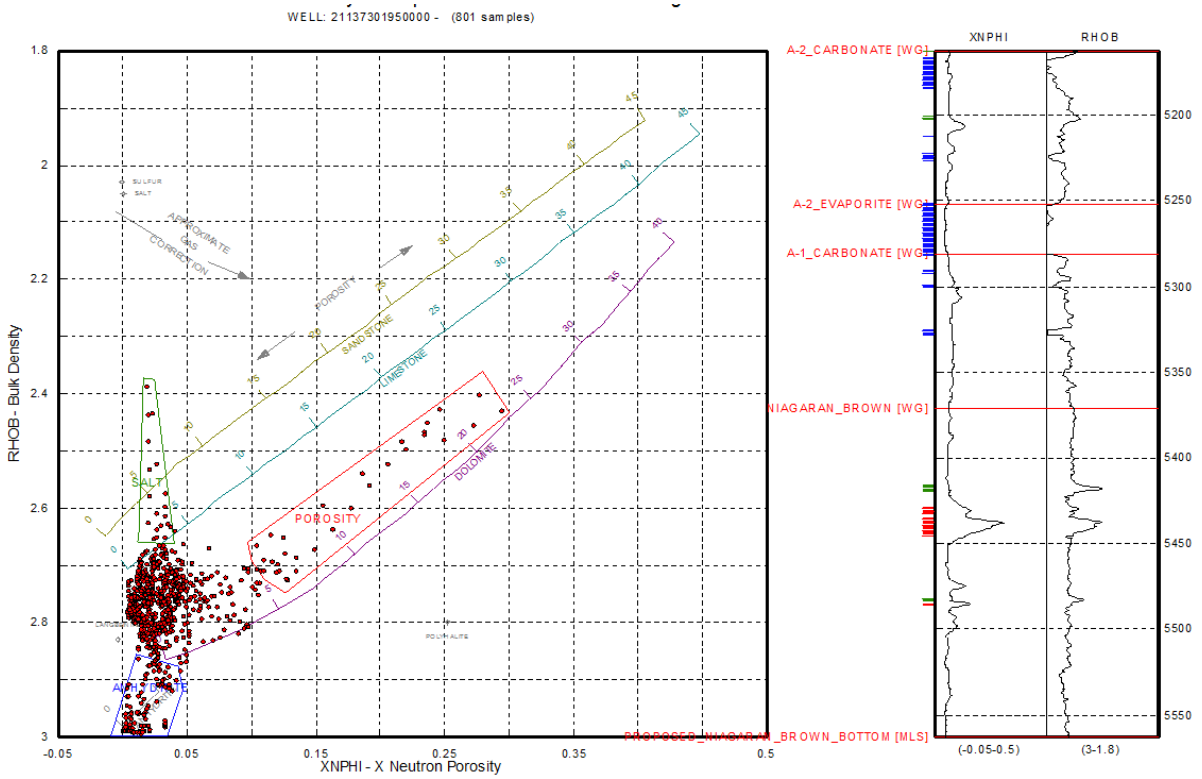


Figure 10-8. Neutron porosity-bulk density crossplot of well 30195 from the A-2 carbonate to the Brown Niagaran showing porosity streaks in the Brown Niagaran (red flags) with potential salt plugging (green flags). Red polygon = porosity >5%, green polygon = salt, blue polygon = anhydrite.

Water saturation was calculated for well 30195 and showed intervals of high resistivity in the presence of evaporites. There was a gradational increase in water saturation toward the base of the Brown Niagaran formation near 5,530 feet MD, which is consistent with the original oil/water contact. On average, the Brown Niagaran had a water saturation of 15%, which increased to 39% below 5,530 feet MD. Figure 10-9 shows the water saturation curve and histogram for well 30195.

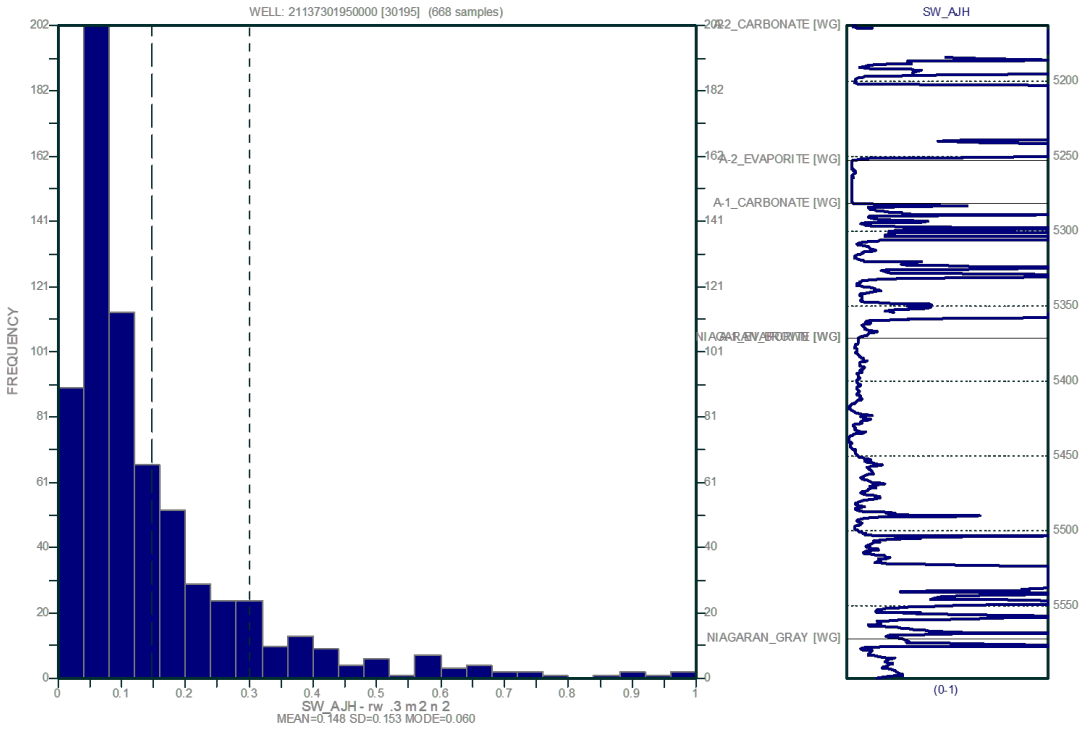


Figure 10-9. Water saturation curve and histogram for well 30195 showing an increase at 5,530 feet MD in the Brown Niagaran.

Well 30203

Well 30203 is located in the northern section of the Charlton 30-31 reef field. Thin intervals of anhydrite were noted in the A-2 carbonate (blue). A salt package was present in the A-2 evaporite and there are thin flags in the Brown Niagaran, indicating potential salt plugs. Minor porosity was observed in the A-1 carbonate with most porosity flags occurring in the Brown Niagaran (red flags). The Brown Niagaran had a significant porosity bloom near 6,010 to 6,140 feet MD where porosity was consistently higher than 5%. Figure 10-10 is the neutron porosity-bulk density crossplot for well 30203.

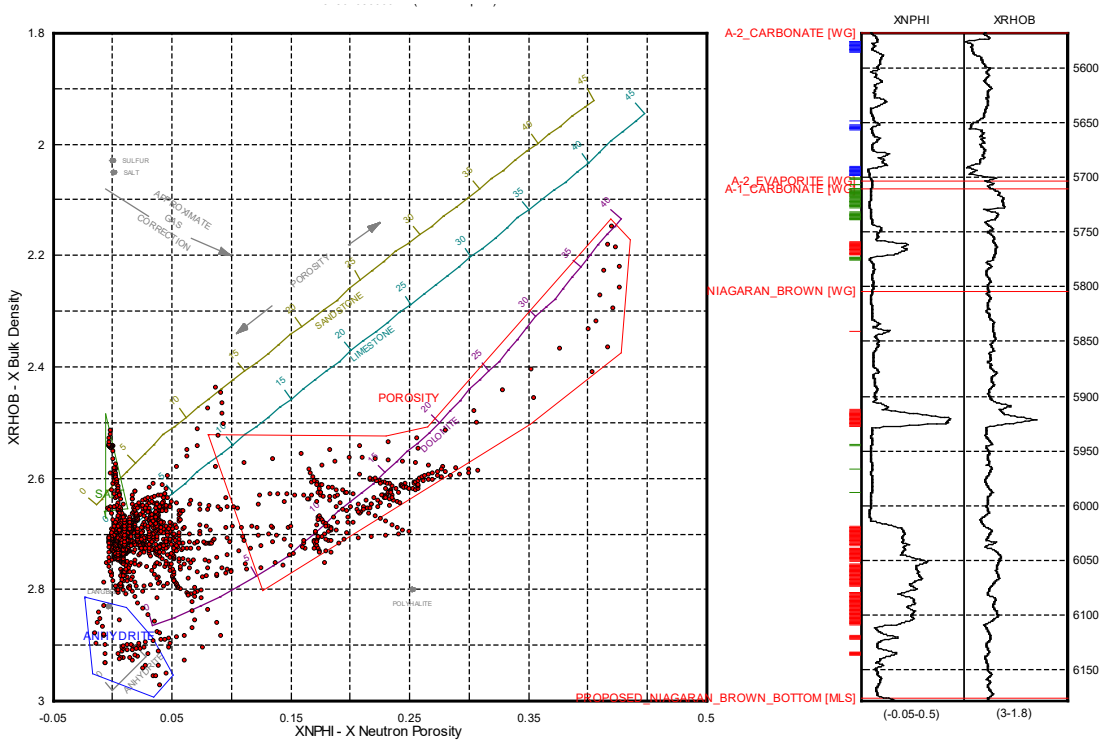


Figure 10-10. Neutron porosity-bulk density crossplot for well 30203 from the A-2 carbonate to the Brown Niagaran showing porosity greater than 5% (red flags) in the Brown Niagaran. Red polygon = porosity >5%, green polygon = salt, blue polygon = anhydrite.

Water saturations calculated for well 30203 showed spikes in saturation in the presence of evaporites. The water saturation curve terminated mid-Brown Niagaran, so a confident oil/water contact could not be established. There was a gradational increase in water saturation leading up to 6,010 feet MD, which could indicate the oil/water contact. If so, the lower porosity bloom would be water-saturated. Figure 10-11 shows the water saturation curve and histogram for well 30203.

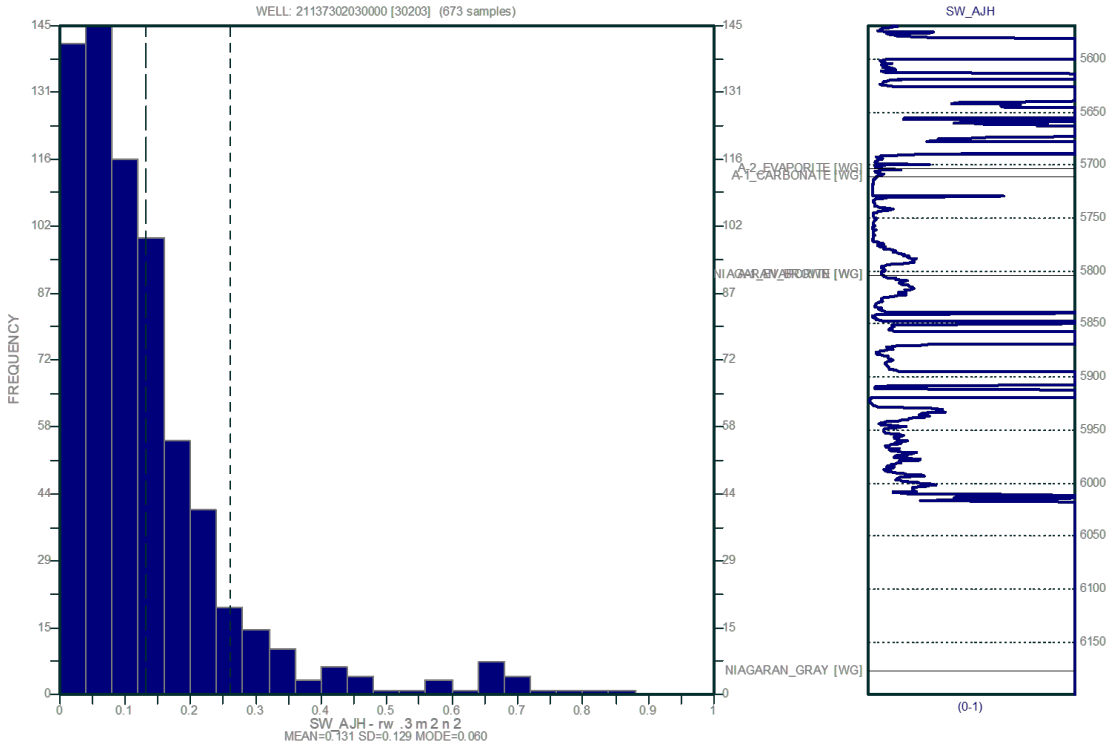


Figure 10-11. Water saturation curve and histogram for well 30203 showing a gradational increase in saturation in the Brown Niagaran before the end of the curve at 6,010 feet MD.

Well 31287

Well 31287 is located in the central-east portion of the Charlton 30-31 reef field. The A-2 carbonate had a mixed limestone-dolomite matrix. The A-1 carbonate plotted as a limestone in this section. The Brown Niagaran had a mixed limestone-dolomite matrix with most of the porosity greater than 5% in the dolomite. Figure 10-12 is the neutron porosity-bulk density crossplot from the A-2 carbonate to the Brown Niagaran. The red rectangle indicates the zones with porosity of greater than 5%, which have been flagged on the neutron porosity and bulk density logs accordingly (the green polygon indicates salt).

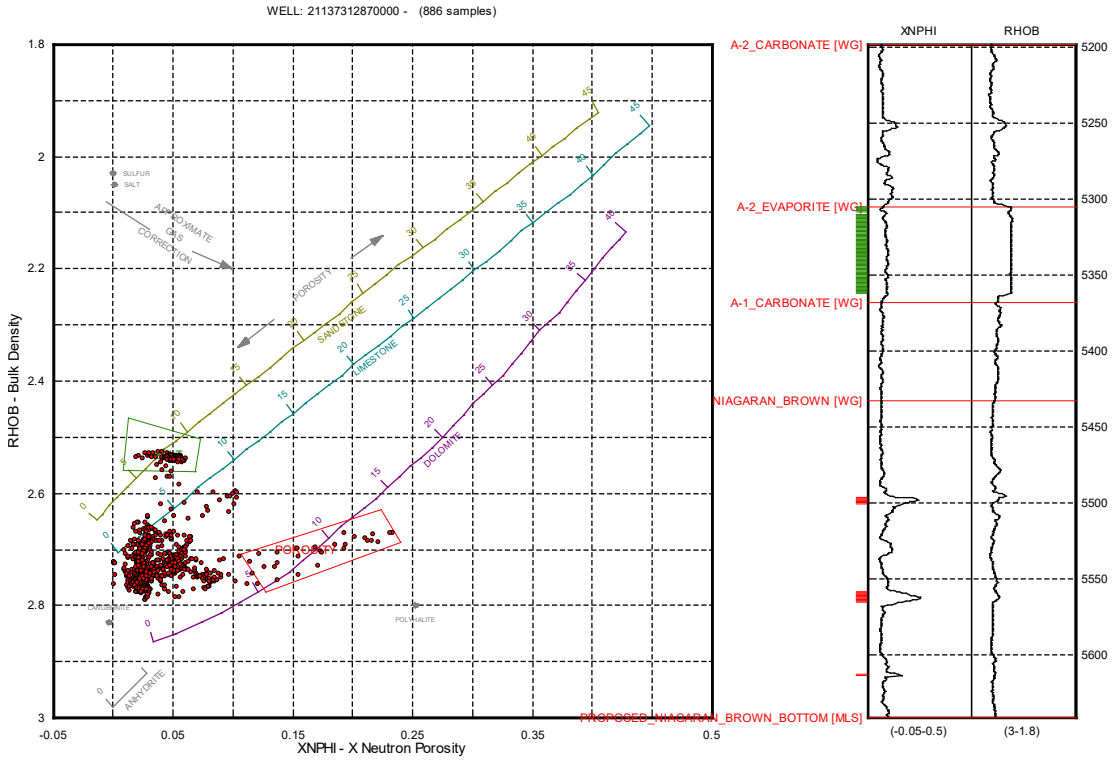


Figure 10-12. Neutron porosity-bulk density crossplot of well 31287 from the A-2 carbonate to the Brown Niagaran showing streaks of porosity in the Brown Niagaran (red flags) and a thick package of salt in the A-2 evaporite (green flags). Red polygon = porosity >5%, green polygon = salt.

Water saturations for well 31287 indicated high saturations in the A-2 carbonate. This could indicate thin evaporite intervals. The water saturation gradually increased mid-Brown Niagaran and remains consistently high below 5,540 feet MD. The oil/water contact was at 5,540 feet MD. The Brown Niagaran had an average water saturation of 40%, which increased to 67% below 5,540 feet MD. There are only thin intervals of high porosity above the water-saturated zone. Figure 10-13 shows the water saturation curve and histogram for well 31287.

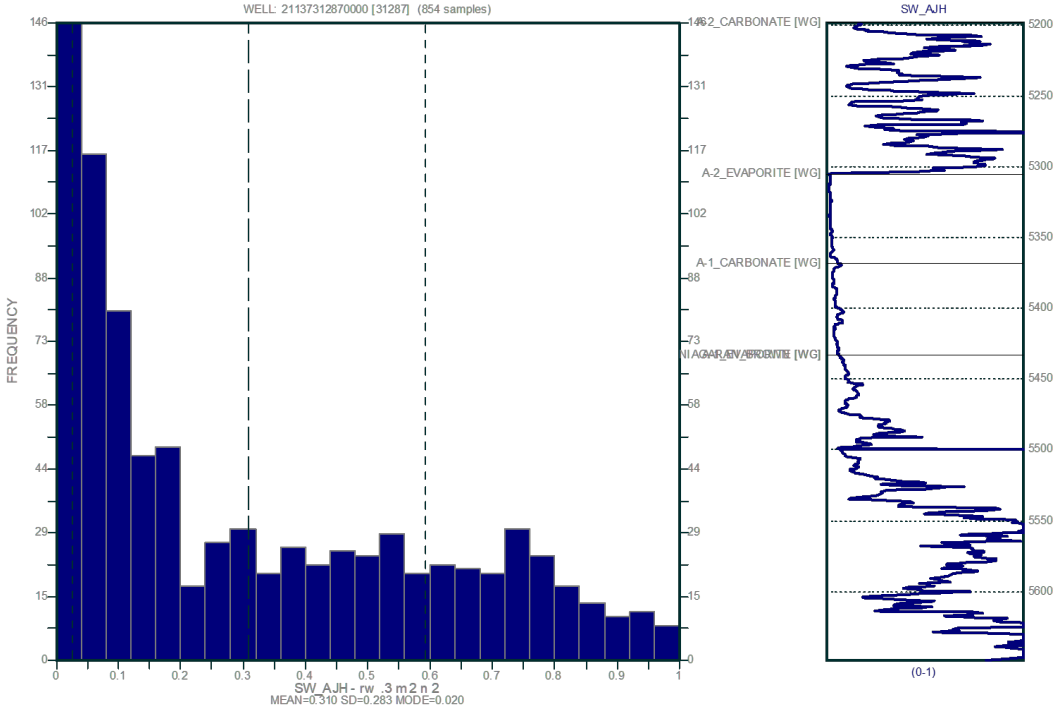


Figure 10-13. Water saturation curve and histogram for well 31287 showing an increase in saturation in the Brown Niagaran at 5,540 feet MD.

Well 32605

Well 32605 is located in the center of the Charlton 30-31 reef field. The A-2 evaporite is composed of anhydrite, and thin anhydritic layers occurred in the A-2 carbonate and A-1 carbonate. Very little salt plugging was observed except for thin intervals in the upper Brown Niagaran and upper A-2 carbonate. Porosity greater than 5% mostly occurred in thin intervals throughout the lower A-1 carbonate and upper Brown Niagaran. The Brown Niagaran is a mixed limestone-dolomite carbonate with significant porosity near the base. Figure 10-14 is the neutron porosity-bulk density crossplot showing porosity >5% (red flags), salt (green flags), and anhydrite (blue flags).

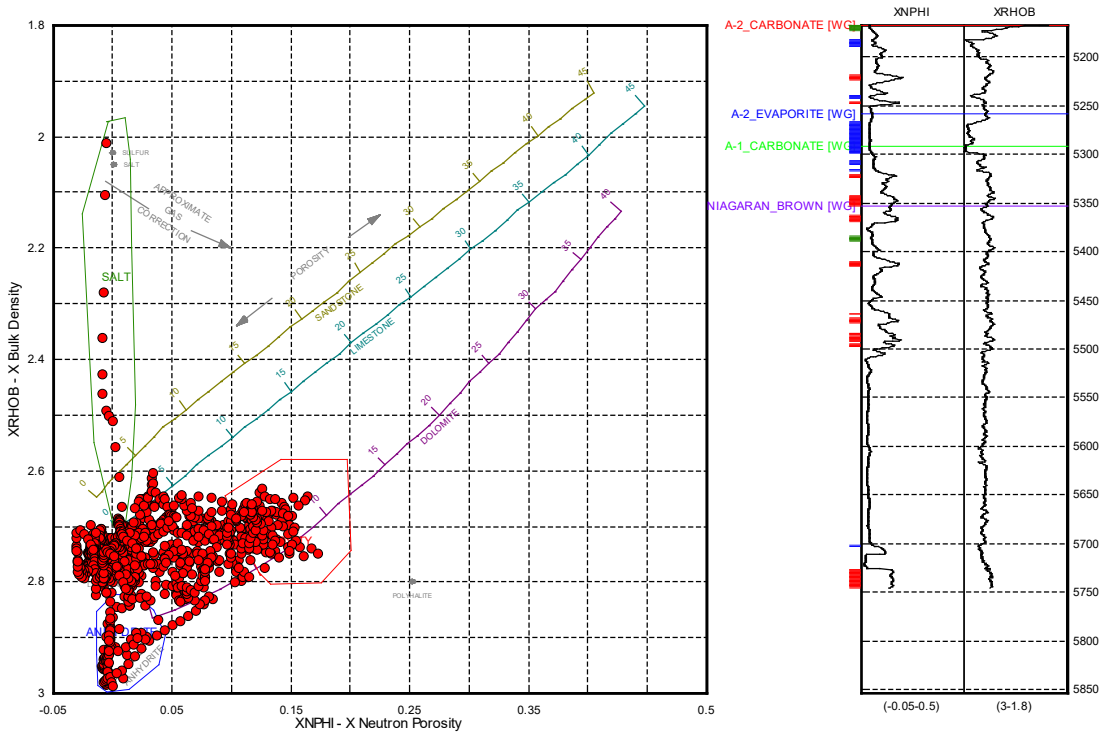


Figure 10-14. Neutron porosity-bulk density crossplot for well 32605 from the A-2 carbonate to the Brown Niagaran showing intervals of porosity greater than 5% in the lower A-1 carbonate and Brown Niagaran. Red polygon = porosity >5%, green polygon = salt, blue polygon = anhydrite.

Water saturations for well 32605 indicated spikes in saturation in the presence of evaporites. There was a significant increase in water saturation at 5,510 feet MD in the mid-Brown Niagaran. The high oil/water contact limits the reservoir potential to the upper Brown Niagaran and lower A-1 carbonate. On average, the Brown Niagaran had a water saturation of 30%, which increased to 49% below 5,510 feet MD. Figure 10-15 shows the water saturation curve and histogram for well 32605.

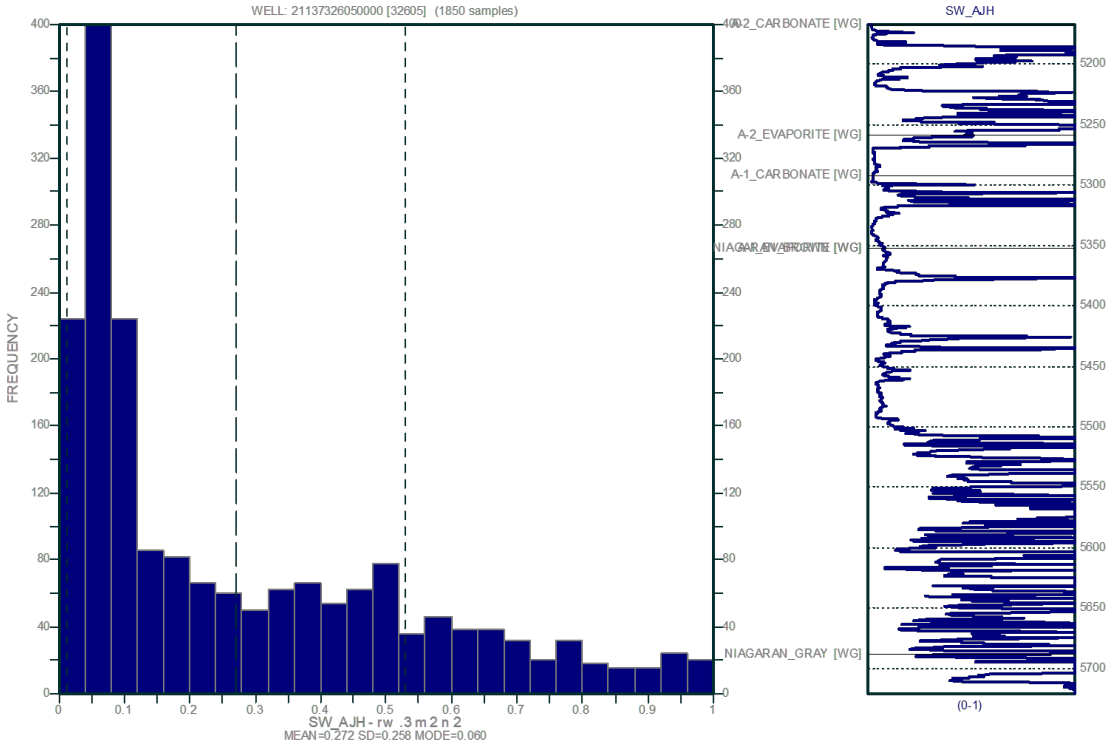


Figure 10-15. Water saturation curve and histogram for well 32605 showing an increase in water saturation mid-Brown Niagaran at 5,510 feet MD.

Well 57916

Well 57916 is located in the central-west portion of the Charlton 30-31 reef field. The A-2 carbonate had a mixed limestone-dolomite matrix and contained some salt intervals in the middle of the formation. The A-1 carbonate is a mixed limestone-dolomite. The Brown Niagaran was predominantly a limestone but at its base was a dolomite. The dolomitic interval was the only area that had porosity greater than 5%. Figure 10-16 shows the neutron porosity-bulk density crossplot from the A-2 carbonate to the Brown Niagaran in well 57916.The red polygon indicates the zones with porosity of greater than 5% and have been flagged on the neutron porosity and bulk density logs accordingly (green indicates salt).

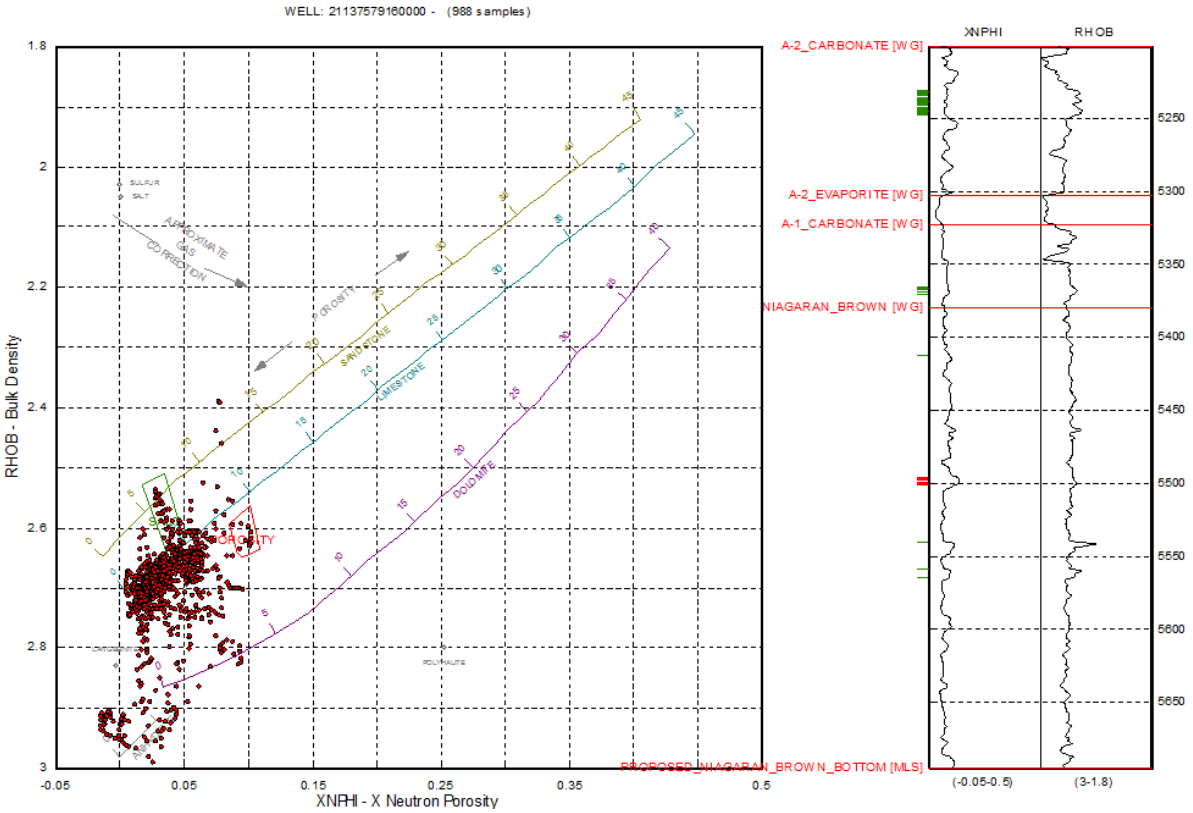


Figure 10-16. Neutron porosity-bulk density crossplot of well 57916 from the A-2 carbonate to the Brown Niagaran showing thin intervals of porosity >5% in the Brown Niagaran (red) with potential salt plugging (green). Red polygon = porosity >5%, green polygon = salt.

Water saturations for well 57916 indicated high saturations in the presence of evaporites. The water saturation increased mid-Brown Niagaran at 5,550 feet MD before decreasing again at 5,630 feet MD. This could indicate a transitional zone, or the oil/water contact could be near 5,550 feet MD. The Brown Niagaran had a relatively low water saturation of 20% with an increase to 30% below 5,550 feet MD. Figure 10-17 shows the water saturation curve and histogram for well 57916.

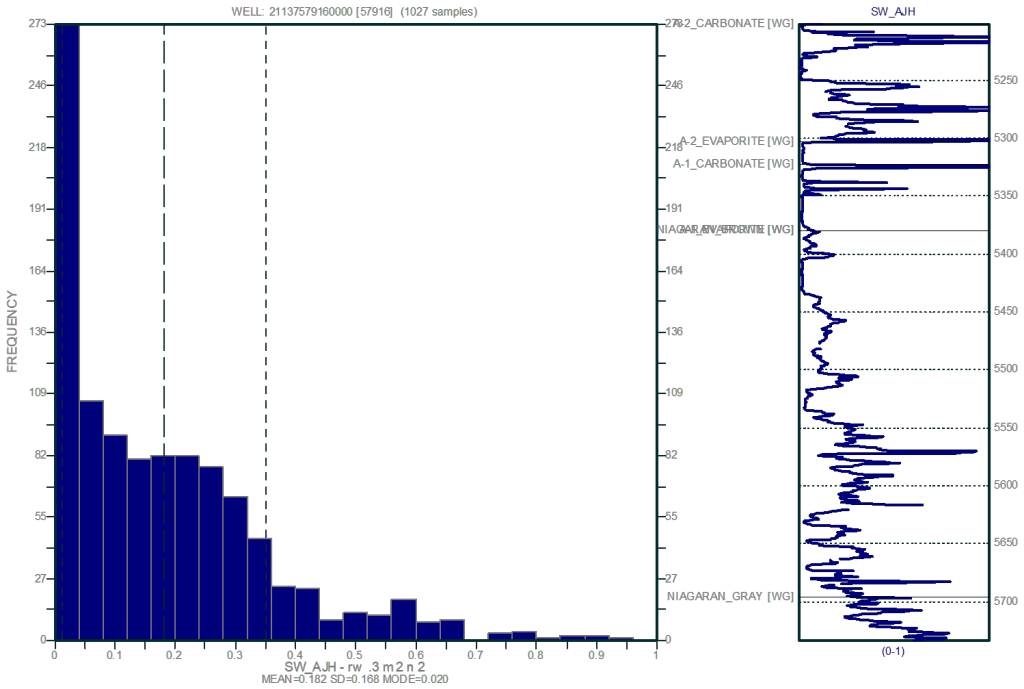


Figure 10-17. Water saturation curve and histogram for well 57916 showing a gradational increase in water saturation mid-Brown Niagaran at 5,550 feet MD.

Well 59048

Well 59048 is located in the south-central portion of the Charlton 30-31 reef field. The A-2 carbonate had a mixed limestone-dolomite matrix. It had anhydrite in the upper horizons and minor amounts of salt in the middle horizons. The A-1 carbonate plotted as a limestone and contained minor amounts of anhydrite in the middle interval. The Brown Niagaran had a mixed limestone-dolostone matrix but was dominated by limestone. It contained all of the porosity greater than 5% in this well, with most of it toward the base of the A-1 carbonate. Figure 10-18 is the neutron porosity-bulk density crossplot from the A-2 carbonate to the Brown Niagaran. The red rectangle indicates the zones with porosity greater than 5% and have been flagged on the neutron porosity and bulk density logs accordingly. The green indicates salt and the blue indicates anhydrite.

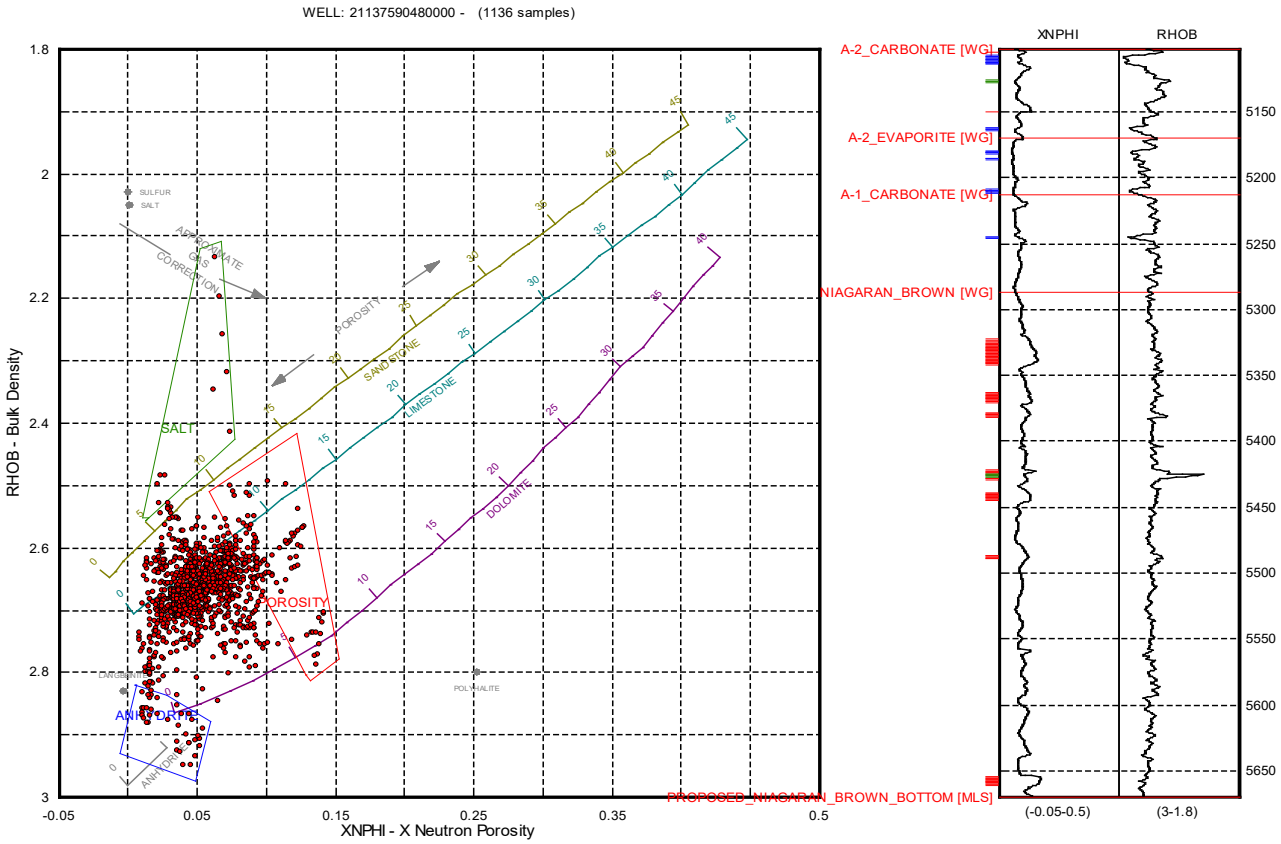


Figure 10-18. Neutron porosity-bulk density crossplot of well 59048 from the A-2 carbonate to the Brown Niagaran showing intervals of porosity >5% (red) in the Brown Niagaran. Red polygon = porosity >5%, green polygon = salt, blue polygon = anhydrite.

Water saturations for well 59048 indicated spikes in saturation in the A-2 carbonate and A-2 evaporite in the presence of evaporites. The saturation levels gradually increase mid-Brown Niagaran at 5,500 feet MD and remain near 50%. The Brown Niagaran had an average saturation of 24% which increased to 39% below 5,500 feet MD. Figure 10-19 shows the water saturation curve and histogram for well 59048.

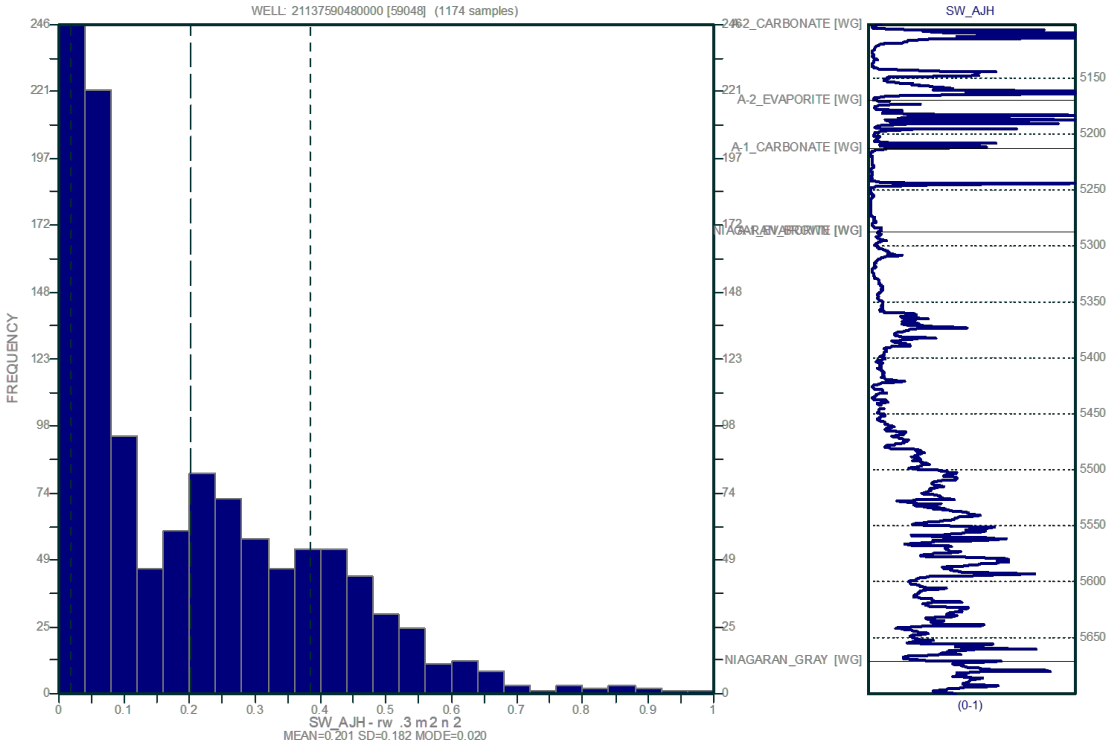


Figure 10-19. Water saturation curve and histogram for well 59048 showing a gradational increase mid-Brown Niagaran near 5,500 feet MD.

10.2.2 Petrophysics Calculations

A-2 Carbonate

The A-2 carbonate is predominantly a mixed limestone-dolomite matrix. The thickness ranged from 172 to 235 feet with an average thickness of 193 feet. The porosity values ranged from 0% to 14% with an average of 4.0%. The net thickness averaged 47 feet with a NTG ratio of 0.24. Salt plugging and anhydrite are commonly found in this formation, which can influence the porosity. A water saturation cutoff of 40% was applied, reducing the average net thickness to 5 feet and the NTG ratio to 0.03, which is representative of a good confining layer (Table 10-3).

Table 10-3. Summary of petrophysical calculations for the A-2 carbonate in the Charlton 30-31 reef field.

Interval: A-2 Carbonate						
Avg. Thickness	**Avg. Porosity**	**Avg. Net Thickness**	**Avg. NTG**	**Avg. SW**	**Avg. Net Thickness (SW<40%)**	**Avg. NTG (SW<40%)**
193 ft	4.0%	47 ft	0.24	32%	5 ft	0.03

A-1 Carbonate

The A-1 carbonate is a mixed limestone-dolomite that is dominated by limestone. The thickness ranged from 51 feet near the crest of the reef system to 90 feet along the flanks. The porosity ranged from 0% to 14% with an average of 4.6%. A porosity cutoff of 5% resulted in an average net thickness of 22 feet with a NTG ratio of 0.34 (Table 10-4). A water saturation cutoff of 40% was applied to eliminate evaporites and saturated rock.

Table 10-4. Summary of petrophysical calculations for the A-1 carbonate in the Charlton 30-31 reef field.

Interval: A-1 Carbonate						
Avg. Thickness	**Avg. Porosity**	**Avg. Net Thickness**	**Avg. NTG**	**Avg. SW**	**Avg. Net Thickness (SW<40%)**	**Avg. NTG (SW<40%)**
67 ft	4.6%	22 ft	0.34	10%	22 ft	0.34

Brown Niagaran

The Brown Niagaran is a mixed limestone-dolomite matrix that is dominated by limestone. The thickness varied from 201 feet along the flanks to 335 feet near the reef crest. The porosity ranged from 0% to 20% with an average of 4.2%. Using a porosity cutoff of 5%, the net thickness is 95 feet with a NTG ratio of 0.32. The oil/water contact is located mid-formation to the base of the Brown Niagaran. A water saturation cutoff of 40% was applied to eliminate water-saturated rock. The net thickness decreased to 73 feet and the NTG ratio to 0.24. Table 10-5 summarizes the petrophysical calculations for the Brown Niagaran.

Table 10-5. Summary of petrophysical calculations for the Brown Niagaran in the Charlton 30-31 reef field.

Interval: Brown Niagaran						
Avg. Thickness	**Avg. Porosity**	**Avg. Net Thickness**	**Avg. NTG**	**Avg. SW**	**Avg. Net Thickness (SW<40%)**	**Avg. NTG (SW<40%)**
288 ft	4.2%	95 ft	0.32	26%	73 ft	0.24

10.3 Seismic Analysis

The Charlton 30-31 field has sharp boundaries in seismic time where the reef has faster arrival times than the surrounding Brown Niagaran surface due to higher elevations. The A-1 carbonate drapes over the Brown Niagaran with little relief observed in seismic time. This is due to similar rock velocities between the A-1 carbonate and Brown Niagaran. There is not enough contrast for separate horizons along the reef crest. The A-2 carbonate has gentle slopes with minor indications of an underlying reef complex. Figure 10-20 through Figure 10-22 show the time surfaces of the seismic horizons.

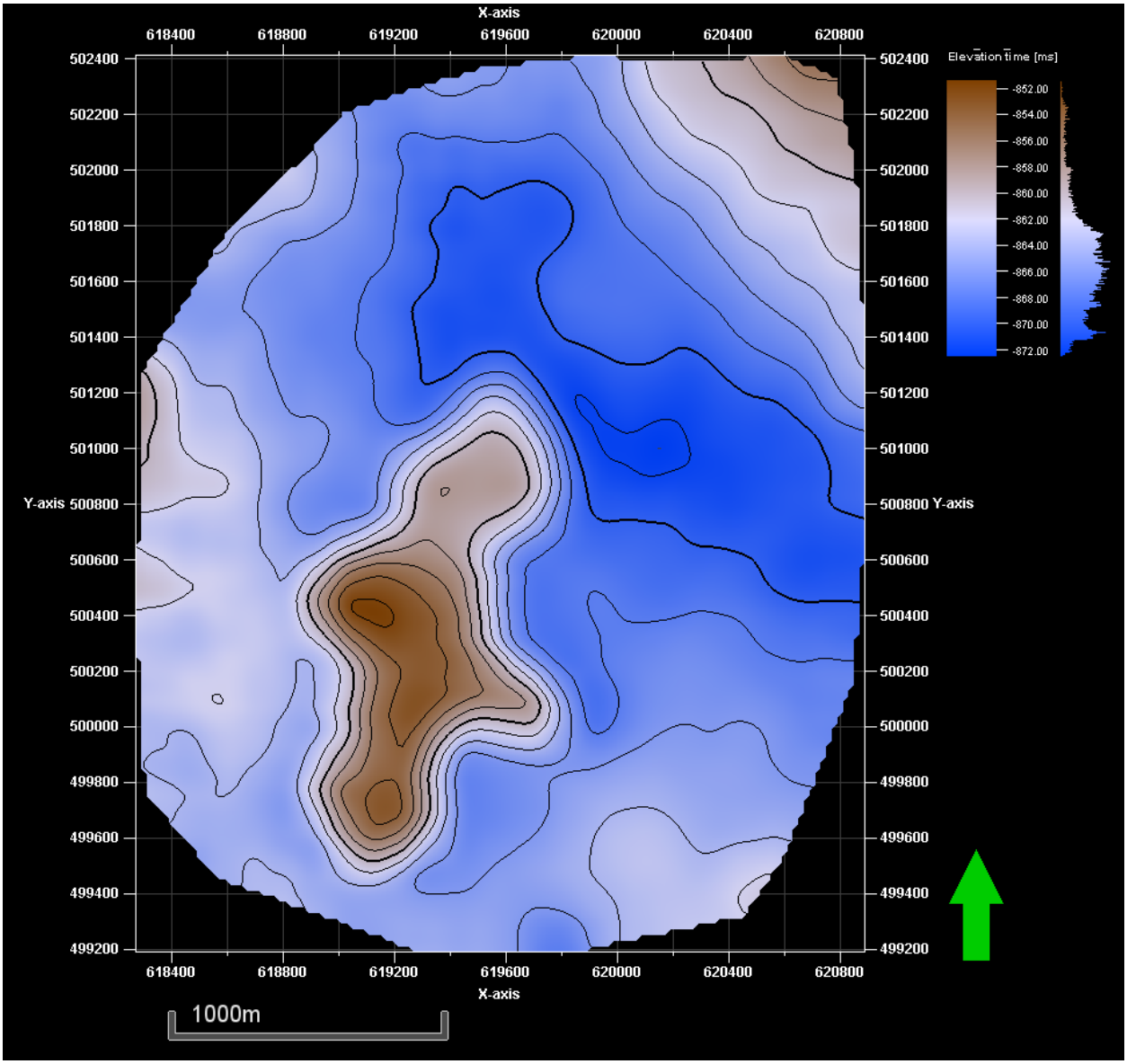


Figure 10-20. Time horizon surface for the A-2 carbonate showing gentle slopes along the edges of the Charlton 30-31 reef field.

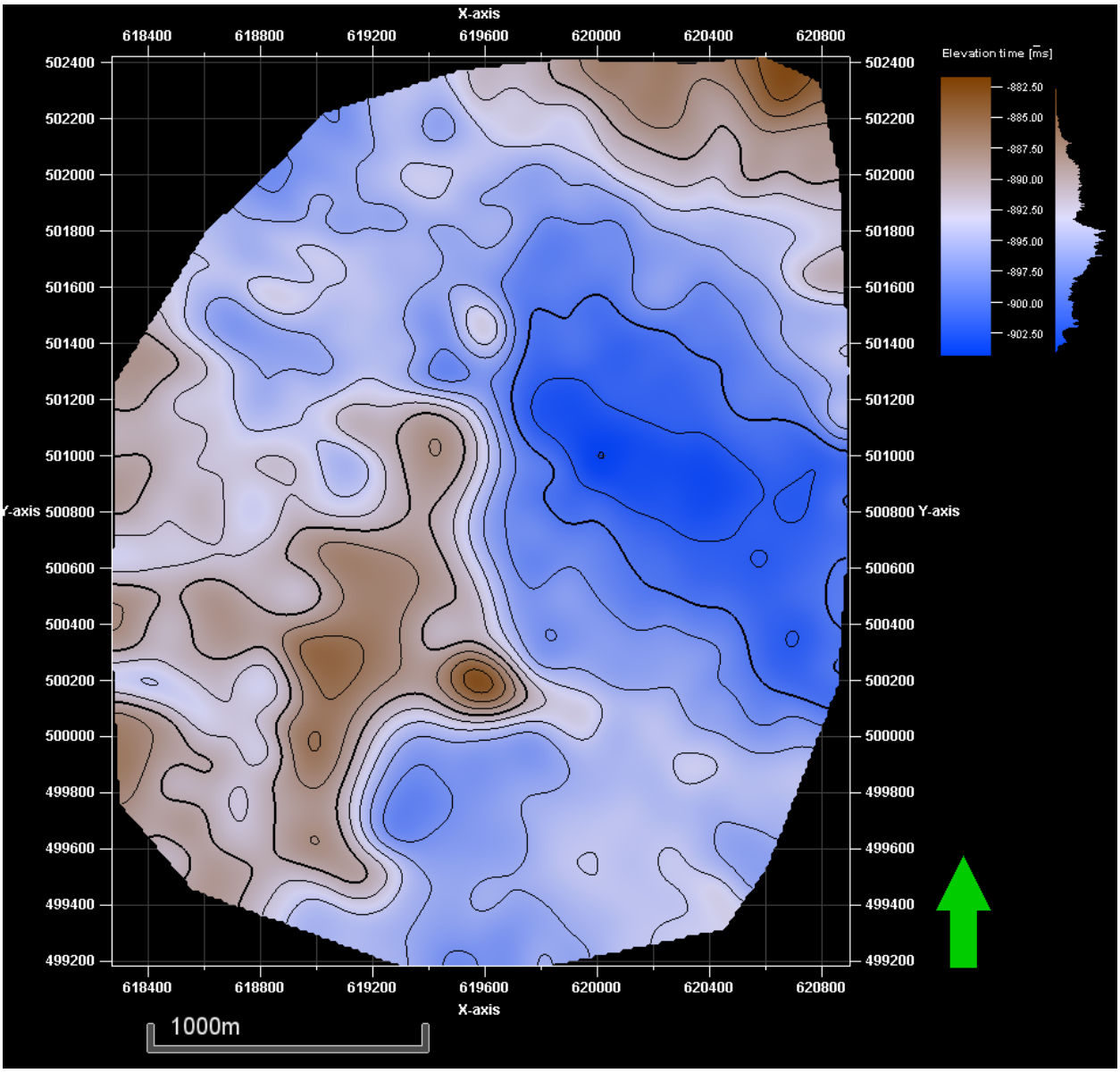


Figure 10-21. Time horizon surface for the A-1 carbonate showing gentle slopes and low relief along the edges of the Charlton 30-31 reef field.

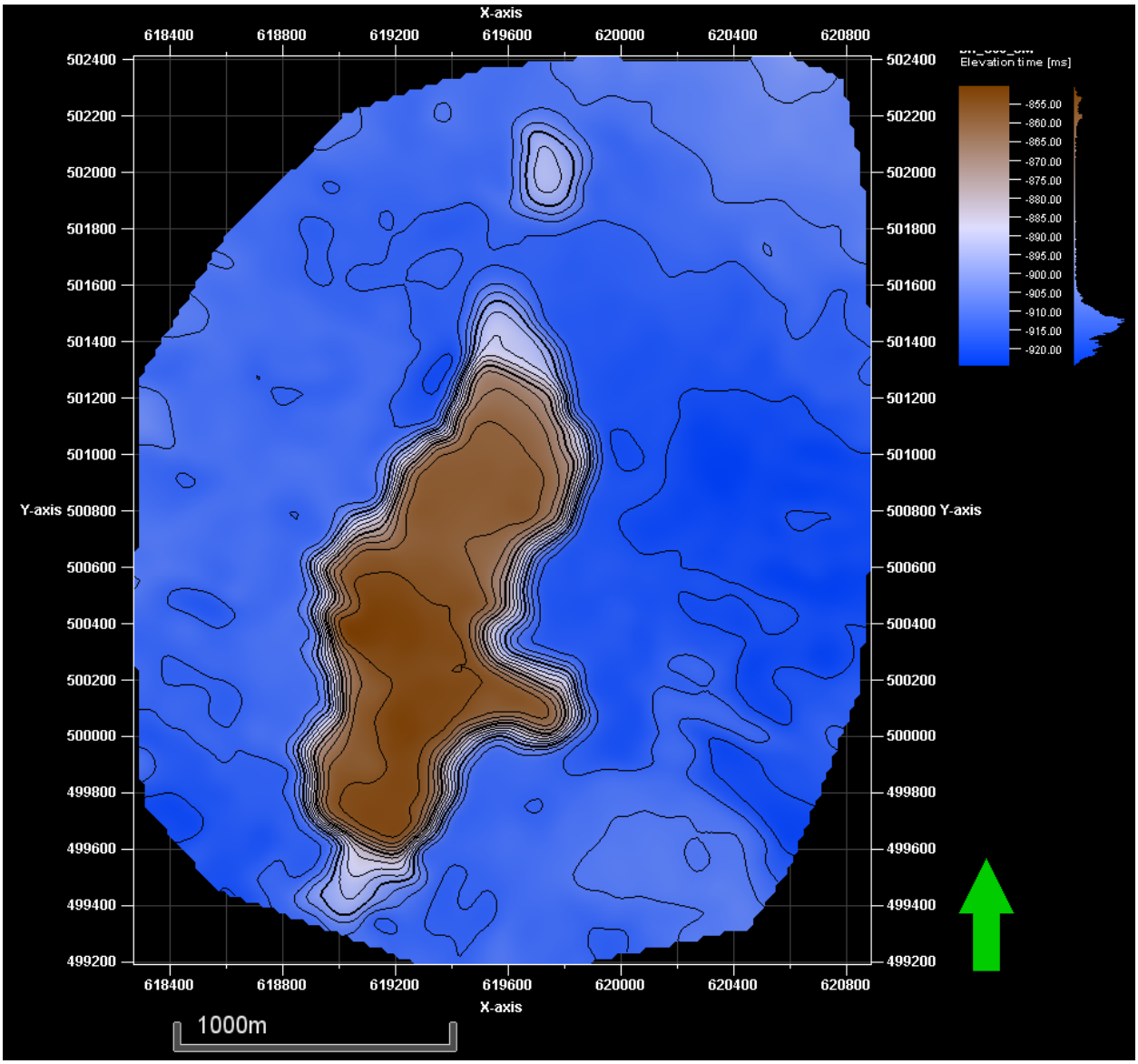


Figure 10-22. Time horizon surface for the Brown Niagaran showing steep slopes along the edges of the Charlton 30-31 reef field.

10.4 Geologic Interpretations

Two cross sections were constructed in the Charlton 30-31 reef field to represent the changes in lithology and lithofacies through the reef (Figure 10-23). Cross section A-A' runs south to north cutting through multiple reef pods (Figure 10-24). Cross section B-B' runs west to east cutting through the middle reef pod and capturing the "thumb" (Figure 10-25). All cross sections were flattened on the top of the A-2 carbonate/ base of the B-salt. Gamma ray, neutron porosity, bulk density, and water saturation logs were used. Flag 1 represents a crossplot porosity greater than 5%, and flag 2 represents porosity greater than 5% with water saturation less than 40%.

Cross Section A-A'

The A-2 carbonate has a consistent high gamma spike mid-formation which marks an interval of carbonate mud. The A-2 evaporite is interbedded anhydrite and carbonate across all wells with no indicators of salt. The thin anhydrite package is consistent with an on-reef well location. The A-1 carbonate has low porosity with thin intervals of porosity flags. Between wells 30203 and 29989, there could be a connected porosity streak in the middle to lower A-1 carbonate. The Brown Niagaran has frequent porosity flags. Well 30203 has a thick interval of high porosity; however, it falls below the oil/water contact.

Cross Section B-B'

The A-2 carbonate has a consistent high gamma spike mid-formation which marks an interval of carbonate mud. The A-2 evaporite is anhydrite in wells 57916, 32605, and 30195. In well 31287, the A-2 Carbonate becomes thicker with a package of salt, which is consistent with a flank position. The A-1 carbonate has thin porosity flags in the middle of the cross section which do not appear to be horizontally connected. The Brown Niagaran has frequent porosity flags above the oil/water contact, with the best porosity observed in the middlemost wells.

The thicknesses of the A-1 carbonate and Brown Niagaran were used to interpret boundaries between lithofacies in the Brown Niagaran formation. The reef core represents the crest of the reef with the thickest Brown Niagaran and thinnest A-1 carbonate. The Brown Niagaran thins in the leeward and windward facies, and the A-1 carbonate thickens. On the flanks of the reefs, salt packages are common. The Charlton 30-31 reef field was interpreted to have three reef pods, with the northern pod less connected than the southernmost pods. The "thumb" in the reef field in well 31287 had a thick package of salt in the A-2 evaporite, which supports it as a flank or off-reef position. Figure 10-26 illustrates the interpreted lithofacies of the Brown Niagaran formation in cross section A-A'.

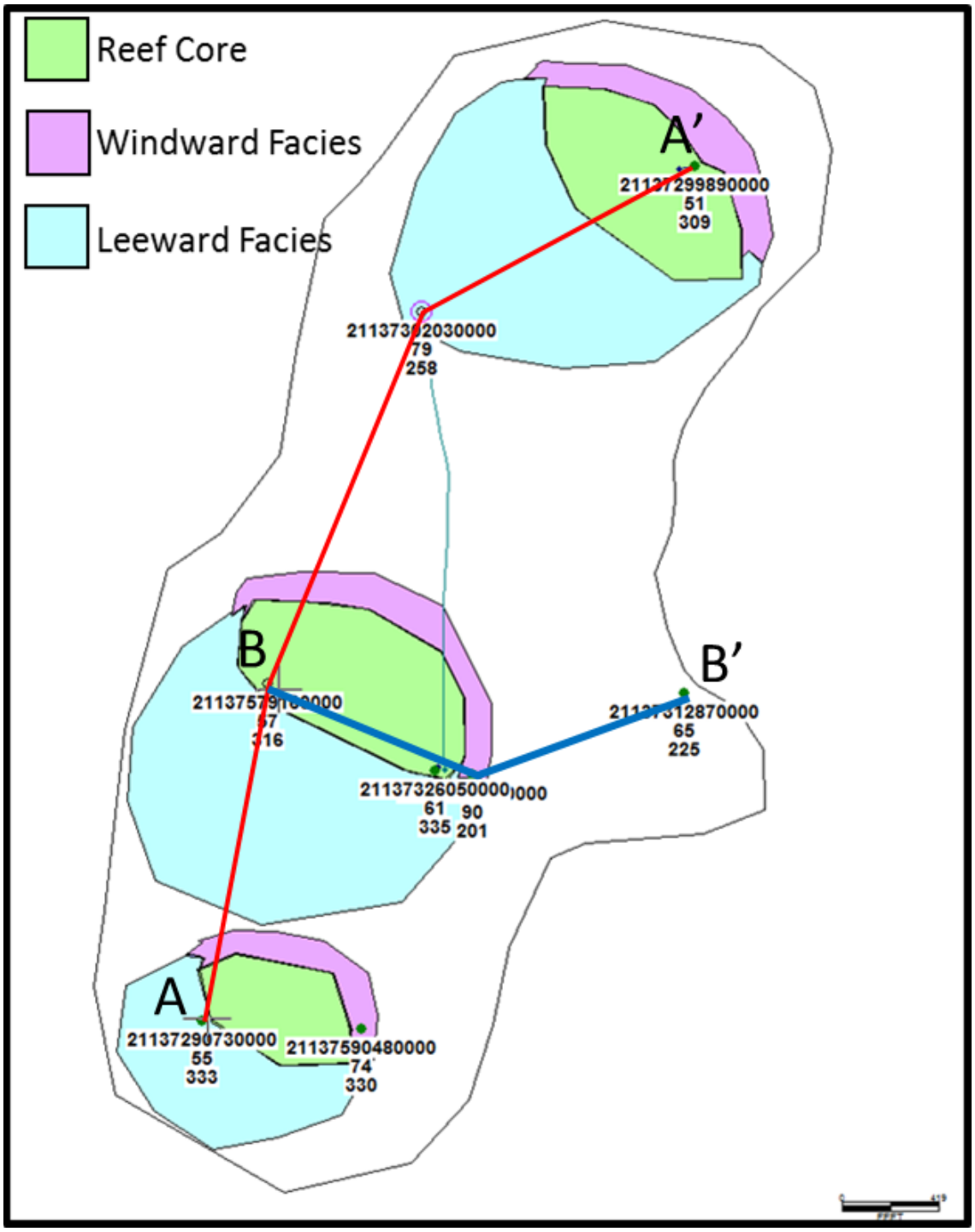


Figure 10-23. Lithofacies of the Brown Niagaran formation in the Charlton 30-31 reef showing three pods.

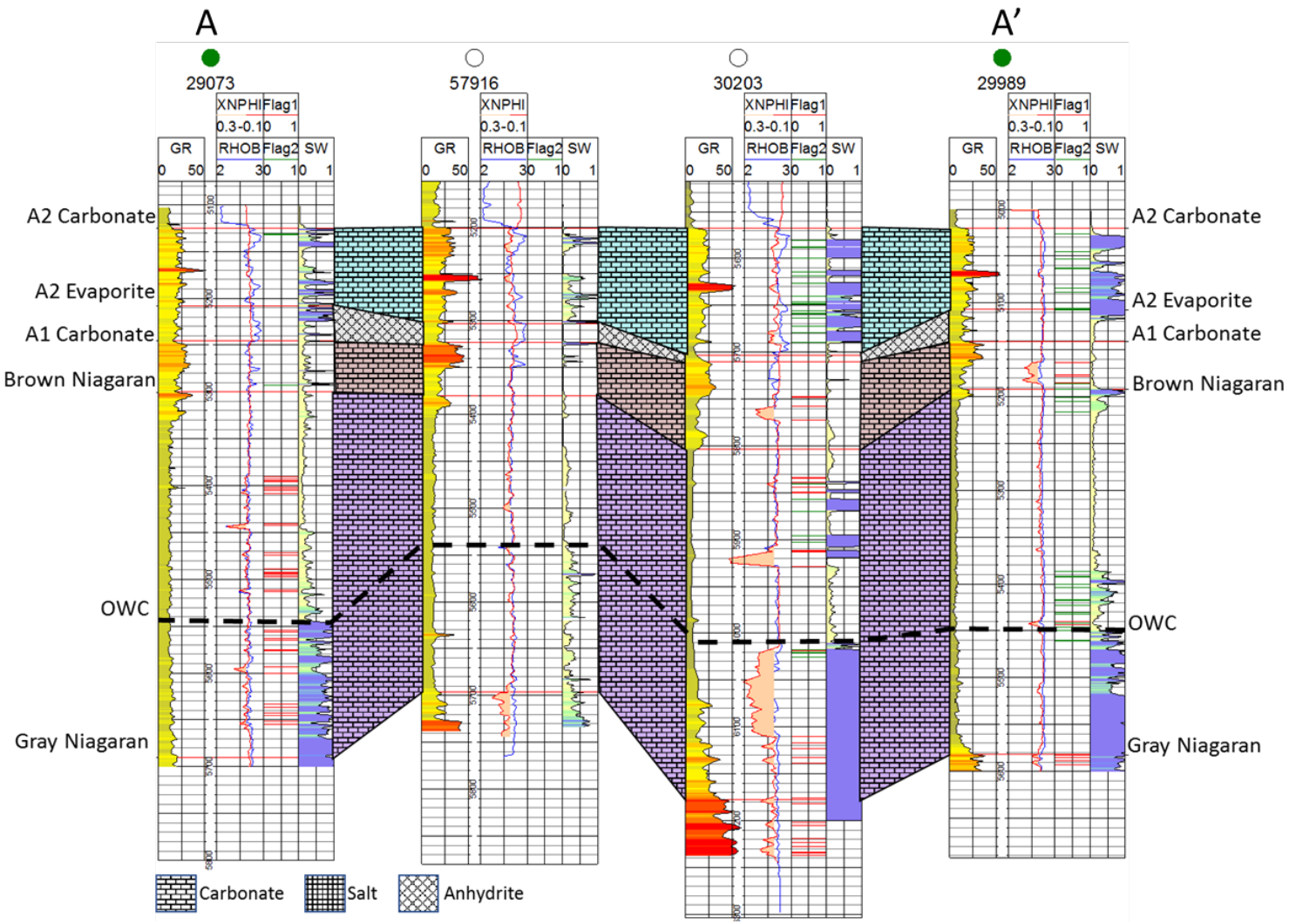


Figure 10-24. Cross section A-A' running south to north through the Charlton 30-31 reef field showing porosity flags (red and green) throughout the Brown Niagaran with an oil/water contact in the lower Brown Niagaran.

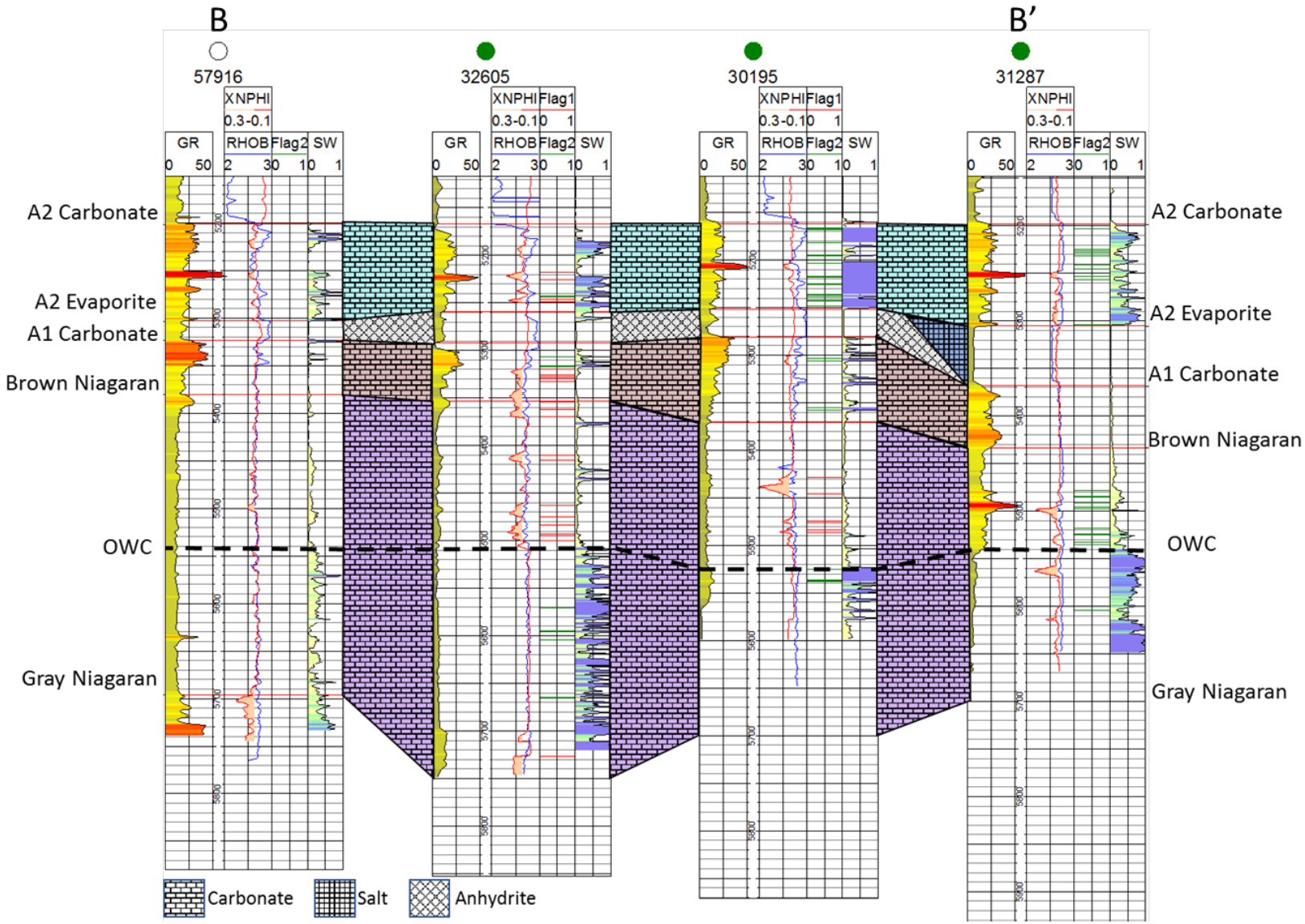


Figure 10-25. Cross section B-B' running west to east through the middle of the Charlton 30-31 reef field showing porosity in the Brown Niagaran and a mid-formation oil/water contact.

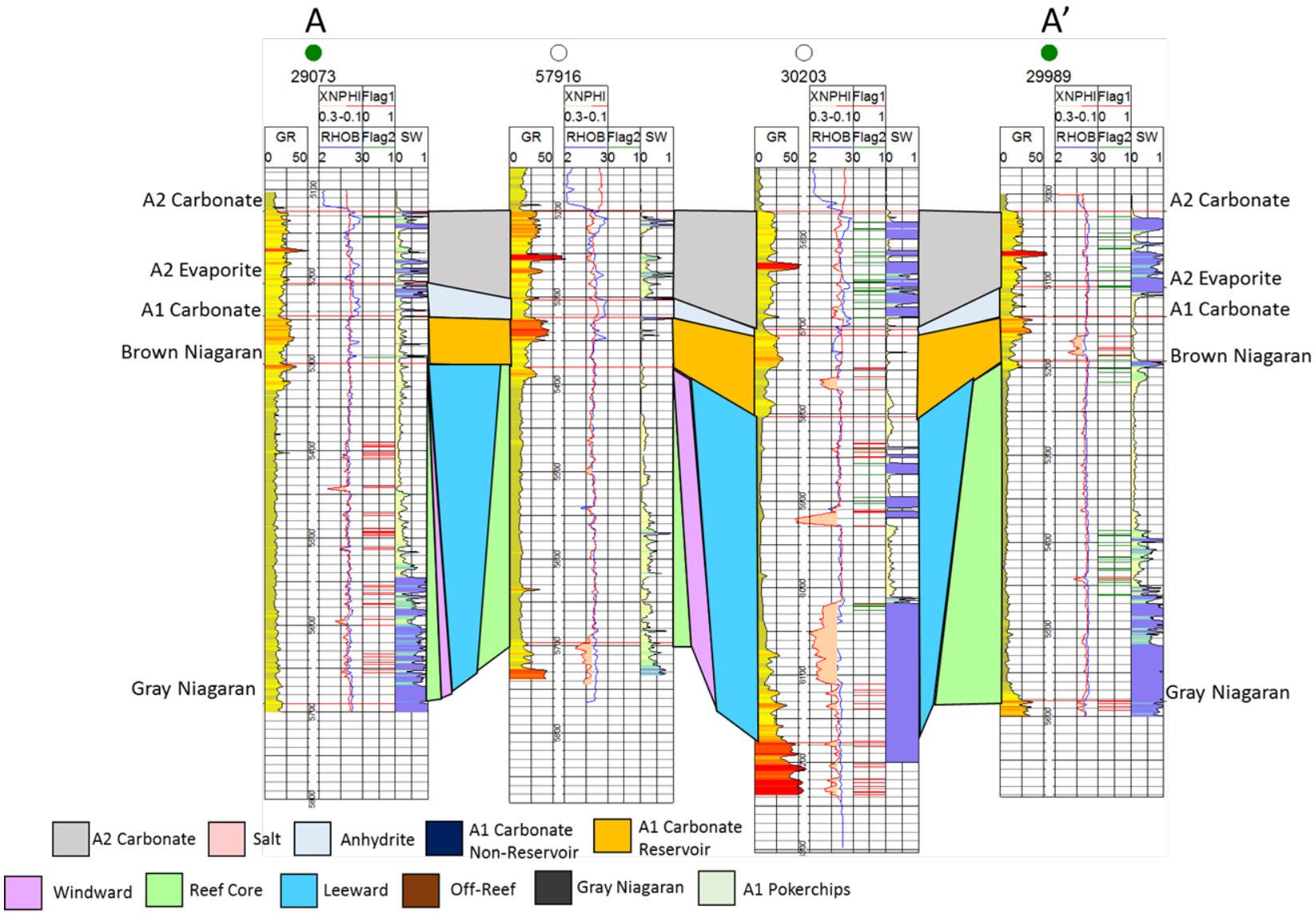


Figure 10-26. Depositional interpretation of the Charlton 30-31 reef field using cross section A-A' showing three closely spaced reefs.

11.0 Charlton 6

11.1 Reef History and Production Review

Production began in the Charlton 6 reef field in 1981 with well 35209. Production peaked in 1983 and then steadily declined through 1995, when operations were halted (Figure 11-1). Cumulative oil production remained relatively flat, around 630,000 bbls. The addition of a second well in 2008 increased oil production and brought the cumulative oil produced to approximately 740,000 bbls. The best producer is well 35209, which accounted for 90% of the total production in the reef. CO_2 EOR has accounted for slightly over 100,000 bbls of oil since 2006. Figure 11-2 shows the cumulative oil and gas production by well in the Charlton 6 reef field.

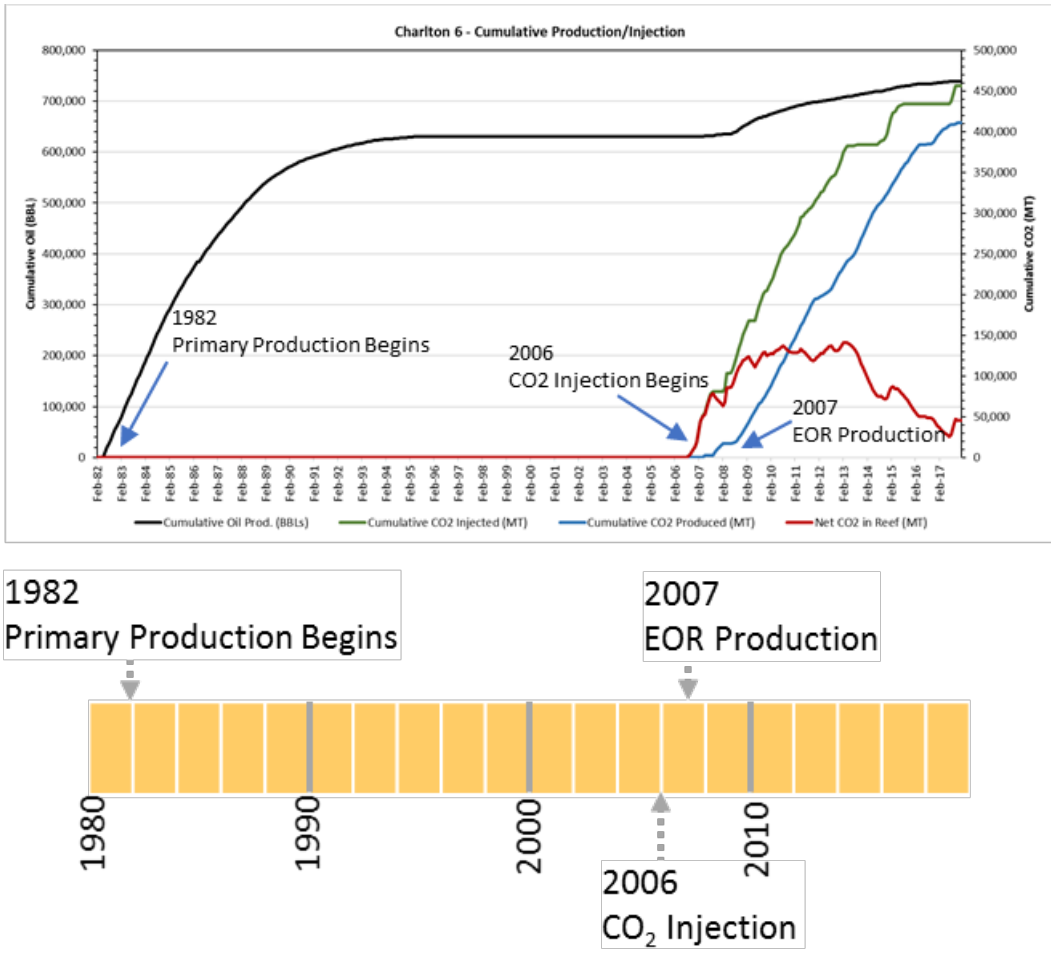


Figure 11-1. Cumulative production in the Charlton 6 reef field from 1982 through 2017 showing an increase in production rates after EOR operations began in 2006.

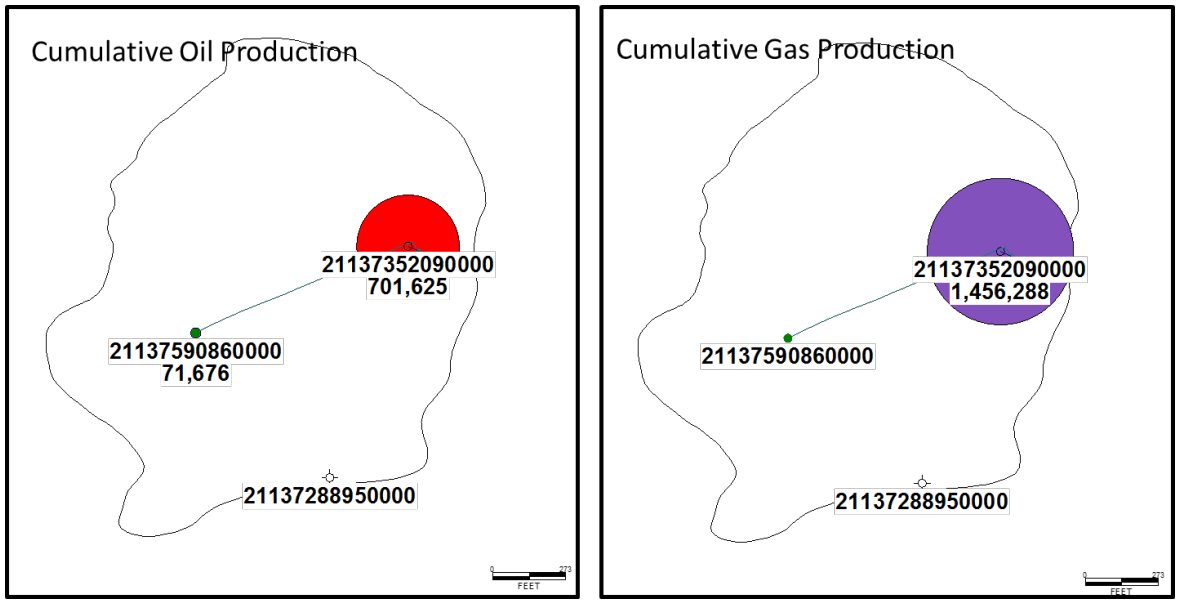


Figure 11-2. Cumulative oil and gas production in the Charlton 6 reef field showing highest production (red) in the northernmost well

The initial (discovery) data for the Charlton 6 reef field, summarized in Table 11-1, consists of OOIP, oil API gravity, discovery pressure and temperature, and fluid saturations. Initial gas saturations were recorded at zero, as gas was produced as it came out of solution during production of oil.

Table 11-1. Summary of initial (discovery) conditions of the Charlton 6 reef field.

		Discovery		Saturation		
OOIP (bbls)	API Gravity	Pressure (psi)	Temperature (ºF)	Oil	Gas	Water
1,700,000	44.2	3,153	98	78.84%	0%	21.16%

11.2 Wireline Log Analysis

Three wells penetrate the Charlton 6 reef field. All three wells have gamma ray, caliper, neutron porosity, bulk density, computed porosity from density (DPHI) and computed average neutron-density porosity (XPHIA) logs that were used in the petrophysical analysis. Table 11-2 lists the available wireline log data for wells that penetrate the Charlton 6 reef field. Figure 11-3 shows a map of the wells within the Charlton 6 reef field.

Table 11-2. Summary of available wireline log data for wells penetrating the Charlton 6 reef field.

	Well UWI	21137288950000	21137352090000	21137590860000
CAL	Caliper			
DT	Sonic			
GR	Gamma Ray			
LLD	Latero-Log Deep (Resistivity)			
LLS	Latero-Log Shallow (Resistivity)			
NPHI	Neutron Porosity			
RES	Resistivity			
RHOB	Bulk Density			
BHP	Bottom Hole Pressure Monitoring			

Note: Green shading indicates logs available by well.

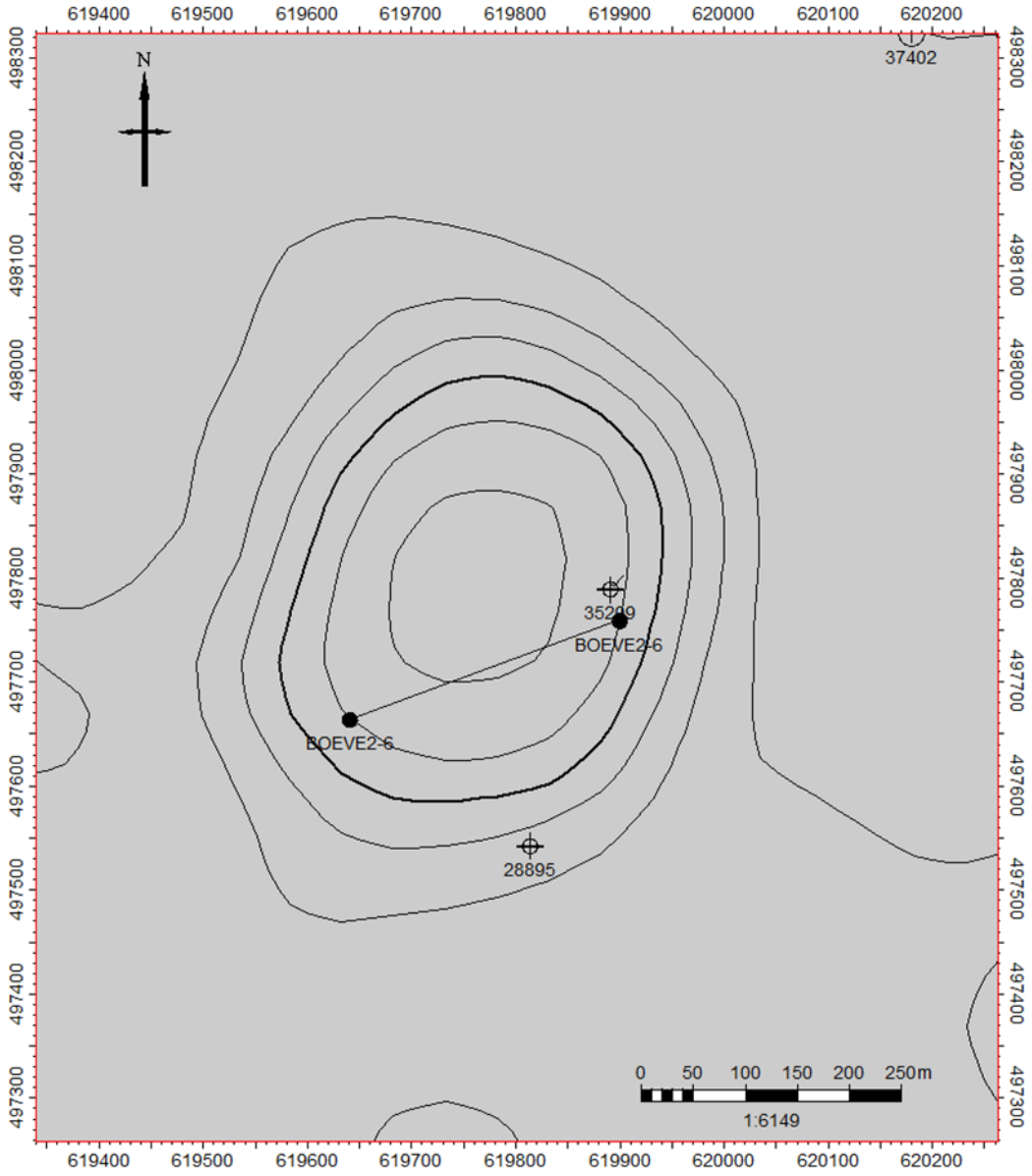


Figure 11-3. Map of the Charlton 6 reef field showing well locations.

11.2.1 Basic Log Interpretation

Well 28895

Well 28895 is located in the south-central portion of the Charlton 6 reef field and is located off the reef proper, as indicated by the thin (28-foot) Brown Niagaran formation. The A-2 carbonate plotted as a limestone with anhydrite and salt plugging at the base and upper intervals. The A-1 carbonate plotted as a limestone with no indications of porosity. The A-1 evaporite plotted as a thick salt package. The Brown Niagaran contained the only porosity in this well, occurring at thin intervals, and plotted as a limestone.

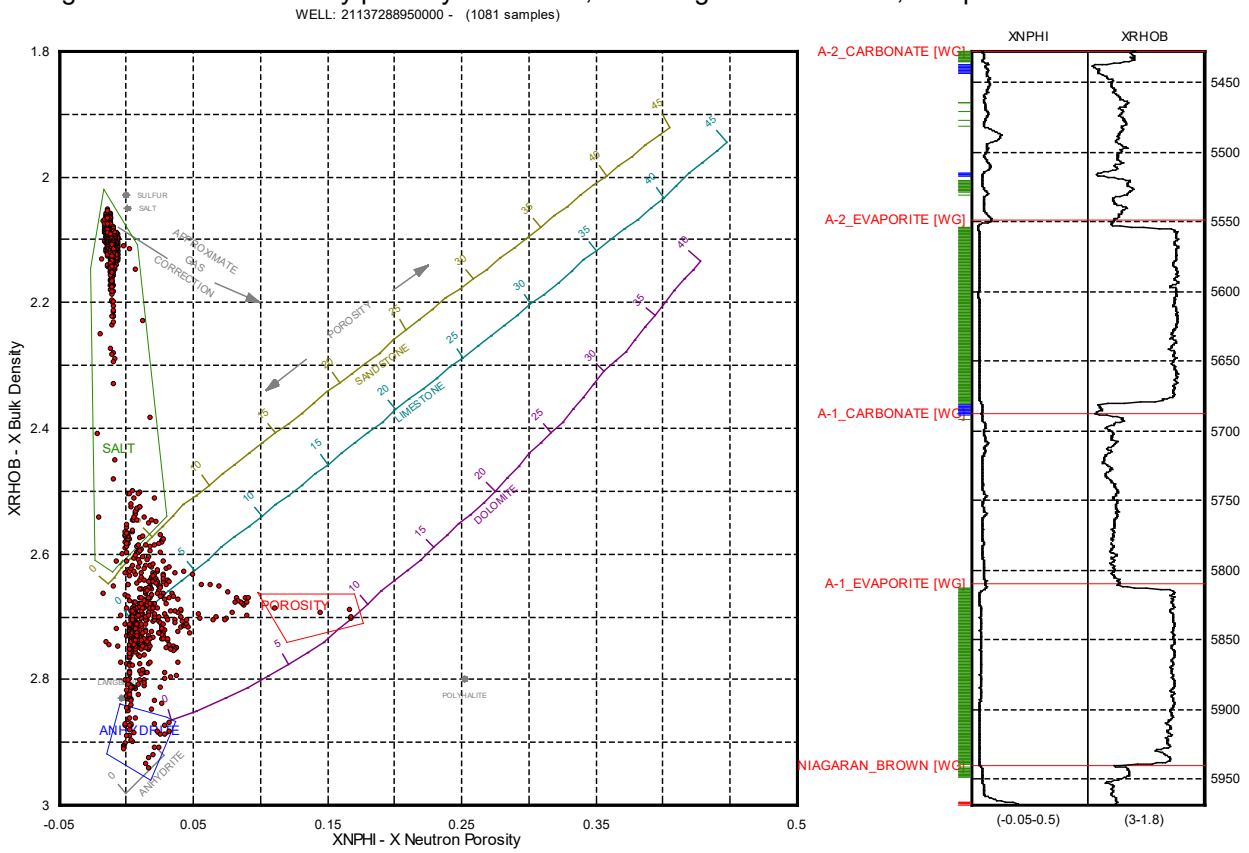


Figure 11-4 shows the neutron porosity-bulk density crossplot from the A-2 carbonate to the Brown Niagaran in well 28895. The red polygon indicates the zones with porosity greater than 5% and have been flagged on the neutron porosity and bulk density logs accordingly, while the blue indicates anhydrite and the green indicates salt.

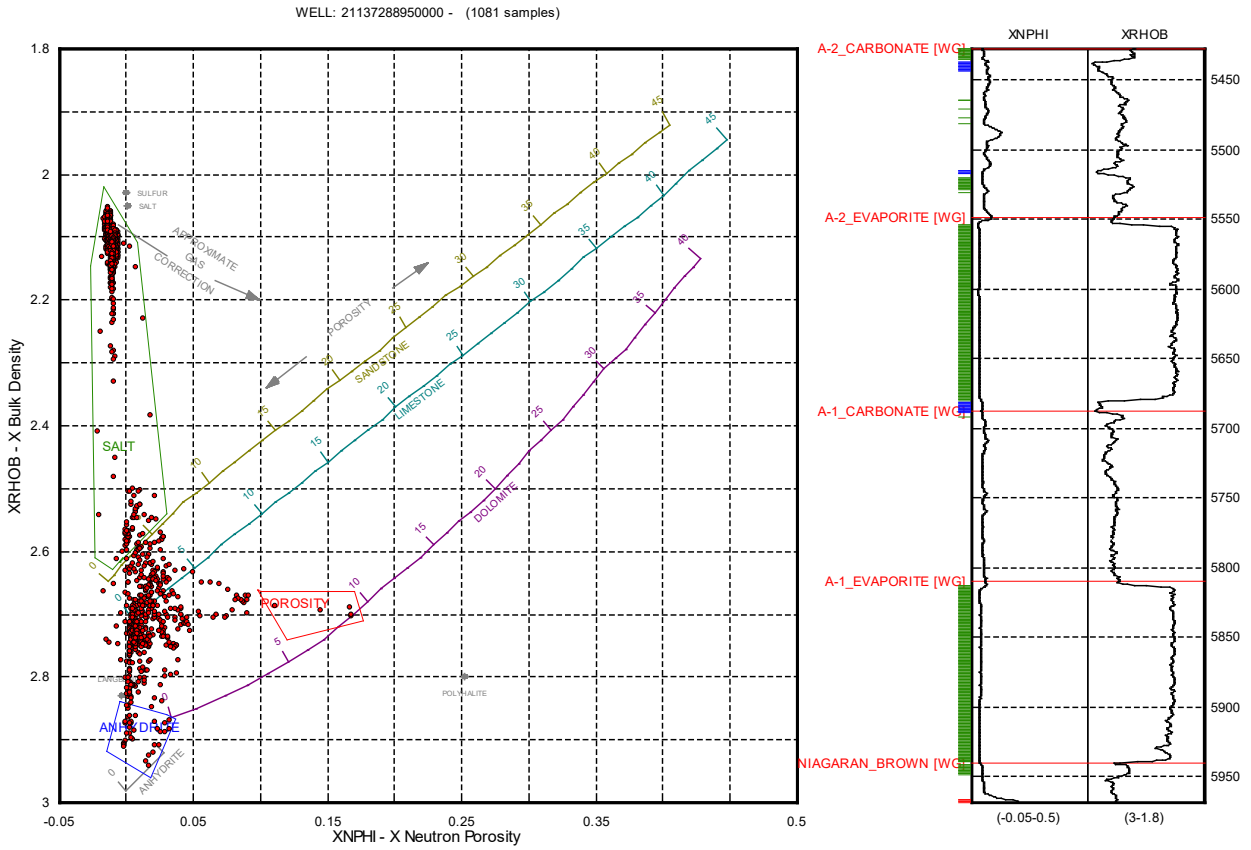


Figure 11-4. Neutron porosity-bulk density crossplot of well 28895 showing very little porosity with thick salt packages. Red polygon = porosity >5%, green polygon = salt, blue polygon = anhydrite.

Water saturations for well 28895 indicate a distinct pattern of erratic saturation spikes in the carbonates and low saturations in the salts. Due to the flank position of this well, the Brown Niagaran and most likely the A-1 carbonate are fully saturated. An oil/water contact is difficult to discern with the thin Brown Niagaran and the influence of evaporites in the flank position. Figure 11-5 shows the water saturation curve and histogram for well 28895.

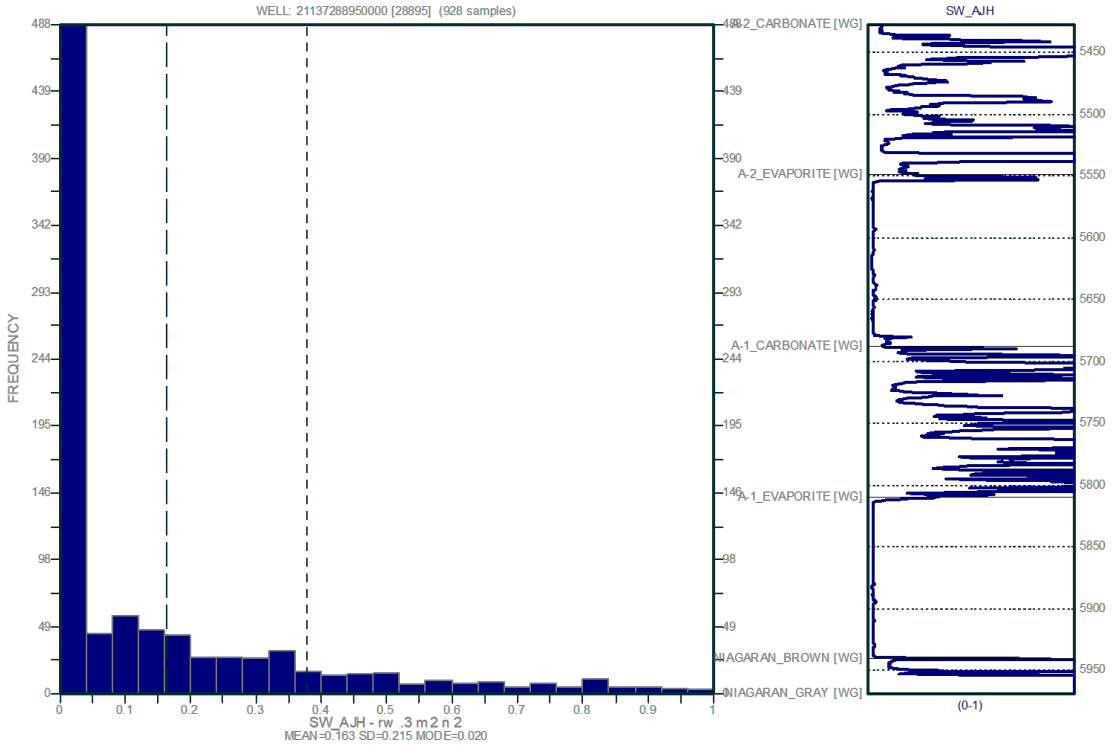


Figure 11-5. Water saturation curve and histogram for well 28895 showing high saturation values and a strong influence of evaporites on the curve.

Well 35209

Well 35209 is located in the northeastern portion of the Charlton 6 reef field. The A-2 carbonate plotted as limestone and contained anhydrite and salt plugging in its upper, middle, and basal intervals. One zone contained porosity greater than 5% around 5,350 feet MD. The A-1 carbonate plotted as a limestone with anhydrite in the upper horizons and no indicators of porosity. The Brown Niagaran plotted as a limestone and contained the most porosity greater than 5%. Most of the porosity was in the middle and basal intervals and contained some salt plugging throughout. Figure 11-6 is the neutron porosity-bulk density crossplot from the A-2 carbonate to the Brown Niagaran in well 35209. The red polygon indicates the zones with porosity of greater than 5% and have been flagged on the neutron porosity and bulk density logs accordingly where blue indicates anhydrite and green indicates salt.

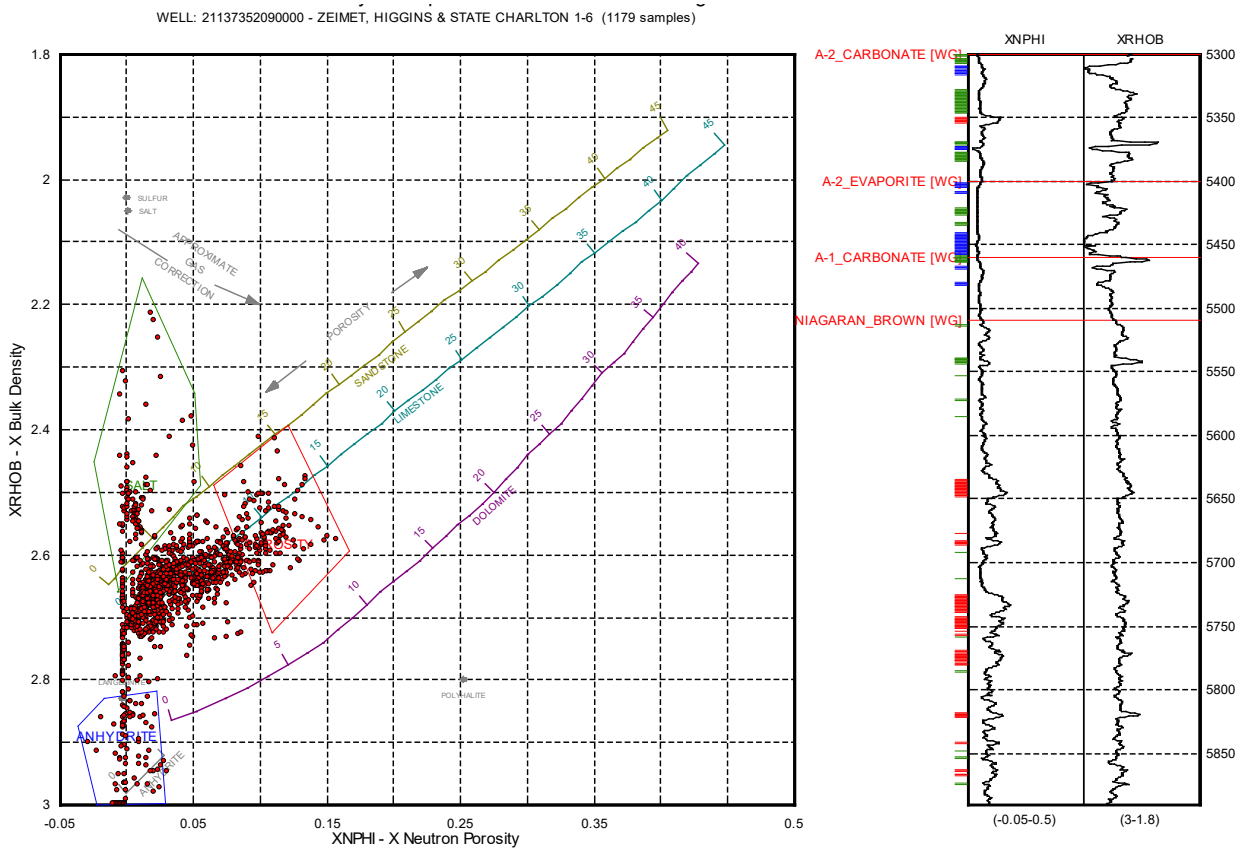


Figure 11-6. Neutron porosity-bulk density crossplot of well 35209 showing porosity >5% in the Brown Niagaran. Red polygon = porosity >5%, green polygon = salt, blue polygon = anhydrite.

Well 59086

Well 59086 is located in the west-central portion of the Charlton 6 reef field. The A-2 carbonate is mostly salt with small intervals of limestone near the base. The A-1 carbonate plotted as a limestone with salt plugging throughout the formation. The Brown Niagaran is dominated by limestone and contains thin intervals of porous dolomite. This formation contained the greatest amount of porosity greater than 5%. While the limestone had more numerous zones of porosity, the dolomite had a higher porosity value. Figure 11-7 shows the neutron porosity-bulk density crossplot from the A-2 carbonate to the Brown Niagaran. The red polygon indicates the zones with porosity greater than 5%, which have been flagged on the neutron porosity and bulk density logs accordingly; green indicates salt.

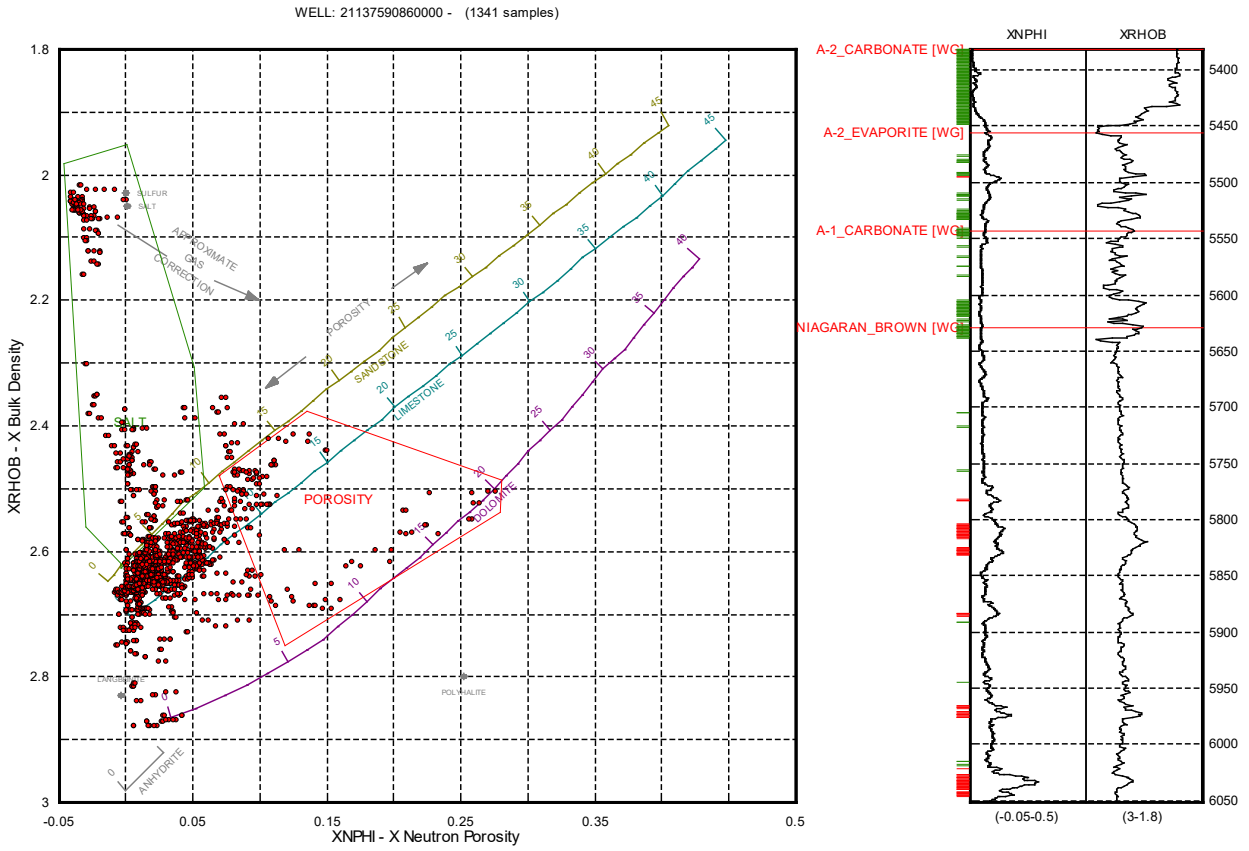


Figure 11-7. Neutron porosity-bulk density crossplot of well 59086 showing intervals of porosity >5% in the Brown Niagaran. Red polygon = porosity >5%, green polygon = salt.

Water saturations for well 59086 indicate high saturations in the presence of evaporites. The water saturation has a sharp increase near the base of the Brown Niagaran formation at 5,945 feet MD. The Brown Niagaran has an average water saturation of 9% with an increase to 21% below 5,945 feet MD. Figure 11-8 shows the water saturation curve and histogram for well 59086.

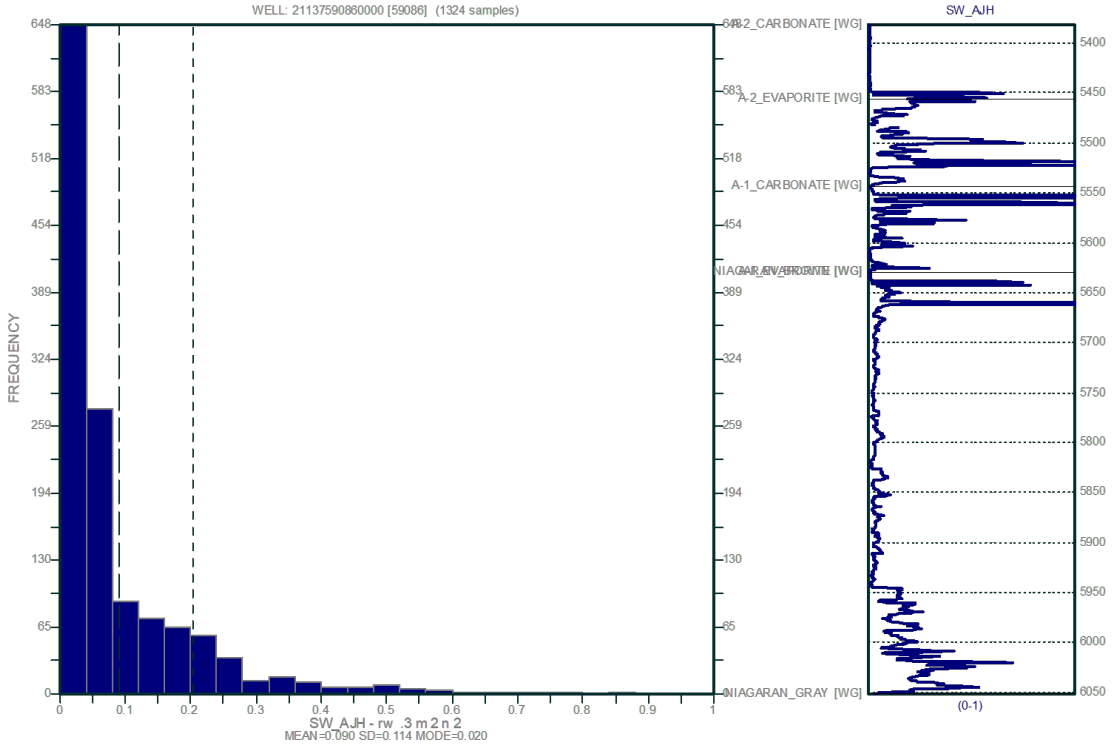


Figure 11-8. Water saturation curve and histogram for well 59086 showing an increase in water saturation at the base of the Brown Niagaran.

11.2.2 Petrophysics Calculations

A-2 Carbonate

The A-2 carbonate contained heavy salt plugging and salt packages with intervals of anhydrite. This formation only had minor amounts of limestone torward its base. The thickness ranged from 67 feet on the crest of the reef to 122 feet toward the flank.The average calculated porosity was 7% (Table 11-3). The average porosities are overestimated due to the presence of salt. The average NPHI values confirm this overestimation and shows little to no porosity. A water saturation cutoff of 40% was applied to eliminate some of the evaporites. The presence of salt skewed the petrophysical calculations.

Table 11-3. Summary of petrophysical calculations for the A-2 carbonate in the Charlton 6 reef field.

Interval: A-2 Carbonate						
Avg. Thickness	**Avg. Porosity**	**Avg. Net Thickness**	**Avg. NTG**	**Avg. SW**	**Avg. Net Thickness (Sw<40%)**	**Avg. NTG (Sw<40%)**
96 ft	7.0%	42 ft	0.49	18%	38 ft	0.51

A-1 Carbonate

The A-1 carbonate contained limestone with minor amounts of anhydrite in the middle horizons. The minimum thickness was 50 feet in well 35209 and the maximum thickness was 122 feet in well 28895. The average porosity was 2.4% (Table 11-4). The porosity was higher when located on the reef (wells 35209 and 59086). The average neutron porosity was also calculated to better interpret porosity due to large amounts of salt found within this reef. The NTG ratio was 0.07 to 0.24. The presence of evaporites skewed the petrophysical calculations.

Table 11-4. Summary of petrophysical calculations for the A-1 carbonate in the Charlton 6 reef field.

Interval: A-1 Carbonate						
Avg. Thickness	**Avg. Porosity**	**Avg. Net Thickness**	**Avg. NTG**	**Avg. SW**	**Avg. Net Thickness (Sw<40%)**	**Avg. NTG (Sw<40%)**
85 ft	2.4%	12 ft	0.16	25%	-	-

Brown Niagaran

The Brown Niagaran plotted as a limestone. The minimum thickness was 28 feet in well 28895 and it was interpreted to be located off-reef. The maximum thickness was 408 feet in well 59086. The average porosity was 5.3% with highs up to 20%. The average neutron porosity was 3.83% and contained a NTG ratio of 0.08 to 0.45 The Brown Niagaran had the greatest porosity and is the most likely reservoir for this reef. Water saturation was only available for one on-reef well which reduced the net thickness in well 35209 from 176 feet to 168 feet. The recorded value only represents one well and is not a true average for the reef. Table 11-5 summarizes the petrophysical calculations for ain the the Brown Niagaran in the Charlton 6 reef field.

Table 11-5. Summary of petrophysical calculations for the Brown Niagaran in the Charlton 6 reef field.

Interval: Brown Niagaran						
Avg. Thickness	**Avg. Porosity**	**Avg. Net Thickness**	**Avg. NTG**	**Avg. SW**	**Avg. Net Thickness (Sw<40%)**	**Avg. NTG (Sw<40%)**
272 ft	5.3%	117 ft	0.32	9%	168 ft	0.41

11.3 Seismic Analysis

The Charlton 6 is a single reef system that is smaller than most of the reef fields. The reef was identified in the west-central portion of the 3D survey with steeply dipping edges. The overlying A-1 carbonate could not be distinguished from the other carbonates and does not show the influence of the reef (Figure 11-9). The A-2 carbonate has a slightly faster arrival time over the location of the reef than the surrounding rocks. The edges are less pronounced but are still visible (Figure 11-10). The edges of the reef/Brown Niagaran were clearly defined and show a single reef system (Figure 11-11).

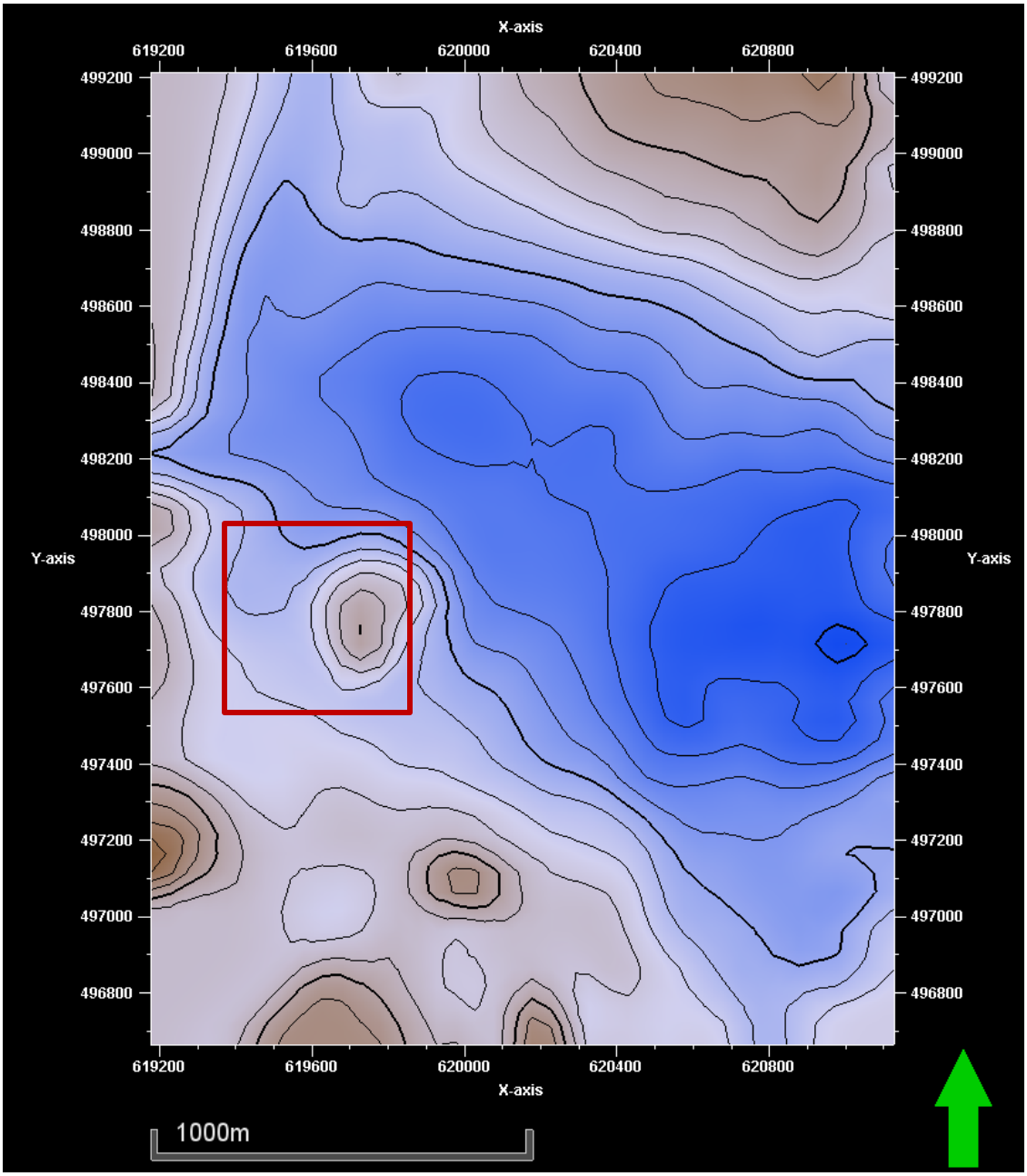


Figure 11-9. Time horizon surface for the A-2 carbonate over the Charlton 6 reef field (red square) showing a slight increase in arrival time over the reef complex.

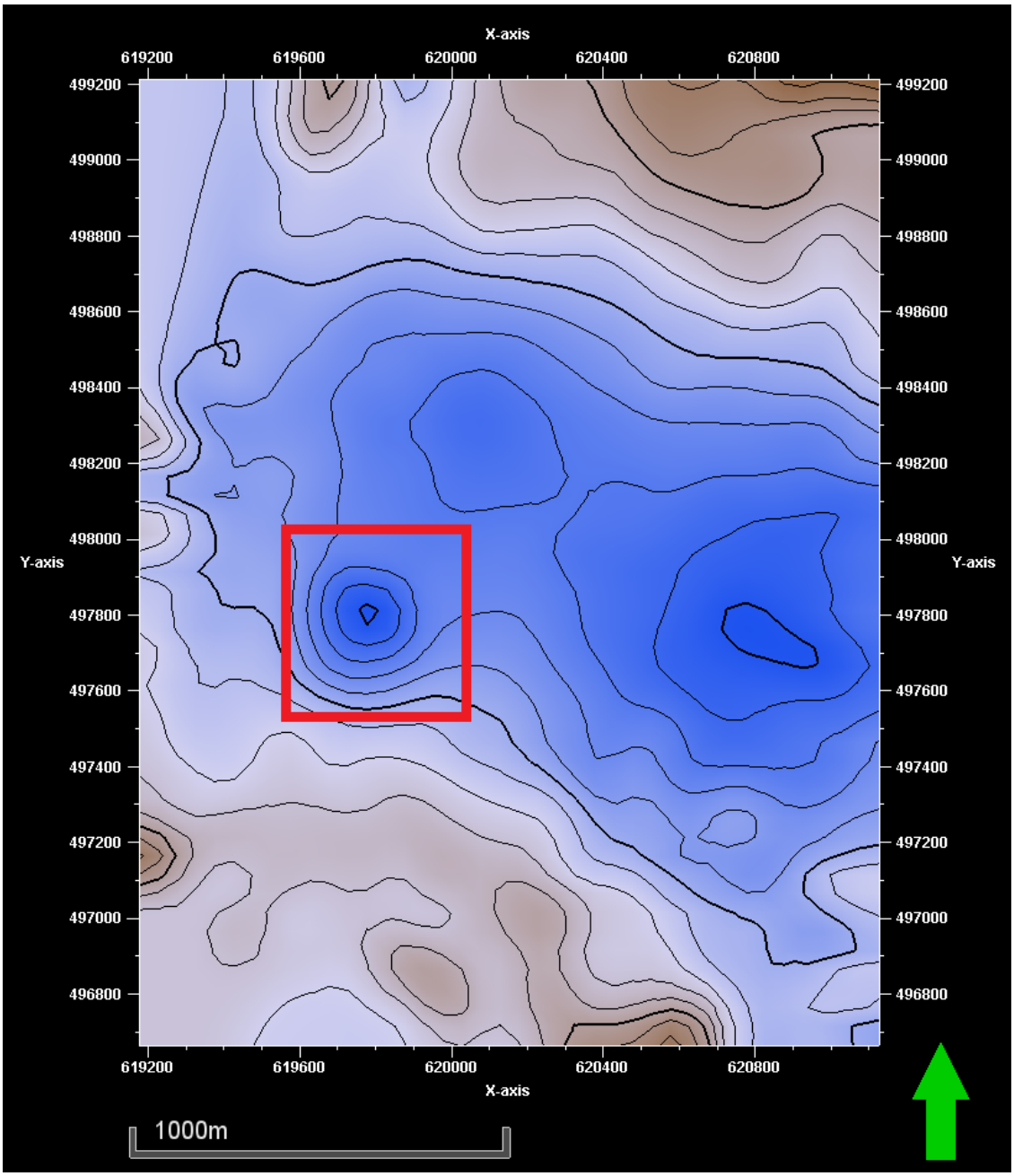


Figure 11-10. Seismic time horizons of the A-1 carbonate over the Charlton 6 reef field (red square) showing no significant changes over the reef complex due to similar lithologies.

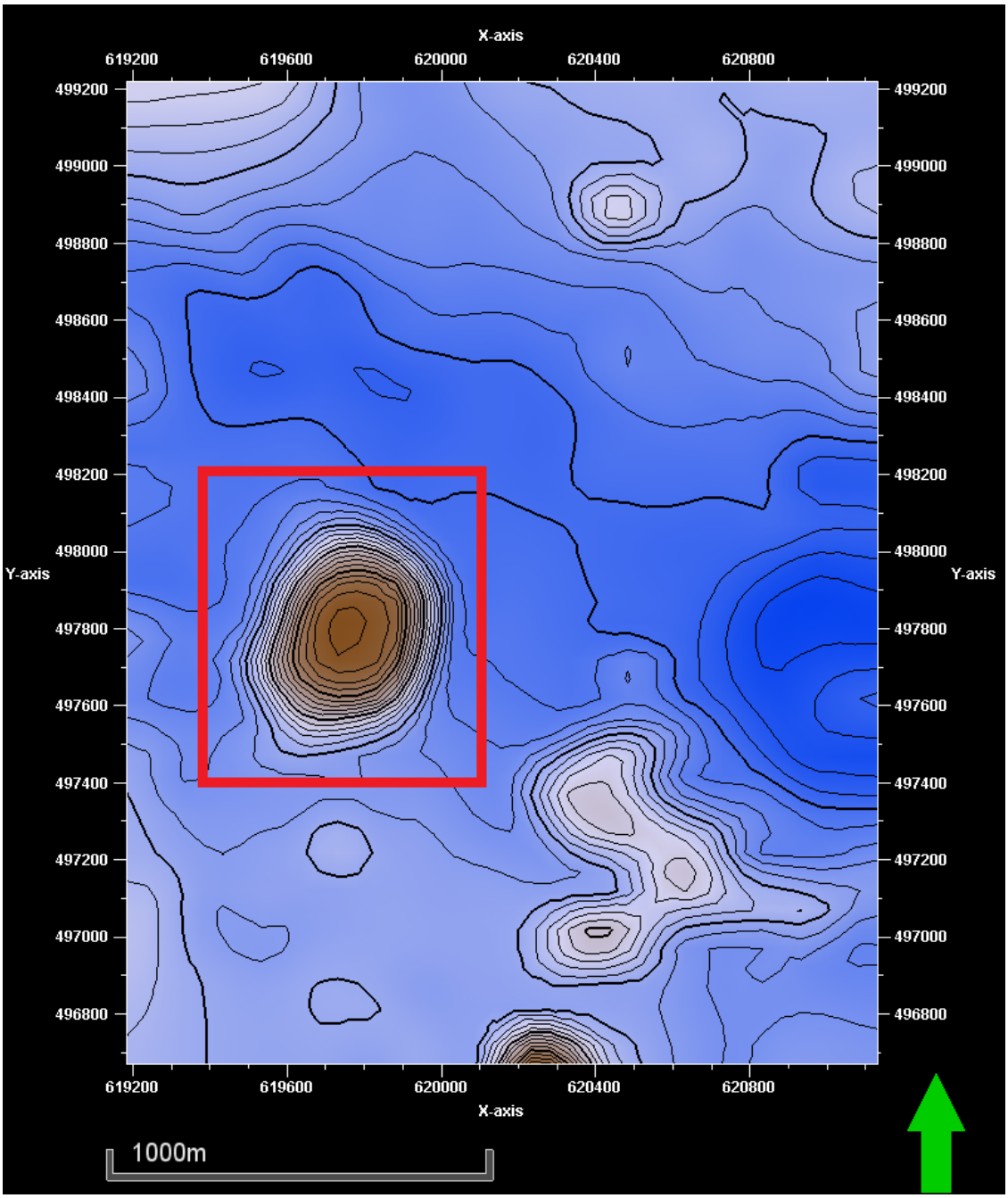


Figure 11-11. Seismic time horizon for the top of the reef structure over the Charlton 6 reef field (red square) showing steep angles along the edges of the reef.

11.4 Geologic Interpretations

Cross section A-A' runs from well 28895 (off-reef) to well 59086 through the main reef structure, ending at well 35209. A lithofacies map of the Brown Niagaran formation in the Charlton 6 reef field (Figure 11-12) shows the path of cross section A-A'. Off-reef has thick packages of salt with a thin Brown Niagaran. As a result, there are very few porosity flags. The oil/water contact is low in this reef, leaving most of the Brown Niagaran available. There are numerous porosity flags in the Brown Niagaran. Wells 59086 and 35209 have porosity flags at similar depths, which could suggest lateral connectivity. The A-1 carbonate has infrequent and thin porosity flags and often was salt plugged. Figure 11-13 shows the cross section A-A' through the Charlton 6 reef field.

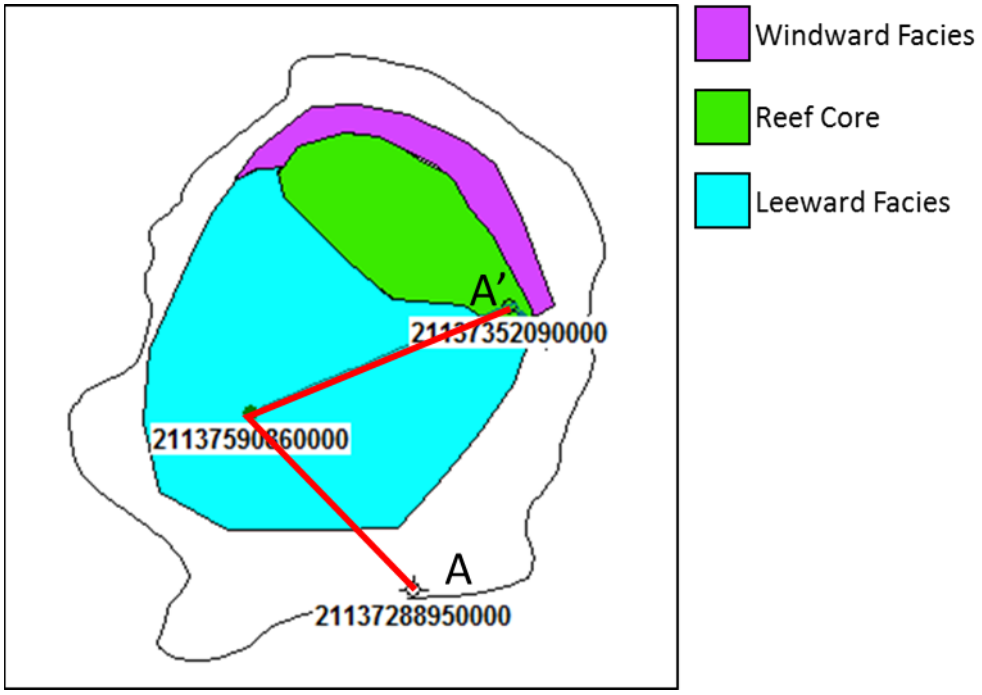


Figure 11-12. Lithofacies map of the Brown Niagaran formation in the Charlton 6 reef field showing a single reef core.

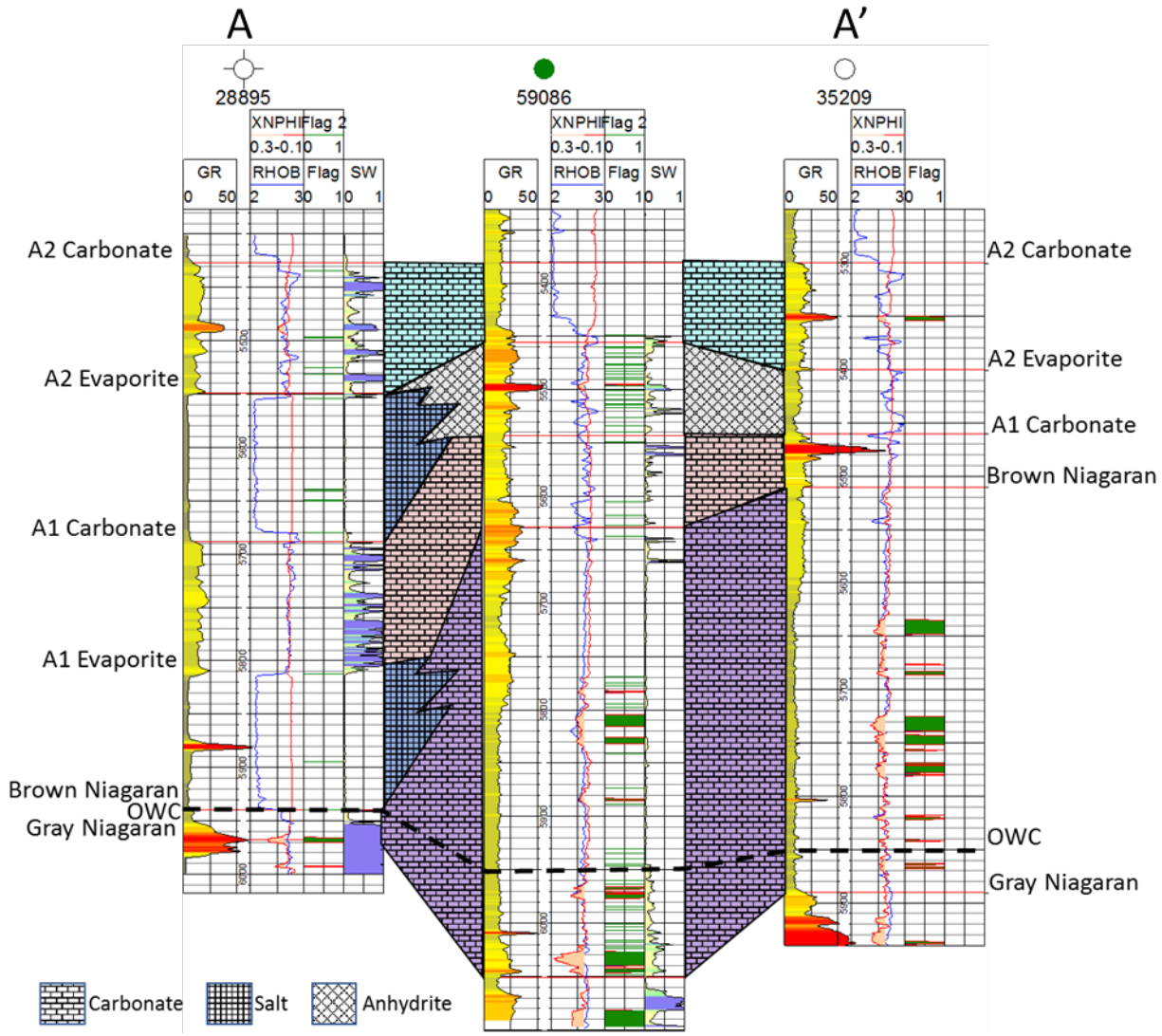


Figure 11-13. Cross section A-A' through the Charlton 6 reef showing frequent porosity flags in the Brown Niagaran and a low oil/water contact.

Charlton 6 was interpreted as a single reef (see Figure 11-12). The boundaries of the Brown Niagaran lithofacies were determined based on thicknesses of the Brown Niagaran and A-1 carbonate. Thick packages of salt in well 28895 with a thin Brown Niagaran indicates an off-reef location. A small reef core (green) covers the northern section of the reef field, and well 35209 is located on the edge. Well 59086 falls in the leeward facies zone in the southern part of the reef. Figure 11-14 illustrates a 2D depositional interpretation of the Charlton 6 reef field.

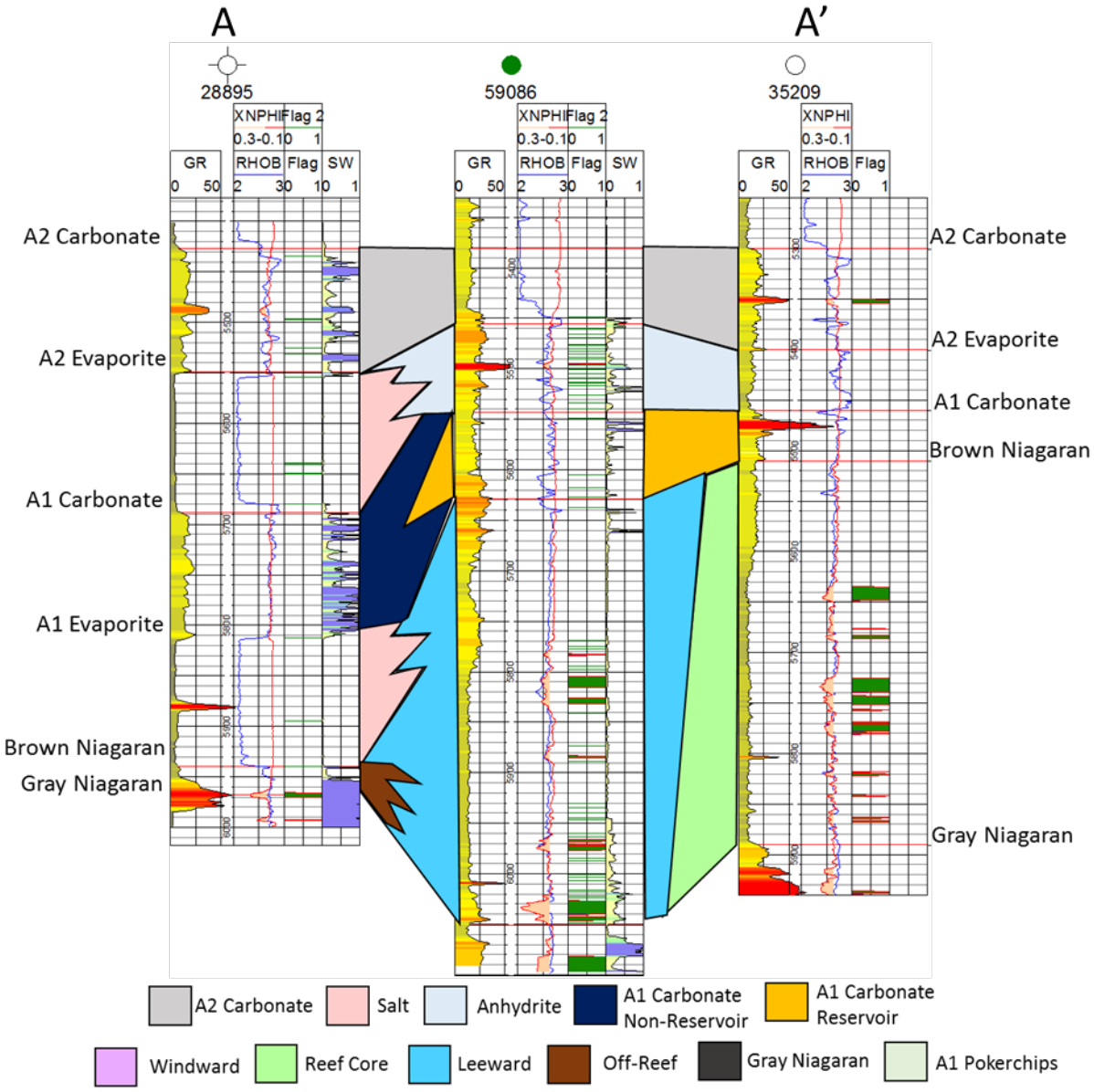


Figure 11-14. Depositional lithofacies interpretation of the Charlton 6 reef field showing one reef pod.

11.0. Charlton 6

12.0 Chester 2

12.1 Reef History and Production Review

Production began in the Chester 2 reef field with the completion of well 28459 in 1971. A total of 37,460 bbls of oil were produced from this well; no gas was produced. Additional wells were drilled with only one good producer. Well 29430 was the only original well to penetrate the dolomitized zone and produced 727,345 bbls of oil. CO_2 injection commenced in 2009, with EOR production following in 2011 (Figure 12-1). As of December 31, 2017, approximately 1,130,800 bbls of oil have been produced from Chester 2. Figure 12-2 shows a map of cumulative production of oil and gas with the best producer located in the west-central area of the reef field. A combination of limited reservoir enhancement by dolomitization and pervasive salt plugging in the upper portion of the reef have impeded the EOR project. Development projects, including two lateral wells, have been low producers when compared to the higher quality reservoir of well 29430, which is currently the CO_2 injector well.

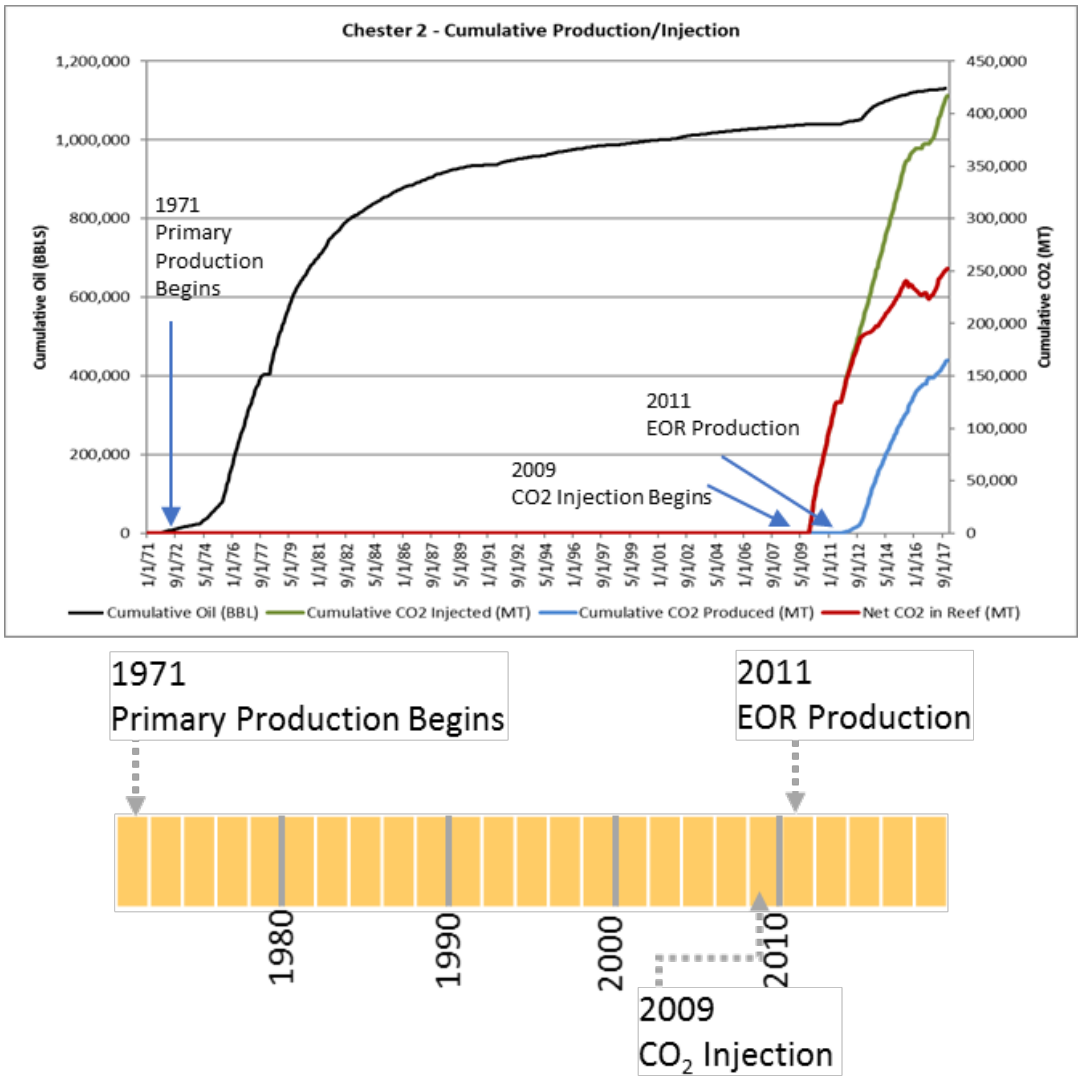


Figure 12-1. Cumulative production in the Chester 2 reef field from 1971 through 2017 showing a slight increase in production after EOR operations began in 2011.

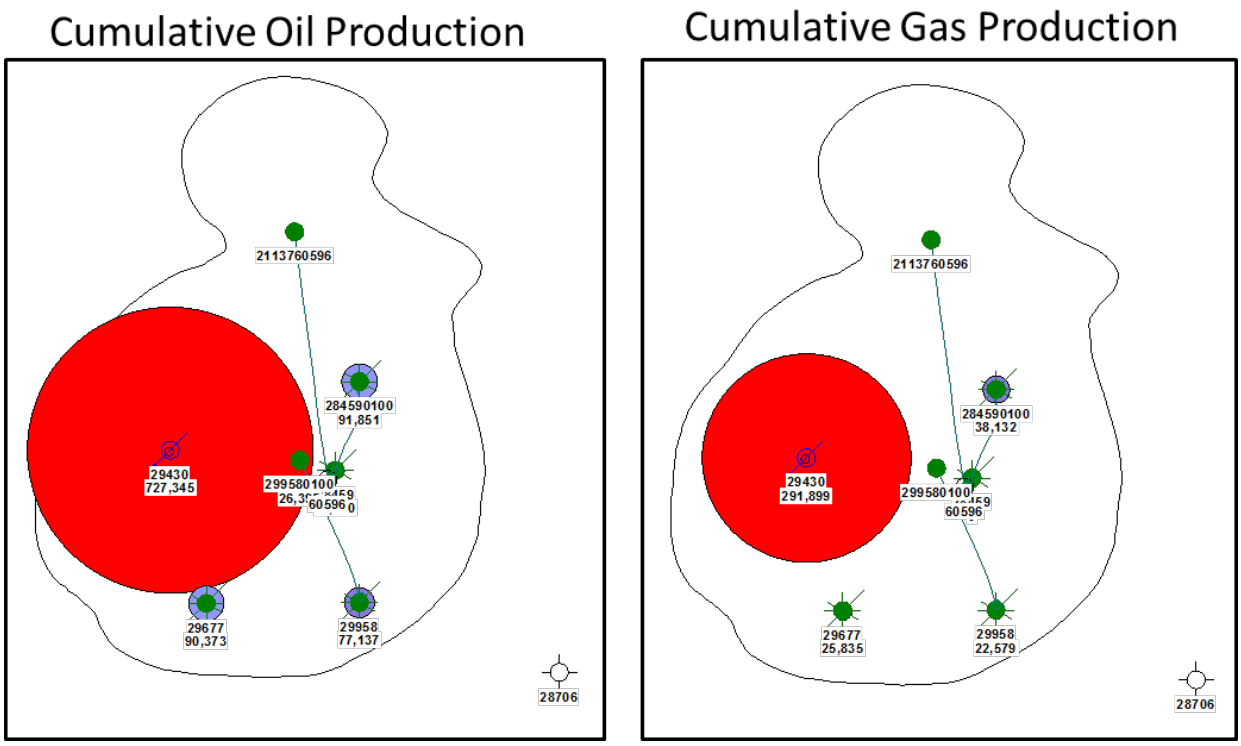


Figure 12-2. Cumulative oil and gas production by well in the Chester 2 reef field showing the best producer is well 29430 (red).

The initial (discovery) data for the Chester 2 reef field, summarized in Table 12-1, consists of OOIP, oil API gravity, discovery pressure and temperature, and fluid saturations. Initial gas saturations were recorded at zero, as gas was produced as it came out of solution during production of oil.

Table 12-1. Summary of initial (discovery) conditions of the Chester 2 reef field.

		Discovery		Saturation		
OOIP (bbls)	API Gravity	Pressure (psi)	Temperature (°F)	Oil	Gas	Water
3,210,000	44.0	3,000	105	61.97%	0%	38.03%

12.2 Wireline Log Analysis

Eight wells penetrate the Chester 2 reef field. All eight have multiple digitized and raster logs available. Of the eight wells, all have gamma ray, seven have neutron porosity, and five have bulk density logs. One well in the Chester 2 reef field has available advanced logs combined with the gamma ray, neutron porosity, sonic, and bulk density digitized logs. Table 12-2 summarizes the log data available for the Chester 2 reef field. Figure 12-3 shows the locations of the wells within the Chester 2 reef field.

Table 12-2. Summary of available wireline log data for wells penetrating the Chester 2 reef field.

	Well UWI	2113728459000	2113728459100	2113728706000	2113729430000	2113729677000	2113729958000	2113729958010	2113760596000
CAL	Caliper	■	■	■	■	■	■		■
DT	Sonic								■
GR	Gamma Ray	■	■	■	■	■	■	■	■
LLD	Latero-Log Deep (Resistivity)				■	■	■		
LLS	Latero-Log Shallow (Resistivity)						■		
NPHI	Neutron Porosity	■	■	■	■	■	■		■
PNC	Pulsed Neutron Capture								2
RES	Resistivity	■			■	■	■		■
RHOB	Bulk Density	■	■		■	■	■		
SNP	Sidewall Neutron Porosity	■			■				
BHP	Bottom Hole Pressure Monitoring				■		■		■

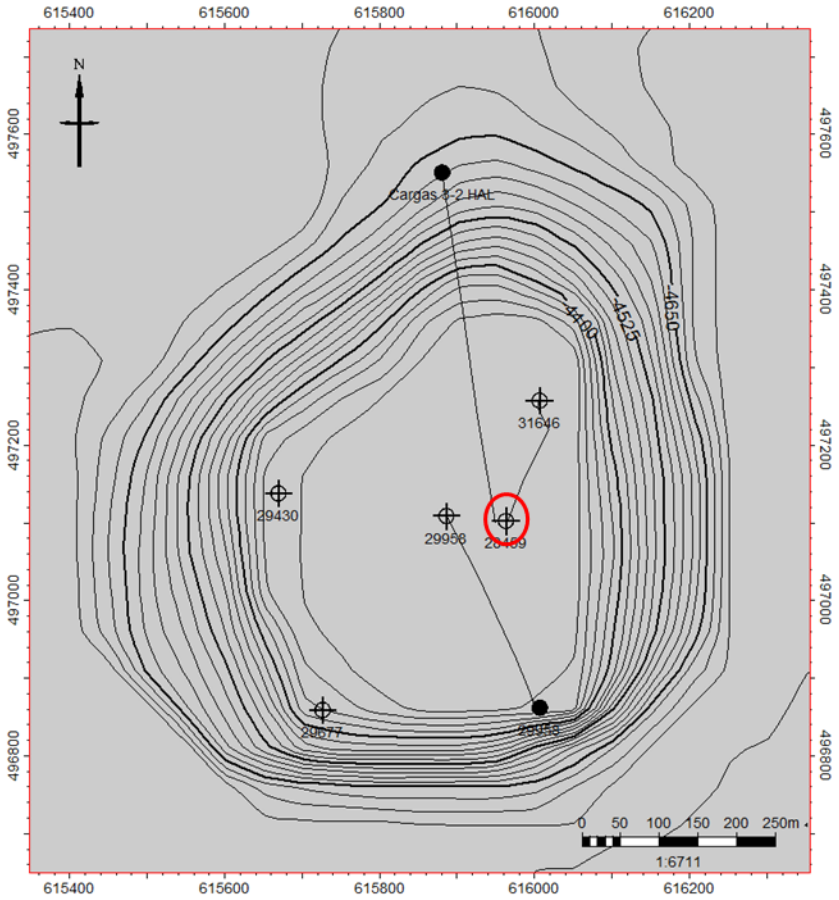


Figure 12-3. Structural map of the Chester 2 reef field showing well locations.

12.2.1 Basic Log Interpretation

Well 28459

Well 28459 is in the middle of the Chester 2 reef field. There are short intervals of greater than 5% porosity within the A-2 carbonate, which plots as a dolomitic limestone containing anhydrite. The A-1 carbonate plotted as a limestone and sandstone, with the trend of data (decreasing bulk density values for the same neutron porosity values) being influenced by salt. The Brown Niagaran plotted as a limestone with a short interval of good porosity in the middle of the formation. Figure 12-4 shows the neutron porosity-bulk density crossplot of the A-2 carbonate through the Gray Niagaran in well 28459.

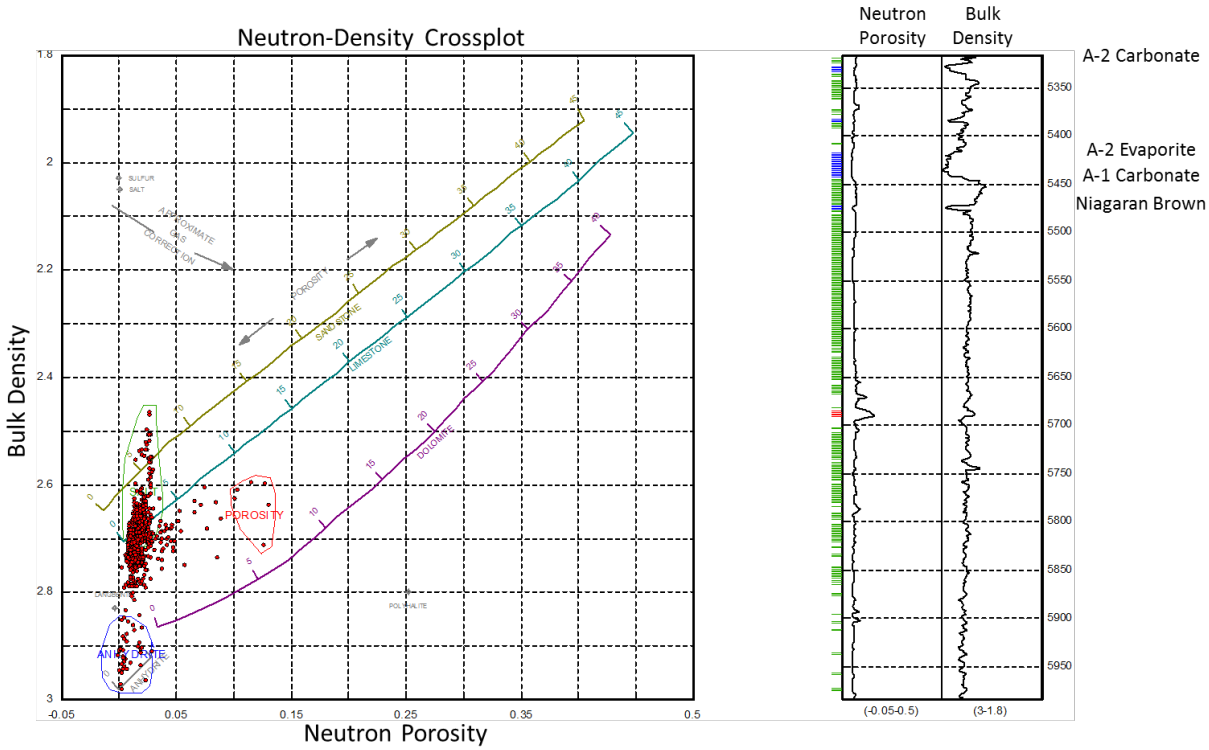


Figure 12-4. Neutron porosity-bulk density crossplot of well 28459 showing porosity in the middle of the Brown Niagaran. Red polygon = porosity >5%, green polygon = salt plugged, blue polygon = anhydrite.

Water saturations for well 28459 indicate frequent spikes in saturation values due to a significant amount of salt plugging. The overall water saturation gradually increases throughout the Brown Niagaran and remains high below 5,830 feet MD. This is consistent with the original estimated oil/water contact, which fell between 5,825 and 5,913 feet MD. On average, the Brown Niagaran had a water saturation of 44% which increased to 74% below 5,830 feet MD. Figure 12-5 shows the water saturation curve and histogram for well 28459.

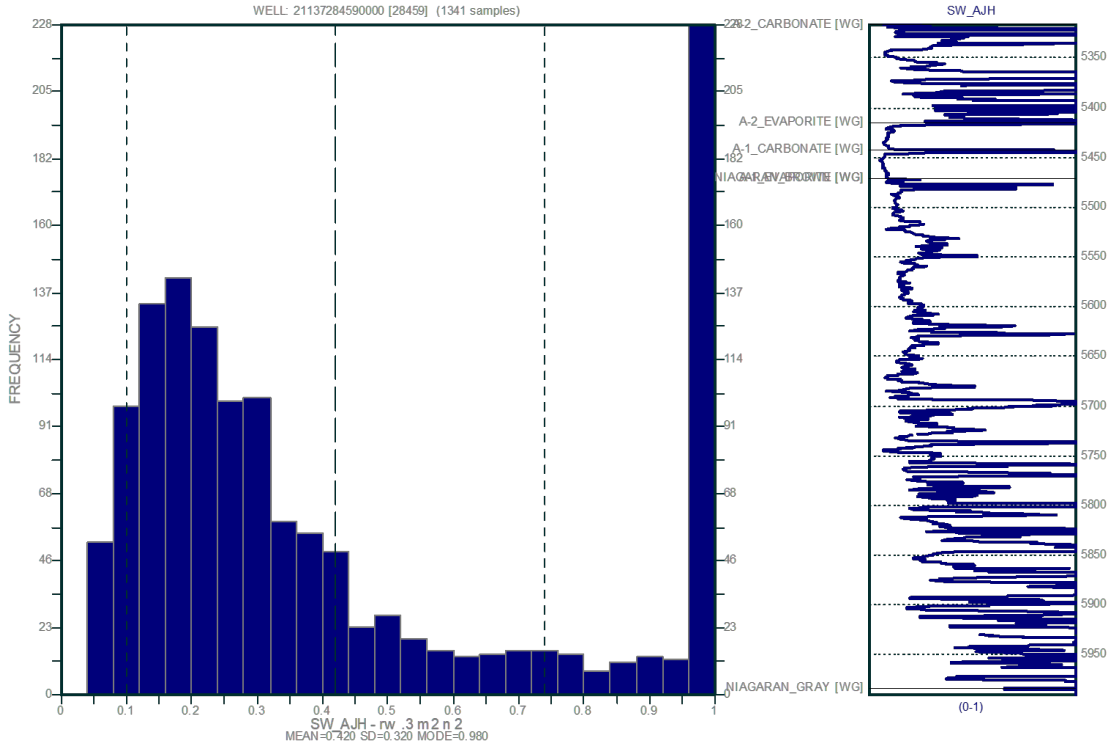


Figure 12-5. Water saturation curve and histogram for well 28459 showing an increase in water saturation toward the base of the Brown Niagaran.

Well 2845901

Well 2845901 is in the middle of the Chester 2 reef field and is dominated by limestone. The A-1 carbonate plots as a limestone, and the A-2 carbonate plots as a dolomitic limestone containing anhydrite. There is no porosity greater than 5% in the A-1 or A-2 carbonates in the Chester 2 reef field. The Brown Niagaran plots mostly as a limestone and has porosity greater than 5% in the middle and lower section. Figure 12-6 shows the neutron porosity-bulk density crossplot of the A-2 carbonate to the Gray Niagaran for well 2845901.

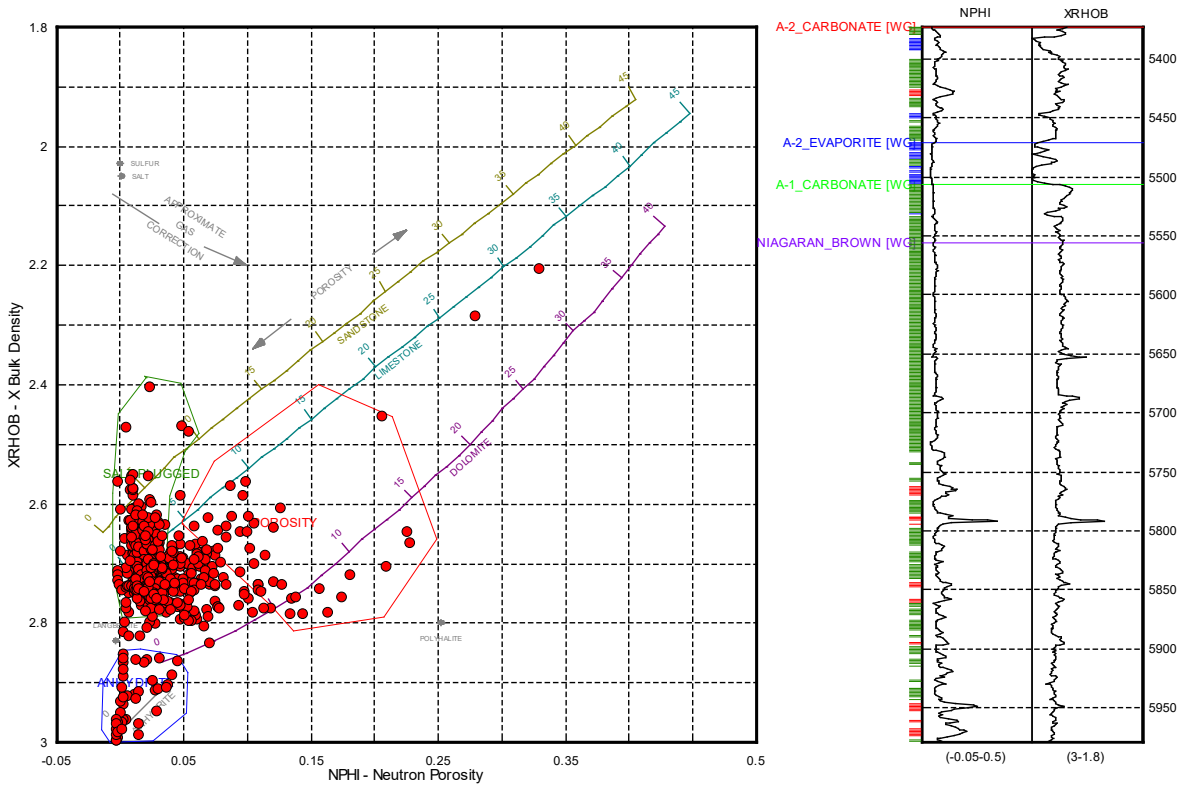


Figure 12-6. Neutron porosity-bulk density crossplot of well 2845901 showing porosity in the A-2 carbonate and in the middle-lower Brown Niagaran.

Well 29430

Well 29430 is on the west-central side of the Chester 2 reef field. The trend of the A-1 carbonate data (decreasing bulk density values for the same neutron porosity values) is due to the presence of salt. The A-2 carbonate plots as a dolomitic limestone and does not contain any porosity greater than 5%. The upper Brown Niagaran plots as a limestone, while the lower section of the formation plots as a dolomite with high porosity. Figure 12-7 shows the neutron porosity-bulk density crossplot of the A-2 carbonate through the Gray Niagaran for well 29430.

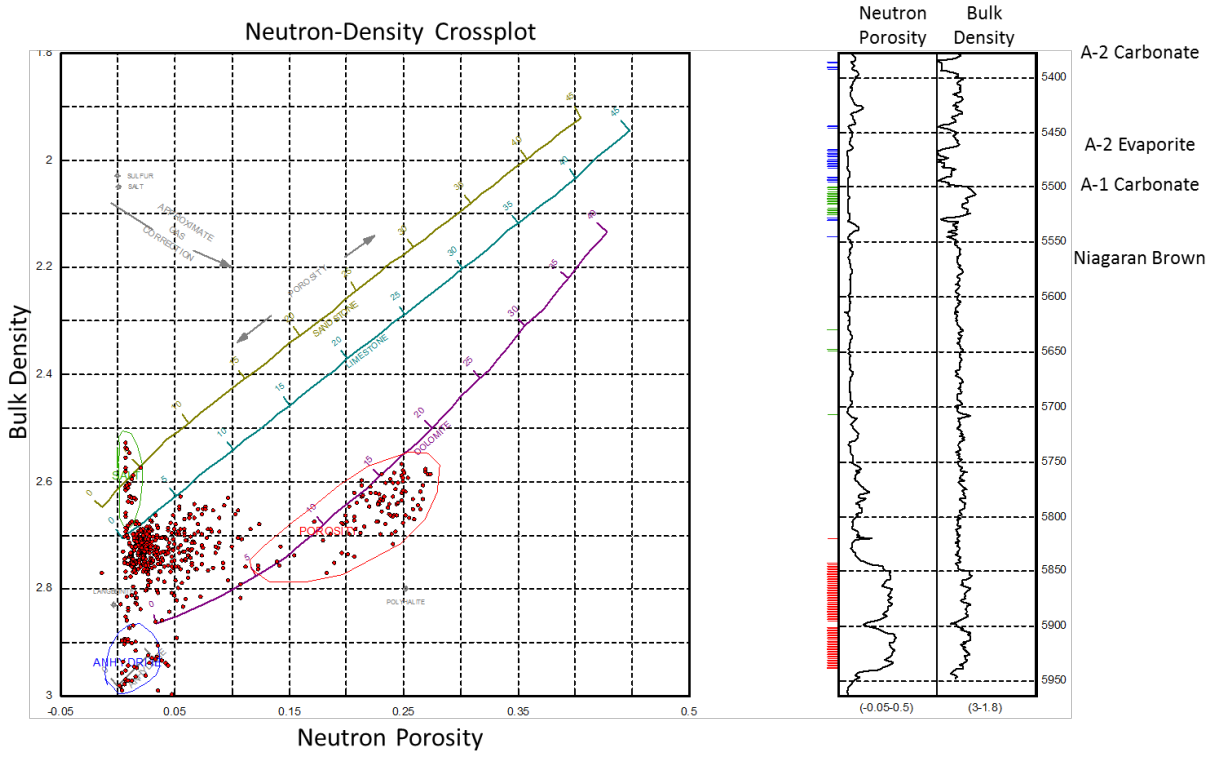


Figure 12-7. Neutron porosity-bulk density crossplot of well 29430 showing porosity in the middle-lower Brown Niagaran.

The water saturations for well 29430 indicate frequent saturation spikes throughout all formations of interest. This is due to the presence of salt. The water saturation shifts near 5,800 feet MD and remains high; this shift is near the recorded oil/water contact of 5,820 to 5,844 feet MD. Figure 12-8 shows the water saturation curve and histogram for well 29430.

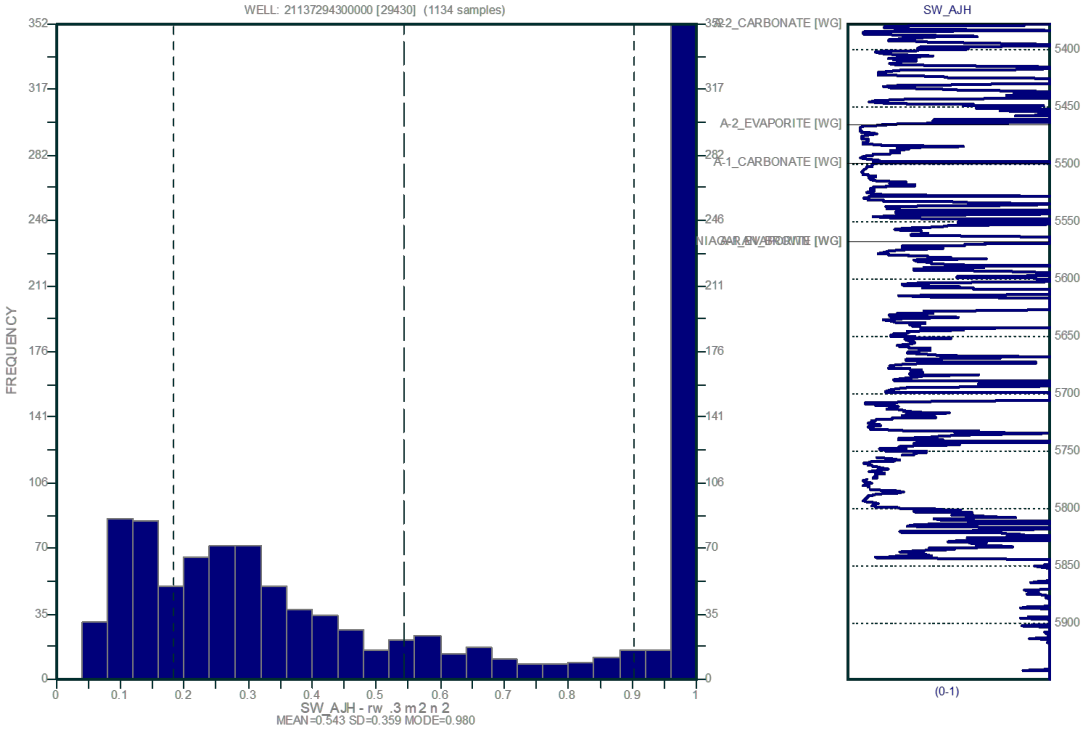


Figure 12-8. Water saturation curve and histogram for well 29430 showing frequent spikes due to evaporites.

Well 29677

Well 29677 is on the southwest edge of the Chester 2 reef field. The A-2 carbonate plots as a dolomitic limestone containing anhydrite. The trend of the A-1 carbonate data (decreasing bulk density values for the same neutron porosity values) is due to the presence salt. The upper half of the A-1 carbonate contains porosity greater than 5%. The Brown Niagaran plots as a limestone with some porosity greater than 5% toward the bottom of the formation. Figure 12-9 shows the neutron porosity-bulk density crossplot of the A-2 carbonate to the Gray Niagaran for well 29677.

Water saturations for well 29677 indicate thin intervals of high water saturation in the presence of evaporites. There is a distinct shift near 5,800 feet MD at the base of the Brown Niagaran. On average, the water saturation in the Brown Niagaran is 30% with an increase to greater than 50% below 5,800 feet MD. Figure 12-10 shows the water saturation curve and histogram for well 29677.

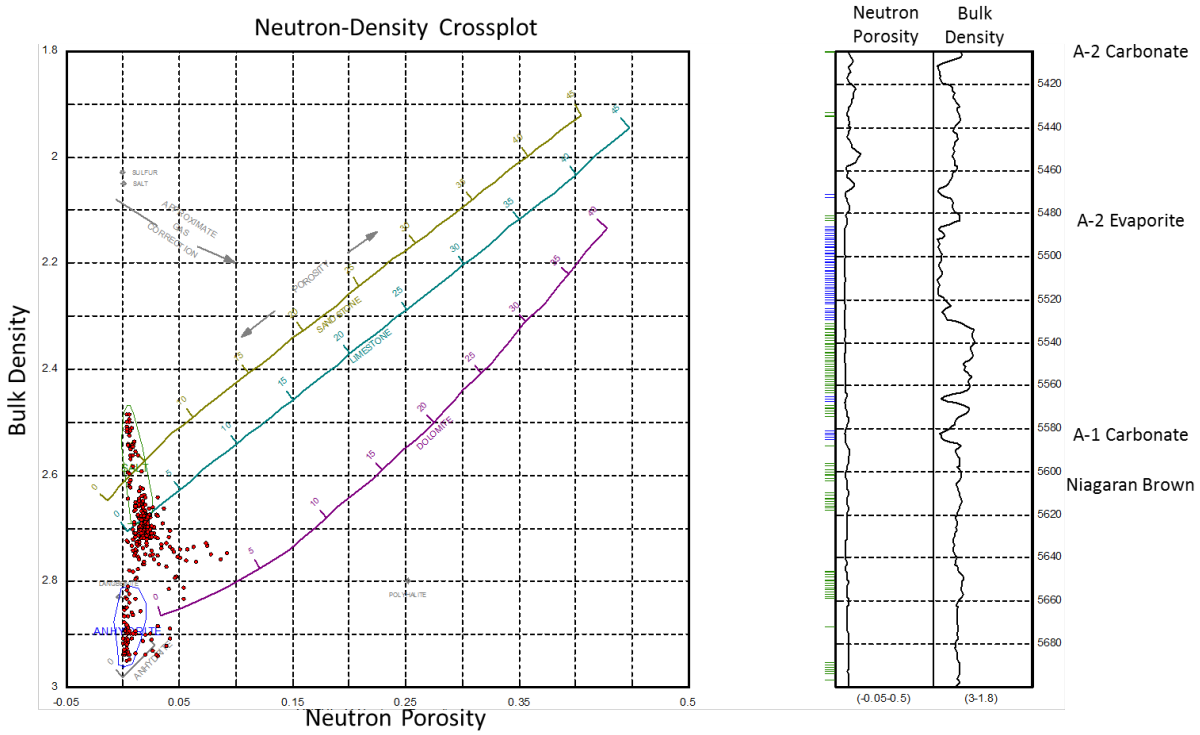


Figure 12-9. Neutron porosity-bulk density crossplot of well 29677 showing porosity in the top half of the A-1 carbonate and in the lower Brown Niagaran.

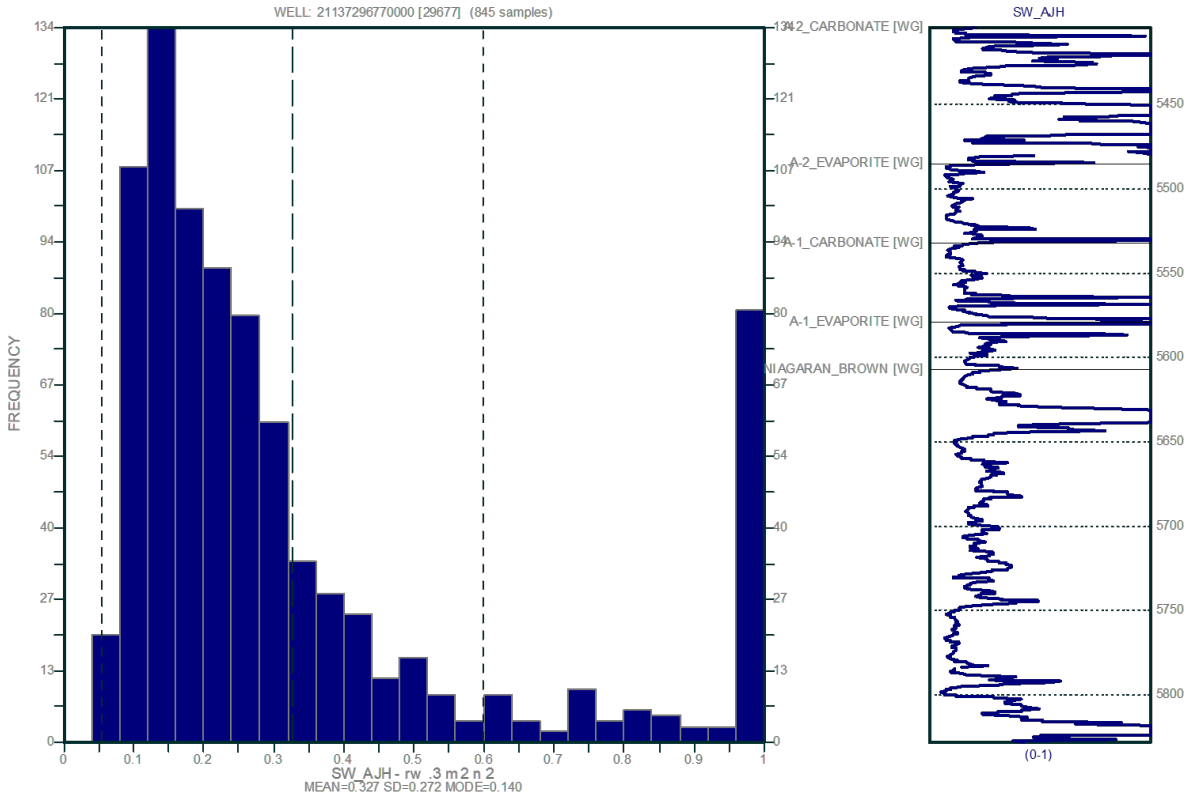


Figure 12-10. Water saturation curve and histogram for well 29677 showing an increase in water saturation near the base of the Brown Niagaran at 5,800 feet MD.

Well 29958

Well 29958 is on the southeast end of the Chester 2 reef field. The A-2 carbonate plots as a salt-plugged limestone containing anhydrite with thin intervals of greater than 5% porosity. The trend of the A-1 carbonate data (decreasing bulk density values for the same neutron porosity values) is due to the presence of salt. The upper section of the A-1 carbonate contains porosity greater than 5%. The Brown Niagaran plots as a limestone with sparse porosity greater than 5%. Figure 12-11 shows the neutron porosity-bulk density crossplot of the A-2 carbonate to the Gray Niagaran in well 29958.

Water saturations for well 29958 indicate thin intervals of high saturations where evaporites are present. Overall, the water saturation remained low with an average of 13%. The oil/water contact was not covered by the logs, so the Brown Niagaran had a low water saturation of 12%. Figure 12-12 shows the water saturation curve and histogram for well 29958.

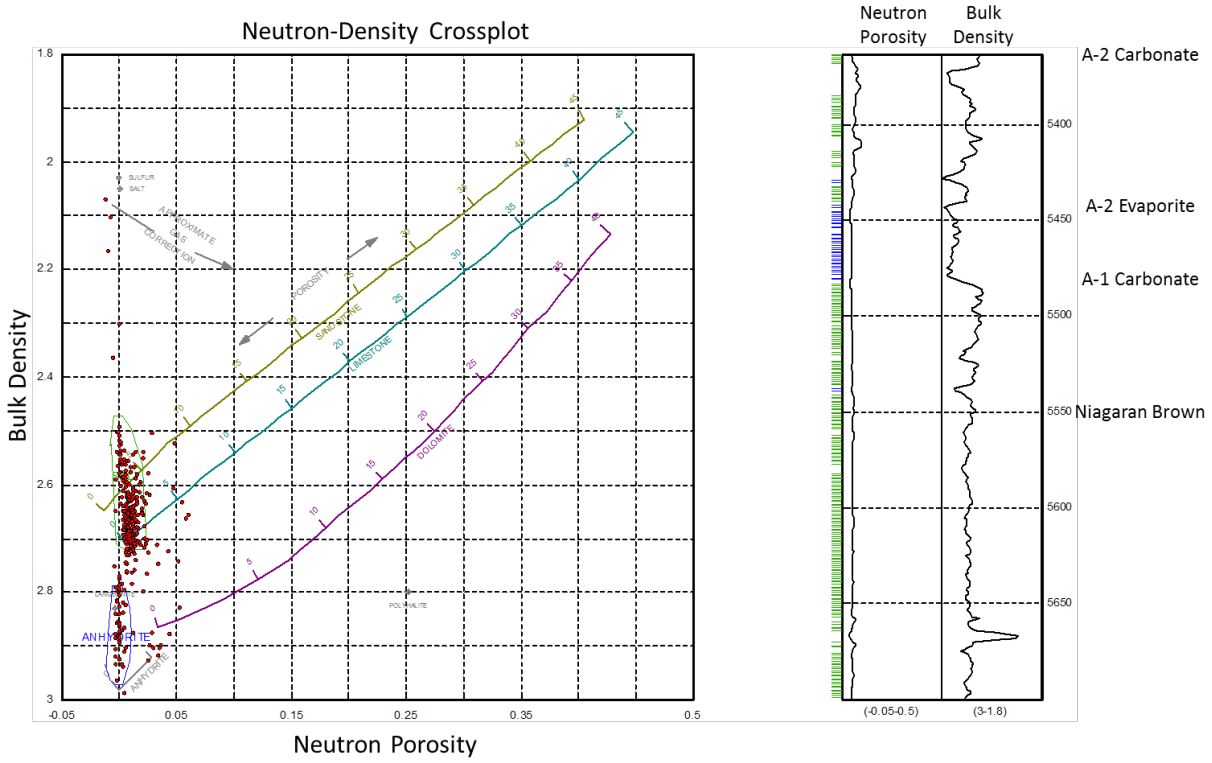


Figure 12-11. Neutron porosity-bulk density crossplot of well 29958 showing porosity in the top half of the A-1 carbonate and in the lower Brown Niagaran.

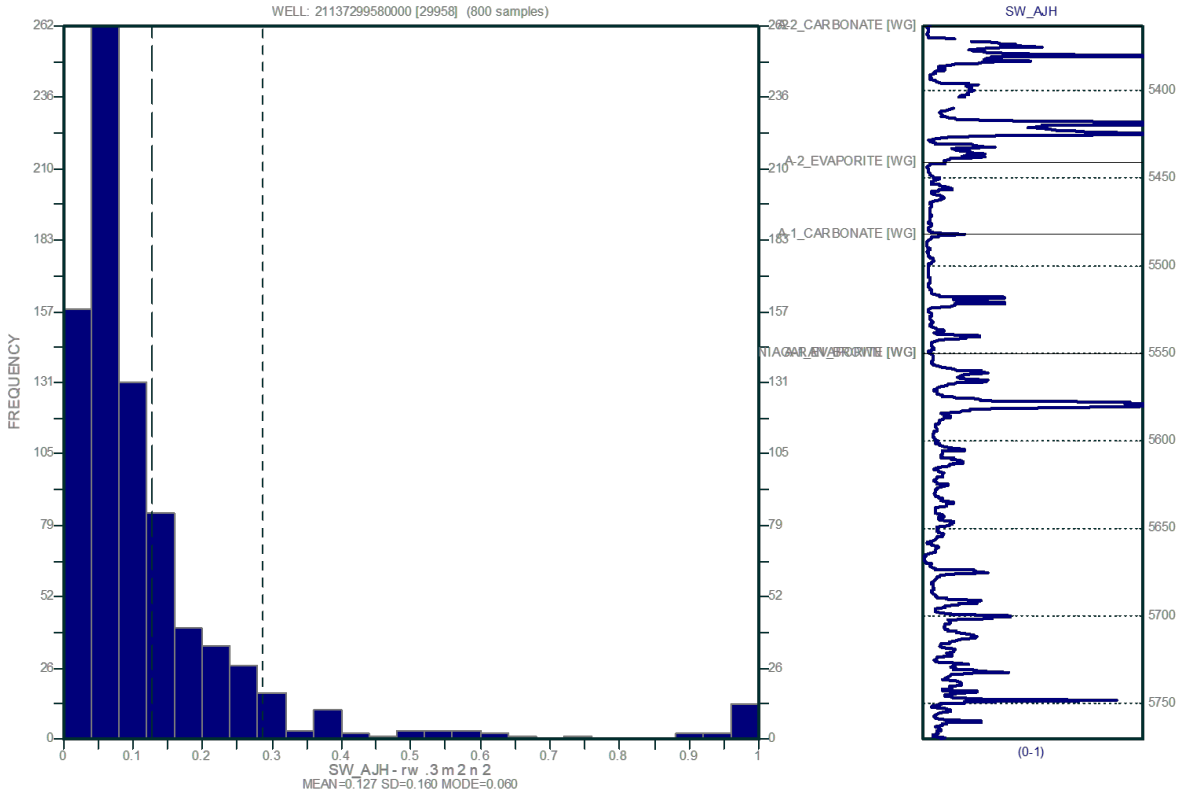


Figure 12-12. Water saturation curve for well 29958 showing relatively low water saturations throughout the intervals of interest.

Well 60596 (Cargas)

Well 60596 is on the north end of the Chester 2 reef field. The A-2 carbonate plots as a salt-plugged limestone containing anhydrite with large intervals of greater than 5% porosity. The trend of the A-1 carbonate data (decreasing bulk density values for the same neutron porosity values) is due to the presence of salt. The Brown Niagaran plots as predominantly a limestone with intervals of porosity greater than 5% throughout. Figure 12-13 shows the neutron porosity-bulk density crossplot of the A-2 carbonate to the Gray Niagaran for well 60596. For more details on well 60596, refer to Attachment 1.

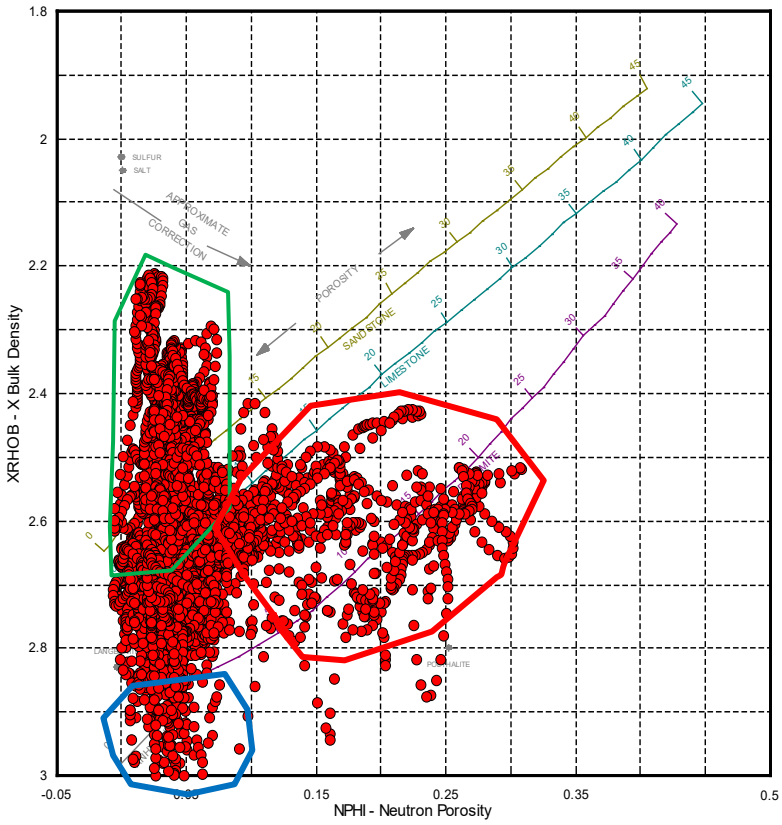


Figure 12-13. Neutron porosity-bulk density crossplot of well 60596 showing high-porosity dolomite in the Brown Niagaran in the northern section of the well. Red polygon = porosity >5%, green polygon = salt, blue polygon = anhydrite.

Water saturations for well 60596 indicate frequent spikes in water saturation up to 100%. The spikes correlate with significant salt plugging and anhydrite. There is an overall increase in water saturation near 6,660 feet MD, where the water saturation remains higher and has more frequent spikes. Overall, the Brown Niagaran had an average water saturation of 23%. Figure 12-14 shows the water saturation curve and histogram for well 60596.

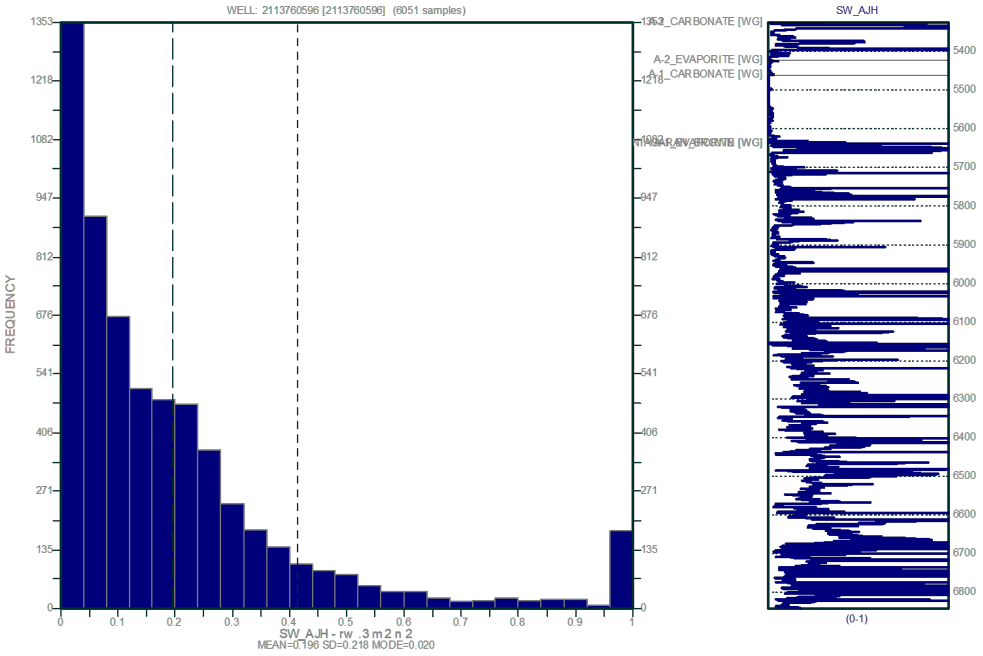


Figure 12-14. Water saturation curve and histogram for well 60596 showing frequent spikes due to the presence of evaporites throughout the formations of interest.

12.2.2 Petrophysics Calculations

A-2 Carbonate

The A-2 carbonate thickness varies from 76 feet on-reef to 108 feet on the flanks. The porosity ranges from 0% to 12% with an average of 4.7%. The spikes in porosity were attributed to the presence of evaporites. Using a porosity cutoff of greater than 5%, the net thickness average was 22 feet with a NTG ratio of 0.25 (Table 12-3). These values are high for a confining unit but are skewed by well 60596, where the porosities are high throughout. After applying a water saturation cutoff of 40% to reduce the influence of evaporites, the net thickness reduced to 20 feet and the NTG ratio to 0.23.

Table 12-3. Summary of petrophysical calculations for the A-2 carbonate in the Chester 2 reef field.

Interval: A-2 Carbonate						
Avg. Thickness	Avg. Porosity	Avg. Net Thickness	Avg. NTG	Avg. SW	Avg. Net Thickness (Sw<40%)	Avg. NTG (Sw<40%)
90 ft	4.7%	22 ft	0.25	41%	20 ft	0.23

A-2 Evaporite

The A-2 evaporite is interbedded anhydrite and carbonate in the Chester 2 reef field and salt on the flanks. Petrophysical calculations were not computed for the A-2 evaporite due to the influence of evaporites on porosity.

A-1 Carbonate

The A-1 carbonate is mostly dolomite with some salt plugging. The thickness ranged from 29 feet on the crest of the reef to 134 feet on the flanks. The porosity ranged from 0% to 18% with an average of 9.5%. Using a porosity cutoff of greater than 5%, the net thickness averages 33 feet with a NTG ratio of 0.43 (Table 12-4). A water saturation cutoff of 40% was applied to eliminate evaporites and water-saturated rock.

Table 12-4. Summary of petrophysical calculations for the A-1 carbonate in the Chester 2 reef field.

Interval: A-1 Carbonate						
Avg. Thickness	Avg. Porosity	Avg. Net Thickness	Avg NTG	Avg. SW	Avg. Net Thickness (Sw<40%)	Avg. NTG (Sw<40%)
72 ft	9.5%	33 ft	0.43	17%	40 ft	0.51

Brown Niagaran

The Brown Niagaran is salt-plugged limestone with some intervals of porous dolomite. The thickness varies from 81 feet on the flank to 422 feet on the crest. The porosity ranged from 0% to 20% with an average of 4%. Using a porosity cutoff of greater than 5% resulted in an average net thickness of 36 feet with a low NTG ratio of 0.12. A water saturation cutoff of less than 40% was applied to eliminate evaporites and water-saturated rock. This reduced the net thickness to 17 feet and the NTG ratio to 0.07 (Table 12-5). The presence of salt plugging greatly reduced the reservoir potential in the Brown Niagaran.

Table 12-5. Summary of petrophysical calculations for the Brown Niagaran in the Chester 2 reef field.

Interval: Brown Niagaran						
Avg. Thickness	Avg. Porosity	Avg. Net Thickness	Avg. NTG	Avg. SW	Avg. Net Thickness (Sw<40%)	Avg. NTG (Sw<40%)
289 ft	4.0%	36 ft	0.12	33%	17 ft	0.07

12.3 Seismic Analysis

The Chester 2 reef field has sharp boundaries in seismic time where the reef has faster arrival times than the surrounding Brown Niagaran surface due to higher elevations (Figure 12-15). The A-1 carbonate drapes over the Brown Niagaran with no relief observed in seismic time (Figure 12-16). This is due to similar rock velocities between the A-1 carbonate and Brown Niagaran. There is not enough contrast for separate horizons along the reef crest. The A-2 carbonate has gentle slopes with minor indications of an underlying reef complex (Figure 12-17).

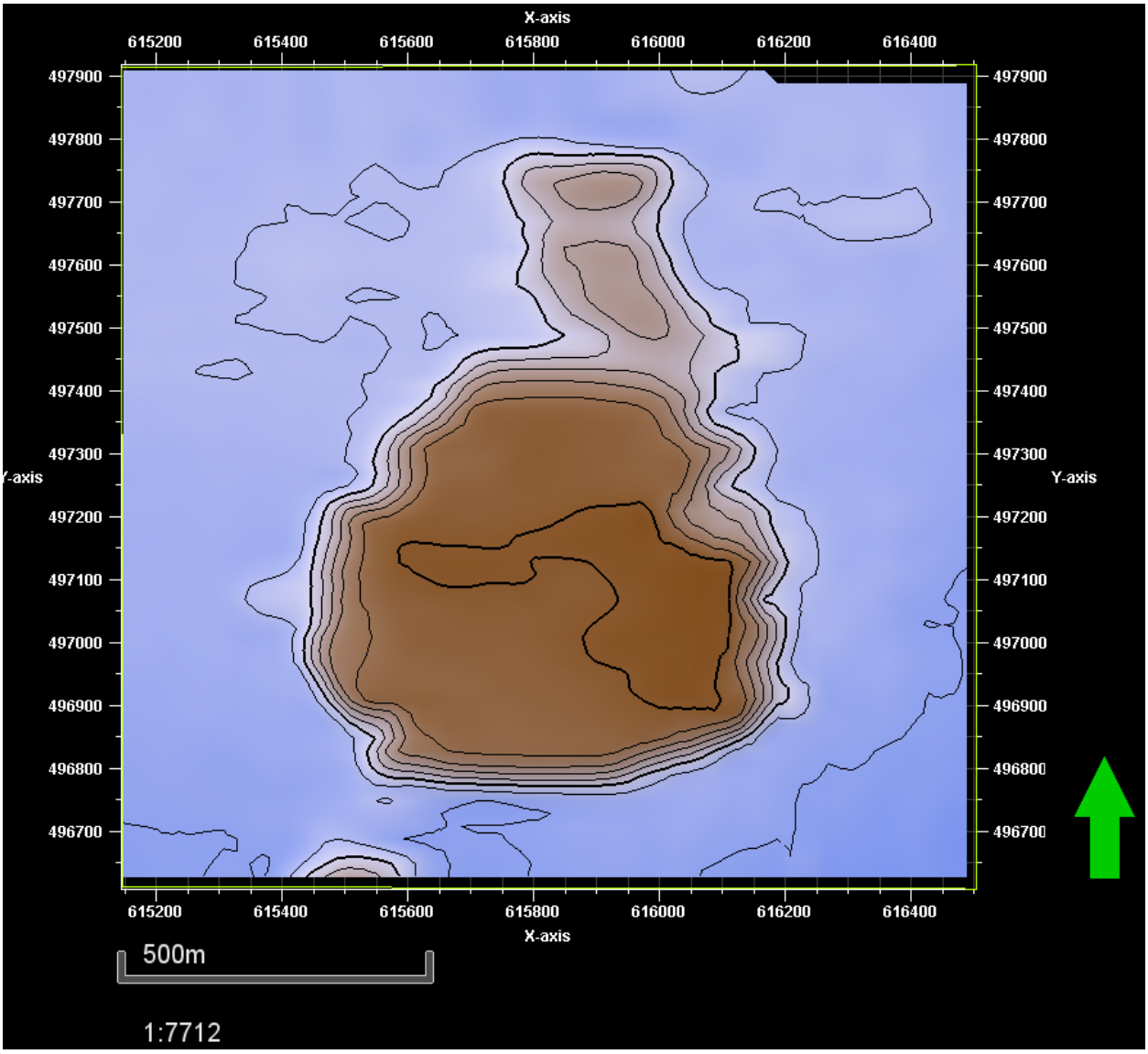


Figure 12-15. Time horizon surface for the Brown Niagaran showing steep slopes along the edges of the Chester 2 reef field.

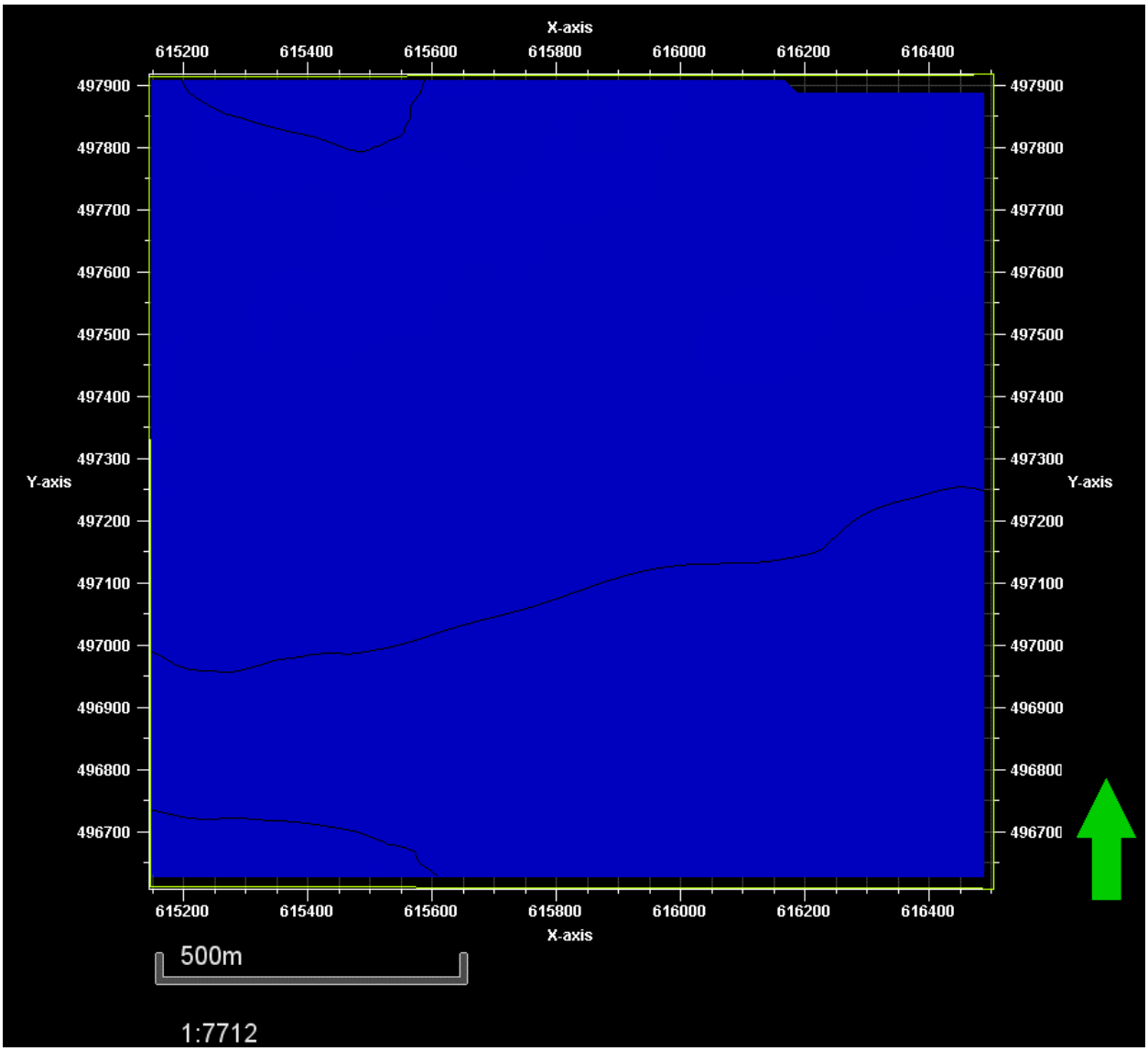


Figure 12-16. Time horizon surface for the A-1 carbonate showing no relief across the Chester 2 reef field due to similar velocities between the A-1 carbonate and Brown Niagaran.

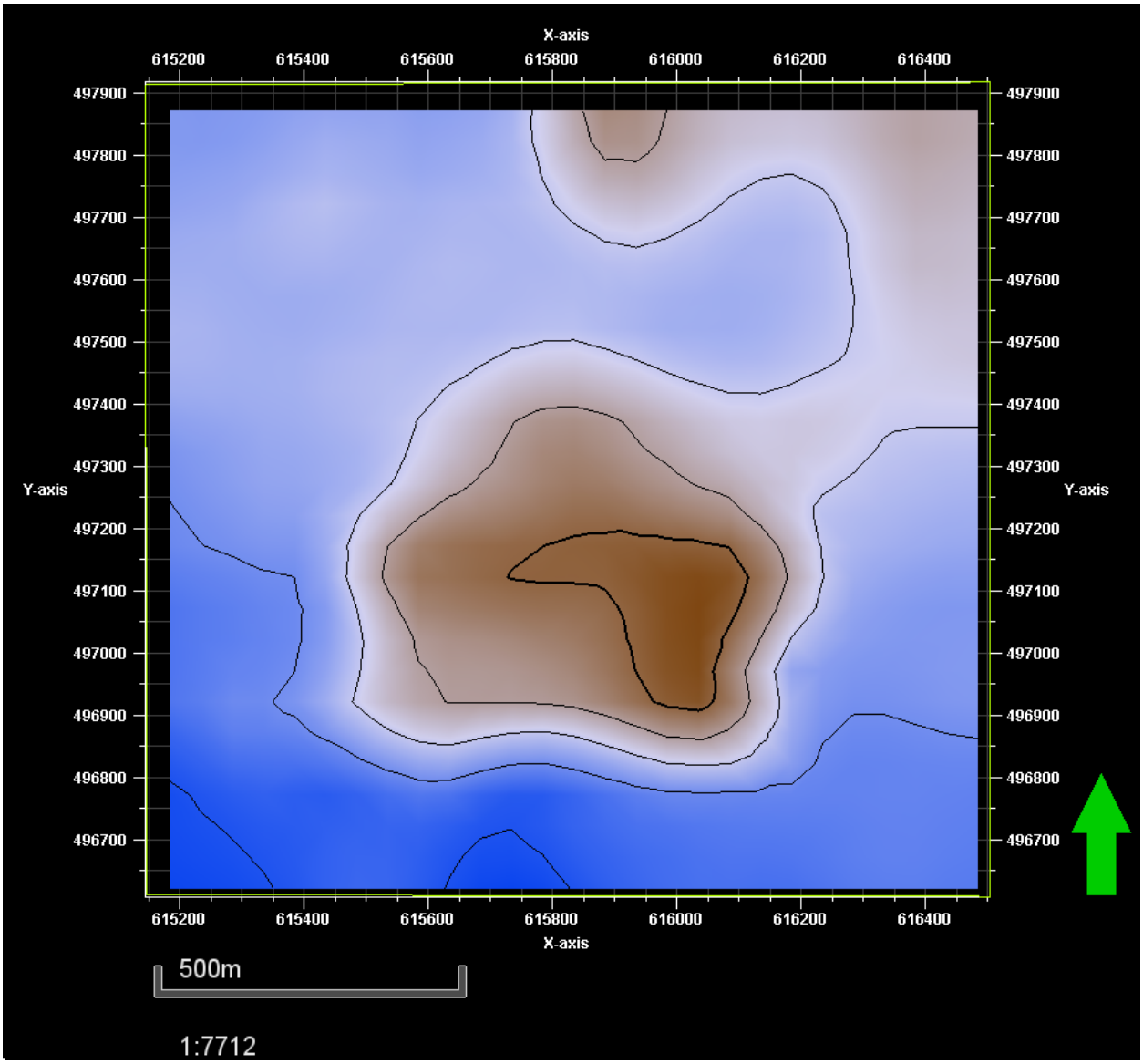


Figure 12-17. Time horizon surface for the A-2 carbonate showing gentle slopes along the edges of the Chester 2 reef field.

Due to the complexity and challenges observed in the Chester 2 reef field, an advanced seismic attribute analysis was conducted by Core Energy, LLC, to better define the reservoir zone within the reef. The results indicate a distinct geobody of higher porosity. Figure 12-18 shows a deviated well and its position within the 3D seismic data. Along the wellbore are discs colored by porosity (hotter represents higher porosity) and a polygon which outlines the extent of the porosity body.

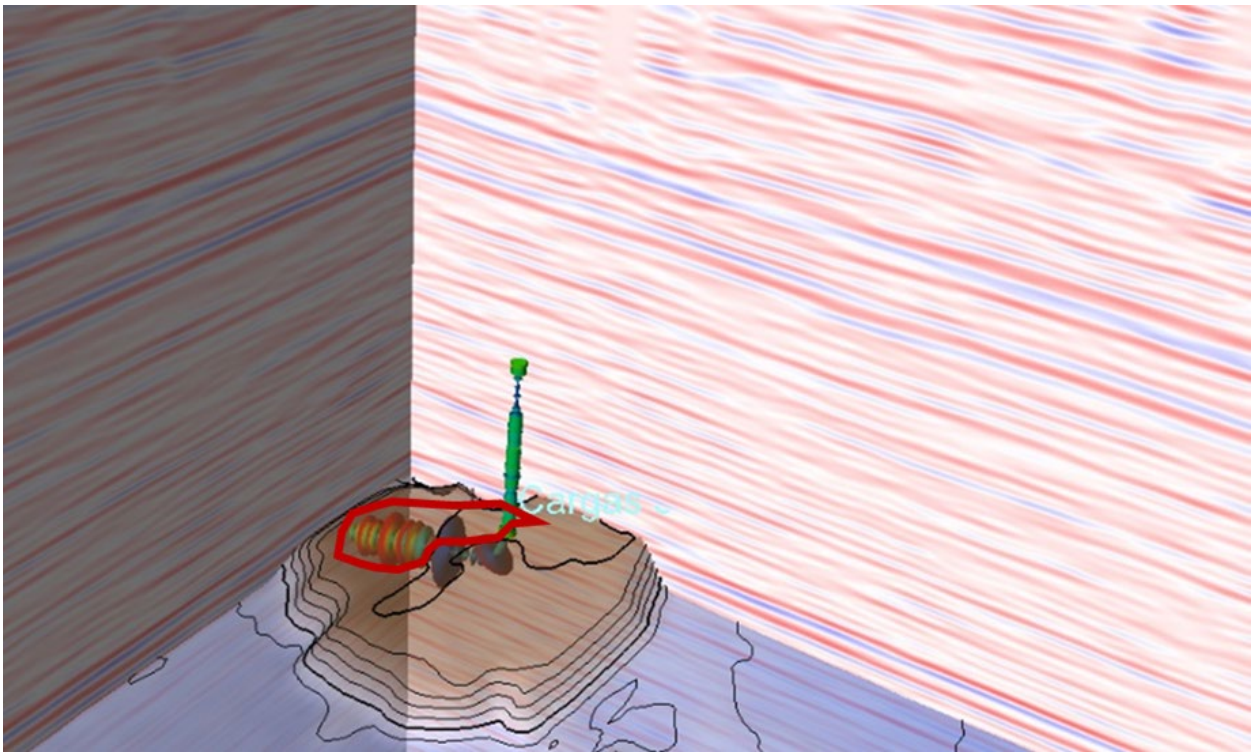


Figure 12-18. Time horizon surface with sections of 3D seismic data and the trajectory of the Cargas well showing a porous zone (red polygon).

12.4 Core Analysis

Whole core was available from well 28459 from a depth of 5,543 feet to 5,625 feet (82 feet long), corresponding to the middle section of the Brown Niagaran in the Chester 2 reef field. Standard core analysis was conducted, which consisted of porosity, permeability, fluid saturation, bulk density, and grain density measurements. The core is salt-plugged throughout (Figure 12-19). Figure 12-3 in Section 12.2 shows the well location of the whole core (red circle).

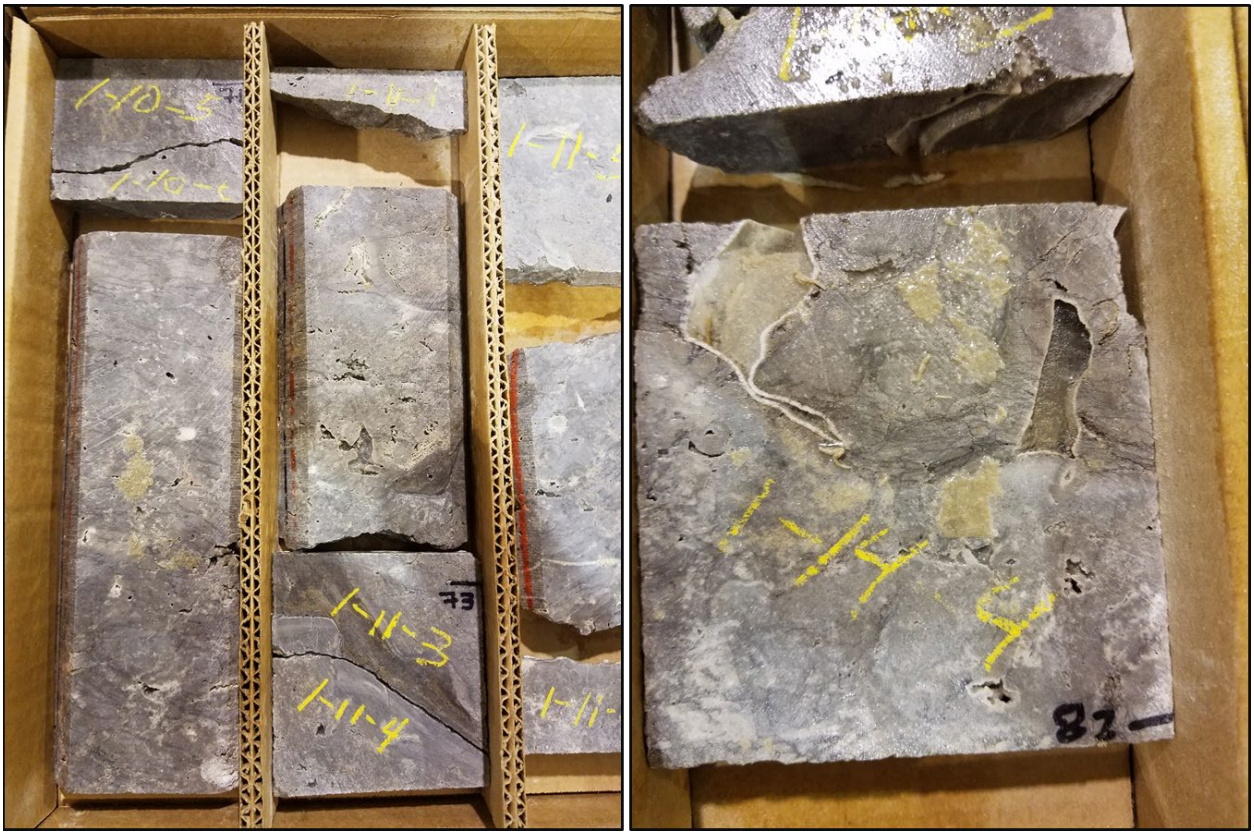


Figure 12-19. Photographs of whole core from Chester 2 showing tight limestone with salt filled vugs and fractures.

Grain Density

The Brown Niagaran has an average grain density of 2.69 g/cm^3, which is consistent with salt-plugged limestone. This interval of the Brown Niagaran had grain densities as low as 2.65 g/cm^3 and as high as 2.74 g/cm^3. Figure 12-20 shows the histogram of the grain density for the whole core interval of the Brown Niagaran in well 28459.

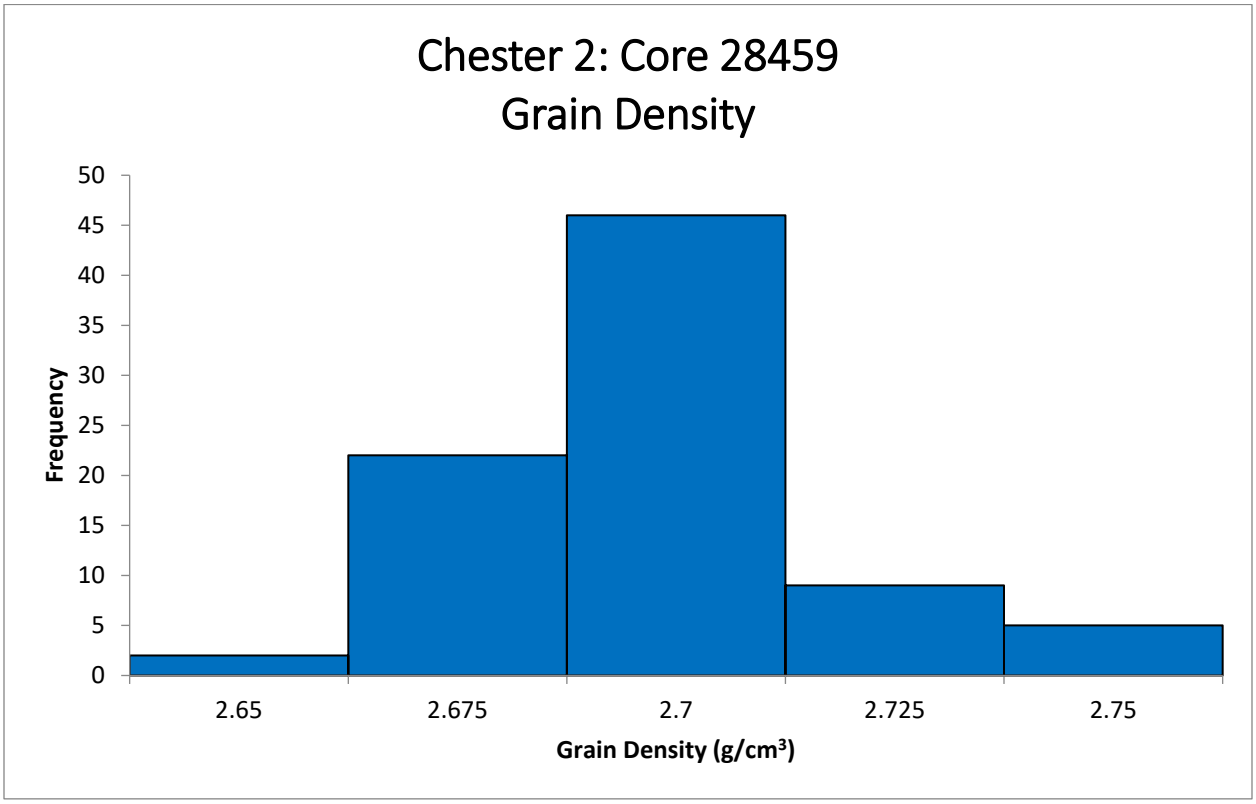


Figure 12-20. Histogram of the grain density for the Brown Niagaran from whole core analysis of well 28459.

Bulk Density

The Brown Niagaran has an average bulk density of 2.68 g/cm^3, which is consistent with salt-plugged limestone and with the grain density values. This interval of the Brown Niagaran had bulk densities as low as 2.63 g/cm^3 and as high as 2.74 g/cm^3. Figure 12-21 shows the histogram of the bulk density for the whole core interval of Brown Niagaran in well 28459.

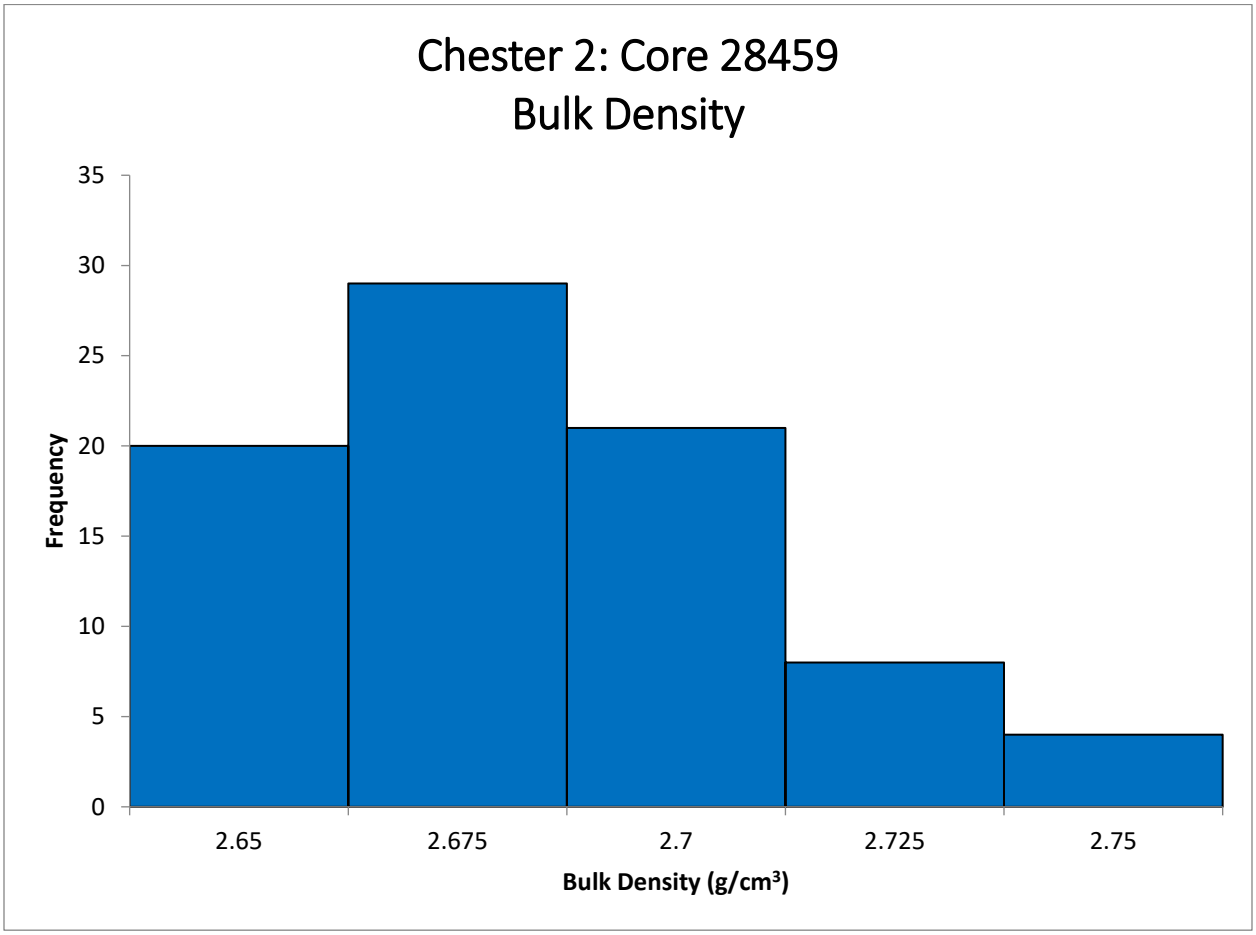


Figure 12-21. Histogram of the bulk density for the Brown Niagaran from whole core analysis of well 28459.

Porosity-Permeability Transform

The Brown Niagaran had a porosity range of 0.5% to 2.7% with permeability ranging from less than 0.1 to 33.8 mD. The data was plotted in Figure 12-22 using the coordinating transform equation represented in Equation 12-1.

$$K_{BN} = 0.1208e^{0.4165\emptyset}$$

Equation 12-1

where:

K_{BN} = permeability of the Brown Niagaran (mD)
ø = porosity (%)

The Brown Niagaran had a poor fitting r^2 value of 0.0064, as can be seen in Figure 12-22.

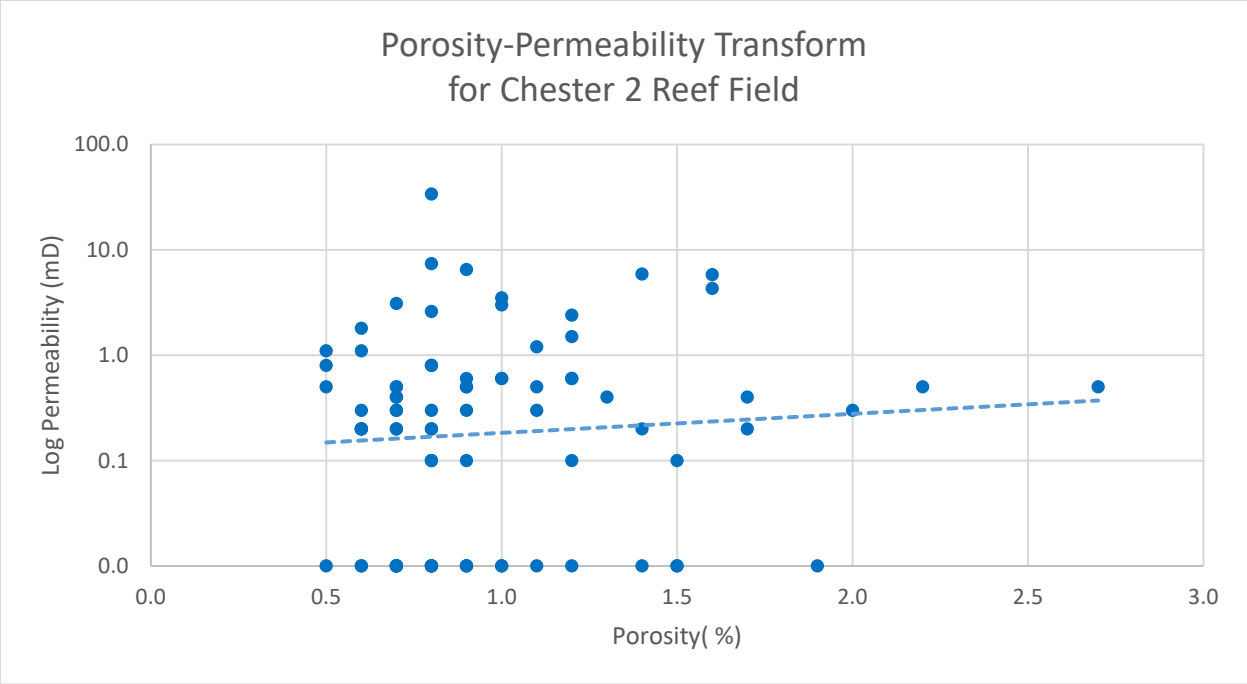


Figure 12-22. Porosity-permeability transform for the A-1 carbonate, A-1 evaporite, and Brown Niagaran from whole core measurements from well 28459.

12.5 Geologic Interpretations

Chester 2 was interpreted as a single reef core (Figure 12-23). The Brown Niagaran was subdivided into three lithofacies: reef core, windward facies, and leeward facies. However, the lithofacies do not describe the flow zones within the Chester 2 reef field. The Chester 2 was highly salt-plugged with an isolated zone of dolomitization. The Brown Niagaran was also subdivided into salt-plugged limestone and reservoir dolomite. Figure 12-23 illustrates the two interpretations based on lithofacies and reservoir quality.

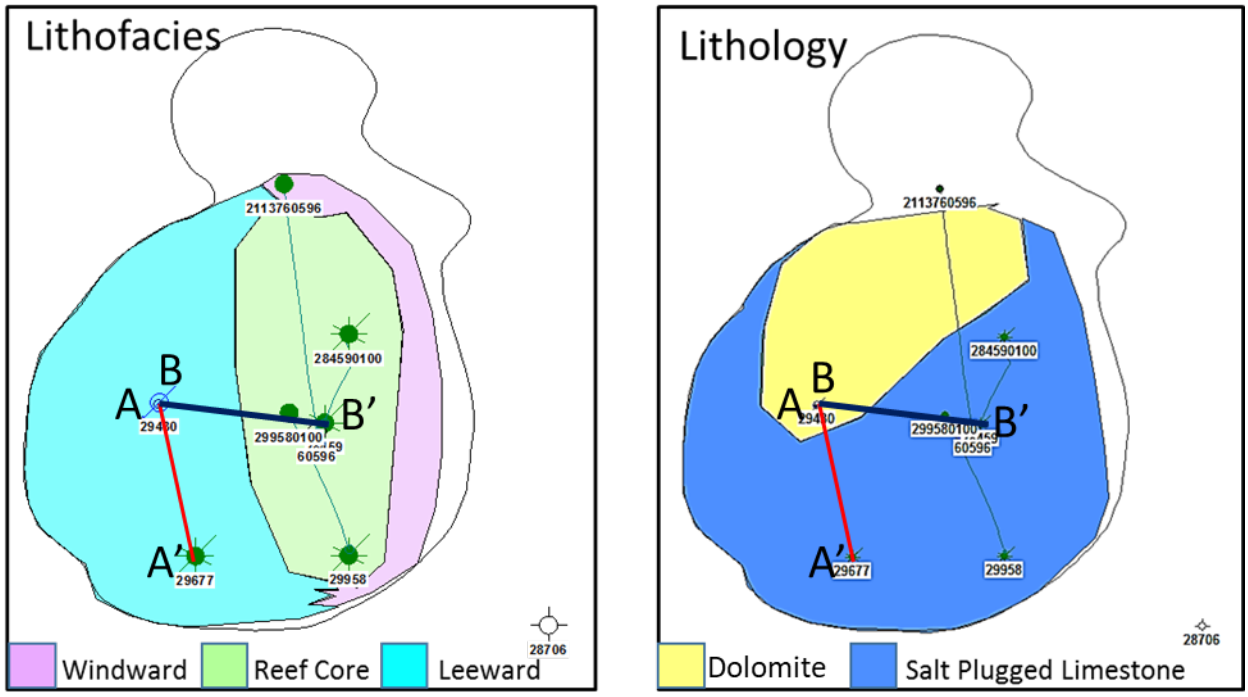


Figure 12-23. Map view of lithofacies and lithology extents in the Chester 2 reef field and locations of cross sections A-A' (red) and B-B'(black).

A single-well cross section of well 60596 was generated to illustrate how it cuts through the reef and into the dolomitized interval (Figure 12-24). Well 60596 (the Cargas well) is a horizontal well which cuts through the major changes in the Chester 2 reef field. The porosity remains high throughout due to the frequent salt plugs. There is an interval at the base of the Brown Niagaran which had increased porosity up to 30% as the well enters the dolomitized zone. The A-1 carbonate has very few porosity flags at this location.

Cross section A-A' runs north to south through the Chester 2 reef field, across the change from dolomite to limestone (Figure 12-25). Cross section B-B' runs west to east across the changes in lithofacies and lithology (Figure 12-26). Both cross sections were flattened on the top of the A-2 carbonate and have neutron porosity, bulk density, gamma ray, porosity flags, and water saturation curves.

Cross section A-A' captures the change from dolomite to salt-plugged limestone. The northern well (29430) penetrates the dolomitized zone; however, it is fully water-saturated at that interval. There is higher porosity in the north than there is in the southern well. The southern well (29677) is composed of salt-plugged limestone with very little reservoir potential. The A-2 carbonate has a gamma spike mid-formation in both wells which could be attributed to carbonate mudstone.

Cross Section B-B' runs west to east across the Chester 2 reef field capturing changes in the lithofacies. The westernmost well (29430) has the dolomitized zone at the base of the Brown Niagaran as part of the leeward reef facies. Moving eastward toward the center of the reef at well 28459, the Brown Niagaran thickens and the A-1 carbonate thins. This is characteristic of the center of the reef in the reef core facies. Very few porosity flags are observed in the central well due to the salt-plugged limestone.

Additionally, Figure 12-27 illustrates the interpreted dolomitized zone in 3D within the Chester 2 reef field. The Cargas 3-2 well (60596) skimmed the top of the zone and the Wolf 1A (29430) penetrated the edge of it.

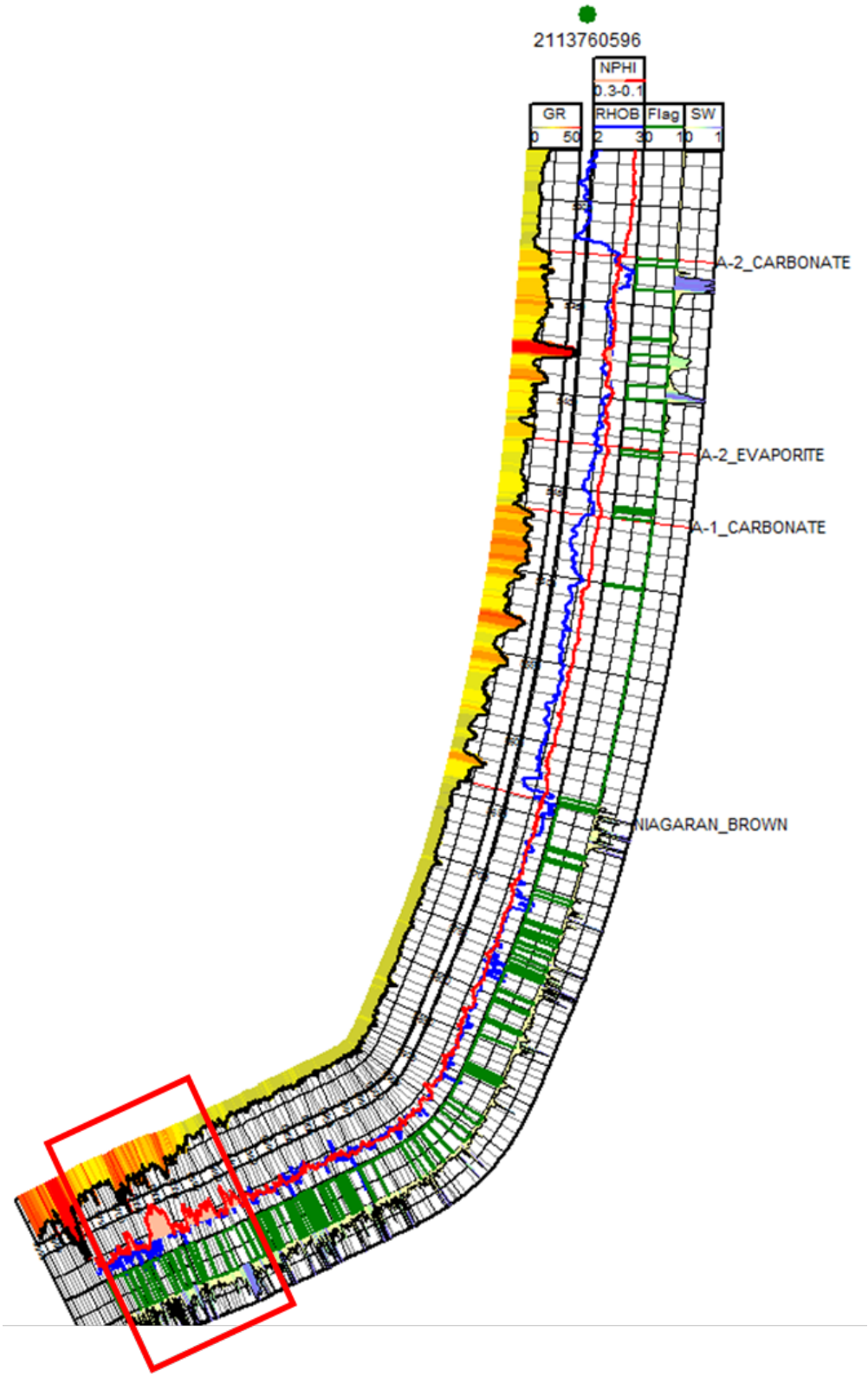


Figure 12-24. Single-well cross section of horizontal well 60596 as it cuts through the Chester 2 reef field. The red rectangle highlights a high-porosity interval which has been identified in the dolomitized zone.

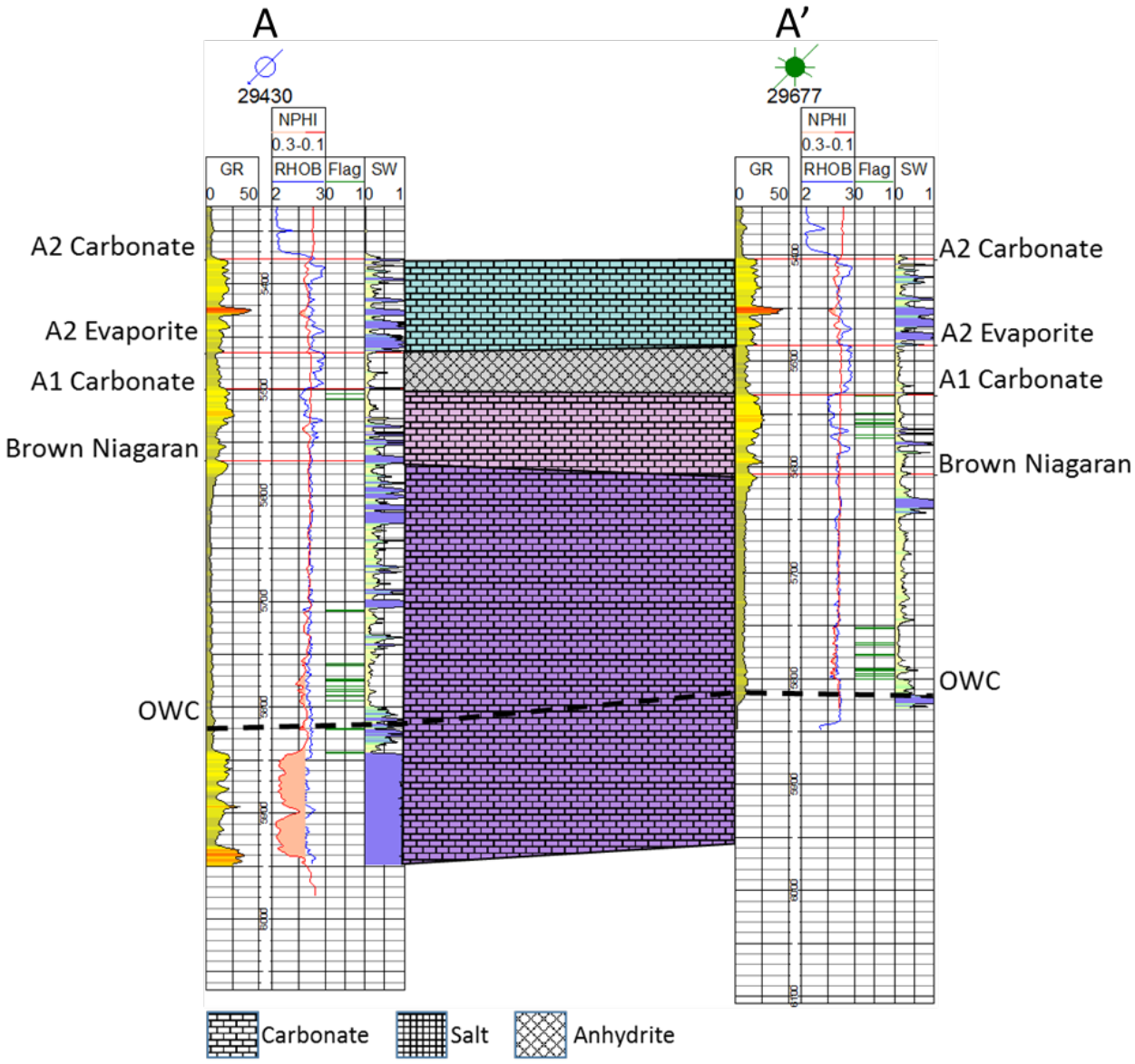


Figure 12-25. Cross section A-A' along the western side of the Chester 2 reef field showing a highly dolomitized zone to the north and little porosity to the south.

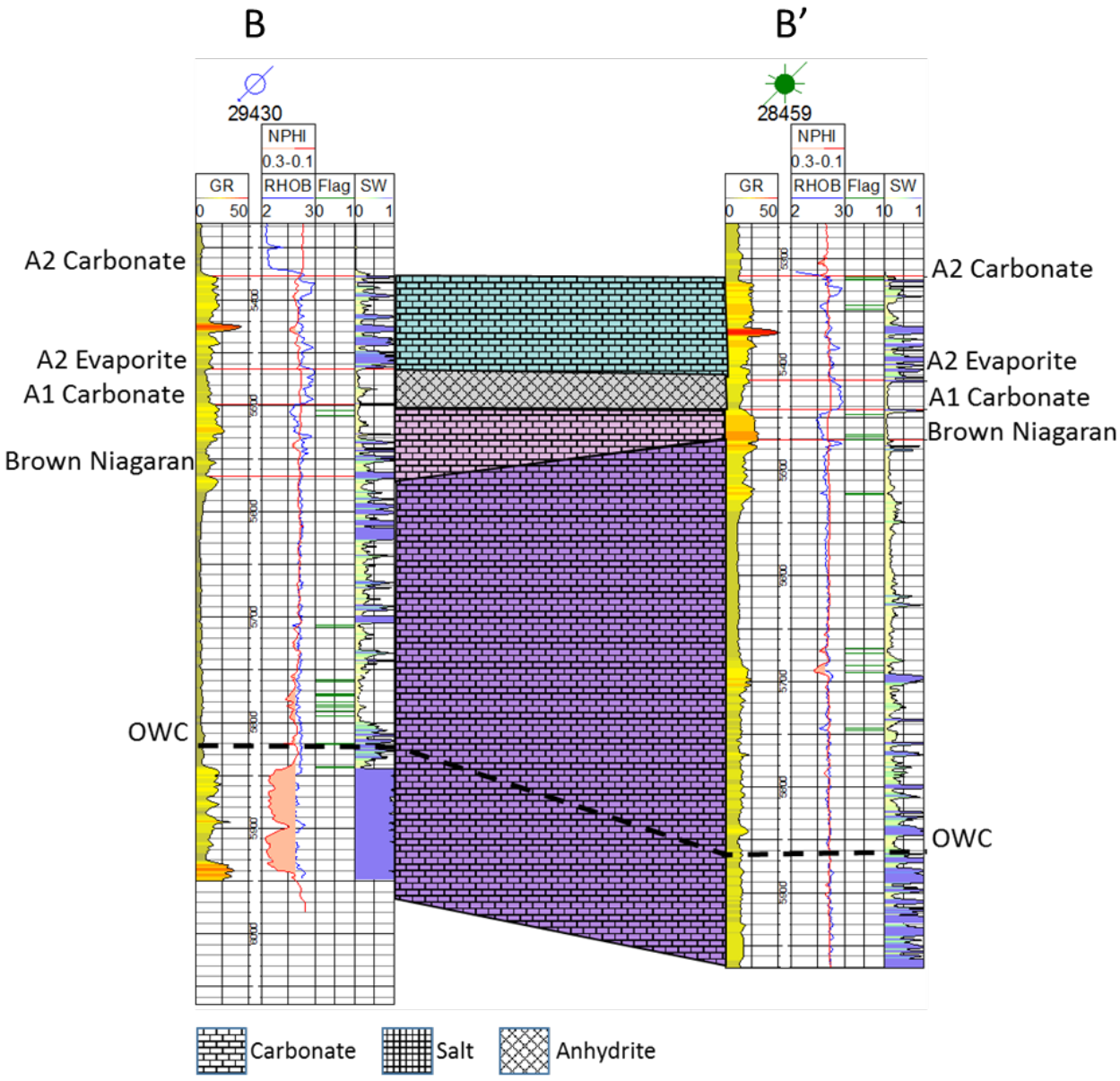


Figure 12-26. Cross section B-B' running west to east through the Chester 2 reef showing the changes in formation thickness transitioning from leeward to reef core positions along with the increased porosity in the dolomitized section in well 29430.

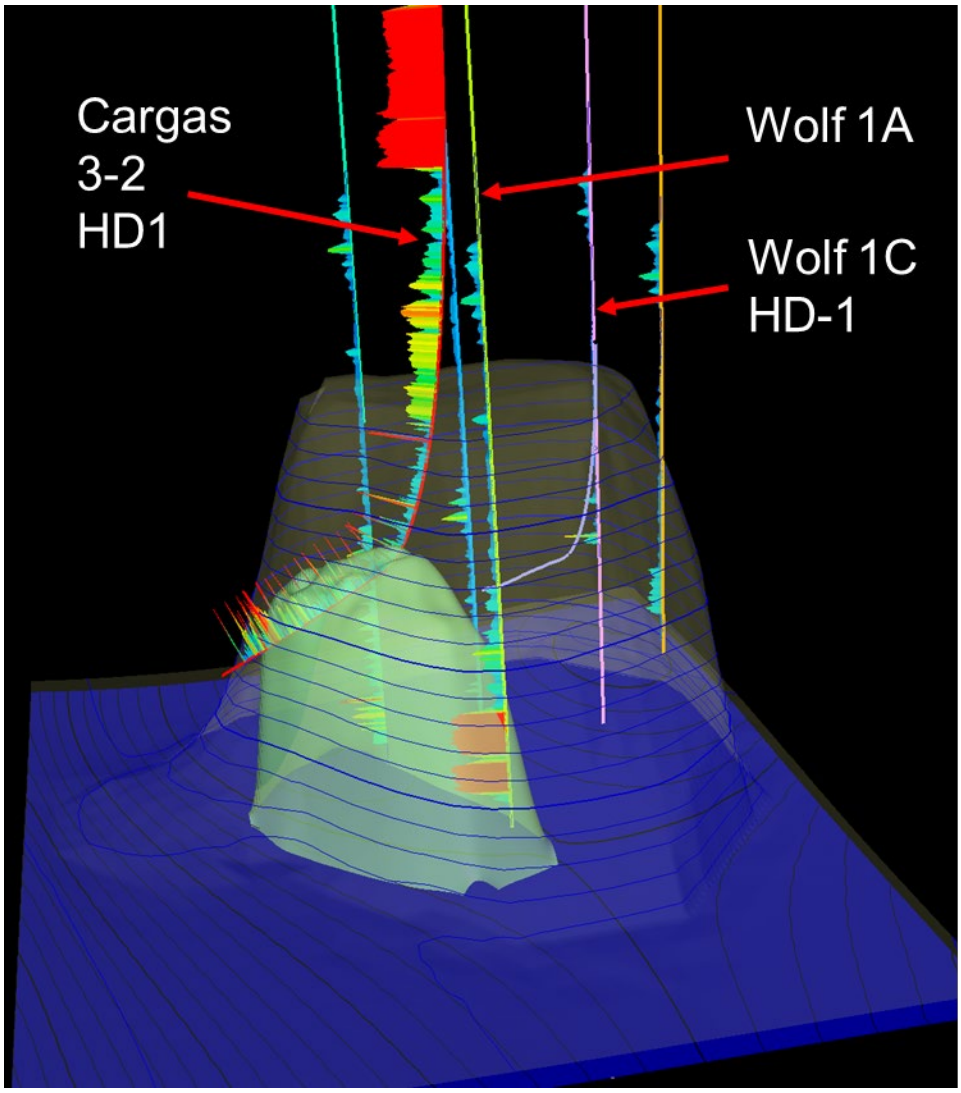


Figure 12-27. 3D interpretation of the dolomitized zone (green) within the Chester 2 reef field showing well locations and trajectories through the 3D volume.

13.0 Chester 5/6

13.1 Reef History and Production Review

Drilling began in the Chester 5-6 reef field in 1973 with well 29067, which produced oil and gas through the late 1980s. Two additional wells, 29234 and 31515, were drilled and produced until 1985. Core Energy, LLC, then took over operations and drilled three new wells: 58926, 59237, and 60833. Well 58926 was originally thought to be a prospect on a separate (new) reef, but pressure data determined that it was a part of the Chester 5/6 pool. There was an initial production spike during Core Energy operations in 2015, followed by a steady decline
(Figure 13-1). Although all of the production is attributed to the EOR, some of the oil produced at 60833 may actually be primary oil production captured from bypassed pay. Well 29067 produced 73% of the primary oil; all other wells had minor production. Cumulative oil production is approximately 1,320,000 bbls as of December 31, 2017, with approximately 110,000 bbls of that total resulting from EOR operations. Figure 13-2 shows the cumulative oil and gas production by well.

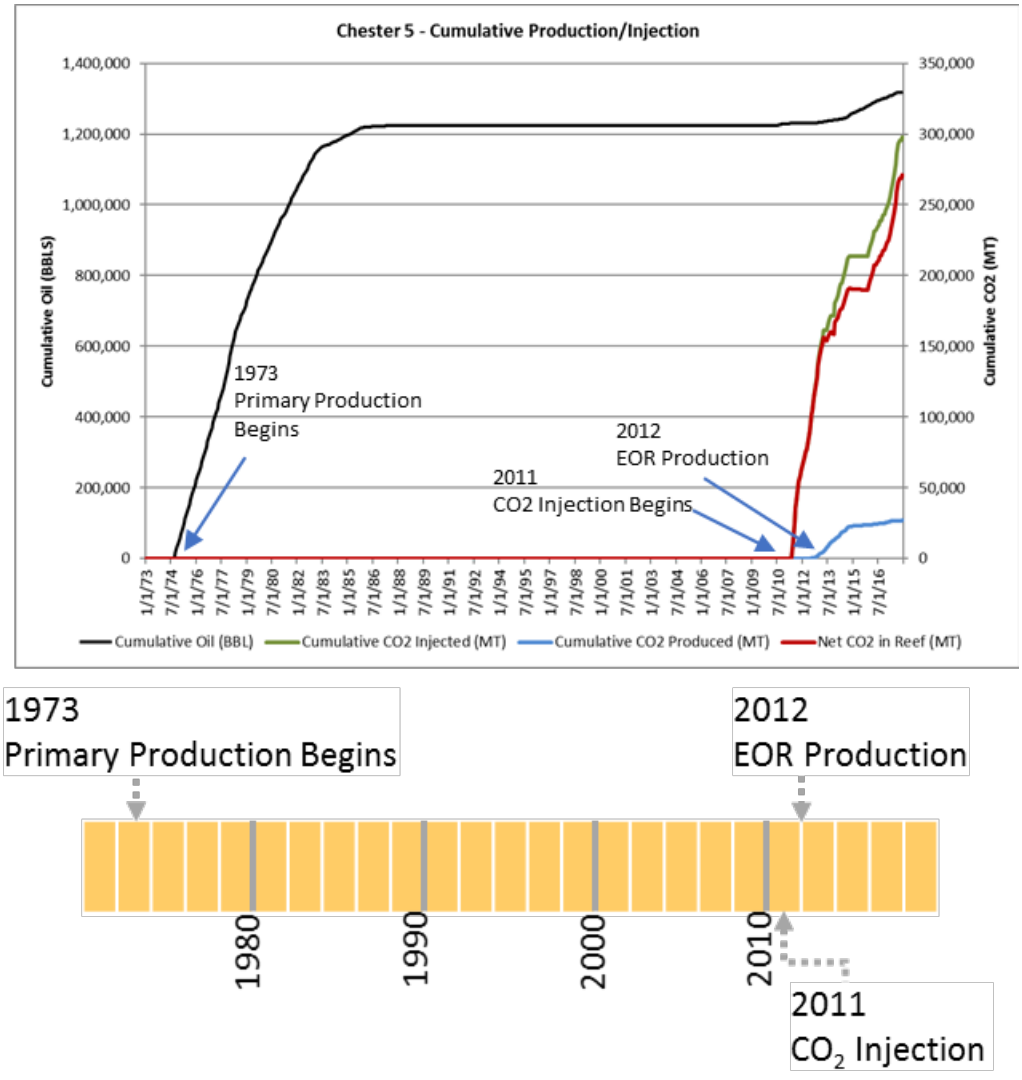


Figure 13-1. Cumulative production in the Chester 5/6 reef field from 1973 through 2017 showing a slight increase in production rates after EOR operations began in 2011.

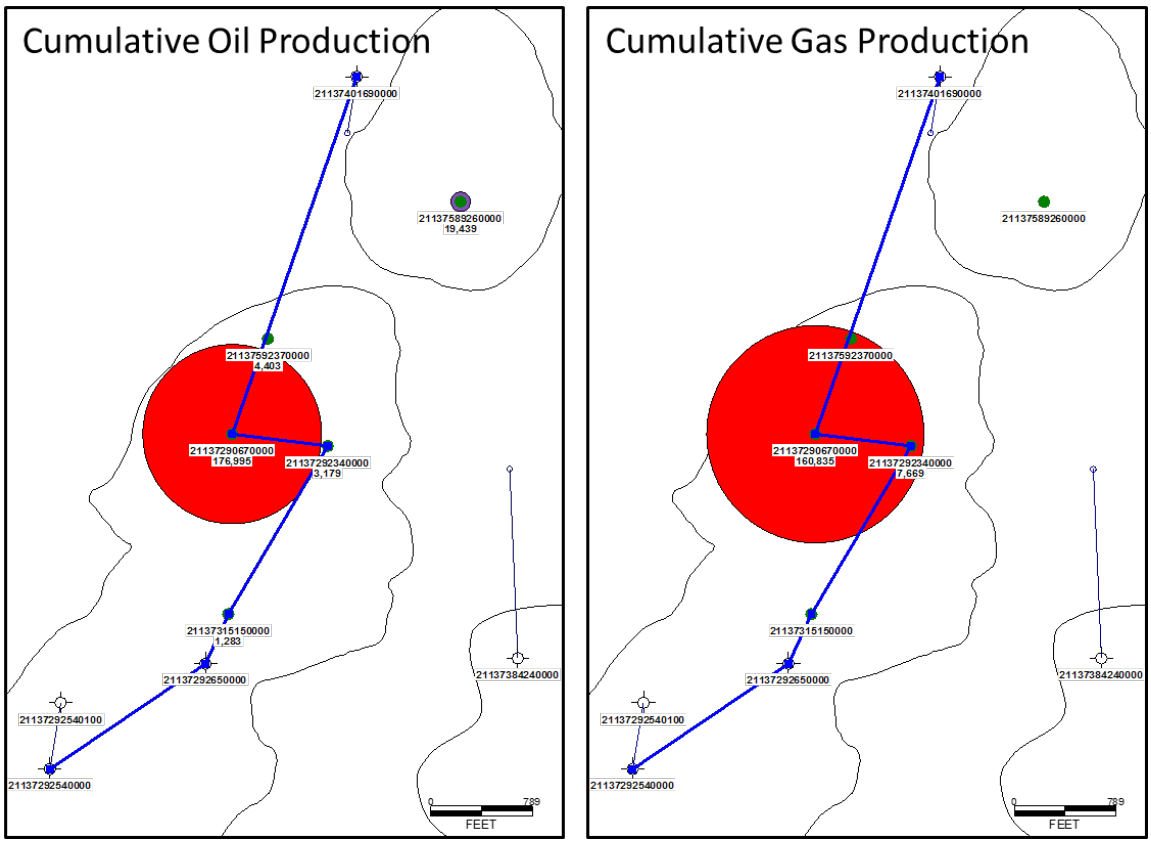


Figure 13-2. Cumulative oil and gas production by well in the Chester 5-6 reef showing the best producer (red) to be well 29067 and cross section line A-A'.

The initial (discovery) data for the Chester 5/6 reef field, summarized in Table 13-1, consists of OOIP, oil API gravity, discovery pressure and temperature, and fluid saturations. Initial gas saturations were recorded at zero, as gas was produced as it came out of solution during production of oil.

Table 13-1. Summary of initial (discovery) conditions of the Chester 5/6 reef field.

		Discovery		Saturation		
OOIP (bbls)	**API Gravity**	**Pressure (psi)**	**Temperature (oF)**	**Oil**	**Gas**	**Water**
2,890,000	43.6	2,896	103	65.00%	0%	35.00%

13.2 Wireline Log Analysis

Ten wells were drilled on the Chester 5-6 reef field. Of these 10 wells, only 6 have viable digital logs or digitized raster logs containing gamma ray, neutron porosity, bulk density, computed bulk density from DT, and caliper logs. Available log data is summarized in Table 13-2. Figure 13-3 shows a map of all wells in the Chester 5-6 reef.

Table 13-2. Summary of available wireline log data for wells penetrating the Chester 5-6 reef field.

	Well UWI	2113729067000	2113729234000	2113729254000	2113729254100	2113729265000	2113731515000	2113738424000	2113740169000	2113758926000	2113759237000
CAL	Caliper	■	■	■		■	■			■	■
DT	Sonic	■	■	■		■					
GR	Gamma Ray	■	■	■		■	■	■	■	■	■
NPHI	Neutron Porosity	■	■			■	■	■	■	■	■
PNC	Pulsed Neutron Capture					1					
RES	Resistivity	■	■	■		■			■	■	■
RHOB	Bulk Density						■	■	■		■
SNP	Sidewall Neutron Porosity										■
BHP	Bottom Hole Pressure Monitoring					■				■	■

Green shading indicates available log and number indicates repeat collected.

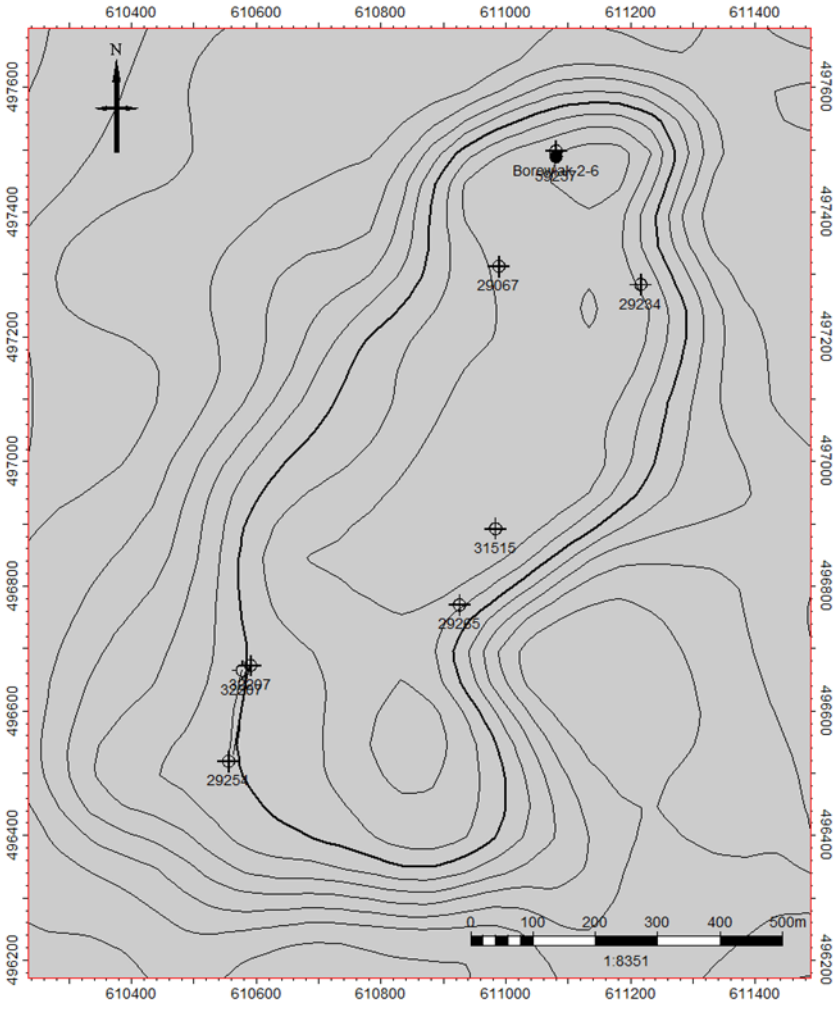


Figure 13-3. Structure map of the Chester 5-6 reef field showing well locations.

13.2.1 Basic Log Interpretation

Well 29067

Well 29067 is in the north-center of the reef field. The A-2 carbonate plotted as a mixed limestone-dolomite matrix and the A-1 carbonate plotted as a dolomite. The A-1 carbonate had the thickest interval of porosity greater than 5%. The Brown Niagaran contained dolomite and some intervals of porosity greater than 5%. This area contained some erroneous data due to the presence of salt and had the highest porosity. Figure 13-4 is the neutron porosity-bulk density crossplot from the A-2 carbonate to the Brown Niagaran in well 29067. The red polygon indicates the zones with porosity greater than 5%, which have been flagged on the neutron porosity and bulk density logs.

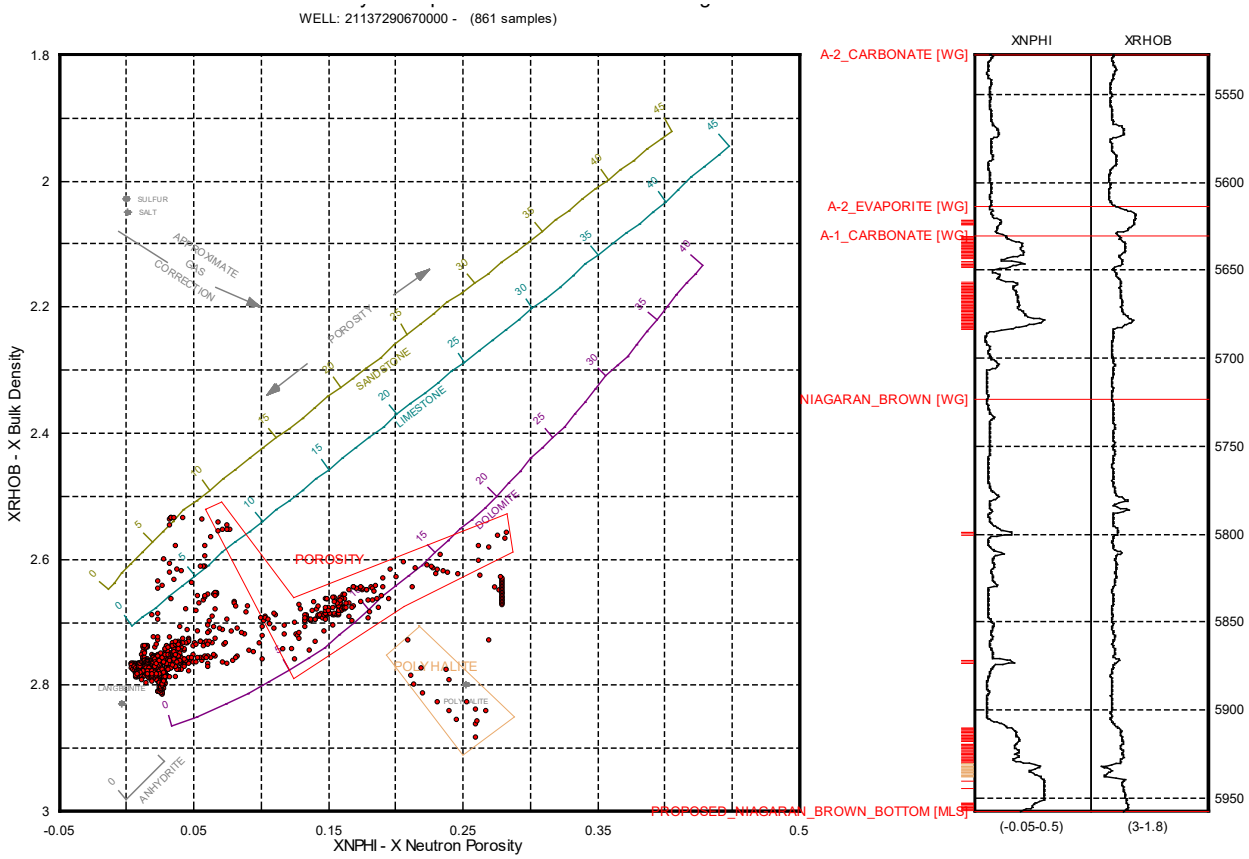


Figure 13-4. Neutron porosity-bulk density crossplot of well 29067 showing porosity in the upper A-1 carbonate and the lower Brown Niagaran with potential polyhalite. Red polygon = porosity >5%, tan polygon = polyhalite.

Water saturations for well 29067 indicate a highly saturated well over the formations of interest. There are frequent saturation spikes in the A-2 carbonate in the presence of evaporites. There is a shift at 5,690 feet MD in the A-1 carbonate where the saturation remains high. This could be the oil/water contact, which limits the available storage space to the upper A-1 carbonate. Figure 13-5 shows the water saturation curve and histogram for well 29067.

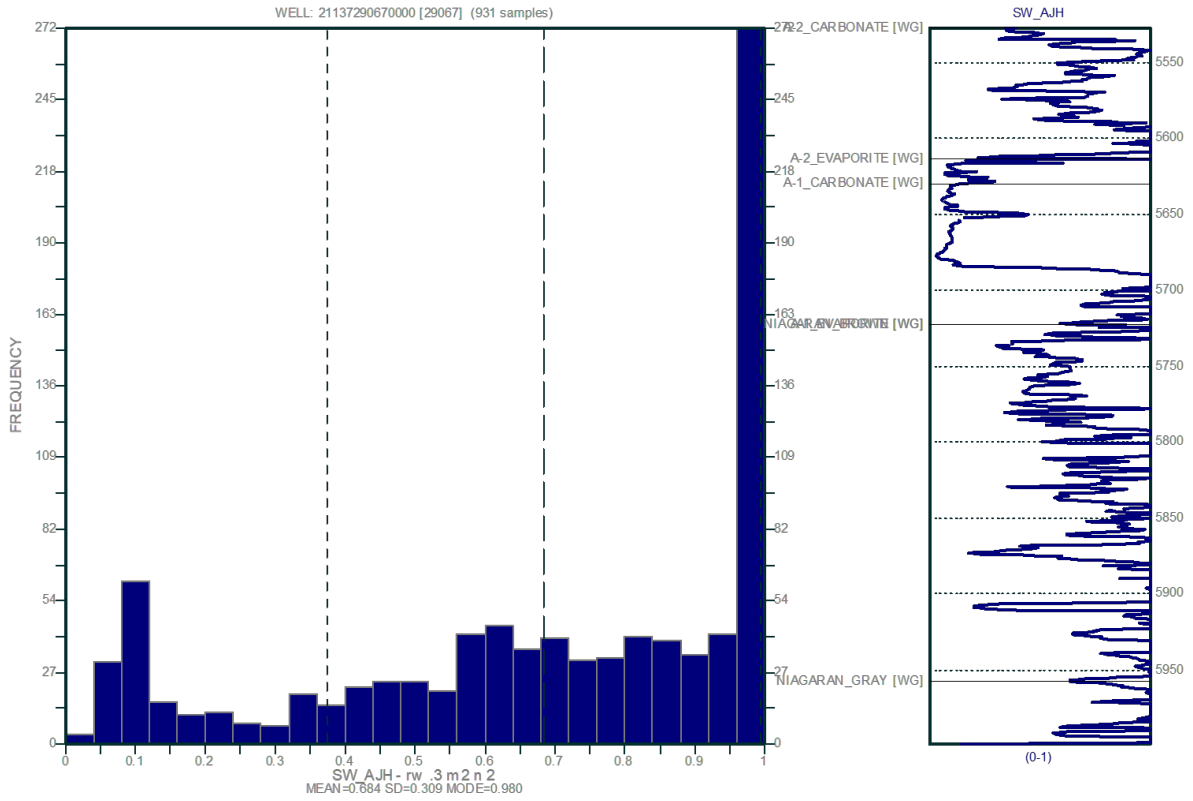


Figure 13-5. Water saturation curve and histogram for well 29067 showing a highly water-saturated well.

Well 29234

Well 29234 is on the east-central side of the reef field. The A-2 carbonate plotted as a mixed limestone-dolomite matrix. The A-1 carbonate plotted as a mixed limestone-dolomite matrix and contained all the porosity for this well. This porosity was in the base of the A-1 carbonate and could have some communication with the Brown Niagaran. The Brown Niagaran plotted as a dolomite and had no porosity greater than 5%. Figure 13-6 shows the neutron porosity-bulk density crossplot for well 29234. The red polygon indicates zones with porosity greater than 5%.

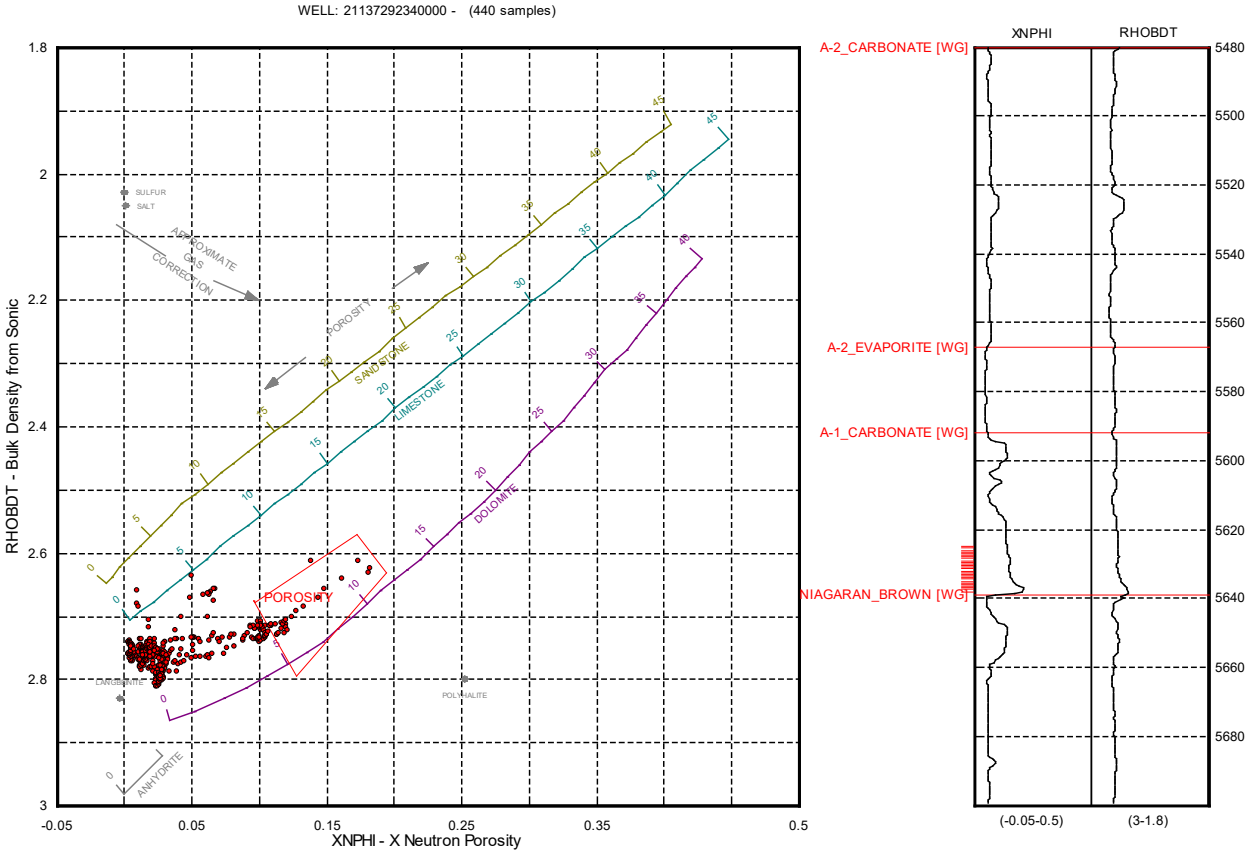


Figure 13-6. Neutron porosity-bulk density crossplot of well 29234 showing porosity flags in the lower A-1 carbonate. Red polygon = porosity >5%.

Water saturations for well 29234 indicate high levels of saturation throughout the well. Saturation spikes in the A-2 carbonate and evaporite could be associated with evaporites. The evaporites were not apparent in the calculated bulk density because bulk density from sonic logs is faulty in evaporites. The water saturation has a shift at 5,640 feet MD at the oil/water contact. The Brown Niagaran is fully saturated, leaving the upper A-1 carbonate with the best reservoir potential. Figure 13-7 shows the water saturation curve and histogram for well 29234.

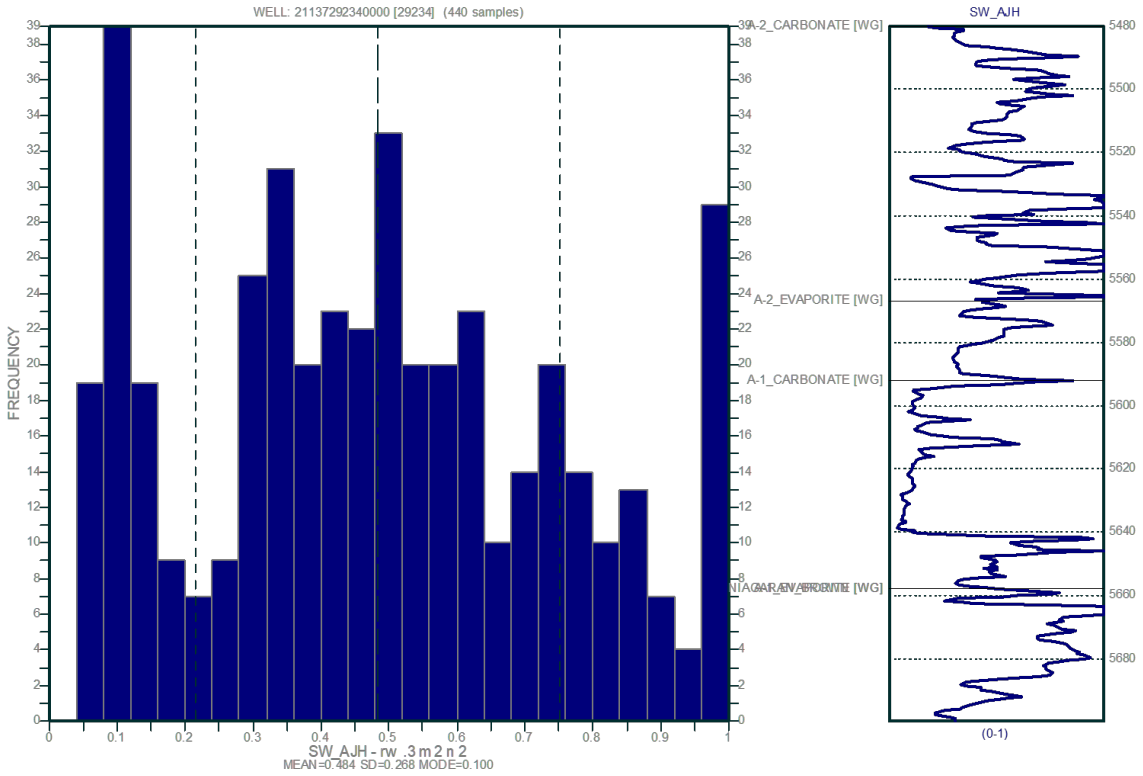


Figure 13-7. Water saturation curve and histogram for well 29234 showing high saturation values and a distinct shift toward the base of the A-1 carbonate.

Well 29265

Well 29265 is in the southern portion of the Chester 5-6 reef field. The A-2 carbonate plotted as a mixed limestone-dolomite matrix. The A-1 carbonate is a dolomite and contained all of the porosity greater than 5%; it could have some potential communication with the Brown Niagaran. The Brown Niagaran is a dolomite and contained less than 5% porosity. Figure 13-8 shows the neutron porosity-bulk density crossplot for well 29265. The red indicates zones with a porosity greater than 5%.

Water saturations for well 29265 indicate high saturation values throughout. The saturation spikes in the A-2 carbonate and A-2 evaporite can be attributed to the presence of evaporites. There is a distinct shift in the A-1 carbonate at 5,680 feet MD where the water saturation remains higher than 50%. The Brown Niagaran is fully saturated, leaving the upper A-1 carbonate with the best reservoir potential. Figure 13-9 shows the water saturation curve and histogram for well 29265.

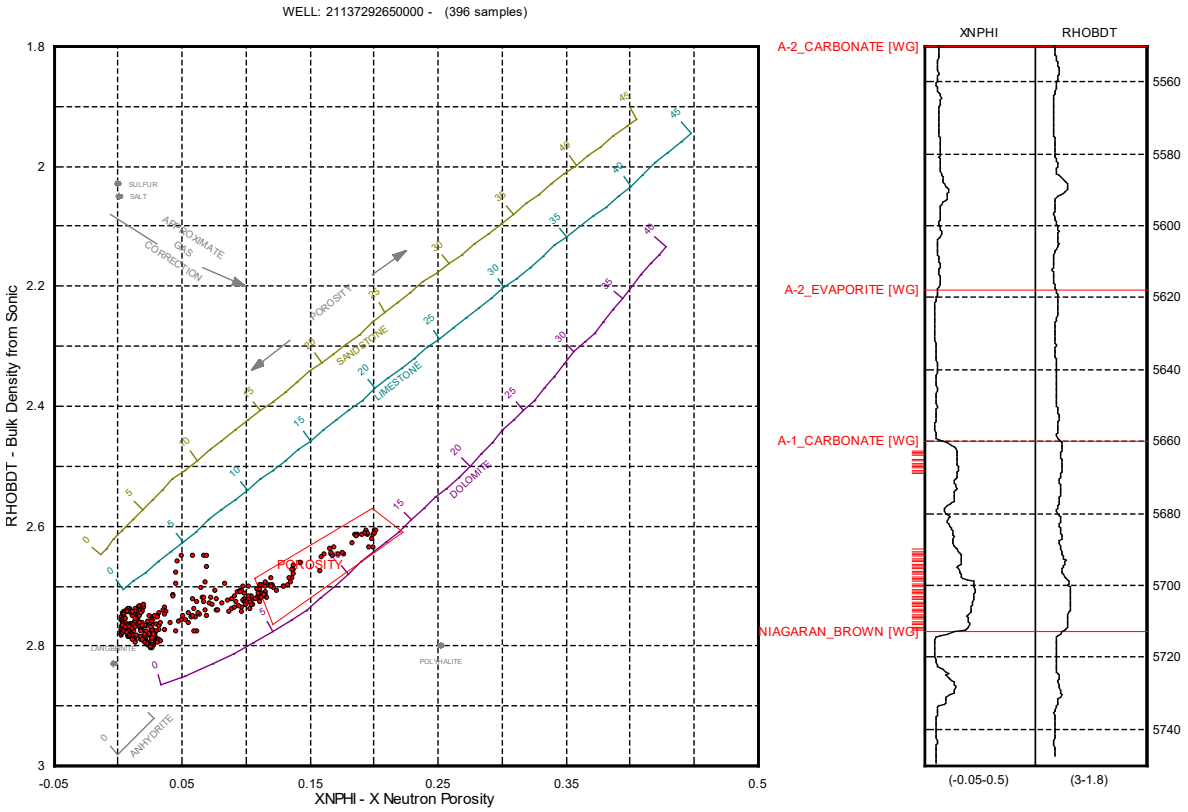


Figure 13-8. Neutron porosity-bulk density crossplot of well 29265 showing porosity flags in the lower A-1 carbonate. Red polygon = porosity >5%.

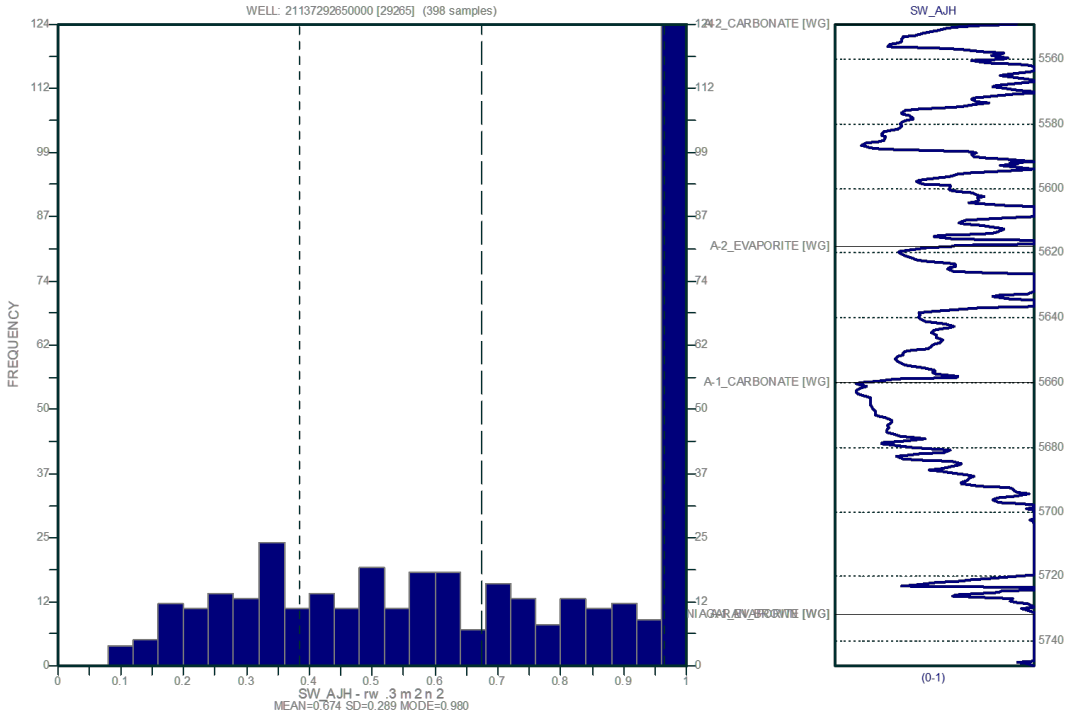


Figure 13-9. Water saturation curve and histogram for well 29265 showing high saturation values and an oil/water contact at 5,680 feet MD.

Well 31515

Well 31515 is in the south-central portion of the Chester 5/6 reef field. The A-2 carbonate plotted as a mixed limestone-dolomite. Anhydrite is dominant in the A-2 evaporite, as indicated by the blue color on the log curves. The A-1 carbonate had a mixed limestone-dolomite matrix. This interval contained the highest and most frequently recorded porosity that is greater than 5%. The Brown Niagaran is a dolomite and contained some porosity greater than 5%. Figure 13-10 shows a neutron porosity-bulk density crossplot for well 31515. The red flags indicate zones with porosities greater than 5%. The blue indicates anhydrite.

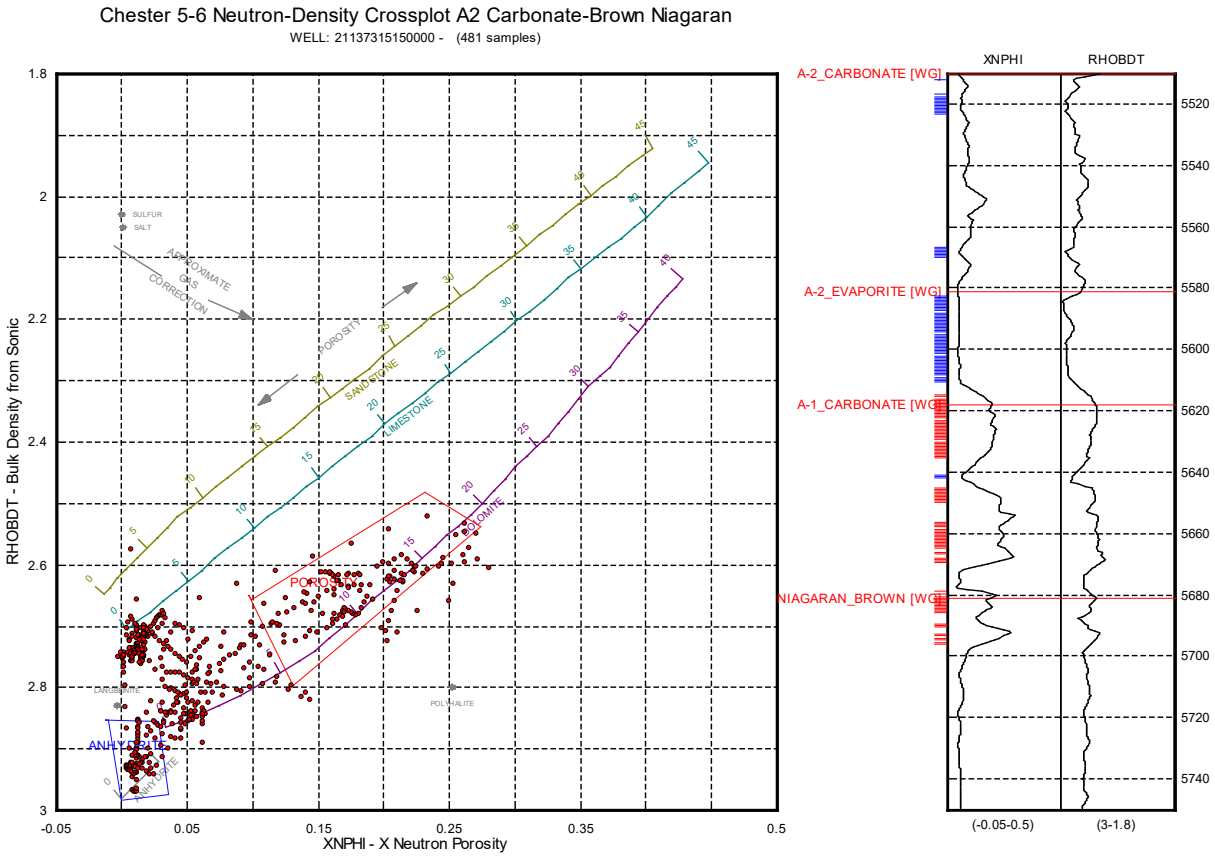


Figure 13-10. Neutron porosity-bulk density crossplot of well 31515 showing porosity flags throughout the A-1 carbonate and top of Brown Niagaran. Red polygon = porosity >5%, blue polygon = anhydrite.

Well 40169

Well 40169 is in the north-central section of the Chester 5/6 reef field. The A-2 carbonate is a mixed dolomite-limestone matrix and contained a minor zone of porosity that is greater than 5%. The A-1 carbonate had a mixed limestone-dolomite matrix and contained two zones of porosity that are greater than 5%. The lower interval of the formation contained anhydrite. The Brown Niagaran had a mixed limestone-dolomite matrix and contained the highest interval of porosity greater than 5%. Figure 13-11 shows the neutron porosity-bulk density crossplot for well 40169. The red flags indicate zones with porosities greater than 5%, blue indicates anhydrite, and green indicates salt.

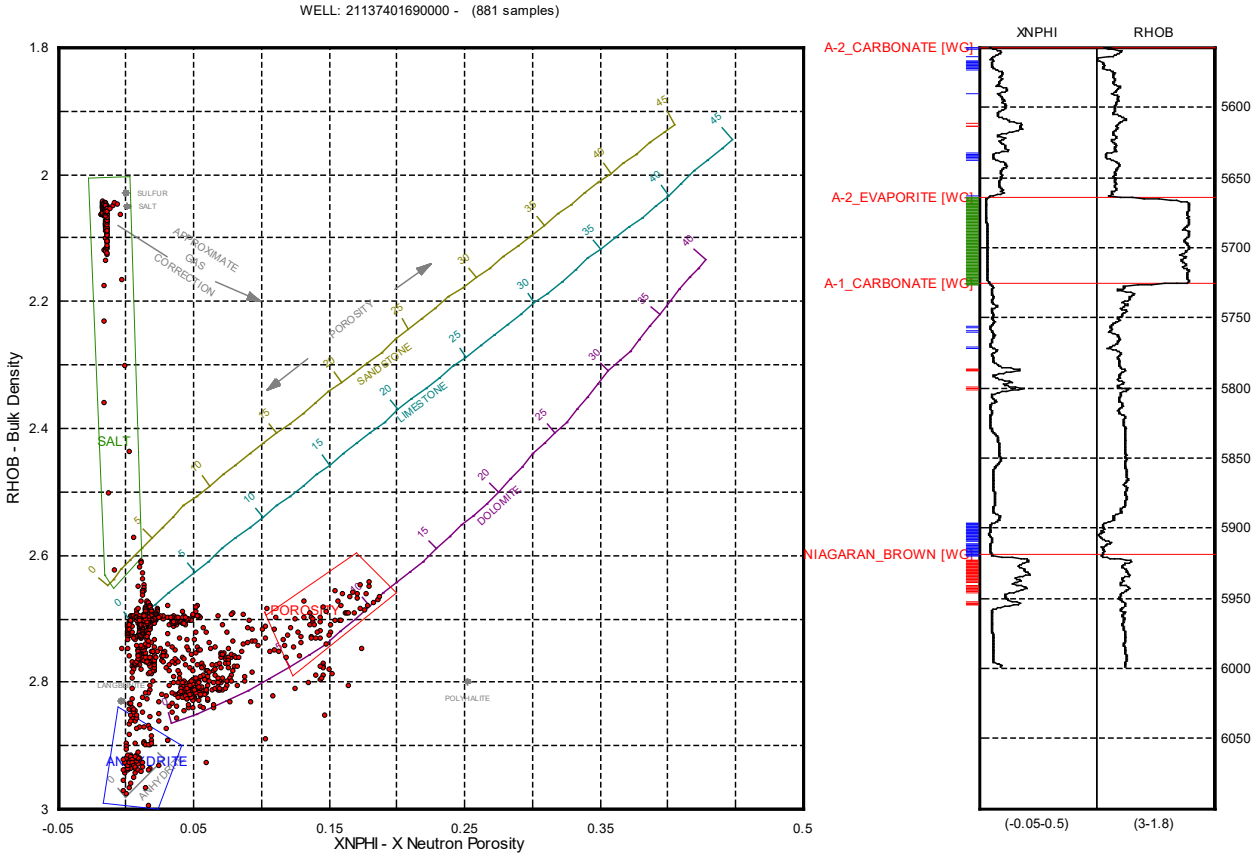


Figure 13-11. Neutron porosity-bulk density crossplot of well 40169 showing porosity flags in the upper Brown Niagaran. Red polygon = porosity >5%, green polygon = salt, blue polygon = anhydrite.

Due to the thin Brown Niagaran and thicker packages of salt, well 40169 is representative of a flank or off-reef well. The water saturation values show a fully saturated well with some fluctuations where evaporites are present. The oil/water contact is high, near the top of the A-1 carbonate at 5,750 feet MD. This results in little to no reservoir potential at this location. Figure 13-12 shows the water saturation curve and histogram for well 40169.

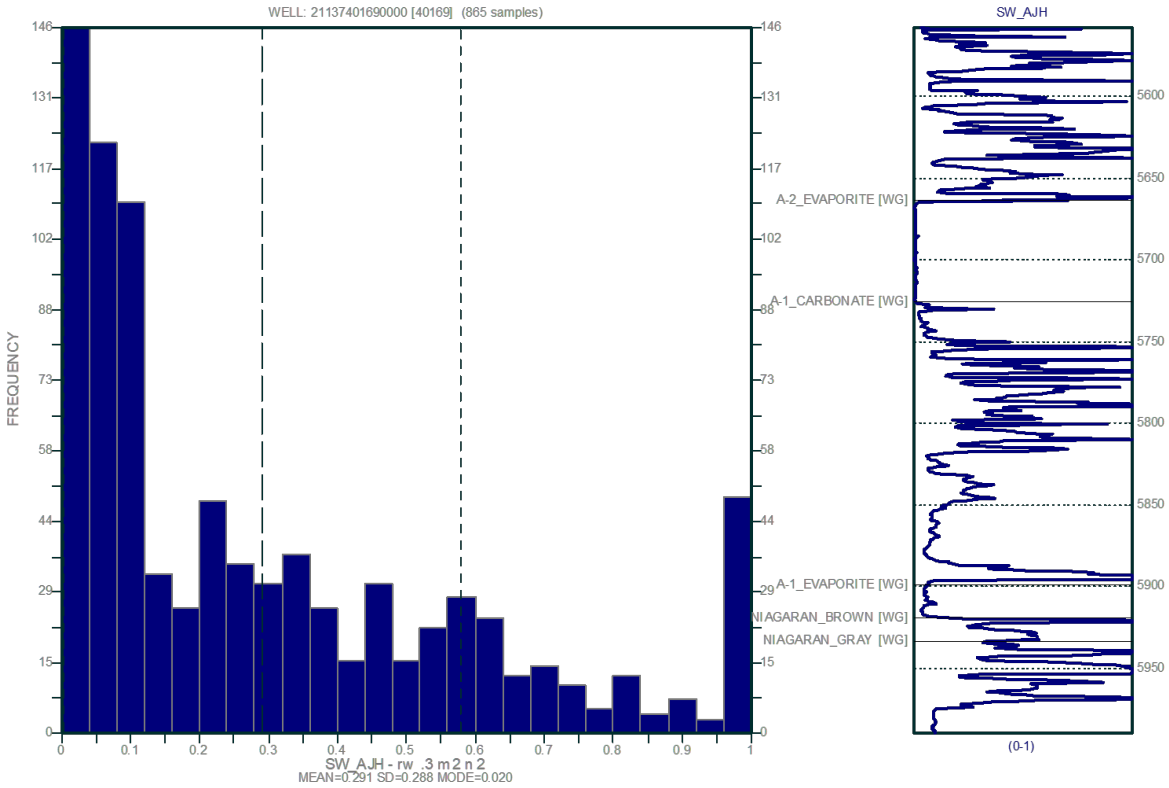


Figure 13-12. Water saturation curve and histogram for well 40169 showing high water saturations throughout.

13.2.2 Petrophysics Calculations

A-2 Carbonate

The A-2 carbonate is a limestone-dolomite matrix. This formation often contained anhydrite in the upper and lower intervals. The average net porosity was 6.4%. The minimum gross thickness was 72 feet in well 31515 and the maximum thickness was 107 feet in well 40169 with an average net thickness of 7 feet. The NTG ratio ranged from 0.057 to 0.101 with an average of 0.076 (Table 13-3).

Table 13-3. Summary of petrophysical calculations for the A-2 carbonate in the Chester 5-6 reef field.

Interval: A-2 Carbonate						
Avg. Thickness	Avg. Porosity	Avg. Net Thickness	Avg. NTG	Avg. SW	Avg. Net Thickness (SW<40%)	Avg. NTG (SW<40%)
84 ft	2.1%	7 ft	0.08	57%	4 ft	0.05

A-1 Carbonate

The A-1 carbonate is a predominantly mixed limestone-dolomite matrix with more dolomite present than limestone. The average net porosity for this formation was 9.62% and ranged from 7.3% to 13.40%. The minimum thickness was 63 feet in well 31515 and the maximum was 193 feet in well 40169. The NTG ratio ranged from 0.53 to 0.79 with an average of 0.55 (Table 13-4).

Table 13-4. Summary of petrophysical calculations for the A-1 carbonate in the Chester 5-6 reef field.

Interval: A-1 Carbonate						
Avg. Thickness	Avg. Porosity	Avg. Net Thickness	Avg. NTG	Avg. SW	Avg. Net Thickness (SW<40%)	Avg. NTG (SW<40%)
97 ft	6.0%	42 ft	0.55	37%	17 ft	0.22

Brown Niagaran

The Brown Niagaran is predominantly a dolomite but in areas of this reef it is a mixed matrix with limestone. The Brown Niagaran had the highest net porosity, which ranged from 10.20% to 11.60% and on average was 11.13%. The minimum thickness was 12.8 feet in well 40169 and the maximum thickness was 234.4 feet in well 29067. The average NTG ratio ranged from 0.211 to 0.824 with an average of 0.436. Table 13-5 summarizes petrophysical calculations.

Table 13-5. Summary of petrophysical calculations for the Brown Niagaran in the Chester 5-6 reef field.

Interval: Brown Niagaran						
Avg. Thickness	Avg. Porosity	Avg. Net Thickness	Avg. NTG	Avg. SW	Avg. Net Thickness (SW<40%)	Avg. NTG (SW<40%)
118 ft	4.2%	32 ft	0.44	75%	32 ft	0.38

13.3 Core Analysis

Whole core was available from the Chester 5-6 reef field in the A-1 carbonate, totaling 59 feet. Standard core analysis was performed, consisting of porosity, permeability, fluid saturation, bulk density, and grain density measurements. The core was described foot by foot, which included lithology and sedimentary structures. High-resolution photographs were taken of each section of core.

Grain Density

The grain density for the Chester 5-6 reef field whole core ranged from 2.71 to 2.87 g/cm^3 with an average of 2.81 g/cm^3. The A-1 carbonate had an average grain density of 2.85 g/cm^3. Salt plugging was recorded in 26 feet of core. The grain density over this interval averaged 2.74 g/cm^3. Table 13-6 summarizes the grain density averages for the Chester 5-6 core;
Figure 13-13 shows a histogram of grain densities.

Table 13-6. Summary of grain density measured from whole core in Chester 5-6 reef field.

Interval	Range (g/cm^3)	Average (g/cm^3)
All Core	2.71-2.87	2.81
A-1 Carbonate	2.77-2.87	2.85
Salt Plugged	2.71-2.79	2.74

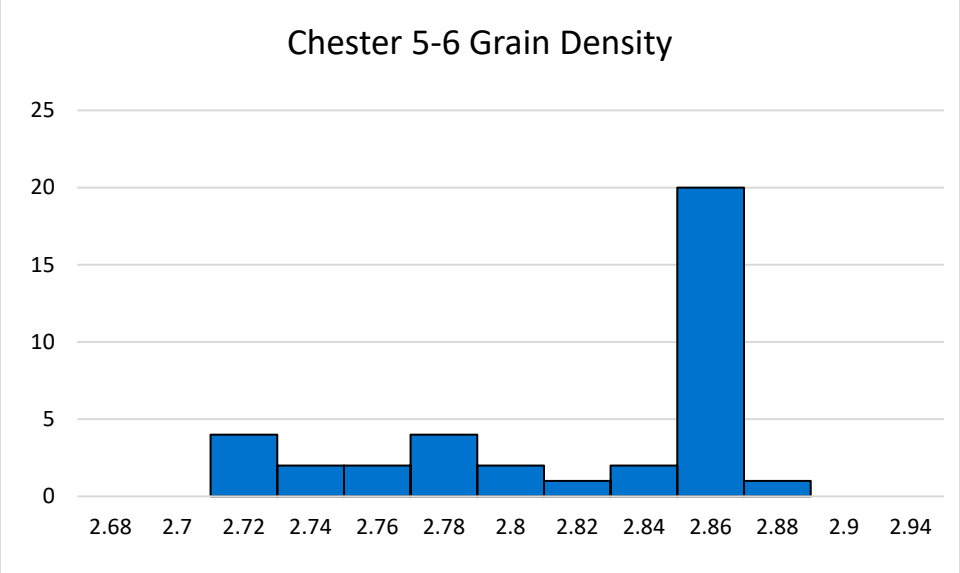


Figure 13-13. Histogram of grain density of the Chester 5-6 reef field.

Porosity-Permeability Transform

The A-1 carbonate had a porosity range from 3.8% to 18.4% with a permeability range from 0.031 to 201.4 mD. Salt plugging decreased the porosity and permeability dramatically. The salt-plugged intervals had a porosity range from 0.4% to 3.4% with a permeability range from 0.00005 to 0.003 mD. This data has been plotted in Figure 13-14 using the coordinating transform equations in Equation 13-1.

$$K_{A1C} = 0.2239e^{0.3387x}$$

Equation 13-1

where:

K_{A1C} = permeability of the A-1 carbonate (mD)
ø = porosity (%)

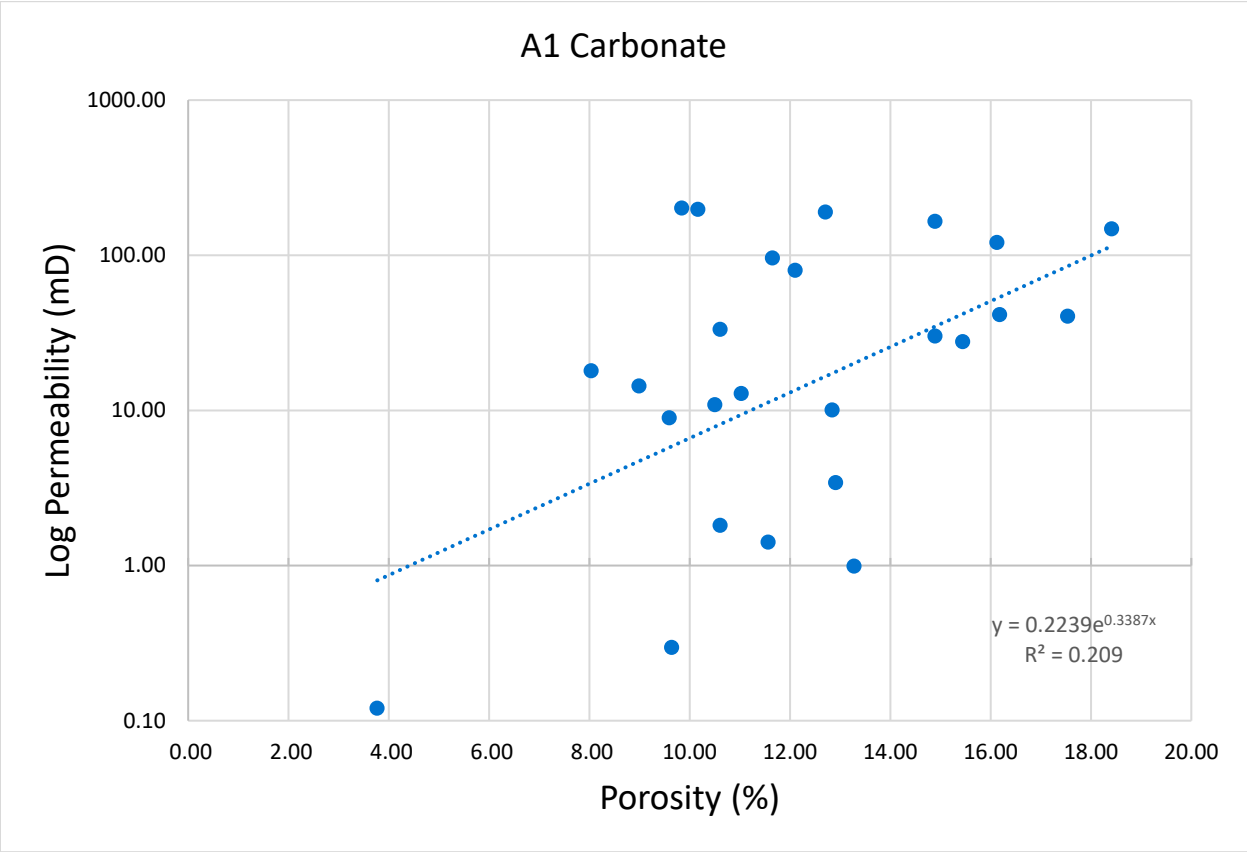


Figure 13-14. Porosity-permeability transform of the Chester 5-6 reef field using whole core measurements.

13.4 Geologic Interpretations

Most wells reached a TD in the upper Brown Niagaran and did not cover the entire formation due to the high oil/water contact. Thicknesses of the A-1 carbonate and changes in evaporites were used to estimate reef position for each well. The Chester 5-6 reef field has at least three reef pods and potentially four, depending on geometry. Although there are multiple pods, the southernmost pods are highly connected through the A-1 carbonate. There may be some minor connectivity between the southern pod and the northern pod through the A-1 carbonate, but there is not enough data to support it. Figure 13-15 illustrates a possible interpretation of reef position for each well in the reef core (green), windward facies (purple), and leeward facies (blue).

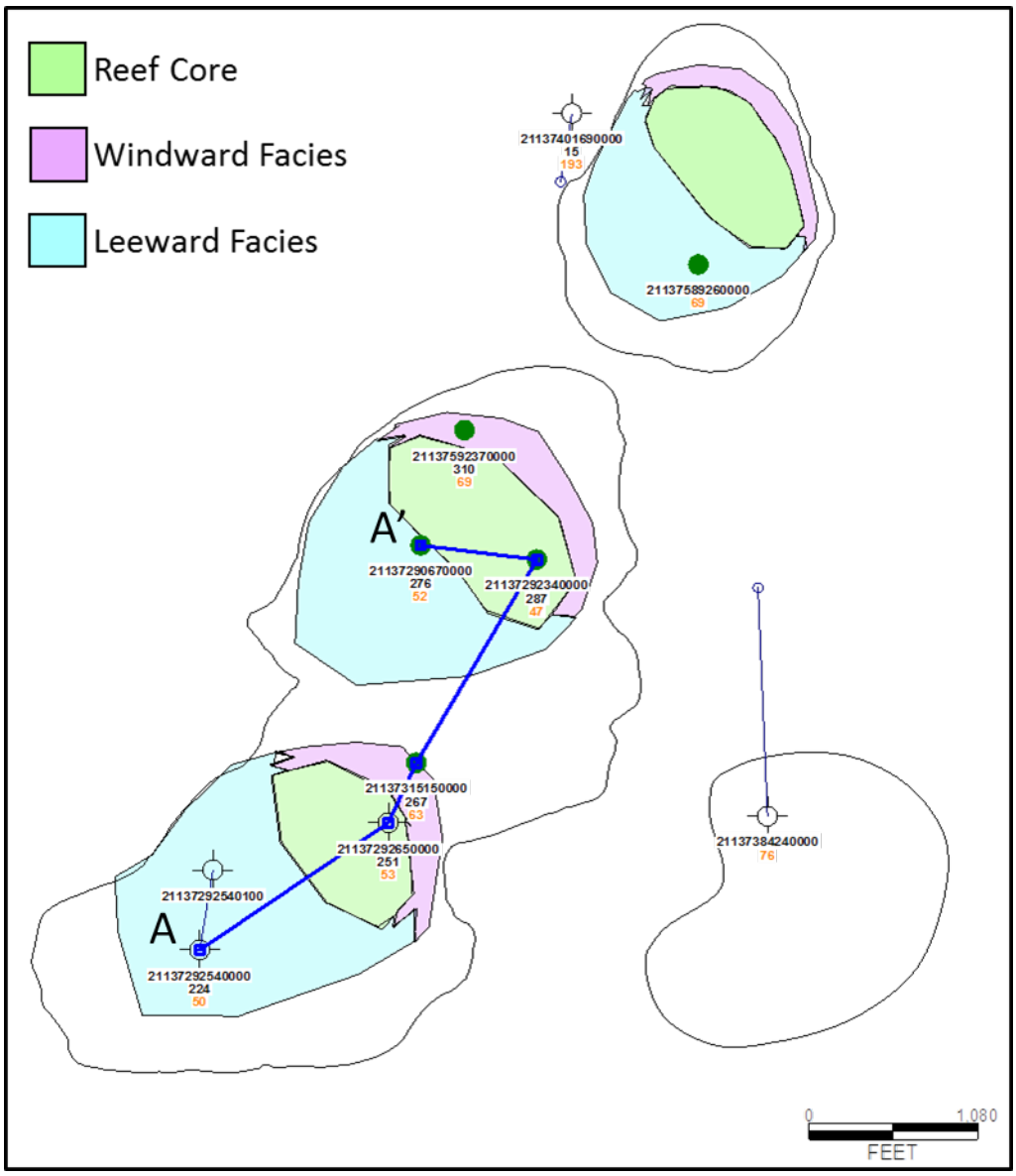


Figure 13-15. Lithofacies interpretation of the Chester 5-6 reef field showing potential locations of reef core, windward facies, and leeward facies. Blue line illustrates cross section line A-A'

Cross section A-A' (see Figure 13-15) runs roughly south to north through the Chester 5-6 reef field. The cross section has wells from different reef pods and ends with well 29067. Most wells did not penetrate far into the Brown Niagaran due to the high oil/water contact. The oil/water contact occurs in the mid-formation A-1 carbonate on top of the reef and the upper A-1 carbonate on the flank of the reef. The A-1 carbonate also shows a continuous high-porosity zone with porosity flags in the upper A-1 carbonate. The A-2 carbonate shows very little porosity with a continuous gamma ray spike mid-formation, which is observed in many reef fields. The presence of a thin salt in the A-2 evaporite in well 29067 suggests that this well is located at the edge of the reef near the flank. Well 40169 illustrates a typical off-reef well with a thick A-1 carbonate and thick salt packages. Cross section A-A' in Figure 13-16 shows porosity trends in the upper A-1 carbonate and a high oil/water contact from well 29254 to well 40169. Figure 13-17 shows the lithofacies interpretation for two of the three reef pods.

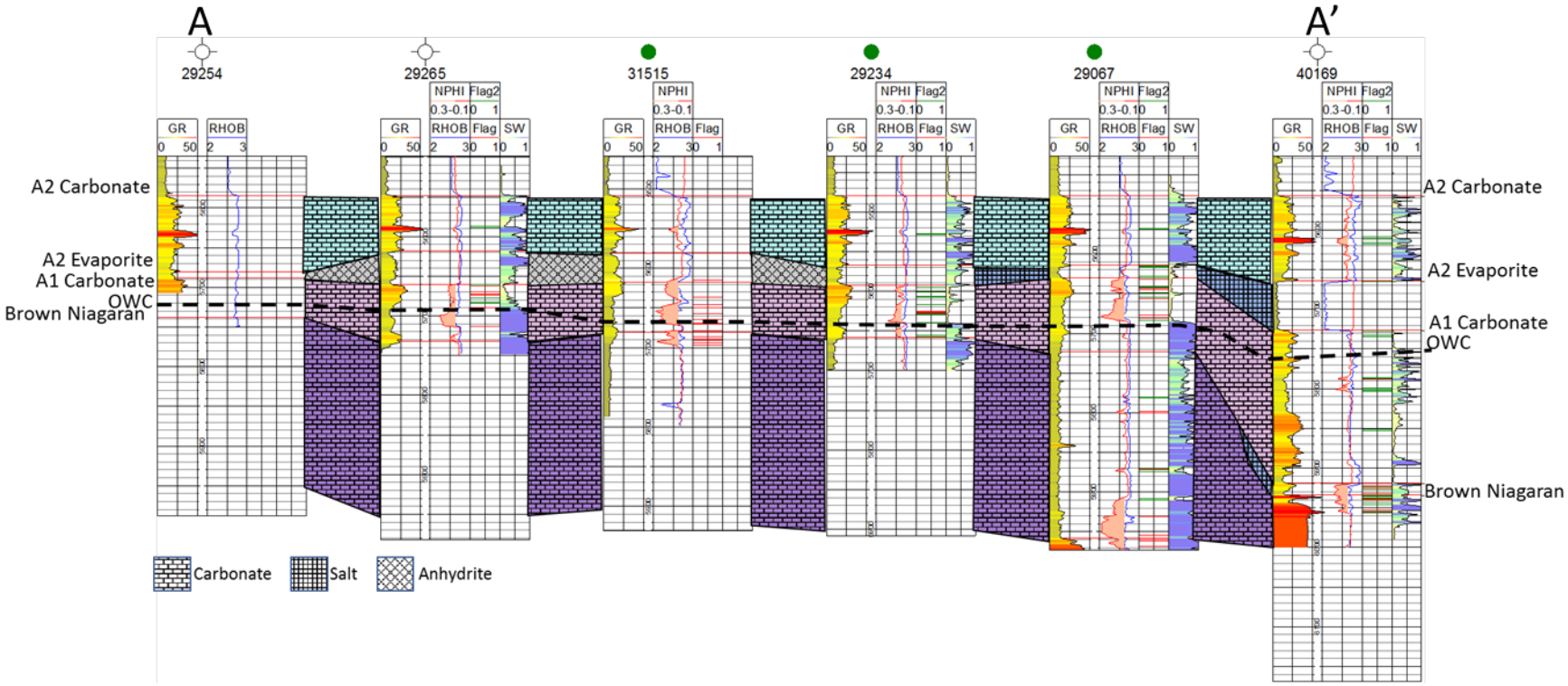


Figure 13-16. Cross section A-A' across the Chester 5-6 reef field showing porosity trends in the upper A-1 carbonate and a high oil/water contact.

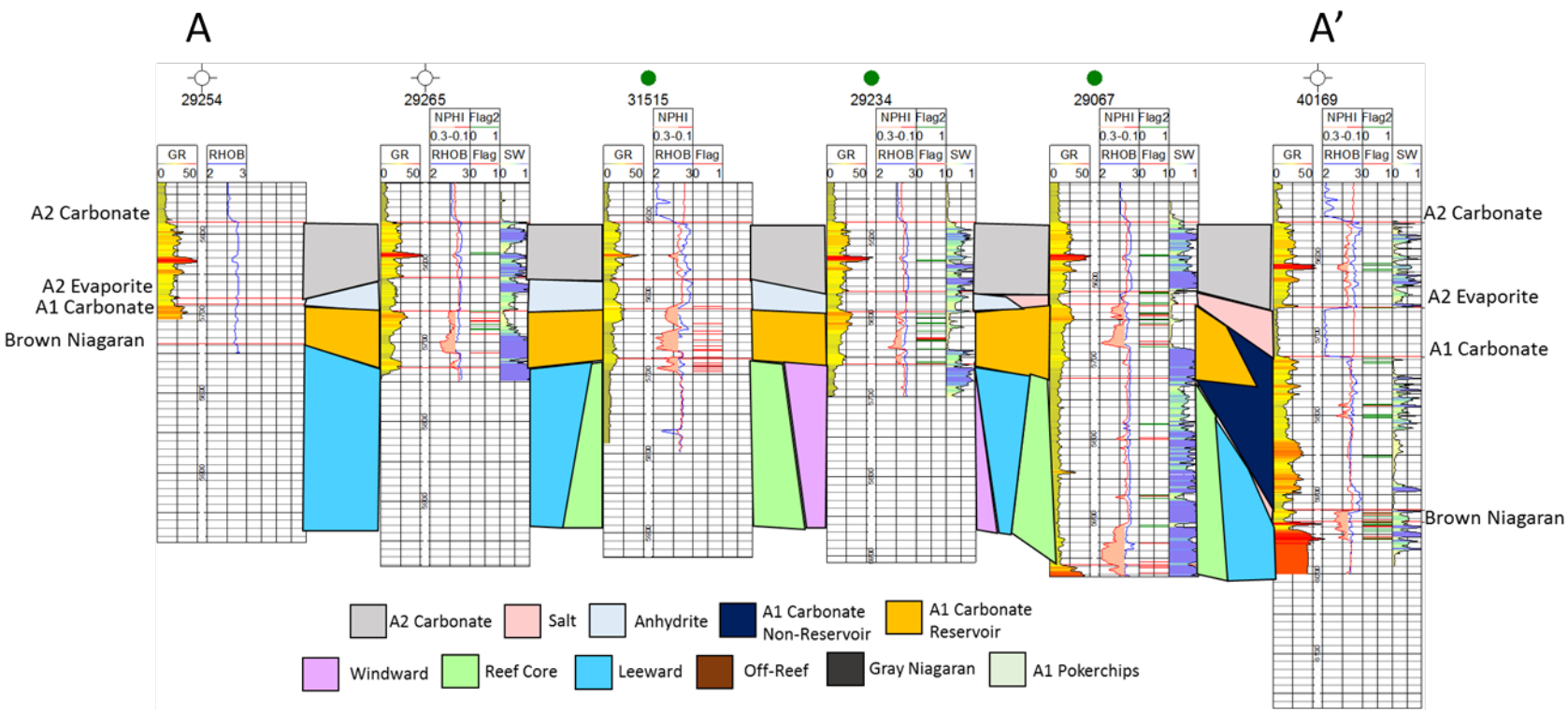


Figure 13-17. Cross section through Chester 5-6 showing lithofacies interpretation with two reef pods represented.

14.0 Geomechanical Assessment

14.1 Introduction

To evaluate the mechanical integrity of a caprock-reservoir system, numerical modeling simulations should be conducted to assess the potential for faulting/fracturing that could lead to CO_2 leakage and/or other consequences.

Before the numerical modeling analysis could be conducted, it is first necessary to characterize the geomechanical properties of the caprock and reservoir formations that is required to evaluate their performance. The main purpose of this task is to study geomechanical properties of Niagaran pinnacle reefs, which have available data to perform geomechanical analysis, in the Michigan basin. This Task is divided into geomechanical characterization, in-situ stress analysis, and a rock mechanical – rock physical experimental data interpretation subtask.

A part of the geomechanical characterization effort includes a subtask that uses dipole sonic log data to define certain fundamental mechanical rock properties. Section 14.2 of this document presents the results of the sonic log analysis task.

As part of geomechanical characterization task, a subtask was conducted to characterize the in-situ stress of the caprock and reservoir formations. Knowledge of the in-situ stress is necessary in order to develop accurate geomechanical and fluid-flow models to predict CO_2 injection, storage, and containment. This included determining the orientation of SH_{max} and magnitude of S_v at multiple well locations to help characterize spatial variability in the mentioned stress parameters. The approach for estimating the orientation of SH_{max} and magnitude of Sv and the results are described in Section 14.3.

Another part of the characterization effort included a subtask that involved performing laboratory testing on core samples of the primary caprock and reservoir geologic units (A-2 carbonate, A-2 anhydrate, A-1 Carbonate, and Brown Niagara) to measure mechanical properties. Rock mechanical properties measured using experimental methods, are critical data for building numerical models to study long-term storage of CO_2 in detail.

This task also includes three appendices on individual well mechanical characterization, formation based mechanical characterization, and shallow formations mechanical characterization.

14.2 Geomechanical Characterization

14.2.1 Introduction

Variation in the rock mechanical properties of formations that are potential injection reservoirs and caprock can affect their injectivity and storage capacity. Rock mechanical properties are key data for building numerical models to study long-term storage of CO_2 in detail. Therefore, it is important to adequately characterize these properties.

A geomechanical characterization was completed using dipole sonic log data collected from five wells. This work was conducted for the purpose of defining the fundamental mechanical rock properties of the primary reservoir and caprock formations. Dynamic elastic parameters (Poisson's ratio, dynamic shear modulus, bulk modulus, and Young's modulus) were defined in six reservoir and caprock formations (Salina, A-2 Carbonate, A-2 Evaporite, A-1 Carbonate, Brown Niagara, and Gray Niagara) and 18 stratigraphically shallower formations.

14.2.2 Calculation of Elastic Properties

Dipole sonic logging tools measure both compressional-wave (DTc) and shear-wave (DTs) slowness (delta time) within a formation. When combined with formation bulk density (ρ), these variables allow for the calculations of dynamic elastic parameters that include, Poisson's ratio, dynamic shear modulus, bulk modulus, and Young's modulus. These four elastic parameters are interrelated such that any one can be expressed in terms of two others and can also be expressed in terms of acoustic-wave velocity and density. Dynamic rock properties should be calibrated to core-derived static (laboratory) properties, because the static measurements more accurately represent the in-situ reservoir mechanical properties.

Poisson's Ratio

When a force is applied to a body, at right angles to the force, a certain amount of lateral (transverse) expansion or contraction takes place. If a solid body is subjected to an axial tension, it contracts laterally; conversely, if it is compressed, the material expands sidewise. Poisson's ratio indicates the relationship between the lateral and axial strain of the rock formation. It is a measure of the geometric change of shape under uniaxial stress. It is expressed by:

$$V = \frac{1\left(\frac{DT_s^2}{DT_c^2}\right) - 2}{2\left(\frac{DT_s^2}{DT_c^2}\right) - 1}$$

Equation 14-1

where:

V = Poisson's ratio (dimensionless);
DT_c = compressional wave slowness (μs/ft); and
DT_s = shear wave slowness (μs/ft).

Dynamic Shear Modulus

Strong internal traverse forces such as torsion (twisting) lead to the permanent deformation of a solid body. The dynamic shear modulus can be used to evaluate a rock formation's ability to resist this deformation (its rigidity to shear stress) and maintain its original configuration. It is calculated as the relationship between the bulk density and the shear wave slowness of a formation (slowness being a unit of measure which is the inverse of velocity). It is expressed by:

$$G = \mathrm{A}\frac{\rho}{DT_s^2}$$

Equation 14-2

where:

G = dynamic shear modulus (10^6 psi);
A = 1.3476x104 (conversion parameter, with units of 10^6 psi/((g/cc)/(μs/ft)^2);
ρ = bulk density (g/cc);
DT_c = compressional wave slowness (μs/ft); and
DT_s = shear wave slowness (μs/ft).

Bulk Modulus

Pressure applied in all directions to a solid body leads to its compression and reduction of volume. The bulk modulus measures the incompressibility of a solid body i.e. its ability to resist reduction in volume when under compression from all sides. It is used in geology to express the resistance of a rock formation to compressive forces. This incompressibility is measured using the relationship between the DT^c and DT^s slowness values, as a conversion factor to convert the units to 106 psi. It is expressed by:

$$K = (1.3476\text{x}10^4)\rho\left(\frac{1}{DT_c^2} - \frac{4}{DT_s^2}\right)$$

Equation 14-3

where:

K = bulk modulus (10^6 psi);
ρ = bulk density (g/cc);
DT_c = compressional wave slowness (μs/ft); and
DT_s = shear wave slowness (μs/ft).

Young's Modulus

Tensional or compressive forces on a solid body lead to it experiencing changes in length. Young's modulus is a measurement of a solid body to withstand changes in length when experiencing tensional or compressive force i.e. its elasticity. In geology, Young's modulus measures a rock formation's elasticity and is calculated using the rock density, shear wave velocity, and compressional wave velocity. It is expressed by:

$$E = 2G(1 + V)$$

Equation 14-4

where:

E = Young's modulus (psi);
G = dynamic shear modulus (psi); and
V = Poisson's ratio (dimensionless).

14.2.3 Results and Discussion

The dynamic elastic parameters calculated in this work are comparable to established standards for the lithologies composing the six formations of interest. A statistical summary of the four dynamic elastic parameters determined within each formation, as an aggregate of all calculated data in Lawnichak 9-33, Cargas 3-2 HD1, Elmac Hills 1-18A, Chester 6-16, and Chester 8-16 is presented in this section. This consisted of the determination of the mean and variance of the aggregate calculated dynamic elastic parameters (Table 14-1 and Figure 14-1). Tables and figures displaying dynamic elastic parameter data calculated for each well can be seen in Appendices A and B.

The mean of the Poisson's ratio values ranged from 0.30 in the Salina and Brown Niagaran Formations to 0.28 in the A-2 Carbonate, A-2 Evaporite, and A-1 Carbonate Formations. Variance of the Poisson's ratio values ranged from 0.0004 in the A-2 Evaporite Formation to 0.0002 in the Salina Formation (Table 14-1, Figure 14-1).

The mean of the Young's modulus values ranged from 12.82x10^6 psi in the A-2 Carbonate Formation to 5.03x10^6 psi in the Salina Formation. The variance of the calculated Young's modulus values ranged from 3.2x10^6 psi in the A-1 Carbonate Formation to 1.68x10^6 psi in the Salina Formation (Table 14-1, Figure 14-1).

Mean values for the dynamic shear modulus range from 5.03 x10^6 psi in the A-2 Carbonate Formation to 1.94 x10^6 psi in the Salina Formation. Variance of the dynamic shear modulus ranged from 0.47 x10^6 psi in the A-1 Carbonate Formation to 0.27 x10^6 psi in the Salina Formation (Table 14-1, Figure 14-1).

Table 14-1. Mean and variance values of geomechanical parameters for each formation combined across wells.

Formation	Number of Wells[a]	Poisson's Ratio		Dynamic Shear Modulus		Bulk Modulus		Young's Modulus	
		Mean	Variance	Mean	Variance	Mean	Variance	Mean	Variance
Salina	5	0.30	0.002	1.94	0.27	4.42	2.30	5.03	1.68
A-2 Carbonate	5	0.28	0.0006	5.03	0.44	9.60	2.45	12.82	2.80
A-2 Evaporite	5	0.28	0.0004	4.92	0.33	9.47	2.38	12.56	2.21
A-1 Carbonate	5	0.28	0.0006	4.40	0.47	8.57	3.34	11.25	3.20
Brown Niagaran	5	0.30	0.0006	4.41	0.38	9.46	2.73	11.42	2.51
Gray Niagaran	3	0.29	0.0005	4.83	0.09	9.74	1.33	12.40	0.48

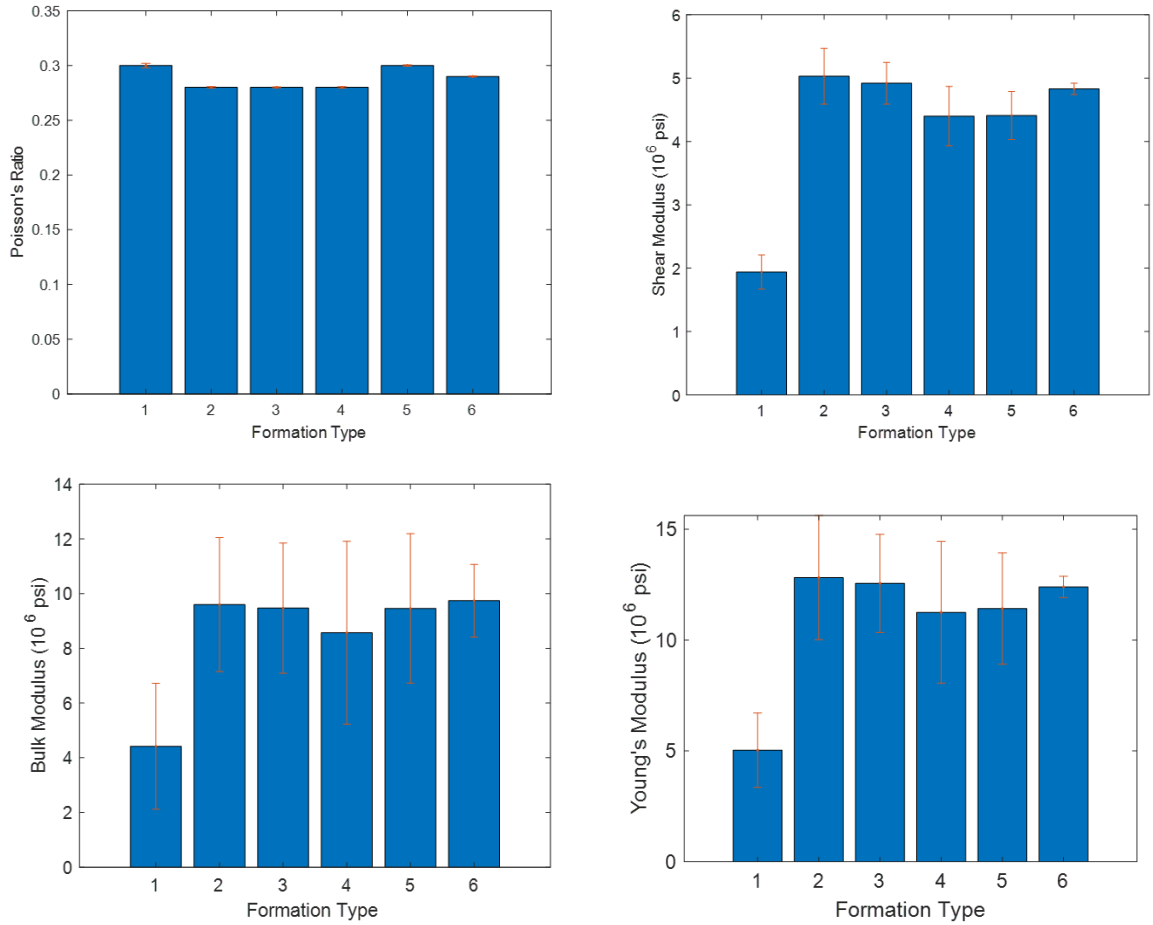


Figure 14-1. Plot of mean and variance for (a) Poisson's ratio (b) Shear Modulus (c) Bulk Modulus (d) Young's Modulus. Formation type number in the figure: 1: Salina, 2: A-2 Carbonate, 3: A-2 Evaporate, 4: A-1 Carbonate, 5: Brown Niagaran, 6: Gray Niagaran.

The mean of the bulk modulus values ranged from 9.47 x10^6 psi in the A-2 Evaporite Formation to 4.42 x10^6 psi in the Salina Formation. Bulk modulus variance ranged from 3.34 x10^6 psi in the A-1 Carbonate Formation to 2.30 x10^6 psi in the Salina Formation (Table 14-1, Figure 14-1).

The variability of the mechanical properties of the Salina Formation and A-2 Evaporite Formation are significantly lower across the four dynamic elastic parameters when compared to the other formations of interest. This indicates that both the Salina Formation and A-2 Evaporite Formation are more homogenous mechanically. The relatively higher levels of variance in the A-2 Carbonate, A-1 Carbonate, and Brown Niagaran Formations indicate that they are more heterogeneous mechanically.

Lower mean values were calculated in the Salina Formation across each of the four dynamic elastic parameters than in any of the other respective formations. This suggests that the Salina Formation is the least resistant to stress between the six formations of interest. The A-2 Carbonate and A-2 Evaporite Formations exhibit similar dynamic elastic property values, that are slightly higher than those calculated in the A-1 Carbonate, Brown Niagara, and Gray Niagara Formations. Differences in the mean values of the dynamic elastic properties in the Salina Formation compared to the other formations is likely attributed to its lithologic composition. Lithology appears to play a smaller role in the mean dynamic elastic property values of the other formations. For instance, the A-2 Carbonate and A-2 Evaporite are mainly composed of dolomite and anhydrite respectively but still exhibit similar dynamic elastic properties. Likewise, the A-1

Carbonate Formation is predominantly composed of dolomite, while the Brown Niagaran Formation could be limestone or dolomite. However, mechanically the two formations appear to be similar.

The Gray Niagaran Formation did not have available sonic density data from the Cargas 3-2 HD1 and El Mac Hills 1-18A wells.

14.2.4 Individual Formation Evaluation Results

Dynamic elastic parameters were calculated in reservoir and caprock formations in five wells. Calculations were used to determine variations in the mechanical rock properties of individual formations in each well. Tables and figures displaying results for each well and formation can be seen in Appendix C.

The mean values of the Salina Formation's dynamic elastic parameters are relatively uniform across each of the five wells, with the expectation of the values calculated from data collected in the El Mac Hills 1-18A well. The bulk modulus mean value calculated in the El Mac Hills 1-18A well was higher than the mean values calculated in each of the other four wells. It is unclear why the mean bulk modulus value for the Salina Formation in El Mac Hills 1-18A is significantly higher than in the other wells of interest.

The A-2 Carbonate Formation is composed predominantly of dolomite. Dynamic elastic parameter mean values for the A-2 Carbonate were within close range across each of the five wells. The lowest dynamic elastic parameter mean values for the A-2 Carbonate were calculated in the Cargas 3-2 HD1 well. Wireline log analysis indicated that in the Cargas 3-2 HD1 well the limestone content of the A-2 Carbonate is higher than in the other wells. The higher limestone content of the A-2 Carbonate in the Cargas 3-2 HD1 well may be affecting the formation mechanically, and potentially explains the lower dynamic elastic parameter mean values calculated in the well.

The A-2 Evaporite Formation is composed mainly of anhydrite and salt. Calculated dynamic elastic parameter mean values were relatively similar in each of the wells except for the Cargas 3-2 HD1 well which displayed notably lower dynamic shear modulus, bulk modulus, and Young's modulus mean values. Data from a neutron density log plot indicates that the A-2 Evaporite Formation in the Cargas 3-2 HD1 well is composed of relatively pure salt and anhydrite. Lower carbonate content in the A-2 Evaporite in Cargas 3-2 HD1 may be affecting the mechanical properties of the formation resulting in lower dynamic elastic parameter mean values. In each of the other wells, the A-2 Evaporite was also characterized as predominantly being composed of anhydrite and salt, but also as having a higher carbonate (dolomite) content. This may be an explanation for the formation having higher generally higher mean dynamic elastic parameter values in the Lawnichak 9-33, El Mac Hills 1-18A, Chester 6-16, and Chester 8-18 wells than those seen in the Cargas 3-2 HD1 well.

The A-1 Carbonate Formation is predominantly composed of porous dolomite and exhibits similar mechanical properties in four of the five wells. Lawnichak 9-33 served as the outlier, as the dynamic elastic parameter mean values calculated for this well were higher than those calculated in the four other wells. The A-1 Carbonate in Lawnichak 9-33 is characterized as being a heterogenous dolomite with minor anhydrite. Formation characterization in the other wells of interest indicates that the A-1 Carbonate has largely the same lithologic composition across each well. This suggests that the difference in the mechanical properties of the A-1 Carbonate in the Lawnichak 9-33 well may be related to other factors than the formations lithology.

The Brown Niagaran Formation could be limestone, dolomite, or mix that exhibits similar mechanical properties in four of the five geomechanically characterized wells. In El Mac Hills 1-18A the mean values for the dynamic shear modulus, bulk modulus, and Young's modulus are all lower than those calculated in the four other wells of interest. Formation characterization of the Brown Niagara displayed significant

lithologic differences in the formation between the five wells. In the Chester 6-16 and Chester 8-16 wells the Brown Niagaran Formation was defined as predominantly limestone, while in the Cargas 3-2 HD1 and Lawnichak 9-33 wells its composition is mixed carbonate with significant amounts of limestones and dolomite. In El Mac Hills 1-18A the Brown Niagaran was characterized as being predominantly composed of dolomite.

14.2.5 Shallow Formation Evaluation Results

In addition to reservoir and caprock formations, sonic log data was collected in formations at stratigraphically shallower depths in the Lawnichak 9-33, Chester 6-16, and Cargas 3-2 HD1 wells. Sonic log data was used to define the mechanical parameters in 17 formations in Lawnichak 9-33, five formations in Chester 6-16, and 11 formations in Cargas 3-2 HD-1. The mean and variance of four dynamic elastic parameters (Poisson's ratio, dynamic shear modulus, bulk modulus, and Young's modulus) were calculated for each identified formation in each well. Tables and figures displaying results for shallow formations of each well can be seen in Appendix C.

Mean values for Poisson's ratio were highest in the Bell Shale and Antrim-Norwood Shale, and lowest in the Bois Blanc Formation and Amherstburg Formation. Both the highest and lowest Poisson's ratio mean values were calculated from formations identified in the Lawnichak 9-33 well. The variance of Poisson's ratio values was largest in the Detroit River Salt Formation in the Lawnichak 9-33 well, and less than one percent in each of the formations identified in the Chester 6-16 and Cargas 3-2 HD1 wells. The highest dynamic shear modulus values were calculated in the Anhydrite Member of the Bass Island Dolomite and Massive Anhydrite Formation, both from the Lawnichak 9-33 well. Dynamic shear modulus values were lowest in the Salina and Glacial Drift Base Formations. Both values were calculated from sonic log data collected in the Cargas 3-2 HD1 well. Dynamic shear modulus variance was highest in the Detroit River Anhydrite and Salina Formation in the Chester 6-16 well, and lowest in the Bass Island Dolomite and Glacial Drift Base Formations in the Cargas 3-2 HD1 well.

Bulk modulus and Young's modulus mean values are highest in the Bass Island Dolomite and Massive Anhydrite Formations and were calculated from data collected in the Lawnichak 9-33 well. The Upper Antrim Shale and Glacial Drift Base Formations both exhibit the lowest values for bulk modulus and Young's modulus and were calculated from data collected in the Lawnichak 9-33 and Chester 6-16 wells respectively. The variance of bulk modulus values was highest in the Detroit River Salt and Traverse Formations in the Lawnichak 9-33 and Cargas 3-2 HD1 wells. Bulk modulus variance was lowest in the Glacial Drift Base Formation in Chester 6-16 and Cargas 3-2 HD1. Young's modulus variance is highest in the Detroit River Salt Formation in the Chester 6-16 and Cargas 3-2 HD1 wells, and lowest in the Glacial Drift Base and Bass Island Dolomite Formations in the Cargas 3-2 HD1 and Chester 6-16 wells.

14.3 In-Situ Stress Analysis

This task aimed to characterize the in-situ state of stress for caprock and reservoir formations in multiple reefs in the Michigan Basin. This included determining the orientation of maximum horizontal stress (SH_{max}) and magnitude of the principal vertical stress (S_v) of multiple formations at multiple well locations to understand the variability of the above mentioned in-situ stress parameters. Knowledge of the stress parameters is necessary in order to develop accurate geomechanical and fluid flow models to predict CO_2 injection, storage, and containment. The ability to characterize the mentioned stress parameters was limited by the available data, particularly for minimum horizontal stress (Sh_{min}). There was sufficient information available to estimate the S_v magnitude and SH_{max} orientation at multiple well locations. Therefore, S_v magnitude and SH_{max} orientation was selected for in-situ stress analysis in this section. In

addition, numerical models were used to estimate changes in Sh_{min} and S_v caused by changes in pressure during CO_2 injection.

14.3.1 SH_{max} Orientation Interpretation

Image Log Analysis of Chester 6-16 and Chester 8-16 Wells

The orientation (azimuth) of the maximum horizontal stress (SH_{max}) could be determined from the orientation of features recorded on image logs, namely drilling-induced fractures (DIFs) and wellbore breakouts (BOs). BOs are a type of wellbore failure that develops when circumferential compressive stress concentrations of the wellbore exceed the required stress needed for compressive failure of the wellbore wall. DIFs develop when circumferential stress concentrations surrounding the wellbore exceed the amount needed for tensile failure of the wellbore wall. Upon development, DIFs are oriented parallel with SH_{max}. Resistivity and acoustic image logs from the Chester 6-16 and Chester 8-16 wells were evaluated for BOs and DIFs. There was a limited amount of DIFs in both wells, with most DIFs occurring in the Bass Island and Salina formations of the 6-16 well (Figure 14-2). There was no evidence of BOs. Based on analysis of the limited DIFs observed, the measured SH_{max} azimuth was between N60E to N80E.

Image Log Analysis of Micro-Frac Results

Four wireline micro-frac tests were conducted in the 8-16 well on January 28, 2017 to generate a fracture from which SH_{max} orientation and other geomechanical parameters (fracture initiation pressure, fracture re-opening pressures, fracture propagation pressures) could be determined. This section presents only a subset of the micro-frac data, namely, before and after micro-frac image logs that show the induced fracture in two of the four tests. In the other two zones, the induced fracture was not visible on the image logs obtained after the micro-frac testing.

The depth of each of the micro-frac tests is given in Table 14-2 along with the name of the formation tested.

Table 14-2. Summary of Open Borehole MicroFrac Tests Performed in Chester 8-16.

Station	Formation	Depth (MD) (ft)	Cycles
1	A-1 Carbonate	5861	3
2	Brown Niagaran	5967	4
3	A-2 Carbonate	5791	5
4	A-2 Carbonate	5765	4

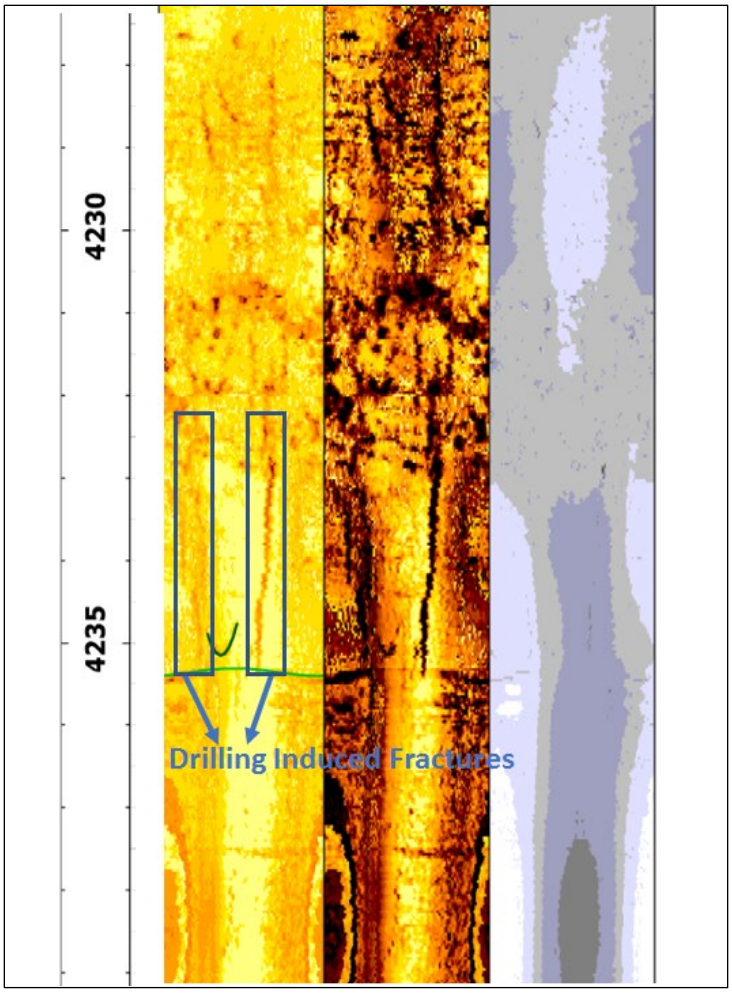


Figure 14-2. Example of DIF recorded on acoustic image of Chester 6-16.

Results of image logs before and after two mini-frac tests in the 8-16 well are shown in Figure 14-3. The interpretation of the induced fracture azimuth indicates that the SH_{max} orientation is N62E and N6E.

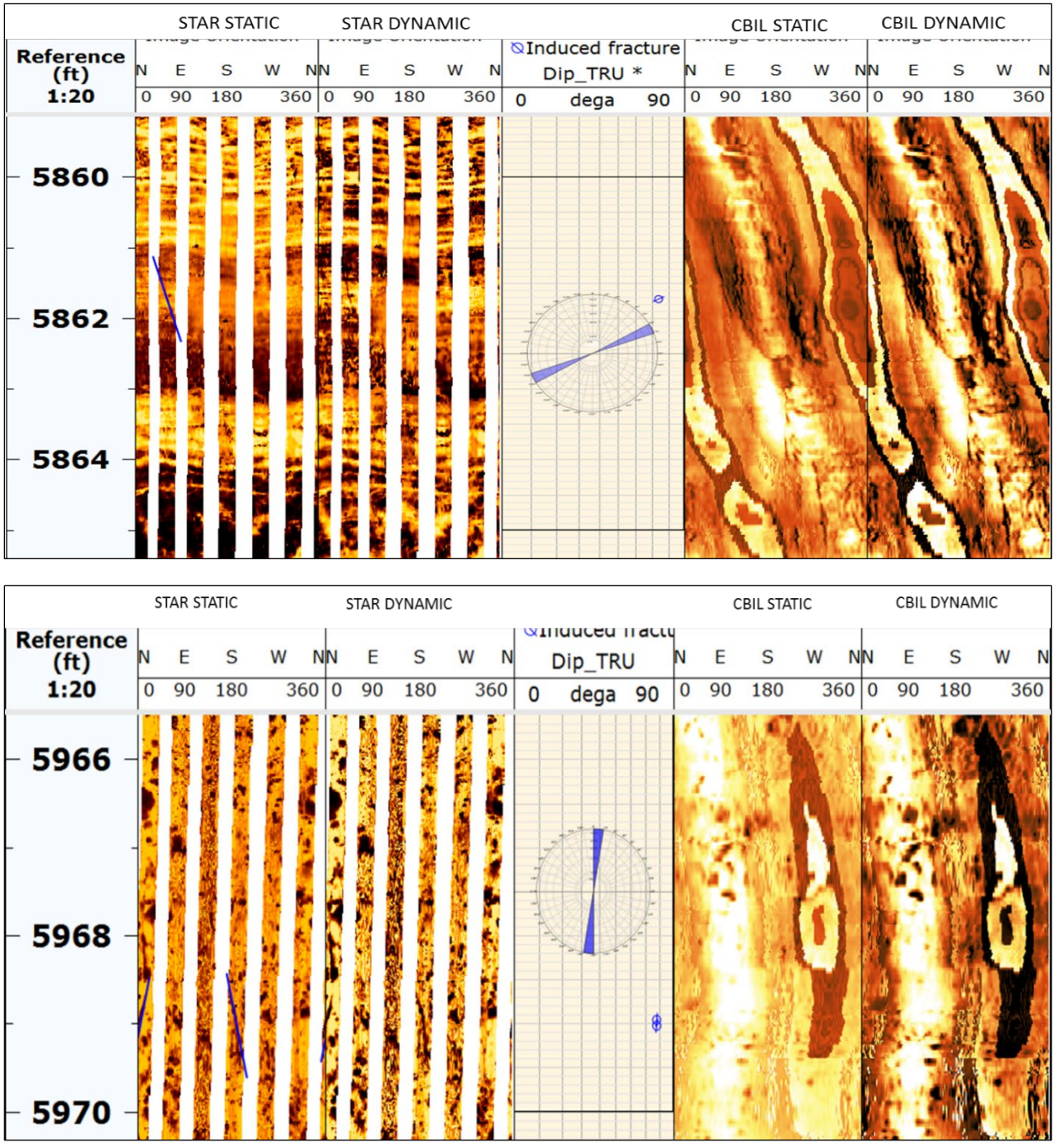


Figure 14-3. Image log interpretation of induced fracture after mini-frac test of A-1 Carbonate (upper) and the Brown Niagara (lower) in the 8-16 well. SH_{max} orientation is N62E and N6E.

SH_{max} Orientation from Shear Wave Anisotropy Data

Multi-receiver sonic instruments measure fast and slow shear wave velocities and the azimuth the of fast shear wave, which are not measured by the conventional dipole sonic logging tool. The advantage of having shear-wave velocity anisotropy data (i.e., fast shear-wave and slow shear-wave velocities) is that it allows for estimating SH_{max} orientation. In Figure 14-4 and Figure 14-5) fast shear-wave azimuth data are shown graphically on two depth plots for two wells (Lawnichak 9-33 and Chester 8-16). SH_{max} orientation can be read directly from the azimuth of the fast shear-wave velocity plot.

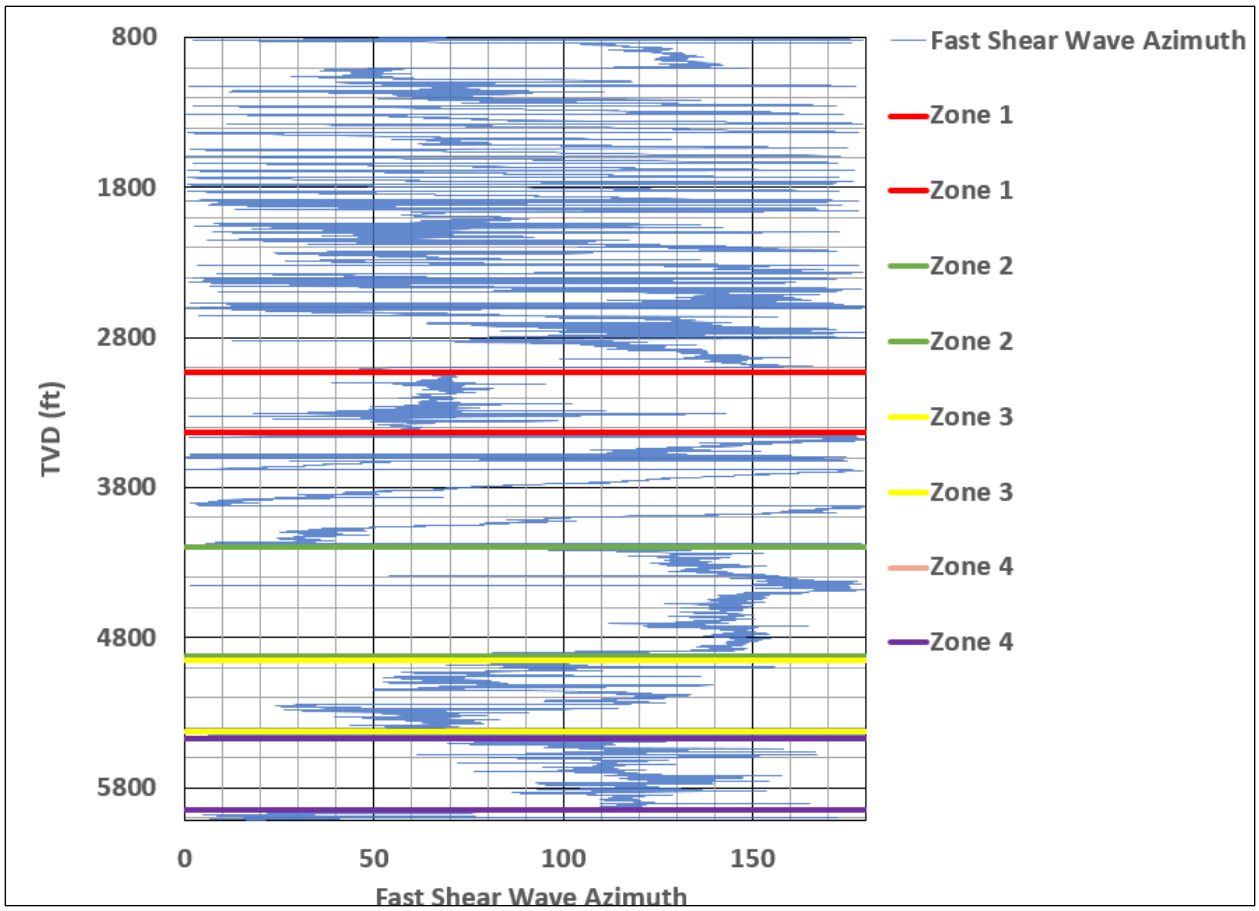


Figure 14-4. Depth plot of fast shear wave anisotropy for Lawnichak 9-33. The depth and formation interval for each zone is mentioned in Table 14-2.

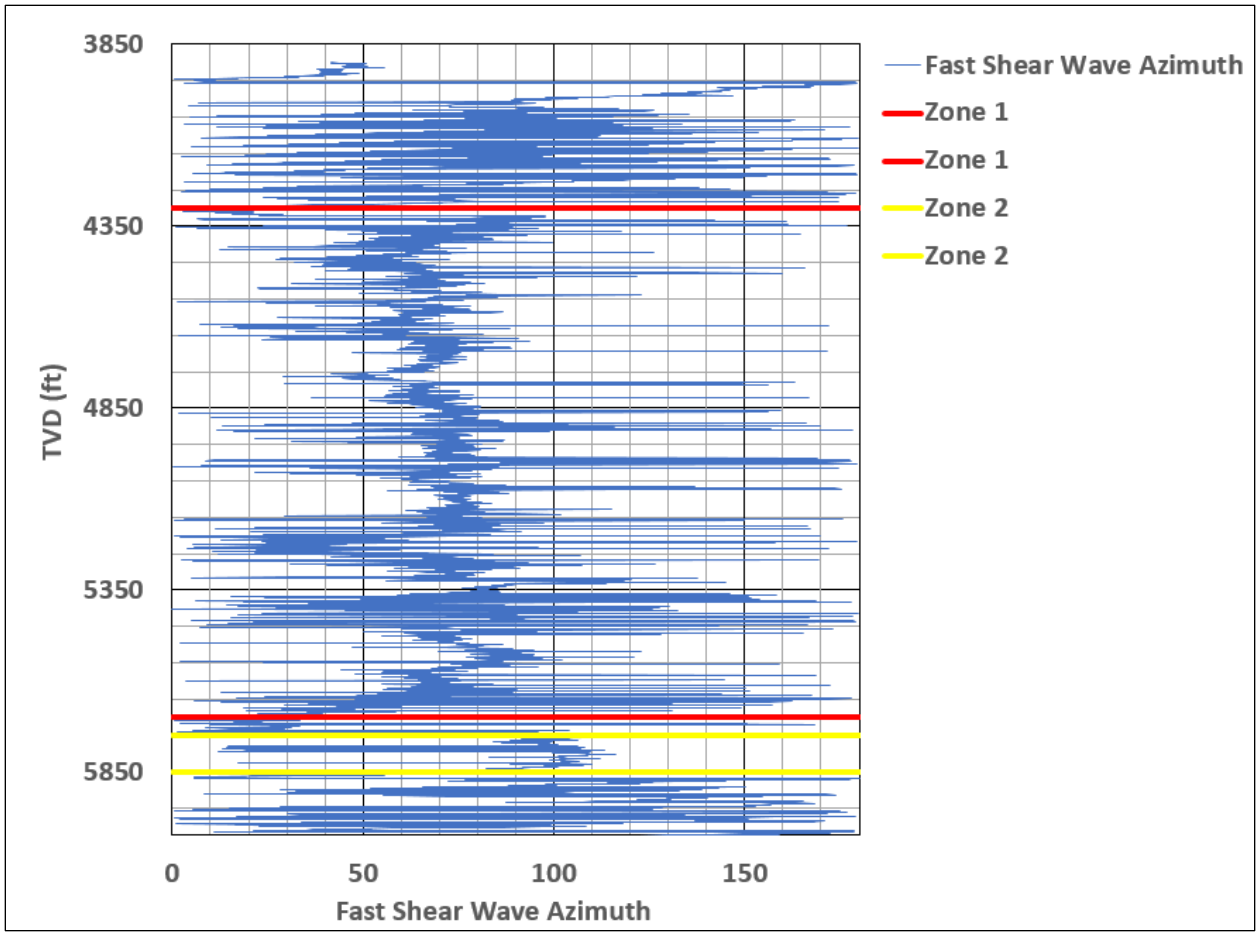


Figure 14-5. Depth plot of fast shear wave anisotropy for Chester 8-16.

The mean and variance of azimuthal data for each zone, shown in Figure 3-3 and Figure 3-4, are summarized in Table 14-3 and Table 14-4. Significant variation of the fast shear wave azimuth is observed moving from one zone to another specifically in Lawnichak 9-33. Zone 2 and zone 4 shows higher values of fast shear wave azimuth, while zone 1 and zone 3 shows lower values of fast shear wave azimuth.

Table 14-3. Fast shear wave azimuth mean and variance for Lawnichak 9-33 (bedding mean azimuth of 68 and fracture azimuth of 61).

Formation		Lawnichak 9-33
		Azimuth Data
Zone1: Bois Blanc-Amherstburg (3028-3436ft)	Mean	65.60
	Variance	14.49
Zone 2: F Salt -B Salt (4200-4923)	Mean	143.00
	Variance	13.75
Zone 3: B Salt -A-1 Carbonate -Brown Niagaran (4950 – 5429)	Mean	81.00
	Variance	28.07
Zone 4: Brown Niagaran -Gray Niagaran (5470 – 5945)	Mean	115.00
	Variance	12.85
All Zones Combined	Mean	107.00
	Variance	35.00

Table 14-4. Fast shear wave azimuth mean and variance for Chester 8-16.

Formation		Chester 8-16
		Azimuth Data
Zone 1: Salt (4300 ft to 5700 ft)	Mean	69.00
	Variance	28.50
Zone 2: A2 Carb (5750 to 5850 ft)	Mean	93.00
	Variance	22.00
All zones	Mean	72.20
	Variance	28.00

A histogram plot of fast shear wave anisotropy data is shown in Figure 14-6 and Figure 14-7. SH_{max} azimuth from shear wave anisotropy data from Lawnichak 9-33 has a mean value of 107°; whereas, the maximum horizontal stress azimuth from Chester 8-16 analysis is 71°. Higher variance is observed for shear-wave anisotropy data for Lawnichak 9-33 (Figure 14-6). The next section discusses the effect of natural fractures and bedding presence which might cause high variance of fast shear wave velocity azimuth.

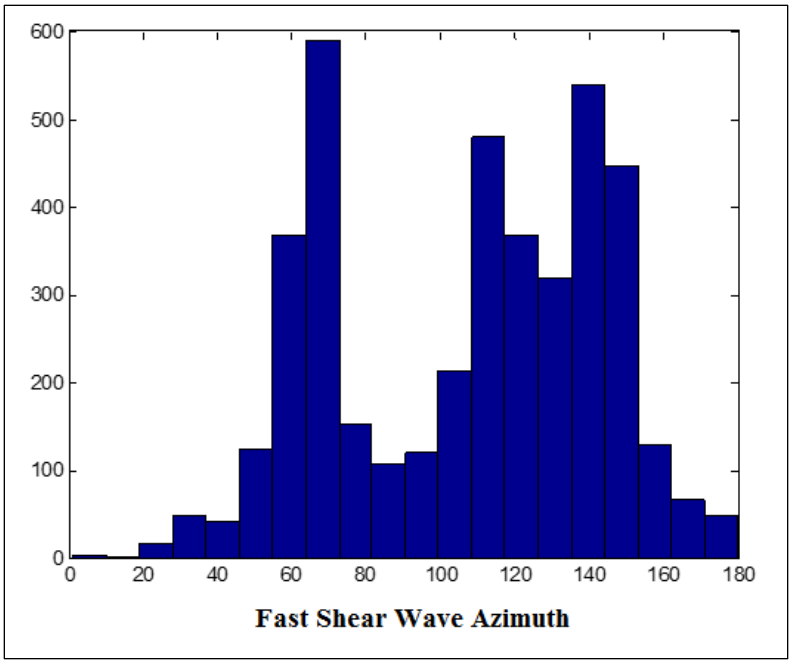


Figure 14-6. Fast shear wave azimuth distribution in Lawnichak 9-33 in all zones mentioned in Table 14-3.

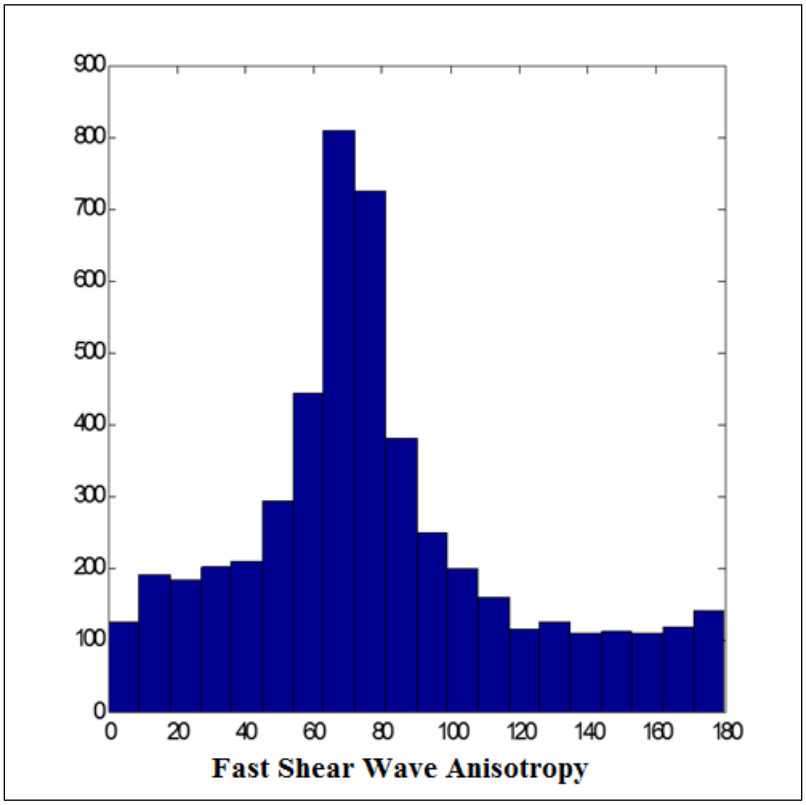


Figure 14-7. Fast shear wave azimuth distribution in Chester 8-16 in all zones mentioned in Table 14-4.

Uncertainly in SHmax Orientation Estimation Using Shear Wave Anisotropy Data in Lawnichak 9-33

Rock fabric changes could cause deviation of fast shear wave orientation from SH_{max} orientation. Figure 14-8 illustrates how rock features such as natural fractures might cause the fast shear-wave azimuth to deviate from the true SH_{max} azimuth. Figure 14-9 shows the presence of natural fractures in Lawnichak 9-33 using image log interpretation. Figure 14-10 shows the azimuth distribution of natural fractures in Lawnichak 9-33 using a rose diagram. The presence and azimuth of natural fractures and bedding planes in Lawnichak 9-33 could cause the deviation of the fast shear wave azimuth away from the SH_{max} azimuth. In fact, the presence of such natural fractures and bedding causes uncertainty in the estimation of the SH_{max} orientation using shear wave anisotropy data. Presence of natural fractures and bedding planes is one of the reasons for the higher variance of the SH_{max} azimuth in Lawnichak 9-33.

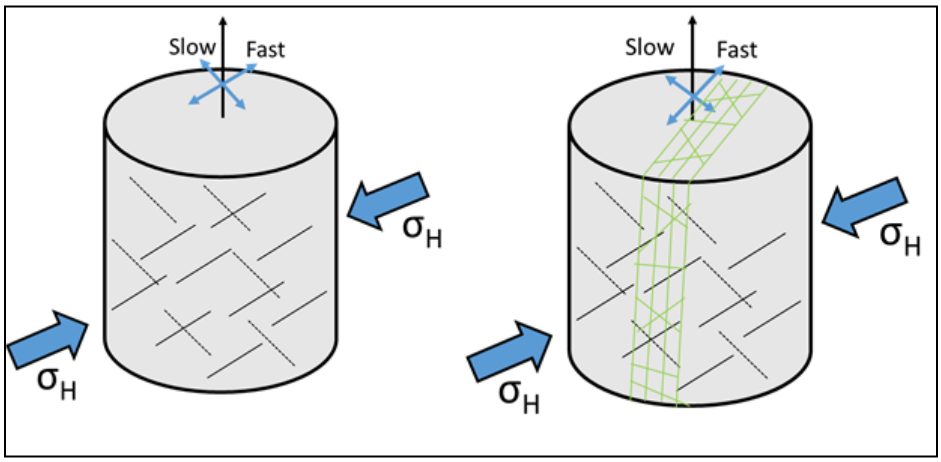


Figure 14-8. Direction of fast shear wave induced by in-situ stress (left) and fractured zones (right).

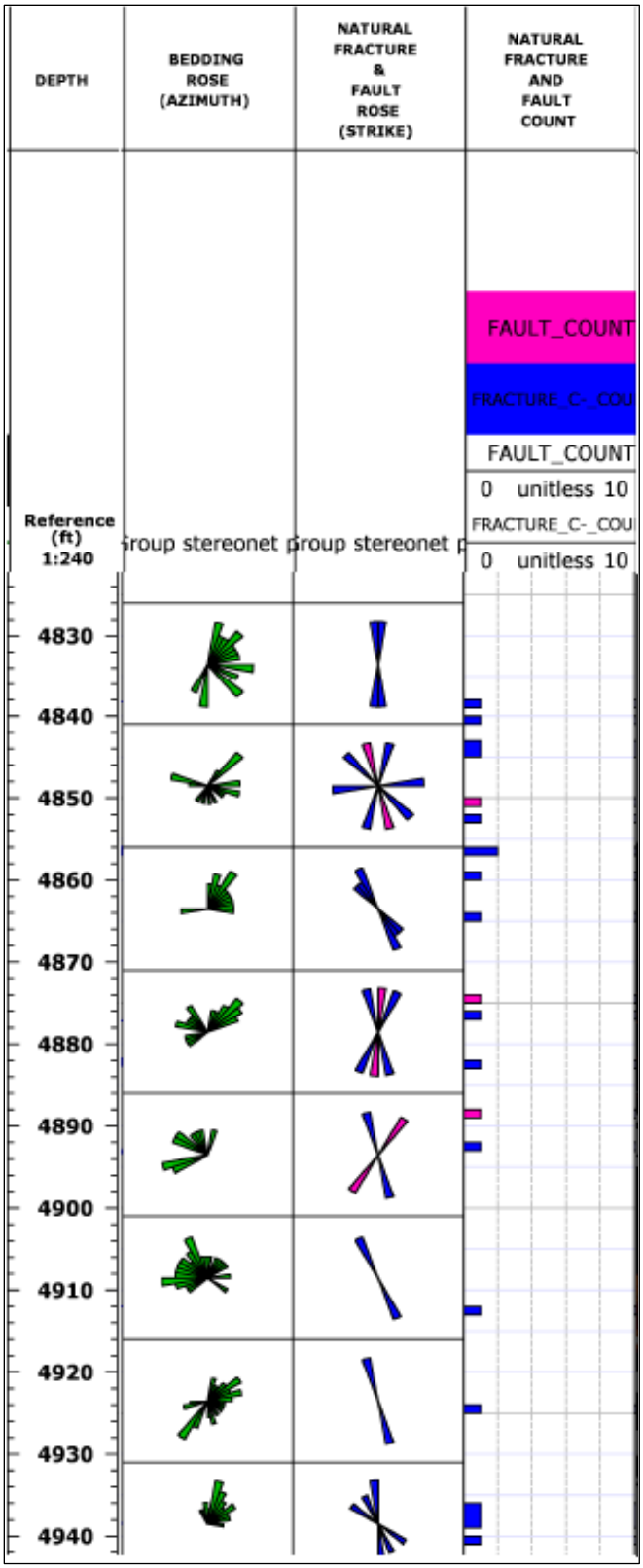


Figure 14-9. Example of natural fractures in Lawnichak 9-33 (1st track: depth, 2nd track: bedding azimuth, 3rd track: fracture azimuth, 4th track: fracture count).

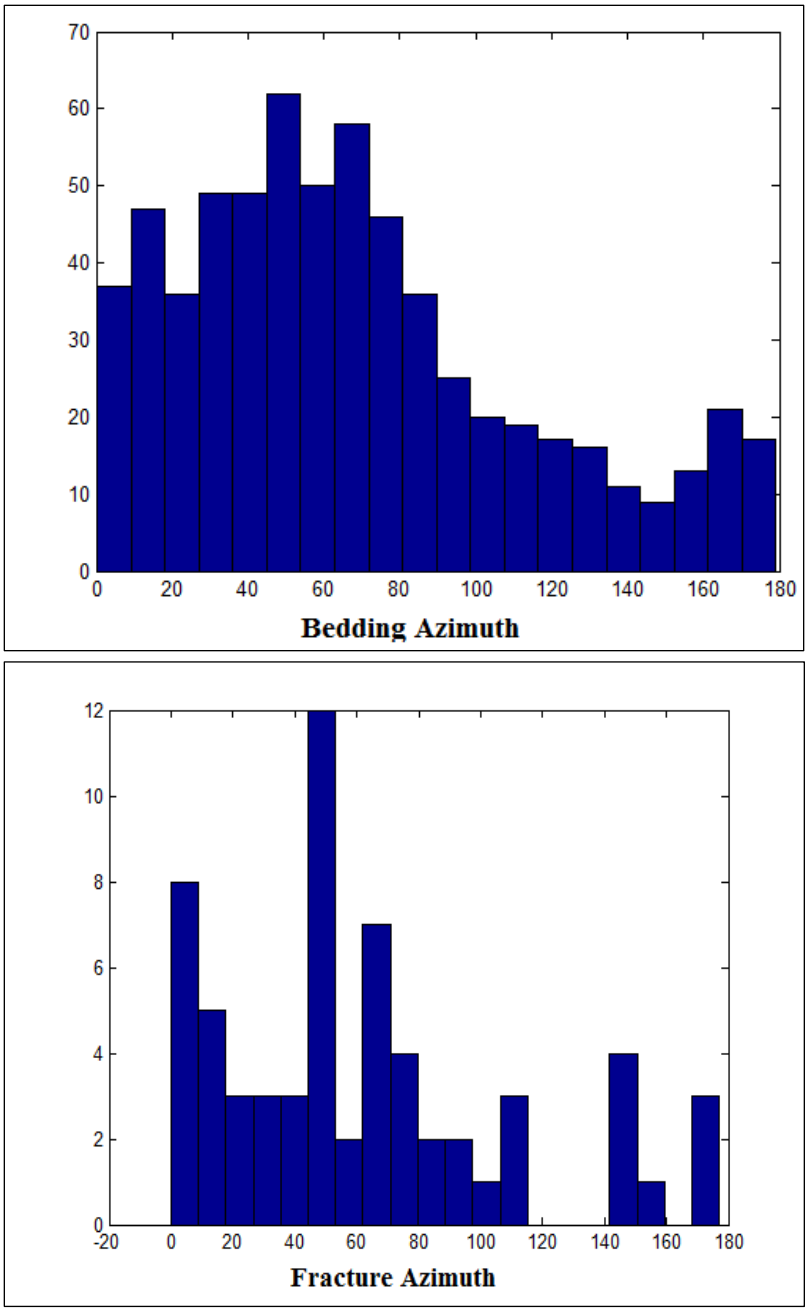


Figure 14-10. Histogram diagram of bedding and natural fracture azimuth in Lawnichak 9-33 (bedding mean azimuth of 68 and fracture azimuth of 61).

14.3.2 Vertical Stress Spatial Variability Analysis

S_v in caprock and reservoir formations of five wells (Lawnichak 9-33, El Mac Hills 1-18A, Cargas 3-2 HD1, Chester 8-16, and Chester 6-16) was estimated to understand its spatial variability across different wells.

The magnitude of S_v is determined by the weight of the overlaying rock material and can be calculated by integrating bulk density from ground surface to the total depth of the well. It is expressed by:

$$\mathrm{Sv} = \Sigma \rho \Delta \mathrm{z} \left(\frac{1 ft^2}{144 in^2} \right)$$

Equation 14-5

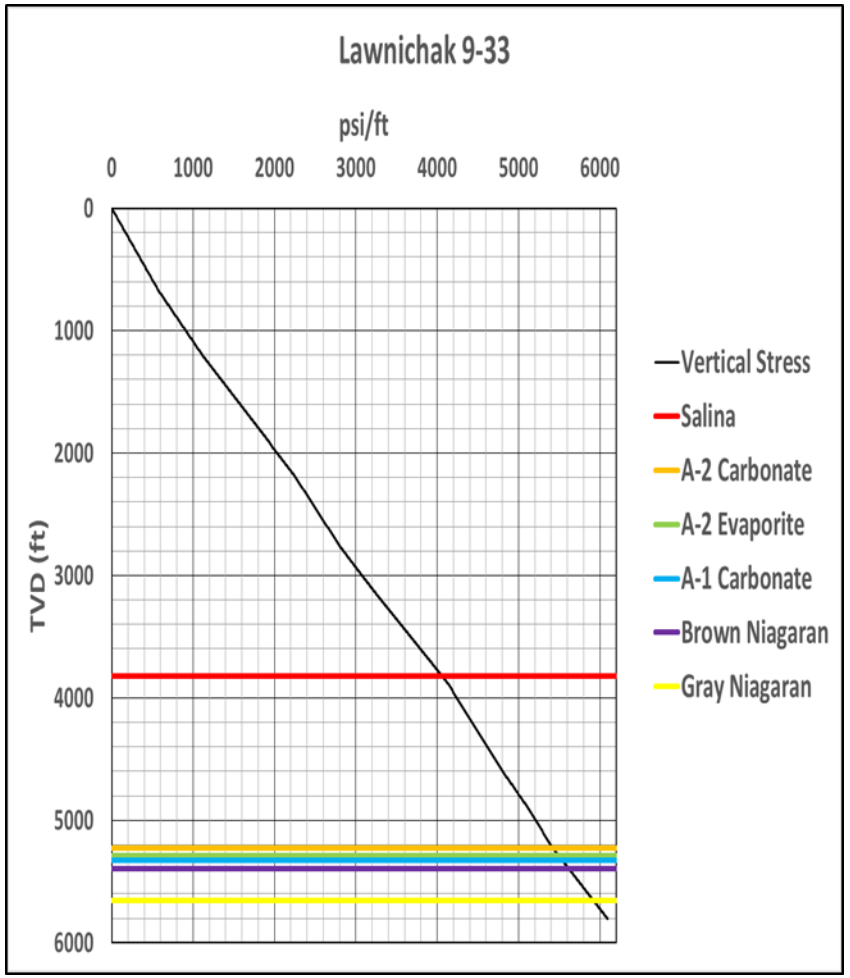
where:

S_v = vertical stress (psi)
ρ = bulk density of the formation measured by geophysical logging tools over a specific depth interval (lbs/ft^3)
Δz = depth interval corresponds to the ρ reading (ft)

Geophysical logs do not start at ground surface; therefore, it is necessary to assume a density for the near-surface interval that was not logged. S_v was calculated in this manner for two wells, Chester 6-16 and Chester 8-16. Geophysical logs for three wells (Lawnichak 9-33, El Mac Hills 1-18A, and Cargas 3-2 HD1) were focused on the caprock and reservoir formations of interest. It was therefore necessary to use an assumed density from ground surface to a depth slightly above the identified top of the Salina Formation. The calculated S_v results are seen Table 14-5 and illustrated in Figure 14-11 through Figure 14-13.

Table 14-5. Summary of calculated S_v values for the five wells characterized in the caprock stress analysis.

Well	Mean S_v (S_v/TVD)
Lawnichak 9-33	1.00
El Mac Hills 1-18A	1.04
Cargas 3-2 HD1	0.99
Chester 8-16	0.99
Chester 6-16	0.97



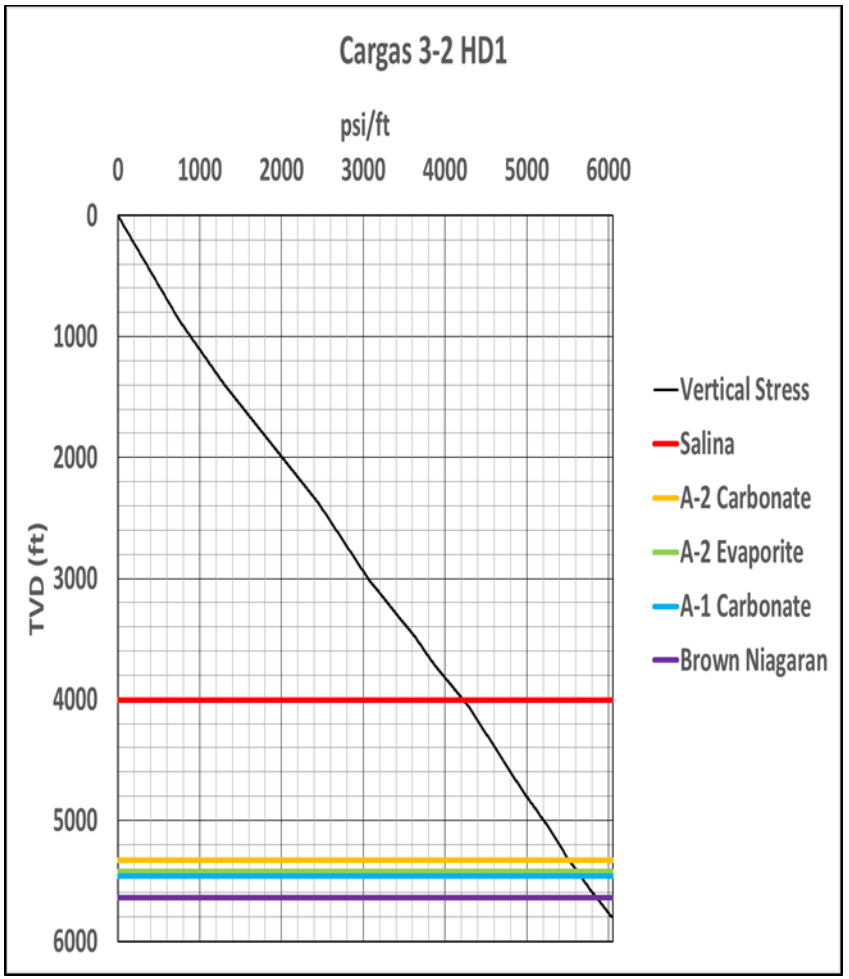


Figure 14-11. Calculated vertical stress magnitude with depth for Lawnichak 9-33 and Cargas 3-2 HD1.

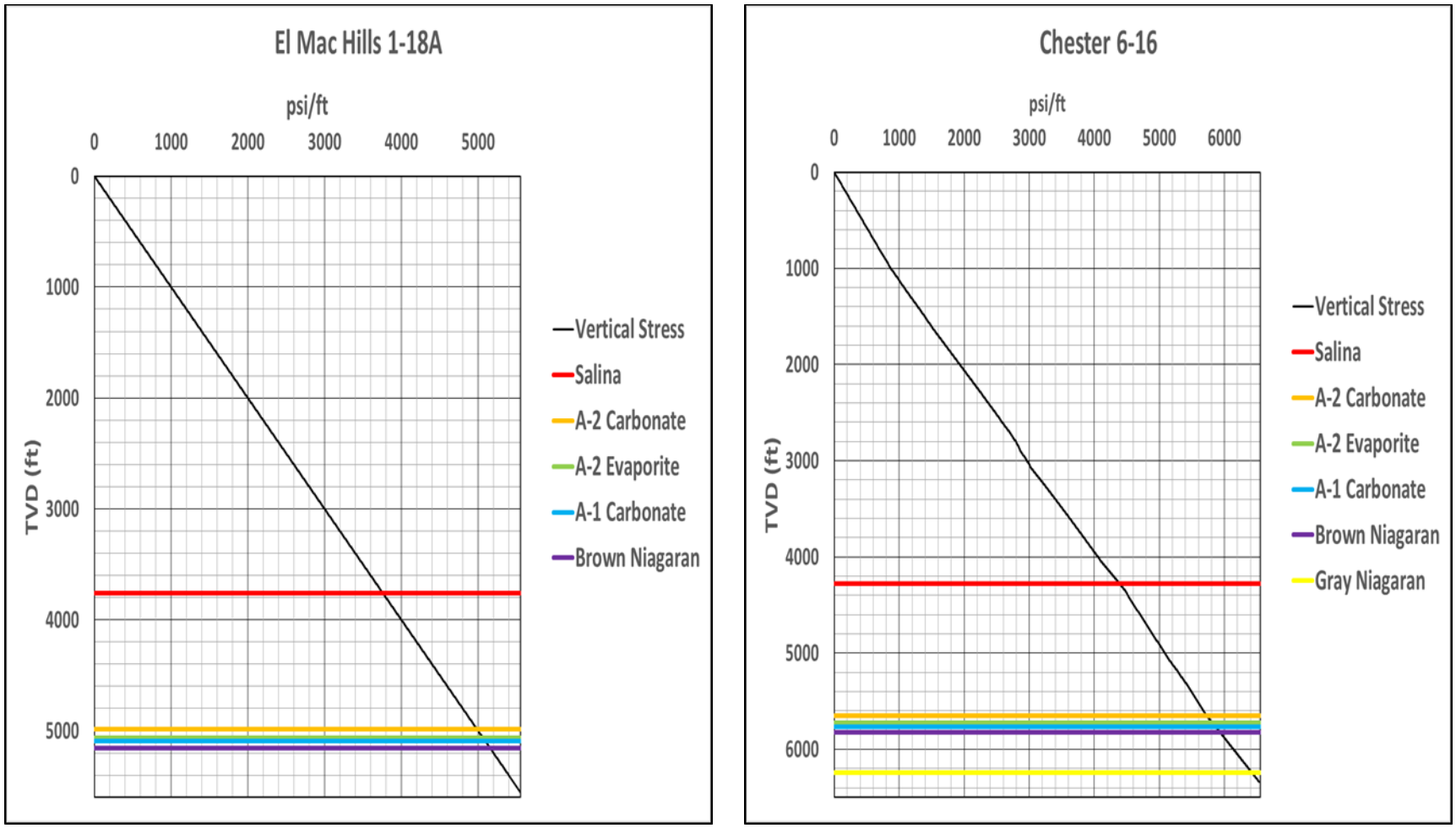


Figure 14-12. Calculated total vertical stress magnitude with depth for El Mac Hills 1-18A and Chester 6-16.

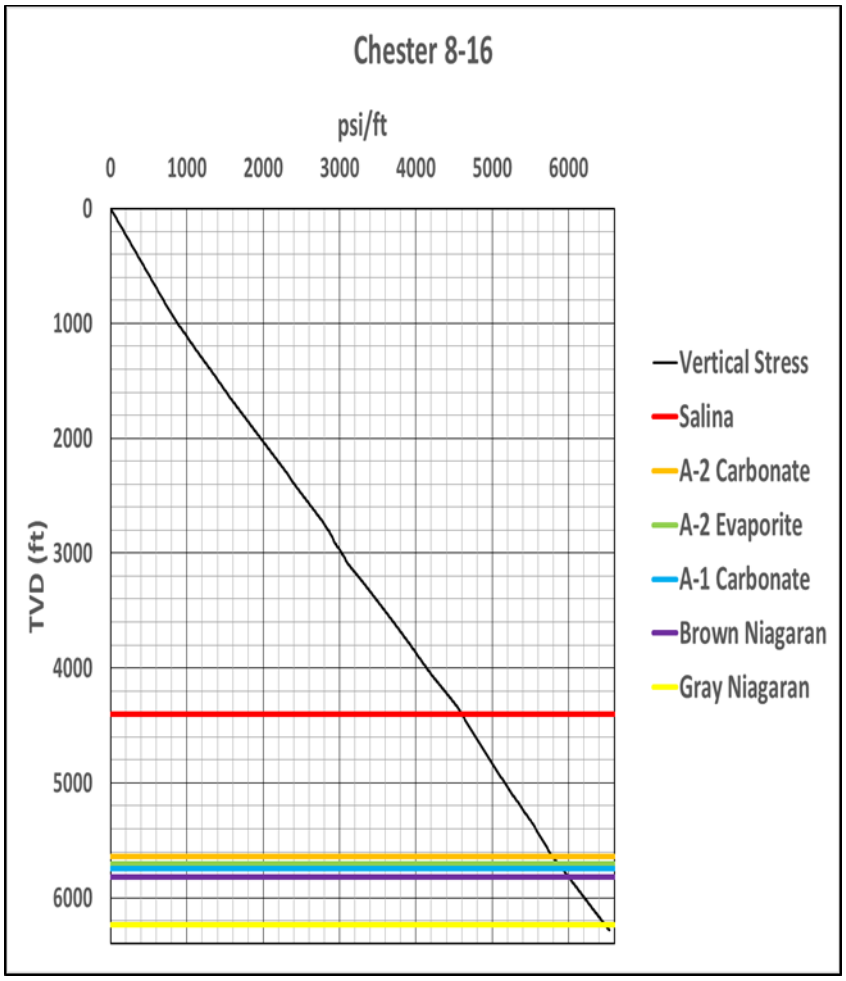


Figure 14-13. Calculated total vertical stress magnitude with depth for Chester 8-16.

14.3.3 In-Situ Stress Changes Due to CO_2 Injection

Injection of CO_2 causes changes in pore pressure which result in changes to Sh_{min} and S_v. It is important to understand the magnitude of these changes because they may affect the storage capacity of the reservoir and/or containment effectiveness of the caprock. In this section, a numerical model was used to estimate changes in Sh_{min} and S_v caused by changes in pressure during CO_2 injection for safe and effective CO_2 storage.

Approach

A 3-D fluid flow simulator, CMG–GEM, was used to model the pressure rise during fluid injection. Next, the geomechanics module of CMG-GEM was used to simulate the poroelastic response during injection. Based on the value of pressure at every time step, the geomechanics module computes stress and deformation in the reservoir and its surrounding formations to determine if and where rock failure might occur. An iterative approach is used for coupling fluid flow and geomechanics. The pressure solution obtained in the reservoir simulator is passed to the geomechanics module to compute deformation, strain, and stress. The solution from the geomechanics module is then passed to the reservoir simulator via a coupling variable such as porosity to obtain new values of pressure.

Geomechanical parameters in each geological layer from reservoir depth to surface, including Young's modulus and Poisson's ratio, were assigned for two caprock-reservoir systems: (1) soft caprock and hard reservoir (2) equal Young's modulus of caprock and reservoir. A simple rectangular prism-shaped model confined by sideburden and overburden layers was built representing a closed reservoir (Figure 14-14). Table 14-6 shows the reservoir-geomechanics parameters used for the numerical model. The change in Sh_{min} and S_v caused by changing pore pressure (poroelastic effect) was numerically estimated under six different pressure scenarios. Results (i.e., increase in Sh_{min} and S_v) are shown in Figure 14-15.

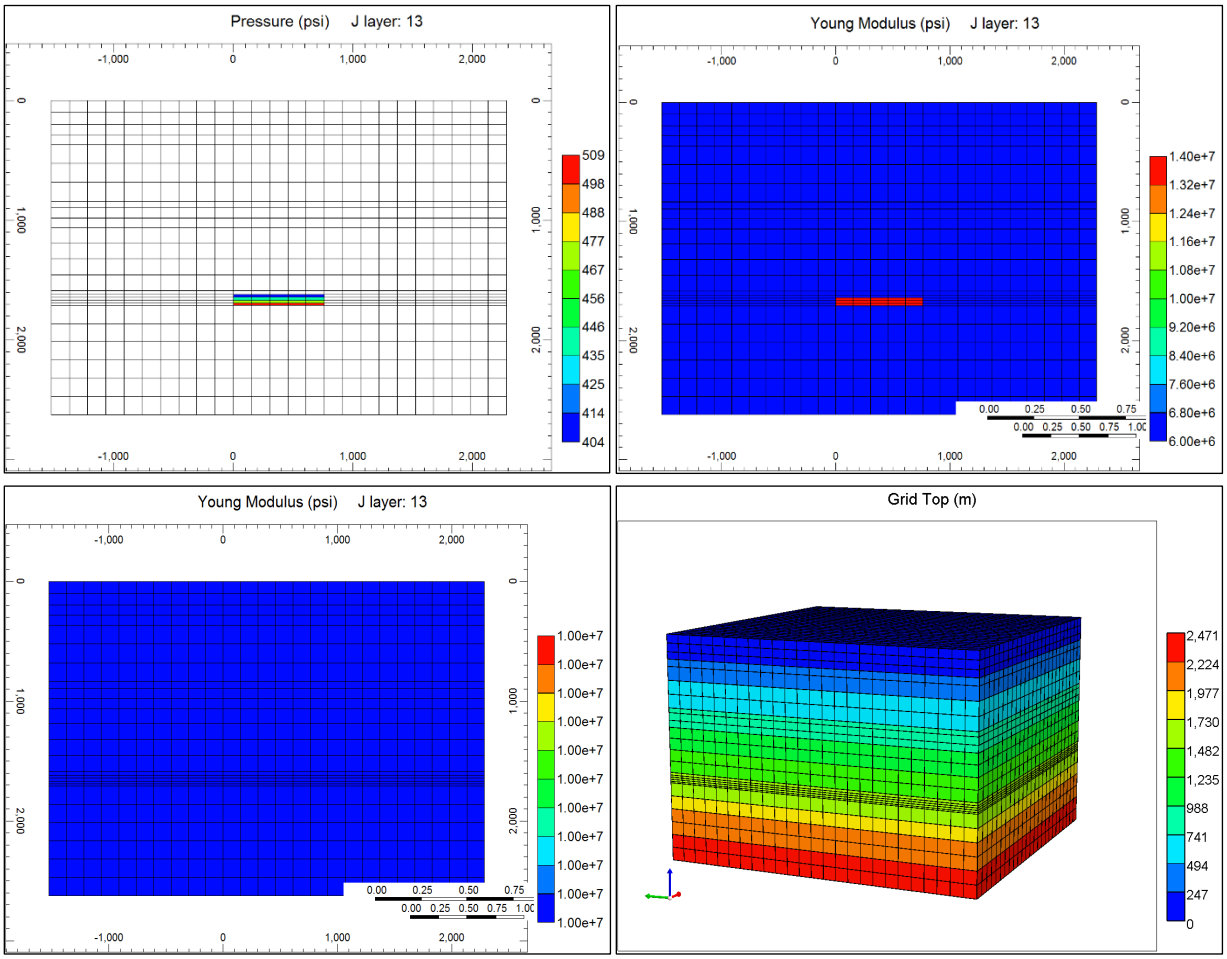


Figure 14-14. (A) Reservoir section in Geomechanics model (B) soft caprock and hard reservoir (C) equal Young's modulus of caprock and reservoir (D) 3D schematic of geomechanical model grid.

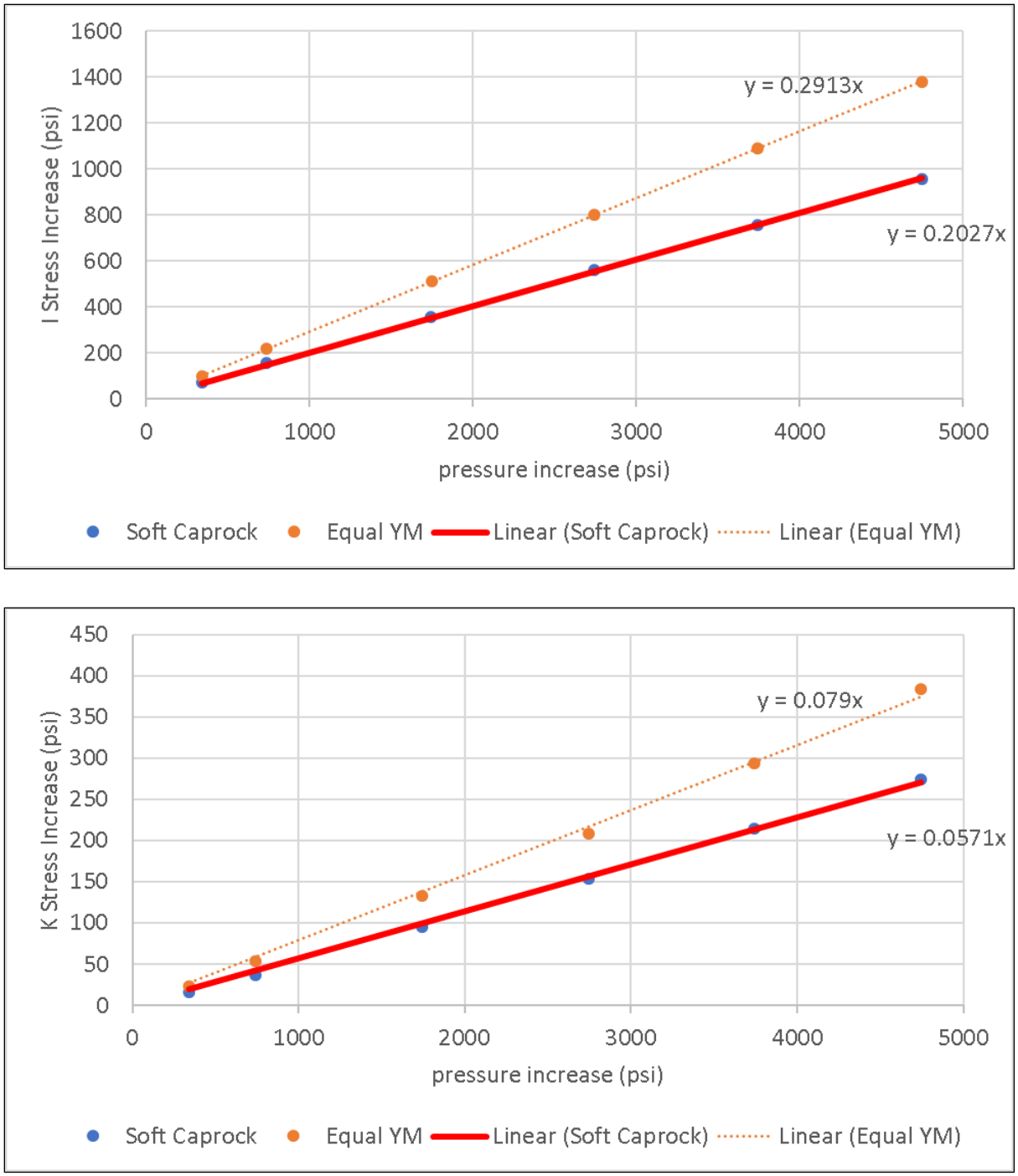


Figure 14-15. Changes in Sh_{min}, stress increase, (top) and Sv, K stress increase, (bottom) as a function of pressure increase.

Table 14-6. Geomechanics Model Parameters

Geomechanics Model Parameters	
Reservoir Top (ft)	5,308
Thickness reservoir (ft)	300 (9 grids in z direction)
Model grid	3D square
Number of grids	21*21*9
Model dimensions (ft)	2500*2500
Property variability, vertical	Varies by layer
Property variability, horizontal	Homogeneous
Porosity reservoir	0.05
Permeability reservoir (mD)	100
Relative permeability	Van Genuchten function with the exponent of 0.457
Injection time	30
Pore pressure gradient (psi)	450
Number of geomechanics cells	25*25*25
Geomechanics model dimensions (ft)	12500 * 12500 * 8600
Rock cohesion (psi),	5,470
Wellbore constraint: pressure (psi)	800, 1200, 2200, 3200, 4200, 5200
Temperature of injected CO_2; ambient reservoir (°C)	50, 50 (isothermal base case)
Reservoir Poisson's Ratio	0.25
Caprock Poisson's Ratio	0.25
Reservoir Young's modulus (psi)	14 *10^6, 10*10^6
Caprock Young's modulus (psi)	6*10^6,10*10^6

Results and Discussion

The results of mini-frac tests of a depleted reef system are shown in Table 14-7 (first row). Using the predicted formula for hard caprock soft reservoir from numerical simulation data, the estimated Sh_{min} at higher pressure scenarios are calculated and shown in Table 14-7.

The results of modeling show that stress increase in the horizontal direction is higher than stress increase in the vertical direction. The reservoir is confined in the horizontal direction, but it is unconfined in the vertical direction. As a result, stress increase in the horizontal direction is higher than the vertical direction as expected. Also, stress increase is lower in the presence of softer caprock specifically in the horizontal direction. The horizontal stress increases from 0.316 psi/ft to 0.49 psi/ft by increasing pressure from 527 psi to 5527 psi for the hard reservoir soft caprock scenario. In contrast, vertical stress increases only from 1 psi/ft to 1.04 psi/ft for the same amount of pressure increase for the same scenario.

Table 14-7. Sh_{min} gradient increase due to increase pressure using hard reservoir and soft caprock scenario.

Scenario	Sh_{min} Gradient (psi/ft)	Sh_{min} (psi)	S_v (psi)	S_v Gradient (psi/ft)	Sh_{min} effective (psi)
pore pressure (527 psi): Measured	0.316	1818.9	5756	1	1555.4
pore pressure (1527 psi): Predicted	0.35	2021.7	5813	1.00	1258.2
pore pressure (2527 psi): Predicted	0.38	2224.4	5870	1.01	960.9
pore pressure (3527 psi): Predicted	0.42	2427.1	5927	1.02	663.6
pore pressure (4527 psi): Predicted	0.45	2629.8	5984	1.03	366.3
pore pressure (5527 psi): Predicted	0.49	2832.5	6041	1.04	69

Sh_{min} effective Is Sh_{min}- ((Biot Coeff)(Pp))

14.4 Rock Mechanical – Rock Physical Experimental Data and Interpretation

14.4.1 Rock Mechanical – Rock Physical Tests

Rock mechanics and rock physics properties are critical data for studying safe storage of CO_2 in reservoir. Rock properties determined from the laboratory testing together with rock properties determined from analysis of geophysical logs and other sources, will be used to develop the numerical models to evaluate the long-term effect of CO_2 storage within the reservoir formations. This section presents the results of the rock physics-rock mechanical laboratory testing performed on rock core samples.

Rock core samples for laboratory testing were obtained from the Dover 33 reef and Chester 16 reef . The samples included whole core plug and rotary sidewall core. Samples submitted for testing included rotary sidewall core samples from the A-2 Carbonate, A-2 Anhydrite, and lower Brown Niagaran formations as well as whole core plug samples from the A-1 Carbonate and upper and lower Brown Niagaran formations. Table 14-8 summarizes the types of tests performed on the core samples and the information that was generated by each test. All core testing was performed by Core Laboratories of Houston, Texas.

Table 14-8. Laboratory tests performed on core samples.

Test	Resulting Information	
Triaxial Test	• Bulk density (g/cc) • Dynamic Elastic Parameters • Dynamic Young's Modulus (x10^6 psi) • Dynamic Poisson's Ratio • Bulk Modulus (x10^6 psi) • Shear Modulus (x10^6 psi) • Ultrasonic Velocity at different stress stage • Acoustic Velocity, compressional wave (ft/sec)	• Acoustic Velocity, shear wave (ft/sec) • Static Elastic Parameters • Static Young's Modulus (x10^6 psi) • Static Poisson's Ratio • Compressive Strength (psi) • State Liquid axial perm during compressive strength test (mD) • Mohr-Coulomb Failure Test
Uniaxial Test	• Static Elastic Parameters • Static Young's Modulus (x10^6 psi) • Static Poisson's Ratio • Unconfined Compressive Strength (psi)	
Brazilian Indirect Tensile Strength Test	• Tensile Strength (psi)	

14.4.2 Rock Mechanical Parameters (Static-Dynamic Correlation)

By definition, the dynamic moduli of rock are those calculated from elastic wave velocity and density, whereas the static moduli are those directly measured in a deformational experiment. The static and dynamic moduli of the same rock may differ significantly from each other. The main reason is likely to be the difference in the deformation (strain) amplitude between the dynamic and static experiments. In the dynamic wave propagation experiment, the strain is about 10^{-7}, while static strain may reach 10^{-2}. The ratio of stress to strain over a large strain measurement (static) is different from the ratio of stress to strain over a small strain measurement (dynamic). More internal deformation will be found over a large strain experiment than over a very small strain cycle because of rock's inelastic and non-linear behavior.

Static moduli are needed for many applications—for example, in wellbore stability and in-situ stress applications to evaluate the possibility of breakouts, elevated pore pressure, and tectonic stress distribution. A common method of calculating the horizontal stress is by assuming that the earth is elastic and does not deform in the horizontal direction. In addition, static moduli are required input to the coupled flow-geomechanical models that were developed for simulating long-term caprock integrity for CO_2 containment.

Static elastic parameters can be obtained through uniaxial or triaxial laboratory experiments performed on rock core. Elastic moduli derived from sonic log data are dynamic moduli. The dynamic elastic modulus can be converted into a static modulus using the correlation between static and dynamic experimental data obtained from triaxial tests of rock core. To develop a correlation between static and dynamic moduli, all triaxial test data from the carbonate formations in the study area were gathered. Table 14-9 and Table 14-10 shows the static and dynamic elastic modulus measurements respectively. The developed correlations for Young's modulus and Poisson's ratio are shown in Figure 14-16. The correlation between Young's Modulus and compressive strength is shown in Figure 14-17.

Table 14-9. Static elastic moduli measured using triaxial test.

Depth (ft)	Well	Pressure (psi)	Compressive Strength (psi)	Young's Modulus (psi)	Poisson's Ratio (psi)
5390.00 (A2 Carb)	Lawnichak 9-33	2685	39836	8.34	0.28
5430.00 (A2 ANH)	Lawnichak 9-33	2710	34079	7.63	0.26
5529.00 (A1 Carb)	Lawnichak 9-33	2765	41122	8.98	0.27
5553.50 (Upper Brown)	Lawnichak 9-33	1555	19779	5.63	0.27
5627.00 (Lower Brown)	Lawnichak 9-33	2820	44758	9.02	0.29
5778.00 (A2 Carb)	Chester 8-16	2200	31087	6.45	0.29
5820.00 (A2 ANH)	Chester 8-16	2200	20256	5.02	0.27
5903.00 (A1 Carb)	Chester 8-16	2200	20858	5.36	0.32
6162.50 (Brown-45)	Chester 8-16	2200	15689	5.38	0.33
6164.50 (Brown-V)	Chester 8-16	2200	27452	6.48	0.29
6338.60 (Gray)	Chester 8-16	2200	24787	4.50	0.27

Table 14-10. Dynamic elastic module measured using triaxial test.

Depth (ft)	Well	Pressure (psi)	Young's Modulus (psi)	Poisson's Ratio (psi)
5390.00 (A2 Carb)	Lawnichak 9-33	2685	13.07	0.308
5430.00 (A2 ANH)	Lawnichak 9-33	2710	12.36	0.294
5529.00 (A1 Carb)	Lawnichak 9-33	2765	13.80	0.300
5553.50 (Upper Brown)	Lawnichak 9-33	1555	10.65	0.284
5627.00 (Lower Brown)	Lawnichak 9-33	2820	13.70	0.292
5778.00 (A2 Carb)	Chester 8-16	2200	13.84	0.287
5820.00 (A2 ANH)	Chester 8-16	2200	13.92	0.256
5903.00 (A1 Carb)	Chester 8-16	2200	10.43	0.332
6162.50 (Brown-45)	Chester 8-16	2200	10.11	0.319
6164.50 (Brown-V)	Chester 8-16	2200	10.45	0.303
6338.60 (Gray)	Chester 8-16	2200	9.69	0.296

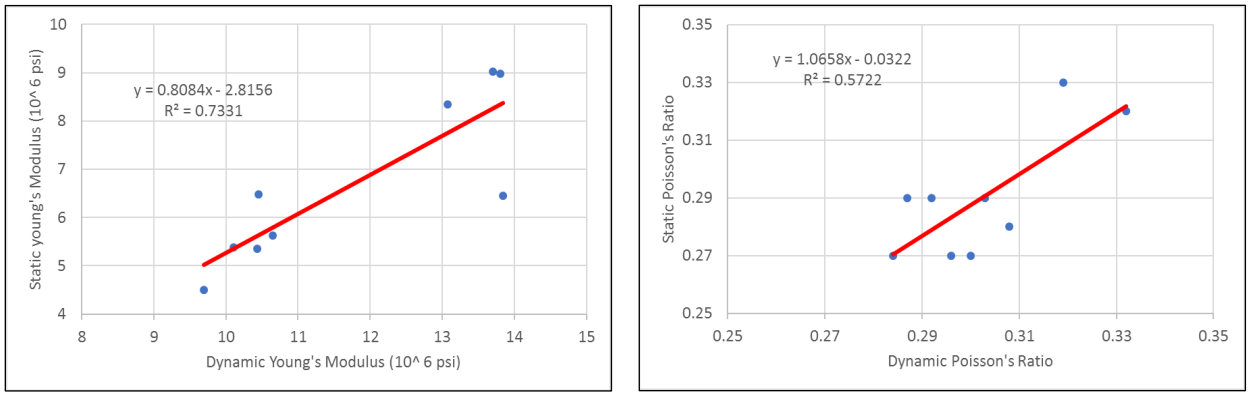


Figure 14-16. Relationship between static and dynamic Young's modulus (b) Relationship between static and dynamic Poisson's Ratio.

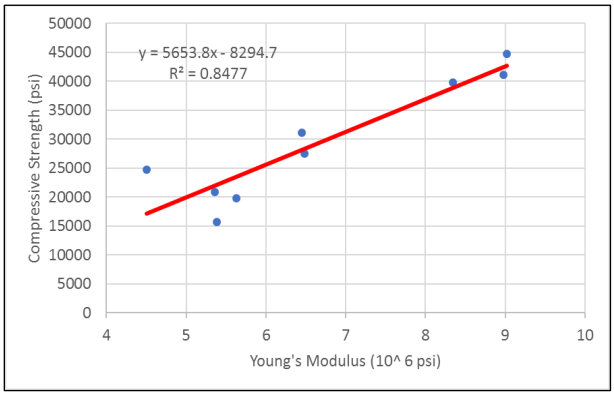


Figure 14-17. Relationship between static Young's modulus and compressive strength.

14.4.3 Biot Coefficient Estimate

Biot's coefficient is one of the most significant hydromechanical parameters used for determining the magnitude of the induced effective stress that governs the mechanical response of a rock formation to variations in pore pressure. Biot coefficient can be expressed as:

$$\alpha = 1 - K^{Rock}/K^{grain}$$

Equation 14-6

where K^{grain} is the grain modulus and K^{Rock} is the bulk modulus. The bulk modulus is measured by monitoring bulk volume change due to changes in confining pressure. Table 14-11 shows the Biot's coefficient estimate for different formations in the study area. Bulk modulus for each formation is measured using a triaxial experiment and grain modulus is estimated for each rock sample using the minerals that composed the sample.

Table 14-11. Estimated Biot's coefficient for each rock sample.

Depth (ft)	Well	Grain Modulus	Grain Modulus	Bulk Modulus	YM	POISSON	Biot Coefficient		Average Biot
		High (psi)	Low (psi)	(10^6) psi	Static (10 ^ 6 psi)	Static	High	Low	
5390.00 (A2 Carb)	Lawnichak 9-33	1.11E+07	9.24E+06	6.318182	8.34	0.28	0.43	0.32	0.37
5430.00 (A2 ANH)	Lawnichak 9-33	9006844	8.12E+06	5.298611	7.63	0.26	0.41	0.35	0.37
5529.00 (A1 Carb)	Lawnichak 9-33	1.38E+07	1.01E+07	6.507246	8.98	0.27	0.52	0.36	0.44
5553.50 (Upper Brown)	Lawnichak 9-33	1.38E+07	1.01E+07	4.07971	5.63	0.27	0.70	0.59	0.65
5627.00 (Lower Brown)	Lawnichak 9-33	1.38E+07	1.01E+07	7.15873	9.02	0.29	0.47	0.29	0.38
5778.00 (A2 Carb)	Chester 8-16	1.11E+07	1.11E+07	5.119048	6.45	0.29	0.54	0.54	0.54
5820.00 (A2 ANH)	Chester 8-16	9006844	8.12E+06	3.637681	5.02	0.27	0.59	0.55	0.57
5903.00 (A1 Carb)	Chester 8-16	1.11E+07	9.24E+06	4.962963	5.36	0.32	0.55	0.46	0.50
6162.50 (Brown-45)	Chester 8-16	1.11E+07	9.24E+06	5.27451	5.38	0.33	0.52	0.43	0.47
6164.50 (Brown-V)	Chester 8-16	1.11E+07	9.24E+06	5.142857	6.48	0.29	0.53	0.44	0.49
6338.60 (Gray)	Chester 8-16	1.11E+07	9.24E+06	3.26087	4.5	0.27	0.70	0.647	0.677

14.4.4 Rock Failure Parameters (UCS and CCS, Mohr-Coulomb Analysis, and Tensile Strength)

The compressive strength test measures geomechanical and physical properties of a rock by applying stress and analyzing the strain response. This includes compressive stress a rock can undergo before failure either under confining pressure (triaxial stress test) or without confining pressure (uniaxial confining pressure). Results of the uniaxial and triaxial tests showing unconfined compressive strength (UCS) and confined compressive strength (CCS) of reservoir and caprock formations are presented in Table 14-12 and Table 14-13.

Table 14-12. Summary of strength parameters determined from uniaxial tests.

		Confining	Measured	Corrected
Depth (ft)	Well	Pressure (psi)	Compressive Strength (psi)	Compressive Strength (psi)
5374.00 (A2-Carb)	Lawnichak 9-33	0	11268	10000
5409.00 (A2-ANH)	Lawnichak 9-33	0	8977	8977
5525.50 (A1-Carb)	Lawnichak 9-33	0	5786	5786
5549.50 (Upper Brown)	Lawnichak 9-33	0	10529	10529
5625.00 (Lower Brown)	Lawnichak 9-33	0	19618	17668
5602.65 (Upper Brown)	Lawnichak 9-33	0	11835	11835
5760.00 (A2 Carb)	Chester 8-16	0	17284	17284
5819.00 (A2 ANH)	Chester 8-16	0	9084	9084
5864.00 (A1 Carb)	Chester 8-16	0	11109	11109
6334.35 (Gray Nia)	Chester 8-16	0	8602	8602
6170.50 (Brown)	Chester 8-16	0	10177	10177

Table 14-13. Summary of strength parameters determined from triaxial tests.

		Confining	Measured	Corrected
Depth (ft)	Well	Pressure (psi)	Compressive Strength (psi)	Compressive Strength (psi)
5390.00 (A2 Carb)	Lawnichak 9-33	2685	39836	39836
5430.00 (A2 ANH)	Lawnichak 9-33	2710	34079	34079
5529.00 (A1 Carb)	Lawnichak 9-33	2765	41122	41122
5553.50 (Upper Brown)	Lawnichak 9-33	1555	19779	19779
5627.00 (Lower Brown)	Lawnichak 9-33	2820	44758	44758
5602.65 (Upper Brown)	Lawnichak 9-33	4215	53122	53122
5602.65 (Upper Brown)	Lawnichak 9-33	1405	28211	28211
5602.65 (Upper Brown)	Lawnichak 9-33	2810	40001	40001
5778.00 (A2 Carb)	Chester 8-16	2200	31087	31087
5820.00 (A2 ANH)	Chester 8-16	2200	20256	20256
5903.00 (A1 Carb)	Chester 8-16	2200	20858	20858
6162.50 (Brown-45)	Chester 8-16	2200	15689	15689
6164.50 (Brown-V)	Chester 8-16	2200	27452	27452
6338.60 (Gray)	Chester 8-16	2200	24787	24787
6176.50(Brown)	Chester 8-16	1150	19656	19656
6178.50(Brown)	Chester 8-16	2300	26960	26960
6180.57(Brown)	Chester 8-16	3450	31447	31447

Mohr-Coulomb Failure Analysis

Accurate failure criteria of reservoir rocks and caprocks based on compressive strength and Mohr-Coulomb failure analysis are critical to evaluating long-term CO_2 injection, storage, and containment. The failure analysis was performed on one sample (four sub samples) of the Brown Niagaran Formation from the Dover 33 Reef and one sample of the Brown Niagaran Formation from the Chester 16 reef. Results of the Mohr-Coulomb failure analysis are presented in Table 14-14 and Figure 14-18 for the Brown Niagaran Formation of the Dover reef and Table 14-15 and Figure 14-19 for the Brown Niagaran Formation of the Chester reef. Key results are the angle of internal friction, coefficient of friction, and cohesion parameter. Both samples show similar unconfined compressive strength and angle of internal friction range. Higher cohesion is observed for Chester sample.

Table 14-14. Mohr-Coulomb failure analysis results for Upper Brown Niagaran Formation in Dover 33 Reef.

Well Name	Sample Depth (ft).	Confining Pressure Pc = σ3 (psi)	Compressive Strength σ1 (psi)	Slope on σ1 vs. σ3	Unconfined Compressive Strength (psi)	Cohesion (psi)	Angle of Internal friction (deg)	Coefficient of Internal Friction
Lawnichak 9-33	5602.65	0	11835	9.94	11345	1799	54.8	1.42
	5602.65	1405	24211					
	5602.65	2810	40001					
	5602.65	4215	53122					

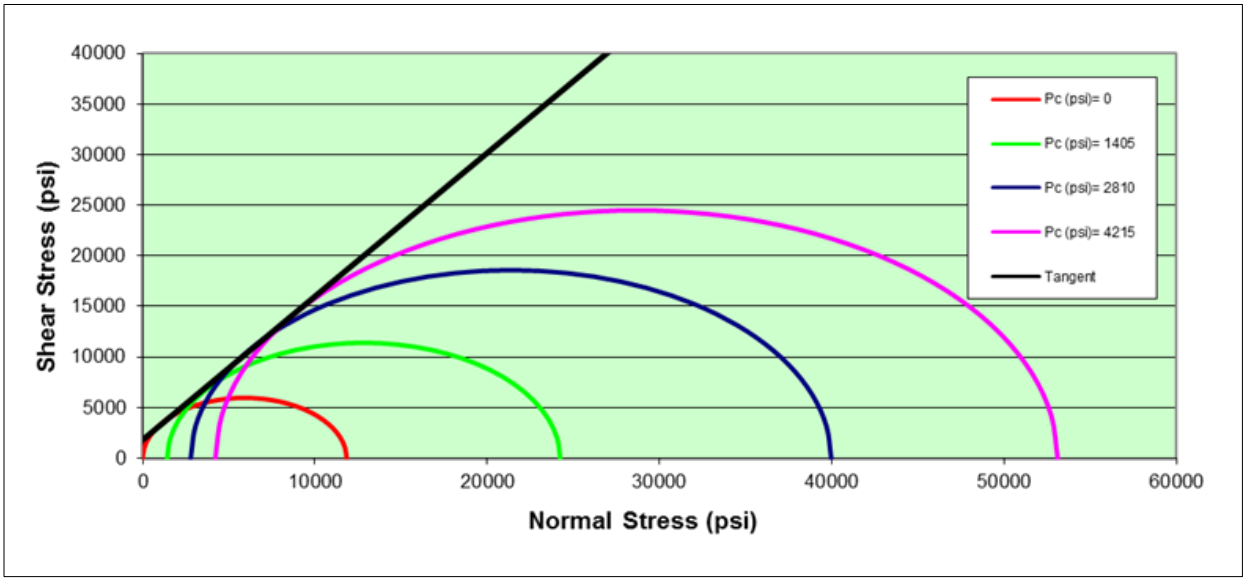


Figure 14-18. Mohr-Coulomb failure analysis.

Table 14-15. Mohr-Coulomb failure analysis results for Brown Niagaran Formation in Chester 16 Reef.

Well Name	Sample Depth (ft).	Confining Pressure Pc = σ3 (psi)	Compressive Strength σ1 (psi)	Slope on σ1 vs. σ3	Unconfined Compressive Strength (psi)	Cohesion (psi)	Angle of Internal friction (deg)	Coefficient of Internal Friction
Chester 8-16	6170.5	0	10177	6.19	11387	2289	46.19	1.04
	6176.5	1150	19642					
	6178.5	2300	26960					
	6180.57	3450	31447					

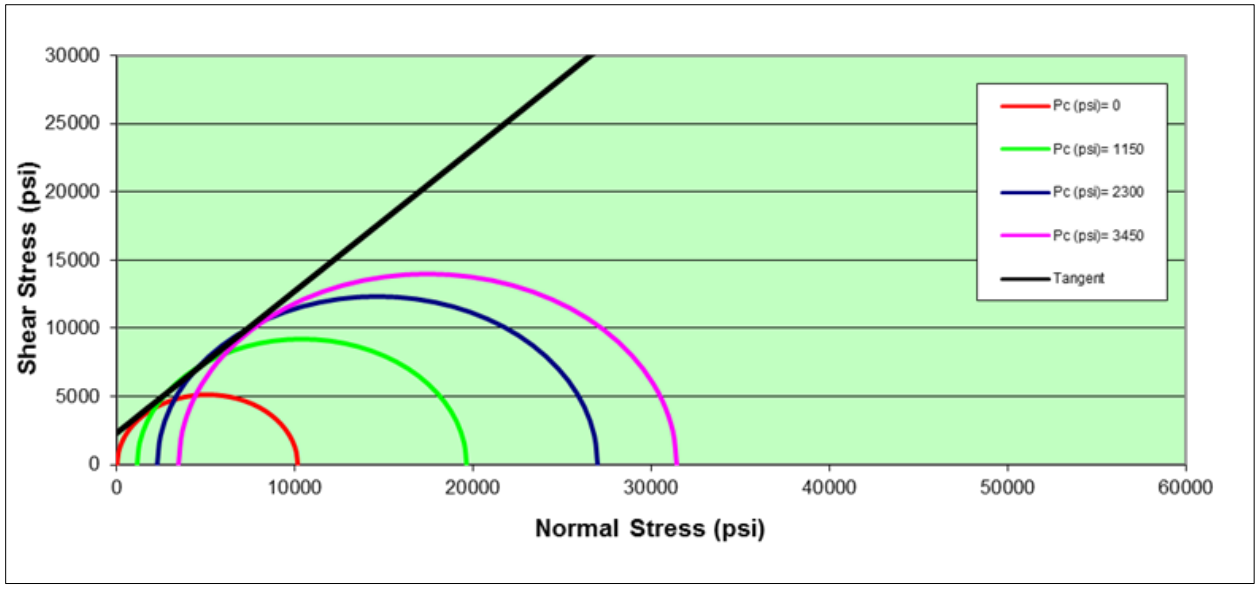


Figure 14-19. Mohr-Coulomb failure analysis.

Rock Tensile Strength Using Brazilian Tensile Test

The Brazilian test is a simple method for determining the tensile strength of a rock sample. In the Brazilian test, a disc of material is subjected to two opposing normal strip loads at the disc periphery and the applied load when the sample fails are used to calculate rock tensile strength. Only one sample from each formation was tested. Summary of tensile strength is shown in Table 14-16. Results of Brazilian Tensile experiments show that A2 carbonate and A2 anhydrate has lower tensile strength in comparison with Brown and Gray Niagaran formation.

Table 14-16. Summary of Brazilian tensile test results.

Depth (ft)	Well Name	Tensile Strength (psi)
5393.00 (A2 Carb)	Lawnichak 9-33	534
5440.00 (A2 ANH)	Lawnichak 9-33	645
5599.60 (Upper Brown)	Lawnichak 9-33	1019
5633.00 (Lower Brown)	Lawnichak 9-33	1112
6168.60 (Brown)	Chester 8-16	1167
6352.80 (Gray)	Chester 8-16	974

14.5 Conclusions

In the geomechanical characterization sub-task, the fundamental rock mechanical properties (bulk modulus, shear modulus, Young's modulus, and Poisson's ratio) of five caprock-reservoir formations were estimated. Data used to conduct this task came from five wells. Results included estimates of the mean and variance of four geomechanical parameters (shear modulus, bulk modulus, Young's modulus, and Poisson's ratio). Estimates of each parameter are provided for each formation for each well location and as an aggregate of data from the five wells. In terms of mechanical properties (shear modulus, bulk modulus, Young's modulus, and Poisson's ratio), the variability of the mechanical properties of the Salina Formation and A-2 Evaporite Formation are significantly lower across the four dynamic elastic parameters when compared to the other formations of interest. This indicates that both the Salina Formation and A-2 Evaporite Formation are more homogenous mechanically. The relatively higher levels of variance in the A-2 Carbonate, A-1 Carbonate, and Brown Niagara Formations indicate that they are more heterogeneous mechanically.

In the stress analysis subtask, the in-situ stress of the caprock and reservoir formations were characterized. This included determining the orientation of SH_{max} and magnitude of Sv at multiple well locations to help characterize spatial variability in the mentioned stress parameters. SH_{max} orientations measured using available image log data as well as shear wave anisotropy data. and Sv magnitude were determined for caprock and reservoir formations for six wells. The analysis provides essential input data (i.e., in-situ stress magnitudes) to model reservoir and caprock behavior during long-term CO_2 injection using numerical simulation. Results of SH_{max} orientations derived from DIFs within caprock formations using image-log analysis show that the orientations of SH_{max} is northeast-southwest. Sv magnitude were determined using bulk density data for 5 wells. The gradient of Sv is ~1 psi/ft. Numerical modeling was performed to predict stress changes by pressure injection. The results of modeling show that stress increase in horizontal direction is higher than stress increase in vertical direction.

In the Rock Mechanical – Rock Physical Experimental Data subtask, laboratory testing of core samples to measure mechanical properties was performed. Cores from the primary caprock and reservoir geologic units including A2 Carbonate, A2 evaporite, A1 carbonate, Brown Niagaran, Gray Niagaran were used to measure unconfined compressive, confined compressive, and tensile strength. Elastic modulus of the rock (Young's modulus and Poisson's ratio) were also measured for samples. A correlation between dynamic and static elastic modulus were built. Also, shear failure parameters (rock cohesion, and internal friction angle) were measured for Brown Niagaran formation. Mechanical rock properties measured using experimental methods, are critical data to study mechanical integrity of formations during CO_2 injection using numerical simulations.

15.0 Well Testing

15.1 Introduction

Well testing is a commonly used tool by geologists and petroleum engineers to measure the dynamic response of a reservoir (Osorio et al., 2017). Analysis of successfully implemented well tests can yield important information regarding the permeability, pressure, and boundaries of a reservoir (Lee, 1982). In addition, certain well tests can also provide geomechanical information, including the fracture pressure of the reservoir and caprock and their state of stress. This information is crucial to properly characterizing the reservoir-caprock system and is used in the construction and correction of reservoir models.

This section discusses several well tests that were conducted during the MRCSP Phase III program to support the geologic characterization of the carbonate pinnacle reefs. The tests were conducted in two wells, one in the Dover 33 reef and the other in the Chester 16 reef and were focused on the A-1 Carbonate and the Brown Niagaran reservoir rocks and the overlying A-2 Carbonate caprock. The well tests were conducted in open (uncased) boreholes (i.e., while the wells were being drilled) because this provides unlimited access to test the rocks intersected by the well. The following well tests were conducted:

- Micro hydraulic fracture (micro-frac) tests were conducted in the 8-16 well to determine fracture pressure, minimum horizontal stress (Sh_{min}) magnitude, and orientation (azimuth) of Sh_{min} and maximum horizontal stress (SH_{max}).
- Hydraulic well testing was used to determine the reservoir pressure, permeability, and reservoir type within one well (Lawnichak 9-33) in the Dover 33 reef and one well (Chester 8-16) within the Chester 16 reef.
- In-situ fluid characterization was performed within the 9-33 well to determine fluid composition at different depths, including presence of CO_2.

A summary of how these well tests were conducted, the type of data generated, and the data analyses performed is provided in this section. The information presented in this section is taken largely from the following three reports by Baker Hughes, which performed the testing and data analysis: BHI (2016), BHI (2017a), and BHI (2017b). These reports are included as attachments to this report.

15.2 Methodology

Well testing was completed in the 9-33 well in the Dover 33 reef from October 28-29, 2016, and in the 8-16 well in the Chester 16 reef from January 26-29, 2017.

15.2.1 Reservoir Pressure

Reservoir pressure is a measurement of pore fluid pressure in a porous reservoir. Testing reservoir pressure is an essential aspect of well testing used in reservoir characterization. Pressure measurements are used in fluid characterization (i.e., fluid contacts), well completion designs, and determination of dynamic reservoir properties. Reservoir pressure is also crucial input for reservoir simulation models.

Prior to conducting hydraulic testing, reservoir pressure measurements were conducted at several depths in the 9-33 well and the 8-16 well to determine current pressure conditions across the reservoir (A-1 Carbonate, Brown Niagaran Formation). Reservoir pressure measurements were completed using the Baker Hughes Reservoir Characterization eXplorer (RCX) tool (Figure 15-1). The RCX was configured

with a single “snorkel” packer-pressure transducer (probe)-piston assembly that is used to make in-situ pressure measurements by conducting small-volume drawdown-buildup tests that produce estimates of reservoir pressure and mobility (permeability divided by viscosity) (Figure 15-2). In order to obtain a representative pressure and mobility measurement, the permeability must be greater than 1 mD. At lower permeabilities, the packer will not seal.

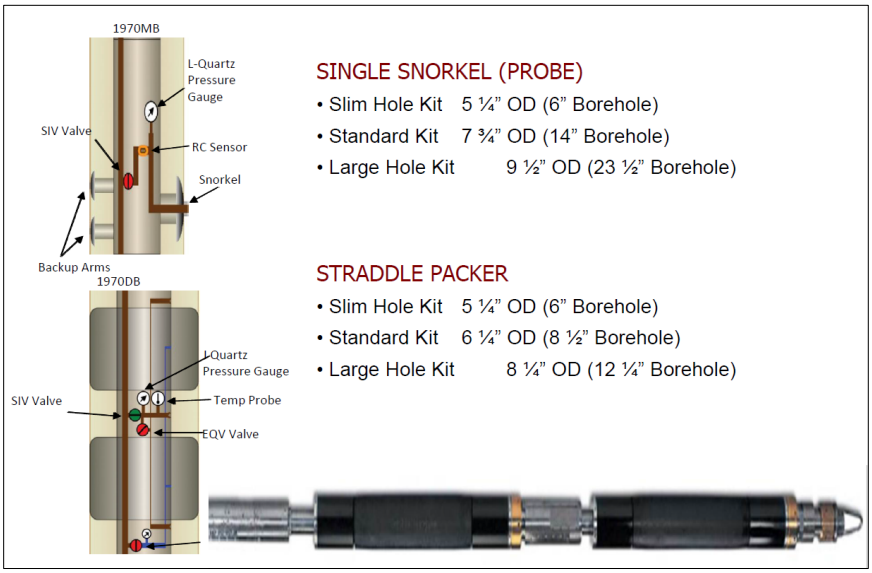


Figure 15-1. RCX configured with single snorkel above straddle packer.

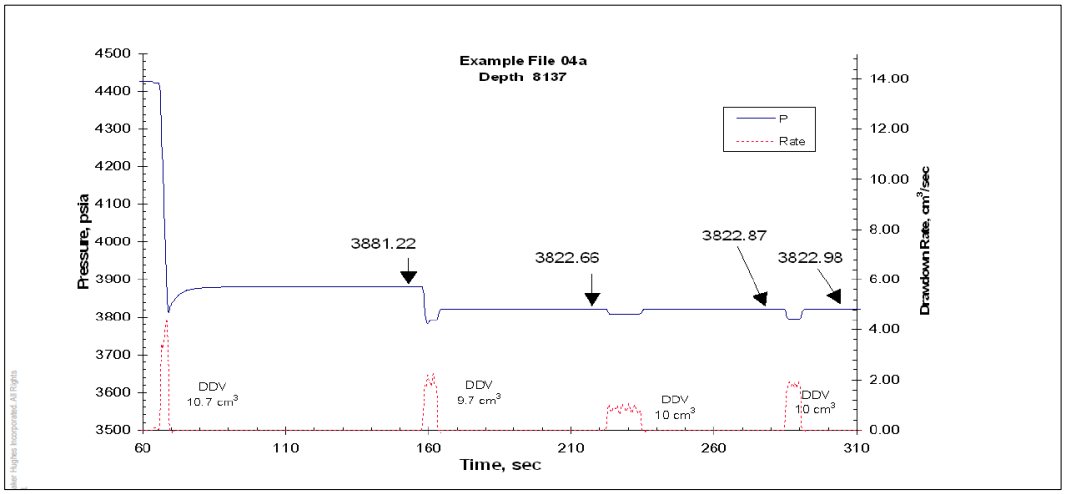


Figure 15-2. Basic pressure testing involving multiple cycles to determine a representative pressure.

15.2.2 Hydraulic Well Testing

Hydraulic drawdown-buildup tests were conducted by Baker Hughes using their RCX tool configured with a straddle packer and an observation probe. The RCX tool as configured for the hydraulic well tests conducted in the 9-33 well and the 8-16 well is illustrated in Figure 15-3. With the packers inflated, the straddle packer isolated a test interval 3.28 ft long within the open borehole. The drawdown-buildup test involves pumping fluid out of the test interval for a predetermined period. Pumping is then stopped, and pressure is allowed to recover to the pre-test condition. Pressure within the test interval is recorded continuously during the test drawdown and buildup periods. For these tests, an observation probe was added to the tool string to record pressure at a location approximately 2 meters above the straddle zone to determine the vertical permeability of the interval between the straddle packer and the observation probe. When the observation probe is included with the primary pressure probe between the packers, Baker Hughes refers to the test as a vertical interference test (VIT) or a local interference test (LIT). When the test is conducted using only the pressure gauge within the straddle packer interval, it is referred to as a mini drill-stem test (mini DST).

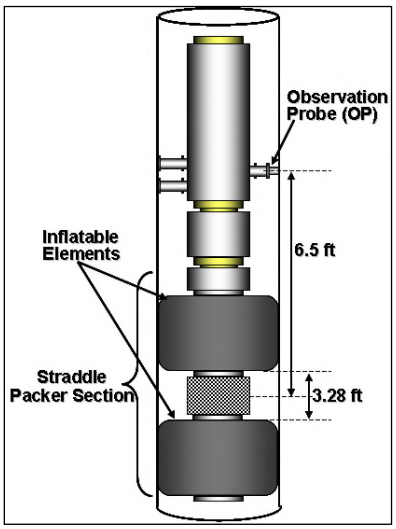


Figure 15-3. Schematic of straddle packer and an observation probe combination for a VIT (also referred to as LIT).

Pressure data from the VIT/LIT tests was analyzed using well test software “Interpret-2010” to study pressure transients. The objective of the tests was to 1) obtain representative estimates of the horizontal and vertical permeability of the reservoir interval, and 2) assess characteristics of the flow regime. As shown in Figure 15-4, expected flow regimes for a mini-DST (no observation probe) include spherical and radial flow. Radial flow provides an estimate of horizontal permeability (kxy). Spherical flow is a function of horizontal and vertical permeability and can be used to isolate vertical permeability if radial flow develops. By adding an observation probe, vertical permeability (of the region between the observation probe and straddle packer interval) can be determined during spherical flow conditions even if radial flow does not develop. Furthermore, simultaneous analysis of two pressure transient sets (i.e., straddle packer and observation probe) reduces the uncertainty in the calculation of reservoir parameters (Figure 15-5 and Figure 15-6).

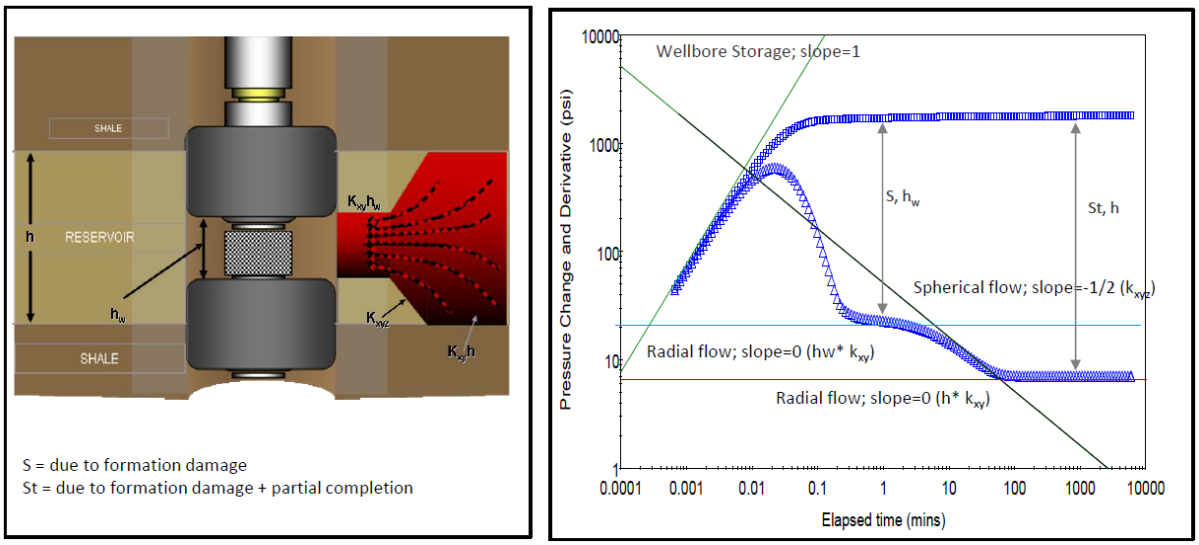


Figure 15-4. Expected flow regimes for a mini-DST (no observation probe). Radial flow provides an estimate of horizontal permeability (kxy); spherical flow is a function of horizontal and vertical permeability and can be used to isolate vertical permeability if radial flow develops.

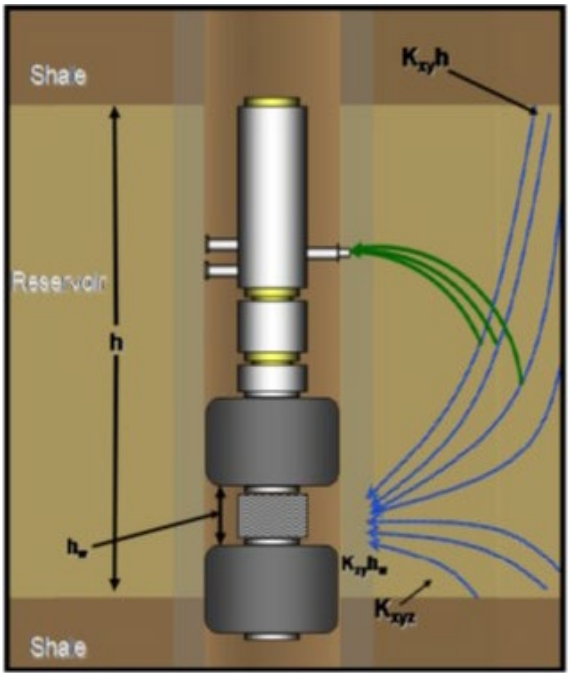


Figure 15-5. Schematic of VIT: tool diagram.

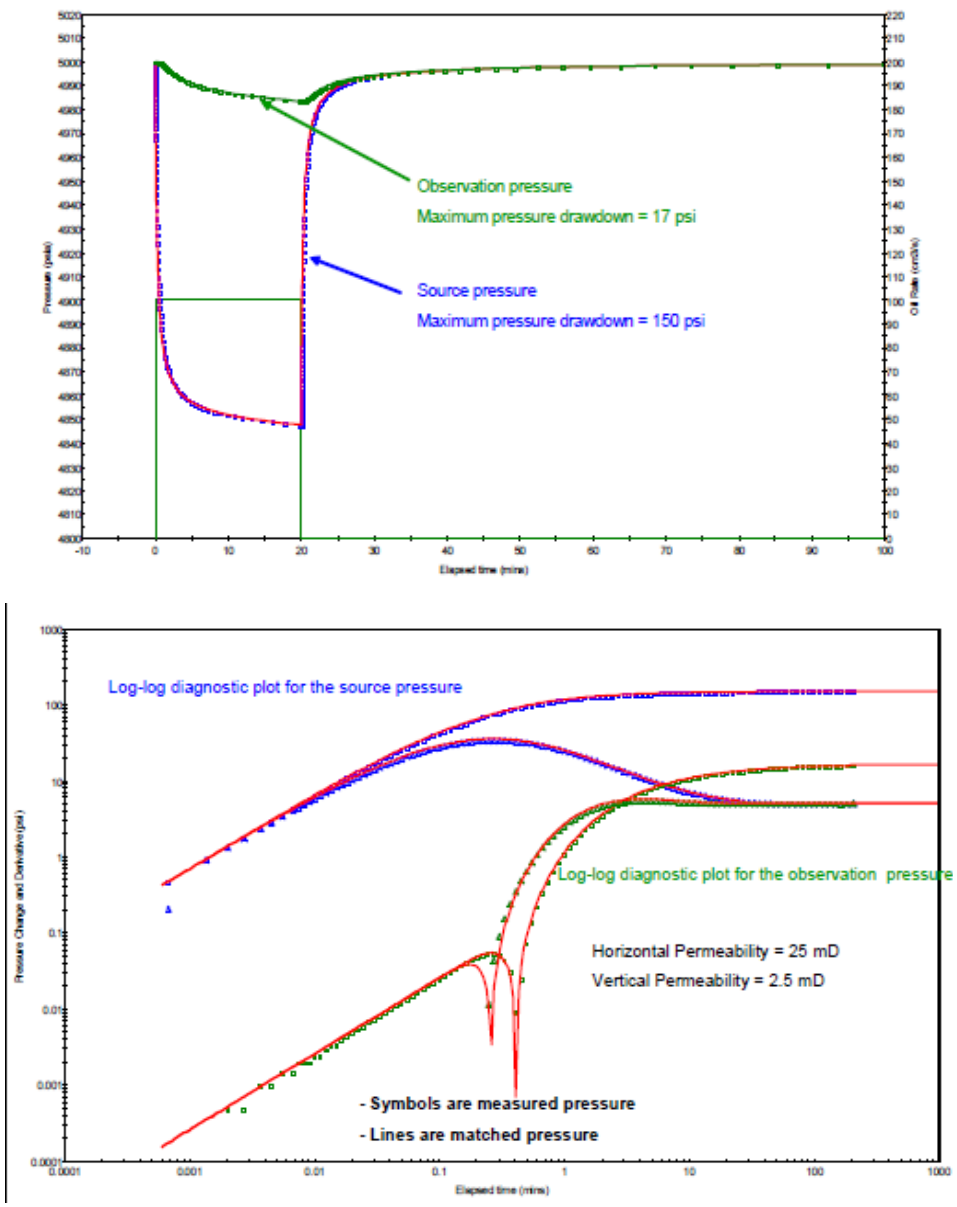


Figure 15-6. Schematic of VIT: example pressure data from straddle packer interval and observation probe (top panel) and pressure/derivative for both intervals (bottom panel).

15.2.3 Micro-Frac Tests

Micro-frac tests are used to determine the magnitude of Sh_{min}. During a micro-frac test, a small hydraulic fracture is created by injecting water into a section of open (uncased) borehole that is isolated with packers. Water is injected at a low but constant rate, causing pressure in the test interval to increase. When the wellbore fluid pressure exceeds the magnitude of Sh_{min}, a hydraulic fracture forms in the direction perpendicular to the Sh_{min} direction—i.e., the direction of SH_{max}. Image logs run after the micro-frac test provide the azimuth of SH_{max} (because the azimuth of Sh_{min} is perpendicular, it is also determined from the image log analysis). The fracture closes when injection is stopped, and the pressure falls below the Sh_{min}. The micro-frac tests are evaluated by analyzing the pressure data from the straddle packer interval.

Figure 15-7 illustrates a micro-frac test showing parameters that can be determined: formation breakdown pressure, fracture reopening pressures, fracture propagation, and fracture closure pressure of the tested formations. Fracture closure pressure is equivalent to Sh_{min}. Micro-frac tests can also be used to calibrate tectonic stress and strain due to pressure depletion in carbonate reservoirs and to improve reservoir deformation modeling and compaction prediction for field development and pressure maintenance decisions.

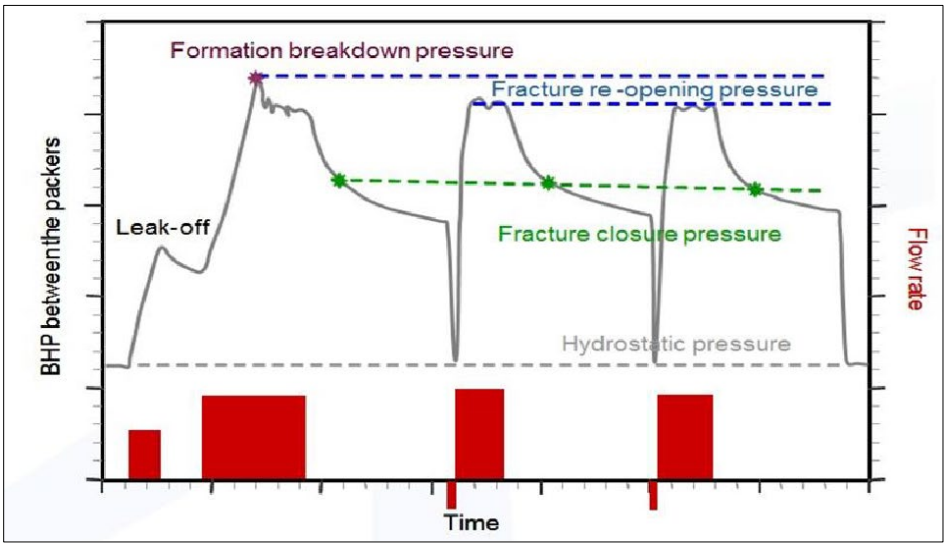


Figure 15-7. Illustration of a typical micro-frac test in which multiple injection-recovery cycles are performed.

Micro-frac testing was completed in the 8-16 well in the reservoir (A-1 Carbonate and Brown Niagaran) and the overlying A-2 Carbonate caprock. The tests were performed by Baker Hughes using their RCX tool configured with a straddle packer (an observation probe was not used in this test). Unlike the hydraulic tests, in the micro-frac test the pump is configured to inject fluid (water) from the borehole above the straddle packer into the test interval (i.e., between the straddle packers) in order to increase reservoir pressure.

The fracture closure pressure (Sh_{min}) was determined by three different methods: (1) pressure decline analysis using the test interval pressure vs. shut-in time; (2) log-log pressure decline analysis using the pressure derivative of the delta pressure and delta time in log-log plot, and (3) G-function analysis by plotting the test interval pressure vs. G-time plot. Each pressure decline method was done using mini-frac software developed by Meyer and Associates (now a Baker Hughes product).

15.2.4 Fluid Characterization

Fluid characteristics were determined in the 9-33 well (Dover 33 reef) at four test depths in the reservoir during the open-borehole testing conducted October 28-29, 2016. Fluid properties were measured in-situ (i.e., without retrieving fluid samples) with the Baker Hughes RCX tool equipped with the In-Situ Fluids eXplorer™ (IFX) module and were used to determine the predominant fluid type present—i.e., water, oil, gas. The tool uses near-infrared (NIR) fluid absorbance spectra and fluorescence spectra (Figure 15-8) to measure continuous refractive index, optical density, and fluorescence (Figure 15-9). A methane detector measures methane directly. In addition, a tuning fork measures fluid density and viscosity and a transducer measures sound speed (slowness) (Figure 15-10). In addition to measured parameters, GOR and fluid compressibility are calculated. GOR is calculated as a function of temperature, pressure, density, and sound speed slowness. GOR is available only when both the tuning fork and the transducer work. In the fluid characterization performed in the 9-33 well, the tuning fork did not work; therefore, the density, viscosity, and GOR measurements were not made. Interpretation of the fluid property measurements allows four fluid types to be determined: oil, dry gas, gas condensate, and formation water.

CO_2 is not measured directly but it is possible to qualitatively determine its presence or absence from the absorbance spectrum; however, this is only possible in the absence of water. Any water presence would greatly affect the reading making it impossible to determine the presence or absence of CO_2.

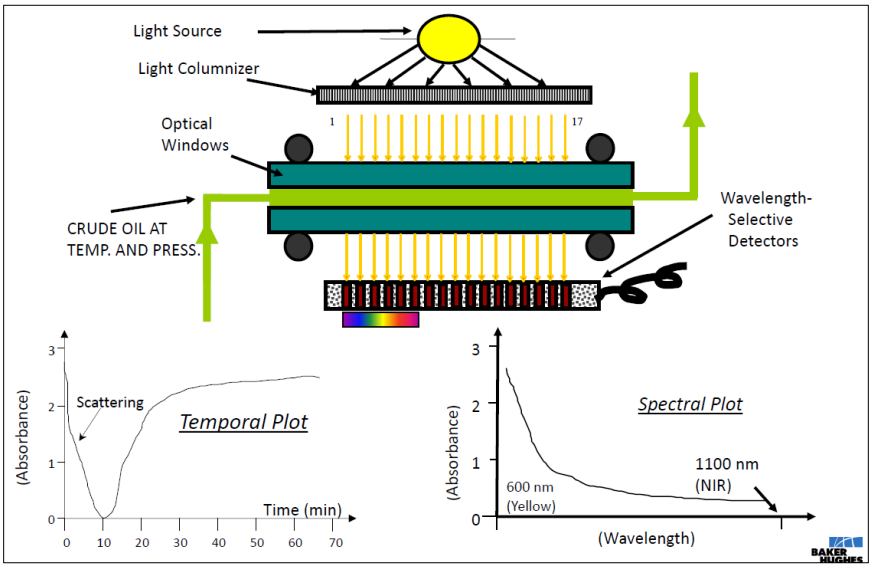


Figure 15-8. Schematic of IFX absorbance analysis.

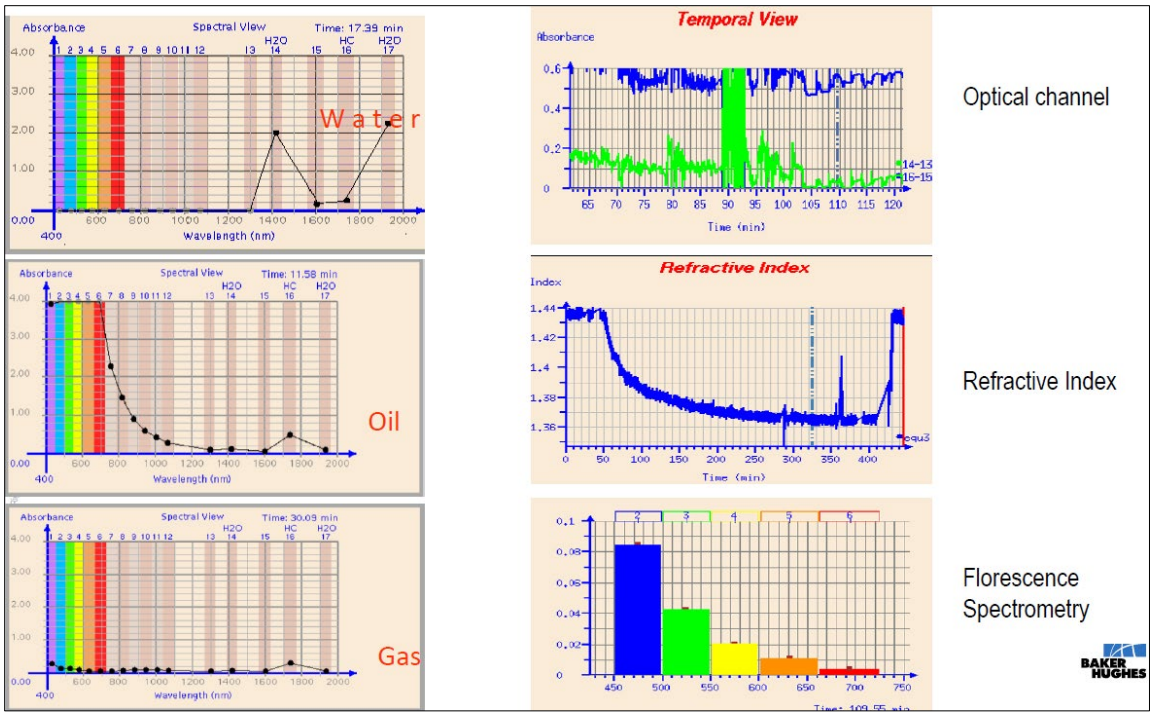


Figure 15-9. Output from spectral absorbance analysis.

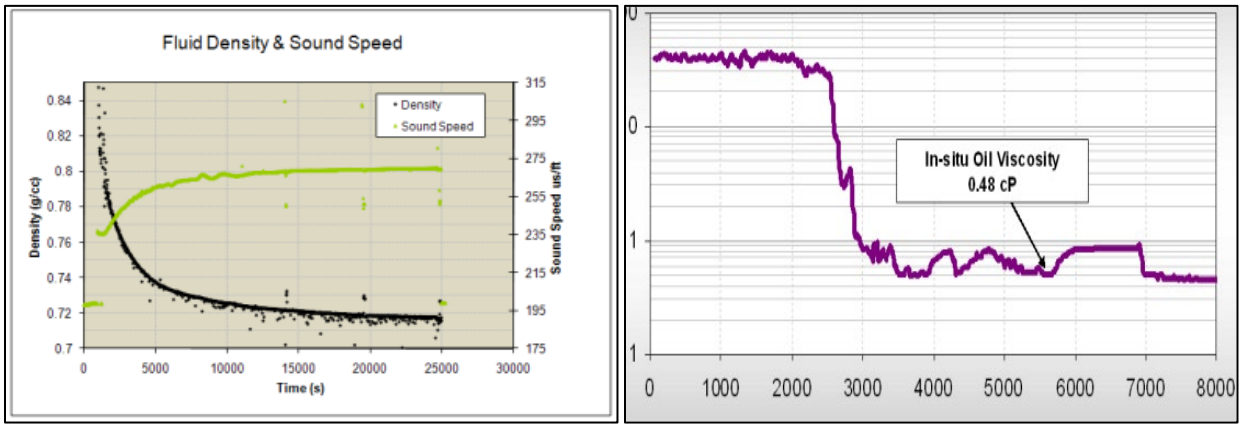


Figure 15-10. Example output from tuning fork (density and viscosity) and transducer (sound speed).

15.3 Lawnichak 9-33 (Dover 33)

15.3.1 Reservoir Pressure

Pressure measurements were attempted at 22 depth locations in the 9-33 well (Table 15-1). Successful tests were achieved at only one depth location, yielding a reservoir pressure of 2920 psi and a mobility of 2.3 mD/cP. The other tests were not successful because the formation permeability was too low (meaning water could not be withdrawn) or a seal was not achieved by the packer (20 of 22 attempts). Baker Hughes attributed the inability to achieve a seal to the standard packer that was used (shown in Figure 15-11; note that it has a smooth face). Baker Hughes recommended using the elongated packer with a lip for subsequent pressure testing of the 8-16 well.

Table 15-1. Pressure and mobility measurements from well 9-33.

Test	MD (ft)	TVD (ft)	Temp (°F)	Minimum Pressure (psi)	Final Build-Up Pressure at End of Test (psig)	Calculated k/mu (mD/cP)	Comment
1	5465.6	5336.7	102.2	---	---	---	No seal
2	5466.0	5337.0	102.6	---	---	---	Tight test
3	5467.2	5337.9	102.8	---	---	---	No seal
4	5494.7	5358.7	102.9	---	---	---	No seal
5	5524.6	5381.4	103.0	---	---	---	No seal
6 (VIT-22)	5527.0	5383.2	103.6	1984.22	2920.57	2.3	Good test
7	5515.7	5374.5	103.6	---	---	---	No seal
8	5571.6	5417.8	103.7	---	---	---	No seal
9	5573.0	5418.9	103.7	---	---	---	No seal
10	5590.3	5432.4	103.8	---	---	---	No seal
11	5589.1	5431.4	103.8	---	---	---	No seal
12	5590.4	5432.4	103.9	---	---	---	No seal
13	5508.7	5445.8	103.9	---	---	---	No seal
14	5639.3	5470.9	104.0	---	---	---	No seal
15	5659.5	5485.9	104.1	---	---	---	No seal
16	5725.5	5539.8	104.2	---	---	---	No seal
17	5787.5	5590.3	104.4	---	---	---	No seal
18	5583.2	5426.8	105.4	---	---	---	No seal
19	5520.7	5378.4	106.1	---	---	---	No seal
20	5620.3	5455.9	105.6	---	---	---	No seal
21	5640.0	5471.5	105.8	---	---	---	No seal
22	5543.3	5395.8	105.5	---	---	---	No seal



Figure 15-11. Packers available for the Baker Hughes RCX single packer probe used to measure reservoir pressure.

15.3.2 Hydraulic Well Tests

Four open-borehole VITs were conducted in the 9-33 well on October 30, 2016: two in the A-1 Carbonate and two in the Brown Niagaran (Table 15-2). This section provides a summary of the four VITs. Table 15-3 lists the properties used in the analysis of VITs.

Table 15-2. Depth of VITs in the 9-33 well.

Test	Formation	Straddle Packer Midpoint (ft, MD)	Observation Probe (ft, MD)
VIT-22	A-1 Carbonate	5527.2	5520.7
VIT-23	Brown Niagaran	5626.8	5620.3
VIT-24	Brown Niagaran	5646.5	5640.0
VIT-25	A-1 Carbonate	5549.8	5543.3

Table 15-3. Reservoir and fluid parameters used in the analysis of the VITs.

Parameter	Unit	VIT-22	VIT-23	VIT-24	VIT-25
Wellbore radius	in	3.9375	3.9375	3.9375	3.9375
Temperature	°F	105	105	105	106
Porosity	%	8	8	7	10
Reservoir thickness	ft	100	100	100	100
Total compressibility	1/psi	7.93E-5	6.8179E-6	6.8416E-6	7.98E-5
CO_2 viscosity	cP	1.25	NA	NA	1.23
Water viscosity	cP	NA	0.77	0.77	NA

The predominant fluid type at test depths #1 and #4 (the two shallowest test points) was determined to be CO_2 (see Section 15.3.3); the predominant fluid type at test depths #2 and #3 was determined to be water. A CO_2 viscosity of 1.25 centipoise (cP), a water viscosity of 0.77 cP, and an average porosity of 8 percent was used in the analyses of VITs. Paradigm's well testing software Interpret-2010 is designed for the simultaneous analysis of pressure data from the straddle packer and observation probes. However, the observation probe did not obtain a seal during any of the four VITs. Therefore, the pressure analyses were conducted using only data from the straddle packer test interval.

VIT-22 (A-1 Carbonate, 5527.2 ft MD)

A total of 60 liters of fluid were pumped (removed) from the straddle packer test interval in 100 minutes, followed by a pressure buildup period that lasted 186 minutes. An average flow rate of 9.9 cubic centimeters per second (cm^3/s) was obtained with the 500-cm^3 pump. The flow rate just before the final buildup period was 11.1 cm^3/s. The maximum pressure drawdown during the flow period was 754 psi in the straddle packer test interval. Figure 15-12 is a plot of the pumping rate and the pressure response in the straddle packer test interval during VIT-22.

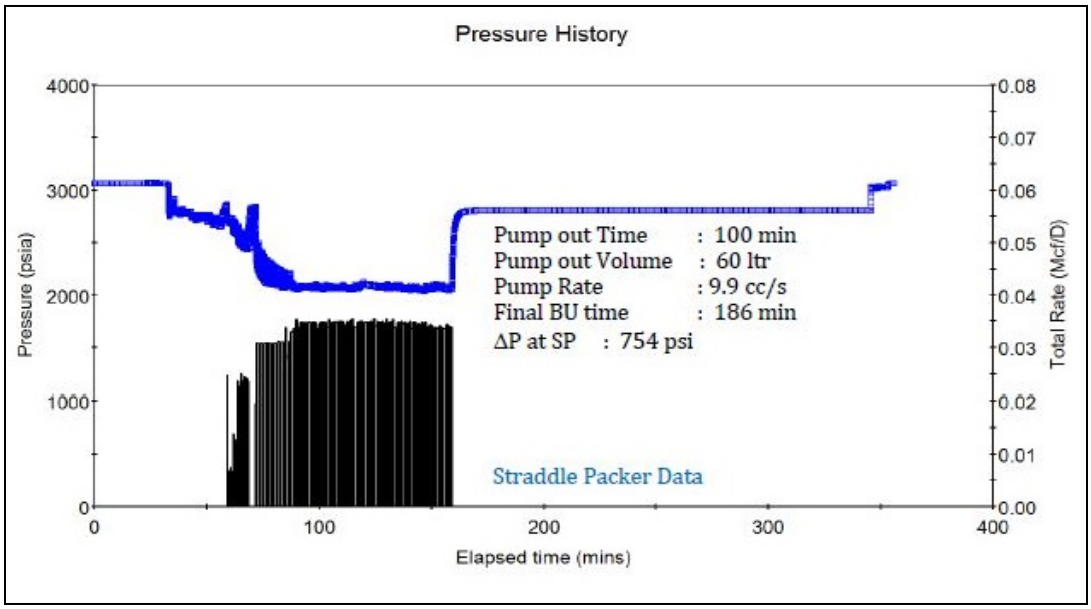


Figure 15-12. Pumping rate and pressure response in the straddle packer interval during VIT-22.

Pressure Transient Analysis (VIT-22)

A diagnostic log-log plot for the straddle packer pressure response data during the buildup period is shown in Figure 15-13 (blue symbols). The straddle packer pressure data (blue squares) and pressure derivative (blue triangles) show that the early-time pressure response was dominated by tool storage and nearby effects of skin. After the tool storage period, the spherical flow regime (slope = -1 on derivative curve) is not well developed. Similarly, the radial flow regime (slope = 0 on derivative curve) is also not well developed. As a result, there is great uncertainty in the pressure transient analysis (PTA) at this station. The properties listed in Table 15-4 were derived from a PTA of the pressure data, assuming spherical and radial flow.

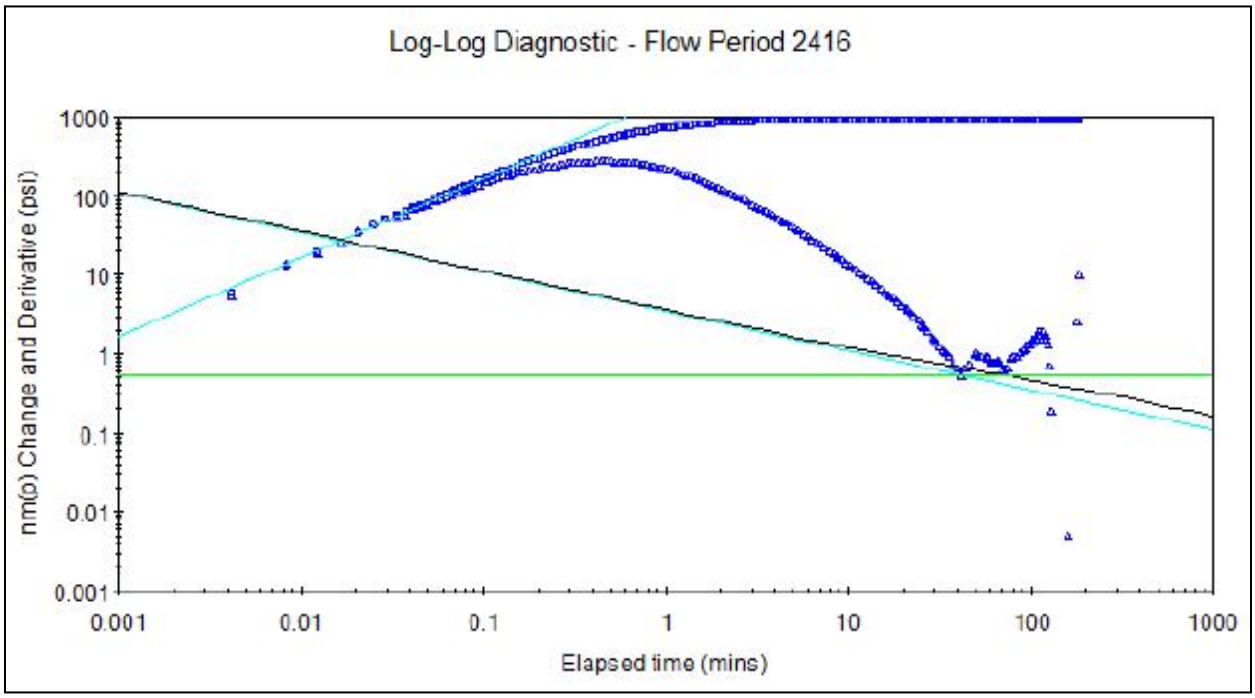


Figure 15-13. PTA of VIT-22; log-log diagnostic plot of straddle packer (blue symbols) pressure response during VIT-22 buildup period, solid lines are shown for wellbore storage (slope = 1), spherical flow (slope = -1) and radial flow (slope = 0) in the straddle packer interval.

Table 15-4. Reservoir properties estimated from PTA of VIT-22 straddle packer pressure data.

Property	Units	Type	Value	Uncertainty
Flow Regime	NA	Spherical Radial	NA	NA
Transmissivity (kh)	mD-ft		968 (avg)	High
Permeability (k)	mD		9.7[a]	High
Reservoir pressure (P[a])	psi		2806[a]	High
Radius of investigation (r)	ft		56	High

[a] Pressure, mobility measured at this depth = 2,920 psi, 2.3 mD/cP.

History Matching (VIT-22)

The VIT-22 pressure data was examined against various vertical well models. The most satisfactory result was obtained with a partially completed well in an infinitely acting homogeneous reservoir model.

Figure 15-14 and Figure 15-15 show the match between modeled data and measured data in a log-log plot of recovery pressure and pressure derivative data (Figure 15-14) and in a Cartesian plot of the entire drawdown-buildup sequence (Figure 15-15). The discrepancy between the actual and calculated pressure data during the pump-out period in Figure 15-15 is attributed to changing wellbore storage that cannot be evaluated with the analytical model; however, the modeled data matches the general trend of the observed pressures.

Model input parameters and reservoir properties derived from the model history match analysis are provided in Figure 15-16.

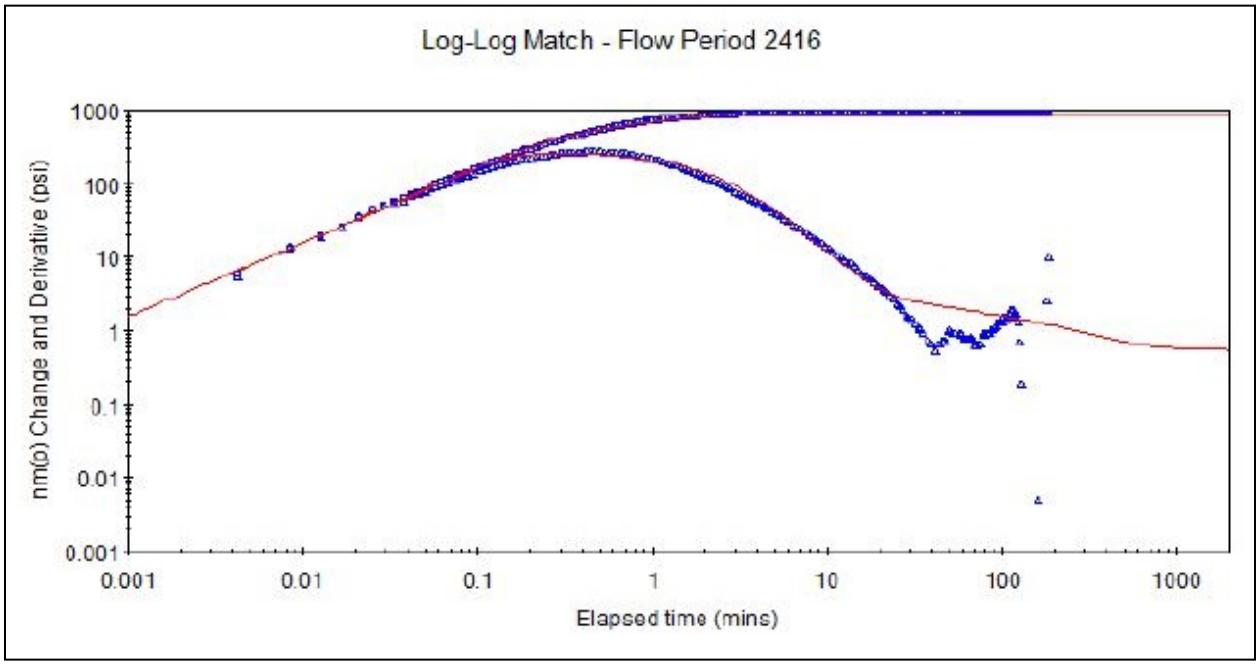


Figure 15-14. Matching of straddle packer data in log-log plot in VIT-22 using "partially completed well in an infinitely acting homogeneous reservoir" model.

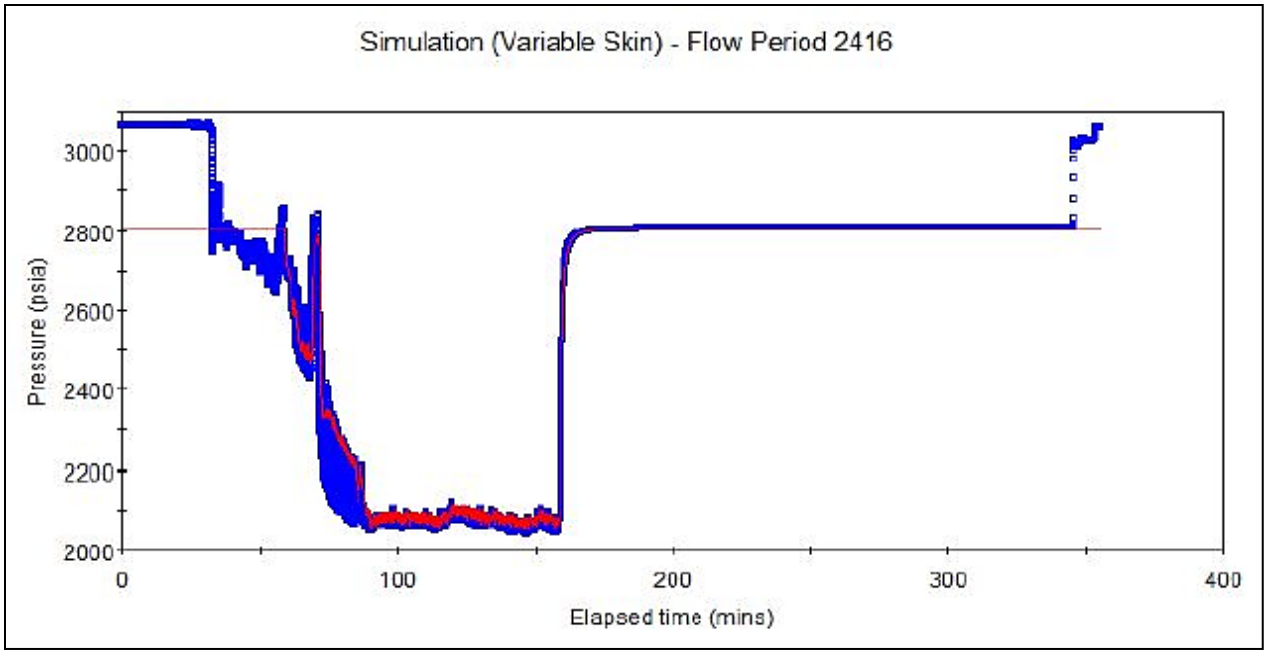


Figure 15-15. Pressure history match of test interval data for the entire VIT-22.

Near Wellbore Effect:	Partially Penetrating Well with C and S
Reservoir Behaviour:	Homogeneous
Boundary Effect:	Infinite Lateral Extent
Initial average reservoir pressure, (pav)i	2806.118 psia
Flowing pressure, pwf	2054.901 psia
Permeability Thickness, kh	967.5 mD.ft
Horizontal Permeability, k(xy)	9.675 mD
Vertical Permeability, k(z)	3.000 mD
First wellbore storage coefficient, C1	2.58E-006 bbl/psi
Second wellbore storage coefficient, C2	5E-006 bbl/psi
Phase redistribution time parameter, Alpha	1.700 s
Phase redistribution pressure change, Dp(C)	22.322 psi
Dimensionless well penetration, hw/h	0.03280
Perforated Interval, Hw	1.00 m
Wellbore skin factor, S(w)	25.03
Completion skin, S(c)	71.88
Total Skin, S(t)	834.95
Distance to Lower Boundary, Zw	55.00 ft
Type of top boundary, Type top	No Flow
Type of bottom boundary, Type bot	No Flow
Radius of investigation (approx), ri	56 ft
Pressure drop due to skin, Dp(S)	678.7 psi

Figure 15-16. Model input parameters and reservoir properties from the model history match analysis for VIT-22.

VIT-23 (Brown Niagaran, 5626.8 ft MD)

For VIT-23, a total of 78 liters of fluid were pumped (removed) from the straddle packer interval in 211 minutes, followed by a pressure recovery period of 55 minutes. An average flow rate of 6.2 cm^3/s was obtained with the 500-cm^3 pump on the RCX tool. The flow rate just before the final buildup period was 7.3 cm^3/s. The pressure drawdown during the flow period was 822 psi in the test interval. There was no seal at the observation probe and no pressure was recorded. Figure 15-17 is a plot of the pumping rate and the pressure response in the straddle packer test interval during VIT-23.

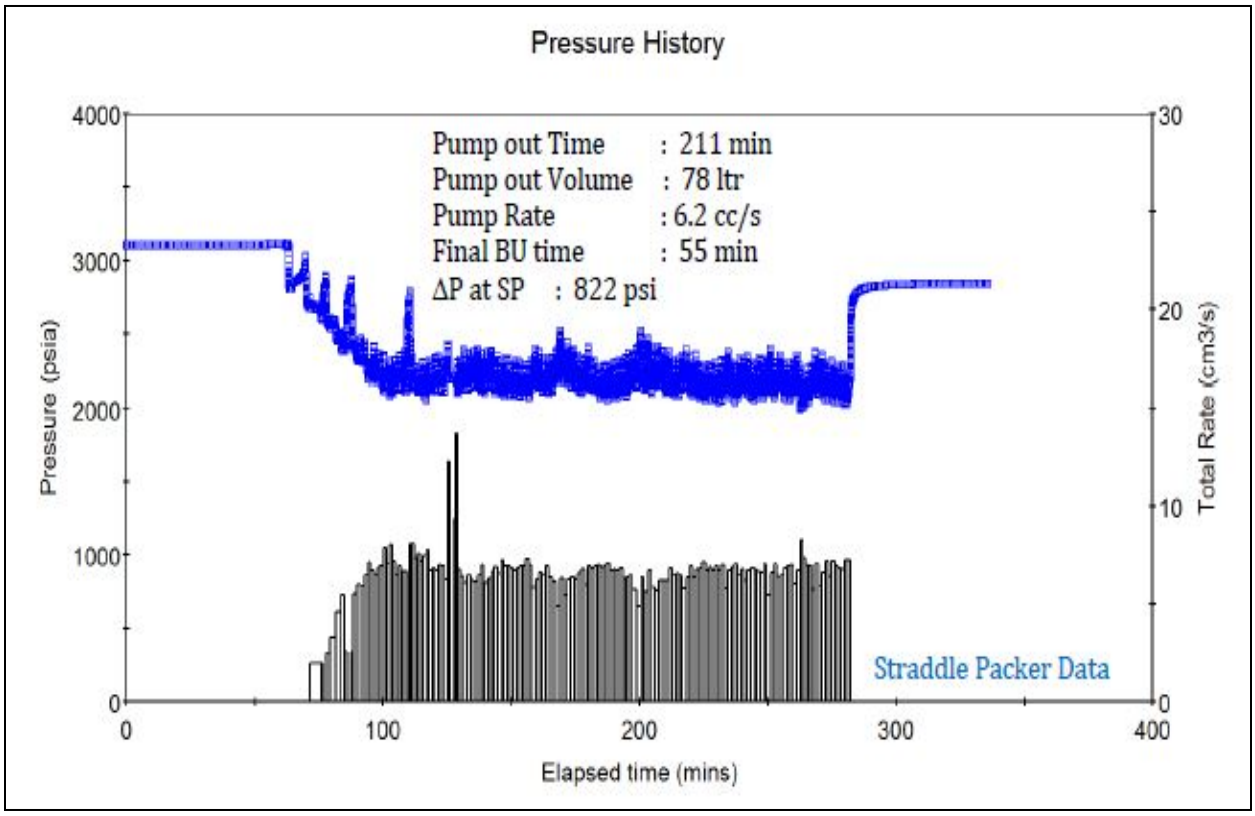


Figure 15-17. Pumping rate and pressure response in the straddle packer interval during VIT-23.

Diagnostic Analysis (VIT-23)

A diagnostic log-log plot for the straddle packer data is shown in Figure 15-18. The early-time pressure response in the straddle packer interval was dominated by tool storage and nearby effects of skin. After the tool storage period, the derivative (blue triangles) shows spherical flow (-1/2 slope derivative) at around 3 minutes. The late-time derivative has a decreasing slope, which may indicate changing reservoir properties (increasing permeability) or a constant pressure boundary, possibly due to CO_2 injection at the nearby 1-33 injection well. Because radial flow was not observed, a PTA was not performed.

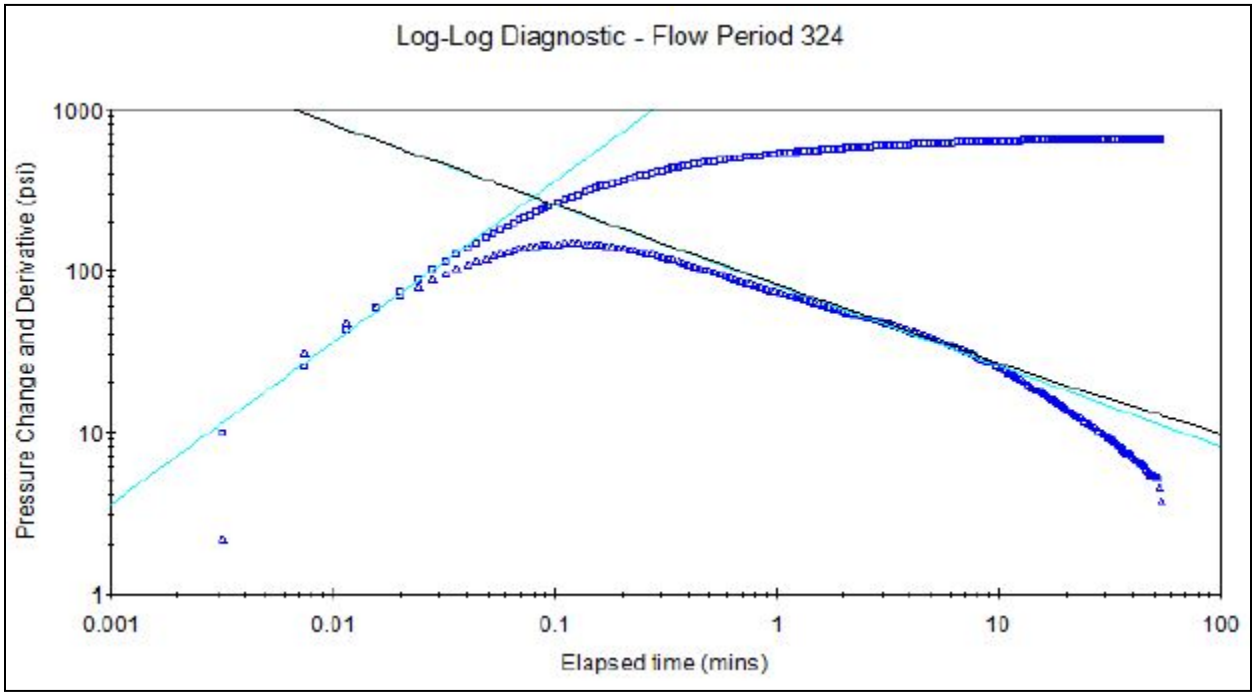


Figure 15-18. PTA of VIT-23; log-log diagnostic plot of straddle packer (blue symbols) pressure response during VIT-23 buildup period; solid lines are shown for wellbore storage (slope = 1) and spherical flow (slope = -1).

History Matching (VIT-23)

For VIT-23, the most satisfactory result was obtained using two models: a partially completed well in a homogeneous reservoir with a constant pressure boundary or a partially completed well in an infinitely acting radial composite reservoir.

Figure 15-19 and Figure 15-20 show the match between modeled data and measured data in a log-log plot of recovery pressure and pressure derivative (Figure 15-19) and in a Cartesian plot of the entire drawdown-buildup sequence (Figure 15-20). In Figure 15-20, the observed pressure spikes during the pump-out period are attributed to slight deformation of the straddle packer. Model input parameters and reservoir properties derived from the model history match analysis are provided in Figure 15-21 (constant pressure boundary model and radial composite model). Both models reasonably match the pressure transient data, and both yield similar transmissivity values (95 and 87 millidarcy-feet [mD-ft]).

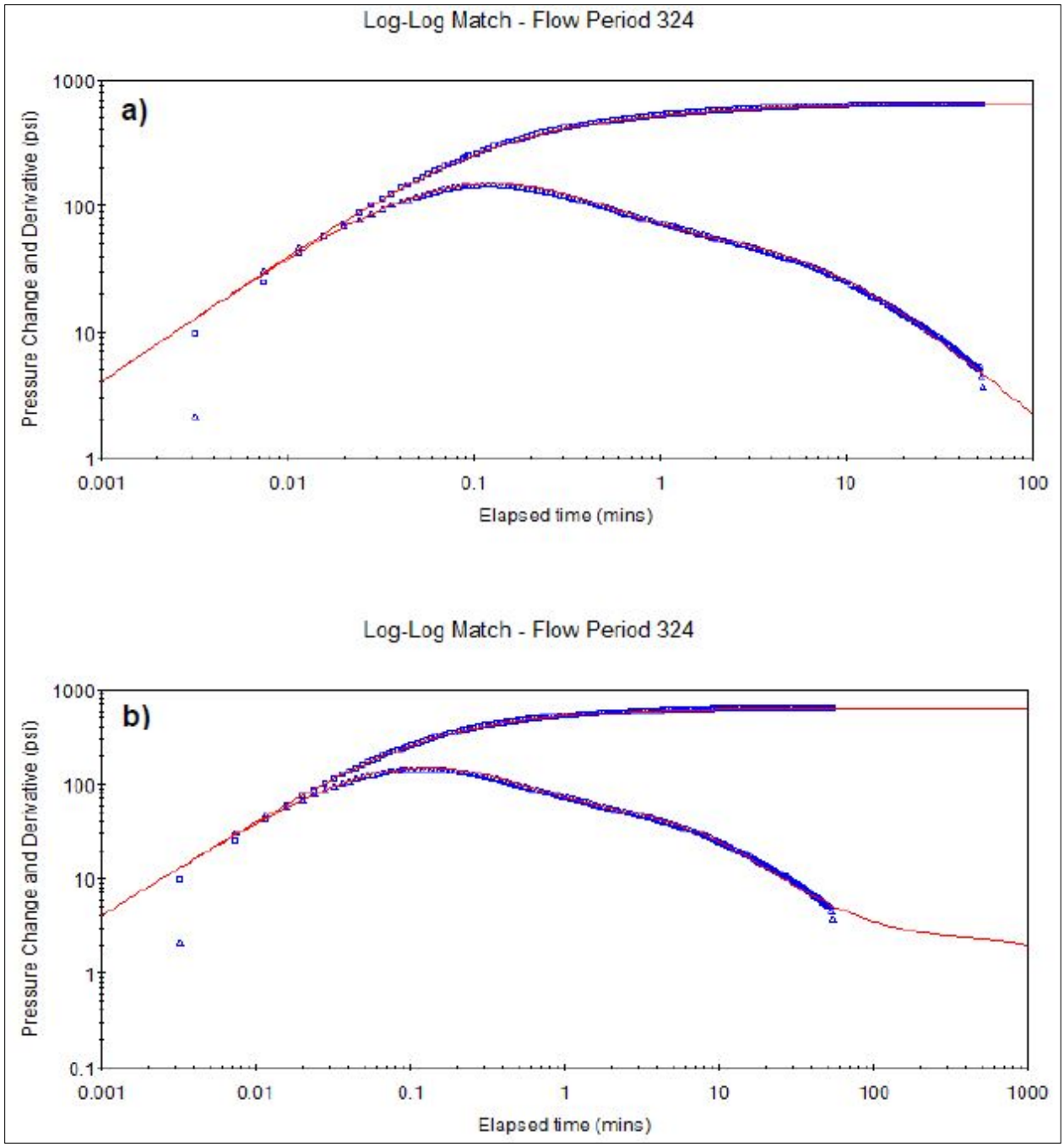


Figure 15-19. Matching of straddle packer data in log-log plot in VIT-23; panel a shows a constant pressure boundary model; panel b shows a radial composite model.

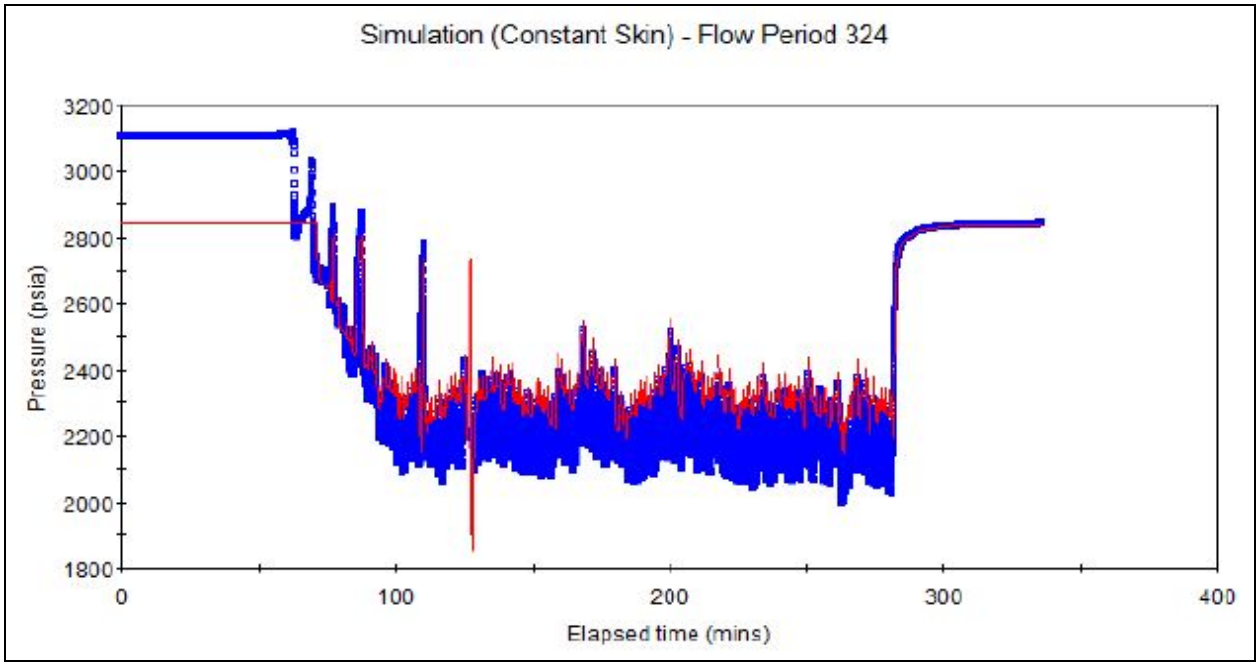


Figure 15-20. Pressure history match of the VIT-23 pumping and buildup periods (both models produce similar results).

MODEL 1 (Constant Pressure Boundary)	
Near Wellbore Effect:	Partially Penetrating Well with C and S
Reservoir Behaviour:	Homogeneous
Boundary Effect:	Single Boundary
Initial average reservoir pressure, (pav)i	2841.554 psia
Flowing pressure, pwf	2195.300 psia
Permeability Thickness, kh	94.51 mD.ft
Horizontal Permeability, k(xy)	0.9451 mD
Vertical Permeability, k(z)	0.02851 mD
Wellbore storage coefficient, C	6.575E-007 bbl/psi
Dimensionless well penetration, hw/h	0.03281
Perforated Interval, Hw	1.00 m
Wellbore skin factor, S(w)	1.41
Completion skin, S(c)	105.29
Total Skin, S(t)	148.16
Distance to Lower Boundary, Zw	19.39 ft
Type of top boundary, Type top	No Flow
Type of bottom boundary, Type bot	No Flow
Distance to first boundary, d1	12.0823 ft
Type of first boundary, Type d1	Const Pres
Distance investigated (approx), Dinv	35 ft
Measured Productivity Index, PI	0.006113 B/D/psi
Steady State Productivity Index, PI-SS	0.006038 B/D/psi
Flow Efficiency, FE	0.7021 fraction
Pressure drop due to skin, Dp(S)	195.0 psi

MODEL 2 (Radial Composite)	
Near Wellbore Effect:	Partially Penetrating Well with C and S
Reservoir Behaviour:	Radial Composite
Boundary Effect:	Infinite Lateral Extent
Initial average reservoir pressure, (pav)i	2843.611 psia
Flowing pressure, pwf	2195.300 psia
Permeability Thickness, kh	88.61 mD.ft
Horizontal Permeability, k(xy)	0.8861 mD
Vertical Permeability, k(z)	0.04211 mD
Wellbore storage coefficient, C	6.5177E-007 bbl/psi
Dimensionless well penetration, hw/h	0.03281
Perforated Interval, Hw	1.00 m
Wellbore skin factor, S(w)	1.25
Completion skin, S(c)	99.39
Total Skin, S(t)	137.63
Distance to Lower Boundary, Zw	12.24 ft
Type of top boundary, Type top	No Flow
Type of bottom boundary, Type bot	No Flow
Composite discontinuity radius, r1	17 ft
Composite storativity ratio, (pch)1/2	0.5410
Composite mobility ratio, (kh/u)1/2	0.2800
Radius of investigation (approx), ri	40 ft
Measured Productivity Index, PI	0.006094 B/D/psi
Flow Efficiency, FE	0.7140 fraction
Pressure drop due to skin, Dp(S)	185.4 psi

Figure 15-21. Model input parameters and reservoir properties from the model history match analysis for VIT-23 (constant pressure boundary model and radial composite model).

VIT-24 (Brown Niagaran, 5646.5 ft MD)

In VIT-24, a total of 14.4 liters of fluid were pumped (removed) from the straddle packer interval in 220 minutes, followed by a pressure recovery period of 134 minutes. An average flow rate of 1.1 cm^3/s was obtained with the 500-cm^3 pump on the RCX tool. The flow rate just before the final buildup period was 1.3 cm^3/s. The pressure drawdown during the flow period was 2073 psi in the test interval. There was no seal at the observation probe, so pressure was not recorded at this location. Figure 15-22 is a plot of the pumping rate and the pressure response in the straddle packer test interval during VIT-24.

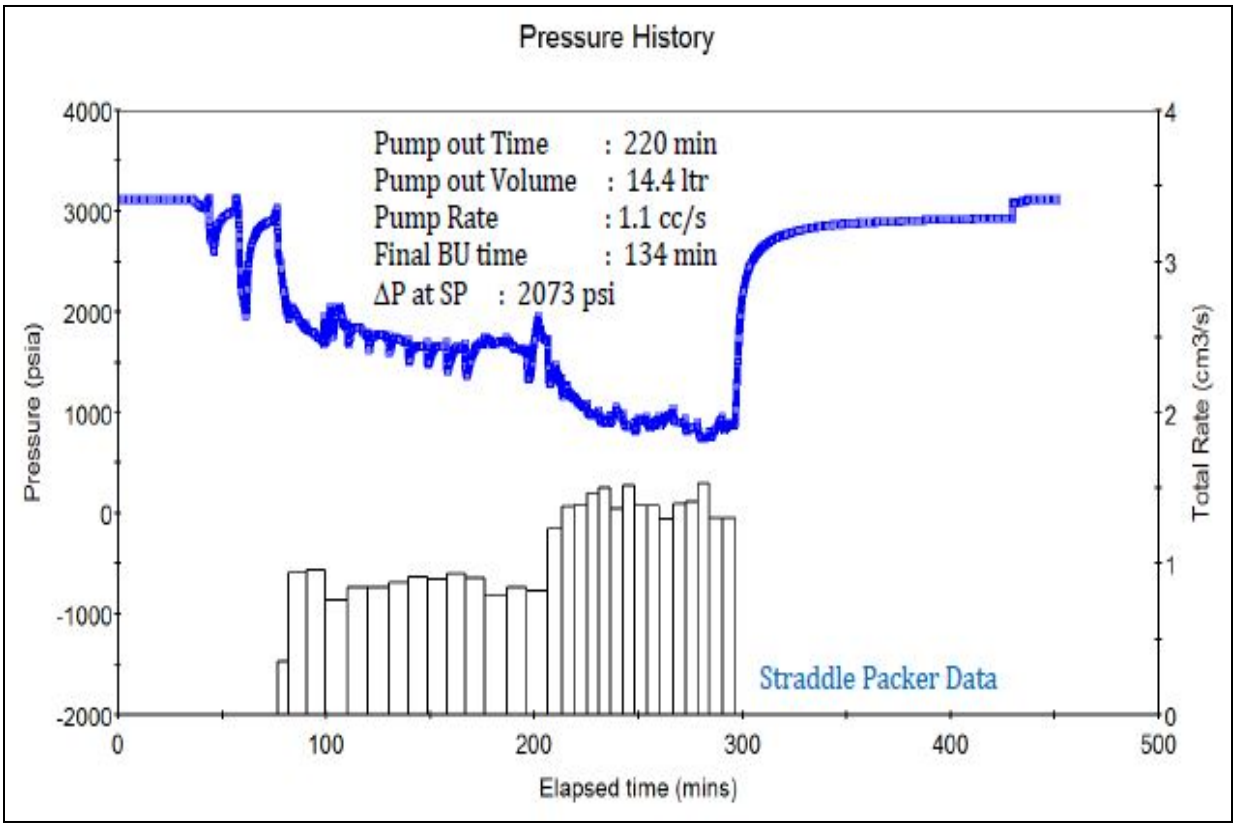


Figure 15-22. Pumping rate and pressure response in the straddle packer interval during VIT-24.

Diagnostic Analysis (VIT-24)

A diagnostic log-log plot for the straddle packer data is shown in Figure 15-23. The early-time pressure response in the straddle packer interval was dominated by tool storage and nearby effects of skin. After the tool storage period, the derivative (blue triangles) shows spherical flow at around 50 minutes of the pressure buildup. Due to the low permeability, the buildup was not extended for stabilization to reach radial flow.

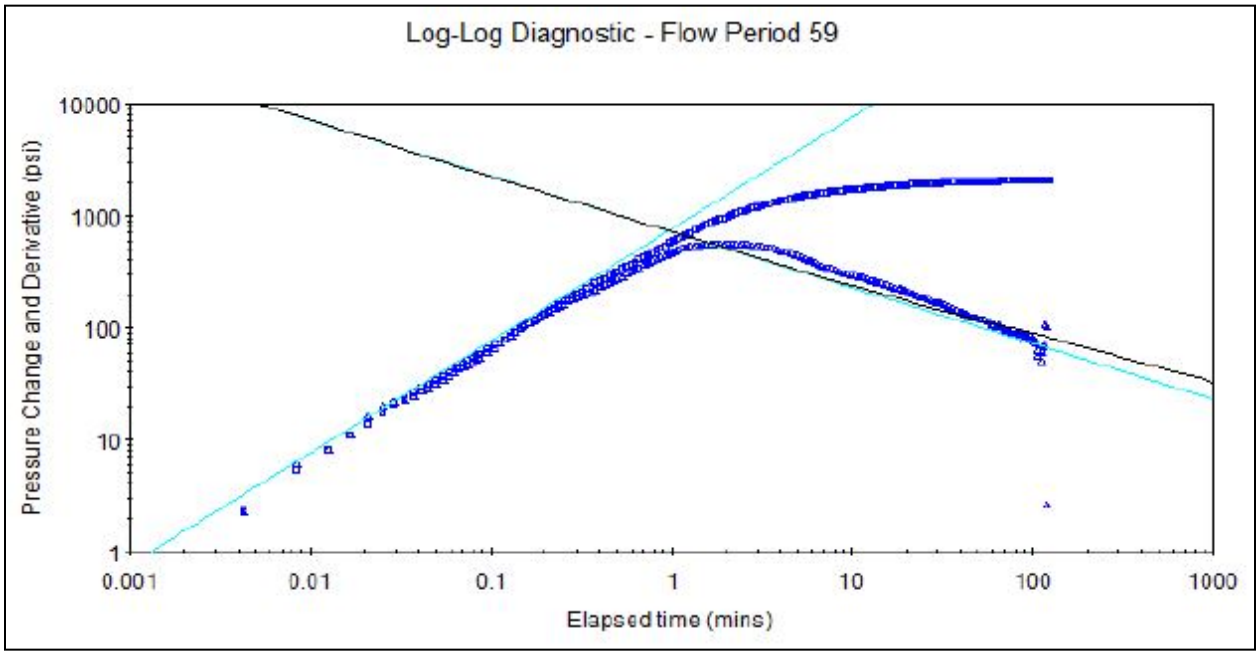


Figure 15-23. Log-log diagnostic plot of the straddle packer (blue symbols) pressure response during VIT-24 buildup period, plus modeled pressure and pressure derivative (solid lines) in the straddle packer interval.

History Matching (VIT-24)

Reservoir properties were estimated by simulating the VIT-24 test data using a model of a partially completed well in a homogeneous reservoir with an infinite lateral extent. Figure 15-24 and Figure 15-25 show the match between modeled data and measured data in a log-log plot of recovery data pressure and pressure derivative (Figure 15-24) and in a Cartesian plot of the entire drawdown-buildup sequence (Figure 15-25).

In Figure 15-25, the observed pressure spikes during the pump-out period are attributed to slight deformation of the straddle packer. Model input parameters and reservoir properties from the model history match analyses are provided in Figure 15-26 (constant pressure boundary model and radial composite model). Both models reasonably match the pressure transient data, and both yield similar transmissivity values (95 and 87 mD-ft).

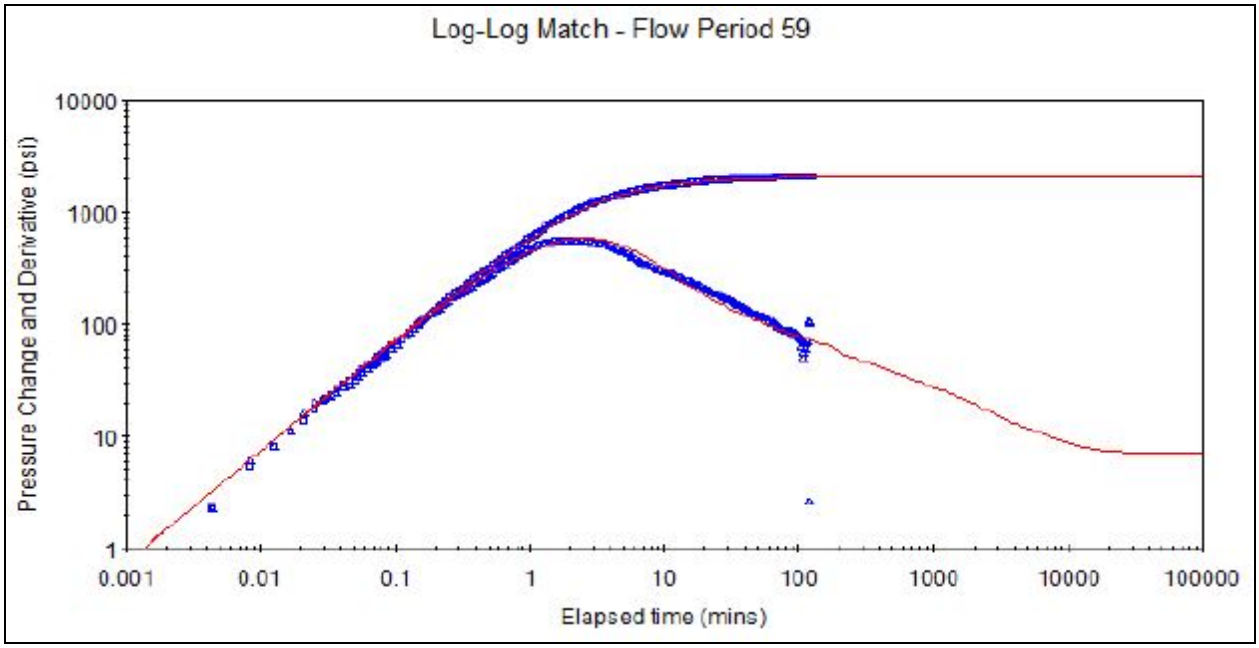


Figure 15-24. Comparison of observed pressure (blue squares) and pressure derivative (blue triangles) data to modeled pressure and pressure derivative (red lines) for the VIT-24 buildup period.

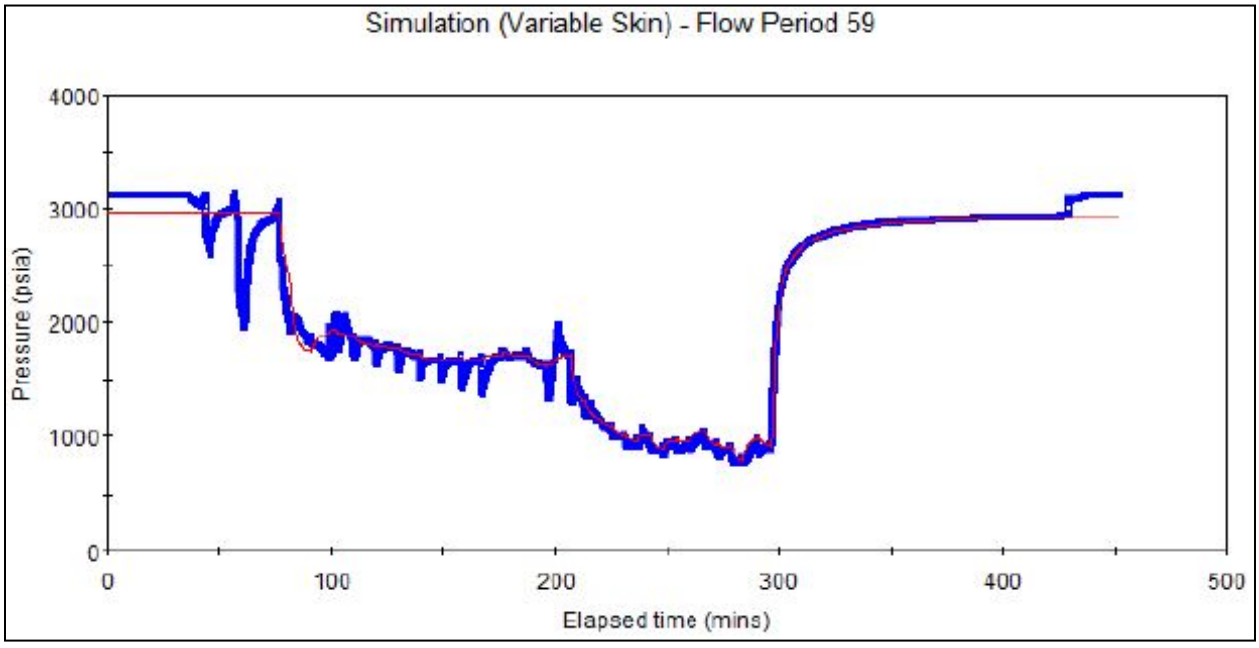


Figure 15-25. Pressure history match of the VIT-24 pumping and buildup periods.

MODEL

Near Wellbore Effect:	Partially Penetrating Well with C and S
Reservoir Behaviour:	Homogeneous
Boundary Effect:	Infinite Lateral Extent

Initial average reservoir pressure, (pav)i	2970.244 psia
Flowing pressure, pwf	876.490 psia
Permeability Thickness, kh	5.450 mD.ft
Horizontal Permeability, k(xy)	0.05450 mD
Vertical Permeability, k(z)	0.006386 mD
Wellbore storage coefficient, C	6.5009E-007 bbl/psi
Dimensionless well penetration, hw/h	0.03281
Perforated Interval, Hw	1.00 m
Wellbore skin factor, S(w)	2.07
Completion skin, S(c)	85.89
Total Skin, S(t)	148.84
Distance to Lower Boundary, Zw	18.54 ft
Type of top boundary, Type top	No Flow
Type of bottom boundary, Type bot	No Flow
Radius of investigation (approx), ri	16 ft
Measured Productivity Index, PI	0.00033682 B/D/psi
Flow Efficiency, FE	0.5769 fraction
Pressure drop due to skin, Dp(S)	885.9 psi

Figure 15-26. Model input parameters and reservoir properties from the model history match analysis for VIT-24.

VIT-25 (A-1 Carbonate, 5549.8 ft MD)

In this test, a total of 106 liters of fluid were pumped (removed) from the straddle packer interval in 157 minutes, followed by a pressure recovery period of 92 minutes. An average flow rate of 11.2 cm^3/s was obtained with the 500-cm^3 pump on the RCX tool. The flow rate just before the final buildup period was 12.6 cm^3/s. The pressure drawdown during the flow period was 152 psi. There was no seal at the observation probe, so pressure was not recorded. Figure 15-27 is a plot of the pumping rate and the pressure response in the straddle packer test interval during VIT-25.

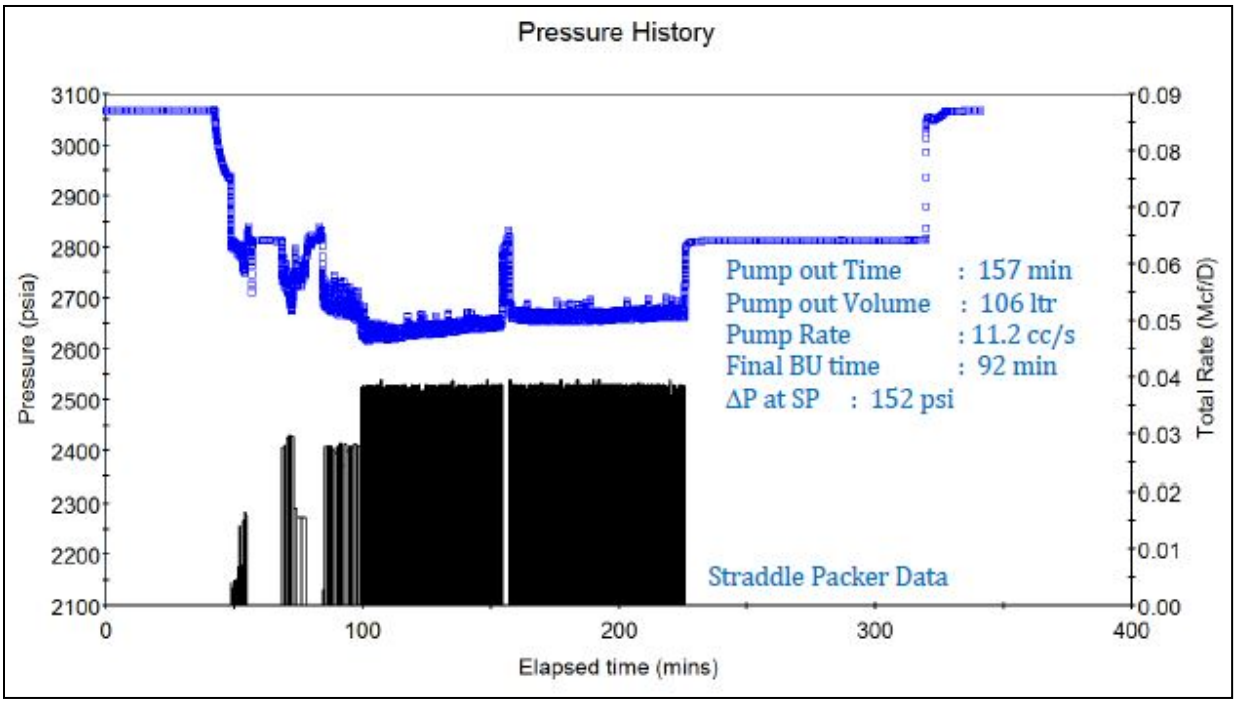


Figure 15-27. Pumping rate and pressure response in the straddle packer interval during VIT-25.

Diagnostic Analysis (VIT-25)

A diagnostic log-log plot for straddle packer data is shown in Figure 15-28. The early-time pressure response in the straddle packer interval was dominated by tool storage and nearby effects of skin. After the tool storage period, the spherical flow is not clearly identifiable. The pressure increase is approximately 153 psi from the shut-in to the end of the buildup. As the pressure increases, the viscosity of supercritical CO_2 also increases from 0.72 to 1.23 cP, which has an influence on the quality of the pressure buildup. Therefore, there is a great uncertainty in the PTA at this station.

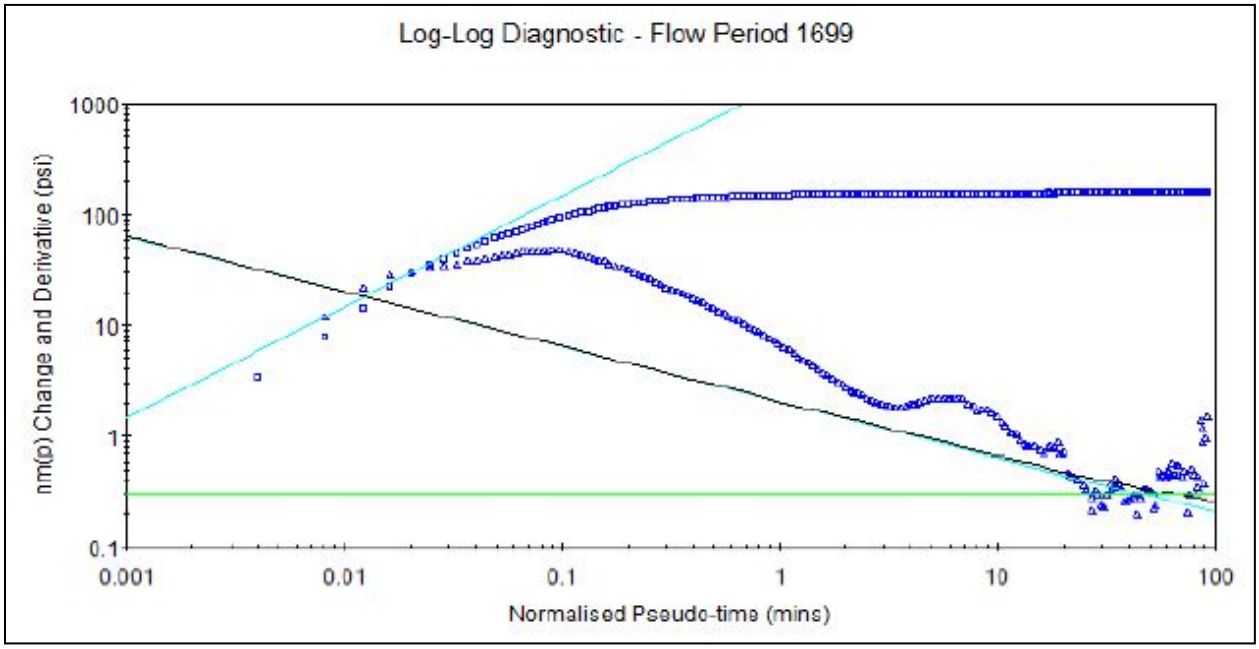


Figure 15-28. Log-log diagnostic plot of the straddle packer (blue symbols) pressure response during VIT-25 buildup period.

History Matching (VIT-25)

Reservoir properties were estimated by simulating the test data using a model of a partially completed well in an infinitely acting homogeneous reservoir model. Figure 15-29 and Figure 15-30 show the match between modeled data and measured data in a log-log plot of recovery data pressure and pressure derivative (Figure 15-29) and in a Cartesian plot of the entire drawdown-buildup sequence (Figure 15-30). Model input parameters and reservoir properties from the model history match analyses are provided in Figure 15-31. This test zone has a higher transmissivity (kh) than the other three tests (1957 mD-ft).

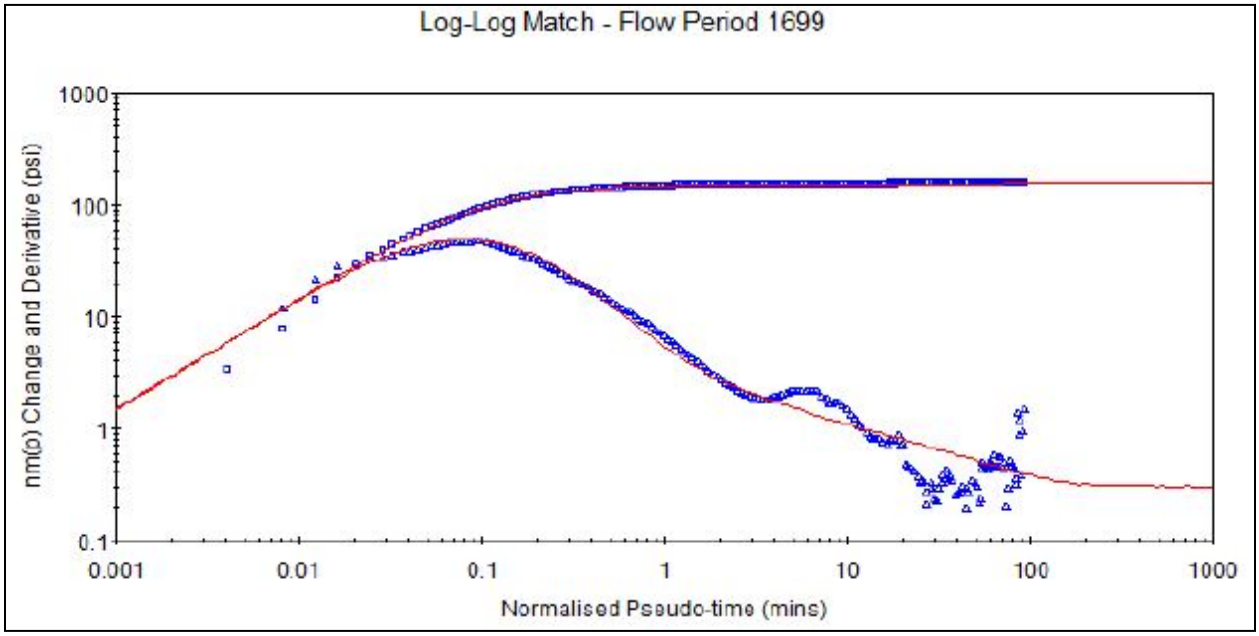


Figure 15-29. Comparison of observed pressure (blue squares) and pressure derivative (blue triangles) data to modeled pressure and pressure derivative (red lines) for the VIT-25 buildup period.

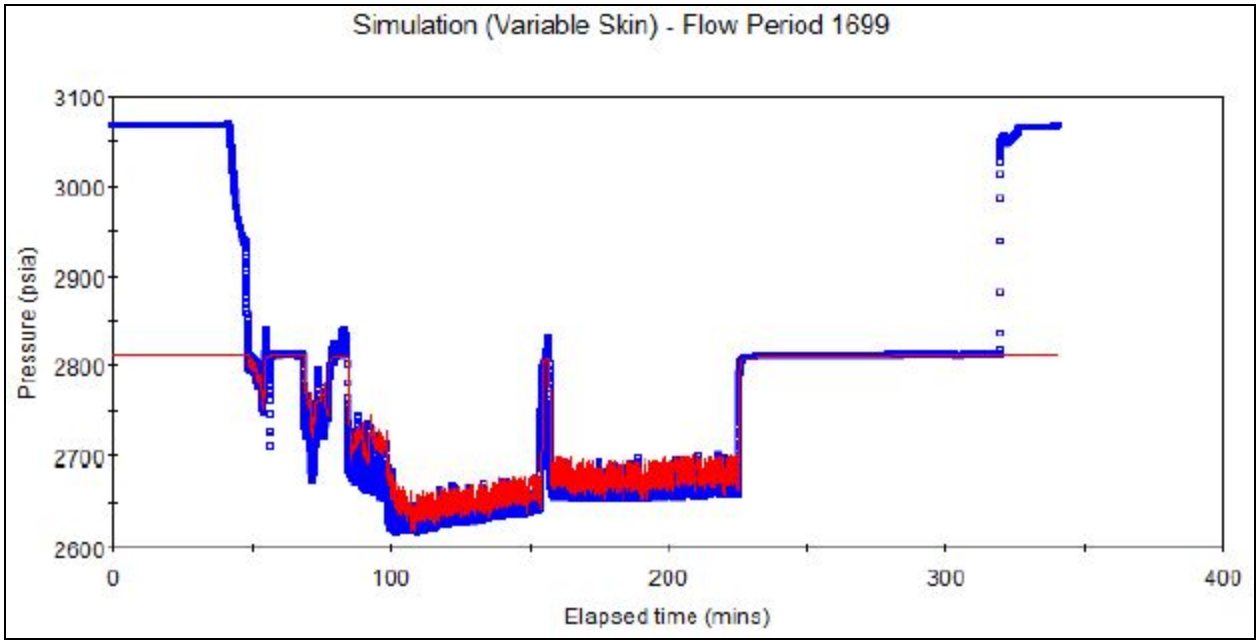


Figure 15-30. Pressure history match of the VIT-25 pumping and buildup periods.

MODEL

Near Wellbore Effect:	Partially Penetrating Well with C and S
Reservoir Behaviour:	Homogeneous
Boundary Effect:	Infinite Lateral Extent

Initial average reservoir pressure, (pav)i	2812.515 psia
Flowing pressure, pwf	2662.348 psia
Permeability Thickness, kh	1957.0 mD.ft
Horizontal Permeability, k(xy)	19.57 mD
Vertical Permeability, k(z)	15.00 mD
First wellbore storage coefficient, C1	2.9868E-006 bbl/psi
Second wellbore storage coefficient, C2	3.2088E-006 bbl/psi
Phase redistribution time parameter, Alpha	0.002358 s
Phase redistribution pressure change, Dp(C)	0.004 psi
Dimensionless well penetration, hw/h	0.03280
Perforated Interval, Hw	1.00 m
Wellbore skin factor, S(w)	6.29
Completion skin, S(c)	60.13
Total Skin, S(t)	251.80
Distance to Lower Boundary, Zw	55.00 ft
Type of top boundary, Type top	No Flow
Type of bottom boundary, Type bot	No Flow
Radius of investigation (approx), ri	51 ft
Pressure drop due to skin, Dp(S)	111.4 psi

Figure 15-31. Model input parameters and reservoir properties from the model history match analysis for VIT-25.

Summary of VIT Results for the 9-33 Well

A summary of the key reservoir properties determined from the VITs is provided in Table 15-5. From this data, the A-1 Carbonate in the Dover 33 reef has significantly higher transmissivity and permeability than the Brown Niagaran. The deepest VIT in the Brown Niagaran yielded the lowest kh.

Table 15-5. Summary of key reservoir properties determined from VITs conducted in the 9-33 well (Dover 33 reef).

Test	Formation	Straddle Packer Midpoint (ft, MD)	Observation Probe (ft, MD)	kh (mD-ft)	kxy (mD)[a]	kz (mD)	Model (see notes)	Radius of Investigation; Inner Boundary (ft)
VIT-22	A-1 Carb	5527.2	5520.7	967	9.7/19	3	1	56
VIT-23	Brown	5626.8	5620.3	94	0.94/1.9	0.03	2	35/12
VIT-23	Brown	5626.8	5620.3	89	0.89/1.8	0.04	3	40/17
VIT-24	Brown	5646.5	5640.0	5.5	0.055/0.11	0.006	1	16
VIT-25	A-1 Carb	5549.8	5543.3	1957	19/38	15	1	51

Notes: kh = transmissivity; kxy = horizontal permeability; kz = vertical permeability; h = reservoir thickness

1. Partially penetrating vertical well in infinite homogeneous reservoir.
2. Partially penetrating vertical well in homogeneous reservoir with constant pressure boundary.
3. Partially penetrating vertical well in radial composite reservoir with infinite lateral extent.

[a] First number is based on h = 100 ft; second number is based on h = 50 ft.

15.3.3 Fluid Characterization

As discussed in Section 15.2.4, fluid characteristics were determined at four test depths in the 9-33 well (Dover 33 reef) during the open-borehole testing conducted October 28-29, 2016. Table 15-6 summarizes the depths of the four sampling stations and the predominant fluid type based on in-situ property measurements made with the Baker Hughes RCX tool equipped with the IFX module. A summary of properties measured at each station is presented below.

Table 15-6. Summary of fluid characterization for the 9-33 well.

Test Depth Number	MD (ft)	TVD (ft)	Formation	Fluid
Station #1	5527.2	5383.4	A-1 Carbonate	CO_2
Station #2	5626.8	5461.0	Brown Niagaran	Water
Station #3	5646.5	5476.6	Brown Niagaran	Water
Station #4	5549.8	5400.8	Brown Niagaran	CO_2

In the fluid characterization performed in the 9-33 well, the tuning fork in the IFX module did not work, so fluid density, viscosity and GOR measurements were not made. Therefore, fluid type was determined based primarily on optical density, using the following guidelines:

- Water is indicated by high values on channels (CH14 and 17).
- Hydrocarbon (oil) is indicated by channel subtraction (16-15).
- Gas (methane) is indicated by channel subtraction of the two methane detectors (M1-M2)
- The presence of CO_2 was estimated from the absorbance spectrum channel (CH21-CH15).

Station #1: 5527.2 ft MD (5383.4 ft TVD)

Figure 15-32 shows the absorbance spectrum for filtrate (top) and sample (bottom) for Station #1. Water channels (CH14 and 17) are dominant in the filtrate spectrum, indicating water-based mud filtrate. Figure 15-32 shows some absorbance in the first three channels, probably due to the solid particles causing interference with the sapphire window. In the sample spectrum, almost all visible and NIR channels do not show absorbance. This is an indication that the formation fluid is not water, oil, or methane gas.

Figure 15-33 shows a temporal plot of the fluid type indicator channels (water) and channel subtractions (oil, gas, and CO_2) during pumping (cleanup) and subsequent recovery (buildup) for Station #1. The hydrocarbon indicator channel subtraction (16-15) yields a low value of 0.07 (green curve). The gas indicator channel subtraction (M1-M2) has a negligible value (red curve). The IFX water indicator channel subtraction (14-13) (blue curve) has a value significantly lower than the start of the pump-out. These findings support the conclusion that the pumped fluid contains water-based mud filtrate to some extent, but no formation oil or methane gas is present during pumping.

Figure 15-34 is a temporal plot of the CO_2 indicator data (channel CH21-CH15). It shows a reading of 0.4 or higher during pumping, indicating the presence of CO_2 gas. This should be used only as a qualitative measurement.

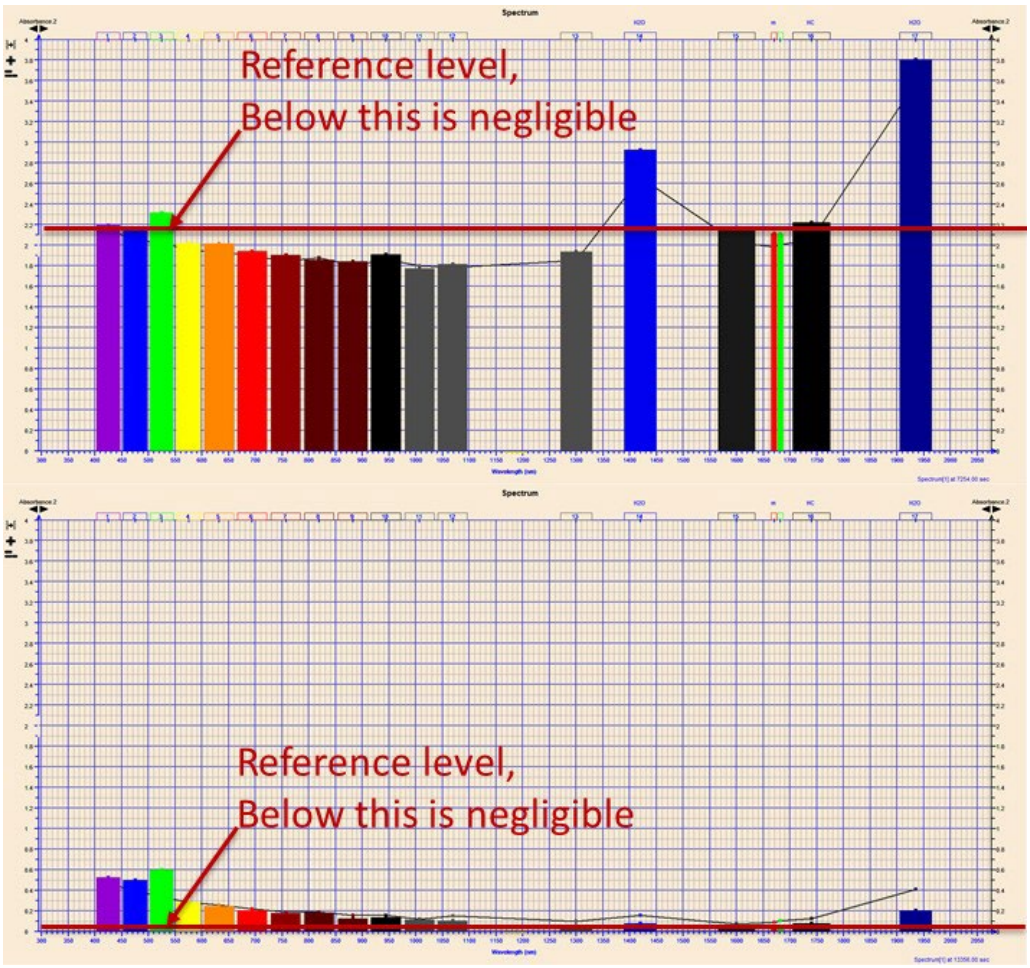


Figure 15-32. Absorbance spectrum for filtrate (top) and sample (bottom) for Station #1.

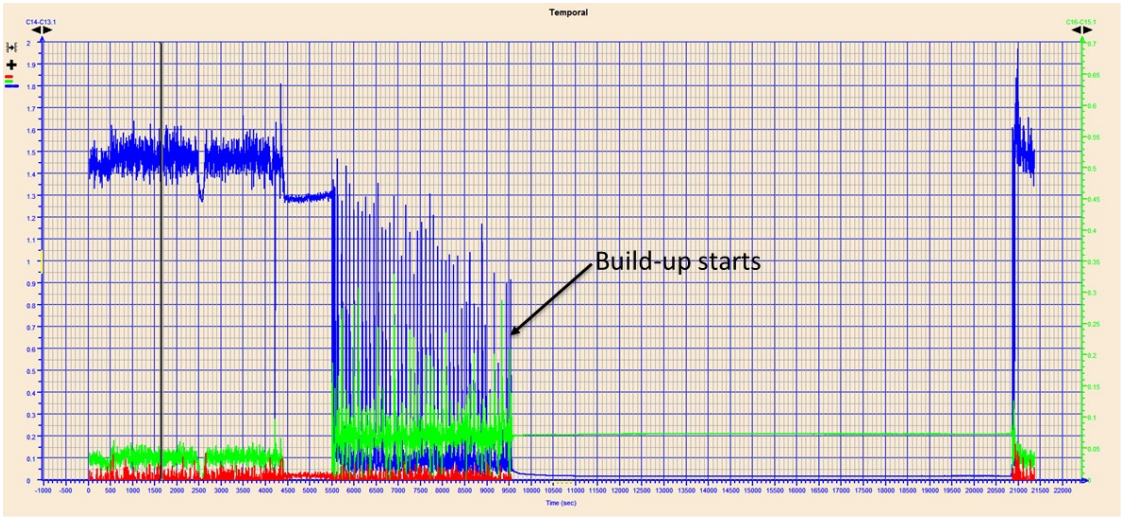


Figure 15-33. Channel subtraction (16-15) for hydrocarbon identification (green curve), gas indicator channel subtraction (M1-M2) (red), and water indicator channel subtraction (14-13) (blue) during pumping and buildup for Station #1.

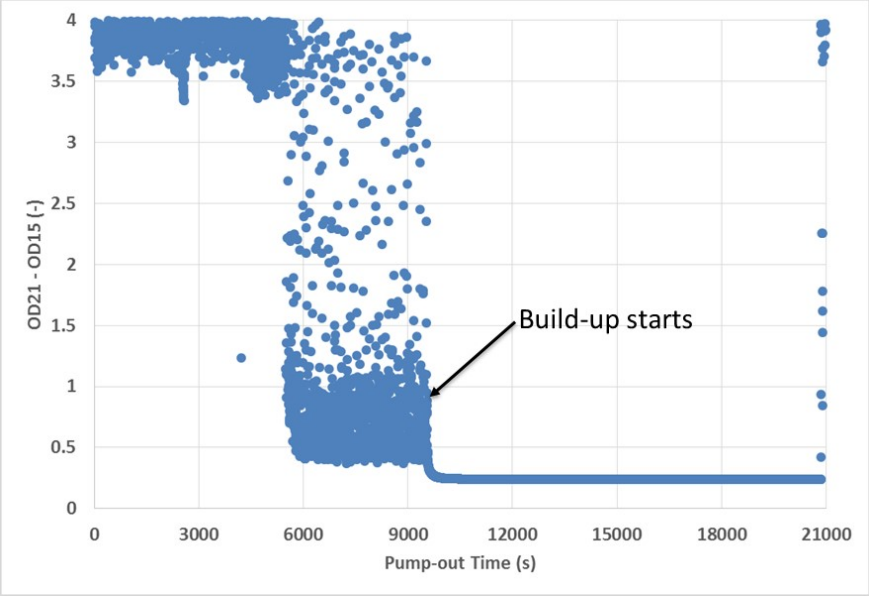


Figure 15-34. CO_2 channel (CH21-CH15) showing a reading of 0.4 or higher during pumping, indicating the presence of CO_2 gas at Station #1.

Station #2: 5626.8 ft MD (5461.0 ft TVD)

Figure 15-35 shows the absorbance spectrum for filtrate (top) and sample (bottom) for Station #2. Water channels (CH14 and 17) are dominant in the filtrate spectrum, indicating water-based mud filtrate. Water channels (CH14 and 17) are also dominant in the sample spectrum, indicating water is the predominant fluid type. Both spectra show some absorbance in the first three channels, likely due to the solid particles causing interference with the sapphire window.

Figure 15-36 shows a temporal plot of the fluid type indicator channels (water) and channel subtractions (oil, gas, and CO_2) during pumping (cleanup) and subsequent recovery (buildup) for Station #2. The hydrocarbon indicator channel subtraction (16-15) yields a low value of 0.05 (green curve). The gas indicator channel subtraction (M1-M2) (red) has a negligible value. The IFX water indicator channel subtraction (14-13) (blue) has a value significantly lower than the start of the pump-out. These findings support the conclusion that the pumped fluid contains formation water with some filtrate contamination, but no formation oil or methane gas is present during pumping.

The CO_2 indicator data (channel CH21-CH15) is not shown because it did not indicate that CO_2 is present.

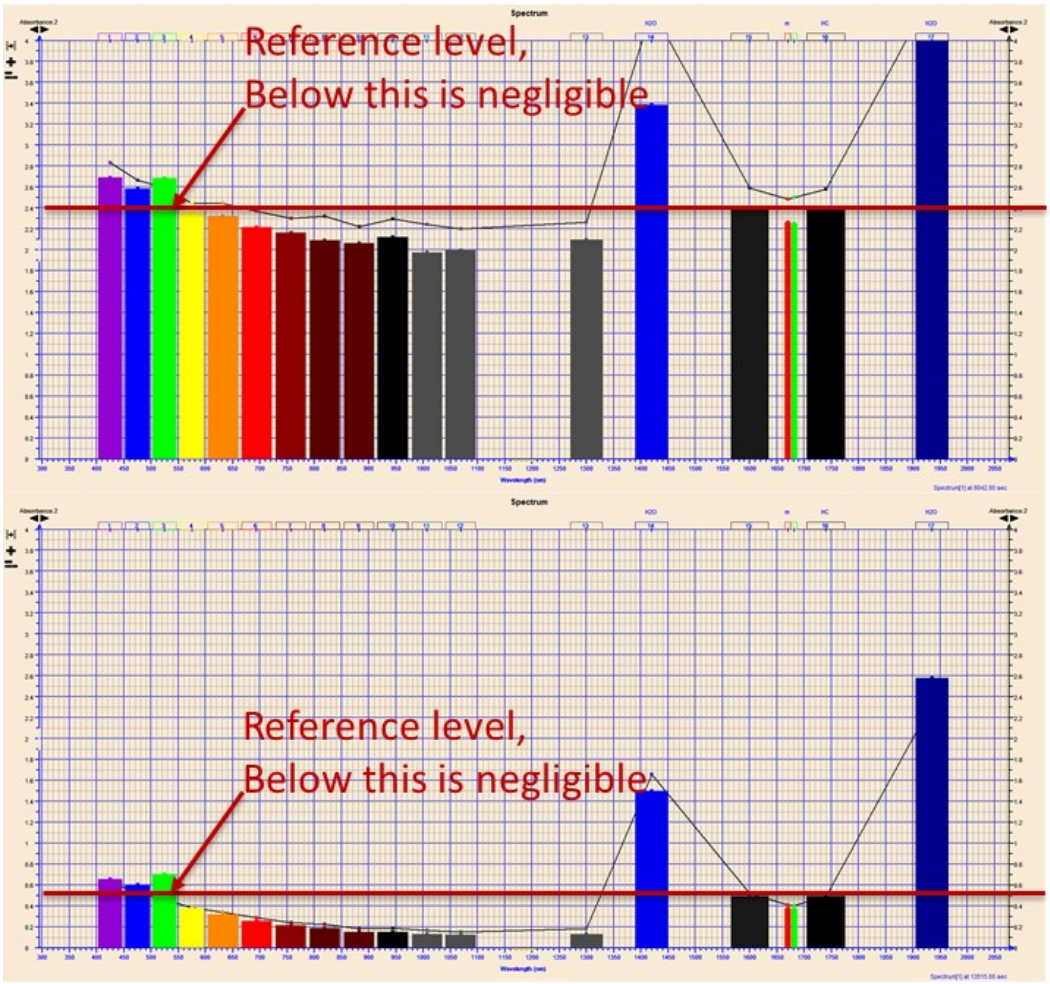


Figure 15-35. Absorbance spectrum for filtrate (top) and sample (bottom) for Station #2.

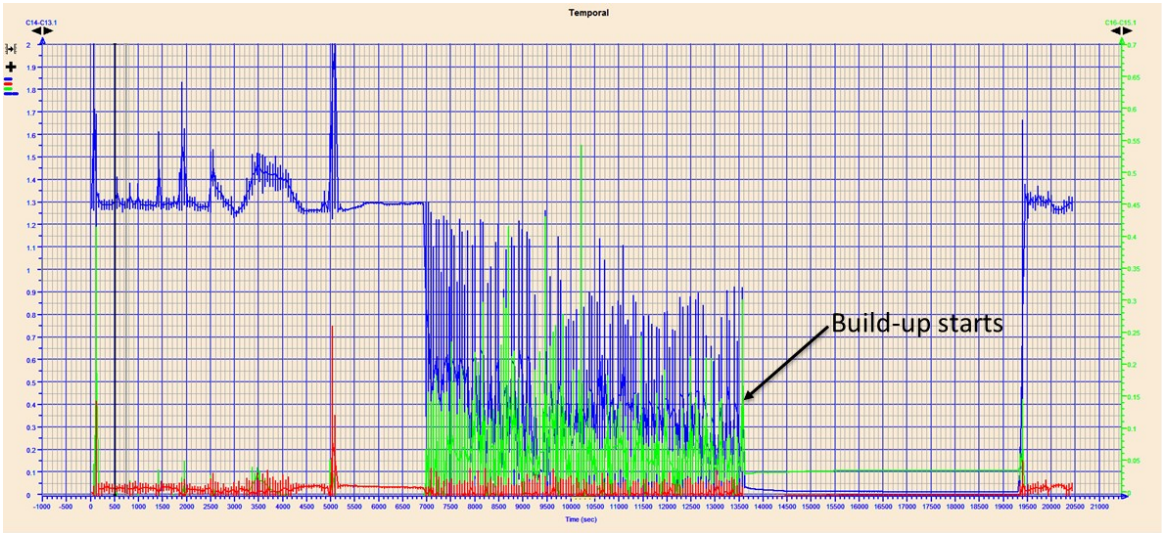


Figure 15-36. Channel subtraction (16-15) for hydrocarbon identification (green curve), gas indicator channel subtraction (M1-M2) (red), and water indicator channel subtraction (14-13) (blue) during pumping and buildup for Station #2.

Station #3: 5646.5 ft MD (5476.6 ft TVD)

Figure 15-37 shows the absorbance spectrum for filtrate (top) and sample (bottom) for Station #3. Water channels (CH14 and 17) are dominant in the filtrate spectrum, indicating water-based mud filtrate. Water channels (CH14 and 17) are also dominant in the sample spectrum, indicating water is the predominant fluid type. As with the other samples, both spectra show some absorbance in the first three (darkness) channels, probably caused by solid particles interfering with the sapphire window.

Figure 15-38 shows a temporal plot of the fluid type indicator channels (water) and channel subtractions (oil, gas, and CO_2) during pumping (cleanup) and subsequent recovery (buildup) for Station #3. The hydrocarbon indicator channel subtraction (16-15) and the gas indicator channel subtraction (M1-M2) yield negligible values. The IFX water indicator channel subtraction (14-13) has a value about the same as the start of the pump-out (blue curve). These findings support the conclusion that the pumped fluid contains mostly filtrate contamination with some formation water, but no formation oil or methane gas is present during pumping.

The CO_2 indicator data (channel CH21-CH15) is not shown because it did not indicate that CO_2 is present.

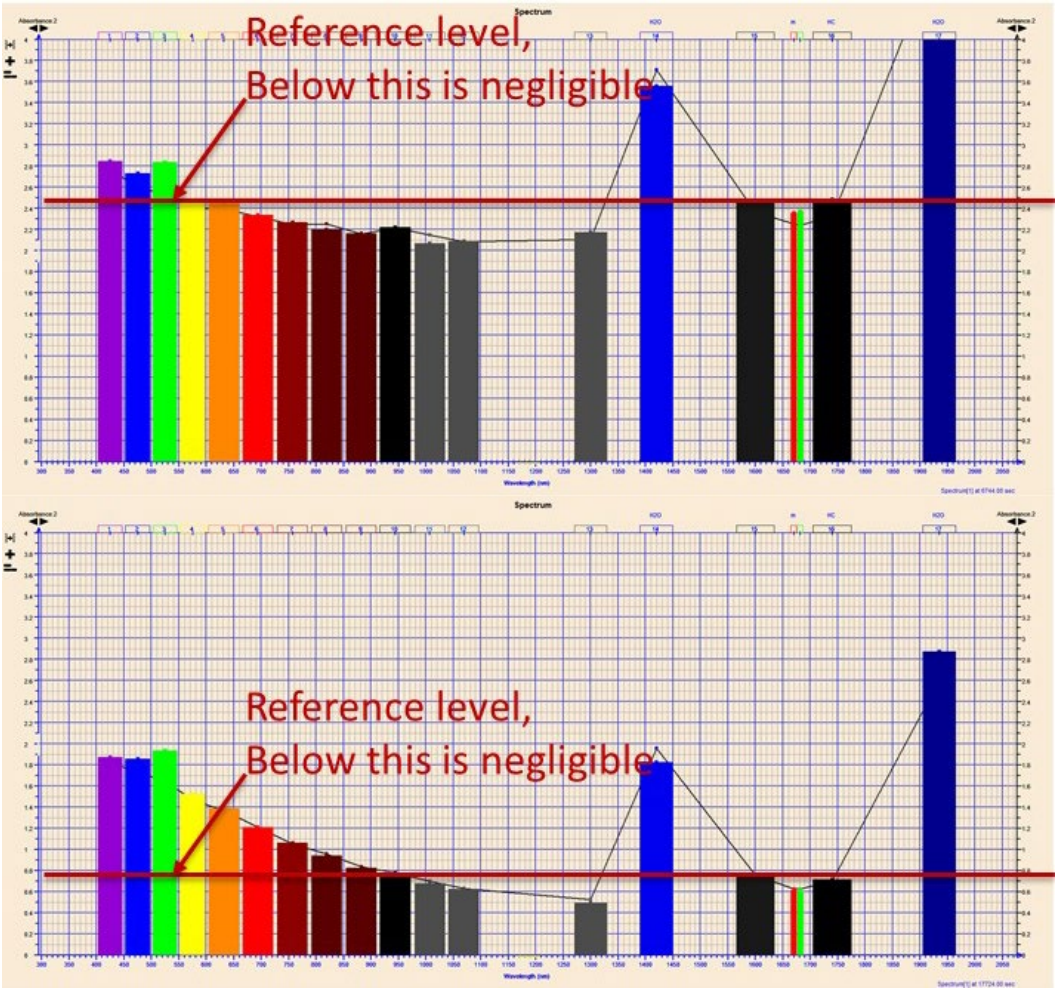


Figure 15-37. Absorbance spectrum for filtrate (top panel) and sample (bottom panel) for Station #3.

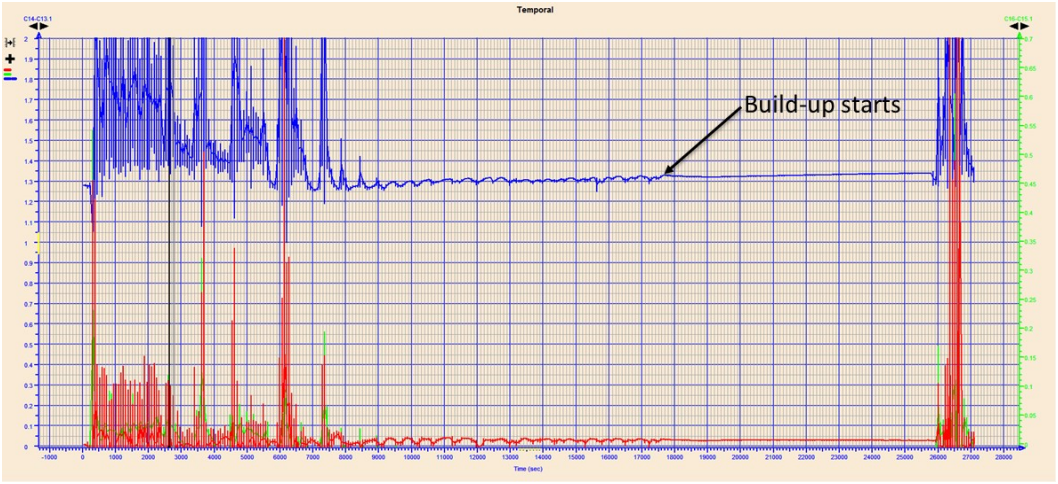


Figure 15-38. Channel subtraction (16-15) for hydrocarbon identification (green curve), gas indicator channel subtraction (M1-M2) (red), and water indicator channel subtraction (14-13) (blue) during pumping and buildup for Station #3.

Station #4: 5549.8 ft MD (5400.8 ft TVD)

Figure 15-39 shows the absorbance spectrum for filtrate (top) and sample (bottom) for Station #4. Water channels (CH14 and 17) are dominant in the filtrate spectrum, indicating water-based mud filtrate. In the sample spectrum, most of the visible and NIR channels show negligible absorbance. The low absorbance on the first few darkness channels is probably due to the solid particles causing interference with the sapphire window. These findings indicate that the formation fluid is not water, oil, or methane gas.

Figure 15-40 shows a temporal plot of the fluid type indicator channels (water) and channel subtractions (oil, gas, and CO_2) during pumping (cleanup) and subsequent recovery (buildup) for Station #4. The hydrocarbon indicator channel subtraction (16-15) yields a low value of 0.05 (green curve). The gas indicator channel subtraction (M1-M2) has a negligible value. The IFX water indicator channel subtraction (14-13) has a value significantly lower than the start of the pump-out (blue curve). These findings support the conclusion that the pumped fluid contains water-based mud filtrate to some extent, but no formation oil or methane gas is present during pumping.

Figure 15-41 is a temporal plot of the CO_2 indicator data (channel CH21-CH15). It shows a reading of 0.4 or higher during pumping, indicating the presence of CO_2 gas.

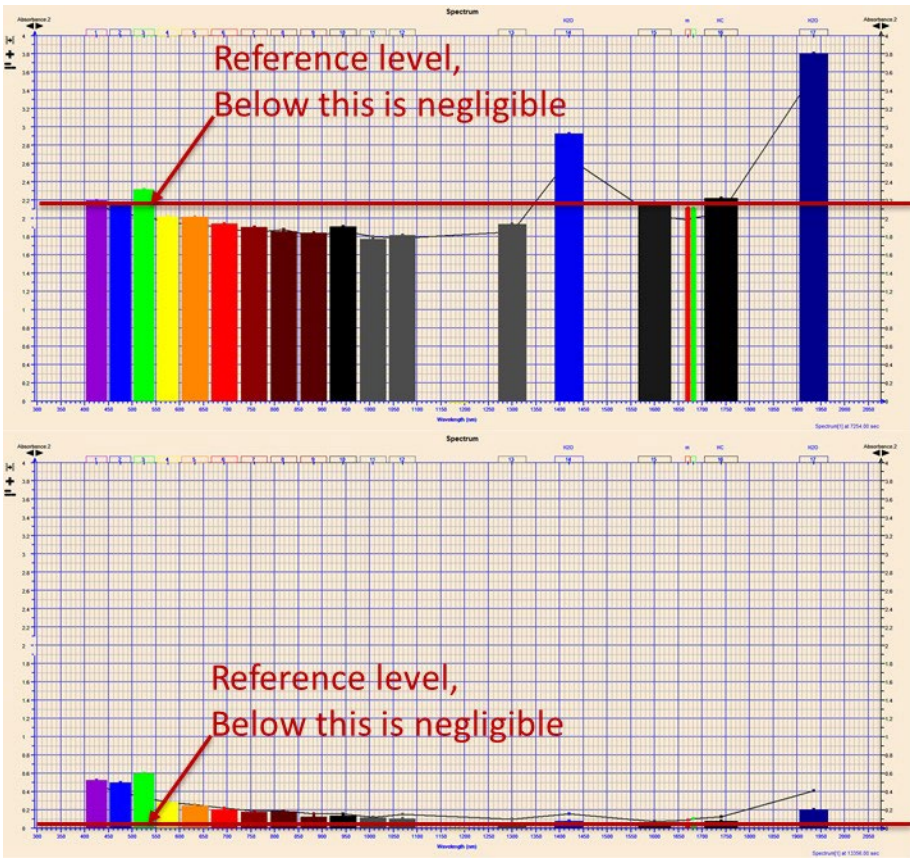


Figure 15-39. Absorbance spectrum for filtrate (top panel) and sample (bottom panel) for Station #4.

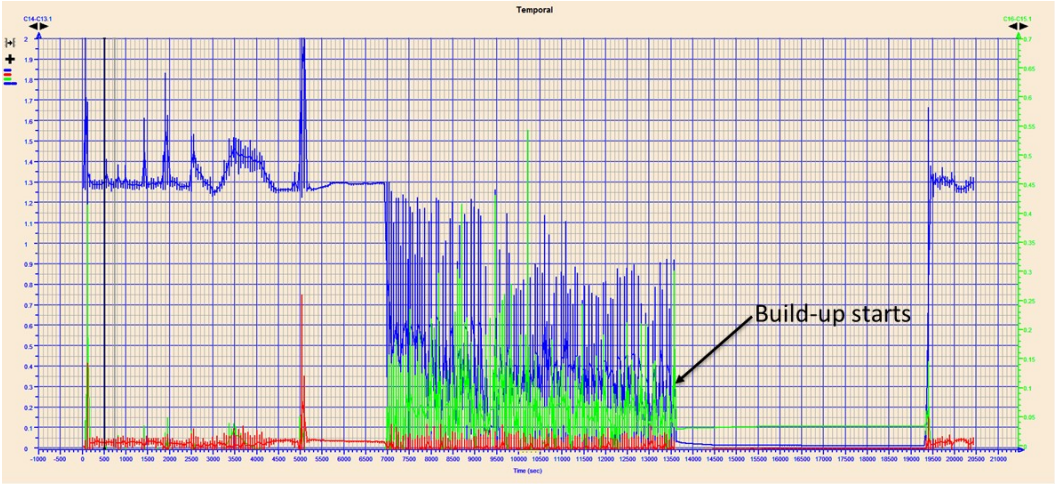


Figure 15-40. Channel subtraction (16-15) for hydrocarbon identification (green curve), gas indicator channel subtraction (M1-M2) (red), and water indicator channel subtraction (14-13) (blue) during pumping and buildup for Station #4.

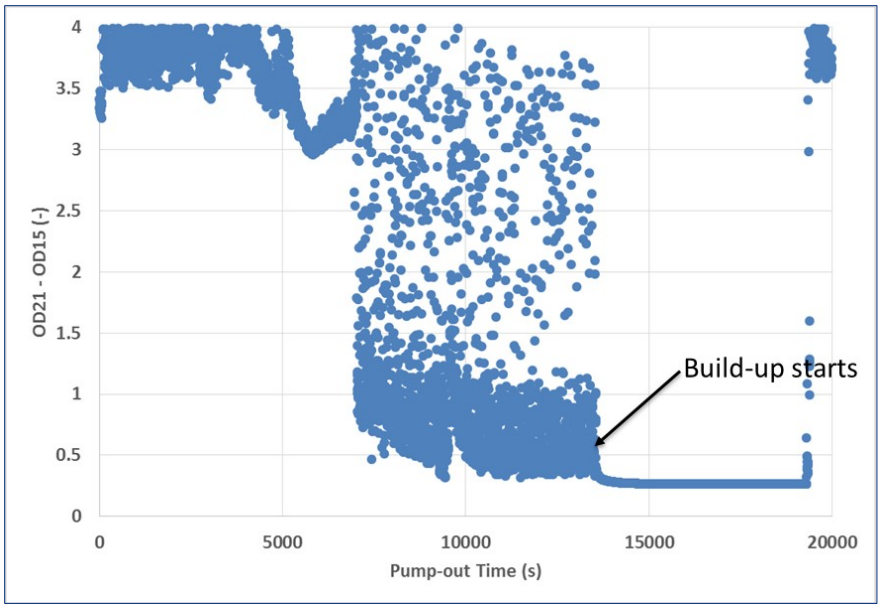


Figure 15-41. CO_2 channel (CH21-CH15) showing a reading of 0.4 or higher during pumping, indicating the presence of CO_2 gas at Station #4.

15.4 Chester 8-16 (Chester 16)

15.4.1 Reservoir Pressure

In-situ reservoir pressure measurements were attempted at 37 depths in the open-borehole section below the A-2 Carbonate in the 8-16 well using the Baker Hughes RCX tool. Successful tests (i.e., yielding a representative pressure and mobility estimate) were achieved at three (3) test depth locations (Table 15-7). Mobility estimates are 6.2 mD/cP, 7.4 mD/cP, and 40 mD/cP. Reservoir pressures are 527, 685, and 528 pounds per square inch gauge (psig). At three other test depth locations, the test was halted before a stable pressure was achieved; however, the pressure readings at the time the test was halted—780 psig, 558 psig, and 650 psig—provide a reasonable (albeit low) estimate of true reservoir pressure at that depth (i.e., since pressure was still recovering (increasing) when the test was halted). The remaining 31 tests were not successful because either the formation permeability was too low (21 depths) (so water could not be withdrawn) or a seal was not achieved by the packer (10 depths). Despite the low number of successful tests, better results were obtained by using a different packer, which helped achieve a seal at more locations compared to the pressure testing performed in the 9-33 well. The standard packer was used for testing in the 9-33 well, while the elongated packer with a lip was used for testing in the 8-16 well.

Figure 15-42 shows the depth of the six pressure values (yellow diamonds) alongside log-porosity. The black symbols (diamonds) on the vertical axis correspond to the depths where pressure measurements were attempted.

Table 15-7. Summary of in-situ reservoir pressure and mobility measurements.

Test	MD (ft)	TVD (ft)	Temp (°F)	Minimum Pressure (psi)	Final BU Pressure at End of Test (psig)	Calculated mobility (k/μ) (mD/cP)	Comment
1	NA						NA
2	NA						NA
3	NA						NA
4	5890.4	5793.6	98.4	---	---	---	Tight test
5	5892.1	5795.4	98.7	---	---	---	Tight test
6	NA						NA
7	5874.8	5778.0	99.0	---	---	---	Tight test
8	5912.2	5815.4	99.2	---	---	---	Tight test
9	5764.5	5667.9	99.2	---	---	---	No seal
10	5750.5	5653.9	98.3				No seal
11	5792.0	5695.3	98.5	---	---	---	Tight test
12	5931.5	5834.7	98.9	---	---	---	Tight test
13	6095.3	5998.6	99.6	---	---	---	Tight test
14	6180.4	6083.6	100.3	---	---	---	No seal
15	6181.4	6084.6	100.2	---	---	---	No seal
16	6182.1	6085.3	101.0	---	---	---	No seal
17	6200.0	6103.2	101.2	---	---	---	Tight test
18	6258.0	6161.2	102.7	---	---	---	Tight test
19	6354.1	6257.3	104.6	---	---	---	Tight test
20	5890.7	5794.0	100.9	---	---	---	Tight test
21 (5)	5884.2	5787.5	100.9	143.17	526.89	47.4	Good test
22 (2)	5911.3	5814.6	101.3	232.98	685.19	7.5	Good test
23	5931.2	5834.4	101.7	---	---	---	Tight test
24	5933.2	5836.4	101.7	---	---	---	Tight test
25-1	6124.1	6027.4	101.8	---	---	---	Tight test
25-2	6138.1	6041.4	101.9	---	---	---	Tight test
26-1	6123.1	6026.3	102.9	---	780[a]	---	Tight test
26-2	6137.1	6040.3	102.1	---	---	---	Tight test
27	NA						NA
28	NA						NA
29 (4)[b]	5858.2	5761.5	101.0	214.01	527.82	8.7	Good test
30	NA						NA
31	NA						NA
32	NA						NA
33	NA						NA
34	5751.1	5654.5	101.1	---	558 [a]	---	Tight test
35-1	5769.2	5672.6	100.7	---	---	---	No seal
35-2	5783.2	5686.5	101.0	---	---	---	No seal
36-1	5787.9	5691.2	100.8	---	---	---	No seal
36-2	5801.9	5705.1	101.1	---	---	---	No seal
37	5792.9	5696.2	101.2	---	650 [a]	---	Tight test

Notes: – indicates parameter could not be determined from test results.
NA indicates pressure not measured
[a] Buildup pressure not stable.
[b] 29(4) results are average of the number of measurements in parentheses (same depth).

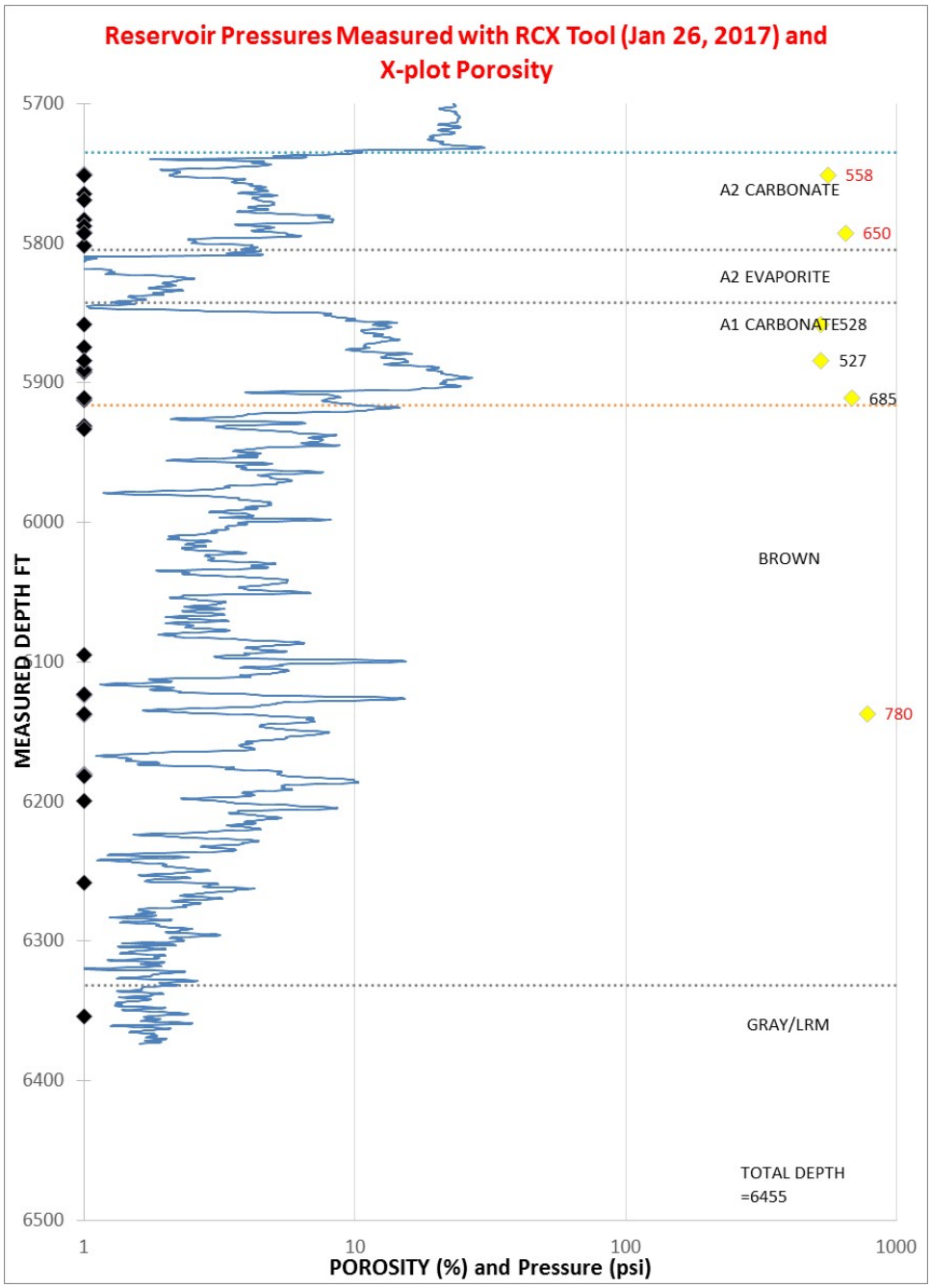


Figure 15-42. Reservoir pressures (yellow diamonds) measured with Baker Hughes RCX tool.

15.4.2 Hydraulic Well Tests

Two open-borehole LITs were conducted in the 8-16 well on January 27, 2017, to determine hydraulic parameters of the primary reservoir interval (the A-1 Carbonate) in the Chester 16 reef. This section provides a summary of the two LITs. Table 15-8 shows the depth of each test.

Table 15-8. Depth of LITs in the Chester 8-16 well.

Test	Formation	Straddle Packer Midpoint (ft, MD)	Observation Probe (ft, MD)
LIT-1	A-1 Carbonate	5890.7	5884.2
LIT-2	A-1 Carbonate	5864.7	5858.2

Pressure communication was observed between the straddle packer and observation probe in both LIT-1 and LIT-2. However, the communication in LIT-2 might be limited by the potential tight streak separating the straddle packer and observation probe.

LIT-1 (A-1 Carbonate, 5890.7 ft MD)

In LIT-1, a total of 57 liters of fluid were pumped (removed) from the straddle packer test interval in 133 minutes, followed by a pressure buildup period that lasted 428 minutes. An average flow rate of 7.2 cm^3/s was obtained with the 434-cm^3 pump. The flow rate just before the final buildup period was 7.5 cm^3/s. The maximum pressure drawdown during the flow period was 453.2 psi in the straddle packer test interval. Figure 15-43 is a plot of the pumping rate and the pressure response in the straddle packer test interval during LIT-1. The pressure response at the observation probe during LIT-1 is shown in Figure 15-44. A pressure drop of 10.2 psi was recorded at the observation probe, indicating good hydraulic communication between the straddle packer interval and the observation probe.

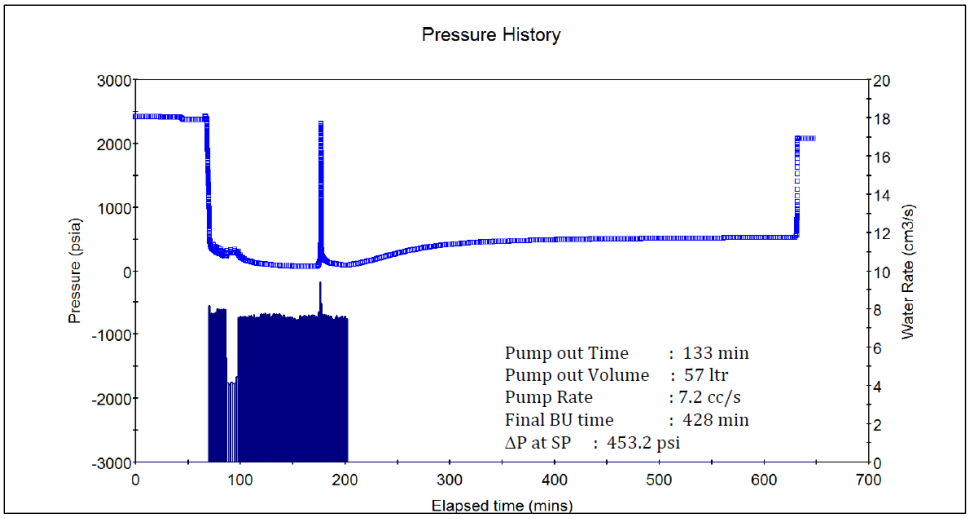


Figure 15-43. Pumping rate and pressure response in the straddle packer interval during LIT-1.

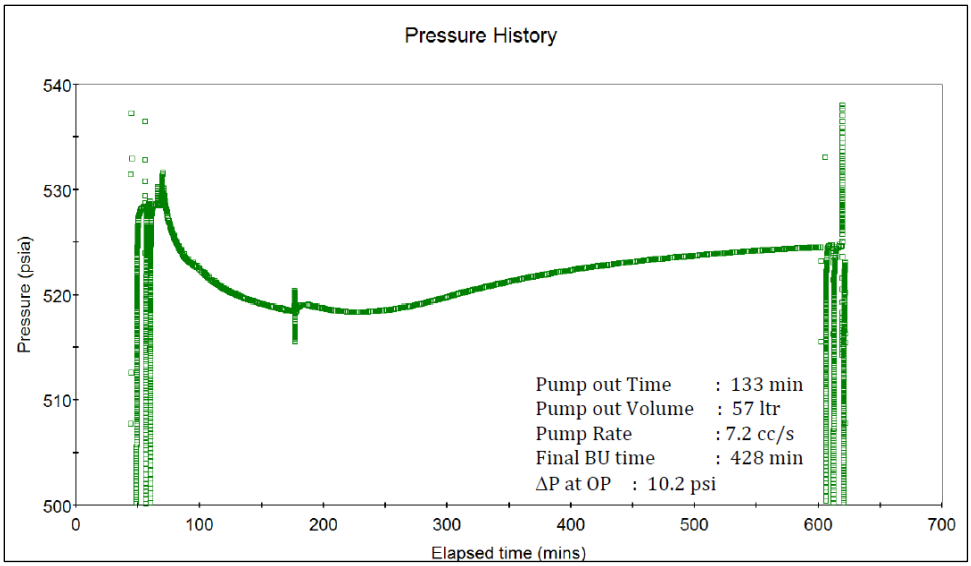


Figure 15-44. Pressure response at the observation probe during LIT-1.

Diagnostic Analysis (LIT-1)

A diagnostic log-log plot for both the straddle packer (blue symbols) and observation probe (green symbols) pressure response data during the buildup period is shown in Figure 15-45. The straddle packer pressure data (blue squares) and pressure derivative (blue triangles) show that the early-time pressure response was dominated by tool storage and nearby effects of skin. After the tool storage period, there is a spherical flow regime around 200 minutes (the red line in Figure 15-45). Infinitely acting radial flow is not observed in the straddle packer interval during the test. The late-time derivative data from the straddle packer interval indicates that the permeability of the tested zone cannot be less than 0.1 mD but a more precise estimate cannot be determined from the straddle packer data alone since infinitely acting radial flow was not observed during the test.

History Matching Analysis

The pressure data was analyzed using a model of a partially penetrating deviated well in an infinitely acting homogeneous reservoir. Because a pressure response was observed at the observation probe, a simultaneous matching analysis of the straddle packer data and observation probe data was possible to provide estimates of the horizontal permeability and the vertical permeability for the reservoir region between the two probe locations.

Figure 15-45 and Figure 15-46 show the match between modeled data and measured data in a log-log plot of recovery data pressure and pressure derivative (Figure 15-45) and in a Cartesian plot of the entire drawdown-buildup sequence (Figure 15-46). Model input parameters and reservoir properties from the model history match analyses are provided in Figure 15-47.

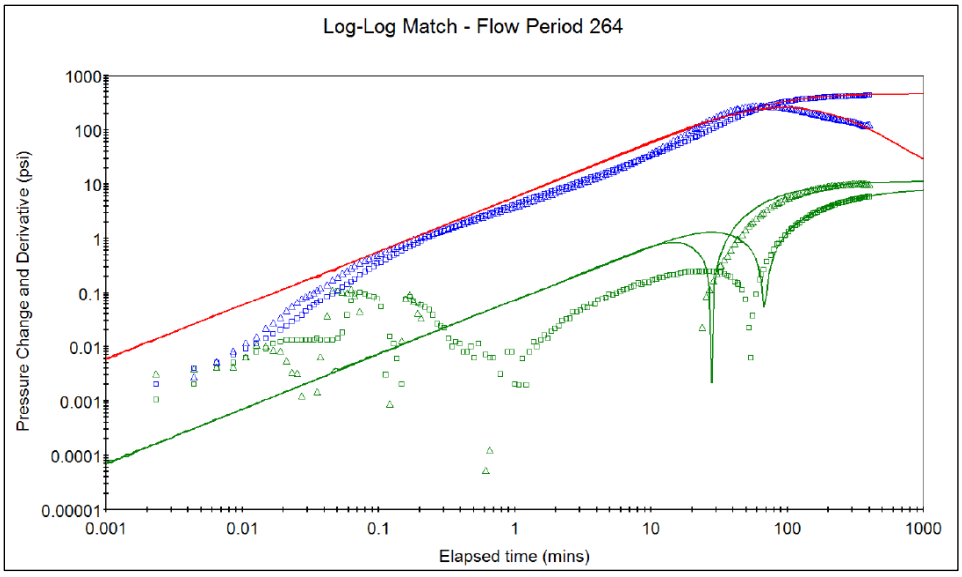


Figure 15-45. Log-log diagnostic plot of straddle packer (blue symbols) and observation probe (green symbols) pressure response during LIT-1 showing modeled response at the straddle packer (red line) and observation probe (green line).

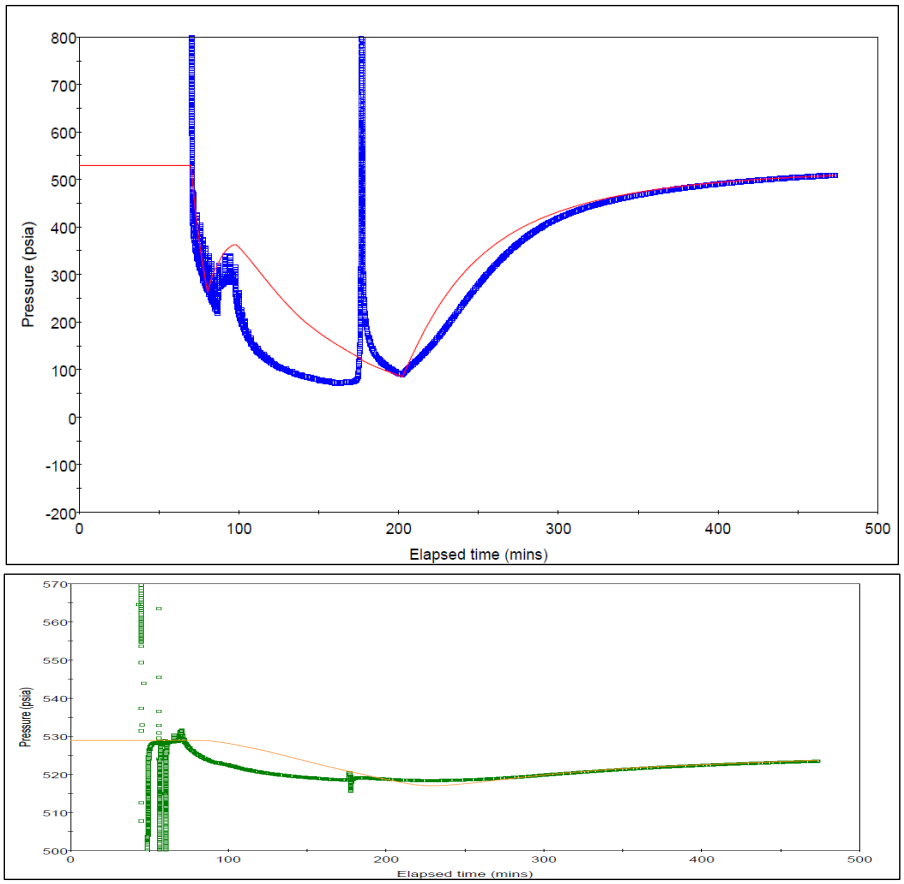


Figure 15-46. Pressure history match of test interval data (top panel) and observation probe data (bottom panel) for the entire LIT-1.

MODEL

Near Wellbore Effect:	Partially Penetrating Deviated Well with C and S
Reservoir Behaviour:	Homogeneous
Boundary Effect:	Infinite Lateral Extent

Initial average reservoir pressure, (pav)i	530.521 psia
Flowing pressure, pwf	89.191 psia
Permeability Thickness, kh	18.10 mD.ft
Horizontal Permeability, k(xy)	0.9050 mD
Vertical Permeability, k(z)	0.01100 mD
Wellbore storage coefficient, C	0.00031652 bbl/psi
Dimensionless well penetration, hw/h	0.1448
Well deviation (degrees), Theta(w)	28
Deviated Well Length, Lw	1.00 m
Wellbore skin factor, S(w)	-0.66
Completion skin, S(c)	17.55
Total Skin, S(t)	17.53
Distance to Lower Boundary, Zw	3.43 ft
Type of top boundary, Type top	No Flow
Type of bottom boundary, Type bot	No Flow
Radius of investigation (approx), ri	78 ft
Measured Productivity Index, PI	0.009174 B/D/psi
Flow Efficiency, FE	1.001 fraction
Pressure drop due to skin, Dp(S)	-0.4639 psi

Figure 15-47. Model input parameters and reservoir properties from the model history match analysis for LIT-1.

LIT-2 (A-1 Carbonate, 5864.7 ft MD)

In this test, a total of 65.1 liters of fluid were pumped (removed) from the straddle packer interval in 190 minutes, followed by a pressure recovery period of 168 minutes. An average flow rate of 5.7 cm^3/s was obtained with the 434-cm^3 pump on the RCX tool. The flow rate just before the final buildup period was 2.7 cm^3/s. The pressure drawdown during the flow period was 352.2 psi in the test interval and 0.5 psi at the observation probe. Figure 15-48 is a plot of the pumping rate and the pressure response in the straddle packer test interval during LIT-2. The pressure response at the observation probe during LIT-2 is shown in Figure 15-49.

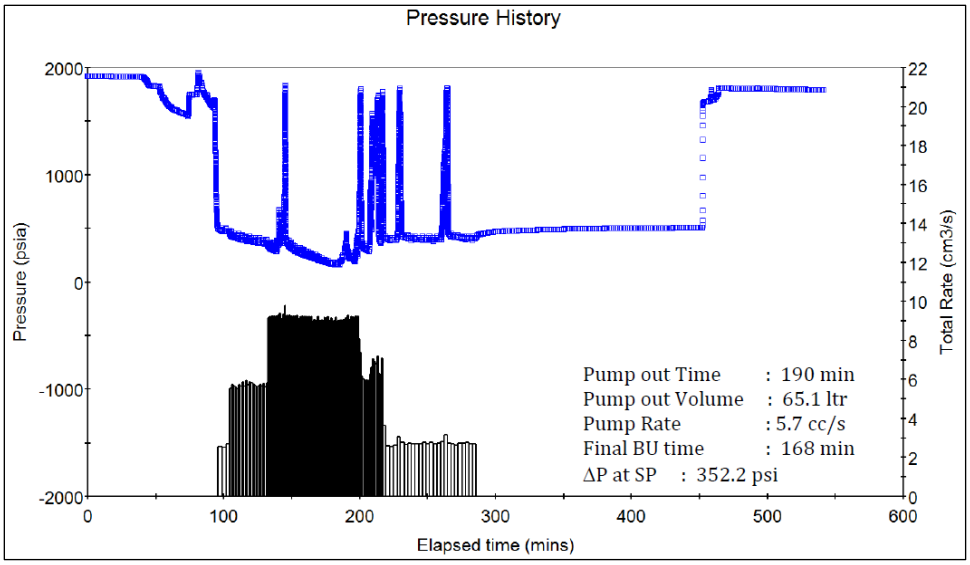


Figure 15-48. Pumping rate and pressure response in the straddle packer interval during LIT-2.

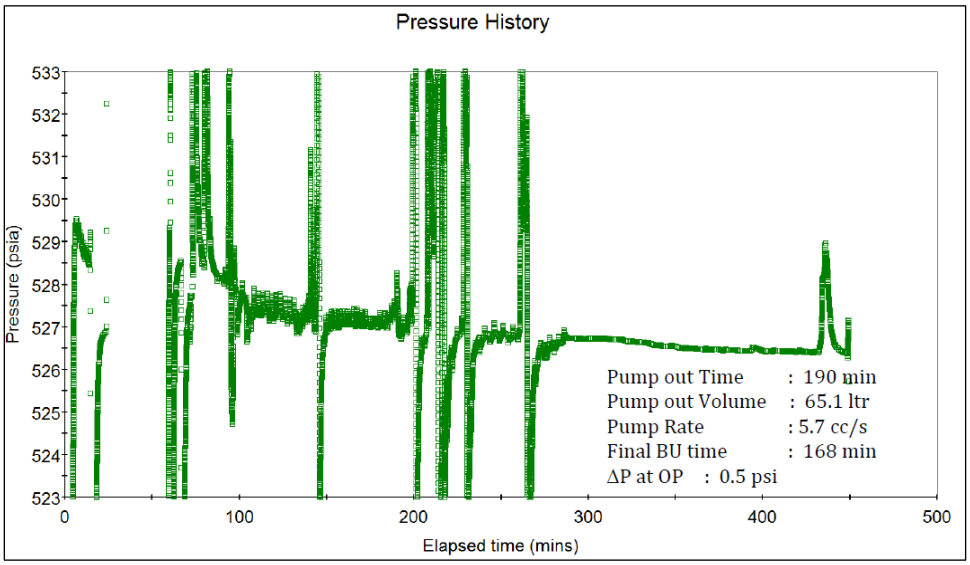


Figure 15-49. Pressure response at the observation probe during LIT-2.

Diagnostic Analysis (LIT-2)

A diagnostic log-log plot for straddle packer data and the observation probe data is shown in Figure 15-50. The observation probe data is not analyzable due to the small pressure drop (0.5 psi). The early-time pressure response in the straddle packer interval was dominated by tool storage and nearby effects of skin. After the tool storage period, the derivative (blue triangles) shows radial flow (horizontal derivative) at around 0.1 minute, followed by an increasing derivative which may indicate changing reservoir properties (decreasing permeability). The late-time derivative has a decreasing slope, suggesting a uniform permeability value farther from the well. Another possible explanation for the shape of the pressure derivative is the existence of a fracture that intersects the test interval. However, there is no evidence of a fracture from the image log or other open-hole logs.

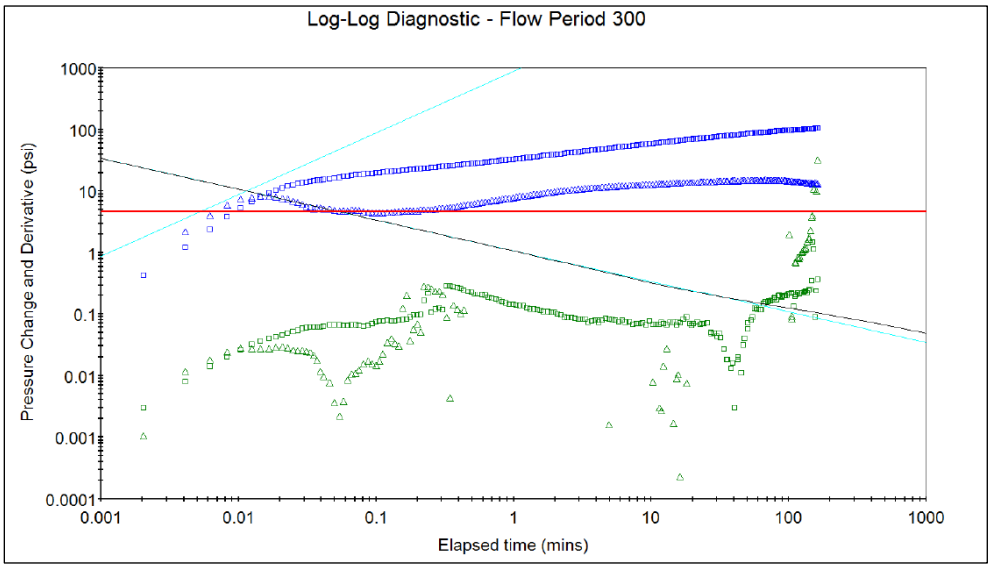


Figure 15-50. Log-log diagnostic plot of straddle packer (blue symbols) and observation probe (green symbols) pressure response during LIT-2 buildup period.

History Match Analysis (LIT-2)

Reservoir properties were estimated by simulating the test data using a model of a partially penetrating deviated well in an infinitely acting radial composite reservoir model (a radial composite reservoir has concentric inner and outer zones with different properties).

Figure 15-51 and Figure 15-52 show the match between modeled data and measured data in a log-log plot of recovery data pressure and pressure derivative (Figure 15-51) and in a Cartesian plot of the entire drawdown-buildup sequence (Figure 15-52). Model input parameters and reservoir properties from the model history match analyses are provided in Figure 15-53.

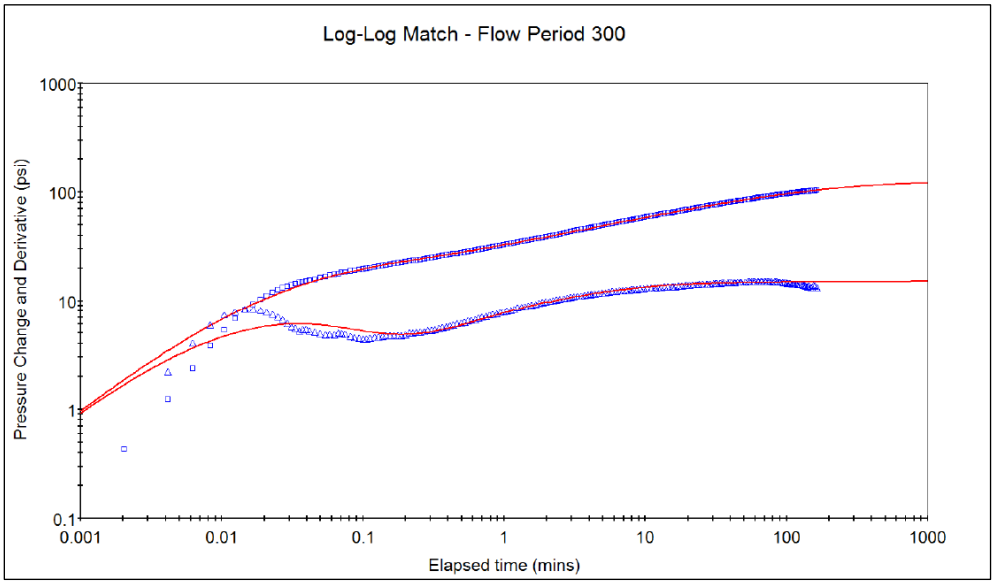


Figure 15-51. Comparison of observed pressure (blue squares) and pressure derivative (blue triangles) data to modeled pressure and pressure derivative (red lines) for the LIT-2 buildup period.

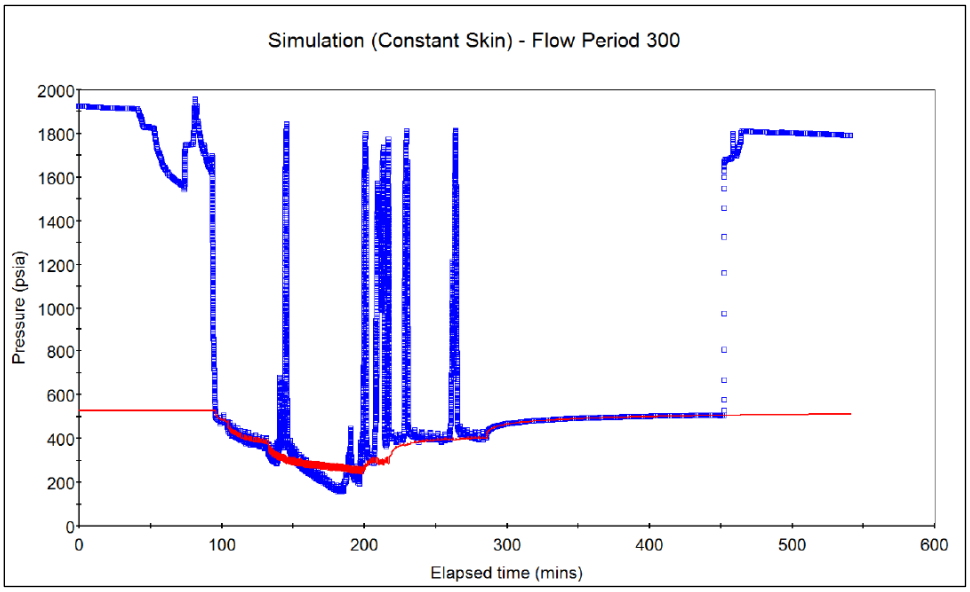
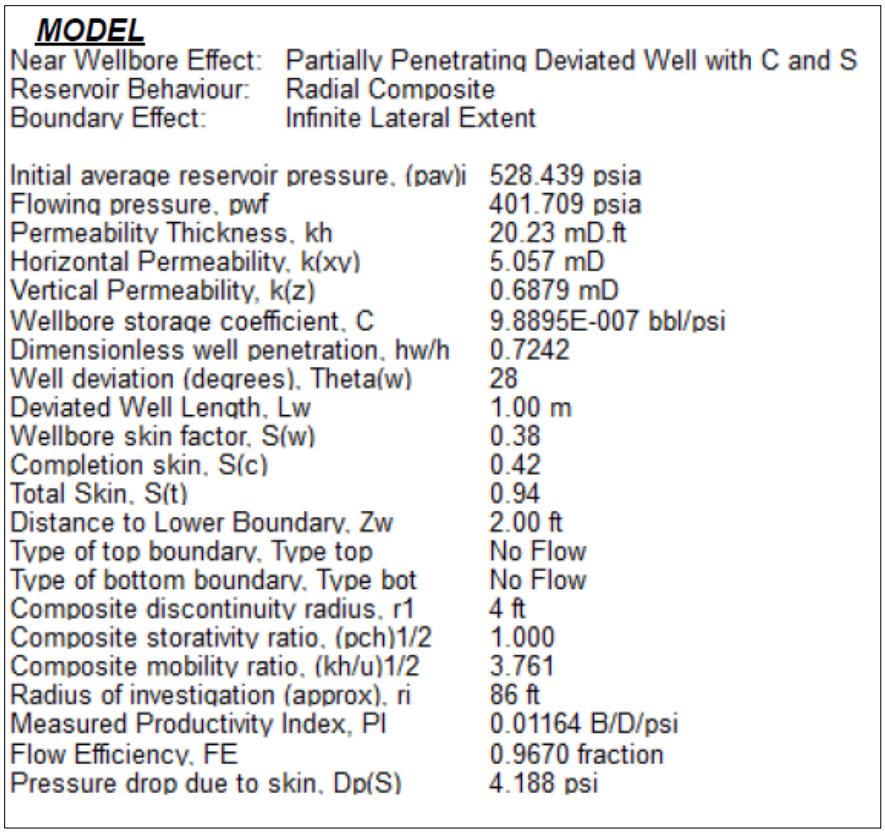


Figure 15-52. Pressure history match of the LIT-2 pumping and buildup periods.



MODEL

Near Wellbore Effect:	Partially Penetrating Deviated Well with C and S
Reservoir Behaviour:	Radial Composite
Boundary Effect:	Infinite Lateral Extent

Initial average reservoir pressure, (pav)i	528.439 psia
Flowing pressure, pwf	401.709 psia
Permeability Thickness, kh	20.23 mD.ft
Horizontal Permeability, k(xy)	5.057 mD
Vertical Permeability, k(z)	0.6879 mD
Wellbore storage coefficient, C	9.8895E-007 bbl/psi
Dimensionless well penetration, hw/h	0.7242
Well deviation (degrees), Theta(w)	28
Deviated Well Length, Lw	1.00 m
Wellbore skin factor, S(w)	0.38
Completion skin, S(c)	0.42
Total Skin, S(t)	0.94
Distance to Lower Boundary, Zw	2.00 ft
Type of top boundary, Type top	No Flow
Type of bottom boundary, Type bot	No Flow
Composite discontinuity radius, r1	4 ft
Composite storativity ratio, (ph)1/2	1.000
Composite mobility ratio, (kh/u)1/2	3.761
Radius of investigation (approx), ri	86 ft
Measured Productivity Index, PI	0.01164 B/D/psi
Flow Efficiency, FE	0.9670 fraction
Pressure drop due to skin, Dp(S)	4.188 psi

Figure 15-53. Model input parameters and reservoir properties from the model history match analysis for LIT-2.

Summary of LIT Results

A summary of the key reservoir properties determined from the two LITs conducted in the 8-16 well is provided in Table 15-9. From these data, the transmissivity of the A-1 Carbonate ranges from 18 to 25 md-ft.

Table 15-9. Summary of key reservoir properties determined from LITs conducted in the Chester 8-16 well.

Test	Formation	Straddle Packer Midpoint (ft, MD)	Observation Probe (ft, MD)	kh (mD-ft)	kxy (mD)	kz (mD)	Model (see notes)	Radius of Investigation; Inner Boundary (ft)
LIT-1	A-1 Carb	5890.7	5884.2	18	0.9[a]	0.01	1	78/NA
LI2-2	A-1 Carb	5864.7	5858.2	20[inner] 24.7[outer]	5.2[b inner] 1.3[a outer]	0.7 [outer]	2	86/4

Notes: kh = transmissivity; kxy = horizontal permeability; kz = vertical permeability; h = reservoir thickness.
1. Partially penetrating deviated well in homogeneous reservoir with infinite lateral extent.
2. Partially penetrating deviated well in radial composite reservoir with infinite lateral extent.
[a] Horizontal permeability is based on h = 20 ft.
[b] Horizontal permeability is based on h = 4 ft.

15.4.3 Micro-Frac Tests

Four wireline micro-frac tests were conducted in the 8-16 well on January 28, 2017. All four tests achieved formation breakdown and showed fracture reopening pressures and good fracture propagation pressures. This section summarizes the micro-frac testing results.

Table 15-10. Summary of open-borehole micro-frac tests performed in the 8-16 well.

Station	Formation	MD (ft)	Cycles
1	A-1 Carbonate	5861	3
2	Brown Niagaran	5967	4
3	A-2 Carbonate	5791	5
4	A-2 Carbonate	5765	4

The depths of the micro-frac tests are given in Table 15-10, along with the name of the formation tested and the number of test cycles performed in the interval. The specific depth interval was based on formation type, borehole quality, formation stress contrast, formation mechanical properties, and in-situ stress conditions. Zones with extensive breakouts that could compromise the sealing capacity of the inflatable elements as well as high-rugosity borehole wall that could deteriorate the rubber during inflating and deflating of elements were avoided. Finally, for optimum fracture containment and proper fracture propagation, it was critical that the inflatable elements were positioned on layers with sufficient stress contrast with respect to the isolated formation interval. This was done in order to avoid sleeve fracturing and early hydraulic communication between the fracture and the hydrostatic pressure.

Micro-Frac Test 1 (A-1 Carbonate, 5861 ft MD)

The first micro-frac test was performed in the A-1 Carbonate at a depth of 5861 ft MD. The test history is illustrated in Figure 15-54. The bottom hole pressure of the isolated interval (APQJ) [psi] is denoted in blue, and the absolute pressure inside the packers (ASPEP) [psi] is denoted in magenta. The flow rate [cm^3/s] is shown with a red line, while the cumulative displaced volume [liters] is shown in green and the bottom hole temperature [°F] is shown in brown.

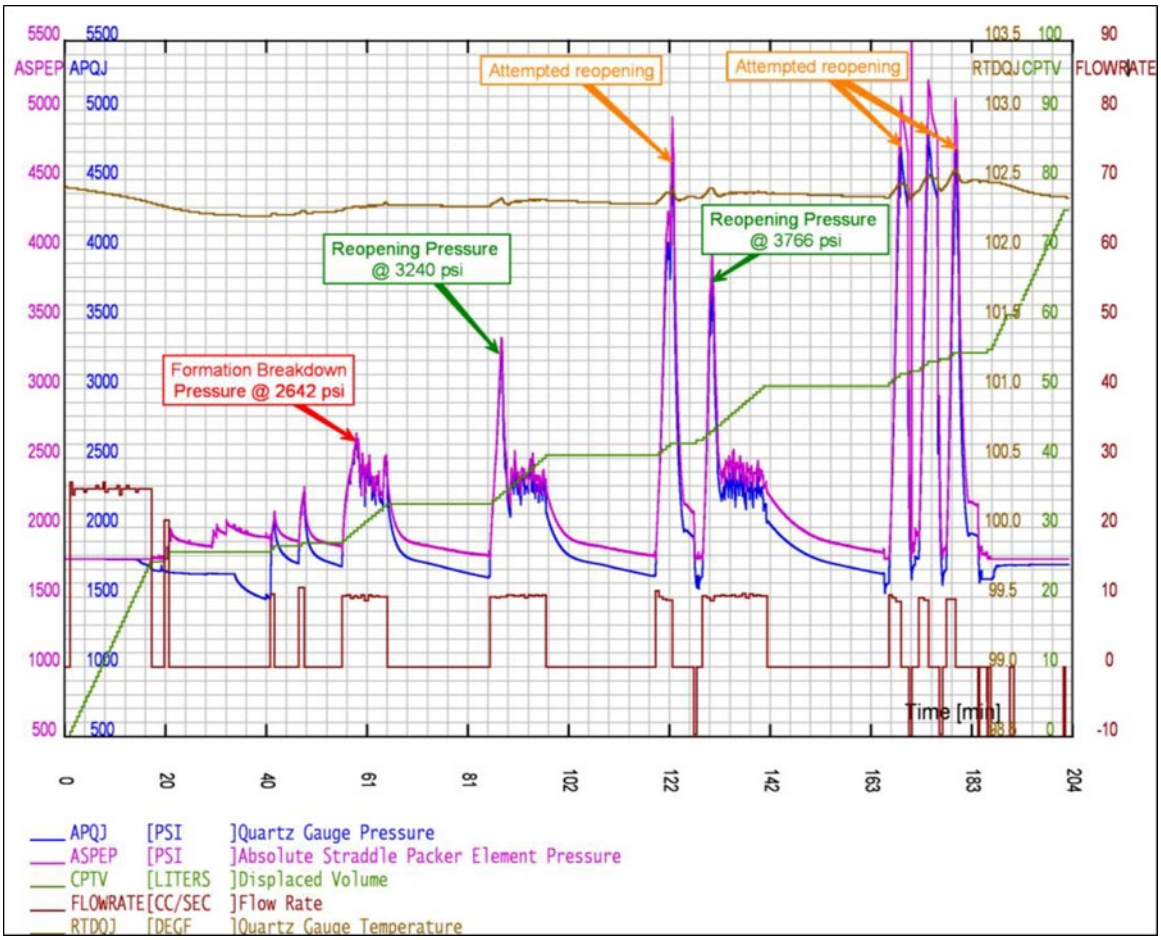


Figure 15-54. Test history for micro-frac test 1 in the A-1 Carbonate at 5861 ft MD.

The straddle packers were inflated in about 17 minutes (with the 1970RB 717-cm^3 pump) with the hydrostatic pressure at 1777.3 psi. Fluid loss was observed in the well, and the hydrostatic pressure kept changing. Once the packers' pressure had stabilized, two packer integrity checks were performed at 2050 psi and 2250 psi, which are equivalent to 273 psi and 473 psi above hydrostatic pressure, respectively. Both packer integrity checks showed good packer seal. Following the integrity tests, three successful injection test cycles were performed. A fourth injection cycle was attempted three times but was not successful at reopening the fracture within the pressure constraints of the packers. The maximum test interval pressure was set at 5,000 psi. If fracturing or reopening could not be achieved within this pressure, injection was halted.

Formation Breakdown Pressure

Formation breakdown was achieved in the first injection cycle (FOT1) (Figure 15-55). The breakdown pressure is 2642 psi, which is 865 psi above the hydrostatic pressure. The fracture was propagated for ~6 minutes after formation breakdown. After shut-in, natural pressure decline was monitored for ~20 minutes.

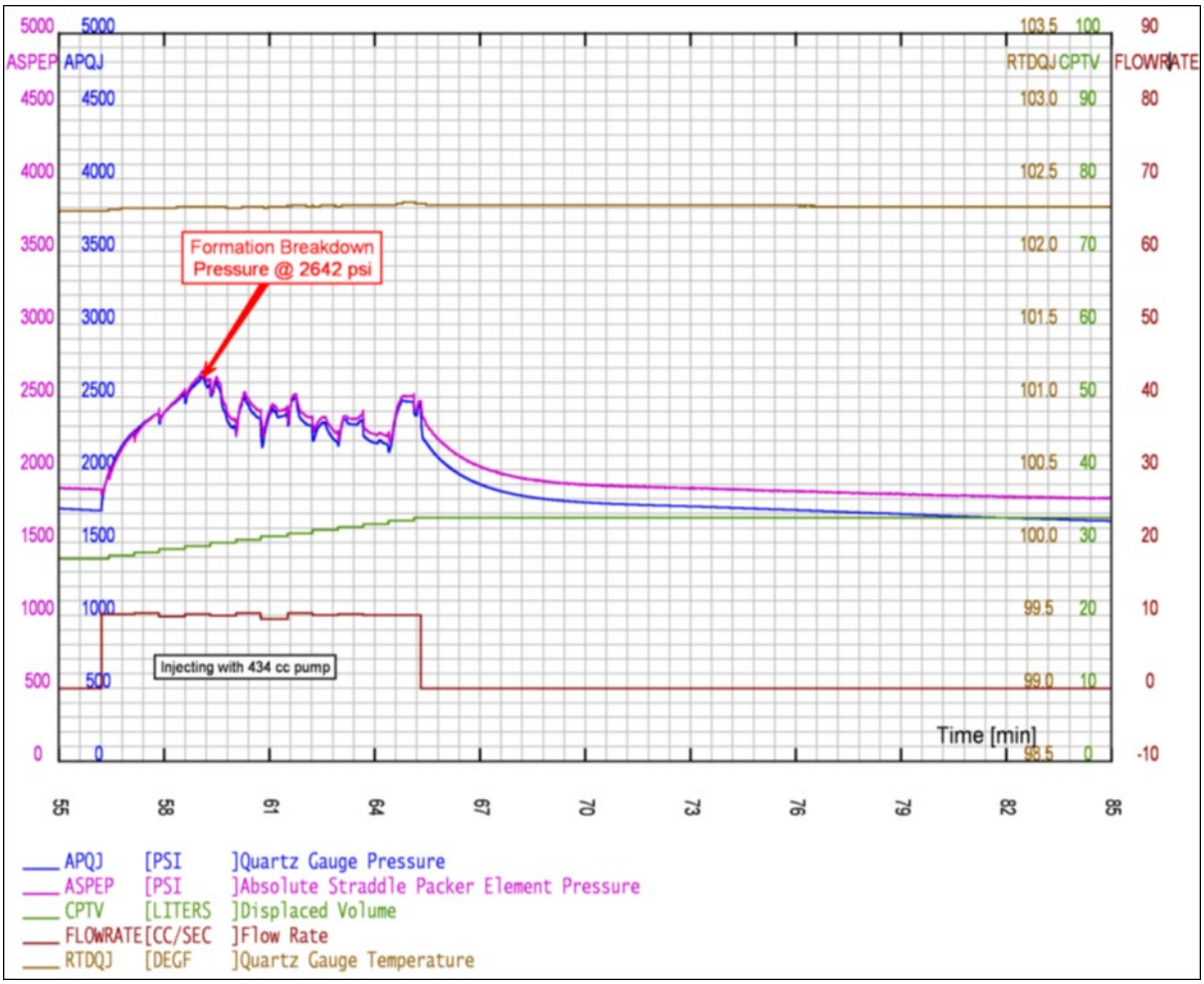


Figure 15-55. Fracture breakdown pressure during FOT1 of micro-frac test 1.

Fracture Reopening Pressure

Fracture reopening pressure was measured in cycles 2 and 3 of micro-frac test 1; reopening pressures were 3240 psi (FOT2) and 3766 psi (FOT3).

An unusual aspect of this test (and the other three micro-frac tests as well) is that the reopening pressure was higher than the breakdown pressure. One possible explanation is that the drilling-mud additives bridged in the fracture, making it harder to reopen the induced fracture. In other words, the particles trapped in the fracture created a restriction that needed to be overcome to reopen the existing fracture. Conversely, the propagation pressure is consistent, suggesting that a new fracture was not created but rather that propagation of the same fracture occurred.

Fracture Propagation Pressure

Fracture propagation pressure was 2300 psi for both FOT2 and FOT3.

Fracture Closure Pressure

The fracture closure pressure was estimated by three different methods: (1) pressure decline analysis using the APQJ pressure vs. square shut-in time; (2) log-log pressure decline analysis using the pressure derivative of the delta pressure and delta time in the log-log plot; and (3) G-function analysis by plotting the APQJ pressure vs. G-time. All three pressure decline analysis methods were performed using mini-frac software developed by Meyer and Associates.

The first method considers a linear regression behavior at the early stage of the shut-in time with the fracture closure pressure occurring at the point where deviation from the linear pressure decline behavior occurs. An example square-root of shut-in time plot is shown in Figure 15-56 for micro-frac station 1/test cycle 1. This method yielded a fracture closure pressure of 1907 psi.

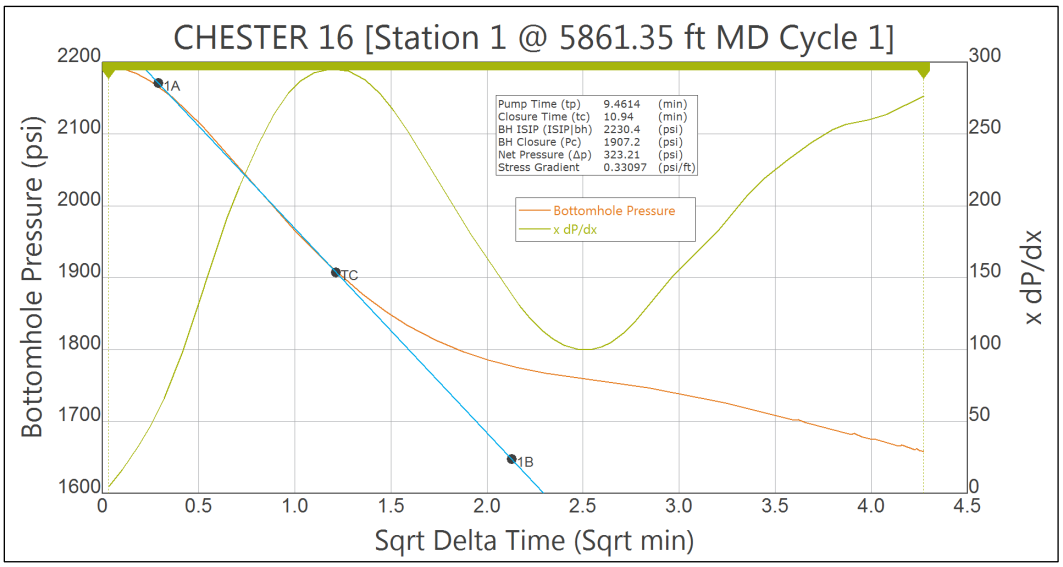


Figure 15-56. Example square root of shut-in-time plot for fracture closure identification in station 1/cycle 1.

The second method looks for a change in the slope of the pressure derivative d(log dP)/d(log dt) from a linear behavior with approximately 0.5 slope into a decreasing trend (the change is associated with fracture closure). The pressure derivative curve must be around 0.5 for a dominant infinite-conductivity fracture flow regime when the fracture is still open; the pressure derivative decreases as the fracture closes. An example log-log of shut-in time plot is shown in Figure 15-57 for micro-frac station 1/test cycle 1. This method yielded a fracture closure pressure of 1896 psi.

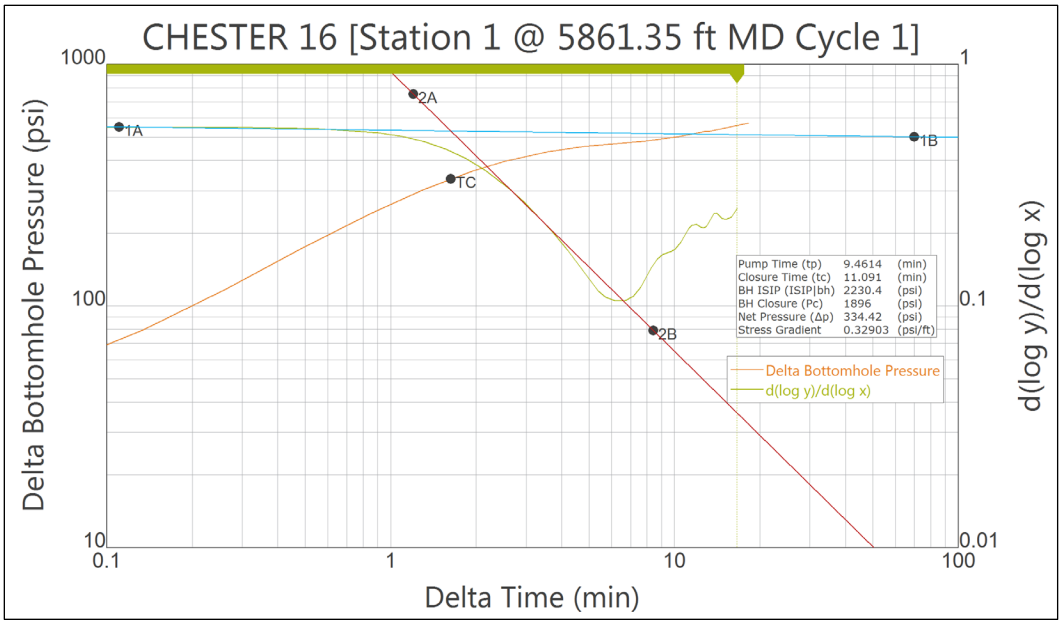


Figure 15-57. Example log-log of shut-in time plot for fracture closure identification in station 1/cycle 1.

The third method looks for a change in the behavior in the pressure vs. G-function plot by identifying the change of slope of the GdP/dG derivative curve (either a linear increasing to flat or a decreasing trend). An example G-function plot is shown in Figure 15-58 for micro-frac station 1/test cycle 1. This method yielded a fracture closure pressure of 1918 psi.

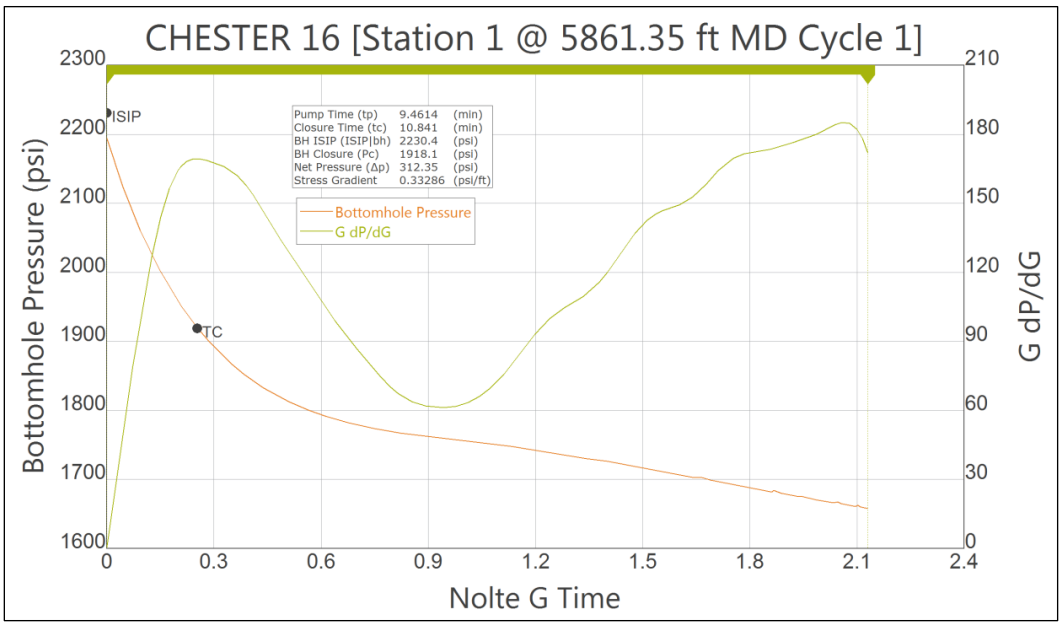


Figure 15-58. Example G-function of shut-in time plot for fracture closure identification in station 1/cycle 1.

The fracture closure pressure is defined in this report as the average of the three pressure decline analysis methods. Table 15-11 summarizes fracture closure pressure values for each of the three injection cycles for micro-frac test 1.

Table 15-11. Fracture closure pressures for micro-frac Station 1 (5861 ft MD).

Pressure Decline Analysis	Flowback Cycle	Fracture Closure (psi)	Fracture Closure Gradient (psi/ft)
Square root of shut-in time	FOT1	1907.2	0.331
Log-log	FOT1	1896.0	0.329
G-function	FOT1	1918.1	0.333
average		1907.1	0.331
Square root of shut-in time	FOT2	1874.0	0.325
Log-log	FOT2	1848.2	0.321
G-function	FOT2	1870.2	0.325
average		1864.1	0.324
Square root of shut-in time	FOT3	1819.1	0.316
Log-log	FOT3	1822.0	0.316
G-function	FOT3	1815.7	0.315
average		1818.9	0.316

Micro-Frac Test 2 (Brown Niagaran, 5967 ft MD)

The second micro-frac test was performed in the Brown Niagaran Formation at 5967 ft MD. The test history is illustrated in Figure 15-59. The straddle packers were inflated in ~17 minutes with the hydrostatic pressure at 1782.5 psi. Once the packers' pressure had stabilized, two packer integrity checks were performed at ~1907.5 psi and 1989.5 psi, which is equivalent to 125 psi and 207 psi above hydrostatic pressure, respectively. Both packer integrity tests showed good packer seal. Subsequently, three successful injection test cycles were performed.

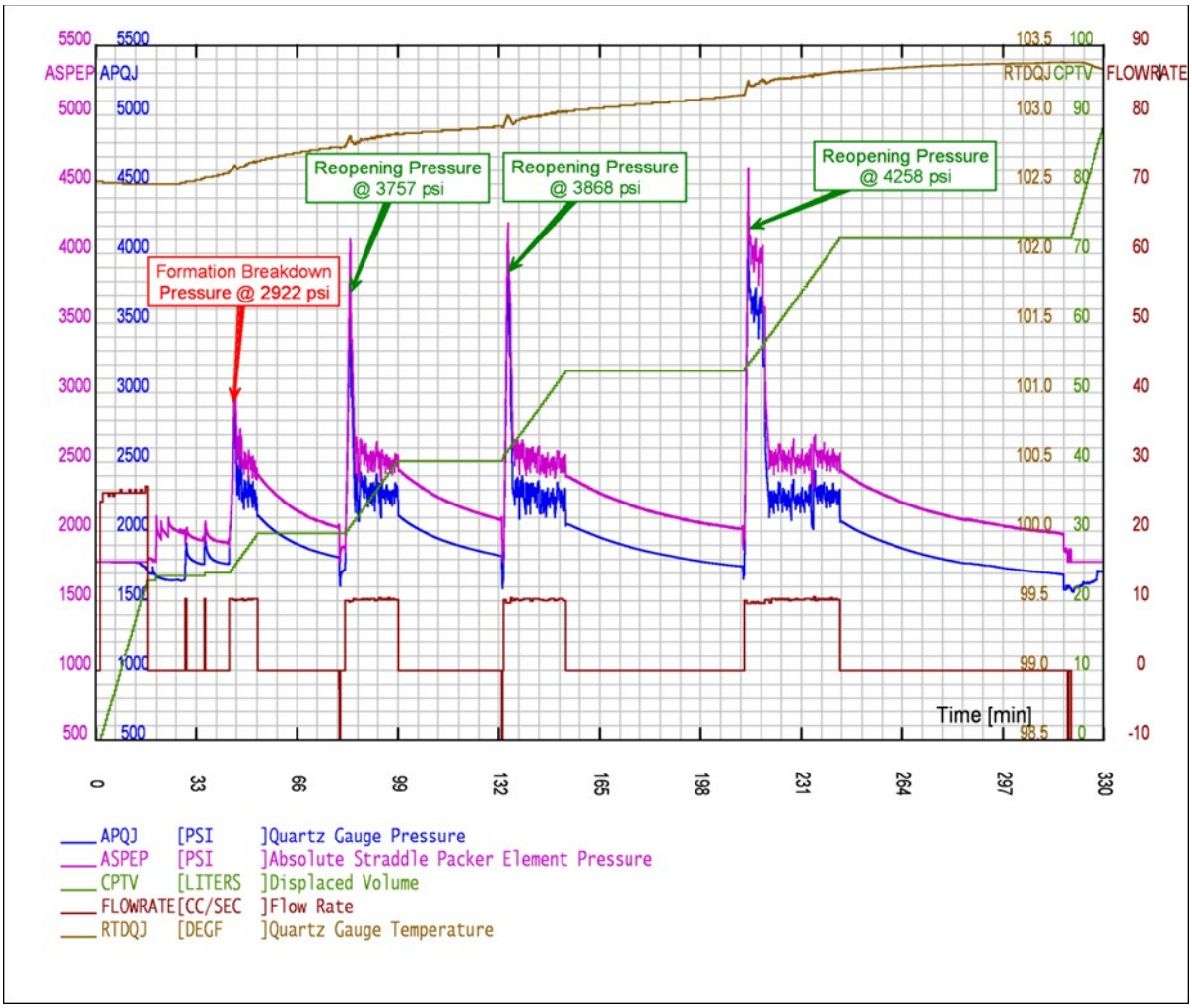


Figure 15-59. Test history for micro-frac test 2 in the Brown Niagaran at 5967 ft MD.

Formation Breakdown Pressure

Formation breakdown was achieved in FOT1 (Figure 15-60). The breakdown pressure, 2922 psi, was 1139.5 psi above the hydrostatic pressure. The fracture was propagated for ~7 minutes after formation breakdown. After shut-in, the fracture was observed with a natural decline for ~28 minutes.

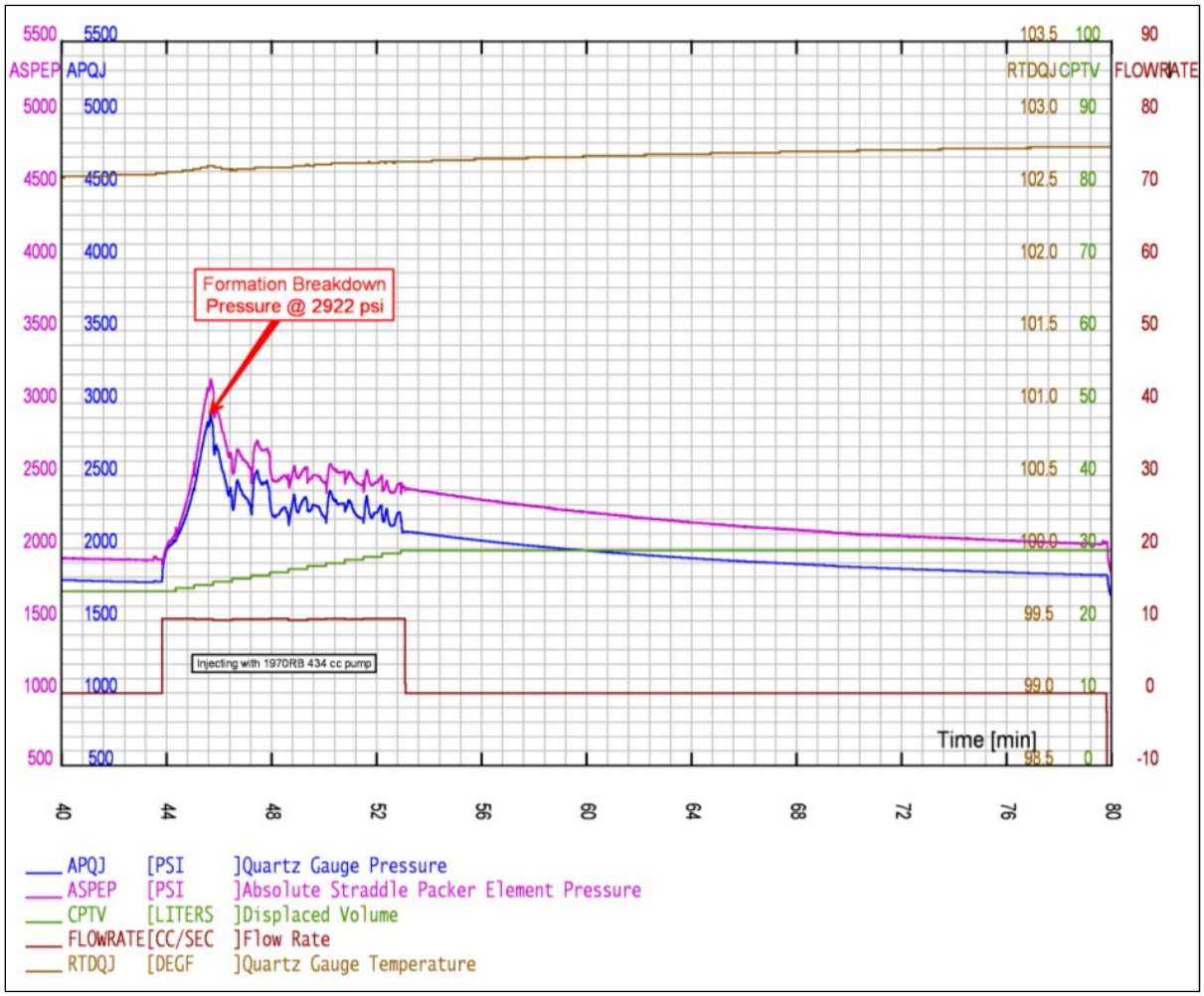


Figure 15-60. Fracture breakdown pressure during the FOT1 of micro-frac test 2.

Fracture Reopening Pressure

Fracture reopening pressure was measured in cycles 2, 3, and 4 of micro-frac test 2. Reopening pressures were 3757 psi (FOT2), 3868 psi (FOT3), and 4258 psi (FOT4). As was the case for micro-frac test 1, the reopening pressure was higher than the breakdown pressure.

Fracture Propagation Pressure

Fracture propagation pressure was measured in cycles 2, 3, and 4 of micro-frac test 2. Fracture propagation pressure was 2300 psi for all three test cycles.

Fracture Closure Pressure

Fracture closure pressure was measured in cycles 2, 3, and 4 of micro-frac test 2. Table 15-12 summarizes the fracture closure pressure measurements for each test cycle determined with the three pressure decline analysis methods.

Table 15-12. Fracture closure pressures for micro-frac Station 2 (5967 ft MD).

Pressure Decline Analysis	Flowback Cycle	Fracture Closure (psi)	Fracture Closure Gradient (psi/ft)
Square root of shut-in time	FOT1	1883.8	0.321
Log-log	FOT1	1886.7	0.322
G-function	FOT1	1883.5	0.321
average		1884.7	0.321
Square root of shut-in time	FOT2	1859.1	0.317
Log-log	FOT2	1857.9	0.317
G-function	FOT2	1857.3	0.316
average		1858.1	0.317
Square root of shut-in time	FOT3	1808.8	0.308
Log-log	FOT3	1802.9	0.307
G-function	FOT3	1806.8	0.308
average		1806.2	0.308
Square root of shut-in time	FOT4	1805.2	0.308
Log-log	FOT4	1792.5	0.305
G-function	FOT4	1800.0	0.307
average		1799.2	0.307

Micro-Frac Test 3 (A-2 Carbonate, 5791 ft MD)

The third micro-frac test was performed in the A-2 Carbonate formation interval at 5791 ft MD. The test history is shown in Figure 15-61. The straddle packers were inflated in ~19 minutes with the hydrostatic pressure at 2849 psi (note: hydrostatic pressure is higher in this test because the borehole was filled with water after micro-frac test 2). Once the packer pressure had stabilized, two packer integrity checks were performed at ~2990 psi and 3198 psi (141 psi and 349 psi above hydrostatic pressure). Both packer integrity tests showed good packer seal.

Following the packer integrity tests, four injection test cycles were performed. Fracture closure pressure could be determined for only the first cycle. During cycle 2, closure pressure could not be determined because the pump stalled. During cycles 3, 4 and 5, the pressure declined after fracturing exhibited an abnormal behavior, which precluded determining closure pressure. However, fracture reopening pressure and fracture propagation pressure were successfully determined for cycles 2, 3, 4, and 5.

Formation Breakdown Pressure

Formation breakdown was achieved in the FOT1 as shown in Figure 15-61. The breakdown pressure, 3790 psi, was 941 psi above the hydrostatic pressure. The fracture was propagated for ~10 minutes after formation breakdown. After shut-in, pressure decline was monitored for ~30 minutes.

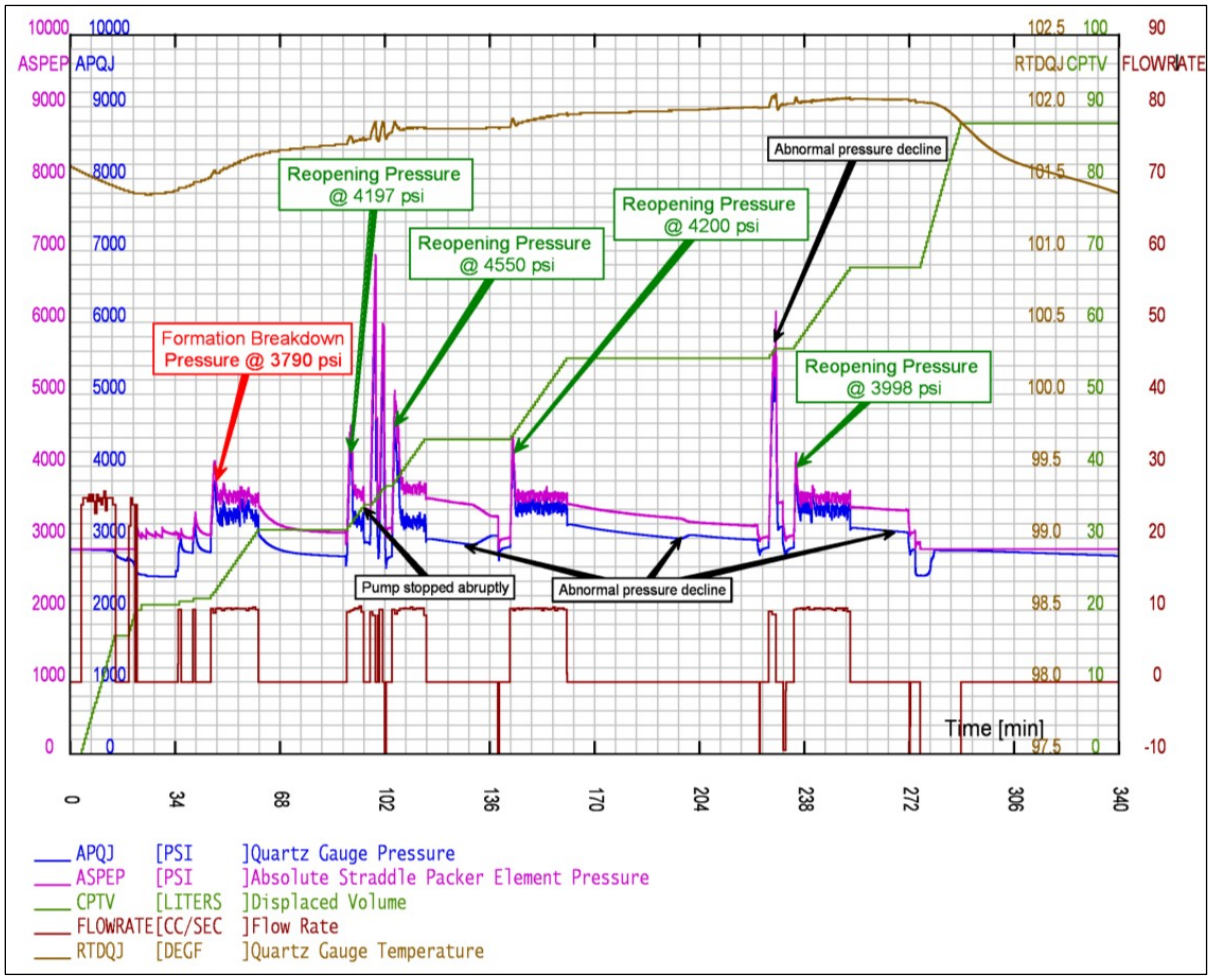


Figure 15-61. Test history for micro-frac test 3 in the A-2 Carbonate at 5791 ft MD.

Fracture Reopening Pressure

Fracture reopening pressure was measured in cycles 2, 3, 4, and 5 of micro-frac test 3. Reopening pressures were 4197 psi (FOT2), 4550 psi (FOT3), 4200 psi (FOT4), and 3998 psi (FOT5). As was the case for micro-frac tests 1 and 2, the reopening pressure was higher than the breakdown pressure.

Fracture Propagation Pressure

Fracture propagation pressure was measured in cycles 2, 3, 4, and 5 of micro-frac test 3. Fracture propagation pressure ranged from 3250 psi to 3400 psi for all four test cycles.

Fracture Closure Pressure

Fracture closure pressure was measured only in cycle 1 of micro-frac test 3. Table 15-13 summarizes the fracture closure pressure measurements determined with the three pressure decline analysis methods.

Table 15-13. Fracture closure pressures for micro-frac Station 3 (5791 ft MD).

Pressure Decline Analysis	Flowback Cycle	Fracture Closure (psi)	Fracture Closure Gradient (psi/ft)
Square root of shut-in time	FOT1	2871.6	0.504
Log-log	FOT1	2876.9	0.505
G-function	FOT1	2864.4	0.503
average		2871.0	0.504

Micro-Frac Test 4 (A-2 Carbonate, 5765 ft MD)

The fourth micro-frac test was performed in the A-2 Carbonate at a depth of 5765 ft MD. The test history is shown in Figure 15-62. The straddle packers were inflated in about 16 minutes under a hydrostatic pressure at 2746 psi. Once the packer pressure had stabilized, two packer integrity checks were done at 3301 psi and 3444 psi (555 and 698 psi above hydrostatic pressure). Both integrity tests showed that the packers had achieved a good seal. Following the integrity tests, four successful test cycles were conducted.

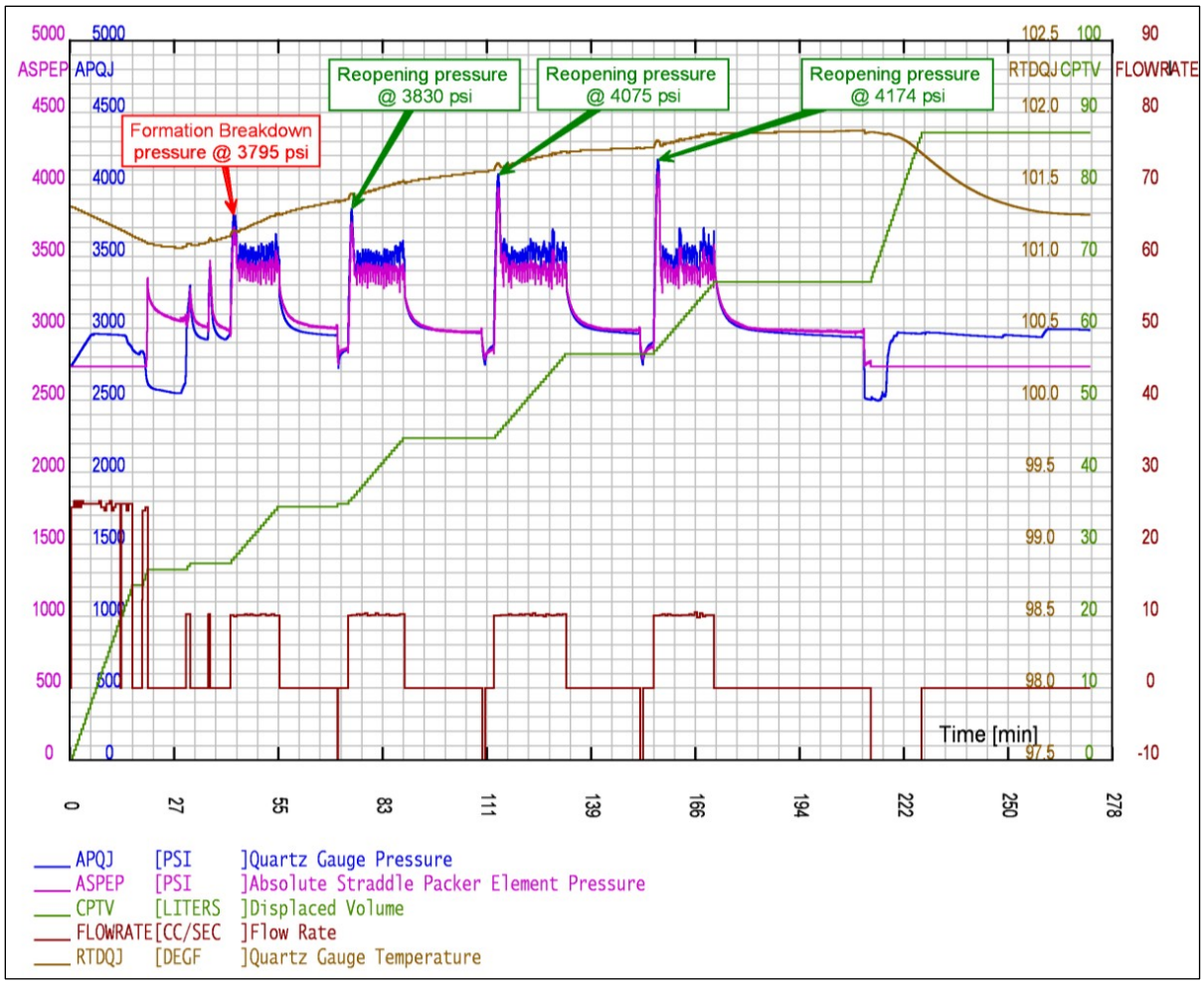


Figure 15-62. Test history for micro-frac test 4 in the A-2 Carbonate at 5765 ft MD.

Formation Breakdown Pressure

Formation breakdown was achieved in FOT1 at 3795 psi (Figure 15-63).

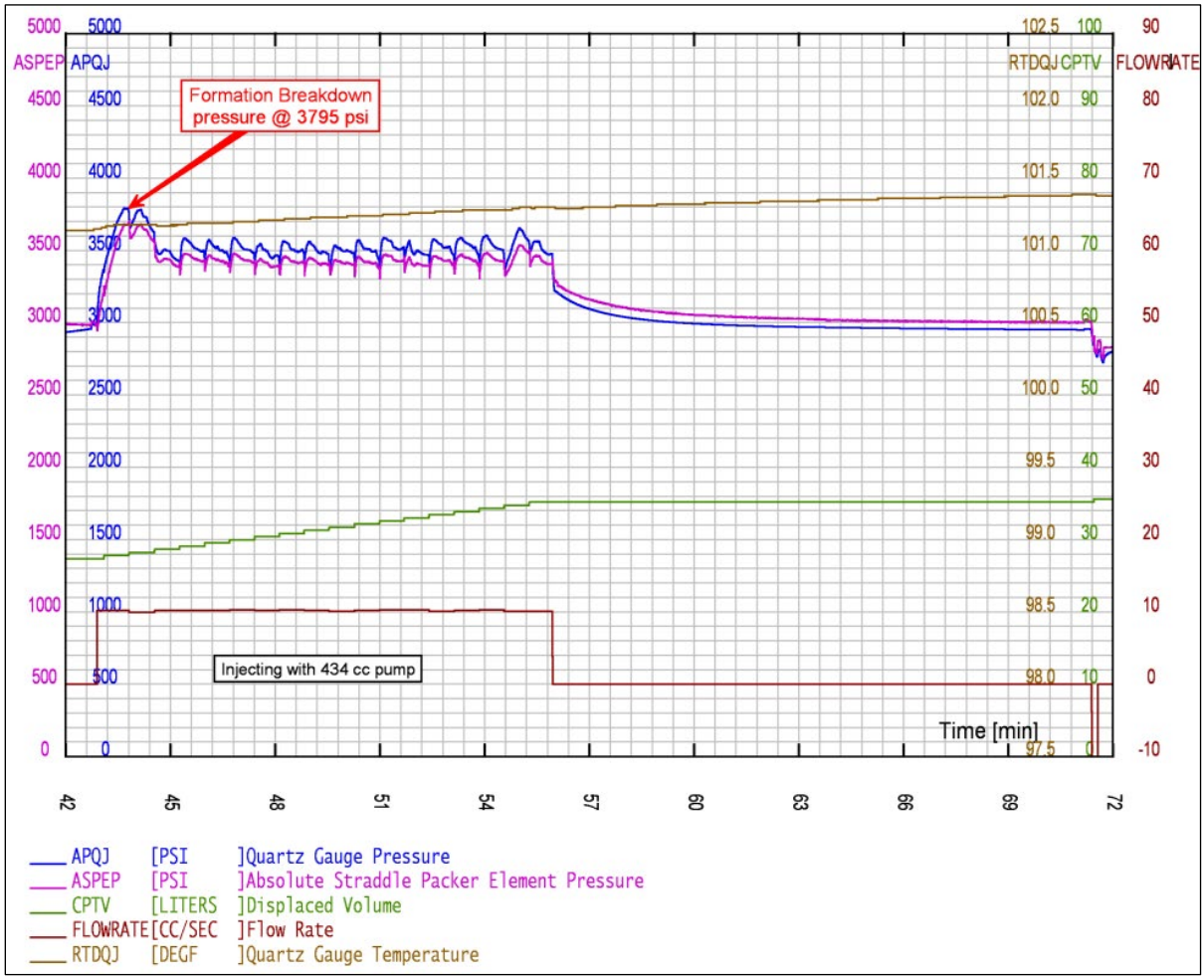


Figure 15-63. Fracture breakdown pressure during the first injection cycle of micro-frac test 4.

Fracture Reopening Pressure

Fracture reopening pressure was measured in cycles 2, 3, and 4 of micro-frac test 4. Reopening pressures were 3830 psi (FOT2), 4075 psi (FOT3) and 4174 psi (FOT4). As was the case for the other micro-frac tests, the reopening pressure was higher than the breakdown pressure.

Fracture Propagation Pressure

Fracture propagation pressure was measured in cycles 2, 3, and 4 of micro-frac test 4. Fracture propagation pressure was 3500 psi for all three test cycles.

Fracture Closure Pressure

Table 15-14 summarizes fracture closure pressure values for each of the four injection cycles for micro-frac test 4.

Table 15-14. Fracture closure pressures for micro-frac test 4 (5765 ft MD).

Pressure Decline Analysis	Flowback Cycle	Fracture Closure (psi)	Fracture Closure Gradient (psi/ft)
Square root of shut-in time	FOT1	3074.7	0.543
Log-log	FOT1	3085.3	0.544
G-function	FOT1	3097.8	0.547
average		3085.9	0.545
Square root of shut-in time	FOT2	3087.4	0.545
Log-log	FOT2	3071.8	0.542
G-function	FOT2	3091.6	0.546
average		3083.6	0.544
Square root of shut-in time	FOT3	3110.3	0.549
Log-log	FOT3	3093.3	0.546
G-function	FOT3	3099.4	0.547
average		3101.0	0.547
Square root of shut-in time	FOT4	3145.0	0.555
Log-log	FOT4	3125.4	0.552
G-function	FOT4	3128.9	0.552
average		3133.1	0.553

Determining Stress Orientation

Before and after image logs of each micro-frac test interval were obtained using the Baker Hughes STAR imaging wireline tool. The objective of obtaining the images was to determine the orientation of the induced fracture, which corresponds to the direction of SH_{max}. Because SH_{max} is perpendicular to Sh_{min}, both SH_{max} and Sh_{min} can be determined from the image analysis. The induced fractures were visible only in Stations 1 (A-1 Carbonate) and 2 (Brown Niagaran). For the two test intervals in the A-2 Carbonate (Stations 3 and 4), the fractures were not visible. This is thought to be due to closing of the fracture before the image log was deployed. The before and after STAR images are shown in Figure 15-64 for Station 1 at 5861 ft and Station 2 at 5967 ft, showing the vertical fracture created by the micro-frac testing. The orientation of the fractures is N62E degrees for Station 1 and N6E degrees for Station 2.

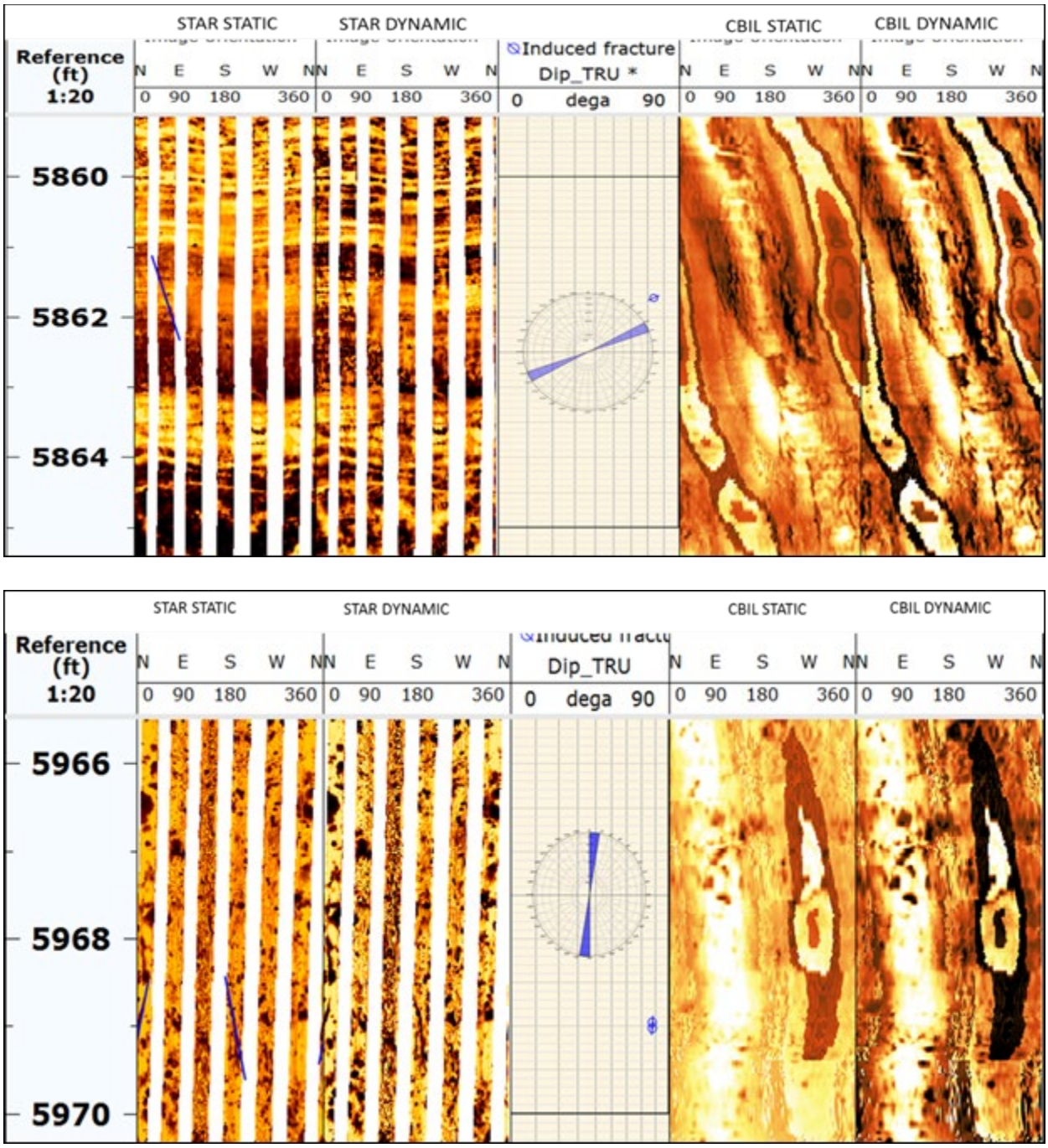


Figure 15-64. Image log interpretation of induced fracture after mini-frac test of Station 1 (A-1 Carbonate, upper) and Station 2 (Brown Niagaran, lower) in the 8-16 well. SH_{max} orientation is N62E and N6E.

Geomechanical Model Calibration

A log-derived geomechanical model provides continuous values for key geomechanical parameters over a depth interval of interest. A geomechanical model for the A-1 Carbonate-Brown Niagaran interval (5735 to 6455 ft) in the 8-16 well in the Chester 16 reef is shown in Figure 15-65. Results of the micro-frac testing were used to confirm (calibrate) values of key parameters (stress parameters) that were derived from log data. The parameters of the geomechanical model include:

- Track 1 shows the gamma ray, borehole caliper, and bit size curves.
- Track 2 shows the neutron-porosity and formation density curves.
- Track 3 shows the borehole acoustic log showing the compressional and shear wave slowness and the vp/vs ratio.
- Track 4 shows the vertical Young's modulus and friction angle and track 5 shows the Poisson's ratio.
- Track 6 shows the unconfined compressive strength (UCS) (estimated from Lal's empirical correlation (Lal, 1999) and Lacy relationships (Lacy, 1997)).
- Track 7 plots the static stiffness tensor components using black for the compressional components, red for the shear components, and green for the off-diagonal components. The rock stiffness conversion from dynamic (acoustically derived) to static (triaxial compression) stiffness was done using the Lacy's empirical correlation (Lacy, 1997) for Young's modulus and a 5 percent reduction was applied for Poisson's ratio. The tensile strength of the formations was estimated as 1/12th of the UCS.
- Track 8 shows the downhole stress profiles which includes the calibration points from the straddle packer micro-frac testing. The red curve is the fracture initiation pressure and the calibration points are the formation breakdown pressures (black diamonds) (the pressure at which the micro-frac will cause the rock formation to fracture hydraulically). The black curve is the minimum horizontal stress and the calibration point is the closure pressure (red diamonds). The blue curve is the formation pore pressure and the calibration point is the pore pressure from formation pressure tests (blue diamonds).
- The minimum horizontal stress was calculated using the static mechanical properties obtained from the acoustic logging tool assuming an isotropic rock model. The minimum horizontal stress was calibrated against the fracture closure and the breakdown pressures measured in all four stations using an external tectonic stress model between -700 to 650 psi in the direction of Sh_{min} and tectonic horizontal stress anisotropy between 0 to 5 percent. The methodology used was to incorporate a non-constant, depth-dependent external tectonic stress model that takes into account the variation in the fracture gradient with depth as a result of tectonic forces. The use of the non-constant depth-dependent external tectonic stress model for this well was due to the effect that if the formations were buried with large difference in depth, the lateral strain would have to change with depth because the deeper formations would be under higher tectonic history than the shallower formations.
- Track 9 shows the stress gradient profiles with the same calibration points expressed as a gradient (i.e., psi/ft).
- Track 10 presents the stress contrast denoting high stresses in red and low stresses in purple.
- Track 11 shows the brittleness profiles.
- The vertical fracture migration curves, shown in track 12, is the delta pressure which is the difference between the fracture closure pressure at each depth and the minimum fracture closure pressure of the interval. This track helps to differentiate between interval with low and high stresses. Low stress zones are denoted in pink and green while high stress zones are denoted in grey and red.

Overall, there is good agreement between the modeled and measured data for all four stations, providing a reliable model to estimate continuous minimum and maximum horizontal stress profiles for this well.

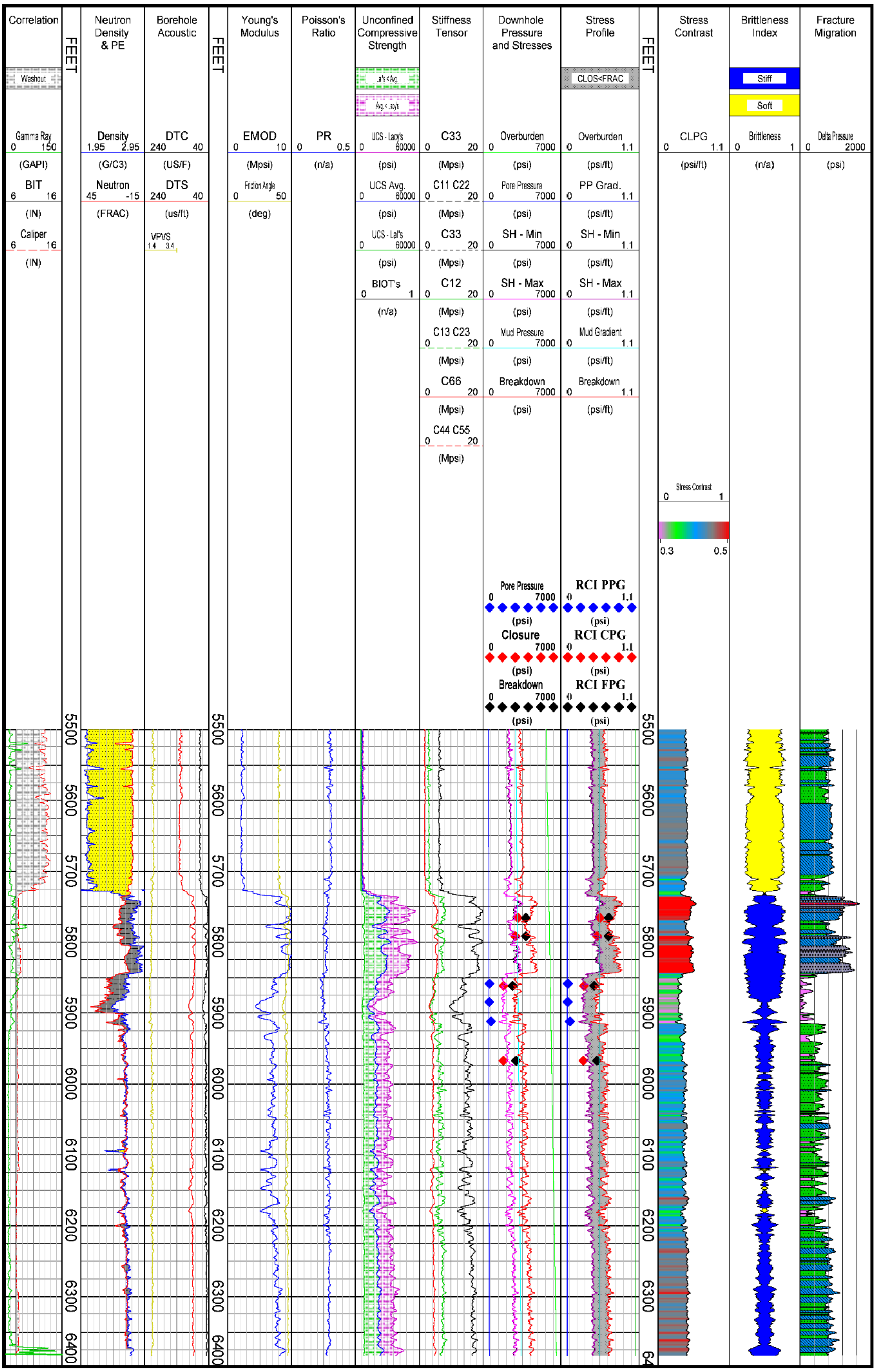


Figure 15-65. Calibration of log-derived stress parameters using measurements from micro-frac testing (see tracks 8 through 12) for the depth interval 5735 to 6455 ft in the 8-16 well. Calibration points from the micro-frac testing are shown in tracks 8 and 9. Note low values of Sh_{min} in the A-1 Carbonate and Brown Niagaran reservoir (sample points below 5850 ft) due to depleted pressure resulting from primary production compared to A-2 Carbonate caprock (sample points above 5850 ft).

15.4.4 Summary

Reservoir Pressure

Pressure measurements were attempted at 22 depth locations in the 9-33 well of the Dover 33 reef. Successful testing was achieved at only one depth location, yielding a reservoir pressure of 2920.57 and a mobility of 2.3 mD/cP. The other tests were not successful because the formation permeability was too low (meaning water could not be withdrawn) or a seal was not achieved by the packer (20 of 22 attempts). Baker Hughes attributed the inability to achieve a seal to the limitations of its standard straddle packer and recommended using the elongated straddle packer with a lip for subsequent testing of the 8-16 well, which produced better results.

In-situ reservoir pressure measurements were attempted at 37 depths in the open-borehole section below the A-2 Carbonate in the 8-16 well using the Baker Hughes RCX tool. Successful tests (i.e., yielding a representative pressure and mobility estimate) were achieved at three (3) test depth locations. Mobility estimates are 6.2 mD/cP, 7.4 mD/cP, and 40 mD/cP. Reservoir pressures are 527, 685, and 528 psig.

Hydraulic Parameters

Four open-borehole VITs were conducted in the 9-33 well on October 30, 2016, to determine hydraulic properties of the primary reservoir interval (the A-1 Carbonate and Brown Niagaran) in the Dover 33 reef. The transmissivity values determined from the VITs are summarized in Table 15-15 and plotted in Figure 15-66. Permeability was calculated by dividing transmissivity by reservoir contributing zone thickness (i.e., kh/h) assuming h = 100 ft. These estimated permeability values are provided in Table 15-15 and plotted in Figure 15-67. From these data, the A-1 Carbonate has significantly higher transmissivity and permeability than the Brown Niagaran.

Table 15-15. Summary of key reservoir properties determined from VITs conducted in 9-33 well (Dover 33 reef).

Test	Formation	Straddle Packer Midpoint (ft, MD)	Observation Probe (ft, MD)	kh (mD-ft)	kxy (mD)[a]	kz (mD)	Model (see notes)	Radius of Investigation; Inner Boundary (ft)
VIT-22	A-1 Carb	5527.2	5520.7	967	9.7/19	3	1	56
VIT-23	Brown	5626.8	5620.3	94	0.94/1.9	0.03	2	35/12
				89	0.89/1.8	0.04	3	40/17
VIT-24	Brown	5646.5	5640.0	5.5	0.055/0.11	0.006	1	16
VIT-25	A-1 Carb	5549.8	5543.3	1957	19/38	15	1	51

Notes: kh = transmissivity; kxy = horizontal permeability; kz = vertical permeability; h = reservoir thickness.
1. Partially penetrating vertical well in infinite homogeneous reservoir.
2. Partially penetrating vertical well in homogeneous reservoir with constant pressure boundary.
3. Partially penetrating vertical well in radial composite reservoir with infinite lateral extent.
[a] First number is based on h = 100 ft; second number is based on h = 50 ft.

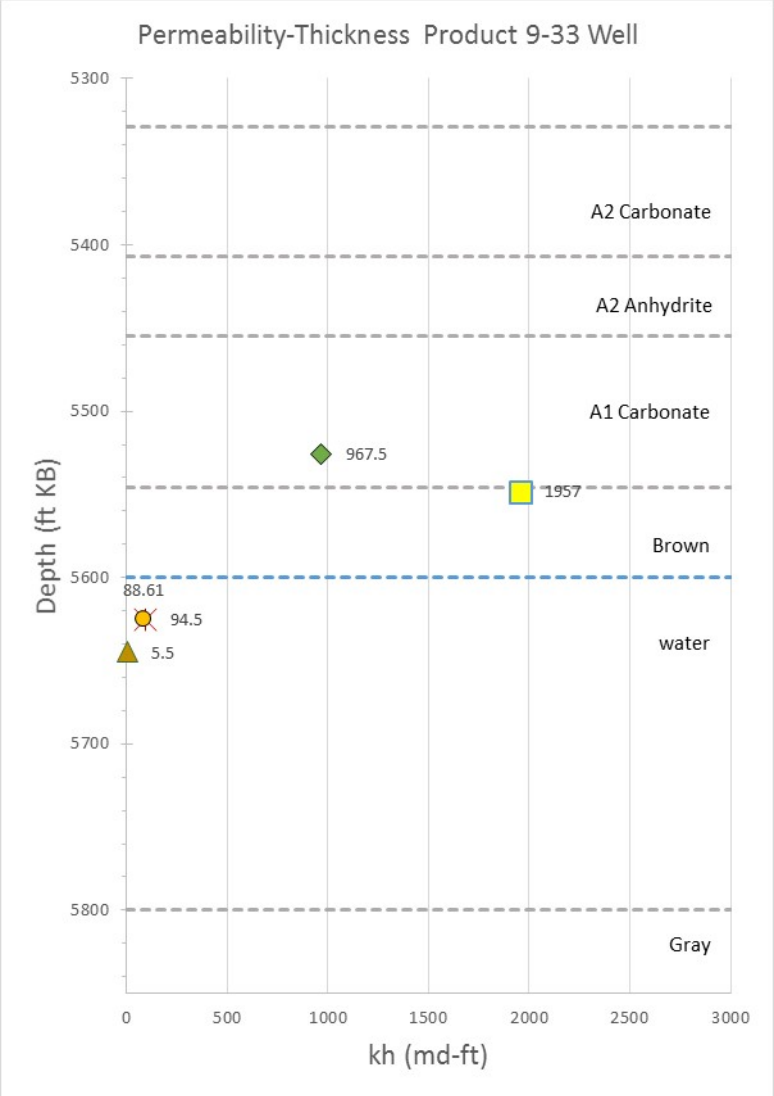


Figure 15-66. Transmissivity values determined from four VITs in the 9-33 well, Dover 33 reef. Each symbol represents a different sample.

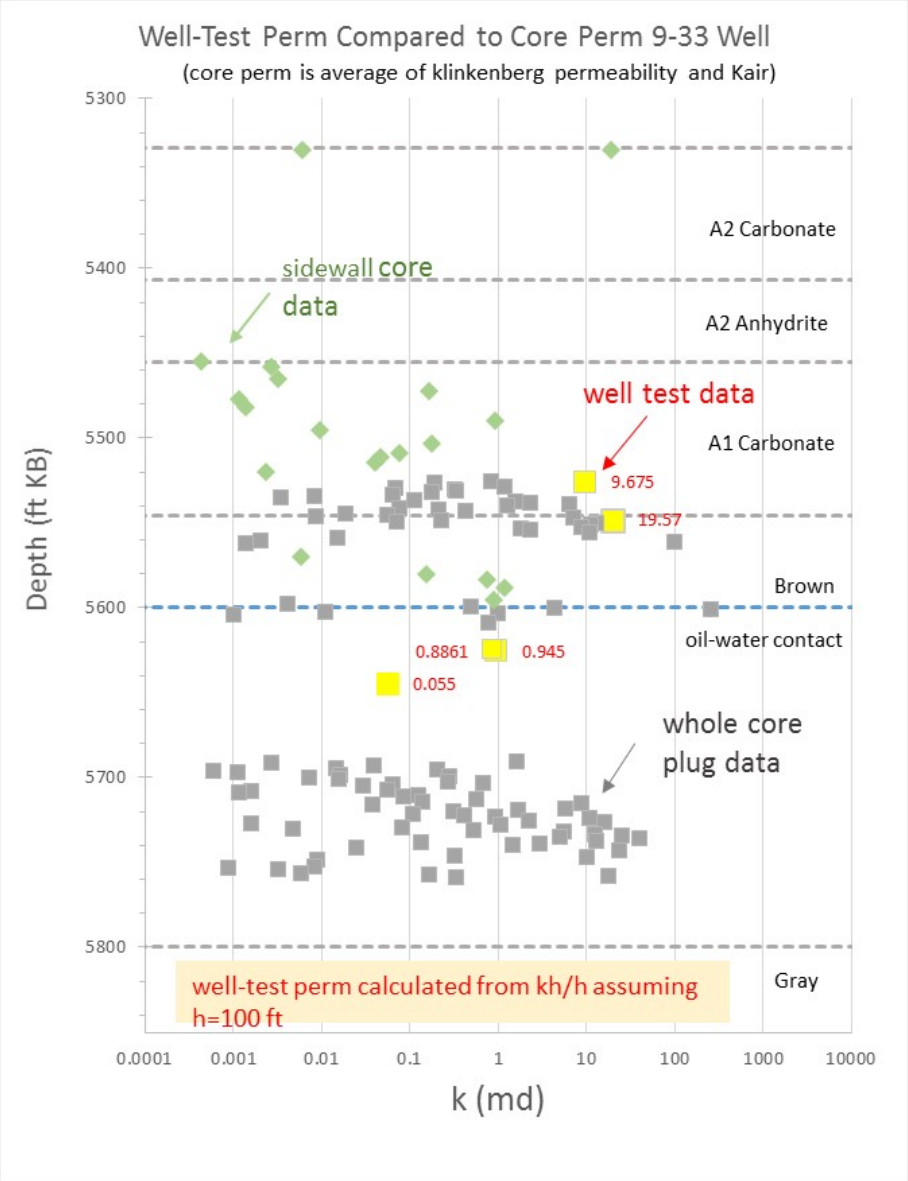


Figure 15-67. Permeability calculated from transmissivity values determined from four VITs in the 9-33 well, Dover 33 reef (assuming h = 100 ft) compared to core permeability.

Two open-borehole LITs were conducted in the 8-16 well on January 27, 2017, to determine hydraulic parameters of the primary reservoir interval (the A-1 Carbonate) in the Chester 16 reef. Transmissivity values determined from the LITs are provided in Table 15-16 and plotted in Figure 15-68. Permeability was calculated by dividing transmissivity by reservoir contributing zone thickness (i.e., kh/h) assuming h = 20 ft. These estimated permeability values are provided in Table 15-16 and plotted in Figure 15-69.

Table 15-16. Summary of key reservoir properties determined from LITs conducted in the 8-16 well (Chester 16 reef).

Test	Formation	Straddle Packer Midpoint (ft, MD)	Observation Probe (ft, MD)	kh (mD-ft)	kxy (mD)	kz (mD)	Model (see notes)	Radius of Investigation; Inner Boundary (ft)
LIT-1	A-1 Carb	5890.7	5884.2	18	0.9[a]	0.01	1	78/NA
LI2-2	A-1 Carb	5864.7	5858.2	20[inner] 24.7[outer]	5.2[b inner] 1.3[a outer]	0.7 [outer]	2	86/4

Notes: kh = transmissivity; kxy = horizontal permeability; kz = vertical permeability; h = reservoir thickness.

1. Partially penetrating deviated well in homogeneous reservoir with infinite lateral extent.
2. Partially penetrating deviated well in radial composite reservoir with infinite lateral extent.

[a] Horizontal permeability is based on h = 20 ft.

[b] Horizontal permeability is based on h = 4 ft.

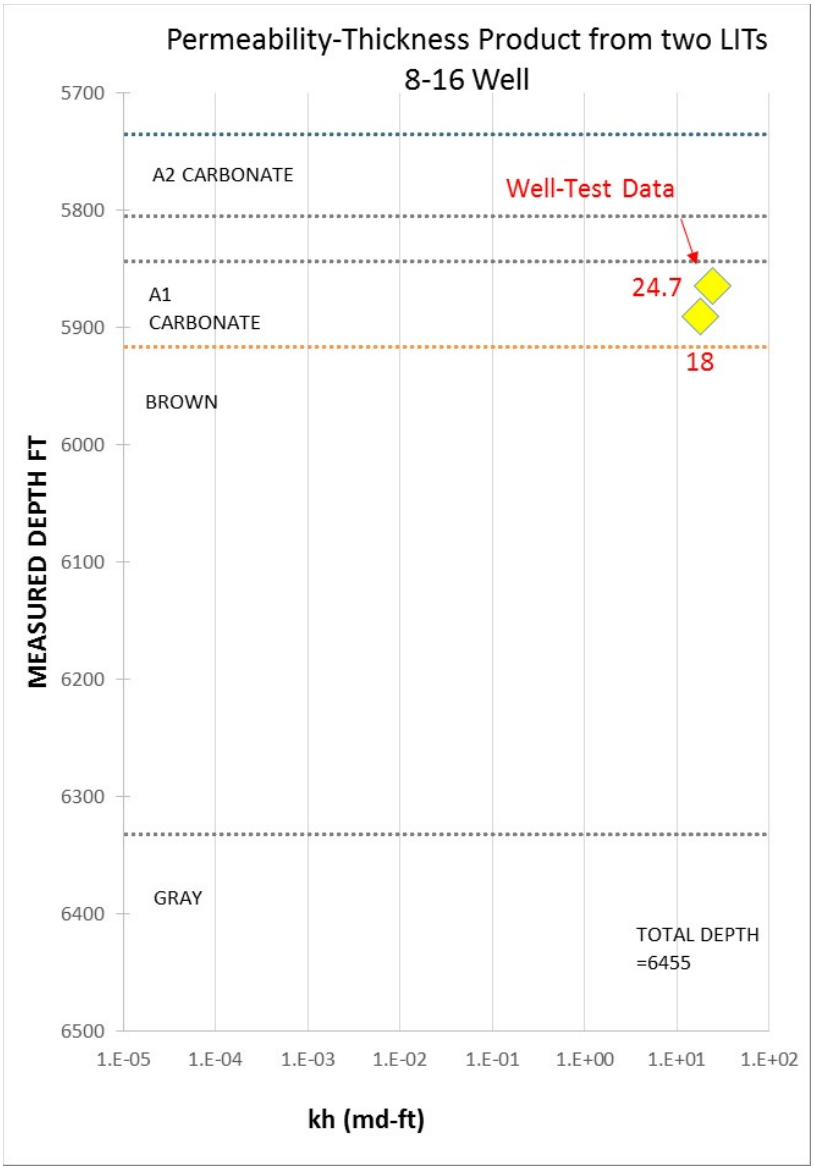


Figure 15-68. Transmissivity values determined from two LITs in the 8-16 well, Chester 16 reef.

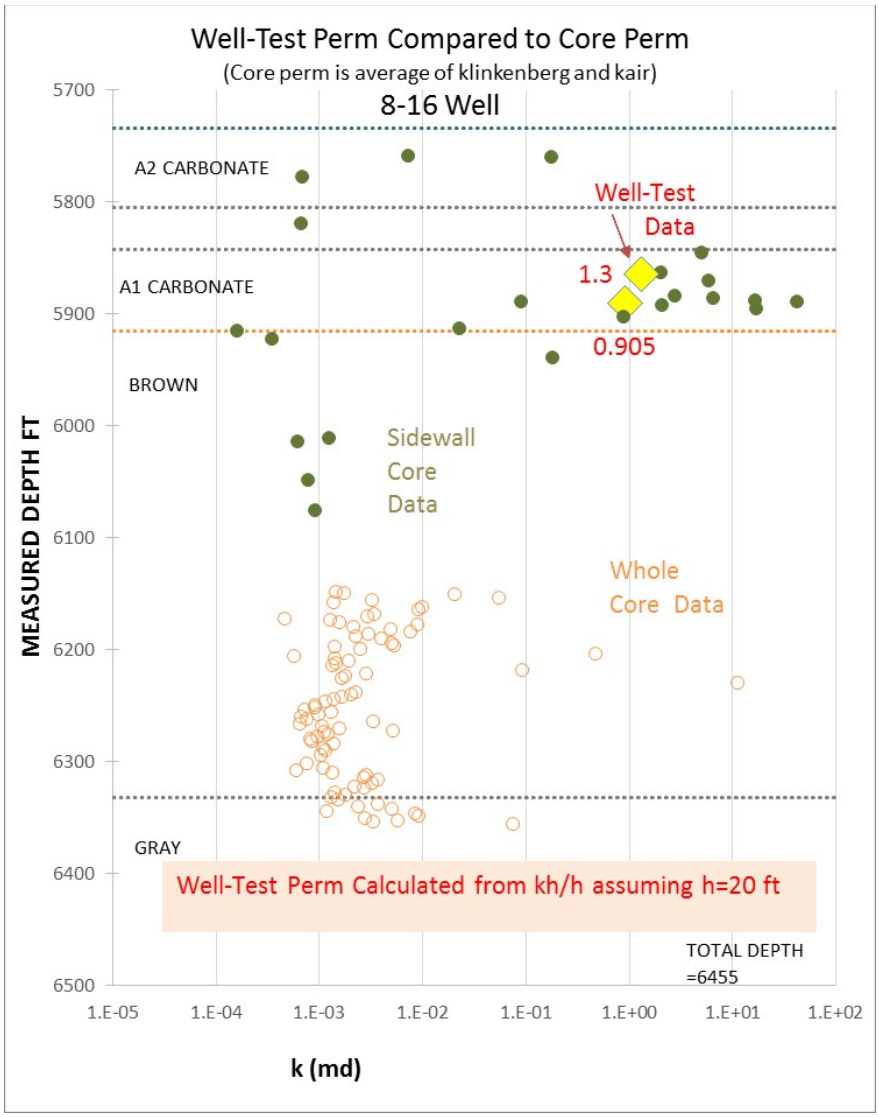


Figure 15-69. Permeability calculated from transmissivity values determined from two LITs in the 8-16 well, Chester 16 reef (assuming h = 20 ft) compared to core permeability.

Fluid Characterization (Dover 33 Reef) Parameters

Fluid characteristics were determined at four test depths in the 9-33 well (Dover 33 reef) during open-borehole testing conducted October 28-29, 2016. Table 15-17 summarizes the depths of the four sampling stations and the predominant fluid type based on in-situ property measurements made with the Baker Hughes RCX tool equipped with the IFX module. A summary of properties measured at each station is presented below.

Table 15-17. Summary of fluid characterization for the 9-33 well.

Test Depth Number	MD (ft)	TVD (ft)	Formation	Fluid
Station #1	5527.2	5383.4	A-1 Carbonate	CO_2
Station #2	5626.8	5461.0	Brown Niagaran	Water
Station #3	5646.5	5476.6	Brown Niagaran	Water
Station #4	5549.8	5400.8	Brown Niagaran	CO_2

Stress Parameters

All four micro-frac tests achieved formation breakdown, fracture reopening, and fracture propagation. The micro-frac test results are summarized in Table 15-18.

Table 15-18. Micro-frac testing results.

Formation	Depth (ft)	Station	Hydrostatic Pressure (psi)	Pore Pressure (psi)	Formation Breakdown Pressure (psi)	Closure Pressure (psi)	Closure Pressure Gradient (psi/ft)
A-1 Carbonate	5861	1	1777	519	2642	1819	0.31
Brown Niagaran	5967	2	1782	528	2922	1799	0.30
A-2 Carbonate	5791	3	2849	512	3790	2871	0.50
A-2 Carbonate	5765	4	2746	510	3795	3084	0.53

Discussion of Low Fracture Pressures in Chester 16 Reef

A noteworthy observation regarding the stress situation in the Chester 16 reef is the finding of extremely low values of Sh_{min} (0.3, 0.31 psi/ft) in the A-1 Carbonate and Brown Niagaran reservoir (sample points below 5850 ft) due to depleted pressure resulting from primary production compared to A-2 Carbonate caprock (reservoir sample points above 5850 ft).

This section analyzes Sh_{min} (and corresponding fracture pressure) increase during the process of filling the reservoir with CO_2 due to the poroelastic effect of injection. To avoid fracturing (tensile fracturing) of the target reservoir, it is necessary to estimate Sh_{min} change by CO_2 injection. The calculated value of Sh_{min}, refined by taking into account anticipated changes in pressure, should be used to set an upper limit on injection pressure to avoid fracturing the reservoir (i.e., “safe” injection pressure). While numerical simulations could be computationally expensive, analytical solutions could be used as an alternative approach to predict stress changes quickly. Such techniques can also be used to estimate changes in Sh_{min} caused by changes in pressure during CO_2 injection and to determine whether the stress state limits the ability of reservoirs to provide for safe and effective CO_2 storage. The change in Sh_{min} caused by changing pore pressure (poroelastic effect) can be approximated by using different techniques such as uniaxial compaction assumption, theory of strain nuclei, theory of inclusion, or theory of inhomogeneity (Fjar et al., 2008, Soltanzadeh and Hawkes, 2009). For example, the Rudnicki model (1999) is used to model the Sh_{min} changes analytically. In this model, the reservoir is assumed to be a spheroid inclusion in an infinite solid medium. By assuming the same elastic parameters in the reservoir and surrounding rock, the Sh_{min} changes can be calculated using inclusion theory as:

$$\frac{\Delta Shmin}{\Delta P} = \alpha \frac{1-2\upsilon}{1-\upsilon}\left[1 - \frac{e}{2\sqrt{(1-e^2)^3}}(\arccos(e) - e\sqrt{1-e^2})\right]$$

Equation 15-1

Where e is the reservoir aspect ratio (thickness-to-diameter ratio) and υ is Poisson's ratio. Direct measurements of Poisson's ratio are available from laboratory triaxial test experiments. Table 15-19 summarizes the triaxial tests performed on Chester 16 Brown Niagaran and Gray Niagaran core. A Poisson's ratio of 0.29 and a Biot coefficient of 0.75 were used to estimate Sh_{min} increase with increasing pore pressure. A schematic of the reef, illustrated in Figure 15-70, shows the reservoir geometry.

Table 15-19. Triaxial test results for Chester 16 cores.

Depth (ft)	Confining Pressure (psi)	Young's Modulus (10^6 psi)	Poisson's Ratio
6162.50	2200	5.38	0.33
6164.50	2200	6.48	0.29
6338.60	2200	4.50	0.27

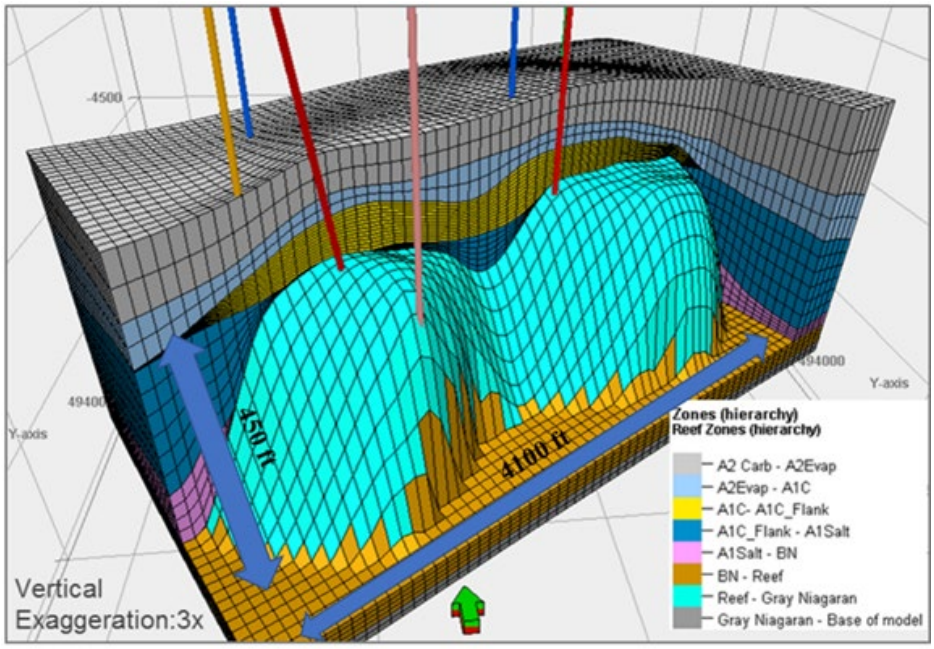


Figure 15-70. Schematic of the Chester 16 reef showing reservoir geometry.

The aspect ratio of the reservoir is approximately calculated using the vertical axis of 450 ft and the horizontal axis of 4100 ft. (450/4100 = 0.1098). Initial Sh_{min} of 1799 psi and pore pressure of 528 psi (Table 15-18) are used to calculate Sh_{min} at higher pressures.

The Sh_{min} increase in the reef, calculated using Eq. (1), is shown in Figure 15-71. This figure shows that by increasing pore pressure from 528 psi to 5298 psi, Sh_{min} increases from 1799 to 3967. Also, Figure 15-71 shows that using uniaxial compaction assumption overpredicts Sh_{min} stress changes since uniaxial compaction assumption considers zero displacement in horizontal directions. In addition to Sh_{min}, effective Sh_{min} (Effective Sh_{min} = Sh_{min} – Biot*Pore Pressure) and fracture pressure (pore pressure at which effective Sh_{min} is zero) are also estimated.

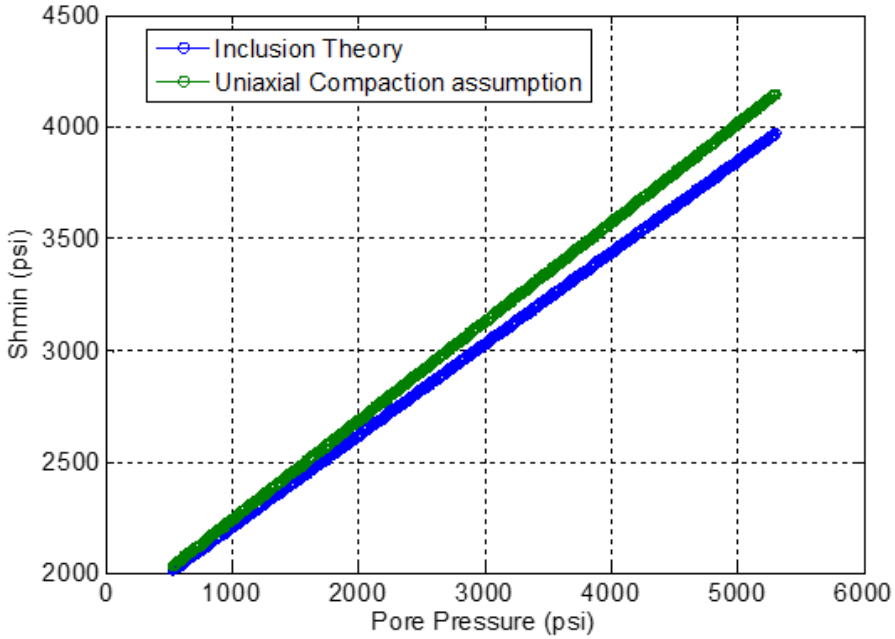


Figure 15-71. Sh_{min} changes as a function of pore pressure.

Figure 15-72 shows the effective Sh_{min} (i.e., Sh_{min} – Biot*Pore Pressure) changes (decrease) due to pore pressure increase. Effective Sh_{min} will be zero at pore pressure of 5288 psi (in other words, the estimated fracture pressure (using Eq. (1) for calculating Sh_{min}) will be 5288 psi due to the poroelastic effect of injection (By assuming rock tensile strength is zero).

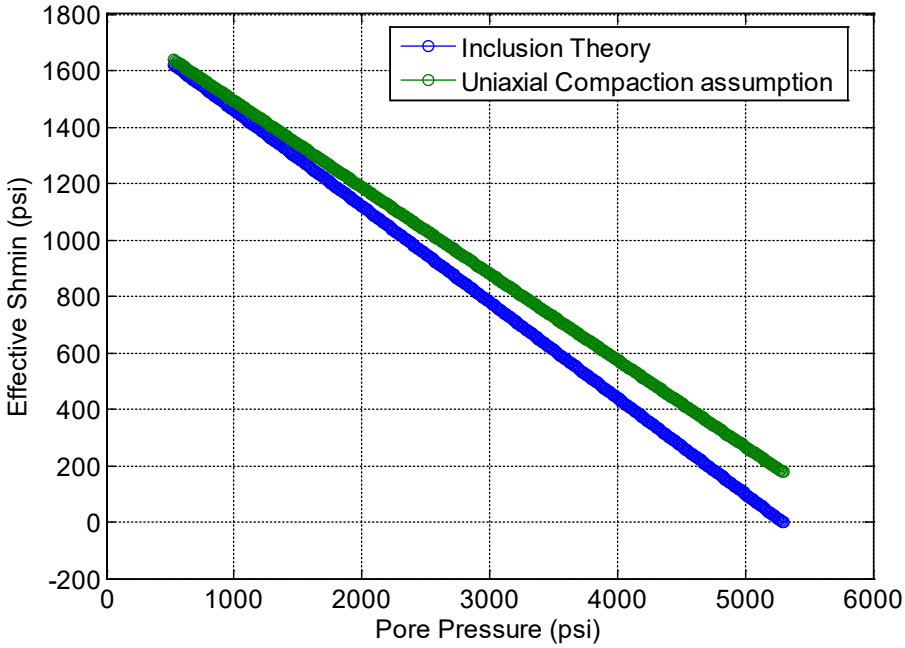


Figure 15-72. Effective Sh_{min} changes as a function of pore pressure. Initial Sh_{min} of 1799 psi and pore pressure of 528 psi (Table 15-18) is used to calculate Sh_{min} at higher pressures.

15.5 Conclusion

Stress data show that primary production significantly lowers the Sh_{min} and the corresponding fracture pressure (FIP) in the reservoir. Because FIP is the threshold used to set the limit on injection pressure for wells regulated under the Underground Injection Control (UIC) program, the amount of CO_2 that can be stored in a depleted reservoir may be limited if regulators use the fracture pressure at the end of primary production to set the limit on injection pressure. Analytical techniques were used to (1) estimate changes in Sh_{min} caused by changes in pressure and temperature during CO_2 injection and (2) determine if the stress limits the amount of CO_2 that can be stored. It was found that fracturing of the reservoir or caprock is not likely because fracture pressure increases as pore pressure increases. We analyzed how Sh_{min} increases during the process of filling the reservoir with CO_2 due to the poroelastic effect of injection; the findings suggest that a ”dynamic fracture pressure” that will not overly constrain the amount of CO_2 that can be injected may be a viable alternative to a fixed FIP limit. This experience is applicable to all depleted reservoirs considered for CO_2 EOR.

16.0 Conclusions

The overall goal of this study was to develop geologic characterization methodologies for complex Niagaran reef reservoirs to better understand reef variability and data applications to inform modeling efforts. Different data types were tested, and advanced data was collected through piggyback operations. These tasks (and their accompanying challenges) led to several important findings, which are summarized below:

Key Challenges and Findings in Developing a Standardized Geologic Characterization Approach

- Data was often of different vintages, vendors, and log types between reef fields (and even within a reef field) due to a long history of oil and gas production. Many wireline logs were digitized, corrected, and checked for quality to remove erroneous data and make logs more comparable. Additionally, industry standard relationships were used to compute missing logs such as bulk density and acoustic travel time.
- Gas effects are a common concern in oil and gas fields; however, most of the logs were collected under pressure conditions where gas was in solution. Little to no gas effects were observed for the reefs.
- The presence of salt, both massive and void-plugging, could greatly influence the bulk density and falsely display as porosity. Standard crossplots could capture larger quantities of salt by vertical trending toward massive salt. Small quantities of salt were not captured. Advanced statistical predictions successfully identified intervals of salt in the Bagley reef field.
- Industry standard analyses, including crossplots, pay flags, and petrophysics on a well-by-well basis, were successful in generating initial assessments of wells and reefs.
- Integration of all data types was crucial to developing geologic interpretations.

Key Challenges and Findings in Assessing Importance of Data Types and Analyses

- Data availability was variable by reef, with datasets ranging from basic to advanced (Table 16-1). Reefs with rich datasets were used to guide interpretations for reefs with less data.
- Well control is a significant challenge with the reefs. Geologic knowledge was used to interpret formation behavior between well locations.
- Wells were often completed in the Brown Niagaran and above the oil/water contact. This prevented a full assessment of the reef thickness and characteristics.
- The Bagley reef field had the least amount of data, including pre-existing basic wireline logs and whole core. The use of analogs and geologic knowledge was critical in developing an interpretation of the reef.
- The Dover 33 and Chester 16 reef fields had the greatest amount of data, which improved the geologic characterization.
- Where seismic data was missing, mapping of reef structure and boundary had to be completed by hand because mapping software algorithms do not consider reef shape. This was done using formation thicknesses, production data, and analog reefs.

- At a minimum, a reef can be characterized using basic wireline logs with the help of an experienced geologist.
- Core data was incomplete over formations and provided only a snapshot of reservoir properties. Core plugs are selected to avoid unstable features such as vugs and fractures, thus can underrepresent secondary porosity

Table 16-1. Summary of data types, analyses, and outcomes used in geologic characterization.

Data Type	Analyses Used	Outcomes
Production	Mapping and well comparisons	Geospatial idea of best producing area
Basic Wireline Logs	Petrophysics and statistics	Individual well characterization for lithology and porosity
Advanced Wireline Logs	Advanced petrophysics	Detailed breakdown of lithology; characterization of vugs, fractures, and textures; and permeability distribution
Whole and Sidewall Core	Routine core analyses, CT scans, geomechanics	Directly measured porosity and permeability, 3D distributions of secondary porosity, and geomechanical properties of formations
3D Seismic	Basic analysis and advanced attribute analysis	Reef boundary and number of pods, location of porosity horizons, and areas of potentially great reservoir potential
Well Tests	Mini-frac	Fracture analysis and estimation of permeability over larger interval

Key Challenges and Findings from Piggyback Wells

- Piggyback wells provided an opportunity to test advanced logs and assess the applicability to the reefs.
- High salinities and relatively low-porosity reservoirs made NMR and elemental spectroscopy challenging. However, with calibration efforts the NMR logged in the Dover 33 reef had permeabilities in the same order of magnitude as core-measured values.
- Deep shear wave was run on three piggyback wells and did not show significant features.
- Image logs were valuable for developing qualitative descriptions of the formations, identifying fractures and vugs, and providing critical information on BO features for geomechanics analyses.
- Core analyses were critical for developing relationships for porosity and permeability and between wireline logs and core.
- Overall, advanced logs proved to be good supplementary data and provided more detail at the well location. The advanced data tested is described in Table 16-2 in order of characterization importance.

Table 16-2. Summary of data tested at piggyback well locations in order of importance for geologic characterization efforts.

Piggyback Data	Limitations	Findings
Whole and Sidewall Core	Selective locations, non in-situ conditions	Reservoir properties
Image Logs	Borehole conditions	Descriptions of rock textures, bedding, vugs, and fractures. Fracture orientation and stress.
NMR	High salinities and lower porosities	If calibrated properly, can provide permeability estimates
Elemental Spectroscopy	High salinities	Detailed lithology breakdown
Deep Shear Wave	Small features	Could not detect any features

Key Challenges and Findings in Assessing Reservoir Controls

- Porosity and permeability are key controls on reservoir quality but can be challenging to characterize without the use of core data (Table 16-3). Porosity logs can be influenced by fluids, salt, logging parameters, and wellbore conditions and need calibration to best represent porosity.
- Secondary processes were determined to be critical in determining reservoir quality; these included salt and anhydrite plugging, dolomitization, and development or enhancement of secondary porosity.
- Reservoir properties were found to be statistically different between lithofacies within the reef field (reef core, windward, and leeward), and dependent on relative position in the A-1 carbonate (crestal or flank).
- A low density of wellbores and incomplete data in a reef field often made it challenging to confidently draw lithofacies boundaries.

Table 16-3. Summary of reservoir controls and identification methods.

Reservoir Control	Identification and Characterization Method
Porosity	Wireline logs provide initial assessment and can be corrected using core-measured porosity
Permeability	Core-measured permeability used to develop porosity-to-permeability relationship. Advanced logs (NMR) can be calibrated using core data to estimate permeability throughout the formation
Lithology	Basic logs provide lithology (limestone, dolostone, salt, anhydrite, etc.)
Salt Plugging	Crossplot analyses can show major salt plugging; advanced analyses (CT, core analyses) can provide distributions of salt plugging
Secondary Porosity	Identified from image logs and whole core, quantified from CT scan analysis
Lithofacies	Combination of log attributes, reef position

Key Findings in Reef Variability

- The reefs under study had a lithology trend which matched the regional interpretation of more dolomitization up-dip. The Dover 33, Bagley, and Charlton 19 reef fields were predominantly dolomitic. The Chester 16, Chester 2, and Charlton 6 were limestone (Figure 16-1).
- Salt plugging was observed to some degree at all reefs but varied from minor (Charlton 19) to extremely pervasive (Chester 2).
- Diagenetically enhanced porosity ranged from extreme (karst) to streaky in the reefs which influenced the reservoir pattern. In dolomitized reefs, porosity trended higher toward the top, while limestone reefs were streakier in nature.
- Production was predominantly recorded from the Brown Niagaran formation; five reef fields also recorded production from the overlying A-1 carbonate.
- Average reef porosity ranged from 1.4% to 11.7%, with average permeabilities up to 94 mD. Dolomitic reefs have higher porosities and NTG ratios in the Brown Niagaran, while limestone reefs are higher in the A-1 carbonate (Figure 16-2).
- The number of pods in a reef field varied from one to four.
- Diagenesis and degree of salt plugging were assigned ranks and plotted with porosity and oil recovery to illustrate reservoir quality. When plotted using porosity, Charlton 19 was ranked as the best reservoir, followed by Dover 33 and Bagley (Figure 16-3). When plotted with percent recovery, Dover 33 and Chester 16 were the highest (Figure 16-4). The porosity method assumes that log porosity is indicative of good reservoir. Percent recovery is a good indicator of reservoir quality; however, it is dependent on well design and estimated OOIP.

Key Challenges and Findings in Confining Unit Assessment

- The immediate confining units are the A-2 evaporite and A-2 carbonate. The A-2 evaporite could be salt (flanks and inter-reef) or anhydrite (overlying reef) with no detectable porosity. The A-2 carbonate varied from dolomitic to limestone with a thin interval of mudstone (A-2 shale). Evaporitic plugging was common in the A-2 carbonate.
- The presence of evaporites made it difficult to assess properties from wireline logs. Porosity was often observed in the A-2 carbonate but unlikely to be effective.
- The ultimate confining unit is the Salina B-salt, which is approximately 300 feet of massive salt with several other saline units overlying it composed of salt, shale, and tight carbonate.
- Geomechanical properties were measured and derived for the confining units. These properties will be used in geomechanical models for a more detailed assessment of confining unit efficiency.

Overall, the geologic characterization efforts conducted under Tasks 3, 4, and 5 provided important insight into reef variability and the importance of reservoir controls. Additionally, the work has demonstrated the different analyses that can be used to interpret a reef. The results will inform the development of SEMs, dynamic models, and geomechanical models, which will assess the reefs in more detail. The lessons learned will also guide the regional assessment of the reefs by identifying important attributes and properties.

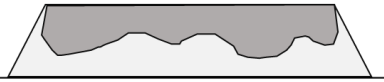
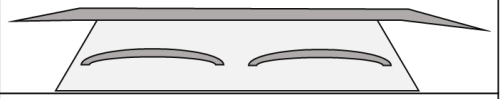
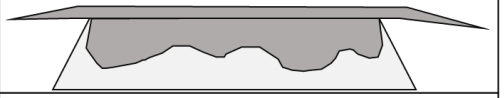
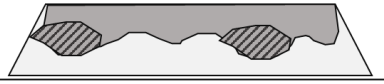
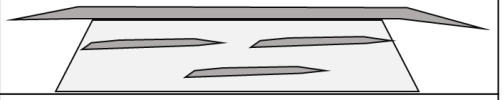
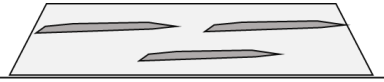
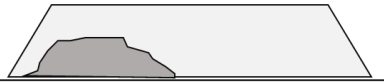
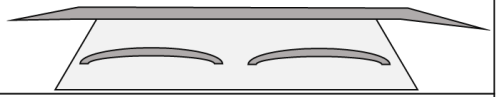
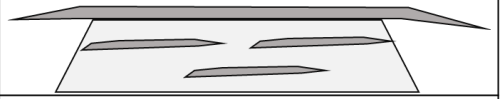
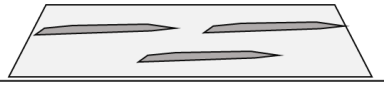
Reef	Petrophysical and Core Properties	Reservoir Attributes	Lithofacies	Production	Reservoir Pattern
Dover 33	Avg. Porosity- 8.2% Avg. Permeability-6.5 mD Lithology-Dolomite	Primary-Brown Niagaran Salt Plugging-Mild Diagenesis-Pervasive # of Reefs- 1		OOIP-3.5 MBBL Oil-1.8 MBBL Gas-1.8 MMCF	
Chester 16	Avg. Porosity- 3.6% (BN), 7.8% (A1C) Avg. Permeability- 23 mD(BN), 7.0 mD(A1C) Lithology- Dolomite (A1C), Limestone (BN)	Primary-BN and A1C Salt Plugging- Minor Diagenesis-Streaky # of Reefs- 2		OOIP-6.9 MBBL Oil-3.0 MBBL Gas-2.6 MMCF	
Bagley	Avg. Porosity- 7.9% (BN), 5.8% (A1C) Avg. Permeability- 94 mD(BN), 7.0 mD(A1C) Lithology-Dolomite	Primary-BN and A1C Salt Plugging-A1C Diagenesis- Pervasive # of Reefs- 4		OOIP-9.0 MMBL Oil- 2.9 MMBL Gas-6.7 MMCF	
Charlton 19	Avg. Porosity-11.7% Avg. Permeability-unknown Lithology-Dolomite	Primary- BN Salt Plugging-Minor Diagenesis- Extreme (Karst) # of Reefs-2		OOIP-2.6 MMBBL Oil-1.1 MMBBL Gas-2.3 MMCF	
Dover 35	Avg. Porosity- 4.7% (BN), 3.1% (A1C) Avg. Permeability-unknown Lithology-mixed carbonate	Primary- BN and A1C Salt Plugging-mild Diagenesis-Streaky # of Reefs-1		OOIP-2.5 MMBBL Oil-1.9 MMBBL Gas-.8 MMCF	
Dover 36	Avg. Porosity-1.4% Avg. Permeability-unknown Lithology- mixed carbonate	Primary-BN Salt Plugging-mild Diagenesis-Streaky # of Reefs-3		OOIP-3.7 MMBBL Oil-1.8 MMBBL Gas-1.2 MMCF	
Chester 2	Avg. Porosity- 4.0% Avg. Permeability-.2 mD Lithology- limestone, dolomitized pod	Primary-BN Salt Plugging-Pervasive Diagenesis- Isolated # of Reefs-1		OOIP- 3.2 MMBBL Oil- 1.1 MMBBL Gas-.7 MMCF	
Chester 5/6	Avg. Porosity- 4.2%(BN), 6.0% (A1C) Avg. Permeability-.8mD (BN), 16 mD (A1C) Lithology- mixed carbonate	Primary-BN and A1C Salt Plugging- mild Diagenesis- streaky # of Reefs-3		OOIP- 2.9 MMBBL Oil- 1.3 MMBBL Gas-1.3 MMCF	
Charlton 30/31	Avg. Porosity-4.6% (A1C), 4.2%(BN) Avg. Permeability-unknown Lithology- limestone	Primary- BN and A1C Salt Plugging- mild Diagenesis- streaky # of Reefs-3		OOIP-6.8 MMBBL Oil- 3.0 MMBBL Gas-3.9 MMCF	
Charlton 6	Avg. Porosity-5.3% Avg. Permeability-unknown Lithology- Limestone	Primary- BN Salt Plugging-Mild Diagenesis- Streaky # of Reefs-1		OOIP-1.7 MMBBL Oil- .7 MMBBL Gas-1.5 MMCF	

Figure 16-1. Reef properties, attributes, lithofacies, production, and reservoir pattern by reef. Green= reef core, purple= windward, and blue= leeward lithofacies.

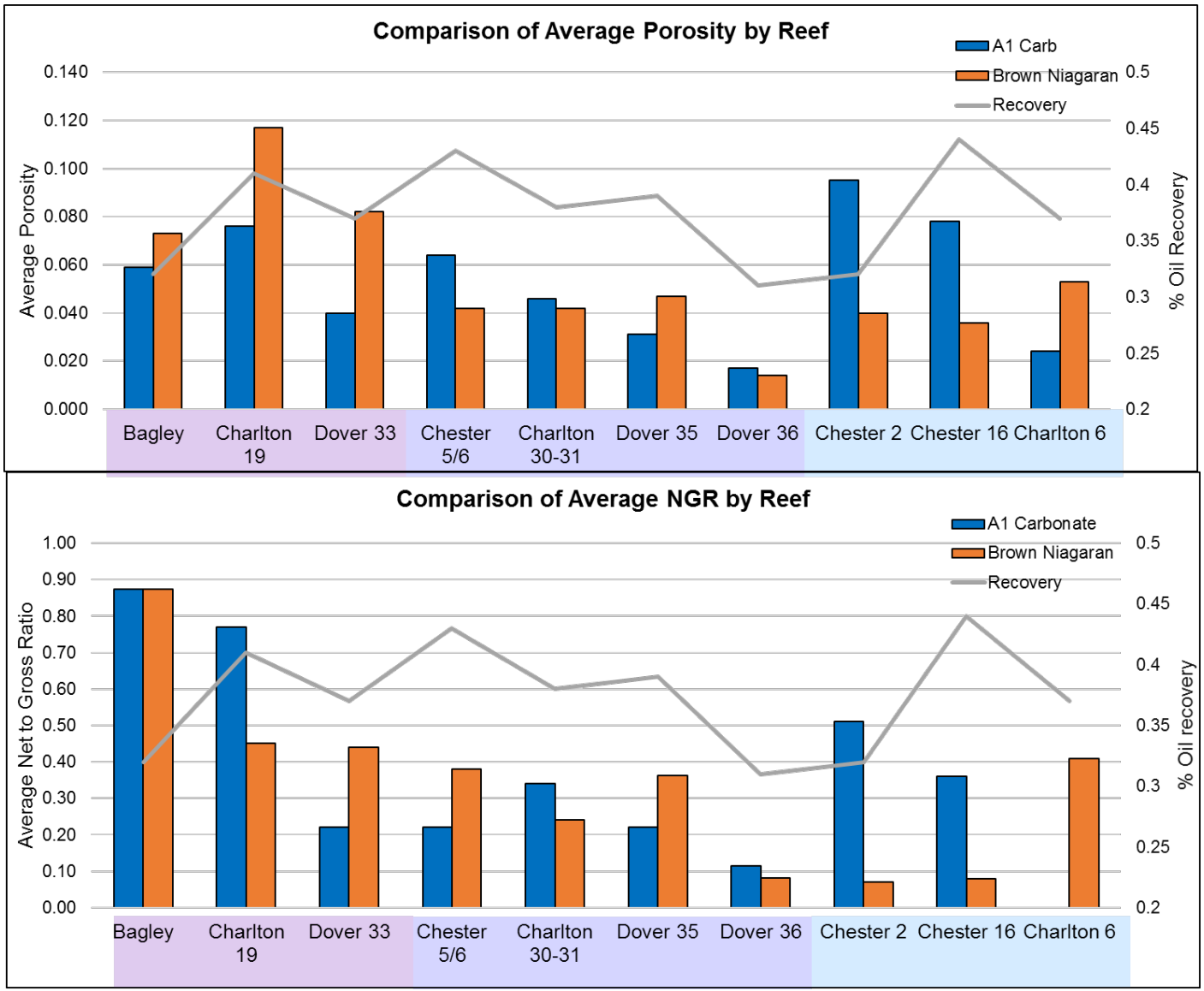


Figure 16-2. Comparison of average porosity, NTG ratio, and percent recovery by reef. Along the horizontal axis, light purple shading (left) = dolomitic, light blue shading (right) = limestone, and lavender (center) = mixed carbonate.

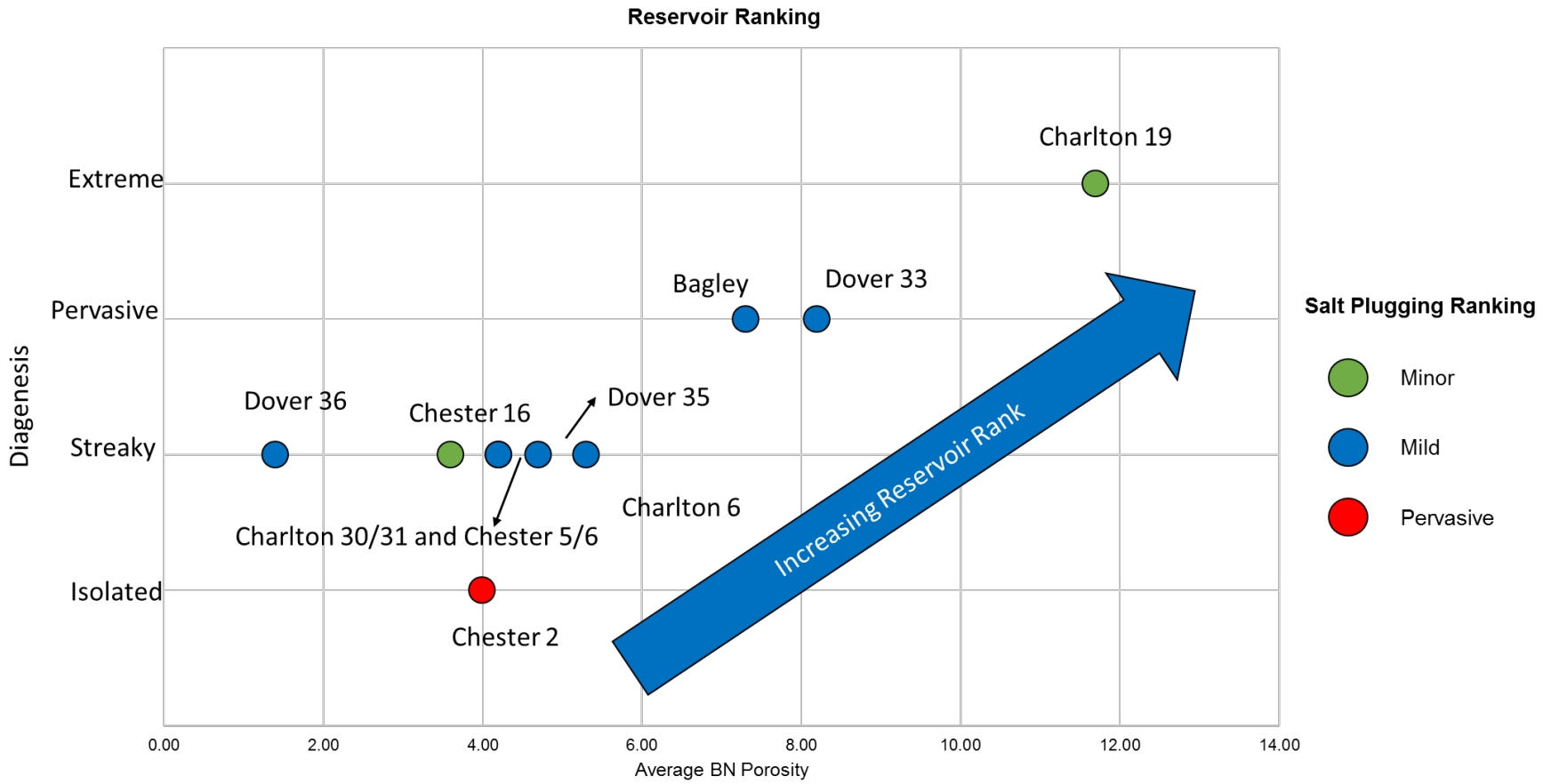


Figure 16-3. Reservoir ranking plot of reefs using diagenesis and salt plugging rank with average porosity.

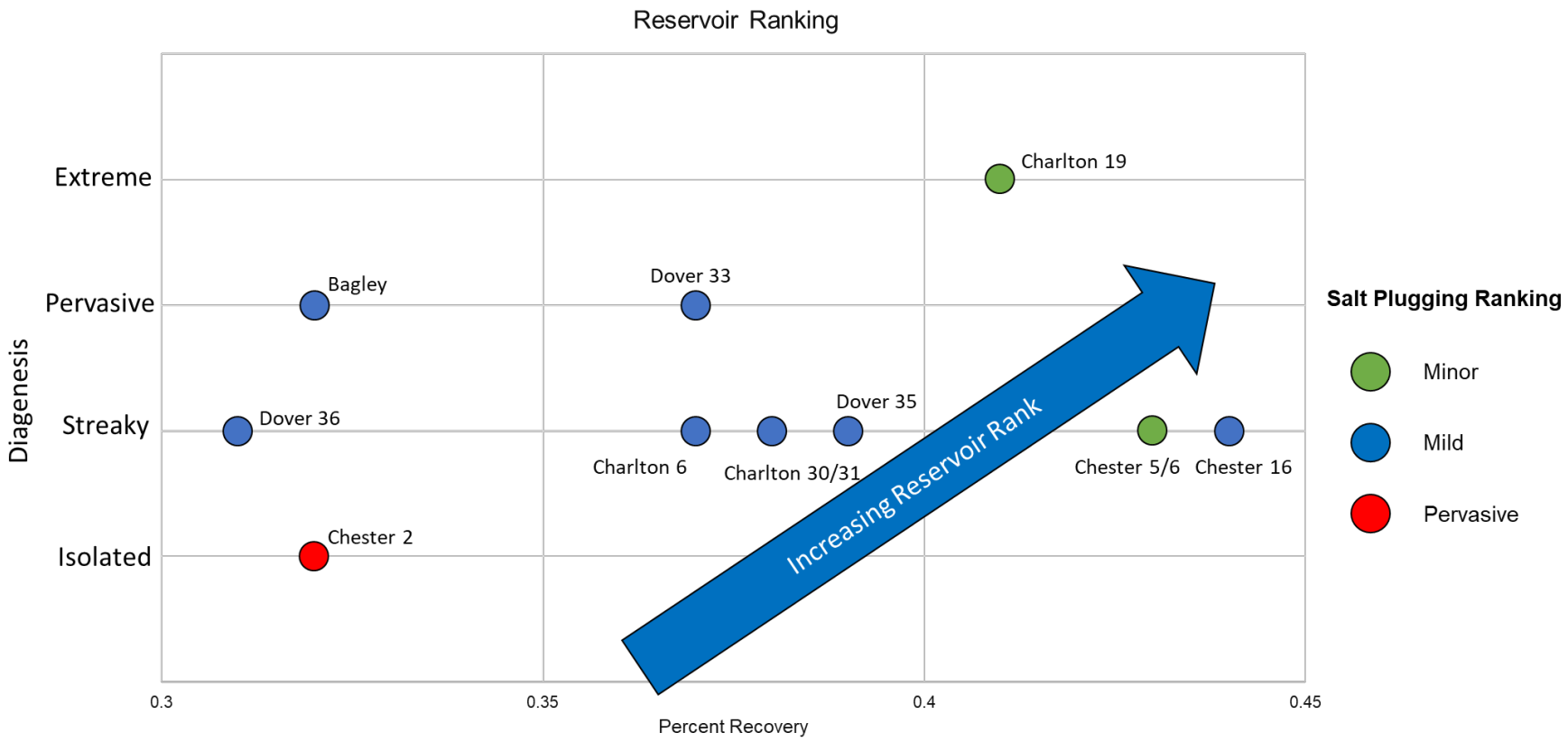


Figure 16-4. Reservoir ranking plot of reefs using diagenesis and salt plugging rank with percent oil recovery.

17.0 References

Barata, J.S.de A.C., 2011, Cementation dynamics in a Middle Eastern carbonate reservoir: Heriot-Watt University. Unpublished thesis, 51pp.

Barnes, D.A., Parris, T.M., and Grammer, G.M., 2008, Hydrothermal Dolomitization of Fluid Reservoirs in the Michigan Basin, USA: AAPG Search and Discovery Article #50087 (2008) Posted July 10, 2008, 25pp.

Barnes, D., Harrison, W. B., III, Grammer, G.M., and Asmus, J., 2013, CO_2/EOR and geological carbon storage resource potential in the Niagaran Pinnacle Reef Trend, lower Michigan, USA: GHGT-11, Energy Procedia, V. 37, pp. 6786-6799.

Ben-Itzhak, L.L., Aharonov, E., Karcz, Z., Kaduri, M., Toussaint, R., 2014, Sedimentary stylolite networks and connectivity in Limestone: Large-scale field observations and implications for structure evolution: Journal of Structural Geology, Elsevier, 2014, pp. 106-123.

BHI, 2016. RCX^{SM} Vertical Interference Test (VIT) Analysis: CORE Energy Well Lawnichak Unit #9-33, November 3, 2016.

BHI, 2017a. RCX^{SM} Vertical Interference Test (VIT) Analysis: CORE Energy Well Chester 16 Unit #8-16; LIT-1 at 5890.7 ft MD in A1 Carbonate Formation; LIT-2 at 5864.7 ft MD in A1 Carbonate Formation; Feb. 2, 2017.

BHI, 2017b. RCI Straddle Packer MicroFrac Testing Sonatrach Exploration, Core Energy LLC, Traverse City, USA; Well name: Chester 16 UNIT 8-16; BHI report: GPE-NA-FRAC-0117; Feb. 10, 2017.

Briggs, L.I., Gill, D., Briggs, D.Z., and Elmore, R.D., 1980. Chapter 17, Transition from open marine to evaporite deposition in the Silurian Michigan Basin, *In* Nissenbaum, A., ed., Hypersaline brines and evaporitic environments: Developments in Sedimentology, Vol. 28, pp. 253-270.

Burgess, R.J., and Benson, A.L., 1969, Exploration for Niagaran reefs in northern Michigan: Ontario Petroleum Institute, v. 8, no. 1, 30 pp.

Carter, K.M., J. Kostelnik, C.D. Laughrey, J.A. Harper, D.A. Barnes, W.B. Harrison III, E.R. Venteris, J. McDonald, J. Wells, L.H. Wickstrom, C.J. Perry, K.L. Avary, J.E. Lewis, M.E. Hohn, A. Stolorow, B.E. Slater, and S.F. Greb, 2010. Characterization of geologic sequestration opportunities in the MRCSP region: Middle Devonian-Middle Silurian formations—MRCSP Phase II Topical Report October 2005-October 2010: U.S. DOE Cooperative Agreement No. DE-FC26-05NT42589, OCDO Grant Agreement No. DC-05-13, 350 pp.

Catacosinos, P.A., Daniels P.A. Jr., and Harrison W.B. III, 1991. Structure, stratigraphy, and petroleum geology of the Michigan Basin; interior cratonic basins, AAPG Memoir 51, pp. 561-601.

Catacosinos, P.A., Harrison, W.B. III, Reynolds, R.F., Westjohn, D.B., and Wollensak, M.S., 2000, Stratigraphic nomenclature for Michigan: Michigan Department of Environmental Quality, Geological Survey Division, 1 sheet.

Catacosinos, P.A., Harrison, W.B. III, Reynolds, R.F., Westjohn, D.B., and Wollensak, M.S., 2001, Stratigraphic Lexicon for Michigan: Michigan Department of Environmental Quality, Geological Survey Division and the Michigan Basin Geological Society, Bulletin 8, 56 pp.

Catuneanu, O., Galloway, W.E., Kendall, C.G. St.C, Miall, A.D., Posamentier, H.W., Strasser, A., and Tucker, M.E., 2011. Sequence Stratigraphy: Methodology and Nomenclature: Newsletters on Stratigraphy, 44, 3, pp. 173-245.

Cercone, K.R., 1984. Diagenesis of Niagaran (middle Silurian) Pinnacle Reefs, Northwest Michigan, Geosciences. Ann Arbor, University of Michigan: 367 pp.

Cercone, K.R., and Lohmann, K.C., 1985, Early diagenesis of Middle Silurian pinnacle reefs, northern Michigan, in Cercone, K.R., and Budai, J.M., eds., Ordovician and Silurian rocks of the Michigan basin and its margins: Michigan Basin Geological Society Special Paper v. 4, pp.109-130.

Cercone, K.R., and Lohmann, K.C., 1987, Late burial diagenesis of Niagaran (Middle Silurian) pinnacle reefs in Michigan basin: The American Association of Petroleum Geologists Bulletin, v. 71, no. 2, pp. 156-166.

Charbonneau, S.L., 1990. Subaerial exposure and meteoric diagenesis in Middle Silurian Guelph Formation (Niagaran) pinnacle reef bioherms of the Michigan Basin: Southwestern Ontario: M.Sc. thesis, Queen's University, Kingston, Ontario, 215 pp.

Conner, A., Place, M., Chace, D., and Gupta, N 2020. Pulsed Neutron Capture for monitoring CO_2 Storage with Enhanced Oil Recovery in Northern Michigan. MRCSP topical report prepared for DOE-NETL project DE-FC26-05NT42589, Battelle Memorial Institute, Columbus, OH

Coniglio, M., R. Frizzel, and B.R. Pratt, 2004. Reef-capping laminites in the Upper Silurian carbonate-to-evaporite transition, Michigan Basin, South-western Ontario: Sedimentology, v. 51, pp. 653-668.

Christie-Blick, N., and Driscoll, N.W., 1995, Sequence stratigraphy: Annual Review of Earth Planetary Sciences, v. 23, pp. 451-478.

Cox, K. and Barnes, D.A., 2016, Anomalous thermal indicators from the authigenic minerals in upper Paleozoic strata of the Michigan Basin: AAPG Search and Discovery Article #10836 (2016).

Davies, G.R. and Smith, L.B. Jr., 2006, Structurally controlled hydrothermal dolomite reservoir facies: An overview: AAPG Bulletin, v. 90/11, pp. 1641-1690.

Dou, Q.F., Sun, Y.F., Sullivan, C., 2009, Seismic detection of a paleokarst system and its influence on carbonate reservoir compartmentalization. SEG Expanded Abstract, pp.1731-1736.

Dunham, R.J., 1962, Classification of carbonate rocks according to depositional texture, *in*, W.E. Ham, ed., Classification of Carbonate Rocks: American Association of Petroleum Geologists Memoir 1, pp.108-121.

Embry, A.F., and Klovan, J.E., 1971, A Late Devonian reef tract on Northeastern Banks Island, NWT: Canadian Petroleum Geology Bulletin, v. 19, pp. 730-781.

Ells, G.D., 1963, Information on Michigan Silurian oil and gas fields: State of Michigan, Department of Conservation, 14pp.

Fjar E., Holt, R., Horsrud, P, Raaen, A., and Risnes, R. 2008. Petroleum Related Rock Mechanics, 2nd edition. Elsevier. ISBN: 978-0-444-50260-5

Frank, T.D., Wilkinson, B.H., and Lohmann, K.C., 1993, Origin of marine pisoliths and the sedimentology of Midwestern Silurian reefs: Journal of Sedimentary Petrology, v. 63, no.6, pp. 1070-1077.

Gardner, W.C., and Bray, E.E., 1984, Oils and source rocks of Niagaran Reefs (Silurian) in the Michigan Basin, *in* Palacas, J.G. ed, Petroleum Geochemistry and Source Rock Potential of Carbonate Rocks: American Association of Petroleum Geologists Studies in Geology 18, pp. 33-44.

Gill, D., 1973. Stratigraphy, facies, evolution and diagenesis of productive Niagaran Guelph reefs and Cayugan sabkha deposits, the Belle River Mills Gas Field, Michigan Basin, University of Michigan, Ann Arbor, MI, United States, Doctoral thesis, 362 pp.

Gill, D., 1979. Differential entrapment of oil and gas in Niagaran pinnacle-reef belt of northern Michigan: American Association of Petroleum Geologists, v. 63, no. 4, pp. 608-620.

Gingras, M.K., Pemberton S.G., Muelenbachs, K., and Machel, H., 2004, Conceptual models for burrow-related, selective dolomitization, with textural and isotopic evidence from the Tyndall Stone (Ordovician) Canada: Geobiology, v. 4, pp. 21-30.

Grammer, G.M., 2006, Topical Report 2005-2006: Summary of research - Establishing the relationship between fracture-related dolomite and primary rock fabric on the distribution of reservoirs in the Michigan Basin: U.S. DOE, Award No. DE-FC26-04NT15513, 167 pp.

Grammer, G.M., 2007, Summary of research through Phase II/Year 2 of initially approved 3 Phase/ 3 Year project—establishing the relationship between fracture-related dolomite and primary rock fabric on the distribution of reservoirs in the Michigan Basin—Final Scientific/Technical Report Oct. 2004-Sept. 2007: U.S. DOE, Award No. DE-FC26-04NT15513, 307 pp.

Grammer, G.M., and Harrison, W.B. III, 2013, Evaluation and modeling of stratigraphic control on the distribution of hydrothermal dolomite away from major fault planes: RPSEA Final Technical Report 08123.12.Final, Contract No. 08123.12, 284 pp.

Grammer, G.M., Karsten, J., Prezbindowski, D., Dattilo, B., and Havens, J., 2017, Reservoir characterization and 3D modeling of Silurian reef slopes: Pipe Creek Jr. Quarry, Grant County, Indiana: Search and Discovery Article #51440 (2017), 45pp.

Grammer, G.M., Thornton, J.E., Robinson, M.E., Feutz, P.J., Schulz, J.E., and Harrison, W.B., III, 2014. Stratigraphic control on the lateral distribution of hydrothermal dolomites away from major fault zones: Part 2: Search and Discovery Article #50964 (2014) Posted May 30, 2014. Adapted from oral presentation to Tulsa Geological Society May 5, 2014.

Haagsma, A., Rine, M., Sullivan, C., Conner, A., Kelley, M., Modroo, A., Larsen, G., and Gupta, N., 2017, Static earth modeling of diverse Michigan Niagara reefs and implications for CO_2 storage: Energy Procedia no. 114, pp. 3353-3363.

Harrison, W.B. III, 2010. “EOR in Silurian-Niagaran reef reservoirs, Michigan,” *In* Evaluation of CO_2-enhanced oil recovery and sequestration opportunities in oil and gas fields in the MRCSP region—MRCSP Phase II Topical Report October 2005-October 2010: U.S. DOE Cooperative Agreement No. DE-FC26-05NT42589, OCDO Grant Agreement No. DC-05-13, pp. 48-54.

Harrison W.B.III, and Voice, P.J., 2018, Evaporite Facies of the Michigan Basin, i*n* Grammer, G.M., Harrison, W.B., III, and Barnes, D.A., eds., Paleozoic Stratigraphy and Resources of the Michigan Basin: Geological Society of America Special Paper, v. 531.pp. 197- 286.

Howell, P. D., and van der Pluijm, B.A., 1990, Early history of the Michigan basin: Subsidence and Appalachian tectonics: Geology, v. 18, pp. 1195–1198.

Howell, P.D., and B.A. van der Pluijm, 1999, Structural sequences and styles of subsidence in the Michigan Basin. Geological Society of America Bulletin, v. 111, no. 7, pp. 974-991.

Huh, J.M., 1973, Geology and diagenesis of the Niagaran pinnacle reefs in the northern shelf of the Michigan Basin. University of Michigan, Ann Arbor, MI, United States, Doctoral thesis.

Huh, J.M., L.I. Briggs, and D. Gill, 1977, Depositional environments of pinnacle reefs, Niagara and Salina Groups, northern shelf, Michigan Basin, *in* J.L. Fischer, ed., Reefs and evaporites-Concepts and depositional models: American Association of Petroleum Geologists Studies in Geology, v. 5, p. 1-21.

Kendall, C.G. St. C., 2003. SEPM STRATA, SEPM Stratigraphy Web. Available at http://www.sepmstrata.org/page.aspx?pageid=1.

Kerans, C., and Tinker S.W., 1997, Sequence Stratigraphy and Characterization of Carbonate Reservoirs: Society of Economic Paleontologists and Mineralogists Short Course Notes no. 40 165 p.

Keister, L.E., 2018, Rock properties of Silurian Niagaran reef carbonates in Michigan after CO_2 injection: Undergraduate thesis: Ohio State University, 48pp.

Lacy, L.L. 1997. Dynamic Rock Mechanics Testing for Optimized Fracture Designs. SPE Paper 38716

Lal, M. 1999. Shale stability: drilling fluid interaction and shale strength. SPE Latin American and Caribbean Petroleum Engineering Conference held in Caracas, Venezuela.

Lee, J. (1982) *Well testing*. Richardson, TX: Society of Petroleum Engineers (SPE textbook series, v. 1).

Leibold, A., 1992, Sedimentological and Geochemical constraints on Niagara/Salina deposition, Michigan Basin: Doctoral Dissertation, University of Michigan, Ann Arbor, Michigan.

Loucks, R.G., Mescher, P.K., and McMechan, G.A., 2004, Three dimensional architecture of a coalesced, collapsed paleocave system in the Lower Ordovician Ellenburger Group, central Texas, AAPG Bulletin, v. 88, no.5, p.545-564.

Lucia, F.J., 1995, Rock fabric/petrophysical classification of carbonate pore space for reservoir characterization: AAPG Bulletin 79, no.5, p.943-961.

Ma, L., Castro, M.C., Hall, C.M., Walter, L.M., 2005, Cross-formational flow and salinity sources inferred from a combined study of helium concentrations, isotopic ratios, and major elements in the Marshall aquifer, southern Michigan: Geochemistry Geophysics Geosystems, v. 6, No. 10, 21 p.

Machel, H.G., 2004, Concepts and models of dolomitization: a critical reappraisal, *in*, C.R.J. Braithwaite, G. Rizzi, and G. Darke, eds., The geometry and petrogenesis of dolomite hydrocarbon reservoirs: Geological Society, Special Publications, vol. 235, London, pp 7–63.

Mazzullo, S.J., and Chilingarian, G.V., 1992, Diagenesis and origin of porosity, *in* G.V. Chilingarian, S.J. Mazzullo, and H.H. Rieke, eds., Carbonate Reservoir Characterization: A Geologic-Engineering Analysis, Part I: Elsevier Publ. Co., Amsterdam, Developments in Petroleum Science 30, p. 199-270.

Miller, J., Sullivan, C., Larsen, G., Kelley, M., Rike, W., Gerst., J., Gupta, N., Paul, D., Pardini, R., and Modroo, A., 2014, Alternative conceptual geologic models for CO_2 injection in a Niagaran pinnacle reef oil field, northern Michigan, USA: Energy Procedia v. 63, pp. 3685-3701.

Moore, C.H., and Wade, W.J, 2013, Carbonate reservoirs: Porosity and diagenesis in a sequence stratigraphic framework: Developments in Sedimentology, v. 67.

Murray, R.C., 1964, Origin and diagenesis of gypsum and anhydrite: Journal of Sedimentary Petrography, v.43, no. 3, pp.512-523.

Murray R.C. and Pray, L.C., 1965, Dolomitization and limestone diagenesis: A symposium: Society of Economic Paleontologists and Mineralogists, SEPM Special Pub 13.

Noack, A., 2008, Analysis of Pore Architecture and Correlation to Sonic Velocity Values in Silurian (Niagaran) Reefs of the Michigan Basin: Thesis (MS), Western Michigan University.

Osorio, R., Sharifi Haddad, A., Stephens, E. and Hamidi, H. (2017) “Geological Interpretation of Channelized Heterolithic Beds through Well Test Analysis,” *Journal of Petroleum Science and Engineering*, 158, pp. 516–528.

Posamentier, H.W., Jervey M. T., and Vail, P. R., 1988, Eustatic controls on clastic deposition I — conceptual framework, in: C. K. Wilgus, B. S. Hastings, C. G. St. C. Kendall, H. W. Posamentier, C. A. Ross and J. C. Van Wagoner, eds., Sea Level Changes - An Integrated Approach: Special Publication no. 42, Society of Economic Paleontologists and Mineralogists, p. 110–124.

Prezbindowski. D.R., Dattilo, B., Havens, J., and Lucas, R., 2018, Silurian reef systems in the Illinois and Michigan basins- What can be learned from modern quarrying operations in north-central Indiana?: AAPG Search and Discovery Article #51343 (2017), posted April 24, 2018.

Purdy, E.G. 1974, Reef configuration: cause and effect. *In* LaPorte, LF, ed. Reefs in Time and Space: Selected Examples from the Recent and Ancient. Society of Economic Paleontologists and Mineralogists Special Publication 18, pp. 9-76.

Qualman, H., 2009, 3-D Interpretation of the Sequence Stratigraphy and Reservoir Property Distribution in the Belle River Mills Silurian (Niagaran) Reef, St. Clair County, Michigan: Thesis (MS), Western Michigan University, Kalamazoo, Michigan, USA, 313 pp.

Rine, M.J., 2015a, Depositional facies and sequence stratigraphy of the Niagaran-Lower Salina reef complex reservoirs of the Guelph Formation, Michigan Basin: Master’s Thesis, Western Michigan University, Kalamazoo, Michigan, USA, 185 pp.

Rine, M.J., Barnes, D., Harrison, W., III, Sullivan, C., Kaczmarek, S., 2015b, Petrophysical and stratigraphic characterization of Michigan Silurian reefs: Search and Discovery Article #30429 (2015), 44pp.

Rine, M.J., J.D. Garrett, and S.E. Kaczmarek, 2017, A new facies architecture model for the Silurian Niagaran pinnacle reef complexes of the Michigan Basin, *in* Characterization and Modeling of Carbonates–Mountjoy Symposium 1: Society of Economic Paleontologists and Mineralogists Special Publication no. 109, pp. 70–86.

Rine, M.J., Kaczmarek, S.E., and Garrett, J.D., 2018, A new sequence model for Silurian A-1 Carbonate (Ruff Formation) of the Michigan Basin, i*n* Grammer, G.M., Harrison, W.B., III, and Barnes, D.A., eds., Paleozoic Stratigraphy and Resources of the Michigan Basin: Geological Society of America Special Paper, v. 531.

Ritter, A.L., 2008, Evaluating the controls on reservoir heterogeneity of Silurian pinnacle reefs, Michigan Basin: M.Sc. thesis, Western Michigan University, Kalamazoo, Michigan, 247 pp.

Rudnicki, J.W. 1999. Alteration of regional stress by reservoirs and other inhomogeneities stabilizing or destabilizing? In 9th ISRM Congress. International Society for Rock Mechanics.

Rullkotter, J.M., P.A. Schaefer, G. Rainer, and K.W. Dunham, 1986, Oil generation in the Michigan Basin: A biological marker and carbon isotope approach: Organic Geochemistry, v. 10, pp. 359-375.

Sarg, J.F., 2001, The sequence stratigraphy, sedimentology, and economic importance of evaporite-carbonate transitions: a review: Sedimentary Geology v. 140, pp. 9-42.

Schlumberger Ltd, 2009, Dolomite: perspectives on a perplexing mineral: Oilfield Review, v. 21, no.3, Autumn 2009, 45pp.

Schlumberger Ltd, 2007, Fundamentals of wettability: Oilfield Review, Summer, 2007, 61pp.

Schlumberger Ltd, 2007, Carbonate reservoirs: https://www.slb.com/~/media/Files/industry_challenges/carbonates/brochures/cb_carbonate_reservoirs_07os003.pdf. Last accessed October 3, 2018.

Schlumberger Ltd, 2005, Confronting the carbonate conundrum: Oilfield Review, Spring 2005, 29pp.

Sears, S.O., and Lucia F.J., 1980, Dolomitization of northern Michigan Niagara reefs by brine refluxion and freshwater/seawater mixing: Society of Economic Paleontologists and Mineralogists Special Publication 28, pp. 215-235.

Shouldice, J. R., 1955, Silurian reefs of southwestern Ontario: Canadian Mineral and Metallurgy Bulletin, v. 48, no. 520.

Suhaimi, A.A., 2016, Pore characterizations and distributions, within the Niagaran lower Salina Reef complex reservoirs in the Silurian northern Niagaran Pinnacle Reef Trend, Michigan basin, Masters thesis: Western Michigan University, 179 pp.

Smith, L., Charbonneau, S.L., and Grimes, D.J., 1993, Karst episodes and permeability development, Silurian reef reservoirs, Southwestern Ontario: Ontario Geological Survey, Open File Report 5850, 320 pp.

Soltanzadeh, M, Hawkes, C, McClellan, P, and Smith, S.A. 2009. Poroelastic Modelling of Production and Injection-Induced Stress Changes in a Pinnacle Reef. Proceedings of the 3rd CANUS Rock Mechanics Symposium, Toronto, Canada, May 2009.

Trout, J.L., 201, Faunal distribution and relative abundance in a Silurian (Wenlock) pinnacle reef complex—Ray Reef, Macomb County, Michigan: Western Michigan University, M.S. Thesis, 300 pp.

Vail, P.R., 1987. Seismic stratigraphy interpretation procedure. In: Bally, A.W. (Ed.), Atlas of Seismic Stratigraphy, vol. 27. American Association of Petroleum Geologists Studies in Geology, pp. 1–10.

Wells, J. W., 1957, Coral reefs: Geol. Soc. Am. Mem. 67, v. 1, pp. 609-631.

Versical, R. T., 1991, Basement control on the development of selected Michigan Basin oil and gas fields as constrained by fabric elements in Paleozoic limestones: M. S. Thesis, Western Michigan University, Kalamazoo, Michigan, 200 pp.

Wold, J.L., 2008, Sequence stratigraphy and 3-D reservoir characterization of a Silurian (Niagaran) reef – Ray Reef Field, Macomb County, Michigan: M.S. Thesis, Western Michigan University, Kalamazoo, Michigan, 104 pp.

Wold, J.L., Grammer, G.M. and Harrison, W.B. III, 2008, Sequence Stratigraphy and 3-D Reservoir Characterization of a Silurian (Niagaran) Reef – Ray Reef Field, Macomb County, Michigan, presented at Eastern Section AAPG, Pittsburgh, PA.

Woods J.R., and Harrison, W.B., 2002, Advanced characterization of fractured reservoirs in carbonate rocks: the Michigan Basin: Final report, DOE DE-AC26-98BC15100, 63pp

Woody, R.E., Gregg, J.M., Koederitz, L.F., 1996, Effect of texture on petrophysical properties of dolomite, evidence from the Cambrian-Ordovician of Southeastern Missouri: AAPG Bulletin v.80, n. 1, pp. 119-132.

Appendix A.
Literature Review of Niagaran Reef Geology

A.1 Introduction

The geology overview provides a review of the geologic setting of the study area and on the structural, sequence stratigraphic, depositional, and diagenetic controls on geologic variability of reservoir and seal development.

Upper Silurian carbonate platforms developed along arches that separate the Michigan, Ohio, and Illinois basins (Sarg, 2001). The Northern Pinnacle Reef Trend (NPRT) developed along the northern slope of the increasingly restricted Michigan Basin (Figure A-1), (Briggs et al., 1980; Harrison III, 2010). The slope reefs range from 2,000 feet to over 6,000 feet deep, with many occurring at depths of 3,500 to 5,000 feet. Individual reefs are closely spaced and compartmentalized from the enclosing rock, and average 50 to 400 acres in area, up to 700 feet in height, with steep flanks of 30° to 45°, thus fitting the definition of pinnacles by Shouldice (1955). Larger reefs commonly consist of coalesced individual pinnacles and mounds; and height of reefs generally increases basinward.

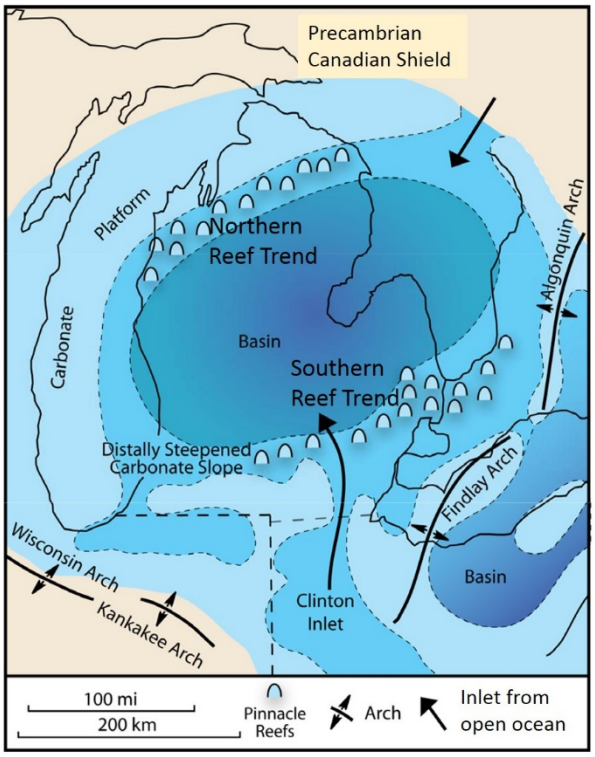
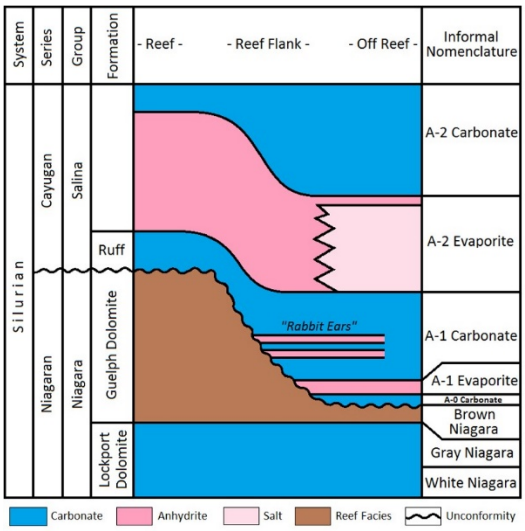


Figure A-1. Silurian Northern Pinnacle Reef Trend within the Michigan Basin (modified from Rine, 2015 and Burgess and Benson, 1969).

Approximately 800 fields in the NPRT, originally developed in the 1970s-1980s, have undergone primary production and some have undergone secondary recovery by water flood and tertiary recovery by CO_2 (Grammer et al., 2009; Harrison III, 2010; Barnes et al., 2013; Haagsma et al., 2017). Fluids in the reefs are generally divided from up-dip to down-dip into gas, oil, and water (Gill, 1979).

Reef reservoir rocks develop in the Brown Niagara lithostratigraphic interval of the Guelph Formation (Figure A-2). Primary reef builders are stromatoporoid sponges, rugose and tabulate corals, plus bryozoans. Additional carbonate producing/trapping organisms include crinoids, brachiopods and algae/ microbial communities (Trout, 2012).

The resulting carbonate buildups may be completely dolomitized, essentially all limestone, or a heterogeneous mix. Porosity types include primary framework voids, interparticle porosity systems, secondary vugs, cavernous and fracture porosity as well as intercrystalline and microcrystalline porosity (Sears and Lucia, 1980). Porosity values of NPRT reefs average between 3% to 12%, with the best porosity and permeability associated with dolomitized reef core and flank facies (Haagsma et al., 2017). The most productive reservoir rocks are characterized by well-developed intercrystalline and vuggy porosity with average permeability values of 3 to 10 millidarcies (mD). Permeability can be significantly higher where fractures intersect voids and matrix porosity.



Period	Epoch	N. American Age	N. American Stage	Michigan		
				Subsurface Group	Subsurface Formation	Informal Literature
Devonian						
Silurian	Late	Pridoli (419-416)	Cayugan	Bass Islands	undiff	
					G	G
		Ludlow (423-419)		Salina	F	F
					E	E
					D	D
					C	C
					B	B
					A-2 Carb	A-2 Carb
					A-2 Evap	A-2 Evap
					Ruff	A-1 Carb
					A-1 Evap	A-1 Evap
					Cain	A-0 Carb
	Middle	Wenlock (428-423)	Niagaran	Niagara	Guelph Dol.	Brown Niagaran
					Lockport Dol.	Gray Niagaran
						White Niagaran
				Manistique	undiff	Manistique
				Burnt Bluff	undiff	Clinton
	Early	Llandovery (444-428)	Alexandrian	Cataract	Cabot Head Sh.	
					Manitoulin Dol.	

Figure A-2. Lithostratigraphy of the Silurian Niagara reef interval, left (after Gill 1973, 1979; and Huh 1973), and comparison of formal and informal lithostratigraphic names, right (modified from Trout 2012).

Reservoir quality is generally enhanced by dolomitization, and upper parts of reefs often, but not always, are more dolomitized than the lower parts. Hydrothermal dolomite is locally present and is related to structure, fractures and migration of deep fluids (Grammer, 2007). Regionally, non-hydrothermal dolomitization of reefs increases updip and salt and anhydrite plugging of porosity is more common in the deeper reefs (Gill, 1979).

The principal source rock for oil accumulation in the NPRT is the off-reef fine-grained facies of the A-1 Carbonate of the Salina Group (Rullkotter et al., 1986; Rine et al., 2017); the Brown Niagara is a secondary source (Gardner and Bray, 1984). Multiple episodes of hydrocarbon migration occurred between the Mississippian and the Middle Jurassic (Cercone and Lohmann, 1987).

Seals for the hydrocarbon reservoirs include the flanking A-1 Evaporite, which transitions from anhydrite near the reefs to halite in the basin center, and the A-2 Evaporite, which overlies the reef, and which is dominantly halite in the NPRT. The A-2 Evaporite thins to zero thickness northward towards the Niagaran carbonate platform that rims the basin margin (Cercone and Lohmann, 1985; Harrison and Voice, 2018). In flanking and off-reef areas, the Rabbit Ears Anhydrites form thin (2-20 feet) vertical baffles and barriers to flow within the A-1 Carbonate.

The following section summarizes: basin structure; Guelph and Ruff lithologies; lithofacies packages and interpreted sequence stratigraphy; evolution of current depositional models of the reef interval; types of porosity and diagenesis; regional trends in diagenesis; and implications for construction of static and dynamic reservoir/seal models.

A.2 Basin Structure

The main structural elements of the Michigan Basin are shown in Figure A-3 The basin appears to have started as an elongate Upper Cambrian to Lower Ordovician continuation of the extensional Reelfoot rift- Illinois Basin (Howell and van der Pluijm, 1990). Howell and van der Pluijm, (1990; 1999) concluded that there were multiple distinct episodes of subsidence in the 200 m.y. history of the Michigan Basin, with several episodes related to the orogenic events in the Appalachian Basin. The episodes of subsidence are as follows: A) early lithospheric extension during the Cambrian to early Ordovician; (B) narrow, basin-centered subsidence during the Early to Middle Ordovician; (C) regional eastward tilting with lack of basin-centered subsidence during the Middle to Late Ordovician, related to Ordovician subduction; (D) renewed broad basin-centered subsidence during the Early to Late Silurian; (E) narrow, basin-centered subsidence from latest Silurian through Middle Devonian; (F) Late Devonian and younger eastward basin tilting. Rine et al. (2018) have documented minor differential subsidence in the North and South Pinnacle Reef Trends during deposition of the A-1 Carbonate.

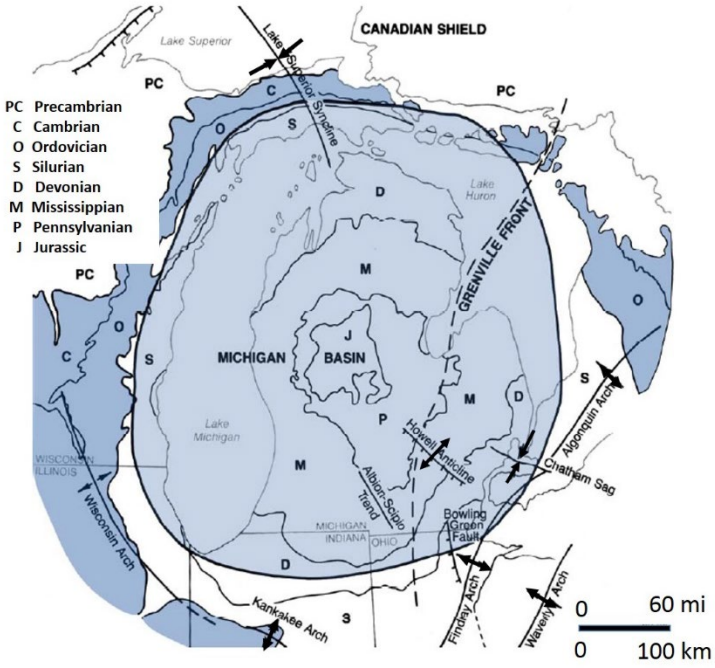


Figure A-3. Main structural elements and age of bedrock in the Michigan Basin (Modified from Rine, 2015 and Catacosinos et al., 1991).

Major faults (Figure A-4) generally trend northwest-southeast. The Howell fault (HL) in southeastern Michigan is an example of a high angle normal fault (Fisher et al., 1988), downthrown to the west, with possibly as much as 800 ft of displacement (Woods and Harrison, 2002). Faults in the Albion-Scorpio (AS) display left lateral wrench fault movement (Grammer and Harrison, 2013). With the exception of the faults in the southeastern part of the basin, most faults appear to terminate at or below middle Devonian age strata (Woods and Harrison, 2002).

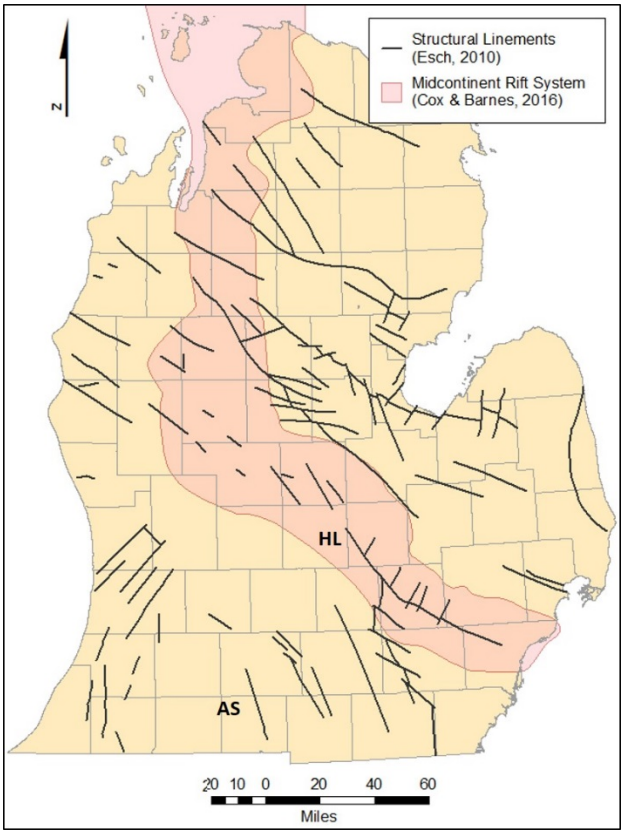


Figure A-4. Major faults in the Michigan Basin. (Modified from Esch, 2010; Cox and Barnes, 2016).

Tectonic lineaments are shown in Figure A-5 and include poorly expressed anticlines and faults. Woods and Harrison (2002) reported that a complex fracture pattern in strata in the center of the Michigan basin is related to the Precambrian Keweenawan rift that extends NW-SE across the central part of the basin. Reactivation of basement faults occurred during the Mississippian (Fisher et al., 1988; Towne et al., 2013) related to northwest/ southeast Alleghenian compression (Woods and Harrison, 2002); later overprints of left-lateral riedel shear movement are due to northeast/southwest compressional stress (Haimson, 1978; Versical, 1991). Distribution and diagenetic overprints of the Niagaran reefs are influenced by structure, with reefs in Oceana County preferentially nucleating on pre-existing wrench- fault related highs, and late-stage hydrothermal dolomitization resulting from fluid migration along faults (Grammer, 2007). Structural mapping and log analysis of the Michigan basin Ordovician Trenton/Black River, Silurian Niagaran, and the Devonian Dundee intervals by Woods and Harrison (2002) and Grammer (2008) indicate that there is a close spatial relationship between gross dolomite distribution and regional scale, wrench-fault related NW-SE and NE-SW structural trends. Most of the Dundee hydrocarbon fields are associated with low relief anticlines on the upthrown side of faults (Woods and Harrison, 2002), and over half of the known Dundee reservoirs appear to have fault-related hydrothermal overprints (Barnes et al., 2008). It should be noted that some of the regional hydrothermal brines have been interpreted to have a chemical overprint from mafic rocks of the Precambrian Keweenawan rift (Cercone 1984; Ma et al., 2005). Cox and Barnes (2016) concluded that anomalous temperature indicators indicate multiple migrations of burial fluids, including Permian age.

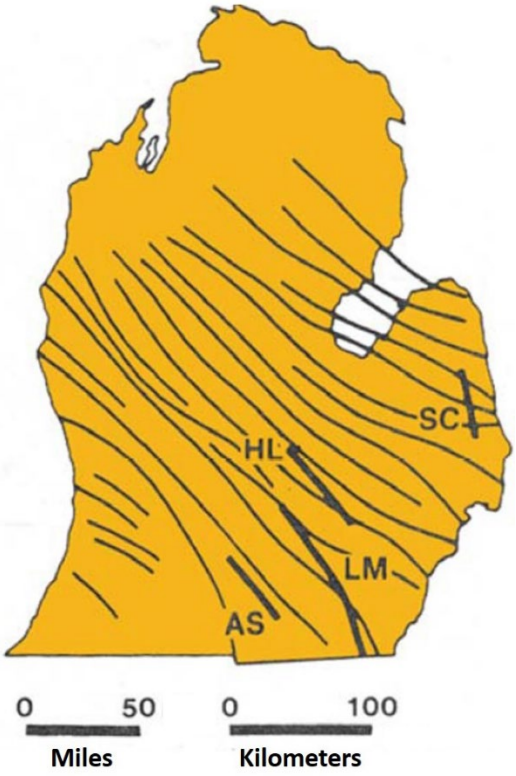


Figure A-5. Lineaments and anticlinal traces in the Michigan Basin area. Labeled faults: AS=Albion-Scipio, HL=Howell, LM=Lucas-Monroe, SC=Sanilac (Modified from Grammer and Harrison, 2013).

Cercone (1984), using petrographic and isotopic data from the Shell State Union 1-8 well in Grand Traverse County, concluded that salt plugging of reefs occurred as multiple events of precipitation and dissolution during the Mississippian or later, and may coincide with reactivation of faults and dissolution of surrounding salt beds. Post-Devonian anticlinal structures in the Overisel field, and six other fields in Allegan County are cored by deformed Silurian A1 salt (Ells, 1963).

A.3 Lithostratigraphy

As shown in Figure A-2, reefs developed in the upper portion of the Niagara Group, which is subdivided into the Guelph Dolomite and Lockport Dolomite Formations (Catacosinos et al., 2000, 2001). Historically, the oil industry subdivides the Niagara Group into Brown, Gray, and White Niagara based on color, texture, and wireline log signature (Carter et al., 2010). The reefal Brown Niagara is stratigraphically equivalent to the Guelph Dolomite, and the underlying Gray and White Niagara are equivalent to the Lockport Dolomite. The reefal buildups in the Brown Niagara are overlain and encased by cyclic carbonate and evaporite beds of the Salina Group.

The Brown Niagara and A-1 Carbonate are the reservoirs in the Silurian reefs (Figure A-6). The Brown Niagara consists of skeletal wackestones, packstones, grainstones, and boundstones/bindstones associated with the organic reef buildups. It includes the off-reef carbonate conglomerate lithofacies below the A-0 Carbonate (Huh, 1973). The distinctive color of the Brown Niagara can be attributed to dolomitization as well as, in some cases, oil staining. The underlying Gray and White Niagara form the base of the reservoir and are characterized by two types of crinoidal wackestones: porous dolomitized wackestones, and low-porosity, undolomitized limestone (Charbonneau, 1990). The Gray and White Niagara reach a thickness of approximately 500 feet near the basin margins and become thinner and have a more reddish color toward the center of the Basin (Huh, 1973; Huh et al., 1977; Charbonneau, 1990). The regional Gray Niagara tends to be slightly thicker below Brown Niagara reefs.

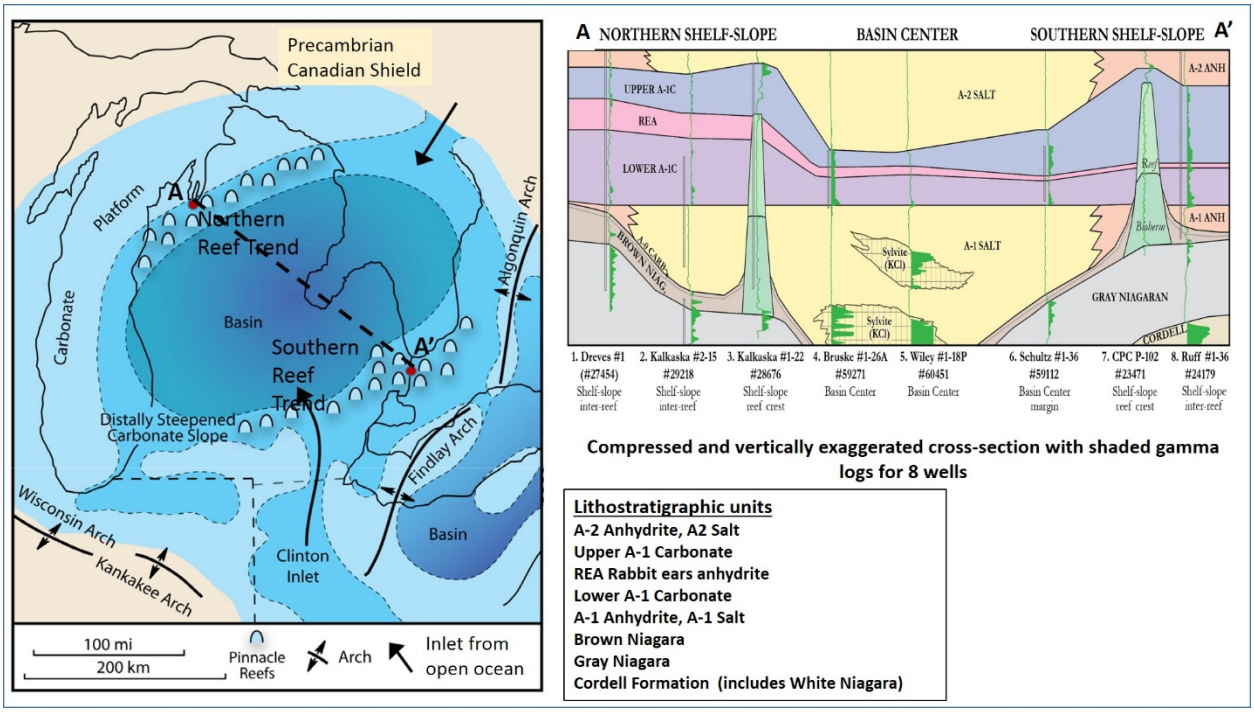


Figure A-6. Geometry of reservoirs and seals in the interval of interest. Modified from Rine, 2015a and Rine et al., 2017.

The A-0 carbonate is a thin (10-40 feet) unit that overlies Brown Niagaran reef-associated conglomerates on reef flanks (Catacosinos et al., 2001; Suhaimi, 2016). The superjacent A-1 Evaporite regionally transitions from halite and sylvite in the basin center to anhydrite on reef flanks, forming a sealing lithology. The A-1 Carbonate, subsurface equivalent to the Ruff Formation, overlies the Brown Niagara on reef crests and overlies the A-1 Evaporite off-reef. It includes laminated, light-brown to tan, fine to medium crystalline dolomitic mudstone, dark shaley “poker-chip” mudstones, and stromatolitic or microbial laminated boundstones, which may show truncation surfaces and rip-up clasts (Huh, 1973; Gill, 1973; Ritter, 2008). Laminated, dolomitic mudstones occur in inter-reef deposits and on the reef; packstones and dolomitic microbial boundstone facies, often displaying anhydritic cements (Gill, 1973) occur on reef crests. Off-reef, the upper part of the A-1 Carbonate includes the thin, regionally correlative Rabbit Ears Anhydrites. The A-1 Carbonate may act as seals on the flanks of the reefs but can develop dolomitic intercrystalline reef top and proximal flank reservoirs as well as microporous reservoirs off-reef. Variations in on-reef upper A-1 Carbonate thickness indicate differential subsidence along the north and south basin margins (Rine et al., 2017).

The A-2 Evaporite occurs as a thin bed of anhydrite or halite above the tops of reefs and as bedded halite in the inter-reef deposits (Huh et al., 1977; Gill, 1977). The A-2 Carbonate is a 100- to 120-foot thick regional tight limestone. Rapid changes in the anhydrite/halite composition of the Niagaran and Salina evaporites surrounding the reefs make the acquisition of a full suite of density and acoustic logs critical in mapping reservoir boundaries and calibrating seismic response.

A.4 Interpreted Sequence Stratigraphy of the Reef Interval

The subdivision of the rock record encountered in an exploration wellbore traditionally is lithostratigraphic and is based on sharp changes in lithology (sandstone, dolostone, limestone, shale, etc.). In contrast, sequence stratigraphy is a method of grouping rock strata based on their depositional relationships, with major boundaries formed by unconformities or their correlative downdip surfaces. Rock units that lie between unconformities are assumed to be more closely related than units that are separated by unconformities.

Stratigraphic sequences contain laterally coeval, shoreline-related deposits within specific systems tracts (Figure A-7). A systems tract is the depositional setting from onshore to offshore; systems tracts are separated by small scale unconformities or depositional facies offsets into lowstand, highstand, and other packages related to the position of sea level, shoreline, and the depositional environment. In essence, stratigraphic sequences are each composed of a succession of genetically laterally-linked strata that reflect deposition in natural depositional systems that are interpreted to have been deposited between eustatic sea-level fall inflection points (Posamentier et al., 1988).

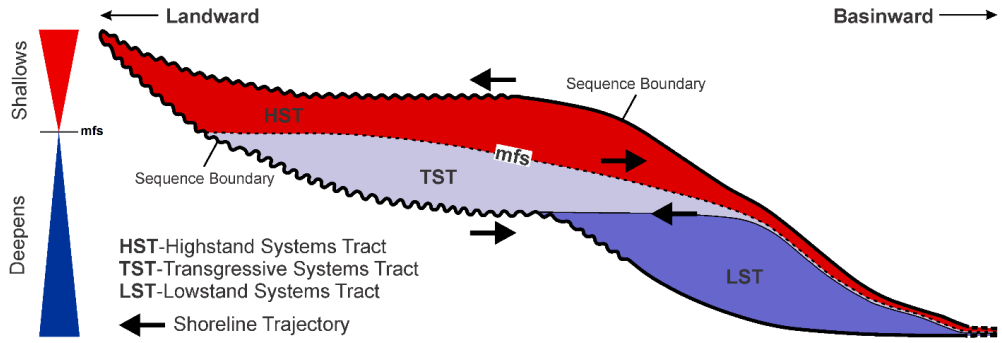


Figure A-7. Geometry of a seismic-scale sequence with three depositional systems tracts (modified after Vail 1987; Christie-Blick and Driscoll 1995). Mfs is maximum flooding surface.

The placement of regional third order, unconformity-bounded sequences generally follows one of two models, as compared in Figure A-8. The older model recognizes three systems tracts as opposed to the newer model of Catuneanu et al. (2011) that separates deposits into four systems tracts, related to relative sea level position: lowstand systems tracts (LST), transgressive systems tracts (TST), high-stand system tracts (HST) and falling stage system tracts (FSST). Both models separate sedimentary rock deposited between regional unconformities, and both recognize lowstand systems tracts as being deposited as sea level is rising, thus forming the basal deposits of the overlying sequence. The more recent model that recognizes falling stage (FFST) deposits is particularly applicable to seismic stratigraphic analysis of siliciclastics in large basins, where during falling sea level, sediment continues to be eroded updip, and deposited in shallow water environments and down-dip in basin floor fans. Correct placement of third order sequence boundaries requires regional data.

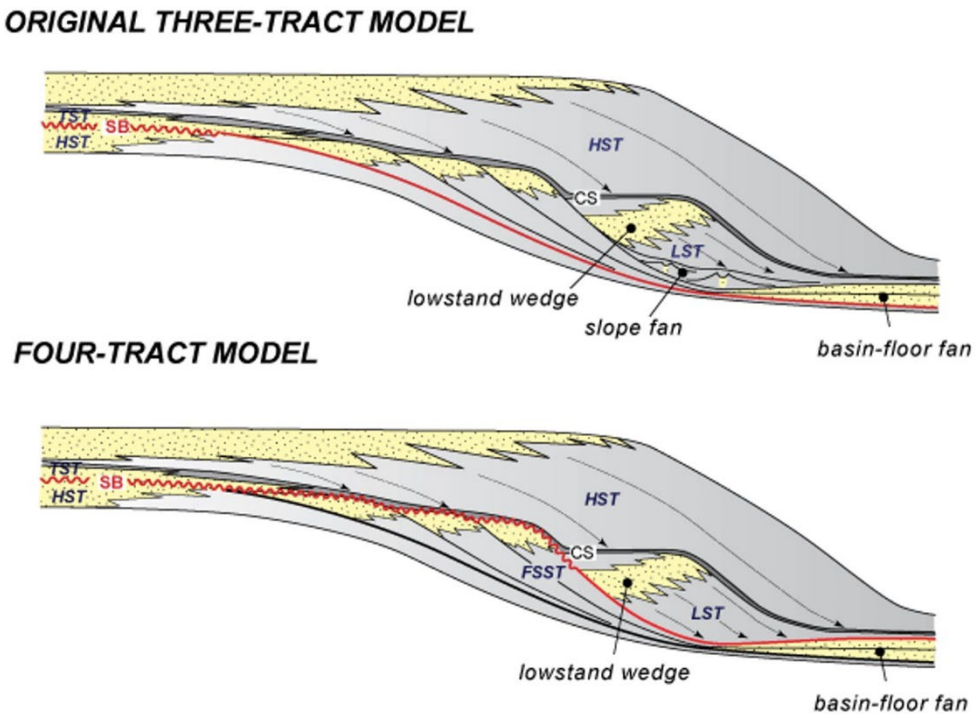


Figure A-8. Comparison of three-tract and four-tract sequence stratigraphic depositional models. Note that deposits formed during sea level fall are included in the lower sequence in the four-tract model. Modified from Catuneanu et al., 2011.

In contrast to siliciclastic systems, shallow water carbonate production on isolated steep-sided reefs may almost completely cease when sea level drops, resulting in flanking breccias and other deposits that are not genetically related to the living reef. Thus, the FSST deposits will likely have very different petrophysical properties from those of HST deposits of a growing reef. Additional information and references on sequence stratigraphy of carbonates can be found in Kendall (2003).

Sequence stratigraphic subdivisions are hierarchical (Figure A-9); in this study, we are concerned with third order sequences that are separated on the reef tops by unconformities, and with facies tracts and fourth-order sequences. In core, fourth-order sequences show vertical progressive changes in depositional environment (such as shallowing from subtidal into the intertidal environment), separated by marked (but not profound) shifts in depositional environment. These fourth-order packages of rock are linked to each other as parts of a vertical and horizontal depositional package, and their recognition helps in definition of internal layering for building reservoir models. Both third- and fourth-order packages commonly have wireline log expression that reflects carbonate-facies stacking patterns. Smaller fifth - order sequences can commonly be identified in core as meter-scale upward shallowing packages, but the development of these sedimentary packages in reefal environments depends on local topographic relief and may be difficult to correlate between wells, even where core exists.

Subsurface sequence stratigraphic analysis may begin with recognizing stratigraphic packages in seismic data or may initiate with examining wireline logs and core to determine sediment stacking packages, abrupt lithofacies offsets, unconformities, and upward shallowing or deepening packages. Carbonate textures, lithologies, and faunal changes are particularly important in determining changes in depositional environment and package boundaries.

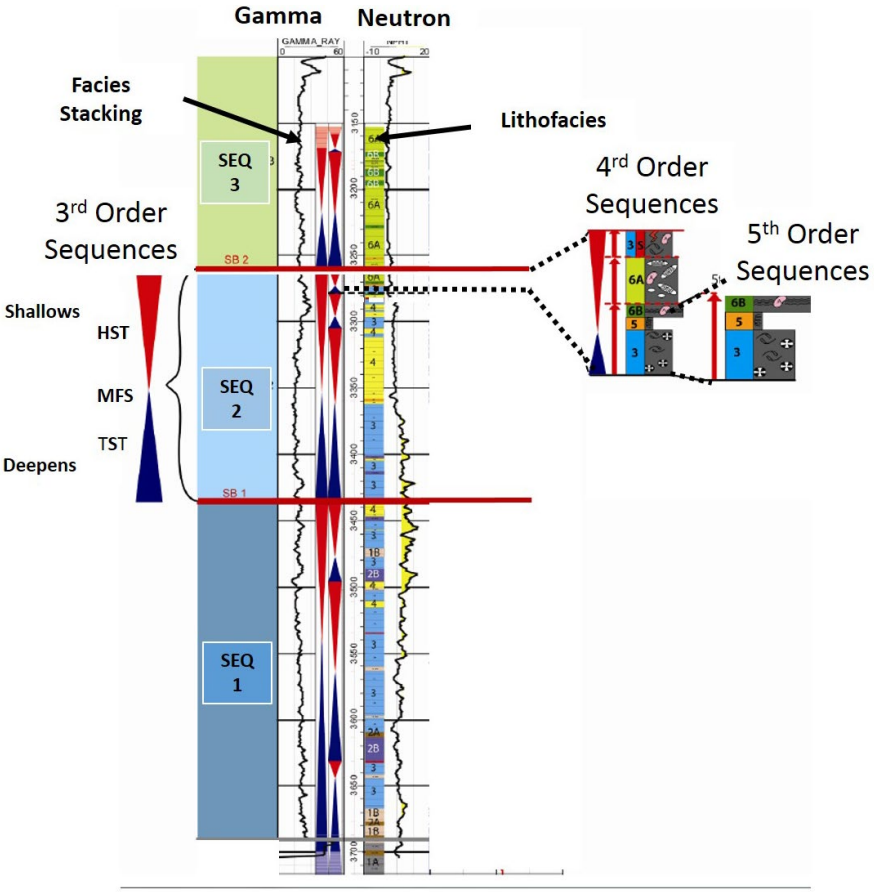


Figure A-9. Hierarchical nature of sequence stratigraphic depositional packages interpreted in the Miller –Fox 1-11 well, Oceana County. Interpretation is based on cored lithofacies, unconformities, flooding surfaces, marine hardgrounds, and wireline-log signatures. Numbered intervals represent lithofacies; red and blue triangles represent upward shallowing and deepening depositional stacking patterns (Modified from Ritter, 2008).

The sedimentary character of the third- and fourth-order sequence stratigraphic units and their lateral and vertical lithologic changes can be explained in terms of control by changes in global/basinal sea level, rate of subsidence, sediment supply, and climate. Reef-associated carbonates are particularly reflective of the changes in depth, wave energy, and sediment supply in their depositional environment, and often accumulate as meter-scale cycles that stack into larger groups. Carbonate lithofacies (Figure A-10) refer to the appearance and characteristics of the rock unit, including rock composition, texture, biotic component, and sedimentary structures. For a sequence stratigraphic study, it is the abrupt juxtaposition of fauna or lithofacies offsets that are not closely associated in nature that help determine the magnitude of an apparent break in the stratigraphic record (Ritter 2008). Lacking indications of upward shallowing packages with minor exposure surfaces, identification of fourth order packages is tenuous within reef core and flanking deposits. Silurian reef outcrops in Illinois and Indiana, illustrated by Prezbindowski et al. (2018), may allow development of criteria for recognition of these packages. In this study, fourth order stacking packages are most recognizable in the off-reef A1 carbonate. Facies tracts (LST, TST, HST), and depositional facies/geobodies (windward fore reef, reef core, leeward back reef) within a given sequence and facies tract, appear to be the most relevant features for constructing models of the internal architecture of the pinnacle reefs.

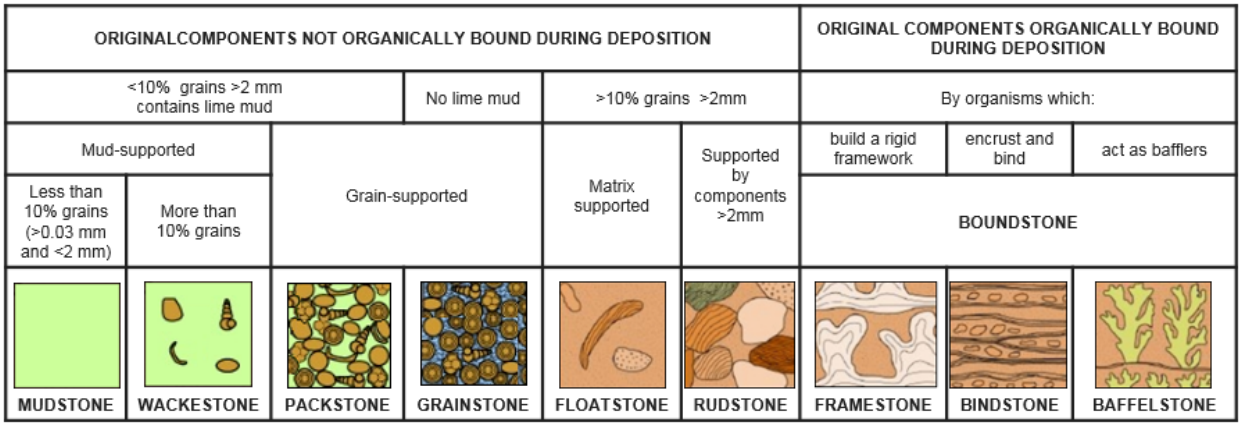


Figure A-10. Carbonate lithofacies, as used in this study, based on classification by Dunham (1962), revised and expanded by Embry and Klovan (1971).

Carbonate lithofacies exhibit original depositional textures and porosity systems that are overprinted by diagenetic events. Identifying the original depositional component provides important information for assigning the spatial distribution of original porosity within the reservoir model. Flow units often, but not always, are bound by fourth or third order boundaries. Intercrystalline dolomite porosity, in particular, may connect porosity systems across unconformities; thus, flow units do not always coincide with sequence stratigraphic or lithostratigraphic units.

Since the 1990s, studies of carbonates have increasingly relied on developing a basin-specific sequence stratigraphic framework within which to build the architecture to constrain models of time-equivalent depositional facies; correlate key facies and sequence surfaces; and identify vertical lithofacies stacking patterns for each identifiable order of cyclicity. The premise is that a sequence stratigraphic framework, including identification of facies tracts, can provide a basis for more accurate lateral and vertical prediction of lithofacies compared to conventional lithostratigraphic analysis. The application of sequence stratigraphy to predict three dimensional development of porosity and seals for carbonate reservoirs is relatively mature (Kerans and Tinker, 1997).

A.4.1 Interpreted Sequence Stratigraphy of the Niagaran Reefs

Sarg (1991) and Liebold (1992) appear to be among the first to apply sequence stratigraphic concepts to the Michigan Basin. Sarg worked on the northern platform and pinnacle reefs; Liebold interpreted a sequence stratigraphic framework for the White Niagara through the Salina B interval, with a focus on changes in sea level and formation of the evaporite deposits. Dr. Michael Grammer and his students at Western Michigan University evaluated the Michigan reef core- and log-based sedimentological work of Huh and others (Huh, 1973, Huh et al., 1977; Gill, 1973) in terms of a sequence stratigraphic framework. Recognition of unconformity-bounded packages by Huh (1973) and Gill (1973) greatly influenced later sequence stratigraphic interpretations. Ritter (2008) applied a sequence stratigraphic approach (See Figure A-9) to facies analysis of cores from five wells in the northern and southern parts of the basin (Figure A-11). Ritter (2008) interpreted three distinct third-order sequences that are separated by erosional unconformities in on-reef wells, and by pronounced lithofacies changes in the cored off-reef southern well Jahn 1-4 (25739).

Grammer's students were also the first to evaluate porosity and permeability trends as they relate to sequence stratigraphically-constrained lithofacies (Ritter, 2008; Noack, 2008.) Importantly, Grammer's students used this type of approach to explore relationships between wireline log data and permeability trends, and to build and populate reservoir models at the Belle River Mills reef complex in the southern reef trend (Wold, 2008; Qualman 2009). Locations of reefs in these studies are shown in Figure A-11.

The results of Huh, Gill, and researchers at MGRRE/Western Michigan University confirm three findings that support the viability of a sequence stratigraphic/lithofacies approach to building static earth models of the Silurian reefs. First, reef-associated organisms change dramatically as the reefs initiated, flourished, and were eventually killed off by basin-wide changes in salinity and connection to the open ocean outside the Michigan Basin. Second, the depositional environment and the shape, size, and mineral composition of the reef organisms have a large influence on the resulting porosity and permeability of the reef rock. Third, within a given stratigraphic interval, wireline logs and computer-generated lithology logs exhibit signatures that can be used to reduce uncertainty on the range of rock types and their petrophysical properties.

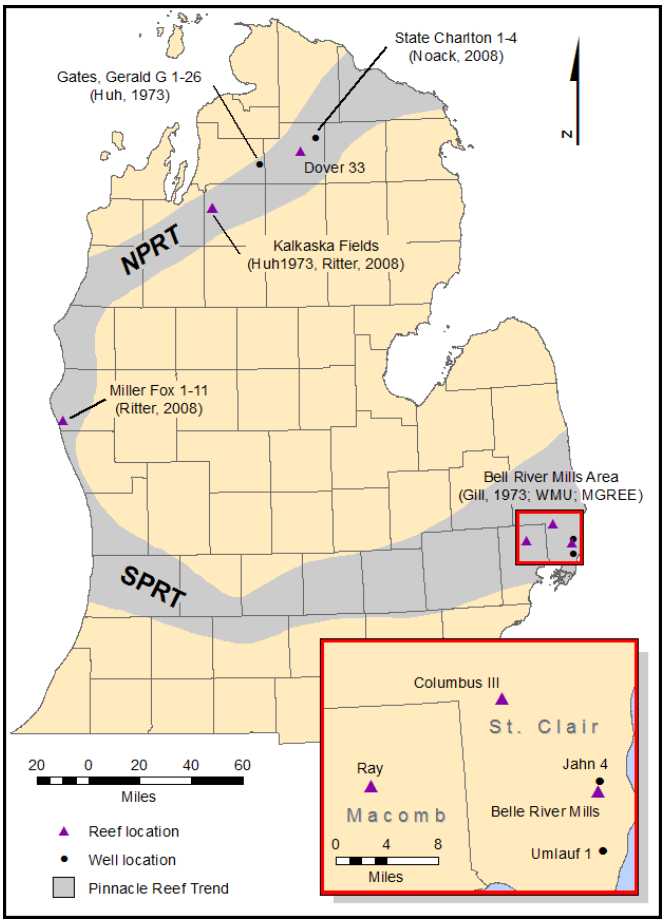
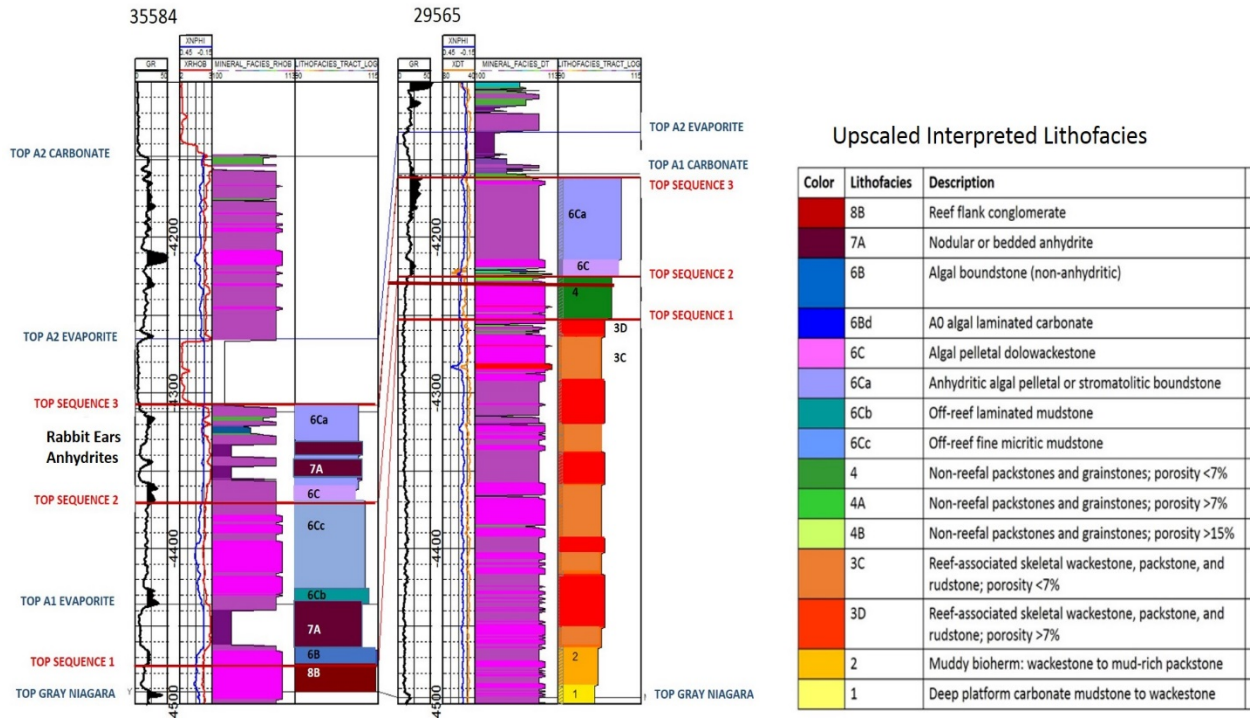


Figure A-11. Location of reefs in Northern and Southern Reef trends mentioned in text. Modified from Miller et al. (2014) and Rine et al. (2017).

As a test of the utility of a sequence stratigraphic framework for construction of static models for the MRCSP Phase III project, Miller et al. (2014) reviewed the sedimentological and lithofacies work of Huh (1973,) Gill (1973), Huh et al. (1977), and students at WMU; correlated wireline log signatures of sequence markers in cored analog wells to uncored wells of the completely dolomitized Dover 33 reef; and interpreted electrofacies from wireline signatures and porosity/permeability transforms from whole core data in sequence stratigraphically constrained lithofacies of reefs studied by Grammer's students. Miller et al. (2014) then constructed and populated parallel static models using lithostratigraphic and sequence stratigraphic frameworks. They concluded that the sequence stratigraphic framework provided an improved approach for reducing uncertainty in lithofacies interpretation where core is lacking, and that the sequence stratigraphic approach provided a basis for interpreting lateral and vertical extent of lithofacies. The challenges of any study of sparsely drilled reefs that lack reef-specific core and rock data include considerable uncertainty on the presence, widths and geometries of depositional windward/leeward and depth-related environments and their resulting primary rock fabric; as well as post-depositional diagenesis. An example of interpreted third order sequences of Miller et al (2014) in on-reef and off-reef wells of the Dover 33 field is shown along with cross-plot electrofacies (petrofacies) and interpreted lithofacies in Figure A-12.



Color	Lithofacies	Description
	8B	Reef flank conglomerate
	7A	Nodular or bedded anhydrite
	6B	Algal boundstone (non-anhydritic)
	6Bd	A0 algal laminated carbonate
	6C	Algal pelletal dolowackestone
	6Ca	Anhydritic algal pelletal or stromatolitic boundstone
	6Cb	Off-reef laminated mudstone
	6Cc	Off-reef fine micritic mudstone
	4	Non-reefal packstones and grainstones; porosity <7%
	4A	Non-reefal packstones and grainstones; porosity >7%
	4B	Non-reefal packstones and grainstones; porosity >15%
	3C	Reef-associated skeletal wackestone, packstone, and rudstone; porosity <7%
	3D	Reef-associated skeletal wackestone, packstone, and rudstone; porosity >7%
	2	Muddy bioherm: wackestone to mud-rich packstone
	1	Deep platform carbonate mudstone to wackestone

Figure A-12. Interpreted third order sequences in a reef flank well (left) and on-reef well (right) from the Dover 33 reef, which lacks core, along with key to interpreted lithofacies. From Miller et al., 2014. These sequence boundaries can be now be adjusted to match recent correlations to additional cored wells by Rine et al., 2017, and Rine et al., 2018.

More recent carbon isotope data allow a more accurate correlation of deposits within reefs, as shown in Figure A-13 for the Columbus 3 reef in the Southern Reef Trend. In addition, an unconformity at the top of the bioherm in this figure is now correlated to a major unconformity between the Niagaran and Salina platform carbonates, as recognized by Smith et al. (1993) on the southeast basin margin. Work by Battelle and WMU students have confirmed a bioherm top unconformity in several wells in the Northern Reef Trend. Smith (1993), working on core from five platform and pinnacle reef fields concluded that a sea-level drop at the end of bioherm development exposed some but not all of the slope bioherms flanking the southern platform, and that platform brines generated at this time dolomitized some but not all of the bioherms. This has important implications for porosity development in the lower Niagaran interval around the northern basin margin as well. Cercone (1984) documented dolomitized intervals that predate burial diagenesis in the lower part of the Niagaran interval of the northern reef Shell Union 1-8 (Grand Traverse County). she interpreted the porous dolomite to have formed during reef exposure and basinal drawdown, rather than post bioherm, pre-reef as specified in the interpretation of Smith et al. (1993).

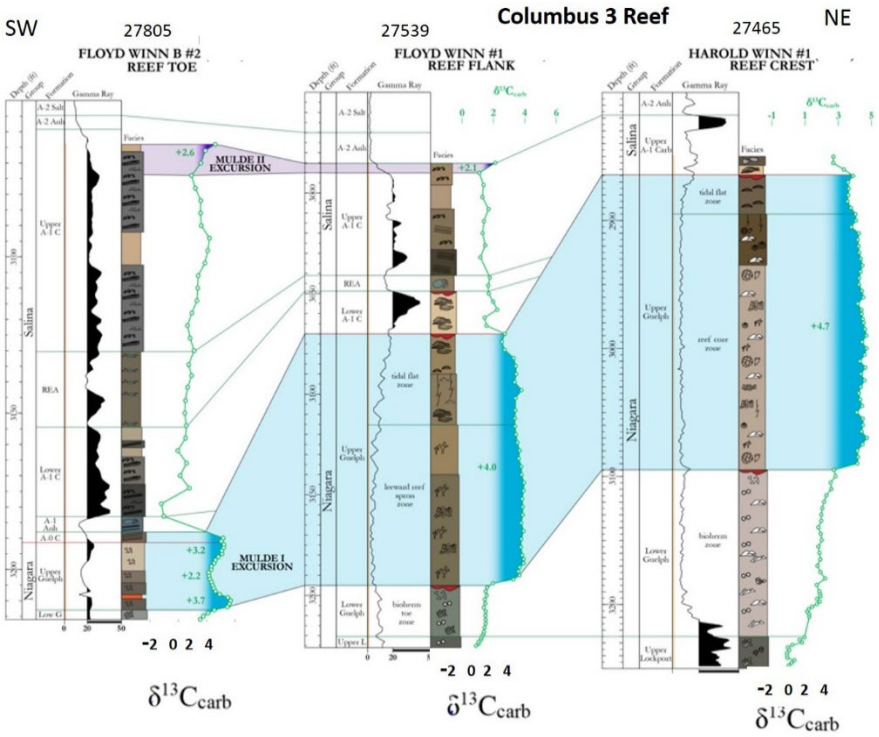


Figure A-13. Relation of the Mulde1 carbon isotope excursion to Niagaran depositional reef facies in the Columbus 3 Reef. Locations of unconformable surfaces are shown in red. Figure is courtesy of Matt Rine.

Recent A1-Carbonate core and carbon isotope data analyzed by Rine et al. (2018) indicate that a sequence boundary within the A-1 carbonate (slightly above the off-reef top Sequence 2 of Miller et al., 2014) coincides with a basin wide sea level drop that resulted in the deposition of the Rabbit Ears Anhydrites (Figure A-14). Thus, the top of the lower A1 Carbonate sequence shown in the work of Miller et al. (2014) should be moved higher to coincide with the findings of Rine et al. (2018). The A1 Carbonate sequences are now recognized as Sequence 3 and 4, in accordance with the recognition of a basin wide sequence boundary on top of the Niagaran bioherm.

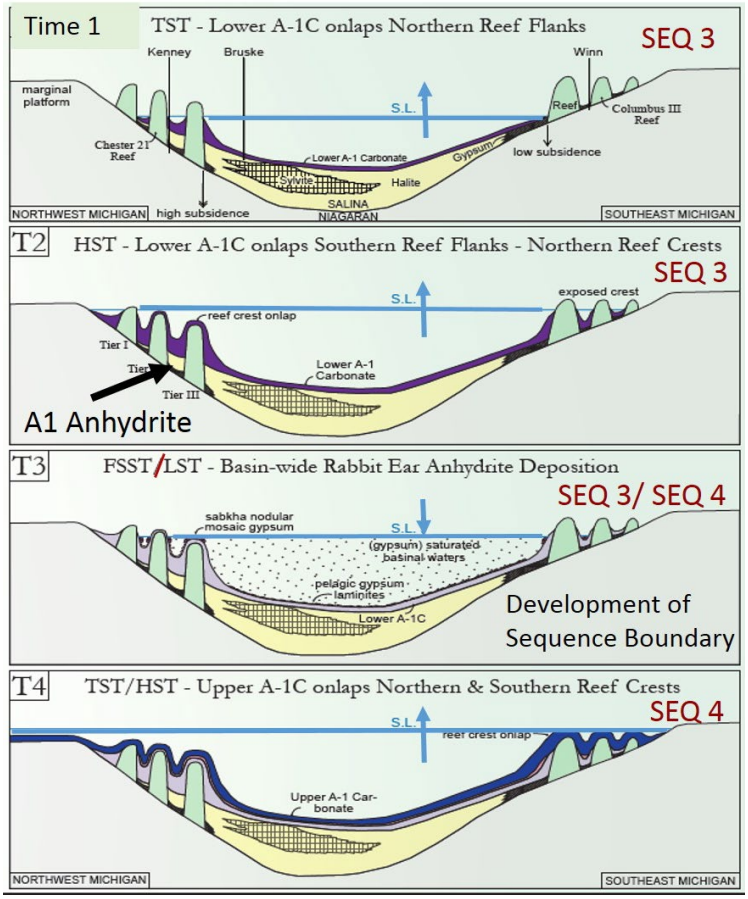


Figure A-14. New sequence stratigraphic interpretation of the A-1 Carbonate. Modified from Rine et al. (2018).

A comparison of third order sequence boundaries from Ritter (2008), Miller et al. 2014), Rine (2015a) and Rine et al. (2018) is projected on Huh's (1973) Kalkaska reef model in Figure A-15. Notably, a basin-wide sequence boundary is recognized on top of the Niagaran bioherms. In addition, Rine et al. (2018), place a third order sequence boundary at an unconformity within the A1 Evaporites, separating evaporites that accumulated during basin drawdown (in the falling stage systems tract) from the overlying A1 evaporites (lowstand systems tract that accumulated as sea level rose over the exposed reefs and the flanking FSST deposits). In addition, Rine et al., (2018) established a basin-wide correlation for the Rabbit Ears Anhydrites (REA), and separated the A1 Carbonate into two sequences, separated by the REA. Finally, current isotopic work by Matt Rine better chronostratigraphy correlates depositional facies between wells. This updated sequence stratigraphic model more correctly constrains basin-wide events, stratigraphic and evaporite relationships, and demonstrates the extremely different nature of falling-stage and lowstand deposits compared to transgressive and highstand carbonate deposits in the Michigan reefs.

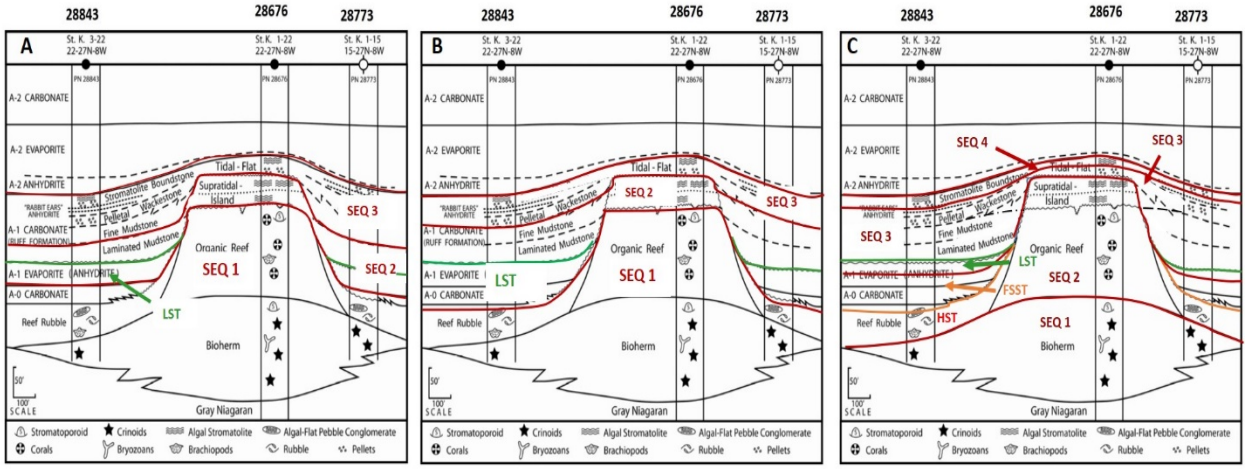


Figure A-15. Comparison of the sequence stratigraphic subdivisions of A) Ritter (2008); (B) Miller et al. (2014), and (C) Rine (2015a), Rine et al. (2017), and Rine et al. (2018), projected onto Huh's (1973) reef model. Subdivisions in C are considered in this report to be most correct.

A summary of current thought on the third order sequences and systems tracts is as follows, in ascending stratigraphic order: the "muddy bioherm" in the lower part of the Brown Niagaran represents the transgressive to highstand systems (HST) tracts of a newly recognized sequence (Sequence 1, see Figure A-13), terminated by a sea level drop that exposed surrounding platforms and the most updip or shallow slope bioherms; with deeper bioherms remaining submerged (Smith et al., 1993). A dolomitizing event accompanied this sea level drop, affecting only some of the exposed and submerged bioherms (Smith et al., 1993). The overlying framework reefs represent the TST and HST of Sequence 2. The A0 Carbonate and lower part of the A1 Evaporite are parts of a falling stage systems tract (FSST) of Sequence 2. Although generally not practical to pick on wireline logs, the upper part of the A-1 evaporite belongs to a lowstand systems tract (LST), and thus is the lower part of a new sequence (Sequence 3), deposited as sea level began to rise along the flanks of the reefs. The off-reef, lower A1 Carbonate (A1C) below the Rabbit Ears Anhydrites represents the transgressive (TST) and highstand systems tracts of Sequence 3. The lowermost A1 Carbonates on top of the northern reefs are laterally equivalent to the uppermost off-reef Sequence 3 highstand carbonate. The reef-flank FSST Rabbit Ears Anhydrites correlate to exposure surfaces on top of the northern reefs. The A1 carbonate above the Rabbit Ears Anhydrite (REA) occurs both on the reef crest and flanks, and is interpreted as the highstand of Sequence 4. Currently, no large relative sea level drop is proposed for the dual- or multi- pronged REA events. The top of the upper A1 Carbonate HST (top of Sequence 4) correlates to the base of the A2 Evaporite (Rine et al., 2017).

A.4.2 Relevance of Sequence Stratigraphic Analysis

The importance of the sequence stratigraphic analysis of the Niagaran reefs is that it allows an understanding of the relative age of the Brown Niagara, the A-0 Carbonate, the A-1 Anhydrite and the A-1 Carbonate, and more realistically allows lateral assignment of lithofacies and petrophysical properties within static models. Establishing relative and isotopic ages eliminated certain depositional models. The correlation of a major platform exposure event (Smith et al., 1993) to the top of bioherm buildups near the southern basin margin provides better understanding of lateral depositional events and the possibility of unexploited dolomite porosity development in reefs within the reef trends. In addition, the recognition by Rine et al. (2018) of an upper and lower A-1 carbonate, separated by the Rabbit Ears Anhydrites and a third- order sequence boundary supports the regional recognition of separate reservoirs in the upper and

lower A-1 Carbonate units. The evolution of the currently used depositional models, based on a sequence stratigraphic approach, is discussed in the following section.

A.5 Evolution of Depositional Models

Both external morphology and internal lithofacies distribution are critical in constructing robust static models, and both had high uncertainty at the beginning of this study. Uncertainty in mapping external morphology is a consequence of Niagaran reef size and steepness of flanks, seismic acquisition challenges and resulting data frequency, velocity contrasts of complex evaporite/carbonate lithologies along reef margins, and sparseness of wellbores. Modern reefs exhibit growth morphologies related to water energy, light/depth, temperature, salinity and sediment input; although much of modern reef morphology may be inherited from karsted Pleistocene precursor reef or carbonate substrate (Purdy, 1974).

Huh (1973) and Gill (1973) examined core and logs from reefs in the Northern Reef Trend (Huh, 1973) and in the Southern Trend (Gill, 1973) to provide ground truth and constraint for reef models. Both researchers identified an initial more mud-rich bioherm, an organic reefal framework, a restricted faunal stage; and both agreed that reef growth ceased prior to deposition of the flanking A-0 Carbonate and A-1 Anhydrite. In contrast to Gill (1973), Huh (1973) found evidence of re-establishment of minor reef-associated communities above the karsted terminal reef surface of his northern reefs (uppermost lower A1 carbonate, Sequence 3 of this study). Their models of the geometry and lithofacies distribution within the Brown Niagara reefs are summarized in Figure A-16.

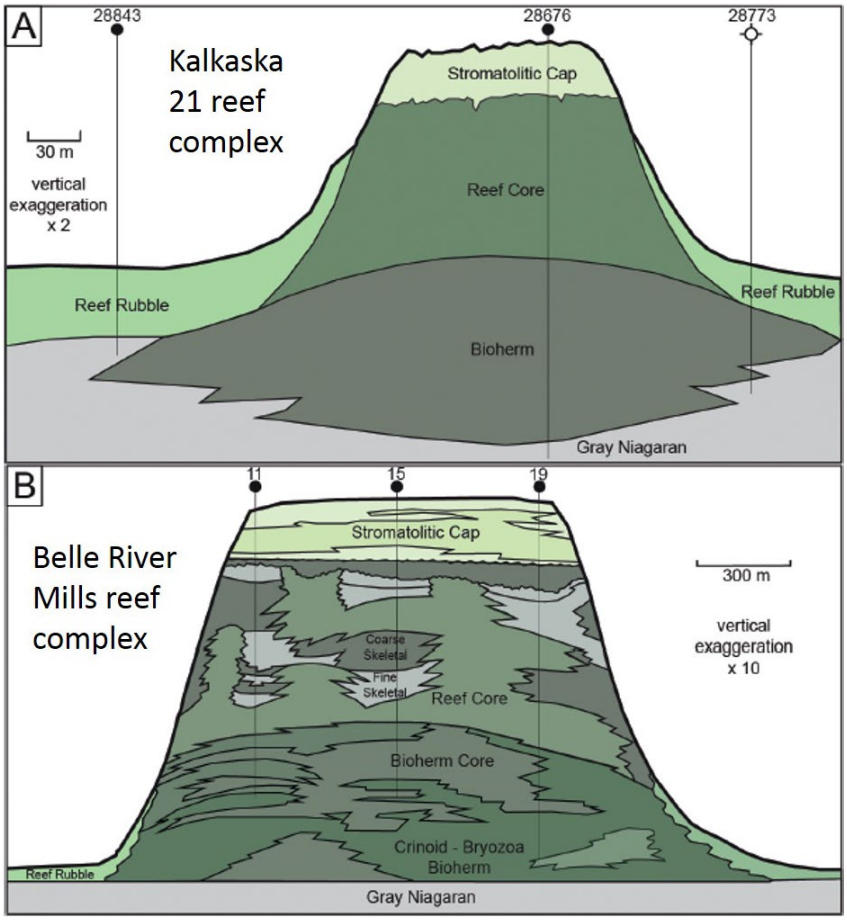


Figure A-16. Simplified geometry and lithofacies distribution in Niagaran reefs by Huh (A) and Gill (B). As shown, these models do not address differences in windward and leeward reef morphologies or facies zonation. Modified from Rine et al. (2017).

Interior reef lithofacies distribution was considered random by Gill et al. (1975). Huh (1973) recognized that lagoonal, leeward debris, reef crest and windward depositional facies were present, and that volumetrically, most of the reef consisted of bioclastic debris, rather than intact growth framework. However, he lacked access to closely spaced cored wells that would allow more definition of external reef morphology, internal reef architecture, and the extent of major reef depositional belts or 3D geobodies.

Niagaran reefs exposed in quarries in Illinois, Michigan and Indiana exhibit differences in windward and leeward morphologies and associated lithofacies (Grammer et al., 2017; Prezbindowski et al., 2018), and the Thornton reef in Chicago displays a windward wave-resistant stromatoporoid ridge. Individual Niagaran reefs in the north and south pinnacle reef trends may exhibit distinctly asymmetric morphologies (Grammer et al., 2010) and may have morphologies that reflect coalescence of individual buildups (Rine et al. (2017). Small relief mounds also exist in the Michigan basin. Observed reef zonation and asymmetry in modern and many ancient reefs include steeper sides and more extensive reef growth on windward margins. Causes for increased reef carbonate accumulation on the windward margin include enhanced growth of carbonate secreting organisms due to higher oxygen levels; removal of fine clogging sediment (Wells, 1957) and reduced nutrient levels (Lukasik and James, 2003); as well as precipitation of marine cement. Very high-energy reef margins may have an encrusting calcareous organism/marine cement pavement (Grammer et al., 2004; Trout, 2012).

Trout (2012) quantified faunal distribution in Niagaran core from eight wells in the Ray Reef Field in the aggregated Belle River Mills field southern reef trend, within three primary depositional environments (windward foreslope, reef crest, and leeward reef), and within three stratigraphic sequences identified by Wold (2008). Primary reef constituents are stromatoporoid sponges, rugose and tabulate corals, and bryozoans. Additional carbonate producing/trapping organisms include favisoid corals, crinoids, brachiopods and algae/microbial communities. Quantified biogenic material consisted of 77% fragmented and 23% insitu organisms. Trout (2012) identified vertically repeated changes in faunal morphology and composition coinciding with upward shallowing lithofacies packages, and differences in faunal abundance, diversity, and morphology related to location on the reef (Figure A-17). Trout concluded that framework organisms were most dominant in the reef crest rather than on the windward margin, and that the preserved reef, above the bioherm, consists mostly of matrix and cement, with lesser amounts of grains and pore space.

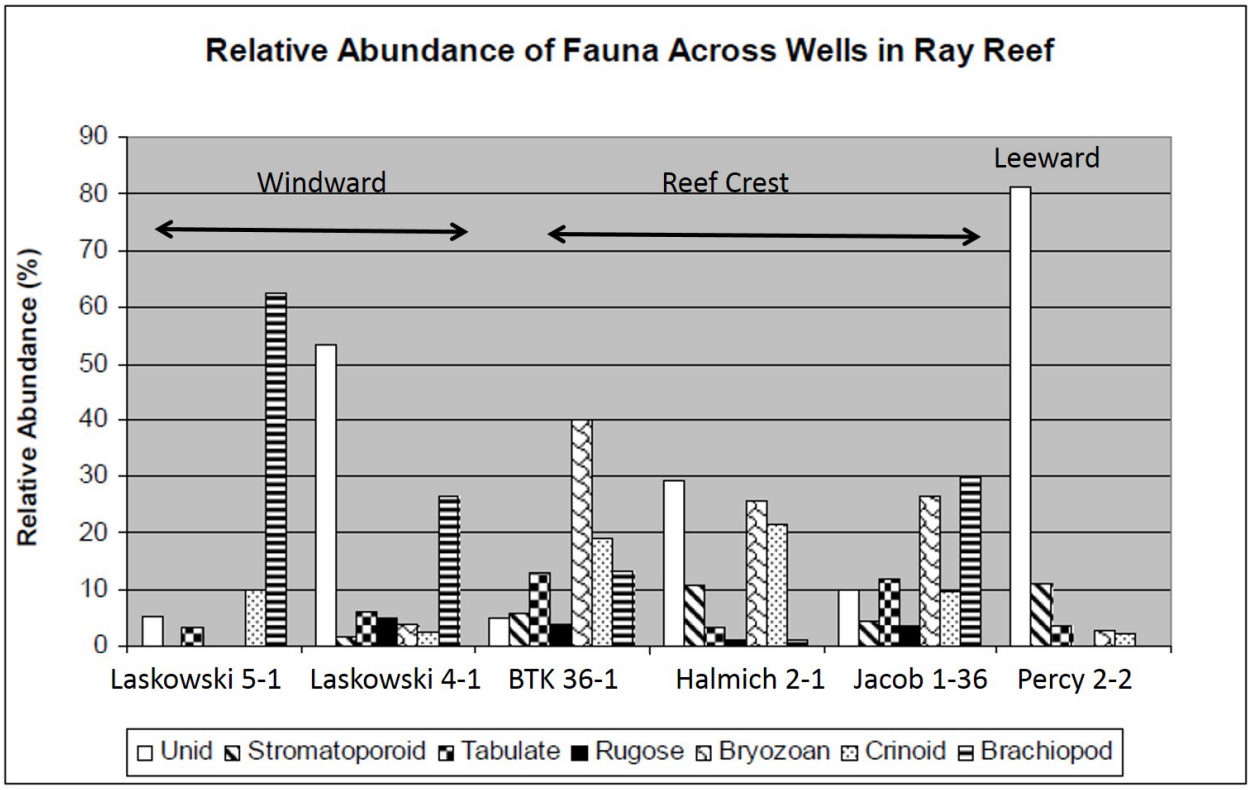


Figure A-17. Niagaran faunal zonation of the Ray Reef in the Southern Reef trend. ***Unid*** *is unidentified skeletal material (Modified from Trout 2012)*

Rine (2015a) studied core from 20 of an original 32 cored wells at the Columbus III reef in the Belle River Mills field in the Southern Reef Trend (see Figure A-11). Twenty nine of the 32 wells had available whole core petrophysical analyses. Many of these wells were regularly spaced with 11 cored wells in reef crest to leeward reef, and nine wells located on reef flank positions. A total of 72 logged wells with supporting well data were used in the analysis.

Rine (2015a) interpreted 16 carbonate lithofacies belonging to 11 reef-associated depositional environments within the three reef growth stages of biohermal complex, reef complex and stromatolitic cap. Rine's (2015a) mapping revealed three-dimensional geobodies strongly controlled by windward and leeward position, with leeward geobodies frequently of much lower reservoir quality. These data allowed the first fully constrained assessment of reef morphology (Figure A-18) and reef depositional facies distribution (Figure A-19).

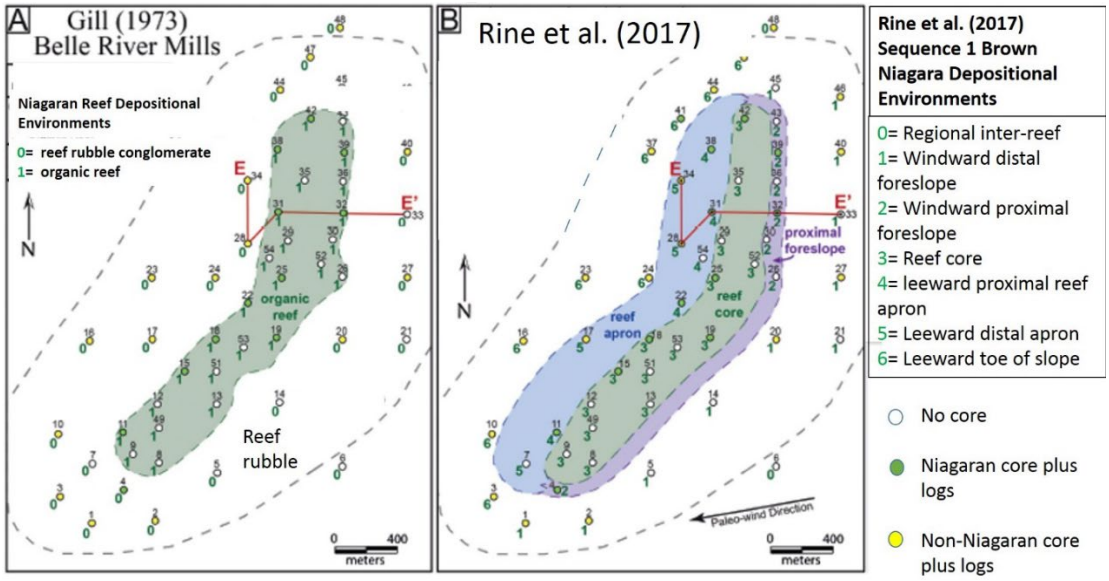


Figure A-18. Comparison of depositional facies belts identified by Gill (1973) and Rine et al. (2017) in the Columbus III reef (St Clair County) in the Belle River Mills Field. Cross section E-E' is shown in the following Figure. Modified from Rine (2015a) and Rine et al. (2017)

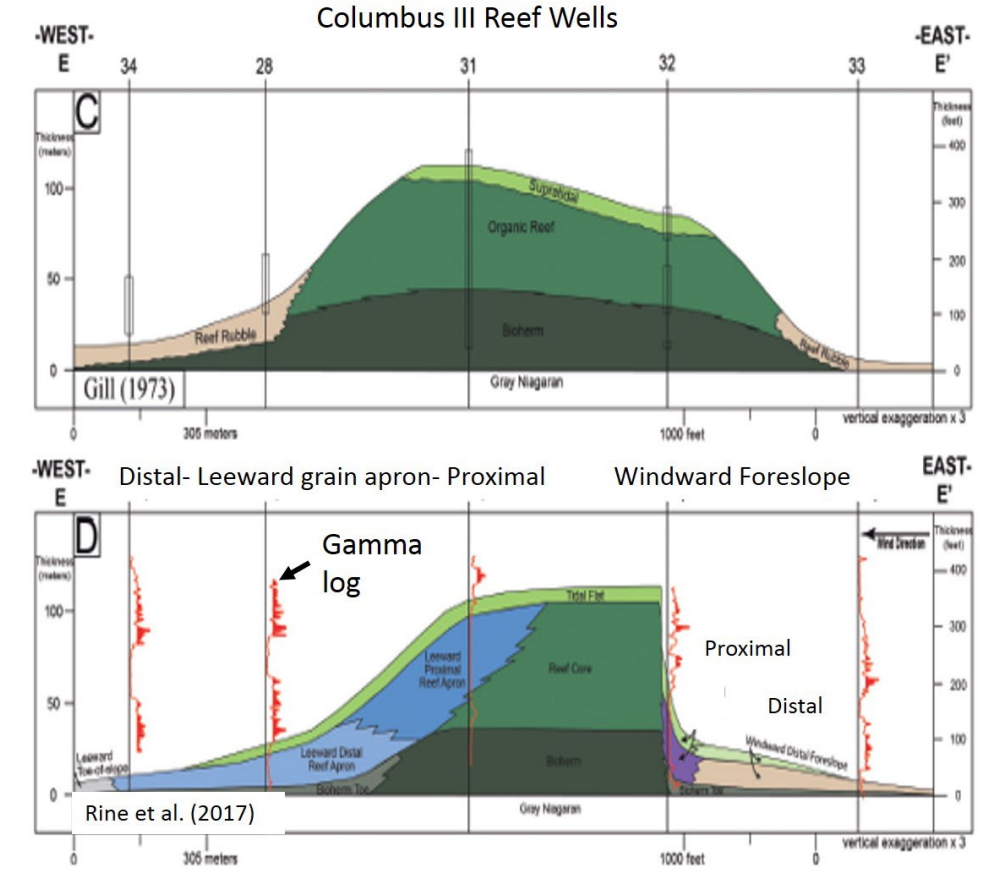


Figure A-19. Comparison of vertical depositional facies distribution and interpreted external reef morphology of the Columbus III reef, Belle River Mills, St. Clair County. Modified from Rine et al. (2017).

Rine et al. (2017) concluded that when tied to core, 3D depositional facies/geobody membership and architecture reflects original and diagenetic textures and petrophysical properties within the Niagaran reef interval of the Columbus III. These data provide both a model and dataset for comparison and prediction of lithofacies, wireline signatures, petrophysical properties (Suhaimi, 2016) and reef morphology of Niagaran reefs in the Northern Reef Trend.

Additional MRCSP studies have shown more complex reef geobody configuration and reservoir compartmentalization resulting from reef coalescence. Coalescence appears have occurred during the development of many of the larger reefs (Rine et al., 2017). Analogous coalescence and geometries of reef apron debris fans are well exposed in the Pipe Creek Junior Silurian reef quarry in Indiana (Grammer et al., 2017, Prezbindowski, et al., 2018)

Disagreement about depositional and age relationships between the Brown Niagaran reef facies and surrounding Salina units (A-0 Carbonate, A-1 Anhydrite, and A-1 Carbonate) has been largely settled through the efforts of researchers at Western Michigan University/MGGRE, using chronostratigraphy of carbon isotope excursions (Rine et al. 2017).

Sequence stratigraphic analysis provides understanding for grouping strata for developing reservoir models. For the Michigan pinnacle reefs, the working groups are: Brown Niagaran depositional reservoir facies (Sequence 1 TST and HST, Sequence 2 TST and HST); A0 plus A1 Evaporite seals (combines FSST and overlying LST); lower A1 Carbonate up to Rabbit Ears Anhydrites, which include source rock, reservoir, and secondary seal (TST and HST of Sequence 3); and upper A1 Carbonate patchy reservoirs and secondary seals above the Rabbit Ears Anhydrites (Sequence 4 TST and HST off reef; HST on-reef).

It should be noted that the original petrophysical properties of depositional geobodies are variably overprinted by diagenetic processes as described in the following section.

A.6 Diagenesis

A.6.1 Introduction and Definition

Diagenesis involves the physical, chemical and biological alteration of sediments into sedimentary rock. Diagenetic processes occur at relatively low temperatures and pressures (in contrast to metamorphism) and change the original mineralogy and texture (rock fabric). Diagenesis redistributes pore space; alters permeability and capillary characteristics; usually, but not always decreases porosity; and can change density, electrical, and acoustic properties (Lucia, 1995; Noack, 2008; Schlumberger, 2009). Original mineralogies of the Silurian reef-associated organisms are shown in Table A-1; and the generalized settings of carbonate diagenetic processes are shown in Figure A-20.

Table A-1. Original mineralogy of Silurian reef organisms. Arag- aragonite, LMC- low magnesium calcite, HMC-high magnesium calcite, Cal-calcite. Modified from Trout, 2012.

Organism	Arag	LMC	HMC	Arag + Cal	Ca Phosphates
Cyanobacteria	x	X	x		
Sponges: Stromatoporoidea	x	X	X		
Corals: Rugosa		X	x		
Corals: Tabulata	x	X	x		
Bryozoa	x	X	x	X	x
Brachiopoda: Articulata		X	x		
Brachiopoda: Inarticulata					X
Mollusca: Bivalvia	X	X		X	
Mollusca: Gastropoda	X	X		x	
Echinodermata			X		

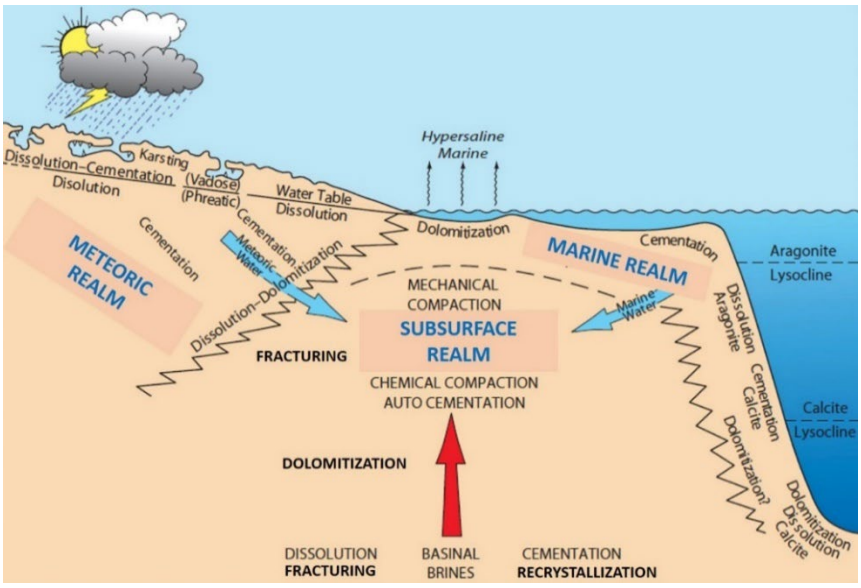


Figure A-20. Realms and processes of carbonate diagenesis. Modified from Moore and Wade (2013)

Many of the basic diagenetic processes can be identified in resulting rock fabrics. Interpretation of original depositional mineralogies and fabric plus diagenetic overprints allows the development of petrophysical rock types (Lucia, 1995), in addition to evaluating carbonate heterogeneity, which exists at scales from pore scale to reservoir scale (Schlumberger, 2005).

Although primary (depositional) porosity includes original reef framework voids, intra fossil voids, and shelter porosity, it is the secondary porosity systems, especially intercrystalline and dissolution that volumetrically dominate the porosity systems of the Silurian reefs. A graphic illustration of primary and secondary porosity types, as used in this study, is shown in Figure A-21.

Intercrystalline, touching pore (including vugs), and fracture porosities dominate higher permeability systems. Figure A-22 illustrates Lucia's (1995) petrophysical classification of porosity and the importance of determining the connections between the various porosity systems in grain-dominated and mud-dominated carbonates. Lucia's (1995) models for estimating permeability from porosity do not apply to vug-touching-vug fabrics.

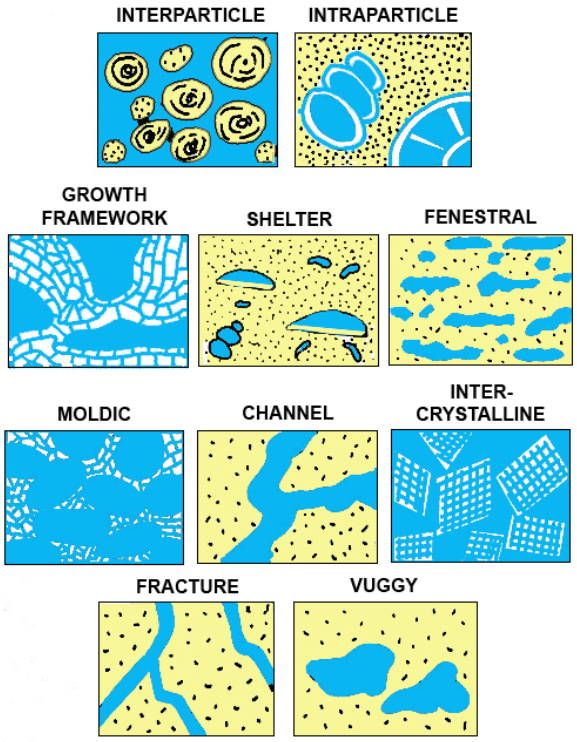


Figure A-21. Carbonate porosity types (modified from Choquette and Pray 1970).

Pore sizes, and pore throat sizes strongly affect reservoir performance. Micropores, with pore-throat diameters less than 0.5 microns (Schlumberger, 2009), can result from shallow or deep burial diagenesis, and may contain gas, or may be completely filled with irreducible water. Micropores have low permeability, and unless fractured, do not contribute to production. Mesopores have pore throat diameters between 0.5 and 5 microns; and macropores have pore throat diameters greater than 5 microns. Fine grained carbonates, and carbonates with clay or organic content, tend to have greater abundances of microporosity. Magnetic resonance logs are helpful (but not infallible) in identifying microporosity as well as secondary porosity; and mercury-injection capillary pressure (MCIP) tests can quantify pore throats, pore geometries, and help separate matrix pore system types on a core-sample scale (Schlumberger 2005).

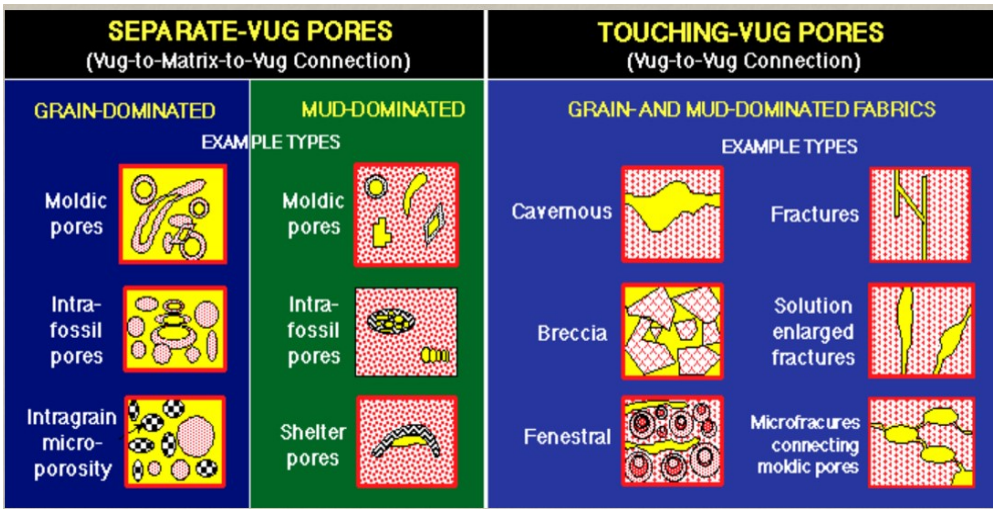


Figure A-22. Petrophysical carbonate porosity classification (after Lucia, 1995). Resulting permeability and reservoir performance depends on connectivity of all porosity systems.

Diagenesis influences brittle behavior, and fracture characteristics and intensity. Most carbonate reservoirs are naturally fractured (Schlumberger, 2007). Fractures occur at multiple scales, and intensities; including grain, bed or layer confined, and through-going joint and fracture swarms that extend

over thousands of feet (Schlumberger 2005). Thus, both matrix and fractures that comprise the multiple-porosity systems and their spatial distribution in carbonate rocks control reservoir porosity, permeability and reservoir behavior (Mazzullo and Chilingarian, 1992). Suhaimi (2016) has recently combined MCIP and petrographic data to characterize the pore types, porosity systems, and relation of porosity to permeability within depositional facies (sensu Rine 2015a) at three dolomitized Kalkaska County reefs.

A.6.2 Diagenetic Processes and Overprints in the Niagaran Reefs

Huh (1973) recognized six major types of diagenetic processes (cementation, dissolution, compaction, dolomitization, pore-filling, and hydrocarbon migration) and 27 diagenetic stages in the Niagaran and Salina A1 cores from Kalkaska, Otsego, and Grand Traverse Counties. Cercone (1984) and Cercone and Lohmann (1985, 1987) recognized 15 diagenetic processes in the Niagaran interval from the Shell Union 1-8 in Grand Traverse County. The relative timing of Cercone's diagenetic processes are summarized in Figure A-23. Note that this diagram does not address gypsum cementation, which according to Huh (1973), occurred after early replacive dolomitization, during A1 Carbonate deposition on the reef top.

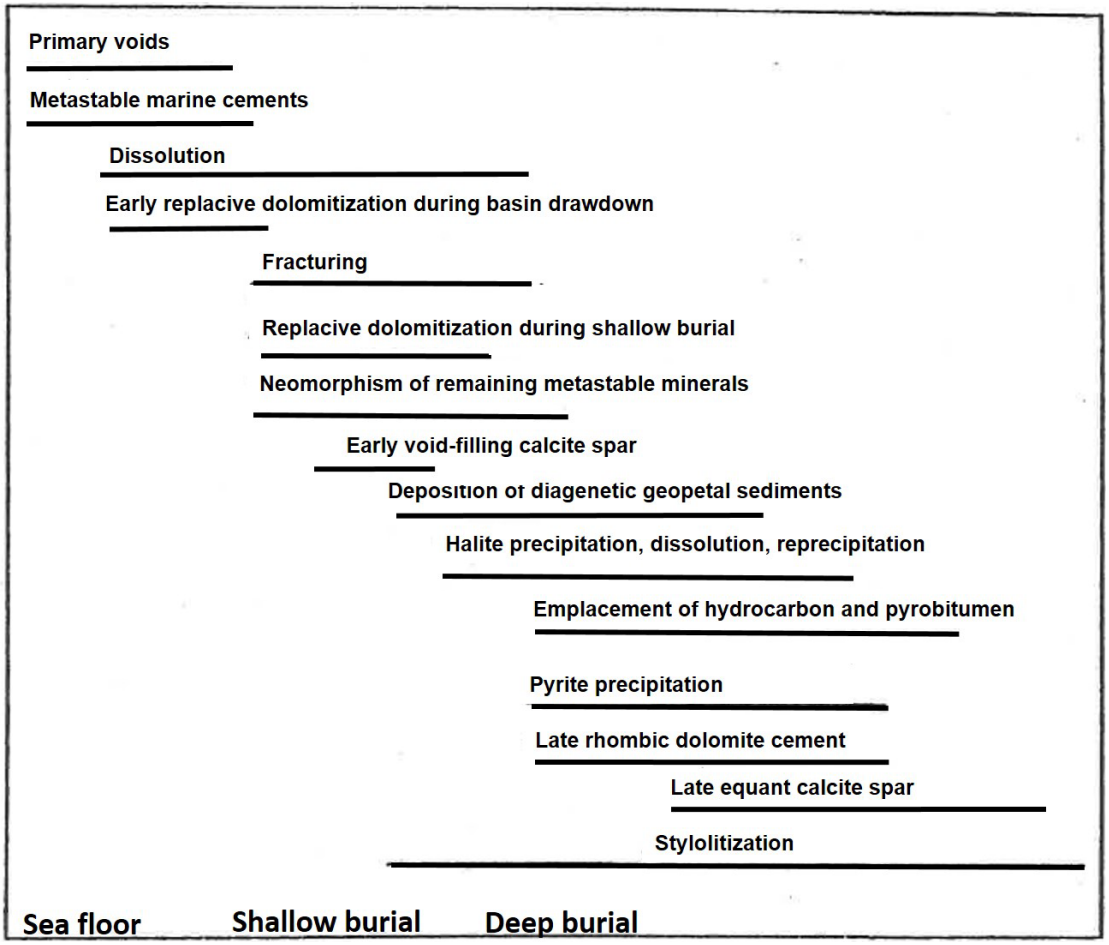


Figure A-23. Relative timing of diagenetic processes identified in the northern reef trend with increasing time towards the right. Modified from Cercone (1984) and Cercone and Lohmann (1985, 1987).

The following diagenetic processes and products are discussed in the following sections: early diagenesis and cementation; compaction, dolomitization and dolomite cements; formation of secondary porosity; anhydrite cement, halite pore filling, and miscellaneous diagenetic minerals and processes.

A.6.3 Early Diagenesis and Cementation

Early diagenesis includes seafloor processes and shallow burial processes in meteoric vadose and meteoric phreatic conditions, as well as processes that occur in mixing zones of marine and meteoric waters, and in shallow burial connate water environments. Post-depositional carbonate detrital components and marine cements include low Mg calcite, and the metastable cements high Mg calcite and aragonite, as well as high Mg micritic cements. Early diagenesis includes stabilization of high Mg calcite to low Mg calcite; and minor calcite, aragonite, and dolomite precipitation at grain contacts in the vadose zone. Caliche may accumulate in evaporative (vadose) surficial deposits (Huh, 1973). Phreatic meteoric diagenesis, as occurs during reef exposure and sea level drop, includes dissolution of high Mg calcite and aragonite (resulting in moldic or vuggy porosity) in updip locations, and stabilization of aragonite and precipitation of calcite if downdip phreatic environments exist (Moore and Wade 2013). Meteoric phreatic diagenesis is most active at the water table. If the phreatic meteoric zone is thin, aragonite and metastable minerals may survive, and karstic cavern formation will be limited.

Within a highstand marine (sea floor) environment, grainstones in windward reef accumulations may remain more porous if grains are coated with carbonate mud, otherwise they are often tightly cemented with isopachous or clotted-micritic (possibly bacterially-associated) marine cement. Trout (2012) reported both highest abundances of marine cement and highest abundances of visible porosity along the steep asymmetric margin of the Ray Reef, St. Claire County, in what she interpreted as windward reef facies.

Beach rock may form along the shoreline and has been interpreted by Battelle in at least one Niagaran core. In contrast, meteoric/marine mixing zone environments are undersaturated; and aragonite, high Mg calcite, and low Mg calcite will dissolve to form moldic, vuggy porosity, and cavernous reef-margin porosity. Replacive dolomite and dolomite cements may also form. Steep windward reef margins are conducive to the development of fractures at this stage (Moore and Wade, 2013).

Mixed siliciclastic/carbonate environments, and shallow carbonate depositional environments with abundant siliceous sponges or windblown quartz silt frequently develop quartz cements and chert. It should be noted that both quartz cements and chert are extremely rare in the pinnacle reefs, but are present in the older Niagaran platform carbonates in Ontario, where a mixed carbonate/quartz silt is present at the top of the biohermal carbonates (Smith et al., 1993).

Moore and Wade (2013) point out that early diagenesis of isolated steep-sided platforms during sea level rise (TST) following reef exposure includes minor marine cementation, dolomitization, and possible minor water table diagenesis. New highstand conditions may preferentially favor carbonate deposition on the windward margins, further accenting reef asymmetry, and arid conditions may cause minor reflux of dense evaporative brines, with precipitation of gypsum/anhydrite plus dolomite cement.

A.6.4 Burial Cementation

Most subsurface waters have very low Mg/Ca ratios (Moore and Wade, 2013). As sediments finally enter burial conditions, low Mg, low inclusion calcite cements may precipitate. These clear spar cements overgrow previously formed diagenetic minerals and cements and can occlude large intergranular and intragranular porosity in the form of syntaxial overgrowth cements of echinoderms. Cercone (1984) determined that in core from the Union 1-8 well from Grand Traverse County, low Mg calcite spar precipitation followed replacive dolomitization (see below) and filled much of the remaining primary porosity.

Burial diagenesis includes the replacement of low Mg calcite with dolomite, and depending on temperature, pressure and fluid chemistry, the continued precipitation of cements. Burial cements include saddle dolomite and calcite. Calcite cements are often Fe- and Mn-rich; and include large multi-pore poikilotopic forms. The cements grow slowly, as fluids evolve through rock/water interactions, and fluid flow tends to be slow, taking place over geologic time. The evolving fluids can reflect lithologies outside of the carbonate area, and oxygen and strontium isotopic signatures can provide important data on the burial environment and source of fluids (Moore and Wade, 2013).

A.6.5 Compaction

Compaction generally causes about 20% loss in porosity prior to lithification, but is the major factor influencing porosity in burial diagenesis (Moore and Wade, 2013). Dolostone resists compaction more than limestone, and presence of siliciclastic clay and organic content decrease resistance to compaction. Interpenetrating grains, stylolites, strain seams, and fractures are common compaction features (Schlumberger 2007).

Stylolites and wispy seams form from pressure dissolution, generally below a burial depth of about 1970 feet (Moore and Wade, 2013), and tend to develop at changes in texture, or increased silt/organic content. They are common in intertidal carbonates, interfaces between grain-rich and grain-poor lithofacies, in reef-debris flanking beds, and in more organic/silt rich maximum flooding zones. They may exist as localized occurrences, long parallel systems or long interconnected systems on scales of kilometers (Ben-Itzhak et al., 2014). Insoluble residues accumulate on irregular stylolitic surfaces and combined with reprecipitation of the carbonate, can generate thin horizontal permeability pathways; or vertical permeability barriers or baffles, sometimes across an entire reservoir (Schlumberger, 2007).

Reefal framestones and boundstones may exhibit little mechanical or pressure solution compaction (although they exhibit microfractures), in contrast to surrounding or underlying facies with higher carbonate mud content. Topographic relief across low-compacting depositional bodies may be accented (Moore and Wade, 2013), and early fractures may form within or between bodies with different resistance to mechanical and chemical compaction, as observable in the Pipe Creek Junior Silurian reef quarry in Indiana (Frank et al., 1993). Cercone (1984) identified fractures within the Shell Union1-8 (Grand Traverse County) Niagaran reefal cores filled with marine cements, confirming early lithification and fracturing.

Compaction and diagenesis of gypsum to anhydrite provides sources of calcium-rich burial fluids (Cercone, 1984). Fluid is also released during the compaction of fine grained muds and shaley intervals such as the poker chip lithofacies of the lower A1 Carbonate.

A.6.6 Dolomitization

Dolomite is both a mineral and a rock (preferred term is dolostone); and occurs both as an original precipitate, post-depositional cement and a replacement mineral. Dolomitization can create intercrystalline porosity and permeability; in contrast, multiple generations of replacive dolomitization, recrystallization or cementation can almost completely occlude porosity. Dolomitization of Niagaran reefs is primarily related to original depositional fabric/stratigraphic identity and original porosity/permeability character; as well as location in the basin, relative to updip sources of dolomitizing fluids; and proximity to faults/fracture systems and volumes of leaching and dolomitizing burial fluids. The following paragraphs describe general types of dolomitization, and timing of dolomitization and types observed in the Niagaran reefs.

Machel (2004) recognized eight main types of diagenetic dolomitization (Figure A-24): surface or near surface dorag; mixing zone of fresh and saline waters; two types of slope convection of normal seawater; and four types of burial diagenetic dolomitization. Surface or shallow burial dolomitization requires seawater or evaporated seawater with high fluxes, long lasting hydrologic flow; burial dolomitization requires large advective flow. As temperature increases, the Mg/Ca ratio required for dolomitization decreases (Grammer and Harrison, 2013).

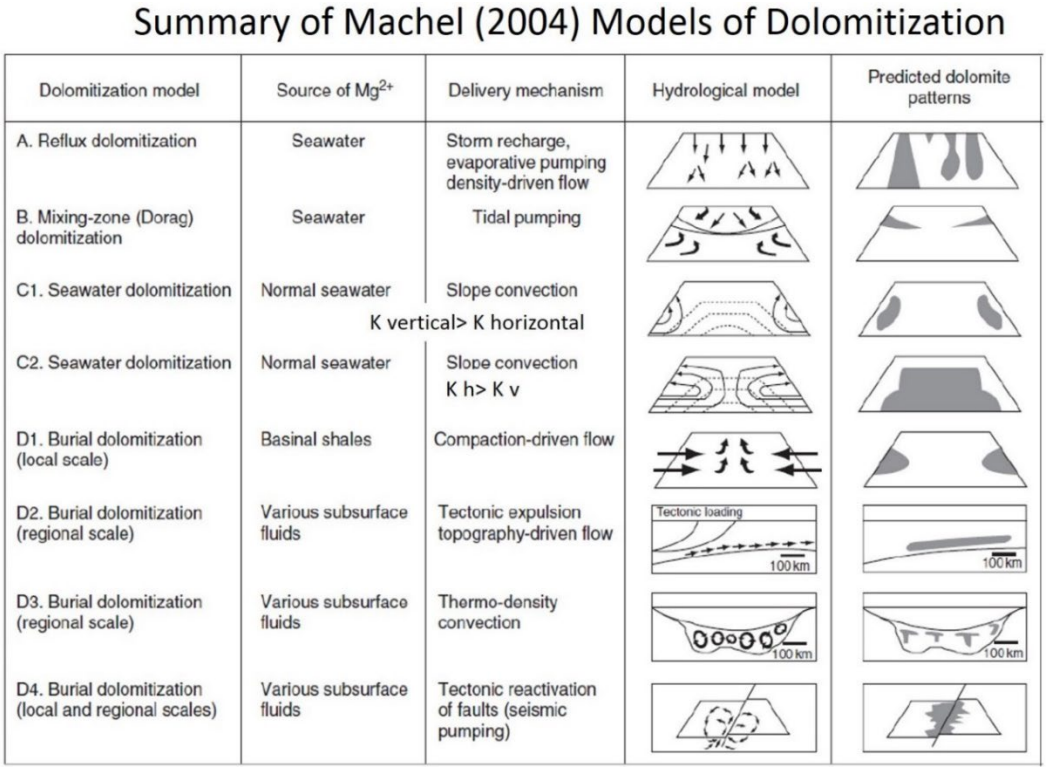


Figure A-24. Major types of dolomitization. Modified from Machel, 2004.

Because fluid temperatures above 70ºC can produce burial dolomitization, fluid migration pathways become the controlling factor on the spatial distribution of burial dolomitization (Grammer 2007). According to Machel (2004), localized burial dolomitization may be connected to expulsion of burial fluids from compaction of muddy or shaley deposits. This may be important in some of the reefs but is largely unexplored. Regional dolomitization may be linked to tectonic expulsion of burial fluids; basin-scale, thermo-density convection; and basinal fluid flow due to reactivation of faults (seismic pumping). With increased temperature, burial dolomitization features exhibit textures and mineralogies associated with hydrothermal (thermobaric) dolomitization, discussed separately. Hydrothermal fluids are defined as those hotter than the surrounding bedrock (Davies and Smith, 2006). The origin of dolomite formation can be aided by analysis of oxygen and strontium isotopes, as well as by fluid inclusion data (Grammer, 2007).

It should be noted that dolomite is metastable and susceptible to dissolution, recrystallization or replacement by calcite, anhydrite, or silica, which can completely destroy visible history of the rock fabric. Huh (1973) documented dedolomitization fabrics in the upper part of the Niagaran reefs of Kalkaska County. In addition, Murray and Pray (1965) found that limestones that have been 80-90% replaced by dolomite have the highest permeabilities. This permeability enhancement is dependent upon original rock fabrics and the distribution of other minerals in the rock (Schlumberger, 2009).

Texture is an important indicator of quality of dolostone reservoirs. Crystal boundary relationships have been used to classify textures into planar and nonplanar. Planar crystal textures include the subdivisions of euhedral and subhedral, with subhedral textures exhibiting more crystal face contact and less porosity. Woody et al. (1996) demonstrated that planar euhedral crystalline (sucrosic) textures, which commonly form in shallow burial diagenetic environments, have a strong relation between porosity and permeability. Nonplanar dolomite textures, which generally form in the subsurface at temperatures in excess of 50°C (Schlumberger, 2009) have no relationship between porosity and permeability. Instead, reservoir quality in nonplanar dolostones is dependent upon development of vuggy porosity and fractures.

Dolomitization of the Niagaran Reef Interval

Dolomitization of the Niagaran interval includes early reflux and mixing zone dolomite cementation during subaerial exposure, and much more pervasive dolomitization by updip, refluxing brines (Cercone, 1985; Grammer, 2007), during shallow burial (Cercone and Lohmann, 1985). Recent work by Rine et al. (2015b) suggests that differences in original porosity and permeability may cause Niagaran reef core lithofacies to dolomitize more readily than muddier leeward grain apron facies; and dolomitized coarser-grained fill in burrowed carbonates can preferentially exhibit higher porosity and permeability (Gingras, et al., 2004; Grammer et al., 2014). In contrast to regional dolomitization, late stage burial dolomitization often shows a relation to fracture and fault related fluid flow, as documented by carbon isotope and fluid inclusion data (Cercone and Lohmann, 1987).

The regional distribution pattern of dolomite in the Niagaran reefs is shown in Figure A-25. Within an area that has both dolostone and limestone, original low permeability lithofacies tend to retain a higher limestone content (Grammer, 2007). Original low permeability/anhydritic tidal flat facies may act as permeability barriers for “surface-down” dolomitization. Figure A-26 illustrates differences in dolomite distribution in three wells from the Chester 16 reef, and Figure A-27 compares the porosity/permeability relationships in dolomite and limestone samples from the reef core depositional facies in the Chester 16 and Chester 21 reefs.

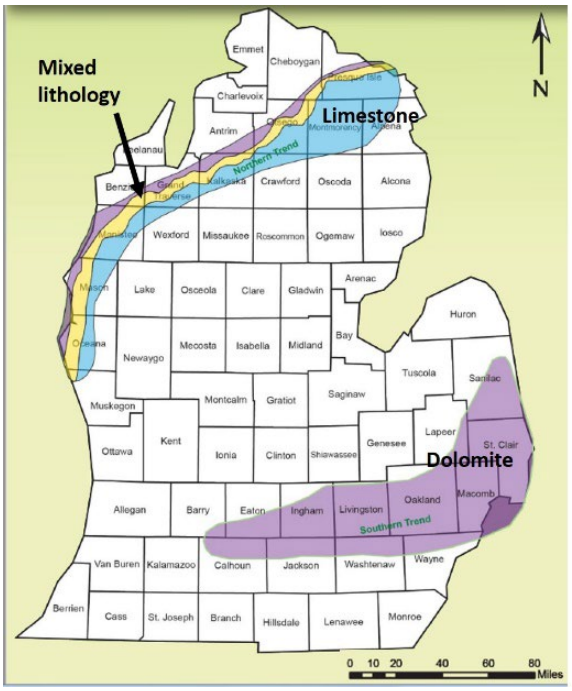


Figure A-25. Generalized distribution of carbonate lithologies in the Niagaran reefs. Modified from Rine 2015b.

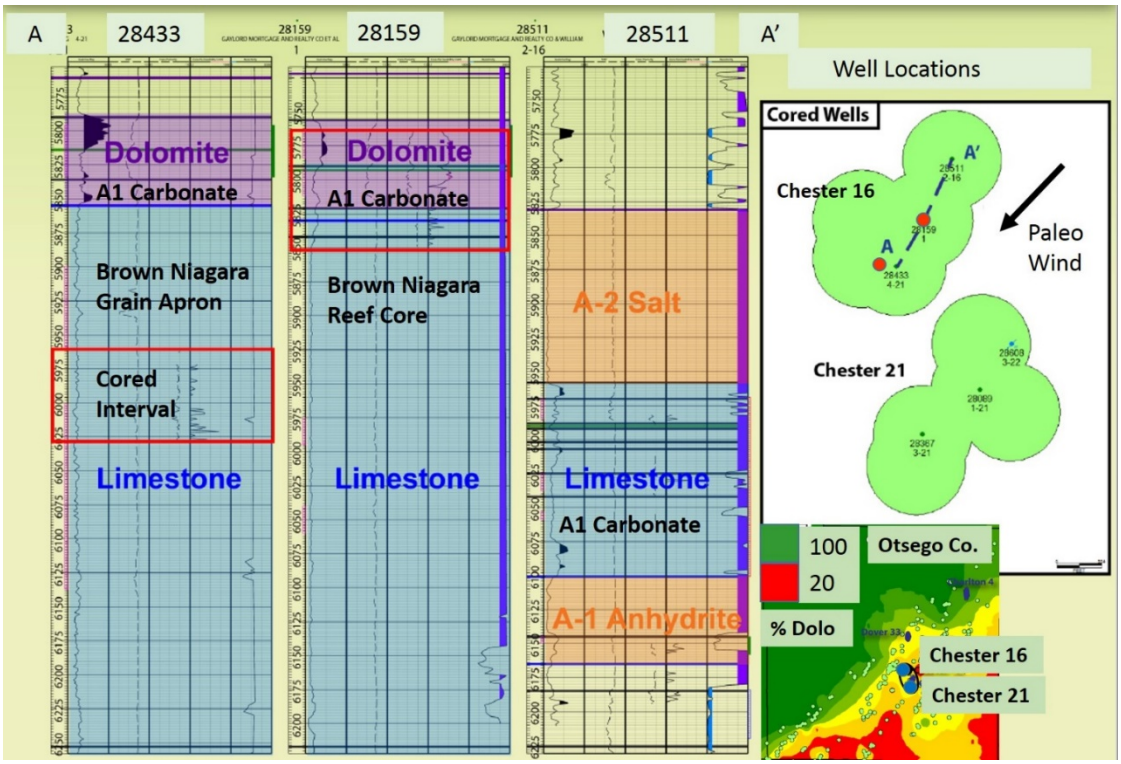


Figure A-26. Distribution of limestone and dolomite lithology in three wells from the Chester 16 reef. Modified from Rine 2015b.

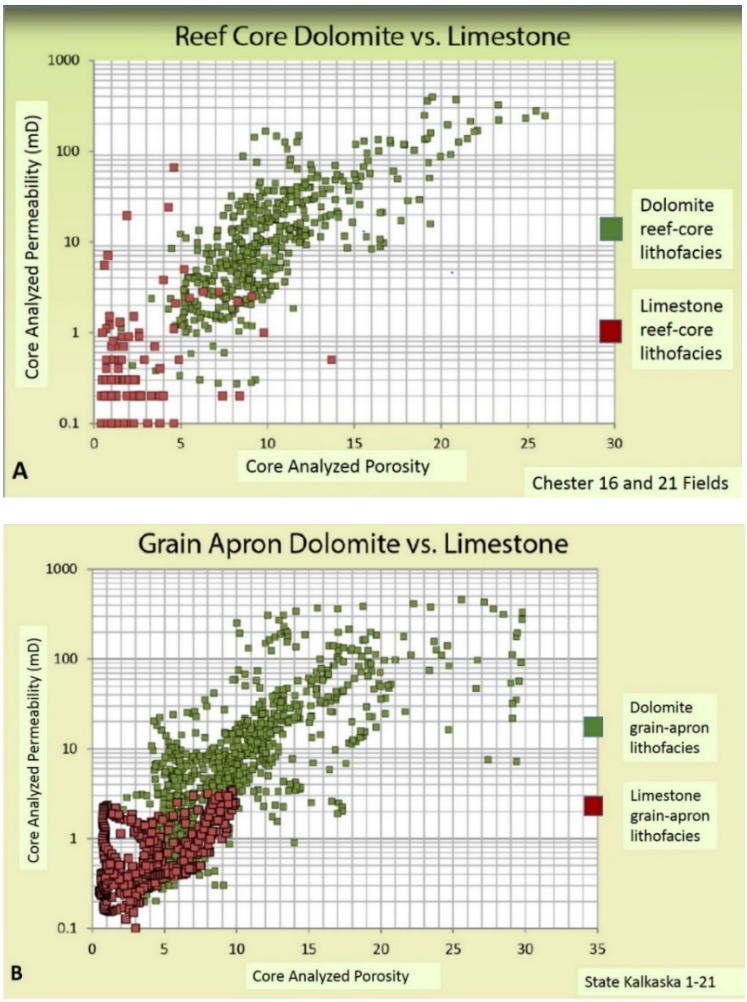


Figure A-27. Comparison of Niagaran reef porosity and permeability in dolomite and limestone whole core samples, grouped by (A) reef-core and (B) leeward grain-apron depositional facies. The Kalkaska 1-21 (28676) is located in Kalkaska County. Modified from Rine, 2015b.

A.6.7 Anhydrite Cements and Salt Plugging

Anhydrite cements commonly reduce or occlude porosity and permeability in on-reef algal/microbial associated lithofacies (often thin limestones) of the A-1 carbonates, as well as in some tidal-flat related lithofacies of the uppermost part of the Brown Niagaran. Huh (1973) concluded that gypsum precipitation occurred during deposition of the upper A1 Carbonate. Timing of conversion of gypsum to anhydrite was not addressed by Huh (1973) or Cercone (1984), but in the Permian basin, appears to occur below a burial depth of a few hundred feet (Murray, 1964).

Hydrothermal induced reaction of sulfates and hydrocarbons can result in the dissolution of anhydrite and the precipitation of baroque (saddle) dolomite. The change from precursor gypsum into anhydrite can release volumes of calcite-rich brines (Cercone, 1984). The presence of anhydrite cements in carbonate increases density and decreases neutron porosity readings.

Salt plugging partially or incompletely occludes porosity in both northern (Huh, 1973) and southern reefs (Rine, 2015a); and may occur in the upper (Berlin reef, St. Claire County), lower (Ray reef, Claire County) or flanks of the reefs (Ells, 1963), as well as in voids in the on-reef A1 Carbonate (Huh, 1973). In petrophysical logs, the presence of halite sharply lowers density, increases density porosity, and decreases neutron porosity. The relation of salt plugging to permeability is shown in Figure A-28 for the reef interval in the Columbus III reef.

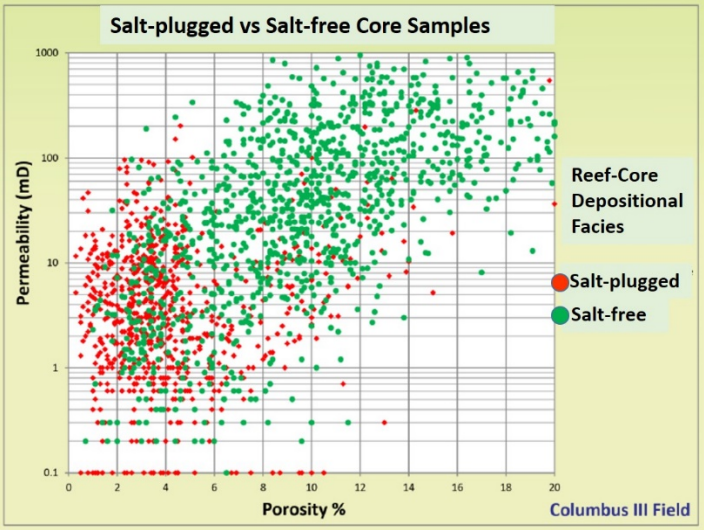


Figure A-28. Effect of salt plugging on reef-core samples from the Columbus III field in the Southern Reef Trend. Modified from Rine, 2015b.

The Salina A2 evaporites consist of anhydrite over the pinnacle reefs, and halite on the distal flanks and in the basin center. These flanking halites are thought to be the source of salt plugging within the Niagaran carbonates, percolating in through fractures. Salt plugging does not usually occlude all porosity; blocky halite cement commonly overlies calcite spar cement in incompletely filled primary pores (Cercone, 1984). Salt plugging appears to have undergone several episodes of precipitation, recrystallization, dissolution and reprecipitation, both before and after hydrocarbon emplacement (Huh, 1973; Cercone and Lohmann, 1987).

A.6.8 Hydrothermal Alteration and Relation to Structure

Hydrothermal (thermobaric) fluids are those that are, at least temporarily, above temperatures and pressures of the surrounding rock (Davies and Smith, 2006). There is a range of processes and fabrics that result from different temperature and pressure regimes and include formation of lead/zinc ore bodies in basinal shale host rock; Mississippi Valley Type (MVT) lead/zinc/dolomite in limestone host rock; as well as structurally controlled hydrothermal dolomite (HDT) with rock fabrics and porosity development influenced to some degree by lateral depositional lithofacies. An awareness of HDT processes and products are of importance in characterizing reservoir and seal potential of the Silurian reefs.

The presence of a hydrothermal setting can be confirmed by stable isotope analyses and fluid inclusion homogenization temperatures (Grammer, 2007). Michigan basin hydrothermal diagenesis has been documented not only in the Silurian Niagaran reefs, but also the in the St. Peter Sandstone, Trenton/ Black River, Burnt Bluff, Bass Islands, and in the Dundee (the most prolific hydrocarbon producer in the Michigan basin) (Barnes et al., 2008). Areas that have documented hydrothermal alteration and dolomitization in northern Michigan are shown in Figure A-29 and include the Bass Islands Dolomite in the State Charlton 4-30 in Otsego County (Barnes et al., 2008). Trenton/Black River homogenization temperatures have been measured between 110-160^{o}C in the Michigan basin (Davies and Smith, 2006)

Hydrothermal dolomite development in the Michigan basin is generally proximal to NW-SE and NE-SW Reidel shears along basement-rooted faults and may be associated with seismic sags (Grammer 2007; Grammer et al., 2014). HDT dolomite fabrics tend to develop along vertical pods near fractures and expand laterally in more permeable zones.

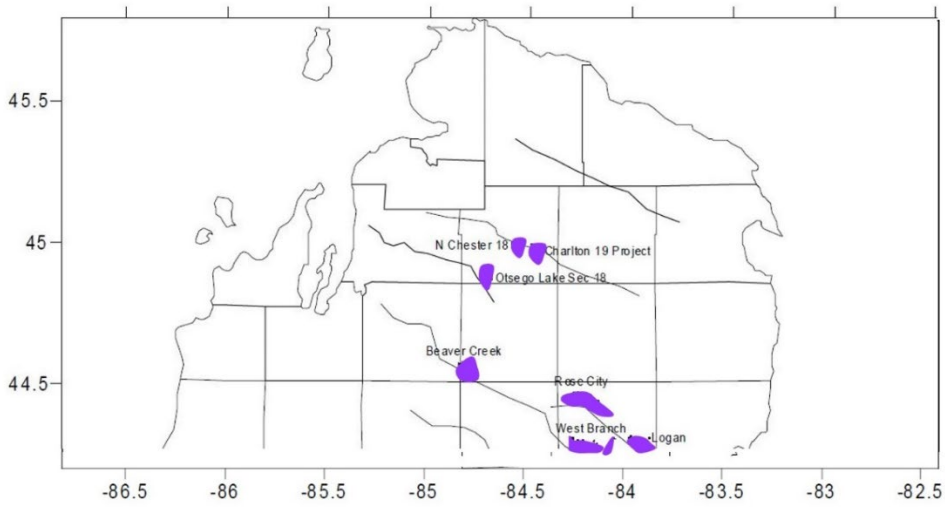


Figure A-29. Faults and documented hydrothermal dolomite in Northern Michigan fields. Modified from Woods and Harrison (2002).

Fluid pathways for dolomitizing basinal fluids through stratigraphic or regional aquifers, and the presence of original lithofacies that possess permeability are important factors in distribution of regional hydrothermal diagenesis (Barnes et al., 2008). In basins where sandstone is a fluid carrier bed, considerable chert/chalcedony/silica cements may precipitate in the dolomites (Davies and Smith, 2006). Hydrothermal fault-associated dolomitizing fluids in the Michigan basin have smaller volumes than regional dolomitizing fluids, and silica cement is extremely low in the Silurian reefs (Huh, 1973; Cercone, 1984; Ritter, 2008).

Structurally-related fluid advection along faults and fractures generally starts with intrusion of undersaturated brines and leaching of limestone and dolostone, followed by matrix dolomitization, hydraulic brecciation and later fluids precipitating saddle dolomite cements (Machel, 2004; Davies and Smith, 2006). This may result in porous and brecciated dolostone near fault zones, surrounded with a halo of tightly cemented dolostone and leached or cemented limestone (Grammer et al., 2014)

Hydrothermal alteration products and processes may include multiple episodes of the following:

- Leaching of limestone, dolomite and other minerals, (including development of microporosity),
- Matrix replacive and fracture-filling dolomite, often with curved “saddle” morphology,
- Recrystallization of limestone and dolostone,
- Precipitation of cements surrounding a proximal dolomitized zone,
- Bedded and fracture-filling chert and chalcedony,
- Dilational breccias and fractures,
- Shear microfractures
- Pore- and fracture-filling anhydrite, calcite, ferroan calcite, drusy quartz, smoky quartz, fluorite, barite, bitumen, authigenic clay minerals, sphalerite, and other sulfides.

Keister (2018) identified fluorite and barite in fractures from the Niagaran interval fin a well in the Dover reef, along with minor replacive potassium feldspar. Huh (1973) identified two morphologies of sphalerite in the Kalkaska reef; these were present only in cores from the bioherm and lower organic reef facies.

A.6.9 Dissolution and Karst

Dissolution

Dissolution products include moldic porosity, vug formation, and fracture enlargement. Occurrence and controls include original mineralogy, and the solubility of the depositional and diagenetic rock fabric. Carbonate dissolution results from contact with undersaturated water, which includes exposure to meteoric water as well as acidic fluids expelled during hydrocarbon generation and deep burial (Moore and Wade, 2013). Pressure related dissolution can result in porosity parallel to pressure seams and incipient fractures, as well as the formation of stylolites, which if perpendicular to fluid flow, may or may not negatively affect permeability (Heap et al., 2013; Ben-Itzhak et al., 2014). Precipitation of carbonate is negatively impacted by the presence of hydrocarbons, and the formation and distribution of stylolites differ before and after hydrocarbon emplacement (Barata, 2011).

Karst

Meteoric karst features form at the interface of the phreatic and vadose zones- i.e., the top of the water table, and are common at or near exposure surfaces, unless the water table is at some depth below the surface. In such cases, limestones tend to develop karst pipes and solution enlarged fractures that extend from the surface to the water table. Rock fabrics formed by karst include in-place, rotated and chaotic breccias, terra rossa and cavern fill, and fractured wall-rock (Loucks et al., 2004). Over time, cavern systems may track falling or rising water tables. Karst features may preferentially form along fracture/joint systems, and may be reactivated by recurrent fracturing or faulting, resulting in multistage coalesced karst features (Loucks et al., 2004). Buried caverns tend to collapse and fill with sediment and carbonate cements (often dolomitized). The resulting karst-related reservoirs may be dominated by fractures. Mixing zone karst may form vuggy or cavernous hydrocarbon reservoirs at reef and platform edges (Dou et al., 2009)

Smith et al. (1993) recognized eight episodes of exposure and karst in reservoirs in the Silurian Fletcher platform, and the Rosedale and Terminus pinnacle reef fields of western Ontario. They recorded thin (up to 6 feet) zones of collapse breccias and overlying paleosol horizons as the most common features. Cavities were partially filled with vadose, phreatic, marine or late-stage calcite, halite and anhydrite cements, and more rarely pyrite and gilsonite. The exposure surfaces compartmentalize reservoirs at three cored fields through evaporite plugging, karstic crusts and paleosols, post- karst marine cements; along with the low permeability stromatolite facies and nodular anhydrite at the top of the Guelph Formation.

Karst breccia fabrics are relatively minor in cored reefs of the Northern Reef Trend, and do not appear to indicate extensive cavern development. Minor karst diagenesis is associated with likely fourth-order exposure surfaces within the reef core interval examined by Ritter (2008). Karst voids and breccias are most common below the top of the Brown Niagaran, and are generally less than 20 feet thick (Ritter, 2008; Wold, 2008; Rine 2015a).

A.6.10 Miscellaneous Diagenetic Mineralization and Processes

Pyrite Mineralization

Pyrite mineralization occurs in reducing conditions, which can be very localized. Huh (1973) reported pyrite occurring as two forms, microcrystalline and massive in his biohermal and organic reef facies. Microcrystalline pyrite was most common along stylolites and small dissolution channels; massive pyrite was commonly associated with vugs, coating late stage dolomite rhombs and gilsonite. The presence of pyrite can decrease resistivity.

Mineralization Associated with Hydrocarbon Generation and Migration

Entry of hydrocarbons into pore systems reduces water saturation and inhibits carbonate cementation; cementation in macropores may cease. When this is combined with continued (typically ferroan calcite) cementation below the oil/water contact, hydrocarbon reservoirs may be baffled or separated from regional hydrodynamic flow (Barata, 2011).

In the Michigan basin, hydrocarbon generation and migration occurred between the Mississippian and Middle Jurassic Periods (Cercone and Lohmann,1987). Huh (1973) interpreted the origin of microcrystalline plus massive yellow sphalerite, pyrite and gilsonite in core samples in his biohermal and lower organic reef facies as being associated with hydrocarbon migration.

Diagenetic Alteration of Wettability

Wettability refers to balance of surface and interfacial forces that result in the affinity of a given solid to be in contact with one fluid rather than another. A water-wet rock with have greater relative permeability to water than to oil, and water-wet reservoirs tend to have thicker transition zones. Although most sandstone reservoirs are strongly water-wet (preferential attachment of rock to water), diagenesis commonly changes water-wet carbonates into mixed wet or oil-wet rocks, which affects their behavior during water floods and reduces sweep efficiency (Schlumberger, 2002). Quartz, calcite and dolomite tend to be water wet prior to oil migration. Carbonate microporosity tends to stay water-wet; pores are usually filled with irreducible water saturation (Schlumberger, 2007). Diagenetic factors that change wettability appear to be most related to hydrocarbon generation or migration and formation of bitumen/pyrobitumen or gilsonite.

A.7 Implications for Constructing Static Models

Structure and Location in Basin

Much of the porosity in the Niagaran reefs is secondary, and both structure and location in the basin have profound influence on lithologies, diagenesis, and associated porosity and permeability development and retention, as well as on height of the reefs and thickness of hydrocarbon column. Rapid changes in the anhydrite/halite composition of the Niagaran and Salina evaporites surrounding the reefs make the acquisition of a full suite of density and acoustic logs critical in calibration and seismic mapping of reservoir boundaries.

Role of Sequence Stratigraphy

In many carbonates, the identification of regional unconformity surfaces or specific systems tracts (TST, HST) is key to predicting porosity development (Kerans and Tinker, 1997), particularly in ramp and platform settings. Carbonates deposited during transgressive systems tracts often have higher carbonate mud content and lower permeability (Grammer, 2010). Ritter (2008) concluded that porosity development was optimized beneath third order sequence boundaries, and that tops of fourth order sequences tend to have reduced porosity and permeability. Grammer (2007) also found that porosity and permeability spikes occurred near the tops of some high frequency (4^{th} and 5^{th} order) packages in the Miller-Fox 1-11 (33500) in Oceana County. However, that model does not uniformly apply to the Niagaran and Lower Salina carbonates. The top of Sequence 1 as most recently interpreted in the Niagaran reef studies is coincidental with an exposure unconformity, or correlative conformity on top of the bioherm. Porosity development is due to early dolomitization and depends on location of the individual bioherm with respect to the margin of the basin and the hydrologic flow of dolomitizing fluids. The top of Sequence 2 is nearly coincidental with the top of the Brown Niagara, and enhanced porosity and permeability is associated with both karsting and dolomitization. On the reef flanks, the top of Sequence 3 is at or near the Rabbit Ears Anhydrite (REA), and is correlative on-reef to an unconformity within the A-1 Carbonate. This boundary is a vertical flow barrier between the off-reef lower and upper A1 Carbonate. Sequence 4 is the relatively thin upper A-1 Carbonate above the REA. On-reef the A1 Carbonate Sequence 4 contains thin reservoirs and is usually anhydrite cemented near the top. Off-reef, grain size and permeability in sequence decrease away from the reef. Third and fourth order sequence membership is important for populating lateral layers in reservoir models of the A-1 Carbonate. Currently, depositional facies/geobody membership (windward versus leeward reef flank; reef core) appears to be the soundest predictor of petrophysical property architecture within Sequences 1 and 2. This combination of stratigraphic/depositional framework is recommended for developing static earth models for the evaluation of the Michigan Niagaran reefs and the A1 Carbonates.

Role of Depositional Facies and Diagenesis

Identification of depositional facies (Rine, 2015a) that recognize differences in original mineral components, textures, and porosity, related to water depth and energy, provide a framework for reservoir and seal architecture within a sequence stratigraphic framework. This framework is valuable for exploring, grouping and predicting petrophysical fabrics and properties used to populate a static earth model (Suhaimi, 2016).

Diagenetic overprints of the Silurian reefs may be confined to or may cross depositional and stratigraphic boundaries. These overprints include cementation, compaction, dolomitization, dissolution, anhydrite and halite cementation, and fracturing associated with surface, near surface and deep burial diagenesis. The presence of evaporite cements in carbonates requires careful petrophysical analysis. Analysis of post-diagenetic petrophysical fabrics and improved prediction of relation of porosity to permeability includes assessing proportions and distribution of porosity types and connectivity. Abundance of microporosity creates a difference between total and effective porosity, and affects reservoir sweep; note that high water saturation in zones of microporosity may still produce low water-cut oil (Schlumberger, 2007). The area of permeability prediction is being actively improved through MICP, dielectric measurements, and other core analyses, as well as modern logging techniques and integrated imaging techniques.

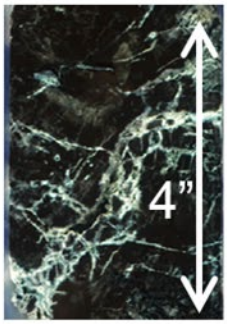
Appendix B.
Detailed Core Descriptions and Photographs

Appendix B provides the photographs and core descriptions for the Lawnichak 9-33 (Dover 33 reef), Chester 8-16 (Chester 16 reef), and Chester 6-16 (Chester 16 reef). The descriptive analyses used the same lithology, sedimentary structure, and diagenesis nomenclature as described in Figure B-1 and Figure B-2.

Lithology Log Legend

- Limestone (~0-10 %POR)
- Limestone (~10-20 %POR)
- Vuggy Limestone
- Dolomitic Limestone
- Vuggy Dolomitic Limestone
- Dolomite
- Porous Dolostone
- Heavy Mineral/Anhydrite
- Plug/Fracture/Rubble

Detail Photo



Abbrv.	Explanation
AL	Algal laminations
ANH	Anhydrite
B	Breccia
BM	Biologic Material
BU	Burrows
FF	Filled fractures
FP	Framework porosity
FP	Flat Pebble clasts
MP	Moldic porosity
OF	Open fractures
OS	Oil stain
PV	Pyrite Filled Vug
R	Rubble/broken core
SLT	Salt
STM	Stromatoporoid
STY	Stylolites
V	Vugs

Figure B-1. Nomenclature and symbology used to describe whole and sidewall cores analyzed under tasks 3, 4, and 5.

Abbrv.	Explanation
AL	Algal laminations
ANH	Anhydrite
B	Breccia
BM	Biologic Material
BU	Burrows
FF	Filled fractures
FP	Framework porosity
MP	Moldic porosity
OF	Open fractures
OS	Oil stain
PV	Pyrite Filled Vug
R	Rubble/broken core
SLT	Salt
STM	Stromatoporoid
STY	Stylolites
V	Vugs

Figure B-2. Rotary sidewall core (RSWC) abbreviation explanation

B.1 Lawnichak 9-33

B.1.1 Whole Core

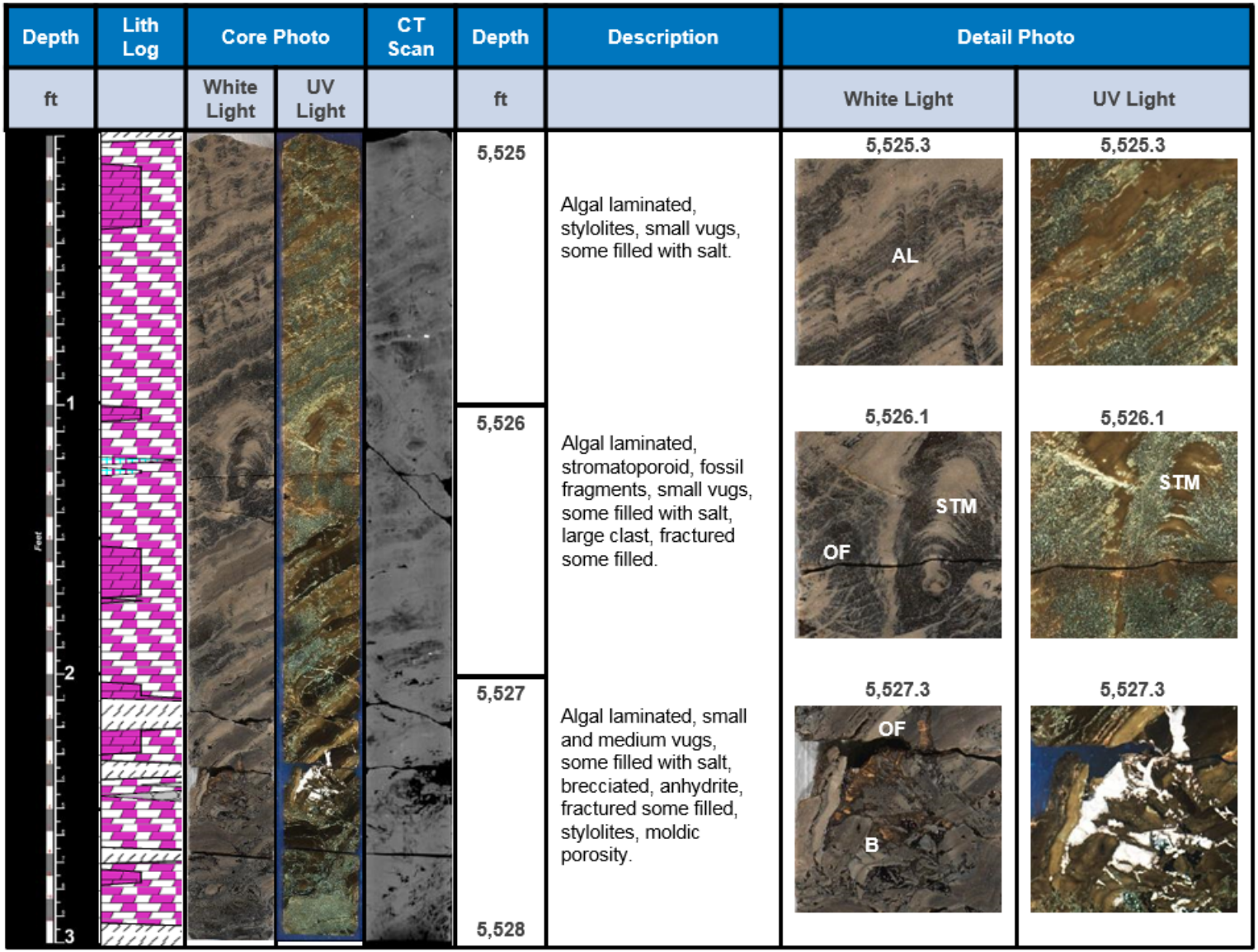


Figure B-3. Compiled illustration of lithology log, core photos (UV and white light), CT scan image, core descriptions, and annotated core images of the A-1 Carbonate for depths 5,525 ft. to 5,528 ft.

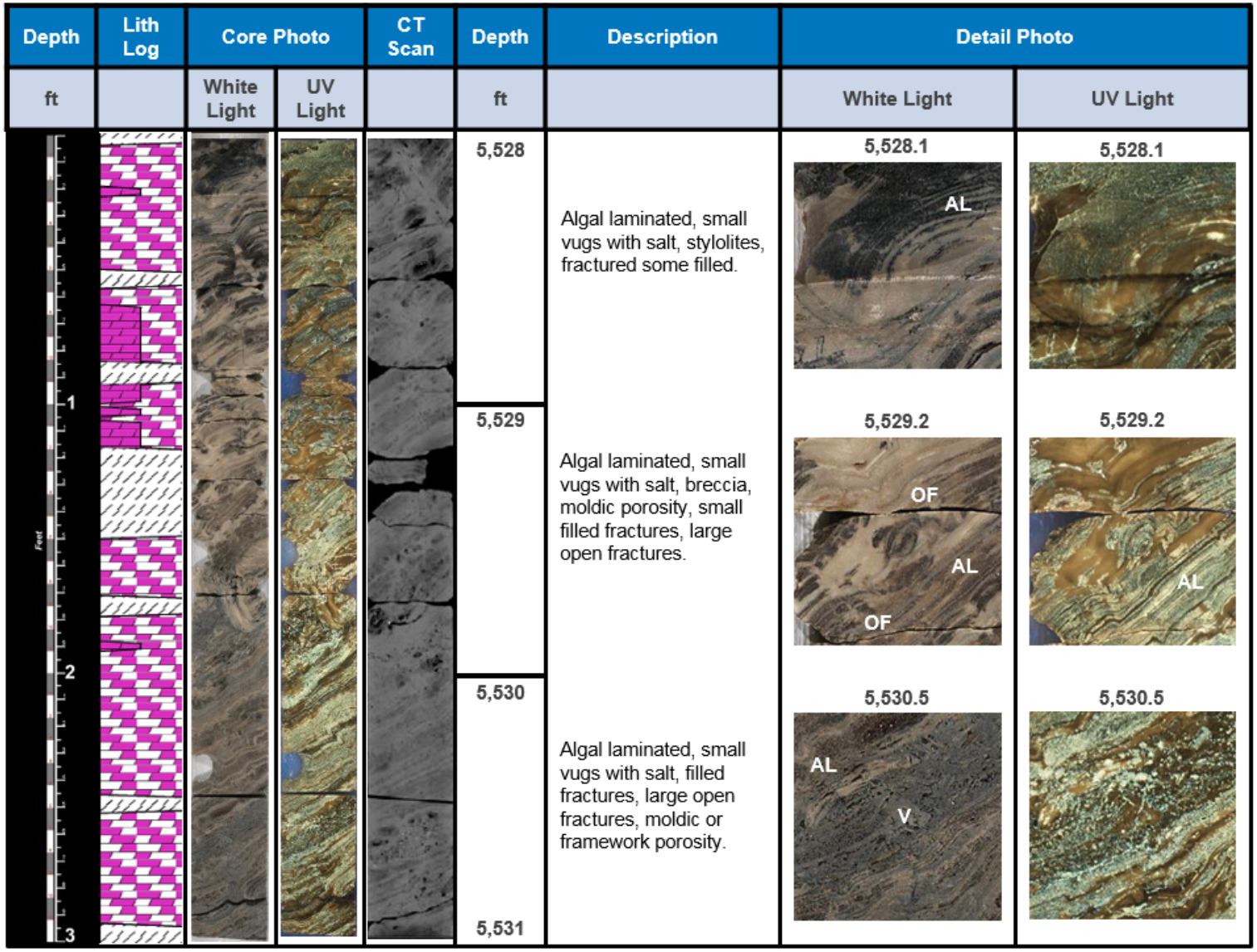


Figure B-4. Compiled illustration of lithology log, core photos (UV and white light), CT scan image, core descriptions, and annotated core images of the A-1 Carbonate for depths 5,528 ft. to 5,531 ft.

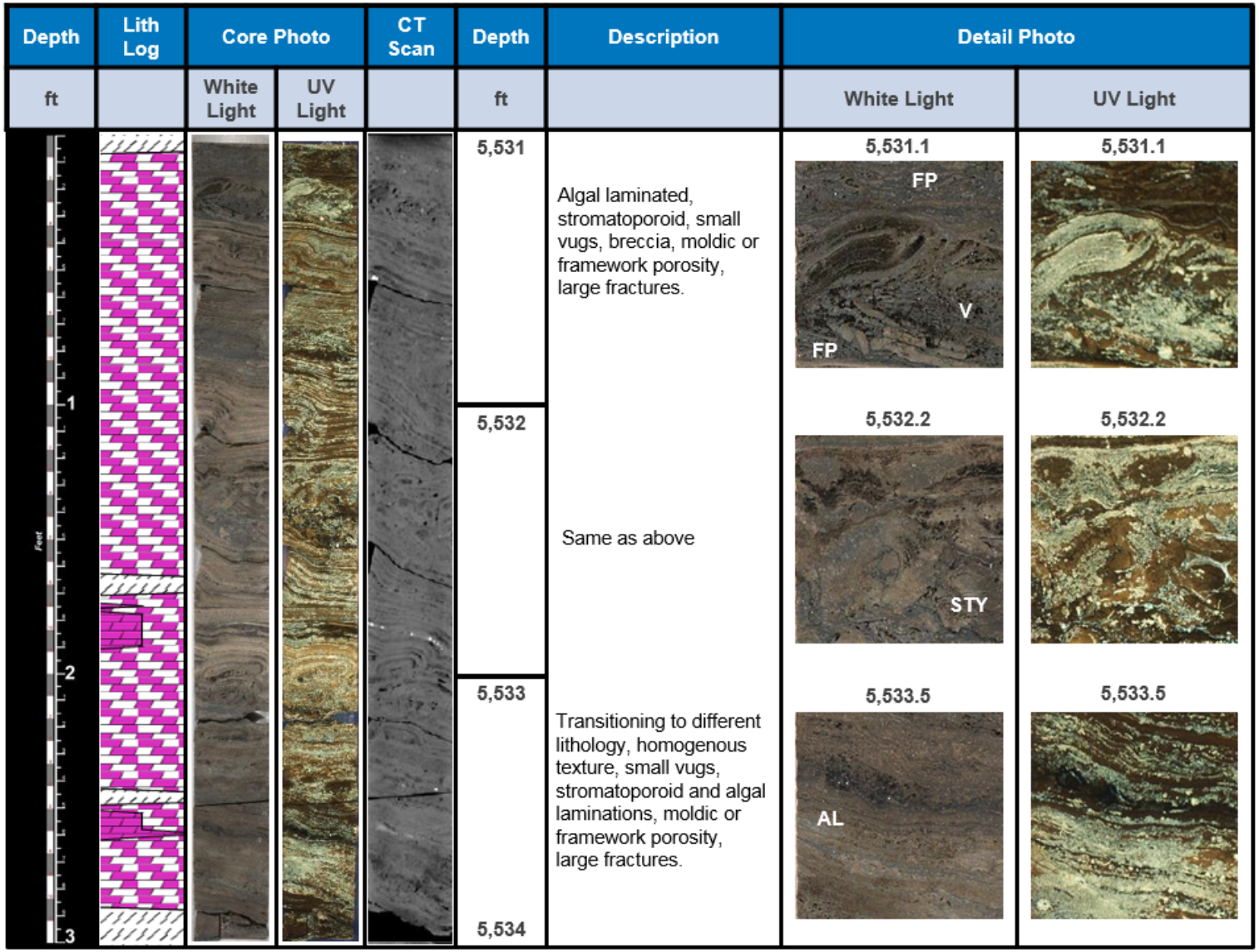


Figure B-5. Compiled illustration of lithology log, core photos (UV and white light), CT scan image, core descriptions, and annotated core images of the A-1 Carbonate for depths 5,531 ft. to 5,534 ft.

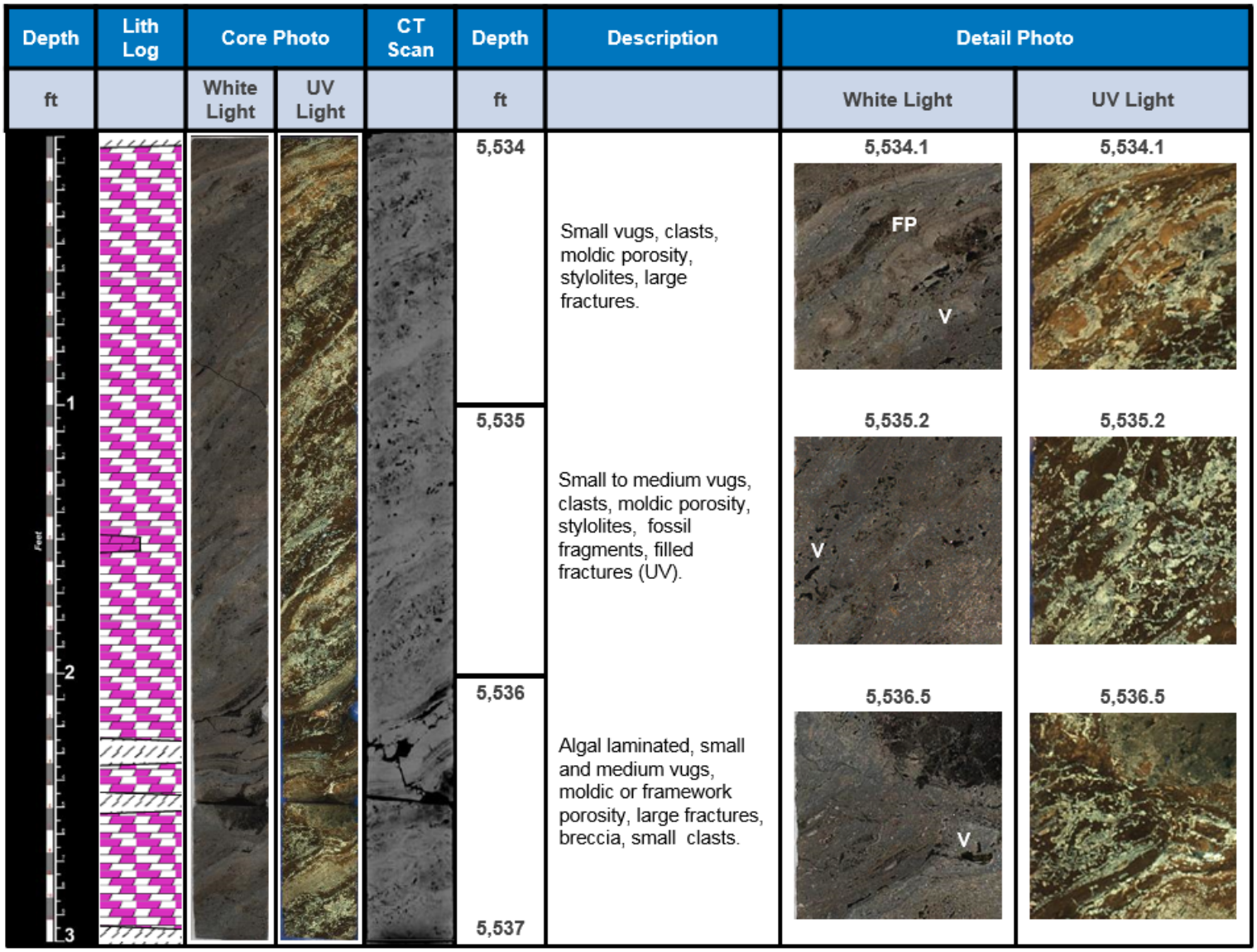


Figure B-6. Compiled illustration of lithology log, core photos (UV and white light), CT scan image, core descriptions, and annotated core images of the A-1 Carbonate for depths 5,534 ft. to 5,537 ft.

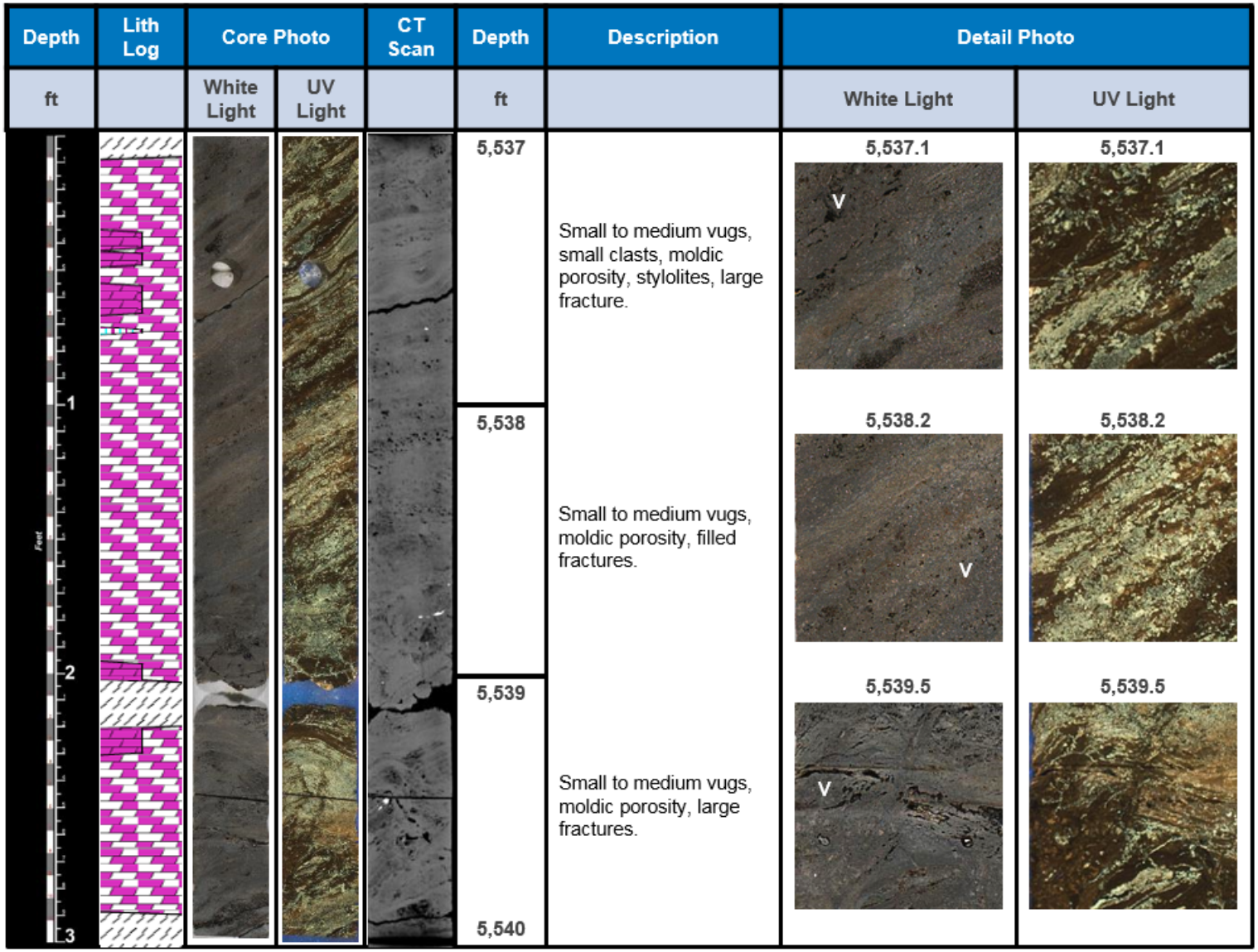


Figure B-7. Compiled illustration of lithology log, core photos (UV and white light), CT scan image, core descriptions, and annotated core images of the A-1 Carbonate for depths 5,537 ft. to 5,540 ft.

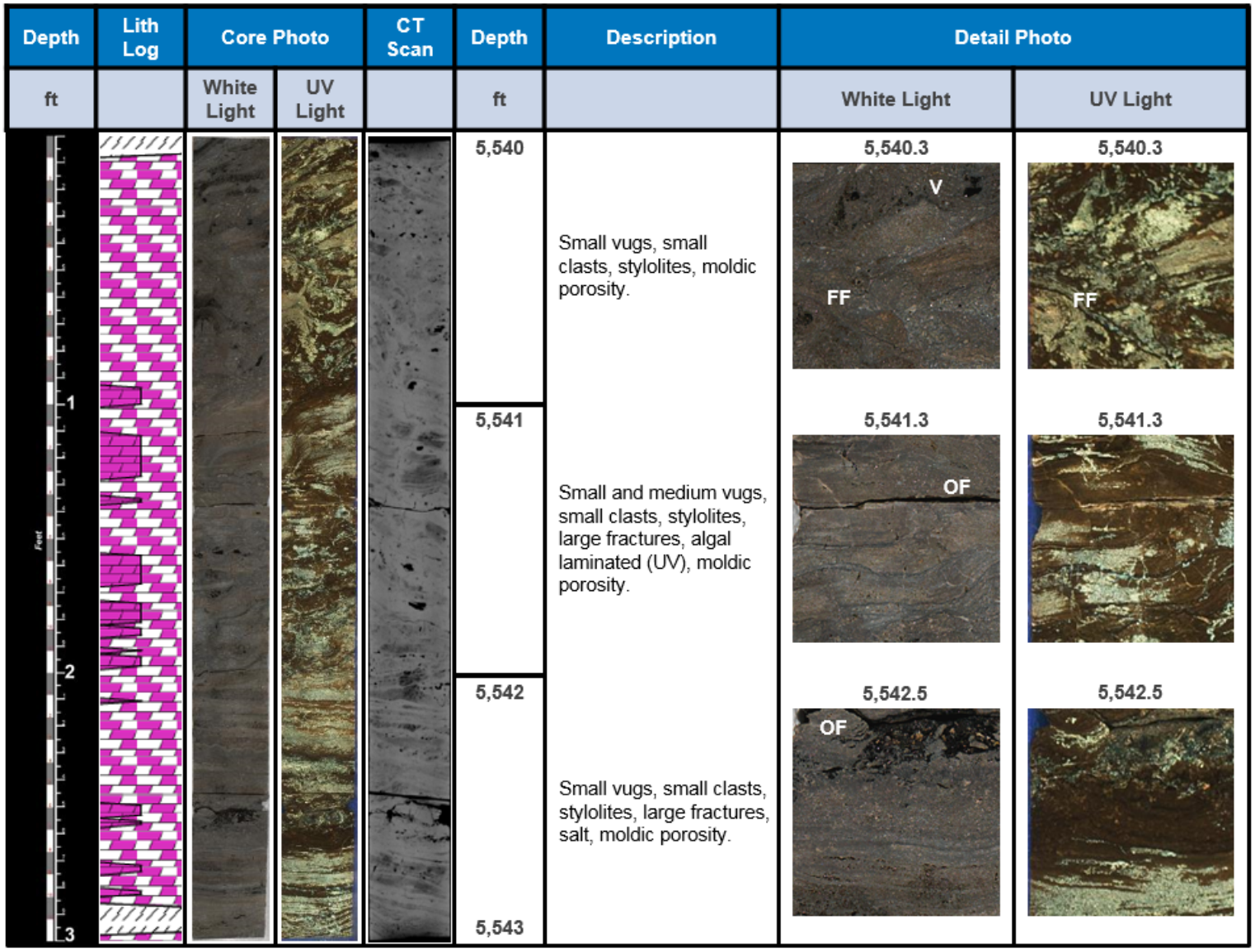


Figure B-8. Compiled illustration of lithology log, core photos (UV and white light), CT scan image, core descriptions, and annotated core images of the A-1 Carbonate for depths 5,540 ft. to 5,543 ft.

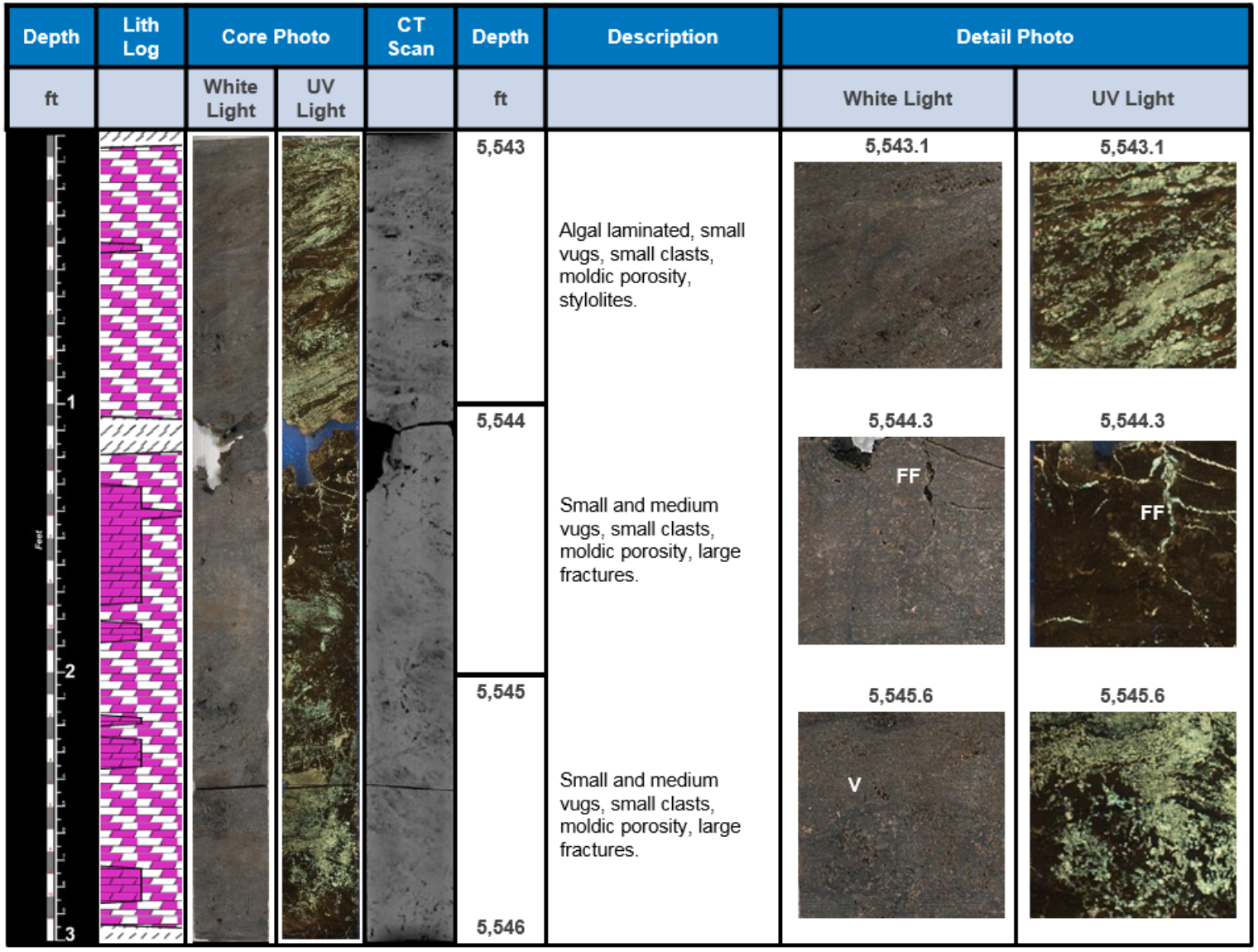


Figure B-9. Compiled illustration of lithology log, core photos (UV and white light), CT scan image, core descriptions, and annotated core images of the A-1 Carbonate for depths 5,543 ft. to 5,546 ft.

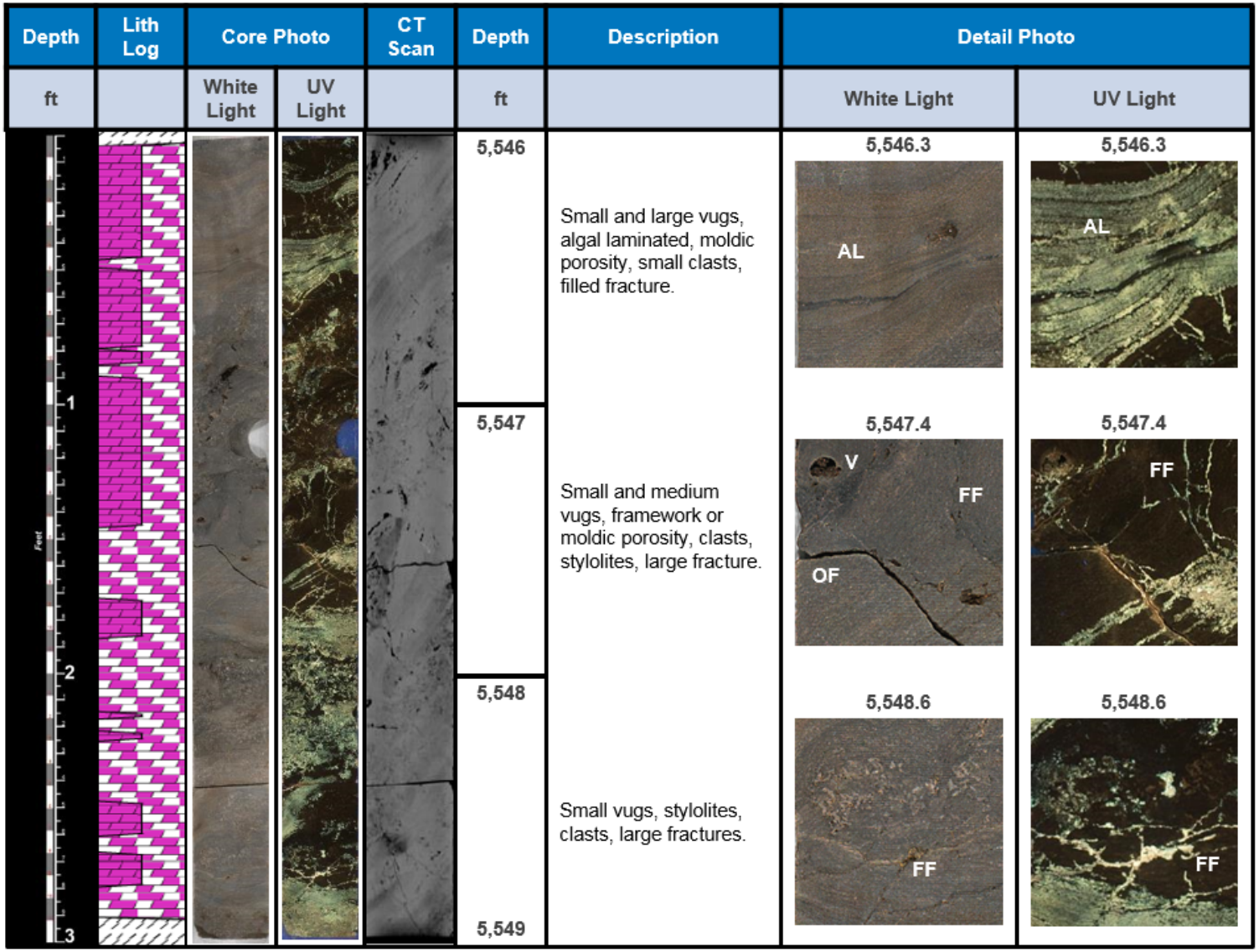


Figure B-10. Compiled illustration of lithology log, core photos (UV and white light), CT scan image, core descriptions, and annotated core images of the Brown Niagaran for depths 5,546 ft. to 5,549 ft.

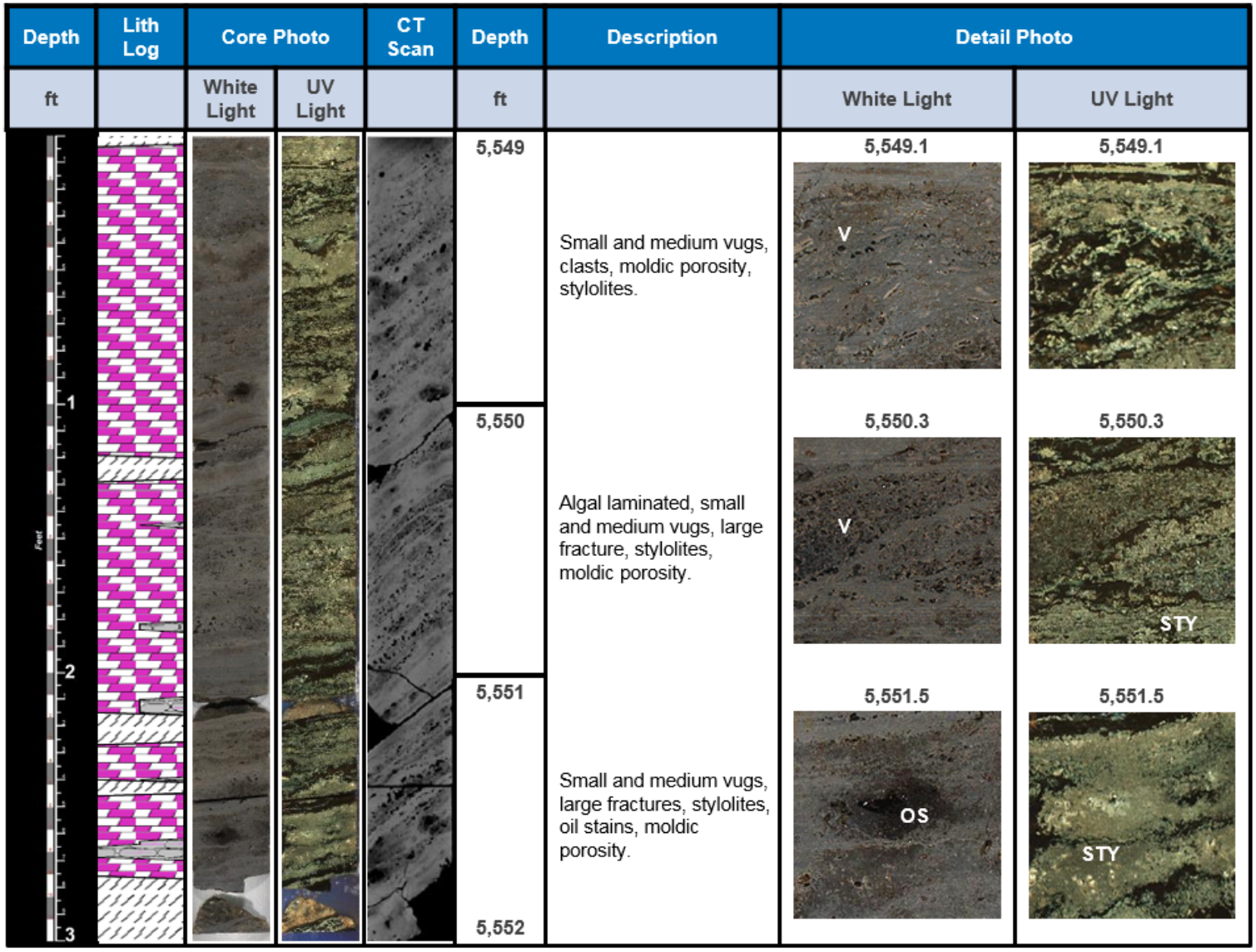


Figure B-11. Compiled illustration of lithology log, core photos (UV and white light), CT scan image, core descriptions, and annotated core images of the Brown Niagaran for depths 5,549 ft. to 5,552 ft.

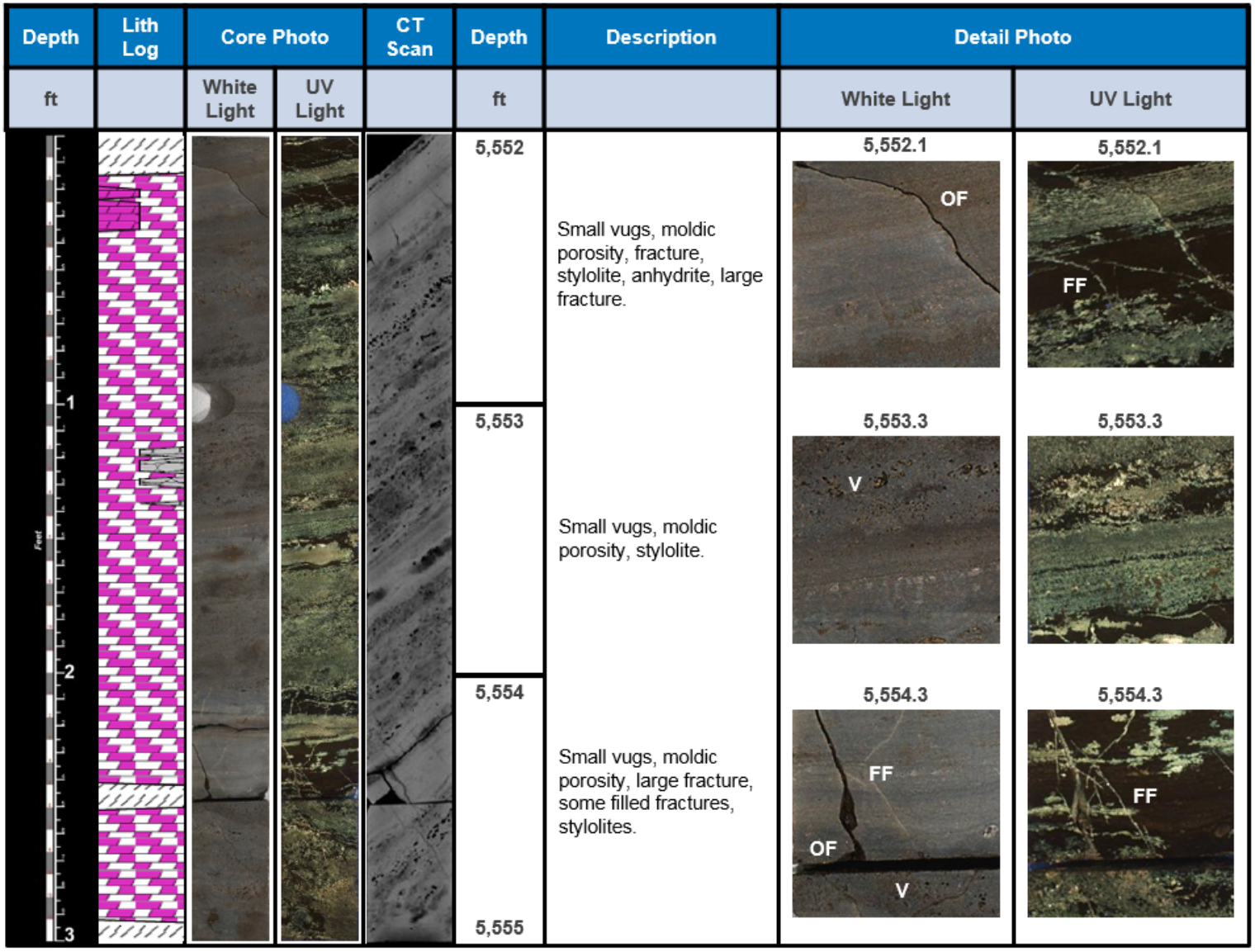


Figure B-12. Compiled illustration of lithology log, core photos (UV and white light), CT scan image, core descriptions, and annotated core images of the Brown Niagaran for depths 5,552 ft. to 5,555 ft

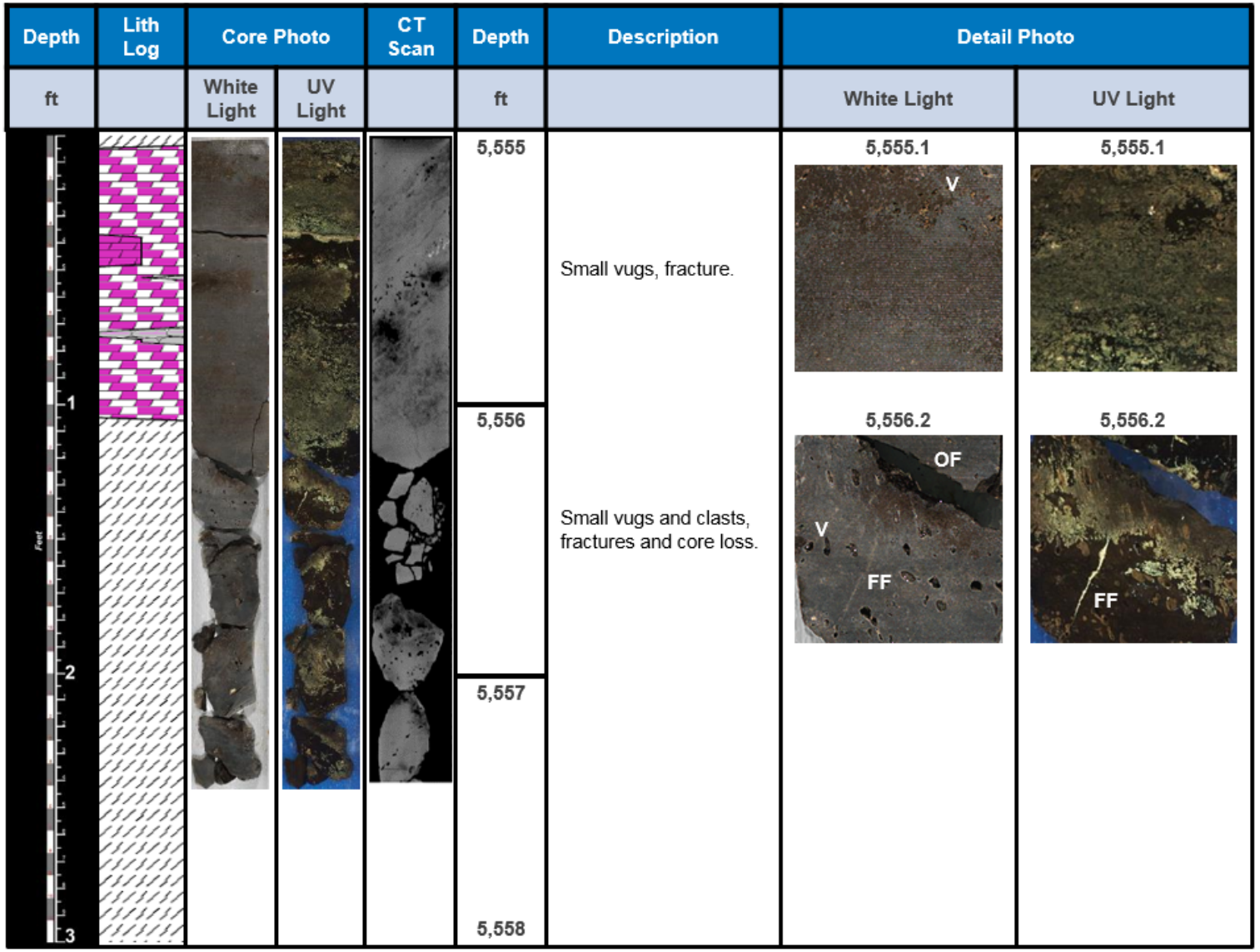


Figure B-13. Compiled illustration of lithology log, core photos (UV and white light), CT scan image, core descriptions, and annotated core images of the Brown Niagaran for depths 5,555 ft. to 5,558 ft.

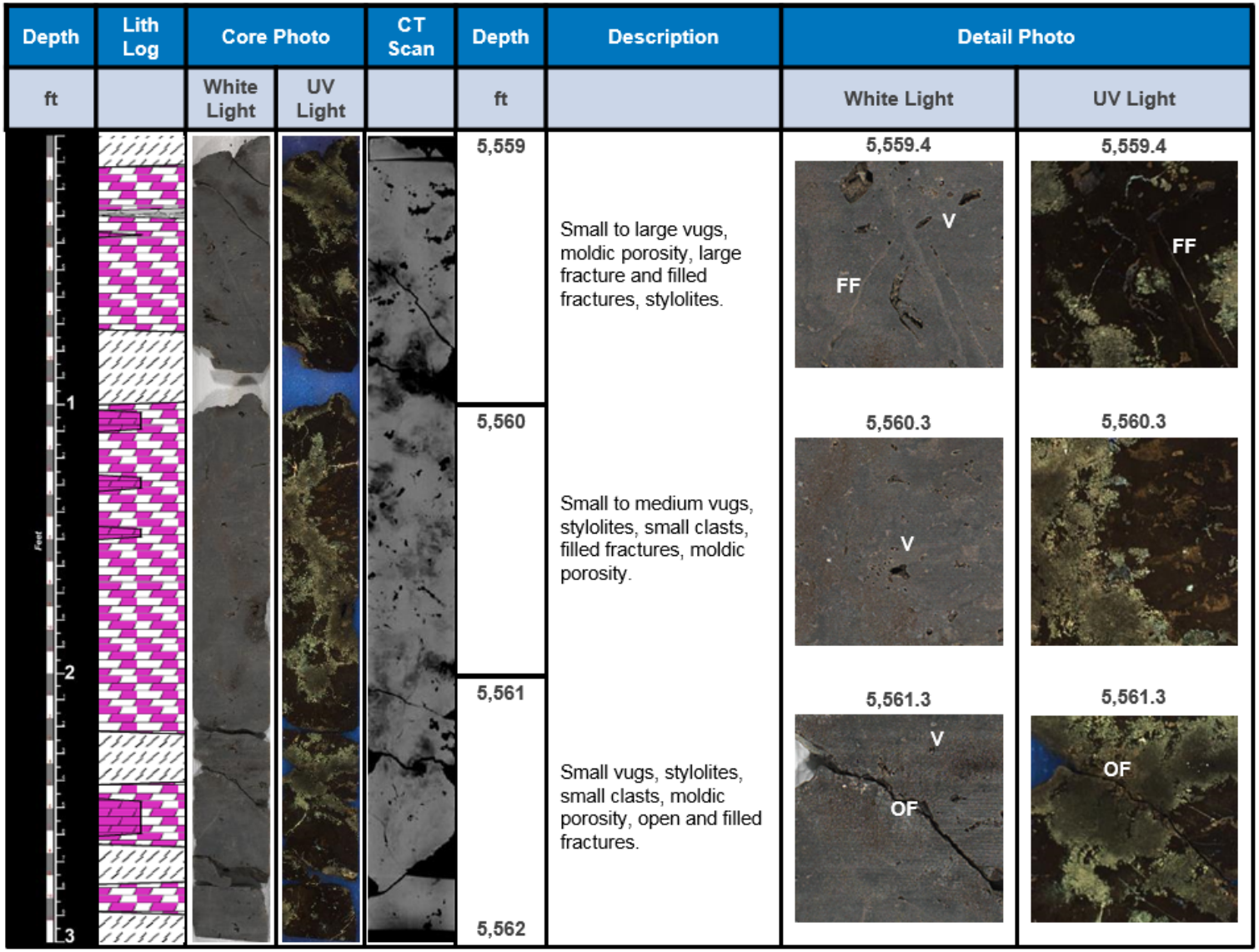


Figure B-14. Compiled illustration of lithology log, core photos (UV and white light), CT scan image, core descriptions, and annotated core images of the Brown Niagaran for depths 5,559 ft. to 5,562 ft.

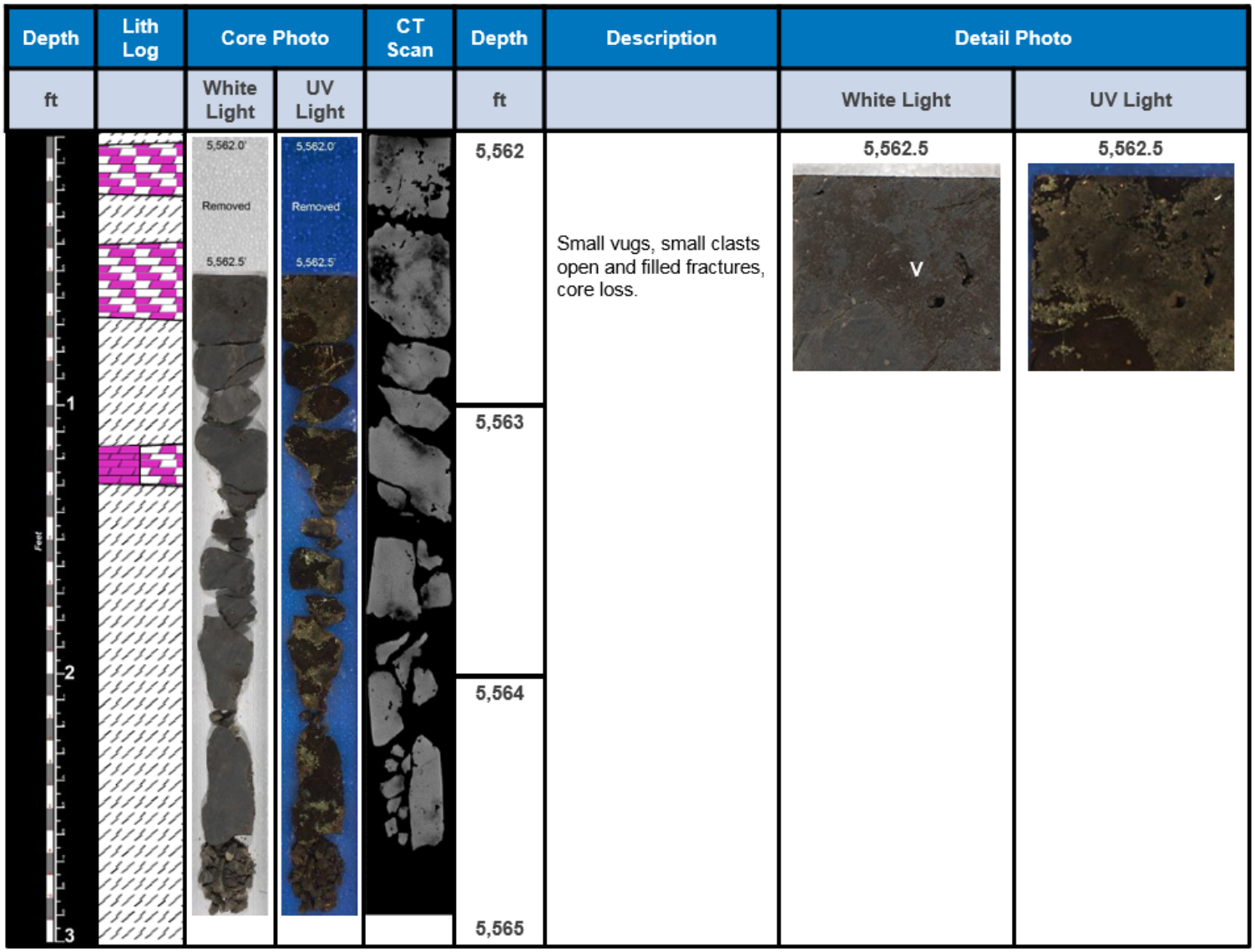


Figure B-15. Compiled illustration of lithology log, core photos (UV and white light), CT scan image, core descriptions, and annotated core images of the Brown Niagaran for depths 5,562 ft. to 5,565 ft.

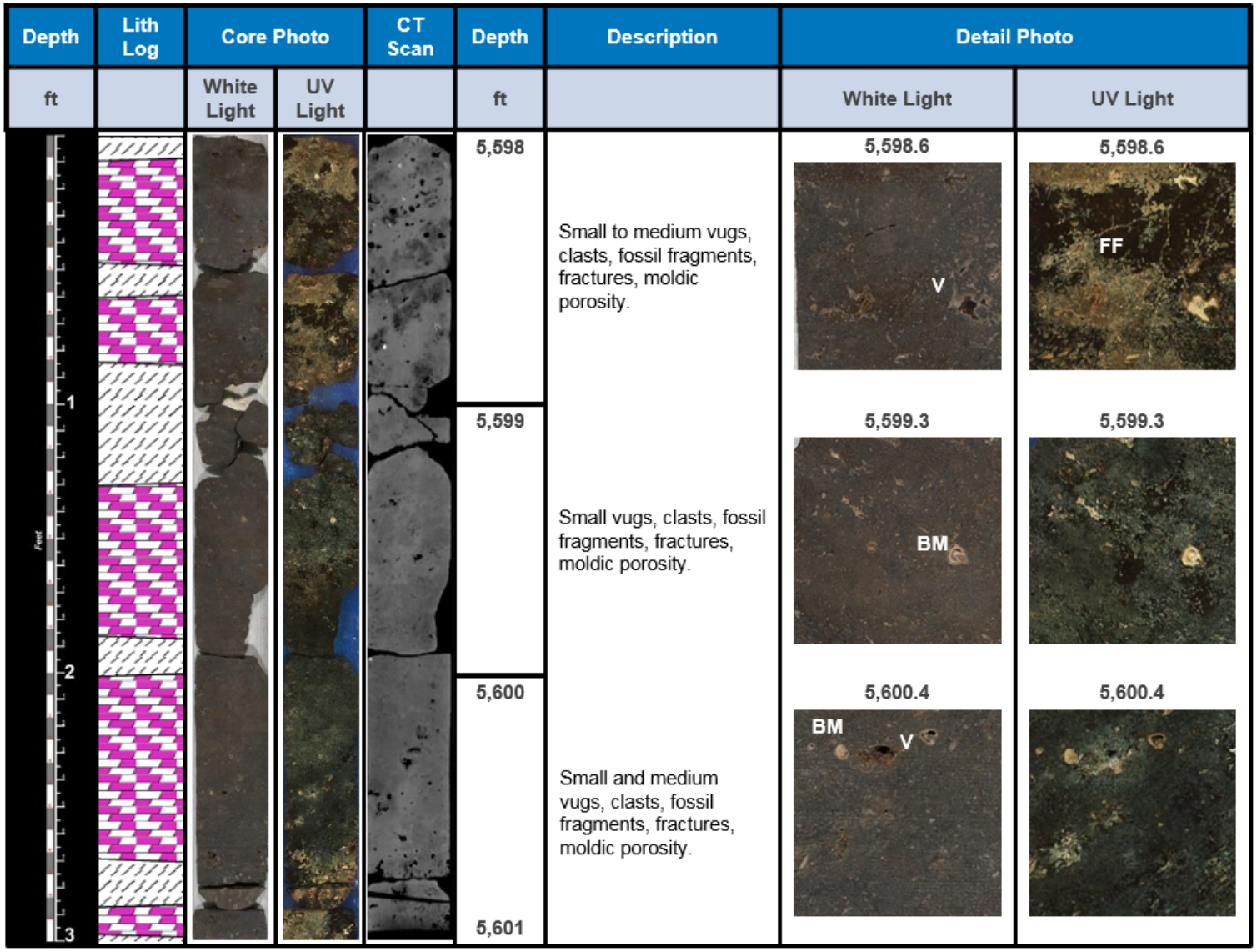


Figure B-16. Compiled illustration of lithology log, core photos (UV and white light), CT scan image, core descriptions, and annotated core images of the Brown Niagaran for depths 5,598 ft. to 5,601 ft.

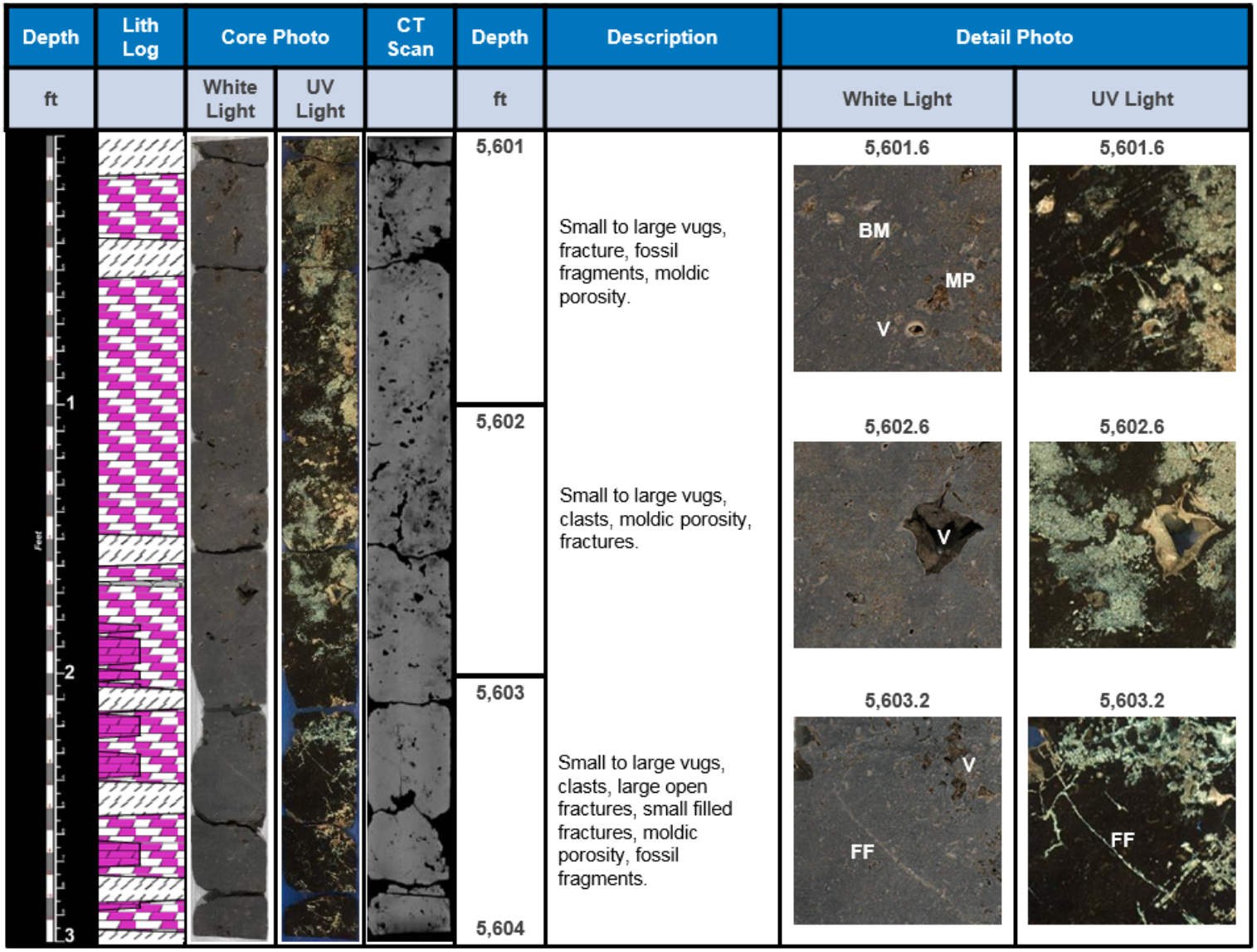


Figure B-17. Compiled illustration of lithology log, core photos (UV and white light), CT scan image, core descriptions, and annotated core images of the Brown Niagaran for depths 5,601 ft. to 5,604 ft.

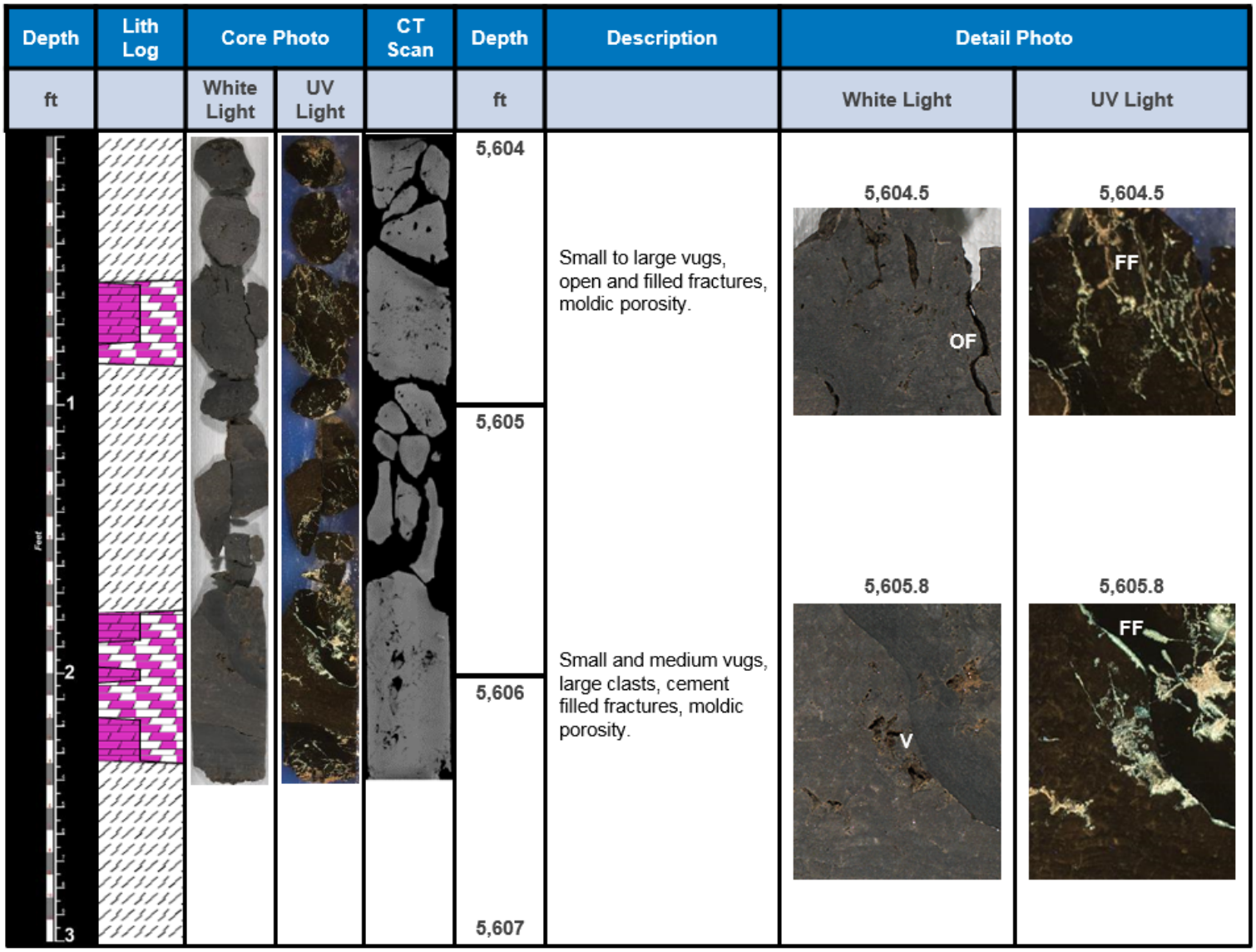


Figure B-18. Compiled illustration of lithology log, core photos (UV and white light), CT scan image, core descriptions, and annotated core images of the Brown Niagaran for depths 5,604 ft. to 5,607 ft.

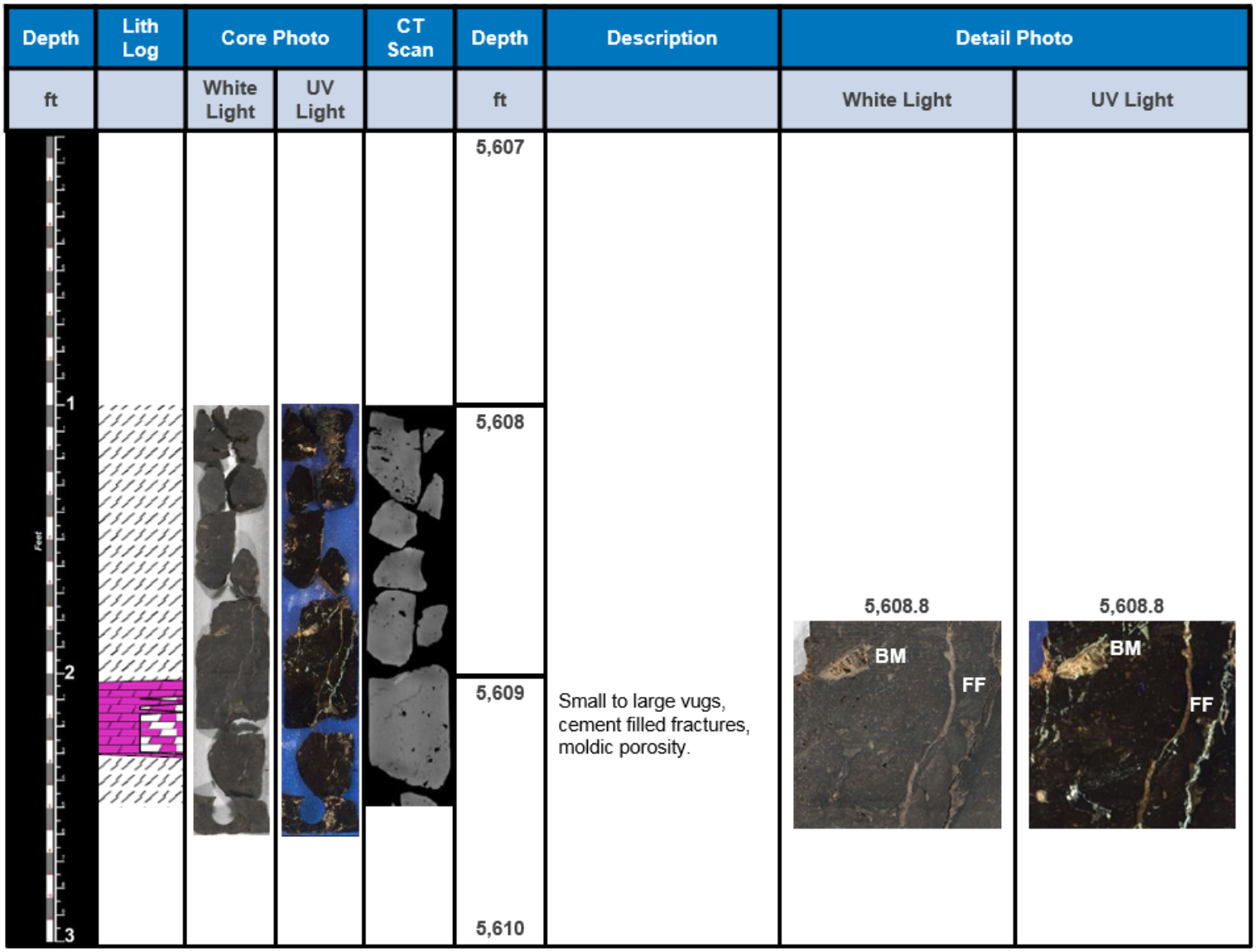


Figure B-19. Compiled illustration of lithology log, core photos (UV and white light), CT scan image, core descriptions, and annotated core images of the Brown Niagaran for depths 5,607 ft. to 5,610 ft.

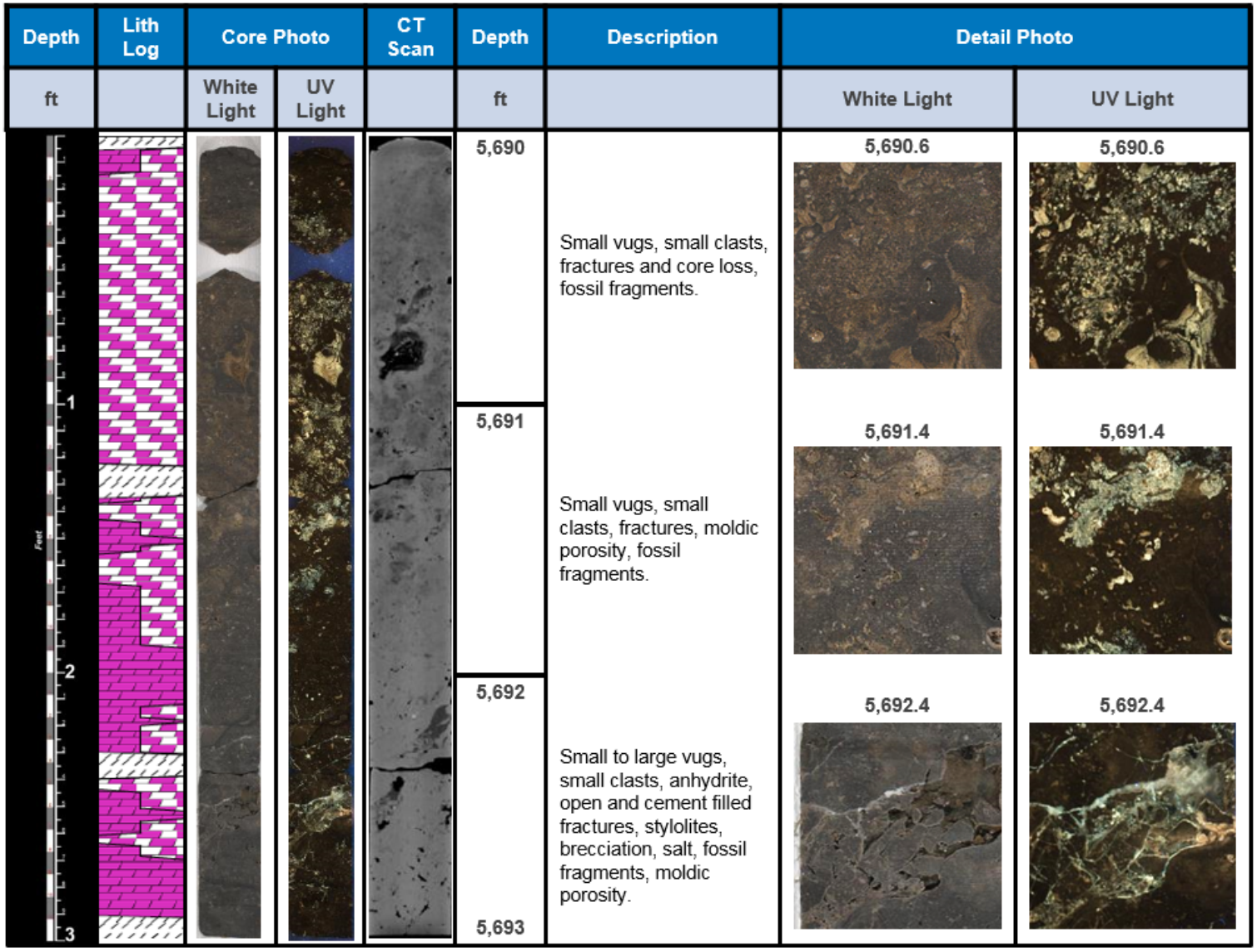


Figure B-20. Compiled illustration of lithology log, core photos (UV and white light), CT scan image, core descriptions, and annotated core images of the Brown Niagaran for depths 5,690 ft. to 5,693 ft.

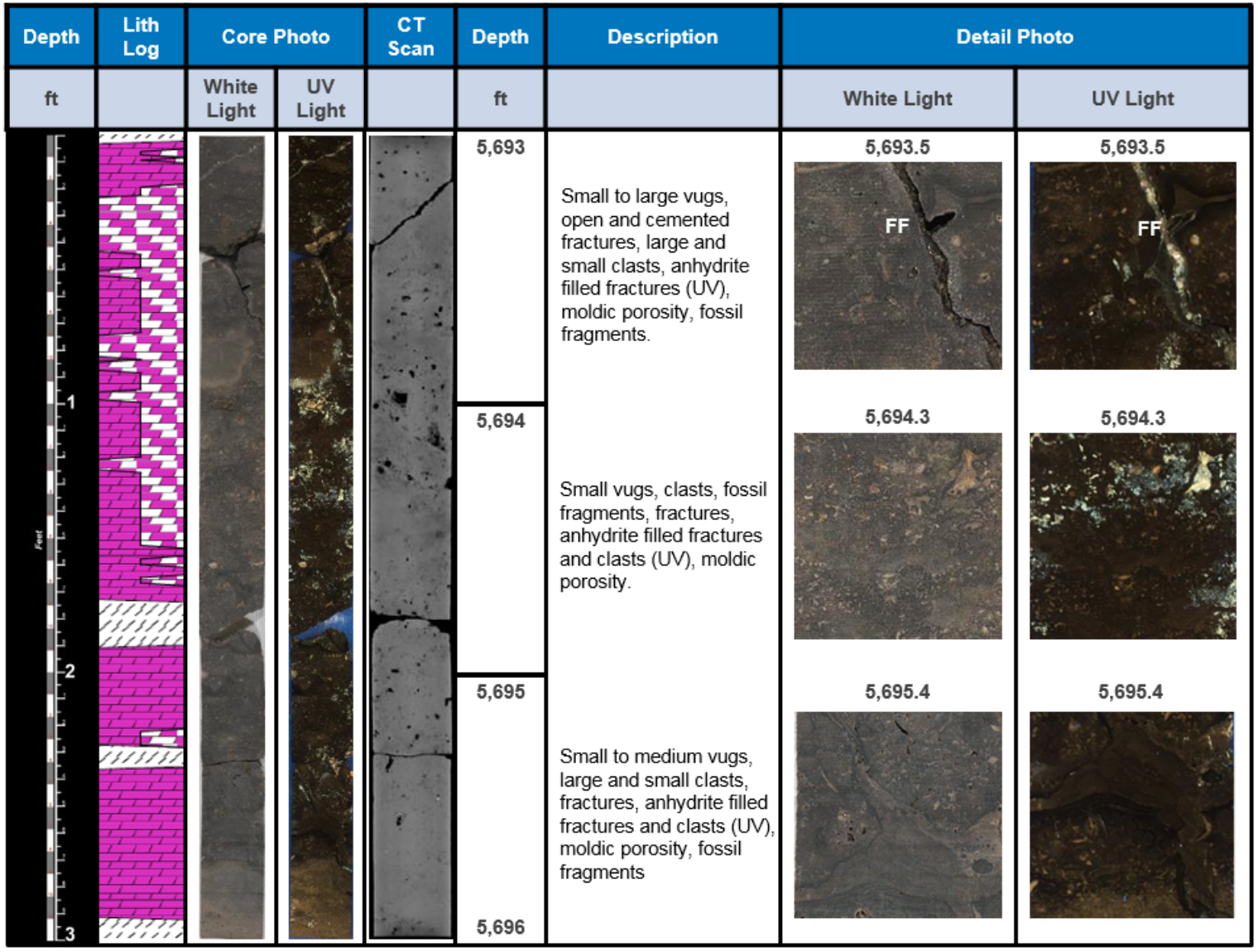


Figure B-21. Compiled illustration of lithology log, core photos (UV and white light), CT scan image, core descriptions, and annotated core images of the Brown Niagaran for depths 5,693 ft. to 5,696 ft.

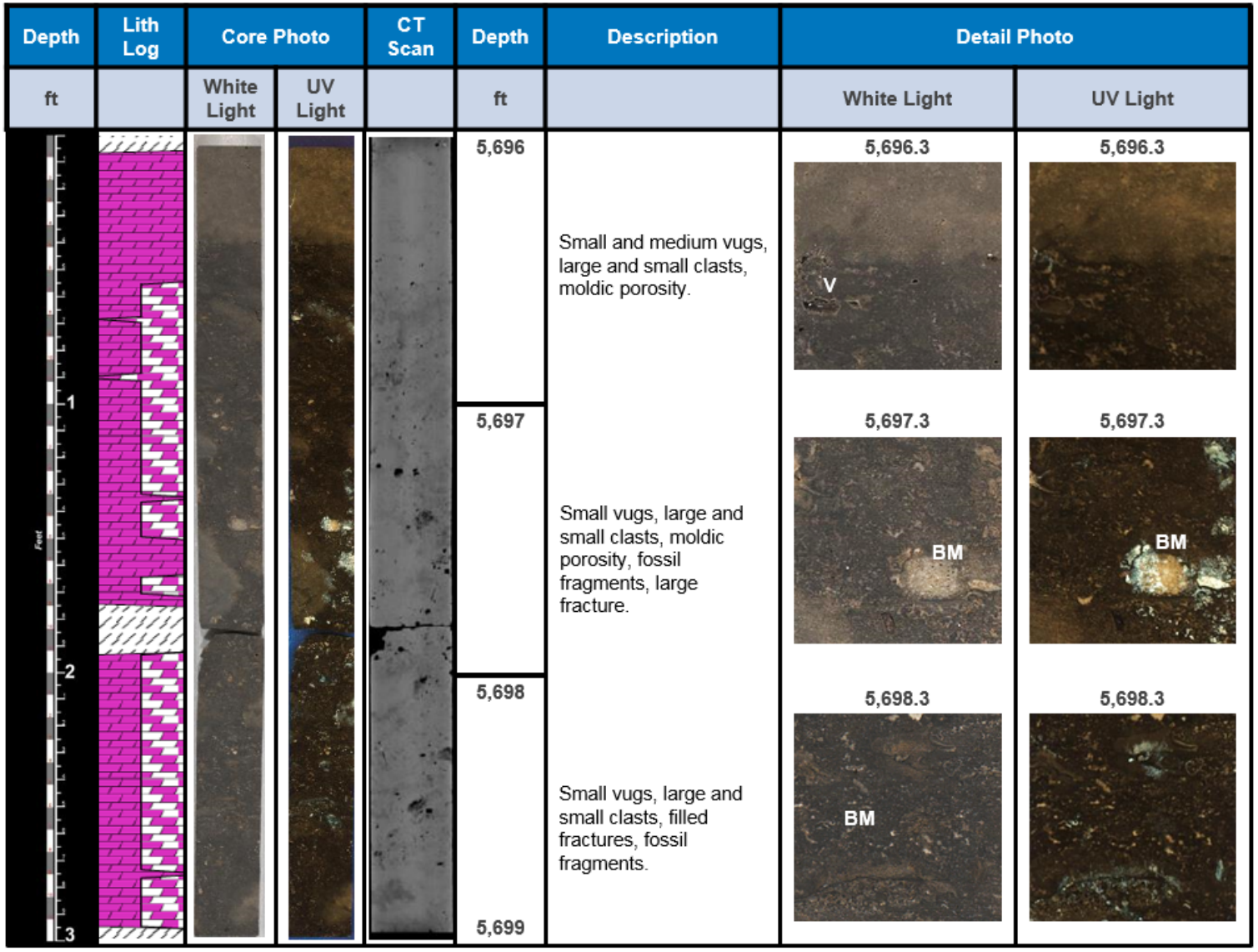


Figure B-22. Compiled illustration of lithology log, core photos (UV and white light), CT scan image, core descriptions, and annotated core images of the Brown Niagaran for depths 5,696 ft. to 5,699 ft.

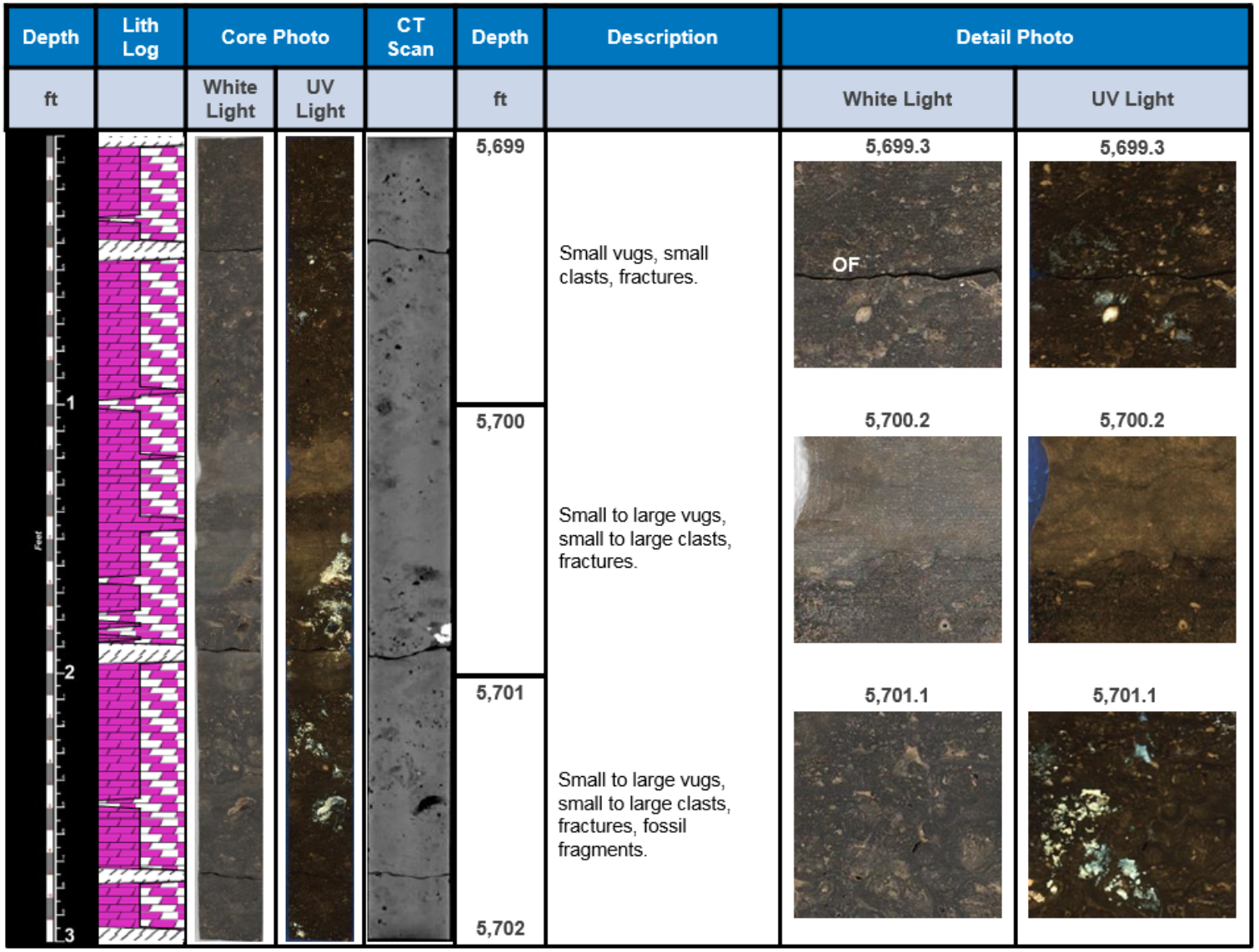


Figure B-23. Compiled illustration of lithology log, core photos (UV and white light), CT scan image, core descriptions, and annotated core images of the Brown Niagaran for depths 5,699 ft. to 5,702 ft.

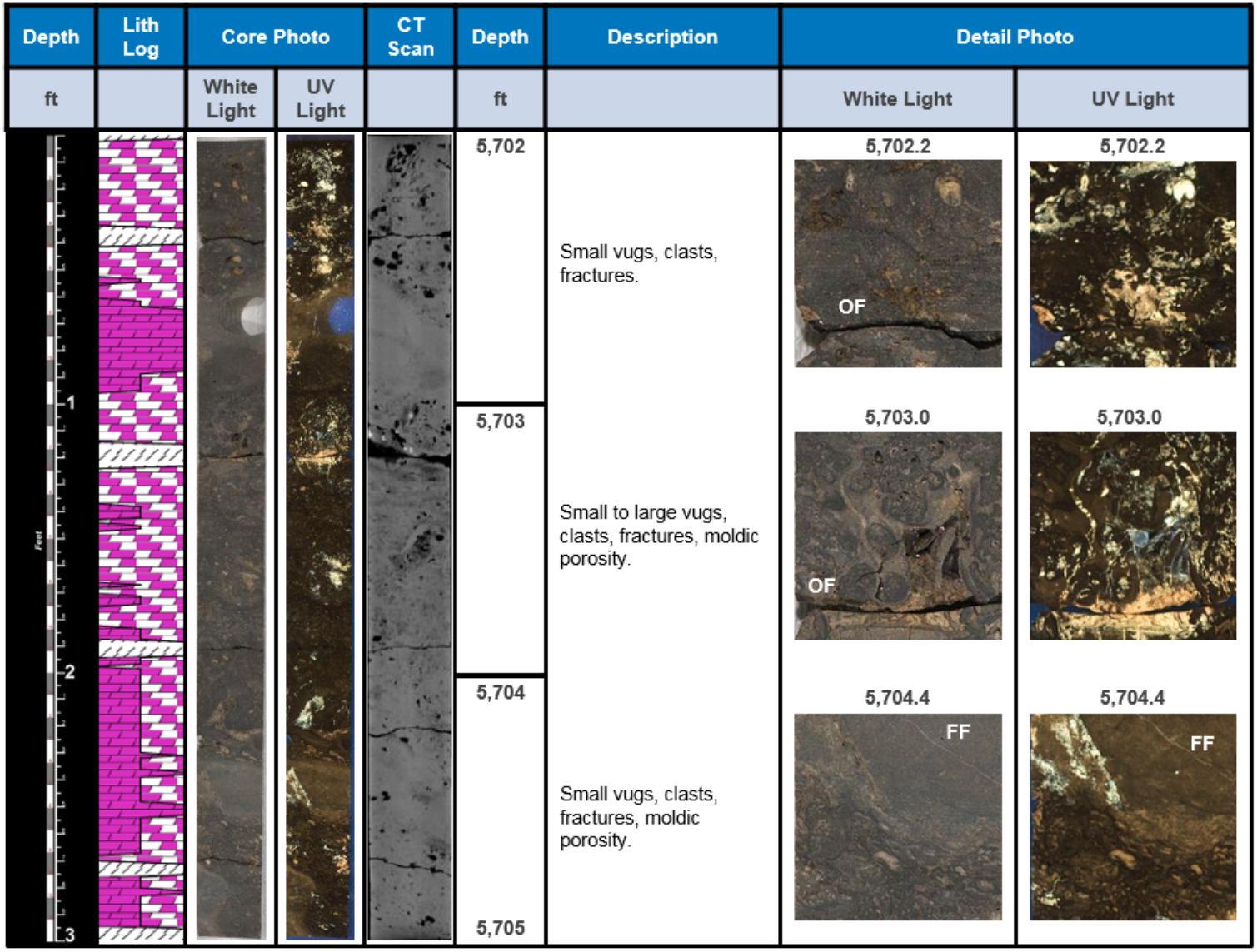


Figure B-24. Compiled illustration of lithology log, core photos (UV and white light), CT scan image, core descriptions, and annotated core images of the Brown Niagaran for depths 5,702 ft. to 5,705 ft.

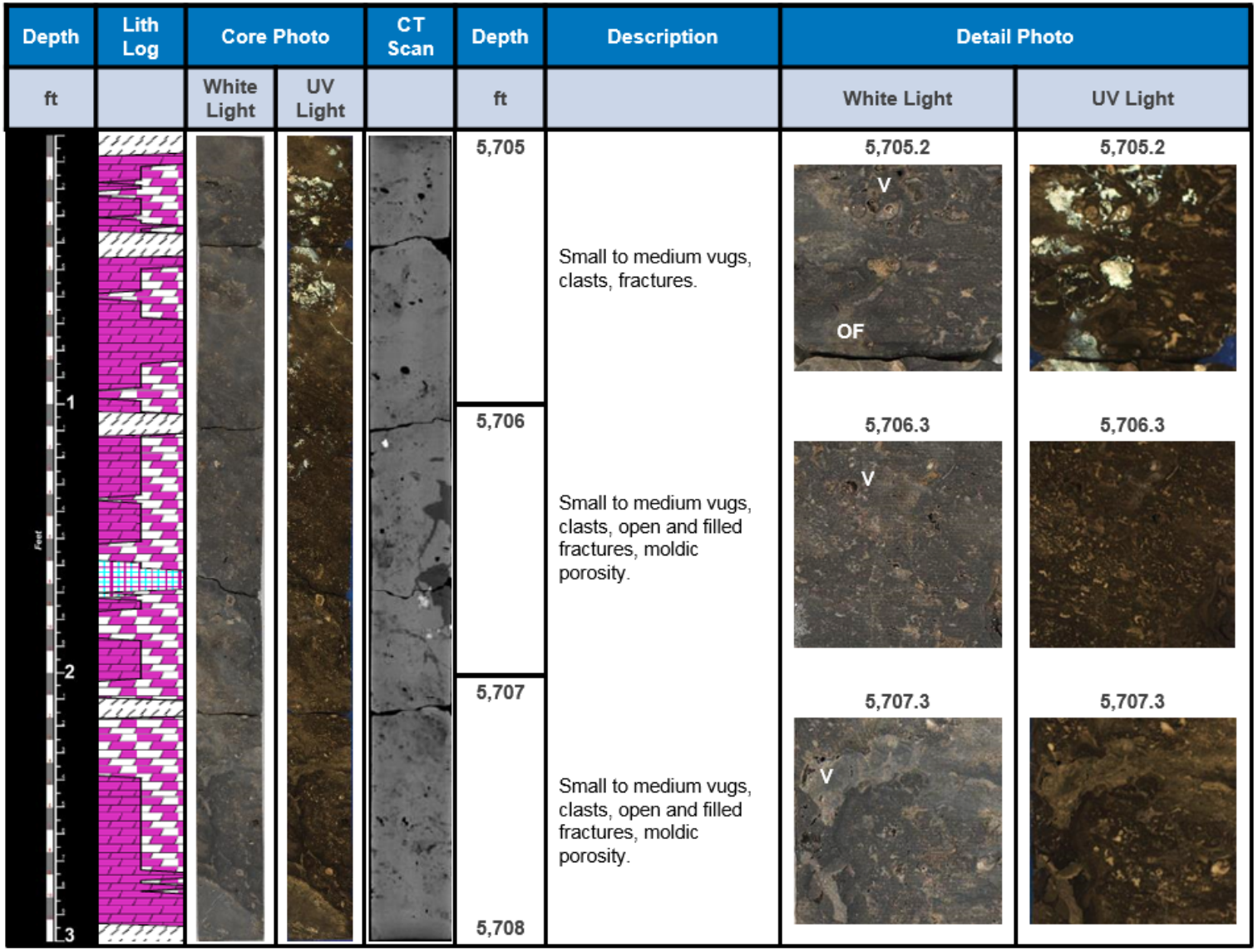


Figure B-25. Compiled illustration of lithology log, core photos (UV and white light), CT scan image, core descriptions, and annotated core images of the Brown Niagaran for depths 5,705 ft. to 5,708 ft.

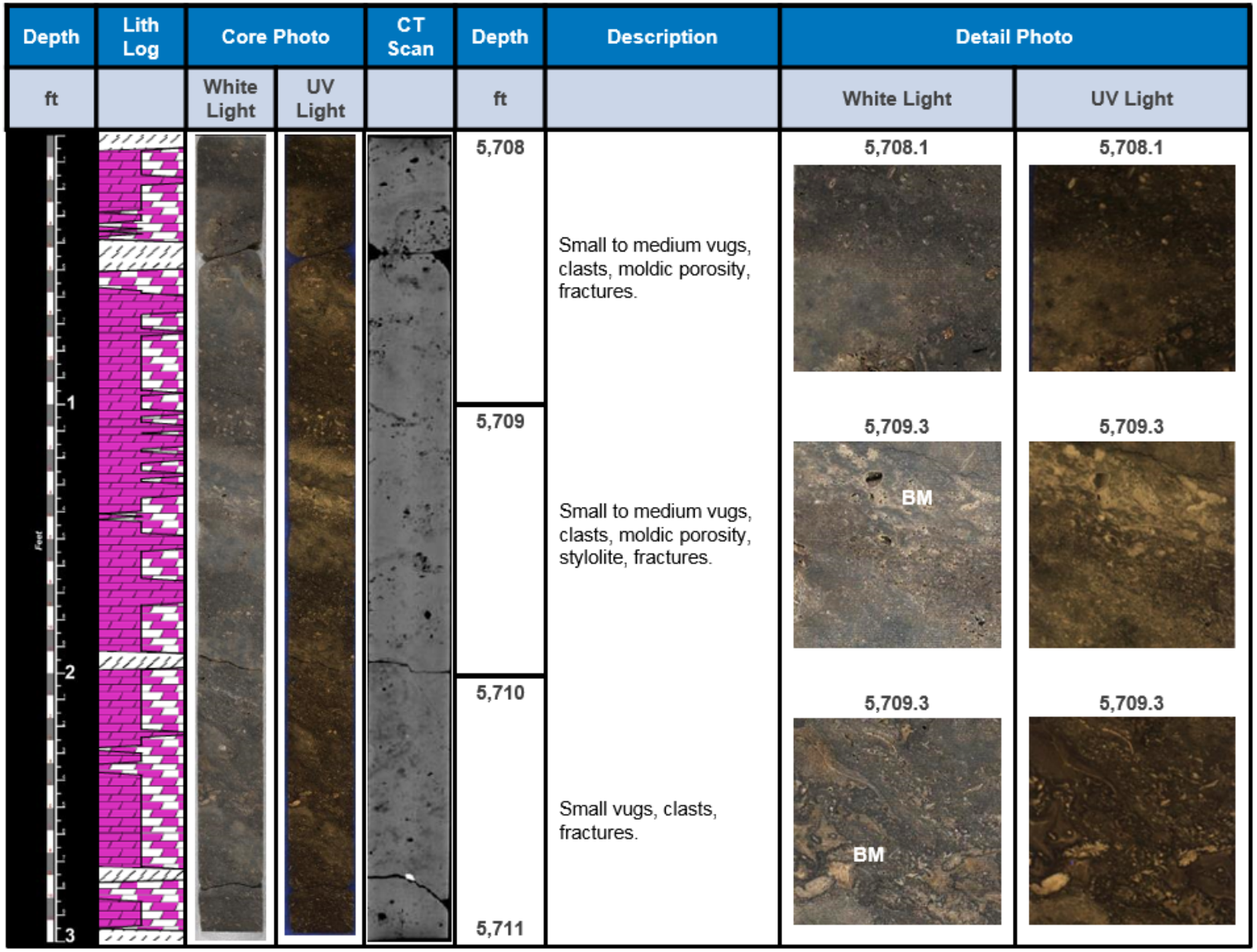


Figure B-26. Compiled illustration of lithology log, core photos (UV and white light), CT scan image, core descriptions, and annotated core images of the Brown Niagaran for depths 5,708 ft. to 5,711 ft.

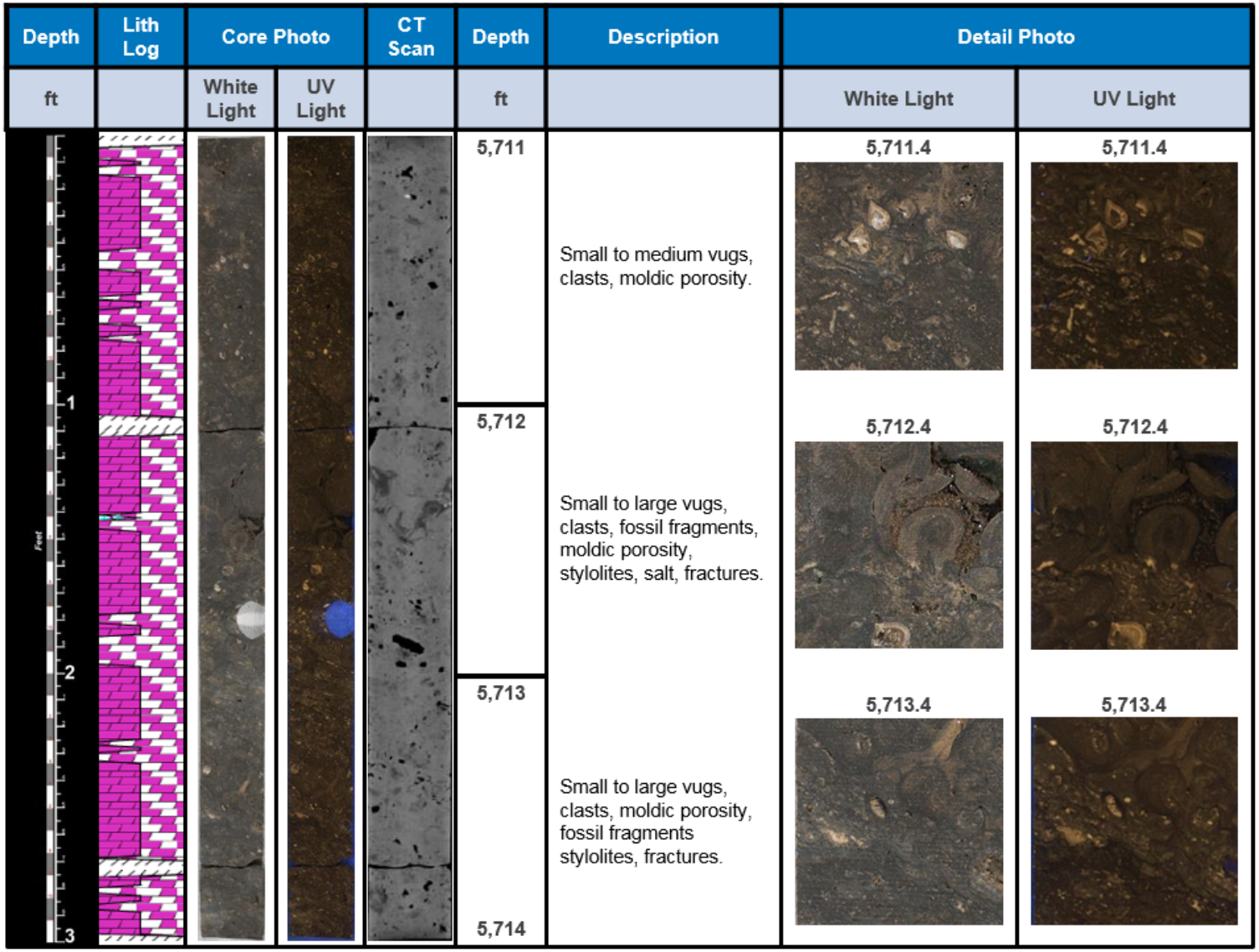


Figure B-27. Compiled illustration of lithology log, core photos (UV and white light), CT scan image, core descriptions, and annotated core images of the Brown Niagaran for depths 5,711 ft. to 5,714 ft.

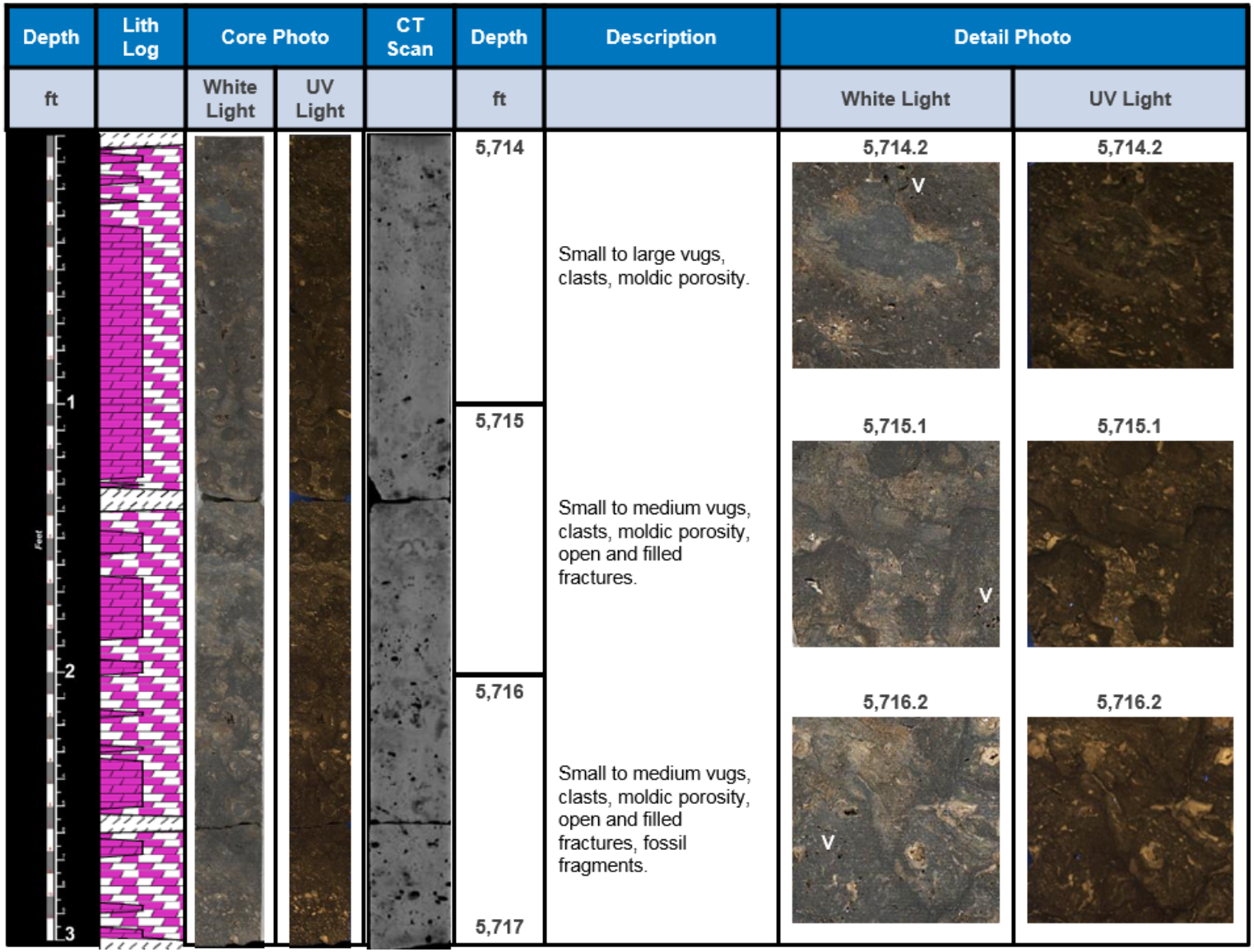


Figure B-28. Compiled illustration of lithology log, core photos (UV and white light), CT scan image, core descriptions, and annotated core images of the Brown Niagaran for depths 5,714 ft. to 5,717 ft.

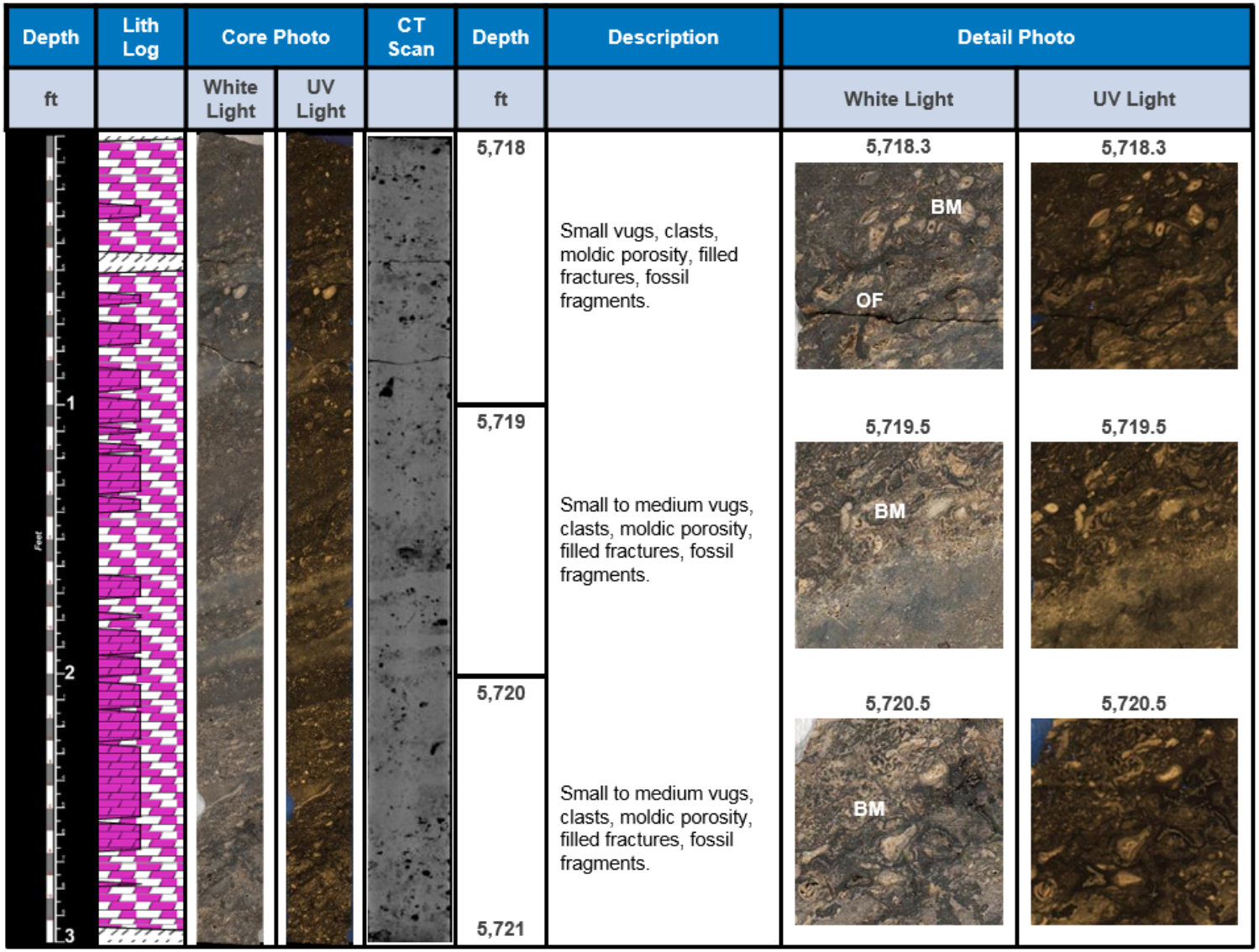


Figure B-29. Compiled illustration of lithology log, core photos (UV and white light), CT scan image, core descriptions, and annotated core images of the Brown Niagaran for depths 5,718 ft. to 5,721 ft.

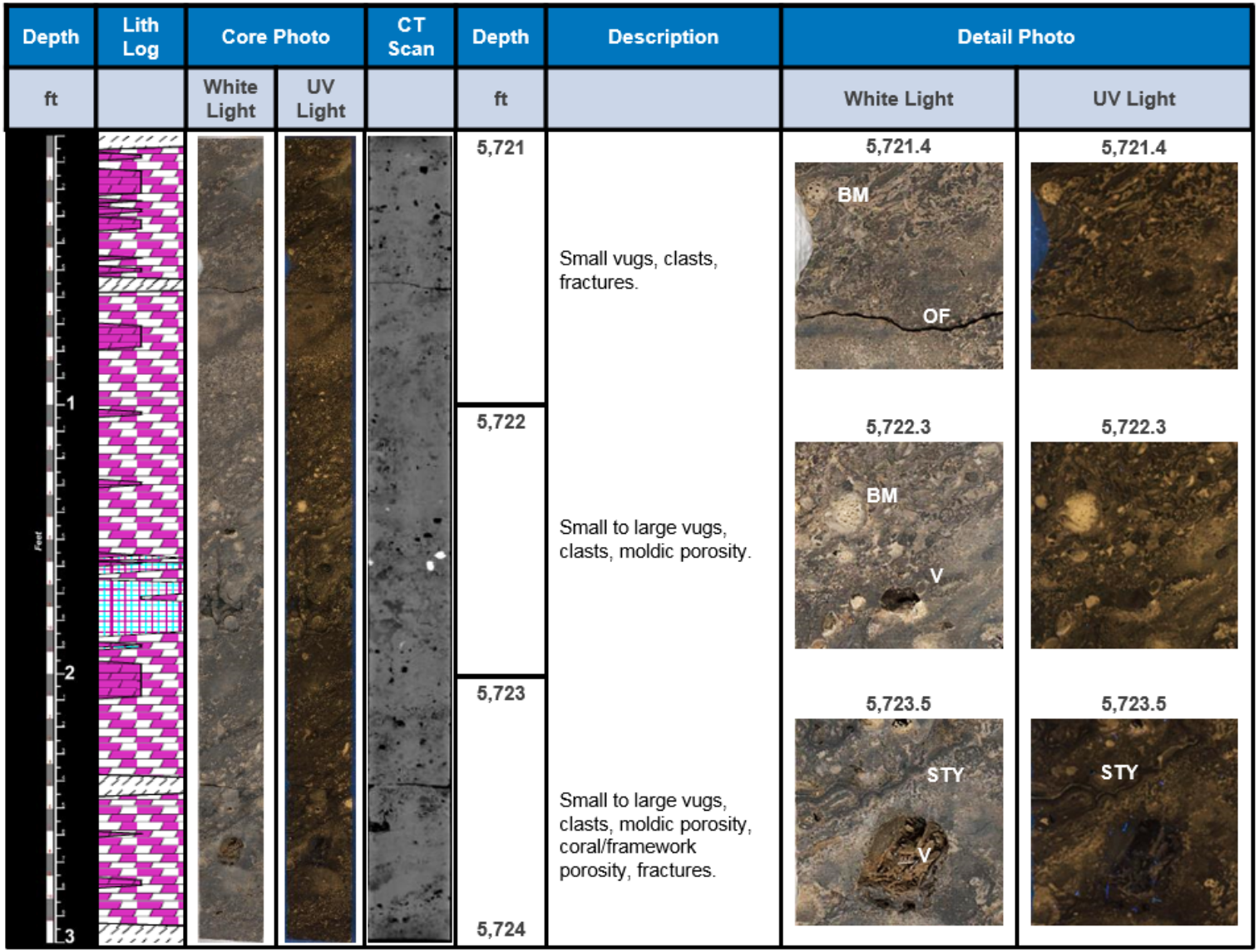


Figure B-30. Compiled illustration of lithology log, core photos (UV and white light), CT scan image, core descriptions, and annotated core images of the Brown Niagaran for depths 5,721 ft. to 5,724 ft.

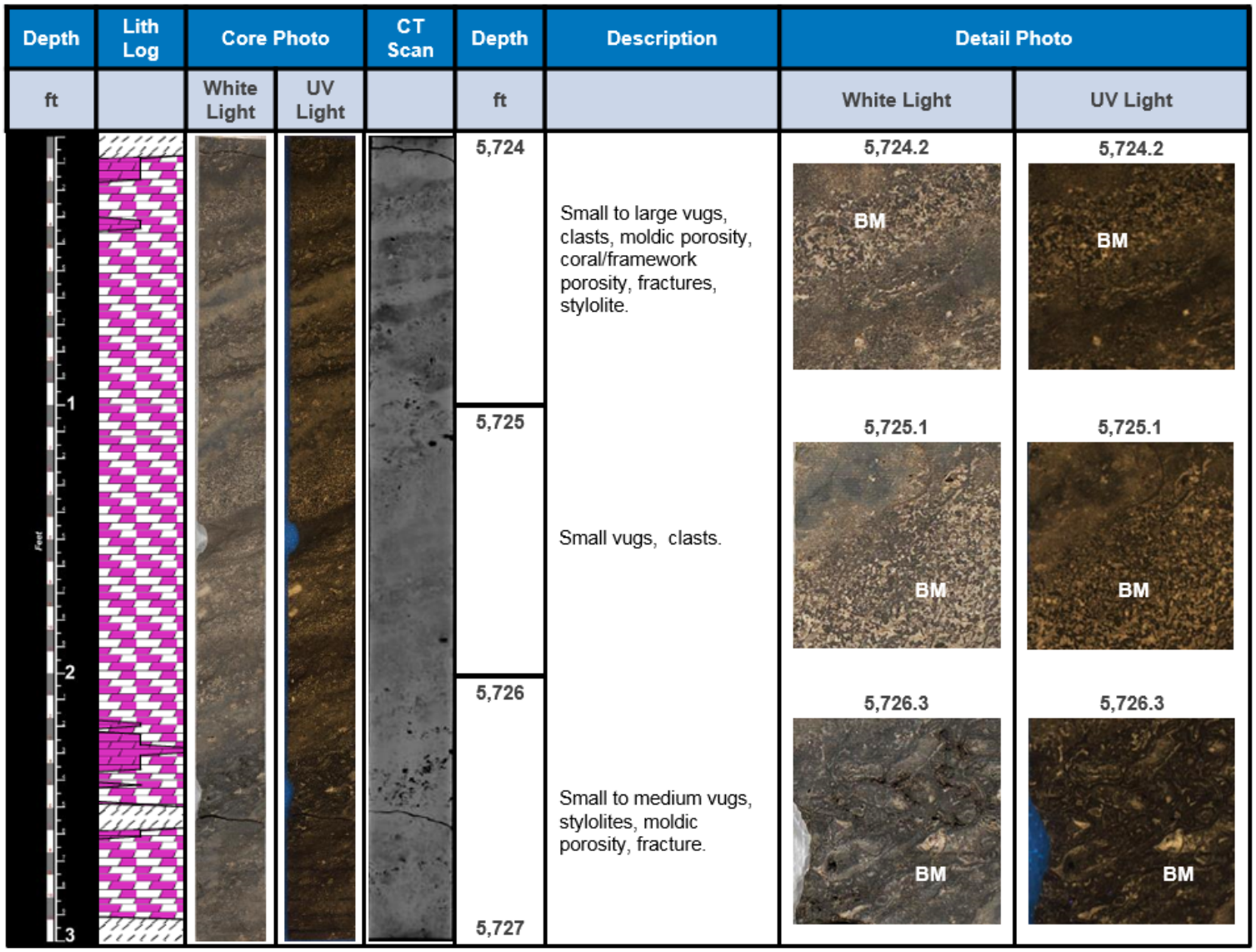


Figure B-31. Compiled illustration of lithology log, core photos (UV and white light), CT scan image, core descriptions, and annotated core images of the Brown Niagaran for depths 5,724 ft. to 5,727 ft.

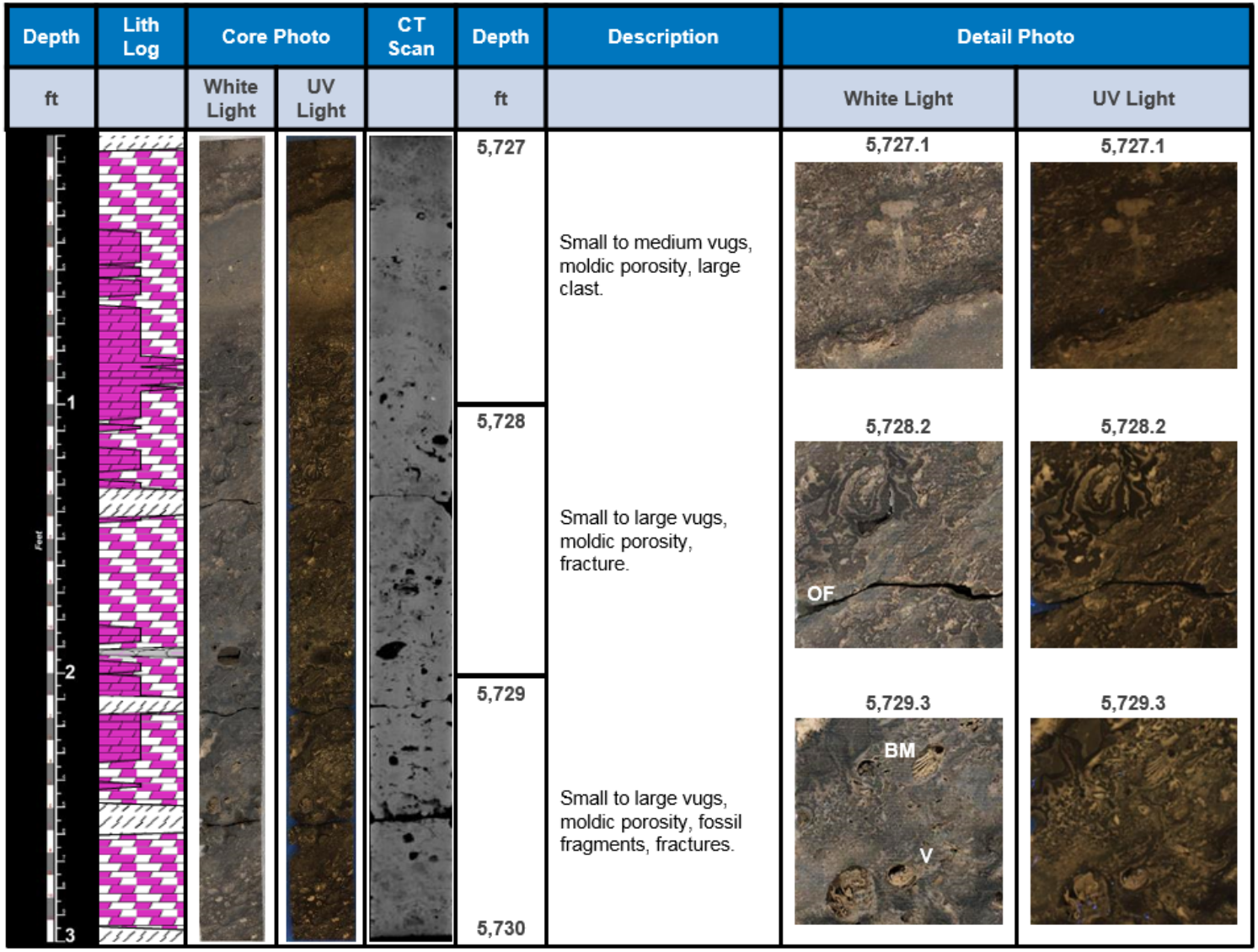


Figure B-32. Compiled illustration of lithology log, core photos (UV and white light), CT scan image, core descriptions, and annotated core images of the Brown Niagaran for depths 5,727 ft. to 5,730 ft.

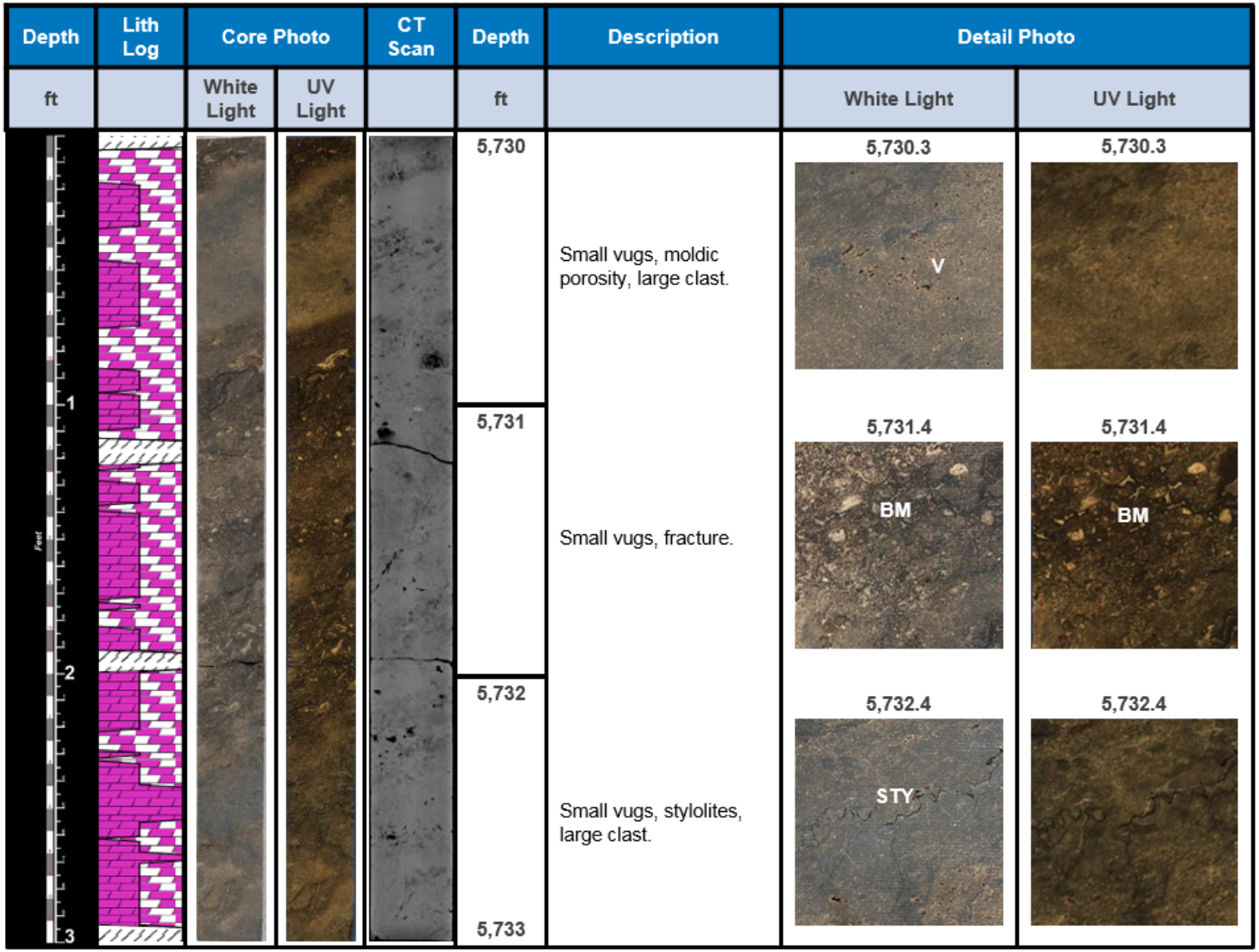


Figure B-33. Compiled illustration of lithology log, core photos (UV and white light), CT scan image, core descriptions, and annotated core images of the Brown Niagaran for depths 5,730 ft. to 5,733 ft.

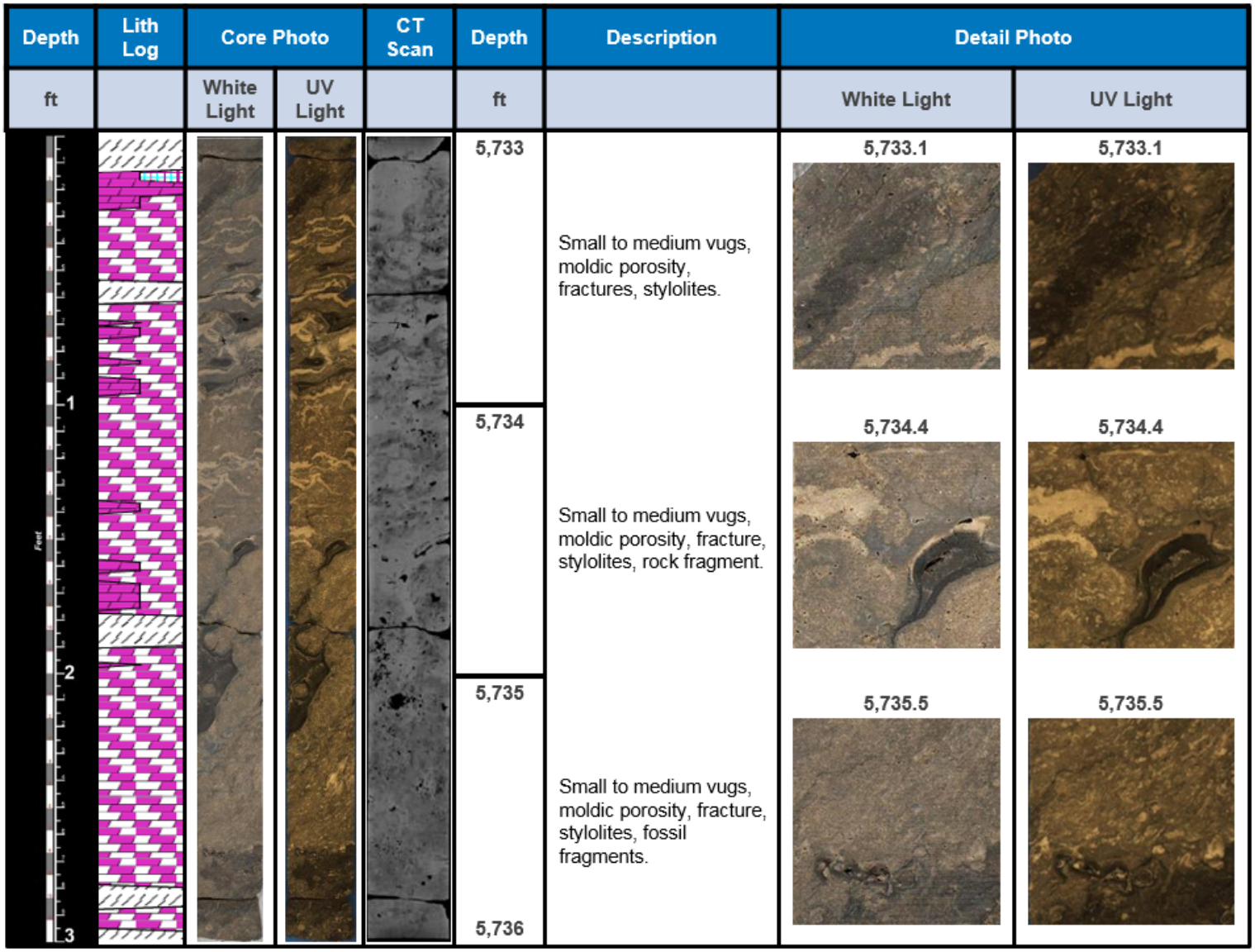


Figure B-34. Compiled illustration of lithology log, core photos (UV and white light), CT scan image, core descriptions, and annotated core images of the Brown Niagaran for depths 5,733 ft. to 5,736 ft.

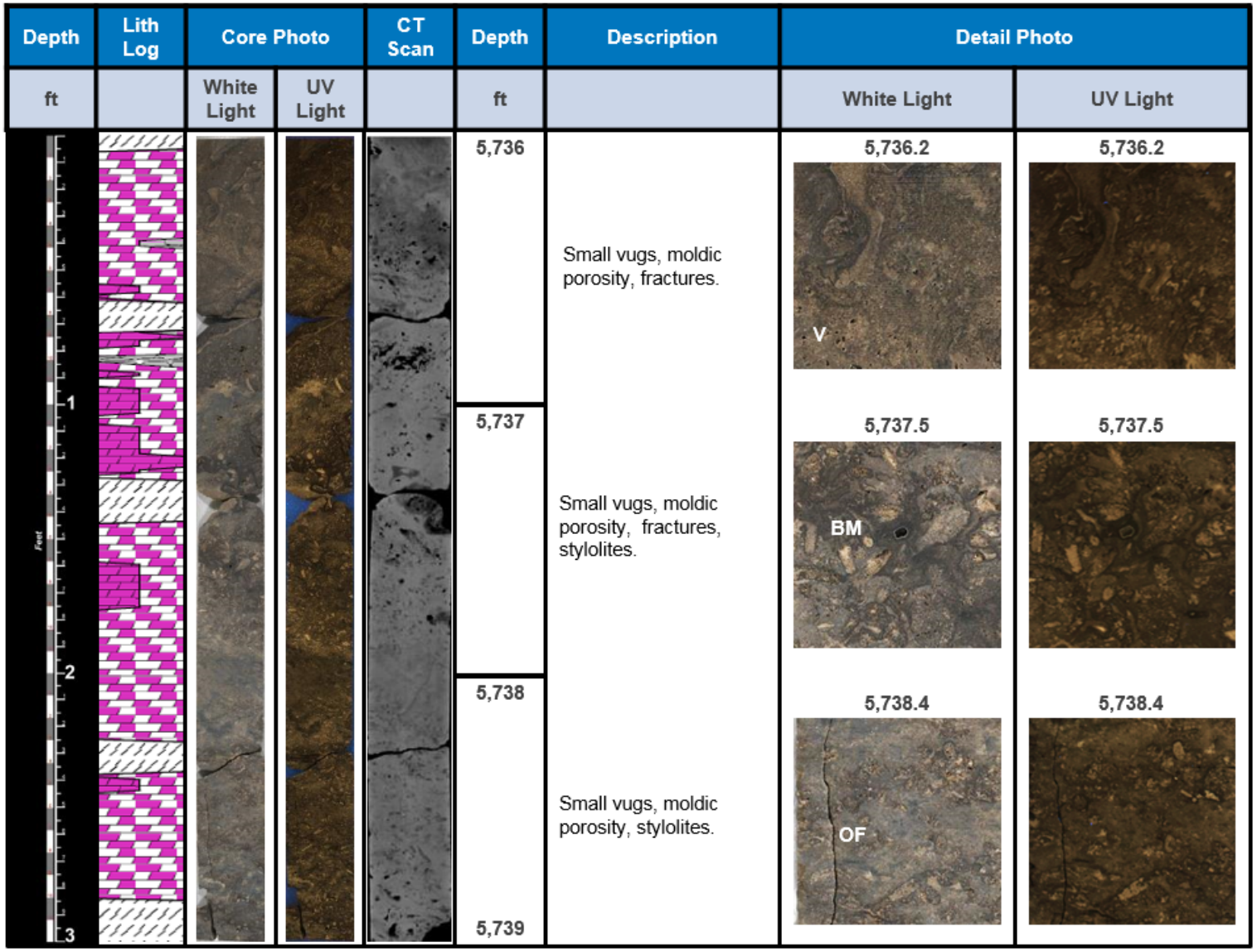


Figure B-35. Compiled illustration of lithology log, core photos (UV and white light), CT scan image, core descriptions, and annotated core images of the Brown Niagaran for depths 5,736 ft. to 5,739 ft.

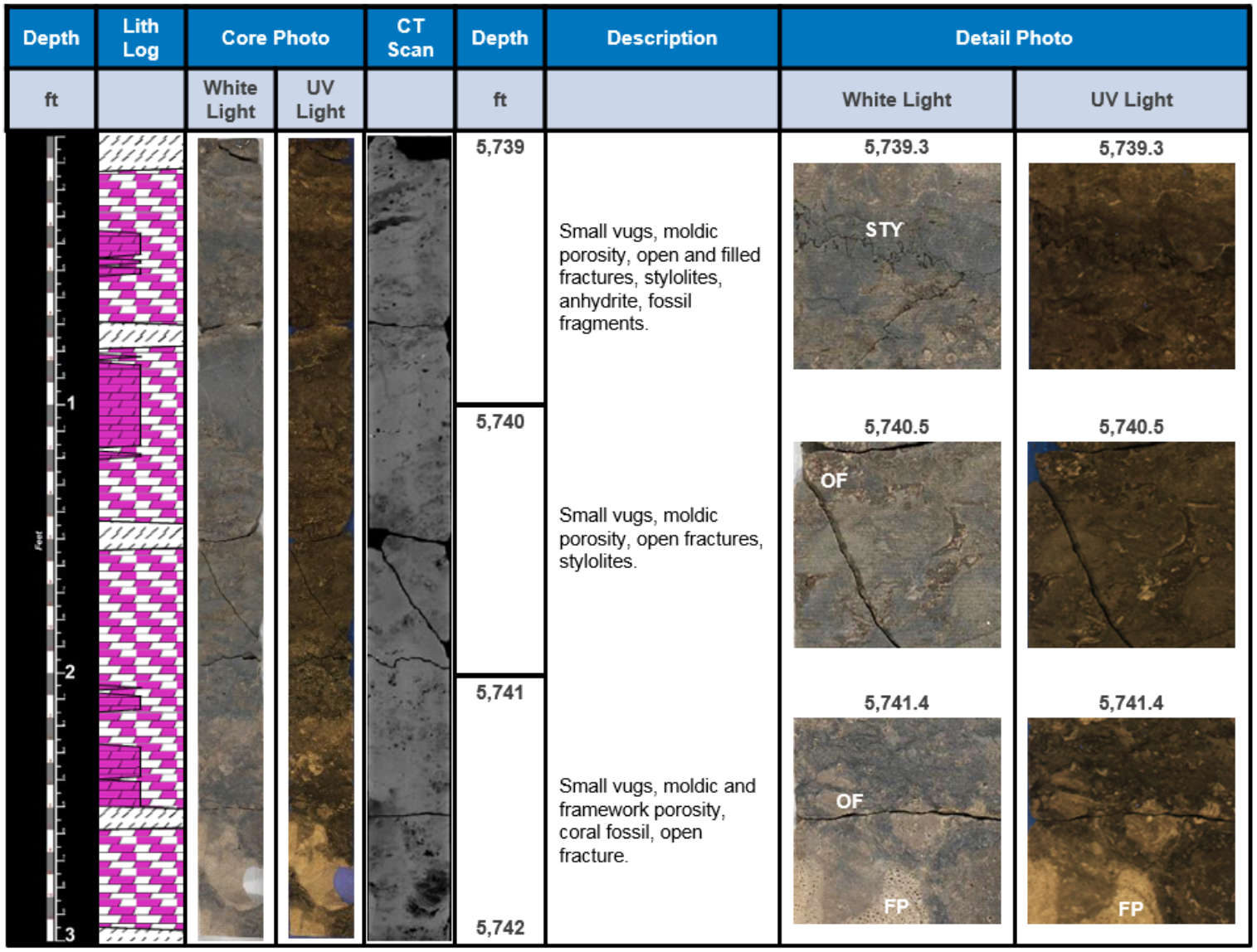


Figure B-36. Compiled illustration of lithology log, core photos (UV and white light), CT scan image, core descriptions, and annotated core images of the Brown Niagaran for depths 5,739 ft. to 5,742 ft.

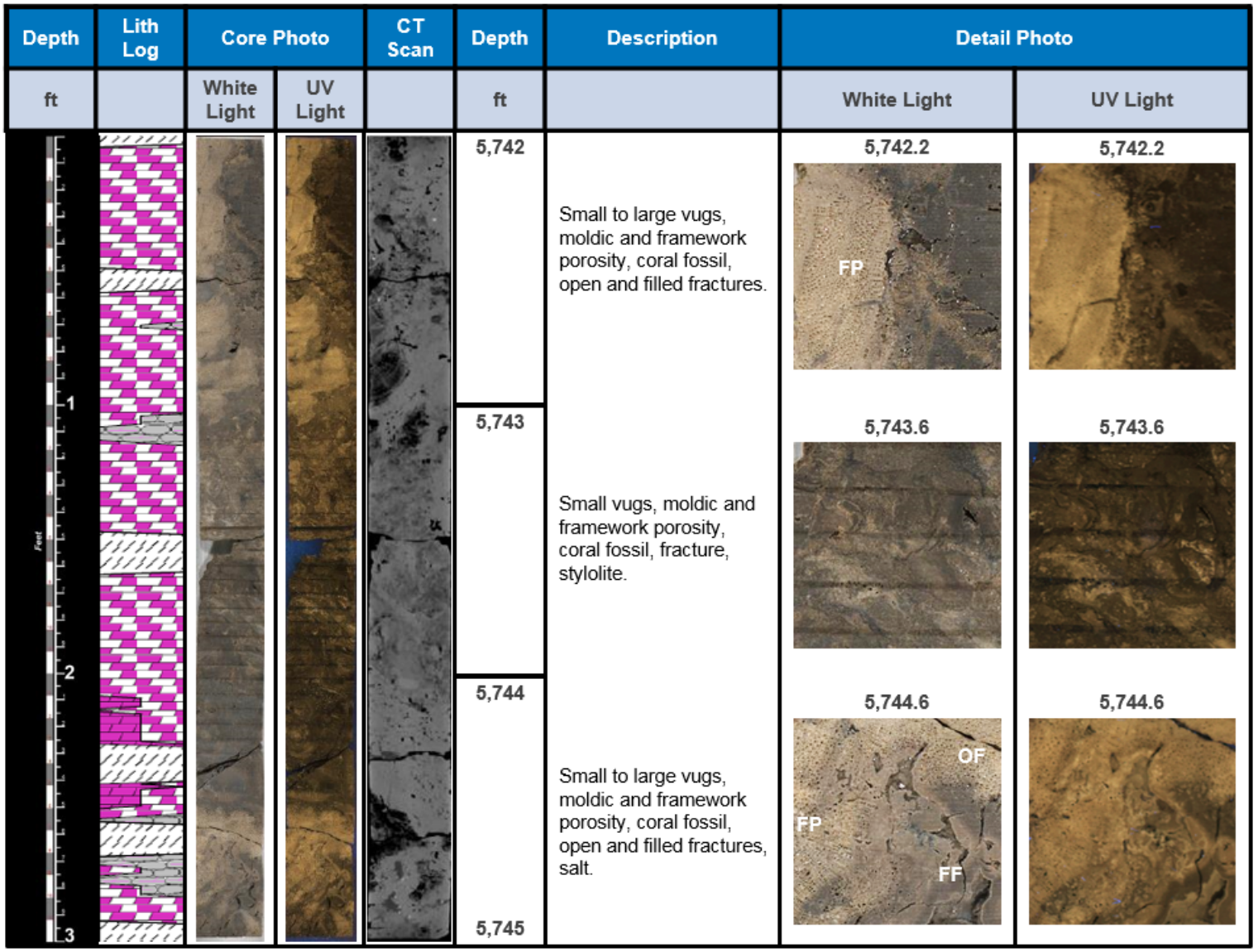


Figure B-37. Compiled illustration of lithology log, core photos (UV and white light), CT scan image, core descriptions, and annotated core images of the Brown Niagaran for depths 5,742 ft. to 5,745 ft.

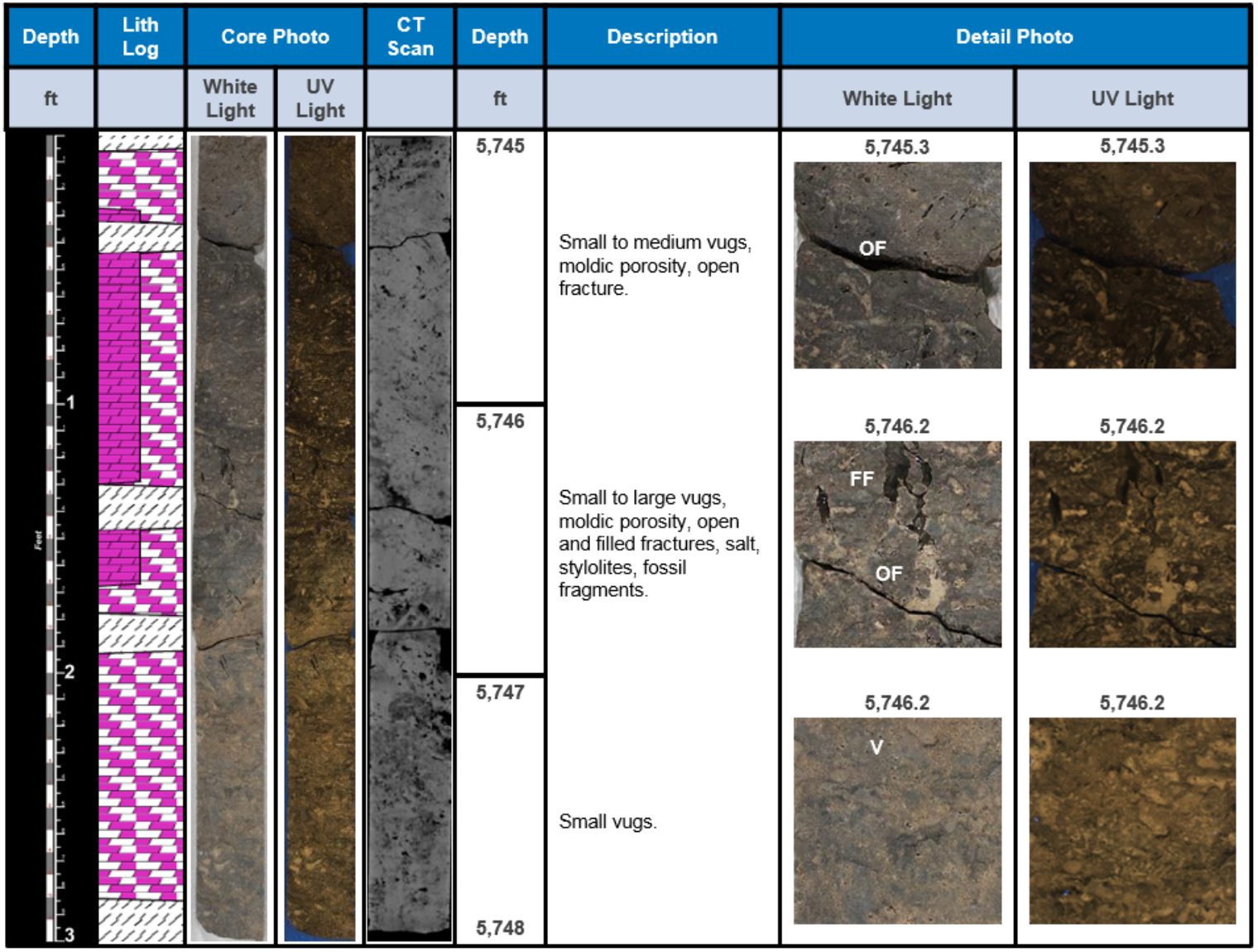


Figure B-38. Compiled illustration of lithology log, core photos (UV and white light), CT scan image, core descriptions, and annotated core images of the Brown Niagaran for depths 5,745 ft. to 5,748 ft.

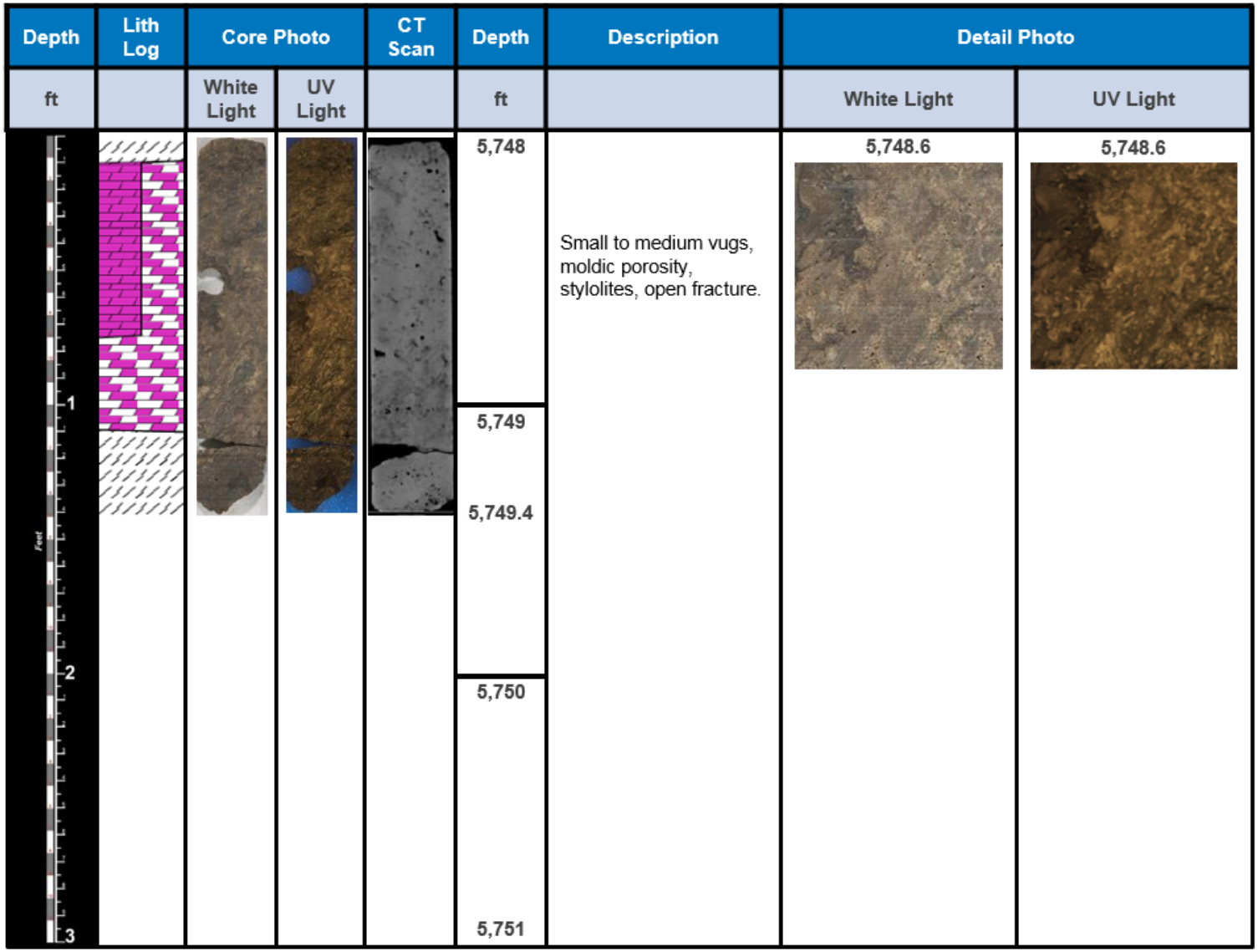


Figure B-39. Compiled illustration of lithology log, core photos (UV and white light), CT scan image, core descriptions, and annotated core images of the Brown Niagaran for depths 5,748 ft. to 5,751 ft.

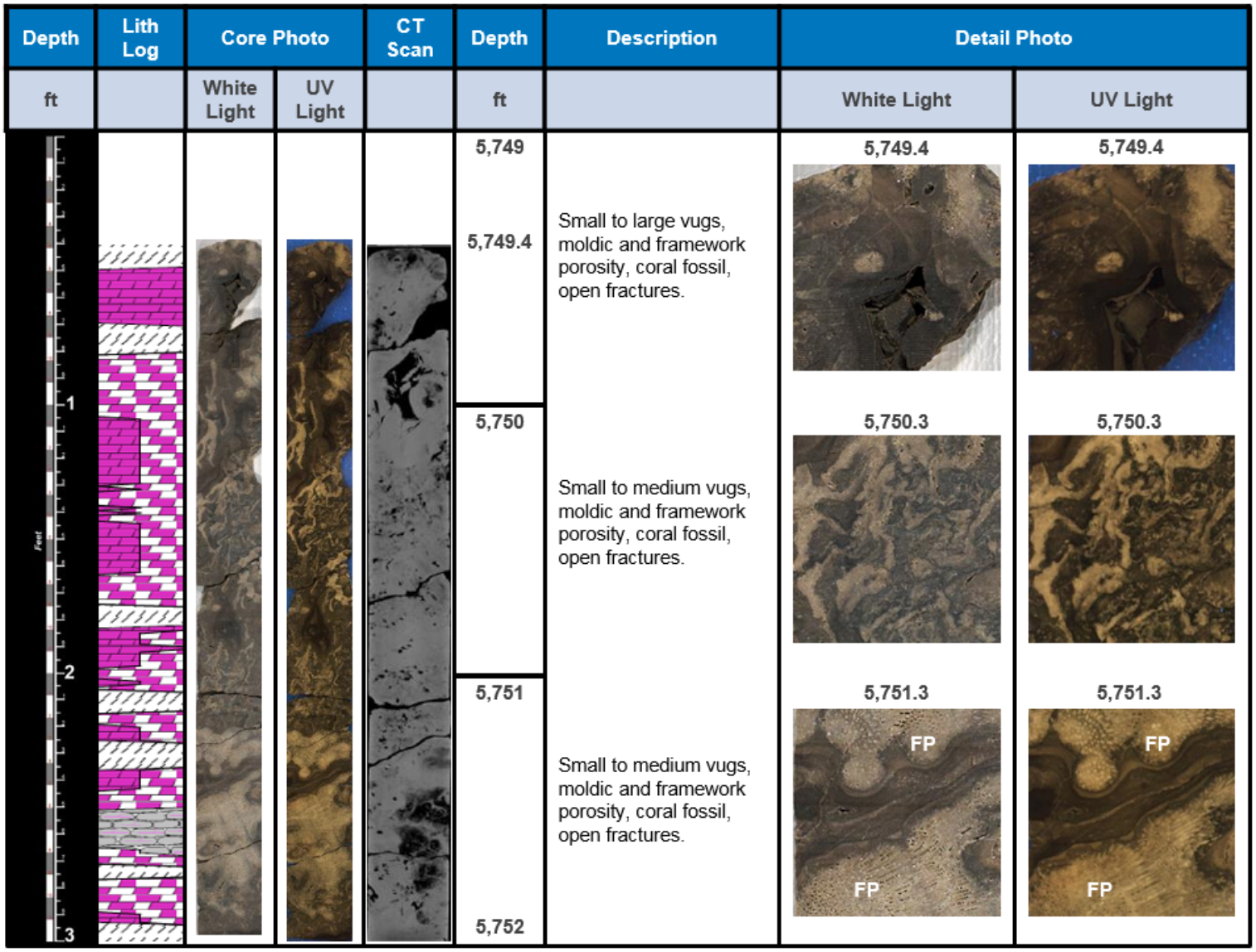


Figure B-40. Compiled illustration of lithology log, core photos (UV and white light), CT scan image, core descriptions, and annotated core images of the Brown Niagaran for depths 5,749 ft. to 5,752 ft.

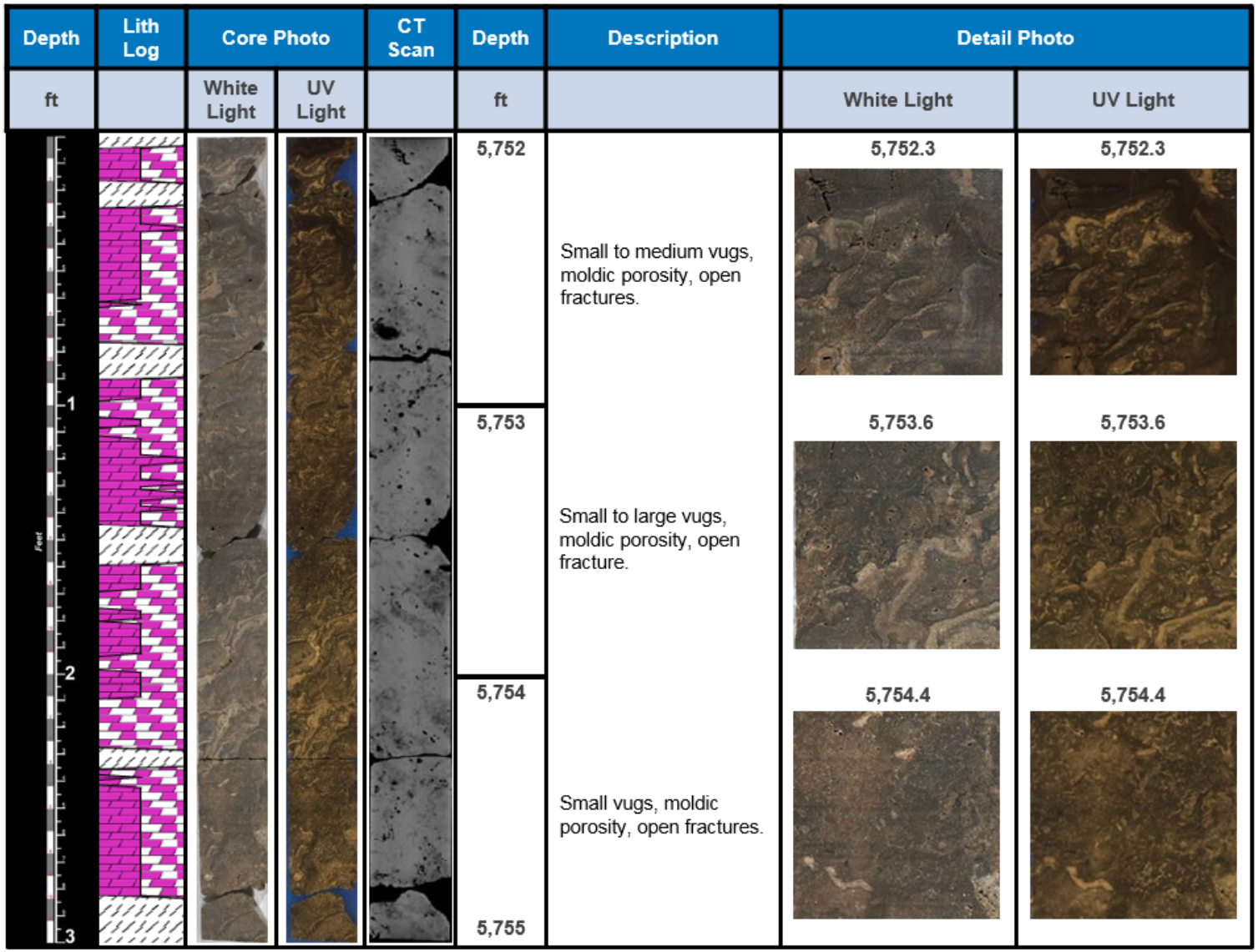


Figure B-41. Compiled illustration of lithology log, core photos (UV and white light), CT scan image, core descriptions, and annotated core images of the Brown Niagaran for depths 5,752 ft. to 5,755 ft.

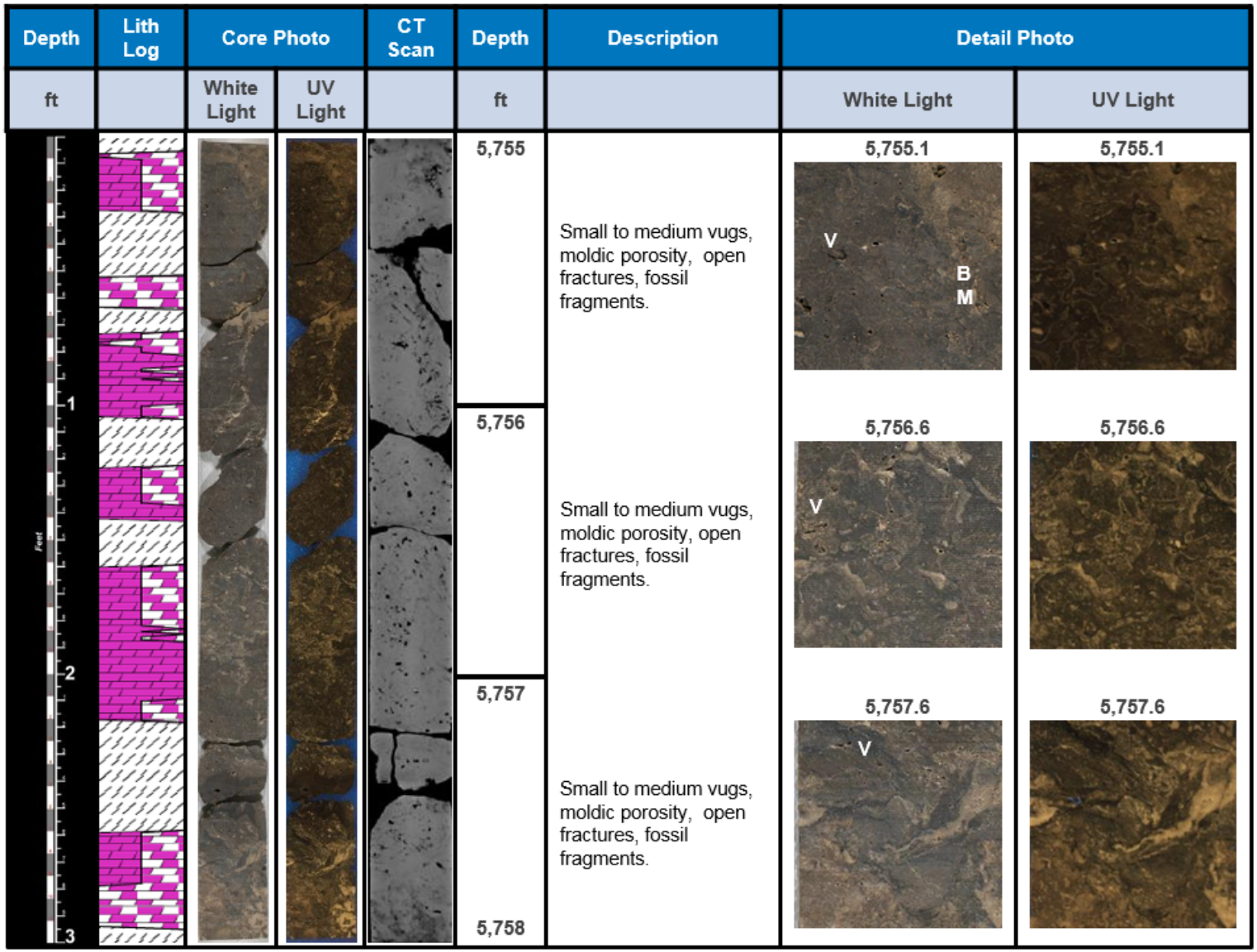


Figure B-42. Compiled illustration of lithology log, core photos (UV and white light), CT scan image, core descriptions, and annotated core images of the Brown Niagaran for depths 5,755 ft. to 5,758 ft.

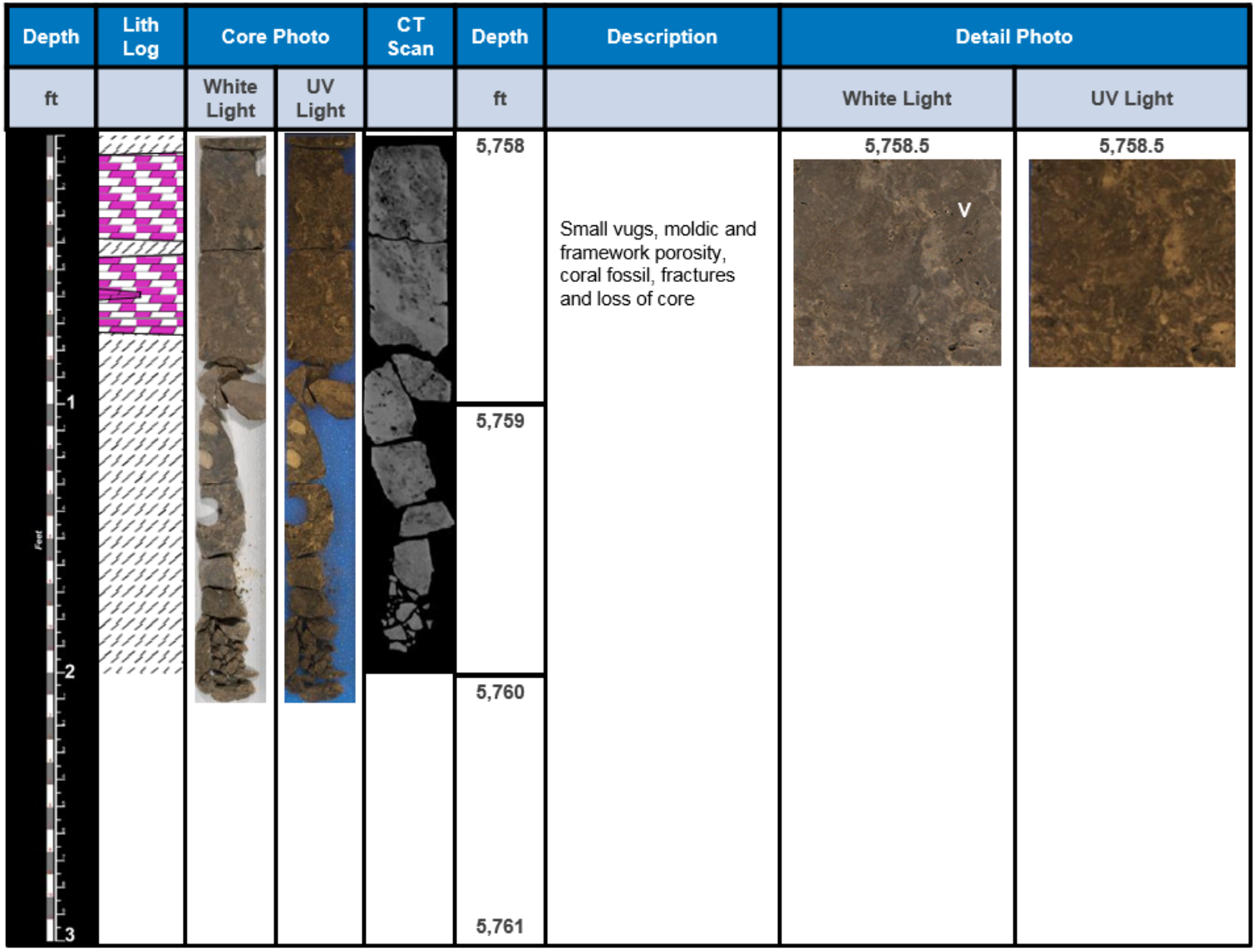


Figure B-43. Compiled illustration of lithology log, core photos (UV and white light), CT scan image, core descriptions, and annotated core images of the Brown Niagaran for depths 5,758 ft. to 5,761 ft.

B.1.2 Lawnichak 9-33 Rotary Sidewall Core

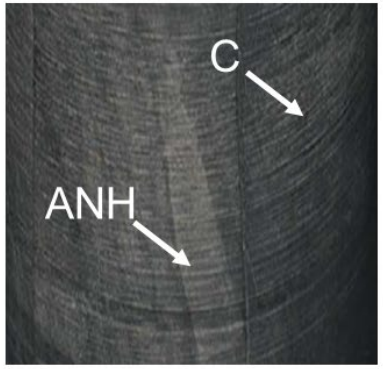
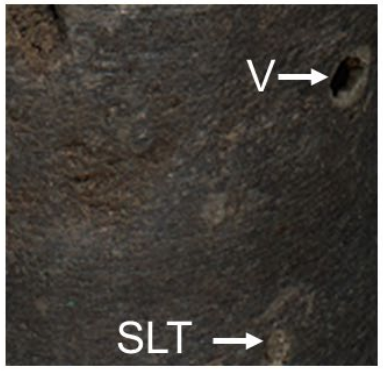
Depth Ft.	White Light Primary Features	UV Light Primary Features	Descriptions
5,330			White Light: Mixed carbonate and anhydrite, alternating light gray and dark layers. UV Light: Alternating light and dark layers.
5,330.5			White Light: Brown carbonate, large vugs, salt plugged vugs. UV Light: Light blue UV response due to potential residual oil, stylolites.

Figure B-44. Annotated RSWC images with corresponding core descriptions of the A-2 Carbonate for depths 5,330 ft. to 5,330.5 ft.

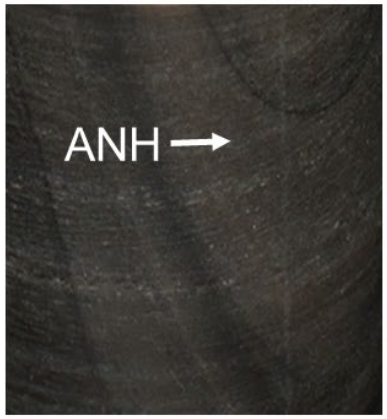
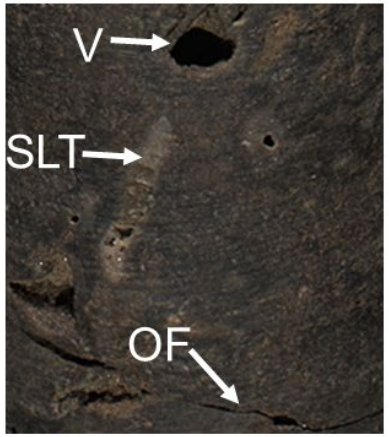
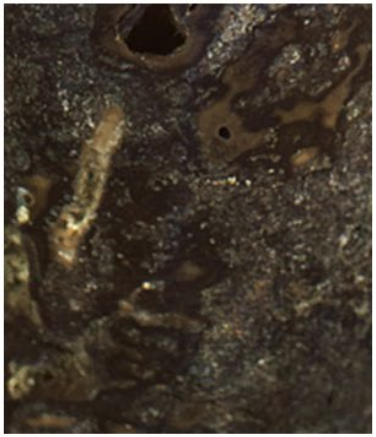
Depth Ft.	White Light Primary Features	UV Light Primary Features	Descriptions
5374			White Light: Mixed anhydrite and carbonate matrix, alternating dark gray and light gray laminations. UV Light: Anhydrite matrix, alternating dark and light laminations.
5374.5			White Light: Brown carbonate, large/small vugs, salt plugged vugs, open fracture. UV Light: Light blue UV response due to potential residual oil.

Figure B-45. Annotated RSWC images with corresponding core descriptions of the A-2 Carbonate for depths 5,374 ft. to 5,374.5 ft.

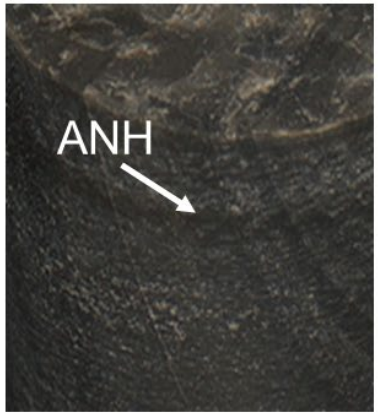
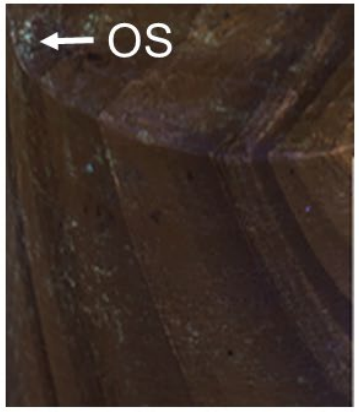
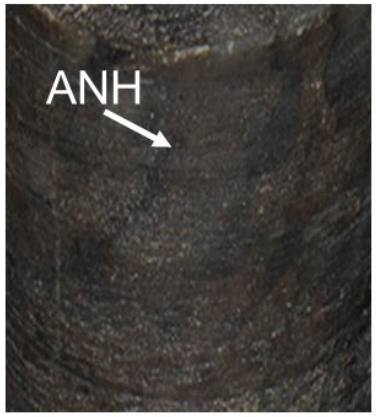
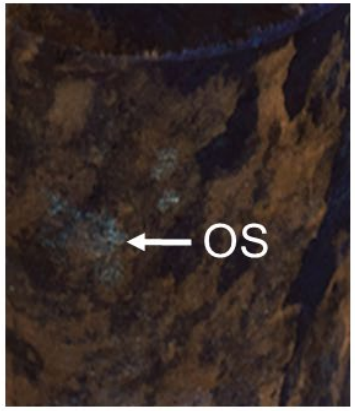
Depth Ft.	White Light Primary Features	UV Light Primary Features	Descriptions
5,378			White Light: Anhydrite matrix, alternating dark gray and light gray laminations. UV Light: Light blue UV response due to potential residual oil.
5,390			White Light: Anhydrite matrix, marbled pattern, dark blotches possibly due to presence of muds. UV Light: Light blue UV response due to potential residual oil.

Figure B-46. Annotated RSWC images with corresponding core descriptions of the A-2 Carbonate for depths 5,378 ft. to 5,390 ft.

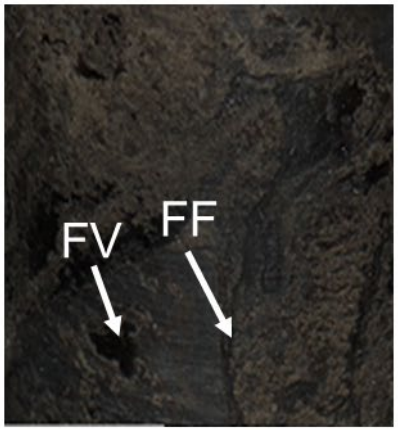
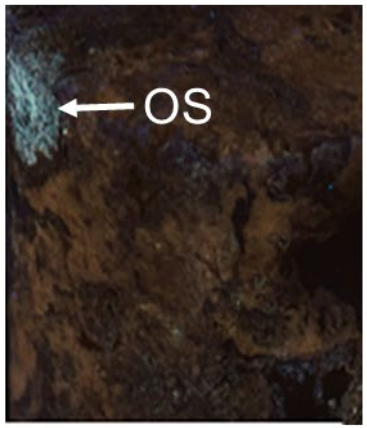
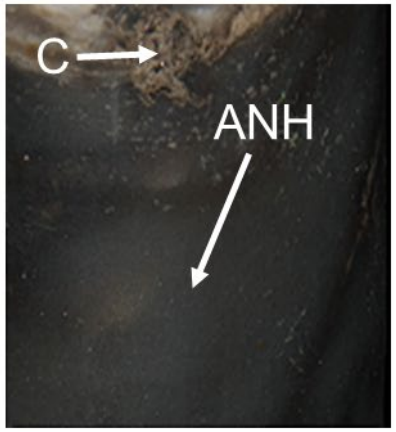
Depth Ft.	White Light Primary Features	UV Light Primary Features	Descriptions
5,393			White Light: Carbonate matrix, mud filled vugs, mud filled fractures. UV Light: Light blue UV response due to potential residual oil.
5,409			White Light: Mixed anhydrite and carbonate matrix. UV Light: Light blue UV response due to potential residual oil.

Figure B-47. Annotated RSWC images with corresponding core descriptions of the A-2 Carbonate and A-2 Evaporite for depths 5,393 ft. and 5,409 ft.

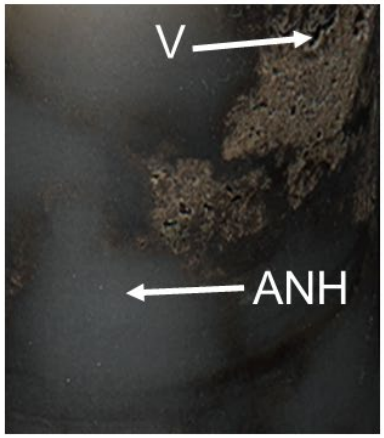
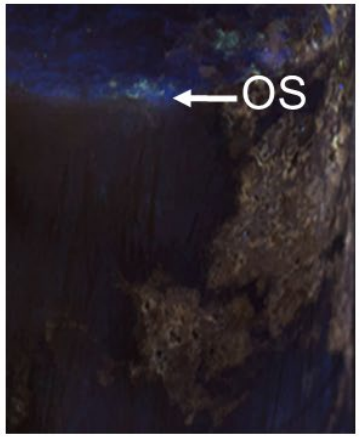
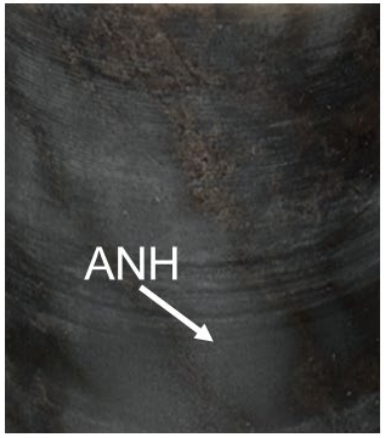
Depth Ft.	White Light Primary Features	UV Light Primary Features	Descriptions
5,415			White Light: Mixed anhydrite and carbonate matrix, small vugs. UV Light: Light blue UV response due to potential residual oil.
5,430			White Light: Mixed anhydrite and carbonate matrix, marbled pattern, some carbonate. UV Light: Light blue UV response due to potential residual oil.

Figure B-48. Annotated RSWC images with corresponding core descriptions of the A-2 Evaporite for depths 5,415 ft. and 5,430 ft.

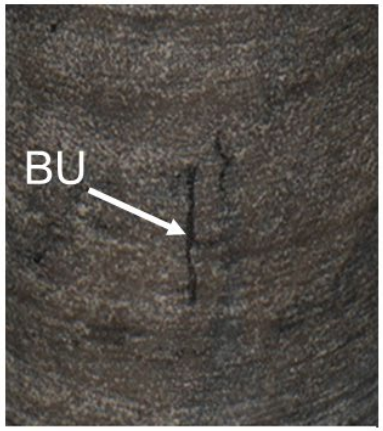
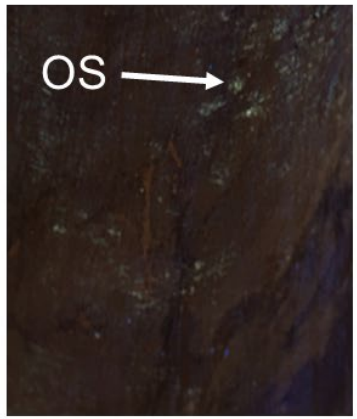
Depth Ft.	White Light Primary Features	UV Light Primary Features	Descriptions
5,440			White Light: Anhydrite matrix, alternating dark gray and light gray laminations. UV Light: Light blue UV response due to potential residual oil.
5,451			White Light: Anhydrite matrix, marbled pattern, dark blotches possibly due to presence of muds, bioturbation. UV Light: Light blue UV response due to potential residual oil.

Figure B-49. Annotated RSWC images with corresponding core descriptions of the A-2 Evaporite for depths 5,440 ft. and 5,451 ft.

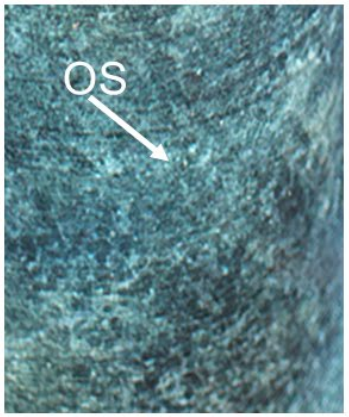
Depth Ft.	White Light Primary Features	UV Light Primary Features	Descriptions
5,454	 A-2 Anhydrite		White Light: Anhydrite matrix, alternating dark gray and light gray laminations. UV Light: Anhydrite matrix, stylolites.
5,455	 A-1 Carbonate		White Light: Gray carbonate. UV Light: Strong light blue UV response due to potential residual oil throughout sample.

Figure B-50. Annotated RSWC images with corresponding core descriptions of the A-2 Evaporite and A-1 Carbonate for depths 5,454 ft. to 5,455 ft.

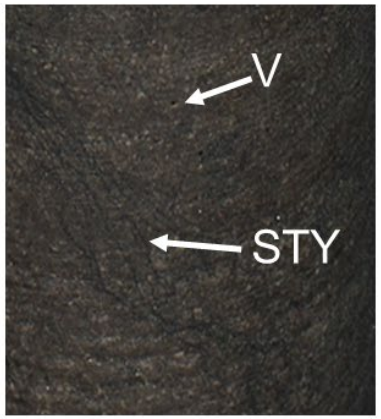
Depth Ft.	White Light Primary Features	UV Light Primary Features	Descriptions
5,456			White Light: Anhydrite matrix, alternating dark gray and light gray laminations, some marble like patterning. UV Light: Anhydrite matrix, stylolites.
5,458			White Light: Gray carbonate, stylolites, small vugs. UV Light: Strong light blue UV response due to potential residual oil throughout sample.

Figure B-51. Annotated RSWC images with corresponding core descriptions of the A-1 Carbonate for depths 5,456 ft. to 5,458 ft.

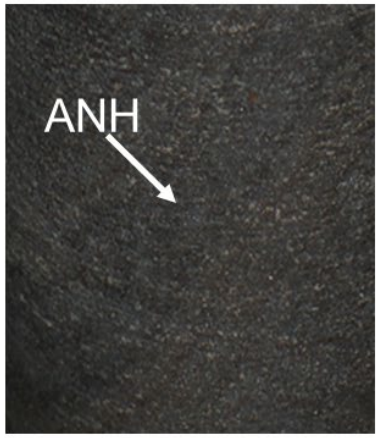
Depth Ft.	White Light Primary Features	UV Light Primary Features	Descriptions
5,465			White Light: Gray carbonate. UV Light: Strong light blue UV response due to potential residual oil throughout sample.
5,467			White Light: Anhydrite matrix, alternating dark gray and light gray laminations. UV Light: Light blue UV response due to potential residual oil.

Figure B-52. Annotated RSWC images with corresponding core descriptions of the A-1 Carbonate for depths 5,465 ft. to 5,467 ft.

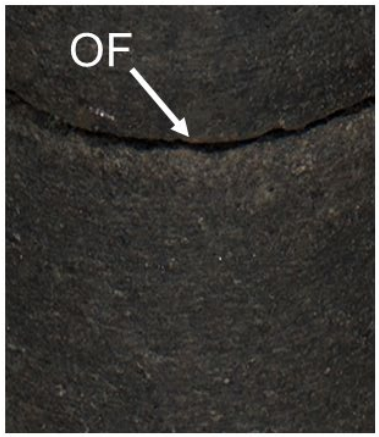
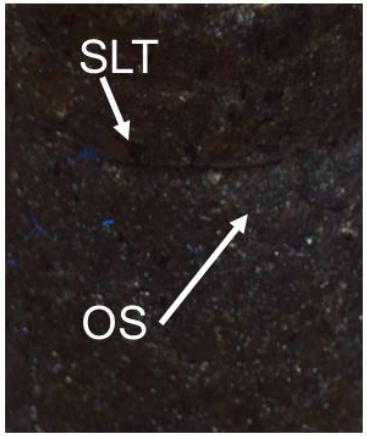
Depth Ft.	White Light Primary Features	UV Light Primary Features	Descriptions
5,472			White Light: Gray carbonate, open fracture. UV Light: Salt filled vugs, light blue UV response due to potential residual oil.
5,477			White Light: Gray carbonate. UV Light: Strong light blue UV response due to potential residual oil throughout sample.

Figure B-53. Annotated RSWC images with corresponding core descriptions of the A-1 Carbonate for depths 5,472 ft. to 5,477 ft.

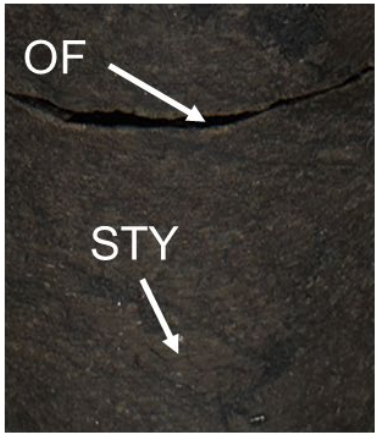
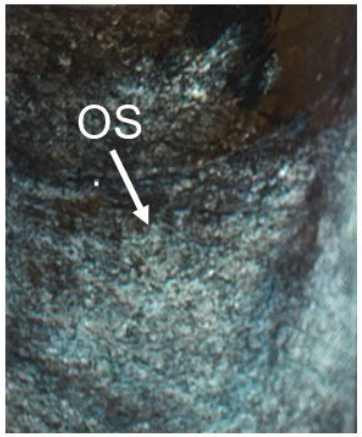
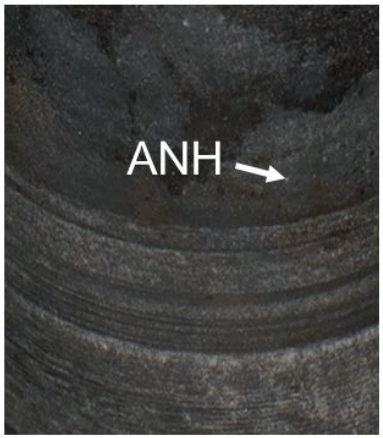
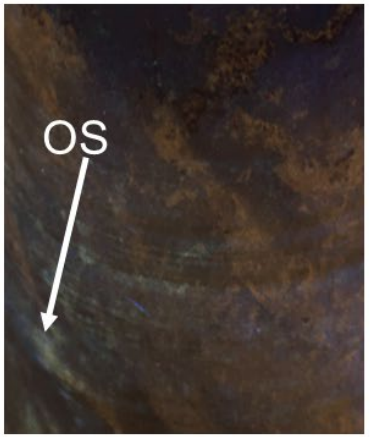
Depth Ft.	White Light Primary Features	UV Light Primary Features	Descriptions
5,482			White Light: Gray carbonate, stylolites, open fractures. UV Light: Strong light blue UV response due to potential residual oil.
5,485			White Light: Anhydrite matrix, some marble like patterning, dark blotches possibly due to presence of muds. UV Light: Light blue UV response due to potential residual oil.

Figure B-54. Annotated RSWC images with corresponding core descriptions of the A-1 Carbonate for depths 5,482 ft. to 5,485 ft.

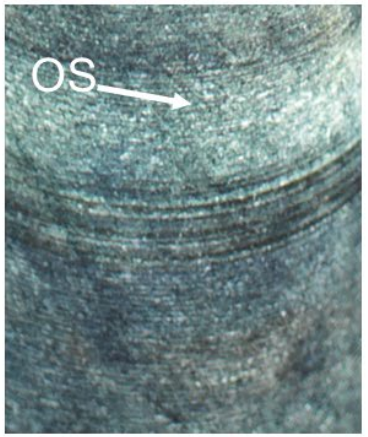
Depth Ft.	White Light Primary Features	UV Light Primary Features	Descriptions
5,490			White Light: Brown carbonate, large/small vugs. UV Light: Light blue UV response due to potential residual oil.
5,495			White Light: Gray carbonate. UV Light: Strong light blue UV response due to potential residual oil throughout sample.

Figure B-55. Annotated RSWC images with corresponding core descriptions of the A-1 Carbonate for depths 5,490 ft. to 5,495 ft.

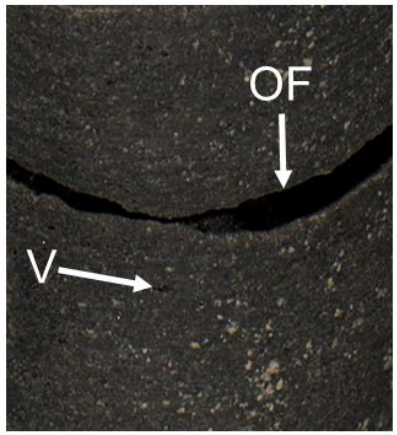
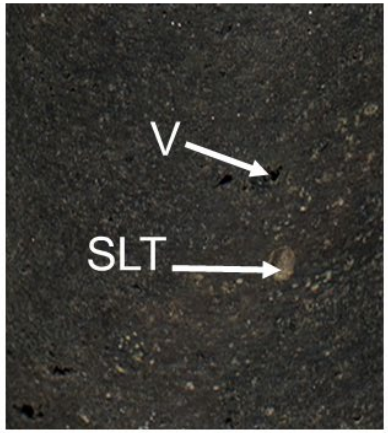
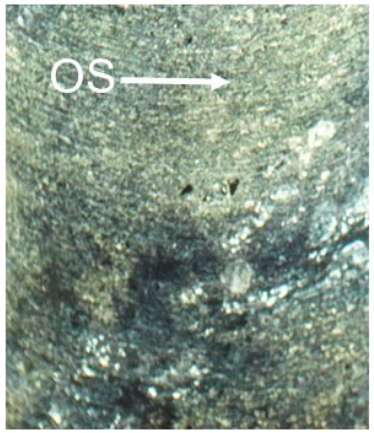
Depth Ft.	White Light Primary Features	UV Light Primary Features	Descriptions
5,503			White Light: Gray carbonate, small vugs, open fracture. UV Light: Strong light blue UV response due to potential residual oil.
5,509			White Light: Gray carbonate, small vugs, salt plugged vugs. UV Light: Strong light blue UV response due to potential residual oil throughout sample.

Figure B-56. Annotated RSWC images with corresponding core descriptions of the A-1 Carbonate for depths 5,503 ft. and 5,509 ft.

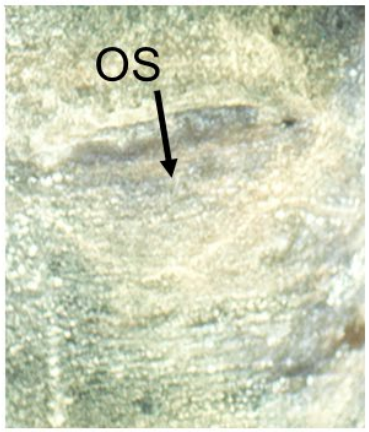
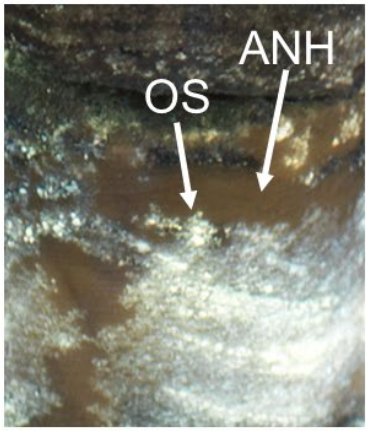
Depth Ft.	White Light Primary Features	UV Light Primary Features	Descriptions
5,511			White Light: Carbonate matrix. UV Light: Strong light blue UV response due to potential residual oil throughout sample.
5,514			White Light: Mixed carbonate and anhydrite matrix, dark areas are possible muds, open fracture. UV Light: Strong light blue UV response due to potential residual oil.

Figure B-57. Annotated RSWC images with corresponding core descriptions of the A-1 Carbonate for depths 5,511 ft. to 5,514 ft.

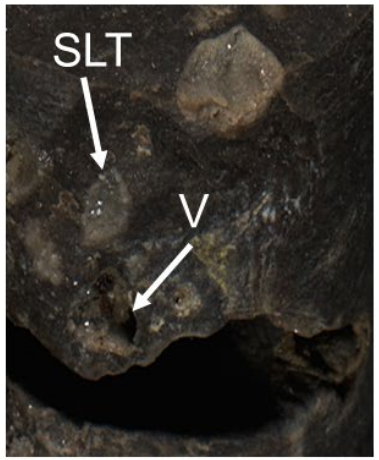
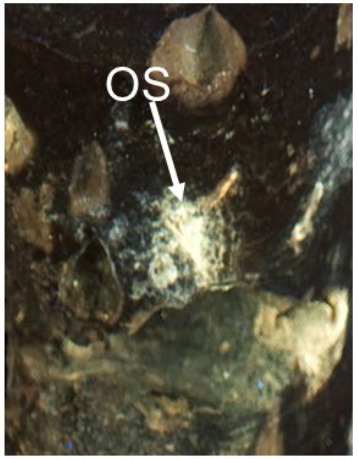
Depth Ft.	White Light Primary Features	UV Light Primary Features	Descriptions
5,520			White Light: Gray carbonate, medium/small vugs, salt plugged vugs. UV Light: Strong light blue UV response due to potential residual oil throughout sample.
5,523			White Light: Gray carbonate, large vugs, salt plugged vugs, broken core. UV Light: Strong light blue UV response due to potential residual oil.

Figure B-58. Annotated RSWC images with corresponding core descriptions of the A-1 Carbonate for depths 5,520 ft. to 5,523 ft.

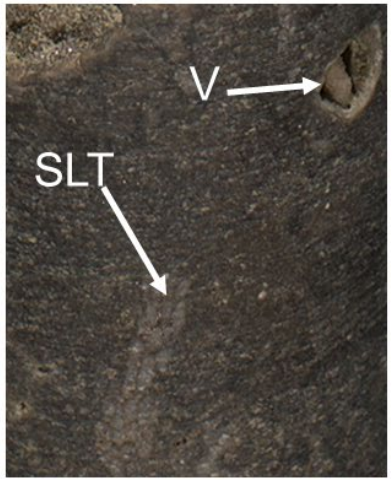
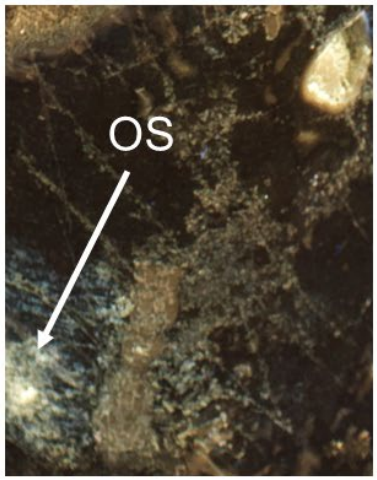
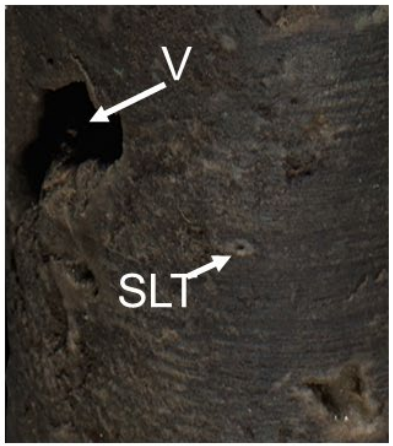
Depth Ft.	White Light Primary Features	UV Light Primary Features	Descriptions
5,570			White Light: Gray carbonate, medium/small vugs, salt plugged vugs. UV Light: Strong light blue UV response due to potential residual oil.
5,576			White Light: Gray carbonate, medium/small vugs, salt plugged vugs. UV Light: Gray carbonate.

Figure B-59. Annotated RSWC images with corresponding core descriptions of the Brown Niagaran for depths 5,570 ft. and 5,576.5 ft.

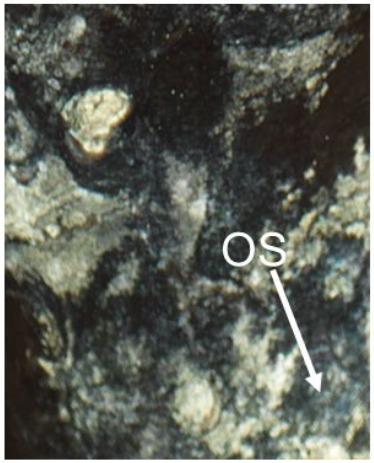
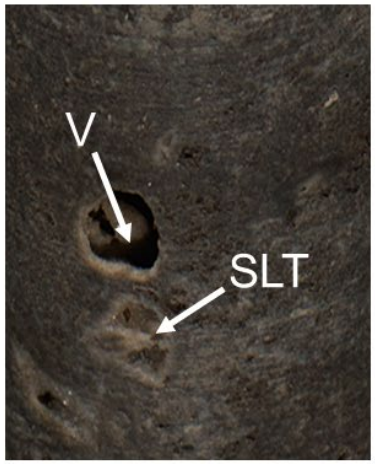
Depth Ft.	White Light Primary Features	UV Light Primary Features	Descriptions
5,580			White Light: Gray carbonate, small vugs, salt plugged vugs. UV Light: Strong light blue UV response due to potential residual oil.
5,583			White Light: Gray carbonate, medium/small vugs, salt plugged vugs. UV Light: Strong light blue UV response due to potential residual oil.

Figure B-60. Annotated RSWC images with corresponding core descriptions of the Brown Niagaran for depths 5,580 ft. to 5,583 ft.

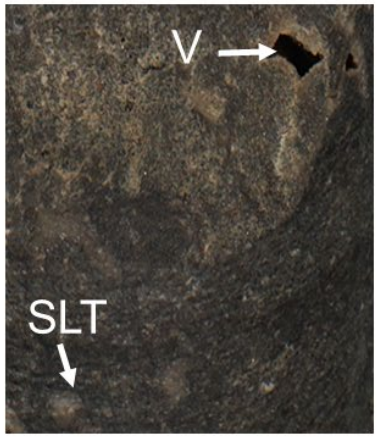
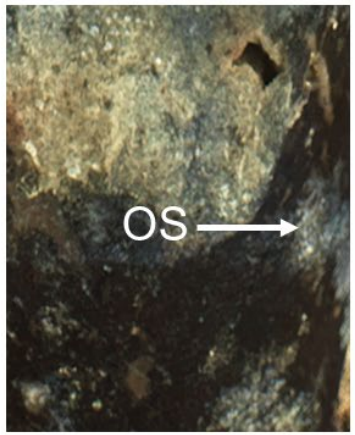
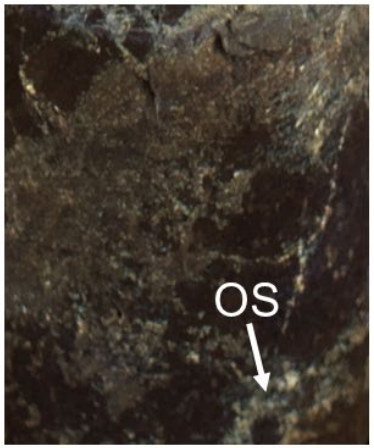
Depth Ft.	White Light Primary Features	UV Light Primary Features	Descriptions
5,587.5			White Light: Gray carbonate, medium/small vugs, salt plugged vugs. UV Light: Strong light blue UV response due to potential residual oil.
5,588			White Light: Gray carbonate, small vugs. UV Light: Strong light blue UV response due to potential residual oil.

Figure B-61. Annotated RSWC images with corresponding core descriptions of the Brown Niagaran for depths 5,587.5 ft. to 5,588 ft.

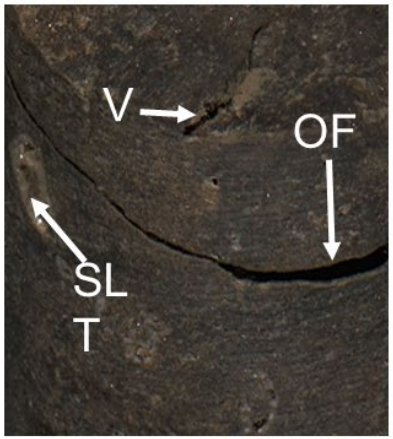
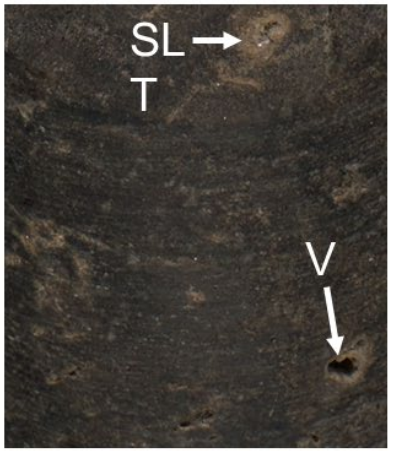
Depth Ft.	White Light Primary Features	UV Light Primary Features	Descriptions
5,595			White Light: Gray carbonate, vugs, salt plugged vugs, open fracture. UV Light: Strong light blue UV response due to potential residual oil.
5,608			White Light: Gray carbonate, large/small vugs, salt plugged vugs. UV Light: Strong light blue UV response due to potential residual oil.

Figure B-62. Annotated RSWC images with corresponding core descriptions of the Brown Niagaran for depths 5,595 ft. and 5,608 ft.

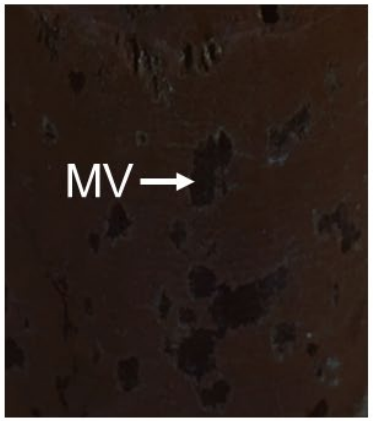
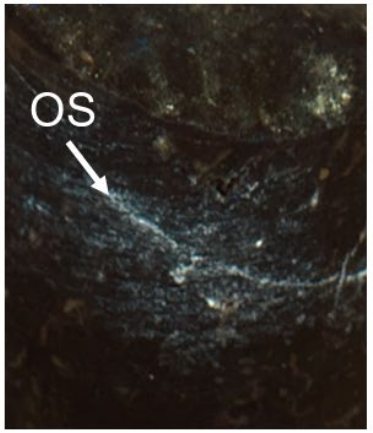
Depth Ft.	White Light Primary Features	UV Light Primary Features	Descriptions
5,615			White Light: Carbonate, filled moldic vugs. UV Light: Carbonate, filled moldic vugs.
5,625			White Light: Gray carbonate, small vugs, salt plugged vugs. UV Light: Strong light blue UV response due to potential residual oil.

Figure B-63. Annotated RSWC images with corresponding core descriptions of the Brown Niagaran for depths 5,615 ft. and 5,625 ft.

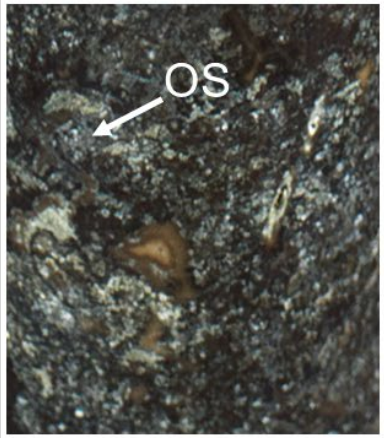
Depth Ft.	White Light Primary Features	UV Light Primary Features	Descriptions
5,627			White Light: Gray carbonate, small vugs, salt plugged vugs. UV Light: Strong light blue UV response due to potential residual oil.
5,630			White Light: Gray carbonate, salt plugged vugs. UV Light: Strong light blue UV response due to potential residual oil.

Figure B-64. Annotated RSWC images with corresponding core descriptions of the Brown Niagaran for depths 5,627 ft. to 5,630 ft.

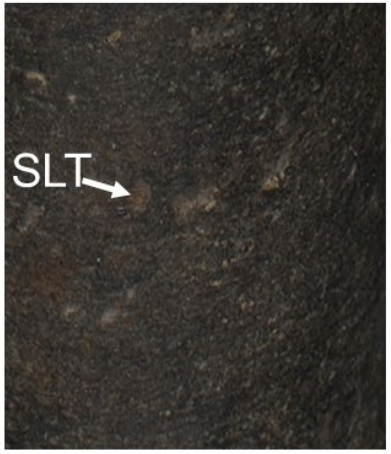
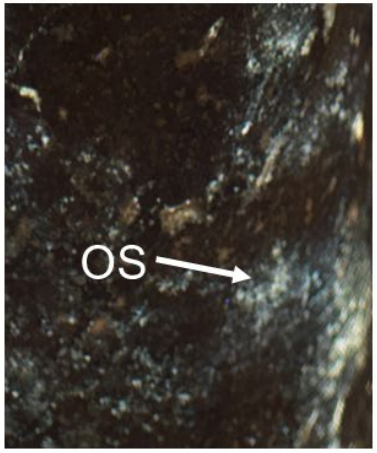
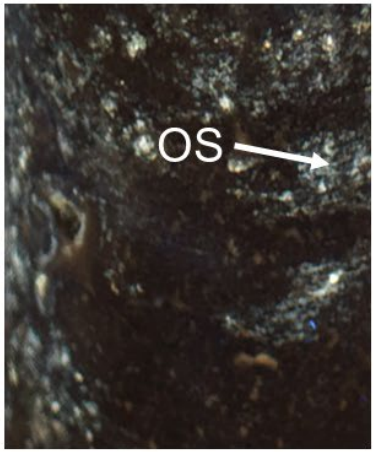
Depth Ft.	White Light Primary Features	UV Light Primary Features	Descriptions
5,633			White Light: Gray carbonate, salt plugged vugs. UV Light: Strong light blue UV response due to potential residual oil.
5,639			White Light: Gray carbonate, large vug, salt plugged vugs. UV Light: Strong light blue UV response due to potential residual oil.

Figure B-65. Annotated RSWC images with corresponding core descriptions of the Brown Niagaran for depths 5,633 ft. and 5,639 ft.

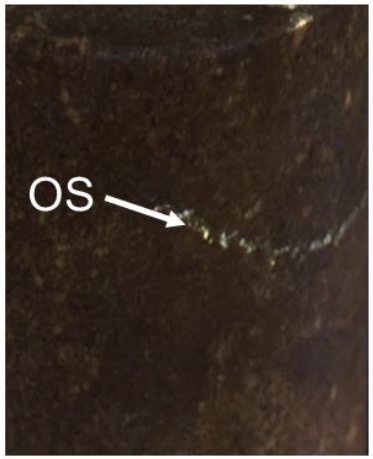
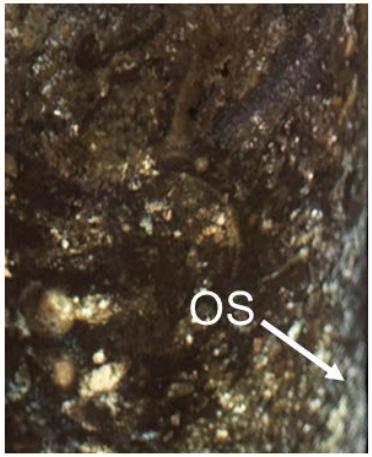
Depth Ft.	White Light Primary Features	UV Light Primary Features	Descriptions
5,643			White Light: Gray carbonate, small vugs. UV Light: Strong light blue UV response due to potential residual oil.
5,647.5			White Light: Gray carbonate, small vugs, salt plugged vugs. UV Light: Strong light blue UV response due to potential residual oil.

Figure B-66. Annotated RSWC images with corresponding core descriptions of the Brown Niagaran for depths 5,643 ft. to 5,647.5 ft.

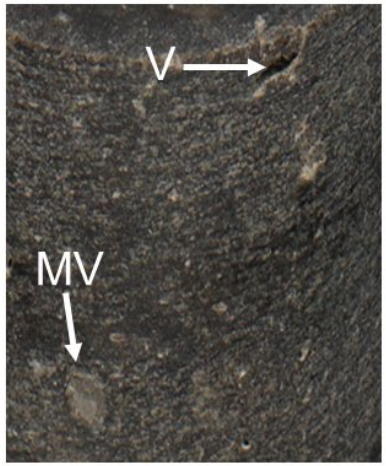
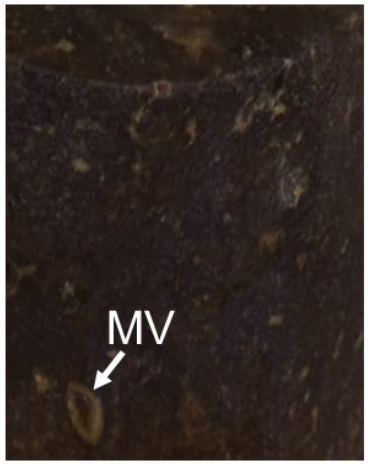
Depth Ft.	White Light Primary Features	UV Light Primary Features	Descriptions
5,655			White Light: Gray carbonate, small vug, filled moldic vugs. UV Light: Filled Moldic vugs.
5,663			White Light: Gray carbonate matrix, bioturbation. UV Light: Gray carbonate matrix.

Figure B-67. Annotated RSWC images with corresponding core descriptions of the Brown Niagaran for depths 5,655 ft. and 5,663 ft.

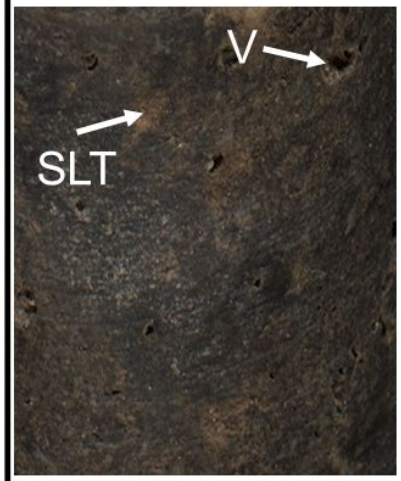
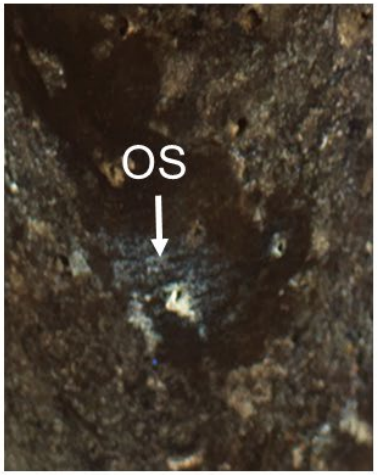
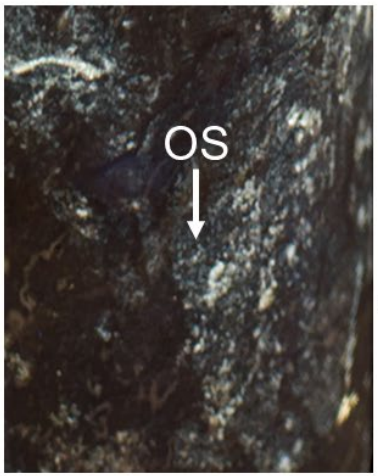
Depth Ft.	White Light Primary Features	UV Light Primary Features	Descriptions
5,665.5			White Light: Gray carbonate, medium/small vugs, salt plugged vugs. UV Light: Strong light blue UV response due to potential residual oil.
5,669			White Light: Gray carbonate, small vugs, salt plugged vugs, bioturbation. UV Light: Strong light blue UV response due to potential residual oil.

Figure B-68. Annotated RSWC images with corresponding core descriptions of the Brown Niagaran for depths 5,665.5 ft. to 5,669 ft.

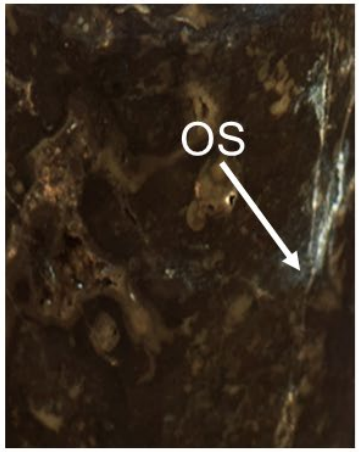
Depth Ft.	White Light Primary Features	UV Light Primary Features	Descriptions
5,676			White Light: Carbonate matrix, some dark gray laminations. UV Light: Carbonate matrix, alternating dark gray and light gray laminations.
5,685			White Light: Gray carbonate, medium/small vugs, salt plugged vugs. UV Light: Strong light blue UV response due to potential residual oil.

Figure B-69. Annotated RSWC images with corresponding core descriptions of the Brown Niagaran for depths 5,676 ft. and 5,685 ft.

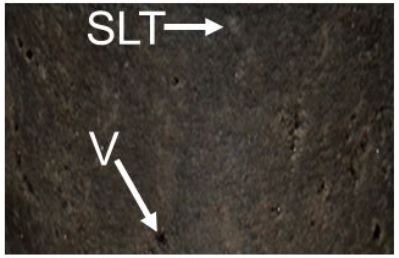
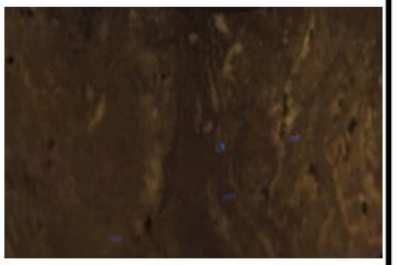
Depth Ft.	White Light Primary Features	UV Light Primary Features	Descriptions
5,773			White Light: Gray carbonate, medium/small vugs. UV Light: Gray carbonate.
5,782			White Light: Gray carbonate, small vugs. UV Light: Gray carbonate.

Figure B-70. Annotated RSWC images with corresponding core descriptions of the Brown Niagaran for depths 5,773 ft. and 5,782 ft.

Depth Ft.	White Light Primary Features	UV Light Primary Features	Descriptions
5,793			White Light: Gray carbonate, small vugs. UV Light: Gray carbonate.
5,800			White Light: Gray carbonate, medium/small vugs. UV Light: Gray carbonate.

Figure B-71. Annotated RSWC images with corresponding core descriptions of the Brown Niagaran for depths 5,793 ft. and 5,800 ft.

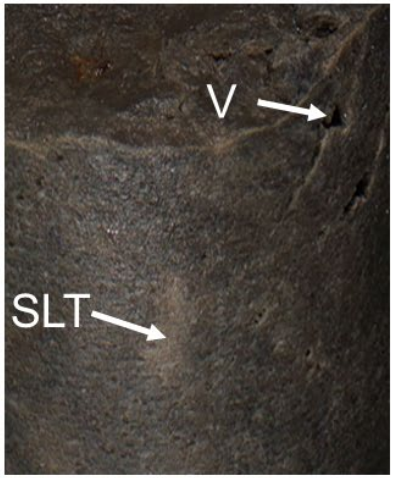
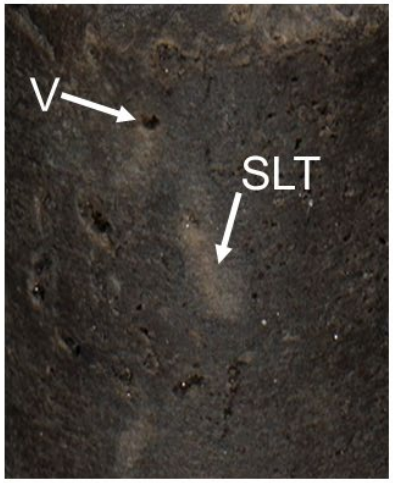
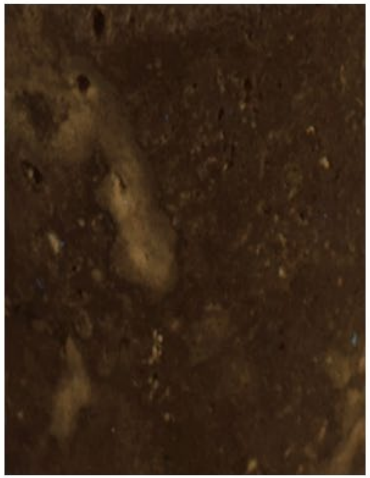
Depth Ft.	White Light Primary Features	UV Light Primary Features	Descriptions
5,805			White Light: Gray carbonate, medium/small vugs, salt plugged vugs. UV Light: Gray carbonate.
5,815			White Light: Gray carbonate, medium/small vugs, salt plugged vugs. UV Light: Gray carbonate.

Figure B-72. Annotated RSWC images with corresponding core descriptions of the Brown Niagaran for depths 5,805 ft. and 5,815 ft.

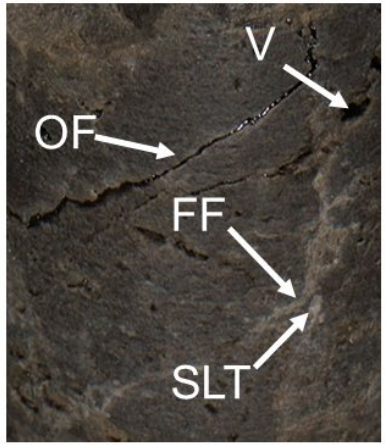
Depth Ft.	White Light Primary Features	UV Light Primary Features	Descriptions
5,817			White Light: Gray carbonate, small vugs, salt plugged vugs. UV Light: Gray carbonate.
5,820			White Light: Gray carbonate, medium/small vugs, salt plugged vugs, open fractures, filled fractures. UV Light: Gray carbonate.

Figure B-73. Annotated RSWC images with corresponding core descriptions of the Brown Niagaran for depths 5,817 ft. to 5,820 ft.

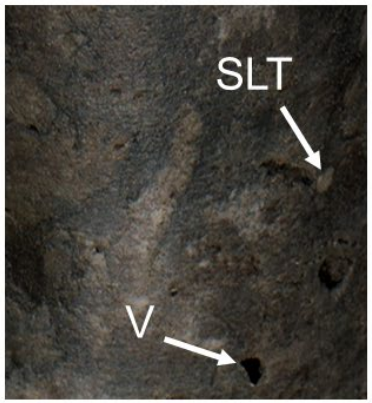
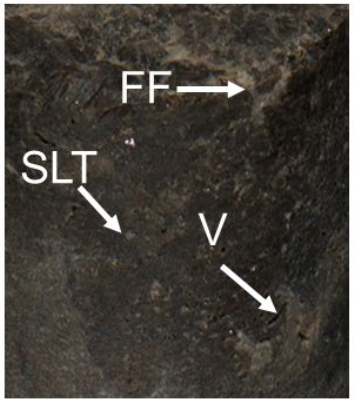
Depth Ft.	White Light Primary Features	UV Light Primary Features	Descriptions
5,830			White Light: Gray carbonate, large/small vugs, salt plugged vugs. UV Light: Gray carbonate.
5,8330			White Light: Gray carbonate, small vugs, salt plugged vugs, filled fractures. UV Light: Gray carbonate.

Figure B-74. Annotated RSWC images with corresponding core descriptions of the Brown Niagaran for depths 5,830 ft. to 5,833 ft.

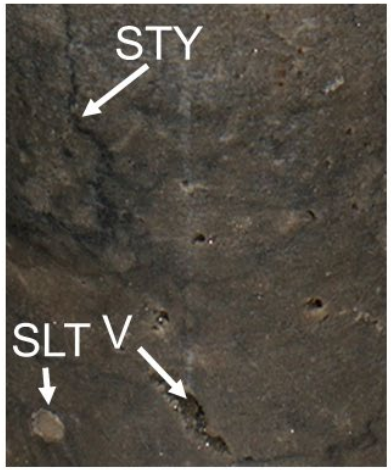
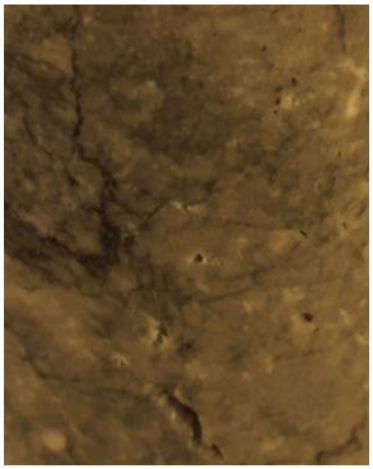
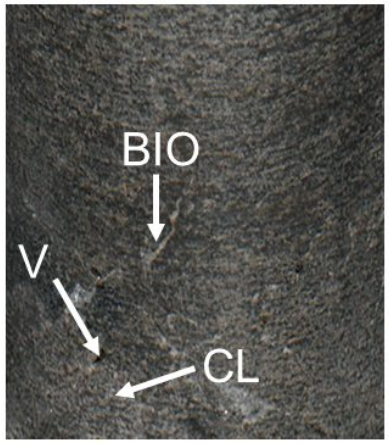
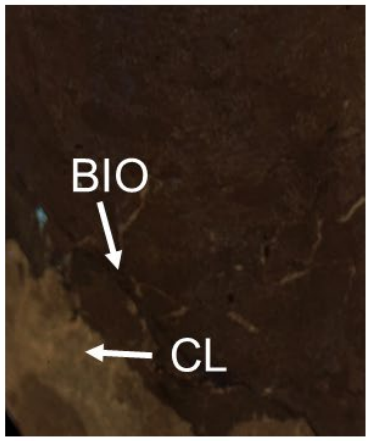
Depth Ft.	White Light Primary Features	UV Light Primary Features	Descriptions
5,847			White Light: Gray carbonate, large/small vugs, salt plugged vugs. UV Light: Gray carbonate.
5,865			White Light: Gray carbonate, small vugs, bioturbation, potential carbonate clast. UV Light: Gray carbonate, bioturbation, potential carbonate clast.

Figure B-75. Annotated RSWC images with corresponding core descriptions of the Brown Niagaran for depths 5,847 ft. and 5,865 ft.

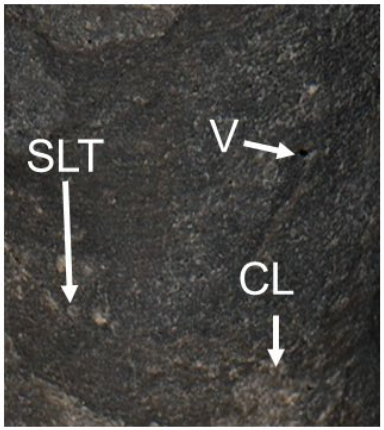
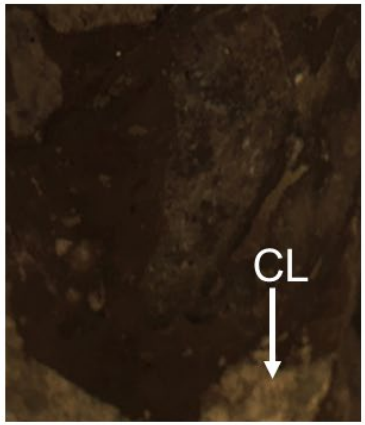
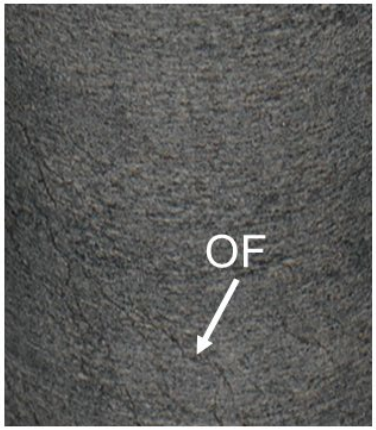
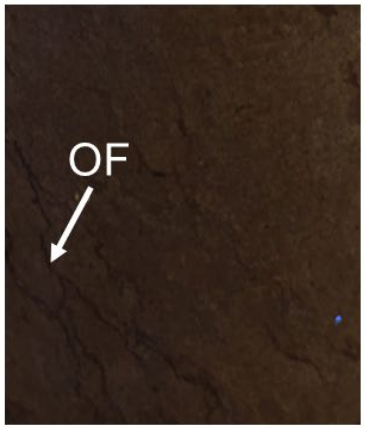
Depth Ft.	White Light Primary Features	UV Light Primary Features	Descriptions
5,867	 Brown Niagara		White Light: Gray carbonate, small vugs, bioturbation, potential carbonate clast. UV Light: Gray carbonate, potential carbonate clast.
5,868	 Gray Niagara		White Light: Gray carbonate, open fractures. UV Light: Gray carbonate, natural fractures.

Figure B-76. Annotated RSWC images with corresponding core descriptions of the Brown Niagaran and Gray Niagaran for depths 5,867 ft. to 5,868 ft.

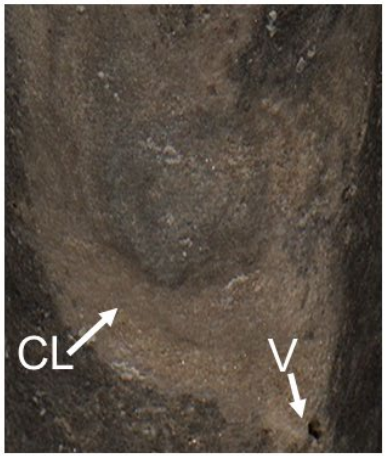
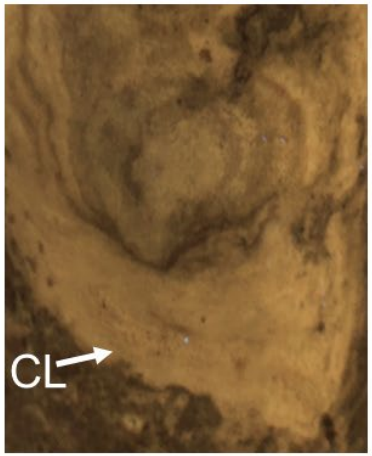
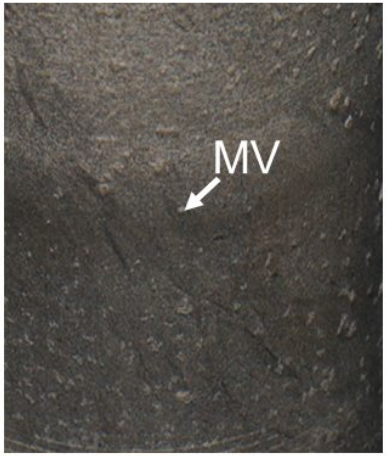
Depth Ft.	White Light Primary Features	UV Light Primary Features	Descriptions
5,873			White Light: Gray carbonate, small vugs, potential carbonate clast. UV Light: Gray carbonate, small vugs, potential carbonate clast.
5,899			White Light: Gray carbonate, filled moldic vugs. UV Light: Gray carbonate, filled moldic vugs.

Figure B-77. Annotated RSWC images with corresponding core descriptions of the Gray Niagaran for depths 5,873 ft. to 5,899 ft.

B.2 Chester 8-16

B.2.1 Whole Core

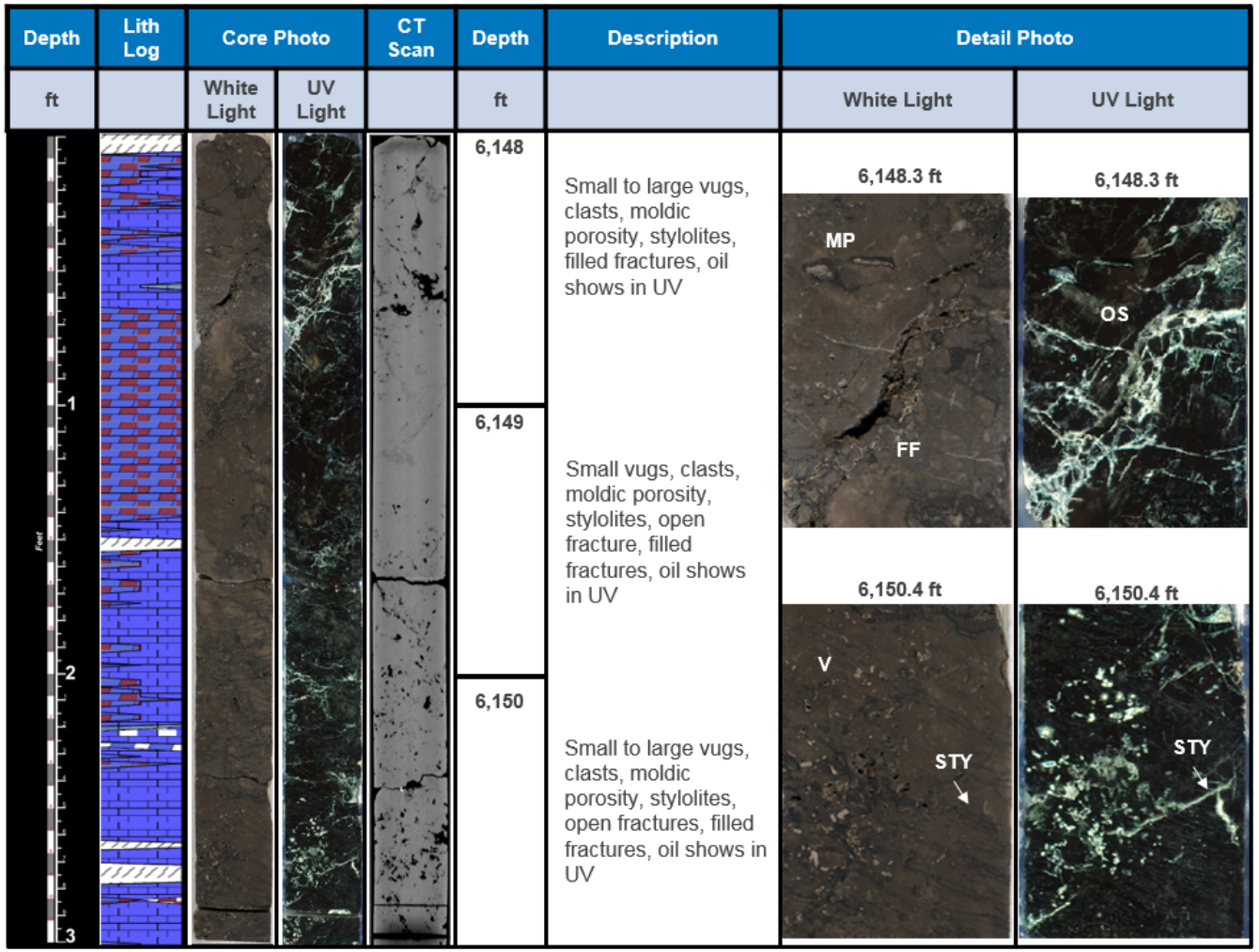


Figure B-78. Compiled illustration of lithology log, core photos (UV and white light), CT scan image, core descriptions, and annotated core images of the Brown Niagaran for depths 6,148 ft. to 6,150 ft.

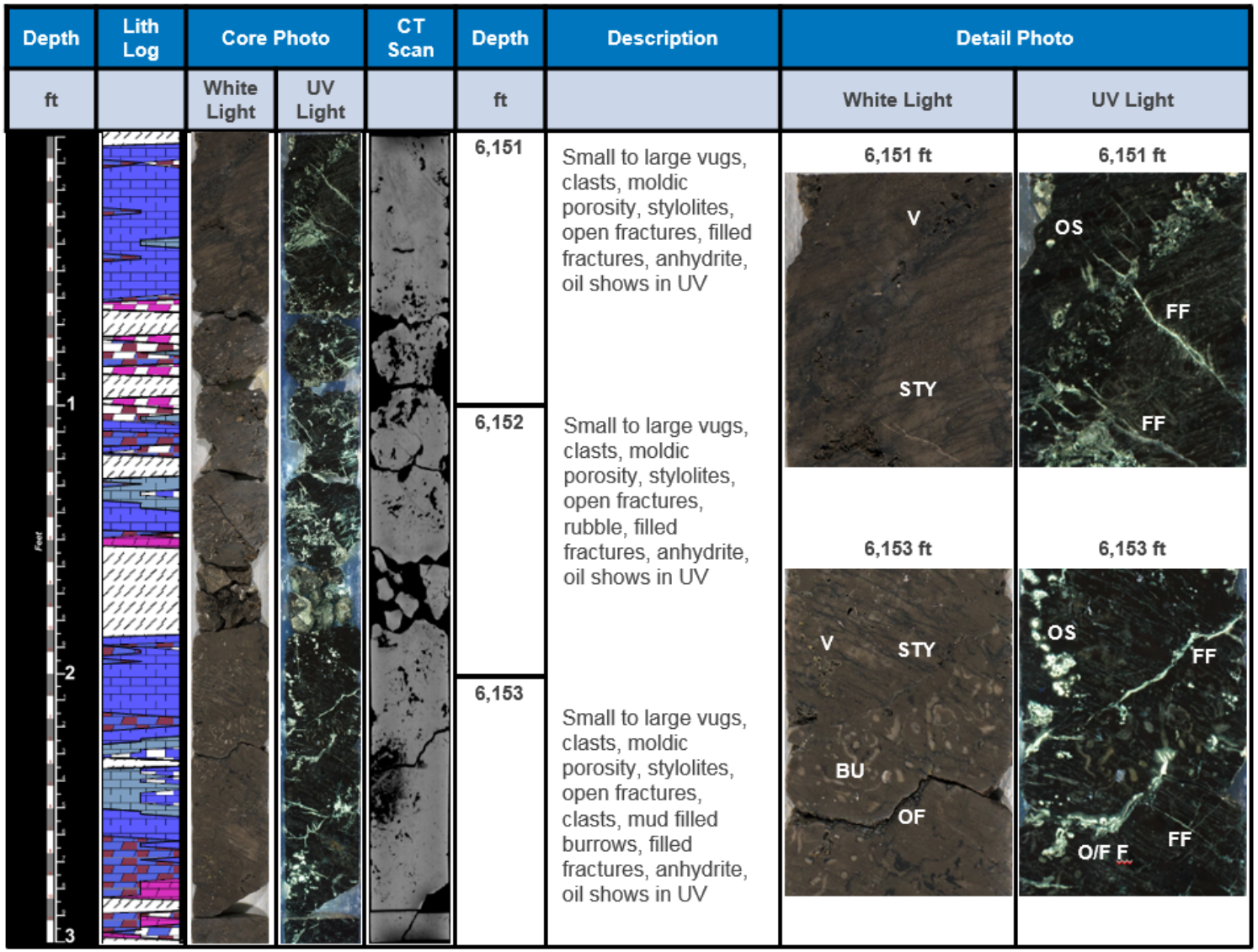


Figure B-79. Compiled illustration of lithology log, core photos (UV and white light), CT scan image, core descriptions, and annotated core images of the Brown Niagaran for depths 6,151 ft. to 6,153 ft.

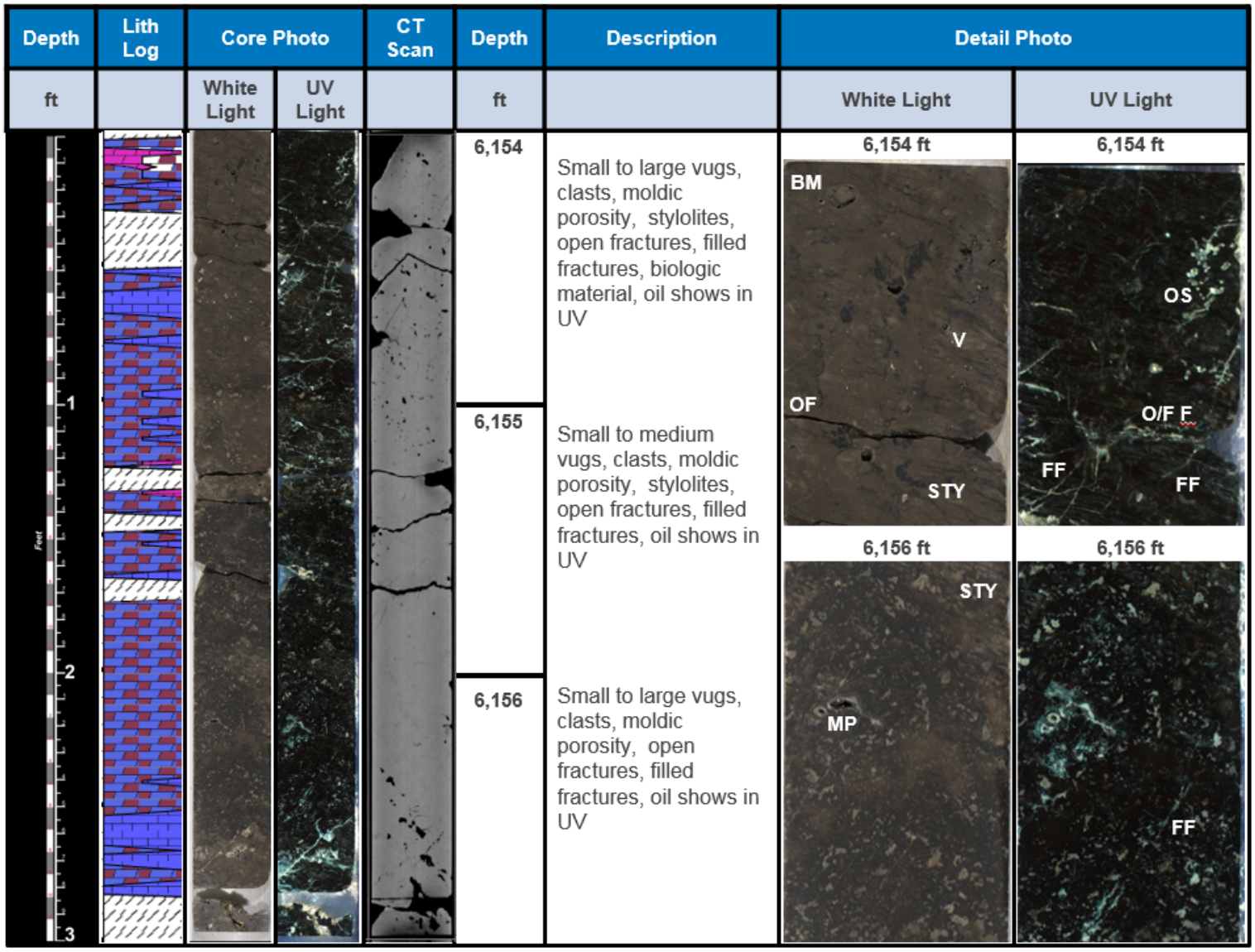


Figure B-80. Compiled illustration of lithology log, core photos (UV and white light), CT scan image, core descriptions, and annotated core images of the Brown Niagaran for depths 6,154 ft. to 6,156 ft.

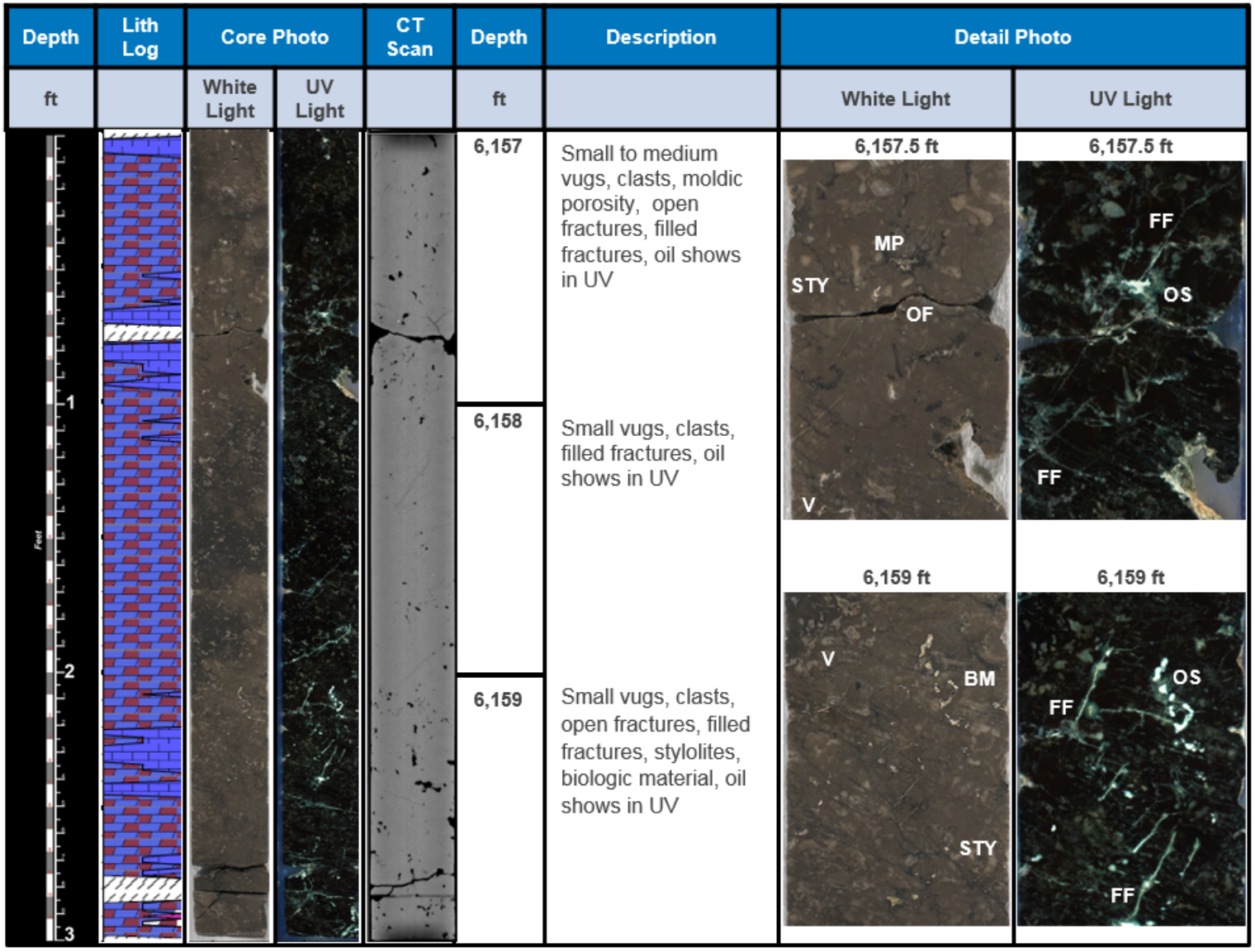


Figure B-81. Compiled illustration of lithology log, core photos (UV and white light), CT scan image, core descriptions, and annotated core images of the Brown Niagaran for depths 6,157 ft. to 6,159 ft.

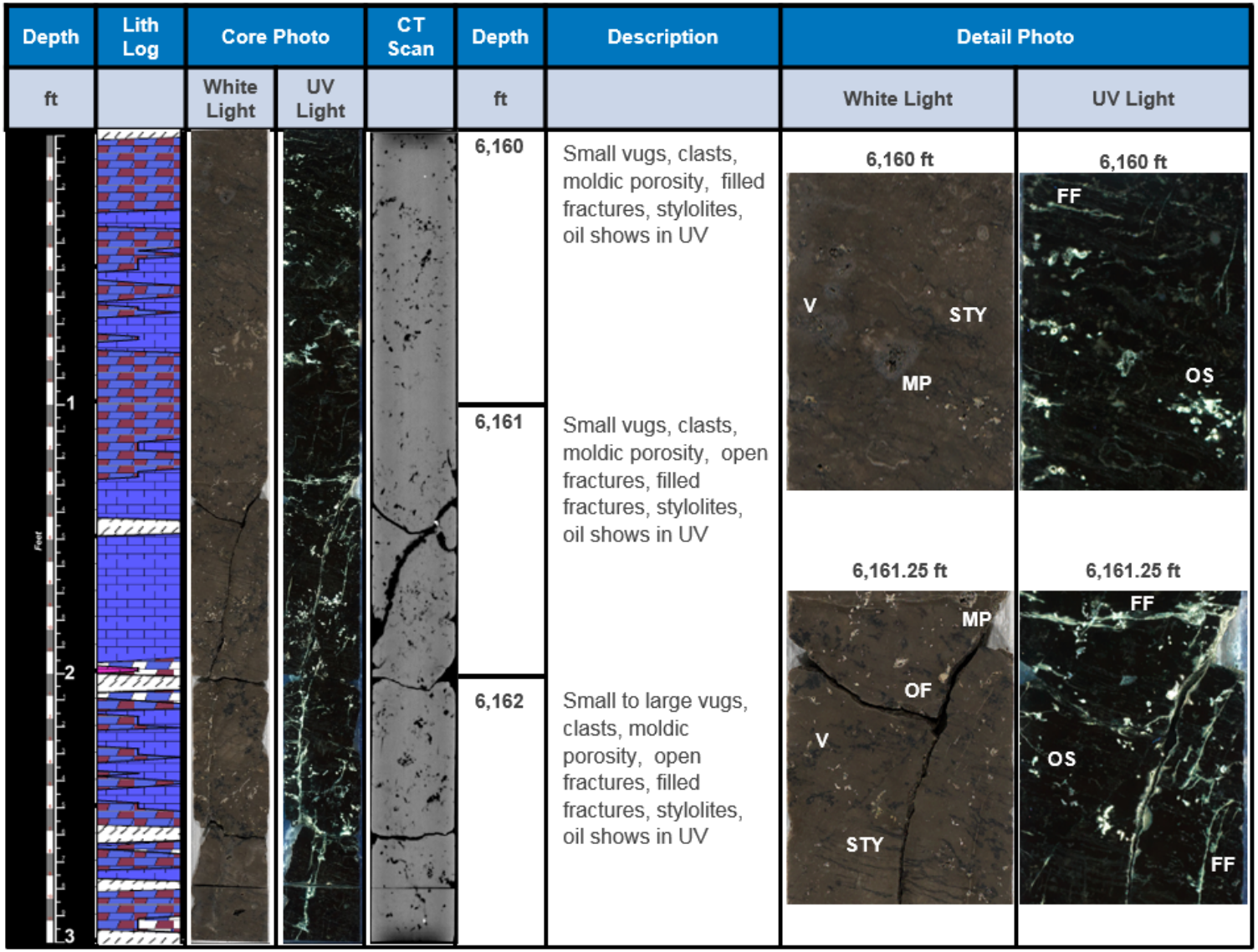


Figure B-82. Compiled illustration of lithology log, core photos (UV and white light), CT scan image, core descriptions, and annotated core images of the Brown Niagaran for depths 6,160 ft. to 6,162 ft.

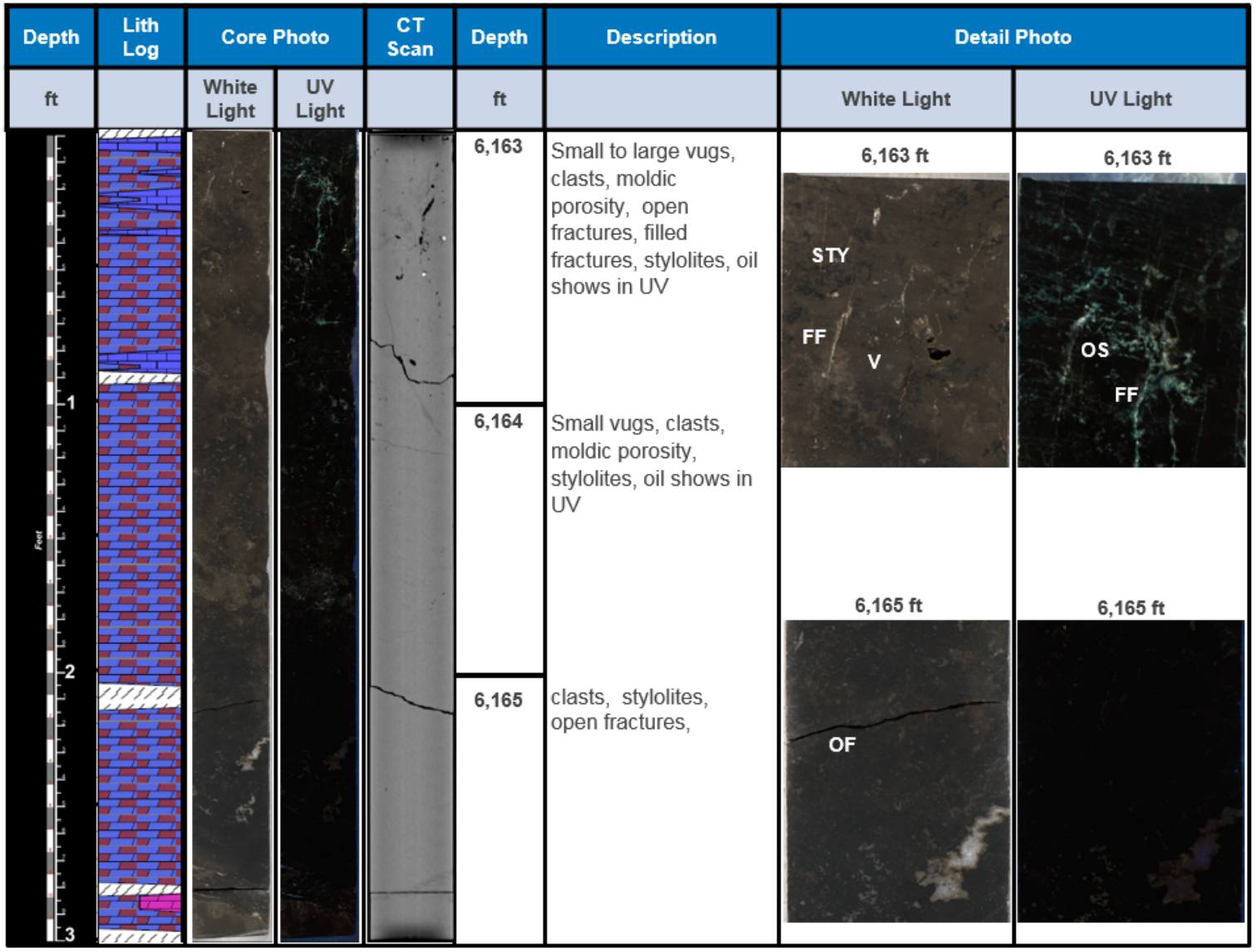


Figure B-83. Compiled illustration of lithology log, core photos (UV and white light), CT scan image, core descriptions, and annotated core images of the Brown Niagaran for depths 6,163 ft. to 6,165 ft.

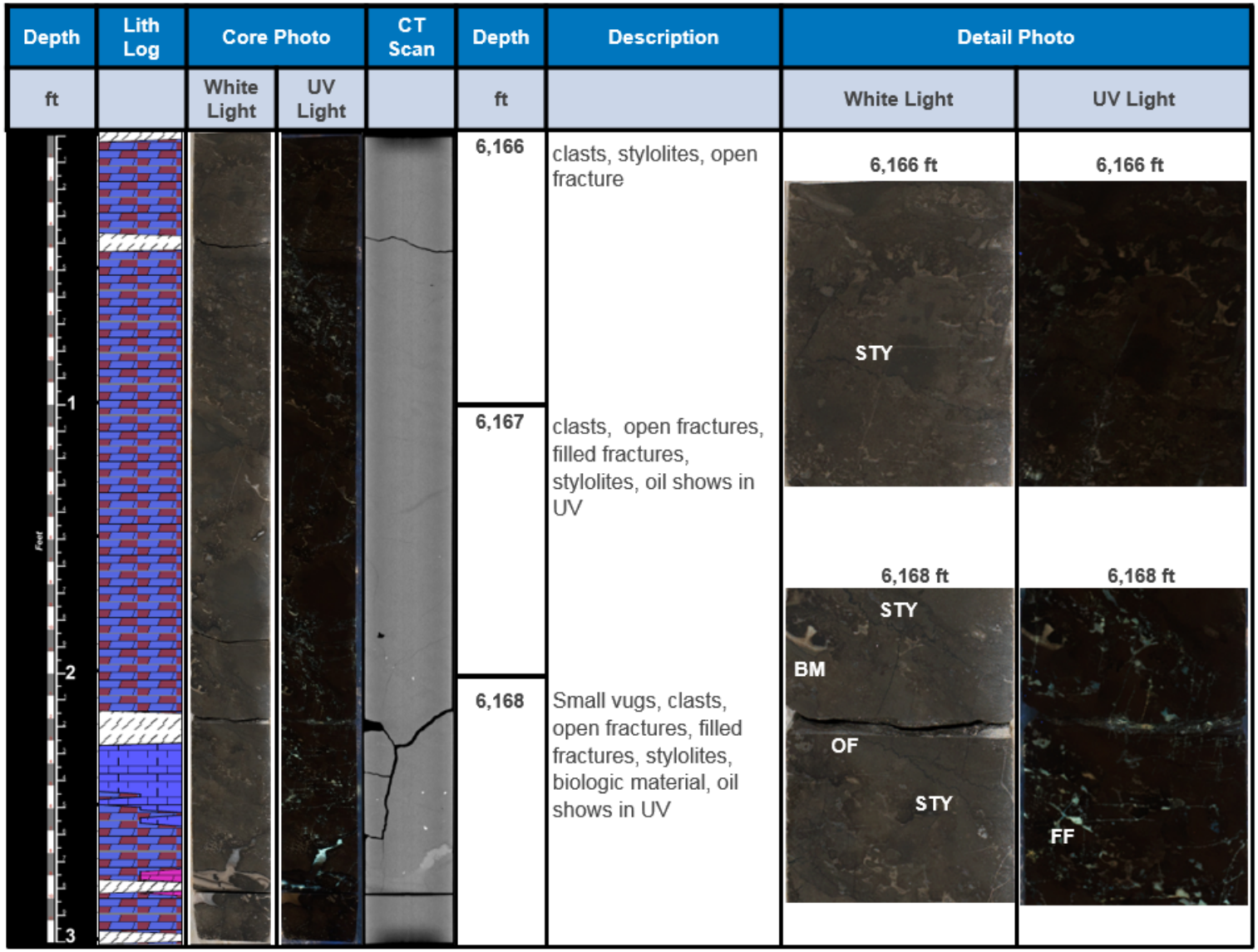


Figure B-84. Compiled illustration of lithology log, core photos (UV and white light), CT scan image, core descriptions, and annotated core images of the Brown Niagaran for depths 6,166 ft. to 6,168 ft.

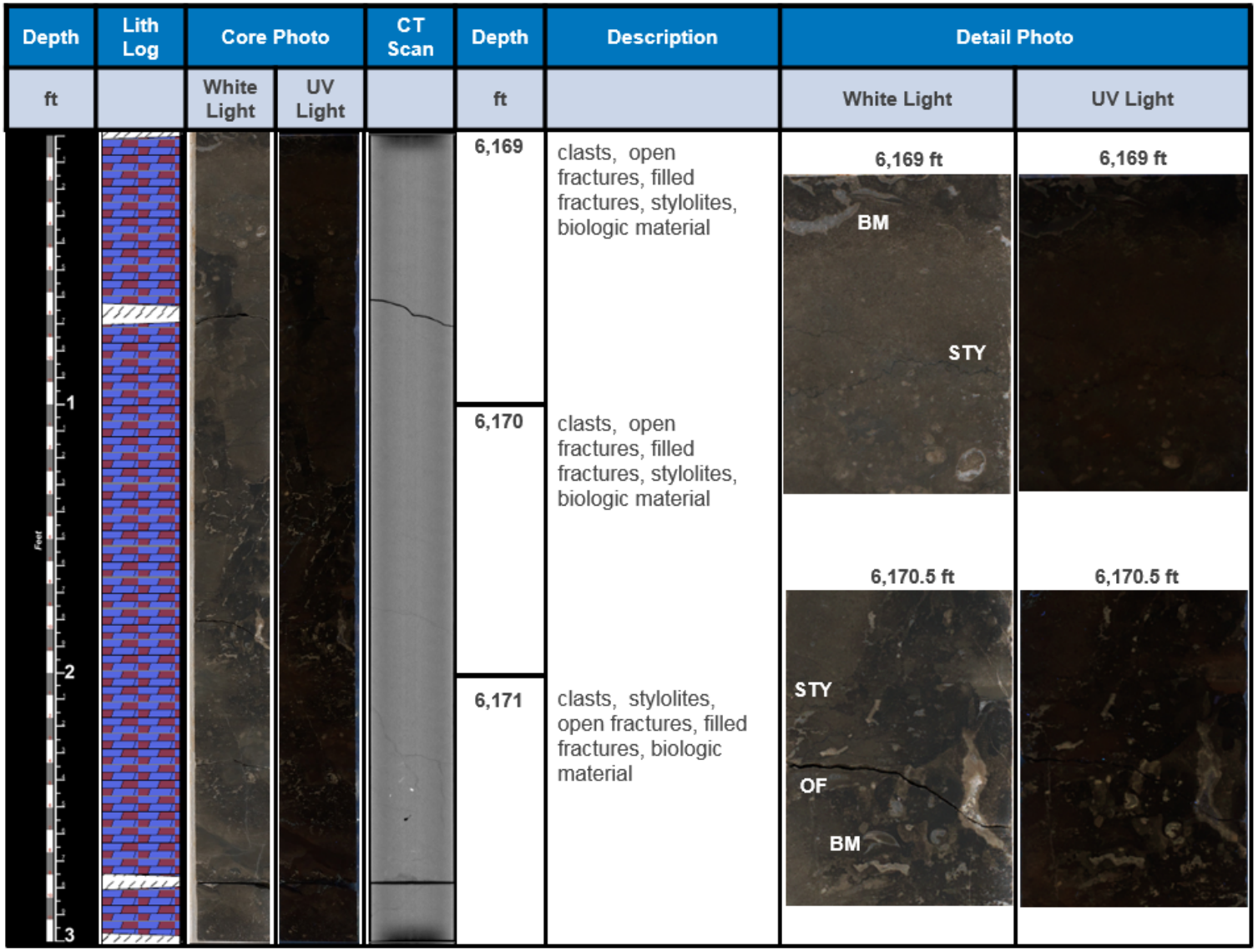


Figure B-85. Compiled illustration of lithology log, core photos (UV and white light), CT scan image, core descriptions, and annotated core images of the Brown Niagaran for depths 6,169 ft. to 6,171 ft.

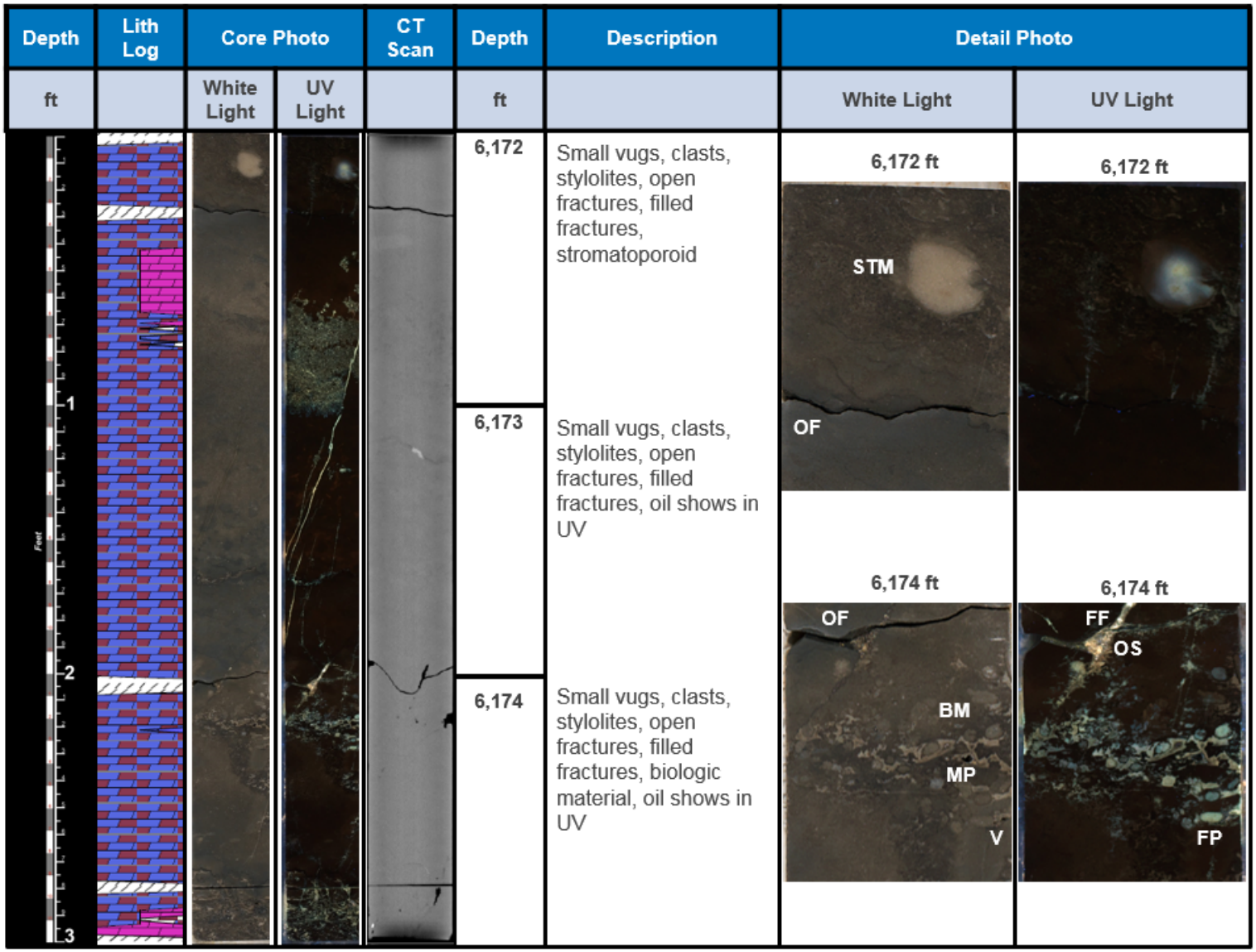


Figure B-86. Compiled illustration of lithology log, core photos (UV and white light), CT scan image, core descriptions, and annotated core images of the Brown Niagaran for depths 6,172 ft. to 6,174 ft.

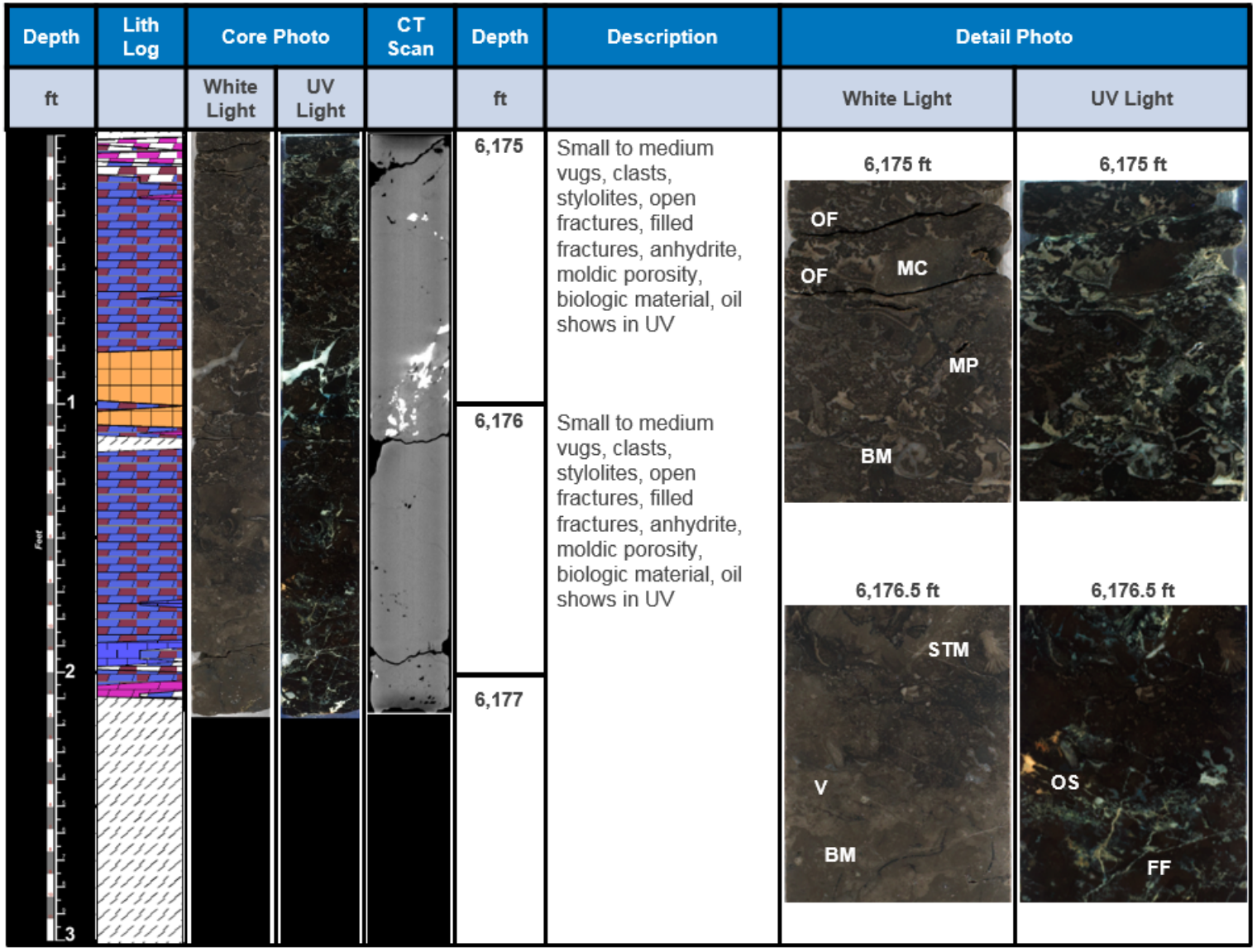


Figure B-87. Compiled illustration of lithology log, core photos (UV and white light), CT scan image, core descriptions, and annotated core images of the Brown Niagaran for depths 6,175 ft. to 6,177 ft.

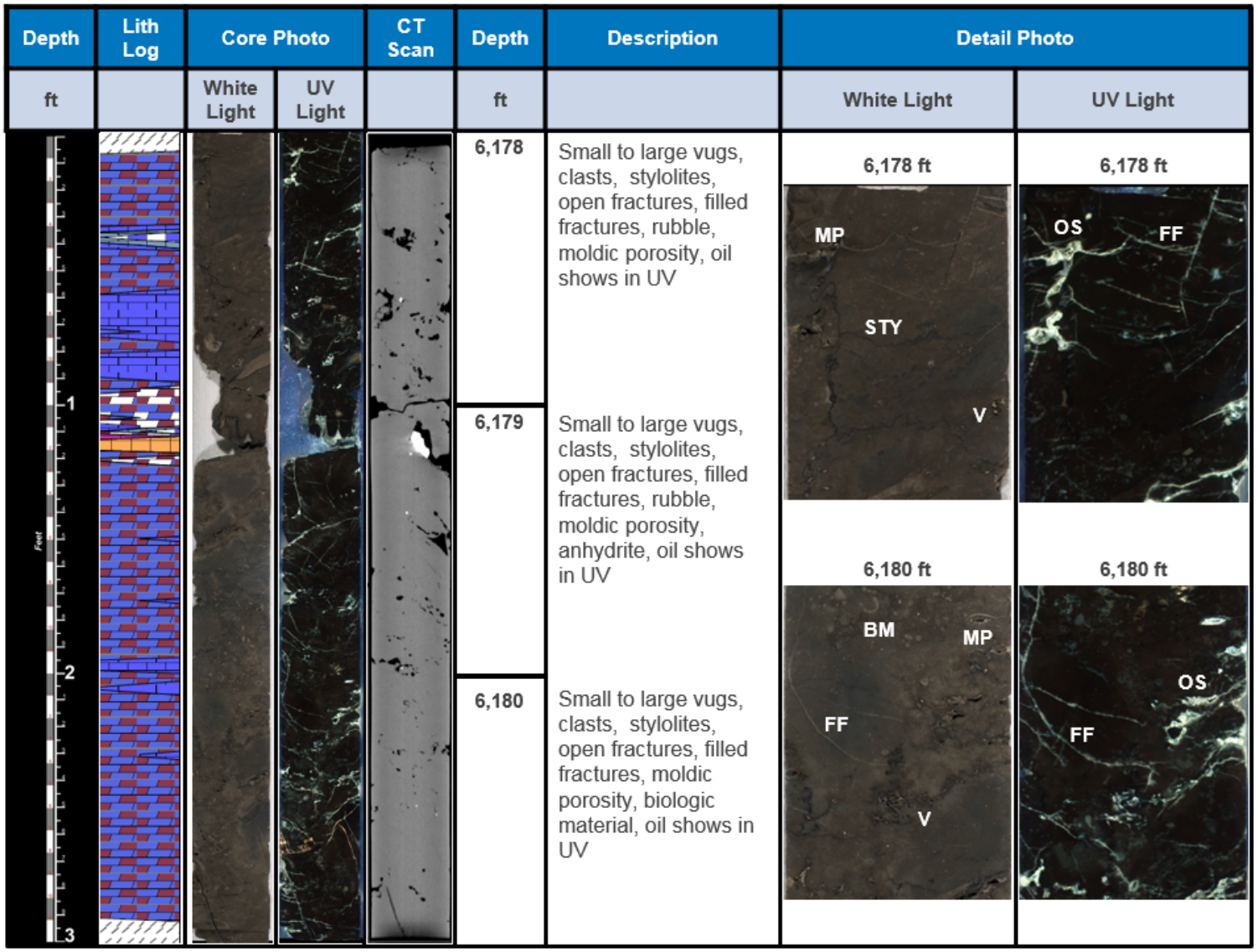


Figure B-88. Compiled illustration of lithology log, core photos (UV and white light), CT scan image, core descriptions, and annotated core images of the Brown Niagaran for depths 6,178 ft. to 6,180 ft.

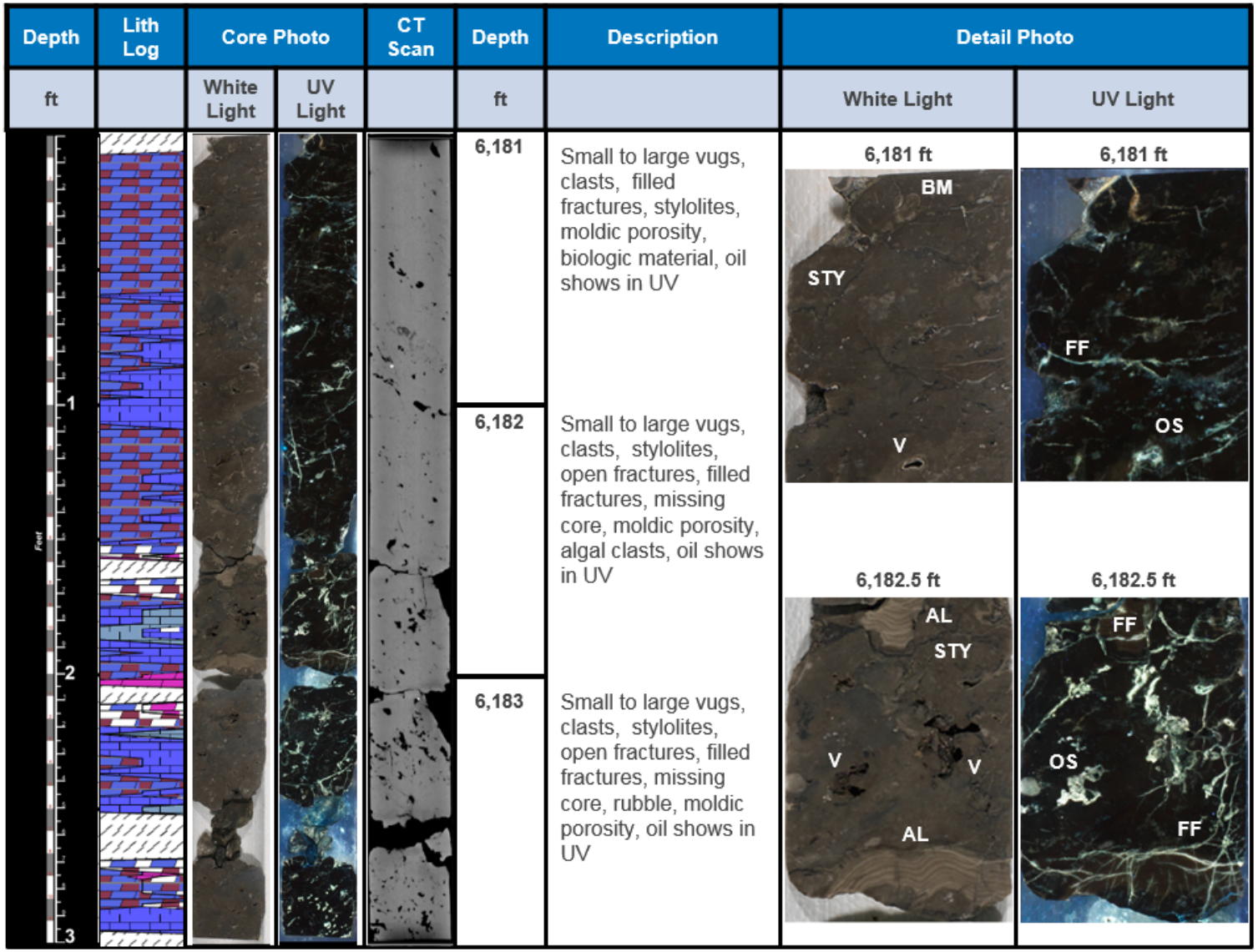


Figure B-89. Compiled illustration of lithology log, core photos (UV and white light), CT scan image, core descriptions, and annotated core images of the Brown Niagaran for depths 6,181 ft. to 6,183 ft.

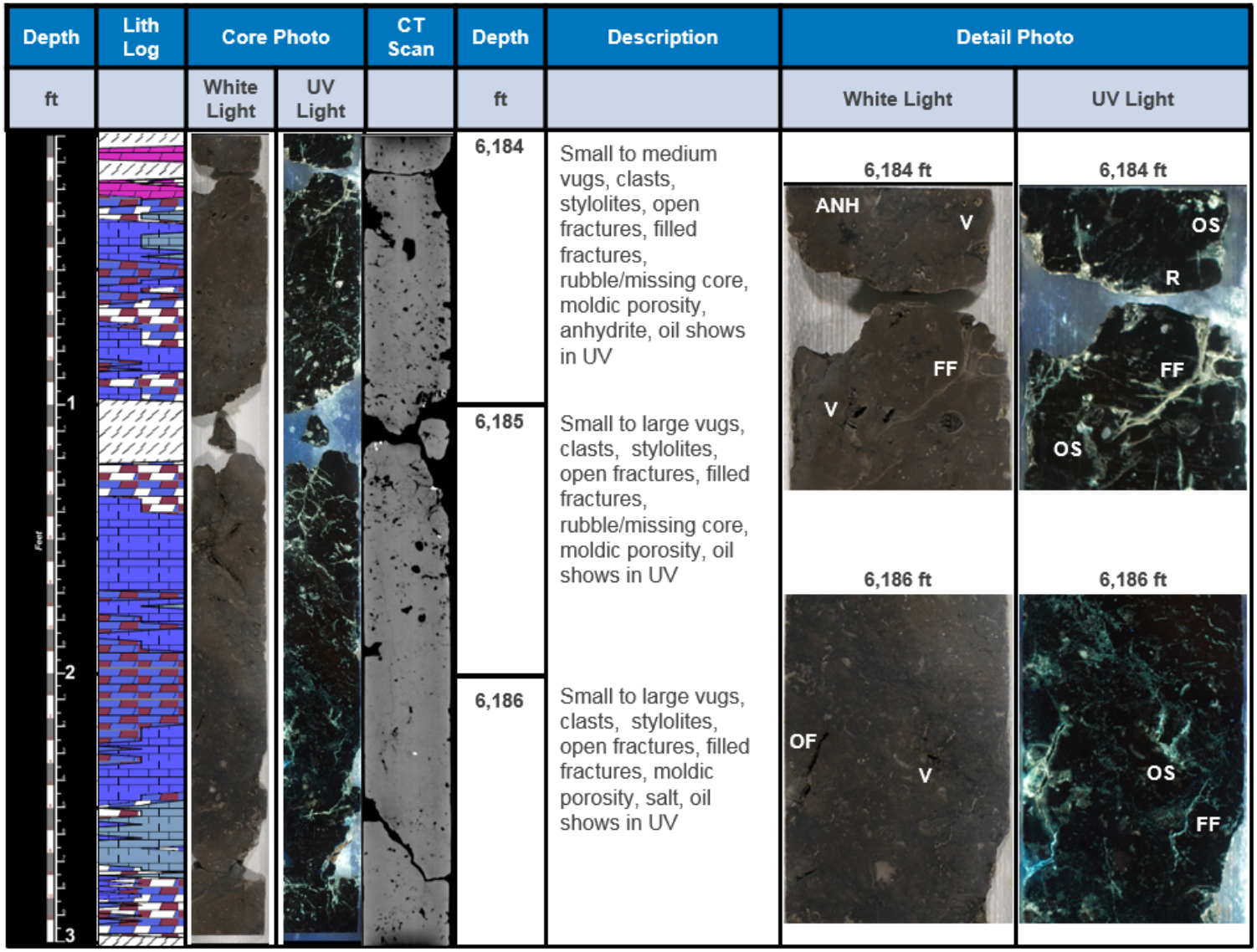


Figure B-90. Compiled illustration of lithology log, core photos (UV and white light), CT scan image, core descriptions, and annotated core images of the Brown Niagaran for depths 6,184 ft. to 6,186 ft.

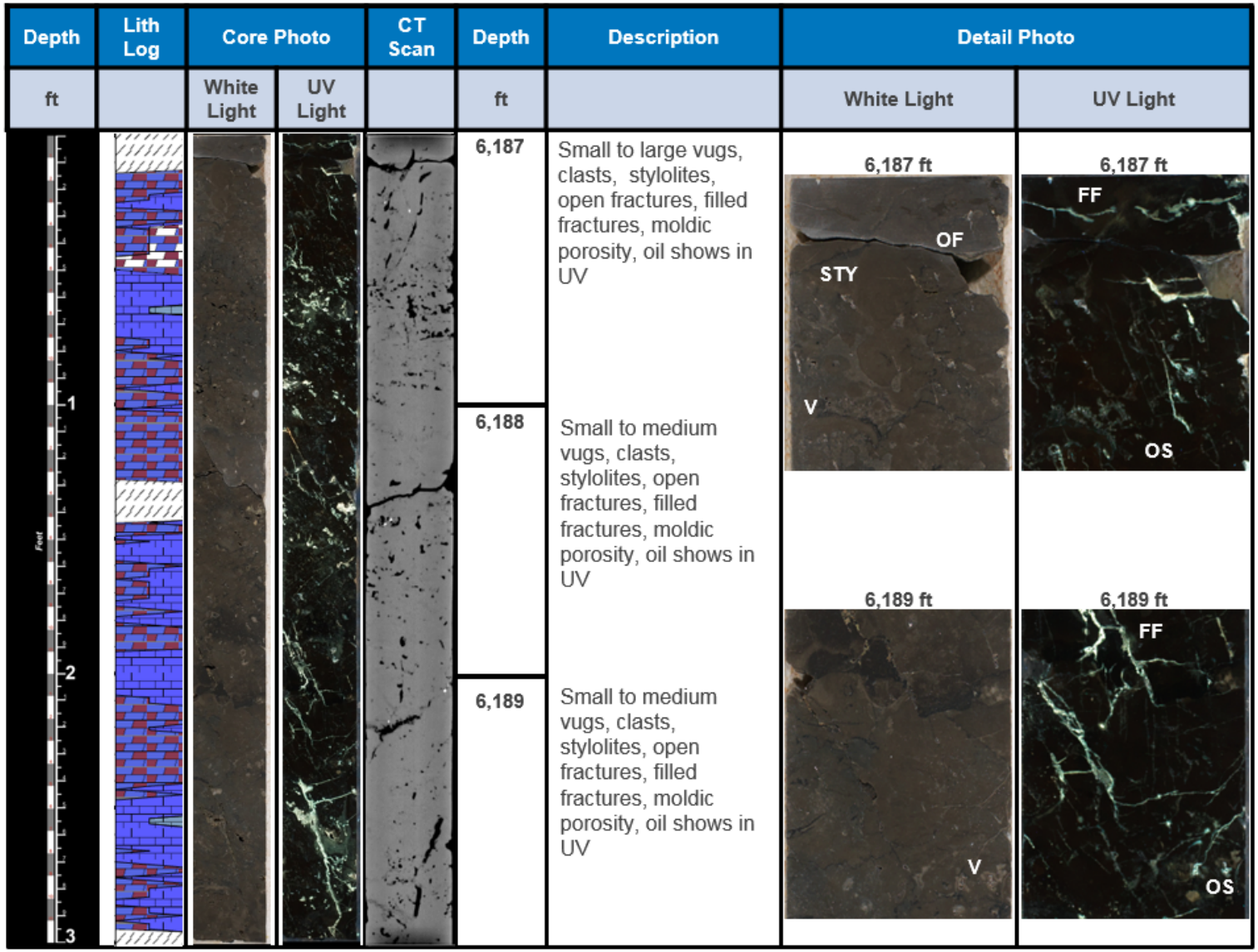


Figure B-91. Compiled illustration of lithology log, core photos (UV and white light), CT scan image, core descriptions, and annotated core images of the Brown Niagaran for depths 6,187 ft. to 6,189 ft.

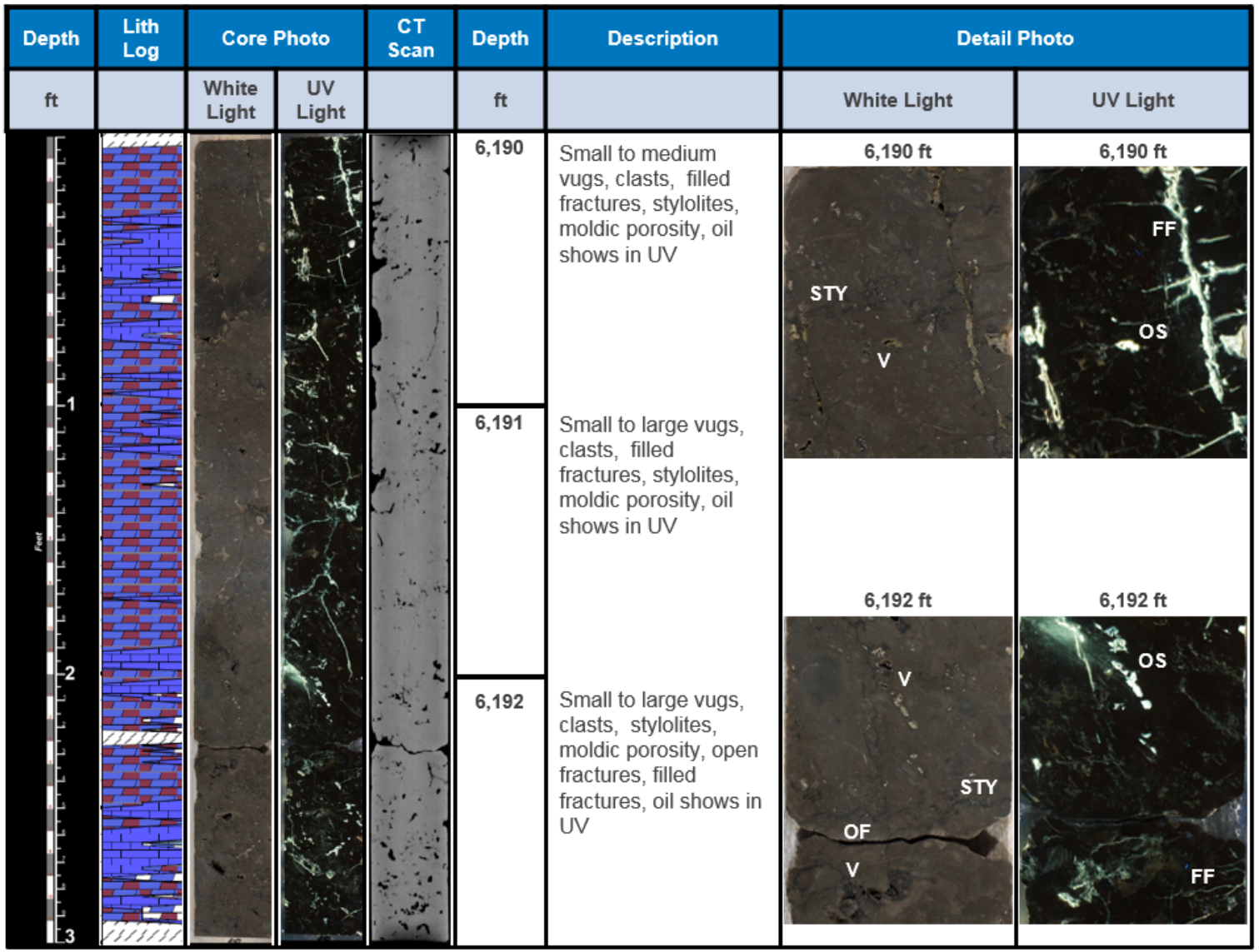


Figure B-92. Compiled illustration of lithology log, core photos (UV and white light), CT scan image, core descriptions, and annotated core images of the Brown Niagaran for depths 6,190 ft. to 6,192 ft.

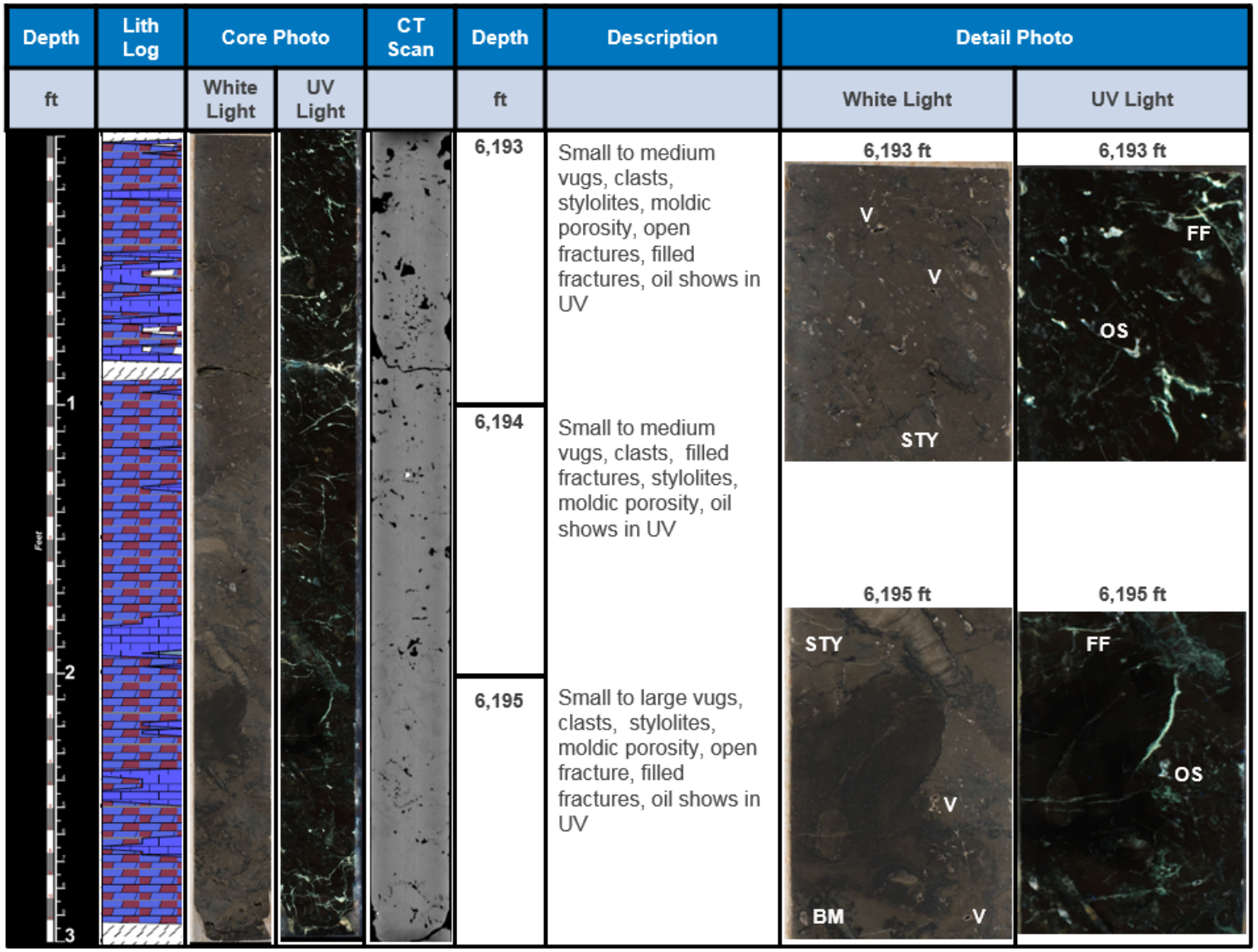


Figure B-93. Compiled illustration of lithology log, core photos (UV and white light), CT scan image, core descriptions, and annotated core images of the Brown Niagaran for depths 6,193 ft. to 6,195 ft.

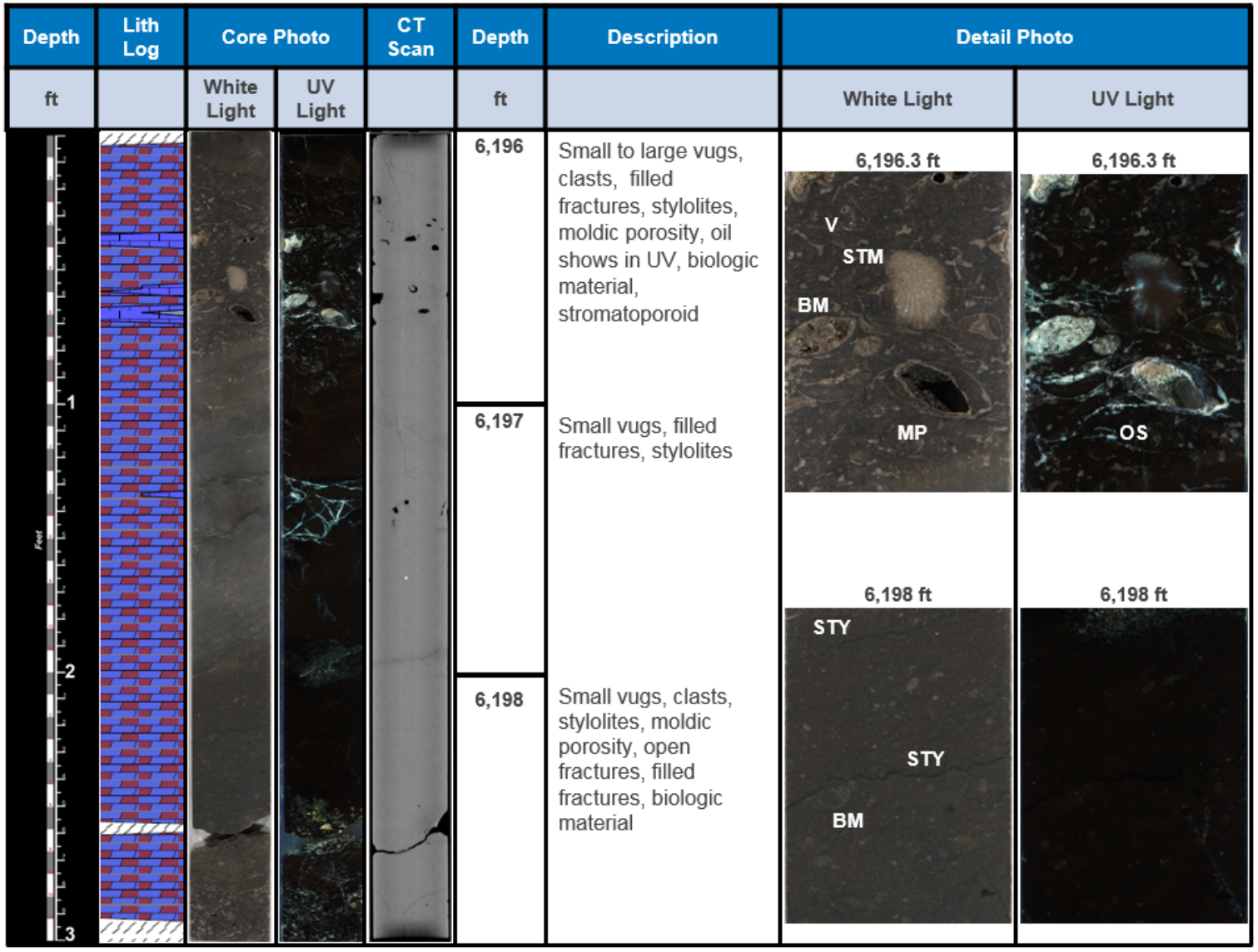


Figure B-94. Compiled illustration of lithology log, core photos (UV and white light), CT scan image, core descriptions, and annotated core images of the Brown Niagaran for depths 6,196 ft. to 6,198 ft.

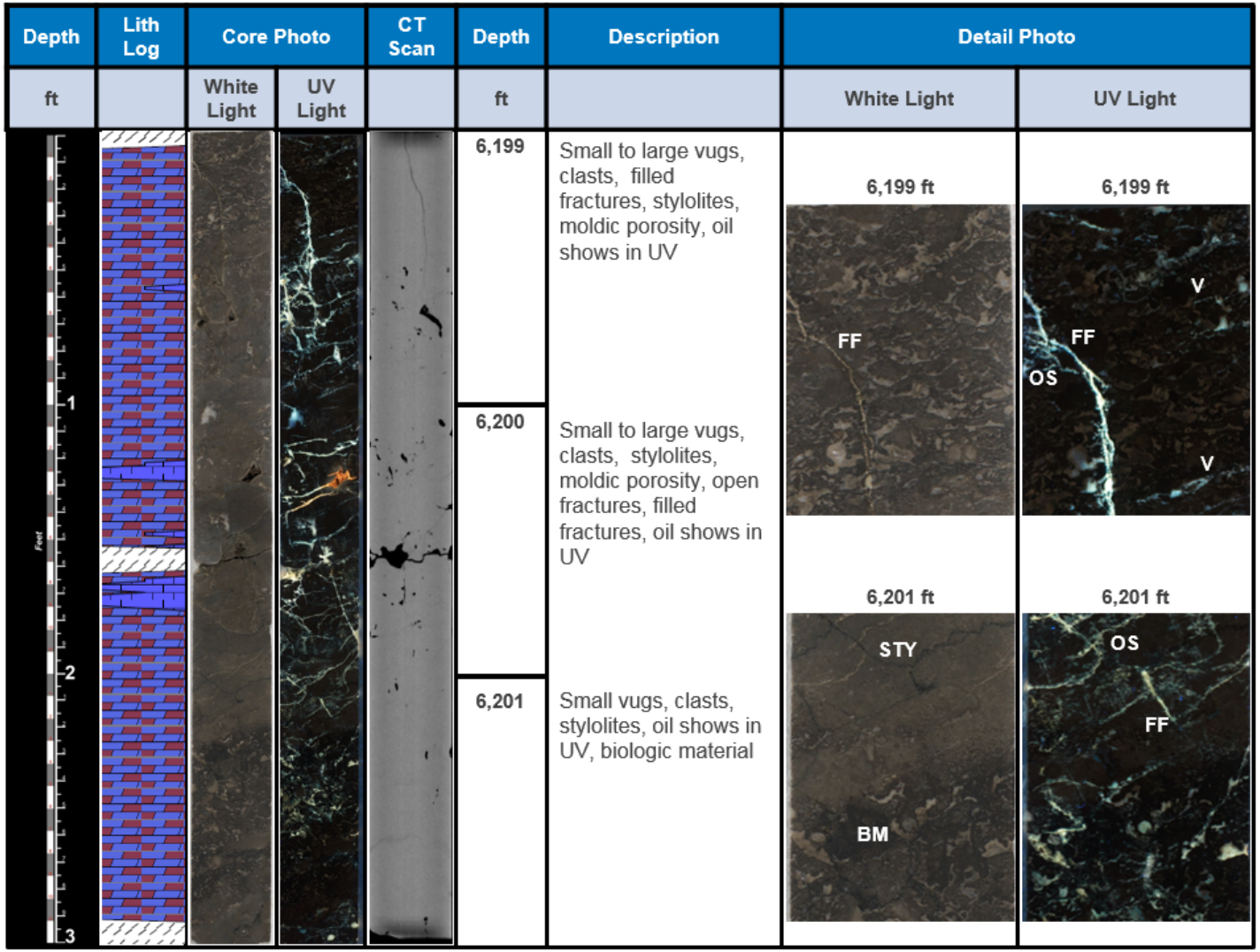


Figure B-95. Compiled illustration of lithology log, core photos (UV and white light), CT scan image, core descriptions, and annotated core images of the Brown Niagaran for depths 6,199 ft. to 6,201 ft.

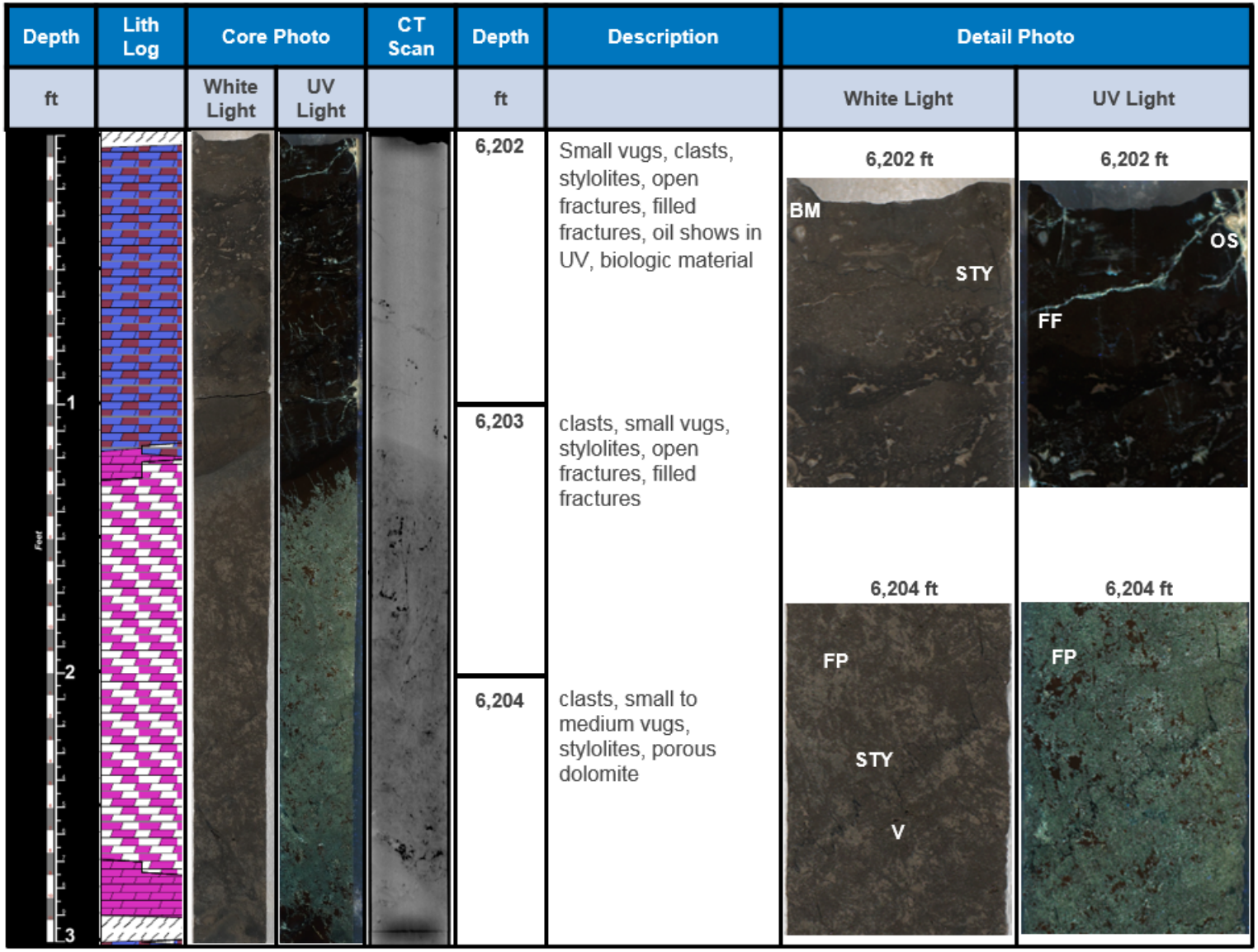


Figure B-96. Compiled illustration of lithology log, core photos (UV and white light), CT scan image, core descriptions, and annotated core images of the Brown Niagaran for depths 6,202 ft. to 6,204 ft.

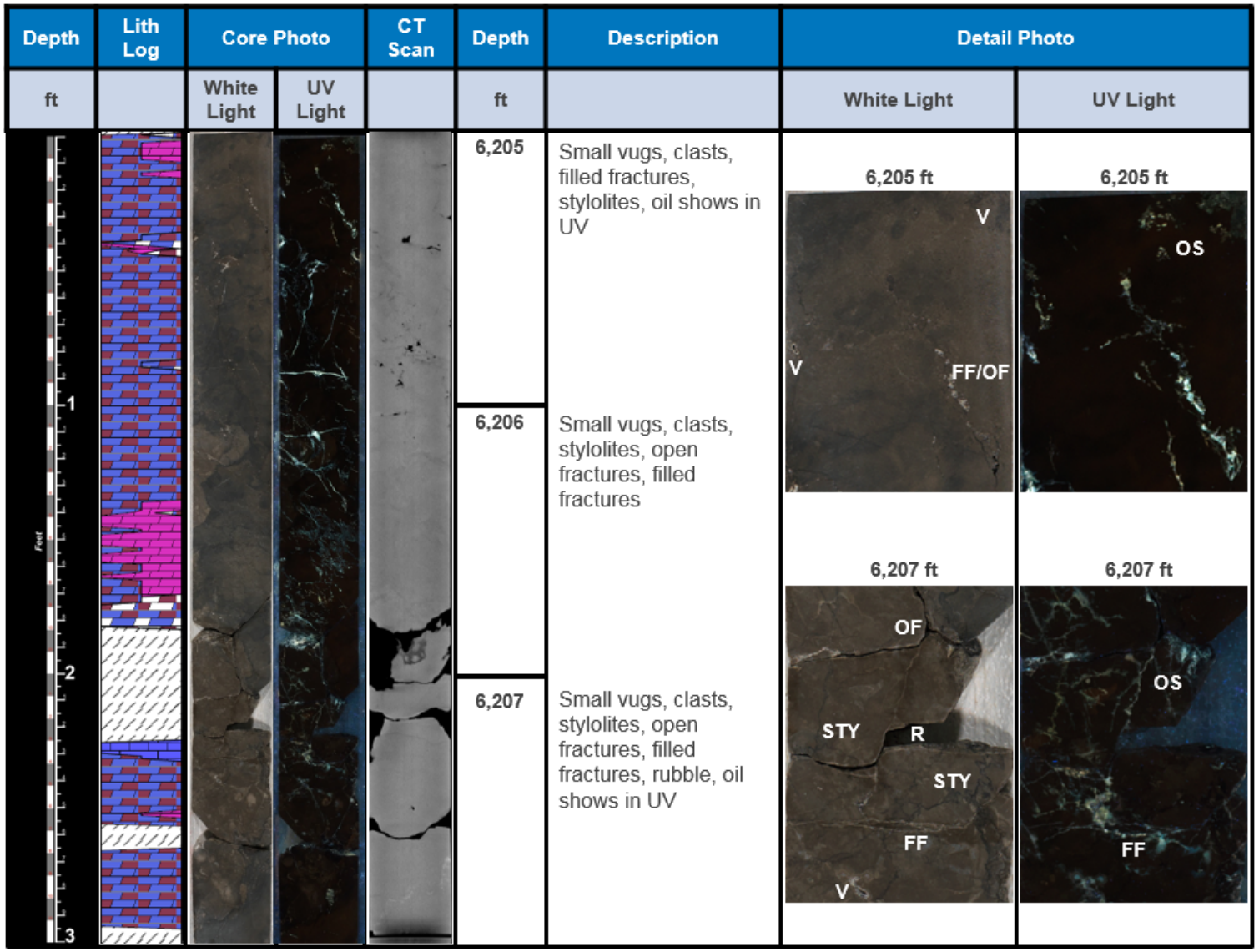


Figure B-97. Compiled illustration of lithology log, core photos (UV and white light), CT scan image, core descriptions, and annotated core images of the Brown Niagaran for depths 6,205 ft. to 6,207 ft.

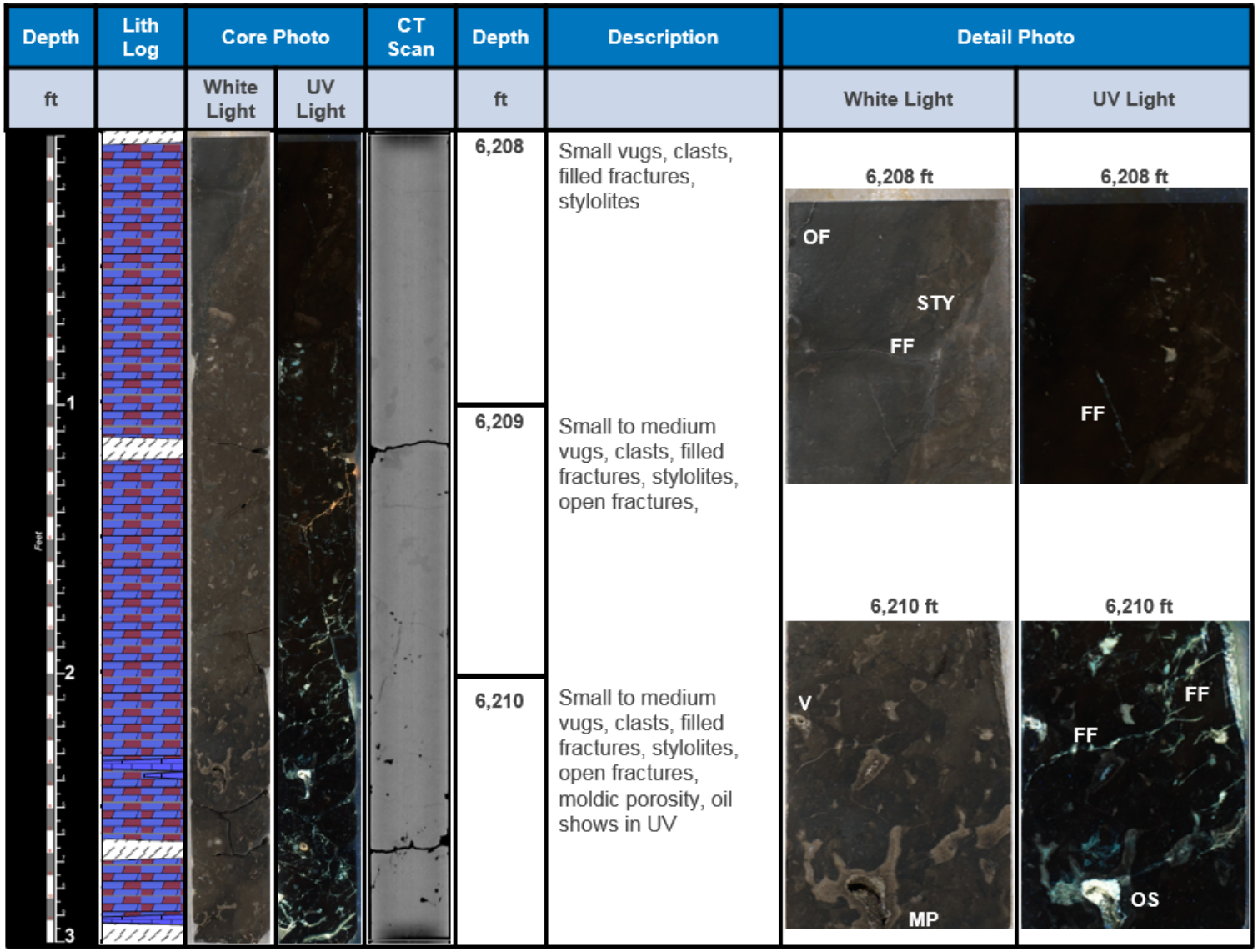


Figure B-98. Compiled illustration of lithology log, core photos (UV and white light), CT scan image, core descriptions, and annotated core images of the Brown Niagaran for depths 6,208 ft. to 6,210 ft.

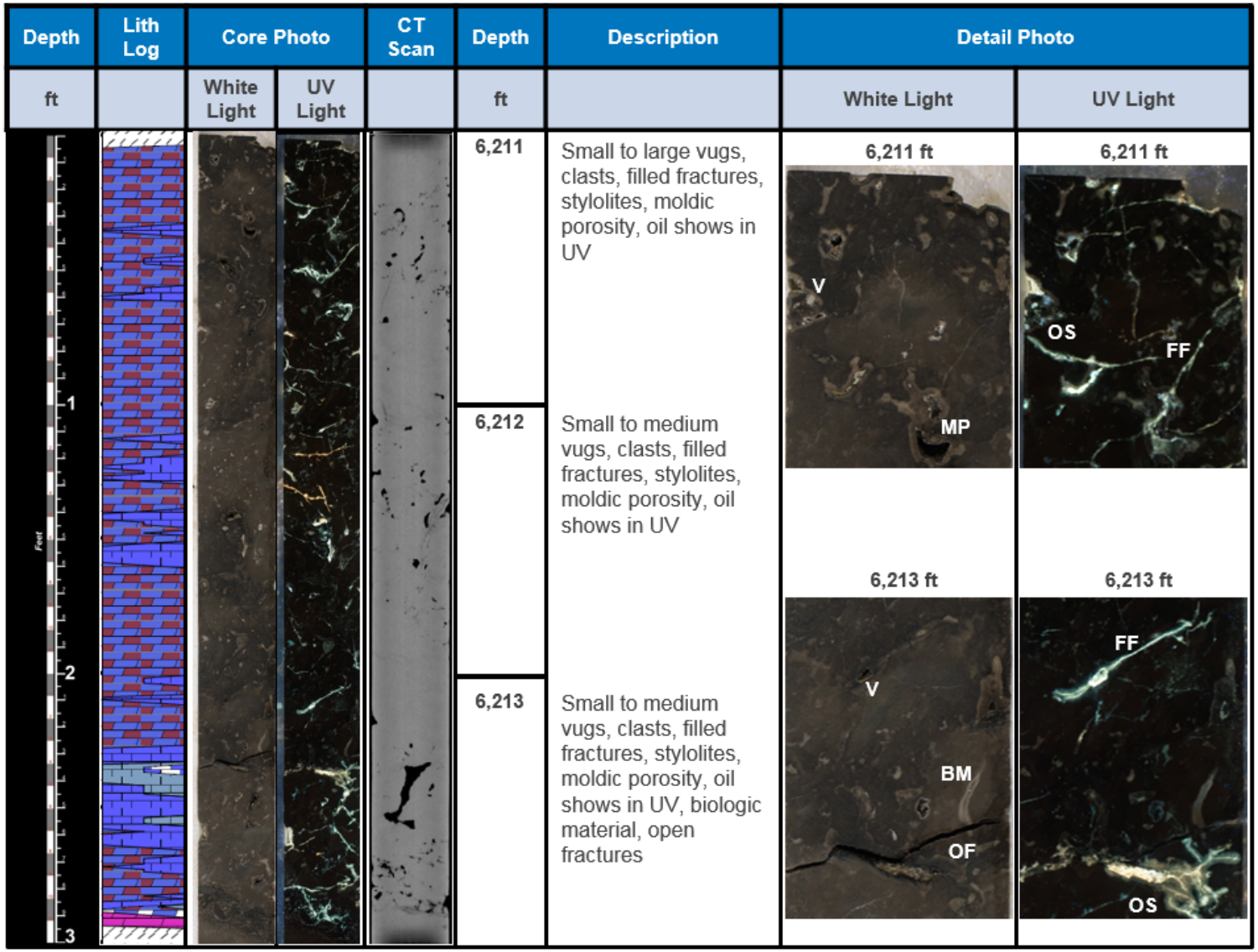


Figure B-99. Compiled illustration of lithology log, core photos (UV and white light), CT scan image, core descriptions, and annotated core images of the Brown Niagaran for depths 6,211 ft. to 6,213 ft.

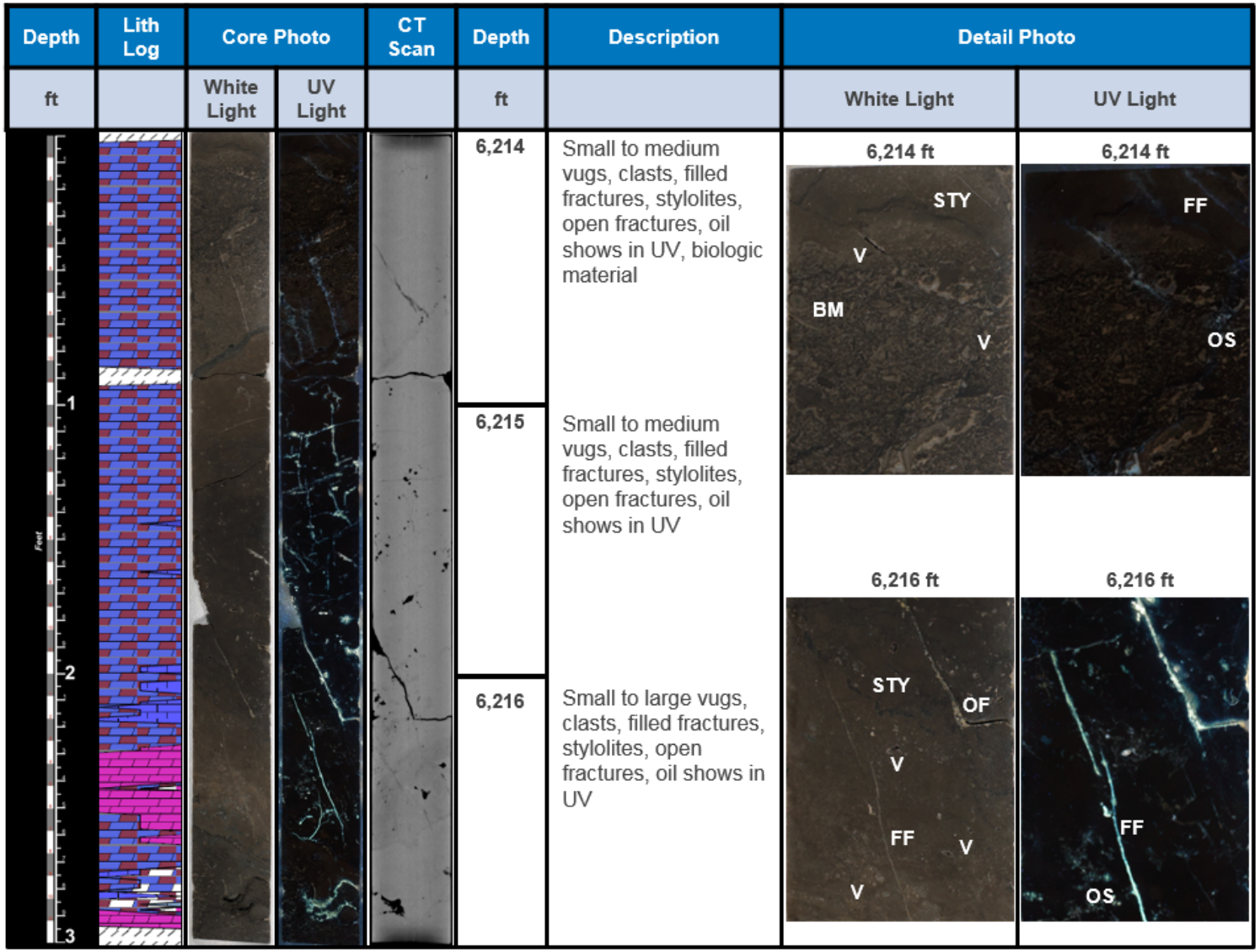


Figure B-100. Compiled illustration of lithology log, core photos (UV and white light), CT scan image, core descriptions, and annotated core images of the Brown Niagaran for depths 6,214 ft. to 6,216 ft.

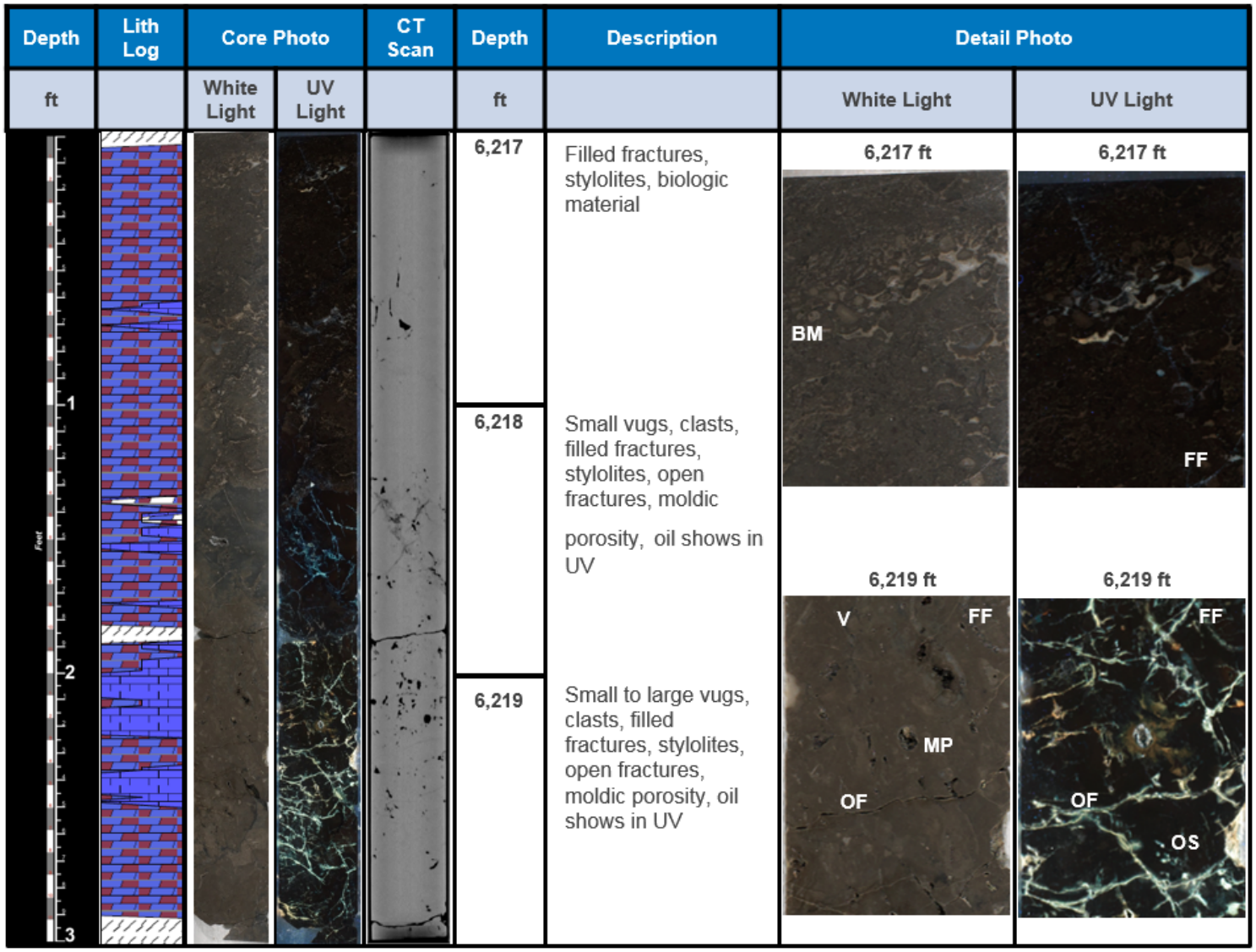


Figure B-101. Compiled illustration of lithology log, core photos (UV and white light), CT scan image, core descriptions, and annotated core images of the Brown Niagaran for depths 6,217 ft. to 6,219 ft.

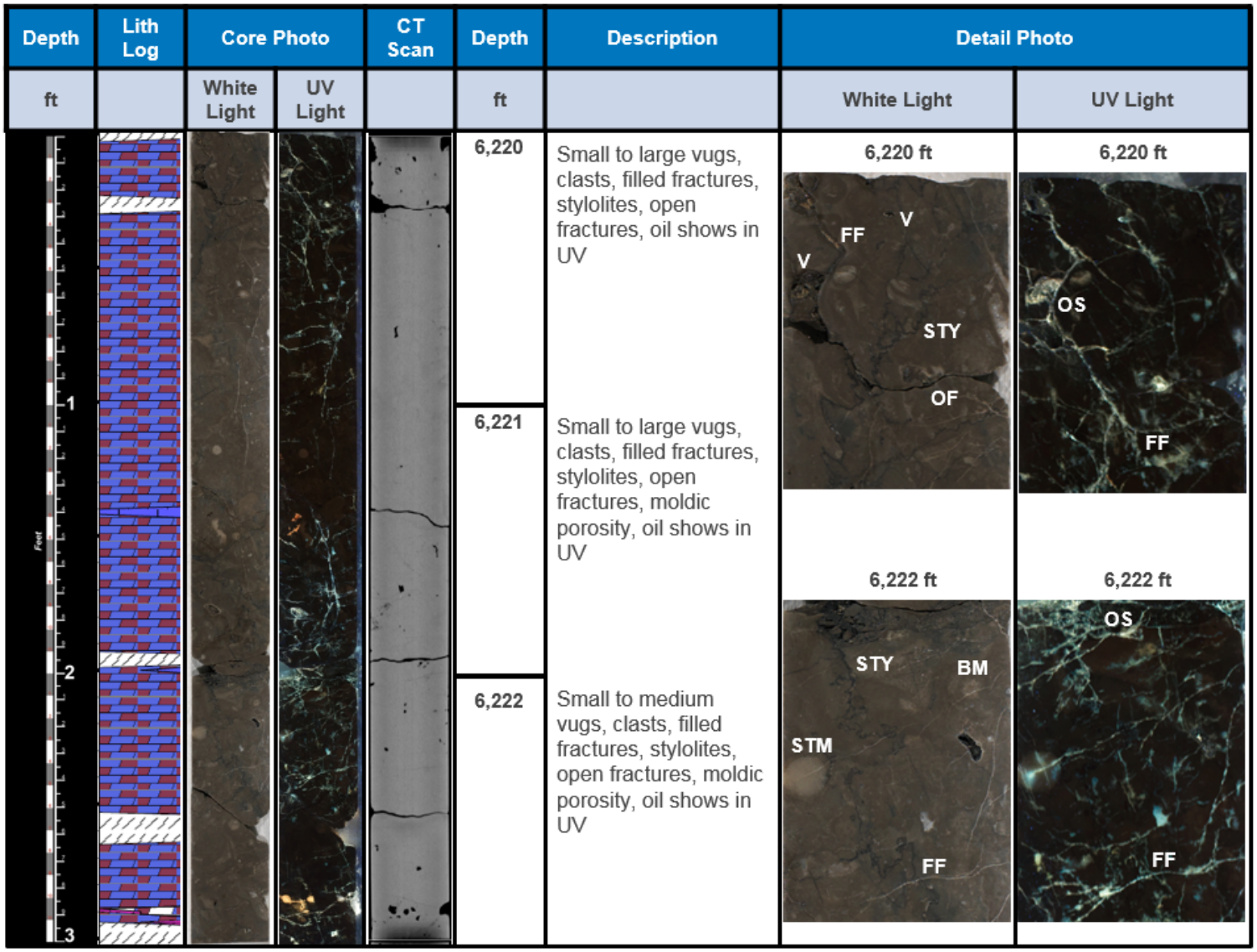


Figure B-102. Compiled illustration of lithology log, core photos (UV and white light), CT scan image, core descriptions, and annotated core images of the Brown Niagaran for depths 6,220 ft. to 6,222 ft.

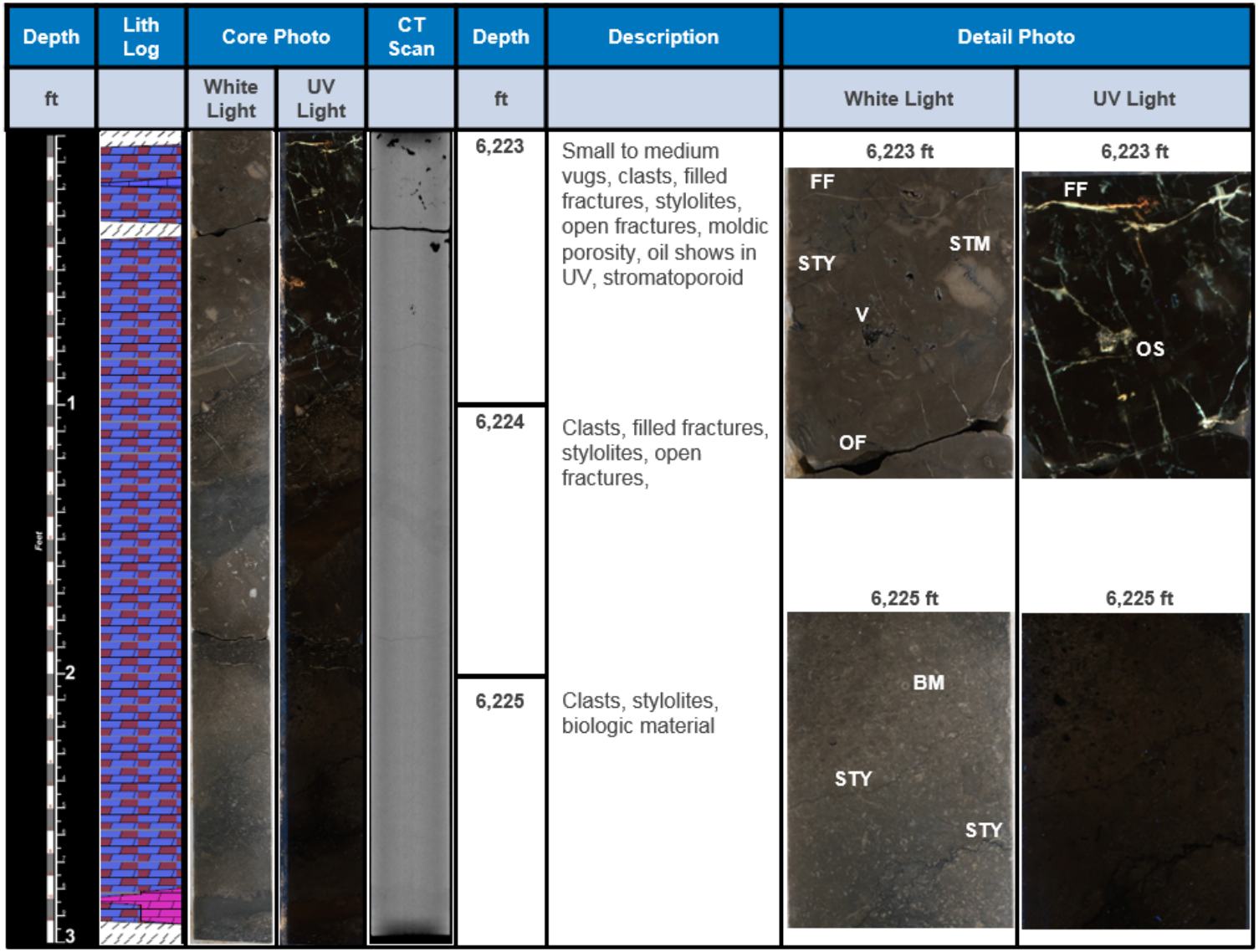


Figure B-103. Compiled illustration of lithology log, core photos (UV and white light), CT scan image, core descriptions, and annotated core images of the Brown Niagaran for depths 6,223 ft. to 6,225 ft.

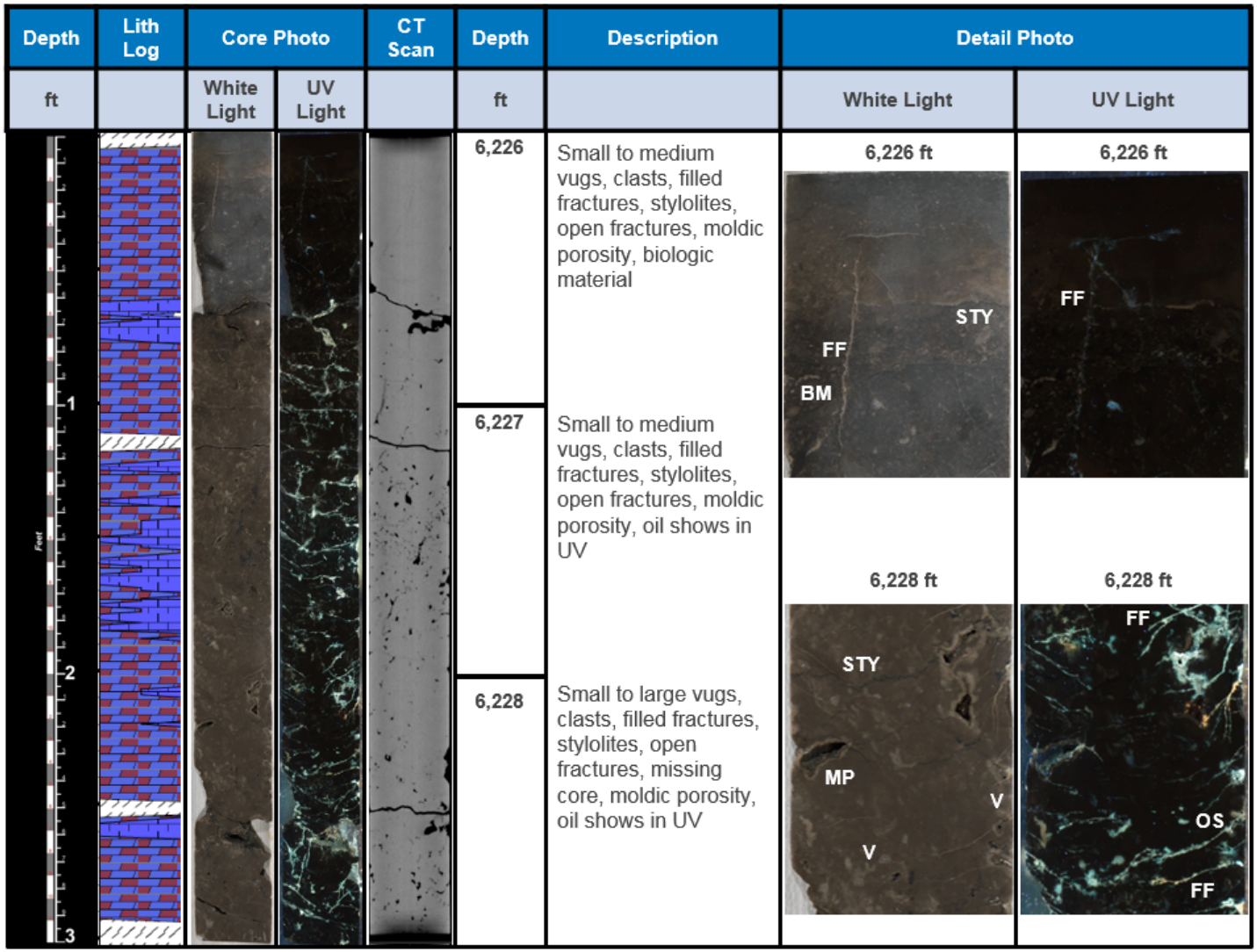


Figure B-104. Compiled illustration of lithology log, core photos (UV and white light), CT scan image, core descriptions, and annotated core images of the Brown Niagaran for depths 6,226 ft. to 6,228 ft.

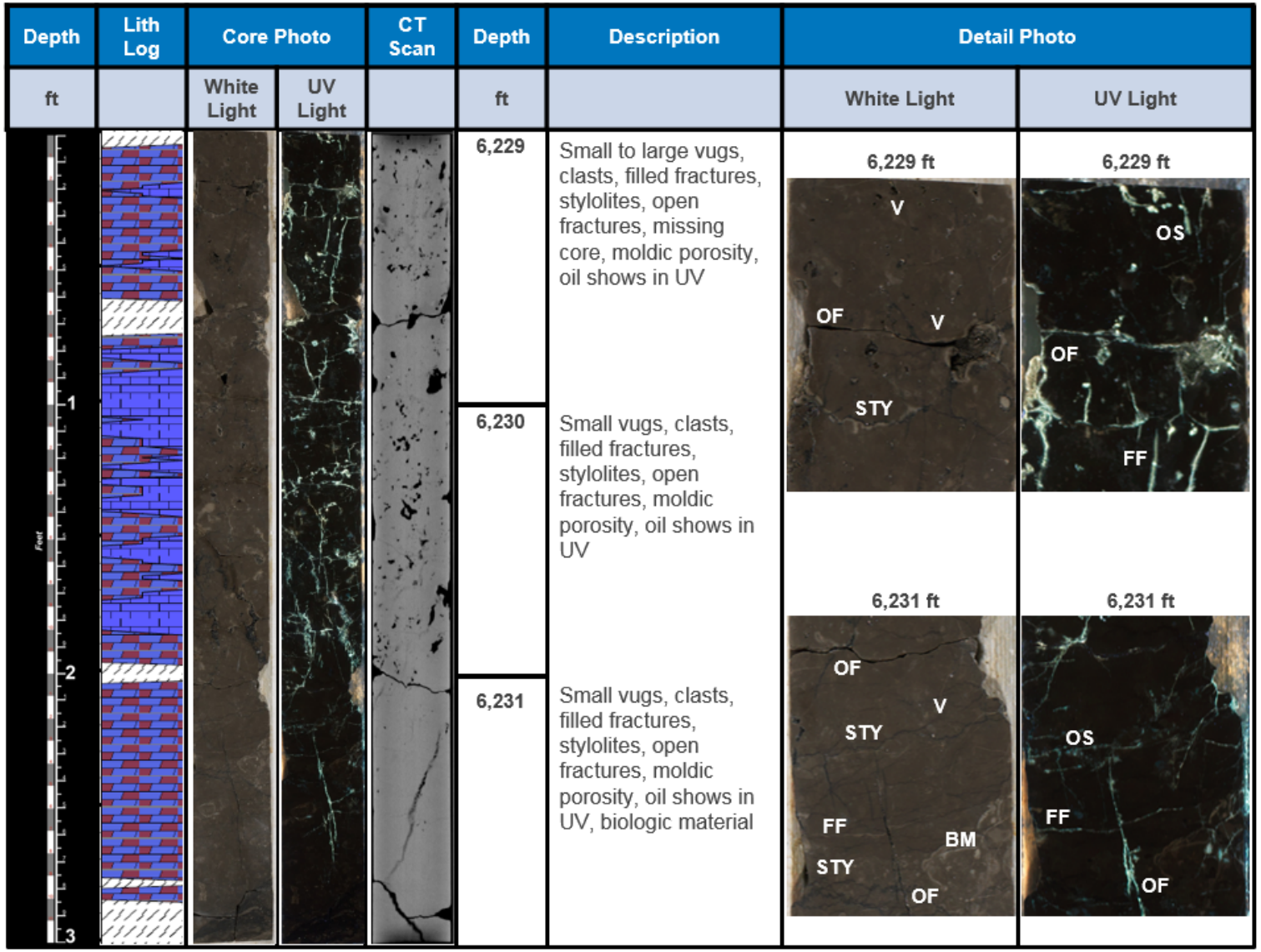


Figure B-105. Compiled illustration of lithology log, core photos (UV and white light), CT scan image, core descriptions, and annotated core images of the Brown Niagaran for depths 6,229 ft. to 6,231 ft.

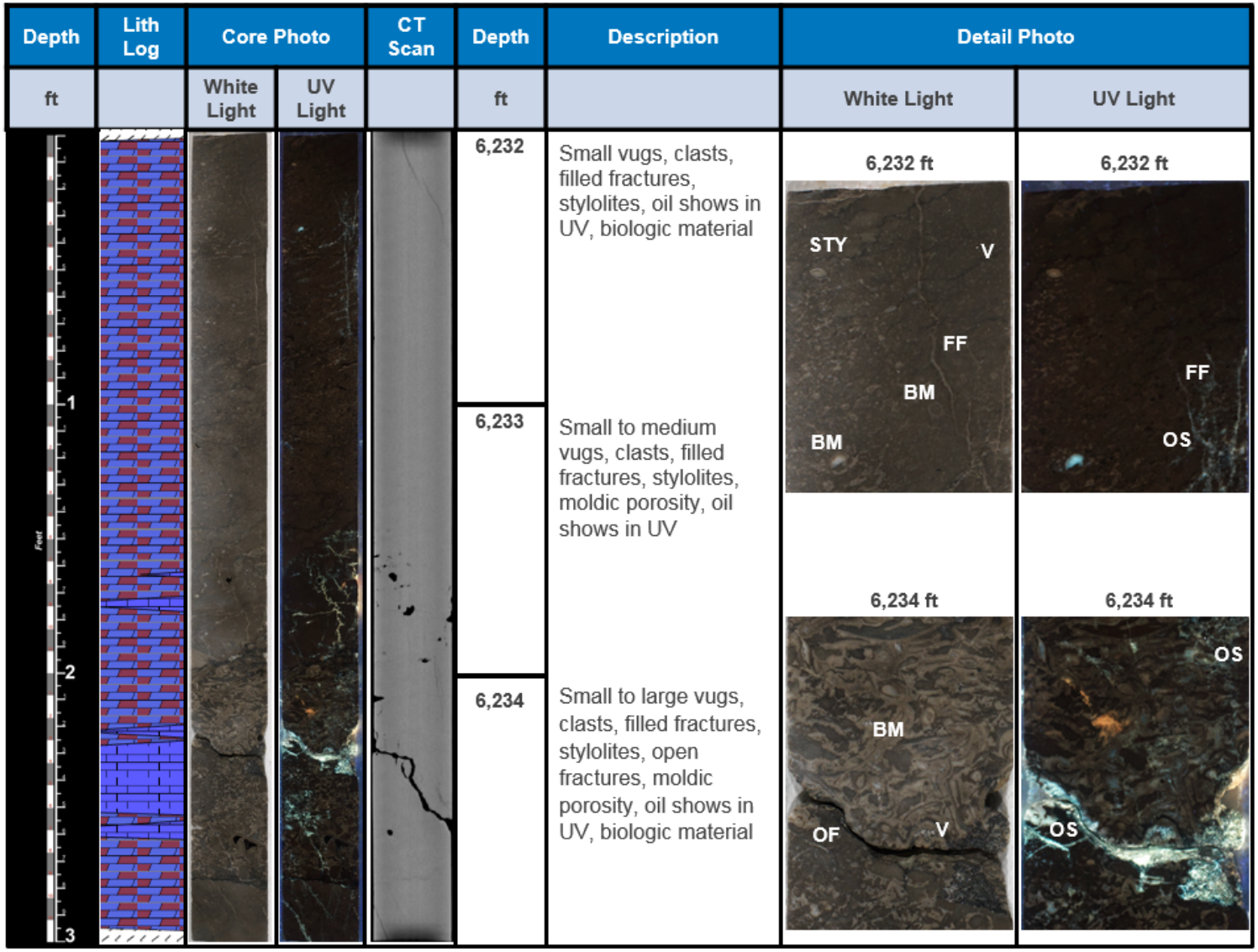


Figure B-106. Compiled illustration of lithology log, core photos (UV and white light), CT scan image, core descriptions, and annotated core images of the Brown Niagaran for depths 6,232 ft. to 6,234 ft.

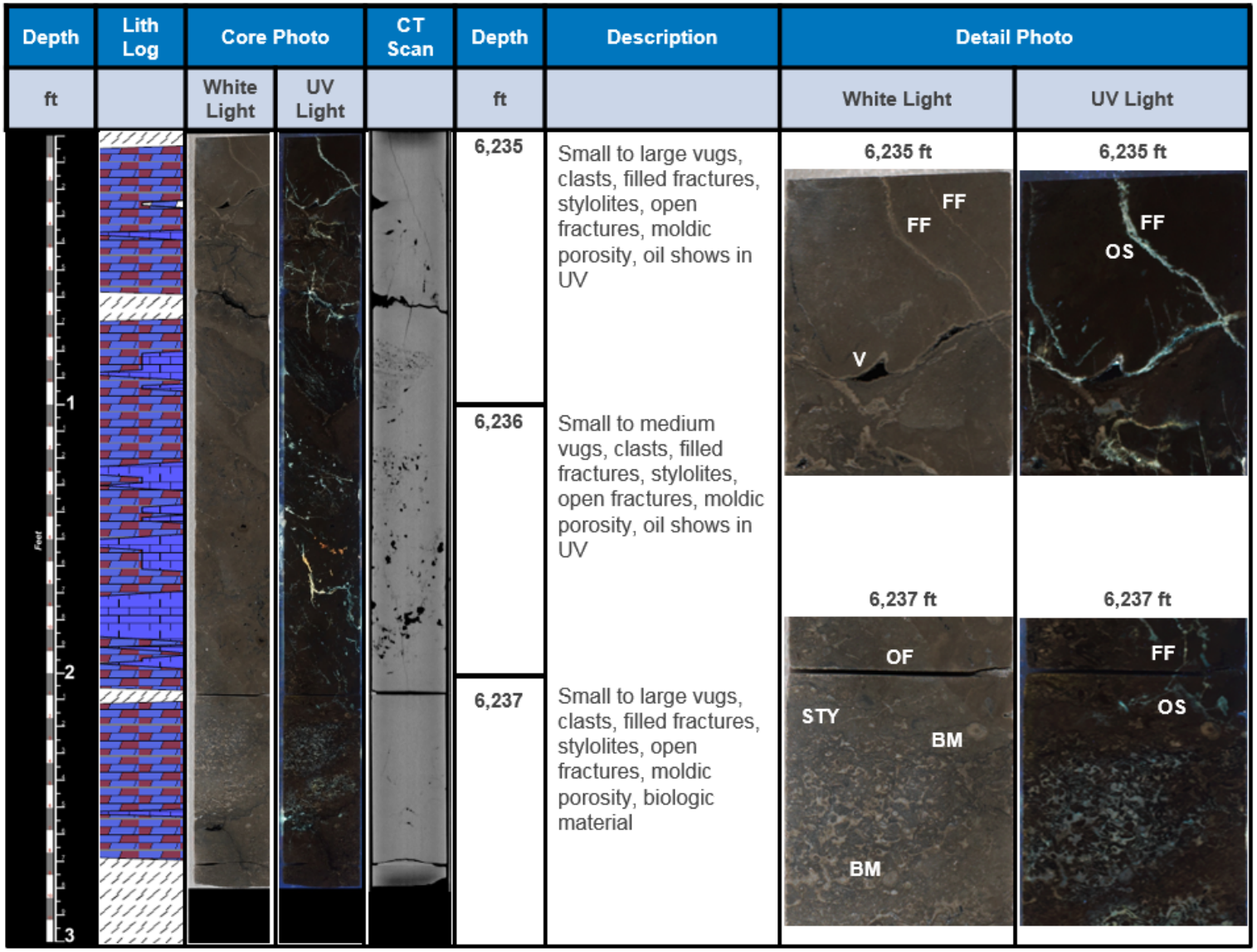


Figure B-107. Compiled illustration of lithology log, core photos (UV and white light), CT scan image, core descriptions, and annotated core images of the Brown Niagaran for depths 6,235 ft. to 6,237 ft.

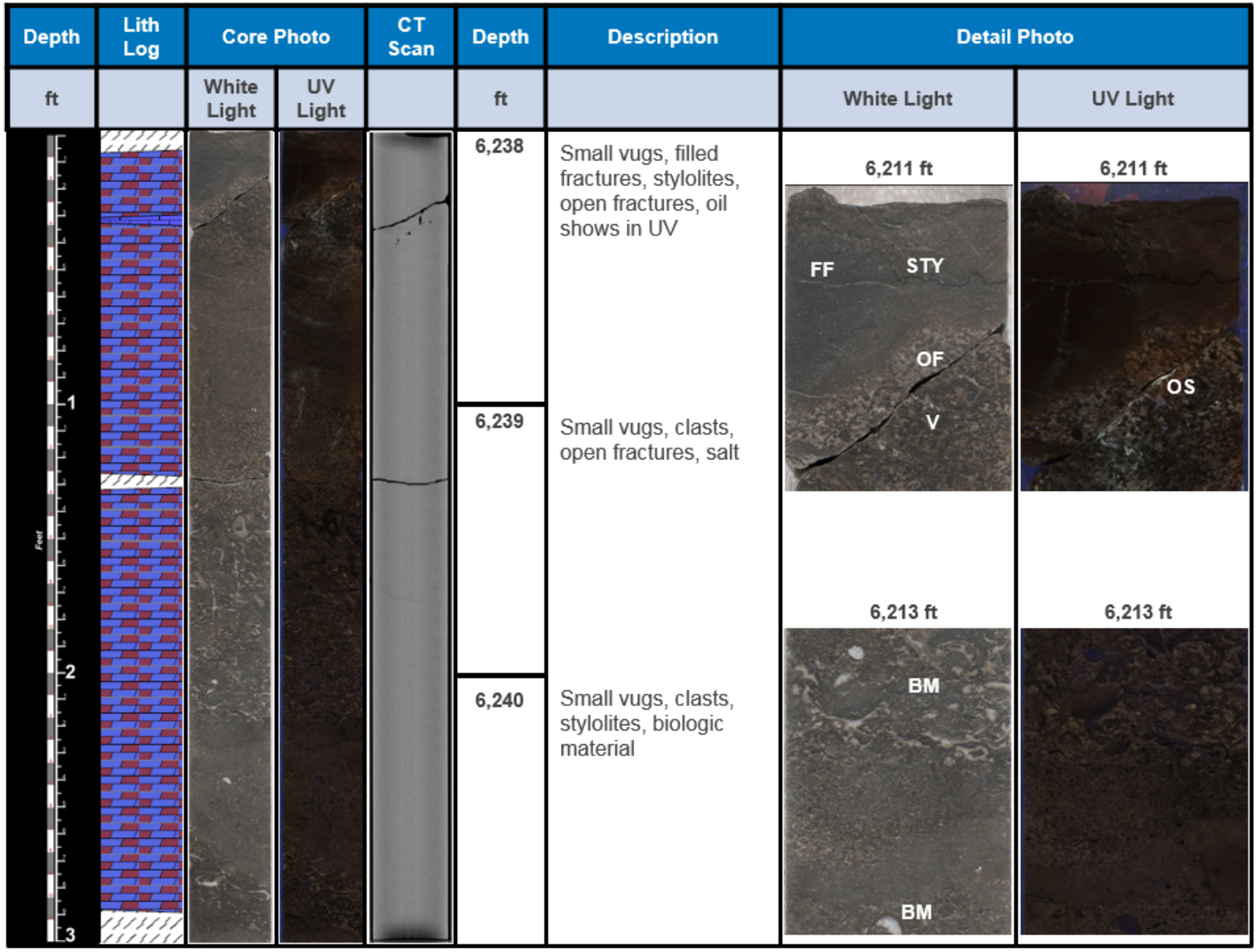


Figure B-108. Compiled illustration of lithology log, core photos (UV and white light), CT scan image, core descriptions, and annotated core images of the Brown Niagaran for depths 6,238 ft. to 6,240 ft.

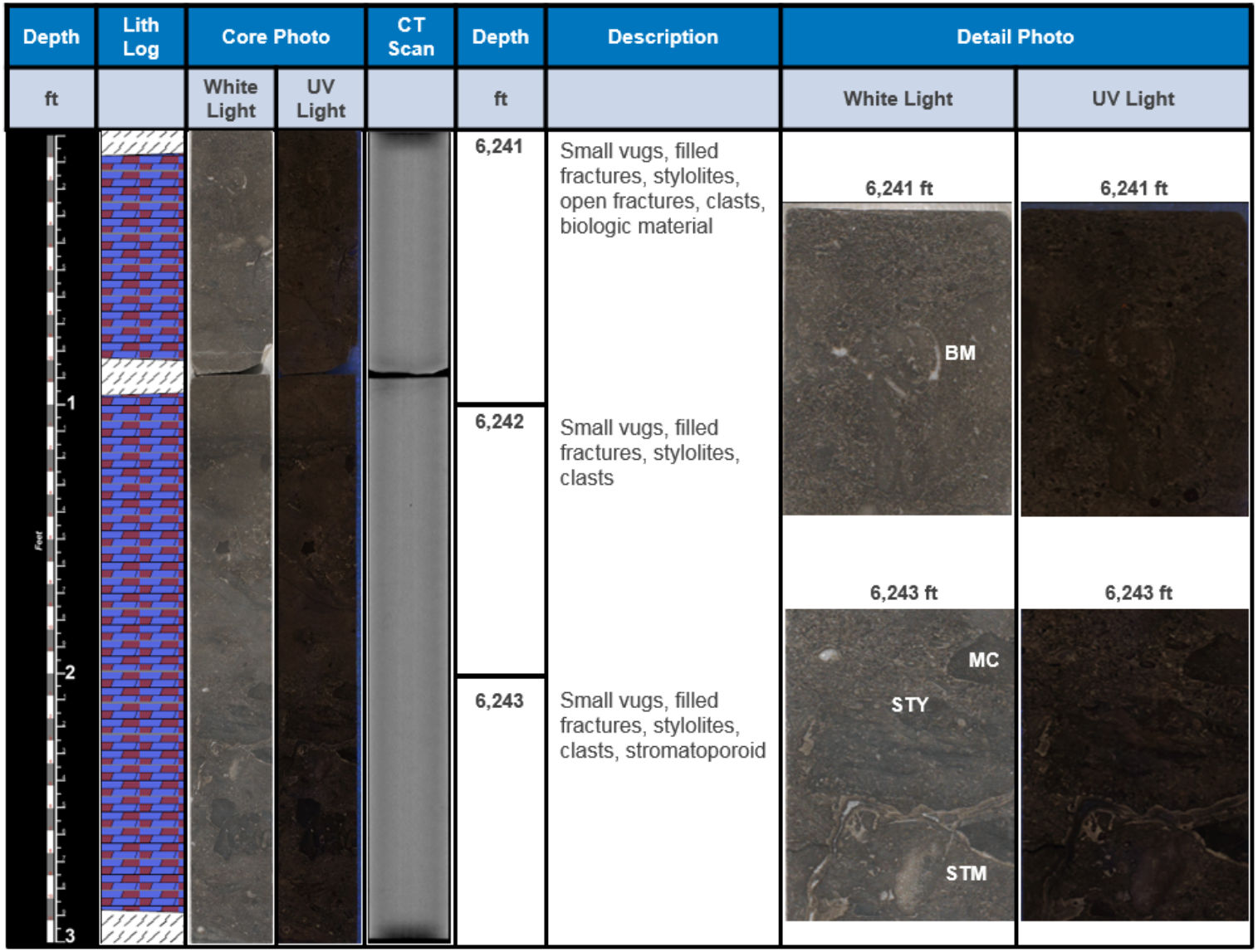


Figure B-109. Compiled illustration of lithology log, core photos (UV and white light), CT scan image, core descriptions, and annotated core images of the Brown Niagaran for depths 6,241 ft. to 6,243 ft.

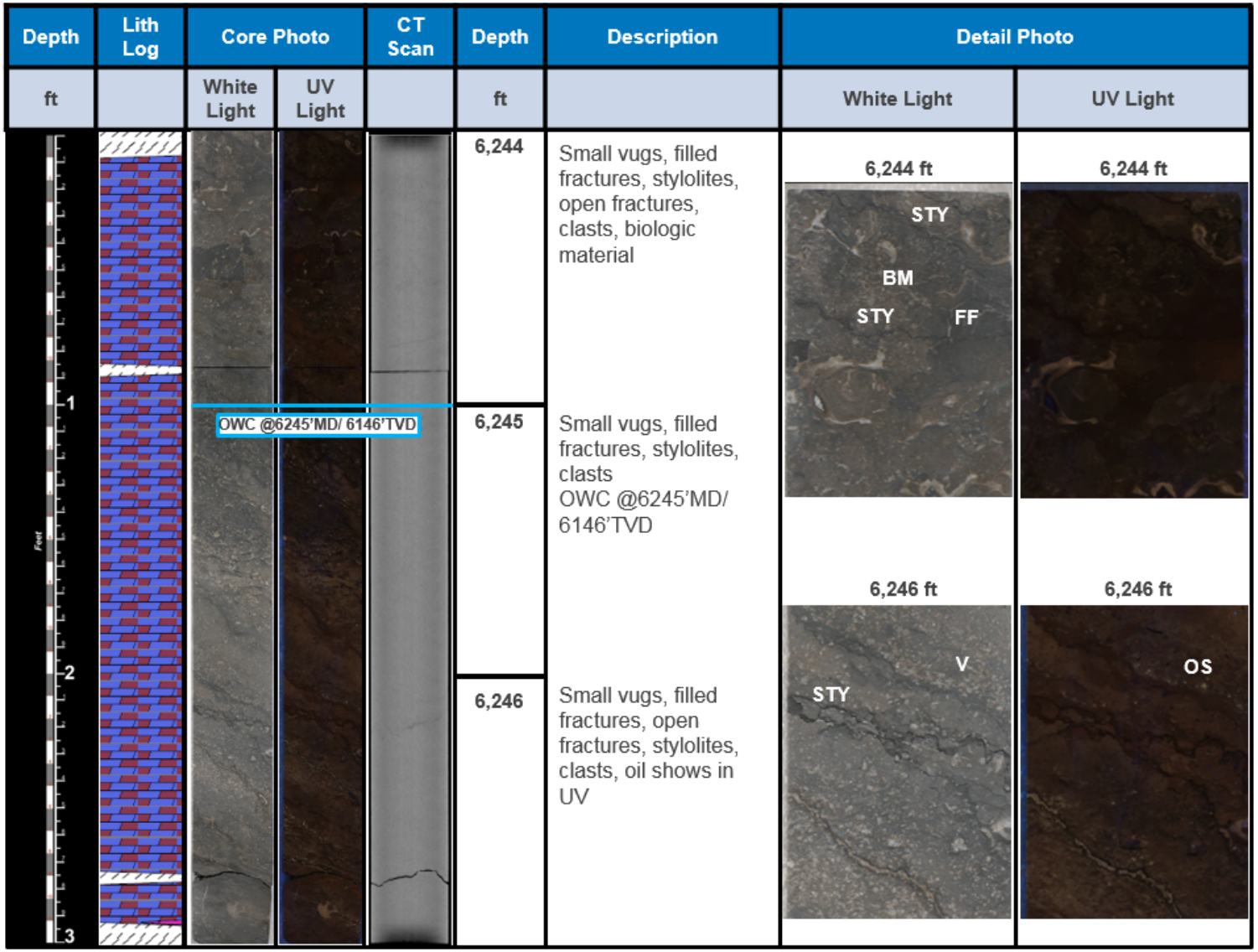


Figure B-110. Compiled illustration of lithology log, core photos (UV and white light), CT scan image, core descriptions, and annotated core images of the Brown Niagaran for depths 6,244 ft. to 6,246 ft.

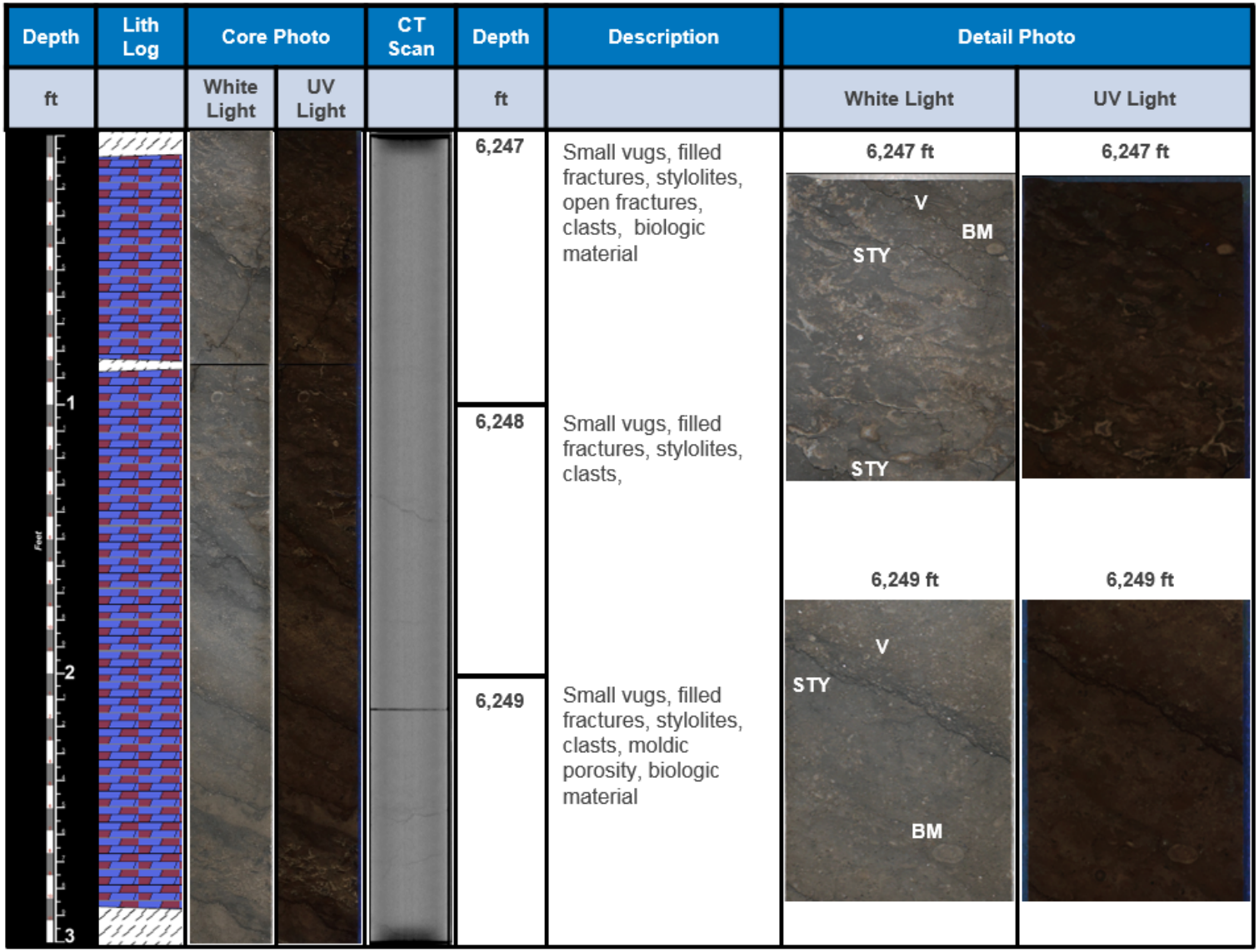


Figure B-111. Compiled illustration of lithology log, core photos (UV and white light), CT scan image, core descriptions, and annotated core images of the Brown Niagaran for depths 6,247 ft. to 6,249 ft.

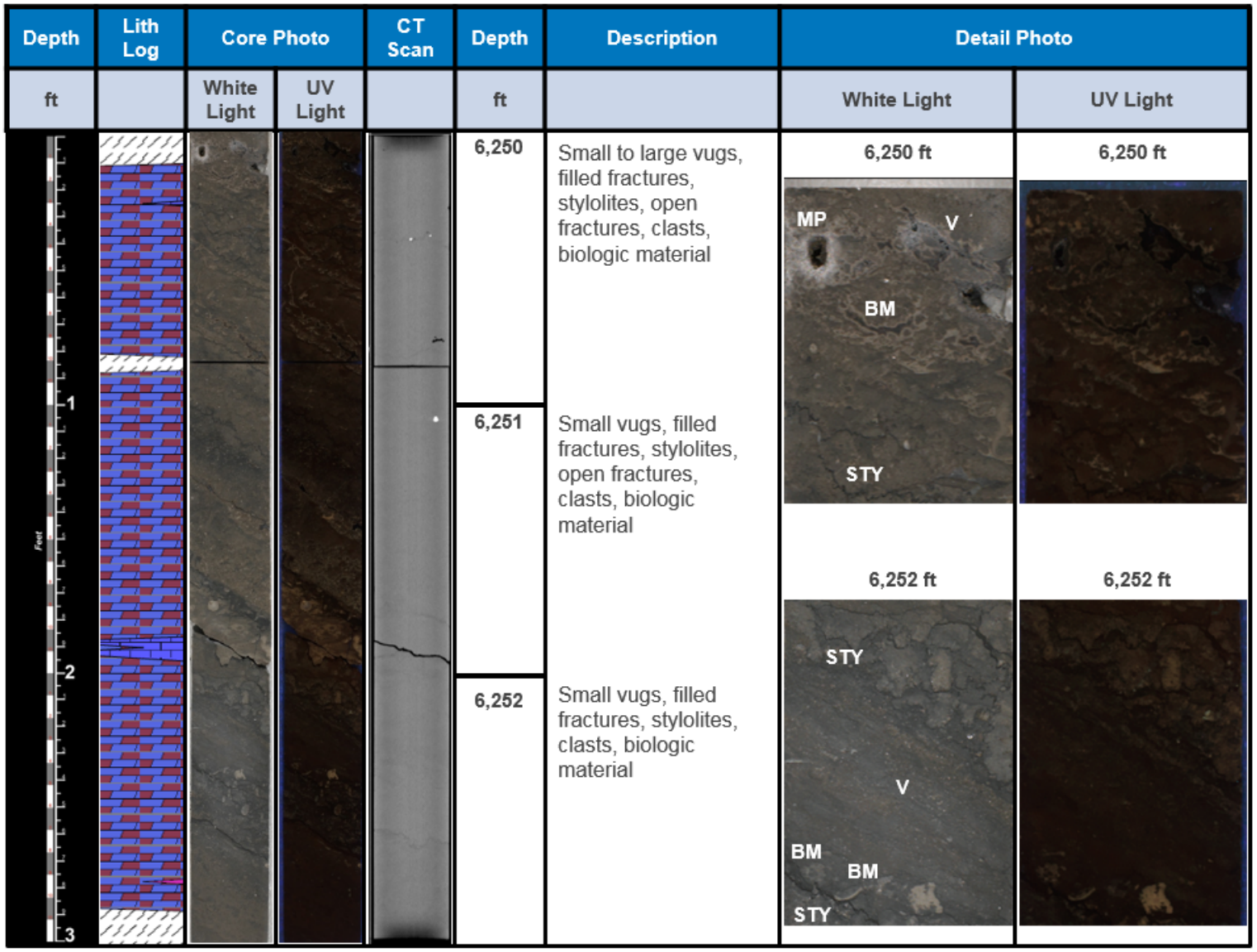


Figure B-112. Compiled illustration of lithology log, core photos (UV and white light), CT scan image, core descriptions, and annotated core images of the Brown Niagaran for depths 6,250 ft. to 6,252 ft.

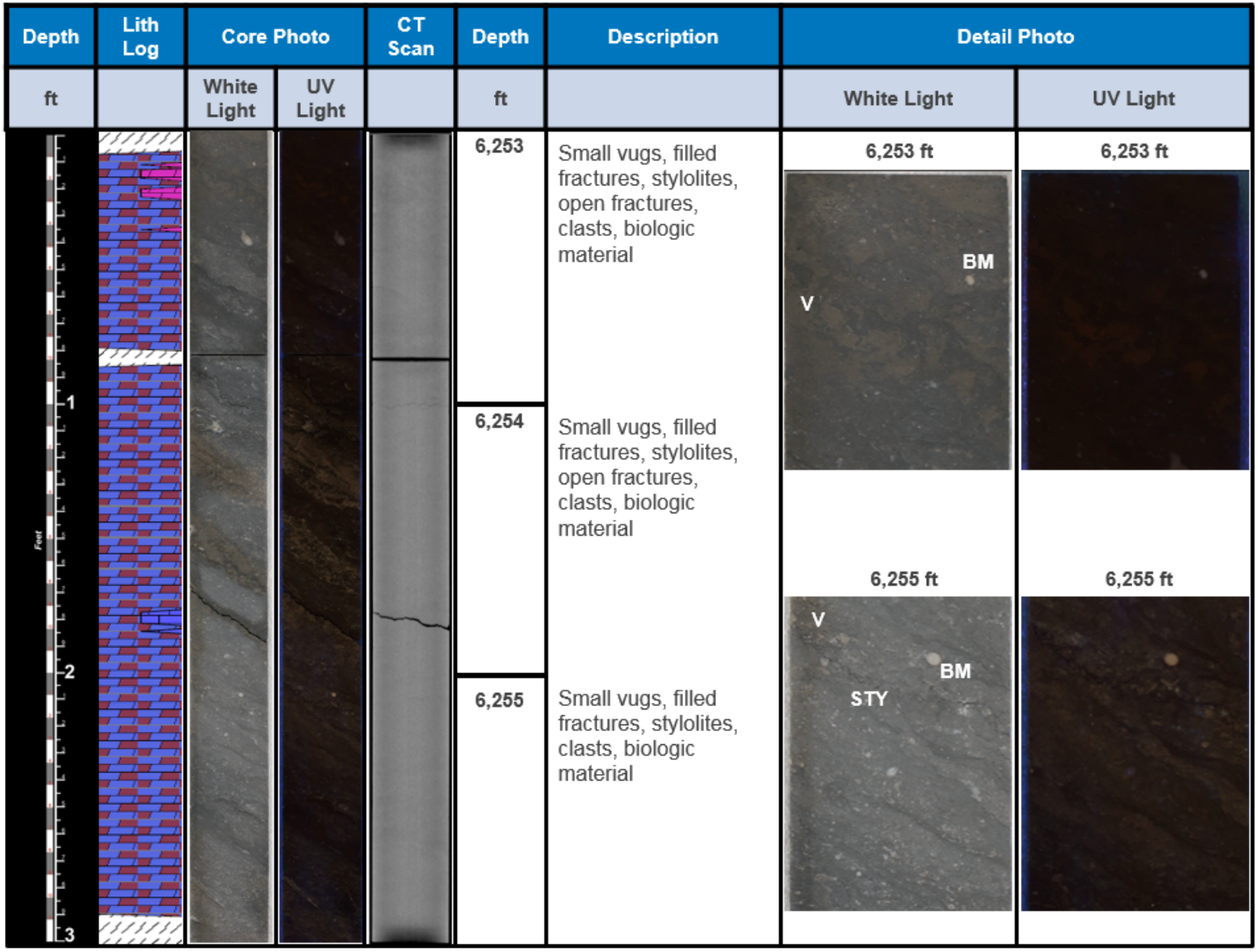


Figure B-113. Compiled illustration of lithology log, core photos (UV and white light), CT scan image, core descriptions, and annotated core images of the Brown Niagaran for depths 6,253 ft. to 6,255 ft.

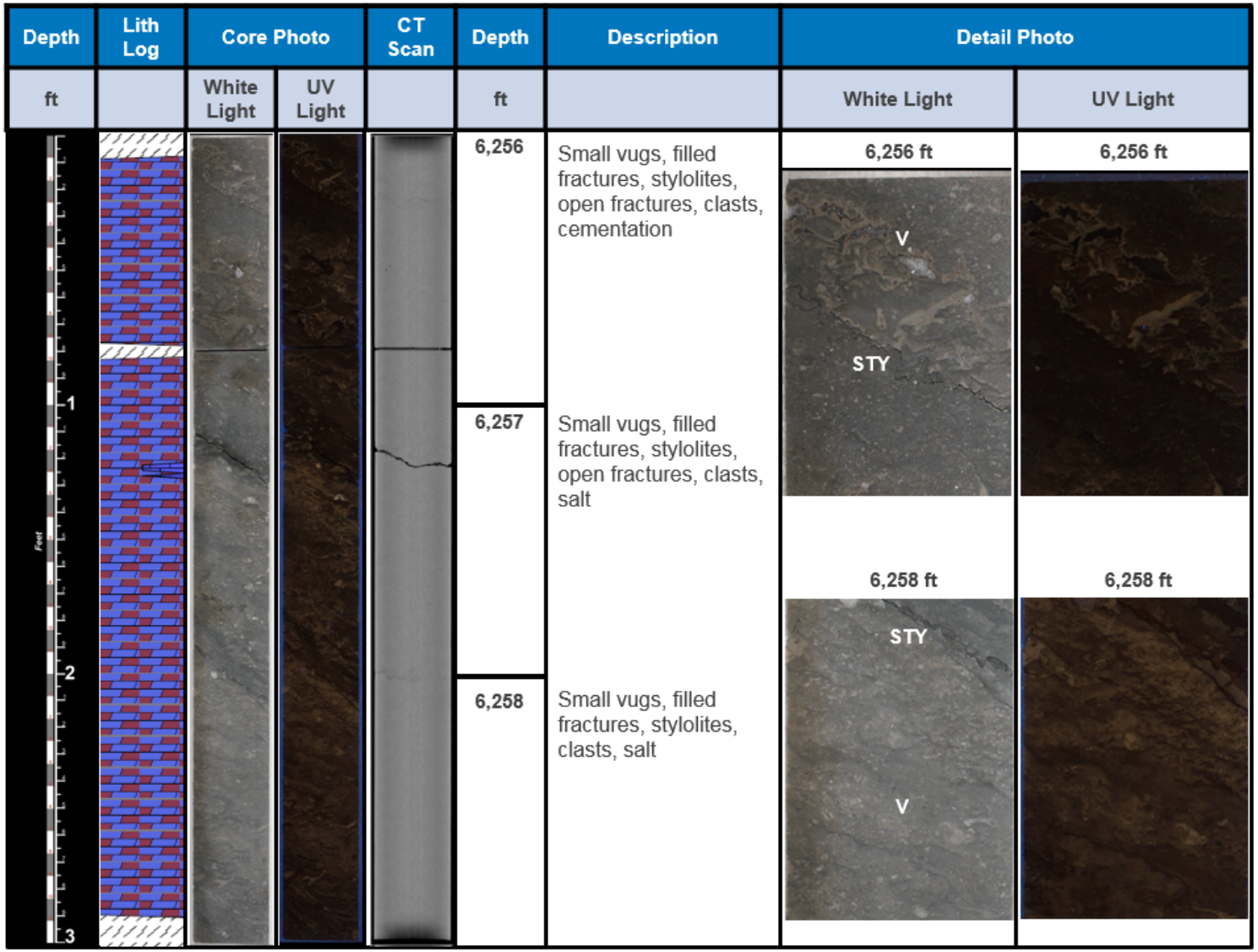


Figure B-114. Compiled illustration of lithology log, core photos (UV and white light), CT scan image, core descriptions, and annotated core images of the Brown Niagaran for depths 6,256 ft. to 6,258 ft.

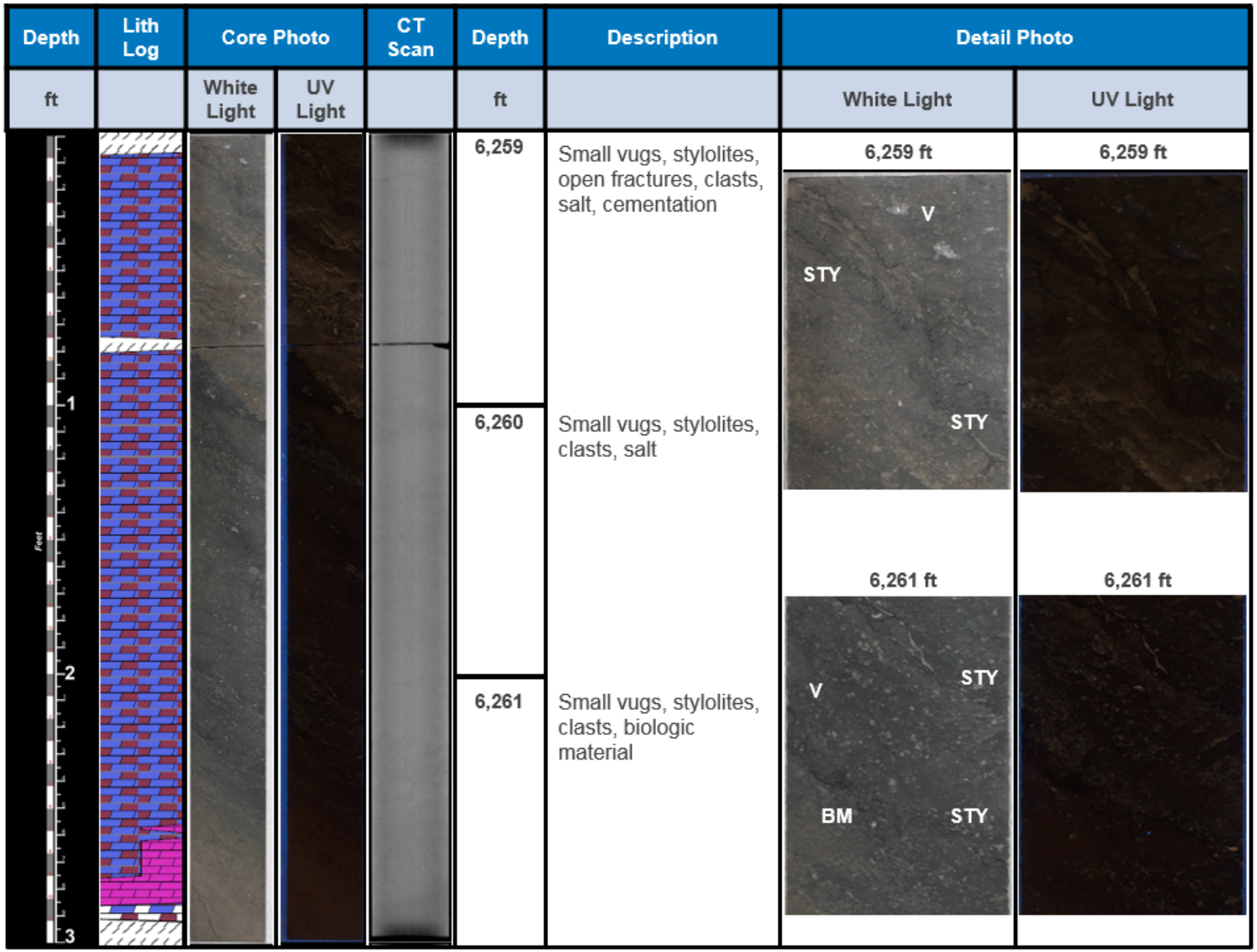


Figure B-115. Compiled illustration of lithology log, core photos (UV and white light), CT scan image, core descriptions, and annotated core images of the Brown Niagaran for depths 6,259 ft. to 6,261 ft.

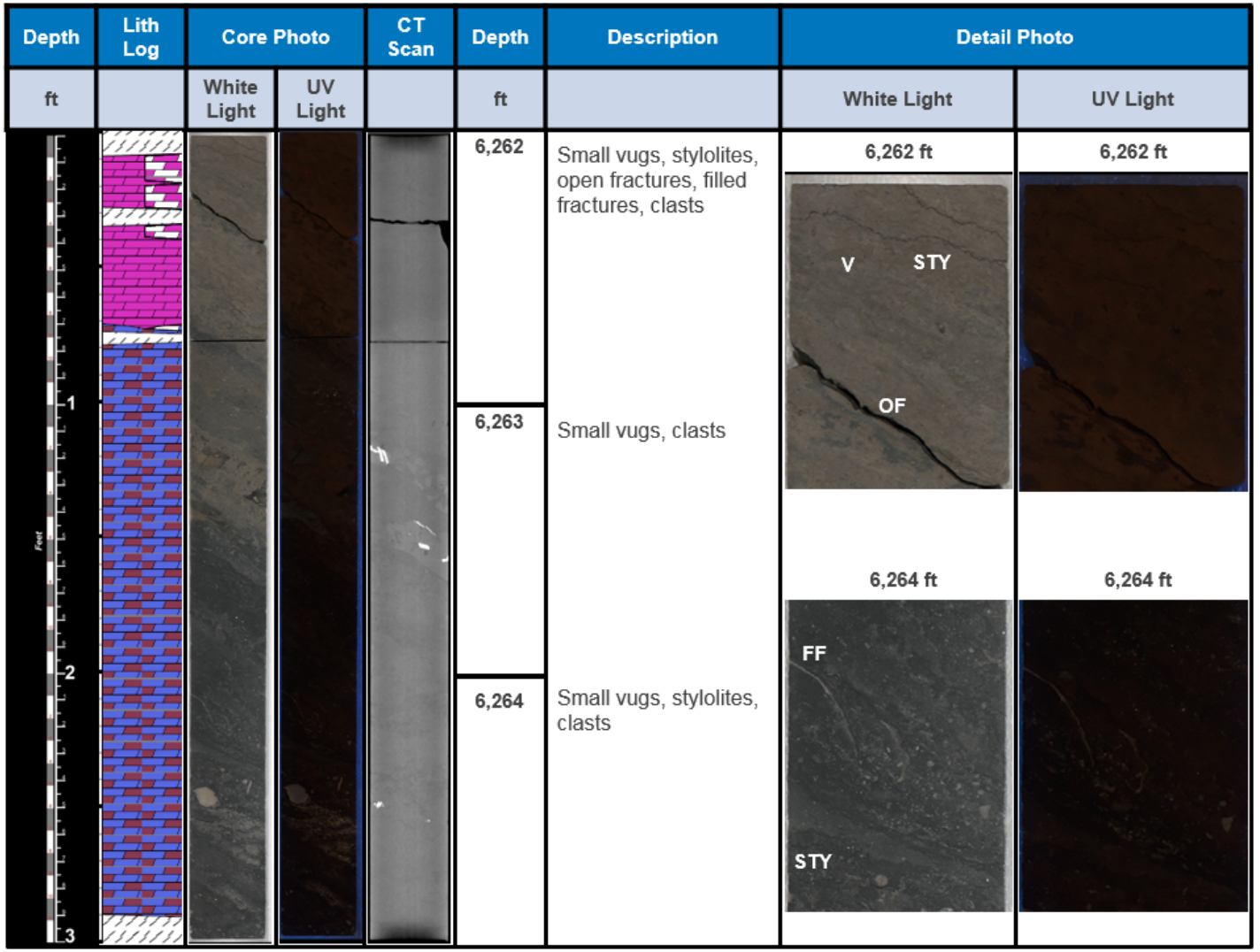


Figure B-116. Compiled illustration of lithology log, core photos (UV and white light), CT scan image, core descriptions, and annotated core images of the Brown Niagaran for depths 6,262 ft. to 6,264 ft.

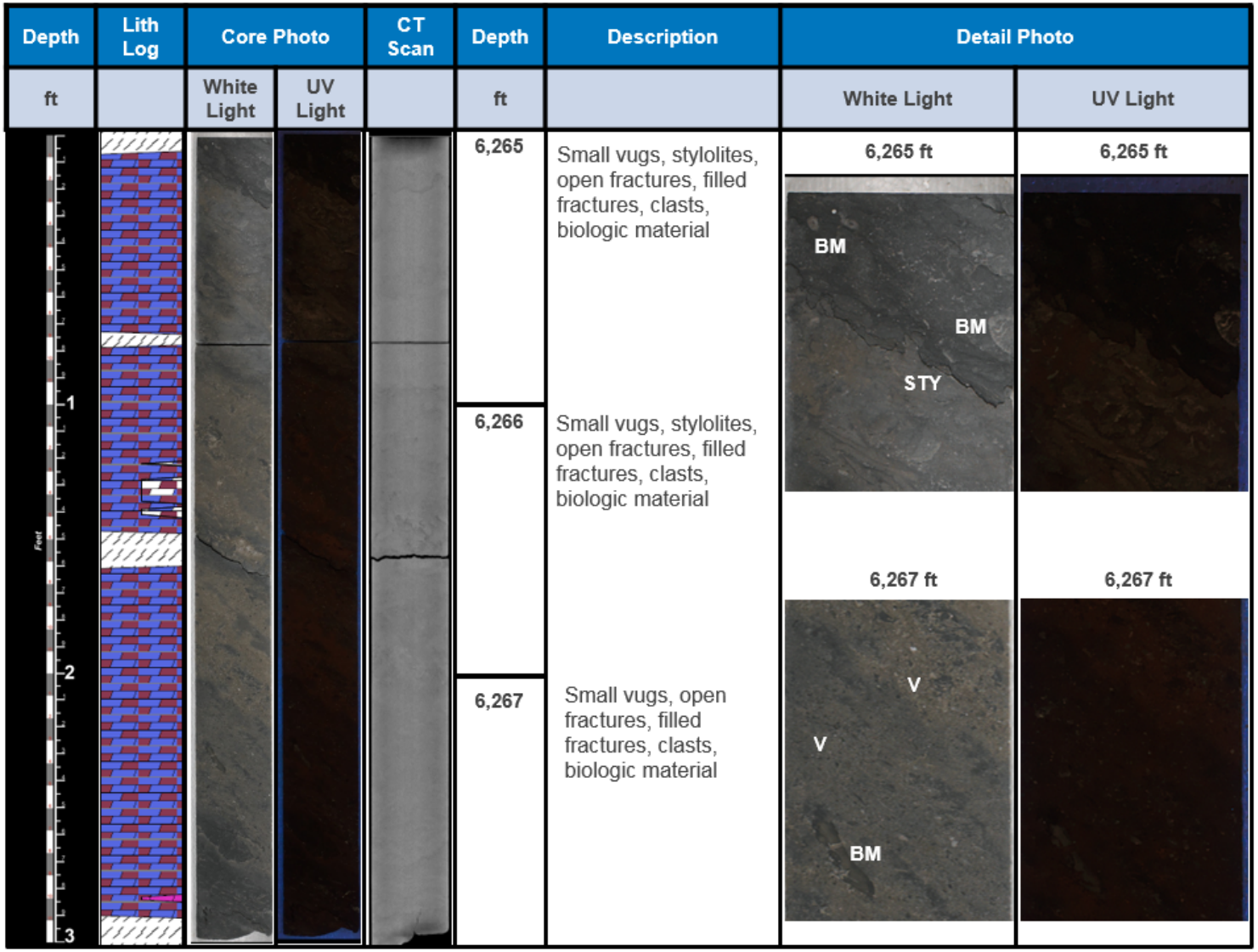


Figure B-117. Compiled illustration of lithology log, core photos (UV and white light), CT scan image, core descriptions, and annotated core images of the Brown Niagaran for depths 6,265 ft. to 6,267 ft.

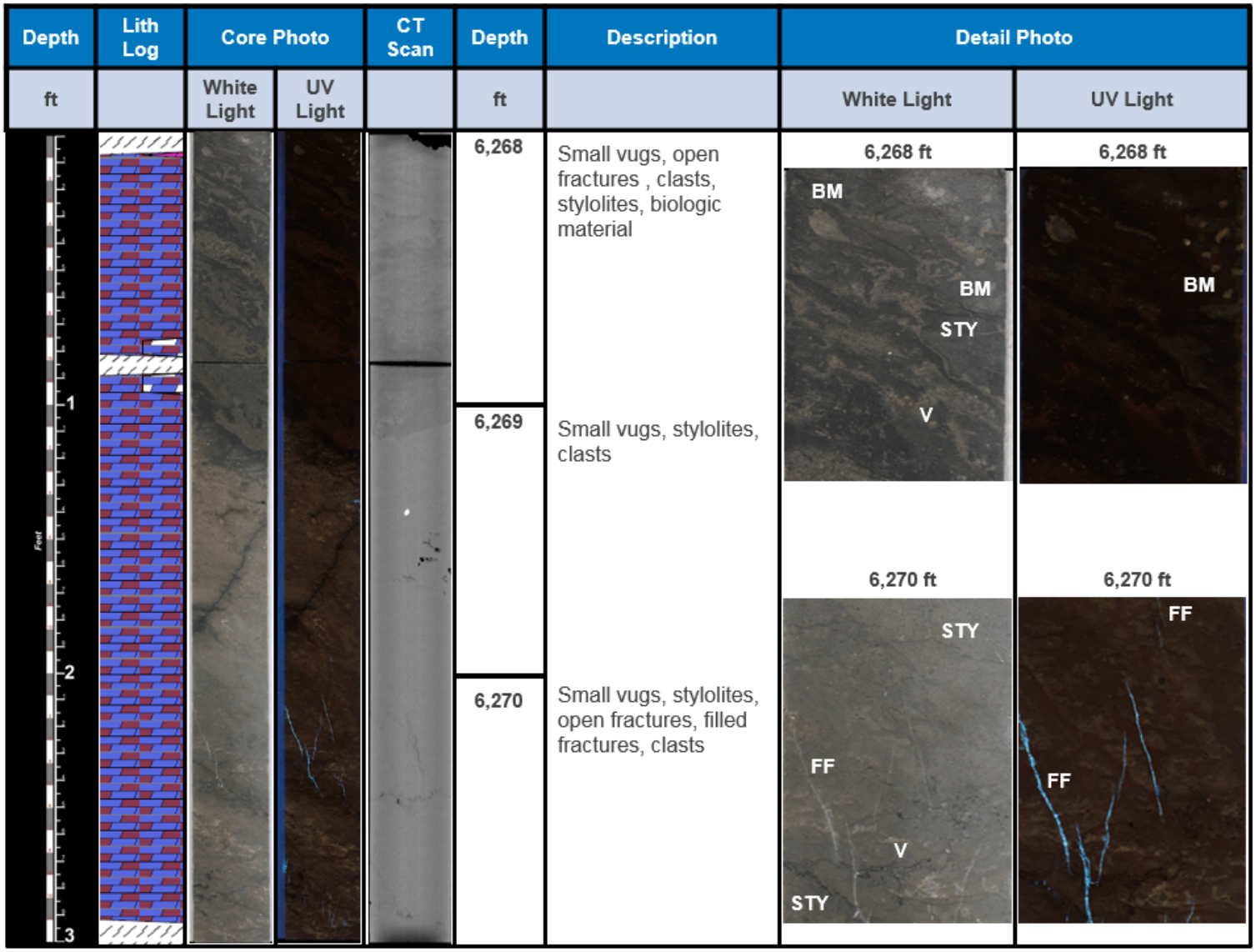


Figure B-118. Compiled illustration of lithology log, core photos (UV and white light), CT scan image, core descriptions, and annotated core images of the Brown Niagaran for depths 6,268 ft. to 6,270 ft.

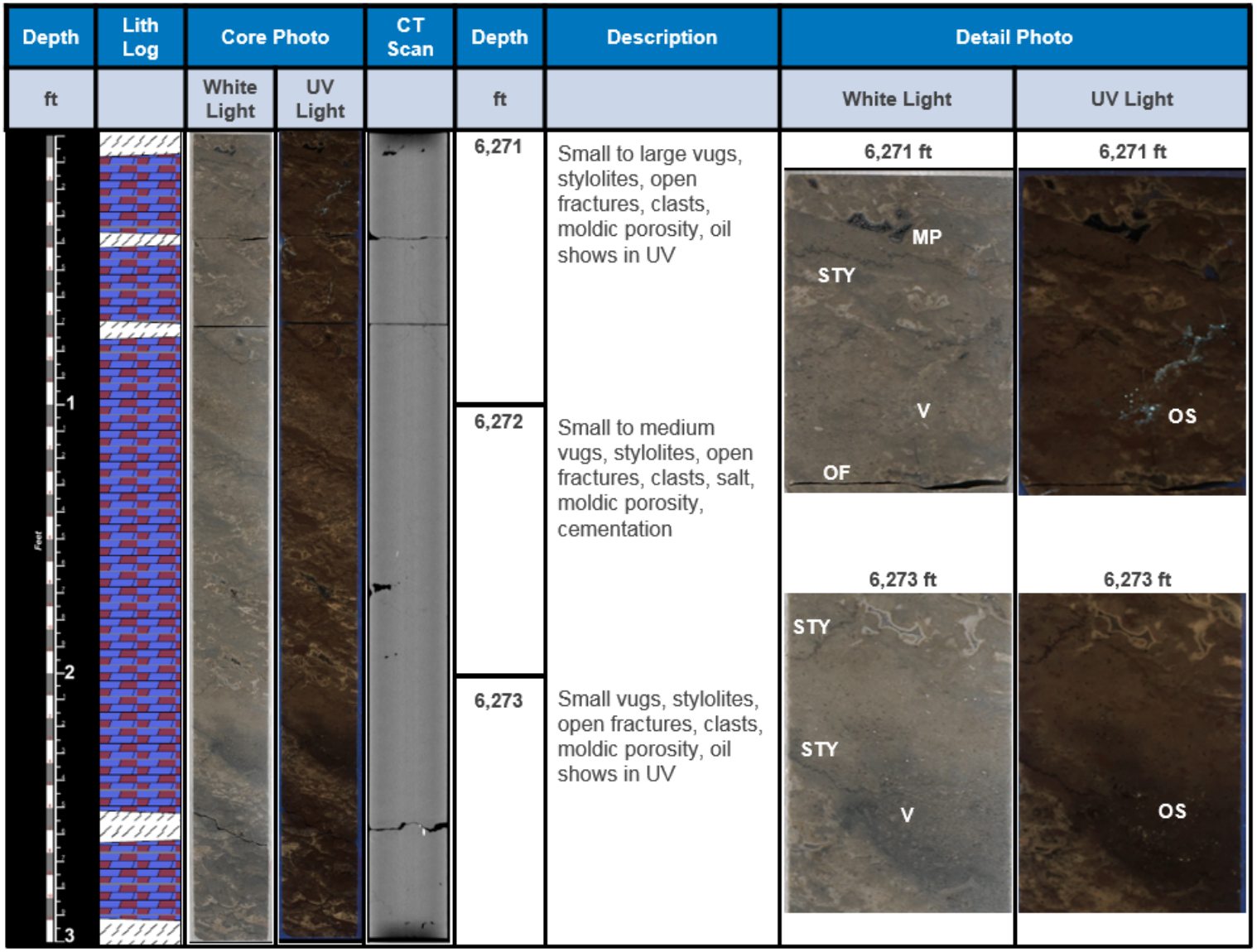


Figure B-119. Compiled illustration of lithology log, core photos (UV and white light), CT scan image, core descriptions, and annotated core images of the Brown Niagaran for depths 6,271 ft. to 6,273 ft.

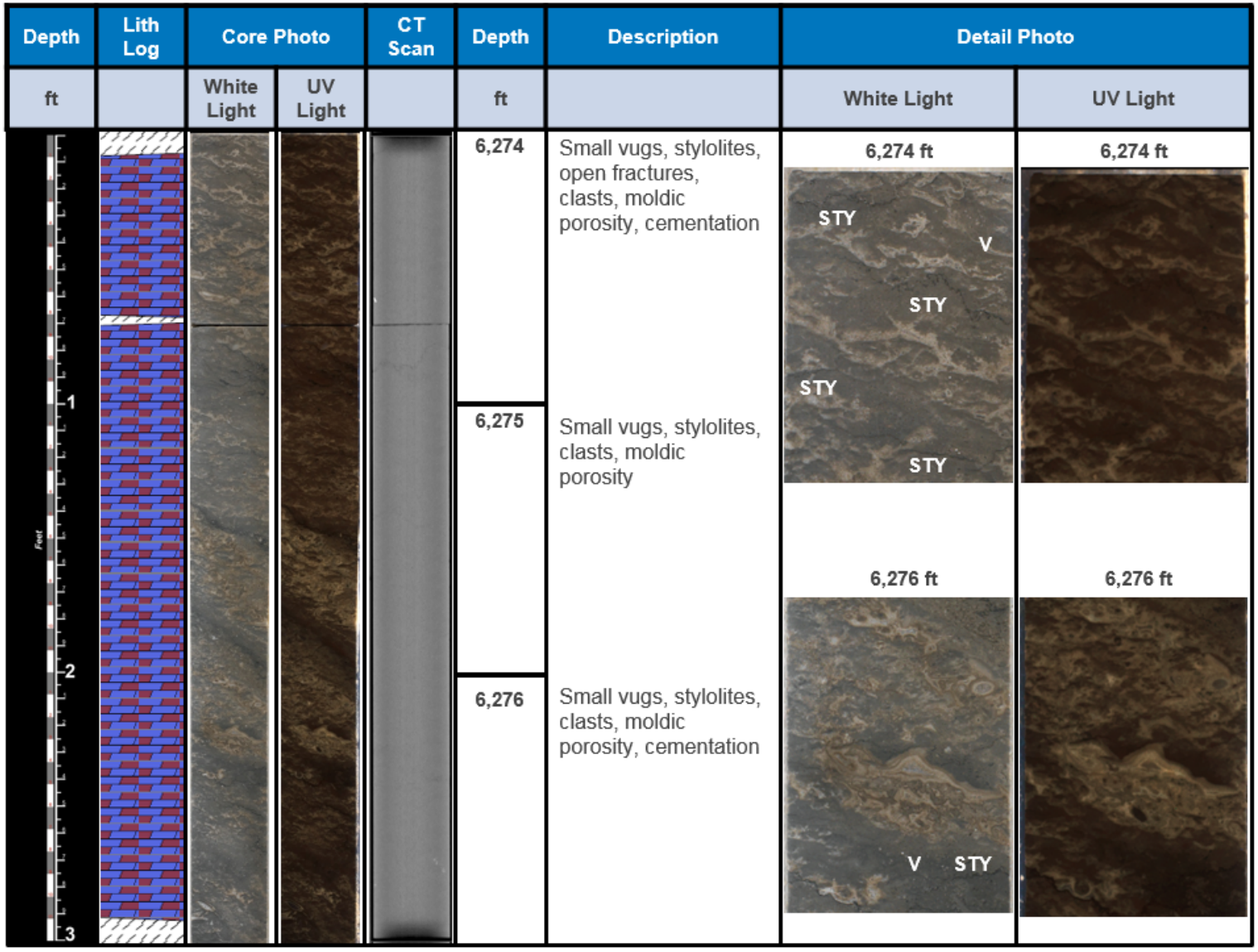


Figure B-120. Compiled illustration of lithology log, core photos (UV and white light), CT scan image, core descriptions, and annotated core images of the Brown Niagaran for depths 6,274 ft. to 6,276 ft.

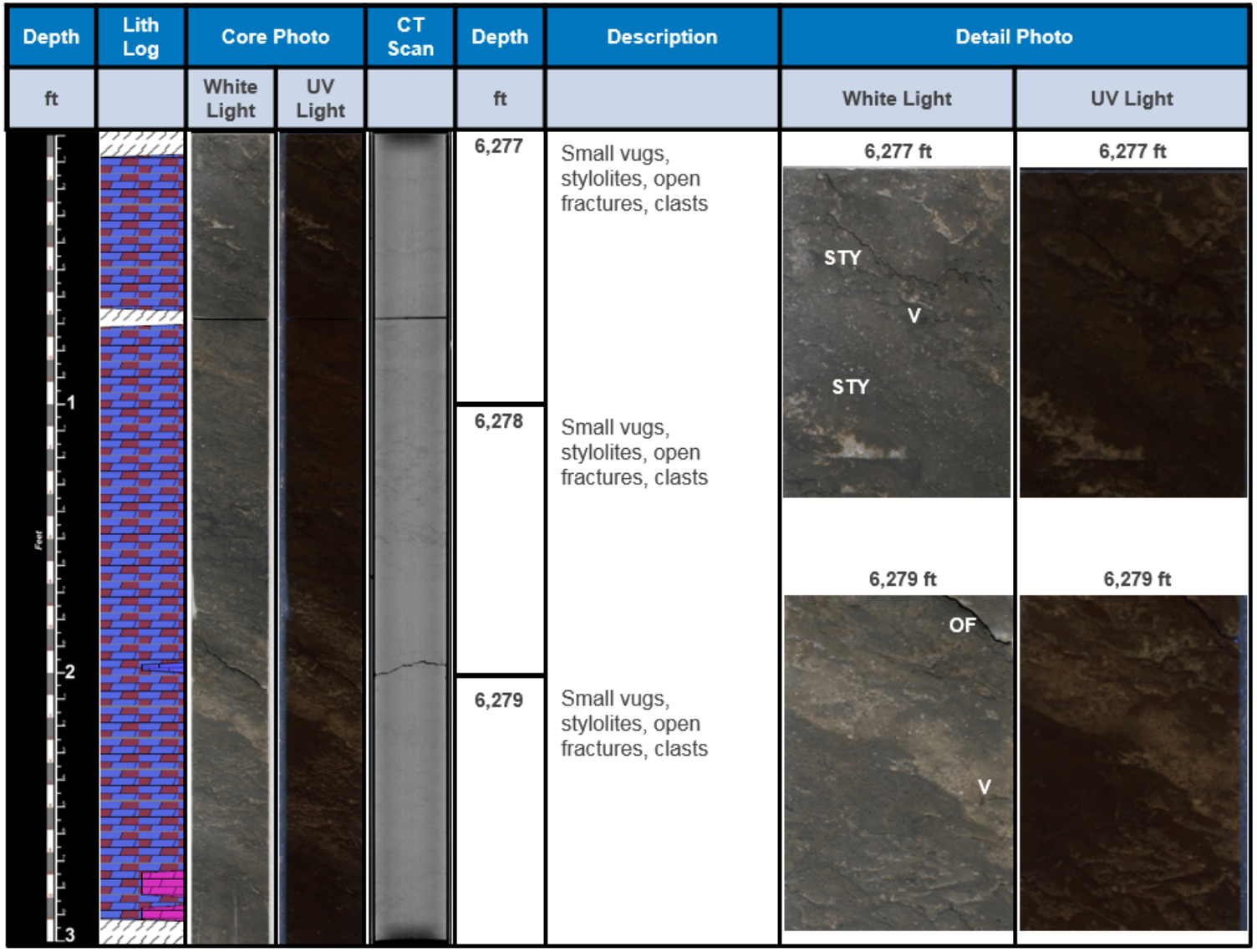


Figure B-121. Compiled illustration of lithology log, core photos (UV and white light), CT scan image, core descriptions, and annotated core images of the Brown Niagaran for depths 6,277 ft. to 6,279 ft.

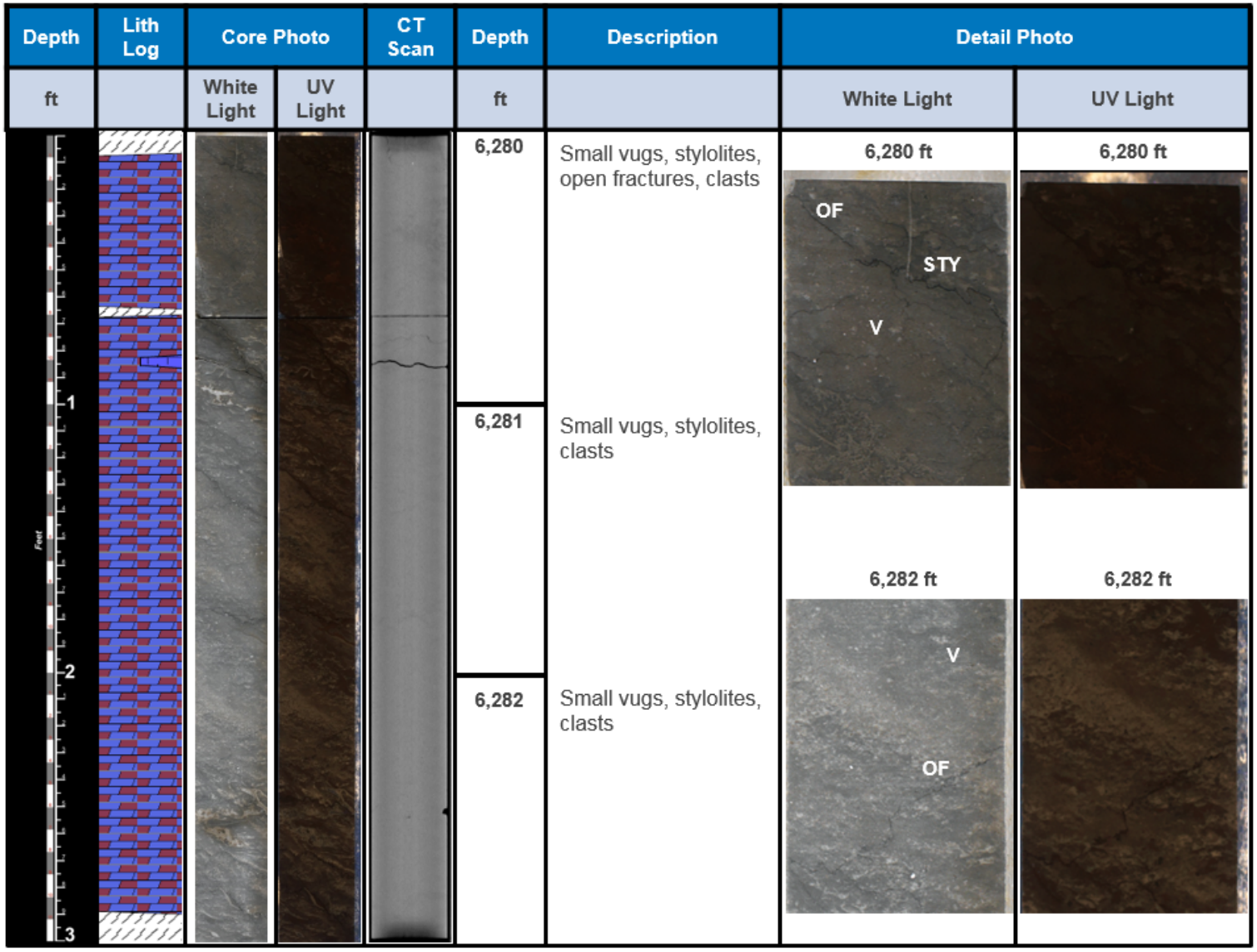


Figure B-122. Compiled illustration of lithology log, core photos (UV and white light), CT scan image, core descriptions, and annotated core images of the Brown Niagaran for depths 6,280 ft. to 6,282 ft.

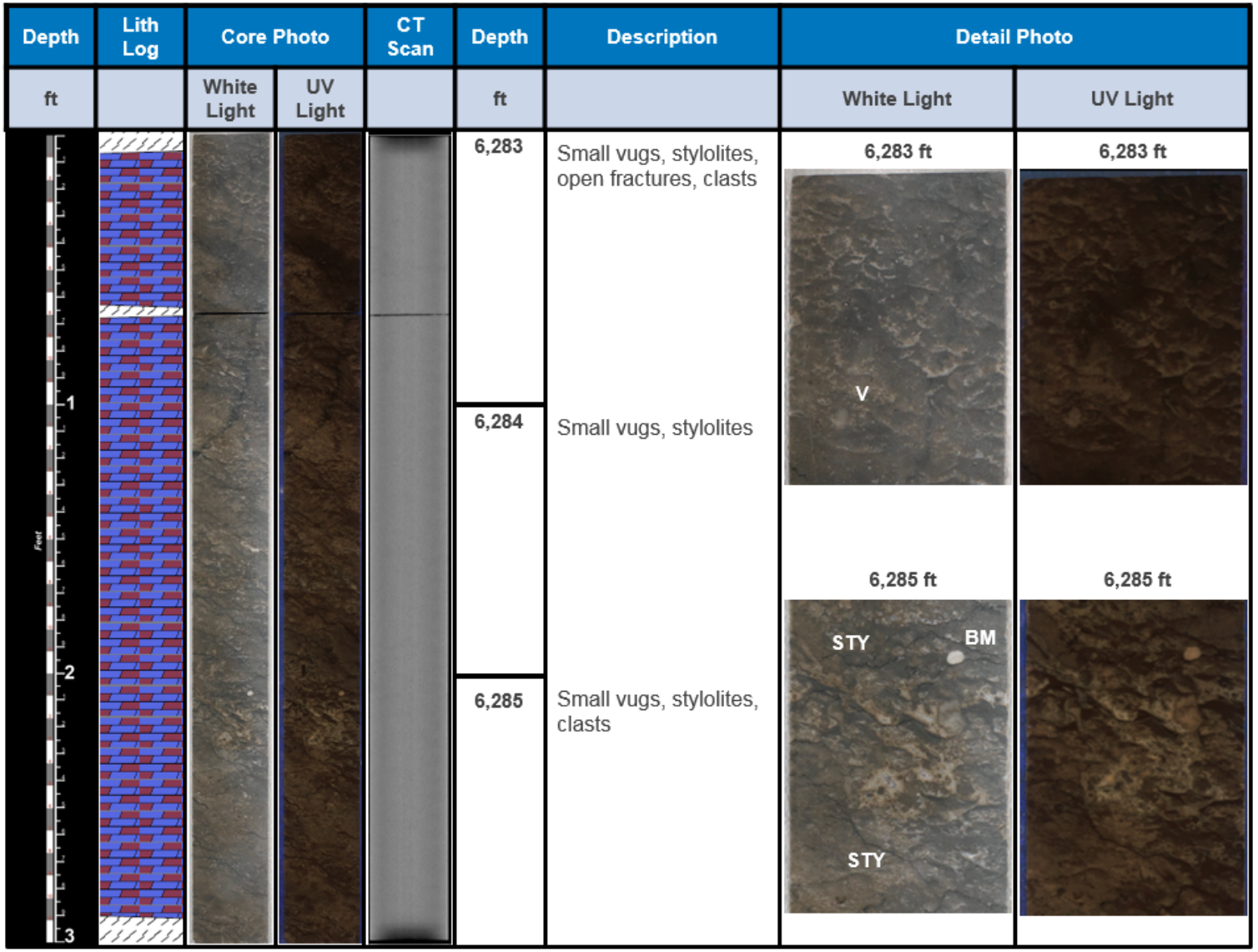


Figure B-123. Compiled illustration of lithology log, core photos (UV and white light), CT scan image, core descriptions, and annotated core images of the Brown Niagaran for depths 6,283 ft. to 6,285 ft.

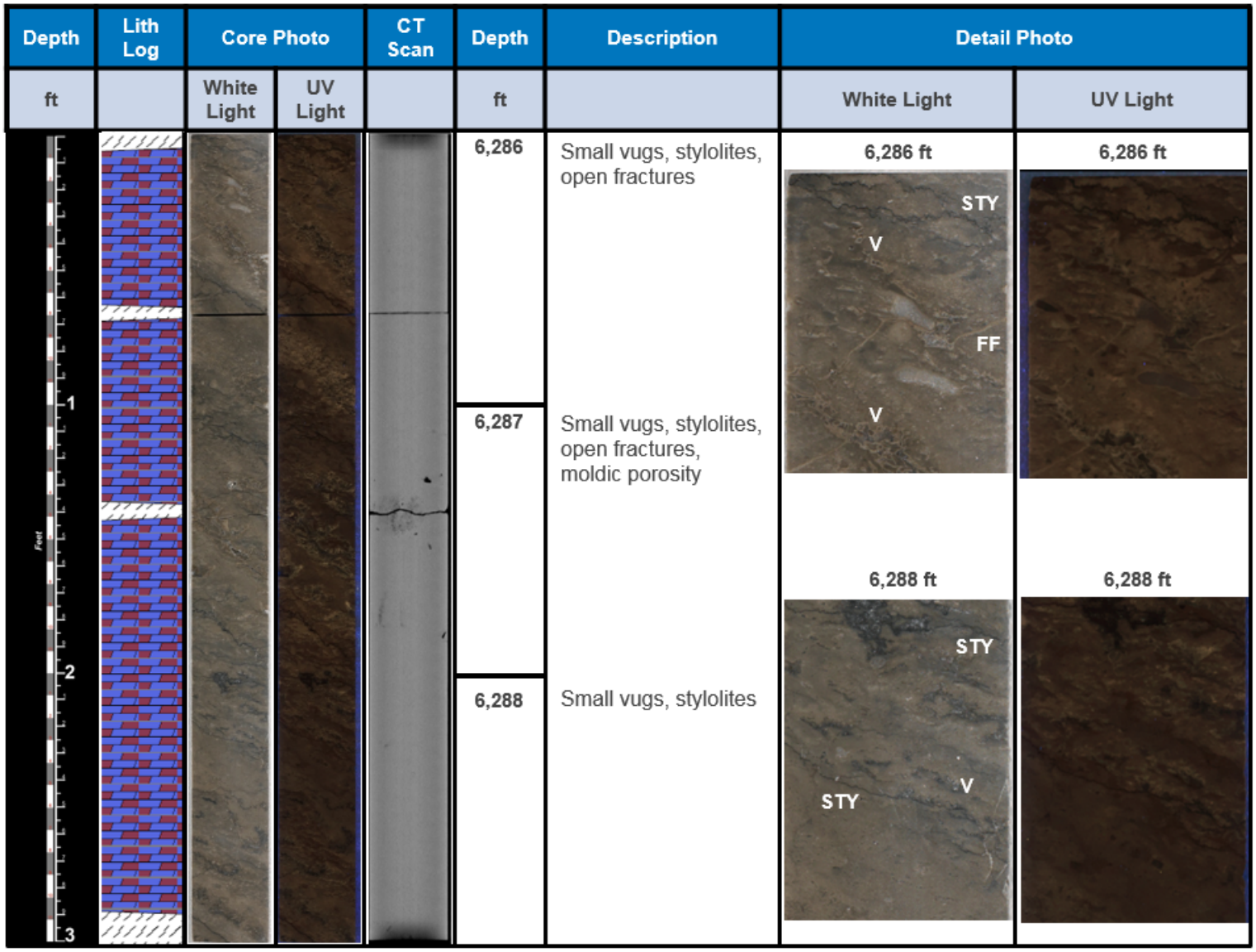


Figure B-124. Compiled illustration of lithology log, core photos (UV and white light), CT scan image, core descriptions, and annotated core images of the Brown Niagaran for depths 6,286 ft. to 6,288 ft.

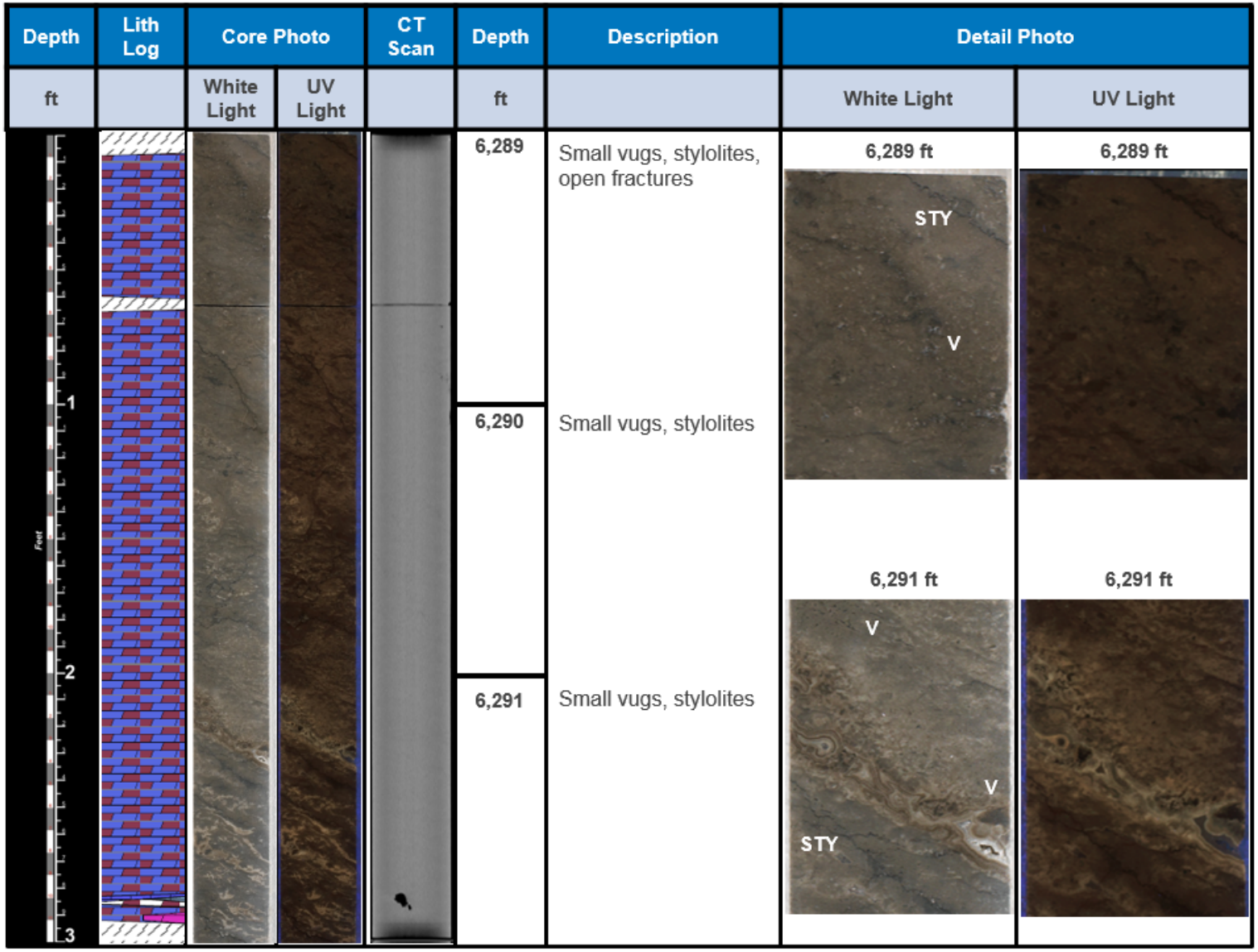


Figure B-125. Compiled illustration of lithology log, core photos (UV and white light), CT scan image, core descriptions, and annotated core images of the Brown Niagaran for depths 6,289 ft. to 6,291 ft.

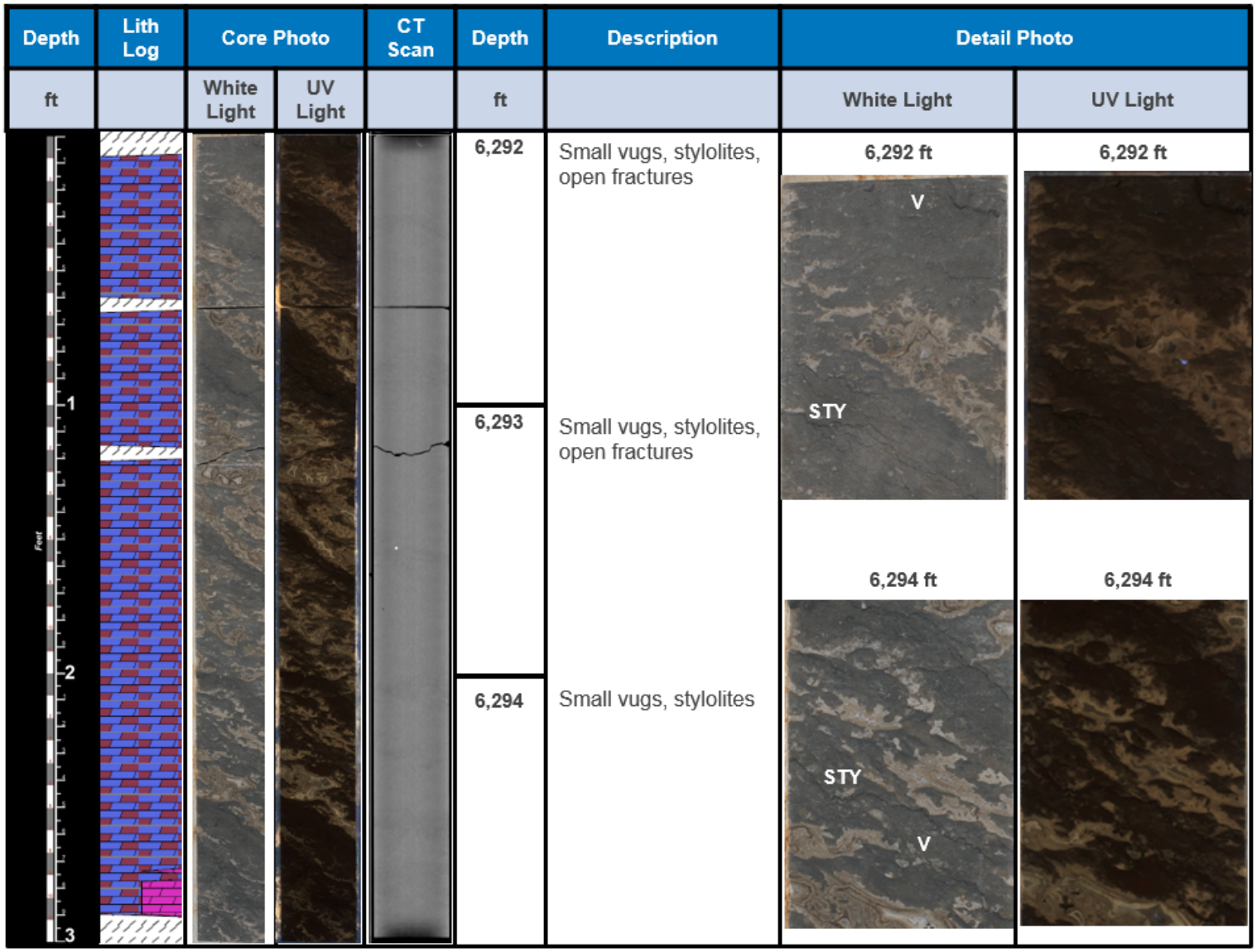


Figure B-126. Compiled illustration of lithology log, core photos (UV and white light), CT scan image, core descriptions, and annotated core images of the Brown Niagaran for depths 6,292 ft. to 6,294 ft.

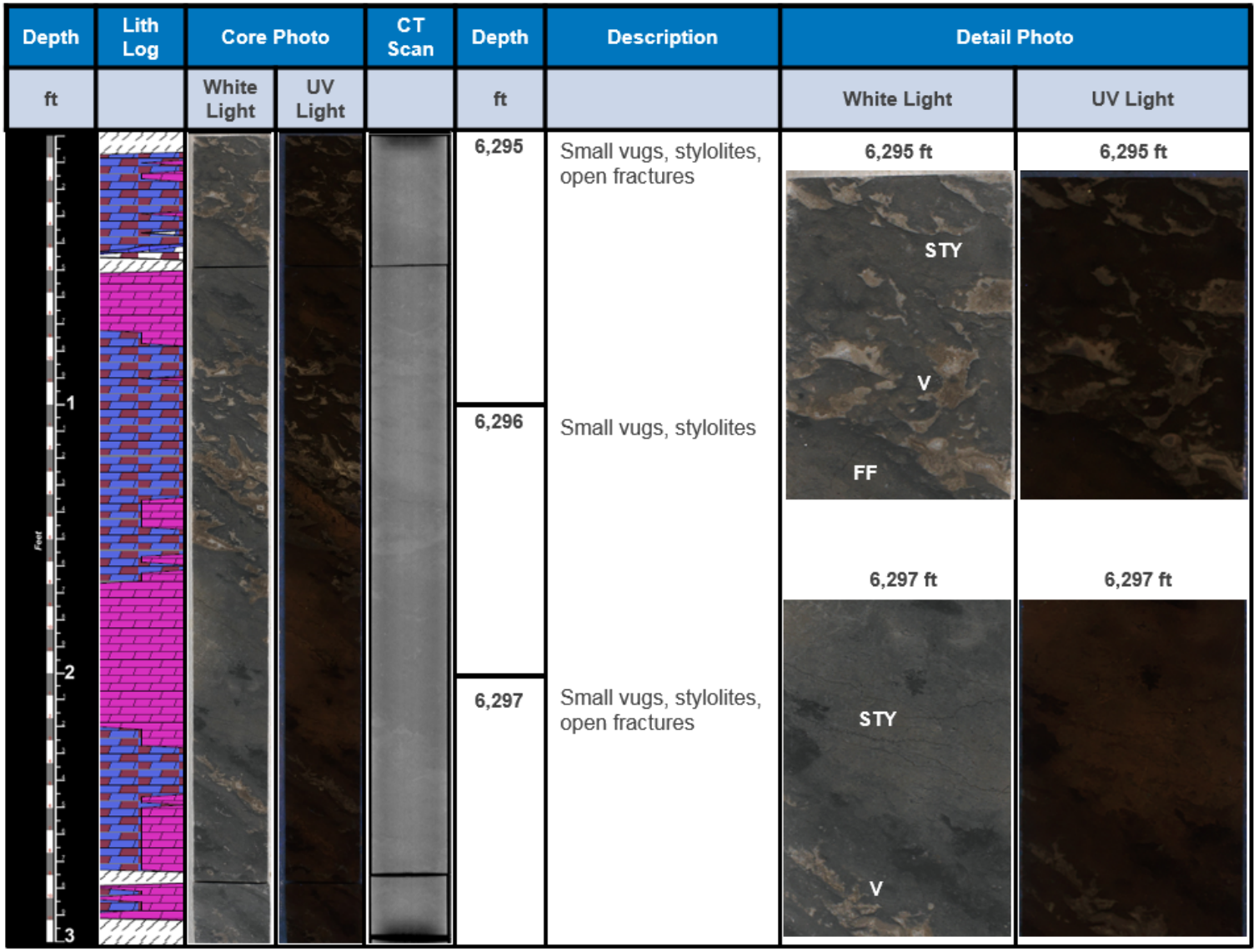


Figure B-127. Compiled illustration of lithology log, core photos (UV and white light), CT scan image, core descriptions, and annotated core images of the Brown Niagaran for depths 6,295 ft. to 6,297 ft.

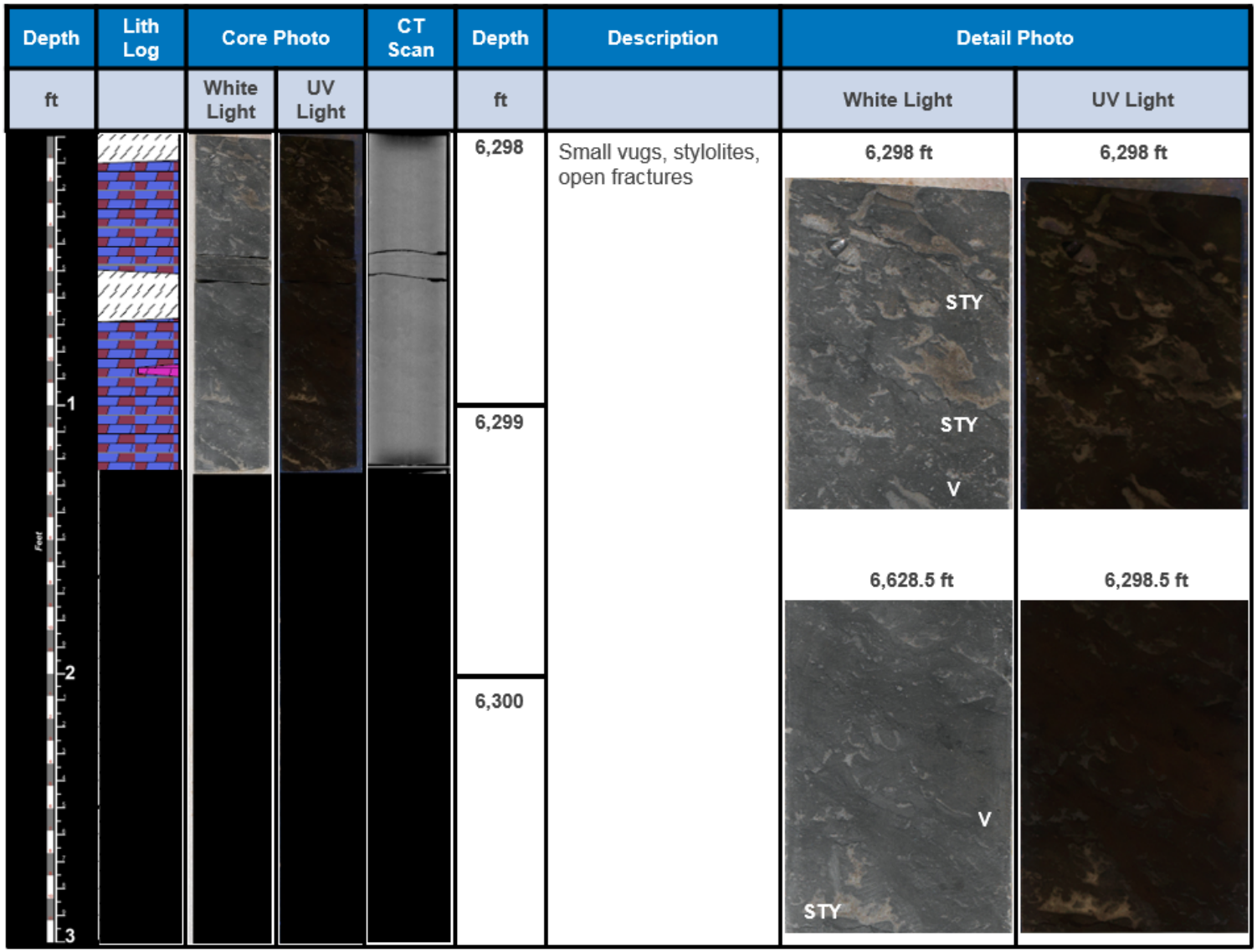


Figure B-128. Compiled illustration of lithology log, core photos (UV and white light), CT scan image, core descriptions, and annotated core images of the Brown Niagaran for depths 6,298 ft. to 6,300 ft.

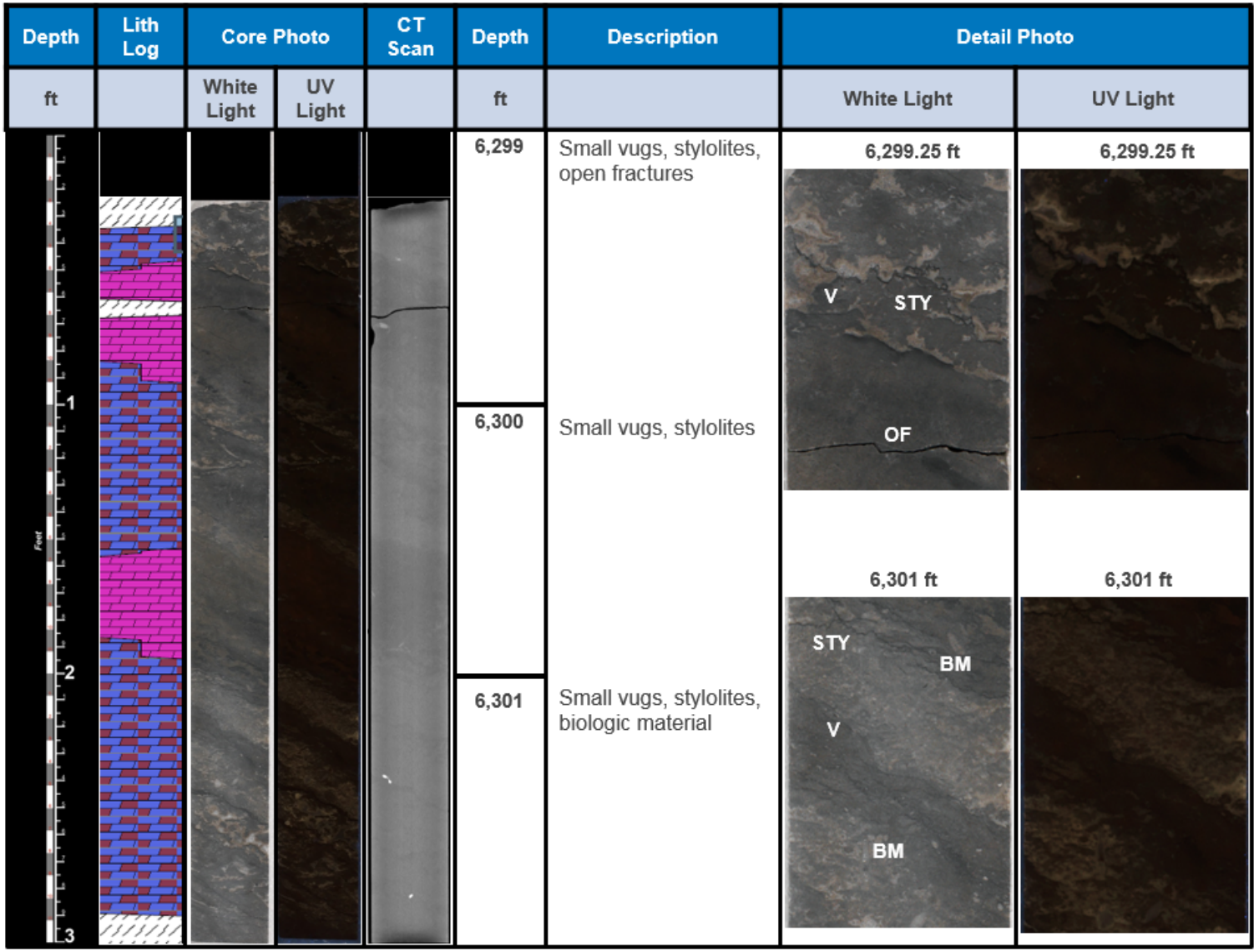


Figure B-129. Compiled illustration of lithology log, core photos (UV and white light), CT scan image, core descriptions, and annotated core images of the Brown Niagaran for depths 6,299 ft. to 6,301 ft.

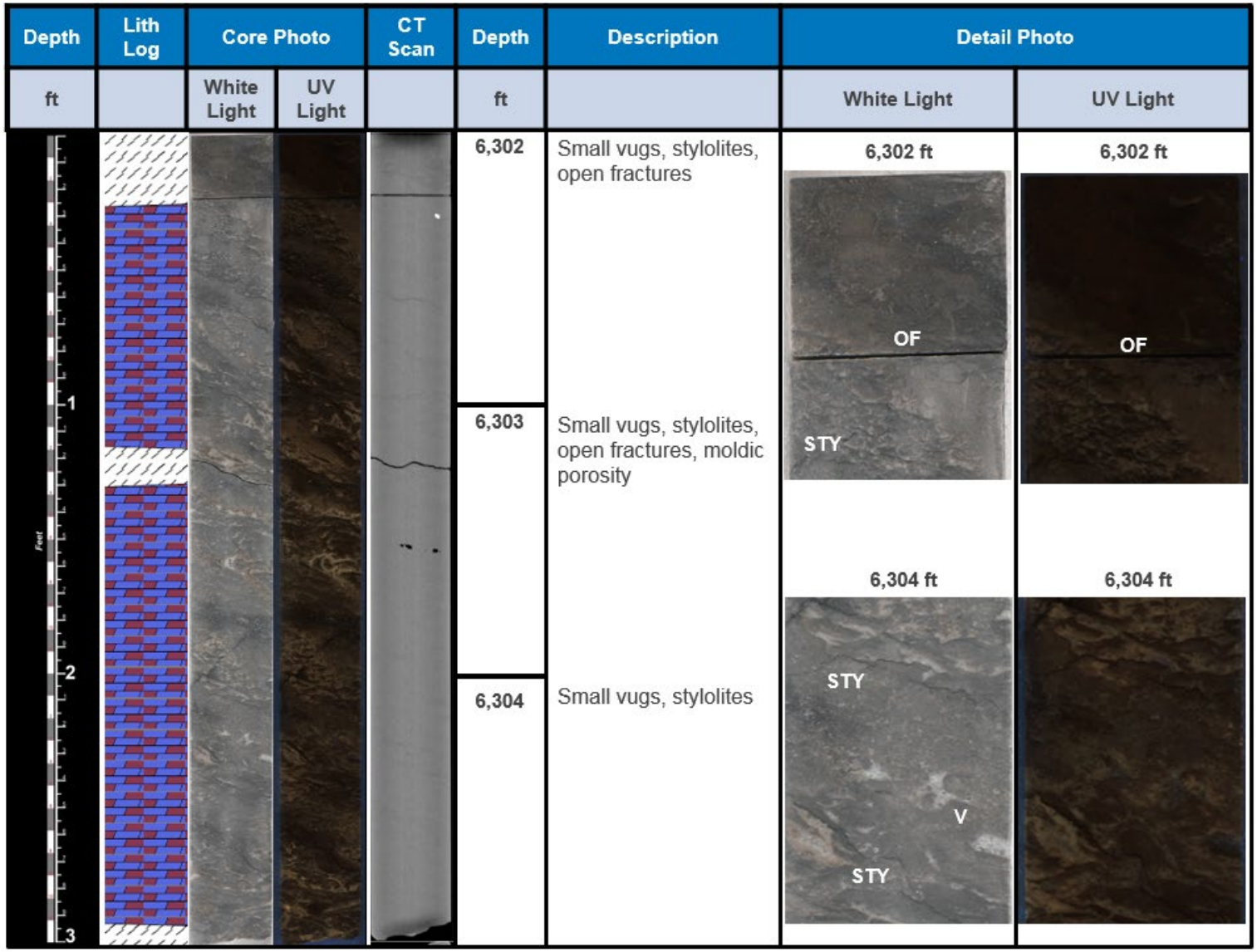


Figure B-130. Compiled illustration of lithology log, core photos (UV and white light), CT scan image, core descriptions, and annotated core images of the Brown Niagaran for depths 6,302 ft. to 6,304 ft.

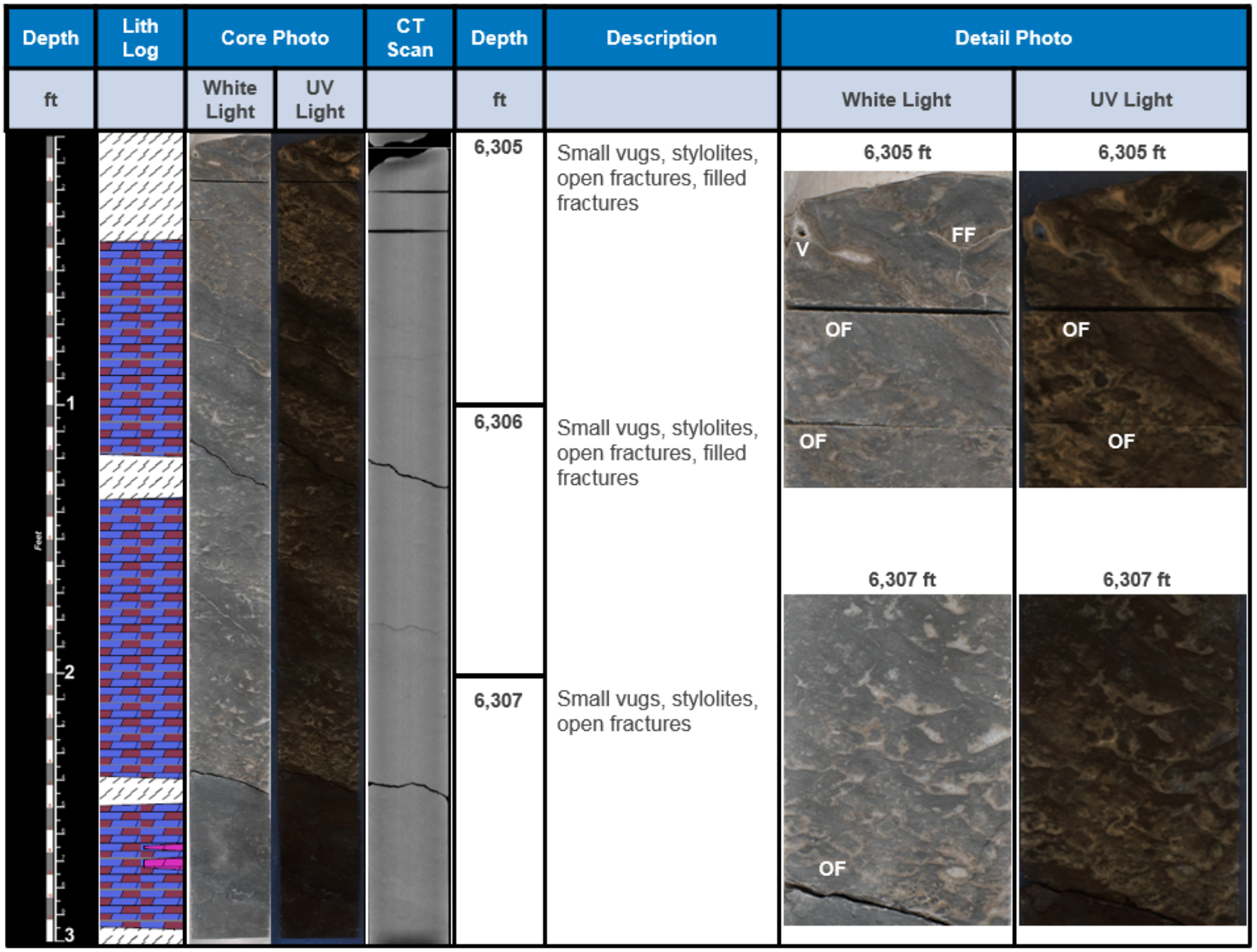


Figure B-131. Compiled illustration of lithology log, core photos (UV and white light), CT scan image, core descriptions, and annotated core images of the Brown Niagaran for depths 6,305 ft. to 6,307 ft.

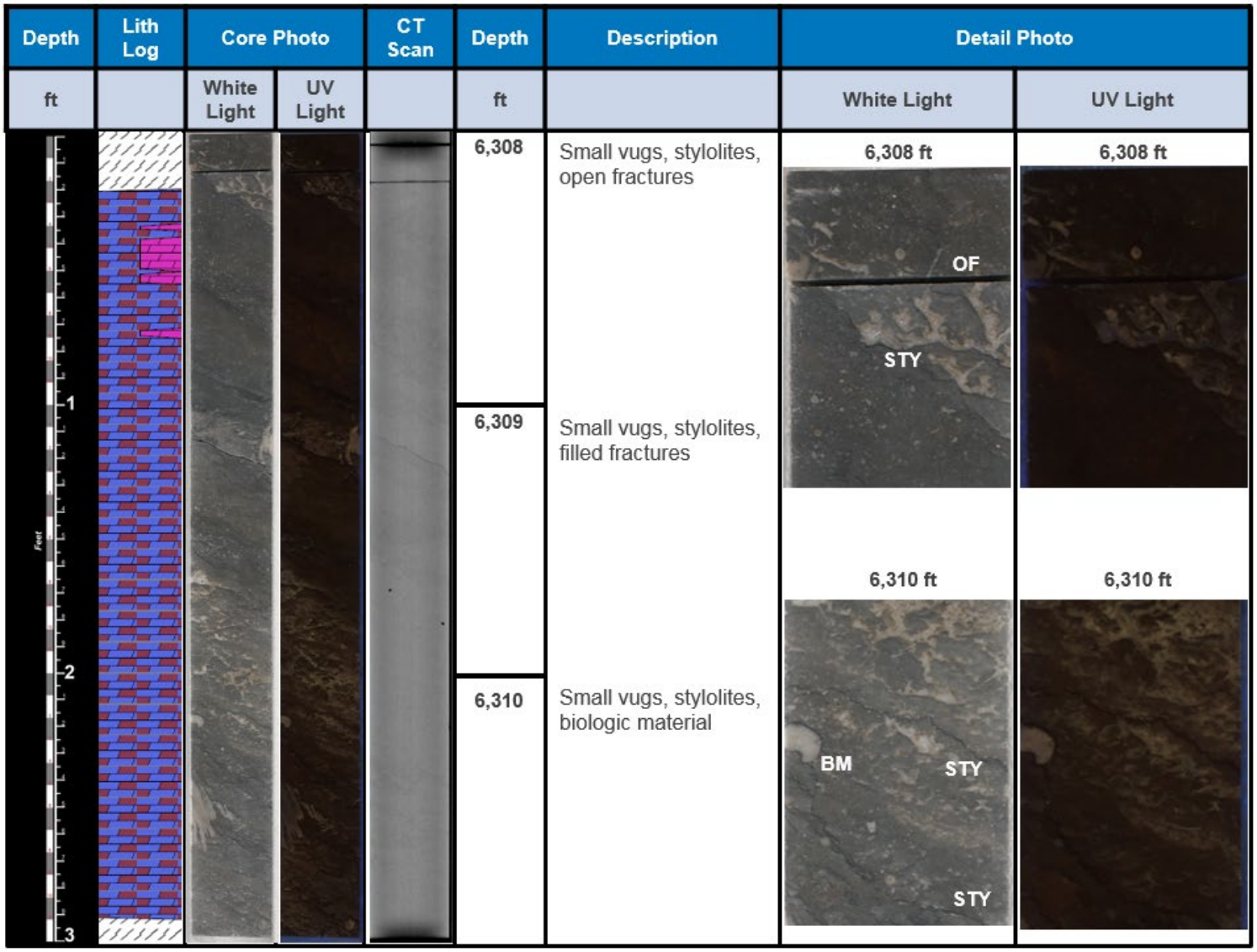


Figure B-132. Compiled illustration of lithology log, core photos (UV and white light), CT scan image, core descriptions, and annotated core images of the Brown Niagaran for depths 6,308 ft. to 6,310 ft.

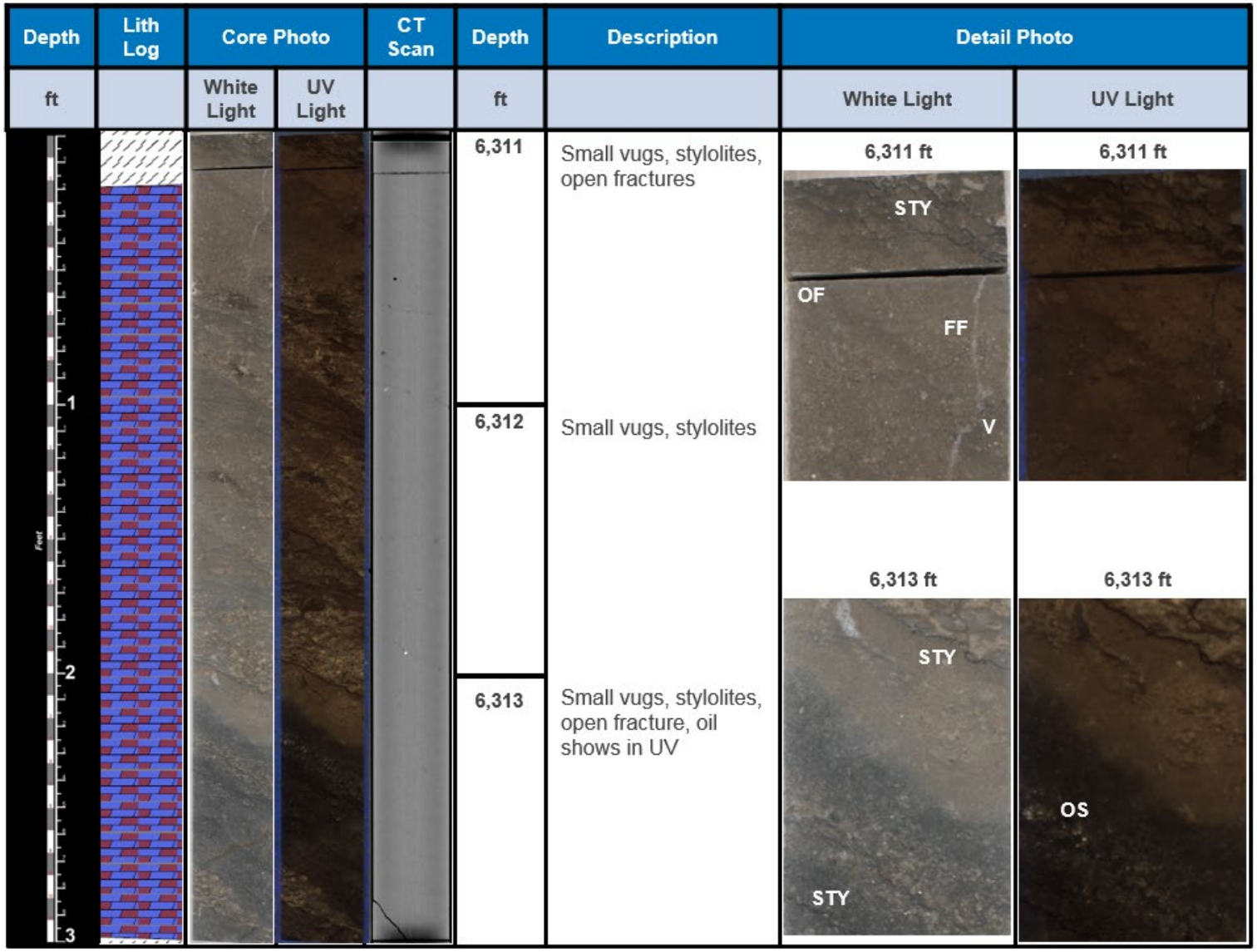


Figure B-133. Compiled illustration of lithology log, core photos (UV and white light), CT scan image, core descriptions, and annotated core images of the Brown Niagaran for depths 6,311 ft. to 6,313 ft.

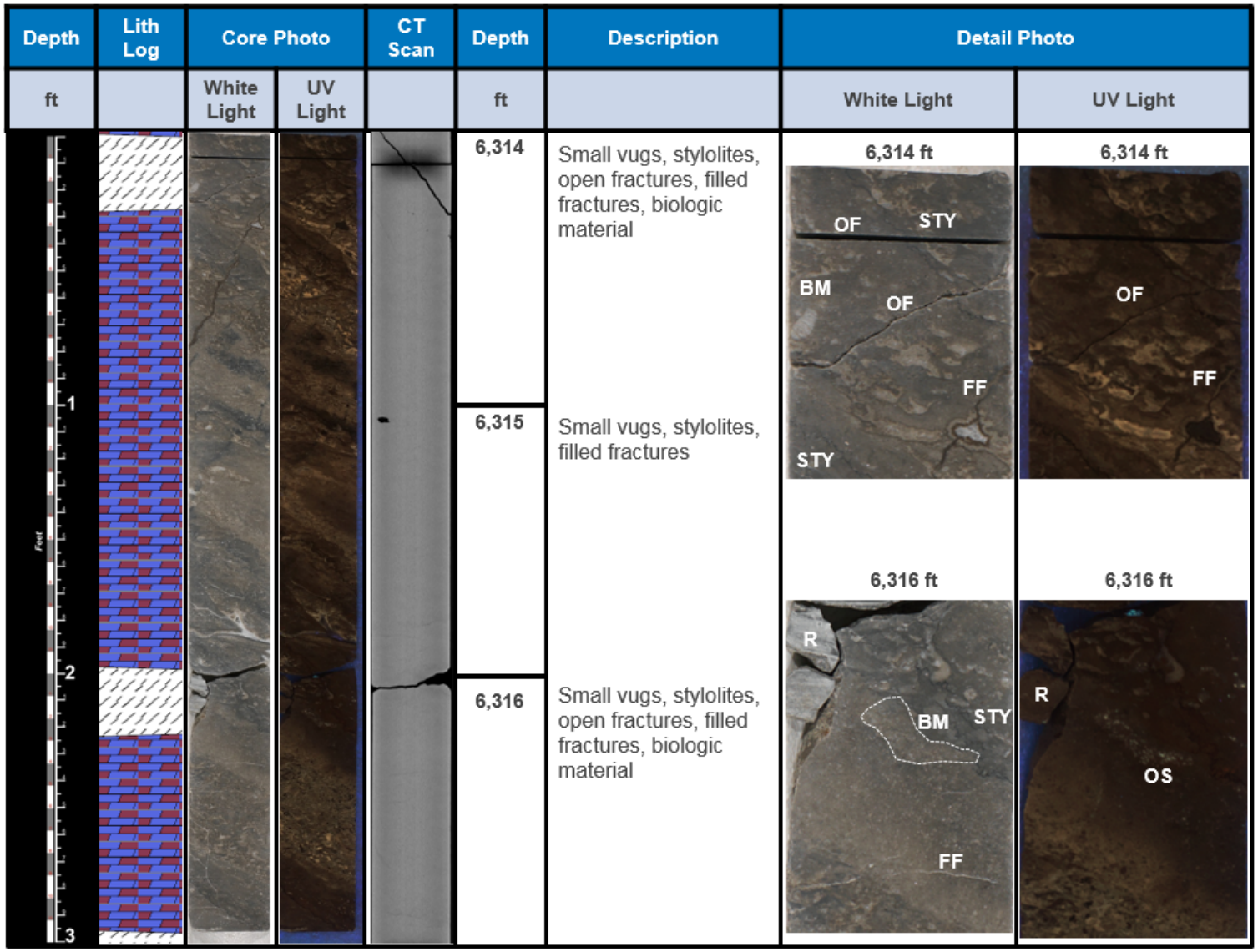


Figure B-134. Compiled illustration of lithology log, core photos (UV and white light), CT scan image, core descriptions, and annotated core images of the Brown Niagaran for depths 6,314 ft. to 6,316 ft.

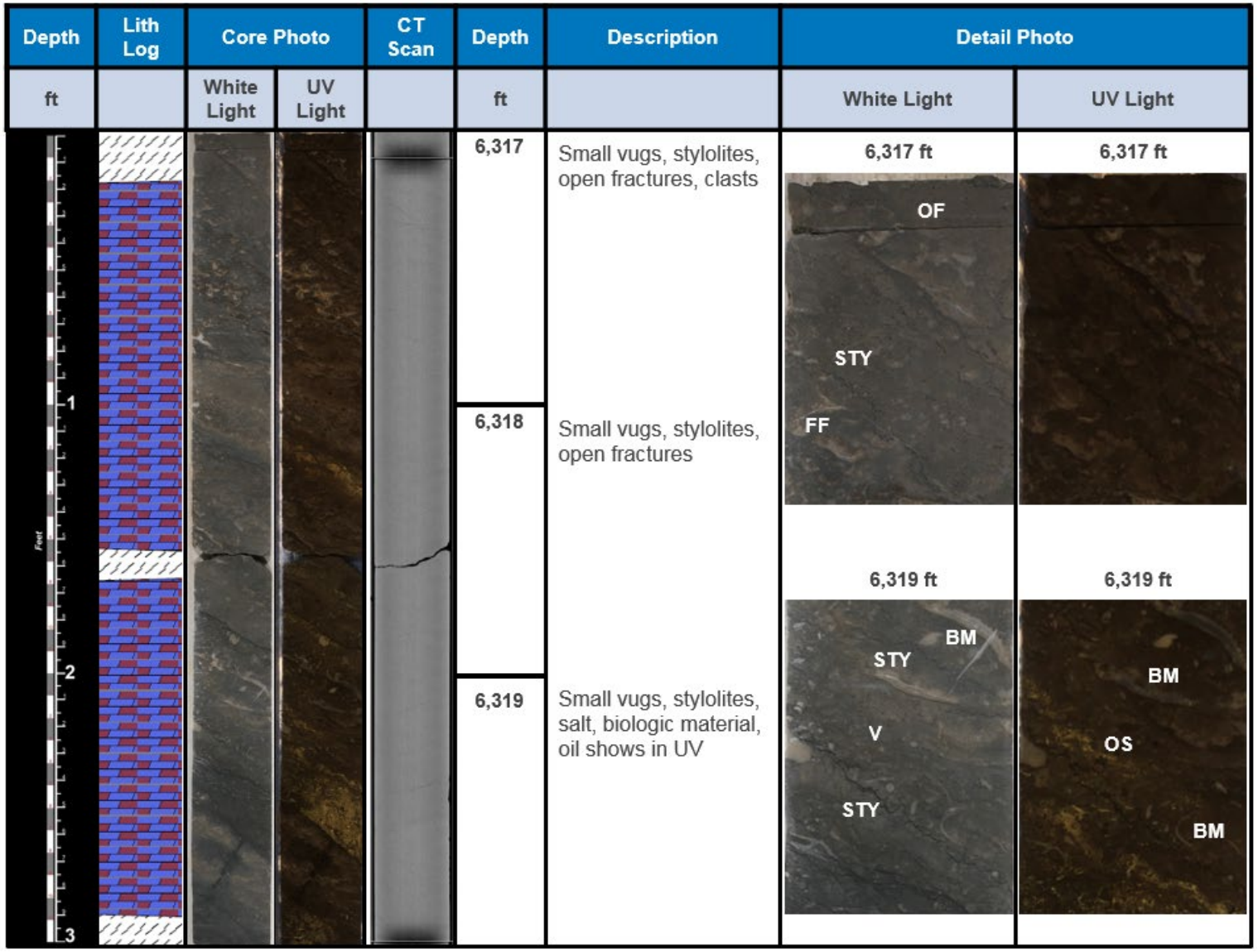


Figure B-135. Compiled illustration of lithology log, core photos (UV and white light), CT scan image, core descriptions, and annotated core images of the Brown Niagaran for depths 6,317 ft. to 6,319 ft.

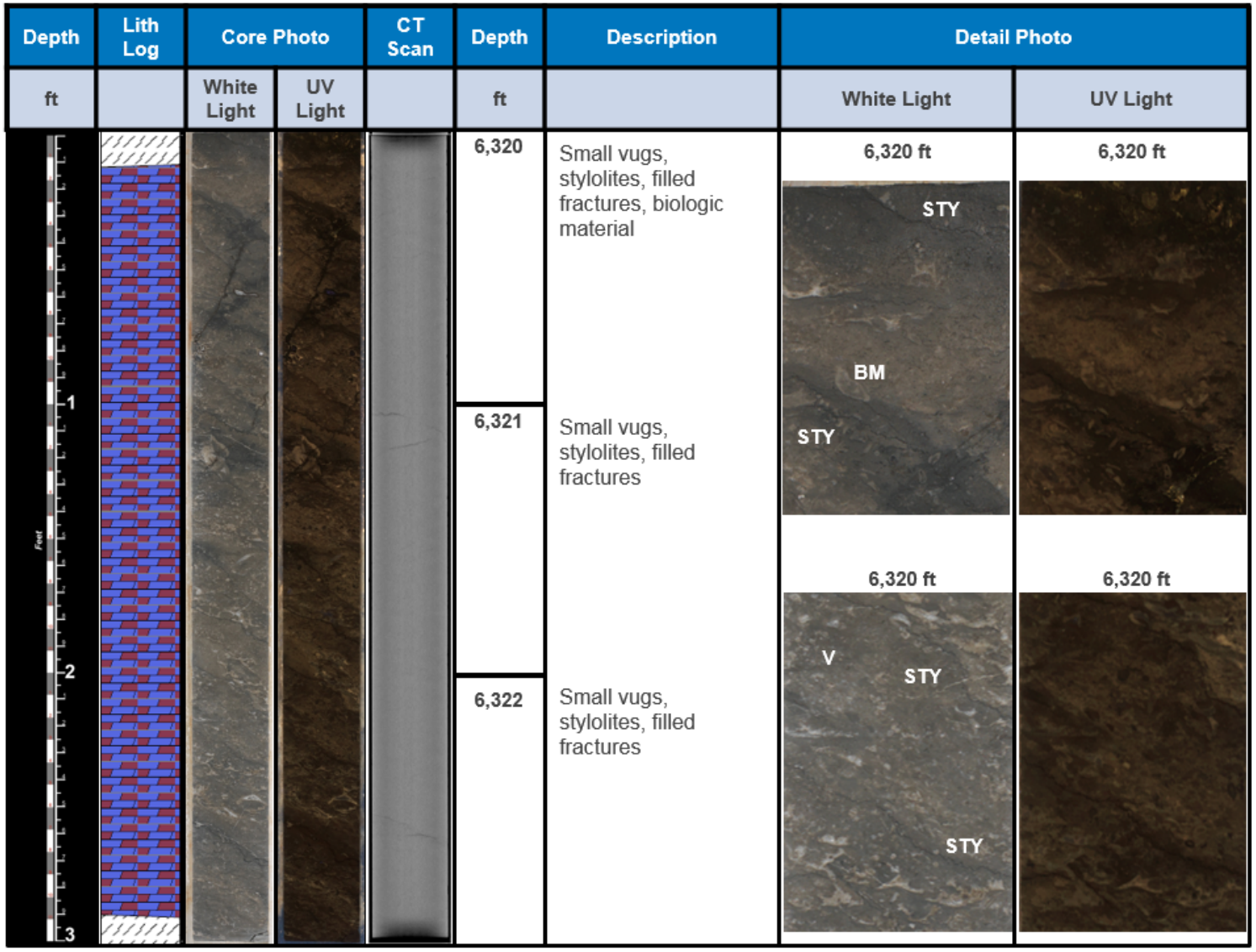


Figure B-136. Compiled illustration of lithology log, core photos (UV and white light), CT scan image, core descriptions, and annotated core images of the Brown Niagaran for depths 6,320 ft. to 6,322 ft.

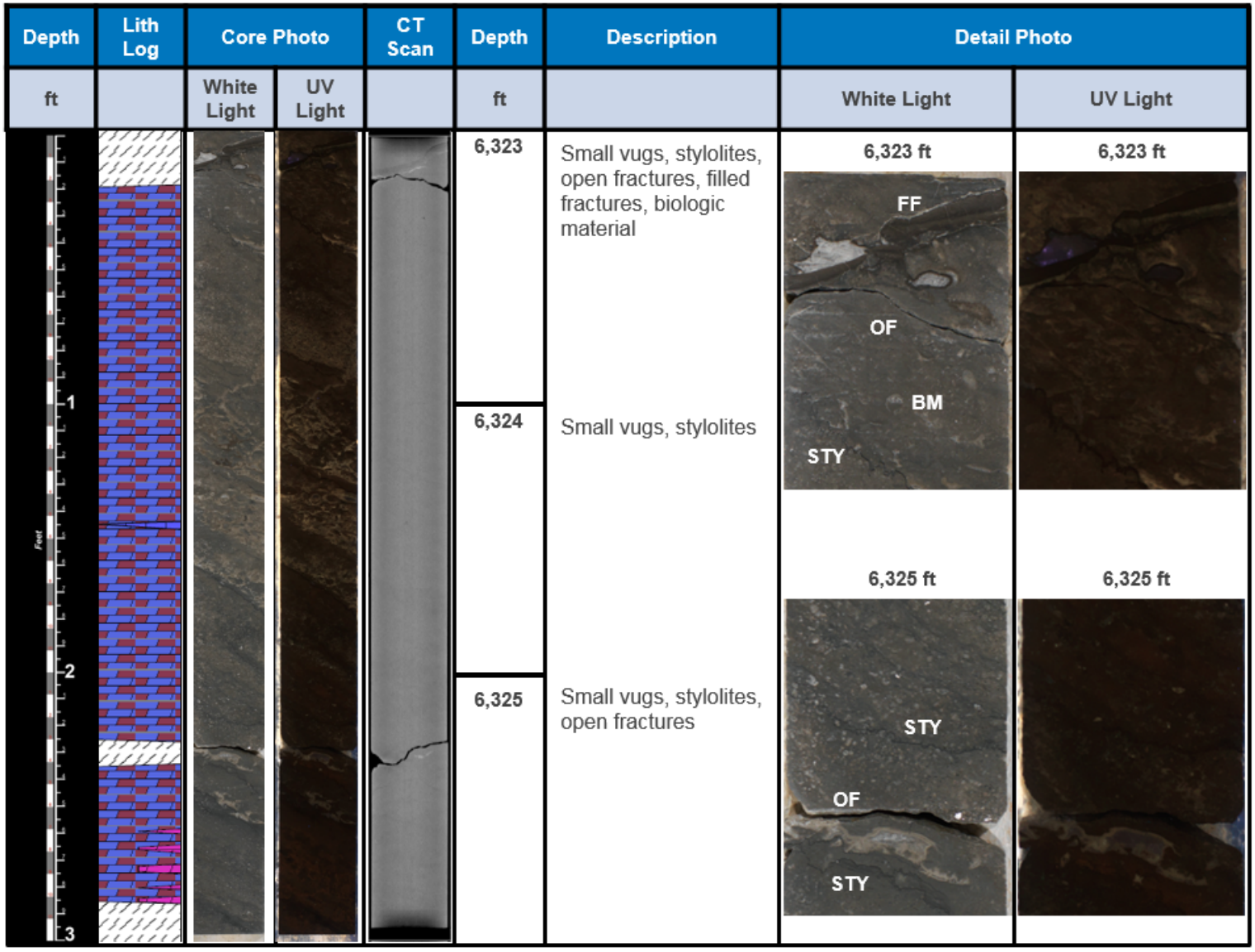


Figure B-137. Compiled illustration of lithology log, core photos (UV and white light), CT scan image, core descriptions, and annotated core images of the Brown Niagaran for depths 6,323 ft. to 6,325 ft.

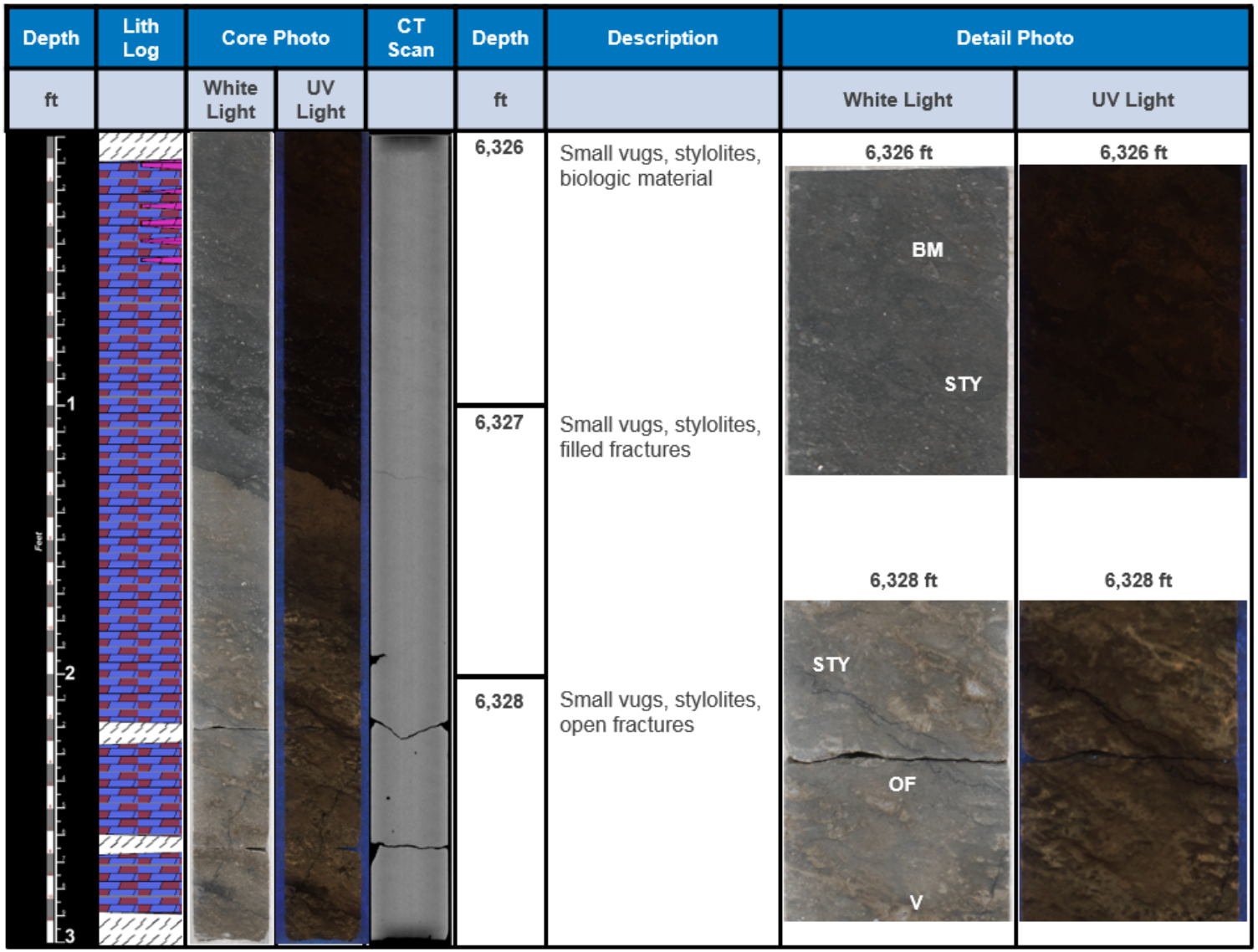


Figure B-138. Compiled illustration of lithology log, core photos (UV and white light), CT scan image, core descriptions, and annotated core images of the Brown Niagaran for depths 6,326 ft. to 6,328 ft.

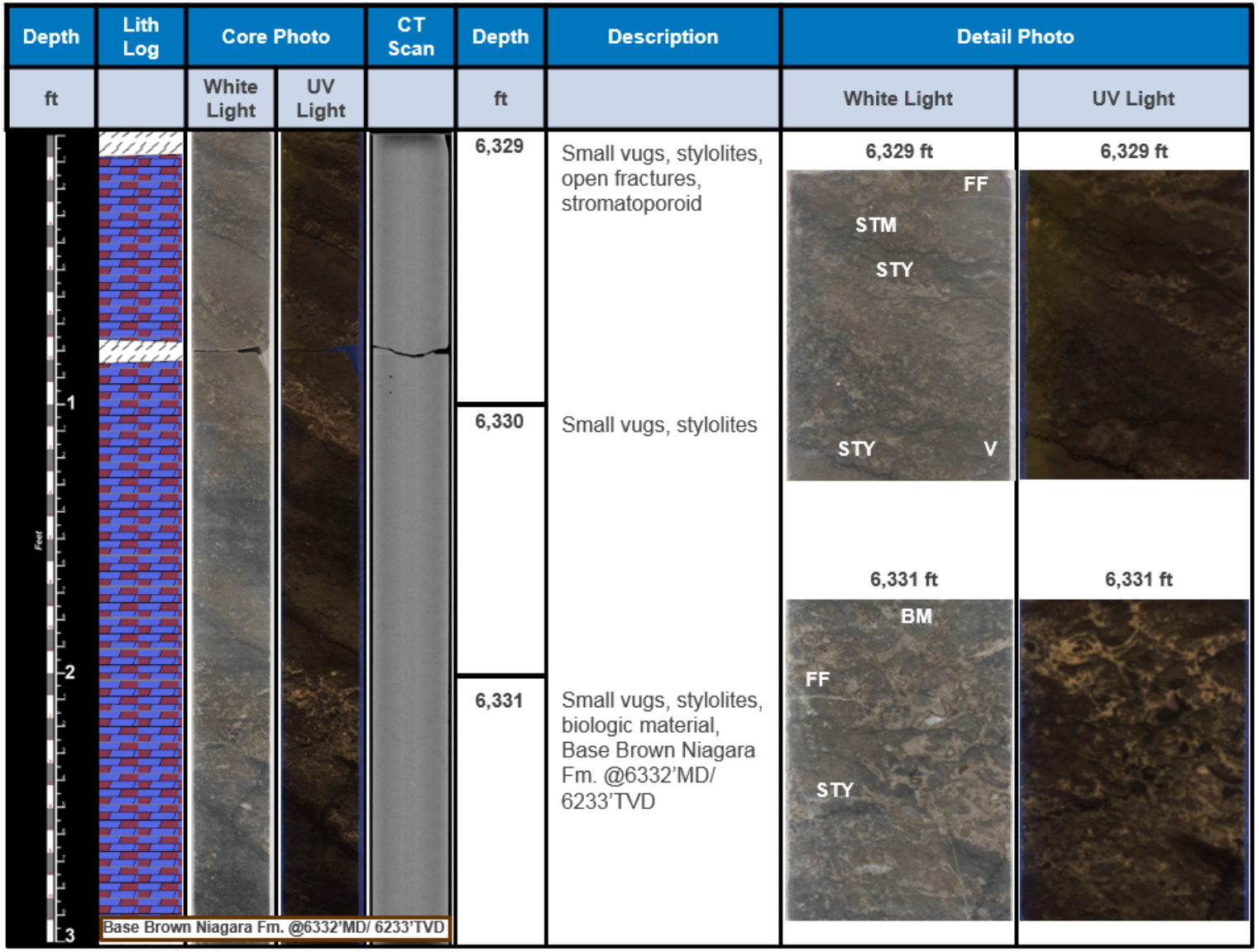


Figure B-139. Compiled illustration of lithology log, core photos (UV and white light), CT scan image, core descriptions, and annotated core images of the Brown Niagaran for depths 6,329 ft. to 6,331 ft.

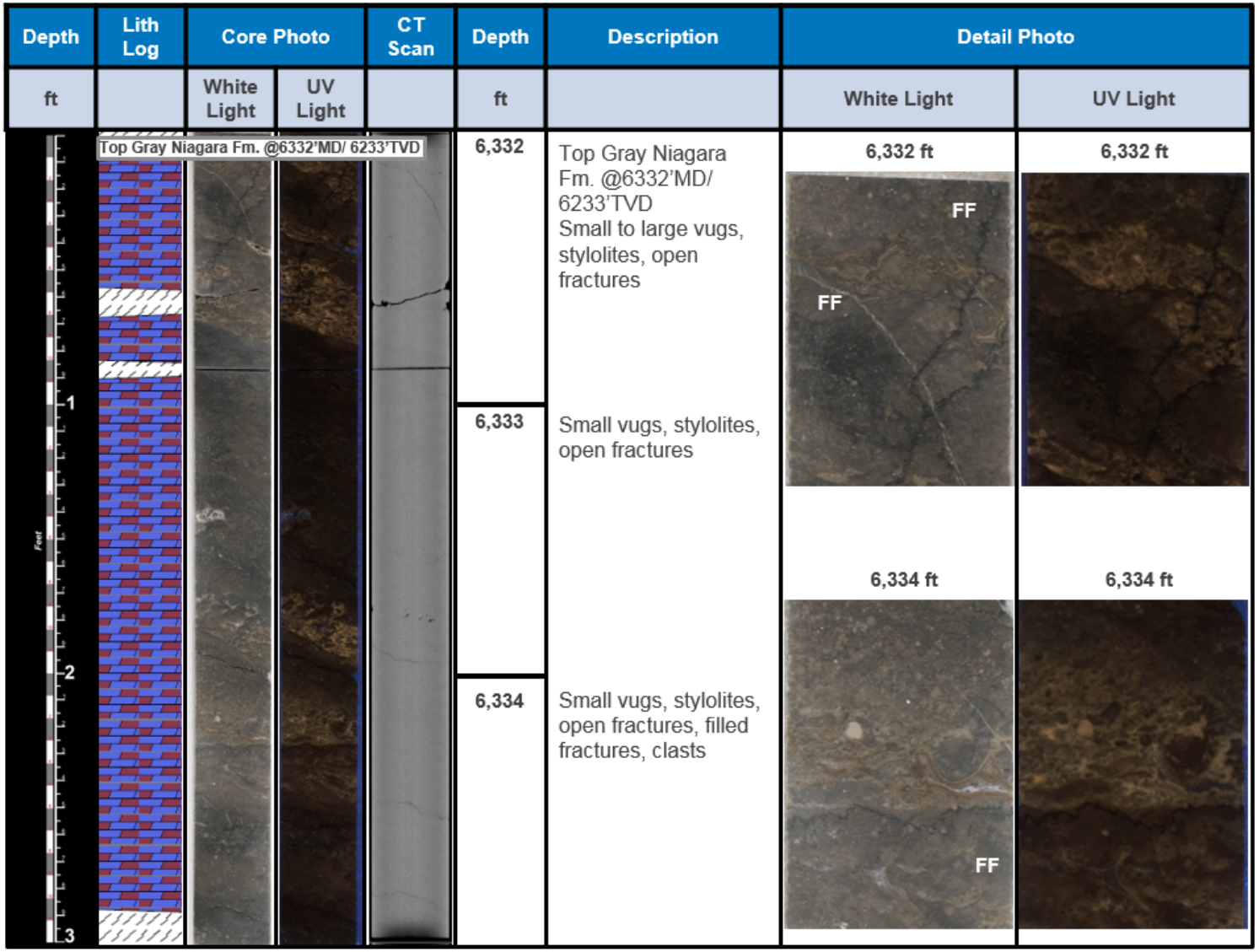


Figure B-140. Compiled illustration of lithology log, core photos (UV and white light), CT scan image, core descriptions, and annotated core images of the Gray Niagaran for depths 6,332 ft. to 6,334 ft.

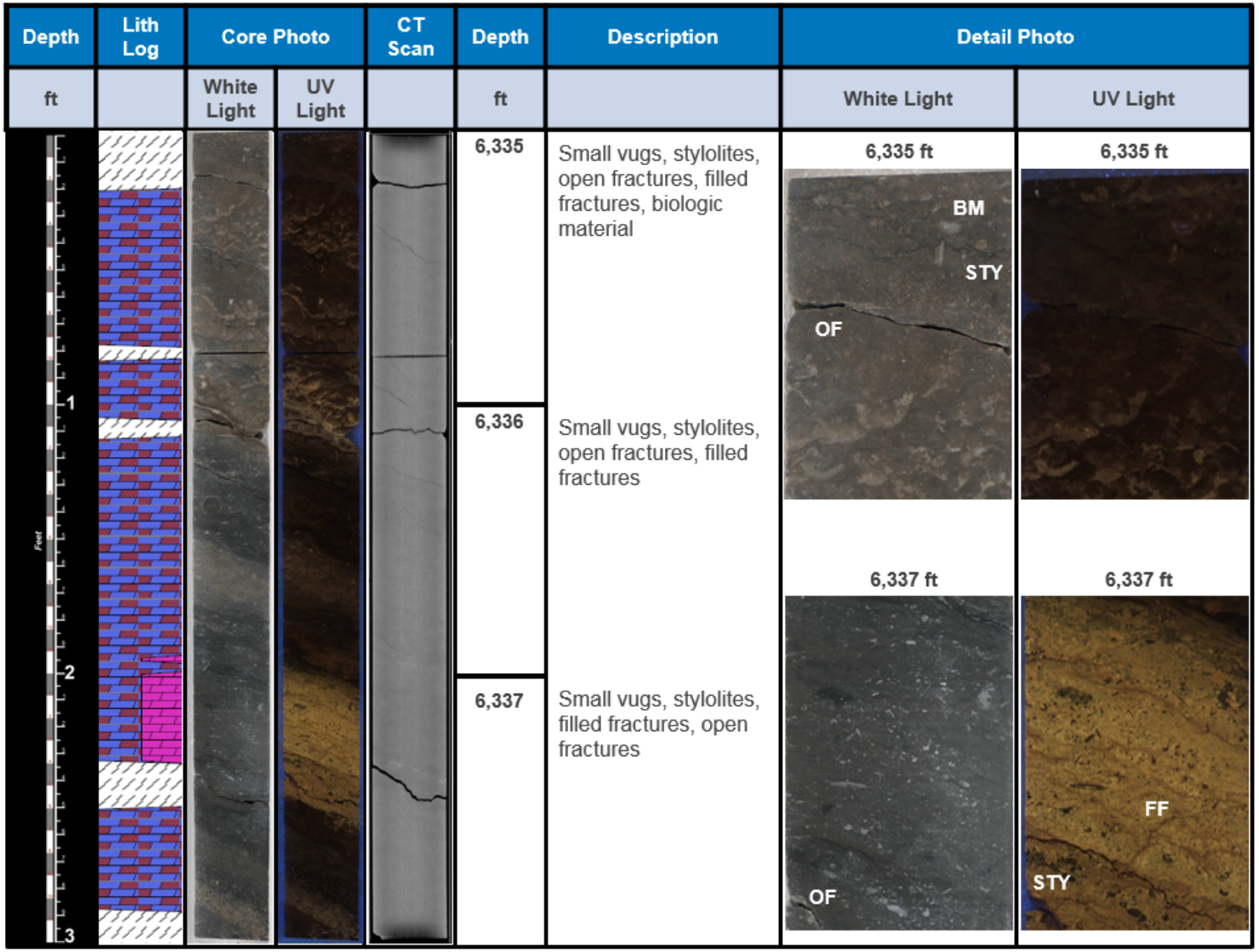


Figure B-141. Compiled illustration of lithology log, core photos (UV and white light), CT scan image, core descriptions, and annotated core images of the Gray Niagaran for depths 6,335 ft. to 6,337 ft.

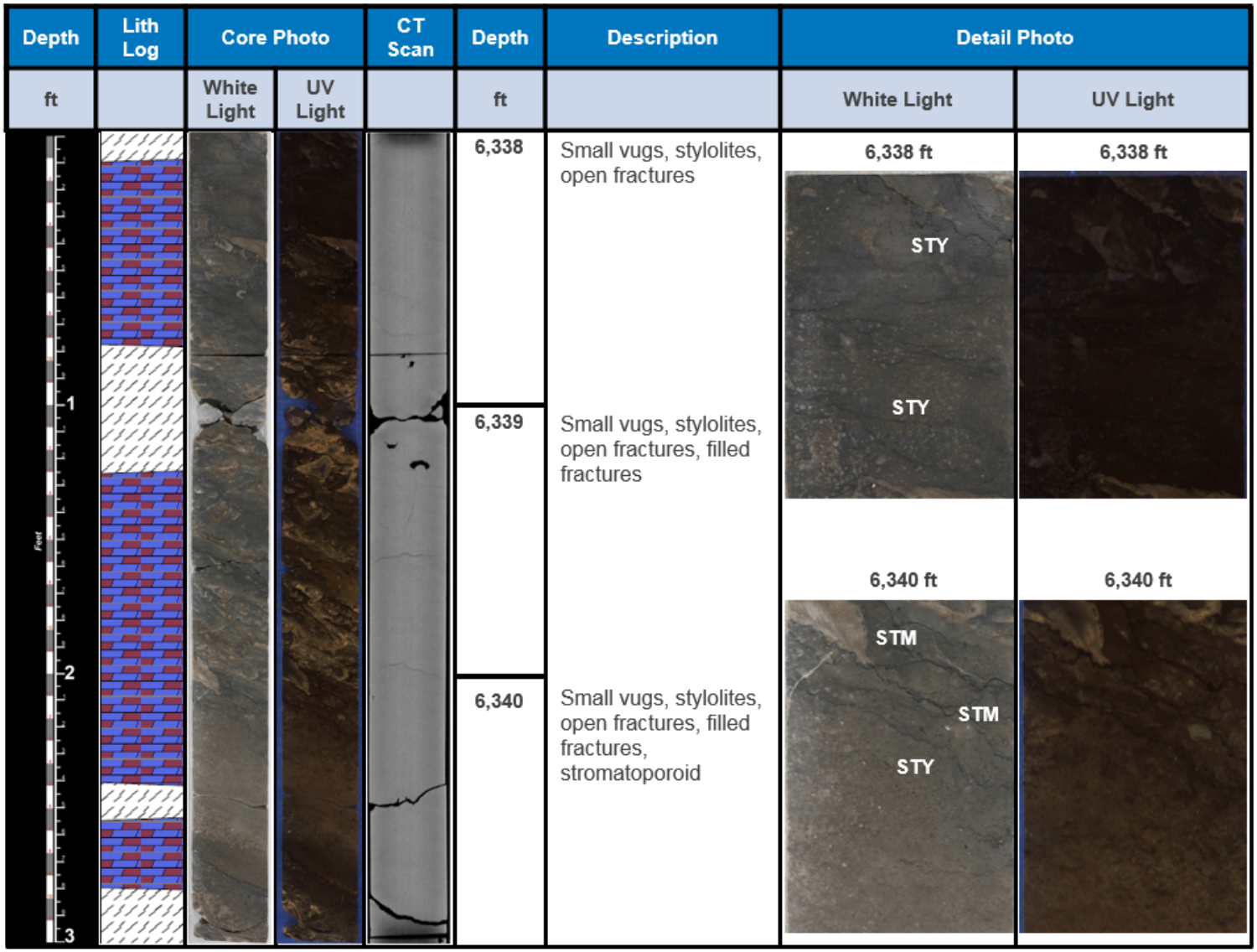


Figure B-142. Compiled illustration of lithology log, core photos (UV and white light), CT scan image, core descriptions, and annotated core images of the Gray Niagaran for depths 6,338 ft. to 6,340 ft.

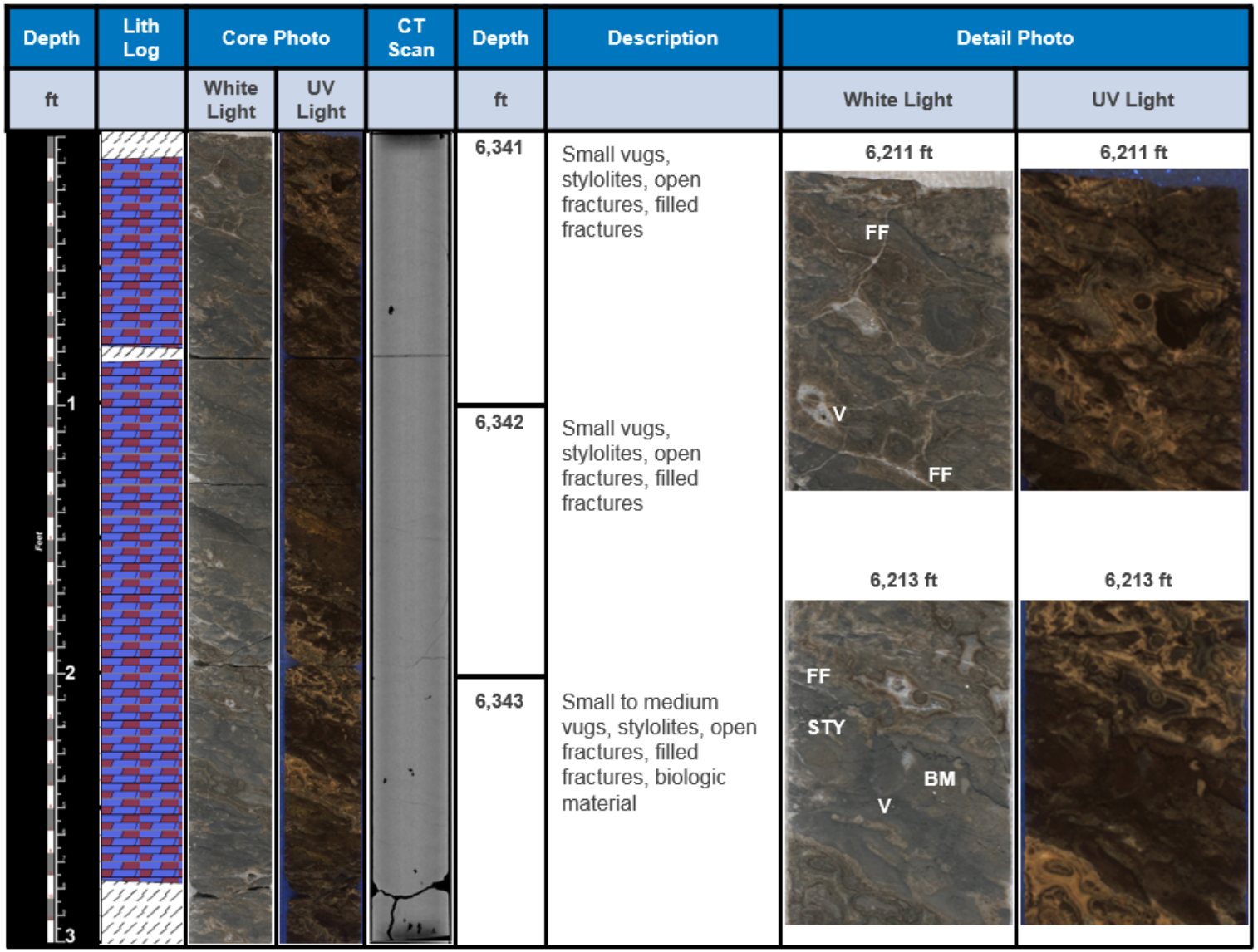


Figure B-143. Compiled illustration of lithology log, core photos (UV and white light), CT scan image, core descriptions, and annotated core images of the Gray Niagaran for depths 6,341 ft. to 6,343 ft.

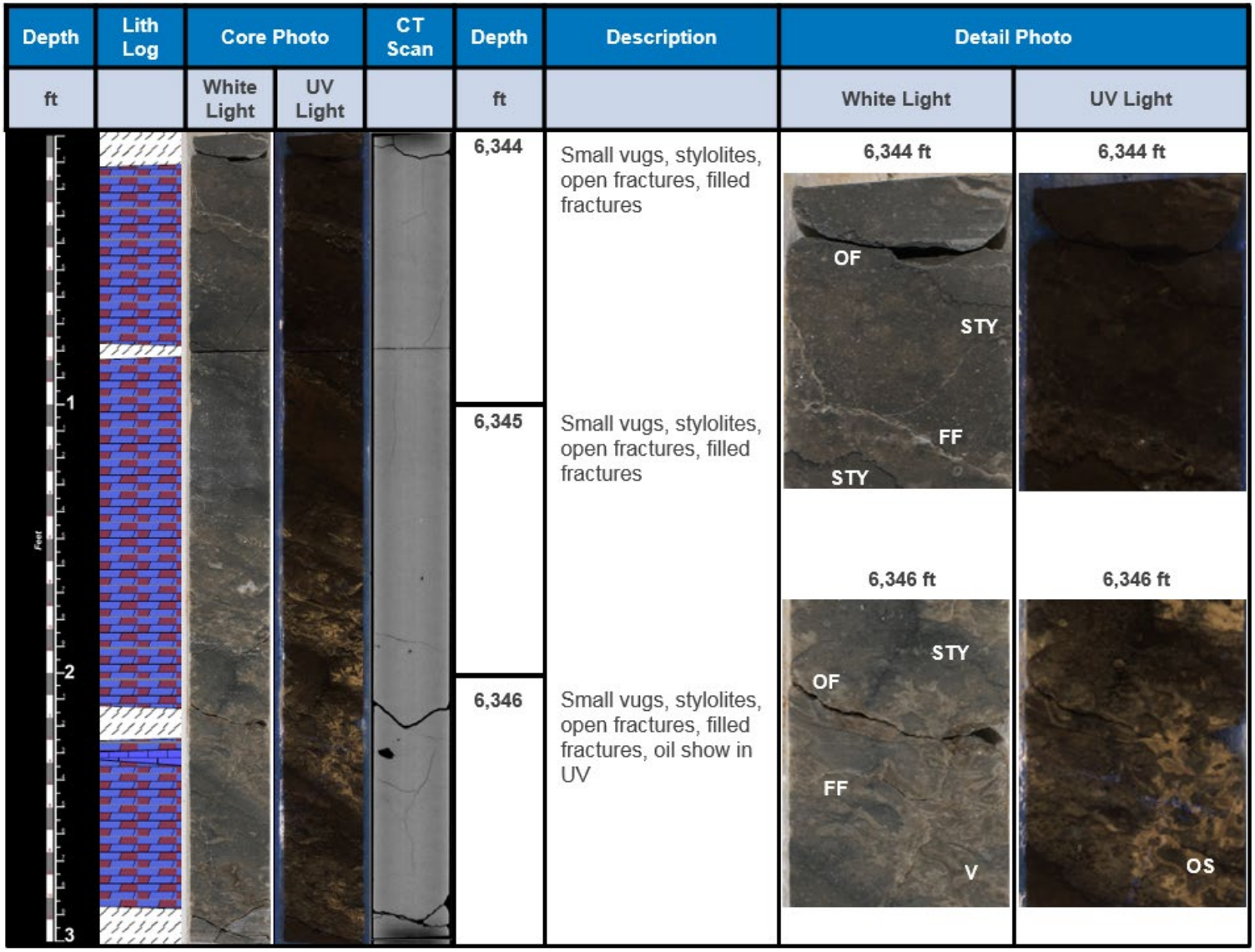


Figure B-144. Compiled illustration of lithology log, core photos (UV and white light), CT scan image, core descriptions, and annotated core images of the Gray Niagaran for depths 6,344 ft. to 6,346 ft.

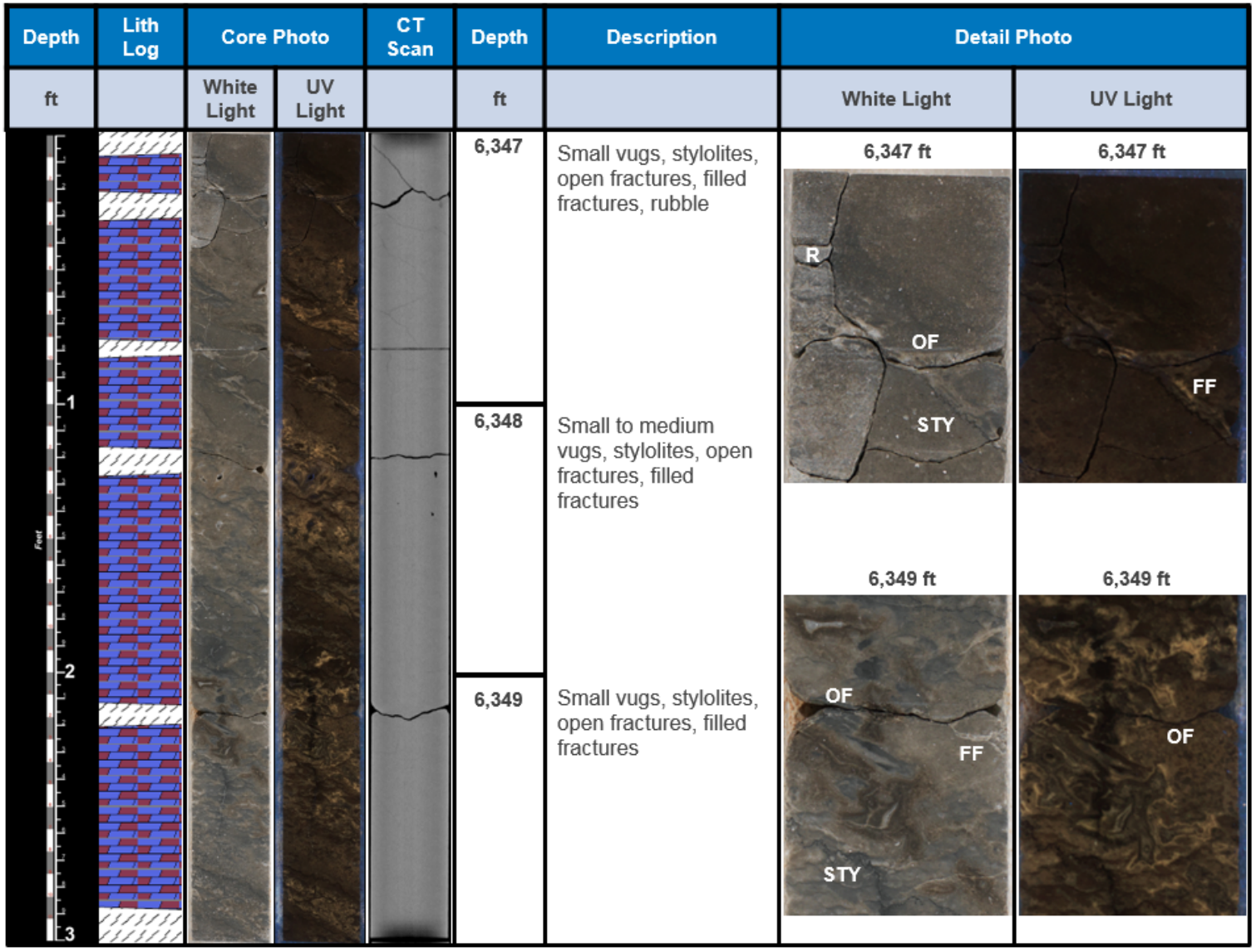


Figure B-145. Compiled illustration of lithology log, core photos (UV and white light), CT scan image, core descriptions, and annotated core images of the Gray Niagaran for depths 6,347 ft. to 6,349 ft.

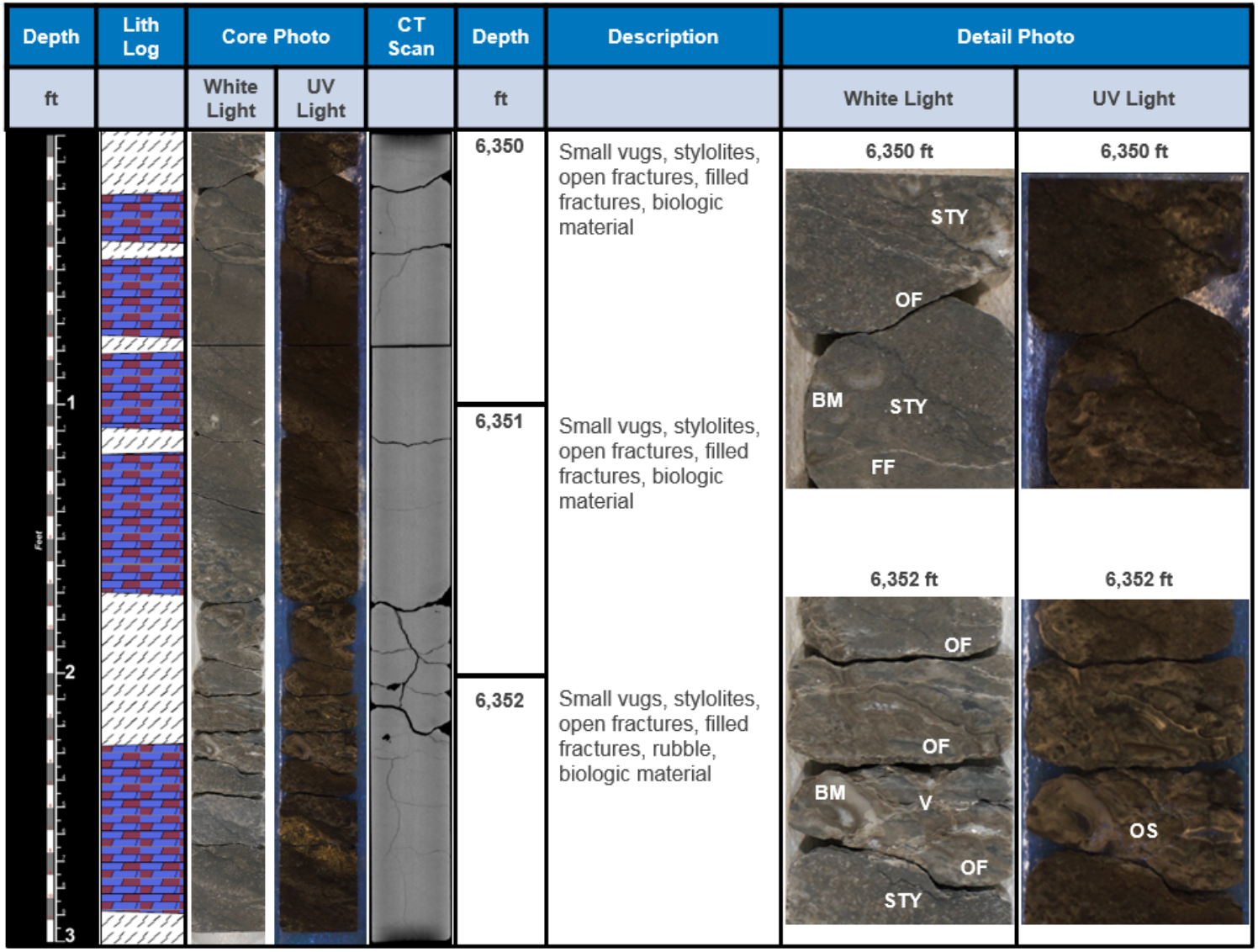


Figure B-146. Compiled illustration of lithology log, core photos (UV and white light), CT scan image, core descriptions, and annotated core images of the Gray Niagaran for depths 6,350 ft. to 6,352 ft.

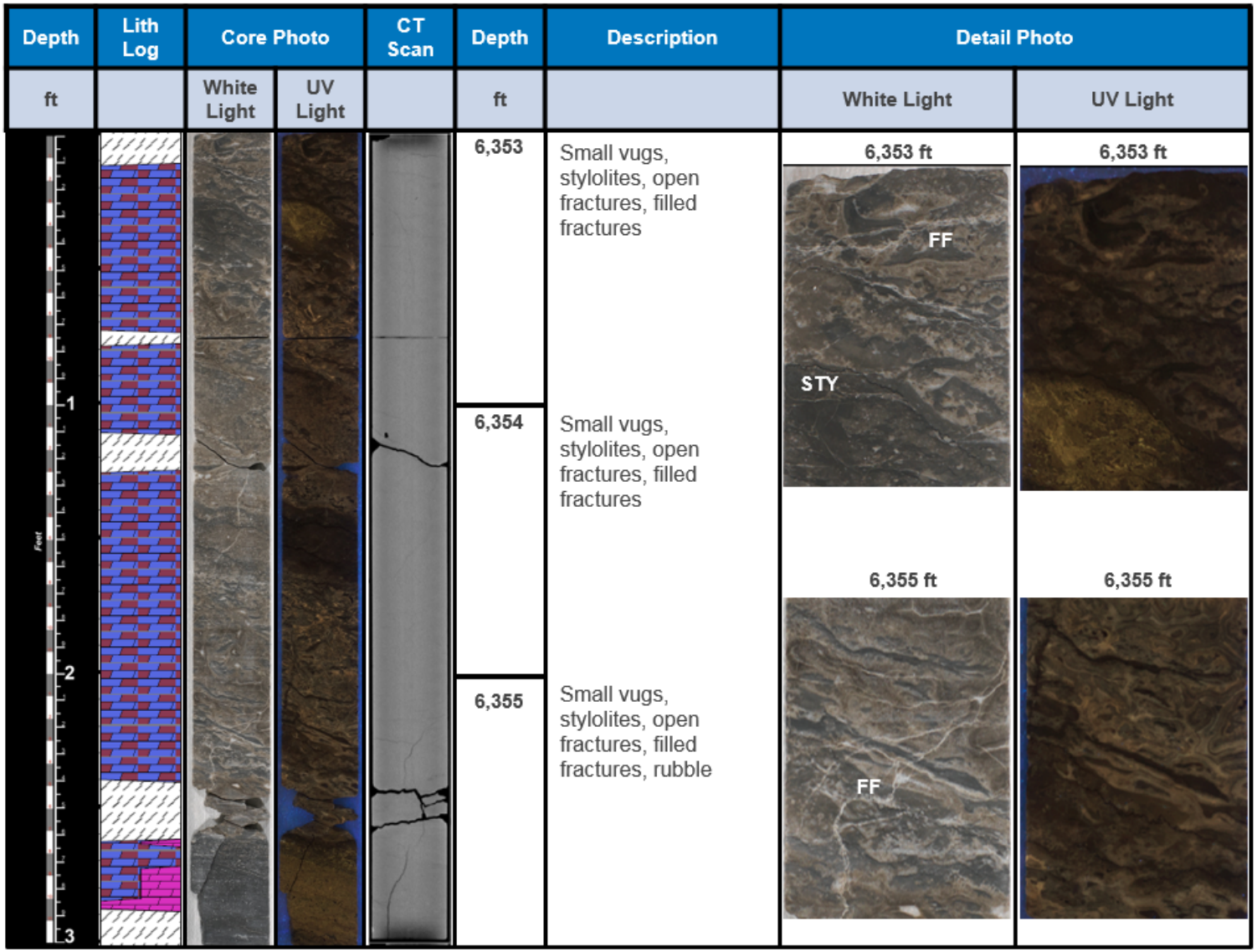


Figure B-147. Compiled illustration of lithology log, core photos (UV and white light), CT scan image, core descriptions, and annotated core images of the Gray Niagaran for depths 6,353 ft. to 6,355 ft.

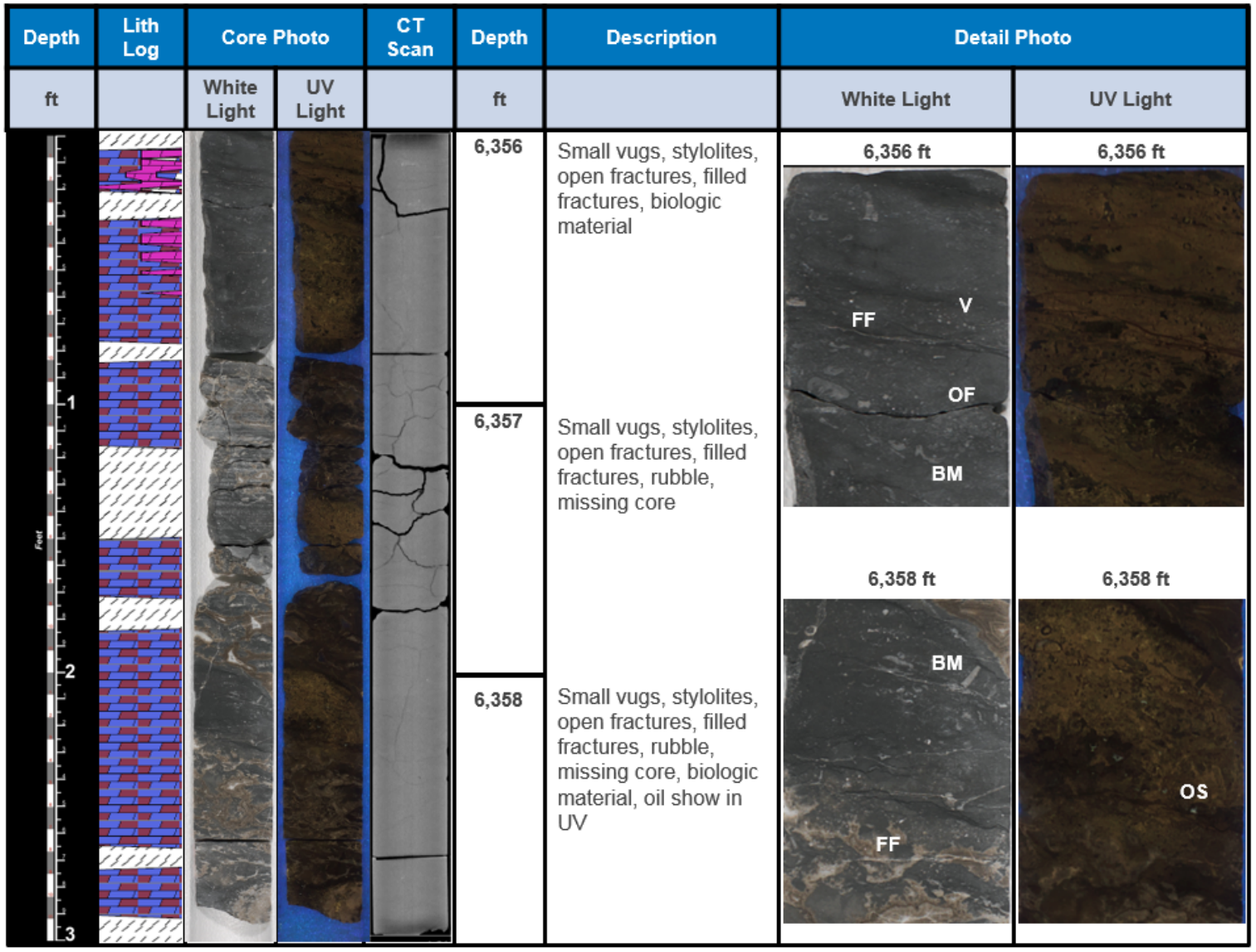


Figure B-148. Compiled illustration of lithology log, core photos (UV and white light), CT scan image, core descriptions, and annotated core images of the Gray Niagaran for depths 6,356 ft. to 6,358 ft.

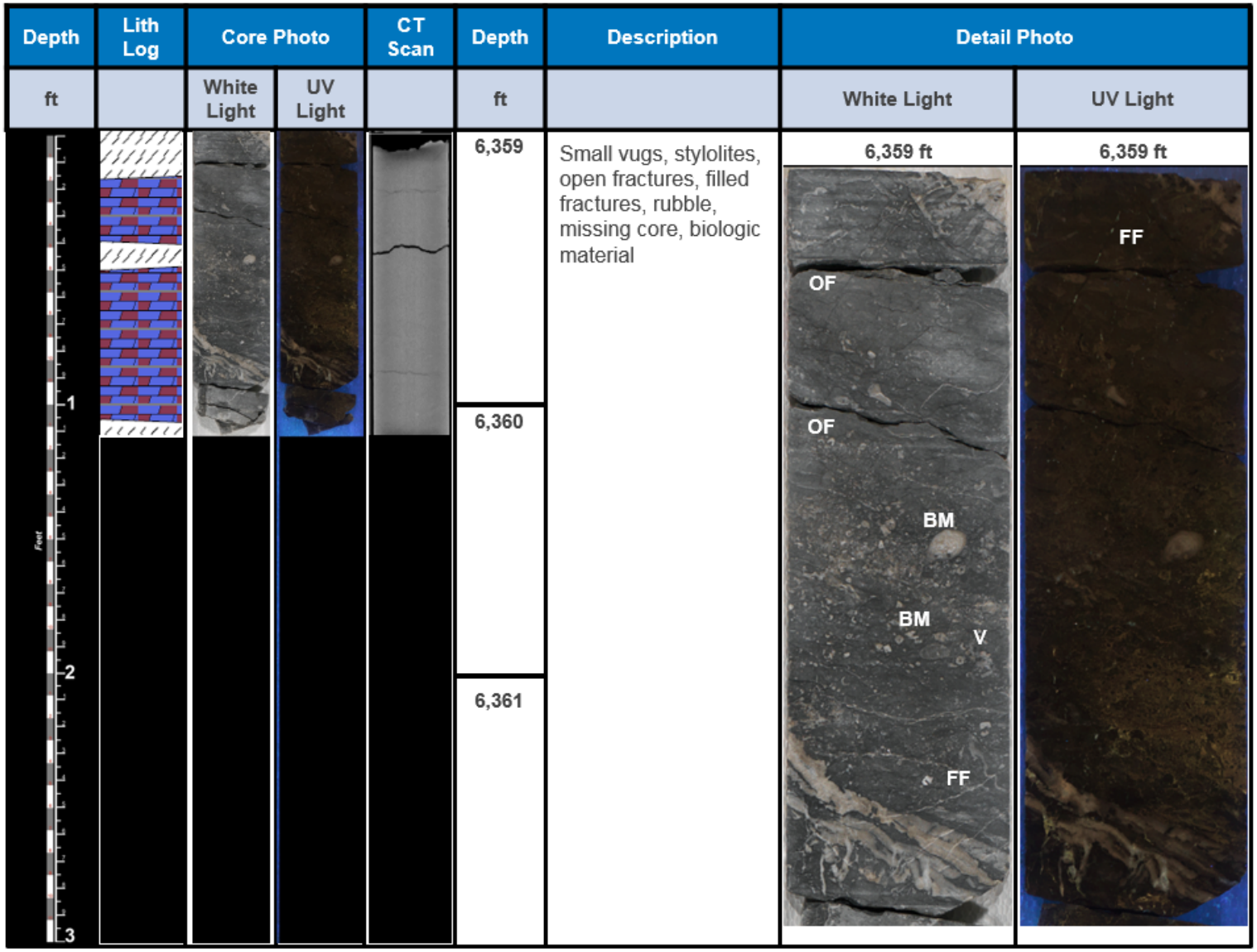


Figure B-149. Compiled illustration of lithology log, core photos (UV and white light), CT scan image, core descriptions, and annotated core images of the Gray Niagaran for depths 6,359 ft. to 6,361 ft.

B.2.2 Chester 8-16 – Rotary Sidewall Core

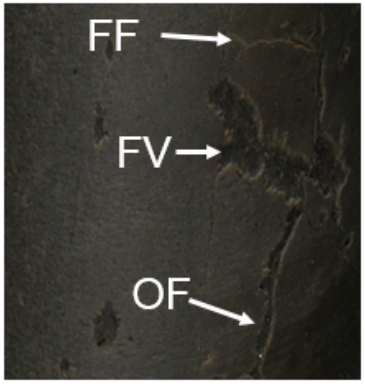
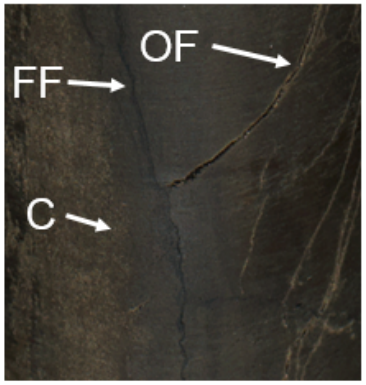
Depth Ft.	White Light Primary Features	UV Light Primary Features	Descriptions
5,760			White Light: Carbonate, mud filled vugs, filled fractures, open fractures. UV Light: Carbonate.
5,760.5			White Light: Carbonate, mud filled vugs, filled fractures, open fractures. UV Light: Carbonate.

Figure B-150. Annotated RSWC images with corresponding core descriptions of the A-2 Carbonate for depths 5,760 ft. to 5,760.5 ft.

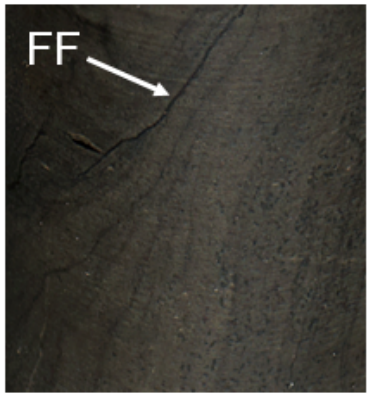
Depth Ft.	White Light Primary Features	UV Light Primary Features	Descriptions
5,761			White Light: Carbonate, filled fractures, alternating dark gray and light gray laminations, opaque mineral crystals. UV Light: Carbonate.
5,778			White Light: Carbonate, alternating dark gray and light gray laminations. UV Light: Carbonate.

Figure B-151. Annotated RSWC images with corresponding core descriptions of the A-2 Carbonate for depths 5,761 ft. and 5,778 ft.

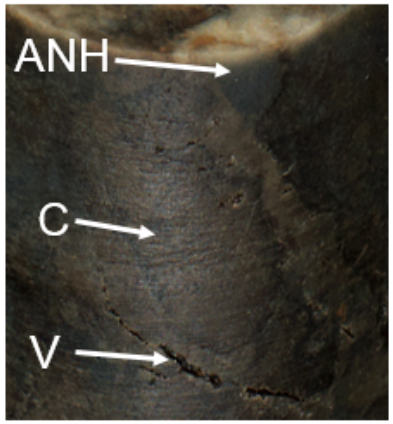
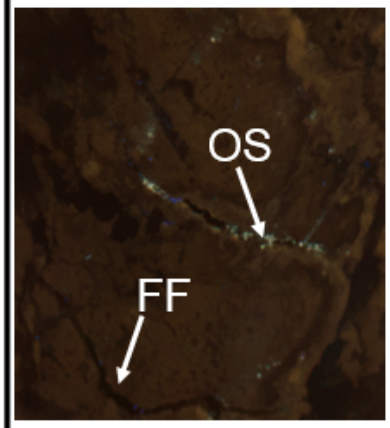
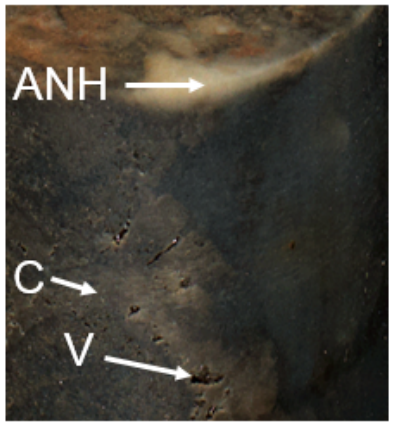
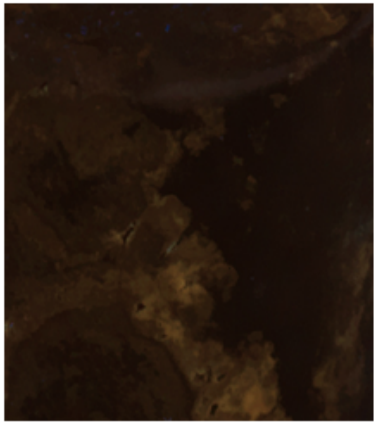
Depth Ft.	White Light Primary Features	UV Light Primary Features	Descriptions
5,819			White Light: Anhydrite and carbonate matrix, filled fractures, small vugs. UV Light: Light blue UV response due to potential residual oil.
5,819.5			White Light: Anhydrite and carbonate matrix, small vugs. UV Light: Anhydrite and carbonate matrix, dark areas are possible muds.

Figure B-152. Annotated RSWC images with corresponding core descriptions of the A-2 Evaporite for depths 5,819 ft. to 5,819.5 ft.

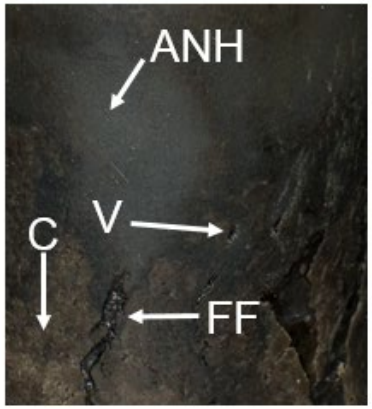
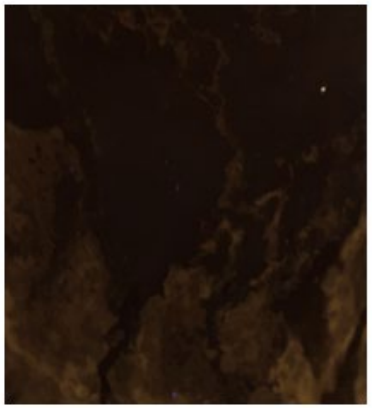
Depth Ft.	White Light Primary Features	UV Light Primary Features	Descriptions
5,820			White Light: Anhydrite and carbonate matrix, small vugs, filled fractures. UV Light: Anhydrite and carbonate matrix, dark areas are possible muds.
5,846			White Light: Gray carbonate, small vugs. UV Light: Strong light blue UV response due to potential residual oil throughout sample.

Figure B-153. Annotated RSWC images with corresponding core descriptions of the A-2 Evaporite and A-1 Carbonate for depths 5,820 ft. to 5,846 ft.

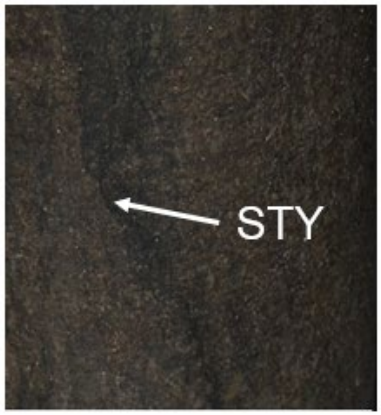
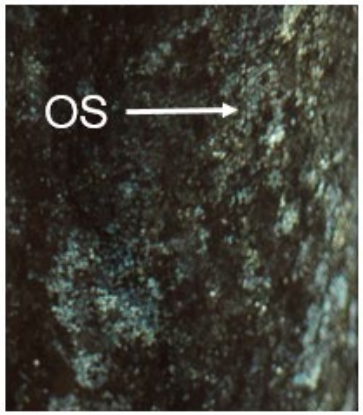
Depth Ft.	White Light Primary Features	UV Light Primary Features	Descriptions
5,884			White Light: Gray carbonate, stylolites. UV Light: Strong light blue UV response due to potential residual oil throughout sample.
5,887			White Light: Gray carbonate. UV Light: Strong light blue UV response due to potential residual oil throughout sample.

Figure B-154. Annotated RSWC images with corresponding core descriptions of the A-1 Carbonate for depths 5,884 ft. to 5,887 ft.

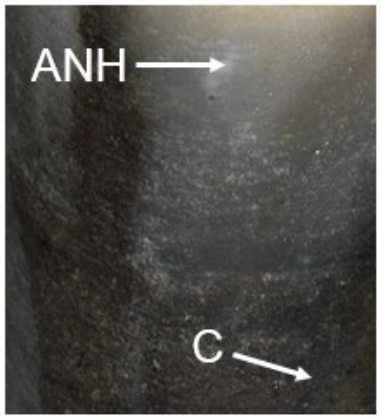
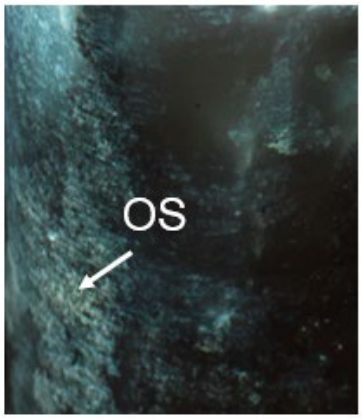
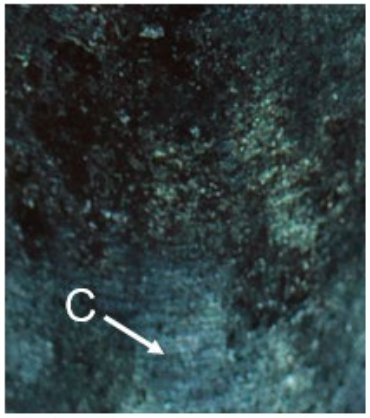
Depth Ft.	White Light Primary Features	UV Light Primary Features	Descriptions
5,864			White Light: Anhydrite and carbonate matrix. UV Light: Strong light blue UV response due to potential residual oil.
5,871			White Light: Gray carbonate, small vugs. UV Light: Strong light blue UV response due to potential residual oil throughout sample.

Figure B-155. Annotated RSWC images with corresponding core descriptions of the A-1 Carbonate for depths 5,864 ft. to 5,871 ft.

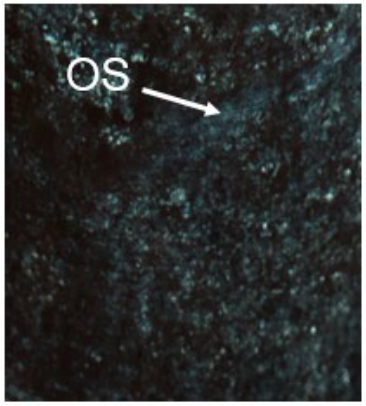
Depth Ft.	White Light Primary Features	UV Light Primary Features	Descriptions
5,889			White Light: Gray carbonate, large/small vugs. UV Light: Strong light blue UV response due to potential residual oil throughout sample.
5,899.5			White Light: Gray carbonate, small vugs. UV Light: Strong light blue UV response due to potential residual oil throughout sample.

Figure B-156. Annotated RSWC images with corresponding core descriptions of the A-1 Carbonate for depths 5,884 ft. to 5,887 ft.

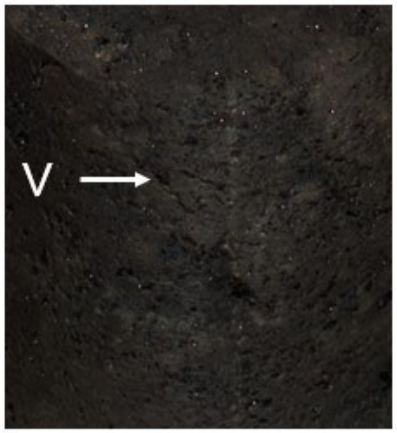
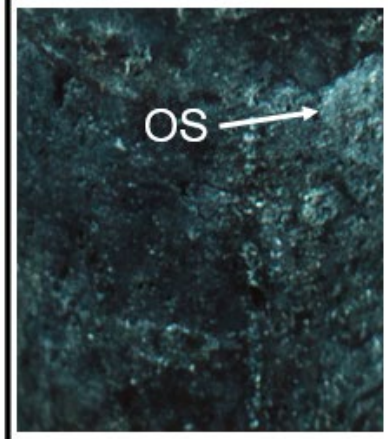
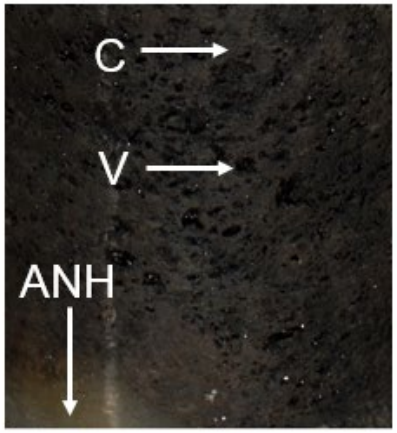
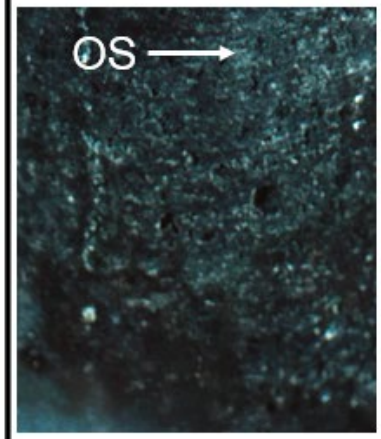
Depth Ft.	White Light Primary Features	UV Light Primary Features	Descriptions
5,890			White Light: Gray carbonate, small vugs. UV Light: Strong light blue UV response due to potential residual oil throughout sample.
5,893			White Light: Gray carbonate, some anhydrite, small vugs. UV Light: Strong light blue UV response due to potential residual oil throughout sample.

Figure B-157. Annotated RSWC images with corresponding core descriptions of the A-1 Carbonate for depths 5,890 ft. to 5,893 ft.

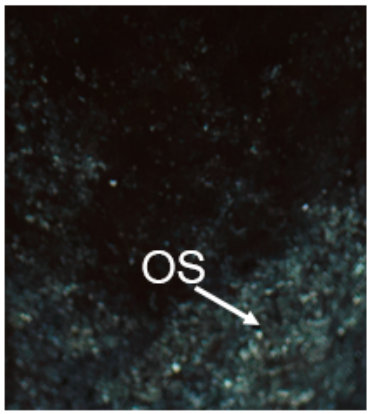
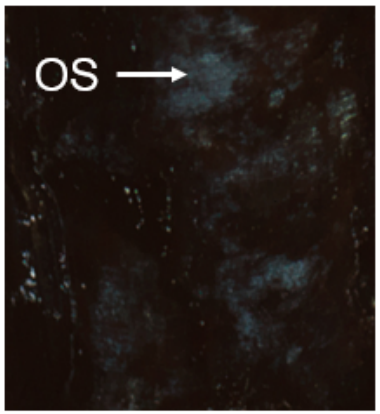
Depth Ft.	White Light Primary Features	UV Light Primary Features	Descriptions
5,896			White Light: Gray carbonate, small vugs. UV Light: Strong light blue UV response due to potential residual oil throughout sample.
5,903			White Light: Carbonate matrix, alternating dark gray and light gray laminations. UV Light: Light blue UV response due to potential residual oil.

Figure B-158. Annotated RSWC images with corresponding core descriptions of the A-1 Carbonate for depths 5,896 ft. to 5,903 ft.

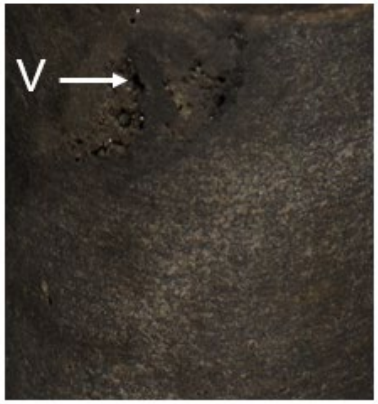
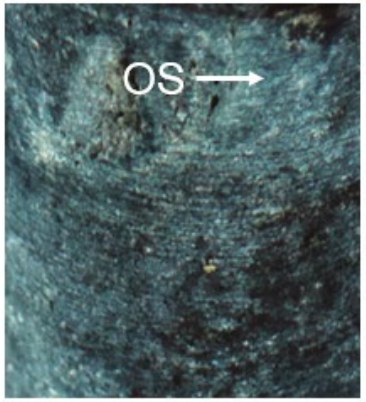
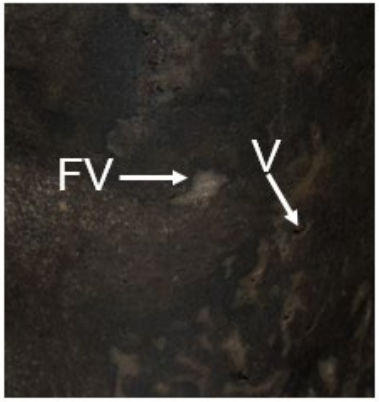
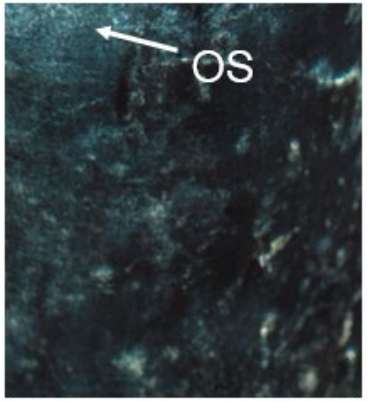
Depth Ft.	White Light Primary Features	UV Light Primary Features	Descriptions
5,914			White Light: Gray carbonate, small vugs. UV Light: Strong light blue UV response due to potential residual oil throughout sample.
5,916			White Light: Gray carbonate, small vugs, salt filled vugs. UV Light: Strong light blue UV response due to potential residual oil throughout sample.

Figure B-159. Annotated RSWC images with corresponding core descriptions of the A-1 Carbonate and the Brown Niagaran for depths 5,914 ft. to 5,916 ft.

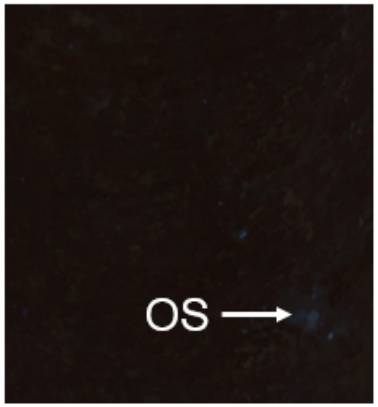
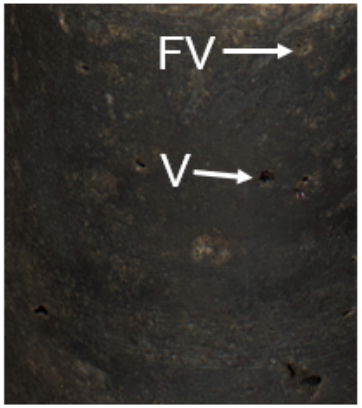
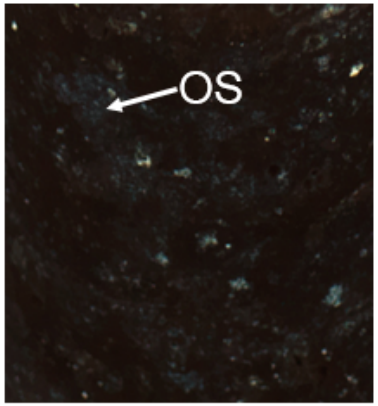
Depth Ft.	White Light Primary Features	UV Light Primary Features	Descriptions
5,923			White Light: Gray carbonate. UV Light: Light blue UV response due to potential residual oil.
5,940			White Light: Gray carbonate, small vugs, salt filled vugs. UV Light: Strong light blue UV response due to potential residual oil.

Figure B-160. Annotated RSWC images with corresponding core descriptions of the Brown Niagaran for depths 5,923 ft. to 5,940 ft.

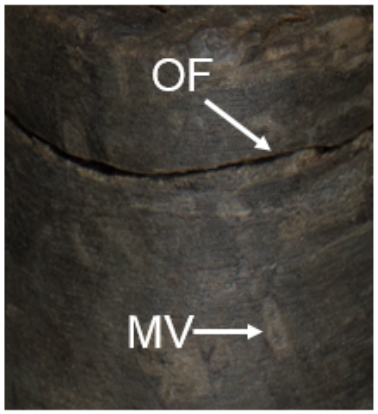
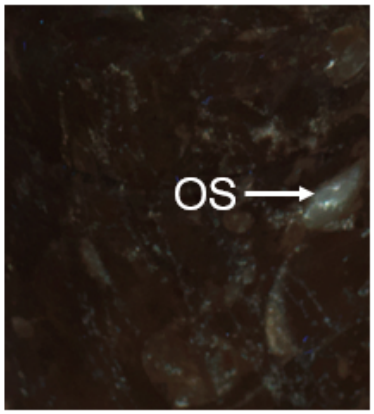
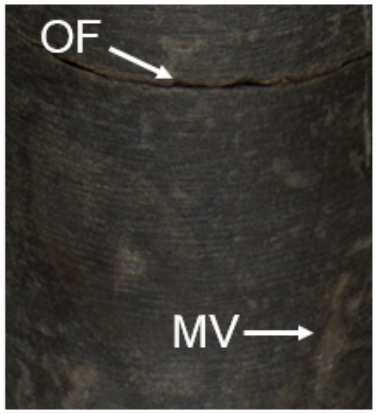
Depth Ft.	White Light Primary Features	UV Light Primary Features	Descriptions
6,012			White Light: Gray carbonate, filled moldic vugs, open fracture. UV Light: Strong light blue UV response due to potential residual oil.
6,015			White Light: Gray carbonate, filled moldic vugs, open fractures, large clast. UV Light: Strong light blue UV response due to potential residual oil throughout sample.

Figure B-161. Annotated RSWC images with corresponding core descriptions of the Brown Niagaran for depths 6,012 ft. to 6,015 ft.

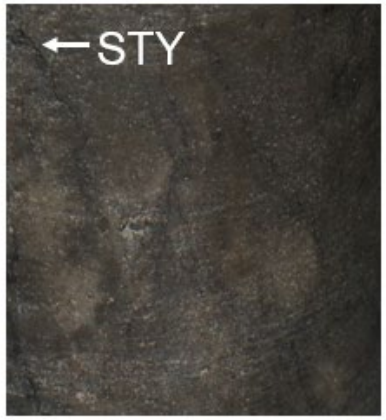
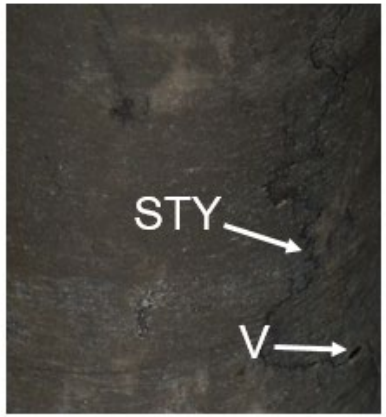
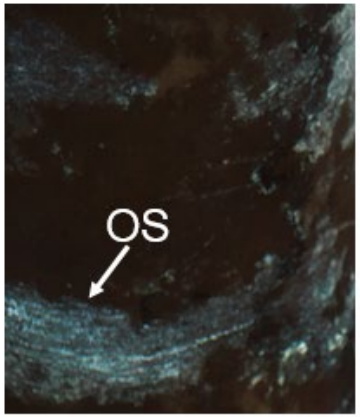
Depth Ft.	White Light Primary Features	UV Light Primary Features	Descriptions
6,049			White Light: Gray carbonate, stylolites. UV Light: Strong light blue UV response due to potential residual oil throughout sample.
6,076			White Light: Gray carbonate, small vugs, stylolites. UV Light: Strong light blue UV response due to potential residual oil.

Figure B-162. Annotated RSWC images with corresponding core descriptions of the Brown Niagaran for depths 6,049 ft. to 6,076 ft.

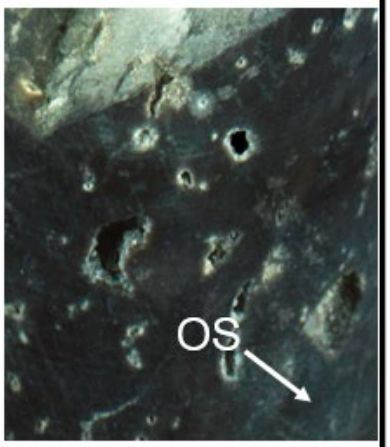
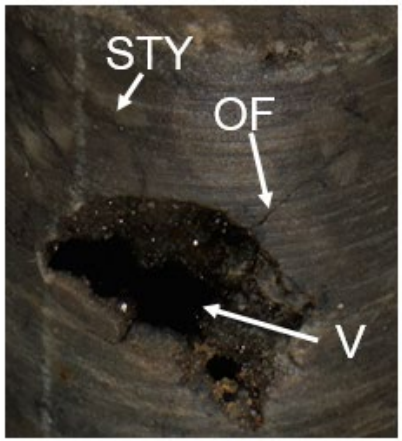
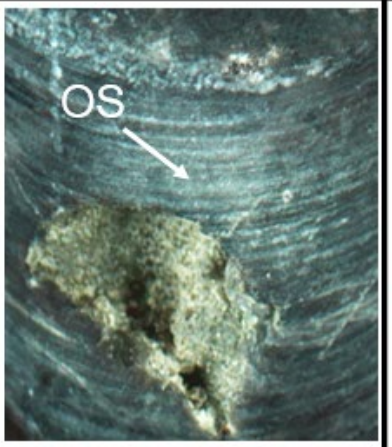
Depth Ft.	White Light Primary Features	UV Light Primary Features	Descriptions
6,095			White Light: Carbonate, medium/small vugs, filled vugs. UV Light: Strong light blue UV response due to potential residual oil throughout sample.
6,121			White Light: Carbonate, large vug, open fractures, stylolites, filled vugs. UV Light: Strong light blue UV response due to potential residual oil throughout sample.

Figure B-163. Annotated RSWC images with corresponding core descriptions of the Brown Niagaran for depths 6,095 ft. to 6,121 ft.

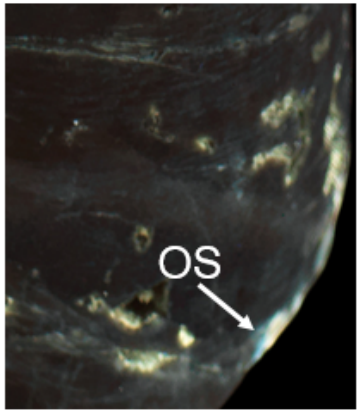
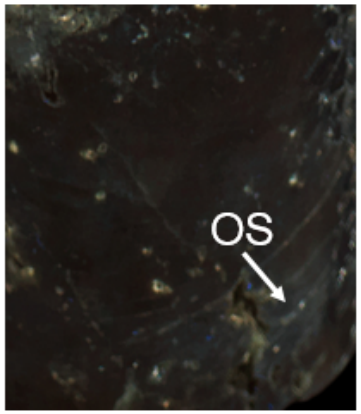
Depth Ft.	White Light Primary Features	UV Light Primary Features	Descriptions
6,137			White Light: Gray carbonate, medium/small vugs, open fracture. UV Light: Strong light blue UV response due to potential residual oil.
6,145			White Light: Gray carbonate, medium/small vugs, stylolites. UV Light: Strong light blue UV response due to potential residual oil.

Figure B-164. Annotated RSWC images with corresponding core descriptions of the Brown Niagaran for depths 6,137 ft. to 6,145 ft.

B.3 Chester 6-16- Rotary Sidewall Core

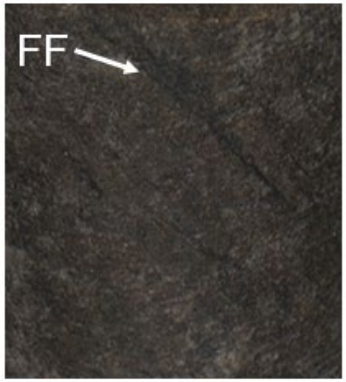
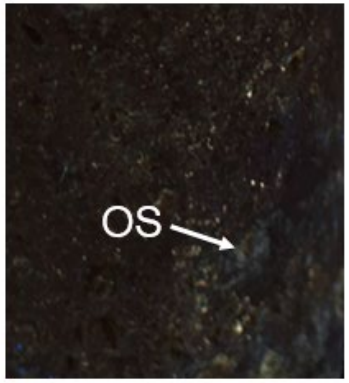
Depth Ft.	White Light Primary Features	UV Light Primary Features	Descriptions
5,927			White Light: Gray carbonate, mud filled fracture. UV Light: Light blue UV response due to potential residual oil.
5,934			White Light: Gray carbonate, small vugs. UV Light: Light blue UV response due to potential residual oil.

Figure B-165. Annotated RSWC images with corresponding core descriptions of the A-1 Carbonate for depths 5,927 ft. and 5,934 ft.

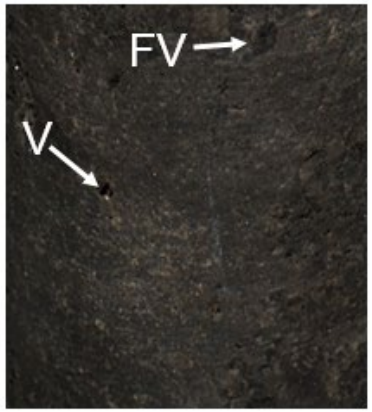
Depth Ft.	White Light Primary Features	UV Light Primary Features	Descriptions
5,938			White Light: Gray carbonate, small vugs, salt filled vugs. UV Light: Light blue UV response due to potential residual oil.
5,961			White Light: Gray carbonate, stylolites. UV Light: Light blue UV response due to potential residual oil.

Figure B-166. Annotated RSWC images with corresponding core descriptions of the A-1 Carbonate for depths 5,938 ft. and 5,961 ft.

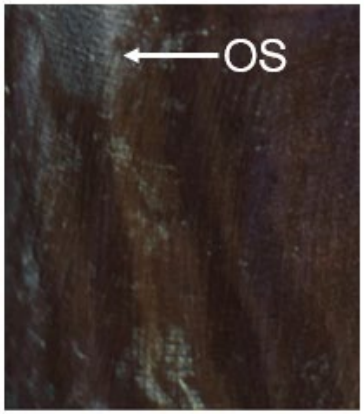
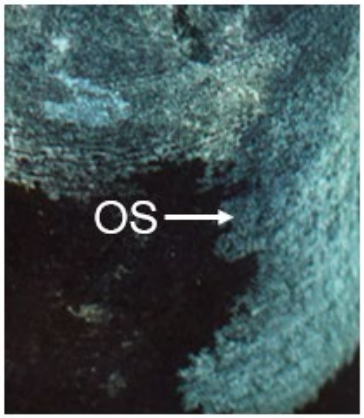
Depth Ft.	White Light Primary Features	UV Light Primary Features	Descriptions
5,962			White Light: Carbonate matrix, filled fracture, alternating dark gray and light gray laminations. UV Light: Light blue UV response due to potential residual oil.
5,968			White Light: Gray carbonate. UV Light: Light blue UV response due to potential residual oil.

Figure B-167. Annotated RSWC images with corresponding core descriptions of the A-1 Carbonate for depths 5,962 ft. and 5,968 ft.

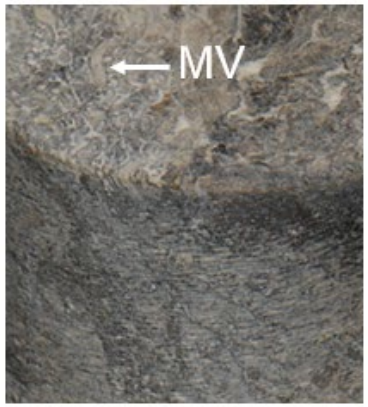
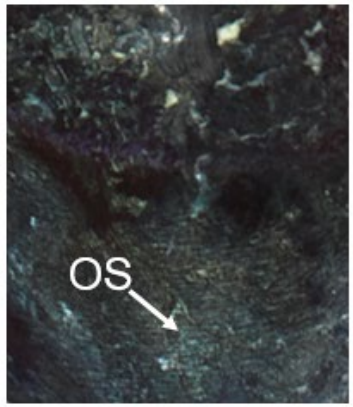
Depth Ft.	White Light Primary Features	UV Light Primary Features	Descriptions
5,970			White Light: Gray carbonate, filled moldic vugs. UV Light: Light blue UV response due to potential residual oil throughout the sample.
5,971			White Light: Gray carbonate, salt filled vugs. UV Light: Light blue UV response due to potential residual oil throughout the sample.

Figure B-168. Annotated RSWC images with corresponding core descriptions of the Brown Niagaran for depths 5,970 ft. to 5,971 ft.

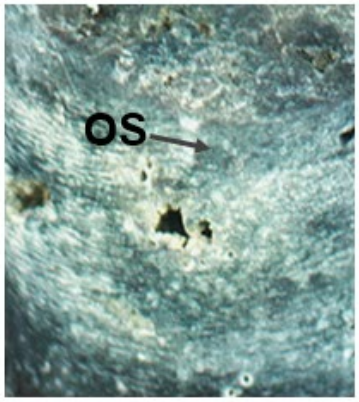
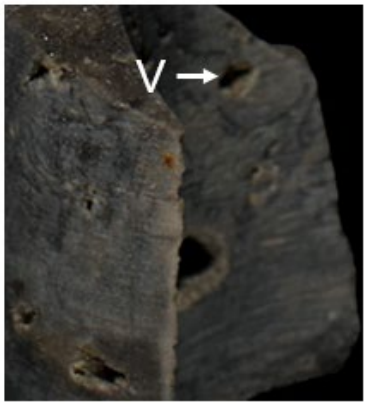
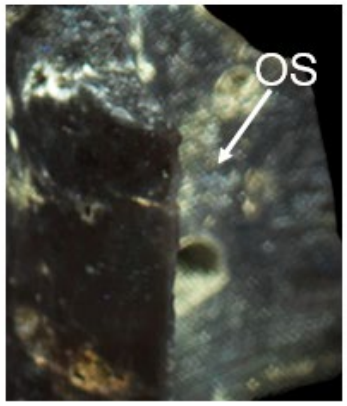
Depth Ft.	White Light Primary Features	UV Light Primary Features	Descriptions
6,015			White Light: Gray carbonate, medium/small vugs. UV Light: Light blue UV response due to potential residual oil throughout sample.
6,032			White Light: Gray carbonate, medium/small vugs, core fragment. UV Light: Light blue UV response due to potential residual oil.

Figure B-169. Annotated RSWC images with corresponding core descriptions of the Brown Niagaran for depths 6,015 ft. and 6,032 ft.

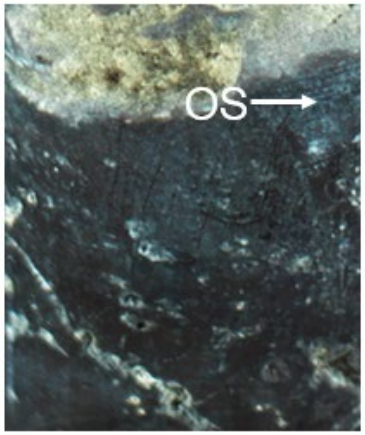
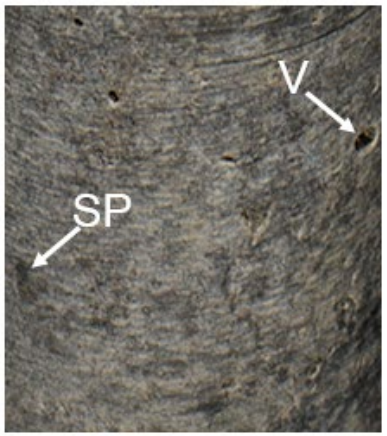
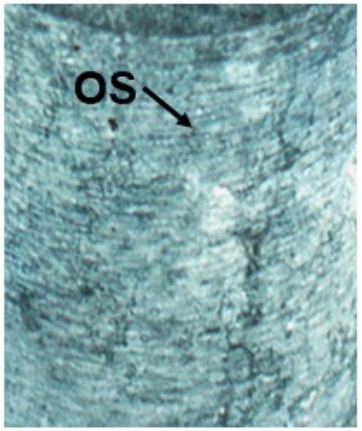
Depth Ft.	White Light Primary Features	UV Light Primary Features	Descriptions
6,032.5			White Light: Gray carbonate, medium/small vugs, fracture. UV Light: Light blue UV response due to potential residual oil throughout sample.
6,033			White Light: Gray carbonate, medium/small vugs, salt filled vugs. UV Light: Light blue UV response due to potential residual oil throughout sample.

Figure B-170. Annotated RSWC images with corresponding core descriptions of the Brown Niagaran for depths 6,032.5 ft. to 6,033 ft.

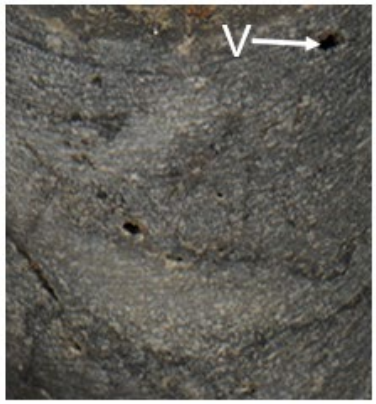
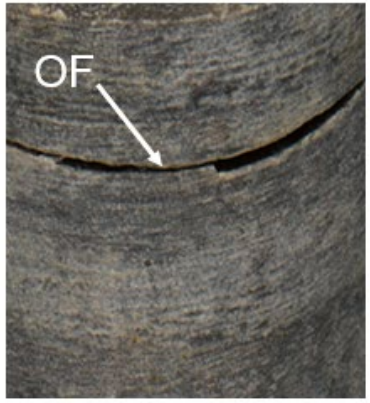
Depth Ft.	White Light Primary Features	UV Light Primary Features	Descriptions
6,033.5			White Light: Gray carbonate, medium/small vugs. UV Light: Light blue UV response due to potential residual oil throughout sample.
6,036			White Light: Gray carbonate, open fractures. UV Light: Light blue UV response due to potential residual oil throughout sample.

Figure B-171. Annotated RSWC images with corresponding core descriptions of the Brown Niagaran for depths 6,033.5 ft. to 6,036 ft.

Appendix C.
Individual Well Geomechanics Evaluation Results

C.1 Individual Well Evaluation

Five wells were subdivided into formations based on the regional nomenclature of the Michigan Basin, and used to produce the following results:

- Depth Plot Summaries: The dynamic elastic parameters (Poisson's ratio, dynamic shear modulus, bulk modulus, and Young's modulus) were calculated for each of the five wells. Individual well data was graphed in depth plots for each individual dynamic elastic parameter. These depth plots were useful to characterize the vertical variations in the elastic properties of each well with respect to variations in depth and formation.
- Histogram Summaries: Individual formation data was aggregated into a single histogram for each well for each respective individual dynamic elastic parameter. These graphs were useful to characterize the variations in the mechanical properties of each formation within each respective individual analyzed well.
- Statistical summaries: A tabulated summary of the mean and variance of each parameter for each formation by well.

C.1.1 Cargas 3-2 HD1

The Cargas 3-2 HD1 well contained five identified formations of interest (Salina, A-2 Carbonate, A-2 Evaporite, A-1 Carbonate, and Brown Niagara). A graphical and statistical summary of the calculated dynamic elastic parameters for the Cargas 3-2 HD1 well are presented in this section.

Depth Plot Summary

Four depth plots in Figure C-1 and Figure C-2 display the mechanical behavior of Cargas 3-2 HD1. Each plot represents one of the four calculated dynamic elastic parameters. Each color on these depth plots represents one of five respective formations of interest in the well.

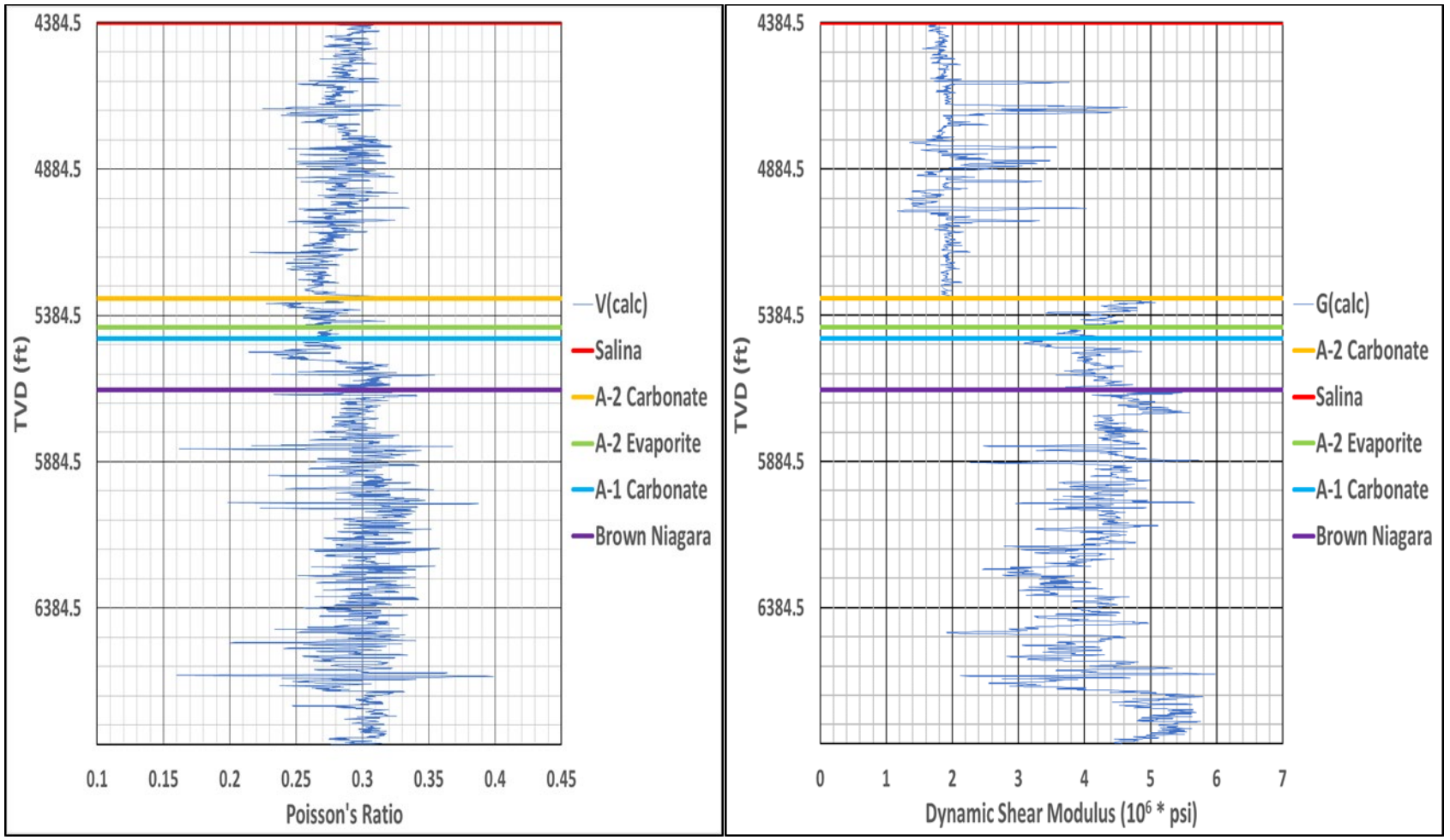


Figure C-1. Depth plots of Poisson's ratio and dynamic shear modulus for Cargas 3-2 HD1.

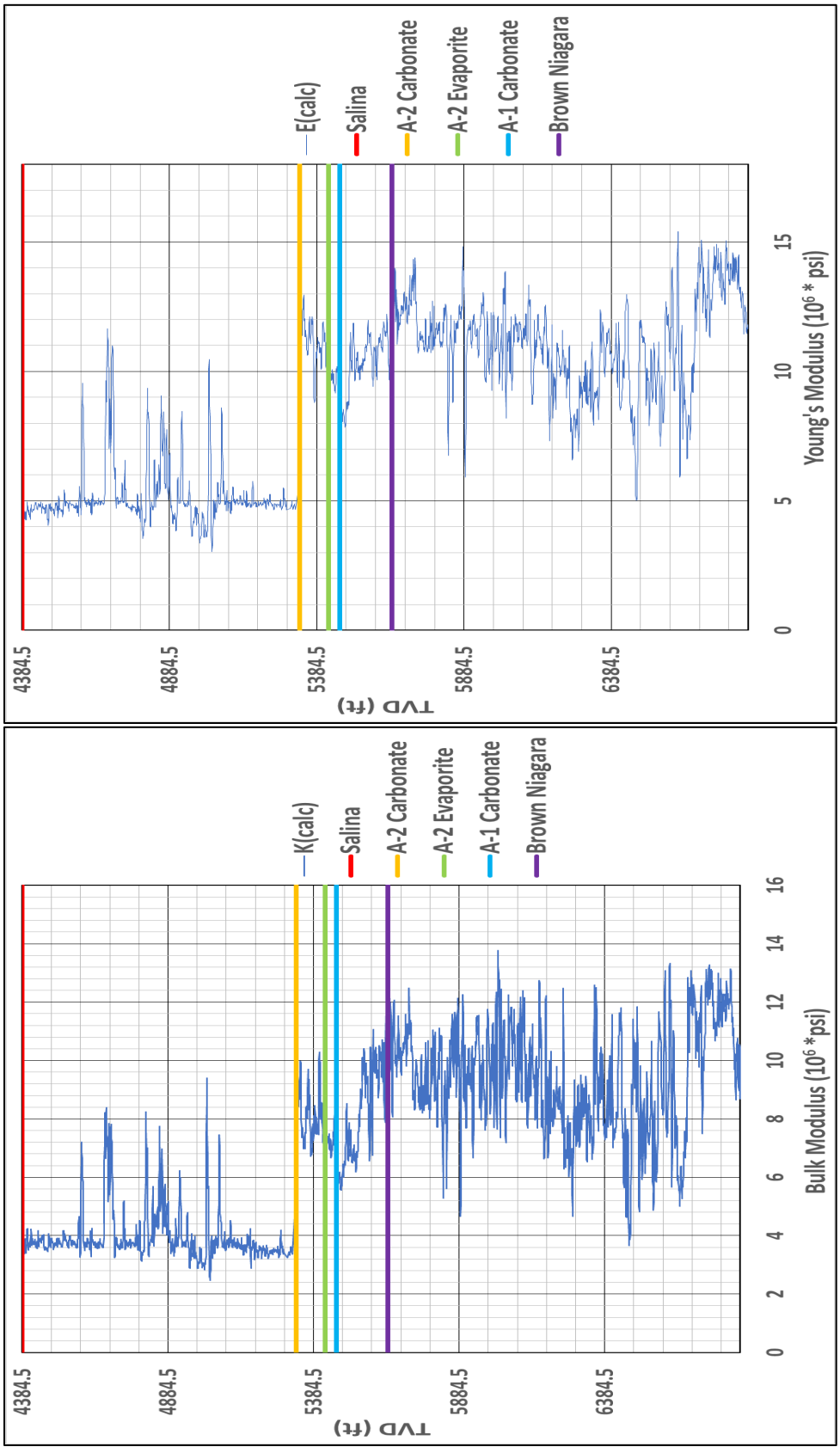


Figure C-2. Depth plots of bulk modulus and Young's modulus for Cargas 3-2 HD1.

Graphical Summary

Eight histograms in Figure C-3 and Figure C-4 display the mechanical behavior of Cargas 3-2 HD1. Two histograms were created for each dynamic elastic parameter, one histogram including the Salina Formation and one histogram omitting it. This was done in consideration of the visual resolution of the histograms of the formations within the reservoir zone. Each color on these histograms represents one of five respective formations of interest in the well.

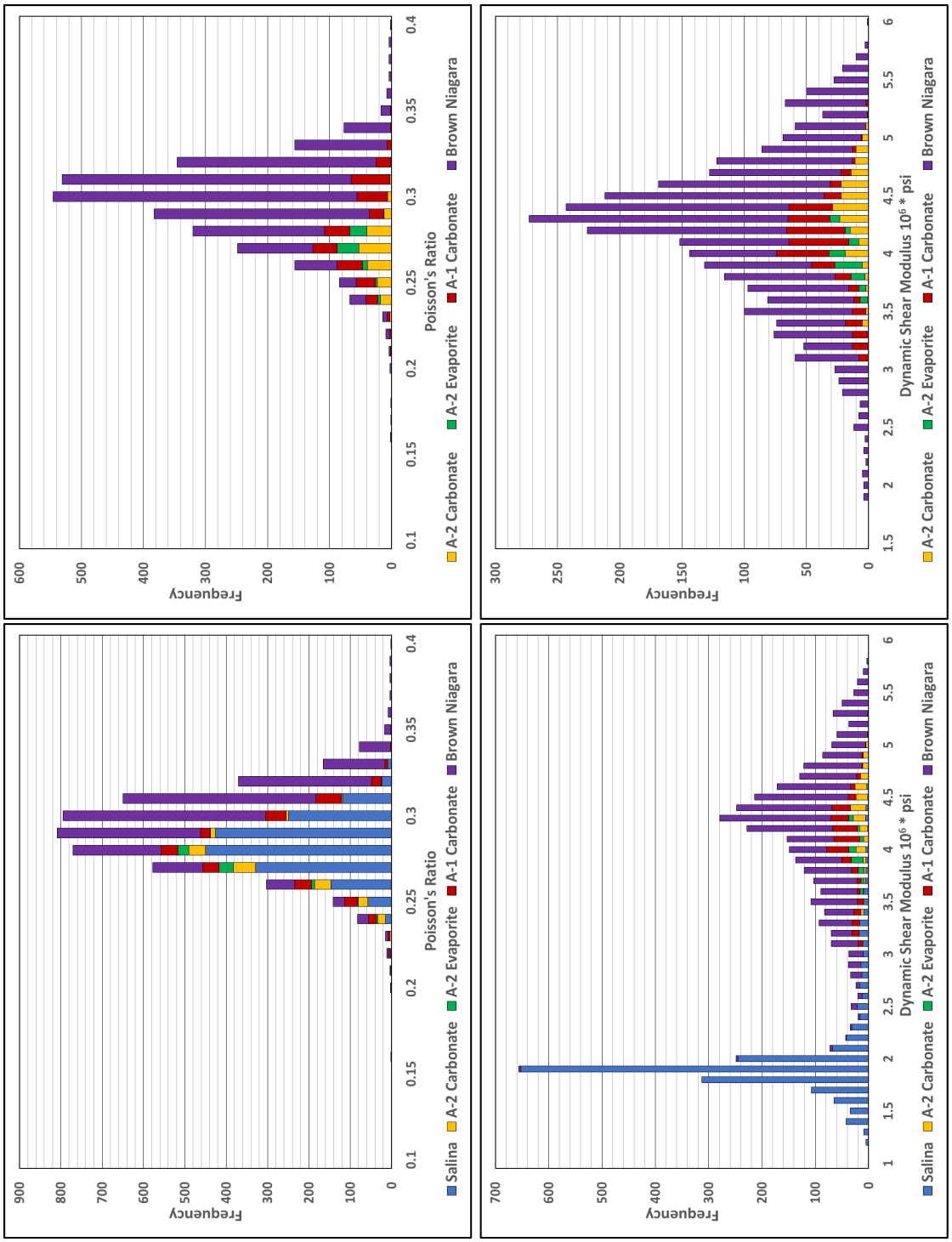


Figure C-3. Histograms of Poisson's ratio and dynamic shear modulus for Cargas 3-2 HD1. Two of the histograms include the Salina Formation, and two of the histograms don't include the Salina Formation for visual resolution purposes.

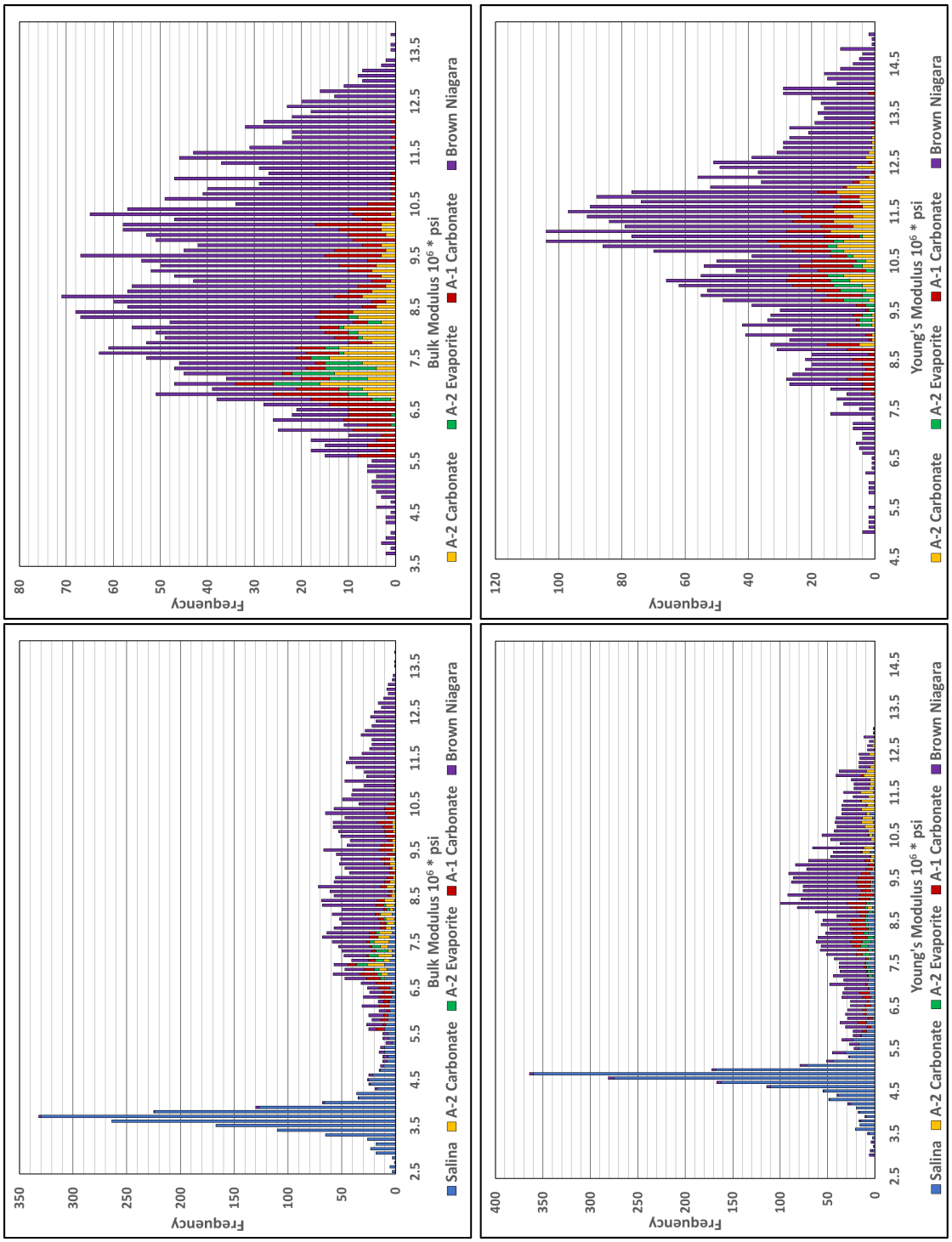


Figure C-4. Histograms of bulk modulus and Young's Modulus for Cargas 3-2 HD1. Two of the histograms include the Salina Formation, and two of the histograms don't include the Salina Formation for visual resolution purposes.

Statistical Summary

Table C-1 presents the mean and variance of each parameter for the formations of interest in Cargas 3-2 HD1.

Table C-1. Mean, variance, and N (number of data values) values of geomechanical parameters within Cargas 3-2 HD1 by formation.

Formation		Cargas 3-2 HD1			
		Poisson's Ratio	Dynamic Shear Modulus	Bulk Modulus	Young's Modulus
Salina	Mean	0.28	2.02	3.99	5.18
	Variance	0.0003	0.24	0.89	1.52
	N	1829	1829	1829	1829
A-2 Carbonate	Mean	0.27	4.38	7.98	11.09
	Variance	0.00	0.12	0.75	0.75
	N	198	198	198	198
A-2 Evaporite	Mean	0.27	3.95	7.26	10.02
	Variance	0.0001	0.04	0.17	0.22
	N	78	78	78	78
A-1 Carbonate	Mean	0.28	4.05	8.16	10.39
	Variance	0.001	0.18	2.53	1.27
	N	350	350	350	350
Brown Niagara	Mean	0.30	4.24	9.36	11.02
	Variance	0.001	0.47	3.47	3.23
	N	2382	2382	2382	2382

C.1.2 El Mac Hills 1-18A

El Mac Hills 1-18A contained five identified formations of interest (Salina, A-2 Carbonate, A-2 Evaporite, A-1 Carbonate, and Brown Niagara). A graphical and statistical summary of the calculated dynamic elastic parameters for El Mac Hills 1-18A are presented in this section.

Depth Plot Summary

Four depth plots in Figure C-5 and Figure C-6 display the mechanical behavior of El Mac Hills 1-18A. Each plot represents one of the four calculated dynamic elastic parameters. Each color on these depth plots represents one of five respective formations of interest in the well.

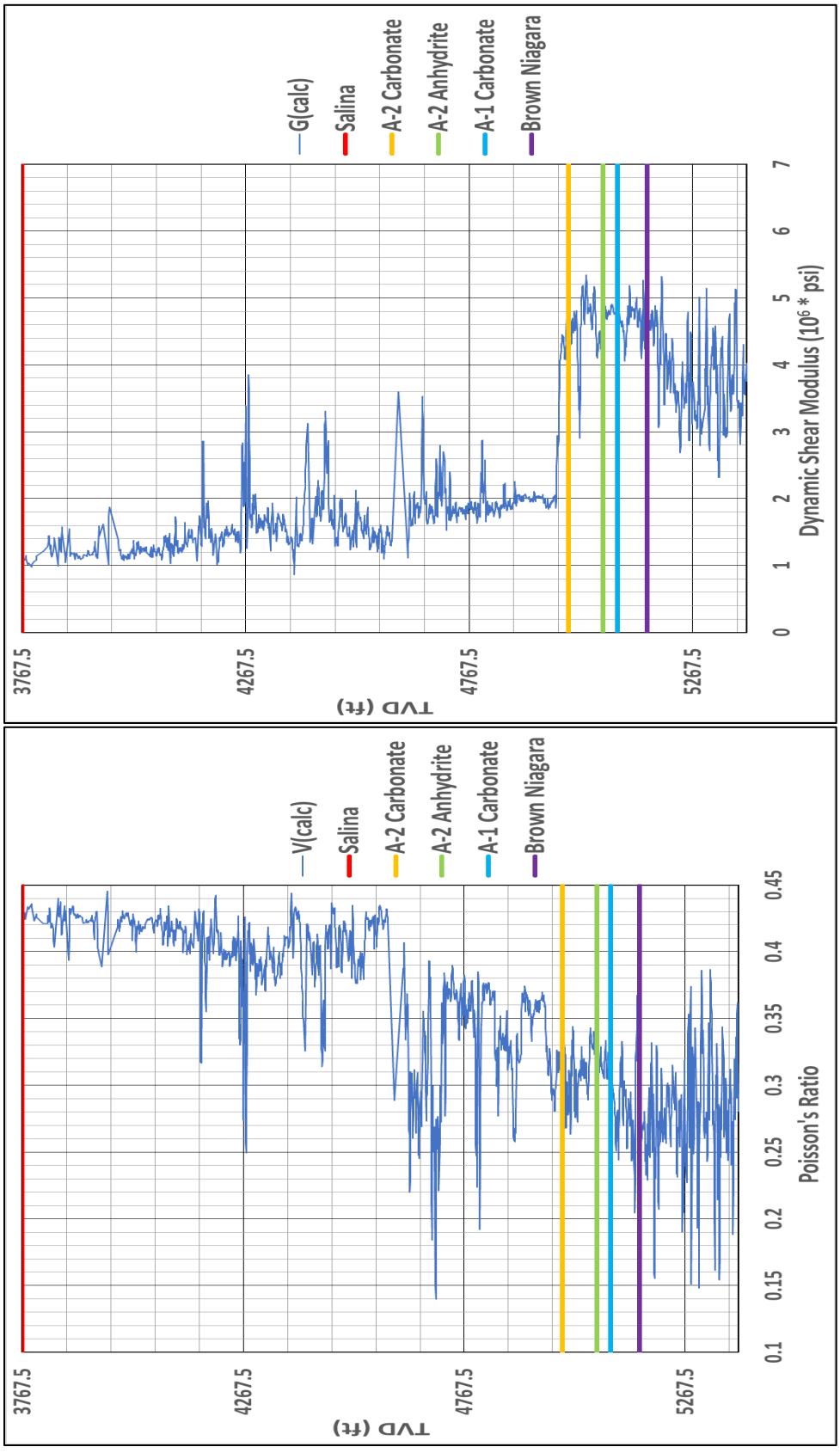


Figure C-5. Depth plots of Poisson's ratio and dynamic shear modulus for El Mac Hills 1-18A.

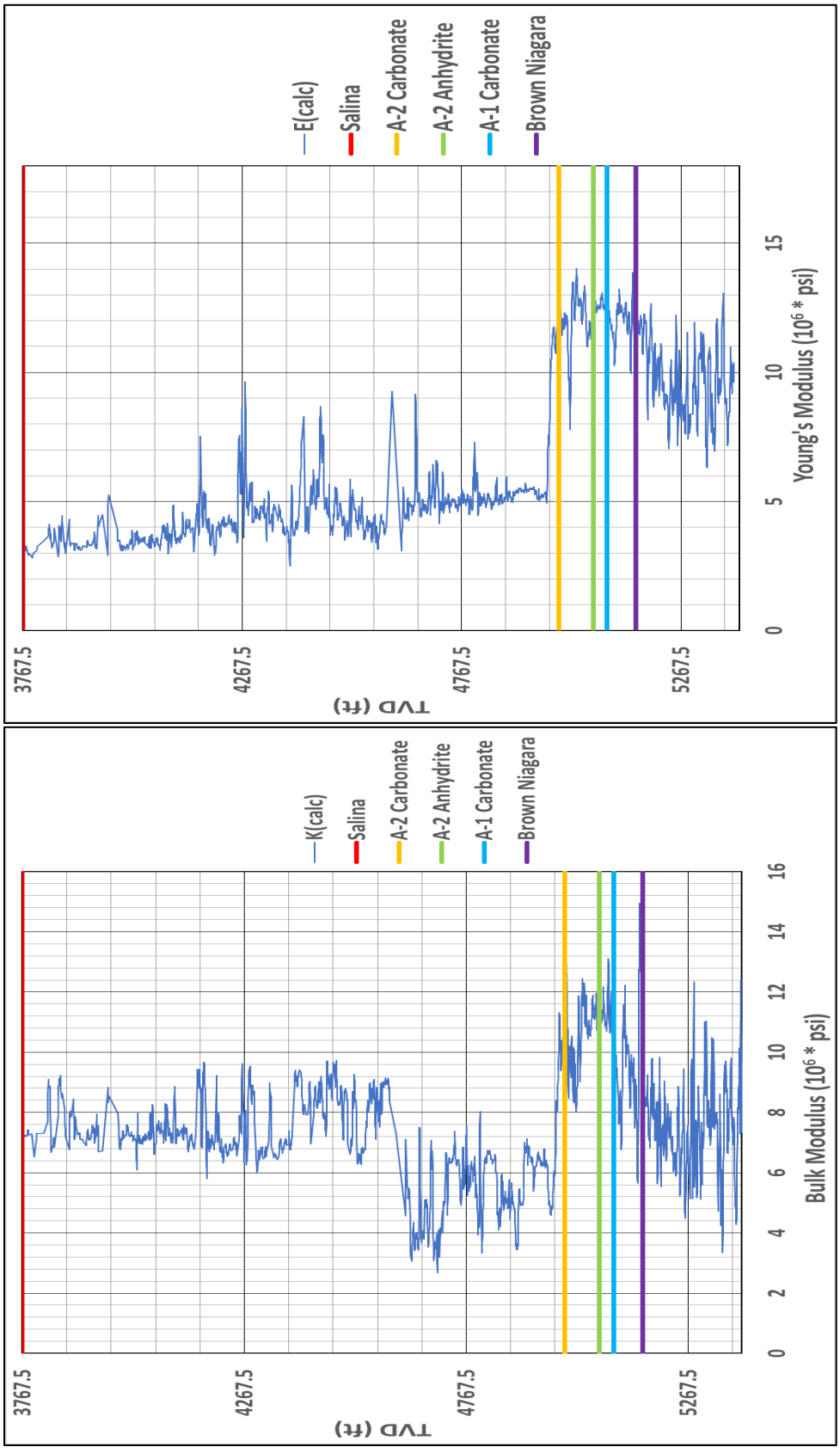


Figure C-6. Depth plots of bulk modulus and Young's modulus for El Mac Hills 1-18A.

Graphical Summary

Eight histograms in Figure C-7 and Figure C-8 display the mechanical behavior of El Mac Hills 1-18A. Two histograms were created for each dynamic elastic parameter, one histogram including the Salina Formation and one histogram omitting it. This was done in consideration of the visual resolution of the histograms of the formations within the reservoir zone. Each color on these histograms represents one of five respective formations of interest in the well.

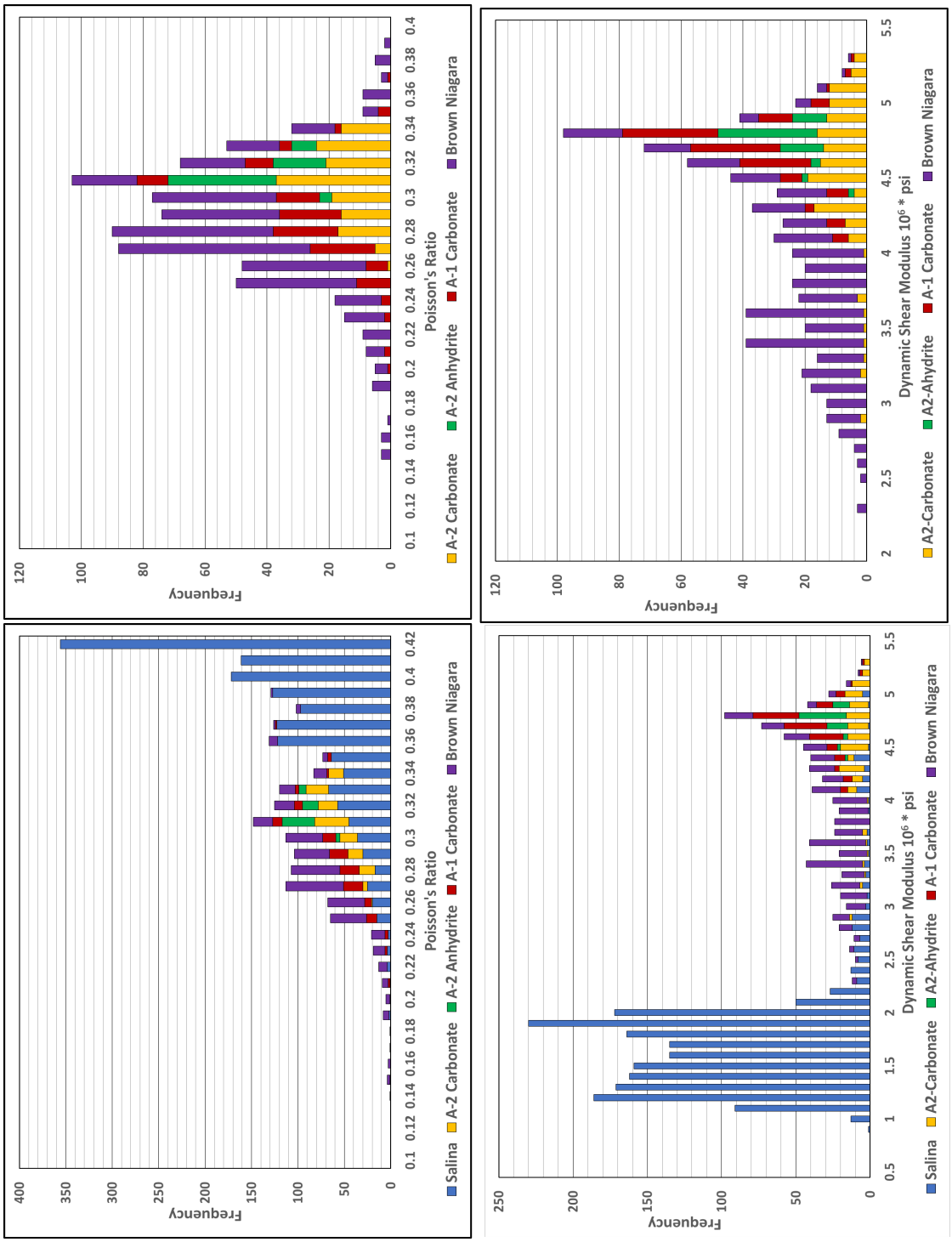


Figure C-7. Histograms of Poisson's ratio and dynamic shear modulus for El Mac Hills 1-18A. Two of the histograms include the Salina Formation, and two of the histograms don't include the Salina Formation for visual resolution purposes.

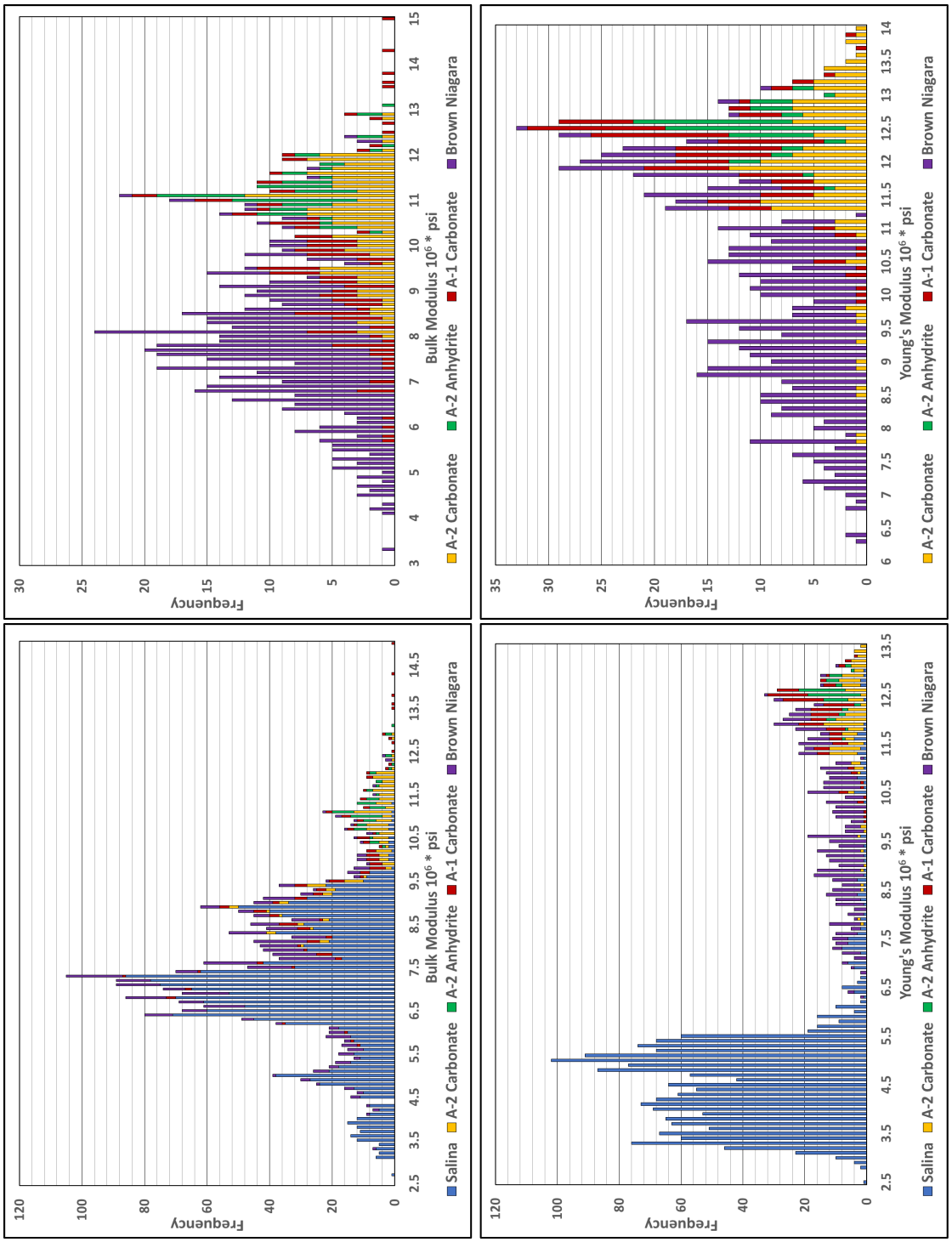


Figure C-8. Histograms of bulk modulus and Young's Modulus for El Mac Hills 1-18A. Two of the histograms include the Salina Formation, and two of the histograms don't include the Salina Formation for visual resolution purposes.

Statistical Summary

Table C-2 presents the mean and variance of each parameter for the formations of interest in El Mac Hills 1-18A.

Table C-2. Mean, variance, and N (number of data values) values of geomechanical parameters within El Mac Hills 1-18A by formation.

Formation		El Mac Hills			
		Poisson's Ratio	Dynamic Shear Modulus	Bulk Modulus	Young's Modulus
Salina	Mean	0.38	1.72	6.98	4.71
	Variance	0.002	0.32	2.27	1.93
	N	1829	1829	1829	1829
A-2 Carbonate	Mean	0.31	4.59	10.56	12.00
	Variance	0.0004	0.21	1.26	1.26
	N	156	156	156	156
A-2 Anhydrite	Mean	0.31	4.76	11.25	12.50
	Variance	0.00	0.01	0.36	0.08
	N	64	64	64	64
A-1 Carbonate	Mean	0.29	4.67	9.54	12.01
	Variance	0.001	0.06	2.96	0.52
	N	132	132	132	132
Brown Niagara	Mean	0.28	3.82	7.54	9.74
	Variance	0.002	0.38	2.03	2.11
	N	427	427	427	427

C.1.3 Lawnichak 9-33

Lawnichak 9-33 contained six identified formations of interest (Salina, A-2 Carbonate, A-2 Evaporite, A-1 Carbonate, Brown Niagara, and Gray Niagara). A graphical and statistical summary of the calculated dynamic elastic parameters for Lawnichak 9-33 are presented in this section.

Depth Plot Summary

Four depth plots in Figure C-9 and Figure C-10 display the mechanical behavior of Lawnichak 9-33. Each plot represents one of the four calculated dynamic elastic parameters. Each color on these depth plots represents one of six respective formations of interest in the well.

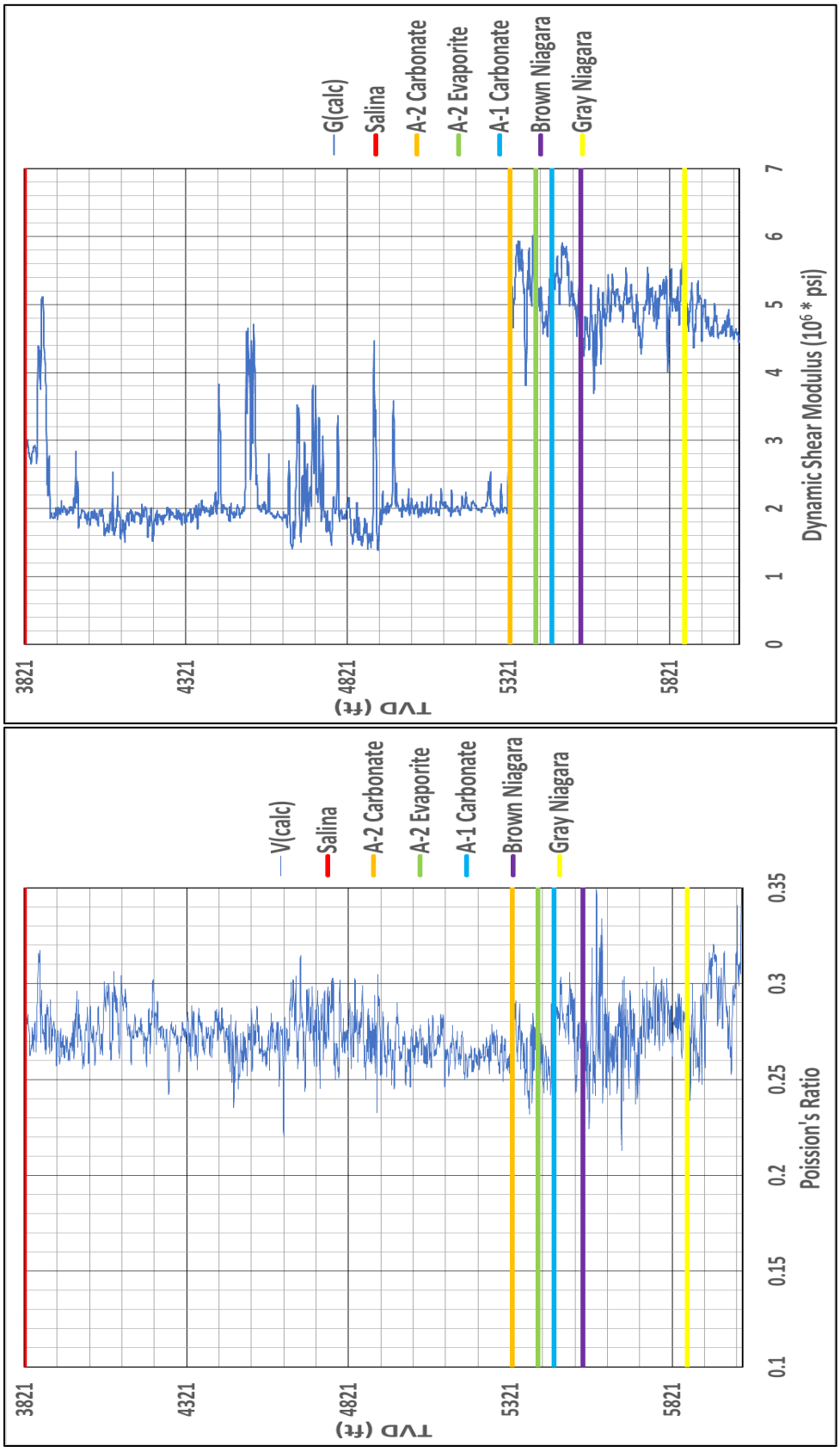


Figure C-9. Depth plots of Poisson's ratio and dynamic shear modulus for Lawnichak 9-33.

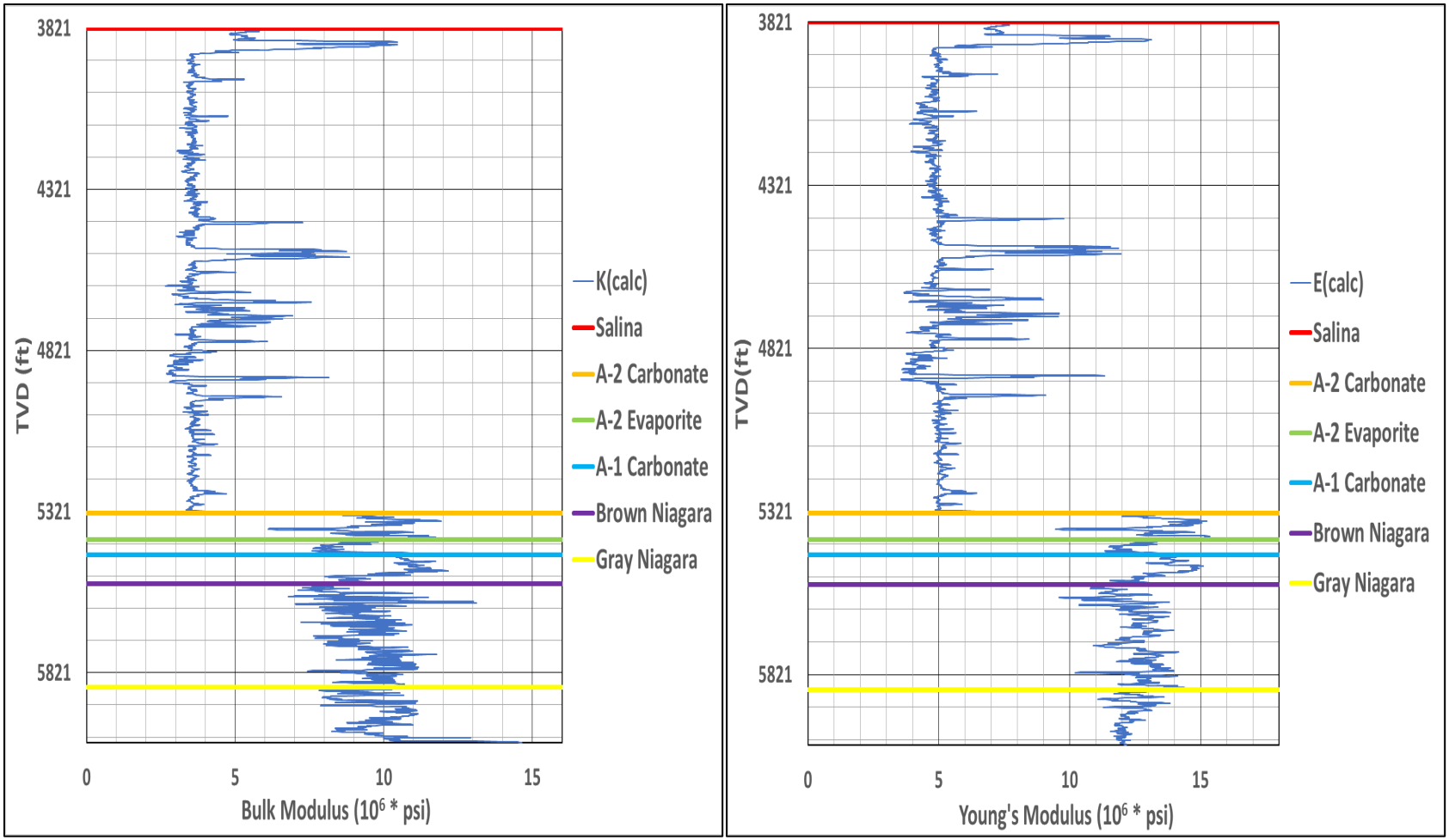


Figure C-10. Depth plots of bulk modulus and Young's modulus for Lawnichak 9-33.

Graphical Summary

Eight histograms in Figure C-11 and Figure C-12 display the mechanical behavior of Lawnichak 9-33. Two histograms were created for each dynamic elastic parameter, one histogram including the Salina Formation and one histogram omitting it. This was done in consideration of the visual resolution of the histograms of the formations within the reservoir zone. Each color on these histograms represents one of five respective formations of interest in the well.

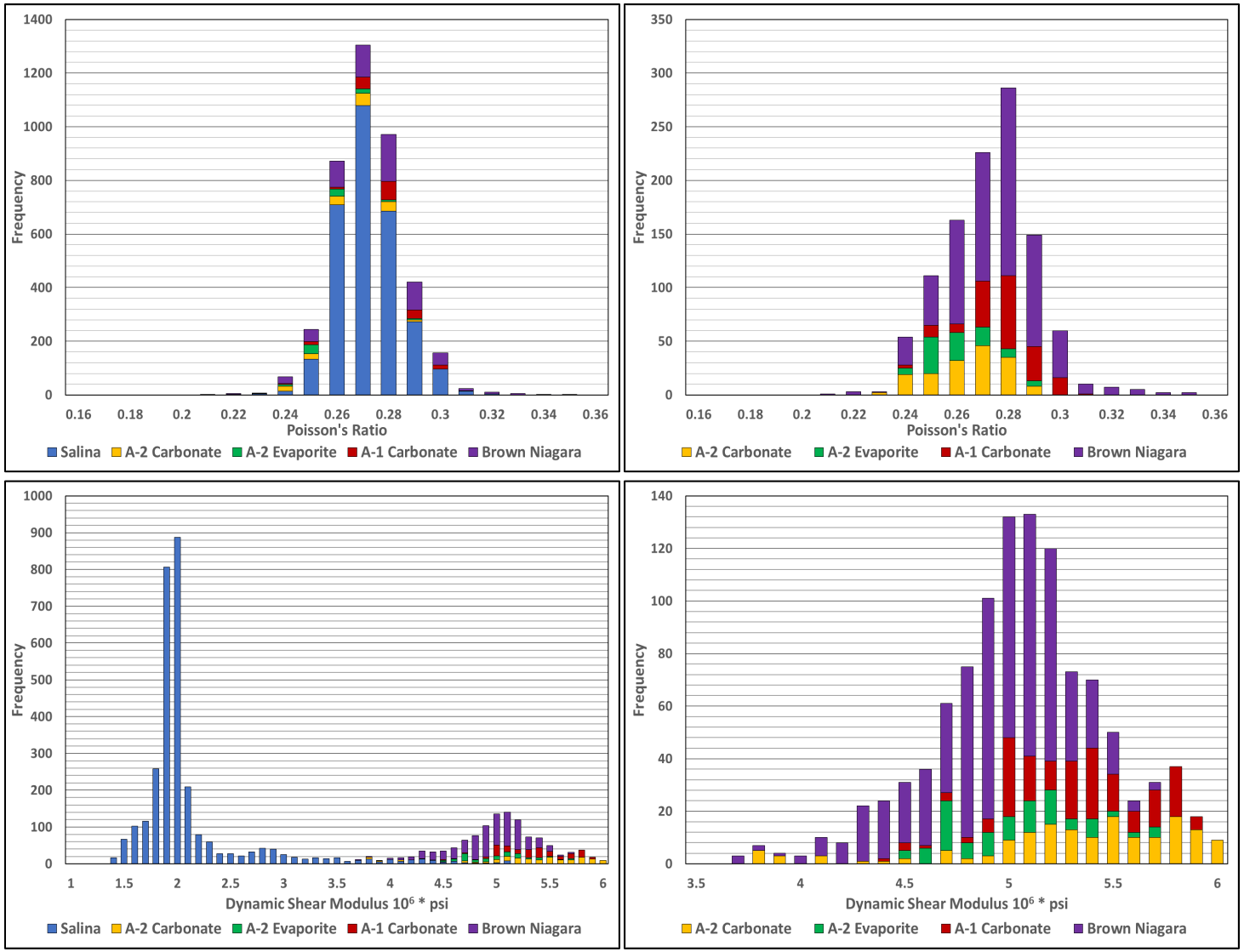


Figure C-11. Histograms of Poisson's ratio and dynamic shear modulus for Lawnichak 9-33. Two of the histograms include the Salina Formation, and two of the histograms don't include the Salina Formation for visual resolution purposes.

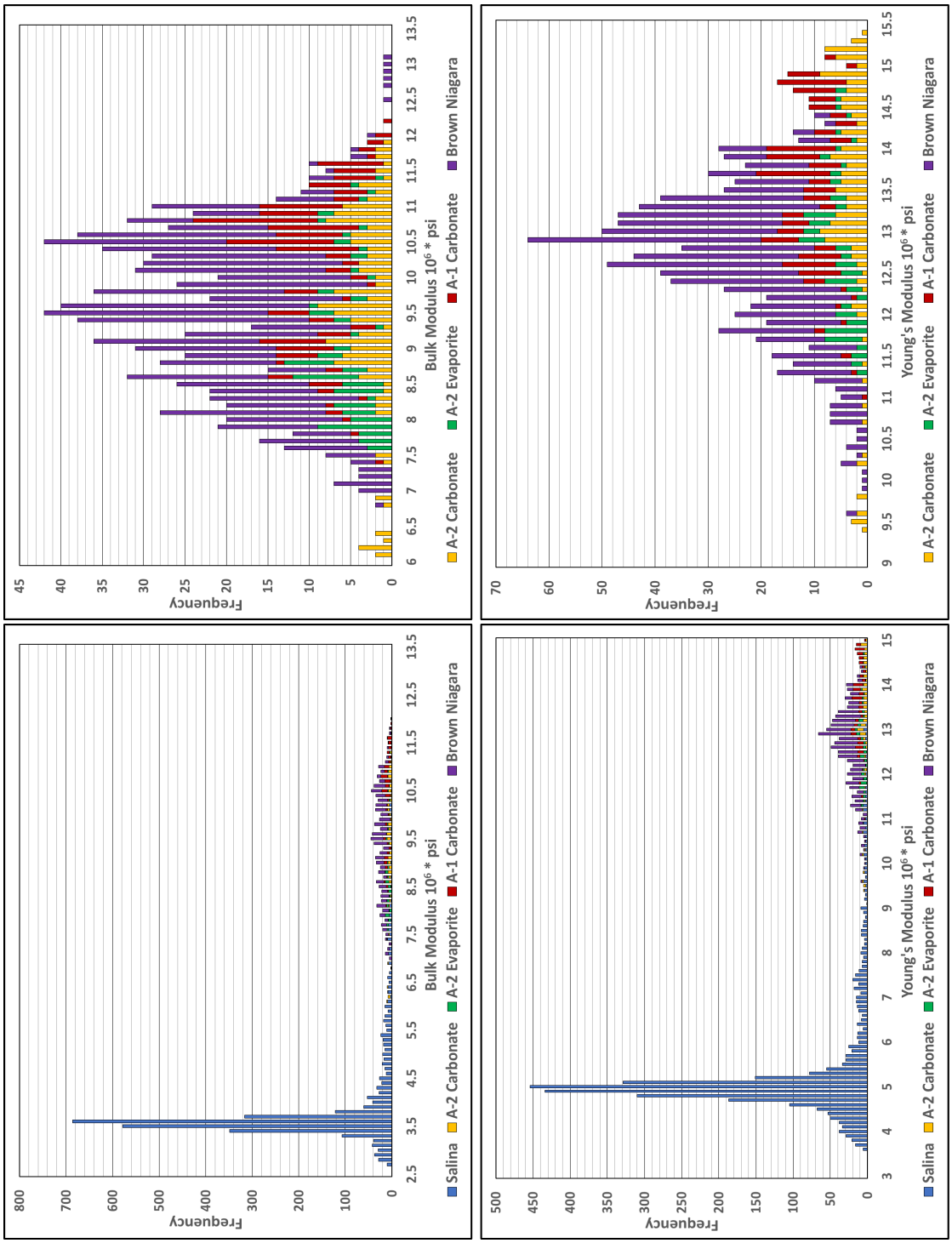


Figure C-12. Histograms of bulk modulus and Young's Modulus for Lawnichak 9-33. Two of the histograms include the Salina Formation, and two of the histograms don't include the Salina Formation for visual resolution purposes.

Statistical Summary

Table C-3 presents the mean and variance of each parameter for the formations of interest in Lawnichak 9-33.

Table C-3. Mean, variance, and N (number of data values) values of geomechanical parameters within Lawnichak 9-33 by formation.

Formation		Lawnichak 9-33			
		Poisson's Ratio	Dynamic Shear Modulus	Bulk Modulus	Young's Modulus
Salina	Mean	0.27	2.10	3.92	5.35
	Variance	0.0001	0.29	1.15	1.91
	N	3010	3010	3010	3010
A-2 Carbonate	Mean	0.26	5.33	9.62	13.48
	Variance	0.0002	0.28	1.78	1.96
	N	162	162	162	162
A-2 Evaporite	Mean	0.26	5.01	8.84	12.63
	Variance	0.0001	0.10	1.01	0.74
	N	96	96	96	96
A-1 Carbonate	Mean	0.28	5.32	10.27	13.60
	Variance	0.0002	0.11	1.07	0.79
	N	182	182	182	182
Brown Niagara	Mean	0.28	4.93	9.40	12.57
	Variance	0.0003	0.11	1.22	0.78
	N	642	642	642	642
Gray Niagara	Mean	0.29	4.75	9.85	12.26
	Variance	0.0005	0.05	1.42	0.25
	N	342	342	342	342

C.1.4 Chester 6-16

Chester 6-16 contained six identified formations of interest (Salina, A-2 Carbonate, A-2 Evaporite, A-1 Carbonate, Brown Niagara, and Gray Niagara). A graphical and statistical summary of the calculated dynamic elastic parameters for Chester 6-16 are presented in this section.

Depth Plot Summary

Four depth plots in Figure C-13 and Figure C-14 display the mechanical behavior of Chester 6-16. Each plot represents one of the four calculated dynamic elastic parameters. Each color on these depth plots represents one of six respective formations of interest in the well.

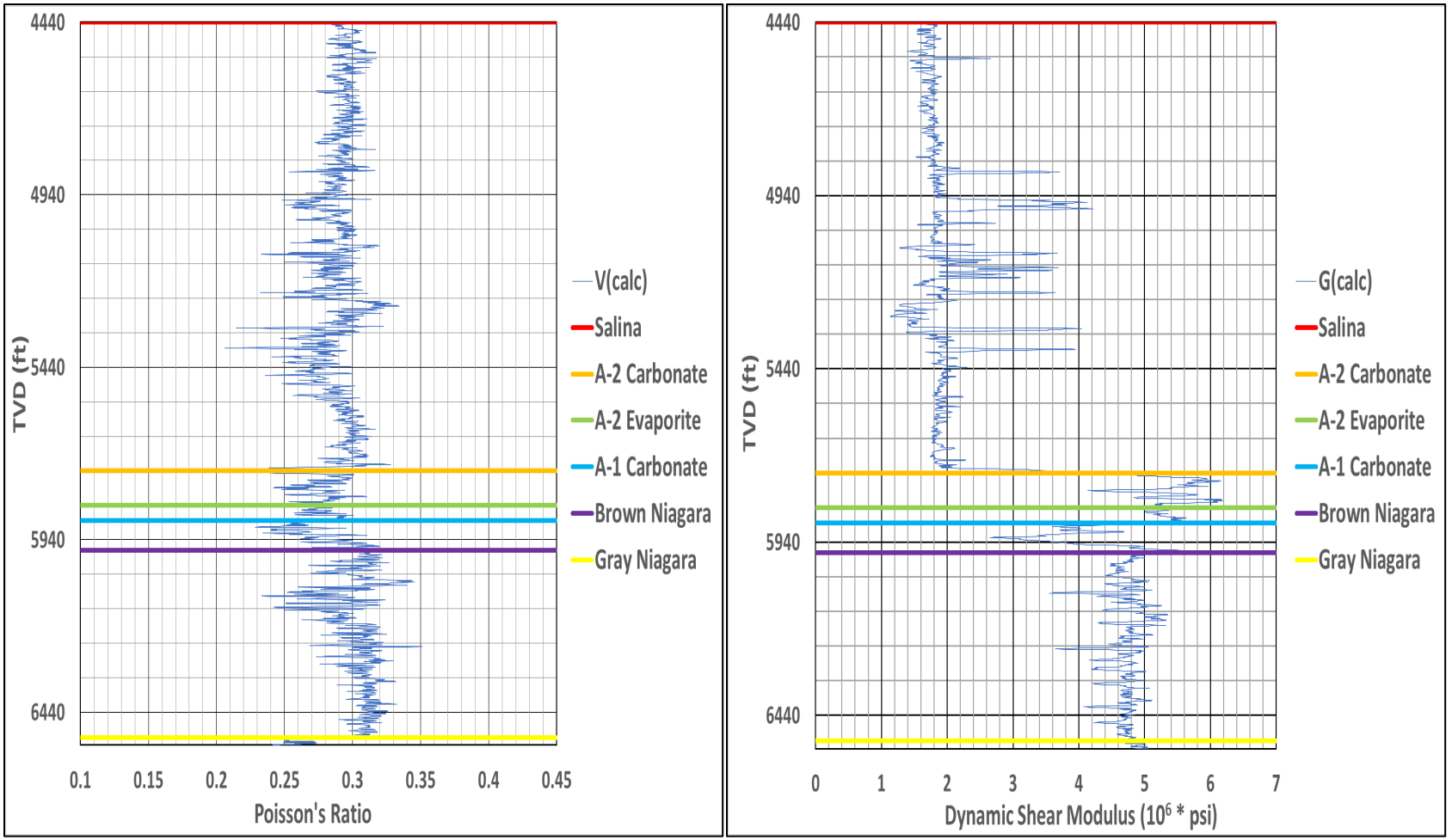


Figure C-13. Depth plots of Poisson's ratio and dynamic shear modulus for Chester 6-16.

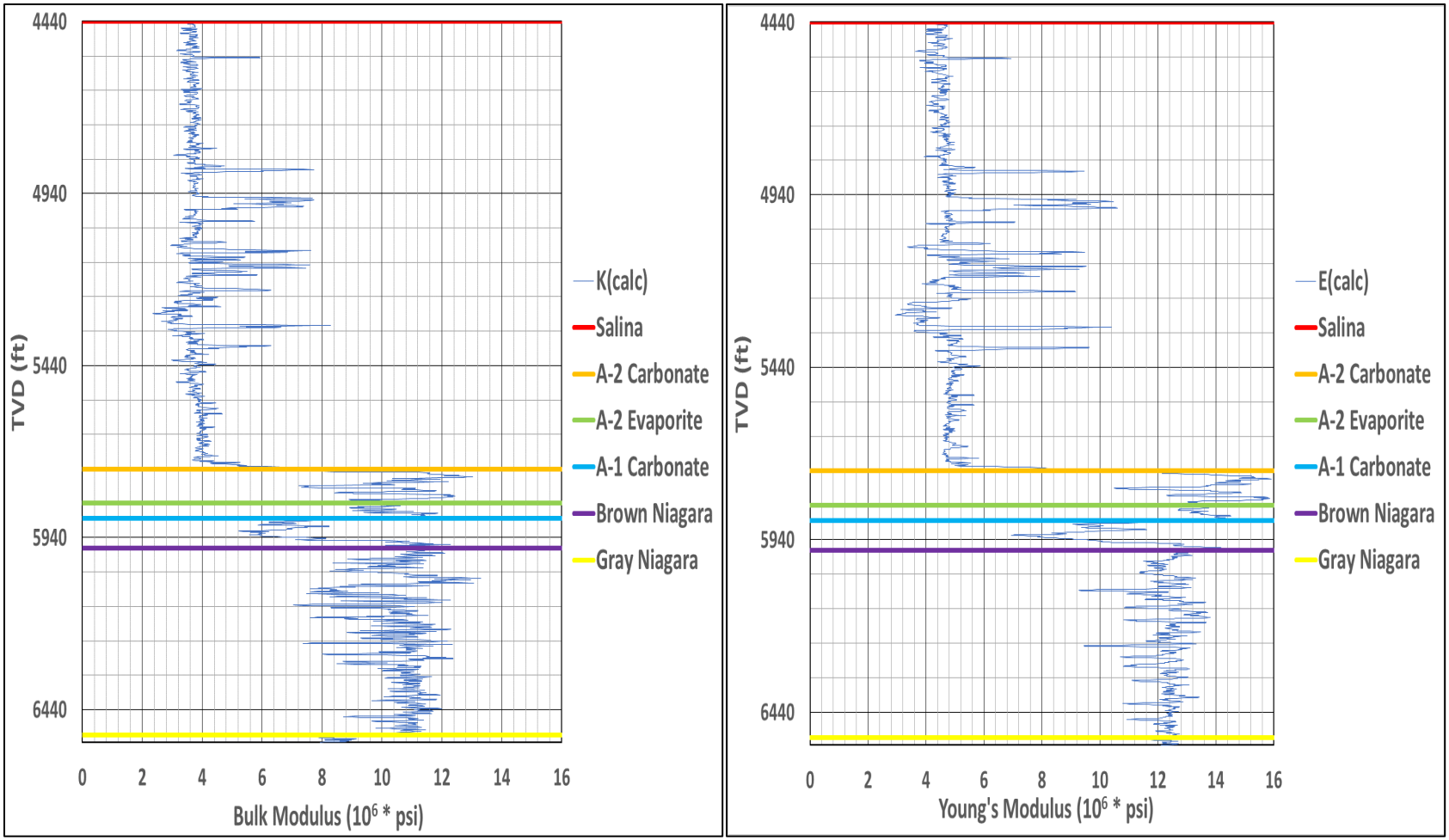


Figure C-14. Depth plots of bulk modulus and Young's modulus for Chester 6-16.

Graphical Summary

Eight histograms in Figure C-15 and Figure C-16 display the mechanical behavior of Chester 6-16. Two histograms were created for each dynamic modulus parameter, one histogram including the Salina Formation and one histogram omitting it. This was done in consideration of the visual resolution of the histograms of the formations within the reservoir zone. Each color on these histograms represents one of five respective formations of interest in the well.

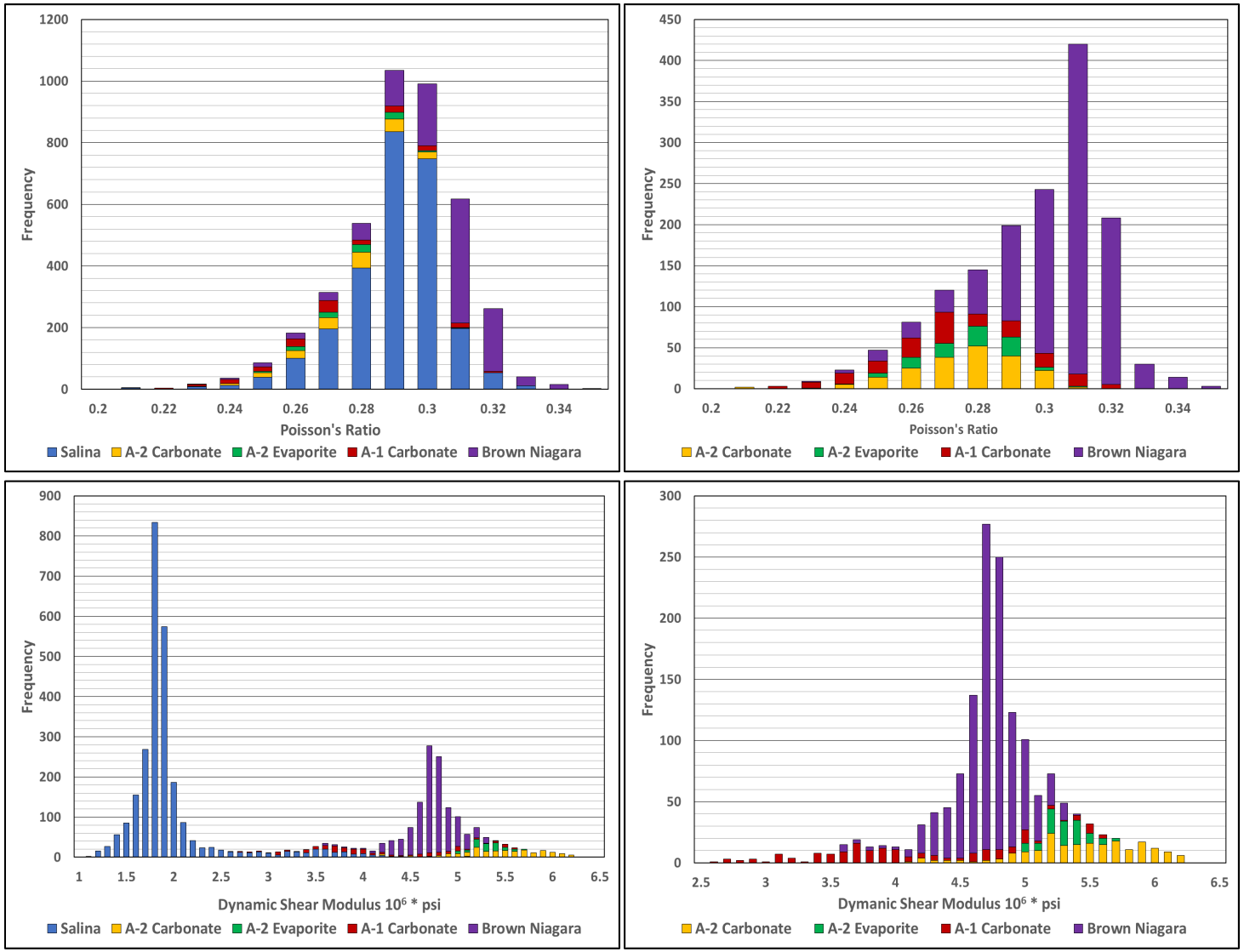


Figure C-15. Histograms of Poisson's ratio and dynamic shear modulus for Chester 6-16. Two of the histograms include the Salina Formation, and two of the histograms don't include the Salina Formation for visual resolution purposes.

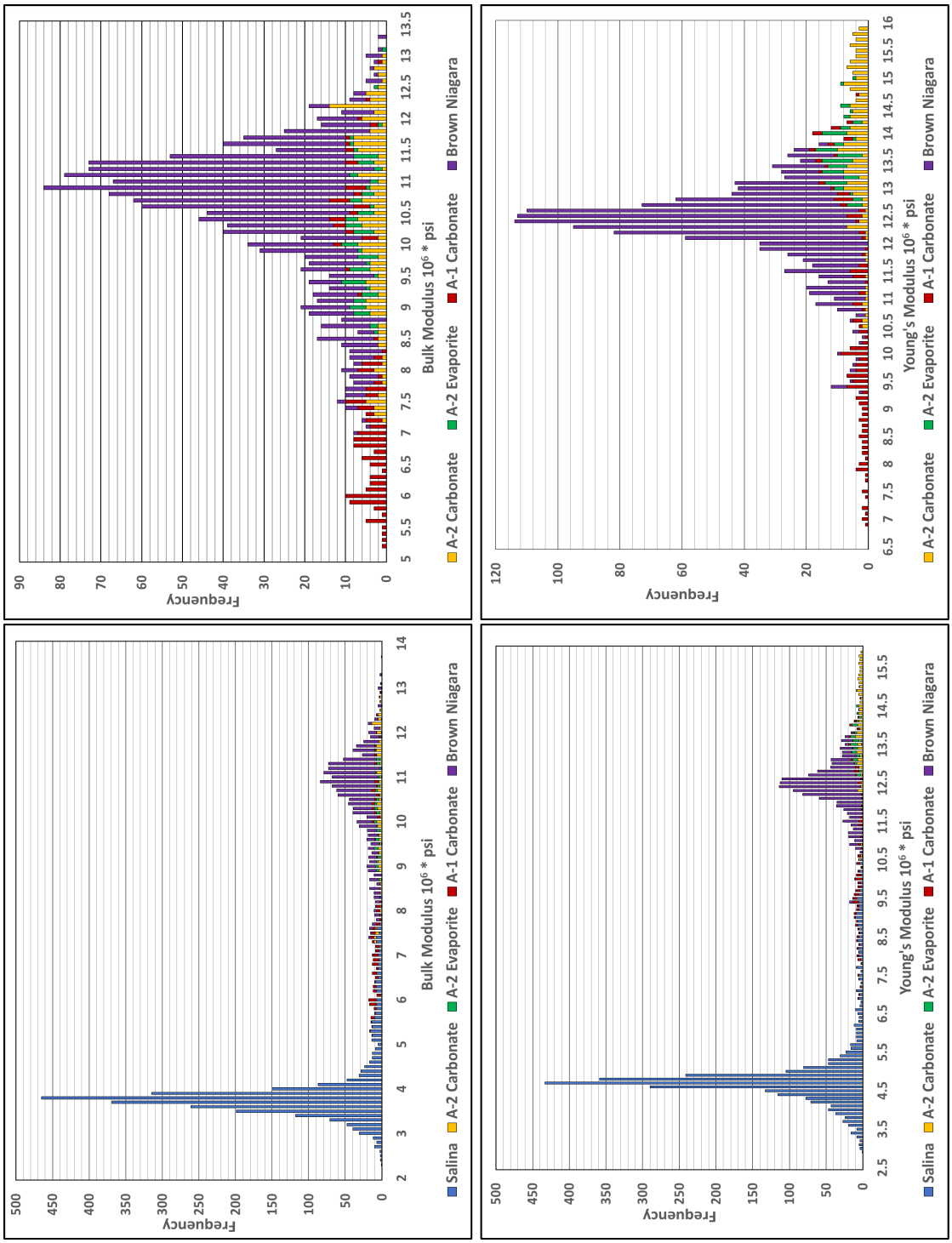


Figure C-16. Histograms of bulk modulus and Young's Modulus for Chester 6-16. Two of the histograms include the Salina Formation, and two of the histograms don't include the Salina Formation for visual resolution purposes.

Statistical Summary

Table C-4 presents the mean and variance of each parameter for the formations of interest in Chester 6-16.

Table C-4. Mean, variance, and N (number of data values) values of geomechanical parameters within Chester 6-16 by formation.

Formation		Chester 6-16			
		Young's Modulus	Poisson's Ratio	Bulk Modulus	Dynamic Shear Modulus
Salina	Mean	5.00	0.29	3.96	1.94
	Variance	1.50	0.0002	0.77	0.24
	N	2600	2600	2600	2600
A-2 Carbonate	Mean	13.90	0.28	10.46	5.44
	Variance	1.61	0.0003	2.26	0.21
	N	201	201	201	201
A-2 Evaporite	Mean	13.56	0.28	10.20	5.31
	Variance	0.25	0.0002	0.92	0.03
	N	88	88	88	88
A-1 Carbonate	Mean	10.54	0.27	7.87	4.14
	Variance	2.20	0.0004	1.28	0.37
	N	172	172	172	172
Brown Niagara	Mean	12.31	0.30	10.58	4.72
	Variance	0.43	0.0003	1.08	0.06
	N	1086	1086	1086	1086
Gray Niagara	Mean	12.03	0.25	8.15	4.80
	Variance	0.43	0.0001	0.46	0.06
	N	45	45	45	45

C.1.5 Chester 8-16

Chester 8-16 contained six identified formations of interest (Salina, A-2 Carbonate, A-2 Evaporite, A-1 Carbonate, Brown Niagara, and Gray Niagara). A graphical and statistical summary of the calculated dynamic elastic parameters for Chester 8-16 are presented in this section.

Depth Plot Summary

Four depth plots in Figure C-17 and Figure C-18 display the mechanical behavior of Chester 8-16. Each plot represents one of the four calculated dynamic elastic parameters. Each color on these depth plots represents one of six respective formations of interest in the well.

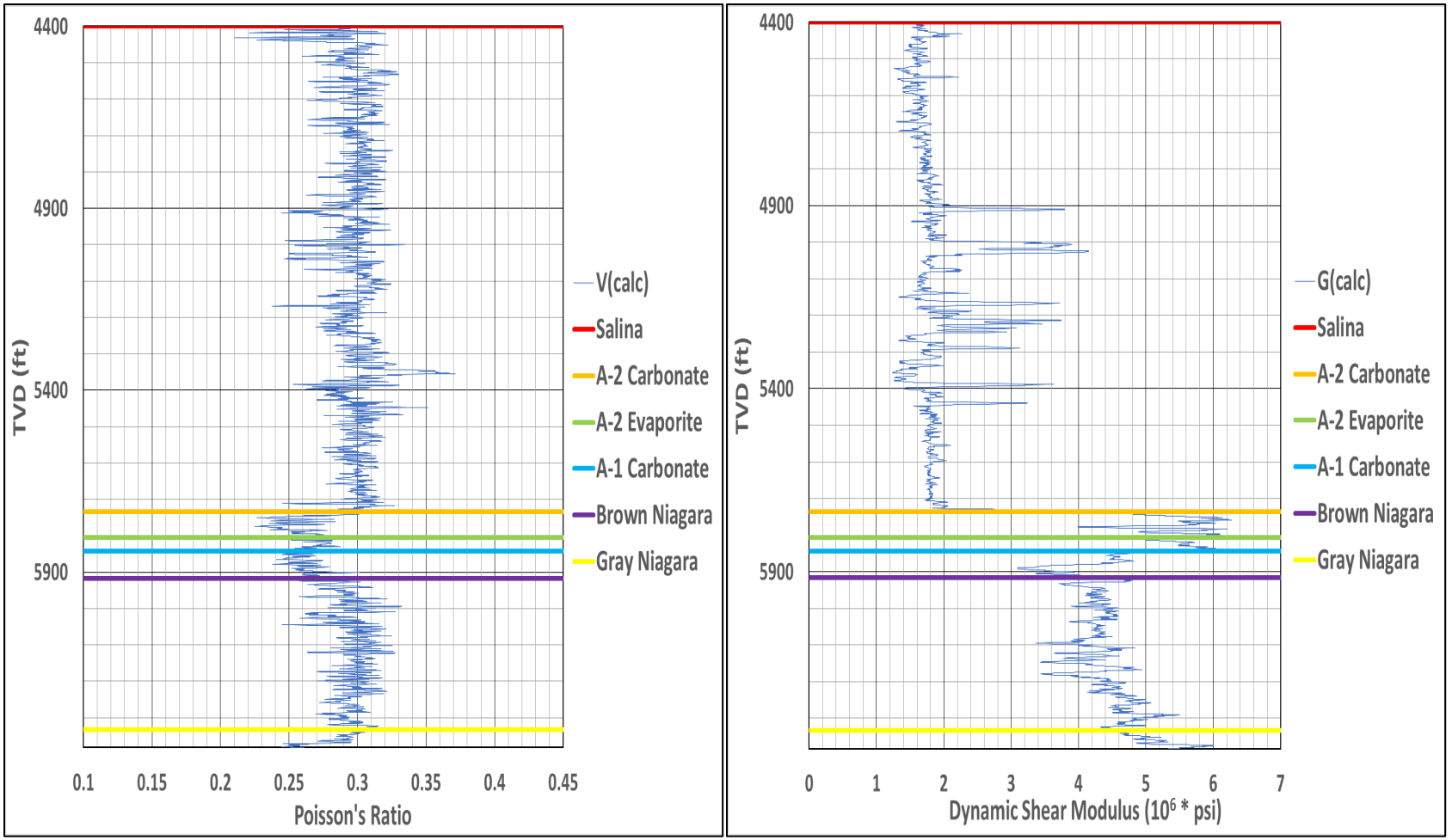


Figure C-17. Depth plots of Poisson's ratio and dynamic shear modulus for Chester 8-16.

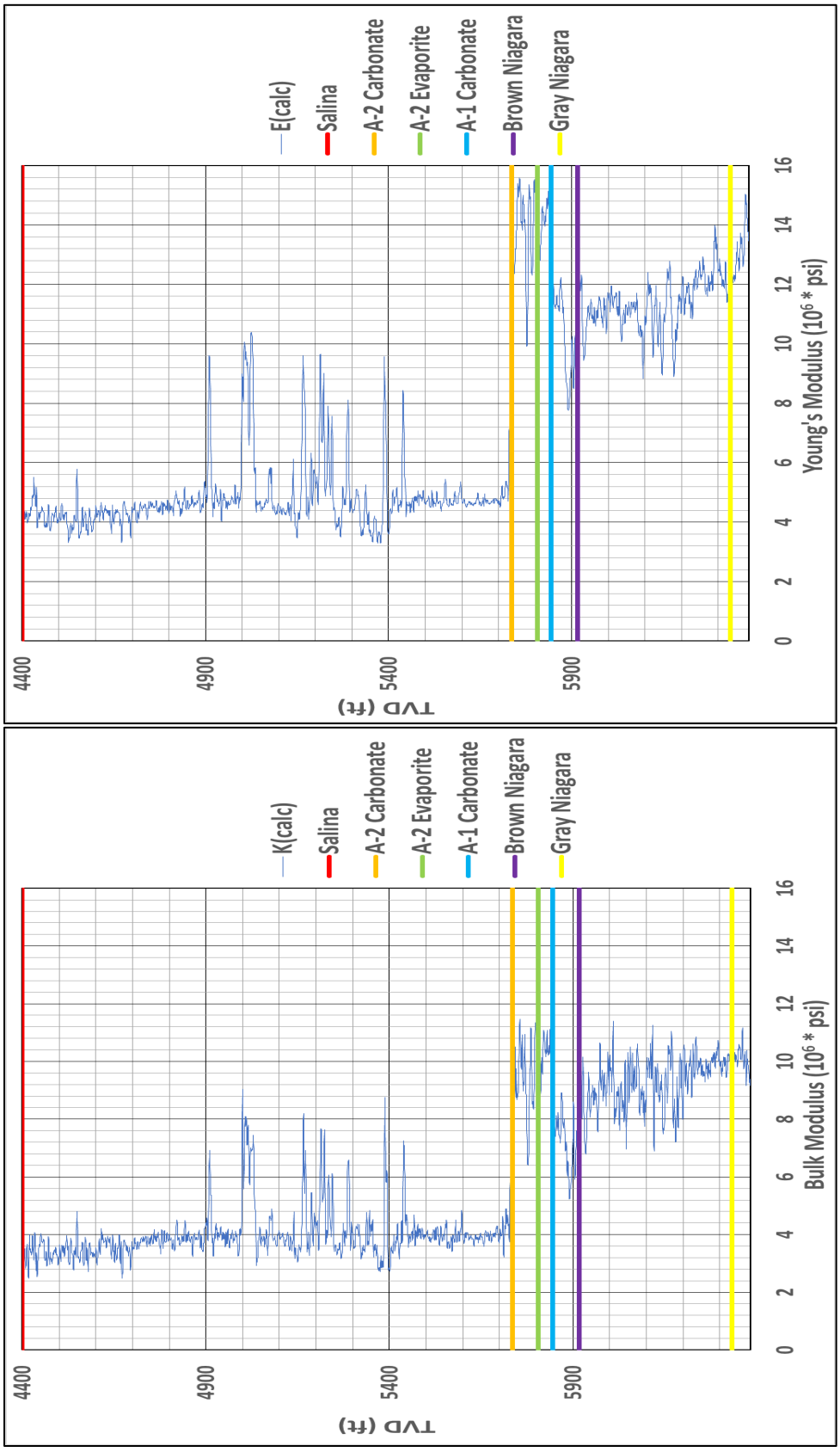


Figure C-18. Depth plots of bulk modulus and Young's modulus for Chester 8-16.

Graphical Summary

Eight histograms in Figure C-19 and Figure C-20 display the mechanical behavior of Chester 8-16. Two histograms were created for each dynamic elastic parameter, one histogram including the Salina Formation and one histogram omitting it. This was done in consideration of the visual resolution of the histograms of the formations within the reservoir zone. Each color on these histograms represents one of five respective formations of interest in this well.

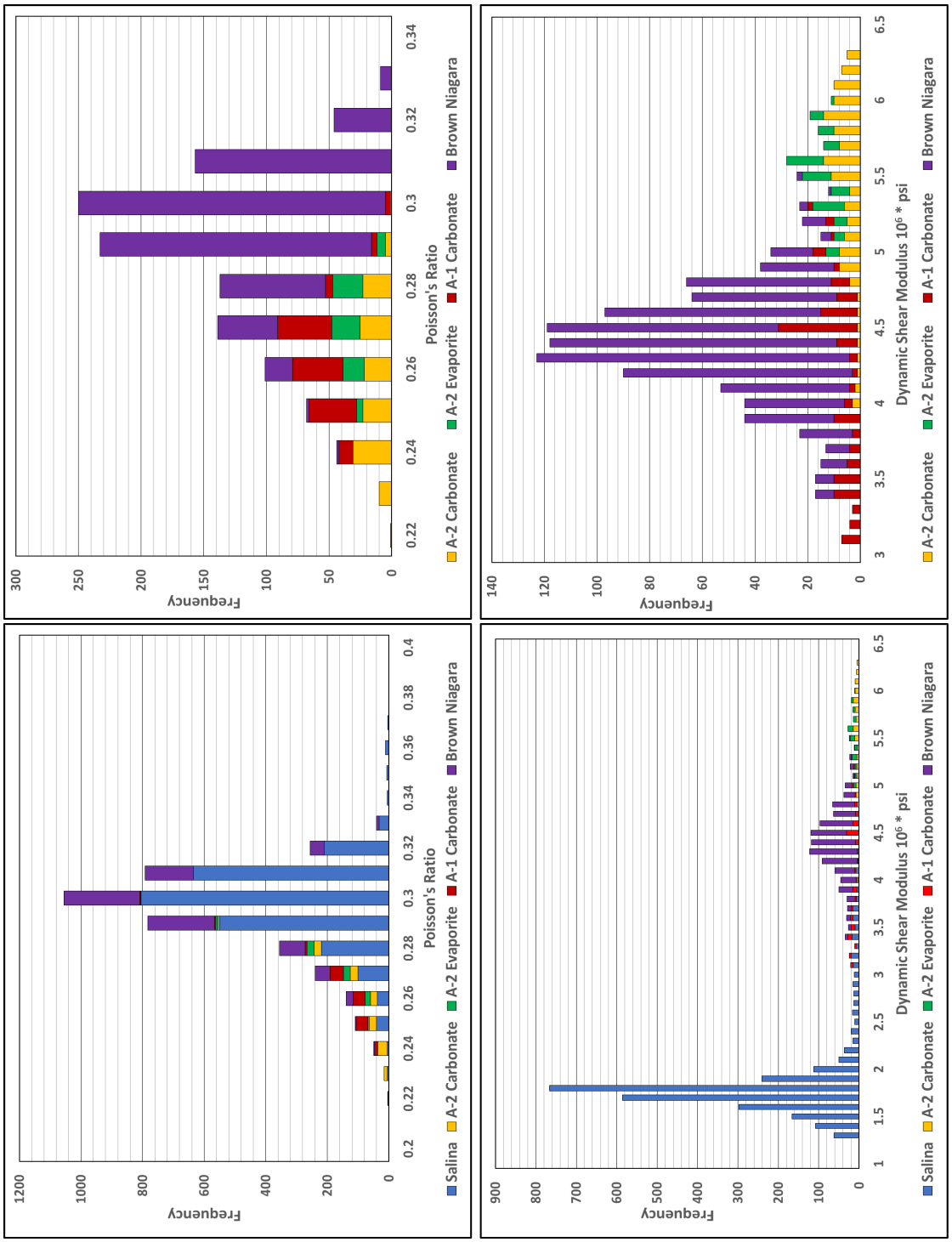


Figure C-19. Histograms of Poisson's ratio and dynamic shear modulus for Chester 8-16. Two of the histograms include the Salina Formation, and two of the histograms don't include the Salina Formation for visual resolution purposes.

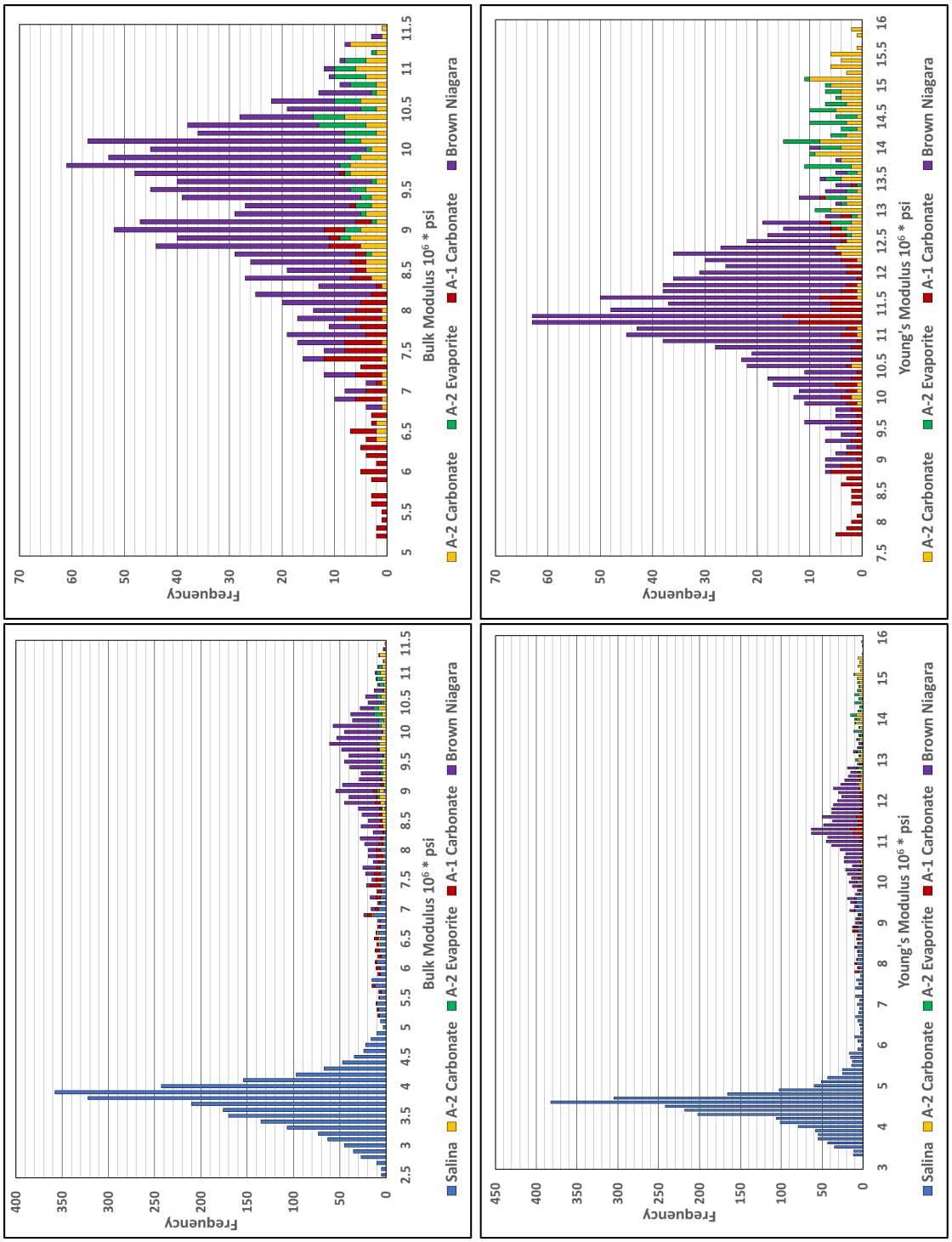


Figure C-20. Histograms of bulk modulus and Young's Modulus for Chester 8-16. Two of the histograms include the Salina Formation, and two of the histograms don't include the Salina Formation for visual resolution purposes.

Statistical Summary

Table C-5 presents the mean and variance of each parameter for the formations of interest in Chester 8-16.

Table C-5. Mean, variance, and N (number of data values) values of geomechanical parameters within Chester 8-16 by formation.

Formation		Chester 8-16			
		Young's Modulus	Poisson's Ratio	Bulk Modulus	Dynamic Shear Modulus
Salina	Mean	4.81	0.30	3.98	1.85
	Variance	1.28	0.0003	0.75	0.20
	N	2670	2670	2670	2670
A-2 Carbonate	Mean	13.84	0.26	9.59	5.50
	Variance	1.92	0.0003	1.49	0.30
	N	141	141	141	141
A-2 Evaporite	Mean	13.95	0.27	10.22	5.48
	Variance	0.42	0.0001	0.42	0.07
	N	76	76	76	76
A-1 Carbonate	Mean	10.53	0.26	7.37	4.17
	Variance	2.15	0.0002	1.07	0.35
	N	146	146	146	146
Brown Niagara	Mean	11.36	0.30	9.30	4.38
	Variance	0.74	0.0002	0.72	0.12
	N	832	832	832	832
Gray Niagara	Mean	13.03	0.28	10.08	5.08
	Variance	0.76	0.0003	0.15	0.17
	N	832	832	832	832

BATTELLE

It can be done

Attachment 1.
Cargas 3-2 HD1
Horizontal Well Wireline and Pipe-Conveyed Log Analysis: Chester 2 Niagaran Reef Piggyback Well

Attachment 1

Cargas 3-2 HD1 Horizontal Well Wireline and Pipe-Conveyed Log Analysis: Chester 2 Niagaran Reef Piggyback Well

Conducted by the Midwest Regional Carbon Sequestration Partnership (MRCSP)

DOE-NETL Cooperative Agreement DE-FC26-05NT42589

Prepared by:

Battelle
505 King Avenue
Columbus, Ohio 43201

Submitted to:

Client
Address
Address

September, 2020

This report is a work prepared for the United States Government by Battelle. In no event shall either the United States Government or Battelle have any responsibility or liability for any consequences of any use, misuse, inability to use, or reliance on any product, information, designs, or other data contained herein, nor does either warrant or otherwise represent in any way the utility, safety, accuracy, adequacy, efficacy, or applicability of the contents hereof.

Table of Contents

Page

List of Acronyms iii
Chapter 1. Well Drilling and Completions 1
1.1 Cargas 3-2 HD1 Well Location and Field Setting 1
1.2 Horizontal Drilling Details 5
1.3 Cargas 3-2 HD1 Petrophysical Logging 6
1.3.1 Wireline Logging and PCL 6
1.3.2 Detailed Description of PCL 7
1.3.3 Cargas 3-2 HD1 PCL and Wireline Logging 7
1.4 Cargas 3-2 HD1 Formation Log Evaluation 12
1.4.1 Salina B Salt 12
1.4.2 Carbonate 12
1.4.3 A-2 Evaporite 12
1.4.4 A-1 Carbonate 12
Appendix A. Daily Report Details of PCL Run 26
Appendix B. Statistics Plots 27

List of Tables

Page

Table 1-1. Wells Drilled Within the Chester 2 reef. 3
Table 1-2. Cargas 3-2 HD1 Log Suite Intervals. 8
Table 1-3. BHI and Mudloggers Log Curve Mnemonics, Common Names, and Uses. 9
Table 1-4. Brown Niagaran Reservoir Zones General Thickness and Porosity. 17

List of Figures

Page

Figure 1-1. Location of Chester 2 Reef Within the Niagaran Reef and Antrim Shale Play Trends 1
Figure 1-2. Core Energy LLC CO2 EOR Pipeline Infrastructure and Active EOR Reef Locations. 2
Figure 1-3. Chester 2 reef with All Well Penetrations. 3
Figure 1-4. Chester 2 Reef West-To-East Cross Section. 4
Figure 1-5. Cargas 3-2 HD1 Directional Well Diagram. 5
Figure 1-6. Deviated Wellbore Cross Section of the Cargas 3-2 HD1. 6
Figure 1-7. Wireline and PCL Schematic. 8

Figure 1-8. Measured Depth Log Curves Plot for Cargas 3-2 HD1. 10
Figure 1-9. Acoustic Log Monopole Compressional Quality Control Correlation Image. 11
Figure 1-10. Salina B Salt to Top Brown Section. 13
Figure 1-11. Neutron Density Cross Plot for the Salina B Salt. 14
Figure 1-12. Neutron Density Cross Plot for the A-2 Carbonate. 14
Figure 1-13. Neutron Density Cross Plot for the A-2 Evaporite. 15
Figure 1-14. Neutron Density Cross Plot for the A-1 Carbonate. 15
Figure 1-15. Brown Niagaran Neutron Density Cross Plot. 16
Figure 1-16. Brown Niagaran Reservoir Zones. 18
Figure 1-17. Upper Niagaran Reservoir Zones Acoustic Logs. 19
Figure 1-18. Middle Niagaran Reservoir Zones Acoustic Logs. 20
Figure 1-19. Lower Niagaran Reservoir Zones Acoustic Logs. 22
Figure 1-20. Scatter Plot of Brown Niagaran Reservoir Zones Mean DTS/DTC Ratio vs DTC 23
Figure 1-21. Chester 2 Reef General Interpretation. 24
Figure B-1. DTC and DTS Boxplot for Cargas 3-2 HD1 Formations, Median Values Shown. 27
Figure B-2. DTC/DTS vs DTC for B Salt 27
Figure B-3. DTC/DTS vs DTC for A-2 Carbonate 28
Figure B-4. DTC/DTS vs DTC for A-2 Evaporite 28
Figure B-5. DTC/DTS vs DTC for A-1 Carbonate 29
Figure B-6. DTC/DTS vs DTC for Brown Niagaran 29
Figure B-7. Compressional Wave Slowness (DTC) 30
Figure B-8. Shear Wave Slowness (DTS) 30
Figure B-9. Vp/Vs Ratio vs. Vp 31
Figure B-10. Vp/Vs Ratio vs. Vp 31
Figure B-11. XRHOB 32
Figure B-12. PE Cross Section 32
Figure B-13. Mean PE vs. Mean Bulk Density 33
Figure B-14. Bulk Density 33
Figure B-15. Compressional Wave Slowness (DTC) 34
Figure B-16. Compressional Wave Slowness (DTS) 34
Figure B-17. Acoustic Porosity 35
Figure B-18. PE Cross Section 35
Figure B-19. Neutron Porosity 36
Figure B-20. Bulk Density 36
Figure B-21. DT24 37

List of Acronyms

Bbl	barrel(s)
BHI	Baker Hughes Inc.
CO2	carbon dioxide
CPPZ	cross plot neutron density porosity
DOE	Department of Energy
DT24	24-inch depth of investigation sonic velocity
DTC	compressional wave slowness
DTS	shear wave slowness
EOR	enhanced oil recovery
MBbl	thousand barrels
MD	measured depth
MMcf/MMCF	million cubic feet
MRCSP	Midwest Regional Carbon Sequestration Partnership
NETL	National Energy Technology Laboratory
PCL	pipe-conveyed logging
PE	photo electric
PNC	pulsed neutron capture
PORA	acoustic porosity
TD	total depth
TVD	total vertical depth
TVT	total vertical thickness
VDL	variable density log
Vp	compressional wave slowness
Vs	shear wave slowness

Chapter 1. Well Drilling and Completions

1.1 Cargas 3-2 HD1 Well Location and Field Setting

The Cargas 3-2 HD1 well is in Otsego County, Michigan (Figure 1-1). The well was drilled semi-horizontally and completed in the Chester 2 Niagaran reef as a part of an ongoing CO_2 EOR (Enhance Oil Recovery) operation being conducted by Core Energy LLC (Figure 1-2). The Antrim Shale gas in the region contains approximately 15 percent CO_2. Antrim Shale operators send the gas to the Chester 10 gas separation plant to separate the CO_2 from the hydrocarbons. Core Energy LLC takes delivery of the CO_2 at its Chester 10 compression facility; from there, the CO_2 is transported north via pipeline to be injected into the reefs for EOR.

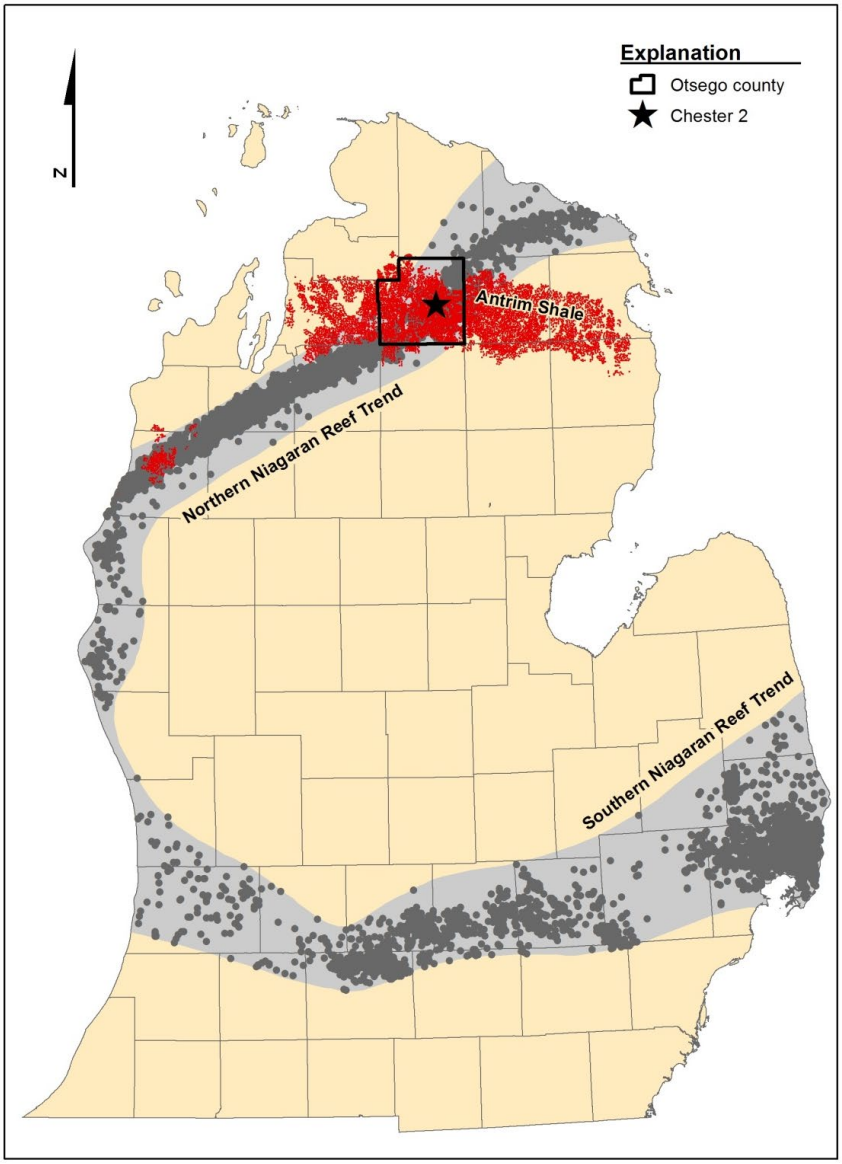


Figure 1-1. Location of Chester 2 Reef Within the Niagaran Reef and Antrim Shale Play Trends

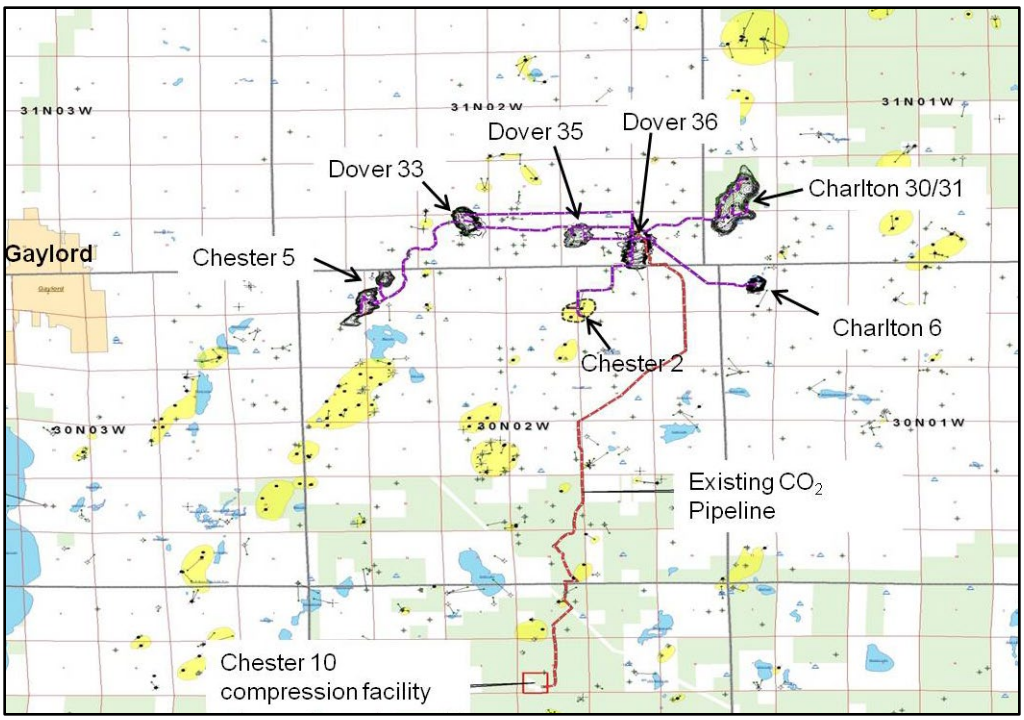
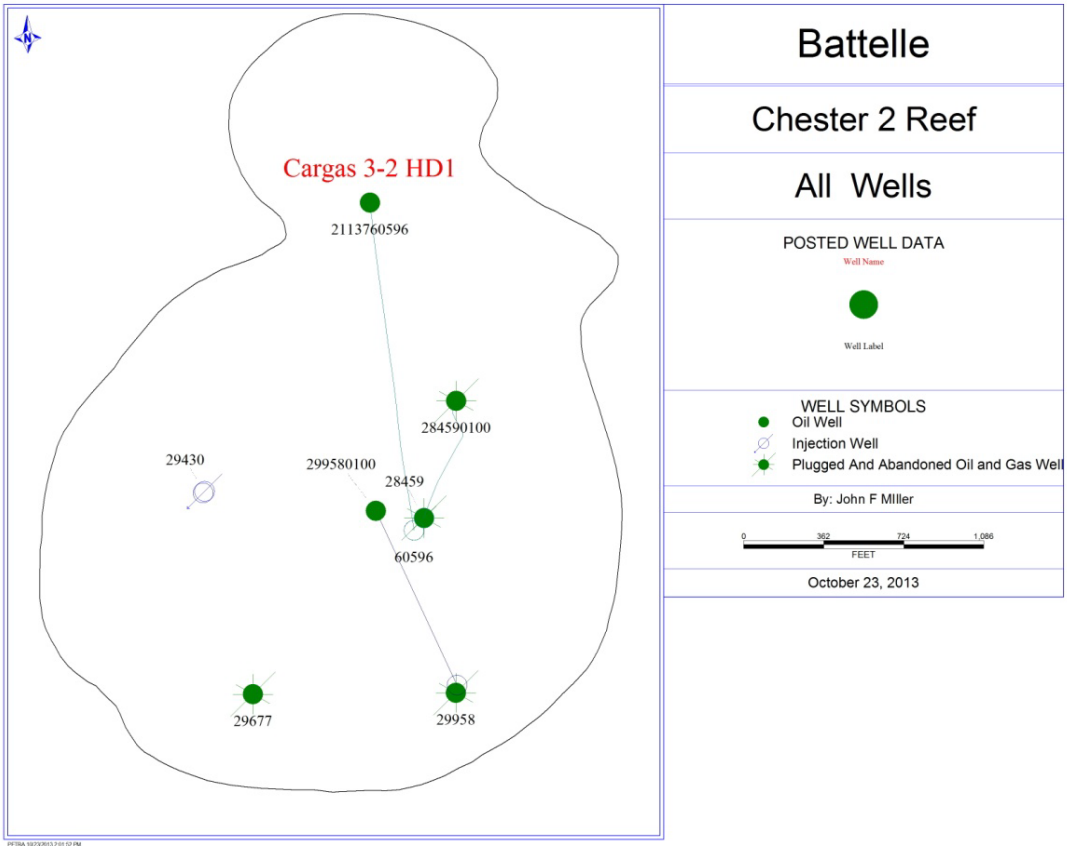


Figure 1-2. Core Energy LLC CO2 EOR Pipeline Infrastructure and Active EOR Reef Locations.

The Chester 2 reef was discovered in 1971. Seven wells (Table 1-1) have been drilled within the reef (Figure 1-3). There is one active CO_2 injection well within the reef, and two producers. The Cargas 3-2 HD1 was drilled in October 2012 to increase the oil production. The cumulative production from 1971 to November 2009 was 1039 thousand barrels (MBbl) oil and 378 million cubic feet (MMCF) gas. CO_2 EOR operations began in November 2009, and cumulative EOR production through September 2013 has been 48 MBbl oil, with a total gross of 4679 MMCF CO_2 injected. Topographical relief of the Chester 2 Niagaran reef from the surrounding regional section is 475 feet (Figure 1-4). The approximate areal extent of the reef as defined by the seismic interpretation is 151 acres (Figure 1-4B). The Chester 2 reef is in the portion of the reef trend where partial dolomitization of the reefs has occurred and is deep enough that salt-plugging is observed in part of the reef.

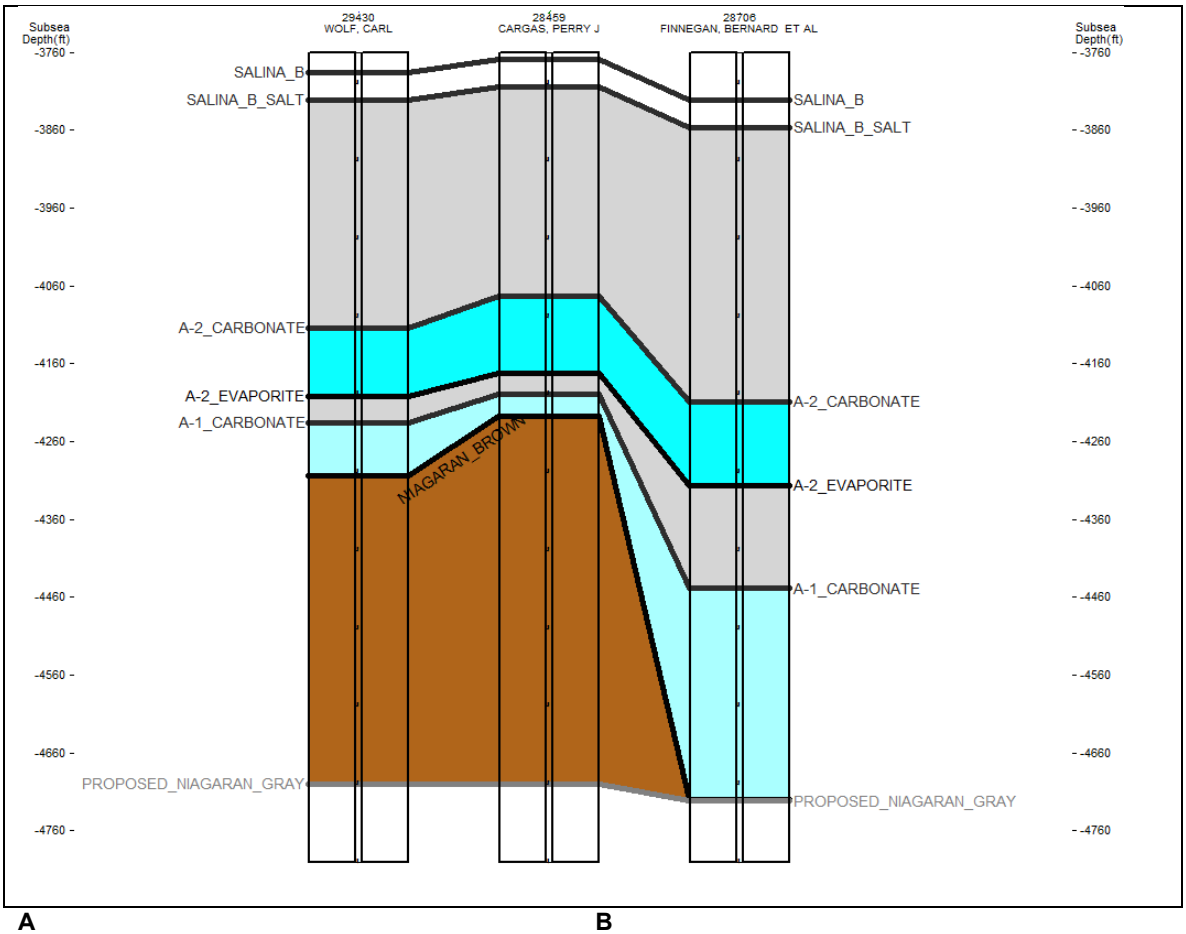
Table 1-1. Wells Drilled Within the Chester 2 reef.

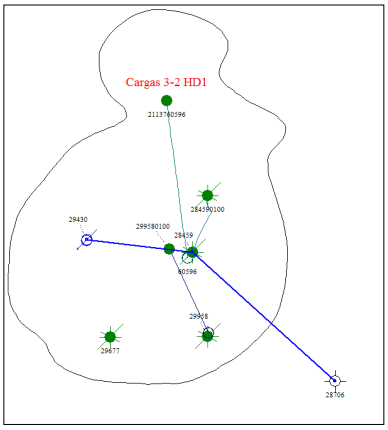
API_WellNo	permit	well_name	well_no	Well Status	Well Type	DTD	Date
21137605960000	60596	CARGAS	3-2 HD-1	Producing	Oil	6962	10/9/2012
21137299580100	2995801	WOLF, CARL ET AL "C"	1 HD1	Producing	Oil	6570	10/9/2001
21137299580000	29958	WOLF, CARL ET AL "C"	1	Producing	Oil	5806	12/9/1974
21137287060000	28706	FINNEGAN, BERNARD ET AL	1	Plugging Approved	Dry Hole	6051	1/6/1972
21137284590000	28459	CARGAS, PERRY J	1	Plugging Approved	Oil	6005	10/4/1971
21137296770000	29677	WOLF, CARL	1-B	Plugging Approved	Oil	5847	6/27/1974
21137294300000	29430	WOLF, CARL	1-A	Active	CO_2 Injector	5973	12/2/1973



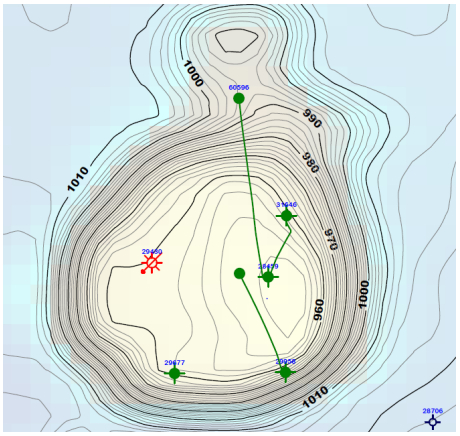
Note: Open circles are surface location on the producers. Filled oil symbol is bottomhole location.

Figure 1-3. Chester 2 reef with All Well Penetrations.





Blue line indicates cross section wells.



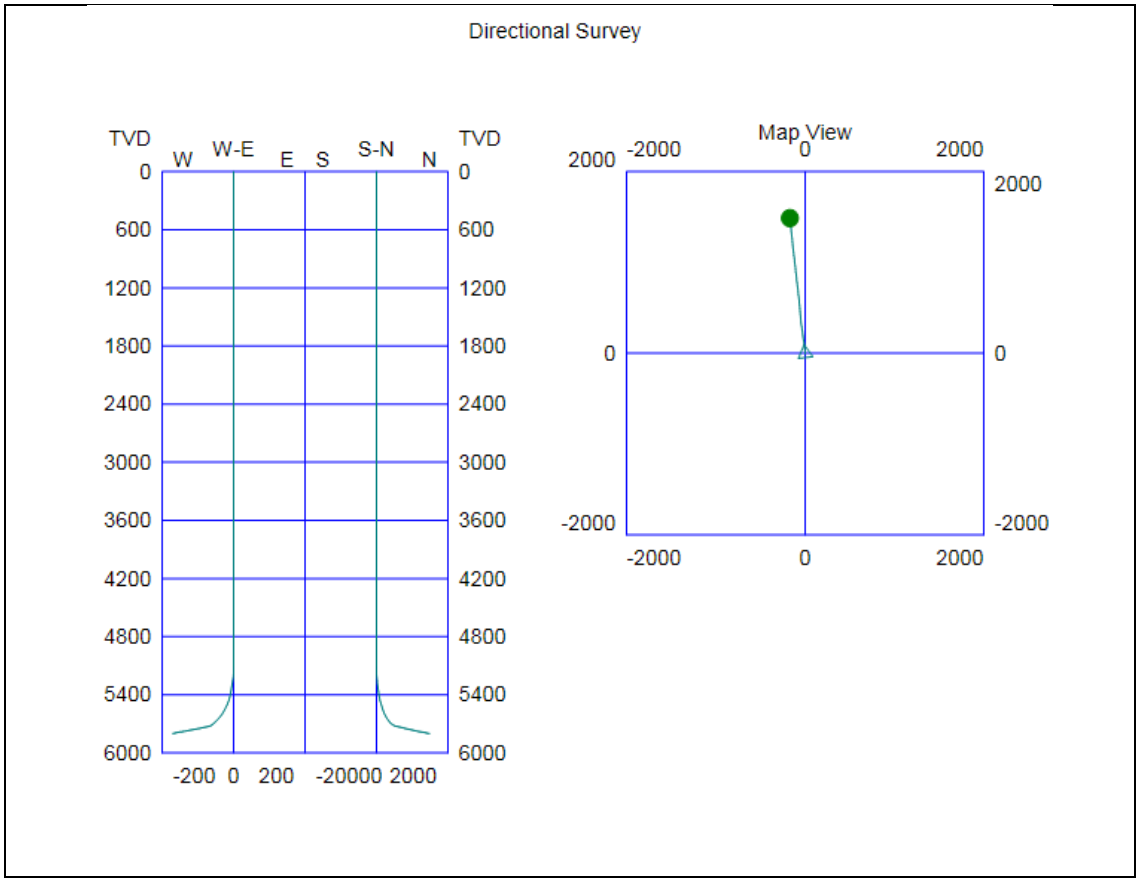
Isochron of the Brown Niagaran from the 3D seismic survey defining the boundaries of the Chester 2 reef. 980 Isochron line defines approximate boundary.

Figure 1-4. Chester 2 Reef West-To-East Cross Section.

1.2 Horizontal Drilling Details

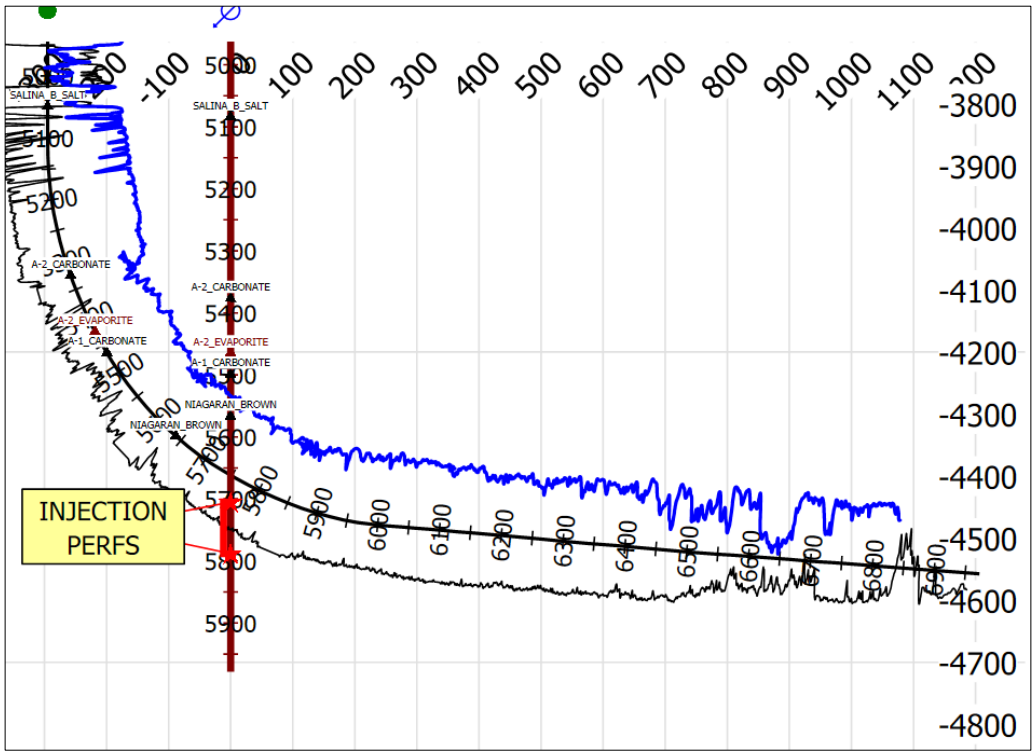
The Cargas 3-2 HD1 semi-horizontal well was spudded on September 17, 2012. Drilling and pipe conveyed logging (PCL) work was completed on October 10, 2012. The horizontal drilling took seven days to complete, and the wireline and PCL took two days. No major drilling issues were encountered beyond monitoring and adjusting mud fluid properties to limit fluid loss into the formation during drilling.

The well was drilled approximately vertical to a kick-off point of 5165 feet MD before turning north at an azimuth of 355 degrees (Figure 1-5). The inclination was gradually built to 85 degrees at 6123 feet MD. The azimuth was then maintained at 355±1 degrees and the inclination angle at 85±1 degrees until total depth (TD) was reached at 6970 feet MD. The total lateral distance from the kick-off point was 1498 feet. The perforated interval in the injection well was the target depth of the semi-horizontal portion of the wellbore (Figure 1-6).



Notes: TVD = Total Vertical Depth.
All units in feet.

Figure 1-5. Cargas 3-2 HD1 Directional Well Diagram.



South **North**

Notes: Figure is parallel to the azimuth of the Cargas 3-2 HD1 with the 29430 injection well projected onto the plane.
Gamma ray curve in black; neutron porosity in blue.
Units along wellbore paths in MD feet; depth units along section in subsea feet.

Figure 1-6. Deviated Wellbore Cross Section of the Cargas 3-2 HD1.

1.3 Cargas 3-2 HD1 Petrophysical Logging

1.3.1 Wireline Logging and PCL

During and after drilling, four main methods are used to convey petrophysical logging tools down the borehole:

1. Conventional wireline: used in vertical or near-vertical wellbores
2. PCL while drilling: limited suite of logs used during drilling to provide information to steer the well, also referred to as Logging While Drilling (LWD)
3. PCL: used in open wellbore after TD is reached to run multiple suite of logs
4. Pump-down logging: small-diameter wireline tools pumped down through tubing

Some logging tools (for example, gamma ray tools) are routinely run during the drilling of a horizontal well in the Michigan Basin. However, for economic efficiency, a full suite of logs to characterize the reservoir is generally run after the wellbore has been drilled. The vertical and lateral heterogeneity observed within Niagaran reef reservoirs makes the full suite of logs critical to understanding the reservoir and seal formation properties. The complete suite of log data in a horizontal well provides several critical insights into the lateral distribution of reservoir changes in the reefs that vertical well cannot provide. The major goals of logging the horizontal sections of the well are to identify vertically oriented, high-permeability zones; detect changes in reservoir properties as the flank of a reef is approached; and determine lateral fluid and gas distribution.

1.3.2 Detailed Description of PCL

The properties of the lateral interval preclude the use of conventional wireline run logging (Figure 1-7A) because the tools are conveyed using gravity. At angles greater than 45 degrees, wireline tools cannot effectively travel within the wellbore. However, for schedule efficiency, conventional wireline logs can be run in the vertical section of the well prior to PCL runs. The PCL and vertical logs should be run for an overlapping interval in order to splice the data from the two logs together after the logging jobs are complete.

PCL is a process where the petrophysical logging tools are attached to the end of drill pipe and moved down (tripped in) the wellbore to the lateral interval (Figure 1-7B). The tools are attached to the end of the drill pipe with a wet connect junction. The drill pipe is then tripped into the hole until the tools are in the lower portion of the vertical section of the wellbore. At this point, a side-entry sub is placed on the drill string at the surface, and the wireline with a sting-in tool are conveyed inside the drill string down to the wet connect. The wireline is “stung-in” into the tools, and the assembly is tested for functionality of the tools and connection. As the drill string continues to be tripped in, the wireline above the side-entry sub is run on the outside of the drill pipe. The drill pipe is tripped in until the tools are positioned just below the lowest depth to be logged. The tools are then activated, and logging occurs as drill pipe is tripped out of the hole.

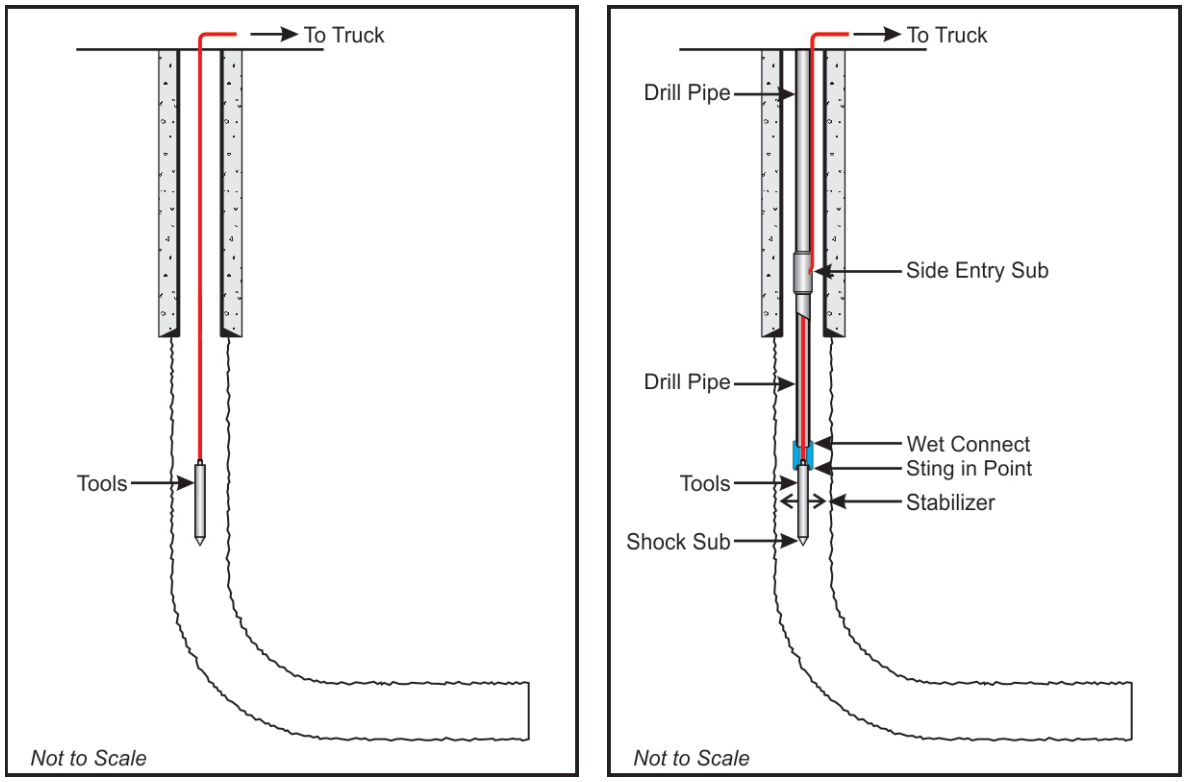
Challenges of PCL include maintaining stable wellbore conditions and logging tool functionality during logging. The main risks include damage or loss of the tools while tripping drill pipe and incomplete data collection, which can be caused by tool connection failures or poor performance of the logging tools due to downhole conditions.

1.3.3 Cargas 3-2 HD1 PCL and Wireline Logging

The Cargas 3-2 HD1 well PCL and wireline logging job was performed by Baker Hughes (BHI) over a 45-hour period after the well reached TD at 6970 feet MD. The wireline logging run in the vertical portion of the well was completed in the first seven hours of the job; the PCL was run in the remaining 38 hours (Appendix A1-A). The logging suites on the wireline and PCL runs (Table 1-2 and Table 1-3) were spliced at a depth of 5632 feet MD. The XMAC dipole sonic logs, RT laterologs, and micro laterologs were only run from TD to 4750 feet (Figure 1-7). The main issues that caused delays during this PCL run were electrical connection issues encountered during the coupling of the wireline to the tools at the wet connect sting-in point and troubleshooting the density tool during logging (Appendix 1-A).

The dipole acoustic logs were processed by Baker Hughes to provide a suite of coherence images for compressional, shear, and Stonely waves along with variable density image logs (Figure 1-8). Stoneley, compressional, and shear measurements allow full reservoir interpretation. This includes cross-dipole azimuthal anisotropy analysis, rock mechanical properties, Stoneley wave permeability analysis, and seismic and log time-depth correlation. Other capabilities include porosity and lithology determination and hydrocarbon detection.

The combination of logs in parallel view provides a visual analysis of reservoir properties based on multiple log characteristics which are then used to segment reservoir for quantitative analysis (Figure 1-9). Going from left to right, the first two panels represent data collected during the drilling of the well, rate of penetration (ROP) while drilling, CO_2 concentrations (in yellow shading), and hydrocarbon shows in red. The other panels include logs collected from the wireline and PCL runs. The logs are visually inspected to correlate zones with hydrocarbon shows and changes in fluid losses during drilling, changes in log properties, and changes in lithology from the drill cuttings descriptions to build the base level interpretation of the full log suite.



A. Wireline Configuration **B. PCL Configuration**

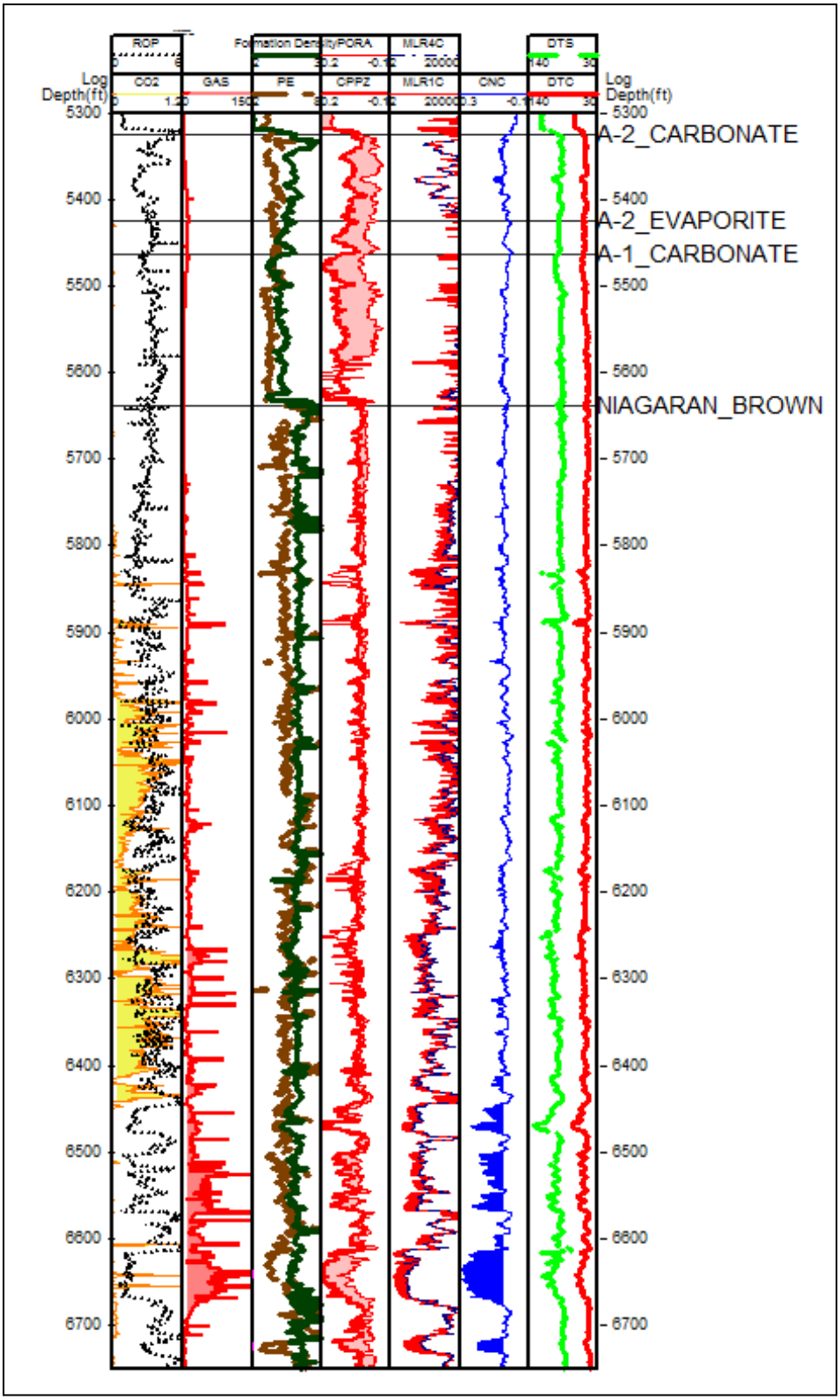
Figure 1-7. Wireline and PCL Schematic.

Table 1-2. Cargas 3-2 HD1 Log Suite Intervals.

BHI Tool Name	Common Tool Name	Logged Interval (feet)	
		Conventional	PCL
X-Multipole Array – XMAC	Dipole and Monopole Sonic	4750-5740	≈ 5200-6954
Compensated X-Densilog	Density	4750-5740	≈ 5200-6954
Compensated Neutron Log	Neutron	4750-5740	≈ 5200-6954
Gamma Ray Log	Gamma	Surface – 5740	≈ 5200-6954
Rt Explorer	Resistivity	4750-5740	≈ 5200-6954
Micro Laterolog	Resistivity	4750-5740	≈ 5200-6954

Table 1-3. BHI and Mudloggers Log Curve Mnemonics, Common Names, and Uses.

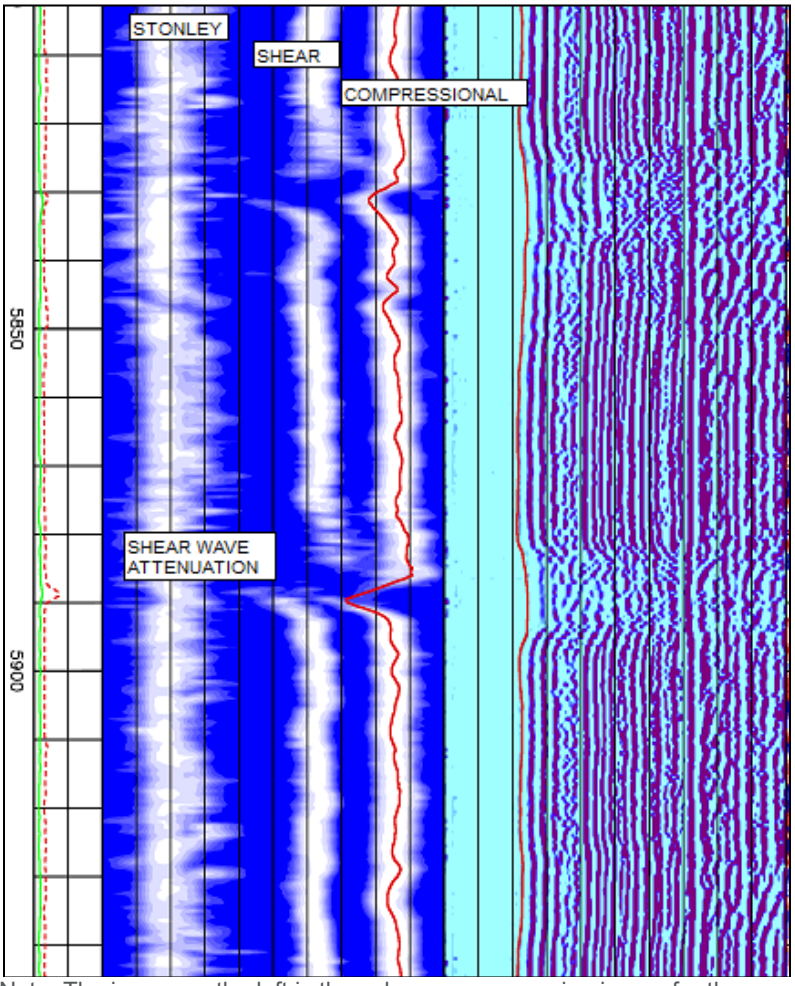
Log Curve Mnemonic	Common Name	Units	Common Analysis
Open Hole Logs			
CAL	CALIPER	INCHES	BOREHOLE DIMENSIONS
CNC	COMPENSATED NEUTRON POROSITY	PU	POROSITY, HYDROCARBON DETECTION
CPPZ	CROSSPLOT POROSITY FROM BULK DENSITY AND NEUTRON	PU	POROSITY
CVOL	CEMENT VOLUME	CUBIC FEET	COMPLETION DESIGN
DT24	ACOUSTIC SLOWNESS OVER 24-INCH INTERVAL	uS/FT	FORMATION MATRIX POROSITY
GR	GAMMA RAY	GAPI	FORMATION CORRELATION
LXOM	MULTILATEROLOG INVERSION LENGTH OF INVASION	INCHES	LATEROLOG INVASION CORRELATION
MLR1C	SHALLOW RESISTIVITY	OHMM	WATER SATURATION, PERMEABILITY
MLR2C	SHALLOW RESISTIVITY	OHMM	WATER SATURATION, PERMEABILITY
MLR3C	MEDIUM RESISTIVITY	OHMM	WATER SATURATION, PERMEABILITY
MLR4C	DEEP RESISTIVITY	OHMM	FORMATION WATER SATURATION, PERMEABILITY
PE	PHOTO ELECTRIC CROSS-SECTION	B/E	FORMATION MINEROLOGY
PORA	ACOUSTIC POROSITY FROM DT24	PU	FORMATION MATRIX POROSITY
PORZ	POROSITY FROM BULK DENSITY	PU	FORMATION POROSITY
RMLL	MICRO LATEROLOG	OHMM	FLUID INVASION AND PERMEABILITY DETECTION
TT	INTEGRATED TRAVEL TIME FROM ACOUSTIC SLOWNESS	MS	SEISMIC MODELLING
ZCOR	DENSITY CORRECTION	G/CC	BULK DENSITY CORRECTION
ZDEN	FORMATION BULK DENSITY	G/CC	POROSITY
DTC	COMPRESSIONAL WAVE SLOWNESS (Vp)	uS/FT	FRACTURE, FLUIDS DETECTION AND MECHANICAL PROPERTIES
DTS	SHEAR WAVE SLOWNESS (Vs)	uS/FT	FRACTURE, FLUIDS DETECTION AND MECHANICAL PROPERTIES
SCRA	Vp/Vs RATIO TO Vp		GAS AND FLUIDS DETECTION, MECHANICAL PROPERTIES
Mud Logs			
ROP	RATE OF PENETRATION	MINUTES/FT	FORMATION EVALUATION WHILE DRILLING
CO_2	CO_2 PERCENT	PU	CO_2 PRESENCE COMING IN HOLE WHILE DRILLING
GAS	TOTAL GAS UNITS		HYDROCARBON SHOWS WHILE DRILLING



Note: See Table 1-3 for log curve mnemonics

Figure 1-8. Measured Depth Log Curves Plot for Cargas 3-2 HD1.

The acoustic logs provide the compressional wave slowness (Vp), shear wave slowness (Vs), the 24-inch depth of investigation formational slowness (DT24), and the correlation coherence and variable density image logs (VDL) (Figure 1-9). The correlation coherence images provide a confidence image of not only the changes in slowness of the reservoir, but also the presence of complete attenuation of the shear or compressional waves in the reservoir. The acoustic logs and images in combination with the other log suites can be used to interpret the orientation of high-permeability fractures or reef facies, discern matrix porosity from vuggy or fracture porosity, and discriminate between potential gas-charged and fluid-charged zones in the well. The acoustic logs can also be used to evaluate the mechanical integrity of seals by determining the homogeneity of the logs over the seal formations. For the purposes of this report, the BHI-derived cross plot neutron density porosity CPPZ will be used as the total formation porosity, and all the porosity curves represent those as calculated using a limestone matrix of 2.71 grams per cubic centimeter.



Note: The image on the left is the coherence processing image for the wave arrivals. The image on the right is the variable density log (VDL).

Figure 1-9. Acoustic Log Monopole Compressional Quality Control Correlation Image.

1.4 Cargas 3-2 HD1 Formation Log Evaluation

1.4.1 Salina B Salt

The Salina B salt is a massive salt section that forms a regional seal at the base of the Salina section above the lower primary seals. The formation is described on the mud log as a clear, frosted salt, with trace interbeds of shale and anhydrite. The total vertical thickness (TVT) encountered in the Cargas well is 272 feet. The bottom of the B salt is shale-free where the top portion (5050 to 5170 feet) has shale stringers identified with gamma and neutron porosity deflections (Figure 1-10). The neutron density crossplot (Figure 1-11) shows a tight cluster around salt point, with some trailing data points toward the limestone and dolomite lines. The trailing data points are also an indication of the previously mentioned shale stringers. The acoustic response (compressional wave slowness [DTC] and shear wave slowness [DTS]) over the entire formation is homogeneous (Figure 1-10; Appendix B, B-1 and B-2). The lack of any changes in acoustic response over the B salt section indicates that it is a thick, homogeneous secondary seal.

1.4.2 Carbonate

The well intersected 99 feet of A-2 carbonate with a TVT of 91 feet. The formation is a relatively tight carbonate with sections of high bulk density toward the top of the formation (5320 to 5340 feet). The mud log description indicates that the top portion of the formation is a light-brown to tan dolomite with abundant anhydrite grading into a medium- to dark-brown limestone at the base. The neutron density crossplot (Figure 1-12) shows a sandy limestone with porosities ranging between 5 and 10 percent. A small amount of the datapoints cluster around the anhydrite indicator. The changes in lithology within the A-2 show very little acoustic changes except within the shale stringer in the middle of the formation (Figure 1-10; Appendix B, B-1 and B-3).

1.4.3 A-2 Evaporite

The well intersected 39 feet of A-2 evaporite with a TVT of 34 feet. The formation is described as a salt-plugged anhydrite in the mud log sample descriptions, and this can be observed by the relatively low bulk density response for an anhydrite (Figure 1-10). The neutron density crossplot (Figure 1-13) demonstrates a somewhat atypical presentation, but the data points plot in between a pure salt and a pure anhydrite, which is consistent with the mud log. The homogeneous acoustic response over the entire interval indicates that it is a good secondary seal (Appendix B, B-1 and B-4).

1.4.4 A-1 Carbonate

The well intersected 175 feet of A-1 carbonate with a TVT of 134 feet. The formation is generally described on the mud log as a light- to medium-brown limestone that grades into a cream color toward the base. The A-1 carbonate has very high resistivity, and relatively low bulk density, photo electric (PE), and neutron porosity, indicating it can probably be classified as a low-density, dolomitic mudstone (Figure 1-10). The neutron density crossplot (Figure 1-14) shows a roughly 5 percent limestone that is highly influenced by salt. The DTC/DTS ratio to DTC plot (Appendix B, B-1 and B-5) indicates that as the DTC decreases, the DTS does not decrease to the same degree. In general, the DTC decreases with depth, as the DTS remains constant (Figure 1-10). These changes parallel a small increase in bulk density toward the base of the formation. The small change in trend of the acoustic response and absence of porosity or

hydrocarbon show that this zone is tight and highly competent, making it the primary seal in the Chester 2 reef.

One zone of potential logging tool error is present in this formation. The zone from 5581 to 5635 has very high acoustic porosity (see Figure 1-10, acoustic porosity curve [PORA]). This zone is where wireline and PCL logs were spliced. None of the other logs appear to have any dramatic changes in this zone, so the acoustic porosity curve may have splicing correlation issues in this zone.

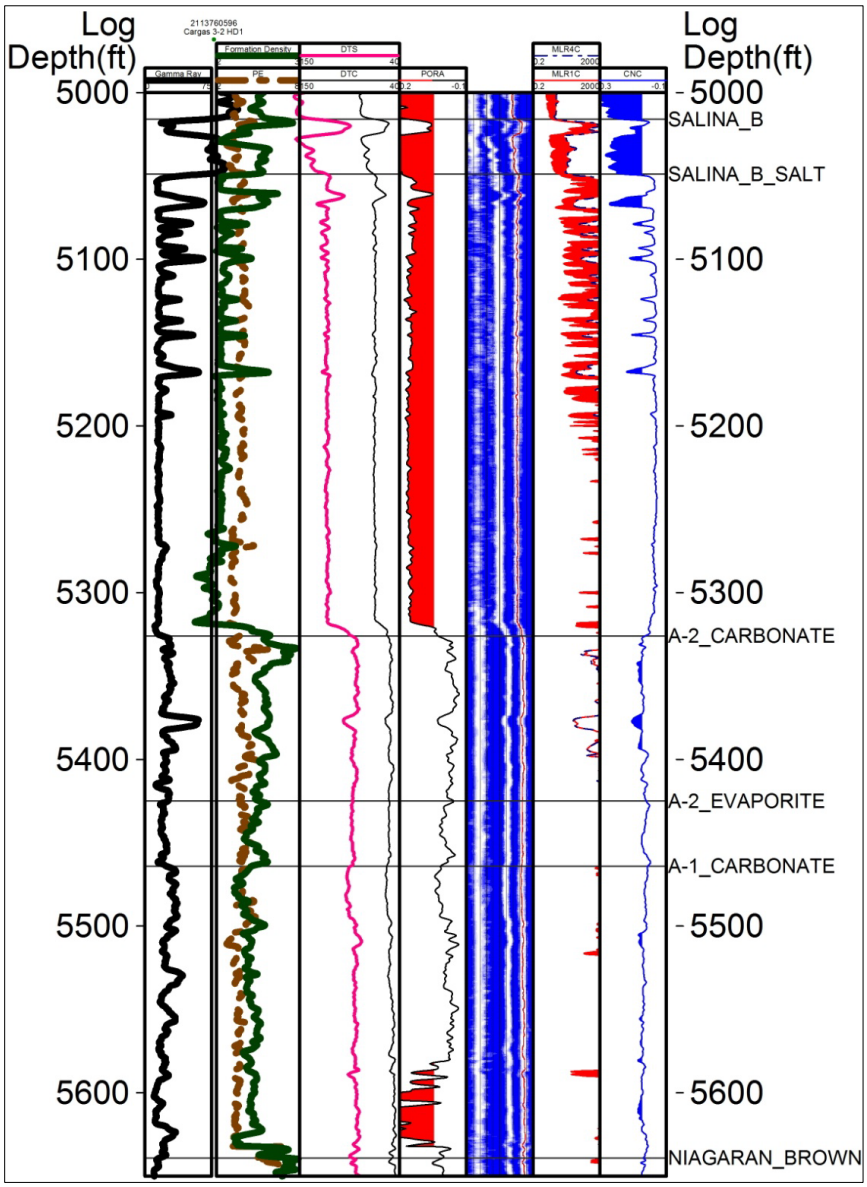


Figure 1-10. Salina B Salt to Top Brown Section.

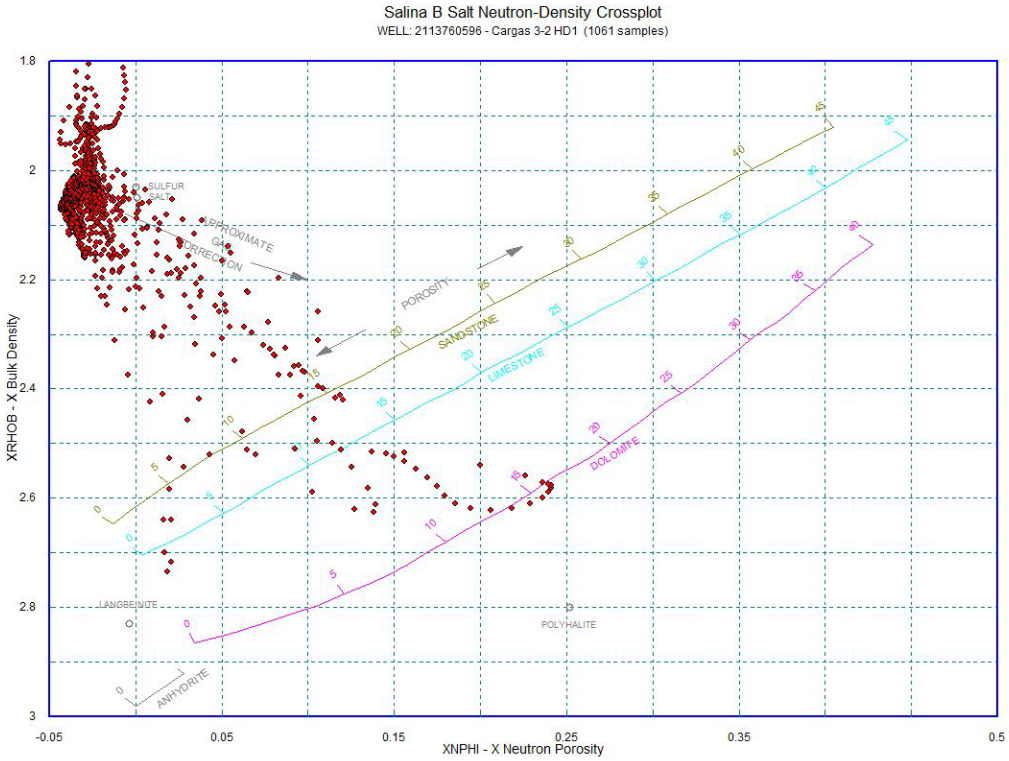


Figure 1-11. Neutron Density Cross Plot for the Salina B Salt.

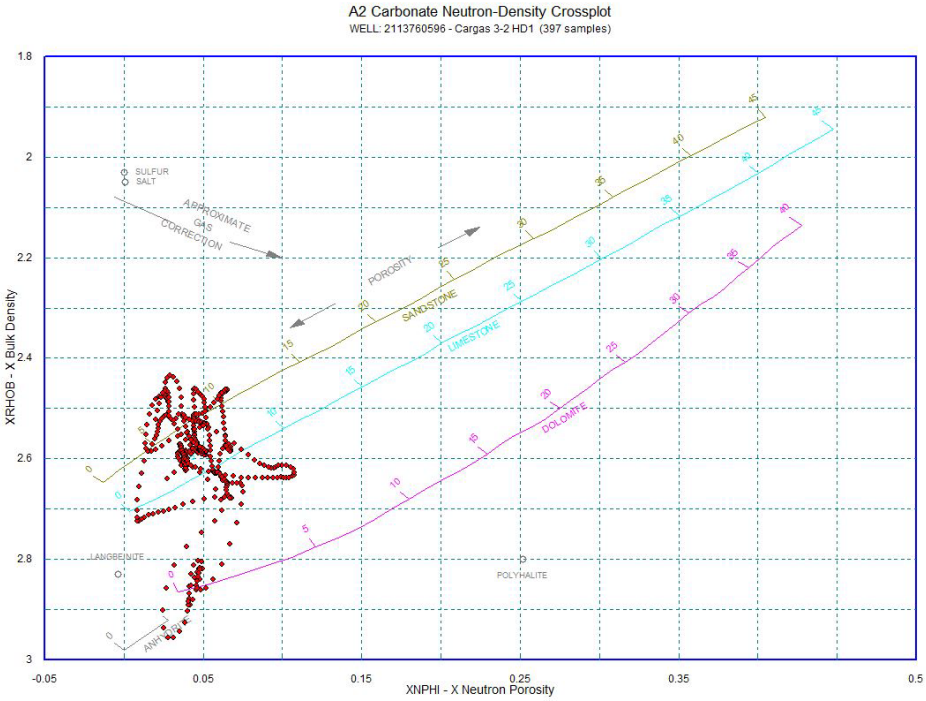


Figure 1-12. Neutron Density Cross Plot for the A-2 Carbonate.

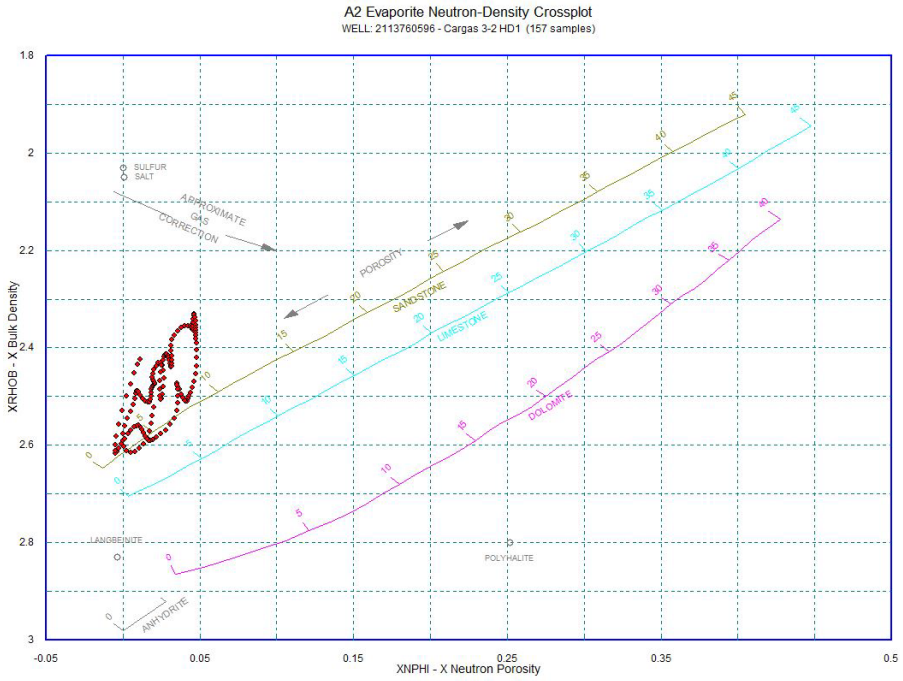


Figure 1-13. Neutron Density Cross Plot for the A-2 Evaporite.

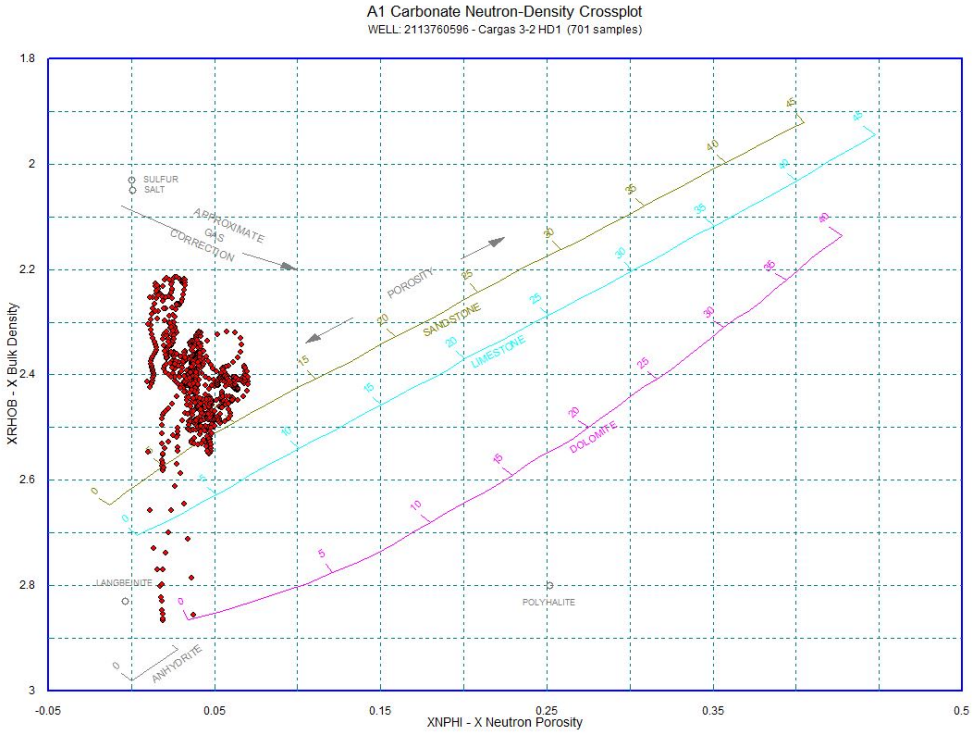


Figure 1-14. Neutron Density Cross Plot for the A-1 Carbonate.

1.4.5 Brown Niagaran

The well intersected 1331 feet of Brown Niagaran with a TVT of 222 feet. The upper portion of the unit is described as a tan to medium-brown limestone with zones of vuggy porosity. From 6510 to 6820 feet, the unit is described as a light- to medium-brown limey dolomite, with zones of sucrosic, vuggy porosity. The crossplot (Figure 1-15) shows mainly a limestone with porosities ranging from 0% to 10% with a few areas of higher porosity, trending up toward 15% to 20%.

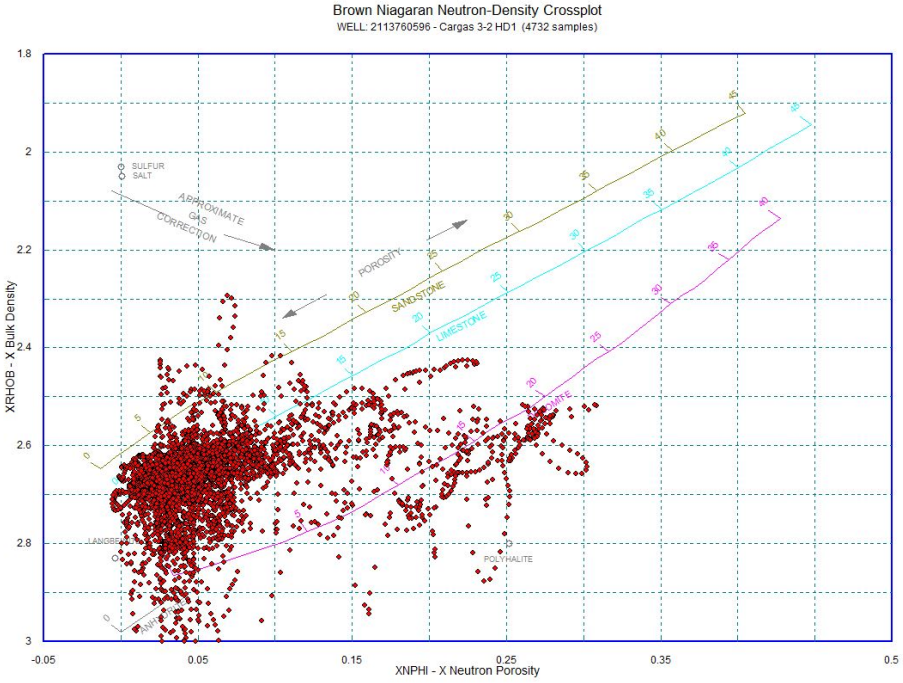


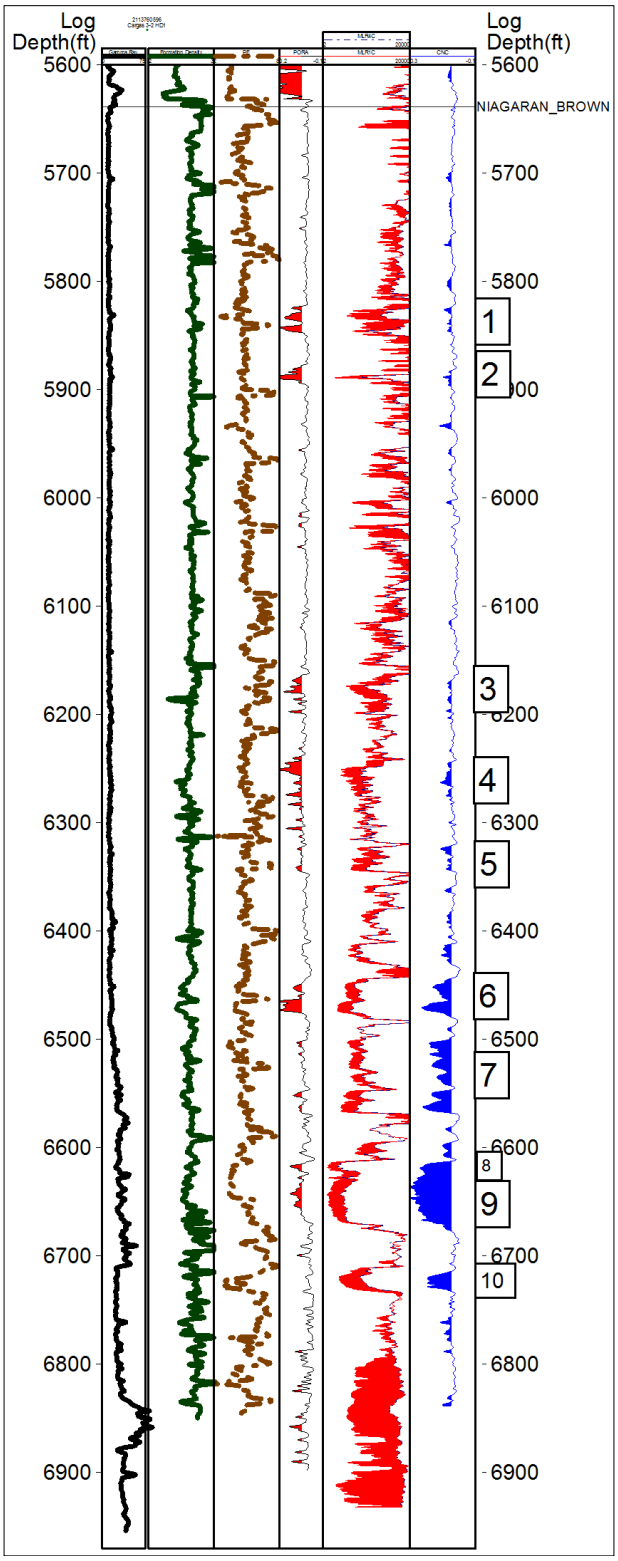
Figure 1-15. Brown Niagaran Neutron Density Cross Plot.

There are a series of high-porosity reservoir zones from 5820 to 6732 feet located in the lateral section of the well as identified on the cross plot porosity curve (CPPZ) and the acoustic porosity curve (PORA) (Figure 1-16; Table 1-4). The thin zones (1 and 2) from 5820 to 5900 feet, in the bottom of the curve portion of the wellbore, are characterized by high resistivity, low neutron porosity, and high shear wave slowness and attenuation (Figure 1-16. These zones had moderate fluid loss during drilling (5 to 10 Bbl/hour), and the mud log indicated spikes of 1 to 2 percent CO_2 and small hydrocarbon shows. The differences in acoustic responses along with the acoustic image logs can be used to interpret angles at which fractures and bedding parallel formational changes intersect the borehole. Fractures oriented perpendicular to the borehole will have little effect on the compressional slowness, but will attenuate the shear wave slowness but fractures oriented oblique to the borehole will attenuate the compressional waves (Morris et al. 1964). Zones 1 and 2 can be interpreted as semi-vertically oriented fractures or vugular zones extending into the CO_2 charged gas cap above the main oil saturated reservoir zones below.

The zones from 6162 to 6347 feet (3, 4, and 5) have lower resistivity with an invasion profile which shows separation between the deep and shallow laterologs (Figure 1-17). These zones also show moderate neutron porosity and high acoustic porosity. The acoustic logs show some changes in compressional and shear wave slowness, but no major attenuations in the shear wave (Figure 1-18). Fluid loss while drilling these zones increased to 60 to 80 Bbl/hour, and a steady show of 1% to 3% CO_2 with small hydrocarbon shows was recorded down to 6440 feet (see Figure 1-11), where it tapered off. These zones can be interpreted as horizontally oriented reef reservoir facies within the portion of the reservoir where CO_2 has been flooded from the injection well. This portion of the reservoir appears to be toward the edge of the CO_2 front.

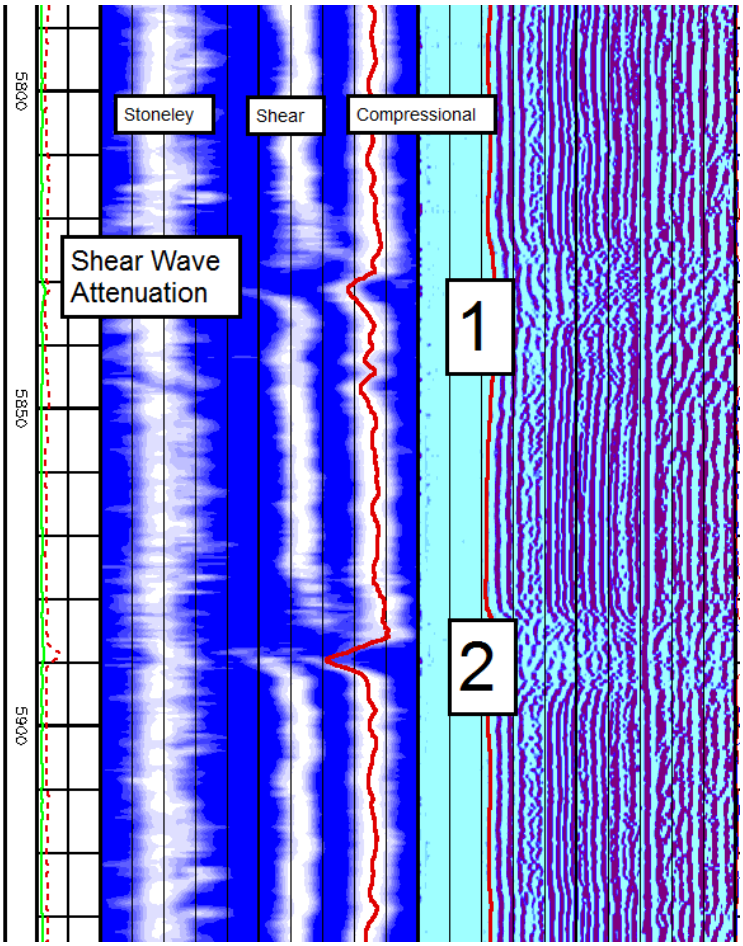
Table 1-4. Brown Niagaran Reservoir Zones General Thickness and Porosity.

Cargas Brown Niagaran Zones	Gross	Net	Porosity Feet	Porosity Average
1	22.5	22	0.823	3.70%
2	13	13	0.465	3.60%
3	33	31.25	1.49	4.80%
4	34	34	2.468	7.30%
5	17	17	0.961	5.70%
6	11	11	1.548	14.10%
7	64	64	6.26	9.80%
8	8	8	0.951	11.90%
9	41	41	6.473	15.80%
10	17	14.25	1.243	8.70%



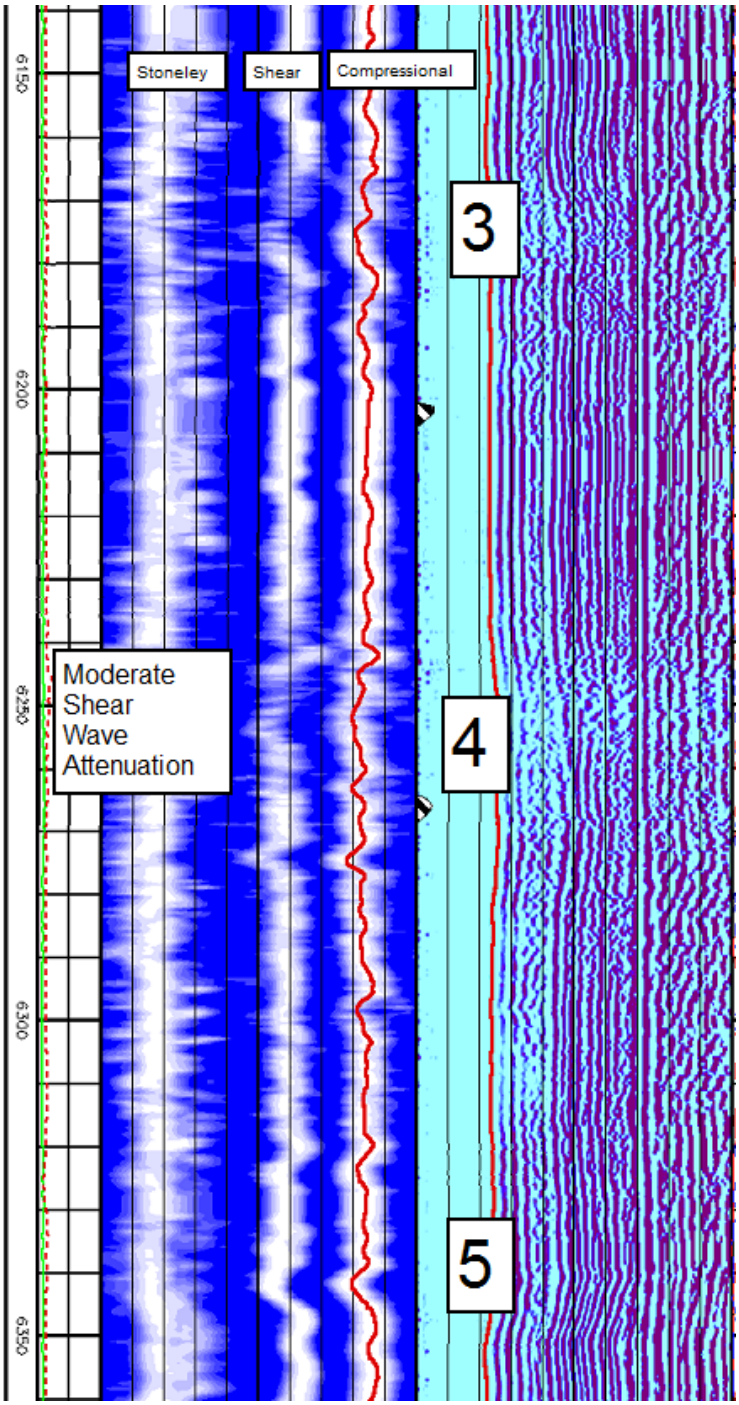
Note: See Table 1-2 for log curve mnemonics.

Figure 1-16. Brown Niagaran Reservoir Zones.



Note: Notice shear wave attenuation in thin zones.

Figure 1-17. Upper Niagaran Reservoir Zones Acoustic Logs.



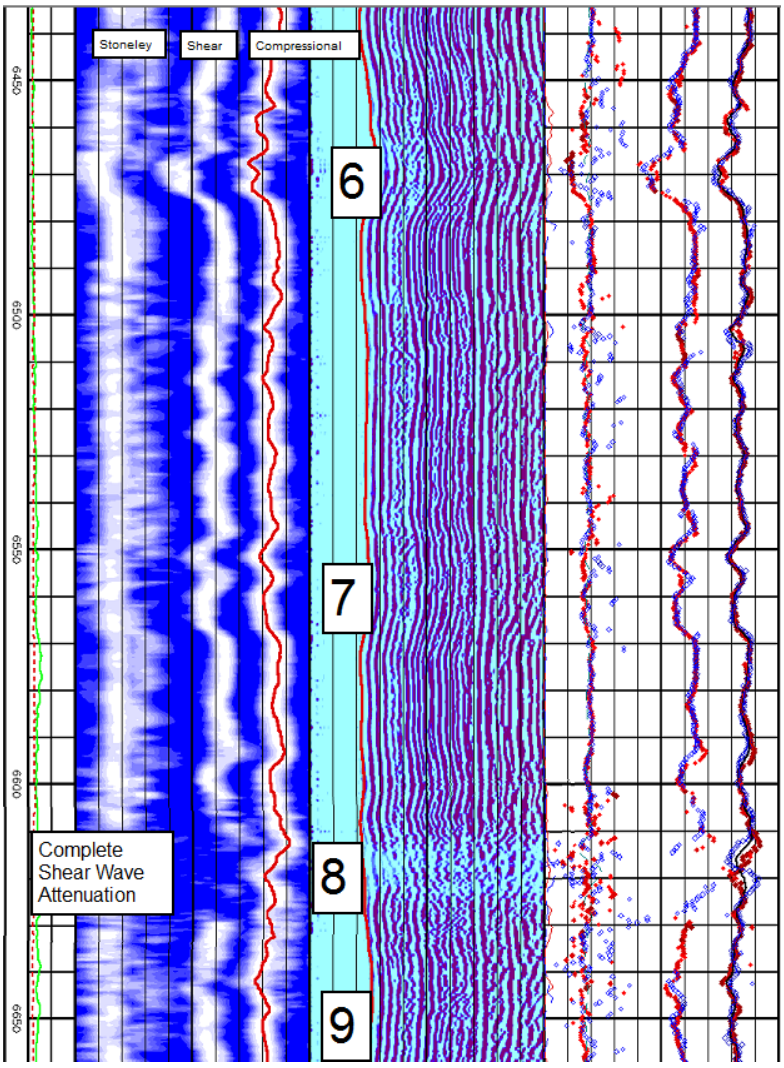
Note: Notice moderate shear wave attenuation.

Figure 1-18. Middle Niagaran Reservoir Zones Acoustic Logs.

The zones from 6448 to 6735 feet (6, 7, 8, 9,and 10) have the lowest resistivity in the Brown Niagaran reservoir zones and the deepest invasion profiles (see Figure 1-16). These zones are characterized by high neutron porosity, rapid changes in formation lithology based on PE and bulk density, and an increase in compressional and shear wave slowness. They also show several thin zones where the shear wave is completely attenuated (Figure 1-19). This portion of the well experienced the highest fluid losses during drilling (80 to 100 Bbl/hour), had the highest hydrocarbon shows, and showed very sharp spikes in the CO_2 percent over the high fluid loss zones. This portion of the reservoir can be characterized as a mixture of high-porosity, dolomitized horizontally oriented reef zones which are intersected by a series of vertically oriented, high-permeability dolomitic vugular zones, or a vertically oriented reef framework structures. The lack of CO_2 indicates that this portion of the reservoir has probably not been adequately swept with CO_2 and has opened new hydrocarbon-bearing zones. The vertically oriented porosity zones may have some connection with the upper gas cap since sharp spikes of CO_2 were detected.

1.4.6 Brown Niagaran Reservoir Zones Discussion

The lateral portion of the wellbore intersected a series of reservoir zones in the Brown Niagaran with varying log characteristics. Ten reservoir zones were identified based on laterolog invasion profiles and acoustic porosity (see Figure 1-16). The full suite of logs was statistically compared to evaluate the changes in reservoir properties in each zone (Appendix B, B-1 and B-6). The crossplot of mean values for the Vp/Vs ratio to Vp for the ten zones indicates that two of the zones (6 and 8) are acoustically different than the other zones (Figure 1-20). Zone 6 shows a distinct slowing of the shear and compressional waves, whereas zone 8 shows little change in the compressional wave, and a complete attenuation of the shear wave (Figure 1-19). Zone 6 also shows little difference between the cross plot porosity and the acoustic porosity. Generally, the acoustic porosity measures the porosity in the rock matrix, and the cross plot porosity derived from the bulk density and neutron curves measures overall porosity. The difference between the two types of porosity is the vuggy or fracture porosity in a carbonate (Asquith and Gibson 1982). Of interest is the lack of fluid loss during drilling in zone 6 and the loss of 80 to 100 Bbl/hour when zone 8 was drilled into. Zone 6 is also at a point in the well where CO_2 is no longer consistently detected on the mud log. Zone 6 can be interpreted as a semi-horizontal stratigraphic zone, with high matrix porosity and potentially low permeability, and zone 8 is a vertically oriented, high-permeability dolomitic vugular zone, or a vertically oriented reef framework structure. Zones 8, 9, and 10 are located along the northern flank of the reef, so these zones may also be a high angle dipping reef flank facies. Continued integration with the seismic and further evaluation are needed to further characterize and interpret the Brown Niagaran reservoir zones.



Note: Notice complete shear wave attenuation.

Figure 1-19. Lower Niagaran Reservoir Zones Acoustic Logs.

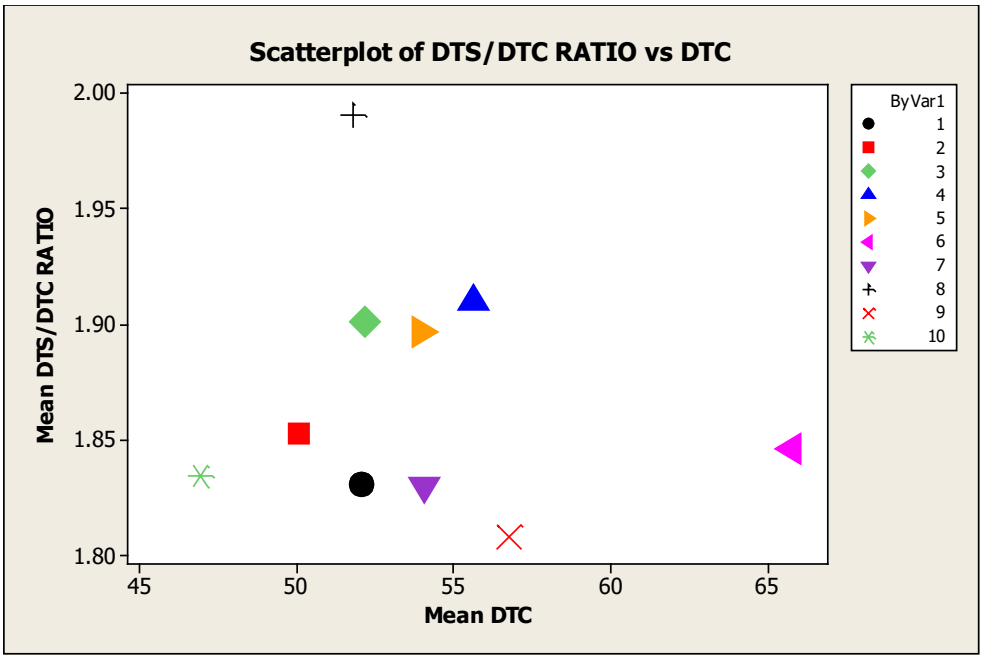


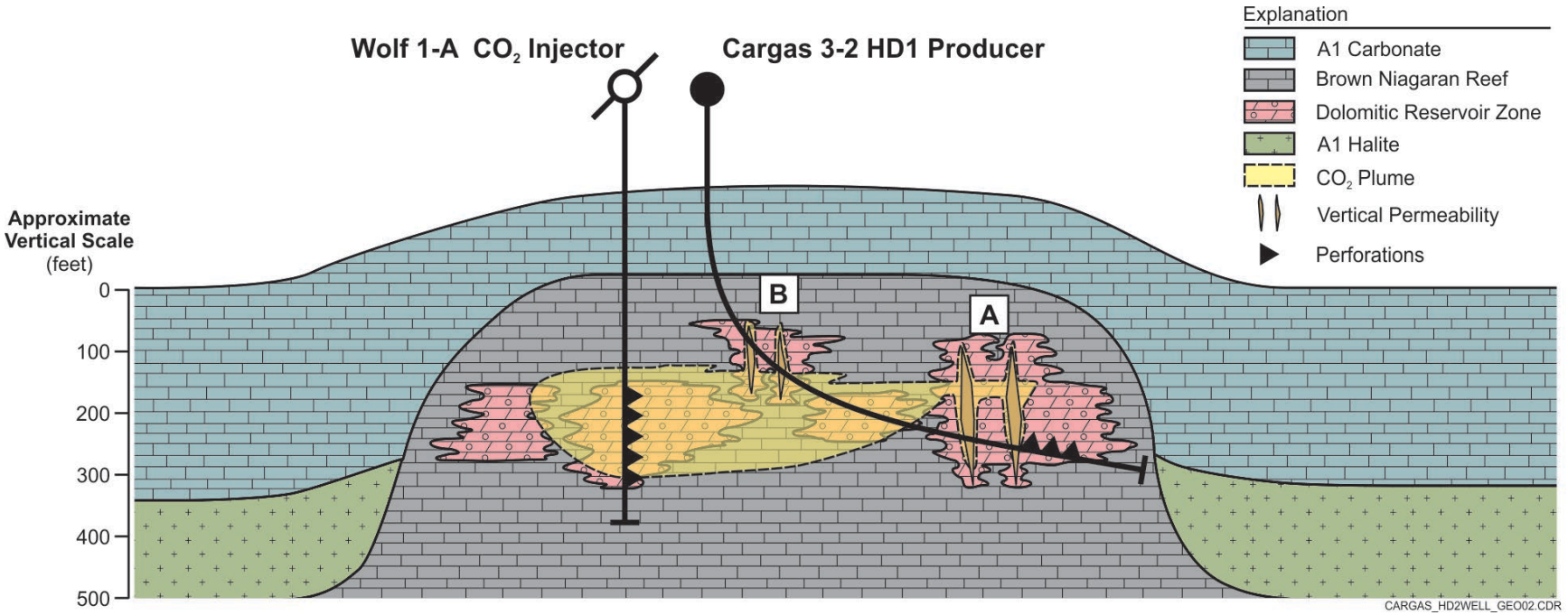
Figure 1-20. Scatter Plot of Brown Niagaran Reservoir Zones Mean DTS/DTC Ratio vs DTC

1.5 Summary and Conclusions

The Cargas 3-2 HD1 semi-horizontal well wireline and PCL suites provide a detailed lithologic interpretation of the lateral distribution of Chester 2 reef reservoir and seal properties. An interpretation of the log suite provides a more detailed picture of the reservoir than can be reconstructed from vertical well logs. The generalized interpretation of the Chester 2 reef (Figure 1-21) shows the vertically oriented, high permeability zones and the horizontally oriented, dolomitized sections of the reef along with the CO_2-charged portion of the reservoir. An individual zone evaluation of isolated reservoir pockets within the reefs has been performed, and the full suite of logs has been integrated with the mud log descriptions. The lateral distribution of reservoir properties will be incorporated into a more detailed static earth model.

The Salina B salt, A-2 carbonate, A-2 evaporite, and A-1 carbonate all have very consistent acoustic shear and compressional slowness, indicating seal integrity. In the Brown Niagaran, 1331 feet MD was intersected in the wellbore over 222 feet TVT, the majority of which was intersected at 85 degrees from vertical. A series of reservoir zones were intersected in the Brown Niagaran which have distinct changes in lithology, fluid invasion, acoustic properties, and porosity. Some of the zones may be interpreted as vertically oriented vugular zones, high-permeability reef framework structures, or steeply dipping reef flank facies. The outer reservoir zones intersected in the well were baffled zones not efficiently swept with the CO_2 injection from the original injector to producer.

The PCL run was performed over a 38-hour period with no major wellbore stability or downhole tool failures.



Note: A. Vertical permeability within reservoir.
B. Vertical permeability extending into upper portion of reef.

Figure 1-21. Chester 2 Reef General Interpretation.

1.6 References

Asquith G., and Gibson, C. (1982). Basic well logging analysis for geologists, American Association of Petroleum Geologists, Methods in Exploration Series, pp. 1-216.

Briggs, L.I., and Briggs, D. (1974). Niagara-Salina relationships in the Michigan Basin, *in* L.I. Briggs and D. Briggs, eds., Silurian Reef-Evaporite Relationships, Lansing, MI: Michigan Basin Geological Society, pp. 1-23.

Cercone, K.R. (1984). Diagenesis of Niagaran (Middle Silurian) pinnacle reefs, Northwest Michigan: Ann Arbor, MI, University of Michigan, 362 pp.

Charbonneau, S.L. (1990). Subaerial exposure and meteoric diagenesis in Middle Silurian Guelph Formation (Niagaran) pinnacle reef bioherms of the Michigan Basin: Southwest Ontario, Kingston, ONT: Queen's University, 208 pp.

Gill, D. (1973). Stratigraphy, facies, evolution and diagenesis of productive Niagaran Guelph reefs and Cayugan sabkha deposits, the Belle River Mills Gas Field, Michigan Basin, University of Michigan, Ann Arbor, MI, United States, Doctoral thesis.

Gill, D. 1977, The Belle River Mills Gas Field: Productive Niagaran Reefs Encased by Sabkha Deposits, Michigan Basin: Michigan Basin Geological Society Special Paper 2, 187 p.

Gill, D. (1979). Differential entrapment of oil and gas in Niagaran pinnacle-reef belt of Northern Michigan, American Association of Petroleum Geologists Bulletin, v. 63, pp. 608-620.

Huh, J.M. (1973). Geology and diagenesis of the Niagaran pinnacle reefs in the Northern Shelf of the Michigan Basin: Ann Arbor, MI, University of Michigan, 253 pp.

Huh, J.M., Briggs, L.I., and Gill, D. (1977). Depositional environments of pinnacle reefs, Niagara and Salina groups, Northern Shelf, Michigan Basin, *in* J.L. Fischer, Reefs and Evaporites - Concepts and Depositional Models. Tulsa. OK: American Association of Petroleum Geologists Studies in Geology, v. 5, pp. 1-21.

Morris, R.L., Grine, D.R., and Arkfeld, T.E. (1964). Using compressional and shear acoustic amplitudes for the location of fractures, Society of Petroleum Engineers, J. Petrol. Technol., 16(6): 623-632.

Ritter, Audrey L. (2008). Evaluating the controls on reservoir heterogeneity of Silurian pinnacle reefs, Michigan Basin. Western Michigan University Kalamazoo, Michigan, United States, Masters thesis, 247 pp.

Appendix A. Daily Report Details of PCL Run

Day 1

7:00 AM	Baker onsite, start rig up.
9:00 AM	Rig up complete, run in with traditional wireline deployed tools (Triple Combo, Resistivity – RTEX, Sonic/Acoustic – XMAC, Dipole Mode).
1:00 PM	Begin to assemble Pipe-Conveyed Logging (PCL) toolstring.
2:00 PM	Wireline deployed logging complete, Rig down wireline deployed tools, Rig up PCL tools.
3:00 PM	Safety meeting with evening rig crew, including Baker Hughes, Inc. (BHI) PCL instructional video.
3:30 PM	Test PCL tools at surface, test failed, troubleshooting revealed damage to part of the wet connect system.
6:30 PM	PCL wet connect system troubleshooting and repair complete, PCL tools tested at surface, successful test.
6:30 PM	4:30 AM (10/10/12) – Trip in hole with PCL tools on drillpipe at 30 ft/min

Day 2

4:30 AM	Wireline tools on bottom, adjust wireline placement with drillpipe to start logging up.
4:30 AM	Pause tripping in drillpipe to set up wireline side door setup, setup PCL wireline system.
6:30 AM	Run in wet connect to test tools at bottom of drillpipe.
7:00 AM	Several attempts made to sting into wet connect system, connection issues.
9:30 AM	Wet connect system functional, continue to trip in to 30' off TD to begin logging. Logging down with some tools for observation of tool functionality.
4:30 PM	Wireline tools on bottom, adjust wireline placement with drillpipe to start logging up.
5:30 PM	Start logging up.
8:00 PM	Pull wireline side entry sub, pull wireline subs and centralizer
10:00 PM	Begin rig down wireline, continue tripping out with drillpipe and wireline tools

Day 3

3:00 AM	PCL Wireline tools out of hole
4:00 AM	Wireline tools rigged down.

Appendix B. Statistics Plots

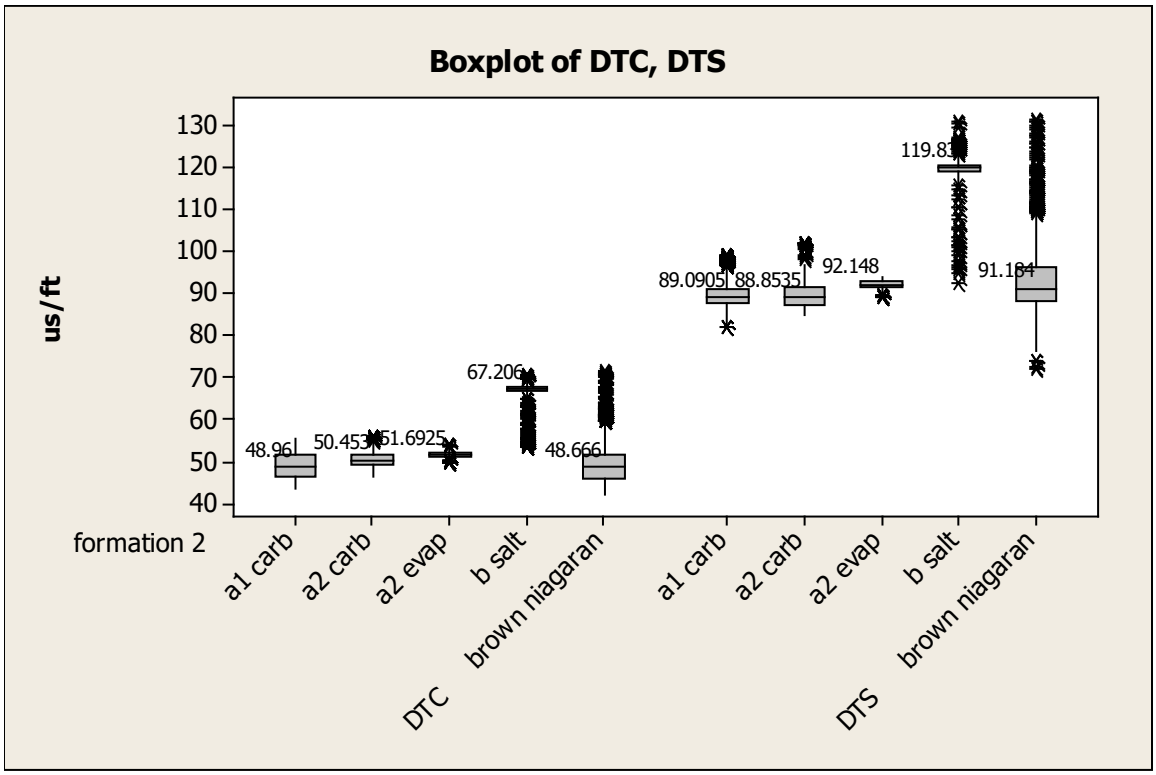


Figure B-1. DTC and DTS Boxplot for Cargas 3-2 HD1 Formations, Median Values Shown.

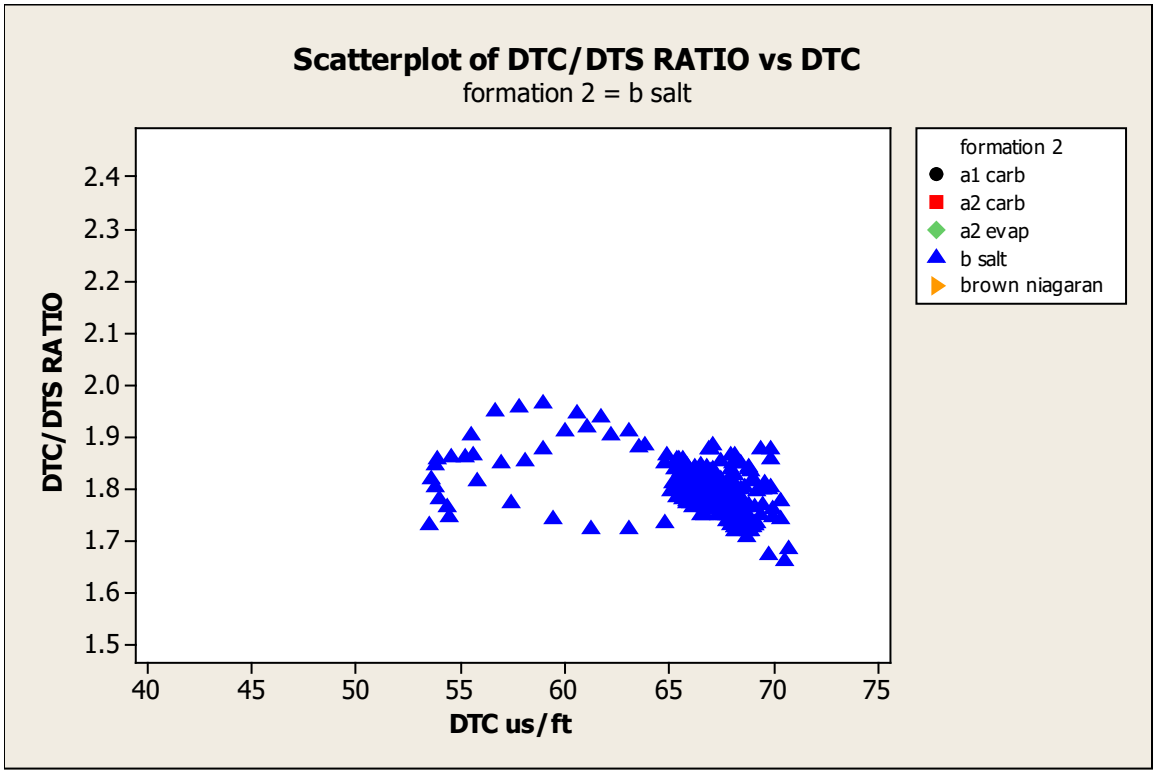


Figure B-2. DTC/DTS vs DTC for B Salt

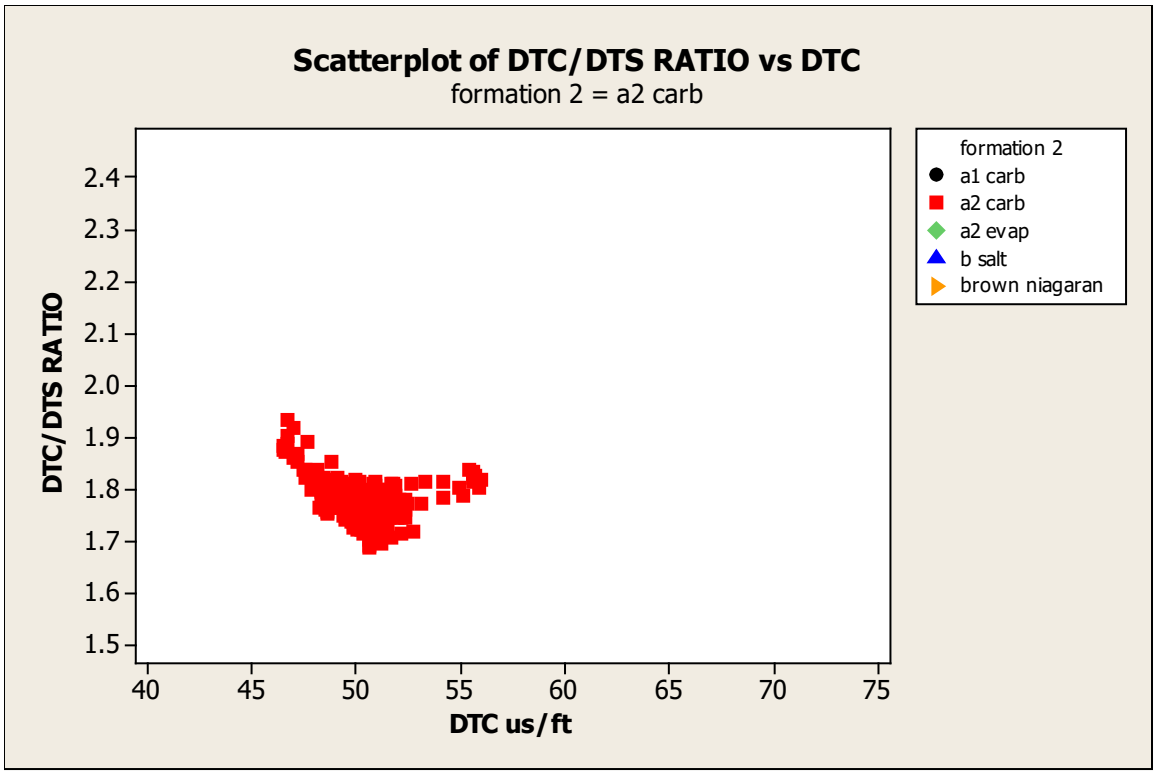


Figure B-3. DTC/DTS vs DTC for A-2 Carbonate

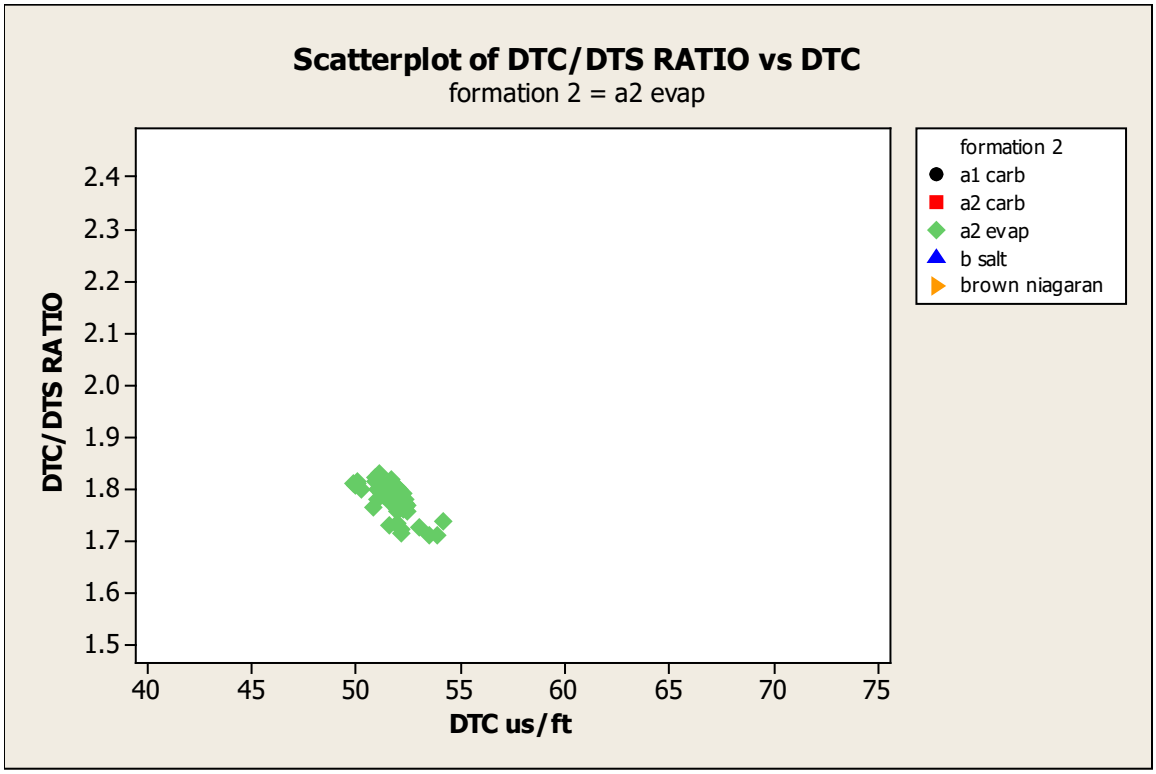


Figure B-4. DTC/DTS vs DTC for A-2 Evaporite

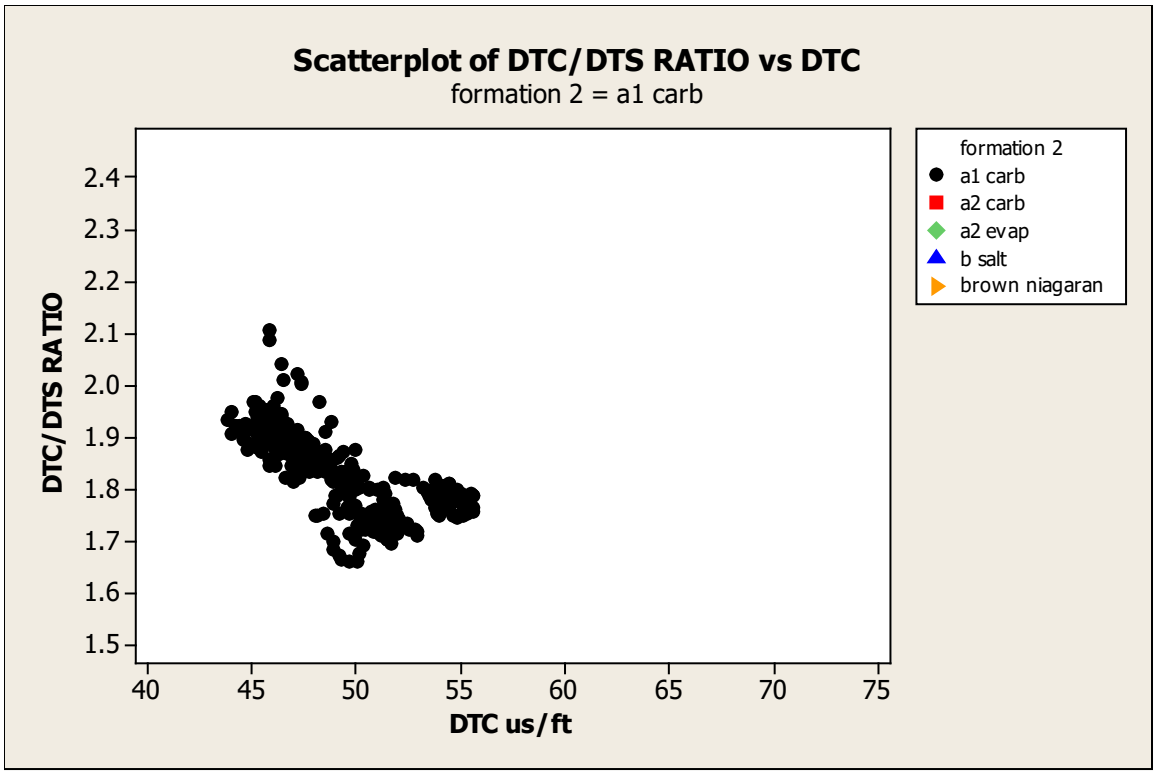


Figure B-5. DTC/DTS vs DTC for A-1 Carbonate

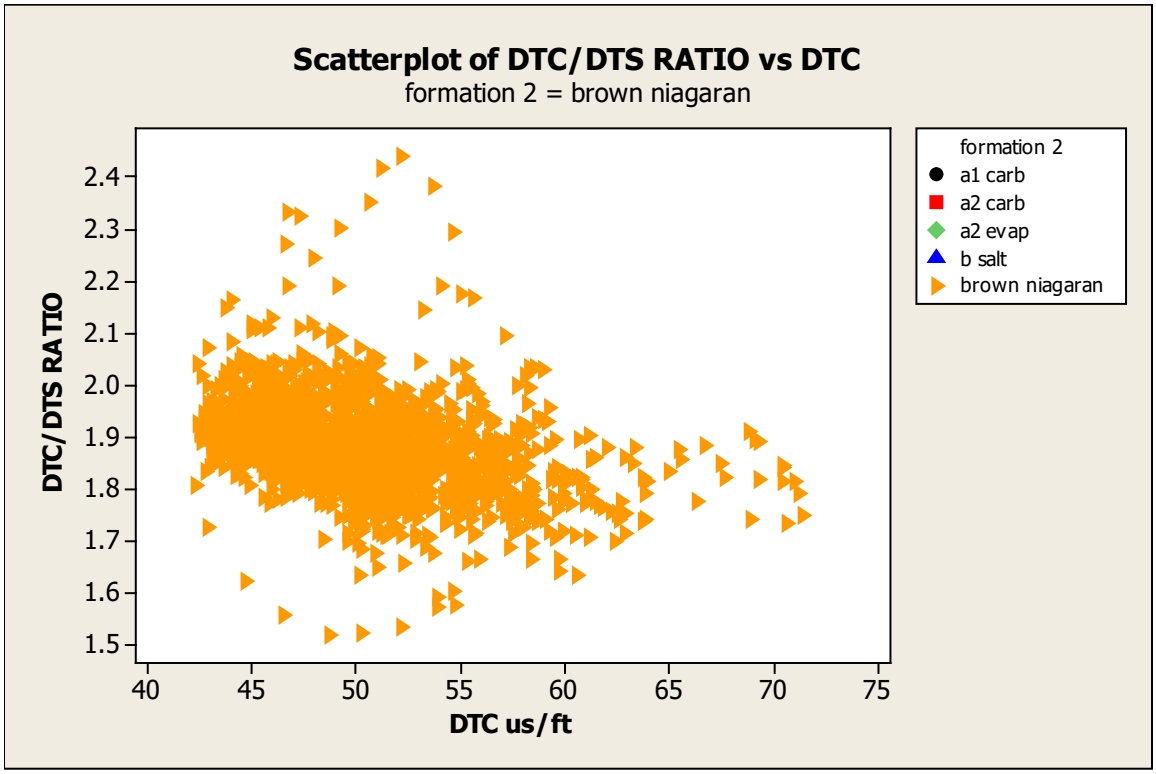


Figure B-6. DTC/DTS vs DTC for Brown Niagaran

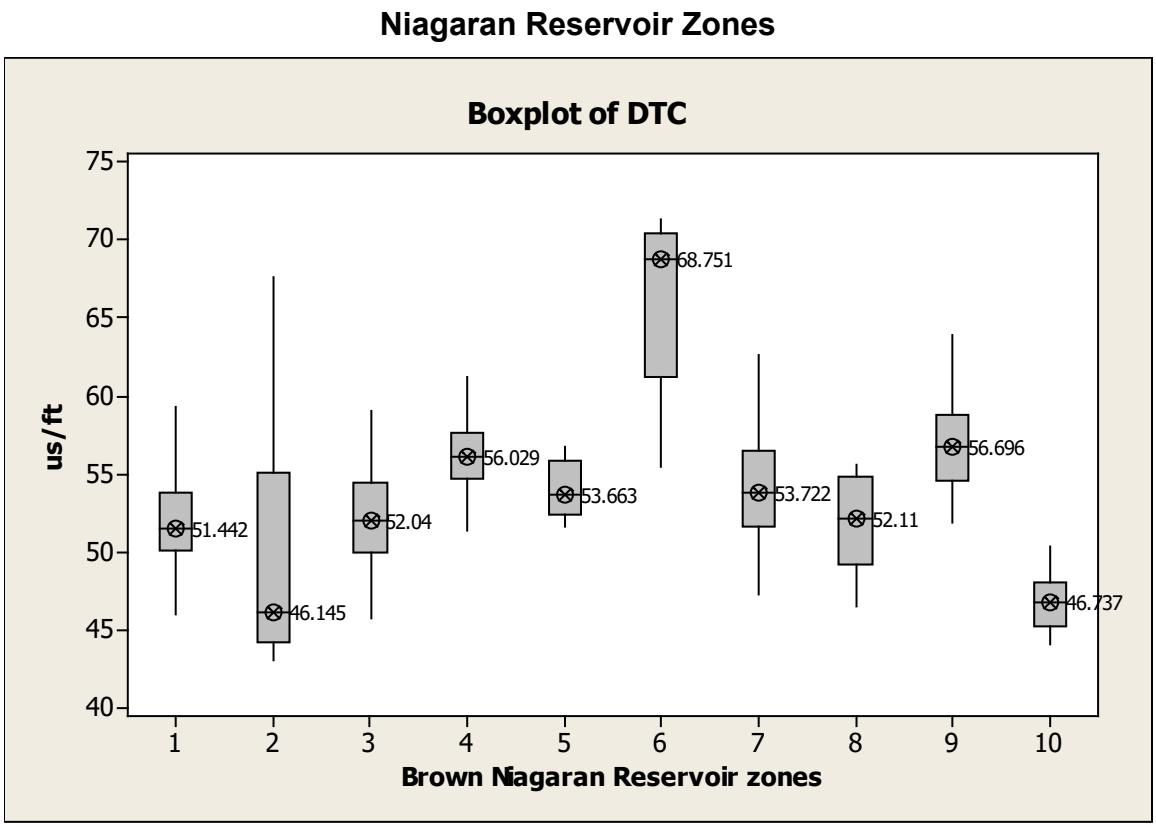


Figure B-7. Compressional Wave Slowness (DTC)

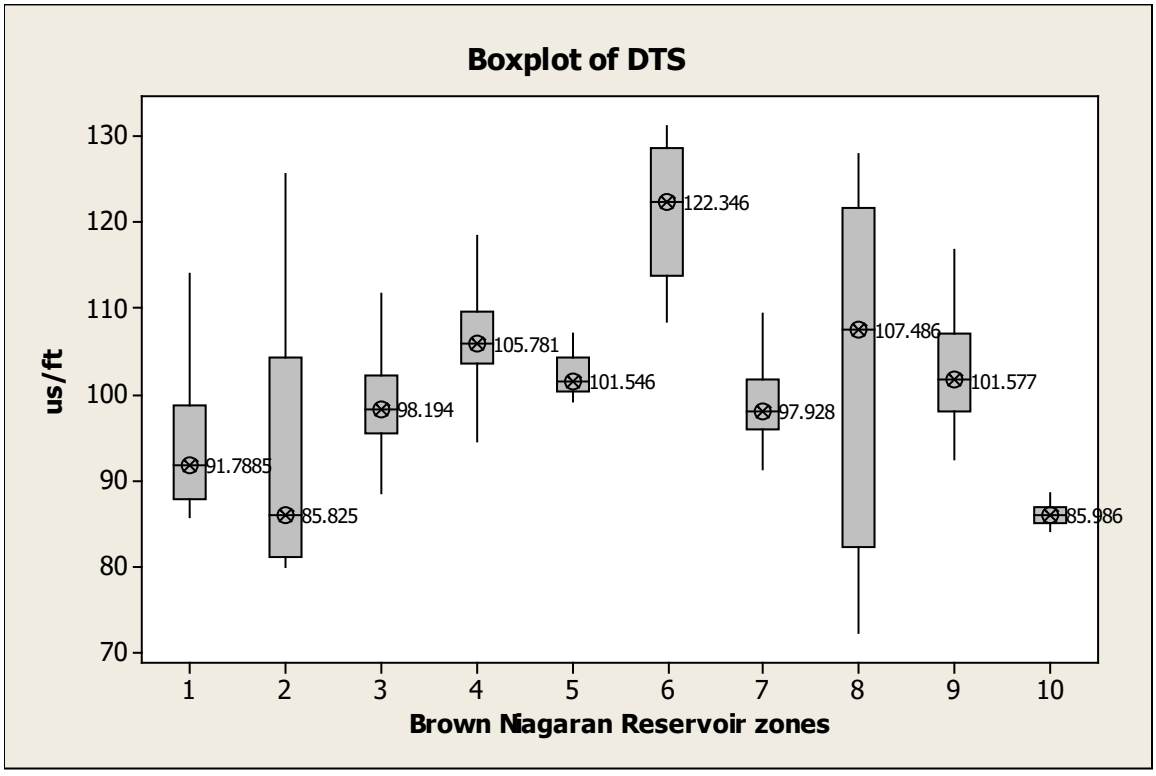


Figure B-8. Shear Wave Slowness (DTS)

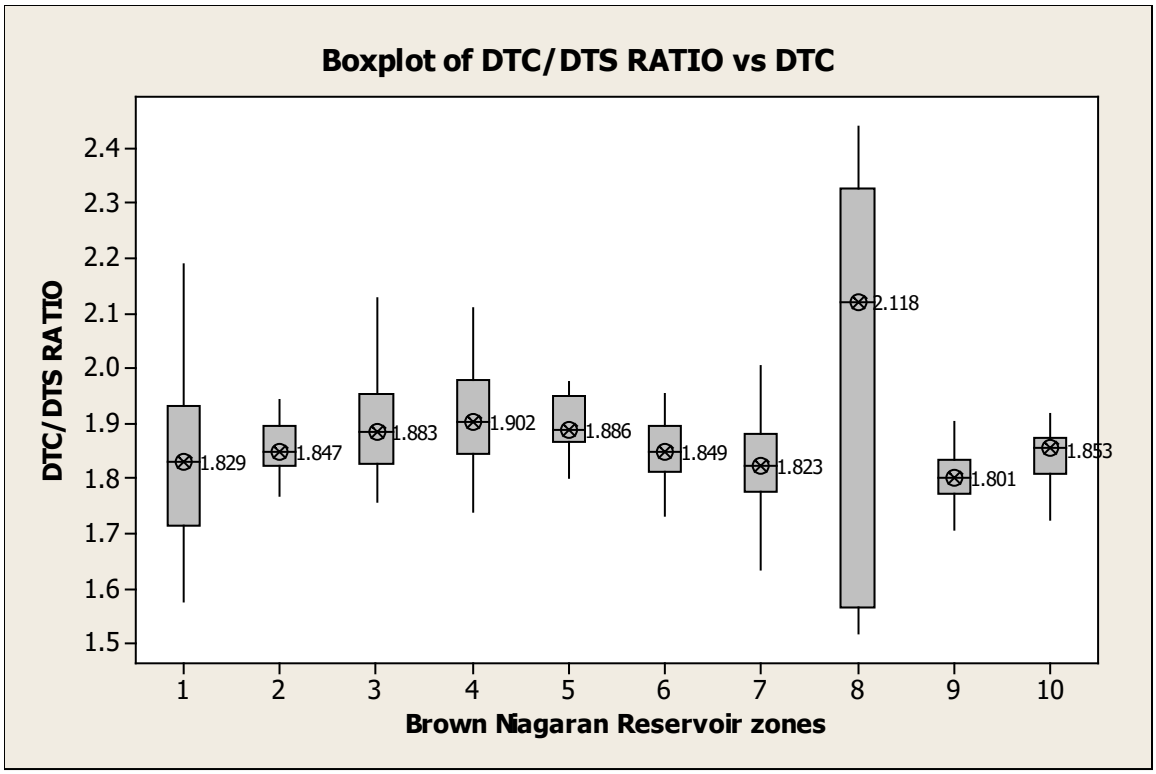


Figure B-9. Vp/Vs Ratio vs. Vp

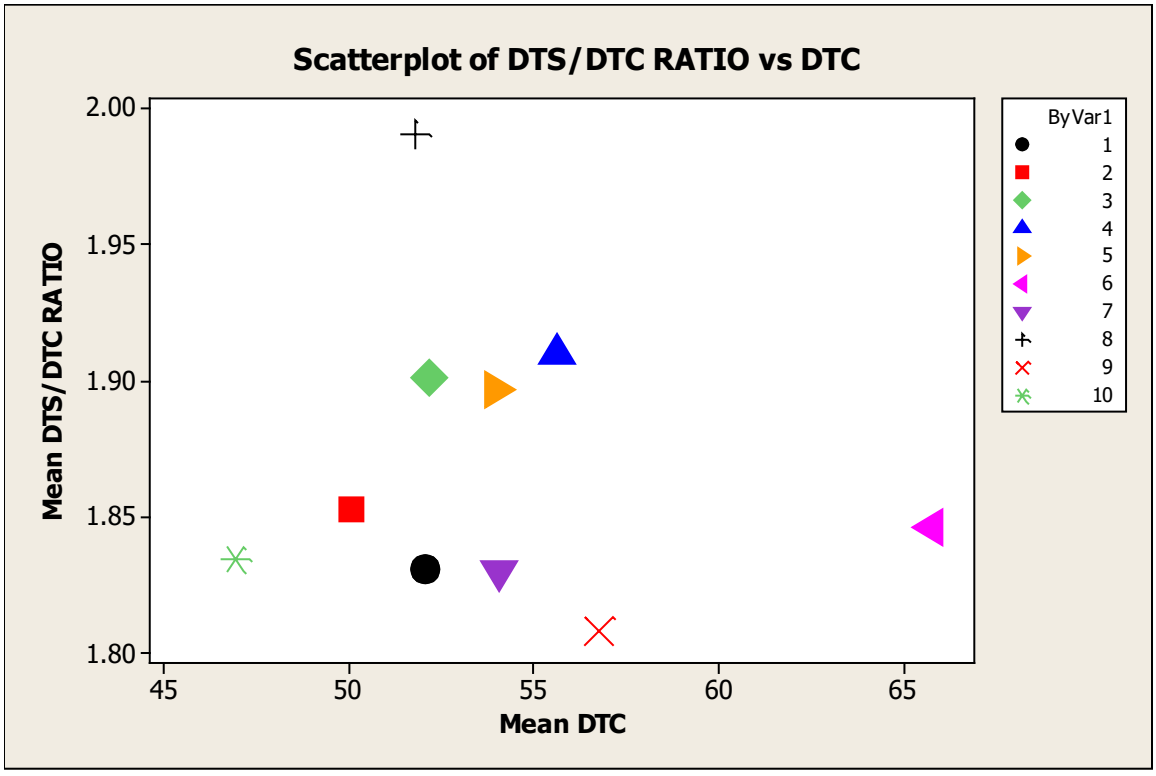


Figure B-10. Vp/Vs Ratio vs. Vp

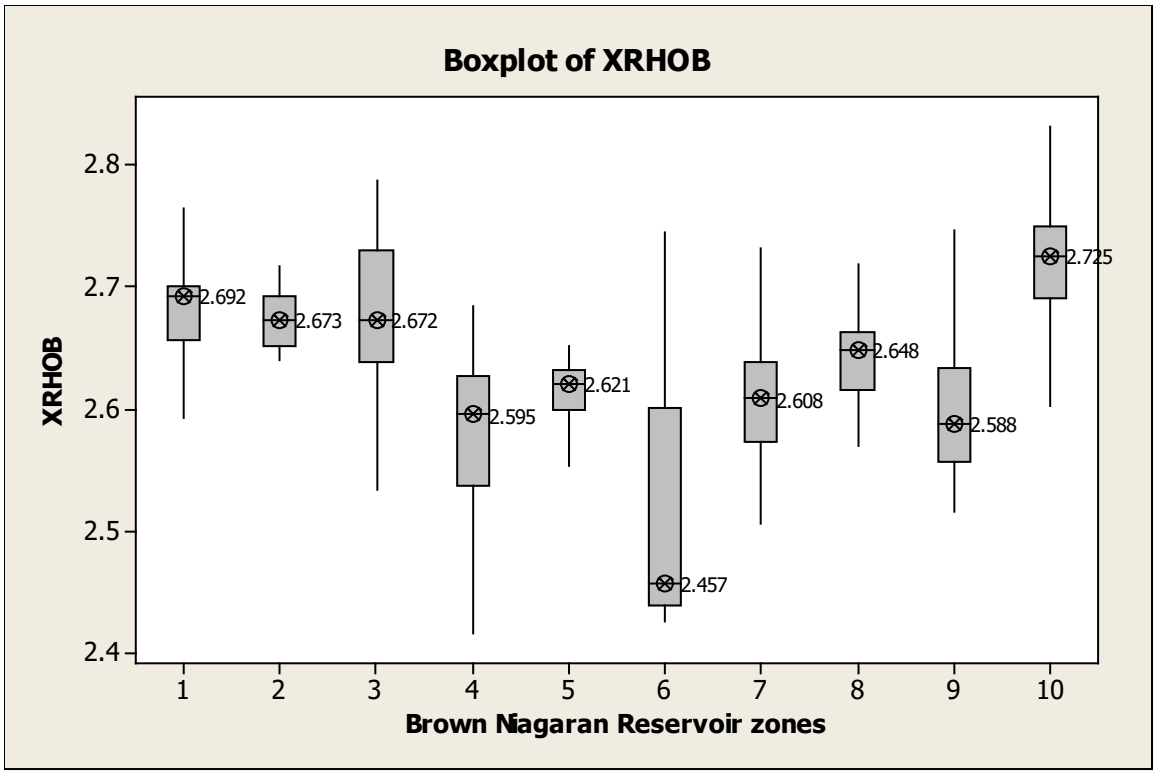


Figure B-11. XRHOB

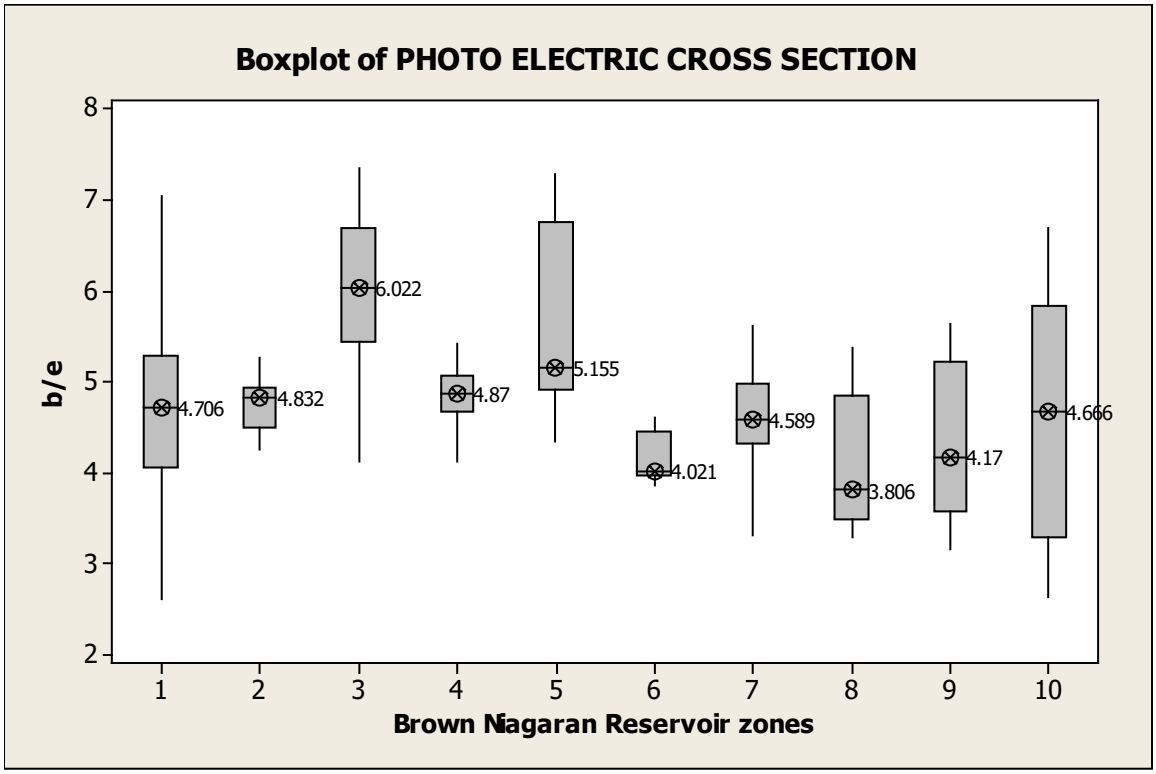


Figure B-12. PE Cross Section

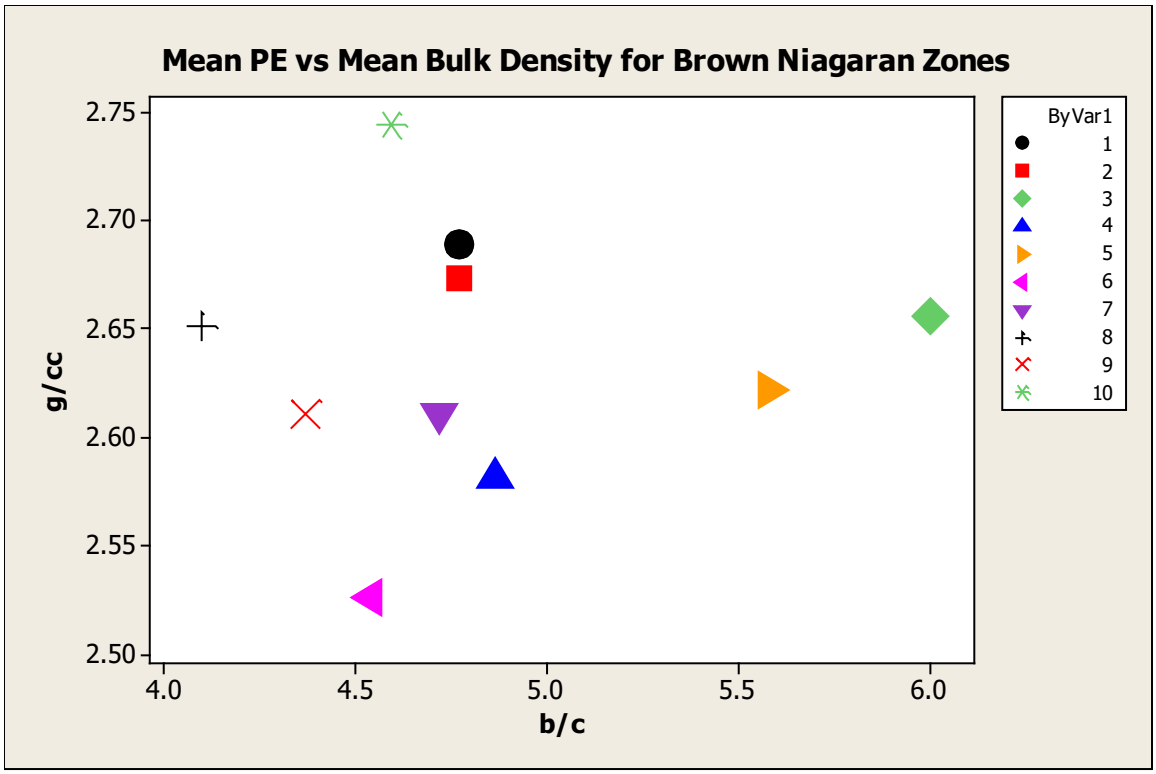


Figure B-13. Mean PE vs. Mean Bulk Density

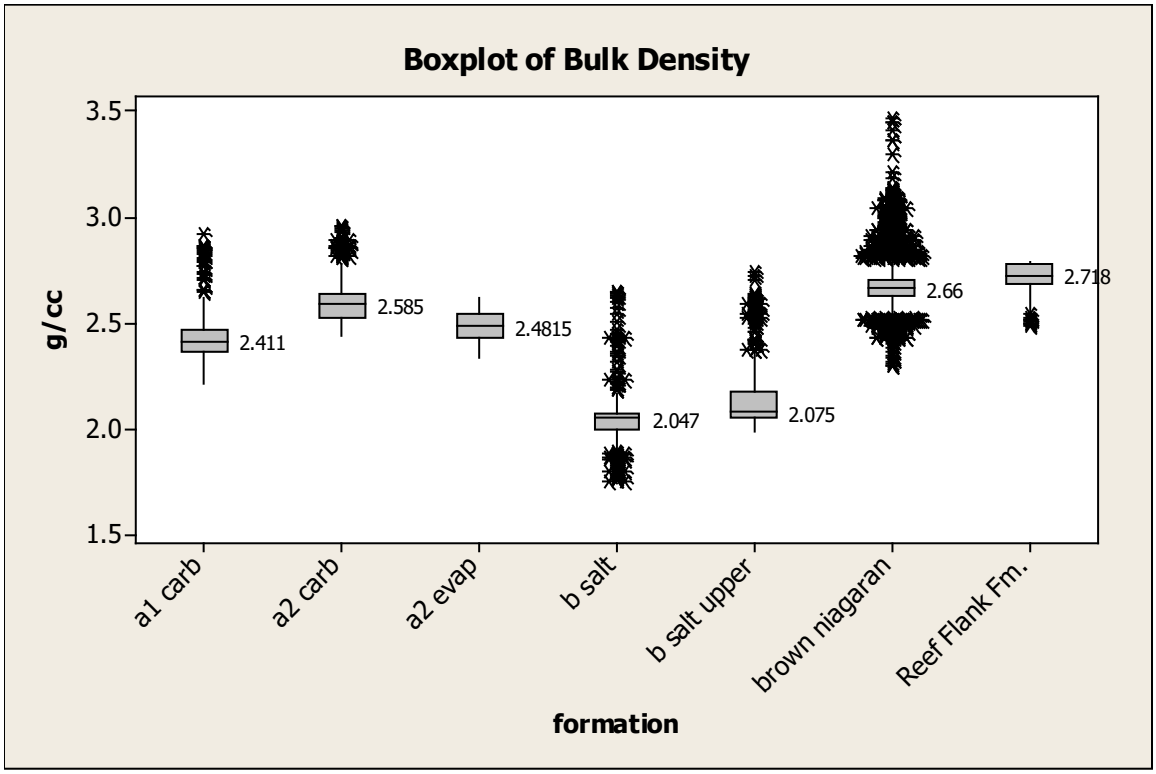


Figure B-14. Bulk Density

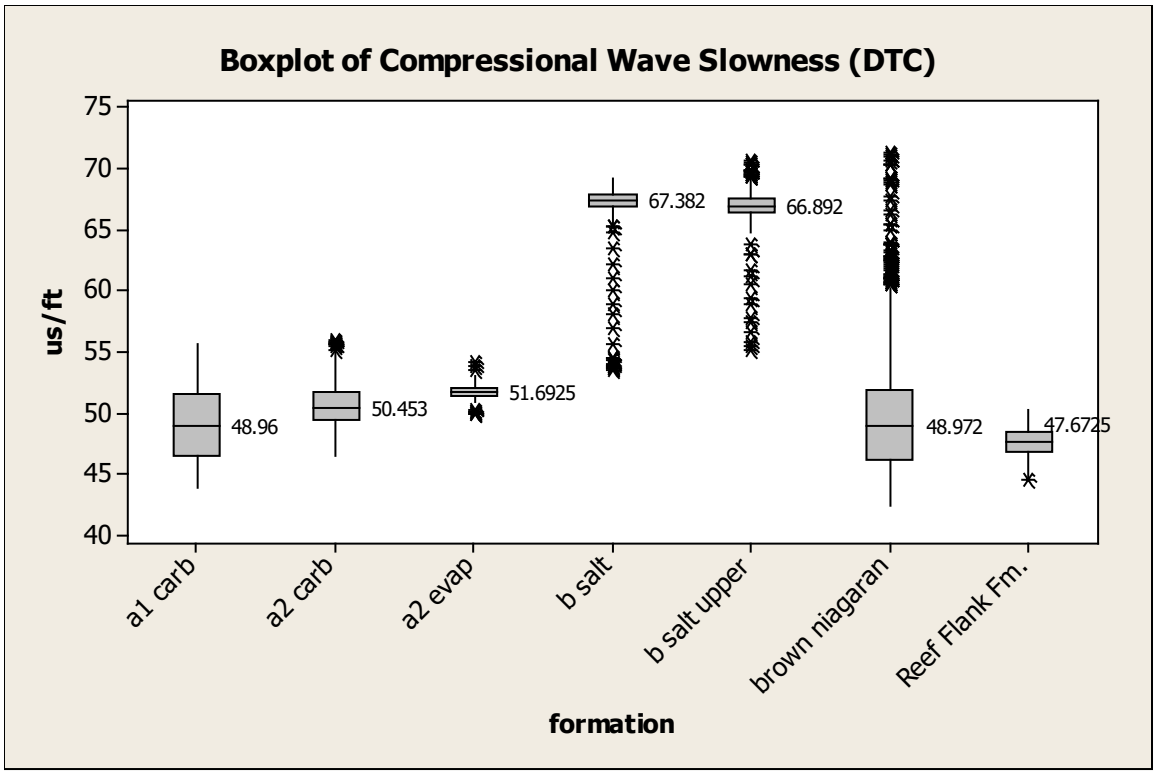


Figure B-15. Compressional Wave Slowness (DTC)

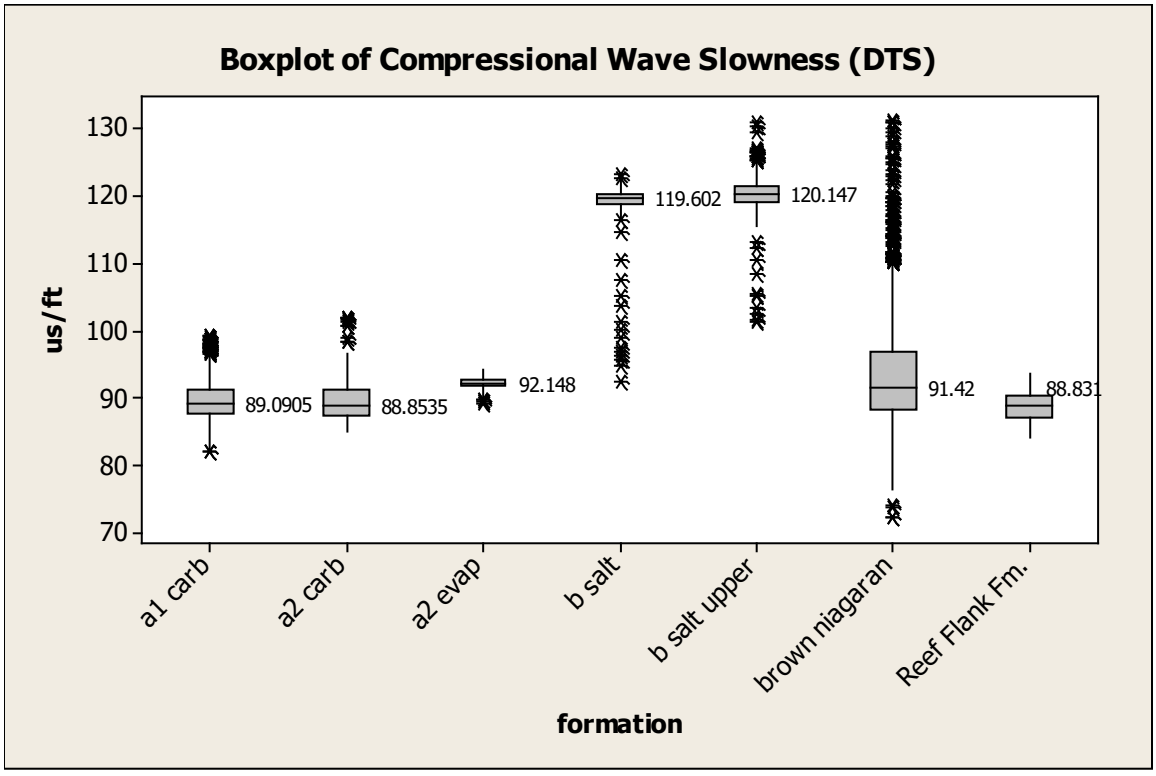


Figure B-16. Compressional Wave Slowness (DTS)

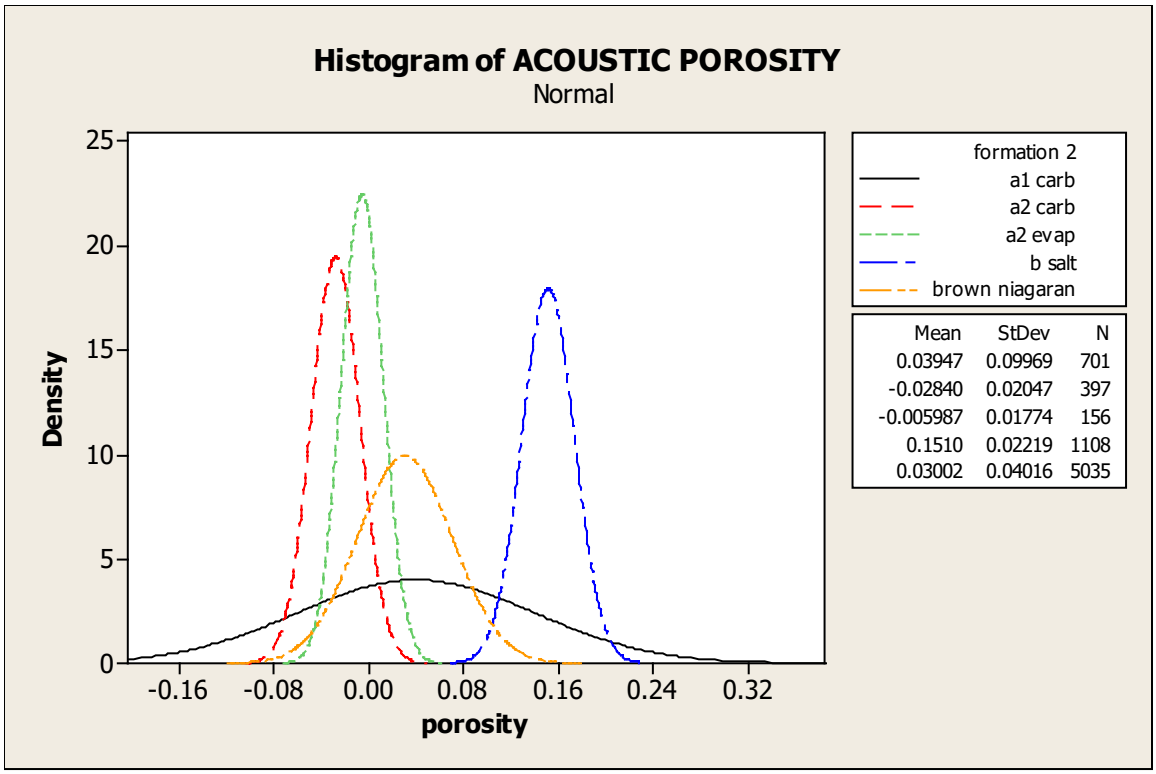


Figure B-17. Acoustic Porosity

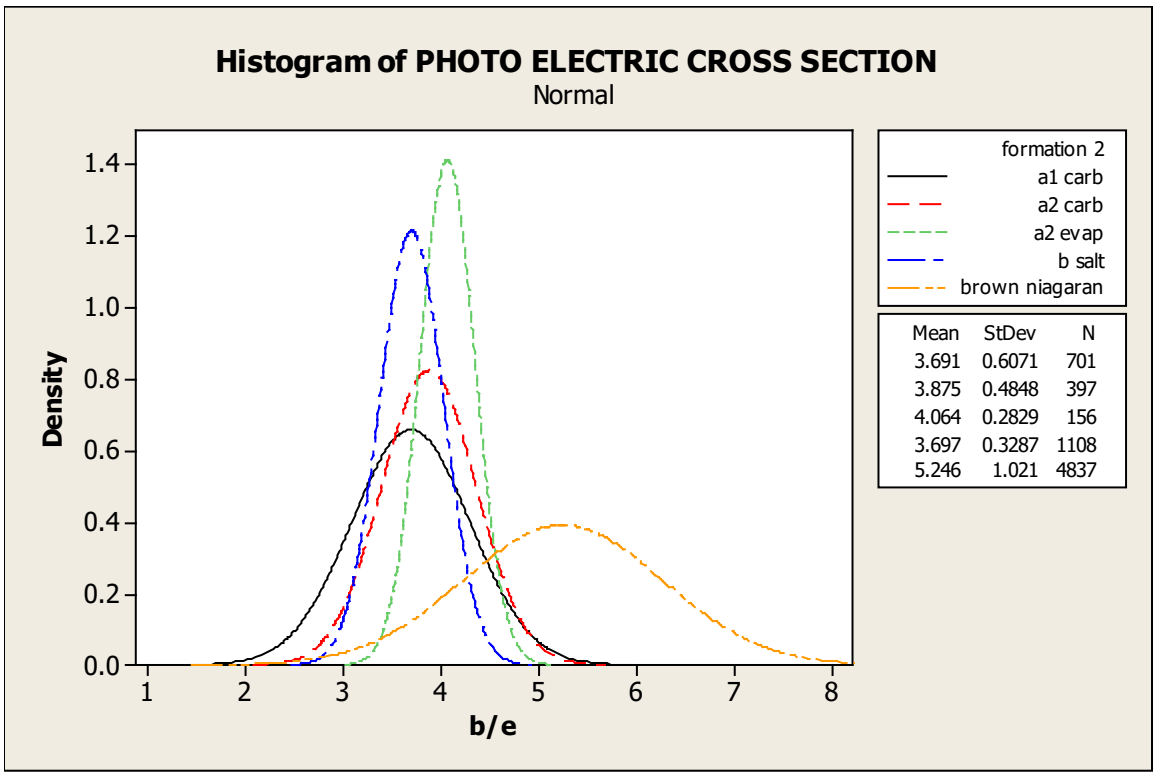


Figure B-18. PE Cross Section

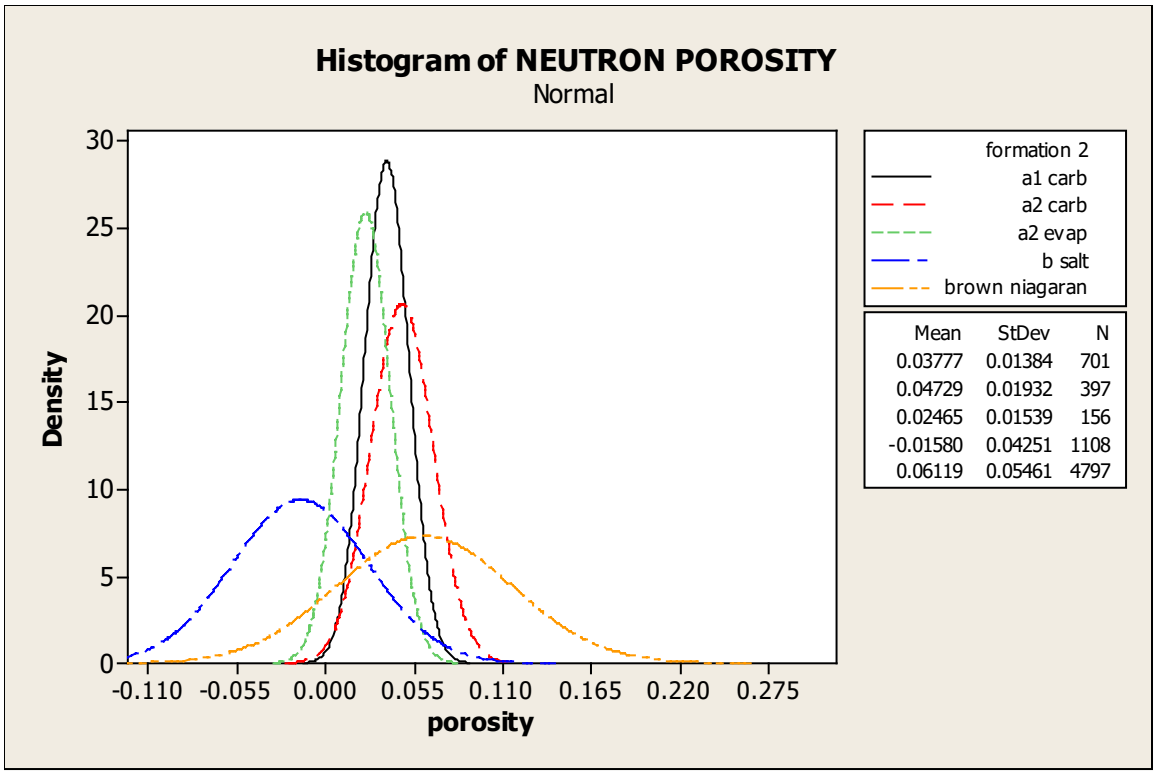


Figure B-19. Neutron Porosity

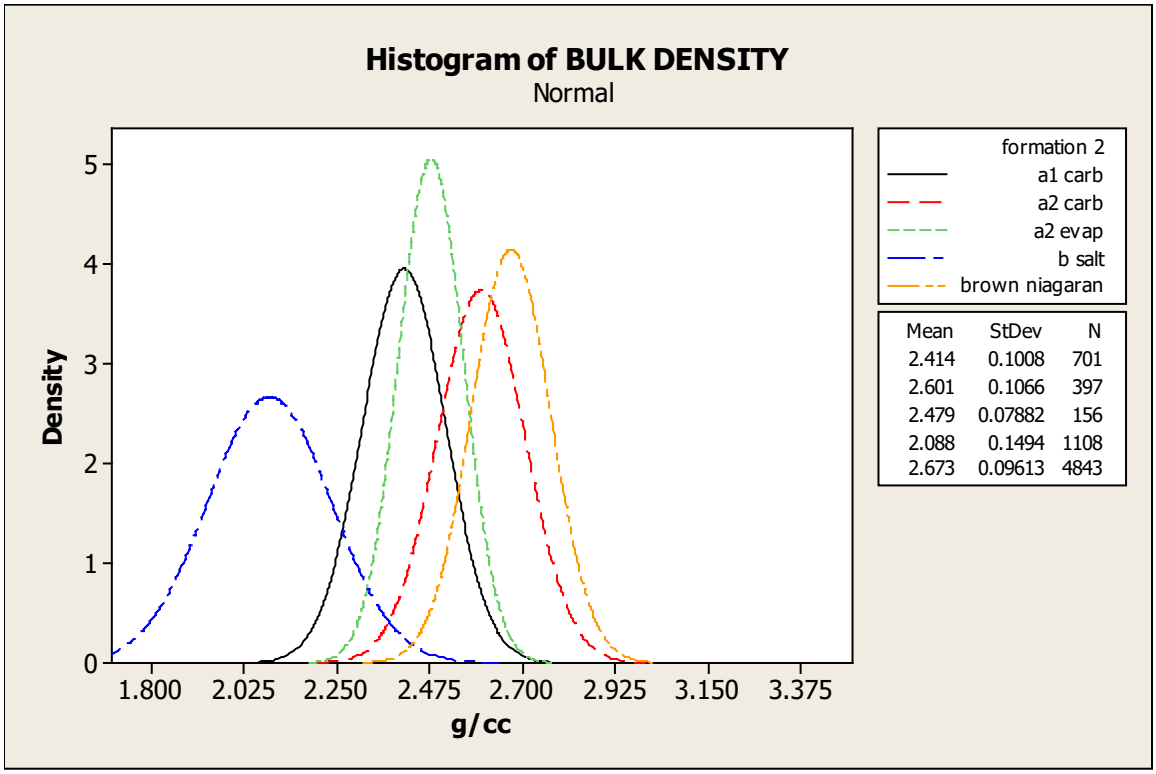


Figure B-20. Bulk Density

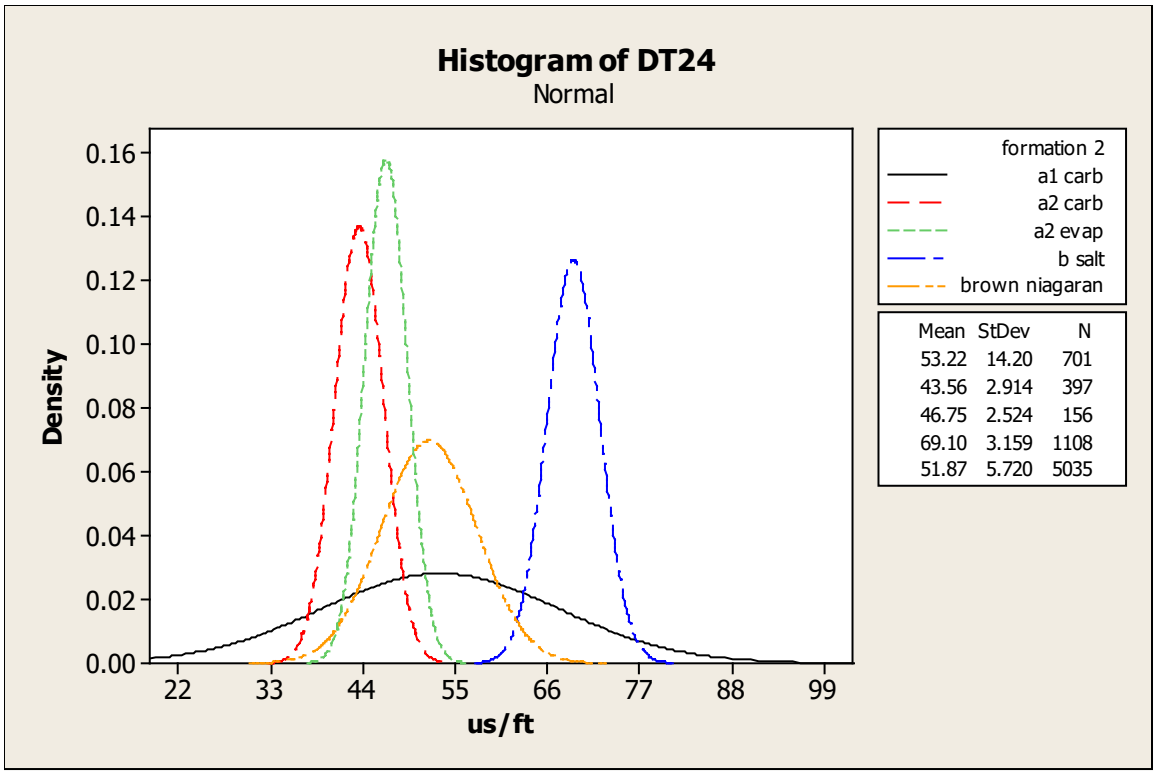


Figure B-21. DT24


BATTELLE
It can be done

Attachment 2.
Lawnichak 9-33
Horizontal Well Wireline and Core Analysis: Dover 33 Niagaran Reef Piggyback Well

Attachment 2

Lawnichak 9-33 Horizontal Well Wireline and Core Analysis: Dover 33 Niagaran Reef Piggyback Well

Conducted by the Midwest Regional Carbon Sequestration Partnership (MRCSP)

DOE-NETL Cooperative Agreement DE-FC26-05NT42589



Prepared by:

Battelle
505 King Avenue
Columbus, Ohio 43201

Submitted to:

Client
Address
Address

April 28, 2019

This report is a work prepared for the United States Government by Battelle. In no event shall either the United States Government or Battelle have any responsibility or liability for any consequences of any use, misuse, inability to use, or reliance on any product, information, designs, or other data contained herein, nor does either warrant or otherwise represent in any way the utility, safety, accuracy, adequacy, efficacy, or applicability of the contents hereof.

Table of Contents

Page

Chapter 1. Well Drilling and Completions 1
1.1 Well Operations Execution 1
1.2 Data Collection 7
1.2.1 Wireline Logs 7
1.2.2 Whole and Sidewall Core 7
Chapter 2. Geologic Characterization 11
2.1 Methodology 11
2.2 Salina Group 15
2.2.1 Basic Wireline Log Analysis 15
2.2.2 Advanced Wireline Log Analysis 16
2.3 A2 Carbonate and A2 Evaporite 21
2.3.1 Basic Wireline Log Analysis and Petrophysical Calculations 21
2.3.2 Advanced Wireline Log Analysis 25
2.3.3 Core Analysis 30
2.4 A1 Carbonate 32
2.4.1 Basic Wireline Log Analysis and Petrophysical Calculations 32
2.4.2 Advanced Wireline Log Analysis 34
2.4.3 Core Analysis 39
2.5 Brown Niagarann 43
2.5.1 Basic Wireline Log Analysis and Petrophysical Calculations 43
2.5.2 Advanced Wireline Log Analysis 47
2.5.3 Core Analysis 59
2.6 Gray Niagarann 62
2.6.1 Basic Wireline Log Analysis and Petrophysical Calculations 62
2.6.2 Advanced Wireline Log analysis 64
2.6.3 Core Analysis 65
2.7 Core Analysis Integration 66
2.7.1 Dual Energy Computed Tomography (CT) Scanning 66
2.7.2 Routine Conventional Core Analysis 68
2.7.3 Routine Sidewall Core Analysis 70
2.7.4 Thin Section Analysis 73
2.7.5 Core Integration Summary 76
Chapter 3. Summary 78

List of Tables

Page

Table 1-1. Wireline Log Intervals 7
Table 1-2. Conventional core acquisition parameters for Lawnichak 9-33 8
Table 1-3. Lawnichak 9-33 RSWC acquisition parameters 8
Table 2-1. Lawnichak 9-33 formation top depths 11
Table 2-2. NMR cross section explanation 13
Table 2-3. A-2 Carbonate zone footages - 5% porosity and 40% water saturation cutoffs 21
Table 2-4. A-2 Evaporite zone footages - 5% porosity cutoff and 40% water saturation cutoff 22
Table 2-5. A-1 Carbonate zone footages - 5% porosity and 40% water saturation cutoff 32
Table 2-6. Brown Niagaran zone footages – 5% porosity and 40% water saturation cutoff 44
Table 2-7. Core grain density summary 68
Table 2-8. Summary of porosity and permeability data from whole core at Lawnichak 9-33 69
Table 2-9. RSWC grain density summary by formation 70
Table 2-10. Summary of RSWC porosity and permeability data 72
Table 2-11. Summary of major whole rock mineralogy 73
Table 2-12. Summary of whole core porosity and permeability data in the Lawnichak 9-33 well 77
Table 2-13. Summary of rotary sidewall core porosity and permeability data in the Lawnichak 9-33 well 77
Table 2-14. Summary of key potential reservoir intervals in the Lawnichak 9-33 well based on whole core analysis and images 77
Table 3-1. Summary of key potential reservoir intervals in the Lawnichak 9-33 well 78

List of Figures

Page

Figure 1-1. Surface hole location for Lawnichak 9-33 marked in red. 2
Figure 1-2. As-built wellbore diagram for Lawnichak 9-33 (not to scale). 3
Figure 1-3. Deviation survey plot for Lawnichak 9-33 well showing the bend near 4500 ft md where the well turns from vertical and angles towards the northeast 4
Figure 1-4. Days vs. depth plot annotated with unscheduled events, casing points, and key geologic horizons for drilling of the Lawnichak 9-33 well. Note that the time required for well completion has not been included. Approximately 9 days, with 7 core runs and 2 different core acquisition vendors, contribute significantly to the time spent on this well. 5
Figure 1-5. Executed formation evaluation program for Lawnichak 9-33 6

Figure 1-6. Lithology log legend and explanation of abbreviations used in the whole core analysis figures. 9
Figure 1-7. RSWC abbreviation explanations. 10
Figure 2-1. Single well cross section comparison of original neutron porosity curve and the corrected neutron porosity curve. Note that the original neutron curve (red) systematically overestimates porosity. The corrected curve has been calibrated to the proper lithology (dolomite) and yields accurate porosity values. 14
Figure 2-2. Single well cross section of the Salina Group in the Lawnichak 9-33 well 15
Figure 2-3. Annotated image log of the Salina D Unit from ~4,810 ft. to 4,825 ft. This texture is described as a massively bedded heterogenous salt with elongated conductive features occurring parallel to the wellbore. 16
Figure 2-4. Annotated image log of the Salina C Shale from ~4,830 ft. to 4,845 ft. The texture is described as largely conductive with distinct bedding planes. This interval is interpreted to be interbedded shale/micrite with fractures and faults resulting from post-depositional compaction. 17
Figure 2-5. Annotated FMI image log of the Salina B Unit from ~4,905 ft. to 4,925 ft. This zone is described as bedded conductive and resistive material that is interpreted to be thinly bedded limestone and shale/micrite. 19
Figure 2-6. Annotated FMI image log of the Salina B Salt from ~5,009 ft. to 5,027 ft. This unit is described as cyclical occurrences of thinly bedded zones of conductive material overlain by thick-to-massively bedded resistive material. 20
Figure 2-7. Neutron-density crossplot of the A-2 Carbonate using the original neutron porosity log. Note that porosity values here are overestimated but lithology is accurate. 21
Figure 2-8. Neutron-density crossplot of the A-2 Carbonate using the calibrated neutron porosity log. Note that porosity values here are accurate but lithology is not. 22
Figure 2-9. Single well cross section of the A-2 Carbonate and A-2 Evaporite in the Lawnichak 9-33 well 23
Figure 2-10. Neutron-density crossplot of the A-2 Evaporite using the original neutron porosity log. Note that porosity values here are overestimated but lithology is accurate. 24
Figure 2-11. Neutron-density crossplot of the A-2 Evaporite using the calibrated neutron porosity log. Note that porosity values here are accurate but lithology is not. 24
Figure 2-12. Formation Lithology Explorer Digital Spectralog (FLeX) log from Lawnichak 9-33 displaying the A-2 Carbonate and A2 Evaporite Formations from 5,326 ft. MD/5,223 ft. TVD to 5,455 ft. MD/5,328 ft. TVD. Select Rotary Side Wall Core (RSWC) samples are shown in both white light (WL) and ultraviolet light (UV) to provide context for lithologic descriptions. Orange box marks zone with high clay mineral content. 26

Figure 2-13. Annotated FMI image log of the A-2 Carbonate from ~5,351 ft. to 5,364 ft. The texture is described as thinly interbedded intervals of materials that exhibit subtle changes in resistivity. 27

Figure 2-14. Annotated FMI image log of the A-2 Evaporite from ~5,417 ft. to 5,427 ft. The texture zone is described as largely resistive with moderate amounts of isolated conductive features occurring throughout and is interpreted to be thickly bedded mixture of anhydrite material 28

Figure 2-15. Cross section of MREX NMR log data, select logs from the triple combo log suite, and pay flags generated from triple combo logs and neutron-density crossplots for the A-2 Carbonate and A-2 Evaporite. NMR effective porosity log is plotted with neutron porosity, density porosity, and average porosity logs derived from the triple combo log suite. Permeability, BVM, BVI, CBW, and T2 distributions are also displayed. 29

Figure 2-16. Annotated RSWC images with corresponding core descriptions of the A-2 Carbonate for depths 5,330 ft. to 5,330.5 ft. 30

Figure 2-17. Annotated RSWC images with corresponding core descriptions of the A-2 Evaporite for depths 5,415 ft. to 5,430 ft. 31

Figure 2-18. Neutron-density crossplot of the A-1 Carbonate using the original neutron porosity log. Note that porosity values here are overestimated but lithology is accurate. 32

Figure 2-19. Neutron-density crossplot of the A-1 Carbonate using the calibrated neutron porosity log. Note that porosity values here are accurate but lithology is not. 33

Figure 2-20. Single well cross section of the A-1 Carbonate in the Lawnichak 9-33 well 34

Figure 2-21. Formation Lithology Explorer Digital Spectralog (FLeX) log from Lawnichak 9-33 displaying the A-1 Carbonate Formation from 5,455 ft. MD/5,328 ft. TVD to 5,546 ft. MD/5,397 ft. TVD. Select Rotary Side Wall Core (RSWC) samples are shown in both white light (WL) and ultraviolet light (UV) to provide context for lithologic descriptions. Orange box marks zone with high sulfur spikes. 35

Figure 2-22. Annotated FMI image log of the A-1 Carbonate from ~5,470 ft. to 5,486 ft. The texture is described as a largely resistive material with cyclical occurrences of conductive features and is interpreted to be bedded mud-supported carbonate material (mudstone, wackestones, packestone etc.). 36

Figure 2-23. Annotated FMI image log of the A-1 Carbonate from ~5,527 ft. to 5,540 ft. This texture zone is described as a bedded heterogenous texture consisting of resistive material with lateral semi-continuous conductive features occurring within bedding planes. 37

Figure 2-24. Annotated FMI image log of the A-1 Carbonate from ~5,538 ft. to 5,550 ft. Note the laminated discontinuous conductive features that occur throughout the resistive matrix, interpreted to be brecciated microbial laminates. 38

Figure 2-25. Cross section of MREX NMR log data, select logs from the triple combo log suite, core porosity and permeability data, and pay flags generated from triple combo logs and neutron-density crossplots for the A-1 Carbonate. NMR effective porosity log is plotted with neutron porosity, density

porosity, and average porosity logs derived from the triple combo log suite as well as core porosity. NMR permeability is displayed with core permeability. BVM, BVI, CBW, and T2 distributions are also displayed. Green box highlights a zone of interest. 39

Figure 2-26. Compiled illustration of lithology log, core photos (UV and white light), CT scan image, core descriptions, and annotated core images of the A-1 Carbonate for depths 5,525 ft. to 5,528 ft. 40

Figure 2-27. Compiled illustration of lithology log, core photos (UV and white light), CT scan image, core descriptions, and annotated core images of the A-1 Carbonate for depths 5,540 ft. to 5,543 ft. 41

Figure 2-28. Annotated RSWC images with corresponding core descriptions of the A-1 Carbonate for depths 5,456 ft. to 5,458 ft. 42

Figure 2-29. Annotated RSWC images with corresponding core descriptions of the A-1 Carbonate for depths 5,520 ft. to 5,523 ft. 43

Figure 2-30. Neutron-density crossplot of the Niagaran Brown using the original neutron porosity log. Note that porosity values here are overestimated but lithology is accurate. 44

Figure 2-31. Neutron-density crossplot of the Brown Niagaran using the calibrated neutron porosity log. Note that porosity values here are accurate but lithology is not. 45

Figure 2-32. Single well cross section of the Brown Niagaran in the Dover 9-33 well 46

Figure 2-33. Elemental spectroscopy log from Lawnichak 9-33 displaying the Brown Niagaran formation from 5,546 ft. to 5,730 ft. Select rotary side wall core samples are shown in both white light (WL) and ultraviolet light (UV) to provide context for lithologic descriptions. Orange arrows indicate zones with high excess carbon. Blue light is the oil-water contact. 47

Figure 2-34. Elemental spectroscopy log from Lawnichak 9-33 displaying the Brown Niagaran formation from 5,710 ft. to 5,900 ft. Select rotary side wall core samples are shown in both white light (WL) and ultraviolet light (UV) to provide context for lithologic descriptions. Orange arrows indicate zones with high excess carbon. 48

Figure 2-35. Annotated FMI image log of the Brown Niagaran from ~5,548 ft. to 5,556 ft. The zone is described as thinly layered conductive and resistive bed and is interpreted to be bedded mudstone. Conductive zones are thought to exhibit vuggy to fenestral porosity. 49

Figure 2-36. Annotated image log of the Brown Niagaran from ~5,564 ft. to 5,575 ft. This texture is described as massive heterogeneously conductive texture where all conductive features occur within a resistive matrix. This zone is interpreted to be massively bedded mudstone with a moderate to high distribution of vuggy porosity. 50

Figure 2-37. Annotated image log of the Brown Niagaran from ~5,580 ft. to 5,588 ft. This texture is described as thin to thickly bedded homogenously conductive and heterogeneously conductive textures and is interpreted to be bedded mudstones and bioclastic wackestones. 51

Figure 2-38. Annotated image log of the Brown Niagaran from ~5,588 ft. to 5,598 ft. This texture is described as massive heterogenous texture with abundant

isolated conductive features held within a resistive matrix material and is interpreted to be massively bedded bioclastic wackestones. 52

Figure 2-39. Annotated image log of the Brown Niagaran from ~5,660 ft. to 5,671 ft. This interval is described as coarsely heterogenous with large discontinuous resistive features held within a conductive matrix and is interpreted to be large rip-up clasts of mudstone held within massively bedded bioclastic wackestone. 53

Figure 2-40. Annotated image log of the Brown Niagaran from ~5,712 ft. to 5,725 ft. This interval is described as inclined interbeds of near-homogenously resistive and conductive materials and is interpreted to be porous, grain-supported packestone/grainstone. 54

Figure 2-41. Annotated image log of the Brown Niagaran from ~5,727 ft. to 5,738 ft. This texture is described as interwoven coarse to fine heterogenous texture and is interpreted to be framestones of reef builder skeletons with reef detritus material infilling cavities. 55

Figure 2-42. Annotated image log of the Brown Niagaran from ~5,772 ft. to 5,785 ft. This interval is described as thin resistive beds interbedded with thickly-to-thinly bedded heterogeneously conductive material and is interpreted to be mudstone interbedded with framestone or bafflestones with syn-depositional cavity filling reef detritus. 56

Figure 2-43. Cross section of NMR log data, select logs from the triple combo log suite, core porosity and permeability data, and pay flags generated from triple combo logs and neutron-density crossplots for the Brown Niagarann. NMR effective porosity log is plotted with neutron porosity, density porosity, and average porosity logs derived from the triple combo log suite as well as core porosity. NMR permeability is displayed with core permeability. BVM, BVI, CBW, and T2 distributions are also displayed. Green boxes highlight zones of interest. 58

Figure 2-44. Compiled illustration of lithology log, core photos (UV and white light), CT scan image, core descriptions, and annotated core images of the Brown Niagaran for depths 5,546 ft. to 5,549 ft. 59

Figure 2-45. Compiled illustration of lithology log, core photos (UV and white light), CT scan image, core descriptions, and annotated core images of the Brown Niagaran for depths 5,749 ft. to 5,752 ft. 60

Figure 2-46. Annotated RSWC images with corresponding core descriptions of the Brown Niagaran for depths 5,580 ft. to 5,583 ft. 61

Figure 2-47. Annotated RSWC images with corresponding core descriptions of the Brown Niagaran for depths 5,847 ft. to 5,865 ft. 62

Figure 2-48. Single well cross section of the Gray Niagaran in the Lawnichak 9-33 well 63

Figure 2-49. Neutron-density crossplot of the Gray Niagaran using the original neutron porosity log. Note that porosity values here are overestimated but lithology is accurate. 64

Figure 2-50. Elemental spectroscopy log from Lawnichak 9-33 displaying the Gray Niagaran Formation from 5,867’MD/5,655’TVD to log TD at 6,046’MD. Select Rotary Side Wall Core (RSWC) samples are shown in both white light (WL) and ultraviolet light (UV) to provide context for lithologic

descriptions. Pink line marks the boundary between Mg dominated dolomite and Ca dominated calcite formation. Orange box marks depths with enhanced kaolinite formation. 65

Figure 2-51. Annotated RSWC images with corresponding core descriptions of the Gray Niagaran for depths 5,873 ft. to 5,899 ft. 66

Figure 2-52. Rock typing results from CT Scan analysis of the Lawnichak 9-33 cores showing mostly porous dolostone and dolomite with some dolomitic chert and halite. 67

Figure 2-53. Histograms of grain density by formation from the Lawnichak 9-33 conventional core 68

Figure 2-54. Core porosity-permeability transform plot for the A-1 Carbonate (yellow circles) and the Brown Niagaran (brown circles) 69

Figure 2-55. Histograms of grain density by formation from the Lawnichak 9-33 RSWCs 71

Figure 2-56. RSWC porosity-permeability transform plot for the A-2 Carbonate (blue circles), A-1 Carbonate (yellow circles), Brown Niagaran (brown circles), and the Gray Niagaran (gray circles) 72

Figure 2-57. Thin section of rotary sidewall core sample at 5,374 ft. (A) shows high-resolution thin section sample of the dolomitic anhydrite sample. Red indicate small anhydrite nodules, yellow arrow indicates micrite-filled fractures, and blue arrows indicate small load casts. (B) is a magnified view of a section of the thin section sample. Dolomites and anhydrites are indicated throughout the thin section with occasional potassium-feldspar (stained yellow) and pyrite minerals. 74

Figure 2-58. Thin section of rotary sidewall core sample at 5,374.50 ft. (A) shows a dolostone with vugs up to 1.5 mm. (B) magnified view of the sample indicating a medium-crystalline dolostone comprised of replacement dolomite with dark matter between small pore spaces. Large euhedral dolomite crystals indicate late stage dolomitization. 75

Figure 2-59. Thin section of rotary sidewall core sample at 5,378 ft. (A) shows light anhydrite dominate anhydritic-dolomitic laminae with darker dolomitic dominated dolomitic-anhydrite laminae. Fractures in the sample were induced during preparation. (B) magnified view of the sample indicating elongated anhydrites intermixed with dolomicrite. There are a few instanced of k-feldspar minerals (yellow stain). 76

Chapter 1. Well Drilling and Completions

Drilling began for the Lawnichak 9-33 well on September 22, 2016 and operated by Core Energy LLC with well evaluation operations contracted by Battelle Memorial Institute on behalf of MRCSP. The surface location of this borehole is marked by a red dot on both a high-resolution aerial photograph and map in Figure 1-1. The final, as-built, wellbore diagram for the sidetrack can be found in Figure 1-2.

This well was directionally drilled from the Kickoff Point (KOP) at 4,305' MD/TVD. The deviation survey plot for Lawnichak 9-33 is shown in Figure 1-3.

1.1 Well Operations Execution

A day vs. depth chart in Figure 1-4 is annotated with unscheduled events that occurred during drilling and completions, casing shoe depths (black triangles), and key formation tops. These unscheduled events are described below:

- Lost returns, the lack of rock samples returning to the surface during drilling, were common across the Northern Michigan Pinnacle Reef Trend, often massive or total, in the intermediate hole section when the mud system was converted from freshwater to brine. Pore pressure within this stratigraphic section must have been at or near the hydrostatic gradient because the drilling fluid density increase caused by adding dissolved salts was sufficient to cause voids to form or open. Drilling with a salt saturated fluid is critical through this interval to prevent hole enlargement and washout while drilling thick salt beds.
  - Lost returns in this hole section at Lawnichak 9-33 started at a depth around 2,020 ft. MD with a high rate of 100bph. These rates were reduced to 20-50bph for the remainder of the interval by periodically circulating and conditioning (C&C) the hole while running Lost Circulation Material (LCM) sweeps.
- An MWD tool failure in the intermediate hole section caused an extra return of the wireline to surface to replace the tool.
- Conventional coring operations at this well were problematic. There were seven total core runs and two separate service providers engaged. Several factors known to decrease the chance of success of coring operations were present, including a deviated well trajectory (nearly 45 degrees inclination in the cored interval), sedimentary beds dipping at high angles relative to the well bore, and the potential for naturally fractured rocks.
  - While entering in hole with the coring BHA to the first core point at 5,525 ft. MD, tight hole was encountered. The BHA made it to bottom by circulating and reaming.
  - Core run #1 jammed at 5,559ft. MD when attempting to resume coring after making a connection. On surface, 33 ft. of core was recovered.
  - Core run #2 jammed at 5,565ft. MD when the "auto-digger" mechanism engaged and suddenly applied an additional 7Klbs weight on bit (WOB). After the jam occurred, an additional 10Klbs WOB was applied, resulting in 3 ft. of milled core at the base, extending to 5,568 ft. MD. The auto-digger tool was disengaged at this point.
  - Core run #3 appears to have jammed after cutting 10 ft., accompanied by increase in standpipe pressure.
  - Switched to 30 ft. core barrels more easily maneuvered by a Kelly driven rig, but core run #4 jammed at 5,608 ft. when the WOB exceeded 5Klbs. 1.6 ft. of 2 ft. cut core is recovered.
  - Core runs numbers 5-7 are conducted by coring vendor Premier instead of ALS.

  - The core barrel for run #7 was made up to a 60 ft. length and jammed after cutting 14 ft. of core.

- While drilling ahead, a drop in pressure was noticed. The team pulled out of hole to locate a suspected hole in the drill string, which was located 18 joints above the drill collar.
- Multiple attempts to collect in situ formation pressure measurements were unsuccessful because of failed seal due to hole condition. While data was eventually collected, more time was lost attempting to resolve continued issues with the straddle packers.

Figure 1-5 shows the executed formation evaluation program for Lawnichak 9-33.

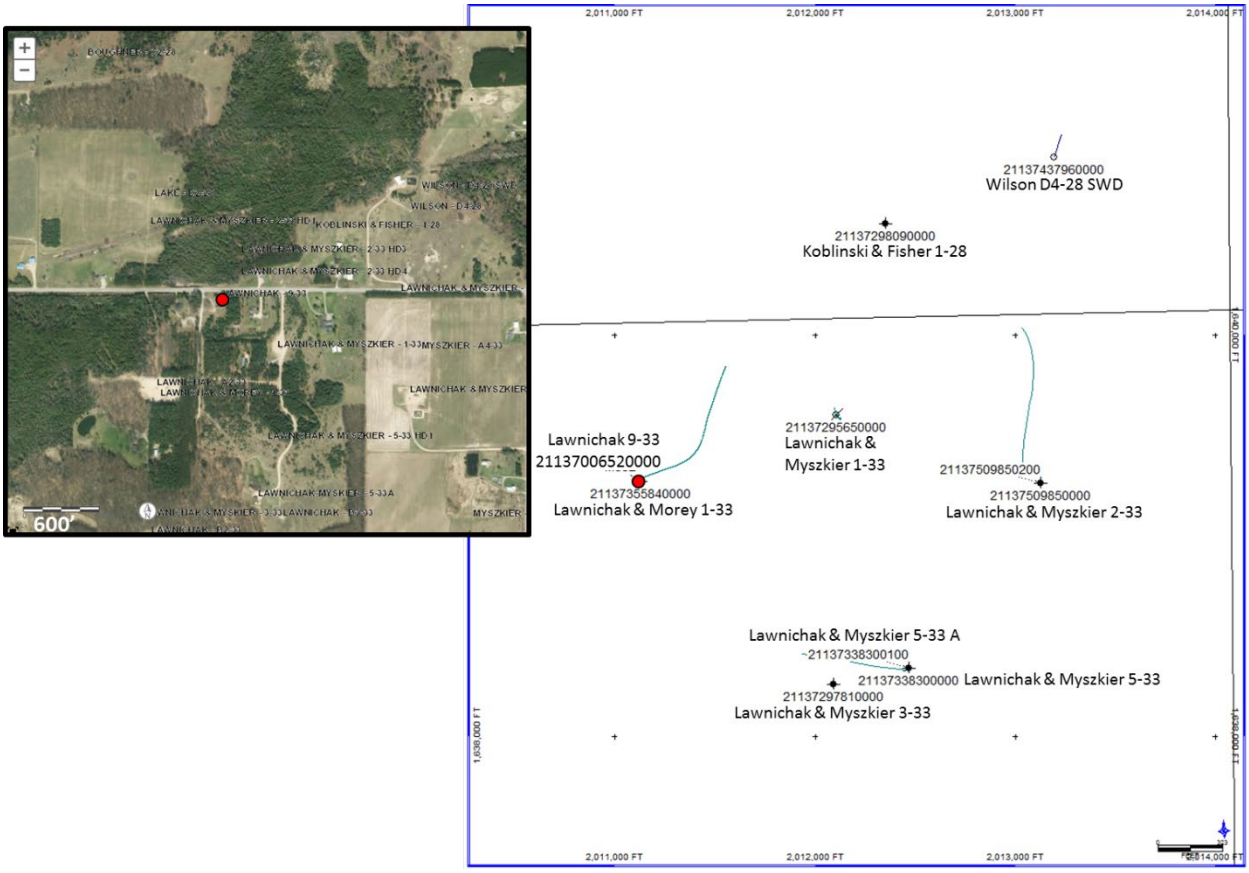


Figure 1-1. Surface hole location for Lawnichak 9-33 marked in red.

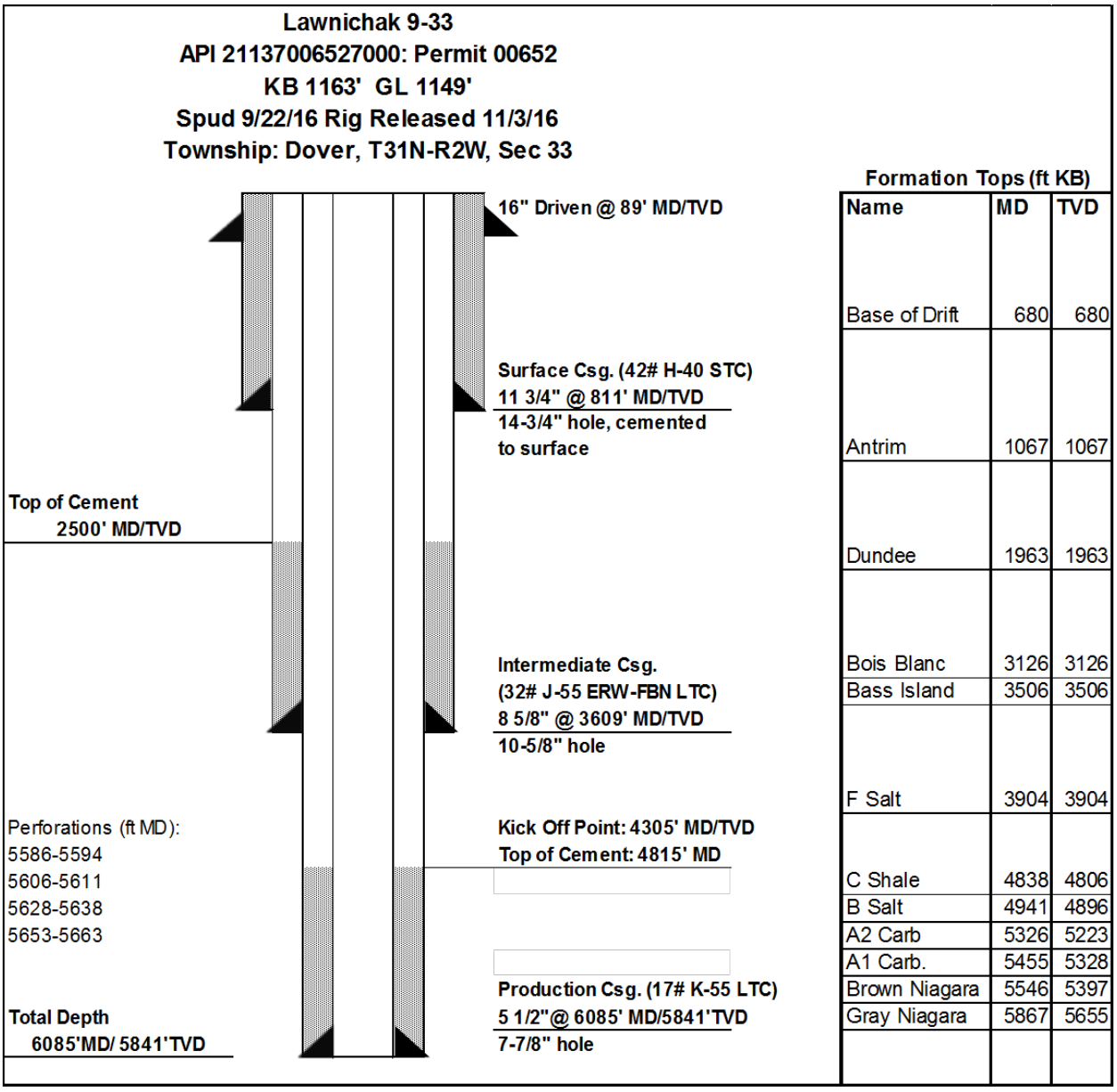


Figure 1-2. As-built wellbore diagram for Lawnichak 9-33 (not to scale).

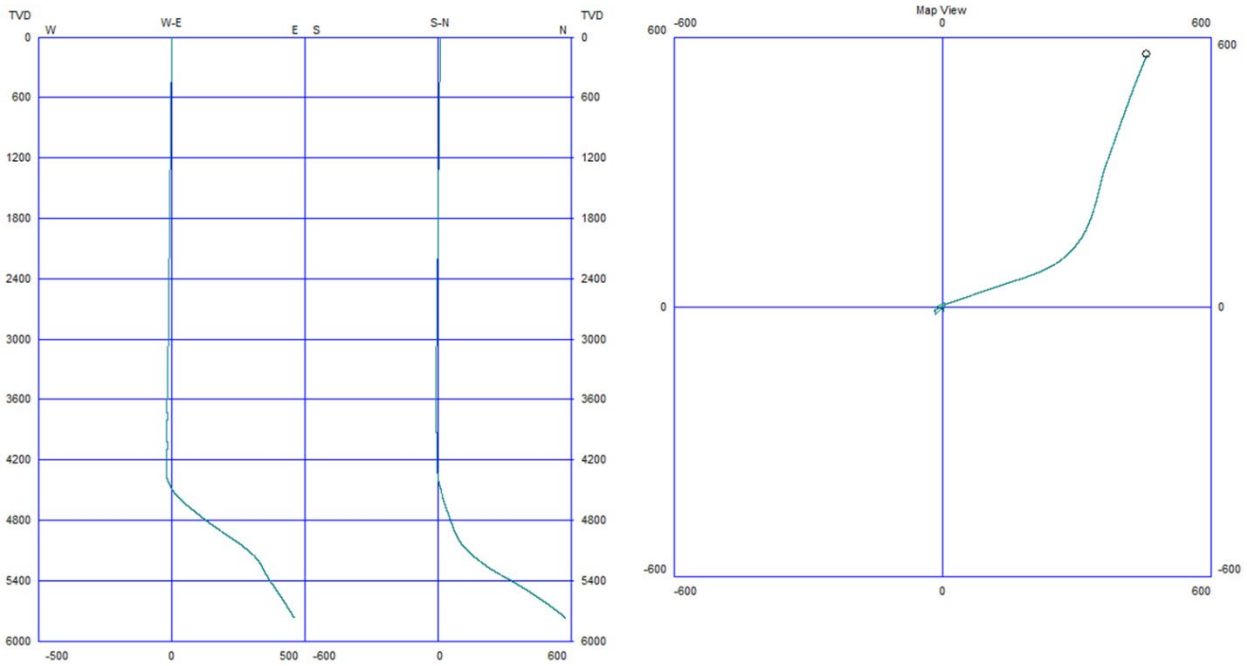


Figure 1-3. Deviation survey plot for Lawnichak 9-33 well showing the bend near 4500 ft md where the well turns from vertical and angles towards the northeast

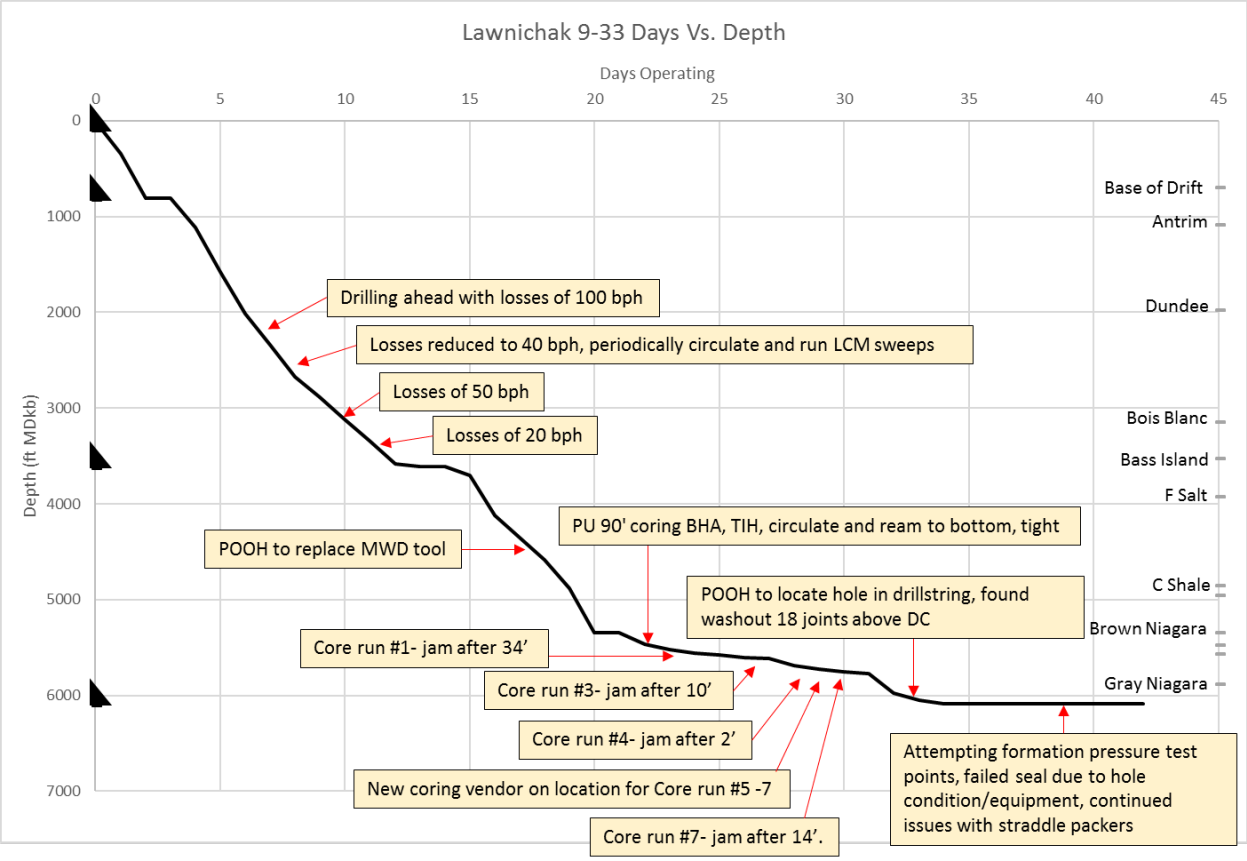


Figure 1-4. Days vs. depth plot annotated with unscheduled events, casing points, and key geologic horizons for drilling of the Lawnichak 9-33 well. Note that the time required for well completion has not been included. Approximately 9 days, with 7 core runs and 2 different core acquisition vendors, contribute significantly to the time spent on this well.

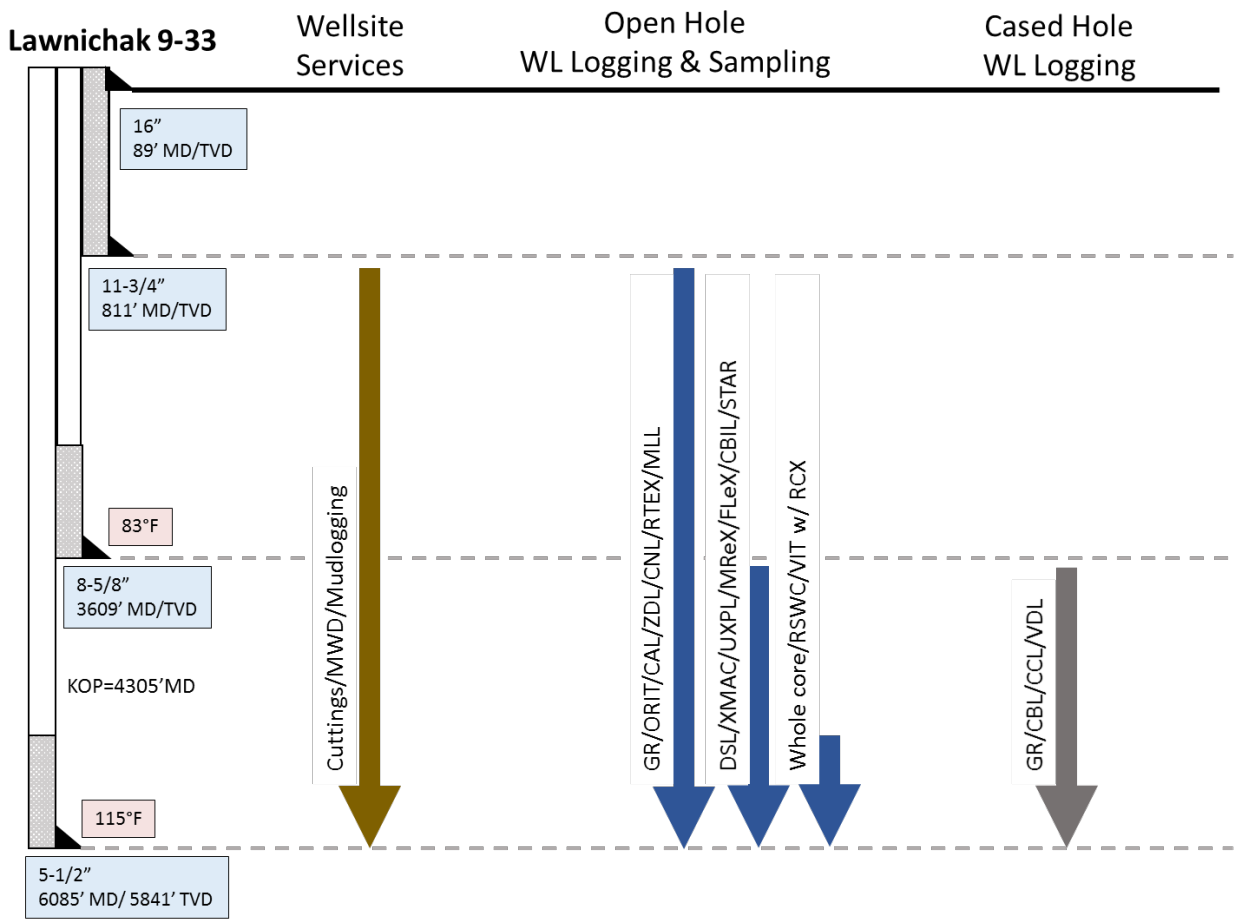


Figure 1-5. Executed formation evaluation program for Lawnichak 9-33

1.2 Data Collection

1.2.1 Wireline Logs

Basic open hole wireline logs and additional advanced logs were collected from the Lawnichak 9-33 well. Table 1-1 provides a summary of logs collected and the interval over which they were collected.

Table 1-1. Wireline Log Intervals

Wireline Log	Interval Run 2 (ft. MD)
Triple Combo	3,560–6,083
Gamma Ray	3,592–6,025
Neutron	3,560–5,860
Density	3,592-6,041
Photoelectric	3,592-6,041
Laterolog	3,598-6,083
Oriented Dipole Acoustic	7,166–8,214
Image Log	4,800-6,060
Nuclear Magnetic Resonance	3,549-6,052
Elemental Spectroscopy	3,602-6,076

The basic open hole log was a standard triple combo, which includes a gamma ray, compensated neutron and density (GR-N-D), photo-electric, laterolog, and caliper. This standard logging suite is used for stratigraphic correlation work and generates reservoir properties such as porosity, fluid content, and formation top interpretation.

The advanced logs provided by Battelle included oriented dipole acoustic, oriented acoustic and resistivity image logs, an elemental spectroscopy log, and a nuclear magnetic resonance (NMR) log. Oriented dipole acoustic logs provide data from which rock mechanics, stress regimes, and an additional derivation of reservoir porosity can be determined. The acoustic and resistivity-derived image log was run in order to determine bedding plane and fracture orientations and rock textures that are used to determine secondary porosity types and interpretive sequence stratigraphic information. The NMR log can be used to derive porosity, permeability, and fluid properties.

1.2.2 Whole and Sidewall Core

Whole Core Data Collection

A total of 118.15 ft. of whole core was recovered from the Lawnichak 9-33 well. The cored interval spans a discontinuous section of the Brown Niagaran Formation from 5,525 ft. to 5763 ft. MD. Drilling occurred between core runs #2 and #3 and between core runs #4 and #5. Acquisition was divided into seven separate coring runs with an average coring rate of penetration (ROP) of 2.7 ft./hr. Depth ranges, recovery rates, and ROP for each run are listed in the table below. Core acquisition at this well was challenging, with runs #1, #2, #3, #4, and #7. Core #7 was aborted due to cores becoming jammed. Due to poor core recovery on core runs 2-4, the coring vendor was changed. After the core jammed on run #7, conventional coring operations were terminated. Table 1-2 summarizes the recovered whole core.

Table 1-2. Conventional core acquisition parameters for Lawnichak 9-33

Core Run #	Coring Vendor	Start Depth	End Depth	Core Cut	Core Recovered	Core Recovery	ROP
		ft MD	ft MD	ft MD	ft MD	%	ft/hr
1	ALS	5525	5559	34	33	97%	5.7
2	ALS	5559	5568	9	5.9	66%	1.5
3	ALS	5598	5608	10	8.4	84%	1.5
4	ALS	5608	5610	2	1.6	80%	0.4
5	Premier	5690	5718	28	27	96%	3.5
6	Premier	5718	5749	31	31.4	101%	3.9
7	Premier	5749	5763	14	10.85	78%	2.2

Sidewall Core Data Collection

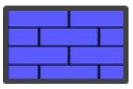
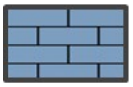
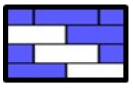
A total of 69 rotary side wall cores (RSWC) were acquired during open hole wireline operations for the Lawnichak 9-33 well using the Baker Hughes MAXCOR tool. The sampling interval, which included the A-2 Carbonate, A-2 Evaporite, A-1 Carbonate, Brown Niagaran and Gray Niagaran Formations (5,330'-5,899'MD), was identified in the field by Battelle technical staff from log signatures. The 1.5in. diameter cores ranged in length between 1.2 in. and 2.5 in., with an average length of 2.06 in. The average time spent coring each sample was ten minutes and ten seconds. Efficiency during this RSWC run was 98.6% with 69 out of 70 cores attempted being recovered (Table 1-3). Additional RSWC samples help compensate for the lack of conventional core in the lowest Brown Niagaran Formation and Gray Niagaran Formation.

Table 1-3. Lawnichak 9-33 RSWC acquisition parameters

Cores Attempted	Cores Recovered	Core Recovery Efficiency	Avg Coring Time (min:sec)	Average Core Length (in.)
70	69	98.6%	10:10	2.06

Conventional Core Description

Descriptions of the conventional core from Dover 9-33 have been made in one-foot intervals and are provided in Appendix A, “Dover-33 Well Report Whole Core Analysis”. Core photographs taken in white light and UV light are included with a correlative CT scan and lithology log. CT scan analysis was used Detail photos highlighting key features are shown at the right side of the figure. Lithology legend and explanation for the core photos is provided in Figure 1-6 and descriptions are summarized by formation in Chapter 2.

Lithology Log Legend
 Limestone (~0-10 %POR)
 Limestone (~10-20 %POR)
 Vuggy Limestone
 Dolomitic Limestone
 Vuggy Dolomitic Limestone
 Dolomite
 Porous Dolostone
 Heavy Mineral/Anhydrite
 Plug/Fracture/Rubble

Abbrv.	Explanation
AL	Algal laminations
ANH	Anhydrite
B	Breccia
BM	Biologic Material
BU	Burrows
FF	Filled fractures
FP	Framework porosity
FP	Flat Pebble clasts
MP	Moldic porosity
OF	Open fractures
OS	Oil stain
PV	Pyrite Filled Vug
R	Rubble/broken core
SLT	Salt
STM	Stromatoporoid
STY	Stylolites
V	Vugs

Figure 1-6. Lithology log legend and explanation of abbreviations used in the whole core analysis figures.

Rotary Sidewall Core Description

Descriptions of the sidewall cores from Dover 9-33 are provided in Appendix A, “Dover-33 Well Report Rotary Sidewall Core Analysis”. Core photographs taken in white light and UV light are included. Descriptions are summarized by formation below and an explanation of abbreviations used in RSWC photos is provided in Figure 1-7.

Abbrv.	Explanation
AL	Algal laminations
ANH	Anhydrite
B	Breccia
BM	Biologic Material
BU	Burrows
FF	Filled fractures
FP	Framework porosity
MP	Moldic porosity
OF	Open fractures
OS	Oil stain
PV	Pyrite Filled Vug
R	Rubble/broken core
SLT	Salt
STM	Stromatoporoid
STY	Stylolites
V	Vugs

Figure 1-7. RSWC abbreviation explanations.

Chapter 2. Geologic Characterization

2.1 Methodology

A standard triple combo logging run was completed for both the intermediate and deep sections of the well bore. The logs included gamma ray, bulk density, neutron porosity and resistivity, as well as tension, caliper, and photo electric effect. Table 2-1 shows the depths and intervals of the key units encountered during the drilling of the Lawnichak 9-33 well based on interpretation from the triple combo log. Log analysis combined this data with regional knowledge to calculate net formation to gross "pay" (net-to-gross) ratios, average porosities for each formation, and to delineate cross plot flags. Detailed petrophysical analysis will be presented for the A-2 Carbonate, A-2 Evaporite, A-1 Carbonate and Brown Niagaran formations. Note that due to limited neutron porosity data collected in the Gray Niagaran, detailed petrophysical calculations were not completed for this formation.

Table 2-1. Lawnichak 9-33 formation top depths

Formation (Lithologies)	Measured Tops (ft.)
Salina G	3,821
Salina F	3,861
Salina F Salt	3,900
Salina E	4,635
Salina D	4,777
Salina C Shale	4,825
Salina B	4,903
Salina B Salt	4,941
A-2 Carbonate	5,326
A-2 Evaporite	5,407
A-1 Carbonate	5,455
Brown Niagarann	5,546
Gray	5,867

Porosity was calculated several ways for the Lawnichak 9-33 formation intervals, including neutron porosity, density porosity and average porosity calculations. Neutron porosity is measured from correlation with the logging tool. A neutron source within the tool measures hydrogen index in the reservoir. As hydrogen atoms are present in water and hydrocarbon reservoirs, measurements of hydrogen allows for the estimation of the amount of liquid-filled porosity. Density porosity is calculated from Equation 2-1:

$$\phi_D = (\rho_{ma} - \rho_b)/(\rho_{ma} - \rho_{fl}) \quad \textbf{(Equation 2-1)}$$

where:

ϕ_D = density porosity

ρ_{ma} = matrix density (based on dolomite density of 2.83 g/cm^3)

ρ_b = bulk density (from the density log)

ρ_{fl} = fluid density (assumed fresh water: 1 g/cm^3)

Average porosity was calculated using both density and neutron porosities with Equation 2-2:

$$\phi_A = (\phi_D + \phi_N) / 2 \quad \textbf{(Equation 2-2)}$$

where:

ϕ_A = average porosity

ϕ_D = density porosity

ϕ_N = neutron porosity

Average porosities are used as representative values of formation porosity because neutron and density log porosity derivations are each susceptible to inaccuracies in certain conditions, such as the presence of gas, washouts, and atypical mineralogy.

Neutron porosity and bulk density data were plotted against each other to generate a crossplot for each formation of interest. Neutron-density crossplots are a graphical analysis technique that can be used to evaluate formation lithology and porosity. Trend lines superimposed on the crossplot represent the log responses calculated for pure sandstone, limestone, and dolomite over a range of porosities (e.g. 0-45%), assuming a fluid density of 1.0 g/cm^3 (fresh water) in the wellbore environment. Crossplot results and data trends can provide insight into lithology and allow for a potential estimate of true, lithology-independent porosity to be determined. Data exhibiting crossplot porosities greater than 5% were flagged, and the flagged data points were depth-denoted on cross-sections for the A-1 Carbonate and the Brown Niagaran formations.

The initial neutron porosity log acquired from Baker Hughes was calibrated incorrectly for the largely dolomitized lithology in this well. This resulted in neutron porosity values being systematically over-estimated (Figure 2-1). Baker Hughes re-calibrated the neutron porosity log and all porosity calculations for this well were made using the updated curve. Due to this re-calibration, Neutron-density crossplots of formations known to be dolomite-dominated generated using the updated neutron curve plot as limestone. In order to resolve this issue, 2 distinct crossplots were generated for formations of interest; one using the original neutron log to show an accurate lithology and one using the updated neutron curve to accurately calculate crossplot porosities and subsequent crossplot porosity flags.

Water saturation calculations were performed to determine the percentage of the pore space that was filled with water and, thus, inversely, what percentage of available pore space is filled with hydrocarbons. Water saturation was calculated using the Archie Equation, a standard oil and gas formula shown in equation 2-3:

$$S_w = \left(\frac{a * R_w}{R_t * \emptyset^m}\right)^{\frac{1}{n}} \qquad \textbf{(Equation 2-3)}$$

where:

S_w = water saturation of the uninvaded zone, %
R_w = formation water resistivity, ohm-ft
R_t = formation resistivity, ohm-ft
Ø = porosity, %
a = tortuosity factor
m = cementation exponent
n = saturation exponent

Pay flags, or high reservoir potential flags, were generated using the following cutoffs; a water saturation calculated lower than 40%, and an average porosity measurement greater than 5%. A water saturation cutoff of 40% ensures the available storage zone is being represented. A minimum average porosity value of 5% was used as a cutoff to identify potential high effective-porosity intervals.

Permeability calculations were performed on the NMR log to further assess the reservoir potential of the key formations of interest and their respective pay zones as flagged by neutron-density crossplot flags and pay flags. Permeability calculations were performed in-house using the T2 relaxation time data from the Baker Hughes MREX NMR log and the Timur Coates permeability equation (equation 2-4):

$$K = \left(\frac{\emptyset}{C}\right)^{m} * \left(\frac{BVM}{BVI}\right)^{n} \quad \textbf{(Equation 2-4)}$$

Where K is permeability in mD, ϕ is effective porosity derived from the MREX tool, C, m, and n are constant parameters provided by Baker Hughes (C = 10, m = 4, and n = 2), BVM is the moveable fluid volume and BVI is the irreducible water volume.

Initial permeability calculations were performed by Baker using a 92 ms T2 cutoff for BVM, though the resulting permeability values when compared to laboratory core permeabilities were inaccurate by orders of magnitude. Thus, in-house permeability calculations were performed using a standard 512 ms T2 cutoff for all depths. The resulting permeability values were largely within the same order of magnitude as the core permeability values and therefore more accurate.

NMR permeability and effective porosity data is displayed in cross section view alongside porosity log data derived from the triple combo log suite and core porosity and permeability data in the advanced wireline log analysis sections for the A-2 Carbonate through the Brown Niagaran. Table 2-2 summarizes the curves and tracks displayed for the NMR data.

Table 2-2. NMR cross section explanation

Track (Curve Color)	Curves	Units
Track 0	Depth	Feet
Track 1	GR	GAPI
Track 2 (brown curve)	Photoelectric index (PE)	Barnes/electron
Track 2 (blue curve)	Density (RHOB)	g/cc
Track 3 (dashed green curve)	Average porosity from density and neutron logs	Percentage
Track 3 (orange x symbols)	Core porosity	Percentage
Track 3 (red dot-dash curve)	Density porosity from density log	Percentage
Track 3 (blue dotted curve)	Neutron porosity log from triple combo	CFCF
Track 3 (black dashed curve)	NMR Effective porosity (MPHEC)	Percentage
Track 4 (purple curve)	Resistivity (RT)	Ohm.m
Track 4 (yellow fill)	NMR Permeability (MPERMC)	Millidarcys
Track 5 (yellow fill)	NMR Clay bound fluid (CBW)	Percentage
Track 5 (brown fill)	NMR Bulk volume moveable(BVM)	Percentage unit
Track 4 (blue fill)	NMR Bulk volume irreducible (BVI)	Percentage unit
Track 5	NMR T2 spectrum	
Track 6 (red flags)	Pay flags (>5% porosity, <40% SW)	
Track 7 (green flags)	Neutron-density crossplot flags	

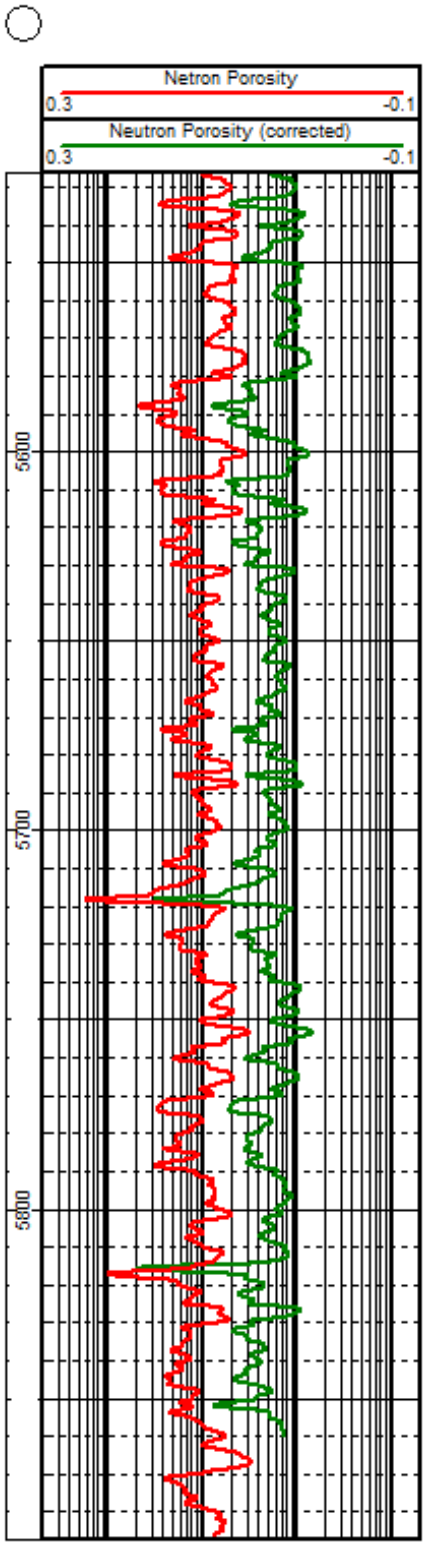


Figure 2-1. Single well cross section comparison of original neutron porosity curve and the corrected neutron porosity curve. Note that the original neutron curve (red) systematically overestimates porosity. The corrected curve has been calibrated to the proper lithology (dolomite) and yields accurate porosity values.

2.2 Salina Group

2.2.1 Basic Wireline Log Analysis

The Salina group is a massively bedded sequence of alternating evaporite and carbonate formations. The Salina Group is considered the regional confining unit for reef reservoirs due to its lithology, thickness, and extent. The Salina Group in the Lawnichak 9-33 well is represented by ~1,200 ft. of evaporite and ~350 ft. of mixed carbonate material. Few pay flags were identified for the entire Salina Group as the water saturation values were too high due to extremely high resistivity readings in the evaporite strata. Few neutron density crossplot flags were identified throughout the Salina. The low porosity and poor reservoir quality of the Salina Group suggests a sufficient confining unit (Figure 2-2).

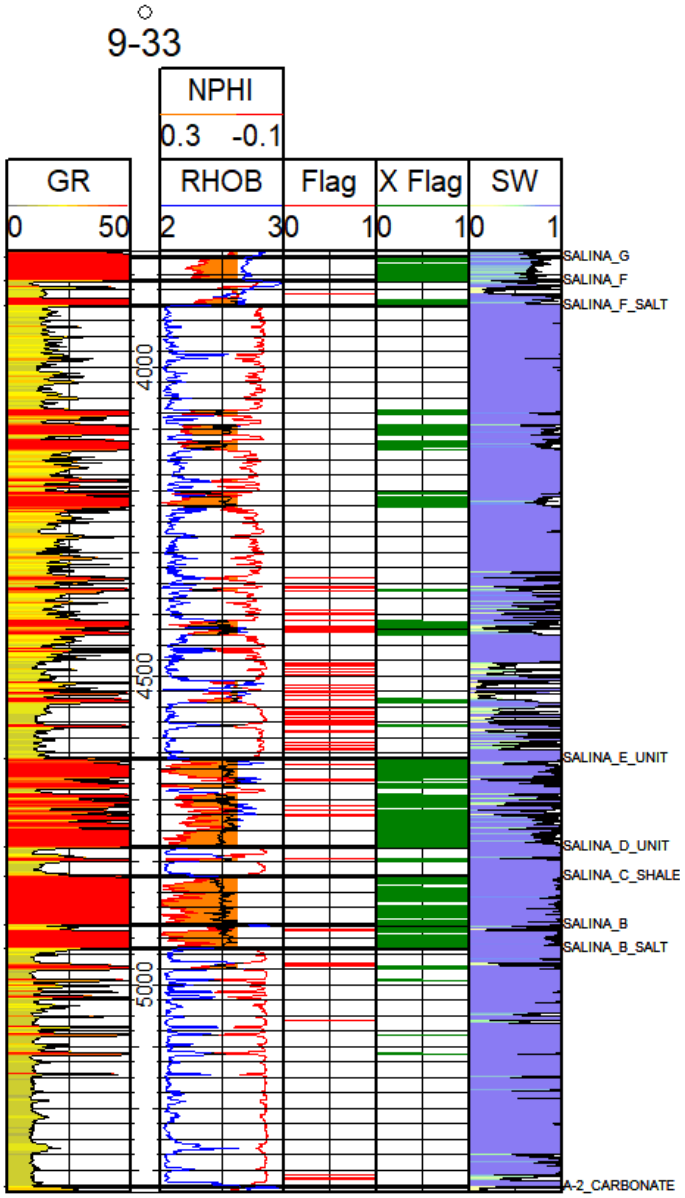


Figure 2-2. Single well cross section of the Salina Group in the Lawnichak 9-33 well

2.2.2 Advanced Wireline Log Analysis

Image Log Analysis

Salina D-Unit

The Salina D-Unit's profile shows as a massively-bedded, heterogenous unit with borehole-parallel elongate conductive features appearing sporadically throughout a resistive material (Figure 2-3). No distinctive bedding planes are encountered in the image log. The texture observed in the EBI image shows a largely resistive profile and a lack of distinctive bedding planes. This paired with the extremely low bulk density observed in the triple combo profile suggests that the Salina D-unit is a massively bedded halite.

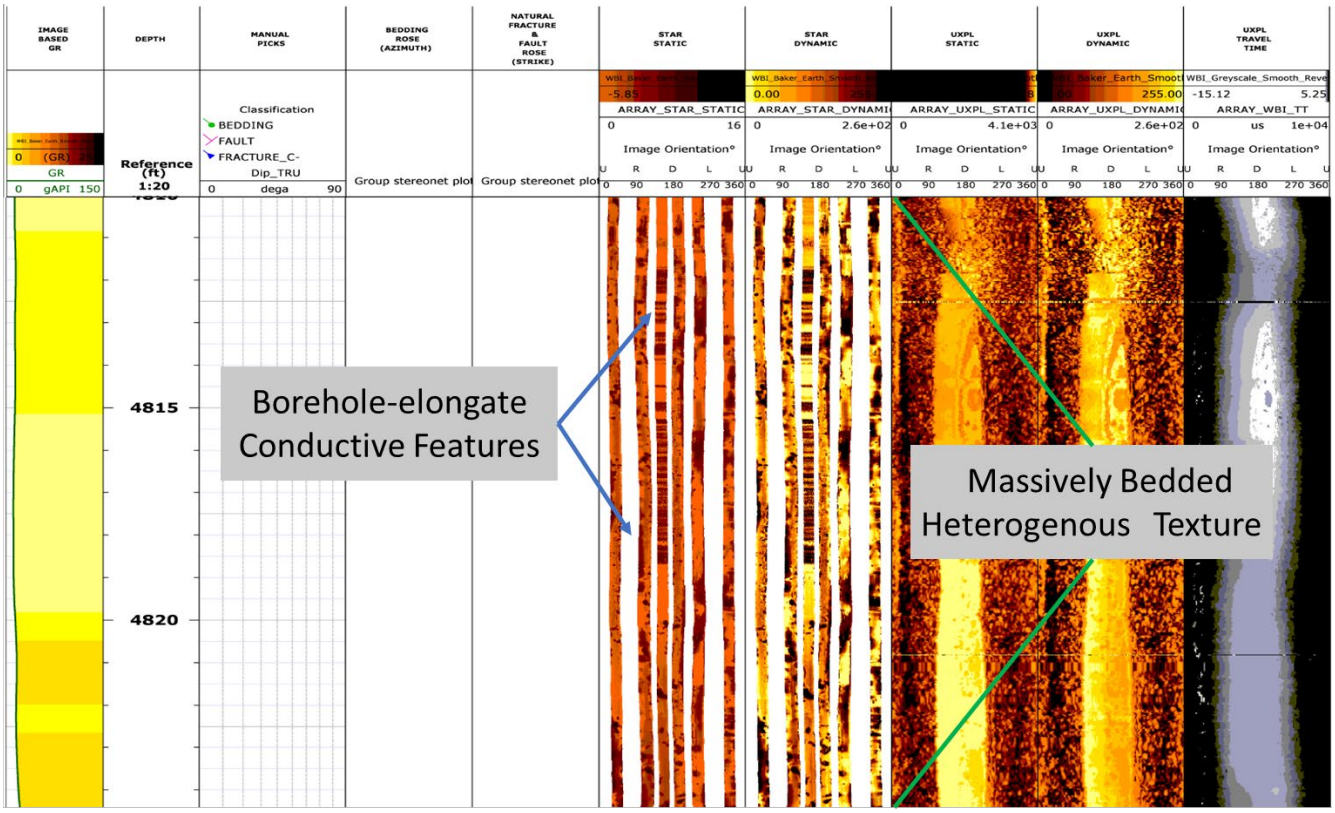


Figure 2-3. Annotated image log of the Salina D Unit from ~4,810 ft. to 4,825 ft. This texture is described as a massively bedded heterogenous salt with elongated conductive features occurring parallel to the wellbore.

Salina C-Shale

The Salina C-shale's EBI profile is observed as a layered conductive, mostly homogenous material (Figure 2-4). Bedding planes easily distinguishes with dipmeter data showing variable dip directions due to the low-angle dips. Faults are seen at 4,874 ft. and 4,850 ft. and natural fractures occur at various depths throughout. Near homogenously conductive EBI textures are interpreted to be thinly bedded shales/micrites, due to their high gamma ray values and uniformly conductive profile (commonly associated with the presence of clay-bound water or microporosity). There are no intervals interpreted to exhibit significant porosity or permeability within the Salina C-shale.

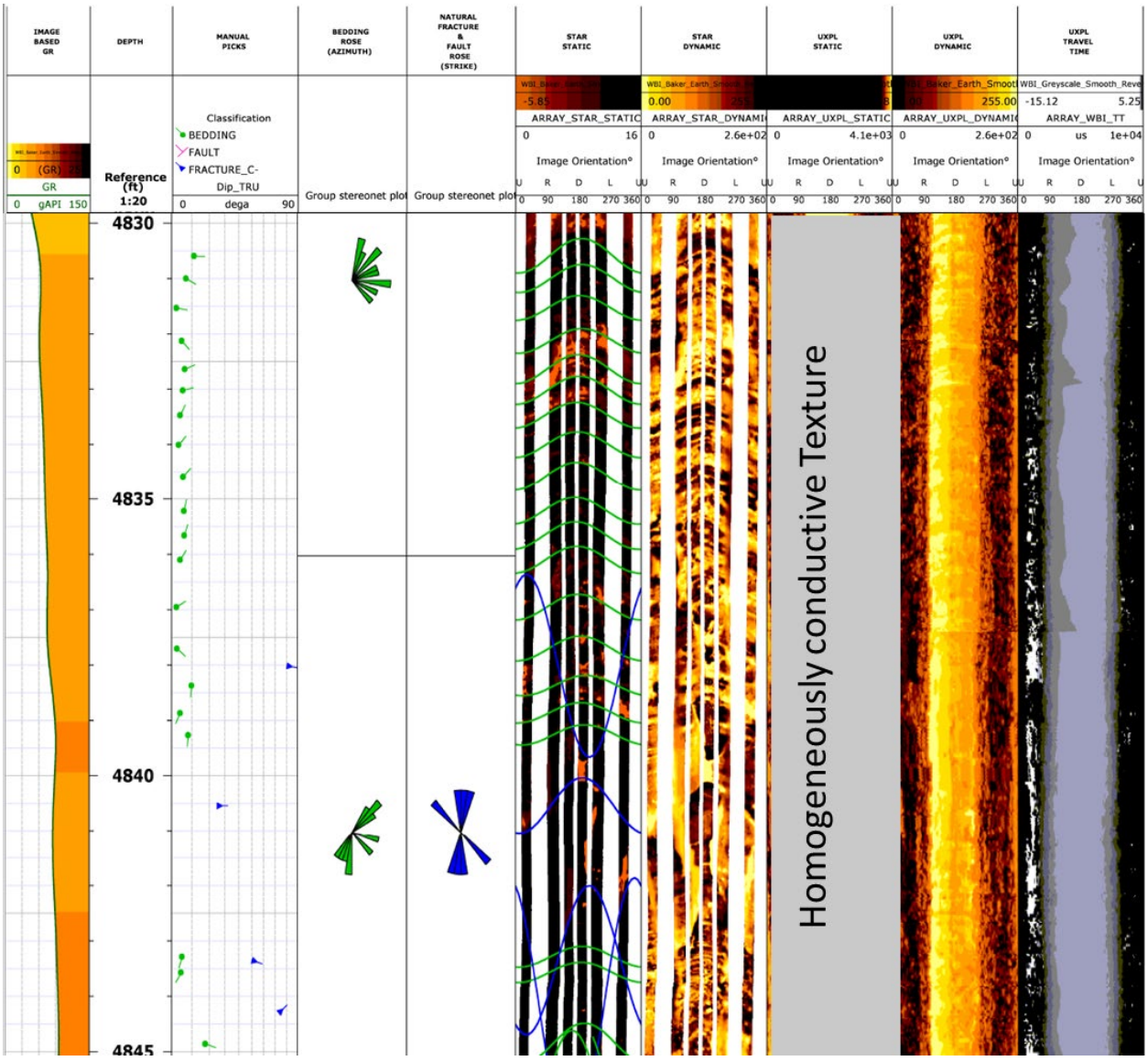


Figure 2-4. Annotated image log of the Salina C Shale from ~4,830 ft. to 4,845 ft. The texture is described as largely conductive with distinct bedding planes. This interval is interpreted to be interbedded shale/micrite with fractures and faults resulting from post-depositional compaction.

Salina B-Unit

The EBI profile of the Salina B-Unit shows a homogenously conductive material bedded with resistive material (Figure 2-5). Dip meter data is collected mostly from conductive zones and are chaotically orientated. Fracture occurrence is constrained to conductive zones. Homogenously conductive zones are interpreted to be micrite/shale due to its high gamma ray and uniformly conductive show (often associated with the presence of clay-bound water or microporosity). Thickly-bedded resistive material is interpreted to be tight limestone/dolostone due to its moderate bulk density value, low gamma ray value and resistive EBI profile. There are no intervals interpreted to exhibit significant porosity or permeability within the Salina B-unit.

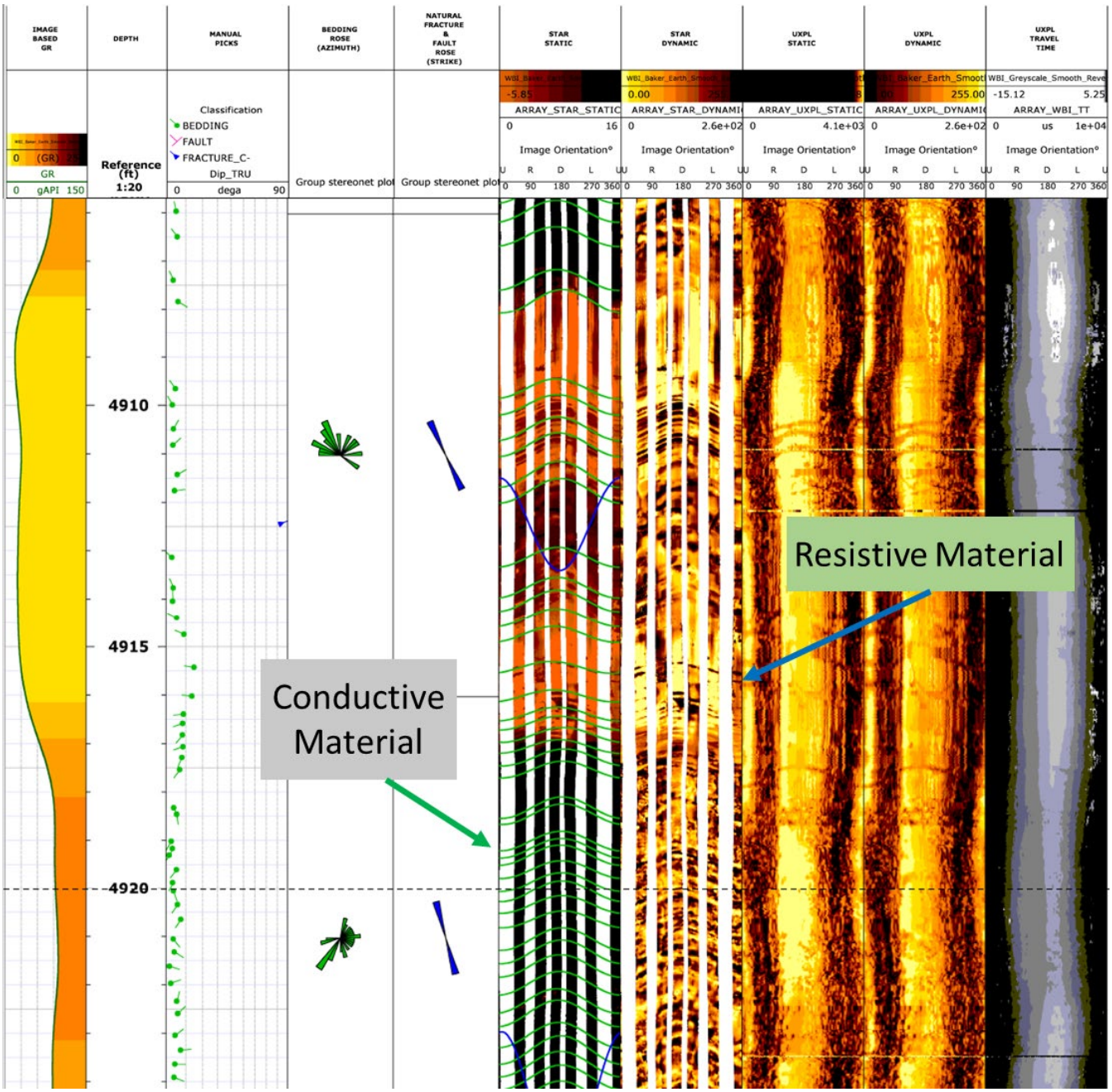


Figure 2-5. Annotated FMI image log of the Salina B Unit from ~4,905 ft. to 4,925 ft. This zone is described as bedded conductive and resistive material that is interpreted to be thinly bedded limestone and shale/micrite.

Salina B-Salt

The EBI texture of the Salina B-Salt is observed as cyclical zones of thin-bedded conductive material overlain by thick-to-massively bedded resistive material (Figure 2-6). The conductive zones have semi-spherical resistive features cross-cutting into conductive beds. The resistive interval is largely uniform, with some small to large irregularly shaped discontinuous conductive features occurring throughout the material. Materials occur cyclically, alternating between relatively thin accumulations of conductive material to thick zones of resistive material. Natural

fractures exist throughout the unit. Fractures dip roughly 80^0 toward the northeast or southeast. Conductive zones are interpreted to be thinly bedded shales/micritic due to their high gamma ray signatures and uniform conductive profiles (often associated with clay bound or microporosity). Resistive intervals are interpreted to be massive deposits of halite due to their low gamma ray and bulk density signatures along with their resistive EBI profile. There are no intervals interpreted to exhibit significant porosity or permeability within the Salina B-salt.

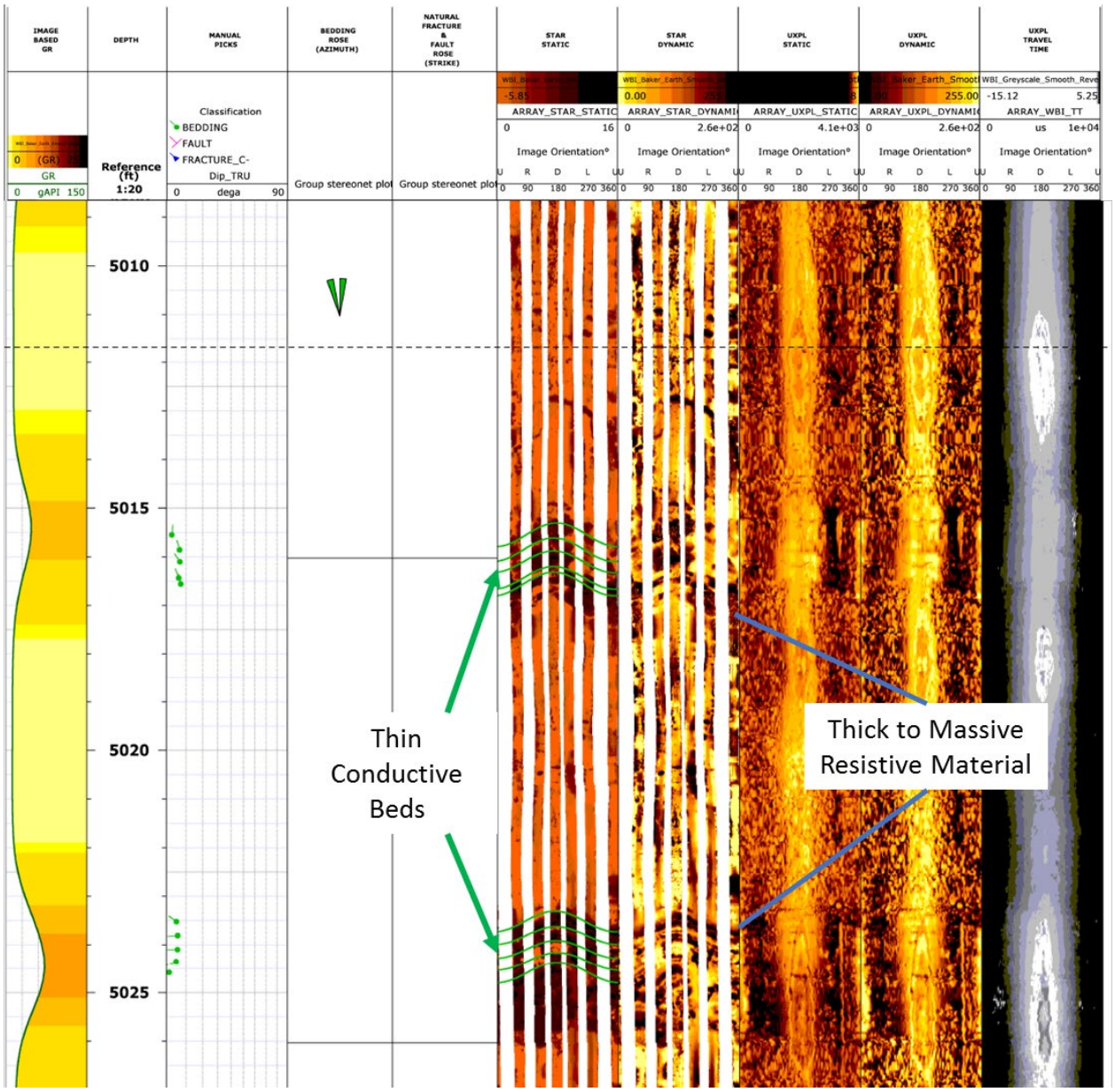


Figure 2-6. Annotated FMI image log of the Salina B Salt from ~5,009 ft. to 5,027 ft. This unit is described as cyclical occurrences of thinly bedded zones of conductive material overlain by thick-to-massively bedded resistive material.

2.3 A2 Carbonate and A2 Evaporite

2.3.1 Basic Wireline Log Analysis and Petrophysical Calculations

The A-2 Carbonate formation was encountered at a depth of 5,326 ft. and extended to a depth of 5,407 ft. for a gross thickness of 81 ft. Basic petrophysical calculations were computed for the A-2 Carbonate using a porosity cutoff of 5% and a water saturation cutoff of 40% (Table 2-3). Net thickness was 2 ft. for a net-to-gross ratio of 2.5%.

The A-2 Carbonate is a fairly heterogenous formation as indicated by the large degree of scattering on the neutron-density crossplot (Figure 2-7) but is dominantly a tight dolomite. Log analysis yielded an average porosity of 1.2% with porosity values ranging from 0-6.6%. Pay flags were identified using a 5% porosity cutoff and a 40% water saturation cutoff (Figure 2-8).

Table 2-3. A-2 Carbonate zone footages - 5% porosity and 40% water saturation cutoffs

Gross Thickness (ft.)	Net Thickness (ft.)	NGR	Porosity ft.	Avg. Porosity
81	2	0.025	0.112	0.056

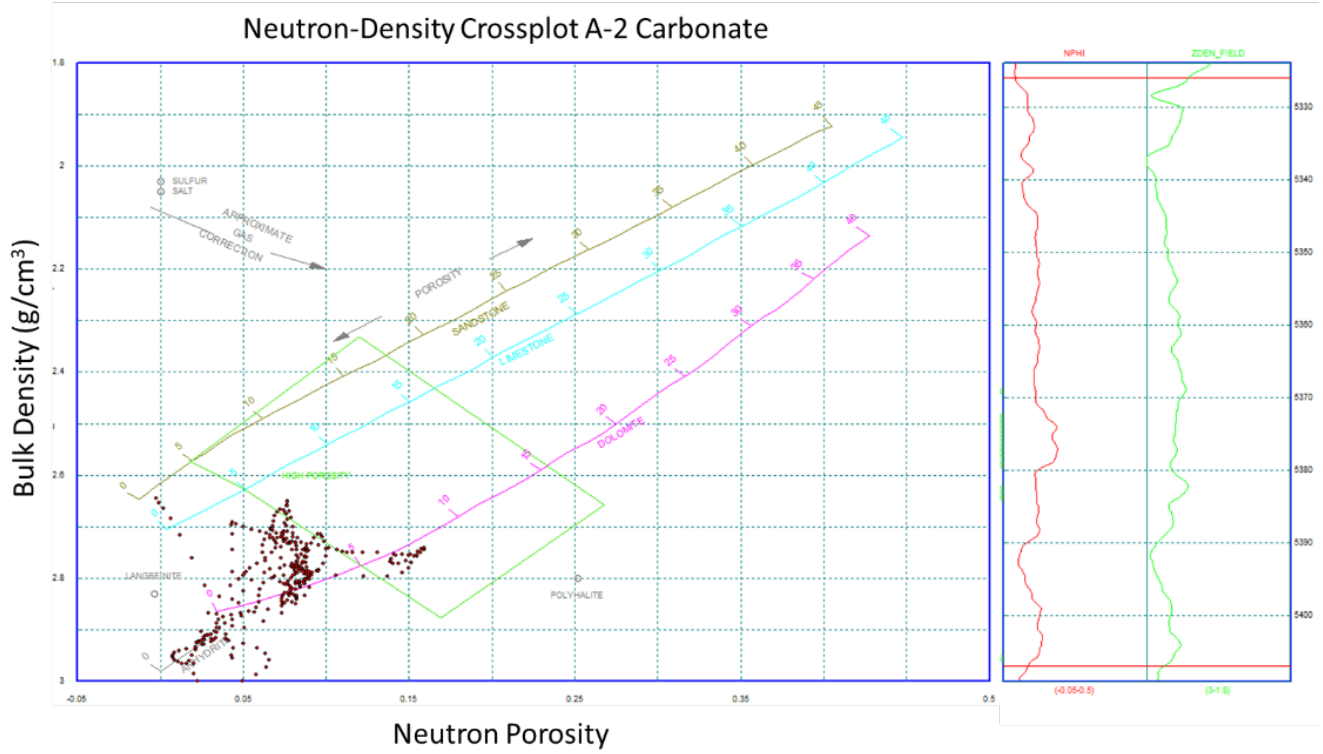


Figure 2-7. Neutron-density crossplot of the A-2 Carbonate using the original neutron porosity log. Note that porosity values here are overestimated but lithology is accurate.

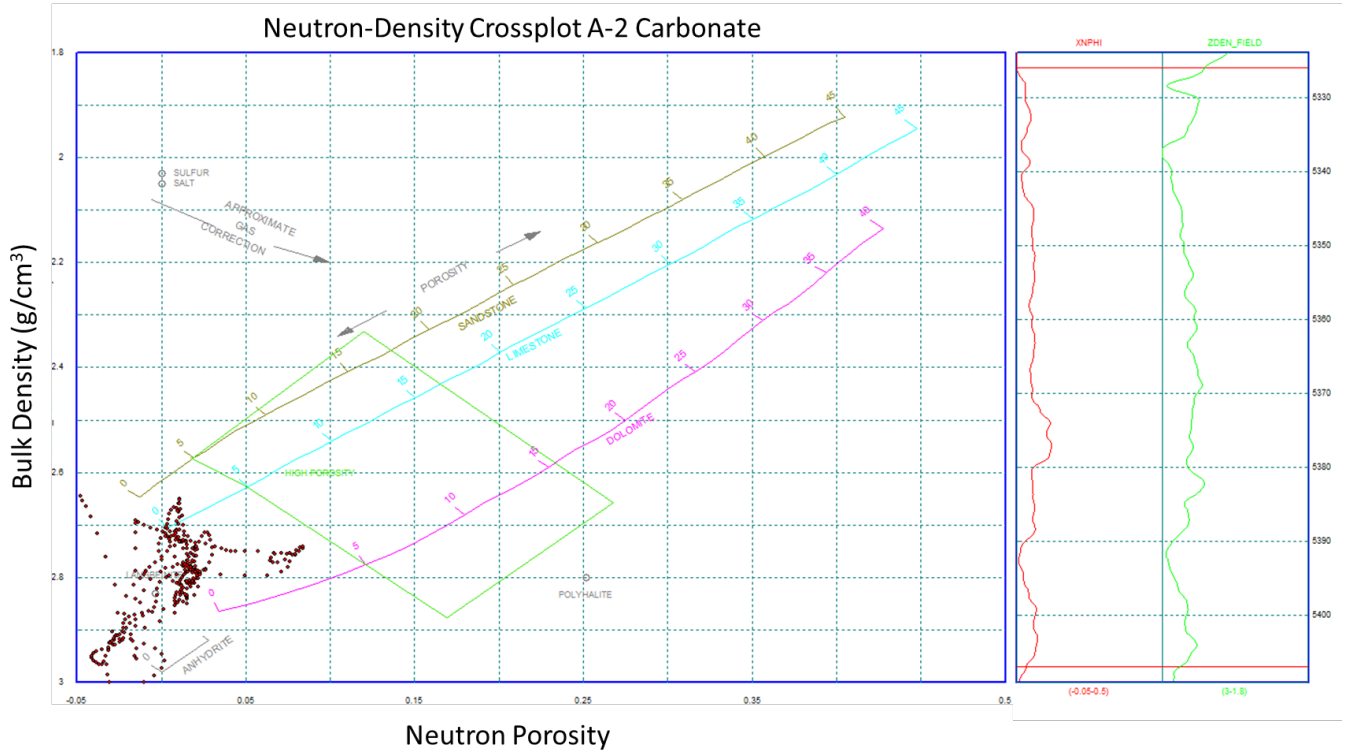


Figure 2-8. Neutron-density crossplot of the A-2 Carbonate using the calibrated neutron porosity log. Note that porosity values here are accurate but lithology is not.

The A-2 Evaporite formation was encountered at a depth of 5,407 ft. and extended to a depth of 5,455 ft. for a gross thickness of 48 ft. Basic petrophysical calculations were computed for the A-2 Evaporite using a porosity cutoff of 5% and a water saturation cutoff of 40% (Table 2-4). Net thickness was 1.75 ft. for a net-to-gross ratio of 3.6%.

The A-2 Evaporite is a heterogenous formation composed largely of anhydrite and evaporite material with strings of dolomite and carbonate (Figure 2-9). Log analysis yielded an average porosity of -0.8% with porosity values ranging from -5.6-5.5%. No crossplot porosity flags or pay flags were identified for this formation (Figure 2-10 and Figure 2-11). Overall, the A-2 Evaporite was anhydrite with little to no porosity, suggesting a sufficient confining unit.

Table 2-4. A-2 Evaporite zone footages - 5% porosity cutoff and 40% water saturation cutoff

Gross Thickness (ft.)	Net Thickness (ft.)	NGR	Porosity ft.	Avg. Porosity
48	1.75	0.036	0.093	-0.008

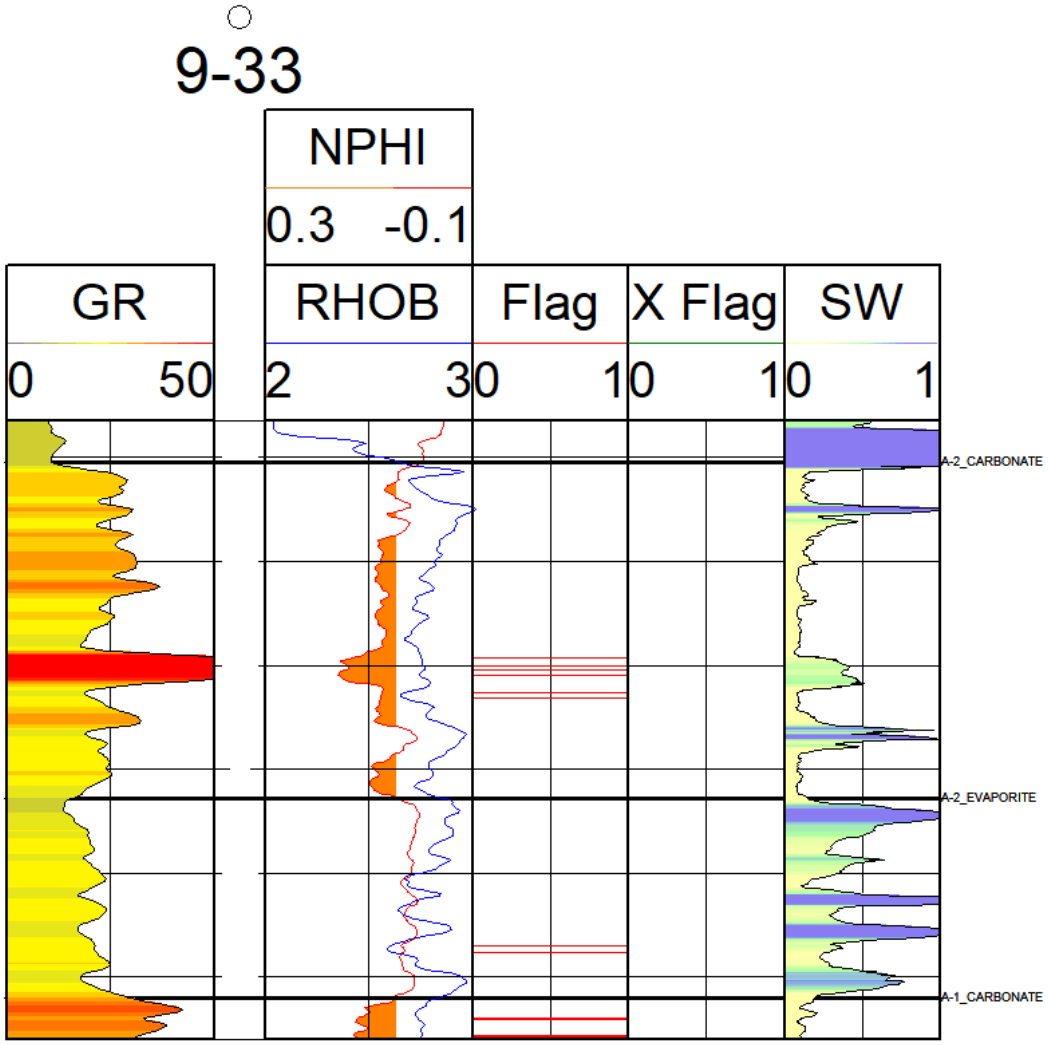


Figure 2-9. Single well cross section of the A-2 Carbonate and A-2 Evaporite in the Lawnichak 9-33 well

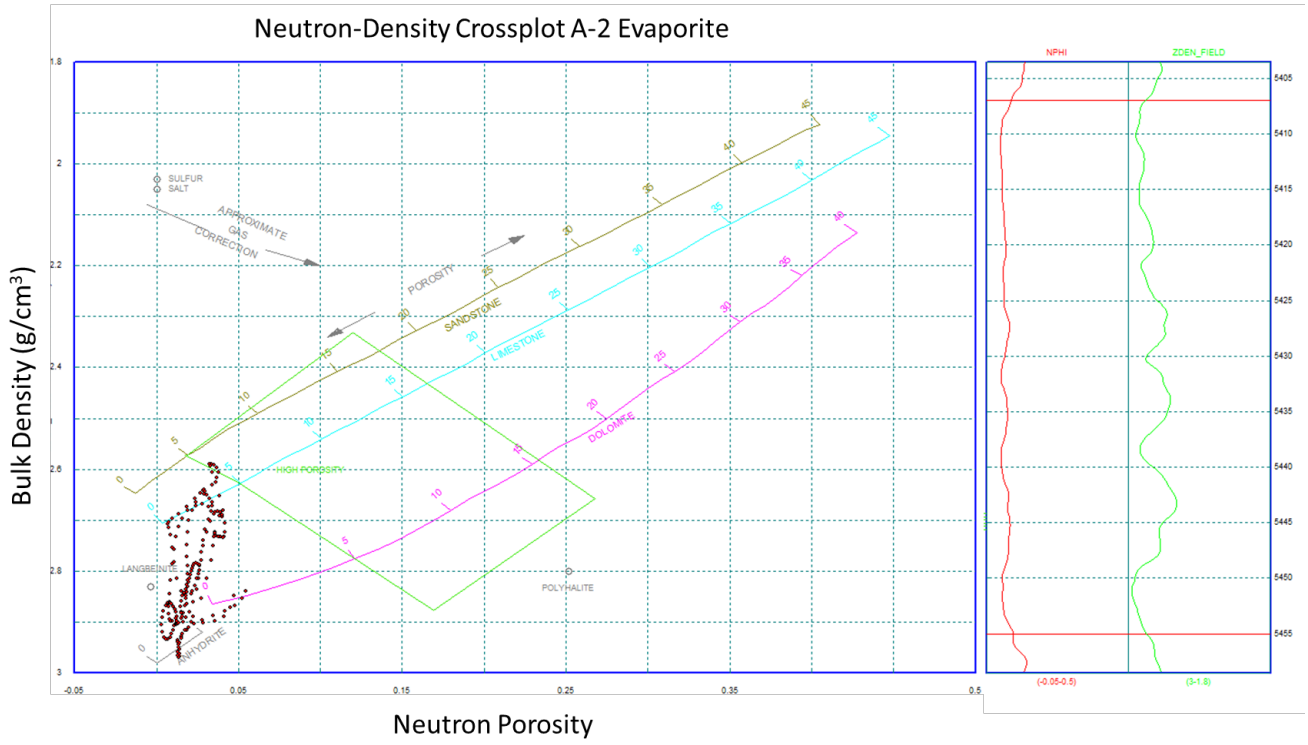


Figure 2-10. Neutron-density crossplot of the A-2 Evaporite using the original neutron porosity log. Note that porosity values here are overestimated but lithology is accurate.

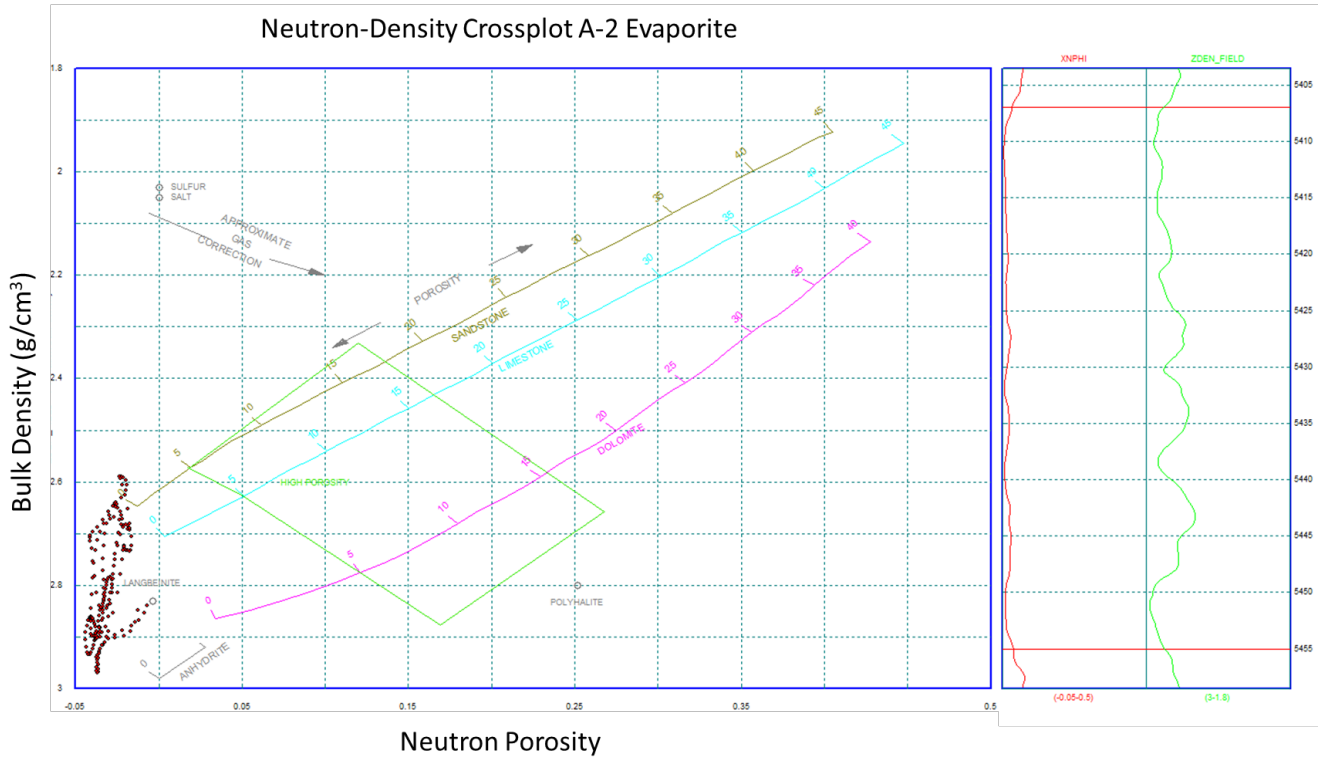


Figure 2-11. Neutron-density crossplot of the A-2 Evaporite using the calibrated neutron porosity log. Note that porosity values here are accurate but lithology is not.

2.3.2 Advanced Wireline Log Analysis

Elemental Spectroscopy Log Analysis

The A-2 Carbonate is a somewhat heterogenous admixture of carbonates, both dolomite and calcite, and evaporite minerals, namely halite and anhydrite, which occurs between 5,326 ft. MD/5,223 ft. TVD and 5,407 ft. MD/5,209 ft. TVD (Figure 2-12). Peaks in sulfur content relative to aluminum, paired with high levels of calcium, indicate anhydrite presence ($CaSO_4$) at Lawnichak 9-33. Examination of white light (WL) and ultraviolet light (UV) photographs of a rotary sidewall core (RSWC) sample collected from within one such enriched sulfur zone at 5,330.5 ft. MD indicates that anhydrite, which exhibits light yellow fluorescence under UV light, is likely filling pore spaces instead of forming massive beds. A marked increase in potassium, as well as associated thorium and aluminum indicates the presence of clay minerals from approximately 5,372 ft. MD to 5,380 ft. MD. This zone is highlighted with a dashed orange box on Figure 2-12. RSWC photographs in Figure 2-12 collected from within this interval at 5,374 ft. MD display fine scale laminations of clay minerals and carbonate rock.

The A-2 Evaporite consists primarily of halite, with minor carbonate and anhydrite that increases towards the top and base (Figure 2-12). This unit extends from 5,407 ft. MD/5,209 ft. TVD to 5,455 ft. MD/5,328 ft. TVD. Predictably, this unit has far less calcium relative to the overlying A-2 Carbonate Formation.

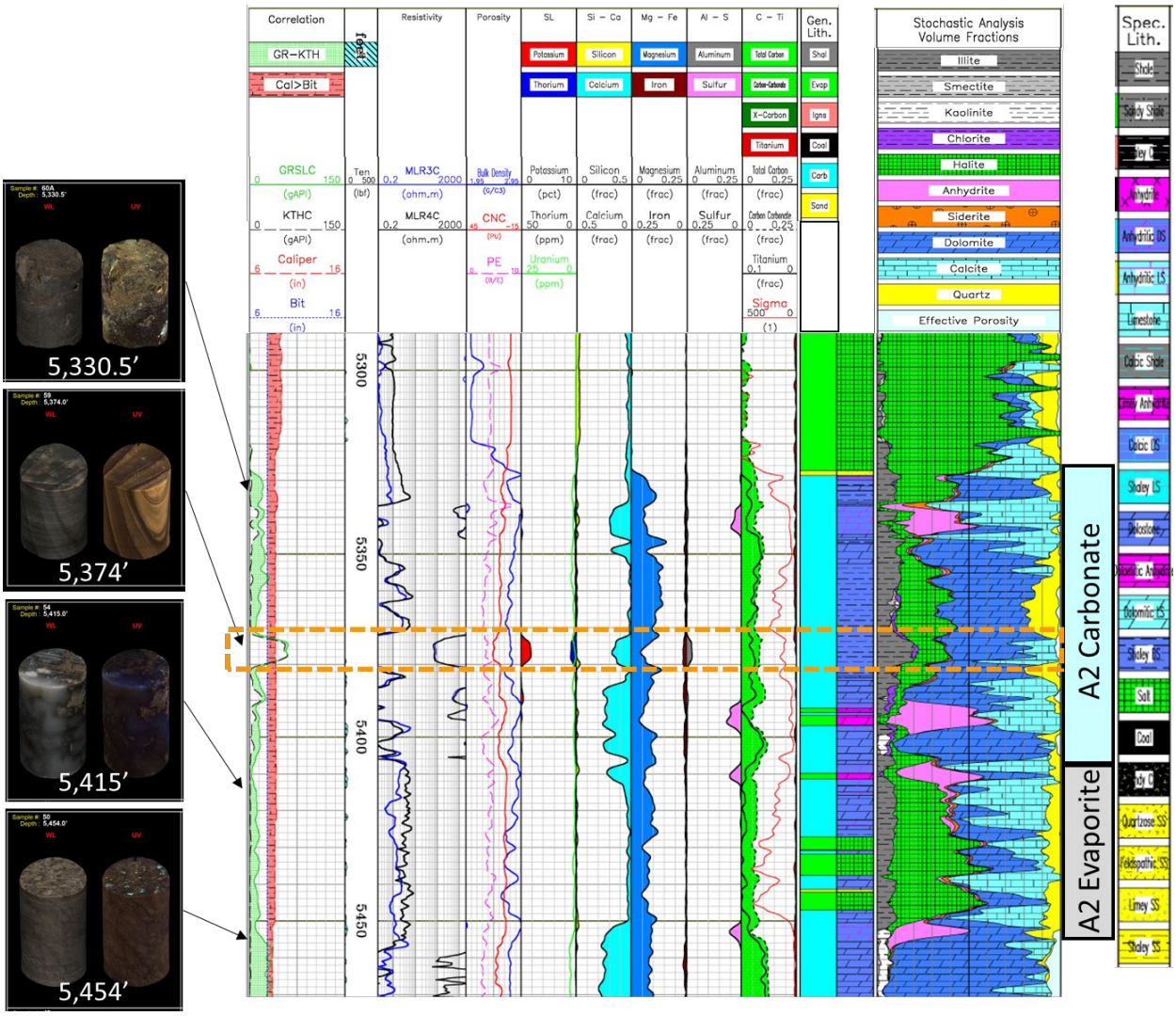


Figure 2-12. Formation Lithology Explorer Digital Spectralog (FLeX) log from Lawnichak 9-33 displaying the A-2 Carbonate and A2 Evaporite Formations from 5,326 ft. MD/5,223 ft. TVD to 5,455 ft. MD/5,328 ft. TVD. Select Rotary Side Wall Core (RSWC) samples are shown in both white light (WL) and ultraviolet light (UV) to provide context for lithologic descriptions. Orange box marks zone with high clay mineral content.

Image Log Analysis

A-2 Carbonate

The A-2 Carbonate is observed as a thinly interbedded interval consisting of materials that exhibit subtle changes in resistivity, only apparent in dynamic profile (Figure 2-13). The unit is thinly to thickly bedded with bedding dipping roughly 10º to the southeast. Fractures exist at various depths throughout, dipping roughly 80º-90º to the northeast. This interval is interpreted to be thinly bedded shales/mudstones interbedded with anhydrite-bearing carbonate materials, due high bulk densities and high photoelectric and fluctuating gamma ray profiles. There are no intervals interpreted to exhibit significant porosity or permeability within the A-2 Carbonate.

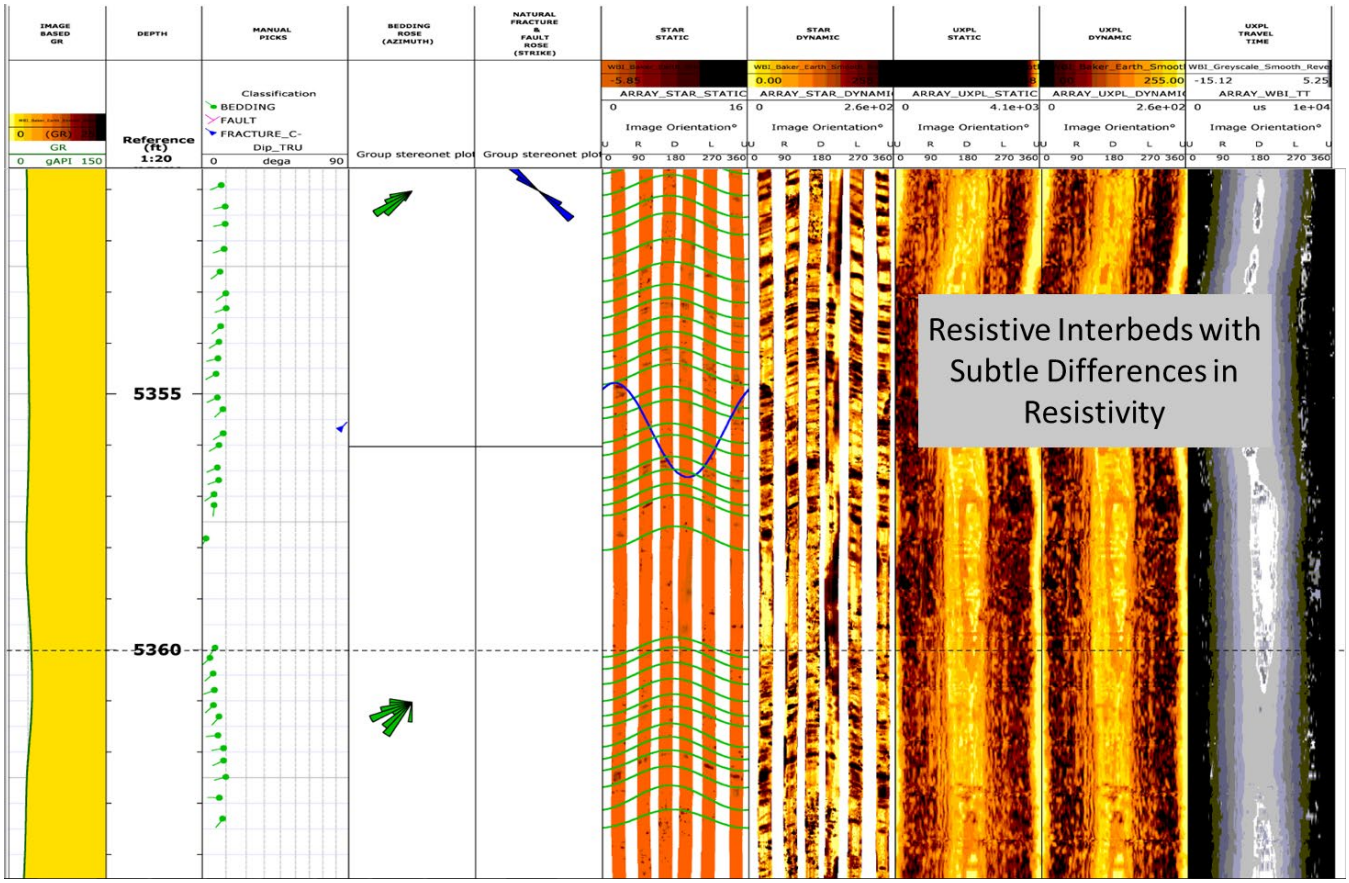


Figure 2-13. Annotated FMI image log of the A-2 Carbonate from ~5,351 ft. to 5,364 ft. The texture is described as thinly interbedded intervals of materials that exhibit subtle changes in resistivity.

A-2 Evaporite

The A-2 Evaporite is observed as resistive material with moderate amounts of isolated conductive features occurring throughout with no distinctive bedding contacts (Figure 2-14). Some conductive features are medium to large sized and are elongated parallel to the borehole. This zone is interpreted to be thickly bedded anhydrite-bearing material (possibly anhydrite/carbonate mixture). Borehole elongate conductive features are interpreted to be spalling features resulting from the well drilling process due to their high conductively and borehole parallel trend. There are no intervals interpreted to exhibit significant porosity or permeability within the A-2 Evaporite.

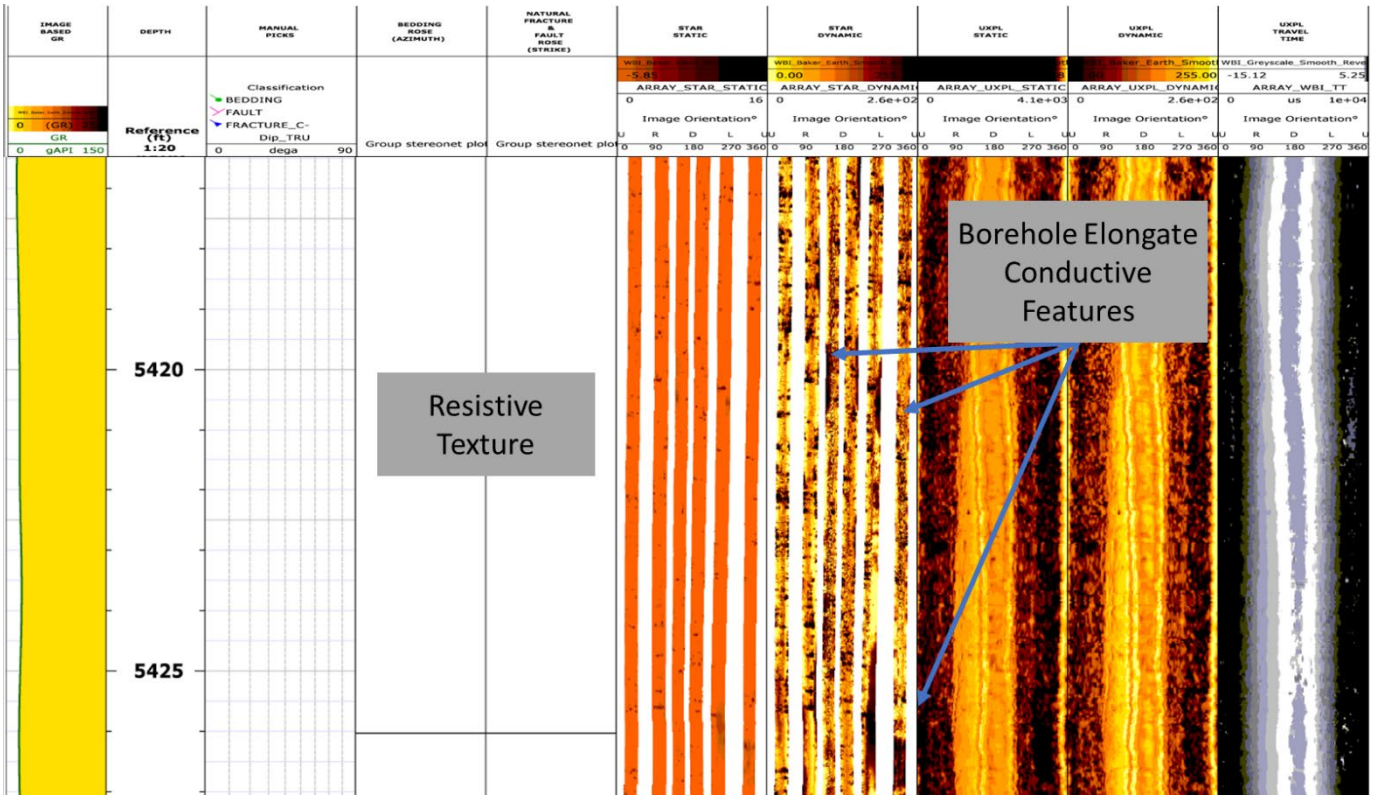


Figure 2-14. Annotated FMI image log of the A-2 Evaporite from ~5,417 ft. to 5,427 ft. The texture zone is described as largely resistive with moderate amounts of isolated conductive features occurring throughout and is interpreted to be thickly bedded mixture of anhydrite material

NMR Log Analysis

The NMR effective porosity and permeability logs for the A-2 carbonate and A-2 Evaporite show no zones of significant porosity or permeability (Figure 2-15). These formations do not provide any significant reservoir quality based on the NMR log as most fluid in pore spaces is either irreducible water or clay-bound water, neither of which are considered moveable fluids.

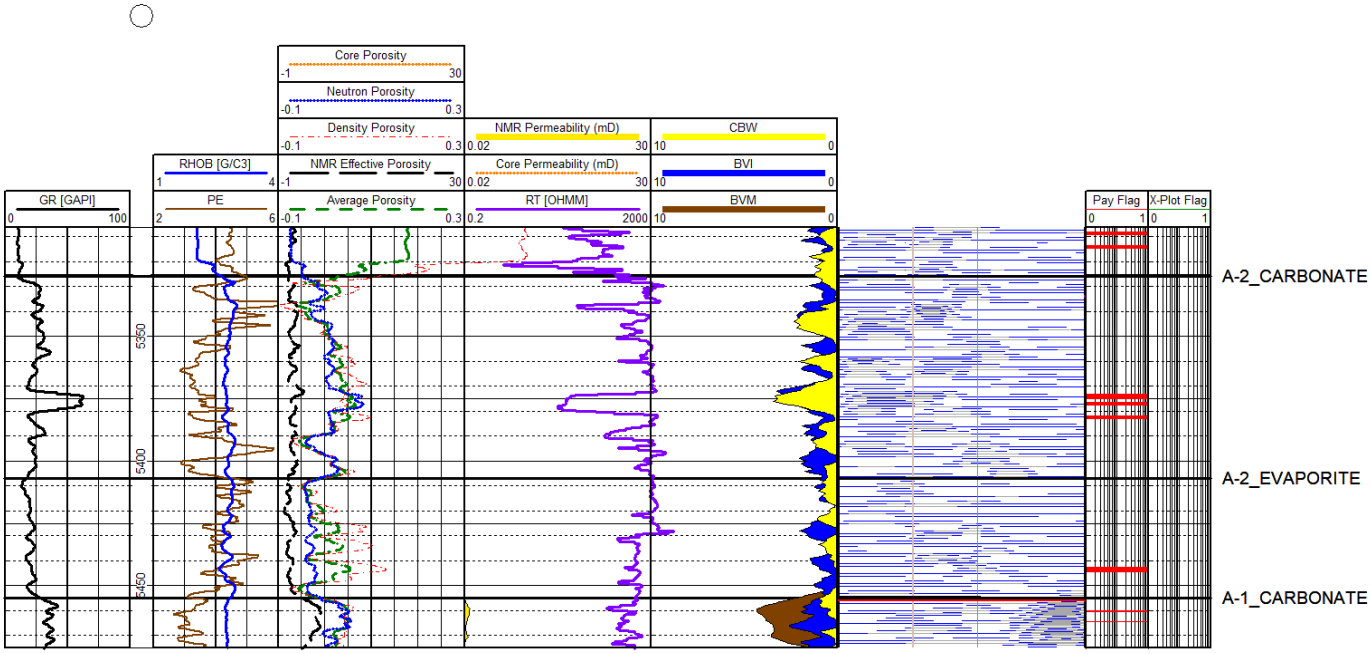


Figure 2-15. Cross section of MREX NMR log data, select logs from the triple combo log suite, and pay flags generated from triple combo logs and neutron-density crossplots for the A-2 Carbonate and A-2 Evaporite. NMR effective porosity log is plotted with neutron porosity, density porosity, and average porosity logs derived from the triple combo log suite. Permeability, BVM, BVI, CBW, and T2 distributions are also displayed.

2.3.3 Core Analysis

Conventional core samples were not recovered for the A-2 Carbonate or the A-2 Evaporite in Dover 9-33. Rotary side wall core (RSWC) samples were recovered for both formations.

A-2 Carbonate

Sidewall core photos of the A-2 Carbonate at Dover 9-33 show a mixed carbonate and anhydrite formation with laminations of alternating light and dark colors (Figure 2-16). UV light images show potential residual oil and stylolites. Small-to-large vugs (some salt plugged), open fractures, and blotches of carbonate mud are present.

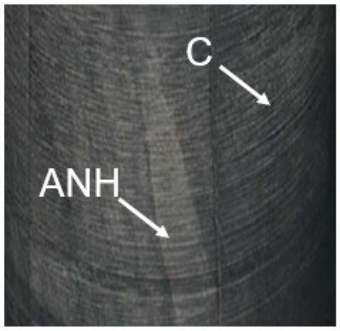
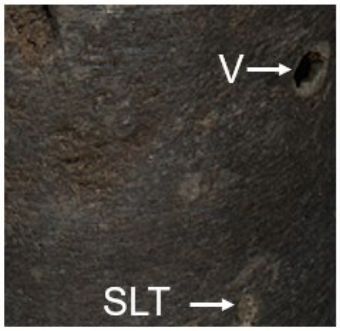
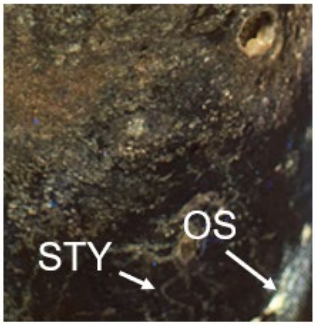
Depth Ft.	White Light Primary Features	UV Light Primary Features	Descriptions
5,330			White Light: Mixed carbonate and anhydrite, alternating light gray and dark layers. UV Light: Alternating light and dark layers.
5,330.5			White Light: Brown carbonate, large vugs, salt plugged vugs. UV Light: Light blue UV response due to potential residual oil, stylolites.

Figure 2-16. Annotated RSWC images with corresponding core descriptions of the A-2 Carbonate for depths 5,330 ft. to 5,330.5 ft.

A-2 Evaporite

Sidewall core photos of the A-2 Evaporite at Dover 9-33 show a predominantly anhydrite matrix with alternating dark and light gray laminations and some minor mixed carbonate matrix. The A-2 Evaporite cores show a relatively homogenous section of anhydrite that is devoid of many sedimentary structures/features (Figure 2-17). UV light images show potential residual oil in some zones.

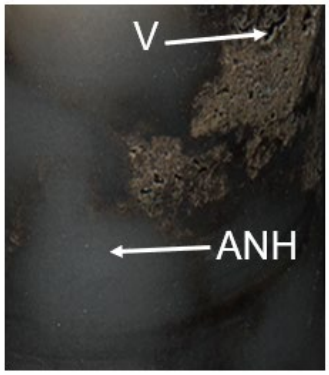
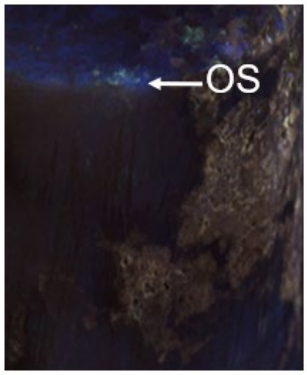
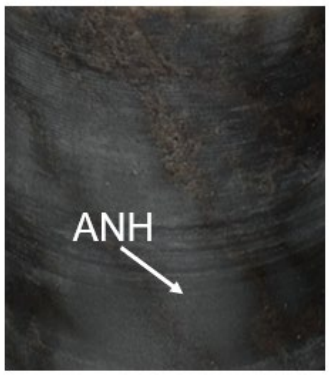
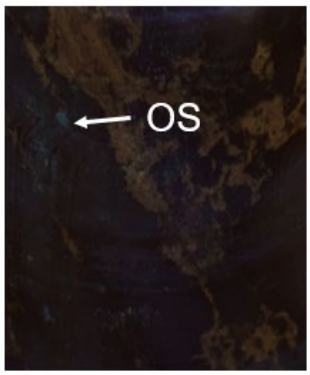
Depth Ft.	White Light Primary Features	UV Light Primary Features	Descriptions
5,415			White Light: Mixed anhydrite and carbonate matrix, small vugs. UV Light: Light blue UV response due to potential residual oil.
5,430			White Light: Mixed anhydrite and carbonate matrix, marbled pattern, some carbonate. UV Light: Light blue UV response due to potential residual oil.

Figure 2-17. Annotated RSWC images with corresponding core descriptions of the A-2 Evaporite for depths 5,415 ft. to 5,430 ft.

2.4 A-1 Carbonate

2.4.1 Basic Wireline Log Analysis and Petrophysical Calculations

The A-1 Carbonate formation was encountered at a depth of 5,455 ft. and extended to a depth of 5,546 ft. for a gross thickness of 91 ft. Basic petrophysical calculations were computed for the A-2 Carbonate using a porosity cutoff of 5% and a water saturation cutoff of 40% (Table 2-5). Net thickness was 5.125 ft. for a net-to-gross ratio of 5.6%.

The A-1 Carbonate is dominantly a relatively low permeability dolomite with minor anhydrite (Figure 2-20). Log analysis yielded an average porosity of 3.1% with porosity values ranging from 0-9.8%. Crossplot porosity flags were generated for data points exceeding 5% crossplot porosity at one distinct interval between ~5,532-5,536 ft. (Figure 2-18 and Figure 2-19). Pay flags were also identified throughout the formation.

Table 2-5. A-1 Carbonate zone footages - 5% porosity and 40% water saturation cutoff

Gross Thickness (ft.)	Net Thickness (ft.)	NGR	Porosity ft.	Avg. Porosity
91	5.125	0.056	0.307	0.06

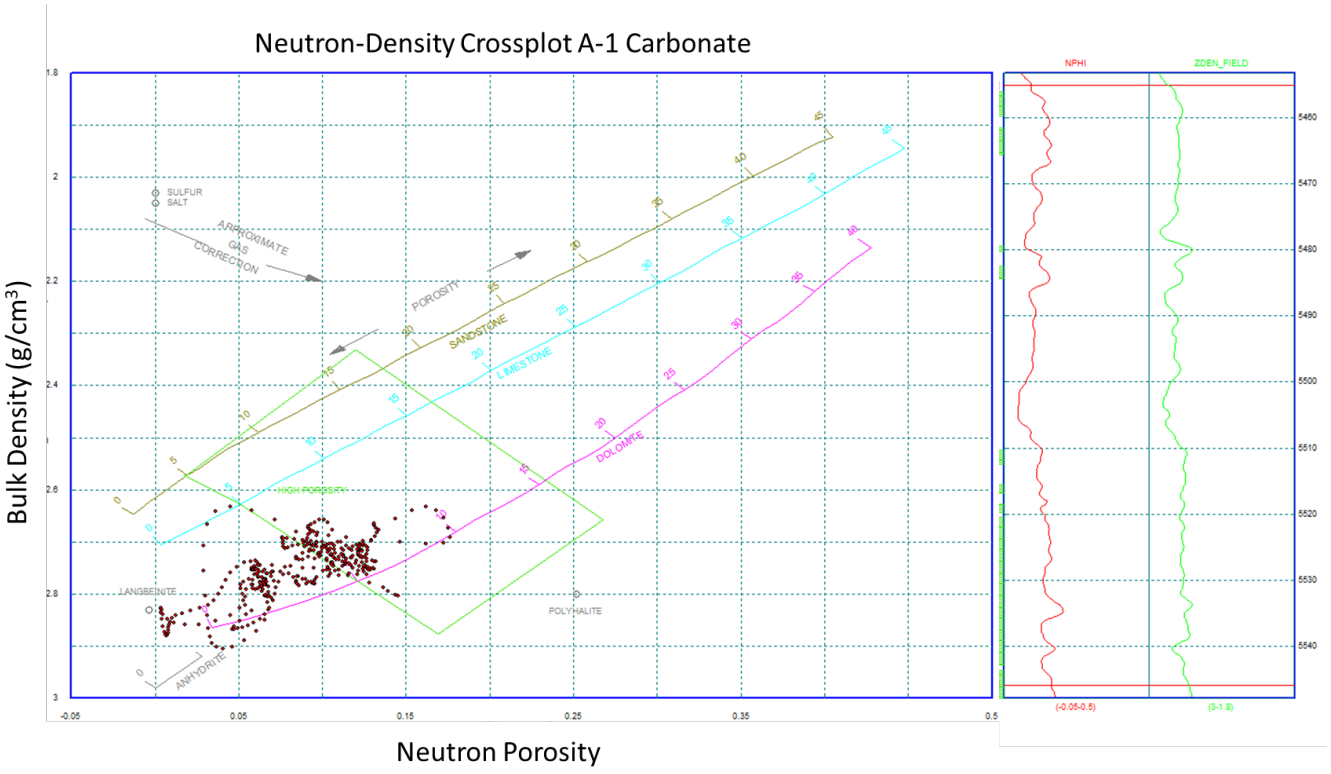


Figure 2-18. Neutron-density crossplot of the A-1 Carbonate using the original neutron porosity log. Note that porosity values here are overestimated but lithology is accurate.

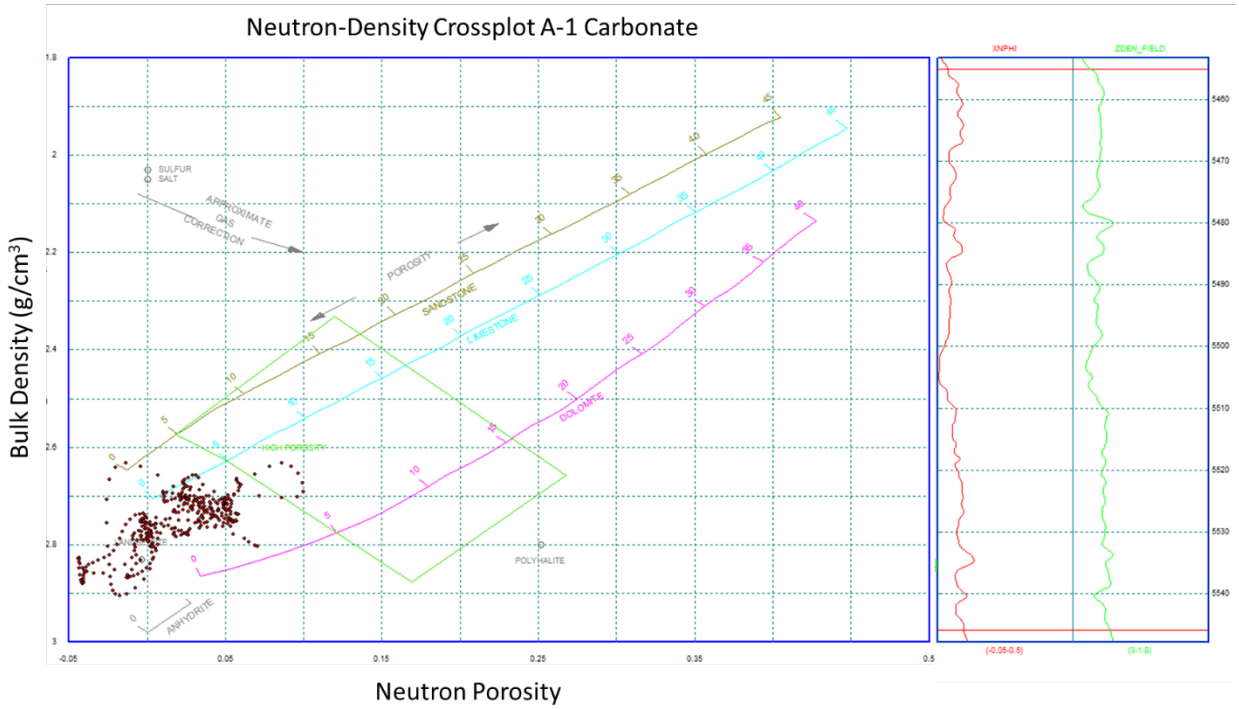


Figure 2-19. Neutron-density crossplot of the A-1 Carbonate using the calibrated neutron porosity log. Note that porosity values here are accurate but lithology is not.

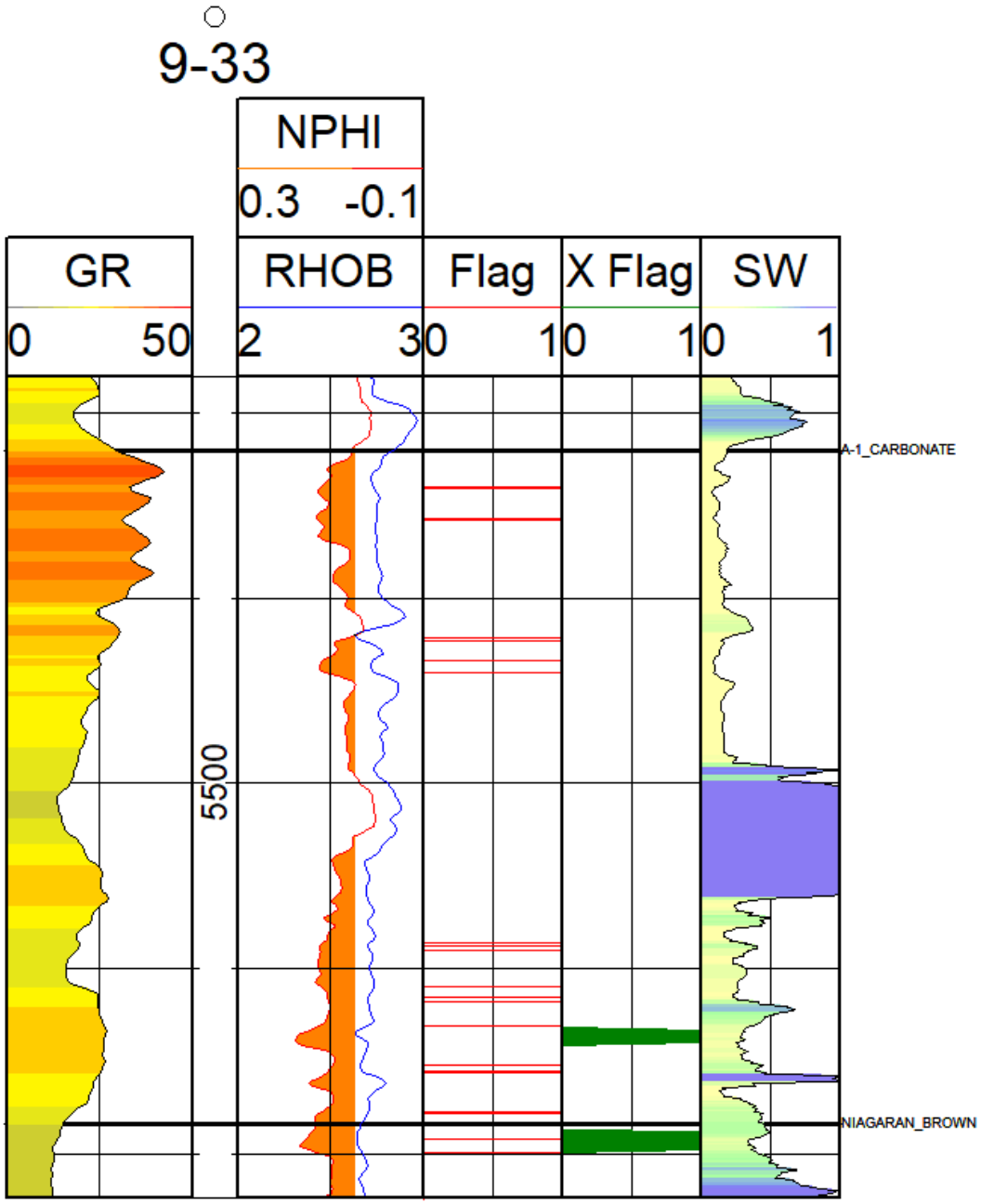


Figure 2-20. Single well cross section of the A-1 Carbonate in the Lawnichak 9-33 well

2.4.2 Advanced Wireline Log Analysis

Elemental Spectroscopy Log Analysis

The A-1 Carbonate Formation ranges from 5,455 ft. MD/5,328 ft. TVD to 5,546 ft. MD/5,397 ft. TVD. It consists primarily of dolomite, with anhydrite and calcite distributed sporadically throughout the upper two thirds of the unit. Examination of white light (WL) and ultraviolet light (UV) photographs of a rotary sidewall core (RSWC) sample collected from a depth correlated to an enriched sulfur zone at 5,503 ft. MD indicates that anhydrite, which exhibits light yellow fluorescence under UV light, is likely filling pore spaces instead of forming massive beds

(Figure 2-21). Likewise, there appears to be dark blue and bluish-green fluorescence present on the UV light photograph of a RSWC collected at 5,485 ft. MD (Figure 2-21). This depth corresponds with the elemental spectroscipy derived interpretation depth of calcite presence, and calcite is known to exhibit a vast array of colors in UV due to impurities. Again, the calcite distribution does not appear to be continuous, but rather concentrated in pore spaces or fracture fills. This zone of the A1 Carbonate with anhydrite and calcite pore plugging is highlighted in Figure 2-21 with a dashed orange box. The A-1 Carbonate from approximately 5,510 ft. MD to 5,546 ft. MD is a relatively homogenous dolomite with trace amounts of clay minerals.

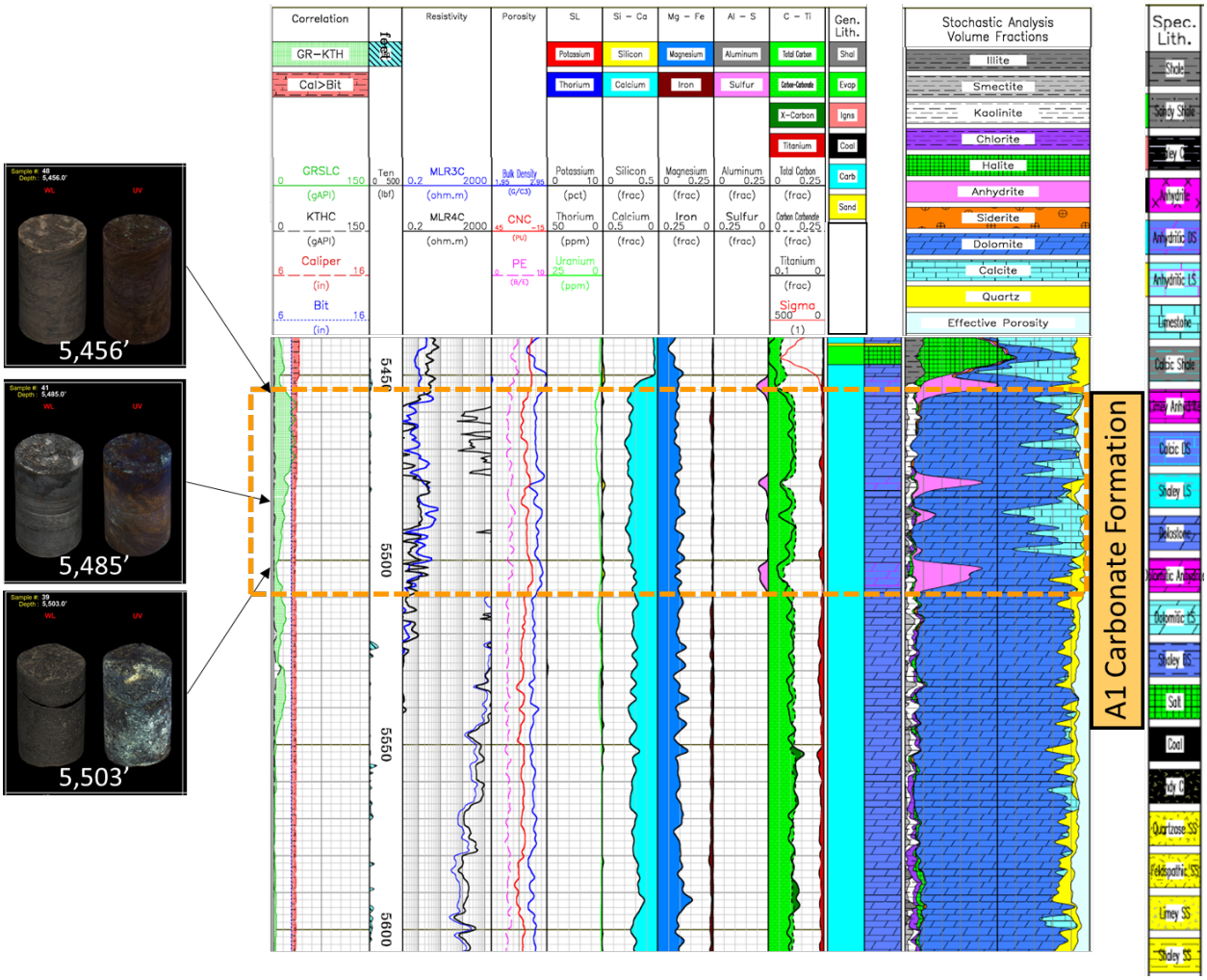


Figure 2-21. Formation Lithology Explorer Digital Spectralog (FLeX) log from Lawnichak 9-33 displaying the A-1 Carbonate Formation from 5,455 ft. MD/5,328 ft. TVD to 5,546 ft. MD/5,397 ft. TVD. Select Rotary Side Wall Core (RSWC) samples are shown in both white light (WL) and ultraviolet light (UV) to provide context for lithologic descriptions. Orange box marks zone with high sulfur spikes.

Image Log Analysis

Three distinct texture zones are observed in the A-1 Carbonate occurring from 5,455 ft. – 5,530 ft., 5,530 ft. – 5,538 ft. and 5,538 ft. to 5,546 ft. (Figure 2-22, Figure 2-23, Figure 2-24). The first texture zone (Figure 2-22) exists from 5455' to 5530' and is a resistive texture with fine, isolated conductive features occurring throughout a resistive matrix material. The occurrence of conductive features seems to be gradational, with a higher concentration occurring at the top of

what is interpreted to be bedding contacts. Large conductive features occur throughout the interval and are elongated parallel to the borehole's axis. This texture is interpreted to be mud-supported carbonate material, due to is moderate gamma reading and the gradational occurrence of conductive features. If conductive features are grain constituents (bioclasts, pellets, or ooids) then this suggests a coarsening upward trend where conductive features result from the dissolution of the constituents. Alternatively, if these conductive features are non-fabric selective vugs, this profile could represent surfaces of sub-areal exposure. Non-fabric selective vuggy form from the evaporation-driven precipitation of salt at sediment interfaces which later is dissolved post-depositionally, creating a non-fabric selective cavity (vug). Either of these interpretations would most likely occur within a peritidal environment, within intertidal to supratidal conditions where periodic sub-areal exposure, karstification or hydraulically-sorted peloids/ooids could be prevalent. This zone is interpreted to exhibit a low to moderate amount porosity development consisting predominantly of non-touching pores.

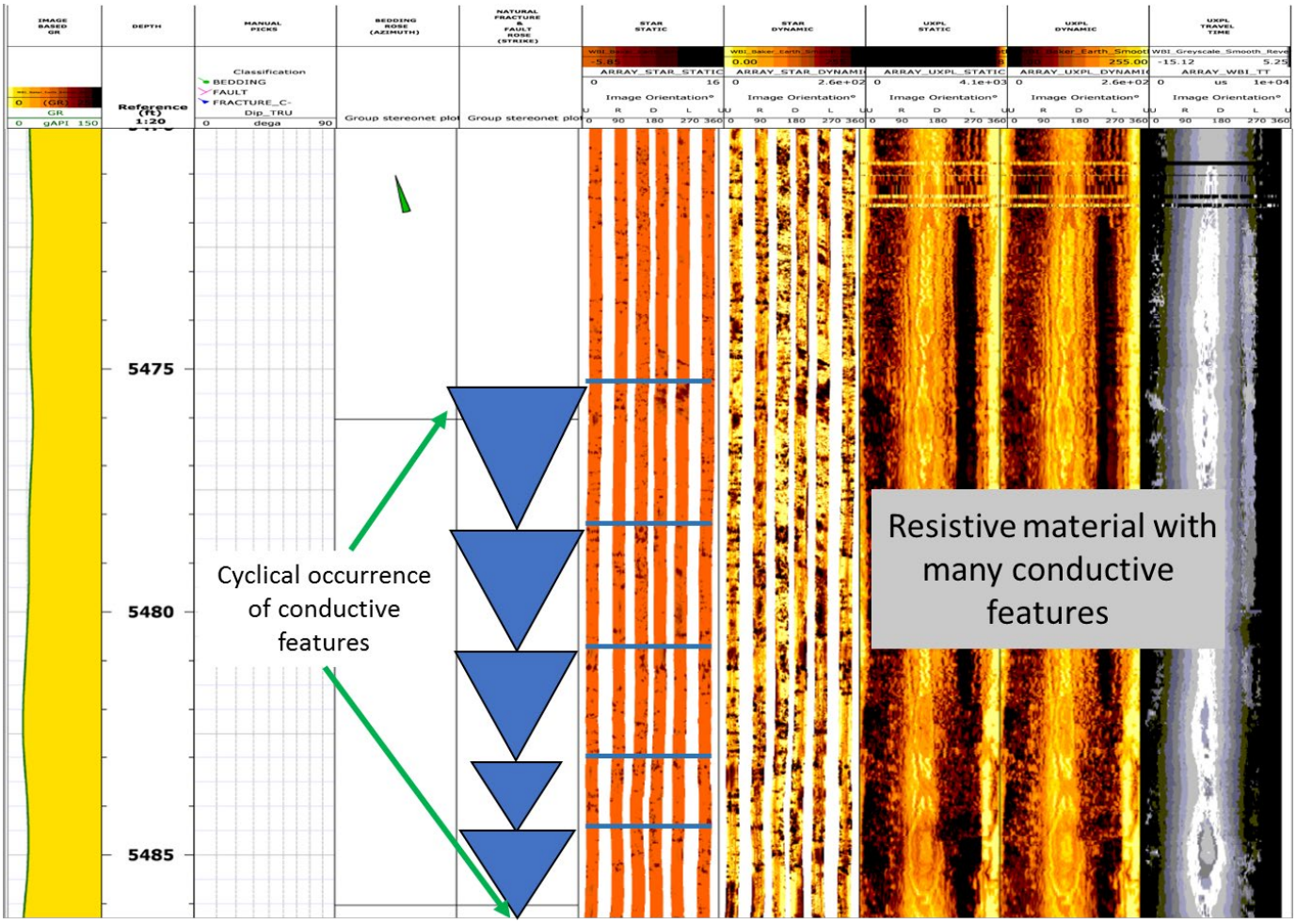


Figure 2-22. Annotated FMI image log of the A-1 Carbonate from ~5,470 ft. to 5,486 ft. The texture is described as a largely resistive material with cyclical occurrences of conductive features and is interpreted to be bedded mud-supported carbonate material (mudstone, wackestones, packestone etc.).

The second texture zone exists from 5,527 ft. to 5,538 ft. and is observed as a bedded heterogeneous texture consisting of resistive material with laterally continuous-to-semi continuous conductive features occurring throughout (Figure 2-23). Within the dynamic profile view, textures appear interwoven suggesting connectivity between features. Within dynamic view, bedded circular-to-linear conductive features appear orientated parallel to sub-parallel of bedding planes. Bedding contacts appear planar and are inclined, dipping 2º-5º to the south-southwest. Conversely, static view shows this zone as largely resistive with few isolated features; this suggests that features observed in dynamic view are subtle changes in resistivity likely related to small pore sizes. This interval has been calibrated to whole core, being identified as laminated microbial mats with abundant fenestrae “birds eye” porosity. This zone is interpreted to exhibit low to moderate reservoir potential due to probable connected fenestrae networks.

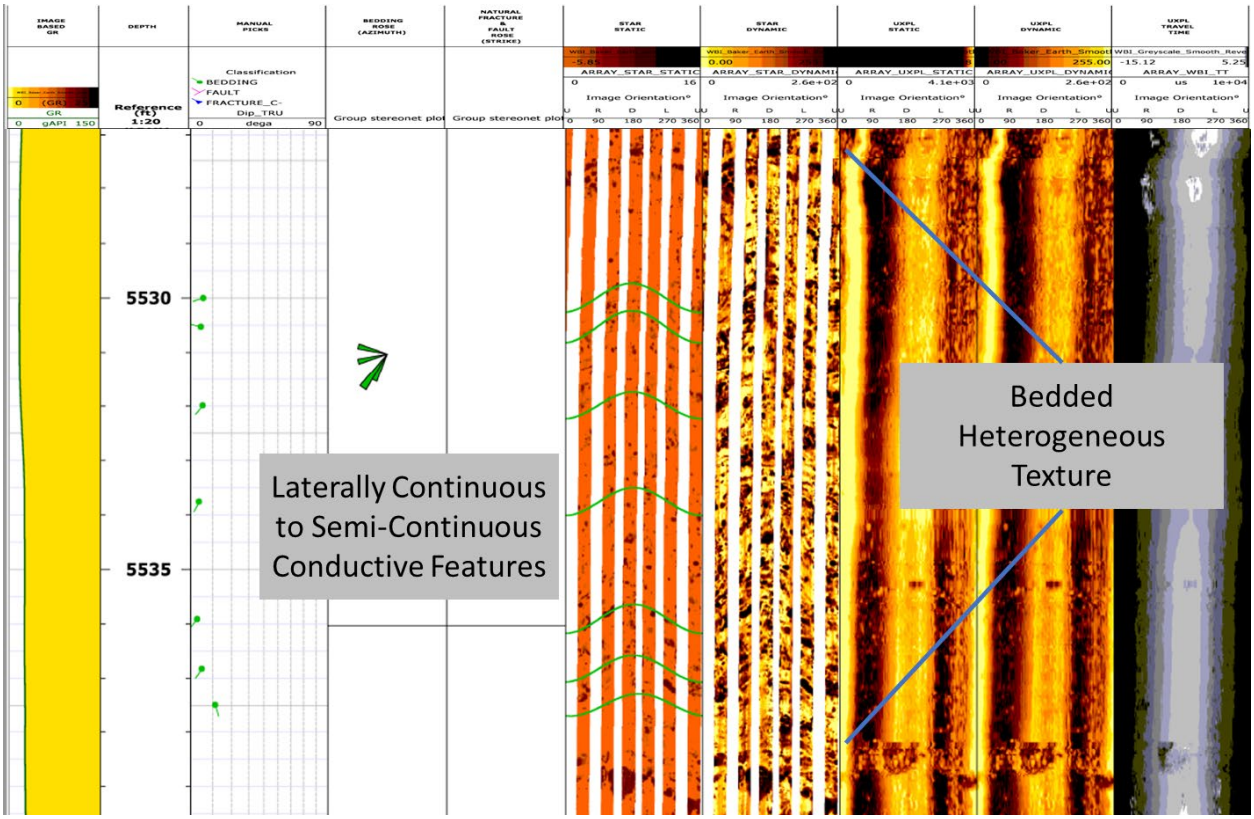


Figure 2-23. Annotated FMI image log of the A-1 Carbonate from ~5,527 ft. to 5,540 ft. This texture zone is described as a bedded heterogenous texture consisting of resistive material with lateral semi-continuous conductive features occurring within bedding planes.

The third texture zone exists from 5,538 ft. to 5,546 ft. and is observed as largely resistive texture with many small-to-large sized conductive features occurring within the matrix material (Figure 2-24). Most of the conductive features are isolated, however some features appear connected. There are no apparent bedding contacts within the interval. Within Dynamic view, the texture looks similar to the overlying texture zone, where conductive features seem bedded and elongate, however the occurrence of these overall are discontinuous to semi-continuous. This interval has been calibrated to whole, being witnessed as stromatolitic conglomerates with brecciated microbial mats held within tight mud matrix material.

Pore types were witnessed to be mainly vuggy or fenestral. This zone is interpreted to display a low potential for injection as it is mud supported and any porous features are discontinuous with a low probability of connectivity.

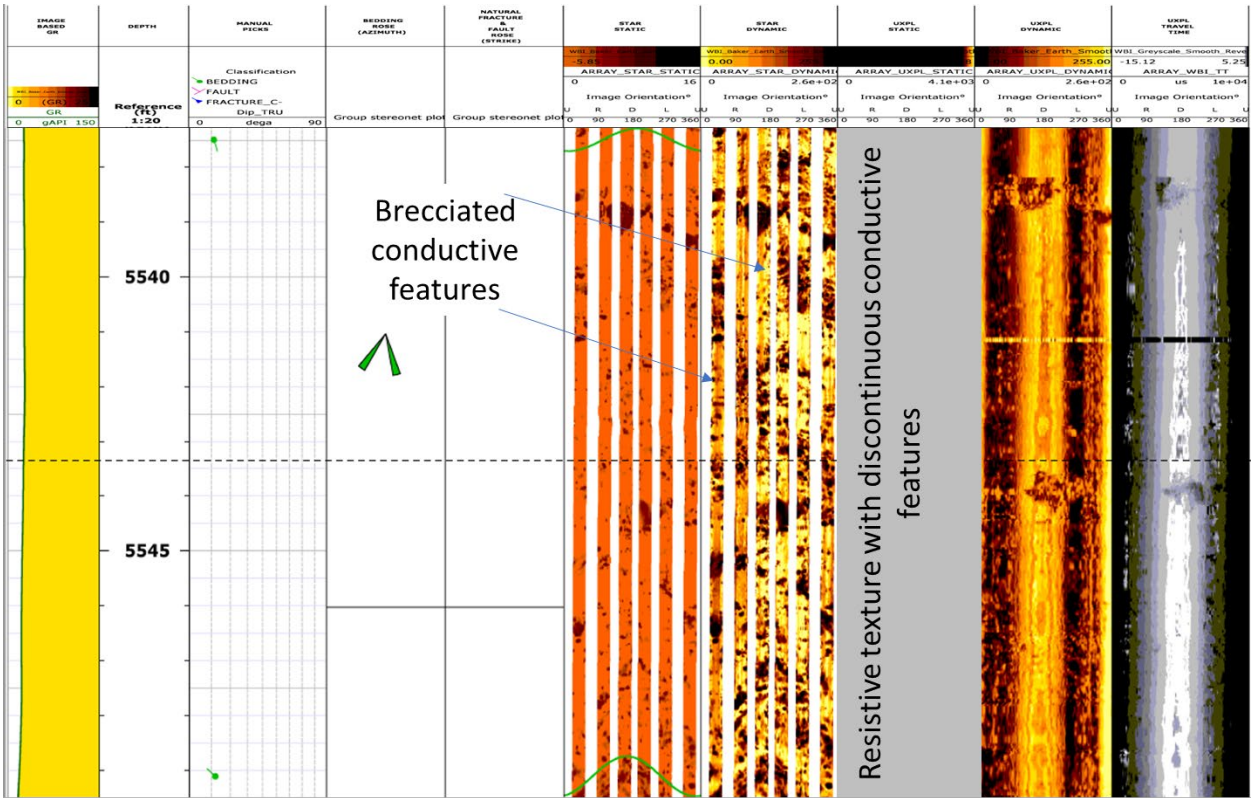


Figure 2-24. Annotated FMI image log of the A-1 Carbonate from ~5,538 ft. to 5,550 ft. Note the laminated discontinuous conductive features that occur throughout the resistive matrix, interpreted to be brecciated microbial laminates.

NMR Log Analysis

One distinct interval within the A-1 Carbonate (highlighted using a green transparent box) exhibits potential reservoir-quality permeability and effective porosity (Figure 2-25). The interval of interest exists at the basal part of the formation from ~5,507 ft. to 5,546 ft. and shows relatively high permeability peaks throughout that coincide with multiple flagged intervals from pay flags and crossplot flags (red and green flags). Like the first zone, the T2 spectrum in this zone suggests that the majority of fluids in place are moveable, having relaxation times equal to or greater than the 512 ms cutoff time. There is very minimal clay bound water in this interval. NMR permeability aligns well with core permeability spikes where core data is available (orange

x-symbols). NMR effective porosity and core porosity are within reasonable agreement as well and show relatively higher porosity throughout this interval.

2.4.3 Core Analysis

Conventional Core

The A-1 Carbonate at Dover 9-33 is mostly porous dolostone with some thin intervals of tighter dolomite (Figure 2-26 and Figure 2-27). The upper ~10 ft. of core was dominated by algal laminations, stromatoporoids, salt-filled fractures, and minor vugs. The lower section of the A-1 transitions to a more homogenous texture with significant zones of small-to-medium vugs, significant moldic/framework porosity, stylolites, large fractures and algal laminations. This section of core is relatively continuous.

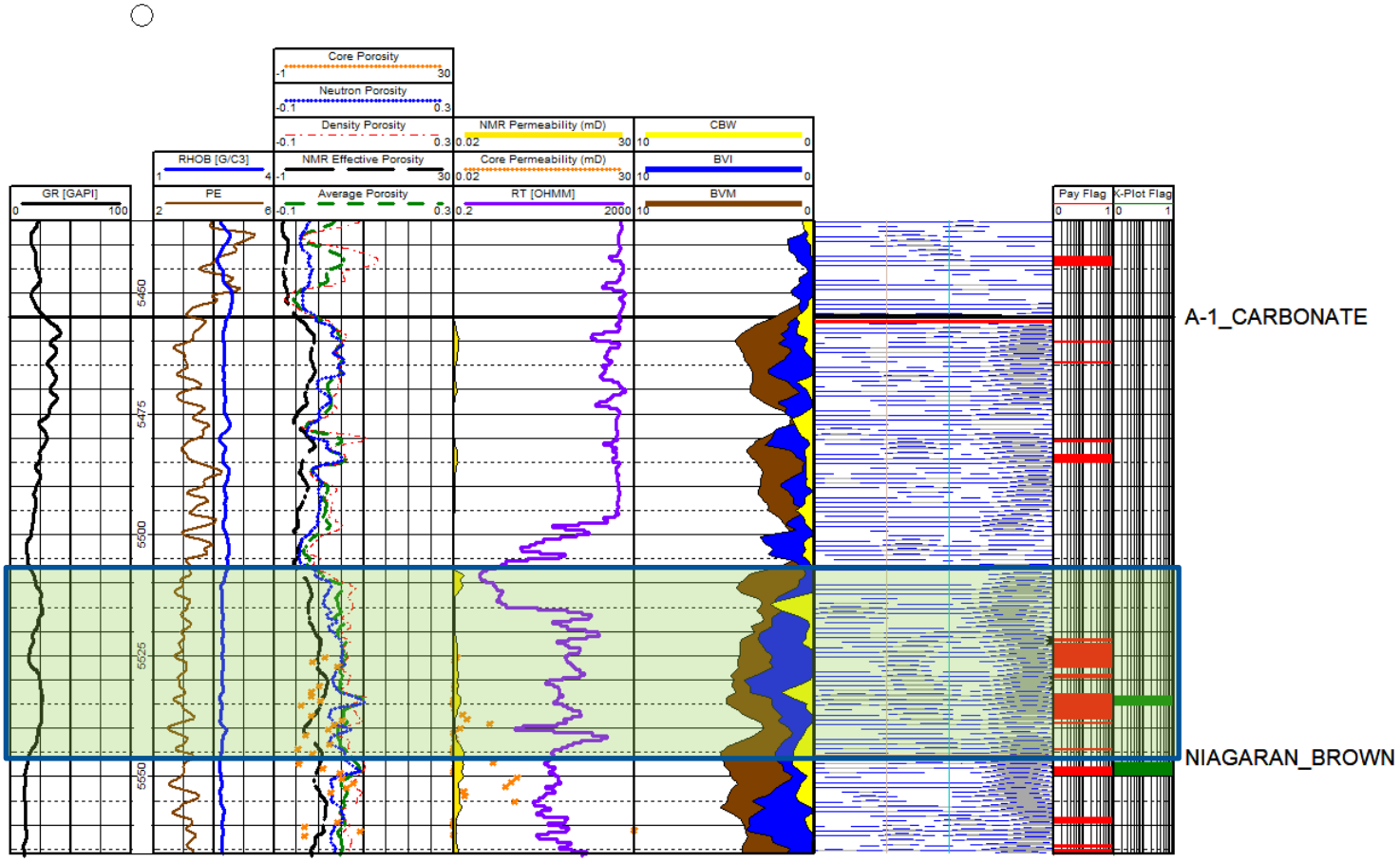


Figure 2-25. Cross section of MREX NMR log data, select logs from the triple combo log suite, core porosity and permeability data, and pay flags generated from triple combo logs and neutron-density crossplots for the A-1 Carbonate. NMR effective porosity log is plotted with neutron porosity, density porosity, and average porosity logs derived from the triple combo log suite as well as core porosity. NMR permeability is displayed with core permeability. BVM, BVI, CBW, and T2 distributions are also displayed. Green box highlights a zone of interest.

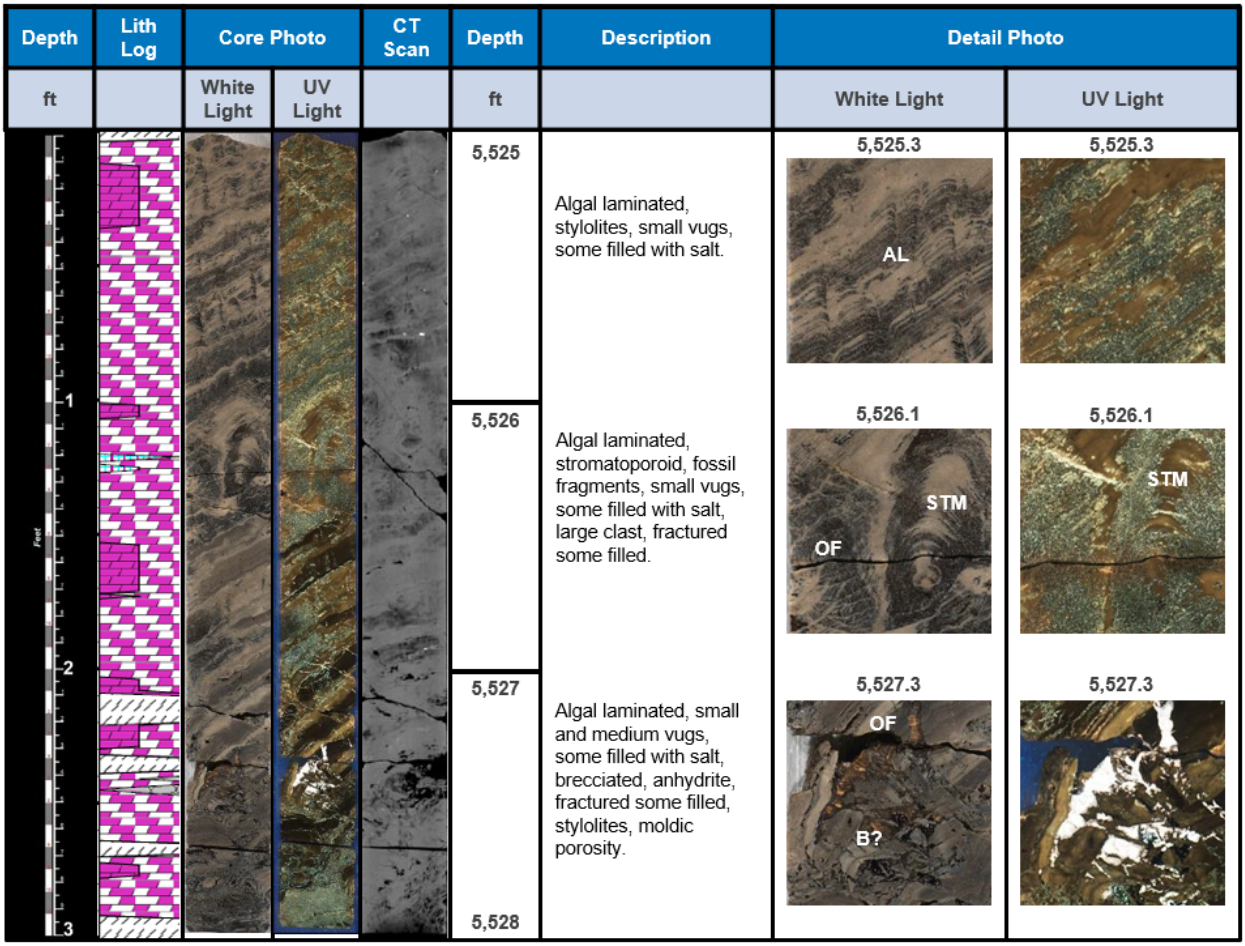


Figure 2-26. Compiled illustration of lithology log, core photos (UV and white light), CT scan image, core descriptions, and annotated core images of the A-1 Carbonate for depths 5,525 ft. to 5,528 ft.

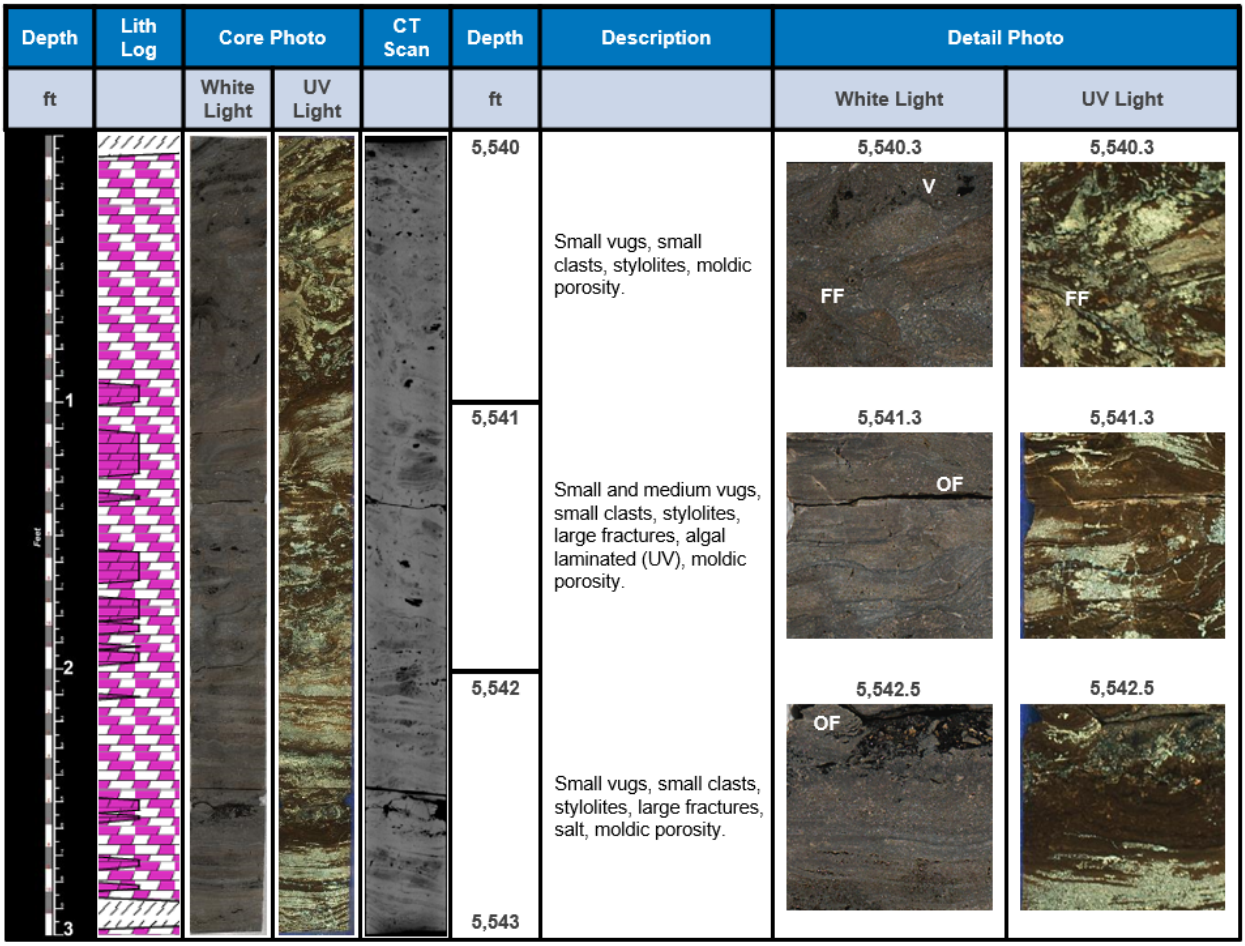


Figure 2-27. Compiled illustration of lithology log, core photos (UV and white light), CT scan image, core descriptions, and annotated core images of the A-1 Carbonate for depths 5,540 ft. to 5,543 ft.

Rotary Sidewall Core

Sidewall core photos of the A-1 Carbonate at Dover 9-33 show the A-1 is predominantly a gray carbonate with some zones of mixed carbonate and anhydrite matrix that transitions to a vuggy gray carbonate toward the basal section of the formation (Figure 2-28 and Figure 2-29). The upper section of the A-1 contains occasional small vugs and open fractures. The lower section of the A-1 contains significant small-to-large vugs, some of which are salt plugged. The UV images show potential residual oil throughout the formation.

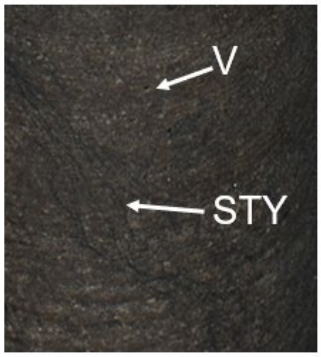
Depth Ft.	White Light Primary Features	UV Light Primary Features	Descriptions
5,456			White Light: Anhydrite matrix, alternating dark gray and light gray laminations, some marble like patterning. UV Light: Anhydrite matrix, stylolites.
5,458			White Light: Gray carbonate, stylolites, small vugs. UV Light: Strong light blue UV response due to potential residual oil throughout sample.

Figure 2-28. Annotated RSWC images with corresponding core descriptions of the A-1 Carbonate for depths 5,456 ft. to 5,458 ft.

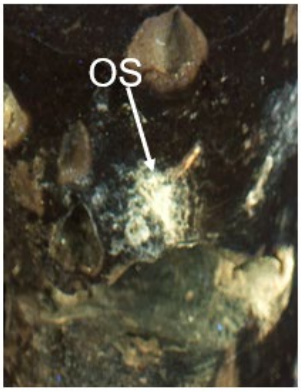
Depth Ft.	White Light Primary Features	UV Light Primary Features	Descriptions
5,520			White Light: Gray carbonate, medium/small vugs, salt plugged vugs. UV Light: Strong light blue UV response due to potential residual oil throughout sample.
5,523			White Light: Gray carbonate, large vugs, salt plugged vugs, broken core. UV Light: Strong light blue UV response due to potential residual oil.

Figure 2-29. Annotated RSWC images with corresponding core descriptions of the A-1 Carbonate for depths 5,520 ft. to 5,523 ft.

2.5 Brown Niagaran

2.5.1 Basic Wireline Log Analysis and Petrophysical Calculations

The Brown Niagaran formation was encountered at a depth of 5,546 ft. and extended to a depth of 5,867 ft. for a gross thickness of 314 ft. Basic petrophysical calculations were computed for the Brown Niagaran using a porosity cutoff of 5% and a water saturation cutoff of 40% (Table 2-6). Net thickness was 136.875 ft. for a net-to-gross ratio of 43.6%. The oil-water contact was observed in the Brown at 5,600 ft.

The Brown Niagaran plots as a homogenous, clean dolomite with zones of significant porosity (Figure 2-33). Log analysis yielded an average porosity of 6.1% with porosity values ranging from 2.1-15%. The neutron-density crossplot shows multiple zones of significant porosity over 5% with a few data points over 10% porosity (Figure 2-30 and Figure 2-31). Multiple pay flags were identified as well throughout most of the formation using a porosity cutoff of 5% and a water saturation cutoff of 40%.

Table 2-6. Brown Niagaran zone footages – 5% porosity and 40% water saturation cutoff

Gross Thickness (ft.)	Net Thickness (ft.)	NGR	Porosity ft.	Avg. Porosity
314	136.875	0.436	9.452	0.069

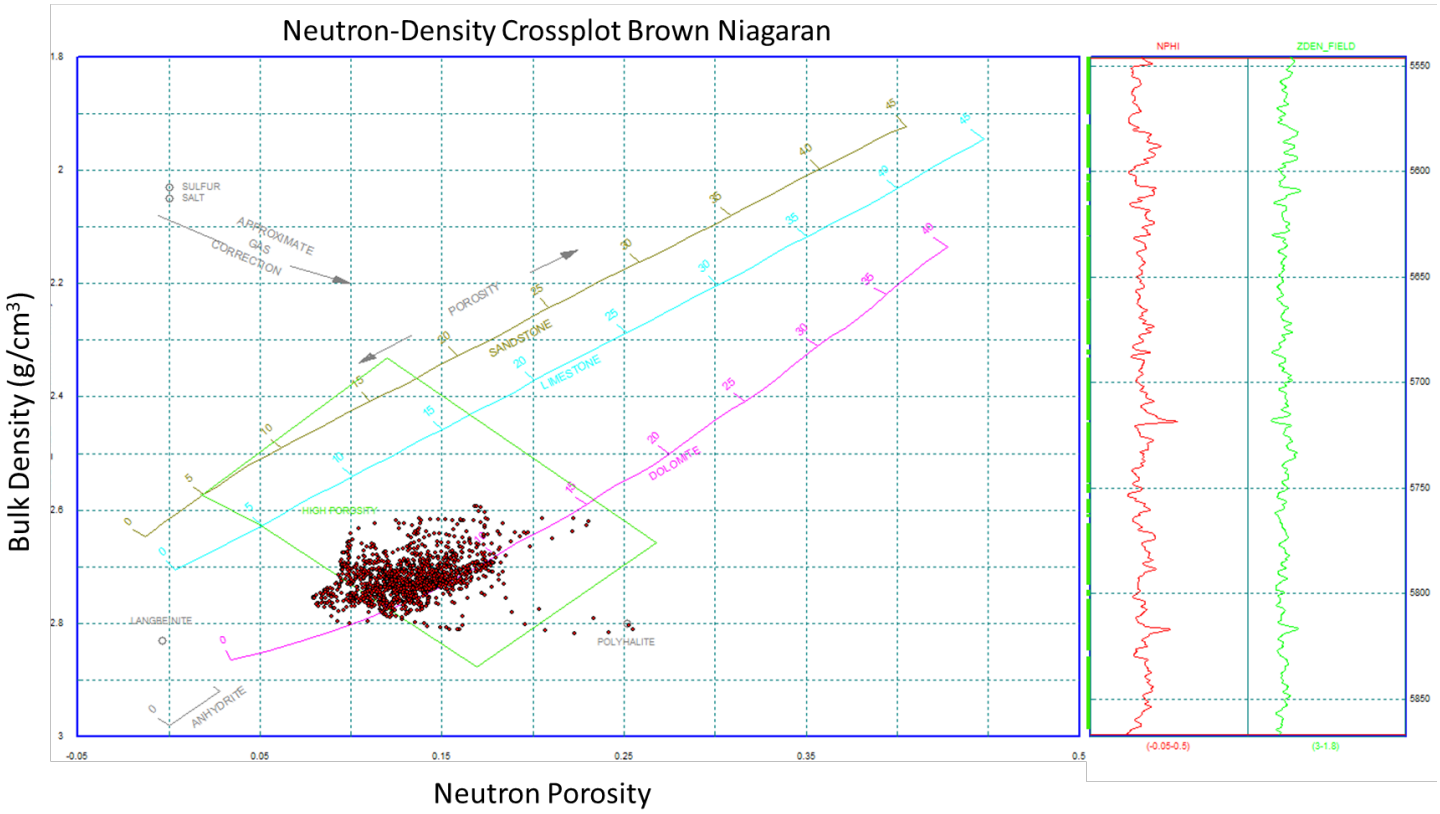


Figure 2-30. Neutron-density crossplot of the Niagaran Brown using the original neutron porosity log. Note that porosity values here are overestimated but lithology is accurate.

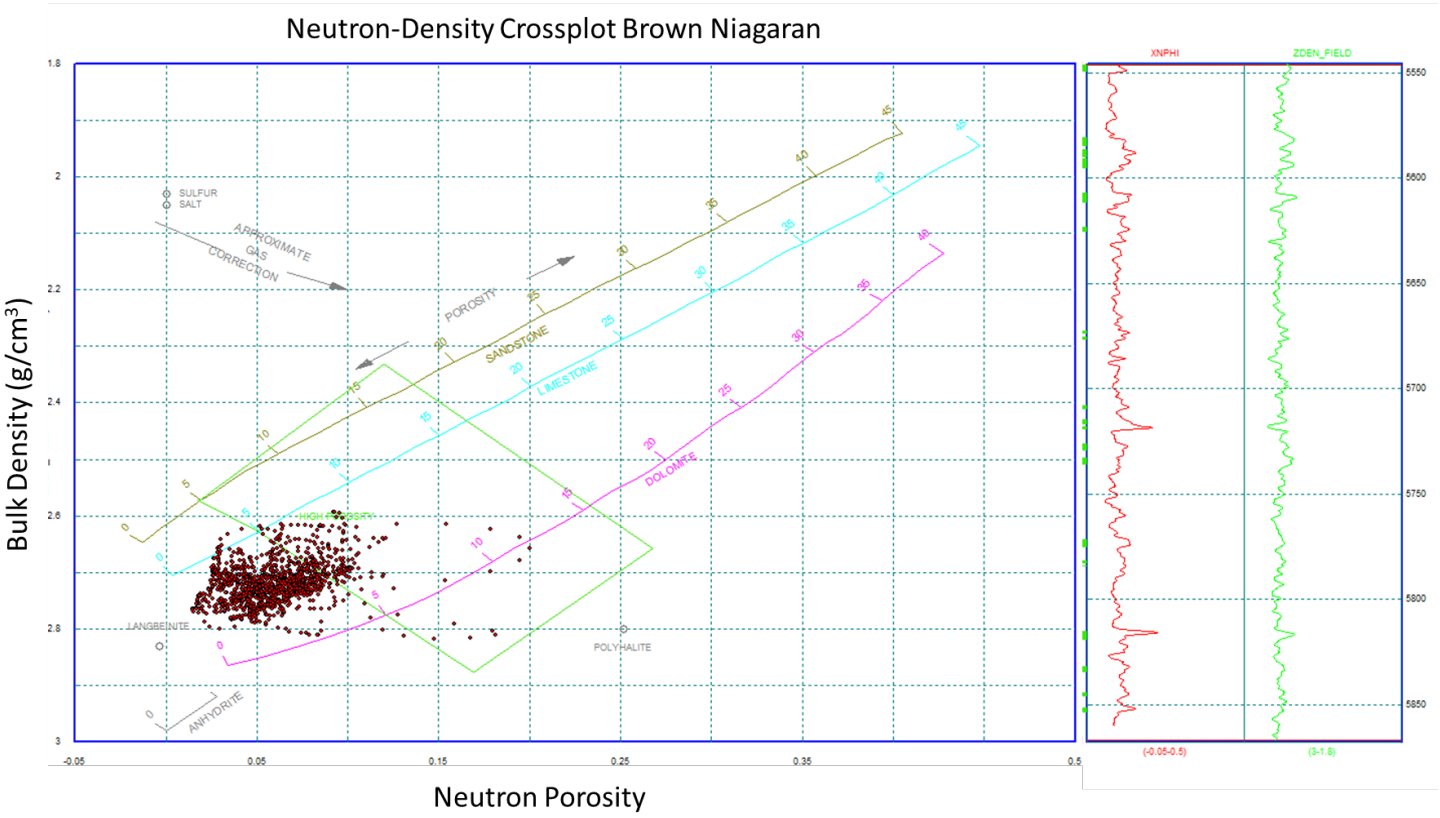


Figure 2-31. Neutron-density crossplot of the Brown Niagaran using the calibrated neutron porosity log. Note that porosity values here are accurate but lithology is not.

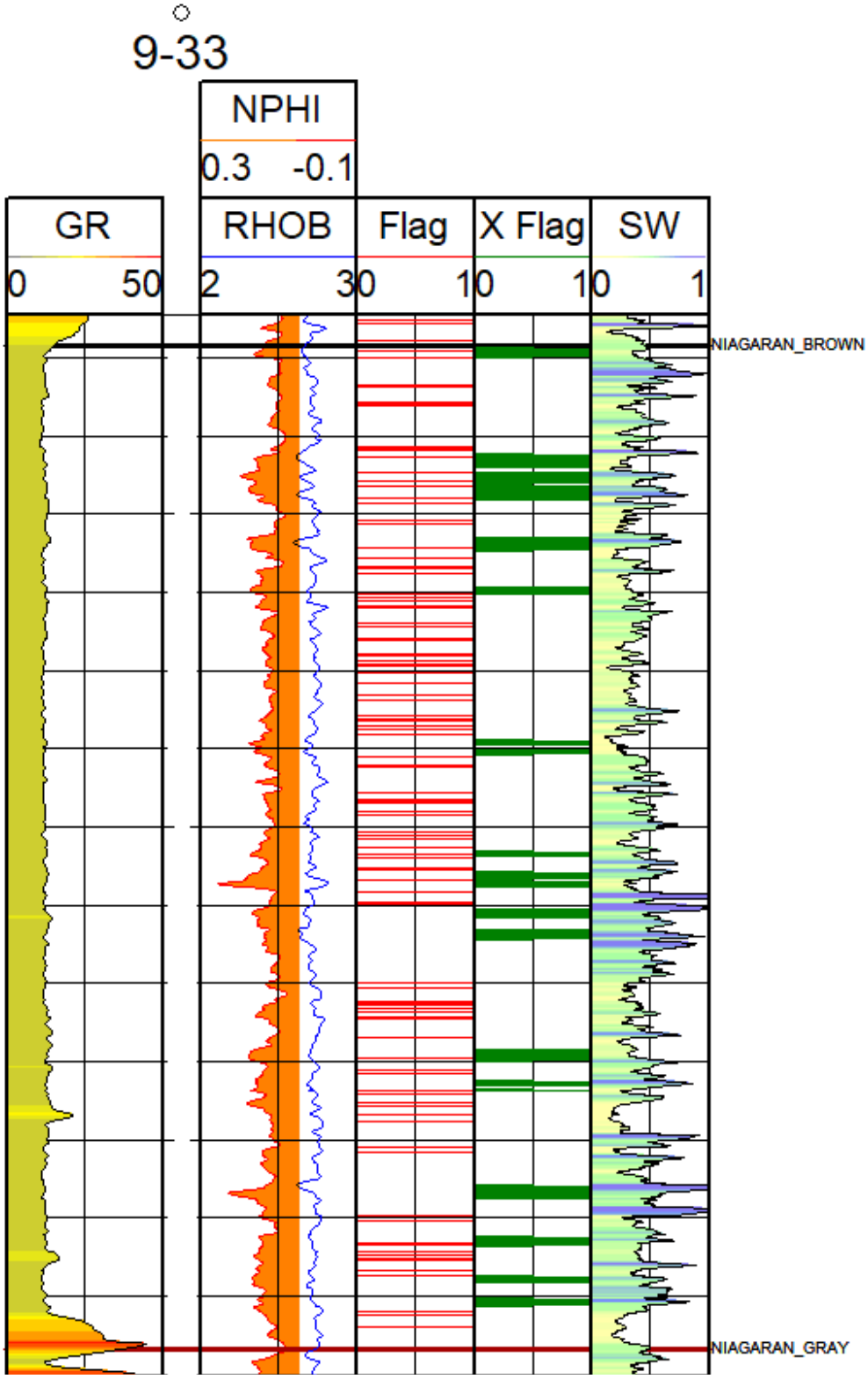


Figure 2-32. Single well cross section of the Brown Niagaran in the Dover 9-33 well

2.5.2 Advanced Wireline Log Analysis

Elemental Spectroscopy Log Analysis

The Brown Niagaran Formation occurs from 5,546 ft. MD/5,397 ft. TVD to 5,867'MD/5,655'TVD. Elemental spectroscopy log analysis reveals this unit to be mineralogically unremarkable. With low concentrations of potassium, thorium, and aluminum, clay minerals are present in only trace amounts. Likewise, stable magnesium to calcium ratios indicate the relative abundances of dolomite and calcite are not changing with depth and the Brown Niagaran is a clean dolomite. One feature of interest highlighted by orange arrows on Figure 2-33 and Figure 2-34 are dark green peaks in the ninth track to the left, called "X-carbon" or excess carbon. This value corresponds to the amount of carbon detected by the tool that has not been accounted for in the mineralogic components of the bulk rock volume and is used to infer total organic carbon (TOC). These peaks imply that there is more organic material present in the Brown Niagaran Formation than the other reservoirs logged in the Lawnichak 9-33 well.

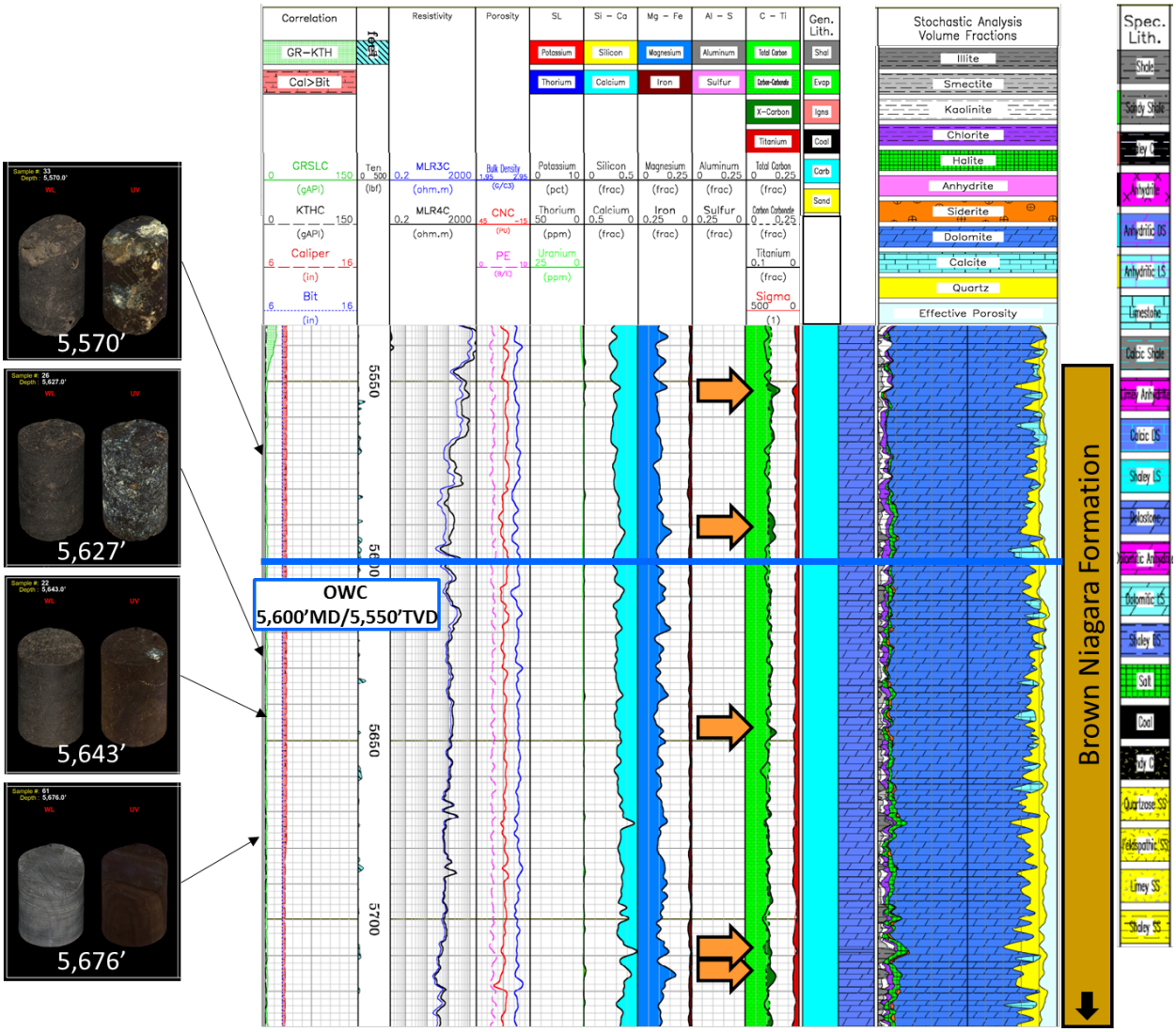


Figure 2-33. Elemental spectroscopy log from Lawnichak 9-33 displaying the Brown Niagaran formation from 5,546 ft. to 5,730 ft. Select rotary side wall core samples are shown in both white light (WL) and ultraviolet light (UV) to provide context for lithologic descriptions. Orange arrows indicate zones with high excess carbon. Blue light is the oil-water contact.

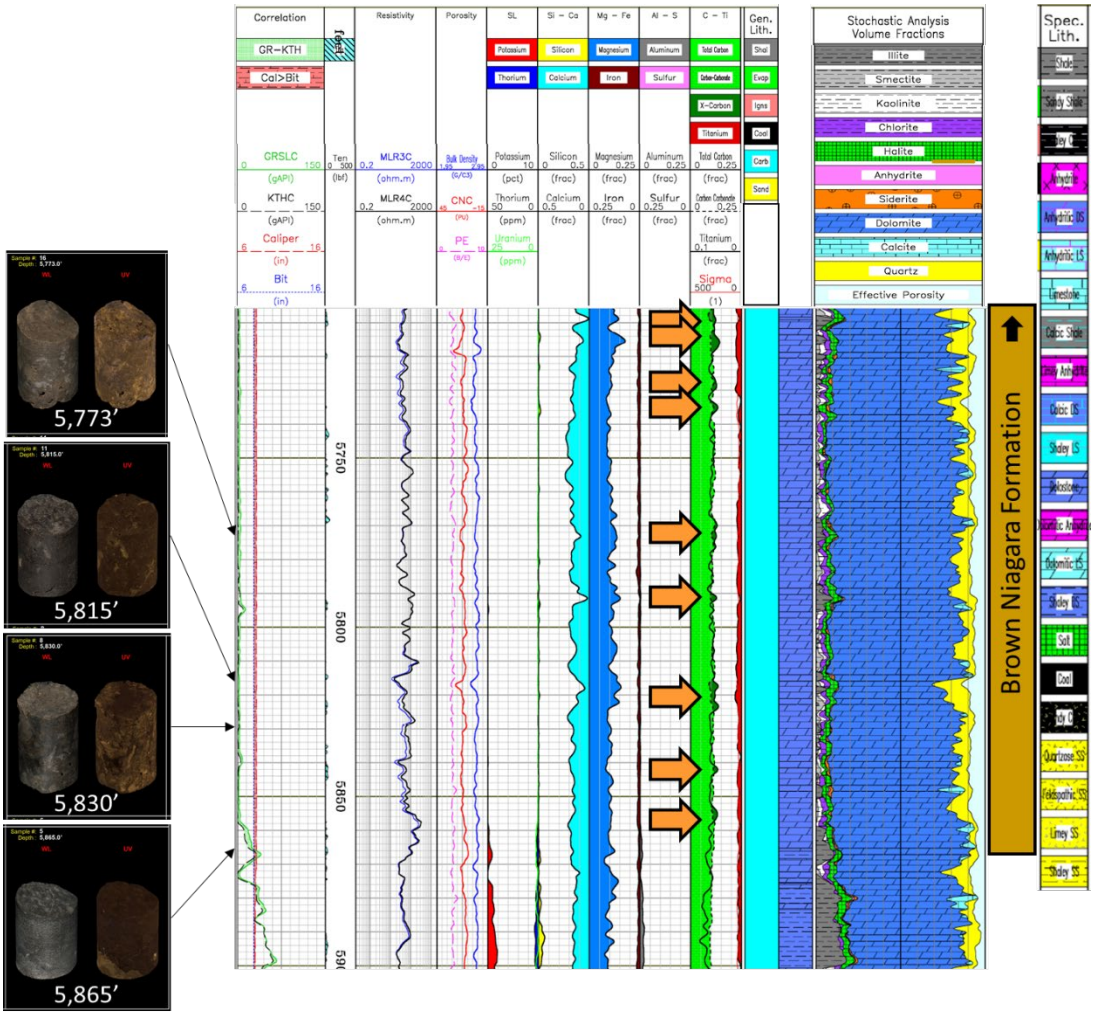


Figure 2-34. Elemental spectroscopy log from Lawnichak 9-33 displaying the Brown Niagaran formation from 5,710 ft. to 5,900 ft. Select rotary side wall core samples are shown in both white light (WL) and ultraviolet light (UV) to provide context for lithologic descriptions. Orange arrows indicate zones with high excess carbon.

Image Log Analysis

Nine distinct texture zones are observed within the Brown Niagaran image log (Figure 2-35 through Figure 2-42). The first texture zone exists from 5,546 ft. to 5,557 ft. and is observed as thinly interbedded resistive-conductive materials (Figure 2-35). Conductive features are bounded by stratigraphic bedding and appear relatively continuous across the bed. Bedding is apparent within the interval with beds dipping 8º-12º west-northwest toward the leeward direction of the reef complex. Conductive features are small to medium in size. This texture zone has been calibrated to core, revealing it to be thinly bedded mudstone interbedded with constrained (bed-bounded) vuggy porosities. The cyclical nature of tight-resistive to vuggy-conductive behavior may be suggestive of periodic sub-areal exposure. This zone is interpreted to be deposited in subtidal to intertidal conditions. This zone is interpreted to exhibit a low to moderate potential for reservoir use due to the development of thin beds with touching vugs.

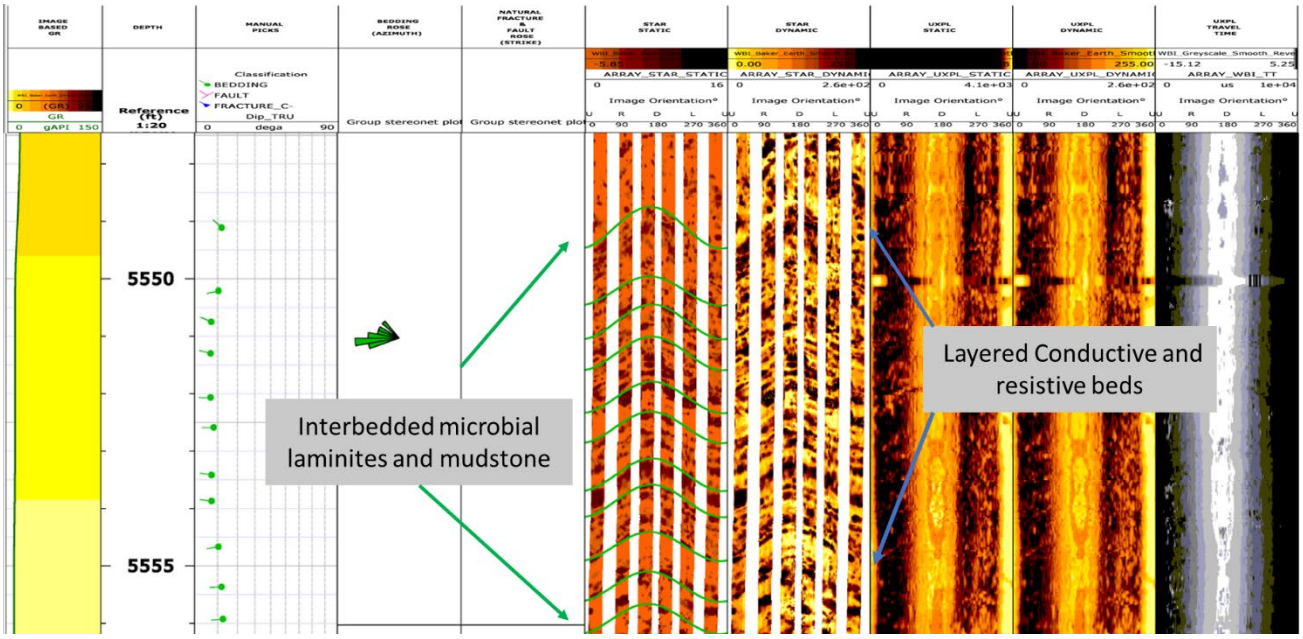


Figure 2-35. Annotated FMI image log of the Brown Niagaran from ~5,548 ft. to 5,556 ft. The zone is described as thinly layered conductive and resistive bed and is interpreted to be bedded mudstone. Conductive zones are thought to exhibit vuggy to fenestral porosity.

The second texture zone exists from 5,557 ft. to 5,580 ft. and is observed as a heterogeneous texture where small-to-medium sized conductive features occur within a resistive matrix (Figure 2-36). The conductive features appear to be interwoven to some degree suggesting connectivity of pores and possible biogenic or diagenetic origin. Most isolated conductive features are shaped irregularly, appearing in a variety of sizes; this behavior is consistent with vuggy porosity. Bedding is not distinct within this interval. Fractures are observed at ~5,560 ft. and 5,770 ft. Fracture features are subtle even in dynamic view, which suggests they are healed fractures. This texture zone is interpreted to be fractured massively bedded mudstone with low to moderate distribution of small to large irregularly shaped vugs. Vuggy porosity appears to be concentrated around fractured zones. This zone is interpreted to be deposited in a subtidal to leeward reef environment. This zone is thought to exhibit low to moderate reservoir potential due the distribution of largely separate vugs.

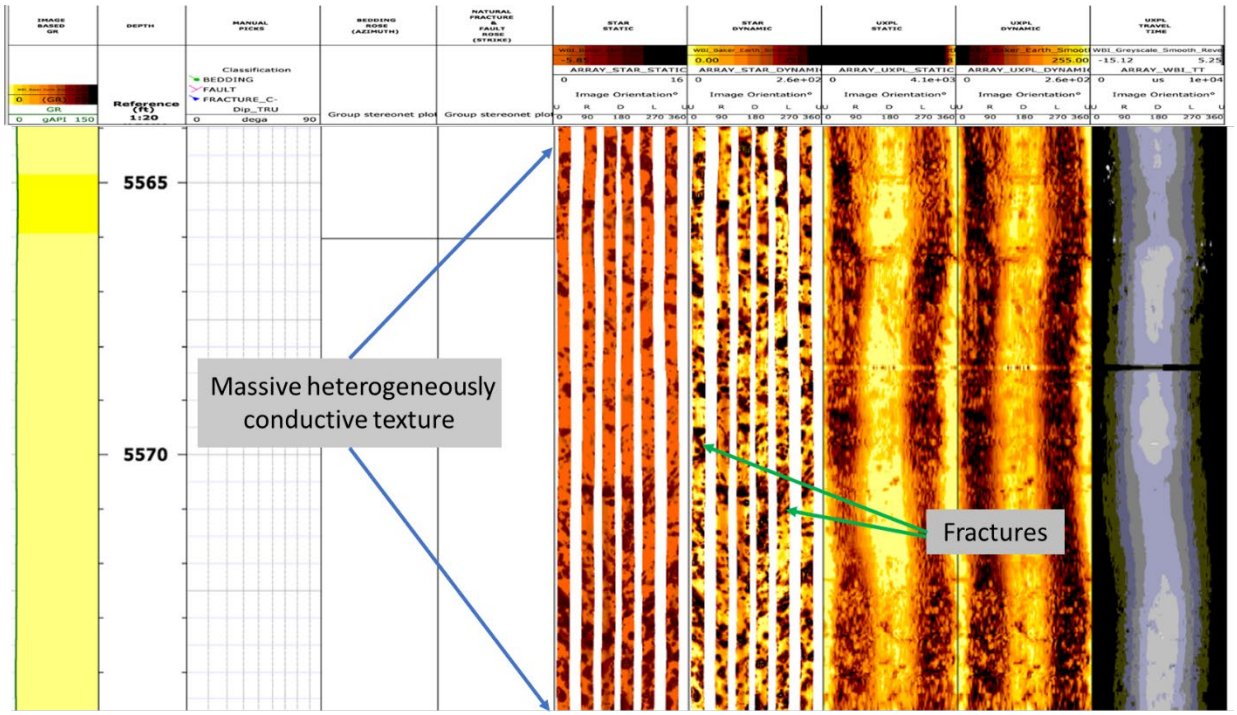


Figure 2-36. Annotated image log of the Brown Niagaran from ~5,564 ft. to 5,575 ft. This texture is described as massive heterogeneously conductive texture where all conductive features occur within a resistive matrix. This zone is interpreted to be massively bedded mudstone with a moderate to high distribution of vuggy porosity.

The third texture zone exists from 5,580 ft. to 5,589 ft. and is observed as a homogenously conductive material interbedded with resistive materials (Figure 2-37). Within this zone, bedding contacts are apparent and dip approximately 60º south-southeast. Generally, the quality of the image log is poor within this interval possibly due to tool sticking or structural stability issues of the wellbore. This zone is interpreted to be tight mudstone possibly interbedded with mud-supported units such as bioclastic wackestones/packestones. Pores are interpreted to be possibly moldic to vuggy. Uniformly conductive zones that are probably associated zones of unplugged microporosity. This texture zone is interpreted to exhibit low reservoir potential.

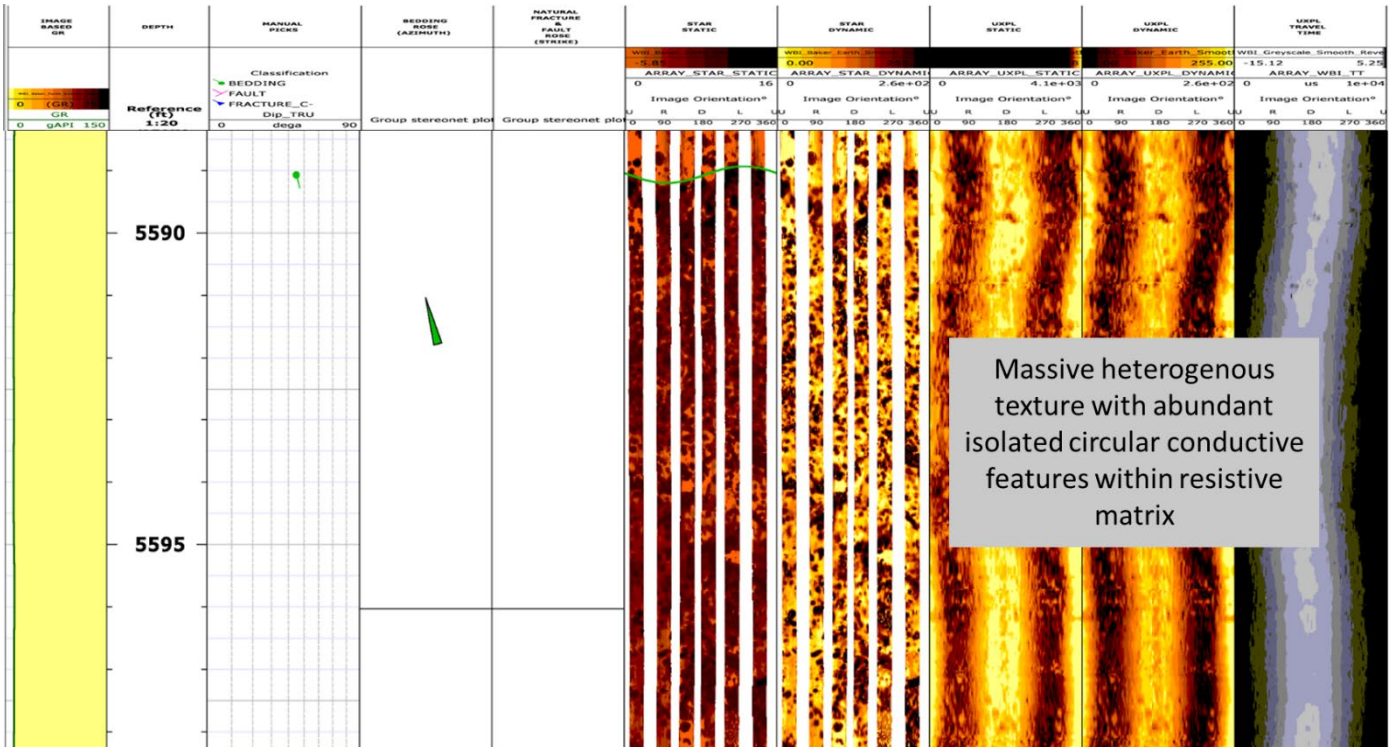


Figure 2-37. Annotated image log of the Brown Niagaran from ~5,580 ft. to 5,588 ft. This texture is described as thin to thickly bedded homogenously conductive and heterogeneously conductive textures and is interpreted to be bedded mudstones and bioclastic wackestones.

The fourth texture zone exists from 5,590 ft. to 5,650 ft. and is observed as a heterogenous texture with significant amounts of isolated conductive features held within a resistive matrix, yielding a largely conductive profile in static and dynamic views (Figure 2-38). Conductive features appear to be small circular to sub-circular in shape, with a random but more structured occurrence, all of which suggest these are possibly fabric selective features. The distribution of conductive features appears to be cyclical from 5,600 ft. - 5,610 ft. Bedding appears to be massive to thickly bedded, dipping steeply up to 60º, with few distinct contacts observed. This zone is interpreted to be composed of mud-supported bioclastic carbonates with abundant fabric selective porosities (moldic, intraparticle shelter etc.). This material is interpreted to have been deposited within the reef apron environment due to the interpreted bioclastic content, degree of dip and extremely low gamma ray. This zone is thought to exhibit a moderate amount of reservoir potential due to distribution and connectivity of conductive features.

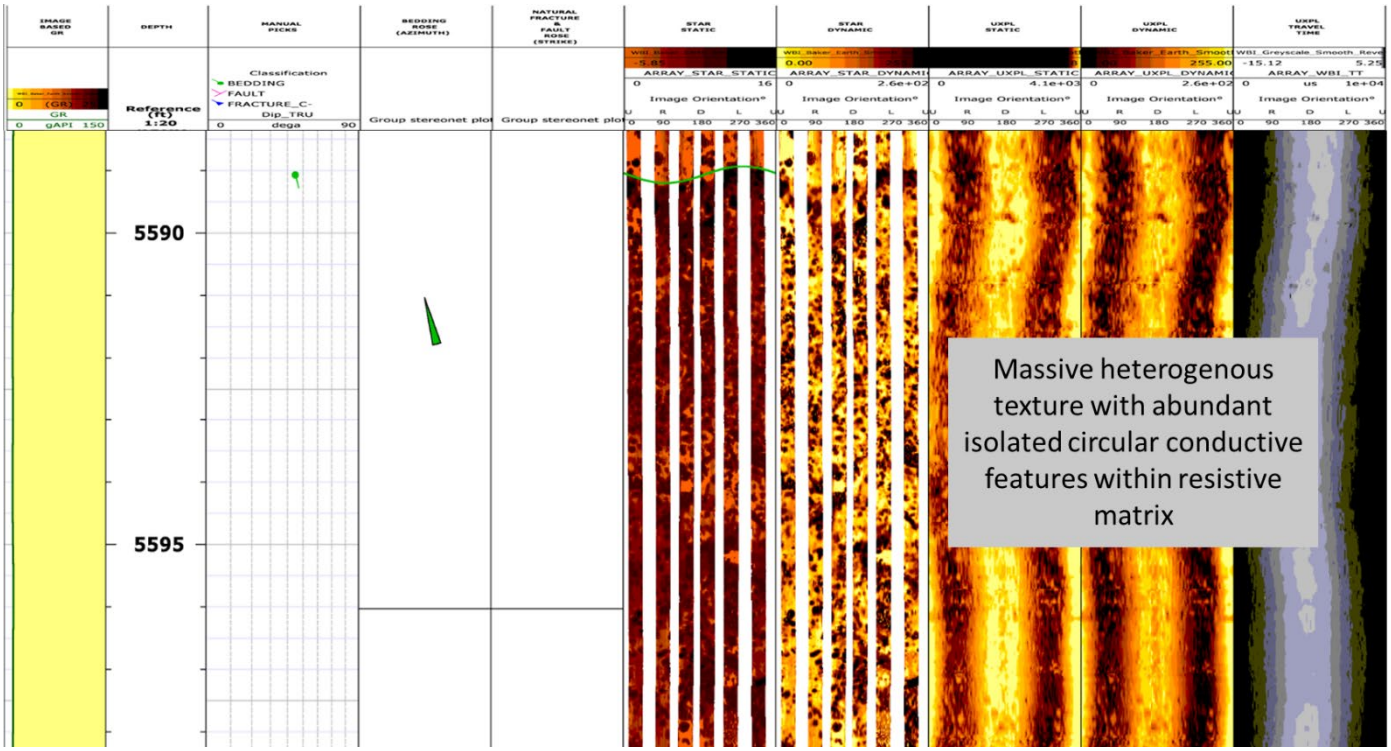


Figure 2-38. Annotated image log of the Brown Niagaran from ~5,588 ft. to 5,598 ft. This texture is described as massive heterogenous texture with abundant isolated conductive features held within a resistive matrix material and is interpreted to be massively bedded bioclastic wackestones.

The fifth texture zone exists from 5,650 ft. to 5,713 ft. and is observed as a coarsely heterogenous texture with medium-to-large sized, discontinuous, circular to semi-circular resistive features occurring within a largely conductive matrix (Figure 2-39). Conductive features seem to be small-to-medium in size and generally semi-circular in shape, suggesting pores are mainly bioclastic in nature. Bedding is not apparent within this zone. Textures like those described in the fourth texture zone occur interbedded with this coarser texture. This zone has been calibrated to whole core revealing the texture to be comprised of discontinuous rip-up clasts of tight resistive mud, held within a wackestone matrix. Pore types are interpreted to be mainly moldic with some vuggy porosity development. Resistive rip-up clasts may potentially be reservoir quality baffles; however, significant porosity is observed within the bioclastic wackestones matrix. This texture has a moderate to high reservoir potential.

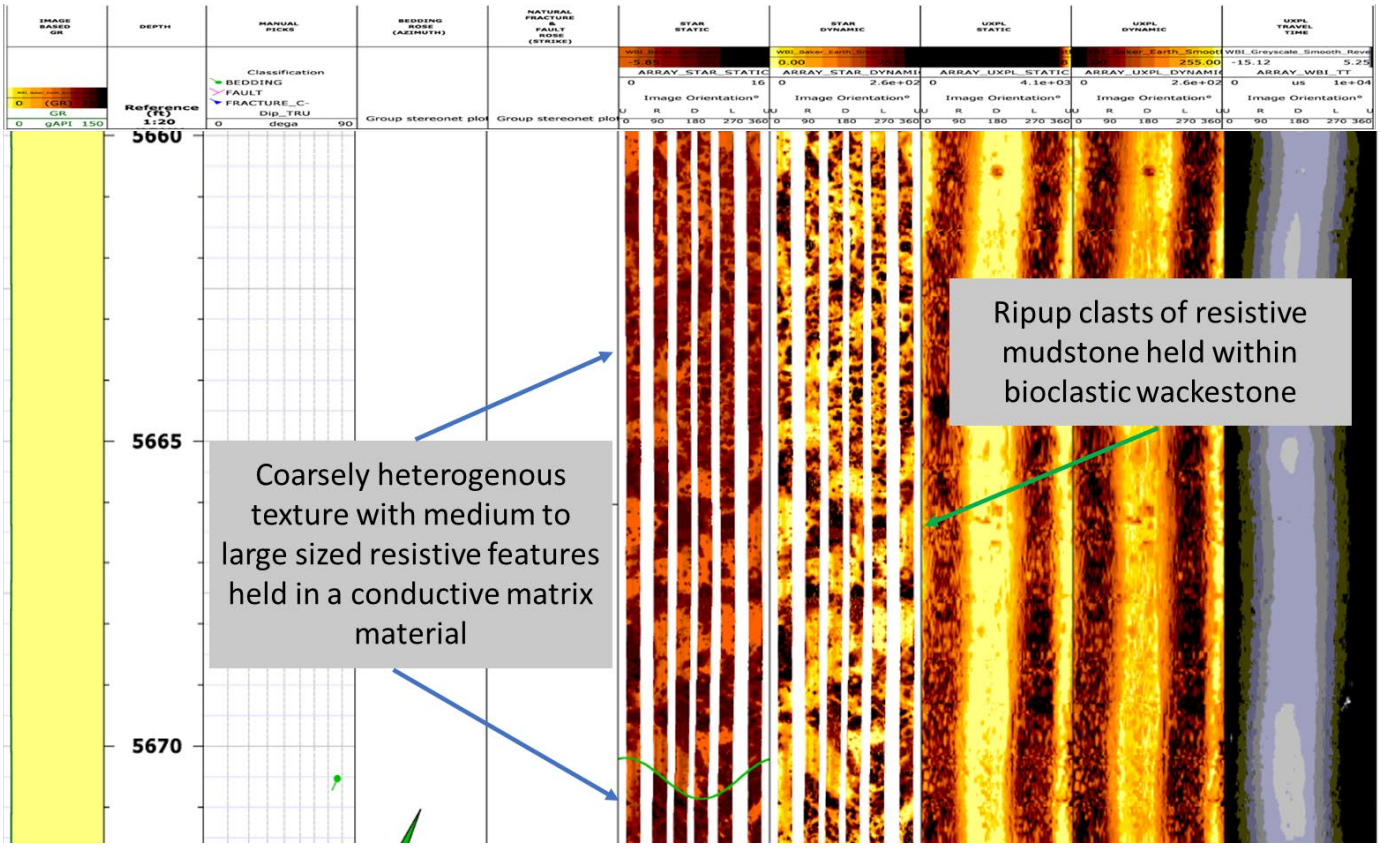


Figure 2-39. Annotated image log of the Brown Niagaran from ~5,660 ft. to 5,671 ft. This interval is described as coarsely heterogenous with large discontinuous resistive features held within a conductive matrix and is interpreted to be large rip-up clasts of mudstone held within massively bedded bioclastic wackestone.

The sixth texture zone exists from 5,713 ft. to 5,726 ft. and may be described as inclined near-homogenously resistive materials interbedded with conductive materials (Figure 2-40). Intervals between resistive beds appear as entirely dark brown to black suggesting the intervals are highly porous and well connected. Stratigraphic bedding dips 20º to 30º to the southwest. This zone has been calibrated to whole core, revealing the texture to be thin beds of tight dolomudstone interbedded with a grain supported packstones or grainstones. These bioclastic beds potentially exhibit intercrystalline, moldic or vuggy pore-types. This texture zone is interpreted to exhibit significant injection potential.

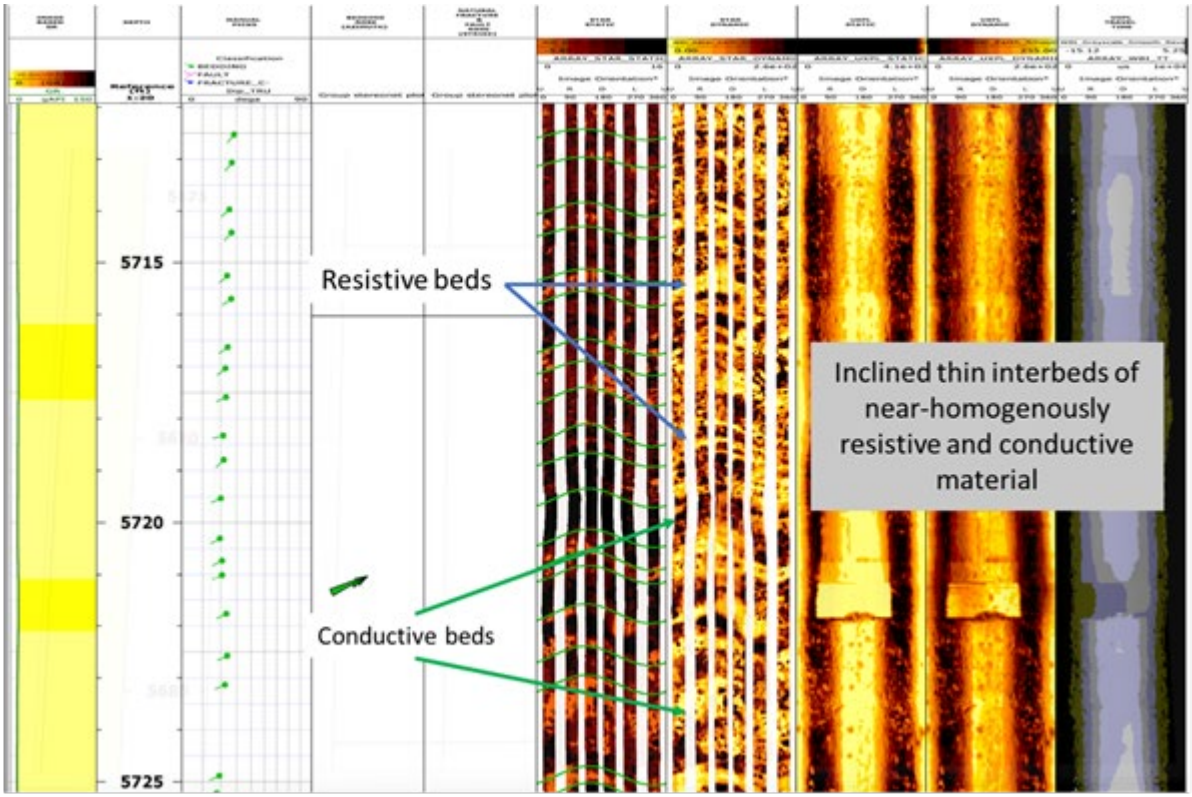


Figure 2-40. Annotated image log of the Brown Niagaran from ~5,712 ft. to 5,725 ft. This interval is described as inclined interbeds of near-homogenously resistive and conductive materials and is interpreted to be porous, grain-supported packestone/grainstone.

The seventh texture zone exists from 5,726 ft. to 5,765 ft. and is marked by a sharp textural contact that may be described as massive, coarse, heterogenous textures gradationally interbedded with fine heterogenous textures (Figure 2-41). Coarse textures exhibit small-to-medium sized conductive features held within a resistive matrix material. Fine texture zones exhibit small but abundant isolated and interwoven (touching) conductive features held within resistive matrix material. In some intervals the abundance of conductive features yields a near uniform conductive profile in static and dynamic view. Stratigraphic bedding is not identifiable which is indicative of gradational changes without dipping beds. If reef building skeletons are in-place, this texture zone interpreted to be framestones with mud-supported reef debris infilling reef cavities. If reef builder skeletons are not in place, the texture is representative of rudstone. Within this zone growth-framework, moldic, shelter and vug pore types are thought to be possible contributors to the EBI conductive profiles. This zone is interpreted to exhibit low to moderate reservoir quality.

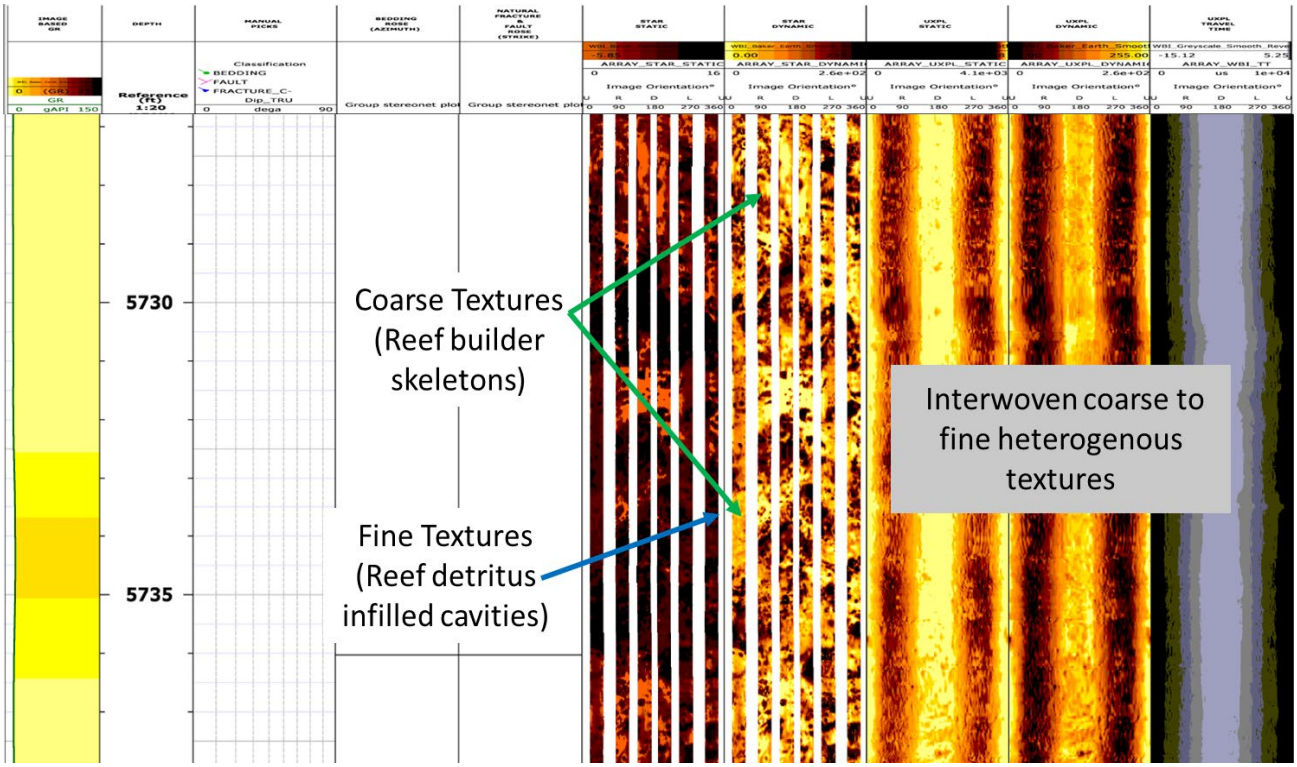


Figure 2-41. Annotated image log of the Brown Niagaran from ~5,727 ft. to 5,738 ft. This texture is described as interwoven coarse to fine heterogenous texture and is interpreted to be framestones of reef builder skeletons with reef detritus material infilling cavities.

The eighth texture zone exists from 5,765 ft. to 5,818 ft. and consists of thin resistive beds interbedded with thickly bedded heterogeneously conductive material (Figure 2-42). The heterogenous intervals exhibit small to medium sized conductive features held within a resistive matrix. These conductive features are semicircular isolated to interwoven. Thin resistive beds are uniformly resistive with few small spherical conductive features occurring within the beds. Natural Fractures occur throughout. These natural fractures are concentrated at contact zones between the beds. Due to its interwoven character, shape and abundance of conductive features, the thickly bedded heterogeneously conductive material is interpreted to be bioclastic in nature, possibly framestone or bafflestones formed syn-depositionally with cavity filling reef detritus. Pore types within this specific texture are interpreted to possibly be a combination of: (1) primary pores such as growth framework, intraparticle and intraparticle, (2) secondary pores such as moldic and intercrystalline and (3) non-fabric selective pores such as fractures and vug. Thin bedded resistive features are interpreted to be tight dolomite dominated by microporosity. Deposition appears to be cyclical with thick buildups of heterogenous material capped by tight resistive muds. This zone is interpreted to exhibit moderate potential for injection, where perforations should be aligned in inter-mud zones.

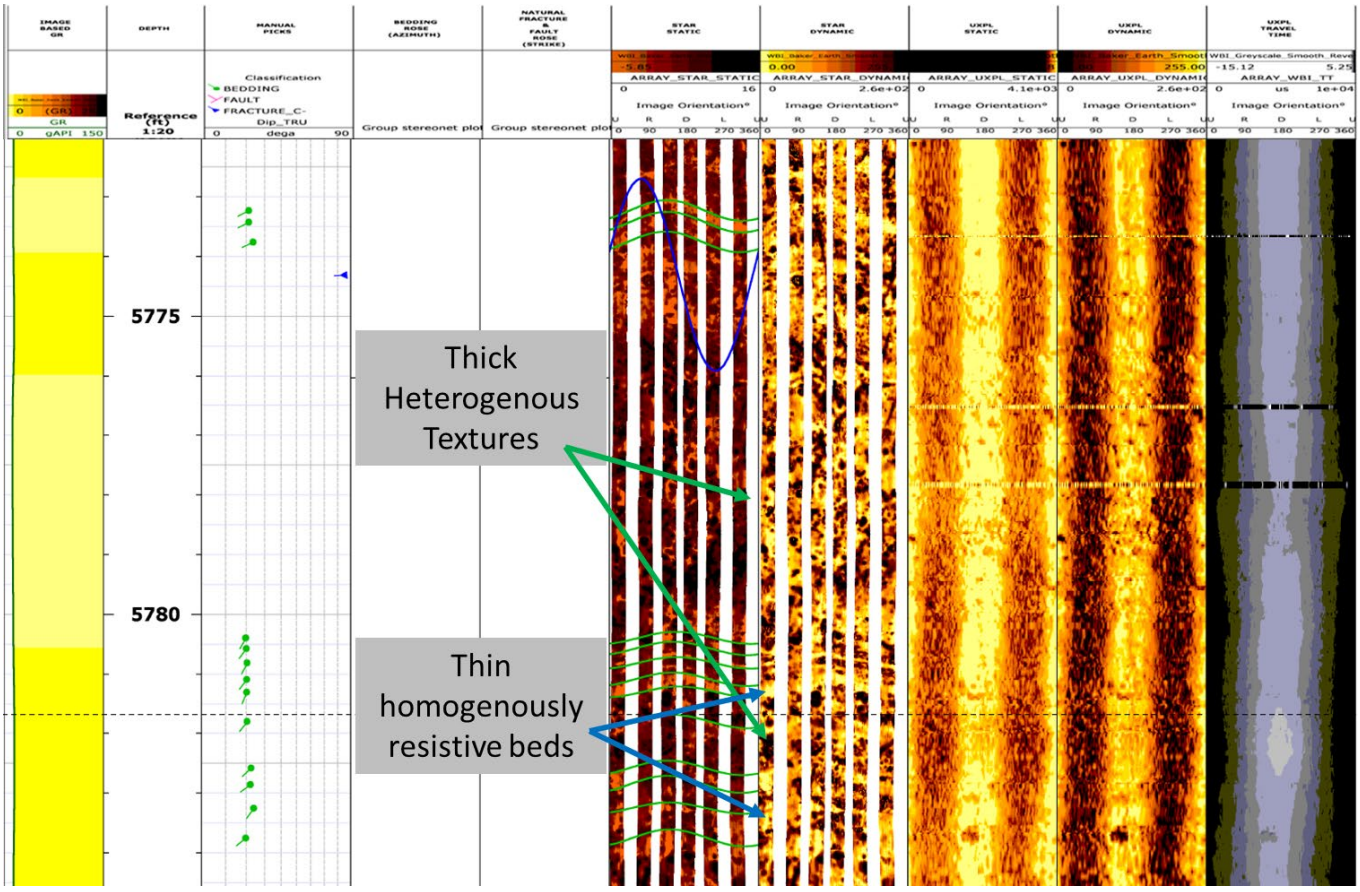


Figure 2-42. Annotated image log of the Brown Niagaran from ~5,772 ft. to 5,785 ft. This interval is described as thin resistive beds interbedded with thickly-to-thinly bedded heterogeneously conductive material and is interpreted to be mudstone interbedded with framestone or bafflestones with syn-depositional cavity filling reef detritus.

The ninth and final texture zone exists from 5,818 ft. to 5,866 ft. and consists a series of unique thickly-to-massively bedded heterogenous textures with small to large interwoven conductive features occurring within a resistive matrix. Within static view much of this section appears as near-uniformly conductive suggesting significant amounts of porosity. Throughout this section, domal shaped resistive features appear that hold small organized conductive features. Bedding is not always apparent within the interval; however sharp contacts occur 5,826 ft. and 5,832 ft. Natural fractures occur at 5,818 ft., 5,827 ft. and 5,860 ft. This texture zone is interpreted to be a thick succession of reef core associated lithofacies such as framestones and bafflestones with reef detritus infilling cavity spaces. This interpretation is derived from the degree of continuity of the textures, the high degree of interwoven conductive features (porosity) and the general character of the image. This zone exhibits a large amount of injection potential shown by the degree of conductive character (porosity) and the interwoven nature of conductive features suggesting good communication between pores.

NMR Log Analysis

Two distinct intervals within the Brown Niagaran (highlighted using green transparent boxes in Figure 2-43) exhibit potential reservoir-quality permeability and effective porosity (Figure 2-43). The first interval exists above the oil-water contact from ~5,546 ft. to 5,640 ft. shows relatively high NMR permeability peaks throughout that coincide with multiple flagged intervals from pay flags and crossplot flags (red and green flags). The T2 spectrum in this zone suggests the majority of fluids in place are moveable, having relaxation times equal to or greater than the 512 ms cutoff time. There is minimal clay bound water in this interval. NMR effective porosity and core porosity are within reasonable agreement as well and show multiple spikes in higher porosity.

The second interval of interest exists below the oil-water contact from ~5,688 ft. to 5,859 ft. and shows relatively high permeability peaks throughout that coincide with multiple flagged intervals from pay flags and crossplot flags (red and green flags). Like the first zone, the T2 spectrum in this zone suggests that the majority of fluids in place are moveable, having relaxation times equal to or greater than the 512 ms cutoff time. There is very minimal clay bound water in this interval. NMR permeability peaks align well with core permeability spikes where core data is available (orange x-symbols). NMR effective porosity and core porosity are within reasonable agreement as well and show multiple large spikes in higher porosity throughout this interval.

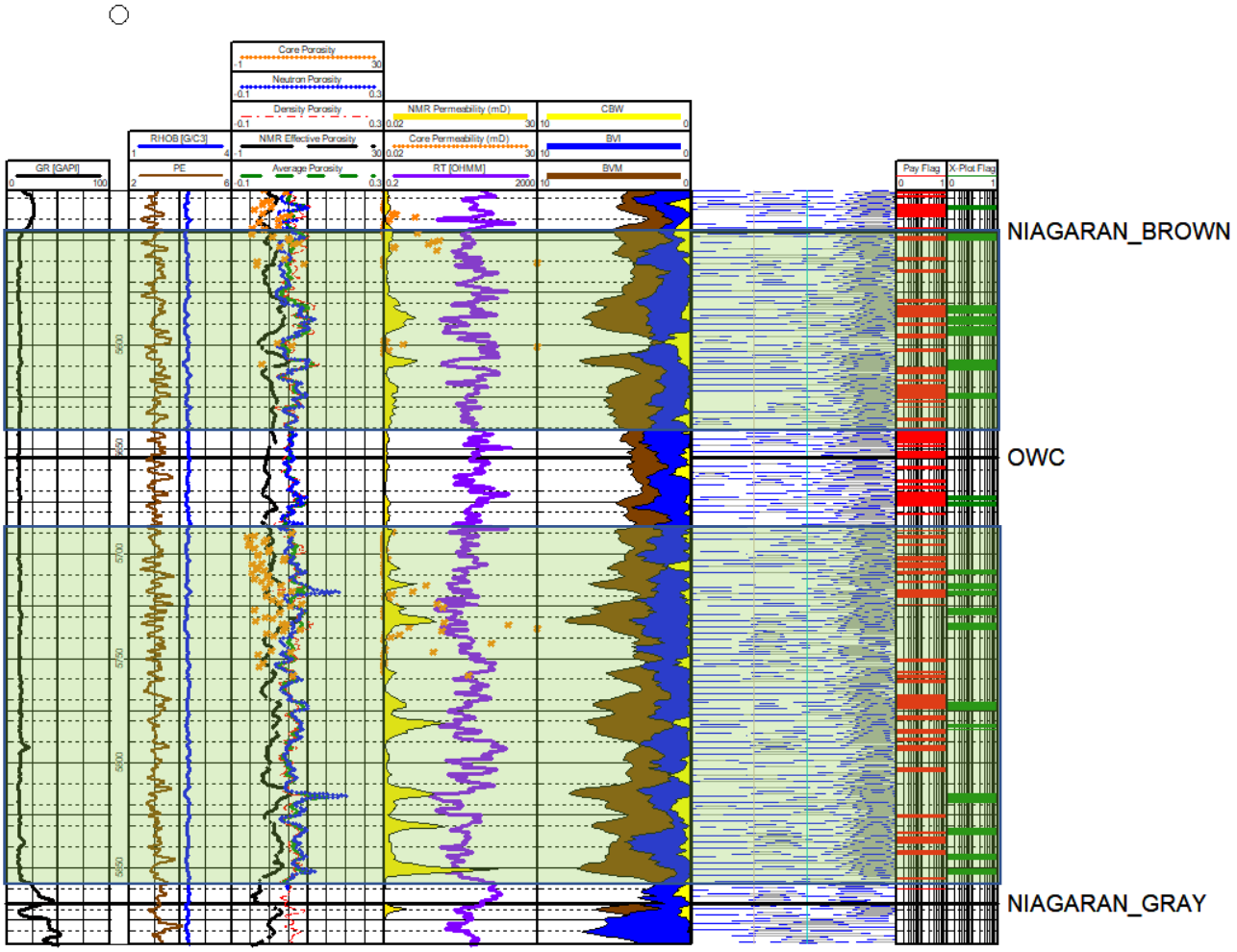


Figure 2-43. Cross section of NMR log data, select logs from the triple combo log suite, core porosity and permeability data, and pay flags generated from triple combo logs and neutron-density crossplots for the Brown Niagarann. NMR effective porosity log is plotted with neutron porosity, density porosity, and average porosity logs derived from the triple combo log suite as well as core porosity. NMR permeability is displayed with core permeability. BVM, BVI, CBW, and T2 distributions are also displayed. Green boxes highlight zones of interest.

2.5.3 Core Analysis

Conventional Core

The Brown Niagaran Formation within the Dover 9-33 reef is mostly porous dolostone with thin intervals of tight dolomite (Figure 2-44 and Figure 2-45). Features such as vugs and fractures result in a heterogeneous reservoir containing isolated zones of high porosity and permeability. Stylolites and bioclastic debris were also present along with fossils and zones of brecciation. UV photos reveal multiple zones of anhydrite-filled fractures and clasts. Zones of reef framework facies with significant porosity were present toward the basal section of the core. Significant sections of core were missing or were present as rubble.

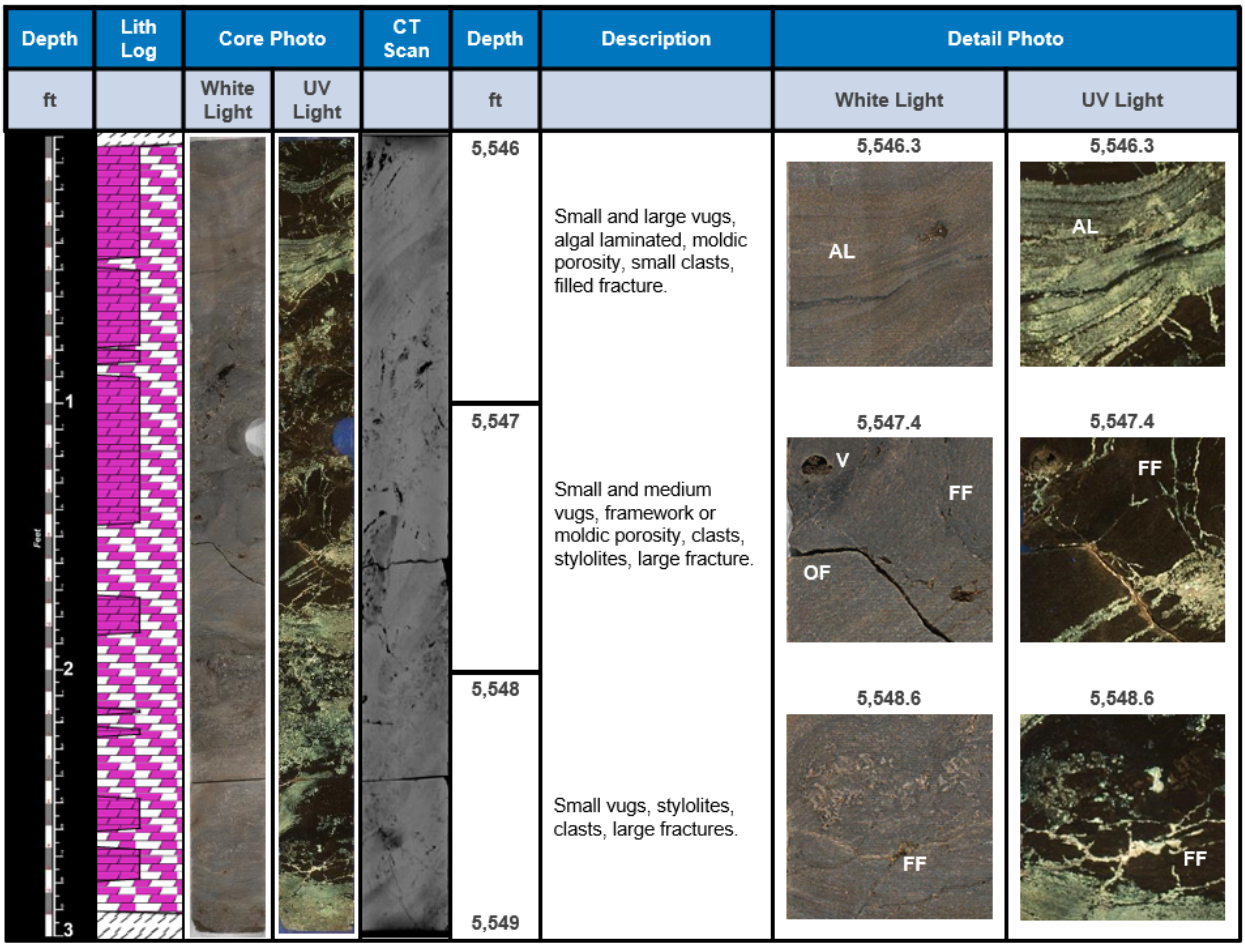


Figure 2-44. Compiled illustration of lithology log, core photos (UV and white light), CT scan image, core descriptions, and annotated core images of the Brown Niagaran for depths 5,546 ft. to 5,549 ft.

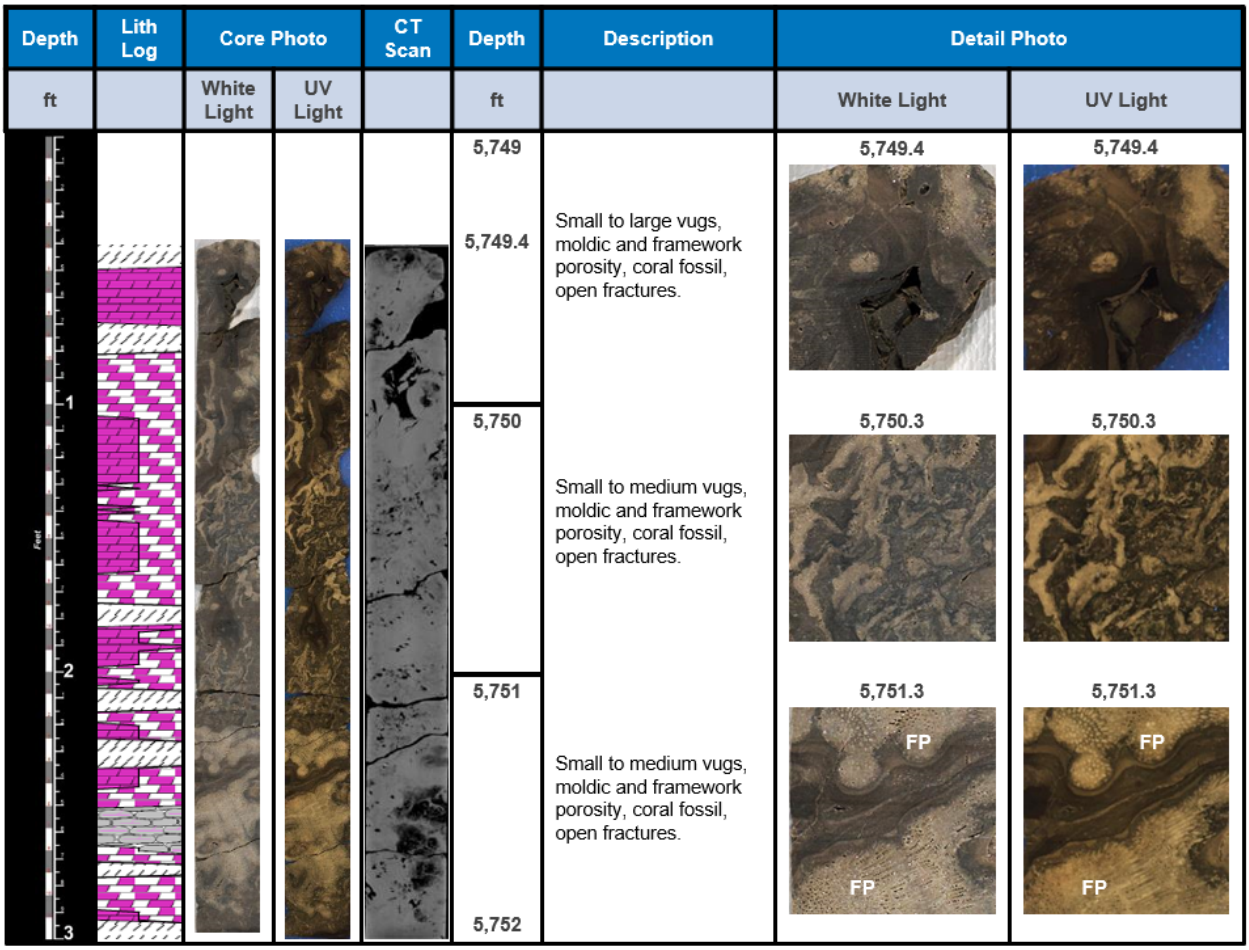


Figure 2-45. Compiled illustration of lithology log, core photos (UV and white light), CT scan image, core descriptions, and annotated core images of the Brown Niagaran for depths 5,749 ft. to 5,752 ft.

Rotary Sidewall Core

Sidewall core photos of the Brown Niagaran at Dover 9-33 show the formation is predominantly a gray carbonate with significant vugular porosity (Figure 2-46 and Figure 2-47). Vugs are present throughout the formation and range from small to large with some filled moldic and some salt-filled vugs. Evidence of minor bioturbation is present sporadically throughout the Brown. The UV images show potential residual oil throughout the formation.

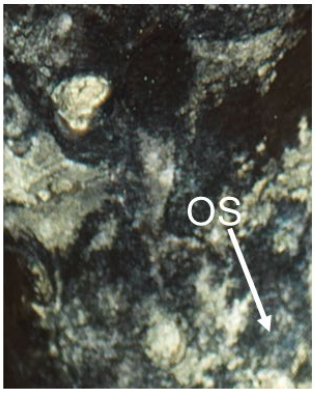
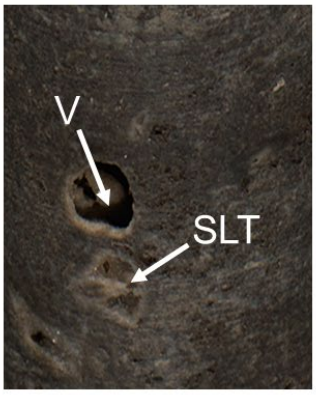
Depth Ft.	White Light Primary Features	UV Light Primary Features	Descriptions
5,580			White Light: Gray carbonate, small vugs, salt plugged vugs. UV Light: Strong light blue UV response due to potential residual oil.
5,583			White Light: Gray carbonate, medium/small vugs, salt plugged vugs. UV Light: Strong light blue UV response due to potential residual oil.

Figure 2-46. Annotated RSWC images with corresponding core descriptions of the Brown Niagaran for depths 5,580 ft. to 5,583 ft.

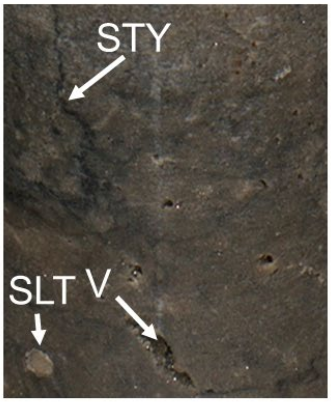
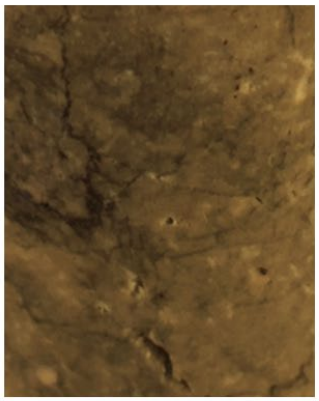
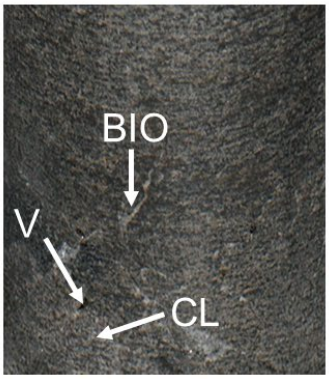
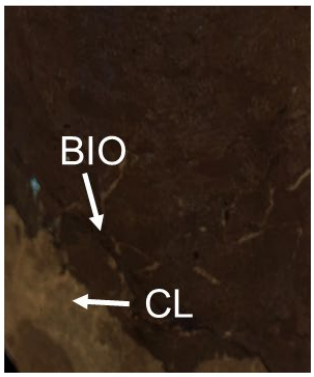
Depth Ft.	White Light Primary Features	UV Light Primary Features	Descriptions
5,847			White Light: Gray carbonate, large/small vugs, salt plugged vugs. UV Light: Gray carbonate.
5,865			White Light: Gray carbonate, small vugs, bioturbation, potential carbonate clast. UV Light: Gray carbonate, bioturbation, potential carbonate clast.

Figure 2-47. Annotated RSWC images with corresponding core descriptions of the Brown Niagaran for depths 5,847 ft. to 5,865 ft.

2.6 Gray Niagaran

2.6.1 Basic Wireline Log Analysis and Petrophysical Calculations

The Gray Niagaran formation was encountered at a depth of 5,867 ft. and the base of the Gray Niagaran was not encountered. Therefore, basic petrophysical calculations (zone footages) could not be calculated for the Gray Niagaran. The updated neutron porosity log coverage did not extend into the Gray Niagaran, so porosity calculations are solely derived from the bulk density curve, expressed as density porosities. Log analysis yielded an average density porosity of 6.3% with porosity values ranging from 3.1% to 9.2% (Figure 2-48). Although the updated neutron log did not extend into the Gray, the original neutron log did and so a crossplot was able to be generated using the original neutron log (Figure 2-49). The neutron-density crossplot shows that the Gray Niagaran is a mixed dolomite/limestone carbonate. GR curve response is also relatively high compared to the Brown Niagaran and suggests that this formation is rich in clay minerals, which is consistent with the elemental spectroscopy log data.

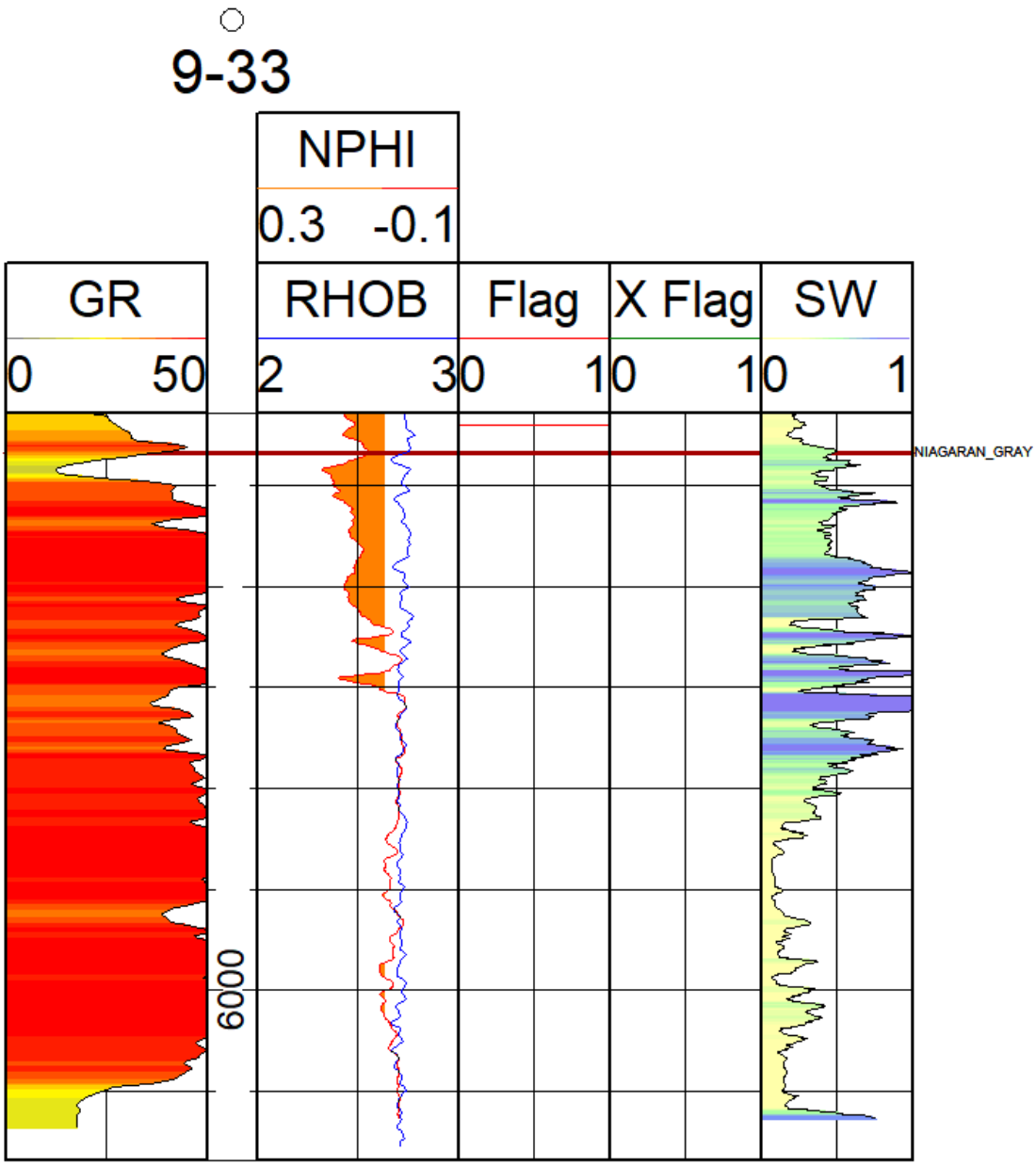


Figure 2-48. Single well cross section of the Gray Niagaran in the Lawnichak 9-33 well

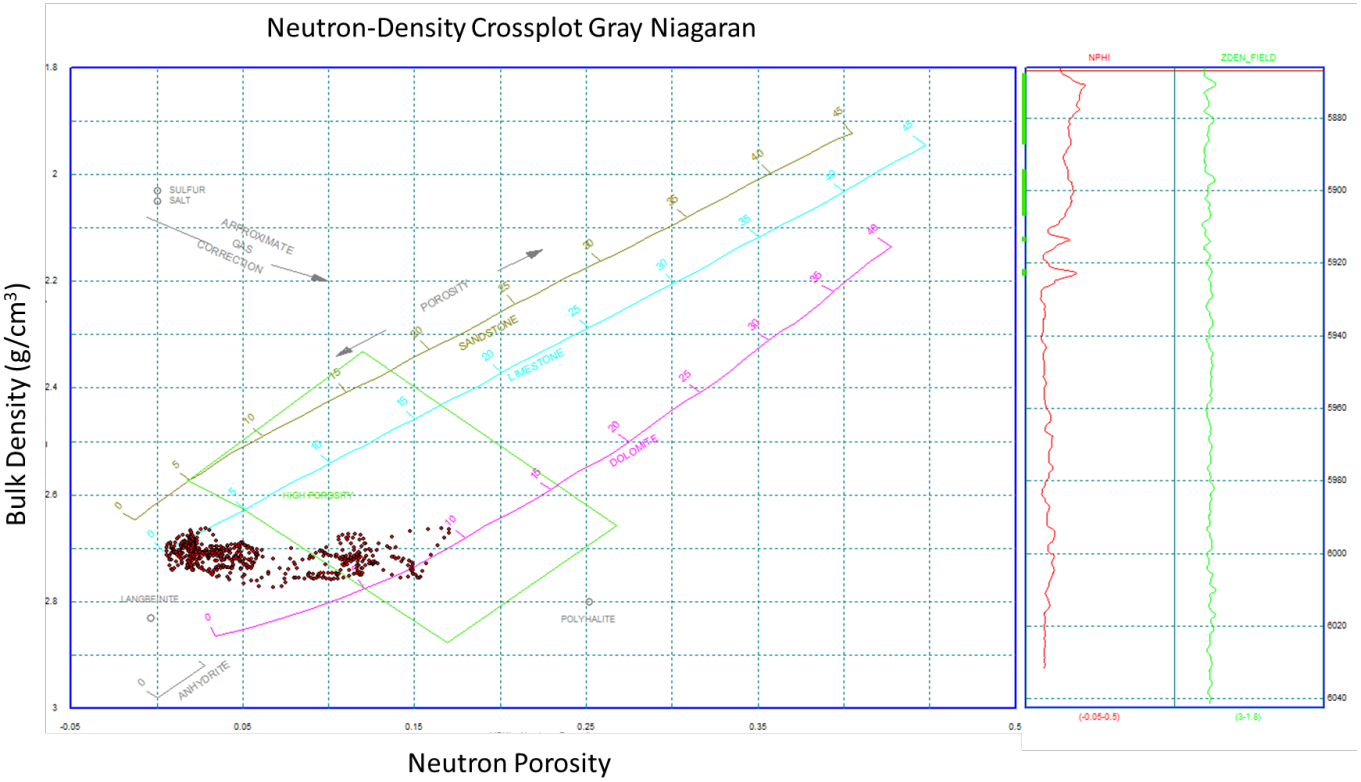


Figure 2-49. Neutron-density crossplot of the Gray Niagaran using the original neutron porosity log. Note that porosity values here are overestimated but lithology is accurate.

2.6.2 Advanced Wireline Log analysis

Elemental Spectroscopy Log Analysis

The Gray Niagaran Formation was logged from a depth of 5,867 ft. MD/5,655 ft. TVD to log TD at 6,046 ft. MD. One key mineralogical difference between this and the other key reservoir units discussed is the persistently high amount of potassium measured in the Gray Niagaran Formation. This translates into high volumetric percentages of clay minerals, with illite ($(K,H_3O)(Al,Mg,Fe)_2(Si,Al)_4O_{10}$) being the dominant form, making up to 25% of the bulk rock volume. However, potassium levels drop in a highly localized fashion, on the order of 1-2-foot sections between 5,912 ft. MD and 5,952 ft. MD, while aluminum values remain high. This indicates the presence of aluminosilicate clay minerals such as kaolinite ($Al_2Si_2O_5(OH)_4$). This kaolinite rich zone is marked on Figure 2-50 with a dashed orange box.

A clear mineralogical boundary within the carbonate system is clearly identifiable from observation of the relative abundance of magnesium and calcium, shown in the 6th and 7th track from the left (Figure 2-50). At 5,905 ft. MD, marked on Figure 2-50 with a pink line, the dolomitic Gray Niagaran Formation switches from nearly 0% to 25-50% calcite bulk rock volume. Nineteen feet deeper, at 5,924 ft. MD, the Gray Niagaran Formation becomes ≥50% calcite through the remainder of the logged interval.

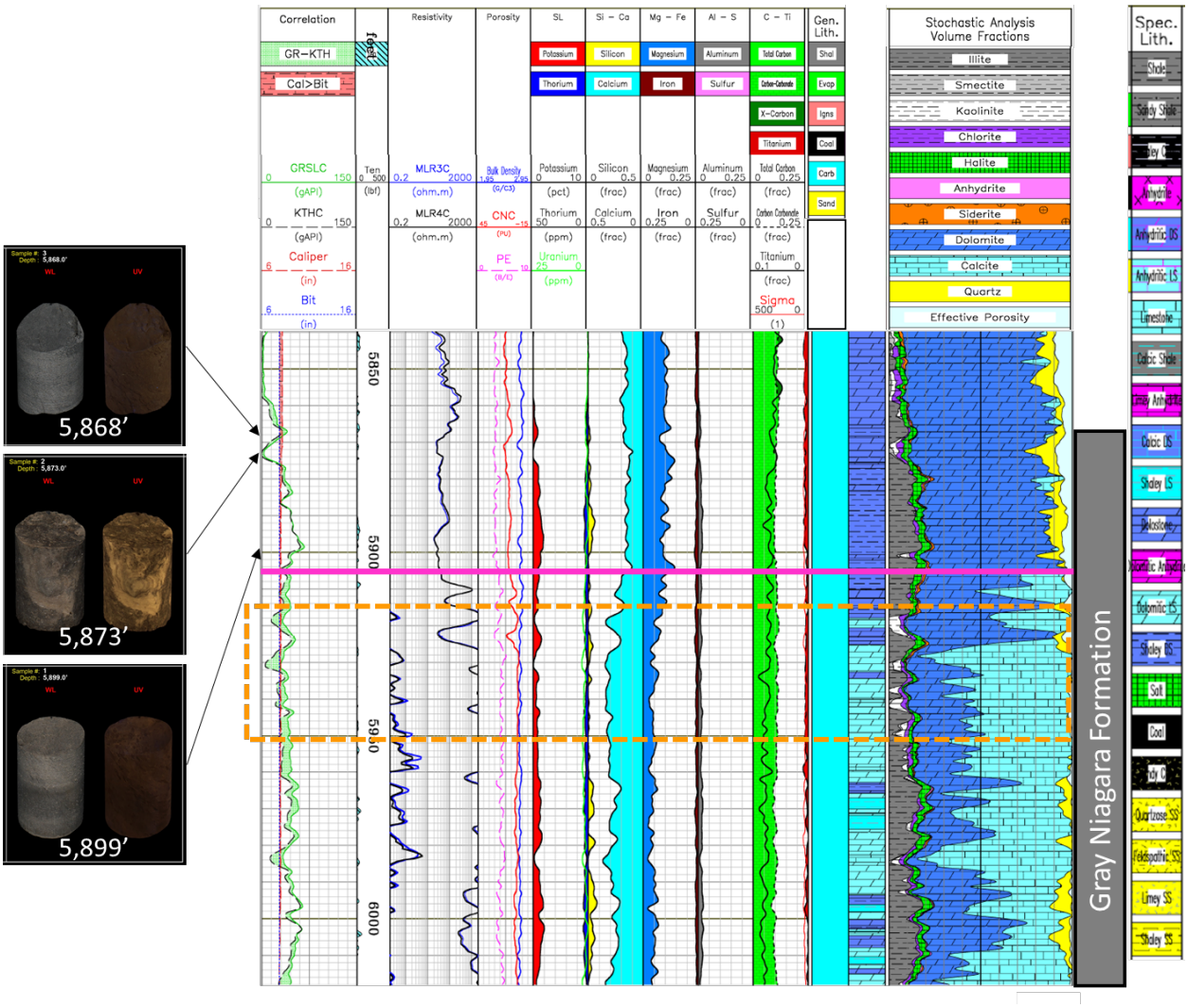


Figure 2-50. Elemental spectroscopy log from Lawnichak 9-33 displaying the Gray Niagaran Formation from 5,867'MD/5,655'TVD to log TD at 6,046'MD. Select Rotary Side Wall Core (RSWC) samples are shown in both white light (WL) and ultraviolet light (UV) to provide context for lithologic descriptions. Pink line marks the boundary between Mg dominated dolomite and Ca dominated calcite formation. Orange box marks depths with enhanced kaolinite formation.

2.6.3 Core Analysis

Rotary side wall core (RSWC) samples were recovered from the Gray Niagaran.

Sidewall core photos of the Gray Niagaran at Dover 9-33 show the Gray is predominantly a gray carbonate that is relatively devoid of sedimentary structures and major secondary porosity (Figure 2-51). Some small vugs and filled moldic vugs are present as well as potential carbonate clasts and minor bioturbation. The UV images show a gray carbonate with filled moldic vugs.

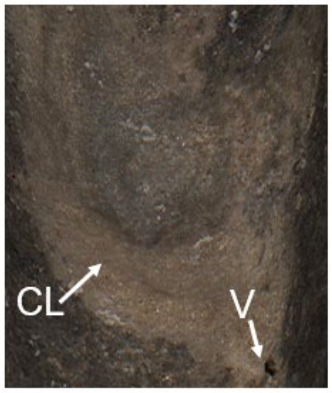
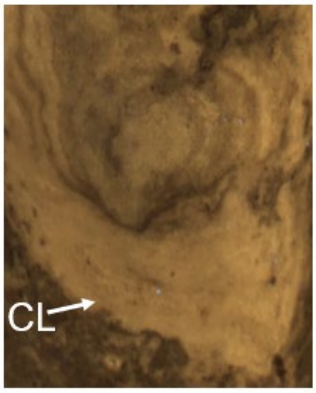
Depth Ft.	White Light Primary Features	UV Light Primary Features	Descriptions
5,873			White Light: Gray carbonate, small vugs, potential carbonate clast. UV Light: Gray carbonate, small vugs, potential carbonate clast.
5,899			White Light: Gray carbonate, filled moldic vugs. UV Light: Gray carbonate, filled moldic vugs.

Figure 2-51. Annotated RSWC images with corresponding core descriptions of the Gray Niagaran for depths 5,873 ft. to 5,899 ft.

2.7 Core Analysis Integration

2.7.1 Dual Energy Computed Tomography (CT) Scanning

Prior to removing the core from the liner, helical CT scans were performed from depths of 5,525 to 5,760 ft., over the A1 Carbonate, and Brown Niagaran Formations by CoreLab in Houston, TX. An X-ray source was set on a helical trajectory around longitudinal sections of cores to derive three-dimensional images of density variations for each core volume. Sample densities are expressed in gray-scale color variations such that light-colored, higher-density areas can be distinguished from darker-colored, low-density areas to identify internal fractures, pore distributions and geometries, and silicate-versus-carbonate mineral variability. These data are essential for the reservoir characterization of rocks with heterogeneous porosity and allow for the accurate sampling of plugs for routine and special core analysis.

In order to model core lithology, two X-ray scans of each core were taken. One scan created images sensitive to bulk density (RHOB) using high energy x-rays. The other scan created an image sensitive to mineralogy using low energy x-rays. These two sets of images were then subjected to a data transform that relates intensity to RHOB and effective atomic number (Zeff). A crossplot of these data from conventional core at Dover 9-33 are shown in Figure 2-52 with

corresponding lithology. The data produced by this tool provide a quantitative understanding of the reservoir potential for the wells and a means by which to correlate wireline log data.

The CT scans revealed frequent intervals with high concentration of vugs, moldic porosity, biologic debris, fractures, stylolites, calcite cement, anhydrite plugs, and regions of massive, tight limestone. Vugular intervals were more frequent in the upper section of core. This transitioned into infrequent, disconnected vugs starting at approximately 5,690 ft. Massive and tight limestone dominated the matrix of the cores with occasional intervals of porosity. Dolostone and porous dolostone have also been identified in the Dover 9-33 well. CT scans and detailed lithology logs spanning the entire cored interval are presented in Appendix A.

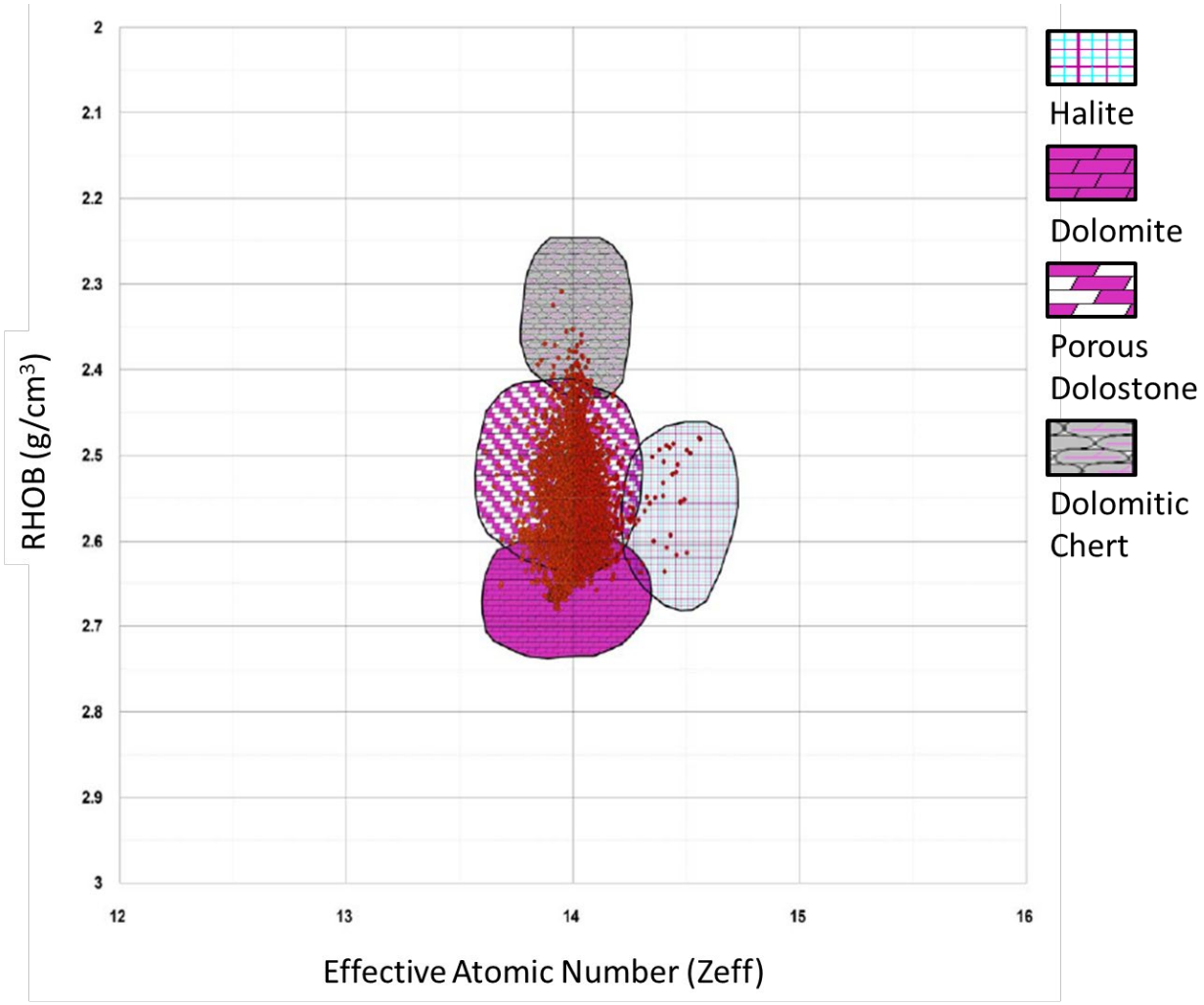


Figure 2-52. Rock typing results from CT Scan analysis of the Lawnichak 9-33 cores showing mostly porous dolostone and dolomite with some dolomitic chert and halite.

2.7.2 Routine Conventional Core Analysis

Routine core analysis was conducted on 1.0 in. diameter plugs drilled from the whole core. These analyses were conducted by Core Lab in Houston, TX. Standard core analysis included porosity, permeability, fluid saturation, bulk density, and grain density measurements.

Grain Density

The grain density for the Dover 9-33 reef core ranged from 2.80 to 2.86 g/cm3. The A-1 Carbonate and the Brown Niagaran had an average grain density of 2.85 g/cm3. Table 2-7 summarizes the grain density averages for the Dover 9-33 core and Figure 2-53 shows grain density histograms by formation.

Table 2-7. Core grain density summary

Interval	Range (g/cm^3)	Average (g/cm^3)
All Core	2.80-2.86	2.85
A-1 Carbonate	2.84-2.85	2.85
Brown Niagarann	2.80-2.86	2.85

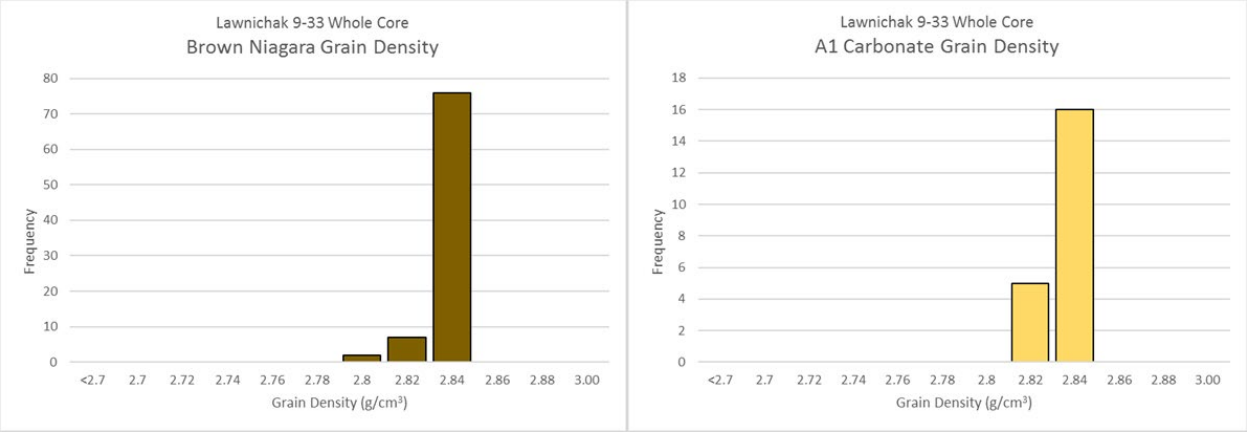


Figure 2-53. Histograms of grain density by formation from the Lawnichak 9-33 conventional core

Porosity and Permeability

The A-1 Carbonate had a porosity range from 3.16% to 10.72% with a permeability range from 0.00 to 6.04 mD (Table 2-8). The Brown Niagaran had a porosity range from 1.51% to 7.14% with a permeability range from .00 to 204.28 mD. This data has been plotted in Figure 2-54 with the coordinating transform equation (Equation 2-5) below:

$$K = 0.2239e^{0.3387\phi} \quad (2\text{-}5)$$

Where K represents the permeability in mD and ϕ is the porosity in percent.

Table 2-8. Summary of porosity and permeability data from whole core at Lawnichak 9-33

Formation	Porosity (%)			Permeability (mD)		
	Min	Max	Average	Min	Max	Average
A-1 Carbonate	3.16	10.72	6.69	0.00	6.04	0.70
Brown Niagarann	1.51	14.16	7.14	0.00	204.28	6.53

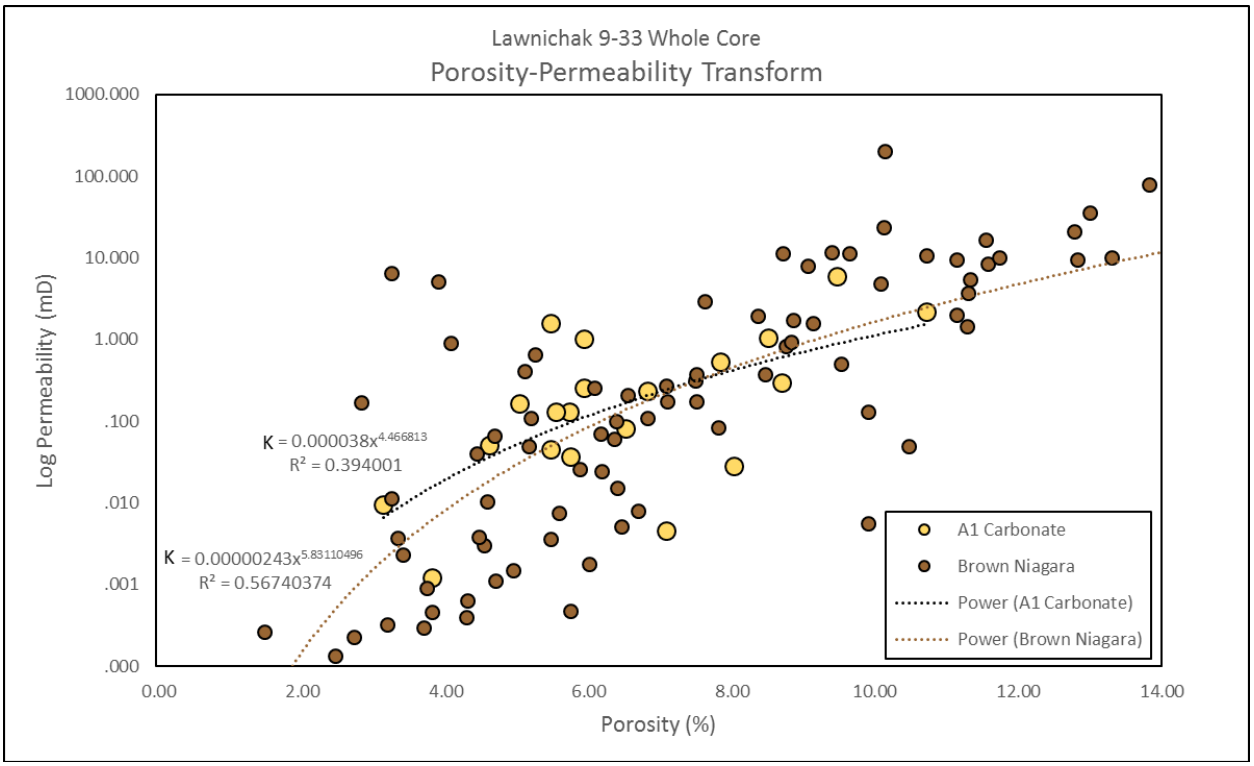


Figure 2-54. Core porosity-permeability transform plot for the A-1 Carbonate (yellow circles) and the Brown Niagaran (brown circles)

2.7.3 Routine Sidewall Core Analysis

Routine core analysis was conducted on 1.5 in. diameter sidewall core samples. These analyses were conducted by Core Lab in Houston, TX. Standard core analysis included porosity, permeability, fluid saturation, bulk density, and grain density measurements.

Grain Density

The grain density for the Dover 9-33 reef sidewall cores ranged from 2.78 to 2.94 g/cm3 with an average of 2.84 g/cm3. The A-2 Carbonate had an average grain density of 2.83 g/cm3. The A-2 Evaporite had an average grain density of 2.89 g/cm3. The A-1 Carbonate had an average grain density of 2.85 g/cm3. The Brown Niagaran had an average grain density of 2.84 g/cm3 and the Gray Niagaran had an average grain density of 2.82 g/cm3. Table 2-9 summarizes the grain density averages for the Dover 9-33 sidewall cores and Figure 2-55 shows grain density histograms for all of Dover 9-33 sidewall cores by formation.

Table 2-9. RSWC grain density summary by formation

Interval	Range (g/cm^3)	Average (g/cm^3)
All Core	2.78-2.94	2.84
A-2 Carbonate	2.82-2.83	2.83
A-2 Evaporite	2.86-2.91	2.89
A-1 Carbonate	2.82-2.94	2.85
Brown Niagarann	2.78-2.90	2.84
Gray Niagarann	2.81-2.84	2.82

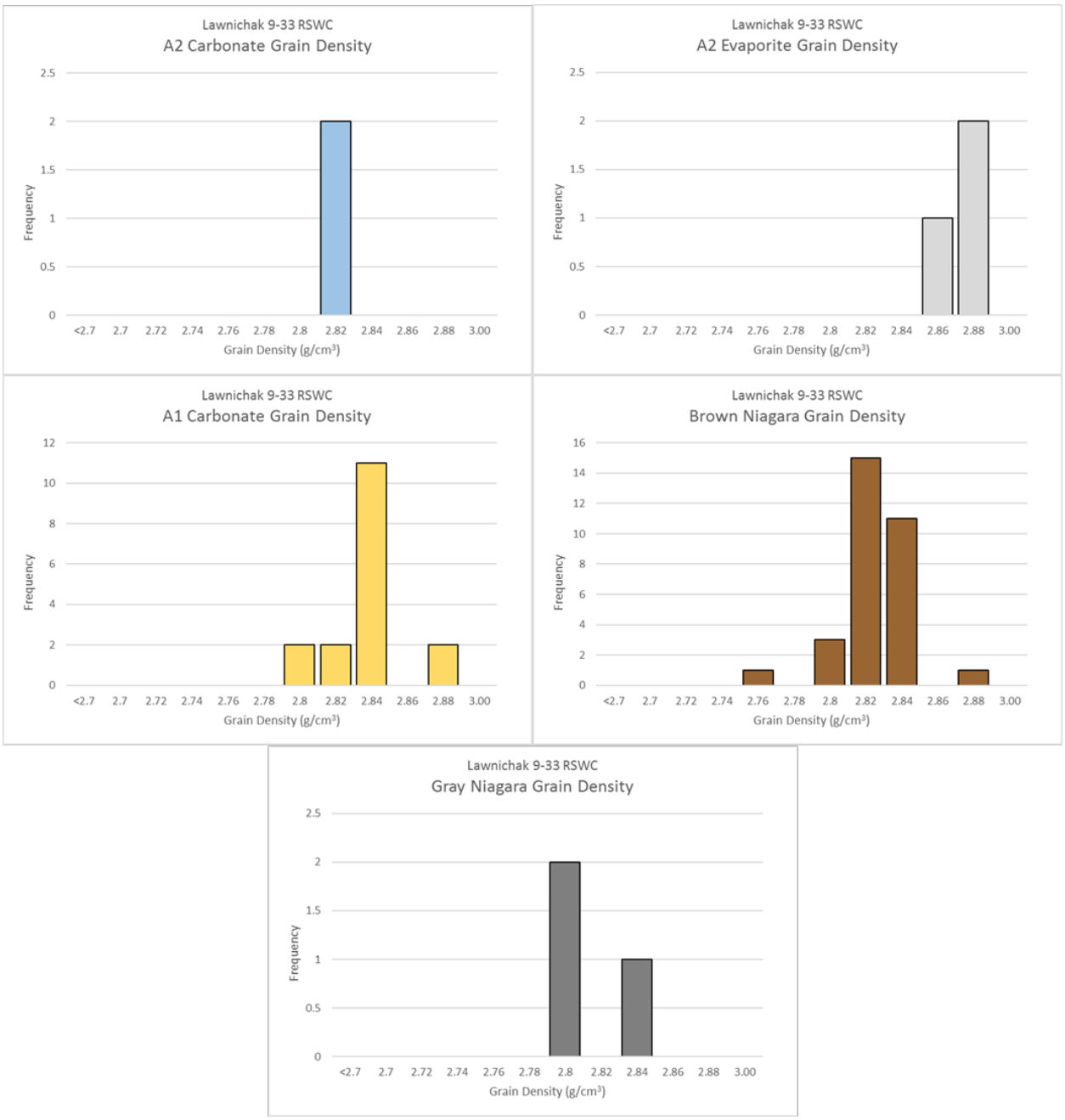


Figure 2-55. Histograms of grain density by formation from the Lawnichak 9-33 RSWCs

Porosity and Permeability

The A-2 Carbonate had a porosity range from 4.3% to 4.7% with a permeability range from 0.00 to 17.7 mD (Table 2-10). The A-2 Evaporite had a porosity range from 0.36% to 0.64%. The A-1 Carbonate had a porosity range from 0.11% to 8.08% with a permeability range from 0.00 to 0.86 mD. The Brown Niagaran had a porosity range from 1.27% to 8.62% with a permeability range from 0.00 to 14.34 mD. The Gray Niagaran had a porosity range from 1.83% to 6.39% with a permeability range from 0.00 to 0.31 mD. This data has been plotted in Figure 2-56 with the coordinating transform equation (equation 2-5) below:

$$K = 0.2239e^{0.3387\phi} \quad (2\text{-}5)$$

Where K represents the permeability in mD and ϕ is the porosity in percent.

Table 2-10. Summary of RSWC porosity and permeability data

Formation	Porosity (%)			Permeability (mD)		
	Min	Max	Average	Min	Max	Average
A-2 Carbonate	4.3	5.1	4.7	0.00	17.7	8.9
A-2 Evaporite	0.36	0.64	0.48	-	-	-
A-1 Carbonate	0.11	8.08	4.19	0.00	0.86	0.09
Brown Niagarann	1.27	8.62	14.88	0.00	14.34	1.646
Gray Niagarann	1.83	6.39	4.72	0.00	0.31	0.10

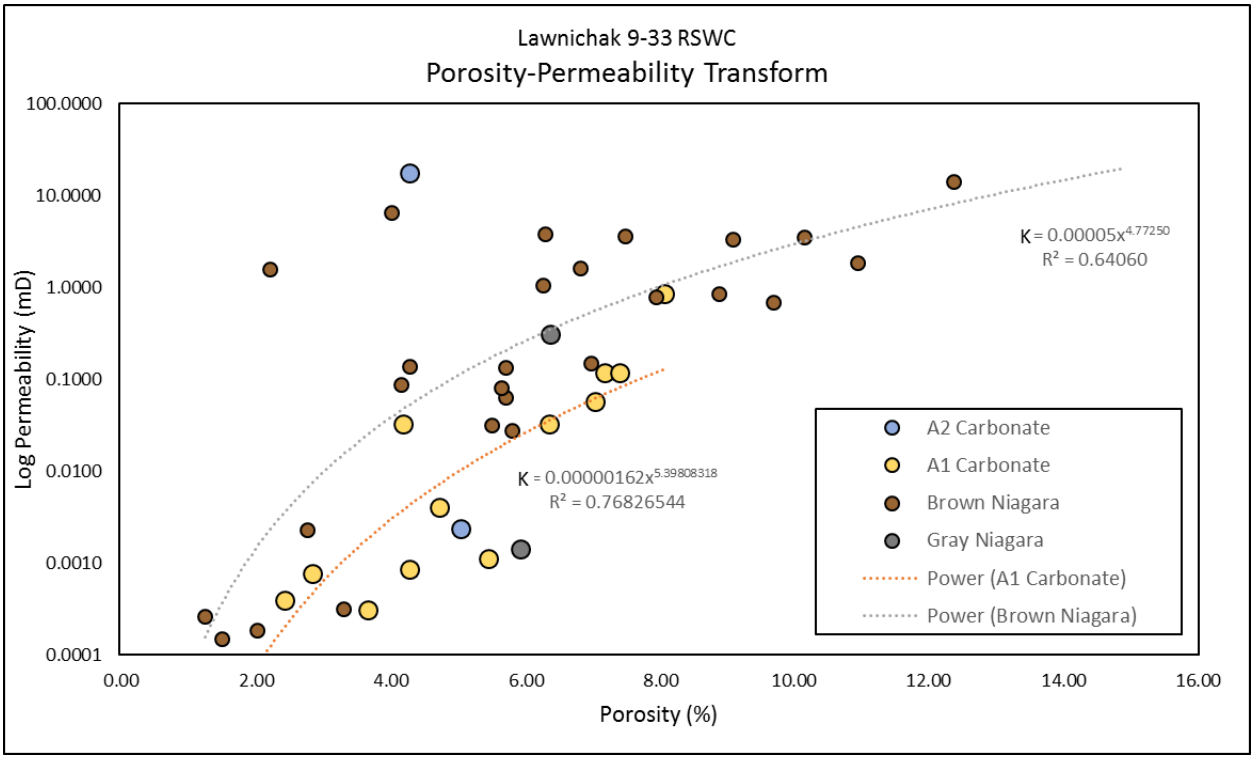


Figure 2-56. RSWC porosity-permeability transform plot for the A-2 Carbonate (blue circles), A-1 Carbonate (yellow circles), Brown Niagaran (brown circles), and the Gray Niagaran (gray circles)

2.7.4 Thin Section Analysis

Core Laboratories performed thin section petrography and X-ray diffraction (XRD) analyses on three rotary sidewall core samples of the colloquially named “A-2 Shale”, which is a higher gamma ray signature of approximately 75 API, within the A-2 Carbonate. The samples were collected from depths of 5,374, 5,374.5, and 5,378 ft. The A-2 Shale has long been referred to as a shale due to its relatively high gamma ray log signature (when compared to surrounding carbonates) though prior to this report, there has been a lack of detailed information and characterization of this stratigraphic unit. Despite the gamma ray signature being relatively higher than the surrounding carbonate intervals, the signature is still not high enough to be consistent with typical shales which tend to show gamma ray signatures of approximately 150 API and higher. Due to the relatively potassium feldspar rich composition and the fact that the A-2 Shale is considered a regional marker bed, some have hypothesized that the A-2 Shale could be a bentonite ash layer. Our preliminary results from thin section analyses suggest that the A-2 Shale is neither shale nor bentonite, but rather a type of dolomitic anhydrite.

Results

The three samples, Figure 2-57, Figure 2-58, and Figure 2-59, are variously identified as two dolomitic anhydrites (5374.00 and 5378.00 ft.) and one dolostone (5374.50 ft.). Using Dunham’s (1962) system for carbonate samples, the sample from 5374.50 ft. classifies as a crystalline dolostone. The two dolomitic anhydrites are not predominately carbonates (based on observation and X–ray diffraction data), so cannot be classified with Dunham’s system. Table 2-11 provides a summary of major whole rock mineralogy.

Table 2-11. Summary of major whole rock mineralogy

Whole Rock Mineralogy (weight %)					
Depth (ft.)	Quartz	K-Feldspar	Dolomite	Anhydrite	Total Clay
5374.00	1.5	0.6	40.1	56.0	1.8
5374.50	0.3	0.0	99.7	0.0	0.0
5378.00	2.1	0.4	39.7	55.2	2.6

Authigenic potassium –feldspar and pyrite are present in the 5,374 ft. and 5,378 ft. samples (Figure 2-57 and Figure 2-59). The potassium–feldspar (stained yellow) is rare in thin section and XRD and replaces some dolomite crystals but not anhydrite. Pyrite is rare in the samples and is visible as small framboids (framboids are spherical structures that are composed of aggregates of minute pyrite crystallites). Samples 5,374 and 5,378 show little to no visible pore spaces. The dolostone sample from 5374.50 ft. (Figure 2-58) shows common amounts of intercrystalline pores. Secondary dissolution has produced minor amounts of moldic pores measuring up to 1.5 mm (small vug–size pore).

Conclusions

Thin section analyses results reveal that the “A-2 Shale” is predominantly a dolomitic anhydrite with little-to-no clay or quartz. Detailed thin section analyses show that anhydrite is not uniformly present and occurs in alternating laminae with dolomite. Authigenic potassium-feldspar is present in the shallowest and deepest samples which replaces some dolomite crystals, but not anhydrite. The source of the potassium-feldspar remains undetermined. For a full, detailed thin section report, see Appendix A.

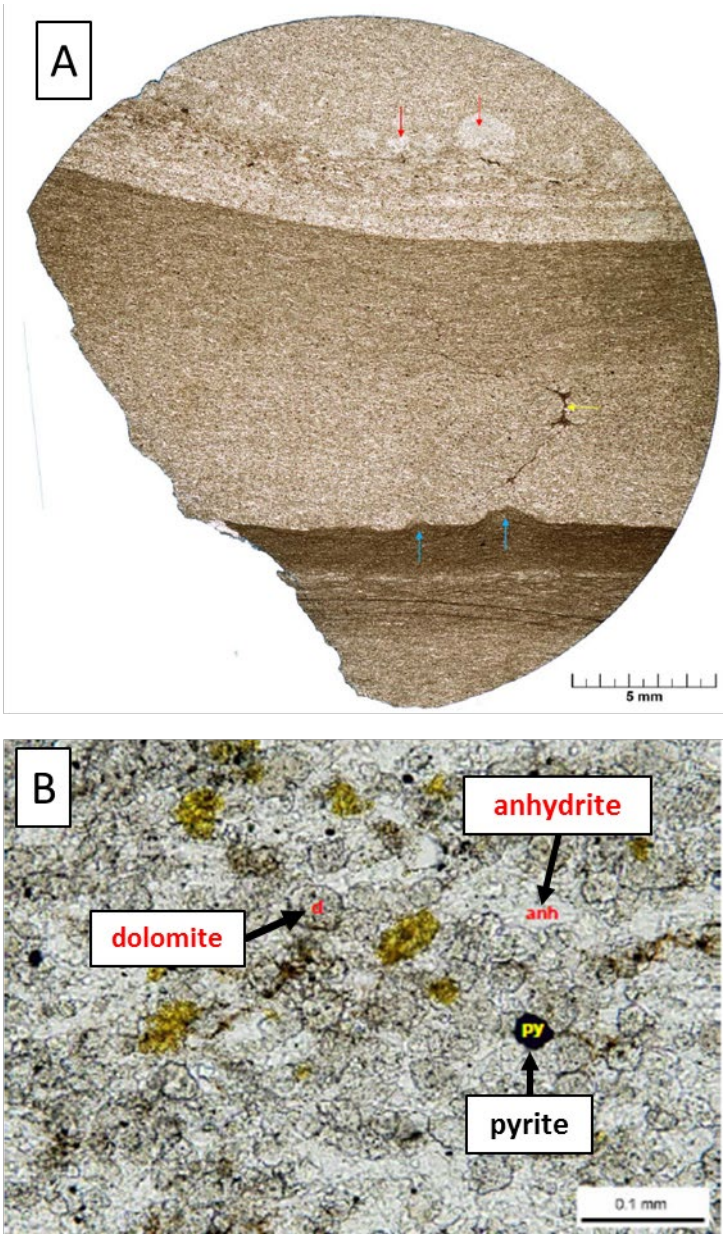


Figure 2-57. Thin section of rotary sidewall core sample at 5,374 ft. (A) shows high-resolution thin section sample of the dolomitic anhydrite sample. Red indicate small anhydrite nodules, yellow arrow indicates micrite-filled fractures, and blue arrows indicate small load casts. (B) is a magnified view of a section of the thin section sample. Dolomites and anhydrites are indicated throughout the thin section with occasional potassium-feldspar (stained yellow) and pyrite minerals.

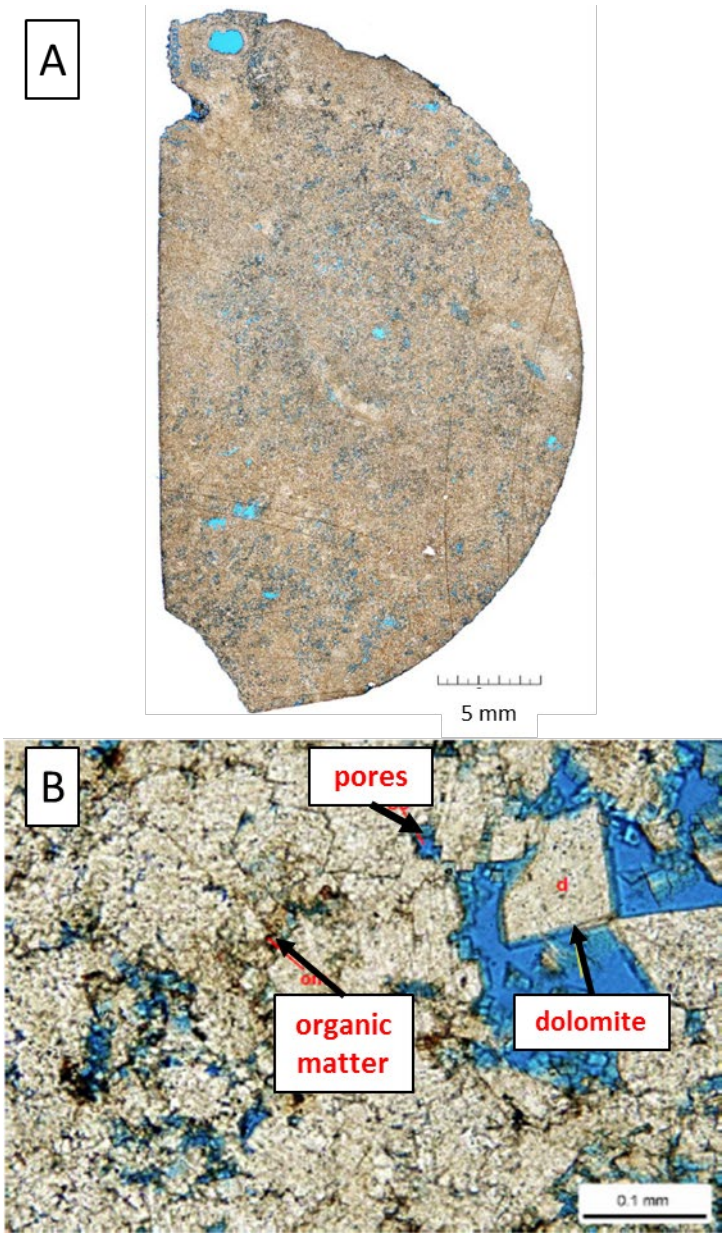


Figure 2-58. Thin section of rotary sidewall core sample at 5,374.50 ft. (A) shows a dolostone with vugs up to 1.5 mm. (B) magnified view of the sample indicating a medium-crystalline dolostone comprised of replacement dolomite with dark matter between small pore spaces. Large euhedral dolomite crystals indicate late stage dolomitization.

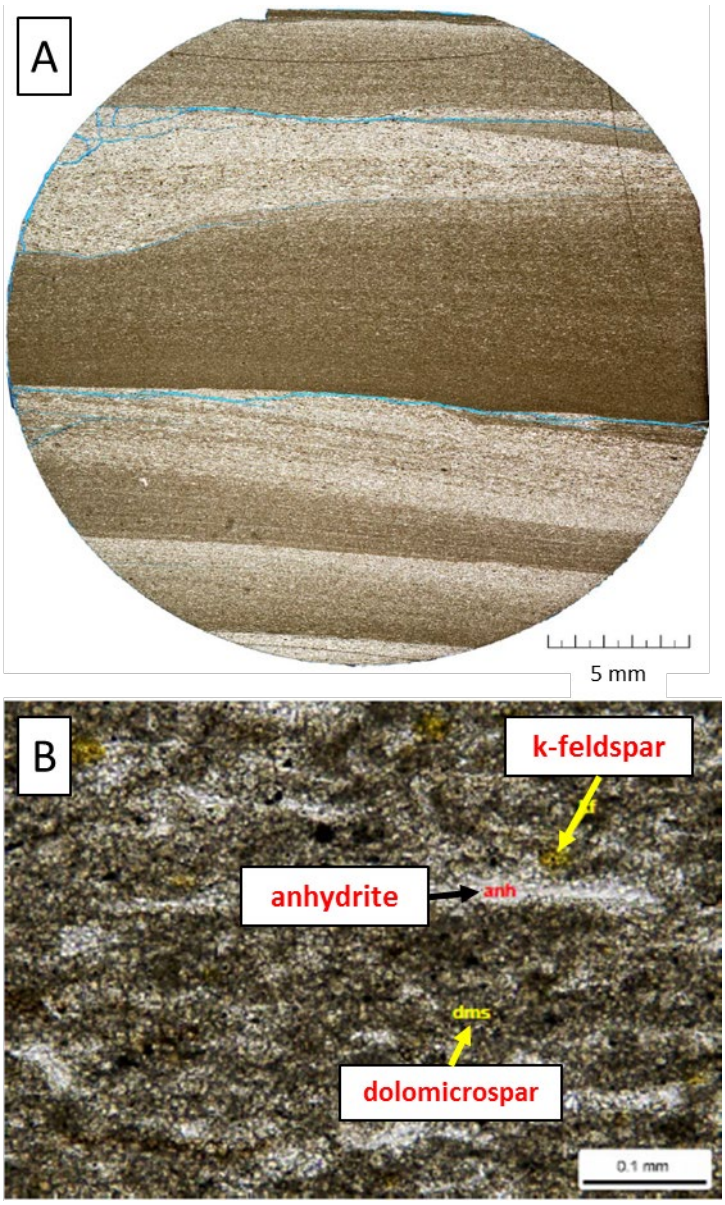


Figure 2-59. Thin section of rotary sidewall core sample at 5,378 ft. (A) shows light anhydrite dominate anhydritic-dolomitic laminae with darker dolomitic dominated dolomitic-anhydrite laminae. Fractures in the sample were induced during preparation. (B) magnified view of the sample indicating elongated anhydrites intermixed with dolomicrite. There are a few instanced of k-feldspar minerals (yellow stain).

2.7.5 Core Integration Summary

Conventional core samples were collected across the A-1 Carbonate and Brown Niagaran formations and rotary sidewall core samples were collected across the A-2 Carbonate, A-2 Evaporite, A-1 Carbonate, Brown Niagaran, and Gray Niagaran formations. Table 2-12 and Table 2-13 show summary statistics of porosity and permeability by formation for conventional and sidewall core, respectively. Table 2-14 shows the depths of key potential reservoir intervals with porosity ≥5% as determined by core analysis and intervals with visible porosity as observed in core images and CT scans. Overall, the 9-33 core is dominated by a porous dolomite

lithology with some isolated zones of high porosity. Visible porosity, as seen on the core images and CT scans, is dominantly in the form of small to medium vugs and significant moldic porosity.

Table 2-12. Summary of whole core porosity and permeability data in the Lawnichak 9-33 well

Formation	Porosity (%)			Permeability (mD)		
	Min	Max	Average	Min	Max	Average
A-1 Carbonate	3.16	10.72	6.69	0.00	6.04	0.70
Brown Niagaran	1.51	14.16	7.14	0.00	204.28	6.53

Table 2-13. Summary of rotary sidewall core porosity and permeability data in the Lawnichak 9-33 well

Formation	Porosity (%)			Permeability (mD)		
	Min	Max	Average	Min	Max	Average
A-2 Carbonate	4.3	5.1	4.7	0.00	17.7	8.9
A-2 Evaporite	0.36	0.64	0.48	-	-	-
A-1 Carbonate	0.11	8.08	4.19	0.00	0.86	0.09
Brown Niagaran	1.27	8.62	14.88	0.00	14.34	1.646
Gray Niagaran	1.83	6.39	4.72	0.00	0.31	0.10

Table 2-14. Summary of key potential reservoir intervals in the Lawnichak 9-33 well based on whole core analysis and images

Formation	Reservoir Intervals [ϕ ≥ 5%] (ft.)	Intervals with visible porosity (ft.)
A-1 Carbonate	5525.5-5534.5, 5536.6-5540.5, 5542.4-5543.5, 5545.5	5527-5528, 5534-5544, 5549-5552
Brown Niagaran	5548.5-5559.5, 5561.5, 5599.5-5602.65, 5609.5, 5690.5, 5693.5-5694.5, 5698.5-5699.5, 5702.5-5704.5, 5708.5, 5710.5-5711.5, 5713.5-5726.5, 5728.5, 5730.5-5731.5, 5733.5-5752.5, 5757.65-5759.4	5549-5555, 5598-5609, 5690-5695, 5697-5725, 5726-5760

Chapter 3. Summary

Well log data from the Lawnichak 9-33 well has provided insight into the local and regional stratigraphy, structure, and petrophysical properties of the potential Northern Pinnacle Reef Trend storage reservoirs and confining units in the Michigan Basin. Independent analyses conducted for five different basic and advanced logs produce complementary results suggesting the A-1 Carbonate and Brown Niagaran formations exhibit reservoir storage potential in the Lawnichak 9-33 well. Additionally, well log data suggests that the A-2 Anhydrite and the very thick, vertically continuous Salina B salt sequence may serve as key confining layers to the underlying reservoir. Table 3-1 lists the formations and their potential injection/storage intervals as determined by crossplot and pay flags, as well as NMR log and core data.

Table 3-1. Summary of key potential reservoir intervals in the Lawnichak 9-33 well

Formation	Potential Reservoir Interval (ft.)
A-1 Carbonate	5,507 – 5,546
Brown Niagaran	5,546 – 5,640
Brown Niagaran	5,688 – 5,859


BATTELLE
It can be done

Attachment 3.
Chester 6-16 Wireline and Core Analysis: Chester 16 Niagaran Reef Piggyback Well

Attachment 3

Chester 6-16 Wireline and Core Analysis: Chester 16 Niagaran Reef Piggyback Well

Conducted by the Midwest Regional Carbon Sequestration Partnership (MRCSP)

DOE-NETL Cooperative Agreement DE-FC26-05NT42589



Prepared by:

Battelle
505 King Avenue
Columbus, Ohio 43201

Submitted to:

Client
Address
Address

April 28, 2019

This report is a work prepared for the United States Government by Battelle. In no event shall either the United States Government or Battelle have any responsibility or liability for any consequences of any use, misuse, inability to use, or reliance on any product, information, designs, or other data contained herein, nor does either warrant or otherwise represent in any way the utility, safety, accuracy, adequacy, efficacy, or applicability of the contents hereof.

Table of Contents

Page

Chapter 1. Well Drilling and Completions 1
1.1 Well Drilling and Completions 1
1.2 Well Operations Execution 1
1.3 Well Logging 2
Chapter 2. Geologic Characterization 9
2.1 Methodology 9
2.1.1 Wireline Log Analysis and Petrophysical Calculations 9
2.1.2 Core Collection and Description 11
2.2 Core Analysis 11
2.2.1 Routine Sidewall Core Analysis 11
2.3 Formation Evaluation 14
2.3.1 A-2 Carbonate and A-2 Evaporite 14
2.3.2 A-1 Carbonate 17
2.3.3 Brown Niagaran 22
2.3.4 Gray Niagaran 28
2.4 Summary 32
Chapter 3. Integrated Geomechanics Analysis 33
3.1 Introduction 33
3.2 Mechanical Parameters Characterization Using Dipole Sonic Log Analysis 33
3.3 In-Situ Stress Analysis 40
3.3.1 Calculating Vertical Stress (Sv) Using Density Logs 40
3.3.2 S_{Hmax} Azimuth Analysis Using Image Log Data 41
3.4 Summary 42
Chapter 4. Summary 44
4.1 Conclusion 44
Appendix A. Core Descriptions 45
A.1 Rotary Side Wall Core Descriptions 46

List of Tables

Page

Table 1-1. Chester 6-16 formation evaluation value of information chart. Logs highlighted in blue represent open hole logs, those highlighted in gray were collected in cased hole. 8
Table 2-1. Formation tops for the Chester 6-16. 9
Table 2-2. Chester 6-16 RSWC acquisition parameters. 11
Table 2-3. Summary of the grain density averages for Chester 6-16 sidewall cores. 11
Table 2-4. Summary of porosity and permeability data from RSWC in Chester 6-16. 13
Table 2-5. Summary of RSWC porosity and permeability data in the Chester 6-16 well. 32
Table 2-6. Summary of key potential reservoir intervals in the Chester 6-16 well based on RSWC analysis and images. 32
Table 3-1. Mean, variance, and N (number of data values) values of geomechanical parameters within Chester 6-16 by formation. 39

List of Figures

Page

Figure 1-1. Surface hole location for Chester 6-16 marked in red. 3
Figure 1-2. As-built wellbore diagram for Chester 6-16 (not to scale). 4
Figure 1-3. Deviation survey plot for well Chester 6-16 showing the degree of deviation from the vertical wellbore (left) and the direction towards the northeast (right). 5
Figure 1-4. Days vs. depth plot annotated with unscheduled events, casing points, and key geologic horizons for drilling and completion of the Chester 6-16 well. 6
Figure 1-5. Executed formation evaluation program for Chester 6-16. 7
Figure 2-1. RSWC abbreviation explanations. 11
Figure 2-2. Histograms of grain density by formation from the Chester 6-16 RSWCs. 12
Figure 2-3. Porosity-permeability transform for the A-1 Carbonate and Brown Niagaran from RSWC measurements in Chester 6-16. Only one point was measurable from Gray Niagaran RSWCs. 13
Figure 2-4. Average porosity histogram of the A-2 Carbonate for Chester 6-16 showing low average porosity of 0.04 %. 14
Figure 2-5. Bulk density and neutron porosity cross plot of the A-2 Carbonate for the Chester 6-16 well showing a tight dolomite with anhydritic layers (blue) and a thin interval of porosity greater than 5% (red). 15
Figure 2-6. Single well cross section over the A-2 Carbonate interval for Chester 6-16 showing relatively low porosity and low water saturation throughout with a high gamma spike mid-formation marking a carbonate shale/mudstone. 16
Figure 2-7. Single well cross section over the A-2 Evaporite interval for Chester 6-16 showing no porosity, high bulk density and water saturation, consistent with anhydrite. 17
Figure 2-8. Average porosity histogram of the A-1 Carbonate for Chester 6-16 showing a bimodal distribution with low porosities at the base of the formation and high porosities mid to upper formation. 18

Figure 2-9. Neutron porosity-bulk density cross plot of the A-1 Carbonate for Chester 6-16 showing mostly porous dolomite (red) and thin intervals of tight dolomite. 18
Figure 2-10. Single well cross section of the A-1 Carbonate for Chester 6-16 showing a thick interval of high porosity (orange shade) with layers of high water saturation attributed to hydrocarbon presence. 19
Figure 2-11. Annotated RSWC images with corresponding core descriptions of the A-1 Carbonate for depths 5,938 ft. to 5,961 ft. 20
Figure 2-12. Annotated RSWC images with corresponding core descriptions of the A-1 Carbonate for depths 5,962 ft. to 5,968 ft. 21
Figure 2-13. Average porosity histogram of the Brown Niagaran for Chester 6-16 showing mostly low porosity with an average of 1.7%. 22
Figure 2-14. Neutron porosity-bulk density cross plot of the Brown Niagaran for Chester 6-16 showing mostly tight limestone with thin intervals of porosity greater than 5% (red). 23
Figure 2-15. Single well cross section of the Brown Niagaran for Chester 6-16 showing thin zones of porosity (red flags) and increasing water saturation towards the OWC (blue dashed line). 24
Figure 2-16. Annotated RSWC images with corresponding core descriptions of the Brown Niagaran for depths 6,015 ft. to 6,032 ft. 25
Figure 2-17. Annotated RSWC images with corresponding core descriptions of the Brown Niagaran for depths 6,173 ft. to 6,177 ft. 26
Figure 2-18. Annotated RSWC images with corresponding core descriptions of the Brown Niagaran for depths 6,197 ft. to 6,310 ft. 27
Figure 2-19. Neutron porosity-bulk density cross plot of the Gray Niagaran for the Chester 6-16 well showing tight limestone with thin intervals of porosity greater than 5% (red flag). 28
Figure 2-20. Single well cross section of the Gray Niagaran for the Chester 6-16 well showing thin intervals of porosity (orange shade) with increasing gamma ray and high water saturation. 29
Figure 2-21. Annotated RSWC images with corresponding core descriptions of the Gray Niagaran for depths 6,516 ft. to 6,549 ft. 30
Figure 2-22. Annotated RSWC images with corresponding core descriptions of the Gray Niagaran for depths 6,550.5 ft. to 6,583 ft. 31
Figure 3-1. Depth plots of Poisson's Ratio and Young's modulus for Chester 6-16. 35
Figure 3-2. Depth plots of dynamic shear modulus and bulk modulus for Chester 6-16. 36
Figure 3-3. Histograms of Poisson's Ratio and Young's Modulus for Chester 6-16. Two of the histograms include the Salina Formation, and two of the histograms don't include the Salina Formation for visual resolution purposes. 37
Figure 3-4. Histograms of dynamic shear modulus and bulk modulus for Chester 6-16. Two of the histograms include the Salina Formation, and two of the histograms don't include the Salina Formation for visual resolution purposes. 38
Figure 3-5. Calculated S_v, SH_{min}, and P_p with depth for Chester 6-16. 41
Figure 3-6. Example of DIF recorded on an acoustic image of the Chester 6-16 well. 42

Figure A-1. RSWC abbreviation explanations. 46
Figure A-2. Annotated RSWC images with corresponding core descriptions of the A-1 Carbonate for depths 5,927 ft. to 5,934 ft. 47
Figure A-3. Annotated RSWC images with corresponding core descriptions of the A-1 Carbonate for depths 5,938 ft. to 5,961 ft. 48
Figure A-4. Annotated RSWC images with corresponding core descriptions of the A-1 Carbonate for depths 5,962 ft. to 5,968 ft. 49
Figure A-5. Annotated RSWC images with corresponding core descriptions of the A-1 Carbonate for depths 5,970 ft. to 5,971 ft. 50
Figure A-6. Annotated RSWC images with corresponding core descriptions of the Brown Niagaran for depths 6,015 ft. to 6,032 ft. 51
Figure A-7. Annotated RSWC images with corresponding core descriptions of the Brown Niagaran for depths 6,032.5 ft. to 6,033 ft. 52
Figure A-8. Annotated RSWC images with corresponding core descriptions of the Brown Niagaran for depths 6,033.5 ft. to 6,036 ft. 53

Chapter 1. Well Drilling and Completions

1.1 Well Drilling and Completions

Drilling of the Chester 6-16 well began on November 7, 2016 and operated by Core Energy LLC with well evaluation operations contracted by Battelle Memorial Institute on behalf of the MRCSP. The surface location of this borehole is marked by a red dot on both a high-resolution aerial photograph and map in Figure 1-1. The final, as-built, wellbore diagram can be found in Figure 1-2.

This well was directionally drilled from the Kick Off Point (KOP) at 4,047' MD/TVD, or the point where the well deviated from vertical The deviation survey plot for Chester 6-16 is shown in Figure 1-3. The maximum angle of inclination is 2.76 degrees and dog leg severity (DLS) does not exceed 1.3 degrees/100' at any point along the well path trajectory.

1.2 Well Operations Execution

A days vs. depth chart in Figure 1-4 is annotated with unscheduled events that occurred during drilling and completions, casing shoe depths (black triangles), and key formation tops. These unscheduled events are described below:

- A drill bit was plugged with cuttings and/or mud while drilling the surface hole section, forcing an extra trip to surface to pick up a new bit.
- Lost returns, or the failure for samples to return to surface during drilling, are common across the Northern Michigan Pinnacle Reef Trend, often massive or total, in the intermediate hole section when the mud system is converted from freshwater to brine. Pore pressure within this stratigraphic section must be at or very near the hydrostatic gradient because the drilling fluid density increase caused by adding dissolved salts is sufficient to cause voids to form or open. Drilling with a salt saturated fluid is critical through this interval to prevent hole enlargement and washout while drilling thick salt beds.
    - Chester 6-16 follows this trend and experienced total losses at 2,724' MD after swapping to brine. The drilling team was able to reach hole section TD at 4,047' MD/TVD while taking losses by: pumping Lost Circulation Material (LCM) sweeps, working/reciprocating the drilling string periodically, and taking time to Circulate and Condition (C&C) the hole.
- While drilling at 5,290' MD, there was a decrease in pump pressure at surface, indicating a potential hole in the drill pipe. The drilling team pulled the pipe out of the hole, inspecting every joint. A hole caused by washout was located 61 stands (30'x2x61=3660') from the surface.
    - During this operation, the last drill collar (DC) was discovered to be missing. The pin that attached the DC to the bottom hole assembly (BHA) had broken. Fishing operations to retrieve the DC were successful.
- Lost returns ranging between 6-10 bph were encountered while drilling from 6,254' MD to 6,660' MD. This interval includes the main section of the Brown Niagaran Formation reservoir and some of the Gray Niagaran Formation.
- The Rotary Side Wall Coring tool (RSWC) became stuck in the hole during the wireline evaluation program, most likely due to differential sticking. The sticking force is the product of a.) the pressure difference between the wellbore fluids and the formation pore pressure and b.) the area over which this difference is applied. Tools that must remain on station for

longer periods of time, such as formation pressure testing tools and coring tools are more likely to fall victim to differential sticking due to the combined effect of time and the breakdown of the mud filtrate barrier on the wellbore wall. The tool was eventually retrieved.

- Rig operations were halted for 3 hours while waiting for a replacement cement head.
- Snow was removed from the location twice during completions operations.

1.3 Well Logging

Wireline logs were run in the intermediate open hole section before running casing from 992' MD to 4,000' MD (Figure 1-5). The caliper was closed from 3067'-2719' MD due to large washouts (widening of the borehole) and sticking in the salt zone. The Micro Laterolog (MLL), or resistivity, data is not valid in this section due to the washout. This interval corresponds to a lost returns zones encountered while drilling. Density and neutron (CN and ZDL) were recorded with respect to a limestone matrix (density =2.71 g/cc).

Wireline logs were also run in the deep open hole section from 4,000'MD to 6,680'MD (Figure 1-5). While logging this hole section, the micro laterolog detection pad was damaged while deployed in the full suite combination. All data in the section labeled "additional log" should be viewed with this knowledge and interpreted carefully.

After the RSWC tool was unstuck and retrieved, 32 out of 33 attempted cores were recovered. The average coring time was under 5 minutes and the average core length was 2.01 inches.

A fiber optic cable was run in conjunction with the 5-1/2" casing string and cemented in place (Figure 1-5). This has allowed for distributed acoustic sensing (DAS) borehole geophysical monitoring over time. Several cased hole logs were run at Chester 6-16 as part of a wellbore integrity study, as well as a baseline Pulsed Neutron Capture log (PNC) for use in monitoring studies.

Table 1-1 lists all data types that were collected during the drilling and completions phase of this well and describes how this data was employed to decrease project and technical uncertainties for MRCSP Phase III research.

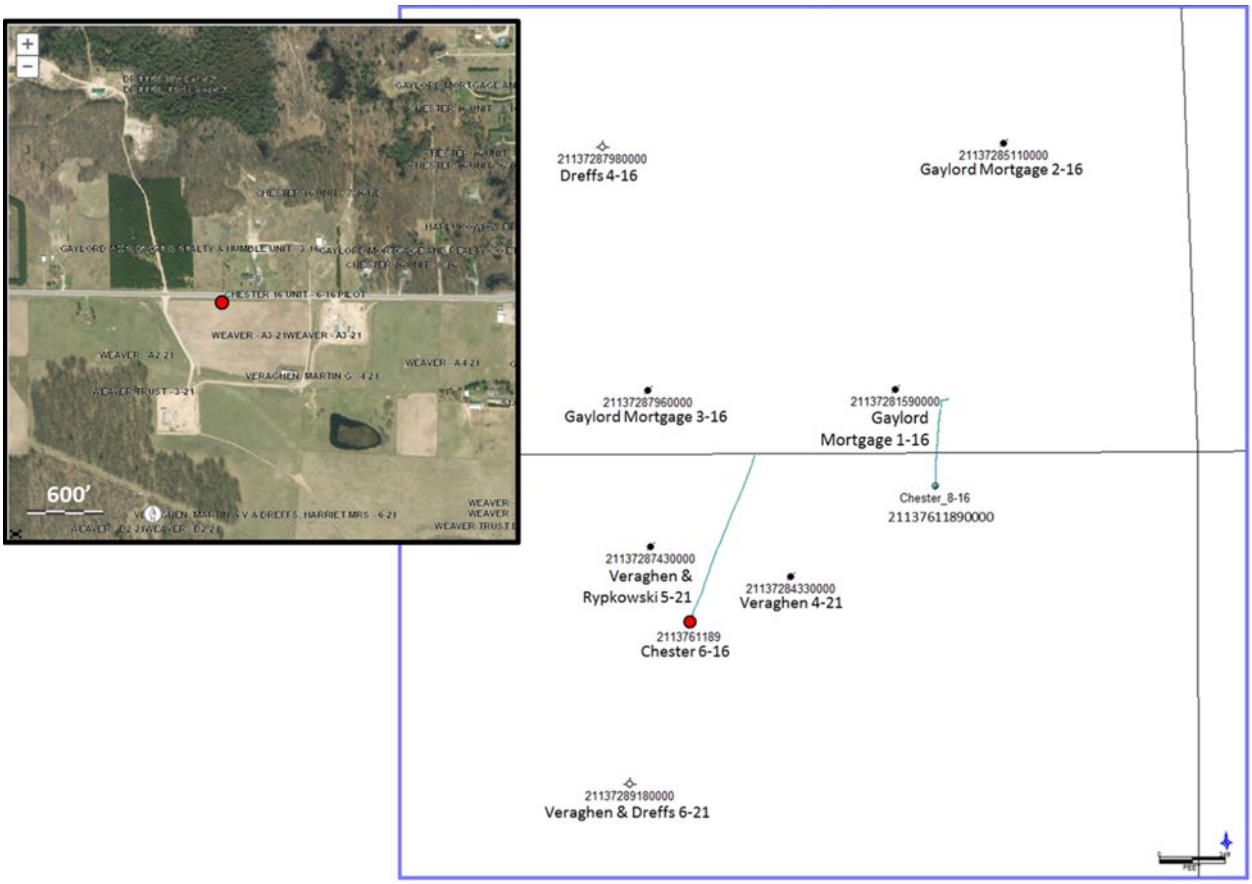


Figure 1-1. Surface hole location for Chester 6-16 marked in red.

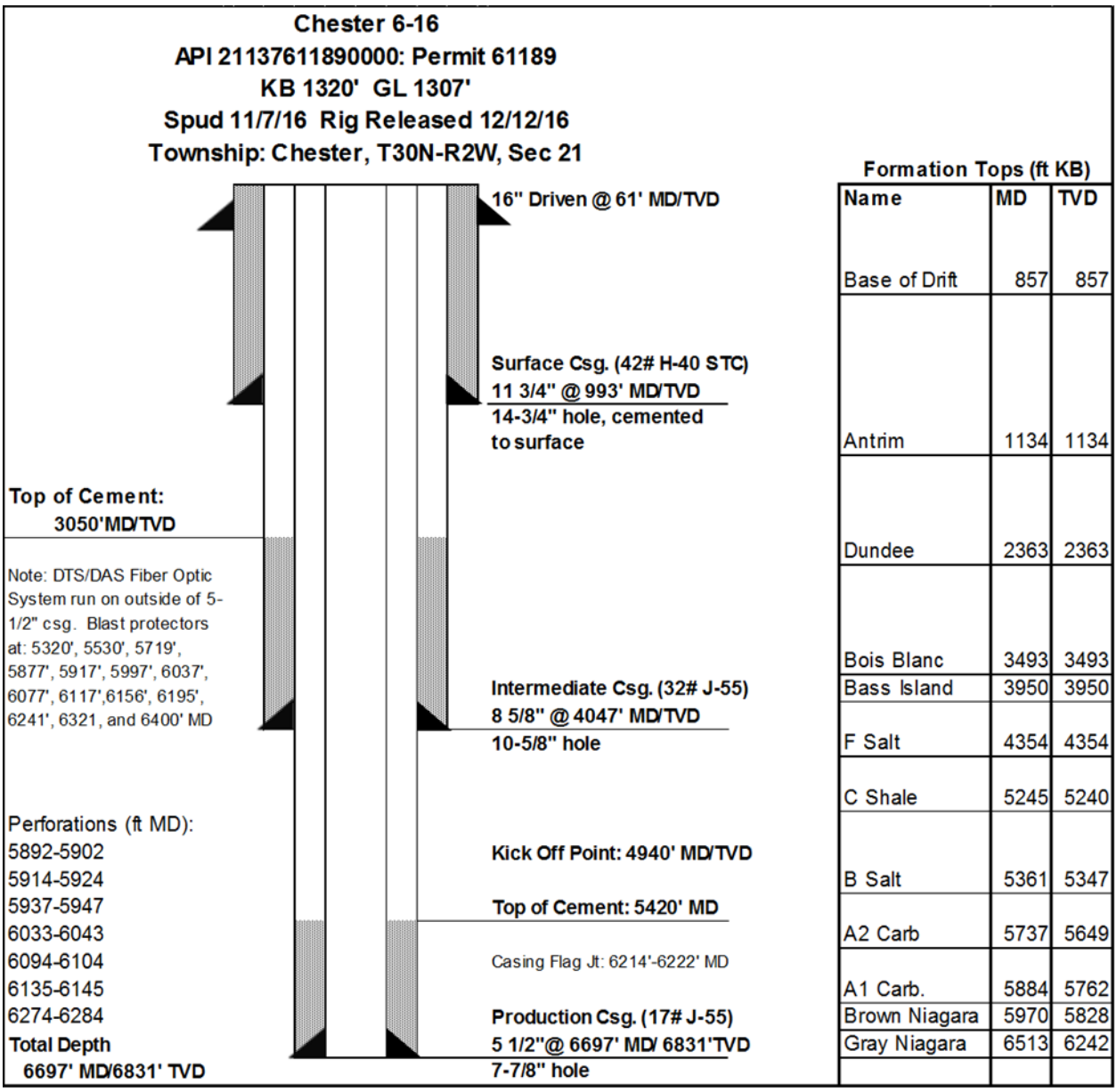


Figure 1-2. As-built wellbore diagram for Chester 6-16 (not to scale).

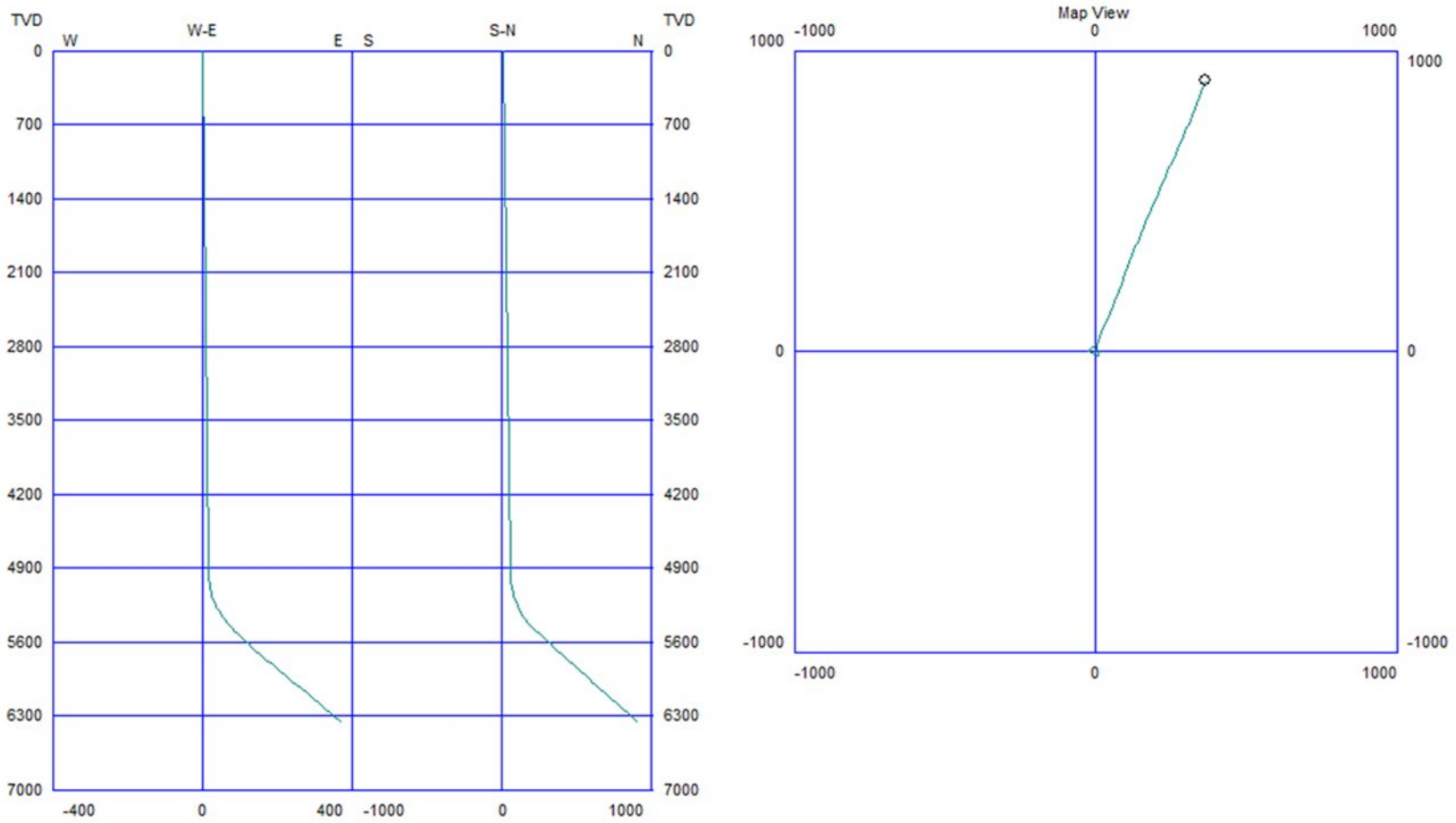


Figure 1-3. Deviation survey plot for well Chester 6-16 showing the degree of deviation from the vertical wellbore (left) and the direction towards the northeast (right).

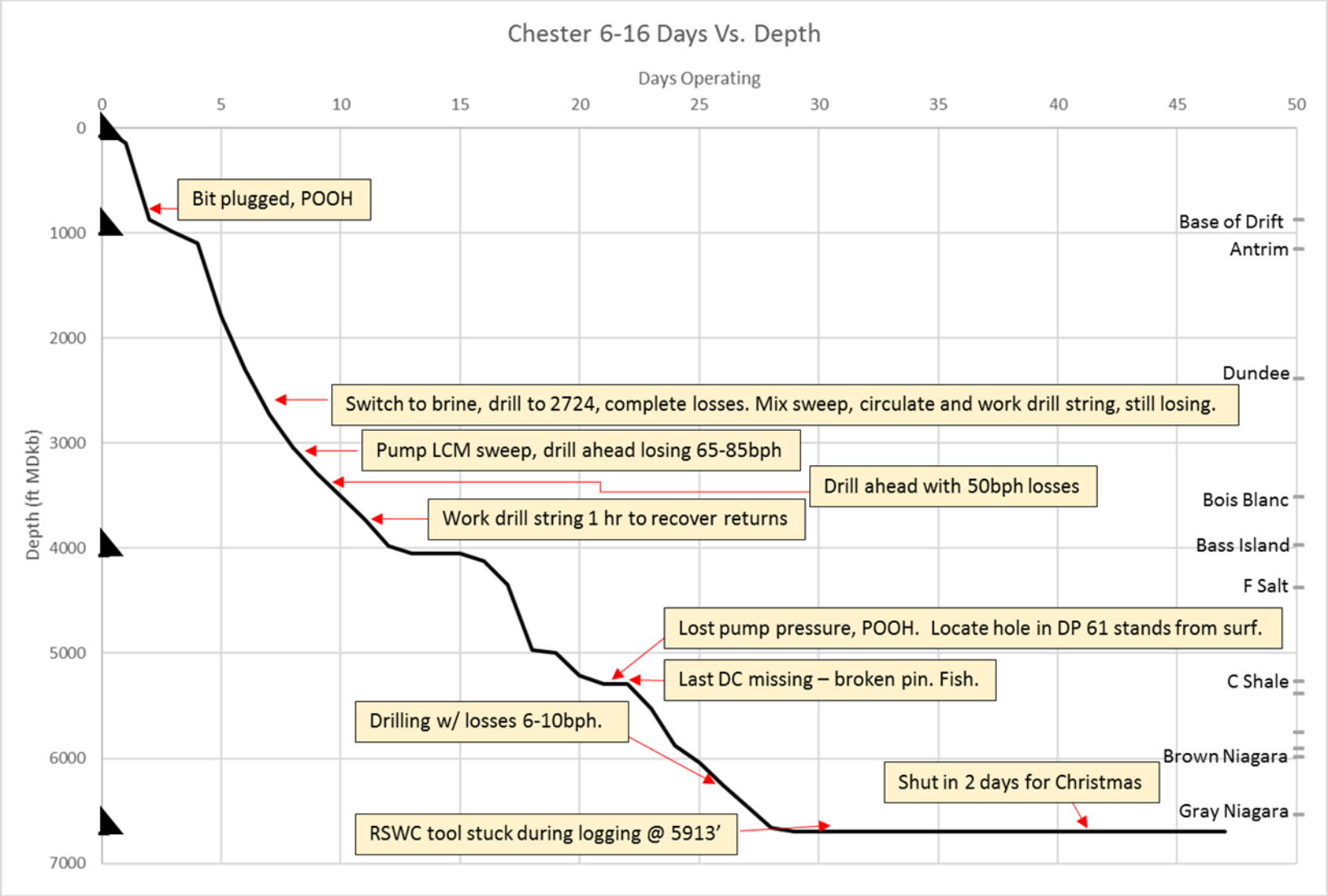


Figure 1-4. Days vs. depth plot annotated with unscheduled events, casing points, and key geologic horizons for drilling and completion of the Chester 6-16 well.

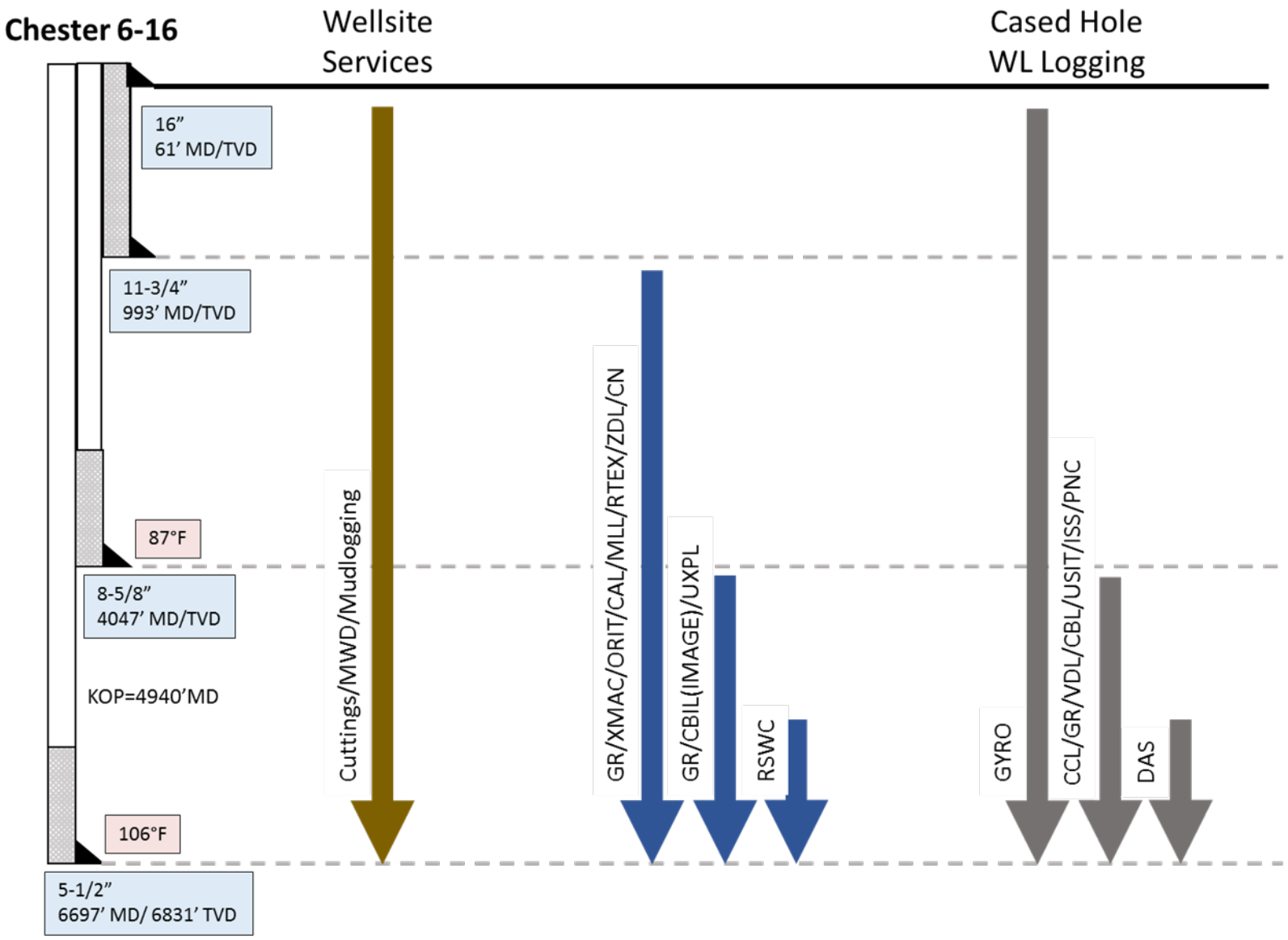


Figure 1-5. Executed formation evaluation program for Chester 6-16.

Table 1-1. Chester 6-16 formation evaluation value of information chart. Logs highlighted in blue represent open hole logs, those highlighted in gray were collected in cased hole.

Log Name and Mnemonic		Value of Information
CAL	Caliper	Provides evidence of borehole size, including enlargement due to washout, which is critical for QA/QC and calibration of many logs.
CBIL	Circumferential Borehole Imaging Log	Used to observe facies/lithology changes, bedding planes, and large vuggy pores to infer depositional settings and correlate with reservoir properties from additional logs for static and dynamic earth models. Identify presence, orientation, attitude of linear features such as fractures and faults to characterize stress fields for geomechanical analyses.
CBL	Cement Bond Log	Evaluates presence of cement behind casing and is used for planning borehole seismic data acquisition.
CCL	Casing Collar Locator	Highlights the presence of metallic casing collars and is used with Gamma Ray tool to correlate cased hole logs on depth and tie in with open hole logs.
CN	Compensated Neutron Log	This tool is used to calculate porosity and identify lithology, by responding to the hydrogen content of the formation. Porosity data is a key input to static and dynamic earth models and CO2 storage estimates.
ECS	Elemental Capture Spectroscopy	This tool measures silicon (Si), iron (Fe), calcium (Ca), sulfur (S), titanium (Ti), gadolinium (Gd), chlorine (Cl), barium (Ba), and hydrogen (H). The data collected were used to make direct observations of in situ formation composition.
DAS	Distributed Acoustic Sensing	DAS borehole seismic data was not collected at the time of drilling or completion, but the distributed optical fiber sensors were cemented on the outside of the casing at Chester 6-16 and 8-16. This will increase the likelihood of repeatability of time-lapse surveys for CO2 monitoring at this reef.
GR	Gamma Ray	Gamma Ray is a standard log that was run in both open hole and cased hole for correlation purposes. This tool identified bed boundaries and informed the interpretation of other petrophysical logs. Interpretations based on this log impacted technical products throughout the project.
GYRO	Gyroscope	This directional survey instrument was run to accurately measure the deviation of the well path from vertical; both inclination and azimuth. This information is critical for applying proper measured depth (MD) or total vertical depth (TVD) datums to geologic surfaces, calculating pressures, and for correlation to other wells.
ISS	Isolation Scanner	Cement evaluation tool that maps the entire annulus. This data was used to evaluate wellbore integrity and identify gas or fluids behind pipe to calibrate PNC logs.
MLL	Micro Laterolog	This is a shallow resistivity tool that was used to evaluate the lithology and fluid content of formations. This information, lithology and (oil/water/gas) was an input to models.
ORIT	Directional Survey	This directional survey instrument was run to accurately measure the deviation of the well path from vertical; both inclination and azimuth. This information is critical for applying proper measured depth (MD) or total vertical depth (TVD) datums to geologic surfaces, calculating pressures, and for correlation to other wells.
PNC	Pulsed Neutron Capture	The cased hole reservoir monitoring tool was run multiple times to measure changes in water, hydrocarbon, and CO_2 saturation over time with CO_2 injection. It was also used to identify salt in reservoir intervals where porosity plugging reduces storage potential. This data was used for baseline reservoir characterization, static earth model input data, and dynamic model history matching.
RSWC	Rotary Side Wall Core	Rotary side wall core plugs are subject to routine and special core analyses that provide lab test based calibration points for petrophysical log interpretation as well as critical values for reservoir modeling that cannot be inferred from downhole logs such as relative permeability and capillary pressure. Unoriented RSWCs can be used to test some geomechanical properties such as Young's modulus and Poisson's ratio.
RTeX	Multi Laterolog Wireline Service	This tool collects resistivity data with four different formation penetration modes and adaptive borehole correction to remove the effects of formation invaded by drilling fluid. Resistivity logs were a basic indicator of fluid type and lithology. Interpretations based on this log impacted technical products throughout the project.
USIT	Ultrasonic Imager tool	The USIT provided a scan of casing condition and cement bond around the entire casing circumference. This data was used to evaluate wellbore integrity and identify gas or fluids behind pipe to calibrate PNC logs.
VDL	Variable Density Scanner	This log was run in the cased hole along with the CBL to assist in its interpretation. It provides the amplitude of the acoustic waveform of the CBL measurement.
XMAC	Cross-Multipole Array Acoustilog	This tool provides full-wave monopole, in-line dipole, and cross-dipole sonic logs. Sonic logs are necessary input parameters for borehole seismic data acquisition planning and processing as well as indicators of rock mechanical properties. They were used in petrophysical analysis of the reefs that was input to the static and dynamic earth models. Deep shear wave image processing was applied to locate and map linear formation features such as fractures and bedding planes.
ZDL	Z Density Log	The density log assists in porosity estimation, lithology determination, seismic data acquisition planning and processing, and geomechanical modeling.

Chapter 2. Geologic Characterization

2.1 Methodology

2.1.1 Wireline Log Analysis and Petrophysical Calculations

Formation evaluations were completed on the A-2 Carbonate, A-2 Evaporite, A-1 Carbonate, Brown Niagaran, and Gray Niagaran formations to complete a geologic characterization of caprock and reservoir formations in Chester 6-16. Formation evaluation included: wireline log analysis and petrophysical calculations, core analysis, elemental spectroscopy analysis, and image log analysis.

A standard triple combo log was run over the intermediate and deep string sections (3878-6637 ft.) of the Chester 6-16 well. The triple combo log suite includes gamma ray, density, neutron porosity and resistivity, as well as tension, caliper, bit, and photo-electric index. Data from the triple combo log was analyzed in the context of the regional geology to identify formation tops, facilitate stratigraphic correlations, and calculate basic formation properties such as net and gross thickness, average porosity, and pay flags delineating potential injection zones. This basic log analysis served as the framework for guiding more advanced characterization efforts.

Five formations and their associated tops were identified for the detailed analyses (Table 2-1). Porosity was evaluated for the formations of interest using neutron porosity, density porosity, and average porosity calculations. Neutron porosity is derived by a neutron source within the logging tool that measures the hydrogen index of the formation. As hydrogen atoms are present in fluids (e.g., brine, oil) residing in the pores of the reservoir, measurements of hydrogen estimated the amount of fluid-filled porosity. The contribution of hydrous minerals (clays) to the logged neutron porosity was evaluated by the gamma ray response of the formation and noted as a potential source of error in neutron porosity measurements. Density porosity was calculated from Equation 1:

Table 2-1. Formation tops for the Chester 6-16.

Formations	Chester 6-16 ft. MD
A2 Carbonate	5737
A2 Evaporite	5839
A1 Carbonate	5884
Brown Niagarann	5970
Gray Niagarann	6513

$$\phi_D = \frac{(\rho_{ma} - \rho_b)}{(\rho_{ma} - \rho_{fl})} \quad \text{(Equation 1)}$$

where:

ϕ_D = density porosity

ρ_{ma} = matrix density (based on limestone density of 2.71 g/cm^3 or grain density data from elemental spectroscopy log)

ρ_b = bulk density (from the density log)

ρ_{fl} = fluid density (assumed fresh: 1.1 g/cm^3 for brine)

Grain density data derived from the weight percentages of minerals detected by the elemental spectroscopy log was used (ρ_{ma}) to calculate density porosity for the formations of interest. Average porosity was calculated using both density and neutron porosities via Equation 2:

$$\phi_A = \frac{(\Phi_D + \Phi_N)}{2} \quad \text{(Equation 2)}$$

where:

ϕ_A = average porosity

ϕ_D = density porosity

ϕ_N = neutron porosity.

Average porosities are used as representative values of formation porosity because neutron and density porosity derivations are each susceptible to inaccuracies in certain conditions, such as the presence of gas, washouts, and atypical mineralogy.

Neutron porosity and bulk density data derived from the triple combo log were plotted against each other to generate a cross plot for each formation. Cross plots are a graphical analysis technique that can be used to evaluate formation lithology and porosity. Trend lines superimposed on the cross plot represent the log responses calculated for pure sandstone, limestone, and dolomite over a range of porosities (e.g. 0-45%), assuming a fluid density of 1.0 g/cm^3 (fresh water) in the wellbore environment. Neutron-density cross plots can provide insight into lithology and allow for a potential estimate of true, lithology-independent porosity to be determined. Data that plotted within cross plot porosities greater than 5% were flagged, and the flagged data points were depth-denoted on cross-sections.

Water saturation calculations were performed to determine the percentage of the pore space that was filled with water and, thus, inversely, what percentage of available pore space is filled with hydrocarbons. Water saturation was calculated using the Archie Equation (Asquith and Krygowski, 2004), a standard oil and gas formula shown in equation 3:

$$S_w = \left(\frac{a \times R_w}{R_t \times \emptyset^m}\right)\frac{1}{n} \quad \text{(Equation 3)}$$

where:

S_w = water saturation of the uninvaded zone, %

R_w = formation water resistivity, ohm-ft

R_t = formation resistivity, ohm-ft

Ø = porosity, %

a = tortuosity factor

m = cementation exponent

n = saturation exponent

Values for formation resistivity (R_t) and porosity (ø) were derived from the wireline logs. Formation water resistivity (R_w) value was determined at each reef field dependent on salinity. Constants a, m, and n were set to industry standard values of a=1, m=2, and n=2.

Pay flags were generated using the following cutoffs; a gamma ray measurement less than 75 API, a water saturation calculated lower than 40%, and a neutron measurement greater than 5%. A gamma ray measurement less than 75 API is a standard indicator of relatively pure sandstone and carbonate reservoirs. A gamma response of 75 API was also used as a maximum cutoff to define the net reservoir thickness. A water saturation cutoff of 40% ensures the available storage zone is being represented. A minimum neutron porosity value of 5% was used as a cutoff to identify potential high effective-porosity intervals.

2.1.2 Core Collection and Description

Rotary Side Wall Core (RSWC) Collection

RSWC's were acquired during open hole wireline operations for the Chester 6-16 well using the Baker Hughes MAXCOR tool. The sampling interval, which included the Brown and Gray Niagaran formations (5,957 ft.-6,583 ft.MD), was identified in the field by Battelle technical staff from log signatures. The 1.5 in. inch diameter cores ranged in length between 1.4 in. inches and 2.5 in. inches, with an average length of 2.01 in. inches. The average time spent coring each sample was four minutes and fifty seconds. Efficiency during this RSWC run was 97.0% with 32 out of 33 cores attempted being recovered. A total of 17 cores were cancelled due to borehole washouts. The RSWC was temporarily stuck in the hole at 5,913 ft.MD but was successfully retrieved. Table 2-2 summarizes the RSWC acquisition parameters for Chester 6-16.

Table 2-2. Chester 6-16 RSWC acquisition parameters.

Cores Attempted	Cores Recovered	Core Recovery Efficiency	Avg Coring Time (min:sec)	Average Core Length (inch)
33	32	97%	4:50	2.01

RSWC Description

Descriptions of the entire inventory of sidewall cores from Chester 6-16 have been made in one-foot intervals and are provided in Appendix A. Core photographs collected in white light and UV light are included. Descriptions abbreviations are summarized below in Figure 2-1.

Abbrv.	Explanation
AL	Algal laminations
ANH	Anhydrite
B	Breccia
BM	Biologic Material
BU	Burrows
FF	Filled Fractures
FP	Framework Porosity
MP	Moldic Porosity
OF	Open Fractures
OS	Oil Stain
PV	Pyrite Filled Vug
R	Rubble/Broken Core
SLT	Salt
STM	Stromatoporoid
STY	Stylolites
V	Vugs

Figure 2-1. RSWC abbreviation explanations.

2.2 Core Analysis

2.2.1 Routine Sidewall Core Analysis

Routine core analysis was conducted on 1.5 in. inch diameter sidewall core samples. These analyses were conducted by Core Lab in Houston, TX, following CMS-300 conventional plug analysis protocol. Standard core analysis included porosity, permeability, fluid saturation, bulk density, and grain density measurements.

Grain Density

The grain density for the Chester 6-16 reef sidewall cores ranged from 2.69 to 2.82 g/cm^3 with an average of 2.74 g/cm^3. The A-1 Carbonate had an average grain density of 2.77 g/cm^3. The Brown Niagaran had an average grain density of 2.73 g/cm^3 and the Gray Niagaran had an average grain density of 2.70 g/cm^3. Table 2-3 summarizes the grain density averages for the Chester 6-16 sidewall core and

Table 2-3. Summary of the grain density averages for Chester 6-16 sidewall cores.

Interval	Range (g/cm^3)	Average (g/cm^3)
All Core	2.69-2.82	2.74
A-1 Carbonate	2.71-2.82	2.77
Brown Niagaran	2.69-2.82	2.73
Gray Niagaran	2.69-2.74	2.70

Figure 2-2 shows grain density histograms for all of the Chester 6-16 sidewall cores and by formation.

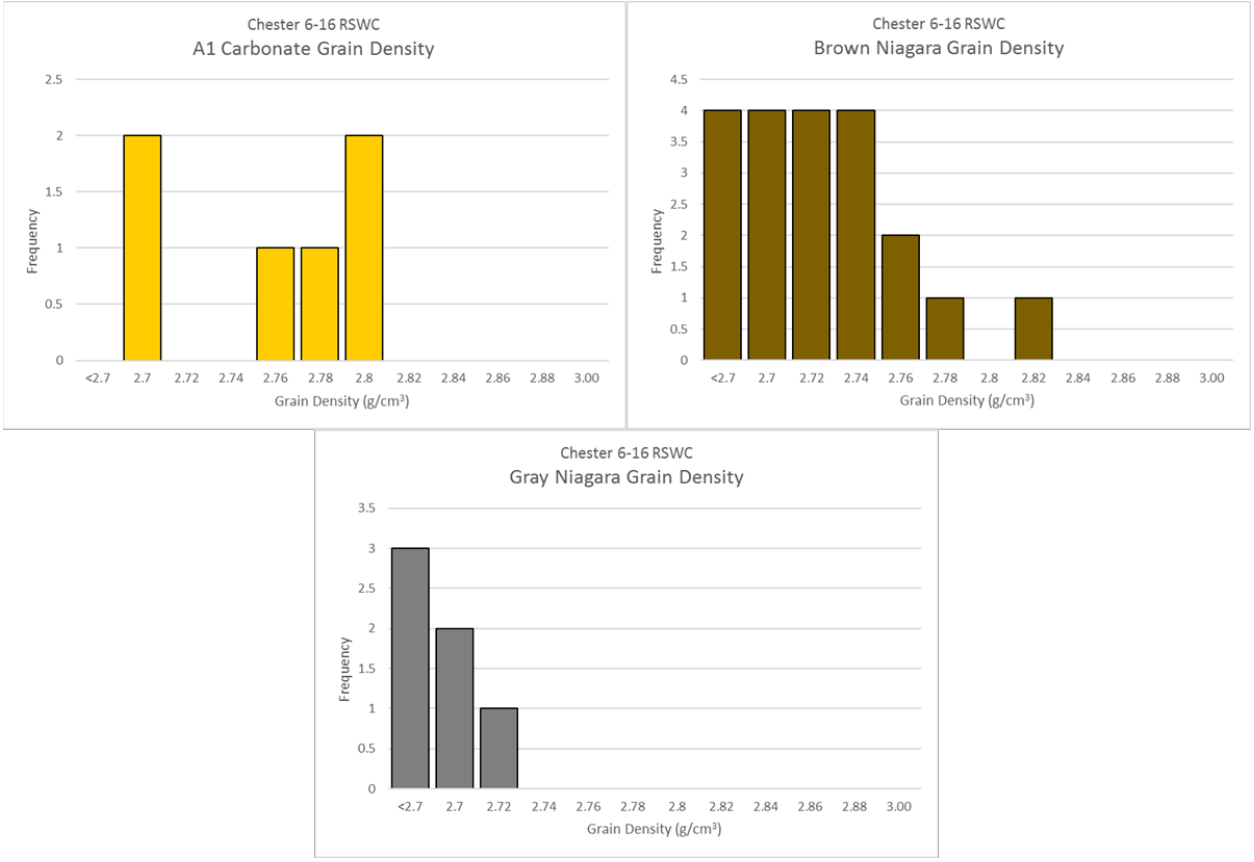


Figure 2-2. Histograms of grain density by formation from the Chester 6-16 RSWCs.

Porosity Permeability

The A-1 Carbonate had a porosity range from 0.29% to 20.08% with a permeability range from 0 to 384.53 mD. The Brown Niagaran had a porosity range from 0.30% to 9.89% with a permeability range from 0 to 3.23 mD. The Gray Niagaran had a porosity range from 0.25% to 1.08% with no apparent detectable permeability. This data has been summarized in Table 2-4 and plotted in Figure 2-3 with the coordinating transform equation in Equation 4.

$$K = 0.2239e^{0.3387x} \qquad \text{Equation 4}$$

Where K represents the permeability in mD and ø is the porosity in percent.

Table 2-4. Summary of porosity and permeability data from RSWC in Chester 6-16.

Formation	Porosity (%)			Permeability (mD)		
	Min	Max	Average	Min	Max	Average
A1 Carbonate	0.29	20.08	4.62	0.00	384.53	4.03
Brown Niagaran	0.30	9.89	2.09	0.00	3.23	0.27
Gray Niagaran	0.25	1.08	0.49	0.00	0.00	0.00

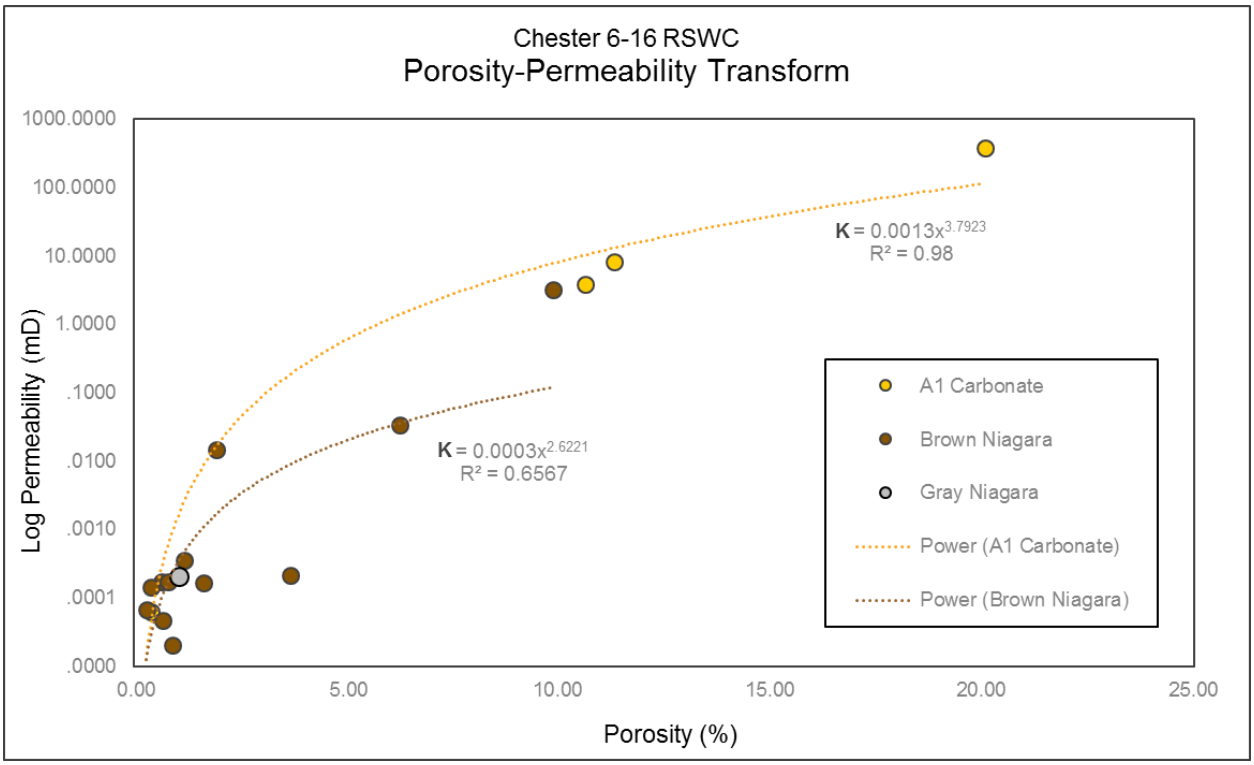


Figure 2-3. Porosity-permeability transform for the A-1 Carbonate and Brown Niagaran from RSWC measurements in Chester 6-16. Only one point was measurable from Gray Niagaran RSWCs.

The extreme heterogeneity of reservoir properties within the A-1 Carbonate is documented by the range of porosity and permeability measured from RSWCs. Permeability up to 384.5 mD with porosity of 20% was measured in a sample with high development of vug structures. The average porosity and permeability values have been calculated without this outlier.

2.3 Formation Evaluation

2.3.1 A-2 Carbonate and A-2 Evaporite

Wireline Log Analysis and Petrophysical Calculations

The A-2 Carbonate was 78 ft. thick in the Chester 6-16 well. The average porosity ranged from 0 to 6.2% with an average of 0.4% (Figure 2-4). The cross-plot porosity was mostly below 5% with an interval 5 ft. thick of greater than 5%. This occurred where the gamma ray was slightly higher and was a carbonate shale (Figure 2-5). The porosity over this interval was representative of microporosity. Additionally, there were intervals with high bulk density (2.9 – 3.0 g/cm^3) which were associated with anhydritic layers (Figure 2-5). Overall, the A-2 Carbonate was a tight dolomite with intervals of carbonate shale and anhydrite.

Basic petrophysical calculations were computed for the A-2 Carbonate using a porosity cutoff of 5% (scenario 1), and a combined cutoff of 5% porosity and 40% water saturation (scenario 2) (Figure 2-6). Both calculations used a gamma ray cutoff of 75 API to eliminate traditional shales. The results for both scenarios yielded the same results; the net thickness was 4.6 ft. with a resulting net to gross ratio of 0.06, and the porosity-ft. was 0.25 %-ft. The petrophysical calculations showed the A-2 Carbonate to have no reservoir potential and, desired values for a confining zone.

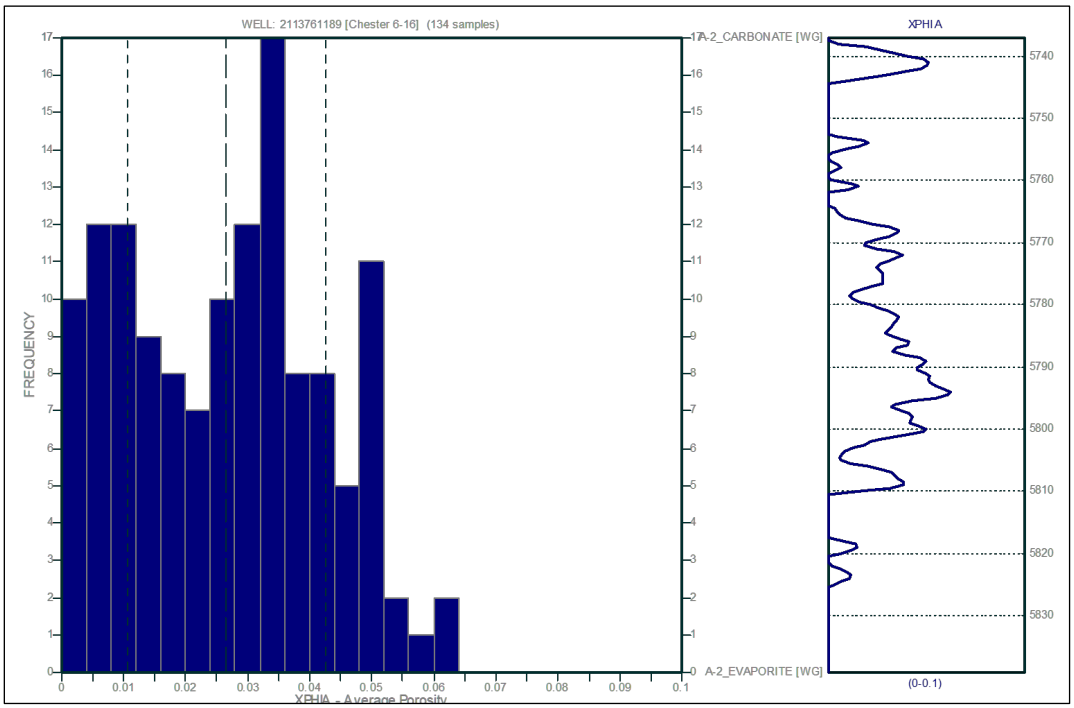


Figure 2-4. Average porosity histogram of the A-2 Carbonate for Chester 6-16 showing low average porosity of 0.04 %.

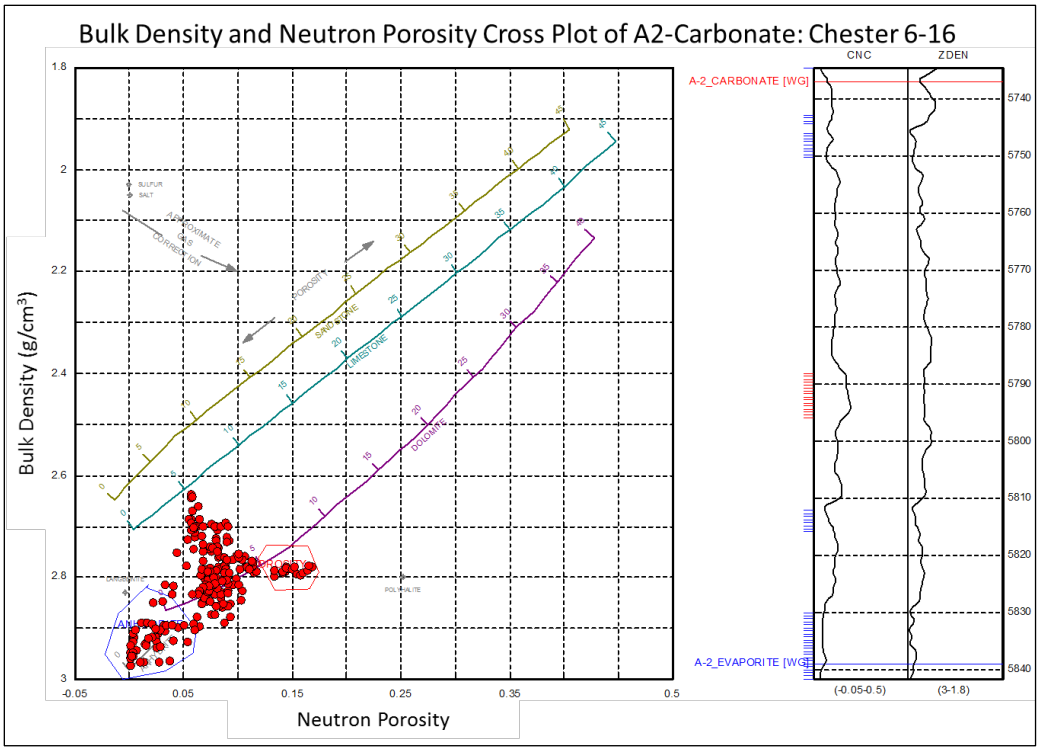


Figure 2-5. Bulk density and neutron porosity cross plot of the A-2 Carbonate for the Chester 6-16 well showing a tight dolomite with anhydritic layers (blue) and a thin interval of porosity greater than 5% (red).

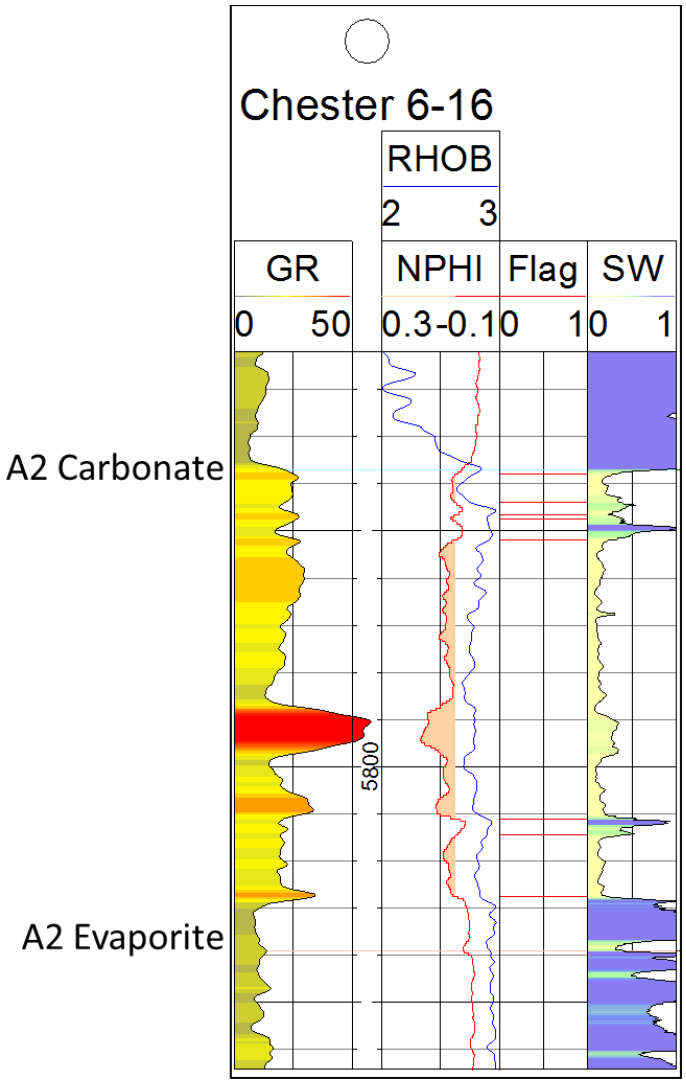


Figure 2-6. Single well cross section over the A-2 Carbonate interval for Chester 6-16 showing relatively low porosity and low water saturation throughout with a high gamma spike mid-formation marking a carbonate shale/mudstone.

The A-2 Evaporite, or A-2 Anhydrite, was 34 ft. thick in Chester 6-16. Porosity was not observed in this formation and the bulk density remained high, consistent with anhydrite. The cross-plot porosity was also at zero with all data points falling into the anhydrite zone (Figure 2-7). The water saturation was high over this interval, averaging at 85% due to the presence of anhydrite. The net thickness was 0 ft with a resulting net to gross of 0 and porosity ft. of 0. Overall, the A-2 Evaporite was mostly anhydrite with no porosity, suggesting a sufficient confining unit.

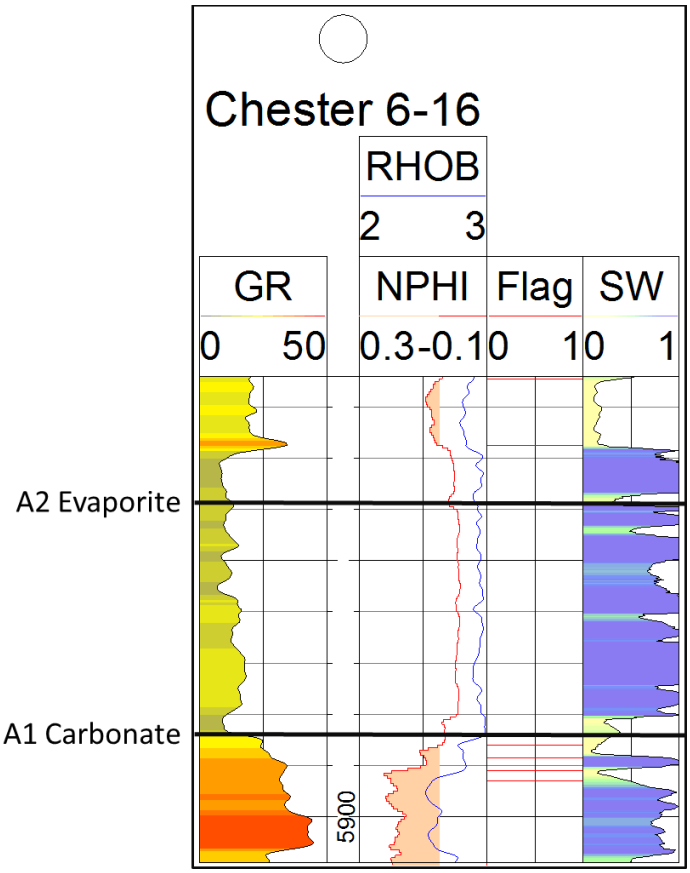


Figure 2-7. Single well cross section over the A-2 Evaporite interval for Chester 6-16 showing no porosity, high bulk density and water saturation, consistent with anhydrite.

Core Analysis

RSWC's were not collected in the A-2 Carbonate or A-2 Evaporite Formations.

2.3.2 A-1 Carbonate

Wireline Log Analysis and Petrophysical Calculations

The A-1 Carbonate was 65 ft. thick in the Chester 6-16 well. The average porosity ranged from 0 to 27.4% with an average of 10.6% (Figure 2-8). The average porosity had a depth dependent bimodal behavior with the lower A-1 Carbonate being less than 4% and the middle to upper being greater than 5%. The cross-plot porosity was mostly above 5% with thin intervals less than 5% (Figure 2-9). The water saturation varied throughout with an average of 52%. This occurred in distinct packages with high porosity (Figure 2-10) which could be a result of hydrocarbon presence. Overall, the A-1 Carbonate plotted as a porous dolomite.

Basic petrophysical calculations were computed for the A-1 Carbonate using a porosity cutoff of 5% (scenario 1), and a combined cutoff of 5% porosity and 40% water saturation (scenario 2). Both calculations used a gamma ray cutoff of 75 API to eliminate traditional shales. The net thickness for scenario 1 was 44 ft. with a resulting net to gross ratio of 0.68 and a porosity footage of 6.7 %-ft. The inclusion of the water saturation cutoff (scenario 2) decreased the net thickness to 13 ft. with a net to gross ratio of 0.20 and a porosity footage of 1.9 %-ft. The water saturation values may be overstated due to poor borehole conditions; therefore the inclusion of

a saturation cutoff may underestimated the potential of the reservoir. The A-1 Carbonate showed strong reservoir potential due to a thick zone of high porosity.

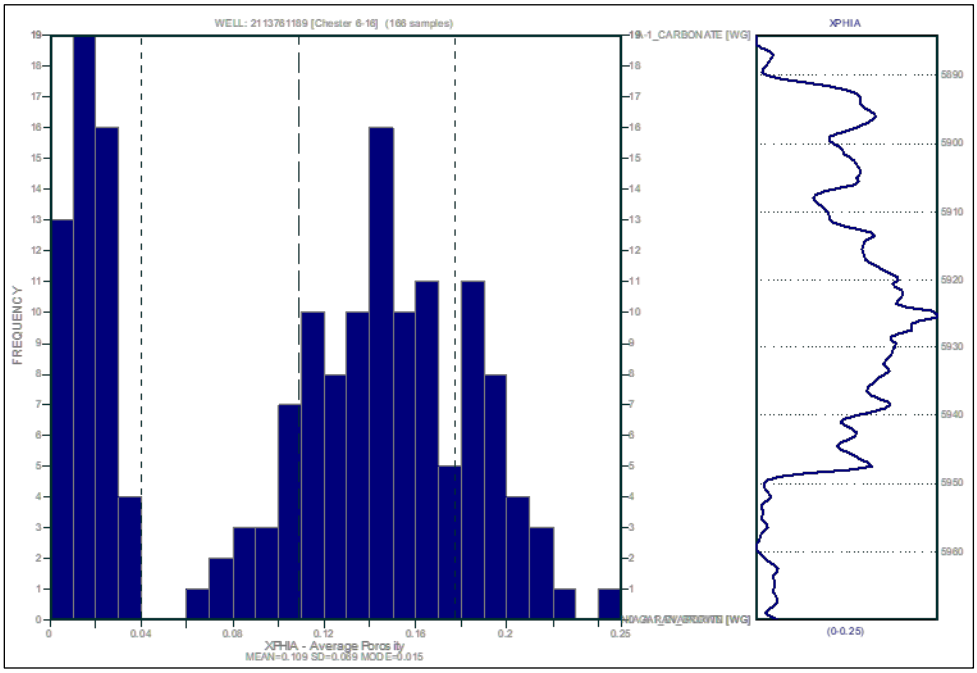


Figure 2-8. Average porosity histogram of the A-1 Carbonate for Chester 6-16 showing a bimodal distribution with low porosities at the base of the formation and high porosities mid to upper formation.

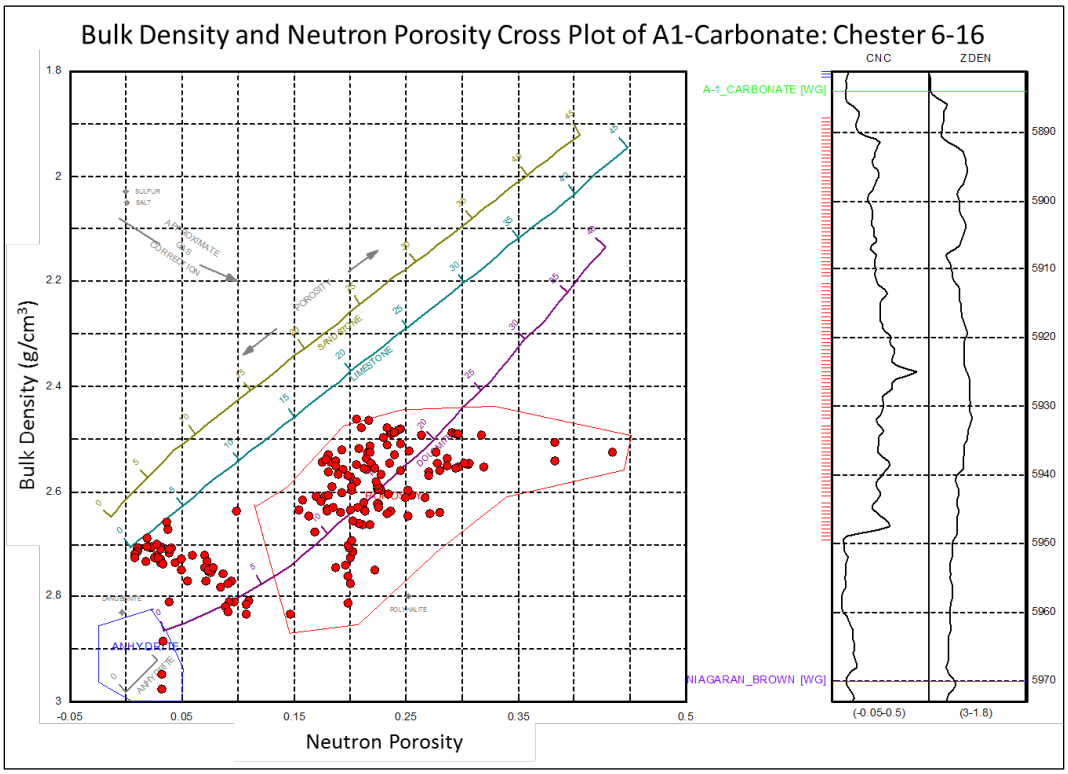


Figure 2-9. Neutron porosity-bulk density cross plot of the A-1 Carbonate for Chester 6-16 showing mostly porous dolomite (red) and thin intervals of tight dolomite.

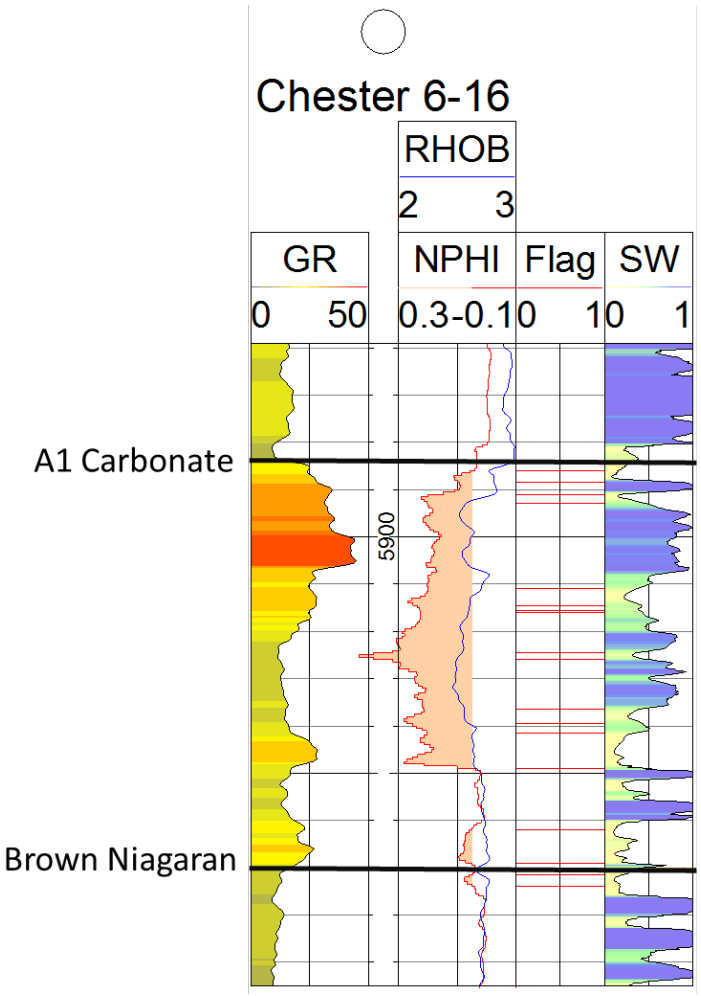


Figure 2-10. Single well cross section of the A-1 Carbonate for Chester 6-16 showing a thick interval of high porosity (orange shade) with layers of high water saturation attributed to hydrocarbon presence.

Core Analysis

Sidewall core photos of the A-1 Carbonate in Chester 6-16 show the A-1 Carbonate is predominantly a gray carbonate with some zones of alternating dark and light gray laminations. Small vugs, some of which are salt-filled, stylolites, and filled fractures are present throughout the core. The UV images show potential residual oil throughout the formation. Figure 2-11 and Figure 2-12 display examples of RSWC sample descriptions of the A-2 Carbonate.

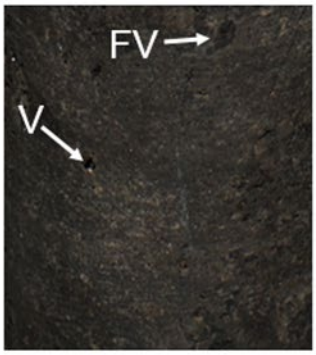
Depth Ft.	White Light Primary Features	UV Light Primary Features	Descriptions
5,938			White Light: Gray carbonate, small vugs, salt filled vugs. UV Light: Light blue UV response due to potential residual oil.
5,961			White Light: Gray carbonate, stylolites. UV Light: Light blue UV response due to potential residual oil.

Figure 2-11. Annotated RSWC images with corresponding core descriptions of the A-1 Carbonate for depths 5,938 ft. to 5,961 ft.

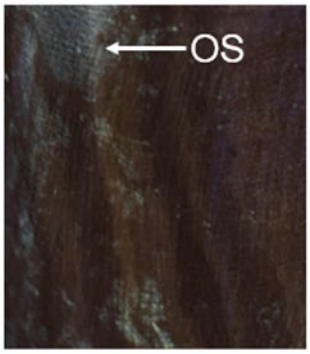
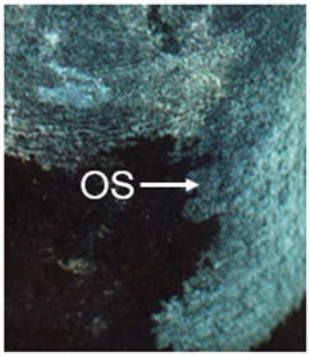
Depth Ft.	White Light Primary Features	UV Light Primary Features	Descriptions
5,962			White Light: Carbonate matrix, filled fracture, alternating dark gray and light gray laminations. UV Light: Light blue UV response due to potential residual oil.
5,968			White Light: Gray carbonate. UV Light: Light blue UV response due to potential residual oil.

Figure 2-12. Annotated RSWC images with corresponding core descriptions of the A-1 Carbonate for depths 5,962 ft. to 5,968 ft.

2.3.3 Brown Niagaran

Wireline Log Analysis and Petrophysical Calculations

The Brown Niagaran was 413 ft. thick in the Chester 6-16 well. The average porosity ranged from 0 to 14.7% with an average of 1.7% (Figure 2-13). The cross-plot porosity was mostly below 5% with thin intervals greater than 5% (Figure 2-14). There was a thin interval (~1-2 ft) in the upper formation which plotted towards salt and could be a result of salt plugging. The oil water contact (OWC) was identified at 6335 ft. MD where there was a shift in the water saturation towards consistently higher values. The interval from 6190 to 6335 ft. had frequent intervals of high water saturation which could be a ROZ (residual oil zone) (Figure 2-15). Overall, the Brown Niagaran was mostly tight limestone with thin (1-2 ft) intervals of high porosity. Only a third of the formation was fully water saturated, leaving the remaining 2/3rds as potential reservoir.

Basic petrophysical calculations were computed for the Brown Niagaran using a porosity cutoff of 5% (scenario 1), and a combined cutoff of 5% porosity and 40% water saturation (scenario 2). Both calculations used a gamma ray cutoff of 75 API to eliminate traditional shales. The net thickness for scenario 1 was 17 ft. with a resulting net to gross ratio of 0.04 and a porosity footage of 1.4 %-ft. The inclusion of the water saturation cutoff (scenario 2) decreased the net thickness to 14 ft. with a net to gross ratio of 0.03 and a porosity footage of 1.1 %-ft. The Brown Niagaran did not show high potential as a reservoir due to thin, intermittent zones of porosity. Results will be compared with advanced logs and sidewall cores to determine full potential of the formation.

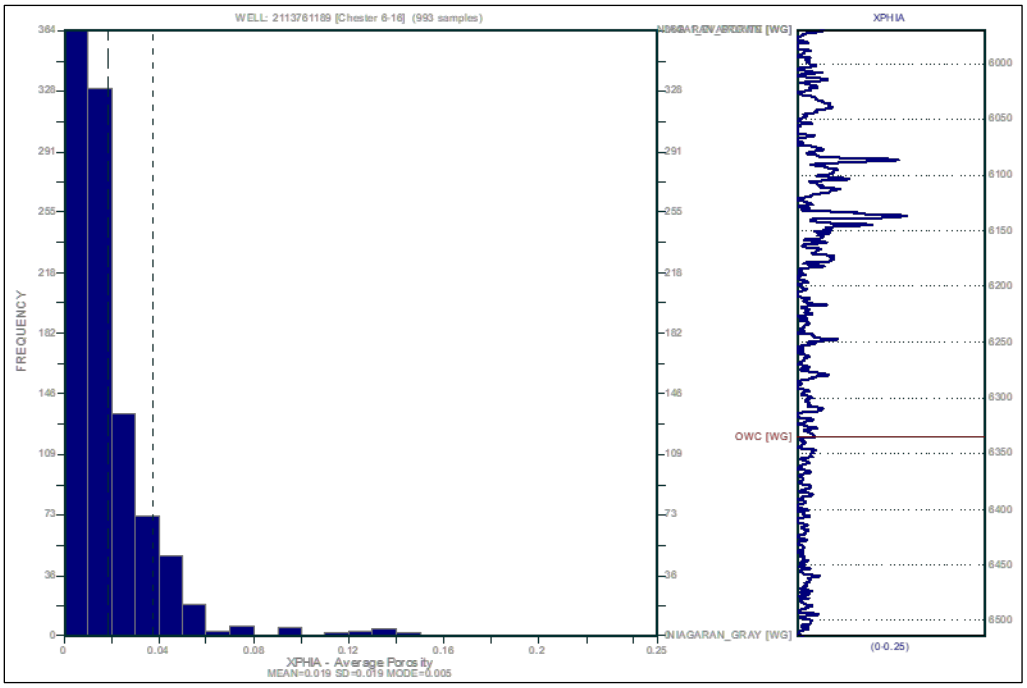


Figure 2-13. Average porosity histogram of the Brown Niagaran for Chester 6-16 showing mostly low porosity with an average of 1.7%.

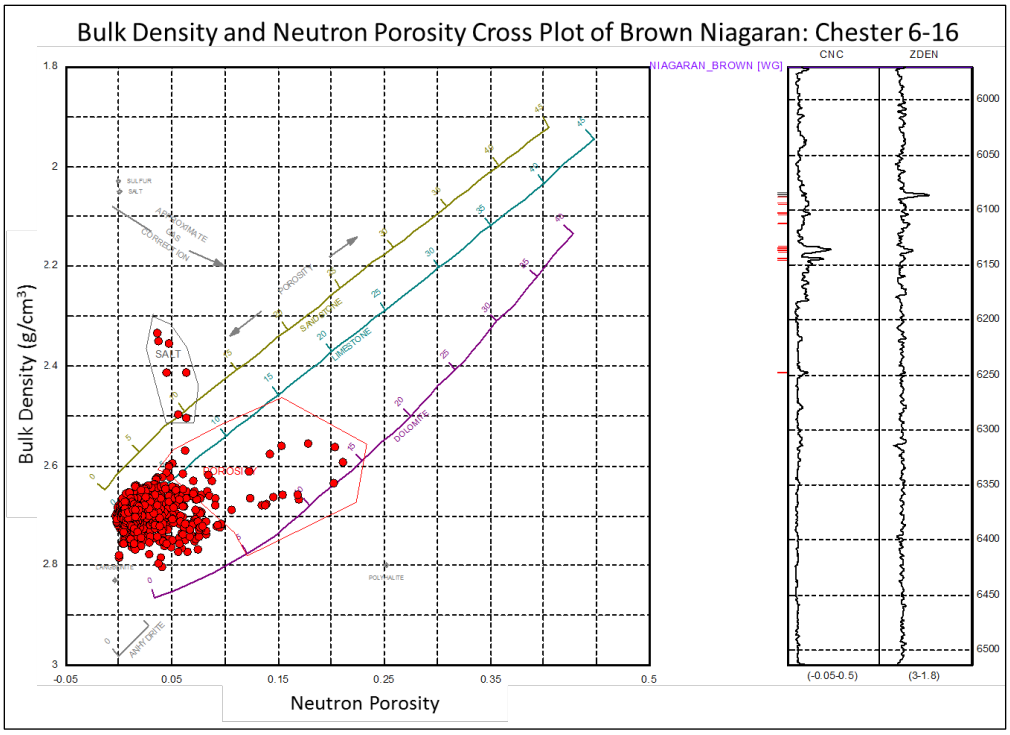


Figure 2-14. Neutron porosity-bulk density cross plot of the Brown Niagaran for Chester 6-16 showing mostly tight limestone with thin intervals of porosity greater than 5% (red).

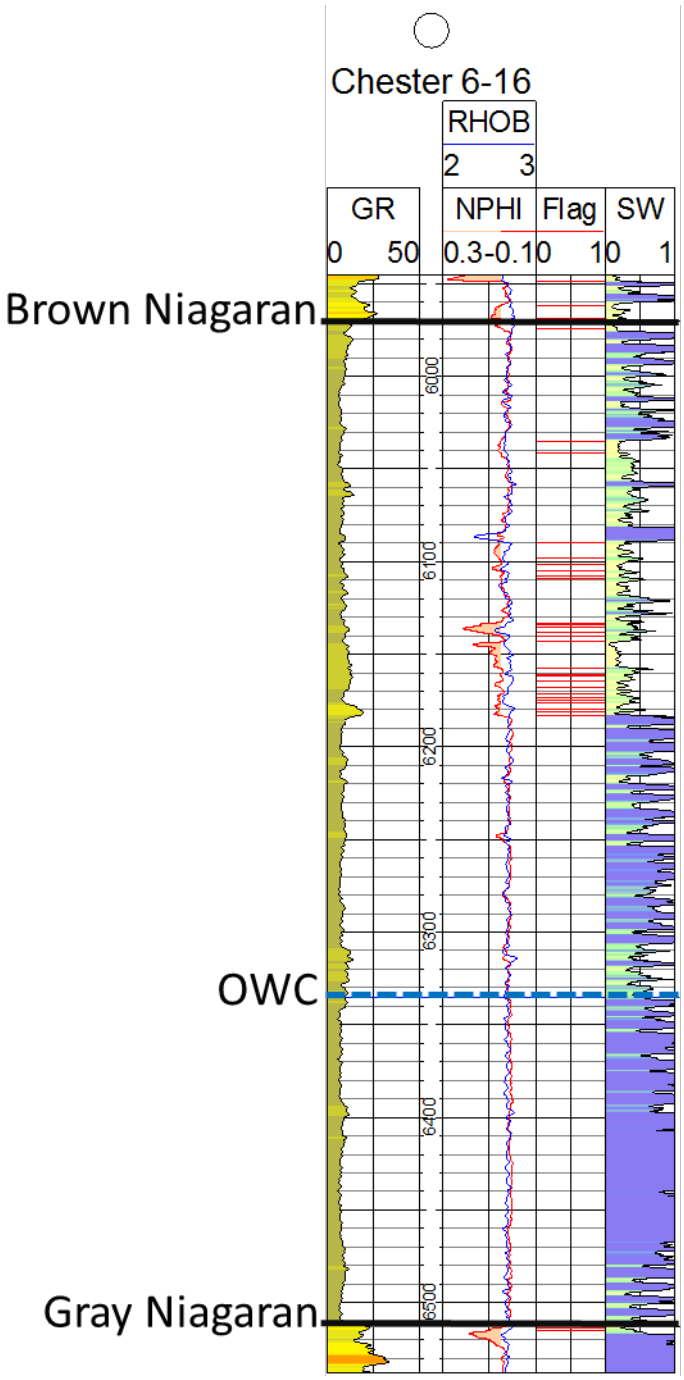


Figure 2-15. Single well cross section of the Brown Niagaran for Chester 6-16 showing thin zones of porosity (red flags) and increasing water saturation towards the OWC (blue dashed line).

Core Analysis

Sidewall core photos of the Brown Niagaran Formation in Chester 6-16 show the Brown Niagaran is predominantly a gray carbonate with significant vugular porosity. Vugs are present throughout the formation, except for the basal section of the Brown Niagaran, and range from small to large with some filled moldic and some salt-filled vugs. Open and filled fractures present throughout as well as minor stylolites. The UV images show potential residual oil throughout the formation. Figure 2-16 through Figure 2-18 display examples of RSWC sample descriptions of the Brown Niagaran Formation.

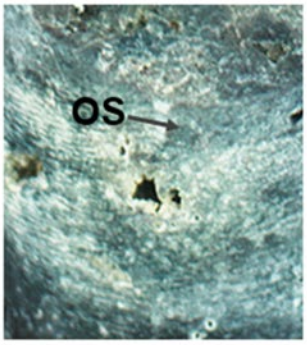
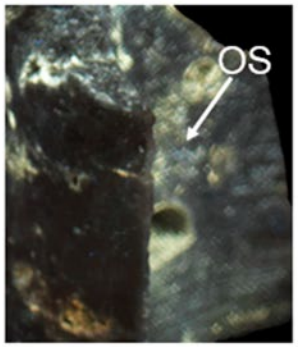
Depth Ft.	White Light Primary Features	UV Light Primary Features	Descriptions
6,015			White Light: Gray carbonate, medium/small vugs. UV Light: Light blue UV response due to potential residual oil throughout sample.
6,032			White Light: Gray carbonate, medium/small vugs, core fragment. UV Light: Light blue UV response due to potential residual oil.

Figure 2-16. Annotated RSWC images with corresponding core descriptions of the Brown Niagaran for depths 6,015 ft. to 6,032 ft.

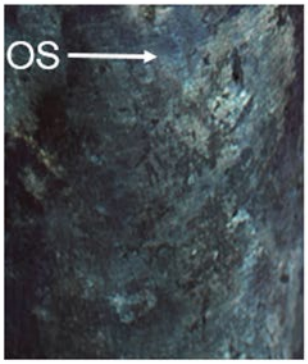
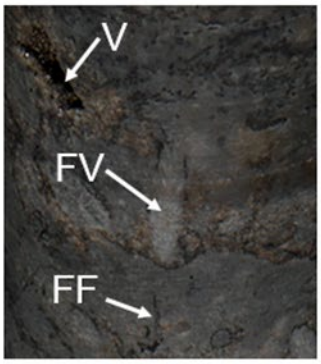
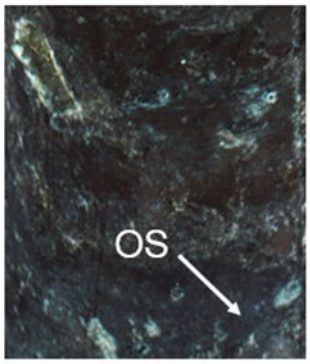
Depth Ft.	White Light Primary Features	UV Light Primary Features	Descriptions
6,173			White Light: Gray carbonate, small vugs. UV Light: Light blue UV response due to potential residual oil throughout sample.
6,177			White Light: Gray carbonate, medium/small vugs, salt filled vugs, filled fractures. UV Light: Light blue UV response due to potential residual oil throughout sample.

Figure 2-17. Annotated RSWC images with corresponding core descriptions of the Brown Niagaran for depths 6,173 ft. to 6,177 ft.

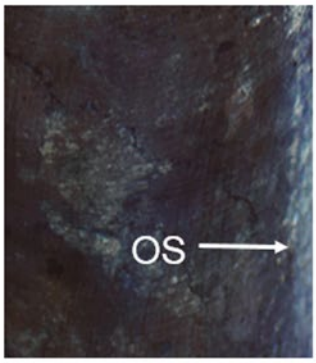
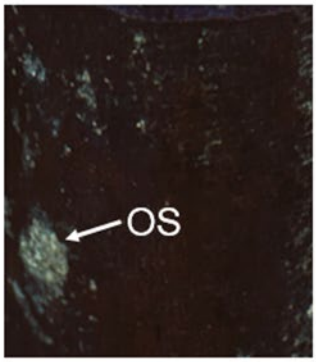
Depth Ft.	White Light Primary Features	UV Light Primary Features	Descriptions
6,197			White Light: Gray carbonate, stylolites. UV Light: Light blue UV response due to potential residual oil.
6,310			White Light: Gray carbonate. UV Light: Light blue UV response due to potential residual oil.

Figure 2-18. Annotated RSWC images with corresponding core descriptions of the Brown Niagaran for depths 6,197 ft. to 6,310 ft.

2.3.4 Gray Niagaran

Wireline Log Analysis and Petrophysical Calculations

Chester 6-16 captured about 60 ft. of the Gray Niagaran with triple combo data. The porosity ranged from 1-11% with an average of 3.4%. The cross-plot porosity was mostly tight limestone with thin intervals (<10 ft) of porosity greater than 5% (Figure 2-19). The formation was fully water saturated with an average of 91% (Figure 2-20). Overall, the Gray Niagaran was a tight limestone which was fully water saturated. Negligible values were calculated using petrophysical techniques, verifying that this was a sufficient underlying confining unit.

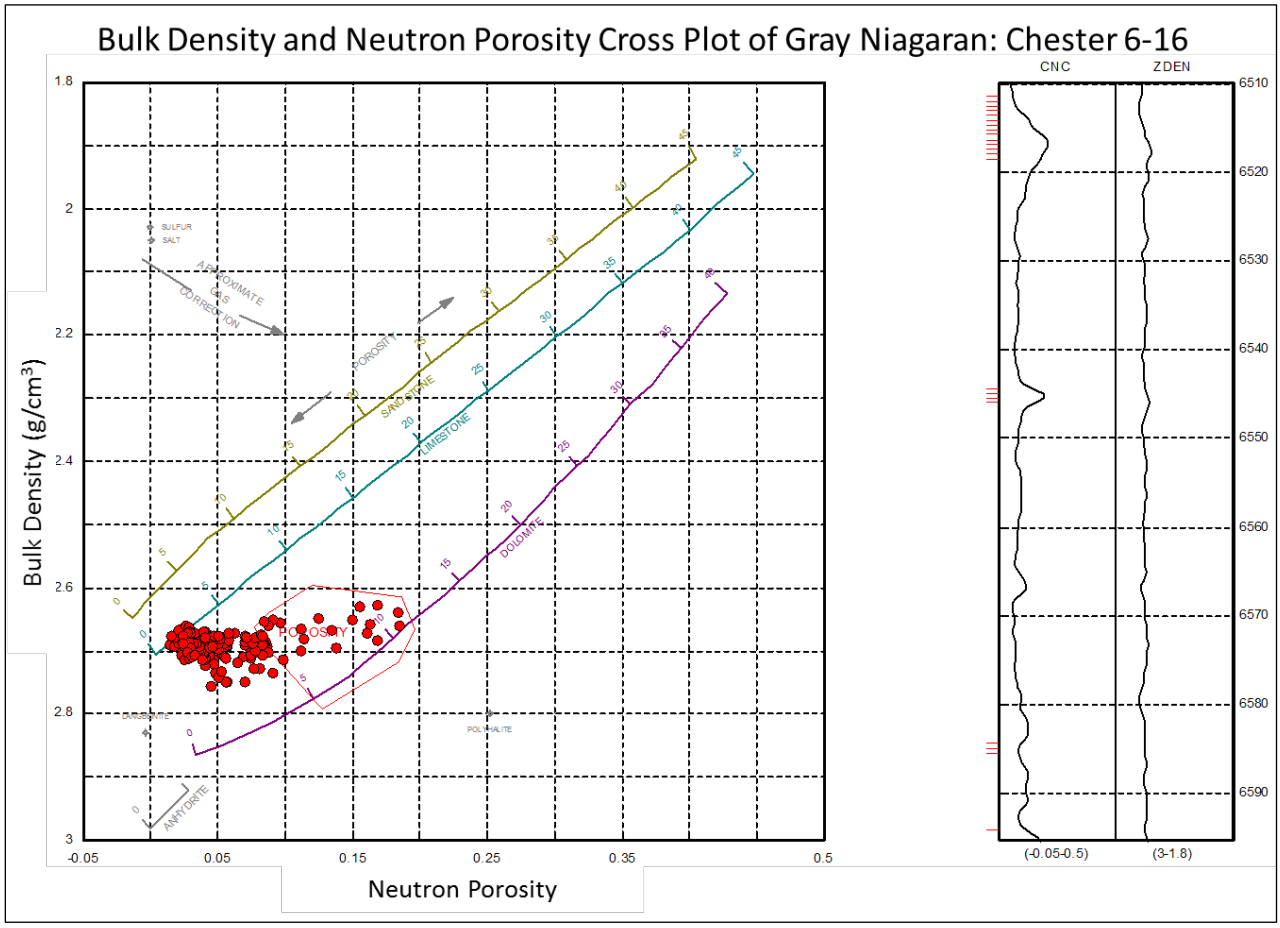


Figure 2-19. Neutron porosity-bulk density cross plot of the Gray Niagaran for the Chester 6-16 well showing tight limestone with thin intervals of porosity greater than 5% (red flag).

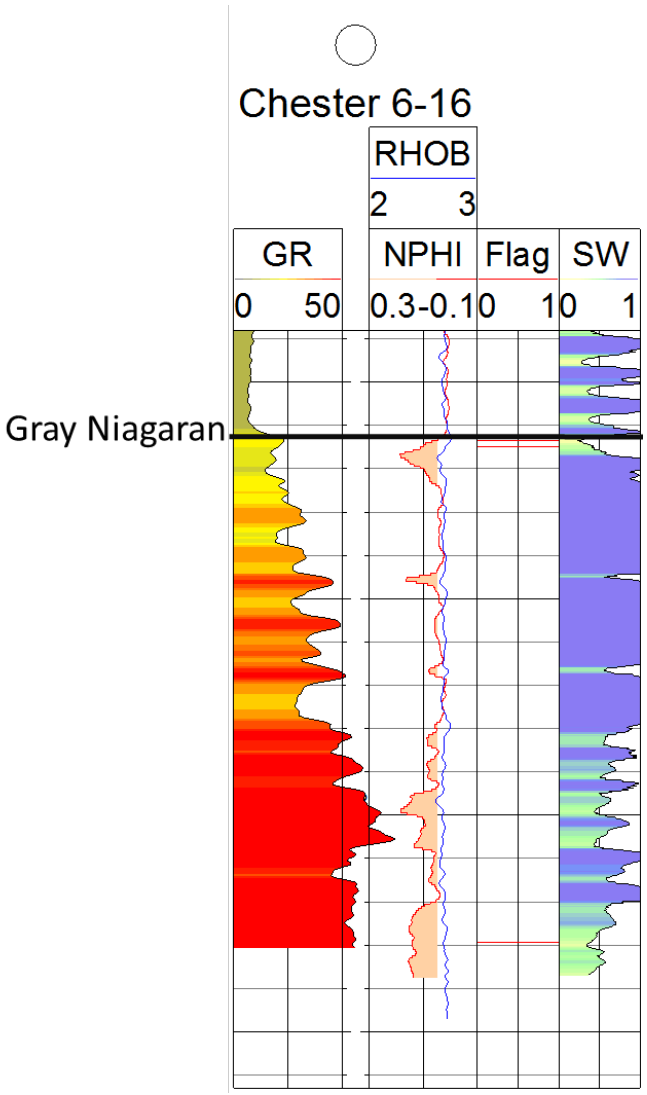


Figure 2-20. Single well cross section of the Gray Niagaran for the Chester 6-16 well showing thin intervals of porosity (orange shade) with increasing gamma ray and high water saturation.

Core Analysis

Sidewall core photos of the Gray Niagaran Formation in Chester 6-16 show the Gray Niagaran is predominantly a homogenous gray carbonate that is relatively devoid of sedimentary structures and major secondary porosity. Stylolites are present throughout the cored interval. The UV images show potential residual oil staining throughout the formation. Figure 2-21 and Figure 2-22 display examples of RSWC sample descriptions of the Gray Niagaran Formation.

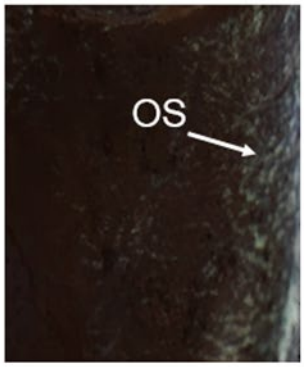
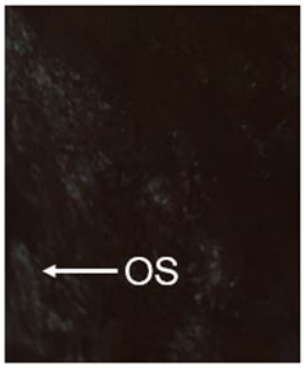
Depth Ft.	White Light Primary Features	UV Light Primary Features	Descriptions
6,516			White Light: Gray carbonate, stylolites. UV Light: Light blue UV response due to potential residual oil.
6,549			White Light: Gray carbonate. UV Light: Light blue UV response due to potential residual oil.

Figure 2-21. Annotated RSWC images with corresponding core descriptions of the Gray Niagaran for depths 6,516 ft. to 6,549 ft.

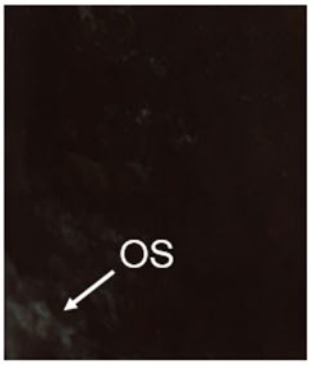
Depth Ft.	White Light Primary Features	UV Light Primary Features	Descriptions
6550.5			White Light: Gray carbonate. UV Light: Light blue UV response due to potential residual oil.
6,583			White Light: Gray carbonate. UV Light: No apparent residual oil staining.

Figure 2-22. Annotated RSWC images with corresponding core descriptions of the Gray Niagaran for depths 6,550.5 ft. to 6,583 ft.

2.4 Summary

RSWC samples were collected across the A-1 Carbonate, Brown Niagaran, and Gray Niagaran formations. Table 2-5 shows summary statistics of porosity and permeability by formation. Table 2-6 shows the depths of key potential reservoir intervals with porosity ≥5% as determined by sidewall core analysis and intervals with visible porosity as observed in core images. Overall, the 6-16 core is dominated by a gray carbonate lithology with some isolated zones of high porosity. Visible porosity, as seen on the core images, is dominantly in the form of small to medium vugs and open fractures. Potential reservoir intervals occur in the A-1 Carbonate and the Brown Niagaran formations above a depth of ~6,200 ft. Generally, core analysis data suggests very minimal reservoir potential in the 6-16 well as only 3 sidewall core samples exhibit porosity at or above 5%.

Table 2-5. Summary of RSWC porosity and permeability data in the Chester 6-16 well.

Formation	Porosity (%)			Permeability (mD)		
	Min	Max	Average	Min	Max	Average
A-1 Carbonate	0.29	20.08	4.62	0.00	384.53	4.03
Brown Niagaran	0.30	9.89	2.09	0.00	3.23	0.27
Gray Niagaran	0.25	1.08	0.49	0.00	0.00	0.00

Table 2-6. Summary of key potential reservoir intervals in the Chester 6-16 well based on RSWC analysis and images.

Formation	Reservoir Intervals [ϕ ≥ 5%] (ft.)	Intervals with visible porosity (ft.)
A-1 Carbonate	5927-5938	5934, 5938
Brown Niagaran	6136	6015, 6032-6036, 6077, 6104, 6113, 6136, 6173, 6177
Gray Niagaran	-	-

Chapter 3. Integrated Geomechanics Analysis

3.1 Introduction

The goal of the geomechanical characterization is to assess the sealing and mechanical integrity effectiveness of the geologic formations that comprise the caprock - reservoir systems for CO_2 storage or CO_2 EOR processes. To evaluate caprock- reservoir performance during CO_2 injection, numerical fluid flow-geomechanical modeling should be conducted to assess the potential for fracturing/ fault activation that could lead to CO_2 leakage. The first step to assess caprock- reservoir performance for CO_2 storage is defining the mechanical properties and in-situ stress parameters of the geologic formations.

This chapter included (1) investigating dipole sonic log data from the Chester 6-16 well to define fundamental mechanical rock properties of the caprock and reservoir formations (2) studying the in-situ stresses in the caprock and reservoir formations by determining the orientation of maximum horizontal stress (S_{Hmax}) and magnitude of the vertical stress using image log data, shear wave anisotropy data, and density log.

3.2 Mechanical Parameters Characterization Using Dipole Sonic Log Analysis

Variation in the physical properties of the geological formations causes changes in rock mechanical parameters. Since rock mechanical parameters are the key data to study safe long-term storage of CO_2, it is important to adequately characterize these properties and study its variations across different formations.

The sonic log analysis was conducted using acoustic data from dipole sonic geophysical logs from the Chester 6-16 well—specifically, compressional-wave and shear-wave slowness (slowness being the inverse of velocity) parameters which were used to calculate rock mechanical properties. Additionally, shear-wave velocity anisotropy data (i.e., fast shear-wave and slow shear-wave velocities) was available for Chester 6-16, and was used to estimate S_{Hmax} azimuth.

Dipole sonic logging tools measure both compressional-wave and shear-wave slowness within a formation. These variables, coupled with formation bulk density (ρ), allow for the calculation of dynamic elastic parameters including Poisson's ratio, Young's modulus, dynamic shear modulus, and bulk modulus.

Poisson's ratio indicates the relationship between the lateral and axial strain of the rock formation. It is expressed by Equation 5:

$$V = \frac{V_p^2 - 2V_s^2}{2*(V_p^2 - V_s^2)} \qquad \text{(Equation 5)}$$

Where:

V = Poisson's ratio

Vp = Compressional velocity

Vs = Shear velocity

Young's modulus is the measure of the stiffness of a material and is calculated using the rock density, shear wave velocity, and compressional wave velocity as shown in Equation 6.

$$E = \frac{\rho V_s^2 (3V_p^2 - 4V_s^2)}{(V_p^2 - V_s^2)} \qquad \text{(Equation 6)}$$

Where:

E = Young's modulus

ρ = Density

The dynamic shear modulus evaluates a rock formation's rigidity to shear stress and is calculated as the relationship between the bulk density and the shear wave slowness of a formation (slowness being a unit of measure which is the inverse of velocity). It is expressed in Equation 7 by:

$$G = A\frac{\rho}{DT_s^2} \quad \text{(Equation 7)}$$

where:

G = dynamic shear modulus (10^6 psi)

A = 1.3476x104 (conversion parameter, with units of 10^6 psi/((g/cc)/(μs/ft)^2)

ρ = bulk density (g/cc)

DT_c = compressional wave slowness (μs/ft)

DT_s = shear wave slowness (μs/ft)

The bulk modulus of a rock formation expresses the resistance of the formation to compression. This incompressibility is measured using the relationship between the DT^c and DT^s slowness values, as a conversion factor to convert the units to 106 psi. It is expressed in equation 8 by:

$$K = (1.3476 \times 10^4)\rho(\frac{1}{DT_c^2} - \frac{4}{DT_s^2}) \quad \text{(Equation 8)}$$

where:

K = bulk modulus (10^6 psi)

ρ = bulk density (g/cc)

DT_c = compressional wave slowness (μs/ft)

DT_s = shear wave slowness (μs/ft)

The results included four dynamic elastic parameters (Poisson's ratio, Young's modulus, dynamic shear modulus, and bulk modulus) calculated for Chester 6-16 (Figure 3-1 and Figure 3-2). Individual well data from Chester 6-16 was aggregated into histograms for each dynamic elastic parameter for each formation to gain an understanding of the variation in the properties of each formation. Results are presented for the five geologic formations (Salina, A-2 Carbonate, A-2 Evaporate, A-1 Carbonate, and Brown Niagaran) in Figure 3-3 and Figure 3-4.

The mean value of Poisson's ratio and Young's modulus within each formation, as an aggregate of data for Chester 6-16 is shown in Table 3-1. In terms of Young's modulus, the Salina Formation has a significantly lower Young's modulus value in comparison to carbonate and evaporite formations. Low Young's modulus was expected to be observed in salt layers due to the high deformation tendency of salt. All geological formations were in the same range in terms of Poisson's ratio (mean Poisson's ratio of 0.27 to 0.30 across different formations).

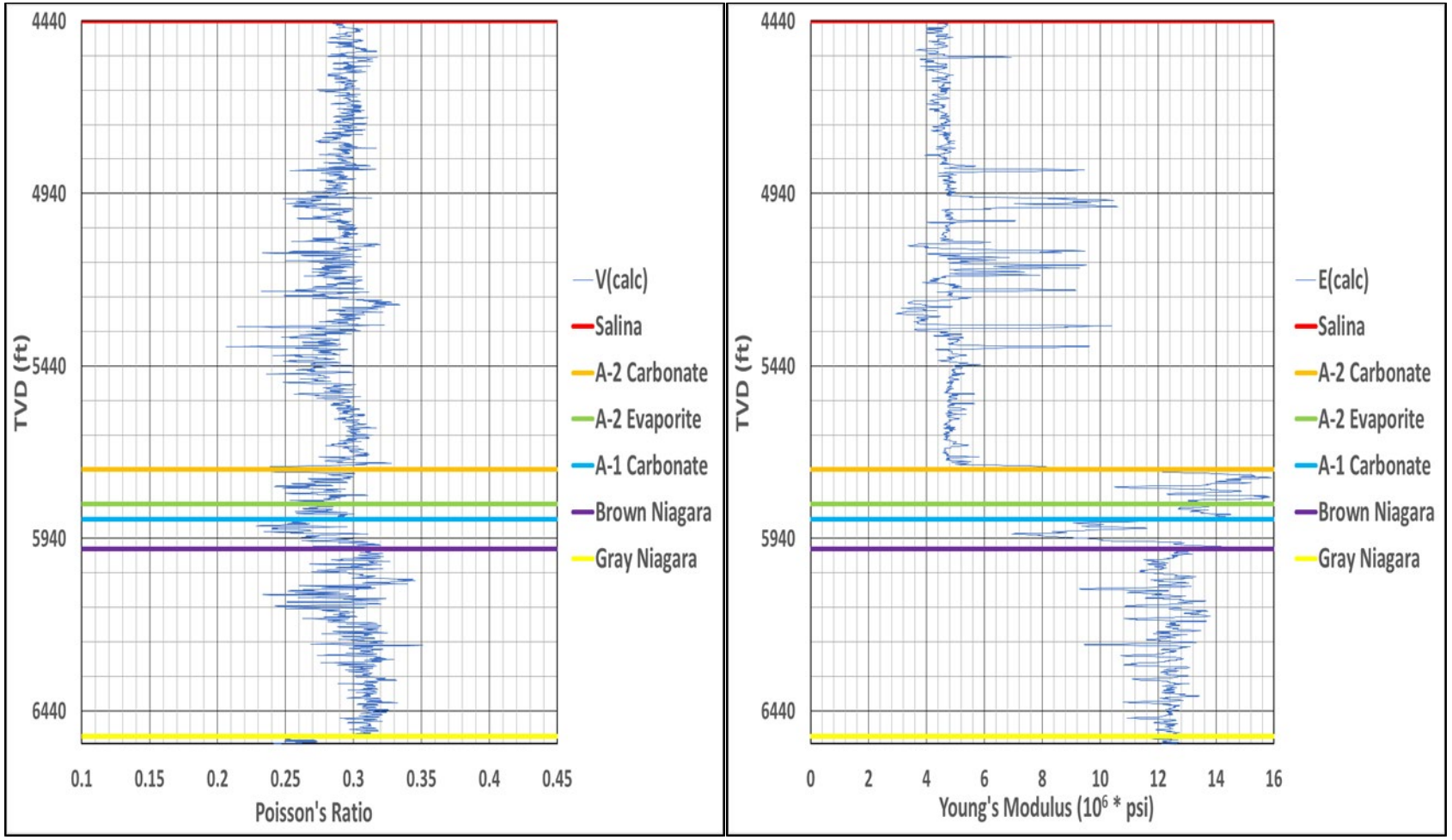


Figure 3-1. Depth plots of Poisson's Ratio and Young's modulus for Chester 6-16.

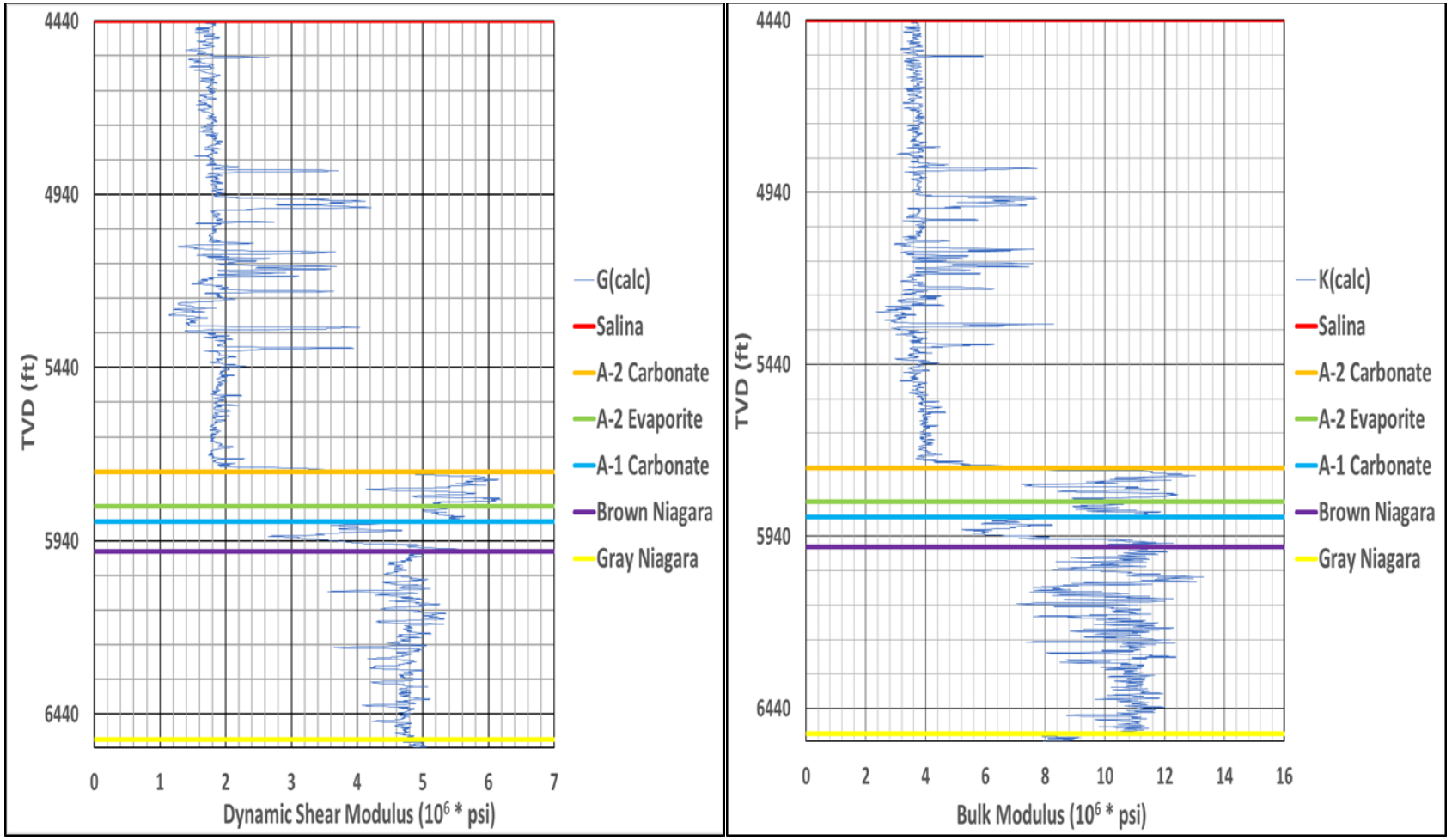


Figure 3-2. Depth plots of dynamic shear modulus and bulk modulus for Chester 6-16.

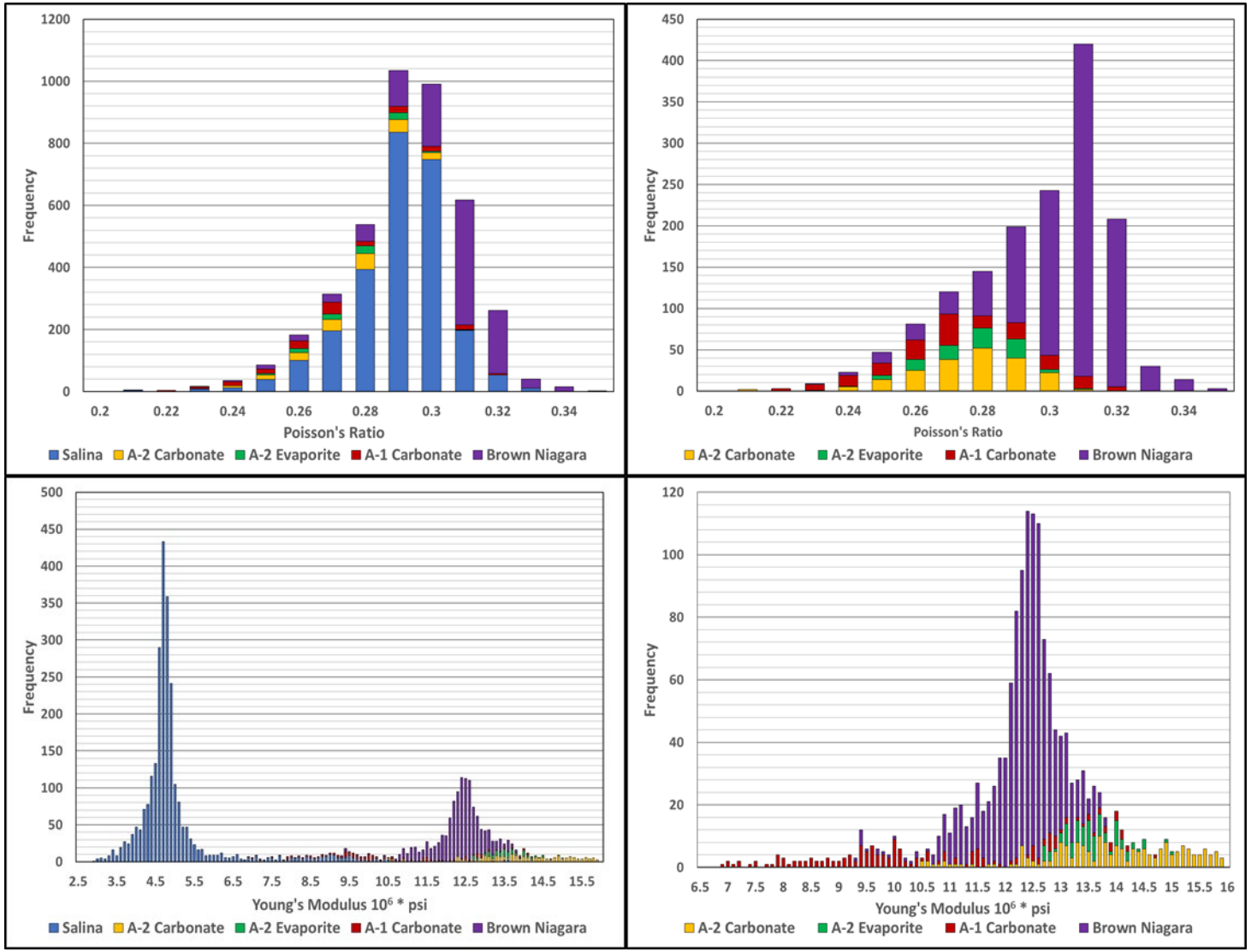


Figure 3-3. Histograms of Poisson's Ratio and Young's Modulus for Chester 6-16. Two of the histograms include the Salina Formation, and two of the histograms don't include the Salina Formation for visual resolution purposes.

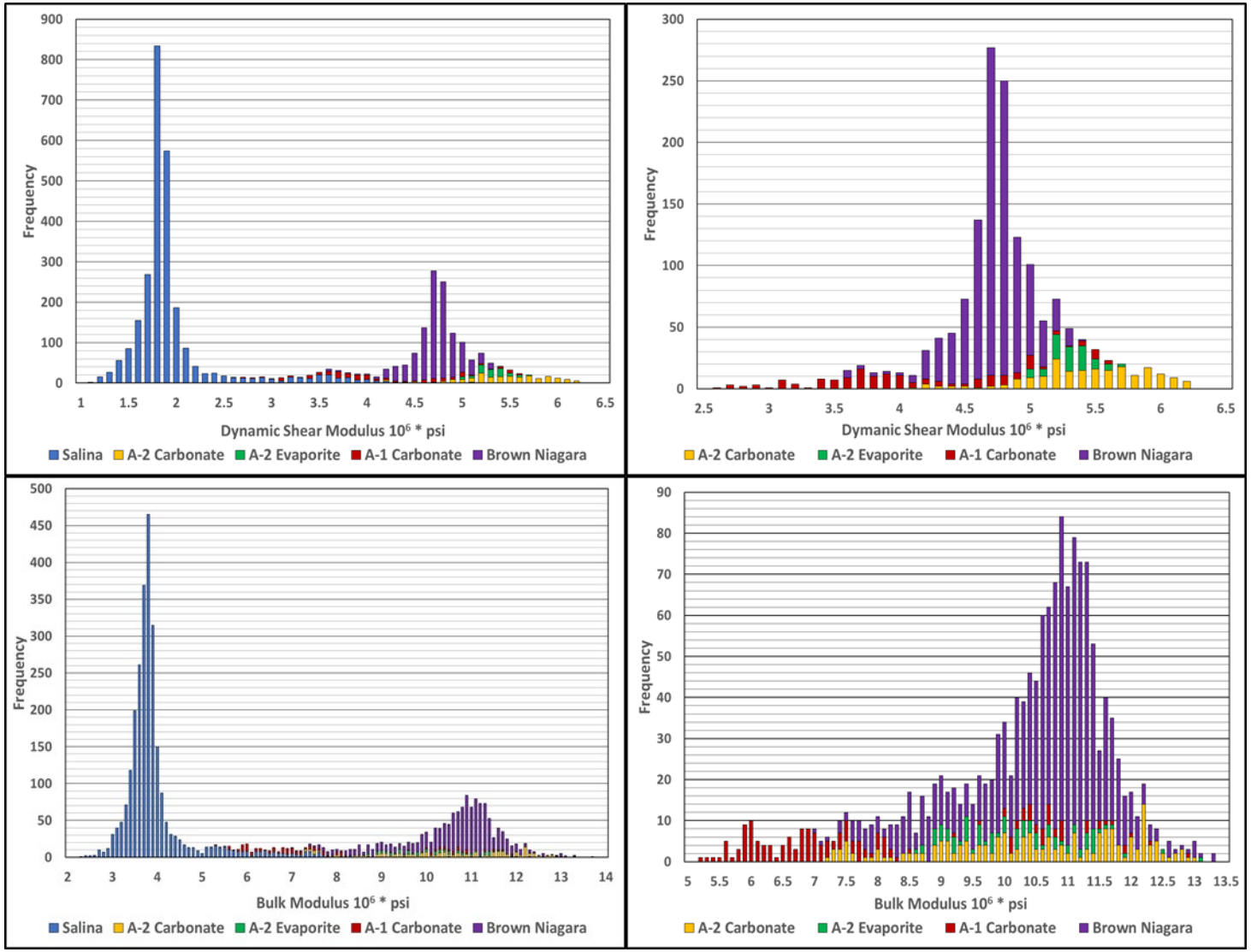


Figure 3-4. Histograms of dynamic shear modulus and bulk modulus for Chester 6-16. Two of the histograms include the Salina Formation, and two of the histograms don't include the Salina Formation for visual resolution purposes.

Table 3-1. Mean, variance, and N (number of data values) values of geomechanical parameters within Chester 6-16 by formation.

Formation		Chester 6-16			
		Young's Modulus	Poisson's Ratio	Bulk Modulus	Dynamic Shear Modulus
Salina	Mean	5.00	0.29	3.96	1.94
	Variance	1.50	0.0002	0.77	0.24
	N	2600	2600	2600	2600
A-2 Carbonate	Mean	13.90	0.28	10.46	5.44
	Variance	1.61	0.0003	2.26	0.21
	N	201	201	201	201
A-2 Evaporite	Mean	13.56	0.28	10.20	5.31
	Variance	0.25	0.0002	0.92	0.03
	N	88	88	88	88
A-1 Carbonate	Mean	10.54	0.27	7.87	4.14
	Variance	2.20	0.0004	1.28	0.37
	N	172	172	172	172
Brown Niagaran	Mean	12.31	0.30	10.58	4.72
	Variance	0.43	0.0003	1.08	0.06
	N	1086	1086	1086	1086
Gray Niagaran	Mean	12.03	0.25	8.15	4.80
	Variance	0.43	0.0001	0.46	0.06
	N	45	45	45	45

3.3 In-Situ Stress Analysis

3.3.1 Calculating Vertical Stress (Sv) Using Density Logs

Formation bulk density (ρ) was used to characterize the in-situ state of stress for caprock and reservoir formations. This involved determining the orientation and magnitude of vertical stress (S_v), least horizontal stress (S_{Hmin}), and pore pressure (P_p)to help characterize variability of the state of stress in Chester 6-16.

The magnitude of S_v is determined by the weight of the overlaying rock material and was calculated by integrating bulk density from ground surface to the total depth of the well. It is expressed by:

$$S_v = \Sigma \rho \Delta z \left(\frac{1ft^2}{144in^2}\right)$$

where:

ρ = bulk density of the formation measured by geophysical logging tools over a specific depth interval (lbs/ft^3)

Δz = depth interval corresponds to the ρ reading (ft)

Geophysical logs do not start at ground surface; therefore, it is usually necessary to assume a density for the near-surface interval that was not logged. S_v was calculated in this manner for Chester 8-16 with an assumed density of 2 lbs/ft^3 being used from ground surface to a depth of 848 ft.

S_{Hmin} was determined by multiplying TVD by an assumed constant of 0.6. It is expressed by:

$$S_{Hmin} = 0.6 \times TVD$$

where:

S_{Hmin} = least horizontal stress (psi)

0.6 = assumed constant

TVD = true vertical depth

P_p was determined by multiplying TVD by an assumed constant of 0.443. It is expressed by:

$$P_p = 0.443 \times TVD$$

where:

P_p = pore pressure (psi)

0.443 = assumed constant

TVD = true vertical depth

S_v, S_{Hmin}, and P_p were each determined from ground surface to total depth in Chester 8-16 and are displayed in Figure 3-5.

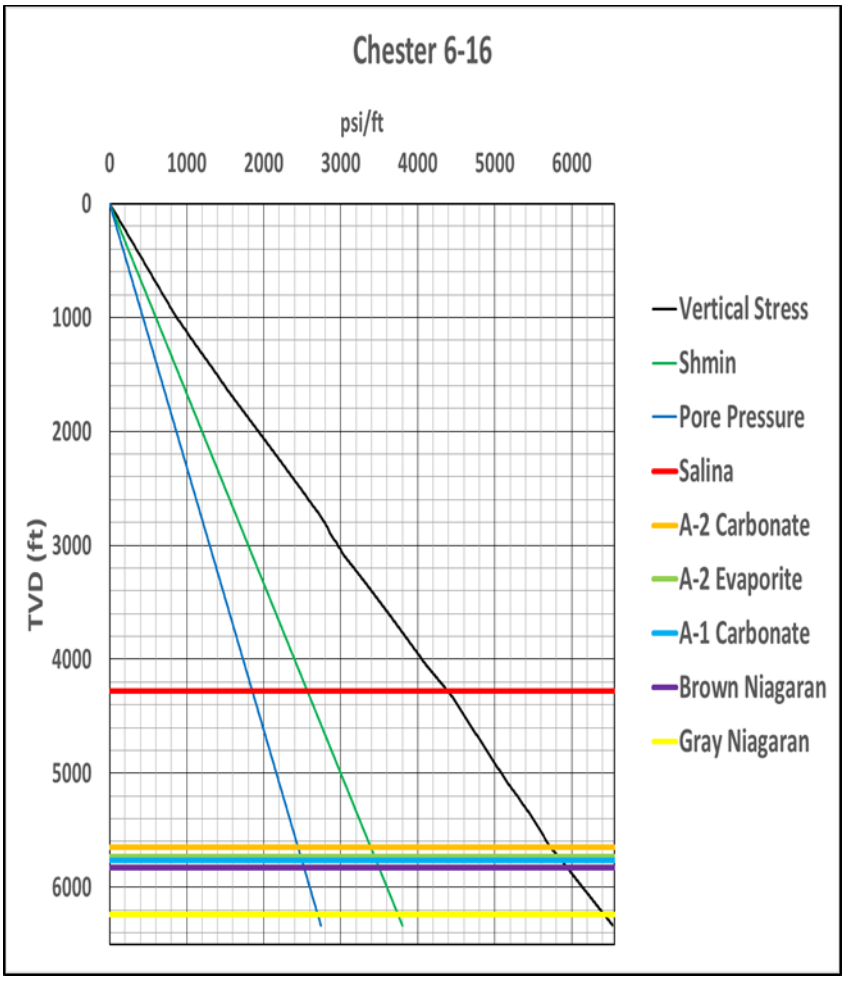


Figure 3-5. Calculated S_v, SH_{min}, and P_p with depth for Chester 6-16.

3.3.2 S_{Hmax} Azimuth Analysis Using Image Log Data

S_{Hmax} orientation (azimuth) was determined from the orientation of features recorded on the image logs, namely drilling-induced fractures (DIFs) and wellbore breakouts (BOs). BOs are a type of wellbore failure that develops when circumferential compressive stress concentrations of the wellbore exceed the required stress needed for compressive failure of the wellbore wall. BOs produce a wellbore profile with symmetric wellbore wall cave-ins oriented perpendicular to the S_{Hmax} orientation. DIFs develop when circumferential stress concentrations surrounding the wellbore exceed the amount needed for tensile failure of the wellbore wall. Upon development, DIFs are oriented parallel with S_{Hmax}. Resistivity and acoustic image log data were collected from the Chester 6-16 well. There were limited occurrences of DIFs mainly located in Bass Island and Salina Salt formations of Chester 6-16. Based on analysis of the limited DIFs occurrence, measured S_{Hmax} azimuth was between N60E to N80E. The changes in geomechanical properties are typically significant from one formation to the another one due to the variation in rock physical parameters. Conversely, the changes in S_{Hmax} azimuth are mainly due to the tectonic history of the basin and the presence of major structural features (e.g. folds and faults). As a result, the similar S_{Hmax} azimuth could be expected in the formations below the Salina Formation.

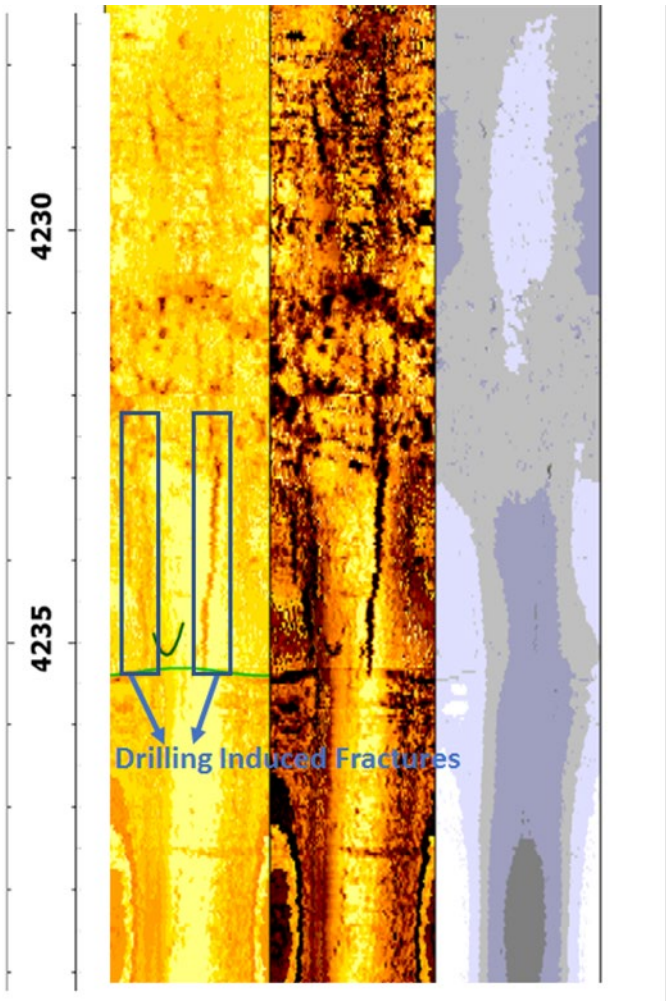


Figure 3-6. Example of DIF recorded on an acoustic image of the Chester 6-16 well.

3.4 Summary

Fundamental rock mechanical properties (Poisson's ratio, Young's modulus, dynamic shear modulus, and bulk modulus) and in-situ stress parameters (S_{Hmax} azimuth and vertical stress) of five caprock-reservoir formations were studied based on available data from the Chester 6-16 well. The data for geomechanics characterization included dipole sonic log, density log, shear wave anisotropy data, and image log data. The geomechanical characterization resulted in the following findings:

- Results included estimates of the Poisson's ratio, Young's modulus, dynamic shear modulus, and bulk modulus for the Chester 6-16 well. The individual well data for Chester 6-16 was aggregated into a single histogram for each dynamic elastic parameter for each formation to gain an understanding of the variation in the properties of the formations. Poisson's ratio values were relatively similar across all formations. The Salina Formation had significantly lower Young's modulus values in comparison to carbonate and evaporite formations.
- There were limited occurrences of DIFs in image log data mainly located in Bass Island and Salina Salt formations of Chester 6-16 well. Based on analysis of the limited DIFs occurrence,

measured S_{Hmax} azimuth was between N60E to N80E. Based on the analysis of the shear wave anisotropy data analysis, the mean orientations of the S_{Hmax} azimuth was N75E.

Chapter 4. Summary

4.1 Conclusion

Well log and well testing data from the Chester 6-16 well has provided insight into the local and regional stratigraphy, structure, geomechanical, and petrophysical properties of potential Northern Pinnacle Reef Trend storage reservoirs and caprocks in the Michigan Basin. Analysis conducted on each formation of interest (Salina, A-2 Carbonate, A-2 Evaporite, A-1 Carbonate, and Brown Niagaran) indicates that sufficient caprock-reservoir performance exists in Chester 6-16 for CO_2 storage. Characteristics identified in the Salina, A-2 Carbonate, and A-2 Evaporite formations indicate that they could potentially serve as effective caprock formations in Chester 6-16. The A-1 Carbonate was characterized as a porous dolostone and exhibits possible potential as a reservoir formation.

Appendix A.

Core Descriptions

A.1 Rotary Side Wall Core Descriptions

Abbrv.	Explanation
AL	Algal laminations
ANH	Anhydrite
B	Breccia
BM	Biologic Material
BU	Burrows
FF	Filled fractures
FP	Framework porosity
MP	Moldic porosity
OF	Open fractures
OS	Oil stain
PV	Pyrite Filled Vug
R	Rubble/broken core
SLT	Salt
STM	Stromatoporoid
STY	Stylolites
V	Vugs

Figure A-1. RSWC abbreviation explanations.

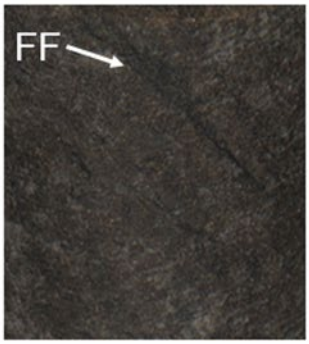
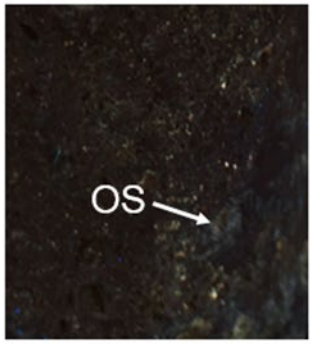
Depth Ft.	White Light Primary Features	UV Light Primary Features	Descriptions
5,927			White Light: Gray carbonate, mud filled fracture. UV Light: Light blue UV response due to potential residual oil.
5,934			White Light: Gray carbonate, small vugs. UV Light: Light blue UV response due to potential residual oil.

Figure A-2. Annotated RSWC images with corresponding core descriptions of the A-1 Carbonate for depths 5,927 ft. to 5,934 ft.

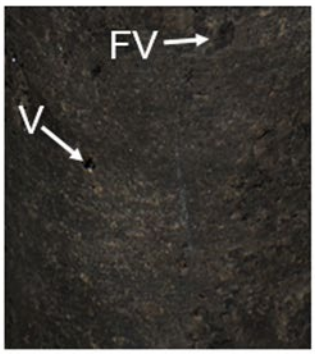
Depth Ft.	White Light Primary Features	UV Light Primary Features	Descriptions
5,938			White Light: Gray carbonate, small vugs, salt filled vugs. UV Light: Light blue UV response due to potential residual oil.
5,961			White Light: Gray carbonate, stylolites. UV Light: Light blue UV response due to potential residual oil.

Figure A-3. Annotated RSWC images with corresponding core descriptions of the A-1 Carbonate for depths 5,938 ft. to 5,961 ft.

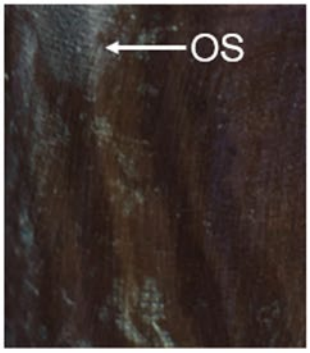
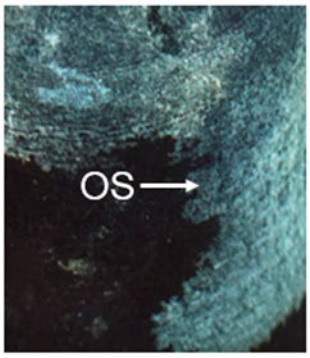
Depth Ft.	White Light Primary Features	UV Light Primary Features	Descriptions
5,962			White Light: Carbonate matrix, filled fracture, alternating dark gray and light gray laminations. UV Light: Light blue UV response due to potential residual oil.
5,968			White Light: Gray carbonate. UV Light: Light blue UV response due to potential residual oil.

Figure A-4. Annotated RSWC images with corresponding core descriptions of the A-1 Carbonate for depths 5,962 ft. to 5,968 ft.

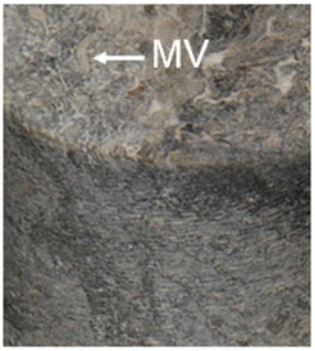
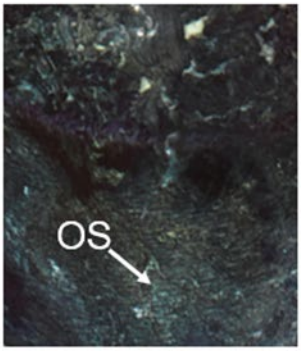
Depth Ft.	White Light Primary Features	UV Light Primary Features	Descriptions
5,970			White Light: Gray carbonate, filled moldic vugs. UV Light: Light blue UV response due to potential residual oil throughout the sample.
5,971			White Light: Gray carbonate, salt filled vugs. UV Light: Light blue UV response due to potential residual oil throughout the sample.

Figure A-5. Annotated RSWC images with corresponding core descriptions of the A-1 Carbonate for depths 5,970 ft. to 5,971 ft.

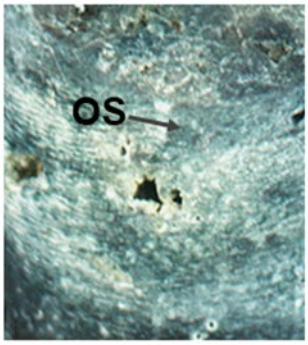
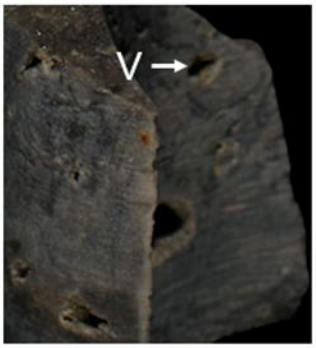
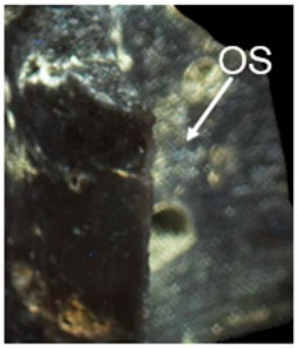
Depth Ft.	White Light Primary Features	UV Light Primary Features	Descriptions
6,015			White Light: Gray carbonate, medium/small vugs. UV Light: Light blue UV response due to potential residual oil throughout sample.
6,032			White Light: Gray carbonate, medium/small vugs, core fragment. UV Light: Light blue UV response due to potential residual oil.

Figure A-6. Annotated RSWC images with corresponding core descriptions of the Brown Niagaran for depths 6,015 ft. to 6,032 ft.

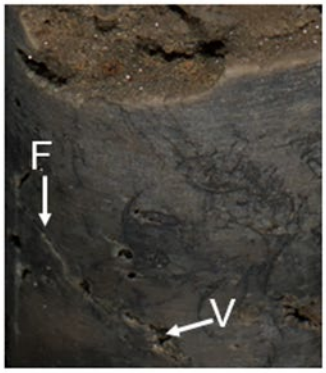
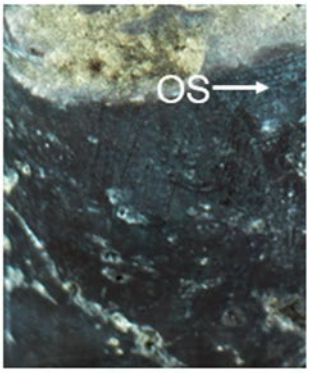
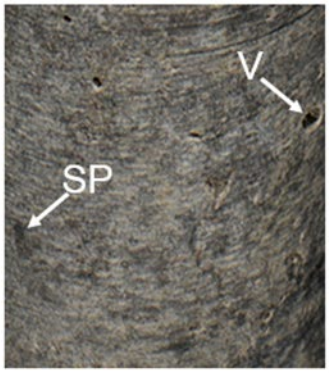
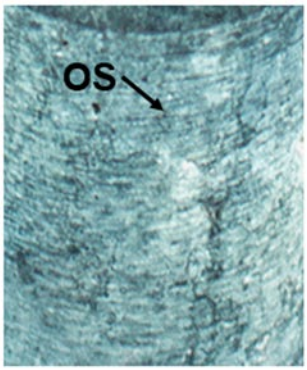
Depth Ft.	White Light Primary Features	UV Light Primary Features	Descriptions
6,032.5			White Light: Gray carbonate, medium/small vugs, fracture. UV Light: Light blue UV response due to potential residual oil throughout sample.
6,033			White Light: Gray carbonate, medium/small vugs, salt filled vugs. UV Light: Light blue UV response due to potential residual oil throughout sample.

Figure A-7. Annotated RSWC images with corresponding core descriptions of the Brown Niagaran for depths 6,032.5 ft. to 6,033 ft.

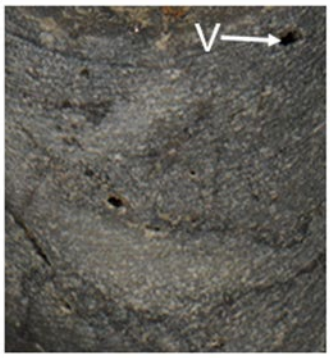
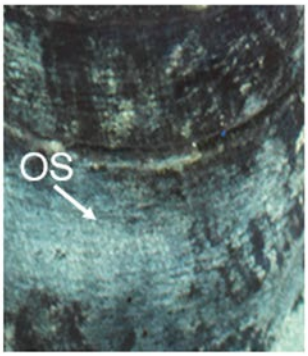
Depth Ft.	White Light Primary Features	UV Light Primary Features	Descriptions
6,033.5			White Light: Gray carbonate, medium/small vugs. UV Light: Light blue UV response due to potential residual oil throughout sample.
6,036			White Light: Gray carbonate, open fractures. UV Light: Light blue UV response due to potential residual oil throughout sample.

Figure A-8. Annotated RSWC images with corresponding core descriptions of the Brown Niagaran for depths 6,033.5 ft. to 6,036 ft.


BATTELLE
It can be done

Attachment 4.
Chester 8-15 Wireline and Core Analysis: Chester 16 Niagaran Reef Piggyback Well

Attachment 4

Chester 8-16 Wireline and Core Analysis: Chester 16 Niagaran Reef Piggyback Well

Conducted by the Midwest Regional Carbon Sequestration Partnership (MRCSP)

DOE-NETL Cooperative Agreement DE-FC26-05NT42589



Prepared by:

Battelle
505 King Avenue
Columbus, Ohio 43201

Submitted to:

Client
Address
Address

April 28, 2019

This report is a work prepared for the United States Government by Battelle. In no event shall either the United States Government or Battelle have any responsibility or liability for any consequences of any use, misuse, inability to use, or reliance on any product, information, designs, or other data contained herein, nor does either warrant or otherwise represent in any way the utility, safety, accuracy, adequacy, efficacy, or applicability of the contents hereof.

Table of Contents

Page

Chapter 1. Well Drilling and Completions 1
1.1 Summary of Drilling and Completions 1
1.2 Well Operations Execution 1
1.3 Well Logging 2
Chapter 2. Geologic Characterization 9
2.1 Methodology 9
2.1.1 Wireline Log Analysis and Petrophysical Calculations 9
2.1.2 Core Collection and Description 11
2.1.3 Elemental Spectroscopy Log Analysis 14
2.1.4 Image Log Analysis 15
2.2 Core Analysis 16
2.2.1 Routine Core Analysis 16
2.2.2 Routine Sidewall Core Analysis 17
2.3 Formation Evaluation 20
2.3.1 A-2 Carbonate and A-2 Evaporite 20
2.3.2 A-1 Carbonate 28
2.3.3 Brown Niagaran 37
2.3.4 Gray Niagaran 50
2.4 Summary 56
Chapter 3. Integrated Geomechanics Analysis 57
3.1 Introduction 57
3.2 Mechanical Parameters Characterization Using Dipole Sonic Log Analysis 57
3.3 In-Situ Stress Analysis 64
3.3.1 Calculating Vertical Stress (S_v) Using Density Logs 64
3.3.2 S_{Hmax} Azimuth Analysis Using Image Log Data 66
3.3.3 S_{Hmax} Azimuth Analysis Using Image Log Data 66
3.4 Summary 68
Chapter 4. Well Testing 69
4.1 Introduction 69
4.1.1 Open-Borehole Formation Testing 69
4.2 Hydraulic Well Tests 71
4.2.1 Local Interference Test #1 (5890.7 ft) 72
4.2.2 Local Interference Test #2 (5864.7 ft) 75

4.2.3 Summary 78
4.3 Micro-Frac Tests 78
4.3.1 MicroFrac Test 1 (5861 Ft MD) 79
4.3.2 MicroFrac Test 2 (5967 ft MD) 86
4.3.3 MicroFrac Test 3 (5791 FT MD) 89
4.3.4 MICROFRAC TEST 4 (5765 FT MD) 90
4.3.5 S_{Hmax} 93
4.3.6 Summary 95
Chapter 5. Summary 97
5.1 Conclusion 97
Chapter 6. References 98

List of Tables

Page

Table 1-1. Chester 8-16 formation evaluation value of information chart. Logs highlighted in blue represent open hole logs, those highlighted in gray were collected in cased hole. 8
Table 2-1. Formation tops identified in Chester 8-16. 9
Table 2-2. Conventional core acquisition parameters for Chester 8-16. 11
Table 2-3. RSWC acquisition parameters for Chester 8-16. 13
Table 2-4. Core grain density summary. 13
Table 2-5. Summary of porosity and permeability data from whole core at Chester 8-16. 17
Table 2-6. RSWC grain density summary by formation. 18
Table 2-7. Summary of RSWC porosity and permeability data. 19
Table 2-8. Summary of whole core porosity and permeability data in the Chester 8-16 well. 56
Table 2-9. Summary of RSWC porosity and permeability data in the Chester 8-16 well. 56
Table 2-10. Summary of key potential reservoir intervals in the Chester 8-16 well based on whole core analysis and images 56
Table 3-1. Mean, variance, and N (number of data values) values of geomechanical parameters within Chester 8-16 by formation 63
Table 4-1. Summary of In-Situ Reservoir Pressure and Mobility Measurements. 69
Table 4-2. Depth of Local Interference Tests. 71
Table 4-3. Reservoir and Fluid Parameters used in the analysis of LIT-1 and LIT-2. 74
Table 4-4. Summary of Reservoir Properties determined from LIT-1 and LIT-2. 78
Table 4-5. Summary of Open Borehole MicroFrac Tests Performed in Chester 8-16. 78
Table 4-6. Fracture Closure Pressures for MicroFrac Station 1 (5861 ft MD). 85

Table 4-7. Fracture Closure Pressures for MicroFrac Station 2 (5967 ft MD). 88
Table 4-8. Fracture Closure Pressures for MicroFrac Station 3 (depth 5791 ft MD). 90
Table 4-9. Fracture Closure Pressures for MicroFrac Test 4 (5765 ft MD). 93
Table 4-10. MicroFrac test program results. 95

List of Figures

Page

Figure 1-1. Surface hole location for Chester 8-16 marked in red. 3
Figure 1-2. As built wellbore diagram for Chester 8-16. (Not to scale.) 4
Figure 1-3. Deviation survey plot for well Chester 8-16 showing deviation path from vertical (left) and northeast orientation (right). 5
Figure 1-4. Days vs depth plot annotated with unscheduled events, casing points, and key geologic horizons for drilling and completion of the Chester 8-16 well. 6
Figure 1-5. Executed formation evaluation program for Chester 8-16. 7
Figure 2-1. Rock typing results from CT Scan analysis of the Chester 8-16 cores showing mostly tight limestone with occasional vugs, dolomite, and anhydrite. 12
Figure 2-2. Lithology log legend and explanation of abbreviations used in the whole core analysis figures. 13
Figure 2-3. RSWC abbreviation explanations. 14
Figure 2-4. FLeX header from well Chester 8-16. 15
Figure 2-5. Histograms of grain density by formation from the Chester 8-16 conventional core. 16
Figure 2-6. Porosity-permeability transform for the Brown Niagaran and Gray Niagaran from whole core measurements at Chester 8-16. 17
Figure 2-7. Histograms of grain density by formation from the Chester 8-16 RSWCs. 18
Figure 2-8. Porosity-permeability transform for the A-2 Carbonate (light blue circle), A-2 Evaporite (magenta circle), A-1 Carbonate (yellow circle), and Brown Niagaran (brown circle) from RSWC measurements. 19
Figure 2-9. Average porosity histogram of the A-2 Carbonate in Chester 8-16 showing a low average porosity of 2% with the highest porosities over the carbonate shale/mudstone interval mid-formation. 21
Figure 2-10. Neutron porosity-bulk density cross plot of the A-2 Carbonate in Chester 8-16 showing tight dolomite with a thin interval of porosity greater than 5% (red). 21
Figure 2-11. Single well cross section of the A-2 Carbonate in Chester 8-16 showing relatively low porosity, low water saturation, and a high gamma interval mid formation indicative of a carbonate shale/mudstone. 22

Figure 2-12. Single well cross section of the A-2 Evaporite in Chester 8-16 well showing low porosity throughout with changes in bulk density and water saturation when the rock changes from anhydrite (top and bottom) to more dolomitic (middle). 23
Figure 2-13. Annotated RSWC images with corresponding core descriptions of the A-2 Carbonate for depths 5,760 ft. to 5,761 ft. 24
Figure 2-14. Annotated RSWC images with corresponding core descriptions of the A-2 Carbonate for depths 5,761 ft. and 5,778 ft. 25
Figure 2-15. Annotated RSWC images with corresponding core descriptions of the A-2 Evaporite for depths 5,819 ft. to 5,820 ft. 26
Figure 2-16. FLeX log from Chester 8-16 displaying the A-2 Carbonate and A-2 Evaporite Formations from 5,735'MD/5,636'TVD to 5,843'MD/5,744'TVD. Select RSWC samples are shown in both WL and UV light to provide context for lithologic descriptions. Core photos by Core Laboratories. 27
Figure 2-17. Average porosity histogram of the A-1 Carbonate for the Chester 8-16 well showing high porosities throughout with an average of 12.5%. 28
Figure 2-18. Neutron porosity-bulk density cross plot of the A-1 Carbonate for the Chester 8-16 well showing mostly high porosity dolomite (red) and thin intervals of porosity less than 5%. 29
Figure 2-19. Single well cross section of the A-1 Carbonate for the Chester 8-16 well showing high porosities (orange shade) throughout with low water saturations. 30
Figure 2-20. Annotated RSWC images with corresponding core descriptions of the A-1 Carbonate for depths 5890 ft. to 5,893 ft. 31
Figure 2-21. Elemental spectroscopy log from Chester 8-16 displaying the A-1 Carbonate from 5,843'MD/5,744'TVD to 5,916'MD/5,817'TVD. Select RSWC samples are shown in both WL and UV to provide context for lithologic descriptions. Core photos by Core Laboratories. 32
Figure 2-22. Uppermost texture zone within the A-1 Carbonate of the Chester 8-16 well. Texture is homogenously resistive with no signs of porosity development. 34
Figure 2-23. Intermediate texture zone of the A-1 Carbonate. The texture is heterogenous with two porosity zones displayed in the figure from 5884'-5888' and 5892'-5903'. 35
Figure 2-24. Lower most textural zone of the A-1 Carbonate of the Chester 8-16 well. 36
Figure 2-25. Average porosity histogram of the Brown Niagaran for the Chester 8-16 well showing relatively low porosity throughout with an average of 3.6%. 37
Figure 2-26. Neutron porosity-bulk density cross plot of the Brown Niagaran for the Chester 8-16 well showing mostly tight limestone with thin intervals of high porosity (red). 38
Figure 2-27. Single well cross section of the Brown Niagaran for the Chester 8-16 well showing thin intervals of porosity (red flags) and an increase in water saturation at the OWC. 39

Figure 2-28. Compiled illustration of lithology log, core photos (UV and white light), CT scan image, core descriptions, and annotated core images of the Brown Niagaran for depths 6,148 ft. to 6,151 ft. 40

Figure 2-29. Compiled illustration of lithology log, core photos (UV and white light), CT scan image, core descriptions, and annotated core images of the Brown Niagaran for depths 6,181 ft. to 6,184 ft. 41

Figure 2-30. Annotated RSWC images with corresponding core descriptions of the Brown Niagaran for depths 6,012 ft. to 6,015 ft. 42

Figure 2-31. Annotated RSWC images with corresponding core descriptions of the Brown Niagaran for depths 6,095 ft. to 6,121 ft. 43

Figure 2-32. Elemental spectroscopy log from Chester 8-16 displaying the Brown Niagaran Formation from 5,916'MD/5,817'TVD to 6,332'MD/6,233'TVD. Select RSWC samples are shown in both white light (WL) and ultraviolet light (UV) to provide context for lithologic descriptions. Core photos by Core Laboratories. 44

Figure 2-33. Textural zone one within the Brown Niagaran Unit of the Chester 8-16 well. Texture is mixed with homogenously resistive and heterogeneous textures. The interval of 5924 ft-5928 ft is a potential zone of significant porosity. 46

Figure 2-34. Textural zone two within the Brown Niagaran Formation of the Chester 8-16 well. Texture is homogenously resistive with some conductive features. At 5992 ft a large isolated semi-spherical conductive body is encountered. 47

Figure 2-35. The third textural zone within the Brown Niagaran Formation of the Chester 8-16 well. Texture is interbedded homogenous and heterogenous materials. Significant porosity zone is displayed from 6141 ft to 6150 ft. Not cyclical packages of homogenously resistive to heterogenous materials. 48

Figure 2-36. The fourth zone of the Brown Niagaran Formation within the Chester 8-16 well. The texture is mixed heterogeneous and homogenously conductive materials. 49

Figure 2-37. Neutron porosity-bulk density cross-plot of the Gray Niagaran for the Chester 8-16 well showing tightly clustered data along the limestone trend with low porosity. 50

Figure 2-38. Single well cross section of the Gray Niagaran for the Chester 8-16 well showing low porosity and high water saturation. 51

Figure 2-39. Compiled illustration of lithology log, core photos (UV and white light), CT scan image, core descriptions, and annotated core images of the Gray Niagaran for depths 6,347 ft. to 6,350 ft. 52

Figure 2-40. Compiled illustration of lithology log, core photos (UV and white light), CT scan image, core descriptions, and annotated core images of the Gray Niagaran for depths 6,356 ft. to 6,359 ft. 53

Figure 2-41. FLeX log from Chester 8-16 displaying the Gray Niagaran Formation from 6,332'MD/6,233'TVD to log TD at 6,447'MD. 54

Figure 2-42. Texture zone of the Gray Niagaran of the Chester 8-16 well. The texture is homogenously resistive interbedded with heterogenous materials. There are no zones of significant porosity. 55
Figure 3-1. Depth plots of Poisson's ratio and Young's modulus for Chester 8-16. 59
Figure 3-2. Depth plots of dynamic shear modulus and bulk modulus for Chester 8-16. 60
Figure 3-3. Histograms of Poisson's ratio and Young's modulus for Chester 8-16. Two of the histograms include the Salina Formation, and two of the histograms don't include the Salina Formation for visual resolution purposes. 61
Figure 3-4. Histograms of bulk modulus and Young's Modulus for Chester 8-16. Two of the histograms include the Salina Formation, and two of the histograms don't include the Salina Formation for visual resolution purposes. 62
Figure 3-5. Calculated S_v, SH_{min}, and P_p with depth for Chester 8-16. 65
Figure 3-6. Anisotropy % (left track), fast shear wave azimuth (middle track), fast and slow shear wave Azimuth (right track) in a section of the Salina Formation of the Chester 8-16 well. 67
Figure 3-7. Rose Diagram of fast shear-wave azimuth data for Chester 8-16 well. 68
Figure 4-1. Reservoir Pressures (yellow diamonds) Measured with Baker Hughes RCX Tool. 70
Figure 4-2. Schematic of Straddle Packer and an Observation Probe combination for a Local Interference Test. ..... 71.
Figure 4-3. Pumping Rate and Pressure Response in the Straddle Packer Interval during LIT-1. 72
Figure 4-4. Pressure Response at the Observation Probe during LIT-1. 72
Figure 4-5. Log-log diagnostic plot of straddle-packer (blue symbols) and observation probe (green symbols) pressure response during LIT-1 showing modeled response at the straddle packer (red line) and observation probe (green line). 74
Figure 4-6. Pressure history match of test interval data (left) and observation probe data (right) for the entire LIT-1 74
Figure 4-7. Pumping Rate and Pressure Response in the Straddle Packer Interval during LIT-2. 75
Figure 4-8. Pressure Response at the Observation Probe during LIT-3. 75
Figure 4-9. Log-log diagnostic plot of straddle-packer (blue symbols) and observation probe (green symbols) pressure response during LIT-2 build-up period, plus modeled pressure and pressure derivative (solid lines) in the straddle packer interval. 76
Figure 4-10. Comparison of observed pressure (blue squares) and pressure derivative (blue triangles) data to modeled pressure and pressure derivative (red lines) for the LIT-2 buildup period. 77
Figure 4-11. Pressure history match of the LIT-2 pumping and buildup periods. 77
Figure 4-12. Test History for MicroFrac Test 1 in the A-1 Carbonate at a depth of 5861 ft MD. 80

Figure 4-13. Fracture Breakdown Pressure During the First Injection Cycle (FOT1) of MicroFrac Test 1. 81
Figure 4-14. Example Square root of Shut-in-time Plot for Fracture Closure Identification in Station 1/Cycle 1. 82
Figure 4-15. Example Log-Log of Shut-in Time Plot for Fracture Closure Identification in Station 1/Cycle 1. 83
Figure 4-16. Example G-Function of Shut-in Time Plot for Fracture Closure Identification in Station 1/cycle 1. 84
Figure 4-17. Test History for MicroFrac Test 2 in the A1 Carbonate at a Depth of 5967 ft MD. 86
Figure 4-18. Fracture Breakdown Pressure During the First Injection Cycle (FOT1) of MicroFrac Test 2. 87
Figure 4-19. Test History for MicroFrac Test 3 in the A1 Carbonate at a Depth of 5791 ft MD. 89
Figure 4-20. Test History for MicroFrac Test 4 in the A-2 Carbonate at a Depth of 5765 ft MD. 91
Figure 4-21. Fracture Breakdown Pressure During the First Injection Cycle of MicroFrac Test 4. 92
Figure 4-22. MicroFrac Testing Station 1 (5861 ft.) Image Logs before and after MicroFrac Testing. 94
Figure 4-23. MicroFrac Testing Station 2 (5967 ft.) Image log before and after MicroFrac Testing. 94

Chapter 1. Well Drilling and Completions

1.1 Summary of Drilling and Completions

Drilling of the Chester 8-16 well began on December 15, 2016 and was operated by Core Energy LLC with well evaluation operations contracted by Battelle Memorial Institute on behalf of MRCSP. The surface location of this borehole is marked by a red dot on both a high-resolution aerial photograph and map in Figure 1-1. The final, as-built, wellbore diagram can be found in Figure 1-2.

This well was directionally drilled from the Kick Off Point (KOP) at 4,342' MD/TVD. The deviation survey plot for Chester 8-16 is shown in Figure 1-3.

1.2 Well Operations Execution

A days vs. depth chart in Figure 1-4 is annotated with unscheduled events that occurred during drilling and completions, casing shoe depths (black triangles), and key formation tops. These unscheduled events are described below:

- Losses into a gravel zone at 768'MD within the surface hole section required the pumping of a lost circulation material (LCM).
- Lost returns are common across the Northern Michigan Pinnacle Reef Trend, often massive or total, in the intermediate hole section when the mud system is converted from freshwater to brine. Pore pressure within this stratigraphic section must be at or very near the hydrostatic gradient because the drilling fluid density increase caused by adding dissolved salts is sufficient to cause voids to form or open. Drilling with a salt saturated fluid is critical through this interval to prevent hole enlargement and washout while drilling thick salt beds.
- Chester 8-16 lost returns at a rate of 40 bph beginning at 2,661'MD before shutting in the well 4 days over the Christmas holiday. The team drilled ahead to 3,833' MD with 15-50 bph losses then stopped to repair mud system pumps. They stopped drilling again for 6 hours to mix and pump LCM sweeps at 4,025'MD with 100 bph losses before calling 10-5/8" hole section TD at 4,065'MD.
- A failed/no test on blind rams (1/6/2017; 4,342'MD) led to additional time for changing seals and subsequent pressure testing.
- The coring bit became stuck at 5,892'MD while running in hole to the first core point at 6,147'MD. The pipe was separated using a depth charge, and fishing operations to retrieve the bit commenced. Ultimately, fishing operations failed after jarring on the stuck coring borehole assembly (BHA) multiple times. The junk in the hole was reamed out from 5,200' to 6,010'MD.
- 10 bph losses occurred while drilling from the end of the last core point (6,355'MD) to well TD at 6,455'MD.
- The production casing cement job locked up while still in the annulus (2/2/2017), preventing cement engineers from completing the job. Engineers attempted to reciprocate the casing with 1500psi. There was no bleed off and casing was free in hole. All cement was in casing.
- Soft cement was drilled out of 4-1/2" casing. (2/5)
- Reverse circulation was initiated and washed out large amounts of LCM. (2/6)
- Cementing was completed. (2/16)

1.3 Well Logging

Wireline logs were run from ~1000'MD to 4,020'MD in the intermediate open hole section before running the 8-5/8" casing string (Figure 1-5). Some logs, such as the acoustic logs were turned on and recording while running through the previous casing string (11-3/4"). Both the compensated neutron (CN) and Z-density log (ZDL) were recorded with respect to a limestone matrix. The caliper log indicated 50'-150' thick zones of borehole enlargement at 2,300'MD, 2,800'MD, and 3,000'MD. These depths are roughly correlative to occurrences of lost returns and may be related.

Wireline logs were also run in the deep open hole section from 4,065'MD to 6,400'MD (Figure 1-5). The elemental spectroscopy tool, containing digital spectralog and simultaneous acoustic and resistivity log, covers only the interval from 4,225' to 6,447'MD. While logging out of the hole, the tool string suffered an electrical short at 4,225'MD and the final 150' was not re-logged. Both the CN and ZDL were recorded with respect to a limestone matrix.

A reservoir characterization tool was used to conduct eight Local Interference Tests (LIT) in the A-1 Carbonate at Chester 8-16 on January 29, 2017. While low permeability was noted within the zone tested, pressure communication between the source and observation probes was observed on two tests.

Out of thirty Rotary Side Wall Cores (RSWC) attempted, thirty were recovered. The average coring time for each was under 9 minutes and the average core length was 2.2 inches.

A fiber optic cable was run in conjunction with the 4-1/2" casing string and cemented in place (Figure 1-5). This has allowed for distributed acoustic sensing (DAS) borehole geophysical monitoring over time. Several cased hole logs were run at Chester 8-16 as part of a wellbore integrity study, as well as a baseline Pulsed Neutron Capture log (PNC) for use in monitoring studies.

Table 1-1 lists all data types that were collected during the drilling and completions phase of this well and describes how this data was employed to decrease project and technical uncertainties for MRCSP Phase III research.

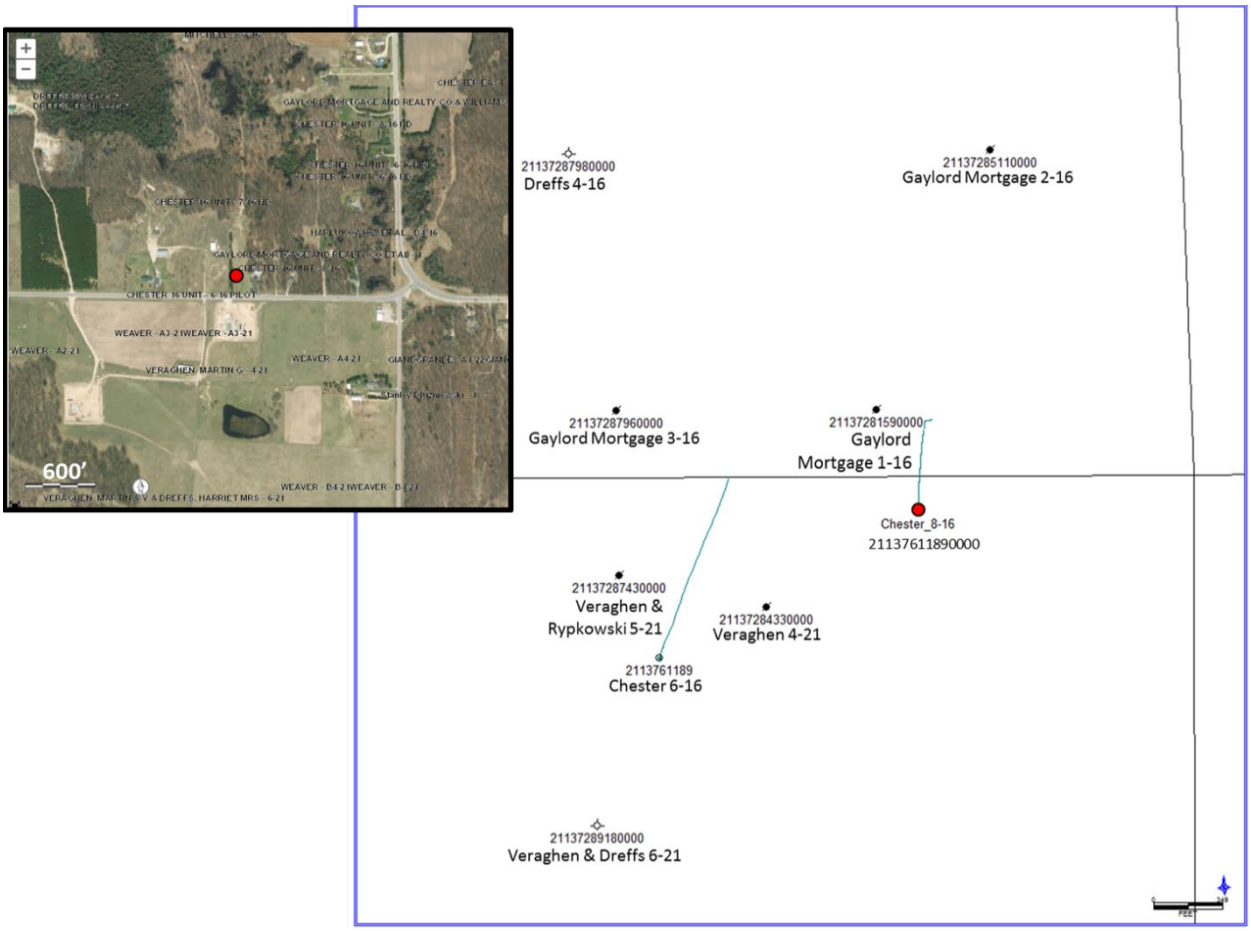


Figure 1-1. Surface hole location for Chester 8-16 marked in red.

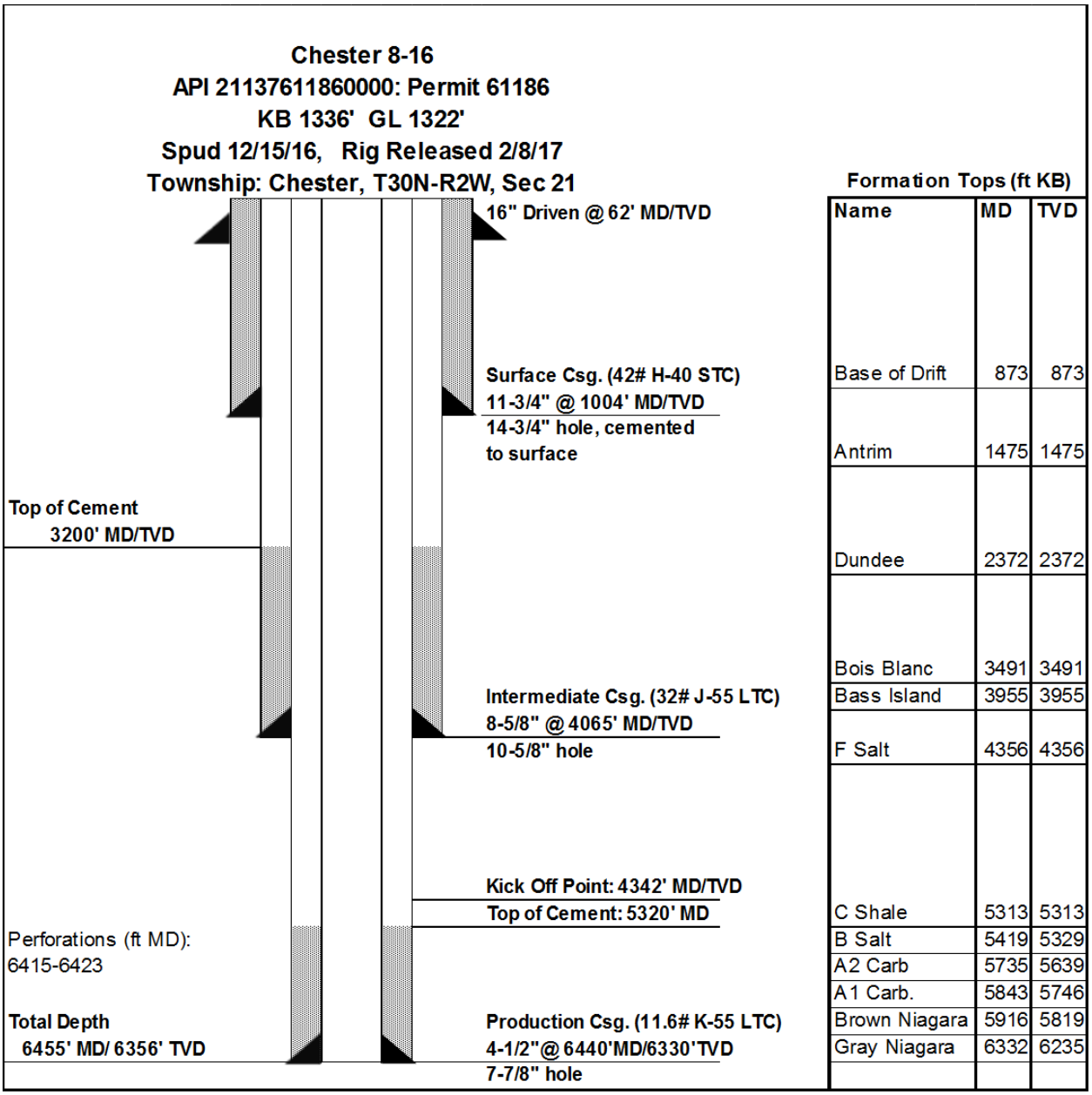


Figure 1-2. As built wellbore diagram for Chester 8-16. (Not to scale.)

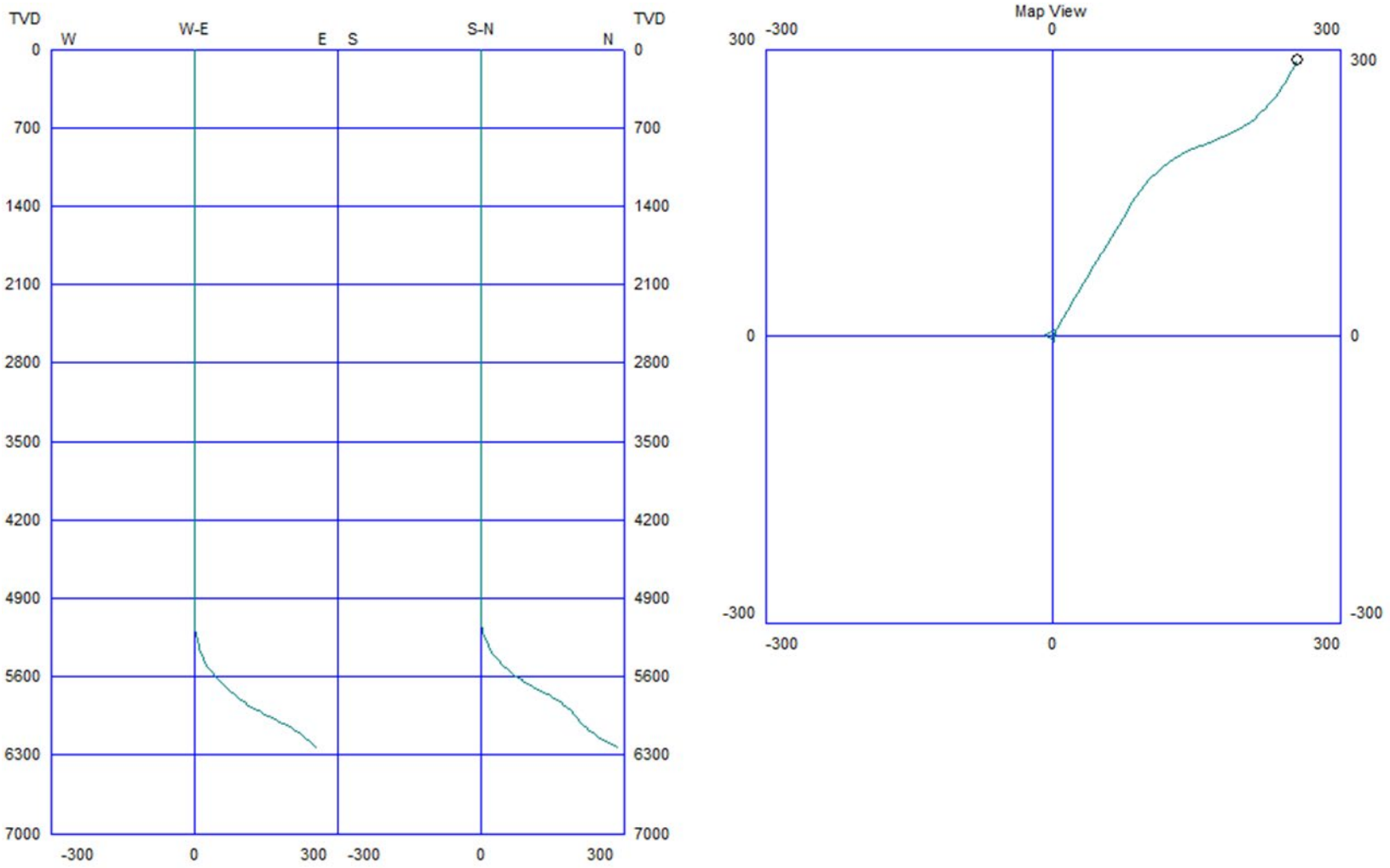


Figure 1-3. Deviation survey plot for well Chester 8-16 showing deviation path from vertical (left) and northeast orientation (right).

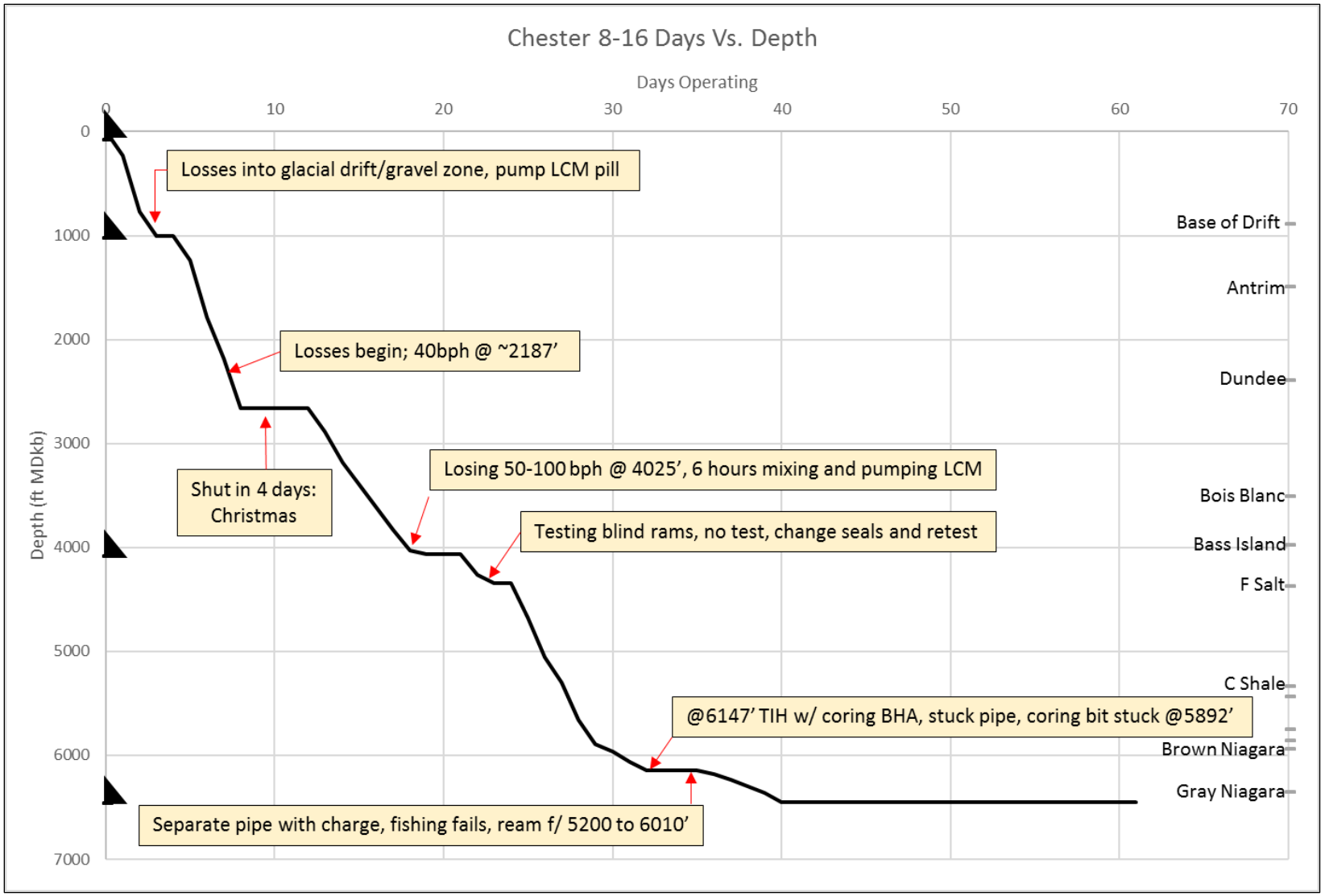


Figure 1-4. Days vs depth plot annotated with unscheduled events, casing points, and key geologic horizons for drilling and completion of the Chester 8-16 well.

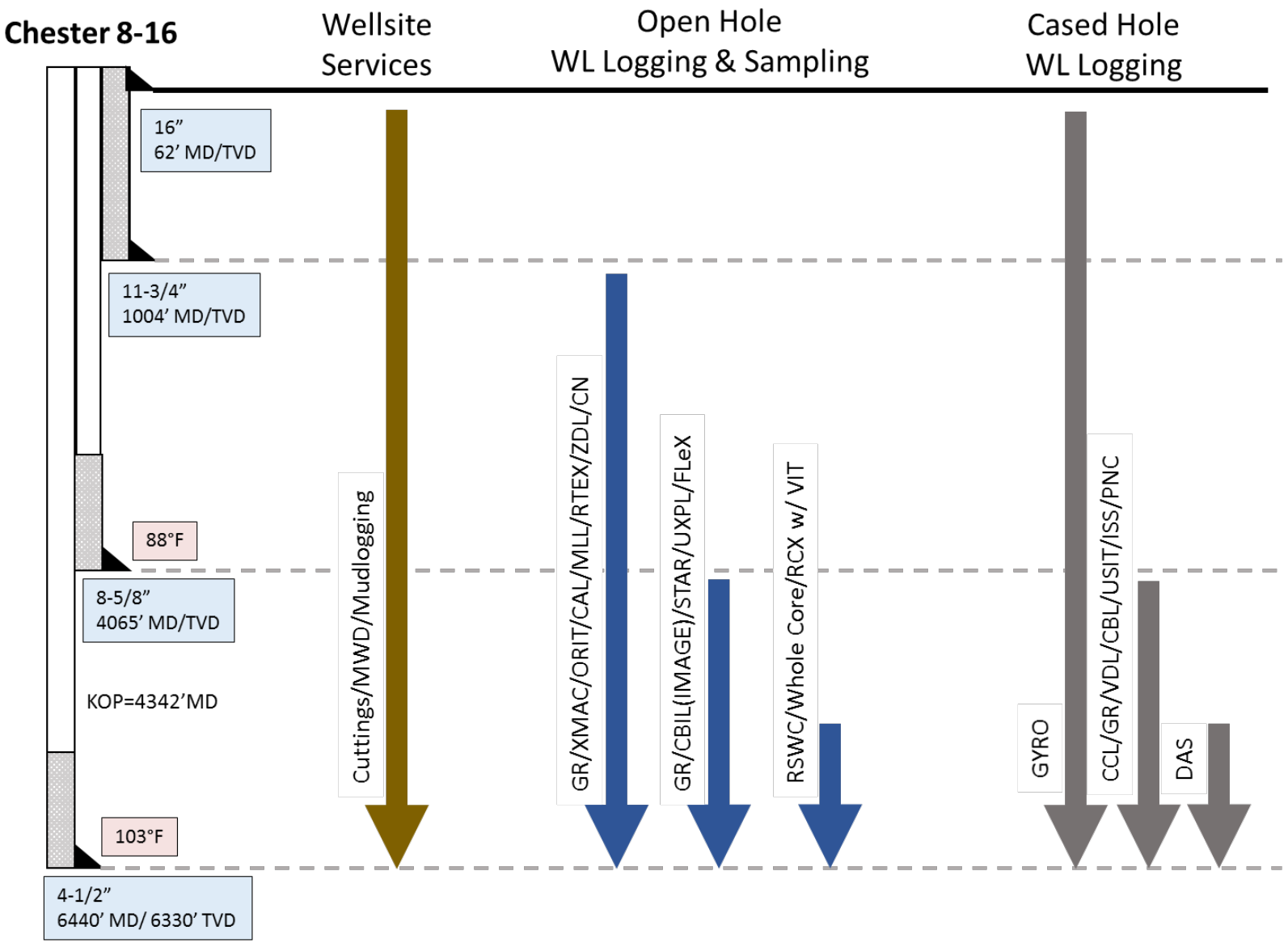


Figure 1-5. Executed formation evaluation program for Chester 8-16.

Table 1-1. Chester 8-16 formation evaluation value of information chart. Logs highlighted in blue represent open hole logs, those highlighted in gray were collected in cased hole.

Log Name and Mnemonic		Value of Information
CAL	Caliper	Provides evidence of borehole size, including enlargement due to washout, which is critical for QA/QC and calibration of many logs.
CBIL	Circumferential Borehole Imaging Log	Used to observe facies/lithology changes, bedding planes, and large vuggy pores to infer depositional settings and correlate with reservoir properties from additional logs for static and dynamic earth models. Identify presence, orientation, attitude of linear features such as fractures and faults to characterize stress fields for geomechanical analyses.
CBL	Cement Bond Log	Evaluates presence of cement behind casing and is used for planning borehole seismic data acquisition.
CCL	Casing Collar Locator	Highlights the presence of metallic casing collars and is used with Gamma Ray tool to correlate cased hole logs on depth and tie in with open hole logs.
CN	Compensated Neutron Log	This tool is used to calculate porosity and identify lithology, by responding to the hydrogen content of the formation. Porosity data is a key input to static and dynamic earth models and CO2 storage estimates.
DAS	Distributed Acoustic Sensing	DAS borehole seismic data was not collected at the time of drilling or completion, but the distributed optical fiber sensors were cemented on the outside of the casing at Chester 6-16 and 8-16. This will increase the likelihood of repeatability of time-lapse surveys for CO2 monitoring at this reef.
ECS	Elemental Capture Spectroscopy	This tool measures silicon (Si), iron (Fe), calcium (Ca), sulfur (S), titanium (Ti), gadolinium (Gd), chlorine (Cl), barium (Ba), and hydrogen (H). The data collected were used to make direct observations of in situ formation composition.
GR	Gamma Ray	Gamma Ray is a standard log that was run in both open hole and cased hole for correlation purposes. This tool identified bed boundaries and informed the interpretation of other petrophysical logs. Interpretations based on this log impacted technical products throughout the project.
GYRO	Gyroscope	This directional survey instrument was run to accurately measure the deviation of the well path from vertical; both inclination and azimuth. This information is critical for applying proper measured depth (MD) or total vertical depth (TVD) datums to geologic surfaces, calculating pressures, and for correlation to other wells.
ISS	Isolation Scanner	Cement evaluation tool that maps the entire annulus. This data was used to evaluate wellbore integrity and identify gas or fluids behind pipe to calibrate PNC logs.
MLL	Micro Laterolog	This is a shallow resistivity tool that was used to evaluate the lithology and fluid content of formations. This information, lithology and (oil/water/gas) was an input to models.
ORIT	Directional Survey	This directional survey instrument was run to accurately measure the deviation of the well path from vertical; both inclination and azimuth. This information is critical for applying proper measured depth (MD) or total vertical depth (TVD) datums to geologic surfaces, calculating pressures, and for correlation to other wells.
PNC	Pulsed Neutron Capture	The cased hole reservoir monitoring tool was run multiple times to measure changes in water, hydrocarbon, and CO_2 saturation over time with CO_2 injection. It was also used to identify salt in reservoir intervals where porosity plugging reduces storage potential.This data was used for baseline reservoir characterization, static earth model input data, and dynamic model history matching.
RSWC	Rotary Side Wall Core	Rotary side wall core plugs are subject to routine and special core analyses that provide lab test based calibration points for petrophysical log interpretation as well as critical values for reservoir modeling that cannot be inferred from downhole logs such as relative permeability and capillary pressure. Unoriented RSWCs can be used to test some geomechanical properties such as Young's modulus and Poisson's ratio.
RTeX	Multi Laterolog Wireline Service	This tool collects resistivity data with four different formation penetration modes and adaptive borehole correction to remove the effects of formation invaded by drilling fluid. Resistivity logs were a basic indicator of fluid type and lithology. Interpretations based on this log impacted technical products throughout the project.
USIT	Ultrasonic Imager tool	The USIT provided a scan of casing condition and cement bond around the entire casing circumference. This data was used to evaluate wellbore integrity and identify gas or fluids behind pipe to calibrate PNC logs.
VDL	Variable Density Scanner	This log was run in the cased hole along with the CBL to assist in its interpretation. It provides the amplitude of the acoustic waveform of the CBL measurement.
VIT	Vertical Interference Test	Vertical interference testing was conducted to determine the level of communication between carbonate layers within the reservoir section. This information is an input to the dynamic earth model and informs understanding of CO_2 flow within a reef.
Whole Core	Whole Core	Whole core was collected to allow for detailed study of facies/lithology changes, bedding planes, and large vuggy pores to infer depositional settings and correlate with reservoir properties from additional logs for static and dynamic earth models. Identify presence, orientation, attitude of linear features such as fractures and faults to characterize stress fields for geomechanical analyses. Furthermore, core plugs were drilled from the whole core that were subject to routine and special core analyses that provide lab test based calibration points for petrophysical log interpretation as well as critical values for reservoir modeling that cannot be inferred from downhole logs such as relative permeability and capillary pressure. Oriented core plugs can be used to test geomechanical properties such as Young's modulus and Poisson's ratio as well as conduct uniaxial-triaxial stress testing.
XMAC	Cross-Multipole Array Acoustilog	This tool provides full-wave monopole, in-line dipole, and cross-dipole sonic logs. Sonic logs are necessary input parameters for borehole seismic data acquisition planning and processing as well as indicators of rock mechanical properties. They were used in petrophysical analysis of the reefs that was input to the static and dynamic earth models. Deep shear wave image processing was applied to locate and map linear formation features such as fractures and bedding planes.
ZDL	Z Density Log	The density log assists in porosity estimation, lithology determination, seismic data acquisition planning and processing, and geomechanical modeling.

Chapter 2. Geologic Characterization

2.1 Methodology

2.1.1 Wireline Log Analysis and Petrophysical Calculations

Formation evaluations were completed on the A-2 Carbonate, A-2 Evaporite, A-1 Carbonate, Brown Niagaran, and Gray Niagaran formations to complete a geologic characterization of caprock and reservoir formations in Chester 8-16. Formation evaluation included: wireline log analysis and petrophysical calculations, core analysis, elemental spectroscopy analysis, and image log analysis.

A standard triple combo log was run over the intermediate and deep string sections (3709-6638 ft.) of the Chester 8-16 well. The triple combo log suite includes gamma ray, density, neutron porosity and resistivity, as well as tension, caliper, and photo-electric effect. Data from the triple combo log was analyzed in the context of the regional geology to identify formation tops, facilitate stratigraphic correlations, and calculate basic formation properties such as net and gross thickness, average porosity, and pay flags (defined intervals of high reservoir quality) delineating potential injection zones. This basic log analysis served as the framework for guiding more advanced characterization efforts.

Five formations and their associated tops were identified for the detailed analyses (Table 2-1). Porosity was evaluated for the formations of interest using neutron porosity, density porosity, and average porosity calculations. Neutron porosity is derived by a neutron source within the logging tool that measures the hydrogen index of the formation. As hydrogen atoms are present in fluids (e.g., brine, oil) residing in the pores of the reservoir, measurements of hydrogen estimated the amount of fluid-filled porosity. The contribution of hydrous minerals (clays) to the logged neutron porosity was evaluated by the gamma ray response of the formation and noted as a potential source of error in neutron porosity measurements. Density porosity was calculated from equation 1:

Table 2-1. Formation tops identified in Chester 8-16.

Formations	Chester 8-16 ft. MD
A-2 Carbonate	5735
A-2 Evaporite	5805
A-1 Carbonate	5843
Brown Niagaran	5916
Gray Niagaran	6332
OWC	6245

$$\phi_D = \frac{(\rho_{ma} - \rho_b)}{(\rho_{ma} - \rho_{fl})} \quad \text{(equation 1)}$$

where:

ϕ_D = density porosity

ρ_{ma} = matrix density (based on limestone density of 2.71 g/cm^3 or grain density data from elemental spectroscopy log)

ρ_b = bulk density (from the density log)

ρ_{fl} = fluid density (assumed fresh: 1.1 g/cm^3 for brine)

Grain density data derived from the weight percentages of minerals detected by the elemental spectroscopy log was used (ρ_{ma}) to calculate density porosity for the formations of interest. Average porosity was calculated using both density and neutron porosities via equation 2:

$$\phi_A = \frac{(\Phi_D + \Phi_N)}{2} \quad \text{(equation 2)}$$

where:

ϕ_A = average porosity

ϕ_D = density porosity

ϕ_N = neutron porosity.

Average porosities are used as representative values of formation porosity because neutron and density porosity derivations are each susceptible to inaccuracies in certain conditions, such as the presence of gas, washouts, and atypical mineralogy.

Neutron porosity and bulk density data derived from the triple combo log were plotted against each other to generate a cross plot for each formation. Cross plots are a graphical analysis technique that can be used to evaluate formation lithology and porosity. Trend lines superimposed on the cross plot represent the log responses calculated for pure sandstone, limestone, and dolomite over a range of porosities (e.g. 0-45%), assuming a fluid density of 1.0 g/cm^3 (fresh water) in the wellbore environment. Neutron-density cross plots can provide insight into lithology and allow for a potential estimate of true, lithology-independent porosity to be determined. Data that plotted within cross plot porosities greater than 5% were flagged, and the flagged data points were depth-denoted on cross-sections.

Water saturation calculations were performed to determine the percentage of the pore space that was filled with water and, thus, inversely, what percentage of available pore space is filled with hydrocarbons. Water saturation was calculated using the Archie Equation, a standard oil and gas formula shown in equation 3:

$$S_w = \left(\frac{a \times R_w}{R_t \times \emptyset^m}\right)\frac{1}{n} \quad \text{(equation 3)}$$

where:

S_w = water saturation of the uninvaded zone, %

R_w = formation water resistivity, ohm-ft

R_t = formation resisitivity, ohm-ft

Ø = porosity, %

a = tortuosity factor

m = cementation exponent

n = saturation exponent

Values for formation resistivity (R_t) and porosity (ø) were derived from the wireline logs. Formation water resistivity (R_w) value was determined at each reef field dependent on salinity. Constants a, m, and n were set to industry standard values of a=1, m=2, and n=2.

Pay flags were generated using the following cutoffs; a gamma ray measurement less than 75 API, a water saturation calculated lower than 40%, and a neutron measurement greater than 5%. A gamma ray measurement less than 75 API is a standard indicator of relatively pure sandstone and carbonate reservoirs. A gamma response of 75 API was also used as a

maximum cutoff to define the net reservoir thickness. A water saturation cutoff of 40% ensures the available storage zone is being represented. A minimum neutron porosity value of 5% was used as a cutoff to identify potential high effective-porosity intervals.

2.1.2 Core Collection and Description

Conventional Core Collection

A total of 210.9' of whole core was recovered from the Chester 8-16 well. The cored interval spans a continuous section of the Brown Niagaran Formation from 6,148'-6,358'MD. Acquisition was divided into four separate coring runs with an average rate of penetration (ROP) of 7.3 ft/hr while coring. Details for depth ranges, recovery rates, and ROP for each run are listed in Table 2-2 below.

Table 2-2. Conventional core acquisition parameters for Chester 8-16.

Core Run #	Coring Vendor	Start Depth	End Depth	Core Cut	Core Recovered	Core Recovery	ROP
		ft MD	ft MD	ft MD	ft MD	%	ft/hr
1	Baker Hughes	6148	6178	30	29.15	97%	7.5
2	Baker Hughes	6178	6238	60	59.83	100%	7.1
3	Baker Hughes	6238	6298	60	61.25	100%	4.8
4	Baker Hughes	6298	6358	60	60.7	100%	10.0

Dual Energy Computed Tomography (CT) Scanning

Before the whole core was removed from liners, helical CT scans were performed from depths of 6,148 to 6,360 ft., over the Brown and Gray Niagaran Formations at CoreLab in Houston, TX. An X-ray source was set on a helical trajectory around longitudinal sections of cores to derive three-dimensional images of density variations for each core volume. Sample densities are expressed in gray-scale color variations such that light-colored, higher-density areas can be distinguished from darker-colored, low-density areas to identify internal fractures, pore distributions and geometries, and silicate-versus-carbonate mineral variability. These data are essential for the reservoir characterization of rocks with heterogeneously distributed porosity and allow for the accurate sampling of plugs for routine and special core analysis.

In order to model core lithology, two X-ray scans of the same core were conducted. One scan created images sensitive to bulk density (RHOB) using high energy x-rays. The other scan created an image sensitive to mineralogy using low energy x-rays. These two sets of images were then independently subjected to a data transform that relates intensity to RHOB and effective atomic number (Zeff). A crossplot of these data from conventional core at Chester 8-16 are shown in Figure 2-1 with corresponding lithology. The data produced by this tool provide a quantitative understanding of the reservoir potential for the wells and a means by which to correlate wireline log data.

The CT scans on the Chester 8-16 core revealed frequent intervals with high concentration of vugs, moldic porosity, biologic debris, fractures, stylolites, calcite cement, anhydrite plugs, and regions of massive, tight limestone. Vugular intervals were more frequent in the upper section of core. This transitioned into infrequent, single, disconnected vugs midway through the core. Massive and tight limestone dominated the matrix of the cores with occasional intervals of porosity. Dolostone and porous dolostone have also been identified in the Chester 8-16 well.

CT scans and detailed lithology logs spanning the entire cored interval are presented in Appendix A.

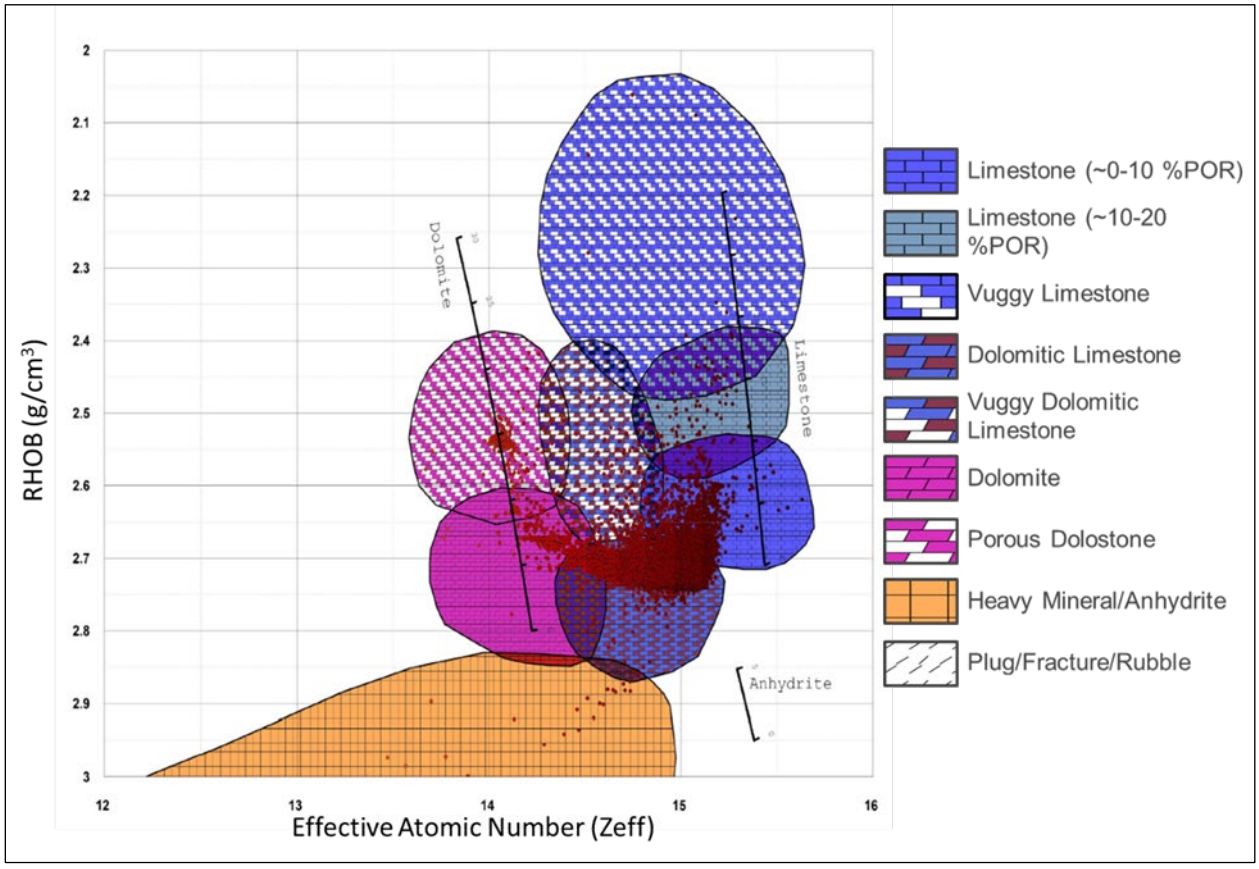


Figure 2-1. Rock typing results from CT Scan analysis of the Chester 8-16 cores showing mostly tight limestone with occasional vugs, dolomite, and anhydrite.

Conventional Core Description

Descriptions of the entire inventory of conventional core from Chester 8-16 were made in one-foot intervals and are provided in Appendix A. Core photographs were collected in white light (WL) and ultra violet (UV) light and are included with a correlative CT scan and lithology log. The lithology log used to describe the conventual core samples is seen below in Figure 2-2.



Abbrv.	Explanation
AL	Algal laminations
ANH	Anhydrite
B	Breccia
BM	Biologic Material
BU	Burrows
FF	Filled fractures
FP	Framework porosity
FP	Flat Pebble clasts
MP	Moldic porosity
OF	Open fractures
OS	Oil stain
PV	Pyrite Filled Vug
R	Rubble/broken core
SLT	Salt
STM	Stromatoporoid
STY	Stylolites
V	Vugs

Figure 2-2. Lithology log legend and explanation of abbreviations used in the whole core analysis figures.

RSWC Collection

Acquisition of 30 RSWC was conducted during open hole wireline operations for the Chester 8-16 well using the Baker Hughes MAXCOR tool. The sampling interval, which included the A-1 Carbonate and Brown Niagaran Formations (5,778 ft.-6,145 ft.MD), was identified in the field by Battelle technical staff from log signatures. The 1.5 in. diameter cores ranged in length between 1.6 in. and 2.5 in., with an average of 2.2 in. The average time spent coring each sample was eight minutes and forty-seven seconds. Efficiency during this RSWC run was 100% with 30 out of 30 cores attempted being recovered on surface. Table 2-3 summarizes the RSWC acquisition parameters for Chester 8-16.

Table 2-3. RSWC acquisition parameters for Chester 8-16.

Cores Attempted	Cores Recovered	Core Recovery Efficiency	Avg Coring Time (min:sec)	Average Core Length (in.)
30	30	100.0%	8:47	2.20

RSWC Description

Descriptions of the entire inventory of sidewall cores from Chester 8-16 have been made in one-foot intervals and are provided in Appendix A. Core photographs collected in white light and UV light are included. Descriptions abbreviations are summarized below in Figure 2-3.

Abbrv.	Explanation
AL	Algal laminations
ANH	Anhydrite
B	Breccia
BM	Biologic Material
BU	Burrows
FF	Filled fractures
FP	Framework porosity
MP	Moldic porosity
OF	Open fractures
OS	Oil stain
PV	Pyrite Filled Vug
R	Rubble/broken core
SLT	Salt
STM	Stromatoporoid
STY	Stylolites
V	Vugs

Figure 2-3. RSWC abbreviation explanations.

2.1.3 Elemental Spectroscopy Log Analysis

Elemental spectroscopy tools operate by generating a pulse of high energy neutrons and measuring the inelastic and captured gamma ray radioactive decay responses of elements in subsurface formations to these neutrons. Analysis of data measurements from the tool consists of plotting weighted fractions of elements on ternary diagrams to derive relative yield measurements of Potassium (K), Thorium (Th), Uranium (U), Silicon (Si), Calcium (Ca), Magnesium (Mg), Iron (Fe), Aluminum (Al), and Sulfur (S) which are common sedimentary rock elements. These measurements are combined with neutron and density porosity, gamma ray, resistivity, and grain density curves, to calculate bulk volumetric mineralogic ratios and conduct in-situ lithological characterization across zones of interest.

The elemental spectroscopy tool logged the Chester 8-16 well on January 24, 2017 from 4,192'MD to 6,447'MD. The tool string shorted while logging out of the hole at 4,225'MD and the remaining 150' of scheduled log was cancelled. Additionally, RockView analysis was conducted by Baker Hughes after logging to provide volumetric fractions of minerals present in the wellbore using a probabilistic approach. Due to the absence of NMR data at the Chester 8-16 well, a simplified clay/feldspar mineralogy model is used.

This well hosted a very high salinity environment that affected the elemental and mineralogical quantification in some zones. Formation water salinity was approximately 286 thousand (k)ppm NaCl. Salinity values from mud chemistry reports averaged 214 kppm for chlorides and 128 kppm for Ca. The unabridged log legend can be found in Figure 2-4, and a shortened version is displayed with the discussion of each formation.

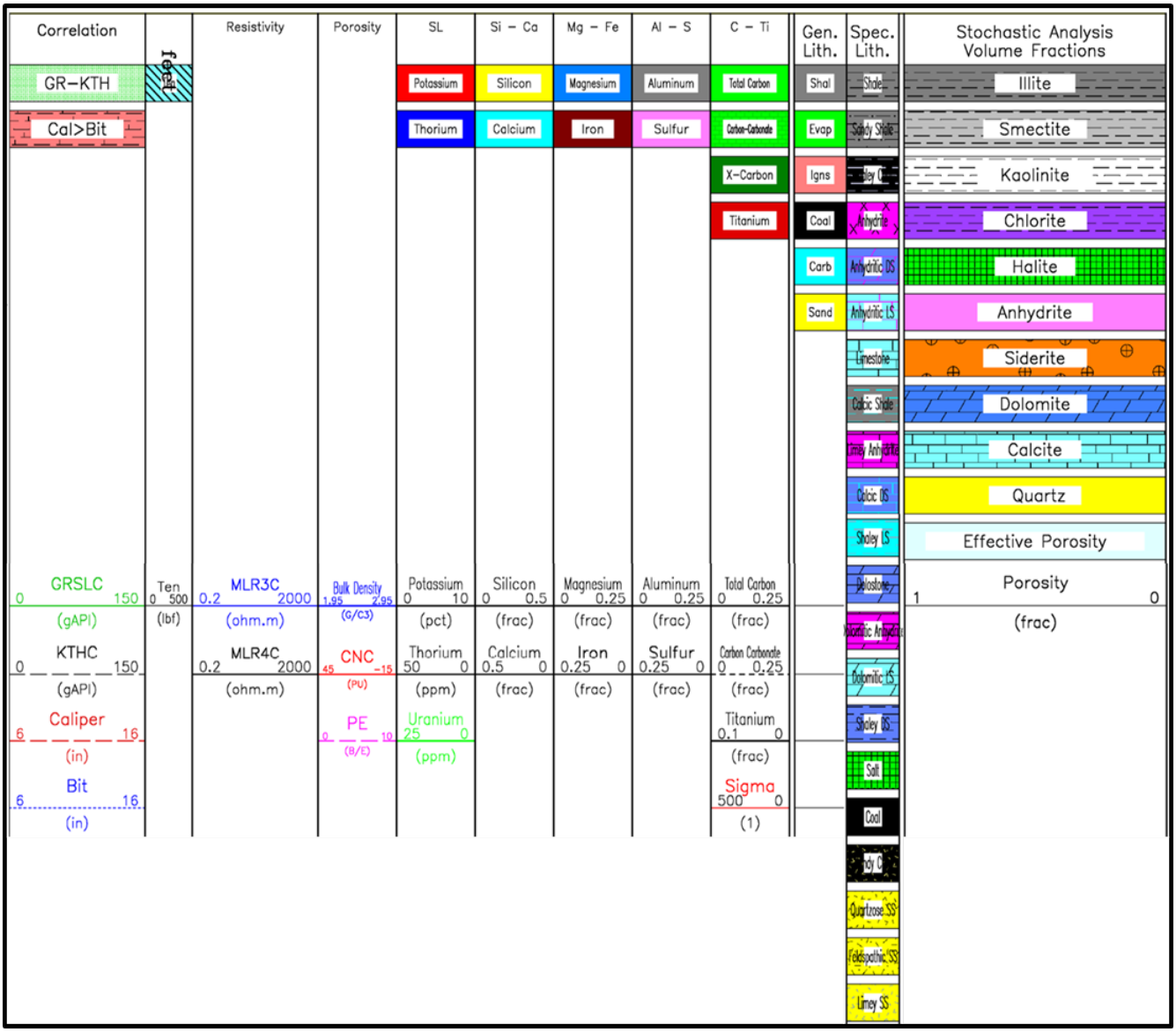


Figure 2-4. FLeX header from well Chester 8-16.

2.1.4 Image Log Analysis

Acoustic and resistivity-derived image logs provide high-resolution, 360-degree wellbore images that can be used to derive structural and sedimentary features for detailed reservoir characterization. Planar features such as faults, fractures, and bedding can be identified, as well as stress fields, bioturbation, soft sediment deformation, and pore spaces. Image logs are instrumental in identifying and characterizing vugular porosity in carbonates, as these pore types are difficult to discern from other basic and advanced log signatures. Image logs can also be used to differentiate breakout and drilling-induced fractures from natural formation features.

2.2 Core Analysis

2.2.1 Routine Core Analysis

Routine core analysis was conducted on 1.0 in. diameter plugs drilled from the whole core. These analyses were conducted by Core Lab in Houston, TX, following CMS-300 conventional plug analysis protocol. Standard core analysis included porosity, permeability, fluid saturation, bulk density, and grain density measurements.

Grain Density

The grain density for the Chester 8-16 reef core ranged from 2.68 to 2.82 g/cm^3. The Brown Niagaran had an average grain density of 2.72 g/cm^3. The Gray Niagaran had an average grain density of 2.71 g/cm^3. Table 2-4 summarizes the grain density averages for the Chester 8-16 core and Figure 2-5 shows grain density histograms by formation.

Table 2-4. Core grain density summary.

Interval	Range (g/cm3)	Average (g/cm3)
All Core	2.68-2.82	2.71
Brown Niagaran	2.68-2.82	2.72
Gray Niagaran	2.70-2.74	2.71

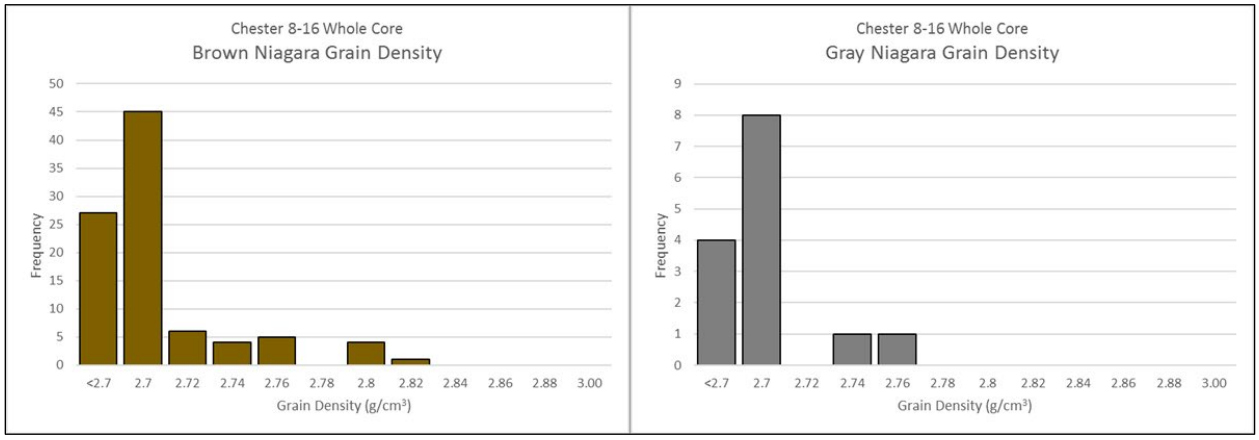


Figure 2-5. Histograms of grain density by formation from the Chester 8-16 conventional core.

Porosity Permeability

The Brown Niagaran had a porosity range from 0.38% to 9.69% with a permeability range from 0.00 to 10.90 mD. The Gray Niagaran had a porosity range from 0.00% to 0.90% with a permeability range from .00 to 0.06 mD. Three points were removed due to anomalously high values for porosity and/or permeability. The Brown Niagaran core plug sampled from 6,204.5 ft. MD contained multiple large vugs, yielding a porosity of 9.69% and permeability of 0.379 mD. The Gray Niagaran core plug sampled from 6,356.5 ft.MD was fractured or chipped and Core Lab indicated that permeability and/or porosity from this sample may be too high. The measurements from this sample indicated a porosity of 0.46% and a permeability of 0.063 mD.

This data has been summarized in Table 2-5 and plotted in Figure 2-6 with the coordinating transform equations in equation 4.

$$K = 0.2239e^{0.3387\Phi} \quad \text{(Equation 4)}$$

Where K represents the permeability in mD and ϕ is the porosity in percent.

Table 2-5. Summary of porosity and permeability data from whole core at Chester 8-16.

Formation	Porosity (%)		Porosity (%)	Permeability (mD)		Permeability (mD)
	Min	Max	Average	Min	Max	Average
Brown Niagaran	0.38	9.69	1.15	0.00	10.90	0.16
Gray Niagaran	0.00	0.90	0.68	0.00	0.06	0.01

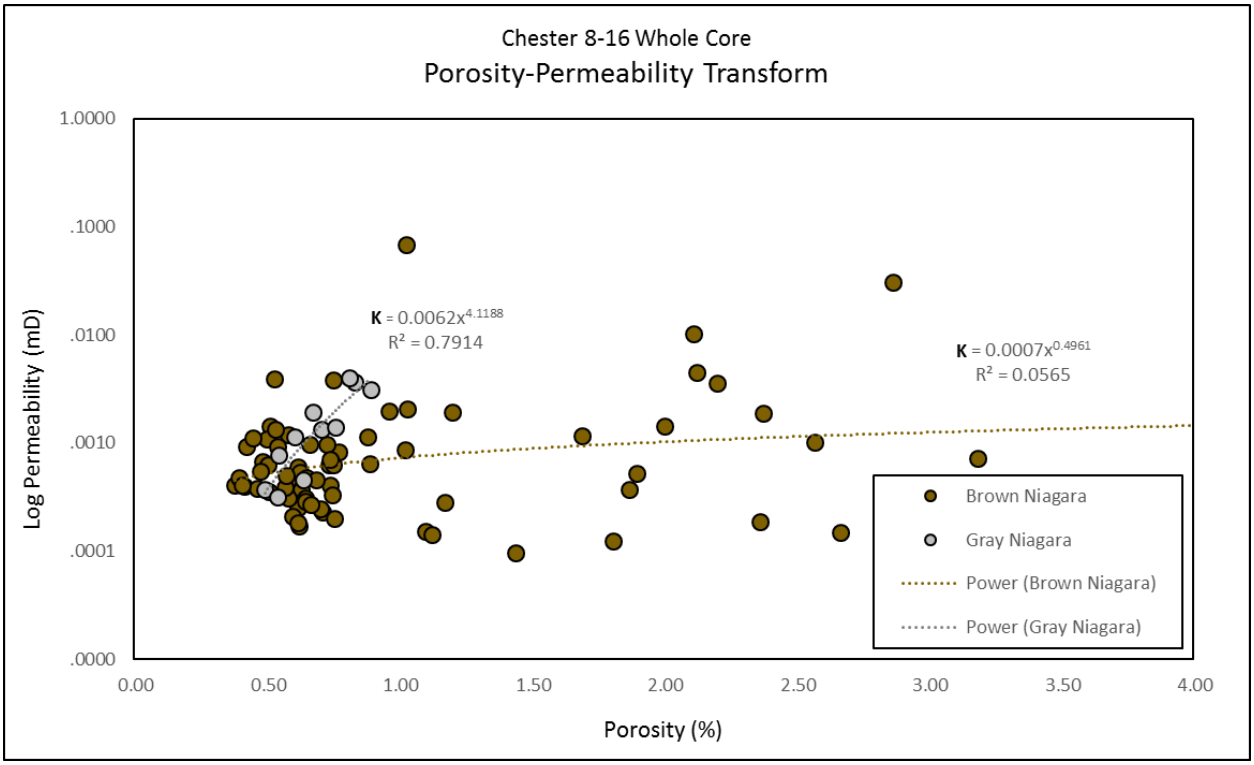


Figure 2-6. Porosity-permeability transform for the Brown Niagaran and Gray Niagaran from whole core measurements at Chester 8-16.

2.2.2 Routine Sidewall Core Analysis

Routine core analysis was conducted on 1.5 in. diameter sidewall core samples. These analyses were conducted by Core Lab in Houston, TX, following CMS-300 conventional plug analysis protocol. Standard core analysis included porosity, permeability, fluid saturation, bulk density, and grain density measurements.

Grain Density

The grain density for the Dover Chester 8-16 reef sidewall core ranged from 2.70 to 2.91 g/cm^3 with an average of 2.78 g/cm^3. The A-2 Carbonate had an average grain density of 2.82 g/cm^3. The A-2 Evaporite had an average grain density of 2.86 g/cm^3. The A-1 Carbonate had an average grain density of 2.80 g/cm^3. The Brown Niagaran had an average grain density of 2.71 g/cm^3. Table 2-6 summarizes the grain density averages for the Chester 8-16 sidewall core and Figure 2-7 shows grain density histograms for all of Chester 8-16 sidewall core and by formation.

Table 2-6. RSWC grain density summary by formation.

Interval	Range (g/cm^3)	Average (g/cm^3)
All Core	2.70-2.91	2.78
A-2 Carbonate	2.73-2.91	2.82
A-2 Evaporite	2.81-2.90	2.86
A-1 Carbonate	2.72-2.87	2.80
Brown Niagaran	2.70-2.79	2.71

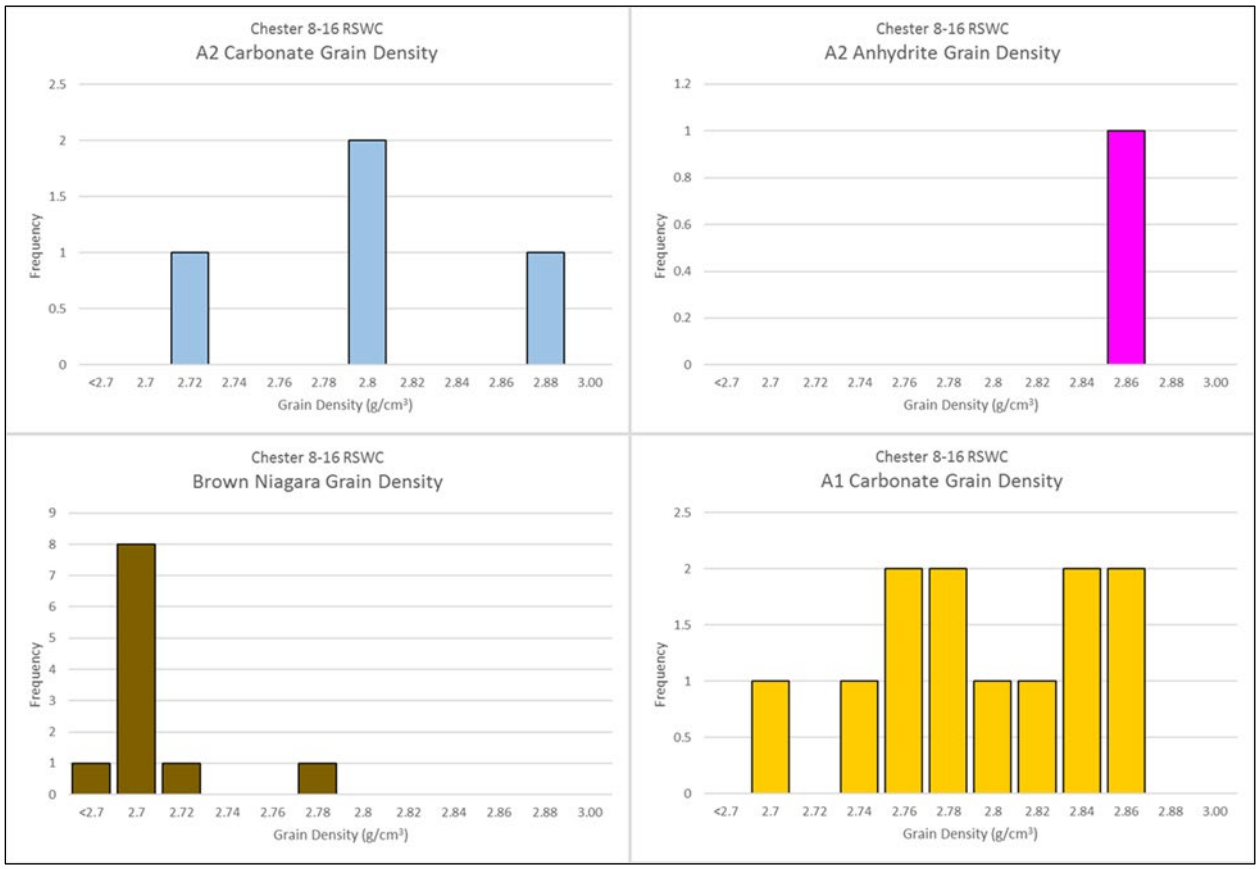


Figure 2-7. Histograms of grain density by formation from the Chester 8-16 RSWCs.

Porosity Permeability

The A-2 Carbonate had a porosity range from 0.21% to 0.62% with a permeability range from 0.00 to 0.13 mD. The A-2 Evaporite had a porosity range from 0.16% to 0.29%. The A-1 Carbonate had a porosity range from 4.72% to 18.18% with a permeability range from 0.01 to 7.87 mD. The Brown Niagaran had a porosity range from 0.47% to 8.62% with a permeability range from 0.00 to 0.02 mD. This data has been summarized in Table 2-7 and plotted in Figure 2-8 with the coordinating transform equations in equation 5.

$$K = 0.2239e^{0.3387\Phi} \quad \text{(Equation 5)}$$

Where K represents the permeability in mD of the and ϕ is the porosity in percent.

Table 2-7. Summary of RSWC porosity and permeability data.

Formation	Porosity (%)			Permeability (mD)		
	Min	Max	Average	Min	Max	Average
A-2 Carbonate	0.21	0.62	0.41	0.00	0.13	0.04
A-2 Evaporite	0.16	0.29	0.24	0.00	0.00	0.00
A-1 Carbonate	4.72	18.18	11.04	0.01	39.65	7.87
Brown Niagaran	0.47	8.62	3.19	0.00	0.14	0.02

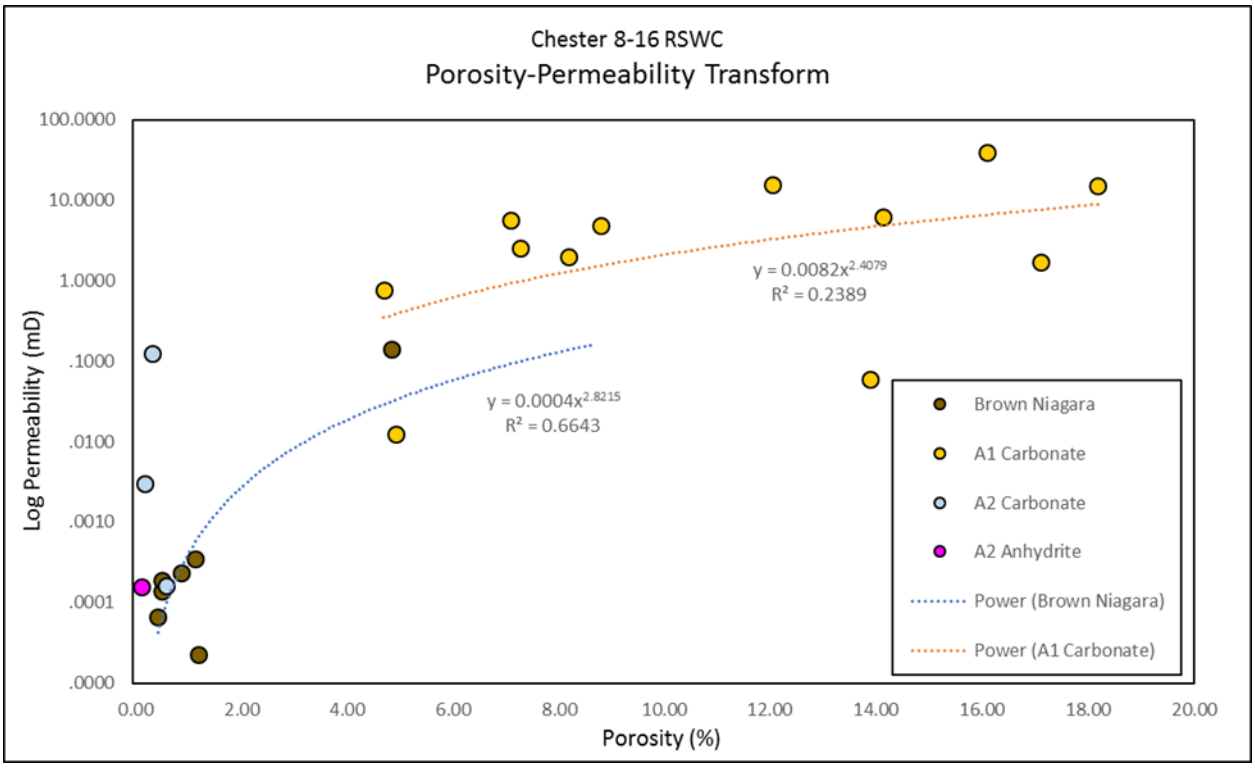


Figure 2-8. Porosity-permeability transform for the A-2 Carbonate (light blue circle), A-2 Evaporite (magenta circle), A-1 Carbonate (yellow circle), and Brown Niagaran (brown circle) from RSWC measurements.

2.3 Formation Evaluation

2.3.1 A-2 Carbonate and A-2 Evaporite

Wireline Log Analysis and Petrophysical Calculations

The A-2 Carbonate was 70 ft. thick in the Chester 8-16 well. The average porosity ranged from 0 to 5.7% with an average of 2% (Figure 2-9). The cross-plot porosity was mostly below 5% with an interval 5 ft. thick of greater than 5% (Figure 2-10). This occurred where the gamma ray was slightly higher and was a carbonate shale (Figure 2-11). The porosity over this interval was representative of microporosity. Overall, the A-2 Carbonate was a tight dolomite with an interval of carbonate shale/mudstone.

Basic petrophysical calculations were computed for the A-2 Carbonate using a porosity cutoff of 5% (scenario 1), and a combined cutoff of 5% porosity and 40% water saturation (scenario 2). Both calculations used a gamma ray cutoff of 75 API to eliminate traditional shales. The results for both scenarios yielded the same results; the net thickness was 5.2 ft. with a resulting net to gross ratio of 0.08, and the porosity-ft. was 0.29 %-ft. The petrophysical calculations showed the A-2 Carbonate to have no reservoir potential and desired values for a confining zone.

The A-2 Evaporite, or A-2 Anhydrite, was 38 ft. thick in Chester 8-16. Porosity was not observed in this formation and the bulk density remained high (Figure 2-12). There was one interval mid-formation where the bulk density shifted towards dolomite (5820-5830 ft.). The cross-plot porosity was also at zero with all data points falling into the anhydrite zone and tight dolomite. The water saturation was high over this interval, averaging near 57% due to the presence of anhydrite. The middle interval had a lower water saturation where the formation became more dolomitic. The net thickness was 0 ft with a resulting net to gross of 0 and porosity ft. of 0. Overall, the A-2 Evaporite was mostly anhydrite with no porosity, suggesting a sufficient confining unit.

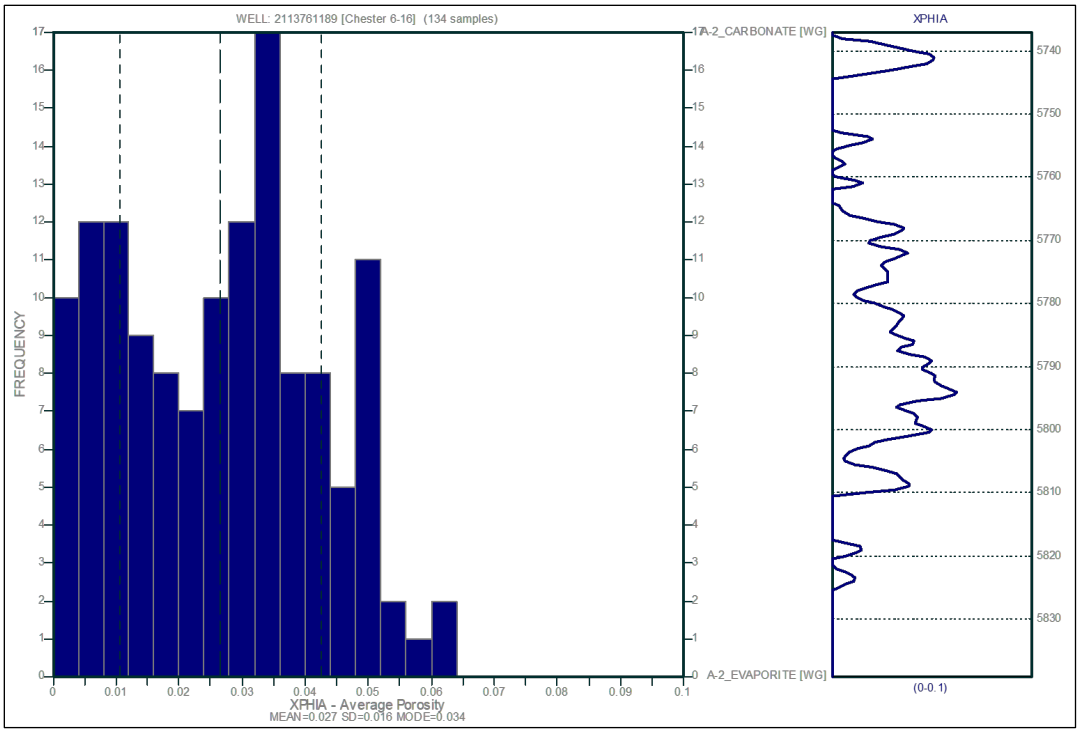


Figure 2-9. Average porosity histogram of the A-2 Carbonate in Chester 8-16 showing a low average porosity of 2% with the highest porosities over the carbonate shale/mudstone interval mid-formation.

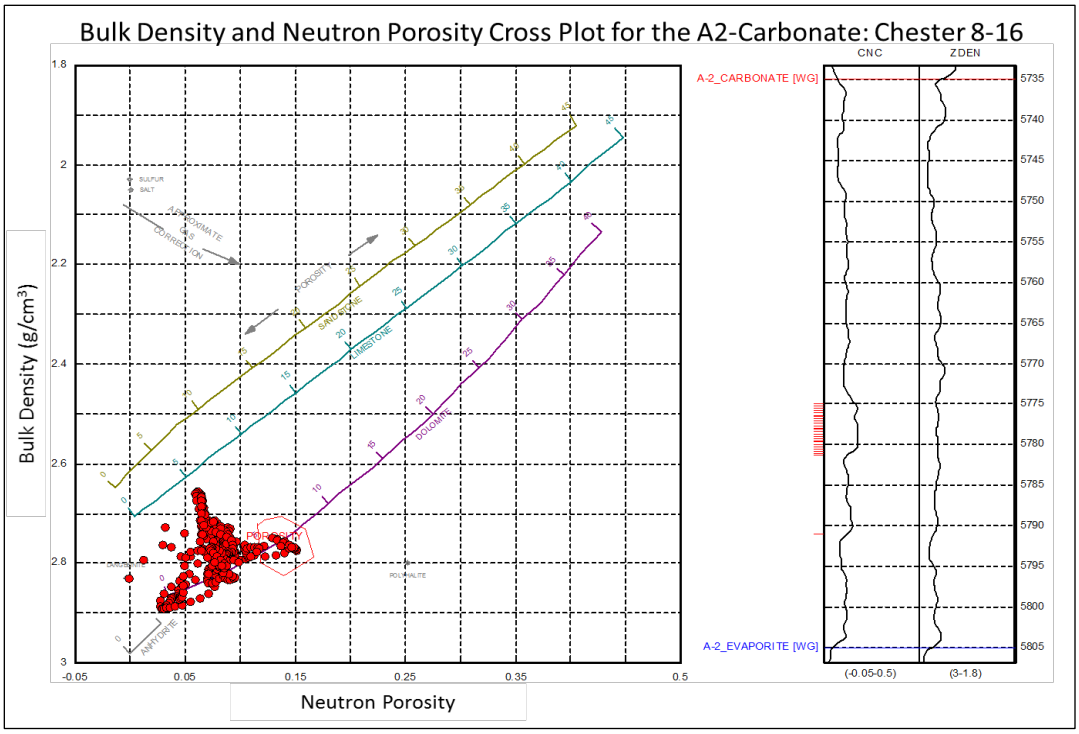


Figure 2-10. Neutron porosity-bulk density cross plot of the A-2 Carbonate in Chester 8-16 showing tight dolomite with a thin interval of porosity greater than 5% (red).

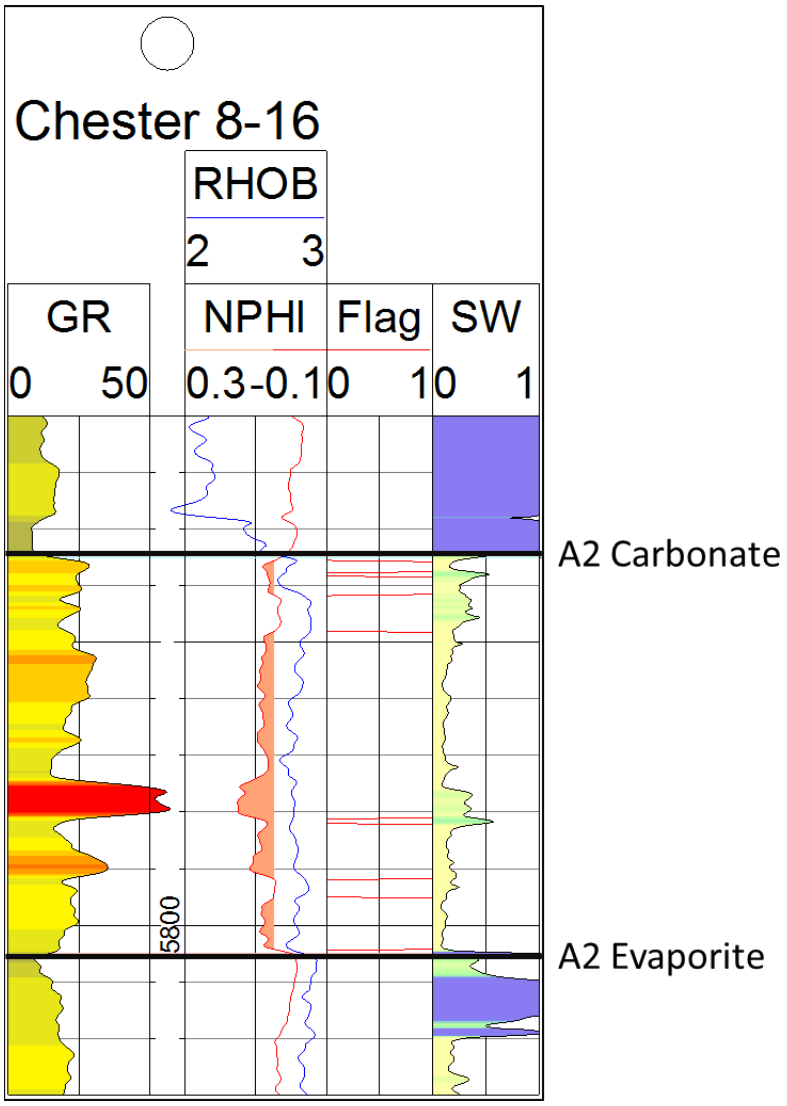


Figure 2-11. Single well cross section of the A-2 Carbonate in Chester 8-16 showing relatively low porosity, low water saturation, and a high gamma interval mid formation indicative of a carbonate shale/mudstone.

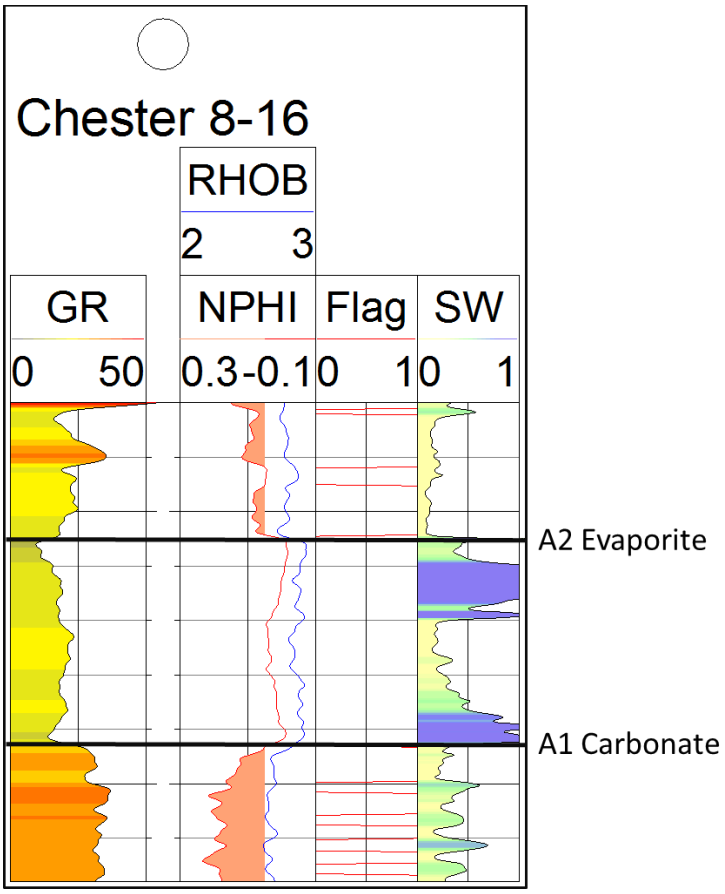


Figure 2-12. Single well cross section of the A-2 Evaporite in Chester 8-16 well showing low porosity throughout with changes in bulk density and water saturation when the rock changes from anhydrite (top and bottom) to more dolomitic (middle).

Core Analysis

Conventional core samples were not recovered for the A-2 Carbonate or A-2 Evaporite in Chester 8-16. RSWC samples however were recovered for both formations.

RSWC photos of the A-2 Carbonate in Chester 8-16 show a carbonate with alternating dark gray and light gray laminations. Mud-filled vugs and fractures are present as well as open fractures. UV light shows minor oil staining. Figure 2-13 and Figure 2-14 display examples of RSWC sample descriptions of the A-2 Carbonate.

RSWC photos of the A-2 Evaporite in Chester 8-16 show a predominantly anhydrite and carbonate matrix. UV light images show minor residual oil staining and areas of possible mud. Filled fractures and small vugs are observed throughout. An example of RSWC samples descriptions from the A-2 Evaporite is displayed in Figure 2-15.

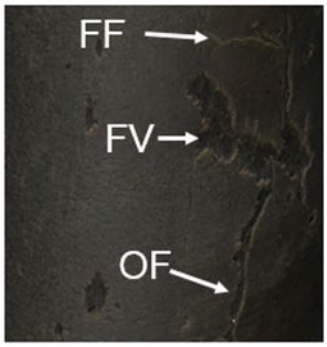
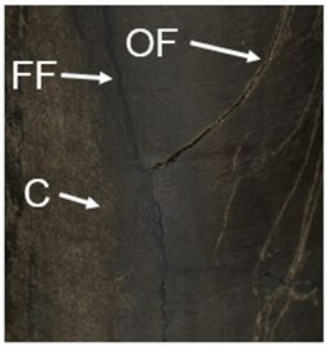
Depth Ft.	White Light Primary Features	UV Light Primary Features	Descriptions
5,760			White Light: Carbonate, mud filled vugs, filled fractures, open fractures. UV Light: Carbonate.
5,760.5			White Light: Carbonate, mud filled vugs, filled fractures, open fractures. UV Light: Carbonate.

Figure 2-13. Annotated RSWC images with corresponding core descriptions of the A-2 Carbonate for depths 5,760 ft. to 5,761 ft.

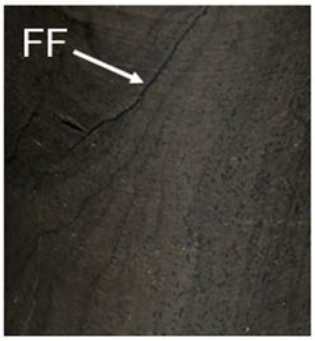
Depth Ft.	White Light Primary Features	UV Light Primary Features	Descriptions
5,761			White Light: Carbonate, filled fractures, alternating dark gray and light gray laminations, opaque mineral crystals. UV Light: Carbonate.
5,778			White Light: Carbonate, alternating dark gray and light gray laminations. UV Light: Carbonate.

Figure 2-14. Annotated RSWC images with corresponding core descriptions of the A-2 Carbonate for depths 5,761 ft. and 5,778 ft.

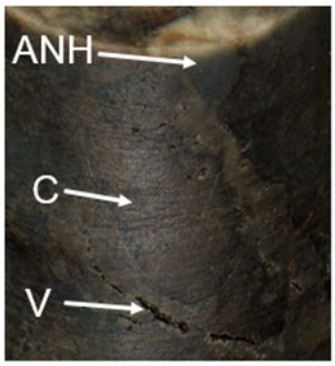
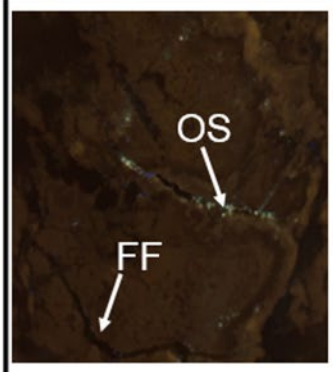
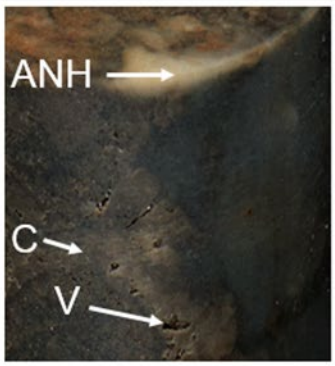
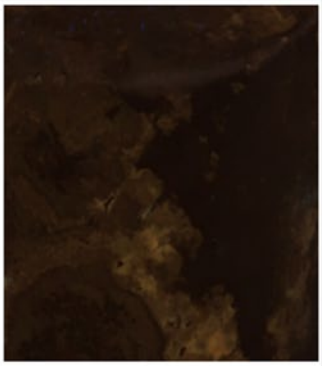
Depth Ft.	White Light Primary Features	UV Light Primary Features	Descriptions
5,819			White Light: Anhydrite and carbonate matrix, filled fractures, small vugs. UV Light: Light blue UV response due to potential residual oil.
5,819.5			White Light: Anhydrite and carbonate matrix, small vugs. UV Light: Anhydrite and carbonate matrix, dark areas are possible muds.

Figure 2-15. Annotated RSWC images with corresponding core descriptions of the A-2 Evaporite for depths 5,819 ft. to 5,820 ft.

Elemental Spectroscopy Log Analysis

Based on elemental spectroscopy logs, the A-2 Carbonate is a mineralogically diverse admixture of limestone, dolostone and evaporite minerals with isolated peaks of K, Al, and S that occurs between 5,735'MD/5,636'TVD and 5,805'MD/5,706'TVD (Figure 2-16). This unit is overlain by salt, causing hole enlargement by washout with drilling mud as circled in red. The two major K peaks at 5,776 and 5,788 coincide with Al enrichment, translating into a bulk volume increase in clay minerals. Examination of WL and UV light photographs of a RSWC sample collected from 5,778'MD reveals fine laminations of clay minerals and carbonates. Similarly, peaks in S curves paired with high Ca levels indicate the presence of anhydrite, CaSO4.

The A-2 Evaporite Formation, consisting largely of salt and limestone from 5,805'MD/5,706'TVD to 5,843'MD/5,744'TVD contains more anhydrite relative to the A-2 Carbonate and has far less dolomite.

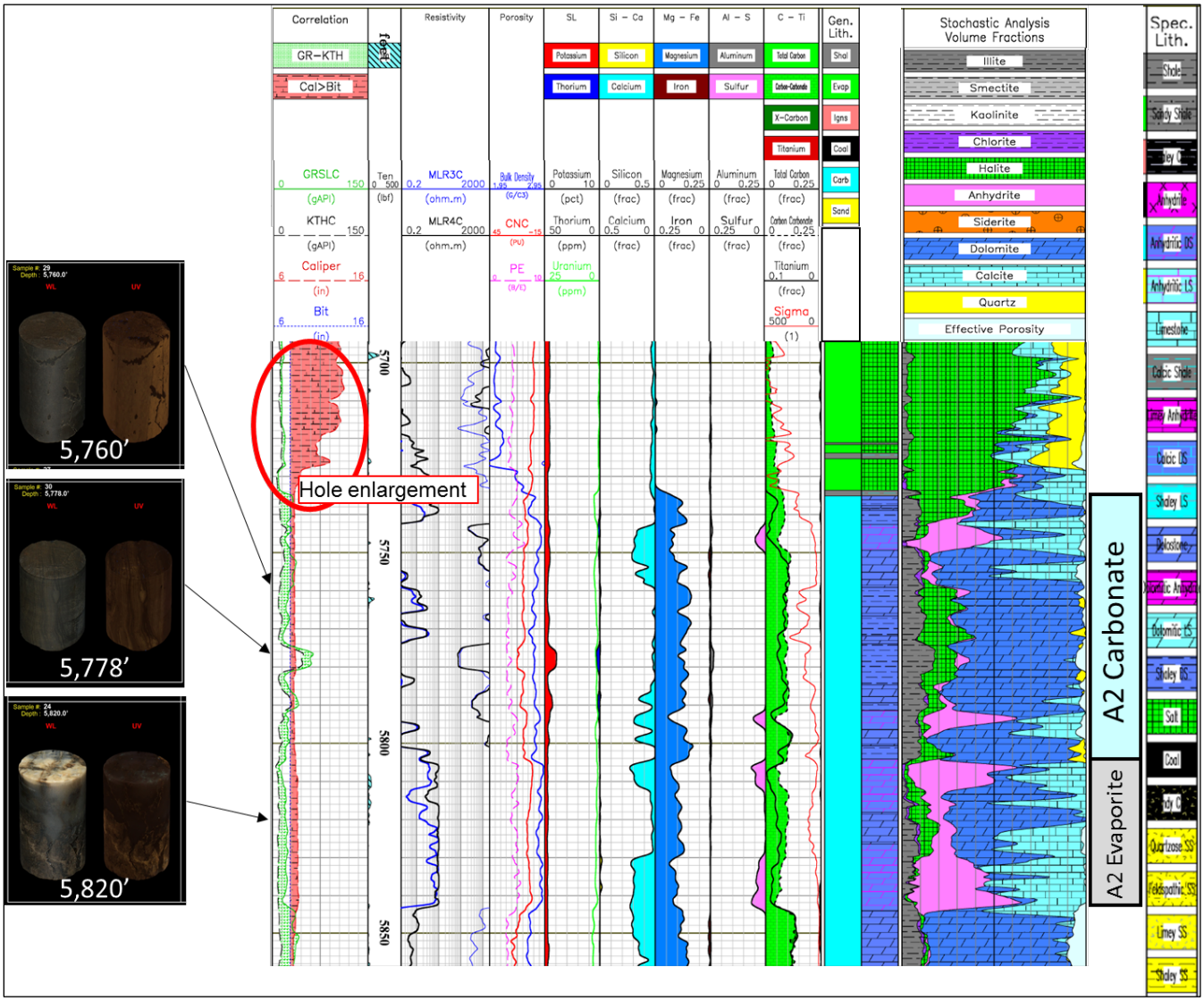


Figure 2-16. FLeX log from Chester 8-16 displaying the A-2 Carbonate and A-2 Evaporite Formations from 5,735'MD/5,636'TVD to 5,843'MD/5,744'TVD. Select RSWC samples are shown in both WL and UV light to provide context for lithologic descriptions. Core photos by Core Laboratories.

Image Log Analysis

The A-2 Carbonate exhibits stratigraphic beds with dips ranging from 5^0 to 23^0 that average 10^0 and deviate from the mean by about 4^0. There are no fractures or significant porosity shows within the A-2 carbonate present in the image log profile.

The A-2 Evaporite exhibits no stratigraphic features, structural features, or porosity shows within the image log profile.

2.3.2 A-1 Carbonate

Wireline Log Analysis and Petrophysical Calculations

The A-1 Carbonate is 73 ft. thick in Chester 8-16. The average porosity ranged from 0 to 26.4% with an average of 12.5% (Figure 2-17). The lower section of the formation had a lower porosity than the middle to upper intervals. The cross-plot porosity was mostly above 5% with thin intervals less than 5% (Figure 2-18). The water saturation varied throughout with an average of 31% (Figure 2-19). Overall, the A-1 Carbonate plotted as a porous dolomite.

Basic petrophysical calculations were computed for the A-1 Carbonate using a porosity cutoff of 5% (scenario 1), and a combined cutoff of 5% porosity and 40% water saturation (scenario 2). Both calculations used a gamma ray cutoff of 75 API to eliminate traditional shales. The net thickness for scenario 1 was 70 ft. with a resulting net to gross ratio of 0.96 and a porosity footage of 9.1 %-ft. The inclusion of the water saturation cutoff (scenario 2) decreased the net thickness to 50 ft. with a net to gross ratio of 0.69 and a porosity footage of 6.8 %-ft. The A-1 Carbonate showed great reservoir potential due to a thick zone of high porosity and low water saturation values.

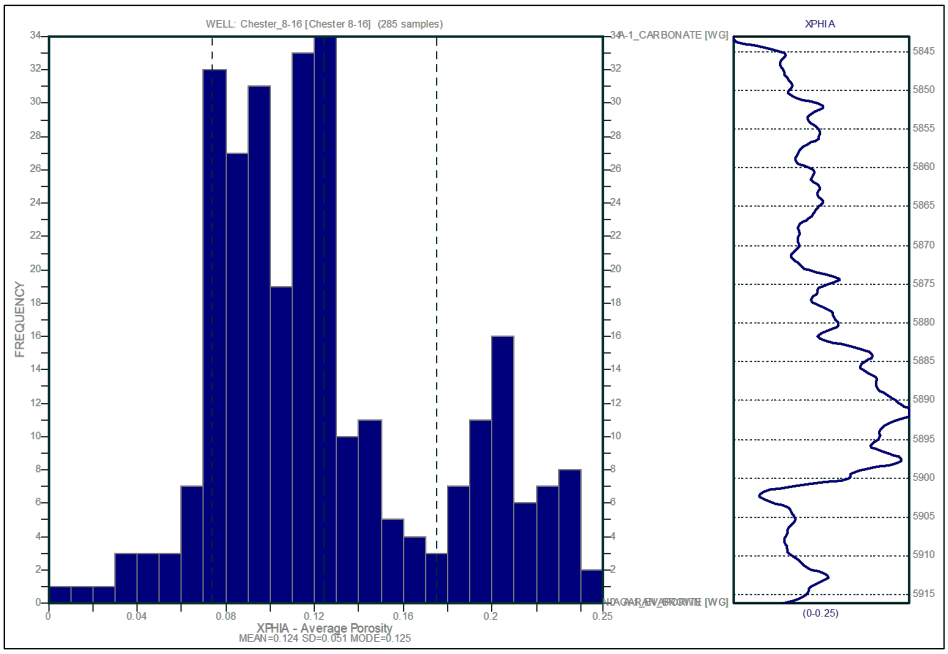


Figure 2-17. Average porosity histogram of the A-1 Carbonate for the Chester 8-16 well showing high porosities throughout with an average of 12.5%.

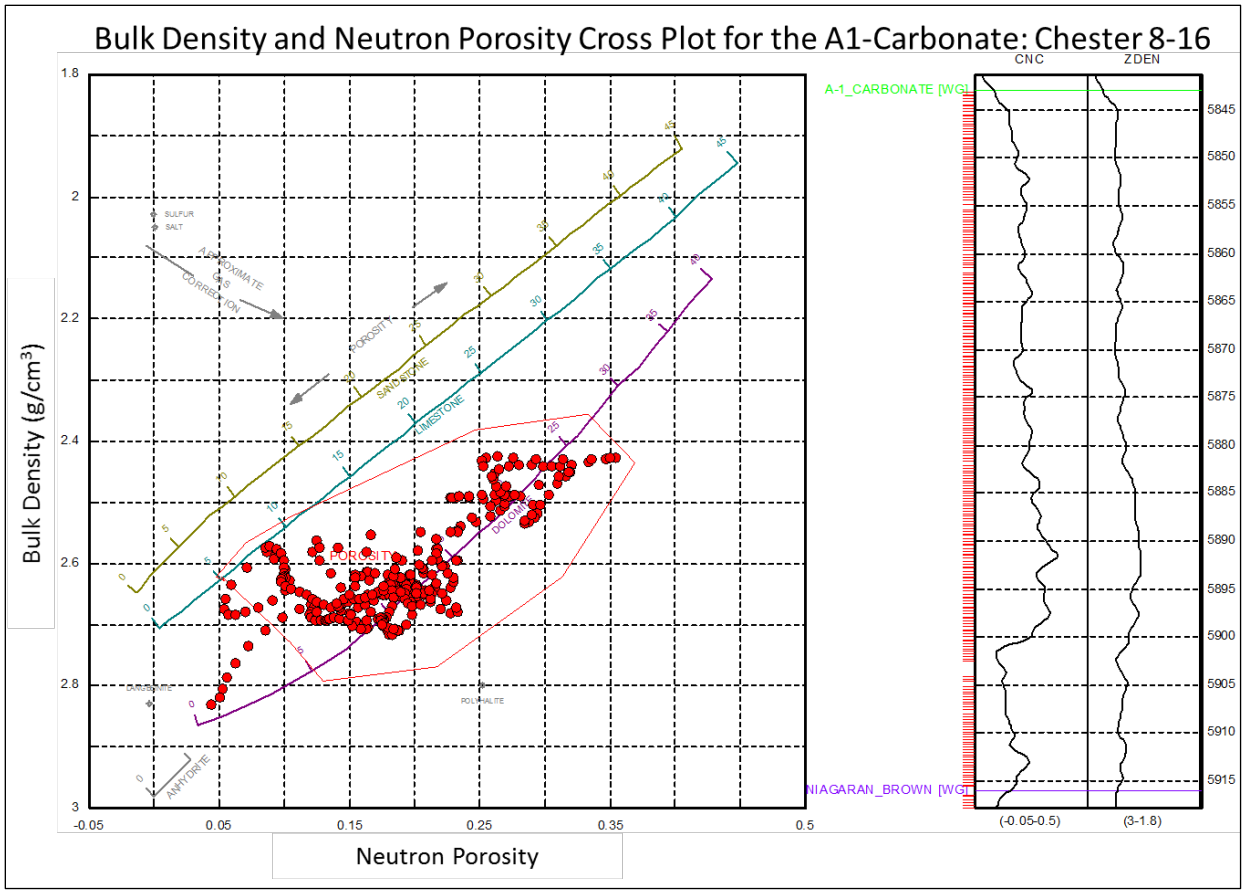


Figure 2-18. Neutron porosity-bulk density cross plot of the A-1 Carbonate for the Chester 8-16 well showing mostly high porosity dolomite (red) and thin intervals of porosity less than 5%.

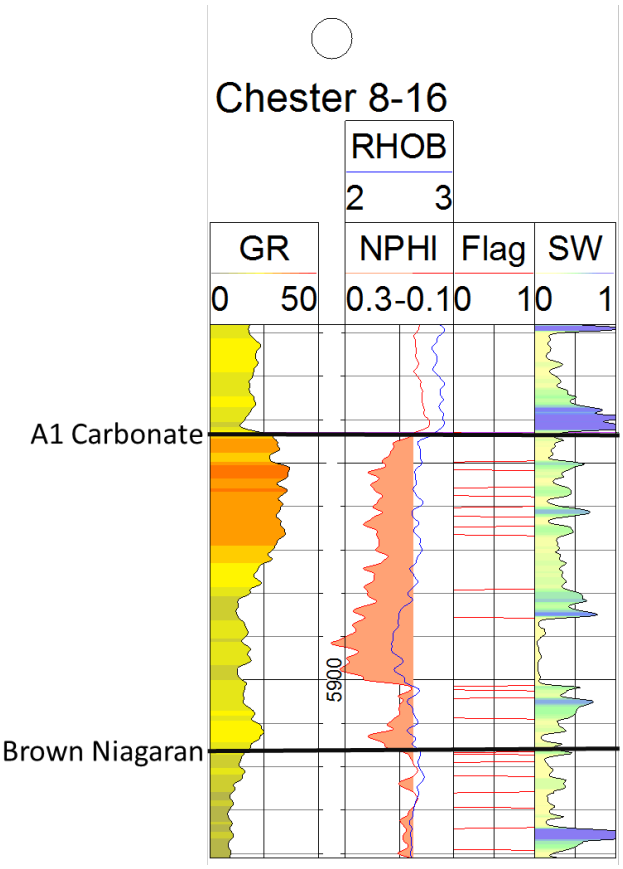


Figure 2-19. Single well cross section of the A-1 Carbonate for the Chester 8-16 well showing high porosities (orange shade) throughout with low water saturations.

Core Analysis

Conventional core samples were not recovered for the A-1 Carbonate Formation in Chester 8-16. However, RSWC samples were recovered and photographed for sample descriptions.

RSWC core photos of the A-1 Carbonate at Chester 8-16 show a predominantly gray carbonate with minor anhydrite matrix. UV light images show potential residual oil throughout the core samples. The core sample collected at 5,820 ft. shows an anhydrite matrix with carbonate mud in both white and UV light. Small vugs observed throughout. An example of RSWC samples descriptions from the A-1 Carbonate is displayed in Figure 2-20.

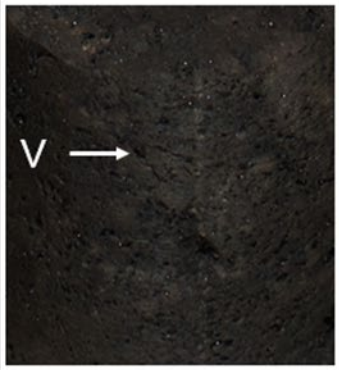
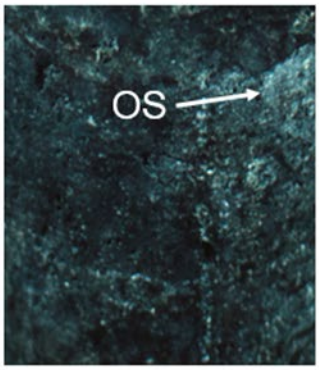
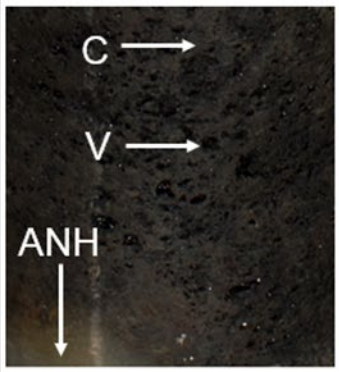
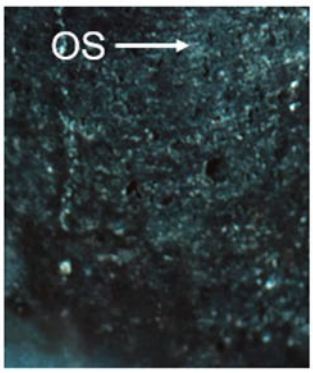
Depth Ft.	White Light Primary Features	UV Light Primary Features	Descriptions
5,890			White Light: Gray carbonate, small vugs. UV Light: Strong light blue UV response due to potential residual oil throughout sample.
5,893			White Light: Gray carbonate, some anhydrite, small vugs. UV Light: Strong light blue UV response due to potential residual oil throughout sample.

Figure 2-20. Annotated RSWC images with corresponding core descriptions of the A-1 Carbonate for depths 5890 ft. to 5,893 ft.

Elemental Spectroscopy Log Analysis

The transition into the A-1 Carbonate Formation at 5,843'MD/5,744'TVD to 5,916'MD/5,817'TVD brings a higher level of magnesium relative to calcium, making the carbonate portion of the lithology nearly completely dolomite until 5,900'MD (Figure 2-21). The A-1 Carbonate has relatively high effective porosity, between 10-20% of bulk rock volume, shown in the lightest blue on the first track from the right. One feature of interest is highlighted by orange arrows on Figure 2-21 are dark green peaks in the fourth track from the right, called "X-carbon" or excess carbon. This value corresponds to the amount of carbon detected by the tool that has not been accounted for in the mineralogic components of the bulk rock volume and is used to infer total organic carbon (TOC). The A-1 Carbonate has the highest X-carbon of any reservoirs in this well and suggests that the A-1 Carbonate may have also provided organic source material.

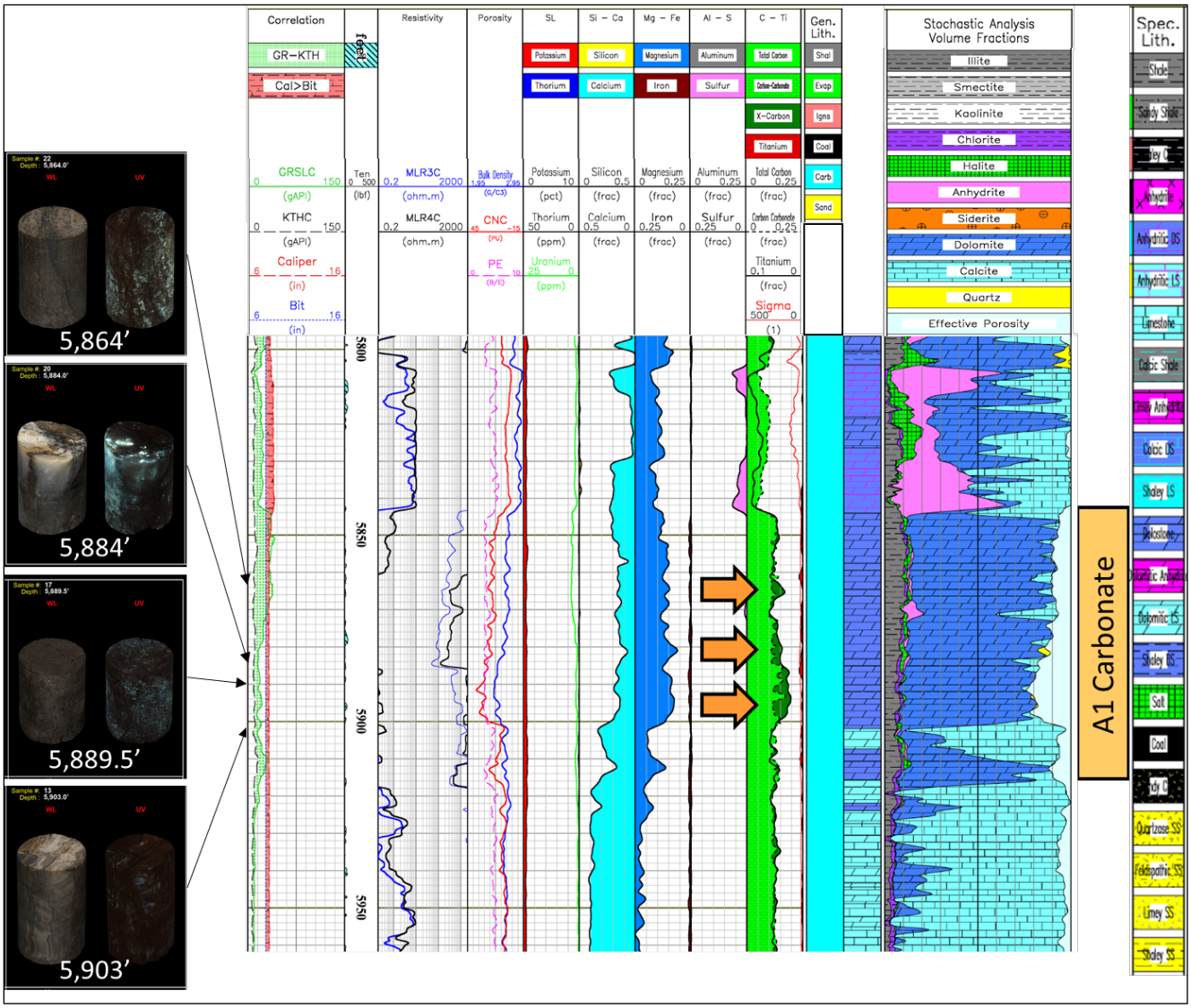


Figure 2-21. Elemental spectroscopy log from Chester 8-16 displaying the A-1 Carbonate from 5,843'MD/5,744'TVD to 5,916'MD/5,817'TVD. Select RSWC samples are shown in both WL and UV to provide context for lithologic descriptions. Core photos by Core Laboratories.

Image Log Analysis

Image log analysis revealed that the A-1 Carbonate can be divided by texture into three zones; the uppermost homogenous zone (Figure 2-22), an interbedded heterogenous zone (Figure 2-23), and a lowermost zone (Figure 2-24) of interbedded heterogenous/homogenously conductive materials occurring in cyclical patterns. The upper most zone exists from 5843’ to 5869’ and is characterized by a homogenously resistive texture with no distinct bedding contacts or features. The intermediate zone, from 5869’ to 5902’, exhibits an interbedded, highly heterogenous resistive/ conductive texture with many conductive features possibly being connected. Bedding within this interval is wavy to planar and is oriented between 142^0 and 301^0 and dips 4^0 to 16^0 NW-SE, however the bedding dip pattern of the interval is complex. Significant porosity zones exist within this texture interval. The third texture zone, from 5902 ft to 5916 ft, shifts to be more homogenous with fewer conductive features. Within the third texture zone, bedding appears to be mostly planar and thickly bedded. Significant amounts of porosity occur within the third texture zone. Stratigraphic bedding dips range from 4^0 to 35^0 with an average dip of 10^0, and a standard deviation of 6^0. The unit is thinly to thickly bedded with generally planar bedding. Some exceptions exist at 5867’ and 5876’ where bedding is wavy. There are no structural features that occur within the A-1 Carbonate interval.

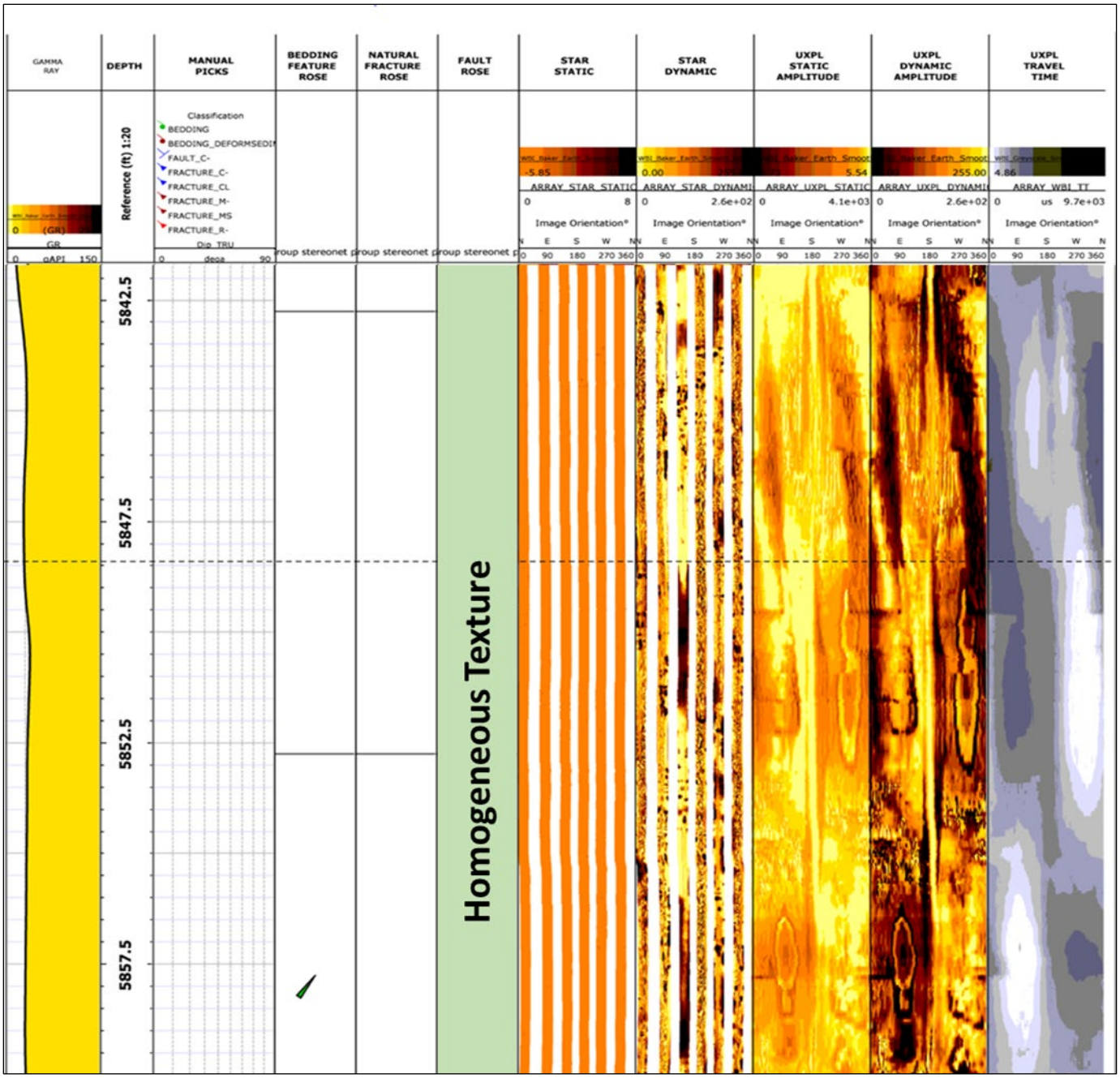


Figure 2-22. Uppermost texture zone within the A-1 Carbonate of the Chester 8-16 well. Texture is homogenously resistive with no signs of porosity development.

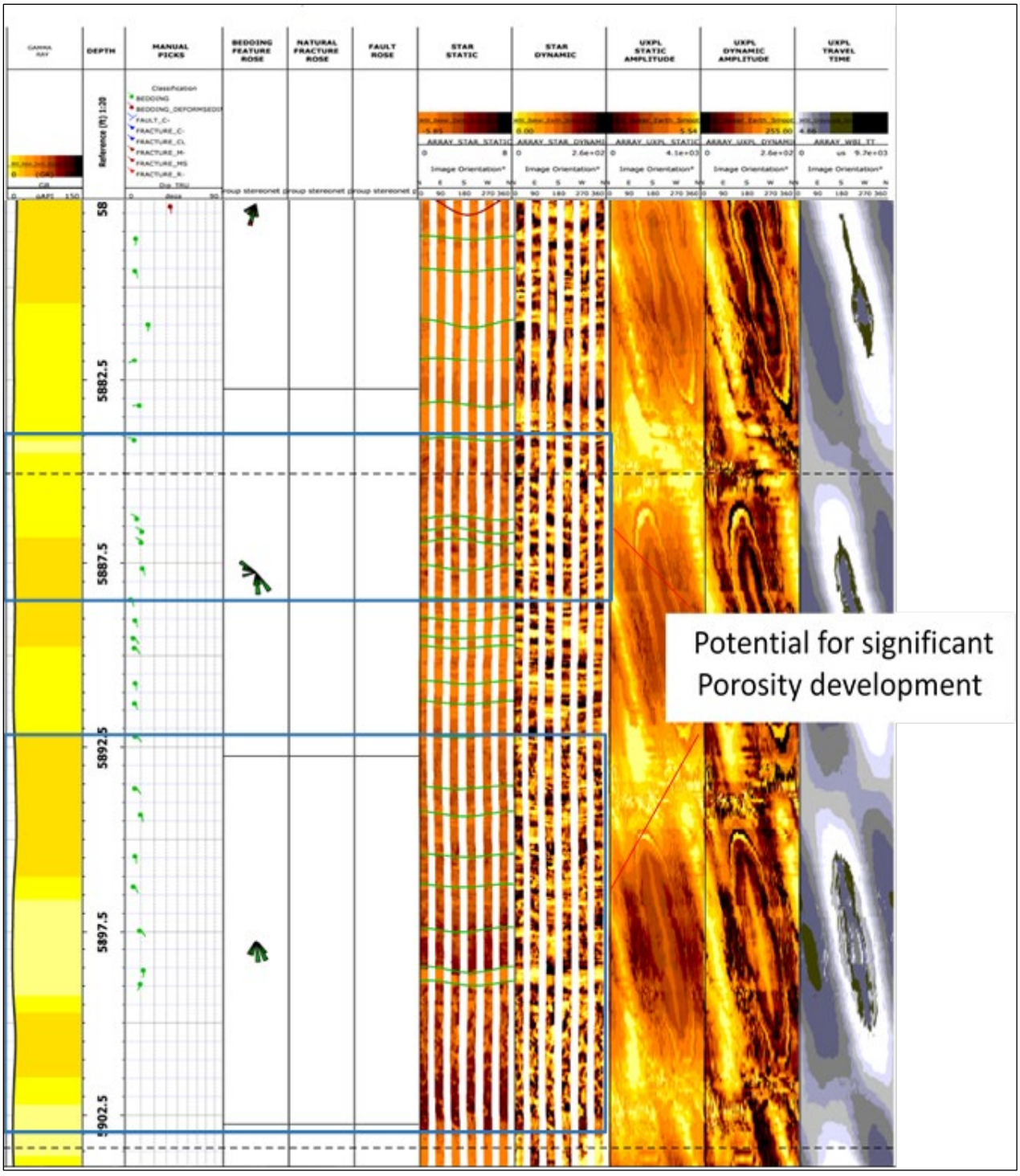


Figure 2-23. Intermediate texture zone of the A-1 Carbonate. The texture is heterogenous with two porosity zones displayed in the figure from 5884'-5888' and 5892'-5903'.

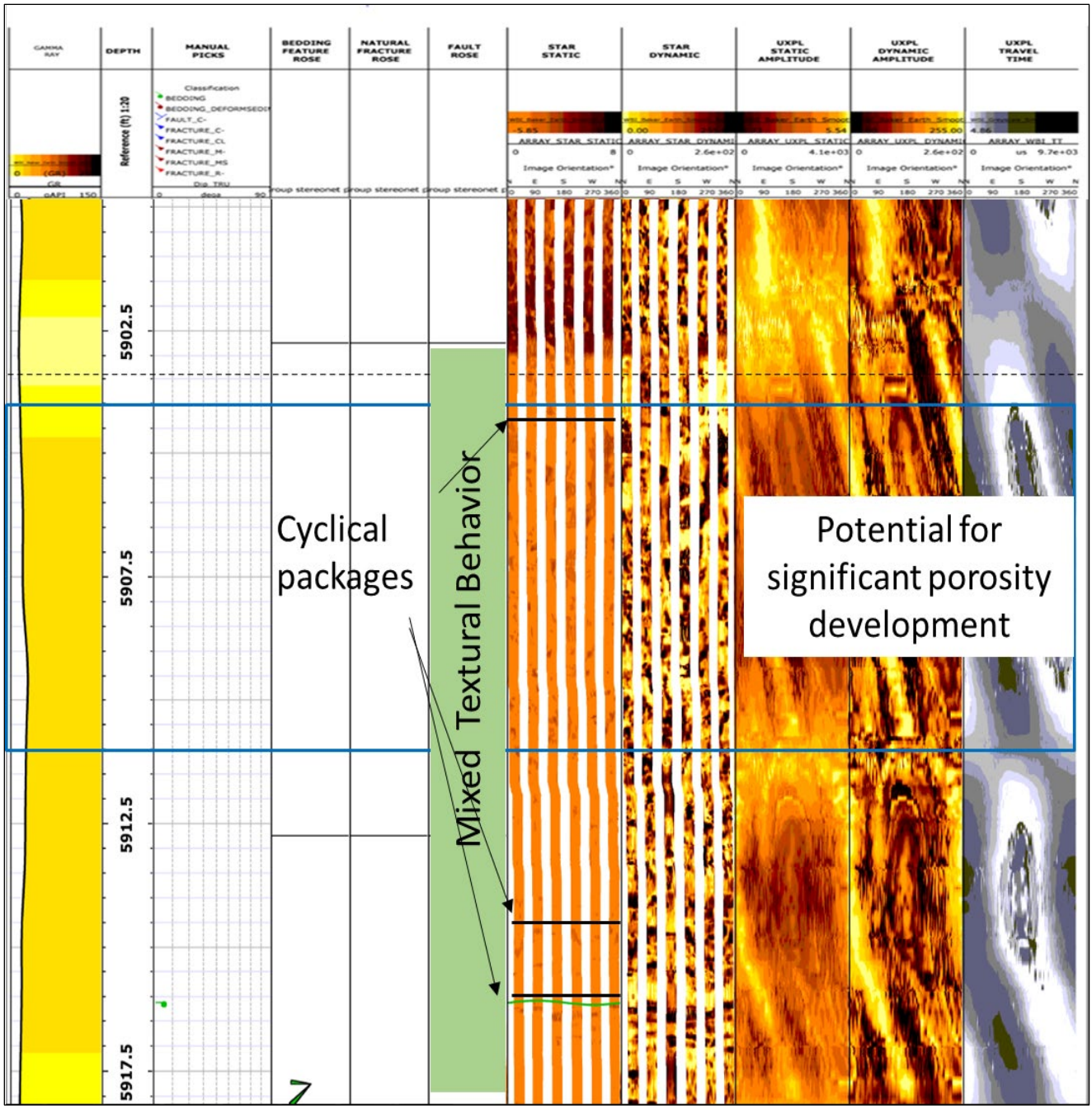


Figure 2-24. Lower most textural zone of the A-1 Carbonate of the Chester 8-16 well.

2.3.3 Brown Niagaran

Wireline Log Analysis and Petrophysical Calculations

The Brown Niagaran is 416 ft. thick in Chester 8-16. The average porosity ranged from 0 to 14.7% with an average of 3.6% (Figure 2-25). The cross-plot porosity was mostly below 5% with thin intervals greater than 5% (Figure 2-26). There was a thin interval (~1-2 ft) in the mid-formation which plotted towards salt and could be a result of salt plugging. The oil water contact (OWC) was identified at 6245 ft. MD where there was a shift in the water saturation towards consistently higher values (Figure 2-27). Overall, the Brown Niagaran is mostly tight limestone with thin (1-2 ft) intervals of high porosity. Only a third of the formation was fully water saturated, leaving the remaining 2/3rds as potential reservoir.

Basic petrophysical calculations were computed for the Brown Niagaran using a porosity cutoff of 5% (scenario 1), and a combined cutoff of 5% porosity and 40% water saturation (scenario 2). Both calculations used a gamma ray cutoff of 75 API to eliminate traditional shales. The net thickness for scenario 1 was 81 ft. with a resulting net to gross ratio of 0.19 and a porosity footage of 5.5 %-ft. The inclusion of the water saturation cutoff (scenario 2) decreased the net thickness to 46 ft. with a net to gross ratio of 0.11 and a porosity footage of 2.8 %-ft. The Brown Niagaran did not show high potential as a reservoir due to thin, intermittent zones of porosity. Results will be compared with advanced logs and sidewall cores to determine the full potential of the formation.

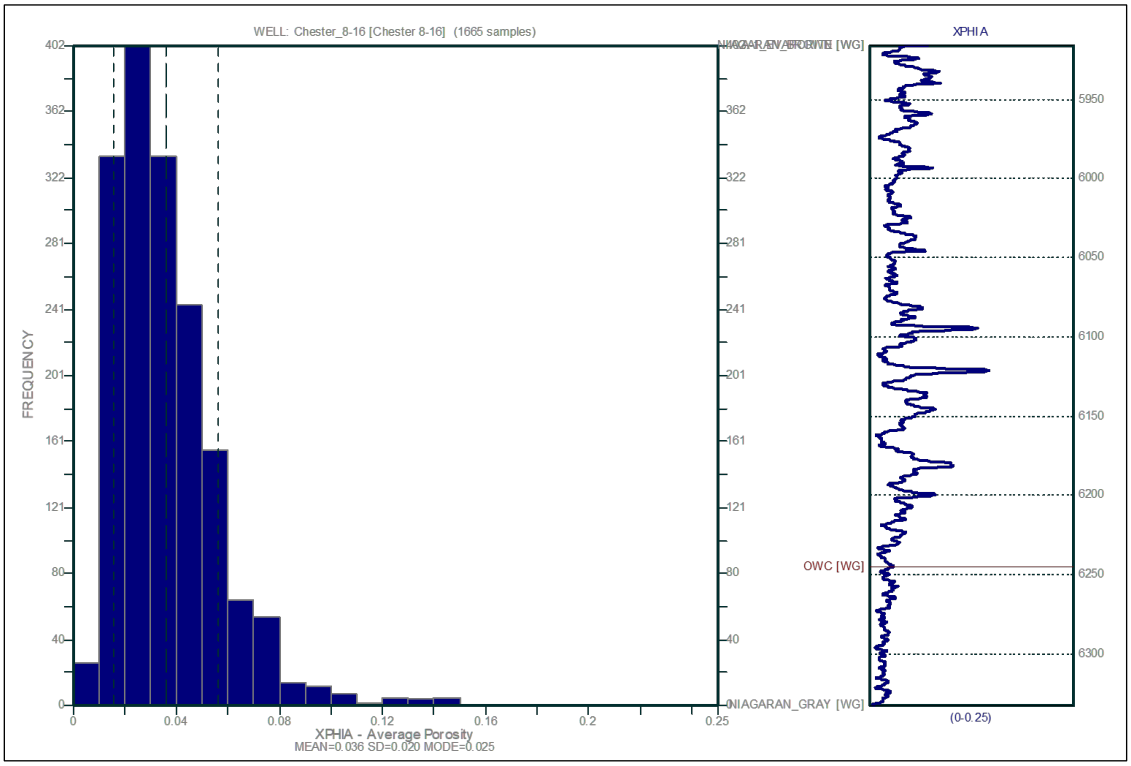


Figure 2-25. Average porosity histogram of the Brown Niagaran for the Chester 8-16 well showing relatively low porosity throughout with an average of 3.6%.

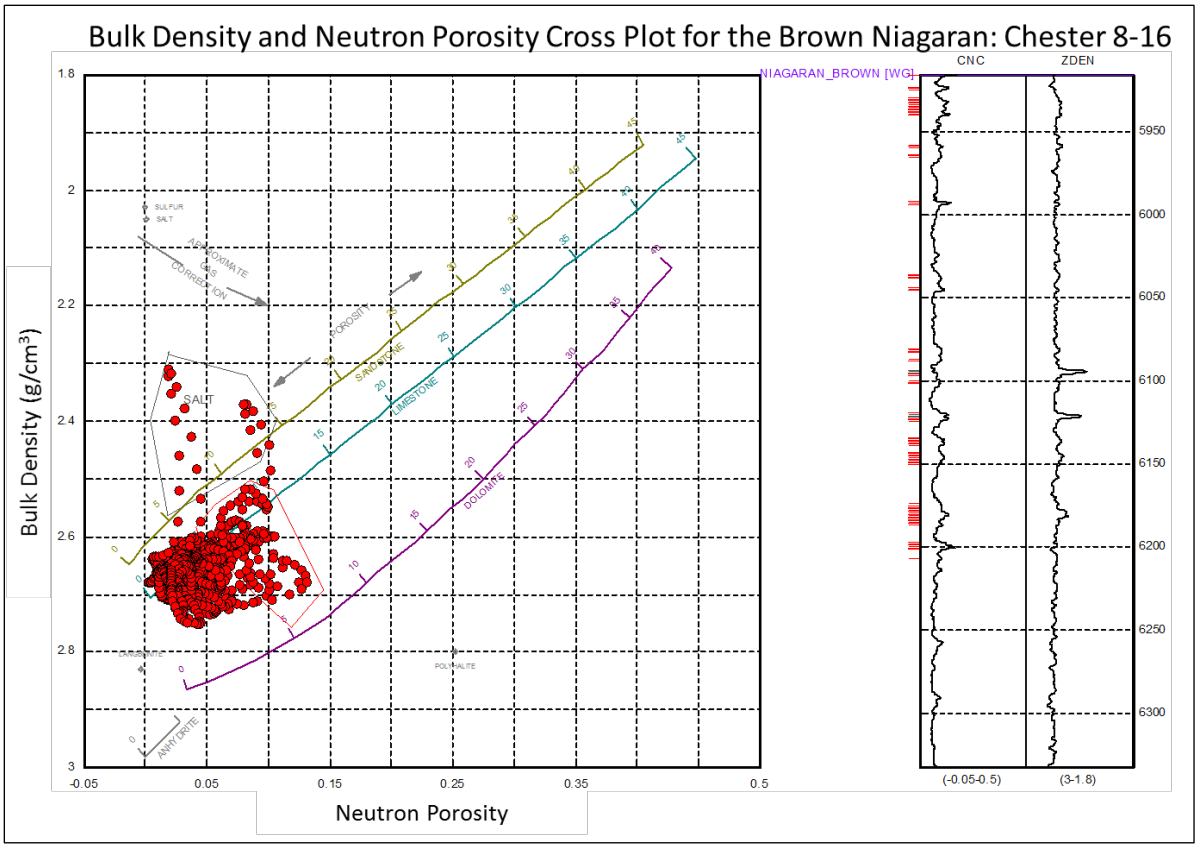


Figure 2-26. Neutron porosity-bulk density cross plot of the Brown Niagaran for the Chester 8-16 well showing mostly tight limestone with thin intervals of high porosity (red).

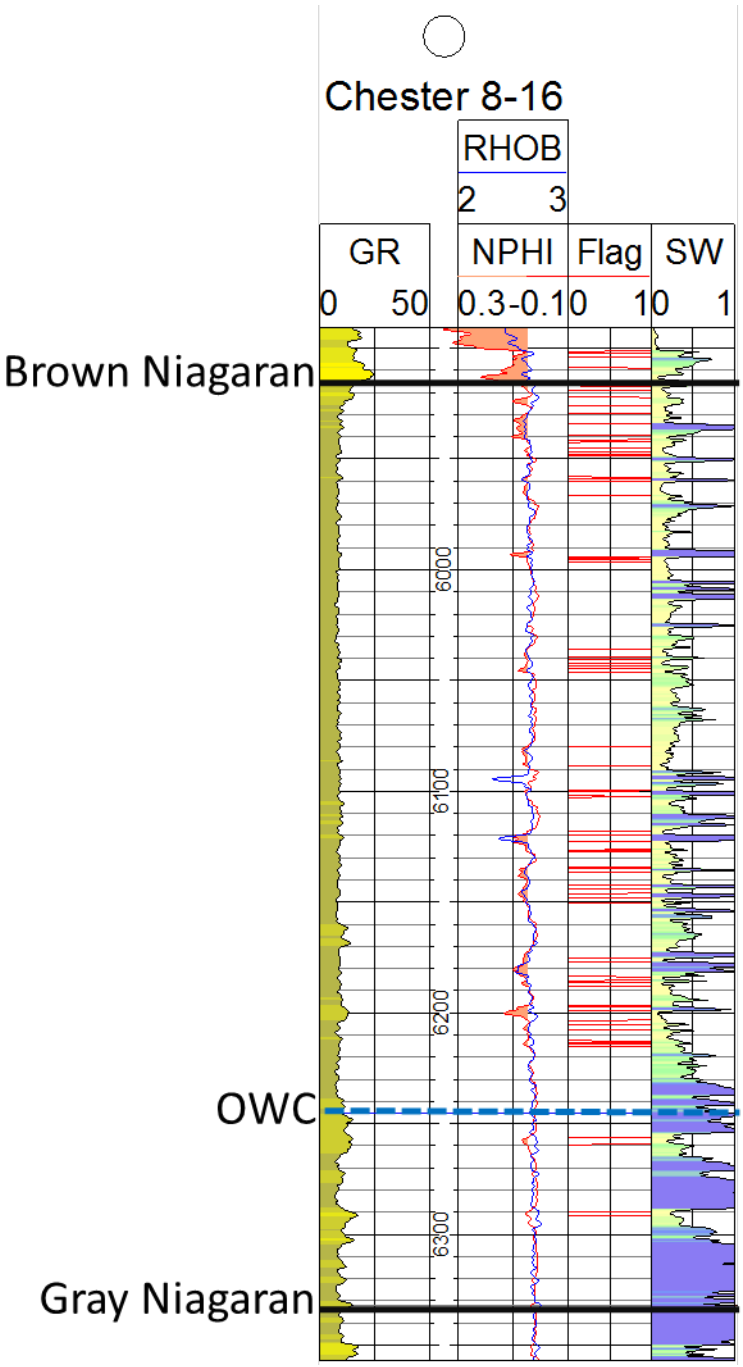


Figure 2-27. Single well cross section of the Brown Niagaran for the Chester 8-16 well showing thin intervals of porosity (red flags) and an increase in water saturation at the OWC.

Core Analysis

The Brown Niagaran Formation at Chester 8-16 is mostly composed of tight dolomitic limestone with thin intervals of dolomite. Features such as vugs and fractures result in a heterogeneous reservoir containing isolated zones of high porosity and permeability. Stylolites and bioclastic debris were observed throughout. Oil shows and salt-filled fractures and vugs observed in the UV light images. Significant moldic porosity observed throughout most of the relatively continuous core. Examples of core descriptions completed for the Brown Niagaran Formation in Chester 8-16 are seen in Figure 2-28 and Figure 2-29.

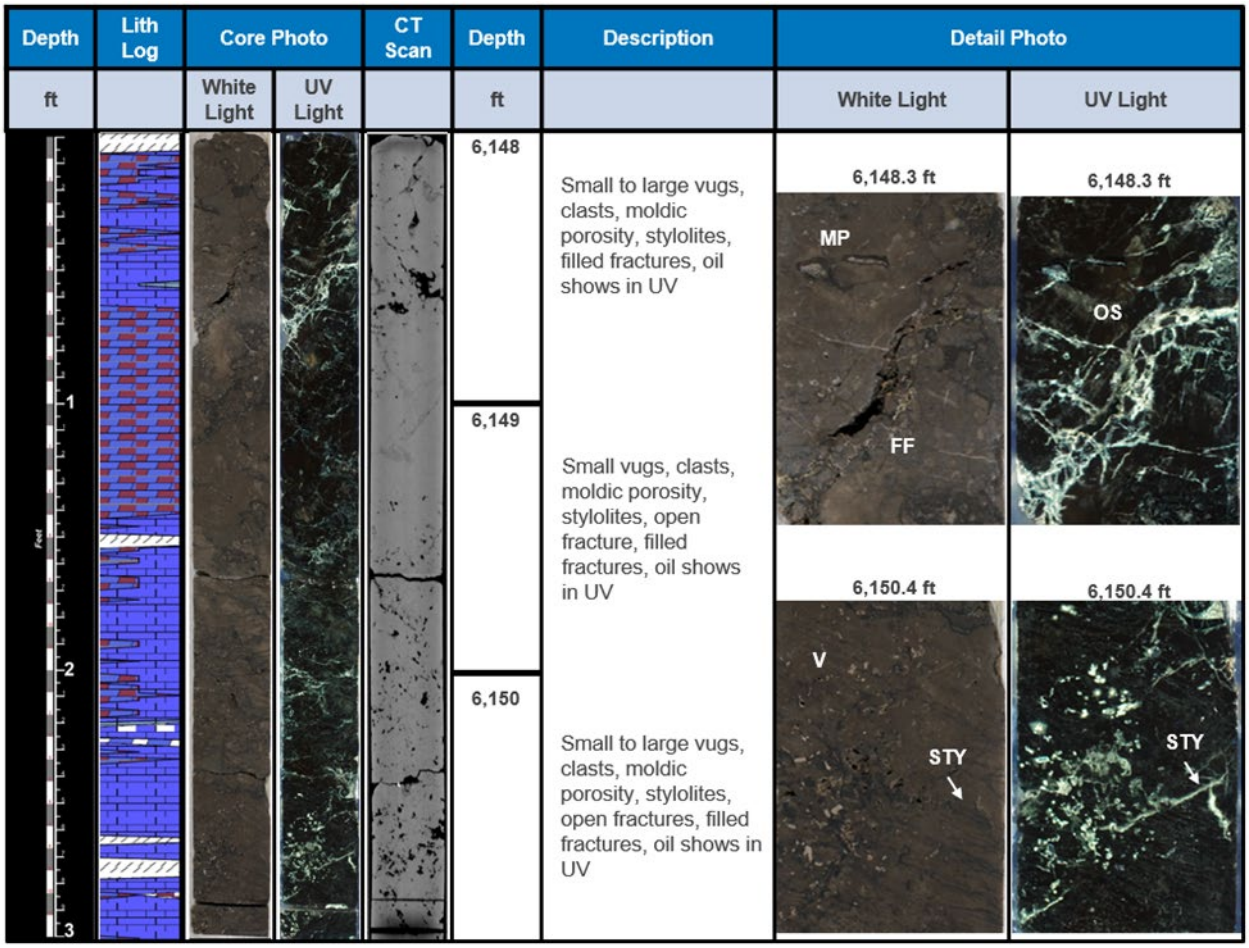


Figure 2-28. Compiled illustration of lithology log, core photos (UV and white light), CT scan image, core descriptions, and annotated core images of the Brown Niagaran for depths 6,148 ft. to 6,151 ft.

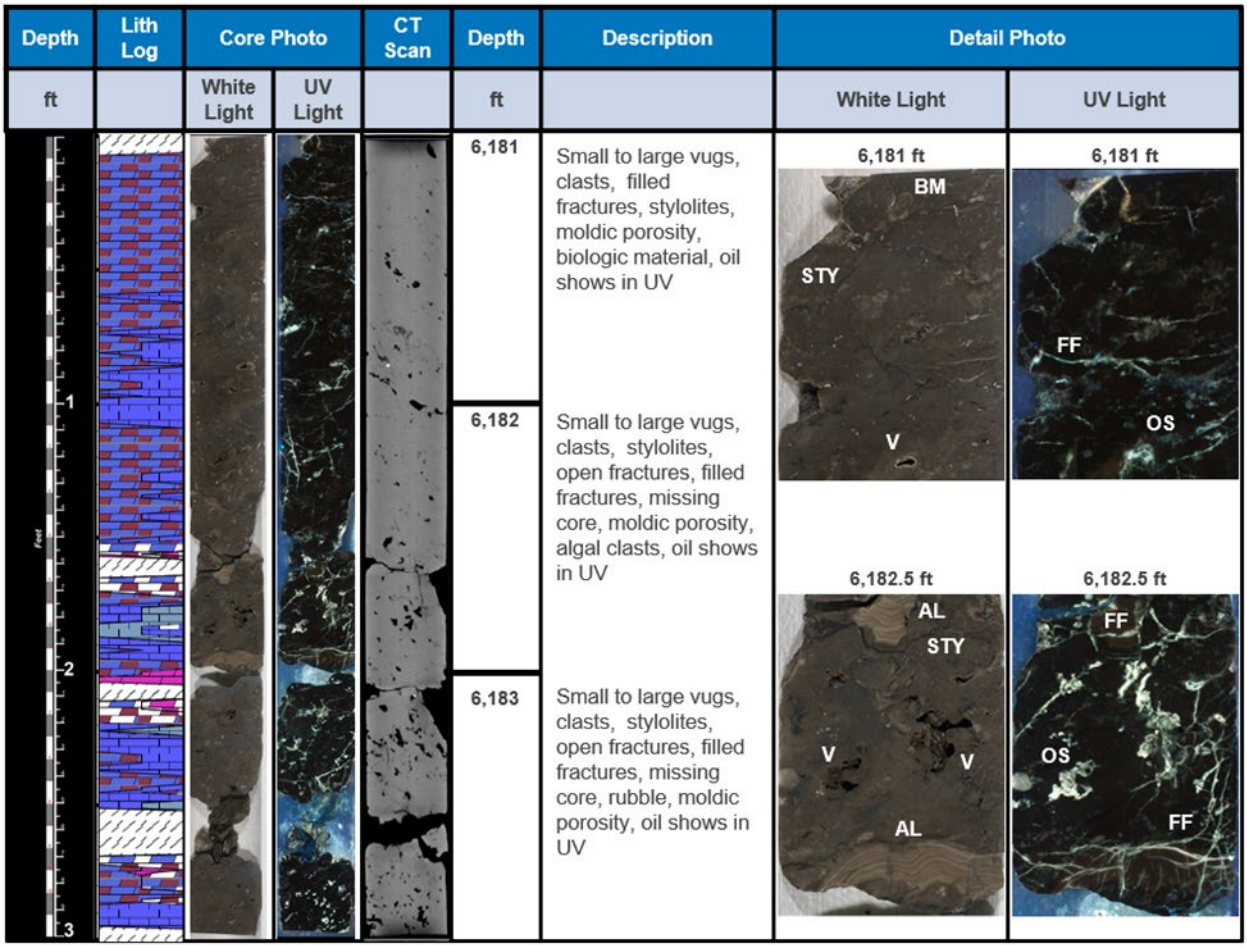


Figure 2-29. Compiled illustration of lithology log, core photos (UV and white light), CT scan image, core descriptions, and annotated core images of the Brown Niagaran for depths 6,181 ft. to 6,184 ft.

RSWC core photos of the Brown Niagaran in Chester 8-16 show a predominantly vuggy gray carbonate. A variety of small-to-large vugs present throughout including open, salt-filled, and filled moldic vugs. Open fractures and stylolites also present in core images. UV light images show potential residual oil throughout the cored interval. Examples of RSWC descriptions completed for the Brown Niagaran Formation in Chester 8-16 are seen in Figure 2-30 and Figure 2-31.

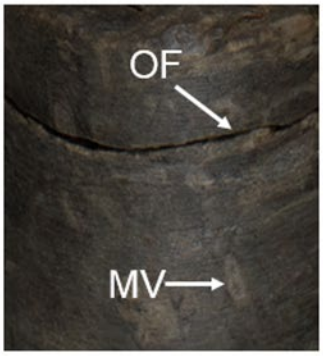
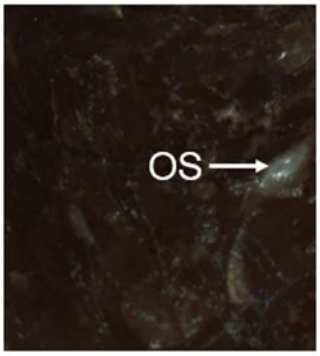
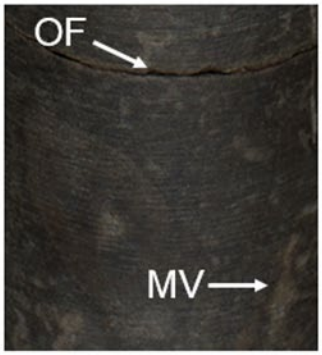
Depth Ft.	White Light Primary Features	UV Light Primary Features	Descriptions
6,012			White Light: Gray carbonate, filled moldic vugs, open fracture. UV Light: Strong light blue UV response due to potential residual oil.
6,015			White Light: Gray carbonate, filled moldic vugs, open fractures, large clast. UV Light: Strong light blue UV response due to potential residual oil throughout sample.

Figure 2-30. Annotated RSWC images with corresponding core descriptions of the Brown Niagaran for depths 6,012 ft. to 6,015 ft.

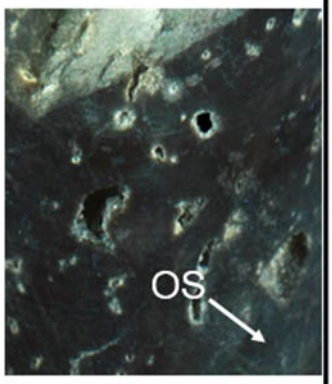
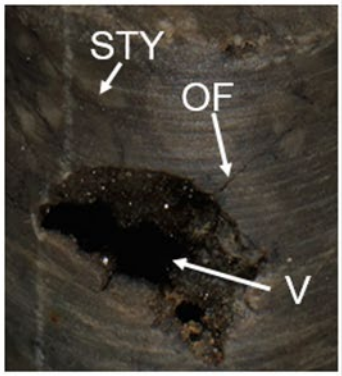
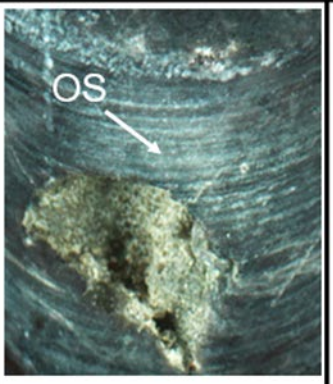
Depth Ft.	White Light Primary Features	UV Light Primary Features	Descriptions
6,095			White Light: Carbonate, medium/small vugs, filled vugs. UV Light: Strong light blue UV response due to potential residual oil throughout sample.
6,121			White Light: Carbonate, large vug, open fractures, stylolites, filled vugs. UV Light: Strong light blue UV response due to potential residual oil throughout sample.

Figure 2-31. Annotated RSWC images with corresponding core descriptions of the Brown Niagaran for depths 6,095 ft. to 6,121 ft.

Elemental Spectroscopy Log Analysis

The Brown Niagaran Formation was logged from 5,916 ft MD/5,817 ft TVD to 6,332 ft MD/6,233 ft TVD. The log indicates a steady magnesium to calcium ratio, with inconsistent spikes of dolomite that increase in frequency and percentage of rock bulk volume towards the OWC at 6,245 ft MD/6,145 ft TVD (Figure 2-32). Peaks on the x-carbon curve indicate that small amounts of higher TOC are seen throughout the Brown Niagaran Formation.

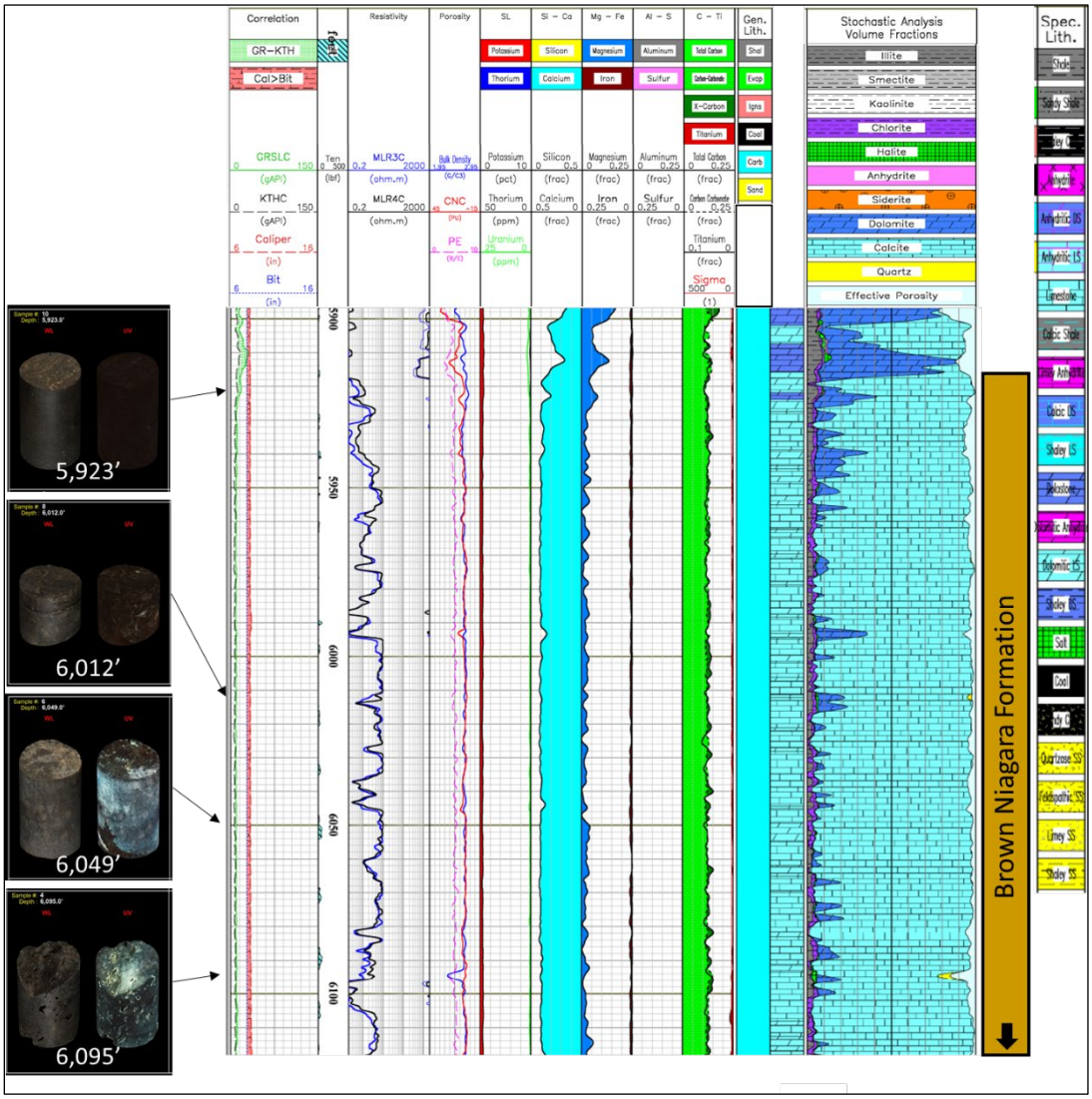


Figure 2-32. Elemental spectroscopy log from Chester 8-16 displaying the Brown Niagaran Formation from 5,916'MD/5,817'TVD to 6,332'MD/6,233'TVD. Select RSWC samples are shown in both white light (WL) and ultraviolet light (UV) to provide context for lithologic descriptions. Core photos by Core Laboratories.

Image Log Analysis

The Brown Niagaran can be divided into four distinct textural zones: (1) mixed heterogeneous/ homogenous texture (Figure 2-33), (2) Homogenous texture with some conductive features (Figure 2-34), (3) Mixed heterogeneous/ homogenous texture (Figure 2-35), (4) mixed heterogeneous/homogenous texture with a chaotic character (Figure 2-36).

The first textural zone exists from 5916 ft to 5934 ft and features planar interbeds of homogenously resistive and heterogeneous materials. This textural behavior is similar and is most likely a continuation of the textures encountered in the lowermost texture zone of the A-1 carbonate. The first textural zone potentially exhibits significant amounts of porosity. The second textural zone exists from 5934 ft-6117 ft and is characterized by a homogenously resistive texture, spotted with a few conductive features scattered throughout and no distinct bedding contacts. Intervals of potential featuring significant amounts of porosity within the second textural zone include: 5992 ft-5995 ft and 6100 ft-6104 ft. The third texture zone exists from 6117 ft to 6194 ft and is characterized by planar to wavy beds with interbedded heterogeneous and homogenously resistive materials. The third textural zone has potential for significant porosity to be present. The fourth textural zone exists from 6194 ft-6332 ft and is characterized by mixed heterogeneous and homogenously resistive intervals with abrupt and consistent wavy bedding. Conductive features within the heterogeneous textures are lenticular and wavy. The fourth textural zone also features a high potential for significant porosity. Bedding within the Brown Niagaran Formation had an average strike of 190^0. Dip angles were measured to range between 5° to 64°, with an average dip of 31°. Dip angles varied by a standard deviation of 11°.

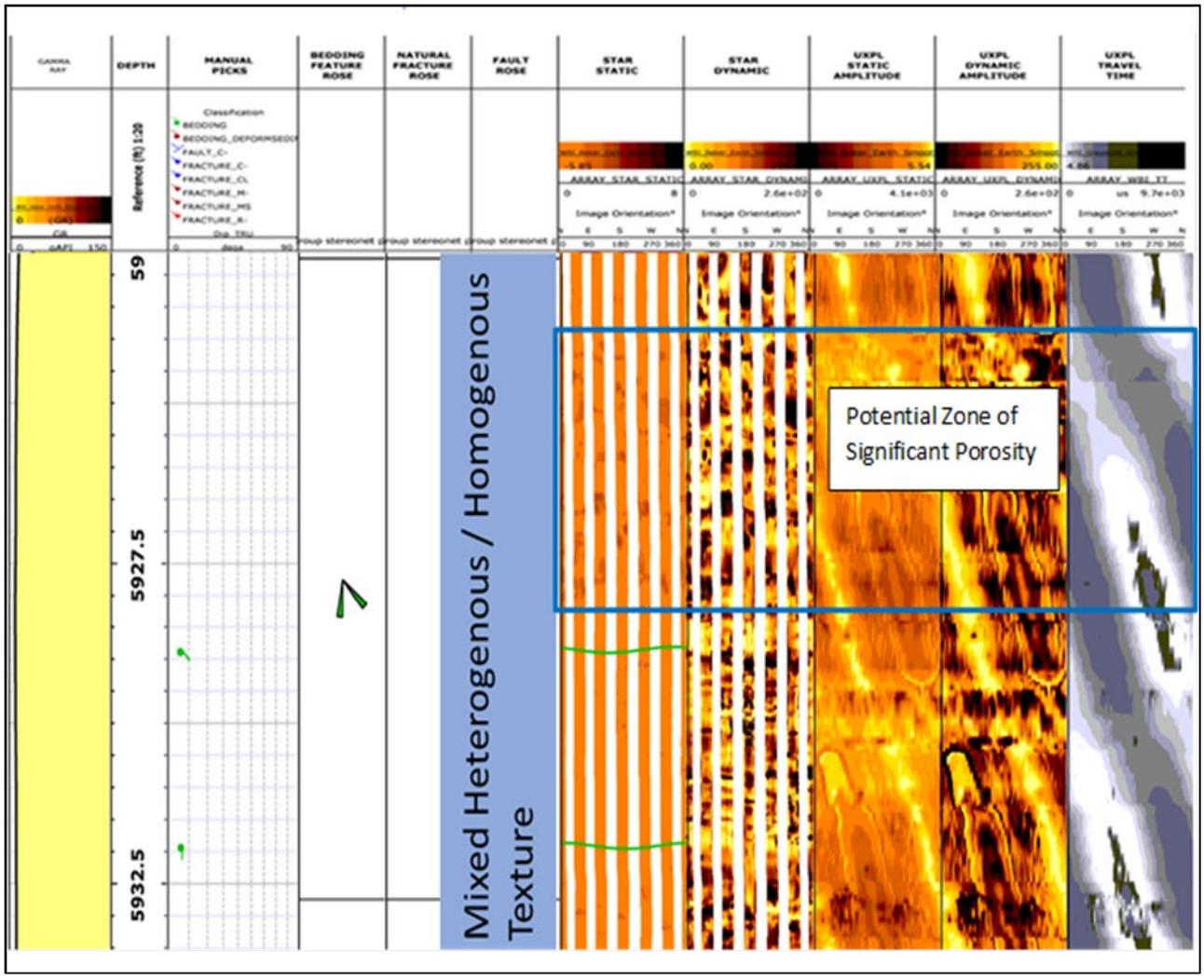


Figure 2-33. Textural zone one within the Brown Niagaran Unit of the Chester 8-16 well. Texture is mixed with homogenously resistive and heterogeneous textures. The interval of 5924 ft-5928 ft is a potential zone of significant porosity.

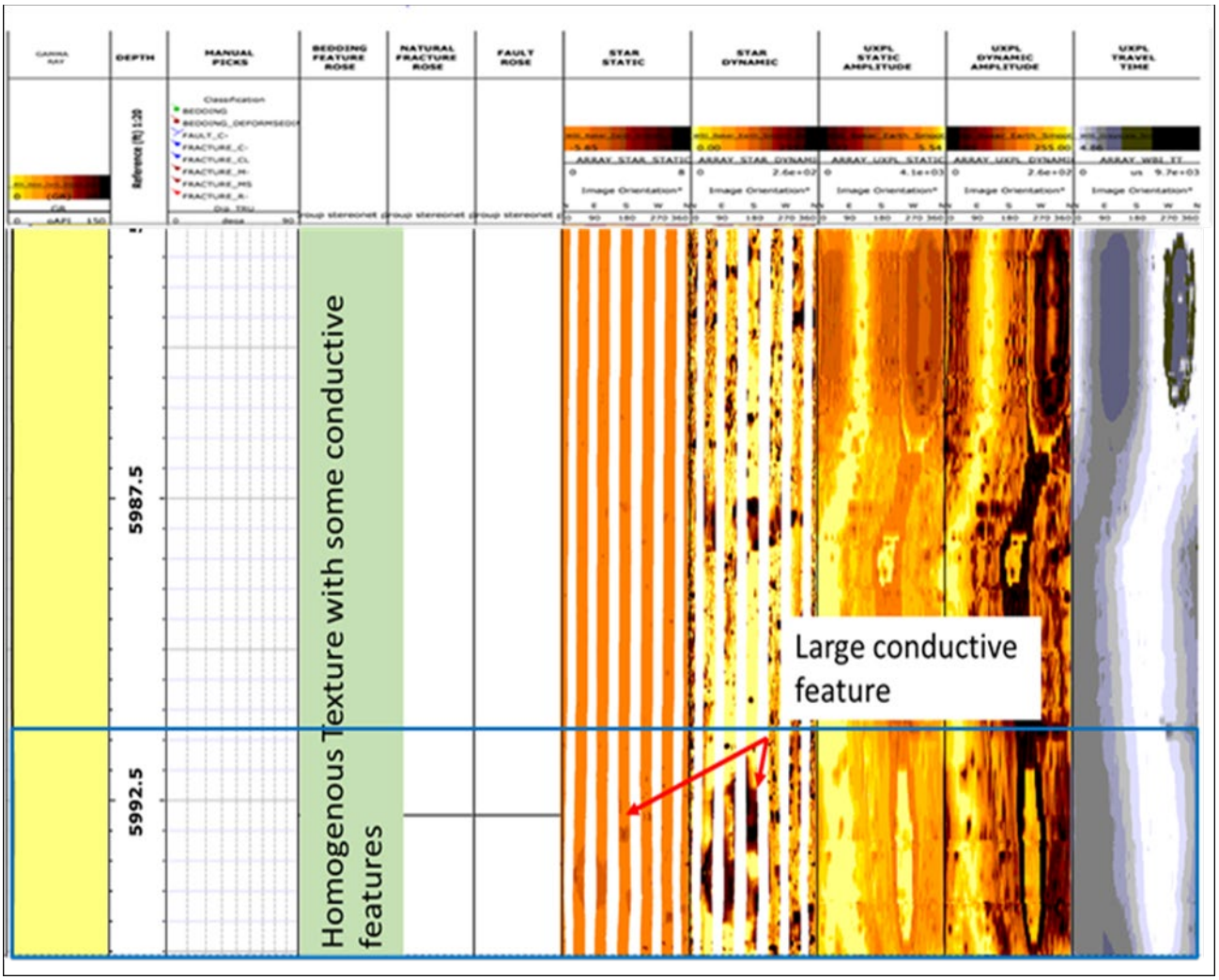


Figure 2-34. Textural zone two within the Brown Niagaran Formation of the Chester 8-16 well. Texture is homogenously resistive with some conductive features. At 5992 ft a large isolated semi-spherical conductive body is encountered.

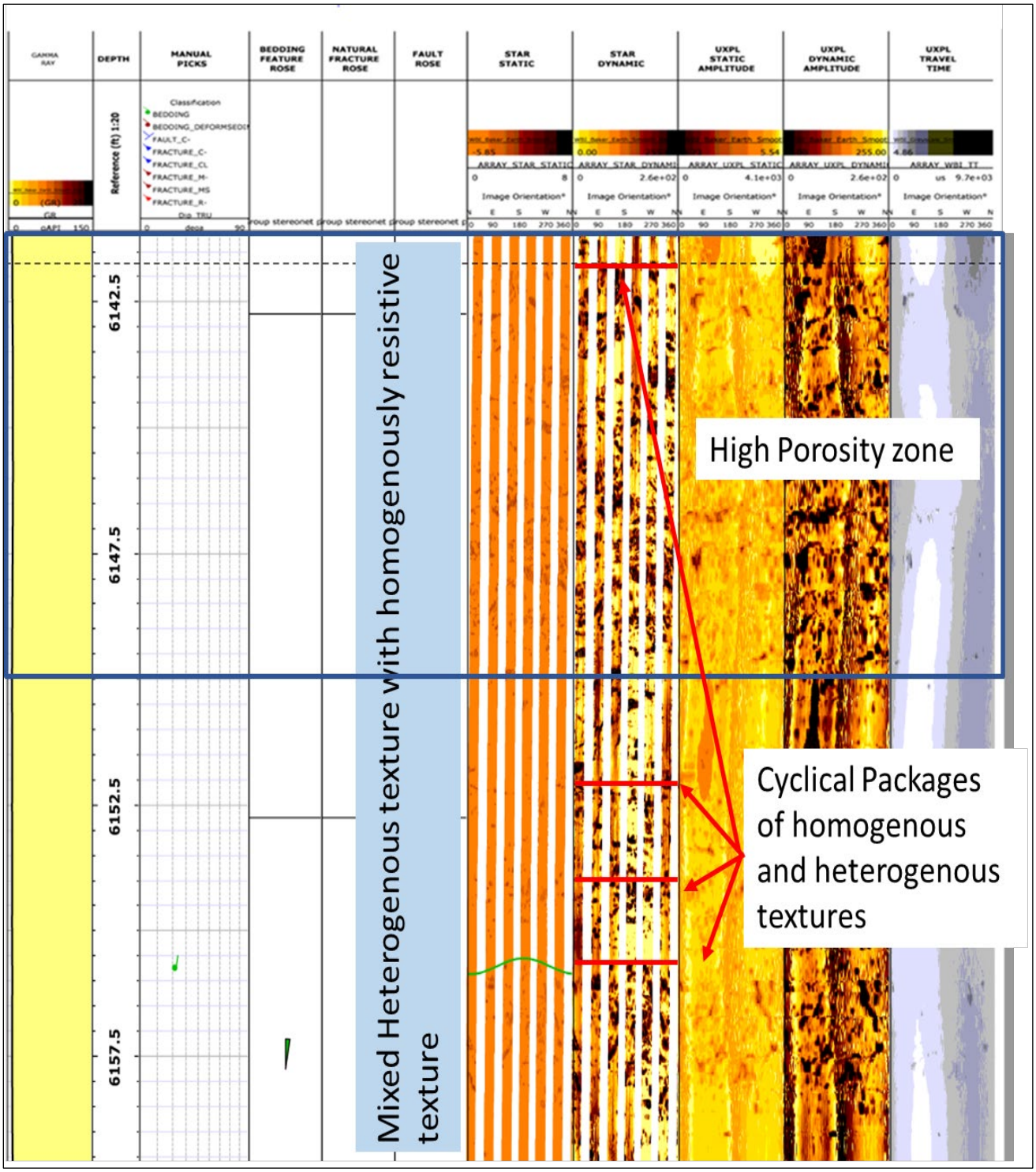


Figure 2-35. The third textural zone within the Brown Niagaran Formation of the Chester 8-16 well.
Texture is interbedded homogenous and heterogenous materials.
Significant porosity zone is displayed from 6141 ft to 6150 ft.
Not cyclical packages of homogenously resistive to heterogenous materials.

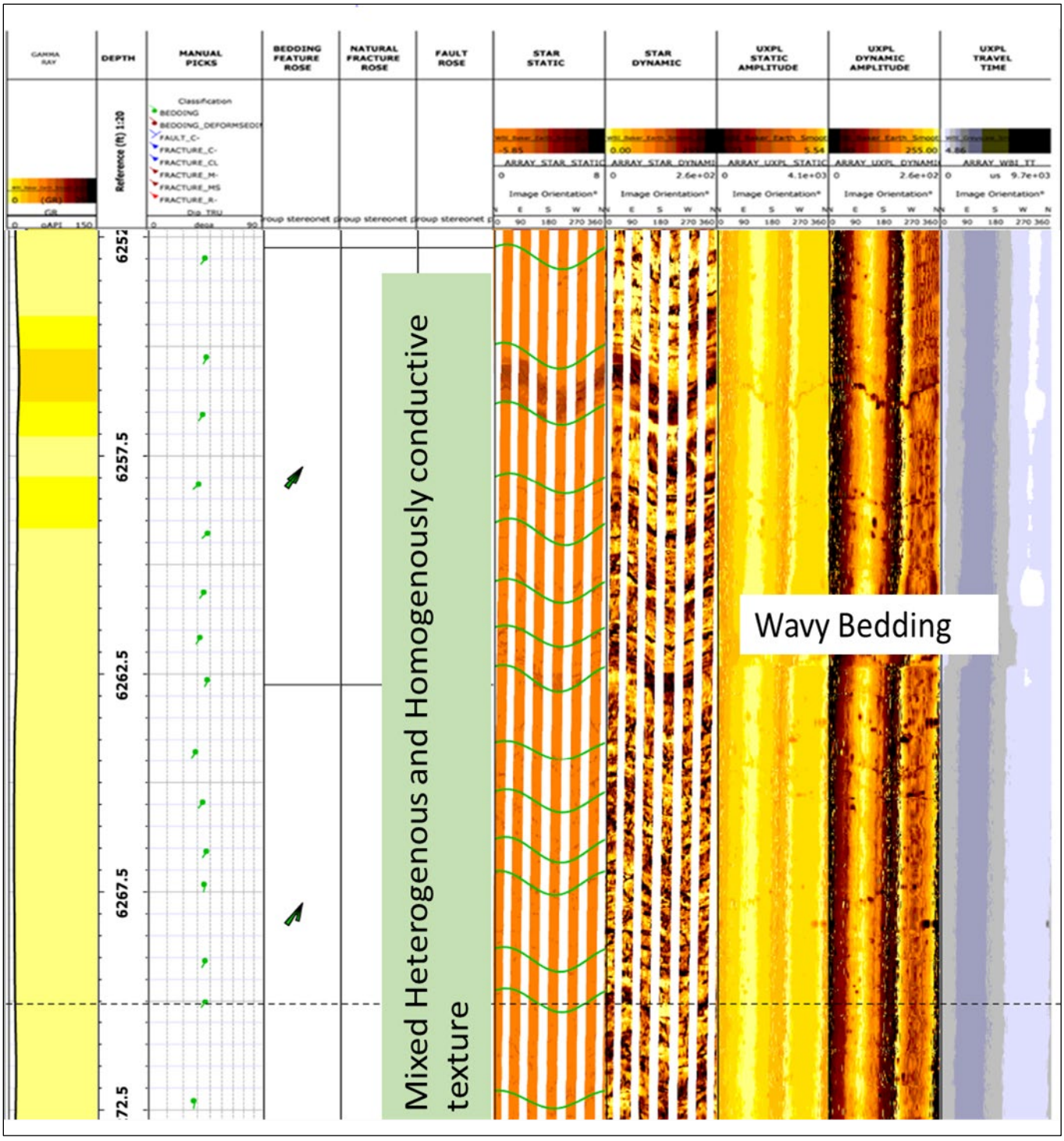


Figure 2-36. The fourth zone of the Brown Niagaran Formation within the Chester 8-16 well. The texture is mixed heterogeneous and homogenously conductive materials.

2.3.4 Gray Niagaran

Wireline Log Analysis and Petrophysical Calculations

The Chester 8-16 well captured 35 ft. of the Gray Niagaran with triple combo data. The porosity ranged from 0 to 2.4% with an average of 1.5%. The cross-plot porosity was all below 5% and tightly clustered along the limestone trend (Figure 2-37). The water saturation was high throughout with an average of 89% indicating a fully saturated formation (Figure 2-38). Overall, the Gray Niagaran was a tight limestone which was fully saturated. Negligible values were calculated using petrophysical techniques, verifying that this was a sufficient underlying confining unit.

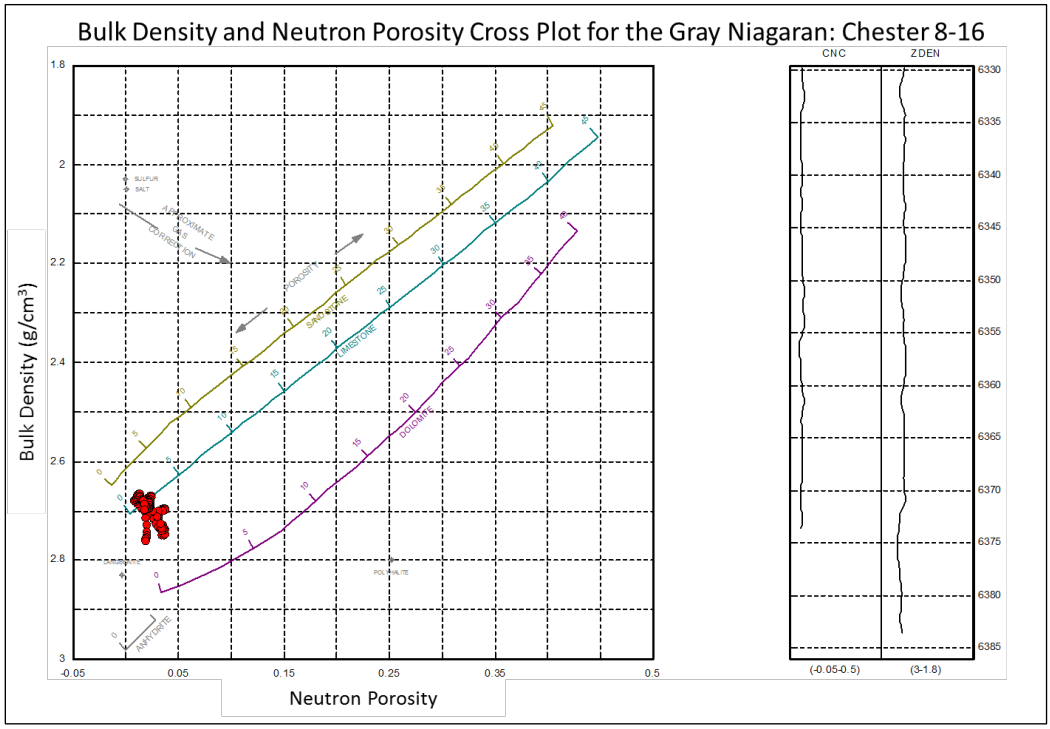


Figure 2-37. Neutron porosity-bulk density cross-plot of the Gray Niagaran for the Chester 8-16 well showing tightly clustered data along the limestone trend with low porosity.

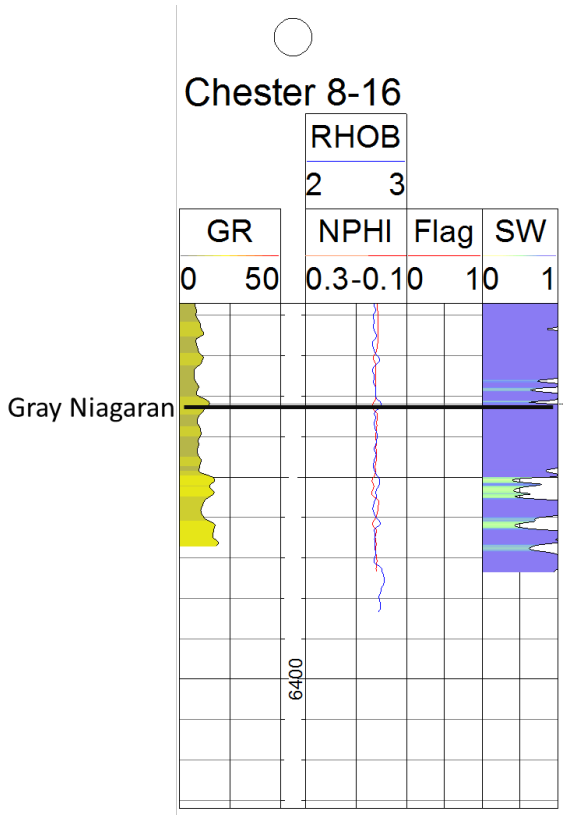


Figure 2-38. Single well cross section of the Gray Niagaran for the Chester 8-16 well showing low porosity and high water saturation.

Core Analysis

The Gray Niagaran formation in Chester 8-16 is mostly composed of tight dolomitic limestone with some thin intervals of dolomite and rubble. Small vugs and open fractures are present throughout the formation, resulting in isolated zones of high porosity. Minor biologic material is present toward the basal section of core. Small oil shows are present toward the base of the core as seen in the UV light image. Overall, the Gray Niagaran Formation in Chester 8-16 is a relatively homogenous section of core. Examples of core descriptions completed for the Gray Niagaran Formation in Chester 8-16 are seen in Figure 2-39 and Figure 2-40.

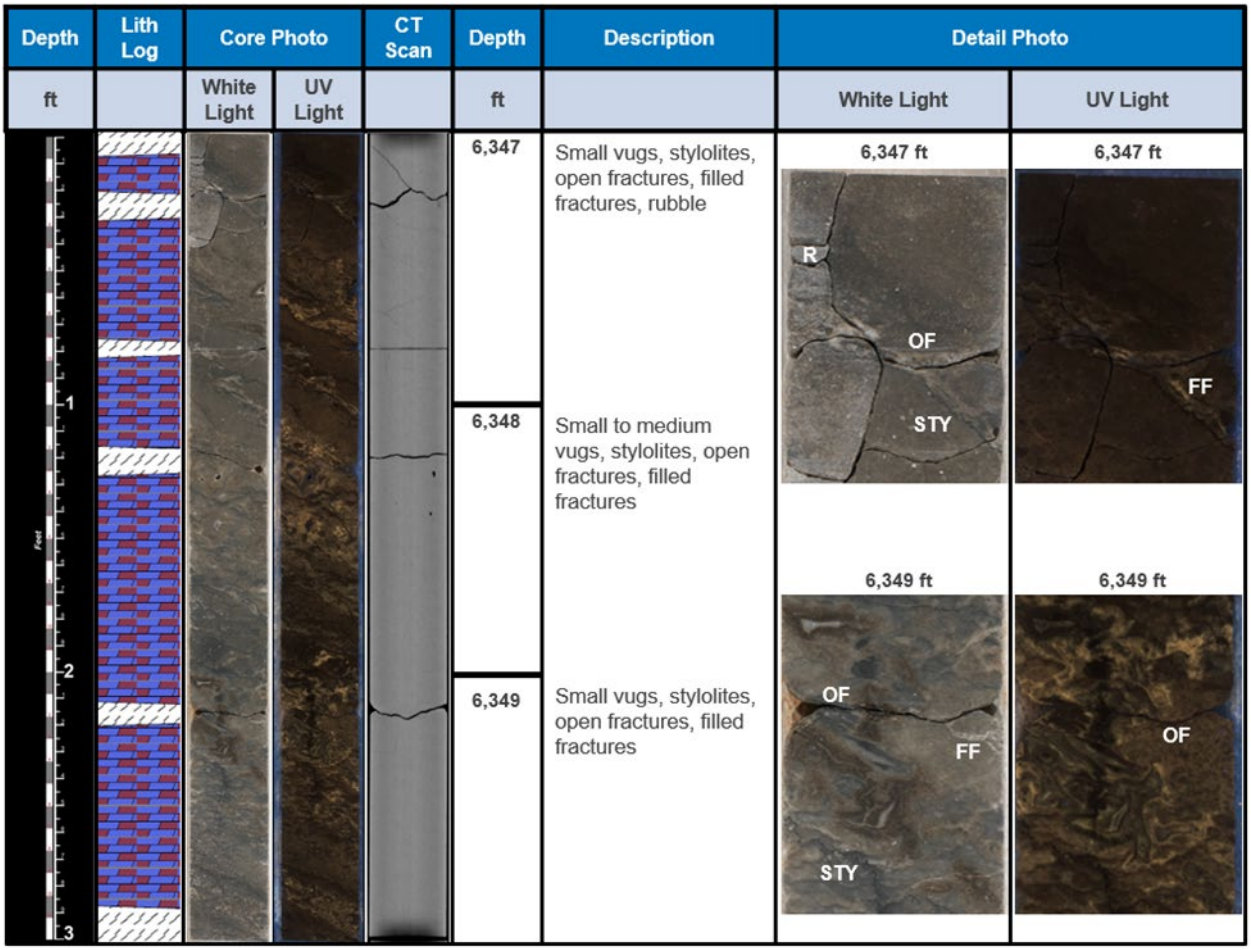


Figure 2-39. Compiled illustration of lithology log, core photos (UV and white light), CT scan image, core descriptions, and annotated core images of the Gray Niagaran for depths 6,347 ft. to 6,350 ft.

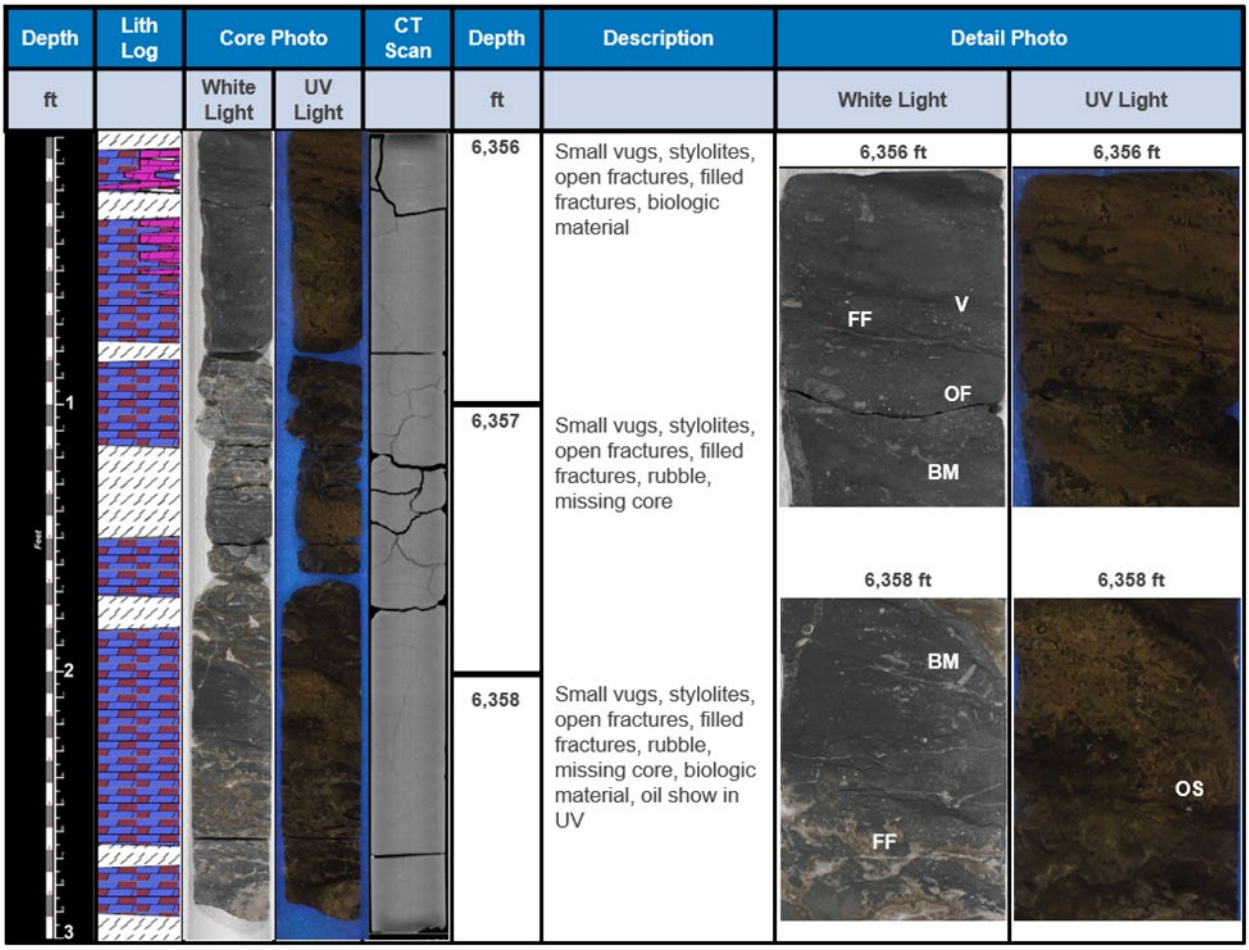


Figure 2-40. Compiled illustration of lithology log, core photos (UV and white light), CT scan image, core descriptions, and annotated core images of the Gray Niagaran for depths 6,356 ft. to 6,359 ft.

Elemental Spectroscopy Log Analysis

Only a small portion of the Gray Niagaran Formation from 6,332'MD/6,233'TVD to log TD at 6,447'MD is captured on the elemental spectroscopy log from Chester 8-16 (Figure 2-41). The logged portion of the Gray Niagaran is unremarkable and consists primarily of calcite with minor dolomite and trace clay minerals.

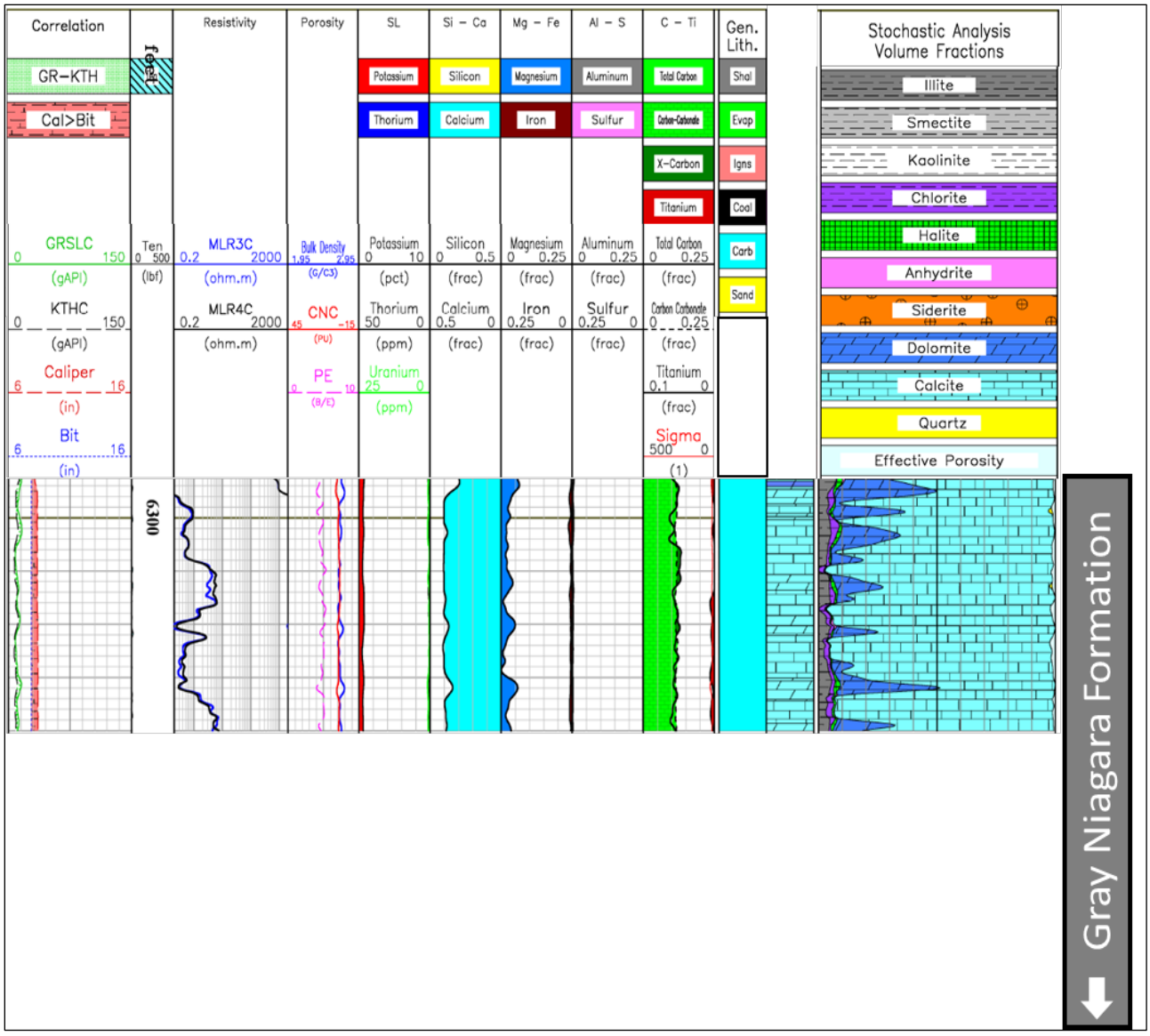


Figure 2-41. FLeX log from Chester 8-16 displaying the Gray Niagaran Formation from 6,332'MD/6,233'TVD to log TD at 6,447'MD.

Image Log Analysis

The Gray Niagaran Formation consists of interbedded limestone and micrite/shales and exhibits two textural zones Figure 2-42. The first textural zone is characterized by a homogenous resistive texture with no distinct bedding planes. The second textural zone is characterized by interbedded homogenously resistive materials with heterogeneous materials, with planar bedding planes (Figure 2-37). Bedding within the Gray Niagaran on average strikes at 190^0 and

dips from 2^0 to 18^0, with an average dip of 8^0. One natural fracture was identified within the formation that has a strike of 215^0 and a dip of 70^0. There are no zones of significant porosity development within the Gray Niagaran.

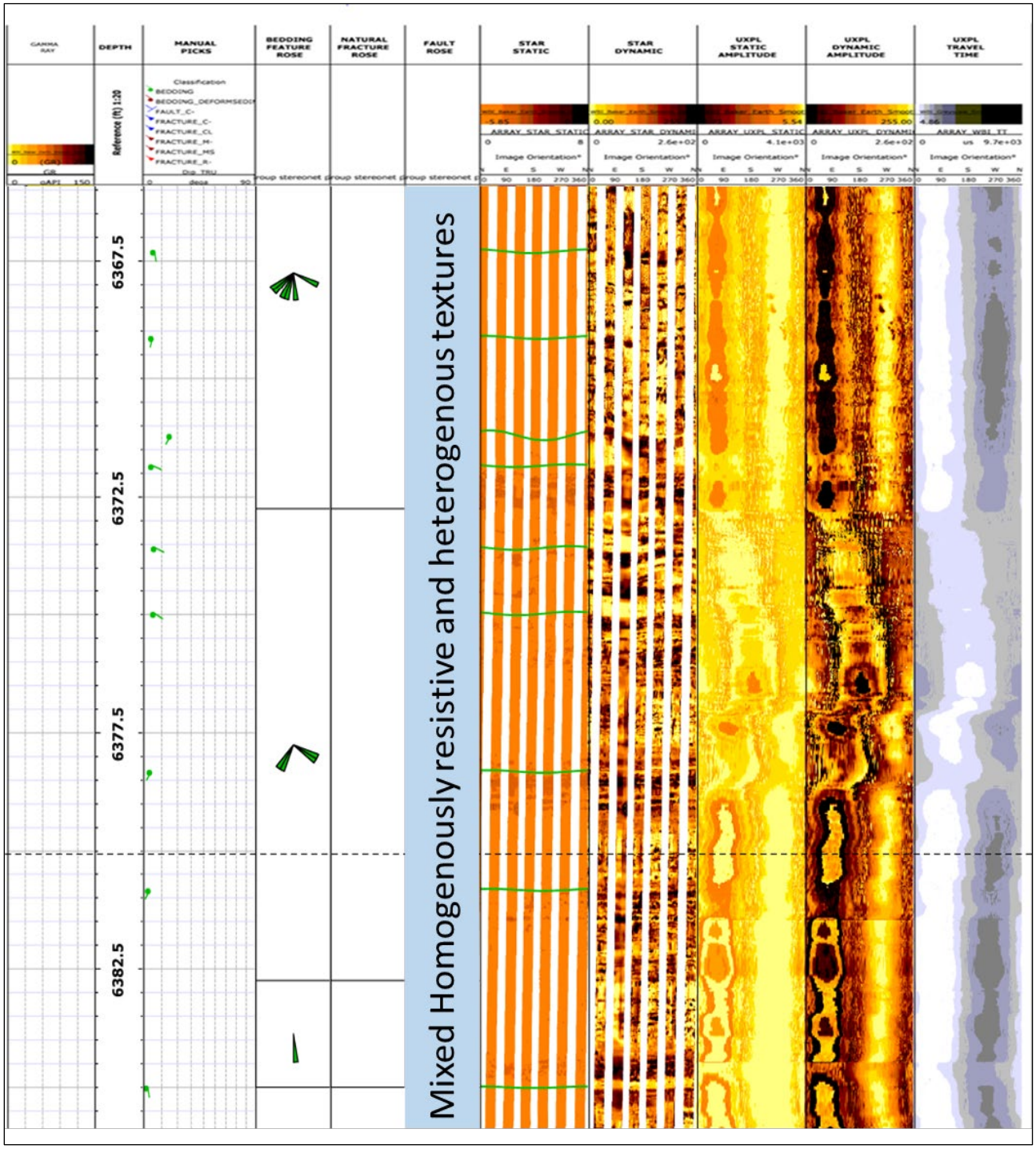


Figure 2-42. Texture zone of the Gray Niagaran of the Chester 8-16 well. The texture is homogenously resistive interbedded with heterogenous materials. There are no zones of significant porosity.

2.4 Summary

Conventional core samples were collected across the Brown Niagaran and Gray Niagaran formations and rotary side wall core samples were collected across the A-2 Carbonate, A-2 Evaporite, A-1 Carbonate, and Brown Niagaran formations. Herein, we present a summary of key reservoir intervals and features as determined from core analysis and images. Table 2-8 and Table 2-9 show summary statistics of porosity and permeability by formation for conventional and sidewall core, respectively. Table 2-10 shows the depths of key potential reservoir intervals with porosity ≥5% as determined by core analysis and intervals with visible porosity as observed in core images and CT scans. Overall, the 8-16 core is dominated by a dolomitic limestone lithology with some isolated zones of tight limestone, tight dolomite, and high porosity. Visible porosity, as seen on the core images and CT scans, is dominantly in the form of small to medium vugs and significant moldic porosity. Potential reservoir intervals occur exclusively in the Brown Niagaran (based on limited whole core data) above a depth of ~6,237 ft. Generally, core analysis data suggests very minimal reservoir potential in the 8-16 well as only 1 conventional core sample exhibits porosity at or above 5%.

Table 2-8. Summary of whole core porosity and permeability data in the Chester 8-16 well.

Formation	Porosity (%)			Permeability (mD)		
	Min	Max	Average	Min	Max	Average
Brown Niagaran	0.38	9.69	1.15	0.00	10.90	0.16
Gray Niagaran	0.00	0.90	0.68	0.00	0.06	0.01

Table 2-9. Summary of RSWC porosity and permeability data in the Chester 8-16 well.

Formation	Porosity (%)			Permeability (mD)		
	Min	Max	Average	Min	Max	Average
A2 Carbonate	0.21	0.62	0.41	0.00	0.13	0.04
A2 Evaporite	0.16	0.29	0.24	-	-	-
A1 Carbonate	4.72	18.18	11.04	0.01	39.65	7.87
Brown Niagaran	0.47	8.62	3.19	0.00	0.14	0.02

Table 2-10. Summary of key potential reservoir intervals in the Chester 8-16 well based on whole core analysis and images.

Formation	Reservoir Intervals [ϕ ≥ 5%] (ft.)	Intervals with visible porosity (ft.)
Brown Niagaran	6204.5	6148-6155, 6156-6164, 6178-6197, 6199-6201, 6203-6205, 6210-6214, 6215-6217, 6218-6220, 6227-6231, 6235-6237
Gray Niagaran	-	-

Chapter 3. Integrated Geomechanics Analysis

3.1 Introduction

The goal of the geomechanical characterization is to assess the sealing and mechanical integrity effectiveness of the geologic formations that comprise the caprock - reservoir systems for CO_2 storage or CO_2 EOR processes. To evaluate caprock- reservoir performance during CO_2 injection, numerical fluid flow-geomechanical modeling should be conducted to assess the potential for fracturing/ fault activation that could lead to CO_2 leakage. The first step to assess caprock- reservoir performance for CO_2 storage is defining the mechanical properties and in-situ stress parameters of the geologic formations.

This chapter included (1) investigating dipole sonic log data from Chester 8-16 to define fundamental mechanical rock properties of the caprock and reservoir formations (2) studying the in-situ stresses in the caprock and reservoir formations by determining the orientation of maximum horizontal stress (S_{Hmax}) and magnitude of the vertical stress using image log data, shear wave anisotropy data, and density log data.

3.2 Mechanical Parameters Characterization Using Dipole Sonic Log Analysis

Variation in the physical properties of the geological formations causes changes in rock mechanical parameters. Since rock mechanical parameters are the key data to study safe long-term storage of CO_2, it is important to adequately characterize these properties and study its variations across different formations.

The sonic log analysis was conducted using acoustic data from dipole sonic geophysical logs from Chester 8-16—specifically, compressional-wave and shear-wave slowness (slowness being the inverse of velocity) parameters which were used to calculate rock mechanical properties. Additionally, shear-wave velocity anisotropy data (i.e., fast shear-wave and slow shear-wave velocities), which were available for the Chester 8-16 well, were used to estimate S_{Hmax} azimuth.

Dipole sonic logging tools measure both compressional-wave and shear-wave slowness within a formation. These variables, coupled with formation bulk density (ρ), allow for the calculation of dynamic elastic parameters including Poisson's ratio, and Young's modulus.

Poisson's ratio indicates the relationship between the lateral and axial strain of the rock formation. It is expressed by:

$$V = \frac{V_p^2 - 2V_s^2}{2*(V_p^2 - V_s^2)} \qquad \text{(equation 6)}$$

Where:

V = Poisson's ratio

Vp = compressional velocity

Vs = Shear velocity

Young's modulus is the measure of the stiffness of a material and is calculated using the rock density, shear wave velocity, and compressional wave velocity.

$$E = \frac{\rho V_s^2 (3V_p^2 - 4V_s^2)}{(V_p^2 - V_s^2)} \qquad \text{(equation 7)}$$

where:

E = Young's Modulus

ρ = Density

The dynamic shear modulus evaluates a rock formation's rigidity to shear stress and is calculated as the relationship between the bulk density and the shear wave slowness of a formation (slowness being a unit of measure which is the inverse of velocity). It is expressed by:

$$G = \mathrm{A}\frac{\rho}{DT_S^2} \quad \text{(equation 8)}$$

where:

G = dynamic shear modulus (10^6 psi)

A = 1.3476x104 (conversion parameter, with units of 10^6 psi/((g/cc)/(μs/ft)^2)

ρ = bulk density (g/cc)

DT_c = compressional wave slowness (μs/ft)

DT_s = shear wave slowness (μs/ft)

The bulk modulus of a rock formation expresses the resistance of the formation to compression. This incompressibility is measured using the relationship between the DT^c and DT^s slowness values, as a conversion factor to convert the units to 106 psi. It is expressed by:

$$K = (1.3476\mathrm{x}10^4)\rho(\frac{1}{DT_C^2} - \frac{4}{DT_S^2}) \quad \text{(equation 9)}$$

where:

K = bulk modulus (10^6 psi)

ρ = bulk density (g/cc)

DT_c = compressional wave slowness (μs/ft)

DT_s = shear wave slowness (μs/ft)

The results included four dynamic elastic parameters (Poisson's ratio, Young's modulus, dynamic shear modulus, and bulk modulus) calculated for Chester 8-16 (Figure 3-1 and Figure 3-2). Individual well data from Chester 8-16 was aggregated into histograms for each dynamic elastic parameter for each formation to gain an understanding of the variation in the properties of each formation. Results are presented for the five geologic formations (Salina, A-2 Carbonate, A-2 Evaporate, A-1 Carbonate, and Brown Niagaran) in Figure 3-3 and Figure 3-4.

The mean value of Poisson's ratio and Young's modulus within each formation, as an aggregate of data for Chester 8-16 is shown in Table 3-1. In terms of Young's modulus, the Salina Formation has a significantly lower Young's modulus value in comparison to carbonate and evaporite formations. Low Young's modulus was expected to be observed in salt layers due to the high deformation tendency of salt. All geological formations were in the same range in terms of Poisson's ratio (mean Poisson's ratio of 0.26 to 0.30 across different formations).

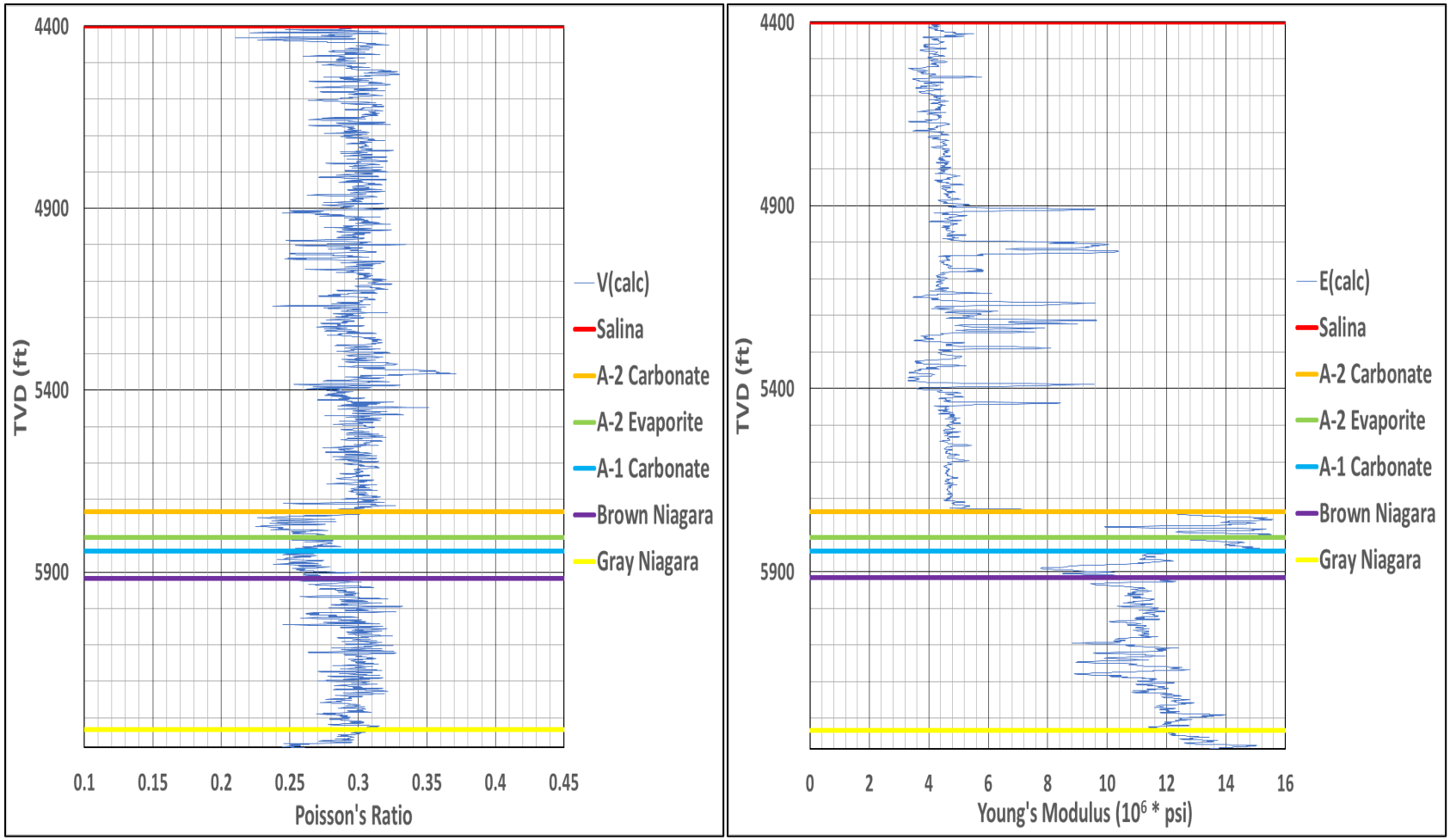


Figure 3-1. Depth plots of Poisson's ratio and Young's modulus for Chester 8-16.

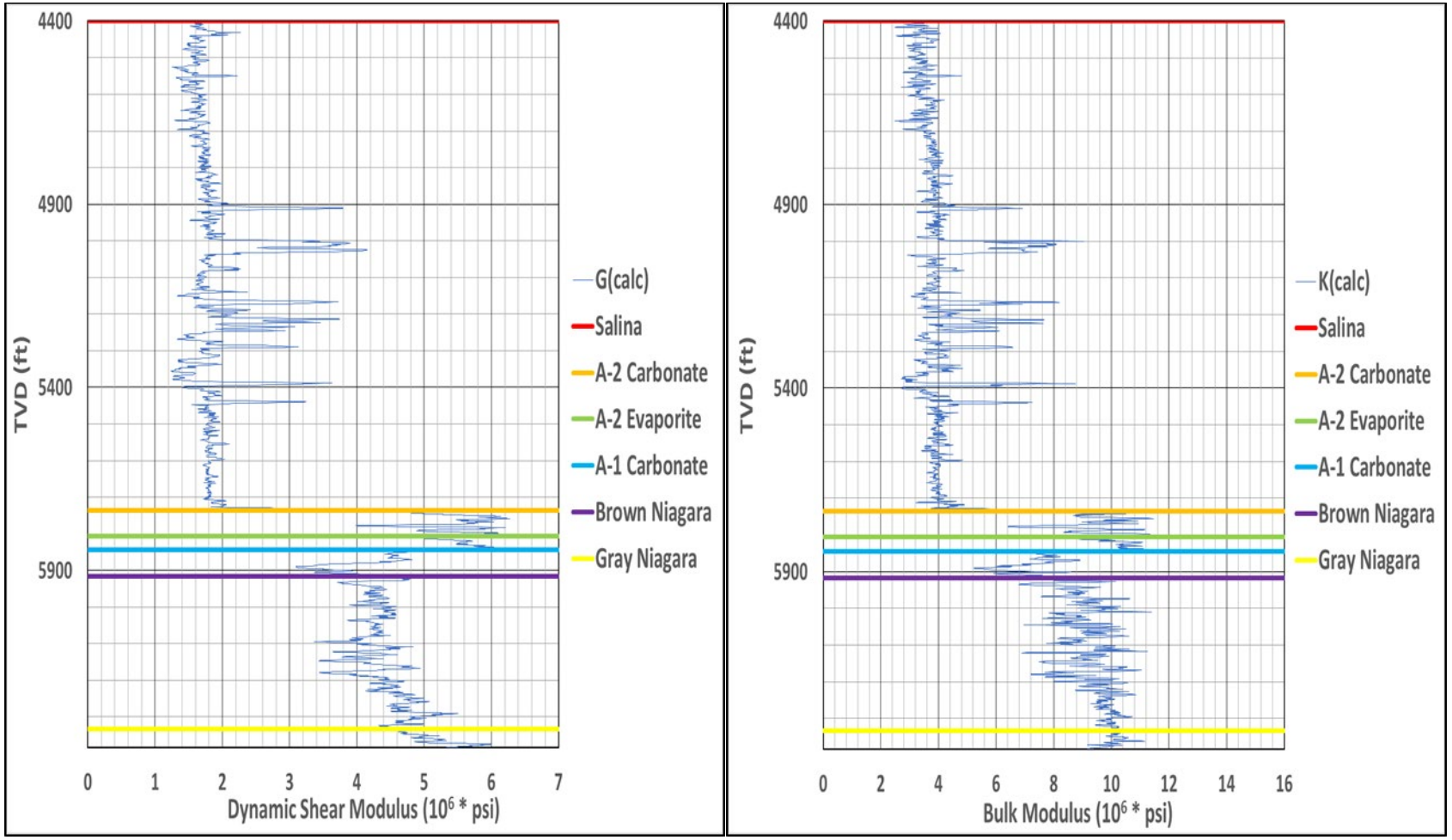


Figure 3-2. Depth plots of dynamic shear modulus and bulk modulus for Chester 8-16.

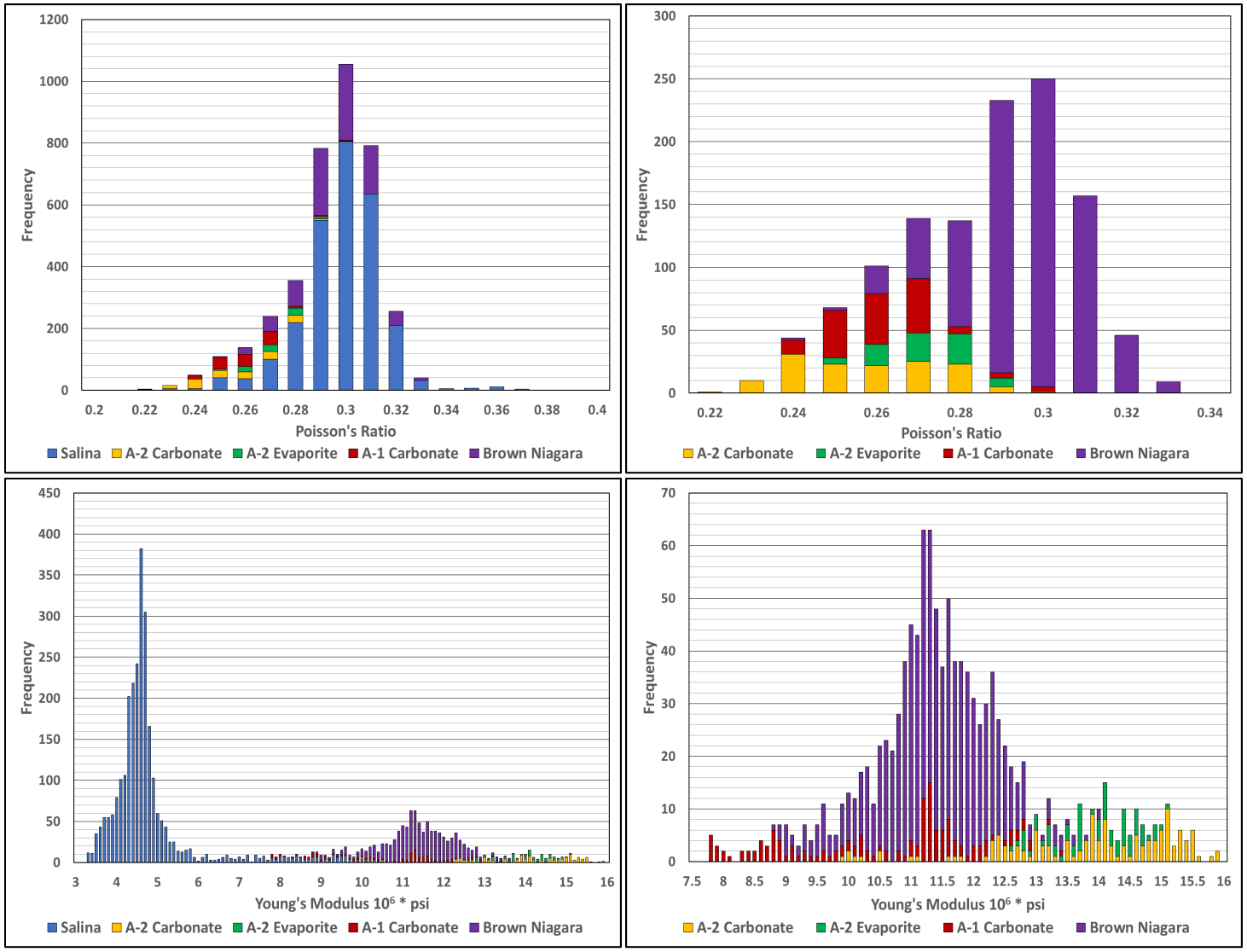


Figure 3-3. Histograms of Poisson's ratio and Young's modulus for Chester 8-16. Two of the histograms include the Salina Formation, and two of the histograms don't include the Salina Formation for visual resolution purposes.

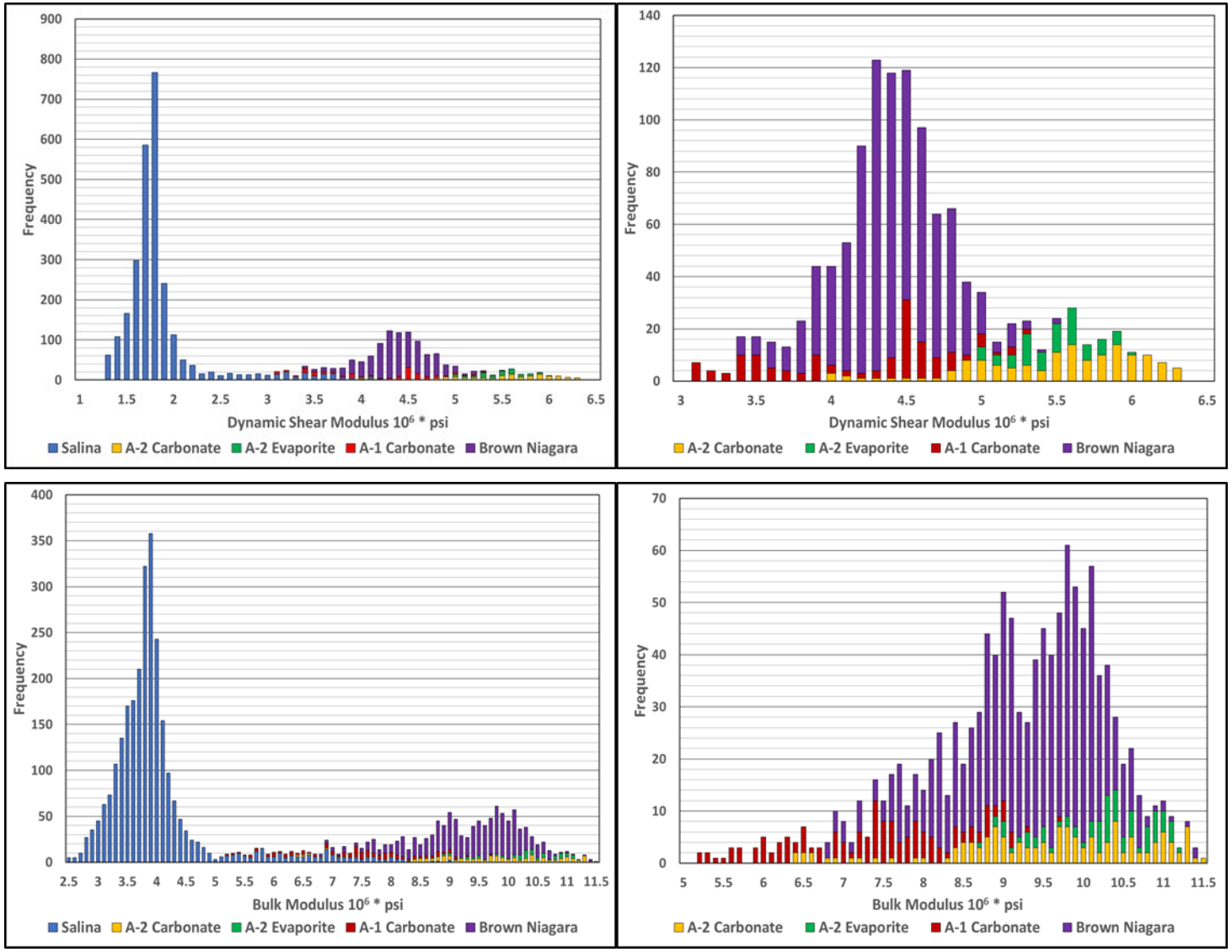


Figure 3-4. Histograms of bulk modulus and Young's Modulus for Chester 8-16. Two of the histograms include the Salina Formation, and two of the histograms don't include the Salina Formation for visual resolution purposes.

Table 3-1. Mean, variance, and N (number of data values) values of geomechanical parameters within Chester 8-16 by formation.

Formation		Chester 8-16			
		Young's Modulus	Poisson's Ratio	Bulk Modulus	Dynamic Shear Modulus
Salina	Mean	4.81	0.30	3.98	1.85
	Variance	1.28	0.0003	0.75	0.20
	N	2670	2670	2670	2670
A-2 Carbonate	Mean	13.84	0.26	9.59	5.50
	Variance	1.92	0.0003	1.49	0.30
	N	141	141	141	141
A-2 Evaporite	Mean	13.95	0.27	10.22	5.48
	Variance	0.42	0.0001	0.42	0.07
	N	76	76	76	76
A-1 Carbonate	Mean	10.53	0.26	7.37	4.17
	Variance	2.15	0.0002	1.07	0.35
	N	146	146	146	146
Brown Niagaran	Mean	11.36	0.30	9.30	4.38
	Variance	0.74	0.0002	0.72	0.12
	N	832	832	832	832
Gray Niagaran	Mean	13.03	0.28	10.08	5.08
	Variance	0.76	0.0003	0.15	0.17
	N	832	832	832	832

3.3 In-Situ Stress Analysis

3.3.1 Calculating Vertical Stress (S_v) Using Density Logs

Formation bulk density (ρ) was used to characterize the in-situ state of stress for caprock and reservoir formations. This involved determining the orientation and magnitude of vertical stress (S_v), least horizontal stress (S_{Hmin}), and pore pressure (P_p)to help characterize variability of the state of stress in Chester 8-16.

The magnitude of S_v is determined by the weight of the overlaying rock material and was calculated by integrating bulk density from ground surface to the total depth of the well. It is expressed by:

$$S_v = \Sigma \rho \Delta z \left(\frac{1ft^2}{144in^2}\right) \quad \text{(equation 10)}$$

where:

S_v = vertical stress (psi)

ρ = bulk density of the formation measured by geophysical logging tools over a specific depth interval (lbs/ft^3)

Δz = depth interval corresponds to the ρ reading (ft)

Geophysical logs do not start at ground surface; therefore, it is usually necessary to assume a density for the near-surface interval that was not logged. S_v was calculated in this manner for Chester 8-16 with an assumed density of 2 lbs/ft^3 being used from ground surface to a depth of 848 ft.

S_{Hmin} was determined by multiplying TVD by an assumed constant of 0.6. It is expressed by:

$$S_{Hmin} = 0.6 \times TVD \quad \text{(equation 11)}$$

where:

S_{Hmin} = least horizontal stress (psi)

0.6 = assumed constant

TVD = true vertical depth

P_p was determined by multiplying TVD by an assumed constant of 0.443. It is expressed by:

$$P_p = 0.443 \times TVD \quad \text{(equation 12)}$$

where:

P_p = pore pressure (psi)

0.443 = assumed constant

TVD = true vertical depth

S_v, S_{Hmin}, and P_p were each determined from ground surface to total depth in Chester 8-16 and are displayed in Figure 3-5.

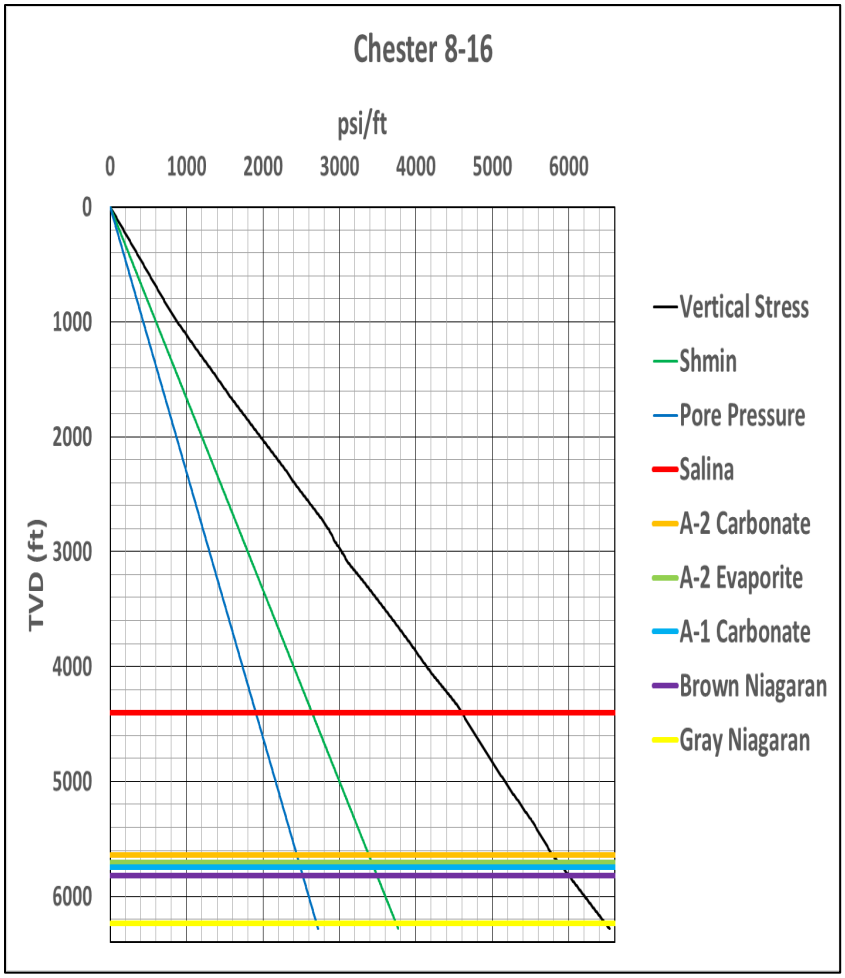


Figure 3-5. Calculated S_v, SH_{min}, and P_p with depth for Chester 8-16.

3.3.2 S_{Hmax} Azimuth Analysis Using Image Log Data

S_{Hmax} orientation (azimuth) is determined from the orientation of features recorded on the image logs, namely drilling-induced fractures (DIFs) and wellbore breakouts (BOs). BOs are a type of wellbore failure that develops when circumferential compressive stress concentrations of the wellbore exceed the required stress needed for compressive failure of the wellbore wall. BOs produce a wellbore profile with symmetric wellbore wall cave-ins oriented perpendicular to the S_{Hmax} orientation. DIFs develop when circumferential stress concentrations surrounding the wellbore exceed the amount needed for tensile failure of the wellbore wall. Upon development, DIFs are oriented parallel with S_{Hmax}. Resistivity and acoustic image log data were collected from the Chester 8-16 well to assess the potential presence and orientation of DIFs and BOs. Neither DIFs nor BOs were identified in the Chester 8-16 well. Changes in geomechanical properties are typically significant from one formation to the another one due to the variation in rock physical parameters. Conversely, the changes in S_{Hmax} azimuth are mainly due to the tectonic history of the basin and the presence of major structural features (e.g. folds and faults). As a result, the similar S_{Hmax} azimuth could be expected in the formations below Salina salt formation.

3.3.3 S_{Hmax} Azimuth Analysis Using Image Log Data

Multi-receiver sonic instruments measure fast and slow shear wave velocities and azimuth of fast shear wave, which are not measured by the conventional dipole sonic logging tool. The example of fast and slow shear wave velocities and azimuth of fast shear wave in Salina salt formation was shown in Figure 3-6. The advantage of having shear-wave velocity anisotropy data (i.e., fast shear-wave and slow shear-wave velocities) is that it allows for estimating maximum horizontal stress orientation (S_{Hmax}) which is a fundamental geomechanical parameter required to characterize the in-situ stress regime. S_{Hmax} orientation can be read directly from the azimuth of the fast shear-wave velocity plot. Fast shear-wave azimuth data were plotted on a rose diagram (Figure 3-7). The diagram included all fast shear measurements made in the caprock-reservoir formations penetrated by the Chester 8-16 well. The fast shear-wave azimuth data showed the mean value of N75E for S_{Hmax} orientation.

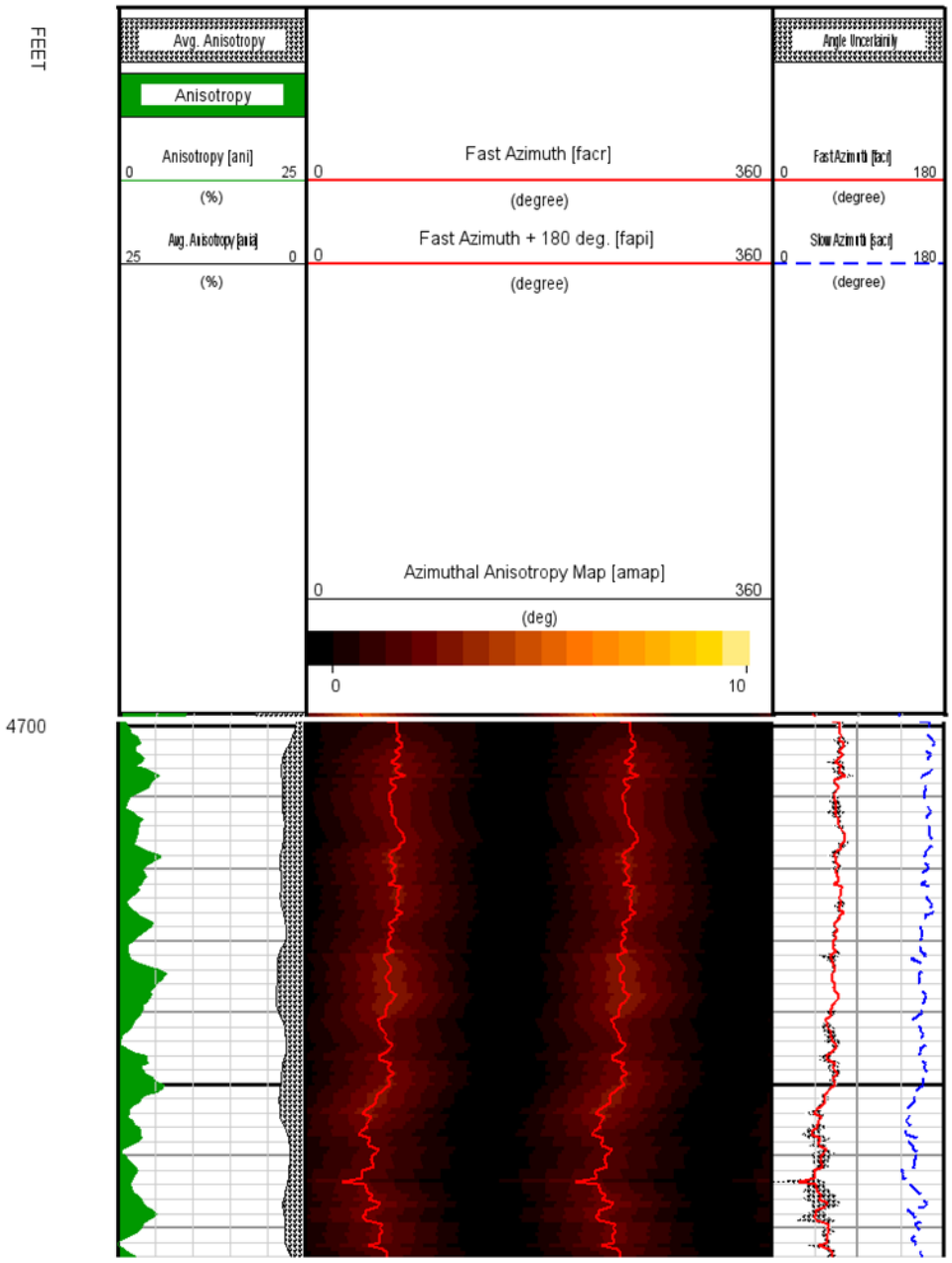


Figure 3-6. Anisotropy % (left track), fast shear wave azimuth (middle track), fast and slow shear wave Azimuth (right track) in a section of the Salina Formation of the Chester 8-16 well.

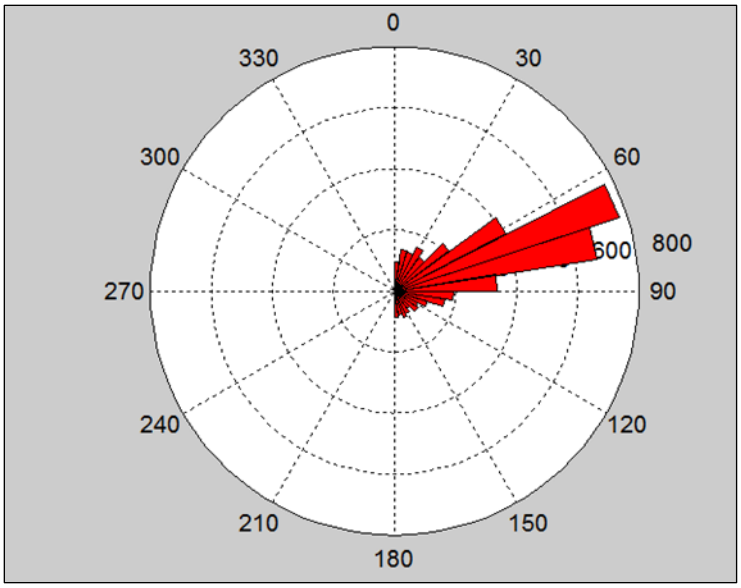


Figure 3-7. Rose Diagram of fast shear-wave azimuth data for Chester 8-16 well.

3.4 Summary

Fundamental rock mechanical properties (Poisson's ratio, Young's modulus, dynamic shear modulus, and bulk modulus) and in-situ stress parameters (S_{Hmax} azimuth and vertical stress) of five caprock-reservoir formations were studied based on available data from the Chester 8-16 well. The data for geomechanics characterization included dipole sonic log, density log, shear wave anisotropy data, and image log data. The geomechanical characterization resulted in the following findings:

- Results included estimates of the Poisson's ratio, Young's modulus, dynamic shear modulus, and bulk modulus for the Chester 8-16 well. The individual well data for Chester 8-16 was aggregated into a single histogram for each dynamic elastic parameter for each formation to gain an understanding of the variation in the properties of the formations. Poisson's ratio values were relatively similar across all formations. The Salina Formation had significantly lower Young's modulus values in comparison to carbonate and evaporite formations.
- Based on the analysis of the shear wave anisotropy data analysis, the mean orientation of the S_{Hmax} azimuth was N75E.

Chapter 4. Well Testing

4.1 Introduction

4.1.1 Open-Borehole Formation Testing

Reservoir Pressure Measurements

In-situ reservoir pressure measurements were attempted at 16 depths in the open borehole section below the A-2 Carbonate using the Baker Hughes Reservoir Characterization eXplorer (RCX) tool. At 10 of the 16 locations, pressure could not be measured because the formation was very tight (poorly permeable), which precluded establishing a seal between the packer and the borehole wall. A stabilized pressure measurement (i.e., pressure recovered to the pre-pumping level) was obtained at three locations, which allowed mobility to be estimated at these depths. At the other three locations, the test was halted before a stable pressure was achieved; however, the pressure reading at the time the test was halted provides a low estimate of true reservoir pressure at that depth (i.e., since pressure was still recovering [increasing] when the test was halted) Table 4-1. Figure 4-1 shows the depth of the six pressure values (yellow diamonds) alongside log-porosity. The black symbols (diamonds) on the vertical axis correspond to the depths where pressure measurements were attempted. The five red vertical lines correspond to the depths where the Sagerider permanent casing mounted pressure gauges were installed.

Table 4-1. Summary of In-Situ Reservoir Pressure and Mobility Measurements.

Depth, MD (ft)	Depth, TVD (ft)	Temperature (F)	Hydrostatic Pressure (psia)	Pumped Volume (L)	Buildup Pressure (psia)	Mobility (mD/cP)
5884.2	5787.5	100.4	2413	3.4	526.894	40.3
5911.3	5814.6	101.3	2056	3.1	685.19	7.4
6137.1	6040.3	102.1	2136	---	780*	ND
5858.2	5761.5	101	1915	1.8	527.82	6.2
5751.1	5654.5	101.1	2987	---	558*	ND
5792.9	5696.2	101.2	2888	---	650*	ND

**buildup pressure not stable*

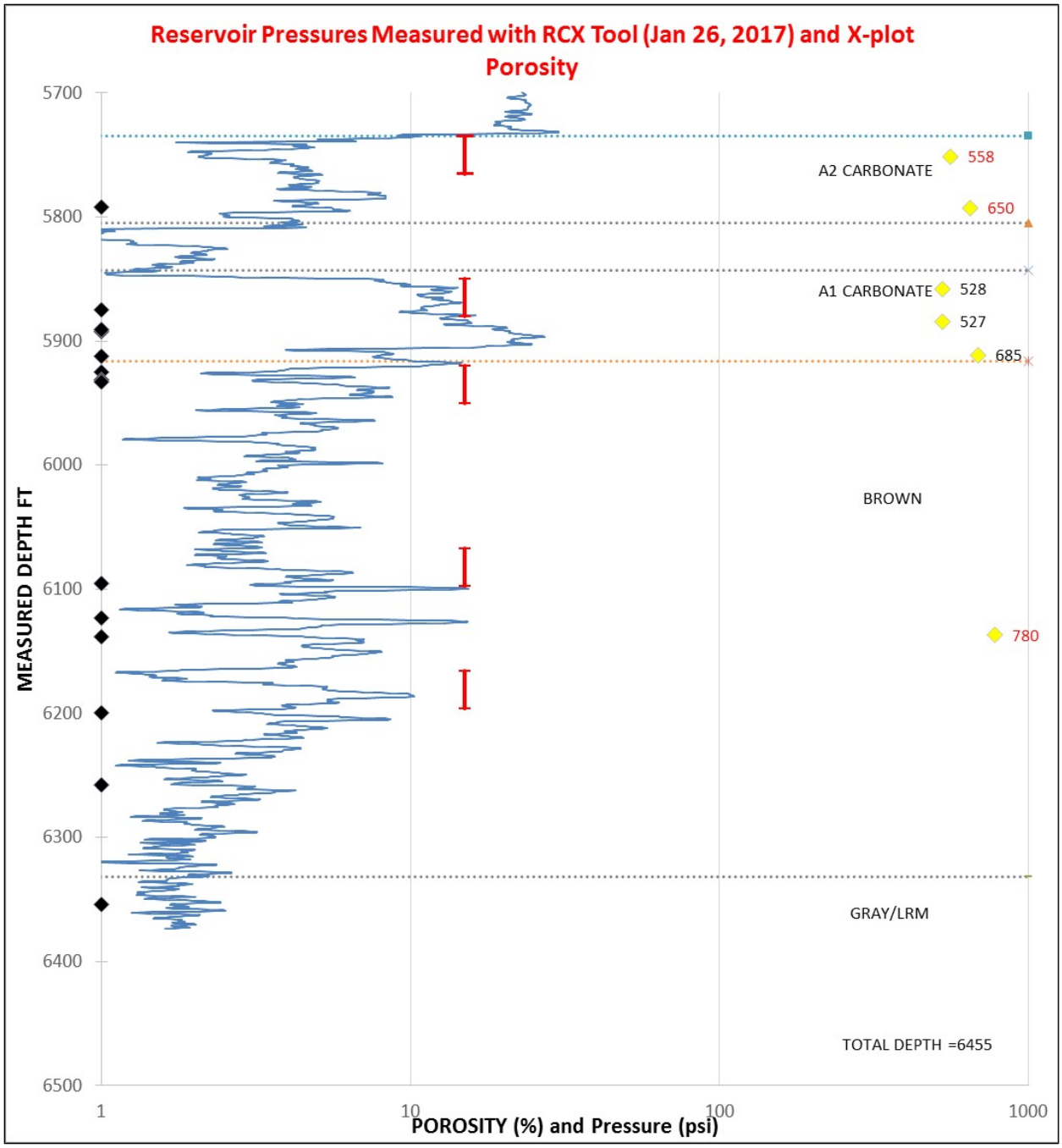


Figure 4-1. Reservoir Pressures (yellow diamonds) Measured with Baker Hughes RCX Tool.

4.2 Hydraulic Well Tests

Two open borehole local interference (withdrawal-buildup) tests were conducted in Chester 8-16 on January 27, 2017 to determine hydraulic parameters of the primary reservoir interval (the A1 Carbonate) in the Chester 16 reef. The tests were performed by Baker Hughes using their RCX tool configured with a straddle packer and an observation probe. The objective of the tests was to obtain representative estimates of the horizontal and vertical permeability of the primary reservoir interval, and to assess characteristics of the flow regime. This section provides a summary of the two LITs.

The RCX tool is illustrated in Figure 4-2. with the packers inflated, the straddle packer isolated a test interval 3.28 ft. in length within the open borehole. The observation probe was positioned 6.5 ft above the center of the straddle-packer interval to provide pressure data to assess the vertical permeability between the top of the straddle packer and the observation probe. The depth of each test is given in Table 4-2.

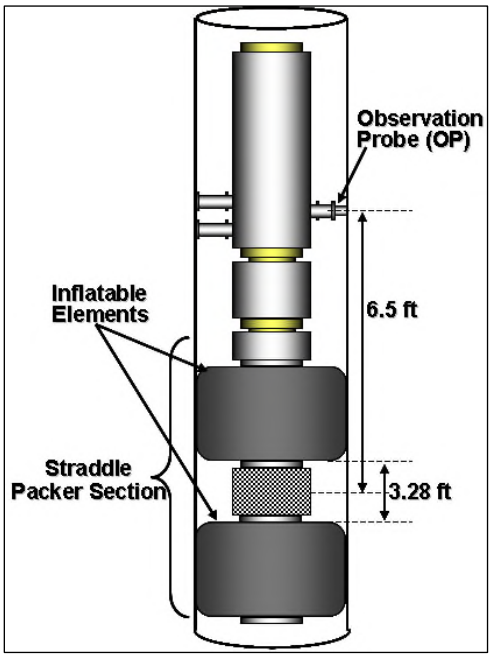


Figure 4-2. Schematic of Straddle Packer and an Observation Probe combination for a Local Interference Test.

Table 4-2. Depth of Local Interference Tests.

Test	Formation	SP-midpoint (ft, MD)	OP (ft, MD)
LIT-1	A1 Carbonate	5890.7	5884.2
LIT-2	A1 Carbonate	5864.7	5858.2

4.2.1 Local Interference Test #1 (5890.7 ft)

A total 57 liters of fluid was pumped (removed) from the straddle packer test interval in 133 minutes which was followed by a pressure buildup period that lasted 428 minutes. An average flow rate of 7.2 cm^3/s was obtained with the 434 cm^3 pump. The flow rate just before the final build up period was 7.5 cm^3/s. The maximum pressure drawdown during flow period was 453.2 psi in the straddle packer test interval. Figure 4-3 is a plot of the pumping rate and the pressure response in the straddle packer test interval during LIT-1. The pressure response at the observation probe during LIT-1 is shown in Figure 4-4. A pressure drop of 10.2 psi was recorded at the observation probe, indicating there was good hydraulic communication between the straddle packer interval and the observation probe.

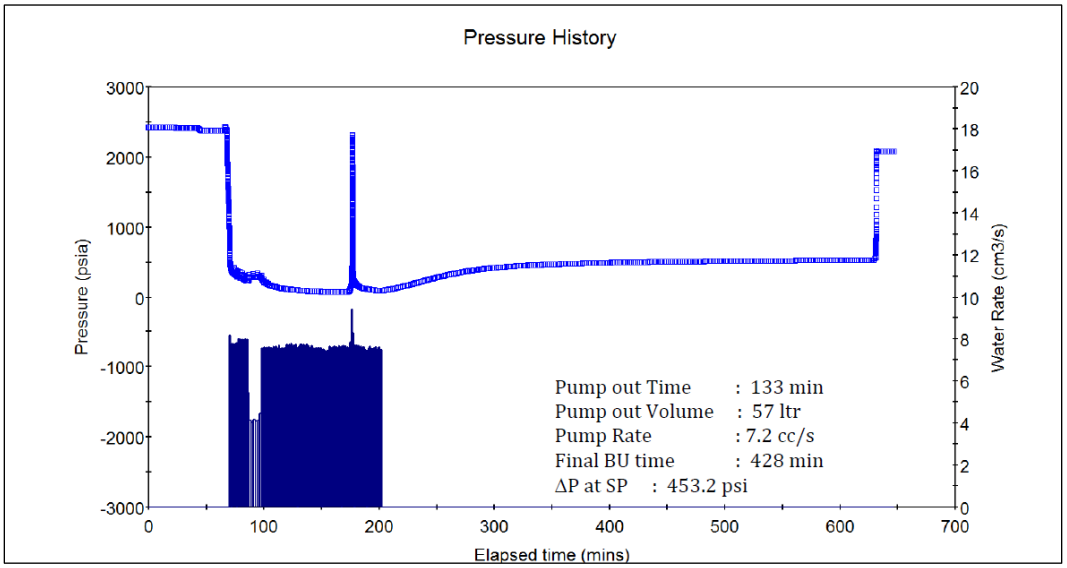


Figure 4-3. Pumping Rate and Pressure Response in the Straddle Packer Interval during LIT-1.

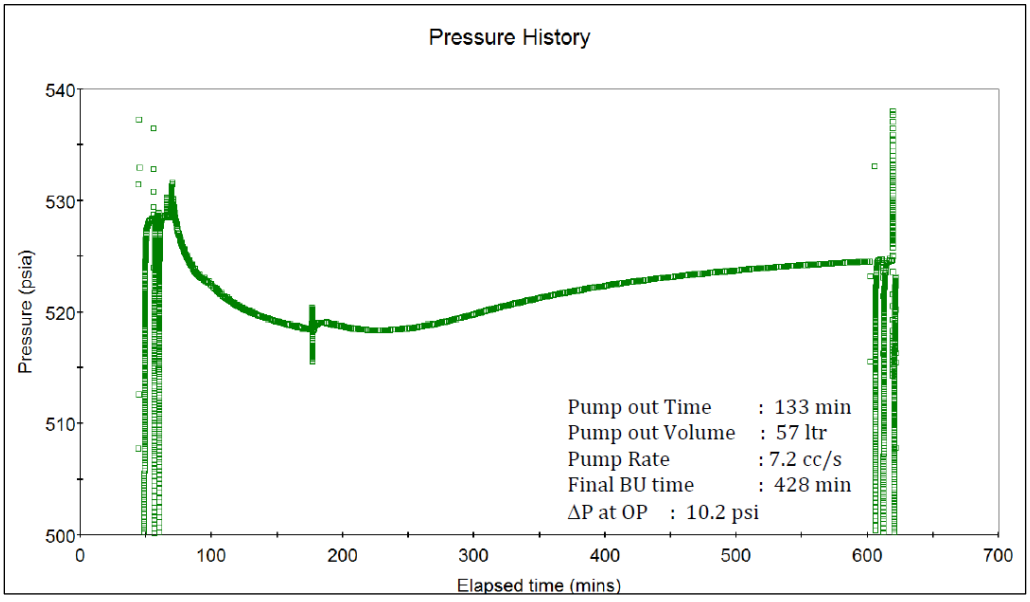


Figure 4-4. Pressure Response at the Observation Probe during LIT-1.

A diagnostic log-log plot for both the straddle packer (blue symbols) and observation probe (green symbols) pressure response data during the buildup period is shown in Figure 4-5. The straddle packer pressure data (blue squares) and pressure derivative (blue triangles) show that the early time pressure response was dominated by tool storage and nearby effects of skin (pressure changes). After the tool storage period, there is a spherical flow regime around 200 minutes (the red line in Figure 4-5). Infinite-acting radial flow is not observed in the straddle packer interval during the test. The late time derivative data from the straddle packer interval indicates that the permeability of the tested zone cannot be less than 0.1 mD but a more precise estimate cannot be determined from the straddle packer data alone since infinite acting radial flow was not observed during the test. However, because a pressure response was observed at the observation probe, a simultaneous matching analysis of the straddle packer data and observation probe data was possible to provide estimates of the horizontal permeability and the vertical permeability for the reservoir region between the two probe locations. The red and green lines in Figure 4-5 show the calculated pressure response at the two probes using an analytical model (pressure data were analyzed with the analytical well test software “Interpret-2010” (Paradigm)) of a partially penetrating deviated well in an infinitely acting homogeneous reservoir. Reservoir parameters derived from the model include:

- vertical permeability (*kz*) of 0.01 mD
- horizontal permeability (*kx*) of 0.9 mD.
- formation pressure (*P**) of 530.5 psia at the straddle packer depth
- radius of investigation of the test of 78 ft.

Figure 4-6 shows the observed and the modeled pressures for the straddle packer interval and the observation probe for the entire test period (Figure 4-5 shows only the buildup period). The discrepancy between the actual and calculated pressure data during the pump-out period is attributed to changing wellbore storage that cannot be simulated by the analytical model; however, the modeled data matches the general trend of the observed pressures. Table 4-3 lists the properties used as input in the analysis of LIT-1 and LIT-2.

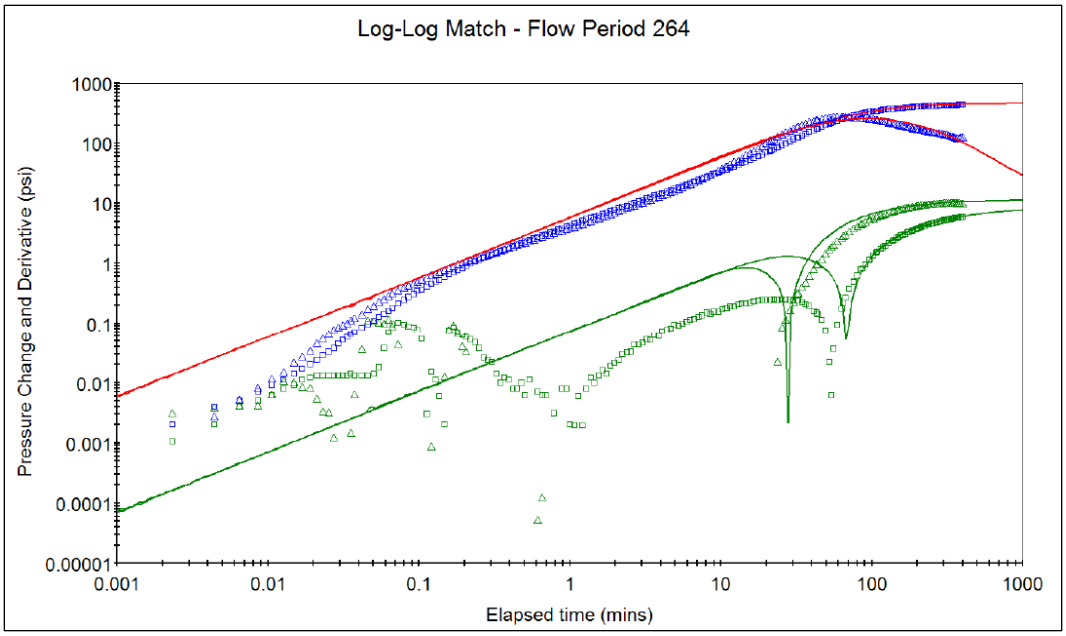


Figure 4-5. Log-log diagnostic plot of straddle-packer (blue symbols) and observation probe (green symbols) pressure response during LIT-1 showing modeled response at the straddle packer (red line) and observation probe (green line).

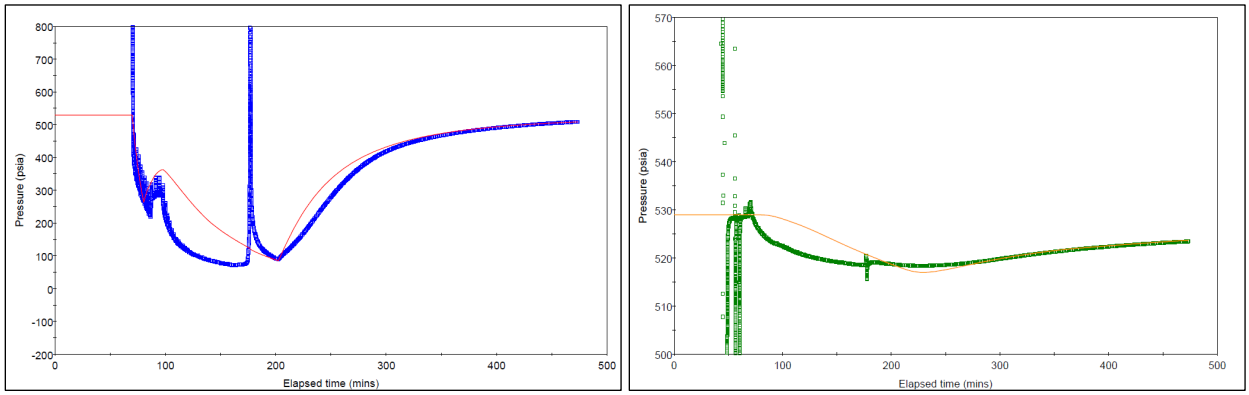


Figure 4-6. Pressure history match of test interval data (left) and observation probe data (right) for the entire LIT-1.

Table 4-3. Reservoir and Fluid Parameters used in the analysis of LIT-1 and LIT-2.

Parameter	Unit	LIT-1	LIT-2	Source
Wellbore radius	in	3.9375	3.9375	Actual
Temperature	^{o}F	101.7	100.9	Measured
Porosity	%	27	27	Log
Reservoir Thickness	ft	20	4	Assumption
Total compressibility	1/psi	7.4456E-6	7.4449E-6	Assumption
Water viscosity	cP	0.79	0.79	(a)

(a) based on empirical fluid property modeling at reservoir pressure and temperature

4.2.2 Local Interference Test #2 (5864.7 ft)

A total 65.1 liters of fluid were pumped (removed) from the straddle packer interval in 190 minutes, which was followed by a pressure recovery period of 168 minutes. An average flow rate of 5.7 cm^3/s was obtained with the 434 cm^3 pump on the RCx tool. The flow rate just before the final build up period was 2.7 cm^3/s. The pressure drawdown during the flow period was 352.2 psi in the test interval and 0.5 psi at the observation probe. Figure 4-7 is a plot of the pumping rate and the pressure response in the straddle packer test interval during LIT-2. The pressure response at the observation probe during LIT-3 is shown in Figure 4-8.

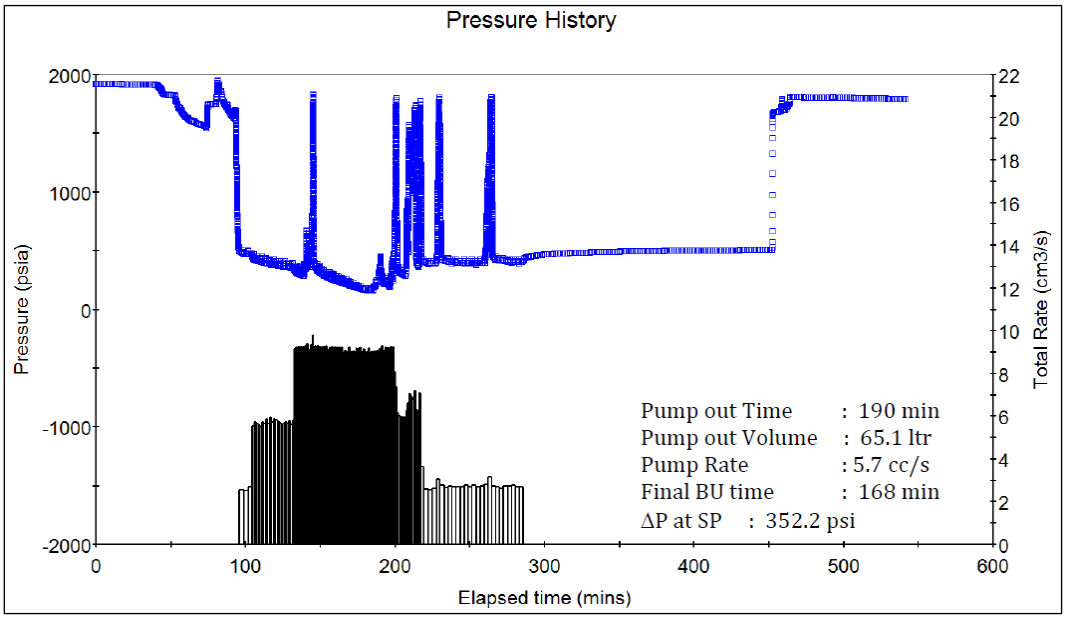


Figure 4-7. Pumping Rate and Pressure Response in the Straddle Packer Interval during LIT-2.

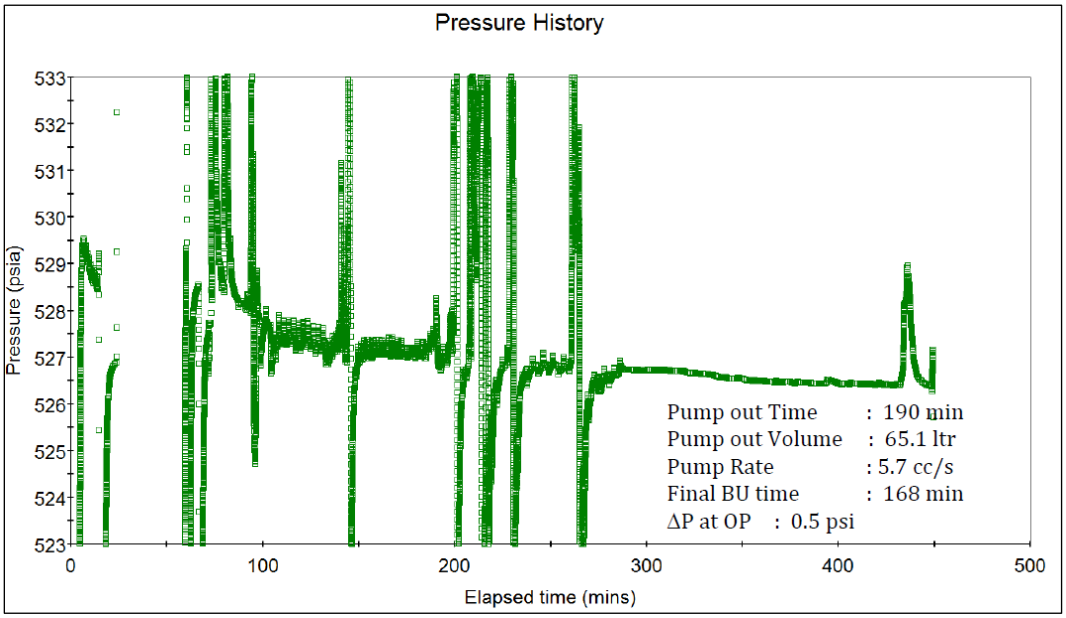


Figure 4-8. Pressure Response at the Observation Probe during LIT-3.

A diagnostic log-log plot for straddle packer data and the observation probe data is shown in Figure 4-9. The observation probe data is not analyzable due to the small pressure drop (i.e. 0.5 psi). The early time pressure response in the straddle packer interval was dominated by tool storage and nearby effects of skin. After the tool storage period, the derivative (blue triangles) shows radial flow (horizontal derivative) at around 0.1 minute, followed by an increasing derivative which may indicate changing reservoir properties (decreasing permeability). The late time derivative has a decreasing slope, suggesting a uniform permeability value further from the well. Another possible explanation for the shape of the pressure derivative is a fracture exists that intersects the test interval. However, there is no evidence of a fracture from the image log or other open hole logs.

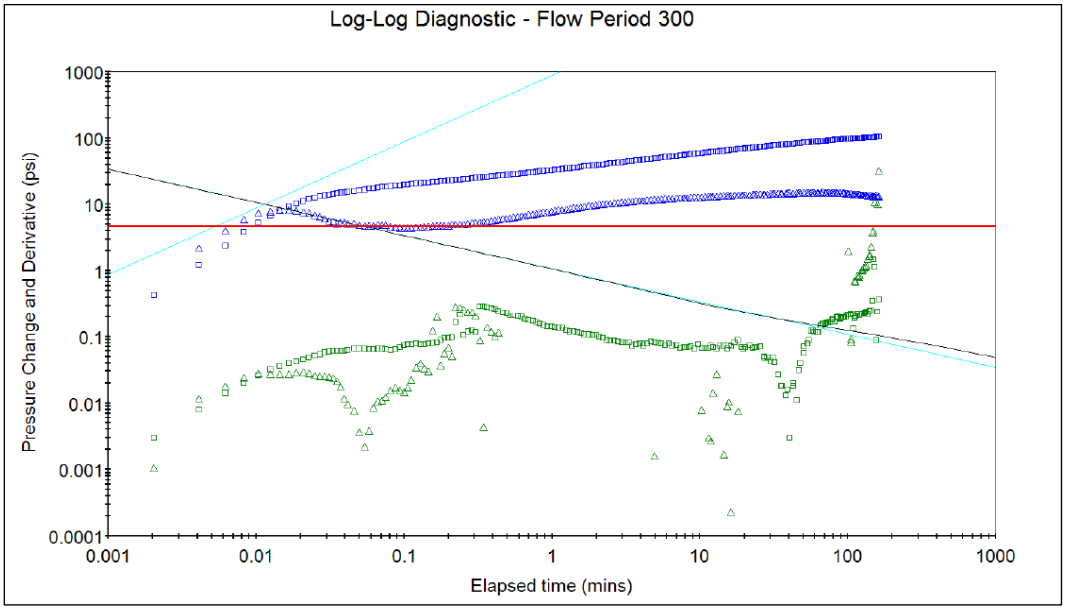


Figure 4-9. Log-log diagnostic plot of straddle-packer (blue symbols) and observation probe (green symbols) pressure response during LIT-2 build-up period, plus modeled pressure and pressure derivative (solid lines) in the straddle packer interval.

Reservoir properties were estimated by simulating the test data using a model of a partially penetrating deviated well in an infinitely acting radial composite reservoir model (a radial composite reservoir has concentric inner and outer zones with different properties). The red lines in Figure 4-10 show the calculated pressure response and pressure derivative for the buildup period in the test interval using the analytical model. Reservoir parameters derived from the model include:

- inner zone *kx* of 5.1 mD
- outer zone *kx* of 1.3 mD
- radius of inner zone of 4 ft
- radius of investigation during the test is 86 ft
- average product of *k*h* for outer zone is 5.2 mD.ft.
- a *P** of 528.4 psia at the straddle-packer depth.

Figure 4-11 compares the observed and the modeled pressure for the entire test period. The discrepancy between the actual and calculated pressure data during the pump-out period is attributed to changing wellbore storage that cannot be evaluated with the analytical model. The observed pressure spikes during the pump-out period are attributed to slight deformation of the

straddle packer. Nevertheless, the modeled data is consistent with the trend in the actual pressure data.

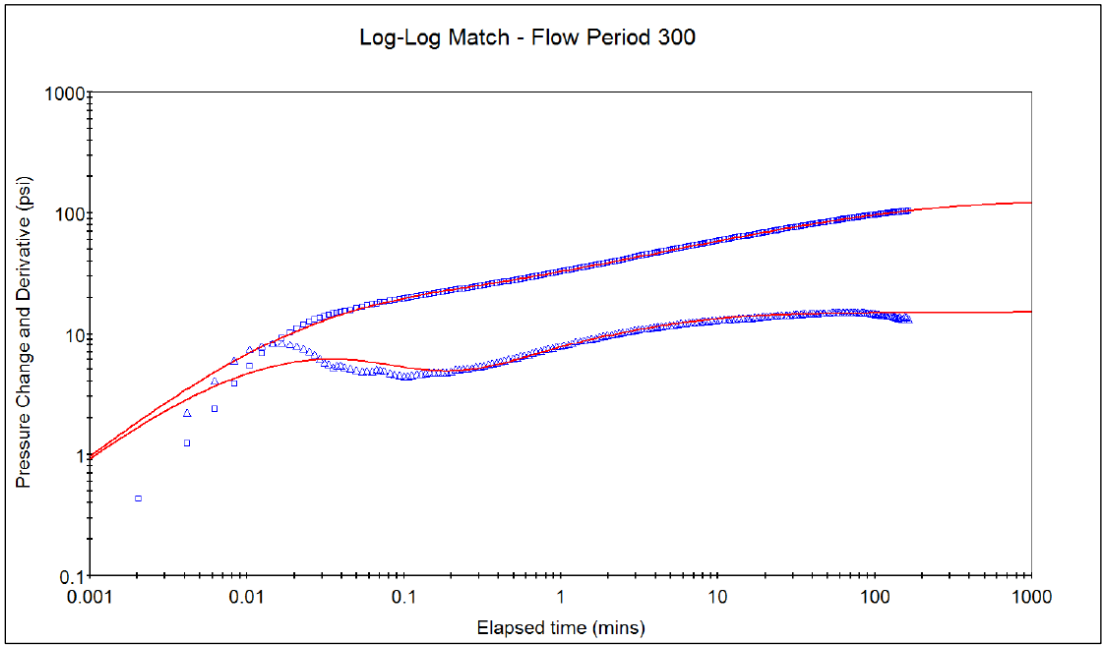


Figure 4-10. Comparison of observed pressure (blue squares) and pressure derivative (blue triangles) data to modeled pressure and pressure derivative (red lines) for the LIT-2 buildup period.

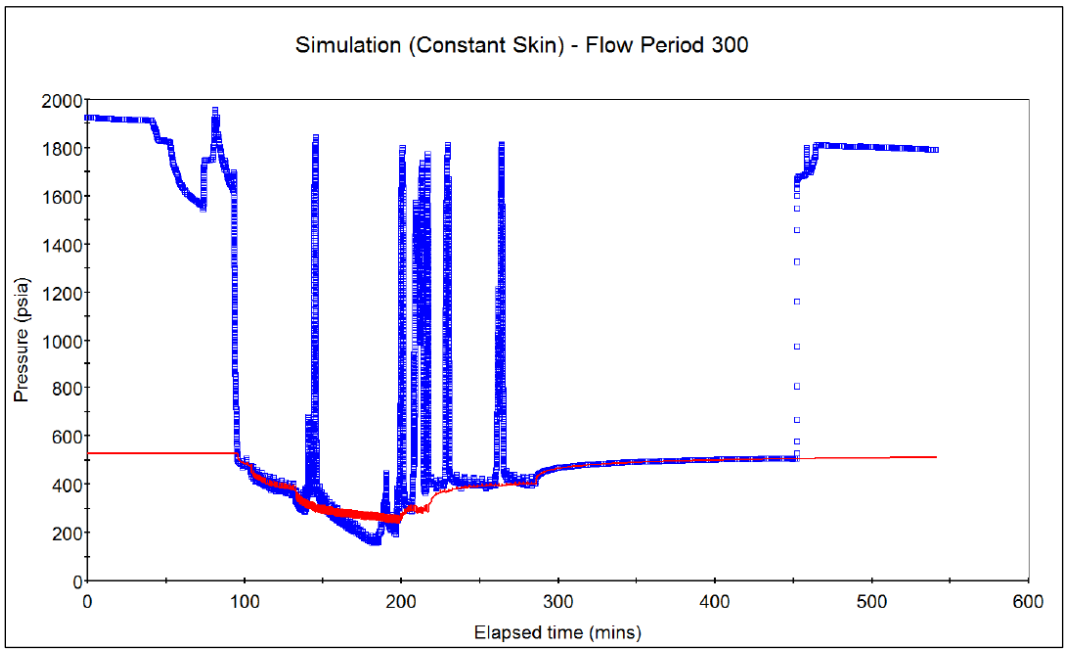


Figure 4-11. Pressure history match of the LIT-2 pumping and buildup periods.

4.2.3 Summary

A summary of the reservoir parameters determined from the two LITs in the A-1 Carbonate is provided in Table 4-4. Analysis of both LIT-1 and LIT-2 indicate that the A-1 Carbonate has low permeability.

Table 4-4. Summary of Reservoir Properties determined from LIT-1 and LIT-2.

Test	Depth (ft)	k_X (mD)	k_Z (mD)	h (ft)	kx*h (mD.ft)	ri (ft)	Model
LIT-1	5890.7	0.9	0.01	20	18	78	Homogeneous Infinite lateral extent
LIT-2	5864.7	5.1 (inner) 1.3 (outer)	N/A[(a)]	4 (inner)[(b)] 19 (outer)	20.4 (inner) 5.2[(c)] (outer) 25.5[(c)] (outer)	4 (inner) 86 (outer)	Radial composite – Infinite lateral extent

(a). Vertical permeability cannot be estimated due to insufficient pressure decline on the observation probe.
(b). Assumes a tight streak with low permeability separates the straddle packer from observation probe is present that slows down the pressure response at the observation probe. The flowing (straddle packer interval) was assumed to be 4 ft for the pressure analysis.
(c). The average product of ***k*h*** for outer zone is 5.2 mD.ft. It should be noted that this value of ***k*h*** represents the 4 ft flow unit where the straddle packer is located. The pre-test conducted in observation probe before the LIT indicates the reservoir zone where the observation probe is located is permeable. The LIT implies that the observation probe is separated from the straddle packer zone by a thin (e.g., 1 ft) low permeability zone. Therefore, the product of ***k*h*** for the 19 ft reservoir zone (excluding the 1 ft thin zone between observation probe and SP) should be higher than the calculated value in this analysis. If the radial composite model is assumed to be valid for all 19-ft. thick reservoir unit the product of ***k*h*** would be 25.5 mD.ft (1.34 mD* 19 ft).

4.3 Micro-Frac Tests

Four (4) wireline MicroFrac tests were conducted in the Chester 8-16 well on January 28, 2017 to measure key geomechanical parameters, including formation breakdown pressure, fracture reopening pressures, fracture propagation, and fracture closure pressure, for the primary reservoir and caprock formation(s). All four tests achieved formation breakdown, showed fracture re-opening pressures and good fracture propagation pressures. The tests were performed by Baker Hughes using their RCX tool configured with a straddle packer. This section provides a summary of the MicroFrac testing results.

The depth of each of the MicroFrac tests is given in Table 4-5 along with the name of the formation tested and the number of test cycles performed in the interval.

Table 4-5. Summary of Open Borehole MicroFrac Tests Performed in Chester 8-16.

Station	Formation	Depth (MD) (ft)	Cycles
1	A-1 Carbonate	5861	3
2	Brown Niagaran	5967	4
3	A-2 Carbonate	5791	5
4	A-2 Carbonate	5765	4

The specific depth interval was based on formation type, borehole quality, formation stress contrast, formation mechanical properties and in-situ stress conditions. Zones with extensive breakouts that could compromise the sealing capacity of the inflatable elements as well as high rugosity borehole wall that could deteriorate the rubber during inflating and deflating of elements were avoided. Finally, it is critical for optimum fracture containment and proper fracture

propagation that the inflatable elements are positioned on layers with sufficient stress contrast with respect to the isolated formation interval in order to avoid sleeve fracturing and early hydraulic communication between the fracture and the hydrostatic pressure.

4.3.1 MicroFrac Test 1 (5861 Ft MD)

The first MicroFrac test was performed in the A-1 Carbonate formation at a depth of 5861 ft MD. The test history is illustrated in Figure 4-12. The bottom hole pressure of the isolated interval (APQJ) and the absolute pressure inside the packers (ASPEP) are denoted in blue and magenta, respectively. The flow rate is presented with a red line [cm^3/sec] while the cumulative displaced volume is shown in green [liters] and the bottom hole temperature is indicated in brown.

The straddle packers were inflated in about 17 minutes (with the 1970RB 717 cm^3 pump) with the hydrostatic pressure at 1777.3 psi. It was observed that there was fluid loss in the well and the hydrostatic pressure kept changing. Once the packers pressure had stabilized, two packer integrity checks were performed at 2050 psi and 2250 psi, which are equivalent to 273 psi and 473 psi above hydrostatic pressure, respectively. Both packer integrity checks showed good packer seal. Following the integrity tests, three successful injection test cycles were performed. A fourth injection cycle was attempted three times but was not successful at reopening the fracture within the pressure constraints of the packers (5,000 psi was used as the maximum test interval pressure, APQJ. Injection was halted if fracturing or reopening could not be achieved within this pressure).

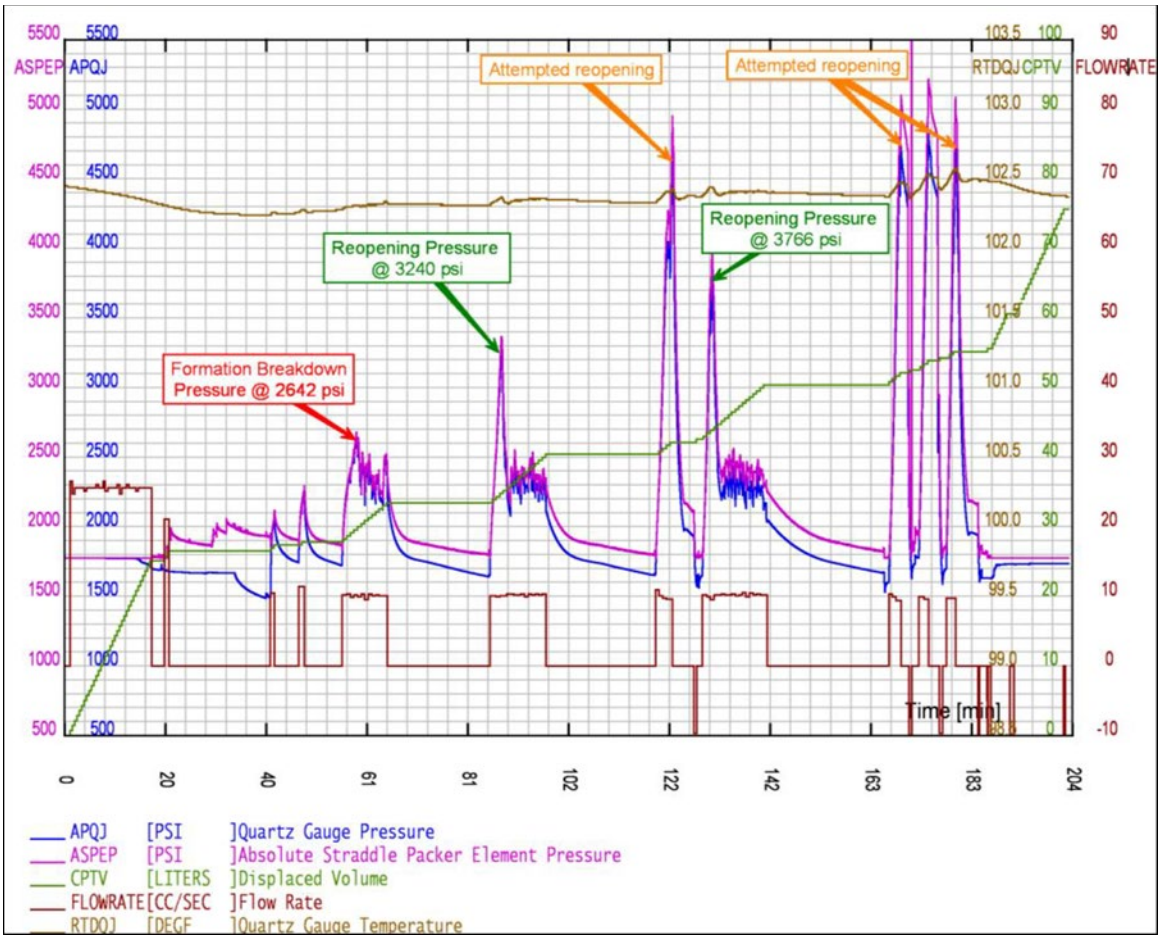


Figure 4-12. Test History for MicroFrac Test 1 in the A-1 Carbonate at a depth of 5861 ft MD.

Formation Breakdown Pressure

Formation breakdown was achieved in the first injection cycle (FOT1) as shown in Figure 4-13. The breakdown pressure is 2642 psi, which is 865 psi above the hydrostatic pressure. The fracture was propagated for ~6 minutes after formation breakdown. After shut-in, natural pressure decline was monitored for ~20 minutes.

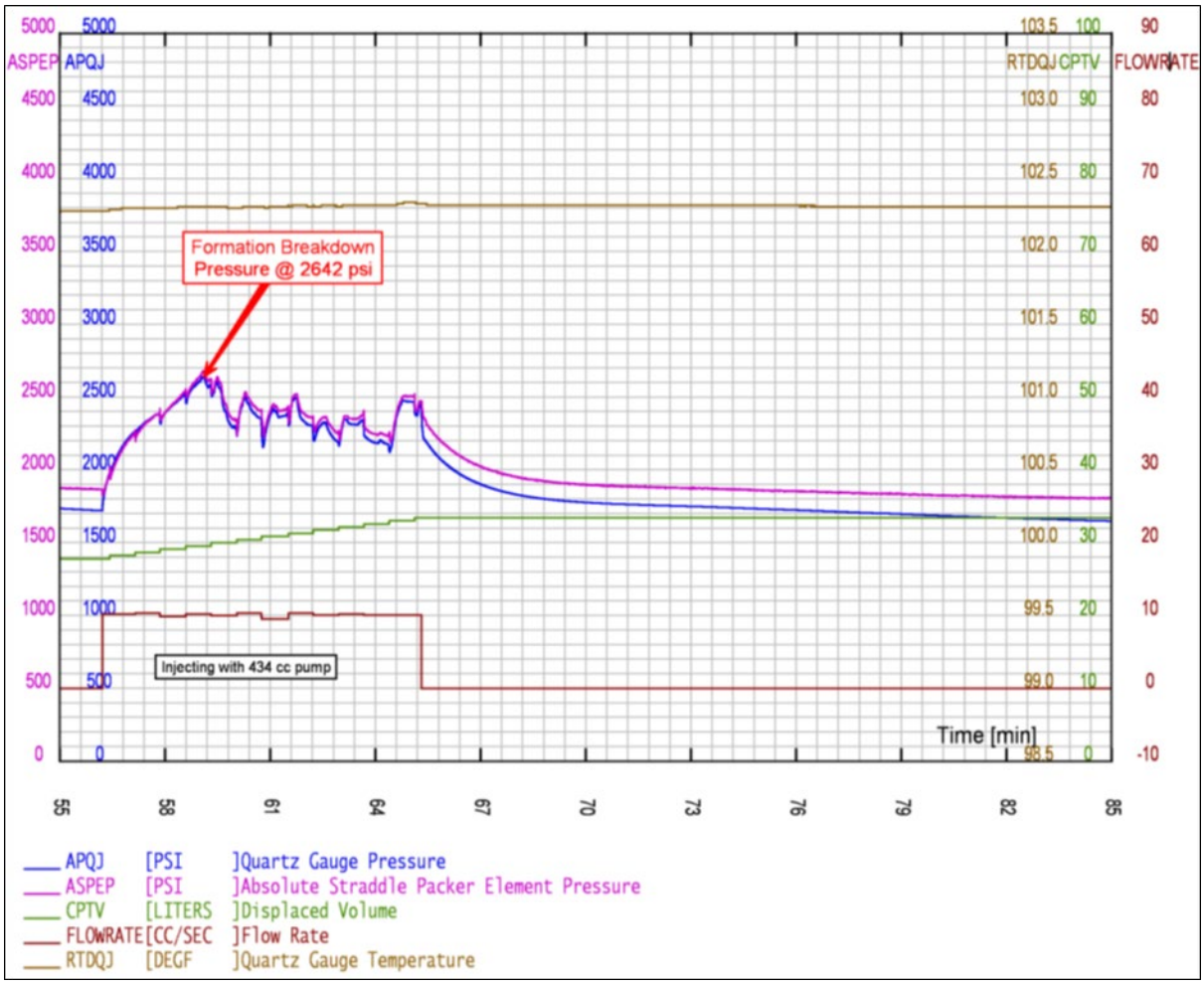


Figure 4-13. Fracture Breakdown Pressure During the First Injection Cycle (FOT1) of MicroFrac Test 1.

Fracture Reopening Pressure

Fracture reopening pressure was measured in cycles 2 and 3 of MicroFrac test 1. Reopening n pressures were 3240 psi (FOT2), 3766 psi (FOT3), and (FOT4).

It was observed that the reopening pressure was higher than the breakdown pressure. This could be a result of the drilling-mud additives bridging in the fracture and making it harder to reopen the induced fracture. Consequently, the particles trapped in the fracture create a restriction that needs to be overcome to reopen the existing fracture. It can also be noted the propagation pressure is consistent, suggesting that no new fracture has been created but rather that propagation of the same fracture occurred.

Fracture Propagation Pressure

Fracture reopening pressure was measured in cycles 2 and 3 of MicroFrac test 1. Fracture propagation pressure was 2300 psi for both FOT2 and FOT3.

Fracture Closure Pressure

The fracture closure pressure was identified by three different methods: (I) Pressure decline analysis using the APQJ pressure vs. shut-in time; (II) Log-Log pressure decline analysis using the pressure derivative of the delta pressure and delta time in log-log plot; and (III) the G-function analysis by plotting the APQJ pressure vs G-time plot. All three pressure decline methods were performed using MinFrac software developed by Meyer and Associates.

The first method considers a linear regression behavior at the early stage of the shut-in time and the fracture closure pressure is associated with the deviation from the linear pressure decline behavior. To identify the peak of the curve, as a guide for fracture closure picking, plot the square-root of shut-in time multiplied by the pressure derivative in the square-root of time (t-½dP/dt-½). An example square-root of shut-in time plot is shown in Figure 4-14 for MicroFrac station 1/test cycle 1. This method yielded a fracture closure pressure of 1907 psi.

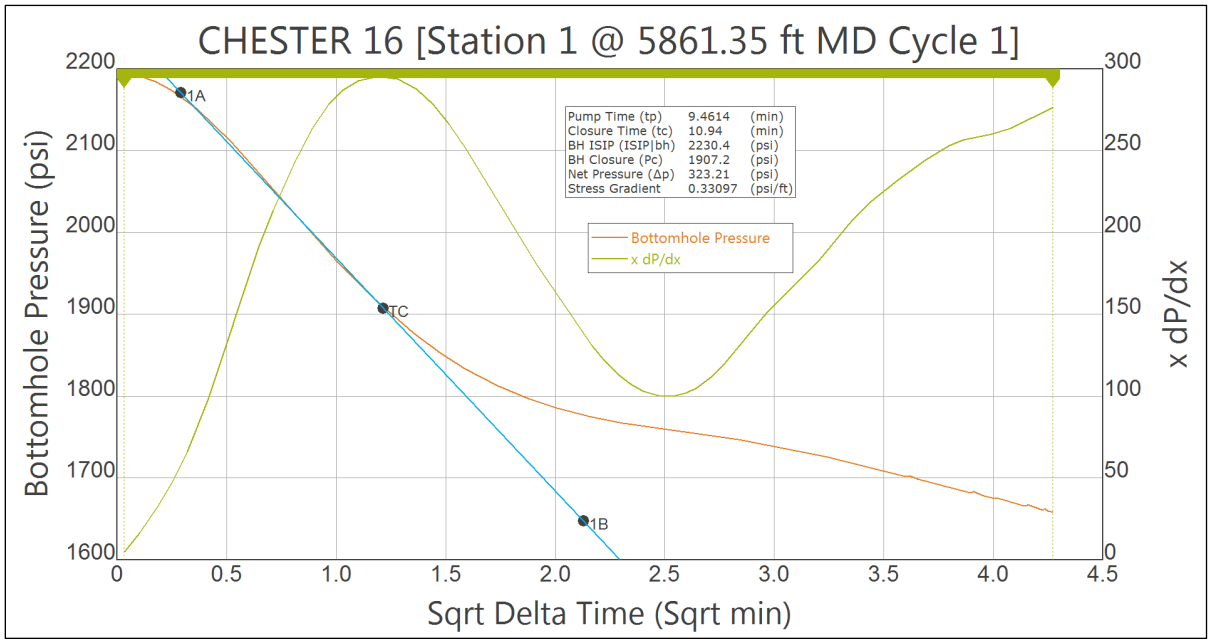


Figure 4-14. Example Square root of Shut-in-time Plot for Fracture Closure Identification in Station 1/Cycle 1.

The second method looks for a change in the slope of the pressure derivative d (log dP)/d (log dt) from a linear behavior around 0.5 slope into a decreasing trend (the change is associated with fracture closure). The pressure derivative curve must be around 0.5 for a dominant infinite-conductivity fracture flow regime when the fracture is still open; the pressure derivative decreases as the fracture closes. An example log-log of shut-in time plot is shown in Figure 4-15 for MicroFrac station 1/test cycle 1. This method yielded a fracture closure pressure of 1896 psi.

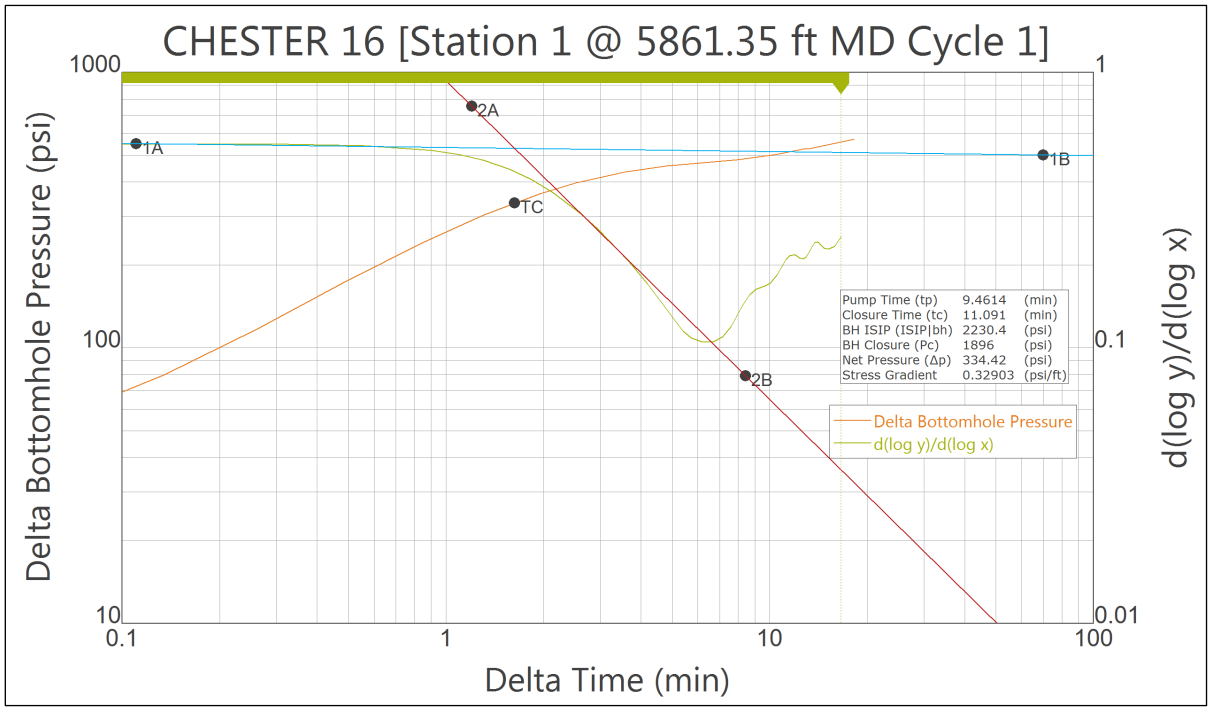


Figure 4-15. Example Log-Log of Shut-in Time Plot for Fracture Closure Identification in Station 1/Cycle 1.

The third method looks for a change in the behavior in the pressure versus G-function plot by identifying the change of slope of the GdP/dG derivative curve from linear increasing to flat or a decreasing trend. An example G-Function plot is shown in Figure 4-16 for MicroFrac station 1/test cycle 1. This method yielded a fracture closure pressure of 1918 psi.

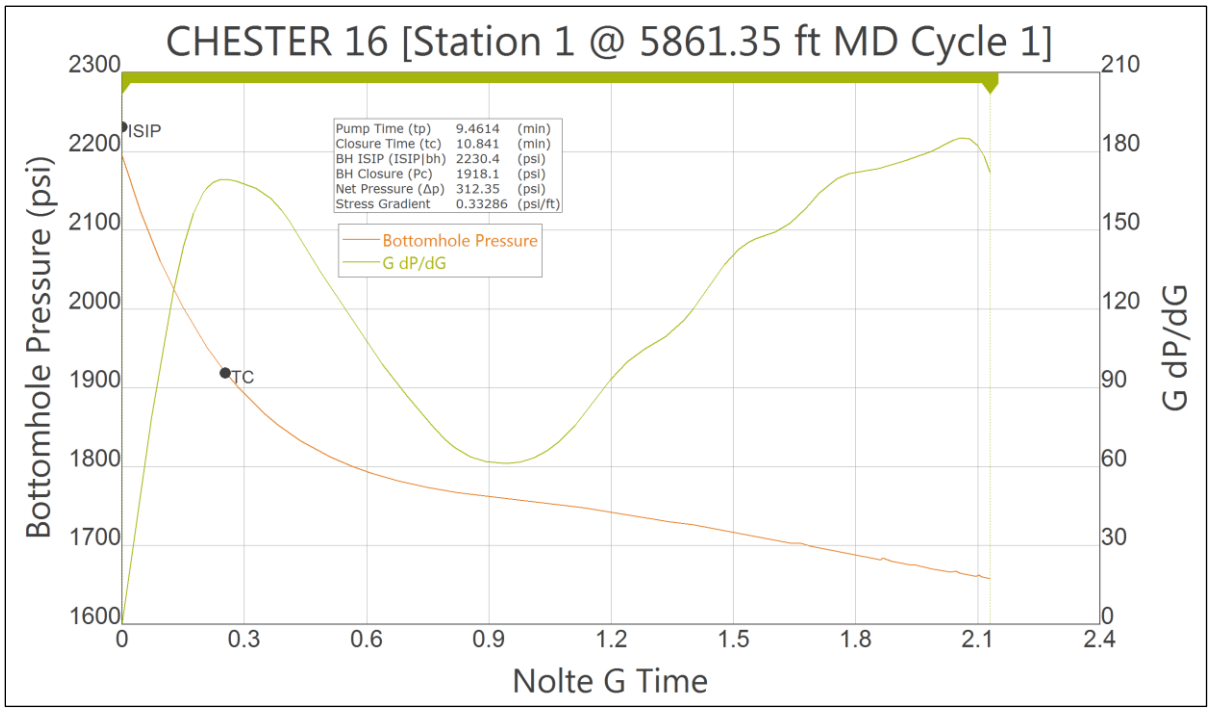


Figure 4-16. Example G-Function of Shut-in Time Plot for Fracture Closure Identification in Station 1/cycle 1.

The fracture closure pressure is defined in this report as the average of the three pressure decline analysis methods. Table 4-6 summarizes fracture closure pressure values for each of the three injection cycles for MicroFrac test 1.

Table 4-6. Fracture Closure Pressures for MicroFrac Station 1 (5861 ft MD).

Pressure Decline Analysis	Flowback Cycle	Fracture Closure, psi	Fracture Closure gradient, psi/ft
Square root of Shut-in Time	FOT1	1907.2	0.331
Log-Log	FOT1	1896.0	0.329
G-Function	FOT1	1918.1	0.333
Fracture closure		1907.1	0.331
Square root of Shut-in Time	FOT2	1874.0	0.325
Log-Log	FOT2	1848.2	0.321
G-Function	FOT2	1870.2	0.325
Fracture closure		1864.1	0.324
Square root of Shut-in Time	FOT3	1819.1	0.316
Log-Log	FOT3	1822.0	0.316
G-Function	FOT3	1815.7	0.315
Fracture closure		1818.9	0.316

4.3.2 MicroFrac Test 2 (5967 ft MD)

The second MicroFrac test was performed in the Brown Niagaran Formation at 5967 ft MD. The test history is illustrated in Figure 4-17. The straddle packers were inflated in ~17 minutes with the hydrostatic pressure at 1782.5 psi. Once the packers pressure had stabilized, two packer integrity checks were performed at ~1907.5 psi and 1989.5 psi, which is equivalent to 125 psi and 207 psi above hydrostatic pressure respectively. Both packer integrity tests showed good packer seal. Subsequently, three successful injection test cycles were performed.

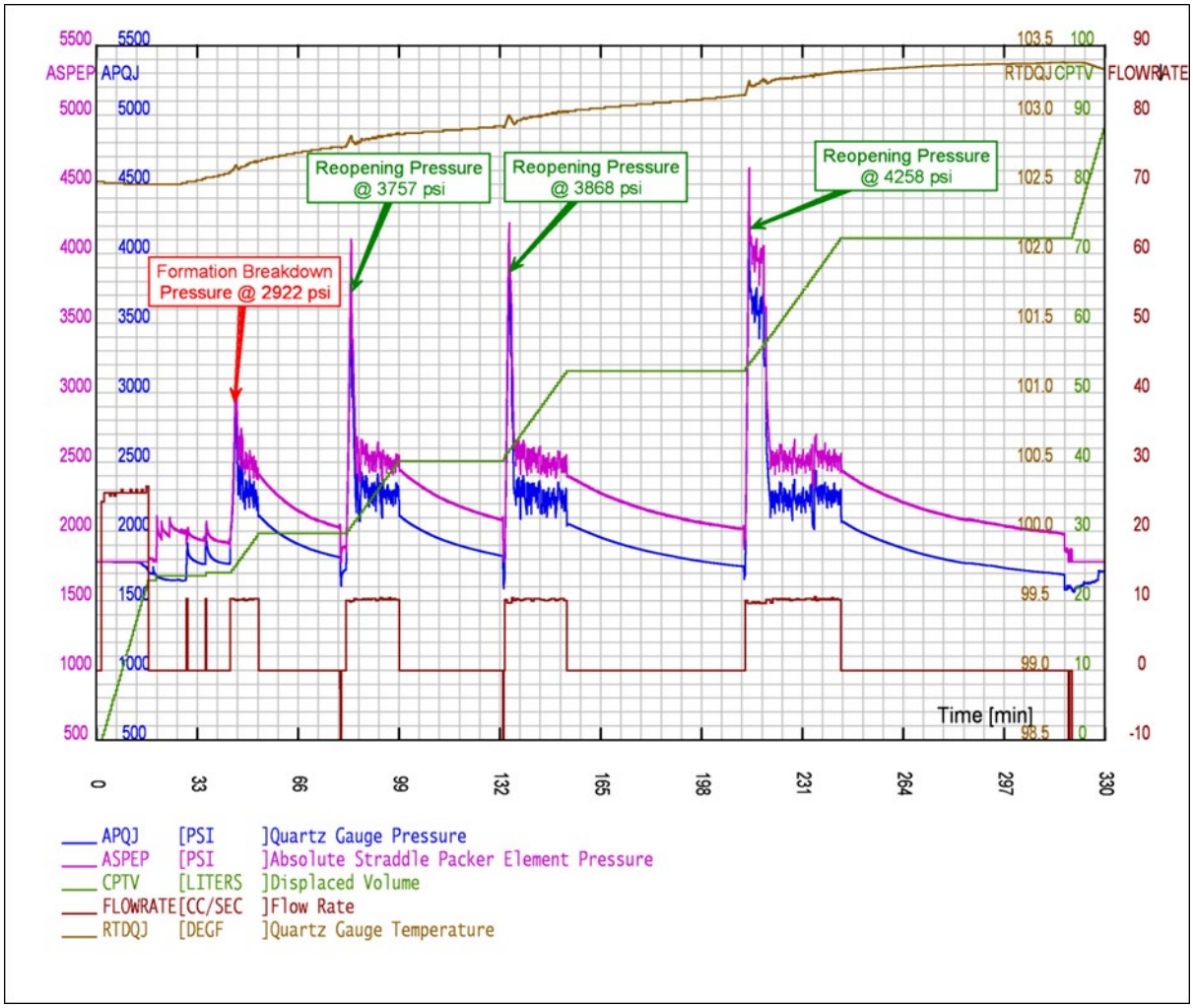


Figure 4-17. Test History for MicroFrac Test 2 in the A1 Carbonate at a Depth of 5967 ft MD.

Formation Breakdown Pressure

Formation breakdown was achieved in the first injection cycle (FOT1) as shown in Figure 4-18 below. The breakdown pressure was 2922 psi, 1139.5 psi above the hydrostatic pressure. The fracture was propagated for ~7 minutes after formation breakdown. After shut-in, fracture pressure was observed with a natural decline for ~28 minutes.

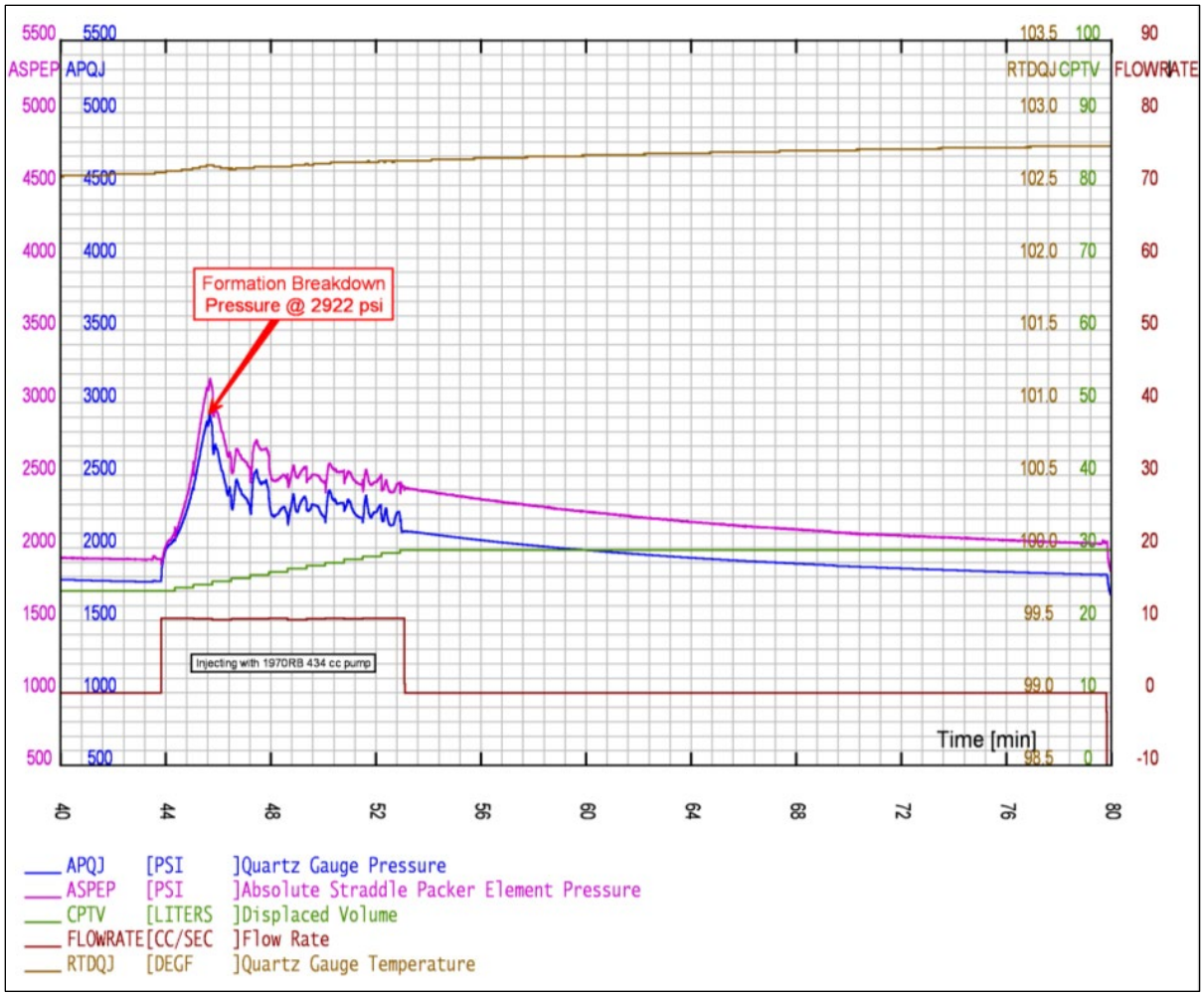


Figure 4-18. Fracture Breakdown Pressure During the First Injection Cycle (FOT1) of MicroFrac Test 2.

Fracture Reopening Pressure

Fracture reopening pressure was measured in cycles 2, 3 and 4 of MicroFrac test 2. Reopening pressures were 3757 psi (FOT2), 3868 psi (FOT3), and 4258 psi (FOT4). As was the case for MicroFrac test 1, the reopening pressure was higher than the breakdown pressure.

Fracture Propagation Pressure

Fracture reopening pressure was measured in cycles 2, 3 and 4 of MicroFrac test 2. Fracture propagation pressure was 2300 psi for all three test cycles.

Fracture Closure Pressure

Fracture closure pressure was measured in cycles 2, 3 and 4 of MicroFrac test 2. Table 4-7 summarizes the fracture closure pressure measurements for each test cycle determined with the three pressure decline analysis methods.

Table 4-7. Fracture Closure Pressures for MicroFrac Station 2 (5967 ft MD).

Pressure Decline Analysis	Flowback Cycle	Fracture Closure, psi	Fracture Closure Gradient, psi/ft
Square root of Shut-in Time	FOT1	1883.8	0.321
Log-Log	FOT1	1886.7	0.322
G-Function	FOT1	1883.5	0.321
Fracture Closure		1884.7	0.321
Square root of Shut-in Time	FOT2	1859.1	0.317
Log-Log	FOT2	1857.9	0.317
G-Function	FOT2	1857.3	0.316
Fracture Closure		1858.1	0.317
Square root of Shut-in Time	FOT3	1808.8	0.308
Log-Log	FOT3	1802.9	0.307
G-Function	FOT3	1806.8	0.308
Fracture Closure		1806.2	0.308
Square root of Shut-in Time	FOT4	1805.2	0.308
Log-Log	FOT4	1792.5	0.305
G-Function	FOT4	1800.0	0.307
Fracture Closure		1799.2	0.307

4.3.3 MicroFrac Test 3 (5791 FT MD)

The third MicroFrac test was performed in the A-2 Carbonate formation interval at 5791 ft MD. The test history is shown in Figure 4-19. The straddle packers were inflated in ~19 minutes with the hydrostatic pressure at 2849 psi (note: hydrostatic pressure is higher in this test because the borehole was filled with water after MicroFrac test 2). Once the packer pressure had stabilized, two packer integrity checks were performed at ~2990 psi and 3198 psi (141 psi and 349 psi above hydrostatic pressure). Both packer integrity tests showed good packer seal.

Following the packer integrity tests, four injection test cycles were performed. Fracture closure pressure could be determined for only the first cycle. During cycle 2, closure pressure could not be determined because the pump stalled. During cycles 3, 4 and 5, the pressure decline after fracturing exhibited an abnormal behavior, which precluded determining closure pressure. However, fracture reopening pressure and fracture propagation pressure were successfully determined for cycles 2, 3, 4, and 5.

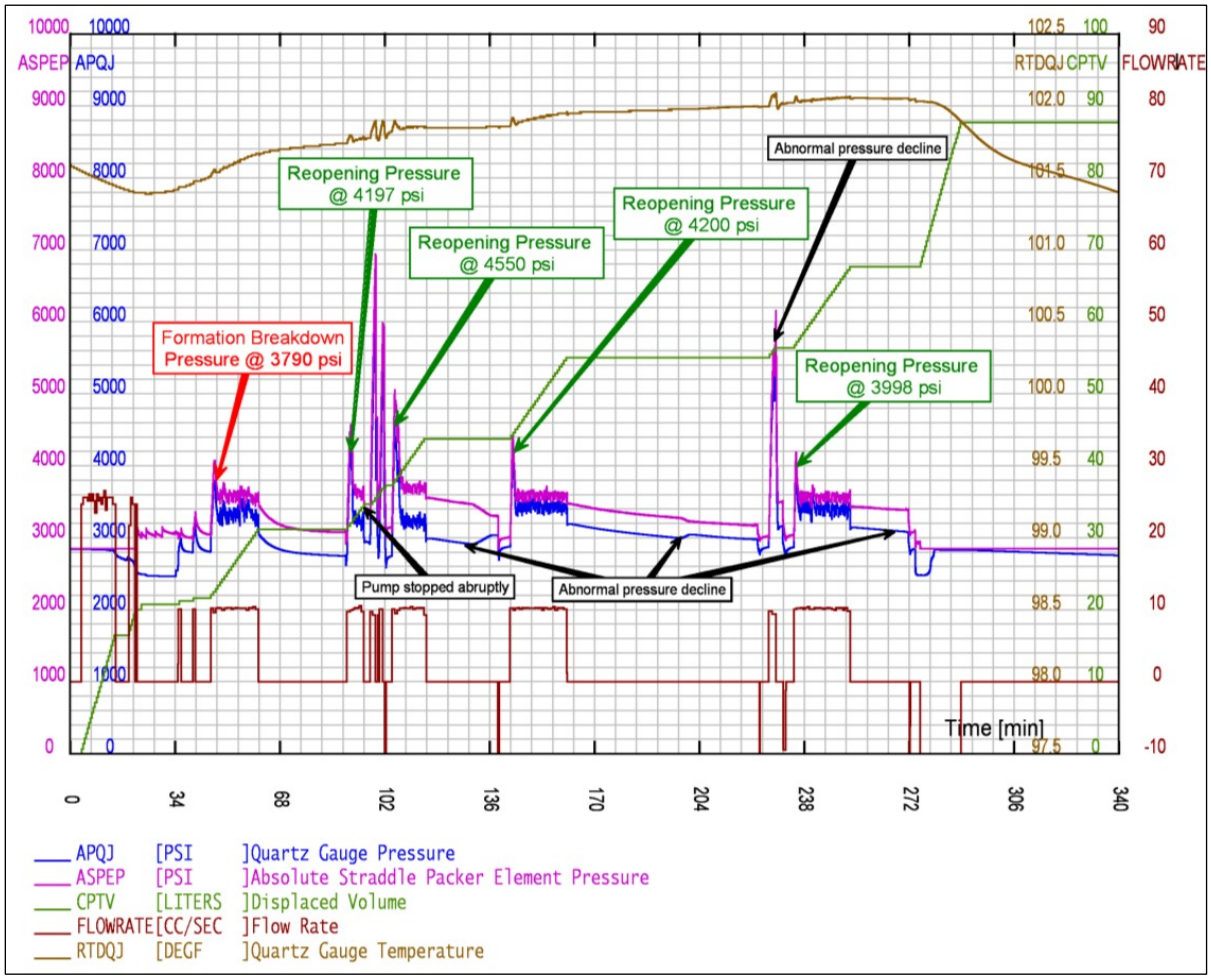


Figure 4-19. Test History for MicroFrac Test 3 in the A1 Carbonate at a Depth of 5791 ft MD.

Formation Breakdown Pressure

Formation breakdown was achieved in the first injection cycle (FOT1) as shown in Figure 4-19. The breakdown pressure was 3790 psi, 941 psi above the hydrostatic pressure. The fracture was propagated for ~10 minutes after formation breakdown. After shut-in, the pressure decline was monitored for ~30 minutes.

Fracture Reopening Pressure

Fracture reopening pressure was measured in cycles 2, 3, 4 and 5 of MicroFrac test 3. Reopening pressures were 4197 psi (FOT2), 4550 psi (FOT3), 4200 psi (FOT4), and 3998 psi (FOT5). As was the case for MicroFrac test 2, the reopening pressure was higher than the breakdown pressure.

Fracture Propagation Pressure

Fracture propagation pressure was measured in cycles 2, 3, 4 and 5 of MicroFrac test 3. Fracture propagation pressure ranged from 3250 psi to 3400 psi for all four test cycles.

Fracture Closure Pressure

Fracture closure pressure was measured only in cycle 1 of MicroFrac test 3. Table 4-8 summarizes the fracture closure pressure measurements determined with the three pressure decline analysis methods.

Table 4-8. Fracture Closure Pressures for MicroFrac Station 3 (depth 5791 ft MD).

Pressure Decline Analysis	Flowback Cycle	Fracture Closure, psi	Fracture Closure Gradient, psi/ft
Square root of Shut-in Time	FOT1	2871.6	0.504
Log-Log	FOT1	2876.9	0.505
G-Function	FOT1	2864.4	0.503
Fracture Closure		2871.0	0.504

4.3.4 MICROFRAC TEST 4 (5765 FT MD)

The fourth MicroFrac test was performed in the A-2 Carbonate at a depth of 5765 ft MD. The test history is shown in Figure 4-20. The straddle packers were inflated in about 16 minutes under a hydrostatic pressure at 2746 psi. Once the packer pressure had stabilized, two packer integrity checks were done at 3301 psi and 3444 psi (555 and 698 psi above hydrostatic pressure). Both integrity tests showed that the packers had achieved a good seal. Following the integrity tests, four successful test cycles were conducted.

Formation Breakdown Pressure

Formation breakdown was achieved in the first injection cycle 1 (FOT1) at 3795 psi as shown in Figure 4-21.

Fracture Reopening Pressure

Fracture reopening pressure was measured in cycles 2, 3 and 4 of MicroFrac test 4. Reopening pressures were 3830 psi (FOT2), 4075 psi (FOT3) and 4174 psi (FOT4). As was the case for the other MicroFrac tests, the reopening pressure was higher than the breakdown pressure.

Fracture Propagation Pressure

Fracture propagation pressure was measured in cycles 2, 3 and 4 of MicroFrac test 4. Fracture propagation pressure was 3500 psi for all four test cycles.

Fracture Closure Pressure

Table 4-9 summarizes fracture closure pressure values for each of the three injection cycles for MicroFrac test 4.

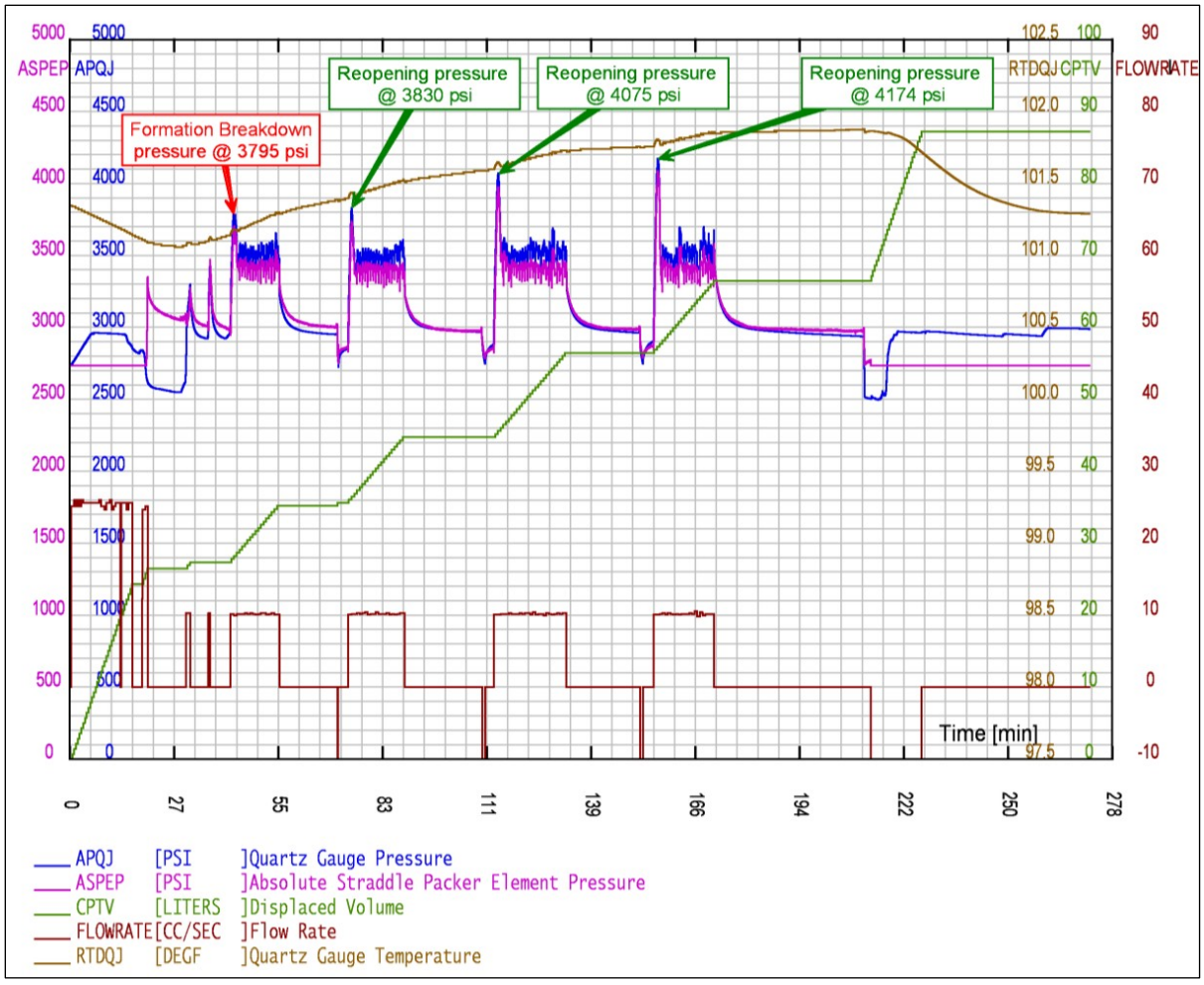


Figure 4-20. Test History for MicroFrac Test 4 in the A-2 Carbonate at a Depth of 5765 ft MD.

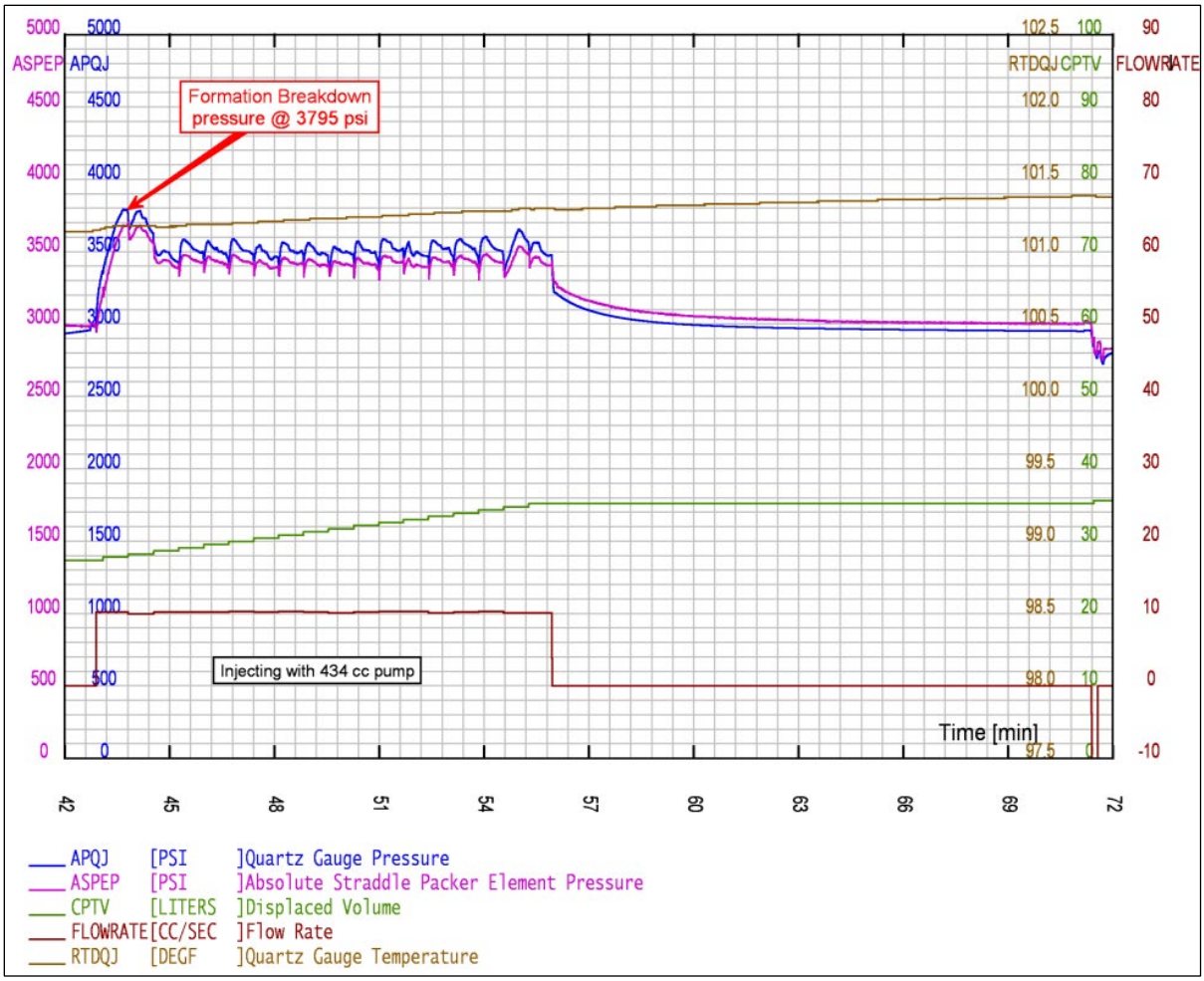


Figure 4-21. Fracture Breakdown Pressure During the First Injection Cycle of MicroFrac Test 4.

Table 4-9. Fracture Closure Pressures for MicroFrac Test 4 (5765 ft MD).

Pressure Decline Analysis	Flowback Cycle	Fracture Closure, psi	Fracture Closure Gradient, psi/ft
Square root of Shut-in Time	FOT1	3074.7	0.543
Log-Log	FOT1	3085.3	0.544
G-Function	FOT1	3097.8	0.547
Fracture Closure		3085.9	0.545
Square root of Shut-in Time	FOT2	3087.4	0.545
Log-Log	FOT2	3071.8	0.542
G-Function	FOT2	3091.6	0.546
Fracture Closure		3083.6	0.544
Square root of Shut-in Time	FOT3	3110.3	0.549
Log-Log	FOT3	3093.3	0.546
G-Function	FOT3	3099.4	0.547
Fracture Closure		3101.0	0.547
Square root of Shut-in Time	FOT4	3145.0	0.555
Log-Log	FOT4	3125.4	0.552
G-Function	FOT4	3128.9	0.552
Fracture Closure		3133.1	0.553

4.3.5 S_{Hmax}

Before and after images of each MicroFrac test interval were obtained using the Baker Hughes acoustic imaging wireline tool. The objective of obtaining the images is to determine the orientation of S_{Hmax}. The induced fractures were visible only in Stations 1 and 2. Post-testing fracture images are shown in Figure 4-22 and Figure 4-23 for Station 1 at 5861 ft and Station 2 at 5967 ft, respectively showing the vertical fracture created during the MicroFrac testing.

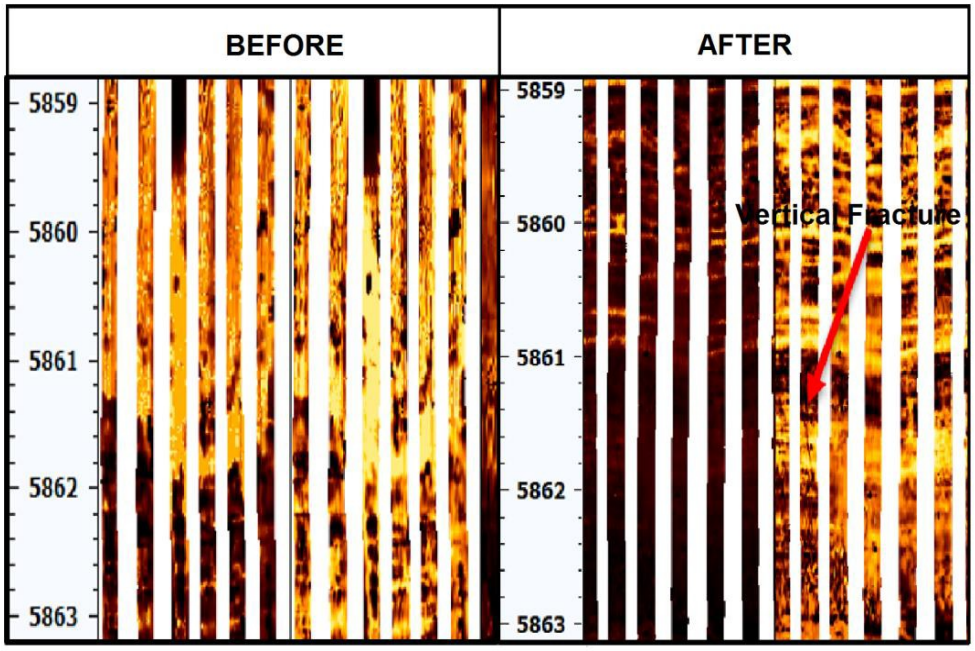


Figure 4-22. MicroFrac Testing Station 1 (5861 ft.) Image Logs before and after MicroFrac Testing.

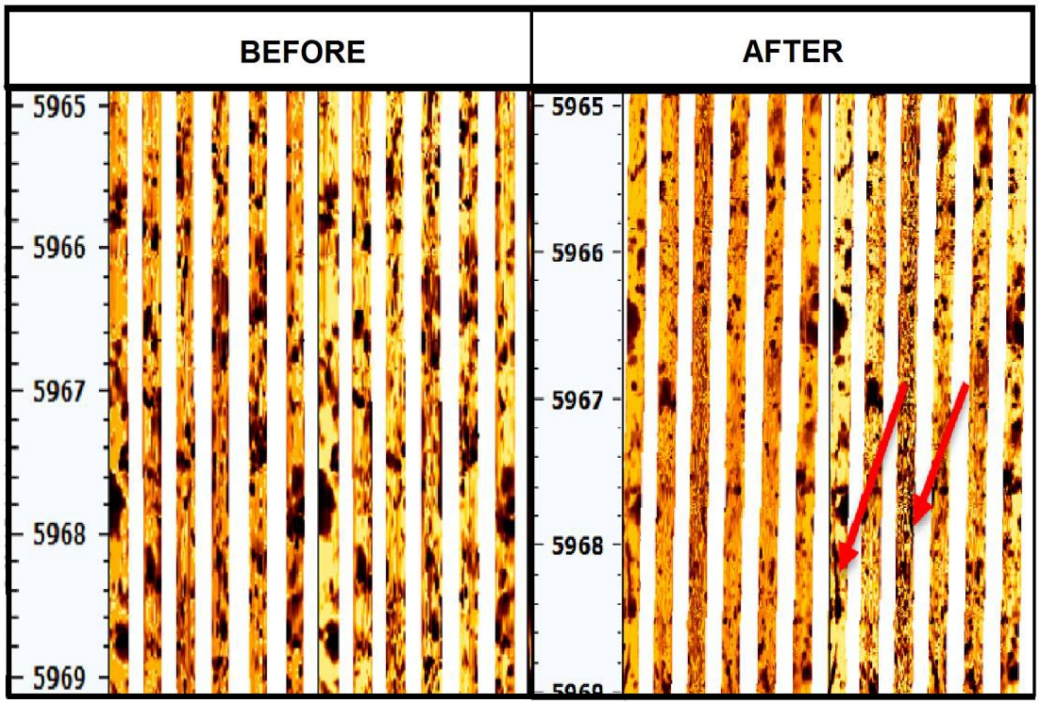


Figure 4-23. MicroFrac Testing Station 2 (5967 ft.) Image log before and after MicroFrac Testing.

4.3.6 Summary

A summary of the MicroFrac test program and the test results are shown in Table 4-10.

Table 4-10. MicroFrac test program results.

Formation	Depth (MD) (ft)	Station	Cycle	Formation Breakdown pressure (psi)	Reopening pressure (psi)	Propagation pressure (psi)	Hydrostatic Pressure (psi)	Closure Pressure (psi)	Comments
A1 Carbonate	5861	1	1	**2642**	-	-	1777	1907.1	Formation breakdown pressure and good propagation.
			2	-	3240	~2300		1864.1	Good propagation and closure pressure.
			3	-	3766	~2300		**1818.9**	Good propagation and closure pressure.
Brown Niagarann	5967	2	1	**2922**	-	-	1782	1884.7	Formation breakdown pressure and good propagation.
			2	-	3757	~2300		1858.1	Good propagation and closure pressure.
			3	-	3868	~2300		1806.2	Good propagation and closure pressure.
			4	-	4258	~2300		**1799.2**	Good propagation and closure pressure.
A2 Carbonate	5791	3	1	**3790**	-	-	2849	**2871.0**	Formation breakdown pressure and good propagation.
			2	-	4197	~3300		-	Pump stalled. No closure pressure measured in this cycle.
			3	-	4550	~3250		-	Abnormal behavior of natural pressure decline. Closure pressure could not be identified.
			4	-	4200	~3400		-	Abnormal behavior of natural pressure decline. Closure pressure could not be identified.
			5	-	3998	~3400		-	Abnormal behavior of natural pressure decline. Closure pressure could not be identified.

Formation	Depth (MD) (ft)	Station	Cycle	Formation Breakdown pressure (psi)	Reopening pressure (psi)	Propagation pressure (psi)	Hydrostatic Pressure (psi)	Closure Pressure (psi)	Comments
A2 Carbonate	5765	4	1	**3795**	-	-	2746	3085.9	Formation breakdown pressure and good propagation.
			2	-	3830	~3500		**3083.6**	Good propagation and closure pressures.
			3	-	4075	~3500		3101.1	Good propagate with slight increase in closure pressures.
			4	-	4174	~3500		3133.1	Good propagation with slight increase in closure pressures.

Chapter 5. Summary

5.1 Conclusion

Well log and well testing data from the Chester 8-16 well has provided insight into the local and regional stratigraphy, structure, geochemical, geomechanical, and petrophysical properties of potential Northern Pinnacle Reef Trend storage reservoirs and caprocks in the Michigan Basin. Analysis conducted on each formation of interest (Salina, A-2 Carbonate, A-2 Evaporite, A-1 Carbonate, and Brown Niagaran) indicates that sufficient caprock-reservoir performance exists in Chester 8-16 for CO_2 storage. Characteristics identified in the Salina, A-2 Carbonate, and A-2 Evaporite formations indicate that they could potentially serve as effective caprock formations in Chester 8-16. The A-1 Carbonate was characterized as a porous dolostone and exhibits strong potential as a reservoir formation.

Chapter 6. References

BHI (2017a). RCX^{SM} Vertical Interference Test (VIT) Analysis: CORE Energy Well Chester 16 Unit #8-16. Prepared by J. X. Haomin.

BHI (2017b). *RCI Straddle Packer MicroFrac Testing (*report reference GPE-NA-FRAC-0117). Traverse City, MI: Core Energy LLC. Prepared by D. Moronkeji.



It can be done

Attachment 5.
El Mac Hills 1-18A
Wireline Log Analysis:
Charlton 19 Niagaran Reef
Piggyback Well

Attachment 5

El Mac Hills 1-18A Wireline Log Analysis: Charlton 19 Niagaran Reef Piggyback Well

Conducted by the Midwest Regional Carbon Sequestration Partnership (MRCSP)

DOE-NETL Cooperative Agreement DE-FC26-05NT42589



Prepared by:

Battelle
505 King Avenue
Columbus, Ohio 43201

Submitted to:

Client
Address
Address

April 28, 2019

This report is a work prepared for the United States Government by Battelle. In no event shall either the United States Government or Battelle have any responsibility or liability for any consequences of any use, misuse, inability to use, or reliance on any product, information, designs, or other data contained herein, nor does either warrant or otherwise represent in any way the utility, safety, accuracy, adequacy, efficacy, or applicability of the contents hereof.

Table of Contents

Page

Chapter 1. Well Drilling and Completions 3
1.1 Well Operations Execution 3
1.2 Well Logging 4
Chapter 2. Geologic Characterization 12
2.1 Methodology 12
2.2 A2 Carbonate and A2 Anhydrite 13
2.3 A1 Carbonate 15
2.4 Brown Niagaran 16
2.5 Triple Combo Log Analysis Conclusions 18

List of Tables

Page

Table 2-1. EMH 1-18A Log Derived Formation Tops 12

List of Figures

Page

Figure 1-1. Surface hole location for El Mac Hills 1-18A marked in red 5
Figure 1-2. As-built wellbore diagram of pre-existing well, El Mac Hills 1-18 6
Figure 1-3. As built wellbore diagram for El Mac Hills 1-18A. (Not to scale.) 7
Figure 1-4. Deviation survey plot for well El Mac Hills 1-18A. 8
Figure 1-5. Days vs depth plot annotated with unscheduled events, casing points, and key geologic horizons for drilling and completion of the El Mac Hills 1-18A well. Remedial cementing operations added approximately 5 days during the completions phase of execution. 9
Figure 1-6. Executed formation evaluation program for El Mac Hills 1-18A. 10
Figure 1-7. El Mac Hills 1-18A formation evaluation value of information chart. Logs highlighted in blue represent open hole logs, those highlighted in gray were collected in cased hole. 11
Figure 2-1. Gamma ray, neutron porosity, bulk density, pay flag, and water saturation log section for the A2 Carbonate and A2 Evaporite. 14
Figure 2-2. Neutron porosity-bulk density cross plot of the A2 Carbonate and A2 Evaporite (Anhydrite) showing low porosity 14
Figure 2-3. Gamma ray, neutron porosity, bulk density, pay flag, and water saturation log section for the A1 Carbonate. 15
Figure 2-4. Neutron porosity-bulk density cross plot of the A1 Carbonate showing low porosity throughout. 16

Figure 2-5. Gamma ray, neutron porosity, bulk density, pay flag, and water saturation log section for the Brown Niagaran. 17
Figure 2-6. Neutron porosity-bulk density cross plot of the Brown Niagaran showing high porosity throughout. 18

Chapter 1. Well Drilling and Completions

The El Mac Hills 1-18A well drilling was initiated on April 27, 2017 and operated by Core Energy LLC with well evaluation operations contracted by Battelle Memorial Institute on behalf of MRCSP. The surface location of this borehole is marked by a red dot on both a high-resolution aerial photograph and map in Figure 1-1. This well was a sidetrack of a pre-existing borehole, El Mac Hills 1-18. A wellbore diagram for the pre-existing well can be found in Figure 1-2. The final, as-built, wellbore diagram for the sidetrack can be found in Figure 1-3.

This well was directionally drilled from the Kickoff Point (KOP) at 761 ft MD/TVD. The deviation survey plot for El Mac Hills 1-18A is shown in Figure 1-4.

1.1 Well Operations Execution

A days vs. depth chart in Figure 1-5 is annotated with unscheduled events that occurred during drilling and completions, casing shoe depths (black triangles), and key formation tops. These unscheduled events are described below:

- Lost returns are common across the Northern Michigan Pinnacle Reef Trend, often massive or total, in the intermediate hole section when the mud system is converted from freshwater to brine. Pore pressure within this stratigraphic section must be at or very near the hydrostatic gradient because the drilling fluid density increase caused by adding dissolved salts is sufficient to cause voids to form or open. Drilling with a salt saturated fluid is critical through this interval to prevent hole enlargement and washout while drilling thick salt beds.
  - El Mac Hills 1-18A experienced losses ranging from 3 to 30 bph in this section from a depth of 2,174 ft MD to hole section TD at 3,362 ft MD.
- Rapid losses (100bph) began in the production hole section at 5,306 ft MD, leading to total losses while drilling from 5,432 ft to 5,483 ft MD. There was no weight on bit while drilling.
- The well was drilled to a total depth of 5,546 ft MD. While a preliminary field pick was called for the top of the Gray Niagaran Formation, further petrophysical log analysis indicated this stratigraphic horizon was not penetrated.
- After reaching total depth, the shut-in casing pressure slowly built to 650psi over 15 hours. After monitoring the well for an additional 6 hours, the well was killed (stopped fluid flow).
  - The drilling team tripped in with a drilling bit and encountered a ledge at 5,480 ft MD. Attempts to drill or ream into the old hole were unsuccessful, with no progress beyond 5,483 ft MD.
  - A streamlined open hole logging program was executed. Pump rates while tripping the BHA were 2-3bpm to maintain overbalance.
  - While preparing to run in with casing, shut-in casing pressure built up to 700psi and stabilized. The well was killed a second time.
- The 5-1/2” production casing string was run to 5,490 ft MD and cemented in place on May 19, 2017.
- Prior to completions operations, interpretation of cased hole wireline logs (SBT/GR) revealed the absence of cement from the plugback TD (PBTD) at 5,421 ft to the external casing packer (ECP). A second log collected while 1000psi was applied to the casing indicated good cement from the ECP to top of cement (TOC) at 4,595 ft MD. This finding necessitated a remedial cement job and squeeze.

- The casing was perforated from 5,018 ft MD to 5,020 ft MD, a cement retainer was placed at 4,890', and cement was pumped. A hesitation squeeze was performed.
- After running in hole and tagging the cement retainer at 4,890 ft MD, the drill bit made 1 foot of progress before falling 4 feet into the hole. This bit was pulled out of hole and inspected. As the traditional bit was "very worn" and had a row of cutters missing, the drilling team decided to swap out for a sand line drill.
- Hard cement was encountered while drilling to 5,015 ft MD and the repeat indicated the presence of good cement from the PBTD at 5,420 ft MD to the squeeze job perforations at 5,018 ft MD.

1.2 Well Logging

Wireline logs were run from ~3,350 ft MD to 5,410 ft MD in the deep open hole section before running the 5-1/2" casing string (Figure 1-6). The acoustic and compensated neutron logs were logged relative to a limestone matrix.

Several cased hole logs were run at El Mac Hills 1-18A for wellbore integrity analysis, as well as a baseline Pulsed Neutron Capture log (PNC) for use in monitoring studies (Figure 1-6).

Figure 1-7 lists all data types that were collected during the drilling and completions phase of this well and describes how this data was employed to decrease project and technical uncertainties for MRCSP Phase III research.



Figure 1-1. Surface hole location for El Mac Hills 1-18A marked in red.

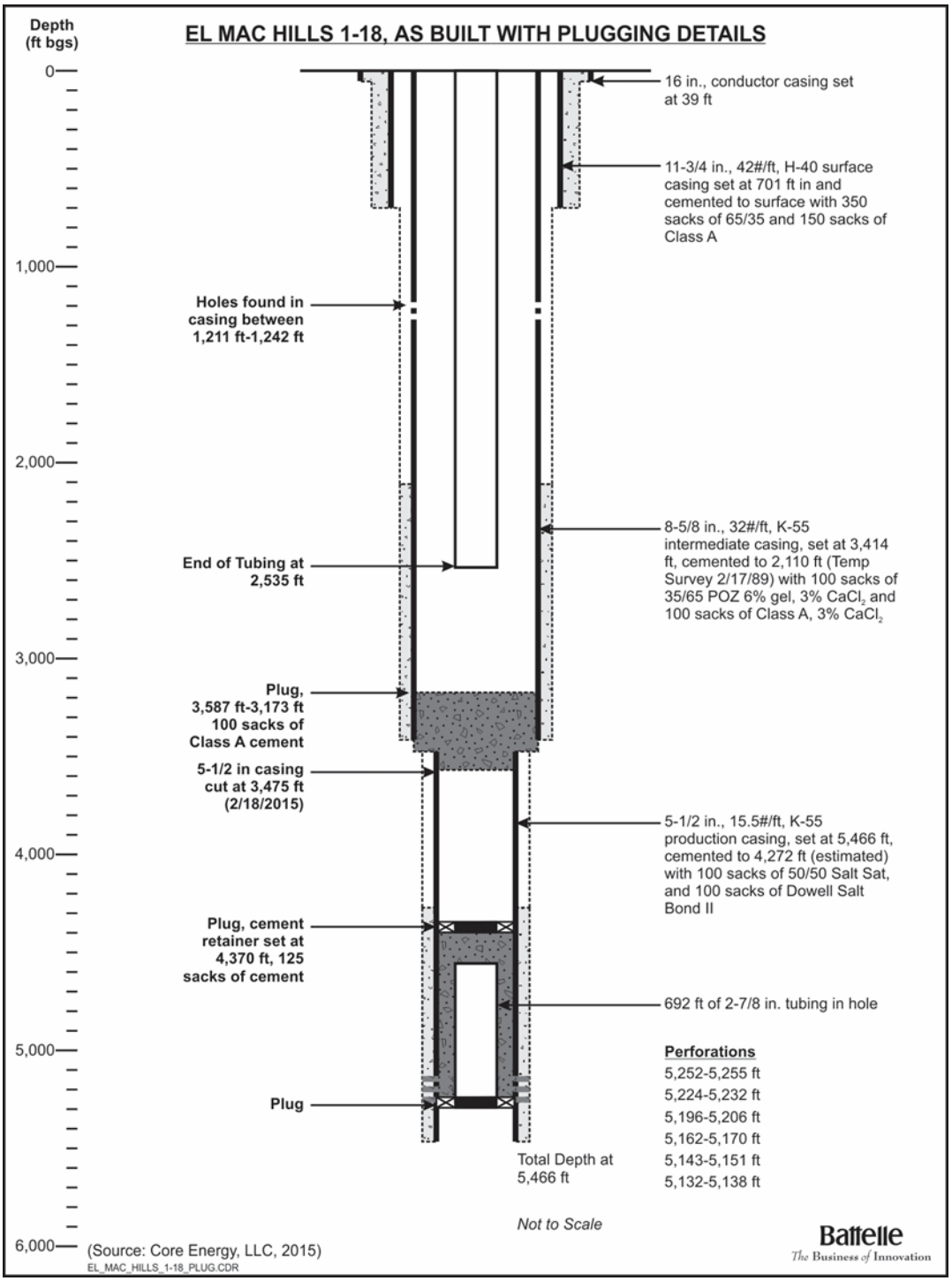
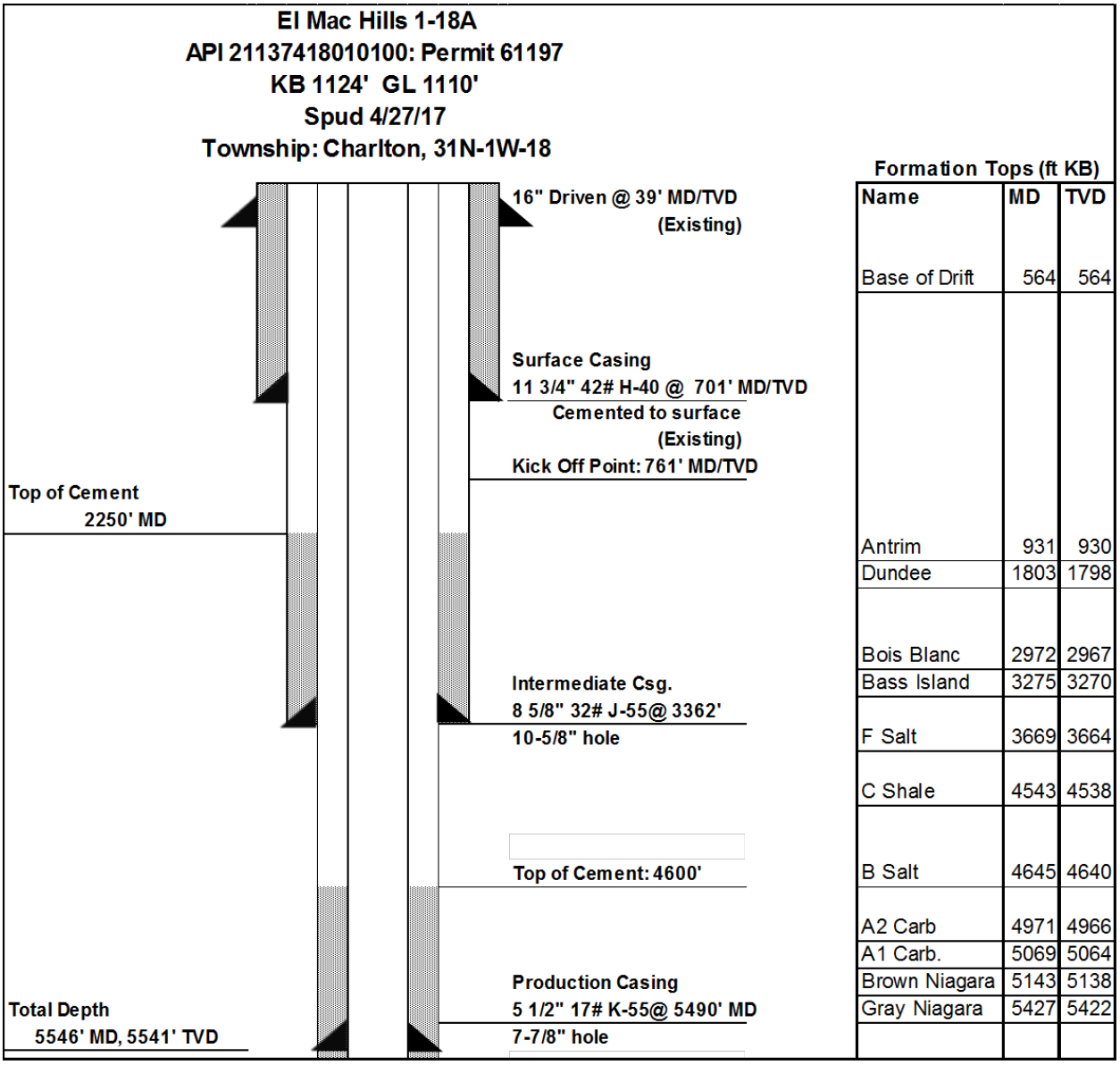


Figure 1-2. As-built wellbore diagram of pre-existing well, El Mac Hills 1-18.



Formation Tops (ft KB)

Name	MD	TVD
Base of Drift	564	564
Antrim	931	930
Dundee	1803	1798
Bois Blanc	2972	2967
Bass Island	3275	3270
F Salt	3669	3664
C Shale	4543	4538
B Salt	4645	4640
A2 Carb	4971	4966
A1 Carb.	5069	5064
Brown Niagara	5143	5138
Gray Niagara	5427	5422

Figure 1-3. As built wellbore diagram for El Mac Hills 1-18A. (Not to scale.)

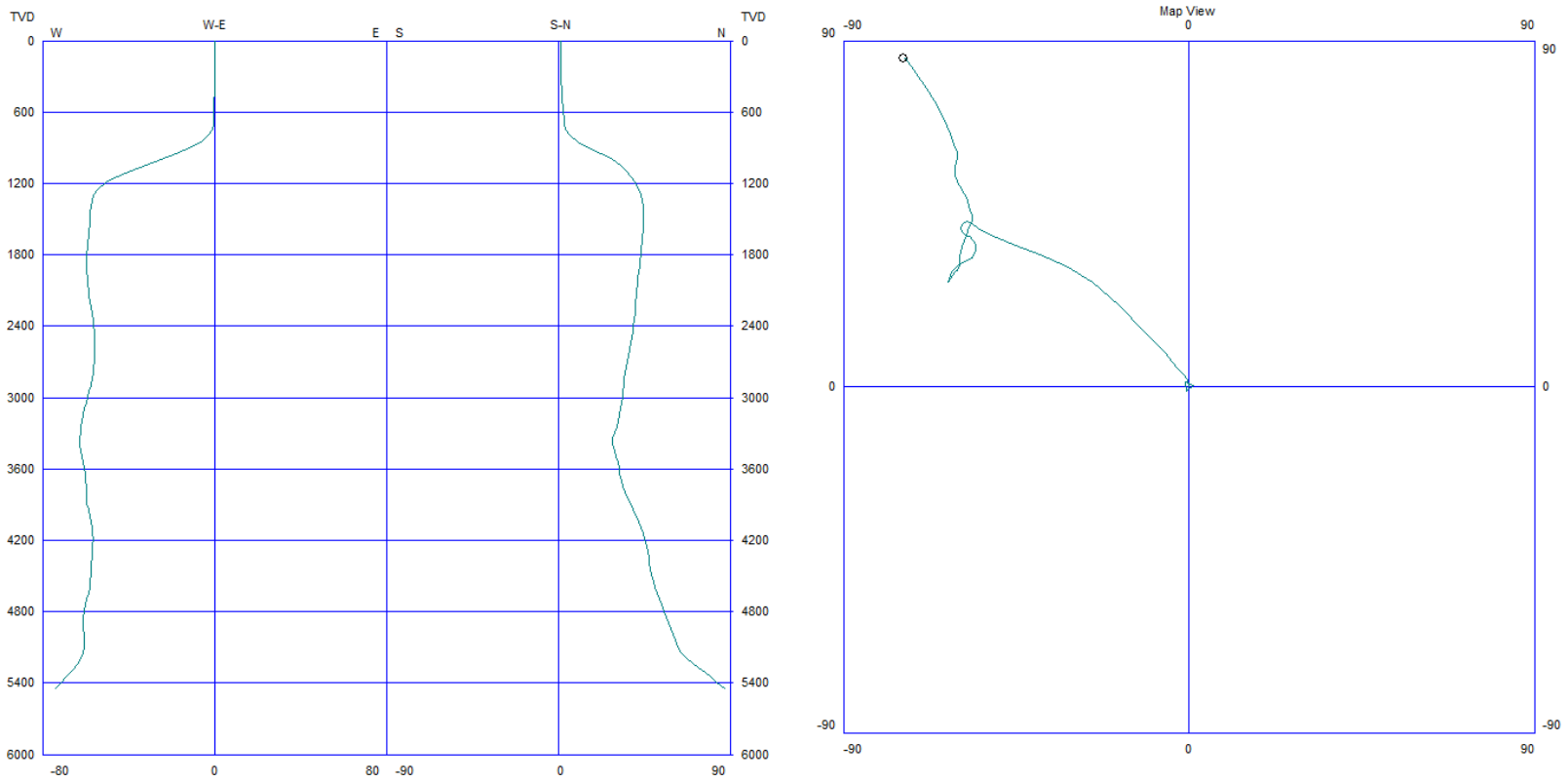


Figure 1-4. Deviation survey plot for well El Mac Hills 1-18A showing deviations from vertical (left) and projection towards the northwest (right).

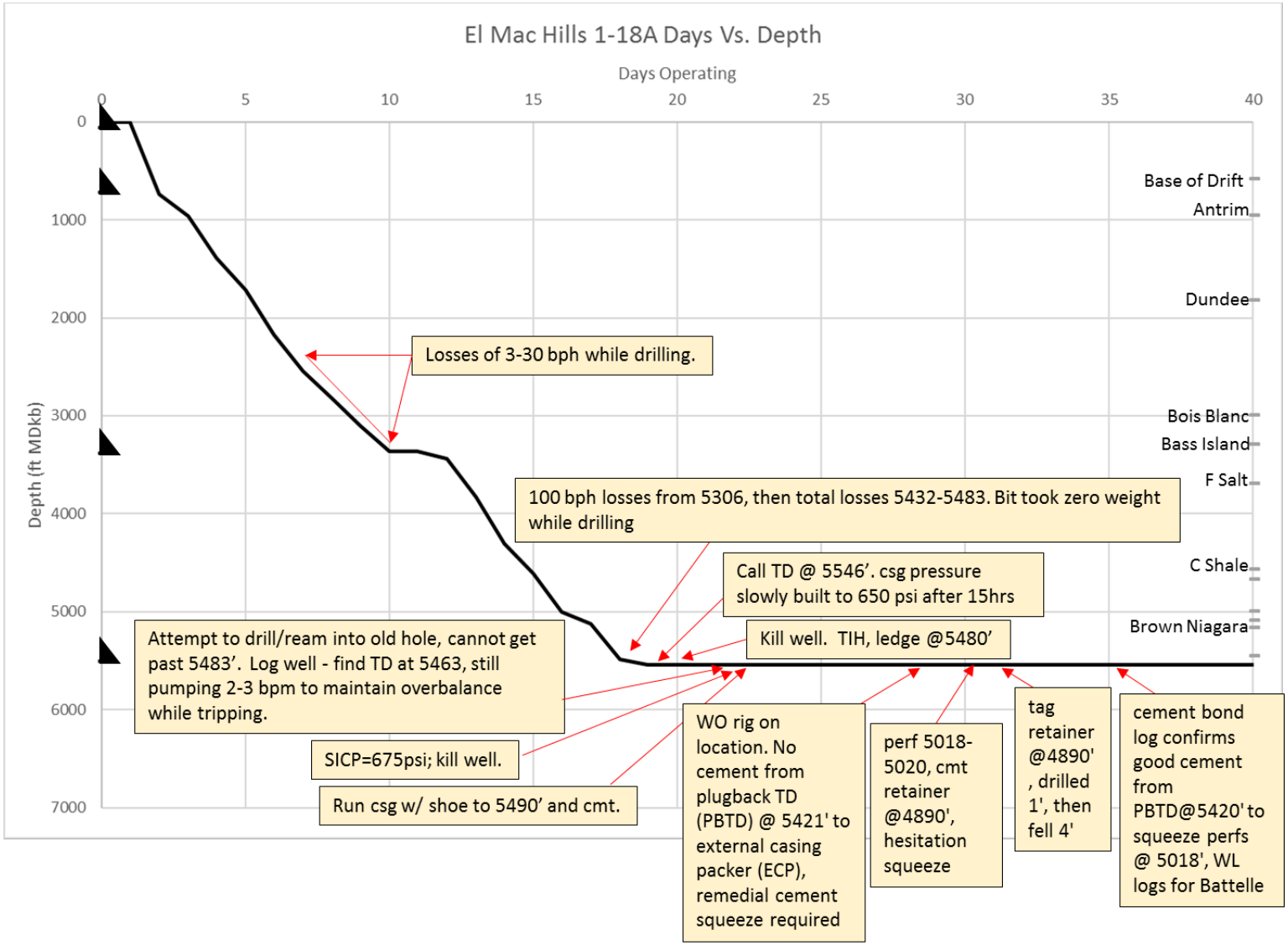


Figure 1-5. Days vs depth plot annotated with unscheduled events, casing points, and key geologic horizons for drilling and completion of the El Mac Hills 1-18A well. Remedial cementing operations added approximately five days during the completions phase of execution.

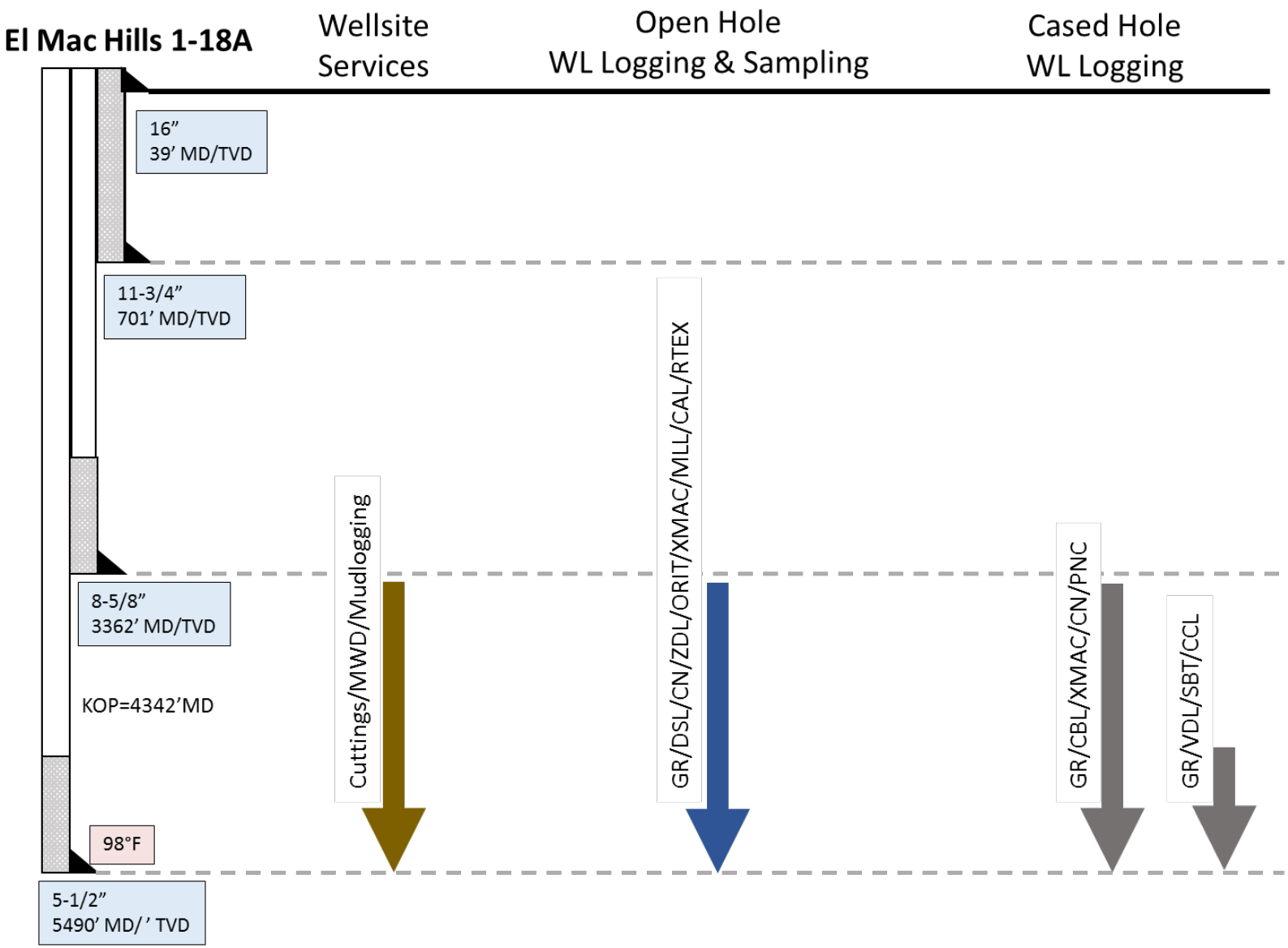


Figure 1-6. Executed formation evaluation program for El Mac Hills 1-18A.

Log Name and Mnemonic		Value of Information
CAL	Caliper	Provides evidence of borehole size, including enlargement due to washout, which is critical for QA/QC and calibration of many logs.
CBL	Cement Bond Log	Evaluates presence of cement behind casing and is used for planning borehore seismic data acquisition.
CCL	Casing Collar Locator	Highlights the presence of metallic casing collars and is used with Gamma Ray tool to correlate cased hole logs on depth and tie in with open hole logs.
CN	Compensated Neutron Log	This tool is used to calculate porosity and identify lithology, by responding to the hydrogen content of the formation. Porosity data is a key input to static and dynamic earth models and CO2 storage estimates.
DSL	Digital SpectraLog	This tool separates the Gamma Ray spectrum into its elemental components of U, Th, and K. This data was used to identify types of clays for reservoir characterization.
GR	Gamma Ray	Gamma Ray is a standard log that was run in both open hole and cased hole for correlation purposes. This tool identified bed boundaries and informed the interpretation of other petrophysical logs. Interpretations based on this log impacted technical products throughout the project.
MLL	Micro Laterolog	This is a shallow resistivity tool that was used to evaluate the lithology and fluid content of formations. This information, lithology and (oil/water/gas) was an input to models.
ORIT	Directional Survey	This directional survey instrument was run to accurately measure the deviation of the well path from vertical; both inclination and azimuth. This information is critical for applying proper measured depth (MD) or total vertical depth (TVD) datums to geologic surfaces, calculating pressures, and for correlation to other wells.
PNC	Pulsed Neutron Capture	The cased hole reservoir monitoring tool was run multiple times to measure changes in water, hydrocarbon, and CO_2 saturation over time with CO_2 injection. It was also used to identify salt in reservoir intervals where porosity plugging reduces storage potential. This data was used for baseline reservoir characterization, static earth model input data, and dynamic model history matching.
RTeX	Multi Laterolog Wireline Service	This tool collects resistivity data with four different formation penetration modes and adaptive borehole correction to remove the effects of formation invaded by drilling fluid. Resistivity logs were a basic indicator of fluid type and lithology. Interpretations based on this log impacted technical products throughout the project.
SBT	Segmented Bond Tool	An acoustic cement evaluation tool that can be used to map localized zones of poor hydraulic isolation across the casing circumference. This data was used to evaluate wellbore integrity and identify gas or fluids behind pipe to calibrate PNC logs.
VDL	Variable Density Scanner	This log was run in the cased hole along with the CBL to assist in its interpretation. It provides the amplitude of the acoustic waveform of the CBL measurement.
XMAC	Cross-Multipole Array Acoustilog	This tool provides full-wave monopole, in-line dipole, and cross-dipole sonic logs. Sonic logs are necessary input parameters for borehole seismic data acquisition planning and processing as well as indicators of rock mechanical properties. They were used in petrophysical analysis of the reefs that was input to the static and dynamic earth models. Deep shear wave image processing was applied to locate and map linear formation features such as fractures and bedding planes.
ZDL	Z Density Log	The density log assists in porosity estimation, lithology determination, seismic data acquisition planning and processing, and geomechanical modeling.

Figure 1-7. El Mac Hills 1-18A formation evaluation value of information chart. Logs highlighted in blue represent open hole logs, those highlighted in gray were collected in cased hole.

Note: Acronyms are Baker Hughes logging tool names

Chapter 2. Geologic Characterization

2.1 Methodology

A standard triple combo log was run over the interval from 3,312–5,370 feet MD in the El Mac Hills 1-18A well (EMH 1-18A). The triple combo log suite includes gamma ray, density, neutron porosity and resistivity, as well as line tension, caliper, and photo-electric effect. Data from the triple combo log was analyzed to identify formation tops, facilitate stratigraphic correlations, and calculate basic formation properties such as net and gross thickness and average porosity. This basic log analysis served as the framework for guiding more advanced characterization efforts.

Five formations and their associated tops were identified for the Silurian interval of the well (Table 2-1). Porosity was evaluated for the formations of interest using neutron porosity (NPHI), density porosity (DPHI), and average porosity (PHIA) calculations. Density porosity was calculated from Equation 1:

Table 2-1. EMH 1-18A Log Derived Formation Tops

Formations	Measured Tops (ft. MD)
Salina B Salt	4,644
A-2 Carbonate	4,971
A-2 Evaporite	5,042
A-1 Carbonate	5,069
Brown Niagaran	5,143
Grey Niagaran	5,427

$$\phi_D = (\rho_{ma} - \rho_b)/(\rho_{ma} - \rho_{fl}) \quad \text{(equation 1)}$$

where:

- ϕ_D = density porosity
- ρ_{ma} = matrix density (based on limestone density of 2.83 g/cm^3 or grain density data from elemental spectroscopy log)
- ρ_b = bulk density (from the density log)
- ρ_{fl} = fluid density (1.15 g/cm^3)

A grain density of 2.81 g/cm3 was used to calculate DPHI for the A-2 Carbonate through the Brown Niagaran. A dolomite density of 2.83 g/cm^3 was the assumed grain density for the A-2 Carbonate to the Brown Niagaran as the log signatures for theses formations are dolomitic in nature. PHIA was calculated using both DPHI and NPHI (run on a dolomite lithology) porosities via Equation 2:

$$\phi_A = (\phi_D + \phi_N) / 2 \quad \text{(equation 2)}$$

where

- ϕ_A = average porosity
- ϕ_D = density porosity
- ϕ_N = neutron porosity.

Average porosities are used as representative values of formation porosity because neutron and density porosity derivations are each susceptible to inaccuracies in certain conditions, such as the presence of gas, washouts, and atypical mineralogy. Average porosity was therefore used to compute footages for each zone.

Neutron porosity and bulk density data derived from the triple combo log were plotted against each other to generate a crossplot for each formation. Trend lines superimposed on the crossplot represent the log responses calculated for pure sandstone, limestone, and dolomite over a range of porosities (e.g. 0-45%). These trend lines assume the logs were run using a limestone lithology and grain density and can provide insight into lithology and allow for a potential estimate of true, lithology-independent porosity to be determined. Data that plotted within crossplot porosities greater than 5% were flagged, and the flagged data points were depth-denoted on cross-sections.

Following industry standard log interpretation guidelines, pay flags were generated using the following cutoffs; a water saturation (Sw) measurement lower than 40% and a neutron measurement greater than 5%. No gamma ray cutoff was applied for the pay flags as all formations contained less than 75 gAPI which is a standard indicator of relatively pure sandstone and carbonate reservoirs.

Cross plot flags indicate intervals of neutron porosity greater than 5%, based on the lithology overlay and not the actual NPHI log values. Pay flags are generated with log value cutoffs assigned to determine where injection zone potential might occur. Neutron porosity was used for pay flags to stay consistent with the crossplot porosity flags.

2.2 A-2 Carbonate and A-2 Evaporite

The A-2 Evaporite unit top is identified at the base of the A-2 Carbonate at 5,042 ft. MD where the neutron porosity decreases by 10% and the density increases to 2.88 g/ft3. The gross thickness of the A-2 Evaporite unit is 27 ft and is considered a baffle to fluid flow. Pay flags are only present in the A-2 Carbonate formation in 4 distinct zones occurring at the top and middle of the formation (Figure 2-1).

The majority of bulk-density and neutron porosity data from the A-2 Carbonate and A-2 Evaporite cluster near the dolomite curve on the crossplot, with lower density values exhibiting scatter towards the limestone and the sandstone curves (Figure 2-2). The A-2 Carbonate apparent crossplot porosities exhibit an average of approximately 1.0% and a range of 0–5%. The A-2 Evaporite data clusters in the lower left corner of the plot where anhydrites plot. These contain little to no porosity. No crossplot porosities above 5% existed and either the A-2 Carbonate or A-2 Evaporite and therefore no crossplot flags were generated.

The A-2 Carbonate and A-2 Evaporite were identified at 4,971–5,069 ft. MD, having a gross thickness of 98 ft. (Figure 2-2). The A-2 Carbonate unit top is identified at the base of the Silurian B Unit at 4,971 ft. MD where the density log increasing to about 2.75 g/ft3. The gross thickness of the A-2 Carbonate unit is 71 ft with a net thickness of 16 ft. resulting in a net-to-gross ratio of 22.5%. An average porosity of 2.7% was derived from density and neutron porosity data.

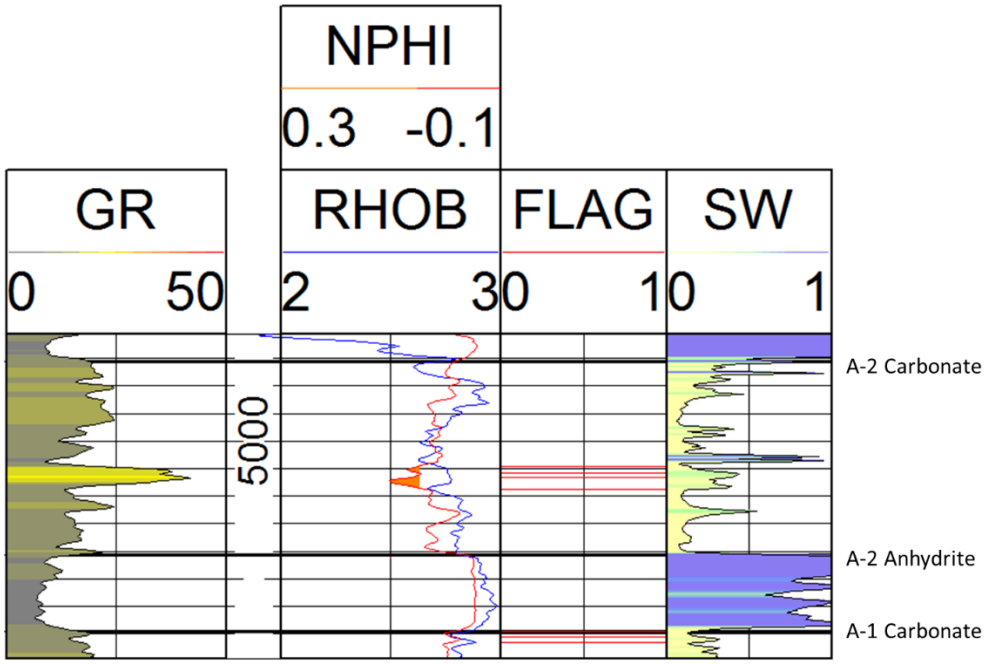


Figure 2-1. Gamma ray, neutron porosity, bulk density, pay flag, and water saturation log section for the A-2 Carbonate and A-2 Evaporite.

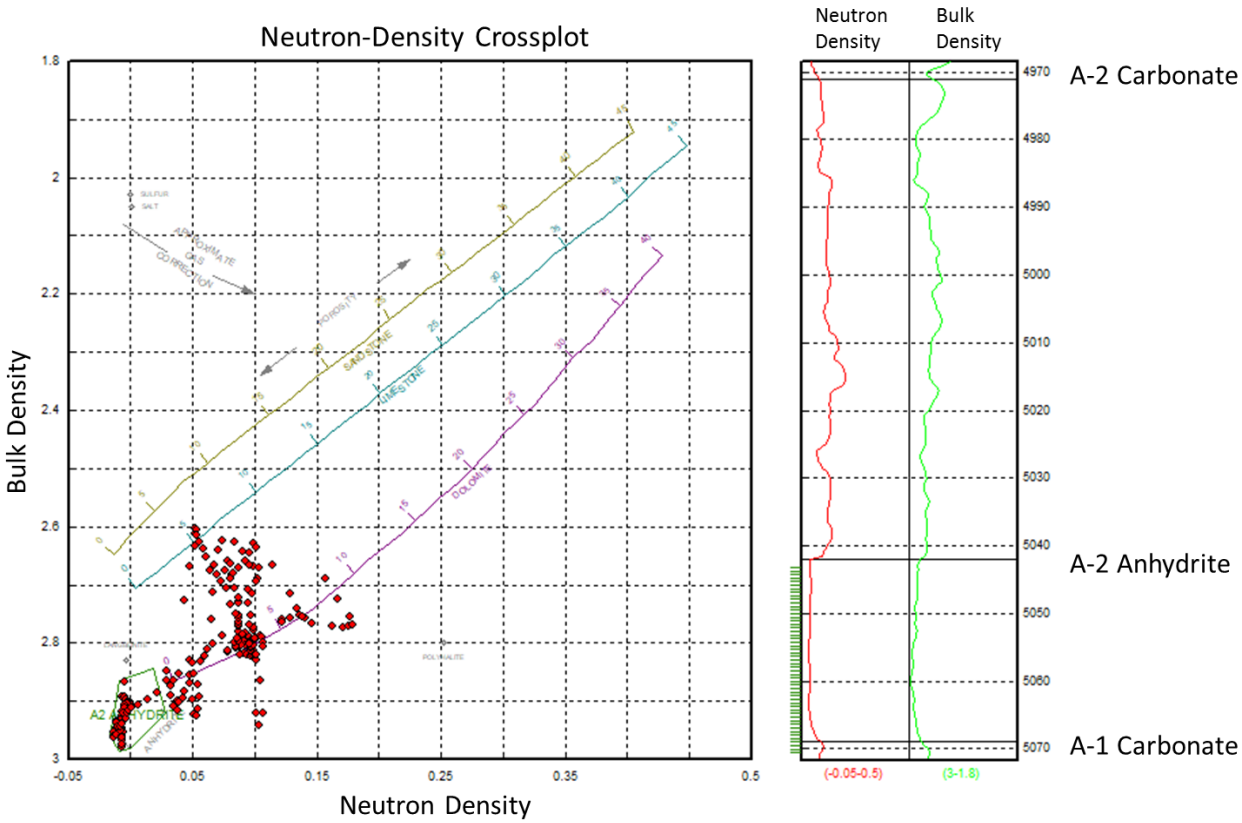


Figure 2-2. Neutron porosity-bulk density cross plot of the A-2 Carbonate and A-2 Evaporite (Anhydrite) showing low porosity.

2.3 A-1 Carbonate

The top of the A-1 Carbonate was identified at the base of the A2 Anhydrite at 5,143 ft. MD where an increase in neutron and density porosities occur as well as a decrease in PE (Figure 2-3). The A-1 Carbonate exhibits a gross thickness of 74 ft. and a net thickness of 17 ft. with a net-to-gross ratio of 23% as defined by an average porosity of greater than5% and a water saturation of less than40%. An average porosity of 3.2% was calculated for the A-1 Carbonate. Pay flags, totaling 17 feet thick, are present in four zones located in the middle of the formation.

Using the dolomite lithology run neutron porosity data shows apparent crossplot porosities ranging from 0.0–4.0%, with an average of ~1.0%. Neutron porosity log values range from 0.0–5.0%. No apparent crossplot porosities are greater than 5% and therefore no crossplot flags were generated (Figure 2-4).

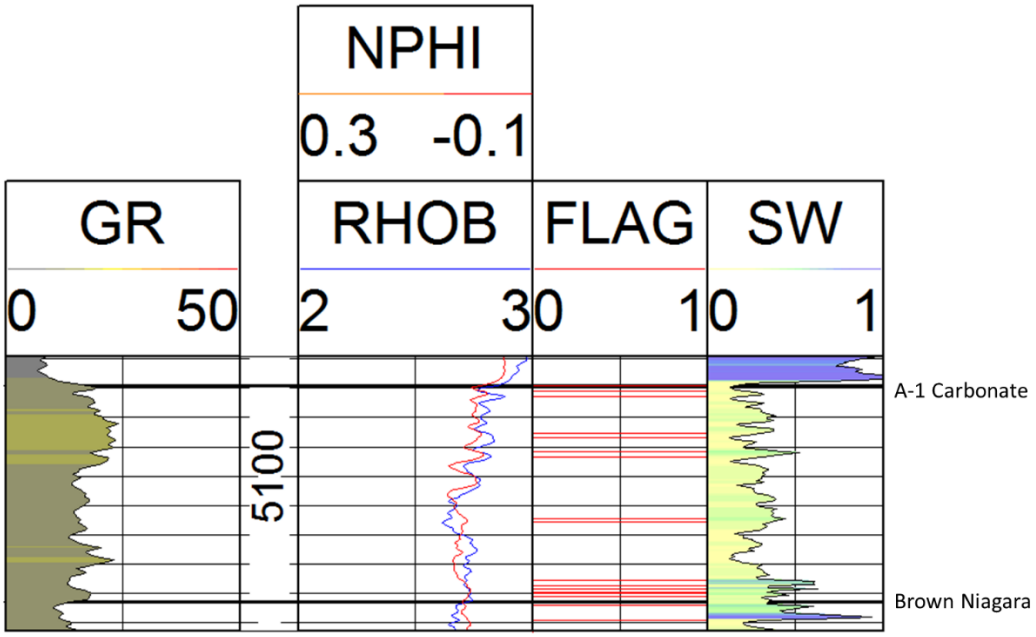


Figure 2-3. Gamma ray, neutron porosity, bulk density, pay flag, and water saturation log section for the A-1 Carbonate.

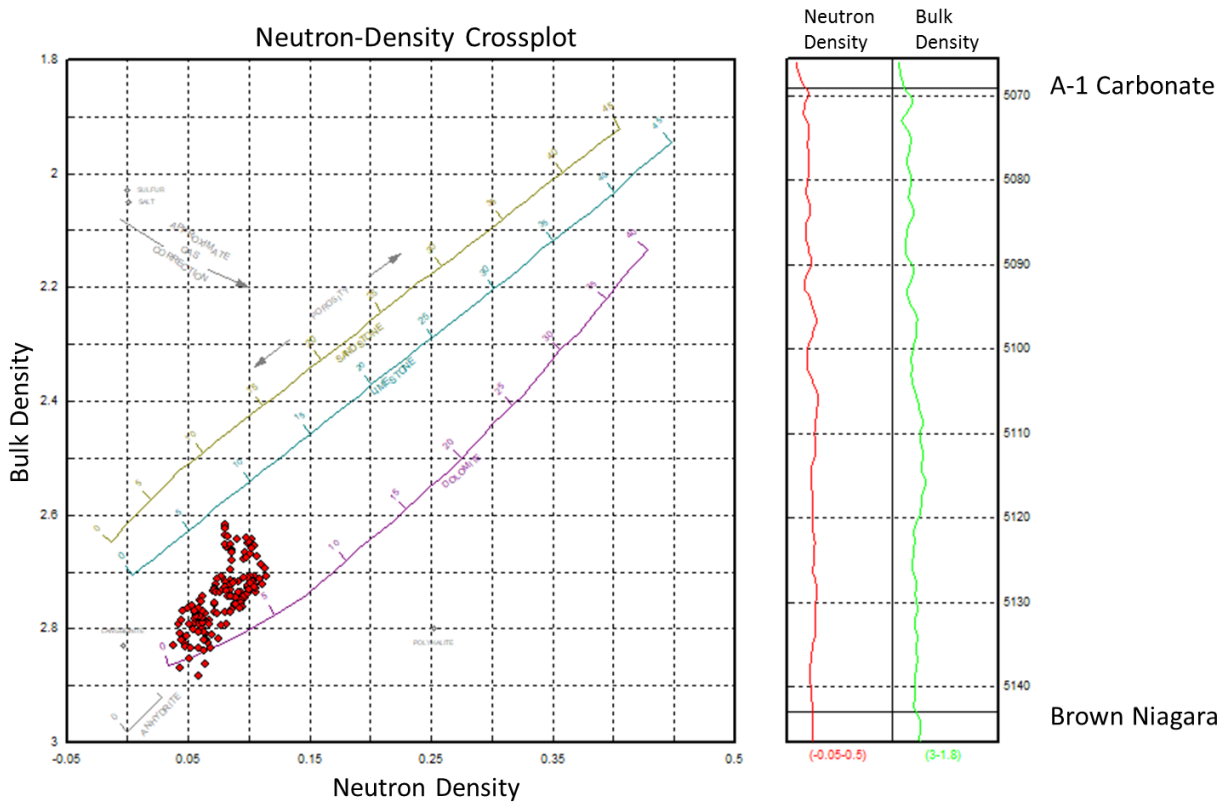


Figure 2-4. Neutron porosity-bulk density cross plot of the A-1 Carbonate showing low porosity throughout.

2.4 Brown Niagaran

The top of the Brown Niagaran was identified at the base of the A-1 Carbonate 5,069 ft. MD (Figure 2-5). The Brown Niagaran exhibits a gross thickness of 284 ft. and a net thickness of 24 ft. with a net-to-gross ratio of 23% as defined by an average porosity of greater than 5% and a water saturation of less than 40%. An average porosity of 10% was calculated for the Brown Niagaran. Pay flags, totally 24 feet thick, are scattered throughout the formation in thin 2-5-foot layers. This scatter is due to the fluctuating water saturation curve from high to low values. It is important to note that the water saturation curve in this well is likely drawn up due to primary production that started in 1988. This well was drilled and logged after primary production in 2017. The logs do not fully penetrate the formation missing ~20 feet of Brown Niagaran. Due to these factors the BN likely has a higher net reservoir than the logs and analysis indicate.

Using the dolomite lithology run neutron porosity data shows apparent cross plot porosities ranging from 0–17%, with an average of ~10%. Neutron porosity log values also range from 0.0–17%. The apparent cross plot porosities greater than 5% were flagged on the cross section in Figure 2-6. Most of the formation is above the apparent cross plot porosity cutoff, but likely the lower half of the formation is too water saturated for storage. Comparison of water saturation curves at initial conditions and extrapolation of the water contact would give a better idea of the net reservoir in the well.

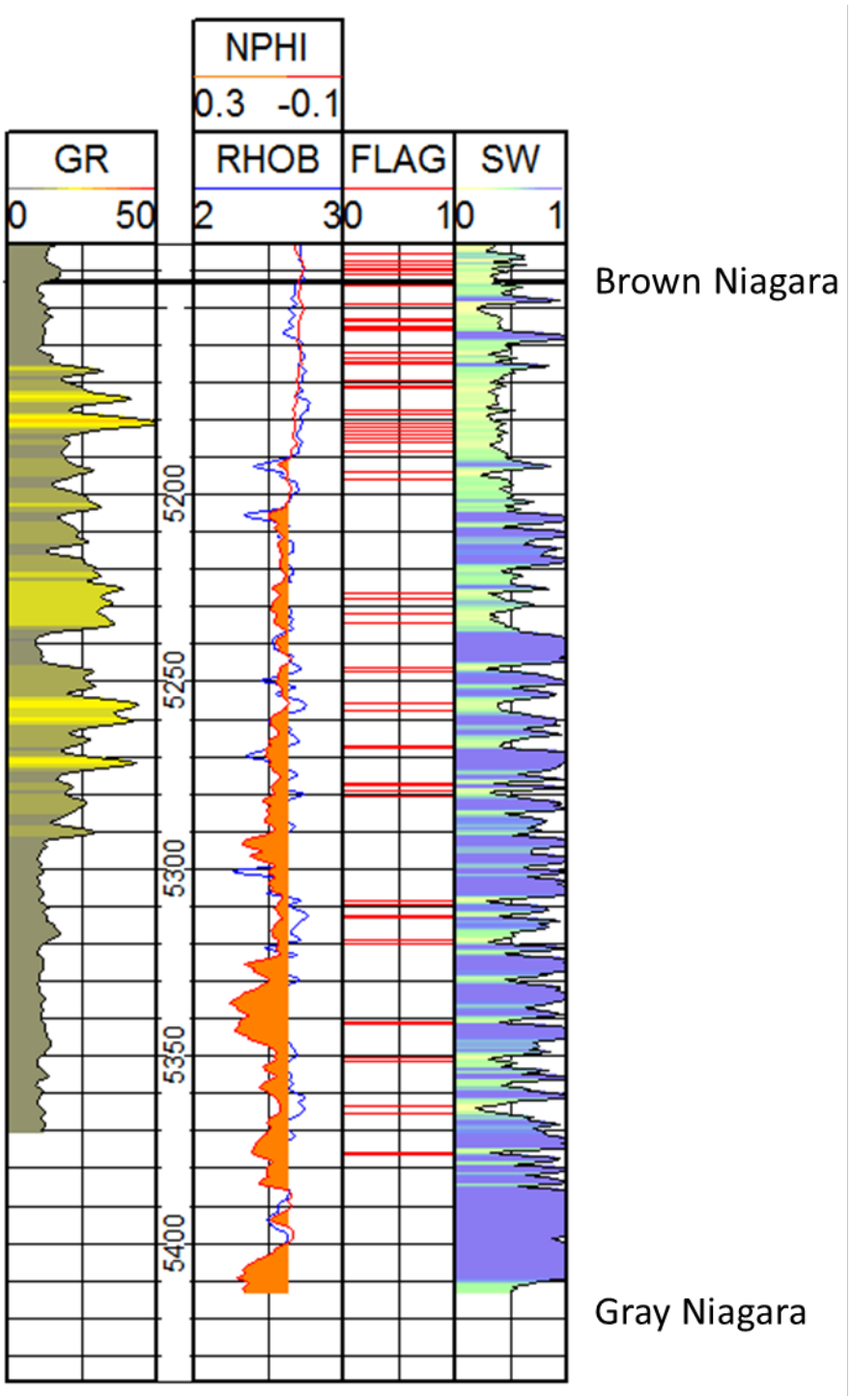


Figure 2-5. Gamma ray, neutron porosity, bulk density, pay flag, and water saturation log section for the Brown Niagaran.

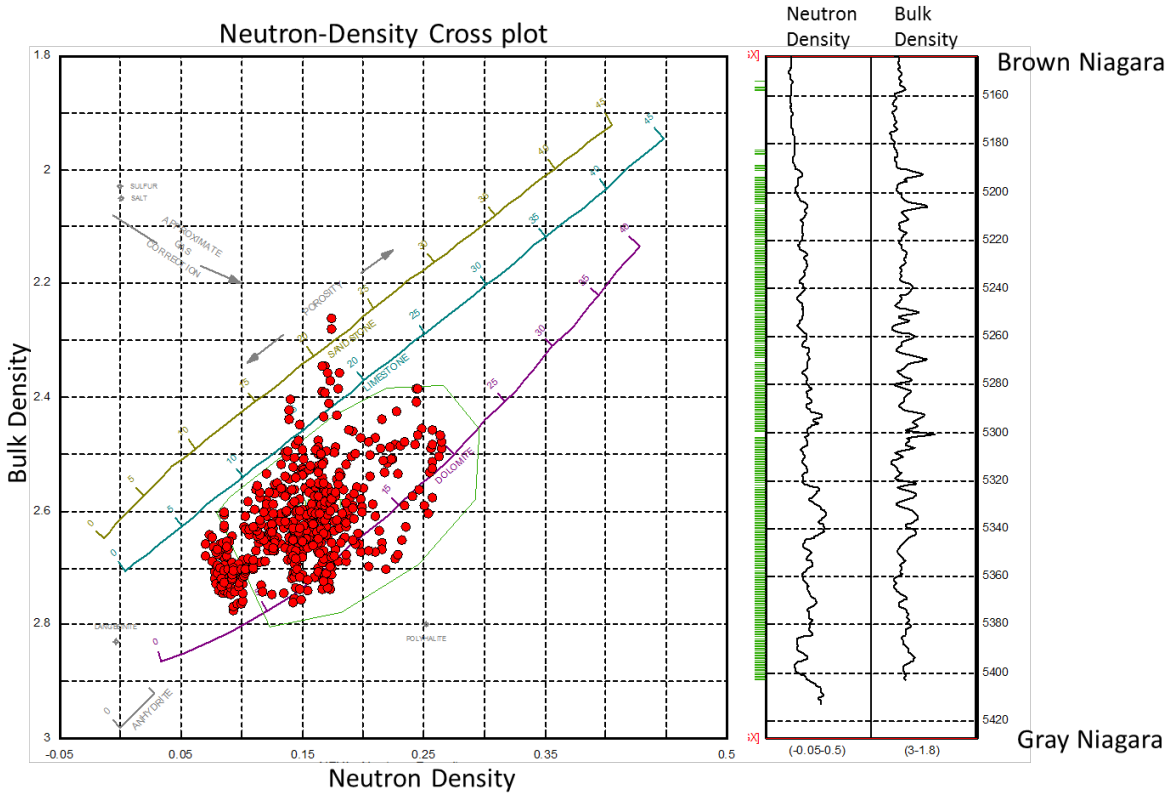


Figure 2-6. Neutron porosity-bulk density cross plot of the Brown Niagaran showing high porosity throughout.

2.5 Conclusions

The A-2 Anhydrite and the thick, vertically continuous character of the Silurian Salina B unit salt sequence is an important factor for assessing their potential to serve as confining layers to the underlying carbonate reservoir. Potential carbonate reservoirs using the pay flag method are the middle of the A-1 Carbonate formation (~17 feet thick each) as well as small scattered zones (1-5 feet thick) in the Brown Niagaran. Using the apparent cross plot flags the only reservoir in the sequence of rock is the Brown Niagaran. This method shows reservoir quality rock starting at 5400 ft. MD all the way to 5190 ft. MD. The lower portion of the Brown Niagaran is water saturated. Drilling records indicate a highly porous zone with potential for karst development.


BATTELLE
It can be done

Attachment 6.
Dover 33 Niagaran Reef Alternative Conceptual Static Earth Models (SEM): Level 1 Lithostratigraphic and Level 2 Sequence Stratigraphic Models

Attachment 6

Dover 33 Niagaran Reef

Alternative Conceptual Static Earth Models (SEM)

Level 1Lithostratigraphic and Level 2 Sequence Stratigraphic Models: Task 3 Depleted Michigan EOR Reef

Prepared by:
Midwest Regional Carbon Sequestration Partnership (MRCSP)
DOE-NETL Cooperative Agreement DE-FC26-05NT42589

Battelle
505 King Avenue
Columbus, Ohio 43201

Submitted to:
The U.S Department of Energy, National Energy Technology Laboratory
3610 Collins Ferry Road
P.O. Box 880
Morgantown, WV 26507-0880

December 3, 2020

This report was prepared by Battelle as part of the Midwest Regional Carbon Sequestration Partnership (MRCSP) program, sponsored by U.S. Department of Energy. Neither Battelle, members of MRCSP, the National Energy Technology Laboratory, the U.S. Department of Energy, nor any person acting on behalf of any of the entities:

a. MAKES ANY WARRANTY OR REPRESENTATION, EXPRESS OR IMPLIED, WITH RESPECT TO THE ACCURACY, COMPLETENESS, OR USEFULNESS OF THE INFORMATION CONTAINED IN THIS DOCUMENT, OR THAT THE USE OF ANY INFORMATION, APPARATUS, METHOD, OR PROCESS DISCLOSED IN THIS DOCUMENT MAY NOT INFRINGE PRIVATELY OWNED RIGHTS, OR

b. ASSUMES ANY LIABILITY WITH RESPECT TO THE USE OF, OR FOR ANY AND ALL DAMAGES RESULTING FROM THE USE OF, ANY INFORMATION, APPARATUS, METHOD, OR PROCESS DISCLOSED IN THIS DOCUMENT.

This topical report contains preliminary findings related to project progress and should not be considered final.

Reference to trade names or specific commercial products, commodities, or services in this report does not represent or constitute an endorsement, recommendation, or favoring by Battelle, or its contractors of the specific commercial product, commodity, or services.

Table of Contents

Page

Chapter 1. Introduction 1
1.1 Objectives 1
1.2 Approach 2
Chapter 2. Geologic Overview 5
Chapter 3. Level 1 Lithostratigraphic Static Earth Model 8
3.1 Well Log Data 10
3.2 Log-Derived Porosity Values 10
3.3 Log-Derived Mineralogy 12
3.4 Dover 33 3D Seismic Data and Interpretation 15
3.5 Construction of 2D Surface Framework 18
3.6 Three Dimensional (3D) Structural Layering 21
3.7 Property Modeling 23
Chapter 4. Level 2 Sequence Stratigraphic Model Construction 29
4.1 Sequence Stratigraphic Overview 30
4.2 Approach 33
4.3 Review of Lithofacies and Sequence Stratigraphic Studies of Michigan Niagaran Reefs 35
4.3.1 Published Key Lithofacies of the Northern Reefs 37
4.3.2 Published Sequence Stratigraphic Studies of the Niagarann Reefs 43
4.4 Interpretation of Sequence Stratigraphy and Lithofacies at the Dover 33 Reef 46
4.4.1 Wireline Log Signatures 46
4.4.2 Cross-plot Mineralogy Logs 48
4.4.3 Computed Lithology Logs 49
4.4.4 Correlation of Third- and Fourth-Order Sequences to the Dover 33 Reef 51
4.4.5 Summary of Interpreted Sequence Boundaries 55
4.5 Lithofacies Interpretation in the Absence of Core 57
4.6 Statistical Analysis of Porosity and Permeability 62
4.6.1 Comparison of Log and Core-derived Porosity/ Permeability Relationships 63
4.6.2 Determination of Best Porosity-Analog Well 63
4.6.3 Multivariate Analysis of Analog Data for Sequence and Lithofacies Conformity 63
4.7 Level 2 Model Construction 64
4.7.1 2D Surface Grid Construction 64

4.7.2 3D Structural Modeling 66
4.7.3 Lithofacies Model Construction 68
Chapter 5. Model Comparisons and Statistical Review 76
5.1 General Statistics 76
5.2 Geometry 79
5.3 Porosity and Permeability Distribution 79
Chapter 6. Summary and Lessons Learned 83
6.1 Seismic Interpretation 83
6.2 Grid and Surface Construction 83
6.3 Porosity and Permeability Modeling 84
6.4 Sequence Stratigraphy and Lithofacies Interpretation 84
6.5 Incorporation of Lithofacies in the Level 2 SEM 87
6.6 Time Effort 88
6.7 Discussion and Recommendations 88
6.7.1 Challenges 88
6.7.2 Key Uncertainties 89
6.7.3 Recommendations 89
Chapter 7. References Cited 91

List of Tables

Page

Table 1-1. Comparison of Level 1 and Level 2 Dover 33 static earth models. 3
Table 3-1. Digital and raster log suites for wells on and adjacent to the Dover 33 reef. 8
Table 3-2. Wells, type of porosity logs, and lithostratigraphic units penetrated. 23
Table 3-3. Variogram modeling data 25
Table 4-1. Sequence 1 variogram final values. 68
Table 4-2. Sequence 2 and Sequence 3 variogram final values. 69
Table 4-3. Permeability transforms for grouped Level 2 lithofacies. 74
Table 5-1. Level 1 and 2 model dimensions. 77
Table 5-2. SEM Level 1 and 2 volume statistics. 77
Table 5-3. SEM Level 1 and 2 porosity statistics. 78
Table 5-4. Level 1 and 2 permeability statistics. 79

List of Figures

Page

Figure 1-1. Location of the Dover 33 pinnacle reef in Otsego County, Michigan, along the Northern Pinnacle Reef Trend. 1

Figure 1-2. General workflow for constructing static earth models with commercial software. 3

Figure 2-1. Generalized lithostratigraphic column showing the vertical and lateral succession of formations adjacent to the Niagarann reef facies. After Catacosinos et al, 2000; and Carter et al., 2010. 5

Figure 2-2. Location, names and permit numbers of wells on the Dover 33 reef. Colored lines indicate lateral sections of wells; red asterix indicates wells immediately south of the displayed map area. 6

Figure 3-1. Lithostratigraphic Formations and zones used in constructing the Level 1 static earth model. 8

Figure 3-2. Workflow for constructing the Level 1 static earth model. 9

Figure 3-3. Sidewall neutron porosity curve (XNPHI) from the 29565 well near the reef center displaying the final 2.5% corrected neutron porosity curve (XNPHI_COR_POS). Note that porosity in anhydrite is truncated at zero porosity units. Depth is in feet, subsea. 11

Figure 3-4. Compensated neutron porosity curve (XNPHI) from the 35195 well with final 6.0% corrected neutron porosity curve (XNPHI_COR_POS) for the CNP values, Negative porosity values are truncated at zero. REA is Rabbit Ears Anhydrite within the A-1 Carbonate.Figure 3-3. Sidewall neutron porosity curve (XNPHI) from the 29565 well near the reef center displaying the final 2.5% corrected neutron porosity curve (XNPHI_COR_POS). Note that porosity in anhydrite is truncated at zero porosity units. Depth is in feet, subsea. 11

Figure 3-4. Compensated neutron porosity curve (XNPHI) from the 35195 well with final 6.0% corrected neutron porosity curve (XNPHI_COR_POS) for the CNP values, Negative porosity values are truncated at zero. REA is Rabbit Ears Anhydrite within the A-1 Carbonate. 11

Figure 3-5. Boxplot statistical comparison of the Dover 33 well 29565 log-derived porosity with the core-derived porosity from other Niagarann reef wells in Michigan (mean value plotted for each well). Figure 3-4. Compensated neutron porosity curve (XNPHI) from the 35195 well with final 6.0% corrected neutron porosity curve (XNPHI_COR_POS) for the CNP values, Negative porosity values are truncated at zero. REA is Rabbit Ears Anhydrite within the A-1 Carbonate. 11

Figure 3-5. Boxplot statistical comparison of the Dover 33 well 29565 log-derived porosity with the core-derived porosity from other Niagarann reef wells in Michigan (mean value plotted for each well). 12

Figure 3-6. Cross-plot mineralogy polygons for bulk density vs neutron porosity in the Dover 33 35195 for the interval from the A-1 Carbonate to TD. Each data point represents a single depth reading on the logs. 13

Figure 3-7. Mineralogy flag logs for two Dover 33 wells, generated from bulk density (RHOB) or sonic (DT) vs neutron porosity cross-plot data. See Table 3-1 for well names; well 35195 is located immediately south of the man reef structure in Figure 2-2. 14

Figure 3-8. Well 29565 synthetic seismogram with extracted traces from the Dover 33 3D seismic volume. 16

Figure 3-9. Power (frequency) and phase spectrum from extracted wavelet from the Dover 33 3D volume. 17

Figure 3-10. Dover 33 3D depth-migrated volume west-to-east arbitrary line in variable amplitude display, showing formation tops in wellbores (small white boxes in wellbore with formation label). Interpreted horizons shown by blue, pink, and green lines. 18

Figure 3-11. 3D seismic and well log data used to build the Brown Niagaran 2D surface. 19

Figure 3-12. Interpreted top of the Brown Niagaran 2D surface from seismic and well log data. Image illustrates how the 2D grid was fitted to the data. Well logs have priority over the seismic during construction of surfaces. 20

Figure 3-13. Resulting lithostratigraphic surfaces interpreted from well log and seismic data. These structural surfaces are input data for generation of the internal 3D grid framework requisite for property modeling. 21

Figure 3-14. Cross-section of structural model showing zones and layers after structural gridding process. Internal cells are not displayed in this image. Cross-section view is to the north. 22

Figure 3-15. Level 1 3D grid at wells, after the “scaling up porosity logs” module had been completed. Only cells that were penetrated by well logs have been assigned porosity values. Each layer is assigned a single porosity value. 24

Figure 3-16. Characteristics of a variogram. Terms are defined in the text. 25

Figure 3-17. Porosity- permeability cross plot used to derive transform for populating the Level 1 SEM. Location of State Kalkaska well is shown in Section 4; Figure 4-4. 26

Figure 3-18. Porosity model, view to the northeast intersection of the south and west planes. Grid cell dimensions in the Brown Niagaran are 10 x 10 meters. 27

Figure 3-19. Permeability model calculated from the upscaled porosity grid. A porosity-to-permeability transform was applied to porosity values in each grid cell to construct the permeability model. Grid cell dimensions of the model are 30 x 30 meters. 28

Figure 3-20. Upscaled porosity model, view to the northeast intersection of the I and J planes. Grid cell dimensions in the Brown Niagaran were upscaled from10 x 10 meters to 30 x 30 meters. 28

Figure 4-1. Workflow for the Level 2 static earth model. 30

Figure 4-2. Two models for placement of a third order sequence boundary. For the Michigan reefs, the A-1 Anhydrite may represent either a falling stage deposit, a lowstand wedge or a combination of the two. HST = highstand systems tracts; SB= sequence boundary; TST = transgressive systems tract; FSST = falling-stage systems tract; LST = lowstand systems tract, CS = composite sequence. From Catuneanu et al., 2011. 31

Figure 4-3. Consecutive three-stage workflow for interpreting a rock and wireline-log-based sequence stratigraphic framework and constrained lithofacies for the Dover 33 Level 2 static earth model. 34

Figure 4-4. Location of the Dover 33 reef relative to key cored wells studied by Huh (1973), Huh et al., 1977), Ritter (2008), and Noack (2008). Petrophysical data were analyzed as part of this study for the State Kalkaska 3-22, permit 288443; Beier #2, 25779; Dietlin #1, 25022; and State Charlton 1-4, 28006. Additional core-based studies conducted by Grammer's students included material from the Belle River Mills Field in the southern reef trend. 35

Figure 4-5. Lithostratigraphy and lithofacies of the Kalkaska reef, as interpreted by Huh (1973). This interpretation, along with core data associated with these wells, contributed to the establishment of a regional sequence stratigraphic framework by Ritter (2008). 36

Figure 4-6. Ideal carbonate lithofacies recognized by Ritter (2008). As arranged here, these lithofacies reflect overall upwards-shallowing depositional conditions (indicated by yellow triangle). 37

Figure 4-7. Muddy bioherm lithofacies 2A of Ritter (2008). Core slab photographs A and B illustrate calcite and anhydrite (black A) cements in stromatactis fabric (SC), carbonate mud (M) and encrusting stromatoporoids (ST). Photographs C and D illustrate carbonate mud (M), anhydrite cement (A), stromatactis fabric (SC) and branching twiggy bryozoans (Z). From Ritter (2008). 38

Figure 4-8. Lithofacies 3, reef facies of Ritter (2008). Slab photographs A and B illustrate stomatoporoid framestones; photographs C and D illustrate coral framestones. Symbols: C - coral; M - mud; ST - stomatoporoid. M-F is the Miller-Fox 1-11, Oceana County; DC is Dietlin Comm. #1, and Br #1 is Beier #1, both from St. Clair County. From Ritter (2008). 39

Figure 4-9. Tidal flat cyanobacterial lithofacies 6A and 6B of Ritter (2008). Slab photographs A and B illustrate cemented breccias (facies 6A); photographs C and D illustrate more growth position boundstones (lithofacies 6B). Symbols: A - Anhydrite; CB -cyanobacterial mats; CM - carbonate cement; FP - "flat-pebble" microbial clasts; and MC - mud cracks. Br-1: Beier #1, St. Clair County; MF1-11 Miller Fox 1-11, Oceana County; ST. K.: State Kalkaska, Kalkaska County. From Ritter 2008. 41

Figure 4-10. Nodular anhydrite lithofacies, grading upward into possible carbonate supratidal deposits. Well permit 27669, from the Columbus III reef in the southern reef trend. Lateral field of view about 3.5 inches; photograph courtesy of Matt Rine. 42

Figure 4-12. Late stage diagenetic fracture fill by halite. Core is from the Kalkaska 1-15, and was studied by both Huh (1973) and Ritter, (2008). Field of view about 3.5 inches; photograph courtesy of Autumn Haagsma..... 43

Figure 4-13. Sequence stratigraphic boundaries for five reefs studied by Ritter (2008). Jahn 4 is an off-reef well; all other wells are located on reef. Jahn 4, Dietlin 2, and Bier 1 are in the Southern Reef Trend..... 44

Figure 4-14. Correspondence of Ritter's unconformity-bounded third order sequences to Huh's (1973) reef stratigraphy. The logs and descriptions from the Kalkaska 3-22 (28843) were important in establishing correlation with the Dover 33 reef. 45

Figure 4-15. Schematic representation of aggrading, prograding, and retrograding carbonate stacking patterns. 47

Figure 4-16. Interpreted aggradational log signatures (black arrows) above the A-1 anhydrite in two off-reef wells at the Dover 33 reef. The gamma curve has been expanded to maximize small deflections common in carbonate logs. 48

Figure 4-17. Electrofacies generated from bulk density (RHOB) or sonic (DT) vs neutron porosity cross-plots. 49

Figure 4-18. Computed ELAN lithology log of the Dover 35584 off-reef well. Changes in computed lithology, calculated porosity and permeability, and free or bound water saturation aid in interpreting sequence and lithofacies boundaries. 50

Figure 4-19. The Kalkaska 3-22 (28843) off-reef well log with lithofacies described by Huh (1973) (left), correlated to the Dover 35584 off-reef well (right). The 35584 well log is vertically stretched for ease of pattern recognition; arrows indicate aggradational log pattern. 51

Figure 4-20. Third- and fourth-order sequences in off-reef well UID #35584 53

Figure 4-21. Correlation of 3rd order sequences in off-reef well 33584 to Dover 33 flank well 50985 with cross-plot mineralogy. Cross-section datum is the top of Sequence 3. 54

Figure 4-22. Third Order Sequence correlation of the Dover 33 off-reef 35584 well (left) to the Dover 33 29565 reef-center well (middle) and to the State Charlton 1-4 cored well in Otsego County (right). 55

Figure 4-23. Huh's lithofacies model, with a comparison of Battelle sequence stratigraphic interpretation (left) with that of Ritter (2008) (right) 57

Figure 4-23. Comparison of on-reef and off-reef sequence interpretation of Ritter (2008) and current study (red). 57

Figure 4-24. Upscaled sequence-restricted lithofacies. 58

Figure 4-25. Comparison of cross-plot and upscaled lithofacies interpretation logs for an off-reef well (35584) and a vertical central reef well (29565) at the Dover 33 reef. Lithofacies 3A and 3B have been combined with Lithofacies 3Cand 3D, based on porosity. 61

Figure 4-26. Cross section across Dover 33 reef with off-reef (Well 35584), central-reef (well 29585), and reef-flank (wells 29809 and 50985. (See Figure 4-24) for upscaled lithofacies color key). 62

Figure 4-27. Sequence 2 upper surface (contour interval = 20 feet). 65

Figure 4-28. Sequence 3 upper surface (contour interval = 20 feet). 65

Figure 4-29. Sequence 1 upper surface (contour interval = 20 feet). 66

Figure 4-30. Zones (Upper) and upscaled layers (Lower) corresponding to the stratigraphic sequences in the Level 2 SEM. 67

Figure 4-31. Facies models from Qualman (2009) with 1,000-foot (A), 500-foot (B), and 50-foot (C) variograms. 70
Figure 4-32. Lithofacies model for the Dover 33 reef. View to the northwest. 71
Figure 4-33. Lithofacies detail on a west-to-east section (green arrow pointing north) showing details such as the “Rabbit Ears” Anhydrite, the A-1 Anhydrite lapping onto the reef flanks, and the building of the reef core. 72
Figure 4-35. Porosity model on west-to-east section (green arrow pointing north)..... 73
Figure 4-34. Porosity model of the Dover 33 reef. View to the northwest. 73
Figure 5-1. Comparison of lithostratigraphic layering (top) to sequence layering (bottom) in west-to-east sections from the Dover 33 Level 1 and Level 2 models. 80
Figure 5-3. Level 2 upscaled porosity model. 81
Figure 5-2. Level 1 upscaled porosity model. 81
Figure 5-5. Level 2 upscaled permeability model. 82
Figure 5-4. Level 1 upscaled permeability model. 82
Figure 6-1. Sequence boundaries in the off-reef Dover 33 35584 well. 86

Chapter 1. Introduction

The Midwest Regional Carbon Sequestration Partnership (MRCSP) is currently conducting its Phase III (commercial-scale) CO_2 injection test in conjunction with Enhanced Oil Recovery (EOR) in a series of Silurian-age (Niagarann) pinnacle reefs in northern Michigan. In the MRCSP Michigan region, CO_2 for large-scale EOR injection is available from Antrim-shale gas processing plants. Some of this CO_2 is already being utilized for oil production from pinnacle reefs in the northern part of the Lower Peninsula of Michigan. About 800 pinnacle reefs have been mapped in the northern reef trend, and carbonates form potential CO_2 storage targets in much of MRCSP region.

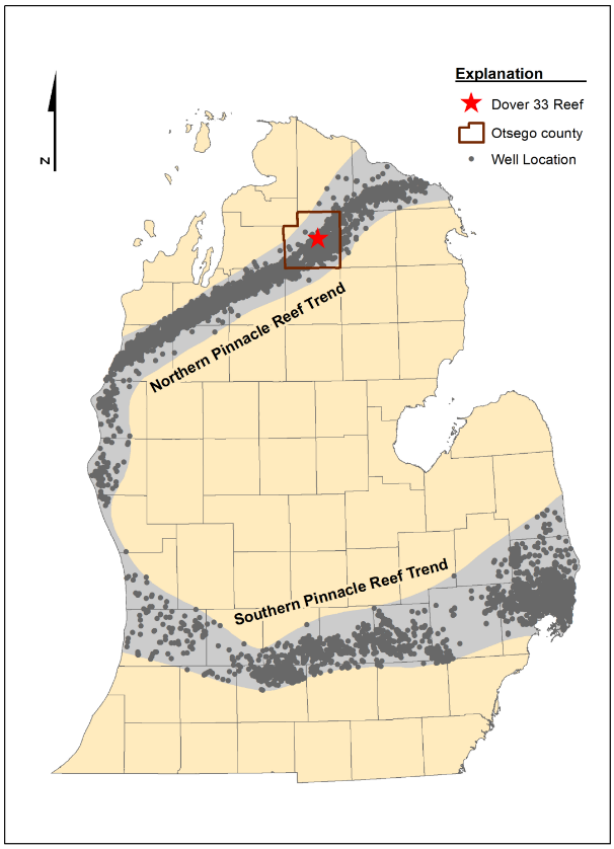


Figure 1-1. Location of the Dover 33 pinnacle reef in Otsego County, Michigan, along the Northern Pinnacle Reef Trend.

The MRCSP Michigan Basin Project examines three operational reef types, categorized by stages in the life cycle of EOR operations. Category 1 reefs are highly depleted and have undergone EOR in the past; Category 2 reefs are actively producing with current EOR; and Category 3 reefs are newly targeted reefs that have not yet undergone EOR (Gupta et al., 2013). A key goal of the MRCSP Phase III program is to develop dynamic numerical reservoir models to simulate the fate of injected CO_2 within each category of reef and to accommodate the geologic variability of the reefs. The Category 1 Dover 33 reef (Figure 1-1) is the first project reef to be studied; CO_2 injection into the Dover 33 reef commenced in April 2013, after completion of characterization and baseline monitoring activities. The success of the dynamic models is contingent upon how well the static earth models (SEMs) capture the reef-specific framework and distribution of reservoir properties, and this report explores the efficacy of two different methodologies, which vary significantly in complexity, for constructing SEMs for Michigan reef reservoirs.

1.1 Objectives

More robust predictions of life-cycle fluid and pressure behavior during CO_2 injection in the Michigan reefs require optimizing structure and property distributions in static earth models. This report details the initial work performed on the Dover 33 reef to construct two separate static earth models that use different methods to determine vertical layering, lateral heterogeneity, and property distribution. The Level 1 model is a traditional lithostratigraphic (Formation)-based model; the Level 2 model is based on a more complex, time-intensive sequence stratigraphic/ lithofacies evaluation. Sequence stratigraphy is a method of determining

laterally linked, coevally deposited strata. Lithofacies refers to lithology, texture, faunal content, and sedimentary structures of a given rock.

The overall objective of the immediate modelling effort is to demonstrate differences in framework and property distribution within the SEMs, and the effect on volumetrics. A comparison of results from the associated dynamic modeling will be presented in a separate report (Mishra, et al., 2020).

Studies of carbonate reservoirs since the 1990's, have increasingly relied on developing a basin-specific sequence stratigraphic framework within which to tie models of depositional facies to chronostratigraphic surfaces (i.e., divide sedimentary strata into time-equivalent, genetically-related rock units). This framework may more accurately capture genetic, deposition-related rock packages; provide a basis for more accurate prediction of lithofacies specific to these depositional packages; and allow a more realistic distribution of porosity/permeability and other petrophysical properties within that framework.

It is recognized that flow units and diagenetic overprints (dolomitization, karst, anhydrite cementation, and salt plugging) may follow or may crosscut these depositional packages and may limit the impact of using a sequence stratigraphic/depositional lithofacies approach. Given the range of lithology and diagenetic overprints in the Michigan reefs, the level of detail required to robustly predict dynamic reservoir behavior is likely to be reef or site specific. Therefore, two things are examined in this study: the feasibility of interpreting sequence stratigraphy and lithofacies in Michigan reefs, and whether this extra effort is justified in a dolomitized reef that lacks core for verification/ calibration of lithofacies. It is anticipated that the sequence stratigraphic/lithofacies methodology provides a more advanced way to reduce uncertainty, but it will have to be tested in reefs with core to fully establish its utility in Silurian reefs of the Michigan basin.

1.2 Approach

Static model development involves construction of reservoir framework and surfaces, and population of that framework with reservoir properties that include porosity and permeability (Figure 1-2). The Dover 33 Level 1 static earth model contains two reef-associated layers, based on lithostratigraphic formations. The Level 2 model uses a sequence stratigraphic approach where the framework of the reef model is defined by wireline signatures that are correlated to regional sequence boundaries, and to interpreted lithofacies as defined in analog reef studies. Reservoir properties are distributed within the sequences and conditioned to the individual lithofacies. A high-level comparison of the two models is shown in Table 1-1. The Level 2 model approach provides more opportunity to analyze 3D spatial details within the reef but is more time and labor intense as compared to the Level 1 model.

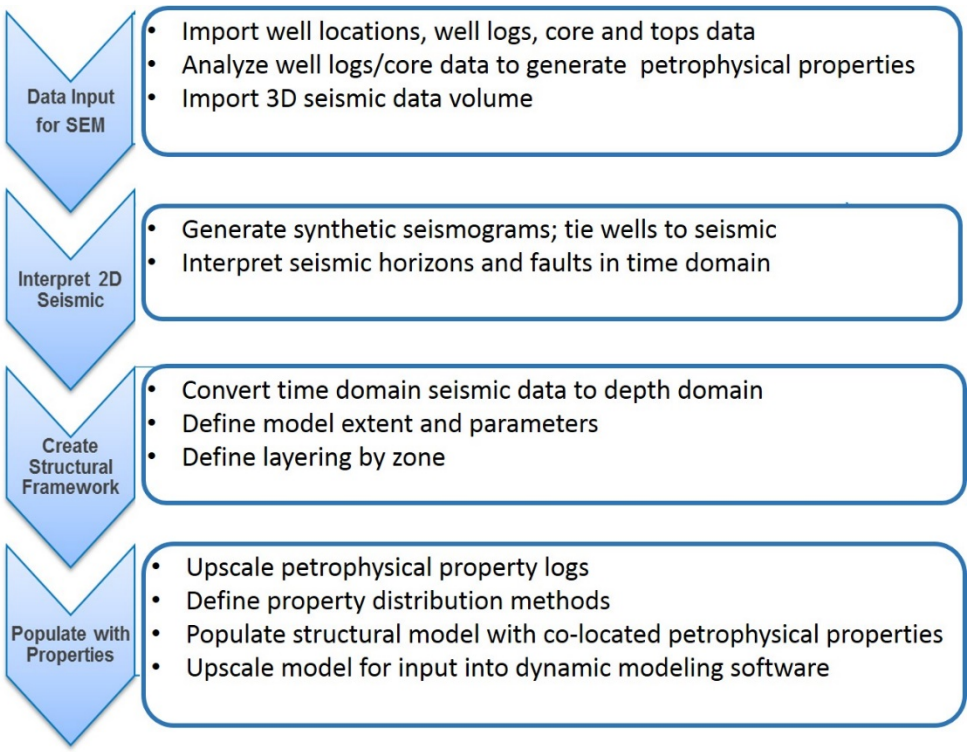


Figure 1-2. General workflow for constructing static earth models with commercial software.

Table 1-1. Comparison of Level 1 and Level 2 Dover 33 static earth models.

Level 1 Static Earth Model (SEM)	Level 2 SEM
• Geologic surfaces based on 3D seismic and well data	• Geologic surfaces within seismic framework based on well data and interpreted regional sequence stratigraphy
• Vertical layering represented by major geologic units (A-1 Carbonate, Brown Niagara, and Gray Niagara)	• Vertical layering represented by major geologic units and interpreted stratigraphic sequences within the Brown Niagara and A-1 Carbonate
• Layer-averaged porosity and permeability (permeability inferred from porosity and well testing)	• Lithofacies-averaged porosity and permeability (wireline log porosity/permeability relationships determined from analog reefs with core)
Reservoir model complexity →	

The following sections review the geology of the Michigan Silurian reefs, and the details of the construction of each static earth model. Unlike the discussion of the Level 1 static earth construction that uses established lithostratigraphic units, the Level 2 discussion includes evaluation of previous work to establish the sequence stratigraphy, depositional environments and lithofacies in Silurian reefs with core data; and the methods used to interpret the stratigraphy and lithofacies of the Dover 33 reef, where there is no core for calibration. Next there is a comparison of the two models and a discussion of the challenges and uncertainties involved with applying each type of static earth model construction to other Silurian reefs in the northern Michigan Basin.

Although the lack of core, at the time, prevented rock-to-log model calibration for the Dover 33 reef, it is expected that the work flows developed in this study would lay the foundation for future reservoir characterization and modeling of these numerous CO_2 sequestration targets; and that a refinement of the sequence stratigraphic/lithofacies approach will optimize prediction and evaluation of dynamics of CO_2 floods across the Northern Michigan reef trend.

Chapter 2. Geologic Overview

Dover 33 is an Early Silurian age subsurface pinnacle reef located in Otsego County, Michigan. The reef is part of the oil-productive Northern Pinnacle Reef Trend (NPRT) on the northern flank of the Michigan Basin (Figure 1-1). Reefs along the NPRT developed in a shallow shelf carbonate depositional system that extended over the Lower Peninsula of Michigan, northern Indiana, northeastern Illinois, eastern Wisconsin, northwestern Ohio, and the Bruce Peninsula of Ontario (Briggs et al., 1980; Coniglio et al., 2004; Harrison III, 2010). These reefs range from 2,000 feet to over 6,000 feet deep, with the majority of the reefs typically occurring at depths of 3,500 to 5,000 feet. They are closely spaced and compartmentalized from the enclosing rock, averaging 50 to 400 acres in area, up to 700 feet in height, and possessing steep flanks (30° to 45°).

Approximately 800 fields in the NPRT, originally developed in the 1970s-1980s, have undergone primary production and, in some cases, secondary recovery by water flood and tertiary recovery by CO_2 (Grammer et al., 2009; Harrison III, 2010; Barnes et al., 2013). The reefs are generally divided in an up-dip direction into gas, oil, and water-saturated (Gill, 1979). The reservoir rocks primarily consist of porous and permeable dolomite and limestone. Reefs may be completely dolomitized, essentially all limestone, or a heterogeneous mix. Dolomitization of reefs increases updip, and salt and anhydrite plugging of porosity is more common in the deeper, down-dip, reefs (Gill, 1979). The upper parts of reefs are often, but not always more dolomitized that the lower parts.

As shown in Figure 2-1, reefs developed in the upper portion of the Niagaran Group, which is subdivided into the Guelph and Lockport Dolomites (Catacosinos et al, 2000; Carter et al., 2010). Historically, the oil industry subdivides the Niagaran Group into Brown, Gray, and White Niagaran based on color, texture, and wireline log signature. The reef facies are referred as the Brown Niagaran, the subsurface equivalent to the Guelph Dolomite (Catacosinos et al., 2000; and Toelle et al., 2008). The underlying Gray and White Niagaran are the subsurface equivalent of the Lockport Dolomite. The Brown Niagaran is overlain and encased by cyclic carbonate and evaporite sequences of the Salina Group.

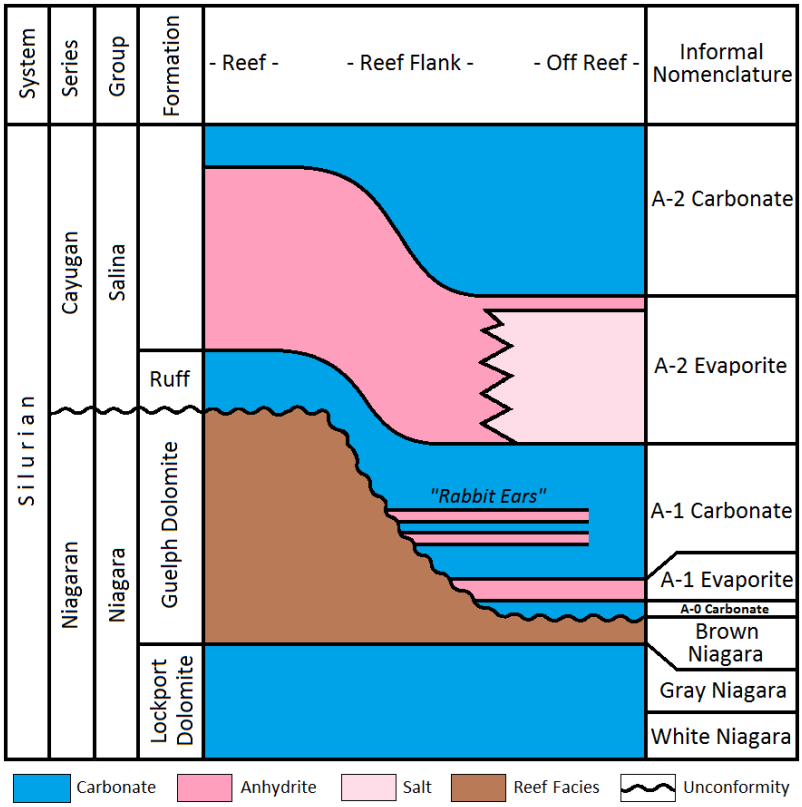
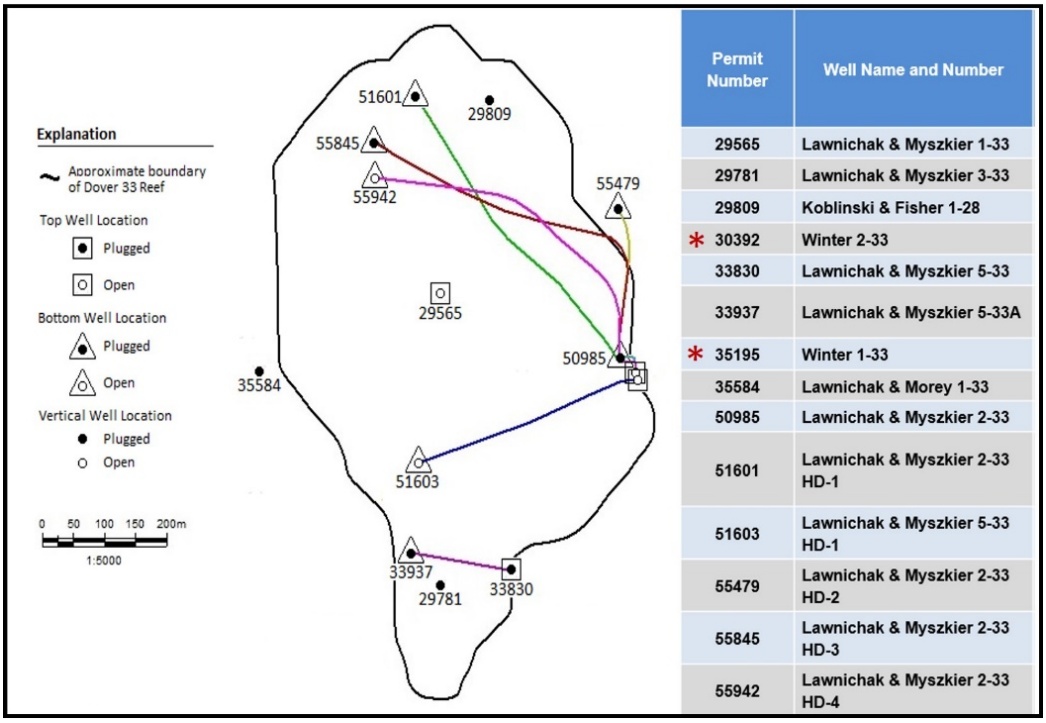


Figure 2-1. Generalized lithostratigraphic column showing the vertical and lateral succession of formations adjacent to the Niagarann reef facies. After Catacosinos et al, 2000; and Carter et al., 2010.

According to Rullkotter et al. (1986), the principal source rock for oil accumulation in the NPRT is the off-reef facies of the A-1 Carbonate. Porosity values of NPRT reefs average about 3% to 12%, with the best porosity and permeability associated with dolomitized reef core and flank facies. The best reservoir rocks are characterized by well-developed intercrystalline and vuggy porosity with average permeability values of 3 to 10 millidarcy (mD). Permeability can be significantly higher where fractures intersect matrix porosity.

Dover 33 (Figure 2-2) is a late-stage EOR reef which has undergone extensive primary and secondary oil recovery and is mostly depleted of oil. The field was discovered in 1974 by Shell Oil with the completion of the Lawnichak-Myszkier well 1-33 (Michigan Department of Environmental Quality [DEQ] permit 29565), which was later converted to a CO_2 injection well in 1996 (Harrison III, 2010). Based on seismic data, the 1-33 well location is near the center of the reef. The reef's depth extends from 5,400 to 5,700 feet, with a maximum height of 280 feet and a total areal extent of 60 acres. Porosity values in the Dover 33 reef wells extend to 24%, but typically range from 3% to 11% with an average of 4% (dolomite-corrected neutron porosity).



Permit Number	Well Name and Number
29565	Lawnichak & Myszkier 1-33
29781	Lawnichak & Myszkier 3-33
29809	Koblinski & Fisher 1-28
* 30392	Winter 2-33
33830	Lawnichak & Myszkier 5-33
33937	Lawnichak & Myszkier 5-33A
* 35195	Winter 1-33
35584	Lawnichak & Morey 1-33
50985	Lawnichak & Myszkier 2-33
51601	Lawnichak & Myszkier 2-33 HD-1
51603	Lawnichak & Myszkier 5-33 HD-1
55479	Lawnichak & Myszkier 2-33 HD-2
55845	Lawnichak & Myszkier 2-33 HD-3
55942	Lawnichak & Myszkier 2-33 HD-4

Figure 2-2. Location, names and permit numbers of wells on the Dover 33 reef. Colored lines indicate lateral sections of wells; red asterix indicates wells immediately south of the displayed map area.

The Brown Niagaran and the overlying A-1 Carbonate are the producing formations of the Dover 33 field. The A-1 anhydrite and A-1 Carbonate anhydrites (“rabbit ears”) form restricted seals on the reef flanks. The A-2 Evaporite forms the regional top seal for the northern trend but is eroded updip. The Brown Niagaran consists of skeletal wackestones, packstones, grainstones, and boundstones/bindstones associated with the organic reef buildups. The Brown Niagaran includes the off-reef carbonate conglomerate lithofacies below the A-0 Carbonate (Huh, 1973). The Brown Niagaran forms the majority of the reservoir rocks associated with producing reefs; the distinctive brown color can be attributed to dolomitization as well as, in some cases, oil staining. The underlying Gray and White Niagaran form the base of the reservoir and are characterized by two types of crinoidal wackestones: porous dolomitized wackestones, and low-porosity, undolomitized limestone (Charbonneau, 1990). The Gray and White Niagaran reach a thickness of approximately 500 feet near the basin margins, become thinner and have a more reddish color toward the center of the Basin, and grade upward into a gray argillaceous, nodular crinoidal wackestone (Huh, 1973; Huh et al., 1977; Charbonneau, 1990).

The A-1 Carbonate, subsurface equivalent to the Ruff Formation, overlies the A-1 Evaporite. It is a light-brown to tan, fine to medium crystalline, laminated, dolomitic mudstone and stromatolitic or microbial laminated boundstones, which may show truncation surfaces and rip-up clasts (Huh, 1973; Gill, 1973; Ritter, 2008). Laminated, dolomitic mudstones occur in inter-reef deposits and on the reef; dolomitic microbial boundstone facies unconformably overlie the Brown Niagarann skeletal deposits (Gill, 1973). The A-1 Carbonate generally seals the flanks of the reefs, but some reservoir zones within the carbonate can be developed on the crests and flanks of the reefs.

The A0 carbonate is a thin (usually less than 10 feet) unit that overlies Brown Niagaran reef-associated conglomerates on reef flanks. The superjacent A-1 Evaporite regionally transitions from halite and sylvite in the basin center to anhydrite on reef flanks, forming a sealing lithology. The A-1 Carbonate, subsurface equivalent to the Ruff Formation, overlies the Brown Niagaran on reef crests and overlies the A-1 Evaporite, off-reef. It includes laminated, light-brown to tan, fine to medium crystalline dolomitic mudstone, dark shaley “poker-chip” mudstones, and stromatolitic or microbial laminated boundstones, which may show truncation surfaces and rip-up clasts (Huh, 1973; Gill, 1973; Ritter, 2008). Laminated, dolomitic mudstones occur in inter-reef deposits and on the reef; packstones and dolomitic microbial boundstone facies, often displaying anhydritic cements (Gill, 1973) occur on reef crests. The upper part of the A-1 Carbonate includes the thin, regionally correlative Rabbit Ears Anhydrites. The A-1 Carbonate may act as seals on the flanks of the reefs, but can develop dolomitic intercrystalline reef top and flank reservoirs as well as microporous reservoirs off reef.

The A-2 Evaporite occurs as a thin bed of anhydrite or halite above the tops of reefs and as bedded halite in the inter-reef deposits (Huh et al., 1977; Gill, 1977). The A-2 Carbonate, above the A-2 Evaporite, is a 100- to 120-foot thick regional tight limestone. Rapid changes in the composition of the A-1 and A-2 Evaporites and the rabbit ears Anhydrites surrounding the reef flanks make the acquisition of a full suite of density and acoustic logs critical in understanding reservoir porosity, seal integrity, and seismic response.

Chapter 3. Level 1 Lithostratigraphic Static Earth Model

The lithostratigraphic units used in the Level 1 static model are shown in Figure 3-1. The wells and available log curves are listed in Table 3-1. Core Energy LLC., supplied the 3D seismic volumes, digital well logs and completion information; additional data were supplied by the Michigan Geologic Survey. Input data include 2.59 square miles of 3D seismic, and 60 well curves from 13 wells (see Table 3-1). Wireline log evaluation and cross section construction was accomplished with HIS Petra software; and Schlumberger's Petrel™ E&P software platform 2013 was used for construction of 3D structural and petrophysical-property models. The workflow for construction of the Level 1 static earth model is shown in Figure 3-2.

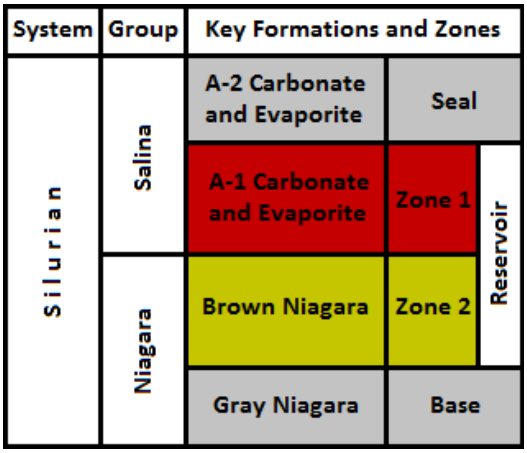


Figure 3-1. Lithostratigraphic Formations and zones used in constructing the Level 1 static earth model.

Table 3-1. Digital and raster log suites for wells on and adjacent to the Dover 33 reef.

API	Permit No.	Common Name	Digital Log Curves	Raster Logs
21137295650000	29565	1-33	CAL, GR, NPHI, DT, RES	Microlaterolog (res), dual laterolog (res), SNP, SON
21137297810000	29781	3-33	CAL, GR, NPHI, DT, RES	Microlaterolog (res), laterolog (res), SNP, SON
21137298090000	29809	1-28	CAL, GR, NPHI, DT, RES	Microlaterolog (res), dual laterolog (res), SNP, SON
21137303920000	30392	Winter 2-33	CAL, GR, NPHI, DT, RES	Dual laterolog (res), SNP, SON
21137309100000	30910	McGinty 4-33	CAL, GR, NPHI, DT, RES	Dual laterolog (res), SNP, SON
21137311080000	31108	Amejka 2-34	CAL, GR, NPHI, DT	SNP, SON
21137338300000	33830	L&M 5-33	CAL, GR, NPHI, DT, RES	Microlaterolog (res), dual laterolog (res), SNP, SON
21137338300100	33937	L&M 5-33A	CAL, GR, NPHI, DT, RES	Microlaterolog (res), dual laterolog (res), SNP, SON
21137351950000	35195	Winter 1-33	CAL, GR, NPHI, RHOB, PE, RES	Triple combo (gr-n-d-pe), micro/dual laterolog (res), four-arm dipmeter
21137355840000	35584	L&M 1-33	CAL, GR, NPHI, RHOB, PE	Triple combo (gr-n-d-pe)

API	Permit No.	Common Name	Digital Log Curves	Raster Logs
21137509850000	50985	2-33	CAL, GR, NPHI, RHOB, PE	Triple combo (gr-n-d-pe), six-arm dipmeter
21137509850100	51601	2-33 HD-1	GR, TPHI, SIGMA	TDT (dual burst thermal decay)
21137509850200	55479	2-33 HD-2	N/A	N/A
21137509850300	55845	2-33 HD-3	N/A	N/A
21137509850400	55942	2-33 HD-4	N/A	N/A
21137516030000	51603	5-33	GR, TPHI, SIGMA	TDT (dual burst thermal decay)

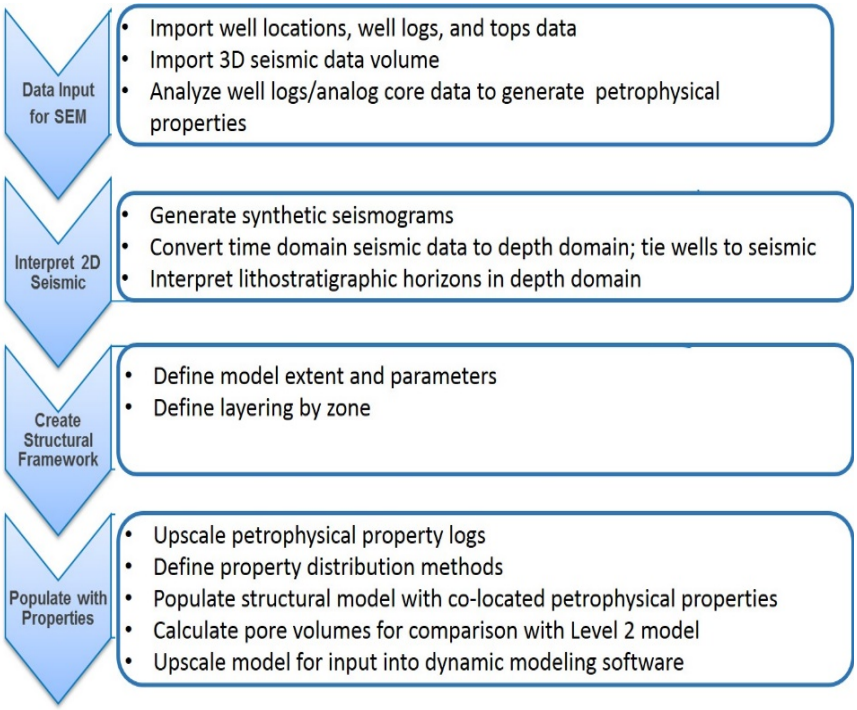


Figure 3-2. Workflow for constructing the Level 1 static earth model.

The initial phase of the project involved collecting and quality control assessment of existing 3D seismic volumes, well logs, completion information, and formation data from Core Energy, LLC, and the Michigan Geologic Survey. The digital well logs and well information were uploaded into the Petra Geologic software modules, and the various log curves were reviewed and repaired if necessary. Formation tops were picked or confirmed, and porosity calculations were generated for intervals to be modeled. Mineralogy logs were generated using standard petrophysical cross-plot methods on wells with limited older suites of logs; full log suites allowed the calculation of computer-generated mineralogy logs (multi-min or ELAN type logs) for four wells. These mineralogy logs, along with gamma ray curves and mud log lithology information permit definition of the lithostratigraphic framework of the reef.

Unlike many standard workflows, the 3D seismic volume was converted from the time domain to the depth domain prior to lithostratigraphic horizon interpretation and mapping. The generation of synthetic seismograms and integration of well and seismic data allowed 2D surface grids and a 3D structural grid to be generated over the entire reef.

In order to populate the framework, petrophysical property models were generated by analyzing wireline log data in Petrel. Various methods of model construction were evaluated to more closely match conceptual reef models. Due to the lack of core in the Dover 33 reef (during the time of this modeling), it was necessary to research analog reefs and wells in the region that have whole core-derived porosity and permeability in order to create porosity-to-permeability transforms for Formations in the Dover 33 reef. The Level 1 model incorporated a single

porosity-to-permeability transform for each of the model zones, based on core data from an analog well. Volume statistics were calculated for comparison with the Level 2 static earth model. After the initial model was completed, it was scaled up to optimize dynamic model run times.

The following sections describe the details of the framework construction and property population of the Level 1 model.

3.1 Well Log Data

The Dover 33 reef discovery wells were drilled in 1974 by Shell Oil Company. The logging company Schlumberger was used on all the discovery and subsequent development wells, so general log consistency is very good with the wells logged over two decades. The initial suites of logs run in the discovery wells consisted of caliper, gamma ray, neutron porosity, sonic (DT), and resistivity (dual laterologs) (Table 3-1). The initial emphasis on logging in the 1970s drilled wells was porosity characterization using the neutron and sonic tools, and hydrocarbon saturations and oil/water contact delineation for oil production. As newer wells were drilled in the 1980s, bulk density and photoelectric (PE) tools were added to further define lithologic details along the flanks of the wells and to better characterize evaporite layers and cementation, and porosity occlusion due to salt plugging.

Dual burst thermal decay (TDT) logs were run in the 1990s on sections of the horizontal and slant wells that were to be used in conjunction with the EOR efforts. These newer logs are used as an estimator of porosity that can be compared with neutron porosity calculated from the vertically logged wells.

The log raster images for the wells were provided by Core Energy and collected from the Michigan DEQ data archives. The majority of the digital las files were previously digitized from paper copy, and provided by Core Energy, while some logs were digitized from the raster images by Battelle geologists using the Petra software package. The digital logs all have 0.5-foot vertical sample spacing.

3.2 Log-Derived Porosity Values

The neutron porosity curves were the sole log that could be used to estimate formation porosity in the wells, based on the curves being present in every vertical well. The original neutron logs were a combination of sidewall neutron porosity (SNP) and compensated neutron porosity (CNP) run on a limestone matrix. The dolomitic nature of the Dover 33 reef, as confirmed in drill cutting samples and determined from cross-plot mineralogy logs leads to an overestimation of porosity based on the original SNP and CNP logs. To correct for a dolomite matrix, Schlumberger has correction charts (Asquith and Gibson, 1982) indicating that a shift of -2.5% for SNP and -6.0% for CNP logs is appropriate. This shift was applied to all wells used in the modeling efforts. Figure 3-3 and Figure 3-4 show an example of a corrected SNP log (Figure 3-3) and a CNP log (Figure 3-4) for the 29565 well and the 35195 well, respectively. The anhydrite or mixed lithology portions of the logs which indicate porosity below 0% were subsequently clipped at zero to remove negative porosity numbers. A statistical comparison of log-derived porosity values for the Dover 33 wells with laboratory-analyzed whole-core core porosity from other Niagaran reefs in the region (Figure 3-5) indicates the normalized Dover 33 log values are within the range of core-derived values. This issue is discussed further in Section 5.0. Note that gamma ray curves have been rescaled from 0 to 50 API units. This narrowed scale greatly enhances correlation of logs in these “clean” carbonates and evaporites.

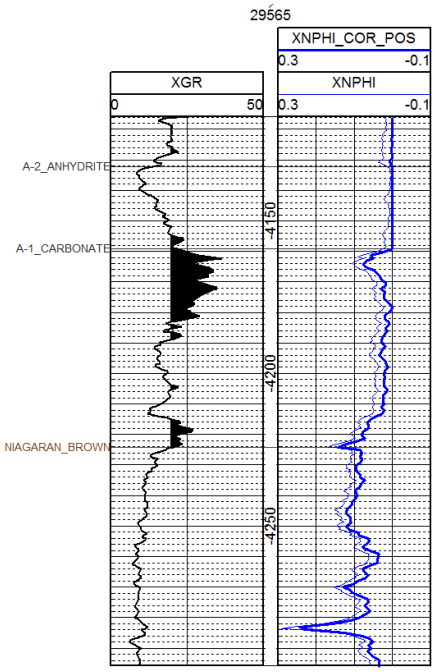


Figure 3-3. Sidewall neutron porosity curve (XNPHI) from the 29565 well near the reef center displaying the final 2.5% corrected neutron porosity curve (XNPHI_COR_POS). Note that porosity in anhydrite is truncated at zero porosity units. Depth is in feet, subsea.

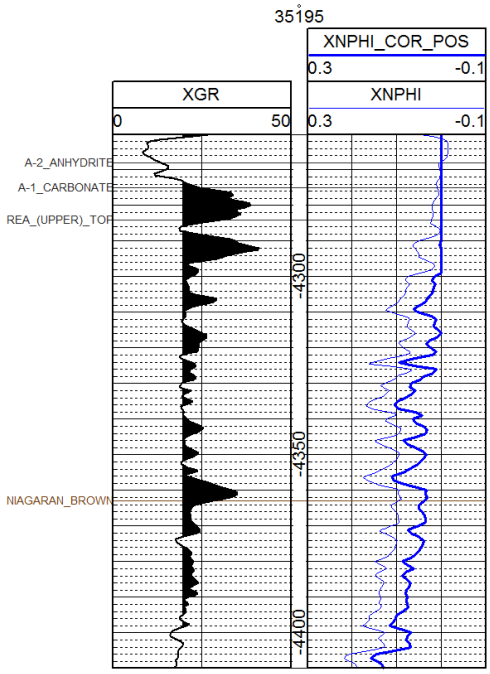


Figure 3-4. Compensated neutron porosity curve (XNPHI) from the 35195 well with final 6.0% corrected neutron porosity curve (XNPHI_COR_POS) for the CNP values, Negative porosity values are truncated at zero. REA is Rabbit Ears Anhydrite within the A-1 Carbonate.

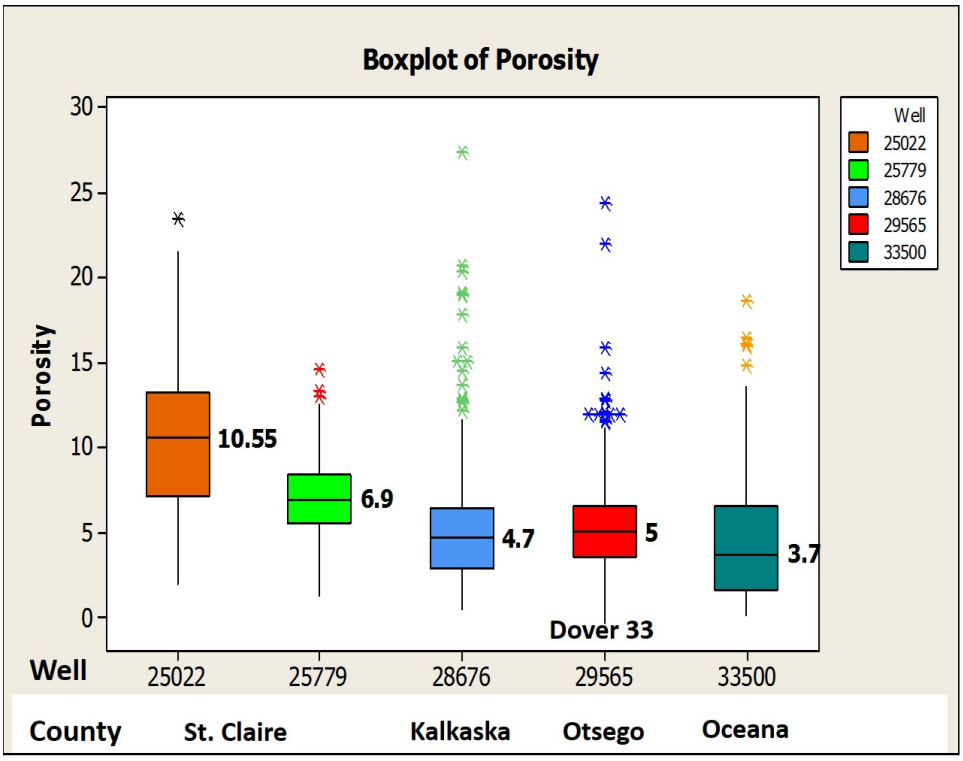


Figure 3-5. Boxplot statistical comparison of the Dover 33 well 29565 log-derived porosity with the core-derived porosity from other Niagarann reef wells in Michigan (mean value plotted for each well).

3.3 Log-Derived Mineralogy

The Northern Michigan Niagarann reefs reservoir facies consist primarily of dolomite and limestone, in variable proportions. Some reefs are completely dolomitized, while others are essentially all limestone. Dolomitization of reefs increases as the reefs become shallower in the subsurface, and salt and anhydrite plugging of porosity is generally more pronounced in the deeper reefs (Gill, 1979). In the absence of cores, the use of logs to identify mineralogy changes within the reef and along its flanks is critical in understanding the porosity framework and lateral extent of layers. Mineralogy flag logs were created from cross-plot-derived mineralogy to facilitate the visual interpretation of the stratigraphic architecture.

The logs needed to perform crossplot mineralogy identification, based on standard chart-book overlays, are available for the wells within the Dover 33 reef. The neutron porosity can be plotted versus the bulk density log or the sonic travel time log (DT). Sandstone, limestone, and dolomite distinctions can then be further subdivided based on the presence of low-density salts and high-density anhydrites (Figure 3-6). The bulk density versus neutron porosity cross-plot in well 31595 (Figure 3-6) shows the majority of values in the dolomite range with minor portions of limestone, anhydrite, and salt. After the cross-plots are completed, a mineralogy flag log is then output, assigning the mineralogy on the cross-plot polygons to the wells (Figure 3-7). The cross-plot analysis confirms the prevailing mineralogy penetrated by the wells on the Dover 33 reef is dominantly low- to high-porosity dolomite.

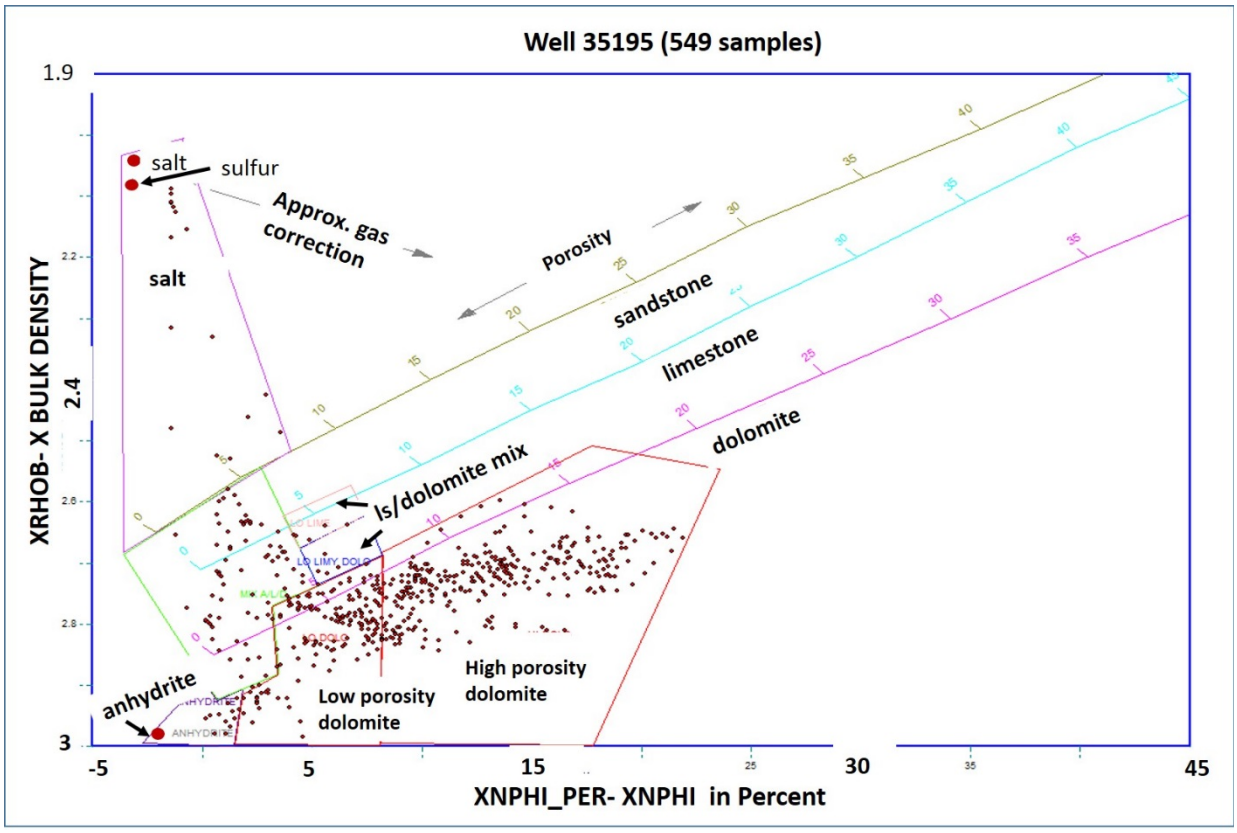
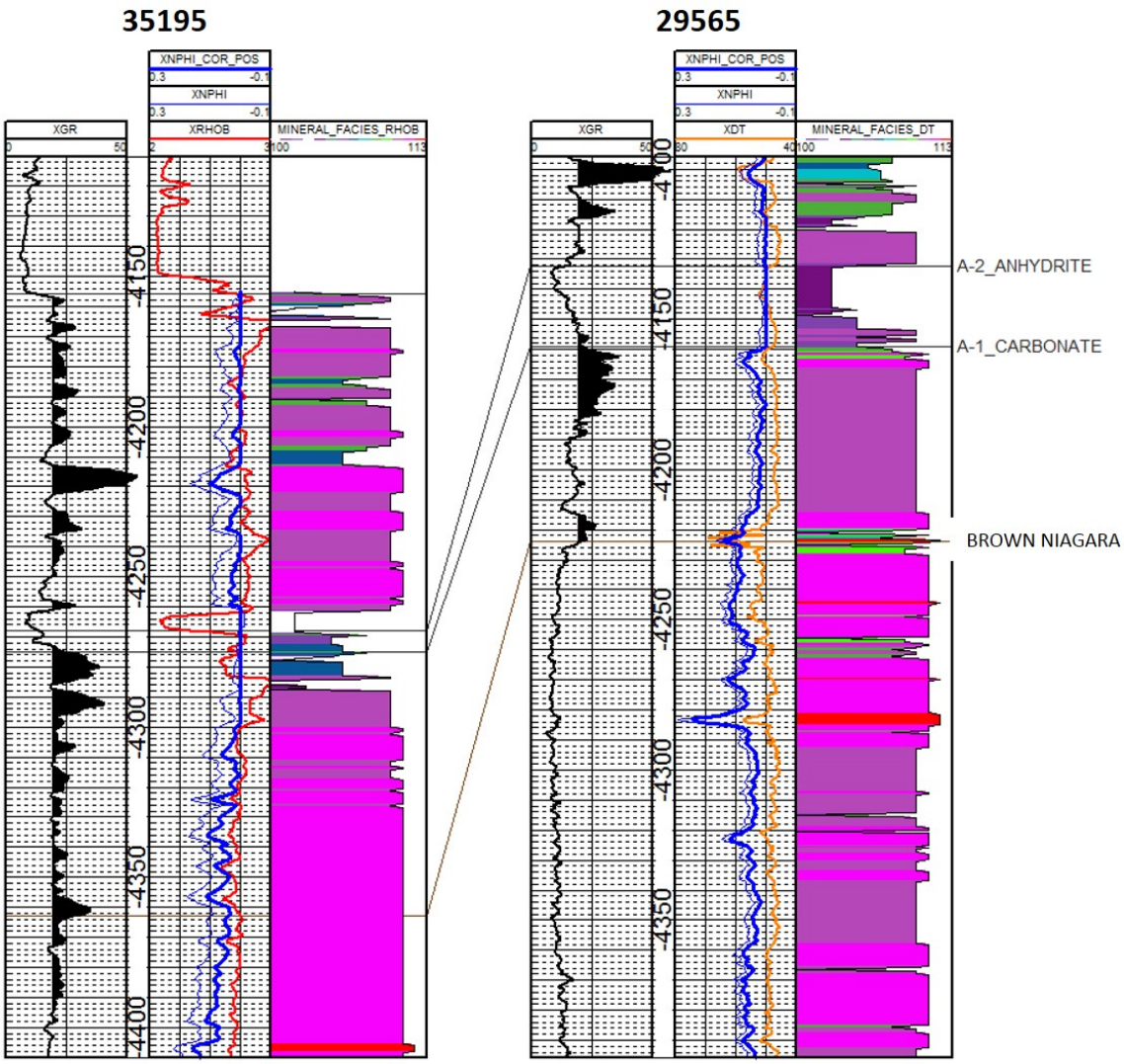


Figure 3-6. Cross-plot mineralogy polygons for bulk density vs neutron porosity in the Dover 33 35195 for the interval from the A-1 Carbonate to TD. Each data point represents a single depth reading on the logs.



	Salt
	Anhydrite
	Mixed Anhydrite/ Limestone / Dolomite
	Low-Porosity Limestone
	High-Porosity Limestone
	Low-Porosity Limey Dolomite
	High-Porosity Limey Dolomite
	Low-Porosity Dolomite
	High-Porosity Dolomite
	Maximum Porosity Dolomite

Figure 3-7. Mineralogy flag logs for two Dover 33 wells, generated from bulk density (RHOB) or sonic (DT) vs neutron porosity cross-plot data. See Table 3-1 for well names; well 35195 is located immediately south of the man reef structure in Figure 2-2.

3.4 Dover 33 3D Seismic Data and Interpretation

A 2.59-square-mile 3D seismic survey was acquired over the Dover 33 reef in 1997 in conjunction with the initial EOR efforts. Core Energy provided the original time-domain migrated 3D data volume and velocity model, which allowed seismic data conversion from travel time-to-depth domain. The depth migration of the 3D seismic volume is an iterative process that includes the following steps:

- Generate synthetic seismograms for wells that have a sonic log (Figure 3-8); evaluate the overall data characteristics of the time-domain migrated 3D to determine the frequency spectrum of the data and overall data quality.
- Use the original Root Mean Square (RMS) migration velocities from the previous time migration to generate a single average RMS function.
- Convert the single RMS function to an average function for the 3D.
- Use the single average function to convert the original time migration volume into depth (10-foot sample interval).
- Apply a static shift of -1,269 feet to the survey.
- Pick the key horizons on the depth-migrated volume (A-2 Carbonate, A-1 Carbonate, and Gray Niagaran) and compare them with the well data to determine how closely the formation tops in the wells within the survey area match the horizon picks from the seismic data.
- Use the final depth-migrated version of the seismic data to pick horizons that become the structural surfaces above and within the Level 1 static earth model.

These depth-converted 3D seismic data were then integrated with the well data to provide a refinement of the geologic structure of the Brown Niagaran, A-1 Carbonate, and enclosing Formations. Note that many of the wells reached total depth just below the interpreted oil/water contact, rather than at the base of the reef.

The flanks of the reefs are particularly difficult to interpret in this portion of the basin due to the presence of anhydrite along the reef flanks. The velocity differences between the high-velocity anhydrites and the carbonates are so small that these lithology changes cannot be imaged with the low-frequency 30-50 hertz data (Figure 3-9). The low frequency content is the result of loss of frequency in the thick layer of glacial till at the surface. The steeply dipping (45- to 60-degree) reef flanks also make imaging and interpreting the reef edges difficult (Figure 3-10). The main horizons picked for inclusion into the Level 1 SEM are the A-2 Carbonate, A-1 Carbonate, Brown Niagaran, and Gray Niagaran. As can be seen in Figure 3-10, the final horizons intersect the formation tops in the wells, indicating good agreement between the seismic data and well data.

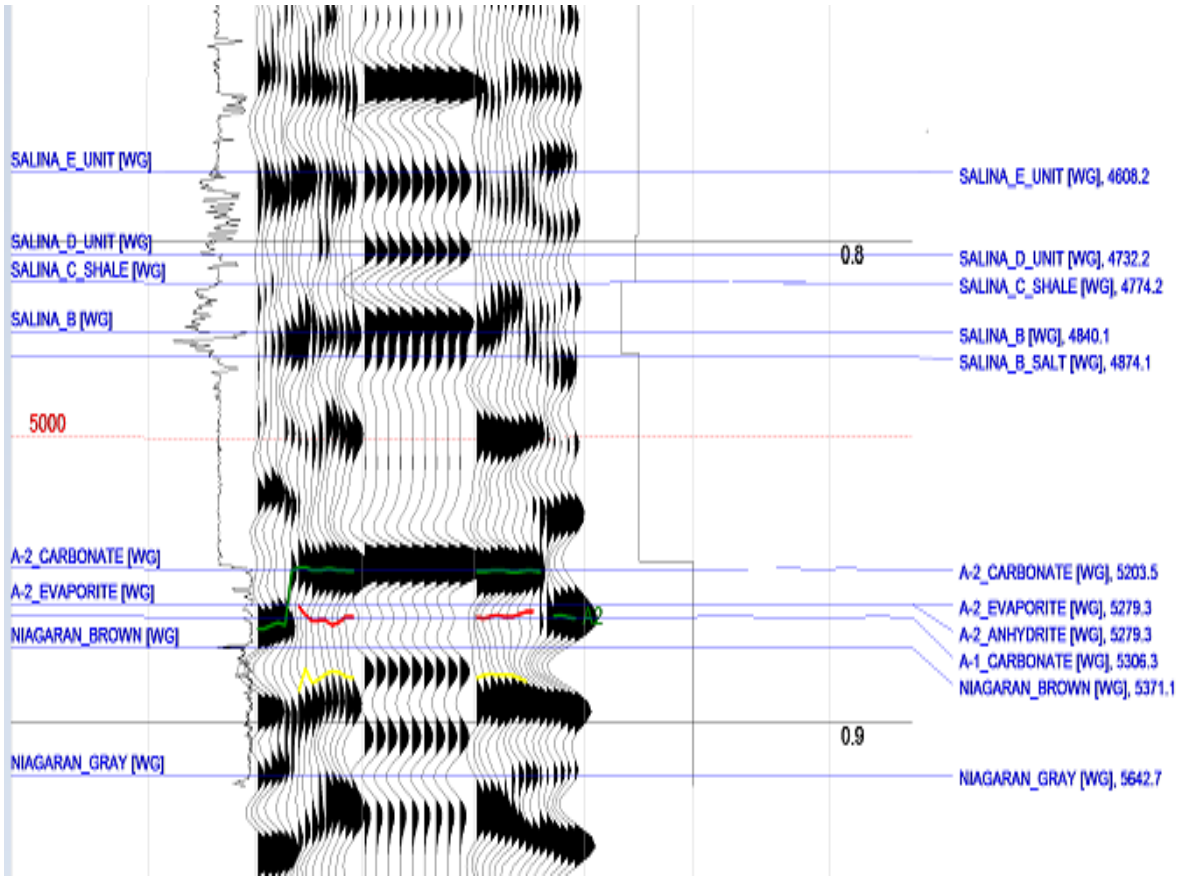


Figure 3-8. Well 29565 synthetic seismogram with extracted traces from the Dover 33 3D seismic volume.

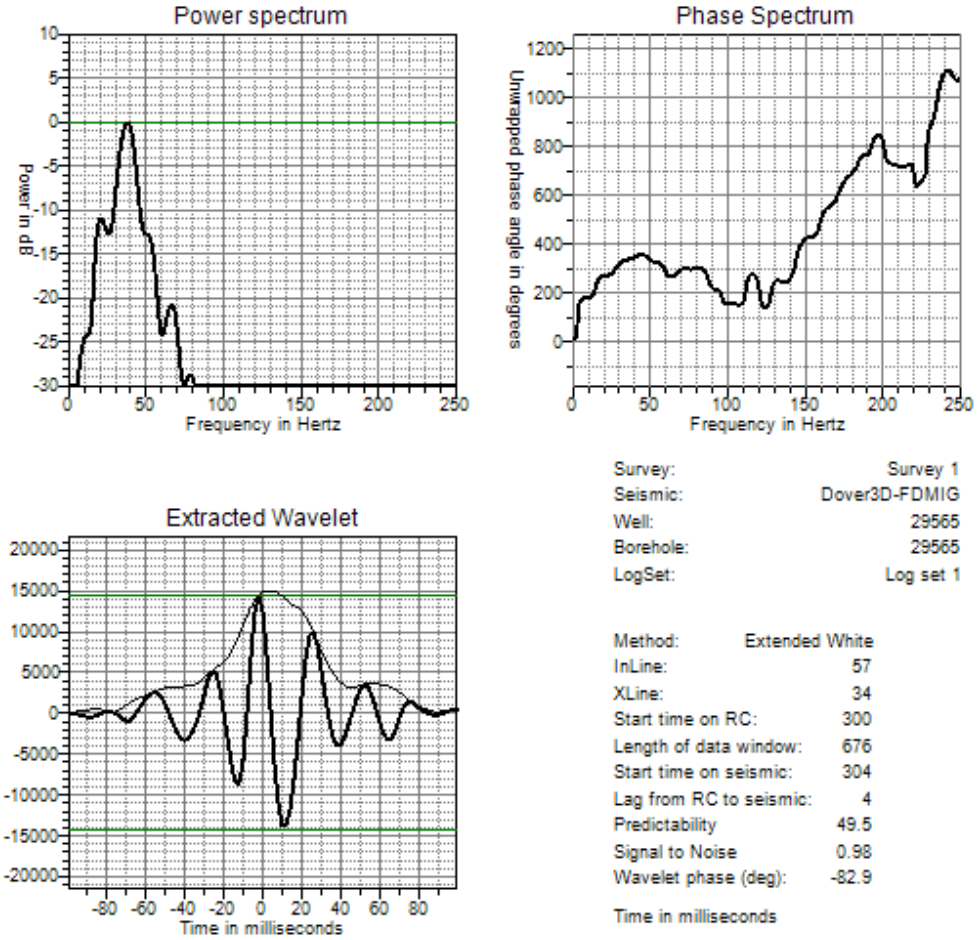


Figure 3-9. Power (frequency) and phase spectrum from extracted wavelet from the Dover 33 3D volume.

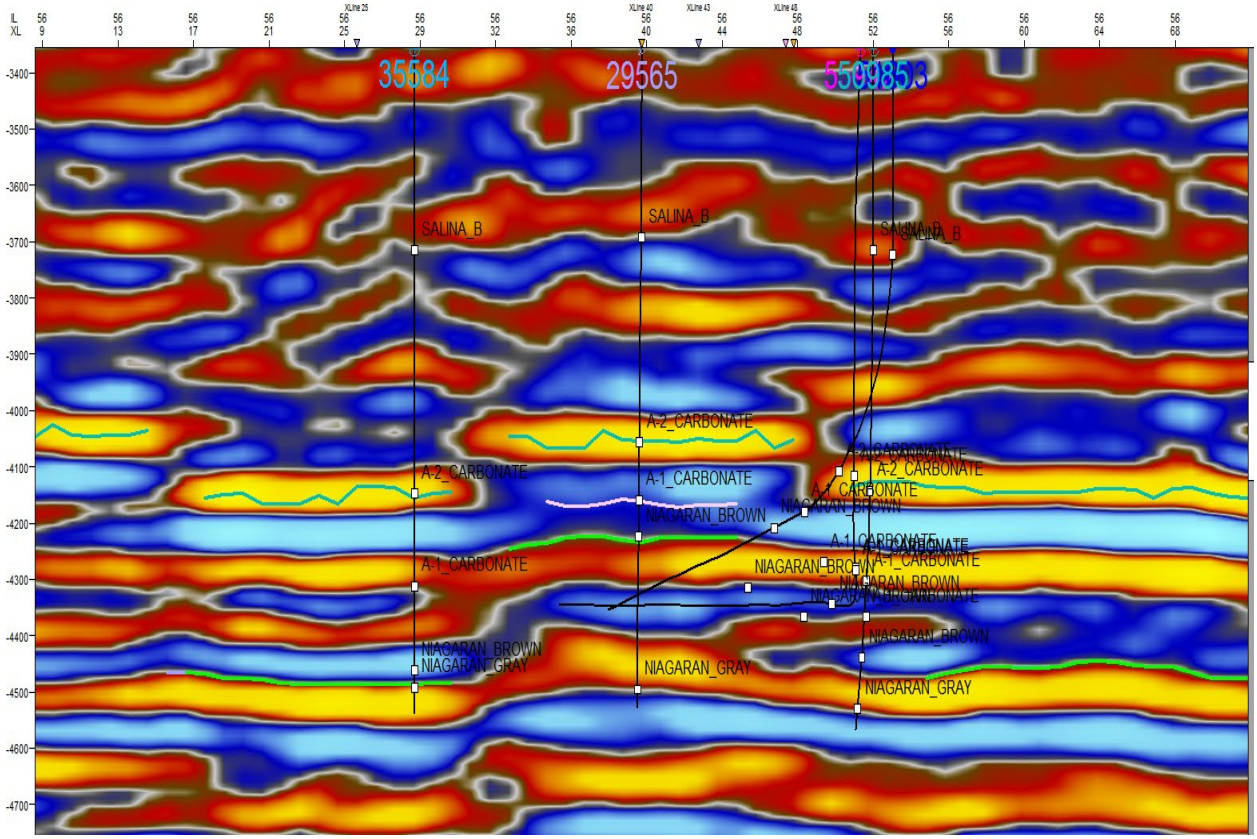


Figure 3-10. Dover 33 3D depth-migrated volume west-to-east arbitrary line in variable amplitude display, showing formation tops in wellbores (small white boxes in wellbore with formation label). Interpreted horizons shown by blue, pink, and green lines.

3.5 Construction of 2D Surface Framework

2D framework surfaces were constructed in Petrel using a convergent interpolation algorithm for each horizon defining the reservoir. Two dimensional (2D) surfaces were made for the A-1 Carbonate, Brown Niagaran, and Gray Niagaran. These three horizons define two lithostratigraphic intervals. The A-1 Carbonate horizon defines the top of the post- reef reservoir interval; the Brown Niagaran horizon is the top of the main reef buildup. The Gray Niagaran horizon defines the reservoir base.

With the exception of the Gray Niagaran, depth-converted seismic was gridded and tied to well log picks. Only the tops of the A-1 Carbonate and the Brown Niagaran were discernible in the 3D seismic. The Brown and Gray Niagaran are dolomites with similar velocities, thus the Gray Niagaran surface could not be interpreted in the seismic data. The Gray Niagaran surface was calculated by subtracting an estimated thickness of non-reef Brown Niagaran from the top of the non-reef Brown Niagaran. The calculated Gray Niagaran surface was adjusted to data measured from four well logs that penetrated the top of the Gray Niagaran below the Dover 33 reef.

Figure 3-11 and Figure 3-12 illustrate the integration of the 3D seismic and well log data to build the Brown Niagaran surface. Figure 3-11 shows depth-converted 3D seismic data as 82.5- x 82.5-foot tiles based on the 3D processing bin size. Numbered vertical gray lines are well paths and permit numbers. Spheres along the well path are the Brown Niagaran tops. Yellow to red

tiles are at the top of the reef facies. Blue to purple tiles are the off-reef Brown Niagaran surface. The gap in seismic data occurring between the top of the reef and the off-reef surfaces is due to the steepness of reef flanks. The tops of the reefs and the inter-reef areas are relatively easy picks due to the semi-horizontal nature of the formations, but the reef-edge locations within the seismic gap are very low-confidence picks.

The gap in the seismic data (Figure 3-11) was used to approximate the lateral extent of the reef facies shown in Figure 3-12. The constructed geologic surfaces (Figure 3-13) were used as input data (horizons) to build the 3D structural framework grid.

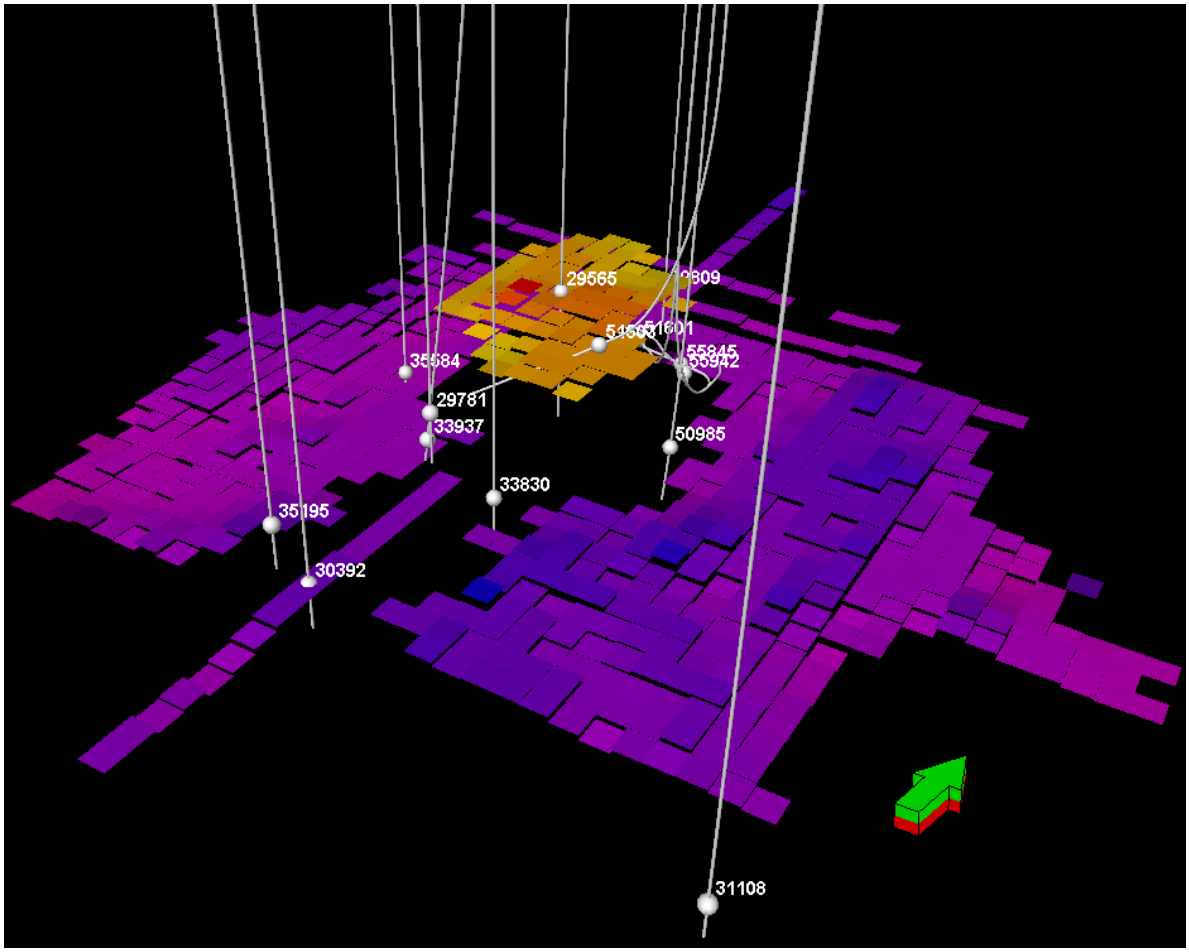


Figure 3-11. 3D seismic and well log data used to build the Brown Niagaran 2D surface.

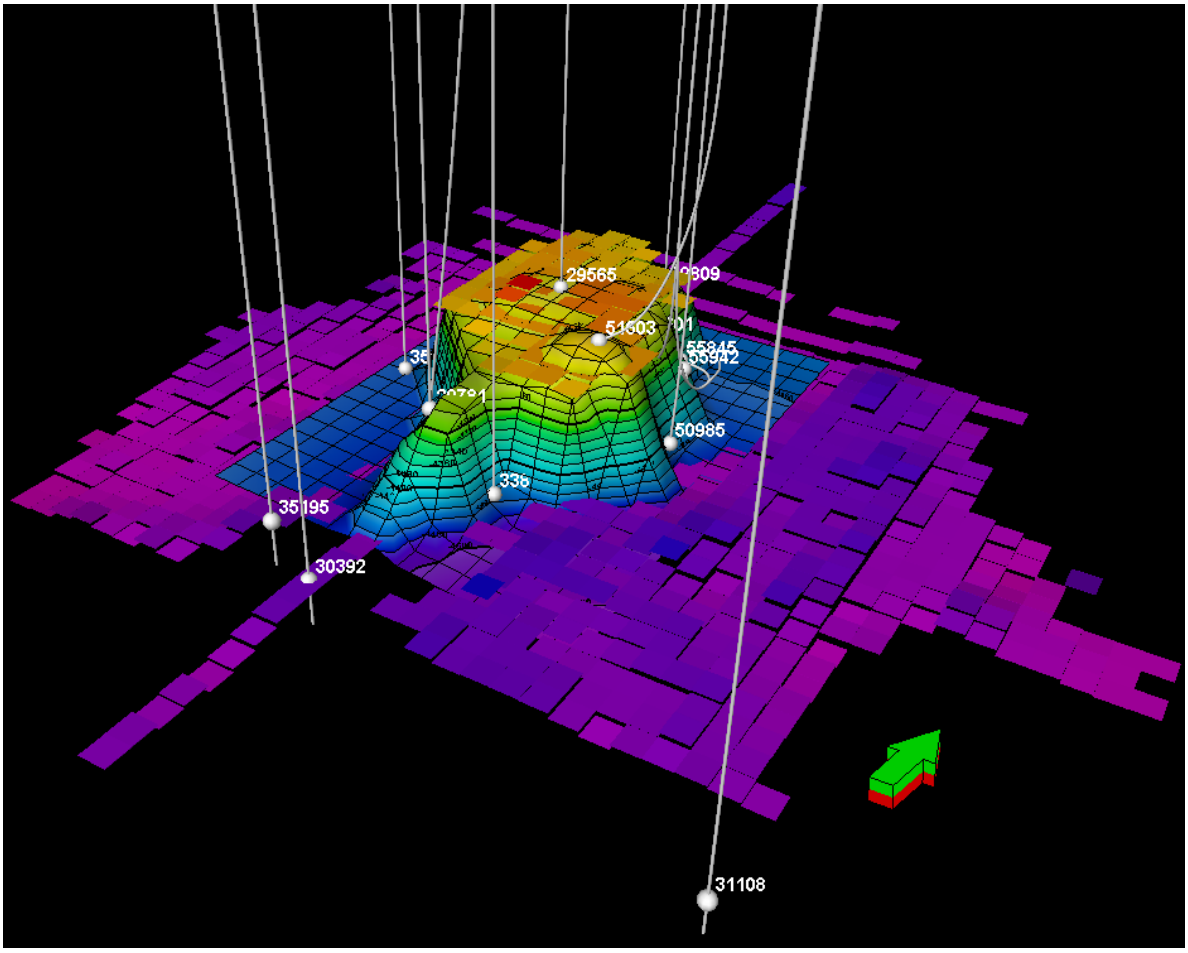


Figure 3-12. Interpreted top of the Brown Niagaran 2D surface from seismic and well log data. Image illustrates how the 2D grid was fitted to the data. Well logs have priority over the seismic during construction of surfaces.

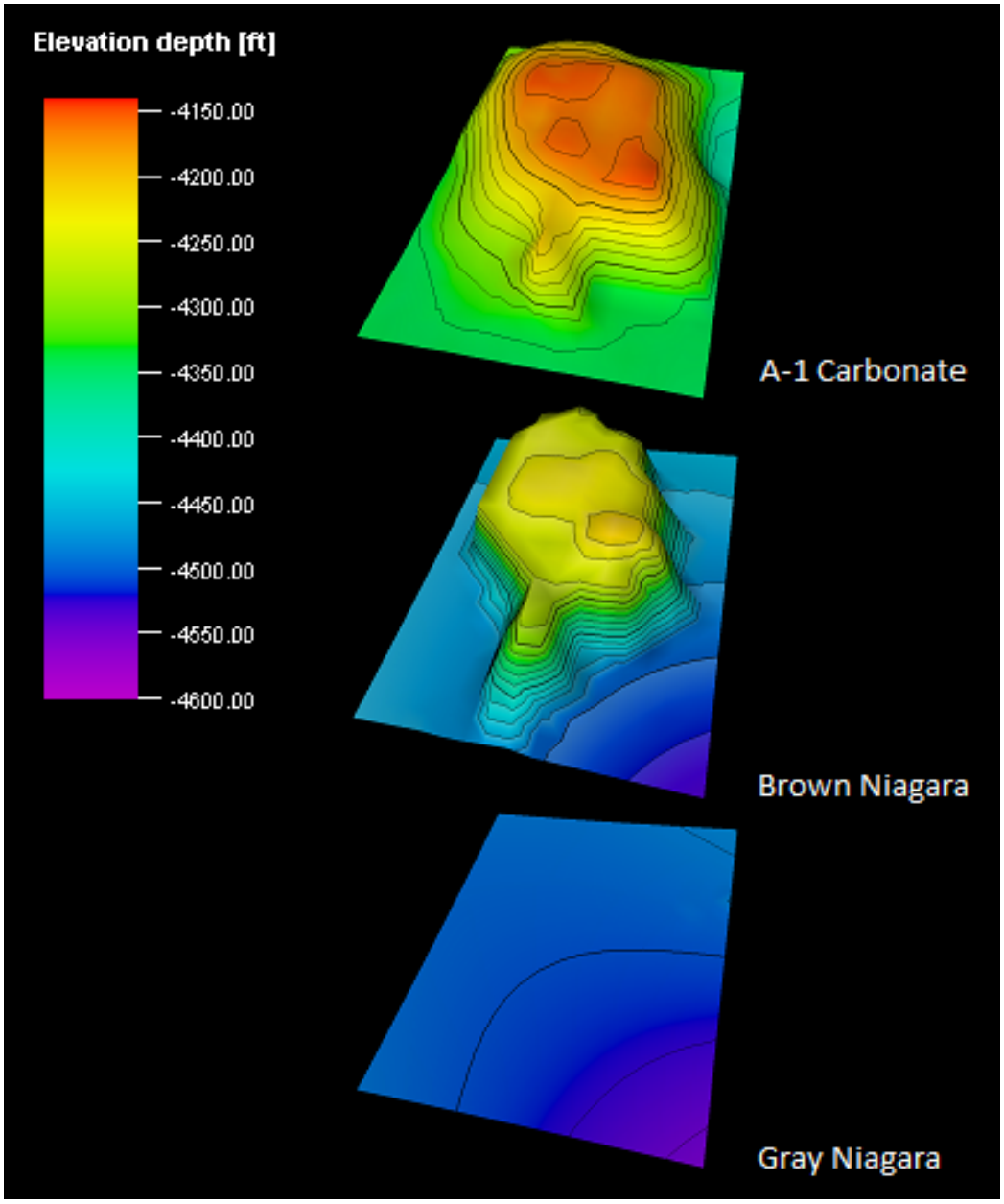


Figure 3-13. Resulting lithostratigraphic surfaces interpreted from well log and seismic data. These structural surfaces are input data for generation of the internal 3D grid framework requisite for property modeling.

3.6 Three Dimensional (3D) Structural Layering

The 3D grid represents the internal framework architecture of the Dover 33 reef model. The process used to build the 3D grid followed the Petrel *Structural framework* workflow that includes: 1) geometry definition, 2) horizon modeling, and 3) structural gridding.

3.6.1 Geometry Definition

Structural modeling was initiated by defining the X-Y resolution of the structural framework grid using the *Geometry definition* process. Note that English units were used in the original calculations, but final definition was made in metric units to simplify input into dynamic modeling software. The Level 1 model grid was constructed with an X-Y resolution and a final grid cell size of 10 meters.

3.6.2 Horizon Modeling

The horizon modeling process imports the 2D lithostratigraphic surfaces as horizons to generate zones between the horizons, within the 3D grid. In Petrel, a horizon is a geological surface in the 3D grid, and a zone is the 3D volume located between two horizons. In the case of the Level 1 SEM, the A-1 Carbonate surface is the top horizon of the 3D grid; the Gray Niagaran is the base horizon; and the Brown Niagaran surface is the horizon the separates the grid representing the reservoir into two zones that will be used for geocellular construction (Figure 3-14). Zone 1 is the volume between the top A-1 Carbonate and top Brown Niagaran horizons, and Zone 2 is the reef volume between the Brown Niagaran and Gray Niagaran horizons.

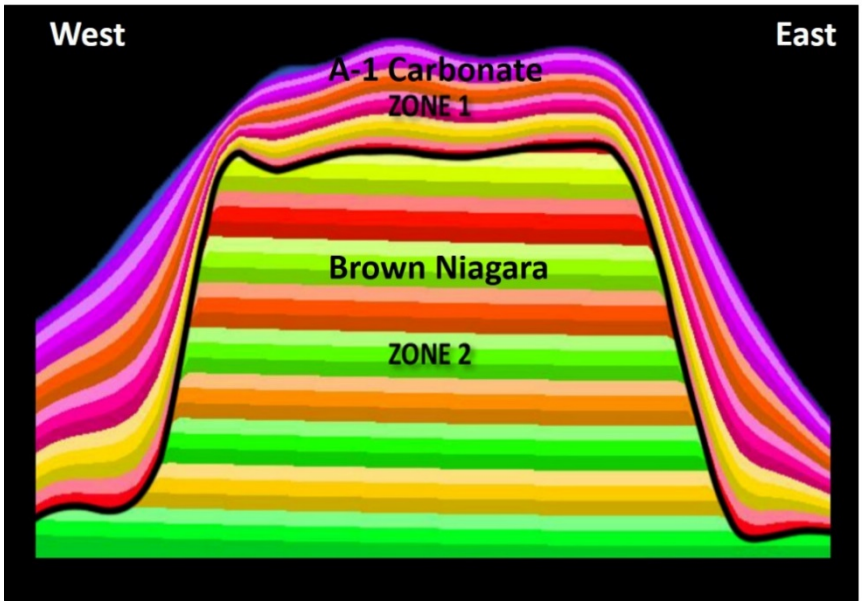


Figure 3-14. Cross-section of structural model showing zones and layers after structural gridding process. Internal cells are not displayed in this image. Cross-section view is to the north.

The boundaries between sedimentary lithostratigraphic Formations are considered to be conformable or unconformable. The top of the Gray Niagaran (the basal horizon) was set as conformable with the overlying Zone 2. The Brown Niagaran horizon was set as erosional (unconformable) so that the internal layers would be truncated by the upper boundary of Zone 1 (unconformable base of the A-1 Carbonate). This constrained the data within each zone, ensuring that property distribution in the cells of Level 1 model honored the conceptual nature of the lithostratigraphic boundaries. The A-1 Carbonate horizon was set as a conformable surface for the top of the model, so that cells within the A-1 Carbonate zone would not be truncated by the lithostratigraphic boundary at the top of the A-1 Carbonate.

3.6.3 Structural Gridding

Structural gridding converts the structural framework grid into a simulation layer grid. This process subdivides the two zones into layers within the zones. Zone 1 was proportionally layered into fifteen layers, building from the bottom. The number of layers was based on dividing

the 150-foot maximum thickness between the A-1 Carbonate and Brown Niagaran horizons by a layer thickness of 10 feet. Thus, the maximum thickness of an individual layer is 10 ft but layers become thinner as the A-1 Carbonate thins. This layering determines the vertical distance over which data are averaged. The Brown Niagaran horizon, the top of Zone 2, was set as an erosional (unconformable) surface truncated by Zone 1. To honor the overlying erosional surface, Zone 2 layering was built from the base with a consistent layer thickness of 10 feet. This ensured that horizontal layering of the zone was truncated at the edges by the sides of the brown Niagaran reef; the layers are truncated by the overlying unconformity at the base of Zone 1 (A-1 Carbonate) (Figure 3-14). The final gridding process produces a geocellular structure; for the Level 1 model, the individual cells of Zone 1, where not truncated, are 10m X 10m; and the Zone 2 cells have a maximum thickness of 3m (note change from English units to metric units).

3.7 Property Modeling

The objective of the property modeling process is to populate the cells of the 3D grid with petrophysical property values (porosity, permeability) to create a realistic geologic representation of the reservoir. The Level 1 property modeling followed a three step process in Petrel: *1) scale up well logs, 2) variogram analysis, and 3) petrophysical modeling.*

3.7.1 Scale Up Well Logs

Scale up well logs is a Petrel software process where property values from well logs are scaled to the resolution of the cells in the 3D grid. In the process, property values are assigned to the grid cells penetrated by well logs. For each grid cell, all log values that fall within the cell are averaged to produce a single value for that cell. Nine porosity logs were scaled up for the Level 1 model using an arithmetic average method for porosity determination (Table 3-2). Note that not all wells penetrate the entire reef; the resulting 3D grid (Figure 3-15) has values only for the grid cells that the wells had penetrated.

Table 3-2. Wells, type of porosity logs, and lithostratigraphic units penetrated.

Permit Number	Well Name and Number	Well Type	Status	Formation Tops Penetrated			Neutron Porosity
				A-1 Carbonate	Brown Niagaran n	Gray Niagaran n	
29565	Lawnichak & Myszkier 1-33	Vertical	Open	X	X	X	SNP
29781	Lawnichak & Myszkier 3-33	Vertical	Plugged	X	X		SNP
29809	Koblinski & Fisher 1-28	Vertical	Plugged	X	X		SNP
30392	Winter 2-33	Vertical	Plugged	X	X		SNP
33830	Lawnichak & Myszkier 5-33	Vertical	Plugged	X	X	X	SNP

Permit Number	Well Name and Number	Well Type	Status	Formation Tops Penetrated			Neutron Porosity
				A-1 Carbonate	Brown Niagaran n	Gray Niagaran n	
33937	Lawnichak & Myszkier 5-33A	Lateral	Plugged	X	X		SNP
35195	Winter 1-33	Vertical	Plugged	X	X		CNL
35584	Lawnichak & Morey 1-33	Vertical	Plugged	X	X	X	CNL
50985	Lawnichak & Myszkier 2-33	Vertical	Plugged	X	X	X	CNL

Note: CNL – compensated neutron porosity SNP – sidewall neutron porosity

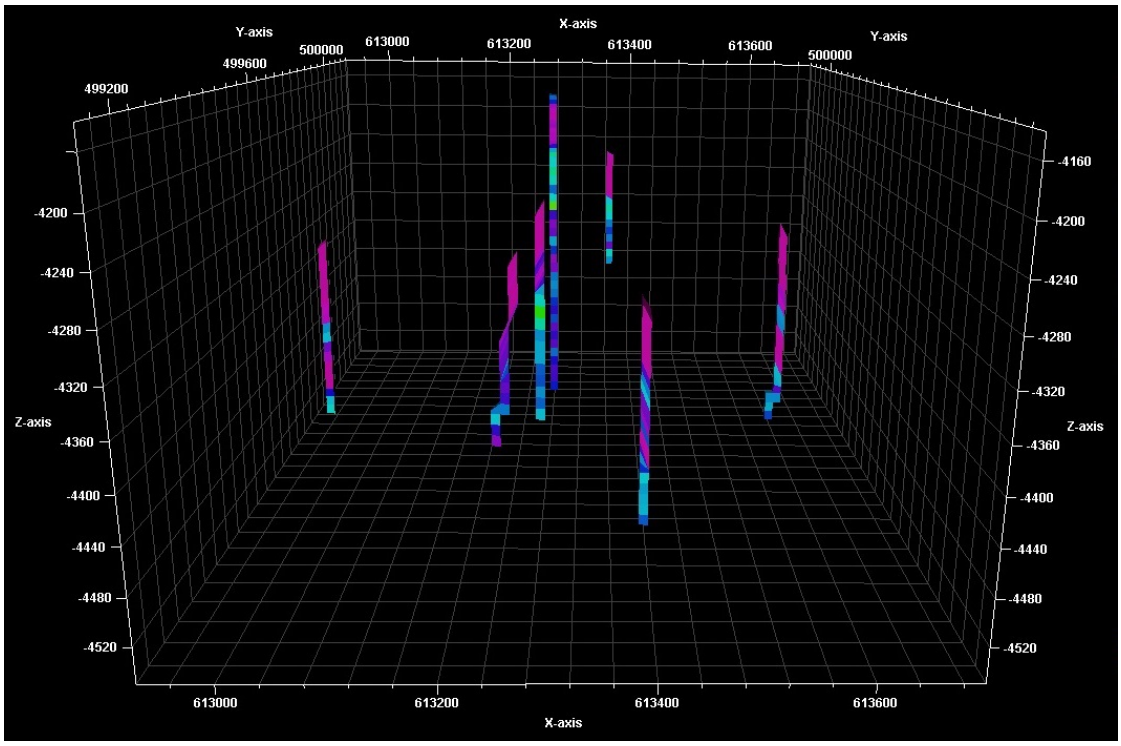


Figure 3-15. Level 1 3D grid at wells, after the "scaling up porosity logs" module had been completed. Only cells that were penetrated by well logs have been assigned porosity values. Each layer is assigned a single porosity value.

3.7.2 Variogram Analysis

The *variogram analysis* process uses variograms to quantify the spatial variation of the petrophysical properties as a function of distance and direction from the well data (Gringarten and Deutsch, 1999). Variogram modeling is used to predict an unknown property value (such as porosity or permeability) at a known location. From determination of the nugget, sill, and range (Figure 3-16), the variogram function can be used to interpolate a property value at a known location. The nugget is the variance where the distance between two measured samples is very close to zero. Sill is the variance value where the variogram levels off. Lag is the separation distance between search points. Range is the lag distance where the variogram reaches the sill value (data dissimilarity is at a maximum).

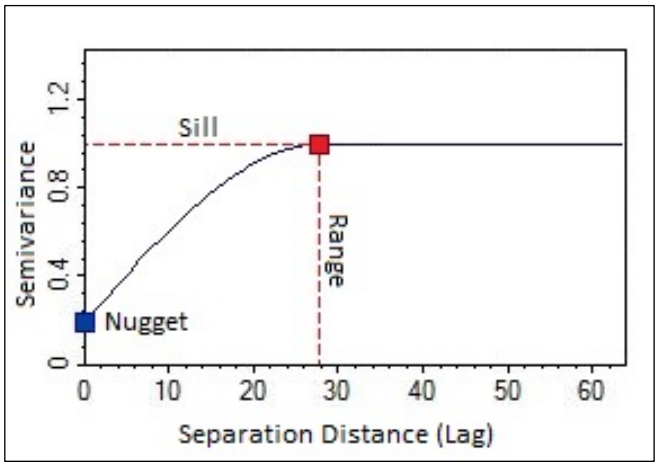


Figure 3-16. Characteristics of a variogram. Terms are defined in the text.

Variogram modeling was applied to the porosity data for both zones of the Level 1 model. Petrel's variogram modeling process analyzes the property data for three spatial directions: major lateral direction, minor lateral direction, and vertical direction. The major lateral direction is where data similarity is at a maximum, and the minor lateral direction is perpendicular to the major direction. The initial major lateral search direction was north-south, and the minor lateral direction was east west based on general reef orientation. Computation results from the data analysis (Table 3-3) show that the range for the A-1 Carbonate is 331^{O} and is 95^{O} for the Brown Niagaran. The A-1 Carbonate zone data have in general a longer correlation lateral distance than the Brown Niagaran internal reef core data. After the sill, nugget, and ranges for the three directions are computed for each zone, a petrophysical model can be constructed for the Level 1 SEM.

Table 3-3. Variogram modeling data

Zone	Type	Nugget	Sill	Range Direction		
				Major ^{O}	Minor ^{O}	Vertical (ft.)
1	Spherical	0	0.997	331.0	221.0	38.8
2	Spherical	0	0.997	95.0	37.8	25.2

Petrophysical Modeling

Petrophysical modeling was undertaken after the densely sampled (0.5 ft) porosity logs were scaled up to the resolution of the 3D grid and variogram analysis on the porosity data was completed. Petrophysical modeling uses the porosity values for each grid cell along the well log trajectory and the results of the variogram analysis to interpolate porosity values for the cells between wells in the 3D grid. The kriging geostatistical method was used to interpolate the distribution of porosity. Kriging is a well-established linear regression deterministic method that relies on the spatial relationships described in the variogram for a particular data set (Hohn, 1999).

Upscale Porosity Model

The final porosity model had 608,608 total grid cells, which was too large for efficient dynamic reservoir simulation modeling. To reduce the number of grid cells in the model to a more manageable size, the level 1 SEM was upscaled. Through the upscaling process, the horizontal dimensions of the grid cells were increased in size from 10 meters to 30 meters. This resulted in a new porosity model with 39,100 total grid cells. The vertical dimension of the cells was not changed.

Permeability Modeling

A permeability model was derived from the upscaled porosity model by calculating permeability from porosity values for each grid cell in the model. Equation 4.1 was the porosity-to-permeability transform used on each grid cell. This equation was derived from the log data, using a statistical regression of core-derived porosity and permeability data from the State Kalkaska #28676 on-reef analog well (Figure 3-17). Location of the state Kalkaska well is shown in Section 4; Figure 4-4, and schematically in Figure 4-5.

(Equation 4.1) $k = (12.83*\phi-0.0432)^{10}$ Where: k = Permeability and ϕ = Porosity (decimal)

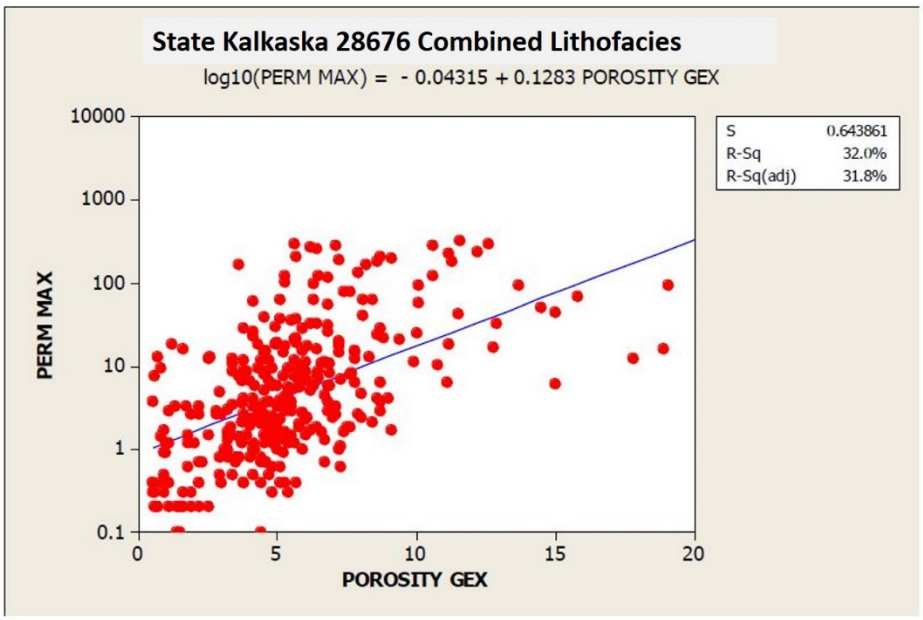


Figure 3-17. Porosity- permeability cross plot used to derive transform for populating the Level 1 SEM. Location of State Kalkaska well is shown in Section 4; Figure 4-4.

Figure 3-18 and Figure 3-20 are the final Level 1 porosity and permeability SEMs. Figure 3-18 is the porosity model with 10- x 10-meter grid cells. Figure 3-19 is the porosity model upscaled to 30- x 30-meter grid cells. Figure 3-20 is the permeability model calculated from the upscaled porosity grid.

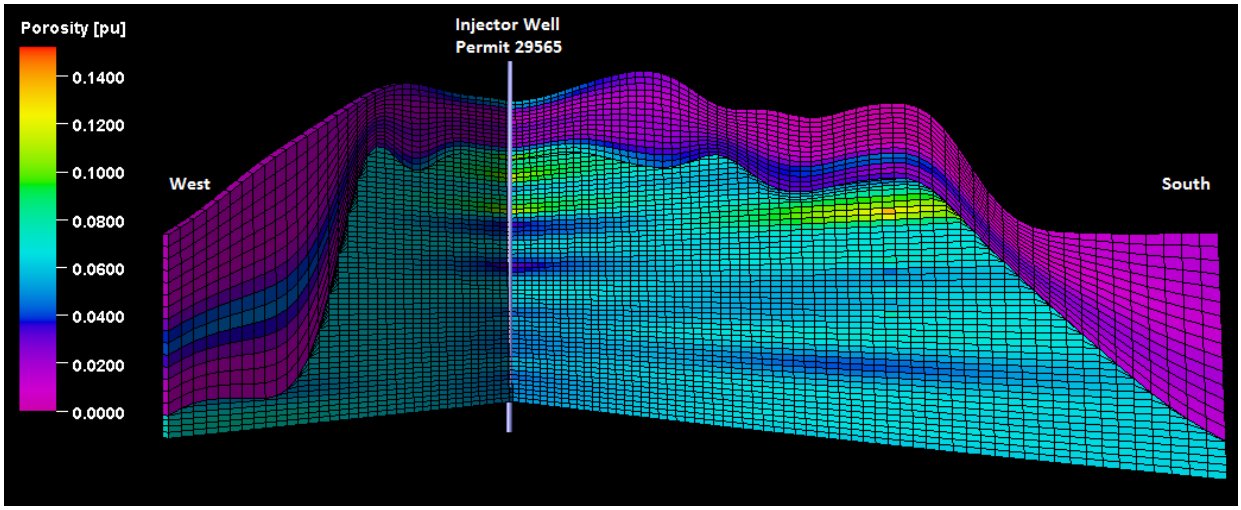


Figure 3-18. Porosity model, view to the northeast intersection of the south and west planes. Grid cell dimensions in the Brown Niagaran are 10 x 10 meters.

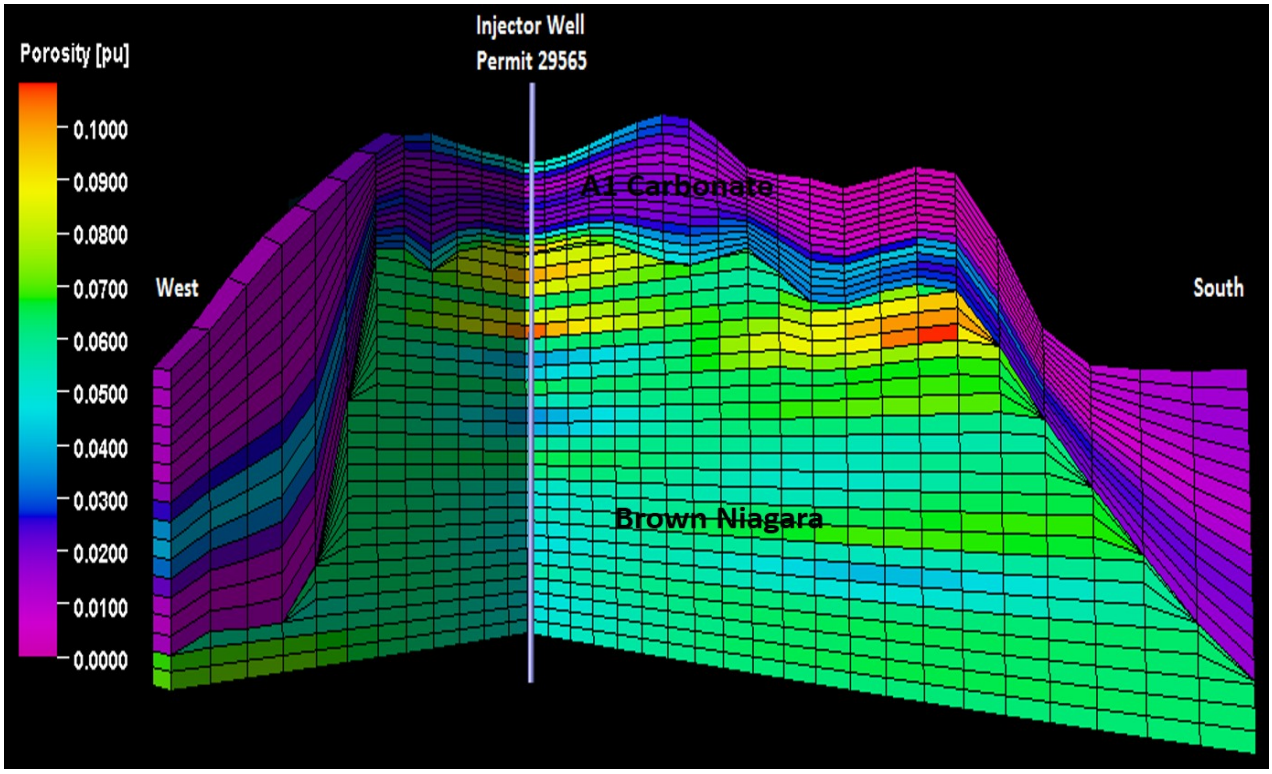


Figure 3-19 Upscaled porosity model, view to the northeast intersection of the I and J planes. Grid cell dimensions in the Brown Niagaran were upscaled from10 x 10 meters to 30 x 30 meters.

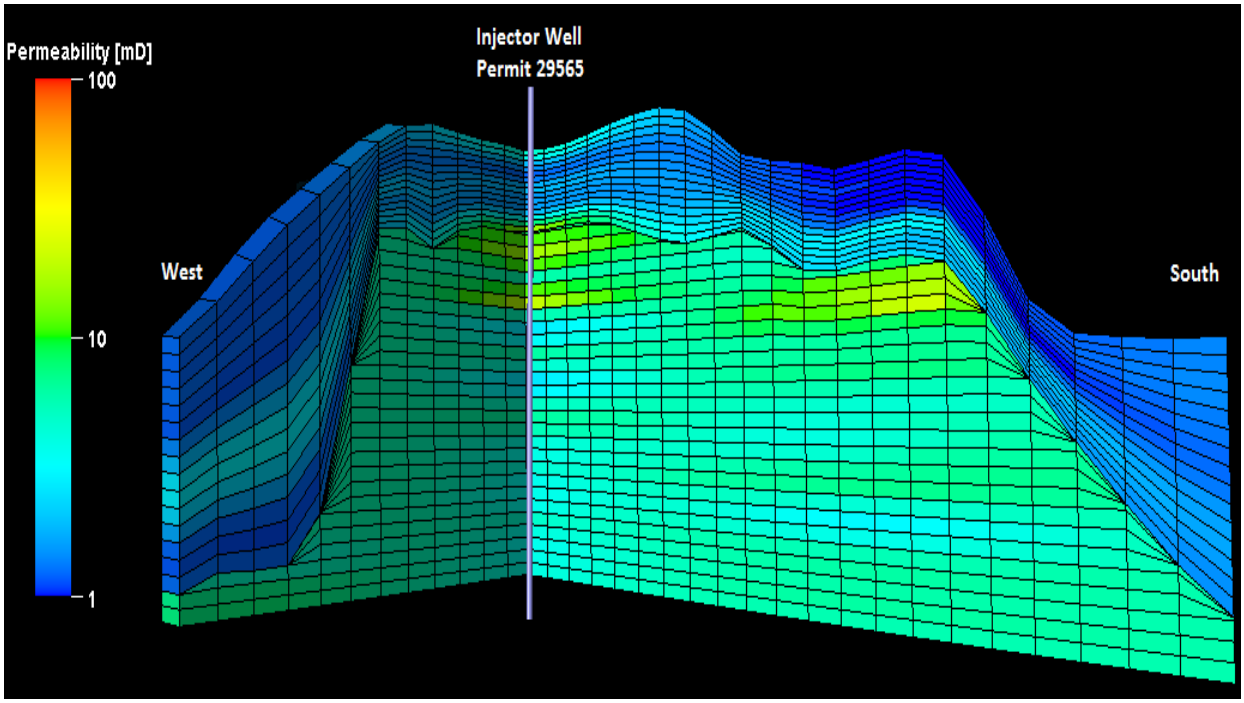


Figure 3-20. Permeability model calculated from the upscaled porosity grid. A porosity-to-permeability transform was applied to porosity values in each grid cell to construct the permeability model.
Grid cell dimensions of the model are 30 x 30 meters.

Chapter 4. Level 2 Sequence Stratigraphic Model Construction

The Level 2 static earth model construction involves creating a stratigraphically constrained 3D lithofacies model for the Dover 33 reef to allow a more realistic quantification and distribution of porosity, permeability, and other petrophysical data. The stratigraphy is primarily based on work by Ritter (2008); lithofacies analogs are primarily from Huh (1973) Ritter (2008) and Noack (2008).

Because core was not available for the Dover 33 reef, it is not possible to independently confirm the published sequence stratigraphic framework for the Michigan Niagaran reef interval. The workflow for construction of the Level 2 static model is shown in Figure 4-1. The previously established sequence stratigraphy for other reefs in northern Michigan was examined in detail and correlated to the Dover 33 reef, based on regional well log correlation. The on-reef and off-reef lithofacies defined in published whole rock core studies were tied to their associated wireline log signatures, and were correlated to the Dover 33 reef. Sequence stratigraphy and associated lithofacies were then interpreted for the Dover 33 reef, based solely on the log signatures and stratigraphic position. Statistical analyses performed on the Dover 33 wireline logs and analog core data allow an evaluation of the relationship between petrophysical properties and interpreted lithofacies. These analyses have uncertainties because of assumption of uniformity and accuracy in lithofacies identification of other authors; correspondence of lithofacies and diagenesis between the analog reefs and the Dover 33; and because the lateral boundaries of leeward and windward depositional lithofacies cannot be distinguished in logs without core-calibration. Petrophysical well-log analysis, as described in the Level 1 workflow, produced mineralogy logs for Dover 33 reef wells through log crossplots and for Schlumberger elemental analysis (Elan) for wells with full suites of logs. These petrophysical data aided in the correlation of previously published sequence boundaries and lithofacies from cored reefs to wells in the Dover 33 reef, and allowed the construction of Dover 33 2-D surface grids for each sequence horizon.

Interpretation of the 3D seismic data, as described in the Level 1 model workflow (Section 3), provided the framework structure for the top and bottom of the Dover 33 Level 2 model; lateral bounds of the reef were constrained by well log signatures within the seismic data gap that was produced by the steep sides of the structure (see Figure 3-11). The process of constructing a 3-D structural framework grid for the Level 2 model defined the model parameters, layering, and the internal architecture and geocellular dimensions. Following the completion of the detailed framework, population of the Level 2 model included constructing a lithofacies model from the lithofacies log interpretation and variogram analysis; constructing a porosity property model by conditioning porosity to the lithofacies; upscaling the porosity model; and calculating a permeability model using porosity-to-permeability transforms for individual lithofacies groups. The subsequent calculation of volumetrics then constituted part of a comparison/evaluation of the two models.

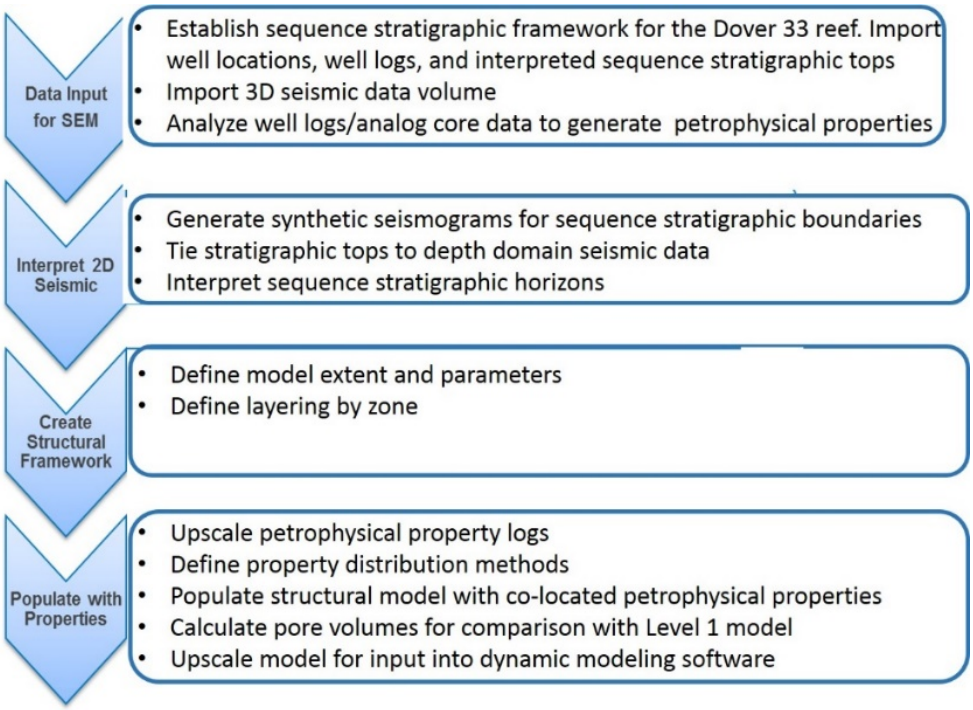


Figure 4-1. Workflow for the Level 2 static earth model.

The following sections provide a background on carbonate sequence stratigraphy, as well as the steps involved in extrapolating the previously defined regional Niagarann reef sequence stratigraphy into the Dover 33 area; and finally, the details of constructing the Level 2 static earth model for the Dover 33 reef.

4.1 Sequence Stratigraphic Overview

The subdivision of the rock record encountered in an exploration wellbore traditionally is lithostratigraphic and is based on sharp changes in lithology (sandstone, dolomite, limestone, shale, etc.). In contrast, sequence stratigraphy is a method of grouping rock strata based on their depositional relationships. Rock units that lie between unconformities are assumed to be more closely related than units that are separated by unconformities. A more general definition from Catuneanu et al. (2009) is “a succession of strata deposited during a full cycle of change in accommodation or sediment supply”.

Sequences contain laterally coeval, shoreline-related deposits within specific systems tracts. A systems tract is the depositional setting from onshore to offshore; systems tracts are separated by small scale unconformities or depositional facies offsets into lowstand, highstand, and other packages related to the position of sea level, shoreline, and the depositional environment. In essence, stratigraphic sequences are each composed of a succession of genetically laterally-linked strata that reflect deposition in natural depositional systems that are interpreted to have been deposited between eustatic sea-level fall inflection points (Posamentier et al., 1988).

The placement of regional third order, unconformity-bounded sequences generally follows one of two models, as shown in Figure 4-2. The older model recognizes three systems tracts, as opposed to the newer model that separates deposits into four systems tracts, related to relative sea level position: lowstand systems tracts (LST), transgressive systems tracts (TST), high-

stand system tracts (HST) and falling stage system tracts (FSST). The most important aspect of these models in relation to the present study relates to grouping deposits that are deposited as part of a continuum. The more recent model of Catuneanu et al. (2011) advocates placing third order sequence boundaries between the falling stage systems tract and the lowstand deposits. This is particularly applicable to seismic stratigraphic analysis of siliciclastics in large basins, where during falling sea level, sediment continues to be eroded updip, and deposited downdip. Correct placement of the sequence boundary requires data on lateral sediment geometries to separate falling stage deposits from the lowstand wedges that were deposited as sea level starts to rise again. In contrast, shallow water carbonate production on isolated steep-sided reefs may almost completely cease when sea level drops, resulting in flanking breccias and other deposits that are not genetically related to the living reef.

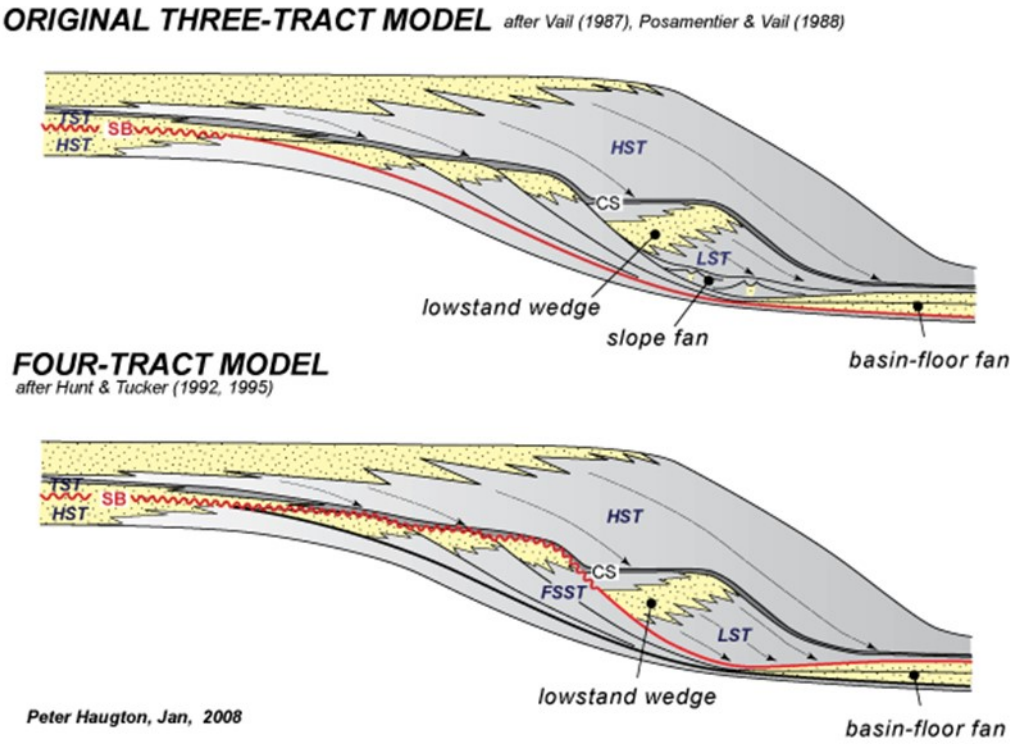


Figure 4-2. Two models for placement of a third order sequence boundary. For the Michigan reefs, the A-1 Anhydrite may represent either a falling stage deposit, a lowstand wedge or a combination of the two. HST = highstand systems tracts; SB= sequence boundary; TST = transgressive systems tract; FSST = falling-stage systems tract; LST = lowstand systems tract, CS = composite sequence. From Catuneanu et al., 2011.

Sequence stratigraphic subdivisions are hierarchical. In this study, we are concerned with third order sequences that are separated on the reef tops by unconformities, and with fourth-order sequences, which in core show vertical progressive changes in depositional environment (such as shallowing into the intertidal environment), separated by marked (but not profound) shifts in depositional environment. Third order boundaries in carbonates may be associated with karst or porosity-occluding diagenetic overprints. The fourth-order packages of rock are linked to each other as parts of a vertical and horizontal depositional package, and their recognition helps in definition of internal layering of reservoir models. Both third- and fourth-order packages commonly have wireline log expression. Smaller 5th-order sequences may be identified in core as meter-scale upward shallowing packages, but the development of these smaller sedimentary

packages depends on local topographic relief and cannot be correlated between wells, even where core exists.

Subsurface sequence analysis may begin with recognizing stratigraphic packages in seismic data or examining wireline logs and core to determine sediment packages, abrupt facies offsets, unconformities, and upward shallowing or deepening packages. Carbonate textures, lithologies, and faunal changes are particularly important in determining changes in depositional environment and package boundaries.

The sedimentary character of the third- and fourth-order sequence stratigraphic units and their lateral and vertical lithologic changes can be explained by changes in global sea level, rate of subsidence, sediment supply, and climate. Reef-associated carbonates are particularly reflective of the changes in depth, wave energy, and sediment supply in their depositional environment. Carbonate lithofacies refer to the appearance and characteristics of the rock unit, including rock composition, texture, biotic component, and sedimentary structures. For a sequence stratigraphic study, it is the abrupt juxtaposition of fauna or lithofacies that are not normally associated in nature that may help determine a break in the stratigraphic record. In reservoir modeling studies, carbonate lithofacies exhibit an original depositional texture and porosity system that is overprinted by diagenetic events. Identifying the original depositional component provides important information for assigning the spatial distribution of original porosity within the reservoir model. Flow units are often bound by fourth or third order boundaries. Sucrosic dolomite may connect porosity systems across unconformities.

Since the 1990s, carbonate reservoir studies have increasingly relied on developing a basin-specific sequence stratigraphic framework to constrain models of time-equivalent depositional facies; correlate key facies and sequence surfaces; and identify vertical depositional patterns for each identifiable order of cyclicity. A sequence stratigraphic framework can provide a basis for more accurate lateral and vertical interpretations of lithofacies compared to conventional lithostratigraphic analysis. The application of sequence stratigraphy to predict lateral and vertical development of porosity and seals for carbonate reservoirs is relatively mature (Kerans and Tinker, 1997).

Michael Grammer and his students at Western Michigan were the first to evaluate the detailed Michigan reef sedimentological work of Huh and others (Huh, 1973, 1977; Gill,1973) in terms of a sequence stratigraphic framework. Grammer's students were also the first to evaluate porosity and permeability trends as they relate to sequence stratigraphically-constrained lithofacies (Ritter, 2008; Noack, 2008) Importantly, Grammer's students used this type of approach to explore relationships between wireline log data and permeability trends, and to build and populate reservoir models at the Ray Reef and Belle River Mills field in the southern reef trend (Wold 2008; Qualman, 2009).

Studies by Huh and Gill and the students at Western Michigan confirm three findings that support the viability of a sequence stratigraphic/lithofacies approach to building static earth models for the Michigan Silurian reefs. First, reef-associated organisms changed dramatically as the reefs initiated, flourished, and were eventually killed off by basin-wide changes in salinity and connection to the open ocean outside the Michigan Basin. Second, the depositional environment and the shape, size, and mineral composition of the reef organisms have a large influence on the resulting porosity and permeability of the reef rock. Third, within a given stratigraphic interval, wireline logs and computer-generated lithology logs exhibit signatures that can be used to reduce uncertainty on possible rock types.

Although the Dover 33 reef had no core with which to calibrate the well logs during the time of these analyses, the goal was not only to establish the stratigraphic framework but also to reduce uncertainty on permeability and other petrophysical properties used to populate that framework.

The challenges of any approach that lacks reef-specific core and rock data include considerable uncertainty on the actual depositional windward/leeward and depth-related environments and their resulting primary rock fabric, as well as post-depositional diagenesis. Reefal carbonates are particularly susceptible to diagenetic changes that create, enhance, or destroy original porosity and permeability. These diagenetic changes are partially constrained in the northern reefs by depositional environment and by stratigraphic position (e.g.., evaporative conditions that produced anhydritic limestone lithofacies are confined to particular stratigraphic intervals). Developing a tool kit for the log-based identification of diagenetic overprints (in particular, salt/anhydrite plugged dolomites within the main reef body) remains one of our biggest challenges to developing predictive relationships between porosity and permeability in the Niagaran carbonates.

4.2 Approach

As detailed in Figure 4-3, the first stage in defining a robust stratigraphic framework and the lithofacies with which to populate that framework, is to determine if the sequence stratigraphic framework established by Ritter (2008), Noack (2008), and Grammer et al.(2010) is viable and internally consistent; and determine if the lithofacies identified by Grammer's students are mutually consistent, and if they are compatible with more detailed studies by Huh (1973) and Gill (1973), and Huh et al. (1977). The second stage is to determine if there are consistent relationships between the whole core porosity/permeability measurements of individual published lithofacies and the sequences to which they belong. The third stage is to correlate the well-log signatures of the published stratigraphic sequences to the Dover 33 reef; determine wireline log-based lithologies within the sequences; interpret log-based lithofacies (electrofacies); and determine porosity-permeability transforms for sequence-constrained lithofacies and electrofacies.

The locations of important cored wells are shown in Figure 4-4. The core described by Noack (2008) at the Charlton 1-4 well is from an Otsego County reef that is relatively close to the Dover 33 reef; and establishing the sequence stratigraphy of that cored well, and the log expression of the lithofacies (which have publicly available foot-by-foot measured porosity and permeability values) were deemed particularly important.

It is anticipated that this general methodology can be updated as new data become available, and expanded to reservoir characterization and modeling of other northern Michigan Silurian reefs. The following sections discuss the individual parts of the sequence stratigraphic workflow, as executed in this study.

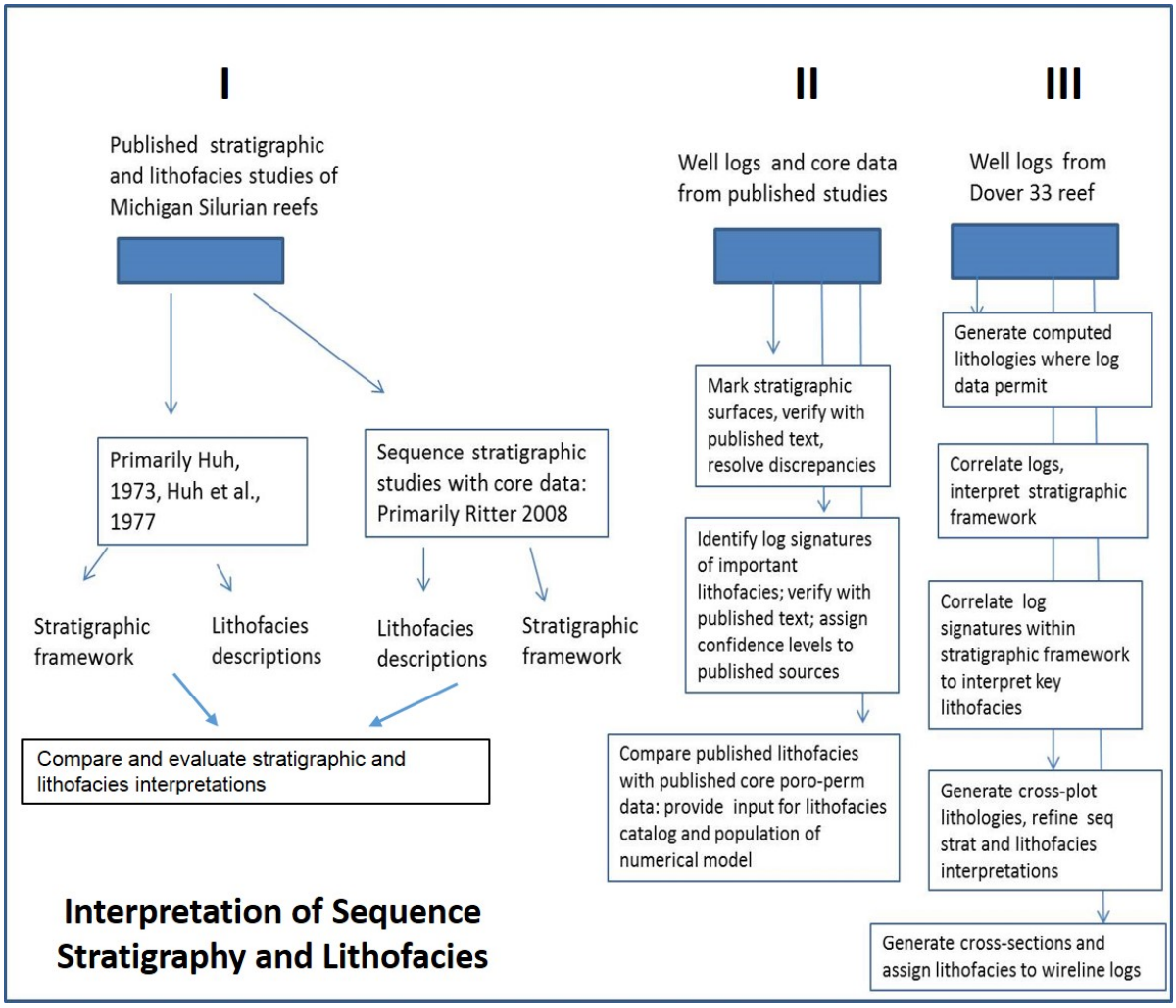


Figure 4-3. Consecutive three-stage workflow for interpreting a rock and wireline-log-based sequence stratigraphic framework and constrained lithofacies for the Dover 33 Level 2 static earth model.

4.3 Review of Lithofacies and Sequence Stratigraphic Studies of Michigan Niagaran Reefs

Interpretation of sequence stratigraphy through core studies is based on lithofacies analysis. Some of the most relevant work on stratigraphic correlation of on-reef and off-reef lithofacies of cored wells of the Silurian reefs was conducted by Huh (1973), Gill (1973), and Ritter (2008). Huh's (1973) important model of the Silurian reefs, based in large part on his core descriptions of a pinnacle reef in Kalkaska County (Figure 4-4), is diagrammatically summarized in Figure 4-5. This three-part, unconformity-separated genetic subdivision of the reef (Bioherm/organic reef, Supratidal island, and Tidal flat) and documentation of stratigraphically controlled lithofacies distribution provided the basis for the innovative sequence stratigraphic interpretation by Ritter (2008). Although Huh's (1973) model does not illustrate differences of windward and leeward reef facies, nor of internal reef geometry, it captures much of the basic current understanding of Michigan reef stratigraphy.

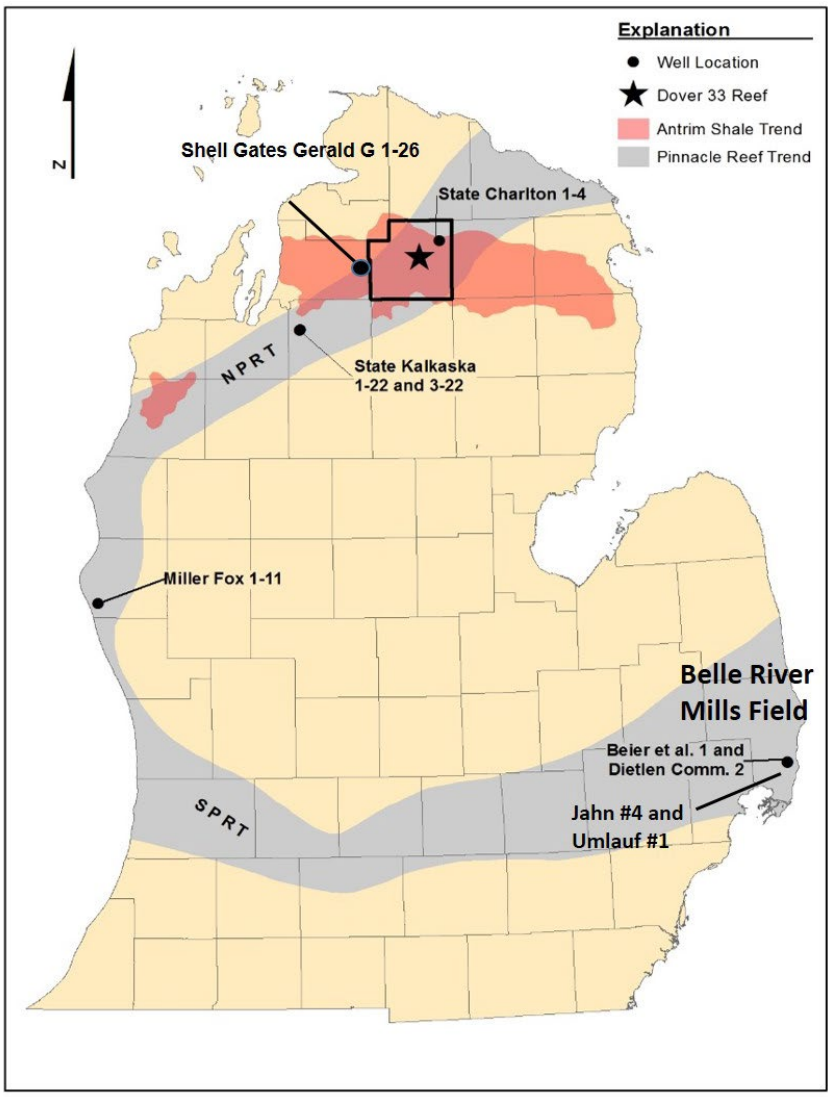


Figure 4-4. Location of the Dover 33 reef relative to key cored wells studied by Huh (1973), Huh et al., 1977), Ritter (2008), and Noack (2008). Petrophysical data were analyzed as part of this study for the State Kalkaska 3-22, permit 288443; Beier #2, 25779; Dietlin #1, 25022; and State Charlton 1-4, 28006. Additional core-based studies conducted by Grammer's students included material from the Belle River Mills Field in the southern reef trend.

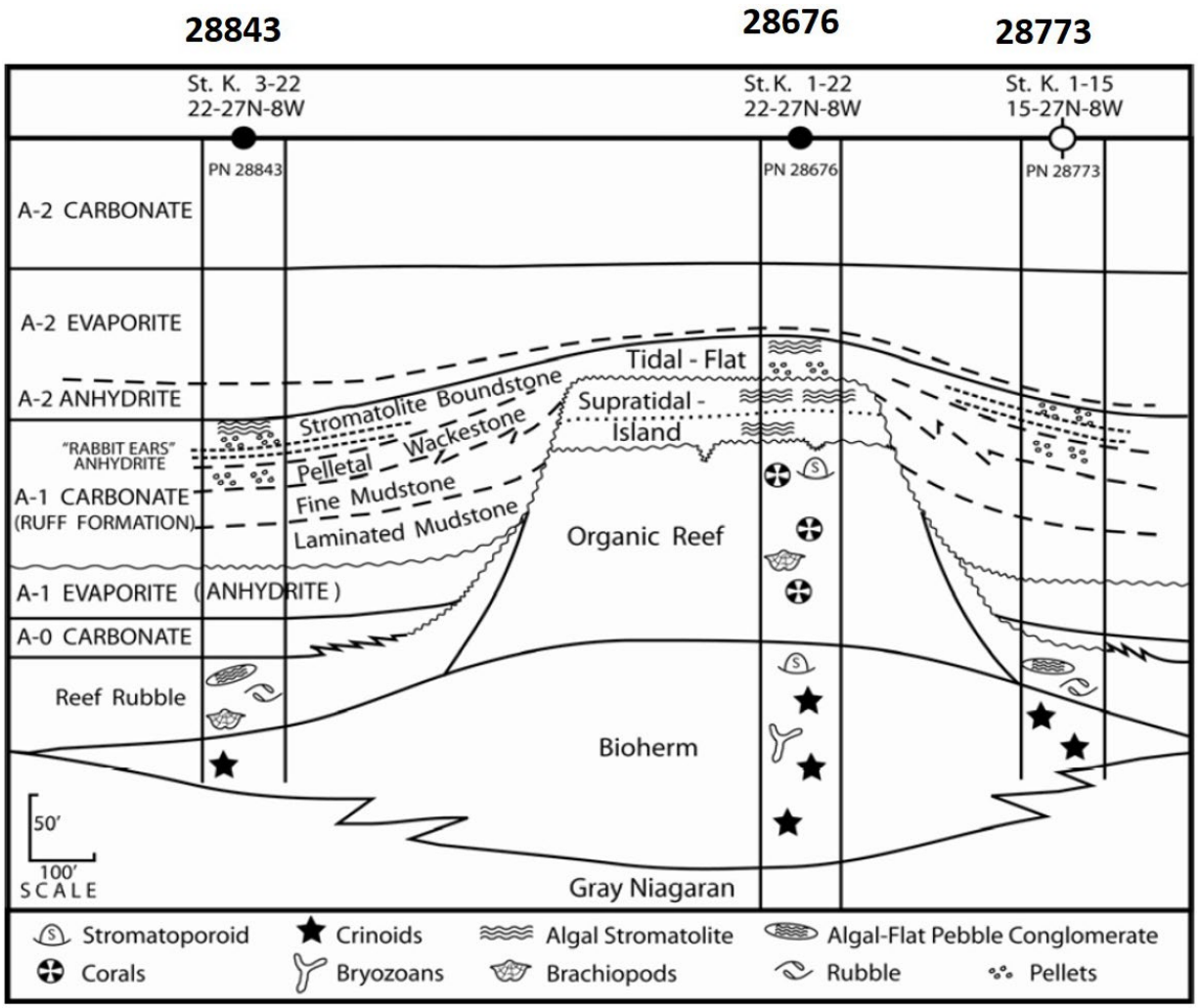


Figure 4-5. Lithostratigraphy and lithofacies of the Kalkaska reef, as interpreted by Huh (1973). This interpretation, along with core data associated with these wells, contributed to the establishment of a regional sequence stratigraphic framework by Ritter (2008).

4.3.1 Published Key Lithofacies of the Northern Reefs

Part of Stage I of the sequence stratigraphic/ lithofacies workflow is to determine the overlap and consistency of published lithofacies descriptions, prior to trying to determine validity of stratigraphic subdivisions and relationships between lithofacies and petrophysical properties. An extensive cross-walk comparison (not shown) of lithofacies descriptions of Huh (1973), Huh et al. (1977), Ritter (2008), and Noack (2008) yielded a total of 52 separately named lithofacies. Most of the lithofacies described by these authors can be lumped into the nine carbonate lithofacies of Ritter (Figure 4-6). Note that Ritter's lithofacies are restricted to carbonates and do not include bedded anhydrite or bedded halite. Because these two lithofacies have distinct and important log and petrophysical properties, they are added to this discussion.

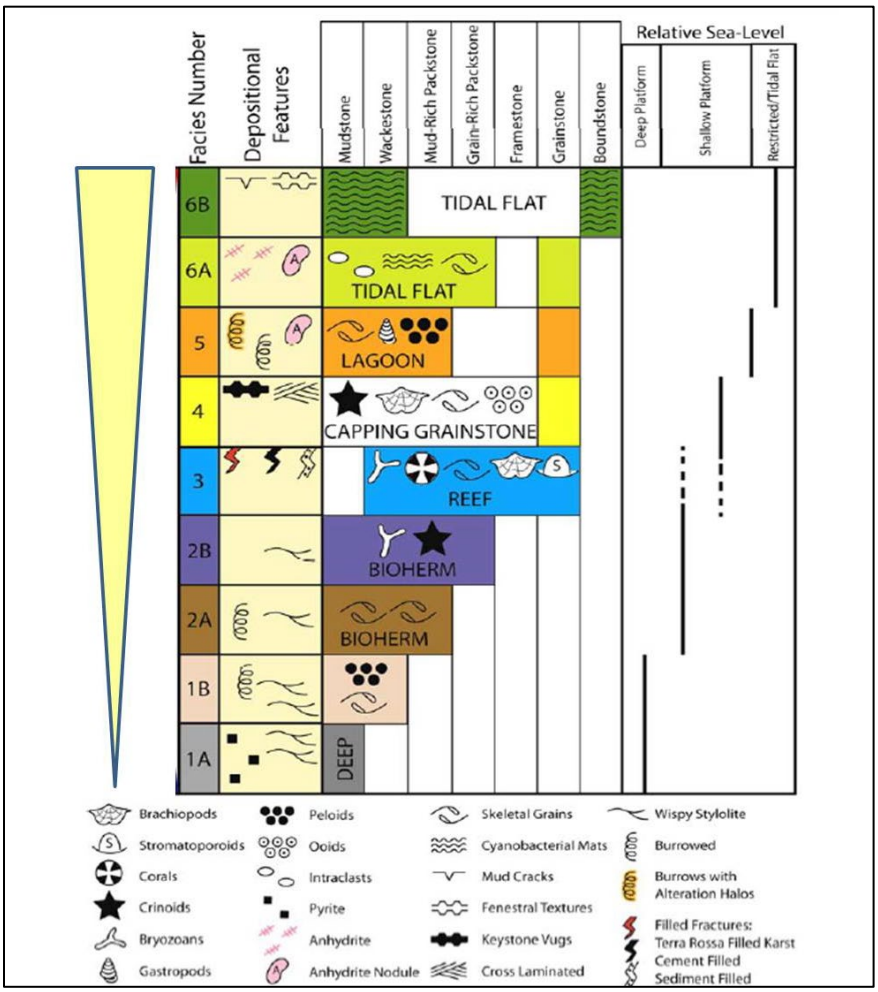


Figure 4-6. Ideal carbonate lithofacies recognized by Ritter (2008). As arranged here, these lithofacies reflect overall upwards-shallowing depositional conditions (indicated by yellow triangle).

Key lithofacies identified in core by Ritter (2008), along with associated porosities and permeabilities as reported by Ritter (2008) are as follows, from deeper water environments of deposition to more shallow environments:

Lithofacies 1A, Deep Platform Mudstone. Dark gray, laminated carbonate mudstone to wackestone (mud-supported, relatively few fossil fragments), interpreted as representing deposition in low-energy water depths greater than 33 feet (below fair-weather wave base). Generally 2-4% porosity and less than1 mD permeability were common.

Lithofacies 1B, Deep Platform Mudstone. Dark gray, burrowed carbonate mudstone to grain-poor packstone (grain supported, with mud matrix). Fossils mostly sand-sized crinoid fragments. Depositional environment: below fair-weather wave base, perhaps adjacent to low-relief organic mounds.

Lithofacies 2A, Muddy Bioherm. Dark gray to brown wackestone with crinoids, delicate branching bryozoans, and stromatactis fabric (marine cement in shelter cavities) (Figure 4-7). Depositional environment: below wave base in bryozoan/crinoid communities forming low-relief organic “mud mounds” or muddy bioherms (mound or lens-shaped organic buildup). Measured porosities are 2-10% and permeabilities range from 0.1 mD to 100 mD.

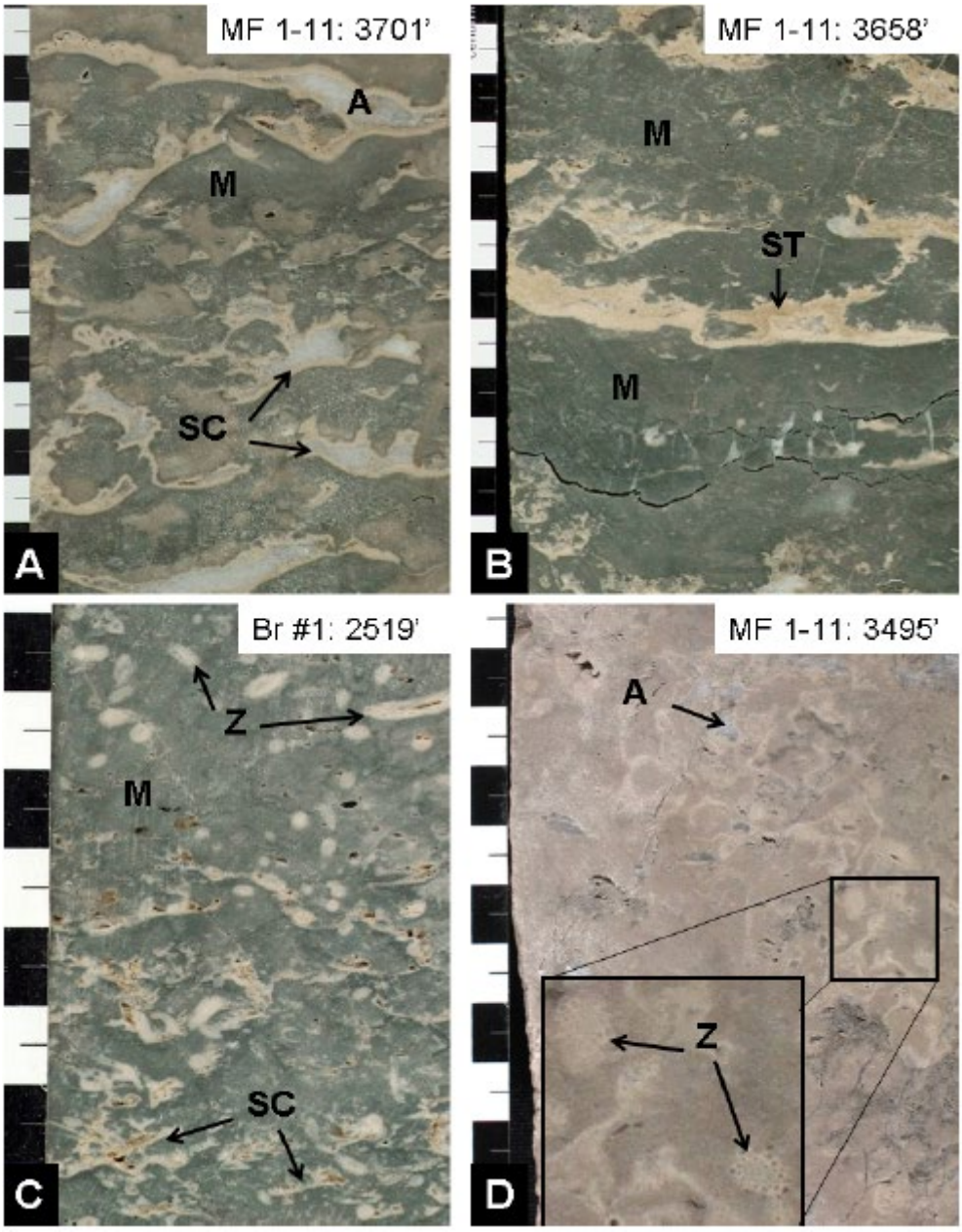


Figure 4-7. Muddy bioherm lithofacies 2A of Ritter (2008). Core slab photographs A and B illustrate calcite and anhydrite (black A) cements in stromatactis fabric (SC), carbonate mud (M) and encrusting stromatoporoids (ST). Photographs C and D illustrate carbonate mud (M), anhydrite cement (A), stromatactis fabric (SC) and branching twiggy bryozoans (Z). From Ritter (2008).

Lithofacies 2B, Muddy Bioherm. Dark gray to brown bryozoan and stromatoporoid (sponge-like organism) wackestone to packstone with increasing diversity and abundance of fossil fragments. Depositional environment: below wave base, in muddy bioherms. Ritter reports both lithofacies 2A and 2B have porosities of 2-10% and permeabilities from 0.1 mD to 100 mD.

Lithofacies 3, Reef Framework. Brown tabulate (colonial) coral and stromatoporoid framestone (cemented reef fossils) with wackestones to grainstones (sand-sized fossil fragments with marine cement and no carbonate mud) infilling the voids between reef fossils (Figure 4-8). Porosity occurs within and between large fossil fragments. Depositional environment: organic reef, water depth within wave base from 33 feet to sea level. Highly variable porosity (2-16%) and permeability (1-25,000 mD).

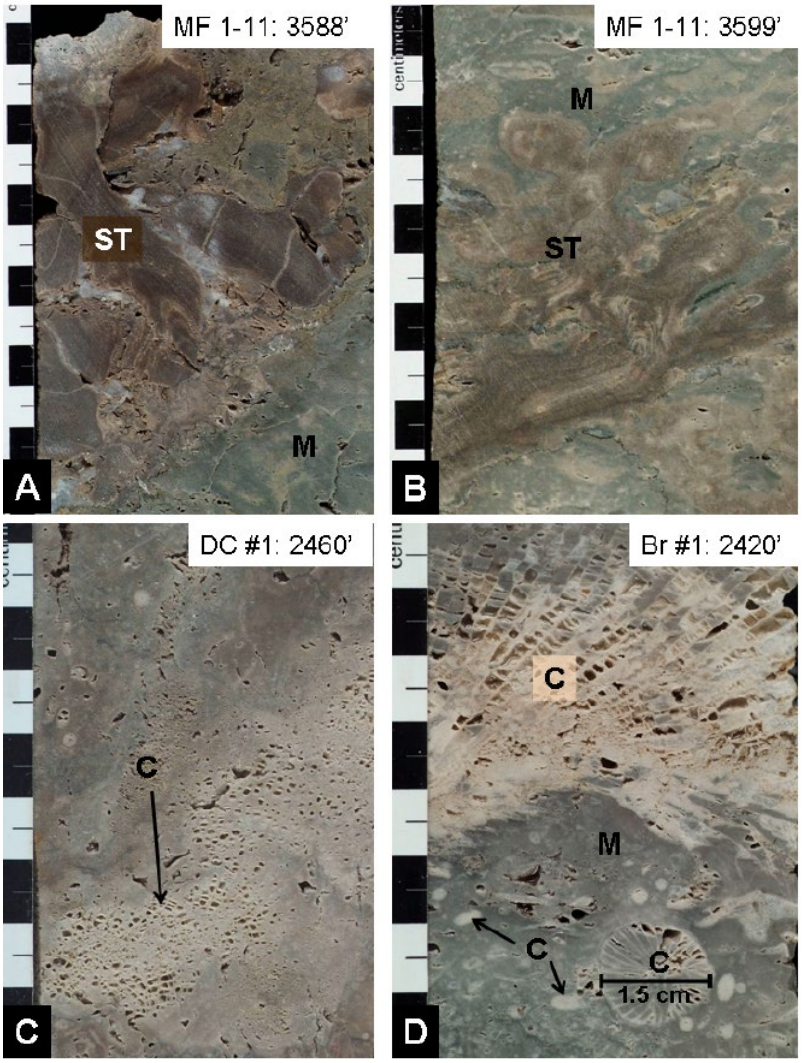


Figure 4-8. Lithofacies 3, reef facies of Ritter (2008). Slab photographs A and B illustrate stomatoporoid framestones; photographs C and D illustrate coral framestones. Symbols: C - coral; M - mud; ST - stomatoporoid. M-F is the Miller-Fox 1-11, Oceana County; DC is Dietlin Comm. #1, and Br #1 is Beier #1, both from St. Clair County. From Ritter (2008).

Lithofacies 4, Reef Capping Grainstone Facies. Brown skeletal grainstones (grain-supported, no mud) to packstones, sand to gravel-sized grains, often cross-stratified. Diverse fauna of brachiopods, crinoids, small solitary corals, fragments of frame builders. Depositional environment: high energy, fore reef, back reef and reef top, near sea level. Depositional porosity may be filled with carbonate cement; porosity generally ranges from 2-14%, and permeability from 0.1-100 mD.

Lithofacies 5, Lagoonal Wackestone Facies. Brown to dark brown, burrowed and bioturbated (texture churned by organisms), wackestone to grain-rich packstone. Dominated by elliptical non-skeletal grains lacking internal structure, similar to crustacean fecal pellets (peloids); moldic porosity common, may be filled by anhydrite or halite. Depositional environment: low energy, restricted shallow water to intertidal/beach. Porosity 1-19%; permeability generally less than 10 mD, but may range higher.

Lithofacies 6A, Tidal Flat Breccia Facies. White to gray, very fine crystalline limestone or dolomite cyanobacterial mat breccia (stromatolite or “algal mat”) with peloidal mud matrix or anhydrite cement (Figure 4-9). Depositional environment: tidal flat, intertidal to supratidal. Porosity generally less than 2%; permeability generally less than 1 mD.

Lithofacies 6B, **Cyanobacterial Boundstone Facies**. White to gray laminated cyanobacterial/microbial boundstone (constituents bound together during deposition), with sparse sand-sized bioclasts, and anhydrite-filled fenestral (window) or bird’s-eye porosity (see Figure 4-9). Depositional environment: tidal ponds, tidal flats. Bird’s eye porosity is almost always filled with evaporites; fenestral moldic porosity can range from 2-10%, with permeability up to 100 mD.

Two additional lithologies/lithofacies, anhydrite and halite, are important but are not carbonate lithologies, and thus are not described by Ritter (2008). Anhydrite occurs as both a depositional lithofacies and diagenetic cement. The two anhydrite depositional lithofacies reported in the Niagaran cores are nodular anhydrite (Figure 4-10) and bedded anhydrite (Figure 4-11). Both bedded and nodular anhydrite occur in the A-1 Evaporite; with bedded anhydrite forming in strongly evaporative subaqueous environments, and nodular anhydrite intertidal, and sabkha (salt flat) very restricted evaporative environments. Nodular (syneresis or “chicken wire”) anhydrite often forms in supratidal sabkha environments, near the groundwater contact.

Halite occurs as beds, deposited as part of the A-1 evaporite in the Michigan basin center, and as late-stage fracture (Figure 4-12) and cavity fill. Halite is seldom a true cement in the reef-associated lithofacies.

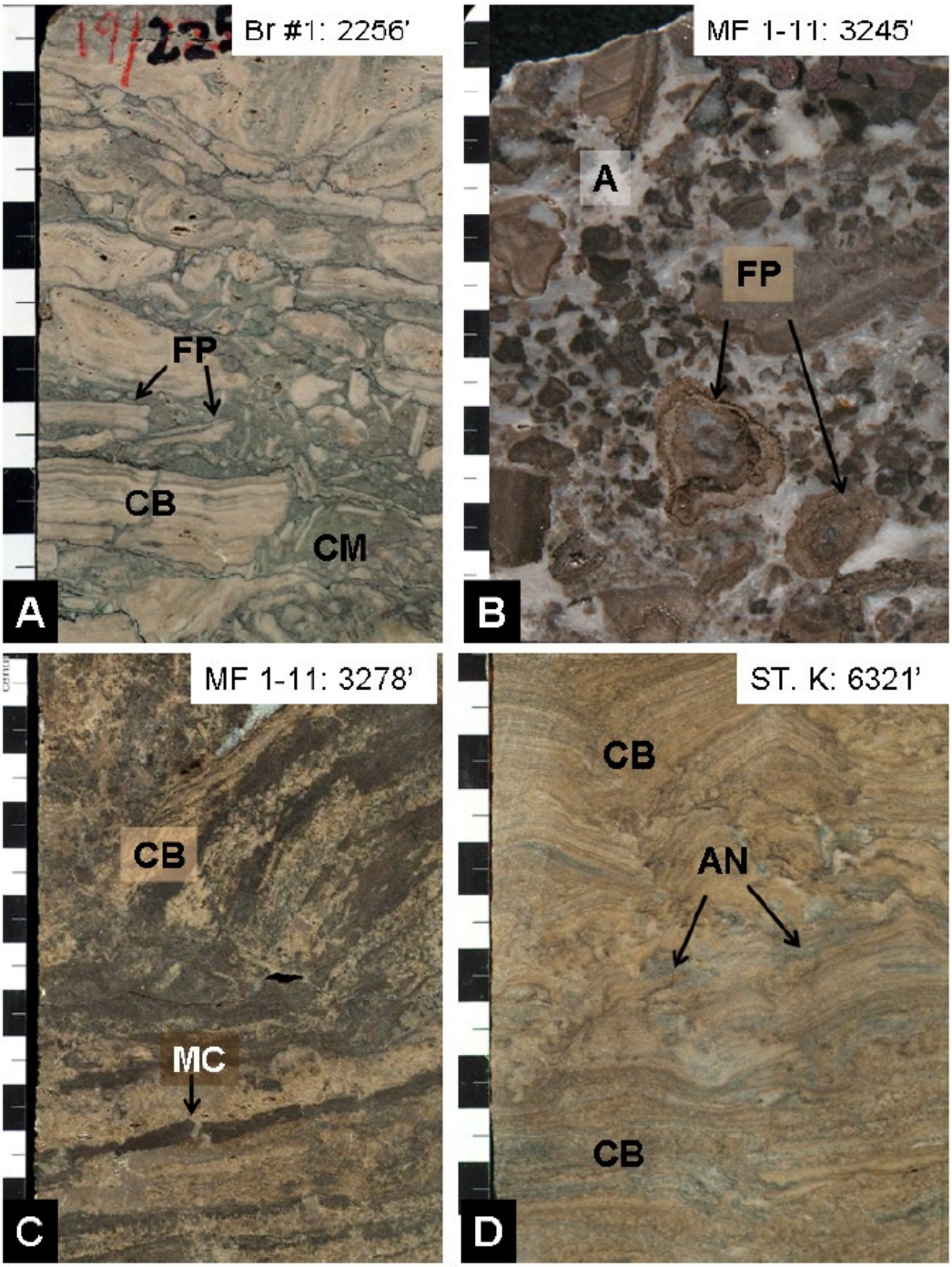


Figure 4-9. Tidal flat cyanobacterial lithofacies 6A and 6B of Ritter (2008). Slab photographs A and B illustrate cemented breccias (facies 6A); photographs C and D illustrate more growth position boundstones (lithofacies 6B). Symbols: A - Anhydrite; CB -cyanobacterial mats; CM - carbonate cement; FP - "flat-pebble" microbial clasts; and MC - mud cracks. Br-1: Beier #1, St. Clair County; MF1-11 Miller Fox 1-11, Oceana County; ST. K.: State Kalkaska, Kalkaska County. From Ritter 2008.



Figure 4-10. Nodular anhydrite lithofacies, grading upward into possible carbonate supratidal deposits. Well permit 27669, from the Columbus III reef in the southern reef trend. Lateral field of view about 3.5 inches; photograph courtesy of Matt Rine.



Figure 4-11. Bedded anhydrite lithofacies from the A-1 Evaporite of the Kalkaska 1-15 well. Lateral field of view about 3.5 inches; photograph courtesy of Autumn Haagsma.

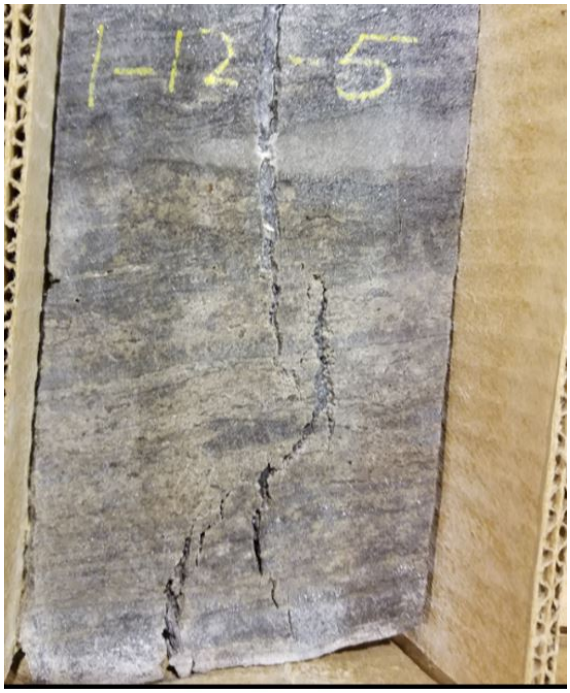


Figure 4-12. Late stage diagenetic fracture fill by halite. Core is from the Kalkaska 1-15, and was studied by both Huh (1973) and Ritter, (2008). Field of view about 3.5 inches; photograph courtesy of Autumn Haagsma.

4.3.2 Published Sequence Stratigraphic Studies of the Niagarann Reefs

Liebold (1992) appears to be the first to apply sequence stratigraphic concepts to the Michigan Basin. He interpreted generalized composite sequence (CS) sets (see Figure 4-2 for illustration) for the White Niagaran through the Salina B interval, with a focus on changes in sea level and formation of the evaporite deposits. Ritter (2008) is the first to apply these concepts to the interval from the base of the Brown Niagaran to the top of the A-1 Carbonate. Third and higher order (shorter time interval) sequence interpretations are based on her core descriptions and include standard criteria of lithofacies stacking patterns, lithofacies offset patterns, and the presence of exposure surfaces. Ritter (2008) interpreted three distinct third-order sequences that are separated by unconformities in both northern and southern reefs. The sequence boundaries as described in her text follow Posamentier and Vail (1988) in placing third order sequence boundaries coincident with erosional surfaces, and below interpreted low stand wedge deposits, which in this case, include the A0 carbonate and A-1 Anhydrite lithostratigraphic units.

Figure 4-13 shows Ritter's (2008) sequence stratigraphic correlation for five regional cored wells, including three southern reefs and two important northern wells (State Kalkaska 1-22 [28676] in Kalkaska County and the Miller-Fox 1-11 [33500] in Oceana County). Ritter's Sequence 1 (on-reef) vertically extends from a basal flooding surface penetrated only in the Beier 1 (25779) core, and encompasses a period of fairly continuous organic growth from muddy bioherm to true organic-reef construction. The sequence is terminated by the lowermost unconformity on top of the reef (as recognized by Huh, 1973).

The correlation of on-reef unconformities to off-reef correlative surfaces has always been difficult (Huh, 1973; Huh et al., 1977). Ritter's illustration (in contradiction to her text) indicates that Sequence 1 contains the off -reef deposits through the lowstand A-1 Anhydrite, thus including the rocks below and above the unconformity that separates Huh's intraclastic reef (growth) debris from the lithoclastic (erosional) reef breccia. Ritter's top Sequence 1 boundary as illustrated above the A-1 Anhydrite would therefore be a composite sequence boundary (see Figure 4-2). Michael Grammer, Ritter's advisor at time of writing her thesis, placed the top of Sequence 1 even lower, below the A0 Carbonate (verbal communication February 2013 to Charlotte Sullivan).

Ritter's Sequence 2, as illustrated in Figure 4-13, includes the thin off-reef A-1 Carbonate interval to the lower "poker chip" shalely layer (described in the Jahn 4 well), as well as the overlying transgressive laminated mudstones recognized by Huh (1973), and thin highstand deposits of mixed non-reef and reef community development on top of previously exposed

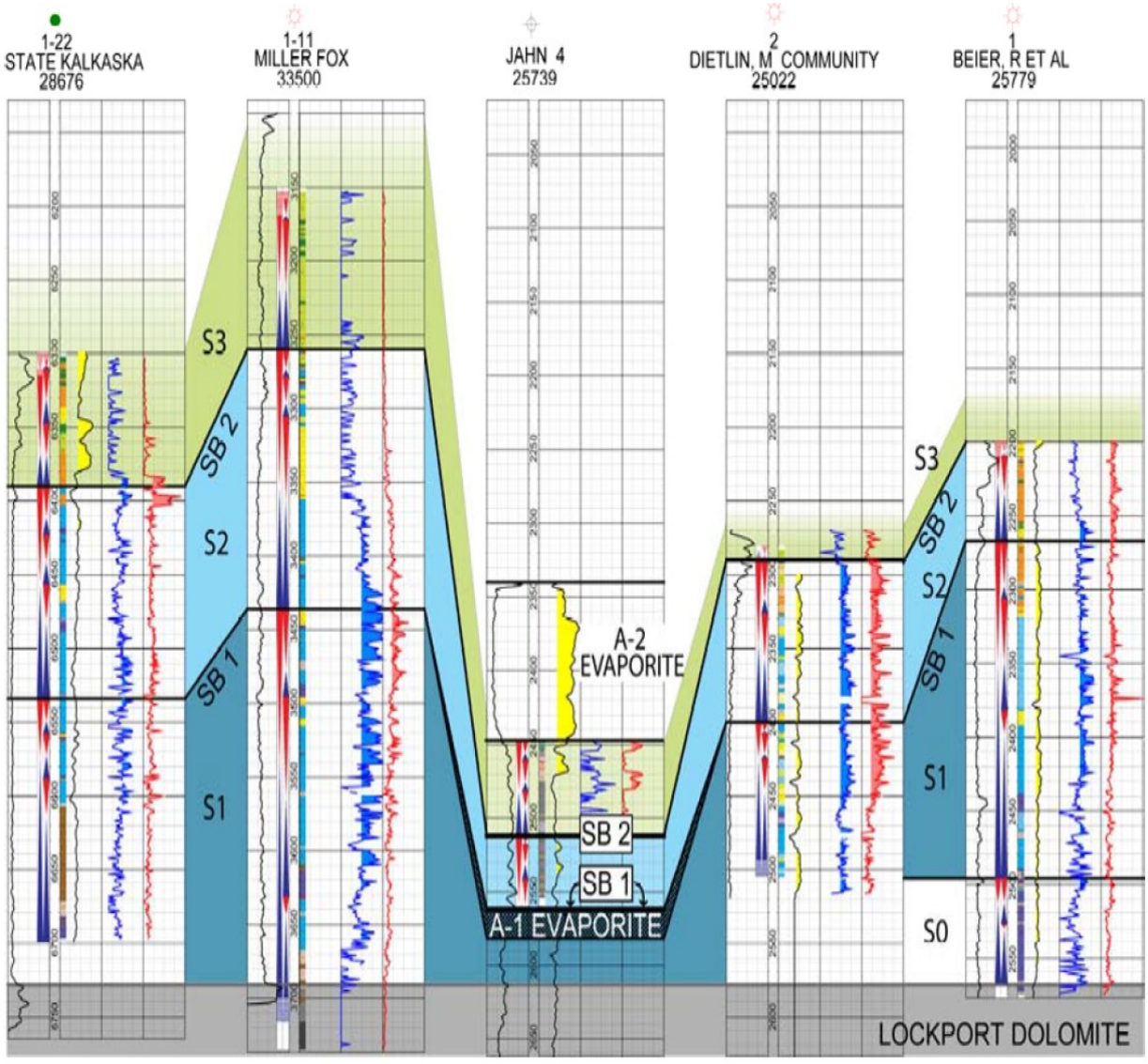


Figure 4-13. Sequence stratigraphic boundaries for five reefs studied by Ritter (2008). Jahn 4 is an off-reef well; all other wells are located on reef. Jahn 4, Dietlin 2, and Bier 1 are in the Southern Reef Trend.

reefs. Ritter's Sequence 2 is topped by an unconformity and a karst surface on reef; this on-reef interval coincides with Huh's (1973) Supratidal Island Stage.

Ritter's on-reef and off-reef Sequence 3 deposits include the rest of the A-1 Carbonate, including the Rabbit Ears Anhydrites, and represent a later period of environmentally stressed, shallow-water carbonate and evaporite deposition, when sea-level shallowly or incompletely covered the reef structures. The top of Sequence 3 coincides with the base of the A-2 Evaporite; the contact which, in places, displays an erosional surface in core (Huh, 1973)

Ritter's on-reef, third-order sequences attempt to correspond to the three on-reef depositional packages of Huh (1973). Figure 4-14 illustrates this relationship.

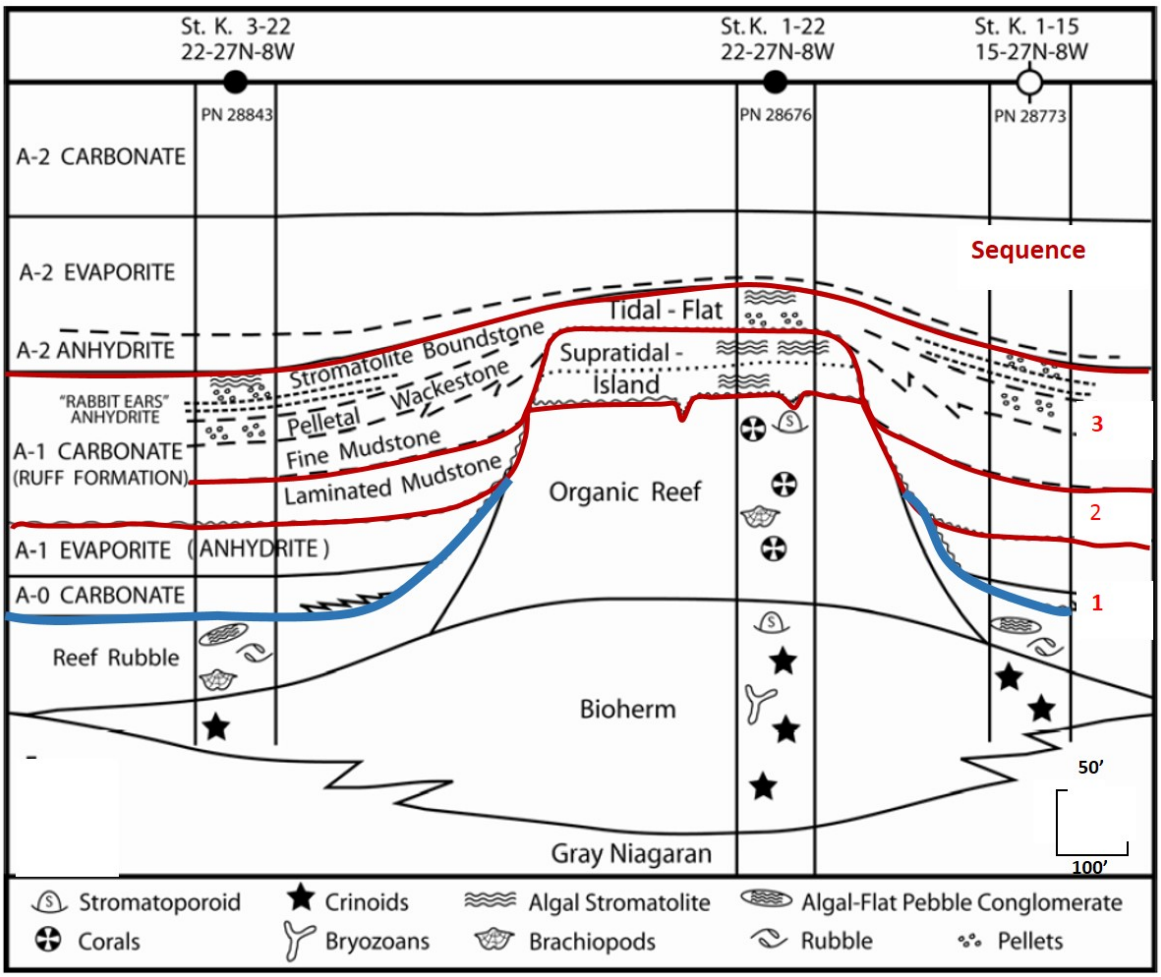


Figure 4-14. Correspondence of Ritter's unconformity-bounded third order sequences to Huh's (1973) reef stratigraphy. The logs and descriptions from the Kalkaska 3-22 (28843) were important in establishing correlation with the Dover 33 reef.

Ritter (2008) placed the off-reef top of Sequence 1 at the top of the A-1 Anhydrite (as seen in our Figure 4-13), but in her thesis text, she places the top of Sequence 1 below the A-1 Anhydrite, above the A0 Carbonate. It appears that she simply did not update her thesis figure to match her text. Grammer's top of off-reef Sequence 1 is below the A-1 Carbonate and is shown in blue.

After examination of the published work by Huh (1973), Gill (1973), Ritter (2008) and Noack (2008), parts of Ritter's off-reef reef stratigraphic model were modified to better conform to the more detailed sedimentological descriptions by Huh (1973). In February 12-13, 2014, a joint partners (Battelle, Core Energy, Western Michigan University) meeting at the MGRRE laboratory allowed examination of cores from the Kalkaska Reef, the Miller Fox 1-11, Jahn 4, and the Charlton 1-4, and a refinement of the stratigraphy and associated lithofacies of Ritter (2008) and Noack (2008).The following section details the tools and methodology used in correlating the stratigraphy of Grammer's students to the wells at the Dover 33 reef; and our evaluation of Ritter's stratigraphy and the optimal placement of sequence boundaries at the State Kalkaska 3-22 and St. Kalkaska 1-15, as well as at the Dover 33 reef. Finally, we discuss the process used in interpreting lithofacies (electrofacies) within the Dover 33 sequences.

4.4 Interpretation of Sequence Stratigraphy and Lithofacies at the Dover 33 Reef

Wireline log patterns, mineralogy identification through wireline log cross plots, and ELAN multi-minerology computed logs are critical in correlating wireline logs and establishing the wireline-based lithofacies (electrofacies) equivalency of stratigraphically constrained lithofacies from cored reefs. These data are essential to building and populating the framework of the Level 2 static earth model. The following sections detail the tools and techniques used in correlating logs and interpreting electrofacies at the Dover 33 reef.

4.4.1 Wireline Log Signatures

The correlation of wireline log signatures is one of the most important tools is establishing stratigraphic equivalency of wells in or between reefs. Wireline signatures reflect lithology (such as anhydrite and halite beds) as well as petrophysical properties of the rocks; and have been used for years to identify depositional environments (Schlumberger, 1989) and carbonate lithofacies stacking patterns (St. C. Kendall, 2003). Expansion of the gamma ray scale is the first step in better identifying subtle but important patterns in "clean" carbonates. Deeper water deposits commonly have a higher gamma ray signature from uranium, as do many flooding surfaces that mark sharp vertical facies offsets. Intertidal deposits may have a very "ratty" gamma and resistivity or density log, reflecting potassium from windblown silt, and higher densities or resistivities in anhydrite cemented carbonate.

Recognition of important genetic depositional packages (as in Huh's 1973 work) or sequence stratigraphic boundaries by Ritter (2008) and others is primarily through lithofacies stacking patterns, from abrupt vertical lithofacies offsets that juxtaposes lithofacies that represent depositional environments that do not naturally occur laterally (i.e., that do not honor Walther's law), or by the presence of surfaces that indicate a hiatus or prolonged non-deposition, followed by renewal of sedimentation. The most common carbonate lithofacies stacking patterns reflected in wireline signatures are ones that reflect deposition in environments that become progressively shallower—for example, due to sediment filling in the depositional environment from below wave base to intertidal environments at sea level. This is commonly referred to as an upward shallowing succession or stacking pattern. Other common stacking patterns (Figure 4-15) include upward-deepening (i.e., retrogradational; transgressive or landward-stepping packages); and aggradational (rate of sea level rise matches rate of sediment accumulation).

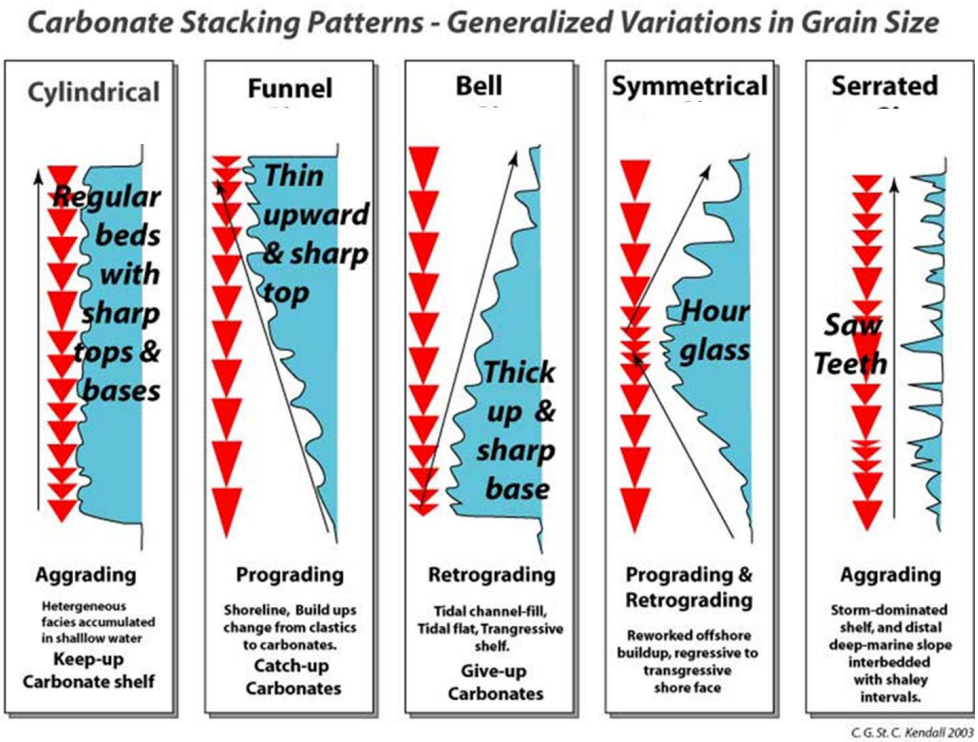


Figure 4-15. Schematic representation of aggrading, prograding, and retrograding carbonate stacking patterns.

The serrated outline represents grain size, which also generally mimics weathering profile and gamma log signature. From St. C. Kendall (2003).
http://www.sepmstrata.org/page.aspx?pageid=1

Figure 4-16 illustrates an aggradational log signature or interpreted stacking pattern of small cycles in two off-reef wells near the Dover 33 reef. These signatures correlate closely with the logs from the Kalkaska 3-22 off-reef well (see Kalkaska reef location in Figure 4-4). The close match of the wireline signatures of the off-reef wells at the Dover 33 reef with the log signatures in the cored off-reef well at the Kalkaska reef (discussed in following sections) allows us to correlate the logs and pick the depths in the Dover 33 reef that correspond to unconformities and lithofacies changes in cores from the off-reef Kalkaska wells that were described by Huh (1973).

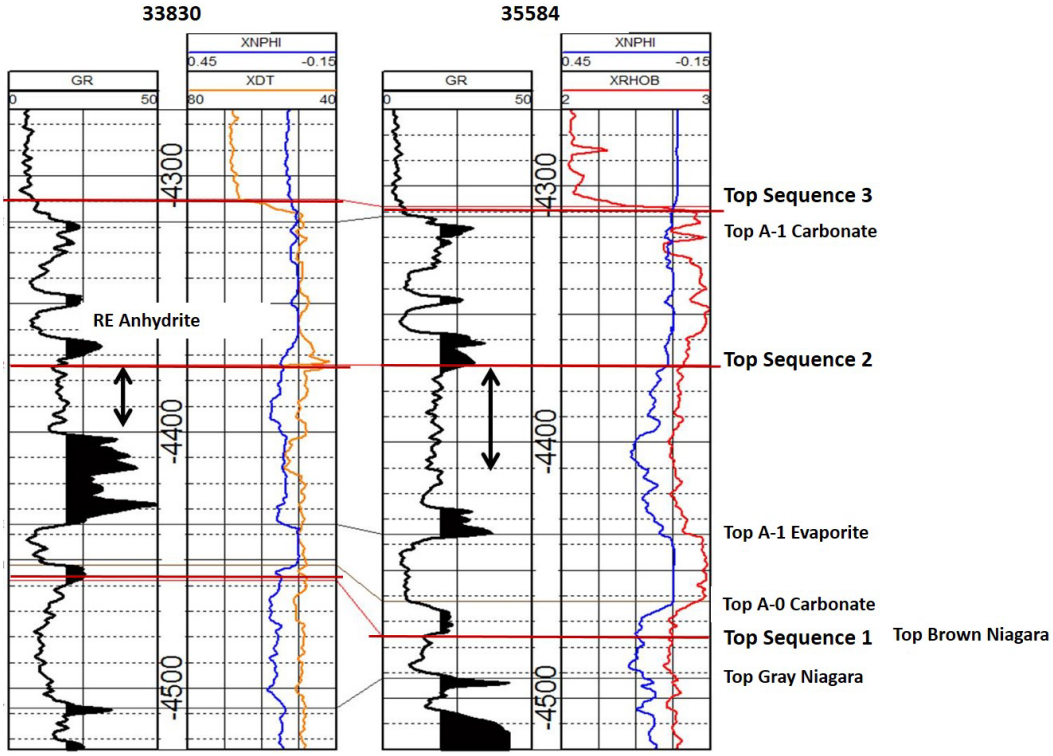


Figure 4-16. Interpreted aggradational log signatures (black arrows) above the A-1 anhydrite in two off-reef wells at the Dover 33 reef. The gamma curve has been expanded to maximize small deflections common in carbonate logs.

Red line above aggradational signature is Battelle's top of Sequence 2, and corresponds to the log pattern of an abrupt lithofacies change and downlap surface described by Huh (1973) in the State Kalkaska 3-22 (28843) well. Interpretation and correlation of sequence boundaries is covered in following sections. Clean gamma ray "bump" below the aggradational package in 35584 appears to regionally correlate with a more grain-rich interval in cores from other A-1 Carbonate wells.

4.4.2 Cross-plot Mineralogy Logs

In the absence of cores, the use of logs to identify mineralogy variation within the reef and along the flanks is critical in the visual wireline correlation of sequence stratigraphic markers and in populating the resulting sequence stratigraphic framework with lithofacies or "electrofacies" (wireline log-based interpretation of lithofacies, *sensu* Serra and Abbot, 1980).

The production of cross-plot mineralogy analysis described in the construction of the Level 1 Model (see Section 3) provides an important means of reducing uncertainty on lithology, electrofacies, and depositional boundaries and lithofacies offsets. Figure 4-17, which is reproduced from Section 3, illustrates lithology differences between the Winter 1-33 (35195, located east of the Dover 33 reef, see Figure 2-2) and the on-reef 29565 well. The electrofacies visually indicate distinct similarities and differences in thickness and lithologies in the logged intervals.

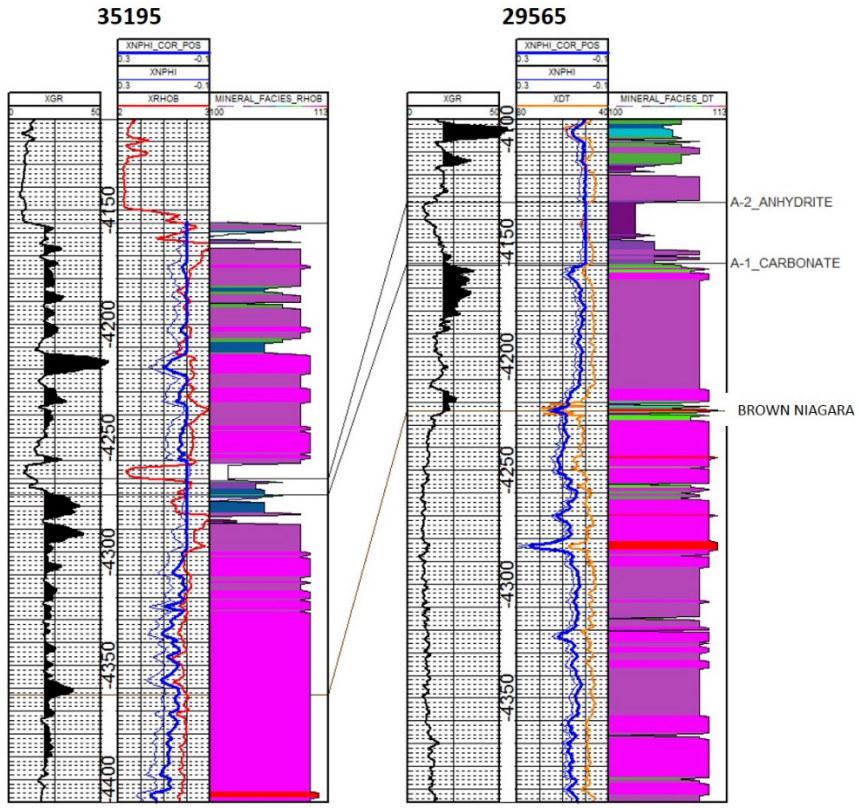


Figure 4-17. Electrofacies generated from bulk density (RHOB) or sonic (DT) vs neutron porosity cross-plots.

4.4.3 Computed Lithology Logs

Four wells had sufficient logs to allow Schlumberger to calculate ELAN lithology logs. These ELAN logs provide much higher resolution and detail on lithologies than do cross-plot generated electrofacies logs. Required input logs include gamma ray, bulk density or sonic travel time, neutron porosity, and photoelectric (PE) cross-section logs. Core and mineral analyses can help calibrate this type of computed logs.

The wells with ELAN logs are:

- 35195 Winter #1-33
- 35584 Lawnichak Morley #1-33
- 37268 St Charlton #2-10
- 50985 Myskier #2-38

Figure 4-18 is an example of an ELAN lithology log for off-reef well Winter 1-33, 35584, located east of the Dover 33 reef. The display in Figure 4-18 includes standard log curves as well as mineral bound water, and unbound zone water (U water). PHIT is total porosity and PIGN is

effective porosity. Note that the ELAN processing produces two measures of permeability that are qualitatively useful, but since they could not be calibrated with core permeability at the Dover 33 reef, they are not used in populating the static earth model. Calibration of ELAN permeability logs in the Michigan reefs is an important area for future reef investigation.

The ELAN lithology logs were used along with the cross-plot mineralogy logs to strengthen interpretation of sequence boundaries and electrofacies based on a) various changes in anhydrite, dolomite, and shale percentage in the off-reef lithofacies; b) changes in the mixed lithology limestones and anhydrites present along the flanks of the reefs; and c) changes in variably porous dolomites of the reef proper. The ELAN logs are particularly helpful in identifying upward shallowing packages of fourth order sequences and in separating thin anhydrite beds from thin tight limestone beds.

In Figure 4-18, the zone with (calculated) illite clay in the A-1 Carbonate (white arrow) correlates to increased gamma and “poker chip” shaley carbonate in the Kalkaska 3-22 well. We interpret this to be a maximum flooding zone, and it appears to correlate to the shaley interval in the Jahn 4 well that Ritter interpreted as a basal flooding zone and her base of Sequence 3.

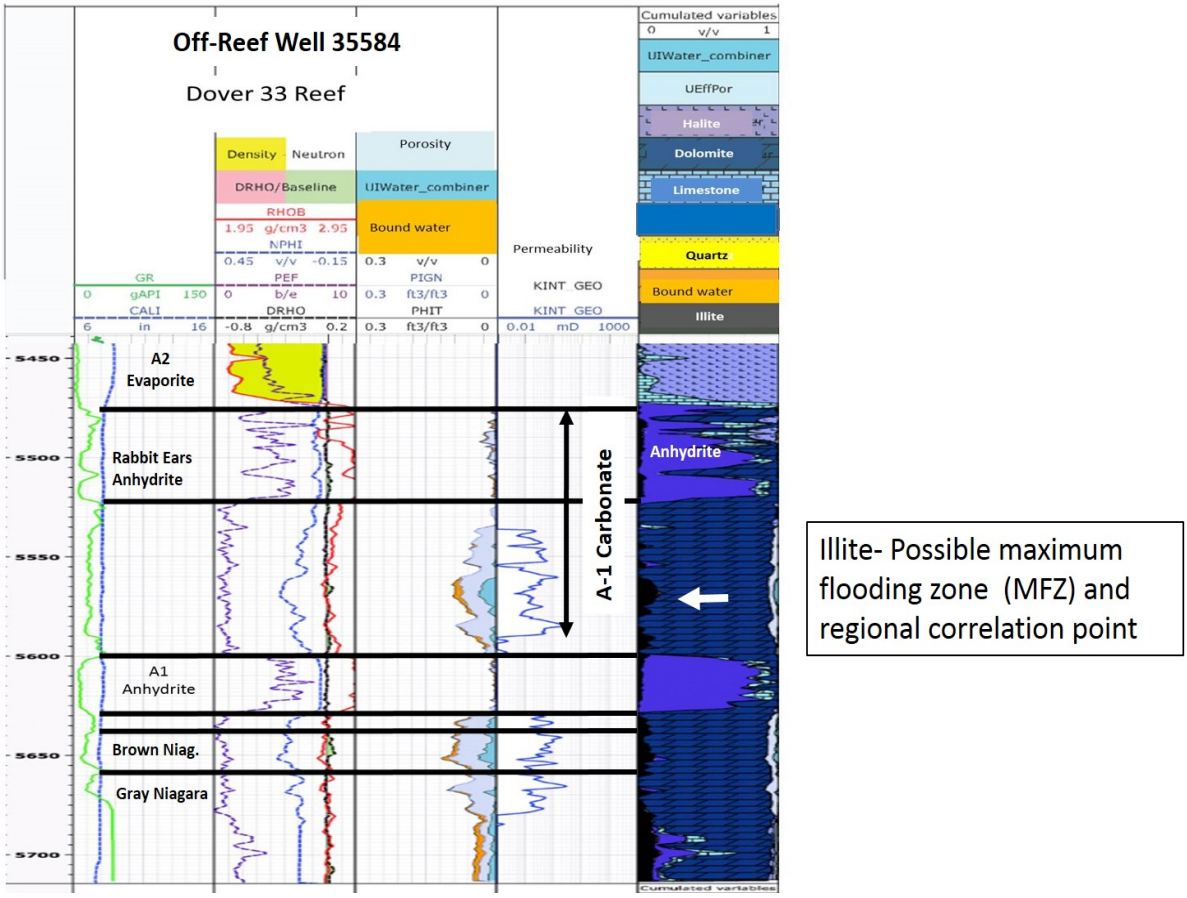


Figure 4-18. Computed ELAN lithology log of the Dover 35584 off-reef well. Changes in computed lithology, calculated porosity and permeability, and free or bound water saturation aid in interpreting sequence and lithofacies boundaries.

4.4.4 Correlation of Third- and Fourth-Order Sequences to the Dover 33 Reef

Correlating the logs of the Kalkaska off-reef well (UID #28843) to the off-reef well (33584) of the Dover 33 reef is the first step in: a) correlating the stratigraphic breaks and associated wireline log signatures recognized by Huh (1973); b) correlating the sequence boundaries established by Ritter; and c) testing the stratigraphic models of Huh and Ritter against the wireline logs and electrofacies in wells at the Dover 33 reef. The Kalkaska 3-22 (28843) well is critical in that it has core that was studied in detail by Huh, and the associated off-reef well log signatures have distinct patterns and character. This correlation is shown in Figure 4-19; interpretation of sequence boundaries is discussed in the following paragraphs.

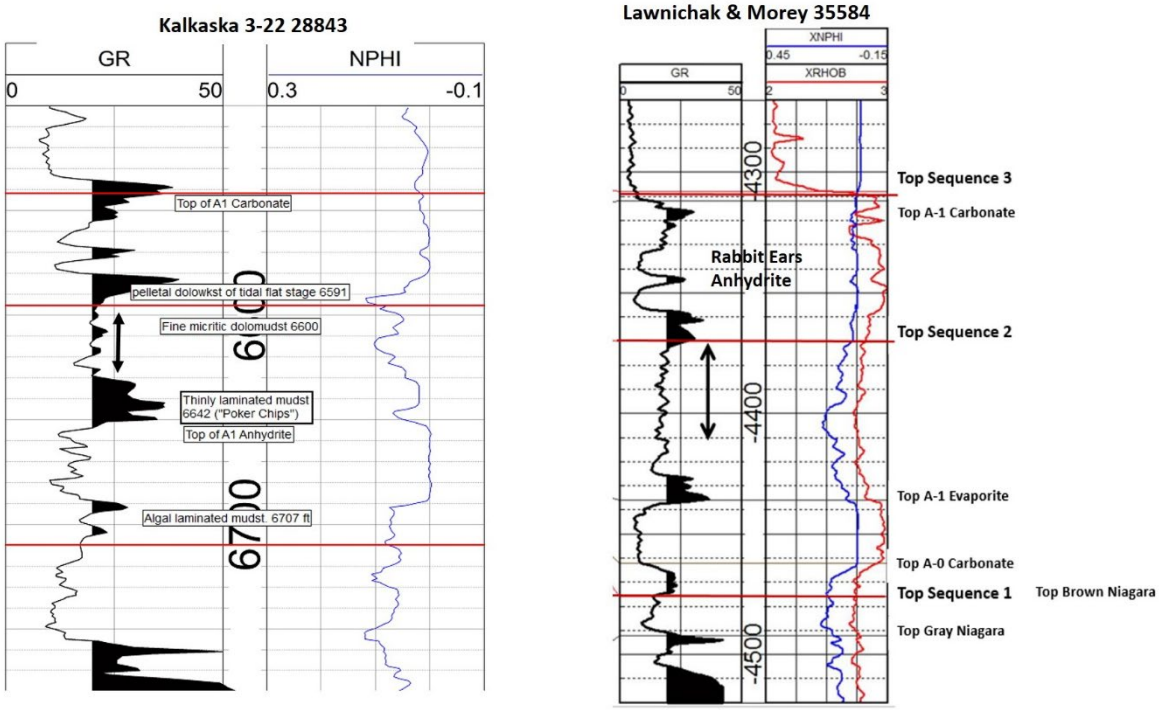


Figure 4-19. The Kalkaska 3-22 (28843) off-reef well log with lithofacies described by Huh (1973) (left), correlated to the Dover 35584 off-reef well (right). The 35584 well log is vertically stretched for ease of pattern recognition; arrows indicate aggradational log pattern.

The close correlation of log signatures provides confidence in recognizing Huh's stratigraphic reef subdivisions. Interpretation of sequence tops is explained in the text.

The placement of sequence boundaries is traditionally initiated by marking the depth of pronounced, but not extreme facies offsets in core and wireline logs. These packages often stack into larger packages whose boundaries display lithology changes or facies offsets of greater magnitude, including possible exposure surfaces. We therefore examined the sedimentological descriptions of Huh for the Kalkaska 3-22 (28843) off-reef core to determine the most likely depths for natural packages in the Dover 33 off-reef wells. Our interpreted stratigraphic boundaries in the log of the Kalkaska 3-22 cored well are as follows:

Top of off-reef Sequence 1:

Huh (1973) recognized the importance of two types of Brown Niagaran conglomerates directly below the A0 carbonate: conglomerate with reef-associated intraclasts, that is, debris from a live reef; and an overlying reefal lithoclastic debris, which is breccia from a dead and eroding reef. Like Huh, we place an unconformity between the two conglomerates, although we cannot define

that contact in Dover 33 wireline logs alone. Huh correlated this unconformable contact to the lowermost unconformity on top of the reef, which marks the end of stromatoporoid/coral reef growth. We place our off-reef top of Sequence 1 (Figure 4-19) at the base of the A0 carbonate, since we cannot differentiate texture or constituents in the underlying carbonate by wireline log alone.

Off-reef Sequence 2:

Huh (1973) and Huh et al. (1977) indicate that no off-reef sediment accumulated during the on-reef Supratidal Island stage (on-reef Sequence 2 of Ritter 2008, and of this study)

Huh (1973) interpreted an upward shallowing package consisting of the A0 and the overlying A-1 Anhydrite, with a gradational contact between the A0 Carbonate and the anhydrite, and an abrupt, and in some cores, an eroded or dissolutional contact on top of the anhydrite. This may be a fourth or third order magnitude surface. Based on regional information, we interpret it as a fourth order package, representing the late (transgressive) lowstand of Sequence 2.

Huh's next younger package of rock in the off-reef Kalkaska 3-22 includes laminated thinly bedded "poker-chip" carbonaceous and calcareous mudstone and fine mudstones. Examination of other off-reef A-1 carbonate cores at the MGRRE core facility indicates that the characteristic clean gamma bump observed in the 35584 well, below a hotter gamma and the aggradational log signature of the fine mudstones (Figure 4-16 and Figure 4-18) is a regionally correlative grain-rich interval with possible porosity and permeability development. We interpret this cleaner gamma "bump" as the top of a fourth order package.

Huh reported a down lap of "large pellet" pelletoidal grainstone onto the aggradational fine mudstone lithofacies described in the Kalkaska 3-22 well. This lithofacies, which has surprisingly large fusiform fecal pellets, was observed by Battelle to occur, as described by Huh (1973), above the off-reef aggradational fine mudstones, and in his on-reef Tidal Flat Stage interval (our Sequence 3). We therefore place the top of Sequence 2 above the aggradational package. We recognize that the downlap might merely represent topping of the reef by sea level and production of highstand carbonates. This is discussed further in later paragraphs.

Huh et al. (1977) show the off reef A0 Carbonate through the A-1 Anhydrite to belong to an unconformity bounded package younger than the on-reef Supratidal Island Stage and older than the Tidal Flat stage; with the total A-1 Carbonate equivalent to the Tidal Flat Stage, and no off-reef sediments coeval with the on-reef deposition of the Supratidal Island stage. We interpret the A-1 carbonate, from the top of the A-1 Anhydrite through the aggradational fine mudstones to be the transgressive part of Huh's Supratidal Island Stage; our Sequence 2.

Huh (1973) considers the entire off-reef A-1 Carbonate to be coeval with sediments deposited during his on-reef Tidal Flat Stage.

Ritter's (2008) off-reef sequence picks were compared as follows:

The results indicate that Ritter's off-reef tops of Sequence 1 and Sequence 2 should be modified to address the more detailed sedimentology reported by Huh (1973). Ritter variously placed the top of Sequence 1 above the A0 Carbonate in her text and above the A-1 Anhydrite (see
Figure 4-13). Huh's confirmation of a major unconformity between the reef intraclast conglomerate /interclast breccia in carbonates immediately below the A-0 carbonate strongly suggests this is the best placement for the off-reef top of Sequence 1. Where the exact depth cannot be determined, the base of the A0 carbonate serves as a proxy for the boundary.

Ritter (2008) places the off-reef top of Sequence 2 below a black shale in the Jahn #4 (25739) well at the position illustrated in Figure 4-13. Huh records "poker chip" shaley carbonates, but no

distinct facies offset, break in sedimentation or erosional surface at this position in the Kalkaska 3-22 (28843). An increase in gamma ray is present in other off-reef wells at this stratigraphic position and we speculate that the facies change recorded in the Jahn #4 well is more likely associated with a fourth order flood-back or maximum flooding zone (MFZ) during sea level rise above the A-1 anhydrite, rather than representing a third order sequence boundary. The magnitude of the observed break between the A-1 Anhydrite and the A-1 Carbonate remains problematic.

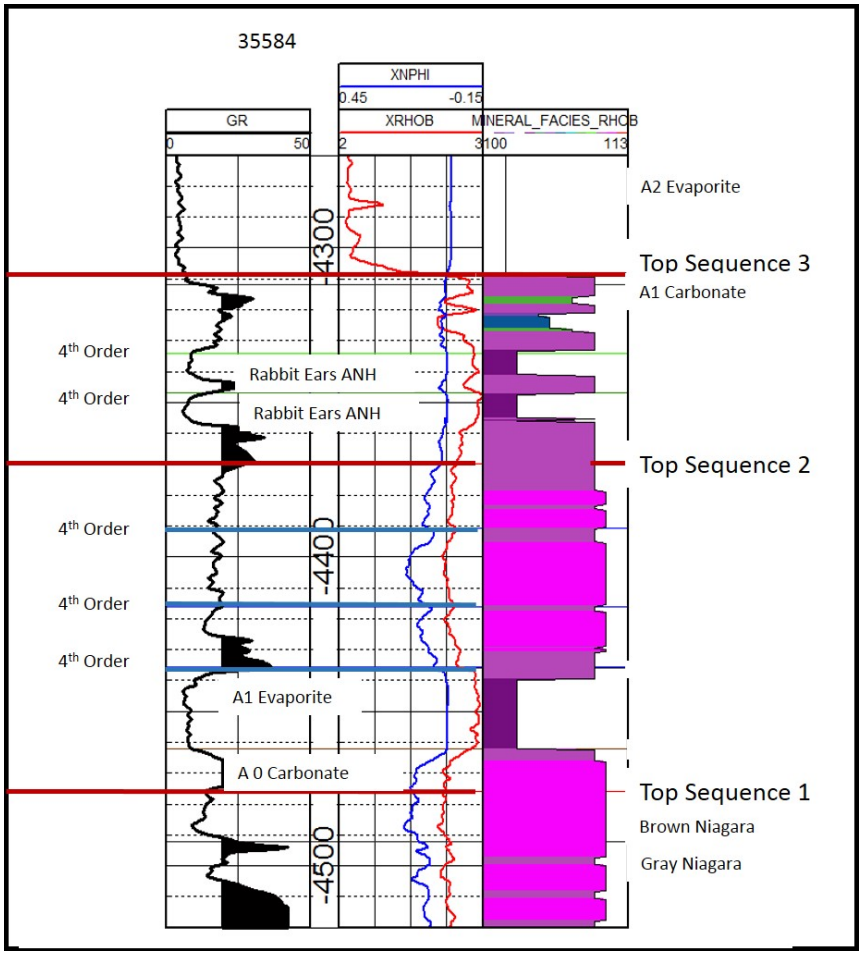


Figure 4-20. Third- and fourth-order sequences in off-reef well UID #35584.

This log serves as the off-reef type-log for this project. The cross-plot mineral facies (colors) reflect the strong relation between stratigraphy and lithology in the off-reef wells. See Figure 4-17 for lithology key.

The top of Sequence 2 in well 35584 (Figure 4-20) is above the aggradational (transgressive) gamma log pattern; and the top of Sequence 3 is placed immediately below the overlying Salina A-2 Evaporite. Ritter interpreted the Rabbit ears Anhydrites to be tops of fourth order sequences; and we concur.

The most correct pick for the off-reef top of Sequence 2 may be improved with additional data.

After interpreting the stratigraphy in the Dover 33 off-reef well (UID #33584); that log was next correlated to the Dover 50985 flank well. Both wells have a computer-generated lithology log, as well as a cross-plot mineralogy log. These logs are important in confirming correlation of Sequence 3 and the top of Sequence 1. The top of Sequence 2 was correlated from the top of the aggradational package identified in the off-reef well 33584. Figure 4-21 illustrates this correlation. The third- and fourth-order sequences were relatively easy to pick in the remaining flank wells at the Dover 33 reef.

Huh (1973) and Huh et al (1977) indicate on their Kalkaska reef model that no off-reef sediments were deposited during the (on-reef) Supratidal Island stage, and indicate all the off-reef deposits of the A-0 Carbonate, A-1 Evaporite, and the overlying A-1 Carbonate were laid down during lowered sea level following deposition of Huh's Supratidal Island Facies (above unconformity at the top of Sequence 2). However, in our work we can physically correlate the log signatures of the upper part of the A-1 Evaporite and the overlying sediments into the Dover

33 flank wells 50983 and 33830, which supports the hypothesis that the A-0 Carbonate and A-1 Evaporite are low stand deposits of Sequence 2 (in agreement with Ritter's methodology), and

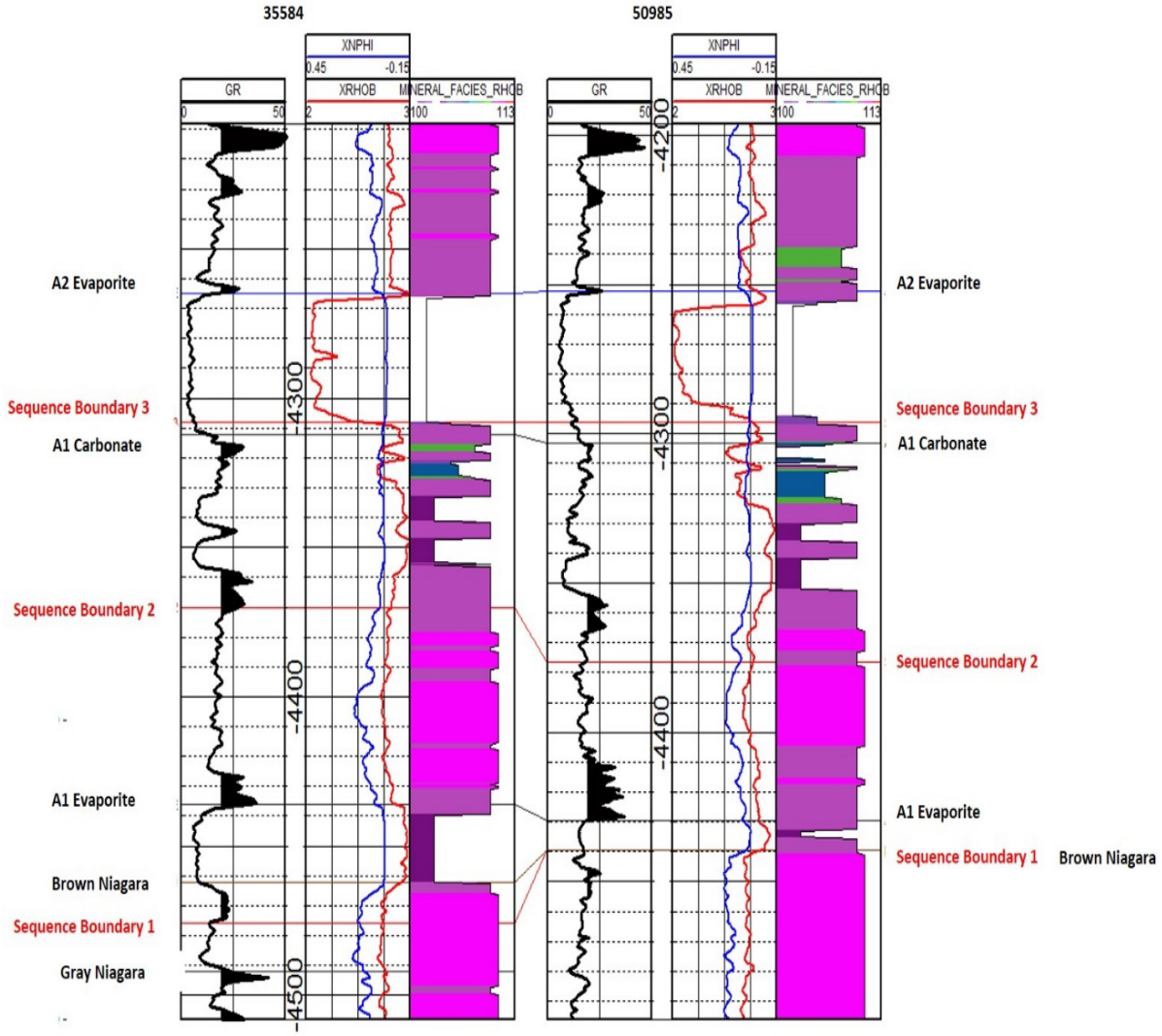


Figure 4-21. Correlation of 3rd order sequences in off-reef well 33584 to Dover 33 flank well 50985 with cross-plot mineralogy. Cross-section datum is the top of Sequence 3.

not part of Sequence 3 deposits.

The most difficult vertical well in Dover 33 to correlate was the reef-top Lawnichak-Myskier 1-33 (UID #29565). Whereas off-reef wells and flank wells have fairly distinctive well signatures (e.g., A-1 anhydrite, aggradational beds, Rabbit Ears anhydrites), wells in the reef center have fewer distinctive signatures and fewer correlation markers. The descriptions by Noack (2008) of core and facies offsets in the closest well with described core, the State Charlton 1-4 well (Otsego County) were crucial to establishing the confidence of the third-order sequence boundary interpretations. Noack identified significant facies offsets as sequence tops in her cored wells, but did not correlate her four sequence boundaries to any published sequences, and did not identify them as to level (fourth- or third-order). However, her detailed foot-by-foot core descriptions, along with her specific and general lithofacies descriptions (e.g., lagoonal grainstones, anhydrite), allowed us to correlate her boundaries to our reef center well log and to

our flank wells where we had greatest confidence in the identification of sequence boundaries and key lithologies. Noack's described lithofacies and facies offsets were verified during the February 12-13, 2014 core workshop at the Michigan Geological Repository for Research and

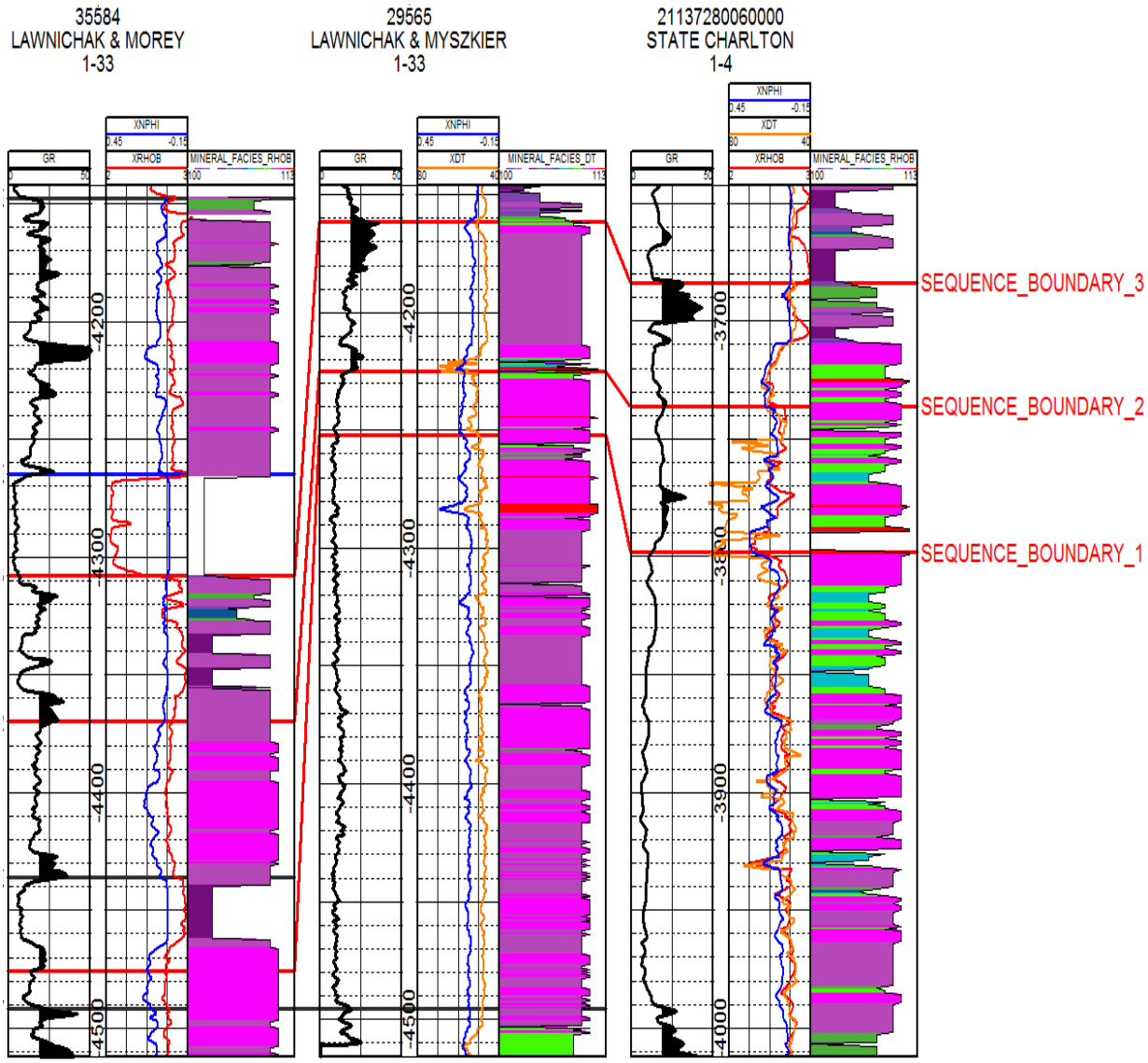


Figure 4-22. Third Order Sequence correlation of the Dover 33 off-reef 35584 well (left) to the Dover 33 29565 reef-center well (middle) and to the State Charlton 1-4 cored well in Otsego County (right).

Determination of sequence boundaries in the State Charlton 1-4 is based on review of Noack's descriptions and examination of the core by Battelle at the MGRRE core facility.
Note the greater abundance of calcareous (limey) dolomite at the State Charlton well.

Education (MGRRE). The resulting correlation of the Charlton 1-4 and the Lawnichak- Myskier 1-33 (Dover 33 reef top well 29565) is shown in Figure 4-22.

4.4.5 Summary of Interpreted Sequence Boundaries

We generally accept the methodology, lithofacies descriptions, and major stratigraphic interpretations of Ritter (2008) but disagree with her placement of the top of Sequence 2 in off-

reef deposits, as well as more minor details on her boundaries of 4th and 5th order cycles. Of the published authors that have described core from the Niagarann reefs, Huh's (1973) work represents the most complete and most detailed evaluation of lithofacies, and in this study we shift some of Ritter's third order off-reef sequence boundaries to better match Huh's lithofacies offsets, as follows. Comparisons with Ritter (2008) are shown in Figure 4-23.

- In this report, we place the off-reef top of Sequence 1 to coincide with the unconformity between the reef conglomerate facies and the overlying A-0 Carbonate, as described by Huh (1973). In practical log correlation, we place the boundary at the base of the A0 Carbonate.
- We place the top of Sequence 2 (the base of Sequence 3) in off-reef wells at a log marker in the State Kalkaska 3-22, just below the onset of Huh's pelletoidal wackestone lithofacies, which he states has a down-lapping relation onto the underlying sediments. We correlate this log marker to the off-reef wells at Dover 33 but note that additional regional data may change the vertical location of this marker.
- We place the on-reef top of Sequence 1 at 6402 ft, and the top of Sequence 2 at 6331ft in the Kalkaska 1-22 (28676), based on examination of core and logs at the MGRRE facility, February 2014.
- A comparison of the pick of the top of our Sequence 1 boundary in the Jahn #4 well is shown on Ritter's (2008, p. 246) cross-section in Figure 4-23. We do not have any basis at this time for identifying the base of Sequence 1 in Dover 33 well logs.

- The off-reef and on-reef assignment of the top of Sequence 3 in this study follows Ritter (2008), and coincides with the top of the A-1 Carbonate.

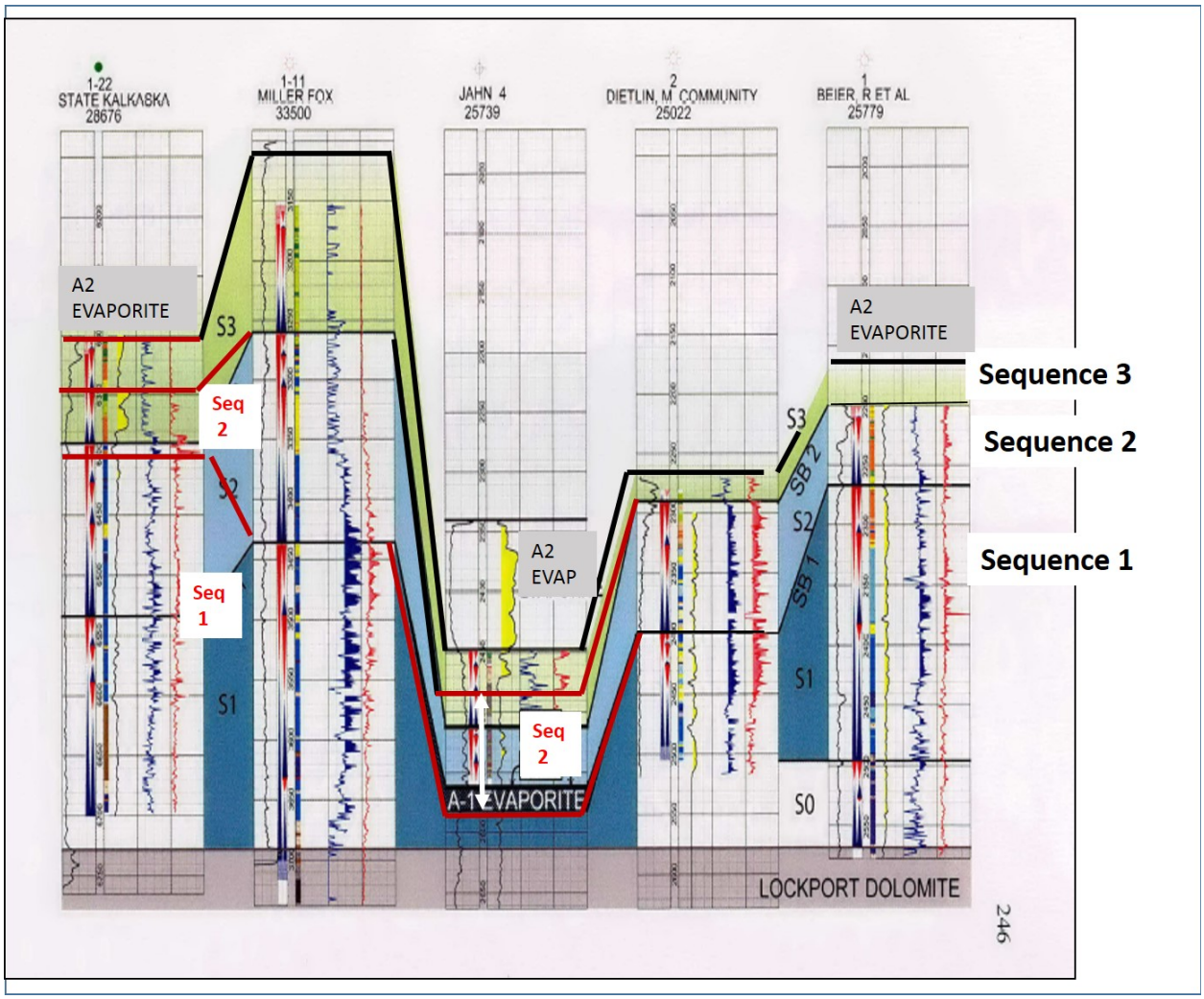


Figure 4-23. Comparison of on-reef and off-reef sequence interpretation of Ritter (2008) and current study (red).

Ritter interprets a thin black shale in the Jahn #4 core as a facies offset and the base of the third-order Sequence 3 genetic package. We interpret the same lithology change as a maximum flooding zone within Sequence 2, and mappable across much of the basin. Ritter places her top of Sequence 1 and 2 on-reef boundaries to be in agreement with Huh (1973). We concur, although the magnitudes of breaks identified in intertidal facies in on-reef core are difficult to establish if not accompanied by karst features.

4.5 Lithofacies Interpretation in the Absence of Core

Interpretation of carbonate lithofacies and depositional environments from only wireline logs presents a challenge but has a long history of “electrofacies” development and calibration (Serra and Abbott, 1980; Zimmerie, 1995). For the northern Michigan Silurian reefs, lithofacies interpretation is greatly simplified by the distinct stratigraphic and third-order, sequence-specific depositional environments and the resulting limited range of lithofacies that developed within each sequence. Because the Niagarann reefs exhibit distinct fauna and lithologies related to extreme changes in environmental conditions through time, many lithofacies are confined to a

particular part of the stratigraphy. For example, anhydrite cemented microbial (algal mat) lithofacies have not yet been described by recent studies of Sequence 1 lithofacies of the

northern reefs (although they could exist); and marine conditions and water depths did not fully reestablish to produce either below-wave-base muddy bioherm or normal reef framework lithofacies on reef tops, after the Sequence 1 sea level drop.

Lithofacies descriptions from Grammer's students (Ritter 2008; Noack, 2008; Grammer et al., 2010) and from Huh (1973) and Huh et al. (1977) were captured in a cross-walk spreadsheet to determine equivalency of lithofacies identified by these authors for the northern reef trend. The resulting 52 lithofacies (not shown) were combined where apparently equivalent, and were then subdivided by sequence, lithology (e.g., dolomite or limestone or anhydrite/carbonate) and dominant biota. Core descriptions and matching porosity/permeability data (as detailed in the respective theses) were examined on a foot-by-foot basis for Ritter's (2008) five wells (Figure 4-23) and for the State Charlton 1-4 well by Noack (2008). It was important to assign these lithofacies to our updated sequence assignments. Lithofacies within a given sequence were merged if they could not be distinguished by log character or mineralogy/computed lithology (for example, stromatorporoid coral framestone versus tabulate coral framestone, or anhydrite-cemented brecciated cyanobacterial mats versus anhydrite-cemented stromatolites). Porous lithofacies described by Grammer's students were each subdivided into low (<7%), medium (7-15%) and high (>15%) measured core porosity, as recorded in MGRRE whole core porosity/permeability data tables. This process resulted in 15 lithofacies (Figure 4-24). Two

Color	Lithofacies	Description	Occurrence
	8B	Reef flank conglomerate	Reef Flank SEQ1
	7A	Nodular or bedded anhydrite	Off-reef, on-reef SEQ 2 and SEQ3
	6B	Algal boundstone (non-anhydritic)	On or off-reef, SEQ 2 and SEQ 3; also below A1 Evaporite SEQ2
	6Bd	A0 algal laminated carbonate	Off-reef, SEQ2
	6C	Algal pelletal dolowackestone	On and off-reef, SEQ3
	6Ca	Anhydritic algal pelletal or stromatolitic boundstone	On and off-reef, SEQ 3
	6Cb	Off-reef laminated mudstone	Off-reef SEQ2
	6Cc	Off-reef fine micritic mudstone	Off-reef SEQ2
	4	Non-reefal packstones and grainstones; porosity <7%	On-reef SEQ2
	4A	Non-reefal packstones and grainstones; porosity >7%	On-reef SEQ 2
	4B	Non-reefal packstones and grainstones; porosity >15%	On-reef SEQ2
	3C	Reef-associated skeletal wackestone, packstone, and rudstone; porosity <7%	On-reef SEQ1
	3D	Reef-associated skeletal wackestone, packstone, and rudstone; porosity >7%	On-reef SEQ1
	2	Muddy bioherm: wackestone to mud-rich packstone	On-reef SEQ1
	1	Deep platform carbonate mudstone to wackestone	SEQ1

Figure 4-24. Upscaled sequence-restricted lithofacies.

Descriptions of lithofacies from cored analog reefs were grouped and assigned to this upscaled classification. The names of the lithofacies, when applied to the Dover 33 wells, are similar to "electrofacies" and represent the most likely rock fabric and biota, based on stratigraphic position and core from analog wells.

Sequence 1, reef framework lithofacies, 3A and 3B were initially separated in modeling, but were later grouped into the upscaled Lithofacies 3C or 3D, depending on their porosity.

These lithofacies (except for anhydrite [Lithofacies 7A], and anhydritic algal boundstones [6Bd, 6B, and 6Ca]) are unique to individual 3rd order sequences. Bedded/nodular anhydrite (Lithofacies 7A) occurs in the interpreted low stand of Sequence 2 off reef (the A-1 anhydrite) and in the off-reef and flank wells of Sequence 3 (the Rabbit Ears Anhydrite). Anhydrite also occurs as a thin bed in Sequence 3 in the on-reef core of the State Charlton 1-4 well where it appears to correlate to the Rabbit Ears Anhydrite. Anhydritic algal mat (boundstone) lithofacies were reported by Huh (1973) below the A-1 Evaporite in Sequence 2 in off-reef lithofacies and on-reef in rocks belonging to Huh's Tidal Flat Stage (Sequence 3). Ritter (2008) reports algal boundstone lithofacies from the upper part of Sequence 2 in the Miller Fox 1-11 in Oceana County.

The upscaled, sequence-specific lithofacies of the cored reefs (and "electrofacies" of the Dover 33 wells) are as follows, generally from deeper water environments of deposition to more shallow environments:

Below Wave Base Sequence 1

Lithofacies 1: Log character similar to that near the base of Sequence 1 in the on-reef Kalkaska 1-22 and the State Charlton 1-4. Depositional environment as interpreted in core of analog wells: deep platform carbonate mudstone to wackestone.

Lithofacies 2. Log character similar to lower part of Sequence 1 in Kalkaska and State Charlton analog wells, above lithofacies 1. Corresponding log character shows slightly more porosity and cleaner gamma than underlying interval. Rock texture and depositional environment as interpreted by Ritter and Noack for cored intervals in the Kalkaska and State Charlton wells: wackestones and packstone textures indicating various low energy, below-wave-base bioherm sub-environments.

Within-wave-base Sequence 1

Lithofacies 3: Dolomites of Sequence 1 with relatively clean gamma ray, occurring above lithofacies 2. Interpreted to be reef-associated in Dover 33 wells, based on stratigraphic position.

Lithofacies 3A: Dolomitic reef framework corresponding to Ritter's Lithofacies 3. Statistically analyzed separately, but not sufficiently distinct; later grouped in Lithofacies 3C or 3D, depending on porosity.

Lithofacies 3B: Bioclastic reefal packstones and wackestones (later grouped by porosity in Lithofacies 3C or 3D). This lithofacies group includes Sequence 1 samples of Ritter's Lithofacies 5, lagoonal deposits.

Described lithofacies in cores from correlative positions in the Kalkaska and State Charlton wells include:

Lithofacies 3C: Either cemented/ evaporite-plugged coral/stromatoporoid framestones or muddy reef debris with porosity less than 7%.

Lithofacies 3D: Coral and stromatoporoid framestone, packstones, and wackestones with porosity greater than 7%.

On-Reef Sequence 2

Lithofacies 4: Dolomites of sequence 2. Interpreted as shallow water, normal marine grainstone/packstone/wackestones that lack coral/stromatoporoid framestone and associated

debris, based on core and core descriptions of the KalkaskA-1-22 and State Charlton 1-4 analogs. This group includes Sequence 2 samples of Ritter's Lithofacies 5, lagoonal deposits. Dover 33 Lithofacies 4 includes:

Lithofacies 4: Bioclastic dolomites with porosity less than 7%.

Lithofacies 4A: Bioclastic dolomites with porosity 7-15%.

Lithofacies 4B: Bioclastic dolomites with porosity greater than 15%.

On-Reef and Off-Reef Sequence 3

Lithofacies 6: Dolomites and anhydritic dolomites of Sequence 3. Interpreted as being deposited in tidal flat to very shallow restricted marine environments, based on observed core at MGRRE as well as on core descriptions by Ritter and Noack. Lithofacies include:

Lithofacies 6B: Low-porosity dolomites, non-anhydritic. Most likely biotic components are mix of cyanobacteria and large fecal pellets in Sequence 3. Ritter described minor low porosity cyanobacterial boundstones in the Miller –Fox 1-11 from the upper part of Sequence 2, in addition to the more common occurrences in Sequence 3. This lithofacies is also assigned to the thin, low-gamma-ray non-anhydritic dolomites immediately above the A-0 Carbonate and below the A-1 anhydrite in off-reef Sequence 2.

Lithofacies 6C: "Pelletoidal" packstones and muddy packstones dominated by large (1- to 4-millimeter) oblong peloids (fecal pellets); has some moldic or matrix porosity development. Huh (1973) states this lithofacies occurs only in his Tidal-Flat Reef Stage (= Sequence 3)

Lithofacies 6Ca: Anhydritic cyanobacterial boundstones/breccias and anhydritic algal/peloidal wackestones and packstones. Generally have very low porosity. These are the uppermost lithofacies in Sequence 3, both on-reef and off-reef.

Reef-Flank Sequence 1

Lithofacies 8B**:** Reef debris conglomerate. Not observed in either the Kalkaska or the State Charlton well; based on log signature and stratigraphic position below the higher-gamma-ray log signature of the A-0 Carbonate. Because this lithofacies has porosity development in some logs, it does not appear to be carbonate wackestones shed from adjacent below-wave-base muddy bioherms. It may be reef talus shed during growth of Sequence 1 reef framework; the uppermost part could be reef breccia, but we have no way to confirm this.

Off-Reef and Reef-Flank Sequence 2

Lithofacies 6: Dolomites of Sequence 2 in off-reef environments; generally lacking anhydrite. Interpreted as being deposited during low stand, transgressive and reef-top shedding of carbonate. Lithofacies include:

Lithofacies 6Bd: A-0 Carbonate, described by Huh (1973) in the Kalkaska 3-22 off-reef well. Fine-grained carbonate with a relatively high gamma ray signature, occurs below the A-1 anhydrite.

Lithofacies 6Cb: Laminated mudstone immediately above the A-1 Anhydrite in the Kalkaska 3-22 core. Overlies what appears to be a dissolution surface or hiatus on top of the A-1 Anhydrite. Observed in other off-reef wells in the same stratigraphic position to develop "poker chip" partings in fissile, dark gray mudstones.

Lithofacies 6Cc: Fine, micritic mudstone with the characteristic aggradational-stacking wireline log signature in Sequence 2 of the cored Kalkaska 3-22, and easily correlated to the off-reef and flank wells at the Dover 33 reef. Huh (1973) reports that the Tidal-Flat Reef Stage "pelletoidal" lithofacies downlaps onto the upper surface of this lithofacies in the Kalkaska 2-33 off-reef well.

Lithofacies 7A: Nodular and bedded anhydrite, based on log signatures and examination of core in the analog State Kalkaska 3-22 off-reef well at the MGRRE core facility. Occurs bedded as the A-1 Anhydrite, and in nodular form in Sequence 3 in the off-reef and reef flank analog wells as the Rabbit Ears Anhydrite.

After the lithofacies descriptions were reviewed for each sequence in the northern wells that had core studied by Ritter, Noack, and Huh, the cross-plot lithologies were examined for each Dover well and compared to cross-plot lithologies in analog wells with core.

Crossplot lithologies and computer-generated ELAN lithology logs (where available) were compared with the assignment of upscaled lithofacies by sequence. The interpreted lithofacies depths were adjusted to match changes in the cross-plot lithology logs. An example of using the cross-plot porosity/lithology logs to fine-tune depths of upscaled lithofacies is shown in Figure 4-25. The final interpretation of all the logs within the project went through several iterations as details were refined during log correlation and cross section construction; and after the February 12-13, 2014 Joint Partners (Battelle, Core Energy, Western Michigan University) meeting at the MGRRE laboratory, where lithofacies in the cores from the Kalkaska Reef, the Miller Fox 1-11, Jahn 4, and the Charlton 1-4 were examined and compared to the logs from the Dover 33 reef.

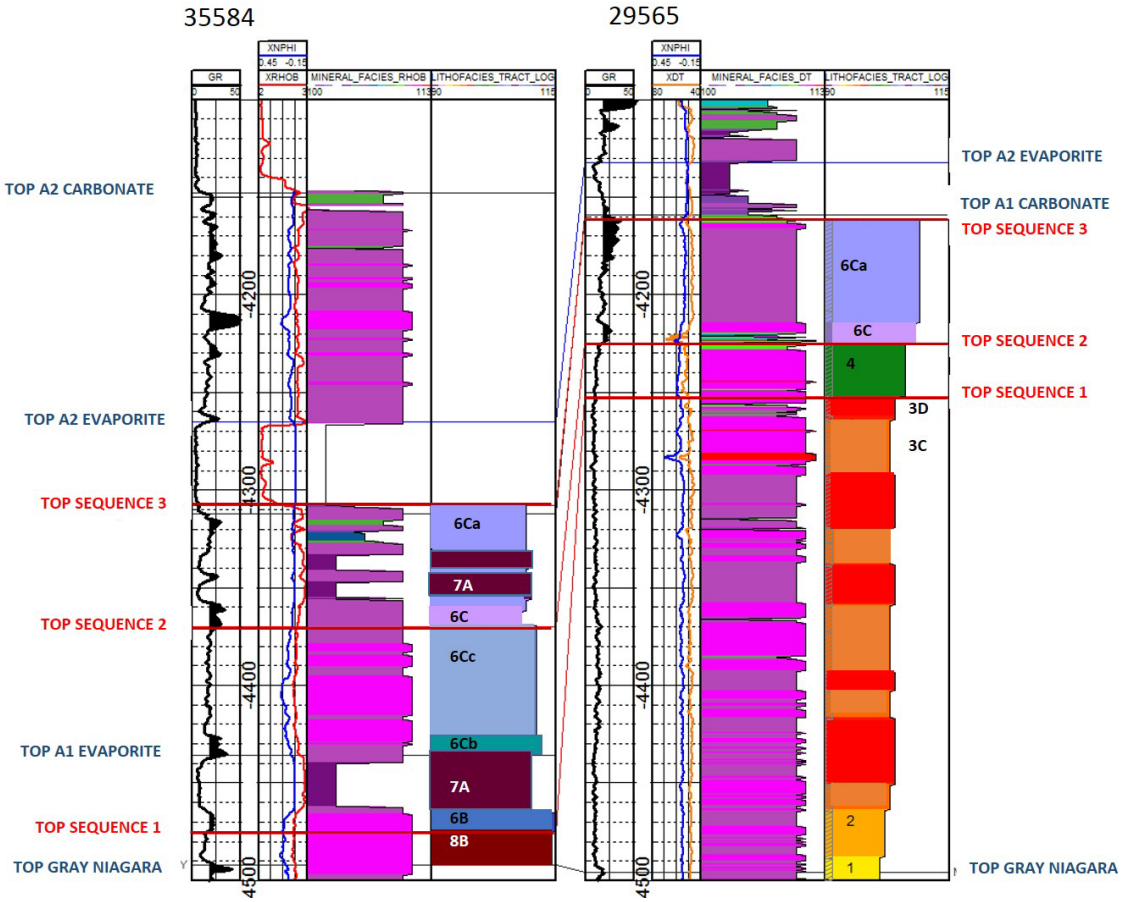


Figure 4-25. Comparison of cross-plot and upscaled lithofacies interpretation logs for an off-reef well (35584) and a vertical central reef well (29565) at the Dover 33 reef. Lithofacies 3A and 3B have been combined with Lithofacies 3Cand 3D, based on porosity.

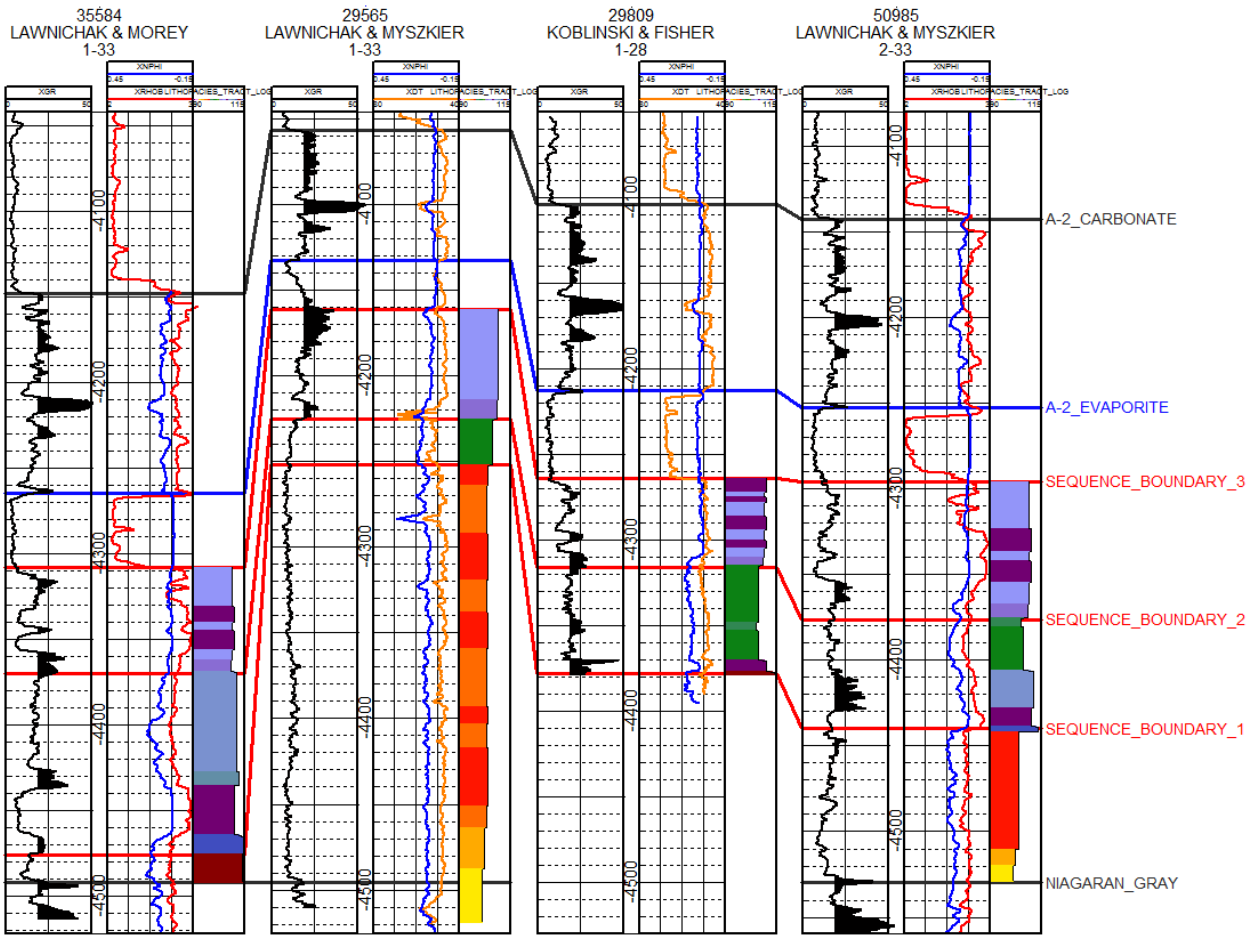


Figure 4-26. Cross section across Dover 33 reef with off-reef (Well 35584), central-reef (well 29585), and reef-flank (wells 29809 and 50985. (See Figure 4-24) for upscaled lithofacies color key).

4.6 Statistical Analysis of Porosity and Permeability

The overall goal of the analysis is to determine whether the wireline log porosity data can be used to predict the permeability in uncored wells with an acceptable level of confidence. Previous studies (Wold, 2008) have shown that the relationship between permeability and log data is likely different between subpopulations of lithofacies, that is, samples from different sequences and depositional environments. The lithofacies used in this analysis are the Battelle upscaled wireline-log based lithofacies (“electrofacies”) in the Dover 33 reef and the upscaled, consistency-checked, core-based lithofacies from wells in the recent (2008-2009) Western Michigan University theses.

Four types of statistical analyses were carried out to justify the level to which log-derived lithofacies can be transformed into permeability.

1. Comparison log-derived and core-analyzed porosity values to determine reliability of relationships between log and core measurements.
2. Comparison of the Dover reef-center Lawnichak and Myszkier 1-33 (29565) log-derived porosity distribution with the MGRRE core-derived porosity distributions to see which reef-center cored wells are most similar to Dover 33.

3. Multivariate analysis of the log curve data from cored wells, along with interpreted sequences, and core lithofacies to see how well the log data conform to previously interpreted lithofacies.
4. Perform a general statistical analysis to evaluate what level of lithofacies subdivision is most robust to transform porosity to permeability.

The details of these analyses are summarized below.

4.6.1 Comparison of Log and Core-derived Porosity/ Permeability Relationships

A comparison of log-based porosity in the Dover 33 main injector with core and log-based porosity and permeability in two recently studied analog wells, the State Charlton 1-4 in Otsego County (Noack, 2008) and in the State Kalkaska 1-22 in Kalkaska County (Ritter, 2008) indicated that porosity ranges were broadly similar in all three wells, and that for the two analog wells, porosity and core-based permeability showed similar trends. However, plots of core-based porosity versus permeability showed considerable scatter for the analog wells around a linear regression line with a correlation of 0.628 and standard error =2.9% in State Kalkaska #1-22, and correlation of 0.642 and standard error =3.79% in the State Charlton #1-4. Thus it appears that a simple transform of non-core-calibrated log porosity to permeability would have considerable uncertainty.

4.6.2 Determination of Best Porosity-Analog Well

Four analog wells (the southern reef wells Beier 25779 and Dietlin 25022, and the northern reef wells State Charlton 1-4 28006 and Miller Fox 1-11 33500) were examined to determine which reef-centered well had a porosity log most similar to the Dover 33 reef-center injector well. The Miller Fox 1-11 (33500) in Oceana County stands out in statistical analyses as having a high number of low-porosity values, unlike the Dover 33 well. The three remaining wells have fairly similar porosity range and frequency distribution (State Kalkaska 1-22 28676, the southern reef well Beier 25779, and the Dover injector 29565). Although the Charlton 1-4 well is the analog well closest in proximity to the Dover 33 reef, the Kalkaska 28676 well porosity range and distribution, particularly that of the Sequence 1 reef core lithofacies, is the most similar northern well to the Dover 33 injector. This finding is used in generating the porosity-to-permeability transform for the Sequence 1 reef interval.

4.6.3 Multivariate Analysis of Analog Data for Sequence and Lithofacies Conformity

The State Charlton 1-4 has the most complete suite of logs. The multivariate analysis of the lithofacies of (Noack 2008), along with sequence stratigraphic interpretation of the State Charlton 1-4 by Battelle provided the data for agglomerative cluster analysis to explore the relation between sequence-constrained lithofacies and wireline log expression. At the coarsest sequence level, there is a correspondence between the log data and the sequence groupings. *In particular, cluster analysis produced individual clusters of lithofacies samples that are restricted to Sequence 1, 2, and 3.* There is also a cluster that contains samples that are similar to each other and that are present in all sequences. From these clustering results, it appears that there is some correspondence between specific sequences and the log data clusters, but at finer levels (i.e., lithofacies and numbered lithofacies), the clusters only identify subsets of similar groupings. We note that statistical analyses of Lithofacies 3A (reef framework) and Lithofacies 3B (reefal packstones, grainstones, and wackstones) were not sufficiently distinct to allow discrimination with wireline logs; thus they were grouped with Lithofacies 3C or 3D, depending on amount of porosity.

The St Clair County southern reef wells Dietlin #2 25022 and Beier et al. #1 25779 (see Figure 4-4) were used in the study to capture reef lithofacies that are rare or not present in the Kalkaska 1-22 28676 and Miller Fox 1-11 33500. Reef flank lithofacies remain under-represented in core data.

In summary, sequence membership greatly reduces the global uncertainty of what lithofacies will occur within a stratigraphic interval; and major depositional environments do produce distinct depositional rock fabrics. However, particularly within Sequence 1 reef core lithofacies, depositional and diagenetic lithofacies produce considerable variation in porosity/permeability relationships, and the uncertainty of lithofacies and associated permeabilities remains high in the absence of core or modern logs.

4.7 Level 2 Model Construction

The level 2 SEM construction involved existing well logs, 3D seismic interpretation of surfaces, and the sequence lithofacies interpretation using Schlumberger's Petrel E&P software platform 2013. The model comprises three sequence horizons and a base horizon of the Gray Niagarann that define three sequence intervals. The Sequence 3 horizon corresponds to the A-1 Carbonate top, and the base is the same as the Level 1 model (Gray Niagarann). This facilitates the final Level 1 and 2 property model comparisons.

The modeling workflow consisted of the following six-step process; 1) build surface grids, 2) construct a 3D structural framework grid, 3) construct a lithofacies model from the lithofacies interpreted logs, 4) construct petrophysical property models conditioned to the lithofacies model, 5) calculate volume statistics for comparison to the level 1 model, and 6) upscale the property models and export for dynamic reservoir simulation. The first three steps are discussed in this section.

4.7.1 2D Surface Grid Construction

The surface construction and wells used in the level 2 SEM are the same as those described in Section 3 for the Level 1 SEM. The main differences between the two models are that the surfaces created in the Level 2 SEM are sequence boundaries, not lithostratigraphic (i.e., formation) boundaries; and that porosity and permeability relations are tied to interpreted lithofacies (electrofacies). The A-1 Carbonate surface was used as a trend surface along with the Sequence 3 tops to create the Sequence 3 upper surface (Figure 4-27), since these surfaces are nearly coincident. This process ensured the bulk volume of the Level 1 and Level 2 models would be similar. The lower surface of the Level 1 and Level 2 SEM, the Gray Niagaran surface, is the same in both models.

The Sequence 3 upper surface was then used as a trend surface to guide the creation of the Sequence 2 upper surface (Figure 4-28) along with the top Sequence 2 picks on the logs. Similarly, the Sequence 2 upper surface was used as a trend surface for Sequence 1 (Figure 4-29). This method of setting surfaces took advantage of the seismic interpretation of the upper surface of the A-1 Carbonate. Using the upper sequence surfaces as trends for the lower sequences created a model that maintains the shape of the general reef structure over the steep flanks of the reef and avoids crossing horizons away from the well data. Some manual manipulation of the final surfaces was needed to smooth the outer corners of the surfaces.

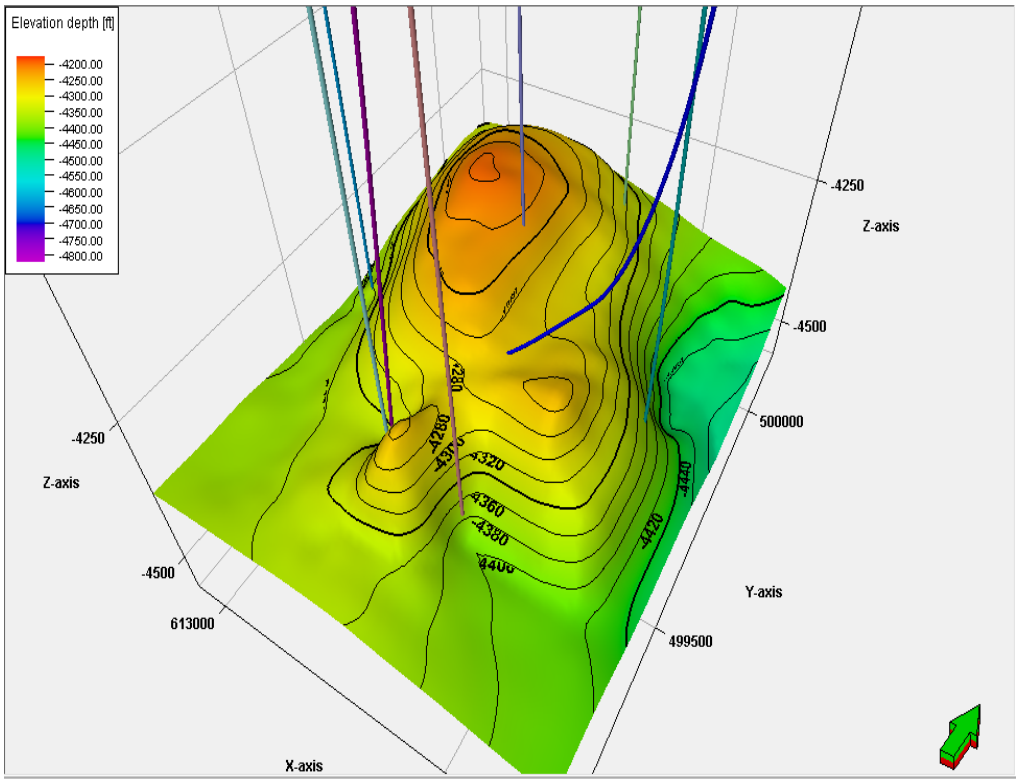


Figure 4-27. Sequence 2 upper surface (contour interval = 20 feet).

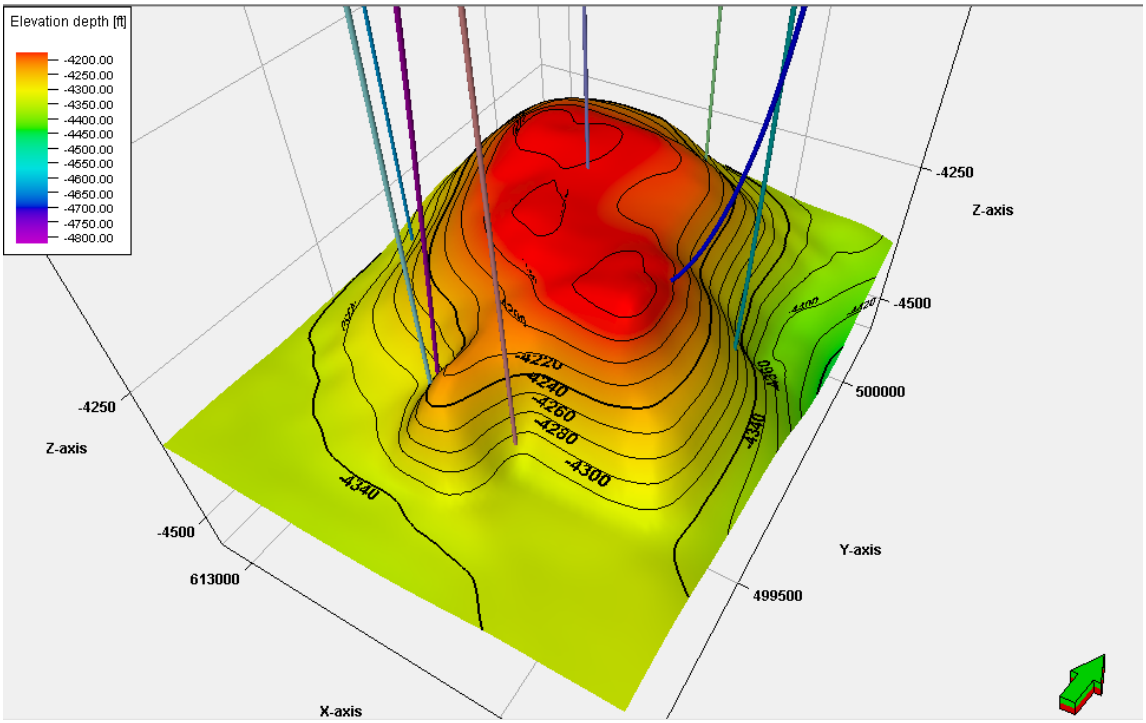


Figure 4-28. Sequence 3 upper surface (contour interval = 20 feet).

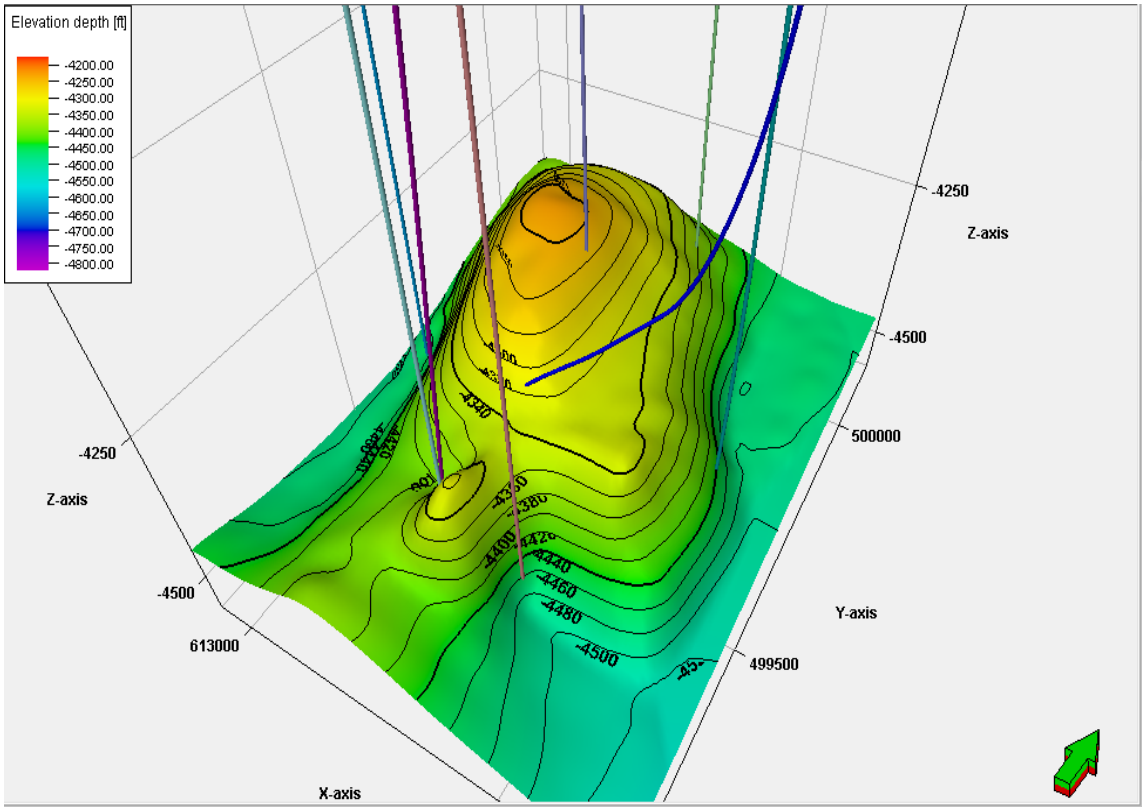


Figure 4-29. Sequence 1 upper surface (contour interval = 20 feet).

4.7.2 3D Structural Modeling

The process for Level 2 structural modeling was basically identical to that for the Level 1 model, and differs only in minor details. The structural model of the Level 2 model consists of 3 zones and 60 layers, including: 30 layers in Zone 1 (Sequence 1), 15 layers in Zone 2 (Sequence 2), and 15 layers in Zone 3 (Sequence 3). This layering scheme was implemented to provide approximate 5-foot thick layers within the center of the reef and the majority of the layers in Sequence 1, which represents the main episode of reef framework growth, and is nearly equivalent to the Brown Niagaran. Layers in Sequence 1 are built from the bottom and are truncated by the unconformable surface at the top of Sequence 1. Layers in Sequence 2 and 3 are built from the bottom, and are proportional, allowing for the variable thickness of lithofacies on the reef top and flanks. This zone, layer, and layer configuration accentuates the growth stages during Sequence 1, and separates the capping facies on the top and flank of the reef in Sequence 2 from the sealing and inter-reef basin infill during Sequence 3 (Figure 4-30).

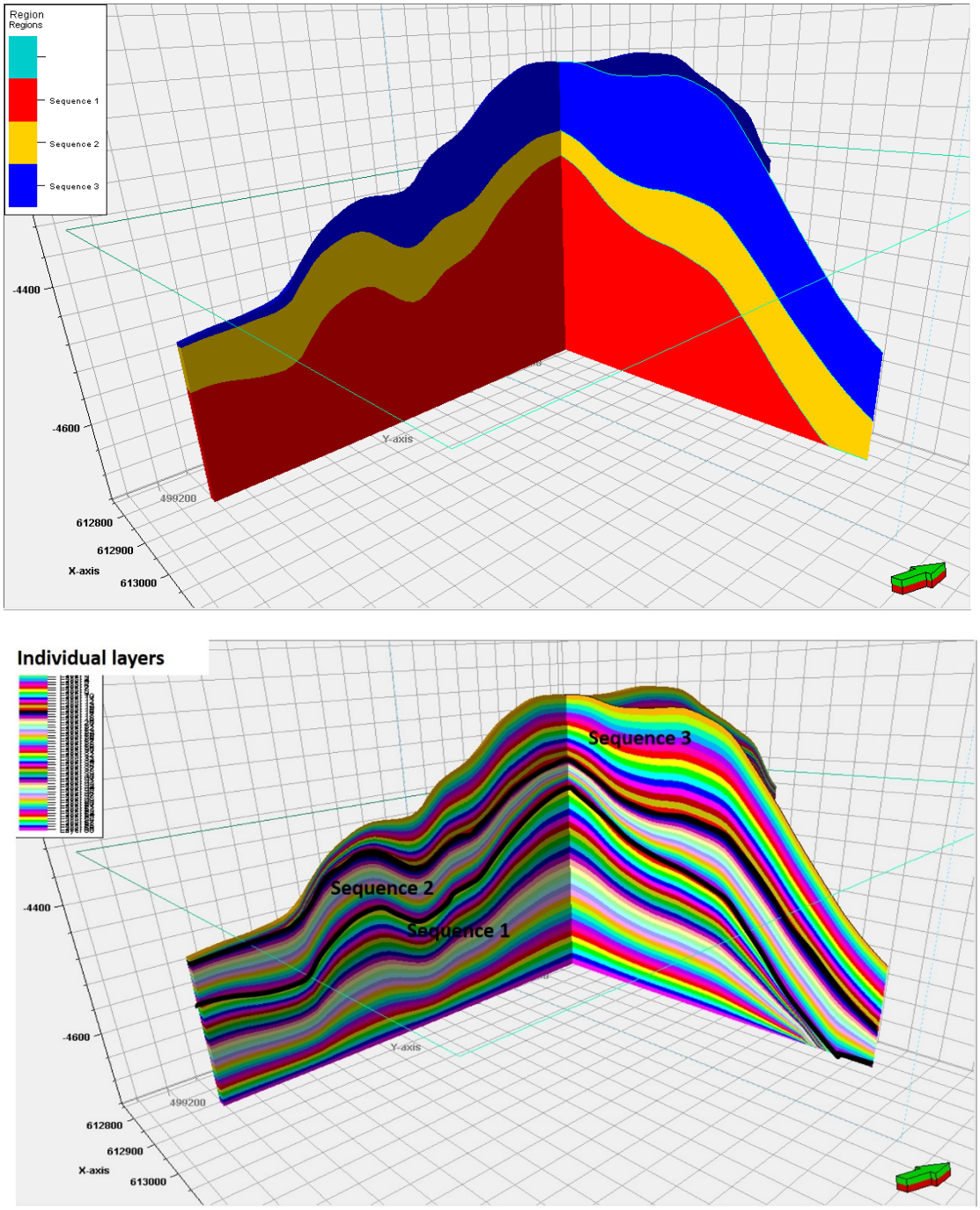


Figure 4-30. Zones (Upper) and upscaled layers (Lower) corresponding to the stratigraphic sequences in the Level 2 SEM.

The final grid includes 77 x 104 x 60 cells. View to the northwest.

4.7.3 Lithofacies Model Construction

The lithofacies model construction is an integral step in the creation of the Level 2 model. The lithofacies distribution within the three sequences is used to condition (i.e., distribute) the porosity and permeability properties within the reef model. The lithofacies model provides a powerful interpretative tool to visualize the important depositional framework of the reef, and the ability to modify small geobodies, or distinctly separate reservoir units, during the iterative static-dynamic modeling process.

Lithofacies Variogram Analysis

The lithofacies logs were imported into Petrel and upscaled in the structural grid. The general variograms were reviewed for the lithofacies on a sequence-by-sequence basis; the variogram analysis is similar to the methodology described for the much more generalized two layers of the Level 1 model. Based on the Level 1 results, the major axis for the Level 2 variogram analysis was set at 330 degrees to provide an identical search cone that is oriented along the slightly northwest-southeast elongated axis of the Dover 33 reef. After an initial generation of the model using the variograms created from the data analysis, it became apparent that some manual manipulation of the variograms is needed for the Level 2 construction, because off-reef Sequence 2 lithofacies were being carried into the reef. The final variogram values are shown in Table 4-1 and Table 4-2.

Table 4-1. Sequence 1 variogram final values.

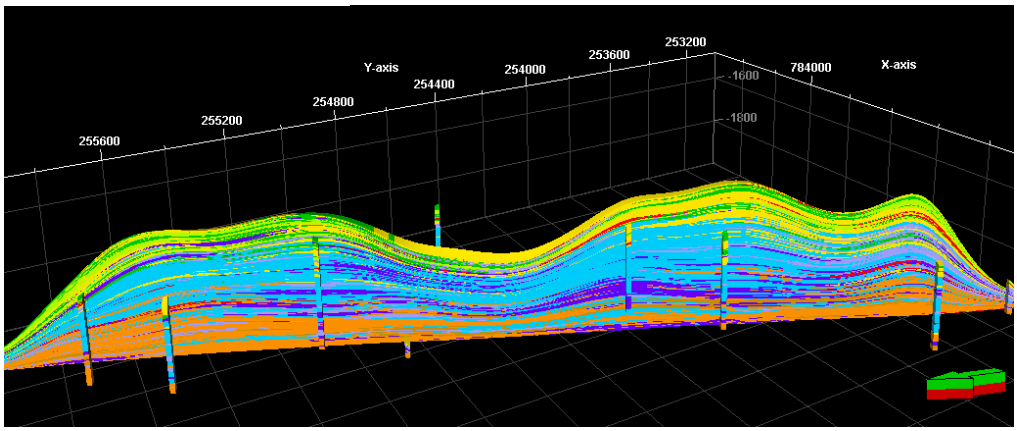
Discrete Layer Number	Facies		Major	Minor	Vertical
SEQUENCE 1					
101	1		393	267	46
102	2		398	267	73
103	3D		551	500	16
104	3C		467	449	34
113	6B		400	270	26
114	8B		100	100	30
115	6Bd		200	200	46

Table 4-2. Sequence 2 and Sequence 3 variogram final values.

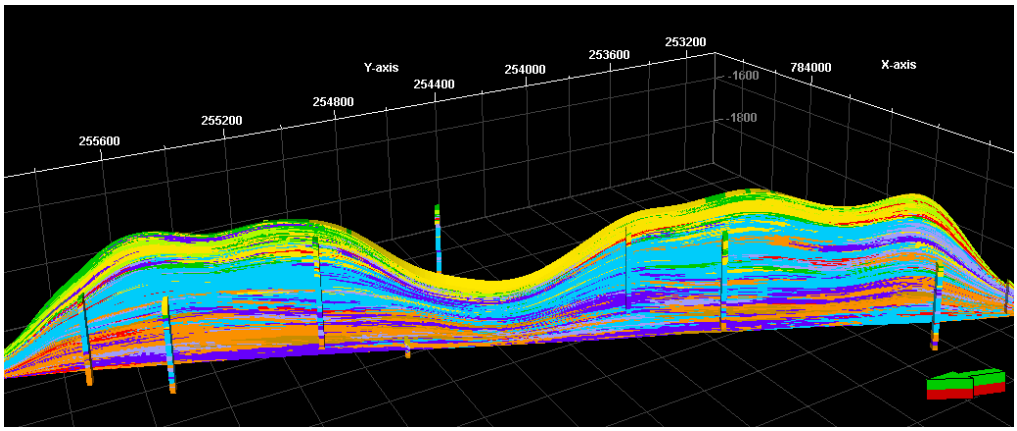
Discrete Layer Number	Facies		Major	Minor	Vertical
SEQUENCE 2					
105	4		344	255	37
106	4A		342	342	52
107	4B		267	251	46
108	6C		376	267	45
109	6Ca		344	270	44
110	7A		490	490	44
111	6Cc		398	398	56
112	6Cb		390	363	37
113	6B		395	267	36
114	8B		384	376	43
115	6Bd		380	380	42
SEQUENCE 3					
108	6C		435	375	45
109	6Ca		468	468	26
110	7A		707	666	30

Qualman (2009) investigated the effect of using different variograms with different correlation lengths on modeled lithofacies distribution within stratigraphic sequences at the Belle River Mills Field in St Clair County, Michigan (Qualman 2009; see location in Figure 4-4) used correlation distances of 50, 500, and 1,000 feet for the variogram major and minor axes (Figure 4-31) and concluded that the 500-foot variogram represented the most geological sound model based on the well spacing of 1,000 feet within the field. For the Dover 33 Level 2 SEM, separate variograms were used for different lithofacies to provide a more fine-tuned approach, where the geology provides an understanding of the general correlation distances of the lithofacies. For example, the off-reef lithofacies 7A (anhydrites) in Sequences 2 and 3 can be correlated on logs over longer distances; thus, a larger correlation distance was used for this lithofacies.

(A) 1,000-foot variogram



(B) 500-foot variogram



(C) 50-foot variogram

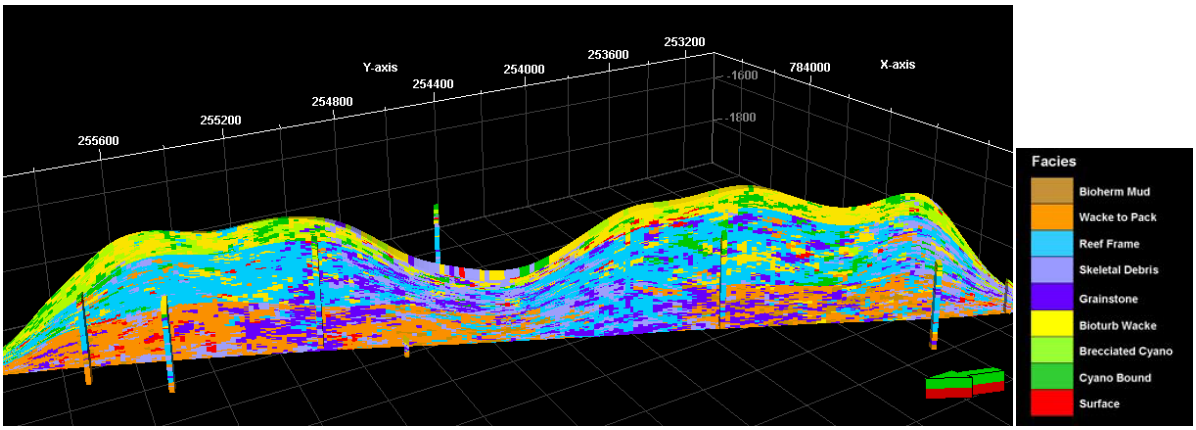


Figure 4-31. Facies models from Qualman (2009) with 1,000-foot (A), 500-foot (B), and 50-foot (C) variograms.

Lithofacies Model Population

The lithofacies model (Figure 4-32) was populated in Petrel using independent indicator kriging for each of the three zones, and using the variograms described in Table 4-1 and Table 4-2 for the lithofacies in each zone (sequence). As described above with the variogram analysis, the process was iterative, in which several models were generated and reviewed to ensure that the geologic progression upward in the sequences was maintained and that the lower Sequence 2 off-reef lithofacies do not extend across the top of the reef. The final model preserves more realistic in some details such as the Sequence 3 “Rabbit Ears” anhydrite interfingering with Sequence 3 reef top anhydritic facies; the A-1 anhydrite lapping onto the reef flanks; and the building of the reef core (Figure 4-33). One detail that is not accurate is that the very thin Sequence 2 Lithofacies 6BD (the A0 Carbonate) is shown as being part of the Sequence 1 reef.

A noteworthy relationship that stands out is the Sequence 2 Lithofacies 4A on-reef Capping Grainstones “spilling” off the eastern side of the reef. This has further implications in the property models because porosity is created in the lower flanks of the reef wedged between anhydrites above and below. This issue is discussed further below.

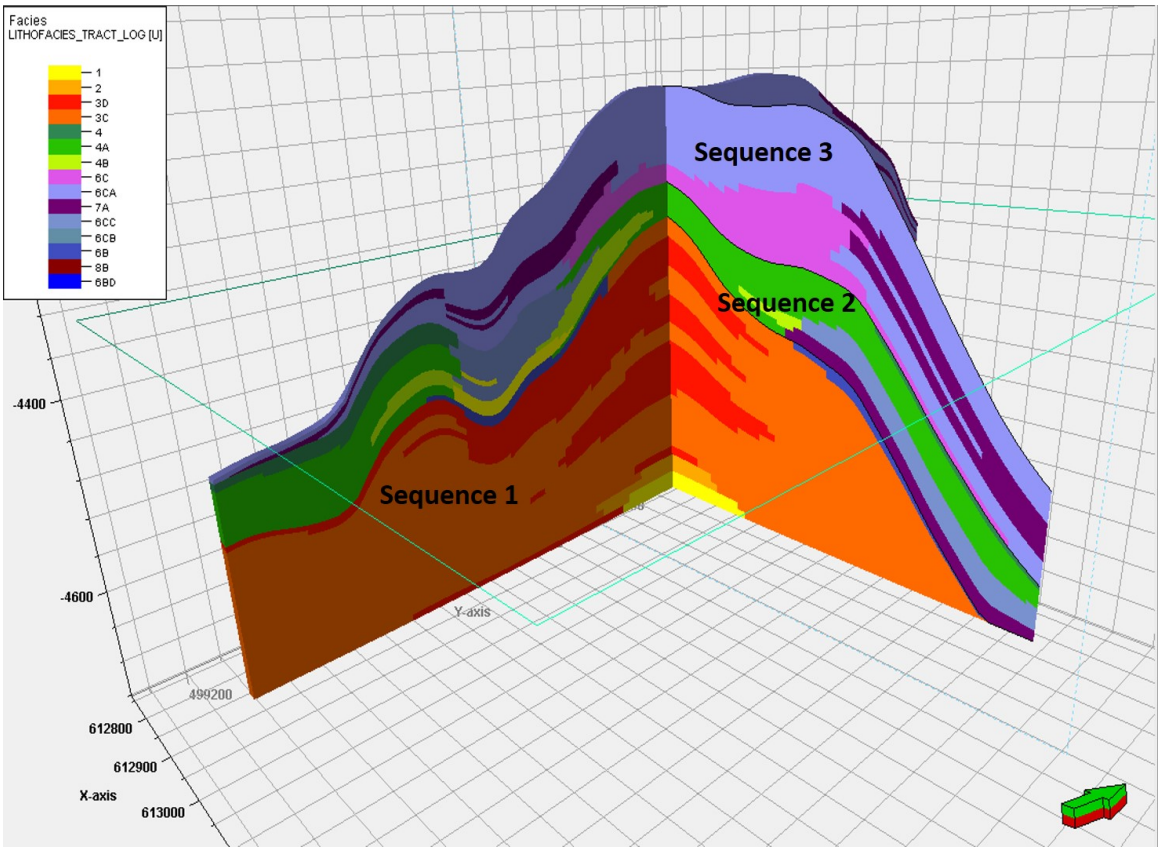


Figure 4-32. Lithofacies model for the Dover 33 reef. View to the northwest.

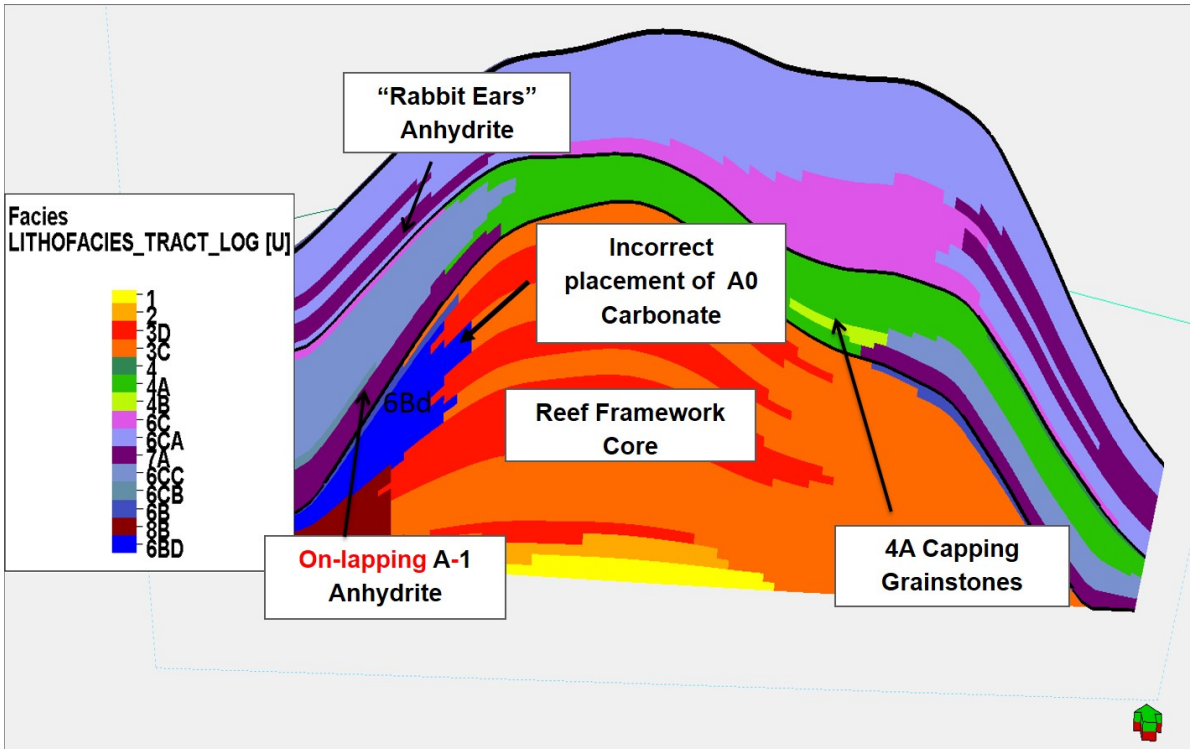


Figure 4-33. Lithofacies detail on a west-to-east section (green arrow pointing north) showing details such as the "Rabbit Ears" Anhydrite, the A-1 Anhydrite lapping onto the reef flanks, and the building of the reef core.

Porosity Model Construction and Population

The porosity model was created by conditioning (connecting) the corrected porosity logs to the corresponding lithofacies assignments in the model. The same porosity logs that were used to construct the Level 1 porosity model were used to construct the Level 2 porosity model. However, new porosity variograms had to be developed for the Level 2 porosity model. As with the Level 1 porosity model, kriging was used to calculate a porosity value for each cell in the 3D grid. The Level 2 porosity model (Figure 4-34 and Figure 4-35) shows a more complex relationship along the flanks of the reef between reservoir and seals than the Level 1 model. The importance of the spatial distribution of the lithofacies is apparent when comparing the porosity model to the lithofacies model (Figure 4-34 and Figure 4-32). This modeling approach of conditioning to the lithofacies results in having the option to iterate after the dynamic models are run to see which lithofacies are potentially most critical to reservoir performance.

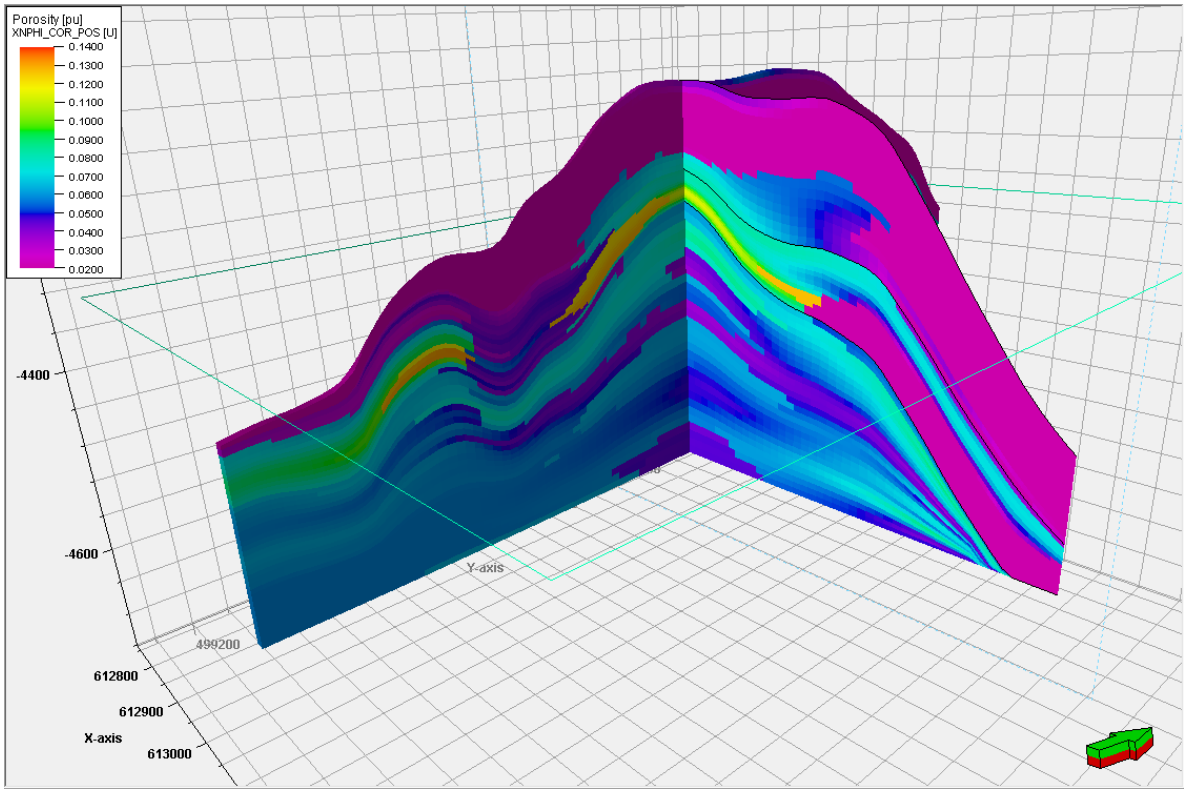


Figure 4-34. Porosity model of the Dover 33 reef. View to the northwest.

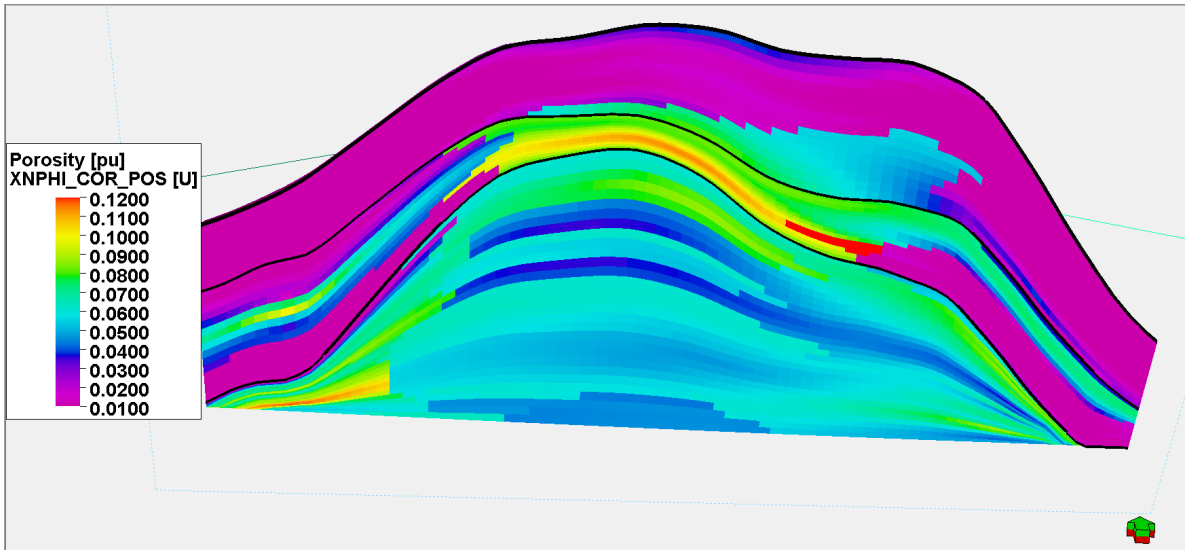


Figure 4-35. Porosity model on west-to-east section (green arrow pointing north).

Permeability Model Construction and Population

A 3D permeability model was created using the porosity-permeability transforms for the numbered lithofacies groups defined in Table 4-1 and Table 4-2 and the kriged porosity value for each individual cell. Porosity and permeability cross-plots of various well and lithofacies groupings were used to select final subdivisions to transform porosity to permeability in the Level 2 model. The individual lithofacies were grouped due to limited permeability data on the individual lithofacies. For the reef framework (Sequence 1), a porosity-permeability transform was used that is based on data from a single well because each well has a distinct diagenetic overprint that produces a large amount of scatter. The State Kalkaska 1-22 (28676) is considered to be the most representative of the reef framework lithofacies and therefore was used to define the transform for the Sequence 1 reef framework. For the other lithofacies groups, porosity-permeability transforms on data subdivided by lithofacies with input data from all five analog wells were used (Table 4-3).The transform used for Group (and Lithofacies) 7, which is anhydrite, does not have permeability values from core; therefore, the transform for Group 6 was used for 7 since these groups are most alike.

Table 4-3. Permeability transforms for grouped Level 2 lithofacies.

Description of group	Numbered lithofacies	Transforms
Reef	3	Log(k)= -0.1217+0.1698(100* ϕ)
Deep platform	1	Log(k)= -0.3027+0.1227(100* ϕ)
Muddy bioherm	2	Log(k)= -0.3264+0.1951(100* ϕ)
Non-reefal skeletal	4	Log(k)= -0.2441+0.1504(100* ϕ)
Anhydritic carbonates	6	Log(k)= -0.2342+0.1272(100* ϕ)
Anhydrite	7	Log(k)= -0.2342+0.1272(100* ϕ)

The final permeability model (Figure 4-36) is similar to the porosity model in that it accentuates the distribution of the lithofacies in the reef and shows a more complex relationship along the reef flanks as compared to the Level 1 model.

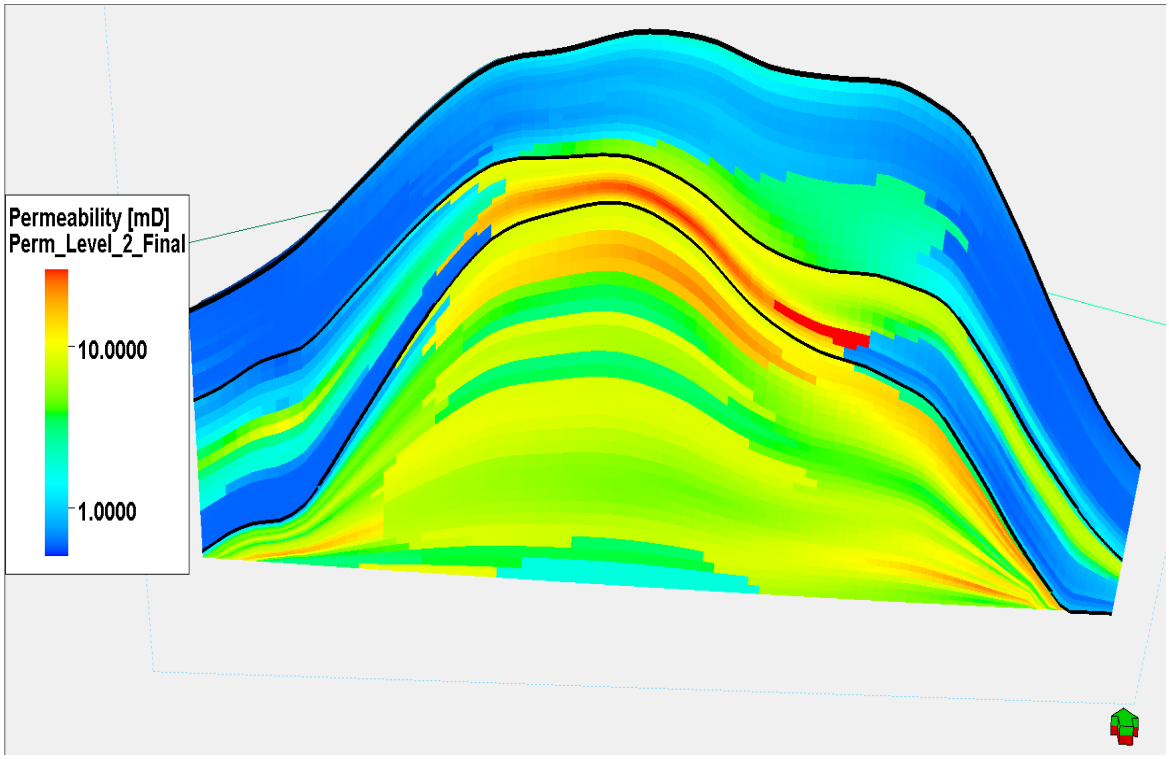


Figure 4-36. Level 2 permeability model on west to east section (green arrow pointing north).

Chapter 5. Model Comparisons and Statistical Review

The overall goal when creating the Level 1 lithostratigraphic and Level 2 sequence stratigraphic models is to determine the level of detail needed to more robustly describe the Niagaran Reef geology. While the models were constructed from the same seismic and log data, different outcomes were achieved through the two approaches. Since there is a much greater time effort involved in creating the sequence stratigraphic interpretation necessary for the Level 2 model, the following section compares the two models in regard to difference in volumetrics, and apparent usefulness for dynamic modeling and for exploration or storage estimation in reefs to be developed.

5.1 General Statistics

The general statistics for the two models are tabulated in Table 5-1 through Figure 5-5. The original Level 1 and Level 2 models have 10- x 10-meter grids with 76 and 60 layers, respectively. The upscaled models have 30- x 30-meter grids with 46 and 40 layers (Table 5-1). The objective in upscaling the models is to converge the layers and bulk volumes on the two models so they were similar in final construction to eliminate layers and volumes as variables for comparison. The final total bulk volume for the two models (1,912,541,601 vs 1,863,934,376 ft^3) varies by 2.5%, mainly due to the upper surface difference (Table 5-2).

The mean porosity values for the Level 1 and 2 models before upscaling are both 4.5% (Table 5-3). When the models are upscaled, the mean porosity for the Level 1 model decreased to 3.9%, while the Level 2 mean stayed at 4.5%. The Level 2 model has less overall smoothing and preserves the values on the high and low end due to the lithofacies conditioning used in the model construction. The total pore volume in the upscaled Level 2 model (75,648,665 ft^3) is 8.9% higher than the Level 1 model (81,255,204 ft^3) (Table 5-4). Again, the conditioning to lithofacies within the sequences has distributed the thin, high-porosity zones on the logs further out into the reef and restricted smoothing.

The permeability differences between the two models follow similar trends to the porosity: the Level 2 model has higher values than the Level 1 model (Table 5-4). The lithofacies permeability transforms used in the Level 2 model have also created a broader range of values within the final upscaled model, 0.6 to 52.9 mD for Level 2 compared to 0.1 to 22.2 mD for Level 1 (Table 5-3). The single transform used in the Level 1 model has a smoothing effect that provides less flexibility. In the Level 1 model, the permeability values can only be scaled up or down as a whole, while the Level 2 model provides the opportunity to adjust the permeabilities for individual lithofacies to see which portions of the reefs have the largest effects.

Table 5-1. Level 1 and 2 model dimensions.

Grid Dimensions						
Model	Grid cells (nI x nJ x nGridLayers) (#)	Horizons (#)	Zones (#)	3D Grids Cells (#)	Layers (#)	Grid Size (meters)
Level 1	77 x 104 x 76	3	2	608,608	76	10 x 10
Level 1 Upscaled	25 x 34 x 46	3	2	39,100	46	30 x 30
Level 2	77 x 104 x 60	4	3	480,480	60	10 x 10
Level 2 Upscaled	25 x 34 x 40	4	3	34,000	40	30 x 30

Table 5-2. SEM Level 1 and 2 volume statistics.

4.23			
Model	Bulk Volume (cubic feet)	Pore Volume (cubic feet)	Ave Porosity PU
Level 1 Total	1,968,424,516	76,969,200	0.039
Level 1 Zone 1	1,041,569,122	19,116,058	0.018
Level 1 Zone 2	926,855,394	57,853,115	0.062
Level 1 Upscaled total	1,912,541,601	75,648,665	0.039
Level 1 Zone 1	993,684,818	18,304,831	0.018
Level 1 Zone 2	918,856,783	57,343,834	0.062
Level 2 Total	1,917,099,397	83,036,401	0.043
Level 2 Zone 1	519,305,677	6,778,891	0.013
Level 2 Zone 2	543,680,668	26,302,516	0.048
Level 2 Zone 3	854,113,052	49,954,994	0.058
Level 2 Upscaled Total	1,863,934,376	81,255,204	0.044
Level 2 Zone 1	499,367,261	6,660,572	0.013
Level 2 Zone 2	521,182,102	25,300,505	0.048
Level 2 Zone 3	843,385,013	49,293,827	0.058

Table 5-3. SEM Level 1 and 2 porosity statistics.

Porosity PU			
Model	**Mean**	**Min**	**Max**
Level 1 Total	0.045	0	0.152
Level 1 Zone 1	0.019	0	0.103
Level 1 Zone 2	0.062	0	0.152
Level 1 Upscaled Total	0.039	0	0.108
Level 1 Zone 1	0.019	0	0.096
Level 1 Zone 2	0.063	0	0.108
Level 2 Total	0.045	0	0.138
Level 2 Zone 1	0.012	0	0.101
Level 2 Zone 2	0.053	0	0.135
Level 2 Zone 3	0.059	0	0.0138
Level 2 Upscaled Total	0.045	0	0.131
Level 2 Zone 1	0.013	0	0.097
Level 2 Zone 2	0.053	0	0.131
Level 2 Zone 3	0.0592	0	0.106

Table 5-4. Level 1 and 2 permeability statistics.

Permeability mD			
Model	**Mean**	**Min**	**Max**
Level 1 Total	4.2	0.9	81.4
Level 1 Zone 1	1.8	0.1	19.0
Level 1 Zone 2	5.8	1.2	81.4
Level 1 Upscaled total	3.6	0.1	22.2
Level 1 Zone 1	1.7	0.9	15.7
Level 1 Zone 2	5.8	2.6	22.2
Level 2 Total	5.5	0.6	165.3
Level 2 Zone 1	1.0	0.6	11.1
Level 2 Zone 2	6.2	0.6	61.7
Level 2 Zone 3	7.6	0.6	165.3
Level 2 Upscaled Total	5.3	0.6	52.9
Level 2 Zone 1	1.0	0.6	10.1
Level 2 Zone 2	5.8	0.6	52.9
Level 2 Zone 3	7.5	0.7	33.9

5.2 Geometry

The general shape on the reef top and outer regions of the Level 1 and Level 2 models are similar, but the reef flanks of the models show considerable differences. The reef flank is steeper in the Level 1 model layers (Figure 5-1). The main reason for this difference is construction of the Level 2, Sequence 2 transition from on-reef to off-reef. Portions of Level 2, Sequence 2 present on the top of the reef are included in the Level 1 model layers that belong to the upper Brown Niagaran, and the off-reef lithofacies in Sequence 2 belong to the A-1 Carbonate zone in the Level 1 model. The on-reef difference is a result of the difference in the "driller's" lithology/log pick of the Brown Niagaran versus the correlation from analog cores that indicates the actual unconformity does not always coincide with the "driller's" pick.

5.3 Porosity and Permeability Distribution

The Level 2 model has a less homogeneous distribution of porosity and permeability and broader ranges of porosity and permeability. Again, as with the geometry discussion, the main differences in the distributions occur in Sequence 2 portion of the Level 2 model (Figure 5-2 through Figure 5-5). The A-1 anhydrites at the base of Sequence 2 form local seals along the flanks; the reef-top capping grainstones (Lithofacies 4) gradually transitions off the reef into lithofacies 6Cc and 6Cb and are ultimately capped by the Sequence 3 "Rabbit Ears" anhydrites. The Level 1 model off-reef porosity zone that occurs in the middle of the A-1 Carbonate is not connected to the higher-porosity reservoir present in the top of the reef, but is isolated from it towards the top of the model (Figure 5-2). This appears to represent a factual situation, based on subsequent examination of regional A-1 Carbonate cores by Battelle and MCGRRE personnel, and appears to represent a totally separate A-1 reservoir. The compartmentalization

of the Dover 33 reservoir is more apparent with the introduction of the sequence interpretation in the Level 2 model.

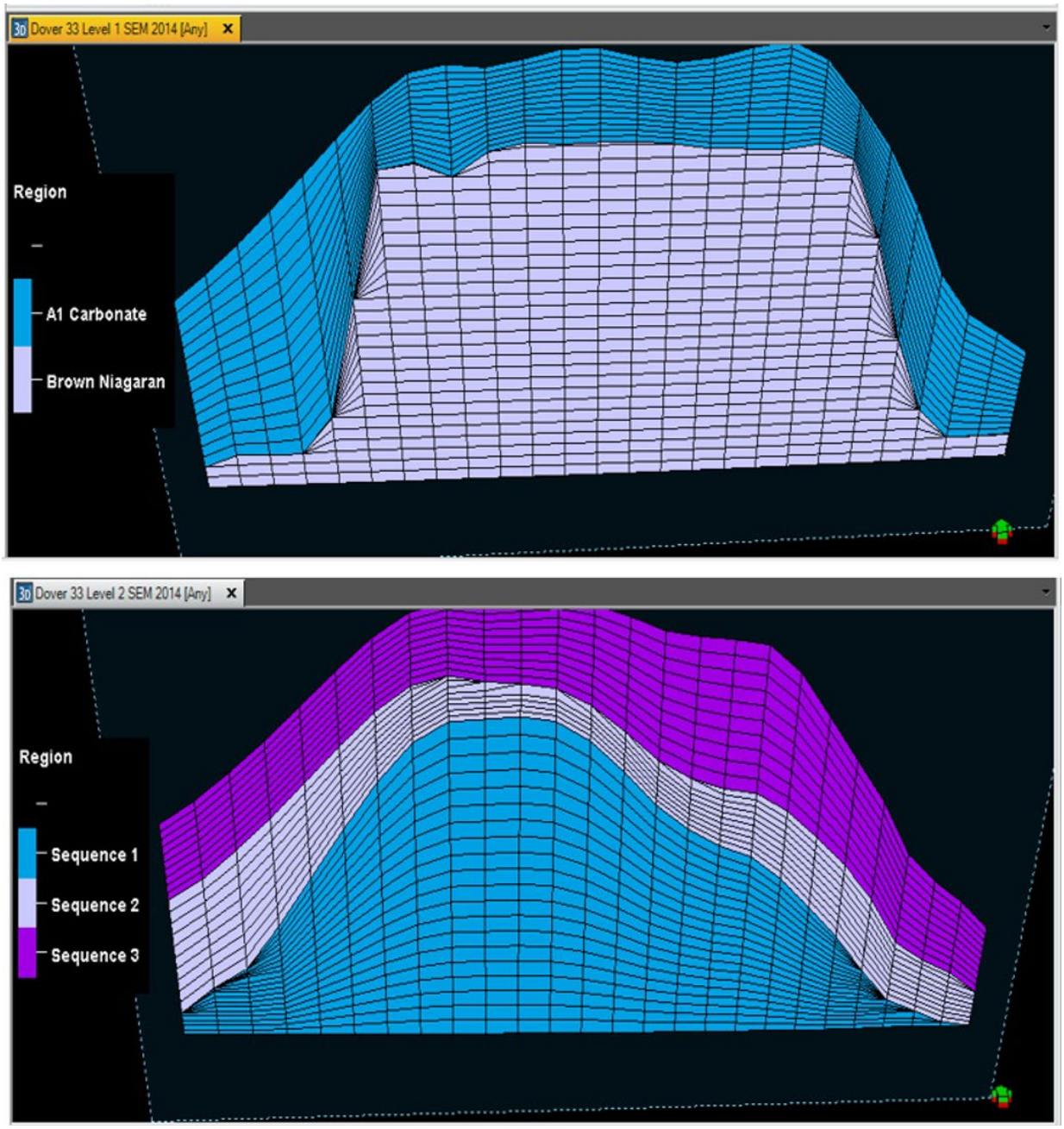


Figure 5-1. Comparison of lithostratigraphic layering (top) to sequence layering (bottom) in west-to-east sections from the Dover 33 Level 1 and Level 2 models.

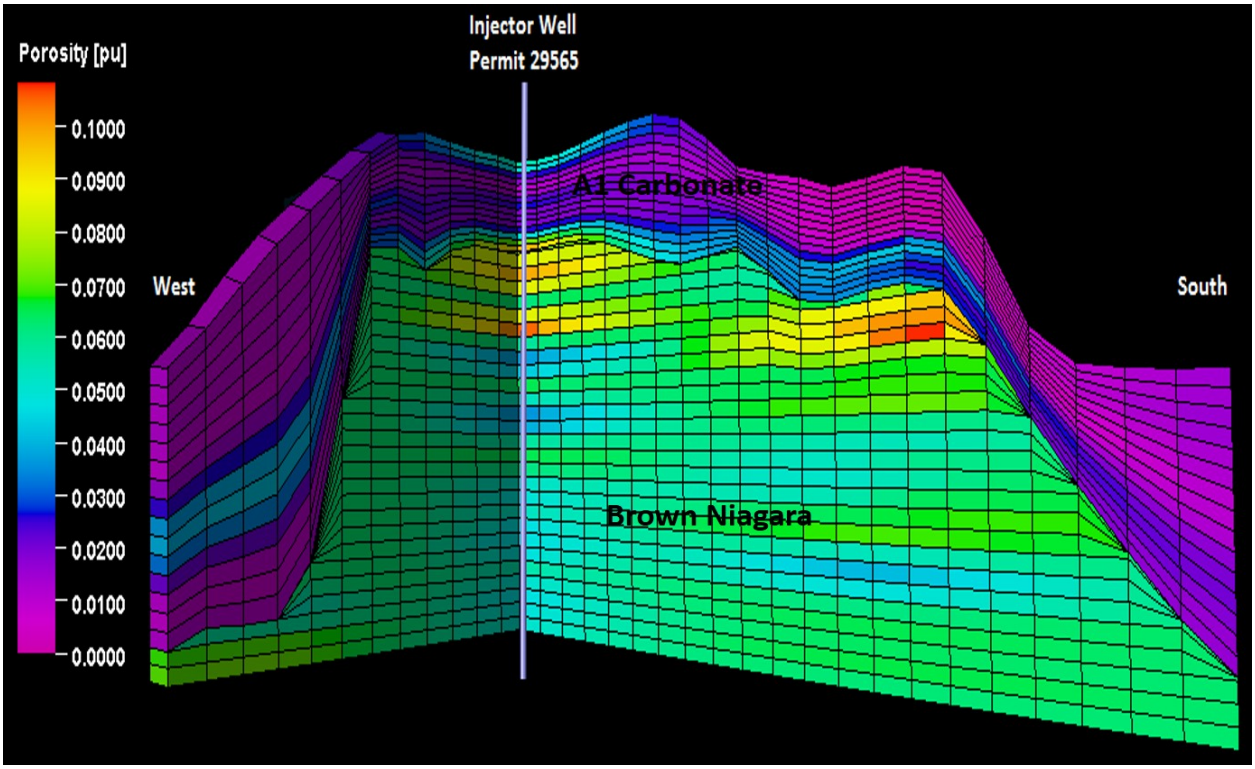


Figure 5-2. Level 1 upscaled porosity model.

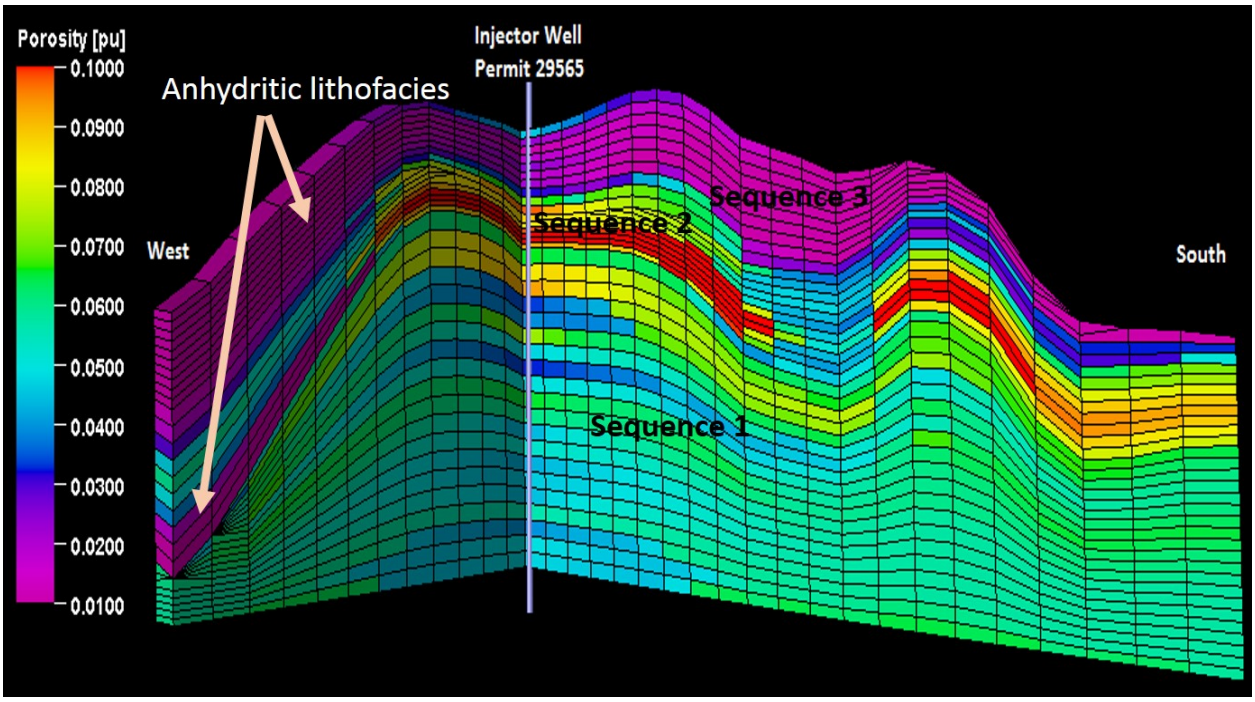


Figure 5-3. Level 2 upscaled porosity model.

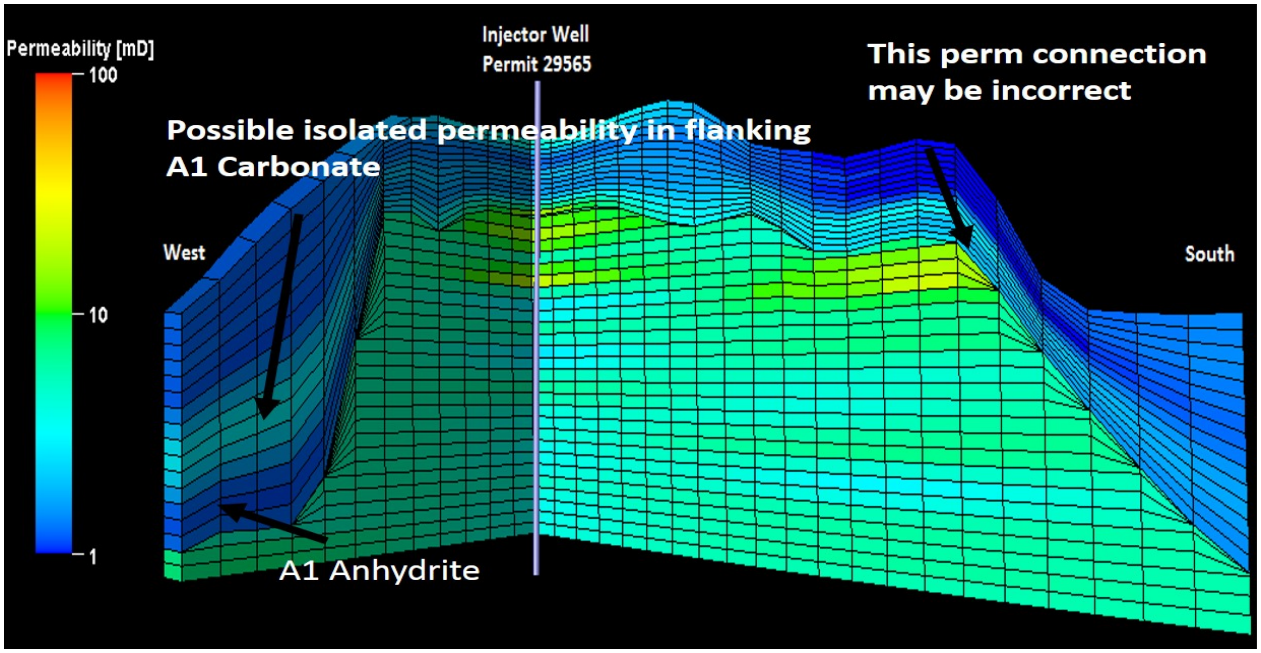


Figure 5-4. Level 1 upscaled permeability model.

The permeability in the flank A-1 carbonate immediately above the A-1 Anhydrite (blue) may not be connected to permeable parts of the A-1 carbonate on top of the reef, but instead, is likely a separate reservoir.

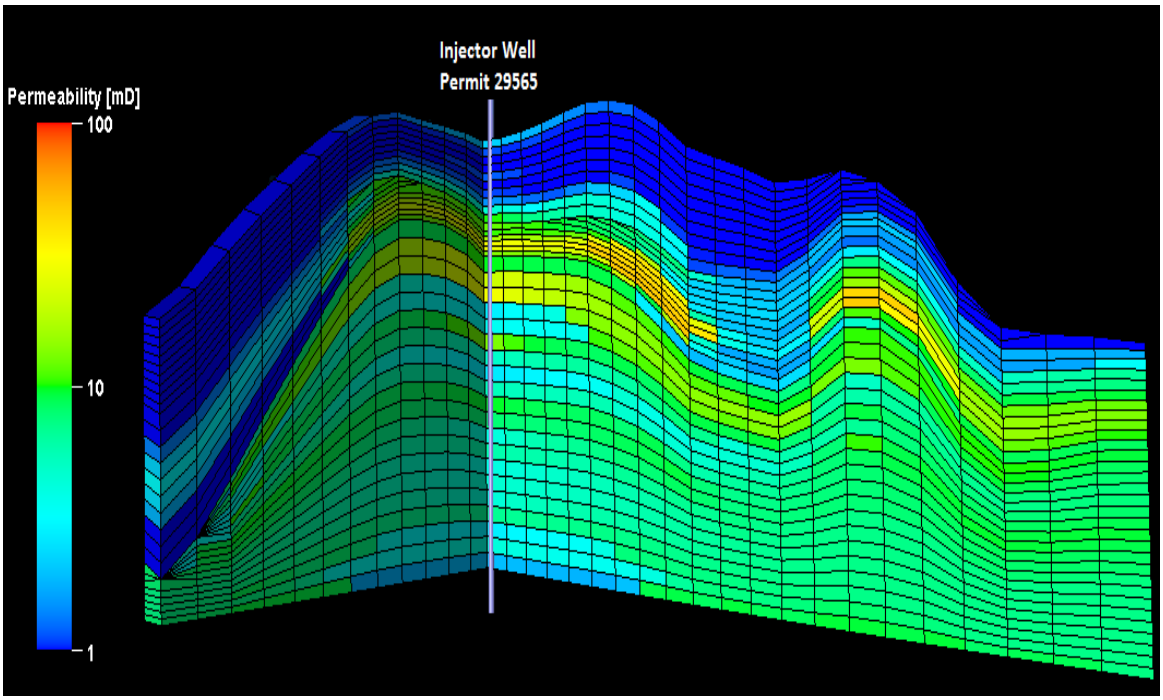


Figure 5-5. Level 2 upscaled permeability model.

Notice the occurrence of permeability in the Sequence 2 reef flank, above the A-1 Anhydrite (blue). This permeability may not be connected to the reef top Sequence 2 lithofacies that is

Chapter 6. Summary and Lessons Learned

This section summarizes the critical insights gained for future modeling on these complex reefs, and includes the challenges, key uncertainties, applicability to numerical reservoir construction, and transferability of the methodologies to other reefs within the Phase III area.

6.1 Seismic Interpretation

The depth-migrated seismic volume was critical in the surface interpretation and the integration of the well log and formation data into the model. Seismic interpretation along the steep flanks of the reef was difficult and did not provide enough detail to model the A-1Carbonate and Brown Niagaran surfaces. A more detailed interpretation (perhaps from Vertical Seismic Profiling [VSP] data) would provide more constraint on the surfaces.

6.2 Grid and Surface Construction

The original SEMs were started at 10- x 10-meter grids to handle the rapid slope changes in the reef flank surfaces and to create lateral formation and lithofacies relationships that appeared realistic based on the cross section analysis. Upscaling to the 30- x 30-meter grid decreased run times in the dynamic models (not shown in this report) and still maintained sections that looked geologically appropriate. A 50- x 50-meter grid was also created (not shown), but it appeared to render overly smooth surfaces and lost detail in the lithofacies model.

The multiple terminated nodes along the steep flanks of the reef caused computational issues in the dynamic models. Future efforts should include further evaluation to determine which layering and zone construction methods will minimize these computational effects.

The layering choices in both SEMs are critical aspects in creating reasonable geologic models in the complex reef system. The conformable (from the bottom) layering in the Level 1 SEM creates relatively flat layering in the internal section of the reef with abrupt termination and no change in orientation at or along the reef flanks. The proportional layering in the Level 2 SEM creates sloping layers in the core of the reef where flat layers may be appropriate. There may be potential to create additional zones within both models that address this issue. The base of the models—the Gray Niagaran— was an estimated surface based on regional log top intervals, due to velocity changes in the seismic data in the vicinity of the reefs. This regional surface does not appear to have large local variation and we conclude that the model base is fairly robust.

Vertical variograms could be calculated due to the high vertical density of log data (porosity, lithofacies) but variograms for the horizontal direction were based on assumed parameters since well spacing is large. In the lithofacies model, the horizontal variograms were edited to manipulate the lateral distribution of the off-reef lithofacies. Variograms for the reef interior has the largest uncertainty. This uncertainty can likely be reduced by additional studies of analog reef that better establish sizes and geometries of depositional reef facies changes: i.e., windward reef margins, reef interior and leeward reef debris belts.

In addition, the choice of statistical method chosen (Kriging) may have considerable influence, and a comparison with Gaussian simulation is suggested for future model runs.

6.3 Porosity and Permeability Modeling

The porosity-to-permeability transforms used to calculate permeability for the Level 1 and Level 2 SEMs are based on relationships in the existing large collection of legacy whole core measurements from analog reefs. Calculations for Level 2 are lithofacies-specific; calculations for Level 1 are Formation-specific. Level 1 sampling over a set log interval may combine measurements from different depositional facies. Cross plots at even the lithofacies-specific level (Level 2) from the analog reefs indicate even these data have a large amount of variability, due to in part to differences in diagenesis as well as to author-specific differences in original assignment of samples to lithofacies categories (lumpers versus splitters). Therefore, calculated permeabilities based on simple linear transforms are likely to have a large amount of uncertainty, for both the Level 1 and Level 2 models. The statistical analysis suggests that each reef has a unique depositional and diagenetic history that affects its porosity and permeability relationships. Samples of a given Level 2 lithofacies tend to have more uniform petrophysical properties when they represent a basin-wide environmental condition, such as very shallow water, evaporative conditions that produce anhydrite-cemented microbial boundstones (Lithofacies 6B). Likewise, lithofacies that represent a more complex depositional environment, such as Lithofacies 3 (reef framework) have considerable variety in lithologic mixes, texture, and porosity systems, which is reflected in the measured porosity/permeability data. Uncertainties and challenges in actual interpretation of lithofacies when no core is available, is discussed in greater detail in a following section

The lateral changes in porosity and permeability are not fully addressed by variograms in either model. Higher-resolution VSP data may provide an additional constraint on horizontal layer distribution within the reef core. The limited logs available for the horizontal well were insufficient to reliably calculate porosity. Acquiring additional logs in horizontal wells might considerably reduce uncertainty and more faithfully replicate the internal reef geology.

6.4 Sequence Stratigraphy and Lithofacies Interpretation

The relation of lithostratigraphic to sequence stratigraphic units is as follows: one or more lithostratigraphic units may form a large scale (low order) sequence stratigraphic unit. Conversely, a single lithostratigraphic unit may turn out to contain more than one lower order sequences and a number of high-order, small -scale sequences. As an example of the latter, the A-1 Carbonate as regionally correlated in the northern reefs contains two 3rd order sequences (Sequence 2 and Sequence 3). On reef, these packages are separated by unconformities that can be recognized in other cored Michigan reefs.

The practical aspect of doing a stratigraphic analysis is to group the rock volumes that are most likely to behave as single units during fluid flow. Our conclusion is that sequence stratigraphic grouping is the best way to start, but we recognize that unconformities may or may not be barriers to flow, and that diagenesis may obscure or may be the dominant control on geometries of flow units. The following paragraphs address details of recognizing sequence boundaries at the Dover 33 reef.

The wireline log markers that coincide with interpreted sequences in the analog wells can be correlated to the Dover reef with reasonable confidence. The third order sequence (Sequence 1) that marks the termination of major reef growth is close to the contact of the A-1 carbonate/Brown Niagaran, and is relatively easy to locate. Picking the on-reef sequence boundaries within logs of the A-1 Carbonate is somewhat more tentative but can be resolved by examining the core and logs of the published analog wells. Huh (1973) concluded that at least one unconformity (separating Sequence 2 and Sequence 3 of Ritter and this study) exists within the A-1 carbonate on-reef. In addition, Huh (1973) noted an erosional contact at the top of the

A-1 carbonate within at least one Kalkaska well. Other authors have indicated a transitional contact between the top of the A-1 carbonate and the overlying Salina evaporate. Because of the sharp facies change, the top of Sequence 3 was placed at this contact.

In cores examined by Ritter and others, there are multiple erosion surfaces in tidal flat lithofacies within the on-reef A-1 carbonate, and in practical core work, it is not always apparent which break within a single core represents a regional unconformity. However, A-1 Carbonate gamma logs tend to have distinct patterns that include the Rabbit Ears Anhydrite off reef, and correlation of gamma markers from wells with cores to reefs without cores is relatively robust for both off-reef wells and on-reef wells. The implication is that as the stratigraphy is refined with future core study, it will be relatively easy to adjust the placement of the boundaries.

The placement of sequences boundaries within the off-reef interval from the A0 to top A-1 carbonate will undoubtedly be refined as more reefs are studied. There is geologic uncertainty in regard to the system tract identity of the A-1 Anhydrite (is it the top of a simple 4th order lowstand transgressive unit? Is the top of the A-1 Anhydrite actually eroded and is the top of an unidentified 3rd order sequence?); the best pick for the top of Sequence 2: and the significance of the thin, but basin-wide Rabbit Ears Anhydrite. Some of the uncertainty of picking sequence boundaries is discussed in the following paragraphs.

A sharp break, and dissolution or possible erosional surface, is present on top of the A-1 Anhydrite in the Kalkaska core studied by Huh (1973). Whether the break represents a fourth order sequence boundary or a new third order boundary is not resolvable with current data. Leibold (1992) interpreted the A-1 Anhydrite as a composite feature, the result of gypsum deposition as sea level was falling (thus a falling stage deposit) and again as sea level was rising (late lowstand, transgressive sea level), just below the poker-chip shale and below the aggrading gamma ray pattern that reflects initiation of carbonate production and marine transgression on the flanks of the eroded reefs. Leibold's evaporite depositional model may be correct, but would suggest that an unconformity should occur within the anhydrite, rather than on top of the anhydrite. Additional core study may resolve this question. This issue is important for basin evolution, and possibly diagenesis, but is not likely to influence construction of static models or behavior of dynamic reservoir models.

The base of Sequence 1 was picked by Ritter (2008) as a flooding surface at the base of the Gray Niagaran, as observed in the Beier 25779 near the Bell River Mills Field. No core-based interpretation of the base of Sequence 1 has been established in the Northern Reef Trend. The top of Sequence 1 coincides with the unconformity at the top of the organic reef buildup, and in cored wells, this unconformity is preceded by a change from reef framework organisms to stromatolitic lithofacies. We have interpreted the off-reef top of Sequence 1 to correlate to the unconformity below the A0 carbonate, on top of the lithoclastic reef-debris conglomerate recognized by both Huh and Ritter.

A more correct pick for the off-reef top of Sequence 2 (Figure 6-1) may be obtained with additional data. Currently, we place the top of Sequence 2 above the aggradational (transgressive) gamma log pattern in the A-1Carbonate, coincident with the downlap surface of pelletoidal grainstone onto the aggradational micritic mudstone lithofacies described by Huh (1973) in the Kalkaska 3-22 well. Although offshore downlap surfaces are commonly associated with sequence boundaries, this downlap surface may actually reflect the change from the transgressive systems tract to a highstand systems tract and initiation of a sudden increase in carbonate production on the reef top. Our placement of the top of the Sequence 2 boundary in off-reef wells is reinforced by the increase in gamma ray that we interpret as an apparent flooding surface below the lowermost Rabbit Ears Anhydrite. The actual top of Sequence 2

could be at the top of either Rabbit Ear (RE) Anhydrite, but we do not have evidence of the magnitude of regional exposure associated with the thin RE anhydrites at this time.

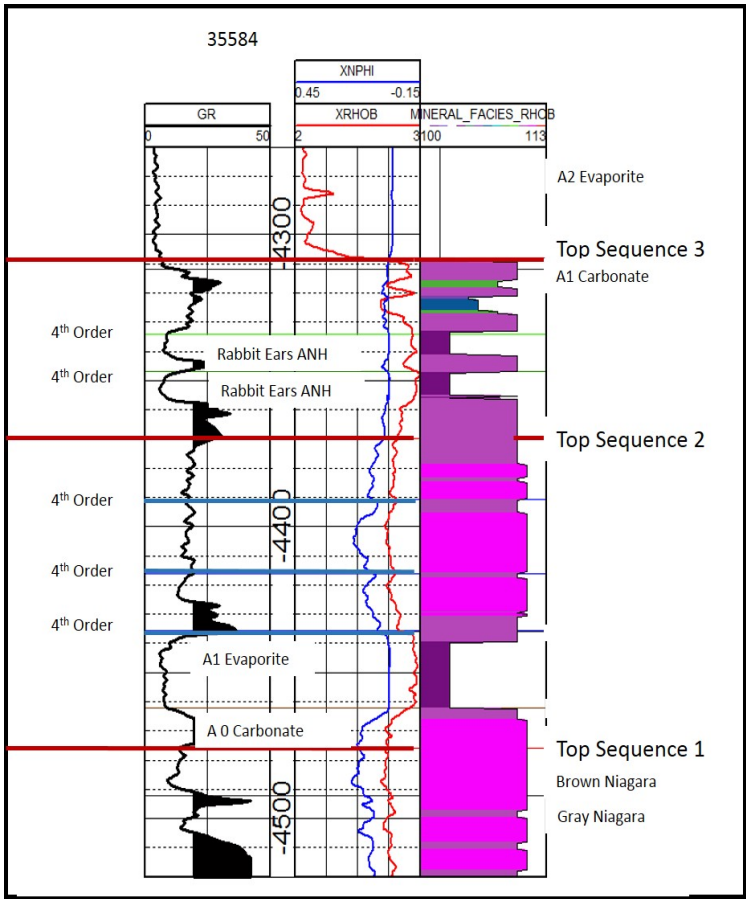


Figure 6-1. Sequence boundaries in the off-reef Dover 33 35584 well.

Electrofacies interpretations have greater uncertainty than major sequence boundary interpretations. Crossplot and computed mineralogy logs are critical in interpreting lithology; ELAN logs reduce uncertainty on identification of lithofacies and the vertical extent of lithofacies cycles, or cycle sets (parasequences). It is important to note that carbonates show cyclic, often meter-scale shallowing upward cycles. Thus a given lithofacies may well be deposited as a cycle that consists of a couplet or triplet, with lithofacies X1, X2, and X3 vertically repeating in .3-.6m beds. In spite of this complication, our review of published core studies indicates that lithofacies (and cycles of lithofacies) are not vertically random. Instead, there are a limited number of lithofacies that occur within each major (possibly 3rd order) sequence; and in the Niagaran reefs, that number becomes especially limited both on-reef and off-reef in Sequence 2 and Sequence 3. Wireline log signatures for off-reef and flank A-1 Carbonate lithologies are particularly well-tied to lithofacies; and these lithofacies have relatively limited variability in porosity/permeability relationships. In contrast, lithofacies assignments for wireline log intervals in Sequence 1 have high uncertainty, both vertically and laterally. Statistical analysis of porosity and permeability data of reef-associated lithofacies that were identified by Ritter and others indicates very weak relationships. Sequence 1 lithofacies have the highest variability in lithology (dolomite versus limestone), porosity types, and diagenetic overprint (possible karst, anhydrite cement, and salt plugging). These lithofacies have the greatest uncertainty when interpreted solely from wireline logs.

Geometries and distribution of lithofacies bodies (depositional facies or geobodies) will be increasingly important in reefs that have mixed limestone/dolomite lithologies, and can be expected to reflect increased marine cementation on windward flanks, and an increased abundance of finer-grained carbonate detrital fabrics on leeward facies, similar to textures and diagenesis of reefs through geologic time (see Glenn-Sullivan, 1989). More generally, many reef buildups throughout the Phanerozoic display lateral zonation related to depth and wave energy. Huh (1973) concluded that windward versus leeward variability exists in the Niagaran reefs, with detrital reef sediment replacing framework organisms in a leeward direction. But without multiple cores or an improved model of windward versus leeward depositional facies geometries,

electrofacies and porosity/permeability relationships within Sequence 1 (except for very low porosity intervals) remain highly uncertain.

Although correlation of sequence boundaries appears to be fairly robust, and lithofacies assignments for Sequence 1 rocks have high uncertainty, the lithofacies descriptions and core photos assembled in this study make it easier to convey geologic ideas about petrophysical property development and property distribution in the reef to other team members and less technical audiences. On-site core workshops and review of the vast core material and associated porosity/permeability data at MGRRE are invaluable for validating the approach, validating and quality-checking lithofacies described by multiple authors, and building consensus on the relation of log signatures to rock character. The observation of apparent microporosity in reef flank (driller's "poker chip", and fine packstones/grainstones) Sequence 2 lithofacies may suggest the need for detailed core plug capillary pressure analysis to better characterize proximal and distal flank permeability.

The process of cross-walking the 152 published lithofacies in the analog studies resulted in delineation of 15 basic lithofacies. This crosswalk and compilation provides the basis for a rock catalog of petrophysical properties. A number of lithofacies described by previous authors, such as diagenetic silica nodules that could be mistaken for reef lithoclasts, reinforces the need for a careful re-inspection of previous descriptions and interpretations of northern reef analog cores plus new descriptions/ core measurements of additional cores for incorporation into the analog database. This work has already been initiated by collaborators at Western Michigan.

A potential area for improvement of reservoir models is better recognition of the presence and distribution of halite-plugged porosity. Although wireline log signatures for bedded evaporites are distinctive, and ELAN mineralogy logs identify anhydrite/limestone mixtures, we do not have a robust method for identifying halite plugging of moldic and vuggy porosity.

6.5 Incorporation of Lithofacies in the Level 2 SEM

Specific remarks related to the Dover 33 Level 2 model include the following:

- The incorporation of the rubble zone (lithofacies 8B) in Sequence 1 along the flanks of the Level 2 reef SEM produces a less steep flank as compared to the Level 1 lithostratigraphic model.
- Combining all algal (microbial) lithofacies in Sequence 1, 2, and 3 into Lithofacies Group 6 may cause obscuring of porosity/permeability relationships, if the off-reef facies have greater microporosity than do the on-reef algal lithofacies. It will be important to identify the amount of microporosity in off-reef facies of analog reefs.
- There appear to be two lithofacies in Sequence 3 that can develop reservoir-quality permeability and porosity. These are Lithofacies 6A and 6C. In addition, Lithofacies 6Ac, anhydrite-cemented algal/tidal flat lithofacies, may develop fenestral porosity: similar variably anhydrite- cemented algal lithofacies form documented "thief zones" in tidal flat carbonates in the Permian Basin and elsewhere (Mutti and Simo, 1993). In contrast, Lithofacies 6C has intercrystalline porosity and greater potential to contribute to reservoir productivity and/or CO_2 storage. The core descriptions of Huh (1973) and other authors of a porous and permeable "pelletoidal" lithofacies (our 6C) in Sequence 3 is important. Although this lithofacies exhibits a similarity in permeability relationships to the porous and permeable packstones in Sequence 2, the pelletoidal Lithofacies 6C appears to be confined to the base of Sequence 3 and is thus an important target to be aware of when evaluating other northern reefs.

- The types of porosity and permeability in flank wells are poorly understood. The petrophysical properties may contribute to reservoir volume or control the nature of boundary conditions. Microporosity may be more common in Sequence 2 A-1 Carbonates. In addition, many larger Niagaran reefs may actually consist of coalesced smaller reefs, and the characteristics of coalescing flank beds may greatly influence compartmentalization and lateral heterogeneity of the reservoir. At the present, we consider the interior of the Dover 33 reef to consist of poorly bedded to generally flat-lying beds, but as we examine additional reefs, we are likely to encounter more extreme changes in lithology (limestone versus dolomite) and compartmentalization (flank versus true reef core and leeward versus windward) within compound or coalesced reefs. Acquisition of image logs in new vertical or horizontal wells is optimal for identifying dipping beds and changes in rock texture associated with different lithofacies.

6.6 Time Effort

A large portion of the time effort involved establishing the stratigraphic framework at the Dover 33 reef; vetting previous work; and finally, interpreting details in the A-1 Carbonate and Sequence 2 and 3 non-reservoir parts of the reef that may not affect the dynamic models. However, the understanding of how off-reef lithofacies affect the reservoir simulations may change over time and with experience on compound, coalesced reefs that internalize off-reef facies.

The Level 2 model provides more opportunity for changes at a finer level of detail as the dynamic models are run.

Having core and core based porosity and permeability in a reef makes many of the steps involved in creating this model much simpler and easier to validate.

We are convinced that a sequence-stratigraphic-constrained lithofacies approach will deliver more realistic static earth models, and that the time effort expended in this project has validated the approach initiated by Grammer's students for characterization of the Michigan Niagaran reefs.

6.7 Discussion and Recommendations

The following section includes an assessment of challenges, key uncertainties, applicability to numerical reservoir construction, and transferability of the methodologies to other reefs within the Phase III area.

6.7.1 Challenges

- Challenges include well and data spacing; depositional facies geometries (windward versus leeward; coalescing small reefs); identification of depositional facies from wireline logs; better identification of carbonate porosity and permeability systems (sensu Lucia, 1995) from well logs (intercrystalline; isolated vug; vug touching vug; fracture), and predictability of diagenetic overprints (dolomite, anhydrite, karst and vug formation; salt plugging, hydrothermal).
- Although wind and energy-related controls on reef zonation and sediment type generation is well recognized in Phanerozoic reefs (Glenn-Sullivan 1989), lateral distribution and boundary definition of depositional facies or geobodies in absence of distinctive seismic signatures or core is problematic. In addition, older log signatures poorly distinguish fine-

scale mixed lithologies. Addition of resistivity-based image logs can add depositional and diagenetic texture information.
- Relation of stratigraphy to flow units: diagenesis can overwhelm original stratigraphic permeability differences and boundaries.

6.7.2 Key Uncertainties

- Lateral extent of lithofacies
- Controls on diagenesis
- Geometry of depositional and diagenetic bodies (including salt plugging)
- Lateral extent of baffles, reservoir compartmentalization
- Total versus effective porosity volumes in reefs with vintage logs
- Contribution and continuity of A-1 Carbonate porosity and permeability
- Heterogeneity and compartmentalization in reefs with mixed lithologies, or that represent coalescing organic buildups.

The level 2 SEM took considerably longer time and more technical effort compared with constructing and populating the level 1 SEM, but now that the sequence stratigraphy and log correlations are defined, and workflows are established, modeling efforts in other reefs in the Northern Michigan Reef Trend should be more rapid. Our lithofacies interpretation of the Dover 33 reef is unique in that it incorporates the transition from on-reef lithofacies into off-reef lithofacies and examines the potential flanking reservoir off the reef core that is bracketed by anhydrites above and below. This sequence stratigraphic modeling approach can be used in larger reefs, where more complex lithologies and internal architecture will demand a higher level of scrutiny.

6.7.3 Recommendations

Data

- Continue to improve VSP and 3D seismic data collection; investigate seismic attributes for helping to define reservoir geobodies (definition of reef margins, reef core versus leeward reef debris; better definition of limestone versus dolomite). It is recognized that gradational lithology boundaries have high uncertainty in imaging, and that marine-cemented limestones can have high seismic velocities, similar to flank anhydrites.
- Collection of full-diameter core is critical for estimating porosity and permeability and for calibrating wireline-log-based lithofacies.
- The combination of modern well logs, such as image logs, isotope logs, advanced sonic logs, and NMR logs, when calibrated with core, is likely to greatly reduce uncertainty on lithology, lithofacies, porosity systems, generation of permeability transforms, and computed wireline permeability logs.

Model Construction

It is important to recognize which characterization elements (thin flow barriers, salt plugging, dolomitization, fractures, karst) are critical in model construction and in dynamic model performance. These elements are reef and scale- specific: the challenge is to efficiently determine relevant vertical and lateral heterogeneity in reservoir properties at the well, multi-well, and field scale.

Several steps have been identified that may further improve model construction.

- Use 3D seismic data (or, more optimally, VSP data) as an attribute to spatially condition porosity.
- Apply a more complex layering scheme to reflect internal and flank reef core deposits.
- Add porosity detail to the lateral wells that are known dry holes and to help estimate low porosity values.
- Test additional statistical methods for building vertical and lateral variograms
- Evaluate dynamic models to compare parameter sensitivities for different models.

Chapter 7. References Cited

Anselmetti, F.S., and G.P. Eberli, 1999. The velocity-deviation log; a tool to predict pore type and permeability trends in carbonate drill holes from sonic and porosity or density logs, AAPG Bulletin 83: 450-466.

Archie, G.E., 1952. Classification of Carbonate Reservoir Rocks and Petrophysical Considerations. Bulletin of the American Association of Petroleum Geologists 36 (2): 278-298.

Asquith G., and C. Gibson, 1982. Basic Well Logging Analysis for Geologists: American Association of Petroleum Geologists, Methods in Exploration Series, pp. 1-216.

Balogh, R.J., 1981. A study of the Middle Silurian Belle River Mills, Peters, and Ray Pinnacle Reefs from the Michigan Basin. Science, Bowling Green State University: 178 pp.

Barnes, D., B. Harrison, G.M. Grammer, and J. Asmus, 2013. CO_2/EOR and geological carbon storage resource potential in the Niagarann Pinnacle Reef Trend, Lower Michigan, USA: GHGT-11, Energy Procedia, V. 37, pp. 6786-6799.

Briggs, L.I., and D.Z. Briggs, 1974a. Niagaran-Salina relationships in the Michigan Basin *in* Silurian reef-evaporite relationships, Kesling (ed), Mich. Basin Geol. Soc., United States 1-23.

Briggs, L.I., and D.Z. Briggs, 1974b. Reefs and evaporites in the Michigan Basin Geotimes 19(8):31.

Briggs, L.I., D. Gill, D.Z. Briggs, and R.D. Elmore, 1980. Chapter 17, “Transition from open marine to evaporite deposition in the Silurian Michigan Basin,” *in* Nissenbaum, A., ed., Hypersaline brines and evaporitic environments: Developments in Sedimentology, V. 28, pp. 253-270.

Carter, K.M., J. Kostelnik, C.D. Laughrey, J.A. Harper, D.A. Barnes, W.B. Harrison III, E.R. Venteris, J. McDonald, J. Wells, L.H. Wickstrom, C.J. Perry, K.L. Avary, J.E. Lewis, M.E. Hohn, A. Stolorow, B.E. Slater, and S.F. Greb, 2010. Characterization of geologic sequestration opportunities in the MRCSP region: Middle Devonian-Middle Silurian formations—MRCSP Phase II Topical Report October 2005-October 2010: U.S. DOE Cooperative Agreement No. DE-FC26-05NT42589, OCDO Grant Agreement No. DC-05-13, 350 pp.

Catacosinos, P.A., P.A. Daniels Jr., and W.B. Harrison III, 1990. Structure, stratigraphy, and petroleum geology of the Michigan Basin; interior cratonic basins, AAPG Memoir, 51, pp. 561-601.

Catacosinos, P.A., W.B. Harrison, R.F. Reynolds, D.B. Westjohn, and M.S. Wollensak, 2000. Stratigraphic nomenclature for Michigan: Michigan Department of Environmental Quality, Geological Survey Division, 1 sheet.

Catacosinos, P.A., D.B. Westjohn, W.B. Harrison, M.S. Wollensak, and R.F. Reynolds, 2001. Stratigraphic lexicon for Michigan: Michigan Department of Environmental Quality, Geological Survey Division, Bulletin 8, 56 pp.

Catuneanu, O, Galloway, WE, Kendall, CGSt.C, Miall, AD, Posamentier, HW, Strasser, A, and Tucker, ME, 2011. Sequence Stratigraphy: Methodology and Nomenclature: Newsletters on Stratigraphy, 44, 3, 173-245.

Caughlin, W.G., F.J. Lucia, and N.L. McIver, 1976. The detection and development of Silurian reefs in northern Michigan. Geophysics 41, (4): 646-658.

Cercone, K.R., 1984. Diagenesis of Niagarann (middle Silurian) Pinnacle Reefs, Northwest Michigan, Geosciences. Ann Arbor, University of Michigan: 367 pp.

Charbonneau, S.L., 1990. Subaerial exposure and meteoric diagenesis in Middle Silurian Guelph Formation (Niagarann) pinnacle reef bioherms of the Michigan Basin: Southwestern Ontario: M.Sc. thesis, Queen's University, Kingston, Ontario, 215 pp.

Coniglio, M., R. Frizzel, and B.R. Pratt, 2004. Reef-capping laminites in the Upper Silurian carbonate-to-evaporite transition, Michigan Basin, South-western Ontario: Sedimentology, Vol. 51, pp. 653-668.

Gill, D., 1973. Stratigraphy, facies, evolution and diagenesis of productive Niagarann Guelph reefs and Cayugan sabkha deposits, the Belle River Mills Gas Field, Michigan Basin, University of Michigan, Ann Arbor, MI, United States, Doctoral thesis, 362pp.

Gill, D., 1977. Salina A-1 sabkha cycles and the Late Silurian paleogeography of the Michigan Basin: Journal of Sedimentary Petrology, v. 47, pp. 979-1017.

Gill, D., 1979. Differential entrapment of oil and gas in Niagarann pinnacle-reef belt of northern Michigan: American Association of Petroleum Geologists, V. 63, No. 4, pp. 608-620.

Gill, D., K.J. Mesolella, J.D. Robinson, L.M. McCormick, and A.R. Ormiston, 1975. Cyclic deposition of Silurian carbonates and evaporites in Michigan Basin discussion and reply, AAPG Bulletin 59 (3): 535-542.

Glenn-Sullivan, E.C., 1989. Foraminifera and associated sedimentary constituents of Holocene and Miocene reefs of the Philippines and Indonesia: PhD dissertation, University of Houston

Grammer, G.M, D.A. Barnes, W.B. Harrison III, A.E. Sandomierski, and R.G. Mannes, 2009. Practical synergies for increasing domestic oil production and geological sequestration of anthropogenic CO_2: An example from the Michigan Basin, *in* M. Grobe, J.C. Pashin, and R.L. Dodge, eds., Carbon dioxide sequestration in geological media—State of the science: American Association of Petroleum Geologists, Studies in Geology 59, pp. 689-706.

Grammer, G.M., A. Noack, H. Qualman, A. Ritter-Varga, J. Wold, A. Sandomierski, and W.B. Harrison III, 2010. Reservoir Characterization of Silurian (Niagarann) "Pinnacle" Reefs in the Michigan Basin. Search and Discovery Article #50286 (2010) Posted July 30, 2010. Adapted from oral presentation at AAPG Annual Convention and Exhibition, New Orleans, Louisiana, April 11-14, 2010.

Gringarten, E., and C.V. Deutsch, 1999. Methodology for variogram interpretation and modeling for improved reservoir characterization: Society of Petroleum Engineers, SPE 56654, 13 pp.

Gupta, N., L. Cumming, M. Kelley, D. Paul, S. Mishra, J. Gerst, M. Place, R. Pardini, A. Modroo, and R. Mannes, 2013. Monitoring and modeling CO_2 behavior in multiple oil bearing carbonate reefs for a large scale demonstration in northern Lower Michigan: Energy Procedia, V. 37, pp. 6800-6807.

Harrison III, W.B., 2010. "EOR in Silurian-Niagarann reef reservoirs, Michigan," *In* Evaluation of CO_2-enhanced oil recovery and sequestration opportunities in oil and gas fields in the MRCSP region—MRCSP Phase II Topical Report October 2005-October 2010: U.S. DOE Cooperative Agreement No. DE-FC26-05NT42589, OCDO Grant Agreement No. DC-05-13, pp. 48-54.

Haynie, J.M., 2009. Characterization and modeling of petrofacies and pore-volume distribution within a gas-storage reservoir, Ray Reef Field, Southern Michigan Basin, Michigan: Masters thesis, University of Colorado, 195pp.

Hohn, M.E. 1999. Geostatistics and Petroleum Geology, second edition. Amsterdam, The Netherlands: Kluwer Academic Publishers, 235pp.

Howell, P.D., and B.A. van der Pluijm, 1999. Structural sequences and styles of subsidence in the Michigan Basin. Geological Society of America Bulletin, 111 (7), pp. 974-991.

Huh, J.M., 1973. Geology and diagenesis of the Niagarann pinnacle reefs in the northern shelf of the Michigan Basin. University of Michigan, Ann Arbor, MI, United States, Doctoral thesis.

Huh, J.M., L.I. Briggs, and D. Gill, 1977. Depositional environments of pinnacle reefs, Niagaran and Salina Groups, northern shelf, Michigan Basin, *in* J.L. Fischer, ed., Reefs and evaporites-Concepts and depositional models: American Association of Petroleum Geologists Studies in Geology, v. 5, p. 1-21.

Kendall, C.G. St. C., 2003. SEPM STRATA, SEPM Stratigraphy Web. Available at http://www.sepmstrata.org/page.aspx?pageid=1.

Kerans, C., and S.W. Tinker, 1997. **Sequence Stratigraphy and Characterization of Carbonate Reservoirs: SEPM Short Course Notes #40.**

Leibold, A., 1992. Sedimentological and Geochemical constraints on Niagaran/Salina deposition, Michigan Basin: Doctoral Dissertation, University of Michigan, Ann Arbor, Michigan.

Lucia, J.F., 1995. Rock-fabric/petrophysical classification of carbonate pore space for reservoir characterization: AAPG Bulletin, v.79, p.1275-1300.

Mitchum, R.M., Jr., P.R. Vail, and S. Thompson, S., III, 1977. Seismic stratigraphy and global changes of sea-level, part 2: the depositional sequence as a basic unit for stratigraphic analysis. In: Payton, C. E. (ed.), Seismic Stratigraphy – Applications to Hydrocarbon Exploration. American Association of Petroleum Geologists Memoir 26, 53–62.

Mutti M., and J.A. Simo, 1993. Stratigraphic patterns and cycle-related diagenesis of upper Yates Formation, Permian, Guadalupe Mountains, in Loucks, R.G., and J.F. Sarg (eds), Carbonate Sequence Stratigraphy: AAPG Memoir 57, 545 pp.

Noack, A., 2008, Analysis of Pore Architecture and Correlation to Sonic Velocity Values in Silurian (Niagarann) Reefs of the Michigan Basin: Thesis (MS), Western Michigan University.

Perez, H.H., and A. Datta-Gupta, 2003. The role of electrofacies, lithofacies, and hydraulic flow units in permeability prediction from well logs: A comparative analysis using classification trees, SPE 84301, Annual Technical Conference and Exhibition, Denver.

Posamentier, H.W., Vail, P. R., 1988. Eustatic controls on clastic deposition. II. Sequence and systems tract models. In: Wilgus, C. K., Hastings, B. S., Kendall, C. G. St. C., Posamentier, H.W., Ross, C. A., Van Wagoner, J. C. (Eds.), Sea Level Changes – An Integrated Approach. SEPM Special Publication **42**, 125–154.

Qualman, H., 2009, 3-D Interpretation of the Sequence Stratigraphy and Reservoir Property Distribution in the Belle River Mills Silurian (Niagarann) Reef, St. Clair County, Michigan: Thesis (MS), Western Michigan University, 313 p.

Riley, R.A., J.A. Harper, W.B. Harrison, III, D.A. Barnes, B.C. Nuttall, K.L. Avary, A.M. Wahr, M.T. Baranoski, B.E. Slater, D.C. Harris, and S.R. Kelly, 2010. Evaluation of CO_2-enhanced oil recovery and sequestration opportunities in oil and gas fields in the MRCSP region—

MRCSP Phase II Topical Report October 2005-October 2010: U.S. DOE Cooperative Agreement No. DE-FC26-05NT42589, OCDO Grant Agreement No. DC-05-13, 177 pp.

Rine, M., Garrett, J., and Kaczmarek, S.E., 2017, A new facies architecture model for the Silurian Niagaran-Lower Salina “Pinnacle” Reef Complexes of the Michigan Basin, In: Advances in Characterization and Modeling of Complex Carbonate Reservoirs – In Memory of Eric Mountjoy (Eds. A. MacNeil, J. Lonnee, and R. Wood) SEPM Special Publication 109, DOI: http://dx.doi.org/10.2110/sepmsp.109.02and Modeling of Complex Carbonate Reservoirs.

Ritter, A.L., 2008. Evaluating the controls on reservoir heterogeneity of Silurian pinnacle reefs, Michigan Basin: M.Sc. thesis, Western Michigan University, Kalamazoo, Michigan, 247 pp.

Rullkotter, J.M., P.A. Schaefer, G. Rainer, and K.W. Dunham, 1986. Oil generation in the Michigan Basin: A biological marker and carbon isotope approach: Organic Geochemistry, Vol. 10, pp. 359-375.

Schlumberger Ltd, 1989. Sedimentary environments from wireline logs. SEF Marketing and Technique. Second edition, 243 pp.

Serra, O., and H.T. Abbott, 1980. The contribution of logging data to sedimentology and stratigraphy, SPE 9270, 55th Annual Fall Technical Conference and Exhibition, Dallas, Texas, 19 pp.

Trout, J.L., 2012. Faunal distribution and relative abundance in a Silurian (Wenlock) pinnacle reef complex—Ray Reef, Macomb County, Michigan: Western Michigan University, M.S. Thesis, 300 pp.

Toelle, B., L. Pekot, D. Barnes, G.M. Grammer, and W. Harrison, 2008. EOR potential of the Michigan Silurian reefs using CO_2: Society of Professional Engineers, SPE 113843-PP, 8 pp.

Vail, PR, 1987. Seismic stratigraphy interpretation procedure. In: Bally, A.W. (Ed.), Atlas of Seismic Stratigraphy, vol. 27. American Association of Petroleum Geologists Studies in Geology, p. 1–10.

Wold, J., G.M. Grammer, and W.B. Harrison, 2008, Sequence Stratigraphy and 3-D Reservoir Characterization of a Silurian (Niagarann) Reef – Ray Reef Field, Macomb County, Michigan, presented at Eastern Section AAPG, Pittsburgh, PA.

Zimmerie, W., 1995. Petroleum Sedimentology: Springer-Verlag, 417 pp.


BATTELLE
It can be done